TTI: 0-7040

Texas A&M Transportation Institute

Evaluation of Corrosion Prevention and Mitigation Approaches Used on Texas Bridges—Volume 1: Steel Girder Bridges

Technical Report 0-7040-R1-Vol1

Cooperative Research Program

TEXAS A&M TRANSPORTATION INSTITUTE
COLLEGE STATION, TEXAS

sponsored by the
Federal Highway Administration and the
Texas Department of Transportation
https://tti.tamu.edu/documents/0-7040-R1-Vol1.pdf

Technical Report Documentation Page

1. Report No.	2. Government Accession No.	3. Recipient's Catalog No.
FHWA/TX-24/0-7040-R1-Vol1		

4. Title and Subtitle	5. Report Date
EVALUATION OF CORROSION PREVENTION AND MITIGATION APPROACHES USED ON TEXAS BRIDGES—VOLUME 1: STEEL GIRDER BRIDGES	Published: July 2024
	6. Performing Organization Code

7. Author(s)	8. Performing Organization Report No.
Stefan Hurlebaus, Anna Birely, Matthew Yarnold, Arash Noshadravan, Arash Rockey, Pushkar Shivechchhu, Seung Hyun Yoon, and Zhen Zhang	Report 0-7040-R1-Vol1

9. Performing Organization Name and Address	10. Work Unit No. (TRAIS)
Texas A&M Transportation Institute The Texas A&M University System College Station, Texas 77843-3135	11. Contract or Grant No. Project 0-7040

12. Sponsoring Agency Name and Address	13. Type of Report and Period Covered
Texas Department of Transportation Research and Technology Implementation Office 125 E. 11th Street Austin, Texas 78701-2483	Technical Report: January 2019–November 2023
	14. Sponsoring Agency Code

15. Supplementary Notes

Project sponsored by the Texas Department of Transportation and the Federal Highway Administration.
Project Title: Evaluation of Corrosion Prevention and Mitigation Approaches Used on Texas Bridges
URL: https://tti.tamu.edu/documents/0-7040-R1-Vol1.pdf

16. Abstract

Corroded steel members cause significant risk to the durability of steel bridges, leading to costly failures and endangering public safety. Thus, it is essential to implement effective corrosion prevention and mitigation strategies to ensure the long-term durability of steel girders and reduce risks associated with corrosion activities. The Texas Department of Transportation uses corrosion-resistant materials and paints steel elements to mitigate corrosion on steel girder bridges. Weathering steel provides excellent corrosion resistance and forms an adhesive oxide layer over time, known as a patina layer, that enhances its resistance to atmospheric corrosion and ultimately results in longer service life. Findings from this study showed weathering steel girders exhibited long-term durability in low to medium corrosive environments. However, an increased volume of akaganeite and splines within the patina decreases the functionality of the rust layer as the corrosivity rises. In such environments, an alternative protection system for steel structures is a zinc-based paint system, known as Paint System III, consisting of three layers of zinc and epoxy coats. The researchers concluded that Paint System III is a durable corrosion prevention and mitigation method for protecting steel structures in high corrosive regions. To identify geographic areas with a higher risk of corrosivity, a corrosion risk assessment map was developed based on factors influencing atmospheric corrosion and was also validated by field inspection results and laboratory examinations. In addition, theoretical modeling based on corrosion fatigue strain-life models was performed to estimate the average service life of weathering steel structures. The researchers concluded that if the corrosion rate of the steel component exceeds 1.5 mils per year, the service life of weathered steel significantly decreases, and a reduction of cyclic loading and fatigue stress on the corroded members is required.

17. Key Words	18. Distribution Statement
Corrosion, Weathering Steel Girders, Painted Steel Girders, Corrosion Prevention and Mitigation Methods, Rust Phase Analysis, Patina Rating Index, Corrosion Fatigue, Corrosion Risk Assessment Map, Service Life of Weathering Steel	No restrictions. This document is available to the public through NTIS: National Technical Information Service Alexandria, Virginia https://www.ntis.gov

19. Security Classif. (of this report)	20. Security Classif. (of this page)	21. No. of Pages	22. Price
Unclassified	Unclassified	1400	

EVALUATION OF CORROSION PREVENTION AND MITIGATION APPROACHES USED ON TEXAS BRIDGES—VOLUME 1: STEEL GIRDER BRIDGES

by

Stefan Hurlebaus, Ph.D.
Research Scientist
Texas A&M Transportation Institute

Arash Rockey, Ph.D.
Postdoctoral Research Associate
Texas A&M Transportation Institute

Anna Birely, Ph.D.
Research Scientist
Texas A&M Transportation Institute

Pushkar Shivechchhu
Graduate Assistant Researcher
Texas A&M Transportation Institute

Matthew Yarnold, Ph.D.
Research Scientist
Texas A&M Transportation Institute

Seung Hyun Yoon
Graduate Assistant Researcher
Texas A&M Transportation Institute

Arash Noshadravan, Ph.D.
Assistant Research Scientist
Texas A&M Transportation Institute

and

Zhen Zhang
Graduate Assistant Researcher
Texas A&M Transportation Institute

Report 0-7040-R1-Vol1
Project 0-7040
Project Title: Evaluation of Corrosion Prevention and Mitigation Approaches Used on Texas Bridges

Sponsored by the
Texas Department of Transportation
and the
Federal Highway Administration

Published: July 2024

TEXAS A&M TRANSPORTATION INSTITUTE
College Station, Texas 77843-3135

DISCLAIMER

This research was sponsored by the Texas Department of Transportation (TxDOT) and the Federal Highway Administration (FHWA). The contents of this report reflect the views of the authors, who are responsible for the facts and the accuracy of the data presented herein. The contents do not necessarily reflect the official view or policies of FHWA or TxDOT. This report does not constitute a standard, specification, or regulation.

This report is not intended for construction, bidding, or permit purposes. The researcher in charge of the project was Stefan Hurlebaus. The United States Government and the State of Texas do not endorse products or manufacturers. Trade or manufacturers' names appear herein solely because they are considered essential to the object of this report.

ACKNOWLEDGMENTS

This project was conducted at Texas A&M University and was supported by TxDOT and FHWA through the Texas A&M Transportation Institute (TTI) as part of Project 0-7040, Evaluation of Corrosion Prevention and Mitigation Approaches Used on Texas Bridges. The authors thank the individuals who were involved with this project and provided invaluable assistance, including Tom Schwerdt (TxDOT, project manager) and the TxDOT Project Monitoring Committee: Johnnie Miller, Steven Austin, Rachel Cano, Robert Owens, Sydney Newman, Teresa Michalk, Niyi Arowojolu, and Kevin Pruski.

TABLE OF CONTENTS

Page

List of Figures ..... **xvii**
List of Tables ..... **li**
1 Introduction **1**
1.1 Background and Significance 1
1.2 Objectives and Scope 2
1.3 Research Plan 3
1.4 Report Outline 3
2 Literature Review **7**
2.1 Introduction 7
2.2 Corrosion in Steel Bridges 8
2.3 Corrosion Risk Assessment for Texas 11
2.4 Mechanism of Steel Corrosion in Atmospheric Conditions 12
2.5 Corrosion Protective System 14
2.5.1 Surface Physical Modification or Surface Treatment 15
2.5.2 Steel Chemical Modification or Corrosion-Resistant Steel 22
2.5.3 Corrosion Prevention and Mitigation Techniques 31
2.5.4 Corrosion Fatigue and Service Life 44
2.6 Synthesis of Research 45
2.7 Summary 46
3 Assessing Corrosion Risk in Texas **47**
3.1 Introduction to Risk Assessment 47
3.2 Methodology 48
3.3 Data Collection and Processing 48
3.4 Texas Corrosion Hazard Assessment 49
3.4.1 Texas Environmental Assessment 50
3.4.2 Texas Contamination Assessment 57
3.5 Texas Corrosion Risk Assessment 60
3.5.1 Atmospheric Corrosion Models 60
3.5.2 Corrosion Risk Assessment Map 61
3.6 Summary 63
4 Field Evaluation to Investigate Effectiveness of Corrosion Mitigation **65**
4.1 Introduction 65
4.2 Selection of Bridges 65
4.3 Selected Mitigation Methods 74
4.3.1 Weathering Steel Bridges 74
4.3.2 Painted Steel Bridges 75
4.4 Field Evaluation 75
4.4.1 Visual Inspection 78
4.4.2 Chloride Test 82
4.4.3 pH Test 82
4.4.4 Ultrasonic Thickness Measurement 83
4.4.5 Tape Adhesion Test 84

4.4.6 Infrared Thermography 85
4.4.7 Pull-Off Adhesion Testing 86
4.4.8 Paint Thickness Measurement 89
4.4.9 Scrape Test 90
4.4.10 Sensor Installation for Continuous Monitoring 90
4.5 Results 92
4.5.1 Visual Inspection 92
4.5.2 Chloride Test 102
4.5.3 pH Test 103
4.5.4 Ultrasonic Thickness Measurement Results 104
4.5.5 Tape Adhesion Results 105
4.5.6 Infrared Thermography 109
4.5.7 Pull-Off Adhesion Results 110
4.5.8 Paint Thickness Measurement 112
4.5.9 Long-Term Monitoring Result 113
4.6 Particle Size Analysis and Development of New PRI 122
4.7 Summary 129
5 Laboratory Testing 131
5.1 Introduction 131
5.2 Experimental Program 131
5.2.1 Scanning Electron Microscopy/Energy-Dispersive X-Ray Spectroscopy 133
5.2.2 X-Ray Photoelectron Spectroscopy 147
5.2.3 Optical Microscopy 154
5.2.4 Powdered X-Ray Diffraction 173
5.3 Summary 187
6 Decision Tool for Selecting Mitigation Methods 189
6.1 Introduction 189
6.2 Decision Analysis Method 189
6.2.1 Weighted Sum Model 189
6.2.2 Description of Criteria 190
6.3 Development of Decision Matrix 200
6.4 Comparison of TxDOT NBI Superstructure Ratings and Normalized Scores from Field and Laboratory Testing 205
6.5 Recommended Mitigation Methods for Steel Bridges 208
6.6 Application of Developed Tool 208
6.7 Summary 211
7 Service Life of Weathering Steel Structures 213
7.1 Introduction 213
7.1.1 Deterioration of Weathering Steel Bridges 213
7.1.2 Corrosion Fatigue Deterioration in Weathering Steel 214
7.1.3 Weldment and Their Effect on Fatigue 218
7.1.4 Damage Indicator and Limit State Function 219
7.1.5 Developed Framework to Predict Service Life of Weathering Steel 222
7.2 Modeling Corrosion Fatigue Degradation for Weathering Steel 223
7.2.1 Material Properties 223
7.2.2 Corrosion Fatigue Simulation Results and Comparative Analysis 224

7.2.3 Corrosion Fatigue Limit State ... 226
7.2.4 Case Studies ... 227
7.2.5 Conclusion ... 263
7.3 Decision Tool Projecting Service Life of Weathering Steel ... 265
7.3.1 Description of Decision Tool ... 265
7.3.2 Application ... 271
7.4 Summary ... 271
8 Summary and Conclusions ... 273
8.1 Conclusions ... 275
8.2 Weathering Steel ... 275
8.3 Paint Steel ... 276
8.4 Service Life of Weathering Steel ... 276
8.5 Recommendations ... 277
References ... 279
Appendix A ... 298
A.1. TYL-PS-02 ... 298
A.1.1. Observed Condition ... 298
A.1.2. NDT Results ... 300
A.1.3. Pull off Adhesion Results ... 303
A.1.4. Optical Microscopy Results ... 305
A.1.5. SEM/EDS Results ... 307
A.2. BRY-PS-01 ... 316
A.2.1. Observed Condition ... 317
A.2.2. NDT Results ... 319
A.2.3. Pull-off Adhesion Result ... 324
A.2.4. Optical Microscopy Results ... 326
A.2.5. SEM/EDS Results ... 329
A.3. ATL-PS-01 ... 336
A.3.1. Observed Condition ... 337
A.3.2. NDT Results ... 339
A.3.3. Pull-off Adhesion Results ... 343
A.3.4. Optical Microscopy Results ... 345
A.3.5. SEM/EDS Results ... 347
A.4. FTW-PS-01 ... 354
A.4.1. Observed Condition ... 355
A.4.2. NDT Results ... 357
A.4.3. Pull-off Adhesion Results ... 362
A.4.4. Optical Microscopy Results ... 364
A.4.5. SEM/EDS Results ... 366
A.5. FTW-PS-02 ... 374
A.5.1. Observed Condition ... 375
A.5.2. NDT Results ... 377
A.5.3. Pull-off Adhesion Results ... 382
A.5.4. Optical Microscopy Results ... 384
A.5.5. SEM/EDS Results ... 386
A.6. AMA-PS-01 ... 394

A.6.1. Observed Condition 395
A.6.2. NDT Results 397
A.6.3. Pull-off Adhesion Results 400
A.6.4. Optical Microscopy Results 401
A.6.5. SEM/EDS Results 403
A.7. AMA-PS-02 408
A.7.1. Observed Condition 408
A.7.2. NDT Results 410
A.7.3. Pull-off Adhesion Results 413
A.7.4. Optical Microscopy Results 414
A.7.5. SEM/EDS Results 415
A.8. AMA-PS-03 419
A.8.1. Observed Condition 419
A.8.2. NDT Results 421
A.8.3. Pull-off Adhesion Results 425
A.8.4. Optical Microscopy Results 426
A.8.5. SEM/EDS Results 428
A.9. WFS-PS-01 435
A.9.1. Observed Condition 435
A.9.2. NDT Results 437
A.9.3. Pull-off Adhesion Results 441
A.9.4. Optical Microscopy Results 443
A.9.5. SEM/EDS Results 444
A.10. WFS-PS-02 446
A.10.1. Observed Condition 446
A.10.2. NDT Results 447
A.10.3. Pull-off Adhesion Results 451
A.10.4. Optical Microscopy Results 453
A.10.5. SEM/EDS Results 454
A.11. WFS-RC-01 460
A.11.1. Observed Condition 460
A.11.2. NDT Results 462
A.11.3. Pull-off Adhesion Results 466
A.11.4. Optical Microscopy Results 468
A.11.5. SEM/EDS Results 470
A.12. WFS-RC-02 476
A.12.1. Observed Condition 476
A.12.2. NDT Results 478
A.12.3. Pull-off Adhesion Results 482
A.12.4. Optical Microscopy Results 484
A.12.5. SEM/EDS Results 486
A.13. DAL-PS-01 490
A.13.1. Observed Condition 490
A.13.2. NDT Results 492
A.13.3. Pull-off Adhesion Results 496
A.13.4. Optical Microscopy Results 498

A.13.5. SEM/EDS Results 499
A.14. YKM-PS-01 506
A.14.1. Observed Condition 506
A.14.2. NDT Results 509
A.14.3. Pull-off Adhesion Results 514
A.14.4. Optical Microscopy Results 516
A.14.5. SEM/EDS Results 519
A.15. CRP-PS-01 535
A.15.1. Observed Condition 535
A.15.2. NDT Results 538
A.15.3. Pull-off Adhesion Results 540
A.15.4. Optical Microscopy Results 542
A.15.5. SEM/EDS Results 544
A.16. TYL-PS-01 550
A.16.1. Observed Condition 550
A.16.2. NDT Results 552
A.16.3. Pull-off Adhesion Results 556
A.16.4. Optical Microscopy Results 558
A.16.5. SEM/EDS Results 560
A.17. ELP-PS-01 576
A.17.1. Observed Condition 576
A.17.2. NDT Results 578
A.17.3. Pull-off Adhesion Results 582
A.17.4. Optical Microscopy Results 584
A.17.5. SEM/EDS Results 585
A.18. HOU-PS-01 600
A.18.1. Observed Condition 600
A.18.2. NDT Results 603
A.18.3. Pull-off Adhesion Results 608
A.18.4. Optical Microscopy Results 610
A.18.5. SEM/EDS Results 612
A.19. BMT-PS-01 618
A.19.1. Observed Condition 618
A.19.2. NDT Results 620
A.19.3. Pull-off Adhesion Results 625
A.19.4. Optical Microscopy Results 627
A.19.5. SEM/EDS Results 629
A.20. BMT-PS-02 646
A.20.1. Observed Condition 646
A.20.2. NDT Results 648
A.20.3. Pull-off Adhesion Results 653
A.20.4. Optical Microscopy Results 655
A.20.5. SEM/EDS Results 657
A.21. AUS-WS-01 676
A.21.1. Observed Condition 676
A.21.2. Field Testing Results and Tape Adhesion Test Results 678

A.21.3. SEM/EDS Results: Exterior Web Girder 682
A.21.4. SEM/EDS Results: Interior Web Girder 695
A.21.5. SEM/EDS Results: Interior Web Girder 700
A.21.6. XPS Result: Exterior Girder 704
A.21.7. XPS Result: Interior Girder 705
A.21.8. XRD Result: Exterior and Interior Girder 706
A.21.9. Particle Size Analysis: Tape Adhesion Results 707
A.22. AUS-WS-03 712
A.22.1. Observed Condition 712
A.22.2. Field Testing and Tape Adhesion Results 713
A.22.3. SEM/EDS Results: Exterior Web Girder 717
A.22.4. SEM/EDS Results: Interior Web Girder 725
A.22.5. SEM/EDS Results: Interior Web Girder 729
A.22.6. XPS Result: Exterior Girder 732
A.22.7. XPS Result: Interior Girder 733
A.22.8. XRD Result: Exterior and Interior Girder 734
A.22.9. Particle Size Analysis: Tape Adhesion Results 735
A.23. AUS-WS-04 740
A.23.1. Observed Condition 740
A.23.2. Field Testing and Tape Adhesion Results 742
A.23.3. SEM/EDS Results: Exterior Web Girder 745
A.23.4. SEM/EDS Results: Interior Web Girder 758
A.23.5. XPS Result: Exterior Girder 767
A.23.6. XPS Result: Interior Girder 768
A.23.7. XRD Result: Exterior and Interior Girder 769
A.23.8. Particle Size Analysis: Tape Adhesion Results 770
A.24. HOU-WS-01 776
A.24.1. Observed Condition 776
A.24.2. Field Inspection Results 777
A.24.3. SEM/EDS Results: Exterior Web Girder 778
A.24.4. XPS Results: Exterior Web Girder 785
A.24.5. XRD Result: Exterior and Interior Girder 786
A.24.6. Particle Size Analysis: Tape Adhesion Results 787
A.25. HOU-WS-02 789
A.25.1. Observed Condition 789
A.25.2. Field Inspection Results 790
A.25.3. SEM/EDS Results: Exterior Web Girder 794
A.25.4. SEM/EDS Results: Interior Web 808
A.25.5. XPS Results: Exterior Web Girder 818
A.25.6. XPS Results: Interior Web Girder 819
A.25.7. XRD Result: Exterior and Interior Girder 820
A.25.8. Particle Size Analysis: Tape Adhesion Results 821
A.26. HOU-WS-03 827
A.26.1. Observed Condition 827
A.26.2. Field Inspection Results 828
A.26.3. SEM/EDS Results: Exterior Web Girder 833

A.26.4. SEM/EDS Results: Interior Web 835
A.26.5. XPS Results: Exterior Web Girder 845
A.26.6. XPS Results: Interior Web Girder 846
A.26.7. XRD Result: Exterior and Interior Girder 847
A.26.8. Particle Size Analysis: Tape Adhesion Results 849
A.27. HOU-WS-04 855
A.27.1. Observed Condition 855
A.27.2. Field Testing and Tape Adhesion Results 856
A.27.3. SEM/EDS Results: Exterior Web Girder 860
A.27.4. SEM/EDS Results: Interior Web 866
A.27.5. XPS Results: Exterior Web Girder 871
A.27.6. XPS Results: Interior Web Girder 872
A.27.7. XRD Result: Exterior and Interior Girder 873
A.27.8. Particle Size Analysis: Tape Adhesion Results 874
A.28. HOU-WS-05 880
A.28.1. Observed Condition 880
A.28.2. Field Inspection Results 881
A.28.3. SEM/EDS Results: Exterior Web Girder 885
A.28.4. SEM/EDS Results: Interior Web 891
A.28.5. XPS Results: Exterior Web Girder 895
A.28.6. XPS Results: Interior Web Girder 896
A.28.7. XRD Result: Exterior and Interior Girder 897
A.28.8. Particle Size Analysis: Tape Adhesion Results 898
A.29. HOU-WS-05* 904
A.29.1. Observed Condition 904
A.29.2. Field Inspection Results 905
A.30. HOU-WS-06 906
A.30.1. Observed Condition 906
A.30.2. Field Testing and Tape Adhesion Results 907
A.30.3. SEM/EDS Results: Exterior Web Girder 912
A.30.4. SEM/EDS Results: Interior Web Girder 919
A.30.5. XPS Results: Exterior Web Girder 923
A.30.6. XPS Results: Interior Web Girder 924
A.30.7. XRD Result: Exterior and Interior Girder 925
A.30.8. Particle Size Analysis: Tape Adhesion Results 927
A.31. HOU-WS-07 934
A.31.1. Observed Condition 934
A.31.2. Field Inspection Results 935
A.31.3. SEM/EDS Results: Exterior Web Girder 939
A.31.4. SEM/EDS Results: Interior Web Girder 951
A.31.5. SEM/EDS Results: Interior Web Girder 952
A.31.6. XPS Results: Exterior Web Girder 959
A.31.7. XPS Results: Interior Web Girder 960
A.31.8. XRD Result: Exterior and Interior Girder 961
A.31.9. Particle Size Analysis: Tape Adhesion Results 962
A.32. CRP-WS-01 967

A.32.1. Observed Condition 967
A.32.2. Field Inspection Results 968
A.32.3. SEM/EDS Results: Exterior Web Girder 973
A.32.4. SEM/EDS Results: Interior Web Girder 977
A.32.5. XPS Result: Exterior Girder 979
A.32.6. XPS Result: Interior Girder 980
A.32.7. XRD Result: Exterior and Interior Girder 981
A.32.8. Particle Size Analysis: Tape Adhesion Results 983
A.33. SAT-WS-01 988
A.33.1. Observed Condition 988
A.33.2. Field Inspection Results 989
A.33.3. Particle Size Analysis: Tape Adhesion Results 994
A.34. ATL-WS-01 1001
A.34.1. Observed Condition 1001
A.34.2. Field Inspection Results 1002
A.34.3. SEM/EDS Results: Exterior Girder 1005
A.34.4. SEM/EDS: Interior Girder 1011
A.34.5. XPS Result: Exterior Girder 1015
A.34.6. XPS Result: Interior Girder 1016
A.34.7. XRD Result: Exterior, Interior, and Bottom Flange of Girder 1017
A.34.8. Particle Size Analysis: Tape Adhesion Results 1019
A.35. ATL-WS-02 1026
A.35.1. Observed Condition 1026
A.35.2. Field Inspection Results 1027
A.35.3. SEM/EDS Results: Exterior Girder Web 1030
A.35.4. SEM/EDS Results: Interior Girder Web 1033
A.35.5. XPS Result: Exterior Girder 1039
A.35.6. XPS Result: Interior Girder 1040
A.35.7. XRD Result: Exterior, Interior, and Bottom Flange of Girder 1041
A.35.8. Particle Size Analysis: Tape Adhesion Results 1043
A.36. ATL-WS-03 1048
A.36.1. Observed Condition 1048
A.36.2. Field Inspection Results 1050
A.36.3. SEM/EDS Results: Exterior Girder Web 1054
A.36.4. SEM/EDS Results: Interior Girder 1064
A.36.5. XPS Result: Exterior Girder 1072
A.36.6. XPS Result: Interior Girder 1073
A.36.7. XRD Result: Exterior and Interior Girder 1074
A.36.8. Particle Size Analysis: Tape Adhesion Results 1075
A.37. LBB-WS-01 1081
A.37.1. Observed Condition 1081
A.37.2. Field Inspection Results 1082
A.37.3. SEM/EDS Results: Exterior Web Girder 1086
A.37.4. SEM/EDS Results: Interior Web Girder 1094
A.37.5. XPS Result: Exterior Girder 1097
A.37.6. XPS Result: Interior Girder 1098

A.37.7. XRD Result: Exterior and Interior Girder 1099
A.37.8. Particle Size Analysis: Tape Adhesion Results 1100
A.38. LBB-WS-02 1107
A.38.1. Observed Condition 1107
A.38.2. Field Inspection Results 1108
A.38.3. SEM/EDS Results: Exterior Web Girder 1113
A.38.4. SEM/EDS Results: Interior Web Girder 1121
A.38.5. SEM/EDS Results: Interior Web Girder 1123
A.38.6. XPS Result: Exterior Girder 1125
A.38.7. XPS Result: Interior Girder 1126
A.38.8. XRD Result: Exterior and Interior Girder 1127
A.38.9. Particle Size Analysis: Tape Adhesion Results 1128
A.39. ELP-WS-01 1134
A.39.1. Observed Condition 1134
A.39.2. Field Inspection Results 1135
A.39.3. SEM/EDS Results: Exterior Web Girder 1140
A.39.4. SEM/EDS Results: Interior Web Girder 1144
A.39.5. XPS Result: Exterior Girder 1154
A.39.6. XPS Result: Interior Girder 1155
A.39.7. XRD Result: Exterior and Interior Girder 1156
A.39.8. Particle Size Analysis: Tape Adhesion Results 1158
A.40. AUS-WS-02 1163
A.40.1. Observed Condition 1163
A.40.2. Field Inspection Results 1165
A.40.3. SEM/EDS Results: Interior Web Girder 1168
A.40.4. SEM/EDS Results: Interior Web Girder 1172
A.40.5. XPS Result: Interior Girder 1180
A.40.6. XRD Result: Exterior and Interior Girder 1181
A.40.7. Particle Size Analysis: Tape Adhesion Results 1182
A.41. FTW-WS-01 1186
A.41.1. Observed Condition 1186
A.41.2. Field Inspection Results 1187
A.41.3. SEM/EDS Results: Exterior Web Girder 1192
A.41.4. SEM/EDS Results: Interior Web Girder 1200
A.41.5. XPS Results: Exterior Web Girder 1202
A.41.6. XPS Results: Interior Web Girder 1203
A.41.7. XRD Result: Exterior and Interior Girder 1204
A.41.8. Particle Size Analysis: Tape Adhesion Results 1206
A.42. FTW-WS-02 1211
A.42.1. Observed Condition 1211
A.42.2. Field Inspection Results 1212
A.42.3. SEM/EDS Results: Exterior Web Girder 1216
A.42.4. SEM/EDS Results: Interior Web Girder 1220
A.42.5. XPS Results: Exterior Web Girder 1222
A.42.6. XPS Results: Interior Web Girder 1223
A.42.7. XRD Result: Exterior and Interior Girder 1224

A.42.8. Particle Size Analysis: Tape Adhesion Results 1226
A.43. FTW-WS-03 1232
A.43.1. Observed Condition 1232
A.43.2. Field Inspection Results 1233
A.43.3. SEM/EDS Results: Exterior Web Girder 1237
A.43.4. SEM/EDS Results: Interior Web Girder 1239
A.43.5. XPS Results: Exterior Web Girder 1241
A.43.6. XPS Results: Interior Web Girder 1242
A.43.7. XRD Result: Exterior and Interior Girder 1243
A.43.8. Particle Size Analysis: Tape Adhesion Results 1245
A.44. DAL-WS-01 1250
A.44.1. Observed Condition 1250
A.44.2. Field Inspection Results 1251
A.44.3. SEM/EDS Results: Exterior Web Girder 1255
A.44.4. SEM/EDS Results: Interior Web Girder 1266
A.44.5. XPS Result: Exterior Girder 1272
A.44.6. XPS Result: Interior Girder 1273
A.44.7. XRD Result: Exterior and Interior Girder 1274
A.44.8. Particle Size Analysis: Tape Adhesion Results 1275
A.45. DAL-WS-02 1280
A.45.1. Observed Condition 1280
A.45.2. Field Inspection Results 1281
A.45.3. SEM/EDS Results: Exterior Web Girder 1285
A.45.4. SEM/EDS Results: Interior Web Girder 1297
A.45.5. XPS Result: Exterior Girder 1303
A.45.6. XPS Result: Interior Girder 1304
A.45.7. XRD Result: Exterior and Interior Girder 1305
A.45.8. Particle Size Analysis: Tape Adhesion Results 1306
A.46. DAL-WS-03 1311
A.46.1. Observed Condition 1311
A.46.2. Field Inspection Results 1312
A.46.3. SEM/EDS Results: Exterior Web Girder 1316
A.46.4. SEM/EDS Results: Interior Web Girder 1324
A.46.5. XPS Result: Exterior Girder 1332
A.46.6. XPS Result: Interior Girder 1333
A.46.7. XRD Result: Exterior and Interior Girder 1334
A.46.8. Particle Size Analysis: Tape Adhesion Results 1335
A.47. PYTHON CODE FOR TAPE TEST ANALYSIS WITH OPENCV AND SCIKIT LEARN 1340

LIST OF FIGURES

Page

Figure 2.1. Collapse of US 35 Highway Bridge (Silver Bridge)—December 15, 1967 (WVDOT, 2023). 9
Figure 2.2. Collapse of 100 Ft Long Section of the Interstate 95 Bridge on Mianus River Greenwich, CT—June 29, 1983 (Cummings, 2017). 10
Figure 2.3. Collapse of IH 35 Bridge Center Section (National Transportation Safety Board, 2008). 10
Figure 2.4. Environmental Characterization and Corrosion Assessment Maps of Texas (Trejo et al., 2009). 12
Figure 2.5. Statewide Environmental Classification Map (TxDOT, 2022). 12
Figure 2.6. Paint System Recommendation for New Construction (Texas Steel Quality Council, 2000). 19
Figure 2.7. Paint System Recommendation for Field Painting for Existing Structures (Texas Steel Quality Council, 2000). 20
Figure 3.1. Local Climatological Station Locations. 49
Figure 3.2. Schematic of Semivariogram. 52
Figure 3.3. Texas Topographical Map (ft) (Daly et al., 1997). 53
Figure 3.4. Texas Environmental Characterizations Map. 54
Figure 3.5. Cross-Validation between Spatial Interpolation Results and True Measurements. 56
Figure 3.6. Texas Salt Application from 1992 to 2015 (lb/year) (Bock et al., 2018). 57
Figure 3.7. Annual Number of FD vs. Salt Application in Texas. 58
Figure 3.8. Chloride Contamination. 59
Figure 3.9. Annual Sulfur Dioxide Deposition (kg/ha) (EPA, 2023). 60
Figure 3.10. Refined Corrosion Risk Assessment Map. 62
Figure 3.11. Countywide Corrosion Risk Assessment Map. 63
Figure 4.1. Map Showing Selected Steel Bridges. 68
Figure 4.2. Selected Weathering Steel Bridges. 69
Figure 4.3. Selected Painted Steel Bridges. 69
Figure 4.4. Distribution of Bridge Age. 70
Figure 4.5. Distribution of Bridges—Region. 70
Figure 4.6. Typically Inspected Locations on Girders. 77
Figure 4.7. Typical Location for Field Testing on Steel Girders. 77
Figure 4.8. Visual Inspection and Tape Adhesion Test. 80
Figure 4.9. Chloride Test and Tape Adhesion Test. 81
Figure 4.10. pH Strips Used for Field Testing. 83
Figure 4.11. Olympus 27 MG Ultrasonic Thickness Gauge. 84
Figure 4.12. Infrared Thermography FLIR T640 Camera. 86
Figure 4.13. Digital and Thermal Image of an Exterior Girder of ATL−PS−01 86
Figure 4.14. Elcometer 510 Automatic Pull-Off Adhesion Testing Kit. 88
Figure 4.15. Pull-off Adhesion Test. 88
Figure 4.16. Cohesive and Adhesive Code. 88
Figure 4.17. Cohesive, Adhesive, and Glue Failure. 89

Figure 4.18. Elcometer 456 Nonferrous Metal Coating Thickness Gauge. 89
Figure 4.19. Scraped Surface for Steel Bridges. 90
Figure 4.20. Installation of Onset HOBO USB Micro Station Data Logger. 91
Figure 4.21. Geographic Locations of Testing Stations. 92
Figure 4.22. Developed Patina on Top Flange of Exterior and Interior Girders. 94
Figure 4.23. Patina Condition on Bottom Flange for Exterior and Interior Girder. 95
Figure 4.24. Developed Patina on Interior and Exterior Girder on CRP−WS−01. 96
Figure 4.25. Developed Patina on Weathering Steel Girders in Austin and Corpus Christi. 97
Figure 4.26. Color Variation of Patina Observed at Joint Near Abutment and Bent Due to Continuous Washing of Patina. 98
Figure 4.27. Paint Failure Observed on TYL−PS−02. 100
Figure 4.28. Development of Corrosion on Harbor Bridge (CRP−PS−01). 100
Figure 4.29. Paint Deterioration on Off-System Bridge (YKM−PS−01). 101
Figure 4.30. Condition of Paint System on Exterior and Interior Girders (ATL−PS−01). 102
Figure 4.31. Patina Condition for WS Bridge in Austin and Corpus Christi with Different Built Year. 107
Figure 4.32. Patina Condition of Interior and Exterior Girder on CRP−WS−01. 108
Figure 4.33. Digital and Thermal Imaging of Painted Girder, AMA−PS−03. 109
Figure 4.34. Digital and Thermal Image of Painted Girder, ATL−PS−01. 110
Figure 4.35. Digital and Thermal Imaging of Painted Girder on AMA−PS−01. 110
Figure 4.36. Comparison of Data from Local Weather Station and Data Measured with Installed TOW Sensor on Exterior Web of ATL−WS−03. 115
Figure 4.37. Comparison of Data from Local Weather Station and Data Measured with Installed TOW Sensor on Interior Web of CRP−WS−01. 116
Figure 4.38. Comparison of Data from Local Weather Station and Data Measured with Installed TOW Sensor on Exterior Web of CRP−WS−01. 117
Figure 4.39. Comparison of Data from Local Weather Station and Data Measured with Installed TOW Sensor on Exterior Web of DAL−WS−02. 118
Figure 4.40. Comparison of Data from Local Weather Station and Data Measured with Installed TOW Sensor on Exterior Web of HOU−WS−07. 119
Figure 4.41. Comparison of Data from Local Weather Station and Data Measured with Installed TOW Sensor on Exterior Web of LBB−WS−01. 120
Figure 4.42. Comparison of TOW. 122
Figure 4.43. Particle Size Analysis. 123
Figure 4.44. Particle Size Analysis Results at A9G1F1 (CRP−WS−01): (a) Top Flange Bottom, (b) Web, (c) Bottom Flange Bottom, (d) Stiffener. 125
Figure 4.45. Particle Size Analysis Results for CRP−WS−01. 126
Figure 4.46. Particle Size Analysis Results for HOU−WS−07. 126
Figure 4.47. Particle Size Analysis Results for ATL−WS−01. 127
Figure 4.48. PDF Developed for Normalized Area of Rust Particles. 128
Figure 5.1. Scanning Electron Microscope with EDS JEOL JSM-7500F. 136
Figure 5.2. SEM Image of Rust Collected from Exterior Web of Weathering Steel Bridge (DAL-WS-02) and Sample Sum Spectrum of the Same Sample. 138
Figure 5.3. SEM Images of Rust Surface Observed on Weathering Steel Bridges in Different Scales (90 μm, 50 μm, and 20 μm). 139

Figure 5.4. SEM Image of Microcracks Detected on Rust Surface of Weathering Steel Bridge on Exterior Web (CRP-WS-01). 139
Figure 5.5. Elemental Compositions (EDS Spectra). 140
Figure 5.6. Sample Elemental Map Showcasing Distribution of Elemental Composition on Weathering Steel Rust Sample. 141
Figure 5.7. Hematite, Goethite, and Lepidocrocite Detected on a Random Rust Sample. 143
Figure 5.8. Microcracks Detected on a Random Rust Sample. 143
Figure 5.9. Phases Compositions of a Weathering Steel Rust Sample. 144
Figure 5.10. SEM Image and EDS Spectrum of Paint Sample (System I) Collected from Exterior Web of WFS−RC−01. 145
Figure 5.11. SEM Image and EDS Spectrum of Zinc-Based Primer (System II) Observed on TYL−PS−01. 146
Figure 5.12. Omicron XPS/UPS System with Argus Detector. 149
Figure 5.13. Fe 2p 3/2 Spectra. 151
Figure 5.14. Adventitious Carbon Curve Fitting for Calibration. 151
Figure 5.15. Fe 2p 3/2 Curve Fitting for Quantification of Avg. FeOOH, Avg. Fe2O3, Avg. FeO, and Fe Metal. 152
Figure 5.16. Olympus DSX500 Opto-Digital Microscope. 156
Figure 5.17. System I Detected on a Random Sample from WFS−RC−01. 157
Figure 5.18. System II Detected on a Random Sample from TYL−PS−02. 157
Figure 5.19. System III Detected on a Random Sample from CRP−PS−01. 158
Figure 5.20. Lead-Based System Detected on a Random Sample from YKM-PS-01. 158
Figure 5.21. Corrosion Detected on the Primer Surface from TYL-PS-01. 159
Figure 5.22. ZBPS Detected on a Random Sample from BRY-PS-02. 160
Figure 5.23. Corrosion Detected on a Random Sample Taken from BRY−PS−01. 161
Figure 5.24. Two-Layer Paint System—ATL-PS-01. 161
Figure 5.25. Corrosion Detected on the Primer Surface of Samples from ATL-PS-01. 162
Figure 5.26. Corrosion Detected within Paint Layers Collected from Top Face of Bottom Flanges—FTW−PS−02. 162
Figure 5.27. Two-Layer Paint System—AMA-PS-01. 163
Figure 5.28. Two-Layer Paint System—AMA-PS-03. 163
Figure 5.29. Severe Corrosion Detected on Samples Collected from AMA-PS-03. 164
Figure 5.30. Severe Corrosion Detected on the Primer Surface of WFS−RC−01. 165
Figure 5.31. Severe Corrosion Detected on Samples Taken from WFS−RC−02. 166
Figure 5.32. Rust spot Detected on the Primer Surface of TYL−PS−02. 166
Figure 5.33. Two-Layer Paint System—ELP-PS-01. 167
Figure 5.34. Two-Layer Paint System—YKM-PS-01. 167
Figure 5.35. Corrosion Detected on Samples Collected from YKM−PS−01. 168
Figure 5.36. Two-Layer Paint System—HOU-PS-01. 168
Figure 5.37. Two-Layer Paint System—BMT-PS-01. 169
Figure 5.38. Rust spot Detected on Samples Collected from BMT-PS-01. 169
Figure 5.39. Two-Layer Paint System—BMT-PS-02. 170
Figure 5.40. BRUKER-AXS D8 Advanced Bragg-Brentano X-Ray Powder Diffractometer. 176
Figure 5.41. Diffracted X-Ray Intensity vs. Diffraction Angle (2θ) from FTW−WS−01. 176
Figure 5.42. Measured and Fitted X-Ray Intensity, Exterior Web of FTW−WS−01. 176

Figure 5.43. Ternary Diagram—Region 1 and Region 2. 178
Figure 5.44. Ternary Diagram—Region 3. 179
Figure 5.45. Ternary Diagram—Region 4. 179
Figure 5.46. Ternary Diagram—Region 6. 180
Figure 5.47. Ternary Diagram—All Regions. 180
Figure 5.48. Comparison between the Goethite and Akaganeite Amount Detected from Samples Collected from Weathering Steel Girders in Region 4 and Region 6. 181
Figure 6.1. Decision Matrix to Assess Performance of Steel Bridges. 200
Figure 6.2. Total Score for Mitigation Methods. 203
Figure 6.3. Total Score for Corrosion Prevention and Mitigation Methods. 204
Figure 6.4. Score for Corrosion Prevention and Mitigation Methods in Each Region. 204
Figure 6.5. Recommended Mitigation System for Steel Bridges. 208
Figure 6.6. Developed Decision Tool. 210
Figure 7.1. AASHTO S-N Curves for Various Fatigue Categories (AASHTO, 2020). 215
Figure 7.2. Strain Amplitude vs. Reversal to Failure. 216
Figure 7.3. Fatigue Hysteresis Loop. 219
Figure 7.4. Steel Plate with Crack Subject to Cyclic Load. 220
Figure 7.5. Energy Interpretation of Neuber's Rule. 221
Figure 7.6. Developed Framework to Predict Service Life of Weathering Steel Bridges. 222
Figure 7.7. Number of Cycles to Failures vs. P_{SWT}. 225
Figure 7.8. Number of Cycles to Failure in Different Corrosive Regions. 226
Figure 7.9. Noncomposite Steel Girder Layout (Barker & Puckett, 2021). 229
Figure 7.10. Service Life of Simple-Span Noncomposite Rolled Steel Beam Bridge in Different Corrosion Regions. 233
Figure 7.11. Composite Steel Section (Barker & Puckett, 2021). 234
Figure 7.12. Service Life of Simple-Span Composite Rolled Steel Beam Bridge in Different Corrosion Regions. 237
Figure 7.13. Two-Span Composite Steel I-Girder Bridge Sketches (Barth, 2022). 238
Figure 7.14. Multiple-Span Composite Steel Section (Barth, 2022). 240
Figure 7.15. Welded Transverse Stiffener Connection (AASHTO, 2010). 241
Figure 7.16. Service Life of Two-Span Continuous Straight Composite Steel I-Girder Bridge in Different Corrosion Regions. 244
Figure 7.17. Three-Span Continuous Horizontally Curved Composite Steel I-girder Bridges Sketches (Rivera & Chavel, 2022). 246
Figure 7.18. Critical Composite Steel Section at G4 (Rivera & Chavel, 2022). 247
Figure 7.19. Service Life of Three-Span Continuous Horizontally Curved Composite Steel Bridge in Different Corrosion Regions. 253
Figure 7.20. Three-Span Continuous Straight Composite Steel Tub Girder Bridge Sketches (Chavel & Carnahan, 2022). 254
Figure 7.21. Critical Composite Steel Section (Chavel & Carnahan, 2022). 257
Figure 7.22. Longitudinal Stiffener on Bottom Flange (Chavel & Carnahan, 2022). 259
Figure 7.23. Unfactored Moment Envelope (Chavel & Carnahan, 2022). 260
Figure 7.24. Service Life of Three-Span Continuous Straight Composite Steel Tub Girder Bridge in Different Corrosion Regions. 263
Figure 7.25. Countywide Service Life Prediction. 266
Figure 7.26. Corrosion Rate vs. Protective Ability Index α/Γ. 267

Figure 7.27. User-Defined Service Life Prediction. 268
Figure A.1. Typical Elevation of TYL-PS-02. 298
Figure A.2. Paint Condition on the Girder of TYL-PS-02. 299
Figure A.3. Digital and Thermal Image of Painted Girder on TYL-PS-02. 300
Figure A.4. Paint System Examined by Optical Microscope TYL–PS–02. 305
Figure A.5. Widespread Corrosion Observed Between Primer and Base Metal (G9F2). 306
Figure A.6 SEM Image and EDS Spectrum of the Paint Collected from Exterior Web of the Girder. 307
Figure A.7 EDS Elemental Mapping of Paint Collected from Exterior Web. 308
Figure A.8. SEM Image and EDS Spectrum of the Paint Collected from Exterior Web of the Girder. 309
Figure A.9. EDS Elemental Mapping of Paint Collected from Exterior Web. 310
Figure A.10. SEM image and EDS Spectrum of the Paint Collected from Exterior Web of the Girder. 311
Figure A.11. EDS Elemental Mapping of Paint Collected from Exterior Web. 312
Figure A.12. SEM Image and EDS Spectrum of the Paint Collected from Interior Web of the Girder. 313
Figure A.13. EDS Elemental Mapping of Paint Collected from Interior Web. 314
Figure A.14. SEM Image and EDS Spectrum of the Paint Collected from Interior Web of the Girder. 315
Figure A.15. EDS Elemental Mapping of Paint Collected from Interior Web. 316
Figure A.16. Typical Elevation of BRY-PS-01 317
Figure A.17. Paint Condition on the Girder of BRY-PS-01. 318
Figure A.18. Digital and Thermal Image of Painted Girder on BRY-PS-01. 319
Figure A.19. Paint System Examined by Optical Microscope (BRY–PS–01 on Girder 1) 326
Figure A.20. Paint System Examined by Optical Microscope (A1G5F1) 327
Figure A.21. Corroded Paint System Examined by Optical Microscope (A1G2F1) 328
Figure A.22. SEM image of Paint and EDS Spectrum of the Paint Collected from Exterior Web of the Girder (A1G1F1) 329
Figure A.23. EDS Elemental Mapping of Paint Collected from Exterior 330
Figure A.24. SEM image of Paint and EDS Spectrum of the Paint Collected from Exterior Web of the Girder (A1G1F1) 331
Figure A.25. EDS Elemental Mapping of Paint Collected from Exterior Girder (A1G1F1) 332
Figure A.26. SEM Image and EDS Spectrum of the Paint Collected from Exterior Web of the Girder (A1G5F1) 333
Figure A.27. EDS Elemental Mapping of Paint Collected from Exterior Girder (A1G5F1) 334
Figure A.28. SEM Image of Paint and EDS Spectrum of the Paint Collected from Exterior Web of the Girder (A1G5F1) 335
Figure A.29. EDS Elemental Mapping of Paint Collected from Exterior Girder (A5G1F1) 336
Figure A.30. Typical Elevation of ATL-PS-01. 337
Figure A.31. Paint Condition on the Girder of ATL-PS-01. 338
Figure A.32. Digital and Thermal Image of Painted Girder on ATL-PS-01. 339
Figure A.33. Two Layer Paint System Examined by Optical Microscope ATL–PS–01. 345
Figure A.34. Corrosion as Observed Between Primer and Base Metal by Optical Microscope ATL–PS–01. 346

Figure A.35. SEM Image of Paint and EDS Spectrum of the Paint Collected from Exterior Web of the Girder. 347
Figure A.36. EDS Elemental Mapping of Paint Collected from Exterior Web. 348
Figure A.37. SEM Image of Paint and EDS Spectrum of the Paint Collected from Exterior Web of the Girder. 349
Figure A.38. SEM Image and EDS Spectrum of the Paint Collected from Exterior Web of the Girder. 350
Figure A.39. SEM Image and EDS Spectrum of the Paint Collected from Exterior Web of the Girder. 351
Figure A.40. SEM Image and EDS Spectrum of the Paint Collected from Interior Web of the Girder. 352
Figure A.41. EDS Elemental Mapping of Paint Collected from Interior Web. 353
Figure A.42. SEM Image and EDS Spectrum of the Paint Collected from Interior Web of the Girder. 354
Figure A.43. Typical Elevation of FTW-PS-01. 355
Figure A.44. Paint Condition on the Girder of FTW-PS-01. 356
Figure A.45. Digital and Thermal Image of Painted Girder on FTW-PS-01. 357
Figure A.46. Two Layer Paint System Examined by Optical Microscope FTW–PS–01 (Int.). 364
Figure A.47. Two Layer Paint System Examined by Optical Microscope FTW–PS–01 (Ext.). 365
Figure A.48. SEM Image and EDS Spectrum of the Paint Collected from Exterior Web of the Girder. 366
Figure A.49. EDS Elemental Mapping of Paint Collected from Exterior Web. 367
Figure A.50. SEM Image and EDS Spectrum of the Paint Collected from Exterior Web of the Girder. 368
Figure A.51. EDS Elemental Mapping of Paint Collected from Exterior Web. 369
Figure A.52. SEM Image of Paint and EDS Spectrum of the Paint Collected from Interior Web of the Girder. 370
Figure A.53. EDS Elemental Mapping of Paint Collected from Interior Web. 371
Figure A.54. SEM Image and EDS Spectrum of the Paint Collected from Interior Web of the Girder. 372
Figure A.55. EDS Elemental Mapping of Paint Collected from Interior Web. 373
Figure A.56. SEM Image and EDS Spectrum of the Paint Collected from Interior Web of the Girder. 374
Figure A.57. Typical Elevation of FTW-PS-02. 375
Figure A.58. Paint Condition on the Girder of FTW-PS-02. 376
Figure A.59. Digital and Thermal Image of Painted Girder on FTW-PS-02. 377
Figure A.60. Two Layer Paint System Examined by Optical Microscope FTW–PS–02. 384
Figure A.61. Corrosion Underneath Paint Layer. 385
Figure A.62. SEM Image and EDS Spectrum of the Paint Collected from Exterior Web of the Girder. 386
Figure A.63. SEM Image and EDS Spectrum of the Paint Collected from Exterior Web of the Girder. 387
Figure A.64. SEM Image and EDS Spectrum of the Paint Collected from Exterior Web of the Girder. 388

Figure A.65. EDS Elemental Mapping of Paint Collected from Exterior Web. 389
Figure A.66. SEM Image of Paint and EDS Spectrum of the Paint Collected from Exterior Web of the Girder. 390
Figure A.67. EDS Elemental Mapping of Paint Collected from Exterior Web 391
Figure A.68. SEM Image and EDS Spectrum of the Paint Collected from Interior Web of the Girder. 392
Figure A.69. EDS Elemental Mapping of Paint Collected from Interior Web. 393
Figure A.70. SEM Image and EDS Spectrum of the Paint Collected from Interior Web of the Girder. 394
Figure A.71. Typical Elevation of AMA-PS-01. 395
Figure A.72. Paint Condition on the Girder of AMA-PS-01. 396
Figure A.73. Digital and Thermal Image of Painted Girder on AMA-PS-01 397
Figure A.74. Paint System Examined by Optical Microscope AMA–PS–01. 401
Figure A.75. Corrosion as Observed Between Primer and Base Metal on Exterior Pile. 402
Figure A.76. SEM Image and EDS Spectrum of the Paint Collected from Exterior Web of the Girder. 403
Figure A.77. EDS Elemental Mapping of Paint Collected from Exterior Web. 404
Figure A.78. SEM Image and EDS Spectrum of the Paint Collected from Interior Web of the Girder. 405
Figure A.79. EDS Elemental Mapping of Paint Collected from Exterior Web. 406
Figure A.80. SEM Image and EDS Spectrum of the Paint Collected from Exterior Web of the Girder. 407
Figure A.81. Typical Elevation of AMA-PS-02. 408
Figure A.82. Paint Condition on the Girder of AMA-PS-02. 409
Figure A.83. Digital and Thermal Image of Painted Girder on AMA-PS-02 410
Figure A.84. Two Layer Paint System Examined by Optical Microscope AMA–PS–02. 414
Figure A.85. SEM Image and EDS Spectrum of the Paint Collected from Exterior Web of the Girder. 415
Figure A.86. EDS Elemental Mapping of Paint Collected from Exterior Web. 416
Figure A.87. SEM Image and EDS Spectrum of the Paint Collected from Interior Web of the Girder. 417
Figure A.88. SEM Image and EDS Spectrum of the Paint Collected from Exterior Web of the Girder. 418
Figure A.89. Typical Elevation of AMA-PS-03 419
Figure A.90. Paint Condition on the Girder of AMA-PS-03 420
Figure A.91. Digital and Thermal Image of Painted Girder on AMA-PS-03 421
Figure A.92. Two Layer Paint System Examined by Optical Microscope AMA–PS–03. 426
Figure A.93. Widespread corrosion and Complete Paint Failure. 427
Figure A.94. SEM Image and EDS Spectrum of the Paint Collected from Exterior Web of the Girder. 428
Figure A.95. EDS Elemental Mapping of Paint Collected from Exterior Web. 429
Figure A.96. SEM Image and EDS Spectrum of the Paint Collected from Exterior Web of the Girder. 430
Figure A.97. EDS Elemental Mapping of Paint Collected from Exterior Web. 431
Figure A.98. SEM Image and EDS Spectrum of the Paint Collected from Exterior Web of the Girder. 432

Figure A.99. SEM Image and EDS Spectrum of the Paint Collected from Exterior Web of the Girder. 433
Figure A.100. EDS Elemental Mapping of Paint Collected from Exterior Web. 434
Figure A.101. Typical Elevation of WFS-PS-01. 435
Figure A.102. Paint Condition on the Girder of WFS-PS-01. 436
Figure A.103. Digital and Thermal Image of Painted Girder on WFS-PS-01. 437
Figure A.104. Two Layer Paint System Examined by Optical Microscope WFS–PS–01. 443
Figure A.105. SEM Image and EDS Spectrum of the Paint Collected from Exterior Web of the Girder. 444
Figure A.106. EDS Elemental Mapping of Paint Collected from Exterior Web. 445
Figure A.107. Typical Elevation of WFS-PS-02. 446
Figure A.108. Digital and Thermal Image of Painted Girder on WFS-PS-02. 447
Figure A.109. Two Layer Paint System Examined by Optical Microscope WFS–PS–02. 453
Figure A.110. SEM Image and EDS Spectrum of the Paint Collected from Exterior Web of the Girder. 454
Figure A.111. EDS Elemental Mapping of Paint Collected from Exterior Web. 455
Figure A.112. SEM Image and EDS Spectrum of the Paint Collected from Interior Web of the Girder. 456
Figure A.113. EDS Elemental Mapping of Paint Collected from Interior Web. 457
Figure A.114. SEM Image and EDS Spectrum of the Paint Collected from Interior Web of the Girder. 458
Figure A.115. EDS Elemental Mapping of Paint Collected from Interior Web. 459
Figure A.116. Typical Elevation of WFS-RC-01. 460
Figure A.117. Paint Condition on the Girder of WFS-RC-01. 461
Figure A.118. Digital and Thermal Image of Painted Girder on WFS-RC-01. 462
Figure A.119. Two Layer Paint System Examined by Optical Microscope WFS–RC–01. 468
Figure A.120. Widespread Corrosion Observed Between Primer and Base Metal. 469
Figure A.121. SEM Image and EDS Spectrum of the Paint Collected from Exterior Web of the Girder. 470
Figure A.122. EDS Elemental Mapping of Paint Collected from Exterior Web. 471
Figure A.123. SEM Image and EDS Spectrum of the Paint Collected from Exterior Web of the Girder. 472
Figure A.124. SEM Image of Paint and EDS Spectrum of the Paint Collected from Exterior Web of the Girder. 473
Figure A.125. SEM Image and EDS Spectrum of the Paint Collected from Interior Web of the Girder. 474
Figure A.126. EDS Elemental Mapping of Paint Collected from Interior Web. 475
Figure A.127. Typical Elevation of WFS-RC-02. 476
Figure A.128. Paint Condition on the Girder of WFS-RC-02. 477
Figure A.129. Digital and Thermal Image of Painted Girder on WFS-RC-02. 478
Figure A.130. Two Layer Paint System Examined by Optical Microscope WFS–RC–02. 484
Figure A.131. Widespread Corrosion Observed under Paint. 485
Figure A.132. SEM Image and EDS Spectrum of the Paint Collected from Exterior Web of the Girder. 486
Figure A.133. EDS Elemental Mapping of Paint Collected from Exterior Web. 487

Figure A.134. SEM Image and EDS Spectrum of the Paint Collected from Exterior Web of the Girder. 488
Figure A.135. EDS Elemental Mapping of Paint Collected from Exterior Web. 489
Figure A.136. Typical Elevation of DAL-PS-01 490
Figure A.137. Paint Condition on the Girder of DAL-PS-01. 491
Figure A.138. Digital and Thermal Image of Painted Girder on DAL-PS-01. 492
Figure A.139. Two Layer Paint System Examined by Optical Microscope DAL–PS–02. 498
Figure A.140. SEM Image of Paint and EDS Spectrum of the Paint Collected from Exterior Web of the Girder. 499
Figure A.141. SEM Image of Paint and EDS Spectrum of the Paint Collected from Exterior Web of the Girder. 500
Figure A.142. EDS Elemental Mapping of Paint Collected from Exterior Web. 501
Figure A.143. SEM Image of Paint and EDS Spectrum of the Paint Collected from Interior Web of the Girder. 502
Figure A.144. EDS Elemental Mapping of Paint Collected from Exterior Web. 503
Figure A.145. SEM image of Paint and EDS Spectrum of the Paint Collected from Interior Web of the Girder. 504
Figure A.146. EDS Elemental Mapping of Paint Collected from Interior Web. 505
Figure A.147. Typical Elevation of YKM-PS-01. 506
Figure A.148. Paint Condition on the Girder of YKM-PS-01. 508
Figure A.149. Digital and Thermal Image of Painted Girder on YKM-PS-01 509
Figure A.150. Two Layer Paint System Examined by Optical Microscope YKM–PS–01 (G1F1). 516
Figure A.151. Two Layer Paint System Examined by Optical Microscope YKM–PS–01 (G3F1). 517
Figure A.152. Paint System Examined by Optical Microscope YKM–PS–01 (G6F1). 518
Figure A.153. SEM Image and EDS Spectrum of the Paint Collected from Exterior Web of the Girder. 519
Figure A.154. EDS Elemental Mapping of Paint Collected from Exterior Web (G1F1). 520
Figure A.155. SEM Image and EDS Spectrum of the Paint Collected from Exterior Web of the Girder. 521
Figure A.156. SEM Image and EDS Spectrum of the Paint Collected from Exterior Web of the Girder. 522
Figure A.157. EDS Elemental Mapping of Paint Collected from Exterior Web. 523
Figure A.158. SEM Image and EDS Spectrum of the Paint Collected from Exterior Web of the Girder. 524
Figure A.159. EDS Elemental Mapping of Paint Collected from Exterior Web. 525
Figure A.160. SEM Image and EDS Spectrum of the Paint Collected from Exterior Web of the Girder. 526
Figure A.161. SEM Image and EDS Spectrum of the Paint Collected from Exterior Web of the Girder. 527
Figure A.162. SEM Image and EDS Spectrum of the Paint Collected from Interior Web of the Girder (G3F1). 528
Figure A.163. SEM Image and EDS Spectrum of the Paint Collected from Interior Web of the Girder (G3F1). 529
Figure A.164. EDS Elemental Mapping of Paint Collected from Interior Web (G3F1). 530

Figure A.165. SEM Image and EDS Spectrum of the Paint Collected from Interior Web of the Girder (G6F1). 531
Figure A.166. EDS Elemental Mapping of Paint Collected from Interior Web (G6F1). 532
Figure A.167. SEM Image of Paint and EDS Spectrum of the Paint Collected from Interior Web of the Girder (G6F1). 533
Figure A.168. SEM Image of Paint and EDS Spectrum of the Paint Collected from Interior Web of the Girder (G6F1). 534
Figure A.169. Typical Elevation of CRP-PS-01 535
Figure A.170. Paint Condition of Bearing, Superstructure, and Truss Members of CRP-PS-01 536
Figure A.171. Paint Condition of Bearing, Superstructure, and Truss Members of CRP-PS-01. 537
Figure A.172. Digital and Thermal Image of Connector Plate and Truss Member on CRP-PS-01. 538
Figure A.173. Two Layer Paint System Examined by Optical Microscope CRP–PS–01. 542
Figure A.174. Corrosion as Observed Between Primer and Base Metal. 543
Figure A.175. SEM Image and EDS Spectrum of the Paint Collected from Exterior Web of the Girder. 544
Figure A.176. EDS Elemental Mapping of Paint Collected from Exterior Web. 545
Figure A.177. SEM Image and EDS Spectrum of the Paint Collected from Exterior Web of the Girder. 546
Figure A.178. EDS Elemental Mapping of Paint Collected from Exterior Web. 547
Figure A.179. SEM Image and EDS Spectrum of the Paint Collected from Exterior Web of the Girder. 548
Figure A.180. EDS Elemental Mapping of Paint Collected from Exterior Web. 549
Figure A.181. Typical Elevation of TYL-PS-01. 550
Figure A.182. Paint Condition on the Girder of TYL-PS-01. 551
Figure A.183. Digital and Thermal Image of Painted Girder on TYL-PS-01. 552
Figure A.184. Two Layer Paint System Examined by Optical Microscope TYL–PS–01. 558
Figure A.185. Spot Rust Observed Between Primer and Base Metal. 559
Figure A.186. SEM Image and EDS Spectrum of the Paint Collected from Exterior Web of the Girder. 560
Figure A.187. EDS Elemental Mapping of Paint Collected from Exterior Web. 561
Figure A.188. SEM Image and EDS Spectrum of the Paint Collected from Exterior Web of the Girder. 562
Figure A.189. SEM Image and EDS Spectrum of the Paint Collected from Exterior Web of the Girder. 563
Figure A.190. EDS Elemental Mapping of Paint Collected from Exterior Web. 564
Figure A.191. SEM Image and EDS Spectrum of the Paint Collected from Exterior Web of the Girder. 565
Figure A.192. EDS Elemental Mapping of Paint Collected from Exterior Web. 566
Figure A.193. SEM Image and EDS Spectrum of the Paint Collected from Exterior Web of the Girder. 567
Figure A.194. EDS Elemental Mapping of Paint Collected from Exterior Web. 568
Figure A.195. SEM Image and EDS Spectrum of the Paint Collected from Exterior Web of the Girder. 569

Figure A.196. SEM Image of Paint and EDS Spectrum of the Paint Collected from Interior Web of the Girder. 570
Figure A.197. SEM Image of Paint and EDS Spectrum of the Paint Collected from Interior Web of the Girder. 571
Figure A.198. SEM Image and EDS Spectrum of the Paint Collected from Interior Web of the Girder. 572
Figure A.199. EDS Elemental Mapping of Paint Collected from Interior Web. 573
Figure A.200. SEM Image of Paint and EDS Spectrum of the Paint Collected from Interior Web of the Girder. 574
Figure A.201. EDS Elemental Mapping of Paint Collected from Interior Web. 575
Figure A.202. Typical Elevation of ELP-PS-01 576
Figure A.203. Paint Condition on the Girder of ELP-PS-01. 577
Figure A.204. Digital and Thermal Image of Painted Girder on ELP-PS-01. 578
Figure A.205. Two Layer Paint System Examined by Optical Microscope ELP-WS-01. 584
Figure A.206. SEM Image and EDS Spectrum of the Paint Collected from Exterior Web of the Girder. 585
Figure A.207. EDS Elemental Mapping of Paint Collected from Exterior Web. 586
Figure A.208. SEM Image and EDS Spectrum of the Paint Collected from Exterior Web of the Girder. 587
Figure A.209. SEM Image and EDS Spectrum of the Paint Collected from Exterior Web of the Girder. 588
Figure A.210. SEM Image and EDS Spectrum of the Paint Collected from Exterior Web of the Girder. 589
Figure A.211. SEM Image and EDS Spectrum of the Paint Collected from Exterior Web of the Girder. 590
Figure A.212. SEM Image and EDS Spectrum of the Paint Collected from Interior Web of the Girder. 591
Figure A.213. SEM Image and EDS Spectrum of the Paint Collected from Interior Web of the Girder. 592
Figure A.214. SEM Image of Paint and EDS Spectrum of the Paint Collected from Interior Web of the Girder. 593
Figure A.215. EDS Elemental Mapping of Paint Collected from Interior Web. 594
Figure A.216. SEM Image and EDS Spectrum of the Paint Collected from Interior Web of the Girder. 595
Figure A.217. SEM Image and EDS Spectrum of the Paint Collected from Interior Web of the Girder. 596
Figure A.218. SEM Image and EDS Spectrum of the Paint Collected from Interior Web of the Girder. 597
Figure A.219. EDS Elemental Mapping of Paint Collected from Interior Web. 598
Figure A.220. SEM Image and EDS Spectrum of the Paint Collected from Interior Web of the Girder. 599
Figure A.221. Typical Elevation of HOU-PS-01 600
Figure A.222. Paint Condition on the Girder of HOU-PS-01 601
Figure A.223. Paint Condition on the Girder of HOU-PS-01 602
Figure A.224. Digital and Thermal Image of Painted Girder on HOU-PS-01. 603
Figure A.225. Two Layer Paint System Examined by Optical Microscope HOU–PS–01 610

Figure A.226. Two Layer Paint System Examined by Optical Microscope HOU–PS–01..... 611
Figure A.227. SEM Image and EDS Spectrum of the Paint Collected from Exterior Web of the Girder. 612
Figure A.228. SEM Image and EDS Spectrum of the Paint Collected from Exterior Web of the Girder. 613
Figure A.229. SEM Image and EDS Spectrum of the Paint Collected from Exterior Web of the Girder. 614
Figure A.230. EDS Elemental Mapping of Paint Collected from Exterior Web. 615
Figure A.231. EDS Elemental Mapping of Paint Collected from Exterior Web. 616
Figure A.232. EDS Elemental Mapping of Paint Collected from Exterior Web. 617
Figure A.233. Typical Elevation of BMT-PS-01 618
Figure A.234. Paint Condition on the Girder of BMT-PS-01. 619
Figure A.235. Digital and Thermal Image of Painted Girder on BMT-PS-01. 620
Figure A.236. Two Layer Paint System Examined by Optical Microscope BMT–PS–01..... 627
Figure A.237. Two Layer Paint System Examined by Optical Microscope BMT–PS–01..... 628
Figure A.238. SEM Image and EDS Spectrum of the Paint Collected from Exterior Web of the Girder. 629
Figure A.239. EDS Elemental Mapping of Paint Collected from Exterior Web. 630
Figure A.240. SEM Image and EDS Spectrum of the Paint Collected from Exterior Web of the Girder. 631
Figure A.241. EDS Elemental Mapping of Paint Collected from Exterior Web 632
Figure A.242. SEM Image and EDS Spectrum of the Paint Collected from Exterior Web of the Girder. 633
Figure A.243. SEM Image and EDS Spectrum of the Paint Collected from Exterior Web of the Girder. 634
Figure A.244. SEM Image and EDS Spectrum of the Paint Collected from Exterior Web of the Girder. 635
Figure A.245. EDS Elemental Mapping of Paint Collected from Exterior Web. 636
Figure A.246. SEM Image and EDS Spectrum of the Paint Collected from Exterior Web of the Girder. 637
Figure A.247. SEM Image and EDS Spectrum of the Paint Collected from Exterior Web of the Girder. 638
Figure A.248. EDS Elemental Mapping of Paint Collected from Exterior Web. 639
Figure A.249. SEM Image and EDS Spectrum of the Paint Collected from Interior Web of the Girder. 640
Figure A.250. EDS Elemental Mapping of Paint Collected from Interior Web. 641
Figure A.251. SEM Image of Paint and EDS Spectrum of the Paint Collected from Interior Web of the Girder. 642
Figure A.252. EDS Elemental Mapping of Paint Collected from Interior Web. 643
Figure A.253. SEM Image and EDS Spectrum of the Paint Collected from Interior Web of the Girder. 644
Figure A.254. SEM Image and EDS Spectrum of the Paint Collected from Interior Web of the Girder. 645
Figure A.255. Typical Elevation of BMT-PS-02 646
Figure A.256. Paint Condition on the Girder of BMT-PS-02. 647
Figure A.257. Digital and Thermal Image of Painted Girder on BMT-PS-02. 648

Figure A.258. Two Layer Paint System Examined by Optical Microscope BMT–PS–02..... 655
Figure A.259. Two Layer Paint System Examined by Optical Microscope BMT–PS–02..... 656
Figure A.260. SEM Image and EDS Spectrum of the Paint Collected from Exterior Web of the Girder. 657
Figure A.261. EDS Elemental Mapping of Paint Collected from Exterior Web. 658
Figure A.262. SEM Image and EDS Spectrum of the Paint Collected from Exterior Web of the Girder. 659
Figure A.263. EDS Elemental Mapping of Paint Collected from Exterior Web. 660
Figure A.264. SEM Image and EDS Spectrum of the Paint Collected from Exterior Web of the Girder. 661
Figure A.265. SEM Image and EDS Spectrum of the Paint Collected from Exterior Web of the Girder. 662
Figure A.266. SEM Image and EDS Spectrum of the Paint Collected from Exterior Web of the Girder. 663
Figure A.267. EDS Elemental Mapping of Paint Collected from Exterior Web. 664
Figure A.268. SEM Image and EDS Spectrum of the Paint Collected from Interior Web of the Girder. 665
Figure A.269. EDS Elemental Mapping of Paint Collected from Interior Web. 666
Figure A.270. SEM Image and EDS Spectrum of the Paint Collected from Interior Web of the Girder. 667
Figure A.271. SEM Image and EDS Spectrum of the Paint Collected from Interior Web of the Girder. 668
Figure A.272. SEM Image and EDS Spectrum of the Paint Collected from Interior Web of the Girder. 669
Figure A.273. EDS Elemental Mapping of Paint Collected from Interior Web. 670
Figure A.274. SEM Image and EDS Spectrum of the Paint Collected from Interior Web of the Girder. 671
Figure A.275. SEM Image and EDS Spectrum of the Paint Collected from Interior Web of the Girder. 672
Figure A.276. SEM Image and EDS Spectrum of the Paint Collected from Interior Web of the Girder. 673
Figure A.277. EDS Elemental Mapping of Paint Collected from Interior Web. 674
Figure A.278. SEM Image of Paint and EDS Spectrum of the Paint Collected from Interior Web of the Girder (G6F1). 675
Figure A.279. Typical Elevation of AUS-WS-01 676
Figure A.280. Patina Condition on Girder of AUS-WS-01. 677
Figure A.281. SEM Image and EDS Spectrum of the Rust Collected from Exterior Web of the Girder. 682
Figure A.282. SEM Image and EDS Spectrum of the Rust Collected from Exterior Web of the Girder. 683
Figure A.283. SEM Image and EDS Spectrum of the Rust Collected from Exterior Web of the Girder. 684
Figure A.284. SEM Image and EDS Spectrum of the Rust Collected from Exterior Web of the Girder. 685
Figure A.285. EDS Elemental Mapping of Rust Collected from Exterior Web. 686

Figure A.286. SEM Image and EDS Spectrum of the Rust Collected from Exterior Web of the Girder. 687
Figure A.287. SEM Image and EDS Spectrum of the Rust Collected from Exterior Web of the Girder. 688
Figure A.288. SEM Image and EDS Spectrum of the Rust Collected from Exterior Web of the Girder. 689
Figure A.289. EDS Elemental Mapping of Rust Collected from Exterior Web. 690
Figure A.290. SEM Image and EDS Spectrum of the Rust Collected from Exterior Web of the Girder. 691
Figure A.291. EDS Elemental Mapping of Rust Collected from Exterior Web. 692
Figure A.292. SEM Image and EDS Spectrum of the Rust Collected from Exterior Web of the Girder. 693
Figure A.293. EDS Elemental Mapping of Rust Collected from Exterior Web. 694
Figure A.294. SEM Image and EDS Spectrum of the Rust Collected from Interior Web of the Girder. 695
Figure A.295. SEM Image and EDS Spectrum of the Rust Collected from Interior Web of the Girder. 696
Figure A.296. SEM Image and EDS Spectrum of the Rust Collected from Interior Web of the Girder. 697
Figure A.297. SEM Image and EDS Spectrum of the Rust Collected from Interior Web of the Girder. 698
Figure A.298. EDS Elemental Mapping of Rust Collected from Interior Web. 699
Figure A.299. SEM Image and EDS Spectrum of the Rust Collected from Interior Web of the Girder. 700
Figure A.300. EDS Elemental Mapping of Rust Collected from Interior Web. 701
Figure A.301. SEM Image and EDS Spectrum of the Rust Collected from Interior Web of the Girder. 702
Figure A.302. EDS Elemental Mapping of Rust Collected from Interior Web. 703
Figure A.303. XPS Spectrum of the Rust Collected from Exterior Web of the Girder. 704
Figure A.304. XPS Spectrum of the Rust Collected from Interior Web of the Girder. 705
Figure A.305. XRD Pattern of Powdered Rust Collected from Exterior Web of the Girder. 706
Figure A.306. XRD Pattern of Powdered Rust Collected from Interior Web of the Girder. 706
Figure A.307. Particle Size Analysis Results at A1G4F2 (a) Top Flange Bottom, (b) Web, (c) Bottom Flange Bottom. 707
Figure A.308. Particle Size Analysis Results at B3G1F1 (a) Top Flange Bottom, (b) Web, (c) Bottom Flange Bottom. 708
Figure A.309. Particle Size Analysis Results at B3G2F2 (a) Top Flange Bottom, (b) Web, (c) Bottom Flange Bottom. 709
Figure A.310. Particle Size Analysis Results at B3G4F2 (a) Top Flange Bottom, (b) Web, (c) Bottom Flange Bottom. 710
Figure A.311. Particle Size Analysis Showing Different Locations Examined. 711
Figure A.312. Typical Picture of AUS-WS-03. 712
Figure A.313. SEM Image and EDS Spectrum of the Rust Collected from Exterior Web of the Girder. 717

Figure A.314. SEM Image and EDS Spectrum of the Rust Collected from Exterior Web of the Girder. 718
Figure A.315. SEM Image and EDS Spectrum of the Rust Collected from Exterior Web of the Girder. 719
Figure A.316. EDS Elemental Mapping of Rust Collected from Exterior Web. 720
Figure A.317. SEM Image and EDS Spectrum of the Rust Collected from Exterior Web of the Girder. 721
Figure A.318. EDS Elemental Mapping of Rust Collected from Exterior Web. 722
Figure A.319. SEM Image and EDS Spectrum of the Rust Collected from Exterior Web of the Girder. 723
Figure A.320. EDS Elemental Mapping of Rust Collected from Exterior Web. 724
Figure A.321. SEM Image and EDS Spectrum of the Rust Collected from Interior Web of the Girder. 725
Figure A.322. SEM Image and EDS Spectrum of the Rust Collected from Interior Web of the Girder. 726
Figure A.323. SEM Image and EDS Spectrum of the Rust Collected from Interior Web of the Girder. 727
Figure A.324. EDS Elemental Mapping of Rust Collected from Interior Web. 728
Figure A.325. SEM Image and EDS Spectrum of the Rust Collected from Interior Web of the Girder. 729
Figure A.326. EDS Elemental Mapping of Rust Collected from Interior Web. 730
Figure A.327. SEM Image and EDS Spectrum of the Rust Collected from Interior Web of the Girder. 731
Figure A.328. XPS Spectrum of the Rust Collected from Exterior Web of the Girder. 732
Figure A.329. XPS Spectrum of the Rust Collected from Interior Web of the Girder. 733
Figure A.330. XRD Pattern of Powdered Rust Collected from Exterior Web of the Girder. 734
Figure A.331. XRD Pattern of Powdered Rust Collected from Interior Web of the Girder. 734
Figure A.332. Particle Size Analysis Results at A1G1F1 (a) Top Flange Bottom, (b) Web, (c) Bottom Flange Bottom. 735
Figure A.333. Particle Size Analysis Results at A1G5F2 (a) Top Flange Bottom, (b) Web, (c) Bottom Flange Bottom. 736
Figure A.334. Particle Size Analysis Results at A1G6F1 (a) Top Flange Bottom, (b) Web, (c) Bottom Flange Bottom. 737
Figure A.335. Particle Size Analysis Results at A1G12F2 (a) Top Flange Bottom, (b) Web, (c) Bottom Flange Bottom (d) Stiffener. 738
Figure A.336. Particle Size Analysis Showing Different Locations Examined. 739
Figure A.337. Typical Elevation of AUS-WS-04 740
Figure A.338. Patina Condition on Girders and Bent Cap of AUS-WS-04 741
Figure A.339. SEM Image and EDS Spectrum of the Rust Collected from Exterior Web of the Girder. 745
Figure A.340. EDS Elemental Mapping of Rust Collected from Exterior Web. 746
Figure A.341. SEM Image and EDS Spectrum of the Rust Collected from Exterior Web of the Girder. 747
Figure A.342. SEM Image and EDS Spectrum of the Rust Collected from Exterior Web of the Girder. 748

Figure A.343. EDS Elemental Mapping of Rust Collected from Exterior Web..... 749
Figure A.344. SEM Image and EDS Spectrum of the Rust Collected from Exterior Web of the Girder. 750
Figure A.345. SEM Image and EDS Spectrum of the Rust Collected from Exterior Web of the Girder. 751
Figure A.346. SEM Image and EDS Spectrum of the Rust Collected from Exterior Web of the Girder. 752
Figure A.347. EDS Elemental Mapping of Rust Collected from Exterior Web..... 753
Figure A.348. SEM Image and EDS Spectrum of the Rust Collected from Exterior Web of the Girder. 754
Figure A.349. SEM Image and EDS Spectrum of the Rust Collected from Exterior Web of the Girder. 755
Figure A.350. SEM Image and EDS Spectrum of the Rust Collected from Exterior Web of the Girder. 756
Figure A.351. EDS Elemental Mapping of Rust Collected from Exterior Web..... 757
Figure A.352. SEM Image and EDS Spectrum of the Rust Collected from Interior Web of the Girder. 758
Figure A.353. SEM Image and EDS Spectrum of the Rust Collected from Interior Web of the Girder. 759
Figure A.354. EDS Elemental Mapping of Rust Collected from Interior Web..... 760
Figure A.355. SEM Image and EDS Spectrum of the Rust Collected from Interior Web of the Girder. 761
Figure A.356. SEM Image and EDS Spectrum of the Rust Collected from Interior Web of the Girder. 762
Figure A.357. SEM Image and EDS Spectrum of the Rust Collected from Interior Web of the Girder. 763
Figure A.358. EDS Elemental Mapping of Rust Collected from Interior Web..... 764
Figure A.359. SEM Image and EDS Spectrum of the Rust Collected from Interior Web of the Girder. 765
Figure A.360. EDS Elemental Mapping of Rust Collected from Interior. 766
Figure A.361. XPS Spectrum of the Rust Collected from Exterior Web of the Girder..... 767
Figure A.362. XPS Spectrum of the Rust Collected from Interior Web of the Girder..... 768
Figure A.363. XRD Pattern of Powdered Rust Collected from Exterior Web of the Girder. 769
Figure A.364. XRD Pattern of Powdered Rust Collected from Interior Web of the Girder. 769
Figure A.365. Particle Size Analysis Results at A1G1F1 (a) Top Flange Bottom, (b) Web, (c) Bottom Flange Bottom (d) Stiffener. 770
Figure A.366. Particle Size Analysis Results at A1G1F2 (a) Top Flange Bottom, (b) Web, (c) Bottom Flange Bottom (d) Stiffener. 771
Figure A.367. Particle Size Analysis Results at A1G2F1 (a) Top Flange Bottom, (b) Web, (c) Bottom Flange Bottom (d) Stiffener. 772
Figure A.368. Particle Size Analysis Results at A1G2F2 (a) Top Flange Bottom, (b) Web, (c) Bottom Flange Bottom (d) Stiffener. 773
Figure A.369. Particle Size Analysis Results at B2G2F1 (a) Top Flange Bottom, (b) Web, (c) Bottom Flange Bottom (d) Stiffener..... 774
Figure A.370. Particle Size Analysis Showing Different Locations Examined. 775

Figure A.371. Typical Picture of HOU-WS-01 776
Figure A.372. SEM Image and EDS Spectrum of the Rust Collected from Exterior Web of the Girder. 778
Figure A.373. SEM Image and EDS Spectrum of the Rust Collected from Exterior Web of the Girder. 779
Figure A.374. SEM Image and EDS Spectrum of the Rust Collected from Exterior Web of the Girder. 780
Figure A.375. EDS Elemental Mapping of Rust Collected from Exterior Web..... 781
Figure A.376. SEM Image and EDS Spectrum of the Rust Collected from Exterior Web of the Girder. 782
Figure A.377. SEM Image and EDS Spectrum of the Rust Collected from Exterior Web of the Girder. 783
Figure A.378. EDS Elemental Mapping of Rust Collected from Exterior Web..... 784
Figure A.379. XPS Spectrum of the Rust Collected from Exterior Web of the Girder..... 785
Figure A.380. XRD Pattern of Powdered Rust Collected from Exterior Web of the Girder. 786
Figure A.381. Particle Size Analysis Results at B8G1F1 (a) Top Flange Bottom, (b) Web, (c) Bottom Flange Bottom (d) Stiffener..... 787
Figure A.382. Particle Size Analysis Results at B6G4F1 (a) Top Flange Bottom, (b) Web, (c) Bottom Flange Bottom (d) Stiffener..... 788
Figure A.383. Typical Picture of HOU-WS-02 789
Figure A.384. SEM Image and EDS Spectrum of the Rust Collected from Exterior Web of the Girder. 794
Figure A.385. SEM Image and EDS Spectrum of the Rust Collected from Exterior Web of the Girder. 795
Figure A.386. SEM Image and EDS Spectrum of the Rust Collected from Exterior Web of the Girder. 796
Figure A.387. SEM Image and EDS Spectrum of the Rust Collected from Exterior Web of the Girder. 797
Figure A.388. SEM Image and EDS Spectrum of the Rust Collected from Exterior Web of the Girder. 798
Figure A.389. EDS Elemental Mapping of Rust Collected from Exterior Web..... 799
Figure A.390. SEM Image and EDS Spectrum of the Rust Collected from Exterior Web of the Girder. 800
Figure A.391. SEM Image and EDS Spectrum of the Rust Collected from Exterior Web of the Girder. 801
Figure A.392. EDS Elemental Mapping of Rust Collected from Exterior Web..... 802
Figure A.393. SEM Image and EDS Spectrum of the Rust Collected from Exterior Web of the Girder. 803
Figure A.394. SEM Image and EDS Spectrum of the Rust Collected from Exterior Web of the Girder. 804
Figure A.395. SEM Image and EDS Spectrum of the Rust Collected from Exterior Web of the Girder. 805
Figure A.396. SEM Image and EDS Spectrum of the Rust Collected from Exterior Web of the Girder. 806
Figure A.397. EDS Elemental Mapping of Rust Collected from Exterior Web..... 807

Figure A.398. SEM Image and EDS Spectrum of the Rust Collected from Interior Web of the Girder. 808
Figure A.399. SEM Image and EDS Spectrum of the Rust Collected from Interior Web of the Girder. 809
Figure A.400. SEM Image and EDS Spectrum of the Rust Collected from Interior Web of the Girder. 810
Figure A.401. SEM Image and EDS Spectrum of the Rust Collected from Interior Web of the Girder. 811
Figure A.402. SEM Image and EDS Spectrum of the Rust Collected from Interior Web of the Girder. 812
Figure A.403. SEM Image and EDS Spectrum of the Rust Collected from Interior Web of the Girder. 813
Figure A.404. SEM Image and EDS Spectrum of the Rust Collected from Interior Web of the Girder. 814
Figure A.405. SEM Image and EDS Spectrum of the Rust Collected from Interior Web of the Girder. 815
Figure A.406. EDS Elemental Mapping of Rust Collected from Interior Web. 816
Figure A.407. SEM Image and EDS Spectrum of the Rust Collected from Interior Web of the Girder. 817
Figure A.408. XPS Spectrum of the Rust Collected from Exterior Web of the Girder. 818
Figure A.409. XPS Spectrum of the Rust Collected from Interior Web of the Girder. 819
Figure A.410. XRD Pattern of Powdered Rust Collected from Exterior Web of the Girder. 820
Figure A.411. XRD Pattern of Powdered Rust Collected from Interior Web of the Girder. 820
Figure A.412. Particle Size Analysis Results at A1G1F1 (a) Top Flange Bottom, (b) Web, (c) Bottom Flange Bottom. 821
Figure A.413. Particle Size Analysis Results at A1G1F2 (a) Top Flange Bottom, (b) Web, (c) Bottom Flange Bottom 822
Figure A.414. Particle Size Analysis Results at A1G1G2 STIFFENER (a) Top Flange Bottom, (b) Web, (c) Bottom Flange Bottom. 823
Figure A.415. Particle Size Analysis Results at A1G2F1 (a) Top Flange Bottom, (b) Web, (c) Bottom Flange Bottom. 824
Figure A.416. Particle Size Analysis Results at A1G3F2 (a) Top Flange Bottom, (b) Web, (c) Bottom Flange Bottom. 825
Figure A.417. Particle Size Analysis Showing Different Locations Examined. 826
Figure A.418. Typical Picture of HOU-WS-03. 827
Figure A.419. SEM Image and EDS Spectrum of the Rust Collected from Exterior Web of the Girder. 833
Figure A.420. EDS Elemental Mapping of Rust Collected from Exterior Web. 834
Figure A.421. SEM Image and EDS Spectrum of the Rust Collected from Interior Web of the Girder. 835
Figure A.422. SEM Image and EDS Spectrum of the Rust Collected from Interior Web of the Girder (G3F1). 836
Figure A.423. EDS Elemental Mapping of Rust Collected from Interior Web (G3F1). 837
Figure A.424. SEM Image and EDS Spectrum of the Rust Collected from Interior Web of the Girder (G3F1). 838

Figure A.425. EDS Elemental Mapping of Rust Collected from Interior Web (G3F1). 839
Figure A.426. SEM Image and EDS Spectrum of the Rust Collected from Interior Web of the Girder. 840
Figure A.427. EDS Elemental Mapping of Rust Collected from Interior Web (G6F1). 841
Figure A.428. SEM Image and EDS Spectrum of the Rust Collected from Interior Web of the Girder. 842
Figure A.429. SEM Image and EDS Spectrum of the Rust Collected from Interior Web of the Girder. 843
Figure A.430. EDS Elemental Mapping of Rust Collected from Interior Web (G6F1). 844
Figure A.431. XPS Spectrum of the Rust Collected from Exterior Web of the Girder. 845
Figure A.432. XPS Spectrum of the Rust Collected from Interior Web of the Girder. 846
Figure A.433. XRD Pattern of Powdered Rust Collected from Exterior Web of the Girder (G1F1). 847
Figure A.434. XRD Pattern of Powdered Rust Collected from Interior Web of the Girder (G6F1). 847
Figure A.435. XRD Pattern of Powdered Rust Collected from Interior Web of the Girder (G3F1). 848
Figure A.436. Particle Size Analysis Results at A1G1F1 (a) Top Flange Bottom, (b) Web, (c) Bottom Flange Bottom (d) StiffenerA1G1F1. 849
Figure A.437. Particle Size Analysis Results at A1G3F1 (a) Top Flange Bottom, (b) Web, (c) Bottom Flange Bottom (d) Stiffener. 850
Figure A.438. Particle Size Analysis Results at A1G5F2 (a) Top Flange Bottom, (b) Web, (c) Bottom Flange Bottom (d) Stiffener. 851
Figure A.439. Particle Size Analysis Results at A1G7F2 (a) Top Flange Bottom, (b) Web, (c) Bottom Flange Bottom (d) Stiffener. 852
Figure A.440. Particle Size Analysis Results at A1G9F2 (a) Top Flange Bottom, (b) Web, (c) Bottom Flange Bottom (d) Stiffener. 853
Figure A.441. Particle Size Analysis Showing Different Locations Examined. 854
Figure A.442. Typical Picture of HOU-WS-04 855
Figure A.443. SEM Image and EDS Spectrum of the Rust Collected from Exterior Web of the Girder. 860
Figure A.444. EDS Elemental Mapping of Rust Collected from Exterior Web. 861
Figure A.445. SEM Image and EDS Spectrum of the Rust Collected from Exterior Web of the Girder. 862
Figure A.446. SEM Image and EDS Spectrum of the Rust Collected from Exterior Web of the Girder. 863
Figure A.447. SEM Image and EDS Spectrum of the Rust Collected from Exterior Web of the Girder. 864
Figure A.448. EDS Elemental Mapping of Rust Collected from Exterior Web. 865
Figure A.449. SEM Image and EDS Spectrum of the Rust Collected from Interior Web of the Girder. 866
Figure A.450. SEM Image and EDS Spectrum of the Rust Collected from Interior Web of the Girder. 867
Figure A.451. EDS Elemental Mapping of Rust Collected from Interior Web. 868
Figure A.452. SEM Image and EDS Spectrum of the Rust Collected from Interior Web of the Girder. 869

Figure A.453. EDS Elemental Mapping of Rust Collected from Interior Web. 870
Figure A.454. XPS Spectrum of the Rust Collected from Exterior Web of the Girder. 871
Figure A.455. XPS Spectrum of the Rust Collected from Interior Web of the Girder. 872
Figure A.456. XRD Pattern of Powdered Rust Collected from Exterior Web of the Girder (G10F2). 873
Figure A.457. XRD Pattern of Powdered Rust Collected from Interior Web of the Girder (G8F2). 873
Figure A.458. Particle Size Analysis Results at A1G1F1 (a) Top Flange Bottom, (b) Web, (c) Bottom Flange Bottom (d) Stiffener. 874
Figure A.459. Particle Size Analysis Results at A1G3F1 (a) Top Flange Bottom, (b) Web, (c) Bottom Flange Bottom (d) Stiffener. 875
Figure A.460. Particle Size Analysis Results at A1G5F1 (a) Top Flange Bottom, (b) Web, (c) Bottom Flange Bottom (d) Stiffener. 876
Figure A.461. Particle Size Analysis Results at A1G7F2 (a) Top Flange Bottom, (b) Web, (c) Bottom Flange Bottom (d) Stiffener. 877
Figure A.462. Particle Size Analysis Results at A1G10F2 (a) Top Flange Bottom, (b) Web, (c) Bottom Flange Bottom (d) Stiffener. 878
Figure A.463. Particle Size Analysis Showing Different Locations Examined. 879
Figure A.464. Typical Picture of HOU-WS-05. 880
Figure A.465. SEM Image and EDS Spectrum of the Rust Collected from Exterior Web of the Girder. 885
Figure A.466. SEM Image and EDS Spectrum of the Rust Collected from Exterior Web of the Girder. 886
Figure A.467. SEM Image and EDS Spectrum of the Rust Collected from Exterior Web of the Girder. 887
Figure A.468. SEM Image and EDS Spectrum of the Rust Collected from Exterior Web of the Girder. 888
Figure A.469. SEM Image and EDS Spectrum of the Rust Collected from Exterior Web of the Girder. 889
Figure A.470. EDS Elemental Mapping of Rust Collected from Exterior Web. 890
Figure A.471. SEM Image and EDS Spectrum of the Rust Collected from Interior Web of the Girder. 891
Figure A.472. SEM Image and EDS Spectrum of the Rust Collected from Interior Web of the Girder. 892
Figure A.473. SEM Image and EDS Spectrum of the Rust Collected from Interior Web of the Girder. 893
Figure A.474. EDS Elemental Mapping of Rust Collected from Interior Web. 894
Figure A.475. XPS Spectrum of the Rust Collected from Exterior Web of the Girder. 895
Figure A.476. XPS Spectrum of the Rust Collected from Interior Web of the Girder. 896
Figure A.477. XRD Pattern of Powdered Rust Collected from Exterior Web of the Girder. 897
Figure A.478. XRD Pattern of Powdered Rust Collected from Interior Web of the Girder. 897
Figure A.479. Particle Size Analysis Results at A1G1F1 (a) Top Flange Bottom, (b) Web, (c) Bottom Flange Bottom (d) Stiffener. 898
Figure A.480. Particle Size Analysis Results at A1G2F2 (a) Top Flange Bottom, (b) Web, (c) Bottom Flange Bottom (d) Stiffener. 899

Figure A.481. Particle Size Analysis Results at A1G3F1 (a) Top Flange Bottom, (b) Web, (c) Bottom Flange Bottom (d) Stiffener. 900
Figure A.482. Particle Size Analysis Results at A1G5F2 (a) Top Flange Bottom, (b) Web, (c) Bottom Flange Bottom (d) Stiffener. 901
Figure A.483. Particle Size Analysis Results at A1G1F1 (77002) (a) Top Flange Bottom, (b) Web, (c) Bottom Flange Bottom (d) Stiffener. 902
Figure A.484. Particle Size Analysis Showing Different Locations Examined. 903
Figure A.485. Typical Picture of HOU-WS-05* 904
Figure A.486. Typical Picture of AUS-WS-06. 906
Figure A.487. SEM Image and EDS Spectrum of the Rust Collected from Exterior Web of the Girder. 912
Figure A.488. EDS Elemental Mapping of Rust Collected from Exterior Web. 913
Figure A.489. SEM Image and EDS Spectrum of the Rust Collected from Exterior Web of the Girder. 914
Figure A.490. SEM Image and EDS Spectrum of the Rust Collected from Exterior Web of the Girder. 915
Figure A.491. SEM Image and EDS Spectrum of the Rust Collected from Exterior Web of the Girder. 916
Figure A.492. SEM Image and EDS Spectrum of the Rust Collected from Exterior Web of the Girder. 917
Figure A.493. EDS Elemental Mapping of Rust Collected from Exterior Web. 918
Figure A.494. SEM Image and EDS Spectrum of the Rust Collected from Interior Web of the Girder. 919
Figure A.495. EDS Elemental Mapping of Rust Collected from Interior Web. 920
Figure A.496. SEM Image and EDS Spectrum of the Rust Collected from Interior Web of the Girder. 921
Figure A.497. EDS Elemental Mapping of Rust Collected from Interior Web. 922
Figure A.498. XPS Spectrum of the Rust Collected from Exterior Web of the Girder. 923
Figure A.499. XPS Spectrum of the Rust Collected from Exterior Web of the Girder. 924
Figure A.500. XRD Pattern of Powdered Rust Collected from Exterior Web of the Girder. 925
Figure A.501. XRD Pattern of Powdered Rust Collected from Interior Web of the Girder. 925
Figure A.502. XRD Pattern of Powdered Rust Collected from Bottom face of Top Flange of the Interior Girder. 926
Figure A.503. Particle Size Analysis Results at A1G1F1 (a) Top Flange Bottom, (b) Web, (c) Bottom Flange Bottom (d) Stiffener. 927
Figure A.504. Particle Size Analysis Results at A1G3F2 (a) Top Flange Bottom, (b) Web, (c) Bottom Flange Bottom (d) Stiffener. 928
Figure A.505. Particle Size Analysis Results at A1G4F1 (a) Top Flange Bottom, (b) Web, (c) Bottom Flange Bottom (d) Stiffener. 929
Figure A.506. Particle Size Analysis Results at A1G8F2 (a) Top Flange Bottom, (b) Web, (c) Bottom Flange Bottom (d) Stiffener. 930
Figure A.507. Particle Size Analysis Results at A1G9F1 (a) Top Flange Bottom, (b) Web, (c) Bottom Flange Bottom (d) Stiffener. 931
Figure A.508. Particle Size Analysis Results at A1G12F2 (a) Top Flange Bottom, (b) Web, (c) Bottom Flange Bottom (d) Stiffener. 932

Figure A.509. Particle Size Analysis Showing Different Locations Examined. 933
Figure A.510. Typical Picture of HOU-WS-07. 934
Figure A.511. SEM Image and EDS Spectrum of the Rust Collected from Exterior Web of the Girder. 939
Figure A.512. SEM Image and EDS Spectrum of the Rust Collected from Exterior Web of the Girder. 940
Figure A.513. SEM Image and EDS Spectrum of the Rust Collected from Exterior Web of the Girder. 941
Figure A.514. EDS Elemental Mapping of Rust Collected from Exterior Web. 942
Figure A.515. SEM Image and EDS Spectrum of the Rust Collected from Exterior Web of the Girder. 943
Figure A.516. EDS Elemental Mapping of Rust Collected from Exterior Web. 944
Figure A.517. SEM Image and EDS Spectrum of the Rust Collected from Exterior Web of the Girder. 945
Figure A.518. EDS Elemental Mapping of Rust Collected from Exterior Web. 946
Figure A.519. SEM Image and EDS Spectrum of the Rust Collected from Exterior Web of the Girder. 947
Figure A.520. EDS Elemental Mapping of Rust Collected from Exterior Web. 948
Figure A.521. SEM Image and EDS Spectrum of the Rust Collected from Exterior Web of the Girder. 949
Figure A.522. EDS Elemental Mapping of Rust Collected from Exterior Web. 950
Figure A.523. SEM Image and EDS Spectrum of the Rust Collected from Interior Web of the Girder. 951
Figure A.524. SEM Image and EDS Spectrum of the Rust Collected from Interior Web of the Girder. 952
Figure A.525. SEM Image and EDS Spectrum of the Rust Collected from Interior Web of the Girder. 953
Figure A.526. EDS Elemental Mapping of Rust Collected from Interior Web. 954
Figure A.527. SEM Image and EDS Spectrum of the Rust Collected from Interior Web of the Girder. 955
Figure A.528. EDS Elemental Mapping of Rust Collected from Interior Web. 956
Figure A.529. SEM Image and EDS Spectrum of the Rust Collected from Interior Web of the Girder. 957
Figure A.530. EDS Elemental Mapping of Rust Collected from Interior Web. 958
Figure A.531. XPS Spectrum of the Rust Collected from Exterior Web of the Girder. 959
Figure A.532. XPS Spectrum of the Rust Collected from Interior Web of the Girder. 960
Figure A.533. XRD Pattern of Powdered Rust Collected from Exterior Web of the Girder. 961
Figure A.534. XRD Pattern of Powdered Rust Collected from Interior Web of the Girder. 961
Figure A.535. Particle Size Analysis Results at A31G1F1 (a) Top Flange Bottom, (b) Web, (c) Bottom Flange Bottom (d) Stiffener. 962
Figure A.536. Particle Size Analysis Results at A31G2F1 (a) Top Flange Bottom, (b) Web, (c) Bottom Flange Bottom (d) Stiffener. 963
Figure A.537. Particle Size Analysis Results at A31G3F2 (a) Top Flange Bottom, (b) Web, (c) Bottom Flange Bottom (d) Stiffener. 964

Figure A.538. Particle Size Analysis Results at A31G4F2 (a) Top Flange Bottom, (b) Web, (c) Bottom Flange Bottom (d) Stiffener. 965
Figure A.539. Particle Size Analysis Showing Different Locations Examined. 966
Figure A.540. Typical Picture of CRP-WS-01. 967
Figure A.541. SEM Image and EDS Spectrum of the Rust Collected from Exterior Web of the Girder. 973
Figure A.542. SEM Image and EDS Spectrum of the Rust Collected from Exterior Web of the Girder. 974
Figure A.543. SEM Image and EDS Spectrum of the Rust Collected from Exterior Web of the Girder. 975
Figure A.544. EDS Elemental Mapping of Rust Collected from Exterior Web. 976
Figure A.545. SEM Image and EDS Spectrum of the Rust Collected from Interior Web of the Girder. 977
Figure A.546. EDS Elemental Mapping of Rust Collected from Interior Web. 978
Figure A.547. XPS Spectrum of the Rust Collected from Exterior Web of the Girder. 979
Figure A.548. XPS Spectrum of the Rust Collected from Interior Web of the Girder. 980
Figure A.549 XRD Pattern of Powdered Rust Collected from Exterior Web of the Girder (G1F1). 981
Figure A.550 XRD Pattern of Powdered Rust Collected from Interior Web of the Girder (G2F1). 981
Figure A.551. XRD Pattern of Powdered Rust Collected from Interior Web of the Girder (G3F2). 982
Figure A.552. Particle Size Analysis Results at A9G1F1 (a) Top Flange Bottom, (b) Web, (c) Bottom Flange Bottom (d) Stiffener. 983
Figure A.553. Particle Size Analysis Results at A9G2F1 (a) Top Flange Bottom, (b) Web, (c) Bottom Flange Bottom (d) Stiffener. 984
Figure A.554. Particle Size Analysis Results at A9G3F2 (a) Top Flange Bottom, (b) Web, (c) Bottom Flange Bottom (d) Stiffener. 985
Figure A.555. Particle Size Analysis Results at A9G4F2 (a) Top Flange Bottom, (b) Web, (c) Bottom Flange Bottom (d) Stiffener. 986
Figure A.556. Particle Size Analysis Showing Different Locations Examined. 987
Figure A.557. Typical Picture of SAT-WS-01. 988
Figure A.558. Particle Size Analysis Results at B5G1F1 (a) Top Flange Bottom, (b) Web, (c) Bottom Flange Bottom (d) Stiffener. 994
Figure A.559. Particle Size Analysis Results at B5G4F1 (a) Top Flange Bottom, (b) Web, (c) Bottom Flange Bottom (d) Stiffener. 995
Figure A.560. Particle Size Analysis Results at B5G7F2 (a) Top Flange Bottom, (b) Web, (c) Bottom Flange Bottom (d) Stiffener. 996
Figure A.561. Particle Size Analysis Results at B6G1F1 (a) Top Flange Bottom, (b) Web, (c) Bottom Flange Bottom (d) Stiffener. 997
Figure A.562. Particle Size Analysis Results at B6G4F1 (a) Top Flange Bottom, (b) Web, (c) Bottom Flange Bottom (d) Stiffener. 998
Figure A.563. Particle Size Analysis Results at B6G7F2 (a) Top Flange Bottom, (b) Web, (c) Bottom Flange Bottom (d) Stiffener. 999
Figure A.564. Particle Size Analysis Showing Different Locations Examined. 1000
Figure A.565. Typical Picture of ATL-WS-01. 1001

Figure A.566. SEM image of Rust and EDS Spectrum of the Rust Collected from Exterior Web of the Girder. 1005
Figure A.567. EDS Elemental Mapping of Rust Collected from Exterior Web..... 1006
Figure A.568. SEM Image and EDS Spectrum of the Rust Collected from Exterior Web of the Girder. 1007
Figure A.569. SEM Image and EDS Spectrum of the Rust Collected from Exterior Web of the Girder. 1008
Figure A.570. SEM Image and EDS Spectrum of the Rust Collected from Exterior Web of the Girder. 1009
Figure A.571. EDS Elemental Mapping of Rust Collected from Exterior Web..... 1010
Figure A.572. SEM Image and EDS Spectrum of the Rust Collected from Interior Web of the Girder. 1011
Figure A.573. EDS Elemental Mapping of Rust Collected from Interior Web..... 1012
Figure A.574. SEM Image and EDS Spectrum of the Rust Collected from Interior Web of the Girder. 1013
Figure A.575. SEM Image and EDS Spectrum of the Rust Collected from Interior Web of the Girder. 1014
Figure A.576. XPS Spectrum of the Rust Collected from Exterior Web of the Girder..... 1015
Figure A.577. XPS spectra of the Rust Collected from Interior Web of the Girder..... 1016
Figure A.578. XRD Pattern of Powdered Rust Collected from Exterior Web of the Girder. 1017
Figure A.579. XRD Pattern of Powdered Rust Collected from Interior Web of the Girder. ... 1017
Figure A.580. XRD Pattern of Powdered Rust Collected from Bottom face of Bottom Flange of the Interior Girder. 1018
Figure A.581. Particle Size Analysis Results at A1G1F1 (a) Top Flange Bottom, (b) Web, (c) Bottom Flange Bottom. 1019
Figure A.582. Particle Size Analysis Results at A1G2F1 (a) Top Flange Bottom, (b) Web, (c) Bottom Flange Bottom. 1020
Figure A.583. Particle Size Analysis Results at A1G3F2 (a) Top Flange Bottom, (b) Web, (c) Bottom Flange Bottom. 1021
Figure A.584. Particle Size Analysis Results at A2G1F1 (a) Top Flange Bottom, (b) Web, (c) Bottom Flange Bottom. 1022
Figure A.585. Particle Size Analysis Results at A3G2F1 (a) Top Flange Bottom, (b) Web, (c) Bottom Flange Bottom. 1023
Figure A.586. Particle Size Analysis Results at A3G2F2 (a) Top Flange Bottom, (b) Web, (c) Bottom Flange Bottom. 1024
Figure A.587. Particle Size Analysis Showing Different Locations Examined. 1025
Figure A.588. Typical Picture of ATL-WS-02. 1026
Figure A.589. SEM Image and EDS Spectrum of the Rust Collected from Exterior Web of the Girder. 1030
Figure A.590. EDS Elemental Mapping of Rust Collected from Exterior Web..... 1031
Figure A.591. SEM Image and EDS Spectrum of the Rust Collected from Exterior Web of the Girder. 1032
Figure A.592. SEM Image and EDS Spectrum of the Rust Collected from Interior Web of the Girder. 1034
Figure A.593. EDS Elemental Mapping of Rust Collected from Interior Web..... 1035

Figure A.594. SEM Image and EDS Spectrum of the Rust Collected from Interior Web of the Girder. 1036
Figure A.595. EDS Elemental Mapping of Rust Collected from Interior Web. 1037
Figure A.596. SEM Image and EDS Spectrum of the Rust Collected from Interior Web of the Girder. 1038
Figure A.597. XPS Spectrum of the Rust Collected from Exterior Web of the Girder. 1039
Figure A.598. XPS spectra of the Rust Collected from Interior Web of the Girder. 1040
Figure A.599 XRD Pattern of Powdered Rust Collected from Exterior Web of the Girder. ... 1041
Figure A.600 XRD Pattern of Powdered Rust Collected from Interior Web of the Girder. 1041
Figure A.601. XRD Pattern of Powdered Rust Collected from Bottom face of Bottom Flange of the Interior Girder. 1042
Figure A.602. Particle Size Analysis Results at B14G1F1 (a) Top Flange Bottom, (b) Web, (c) Bottom Flange Bottom. 1043
Figure A.603. Particle Size Analysis Results at B14G3F2 (a) Top Flange Bottom, (b) Web, (c) Bottom Flange Bottom. 1044
Figure A.604. Particle Size Analysis Results at B15G1F1 (a) Top Flange Bottom, (b) Web, (c) Bottom Flange Bottom. 1045
Figure A.605. Particle Size Analysis Results at B15G3F2 (a) Top Flange Bottom, (b) Web, (c) Bottom Flange Bottom. 1046
Figure A.606. Particle Size Analysis Showing Different Locations Examined. 1047
Figure A.607. Typical Picture of ATL-WS-03. 1048
Figure A.608. Fiels Inspection Picture of ATL-WS-03. 1049
Figure A.609. SEM Image and EDS Spectrum of the Rust Collected from Exterior Web of the Girder. 1054
Figure A.610. SEM Image and EDS Spectrum of the Rust Collected from Exterior Web of the Girder. 1055
Figure A.611. SEM Image and EDS Spectrum of the Rust Collected from Exterior Web of the Girder. 1056
Figure A.612. EDS Elemental Mapping of Rust Collected from Exterior Web. 1057
Figure A.613. SEM Image and EDS Spectrum of the Rust Collected from Exterior Web of the Girder. 1058
Figure A.614. EDS Elemental Mapping of Rust Collected from Exterior Web. 1059
Figure A.615. SEM Image and EDS Spectrum of the Rust Collected from Exterior Web of the Girder. 1060
Figure A.616. SEM Image and EDS Spectrum of the Rust Collected from Exterior Web of the Girder. 1061
Figure A.617. SEM Image and EDS Spectrum of the Rust Collected from Exterior Web of the Girder. 1062
Figure A.618. EDS Elemental Mapping of Rust Collected from Exterior Web. 1063
Figure A.619. SEM Image and EDS Spectrum of the Rust Collected from Interior Web of the Girder. 1064
Figure A.620. EDS Elemental Mapping of Rust Collected from Interior Web. 1065
Figure A.621. SEM Image and EDS Spectrum of the Rust Collected from Interior Web of the Girder. 1066
Figure A.622. EDS Elemental Mapping of Rust Collected from Interior Web. 1067

Figure A.623. SEM Image and EDS Spectrum of the Rust Collected from Interior Web of the Girder. 1068
Figure A.624. EDS Elemental Mapping of Rust Collected from Interior Web. 1069
Figure A.625. SEM Image and EDS Spectrum of the Rust Collected from Interior Web of the Girder. 1070
Figure A.626. EDS Elemental Mapping of Rust Collected from Interior Web. 1071
Figure A.627. XPS Spectrum of the Rust Collected from Exterior Web of the Girder. 1072
Figure A.628. XPS Spectrum of the Rust Collected from Interior Web of the Girder. 1073
Figure A.629. XRD Pattern of Powdered Rust Collected from Exterior Web of the Girder. 1074
Figure A.630. XRD Pattern of Powdered Rust Collected from Interior Web of the Girder. ... 1074
Figure A.631. Particle Size Analysis Results at B10G1F1 (a) Top Flange Bottom, (b) Web, (c) Bottom Flange Bottom. 1075
Figure A.632. Particle Size Analysis Results at B10G2F1 (a) Top Flange Bottom, (b) Web, (c) Bottom Flange Bottom. 1076
Figure A.633. Particle Size Analysis Results at B11G1F1 (a) Top Flange Bottom, (b) Web, (c) Bottom Flange Bottom. 1077
Figure A.634. Particle Size Analysis Results at B11G2F1 (a) Top Flange Bottom, (b) Web, (c) Bottom Flange Bottom. 1078
Figure A.635. Particle Size Analysis Results at B11G3F2 (a) Top Flange Bottom, (b) Web, (c) Bottom Flange Bottom. 1079
Figure A.636. Particle Size Analysis Showing Different Locations Examined. 1080
Figure A.637. Typical Picture of LBB-WS-01 1081
Figure A.638. SEM Image and EDS Spectrum of the Rust Collected from Exterior Web of the Girder. 1086
Figure A.639. EDS Elemental Mapping of Rust Collected from Exterior Web. 1087
Figure A.640. SEM Image and EDS Spectrum of the Rust Collected from Interior BF Bottom of the Girder. 1088
Figure A.641. SEM Image and EDS Spectrum of the Rust Collected from Interior BF Bottom of the Girder. 1089
Figure A.642. EDS Elemental Mapping of Rust Collected from Interior BF Bottom. 1090
Figure A.643. SEM Image and EDS Spectrum of the Rust Collected from Interior BF Bottom of the Girder. 1091
Figure A.644. SEM Image and EDS Spectrum of the Rust Collected from Interior BF Bottom of the Girder. 1092
Figure A.645. EDS Elemental Mapping of Rust Collected from Interior BF Bottom. 1093
Figure A.646. SEM Image and EDS Spectrum of the Rust Collected from Interior Web of the Girder. 1094
Figure A.647. SEM Image and EDS Spectrum of the Rust Collected from Interior Web of the Girder. 1095
Figure A.648. EDS Elemental Mapping of Rust Collected from Interior Web. 1096
Figure A.649. XPS Spectrum of the Rust Collected from Exterior Web of the Girder. 1097
Figure A.650. XPS Spectrum of the Rust Collected from Interior Web of the Girder. 1098
Figure A.651. XRD Pattern of Powdered Rust Collected from Exterior Web of the Girder. 1099
Figure A.652. XRD Pattern of Powdered Rust Collected from Interior Web of the Girder. ... 1099

Figure A.653. Particle Size Analysis Results at B5G1F1 (a) Top Flange Bottom, (b) Web, (c) Bottom Flange Bottom (d) Stiffener. 1100
Figure A.654. Particle Size Analysis Results at B5G2F1 (a) Top Flange Bottom, (b) Web, (c) Bottom Flange Bottom (d) Stiffener. 1101
Figure A.655. Particle Size Analysis Results at B5G4F2 (a) Top Flange Bottom, (b) Web, (c) Bottom Flange Bottom (d) Stiffener. 1102
Figure A.656. Particle Size Analysis Results at B6G1F1 (a) Top Flange Bottom, (b) Web, (c) Bottom Flange Bottom (d) Stiffener. 1103
Figure A.657. Particle Size Analysis Results at B6G2F1 (a) Top Flange Bottom, (b) Web, (c) Bottom Flange Bottom (d) Stiffener. 1104
Figure A.658. Particle Size Analysis Results at B6G4F2 (a) Top Flange Bottom, (b) Web, (c) Bottom Flange Bottom (d) Stiffener. 1105
Figure A.659. Particle Size Analysis Showing Different Locations Examined. 1106
Figure A.660. Typical Picture of LBB-WS-02 1107
Figure A.661. SEM Image and EDS Spectrum of the Rust Collected from Exterior Web of the Girder. 1113
Figure A.662. EDS Elemental Mapping of Rust Collected from Exterior Web. 1114
Figure A.663. SEM Image and EDS Spectrum of the Rust Collected from Exterior Web of the Girder. 1115
Figure A.664. EDS Elemental Mapping of Rust Collected from Exterior Web. 1116
Figure A.665. SEM Image and EDS Spectrum of the Rust Collected from Exterior BF Bottom of the Girder. 1117
Figure A.666. EDS Elemental Mapping of Rust Collected from Exterior BF Bottom. 1118
Figure A.667. SEM Image and EDS Spectrum of the Rust Collected from Exterior BF Bottom of the Girder. 1119
Figure A.668. EDS Elemental Mapping of Rust Collected from Exterior BF Bottom. 1120
Figure A.669. SEM Image and EDS Spectrum of the Rust Collected from Interior Web of the Girder. 1121
Figure A.670. EDS Elemental Mapping of Rust Collected from Interior Web. 1122
Figure A.671. SEM Image and EDS Spectrum of the Rust Collected from Interior Web of the Girder. 1123
Figure A.672. EDS Elemental Mapping of Rust Collected from Interior Web. 1124
Figure A.673. XPS Spectrum of the Rust Collected from Exterior Web of the Girder. 1125
Figure A.674. XPS Spectrum of the Rust Collected from Interior Web of the Girder. 1126
Figure A.675. XRD Pattern of Powdered Rust Collected from Exterior Web of the Girder. 1127
Figure A.676. XRD Pattern of Powdered Rust Collected from Interior Web of the Girder. ... 1127
Figure A.677. Particle Size Analysis Results at B3G1F1 (a) Top Flange Bottom, (b) Web, (c) Bottom Flange Bottom (d) Stiffener. 1128
Figure A.678. Particle Size Analysis Results at B3G2F2 (a) Top Flange Bottom, (b) Web, (c) Bottom Flange Bottom (d) Stiffener. 1129
Figure A.679. Particle Size Analysis Results at B3G4F2 (a) Top Flange Bottom, (b) Web, (c) Bottom Flange Bottom (d) Stiffener. 1130
Figure A.680. Particle Size Analysis Results at B4G3F1 (a) Top Flange Bottom, (b) Web, (c) Bottom Flange Bottom (d) Stiffener. 1131

Figure A.681. Particle Size Analysis Results at B4G4F2 (a) Top Flange Bottom, (b) Web, (c) Bottom Flange Bottom (d) Stiffener. 1132
Figure A.682. Particle Size Analysis Showing Different Locations Examined. 1133
Figure A.683. Typical Picture of ELP-WS-01 1134
Figure A.684. SEM Image and EDS Spectrum of the Rust Collected from Exterior Web of the Girder. 1140
Figure A.685. SEM Image and EDS Spectrum of the Rust Collected from Exterior Web of the Girder. 1141
Figure A.686. SEM Image and EDS Spectrum of the Rust Collected from Exterior Web of the Girder. 1142
Figure A.687. EDS Elemental Mapping of Rust Collected from Exterior Web. 1143
Figure A.688. SEM Image and EDS Spectrum of the Rust Collected from Interior Web of the Girder. 1144
Figure A.689. EDS Elemental Mapping of Rust Collected from Interior Web. 1145
Figure A.690. SEM Image and EDS Spectrum of the Rust Collected from Exterior Web of the Girder. 1146
Figure A.691. SEM Image and EDS Spectrum of the Rust Collected from Exterior Web of the Girder. 1147
Figure A.692. SEM Image and EDS Spectrum of the Rust Collected from Exterior Web of the Girder. 1148
Figure A.693. EDS Elemental Mapping of Rust Collected from Exterior Web. 1149
Figure A.694. SEM Image and EDS Spectrum of the Rust Collected from Exterior Web of the Girder. 1150
Figure A.695. EDS Elemental Mapping of Rust Collected from Exterior Web. 1151
Figure A.696. SEM Image and EDS Spectrum of the Rust Collected from Exterior Web of the Girder. 1152
Figure A.697. EDS Elemental Mapping of Rust Collected from Exterior Web. 1153
Figure A.698. XPS Spectrum of the Rust Collected from Exterior Web of the Girder. 1154
Figure A.699. XPS Spectrum of the Rust Collected from Interior Web of the Girder. 1155
Figure A.700. XRD Pattern of Powdered Rust Collected from Exterior Web of the Girder. 1156
Figure A.701. XRD Pattern of Powdered Rust Collected from Interior Web of the Girder. 1156
Figure A.702. XRD Pattern of Powdered Rust Collected from Bottom face of Bottom Flange of the Interior Girder. 1157
Figure A.703. XRD Pattern of Powdered Rust Collected from Bottom face of Bottom Flange of the Exterior Girder. 1157
Figure A.704. Particle Size Analysis Results at A1G1F1 (a) Top Flange Bottom, (b) Web, (c) Bottom Flange Bottom (d) Stiffener. 1158
Figure A.705. Particle Size Analysis Results at A1G3F1 (a) Top Flange Bottom, (b) Web, (c) Bottom Flange Bottom (d) Stiffener. 1159
Figure A.706. Particle Size Analysis Results at A1G5F2 (a) Top Flange Bottom, (b) Web, (c) Bottom Flange Bottom (d) Stiffener. 1160
Figure A.707. Particle Size Analysis Results at A1G12F1 (a) Top Flange Bottom, (b) Web, (c) Bottom Flange Bottom (d) Stiffener. 1161
Figure A.708. Particle Size Analysis Showing Different Locations Examined. 1162
Figure A.709. Typical Picture of AUS-WS-02. 1163

Figure A.710. SEM Image and EDS Spectrum of the Rust Collected from Interior Web of the Girder. 1168
Figure A.711. EDS Elemental Mapping of Rust Collected from Interior Web. 1169
Figure A.712. SEM Image and EDS Spectrum of the Rust Collected from Interior Web of the Girder. 1170
Figure A.713. SEM Image and EDS Spectrum of the Rust Collected from Interior Web of the Girder. 1171
Figure A.714. SEM Image and EDS Spectrum of the Rust Collected from Interior Web of the Girder. 1172
Figure A.715. EDS Elemental Mapping of Rust Collected from Interior Web. 1173
Figure A.716. SEM Image and EDS Spectrum of the Rust Collected from Interior Web of the Girder. 1174
Figure A.717. SEM Image and EDS Spectrum of the Rust Collected from Interior Web of the Girder. 1175
Figure A.718. SEM Image and EDS Spectrum of the Rust Collected from Interior Web of the Girder. 1176
Figure A.719. EDS Elemental Mapping of Rust Collected from Interior Web. 1177
Figure A.720. SEM Image and EDS Spectrum of the Rust Collected from Interior Web of the Girder. 1178
Figure A.721. EDS Elemental Mapping of Rust Collected from Interior Web. 1179
Figure A.722. XPS Spectrum of the Rust Collected from Interior Web of the Girder. 1180
Figure A.723. XRD Pattern of Powdered Rust Collected from Interior Web of the Girder. ... 1181
Figure A.724. Particle Size Analysis Results at B16G4F1 (a) Top Flange Bottom, (b) Web, (c) Bottom Flange Bottom. 1182
Figure A.725. Particle Size Analysis Results at B16G5F1 (a) Top Flange Bottom, (b) Web, (c) Bottom Flange Bottom. 1183
Figure A.726. Particle Size Analysis Results at B16G7F2 (a) Top Flange Bottom, (b) Web, (c) Bottom Flange Bottom. 1184
Figure A.727. Particle Size Analysis Showing Different Locations Examined. 1185
Figure A.728. Typical Picture of FTW-WS-01. 1186
Figure A.729. SEM Image and EDS Spectrum of the Rust Collected from Exterior Web of the Girder. 1192
Figure A.730. SEM Image and EDS Spectrum of the Rust Collected from Exterior Web of the Girder. 1193
Figure A.731. SEM Image and EDS Spectrum of the Rust Collected from Exterior Web of the Girder. 1194
Figure A.732. SEM Image and EDS Spectrum of the Rust Collected from Exterior Web of the Girder. 1195
Figure A.733. SEM Image and EDS Spectrum of the Rust Collected from Exterior Web of the Girder. 1196
Figure A.734. EDS Elemental Mapping of Rust Collected from Exterior Web. 1197
Figure A.735. SEM Image and EDS Spectrum of the Rust Collected from Exterior Web of the Girder. 1198
Figure A.736. EDS Elemental Mapping of Rust Collected from Exterior Web. 1199
Figure A.737. SEM Image and EDS Spectrum of the Rust Collected from Interior Web of the Girder. 1200

Figure A.738. EDS Elemental Mapping of Rust Collected from Interior Web. 1201
Figure A.739. XPS Spectrum of the Rust Collected from Exterior Web of the Girder. 1202
Figure A.740. XPS Spectrum of the Rust Collected from Interior Web of the Girder. 1203
Figure A.741. XRD Pattern of Powdered Rust Collected from Exterior Web of the Girder. 1204
Figure A.742. XRD Pattern of Powdered Rust Collected from Interior Web of the Girder. ... 1204
Figure A.743. XRD Pattern of Powdered Rust Collected from Bottom face of Bottom Flange of the Interior Girder. 1205
Figure A.744. Particle Size Analysis Results at A1G1F1 (a) Top Flange Bottom, (b) Web, (c) Bottom Flange Bottom (d) Stiffener. 1206
Figure A.745. Particle Size Analysis Results at A3G7F1 (a) Top Flange Bottom, (b) Web, (c) Bottom Flange Bottom (d) Stiffener. 1207
Figure A.746. Particle Size Analysis Results at A3G9F2 (a) Top Flange Bottom, (b) Web, (c) Bottom Flange Bottom (d) Stiffener. 1208
Figure A.747. Particle Size Analysis Results at A3G11F2 (a) Top Flange Bottom, (b) Web, (c) Bottom Flange Bottom (d) Stiffener. 1209
Figure A.748. Particle Size Analysis Showing Different Locations Examined. 1210
Figure A.749. Typical Picture of FTW-WS-02. 1211
Figure A.750. SEM Image and EDS Spectrum of the Rust Collected from Exterior Web of the Girder. 1216
Figure A.751. EDS Elemental Mapping of Rust Collected from Exterior Web. 1217
Figure A.752. SEM Image and EDS Spectrum of the Rust Collected from Exterior Web of the Girder. 1218
Figure A.753. SEM Image and EDS Spectrum of the Rust Collected from Exterior Web of the Girder. 1219
Figure A.754. SEM Image and EDS Spectrum of the Rust Collected from Interior Web of the Girder. 1220
Figure A.755. EDS Elemental Mapping of Rust Collected from Interior Web. 1221
Figure A.756. XPS Spectrum of the Rust Collected from Exterior Web of the Girder. 1222
Figure A.757. XPS Spectrum of the Rust Collected from Interior Web of the Girder. 1223
Figure A.758. XRD Pattern of Powdered Rust Collected from Exterior Web of the Girder. 1224
Figure A.759. XRD Pattern of Powdered Rust Collected from Interior Web of the Girder. ... 1224
Figure A.760. XRD Pattern of Powdered Rust Collected from Bottom face of Bottom Flange of the Interior Girder. 1225
Figure A.761. Particle Size Analysis Results at A1G1F1 (a) Top Flange Bottom, (b) Web, (c) Bottom Flange Bottom (d) Stiffener. 1226
Figure A.762. Particle Size Analysis Results at A1G1F2 (a) Top Flange Bottom, (b) Web, (c) Bottom Flange Bottom (d) Stiffener. 1227
Figure A.763. Particle Size Analysis Results at A1G2F1 (a) Top Flange Bottom, (b) Web, (c) Bottom Flange Bottom (d) Stiffener. 1228
Figure A.764. Particle Size Analysis Results at A3G1F1 (a) Top Flange Bottom, (b) Web, (c) Bottom Flange Bottom (d) Stiffener. 1229
Figure A.765. Particle Size Analysis Results at A3G2F1 (a) Top Flange Bottom, (b) Web, (c) Bottom Flange Bottom (d) Stiffener. 1230
Figure A.766. Particle Size Analysis Showing Different Locations Examined. 1231

Figure A.767. Typical Picture of FTW-WS-03. 1232
Figure A.768. SEM Image and EDS Spectrum of the Rust Collected from Exterior Web of the Girder. 1237
Figure A.769. EDS Elemental Mapping of Rust Collected from Exterior Web. 1238
Figure A.770. SEM Image and EDS Spectrum of the Rust Collected from Interior Web of the Girder. 1239
Figure A.771. EDS Elemental Mapping of Rust Collected from Interior Web. 1240
Figure A.772. XPS Spectrum of the Rust Collected from Exterior Web of the Girder. 1241
Figure A.773. XPS Spectrum of the Rust Collected from Interior Web of the Girder. 1242
Figure A.774. XRD Pattern of Powdered Rust Collected from Exterior Web of the Girder. 1243
Figure A.775. XRD Pattern of Powdered Rust Collected from Interior Web of the Girder. ... 1243
Figure A.776. XRD Pattern of Powdered Rust Collected from Bottom face of Bottom Flange of the Interior Girder. 1244
Figure A.777. Particle Size Analysis Results at A1G1F1 (a) Top Flange Bottom, (b) Web, (c) Bottom Flange Bottom (d) Stiffener. 1245
Figure A.778. Particle Size Analysis Results at A1G3F1 (a) Top Flange Bottom, (b) Web, (c) Bottom Flange Bottom (d) Stiffener. 1246
Figure A.779. Particle Size Analysis Results at A1G4F2 (a) Top Flange Bottom, (b) Web, (c) Bottom Flange Bottom (d) Stiffener. 1247
Figure A.780. Particle Size Analysis Results at A1G6F2 (a) Top Flange Bottom, (b) Web, (c) Bottom Flange Bottom (d) Stiffener. 1248
Figure A.781. Particle Size Analysis Showing Different Locations Examined. 1249
Figure A.782. Typical Picture of DAL-WS-01. 1250
Figure A.783. SEM Image and EDS Spectrum of the Rust Collected from Exterior Web of the Girder. 1255
Figure A.784. SEM Image and EDS Spectrum of the Rust Collected from Exterior Web of the Girder. 1256
Figure A.785. SEM Image and EDS Spectrum of the Rust Collected from Exterior Web of the Girder. 1257
Figure A.786. SEM Image and EDS Spectrum of the Rust Collected from Exterior Web of the Girder. 1258
Figure A.787. EDS Elemental Mapping of Rust Collected from Exterior Web. 1259
Figure A.788. SEM Image and EDS Spectrum of the Rust Collected from Exterior Web of the Girder. 1260
Figure A.789. SEM Image and EDS Spectrum of the Rust Collected from Exterior Web of the Girder. 1261
Figure A.790. SEM Image and EDS Spectrum of the Rust Collected from Exterior Web of the Girder. 1262
Figure A.791. SEM Image and EDS Spectrum of the Rust Collected from Exterior Web of the Girder. 1263
Figure A.792. SEM Image and EDS Spectrum of the Rust Collected from Exterior Web of the Girder. 1264
Figure A.793. EDS Elemental Mapping of Rust Collected from Exterior Web. 1265
Figure A.794. SEM Image and EDS Spectrum of the Rust Collected from Interior Web of the Girder. 1266

Figure A.795. EDS Elemental Mapping of Rust Collected from Interior Web. 1267
Figure A.796. SEM Image and EDS Spectrum of the Rust Collected from Interior Web of the Girder. 1268
Figure A.797. EDS Elemental Mapping of Rust Collected from Interior Web. 1269
Figure A.798. SEM Image and EDS Spectrum of the Rust Collected from Interior Web of the Girder. 1270
Figure A.799. EDS Elemental Mapping of Rust Collected from Interior Web. 1271
Figure A.800. XPS Spectrum of the Rust Collected from Exterior Web of the Girder. 1272
Figure A.801. XPS Spectrum of the Rust Collected from Interior Web of the Girder. 1273
Figure A.802. XRD Pattern of Powdered Rust Collected from Exterior Web of the Girder. 1274
Figure A.803. XRD Pattern of Powdered Rust Collected from Interior Web of the Girder. ... 1274
Figure A.804. Particle Size Analysis Results at A1G1F1 (a) Top Flange Bottom, (b) Web, (c) Bottom Flange Bottom (d) Stiffener. 1275
Figure A.805. Particle Size Analysis Results at A1G3F1 (a) Top Flange Bottom, (b) Web, (c) Bottom Flange Bottom (d) Stiffener. 1276
Figure A.806. Particle Size Analysis Results at A1G4F2 (a) Top Flange Bottom, (b) Web, (c) Bottom Flange Bottom (d) Stiffener. 1277
Figure A.807. Particle Size Analysis Results at A1G6F2 (a) Top Flange Bottom, (b) Web, (c) Bottom Flange Bottom (d) Stiffener. 1278
Figure A.808. Particle Size Analysis Showing Different Locations Examined. 1279
Figure A.809. Typical Picture of DAL-WS-02. 1280
Figure A.810. SEM Image and EDS Spectrum of the Rust Collected from Exterior Web of the Girder. 1285
Figure A.811. SEM Image and EDS Spectrum of the Rust Collected from Exterior Web of the Girder. 1286
Figure A.812. SEM Image and EDS Spectrum of the Rust Collected from Exterior Web of the Girder. 1287
Figure A.813. SEM Image and EDS Spectrum of the Rust Collected from Exterior Web of the Girder. 1288
Figure A.814. SEM Image and EDS Spectrum of the Rust Collected from Exterior Web of the Girder. 1289
Figure A.815. EDS Elemental Mapping of Rust Collected from Exterior Web. 1290
Figure A.816. SEM Image and EDS Spectrum of the Rust Collected from Exterior Web of the Girder. 1291
Figure A.817. SEM Image and EDS Spectrum of the Rust Collected from Exterior Web of the Girder. 1292
Figure A.818. SEM Image and EDS Spectrum of the Rust Collected from Exterior Web of the Girder. 1293
Figure A.819. EDS Elemental Mapping of Rust Collected from Exterior Web. 1294
Figure A.820. SEM Image and EDS Spectrum of the Rust Collected from Exterior Web of the Girder. 1295
Figure A.821. SEM Image and EDS Spectrum of the Rust Collected from Exterior Web of the Girder. 1296
Figure A.822. SEM Image and EDS Spectrum of the Rust Collected from Interior Web of the Girder. 1297

Figure A.823. EDS Elemental Mapping of Rust Collected from Interior Web. 1298
Figure A.824. SEM Image and EDS Spectrum of the Rust Collected from Interior Web of the Girder. 1299
Figure A.825. SEM Image and EDS Spectrum of the Rust Collected from Interior Web of the Girder. 1300
Figure A.826. EDS Elemental Mapping of Rust Collected from Interior Web. 1301
Figure A.827. SEM Image and EDS Spectrum of the Rust Collected from Interior Web of the Girder. 1302
Figure A.828. XPS Spectrum of the Rust Collected from Exterior Web of the Girder. 1303
Figure A.829. XPS Spectrum of the Rust Collected from Interior Web of the Girder. 1304
Figure A.830. XRD Pattern of Powdered Rust Collected from Exterior Web of the Girder. 1305
Figure A.831. XRD Pattern of Powdered Rust Collected from Interior Web of the Girder. ... 1305
Figure A.832. Particle Size Analysis Results at A1G1F1 (a) Top Flange Bottom, (b) Web, (c) Bottom Flange Bottom (d) StiffenerA1G1F1. 1306
Figure A.833. Particle Size Analysis Results at A1G2F1 (a) Top Flange Bottom, (b) Web, (c) Bottom Flange Bottom (d) Stiffener. 1307
Figure A.834. Particle Size Analysis Results at A1G3F2 (a) Top Flange Bottom, (b) Web, (c) Bottom Flange Bottom (d) Stiffener. 1308
Figure A.835. Particle Size Analysis Results at A1G4F2 (a) Top Flange Bottom, (b) Web, (c) Bottom Flange Bottom (d) Stiffener. 1309
Figure A.836. Particle Size Analysis Showing Different Locations Examined. 1310
Figure A.837. Typical Picture of DAL-WS-03. 1311
Figure A.838. SEM Image and EDS Spectrum of the Rust Collected from Exterior Web of the Girder. 1316
Figure A.839. SEM Image and EDS Spectrum of the Rust Collected from Exterior Web of the Girder. 1317
Figure A.840. SEM Image and EDS Spectrum of the Rust Collected from Exterior Web of the Girder. 1318
Figure A.841. EDS Elemental Mapping of Rust Collected from Exterior Web. 1319
Figure A.842. SEM Image and EDS Spectrum of the Rust Collected from Exterior Web of the Girder. 1320
Figure A.843. EDS Elemental Mapping of Rust Collected from Exterior Web. 1321
Figure A.844. SEM Image and EDS Spectrum of the Rust Collected from Exterior Web of the Girder. 1322
Figure A.845. EDS Elemental Mapping of Rust Collected from Exterior Web. 1323
Figure A.846. SEM Image and EDS Spectrum of the Rust Collected from Interior Web of the Girder. 1324
Figure A.847. SEM Image and EDS Spectrum of the Rust Collected from Interior Web of the Girder. 1325
Figure A.848. SEM Image and EDS Spectrum of the Rust Collected from Interior Web of the Girder. 1326
Figure A.849. EDS Elemental Mapping of Rust Collected from Interior Web. 1327
Figure A.850. SEM Image and EDS Spectrum of the Rust Collected from Interior Web of the Girder. 1328
Figure A.851. EDS Elemental Mapping of Rust Collected from Interior Web. 1329

Figure A.852. SEM Image and EDS Spectrum of the Rust Collected from Interior Web of the Girder. 1330
Figure A.853. EDS Elemental Mapping of Rust Collected from Interior Web. 1331
Figure A.854. XPS Spectrum of the Rust Collected from Exterior Web of the Girder. 1332
Figure A.855. XPS Spectrum of the Rust Collected from Interior Web of the Girder. 1333
Figure A.856. XRD Pattern of Powdered Rust Collected from Exterior Web of the Girder. 1334
Figure A.857. XRD Pattern of Powdered Rust Collected from Interior Web of the Girder. ... 1334
Figure A.858. Particle Size Analysis Results at A6G1F1 (a) Top Flange Bottom, (b) Web, (c) Bottom Flange Bottom (d) Stiffener. 1335
Figure A.859. Particle Size Analysis Results at A6G3F1 (a) Top Flange Bottom, (b) Web, (c) Bottom Flange Bottom (d) Stiffener. 1336
Figure A.860. Particle Size Analysis Results at A6G5F2 (a) Top Flange Bottom, (b) Web, (c) Bottom Flange Bottom (d) Stiffener. 1337
Figure A.861. Particle Size Analysis Results at A6G8F2 (a) Top Flange Bottom, (b) Web, (c) Bottom Flange Bottom (d) Stiffener. 1338
Figure A.862. Particle Size Analysis Showing Different Locations Examined. 1339

LIST OF TABLES

Page

Table 2-1. Evolution of Paint System Used in Texas. 16
Table 2-2. Results of Literature Review on Paint System. 40
Table 2-3. Appearance Guidelines for Color of Patina (Albrecht et al., 1989). 41
Table 2-4. Appearance Guidelines for Texture of Oxide Layer (Albrecht et al., 1989). 41
Table 2-5. Appearance Index of Oxide Layers (Hara et al., 2007). 42
Table 2-6. Appearance Index of Oxide Layers (Hara et al., 2007). 43
Table 2-7. Proposed Patina Evaluation Rating Scale (Crampton & Holloway, 2015) 44
Table 4-1. Weathering Steel Bridge. 71
Table 4-2. Painted Steel Bridge Information. 73
Table 4-3. Field Tests Performed on Steel Bridges. 76
Table 4-4. Description of Rusting Ratings for Painted Bridges (ASTM D610, 2019). 79
Table 4-5. PRI Scale. 85
Table 4-6. Selected Bridges for Datalogger Installation. 91
Table 4-7. Chloride Test Result. 103
Table 4-8. pH Test Results for All Steel Bridges. 104
Table 4-9. Thickness Measurement with Ultrasonic Testing. 105
Table 4-10. Pull-Off Adhesion Test Results, TYL−PS−01 (A4-G1F1 Web). 111
Table 4-11. Pull-off Adhesion Test Results, YKM−PS−01 (Web). 112
Table 4-12. Dry Film Thickness Results. 113
Table 4-13. Sensor Measurements and Calculated Wetness Time Based on ISO-9223. 121
Table 4-14. Calculated Wetness Time from Local Weather Station Based on ISO-9223. 121
Table 4-15. PRI Based on Particle Size Analysis. 128
Table 5-1. Chemical Formulas of Rust Layers (Schwertmann & Cornell, 2000). 133
Table 5-2. Chemical Composition of Different Types of Weathering Steel (Weight %). 134
Table 5-3. Technical Specifications for JSM—7500F. 135
Table 5-4. Elemental Composition of Spectrum 2, Spectrum 3, and Sum Spectrum Obtained from EDS Analysis on Rust Surface of Weathering Steel Sample. 141
Table 5-5. XPS Curve-Fitting Quantitative Results in Area Percent. 153
Table 5-6. Optical Microscopy Analysis on Collected Paint Samples. 171
Table 5-7. Classification of Patina. 177
Table 5-8. Quantitative Phase Analysis Results of Weathering Steel Rust. 182
Table 5-9. Patina Condition for Weathering Bridges Based on XRD Phase Analysis. 185
Table 6-1. Score Values—Weathering Steel Bridge. 192
Table 6-2. Score Values—Painted Steel Bridge. 194
Table 6-3. Upfront and Maintenance Cost for System I in Region 1 and Region 2 (American Galvanizers Association, 2023). 195
Table 6-4. Upfront and Maintenance Cost for System I in Region 3 And Region 4 (American Galvanizers Association, 2023). 195
Table 6-5. Upfront and Maintenance Cost for System I in Region 5 and Region 6 (American Galvanizers Association, 2023). 196
Table 6-6. Upfront and Maintenance Cost for System II in Region 1 and Region 2 (American Galvanizers Association, 2023). 196

Table 6-7. Upfront and Maintenance Cost for System II Region 3 and Region 4 (American Galvanizers Association, 2023). 197
Table 6-8. Upfront and Maintenance Cost for System II Region 5 and Region 6 (American Galvanizers Association, 2023). 197
Table 6-9. Upfront and Maintenance Cost for System III-A in Region 1 and Region 2 (American Galvanizers Association, 2023). 198
Table 6-10. Upfront and Maintenance Cost for System III-A Region 3 and Region 4 (American Galvanizers Association, 2023). 198
Table 6-11. Upfront and Maintenance Cost for System III-A Region 5 and Region 6 (American Galvanizers Association, 2023). 198
Table 6-12. Cost Table for Corrosion Protection Systems. 199
Table 6-13. Linear Scale for Cost Scores. 199
Table 6-14. Calculated Cost Scores for Corrosion Protection Systems in Different Regions. 200
Table 6-15. Categories and Weight Factors for Durability-Driven Scenario. 201
Table 6-16. Comparison of TxDOT Inventory Superstructure Rating with the Research Findings for Weathering Steel Bridges. 206
Table 6-17. Comparison of TxDOT Inventory Superstructure Rating with the Research Findings for Painted Steel Bridges. 207
Table 7-1. Fatigue Category and Threshold (AASHTO, 2020). 215
Table 7-2. Stress Concentration Factor of Different Welds (Dimitrakis & Lawrence, 2001; Veritas, 2001; Spotts et al., 2004). 219
Table 7-3. A588/A709W Mechanical Parameters. 224
Table 7-4. Load Factors for Corrosion Fatigue Limit State (Nowak, 1999; Kulicki, 2015). 227
Table 7-5. Maximum Unfactored Moments and Shears (Barker & Puckett, 2021). 230
Table 7-6. Fraction of Trucks in Traffic (AASHTO, 2020). 230
Table 7-7. Fraction of Single-Lane Truck Traffic (AASHTO, 2020). 230
Table 7-8. Cycles Per Truck Passage for Simple Span and Continuous Girders (AASHTO, 2020). 232
Table 7-9. Short-Term and Long-Term Composite Section Properties at Mid-span (Barker & Puckett, 2021). 235
Table 7-10. Maximum Unfactored Moments and Shears (Barker & Puckett, 2021). 235
Table 7-11. Composite Section Properties at Negative Moment Region (Barth, 2022). 241
Table 7-12. Composite Section Properties at Positive Moment Region (Barth, 2022). 241
Table 7-13. Composite Section Properties at Negative Moment Region (Rivera & Chavel, 2022). 248
Table 7-14. Composite Section Properties at Positive Moment Region (Rivera & Chavel, 2022). 248
Table 7-15. Maximum Unfactored Dead Moments on Different Regions. 250
Table 7-16. Composite Section Properties at Negative Moment Region (Chavel & Carnahan, 2022). 258
Table 7-17. Composite Section Properties at Positive Moment Region (Chavel & Carnahan, 2022). 258
Table 7-18. Summarized Results of Case Studies. 264
Table 7-19 Provided Descriptions. 269
Table A-1.Field Inspection Results for TYL-PS-02. 301

Table A-2. Field Inspection Results for TYL-PS-02. 302
Table A-3. Pull off Adhesion Results for TYL-PS-02. 303
Table A-4. Pull off Adhesion Results for TYL-PS-02. 304
Table A-5. Field Inspection Results for BRY-PS-01 320
Table A-6. Field Inspection Results for BRY-PS-01 321
Table A-7. Field Inspection Results for BRY-PS-01 322
Table A-8. Field Inspection Results for BRY-PS-01 323
Table A-9. Paint System Information 323
Table A-10. Pull-off Adhesion Results for BRY-PS-01 324
Table A-11. Pull-off Adhesion Results for BRY-PS-01 325
Table A-12. Field Inspection Results for ATL-PS-01. 340
Table A-13. Field Inspection Results for ATL-PS-01. 341
Table A-14. Paint System Information - 2-Layer System. 342
Table A-15. Pull-off Adhesion Results for ATL-PS-01. 343
Table A-16. Pull-off Adhesion Results for ATL-PS-01. 344
Table A-17. Field Inspection Results for FTW-PS-01. 358
Table A-18. Field Inspection Results for FTW-PS-01. 359
Table A-19. Field Inspection Results for FTW-PS-01. 360
Table A-20. Paint System Information: Exterior Girders (3-Layers). 360
Table A-21. Paint System Information: Interior Girders (2-Layer). 361
Table A-22. Pull-off Adhesion Results for FTW-PS-01. 362
Table A-23. Pull-off Adhesion Results for FTW-PS-01. 363
Table A-24. Paint System Information: Interior Girders (2-Layer). 378
Table A-25. Field Inspection Results for FTW-PS-02. 379
Table A-26. Field Inspection Results for FTW-PS-02. 380
Table A-27. Field Inspection Results for FTW-PS-02. 381
Table A-28. Pull-off Adhesion Results for FTW-PS-02. 382
Table A-29. Pull-off Adhesion Results for FTW-PS-02. 383
Table A-30. Paint System Information: (2-Layer Lead-Based). 398
Table A-31. Field Inspection Results for AMA-PS-01. 399
Table A-32. Pull-off Adhesion Results for AMA-PS-01. 400
Table A-33. Paint System Information. 411
Table A-34. Field Inspection Results for AMA-PS-02. 412
Table A-35. Pull-off Adhesion Results for AMA-PS-02. 413
Table A-36. Field Inspection Results for AMA-PS-03. 422
Table A-37. Field Inspection Results for AMA-PS-03. 423
Table A-38. Paint System Information: (2-Layer Zinc-Based). 424
Table A-39. Pull-off Adhesion Results for AMA-PS-03. 425
Table A-40. Field Inspection Results for WFS-PS-01 438
Table A-41. Field Inspection Results for WFS-PS-01 439
Table A-42. Field Inspection Results for WFS-PS-01 440
Table A-43. Paint System Information. 440
Table A-44. Pull-off Adhesion Results for WFS-PS-01 441
Table A-45. Pull-off Adhesion Results for WFS-PS-01 442
Table A-46. Field Inspection Results for WFS-PS-02 448
Table A-47. Field Inspection Results for WFS-PS-02 449

Table A-48. Field Inspection Results for WFS-PS-02. 450
Table A-49. Paint System Information. 450
Table A-50. Pull-off Adhesion Results for WFS-PS-02. 451
Table A-51. Pull-off Adhesion Results for WFS-PS-02. 452
Table A-52. Field Inspection Results for WFS-RC-01. 463
Table A-53. Field Inspection Results for WFS-RC-01. 464
Table A-54. Field Inspection Results for WFS-RC-01. 465
Table A-55. Paint System Information. 465
Table A-56. Pull-off Adhesion Results for WFS-RC-01. 466
Table A-57. Pull-off Adhesion Results for WFS-RC-01. 467
Table A-58. Field Inspection Results for WFS-RC-02. 479
Table A-59. Field Inspection Results for WFS-RC-02. 480
Table A-60. Field Inspection Results for WFS-RC-02. 481
Table A-61. Pull-off Adhesion Results for WFS-RC-02. 482
Table A-62. Pull-off Adhesion Results for WFS-RC-02. 483
Table A-63. Field Inspection Results for DAL-PS-01. 493
Table A-64. Field Inspection Results for DAL-PS-01. 494
Table A-65. Field Inspection Results for DAL-PS-01. 495
Table A-66. Pull-off Adhesion Results for DAL-PS-01. 496
Table A-67. Pull-off Adhesion Results for DAL-PS-01. 497
Table A-68. Field Inspection Results for YKM-PS-01. 510
Table A-69. Field Inspection Results for YKM-PS-01. 511
Table A-70. Field Inspection Results for YKM-PS-01. 512
Table A-71. Field Inspection Results for YKM-PS-01. 513
Table A-72. Pull-off Adhesion Results for YKM-PS-01. 514
Table A-73. Pull-off Adhesion Results for YKM-PS-01. 515
Table A-74. Field Inspection Results for CRP-PS-01. 539
Table A-75. Pull-off Adhesion Results for CRP-PS-01. 540
Table A-76. Pull-off Adhesion Results for CRP-PS-01. 541
Table A-77. Field Inspection Results for TYL-PS-01. 553
Table A-78. Field Inspection Results for TYL-PS-01. 554
Table A-79. Field Inspection Results for TYL-PS-01. 555
Table A-80. Pull-off Adhesion Results for TYL-PS-01. 556
Table A-81. Pull-off Adhesion Results for TYL-PS-01. 557
Table A-82. Field Inspection Results for ELP-PS-01. 579
Table A-83. Field Inspection Results for ELP-PS-01. 580
Table A-84. Field Inspection Results for ELP-PS-01. 581
Table A-85. Pull-off Adhesion Results for ELP-PS-01. 582
Table A-86. Pull-off Adhesion Results for ELP-PS-01. 583
Table A-87. Paint System Information. 604
Table A-88. Field Inspection Results for HOU-PS-01. 605
Table A-89. Field Inspection Results for HOU-PS-01. 606
Table A-90. Field Inspection Results for HOU-PS-01. 607
Table A-91. Pull-off Adhesion Results for HOU-PS-01. 608
Table A-92. Pull-off Adhesion Results for HOU-PS-01. 609
Table A-93. Paint System Information. 621

Table A-94. Field Inspection Results for BMT-PS-01. 622
Table A-95. Field Inspection Results for BMT-PS-01. 623
Table A-96. Field Inspection Results for BMT-PS-01. 624
Table A-97. Pull-off Adhesion Results for BMT-PS-01. 625
Table A-98. Pull-off Adhesion Results for BMT-PS-01. 626
Table A-99. Paint System Information. 649
Table A-100. Field Inspection Results for BMT-PS-02. 650
Table A-101. Field Inspection Results for BMT-PS-02. 651
Table A-102. Field Inspection Results for BMT-PS-02. 652
Table A-103. Pull-off Adhesion Results for BMT-PS-02. 653
Table A-104. Pull-off Adhesion Results for BMT-PS-02. 654
Table A-105. Field Inspection Results for AUS-WS-01. 678
Table A-106. Field Inspection Results for AUS-WS-01. 679
Table A-107. Field Inspection Results for AUS-WS-01. 680
Table A-108. Field Inspection Results for AUS-WS-01. 681
Table A-109. Field Inspection Results for AUS-WS-03. 713
Table A-110. Field Inspection Results for AUS-WS-03. 714
Table A-111. Field Inspection Results for AUS-WS-03. 715
Table A-112. Field Inspection Results for AUS-WS-03. 716
Table A-113. Field Inspection Results for AUS-WS-04. 742
Table A-114. Field Inspection Results for AUS-WS-04. 743
Table A-115. Field Inspection Results for AUS-WS-04. 744
Table A-116. Field Inspection Results for HOU-WS-01 777
Table A-117. Field Inspection Results for HOU-WS-02 790
Table A-118. Field Inspection Results for HOU-WS-02 791
Table A-119. Field Inspection Results for HOU-WS-02 792
Table A-120. Field Inspection Results for HOU-WS-02 793
Table A-121. Field Inspection Results for HOU-WS-03 828
Table A-122. Field Inspection Results for HOU-WS-03 829
Table A-123. Field Inspection Results for HOU-WS-03 830
Table A-124. Field Inspection Results for HOU-WS-03 831
Table A-125. Field Inspection Results for HOU-WS-03 832
Table A-126. Field Inspection Results for HOU-WS-04 856
Table A-127. Field Inspection Results for HOU-WS-04 857
Table A-128. Field Inspection Results for HOU-WS-04 858
Table A-129. Field Inspection Results for HOU-WS-04 859
Table A-130. Field Inspection Results for HOU-WS-05 881
Table A-131. Field Inspection Results for HOU-WS-05 882
Table A-132. Field Inspection Results for HOU-WS-05 883
Table A-133. Field Inspection Results for HOU-WS-05 884
Table A-134. Field Inspection Results for HOU-WS-05* 905
Table A-135. Field Inspection Results for HOU-WS-06 907
Table A-136. Field Inspection Results for HOU-WS-06 908
Table A-137. Field Inspection Results for HOU-WS-06 909
Table A-138. Field Inspection Results for HOU-WS-06 910
Table A-139. Field Inspection Results for HOU-WS-06 911

Table A-140. Field Inspection Results for HOU-WS-07..... 935
Table A-141. Field Inspection Results for HOU-WS-07..... 936
Table A-142. Field Inspection Results for HOU-WS-07..... 937
Table A-143. Field Inspection Results for HOU-WS-07..... 938
Table A-144. Field Inspection Results for CRP-WS-01..... 968
Table A-145. Field Inspection Results for CRP-WS-01..... 969
Table A-146. Field Inspection Results for CRP-WS-01..... 970
Table A-147. Field Inspection Results for CRP-WS-01..... 971
Table A-148. Field Inspection Results for CRP-WS-01..... 972
Table A-149. Field Inspection Results for SAT-WS-01..... 989
Table A-150. Field Inspection Results for SAT-WS-01..... 990
Table A-151. Field Inspection Results for SAT-WS-01..... 991
Table A-152. Field Inspection Results for SAT-WS-01..... 992
Table A-153. Field Inspection Results for SAT-WS-01..... 993
Table A-154. Field Inspection Results for ATL-WS-01. 1002
Table A-155. Field Inspection Results for ATL-WS-01. 1003
Table A-156. Field Inspection Results for ATL-WS-01. 1004
Table A-157. Field Inspection Results for ATL-WS-02. 1027
Table A-158. Field Inspection Results for ATL-WS-02. 1028
Table A-159. Field Inspection Results for ATL-WS-02. 1029
Table A-160. Field Inspection Results for ATL-WS-03. 1050
Table A-161. Field Inspection Results for ATL-WS-03. 1051
Table A-162. Field Inspection Results for ATL-WS-03. 1052
Table A-163. Field Inspection Results for ATL-WS-03. 1053
Table A-164. Field Inspection Results for LBB-WS-01. 1082
Table A-165. Field Inspection Results for LBB-WS-01. 1083
Table A-166. Field Inspection Results for LBB-WS-01. 1084
Table A-167. Field Inspection Results for LBB-WS-01. 1085
Table A-168. Field Inspection Results for LBB-WS-02. 1108
Table A-169. Field Inspection Results for LBB-WS-02. 1109
Table A-170. Field Inspection Results for LBB-WS-02. 1110
Table A-171.Field Inspection Results for LBB-WS-02. 1111
Table A-172. Field Inspection Results for LBB-WS-02. 1112
Table A-173. Field Inspection Results for ELP-WS-01. 1135
Table A-174. Field Inspection Results for ELP-WS-01. 1136
Table A-175. Field Inspection Results for ELP-WS-01. 1137
Table A-176. Field Inspection Results for ELP-WS-01. 1138
Table A-177. Field Inspection Results for ELP-WS-01. 1139
Table A-178. Field Inspection Results for AUS-WS-02. 1165
Table A-179. Field Inspection Results for AUS-WS-02. 1166
Table A-180. Field Inspection Results for AUS-WS-02. 1167
Table A-181. Field Inspection Results for FTW-WS-01. 1187
Table A-182. Field Inspection Results for FTW-WS-01. 1188
Table A-183. Field Inspection Results for FWA-WS-01. 1189
Table A-184. Field Inspection Results for FWA-WS-01. 1190
Table A-185. Field Inspection Results for FWA-WS-01. 1191

Table A-186. Field Inspection Results for FTW-WS-02. 1212
Table A-187. Field Inspection Results for FTW-WS-02. 1213
Table A-188. Field Inspection Results for FWA-WS-02. 1214
Table A-189. Field Inspection Results for FTW-WS-02. 1215
Table A-190. Field Inspection Results for FTW-WS-03. 1233
Table A-191. Field Inspection Results for FTW-WS-03. 1234
Table A-192. Field Inspection Results for FTW-WS-03 1235
Table A-193. Field Inspection Results for FTW-WS-03 1236
Table A-194. Field Inspection Results for DAL-WS-01. 1251
Table A-195. Field Inspection Results for DAL-WS-01. 1252
Table A-196. Field Inspection Results for DAL-WS-01. 1253
Table A-197. Field Inspection Results for DAL-WS-01. 1254
Table A-198. Field Inspection Results for DAL-WS-02. 1281
Table A-199. Field Inspection Results for DAL-WS-02. 1282
Table A-200. Field Inspection Results for DAL-WS-02. 1283
Table A-201. Field Inspection Results for DAL-WS-02. 1284
Table A-202. Field Inspection Results for DAL-WS-03. 1312
Table A-203. Field Inspection Results for DAL-WS-03. 1313
Table A-204. Field Inspection Results for DAL-WS-03. 1314
Table A-205. Field Inspection Results for DAL-WS-03. 1315

1 INTRODUCTION

1.1 BACKGROUND AND SIGNIFICANCE

Steel corrosion has been recognized as a challenging problem by most departments of transportation (DOTs) across the nation. In Texas, corrosion-related issues cost the state agency millions of dollars and have a significant impact on overall financial obligations and resources allocated to maintenance and repairs. The Texas Department of Transportation (TxDOT) implemented a routine inspection and maintenance program to ensure the safety of state steel bridges, including using *weathering steel* girders and *painting steel* girders. These systems are susceptible to potential corrosion failure if inspection, maintenance, and repairs are neglected or delayed.

The selection of either of these two systems as a corrosion prevention and mitigation method to protect steel girders from corrosion relies on several factors, including the corrosivity of the environment and the overall cost associated with long-term maintenance and repairs. Painted systems are more common in Texas, and they include *on-system* and *off-system* bridges. On-system bridges are built mostly in urban and metropolitan areas with high volume traffic, such as Houston and Dallas. TxDOT more commonly uses weathering steel in the construction of steel girders in these metropolitan areas. However, off-system bridges using painted steel girders are more common in low traffic environments such as rural areas. The latter system is more susceptible to corrosion failure because an intense maintenance and repair program has not been implemented for the off-system structures. Weathering steel, to some extent, provides a cost-effective solution in the construction of bridge structures due to its corrosion-resistant properties, yet the durability of the system is suspect in regions with high chloride deposition.

A review of existing literature revealed that a risk assessment map describing the potential for corrosion in the state's environment is needed to provide guidance to the state agency and affiliated departments on selecting proper corrosion prevention and mitigation methods for steel girders. In addition, most maintenance and repairs programs are limited to visual inspections that significantly rely on the inspector's expertise and professional judgment. Therefore, new guidelines needed to be developed and the existing standards needed to be revised to improve the results of inspections and field examinations. To that end, a new Patina Rating Index (PRI) was

developed to enhance field evaluation of weathering steel, and a lab procedure to quantitatively analyze the results of field inspections was created.

This research investigated whether corrosion prevention and mitigation methods employed in steel bridges exhibited satisfactory durability and performance. It also determined whether the performance of the mitigation techniques varies in different geographic areas with cold, arid, or humid environments. Additionally, it addresses the effectiveness of the corrosion prevention and mitigation methods in enhancing corrosion resistance of steel girders constructed in each individual county across the state, and it offers tools and guidelines that can inform the decision-making process.

1.2 OBJECTIVES AND SCOPE

The major objectives of this study are listed below:

- Review and document studies performed in the past, the state-of-the-practice, and state-of-the-art on the evaluation of corrosion prevention and mitigation approaches on steel girders.
- Utilize knowledge of worldwide field investigations for the performance of corrosion mitigation techniques applied in weathering and painted steel bridges.
- Conduct a comprehensive field evaluation study to further understand the performance of various corrosion prevention and mitigation techniques previously implemented by TxDOT, including zinc-rich primer paint systems and corrosion-resistant steel (weathering steel).
- Conduct laboratory testing to investigate the effectiveness of corrosion mitigation methods employed in steel structures and obtain better understanding of corrosion prevention and mitigation techniques.
- Update the Texas corrosion risk assessment map by considering factors such as wetness duration and effectiveness of pollutants such as airborne chloride in marine environments, deicing salt during freezing days, and sulfur dioxide deposition in industrial environments.
- Develop a decision support tool using a multidimensional, multicriterion ranking and scoring process to effectively evaluate the performance of corrosion prevention for new construction and corrosion mitigation for maintenance of existing structures.

- Develop a tool for predicting the service life of weathering steel structures based on (a) the literature review, (b) a field evaluation of weathering steel bridges, and (c) the results of laboratory testing that enables engineers to evaluate the service life of existing as well as planned weathering steel structures and develop long-term plans for maintenance and replacement of the existing inventory.

1.3 RESEARCH PLAN

To accomplish the outcome of this research study, the following tasks were conducted:

- Task 1: Project Management and Research Coordination.
- Task 2: Review State-of-the-Art and State-of-the-Practice.
- Task 3: Field Evaluation to Investigate Effectiveness of Corrosion Mitigation.
- Task 4: Perform Laboratory Tests.
- Task 5: Develop Decision Tool for Effective Corrosion Prevention and Mitigation.
- Task 6: Develop Decision Tool Projecting Service Life of Weathering Steel Structures.

This document, Volume 1 of a two-volume report, provides comprehensive findings of field inspections and laboratory testing in addition to recommendations for corrosion prevention and mitigation strategies applied to steel girder bridges.

1.4 REPORT OUTLINE

The report is divided into eight chapters. Chapter 1 describes the motivation, significance, and objectives of the research. Chapter 2 presents a comprehensive literature review on corrosion prevention and mitigation methods implemented on TxDOT steel girders. In addition, a review of new paint systems that have been applied on steel girders worldwide, or evaluated in the laboratories, were also included in this chapter.

Chapter 3 describes a corrosion risk assessment map for Texas that was developed based on environmental parameters, including average annual temperature and relative humidity (RH). These parameters were employed to predict wetness duration for a given environment across the state. Further, the assessment considered the effect of airborne chloride and deicing salt. In addition, to demonstrate the impact of industrial activities, sulfur dioxide was also included in the compilation of the final map.

Chapter 4 summarizes field inspections of weathering and painted steel. It discusses the examinations performed during the field inspection of 45 steel bridges across the state. Field evaluation of weathering steel included analyzing the state of the patina layer using a tape adhesion test, image analysis techniques, and thermal imaging. A new patina index rating is proposed that can be used for the inspection of weathering steel girders. A comparison is also given between true time of wetness (TOW) and theoretical estimation defined by ISO 9223. Field inspection of painted systems comprised visual inspection, performing field tests such as thickness measurement, and thermal imaging.

Chapter 5 presents the results of laboratory tests conducted on samples obtained from weathering and painted steel girders. Scanning electron microscopy (SEM) with energy-dispersive spectroscopy (EDS; hereafter, SEM/EDS), X-ray photoelectron spectroscopy (XPS), and X-ray diffraction (XRD) are the examinations performed on samples collected from weathering steel structures. This chapter introduces the use of ternary diagrams to identify whether the state of the patina is protective or not. SEM/EDS and optical microscopy were conducted on scraped samples from painted steel girders. This chapter also describes the extent of corrosion within the paint layers (between the primer and steel substrate) and discusses methods of identifying the coating systems implemented on steel girders.

Chapter 6 provides a description of a decision support tool that can be used for the selection of proper corrosion prevention and mitigation methods for both existing and new structures. The chapter discusses using the PRI, chloride phase ratio, and protective phase ratio to identify the durability of weathering steel girders. It also explains how to factor in the pull-off adhesion test, paint thickness measurements, and chloride concentration within painting layers to determine the durability of the painted steel structures. Another parameter that is discussed in detail is the cost of corrosion prevention and mitigation techniques. In the end, the total score, which includes the sum of durability and cost scores for each individual mitigation method, is provided in this chapter.

Chapter 7 describes theories and background required to predict the average service life of weathering steel due to corrosion attacks. It discusses the effect of corrosion fatigue on reducing the functionality of weathered components. Based on limit state function, the proposed approach estimates the average service life of weathering steel structures by considering potential mechanical failures and influential environmental factors. Five case studies are presented at the

end of the chapter to illustrate the implementation of this approach on designing new structures and estimating required maintenance and repairs.

Finally, Chapter 8 presents the summary and conclusions derived from the current research. According to the findings obtained from the study, recommendations are provided on the application of corrosion prevention and mitigation methods for steel bridge structures. Conclusions about the performance of the systems implemented on TxDOT steel girders are provided. Some recommendations for future studies are also proposed in this chapter. In addition to the above chapters, the report also has an appendix for each bridge inspected as part of this study that provides the details of the experimental results, including the field examinations and laboratory testing.

2 LITERATURE REVIEW

2.1 INTRODUCTION

Corrosion is a process involving electrochemical reactions that occur between metal and its surrounding environment that leads to the deterioration of the metal. As corrosion reactions progress, metal is converted to metal oxides. The presence of corrosive agents such as chloride and sulfur accelerate the corrosion process, causing the metal to deteriorate at a faster rate. Corrosion of steel appears in different forms that are classified into the following categories: uniform corrosion, galvanic corrosion, underfilm corrosion, pitting corrosion, intergranular corrosion, erosion corrosion, and stress corrosion.

Uniform corrosion is a consistent loss of metal thickness over the large area of a steel member, while pitting corrosion occurs as a narrow pit with a radius of equal or lesser depth. Pitting corrosion is destructive and is the most prevalent type of corrosion in steel. Crevice corrosion is a localized corrosion and can be found in narrow crevices. Galvanic corrosion occurs when two metals with different potential are in contact, thereby causing a closed circuit. Intergranular corrosion is a form of localized corrosion in which the corrosion propagates within the crystalline structure of material, and no significant corrosion occurs on other parts. Erosion corrosion happens as the surface is exposed to mechanical wear, leading to the metal loss of steel members. Cavitation corrosion is often associated with fluid dynamics conditions—such as pressure variations due to high velocities—in water turbines, propellers, and pump rotors. Another type of corrosion is fretting corrosion, which occurs at the interface of two metal components subjected to repeated relative motion. Stress corrosion cracking occurs due to an extensive amount of tensile stress and progress of pitting corrosion. Finally, atmospheric corrosion occurs when the steel member is exposed to dust and solid particles, moisture, and airborne chloride in the atmosphere.

Corrosion protection of steel girders is a complicated process because of the existence of welded sections and bolted members. The structure must be designed so that runoff water, debris, and deicing salt easily wash away from the steel surface. For example, Kogler (2015) recommended that integral abutments must be employed in steel structures instead of expansion joints to reduce the maintenance and extend the service life of steel bridges. Kogler also noted that lateral and vertical splash areas and I-shaped bottom flanges are more susceptible to corrosion and

must be adequately protected. The author specified that the destructive effect of sunlight can be a factor in diminishing the durability of coating components, and consideration should be given explicitly to fascia elements. According to this study, painted steel cannot correctly protect peripheral members such as gratings, bearings, and curbs, and the preference is to alloy those members with corrosion-resistant metals.

2.2 CORROSION IN STEEL BRIDGES

Steel bridges can be significantly impacted by corrosion, and the gradual degradation of their structural elements can lead to catastrophic failure or collapse of the system. Incidents of this nature not only result in monetary damage but also pose a significant risk to human life. Steel girders are the primary components of superstructures and are particularly vulnerable to corrosion.

Steel bridges are frequently employed in the construction of medium-to-long span structures. These types of bridges are not only cost effective, but they also reduce the weight of the overall structure, simplifying maintenance and repair procedures and expediting construction processes. There are several different classifications of steel bridges, such as rolled beam bridges, welded plate girder bridges, truss bridges, arch bridges, cable-stayed bridges, and cable suspension bridges. These structures can be further divided into three categories: uncoated weathering steel, painted carbon steel, and stainless steel bridges. Painted steel bridges are frequently constructed in regions with elevated chloride concentrations. Unfortunately, a substantial maintenance cost is required over the operational lifespan of the steel girders due to the need for regular maintenance and repainting. In addition, the cost associated with construction of steel bridges with stainless steel is also high. Therefore, weathering steel girders are commonly preferred in bridge construction. Weathering steel can resist atmospheric corrosion, which eliminates the cost associated with protective coating systems. However, the utilization of uncoated weathering steel is not advised in areas with elevated chloride concentration, such as coastal regions with substantial levels of airborne chloride and bridge structures subjected to massive amounts of deicing salt. Despite the fact that stainless steel offers excellent corrosion resistance, the high cost associated with stainless steel limits its application in primary bridge components.

Based on the inventory data provided by TxDOT (TxDOT, 2023), 110 steel bridges in Texas are classified as substandard superstructures, while an additional 544 bridges are categorized as moderate superstructures. The bridges classified as substandard indicating gradual degradation

of steel components due to corrosion and fatigue. Therefore, the utilization of corrosion prevention systems, such as galvanizing, is recommended to ensure the durability of these bridges. Figure 2.1 shows the collapse of US 35 highway bridge.



Figure 2.1. Collapse of US 35 Highway Bridge (Silver Bridge)—December 15, 1967 (WVDOT, 2023).

Inadequate mitigation of corrosion can result in structural replacement or complete structural failure if repairs are not performed on time. An example of tragic structural failure that led to the loss of 46 individuals is the collapse of a US 35 highway bridge, known as the Silver Bridge in 1967. The cause of the failure of the system was corrosion fatigue and stress corrosion cracking in the lower limb of an eyebar joint (Lichtenstein, 1993). Another example is the collapse of US 43 Chickasawbogue Creek Bridge in 1985; the steel pile failed and led to the structural collapse. The failure was due to severe corrosion and significant reduction in the cross-section thickness of the web and flanges of the steel H-piles (National Transportation Safety Board, 1986). The collapse of the Interstate Route 95 Highway Bridge as shown in Figure 2.2 in Greenwich, Connecticut, in 1983, also happened because of corrosion attacks. The suspended span of the bridge collapsed into the Mianus River as a result of lateral displacement of the hangers within the pin and hanger suspension assembly (Bell, 2022).

Steel bridges are vulnerable to corrosion despite their cost effectiveness and ease of construction. The selection of appropriate materials, implementation of effective maintenance practices, and utilization of corrosion prevention systems are essential to minimize the corrosion

initiation on steel members and improve the operational lifespan of bridges. The failure to address corrosion on steel girders can result in structural failure or collapse.



Figure 2.2. Collapse of 100 Ft Long Section of the Interstate 95 Bridge on Mianus River Greenwich, CT—June 29, 1983 (Cummings, 2017).



Figure 2.3. Collapse of IH 35 Bridge Center Section (National Transportation Safety Board, 2008).

The 2007 collapse of the I-35W bridge over the Mississippi River as shown in Figure 2.3 in Minneapolis, Minnesota provides a recent example of a catastrophic steel bridge failure. Although the National Transportation Safety Board concluded that design flaws were the likely

primary cause, yet corrosion damage was also found on critical gusset plates and may have been a contributing factor of the failure (National Transportation Safety Board, 2008).

2.3 CORROSION RISK ASSESSMENT FOR TEXAS

Trejo et al. (2009) developed an environmental characterization map to assess the level of corrosivity in all the state districts. This map was created based on environmental factors such as the annual average of temperature, the annual amount of precipitation, the yearly average RH, and total number of freeze days (FD) (Figure 2.4). The authors estimated the volume of deicing salt used on roads and airborne chloride deposition by introducing a chloride frequency factor and developed a total corrosion risk factor by summing all the individual factors for each individual district. However, the environmental characterization map proposed by Trejo et al. (2009) does not consider the effect of the TOW and the influence of industrial contaminants (like sulfur dioxide) recommended by international standards such as ISO 9223 (2012). An overlap of parameters also exists between the total number of FD and the so-called chloride frequency factor. Note that low temperature does not directly cause an increase in the rate of corrosion on steel components, but it leads to an increased demand for the use of deicing salt on the roads.

The TxDOT Bridge Division proposed the statewide environmental classification map shown in Figure 2.5 to help guide engineers to foresee proper corrosion prevention and mitigation methods in the design and construction of bridge structures (TxDOT, 2022). The guideline offers four zones for the state—mild, moderate, aggressive, and marine. These zones were designated based on historical performance of bridge structures and meteorological data. The state agency recommends districts and local authorities evaluate the use of corrosion prevention and mitigation methods employed in the bridge structures by considering environmental risks; in particular, structures located in a marine environment should be assessed on a case-by-case basis.

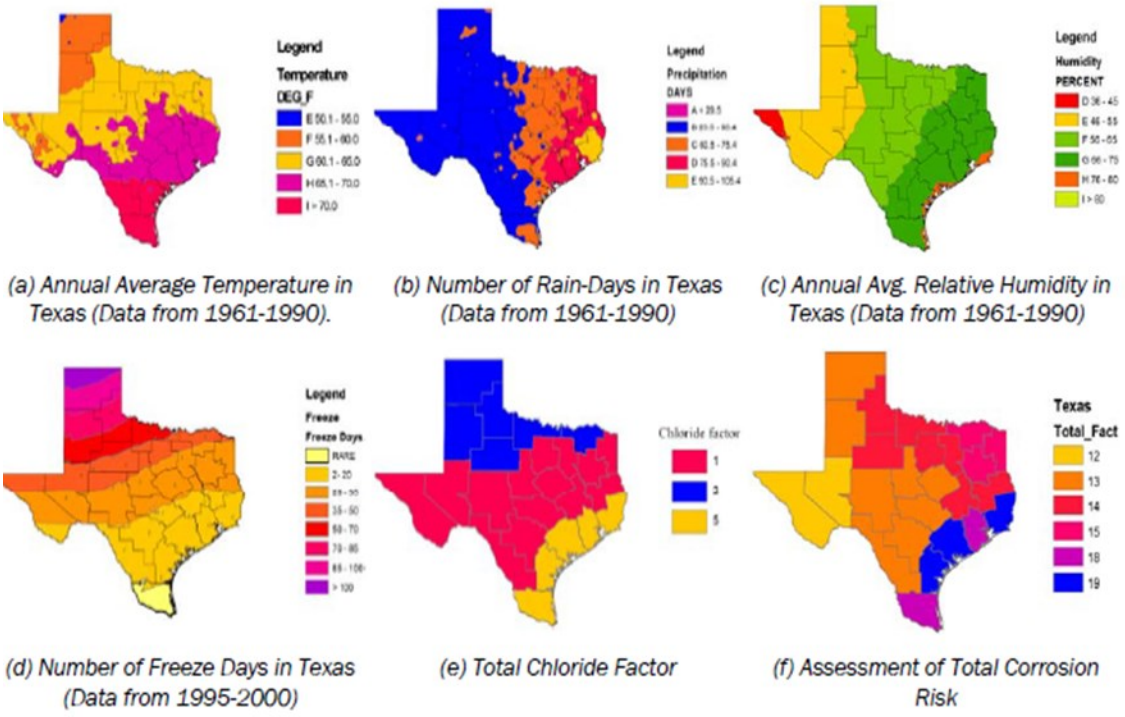


Figure 2.4. Environmental Characterization and Corrosion Assessment Maps of Texas (Trejo et al., 2009).

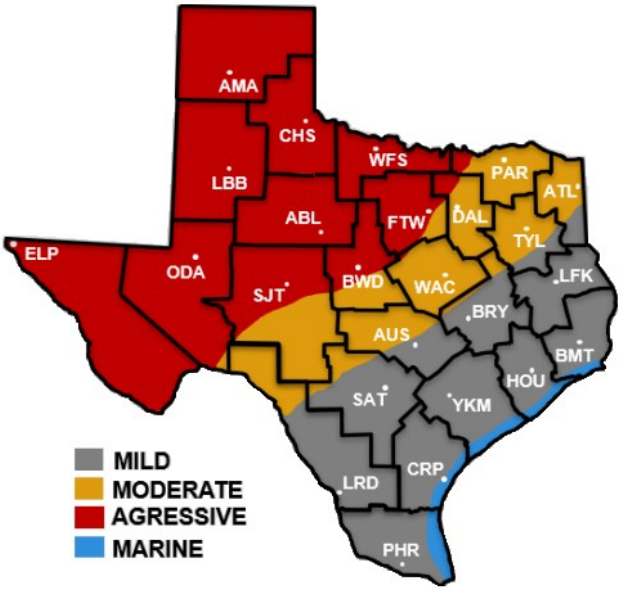


Figure 2.5. Statewide Environmental Classification Map (TxDOT, 2022).

2.4 MECHANISM OF STEEL CORROSION IN ATMOSPHERIC CONDITIONS

Steel corrosion involves an oxidation reaction (anodic reaction) and a reduction reaction (cathodic reaction). In an oxidation reaction, steel dissolves into an ionic state and releases

electrons. Simultaneously, the reduction reaction consumes free electrons. The redox reactions proceed when anodic and cathodic sites are electrically connected through electrolytes, such as a thin film of moisture.

Atmospheric corrosion is the primary corrosive process for steel bridges. It occurs when the structural elements are exposed to gaseous atmospheric substances, like oxygen, carbon dioxide, water vapor, and chlorine or sulfur compounds. This type of corrosion is highly dependent on the environmental parameters of the structure since the electrolyte is typically moist from sea spray, precipitation, fog, and other forms of moisture prevalent in the structure's location.

The reactions of the steel members at the wet surface, as described by Broomfield (2023), are:

Anodic half-cell:

$$Fe \rightarrow Fe^{2+} + 2e^{-} \tag{2.1}$$

Cathodic half-cell:

$$2H_2O + O_2 + 4e^{-} \rightarrow 4OH^{-} \tag{2.2}$$

Then, rust forms as follows:

$$Fe^{2+} + 2OH^{-} \rightarrow Fe(OH)_2 \tag{2.3}$$

where ferrous hydroxide $Fe(OH)_2$ is oxidized (iron hydroxide) and further to hydrous ferric oxide at the outer rust layer:

$$4Fe(OH)_2 + O_2 + 2H_2O \rightarrow 4Fe(OH)_3 \tag{2.4}$$

$$2Fe(OH)_3 \rightarrow Fe_2O_3.H_2O + 2H_2O \tag{2.5}$$

According to Saha (2012), rust is transformed into crystalline compounds such as hematite, magnetite, and oxyhydroxides (FeOOH) in weathering steel. The mild layer of rust cannot protect structures since it is porous, and air and water can easily penetrate the protective layer. Nevertheless, alloying weathering steel with metals like Copper (Cu), Phosphorus (P), Chromium (Cr), and Nickel (Ni) can alter the oxyhydroxide rust layer, preventing oxygen attacks and helping in the formation of a deep and protective rust layer, which is adhered to the steel substrate. Note

that the particle size distribution of FeOOH in the rust of weathering steel is continuous (Kamimura et al., 2006).

Moisture and RH are the most crucial elements that influence atmospheric corrosion. The basic humidity level for steel in an unpolluted atmosphere is 60 percent. As the RH exceeds this threshold, corrosion increases due to a moisture film appearing on the metallic surface and produces countless galvanic cells. Schindelholz et al. (2014) advised a lower critical humidity for steel structures in maritime environments because salt crystals deposited on steel surfaces can absorb water, function as an electrolyte, and cause pitting corrosion.

Chlorides can reduce the protection of corrosion product film. The chloride in the atmosphere depends on the distance to the seacoast, the season, and the strength of the prevailing wind. The effect of chloride on steel is most severe in areas located 0.3–0.6 mi (0.5–1.0 km) from the coastline. Steel also reacts with sulfur dioxide in the atmosphere, produced by fossil fuel combustion in industrial areas, and forms ferrous sulfate. Sulfur dioxide can accelerate corrosion by impairing the protective nature of the rust films by forming ferrous sulfate nests (Revie, 2011).

2.5 CORROSION PROTECTIVE SYSTEM

Preventing or mitigating corrosion on steel components in bridge superstructures is a significant challenge for state transportation agencies. Implementing strategies to extend the service life of steel girders can be critical and expensive. As such, it is imperative to adopt cost-effective materials and maintenance practices to delay the onset of bridge corrosion in different environments. The performance of a corrosion protection system depends on micro- and macroenvironmental exposure conditions that can be classified into three types: mild or rural (having little to no exposure to natural airborne or deicing salts), moderate or industrial (having some instance of exposure to airborne or deicing salts), and severe or marine (high salt concentration from proximity to the seacoast or from deicing salts and high humidity and moisture). The microenvironment depends on the material, configuration, orientation relative to runoff, and exposure to direct sunlight. Corrosion protection for steel bridges includes zinc-rich primer paint systems, thermal spray metalizing, hot-dip galvanizing, and corrosion-resistant steel (weathering and stainless steel).

Climate and exposure regions vary significantly in the United States in terms of humidity, temperature, pollution, airborne Chloride and ultraviolet radiation from the sun. Thus, the

effectiveness of structural steel protection systems (protective coating systems or corrosion-resistant alloys) will depend on site conditions. The performance of corrosion protection systems is directly influenced by the macroenvironment (mild, moderate, and severe) and microenvironment. The macroenvironment includes local weather conditions, such as rainfall, and contaminant levels, such as chloride and sulfur dioxide. The microenvironment includes material, configuration, and orientation relative to runoff and exposure to direct sunlight. Thus, the selection of a corrosion protection approach for steel girders is determined based on cost, fabrication, and expected maintenance. Corrosion protection methods can be classified into two groups:

1. Surface physical modification or surface treatment (zinc-rich primer paints, metalizing, and galvanizing).
2. Steel chemical modification or corrosion-resistant steel (weathering and stainless steel).

2.5.1 Surface Physical Modification or Surface Treatment

2.5.1.1 History of Used Paint System

In Texas, the paint system has evolved over the decades from lead and aluminum-based paint system to zinc and epoxy-based paint system to achieve better performance, durability, aesthetics, and less health risk while application and maintenance repaint.

The 1952 specifications mention the use of red lead paste and aluminum paint coats for application on steel bridges. The red lead paste contained 92–94 percent red lead and 6–8 percent linseed oil which acts as a corrosion resistant filler that adhered well to the steel surface. Aluminum based paint system was composed of aluminum pigments suspended in oil or solvent based binders and was used for uniform color appearance (TxDOT, 1952). The application techniques used for painting applications were spray, brush, and roller method of painting. In 1962, the paint systems specified became more complex with an addition of new zinc-based paint system containing Organic zinc-rich primer (OZ) coat formed by mixing zinc dust in organic binder. This coating provided superior corrosion protection due to its sacrificial nature of zinc. The specification also mentions the color of appearance coat that were used. The color used were metallic (Aluminum and oil-based paint), gray, and green (TxDOT, 1962).

The 1972 specifications brought several changes for example, the application of different paint system were categorized based on blast-cleaning classes, Aluminum coat could be either slow dried or fast dried, color used for paint pigments were gray green, and metallic (Aluminum),

and use of weathering steel was mentioned as a separate category which did not required painting due to its inherent corrosion resistance (TxDOT, 1972). The 1982 paint specifications had the same general information about the different corrosion protection paint system except that each paint system was customized to address different protection needs depending on the severity of the environment (TxDOT, 1982).

In the 1993 specifications a comprehensive approach regarding all the paint system was listed. The type of primer coat, thickness and paint specifications varied based on the required protection level. The specification also lists urethane-based paint (concrete gray color) as appearance coat to maximize protection, durability, and aesthetics. The paint systems included zinc and aluminum as sacrificial coating to improve corrosion resistance of the steel. The standards also mentioned that weathering steel should be left uncoated unless specified in the plan (TxDOT, 1993).

Table 2-1. Evolution of Paint System Used in Texas.

Time Period	Paint Colors	Primary Pigments	Key Developments
1952	Red Lead, Aluminum	Red Lead, Aluminum Pigments	Introduction of basic red lead paste and aluminum coatings, applied via spray, brush, or roller.
1962	Aluminum, Green, Gray, Brown	Aluminum, Zinc, Resins	OZ-rich prime coats; resin-based appearance coats in diverse colors; various application methods.
1972	Aluminum, Green, Gray, Weathering Steel	Aluminum, Zinc	Categorization based on blast-cleaning classes; weathering steel recognized for its natural corrosion resistance.
1982	Aluminum, Green, Gray	Aluminum, Resins	Refinement of prime coat systems based on blast-cleaning classes; expansion of appearance coat options.
1993	Aluminum, Green, Gray, Concrete Gray (Urethane)	Aluminum, Zinc, Urethane	Specific prime coat systems with tailored paint types; introduction of concrete gray urethane appearance coat.

Kline (2008) documented the historical development of paint systems employed on steel bridges. According to the author, lead-based paint was initially utilized as the primary form of coating for the purpose of preventing corrosion. Lead-based pain systems were the predominant coating applied to steel bridges starting in the late 19th century. These systems contained lead and chromium pigments that helped prevent corrosion by passivating the steel surface. Lead-based paints were low cost, easy to apply, and adhered well to mill scale on the steel. However, they had

a relatively short lifespan when exposed to harsh environments, particularly a thicker coating would make the paint system brittle. Moreover, lead is toxic, and its application declined overtime. This concluded to use more advanced coating systems to protect steel bridges.

During the 1970s, there was a notable shift toward the adoption of zinc-rich systems, which subsequently emerged as the prevailing industry norm for protecting steel against corrosion. The paint system consisted of a primer with a high zinc content subsequently followed by several layers of coating. The zinc-rich primer applied on steel as a sacrificial anode, providing galvanic protection to the steel substrate. The subsequent topcoats also provided a protective barrier for the primer, effectively preventing its exposure to the surrounding atmosphere. According to Kline (2008), zinc-rich systems can benefit to protect steel girders, such as extended durability, enhanced functionality in challenging conditions, and decreased toxicity, in comparison to lead-based paint. (Kline, 2008).

Currently, zinc-rich systems remain the prevailing paint system for steel bridges. These systems offer a variety of coating types that can effectively protect steel substrate in different exposure conditions and service environments. The coatings encompass a range of materials such as epoxies, polyurethanes, polysiloxanes, fluoropolymers, acrylics, and various others. Kline (2008) noted that there is still an ongoing debate among experts regarding the most suitable type of coating for different circumstances. Additionally, there is a lack of comprehensive and extensive field data regarding the long-term effectiveness and durability of coatings, and additional research is required to obtain the targeted 100-year service life for steel bridges through coating. Lead-based paint coatings were commonly used on steel bridges in the early 20th century. However, concerns raised about their environmental and health impacts.

Paglia et al. (2021) investigated the condition of lead-painted steel bridges by conducting mechanical, chemical, and visual evaluations of the steel and coatings. The steel primarily displayed superficial, uniform corrosion, and some areas showed more advanced corrosion from moisture and organic buildup. The authors concluded that the lead-based coatings demonstrated reasonable durability over time. However, they reported that these paint system should be replaced with modern, safer coating systems which will address environmental and health worries while maintaining bridge integrity (Paglia et al., 2021).

2.5.1.2 Protective Mechanism of Anticorrosive Coatings

Anticorrosive coatings can be classified in three protection systems: *barrier coating*, *inhibitive coating*, and *sacrificial coating*. Barrier coating prevents reactions of corrosive agents with steel substrate. Inhibitive coating provide protection by interacting with the surrounding environment, forming a protective film or barrier on the metal surface. Inhibitive pigments, commonly inorganic salts with slight water solubility, are frequently employed in this type of coating. Sacrificial coating protects steel substrate by utilizing the principle of galvanic corrosion (Sørensen et al., 2009; Faccini et al., 2021).

2.5.1.3 Zinc-Rich Primer

Zinc-rich primer-based coating has been used on most paint-steel bridges in the United States. The zinc-rich primer coating can be organic zinc (OZ) or inorganic zinc (IOZ) that is a type of sacrificial cathodic protection typically consisting of two or three layers of paint with the primer coat. OZ primers are made by mixing zinc metal pigment into organic resin, epoxy, or urethane, while IOZ primers are made by mixing zinc metal powder and inorganic silicate paint binder such as ethyl silicate (solvent-borne) or alkali silicate (waterborne). The durability of zinc-rich primer depends on surface preparation, adherence to mixing, and curing conditions.

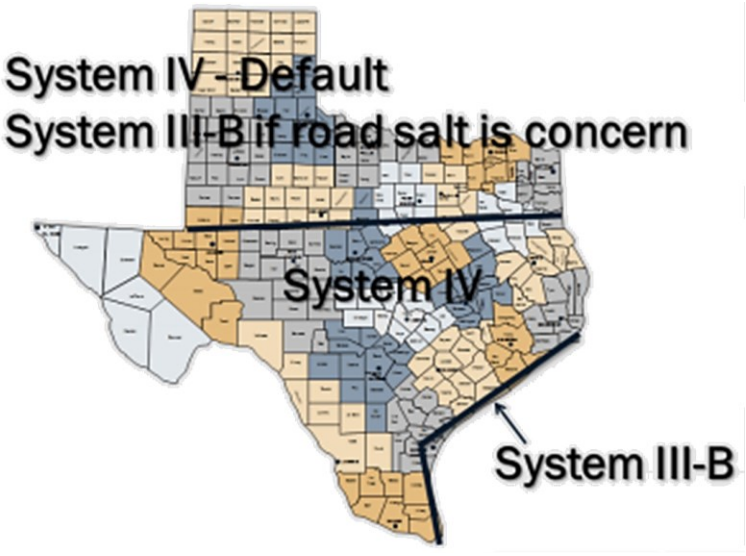
TxDOT uses the following standard paint systems for painting new and existing steel bridges. The primer and appearance coats for Systems I and II must meet Department Materials Specification D-9-8100:

- System I-A (Overcoating, One Coat): The system consists of one coat of overcoat applied with at least 4 mils dry film thickness (DFT) to all surfaces.
- System I-B (Overcoating): The paint system is a 3-coat system that applies 0.5–1.0 mils DFT of penetrating sealer, 4.0–8.0 mils DFT of epoxy intermediate primer, and 2.0–6.0 mils DFT of polyurethane appearance coat to all painted surfaces. The paint system I-B was the preferred choice in a highly corrosive environment.
- System II (Field Painting): This paint system is a two-coat system composed of primer and appearance coats. The primer coat contains an application of organic zinc (OZ) primer of 3.5–10.0 mils thickness in at least two coats, while the appearance coat consists of 2.0–5.0 mils of acrylic latex. The system is the default paint system widely used for field painting steel bridges all over Texas except in coastal regions.

TxDOT uses more extensive paint coating systems classified as Level III. Paints for System III shall agree with D-9-8101. Provided below are the explanations of the System III coating:

- System III-A (Field Painting): The paint system is three coats consisting of a primer coat containing epoxy zinc of at least 3.5 mils DFT, a stripe coat of intermediate epoxy coating (which is usually not counted as part of the coating system), an intermediate epoxy coat of at least 2 mils DFT, and a polyurethane appearance coat of at least 2 mils. This paint system is applied in field painting of coastal bridges and to bridges experiencing corrosion due to deicing salts.
- System III-B (Shop Painting): The paint system consists of IOZ primer of at least 3 mils DFT, a stripe coat of intermediate epoxy coating, an intermediate epoxy coat of at least 2 mils DFT, and a polyurethane appearance coat of at least 2 mils DFT. The paint system finds application in shop painting of new steel bridges intended for use in coastal regions and regions where corrosion from deicing salt is an issue.
- System IV-A (Shop Painting): The paint system consists of an IOZ primer coat of at least 3 mils DFT and an acrylic latex appearance coat of at least 2 mils DFT. The paint system is used in shop painting of new steel bridges and is not suitable for bridges located in the coastal regions.

Figure 2.6 and Figure 2.7 show the recommended paint systems for new construction and existing structures, respectively.



3

Figure 2.6. Paint System Recommendation for New Construction (Texas Steel Quality Council, 2000).

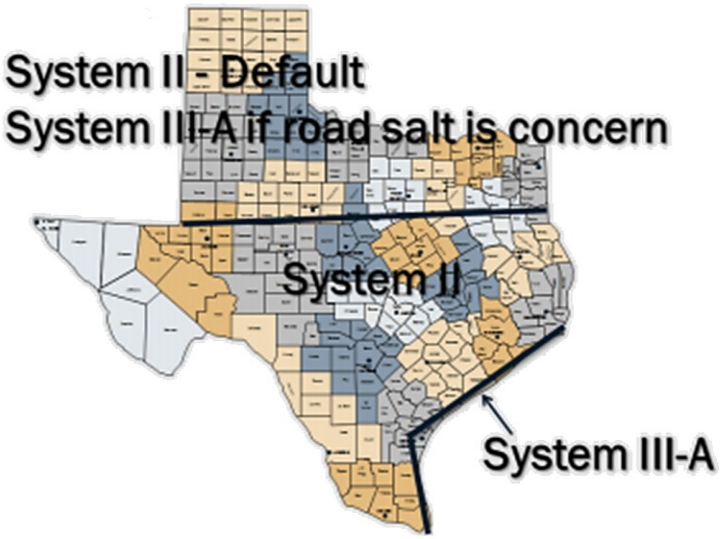


Figure 2.7. Paint System Recommendation for Field Painting for Existing Structures (Texas Steel Quality Council, 2000).

Three-coat systems have improved corrosion resistance of steel bridges across the nation. However, demand for superior and more economical paint systems has led to the development of two-coat paint systems with similar performance and lower cost. Although zinc-rich primer systems offer reliable corrosion protection, they come with certain limitations, such as the drying and curing time of each individual coat (Munger et al., 2022). These limitations increase the fabrication costs of steel members and make them vulnerable to contamination in both the shop and field environment. Therefore, coatings requiring less drying and curing time are desirable.

While coating can provide perfect adhesion to the substrate, improper surface preparation can lead to delamination of the coating layers (Jamali & Mills, 2014). Hence, the protective coating system is less effective on weathering steel exposed to some extent of corrosion because the surface cleaning techniques cannot completely remove corrosive agents such as chloride contaminants from the bases of pits in the steel (Appleman et al., 1995).

2.5.1.4 Thermal Spray Metalizing

Thermal spray metalizing is a form of the sacrificial cathodic process to provide bridge corrosion protection. The process involves melting pure zinc—or an alloy that has 85 percent zinc and 15 percent aluminum—using a heat source and spraying the molten metal onto the target surface (steel surface). As the molten metal hits the surface, it solidifies and forms a hard sacrificial metal coating. The coating consists of a series of overlapping *splats* of metal. Kogler (2015) noted

that several concerns have held back the use of metalizing in the bridge industry. Some concerns include the cost and productivity of the metalizing process.

The metalizing application is not very complex, yet it does require expertise and a heat source to produce an excellent protective coating. The rate of the metalizing application (100–200 sq ft per man hour) is slower than spray painting (1000 sq ft of surface per man hour) (Ault & Farschon, 2009). In the case of multiple coats (typically three), the metalizing and painting application rates are similar because of the coating curing time. Kogler (2015) noted that the thickness of the coating is directly related to its service life. The author also suggested a thick coating because metalizing is a porous coating. Achieving a sufficient coating thickness is essential for an effective corrosion protection system. The American Welding Society (1993) recommended no less than a sealer coat and often a sealer and finish coat over metalizing to enhance the system's durability in a marine environment. A sealer coat is a low-viscosity epoxy or urethane applied on the metalizing layer, while a sealer and finish coat are an epoxy midcoat with a polyurethane topcoat.

2.5.1.5 Hot-Dip Galvanizing

Mechanically deposited galvanizing, *continuous (sheet) galvanizing*, and *hot-dip galvanizing* are three forms of the galvanizing process. All these processes deposit a continuous layer of pure zinc on the steel surface. In mechanical galvanizing, a thick zinc coating is applied over steel at room temperature. However, this process is limited to a steel fastener, while continuous galvanizing is durable and used in automobiles and other industries.

Hot-dip galvanizing is a process of soaking steel components in several baths to achieve a pure zinc layer on the surface of the substrate. These steps include *degreasing and rinsing*, *pickling and rinsing*, *flux solution*, *drying*, *zinc bath*, and *cooling and inspection*. The steel component is immersed in molten zinc with a temperature ranging from 820 to 900°F. Due to heat, a metallurgical bond develops between the steel, zinc, and a layer of sacrificial coating. The hot-dipped galvanizing process cannot be deployed in the field. Another drawback to hot-dip galvanizing is that the designer could not specify the desired coating thickness of the hot-dipped galvanized component because the thickness and composition of zinc layers depends on the steel chemical composition, as noted by Kogler (2015).

Galvanizing reactive steel consists of silicon (Si) levels in a range from 0.04 percent to 0.15 percent or even above 0.22 percent. The problem associated with such steel is that the entire galvanized layer is composed of a zinc/iron intermetallic that may be very thick (10 mils) and brittle. However, the layer thickness is around 4 mils thick for nonreactive steel because the intermetallic forms with a gradient in zinc/iron ratio. The ratio is nearer to the steel surface and decreases through the thickness of the outer layer, which becomes pure zinc. ASTM A123 provides the minimum thickness criteria for various classes of material and recommends a minimum galvanized coating of 3.9 mils for steel bridges (ASTM A123/A123M, 2017).

The durability of galvanized steel in a corrosive environment is directly related to the thickness of the zinc coating, and the service life of the system ranges between 15 years for an aggressive industrial environment and 780 years for a rural environment. Zinc has quite a slow corrosion rate in most natural environment conditions, but it can increase from 0.1 to 0.4 mils per year (mpy) or to as high as 0.5 mpy in a humid and salt-rich environment. Additionally, microenvironmental factors may extremely influence the durability of the coating (Kogler, 2015).

Topcoating after galvanizing provides extra corrosion resistance and enhances the durability of the system. However, errors made in surface preparation can result in poor performance. Therefore, the specification of the topcoat of paint over hot-dip galvanizing must follow ASTM D6386 (2022).

2.5.2 Steel Chemical Modification or Corrosion-Resistant Steel

Corrosion-resistant steel is another option to protect steel bridge structures from corrosive environments. The typical selections for corrosion-resistant steel are stainless steel and weathering steel. The use of stainless steel in steel bridges is relatively low due to its high cost and the difficulty of welding components. However, weathering steel is the most common corrosion-resistant steel in North American steel bridges because it is a cost-effective solution for structural steel corrosion resistance.

Weathering steel is an alloy of copper (Cu), Cr, nickel (Ni), and other metals. After exposing the metal to air, a dark-brown protective oxide rust appears on the steel surface that adheres to the substrate and inhibits further corrosion. Three common types of weathering steel utilized in the industry are ASTM A242, ASTM A588, and ASTM A709. Developing a durable

patina can take six to 24 months depending on moisture, RH, and climatic conditions (ASTM A242/A242M, 2018; ASTM A588/A588M, 2019; ASTM A709/A709M, 2021).

Although weathering steel bridges are suitable for most places, they may not function well in extreme settings such as harsh coastal environments, continually wet and dry climates, and some harsh industrial environments. Stephens et al. (2019) recommended avoiding these conditions or applying zinc-rich primer coating to boost the corrosion resistance of such bridges. Kogler (2015) highlighted the utilization of weathering steel in bridge superstructures because of the steel superior corrosion resistance compared to carbon steel. However, proper detailing, surface preparation, and maintenance procedures are essential to ensure optimal performance in different corrosive environments.

TxDOT conducted a study in 2000 to evaluate weathering steel performance. The study revealed that uncoated weathering steel is an excellent material for steel bridge construction because it forms a protective oxide film that prevents further corrosion. However, concerns have been raised and reported regarding the use of uncoated weathering steel in coastal areas with high salt concentrations or in regions where deicing salt is frequently applied. McDad et al. (2000) suggested sandblast cleaning and removing the accumulated dirt and salt from all exterior surfaces, including the underside of the bottom flange of beams and bent caps. They advised applying a suitable coating system to weathering steel in areas where the surface may come in contact with standing water. Corrosion protection coating systems were also recommended for steel embedded in soil or a gravel pocket.

2.5.2.1 Historical Use of Weathering Steel

Weathering steel has been the prevalent material in the construction of steel bridges across the United States since the mid-1960s. It can generate a protective surface layer that delays corrosion and eliminates repainting of steel girders, thereby potentially resulting in substantial savings in life-cycle expenses. If weathering steel alloys with Cu, Cr, Ni, and Si, it can provide superior resistance to atmospheric corrosion (Albrecht & Naeemi, 1984).

Four types of weathering steel that are commonly utilized in the construction of steel bridges are ASTM A242, ASTM A588, ASTM A709, and ASTM A852. ASTM A242 steel was first introduced in 1941 and is classified in two grades. Type 1 has a nominal yield strength of 50 ksi, with a minimum Cu content of 0.20 percent, while Type 2 also has a nominal yield strength

of 50 ksi but has a higher minimum Cu content of 0.40 percent. Type 2 exhibits lower phosphorus (P) and sulfur contents than Type 1, thus enhancing its toughness and weldability. Type 1 is commonly used for architectural purposes, whereas Type 2 is more suitable for bridges.

ASTM A588 steel was developed in the late 1960s. The steel provides higher strength and better corrosion resistance than A242 steel. It consists of five grades: A, B, C, D, and E, each with a nominal yield strength of 50 ksi and a minimum Cu content of 0.20 percent. Grade A is common in construction of steel bridges. Fraction of P content is more in grade B that improves the steel weldability and toughness. Grade C contains lower carbon content, so it is improving the weldability and notch toughness of the steel. Grade D has higher Ni content, thus enhancing corrosion resistance in marine environments. Finally, Grade E contains Cr and Si contents, thus improving corrosion resistance in industrial environments.

ASTM A709 steel is a general specification steel for bridge construction that consists of carbon, high-strength low-alloy, and quenched and tempered alloy steel. ASTM A709 steel comprises eight grades. Grades 36, 50, and 50S are ordinary carbon steel lacking enhanced atmospheric corrosion resistance. Grades 50W and HPS50W are weathering steel corresponding to A588 Grade A and a modified A588 Grade B, respectively. Grades HPS70W, 100, and 100W are quenched and tempered alloy steels that provide higher yield strengths than weathering steels but exhibit lower corrosion resistance (Albrecht et al., 1989).

ASTM A852 steel represents a novel specification consisting of quenched and tempered high-strength low-alloy structural steel plates designed for welded bridges. It features one grade with a nominal yield strength of 70 ksi and a minimum Cu content of 0.20 percent. The specification allows for Cr, Ni, Si, vanadium, and columbium variations within specified limits, offering flexibility in chemical composition and enhancing durability of the metal.

Albrecht et al. (1989) reported that most DOTs utilizing weathering steel in bridge structures have established their own design criteria to enhance corrosion performance of the system. These criteria include limiting weathering steel to rural areas, avoiding using it in construction in coastal areas and heavily salted highway environments, painting joints, conducting blast cleaning of steel before erection, implementing effective drainage systems, safeguarding concrete against rust staining, galvanizing scuppers, using bearings and expansion devices, and avoiding the use of hinges or sliding plates.

In Europe, the decision to utilize weathering steel in construction of steel bridges depends on the location of the structure, and it is not common in marine, industrial, or humid environments. The erosion performance of weathering steel in Europe is commonly better than in the United States due to lower levels of air pollutants and increased sun exposure. In Germany, for example, weathering steel was almost entirely prohibited in 1979 for bridges on the federal system because of concerns about corrosion and inspection. Only two exemptions were granted for composite girder bridges over electrified railways. The German specifications categorize the environments according to their corrosiveness and suggest minimum thicknesses and inspection intervals for weathering steel (Albrecht & Naeemi, 1984) .

In Japan, a total of 115 weathering steel bridges were built before 1979, out of which only five bridges were not painted. The primary incentive for employing weathering steel was to extend the life of the system in industrial and coastal areas with high humidity and rainfall. The Japanese experience of using weathering steel in the construction of steel girders shows that meticulous design and selective use of protective coatings can overcome the negative effects of marine exposure on weathering steel (Albrecht & Naeemi, 1984).

2.5.2.2 Unsatisfactory Performance of Weathering Steel

Multiple factors such as a humid environment, industrial contaminants, and the application of deicing salts can contribute to the unsatisfactory performance of weathering steel bridges. In marine environments, salt particles in the air or mixed with water accelerate corrosion rates in such a humid environment that it can lead to break protective oxide layers. The duration of moisture films on steel surfaces (TOW) affects oxide formation and increases the rate of redox reactions on steel surfaces. Industrial contaminants, such as sulfur dioxide and acids, disrupt oxide formation and cause accumulation of deposits and stains on weathering steel; consequently, bridges near industrial plants or urban areas are at greater risk of industrial corrosion. Deicing salt that is employed to melt ice on roadways can also contaminate weathering steel bridges with chloride ions and increase the rate of corrosion. Bridges on heavily salted highways or with poor drainage systems are more susceptible to corrosion as a result of deicing salt applications. Other factors that can also contribute to unsatisfactory performance of weathering steel include water leakage in expansion joints, mill scale pitting, poultices, crevices in bolted connections or welds, in addition to contamination during shipping and storage.

When RH is greater than a critical value, the corrosion rate of steel increases. The rate is also influenced by the concentration of pollutants and contaminants deposited on steel surface. For example, the rate of corrosivity in rural areas with a low-level-aggressive pollutant environment is high when RH exceeds 70 percent. However, the rate increases when RH exceeds 60 percent in industrial areas, with atmospheric pollutants like sulfur and nitrogen oxides. This is because of the formation of acidic solutions from anions dissolved in moisture films. The marine environment also accelerates the corrosion process of steel due to the deposition of airborne chloride, which can break the protective oxide layers. Marine environments are highly corrosive, especially in regions with high humidity and rainfall (Albrecht & Naeemi, 1984; Albrecht et al., 1989).

Microenvironmental factors influence atmospheric corrosion of steel girders. The initial climatic conditions during installation, including exposure to sea salt spray, can impact corrosion behavior. It can be argued that the location of steel surfaces also contributes to the rate of corrosion. In general, it is expected that south-facing surfaces experience less corrosion than north-facing or sheltered surfaces. Other factors such as the exposure angle of sunlight and wind relative to the horizontal, proper drainage, and rain washing can influence the rate of corrosion. The accumulation of salt and debris on steel surfaces traps moisture and increases the TOW, essentially increasing the rate of corrosion.

2.5.2.3 Weathering Steel Alloy and Its Effect on Corrosion Resistance

Metallic components that significantly enhance weathering steel properties and its ability to resist corrosion are Cu, P, Cr, Ni, and Si. These elements promote the generation of amorphous substances within the inner rust layer, which consequently results in decreasing the rate of reactions between iron ions and water and oxygen compounds, which are effective factors in the corrosion process. A stable Cu-oxide or hydroxide acts as a barrier against further oxidation and improves the corrosion resistance of weathering steel. It promotes formation of a compact and adherent rust layer that diminishes the permeability of water and oxygen. The optimal Cu amount in weathering steel varies from 0.2 wt.% to 0.5 wt.%. P increases corrosion resistance of weathering steel. Phosphoric oxide or hydroxide interacts with iron and generates stable compounds that can protect steel substrate from aggressive environment. The P substances in weathering steel ranges from 0.03 wt.% to 0.15 wt.%. Cr also improves the corrosion resistance of weathering steel by producing a protective layer of Cr-oxide or hydroxide. This layer acts as a

barrier against further oxidation and improves the hardness and wear resistance of weathering steel. The Cr fraction in weathering steel typically ranges between 0.5 wt.% and 1.5 wt.%. Ni is also an element that increases the corrosion resistance of weathering steel. The Ni-oxide or hydroxide interacts with iron to produce a stable compound and enhances the toughness and ductility of weathering steel. Corrosion resistant steel often contains of 0.5 wt.% to 1.5 wt.% of Ni substances. Although Si does not directly enhance the corrosion resistance of weathering steel, a silica gel or oxide can react with iron and produce stable compounds. Weathering steel typically contains 0.25 wt.% to 0.75 wt.% of Si (Albrecht & Naeemi, 1984; Albrecht et al., 1989).

Extensive research has been conducted on the impact of alloying elements on the corrosion resistance of weathering steel. Liu et al. (2019) suggested that the addition of cerium (Ce) and lanthanum (La) to weathering steels leads to significant improvements in corrosion resistance of the steel, particularly pitting corrosion resistance. These elements facilitate the formation of protective oxyhydroxides like goethite within the rust layer. The protective phase of iron oxide enhances the adhesion and compactness of the patina (the rust layer) and blocks penetration of corrosive ions (Liu et al., 2019).

Cano et al. (2014) examined the impact of alloying elements on the corrosion resistance of weathering steel. The authors reported that a Ni content ranging from 1 wt.% to 3 wt.% in weathering steel enhances its resistance to corrosion in marine environments due to the formation of nanophase goethite in large volume, or combined with ferrihydrite and low crystallized maghemite, in the inner rust layer. The authors also suggested that Cr alloyed with weathering steel improves corrosion resistance by accumulating within the inner rust layer and subsequently forming dense oxide layers consisting of Cr-goethite. However, Cano et al. (2014) observed that Cu expedites the process of development of an oxide layer, particularly during the initial phases of atmospheric corrosion.

Hou and Liang (1999) conducted a comprehensive investigation on atmospheric corrosion effects on weathering steel. The researchers concluded that the inclusion of Cu and P alloying with iron significantly enhances the corrosion-resistant properties of weathering steel. Additionally, alloying elements such as Cr, Mn, Mo, and Ni with iron improve the corrosion resistance of weathering steel through the formation of a durable rust layer. The corrosion resistance of weathering steel is minimally influenced by carbon, manganese, and silicon, with their primary impact being on the mechanical properties and weldability of the steel (Hou & Liang, 1999).

Wu et al. (2020) examined the impact of different alloys, with a specific focus on Ni, on the corrosion resistance of weathering steel in a tropical marine environment. The researchers concluded that weathering steel containing 3 percent Ni demonstrated great corrosion resistance, and corrosion product films are superior in comparison to both conventional weathering steel and carbon steel. The refined crystal phases observed in the inner corrosion product film can be attributed to the presence and aggregation of $NiFe_2O_4$. This aggregation led to the transformation of γ-FeOOH into fine-grained α-FeOOH. Additionally, the formation of an electronegative inner layer due to the presence of $NiFe_2O_4$ effectively hindered the penetration of chloride ions. The research findings indicate that the addition of Ni as an alloying element significantly improves the ability of weathering steel to resist corrosion in marine environments. The study suggests that a Ni content of 3 percent is the most effective concentration for achieving optimal corrosion resistance (Wu et al., 2020).

Morcillo et al. (2013) reviewed studies have been conducted on atmospheric corrosion and its effect on weathering steel. The authors emphasized the influence of alloying elements such as Cu, Cr, Ni, P, Si, and Mn on the corrosion resistance of weathering steel. According to Morcillo et al. (2013), Cr and Ni enhance the adhesion and protective characteristics of this rust layer. The existence of P within steel components affects the structure and arrangement of the rust layer, while Si improves resistance against oxidation and increases susceptibility to pitting corrosion. Additionally, manganese contributes to both the mechanical properties and resistance to atmospheric corrosion of the steel.

Cheng et al. (2017) examined the impact of different alloy elements, such as Ni, on the corrosion resistance of weathering steel in acidic environments. The researchers reported inclusion of Ni in weathering steel resulted in enhanced corrosion resistance. Specifically, a Ni content of 3.5 wt.% was the most effective in acidic environments and was found to enhance the initiation of $Fe(O,OH)_6$ (Iron(III) oxide-hydroxide) nano-network, promote the development of a dense rust layer, impeding the expansion of Fe_2NiO_4 (Iron nickel oxide). Moreover, the addition of Cu and Cr has been observed to improve the ability of weathering steel to resist atmospheric corrosion. This feature is achieved by promoting the development of a protective rust layer and the formation of spinel oxides within the rust layer, respectively.

The corrosion behavior of weathering steel and Ni-advanced weathering steel (NAWS) in a tropical marine atmosphere was studied by Wu et al. (2018). The corrosion rate of NAWS was

lower than ordinary weathering steel, although its corrosion potential was found to be higher. NAWS provides fine-grained goethite with less lepidocrocite and akaganeite; the product is a dense film and free from cracks. Ni was found to positively impact refining the grain structure, facilitating the conversion of lepidocrocite to goethite, and preventing chloride ions from penetrating the inner film. These effects collectively led to an improvement in corrosion resistance (Wu et al., 2018).

Diaz et al. (2013) highlighted the significant impact of alloying elements with iron to increase the corrosion resistance of weathering steel, with particular emphasis on the role of Ni. The researchers reported that Ni promotes the development of nanophase goethite, which functions as a barrier within the inner rust layer. In addition, Ni alters the surface charge of rust, thus hindering the ingress of chloride ions and reducing the likelihood of pitting corrosion. The corrosion rate of weathering steel exhibited a downward trend as the Ni content was elevated from 1 percent to 3 percent.

The influence of Cr content on the electrochemical behavior of weathering steels was investigated by Qian et al. (2013). The steel ability to passivate and resist corrosion can be enhanced by Cr. Steel with an elevated level of Cr demonstrated passivation characteristics and reduced corrosion current density. Introducing pre-rusting to steels with elevated Cr content led to notable changes in polarization behavior and improved corrosion resistance, which can be attributed to forming a rust layer consisting of a higher fraction of goethite. Other studies (Chen et al. (2005); Raja et al. (2021); Cano et al. (2018)) also concluded that Ni and Cr enhance the corrosion resistance of weathering steel. McCuen and Albrecht (2005) developed an exponential model designed to predict the thickness loss of weathering steel, considering factors such as alloy composition and duration of exposure. The authors found that Cu can have significant impact on improving corrosion resistance, although its effectiveness decreases with higher Cu concentrations. Ni, Cr, and Si decreased the thickness loss, whereas P did not demonstrate a notable impact.

In another research, Townsend (2001) studied the effect of different alloying elements on the corrosion performance of weathering steel in industrial environments and concluded that the addition of alloying element P considerably increased corrosion resistance. Improving corrosion resistance was observed by alloying weathering steel with elements such as Si, Cr, Sn, while C, Cu, and Ni also showed improvement in material properties. Further, the study argued that no

reliable conclusion regarding corrosion resistance could be made for elements like vanadium, manganese, aluminum, cobalt, arsenic, and tungsten. In a different research (Wang et al., 2021), the impact of alloying elements like Cu and P on the initial rust composition was studied in a simulated environment which showed that Cu had an exceptional influence on reducing the anodic and cathodic reduction reactions that encourages the development of goethite within the internal rust layer. Moreover, a lower corrosion rate was observed if both Cu and P were present as alloying element in the steel because they of their combined effect on the dispersion of goethite within the inner rust layer.

In a review paper on weathering steel, Morcillo et al. (2019a) compared the performance of weathering steel with carbon steel and the study showed enhanced corrosion performance due to use of several alloying elements like Cu, Cr, Ni, P, and others which helps in the formation of protective rust layer containing goethite that protects the steel substrate. Moreover, the authors further explored and explained the reason for enhanced corrosion resistance because of addition of chromium element. The study found that adding chromium in small amounts helped in development of patina layer made of nanoparticles of Cr-substituted goethite which blocks aggressive anions like chloride and sulfate effectively from contacting the steel surface.

The corrosion behavior of three weathering steels with different alloy contents was investigated by (Liu et al., 2020) in a study that also included a comparison with Q345 steel. The study was conducted under simulated industrial atmosphere conditions. The combination of Cr and P had a combined impact on improving the weathering steel resistance. This result led to the development of a cohesive and consistent layer of rust, as well as a decrease in the occurrence of hydrogen evolution during cathodic reactions. Nevertheless, Cu and Mn had an adverse impact on the corrosion resistance of the steel. These elements impeded the development of a stable goethite phase within the rust layer, while simultaneously promoting the hydrolysis reaction catalyzed by Cr ions. Elevated concentrations of Cr and P demonstrated the most favorable corrosion characteristics, while a combination of Cr, Mn, and Cu exhibited the least desirable corrosion behavior when exposed to a simulated industrial atmosphere.

A study conducted by Kim et al. (2002) focused on investigating the influence of Si content on the corrosion characteristics of calcium-modified weathering steel in an environment with a high chloride concentration. Researchers reported that the addition of calcium in weathering steel enhances the development of a compact layer of rust, thus providing an effective protective barrier

against corrosion for the steel. However, Si might also decrease corrosion resistance of the protection layer because Si facilitates the creation of amorphous oxides, subsequently reducing the alkaline nature of the water film on the steel substrate.

2.5.3 Corrosion Prevention and Mitigation Techniques

McDad et al. (2000) assessed the performance of weathering steel in Texas. The study involved a field evaluation of 40 bridges located in different environments. The selection of bridges was based on severe coastal areas with a high salt atmosphere, industrial zones, urban zones over rivers and highways, and suburban and rural zones. As determined by a visual inspection, the color of weathering steel bridges varied from light- to darker-brown. Most bridges were found to have mill scales on their bottom flanges, exposed top flanges of bent caps, and webs. The research found that the performance of exposed surfaces of weathering steel in coastal regions was comparable to that in other environments. However, the performance of non-exposed surfaces, particularly near the coastline, was poor because bigger rust flakes were observed on the steel surface.

According to McDad et al. (2000), rusting steel structures contribute to bridge staining, and poorly designed and installed drip plates were ineffective. Drip pans were also found to be ineffective. In addition, the study revealed that proper detailing was necessary for effective weathering steel performance. The study found that ponding water increases the corrosion rate, and accumulated debris tends to absorb moisture and obstruct the flow of runoff water. The researchers assessed the effectiveness of weather-resistant steel using ultrasonic thickness measurement data acquired from three bridges. Ultrasonic thickness measurement was inadequate for measuring performance prior to the onset of severe corrosion because steel expands after corrosion, and estimating the initial thickness of the steel plate was frequently inaccurate. The author mentioned that when deicing salts are frequently used, weathering steel demonstrates good performance if precautions are taken to minimize runoff onto the steel and utilize noncorrosive deicing chemicals. To attain a consistent and aesthetically pleasing look, it is important to blast-clean all exposed surfaces, including fascia and other areas exposed to weather conditions, using SSPC-SP6. The authors also compared the TxDOT blast-cleaning specifications with SSPC blast-cleaning recommendations and recommended using the SSPC-SP6 *commercial blast* for weathering steel for achieving a smooth, uniform patina.

Barth et al. (2005) studied the weathering performance of West Virginia steel bridges. The authors discovered that although the literature on weathering steel emphasizes the significance of wet and dry cycles for forming a stable patina, the dry phase of this cycle is more effective. The study also examined the applicability and benefits of installing drip plates. The results showed that drip plates can cause accumulation of debris and retain water, which affects corrosion rates. The authors concluded that weathering steel bridges in West Virginia generally perform well. The study also reported a significant corrosion occurred on the underside of steel components, where the corrosion rate of weathering steel ranged from 0.04 to 0.2 mm/year. The authors suggested painting the end of the girders over a length, which is equal to the depth of the girder, to reduce the deterioration rate.

Urban et al. (2015) introduced an analytical corrosion prediction model to quantify corrosion losses and explain the degree of correlation dependence between corrosion losses and thickness of corrosion products on a bridge in Ostrava, Czech Republic, that spanned a railroad track. The investigation revealed that corrosion products generated more rapidly on the upper surfaces of bottom flanges than on the web.

Crampton et al. (2013) completed a project for Iowa DOT and the Federal Highway Administration (FHWA) in which they evaluated the performance of weathering steel bridges and developed efficient inspection and maintenance systems. The research included the field inspection approach, methods, and results for 31 weathering steel bridges. It was concluded that the performance of weathering steel bridges is dependent on the proper formation of a dense, protective patina layer on the steel surface. Weathering steel initially corrodes at a rate similar to carbon steel, but cycles of wetting and drying cause the formation of the oxide layer (patina) that slows the rate of corrosion. The report recommended both visual inspection and tape adhesion testing during routine bridge inspections to evaluate the patina condition overtime. Visual inspection mainly includes patina color, uniformity, texture, and flake size, but tape testing provides physical samples to verify and improve visual ratings. A rating system from 3 (serious) to 8 (excellent) was proposed to quantify the patina condition. The authors recommended the ratings be assigned for overall condition and noted at typical locations and problem areas. The authors also suggested high-pressure washing (from 3500 to 5000 psi) that can be effective to remove contaminants such as chlorides, dirt, and loose flakes. These contaminants retain moisture and hinder the formation of protective layer. Urban bridges with high traffic below were the highest

priority, with washing intervals of 1–2 years. Suburban and rural bridges were lower priority, with longer intervals of 3–10 years. Moreover, chloride testing was found to be of limited utility, making it difficult to make quantitative comparisons between patina.

Granata et al. (2017) conducted a study to determine the applicability of weathering steel in Florida. The researchers conducted a field study on Florida steel bridges to produce a guideline for selecting weathering steel as a bridge material. This study was conducted by analyzing data that included measurements of thickness loss and meteorological conditions from 30 monitoring stations. The corrosion rate of weathering steel was found to be minimal in Florida. The study proposed an alternative method for a simplified and rapid evaluation of weathering steel.

Ault and Farschon (2009) reported in a study conducted for New Jersey DOT that evaluated the performance of 47 different experimental coating systems. The coatings were applied to different spans of the Mathis Bridge between 1986 and 1987. After 20 years of exposure, the results showed that pure zinc and 85 percent zinc and 15 percent aluminum metalizing (with topcoats) were the best-performing systems, with each rating 9 according to the ASTM D610 standard. Brevoort et al. (1996) proposed a lifespan of 17.5 years for zinc metalizing in a marine environment. The results obtained from that study agree with the data from the AWS on the corrosion rate of metalizing (American Welding Society, 1974). The AWS conducted a 19-year study in which test panels of metalized coatings were placed at seven different locations. The metalized coatings used in the study were thermal sprayed with pure aluminum, pure zinc, or zinc/aluminum alloy; untreated; and sealed with aluminum vinyl or chlorinated rubber. Note that aluminum metalizing did discolor and had a blotchy appearance, while a 9 mils thick coating was enough to protect the base metal in all the exposure sites. For aluminum vinyl-sealed zinc with 3-mils thickness, the base metal and zinc were not affected at any exposure sites.

Kain and Baker (1987) reported that 27 metalized coatings of single and multimetal compositions. The study examined and compared 10 different proportions of zinc and aluminum mixed with individual powders of each alloy that were alloyed together, then powdered or applied individually. The study concluded that an alloy containing more than 50 percent aluminum exhibited the best performance, and zinc alone required 6 mils of thickness to be effective. Aluminum alone required only 3 mils of thickness for an effective performance. The results of both the AWS and Cambridge University studies were found to be in good agreement with each

other, and the results showed that a higher percentage of aluminum in the metalizing performed better than a higher percentage of zinc for the same thicknesses (Brevoort et al., 1996).

In 1997, FHWA conducted exposure studies on unsealed and sealed test panels with zinc and zinc/aluminum coating systems in marine locations in Louisiana and New Jersey for over 5 and 6.5 years, respectively, and found metalizing to be some of the best performing coating systems. After analyzing the rust data, the researcher predicted a life of 30 years for coatings in marine environments. FHWA also conducted a 4-year study evaluating the performance of eight different protective coating systems on weathering steel bridges: an epoxy zinc-rich system, a urethane zinc-rich system, an epoxy mastic system, an ethyl silicate zinc/vinyl system, a waterborne alkali silicate/acrylic system, an oil-alkyd control, a thermally sprayed zinc (TSZ) system, and a low volatile organic compound (VOC) ethyl silicate system. Three bridges in Michigan, Pennsylvania, and Louisiana were selected for the study. The results indicate that wet and dry surface preparation methods (dry abrasive blasting, wet abrasive blasting, and power-tool cleaning using rotary peening and nonwoven abrasive discs) can remove sufficient contamination to ensure the high performance of coating systems. This study also recommended selecting coating systems based on the classification of steel condition and the exposure condition (Appleman et al., 1995).

Brevoort et al. (1996) predicted the cost and service life of protective coatings. The study estimated the service life of 89 coatings until the first maintenance action, along with their costs. The authors found that pure zinc metalizing had an estimated life of 33, 22, and 16 years in rural, industrial, and heavy industrial environment, respectively, and 17.5 years in a marine environment. Leyland et al. (2006) later studied different coating systems on Maine and Connecticut bridges and found that Brevoort's prediction was conservative.

Toubia and Emami (2016) performed a research study for Ohio DOT to evaluate the performance of five structural steel coating systems. Four of these coatings were classified as two-coat systems composed of a zinc-rich primer and a polysiloxane topcoat, and another one was a three-coat system made up of IOZ/OZ, epoxy, and urethane. A series of tests was conducted to evaluate properties of the coatings, such as adhesion, bending, chipping, abrasion, water resistance, weathering, corrosion, flexibility, and chipping resistance. Based on the findings presented in the report, the two-coat system demonstrated an equivalent performance to the three-coat system.

Moreover, the utilization of a two-coat system presented several benefits, including cost reduction and simplified application procedure.

Kodumuri and Lee (2011) conducted a research study focusing on the identification and evaluation of coating systems for steel bridge structures. The primary objective of this study was to assess the potential of these coating systems to provide a service life of 100 years with minimal maintenance requirements. The authors suggested that the three-coat IOZ control system displayed superior resistance to corrosion. They also analyzed the performance of one coat with a high-ratio calcium sulfonate alkyd that showed promising outcomes. The TSZ system consisting of two coats demonstrated acceptable performance, yet excessive blistering, and peeling was reported for this coating system.

The research study conducted by Hoang et al. (2022) focused on investigating the application of flake zinc-aluminum (ZnAl) alloy pigment in silicate coating. Because of drawbacks associated with conventional zinc-rich coating, the authors suggested employing flake ZnAl alloy pigment. Silicate coatings containing different concentrations of flake ZnAl alloy were fabricated and subsequently deposited onto carbon steel specimens through a spray-coating technique. The evaluation of the coating resistance to corrosion was conducted using electrochemical measurements, salt spray tests, pull-off tests, and an analysis of surface morphology. The findings of the study indicate that the silicate coating containing 25 wt% flake ZnAl alloy demonstrated superior corrosion protection capabilities, as was evidenced by a lower corrosion current density, higher total resistance, longer duration before the onset of rust, and minimal adhesion loss following exposure to salt spray.

Knudsen et al. (2012) examined the TSZ duplex coating system to protect steel structures from corrosion activities in offshore and coastal environments. Based on the results of field testing and laboratory examinations, the author concluded that TSZ duplex coating is a superior coating system compared to thermally sprayed aluminum (TSA) and conventional paint systems. This conclusion was made because of the great overall performance and less required maintenance of the proposed coating system. In a different study, the effectiveness and deterioration of duplex coating systems made up of TSZ and organic paint on steel bridges in Norway was carried out by Knudsen et al. (2016). Seven bridges investigated by the authors that had different sets of exposure time, condition, and coating methods. The corrosion damage on the zinc layer reported in this study was either large in area or isolated in some spots that can be described as pinholes in the

paint. The researchers discussed mechanisms and causes of pinhole formation and corrosion initiation in detail.

Darden (2016) examined fluoropolymer coating for Japanese steel bridges and investigated if the coating withstood atmospheric corrosion. Fluoropolymer coating showed corrosion protection and cost effectiveness. The report also explained the development of the national specification for bridge coatings in Japan, emphasizing the requirement for fluoropolymer topcoats for both new construction and field maintenance projects. Dallin et al. (2018) also focused on the application of duplex zinc coating to protect steel structures from corrosion. Duplex zinc coating, which is a metallic zinc layer and a paint topcoat, exhibited higher corrosion resistance. The report also illustrated successful applications of duplex coating on steel structures such as bridges, transmission poles, light rail networks, and NASA facilities.

Seré et al. (2014) compared the performance of hot-dip galvanized steel and coated steel with a 55 percent Al-Zn alloy by evaluating their corrosion-resistant and adhesive characteristics. The authors reported that silane enhances paint adherence, particularly on hot-dip galvanized steel, if it is applied on the substrate during the pretreatment, although blistering can cause the paint coat to peel, leaving the substrate susceptible to corrosion. According to this study, silane pretreatment significantly improves adhesion and works better in saltine environments.

Chavan et al. (2013) examined the corrosion resistance of cold-sprayed zinc coating applied to mild steel substrates. The authors concluded that a thick and dense layer of cold-sprayed zinc coating can provide effective protection against corrosion for steel. The coating exhibited strong adhesion to the substrate, although the possibility of cracks and pores was not ruled out. Additionally, the authors suggested a heat treatment at 150°C to reduce the porosity of the coating.

Stojanović et al. (2022) assessed corrosion-resistant waterborne coatings that have been dried using both traditional atmospheric conditions and accelerated infrared (IR) technology. The authors concluded that the utilization of IR drying technology reduces drying durations while maintaining the integrity and quality of waterborne coatings. However, it was concluded that solvent-borne coatings continue to demonstrate superior durability when exposed to harsh marine environments.

Boidot et al. (2022) studied the effectiveness of waterborne, hybrid-organic-IOZ-rich coatings in reducing corrosion resistance of the metals. The authors observed a medium to high fraction of aluminum results in the corrosion byproducts without improving the protective barrier,

yet the addition of precise quantities of aluminum flakes substantially improves the coating's ability to prevent corrosion.

Kakaei et al. (2013) evaluated the effectiveness of waterborne IOZ-rich silicate paint in mitigating corrosion in steel structures. The coating employed was potassium silicate as a binding agent. In addition, zinc and micaceous iron oxide were also used as pigments. The impact of a cyclic dry-wet environment on the coating was examined during laboratory testing. It was found that substituting a mix of zinc with micaceous iron oxide can potentially lead to a decrease in cathodic protection.

Knudsen et al. (2019) examined the effectiveness and long-term viability of TSZ duplex coatings to protect steel bridges located in Norway. The corrosivity of five road bridges with varying climatic conditions was assessed, and the progress of corrosion product development was examined for 56 bridges. These structures were built between 1967 and 1995. Severe corrosion and pinholes, particularly in structures located in a marine environment, were observed in thin layers of the TSZ duplex coating. It was concluded that the coating can be a promising protection system for a period of up to 50 years, especially in environments with low levels of corrosivity.

Knudsen et al. (2022) also examined the use of TSZ duplex coatings on steel bridges in coastal areas of Norway. To evaluate the performance of 61 substantial steel bridges built before 1995, the researchers examined the state of the coatings on each individual bridge. According to the findings, the longevity of coatings relies on the corrosivity of the environment. The authors reported that the lifespan of the coatings reduces with increasing corrosivity, and in a highly corrosive environment, it drops to about 25 years, while the durability of coatings is 100 years in a low corrosive environment. The authors also compared TSZ duplex coatings to rich zinc-based paint systems (ZBPSs). According to the results, TSZ duplex coatings have significantly longer lifespans, with lower maintenance cost.

Eriksen et al. (2020) performed a study on different coating systems to improve corrosion resistance of Scandinavian Road bridges. Their main objective was to address the cost of corrosion problems on steel bridges and highlight the significance of choosing durable coatings to save maintenance costs. In this study, the authors assessed the quality of IOZ with an organic topcoat, duplex TSZ with an alkyd coating, and an OZ epoxy primer coating. The authors collected coating conditions of 82 Norwegian and 32 Swedish steel bridges, corrosive environments, and maintenance costs. In particular, it was found that TSZ duplex coatings shows great performance

and required less maintenance in low corrosive regions, while IOZ coating systems showed less durability and required careful inspection. It was also concluded that OZ coating systems could be protective with moderate durability, but with a reasonable maintenance and repair cost.

Momber and Irmer (2013) assessed the performance of eight distinct organic coating systems designed for offshore structures located in Arctic regions. The authors evaluated the efficacy of corrosion protection, mechanical characteristics, and performance under different environmental conditions, including low temperatures, UV radiation, salt spray exposure, and dry-wet cycles. A zinc-dust-based coating, polyurethane, demonstrated superior corrosion resistance compared to other coatings. Besides polyurethane's performance, a rubber-based polyester coating also exhibited decent protection. The authors also studied the impact of the aging, wetting properties, and development of rime ice on the durability and extended lifespan of the coatings. The researchers concluded that the effectiveness of organic coatings in Arctic environments relies on several factors, such as the type of the coat, the filler material, the composition of the layers, the thickness of the film, and the method of application.

Galedari et al. (2019) studied corrosion resistance of thermally sprayed protective coatings that are commonly applied to steel structures. The authors mainly investigated five types of thermally sprayed coating: aluminum-based, zinc-based, Ni-based, chrome-based, and ceramic based. Aluminum-based coatings are frequently employed to protect steel from corrosion due to their anodic nature and the formation of a passive layer. Wire arc spraying, flame spraying, cold gas-dynamic spraying, and high-velocity air-fuel spraying are some of the thermal spraying techniques. The addition of alloying elements such as magnesium, zinc, Si, and rare earth elements can elevate the mechanical and corrosion properties of these coatings. Aluminum-based coatings exhibit self-sealing properties, thereby preventing further electrolyte penetration. However, these coatings fail due to pitting and mechanical damage, and they are not recommended as a protection system in corrosive or high-temperature environments.

Ni-based coatings show corrosion protection at elevated temperatures. High-velocity oxy-fuel spraying, air or vacuum plasma spraying, plasma-transferred arc spraying, and plasma electrolytic oxidation are some of the thermal spraying techniques. Cr, boron, Si, titanium, and tungsten carbide are used as alloying elements to improve the coating's hardness, oxidation resistance, and attrition resistance. However, depending on the corrosive environment, Ni-based coatings may be vulnerable to selective corrosion of the binder phase or the hard particulates.

According to Galedari et al. (2019), a zinc-based coating is a sacrificial anodic system and can be applied to steel via thermal spraying techniques, including wire arc spraying, flame spraying, and cold gas-dynamic spraying. Zinc-based coatings show limited resistance to high humidity and aggressive ions such as chloride and sulfate and may dissolve rapidly in such solutions, instead the chrome-based coatings can provide protection to steel against corrosion. In general, it was concluded that nickel, chromium (II) carbide, tungsten carbide, and cobalt can enhance both the coating hardness and erosion resistance, as well as resistance to oxidation.

As a maintenance procedure, it is common to perform high-pressure washing of steel girders to remove dirt, debris, and loose rust flakes. However, it was seen that this approach does not significantly eliminate chlorides within the patina layers (Crampton et al., 2013). Painting steel girders can be a better choice over weathering steel when the structure is located in aggressive environments, such as coastal areas. Visual inspection can be an immediate solution to assess the rust condition and estimate the extent of corrosion on steel surfaces, yet the accuracy of the results depends on the skill of the inspectors. The performance of nondestructive evaluation to assess the status of corrosion of steel girders in service can also be a challenge. For example, in the case of ultrasonic measurements, the original thickness of the specific testing object (steel plate) is typically unknown, making it difficult to obtain accurate results since a reference point is unavailable. However, Infrared Thermography (IR) may be used to detect concealed flaws under the paint of steel columns. Note that there is a study reporting the limited application of IRT in identifying defects on bridge structures (Sidelev, 2014).

In terms of metalizing, aluminum coating exhibited a great ability to increase corrosion resistance of steel plates. A TSZ duplex coating has also been shown to be an excellent protection system against corrosion and can also lower life-cycle costs. Heat treatment and infrared drying technology can increase the corrosion resistance and improve the overall performance of the coatings (Chavan et al., 2013; Stojanović et al., 2022). Some studies have suggested the use of aluminum flakes to improve the corrosion resistance of the coatings, but research in this area is still in progress (Galedari et al., 2019; Boidot et al., 2022). Table 2-2 summarizes the literature review for different types of paint system.

Table 2-2. Results of Literature Review on Paint System.

Study	Test, Location	Findings: Greater Corrosion Resistance	Reference
2-coat (ZE + PS) 3-coat (IOZ) OZ primer, E, urethane topcoat	Laboratory Test: ACT, Adhesion Test, Ohio	Two-coat system: ZE + PS	Toubia and Emami (2016)
3-coat (IOZ + E+ PU) 3-coat (MCU + E + PU) 3-coat (MCU + E + F) 2-coat (ZE + PU) 2-coat (Zn + PS) 2-coat (TSZ + LE) 2-coat (ZnE + LE) 1-coat (HRCSA)	Laboratory Test: ACT, Virginia	Three-coat system: IOZ/E/PU + ZE/E/PU One coat system: HRCSA	Kodumuri and Lee (2011)
Silicate coating with flake ZnAl alloy	Laboratory Test: EIS, Vietnam	Silicate coating with 25 wt% flake ZnAl alloy	Hoang et al. (2022)
TSZ duplex coating, TSA duplex coating IOZ/OZ paint system	Field + Lab Test: Norway	TSZ duplex coating	Knudsen et al. (2012)
TSZ duplex coating OZ coating	Field Test: 7 Bridges, Norway	TSZ duplex coating	Knudsen et al. (2016)
Cold-sprayed zinc coating	Laboratory Test: India	Promising performance	Chavan et al. (2013)
Waterborne IOZ-rich silicate paint	Laboratory Test: (EIS), Iran	Promising performance	Kakaei et al. (2013)
TSZ duplex coating (marine environment)	Field Test: 56 Bridges, Norway	Promising performance and durable for 50 years	Knudsen et al. (2019)
TSZ duplex coating (coastal region)	Field Test: 61 Bridges, Norway	Promising performance and long lifespans	Knudsen et al. (2022)
IOZ + OZ topcoat Duplex TSZ with an alkyd coating OZ + E primer coating	Field Test: 82 Bridges, Norway; 32 bridges, Sweden	Duplex TSZ coating with an alkyd coating	Eriksen et al. (2020)

Note:
E: epoxy
F: flourourethane
LE: linear epoxy
PU: polyurethane
PS: polysiloxane
Zn: inorganic zinc (IOZ) primer
ZE: zinc-rich epoxy primer
ZnE: experimental zinc primer
MCU: moisture-cured urethane zinc primer
TSA: thermally sprayed aluminum
TSZ: thermally sprayed zinc primer
HRCSA: high-ratio calcium sulfonate alkyd
ACT: accelerated corrosion test
EIS: electrochemical impedance spectroscopy

2.5.3.1 Performance Assessment of Weathering Steel Bridges

Weathering steel without a well-formed protective patina can lead to advanced corrosion and often negates cost savings. Therefore, early detection of the problematic areas is the key to save weathering steel bridges from further deterioration and ultimately saving on maintenance costs. Several researchers have performed studies to assess the patina performance and classify it based on visual inspection and the tape adhesion test (Albrecht et al., 1989; Hara et al., 2007; Crampton & Holloway, 2015). Albrecht et al. (1989), in NCHRP Report 314, presented the guidelines to assess the patina (oxide layer) condition of weathering steel structures. The guidelines use color and texture as the criteria for evaluating the nature of the patina (i.e., if the patina is protective or not). However, the authors cautioned that visual inspection alone can be misleading and recommended using hammer tapping or wire brushing to check if the layer is adherent or loosely attached. Moreover, the study also recommended that inspectors should understand the appearance of patina in different microclimates and environmental conditions. The authors' recommendations are summarized in Table 2-3 and

Table 2-4. Table 2-3 provides the appearance guidelines for evaluating the patina based on color, while

Table 2-4 summarizes the guidelines for evaluating patina based on texture.

Table 2-3. Appearance Guidelines for Color of Patina (Albrecht et al., 1989).

Color	Condition
Yellow-orange	Initial stage of exposure
Light-brown	Early stage of exposure
Chocolate-brown to purple-brown	Development of protective oxide
Black	Nonprotective oxide

Table 2-4. Appearance Guidelines for Texture of Oxide Layer (Albrecht et al., 1989).

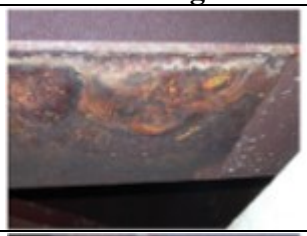
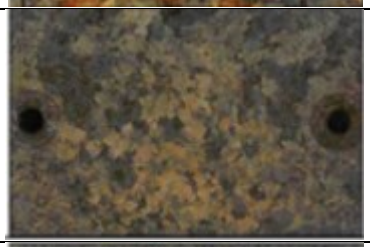
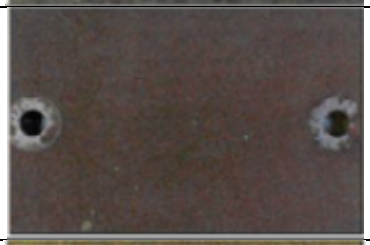
Texture	Condition
Tightly adherent, capable of withstanding hammering or vigorous wire brushing	Protective oxide
Dusty	Early stages of exposure; should change after a few years
Granular	Possible indication of problem depending on length of exposure and location of structure
Small flakes, 6 mm in diameter	Initial indication of nonprotective oxide
Large flakes, 12 mm in diameter or greater	Nonprotective oxide
Laminar sheets or nodules	Nonprotective oxide, severe corrosion

Table 2-5. Appearance Index of Oxide Layers (Hara et al., 2007).

Appearance Index Rating	Oxide Layer Thickness	Description	Rust Flake Size
1	> 800 μm	Large swelling and laminated flaky layer	> 25 mm
2	> 400 μm	Partial swelling and flaky layer	5 mm to 25 mm
3	> 400 μm	Non-uniform rust	1 mm to 5 mm
4	> 400 μm	Adherent and uniform dark-brown rust	Fine < 1 mm
5	< 200 μm	Light-brown rust	Fine

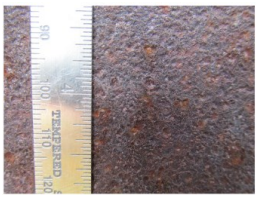
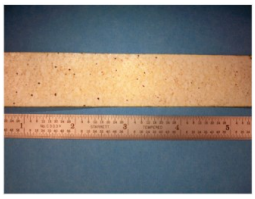
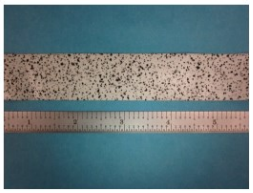
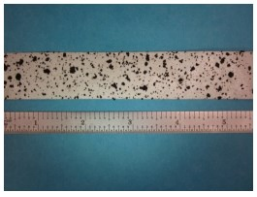
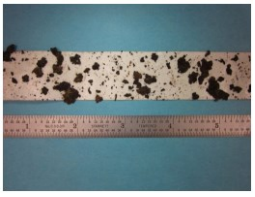
In a study conducted in Japan, Hara et al. (2007) developed a straightforward visual rating system—known as an appearance index rating (Table 2-5)—to assess the protective ability and durability of the rust patina formed on the weathering steel surface (Table 2-6). The system assigns a rating from 1 to 5 based on the color and texture of the patina (oxide layers). Whereas an appearance index of 3 or 4 indicates the patina has a protective, stable rust layer in which corrosion has been minimized, an appearance index of 1 or 2 indicates a nonprotective patina with thick rust formation. The researchers suggested that the appearance index directly correlates with the actual corrosion rate of the weathering steel, which means a lower index value corresponds to a higher corrosion rate and vice versa.

Table 2-6. Appearance Index of Oxide Layers (Hara et al., 2007).

Appearance Index	Appearance of coupon	Description of Characteristic	Appearance of Rust in Bridge
1		Large swelling and laminated flaky layer Thick>800 μm	
2		Rust Size: 5-25 mm Partial swelling and flaky layer Thick>400 μm	
3		Rust Size: 1-5 mm Not fine not unifrom rust Thick>400 μm	
4		Rust size: fine, adherent and uniform rust Color: dark brown Thick<400 μm	
5		Rust size: fine Color: light brown Thick<200 μm Thin rust	

More recently, a similar study was conducted in Iowa by Crampton and Holloway (2015). In this study, a system was developed known as the patina rating system. The system recommends using a patina rating scale between 3 to 8 in which a rating value of 8 represents very *good* condition and 3 represents *serious* condition. Several factors, such as color, texture, rust flake size, and the tape adhesion test, were considered for developing this rating scale. Table 2-7 summarize the proposed patina evaluation rating scale based on color, texture, particle size, and the tape adhesion test.

Table 2-7. Proposed Patina Evaluation Rating Scale (Crampton & Holloway, 2015)

Patina Rating	Color	Texture	Flake Size (mm)	Example Condition	Example Tape Test Specimen
8	Dark brown with lighter reddish-brown, metallic and purple-brown spots, Uniform color	Texture may be dimpled or rough but uniform in pattern	<1		
7	Uniform color pattern, dark brown with lighter reddish-brown, metallic and purple-	Texture may be dimpled or rough but uniform in pattern	<1		
6	Dark brown color with minor Variation	Texture more granular and loose flakes	1-5		
5	Dark brown with black and some color variation	Layer beneath flakes thicker and more permeable	5-25		
4	Color is dark brown and black but nonuniform	Poultice areas have thin delamination sheets	>25		
3	Blackish, stained, blotchy appearance	Formation of laminar sheets with deeply pitted semi-adherent layer beneath	>25		

2.5.4 Corrosion Fatigue and Service Life

Corrosion fatigue refers to the combined action of deterioration of steel members as a result of alternating cycling stresses in a corrosive environment (Harlow & Wei, 1994). The phenomenon

can be divided into the following stages: the corrosion initiation and the formation of pitting corrosion; pitting and fatigue crack growth rate, which can be defined as the surface cracking resulting from the pitting (Kondo, 1989); and when crack growth rate exceeds the pitting growth rate. During the final stage, the crack will grow at a higher rate than it does in a noncorrosive environment until the failure criteria is realized (Shi & Mahadevan, 2001).

The research on steel structures and intended civil engineering applications is limited due to a lack of understanding because of limited experimental research and the complexity of study. Novak (1983) investigated the corrosion fatigue cracking in four classes of carbon steel: AS6, A588-A, A517-F, and V-150. The researcher's main observations were that the fatigue strength of all steel samples in corrosive environments declined in varying degrees, and there is no clear corrosion fatigue crack initiation threshold of corroded samples. Additionally, further experiments were conducted for full scale weathering steel specimens that were subjected to cyclic loading and a corrosive environment (Albrecht et al., 1989; Albrecht & Sidani, 1989; Albrecht & Shabshab, 1994; Albrecht & Lenwari, 2009). Apart from these experiments, Zuraski and Johnson (1990) conducted a fatigue test on the tension flange of the truss stringers from abandoned bridges that showed a faster deterioration rate of specimens because of the corrosive environment. In terms of a corrosion fatigue model, El Aghoury and Galal (2014) related the corrosivity with the fatigue strength and calibrated the strain-life model by the experimental results. Similarly, Adasooriya et al. (2020) introduced the environmental reeducation factor to adjust the fatigue strength of corroded tubular joints that can be used to evaluate the corrosion fatigue resistance of corroded steel members without delving into the details regarding pitting nucleation, transition, and crack propagation rate.

2.6 SYNTHESIS OF RESEARCH

Steel girders that are located in regions with high airborne chloride and perhaps the frequent use of deicing salt experience severe corrosion. This can lead to costly repairs and reduce the service life of the steel girder. Improper installation of drip plates and waterlogging intensifies corrosion problems by extending the time of wetness duration. Current inspection procedures lack reliable methods to evaluate corrosion prevention and mitigation performance of steel girders. Inspectors primarily rely on visual assessments for weathering and painted steel bridges that provide only qualitative data. To this end, more objective field testing is needed to improve field

evaluations. Therefore, a research study is needed to develop a comprehensive guideline to assess corrosion prevention and mitigation methods employed on weathering and painted steel girders across Texas. This report provides assessment of corrosion resistance of existing steel girders, and provides recommendations that can be used on new structures.

2.7 SUMMARY

Corrosion can cause a risk of localized failure or even complete collapse of the steel girders; hence, it is essential to inspect the quality of steel and the extent of corrosion overtime. Electrochemical reactions required for the corrosion process will be initiated as corrosive agents such as oxygen, carbon dioxide, chloride, and sulfur ions contact the steel surface. The composition of the rust layer differs from mild steel to weathering steel because the patina layer in weathering steel is uniformly distributed oxyhydroxides on the steel surface. The patina layer reduces the rate of corrosion in steel substrate unless sulfur dioxide and chloride ions contact the rust layer that leaves the protection system less effective.

A proper coating system such as zin-painting can provide corrosion protection for decades. Both inorganic and OZ-rich paint systems have demonstrated good performance even in difficult marine environments. Note that three coats have showed greater performance in an aggressive environment—such as coastlines. Galvanized and metalized coatings have also demonstrated excellent performance and also require less maintenance. In general, a service life of 20 years in maritime environments, and even longer for structures located in low corrosion risk environments, is expected for the above coating systems.

3 ASSESSING CORROSION RISK IN TEXAS

Steel girders and reinforced concrete decks are constantly exposed to environmental factors that can lead to corrosion initiation and propagation on steel members. These factors including humidity and air pollution can eventually pose risks to the functionality of the steel and concrete bridges. Deciding effective mitigation techniques that should be considered for a particular sub- and super structures requires understanding of risks associated with environmental factors causing corrosion. This section presents a comprehensive study that aims to estimate the risk of atmospheric corrosion across Texas. By integrating climate data and pollution information, a corrosion risk assessment map was developed that considers the factors influencing corrosion of steel and aids in identifying highly corrosive environments across the state.

3.1 INTRODUCTION TO RISK ASSESSMENT

Risk refers to the potential of damage or failure that happens because of an event or activity. To predict a risk associated with a phenomenon, both likelihood and impact of an undesirable outcome must be considered in the calculation (Ang & Tang, 1984; Kumpulainen, 2006; Porter, 2015). Risk can be defined in terms of *hazard*:

$$\text{Risk} = \text{Hazard} \tag{3.1}$$

In this report, a hazard is a natural event (such as corrosion) that can cause or contribute to initiation of an unwanted event or adverse outcome, like the collapse of a bridge structure (Rodriguez et al., 1994; Kumpulainen, 2006).

As a bridge structure ages, the vulnerability to damage as the result of corrosion increases, particularly in aggressive environments. Major factors that can influence bridge structures are classified as corrosion hazards, including *atmospheric pollution* and *industrial contamination*. Atmospheric pollution includes the temperature and RH of the environment in which the structure is located. It can be defined in terms of TOW and annual number of FD. Industrial contamination incorporates airborne chloride produced from industrial activities. Sulfur dioxide, carbon monoxide, and nitrite dioxide are examples of air pollutants in urban and industrial areas (Morcillo et al., 2013; Leygraf et al., 2016). An additional significant source of a corrosion hazard that is most applicable to steel and concrete bridges is the use of deicing salt on bridge decks during winter.

3.2 METHODOLOGY

The methodology employed in this study was divided into two parts: documenting environmental factors that impact the corrosion process on steel, according to ISO 9223; and developing mathematical models to predict risk associated with atmospheric corrosion. The national climate database was used to collect the temperature and RH data that were later used to determine the annual number of FD and TOW across the state. The corrosion risk assessment map was developed based on spatial interpolation techniques, such as kriging and co-kriging. To calculate risk associated with corrosivity, two sets of chloride data were developed for the usage of deicing salt on state roads in addition to airborne chloride deposition at the coastline. The Environmental Protection Agency (EPA) dataset was also used to consider the effect of sulfur dioxide in the risk analysis conducted in this research (Pickard et al., 2015). Finally, the Klinesmith et al. (2007) corrosion model was employed to predict the potential weight loss of steel without the use of any protection by incorporating the environmental and contamination factors. The result of weight loss calculated from Klinesmith's model was used to demonstrate the potential hazard for steel girders and concrete bridges (Klinesmith et al., 2007). The corrosion risk assessment map for Texas was generated by influencing hazard outcomes.

3.3 DATA COLLECTION AND PROCESSING

The main source of data collected in this research was from a local climatological dataset (LCD) that provided a comprehensive data point of daily temperature, precipitation, and wind. The locations of climate stations from which data were recorded is given in Figure 3.1. As shown in this figure, in addition to all climate stations across the state, the data from certain stations in New Mexico, Oklahoma, Arkansas, Louisiana, and several stations in Mexico were added to the dataset to improve the result of spatial interpolation.

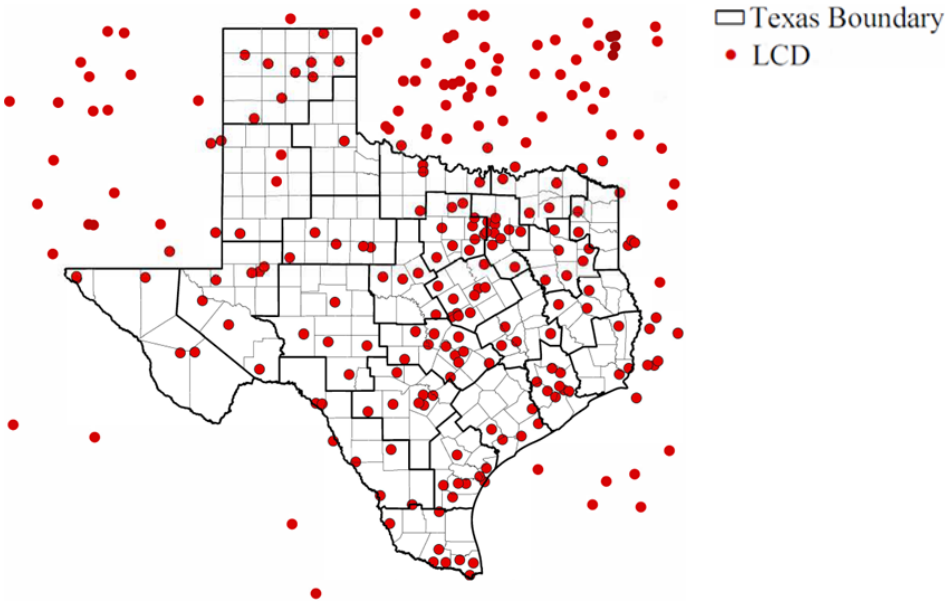


Figure 3.1. Local Climatological Station Locations.

After the collection of data, an interpolation technique was employed to estimate or substitute missing values based on neighboring observations or supporting data sources. Climate data were collected at various temporal resolutions ranging from hourly measurements to daily or monthly recordings. Therefore, it was required to adjust the time scale to ensure consistency and comparability across different datasets. In this research, the definition proposed by ISO 9223 (2012) was used to calculate TOW—that is, analyzing the hourly temperature and hourly RH data. According to ISO 9223 (2012), TOW is the time when the air temperature is higher than 32°F and the RH is greater than 80 percent. Another factor considered in this study was the number of FD, which can significantly impact corrosion initiation on steel structures. *Freeze day* refers to the time when the air temperature is lower than 32°F. To ensure safe passage for vehicles and reduce ice and snow on roads, deicing salts are applied to roads if the temperature will drop below 32°F (Lee, 2017). Thus, this temperature was considered as a reference to calculate the annual number of FD.

3.4 TEXAS CORROSION HAZARD ASSESSMENT

Spatial interpolation techniques such as kriging and co-kriging were applied to generate environmental characteristics of Texas to further refine the corrosion risk assessment. Pollution maps were created by focusing on chloride and sulfur dioxide levels—which are major contributors to steel and concrete bridge corrosion. The relationship between deicing chloride and

the annual number of FD was examined and assumptions were validated. Finally, sulfur dioxide data were collected from a widely used environmental pollution atlas and factored in the calculation.

3.4.1 Texas Environmental Assessment

A review of the spatial interpolation method, including kriging and co-kriging, is provided in this section. This method was used to develop detailed maps to assess corrosion hazard potential across the state. The four environmental factors considered in this study are annual average temperature, RH, the total annual number of FD, and TOW.

3.4.1.1 Kriging and Co-Kriging Methods

Kriging has proved to be a promising interpolation approach in terms of accuracy and bias reduction (Li & Heap, 2008; Samanta et al., 2012). It can estimate the spatial variation structure by using variograms, which incorporate spatial autocorrelation. Unlike nongeostatistical methods, kriging considers the inherent spatial relationships between data points, resulting in more reliable and precise estimations. The underlying principle of kriging involves determining a linear combination of weights based on the spatial variation structure.

The kriging method predicts unmeasured value by assigning different weight to the neighboring datapoints:

$$\hat{Z}(S_0) = \sum_{i=1}^{N} \lambda_i Z(S_i) \tag{3.2}$$

where $\hat{Z}(S_0)$ refers to the predicted value at the target location (S_0); $Z(S_i)$ refers to the measurement at the neighboring location (S_i); and λ_i denotes the weights assigned to neighboring points that are determined during the spatial autocorrelation. The empirical semivariogram and covariance function are developed before the prediction to quantify the spatial autocorrelation. If the stationary mean (μ) is known, Equation (3.3) can be modified:

$$\hat{Z}(S_0) - \mu = \sum_{i=1}^{N} \lambda_i [Z(S_i) - \mu(S_0)] \tag{3.3}$$

and the semivariance γ of function Z between two points can be expressed as:

$$\gamma(S_i, S_j) = \gamma(h) = \frac{1}{2} var[Z(S_i) - Z(S_j)] \tag{3.4}$$

where the parameter "*h*" is the distance between two points (S_i and S_j). If several sample points are selected within the range, the semivariance ($\hat{\gamma}$) can be estimated, like so:

$$\hat{\gamma}(h) = \frac{1}{2n}\sum_{i=1}^{n}[Z(S_i) - Z(S_i + h)]^2 \tag{3.5}$$

where n is the number of sample points within the distance h.

Figure 3.2 shows a schematic experimental variogram that reflects a fundamental principle: that the objects or locations closer to each other tend to be more similar than objects or locations farther apart. This principle forms the foundation for understanding and analyzing spatial patterns and relationships in geographical data. Additionally, several essential features can be highlighted in the semivariogram. The nugget C_0 is the residual at the distance close to 0. The range refers to the distance where the sill is reached or the model first flattens (Webster & Oliver, 2007).

Exponential function was selected in this study to fit the semivariogram datapoints:

$$\hat{\gamma}(h) = \begin{cases} \mathrm{C}_0 + \mathrm{C}_1\left(1 - e^{\frac{-h}{a}}\right) & h > 0 \\ 0 & h = 0 \end{cases} \tag{3.6}$$

where *a* is the best fitting coefficient, and C_1 is the covariance function. Once the empirical semivariogram function is determined, the weight λ_i can be estimated by minimizing the variance:

$$\begin{aligned} &\min_{1,\dots n}\{\mathrm{var}[\hat{Z}(S_0)]\} = \min_{1,\dots \mathrm{n}}\left\{\mathrm{E}\left[\{\hat{Z}(S_0) - Z(S_0)\}^2\right]\right\} \\ &= \min_{1,\dots n}\left\{\mathrm{E}\left[\left(\hat{Z}(S_0)\right)^2 + \left(Z(S_0)\right)^2 - 2\hat{Z}(S_0)Z(S_0)\right]\right\} \\ &= \min_{1,\dots n}\left\{\sum_{i=1}^{n}\sum_{j=1}^{n}\lambda_i\lambda_j\mathrm{C}(S_i - S_j) + \mathrm{C}_1(S_i - S_0) - 2\sum_{i=1}^{n}\lambda_i\mathrm{C}_1(S_i - S_0)\right\} \end{aligned} \tag{3.7}$$

Among them, the parameter C_1 refers to the covariance function of $Z(S_i)$ and $Z(S_j)$,

$$\mathrm{C}_1(S_i - S_j) = \mathrm{Cov}[Z(S_i), Z(S_j)] \tag{3.8}$$

Another spatial interpolation method is the co-kriging approach, which can provide more accurate and reliable predictions than standard kriging methods. The cross-variogram (cross-correlation) between primary and secondary variables is described in the following equation:

$$\hat{\gamma}_{12}(h) = \frac{1}{2n}\sum_{i=1}^{n}[z_1(x_i) - z_1(x_i + h)]\,[z_2(x_i) - z_2(x_i + h)] \tag{3.9}$$

In co-kriging, the primary variable is interpolated using a weighted combination of the primary and secondary variables. The weights assigned to each variable are determined based on their spatial cross-correlation and the covariance matrix derived from the semivariogram models. Hence, the predicated value $\hat{Z}(S_0)$ can be modified to the following:

$$\hat{Z}(S_0) - \mu_1 = \sum_{i_1=1}^{n_1} \lambda_{i_1}[Z_1(S_{i_1}) - \mu_1(S_{i_1})] + \sum_{j=2}^{n_v} \sum_{i_j=1}^{n_j} \lambda_{i_j}\left[Z_j\left(S_{i_j}\right) - \mu_j\left(S_{i_j}\right)\right] \quad (3.10)$$

where μ_1 is the stationary mean of the preliminary variable; n_1 refers to the number of measurements included in the estimation; λ_{i_1} is the weight for the preliminary variable; λ_{i_j} is the weight of the secondary variable; $\mu_1(S_{i_1})$ refers the mean of the selected surrounding measurements; $\mu_j(S_{i_j})$ denotes the mean of the sample of j^{th} secondary variable selected to predict; $Z_1(S_{i_1})$ is the value of the primary variable at the i_1th point; and $Z_j(S_{i_j})$ is the data at the i_jth point of the j^{th} secondary variable.

Co-kriging accounts for the spatial relationships between the primary and secondary variables. Co-kriging can find patterns that results in more accurate predictions by considering the cross-correlation between all the variables (Knotters et al., 1995).

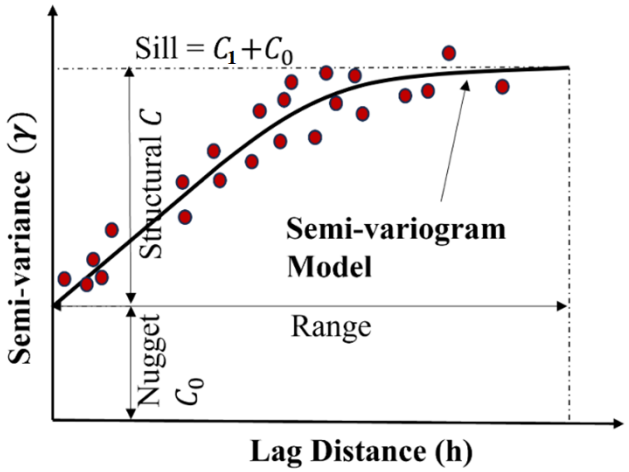


Figure 3.2. Schematic of Semivariogram.

3.4.1.2 Spatial Interpolation Results

After initial data preprocessing, a selection of 255 local climate stations was made for the purpose of spatial interpolation. The primary processing step involved utilizing the geostatistical wizard tool within the ArcGIS Pro 3.1 software. Ordinary kriging was used for mapping RH and

the annual number of FD in Texas. The temperature map was generated by using the co-kriging method and considering elevation as the secondary variable. This process provided the spatial distribution of temperature patterns in Texas. Samanta et al. (2012) also used elevation as a secondary variable, and the authors suggested that this adjustment enhances the accuracy and precision of temperature predictions. The elevation data with 0.5-mile grid resolution was obtained from the PRISM program, as shown in Figure 3.3 (Daly et al., 1997).

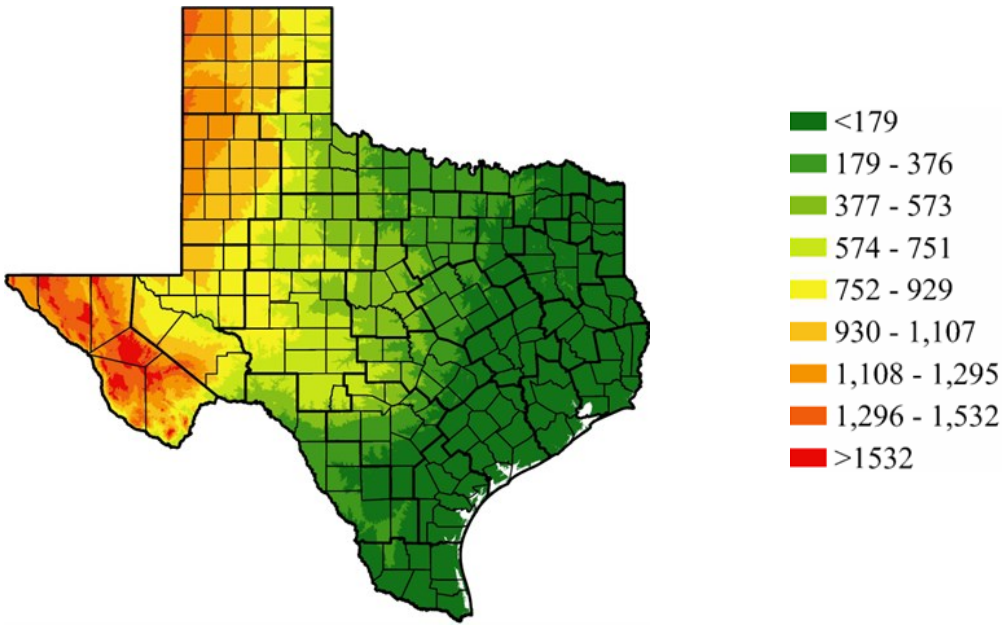
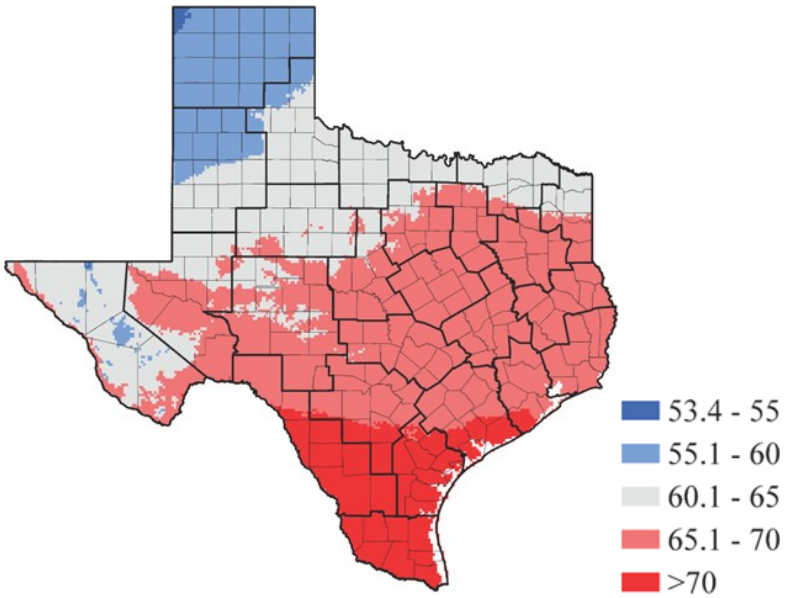


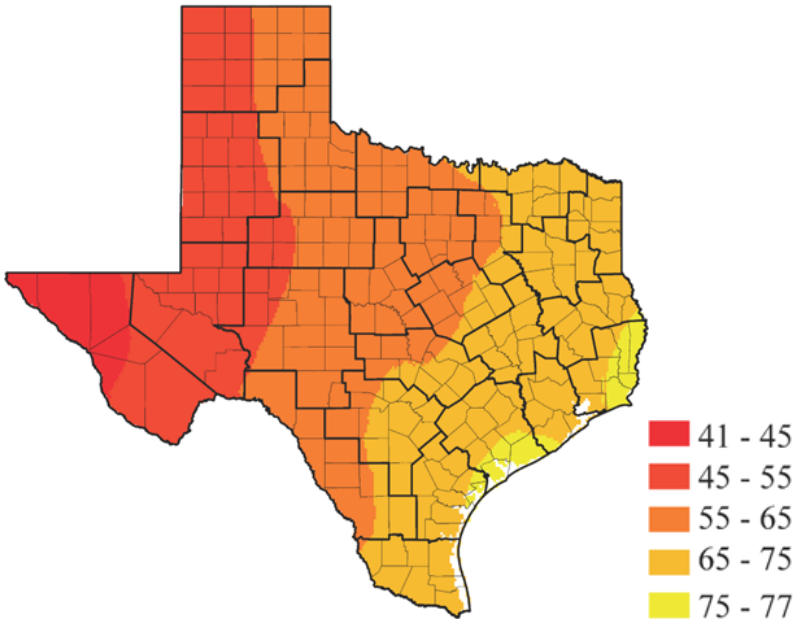
Figure 3.3. Texas Topographical Map (ft) (Daly et al., 1997)

The TOW was estimated by using the co-kriging method, with RH as the secondary variable. By incorporating the spatial cross-correlation between RH and average temperature, the co-kriging technique predicted wetness duration for different locations across the state. Texas environmental maps are shown in Figure 3.4.

Figure 3.4(a) shows the annual average temperature for Texas. As shown in this figure, the average temperature is over 70°F in the south and a little less than 55°F in the north. The amount of water vapor in the air significantly decreases at the climate stations located far from the coastline because RH drops by 40 percent. Thus, the El Paso District exhibits more dry seasons, while the average RH reaches more than 75 percent at the coastline (Figure 3.4[b]). Consequently, the annual number of FD is over 100 days a year for the northern part of the state, but freezing is rare for most southern counties (Figure 3.4[c]). The average annual TOW is less than 500 hours/year in the El Paso District, and it is over 4500 hours/year for the coastline (Figure 3.4[d]).

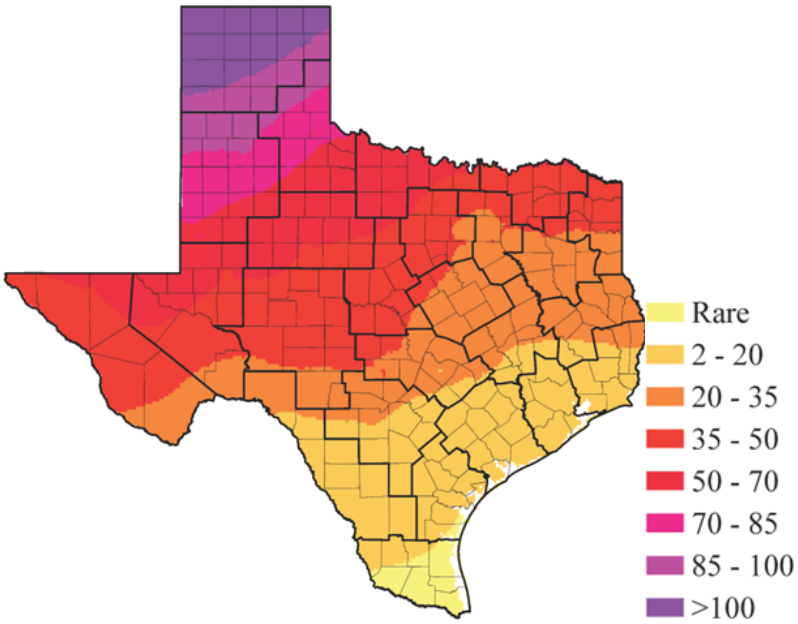


(a) Annual Average Temperature (°F) (2000–2018)

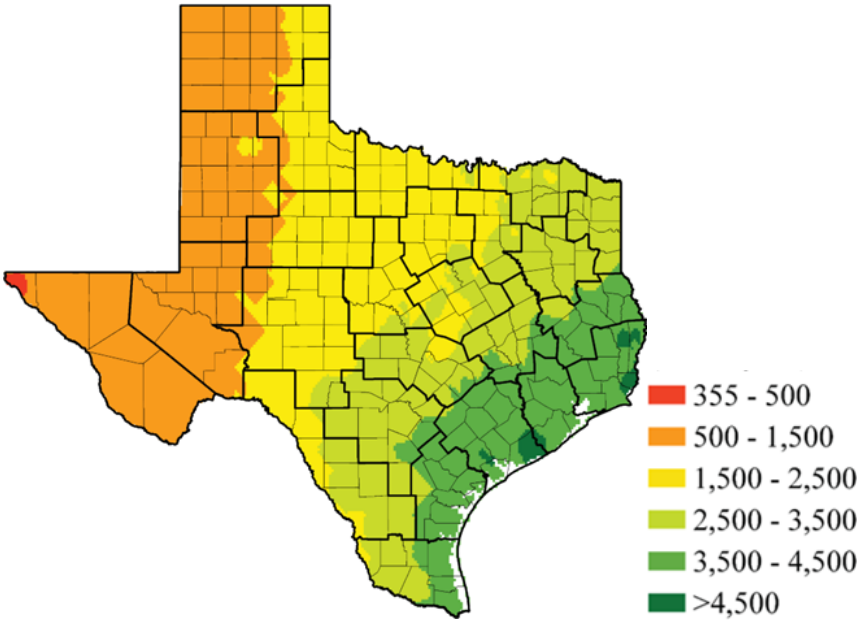


(b) Annual Average RH (%) (2000–2018)

Figure 3.4. Texas Environmental Characterizations Map.



(c) Annual Number of FD (2000–2018)



(d) Annual Average TOW (hours/year) (2000–2018)

Figure 3.4. Texas Environmental Characterizations Map (Cont.).

After analyzing the spatial interpolation results, a positive correlation was obtained between the predicted results from special interpolation procedure and the corresponding observed values collected for 250 stations from LCDs (Figure 3.5). As shown in Figure 3.5(a), the annual average temperature variations ranged between 40°F to 80°F, with a clustered data distribution between 40°F to 80°F. The annual average RH ranged from 40 percent to 80 percent (Figure 3.5[b]). The annual number of FD ranged from 0 to 250 days (Figure 3.5[c]), and TOW was distributed across 1000 to 8000 hours/year (Figure 3.5[d]).

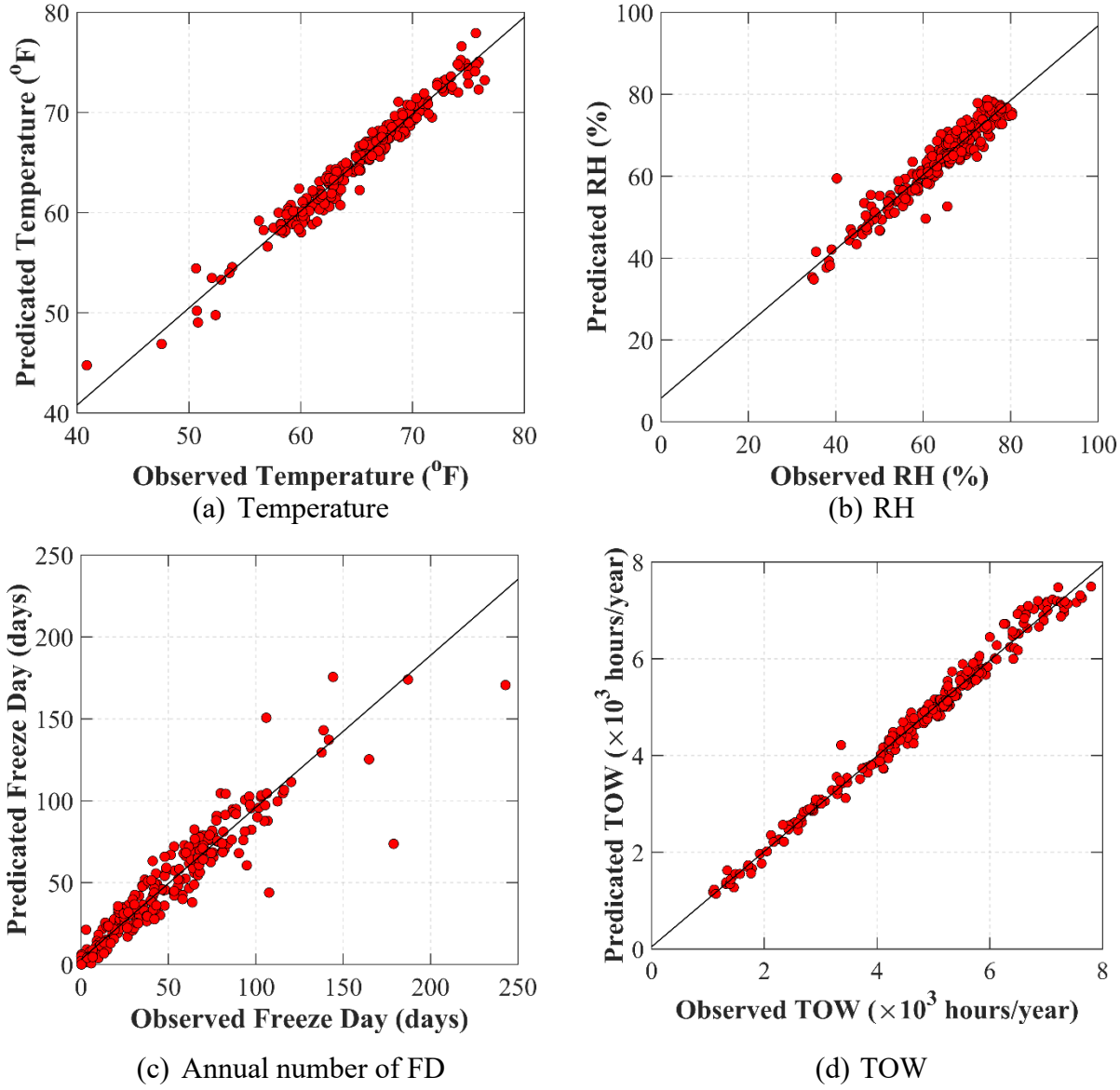


Figure 3.5. Cross-Validation between Spatial Interpolation Results and True Measurements.

3.4.2 Texas Contamination Assessment

Airborne chloride and sulfur dioxide are two parameters that intensify atmospheric corrosion on steel members. The ISOCORRAG Program (Knotkova et al., 1995) collected and documented a dataset of these two ambient air pollutants and obtained their relationship with metal loss. These two pollutants were also considered in this research to develop the corrosion risk assessment map. Deicing salt and a marine environment are two major sources of chloride that cause corrosion in steel girders and concrete decks. Bock et al. (2018) reported the annual estimation of road salt application in the United States, as shown in Figure 3.6.

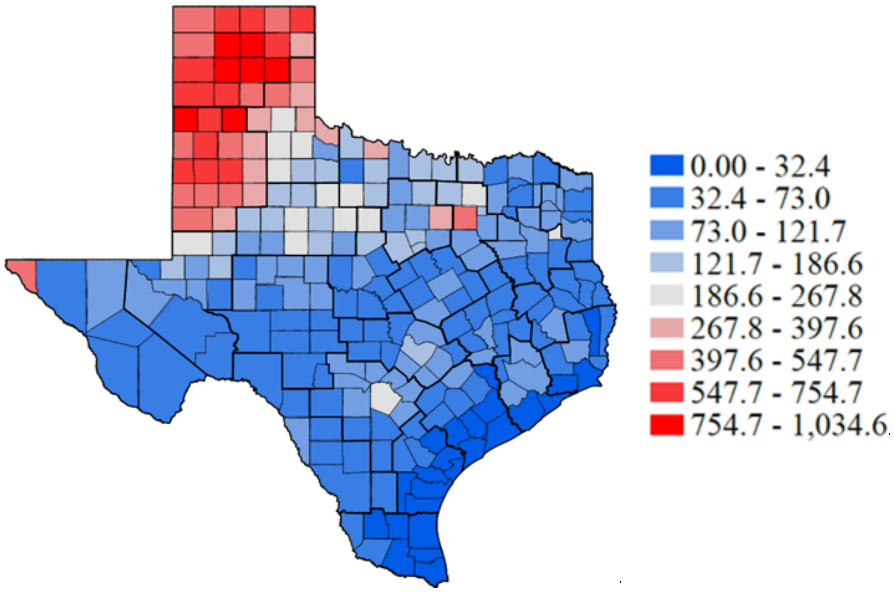


Figure 3.6. Texas Salt Application from 1992 to 2015 (lb/year) (Bock et al., 2018).

A nonlinear relationship exists between the approximate deicing salt used in each Texas county and the corresponding annual number of FD. As shown in Figure 3.7, a longer period of freezing air temperature resulted in more application of deicing salt. Therefore, it was expected that the amount of salt used on Texas roads and annual number of FD exhibit a logarithmic pattern. To predict refined data of deicing usage across Texas, an exponential relationship between deicing salt (Cl_{ds}) and the annual number of FD was developed using regression analysis:

$$Cl_{ds} = \frac{12\vartheta}{b} e^{0.03\,FD+2} \tag{3.11}$$

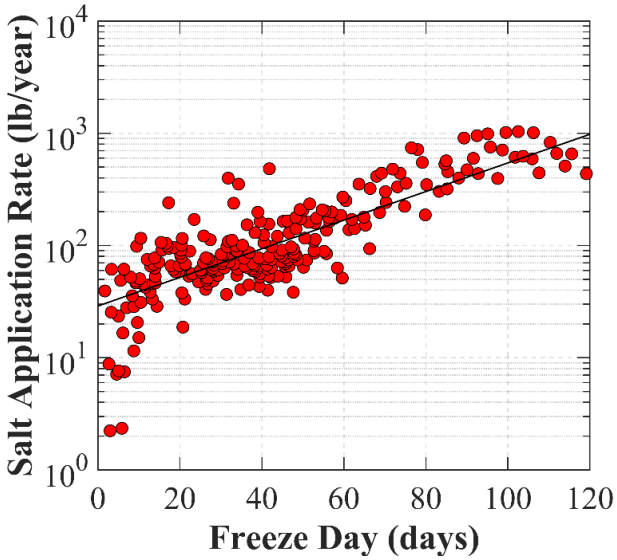
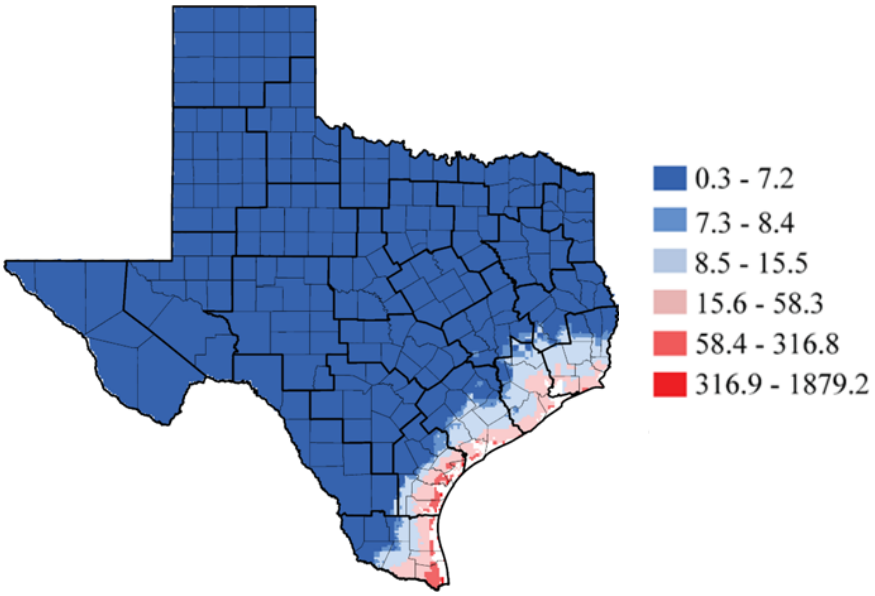


Figure 3.7. Annual Number of FD vs. Salt Application in Texas.

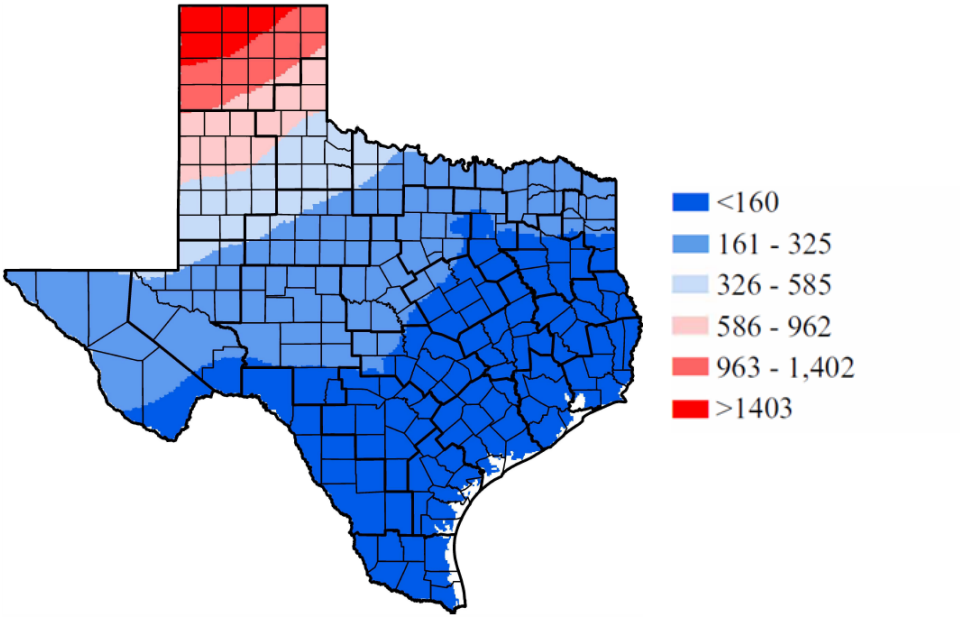
The associated R-squared value determined for this model was 0.67. The parameter b in Equation (3.11) is the average width of the roads (assumed to be 12 ft), and the factor ϑ modifies the amount of chloride deposition left over on the road over time. Tempest et al. (2014) proposed that the leftover salt on roads that can cause further corrosion problems is about 1 percent of the applied deicer; thus, the factor (ϑ) was assumed to be 0.01 for the case of using the mixture of salt and sand on the roads. Alcántara et al. (2015) proposed an empirical model to estimate the airborne chloride (Cl_a) (mg/m^2/day) at the coastline (up to 3300 ft [1000 m] from the coast). The authors proposed different models describing the airborne deposition over three-month periods. In the current study, researchers decided to use the model that gives slightly higher values of chloride deposition:

$$Cl_a = 1.63 \times 10^5 \, e^{-X/71.25} + 83.03 \qquad (3.12)$$

where X is distance from the shore in meters. Figure 3.8 shows the prediction of airborne chloride deposition and deicing salt usage in Texas. Because airborne chloride deposition significantly decreases as it moves farther away from the coastline (more than 3300 ft), researchers decided to exponentially reduce the pollutant values to low levels in the north.



(a) Airborne Chloride Deposition (mg/m^2/day)



(b) Deicing Salt Usage (mg/m^2/day)

Figure 3.8. Chloride Contamination.

Another pollutant considered in this research was annual sulfur deposition, which can come from the combustion of fossil fuels. Pickard et al. (2015) proposed mathematical models and integrated the annual average sulfate deposition rates, as shown in Figure 3.9. Note that the values represented in Figure 3.9 should be converted to volumetric deposition ($\mu g/m^3$) according to the model outlined in ISO 9223 (2012) and the ISOCORRAG Program (Knotkova et al., 1995).

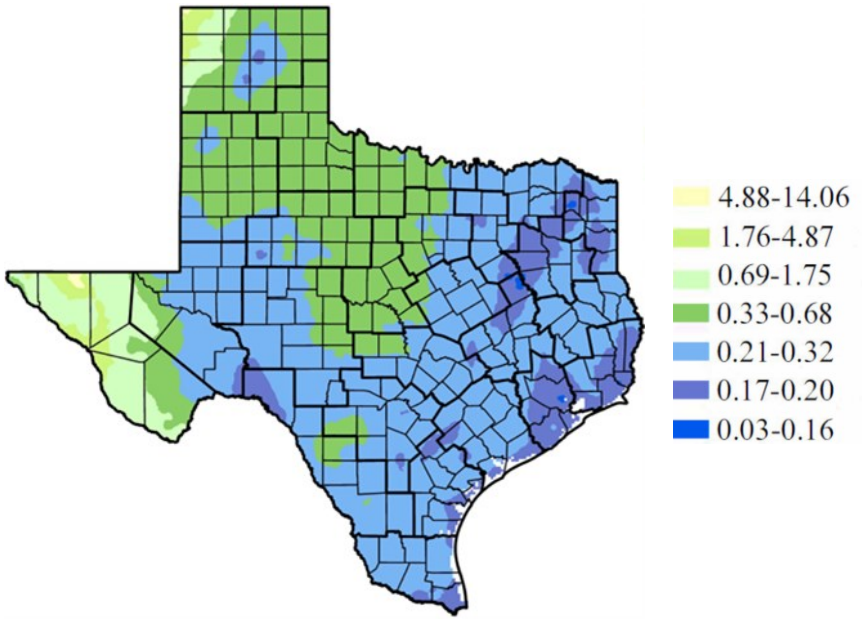


Figure 3.9. Annual Sulfur Dioxide Deposition (kg/ha) (EPA, 2023).

3.5 TEXAS CORROSION RISK ASSESSMENT

3.5.1 Atmospheric Corrosion Models

Wagner (1959) introduced the theory of ideal ionic diffusion-controlled oxidation in pure metals and suggested a time-dependent nonlinear behavior of the oxidation rate. Fontana and Greene (1967) explored Wagner's theories and suggested the use of power laws to predict the oxidation rate of iron in a diffusion-controlled environment, which were in good agreement with the experimental results. Since then, power law has been used in many studies to model the corrosion rate of metals. Fontana and Greene (1967) also addressed negative impacts of atmospheric corrosion for metals. They divided the atmosphere into marine, industrial, and rural and determined the corrosion rate of iron on the coast is 500 times higher than in other environments due to the influence of airborne chloride deposition. The rate in an industrial environment is 100 times higher than in desert and rural areas mainly because of corrosive

contaminants such as sulfur dioxide. In the 1980s, the ISOCORRAG Program was designed through collaboration of several laboratories around the world to study the effect of atmospheric corrosion in different environments (Knotkova et al., 1995; Chico et al., 2017). The findings of the study were used to develop an international standard, ISO 9223, that addressed the corrosivity of atmospheres and corrosion of metals and alloys. The ISOCORRAG Program also offered a few mathematical models to predict corrosion rates of different metals, including iron. However, these models neither considered all environmental factors that control oxidation of the metals in atmospheric conditions nor accurately predicted the rate of corrosion. Similarly, other modeling attempts (Guttman & Sereda, 1968; Haynie & Upham, 1974; Barton, 1980; Hakkarainen & Yläsaari, 1982; Knotkova et al., 1995) did not consider all the factors that impact the atmospheric corrosion of iron and often focused on just one or two specific parameters.

However, by analyzing the ISOCORRAG Program database, (Klinesmith et al., 2007) introduced a mathematical model to predict the corrosion rate of iron based on environmental factors such as TOW, sulfur dioxide concentration, salinity, and air temperature. The Klinesmith model considers a linear change of corrosion rate with time, which is a departure from the power model proposed in the past. (Landolfo et al., 2010) studied corrosion models proposed by Klinesmith et al. and concluded that although long-term predictions of Klinesmith's model are questionable, it accurately approximates the thickness loss of metals for one year of exposure. As far as current research is concerned, this model was used to estimate the risk of corrosion in different environments by considering the potential environmental factors that can impact corrosion rate of bridge structures.

3.5.2 Corrosion Risk Assessment Map

The corrosion risk assessment map developed in this study considers atmospheric corrosion based on environmental factors and airborne contamination pollutants. This map can be used to predict the potential risk of corrosivity associated with the location of bridge structures. Klinesmith et al. (2007) used the ISOCORRAG Program database to propose an empirical model to estimate weight loss of the metallic components as the result of environmental factors, including TOW, sulfur dioxide, salinity, and temperature:

$$w(t) = 13.4 \times t^{0.98} \left(\frac{\mathrm{TOW}}{3800}\right)^{0.46} \left(1 + \frac{\mathrm{SO_2}}{20}\right)^{0.62} \left(1 + \frac{\mathrm{Cl}}{50}\right)^{0.34} e^{0.016(T+20)} \tag{3.13}$$

where w is weight loss (μm), t is time (year), and T is temperature (°C). The chloride in Equation (3.13) is the summation of the amount of deicing salt and airborne chloride deposition for a given point in mg/m^2/day. Considering weight loss as a hazard, the final corrosion risk can be estimated as:

$$Risk = w(t) \tag{3.14}$$

Figure 3.10 depicts the predictions developed for the Corrosion Risk Assessment Map for Texas. This map represents the corrosivity risk environment based on different parameters discussed in this section for six divided regions. Region 1 and Region 2 designate low-risk environments in southwest Texas. Region 3 and Region 4 demonstrate the areas with medium risk of corrosivity, and Region 5 and Region 6 show the locations with a high risk of corrosion attacks. As shown in this figure, the severity of corrosion is relatively high both in the north of the state (because of the excessive amount of deicing usage) and at the coastline (because of the higher range of TOW, greater deposition of airborne chloride, and industrial activities). Figure 3.11 shows a countywide corrosion risk assessment map that was developed by averaging the prediction values for each individual county. The final results represented in this figure will aid state agencies in identifying associated risks with the new and existing steel girders and concrete decks.

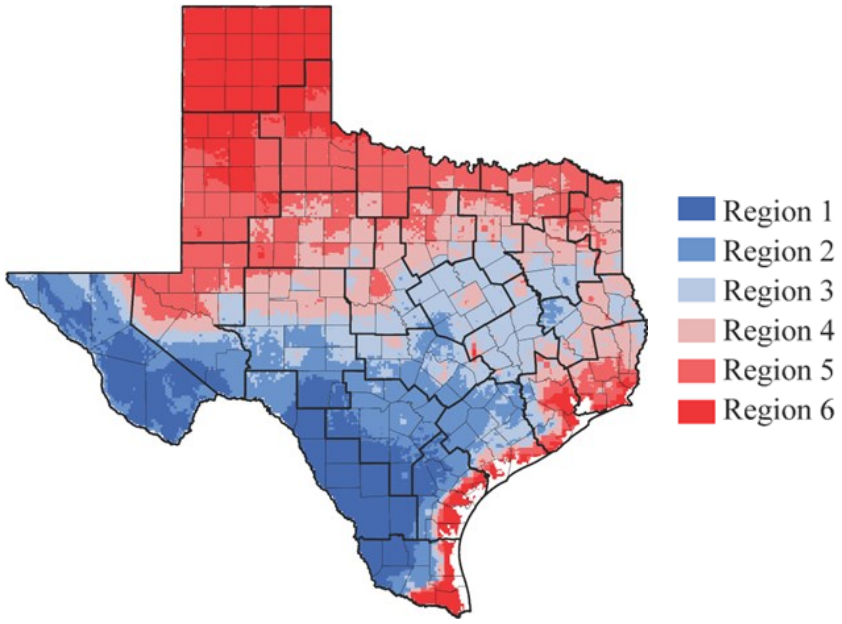


Figure 3.10. Refined Corrosion Risk Assessment Map.

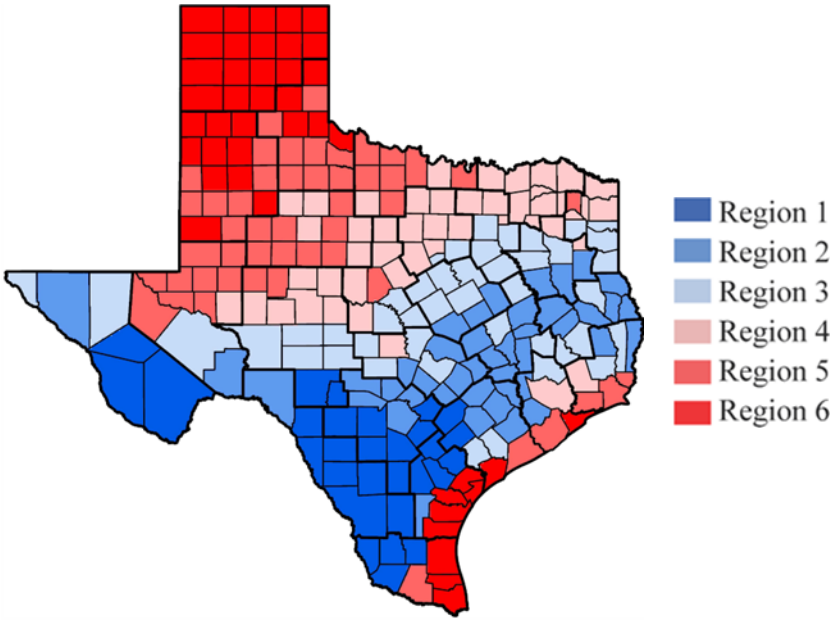


Figure 3.11. Countywide Corrosion Risk Assessment Map.

3.6 SUMMARY

Using environmental parameters, a corrosion risk assessment map was developed for Texas. The map is divided into six corrosive risk environments that can be used to identify potential corrosion hazard for bridge structures across the state. Findings suggest that the annual number of FD substantially impacts the usage of deicing salt on roads. This phenomenon typically occurs in counties located in the north of the state. In addition, the risk of corrosion is also high at the coastline as the result of airborne chloride deposition. Moreover, airborne pollutants such as sulfur dioxide can also intensify the corrosion rate of steel components in urban and industrial environments.

4 FIELD EVALUATION TO INVESTIGATE EFFECTIVENESS OF CORROSION MITIGATION

4.1 INTRODUCTION

A field evaluation was conducted in this study to understand the performance of corrosion mitigation methods used on steel bridges. This chapter describes an analysis and evaluation of the effectiveness of these techniques in different corrosion risk environments across the state and provides a detailed discussion on the performance of patina layers and paint coatings having been in service for several years.

Selecting 45 steel bridges across the state, the field evaluation commenced by visiting the selected steel girders and followed by visual inspection, field testing, and samples collections for laboratory examinations. Section 4.2 presents the initial results and discussion related to the field inspection. It highlights the findings regarding weathering steel and paint systems, especially in regard to spotting localized and poultice corrosion and investigating delamination of the patina or paint coating layers. It also provides details on patina conditions among different districts and bridge locations. The impact of environmental factors, such as chloride deposition and deicing salt usage, is also discussed. Section 4.3 offers a comprehensive analysis and discussion of the results obtained from the field inspection of steel bridges. This section highlights the results of the field evaluation of patina coatings, including the tape adhesion test, image analysis techniques, and thermal imaging. The challenges associated with measuring TOW and the proposed patina rating system are also addressed.

4.2 SELECTION OF BRIDGES

According to the TxDOT bridge database, Texas has 57,518 bridges, of which 6778 are steel girder bridges (TxDOT, 2023). For this study, it was not possible to visit all steel girders in Texas; therefore, a selection of bridges had to be made. Researchers concentrated on district and bridge selection in environments that are aggressive in nature, including marine, dry-wet cycling, and areas subjected to frequent applications of deicing salt. The aim of this task was to target steel girders with a high propensity for corrosion. To that end, Texas environmental characterization and contamination maps were used in the selection process of steel girders for field inspection and subsequent evaluation of mitigation strategies.

The effectiveness of corrosion protection systems relies on micro- and macro-environmental conditions. Macroenvironments include mild or rural (minimal to negligible exposure to airborne chlorides or deicing salts), moderate or industrial (occasional exposure to airborne chloride or deicing salts), and severe or marine (high TOW, high concentration of airborne salt deposition, or heavy usage of deicing salts). However, microenvironment refers factors such as material, layout, orientation relative to runoff, and exposure to direct sunlight.

A total of 25 weathering and 20 painted steel girders were selected across the state. This selection was based on factors such as the age of the girders, the type of superstructures, and the corrosion mitigation techniques. In the selection process, the decision was made to target girders distributed across 15 districts in Texas to account for environmental parameters that may impact the corrosion process on steel structures. These parameters were temperature, humidity, areas with high airborne chloride concentration, and urban and rural environmental conditions.

As illustrated in Figure 3.4, Figure 3.6, Figure 3.8, and Figure 3.9, Amarillo, Lubbock, and Wichita Falls Districts experience lower average annual temperatures, a higher number of annual numbers of FD, frequent use of deicing salts, and elevated airborne sulfate concentration. A total of seven steel bridges were selected from these districts. Six bridges were located in northeast Texas, including three painted and three weathering steel bridges in the Atlanta and Tyler Districts. Nine steel bridges, including six weathering and three painted steel bridges, were located in Dallas and Fort Worth Districts because they featured excessive usage of deicing salt and high average annual temperature and RH. Thirteen steel bridges with a marine environment and high concentration of airborne chloride were chosen in the Beaumont, Corpus Christi, Houston, and Yoakum Districts. Figure 4.1 shows the location of selected steel bridges inspected in this study.

Weathering steel girders were selected based on the corrosion risk assessment map introduced in Chapter 2. Two bridges were chosen for low-risk corrosion environments (Region 2) that were located in rural areas. Twenty bridges were selected for moderate risk environments (Region 3 and Region 4), and three bridges in aggressive environmental conditions with sulfur and chloride contaminants (Region 6) were selected. The majority of the bridges were located in low- to medium-corrosive risk environments because the construction of weathering steel bridges in coastal areas and regions where deicing salt is not recommended by most DOTs. Out of 25 weathering steel girder bridges (Figure 4.2), 15 structures were less than 30 years of age, and 10

were older than 30 years. All the selected bridges had a superstructure condition rating between 4 and 8 in the Texas bridge database. Details on the selected bridges can be found in Table 4-1.

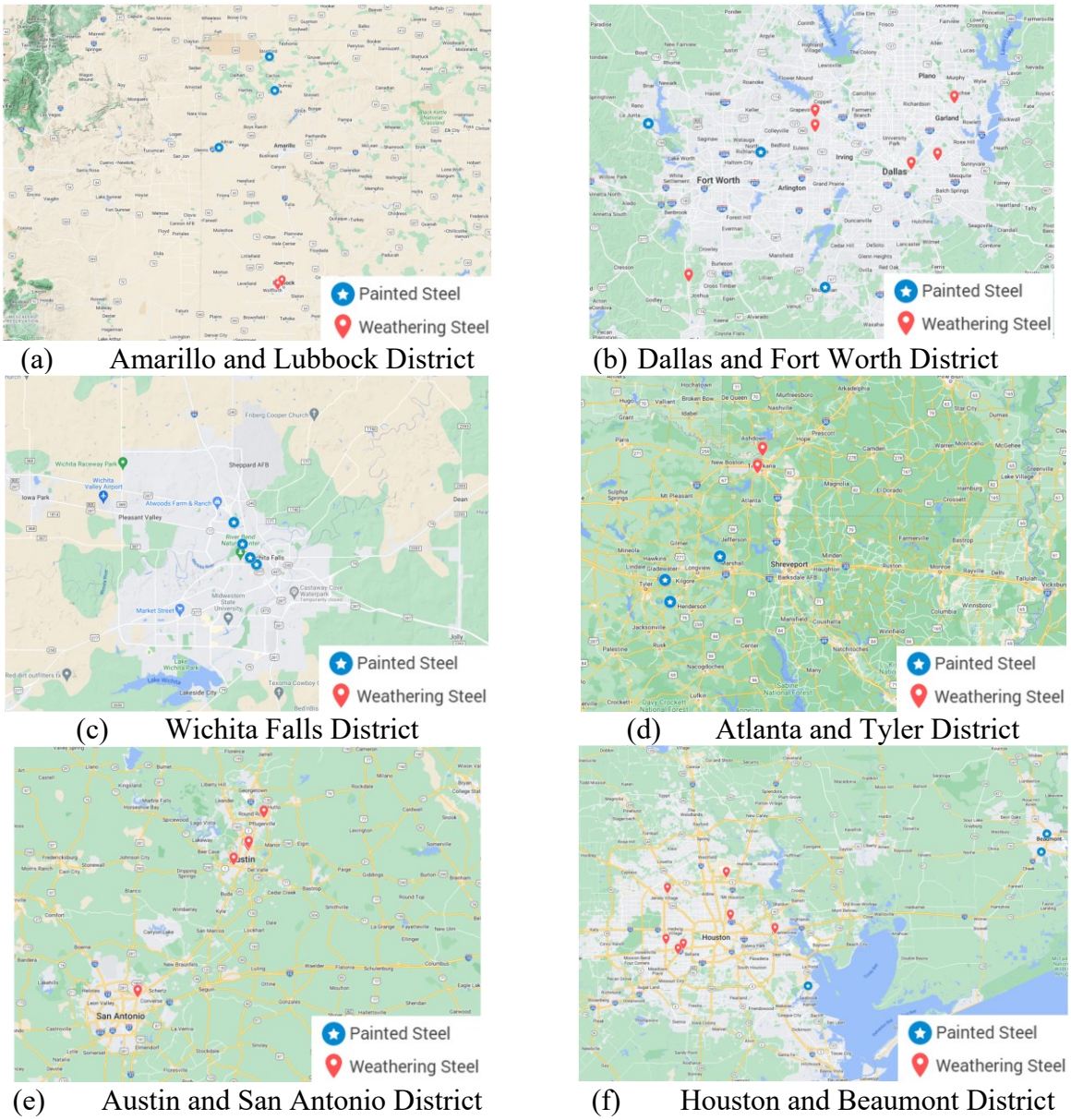
In terms of painted bridges, researchers selected one individual steel girder bridge in a low corrosion risk area (Region 2), eight in moderate risk regions (Region 3 and Region 4), and eleven in high-risk regions. Figure 4.3 shows the locations of all the painted steel bridges. Table 4-1 also provides detailed information about the selected steel girder bridges, including the location of these bridges. A total of 20 painted bridges were selected, including 13 painted bridges built after 1995 and seven of them built before 1995 (Figure 4.3). In this project, the ZBPS, which was used in Texas after 1995, was used as one of the selection criteria for the painted steel bridges. Similar to weathering steel bridges, all of the selected painted steel girder bridges, including three off-system bridges and 17 on-system bridges, had superstructure condition ratings between 4 and 8. The map in Figure 4.3 gives the locations of the painted steel bridges.

Six painted steel bridges built over water bodies like rivers or creeks were inspected to assess the performance of the paint system in this environmental condition. Researchers selected two bridges in coastal areas (i.e., Corpus Christi and Beaumont District) to account for the aggressive environmental condition due to the high airborne chloride deposition rate. More information about these bridges can be found in Table 4-2.

Among the selected painted steel bridges, three off-system structures selected in Atlanta (Region 3), Bryan (Region 2), and Yoakum (Region 5) Districts had a superstructure condition rating of 5, with severe paint deterioration. Two of these three bridges had painted steel piles and one had steel girders. In addition, researchers conducted field inspection on two reinforced concrete bridges with steel girders located in Wichita Falls and three bridges in Amarillo Districts. Two of these bridges had painted steel piles and one had painted steel girders.

For long-term monitoring of environmental condition and their effects on steel components, a datalogger equipped with sensing devices to measure temperature and RH was installed on five bridges located in different environments. The sensor was an Onset HOBO S-LWA-M003 Leaf Wetness Smart Sensor that was also capable of estimating TOW. The five steel girders were located in Atlanta (Region 4), Corpus Christi (Region 6), Dallas (Region 3), Houston (Region 4), and Lubbock (Region 6) Districts. These structures were selected to study the effect of different parameters, such as high RH in Atlanta District, deicing salt usage in Dallas and Lubbock Districts, and airborne chloride concentration near coastal areas in Houston and Corpus

Christi Districts. The objective of measuring temperature, RH, and TOW was to validate the environmental data from weather stations located close to the bridges. Figure 4.4 and Figure 4.5 shows bar chart for weathering and painted steel representing distributing of bridge age and distribution of bridges across all the regions respectively.



(a) Amarillo and Lubbock District (b) Dallas and Fort Worth District

(c) Wichita Falls District (d) Atlanta and Tyler District

(e) Austin and San Antonio District (f) Houston and Beaumont District

Figure 4.1. Map Showing Selected Steel Bridges.

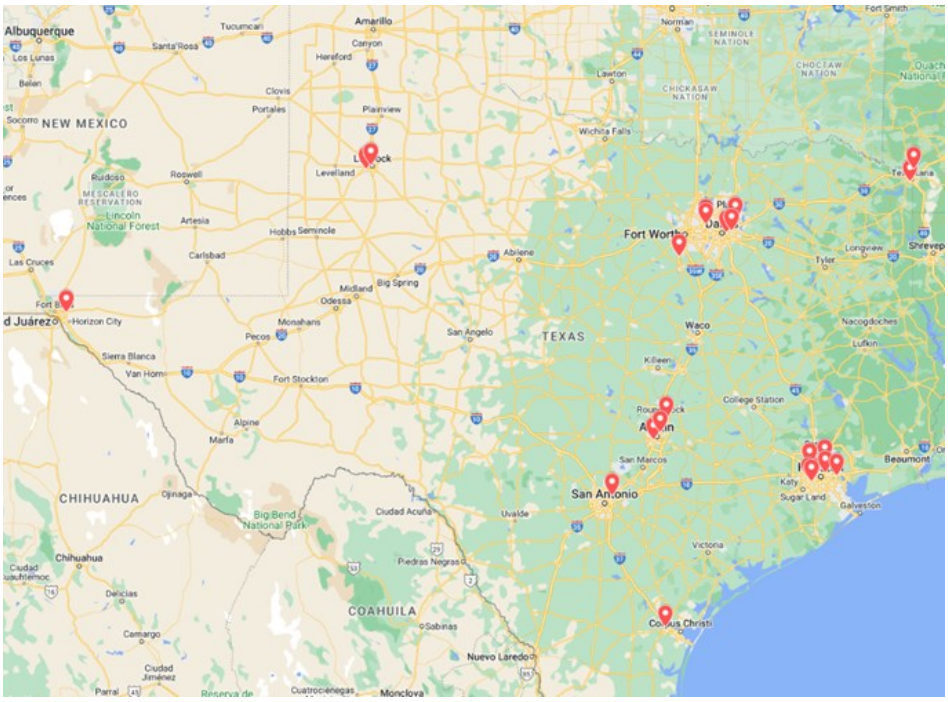


Figure 4.2. Selected Weathering Steel Bridges.

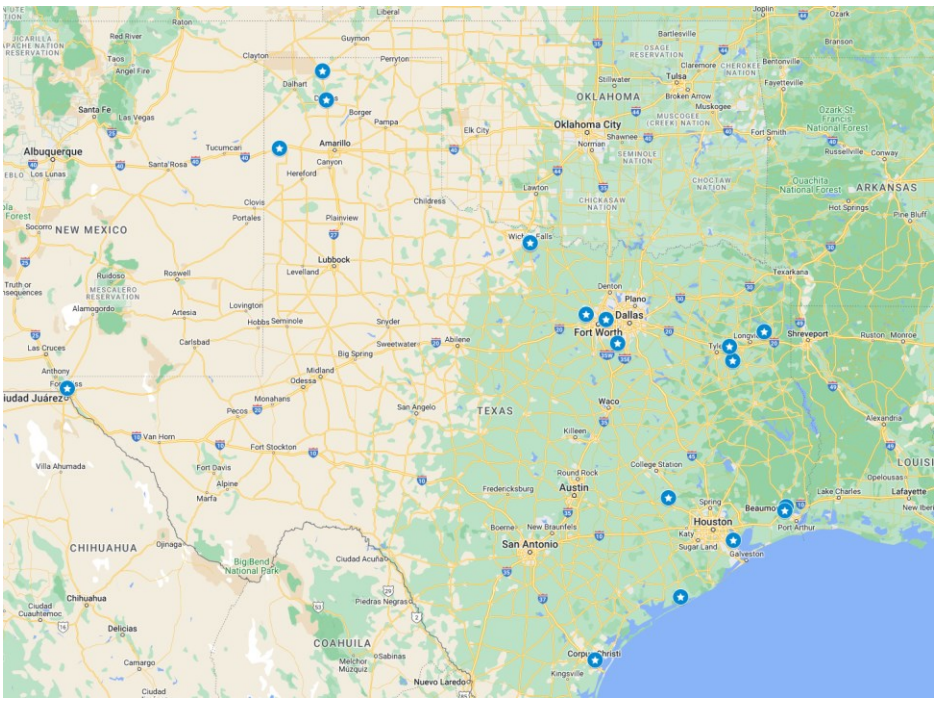


Figure 4.3. Selected Painted Steel Bridges.

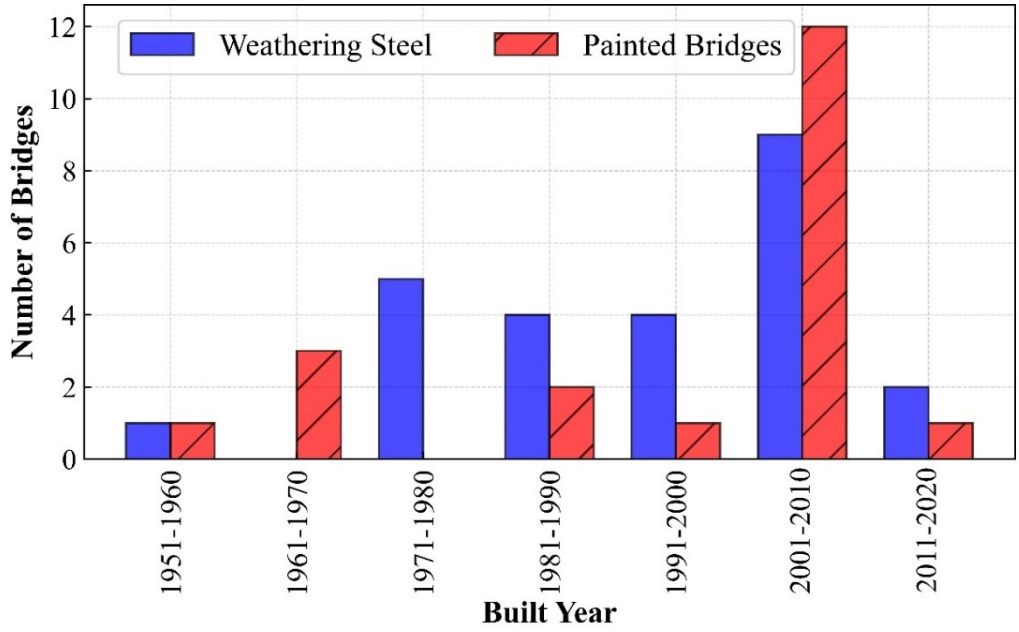


Figure 4.4. Distribution of Bridge Age.

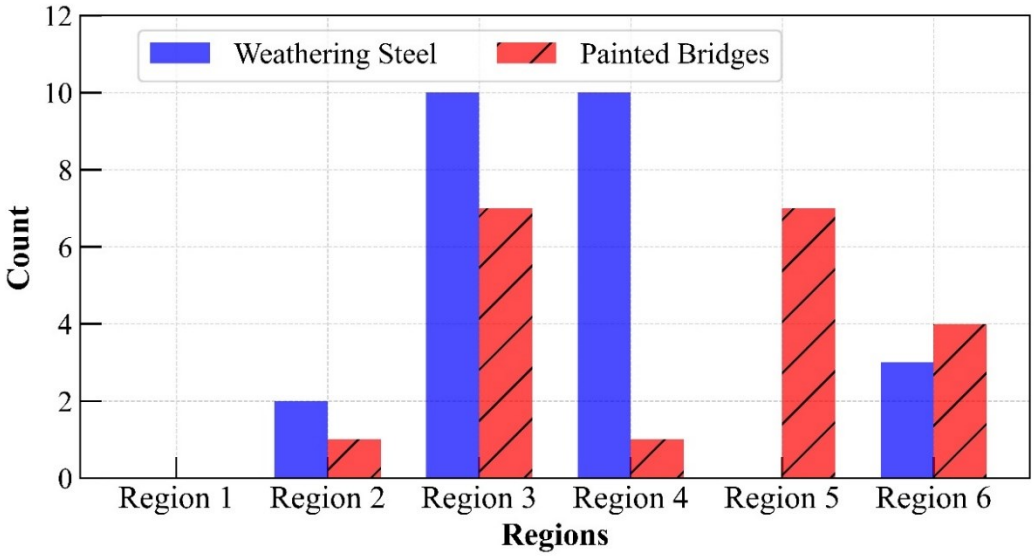


Figure 4.5. Distribution of Bridges—Region.

Table 4-1. Weathering Steel Bridge.

Bridge Name	Bridge ID	Built Year	Facility Carried and Intersected	Member Type
ATL−WS−01	190190205003072	2004	LP 151 SB over SH 93	Box Girder
ATL−WS−02	190190205003074	2004	US 59 NB TO IH 369 NB over LP 151 SH 93 Corral Creek	Box Girder
ATL−WS−03	190190021701007	1976	US 59/71 SB over Red River	Plate Girder
AUS−WS−01	142270001513363	1977	IH 35 N T/A @ 51st over IH 35	Plate Girder
AUS−WS−02	142270011313114	1997	US 290 EB over Manchaca/Westgate Blvd.	Plate Girder
AUS−WS−03	142270068307073	2006	Heathewilde Blvd. over SH 45	Plate Girder
AUS−WS−04	142270001513451	2002	IH 35 NB to US 290 EB over IH 35 NB FR	Box Girder
CRP−WS−01	161780037301038	2007	FM 624 Conn over US 77 SB	Plate Girder
DAL−WS−01	1805709F4360012	1973	S Fitzhugh Ave. SB over UP RR	Box Girder
DAL−WS−02	180570296406467	2011	SH 190 EB On-Ramp over SH 190 EB Off-Ramp	Plate Girder
DAL−WS−03	180570000911373	1960	Big Town Blvd. SB over IH 30	I-Beam
ELP−WS−01	240720037402084	2003	LP 375 over US 62 (Montana Ave)	Plate Girder
FTW−WS−01	22200BB0985007	1974	N Intl Pkwy 1-1E over Ramps C-1S C-1N	Plate Girder
FTW−WS−02	22200F00189003	1974	N Intl Pkwy (2-5E) over Crossunder #6 Road	Plate Girder

Table 4 1. Weathering Steel Bridge (Cont.).

Bridge Name	Bridge ID	Built Year	Facility Carried and Intersected	Member Type
FTW−WS−03	21270050405501	2014	SH 121 (NTTA) over FM 1902B	Plate Girder
HOU−WS−01	121020002713209	1993	US 59 SBML over Westpark Dr.	Plate Girder
HOU−WS−02	121020TOL010109	2006	IAH Conn Ramp over JFK Blvd.	Box Girder
HOU−WS−03	121020325601192	1990	BW 8 NB over West Road	Plate Girder
HOU-WS-04	121020125804124	1987	BW 8 SB over Westheimer Pkwy. (FM 1093)	I-Beam
HOU−WS−05	121020B40177001	1989	Lockwood Dr. NB over HB&T RR	Plate Girder
HOU−WS−06	121020002713240	1992	IH 69 / US 59 NBML over Bellaire Blvd.	Plate Girder
HOU−WS−07	121020050801447	1994	CON IH 10 EB-BW8 SB over IH 10 EBFR/BW8 SBFR/UP RR	Plate Girder
LBB−WS−01	51520038001002	2009	US 82 EB DIR Conn over LP 289 FR US 82 FR	Plate Girder
LBB−WS−02	51520038001038	2009	4th East Ramp over US 82	Plate Girder
SAT−WS−01	150150001710329	1983	IH 35 SBML over IH 410 Conn & Randolph	Plate Girder

Table 4-2. Painted Steel Bridge Information.

Bridge Name	Bridge ID	Built Year	Facility Carried and Intersected	Member Type
AMA−PS−01	42110006603025	1986	US 287 NB over Coldwater Creek	Steel Piles
AMA−PS−02	41710006604020	1981	US 287 NB over South Palo Duro Creek	Steel Piles
AMA−PS−03	41800009002031	1961	IH 40 EB over Ivy Road	I-Beam
ATL−PS−01	191030AA0109001	2004	CR 4106 over Bear Creek	I-Beam
BMT−PS−01	201240020011132	1966	US 69-96-287 NB over US 69 SB Conn to IH 10 EB	I-Beam
BMT−PS−02	201240073902013	1961	Walden Road over IH 10 WB	I-Beam
BRY−PS−01	172390AA0291001	2004	Running River Ln. over Doe Run Creek	I-Beam
CRP−PS−01	161780010106041	1959	US 181 over CC Ship Channel	Truss
DAL−PS−01	180710026101225	2007	Ramp L (to US 67 NB) over US 287 BUS	I-Beam
ELP−PS−01	240720104603116	2000	Carrington Road over Spur 601	Plate Girder
FTW−PS−01	22200000813420	2002	IH 820 Ramp K over SH 121	Plate Girder
FTW−PS−02	22200017104049	2007	SH 199 EB over FM 730	I-Beam
HOU−PS−01	121020038905356	2016	SH 146 NB Connector over UP RR Frtg. Road	Plate Girder

Table 4 2. Painted Steel Bridge Information (Cont.).

Bridge Name	Bridge ID	Built Year	Facility Carried and Intersected	Member Type
TYL−PS−01	102120024507306	2009	SH 64 over SH 135	Plate Girder
TYL−PS−02	102120049506385	2009	CR 3100 over IH 20	I-Beam
WFS−PS−01	32430004309191	2001	IH 44 SB over Maurine St.	I-Beam
WFS−PS−02	32430004309193	2001	IH 44 SB over N 8th St.	I-Beam
WFS−RC−01	32430004309188	2001	IH 44 NB over 6th St.	I-Beam
WFS−RC−02	32430004309202	2001	IH 44 SB	I-Beam
YKM−PS−01	131580AA0220001	2004	N Gulf Rd./CR 244 over Little Boggy Creek	I-Beam

4.3 SELECTED MITIGATION METHODS

Adopting a cost-effective mitigation technique that provides better corrosion resistance and delays the onset of steel girders' deterioration due to a corrosive environment is a major challenge affecting the service life of bridge structures in different micro- and macroenvironmental conditions. This section describes corrosion protective systems adopted by TxDOT for use in weathering and painted steel bridges. These mitigations include corrosion-resistant steel, weathering steel, and zinc-rich primer paint systems.

4.3.1 Weathering Steel Bridges

Weathering steel is a low-alloy steel and offers corrosion protection if the protective layer (patina) is properly developed on the steel surface. The patina layer adheres to the surface and prevents further corrosion activities on the steel substrate. TxDOT allows construction of weathering steel bridges across the state except in coastal locations. In the past, ASTM A242 (2018) and ASTM A588/A588M (2019) Grade 50 were the steel used in these types of steel

bridges, but the state agency decided to use modern weathering steel for new constructions, such as ASTM A709/A709M (2021) Grade HPS 50W, ASTM A709/A709M (2021) Grade 50S, and ASTM A709/A709M (2021) Grade HPS 70W.

4.3.2 Painted Steel Bridges

TxDOT employs standardized paint systems for the application of primer and appearance coats to protect both newly constructed and pre-existing steel bridges from a corrosive environment. System I and System II adhere to the guidelines outlined in department materials specifications (DMSs) (DMS 8100, 2004; DMS 8101, 2007).

System I-A consists of a single layer overcoat with a DFT of no less than 4.0 mils. System I-B is designed to be used on steel surfaces that are more susceptible to corrosion damage. This system consists of three distinct layers—a penetrating sealer, an epoxy intermediate primer, and a polyurethane appearance coat. Each layer is applied with a different DFT range. System II is a common paint system employed in steel girders for field painting across the state except for coastal areas. This system consists of two coats: an epoxy zinc primer and an acrylic latex appearance coat. In addition, TxDOT recommends the use of paint coating systems, according to DMS-8101 standard, classified as Level III for structures located in highly corrosive environments. System III-A is designed for use on coastal bridges and on structures subjected to the corrosive effects of deicing salts. This system includes a primer, intermediate epoxy coatings, and a polyurethane appearance coat. System III-B is specifically designed for painting newly constructed steel bridges located in coastal regions. This system consists of an IOZ primer and epoxy coatings. System IV-A is a recommended method for applying paint to newly fabricated steel structures in noncoastal areas. This system consists of two layers: an initial layer of IOZ primer followed by a topcoat of acrylic latex paint.

4.4 FIELD EVALUATION

The field inspection conducted in this research includes both visual inspection and nondestructive testing. The examinations performed in the field include a visual inspection, a tape adhesion test, a chloride test, a pH test, an ultrasonic thickness gauge measurement, pull-off adhesion tests, documentation of any crack or section loss of a member, and collection of patina

and paint samples from the web of the exterior and interior girders for future laboratory evaluation. Table 4-3 provides summarizes the field tests performed on weathering and painted steel.

Table 4-3. Field Tests Performed on Steel Bridges.

Field Inspection Tests	Weathering Steel	Painted Steel
Visual inspection	Yes	Yes
Chloride test	Yes	Yes
pH test	Yes	Yes
Ultrasonic thickness measurement	Yes	Yes
Scrape test	Yes	Yes
Tape adhesion test	Yes	No
Pull-off adhesion testing	No	Yes
IR thermography	No	Yes

Field examinations were performed at the locations shown in Figure 4.6 and Figure 4.7 for the steel girders, including 2 to 4 ft from the abutment or bent. Inspections were performed on the exterior and interior girders to account for microclimatic conditions. For example, the paint coating or developed patina layers on exterior girders becomes more quickly wet and dry than the protective layers on interior girders. Additionally, the paint and patina can be more easily washed away by rain on exterior girders than on interior girders. Temperature and RH are also different on the fascia because of direct exposure to sunlight, wind, and rain.

Acronyms used in Figure 4.6 are “A1” for Abutment 1, “B2” for Bent 2, and “G1” for Girder 1, according to as-built drawings. “F1” is the exterior face (or face parallel to the exterior face) of Girder 1. “F2” is the interior face (or face parallel to the interior face) of Girder 1, as shown in Figure 4.6. A total of four faces (two interior and two exterior) were typically selected for field testing. For example, in Figure 4.6, the four faces selected for inspection were G1F1, G5F1, G9F2, and G18F2. Figure 4.7 shows more detail on locations of field testing on steel bridge girders inspected during this research.

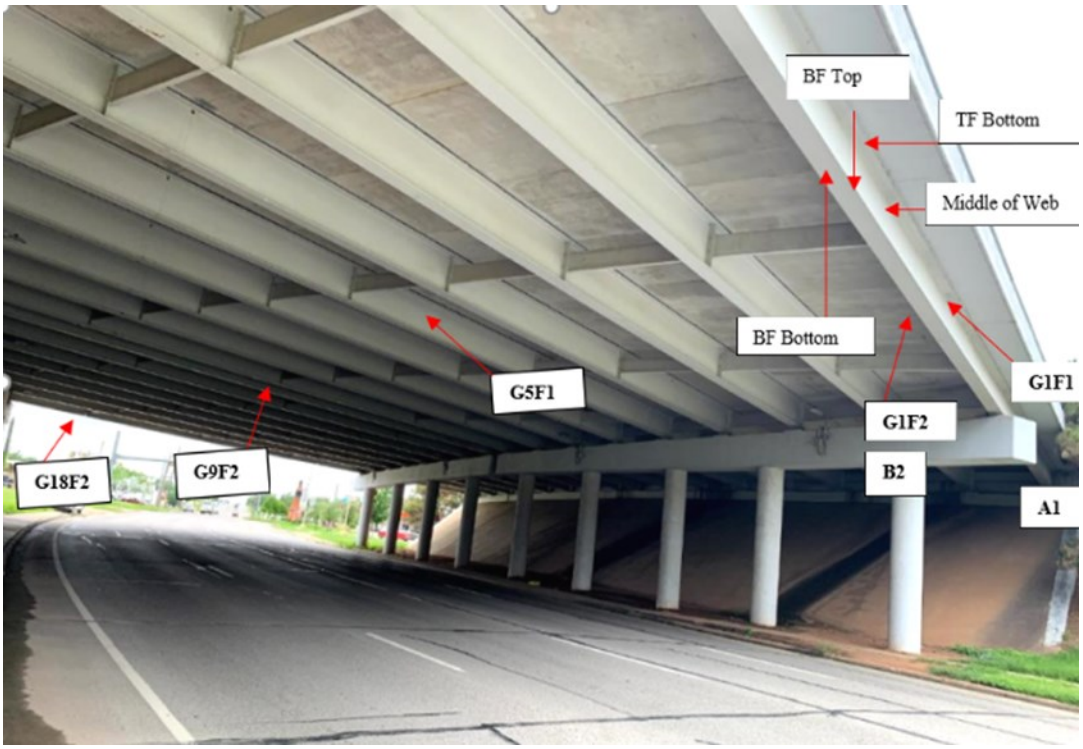


Figure 4.6. Typically Inspected Locations on Girders.

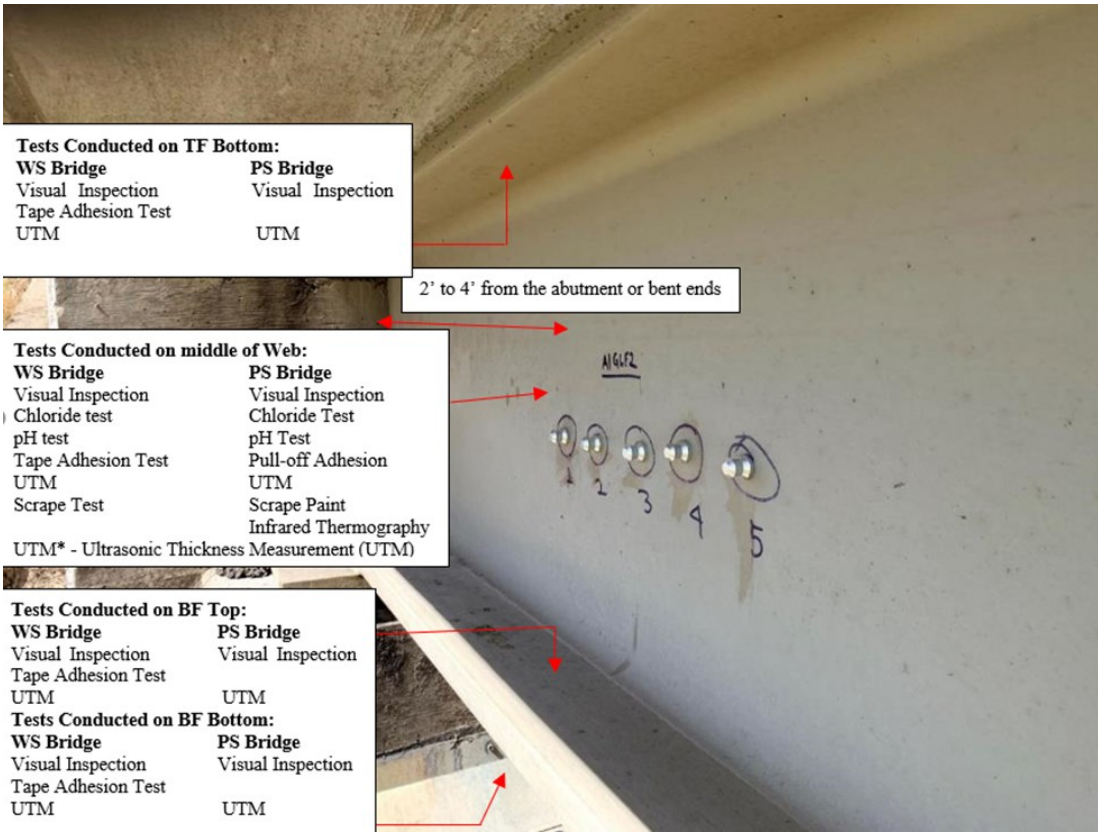


Figure 4.7. Typical Location for Field Testing on Steel Girders.

4.4.1 Visual Inspection

Visual inspection is a fast and effective way to assess patina conditions for weathering steel bridges. In this study, visual inspection was performed on the top flange/bottom face, web, bottom flange/top face, and bottom flange/bottom face of selected steel girders, and the results, including corrosion-related issues, delamination of the rust layers, poultices corrosion, and pitting corrosion, were documented for further analysis. Figure 4.8 and Figure 4.9 (a), (b) and (c) shows an example of a visual inspection of a weathering steel girder.

Visual inspection was conducted to assess the performance of painted steel girders, as well. This examination included rating the degree of rust on a 0-to-10 scale, as stated in ASTM D610 (2019); evaluating the degree of checking (ASTM D660 (2019); assessing the degree of erosion, as outlined in (ASTM D662, 2019); and determining the degree of blistering (ASTM D714, 2017). Besides rust—which was observed to develop on the steel surface—other types of corrosion did not occur on steel girders inspected in this research. The ASTM D610 (2019) classifies rust into four categories: spot rust (S), general rust (G), pinpoint rust (P), and hybrid rust (H). In addition, ASTM D610 (2019) describes the rust rating and provides pictorial examples of rusted areas in percentages to determine the severity of developed rust on steel surfaces. Table 4-4 provides the criteria for evaluation of paint systems' performance based on rusted surfaces of the structural member.

Table 4-4. Description of Rusting Ratings for Painted Bridges (ASTM D610, 2019).

Rust Grade	Percent of Surface Rusted	Visual Examples		
		Spots (S)	General (G)	Pinpoint (P)
10	Less than or equal to 0.01%	None		
9	Greater than 0.01% and up to 0.03%	9-S	9-G	9-P
8	Greater than 0.03% and up to 0.1%	8-S	8-G	8-P
7	Greater than 0.1% and up to 0.3%	7-S	7-G	7-P
6	Greater than 0.3% and up to 1.0%	6-S	6-G	6-P
5	Greater than 1.0% and up to 3.0%	5-S	5-G	5-P
4	Greater than 3.0% and up to 10.0%	4-S	4-G	4-P
3	Greater than 10.0% and up to 16.0%	3-S	3-G	3-P
2	Greater than 16.0% and up to 33.0%	2-S	2-G	2-P
1	Greater than 33.0% and up to 50.0%	1-S	1-G	1-P
0	Greater than 50%	None		



(a) Developed Patina (Exterior Girder)



(b) Developed Patina (Top Flange of the Interior Girder)



(c) Plate Girder



(d) Patina Condition of Bent Cap



(e) Tape Adhesion Test

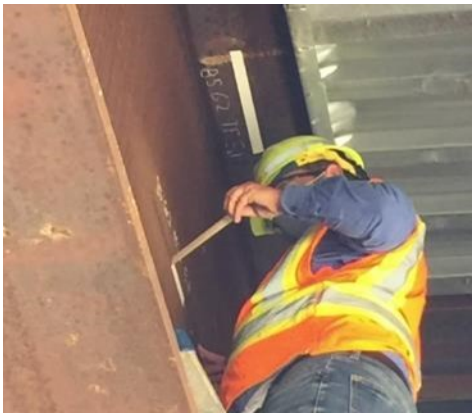


(f) Box Girder

Figure 4.8. Visual Inspection and Tape Adhesion Test.



(a) Top Flange (Exterior Girder Near Abutment)



(b) Removal of Tape (Adhesion Testing)



(c) Exterior Girder Near Bent Cap



(d) Chloride Test Kit



(e) Chloride Testing (Web of Exterior Girder)



(f) Sleeve Attached to the Girder Surface

Figure 4.9. Chloride Test and Tape Adhesion Test.

4.4.2 Chloride Test

To correlate chloride ion concentrations measured on the web of the exterior and interior girder of weathering and painted steel bridges, an eCHLOR*TEST© chloride testing kit was used in the field, as shown in Figure 4.9(d) and Figure 4.9(f). Typically, the test is performed at locations shown in Figure 4.6 and Figure 4.7.

The test procedure for conducting the eCHLOR*TEST is as follows:

1. Select the examining location and prepare the surface to which the sleeve will adhere.
2. Remove the extraction solution into the latex test sleeve.
3. Peel the backing from the adhesive foam at the mouth of the sleeve.
4. Remove excess air from the sleeve and seal the mouth to the weathered surface.
5. Manipulate the solution for 2 minutes.
6. Capture the solution in the lower free end of the sleeve.
7. Remove the sleeve from the surface and return it to the original location in the kit.
8. Remove the plunger from the auto-vial filter assembly and place the funnel into the auto-vial filter assembly.
9. Pour the extract solution from the sleeve through the funnel into the filter.
10. Collect the filtered liquid into the bottle.
11. Titrate the liquid with silver nitrate solution and test in an electronic chloride tester for chloride concentration.

4.4.3 pH Test

The pH level is effective in developing a stable protective layer on weathering steel structures. Goethite that is amorphous oxyhydroxide can form in an alkaline environment with a pH level at 12.5 to 13.5, but lepidocrocite can develop at a pH around 6.0–6.5 ((Misawa et al., 1974; Yamashita et al., 1994). Chen et al. (2010) noted that acidity or alkalinity of the steel surface directly influences a continuous and dense protective patina layer. The pH level affects the ability of zinc-based coatings to maintain protection against corrosion. Some researchers (Wilmot, 2007; Goodwin, 2018) suggested that the corrosion rate of zinc varies with the pH level, and the attack is most severe at a pH below 6 and above 12.5. Figure 4.10 shows pH stripes used during field testing. The pH test locations are shown in Figure 4.6 and Figure 4.7, and the test procedure is outlined below:

1. Clean the surface with a brush to remove dirt and debris.
2. Spray deionized water on the testing area.
3. Keep the pH testing strips in contact with the wet surface for 30 seconds to 60 seconds.
4. Use two pH strips at each location for consistency in measurements.



Figure 4.10. pH Strips Used for Field Testing.

4.4.4 Ultrasonic Thickness Measurement

The ultrasonic thickness gauge (Olympus 27 MG©) was employed to measure thickness of both flanges and the web of selected steel girders (Figure 4.11). Overall, three thickness measurements were taken at four locations on the exterior and interior girders as per ASTM E797/797M (2021). These spots were the bottom face of the top flange, the web, the top face of the bottom flange, and the bottom face of the bottom flange, as shown in Figure 4.6 and Figure 4.7.

Provided below is the procedure for taking ultrasonic thickness measurements:

1. Attach the dual transducer at the top of the thickness gauge.
2. Calibrate the thickness gauge with the given test block.
3. Apply the couplant between the transducer and measuring surface.
4. Document the readings.



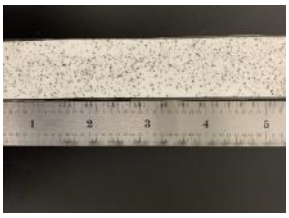
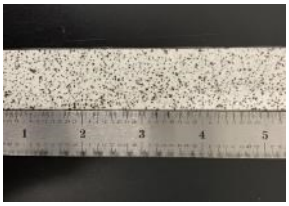
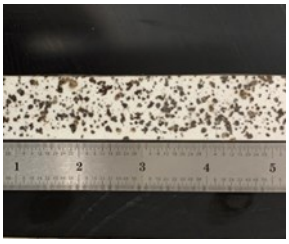
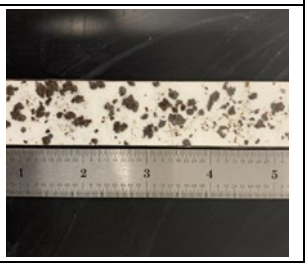
Figure 4.11. Olympus 27 MG Ultrasonic Thickness Gauge.

4.4.5 Tape Adhesion Test

A tape adhesion test was only conducted on weathering steel, and it provided details on the adherence property of the patina layer, rust flake size, and rust spatial distribution. Elcometer 99© crosshatch tape was used since it is equivalent to the Permacell P-99 tape recommended by ASTM D3359 (2017). Note that the production of Permacell P-99 crosshatch tape stopped in 2009. Figure 4.8(e), Figure 4.9(a), and Figure 4.9(c) show the tape adhesion testing being conducted in the field. Figure 4.6 and Figure 4.7 show the tape adhesion test locations. Table 4-5 shows the patina rating observed during field inspection. The outlined procedure below describes the tape adhesion test:

1. Attach 6- to 12-in. long strip to the patina surface.
2. Peel off the tape from the surface quickly and smoothly (after one minute).
3. Preserve the rust information on the tape.
4. Apply transparent tape to the face where the rust particles attached to the initial tape.
5. Remove the extra clear tape from the sides.
6. Store tape specimens inside the sample bags for future assessment and reference.
7. Assign a patina index rating based on the rust size and density of the collected tape test specimen.

Table 4-5. PRI Scale.

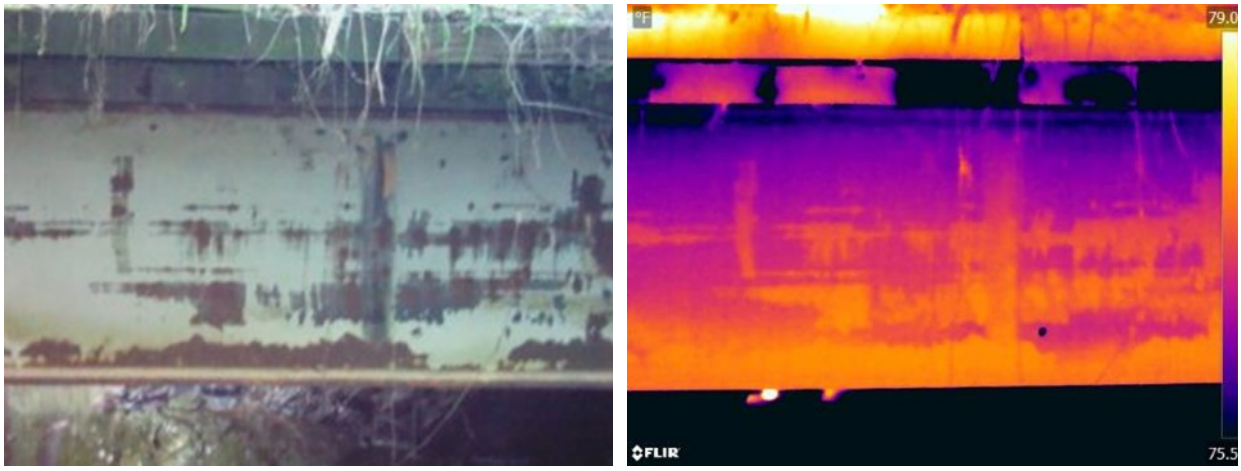
Iowa-Based PRI	Rust Particle Size	Field Condition	Tape Test
8	< 39.4 mils		
7	< 39.4 mils		
6	39.4–196.9 mils		
5	196.9–984.3 mils		

4.4.6 Infrared Thermography

Infrared thermography was performed on painted steel bridges to determine subsurface defects on underlying paint coatings such as internal rusting, blistering, erosion, and cracking. A FLIR T640© camera (Figure 4.12) was used to document the paint condition of exterior and interior girders, steel piles, and angles or stiffeners between girders. Figure 4.13 shows an example of digital and thermal imaging of an external girder taken from steel components of an off-system bridge in the Atlanta District (ATL−PS−01).



Figure 4.12. Infrared Thermography FLIR T640 Camera.



(a) Digital Image (b) Thermal Image

Figure 4.13. Digital and Thermal Image of an Exterior Girder of ATL−PS−01

4.4.7 Pull-Off Adhesion Testing

As in ASTM D4541 (2017), a pull-off adhesion test was conducted on painted steel bridges to evaluate the pull-off strength of the coatings on the web of the exterior and interior girders. A pull-off adhesion tester (Elcometer 510 automatic pull-off adhesion tester© (Figure 4.14)) in addition to at least five dollies was employed to determine the maximum pull force of paint coatings. Typically, the test is performed at locations shown in Figure 4.6 and Figure 4.7

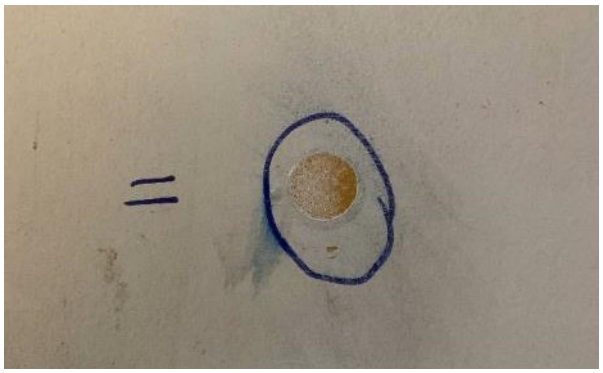
The test procedure performed during the field examination was as follows:

1. Prepare the testing area by using sandpaper to slightly abrade and a cloth or paper towel to clean the surface.
2. Apply Loctite Liquid professional super glue on 0.78 in. diameter dollies.
3. Remove the excess glue after attaching it to the examined surface.
4. Apply low pressure to the dollies for 2–3 minutes to allow setting of the epoxy super glue.
5. Pull the dollies with a pull-off adhesion tester (Elcometer 510).
6. Document the paint pull-off strength reading and failure conditions.
7. Record any failures by examining the dollies' faces and the test area.

Failure can occur within the glue, coating system, and steel substrate. Three failure modes are expected to happen, including *cohesive failure*, *adhesive failure*, and *glue failure*. Cohesive failure occurs when the coating fails within the body of the coating layer, leaving the same coat on the dolly and the testing area. Adhesive failure occurs at the interface between layers when one layer pulls away from the other. Thus, the coating sample attached to the dolly is different from the coating on the testing area. Glue failure occurs when no coating is present on the dolly. That event may occur due to insufficient glue curing or incompatibility between the adhesive coating, dolly, and testing surface. Figure 4.15 depicts a pull-off adhesion test conducted on selected steel girders during field examinations. Predicting the potential failure of the paint system can be achieved by examining the face of the dolly and the test area (Figure 4.16 and Figure 4.17). The cohesive and adhesive codes are given in Figure 4.16. "A" represents base metal, while "B," "C," "D," "E," and "F" indicate different layers of paint starting from the first layer to the fifth layer, respectively. The symbol "Y" symbolizes glue and "Z" denotes the dolly. Adhesive failure between the glue and dolly (also known as glue failure) is referred to as "Y/Z," while adhesive failure between the fourth and fifth layers (adhesive failure of paint) is denoted as "E/F."



Figure 4.14. Elcometer 510 Automatic Pull-Off Adhesion Testing Kit.



(a) Close-up Picture of Painted Surface after Pull-off Adhesion Test



(b) Close-up Picture of Dolly Surface after Pull-off Adhesion Test

Figure 4.15. Pull-off Adhesion Test.

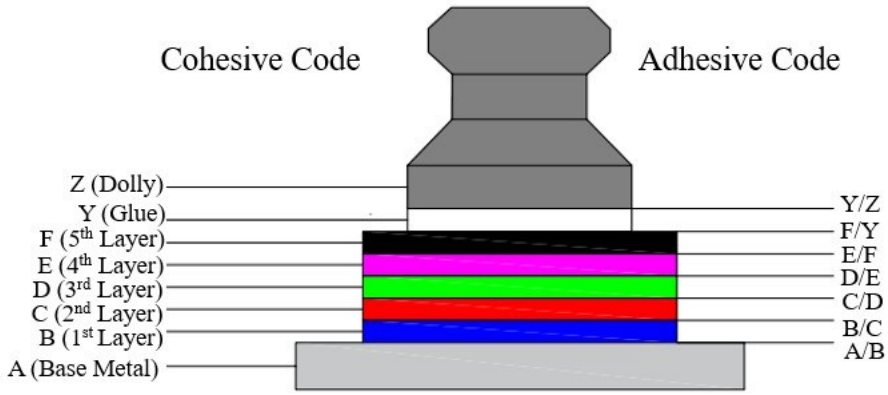


Figure 4.16. Cohesive and Adhesive Code.

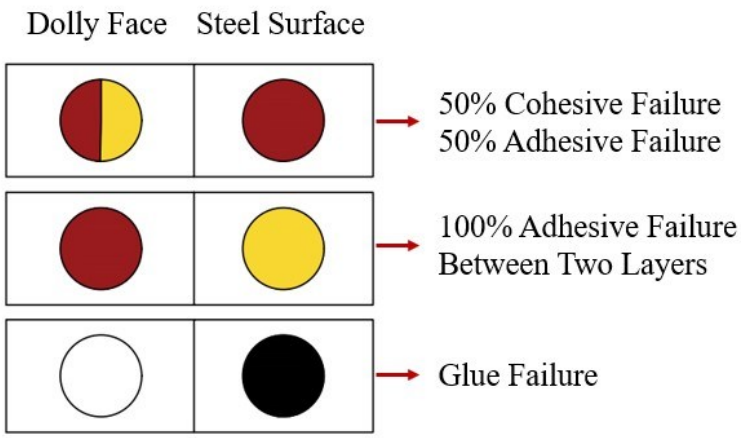


Figure 4.17. Cohesive, Adhesive, and Glue Failure.

4.4.8 Paint Thickness Measurement

An Elcometer 456 nonferrous metal coating thickness gauge© was used to measure the thickness of paint coatings (Figure 4.18). The measurements were conducted particularly on areas that were susceptible to corrosion. The results were documented for further analysis. Typically, the test is performed at locations shown in Figure 4.6 and Figure 4.7, as per ASTM 7091 (2022). The device was also used to measure patina thickness on some of the weathering steel bridges.



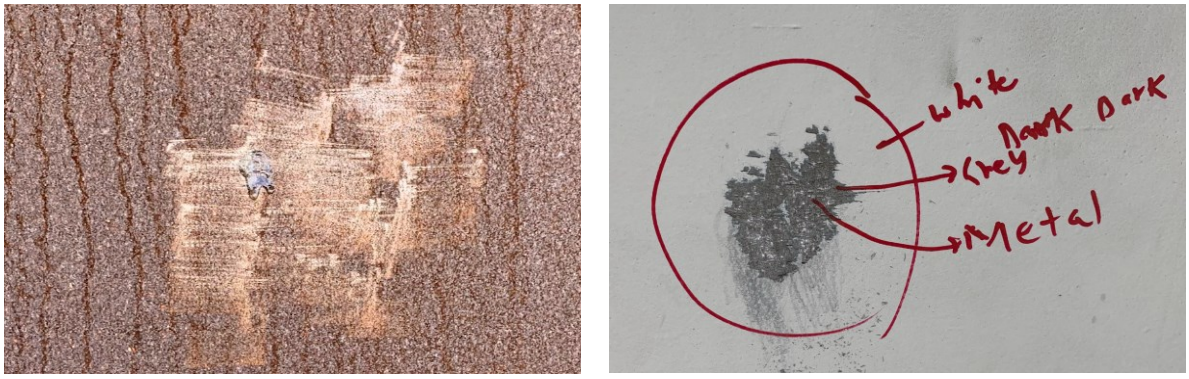
Figure 4.18. Elcometer 456 Nonferrous Metal Coating Thickness Gauge.

4.4.9 Scrape Test

A scrape test was performed in the middle of the web for exterior and interior girders, and samples were collected and carefully stored for laboratory evaluation of rust particles (Figure 4.19). As in ASTM E1729 (2020), the sample collection was conducted on both weathering and painted steel girders. Typically, the test is performed at locations shown in Figure 4.6 and Figure 4.7.

The procedure for the scrape test and sample collection is as follows:

1. Attach a white paper with clear tape to the testing area and make a funnel.
2. Collect the patina samples from the surface using the funnel.
3. Use a scraping blade or knife to scrape rust particles from the web surface.
4. Store the rust particles in plastic bags.



(a) Weathering Steel Scraped Surface (b) Painted Steel Scraped Surface

Figure 4.19. Scraped Surface for Steel Bridges.

4.4.10 Sensor Installation for Continuous Monitoring

Multiple studies (Morcillo et al., 2013; Jaén et al., 2014; Thee et al., 2015; Kubzová et al., 2020) suggested that atmospheric corrosion will intensify the deterioration of weathering steel as the duration of the wetness of the steel surface increases. ISO 9223 (2012) proposed an approach to determine TOW based on temperature and RH. In this study, to assess the impact of TOW on weathering steel members, data loggers were installed and used to continuously record one year of data of the environment at five locations (Table 4-6). Two bridges were located near coastal regions in the Houston and Corpus Christi area; two were located in the Lubbock and Dallas Districts, which have a higher usage of deicing salts; one was located in the Atlanta District and had the highest rainfall.

Table 4-6. Selected Bridges for Datalogger Installation.

Bridge Name	Year Built	Environmental Characteristic
ATL−WS−03	1976	High Rainfall
CRP−WS−01	2007	Airborne Chloride
DAL−WS−02	2011	Deicing Salt
HOU−WS−07	1994	Airborne Chloride
LBB−WS−01	2009	Deicing Salt

Onset HOBO® S-LWA-M003 Leaf wetness smart sensors© were used to estimate TOW because painting and preconditioning is not needed for consistent measurement. Onset HOBO® S-THB-M002/12-bit Temperature/Relative Humidity Smart Sensor© was also used to continuously record temperature and humidity data. Onset HOBO USB Micro Station Data Logger© stored environmental data based on a measurement frequency of every 10 minutes (Figure 4.20). The geographic locations of the testing sites are given in Figure 4.21.

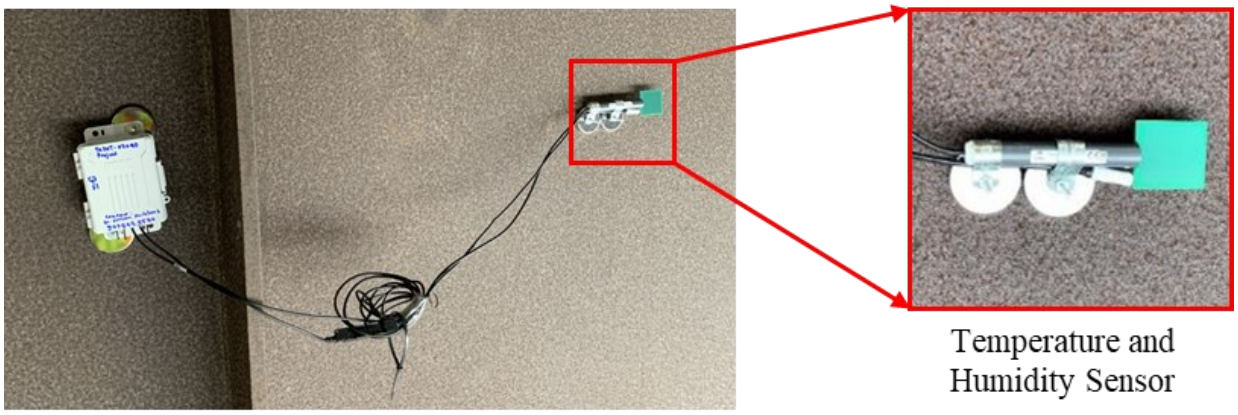


Figure 4.20. Installation of Onset HOBO USB Micro Station Data Logger.

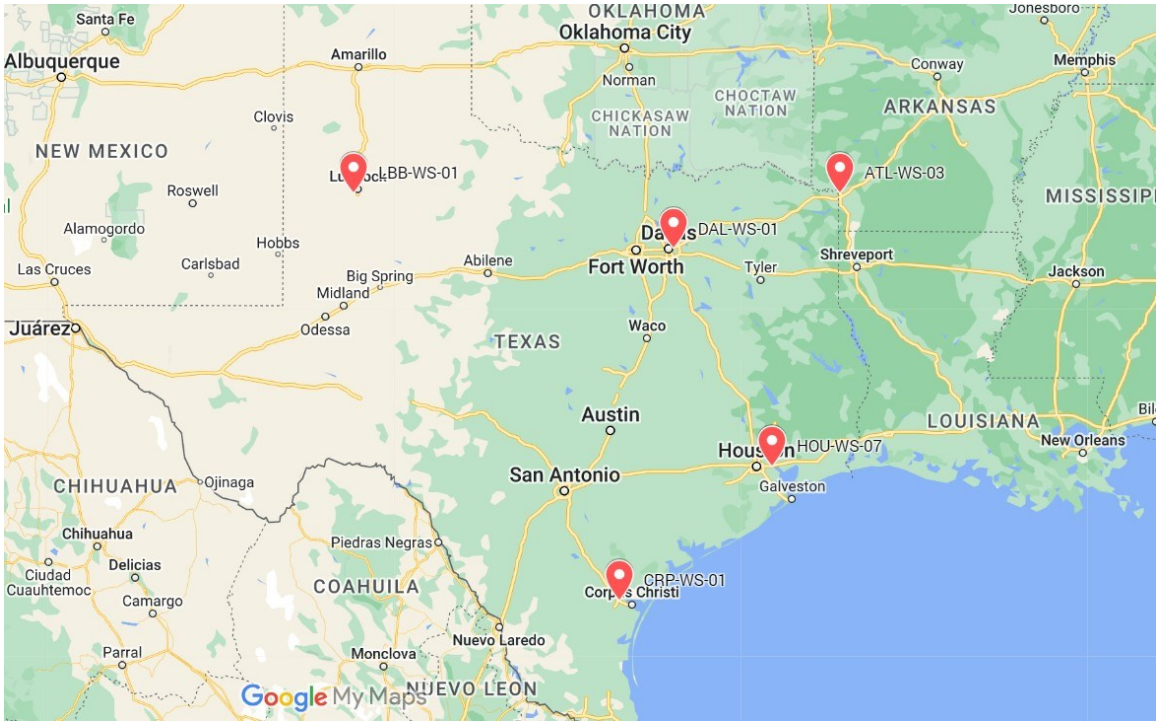


Figure 4.21. Geographic Locations of Testing Stations.

4.5 RESULTS

This section presents discussion and analysis performed on the test results of field examinations. It includes an analysis of the visual inspection of weathering and painted steel girders as well as an assessment of the data collected during the chloride test, pH test, ultrasonic thickness measurement, tape adhesion test, IR thermography, pull-off adhesion examination, paint thickness measurement, and environmental data collection.

4.5.1 Visual Inspection

4.5.1.1 Weathering Steel Bridges

The performance of weathering steel is influenced by factors such as airborne chloride deposition and deicing salt usage during winter. The age of bridge components can also contribute to the performance of the patina layer whether it is protective or not. The color of the patina observed on inspected weathering steel bridges ranged from orange to brown to black, as shown in Figure 4.22. Localized delamination of the patina was also observed on the bottom face of the top flange (Figure 4.22[a] and Figure 4.22[d]). Poultice corrosion due to dirt accumulation was usually found on the top face of the bottom flange of interior girders, while less poultice corrosion

and a little dirt accumulation was observed on exterior girders, as shown in Figure 4.23. Another conclusion was that poultice corrosion (sometimes with localized pitting) was prevalent along the length of the girder's top face of the bottom flange (Figure 4.23[e] and Figure 4.23[f]). It was concluded that a stable patina was developed on the web as well as on the top and bottom flange of trapezoidal box girders. However, some differences were observed between the developed patina on interior and exterior surfaces. Figure 4.24 demonstrates the differences between the developed patina on the interior and exterior girder of CRP−WS−01, with the interior girder showing widespread pitting corrosion and loose rust flakes, while the exterior face maintains a stable patina condition. Variations in patina color were also observed for weathering steel bridges on AUS-WS-01 and AUS-WS-04. The patina layer was found to be stable and protective for AUS-WS-01 and AUS-WS-04 bridges located in the Austin District in comparison to the CRP-WS-01 in Corpus Christi. Figure 4.25 shows a variation of the developed patina based on the age of weathered steel for the exterior and interior faces of steel girders. Staining was also observed underneath the face of the steel bent cap. It was concluded that the exterior web of the girder facing away from the bridge typically shows a uniform and well-maintained patina, while some color variation occurred near the abutments and bent caps due to leakage of rainwater (Figure 4.26). In addition, the interior web generally exhibited a uniform and well-preserved patina, with occasional dirt accumulation on the surface (Figure 4.23[e], Figure 4.26[c], and Figure 4.26[e]).



(a) Color Variation of Patina, Exterior Girder (CRP−WS−01)



(b) Color Variation of Patina, Interior Box Girder (HOU−WS−02)



(c) Black Color Patina, Interior Girder (HOU−WS−03)



(d) Black Patina, Interior Girder (HOU−WS−03)

Figure 4.22. Developed Patina on Top Flange of Exterior and Interior Girders.



(a) Dirt Accumulated on Bottom Flange, Interior Girder (HOU−WS−03)



(b) Drip Plates with No Dirt, Exterior Girder (HOU−WS−03)



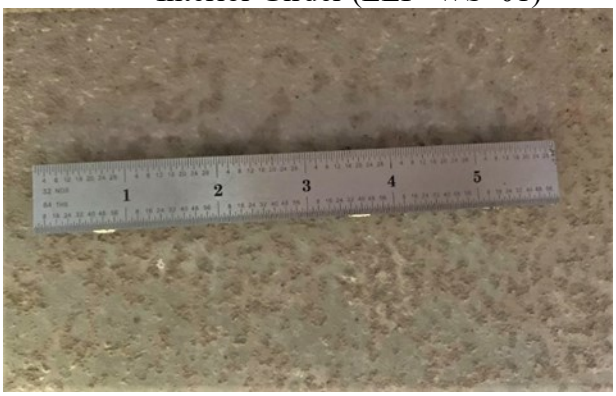
(c) Accumulation of Dirt, Interior Girder (ELP−WS−01)



(d) Bird Feces and Dirt Accumulation, Interior Girder (ELP−WS−01)

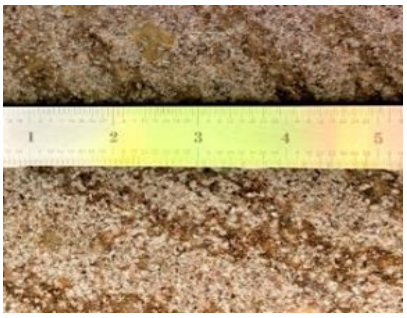


(e) Poultice corrosion with Accumulation of Dirt (SAT−WS−01)



(f) Poultice Corrosion (SAT−WS−01)

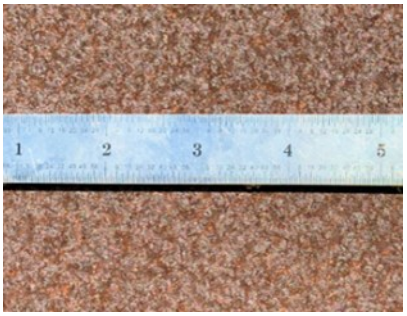
Figure 4.23. Patina Condition on Bottom Flange for Exterior and Interior Girder.



(a) Bottom Face of Top Flange, Exterior Girder



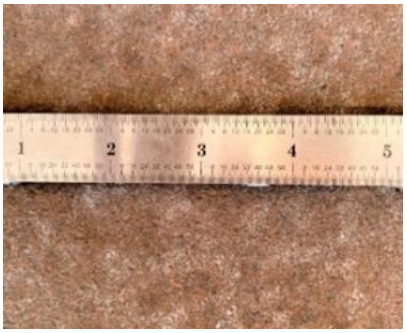
(b) Bottom Face of Top Flange, Interior Girder



(c) Web Exterior Girder



(d) Web Interior Girder



(e) Top Face of Bottom Flange, Exterior Girder



(f) Top Face of Bottom Flange, Top Interior Girder

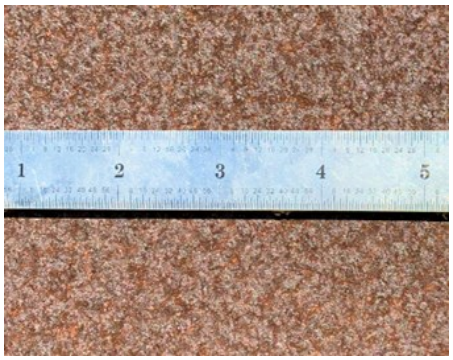


(g) Bottom Face of Bottom Flange, Exterior Girder



(h) Bottom Face of Bottom Flange, Interior Girder

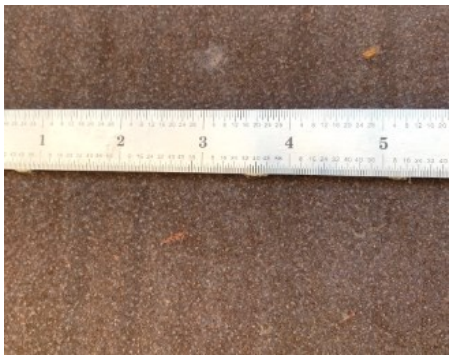
Figure 4.24. Developed Patina on Interior and Exterior Girder on CRP−WS−01.



(a) Exterior Girder Web, CRP−WS−01, Year Built—2007



(b) Interior Girder Web, CRP−WS−01, Year Built—2007



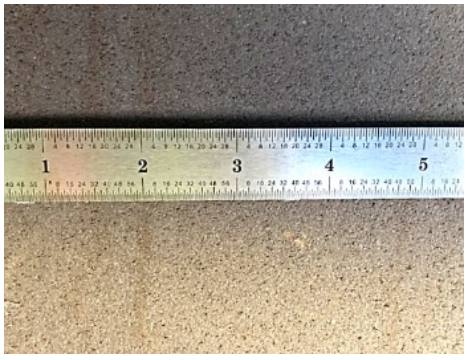
(c) Exterior Girder Web, AUS−WS−04, Year Built—2002



(d) Interior Girder Web, AUS−WS−04, Year Built—2002



(e) Exterior Girder Web, AUS−WS−01, Year Built—1977



(f) Interior Girder Web, AUS−WS−01, Year Built—1977

Figure 4.25. Developed Patina on Weathering Steel Girders in Austin and Corpus Christi.



(a) Patina on Exterior Girder (FTW−WS−01)



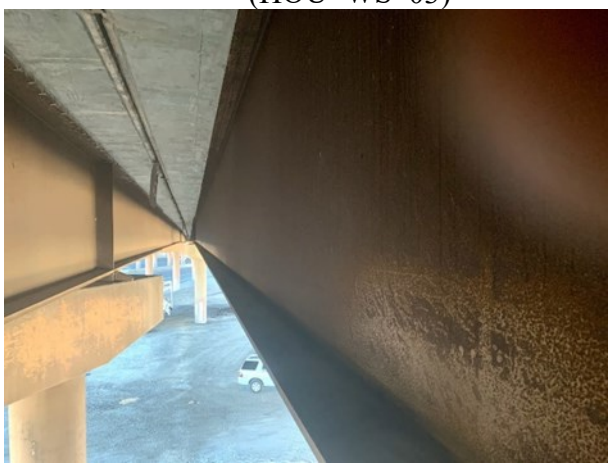
(b) Patina on Exterior Girder (ELP−WS−01)



(c) Patina on Interior Girder (HOU−WS−03)



(d) Patina on Exterior Girder (ELP−WS−01)



(e) Patina on Exterior Girder (SAT−WS−01)



(f) Patina on Exterior Girder (SAT−WS−01)

Figure 4.26. Color Variation of Patina Observed at Joint Near Abutment and Bent Due to Continuous Washing of Patina.

4.5.1.2 TxDOT On-System Painted Bridges

The field inspection revealed that on-system bridges were generally in good condition without any paint defects. However, minor rust spots were noticed on connections and the bottom flange (Figure 4.27). The accumulation of dirt was found on the top of the bottom flange. The pull-off adhesion strength values for these bridges ranged from 800 psi to 2700 psi, which was significantly higher than off-system painted bridges. Moreover, researchers concluded that the results of pull-off adhesion tests were superior to visual examinations. For example, during the visual inspection of FTW−PS−02, the exterior face girder exhibited no signs of corrosion, but scraping off the paint revealed corrosion and rust over the exterior face. No corrosion was observed on the interior girder after paint removal. Only the primer coating with the white overcoat missing was found on TYL−PS−02 painted with System II. Corrosion was also observed at the edge of the top and bottom flanges, although the overall affected area was minimal (Figure 4.27). Corrosion at the joints and structural members was observed on CRP−PS−01 directly over water. The girder is painted with System III designed for salt-laden coastal conditions (Figure 4.28). Researchers also determined that blistering and cracking did not happen on any of the on-system bridges but did occur on a few observed off-system bridges.



(a) Edge of Flange Undergoing Corrosion

(b) Staining on Edge of Girder Flange



(c) Paint Failure at Joints Near Abutment

(d) Paint Failure and Corrosion at Joints

Figure 4.27. Paint Failure Observed on TYL−PS−02.

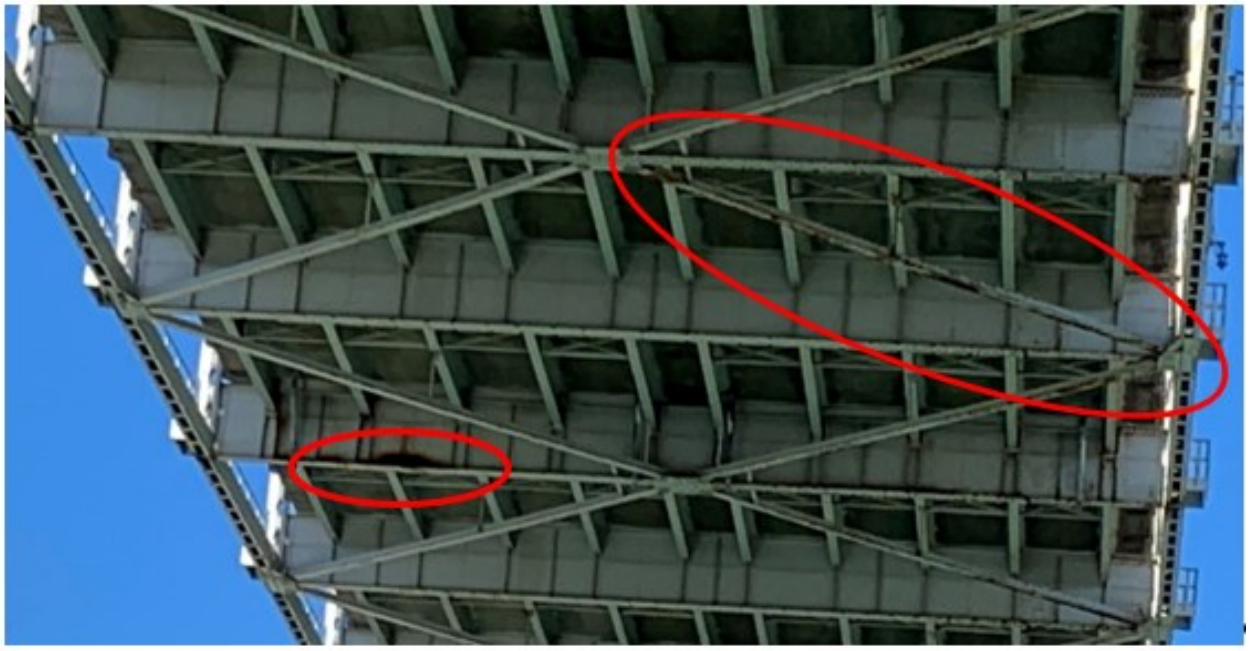


Figure 4.28. Development of Corrosion on Harbor Bridge (CRP−PS−01).

4.5.1.3 TxDOT Off-System Painted Bridges

The paint system utilized on off-system bridges often remains unidentified, and these bridges can employ multiple types of paint systems for corrosion protection, as demonstrated in Figure 4.29(d). During field inspections of three off-system bridges, paint failure was observed over the top and bottom flanges, along with paint failure on the web, as depicted in Figure 4.29 and Figure 4.30. In addition, Figure 4.29(c) illustrates the accumulation of debris within interior girders due to flooding. The build-up of dirt over the top of the bottom flange has resulted in accelerated paint deterioration and poultice corrosion. All inspected girders exhibited rusted surfaces and pitting corrosion to some extent. It was concluded, based on visual examinations, and documented testing results, that the frequent occurrence of flooding might be a contributor to the deterioration of the paint system.



(a) Rusting on Flange and Web



(b) Rusting on Steel Piles



(c) Rusting on Flange and Web



(d) Interior Girder with Different Paint

Figure 4.29. Paint Deterioration on Off-System Bridge (YKM−PS−01).



(a) Paint Failure on Exterior Girder (b) Paint Failure on Interior Girder

(c) Debris Collected between the Girders (d) Paint Failure on Interior Girder

Figure 4.30. Condition of Paint System on Exterior and Interior Girders (ATL−PS−01).

4.5.2 Chloride Test

During the field inspection, researchers measured chloride concentration on weathering steel patina ranging from 0 ppm to 13 ppm. However, the extent of deterioration identified by the size of the rust flake and the patina index was not consistent with the measured chloride concentration. For instance, the average chloride concentration recorded for the steel girders located in Corpus Christi was 1 ppm, but the bridge is located in an area with high airborne chloride concentrations. Nonetheless, the average chloride concentration recorded for the steel girders in Austin was higher than in Corpus Christi. Similarly, bridges in Beaumont showed a lower value of chloride concentrations.

The patina layer on weathering steel bridges varied in terms of permeability. As corrosion-related deterioration progresses, the oxide layer of the patina becomes thicker and more porous. Note that chlorides ions deposited during patina development react with hydroxide and form new

corrosion products. Therefore, it is essential to measure not only the amount of iron oxide, such as Akaganeite, but also the level of chloride ions within or beneath the patina layer. Findings indicated that the field chloride testing is inconclusive, and further lab testing must be conducted to study the state of the patina layer and determine if it is protective or not. Chloride concentrations accumulated on steel surfaces are given in Table 4-7 for inspected steel girders. It was concluded that field measurement of chloride content is not a reliable approach to predict durability and long-term performance of weathering steel girders.

Table 4-7. Chloride Test Result.

Bridge Name	Exterior (ppm)	Interior (ppm)	Bridge Name	Exterior (ppm)	Interior (ppm)
ATL−WS−01	1	1	BMT−PS−01	1	1
ATL−WS−02	6	10	BMT−PS−01	0	1
ATL−WS−03	1	2	HOU−PS−01	1	1
AUS−WS−01	1	1	TYL−PS−01	1	1
AUS−WS−02	0	2	TYL−PS−02	0	0
AUS−WS−03	1	1	BRY−PS−01	1	1
AUS−WS−04	3	3	ATL−PS−01	1	1
DAL−WS−01	1	1	FTW−PS−01	0	1
DAL−WS−02	0	0	FTW−PS−02	1	1
DAL−WS−03	1	1	AMA−PS−01	1	1
FTW−WS−01	1	1	AMA−PS−02	1	1
FTW−WS−02	1	1	AMA−PS−03	1	1
FTW−WS−03	6	0	WFS−PS−01	1	2
SAT−WS−01	1	1	WFS−PS−02	3	2
ELP−WS−01	1	1	WFS−RC−01	1	1
HOU−WS−01	—	1	WFS−RC−02	—	1
HOU−WS−02	0	0	DAL−PS−01	—	0
HOU−WS−03	0	1	YKM−PS−01	1	0
HOU−WS−04	1	1	CRP−PS−01	1	1
HOU−WS−05	1	0	ELP−PS−01	2	5
HOU−WS−06	1	1			
HOU−WS−07	1	1			
LBB−WS−01	11	13			
LBB−WS−02	6	2			
CRP−WS−01	1	1			

Note:
— No measurements were made

4.5.3 pH Test

Similar to field chloride testing, the results of pH testing were not promising, and the test is not recommended for field inspections. All the pH strips used on the selected steel bridges

yielded a constant value of 5, which represented a natural to slightly acidic environment. Table 4-8 provides the results of pH tests performed on some steel girders.

Table 4-8. pH Test Results for All Steel Bridges.

Bridge Name	Exterior	Interior	Bridge Name	Exterior	Interior
ATL−WS−01	5	5	BMT−PS−01	5	5
ATL−WS−02	5	5	BMT−PS−01	5	5
ATL−WS−03	5	5	HOU−PS−01	5	5
AUS−WS−01	5	5	TYL−PS−01	5	5
AUS−WS−02	5	5	TYL−PS−02	5	6
AUS−WS−03	5	5	BRY−PS−01	5	5
AUS−WS−04	5	5	ATL−PS−01	5	5
DAL−WS−01	5	5	FTW−PS−01	5	5
DAL−WS−02	5	5	FTW−PS−02	5	5
DAL−WS−03	5	5	AMA−PS−01	5	5
FTW−WS−01	5	5	AMA−PS−02	5	5
FTW−WS−02	5	5	AMA−PS−03	5	5
FTW−WS−03	5	5	WFS−PS−01	5	5
SAT−WS−01	5	5	WFS−PS−02	5	5
ELP−WS−01	5	5	WFS−RC−01	5	5
HOU−WS−01	5	5	WFS−RC−02	5	5
HOU−WS−02	5	5	DAL−PS−01	5	5
HOU−WS−03	5	5	YKM−PS−01	5	5
HOU−WS−04	5	5	CRP−PS−01	5	5
HOU−WS−05	5	5	ELP−PS−01	5	5
HOU−WS−06	5	5			
HOU−WS−07	5	5			
CRP−WS−01	5	5			
LBB−WS−01	5	5			
LBB−WS−02	5	5			

4.5.4 Ultrasonic Thickness Measurement Results

Using ultrasonic thickness measurements, researchers measured the thickness loss of steel plates at several locations on the web, bottom face of the top flange (TF), and top and bottom face of the bottom flange (BF), as shown in Figure 4.6 and Figure 4.7. Table 4-9 shows ultrasonic thickness measurements at various location for HOU−WS−06. Thickness measurements were generally greater than the original design thickness, though there were a few locations where the thickness on the bottom face of the bottom flange was lower than the design thickness. The reduction in thickness was found to be fairly small. Steel plates are typically rolled with a thickness greater than their nominal value, and the formation of rust on steel surfaces results in an increased

thickness. The initial oversizing of the metal with an additional rust layer contribute to a greater thickness measurement than the nominal values. Sener et al. (1998) also concluded that the original thickness of the steel plate must be known to ensure the accuracy of ultrasonic testing measurements. The authors reported an average 1.914 percent increase in thickness per decade.

Table 4-9. Thickness Measurement with Ultrasonic Testing.

Bridge	Girder	Location	Plan Thickness	Average Thickness (Field)	Difference	Thickness Change (%)	Year Built
HOU−WS−06	A1G1F1	TF Bottom	1.00	1.039	0.039	3.93	1992
		Web	0.50	0.539	0.039	7.73	
		BF Bottom	1.00	0.999	0.001	−0.13	
	A1G3F1	TF Bottom	1.00	1.007	0.007	0.70	
		Web	0.50	0.530	0.030	5.93	
		BF Bottom	1.00	1.016	0.016	1.57	
	A1G4F2	TF Bottom	1.00	1.018	0.018	1.83	
		Web	0.50	0.537	0.037	7.47	
		BF Bottom	1.00	1.020	0.020	1.97	
	A1G8F2	TF Bottom	1.00	1.004	0.004	0.37	
		Web	0.50	0.500	0.000	0.07	
		BF Bottom	1.00	0.995	0.005	−0.47	
	A1G9F1	TF Bottom	1.00	0.998	0.002	−0.20	
		Web	0.50	0.505	0.005	0.93	
		BF Bottom	1.00	1.001	0.001	0.10	
	A1G12F2	TF Bottom	1.00	1.001	0.001	0.10	
		Web	0.50	0.505	0.005	0.93	
		BF Bottom	1.00	0.996	0.004	−0.40	

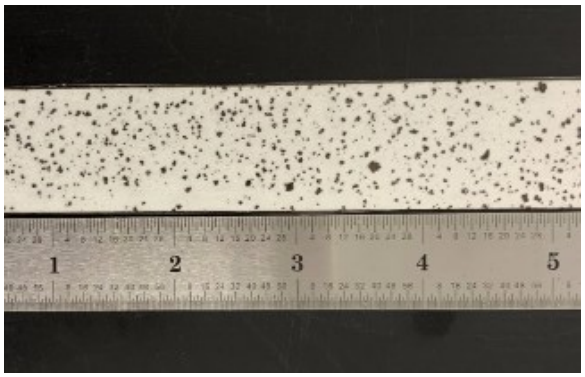
4.5.5 Tape Adhesion Results

The tape adhesion test proved to be a highly efficient technique for acquiring the field condition of patina coatings. Particularly, quantification of flakes removed by the tape provided insights into the overall adherence of the protective layer. Note that the test failed when surfaces were heavily chalked and contained dirt buildup. The findings of the tape test were analyzed for different patina using scaling systems ranging from Category 5 to Category 8 on the Iowa patina rating scale. Using the recorded data of the tape adhesion test, this Iowa ranking system was modified with new rating index from Category 0 to Category 10. Image analysis techniques were utilized to assess tape adhesion test results by examining rust particle size and distribution. The analysis involved thresholding and masking methods to isolate and segment rust particles within

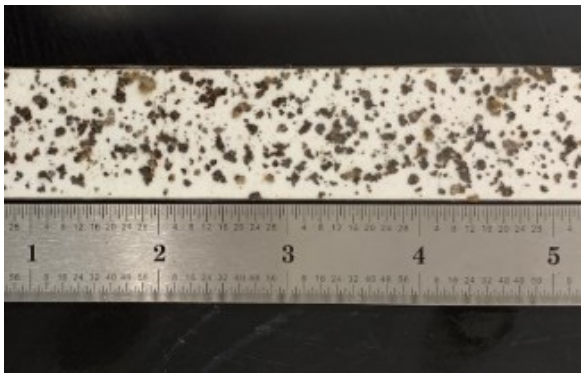
images and determine their size, area, shape, etc. Specifically, *Yen thresholding* and *binary masking* were implemented. Yen thresholding calculates an optimal threshold value that maximizes interclass variance between particle and background pixels, thereby separating the two regions (Yen et al., 1995). This threshold creates a binary mask wherein pixels above the threshold represent foreground rust particles, and pixels below constitute the background (Sezgin & Sankur, 2004). Thresholding and masking approaches like Yen's enable common image analysis tasks to extract particles from background regions for measurement and characterization. Detailed test results are documented for each individual bridge in the appendix.

Tape profiles documented in this research can be used to assess the quality of patina. These profiles were obtained from the exterior fascia girder and the interior girders located near the abutments and bent caps. It was determined that the exposed exterior surfaces of the fascia exhibited greater performance, showing minimal or no deterioration in the protective oxide layer. On the contrary, the interior surfaces of the girders showed considerably more rust flaking. This flaking occurred particularly at the bottoms (i.e., the bottom of the web and bottom flange), and especially at the top of the bottom flanges, where significant poultice corrosion was observed.

Figure 4.31 illustrates the tape test results for both the exterior and the interior webs of CRP−WS−01, AUS−WS−04, and AUS−WS−01. The condition of patina developed on AUS−WS−01 was excellent for both the exterior and interior surfaces. However, the tape adhesion test revealed the presence of loosely attached rust flakes of larger sizes in the exterior face of the girder of CRP−WS−01. The tape adhesion results for AUS−WS−01 were similar for both the exterior and interior surfaces, although the size and density of rust flakes were larger than those observed in AUS−WS−04. Figure 4.32 compares the patina condition for the exterior and interior surfaces of the girder at different locations on CRP−WS−01. Smaller-sized rust flakes were seen on the exterior girder in comparison to the interior girders except for the bottom face of the bottom flange.



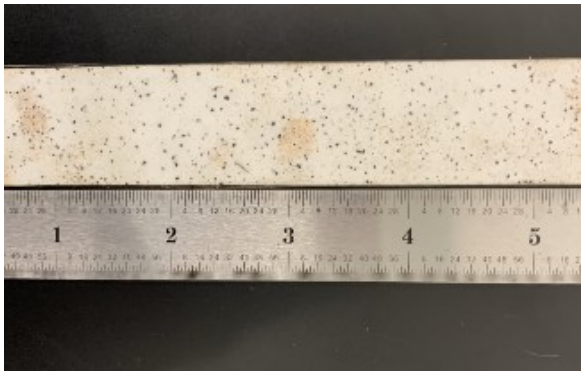
(a) Exterior Girder Web (CRP−WS−01)
Year Built—2007



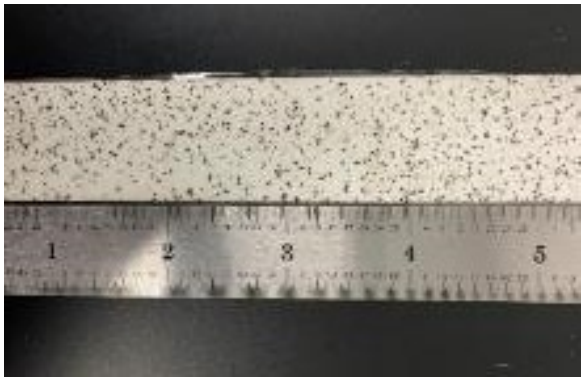
(b) Interior Girder Web (CRP−WS−01)
Year Built—2007



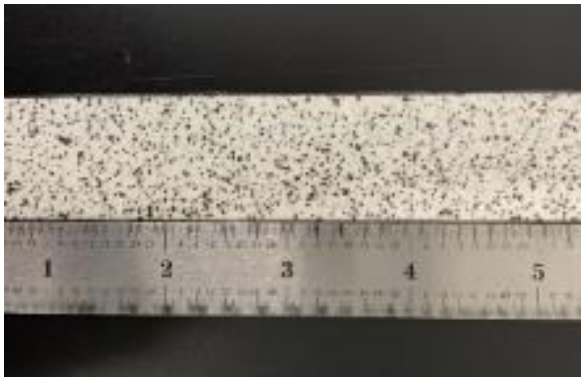
(c) Exterior Girder Web (AUS−WS−04)
Year Built—2002



(d) Interior Girder Web (AUS−WS−04)
Year Built—2002

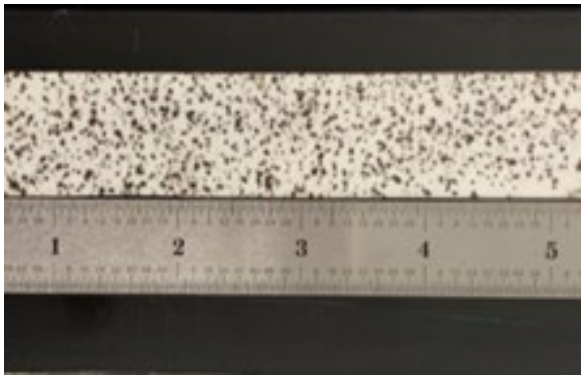


(e) Exterior Girder Web (AUS−WS−01)
Year Built—1977

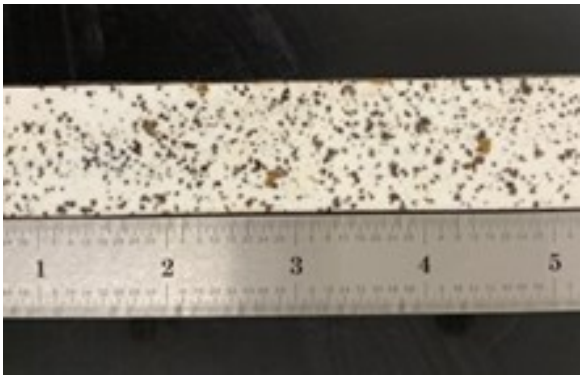


(f) Interior Girder Web (AUS−WS−01)
Year Built—1977

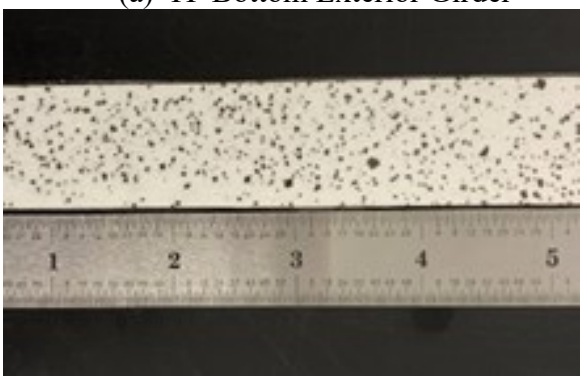
Figure 4.31. Patina Condition for WS Bridge in Austin and Corpus Christi with Different Built Year.



(a) TF Bottom Exterior Girder



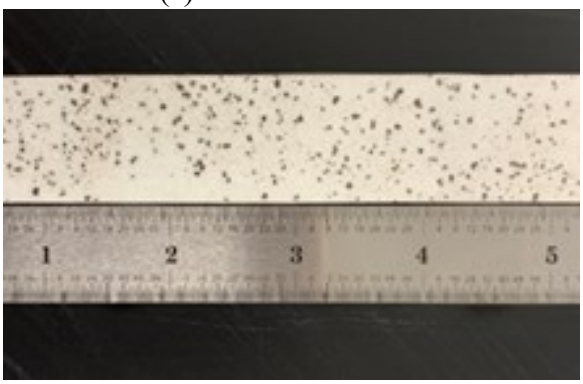
(b) TF Bottom Interior Girder



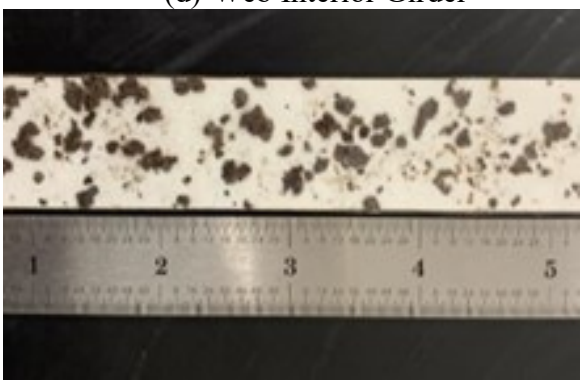
(c) Web Exterior Girder



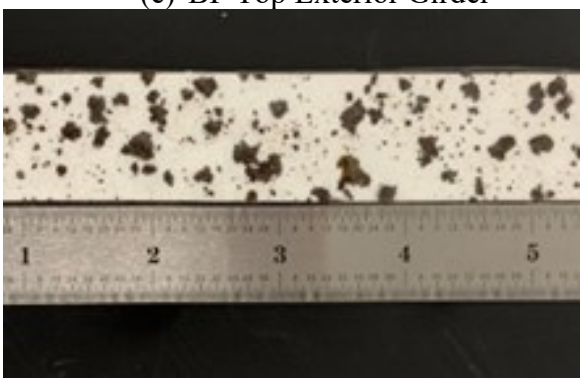
(d) Web Interior Girder



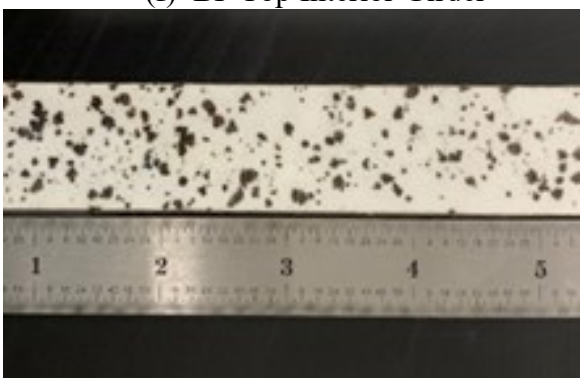
(e) BF Top Exterior Girder



(f) BF Top Interior Girder



(g) BF Bottom Exterior Girder

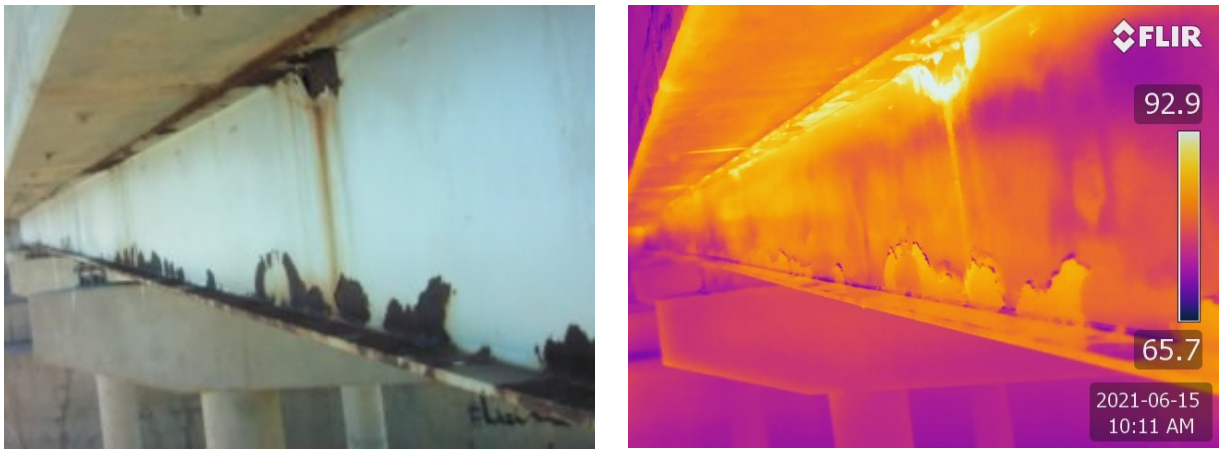


(h) BF Bottom Interior Girder

Figure 4.32. Patina Condition of Interior and Exterior Girder on CRP−WS−01.

4.5.6 Infrared Thermography

Thermal imaging successfully detected the locations where defects had occurred in Paint System II. As shown in Figure 4.33, a thermogram has been constructed for a painted steel girder in Amarillo (AMA−PS−03) and detected the location of defects and the state of corrosion. Thermal imaging developed for ATL−PS−01 indicates severe paint deterioration and rusting (Figure 4.34). Paint deterioration on System II was also detected on the steel pier of AMA−PS−01 and is depicted in Figure 4.35. Note that the quality of thermal imaging was not optimal, primarily due to variations in the timing of thermal imaging captured during the field inspections of steel bridges. The direction and intensity of sunlight can significantly impact the quality of thermal photos. In addition, if the target area is classified as sheltered regions, this can also affect and reduce the quality of thermal imaging. However, despite these challenges, it was decided to include the results of thermal imaging in this report to provide the reader a comprehensive overview. The results of IR thermography were still found to be useful to detect and identify paint deterioration in some cases, as shown in Figure 4.33 to Figure 4.35.



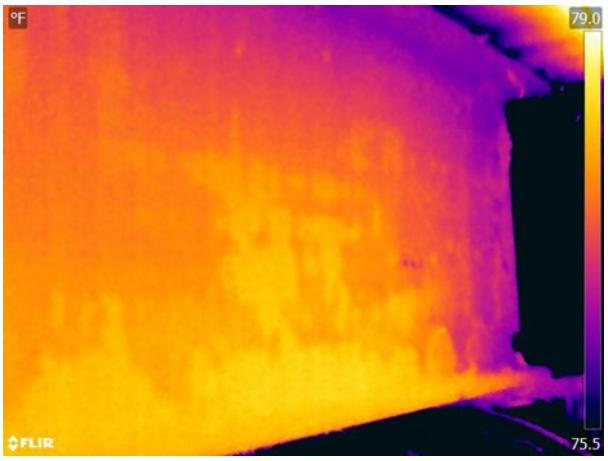
(a) Digital Image of Exterior Face of Girder Near Abutment Ends

(b) Thermal Image of Exterior Face of Girder Near Abutment Ends

Figure 4.33. Digital and Thermal Imaging of Painted Girder, AMA−PS−03.



(a) Digital Image of Exterior Face of I-Beam

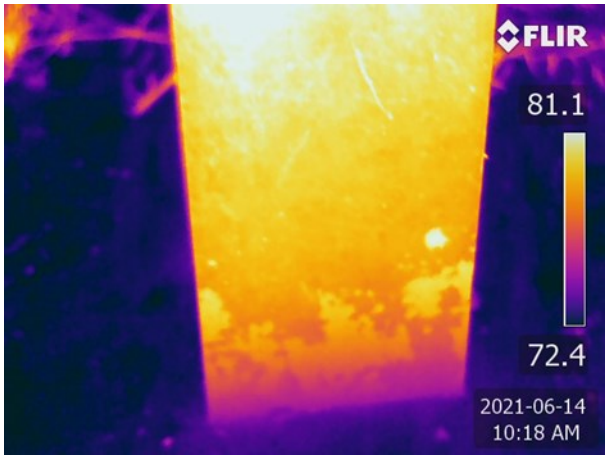


(b) Thermal Image of Exterior Face of I-Beam

Figure 4.34. Digital and Thermal Image of Painted Girder, ATL−PS−01.



(a) Digital Image of Pier Paint Deterioration



(b) Thermal Image of Pier Paint Deterioration

Figure 4.35. Digital and Thermal Imaging of Painted Girder on AMA−PS−01.

4.5.7 Pull-Off Adhesion Results

Table 4-10 provides the pull-off adhesion test results documented for the exterior web of TYL−PS−01, which is an on-system painted steel bridge. The pull-off results and the imaging of the dolly and the testing area (steel substrate) are given in Table 4-10. The paint system examined on the exterior web of TYL−PS−01 is classified as System II without a topcoat. The pull-off results indicate that the bond between paint coats and steel substrate is strong and long-lasting; hence, it was determined that the protection system was durable.

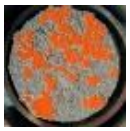
Table 4-11 shows examples of an off-system bridge (YKM−PS−01) whose examination was carried out on the web. It was determined that the paint system used on its steel girders is most likely a lead-based paint system (LBPS). Based on the pull-off results obtained for this bridge, researchers concluded that the bond between paint coats and steel substrate is not adhesive because the protective layer was easily detached from the metal surface.

Table 4-10. Pull-Off Adhesion Test Results, TYL−PS−01 (A4-G1F1 Web).

Dolly Face	Substrate Face	Result (psi)	Attributes	Failure Type
		1856	30% Y/Z 70% A/B	Adhesive Failure
		2181	0% Y/Z 100% A/B	Adhesive Failure
		2415	0% Y/Z 90% A/B	Adhesive Failure
		2676	0% Y/Z 90% A/B	Adhesive Failure
		2117	10% Y/Z 90% A/B	Adhesive Failure

Note:
A: Base metal or substrate on which the paint system has been applied
B: First layer of paint close to the substrate or bottom layer of paint
Y: Glue
Z: Dolly
Y/Z: Glue failure vs. the adhesive failure
A/B: Adhesive failure between substrate and the primer (i.e., bottom layer of paint)
*The pull-off adhesion result attributes in Table 4-10 show the type of failure to its nearest 10%.

Table 4-11. Pull-off Adhesion Test Results, YKM−PS−01 (Web).

Dolly Face	Substrate Face	Result (psi)	Attributes	Failure Type
		494	20% C 80% B/C	Cohesive—Adhesive
		465	70% C 30% B/C	Cohesive—Adhesive
		421	90% C 10% B/C	Cohesive—Adhesive
		491	90% C 10% B/C	Cohesive—Adhesive
		429	50% C 50% B/C	Cohesive—Adhesive

Note:
B: First layer (i.e., primer) close to the substrate
C: Second layer of paint (topcoat in this case)
B/C: Adhesive failure between primer and topcoat from the based metal

4.5.8 Paint Thickness Measurement

The protective coating should be sufficiently thick to preserve steel from corrosion to provide strong adhesion between the paint layer and steel substrate. Therefore if Table 4-12 provides the results of paint thickness measurements that were recorded from steel girders on TYL−PS−01. The lowest and highest thickness measured on the top flange of the steel girders ranged between 2.7 mils and 8.1 mils, and the thickness of the web ranged between 3.6 mils and 7.8 mils. For the bottom flange, the minimum and maximum thicknesses were measured as being between 2.7 mils and 7.5 mils.

Table 4-12. Dry Film Thickness Results.

Bridge	Girder	Location	Reading 1 (mils)	Reading 2 (mils)	Reading 3 (mils)	Average (mils)
TYL−PS−01	A5G1F1	TF Bot.	5.9	5.8	6.1	5.9
		Web	7.9	7.3	7.8	7.7
		BF Top	8.1	7.4	7.5	7.6
		BF Bot.	7.2	7.4	6.4	7.0
	A5G3F1	TF Bot.	4.4	4.1	4.0	4.2
		Web	6.6	5.7	5.6	5.9
		BF Top	5.5	5.6	7.0	6.0
		BF Bot.	4.0	4.1	4.6	4.2
	A5G5F2	TF Bot.	2.7	3.2	3.9	3.3
		Web	5.6	5.2	4.6	5.1
		BF Top	4.8	4.4	4.5	4.5
		BF Bot.	3.9	3.5	3.9	3.8
	A5G9F2	TF Bot.	3.3	2.7	2.7	2.9
		Web	2.7	3.6	4.1	3.5
		BF Top	4.2	4.3	4.6	4.4
		BF Bot.	2.9	3.1	3.4	3.1

4.5.9 Long-Term Monitoring Result

The data collected from the Onset HOBO S-LWA-M003 Leaf Wetness Smart Sensor was analyzed for temperature and RH. Then, the results were compared to an LCD from a nearby station close to the steel bridge sites to assess the accuracy of the sensor measurements and validate the reliability of the collected data.

The data collection process included the use of three sensors in addition to a datalogger to record and document environmental data. The Onset HOBO S-LWA-M003 Leaf Wetness Smart Sensor was used to measure TOW, while the Temperature/Relative Humidity (2 m cable) Smart Sensor was employed to collect the temperature and RH of each site. The HOBO USB Micro Station Data Logger was used to store all the recordings.

Two approaches have been widely accepted in the literature for the estimation of TOW: (1) using a capacitive grid sensor on a metal surface to directly measure TOW, or (2) using the environmental condition (when RH is greater than 80 percent, and temperature is greater than 32°F). As demonstrated in Figure 4.36(a) and Figure 4.36(b), there was a comparative assessment of temperature and RH data procured from both sensors and the local weather station. Figure 4.36(c) depicts the actual wetness period measured by the leaf wetness sensor that correlates to the

data garnered from the sensors and the local weather station. The bridge (ATL−WS−03) is located in the northeast region of Texas, the area with high rainfall and elevated RH.

Figure 4.37 shows both the sensor data from the interior girder of CRP−WS−01 and the local weather station recordings. Although a malfunction in the datalogger limited the data collection for a period of three months, the sensor readings align with the weather station data. A comparison between Figure 4.38 and Figure 4.37 illustrates a strong agreement in temperature, RH, and TOW, both for exterior and interior girders.

In Figure 4.38, a data comparison was obtained between temperature, RH, and TOW recordings from the sensor for the exterior girder of CRP−WS−01 and the environmental data documented by the local weather station. A strong correlation is evident between the sensor recordings and local weather station data (Figure 4.38[a]). Note that the bridge is located in Region 6, close to coastal areas, with high RH (Figure 4.38[b]).

Figure 4.39 shows the sensor reading for DAL−WS−02. A good correlation was observed between the sensor's recordings and environmental data collected from the local weather station. The Dallas weathering steel bridge is located in Region 4, which is a medium to high corrosive environment. Figure 4.40 shows the environmental data recorded from steel girders on HOU−WS−07, which is located near the coast. The data logged for temperature was lower than data documented by the local weather station because the sensor was positioned on an interior girder without exposure to sunlight, but the RH readings from the sensor and local weather station followed a similar trend for several months. Figure 4.41 represents results for LBB−WS−01, which is located in Region 6 and is subjected to deicing salt during winter. Despite the results documented for RH, a shift was noticed in the temperature readings, wherein the sensor registered higher temperature readings than the local weather station data.

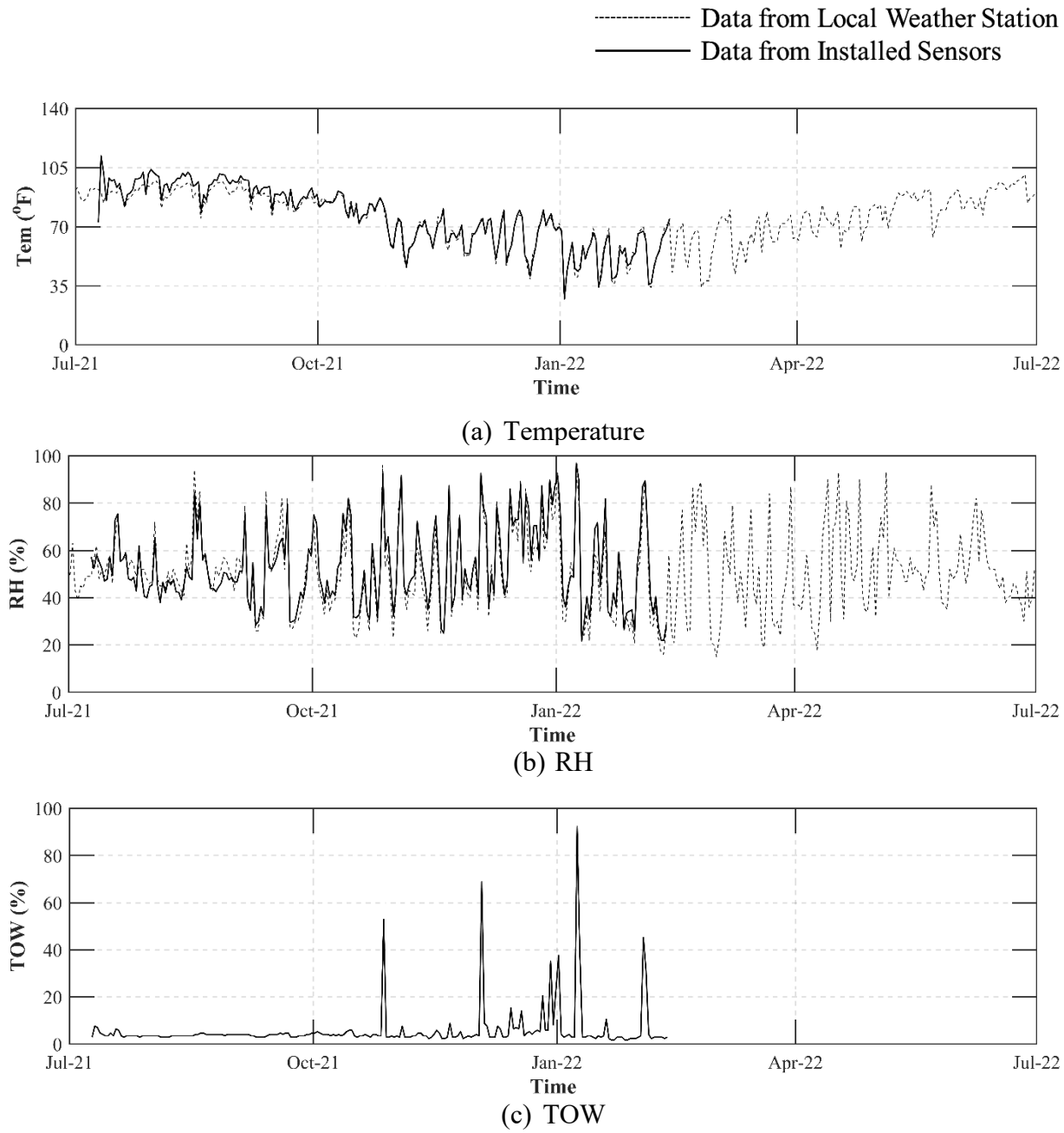


Figure 4.36. Comparison of Data from Local Weather Station and Data Measured with Installed TOW Sensor on Exterior Web of ATL−WS−03.

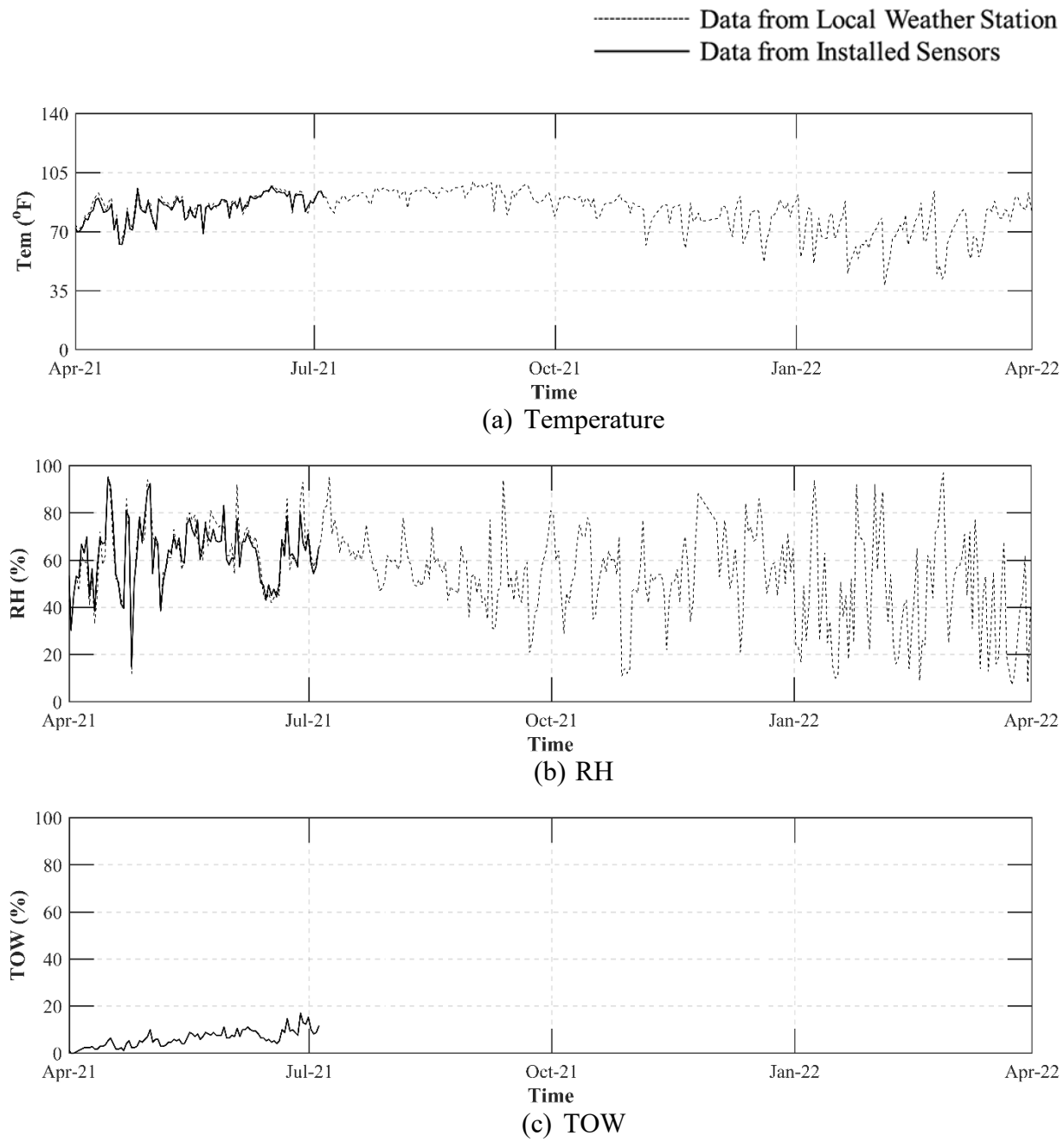


Figure 4.37. Comparison of Data from Local Weather Station and Data Measured with Installed TOW Sensor on Interior Web of CRP−WS−01.

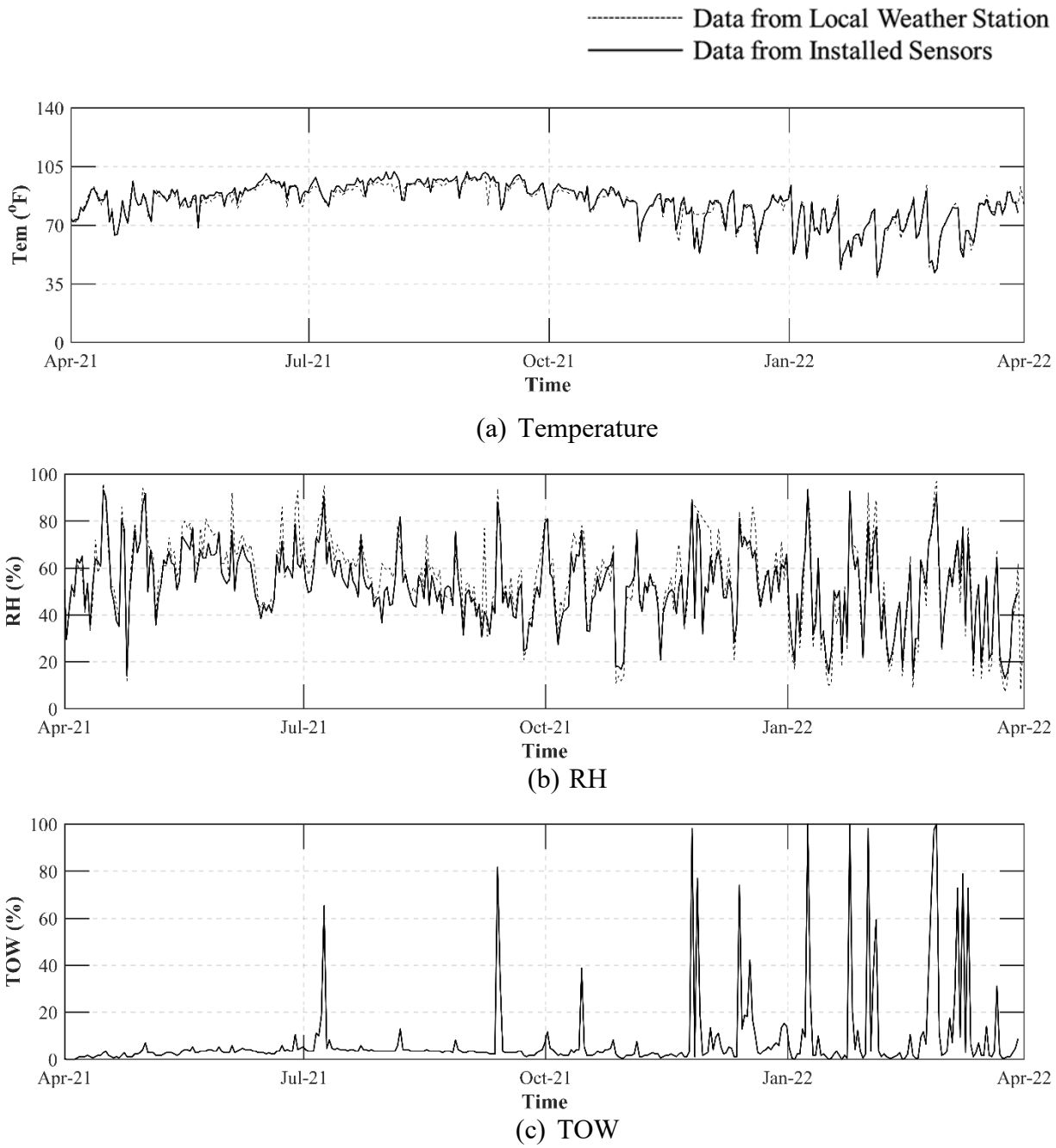


Figure 4.38. Comparison of Data from Local Weather Station and Data Measured with Installed TOW Sensor on Exterior Web of CRP−WS−01.

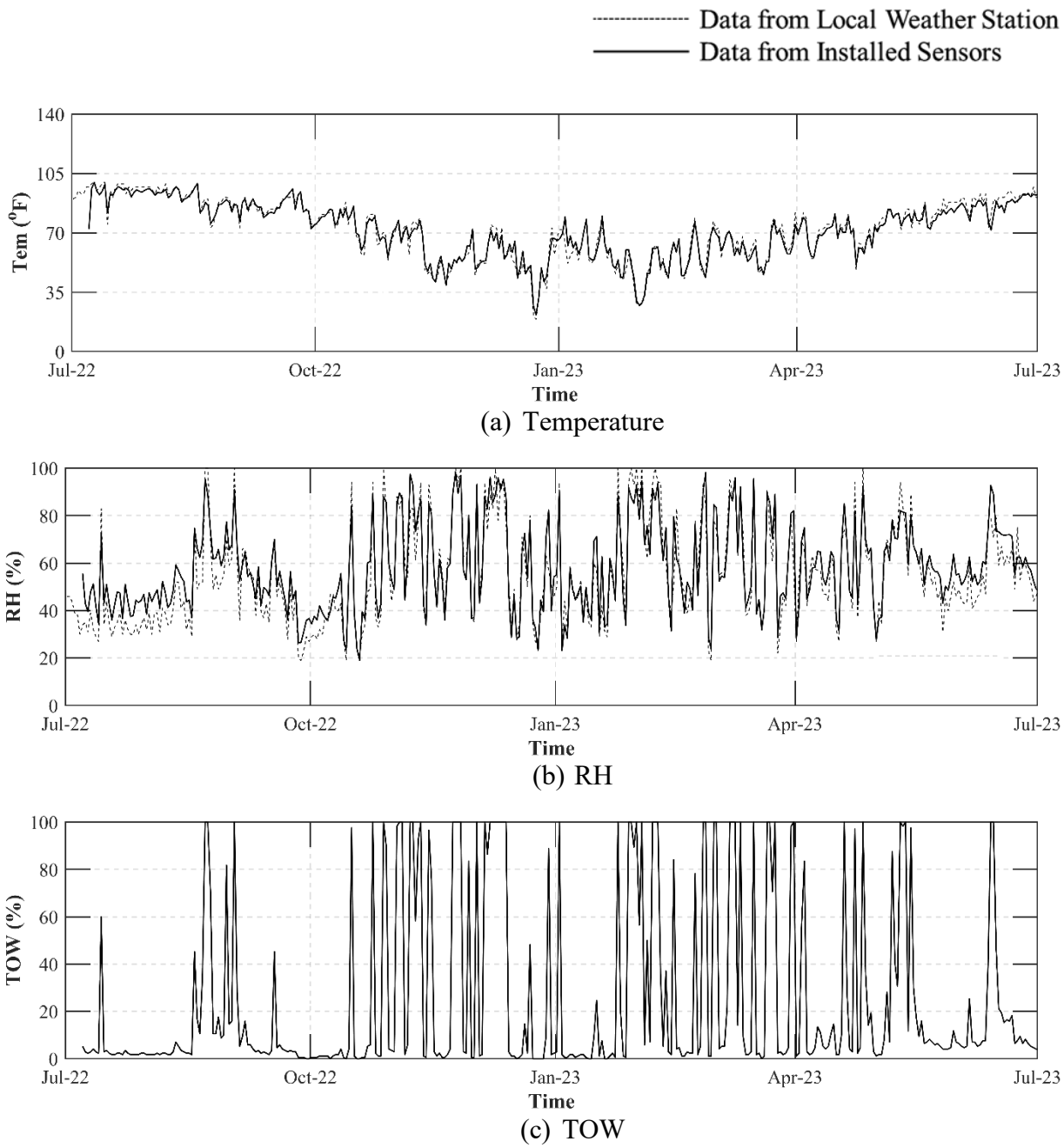


Figure 4.39. Comparison of Data from Local Weather Station and Data Measured with Installed TOW Sensor on Exterior Web of DAL−WS−02.

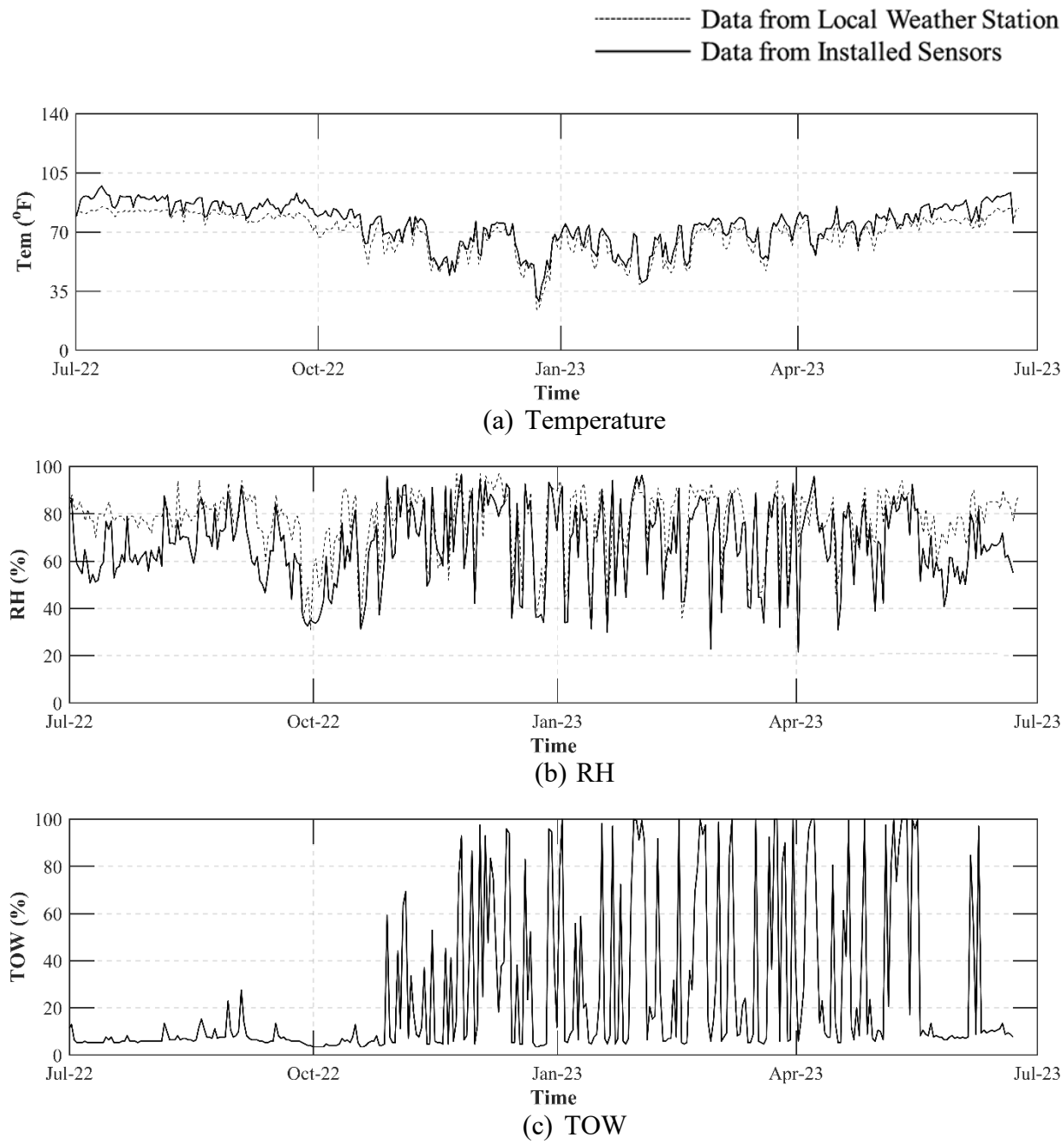


Figure 4.40. Comparison of Data from Local Weather Station and Data Measured with Installed TOW Sensor on Exterior Web of HOU−WS−07.

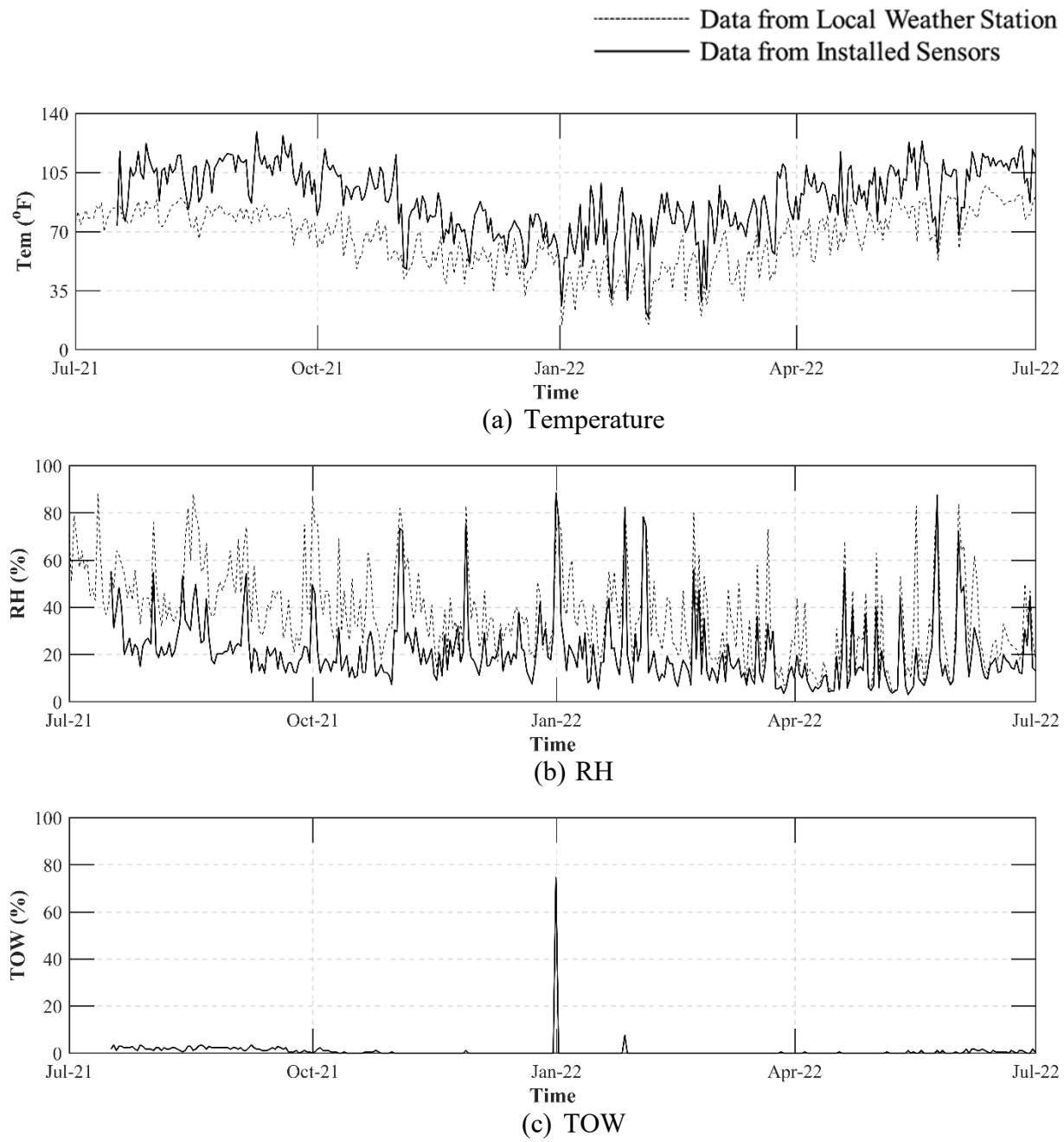


Figure 4.41. Comparison of Data from Local Weather Station and Data Measured with Installed TOW Sensor on Exterior Web of LBB−WS−01.

A significant difference was observed between wetness duration readings from a capacitive grid sensor and the TOW estimated according to the standard proposed by ISO 9223 (2012). The actual wetness probably varies from the definition proposed by the standard because ISO 9223 (2012)does not account for the location of the metals, whether they are sheltered or unsheltered, and their exposure to wind and sunlight in its calculation of wetness duration. Table 4-13 provides

the TOW recorded from the capacitive grid sensor and the calculated wetness from recorded temperature and RH. In the majority of cases, the TOW derived from the sensor exhibited significantly lower readings than calculated values according to the definition outlined in the ISO 9223 (2012)standard. Table 4-14 shows the duration of wetness that is computed based on environmental data collected from local weather stations. Note that the orientation of the sensor installation can also contribute to the final TOW recordings. TOW readings can greatly vary depending on sensor position, as noted in the sensing device manual.

Table 4-13. Sensor Measurements and Calculated Wetness Time Based on ISO-9223.

Bridge Name	Location	Duration (year)	TOW (hours/year)	Temperature (°F)	RH (%)	TOW ISO (hours/year)
ATL−WS−03	Exterior	0.60	879	67.5	69	2850
CRP−WS−01	Interior	0.27	749	78.7	75	4158
CRP−WS−01	Exterior	1.01	2352	75.7	69	3388
DAL−WS−02	Exterior	1.03	2469	65.0	71	2878
HOU−WS−07	Exterior	1.25	2267	74.1	70	3106
LBB−WS−01	Exterior	1.20	146	71.1	41	313

Table 4-14. Calculated Wetness Time from Local Weather Station Based on ISO-9223.

Bridge Name	Location	TOW (hours/year)	Temperature (°F)	RH (%)
ATL-WS-03	Exterior	3171	63.4	71
CRP−WS−01	Interior G2F1	4011	72.3	74
CRP−WS−01	Exterior G1F1	4011	72.3	74
DAL−WS−02	Exterior	2712	65.6	70
HOU−WS−07	Exterior	3151	70.7	71
LBB−WS−01	Exterior	1365	60.7	54

Schindelholz et al. (2013) investigated the actual TOW collected from sensing devices at sheltered locations and reported similar findings—that actual duration of wetness is lower than the results obtained by ISO 9223 (2012). The study indicated that factors such as wettability, electrode spacing, aerosol size, and loading density impacted the wetness accuracy measured by sensors. It was also reported that the grid sensors were more responsive at lower RH levels. These factors might have also contributed to the lower wetness measurements recorded from the leaf wetness sensor in this study. Figure 4.42 illustrates a comparison between the recorded wetness duration

from the sensing device, calculated TOW based on ISO 9223 (2012) from temperature and RH readings logged by the sensor, and calculated TOW based on ISO 9223 (2012) from environmental data documented by local weather stations. TOW recorded from the leaf wetness sensor was noticeably lower than calculated wetness duration from ISO 9223 (2012).

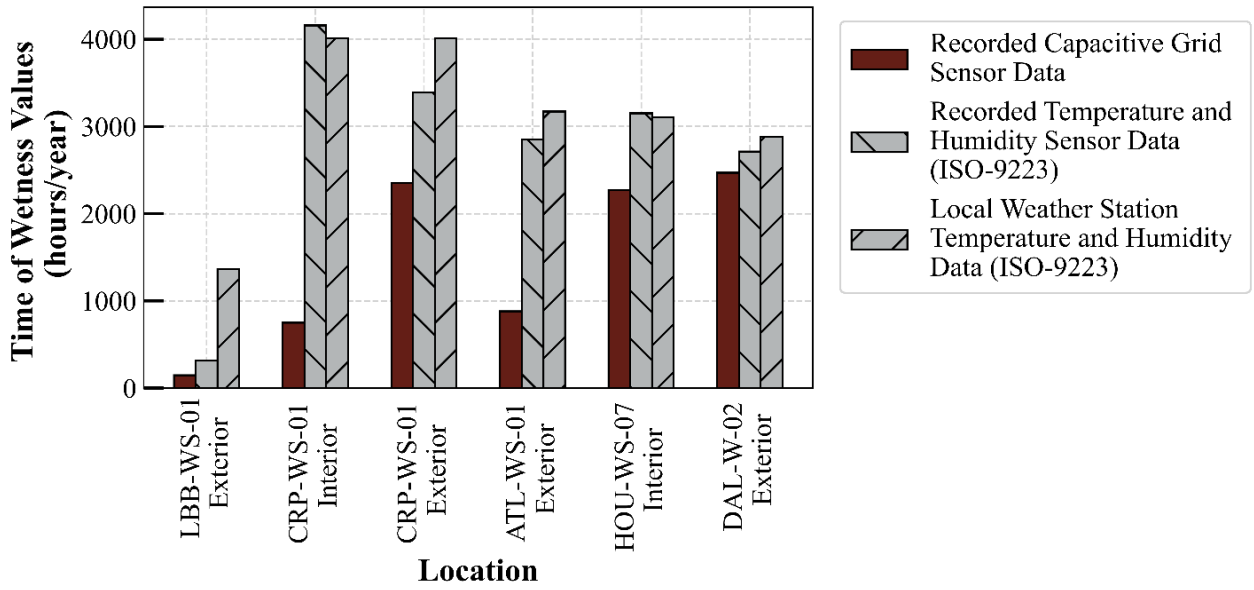


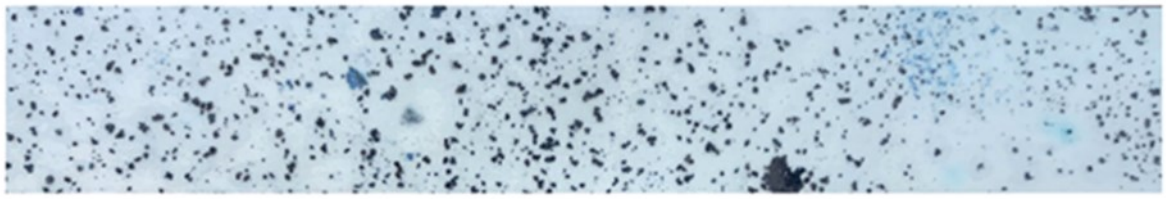
Figure 4.42. Comparison of TOW.

4.6 PARTICLE SIZE ANALYSIS AND DEVELOPMENT OF NEW PRI

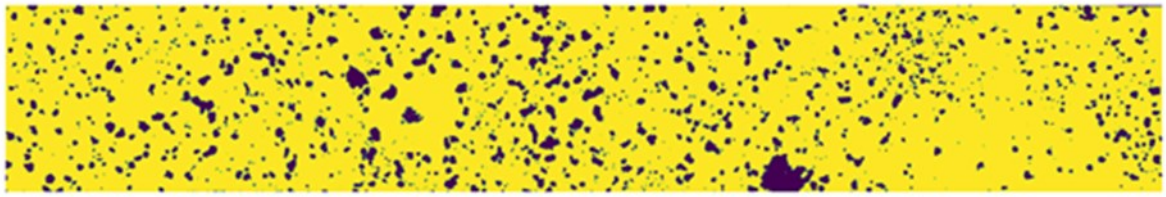
Image analysis was carried out to evaluate tape adhesion test results in terms of particle size and distribution of rust density. The analysis included thresholding and a masking technique to segment the particles from an image and count their size, area, shape, etc. In this case, Yen thresholding and binary masking techniques were used. Image analysis techniques like Yen thresholding and masking are commonly used to isolate and study particles from background regions in images. Yen thresholding determines an optimal threshold value that separates particle pixels from background pixels by maximizing interclass variance between the two regions (Yen et al., 1995). The threshold is then used to create a binary mask in which pixels above the threshold are classified as foreground particles and pixels below are background (Sezgin & Sankur, 2004).

The binary mask from thresholding is applied to the original image to extract only the particles of interest by setting background pixels to zero intensity (Russ, 2011). This masking process eliminates background regions and retains particles in their original form, ready for further analysis like measuring size, area, shape parameters, etc., or using advanced segmentation methods

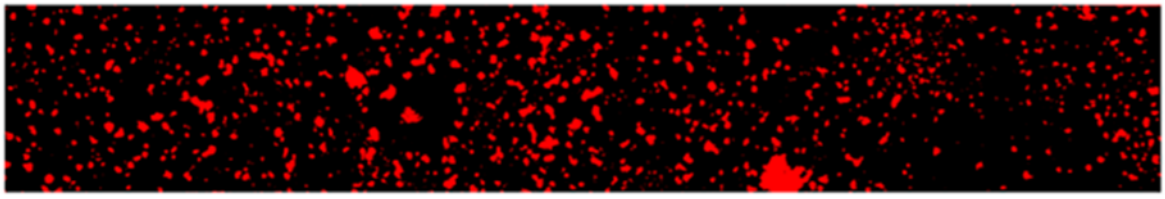
(Soille, 1999). Together, Yen thresholding classifies pixels into particle and background regions, while masking eliminates the background and retains just the particles for characterization and quantification in particle size analysis (Cao et al., 2021). For analyzing the particle size, a python script was developed using several libraries, such as pandas (McKinney, 2011), OpenCV (Bradski & Kaehler, 2000), and scikit-image (Van der Walt et al., 2014), to perform image segmentation using thresholding and masking and to then calculate the size, shape, and area of rust particles. Yen's thresholding method (Yen et al., 1995) was implemented to detect the particles with good accuracy. However, it was decided to combine Yen's thresholding with masking that involves isolating and separating targeted particles from the background to further enhance the precision of particle detection and perform statistical analysis. Thresholding-based binary masks were also implemented to segment and extract particles from images.



(a) Raw Image



(b) Threshold Image Using Yen Thresholding



(c) Masked Image for Particle Size Analysis

Figure 4.43. Particle Size Analysis.

Figure 4.43(a) shows a raw image of the data recorded on adhesive tapes with dimensions of 5 in. by 1 in., while Figure 4.43(b) illustrates Yen's thresholding results that converted an input image into a binary image based on the image histogram and optimal threshold values. As shown

in Figure 4.43(b), the thresholding technique accurately selected rust particles and differentiated them from the background by maximizing between-class variance. Figure 4.43(c) shows the masking results precisely detecting the surrounding rust particles. Particle size analysis was conducted within the targeted areas to convert image data into numerical values.

The process involved evaluating each individual tape by documenting the count, size, and shape of rust particles. In addition, the distribution, area, and density of rust particles were calculated using the python script. Figure 4.44 shows the particle size analysis for CRP−WS−01, including results computed for the top flange, web, bottom face of bottom flange, and stiffener. Note that the recorded data from the top face of bottom flange was not included in image analysis since dirt and debris collected on the top face inhibited the adherence of rust particles to the tape. Figure 4.45 and Figure 4.46 show the image analysis results of the count and size of the rust particles developed on steel girders located in a marine environment. An analysis of the results obtained for CRP−WS−01 and HOU−WS−07 showed that large rust flakes developed on steel girders, which represented unstable patina for these two structures because of the deposition of airborne chloride and elevated RH. Figure 4.47 demonstrates the results of image analysis for steel girders of ATL−WS−01, which depicts stable patina formation on weathering steel girders.

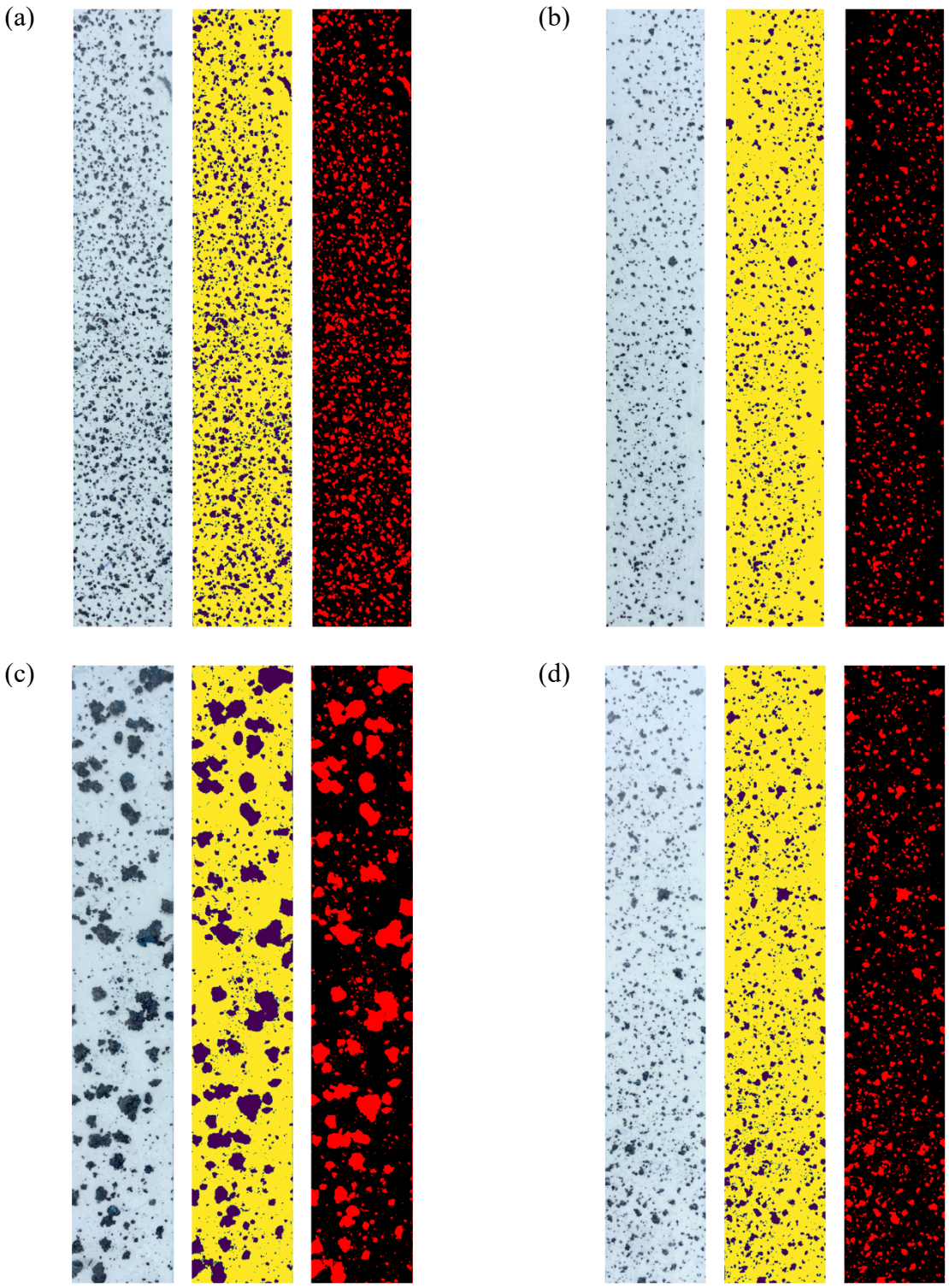


Figure 4.44. Particle Size Analysis Results at A9G1F1 (CRP−WS−01): (a) Top Flange Bottom, (b) Web, (c) Bottom Flange Bottom, (d) Stiffener.

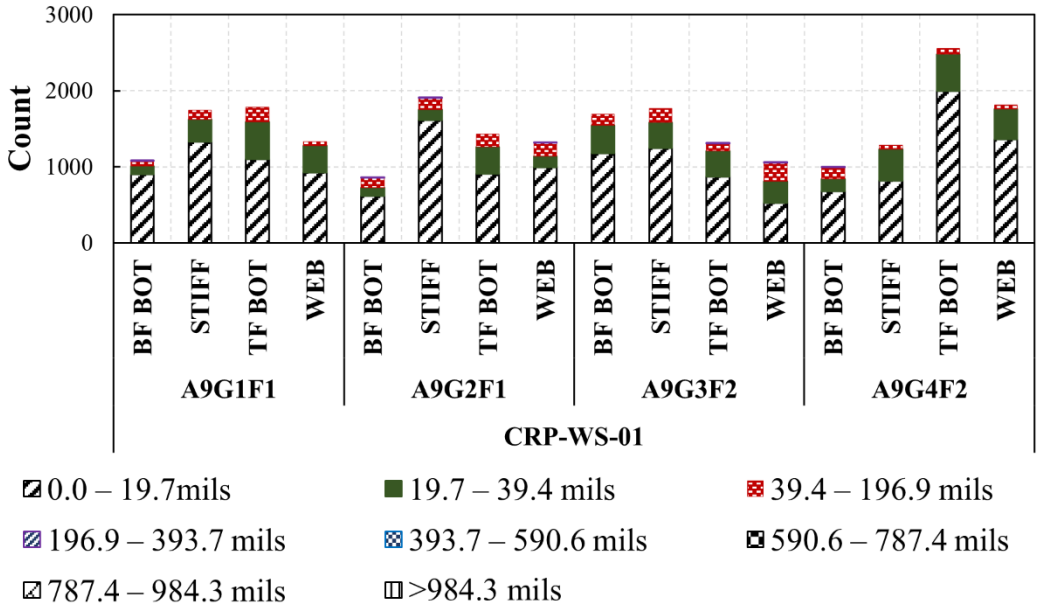


Figure 4.45. Particle Size Analysis Results for CRP−WS−01.

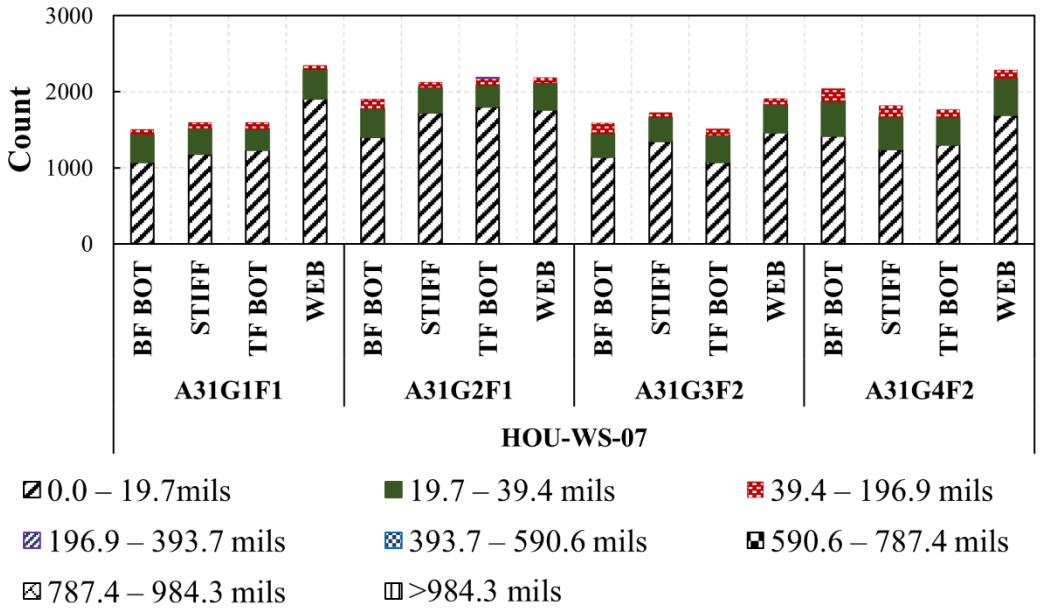


Figure 4.46. Particle Size Analysis Results for HOU−WS−07.

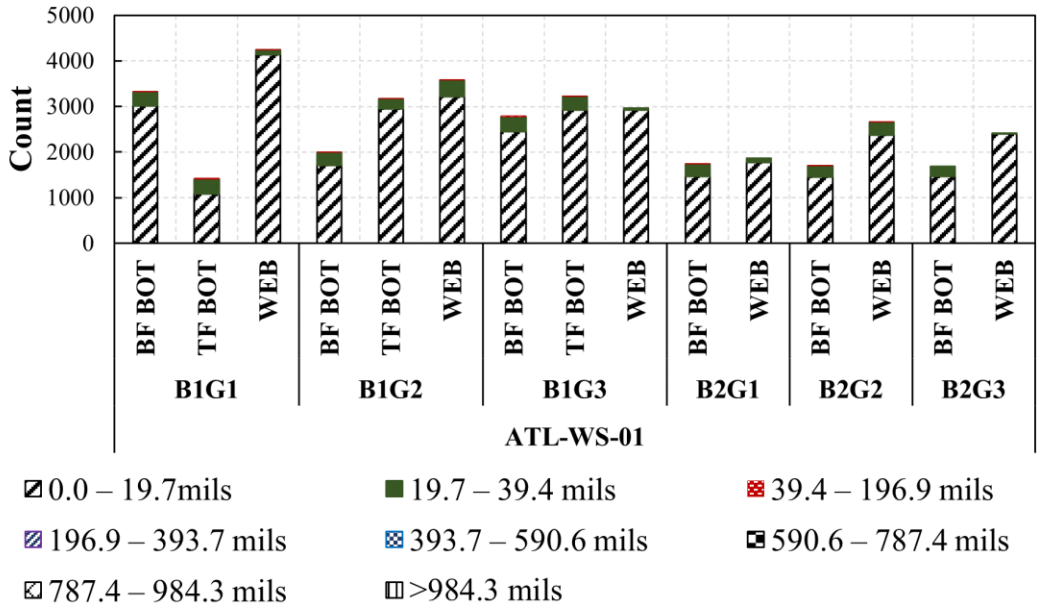


Figure 4.47. Particle Size Analysis Results for ATL−WS−01.

A proposed PRI developed in this study is given in Table 4-15. This rating system is based on our findings from 25 weathering steel girder bridges inspected across the state. The inspected structures were located in both low and moderate corrosive risk regions, as well as in places with a marine environment or in places with a high usage of deicing salt. A total of 354 tape adhesion samples were documented during field inspections, and the proposed patina rating was developed that can be used to evaluate patina on weathering steel bridges.

The new rating index modifies the Iowa PRI system by considering scores ranging from 0 to 10 that are determined in relation to the area of the rust particles on tape samples and flake particle size. By analyzing the recorded data documented during the inspection of weathering steel girders, researchers concluded that the normalized area of rust particles on testing strips can be used to determine the condition of the patina. If the developed patina on the steel surface is stable, the normalized area of rust particles on the testing strip must be less than 10 percent; otherwise, the protective rust layer is probably not stable. Another factor considered in the new rating index is the size of flake particles collected on the testing strip. If the largest flake size recorded on tape is less than 196.9 mils (5 mm), then a stable patina has formed that adheres to the steel substrate.

Table 4-15. PRI Based on Particle Size Analysis.

PRI	Iowa PRI	Normalized Area (%)	Largest Flake Size (mils)	Patina Category
10	8	Small (<10)	0.0–19.7	Excellent
9	8	Large (10–30)	0.0–19.7	Excellent
8	7	Small (<10)	19.7–39.4	Good
7	7	Large (10–30)	19.7–39.4	Good
6	6	Small (<10)	39.4–196.9	Satisfactory
5	6	Large (10–30)	39.4–196.9	Fair
4	5	Small (<10)	196.9–984.3	Poor
3	5	Large (10–30)	196.9–984.3	Serious
2	4	Small (<10)	> 984.3	Very Serious
1	4	Large (10–30)	> 984.3	Very Serious
0	3	Large (>30)	> 984.3	Very Serious

Figure 4.48 shows the probability distribution function (PDF) developed for the results of the tape adhesion test conducted in this research. Normal distribution was applied to determine the best fit curve to the normalized area of rust particles, wherein mean and standard deviation were 7.5 percent and 4.6 percent, respectively. Two-thirds of the sample strips collected during field inspection had a normalized area of less than 10 percent.

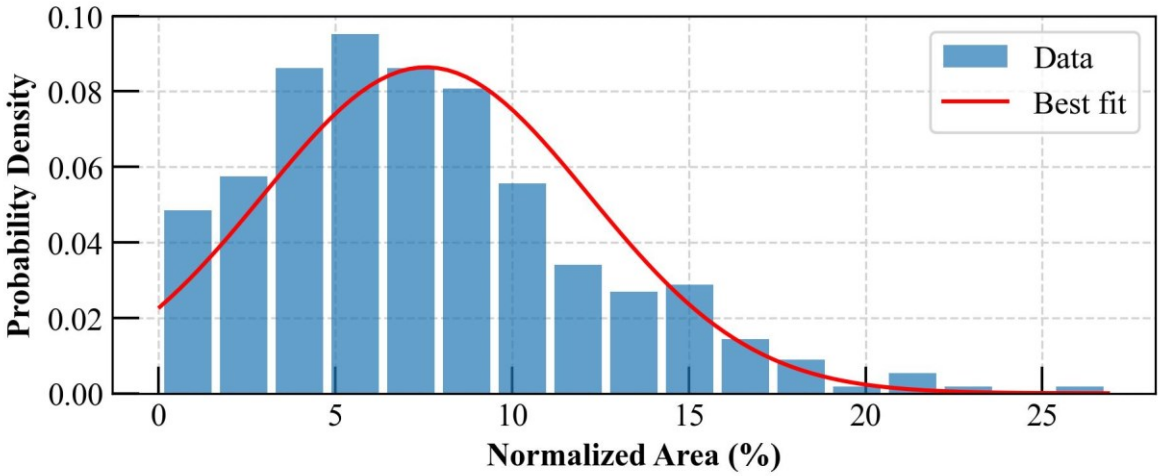


Figure 4.48. PDF Developed for Normalized Area of Rust Particles.

4.7 SUMMARY

The results from the field examinations provided a comprehensive evaluation of the weathering steel and paint coatings applied on steel girders across the state. Factors like airborne chloride deposition, usage of deicing salts, and the age of the bridge are identified as influential elements impacting the performance of weathering steel. The patina color observed on the inspected steel girders varied from orange to brown to black, and stains were sometimes visible on the steel components of bent caps. The exterior girders typically displayed a well-preserved and stable patina, while the interior girders showed a consistent rust film but with sporadic dirt build-up. Poultice corrosion and localized delamination of the patina was observed on some surfaces. The condition of the patina was found to be more stable in some districts than others. For example, patina developed on weathering steel bridges in Austin District generally exhibited more stability than ones in Corpus Christi.

On-system bridges predominantly showed good corrosion resistance with less paint defects. However, it is worth noting that minor rust spot and dirt accumulation were visible on connections and the bottom flange. The inspected off-system bridges demonstrated extensive paint failure on the top and bottom flanges, with rust and pitting evident on the web. It was concluded that flooding and water logging accelerated the paint deterioration for off-system structures. An LBPS was also applied on some of these bridges that was found to be degraded to some extent. Corrosion was observed in certain areas, particularly under salt-laden coastal conditions.

The chloride test measurements performed in the field did not align with expected results from visual inspections and varied within protective patina developed on weathering steel. The field examination can determine the amount of surface chloride on steel, but it fails to determine details of rust particles such as the amount of akaganeite, a mineral containing a chloride-containing iron (III) oxide-hydroxide, within the patina later. A pH test was also conducted during each field examination and showed a slightly acidic environment on inspected steel girders. Thermal imaging documented during the field inspections helped identify areas with paint defects and rusting. In addition, sensors and data loggers installed on some steel girders showed an inconsistency between the recorded wetness duration and the calculated duration based on ISO 9223. It was concluded that the tape adhesion test can be an effective approach to evaluate the patina layer formed on weathering steel. From the test results conducted in this study, it was concluded that the exterior surfaces of steel girders typically demonstrated superior corrosion

resistance, while the interior surfaces displayed more rust flaking and poultice corrosion. Tape adhesion test results were analyzed via image analysis techniques such as Yen's thresholding and masking, which aided in determining particle size and enhanced the patina rating. The proposed patina rating considers factors like particle size and rust area percentage and assigns a rating on a scale of 0 (very serious) to 10 (excellent).

5 LABORATORY TESTING

5.1 INTRODUCTION

This chapter describes laboratory testing performed on weathering and painted steel girders of TxDOT bridges. After collecting samples (scraped rust from the web of the fascia and interior girders of weathering steel), three sets of experiments were conducted to analyze the chemical and phase composition of the rust samples. Analysis of the collected rust particle revealed if the developed patina was active, inactive, or protective. These experiments included SEM/EDS, XPS, and XRD. This chapter also provides a classification of different paint systems applied on steel bridges in Texas. Similar to with the weathering steel, samples (scraped paint) were collected from the fascia and interior web of painted steel girders during the field inspection. The laboratory testing utilized during the examination of scraped paints includes optical microscopy and SEM/EDS. The primary objective of these tests was to determine the number of layers used in a specific paint system and identify existing pigments in each layer. Finally, studying the results of the laboratory examinations aided to differentiate between an LBPS, a ZBPS, and an epoxy paint system without zinc or lead.

5.2 EXPERIMENTAL PROGRAM

Corrosion products known as rust or patina form on weathering steel because of their interaction with iron and its surrounding environment. When the rust layer adheres to the surface of the steel substrate, it effectively prevents further corrosion. However, the rust particles do not protect steel from undergoing corrosion if they are loosely attached to the substrate (or the formed patina is non-adherent). The rust typically contains oxides, hydroxides, and oxyhydroxides that can be crystalline or amorphous. Rust may occur from either the substrate (endogenous products) or the surrounding environment (exogenous products). The formation of each individual component within the rust layer relies on the material composition, exposed environmental conditions, and changes in climatological factors such as rain, temperature, and pollution condition.

Schwertmann and Cornell (2000) suggested common corrosion products given in Table 5-1 that can form in the patina layer. Note that other compounds such as iron(II) sulfur heptahydrate, tetrahydrate, or hydrated iron(III) sulfate can also form, particularly in urban and

industrial environments. Alternatively, components such as iron(II) chloride, iron(II) chloride tetrahydrate ($FeCl_2.4H_2O$), and iron(III) chloride hexahydrate can form in marine atmospheres. These products, which contain sulfur and chloride ions, can contribute to the initiation and propagation of corrosion on steel. Iron compounds in lower or higher concentrations can be detected by examining the rust layers. Iron chlorides and sulfates are water-soluble and can easily be washed away by rainwater; thus, they are low in concentration in test samples. Conversely, iron oxides and iron(III) hydroxide are insoluble in water and can be found in higher concentration (Linke & Seidell, 1958).

Typical iron oxide minerals that over time can form in the rust layer are goethite (α–FeOOH), akaganeite (β–FeOOH), lepidocrocite (γ–FeOOH), and magnetite (Fe_3O_4). For example, in urban, rural, or industrial areas having low chloride deposits, α–FeOOH and γ–FeOOH are common corrosion products. However, in a high chloride environment, akaganeite (β–FeOOH) and spline also form in the rust layer. Keiser et al. (1982) studied the electrochemical reduction of iron oxide minerals and amorphous FeOOH and monitored the reaction products by using Raman and IR thermography. The researchers concluded that goethite resists electrochemical reduction, while other minerals such as lepidocrocite and amorphous FeOOH could be reduced to magnetite (Fe_3O_4).

Yamashita et al. (1998) noted that the amount of α–FeOOH and γ–FeOOH is a function of exposure time in industrial and rural environment. The authors also reported that the ratio of α/γ increases proportionally with an increase in the exposure period. Yamashita et al. (1994) studied the characteristic features of the rust layers on weathering steel and mild steel exposed to an industrial atmosphere for 26 years. Yamashita et al. found that the rust layer formed on weathering steel consists of two distinct layers: an inner layer composed of densely packed nanoparticles of α–FeOOH adhering to the steel surface, and an outer layer consisting of γ–FeOOH. The inner layer that was composed of α–FeOOH and enriched Cr was stable and protective. The primary component of this layer was initially γ–FeOOH, which formed within a few years and gradually transformed to α–FeOOH over time. Yamashita et al. (1994) concluded that the ferric oxyhydroxide of α–FeOOH is the final stable corrosion product in an atmospheric environment. When the densely packed, nano-sized α–FeOOH formed by the enrichment of Cr covers the weathering steel surface, it aids in reducing cracks and voids in the rust layer. In fact, the nano size α–FeOOH layer produced over decades exhibits a great ability to provide protection against an

atmospheric attack in an industrial environment. Another important fact reported by Yamashita et al. (1994) is that Cu and phosphate were not concentrated in the protective inner α–FeOOH layer, whereas Cr had a relatively high concentration after 26 years of exposure. However, the existence of Cu and phosphate has been noted to be beneficial for a protective rust layer on weathering steel (Morcillo et al., 2014).

Aside from weathering steel, TxDOT also uses paint systems to protect steel bridges from corrosion. Environmental conditions directly influence the decision of whether a particular type of system should be used to protect steel bridges from corrosion or not. The paint systems applied to steel bridges in Texas include System I, which is an epoxy-based paint system, as well as System II, System III, and System IV, which are OZ primers with a polyurethane coating. The results obtained from the laboratory testing helped identify colors, number of layers, and main elements of each paint system, such as zinc and lead.

Table 5-1. Chemical Formulas of Rust Layers (Schwertmann & Cornell, 2000).

Oxides	Formula	Hydroxides	Formula	Others	Formula
Hematite	α–Fe_2O_3	Goethite	α–FeOOH	Ferrous Chloride	$FeCl_2$
Maghemite	γ–Fe_2O_3	Akaganeite	β–FeOOH	Ferric Chloride	$FeCl_3$
Magnetite	Fe_3O_4	Lepidocrocite	γ–FeOOH	Ferrous Sulfate	$FeSO_4$
Ferrihydrite	$Fe_5HO_8.4H_2O$	Feroxyhyte	δ–FeOOH	Ferric Sulfate	$Fe_2(SO_4)_3$

5.2.1 Scanning Electron Microscopy/Energy-Dispersive X-Ray Spectroscopy

Using a focused beam of high-energy electrons, SEM recorded signals emitted from the surface of the examined sample. Electron-sample interactions reveal information on the sample's surface morphology (texture), chemical composition, crystalline structure, and material orientation. Data were usually collected throughout a defined region of the surface of the sample. Two-dimensional images were documented for any changes of sample properties. These images can be taken in two imaging modes—backscattered electron and secondary electron imaging (SEI) modes. Secondary imaging provides information about the surface topography, fractures, and crystal deposits, while backscattered electron imaging provides compositional information. When the sample is subjected to an electron beam, it generates specific X-rays that can be utilized through EDS analysis to identify the elemental composition of elements that are heavier than carbon.

SEM/EDS was used to identify the morphology and determine the elemental composition of weathering steel rust and paint samples. The chemical composition of weathering steel is listed

in Table 5-2. According to ASTM A242, A588, and A709, carbon (C) should range from 0.12 to 0.23 percent, Si (Si) from 0.25 to 0.50 percent, manganese (Mn) from 0.20 to 1.60 percent, P from 0.01 to 0.035 percent, sulfur (S) from 0.030 to 0.045 percent, Cr from 0.35 to 1.25 percent, Cu from 0.25 to 0.60 percent, vanadium (V) from 0.02 to 0.15 percent, and Ni from 0.40 to 0.65 percent by weight for different types of weathering steel. Note, vanadium is not mentioned in ASTM A242, which is signified by a dash in the table.

Table 5-2. Chemical Composition of Different Types of Weathering Steel (Weight %).

Grade	C	Si	Mn	P	S	Cr	Cu	V	Ni
ASTM A242	0.12	0.25–0.75	0.20–0.50	0.01–0.2	0.03	0.50–1.25	0.25–0.55	—	0.65
ASTM A588	0.16	0.30–0.50	0.80–1.25	0.03	0.03	0.40–0.65	0.25–0.40	0.02–0.10	0.40
ASTM A709	0.23	0.40	0.50–1.6	0.035	0.045	0.35	0.60	0.15	0.45

Raman et al. (1989) studied the morphology and growth characteristics of rust phases developed on ASTM A-588 weathering steel modeling tropical environmental conditions in three laboratory examinations: (1) accelerated atmospheric exposure simulation tests (AAEST), (2) salt fog tests, and (3) continuous immersion tests in plain and salt water. The authors analyzed the morphology and particle characteristics of the patina using microstructural data from SEM. It was reported that magnetite was detected under constant humid conditions, but it was also noted that over time, magnetite (Fe_3O_4) could convert to goethite (α–FeOOH). The predominant phase in AAEST was α–FeOOH, while amorphous bulk appeared as an adherent "cotton bolls" layer. It was also reported that a sedimentary layer formed on the steel surface during continuous immersion. All phase compositions of iron oxide (including α–, δ–, γ–FeOOH, and γ–Fe_20_3) were found to be crystalline. In addition, magnetite that was converted to α–FeOOH through whiskers and rods was observed during the salt fog test.

For weathering steel and painted steel, the main objectives of SEM/EDS are as follows:

1. To examine the morphological details of rust and paint samples.
2. To determine the elemental composition of rust and paint samples.
3. To compare pollutants such as sulfur and chlorine on the exterior and interior faces of girders.

4. To examine if the distribution of contaminants is uniform (homogenous) or not.
5. To distinguish between lead-based, zinc-based, and epoxy paint systems.

5.2.1.1 Experimental Setup

Figure 5.1 shows JEOL JSM-7500F, an ultra-high-resolution, field-emission-scanning electron microscope equipped with a high brightness conical FE gun and a low aberration conical objective lens; it was the equipment used for conducting SEM/EDS on collected rust and paint samples. The lens improves the overall stability of the JSM-7500F and enables observations of the sample at magnifications up to 10,000,000x with a guaranteed resolution of 3.93700787 × 10^{-8} mils (1 nm). The instrument is also equipped with an energy filter to observe the fine surface morphology of nanostructures. The technical specifications for JSM-7500F are shown in Table 5-3.

Table 5-3. Technical Specifications for JSM—7500F.

Source	**Cold cathode ultrahigh voltage field emission conical anode gun**
Resolution	3.9 × 10^{-5} mils guaranteed at 15 kV; 8.6 × 10^{-5} mils guaranteed at 1.0 kV
Acc. voltage	0.5 to 30 kV (SEM or low magnification [LM] mode); 10 V steps from 0.5 to 2.9 kV; 100 V steps from 2.9 to 30 kV
Magnification range	25x to 19,000x in LM mode; 100x to 650,000x in SEM mode
Probe current	1×10^{-13} order to > 2×10^{-9} amps (continuous)

For weathering steel samples, the corrosion products formed on the surface of steel were scraped off with a blade. These samples were later analyzed with JEOL JSM-7500F. Prior to the laboratory analysis, the powdered rust was dried off and pressed over carbon tape mounted on the cylindrical sample. For painted steel samples, samples were similarly scraped off with a blade and analyzed with JEOL JSM-7500F. Prior to the laboratory analysis, the paint sample was dried and pressed over carbon tape mounted on the cylindrical sample.



Figure 5.1. Scanning Electron Microscope with EDS JEOL JSM-7500F.

The following procedure was followed during the SEM/EDS analysis:

1. Mount a small piece of clean Cu next to the sample for quant optimization.
2. Load the sample, close the airlocks, and wait until the vacuum pressure reads 5.22×10^{-8} (3.6×10^{-4}) Pa.
3. Select input voltage for acceleration voltage (start with 5 kV).
4. Turn on the acceleration voltage and watch for emission current to increase (usually 20 μA).
5. Check probe current setting.
6. Use LM setting to find the area of interest on sample and have it centered.
7. Auto-adjust contrast and brightness.
8. Focus enough to identify the site of interest of the sample.
9. Turn off LM and select SEM mode.
10. Select the desired working distance.
11. Align the beam using operational panel.
12. Set the magnification to ~ 100000X and focus the image.

13. Turn wobbler on and correct for image shifts and then turn off the wobbler.
14. Increase the magnification and focus to check for any astigmatism. Correct the astigmatism if necessary.
15. Use freeze mode to acquire the images.
16. Set the acceleration voltage to 20 kV, the emission current to 20 μA, and adjust current value between 12 to 14 μA for EDS analysis probe to get a good image.
17. Insert Labe detector.
18. Use SEI mode and select the sample location.
19. Adjust the magnification, focus, and astigmatism; also, adjust the contrast and brightness of the image.
20. Check the acquisition setup to achieve more than 250,000 counts.
21. Perform quant optimization. This is done on the clean Cu tape mounted next to the sample collected data for 60 seconds (twice), and the beam length is measured. If it is close to 100 percent of the previous measurement, then the beam is considered stable. Start taking the measurements for EDS analysis.
22. Move to the site of interest and select the area for EDS analysis.
23. Acquire spectra and elemental composition.

5.2.1.2 Experimental Results: Weathering Steel

The EDS analysis provided the elemental composition of rust for exterior and interior girders of all the weathering steel bridges, while the SEM analysis provided images of the rust surface at different magnification, which helped when studying the morphology and surface characteristics of the collected rust. Figure 5.2 shows the SEM image of rust collected from an exterior steel girder along with the associated sum spectrum obtained from EDS analysis. In this examples, microcracks were also detected on the examined surfaces, as indicated in Figure 5.2 and Figure 5.4. The prepared rust surface was examined at different magnification to investigate the morphological details shown in Figure 5.3. If the surface properties varied with composition, then the EDS spectrum was particularly obtained to examine the change in elemental composition (Figure 5.5).

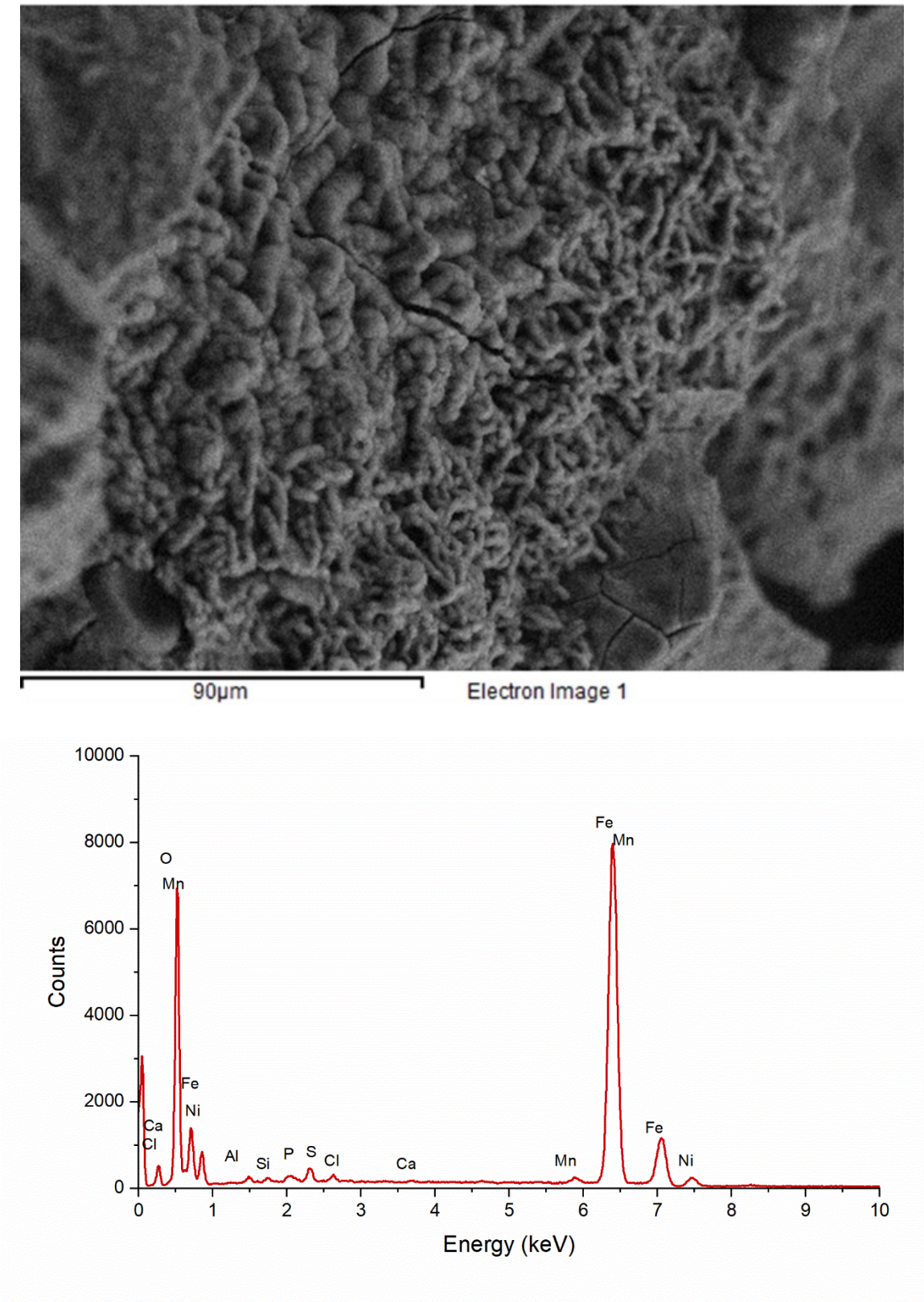


Figure 5.2. SEM Image of Rust Collected from Exterior Web of Weathering Steel Bridge (DAL-WS-02) and Sample Sum Spectrum of the Same Sample.

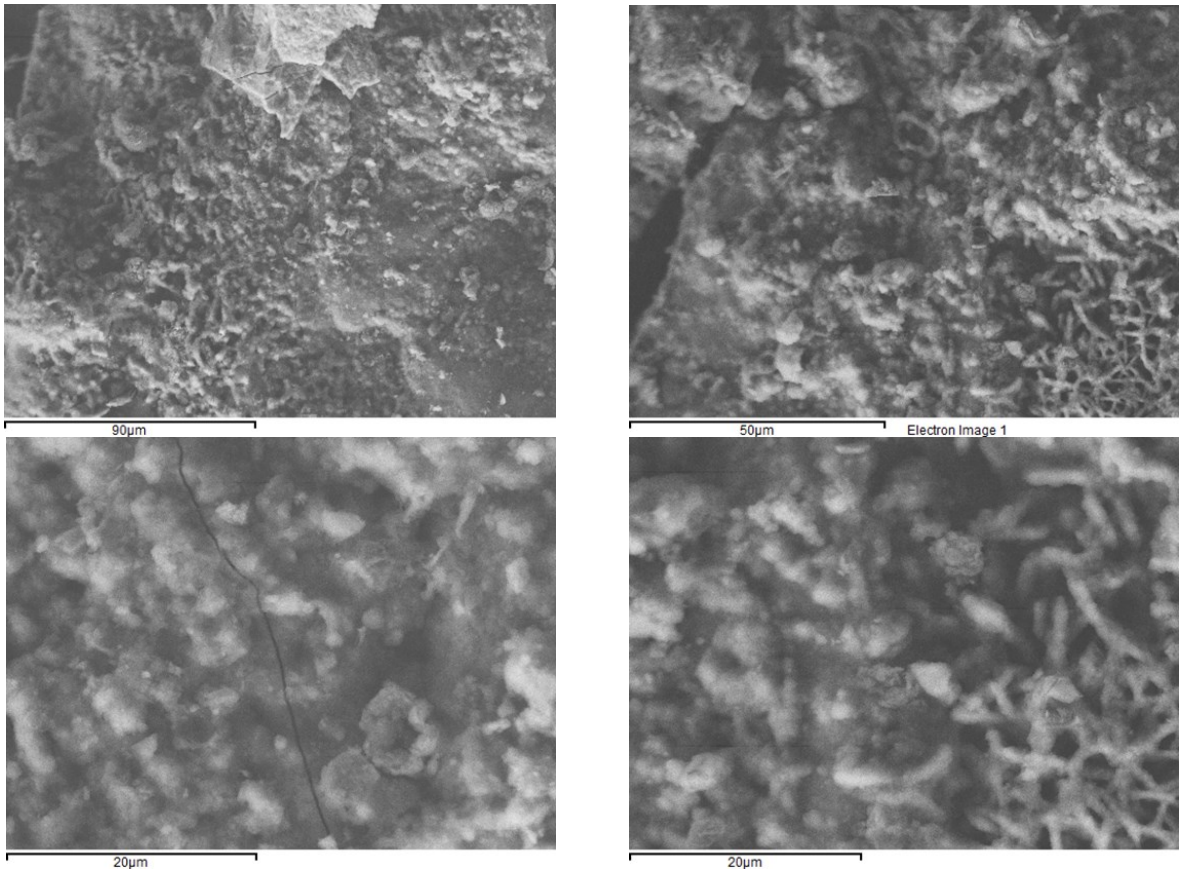


Figure 5.3. SEM Images of Rust Surface Observed on Weathering Steel Bridges in Different Scales (90 µm, 50 µm, and 20 µm).

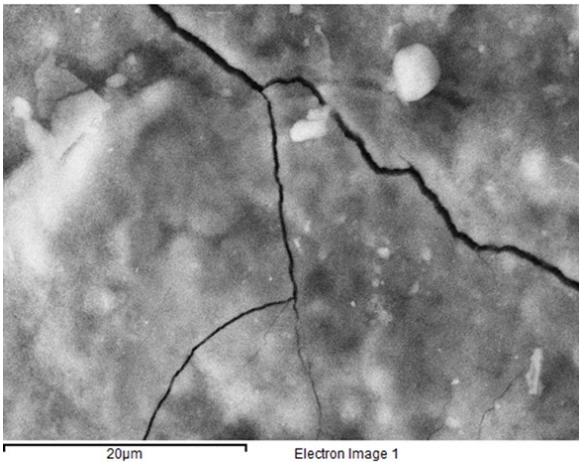


Figure 5.4. SEM Image of Microcracks Detected on Rust Surface of Weathering Steel Bridge on Exterior Web (CRP-WS-01).

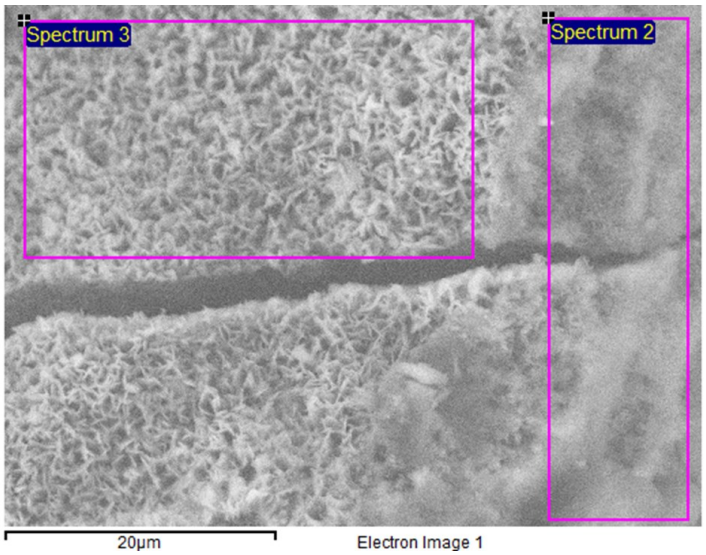


Figure 5.5. Elemental Compositions (EDS Spectra).

Figure 5.5 shows the morphological characteristics of the patina surface. A total of three EDS analysis results are shown in Table 5-4 and Figure 5.5. Table 5-4 gives elemental compositions of Spectrum 2, Spectrum 3, and the sum of spectra collected over entire area. A change in surface characteristics can be seen in Figure 5.5, indicating that the elemental composition was not only uniform over the entire rust surface, but it was also nonuniform due to the formation of iron oxides or hydroxides discussed earlier. Figure 5.6 shows the sample elemental map obtained from EDS analysis. This elemental map provides details about the distribution of all the elements that existed on the examined surface and validates whether the particular element was uniformly distributed throughout the surface or not.

Table 5-4. Elemental Composition of Spectrum 2, Spectrum 3, and Sum Spectrum Obtained from EDS Analysis on Rust Surface of Weathering Steel Sample.

Element	Spectrum 2	Spectrum 3	Sum Spectrum
Element	**Weight %**	**Weight %**	**Weight %**
O K*	27.8	45.5	43.5
Al K	1.39	0.93	1.44
Si K	1.73	1.03	2.36
S K	0.31	0.41	0.86
Cl K	0.52	0.57	0.76
Cr K	0.27	—	—
K K	—	—	0.19
Ca K	—	—	0.15
Mn K	0.58	0.41	1.11
Fe K	67.3	51.2	49.4
Cu K	0.10	—	0.26

Note:
Chlorine and Sulphur detected during EDS analysis.

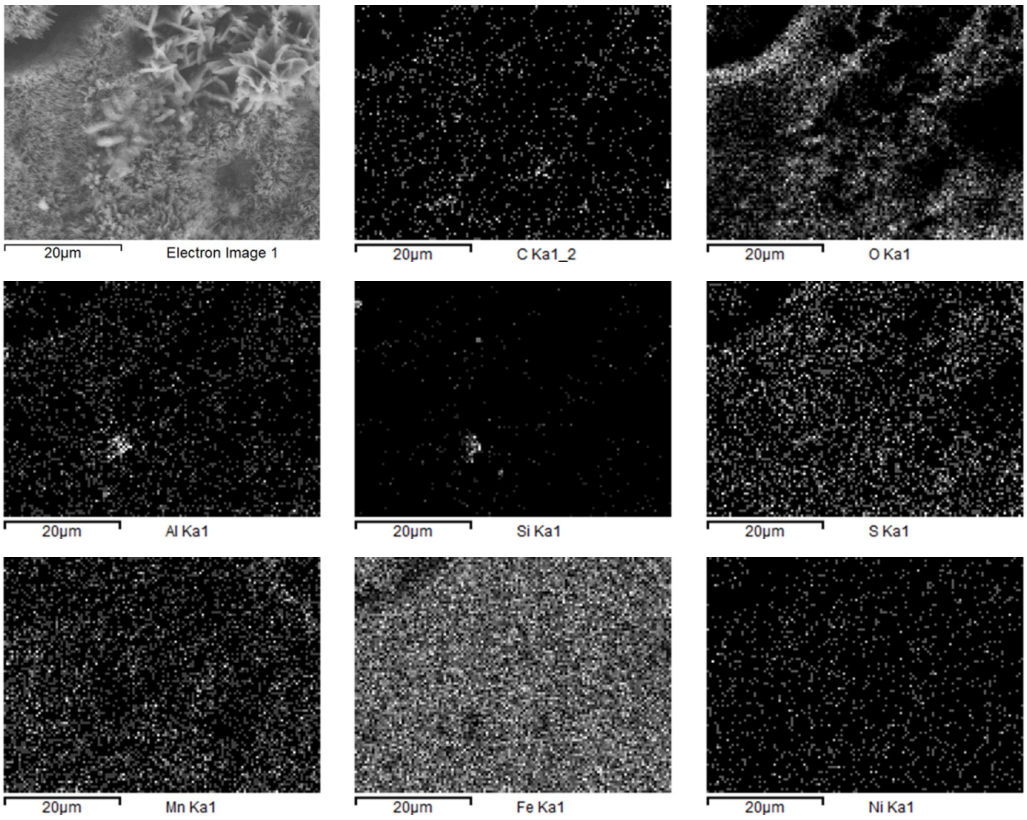
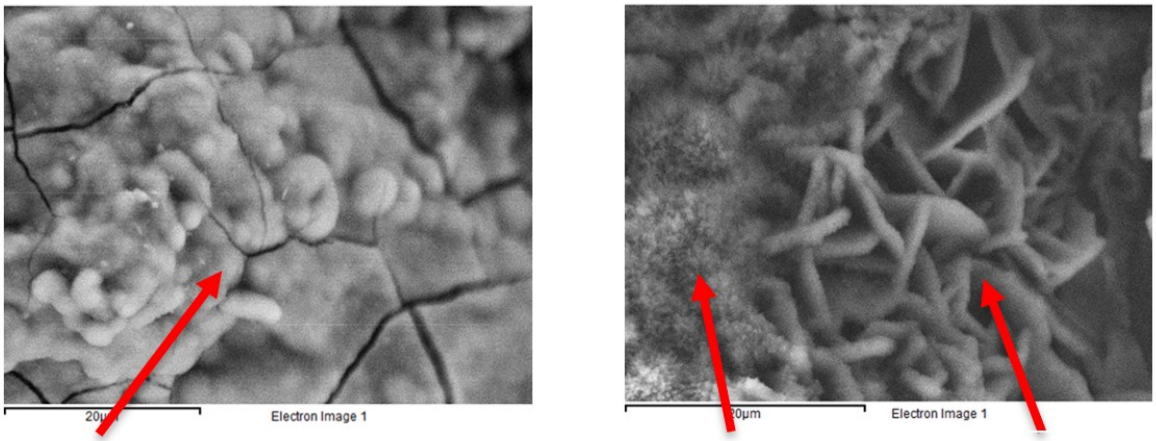


Figure 5.6. Sample Elemental Map Showcasing Distribution of Elemental Composition on Weathering Steel Rust Sample.

Iron and oxygen were found to be the primary elements in the rust layer, but sulfur and chlorine were typically found in low quantities. Chlorine was detected in a few cases but was mostly absent in examined areas of ELP-WS-01. Additionally, minor amounts of Si, P, Cr, Cu, calcium, and sodium were frequently detected by EDS. Components of weathering steel were determined to be Mn, Cr, Ni, and Cu. Moreover, the steel was composed by the addition of a small amount of silicon as an alloying material. Calcium was also found on the specimens, though it might have been from debris mixed with the rust sample. Microcracks were also observed on the rust surface.

Figure 5.7(a) depicts an SEM image illustrating the presence of hematite, while Figure 5.7(b) illustrates the existence of goethite and lepidocrocite within the rust sample obtained from the AUS−WS−04 bridge. The coexistence of goethite and lepidocrocite in the rust layer from the exterior girder implies the formation of a protective oxide. In contrast, the presence of hematite on samples taken from the interior girder indicates the inadequate protective capabilities of the patina layer. Figure 5.8 further supports these findings by visually demonstrating the formation of goethite and lepidocrocite on the exterior girder, thereby confirming the existence of a protective rust phase, while the interior girder exhibits the formation of nonprotective hematite. Figure 5.7(a), Figure 5.8(a), and Figure 5.8(b) also show microcracks that are a dominant factor in severe environments, such as Region 6. Elevated chloride concentrations (from deicing salt usage or airborne chloride in a marine environment) in the patina layer accelerates the corrosion rate of the metal. The accelerated corrosion process is attributed to the formation of Akaganeite (β–FeOOH). Iron oxyhydroxide blocks the formation of goethite (α–FeOOH), which is an essential component for a protective oxide layer.



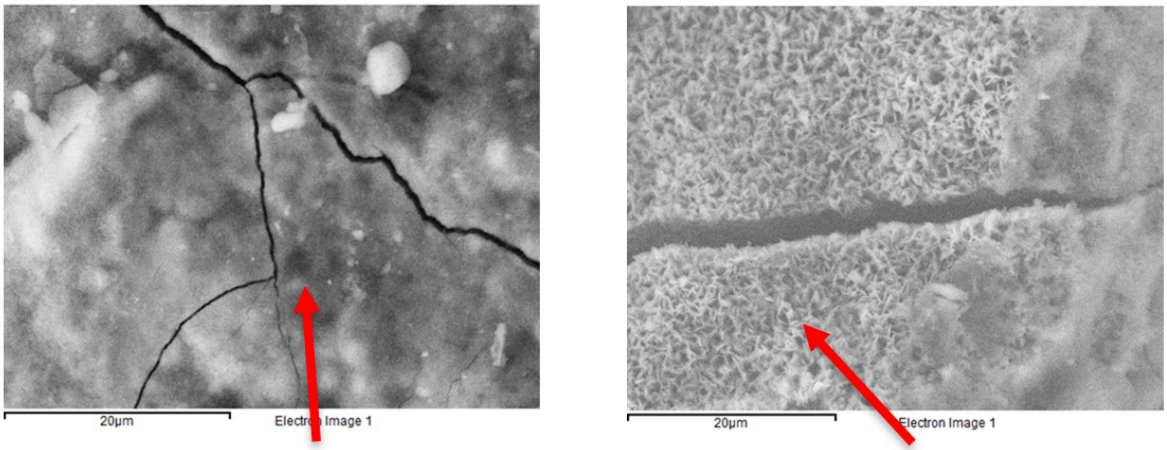
Hematite (α-Fe_2O_3)

Goethite (α-FeOOH)

Lepidocrocite (γ-FeOOH)

(a) AUS−WS−04 (Interior Girder) (b) AUS−WS−04 (Exterior Girder)

Figure 5.7. Hematite, Goethite, and Lepidocrocite Detected on a Random Rust Sample.



Hematite (α-Fe_2O_3)

Lepidocrocite (γ-FeOOH) + Goethite (α-FeOOH)

(a) CRP−WS−01 (Interior Girder) (b) CRP−WS−01 (Exterior Girder)

Figure 5.8. Microcracks Detected on a Random Rust Sample.

Figure 5.9 shows the chemical and phase compositions of a random sample of a patina collected from weathering steel. As discussed, a patina layer may consist of different components. Goethite—a protective iron oxide—forms dense and nano-sized crystalline layers. Additionally, the γ-phase or lepidocrocite, exhibits a planar crystalline structure that is less dense than goethite. Figure 5.9 also shows Akaganeite, characterized by its monoclinic crystal structure, and brittle layers of hematite. The presence of hematite in the form of brittle layers increases the likelihood of microcrack initiations within the rust layer.

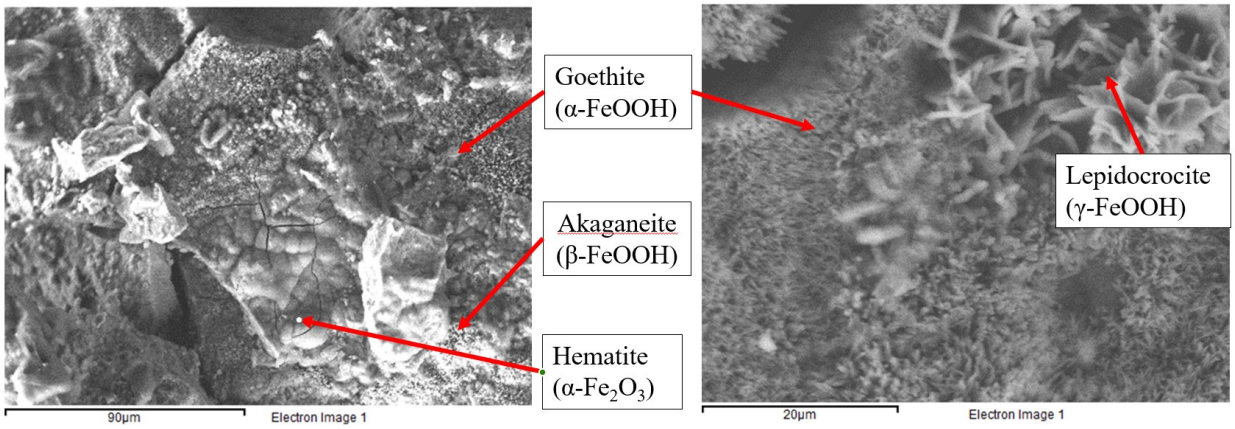
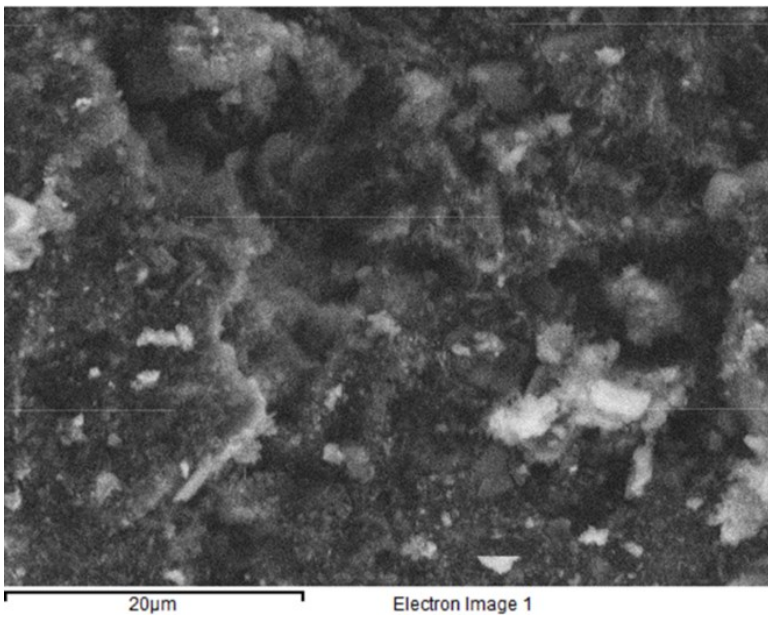


Figure 5.9. Phases Compositions of a Weathering Steel Rust Sample.

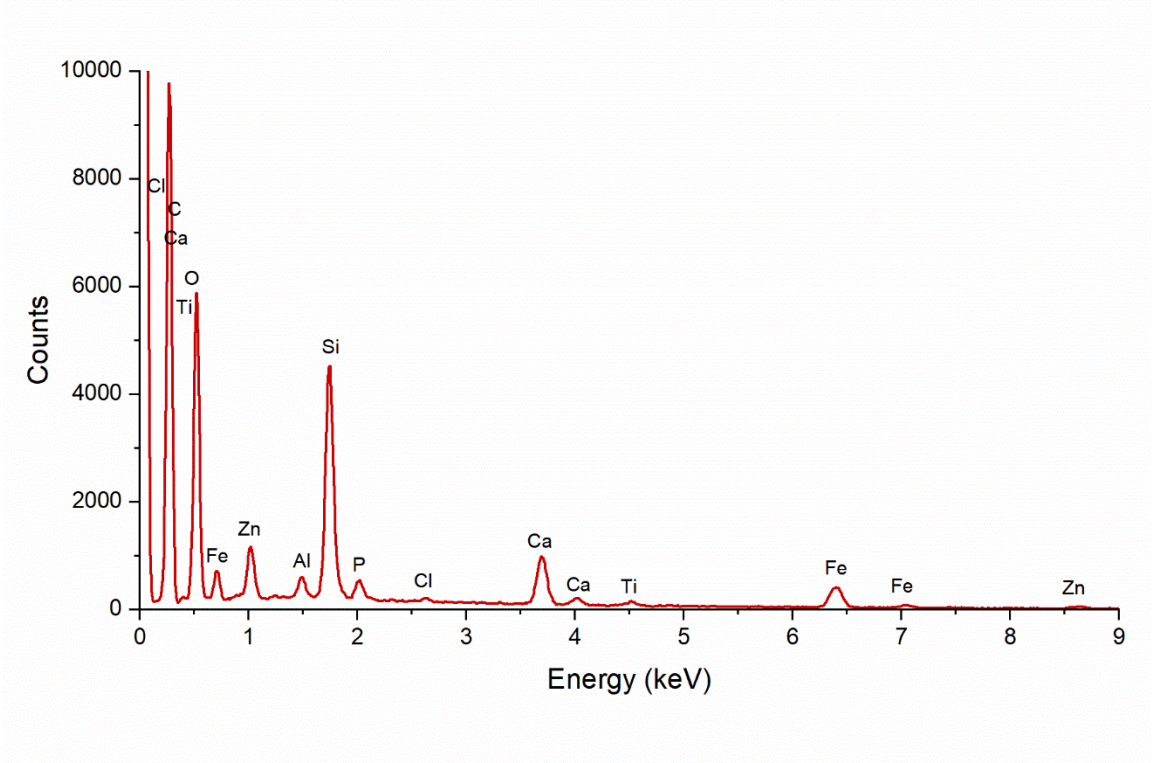
5.2.1.3 Experimental Results: Painted Steel

Typical results of the SEM/EDS analysis of paint samples are shown in Figure 5.10 and Figure 5.11. The results show a higher percentage of carbon in System I and System II. The higher percentage might be due to the epoxy layer of paint that consisted of carbon; carbon was also deposited on the prepared surface during the SEM/EDS analysis. When analyzing the primer of System II, zinc was observed in a significant amount, which aided in differentiating System II from System I. Elements such as sulfur (S), chlorine (Cl), oxygen (O), aluminum (Al), silicon (Si), phosphorous (P), calcium (Ca), titanium (Ti), iron (Fe), and zinc (Zn) were found in the EDS spectrum analysis. Sulfur deposition was observed on six bridges located mostly in industrial areas. Chlorine was observed in low amounts in 11 of the painted steel bridges. Chlorine deposition might be due to airborne chloride or the use of deicing salts in winter. Titanium observed in SEM/EDS images designates the use of white pigments in painted layers. For two painted bridges, AMA-PS-01 and YKM-PS-01, the EDS analysis revealed the presence of lead, which helped differentiate LBPSs from zinc and epoxy-based paint systems. Note that the SEM/EDS analysis only shows the grayscale image of paint and does not show the true colors of pigments.



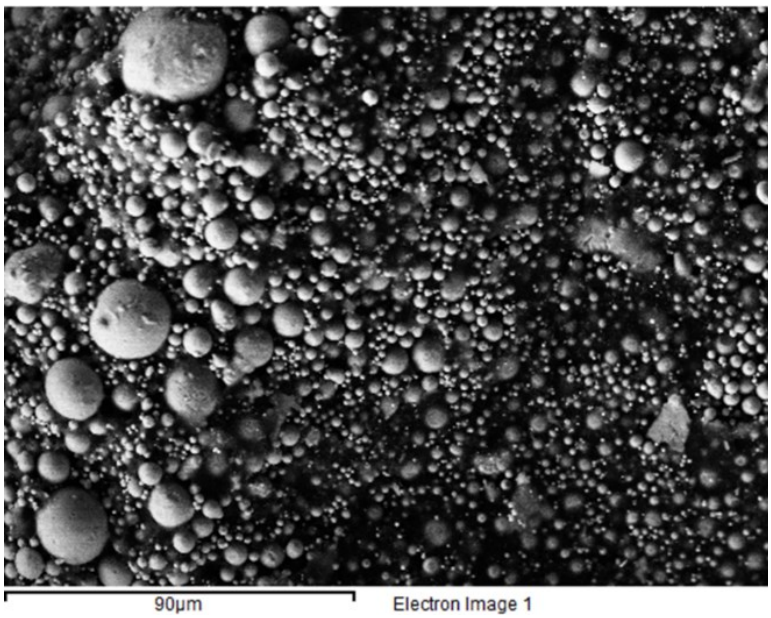
Element	Weight%	Atomic%
C K	51.7	61.1
O K	40.0	35.5
Al K	0.34	0.18
Si K	3.89	1.97
P K	0.37	0.17
Cl K	0.07	0.03
Ca K	1.33	0.47
Ti K	0.16	0.05
Fe K	1.70	0.43
Zn K	0.44	0.09

(a) SEM Image of Paint (20 µm)



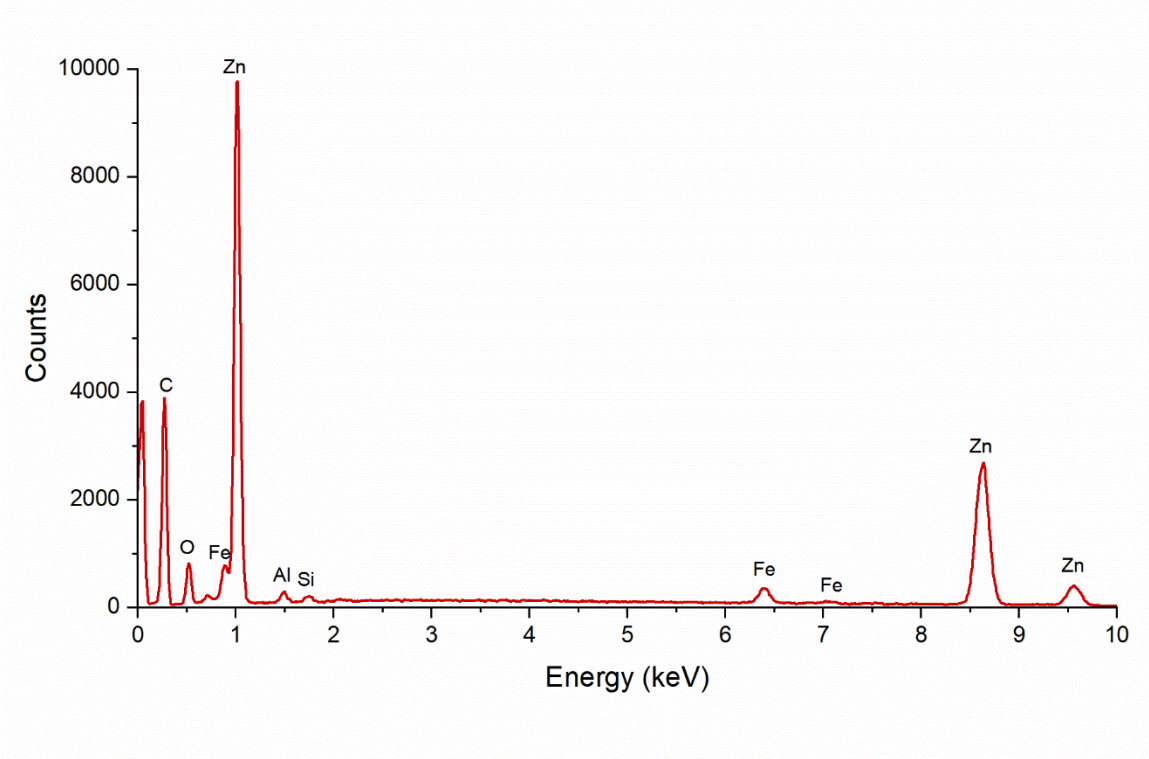
(b) EDS Spectrum of Paint Showing Elemental Peaks

Figure 5.10. SEM Image and EDS Spectrum of Paint Sample (System I) Collected from Exterior Web of WFS−RC−01.



Element	Weight%	Atomic%
C K	51.5	79.2
O K	7.77	8.97
Al K	0.39	0.27
Si K	0.21	0.14
Fe K	1.46	0.48
Zn K	38.7	10.9

(a) SEM Image of Paint (90 µm)



(b) EDS Spectrum of Rust Showing Elemental Peaks

Figure 5.11. SEM Image and EDS Spectrum of Zinc-Based Primer (System II) Observed on TYL−PS−01.

SEM images provided morphological surface characteristics of rust, and EDS analysis revealed the elemental composition of rust samples taken from weathering steel bridges. The analysis showed iron and oxygen were major constituents of the patina samples. A small amount of chlorine and sulfur were observed on 22 of the weathering steel bridges. Microcracks were also observed on the rust surface, but this analysis did not give any information about the type of oxides that formed on the rust surface. Therefore, the quantitative information about α–FeOOH, β–FeOOH, γ–FeOOH, δ–FeOOH, and Fe_3O_4 were obtained by using XPS and XRD analysis.

SEM/EDS analysis was able to distinguish between paint systems used in the TxDOT bridges, such as LBPSs, ZBPSs, and epoxy-based paint systems. However, the SEM images did not provide details about the true colors of pigments that is necessary for identifying and characterizing paint systems. Consequently, optical microscopy was also performed in order to identify the pigments present in the paint sample.

5.2.2 X-Ray Photoelectron Spectroscopy

X-ray photoelectron spectroscopy (XPS)/ Ultraviolet photoelectron Spectroscopy (UPS) is widely used to identify the chemical state of elements. In the patina, high-spin Fe(II) and Fe(III) contain unpaired electrons and exhibit multiplet splitting. Biesinger et al. (2011) outlined a spectral curve fit procedure for different transition metals (Fe, Co, Ni, Cr, Mn) to quantitatively determine the chemical state of the components. In addition to this reference, a binding energy database (NIST database) provides sufficient information for chemical state determination of single peak spectra.

The initial step in the analysis of 2p spectra for transition metal was to separate 2p3/2 and 2p1/2 spin orbit split components. It was observed that the separation between 2p3/2 and 2p1/2 was sufficiently large to detect intense 2p3/2 signals that consisted of multiple peaks. Pratt et al. (1994) used a set of multiplet peaks to curve fit oxidized iron sulfide (pyrrhotite surfaces). Gupta and Sen (1975) provided fitting parameters for Fe(II) (high-spin only) and Fe(III) species. Grosvenor et al. (2004a) used a near approximation of the Gupta and Sen (1975)multiplet structure to fit the different iron oxide, hydroxide, and halide peak forms. Note that ligands had different peak spacing and intensity, but all high-spin compounds have broad satellite peaks of variable intensities at binding energies above the primary Fe 2p 3/2 structure in their spectra.

Biesinger et al. (2011) proposed all fitting parameters needed for curve fitting, which included the multiplet and satellite structure. The authors employed a Shirley background covering for these fits that was only the 2p3/2 region of the spectrum. The fitting values and reference spectra helped identify pure oxide or hydroxide species. However, the overlapping spectrum also made the curve fitting for mixed systems complicated. Since Fe (III) compounds have similar Fe 2p binding energies but distinct peak and intensities, multiple Fe(III) species cannot be correctly matched to a spectrum. Therefore, Fe is a difficult metal to curve fit because of substantial numbers of potential species.

Biesinger et al. (2011) also introduced a method of fitting parameters for the quantitative determination of iron oxides, hydroxides, and metal. For quantitative estimation, the Fe 2p 3/2 spectrum was then curve fitted to obtain the quantitative information on rust surfaces for Fe metal, avg. FeO, avg. Fe_2O_3, and avg. FeOOH.

The main objective of XPS analysis was to quantify the various oxides, hydroxides, and oxyhydroxides that lead to determining the Protective Ability Index (PAI) of the patina in terms of the α/γ ratio and α/Γ ratio. Because curve fitting of Fe spectra is a complex task and may contribute to significant error due to overlapping binding energies of various species, such as Fe_2O_3, FeOOH, Fe_3O_4, $FeCr_2O_4$, and FeO, it was decided, similar to previous studies, to curve fit the spectra for only four species—FeO, avg. FeOOH, avg. Fe_2O_3, and Fe metal (Gupta & Sen, 1975; McIntyre & Zetaruk, 1977; Pratt et al., 1994; Grosvenor et al., 2004b).

5.2.2.1 Experimental Setup

An Omicron XPS/UPS system with an Argus detector was utilized for the XPS study of weathering steel rust samples. The device employed the dual Mg/Al DAR 400 X-ray source from Omicron for XPS measurement. This device was outfitted with a 128-channel microchannel plate Argus detector with 0.8 eV resolution, allowing for imaging of a 6 mm by 6 mm region with high sensitivity and snapshot XPS. This system was also equipped with a CN10 charge neutralizer to reduce charging and an NGI3000 Argon ion sputter for surface cleaning.

In this study, the corrosion products collected from the surface of external and internal weathering steel were analyzed with the Omicron XPS/UPS system equipped with Argus detector. Prior to the laboratory analysis, the powdered rust was dried off and pressed over carbon tape that was attached to the cylindrical sample.

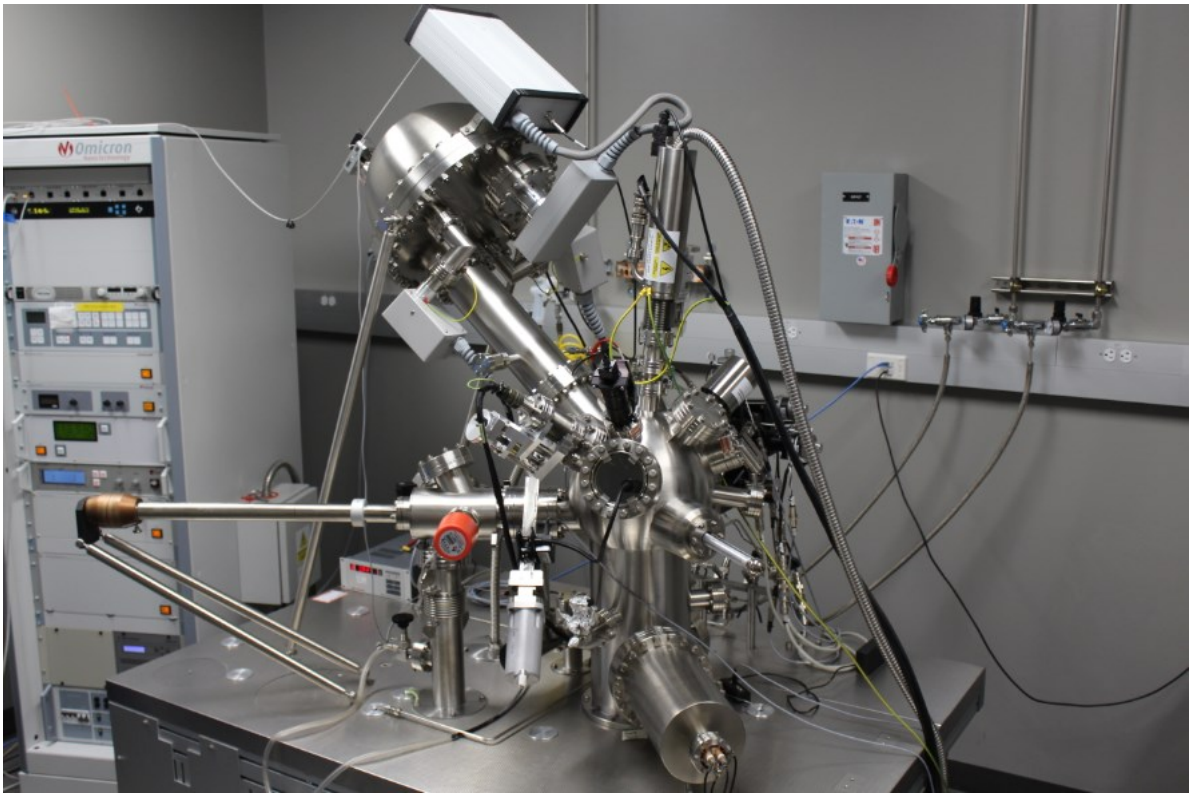


Figure 5.12. Omicron XPS/UPS System with Argus Detector.

The procedure outlined below was followed during the XPS analysis for preparing and transferring the sample from the loading chamber to the analysis chamber:

1. Verify the pressure of the analysis chamber. It should be less than 8.7×10^{-11} psi or 6×10^{-7} Pa. Press the Close Valve followed by the Turbo to shut off the turbo pump and allow it to escape.
2. Wipe the sample holder with isopropyl alcohol or acetone.
3. Unlock the sample loading door and remove liquid nitrogen from the system and shut the vent valve.
4. Open the sample loading door and load the specimen into the sample holder.
5. Clean the inside of the transfer chamber and seal the door. Ensure the turbo vent light is illuminated. Press Turbo to engage the turbo pump, and then press Open Valve to open the turbo valve instantly.
6. Wait until the pressure in the transfer chamber (as shown by the bench gauge) falls below 1.01×10^{-10} psi or 7×10^{-7} (typically 30 minutes).

7. Open the gate valve for the sample transfer and monitor the pressure in the analysis chamber. Note that when the gate valve is fully open, chamber pressure should not exceed 2.9×10^{-11} psi or 2×10^{-7} Pa.
8. Transfer the sample holder into the chamber for analysis. The transfer arm should not rotate, or the sample puck will fall off.
9. Position the transfer arm lock.
10. Pull back the transfer arm and shut the gate valve.
11. Collect survey spectrum and then collect Fe 2p3/2, C-1s, O-1s, and Fe 3p spectrum.

The collected spectra were analyzed using CasaXPS software. Gaussian (Y%) - Lorentzian (X%) was defined in Casa as GL(X). Peak shapes and peak binding energy comparisons were made to determine the oxide composition based on previous findings in the literature (Gupta & Sen, 1975; Grosvenor et al., 2004a; Biesinger et al., 2011).

5.2.2.2 Experimental Results

During the XPS examination, Fe 2p 3/2 spectra C-1s spectra, which is the inner most orbit of a carbon atom, and O-1s spectra were observed in collected rust samples. The raw XPS data were documented for Fe 2p 3/2, shown in Figure 5.13, whereas the data calibrated for intensity with phi transmission coefficients (a = 304.3, b = 0.91) and energy calibrated using adventitious carbon curve fitting are shown in Figure 5.14. For the quantitative determination of iron oxides, hydroxides, and Fe metal, a complex curve fitting using Biesinger et al. (2011) fitting parameters to fit Fe 2p 3/2 spectra was derived, as shown in Figure 5.15. Table 5-5 shows the quantitative results obtained after curve fitting Fe 2p 3/2 spectra for all the collected rust samples. The curve-fitting plots for the weathering steel girders inspected in this research are provided in the Appendix.

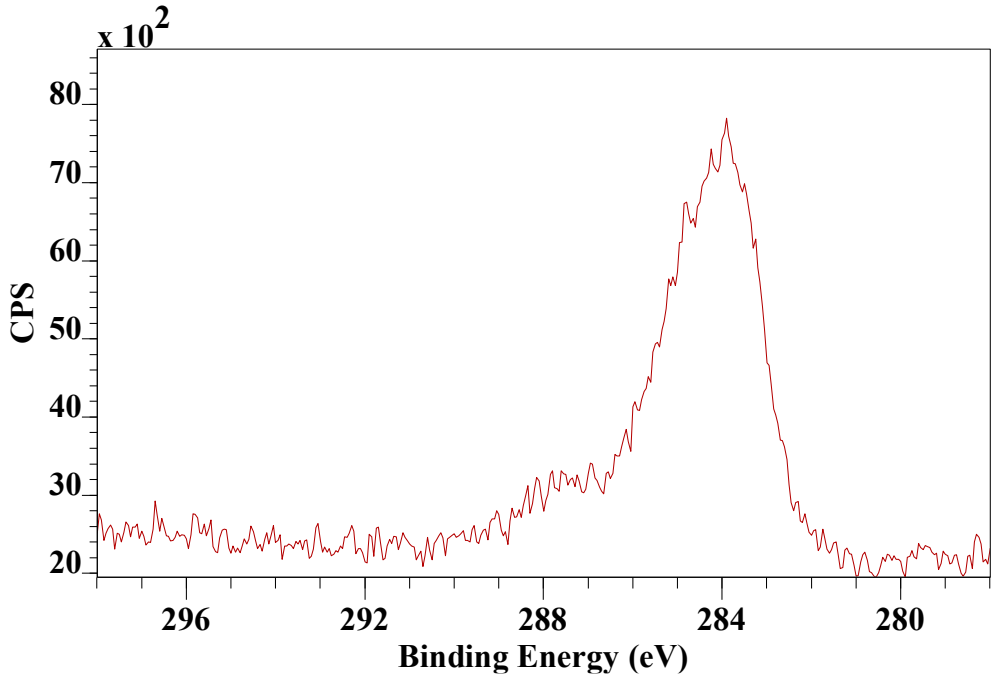


Figure 5.13. Fe 2p 3/2 Spectra.

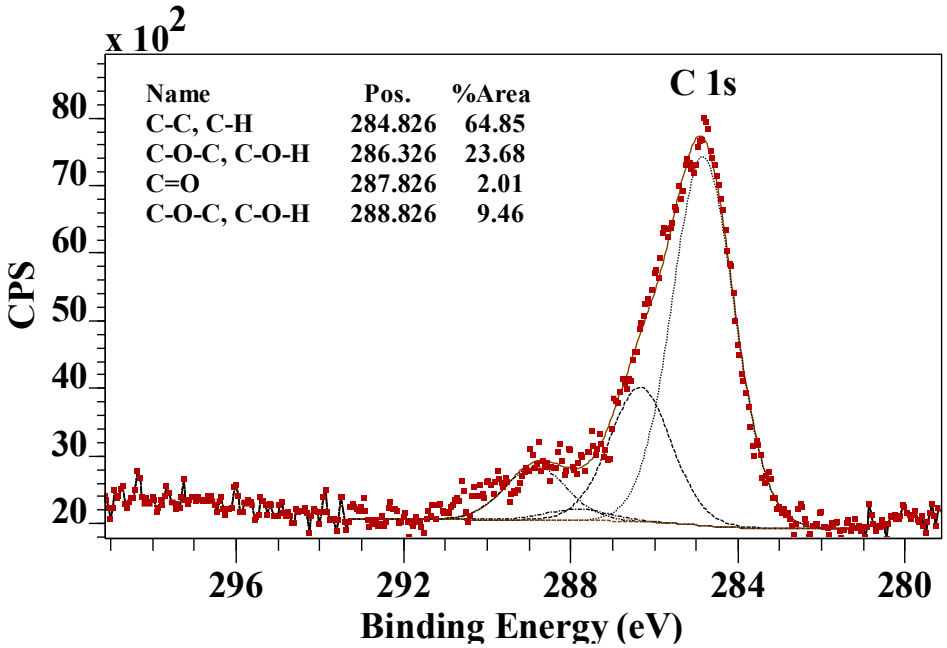


Figure 5.14. Adventitious Carbon Curve Fitting for Calibration.

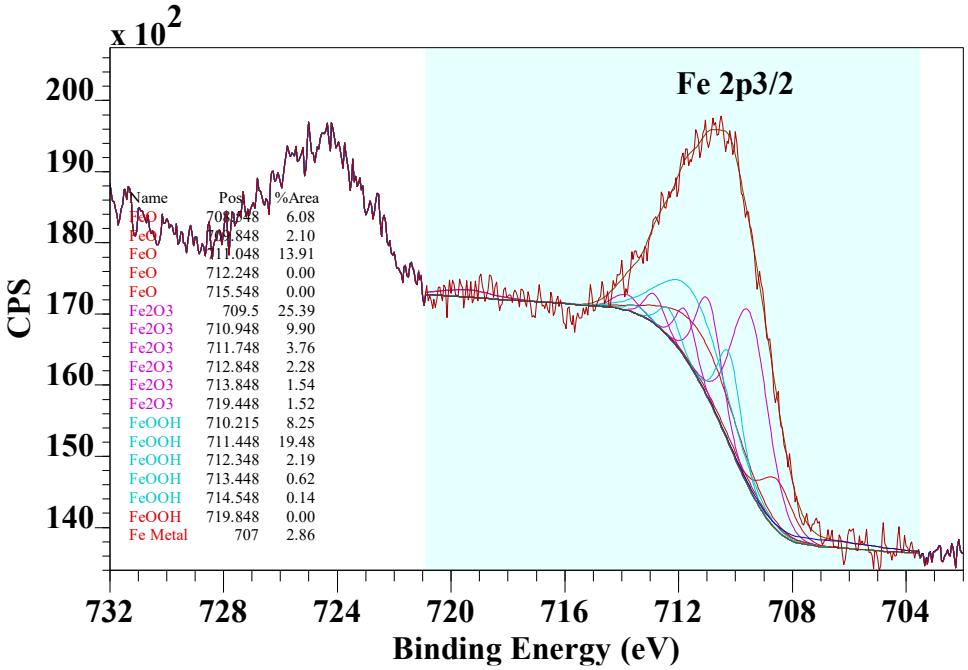


Figure 5.15. Fe 2p 3/2 Curve Fitting for Quantification of Avg. FeOOH, Avg. Fe2O3, Avg. FeO, and Fe Metal.

Table 5-5. XPS Curve-Fitting Quantitative Results in Area Percent.

Bridge Name	Location	FeO (Area %)	Fe_2O_3 (Area %)	FeOOH (Area %)	Fe Metal (Area %)
ATL-WS-01	EXT	17.4	36.0	45.9	0.00
	INT	22.8	45.5	31.0	0.68
ATL-WS-02	EXT	3.96	24.4	71.0	0.00
	INT	69.8	16.0	14.2	0.00
ATL-WS-03	EXT	34.0	26.3	39.2	0.55
	INT	32.8	19.2	48.1	0.00
AUS-WS-01	EXT	7.58	35.4	57.0	0.00
	INT	3.91	73.6	22.2	0.30
AUS-WS-02	EXT	25.9	24.7	48.0	1.51
	INT	24.2	25.8	50.0	0.00
AUS-WS-03	EXT	12.7	25.9	61.4	0.00
	INT	7.31	19.6	73.0	0.00
AUS-WS-04	EXT	12.9	36.6	47.6	2.99
	INT	12.1	64.4	23.5	0.00
CRP-WS-01	EXT	2.88	60.5	36.7	0.00
	INT	27.8	46.3	25.4	0.53
ELP-WS-01	EXT	11.0	43.9	43.8	1.28
	INT	14.6	34.2	51.2	0.00
FTW-WS-01	EXT	28.3	24.8	46.9	0.00
	INT	8.82	39.0	52.2	0.00
FTW-WS-02	EXT	21.8	11.4	66.8	0.00
	INT	16.4	37.5	45.6	0.57
FTW-WS-03	EXT	4.98	27.1	67.1	0.81
	INT	7.80	27.2	65.0	0.00
HOU-WS-07	EXT	17.8	48.1	33.5	0.62
	INT	7.88	11.0	81.1	0.00
HOU-WS-03	EXT	14.3	33.9	51.8	0.00
	INT	14.3	35.4	50.0	0.00
HOU-WS-01	EXT	13.5	42.0	44.5	0.00
	INT	—	—	—	—
HOU-WS-06	EXT	14.4	16.7	68.9	0.00
	INT	5.28	46.5	48.3	0.00
HOU-WS-04	EXT	13.1	34.7	50.6	1.58
	INT	29.3	16.1	54.6	0.00
HOU-WS-02	EXT	29.3	25.8	44.6	0.29
	INT	25.6	30.3	44.1	0.00
HOU-WS-05	EXT	11.3	43.9	44.4	0.48
	INT	20.4	37.9	41.8	0.00

Table 5-5. XPS Curve-Fitting Quantitative Results in Area Percent (Cont.).

Bridge Name	Location	FeO (Area %)	Fe_2O_3 (Area %)	FeOOH (Area %)	Fe Metal (Area %)
LBB-WS-01	EXT	26.0	36.0	36.7	1.40
	INT	41.3	19.4	38.0	1.30
LBB-WS-02	EXT	24.6	35.9	39.5	0.00
	INT	11.1	32.7	56.2	0.00
DAL-WS-01	EXT	15.8	32.9	51.3	0.00
	INT	12.9	44.3	43.4	0.00
DAL-WS-02	EXT	4.07	28.6	66.8	0.58
	INT	13.4	39.0	47.7	0.00
DAL-WS-03	EXT	12.7	14.8	71.3	1.23
	INT	14.8	38.6	46.6	0.00

The XPS analysis of rust samples of the inspected weathering steel girders confirmed the presence of iron oxide (FeO and Fe2O3), iron hydroxides (FeOOH), and iron metal. The composition of these constituents varied among samples taken from exterior and interior girders. Additionally, it was observed that the age of the bridges and the environmental conditions had an impact on the composition of the samples. Since XPS analysis only confirmed iron oxides and hydroxides, and it was not suitable to quantify the amount of α–FeOOH, β–FeOOH, γ–FeOOH, δ–FeOOH, and Fe_3O_4, XRD analysis was also needed to evaluate the PAI by quantifying the amount of these oxyhydroxides and magnetite.

5.2.3 Optical Microscopy

Optical microscopes are commonly used to study the surface characteristics of coating systems. By magnifying the sample image, the pigment color, precise thickness, and height measurement of paint layers can be determined. In this study, optical microscopes were employed to determine the quantity, thickness, and color sequence of layers in paint fragments. Additionally, the microscopes were also employed to identify textures and the basic characteristics of pigment and extender combinations. Note that polarized light microscopy (incident and transmitted light) up to a 1000x magnification is typically used for normal paint evaluations (Hamer, 1982; Kilbourn & Marx, 1994; Stoecklein & Tuente, 1994; Caddy, 2001).

The main objective in using optical microscopy was to study the surface characteristics of scraped paint samples and identify color pigments, determine layers of paint, and measure the thickness of the layers of paint.

5.2.3.1 Experimental Setup

Two sets of lenses were used in the optical microscope: namely MPLFLN10XBDP with 10x optical zoom, and MPLFLN50XBDP with 50x optical zoom. The images of paint samples were examined by using the mix observation mode, including bright-field and dark-field observation methods. The bright-field was used for observation, and the dark-field was used for detection. The experiment began by preparing and placing the paint samples on the cylindrical mount. To identify pigment color, scan of the paint samples was performed by utilizing 10x optical zoom. The selected particles were finally scanned with a combination of10x and 50x optical zoom in a mix observation mode, which consisted of bright-field and dark-field, to determine the thickness of paint layers. The experiment was conducted at multiple locations and average thickness was documented for further analysis.

5.2.3.2 Experimental Results

The paint samples collected during the field inspection of bridges were examined using the Olympus DSX500 to identify the type of paint systems and paint layers. TxDOT uses four types of paint systems: System I, System II, System III, and System IV. System I is the only epoxy-based paint system, and the other three are ZBPSs. The aging bridges are expected to utilize LBPS since the application of ZBPS only started in the past 25 years. These structures are typically off-system bridges that are not subjected to heavy loads. Note that the LBPS was extensively used in the past because of the durability of the paint; however, the lead-based paint was replaced with zinc-based paint due to its environmental hazards in recent years.

Using Olympus DSX500 (Figure 5.16), it was possible to identify the type of paint systems used on TxDOT-painted steel girders that were rarely reported in as-built drawings. Thus, the optical microscopy results of seven documented painted bridges (WFS-RC-01, WFS-RC-02 [System I], TYL-PS-01, TYL-PS-02, WFS-PS-01, WFS-PS-02 [System II], and CRP-PS-01 [System III]) were used to make a comparison with other painted bridges and to identify the unknown paint systems. After completing the laboratory examination and analyzing the results, the type of paint layers and primer layers were classified into three categories: epoxy, zinc-based, and lead-based paint. The thickness of individual layers was also documented using an optical microscope. In addition, spot corrosion was observed on samples taken from steel girders of CRP-PS-01 and FTW-PS-02.



Figure 5.16. Olympus DSX500 Opto-Digital Microscope.

Figure 5.17 shows an identified Paint System I that was obtained from the steel girder of WFS−RC−01. This sample consisted of two layers of paint with no sign of zinc-based primer detected in the paint layers. An example of System II was observed on TYL-PS-01, as shown in Figure 5.18. This system was composed of two layers: a primer layer with a metallic green color and a topcoat with a white color. Figure 5.19 represents a sample collected from CRP-WS-01 (Harbor Bridge) that was identified as System III. Finally, an example of an LBPS is shown in Figure 5.20. Analyzing the results of optical microscopy provided remarkable detail regarding the performance of paint systems applied to TxDOT steel bridges. Figure 5.19 demonstrates the deterioration of the paint layers caused by both rust-spot and microcracks. Similarly, Figure 5.21 shows the significant accumulation of corrosion products beneath the primer surface. The formation of corrosion within painted systems can be a result of chemical and environmental pollutants, exposure to moisture, poor surface preparation, inadequate thickness of paint, or use of unsuitable paint system.

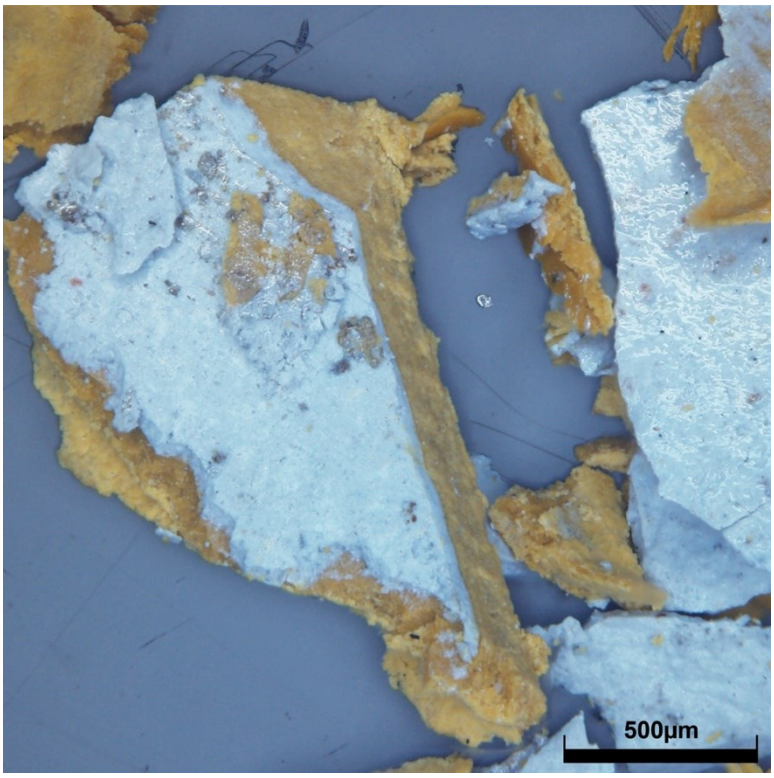


Figure 5.17. System I Detected on a Random Sample from WFS−RC−01.

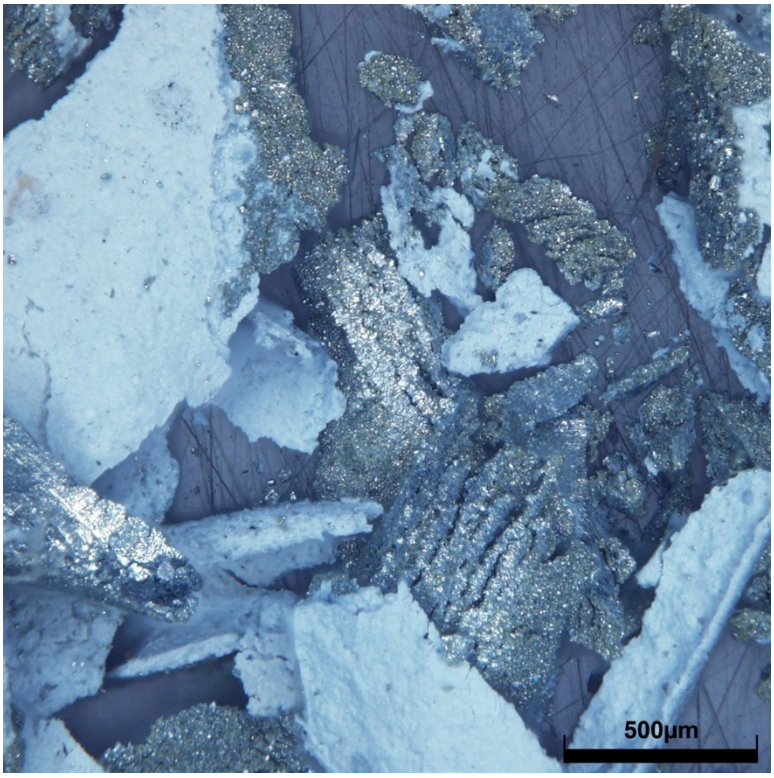


Figure 5.18. System II Detected on a Random Sample from TYL−PS−02.

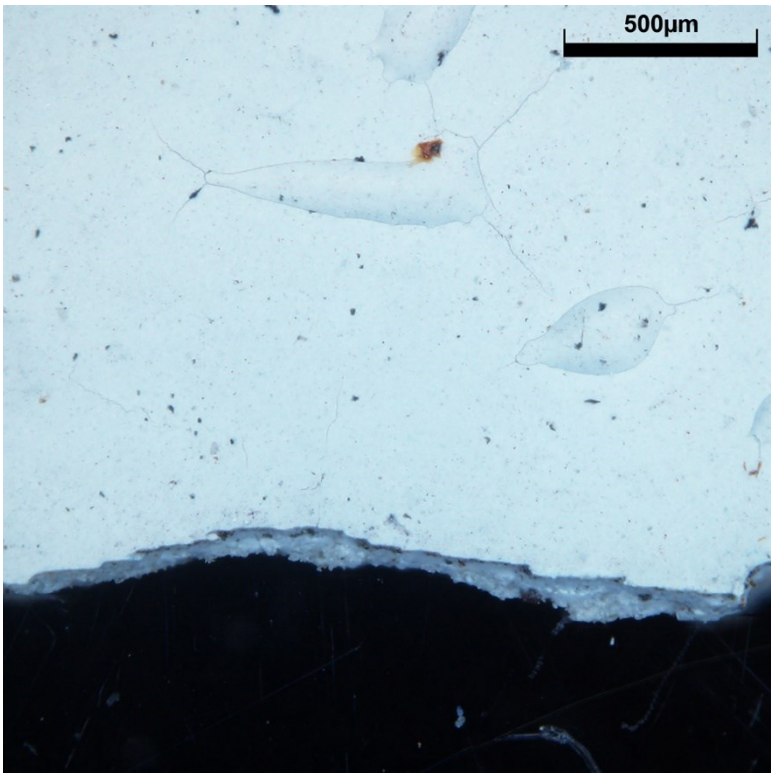


Figure 5.19. System III Detected on a Random Sample from CRP−PS−01.

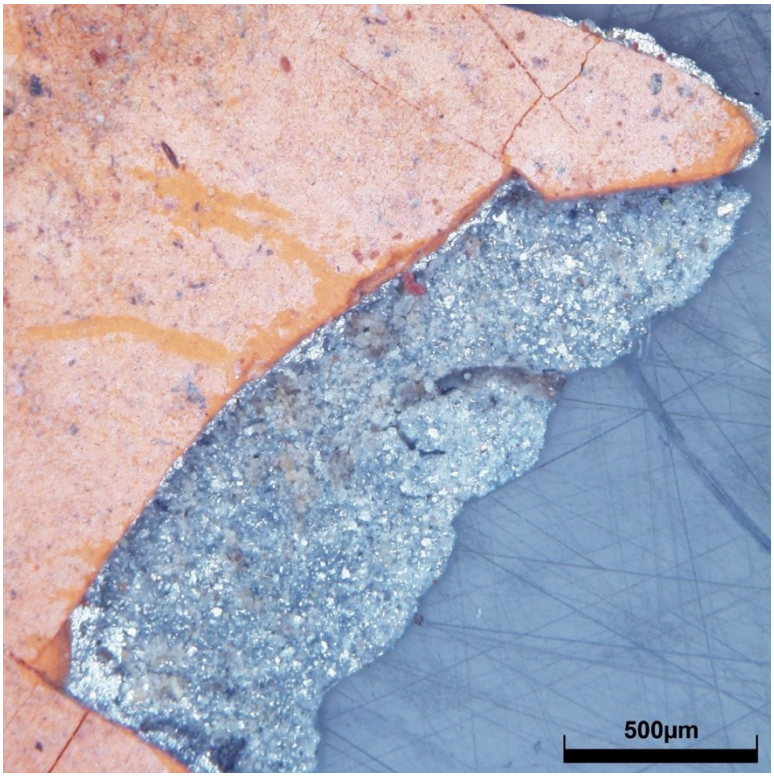


Figure 5.20. Lead-Based System Detected on a Random Sample from YKM-PS-01.

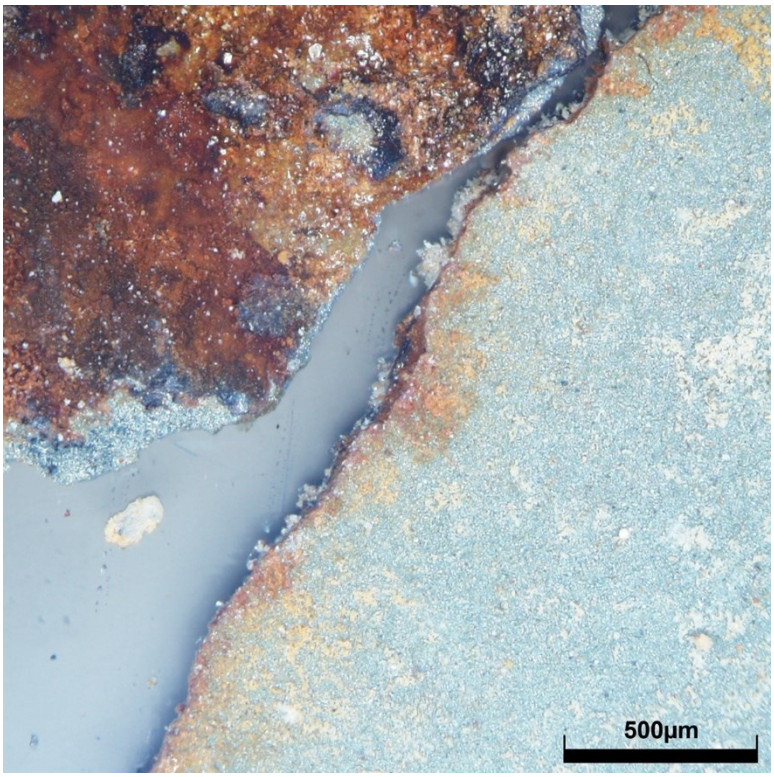


Figure 5.21. Corrosion Detected on the Primer Surface from TYL-PS-01.

Two paint samples shown in Figure 5.22 and Figure 5.23 were obtained from the same bridge (BRY-PS-01 and BRY-PS-02). It was determined that distinct paint systems were applied to the steel girders, and no visible signs of corrosion, either on the surface or within the coating, were observed for a ZBPS depicted in Figure 5.22. On the contrary, extensive corrosion was detected on samples taken from the second girder, as shown in Figure 5.23. This finding emphasizes the challenge associated with detecting localized corrosion problems and the need for regular inspections. Two paint samples taken from off-system steel bridges in the Atlanta District (ATL−PS−01) are depicted in Figure 5.24 and Figure 5.25. The optical microscopy results agreed with the conclusions drawn from visual inspection. The paint layers with extensive deterioration were found only on certain locations of the exterior web. Figure 5.24 illustrates the presence of a two-layered paint, consisting of a metallic topcoat and a greenish-color primer. Corrosion products were observed within the primer, as shown in Figure 5.25. Figure 5.26 represents a random sample of System II obtained from FTW−PS−02 in the Fort Worth District. Corrosion products were detected within the paint layers on the top face of the bottom flange near the supports of this bridge. It was concluded that most of paint systems used in Amarillo District are relatively old since LBPSs were observed on steel girders inspected in this area (Figure 5.27 to Figure 5.29). Further,

the optical microscopy results of AMA−PS−03 revealed significant deterioration of paint layers and extensive corrosion failure.

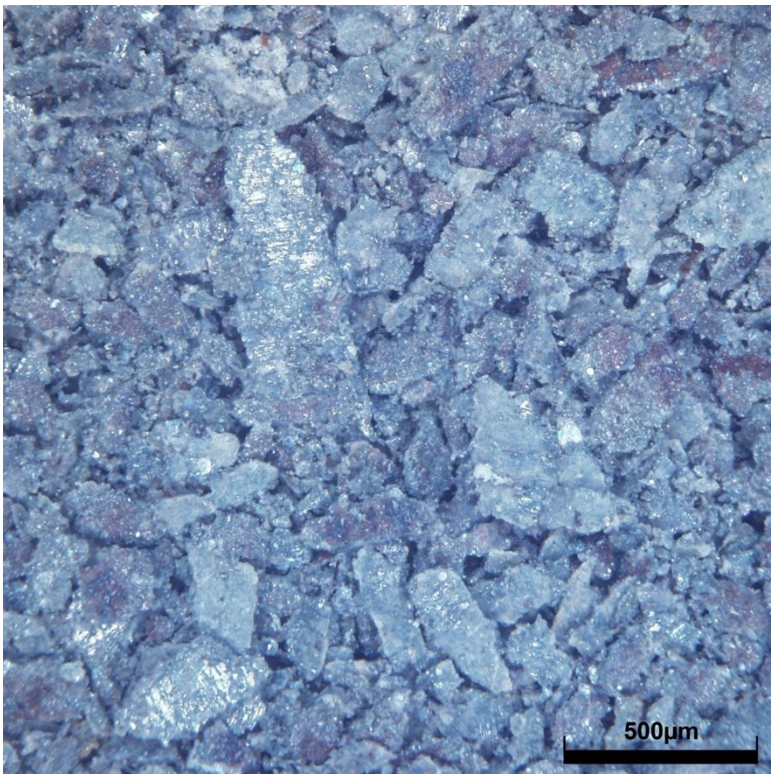


Figure 5.22. ZBPS Detected on a Random Sample from BRY-PS-02.

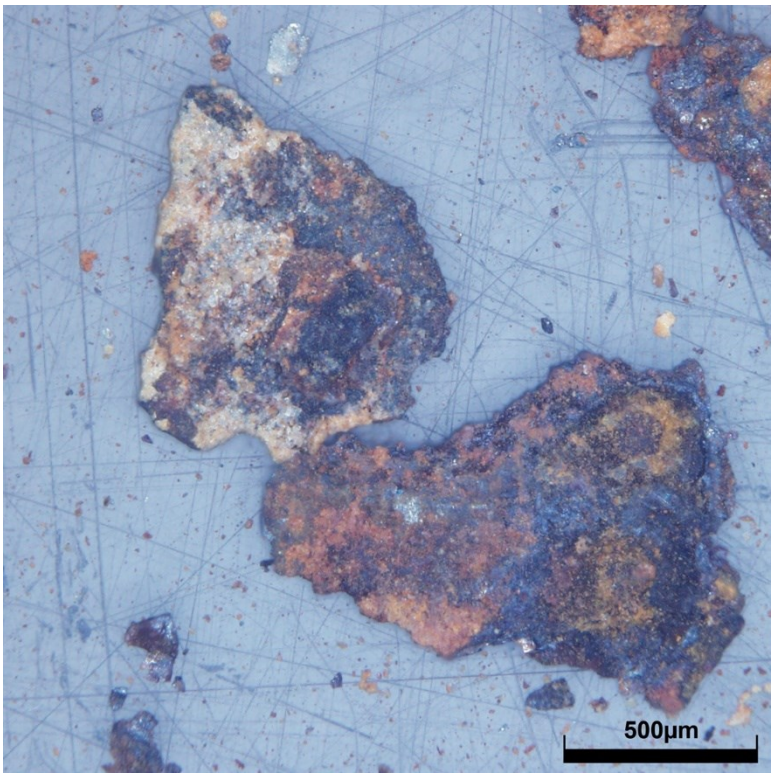


Figure 5.23. Corrosion Detected on a Random Sample Taken from BRY−PS−01.

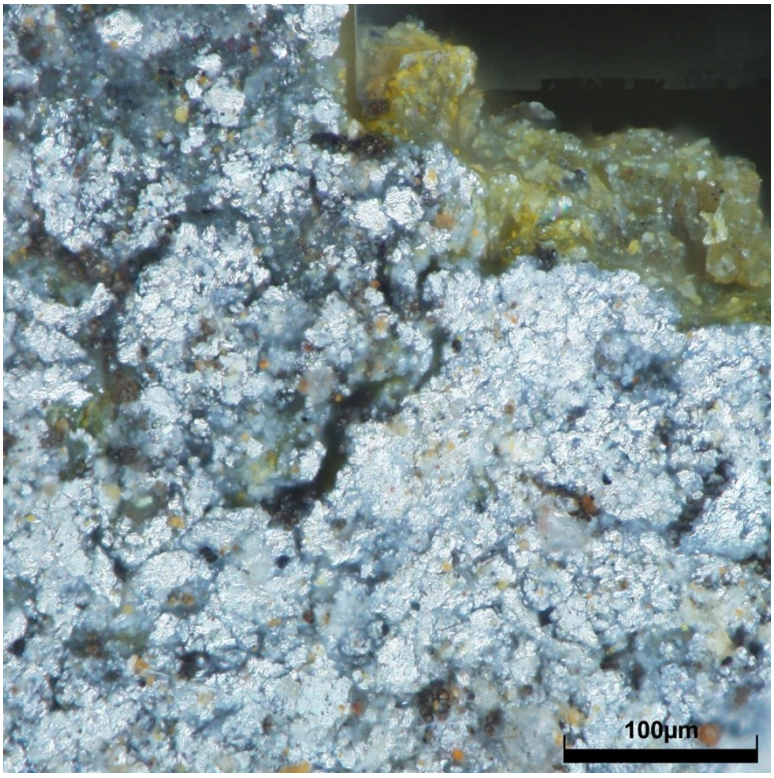


Figure 5.24. Two-Layer Paint System—ATL-PS-01.

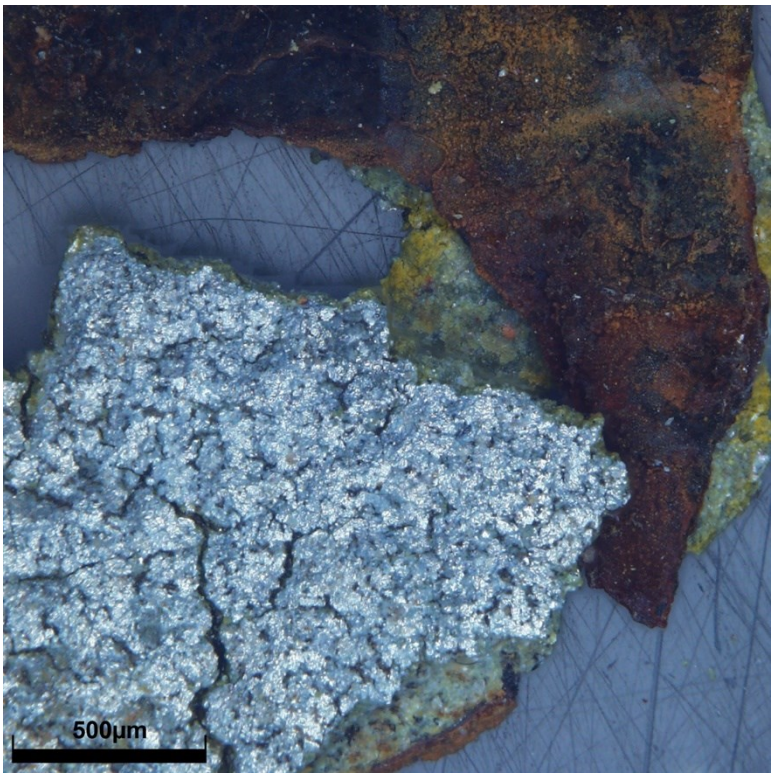


Figure 5.25. Corrosion Detected on the Primer Surface of Samples from ATL-PS-01.

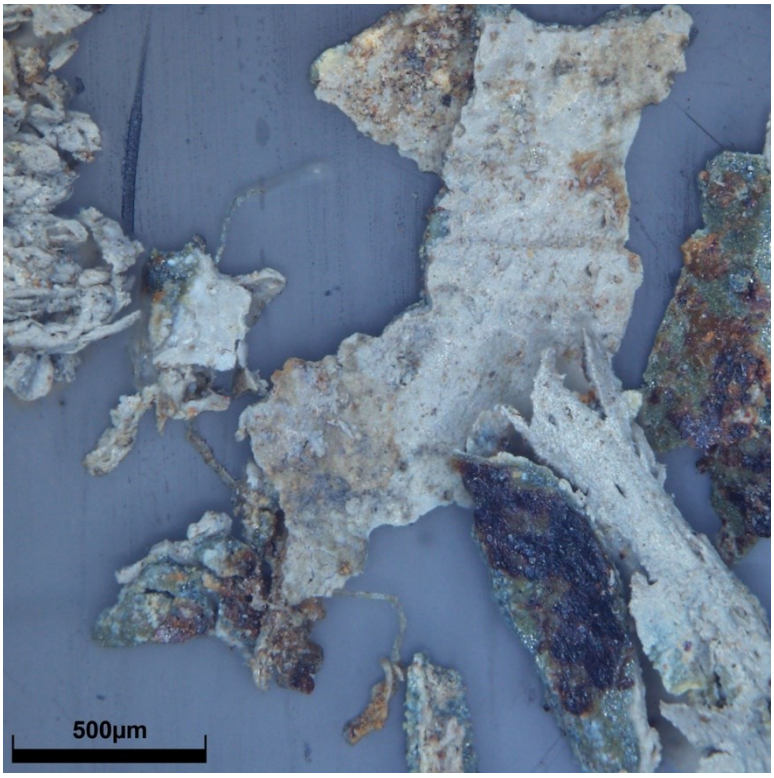


Figure 5.26. Corrosion Detected within Paint Layers Collected from Top Face of Bottom Flanges—FTW−PS−02.

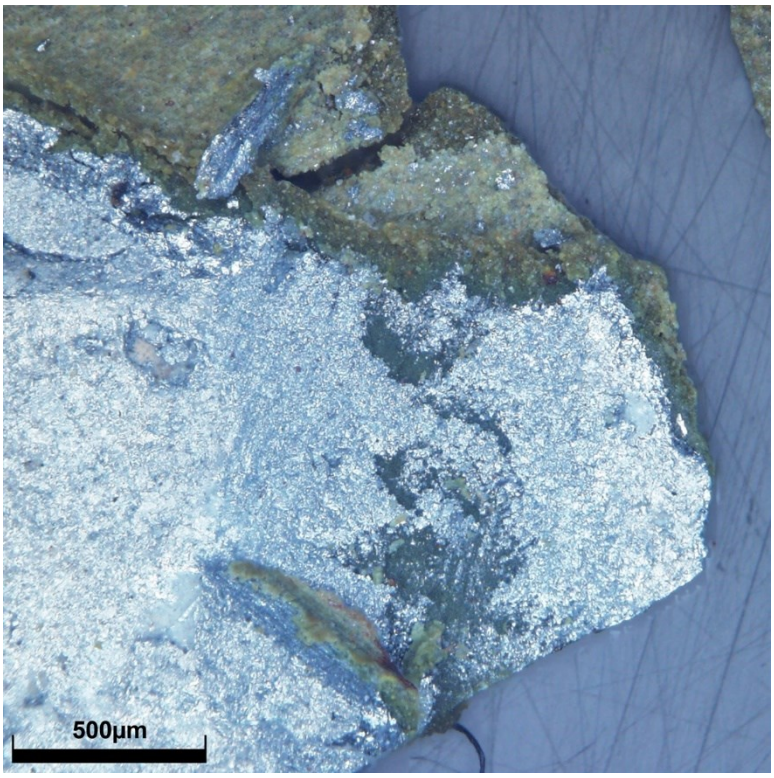


Figure 5.27. Two-Layer Paint System—AMA-PS-01.

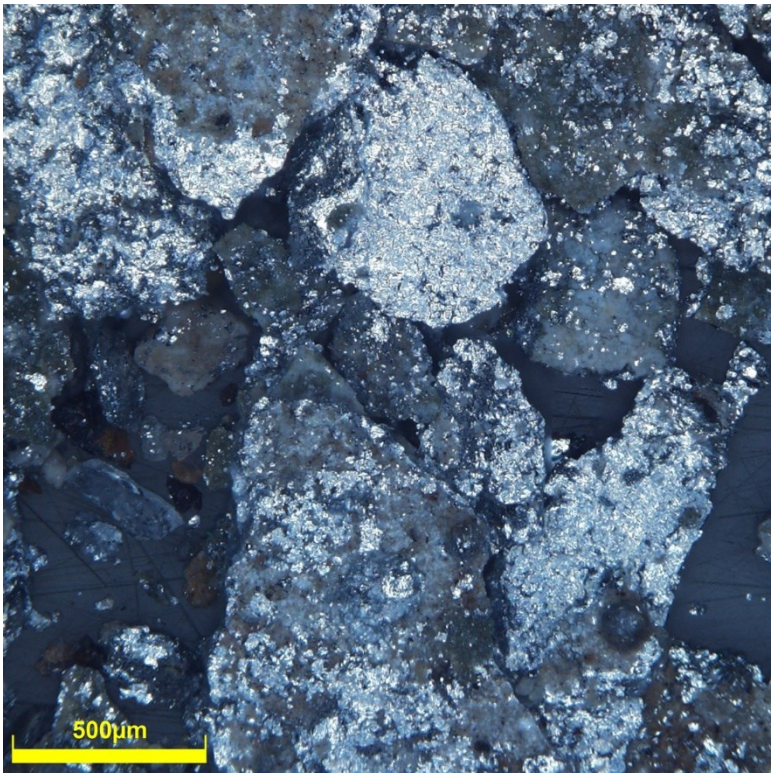


Figure 5.28. Two-Layer Paint System—AMA-PS-03.

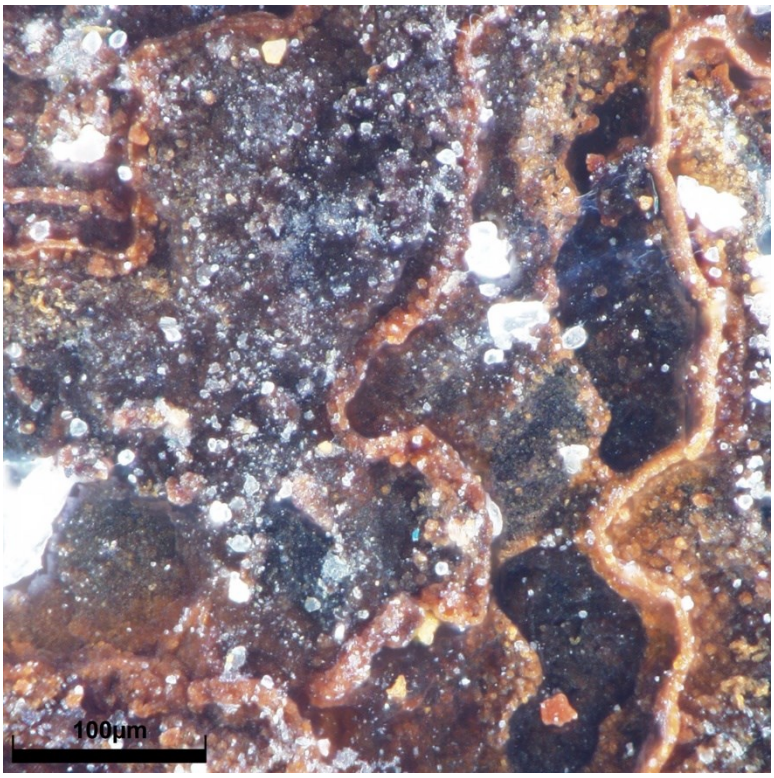


Figure 5.29. Severe Corrosion Detected on Samples Collected from AMA-PS-03.

Figure 5.30 and Figure 5.31 illustrate the severity of corrosion initiation and propagation within the primers of WFS−RC−01 and WFS−RC−02. It was concluded that System I was utilized to mitigate the electrochemical impact of the corrosive environment for both bridges. Note that the paint samples were scraped from the top face of the bottom flange of the interior girder in close proximity to the abutments.

Rust spot was detected on System II samples taken from TYL−PS−02 (Figure 5.32). The paint system was classified as an OZ-based primer. Figure 5.33 illustrates the System I observed on ELP−PS−01, an epoxy-based paint system without any zinc-based primer. An LBPS was detected on an off-system steel bridge in Yoakum District, shown in Figure 5.34 and Figure 5.35. Extensive corrosion products were detected between the coated layer and steel substrate of this bridge, as illustrated in Figure 5.35. Additionally, System II was identified on two painted steel bridges located in the Houston and Beaumont District—HOU−PS−01 and BMT−PS−01. Figure 5.36 represents a two-layer ZBPS consisting of a blue epoxy topcoat and a metallic green primer as the bottom coat, and Figure 5.37 shows a ZBPS with a white epoxy topcoat and a metallic green zinc primer. Rust spot was observed within the primer coat of the paint system shown in Figure 5.37. System II was also identified in the analysis of samples obtained from BMT−PS−01 and

BMT−PS−02. Figure 5.38 highlights spot corrosion that was observed within the primer coat, and Figure 5 39 illustrates the two-layer ZBPS that was applied to the steel girders of BMT−PS−02.

The final results of the optical microscopy are given in Table 5-6. Due to the difficulty in determining the type of paint systems applied to steel bridges, further analysis was conducted using SEM/EDS to identify the type of paint systems, whether epoxy, lead-based, or ZBPS.

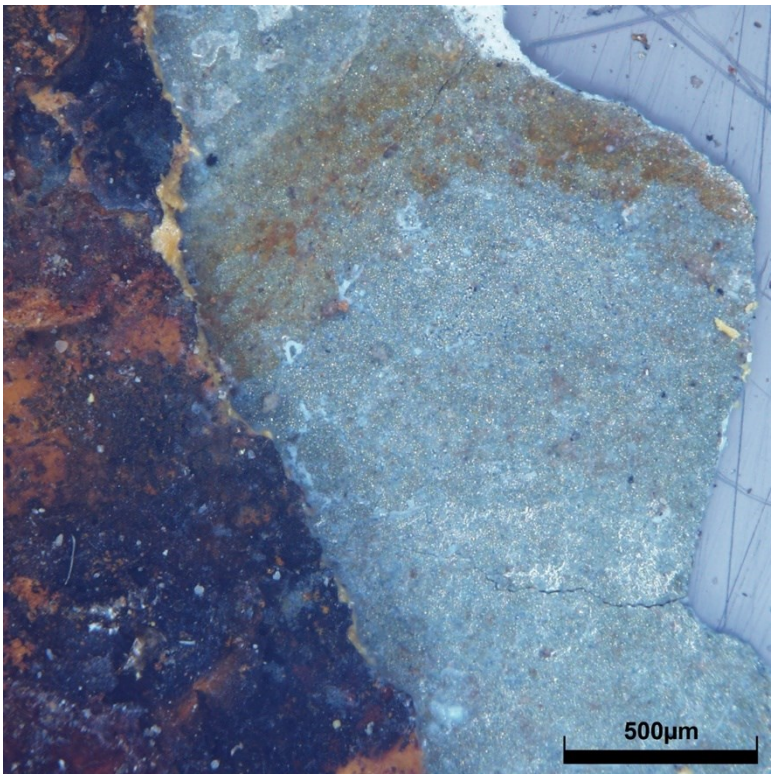


Figure 5.30. Severe Corrosion Detected on the Primer Surface of WFS−RC−01.

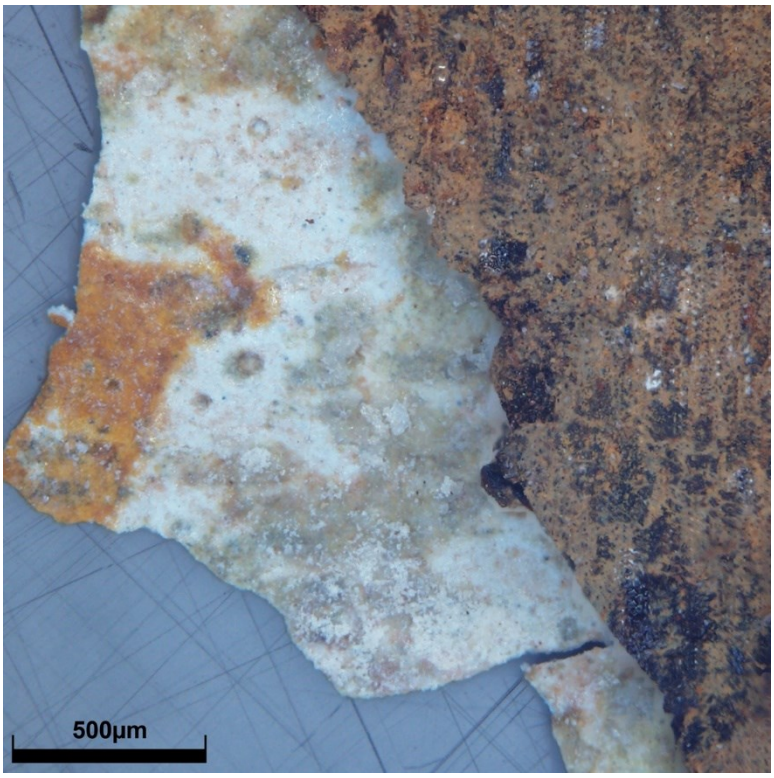


Figure 5.31. Severe Corrosion Detected on Samples Taken from WFS−RC−02.

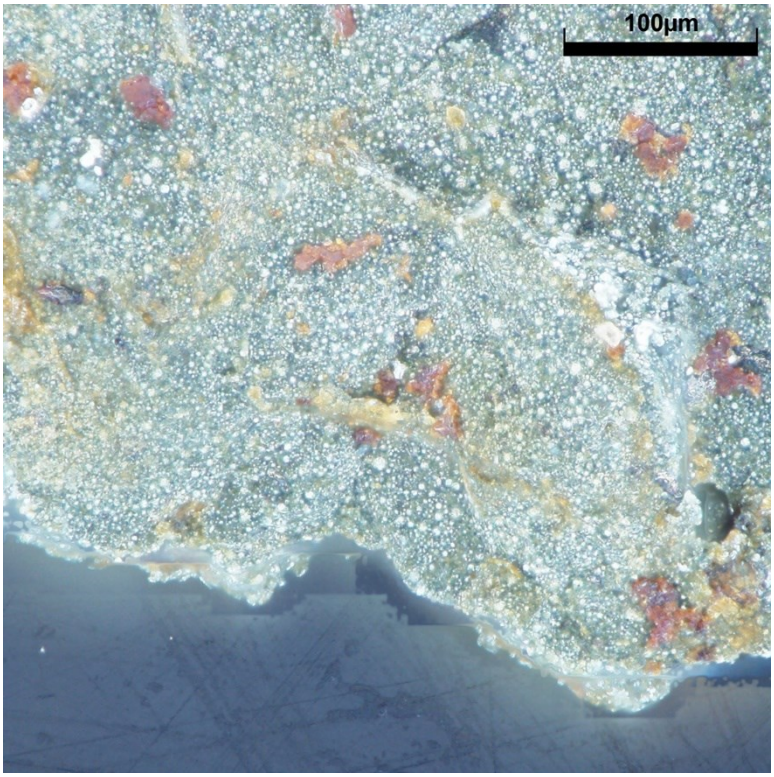


Figure 5.32. Rust spot Detected on the Primer Surface of TYL−PS−02.

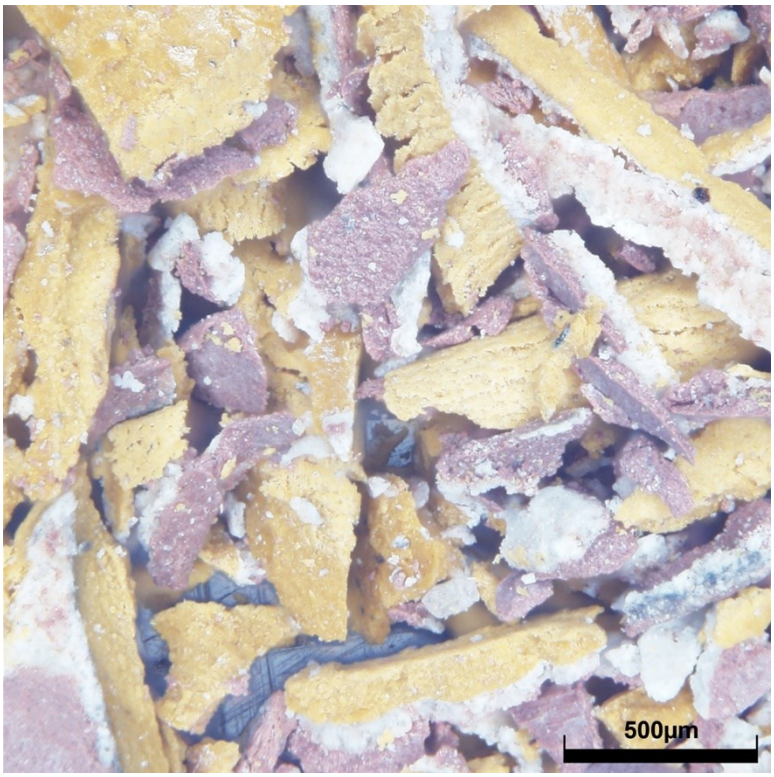


Figure 5.33. Two-Layer Paint System—ELP-PS-01.

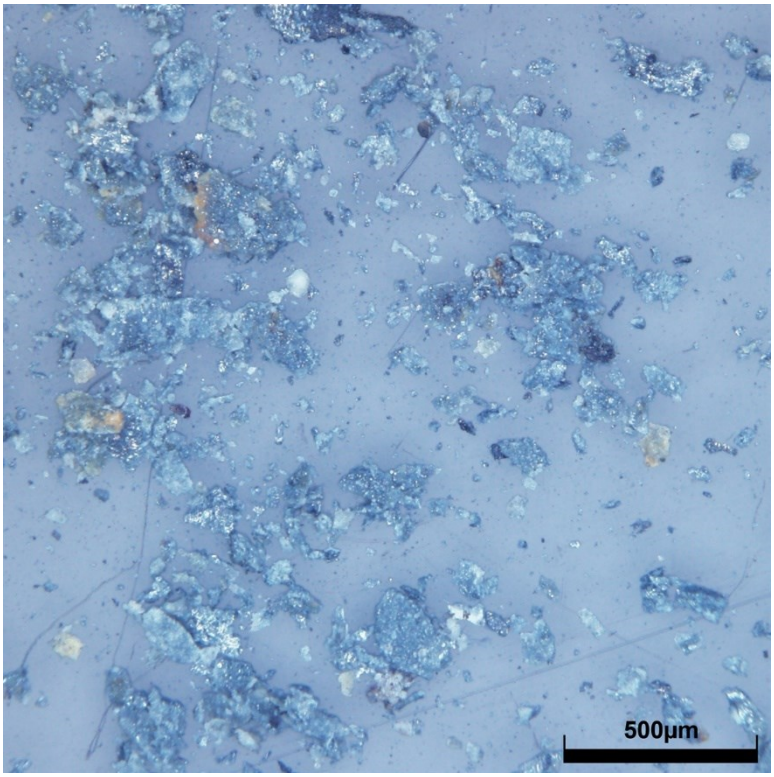


Figure 5.34. Two-Layer Paint System—YKM-PS-01.

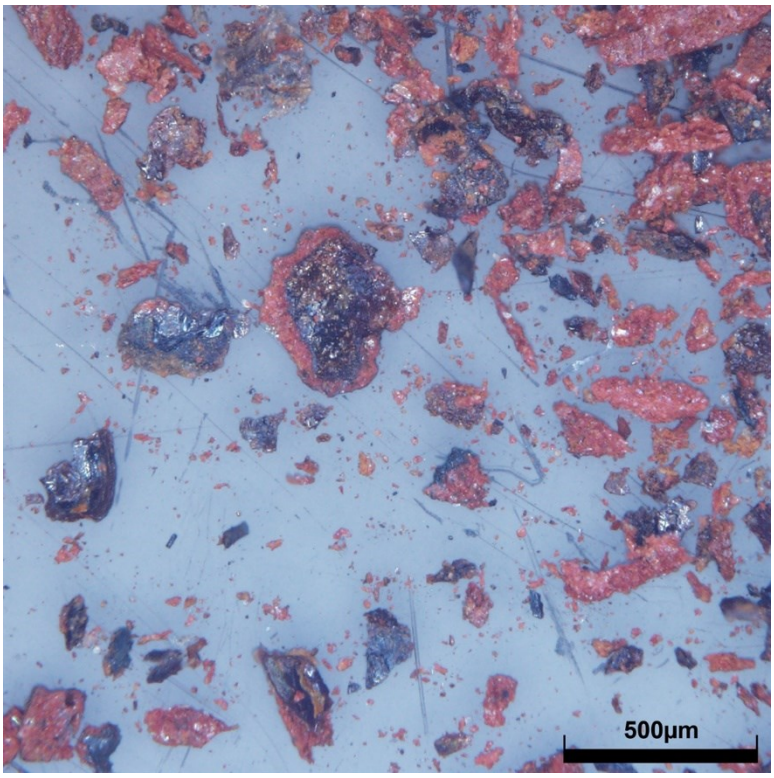


Figure 5.35. Corrosion Detected on Samples Collected from YKM−PS−01.

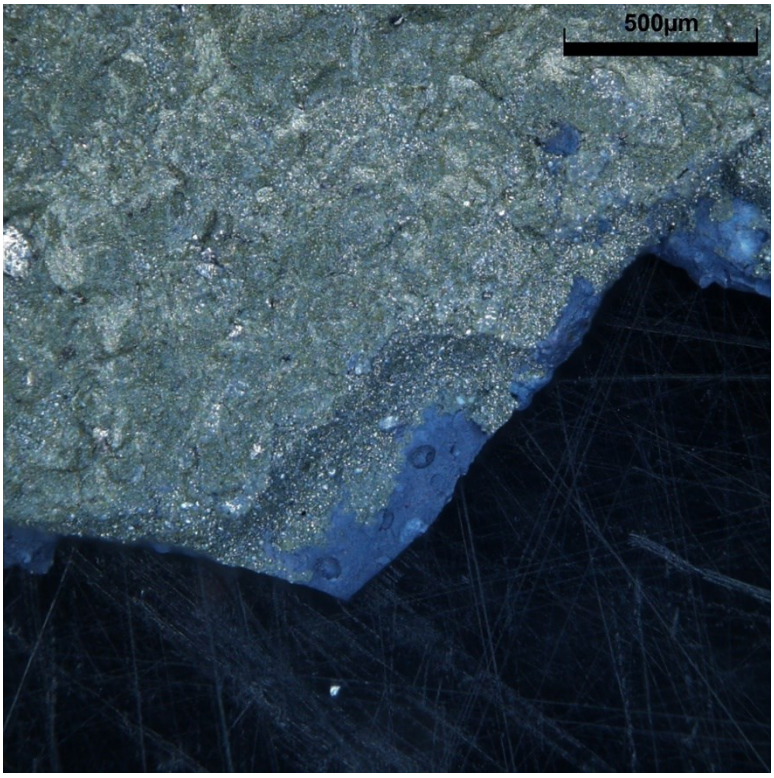


Figure 5.36. Two-Layer Paint System—HOU-PS-01.

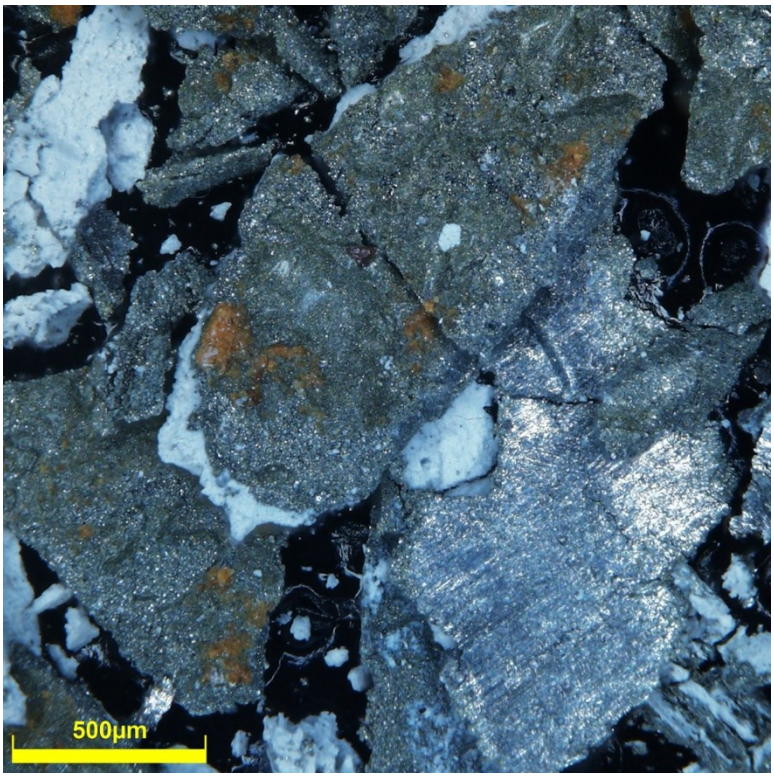


Figure 5.37. Two-Layer Paint System—BMT-PS-01.

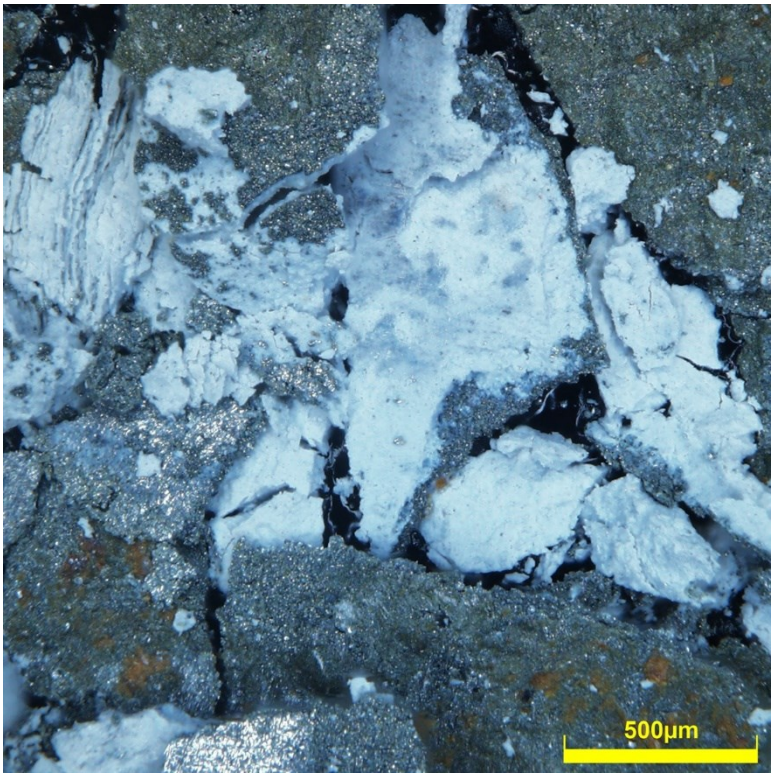


Figure 5.38. Rust spot Detected on Samples Collected from BMT-PS-01.

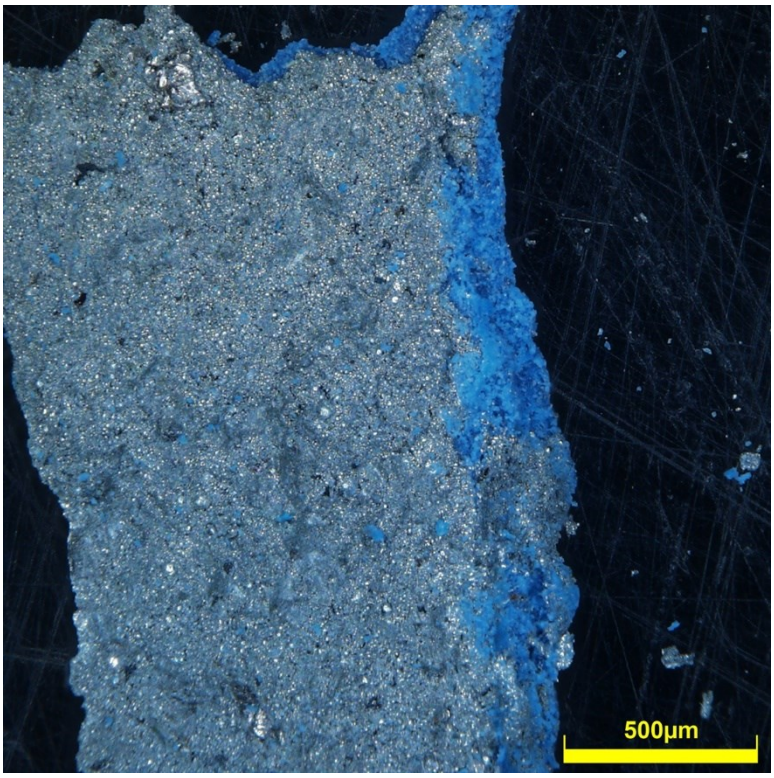


Figure 5.39. Two-Layer Paint System—BMT-PS-02.

Table 5-6. Optical Microscopy Analysis on Collected Paint Samples.

Bridge	Visual Inspection	Optical Microscope	Paint System	Detection of Corrosion	Optical Microscopy Thickness (mils)
ATL-PS-01	Two-Layer TC: NV Primer: GE	Two-Layer TC: MC Primer: Green	Epoxy-Based	Widespread rusting	TC:2.5 Primer:20.9
AMA-PS-01	Two-Layer TC: MC Primer: GE	Two-Layer TC: MC Primer: GE	LBPS	Yes	TC: 2.4 Primer:2.1
AMA-PS-02	Two-Layer TC: WE Primer: MC	Two-Layer TC: WE Primer: MC	ZBPS System II	No	TC: 10.5 Primer: 7.3
AMA-PS-03	Two-Layer TC: MC Primer: GE	Two-Layer TC: MC Primer: GE	LBPS	No	TC + Primer: 12.0
BRY-PS-01	G1: One Layer TC: MG G5: Two-Layer TC: WE Primer: NV	G1: One Layer TC: MG G5: Two-Layer TC: WE Primer: NV	ZBPS System II	Widespread rusting	A1G1F1: Primer:3 A5G1F1: Primer:8.4 A1G2F1: TC + Primer:5.9
BMT-PS-01	Two-Layer TC: WE Primer: MG	Two-Layer TC: WE Primer: MG	ZBPS System II	Rust between base metal and primer	TC + Primer:8.7
BMT-PS-02	Two-Layer TC: BE Primer: MG	Two-Layer TC: BE Primer: MG	ZBPS System II	No	TC + Primer: 10.6
CRP-PS-01	Two-Layer TC: WE Primer: MG	Two-Layer TC: WE Primer: MG	ZBPS System III	No	TC + Primer: 18.3
DAL-PS-01	Two-Layer TC: WE Primer: YE	Two-Layer TC: WE Primer: YE	Not ZBPS	No	TC: 2.0 Primer: 7.2
ELP-PS-01	Two-Coat TC: YE Primer: MG	Three Layer TC: YE MC: WE Primer: MG	System I	No	TC: 1.0 Primer:7.7
FTW-PS-01	FG: Two-Layer TC: Maroon Primer: MG IG: Two-Layer TC: WE Primer: MG	FG: Two-Layer TC: Maroon Primer: MG IG: Two-Layer TC: WE Primer: MG	ZBPS System II	No	FG: − TC: 3.1 MC: 3.1 Primer: 7.6 IG: − TC: 0.5 Primer: 8.3

Table 5 6. Optical Microscopy Analysis on Collected Paint Samples (Cont.).

Bridge	Visual Inspection	Optical Microscope	Paint System	Detection of Corrosion	Optical Microscopy Thickness (mils)
FTW-PS-02	Two-Layer TC: WE Primer: MG	Two-Layer TC: WE Primer: MG	ZBPS System II	No	TC: 4.3 Primer: 15.6
HOU-PS-01	Two-Layer TC: BE Primer: MG	Two-Layer TC: BE Primer: MG	ZBPS System II	No	TC: 5.9 Primer: 7.0
TYL-PS-01	Two-Layer TC: NV Primer: MG	Two-Layer TC: WE Primer: MG	ZBPS System II	Rust between base metal and primer	TC: 7.6 Primer: 2.6
TYL-PS-02	Two-Layer TC: WE Primer: MG	Two-Layer TC: WE Primer: MG	ZBPS System II	Rust between base metal and primer	TC: 5.7 Primer: 20.9
WFS-PS-01	Two-Layer TC: WE Primer: MG	Two-Layer TC: WE Primer: MG	ZBPS System II	No	TC: 2.4 Primer: 12.5
WFS-PS-02	Two-Layer TC: WE Primer: MG	Two-Layer TC: WE Primer: MG	ZBPS System II	No	TC: 4.3 Primer: 8.3
WFS-RC-01	Two-Layer TC: WE Primer: YE	Two-Layer TC: WE Primer: YE	Not ZBPS System I	No	TC: 1.5 Primer: 8.9
WFS-RC-02	Two-Layer TC: WE Primer: YE	Two-Layer TC: WE Primer: YE	Not ZBPS System I	Rust between base metal and primer	TC: 8.2 Primer: 11.9
YKM-PS-01	G1: TC: NV Primer: GE G3: TC: RE Mid. Coat: MC Primer: GE G6: TC: RE	G1: TC: WE Primer: GE G3: TC: RE Mid. Coat: MC Primer: GE G6: TC: RE	LBPS	Rust found within Paint layer	A1G1F1: TC: − Primer: 8.7 A1G3F1: TC: 12.3 Primer: 4.9 A1G6F1: TC: 4.1

Note:
NV: Not Visible
FG: Fascia Girder, IG: Interior Girder
TC: Topcoat, MC: Metallic Coat, MG: Metallic Green
GE: Green Epoxy, BE: Blue Epoxy, RE: Red Epoxy, WE: White Epoxy, YE: Yellow Epoxy, ME: Maroon Epoxy
ZBPS: Zinc-Based Paint System
LBPS: Lead-Based Paint System
System I: Two-Layer Epoxy-Based Paint System
System II: Zinc-Based Two-Layer Paint System
System III: ZBPS

Using optical microscopy, researchers identified the colors of individual layers of the paint samples applied to TxDOT steel girders. It also helped identify rust spot within primer and topcoat. However, it was not effective in differentiating between System II and System III due to the similarity in color between the top layer and the primer coat used in these systems. The optical microscopy aided in accurately identifying ZBPSs, but it was also not effective distinguishing lead-based paint. Therefore, SEM/EDS was employed to distinguish lead-based, zinc-based, and epoxy-based paint systems.

5.2.4 Powdered X-Ray Diffraction

The corrosion properties of weathering steel are directly influenced by the chemical composition of the patina that forms on the surface of weathering steel (Kubzova et al., 2017). The patina layer made up of iron oxides and hydroxides has a phase-complex composition consisting of various crystalline and amorphous components (Cook, 2005; Mizoguchi et al., 2005). Goethite (α–FeOOH) is the primary and most stable corrosion product that forms on weathering steel. As the volume of densely packed goethite increases in the patina, the corrosion resistance of the protection layer improves because goethite effectively limits the diffusion of moisture within the rust layer (Okada et al., 1969; Waseda & Suzuki, 2006). Lepidocrocite (γ–FeOOH) is another corrosion product developed in the early stage of patina formation. The iron oxide forms in a laminated crystalline structure, and it is not as protective as goethite. Other oxides that can be found within the patina that are not effective mitigating corrosion are magnetite (spinel, Fe_3O_4), maghemite (γ–Fe_2O_3), and ferrihydrite ($5Fe_2O_3.9H_2O$).

There are also hydroxides that can form in the patina and increase the rate of corrosion on weathering steel. Akaganeite (β–FeOOH) can form due to chemical reactions between iron hydroxide and chloride ions (Asami & Kikuchi, 2003), while hematite (α–Fe_2O_3) can result from reactions involving sulfur dioxide (de la Fuente et al., 2011; Aramendia et al., 2013). The formation of a significant volume of these minerals in the patina layer indicates whether the rust is protective or not (Hara et al., 2006; Hara et al., 2007).

A dense patina layer gradually forms on weathering steel under the influence of wetting and drying cycles. After exposure to a weathering cycle, lepidocrocite (γ–FeOOH) is the primary oxide that forms on steel. However, the transformation of lepidocrocite to stable goethite occurs over time, which reduces the corrosion rate of the steel. The PAI defining the volume of goethite

in the patina can be calculated from the mass fractions of goethite and lepidocrocite (α/γ). A high α/γ ratio indicates that a desired protective layer has been reached against corrosion. Some studies (Corbun & Kim 3rd, 1990; Scott & Eggert, 2009) suggested that the corrosion rate of weathering steel is equivalent to carbon steel in humid environments. In fact, the transformation of lepidocrocite to goethite requires a drying cycle, and without it the oxide film will not provide sufficient protection.

Li et al. (2008) expressed the PAI_α and PAI_β as a mass fraction of phase compositions in the patina layer:

$$PAI_\alpha = \frac{\alpha}{s+\beta+\gamma} \tag{5.1}$$

$$PAI_\beta = \frac{\beta+s}{s+\beta+\gamma} \tag{5.2}$$

where α represents the mass fraction of goethite (α–FeOOH); β is the mass fraction of akaganeite (β–FeOOH); γ denotes the mass fraction of lepidocrocite (γ–FeOOH); and s is the sum of the mass fraction of hematite (α–Fe_2O_3) and maghemite (γ–Fe_2O_3). The PAI (PAI_α and PAI_β) can be used as a metric to evaluate the effectiveness of the patina layer in minimizing corrosion activity on weathering steel. Hara et al. (2007) suggested that the corrosion rate of the steel substrate should be considered less than 0.39 mils/year (0.01 mm/year) if the PAI_α is greater than 1. Otherwise, the corrosion rate of the steel substrate can be estimated using PAI_β, in which the rate still remains below 0.39 mils/year (0.01 mm/year) if the PAI_β is less than or equal to 0.5.

Hara et al. (2007) proposed the following criteria to identify the condition of the patina layer—whether active, inactive, or protective:

1. If the iron-oxidized layer consists of reactive elements other than goethite (as indicated by $PAI_\alpha < 1$) and PAI_β is greater than or equal to 0.5, the patina is not protective but active. The thickness of the rust is about 15.75 mils (400 μm).
2. If the iron-oxidized layer consists of reactive components other than goethite (as indicated by $PAI_\alpha < 1$) and PAI_β is less than 0.5, it implies a substantial proportion of lepidocrocite (γ–FeOOH) in the patina layer. The oxide film will eventually convert to goethite under favorable conditions (dry/wet cycles) if the chloride concentration is low in the patina layer. The thickness of the rust is typically below 15.7 mils (400 μm) in this inactive condition.

3. If the iron-oxidized layer consists of goethite ($PAI_{\alpha} > 1$), the patina is protective. The layer is uniform and compact layer.

5.2.4.1 Experimental Setup

Figure 5.40 shows apparatus (Bruker-AXS D8 Vario X-ray Powder Diffractometer) used during examinations of patina samples. The XRD data were collected with θ–2θ scanning in a 2θ range of 10° to 75° at a scanning speed of 0.02°/s. A semiquantitative analysis was performed using the reference intensity ratio method. The whole rust layer was scraped from the sample surface using a knife and subsequently ground into a homogeneous fine powder with a mortar. The powder was characterized by using XRD to identify the phase constituents.

The material was initially pounded into a fine powder using a mortar and pestle to ensure that the particles were sufficiently small to produce an accurate diffraction pattern. The X-ray diffractometer was calibrated using a known diffraction pattern from a standard material provided by Crystallography Open Database and American Mineralogist Crystal Structure Database. When the calibration procedure finished, samples were placed within the instrument and exposed to X-ray beams for data collection. The dispersed X-rays were then analyzed using PROFEX software to determine the crystalline structure of the material.

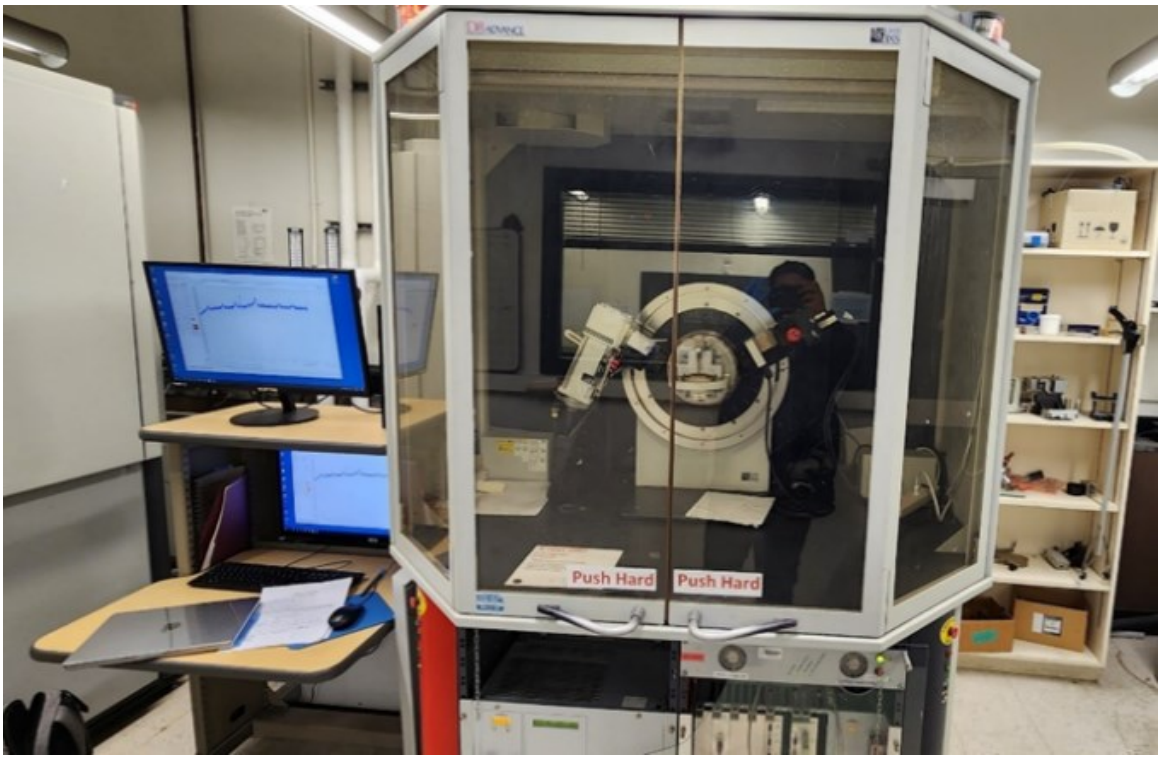


Figure 5.40. BRUKER-AXS D8 Advanced Bragg-Brentano X-Ray Powder Diffractometer.

5.2.4.2 Experimental Results

The graphical representation of powdered XRD data, depicted in Figure 5.41, displays the intensity of diffracted X-rays as a function of a diffraction angle (also known as the two-theta (2θ) angle). Figure 5.42 also shows phase quantification outcomes attained via Rietveld refinement. The analysis involved measuring X-ray intensity as the input parameter for quantifying all the distinct phases in the rust sample, such as goethite, Akaganeite, maghemite, hematite, ferrihydrite, and magnetite.

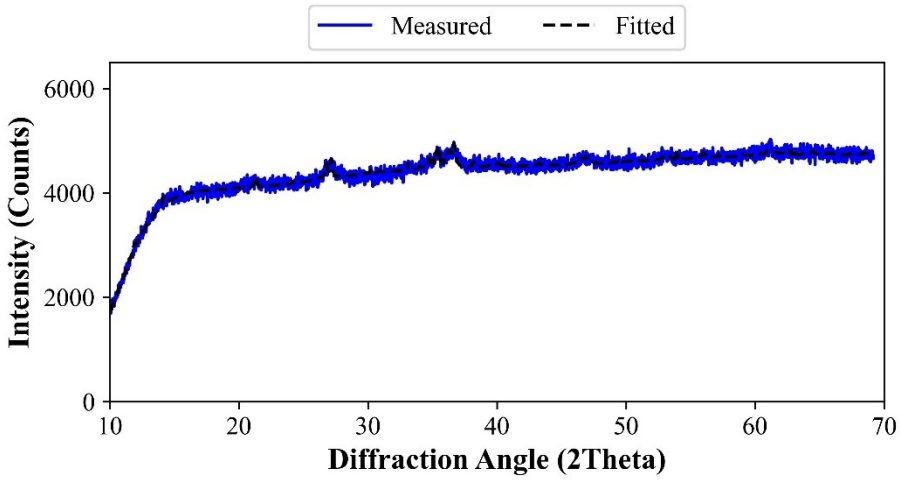


Figure 5.41. Diffracted X-Ray Intensity vs. Diffraction Angle (2θ) from FTW−WS−01.

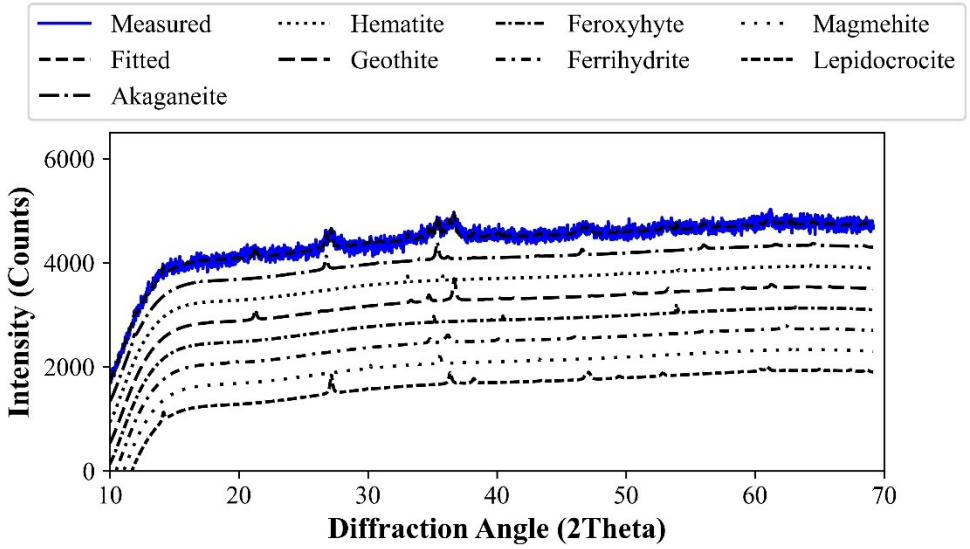


Figure 5.42. Measured and Fitted X-Ray Intensity, Exterior Web of FTW−WS−01.

The results obtained from the quantitative phase analysis were summarized and presented in ternary diagrams shown in Figure 5.43 to Figure 5.47. Three axes of the diagrams represent goethite (α–FeOOH), lepidocrocite (γ–FeOOH), and minerals such as akaganeite (β–FeOOH) and spinel; the latter is composed of hematite (α–Fe_2O_3) and maghemite (γ–Fe_2O_3). In these diagrams, the combined mass fraction of α, β+s, and γ phases of the patina is denoted by σ, while the combined mass fraction of β+s and γ phases of the rust is denoted by Γ. Each diagram was divided into three distinct areas: the protective zone (shaded in green), the inactive zone (shaded in yellow), and the active zone (shaded in red), as also indicated in Table 5-7. Moreover, a corrosion rate of 0.39 mils/year (0.01 mm/year) was highlighted as a threshold to differentiate between the active and inactive regions, similar to the approach of Hara et al. (2007). The size of the marker in ternary diagrams represents the bridge age, with smaller markers indicating newly constructed bridges and larger markers representing older bridges.

Table 5-7. Classification of Patina.

Category	Condition	Definition
Protective	$PAI_\alpha > 1$	Corrosion rate of steel is less than 0.39 mils/year
Inactive	$PAI_\alpha < 1$ & $PAI_\beta < 0.5$	Corrosion rate of steel is less than 0.39 mils /year
Active	$PAI_\alpha < 1$ & $PAI_\beta > 0.5$	Corrosion rate of steel is greater than 0.39 mils /year

Figure 5.43 shows the results obtained for inspected bridges in Region 2, where the exterior girders had a protective patina. However, the interior girders had an inactive patina, which can stem from trapped water that can increase the wetness duration (TOW) for the interior girders. Figure 5.44 and Figure 5.45 show ternary diagrams developed for weathering steel bridges in Region 3 and Region 4, respectively. It was evident that the patina layer was protective in most bridges in these regions. However, the application of deicing salt might have resulted in an inactive patina in a medium corrosive environment in which, during an XRD examination, a higher volume of akaganeite and spinel was detected in samples.

Figure 5.46 presents a ternary diagram developed for three weathering steel bridges: CRP−WS−01—located in a marine environment, and LBB−WS−01 and LBB−WS−02—located in industrial zones in the Permian Basin. In the marine environment, the deposition of airborne chloride can lead to the formation of large rust flakes on the steel surface. In industrial regions, the

extensive usage of deicing salt, combined with the potential deposition of sulfur dioxide, can contribute to a significant increase in corrosion levels. Note that unlike the protective patina layer, the rust flakes are not adherent to substrate and readily detach from steel.

The results obtained from the ternary diagram agree with the findings from the field inspection of the steel girders in Region 6. Figure 5.47 summarizes all the results of a quantitative phase analysis obtained for all the weathering steel bridges inspected in this study; they are also tabulated in Table 5-8.

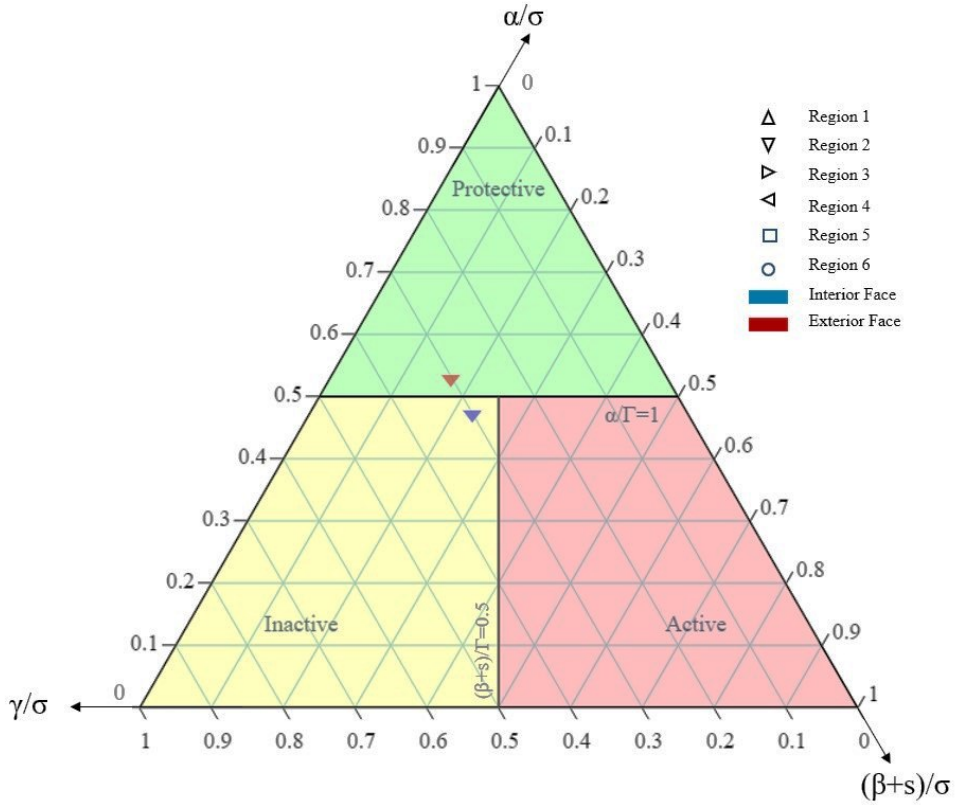


Figure 5.43. Ternary Diagram—Region 1 and Region 2.

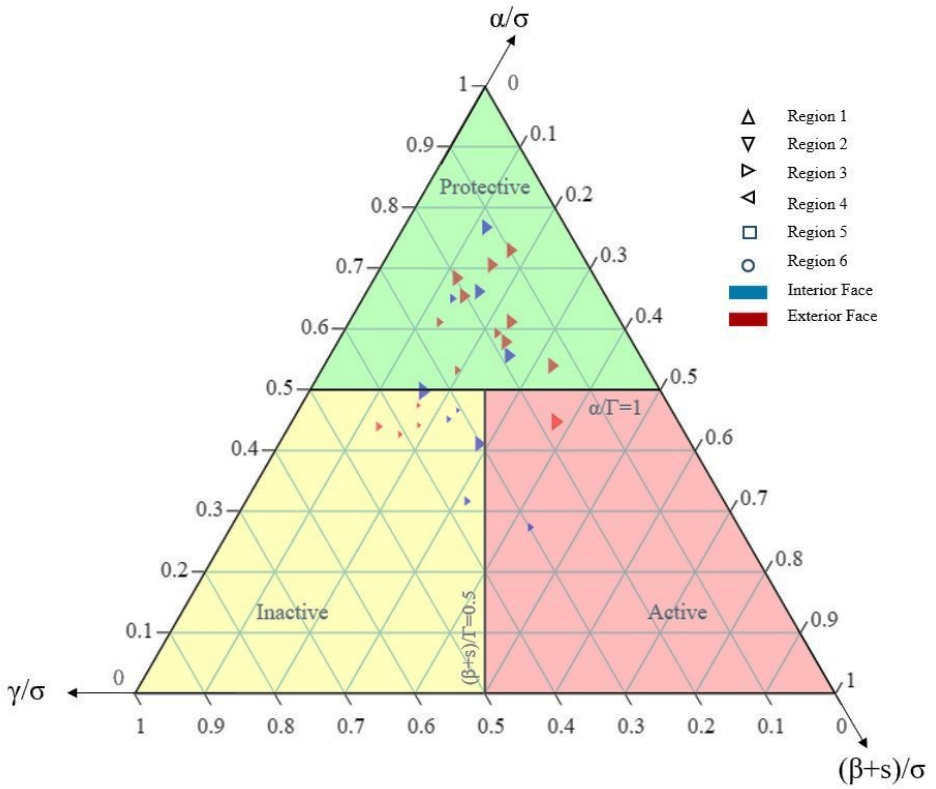


Figure 5.44. Ternary Diagram—Region 3.

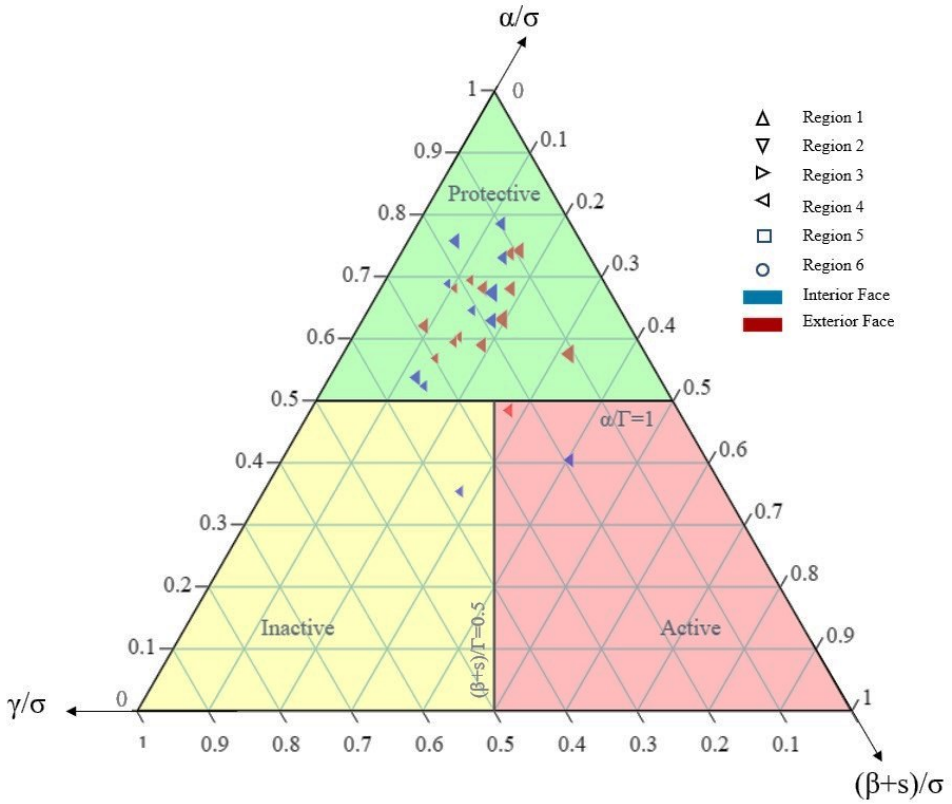


Figure 5.45. Ternary Diagram—Region 4.

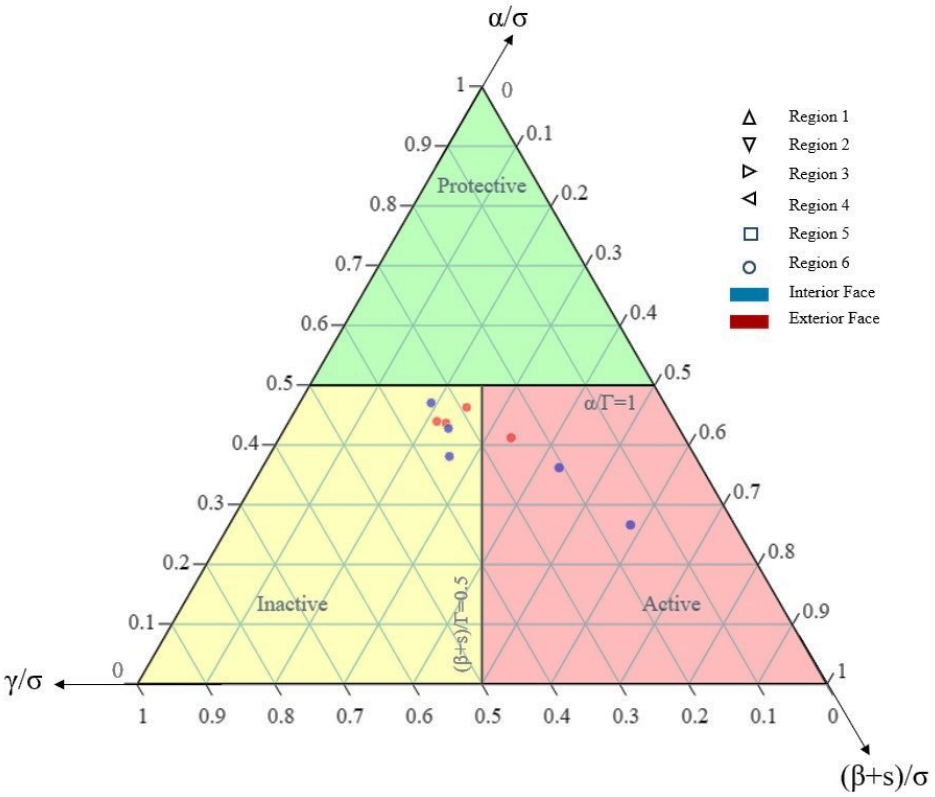


Figure 5.46. Ternary Diagram—Region 6.

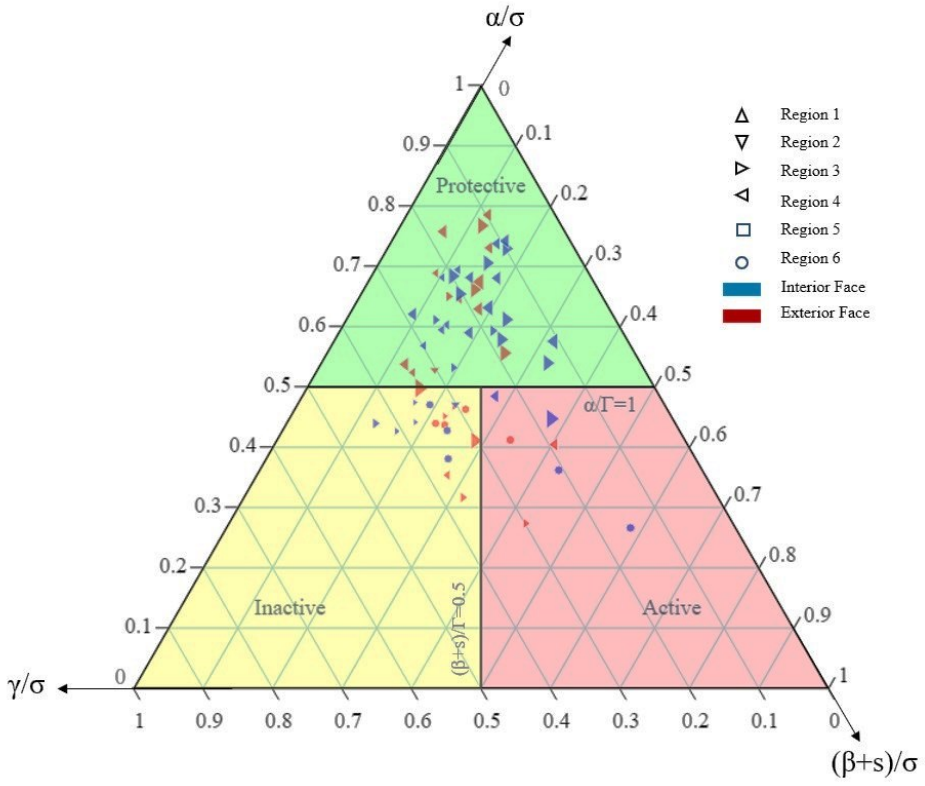


Figure 5.47. Ternary Diagram—All Regions.

Figure 5.48 shows a comparison between the amount of goethite (α-phase of iron oxide) and akaganeite (β-phase of iron oxide) in addition to spline detected during XRD examination of patina samples taken from weathering steel girders in Region 4 and Region 6. The fraction of goethite species generally was more prevalent in samples taken from girders in Region 4 compared to samples from Region 6, where the fraction of akaganeite and spline were found to be higher. The extended amount of akaganeite and spline indicates that the patina layer is not protective, and it is vulnerable to corrosion activities and susceptible to the protective layer instability. In Region 5 and Region 6, the elevated amount of chloride or other pollutant ions within the patina layer causes the formation of β-phase of iron oxide and other nonprotective minerals such as spline. In addition, it is evident that the fraction of lepidocrocite (γ-phase of iron oxide) was also greater for samples extracted from steel girders in Region 6. As discussed, lepidocrocite layers do not adhere to steel substrate, and they can easily fall off from the surface. The fact that the fraction of γ-phase of iron oxide is greater for several specimens in Region 6, it can also indicate lack of sufficient wetting and drying cycles required for the formation of protective patina layer. Note that samples studied in this research were taken within a distance of 12 ft from the girder joints.

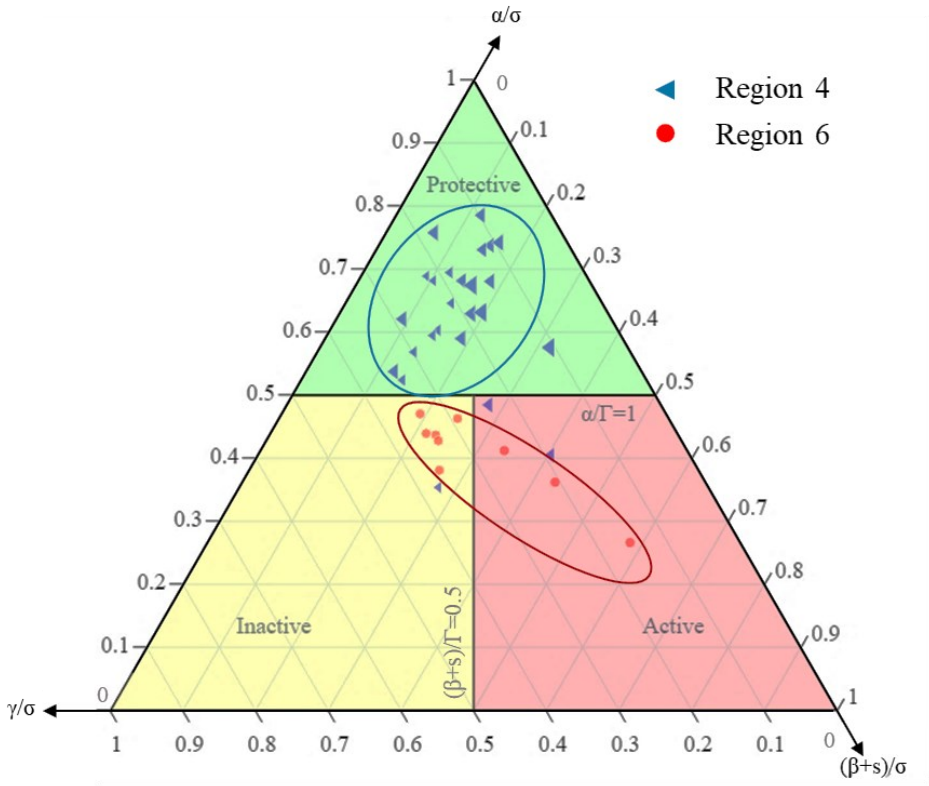


Figure 5.48. Comparison between the Goethite and Akaganeite Amount Detected from Samples Collected from Weathering Steel Girders in Region 4 and Region 6.

XRD analysis provided a deeper understanding of rust composition. It helped to classify the patina into three categories: active, inactive, and protective. It was also observed that the microenvironmental condition can affect the TOW and increase the rate of corrosion. This phenomenon was the case for weathering steel bridges inspected in a low-risk corrosive environment such as Region 1 and Region 2, where high concentrations of chlorides and sulfur dioxide are not expected. Researchers also concluded that most bridges located in Region 3 and Region 4 had a protective patina, which indicated the effectiveness of weathering steel in that environment. However, the few data points that found the patina active suggest local issues caused localized corrosion. Using a quantitative phase analysis, researchers further concluded that none of the examined rust samples taken from weathering steel bridges located in high corrosive environments such as Region 6 were protective in nature.

Table 5-8. Quantitative Phase Analysis Results of Weathering Steel Rust.

Bridge Name	Age	Face	Location	β–FeOOH Akaganeite	α–Fe2O3 Hematite	α–FeOOH Goethite	δ–FeOOH Feroxyhyte	Fh Ferrihydrite	γ–Fe2O3 Maghemite	γ–FeOOH Lepidocrocite
ATL-WS-01	19	EXT	Web	6.08	3.76	47.0	7.64	2.53	2.97	30.1
ATL-WS-01	19	EXT	BF Bot	22.4	2.00	34.7	0.00	1.90	2.60	36.4
ATL-WS-01	19	INT	Web	4.92	5.01	55.5	5.00	3.02	3.82	22.8
ATL-WS-01	19	INT	BF Bot	5.69	2.36	52.1	7.70	0.59	4.20	27.3
ATL-WS-02	19	EXT	Web	6.17	5.01	53.2	12.1	5.55	0.90	17.1
ATL-WS-02	19	INT	BF Stiff	4.62	4.14	61.0	9.50	2.69	1.77	16.3
ATL-WS-02	19	INT	Web	4.03	4.15	54.0	7.90	1.26	5.12	23.5
ATL-WS-03	47	INT	BF Stiff	15.8	4.77	49.7	8.20	5.44	6.84	9.20
ATL-WS-03	47	EXT	Web	4.67	4.51	57.3	11.2	3.87	4.50	14.0
ATL-WS-03	47	INT	Web	9.98	4.36	55.5	9.20	2.80	2.90	15.2
AUS-WS-01	46	EXT	Web	6.57	4.93	58.5	10.1	1.52	2.64	15.8
AUS-WS-01	46	INT	Web	6.80	2.86	59.7	9.40	5.97	3.56	11.7
AUS-WS-02	26	INT	Web	6.13	4.86	51.4	10.3	3.06	8.10	16.2
AUS-WS-03	17	EXT	Web	8.06	2.70	48.6	7.50	0.55	4.80	27.8
AUS-WS-03	17	INT	Web	12.3	4.92	42.9	7.00	2.03	3.48	27.4
AUS-WS-04	21	EXT	Web	0.81	5.21	54.9	11.4	4.21	4.80	18.7
AUS-WS-04	21	INT	Web	4.00	3.10	52.7	9.10	4.58	4.02	22.4
CRP-WS-01	16	EXT	Web	23.1	3.30	37.0	5.10	5.01	3.78	22.6
CRP-WS-01	16	INT	Web	30.5	12.1	24.1	1.18	8.29	10.1	13.7

Table 5-8. Quantitative Phase Analysis Results of Weathering Steel Rust (Cont).

Bridge Name	Age	Face	Location	β–FeOOH Akaganeite	α–Fe2O3 Hematite	α–FeOOH Goethite	δ–FeOOH Feroxyhyte	Fh Ferrihydrite	γ–Fe2O3 Maghemite	γ–FeOOH Lepidocrocite
CRP-WS-01	16	INT	Web	13.0	9.23	32.7	7.80	1.80	16.7	18.7
CRP-WS-01	16	INT	Web	13.0	9.23	32.7	7.80	1.80	16.7	18.7
DAL-WS-01	50	EXT	Web	16.6	3.11	50.2	6.40	3.38	3.33	17.0
DAL-WS-01	50	INT	Web	10.8	6.80	55.8	4.10	4.60	3.40	14.4
DAL-WS-01	50	INT	Web	15.1	4.85	50.8	9.00	3.26	1.06	16.0
DAL-WS-02	12	EXT	Web	11.4	1.56	41.9	5.10	2.14	7.61	30.3
DAL-WS-02	12	INT	Web	10.0	0.49	38.8	5.30	3.67	4.63	37.2
DAL-WS-03	63	EXT	Web	9.43	1.69	43.6	7.30	5.12	3.09	29.7
DAL-WS-03	63	INT	Web	2.11	20.7	39.9	8.70	2.03	10.8	15.7
ELP-WS-01	20	EXT	BF Bot	15.2	3.83	28.4	4.70	5.68	9.30	33.0
ELP-WS-01	20	EXT	Web	32.6	0.00	21.5	13.3	8.12	0.97	23.5
ELP-WS-01	20	INT	BF Bot	10.9	0.00	43.9	0.00	0.00	1.90	43.2
ELP-WS-01	20	INT	Web	11.6	0.88	47.8	6.30	3.94	4.96	24.6
FTW-WS-02	49	INT	BF Bot	6.31	5.02	59.1	10.4	8.53	2.54	8.02
FTW-WS-02	49	EXT	Web	20.7	2.59	36.6	2.97	8.00	2.16	27.0
FTW-WS-02	49	INT	Web	12.0	5.70	45.1	12.1	4.33	9.50	11.3
FTW-WS-03	9	INT	BF Bot	11.2	4.17	39.9	3.50	6.14	1.30	33.8
FTW-WS-03	9	EXT	Web	12.3	1.97	43.1	3.35	4.28	6.81	28.3
FTW-WS-03	9	INT	Web	10.3	0.00	40.1	9.80	5.56	3.86	30.3
FTW-WS-01	49	EXT	Web	0.89	5.41	67.0	10.7	2.02	3.92	10.1
FTW-WS-01	49	INT	BF Bot	3.88	4.95	59.9	9.20	3.31	1.44	17.4
FTW-WS-01	49	INT	Web	6.24	1.79	57.3	10.0	2.35	4.40	17.8
HOU-WS-07	29	EXT	Web	6.41	4.98	63.9	8.90	3.70	1.49	10.7
HOU-WS-07	29	INT	Web	6.29	3.17	63.6	12.0	1.70	3.84	9.32
HOU-WS-02	17	EXT	Web	5.94	1.72	59.8	10.3	2.92	0.23	19.1
HOU-WS-02	17	INT	Web	6.15	3.11	60.7	7.60	3.39	0.00	19.1
HOU-WS-03	33	EXT	Web	7.02	3.80	51.5	0.30	3.92	0.89	32.6
HOU-WS-03	33	INT	Web	3.97	1.06	55.1	8.40	2.84	3.14	25.5
HOU-WS-03	33	INT	Web	6.01	5.79	58.1	12.2	2.44	3.85	11.6
HOU-WS-01	30	EXT	Web	3.30	22.6	36.1	7.80	2.97	10.1	17.1
HOU-WS-06	31	EXT	Web	5.03	4.25	67.0	9.90	4.75	0.77	8.25
HOU-WS-06	31	INT	Web	6.21	4.60	60.0	8.50	3.38	1.86	15.4
HOU-WS-06	31	INT	TF Bot	4.24	8.23	43.6	9.80	0.12	12.6	21.3
HOU-WS-04	36	EXT	Web	8.97	2.07	55.5	10.1	1.64	5.06	16.6

Table 5-8. Quantitative Phase Analysis Results of Weathering Steel Rust (Cont).

Bridge Name	Age	Face	Location	β–FeOOH Akaganeite	α–Fe2O3 Hematite	α–FeOOH Goethite	δ–FeOOH Feroxyhyte	Fh Ferrihydrite	γ–Fe2O3 Maghemite	γ–FeOOH Lepidocrocite
HOU-WS-04	36	INT	Web	7.12	3.53	62.3	14.8	1.23	3.16	7.83
HOU-WS-05	34	EXT	Web	2.33	3.44	65.2	11.7	2.27	0.00	15.1
HOU-WS-05	34	INT	Web	9.48	2.90	53.4	8.40	1.05	4.68	20.1
LBB-WS-01	14	EXT	Web	13.8	3.42	41.4	7.00	3.55	4.84	26.0
LBB-WS-01	14	INT	BF Bot	16.0	1.07	36.4	0.00	4.48	8.00	34.1
LBB-WS-01	14	INT	Web	11.9	1.48	41.0	8.70	4.23	3.31	29.5
LBB-WS-02	14	EXT	BF Bot	16.5	0.83	37.3	5.40	9.09	2.21	28.5
LBB-WS-02	14	EXT	Web	12.0	1.10	38.4	6.60	5.92	5.65	30.2
LBB-WS-02	14	INT	Web	13.6	1.60	40.0	4.10	2.42	7.00	31.3

Note:
INT: Interior Girder; EXT: Exterior Girder
BF: Bottom Flange; BOT: Bottom Face
STIFF: Stiffener

Table 5-9 presents α/Γ and (β+s)/Γ ratios that were used to classify the patina layer into three categories: active, inactive, and protective. These results are also given in ternary diagrams in Figure 5.43 to Figure 5.47 for different corrosive regions in Texas. The corrosion rate is the lowest for a protective patina, with steel losing less than 0.39 mils/year and the α/Γ ratio (PAI_α) is greater than 1. An inactive patina layer also exhibits a low corrosion rate, with a corrosion loss of less than 0.39 mils/year, which is observed when the PAI_α is less than 1, but the (β+s)/Γ ratio (PAI_β) is less than 0.5. An active patina, with a corrosion rate higher than 0.39 mils/year, happens when the PAI_α is less than 1, but the PAI_β exceeds 0.5. Based on the XRD results for weathering steel bridges, researchers observed that the corrosion resistance of steel members varies significantly even between bridges of similar age. For instance, the 17-year-old AUS-WS-03 exhibits inactive corrosion on the interior web, whereas the 17-year-old HOU-WS-02 displays a protective patina across all locations, thus signifying excellent corrosion resistance. Some of the oldest bridges, such as the 49-year-old FTW-WS-01 and 50-year-old DAL-WS-01, mostly maintain a protective patina, whereas the 16-year-old CRP-WS-01 displays the worst corrosion, with active patina at all locations as a result of high airborne chloride concentration in coastal areas.

Interior web surfaces often exhibit worse corrosion, such as the active patina occurring on the interior of AUS-WS-03, DAL-WS-03, and HOU-WS-06, despite having a protective exterior patina. The possible reason for the change in corrosion rate between interior and exterior surfaces is because of the extended TOW on the interior girder and the fact that more dirt accumulation on the interior girder leads to trapped, moisture-laden air. However, certain bridges, such as AUS-WS-04, HOU-WS-04 and HOU-WS-07, exhibit protective patina across all exterior and interior faces, thus highlighting excellent corrosion performance. LBB-WS-01 and LBB-WS-02 have an inactive patina condition because the lack of proper alternating wet and dry cycles prevents the sufficient time required for the formation of a protective patina.

Researchers concluded that the age of the bridge does not directly influence the corrosion resistance of weathering steel girders. Both older and newer bridges exhibited effective and poor patina layers. The protective capability of the patina layer relies on environmental factors, as well as on whether contaminants such as sulfur dioxide and chloride come into contact with rust. Therefore, a careful inspection of all faces of the girders is necessary to accurately investigate corrosion patterns on weathering steel members.

Table 5-9. Patina Condition for Weathering Bridges Based on XRD Phase Analysis.

Bridge Name	Age	Face	Location	α/Γ	(β+s)/Γ	Patina Condition
ATL-WS-01	19	EXT	Web	1.10	0.29	Protective Patina
ATL-WS-01	19	EXT	BF Bot	0.55	0.43	Inactive Patina
ATL-WS-01	19	INT	Web	1.52	0.38	Protective Patina
ATL-WS-01	19	INT	BF Bot	1.32	0.31	Protective Patina
ATL-WS-02	19	EXT	Web	1.82	0.41	Protective Patina
ATL-WS-02	19	INT	BF Stiff	2.27	0.39	Protective Patina
ATL-WS-02	19	INT	Web	1.47	0.36	Protective Patina
ATL-WS-03	47	INT	BF Stiff	1.36	0.75	Protective Patina
ATL-WS-03	47	EXT	Web	2.07	0.49	Protective Patina
ATL-WS-03	47	INT	Web	1.71	0.53	Protective Patina
AUS-WS-01	46	EXT	Web	1.96	0.47	Protective Patina
AUS-WS-01	46	INT	Web	2.40	0.53	Protective Patina
AUS-WS-02	26	INT	Web	1.46	0.54	Protective Patina
AUS-WS-03	17	EXT	Web	1.12	0.36	Protective Patina
AUS-WS-03	17	INT	Web	0.89	0.43	Inactive Patina
AUS-WS-04	21	EXT	Web	1.86	0.37	Protective Patina
AUS-WS-04	21	INT	Web	1.57	0.33	Protective Patina

Table 5 9. Patina Condition for Weathering Bridges Based on XRD Phase Analysis (Cont.).

Bridge Name	Age	Face	Location	α/Γ	(β+s)/Γ	Patina Condition
CRP-WS-01	16	EXT	Web	0.70	0.57	Active Patina
CRP-WS-01	16	INT	Web	0.36	0.79	Active Patina
CRP-WS-01	16	INT	Web	0.57	0.68	Active Patina
DAL-WS-01	50	EXT	Web	1.25	0.58	Protective Patina
DAL-WS-01	50	INT	Web	1.58	0.59	Protective Patina
DAL-WS-01	50	INT	Web	1.37	0.57	Protective Patina
DAL-WS-02	12	EXT	Web	0.82	0.40	Inactive Patina
DAL-WS-02	12	INT	Web	0.74	0.29	Inactive Patina
DAL-WS-03	63	EXT	Web	0.99	0.32	Inactive Patina
DAL-WS-03	63	INT	Web	0.81	0.68	Active Patina
ELP-WS-01	20	EXT	BF Bot	0.46	0.46	Inactive Patina
ELP-WS-01	20	EXT	Web	0.38	0.59	Active Patina
ELP-WS-01	20	INT	BF Bot	0.78	0.23	Inactive Patina
ELP-WS-01	20	INT	Web	1.14	0.41	Protective Patina
FTW-WS-02	49	INT	BF Bot	2.70	0.63	Protective Patina
FTW-WS-02	49	EXT	Web	0.70	0.49	Inactive Patina
FTW-WS-02	49	INT	Web	1.17	0.71	Protective Patina
FTW-WS-03	9	INT	BF Bot	0.79	0.33	Inactive Patina
FTW-WS-03	9	EXT	Web	0.87	0.43	Inactive Patina
FTW-WS-03	9	INT	Web	0.90	0.32	Inactive Patina
FTW-WS-01	49	EXT	Web	3.30	0.50	Protective Patina
FTW-WS-01	49	INT	BF Bot	2.16	0.37	Protective Patina
FTW-WS-01	49	INT	Web	1.89	0.41	Protective Patina
HOU-WS-07	29	EXT	Web	2.71	0.55	Protective Patina
HOU-WS-07	29	INT	Web	2.81	0.59	Protective Patina
HOU-WS-02	17	EXT	Web	2.21	0.29	Protective Patina
HOU-WS-02	17	INT	Web	2.14	0.33	Protective Patina
HOU-WS-03	33	EXT	Web	1.16	0.26	Protective Patina
HOU-WS-03	33	INT	Web	1.64	0.24	Protective Patina
HOU-WS-03	33	INT	Web	2.13	0.57	Protective Patina
HOU-WS-01	30	EXT	Web	0.68	0.68	Active Patina
HOU-WS-06	31	EXT	Web	3.66	0.55	Protective Patina
HOU-WS-06	31	INT	Web	2.14	0.45	Protective Patina
HOU-WS-06	31	INT	TF Bot	0.94	0.54	Active Patina
HOU-WS-04	36	EXT	Web	1.70	0.49	Protective Patina
HOU-WS-04	36	INT	Web	2.88	0.64	Protective Patina
HOU-WS-05	34	EXT	Web	3.13	0.28	Protective Patina
HOU-WS-05	34	INT	Web	1.44	0.46	Protective Patina

Table 5-9. Patina Condition for Weathering Bridges Based on XRD Phase Analysis (Cont).

Bridge Name	Age	Face	Location	α/Γ	(β+s)/Γ	Patina Condition
LBB-WS-01	14	EXT	Web	0.86	0.46	Inactive Patina
LBB-WS-01	14	INT	BF Bot	0.62	0.42	Inactive Patina
LBB-WS-01	14	INT	Web	0.89	0.36	Inactive Patina
LBB-WS-02	14	EXT	BF Bot	0.78	0.41	Inactive Patina
LBB-WS-02	14	EXT	Web	0.78	0.38	Inactive Patina
LBB-WS-02	14	INT	Web	0.75	0.41	Inactive Patina

5.3 SUMMARY

The laboratory analysis of patina samples collected from TxDOT weathering steel bridges include XPS, SEM, EDS, and XRD data. These experiments were essential for investigating the composition and morphology of rust formed on steel surfaces. The results revealed that the rust constituents varied depending on the bridge location, age, and whether the samples were taken from exterior or interior girders. While XPS analysis confirmed the presence of iron oxides and hydroxides, it could not sufficiently quantify the amounts of specific rust components necessary for evaluating the quality of the patina, such as α–FeOOH, β–FeOOH, γ–FeOOH, δ–FeOOH, α–Fe_2O_3, γ– Fe_2O_3 and Fe_3O_4. Therefore, XRD analysis was essential to obtain quantitative data on these crystalline rust components. SEM image analysis provided a detailed examination of the morphological surface characteristics of the rust, while EDS analysis delivered valuable insights on the elemental composition.

The findings of this study emphasize the effectiveness of using powdered XRD quantitative phase analysis in combination with ternary diagrams to characterize the corrosion components of the patina layer formed on weathering steel bridges. This approach proved to be valuable in providing comprehensive insights into the composition and distribution of the corrosion products and classifying them into active, inactive, and protective categories. The results also revealed that bridges in Region 6 exhibited nonprotective patina formation, likely due to an aggressive environment and inadequate girder washing, whereas the majority of bridges in Regions 3 and 4 exhibited the formation of a protective patina.

A combination of SEM/EDS and optical microscopy was employed to analyze and determine the type of painting systems used in TxDOT steel girders. The SEM/EDS analysis successfully differentiated between lead-based, zinc-based, and epoxy-based paint systems. Additionally, optical microscopy was employed to identify the pigments in the paint samples and

determine the individual layer colors. However, the examination was not effective differentiating between System II and System III paint systems due to their similar color and features of the topcoats and primers. Although the identification of the ZBPS was accurate using the optical microscope, further validation was necessary to confirm the presence of lead in the paint systems. EDS analysis showed lead and zinc in the paint samples, indicating that the combination of SEM/EDS and optical microscopy analysis can provide comprehensive understanding of the paint systems. During the analysis of the results of tests performed in this study, rust spot was also detected between the base metal and primer surface.

6 DECISION TOOL FOR SELECTING MITIGATION METHODS

6.1 INTRODUCTION

This chapter describes a set of metrics developed in this work to evaluate the performance of corrosion prevention and mitigation methods for steel girders. These metrics enable assessment and ranking of different methods based on performance scores. The primary objective of these metrics is to provide users with a reliable approach for selecting the most optimal corrosion mitigation method for steel girder bridges. To achieve this purpose, a weighted sum model (WSM) was employed to rank the effectiveness of corrosion prevention and mitigation techniques used on both weathering steel and painted steel girders of Texas bridges.

6.2 DECISION ANALYSIS METHOD

In this research, a decision support tool was developed to effectively evaluate the performance of corrosion prevention and mitigation methods for weathering steel and painted steel girders. The tool utilizes a multidimensional, multicriterion ranking and scoring process and incorporates the outcomes of field inspection and laboratory experiments.

6.2.1 Weighted Sum Model

The WSM has been utilized in previous studies for decision-making and evaluating available options based on multiple criteria. It involves taking the weighted sum of all criterion values and assigning scores to each option (Triantaphyllou & Mann, 1989; Wang & Triantaphyllou, 2008; Mateo, 2012; Hurlebaus et al., 2017). The WSM is easy to comprehend and implement in different scenarios, making it suitable to use on multivariable problems (Triantaphyllou & Mann, 1989; Triantaphyllou, 2000).

A method suggested by Fishburn (1967) was utilized in this section to calculate the overall score (A) in terms of the available options (M) and criteria (N). According to this definition, the overall score is obtained by summing the weights (w_j) that were applied to each possible option (a) across all criteria:

$$A_j = \sum_{i=1}^{N} a_i w_i , \quad j = 1,2,3,\ldots,M \tag{6.1}$$

In this study, options are corrosion prevention and mitigation methods, and parameter a represents testing evaluation results, respectively.

A scoring system ranging from 0 to 10 was also employed for ranking mitigation techniques applied to steel girders. In this system, a score of 0 indicates the least favorable outcome, while a score of 10 reflects the most desirable outcome. The decision tool developed in this research aimed to evaluate four corrosion prevention and mitigation systems applied to steel girder bridges and evaluate weathering steel and painted steel (System I, System II, and System III) for their effectiveness in enhancing the corrosion resistance of steel components in different corrosion risk environments across Texas.

6.2.2 Description of Criteria

Durability and cost were two primary criteria considered in designing the decision tool for steel girders. The framework of scoring corrosion prevention and mitigation methods for weathering and painted steel girders was established based on the findings from both field investigations and laboratory experiments. Because of the differences between the laboratory tests and field inspections conducted for weathering steel and painted steel, it was necessary to consider separate criteria for evaluating these corrosion prevention and mitigation methods.

The durability scores for weathering steel were mainly developed based on the PRI that was computed from the results of both field evaluations and laboratory tests. The condition of the patina on the surface of weathering steel plays a significant role in assessing the condition of the steel components, and thus it was considered in the scoring system. In the case of painted steel, the durability score was determined in accordance with ASTM D610 (2019) by considering factors such as the pull-off adhesion test, paint thickness, chloride concentration, and the extent of corrosion.

6.2.2.1 Weathering Steel Durability Score

Durability scores incorporate the PRI, the protective rust ratio based on the mass fraction of goethite in the rust phase, and the chloride phase ratio determined by the mass fractions of Akaganeite, maghemite, and hematite in the rust phase.

6.2.2.1.1 Patina Rating Index

The PRI was employed as a decision metric to evaluate the performance of weathering steel, as discussed in Section 4.6. The quality of the protective patina formed on the steel surface was ranged between 0 and 10, where a score of 10 indicates a highly effective and adherent patina, and a score of 0 implies a nonprotective patina with poor adhesion. The calculation of the PRI includes color, texture, particle size, density, and adhesion properties of the paint layer. Note that data collection was conducted for both exterior and interior girders to account for microenvironmental conditions.

6.2.2.1.2 Chloride Phase Ratio

The formation of the Akaganeite on the steel surface accelerates the corrosion process and causes the deterioration of the patina layer formed on weathering steel. Akaganeite forms in chloride-rich environments and represents a nonprotective phase of rust layers. As discussed in Chapter 5, the chloride phase ratio that is determined by the mass fraction of akaganeite (β-FeOOH) and the combined mass fractions of hematite and maghemite within patina layer can be used to assess of the condition of the protective layer. In this section, the chloride phase ratio was used as a scale distributed from 0 to 10. A score of 0 denotes a severe degradation of patina with minimal or no protective capabilities. This condition designates an elevated percentage of akaganeite and can lead to an intensifying corrosion rate. A score of 10 indicates a well-formed and protective patina that occurs when the chloride phase ratio is 0 or negligible.

6.2.2.1.3 Protective Phase Ratio

In contrast to the chloride phase ratio, the evaluation of the protective ability of the patina layer heavily relies on the mass fraction of goethite (α-FeOOH). This element is determined by the protective phase ratio, which considers the relative mass fraction of goethite to the combined mass fractions of all elements (goethite, akaganeite, maghemite, hematite, and lepidocrocite). This ratio, ranging between 0 and 1, used as an indicator of the effectiveness of the patina in providing corrosion protection, from a nonprotective state to optimal protection. In terms of the scoring system, scores are assigned on a scale from 0 to 10. A score of 10 represents an excellent level of protection provided by the presence of goethite, while a score of 0 indicates either the absence of the α-phase of the rust product or its formation in a negligible amount.

Table 6-1 provides an overview of the criteria employed in this study to evaluate the performance of weathering steel. Uniform weights were used in the calculation of overall durability scores. The scores obtained for the three criteria discussed above were accumulated separately for both exterior and interior girders and subsequently normalized to a scale ranging from 0 to 10.

Table 6-1. Score Values—Weathering Steel Bridge.

Weight	W_1		W_2		W_3	
Scores	PRI		Chloride Phase Ratio		Protective Phase Ratio	
	Interior	Exterior	Interior	Exterior	Interior	Exterior
0	0	0	1	1	0	0
1	1	1	0.9	0.9	0.1	0.1
2	2	2	0.8	0.8	0.2	0.2
3	3	3	0.7	0.7	0.3	0.3
4	4	4	0.6	0.6	0.4	0.4
5	5	5	0.5	0.5	0.5	0.5
6	6	6	0.4	0.4	0.6	0.6
7	7	7	0.3	0.3	0.7	0.7
8	8	8	0.2	0.2	0.8	0.8
9	9	9	0.1	0.1	0.9	0.9
10	10	10	0	0	1.0	1.0

6.2.2.2 Painted Steel Durability Scores

The durability scores for painted steel both exterior and interior girders were determined based on four criteria: including the pull-off adhesion test, paint thickness measurements, the chloride concentration in paint systems, and the qualitative determination of the corroded area. To calculate an overall durability score for the painted steel, the scores obtained from each criterion were combined according to ASTM D610 (2019). The overall score developed in this research reflects the condition of the paint systems and their ability to withstand environmental factors, and the fact that they can protect the underlying steel substrate. To ensure a fair evaluation, uniform weights were assigned to each criterion in the calculation of the overall durability score.

6.2.2.2.1 Pull-off Adhesion

The adhesion of paint systems was evaluated to assess the long-term performance of the protective layer and ensure overall durability and corrosion resistance of steel girders. To this end, the procedure outlined in ASTM D4541 (2017) was used to quantify the adhesive strength of the

painted layers by measuring the force needed for detaching dollies from the surface of the paint. The results from the pull-off adhesion tests conducted on steel girders across the state exhibited a normal distribution pattern. Consequently, a percentile scale based on the pull-off adhesion test was used to create a ranking system for analyzing the performance of paint systems.

Table 6-2 provides the scoring system—corresponding to different percentile ranges—developed for the decision tool. As an example, the mitigation method was assigned a score of 0 if the pull-off force was less than 600 psi, thereby indicating poor adhesion of the painted layer. However, the paint system received a score of 10 if the pull-off force exceeded 2400 psi, which represents excellent adhesion.

6.2.2.2.2 Paint Thickness Measurement

The protective paint layers undergo gradual deterioration, resulting in less corrosion resistance and protective capability. Thus, to reduce the risk of corrosion, it is essential to establish a protective barrier by consistently renewing the painting of steel structures. The results of paint thickness measurements obtained during field inspections were used to evaluate the effectiveness of the protective layers. It was observed that thicker coating layers provide decent protection. To establish a standardized evaluation, a percentile scale ranging from 0 to 10 was developed, with a score of 10 denoting good performance and a score of 0 denoting poor performance of the painting system (Table 6-2).

6.2.2.2.3 Chloride Concentration

Chloride ions speed up the corrosion process and reduce the corrosion resistance of the coating barrier. This is particularly pronounced in zinc coating, which is a sacrificial protective paint system. Therefore, reducing the chloride concentration on the steel surface is necessary for mitigating corrosion in steel bridges. In this study, the chloride concentration in protective layers was assessed by conducting EDS analysis on paint samples extracted from the steel girders. Table 6-2 provides criteria for scoring based on different chloride concentration levels. A linear scale ranging from 0 to 1 was used to assess the coating quality in relation to the chloride concentration, resulting in scores from 0 to 10. Higher scores indicate better performance.

6.2.2.2.4 Corroded Area ASTM D610

The analysis conducted to study the extent of corroded areas on steel girders in accordance to ASTM D610 (2019) was used as another parameter to assess the performance of paint systems in mitigating corrosion. This evaluation enabled the ranking of paint system performance and identification of vulnerable areas. To evaluate the performance of the paint layers, a scoring system ranging from 0 to 10 was developed based on the extent of corroded areas. A score of 10 corresponds to a lower or non-existent corroded surface (indicating effective corrosion protection), while a score of 0 reflects inadequate protection against corrosive agents (Table 6-2).

Table 6-2. Score Values—Painted Steel Bridge.

Weight	**W_1**	**W_2**	**W_3**	**W_4**
Scores	**Pull-off Adhesion (psi)**	**Thickness Measurement (mils)**	**Chloride Concentration (%)**	**Corroded Area ASTM D610**
	Int./Ext.	**Int./Ext.**	**Int./Ext.**	**Int./Ext.**
0	<600	<3.35	>1.0	≥ 50%
1	600–800	3.35–4.33	0.9–1.0	33%–50%
2	800–1000	4.33–5.31	0.8–0.9	16%–33%
3	1000–1200	5.31–6.30	0.7–0.8	10%–16%
4	1200–1400	6.30–7.28	0.6–0.7	3.0%–10%
5	1400–1600	7.28–8.27	0.5–0.6	1.0%–3.0%
6	1600–1800	8.27–9.25	0.4–0.5	0.30%–1.0 %
7	1800–2000	9.25–10.24	0.3–0.4	0.10%–0.30%
8	2000–2200	10.24–11.22	0.2–0.3	0.03%–0.10%
9	2200–2400	11.22–12.20	0.1–0.2	0.01%–0.03%
10	>2400	>12.20	<0.1	CA ≤ 0.01%

6.2.2.3 Cost

A 100-year period reported by the American Galvanizers Association (2023) was considered to develop a cost scaling system. During this period, epoxy-based paint and ZBPSs were considered as common paint systems having applied on steel girders. The cost evaluation includes upfront painting, touch-up, and maintenance costs. However, the dataset used by the American Galvanizers Association did not consider factors such as inflation and interest rates. In this study, we revisited the cost assessment and incorporated the impact of inflation on prices.

The cost data for different corrosion mitigation techniques are listed in Table 6-3, Table 6-4, and Table 6-5. The cost is listed for touch-up painting done at different intervals (e.g., Year 13, 17, 23), maintenance repainting at different intervals (e.g., Year 19, 25, 34), and full repainting at different intervals (e.g., Year 26, 34, 46). The cost of touch-up and maintenance repainting is the same in all regions and years, at $2.28 and $3.99, respectively. The cost of a full repaint is constant at $7.70.

Table 6-3. Upfront and Maintenance Cost for System I in Region 1 and Region 2 (American Galvanizers Association, 2023).

Paint Application	Cost ($/ft^2)	In-Service (year)
Original Paint	5.70	—
Touch-Up	2.28	23
Maintenance Repaint	3.99	34
Full Repaint	7.70	46
Touch-Up	2.28	69
Maintenance Repaint	3.99	80
Full Repaint	7.70	92

Table 6-4. Upfront and Maintenance Cost for System I in Region 3 And Region 4 (American Galvanizers Association, 2023).

Paint Application	Cost ($/ft^2)	In-Service (year)
Original Paint	5.7	—
Touch-Up	2.28	17
Maintenance Repaint	3.99	25
Full Repaint	7.7	34
Touch-Up	2.28	51
Maintenance Repaint	3.99	59
Full Repaint	7.7	69
Touch-Up	2.28	85
Maintenance Repaint	3.99	93

Table 6-5. Upfront and Maintenance Cost for System I in Region 5 and Region 6 (American Galvanizers Association, 2023).

Paint Application	Cost ($/ft^2)	In-Service (year)
Original Paint	5.7	—
Touch-Up	2.28	13
Maintenance Repaint	3.99	19
Full Repaint	7.7	26
Touch-Up	2.28	39
Maintenance Repaint	3.99	45
Full Repaint	7.7	52
Touch-Up	2.28	65
Maintenance Repaint	3.99	71
Full Repaint	7.7	78
Touch-Up	2.28	91
Maintenance Repaint	3.99	97

Table 6-6, Table 6-7, and Table 6-8 show the costs for touch-up, repairs, and full repainting for System II in different regions. The original paint cost in Region 2 is $4.49, touch-up costs $1.79 in Years 24 and 72, and maintenance repainting costs $3.14 in Years 36 and 84. A full repainting in Region 2 costs $6.06 in Years 48 and 96. Regions 3 and Region 4 have the same touch-up, maintenance, and full repainting costs as Region 2, but with a different year interval (Years 17, 25, 34, etc., for Region 3 and Years 18, 26, 35, etc., for Region 4). Similarly, Regions 5 and 6 have the same costs as the other regions, but repainting will be scheduled in different years (Years 11, 16, 22, etc., for Region 5 and Years 12, 17, 23, etc., for Region 6).

Table 6-6. Upfront and Maintenance Cost for System II in Region 1 and Region 2 (American Galvanizers Association, 2023).

Paint Application	Cost ($/ft^2)	In-Service (year)
Original Paint	4.49	—
Touch-Up	1.79	24
Maintenance Repaint	3.14	36
Full Repaint	6.06	48
Touch-Up	1.79	72
Maintenance Repaint	3.14	84
Full Repaint	6.06	96

Table 6-7. Upfront and Maintenance Cost for System II Region 3 and Region 4 (American Galvanizers Association, 2023).

Paint Application	Cost ($/ft^2)	In-Service (year)
Original Paint	4.49	—
Touch-Up	1.79	17
Maintenance Repaint	3.14	25
Full Repaint	6.06	34
Touch-Up	1.79	51
Maintenance Repaint	3.14	59
Full Repaint	6.06	68
Touch-Up	1.79	85
Maintenance Repaint	3.14	93

Table 6-8. Upfront and Maintenance Cost for System II Region 5 and Region 6 (American Galvanizers Association, 2023).

Paint Application	Cost ($/ft^2)	In-Service (year)
Original Paint	4.49	—
Touch-Up	1.79	11
Maintenance Repaint	3.14	16
Full Repaint	6.06	22
Touch-Up	1.79	33
Maintenance Repaint	3.14	38
Full Repaint	6.06	44
Touch-Up	1.79	55
Maintenance Repaint	3.14	60
Full Repaint	6.06	66
Touch-Up	1.79	77
Maintenance Repaint	3.14	82
Full Repaint	6.06	88
Touch-Up	1.79	99

Table 6-9, Table 6-10, and Table 6-11 provide cost information for touch-up, repairs, and full repainting applications for System III-A in different regions. In Region 2, the original paint cost is $5.77. In this and other regions, touch-up costs are $2.31, maintenance repainting costs are $4.04, and full repainting costs are $7.79. The timing of these repainting and maintenance differs by region. For example, repainting of steel girders located in Region 2 is foreseen to occur after 29, 43, and 58 years of service. In Region 3 and Region 4, the costs calculated for repainting girders are the same; but touch-ups, maintenance repaints, and full repaints happen at different intervals, after 20, 30, and 40 years of service. Similarly, the costs stay the same for girders in Regions 5 and Region 6, but repainting will be predicted to be after 14, 21, and 28 years of service.

Table 6-9. Upfront and Maintenance Cost for System III-A in Region 1 and Region 2 (American Galvanizers Association, 2023).

Paint Application	Cost ($/ft^2)	In-Service (year)
Original Paint	5.77	—
Touch-Up	2.31	29
Maintenance Repaint	4.04	43
Full Repaint	7.79	58
Touch-Up	2.31	87

Table 6-10. Upfront and Maintenance Cost for System III-A Region 3 and Region 4 (American Galvanizers Association, 2023).

Paint Application	Cost ($/ft^2)	In-Service (year)
Original Paint	5.77	—
Touch-Up	2.31	20
Maintenance Repaint	4.04	30
Full Repaint	7.79	40
Touch-Up	2.31	60
Maintenance Repaint	4.04	70
Full Repaint	7.79	80

Table 6-11. Upfront and Maintenance Cost for System III-A Region 5 and Region 6 (American Galvanizers Association, 2023).

Paint Application	Cost ($/ft^2)	In-Service (year)
Original Paint	5.77	—
Touch-Up	2.31	14
Maintenance Repaint	4.04	21
Full Repaint	7.79	28
Touch-Up	2.31	42
Maintenance Repaint	4.04	49
Full Repaint	7.79	56
Touch-Up	2.31	70
Maintenance Repaint	4.04	77
Full Repaint	7.79	84
Touch-Up	2.31	98

According to Kogler and Ocel (2022), the price for weathering steel was $1 per pound in 2013. An annual inflation rate of 2.4 percent (US Bureau of Labour Statistics, 2023) was added to calculate the present cost, which is $1.27 per pound, whereas carbon steel costs $0.41 per pound (Leeco Steel, 2023). To calculate the cost difference, 1 in. thick steel plate with a density of 490 pounds per cubic ft is used. The cost difference of $0.86 per pound is then multiplied by the density and thickness of steel plate to calculate the cost difference between weathering steel and carbon

steel, which is about $35.1 per square ft. For steel girders located in Region 6, it was assumed that the weathering steel girders should be painted after 20 years of service to protect the steel substrate from corrosion attacks. This rough estimation was based on the past observations of the performance of weathering steel girders in this region; for example, SH 124 over the intercoastal canal was blasted and repainted after 20 years of service. This also agrees with the theoretical calculation conducted in Chapter 7 of this report. Therefore, the total cost for weathering steel during its assumed service life of 100 years that includes an upfront cost ($35.1/ft^2) and the cost of maintaining Paint System III over 80 years of service. Table 6-12 provides cost information for a variety of protection systems typically used in TxDOT steel bridges, including weathering steel and different types of paint systems.

Table 6-12. Cost Table for Corrosion Protection Systems.

Corrosion Protection System	Region 1–2 ($/ft^2)	Region 3 ($/ft^2)	Region 4 ($/ft^2)	Region 5 ($/ft^2)	Region 6 ($/ft^2)
Weathering Steel	35.1	35.1	35.1	35.1	67.4
System I	28.6	39.0	39.0	51.6	51.6
System II	21.4	30.8	30.8	48.8	48.8
System III	22.0	34.0	34.0	48.8	48.8

The additional costs associated with repainting and maintenance of weathering steel were factored in, and a linear scale ranging from 0 to 10 was used to convert the costs into a ranking system given in Table 6-13. Additionally, Table 6-14 provides the overall scores used to rank the corrosion prevention and mitigation methods based on their cost.

Table 6-13. Linear Scale for Cost Scores.

Cost ($/ft^2)	Score Cost
20	10
25	9
30	8
35	7
40	6
45	5
50	4
55	3
60	2
65	1
>70	0

Table 6-14. Calculated Cost Scores for Corrosion Protection Systems in Different Regions.

Corrosion Protection System	Region 1–2	Region 3	Region 4	Region 5	Region 6
Weathering Steel	6.98	6.98	6.98	6.98	0.52
System I	8.28	6.2	6.2	3.68	3.68
System II	9.72	7.84	7.84	4.24	4.24
System III	9.60	7.2	7.2	4.24	4.24

6.3 DEVELOPMENT OF DECISION MATRIX

A scoring system depicted by the decision matrix in Figure 6.1 was designed to evaluate the effectiveness of mitigation methods employed in steel girder bridges. The decision tool was built upon two key criteria: durability and cost. Scores were assigned accordingly by assessing the accuracy and precision of each corrosion prevention and mitigation method. Furthermore, the integration of six corrosion risk regions introduced an additional dimension to the decision matrix. Finally, the results of the three-dimensional decision matrix were used to analyze the performance of each of the forementioned corrosion mitigations in different risk environments.

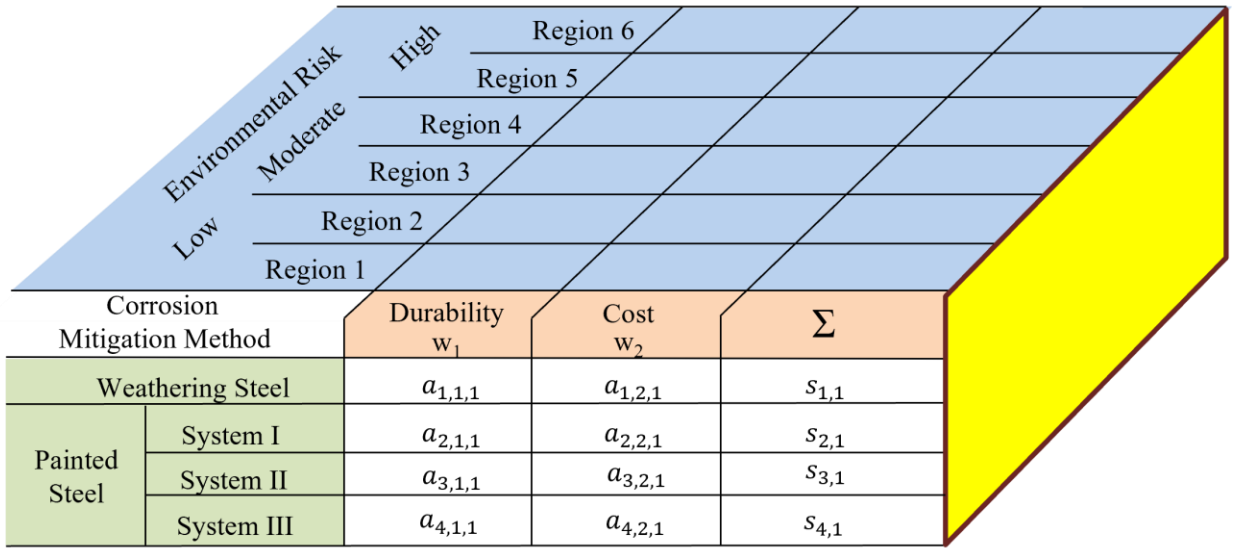


Figure 6.1. Decision Matrix to Assess Performance of Steel Bridges.

The overall scores of each corrosion prevention and mitigation method are depicted in stacked bar charts in Figure 6.2(a) to Figure 6.2(e) These charts reflect the environmental corrosion risk associated with the location of the inspected steel bridges. The decision-making process discussed in this section relies on a durability-driven approach, wherein durability carries a weight of 70 percent and cost carries a weight of 30 percent, as specified in Table 6-15. This

weighting scheme highlights the greater importance of durability in the selection of corrosion prevention and mitigation methods, thus prioritizing safety considerations. Although variations in cost among the methods are considered, they have a relatively smaller impact on the decision-making process than durability.

Table 6-15. Categories and Weight Factors for Durability-Driven Scenario.

Weighted Category	Durability-Driven Scenario	
Durability	W_1	70%
Cost	W_2	30%

In low corrosion risk environments, such as Region 1 and Region 2, weathering steel was a promising corrosion prevention and mitigation method, with an overall score of 7. When considering the durability of steel girders in these environments, weathering steel outperformed painted steel. Among painted steel girders, System III exhibited higher overall scores for both durability and cost factors. System II, on the other hand, has performed comparably well to System III. Figure 6.2(a) provides visual representations of these findings. Although System III exhibited higher durability among the painted steel options, it is important to consider the cost factor in the decision-making process. In low corrosion risk environments, System II is recommended as a cost-effective alternative despite receiving a slightly lower score than System III.

In Region 3 and Region 4, where the risk of corrosion increases, weathering steel continued to outperform paint systems, obtaining higher scores. Additionally, the cost of weathering steel is comparable to that of painted steel. The durability performance of both System II and System III exhibited similar results. While the cost factor, including maintenance costs, should be considered, System II received a slightly better score in Region 4 than System III. The use of weathering steel generally is recommended because of the superior performance and effectiveness of weathering steel in mitigating corrosion in these regions, as illustrated in Figure 6.2(b) and Figure 6.2(c).

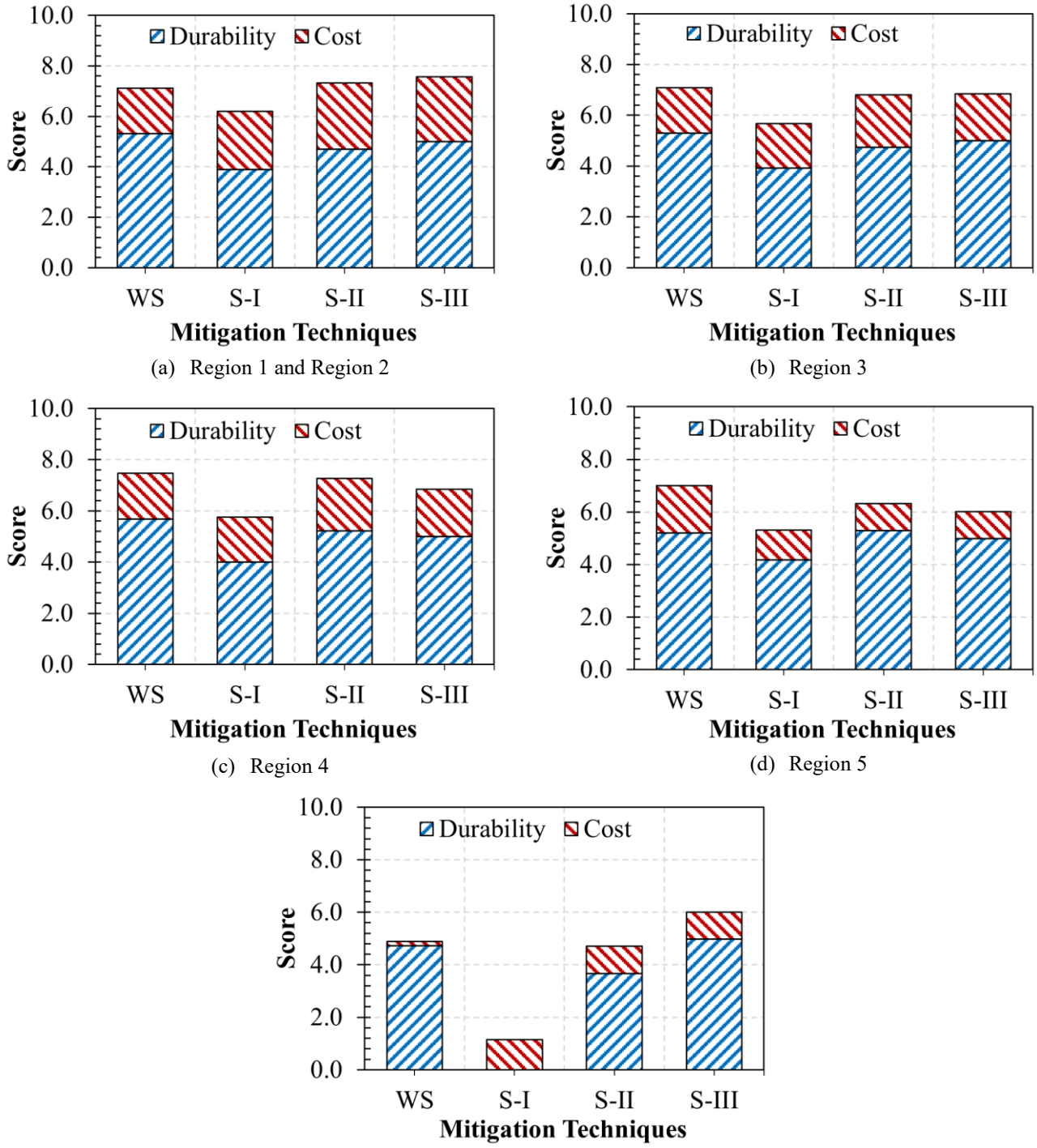
Region 5 is classified as a high-risk corrosive environment, where the overall performance of weathering steel, as well as Systems II and III, declined for steel girders located in this region (Figure 6.2(d)). Weathering steel received a higher cost score, which resulted in a better overall score in the ranking developed in this study. The decision to select weathering steel over System III ultimately depends on the bridge owner's judgment, and it depends on cost considerations. It is

anticipated that steel bridges located in this region will require additional repainting due to the increased likelihood of corrosion.

In a severe corrosive environment such as the industrial area located around the Gulf of Mexico, there was a significant decrease in the durability performance of weathering steel. As a result, it is not recommended to use weathering steel in this region. However, if weathering steel has already been utilized, regular inspection and maintenance are highly encouraged to mitigate corrosion risks. Similarly, the performance of System II also decreased in this harsh corrosive environment. The cost score of System II is estimated to be higher than that of System III due to the increased likelihood of requiring additional repainting on steel components. System III demonstrated better performance in Region 6 and is therefore recommended as the corrosion prevention and mitigation method to utilize in this region.

In general, System I exhibited poor performance. This paint system is primarily used for repairs and is not commonly employed on a large scale. During field inspections in Region 6, no cases were observed wherein System I was employed on steel components. In Region 5, wherever System I was found, the durability performance was estimated to be lower than for other paint systems and weathering steel. Additionally, TxDOT also uses System IV, which is a shop paint system. However, it was challenging to differentiate this system from System II or System III; therefore, it was not considered in the analysis conducted in this research.

Note that corrosion is a localized problem that can occur regardless of the environment. If the conditions become favorable for electrochemical reactions, corrosion can initiate or if it exists can propagate even in low-risk corrosion environments. Therefore, regular inspections of steel girders are recommended to identify any localized corrosion and metal degradation issues. Figure 6.3 presents a single bar chart summarizing the overall scores of corrosion prevention and mitigation methods used in inspected steel girders, including weathering steel and paint systems. This figure enables the reader to assess the performance of the mitigation techniques in different corrosion risk environments across the state. Additionally, Figure 6.4 shows the performance of each corrosion prevention and mitigation method employed in TxDOT steel girders across different regions.



(a) Region 1 and Region 2

(b) Region 3

(c) Region 4

(d) Region 5

(e) Region 6

Note: WS, S-I, S-II, and S-III Denote Weathering Steel, Paint System I, Paint System II, and Paint System III.

Figure 6.2. Total Score for Mitigation Methods.

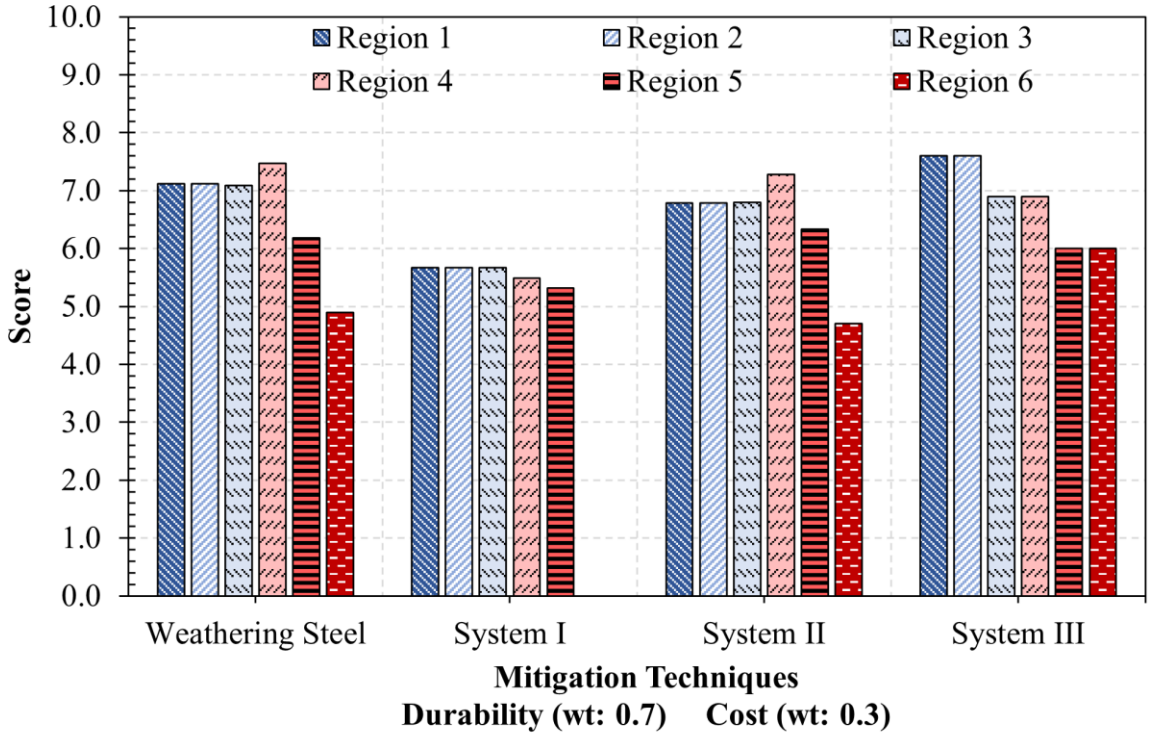


Figure 6.3. Total Score for Corrosion Prevention and Mitigation Methods.

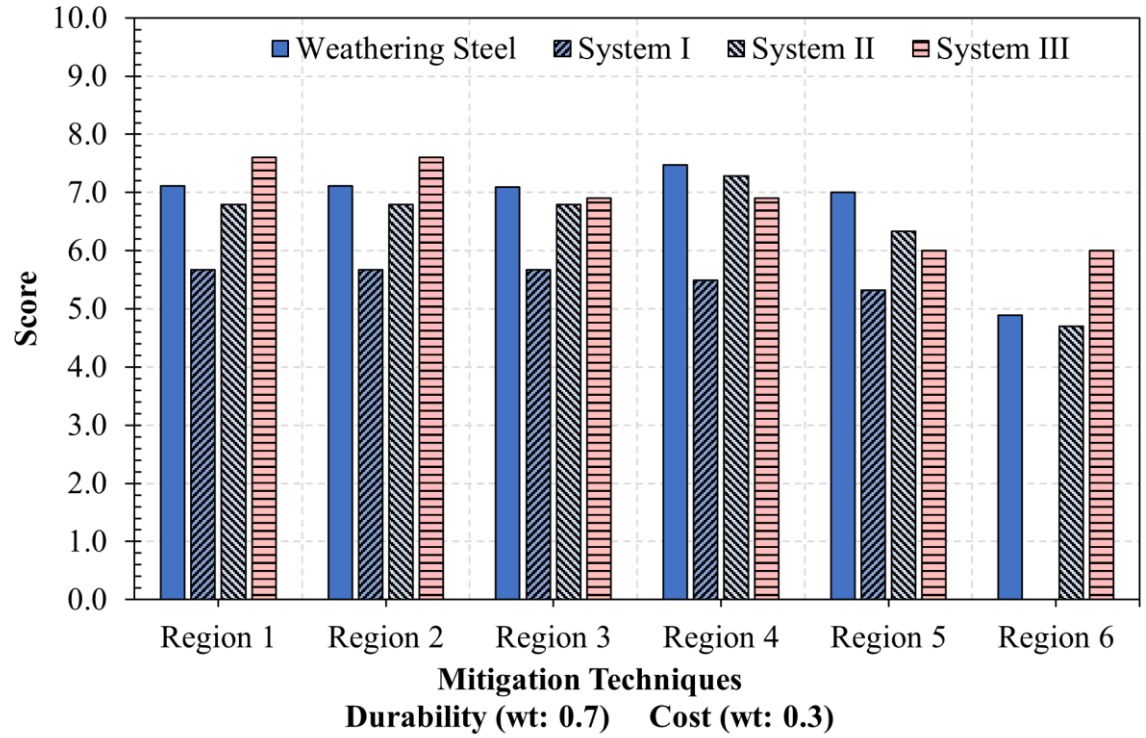


Figure 6.4. Score for Corrosion Prevention and Mitigation Methods in Each Region.

6.4 COMPARISON OF TXDOT NBI SUPERSTRUCTURE RATINGS AND NORMALIZED SCORES FROM FIELD AND LABORATORY TESTING

Table 6-16 gives a list of inspected bridges in this research and the condition of their superstructures. In particular, the table contains the age of each bridge in years, its TxDOT superstructure rating, and a normalized score for each individual bridge. The TxDOT superstructure rating represents the overall condition of the superstructure on a 0 to 9 scale where 0 represents *failed condition* and 9 represents *excellent condition*.

The TxDOT superstructure rating suggest an assessment of the general condition of the bridge superstructures. In contrast, the normalized score obtained from specific field and lab testing in this research relates to corrosion and corrosion-induced damage. These tests involve tape adhesion testing to quantify the performance of the patina and powdered XRD phase analysis to identify the different phases of the rust. The normalized score is directly aimed on quantifying the performance of the weathering steel patina and whether it is protective. Comparing the TxDOT superstructure rating to the normalized score highlights some significant similarities and also differences. For example, AUS-WS-02 has been rated as 5 in the TxDOT rating, indicating potential structural deterioration, but the normalized score obtained for this bridge in this work is 8.2, indicating a well-formed protective patina with no corrosion issues. Conversely, both the TxDOT rating and the normalized score for DAL-WS-03 and HOU-WS-02 suggests that both the overall bridge condition and the corrosion resistance of steel members are within acceptable limits.

Table 6-16. Comparison of TxDOT Inventory Superstructure Rating with the Research Findings for Weathering Steel Bridges.

Bridge Name	Bridge Number	Bridge Age (years)	TxDOT Superstructure Rating	Normalized Score
ATL-WS-01	190190205003072	19	8	8.2
ATL-WS-02	190190205003074	19	7	8.3
ATL-WS-03	190190021701007	47	6	8.0
AUS-WS-01	142270001513363	46	8	8.0
AUS-WS-02	142270011313114	26	5	8.2
AUS-WS-03	142270068307073	17	8	7.6
AUS-WS-04	142270001513451	21	6	7.6
CRP-WS-01	161780037301038	16	8	6.0
DAL-WS-01	1805709F4360012	50	6	7.3
DAL-WS-02	180570296406467	12	7	7.1
DAL-WS-03	180570000911373	63	8	7.3
ELP-WS-01	240720037402084	20	8	7.0
FTW-WS-01	022200BB0985007	49	7	7.3
FTW-WS-02	022200F00189003	49	7	7.4
FTW-WS-03	21270050405501	9	8	8.5
HOU-WS-01	121020002713209	30	7	8.3
HOU-WS-02	121020TOL010109	17	7	8.7
HOU-WS-03	121020325601192	33	7	8.0
HOU-WS-04	121020125804124	36	7	7.3
HOU-WS-05	121020B40177001	34	8	7.8
HOU-WS-06	121020002713240	31	8	8.4
HOU-WS-07	121020050801447	29	6	8.3
LBB-WS-01	51520038001002	14	8	7.5
LBB-WS-02	51520038001038	14	8	7.3
SAT-WS-01	150150001710329	40	7	8.2

Table 6-17 provides a comparison of the TxDOT NBI (National Bridge Inventory) superstructure rating with the normalized score, which is based on ASTM D662 rating, paint thickness, pull-off adhesion results, and chloride concentration from EDS analysis. The normalized score reported in this study gives a quantitative corrosion assessment of a bridge superstructure condition than the TxDOT qualitative NBI rating. This provides the overall damage and performance of the superstructures, including cracking, section loss, and deterioration of structural members; the condition of bearings and joints; alignment problems such as settlement or deformation; connection failures; the level of damage or deterioration present in the deck that could affect the superstructure; and the state of any fracture critical components.

Similar to the conclusions drawn from the scores developed for weathering steel, it was obtained instances where two scores closely align; for example, FTW-PS-02 has both an NBI superstructure rating of 7 and a normalized score of 7.1. However, there were also several cases where a significant difference was seen between the two rating systems. For example, AMA-PS-02 is rated 6 in the NBI rating, which implies acceptable condition; however, the normalized score of the bridge developed in this study is 5.3 for this girder, which indicates a low level of corrosion resistance. Another example is CRP-PS-01, which is rated 5 in NBI rating system, suggesting the steel bridge was in poor condition. However, the normalized score of the steel girders is 7.1, indicating a good corrosion resistance of the superstructure. Note that these two rating systems assess different aspects of the bridge conditions: the normalized score focuses on the paint system quality, and the Texas NBI superstructure rating considers the overall superstructure condition.

Table 6-17. Comparison of TxDOT Inventory Superstructure Rating with the Research Findings for Painted Steel Bridges.

Bridge Name	Bridge Number	Bridge Age (years)	Paint System	Texas Superstructure Rating	Normalized Score
AMA-PS-01	42110006603025	37	Lead-Based	7	4.3
AMA-PS-02	41710006604020	42	System II	6	5.3
AMA-PS-03	41800009002031	62	Lead-Based	6	4.0
ATL-PS-01	191030AA0109001	19	Epoxy-Based	6	2.6
BMT-PS-01	201240020011132	57	System II	6	4.7
BMT-PS-02	201240073902013	62	System II	6	8.6
BRY-PS-01	172390AA0291001	19	System II	6	3.8
CRP-PS-01	161780010106041	64	System III	5	7.1
DAL-PS-01	180710026101225	16	System I	7	5.6
ELP-PS-01	240720104603116	23	System I	8	5.6
FTW-PS-01	22200000813420	21	System II	7	6.8
FTW-PS-02	22200017104049	16	System II	7	7.1
HOU-PS-01	121020038905356	7	System II	7	7.5
TYL-PS-01	102120024507306	14	System II	7	7.4
TYL-PS-02	102120049506385	14	System II	7	5.9
WFS-PS-01	32430004309191	22	System II	7	8.6
WFS-PS-02	32430004309193	22	System II	7	8.4
WFS-RC-01	32430004309188	22	System I	7	6.8
WFS-RC-02	32430004309202	22	System I	7	5.2
YKM-PS-01	131580AA0220001	19	Lead-Based	6	1.0

6.5 RECOMMENDED MITIGATION METHODS FOR STEEL BRIDGES

Based on an analysis of durability and cost scores, a recommendation for the application of corrosion prevention and mitigation systems on both new and existing steel structures is given in Figure 6.5 for each respective county. The map demonstrates the utilization of weathering steel in low to medium corrosive environments (Region 1 to Region 3), while System II (or System IV for new structures) is suggested for steel girders in Region 4. As corrosivity increases (Region 5 and Region 6), the use of Paint System III-A (or System III-B for new structure) is recommended.

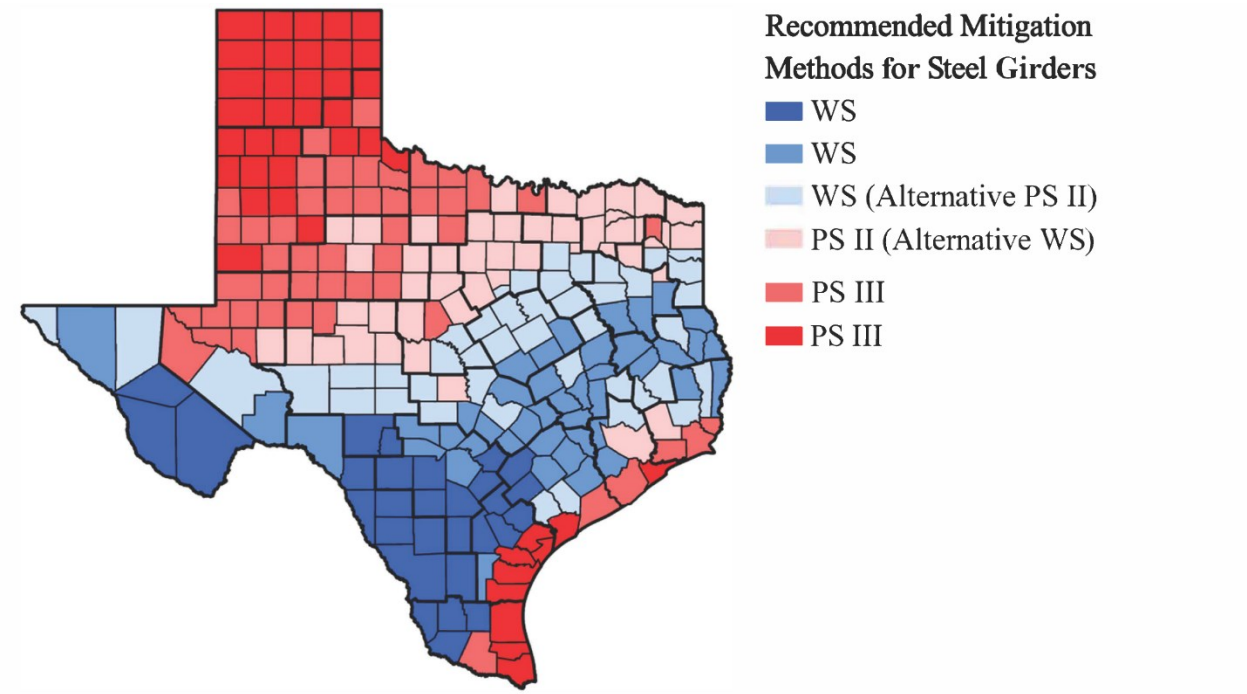


Figure 6.5. Recommended Mitigation System for Steel Bridges.

6.6 APPLICATION OF DEVELOPED TOOL

A spreadsheet was developed to analyze the performance of corrosion prevention and mitigation methods in TxDOT steel girders. The program enables users to evaluate different aspects of the decision framework established in this study. Figure 6.6 shows a screenshot of the program's interface. Within the program, users have the ability to select specific corrosion risk regions and assess the effectiveness of the corrosion prevention and mitigation techniques for different county. The program generates informative charts and graphs, providing an overview of the overall scores and performance of different methods across different regions in Texas. For instructions on how to effectively utilize the program, the reader is referred to the user guide or

documentation included within the spreadsheet that provides detailed guidance on the program features for the purpose of decision-making and evaluation of corrosion prevention and mitigation methods.

Input

Bridge Type Concrete / Steel

County Nueces

Run

	Weight
Durability	70 %
Cost	30 %

(Insert desired Durability %)

Output

Priority Rating Table

Corrosion Risk Region	6		
Mitigation	**Weighted Durability**	**Weighted Cost**	**Total Score**
System III	5.0	1.0	6.0
WS	4.7	0.2	4.9
System II	3.7	1.0	4.7
System I	0.0	1.1	1.1

Priority Rating Plot

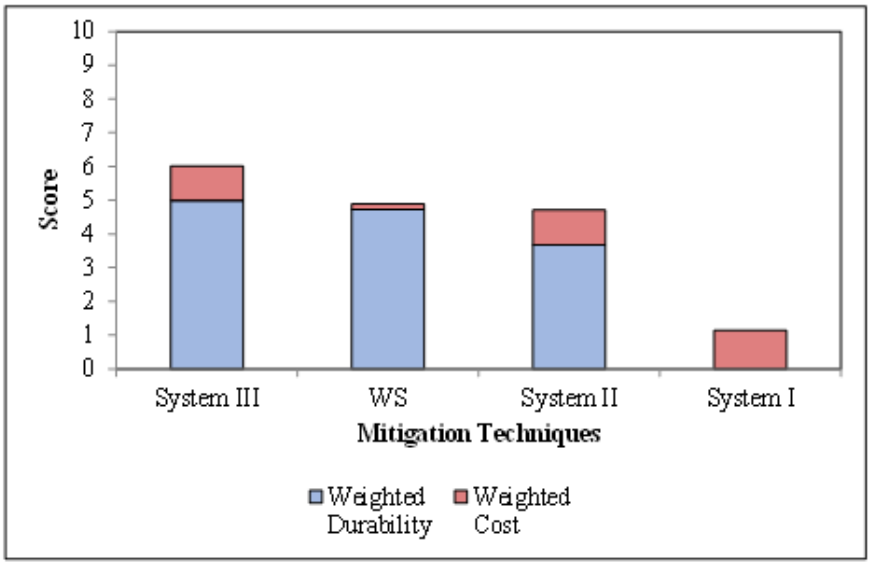


Figure 6.6. Developed Decision Tool.

6.7 SUMMARY

The proposed criteria-based evaluation presented in this study provides a comprehensive assessment of the durability of corrosion mitigation methods used on TxDOT steel girder bridges. Researchers concluded that all mitigation techniques performed well in low-risk environments. However, weathering steel is recommended for steel bridges located in Region 3 and Region 4, which are medium risk environments. As the risk of corrosion increases, particularly in aggressive environments classified as Region 5 and Region 6, System III exhibited better performance than other mitigation techniques. Therefore, researchers recommend prioritizing the use of System III over other techniques in regions with elevated corrosion risk. Weathering steel demonstrated poor performance in Region 6; consequently, this mitigation technique is not recommended for this region.

7 SERVICE LIFE OF WEATHERING STEEL STRUCTURES

7.1 INTRODUCTION

This chapter describes a mathematical model to predict the service life of weathering steel girder bridges as a result of corrosion attacks. It provides a review of modern weathering steel degradation and highlights the mechanism of corrosion fatigue—the most critical deterioration occurring on this type of structures. It discusses corrosion fatigue models and the failure of welded connections due to corrosion fatigue. A mathematical model was used based on geometrical mean of stress range and maximum tensile stress to predict the fatigue limit of weathering steel components. Finally, this chapter presents a framework to predict the average service life of weathering steel structures using Miner's damage rule.

7.1.1 Deterioration of Weathering Steel Bridges

Weathering steel girders are designed to develop a protective rust layer that helps to mitigate corrosion and extend the service life of the structure. However, a high salt environment can impact the long-term durability of weathering steel bridges. Corrosive agents cause the failure of the protective layer, leading to an accelerated corrosion process on the steel substrate (Morcillo et al., 2019a). Uniform corrosion, which commonly occurs on weathering steel girders, reduces the section thickness and consequently results in lower structural capacity of the system. Damgaard and Walbridge (2009) investigated the reduction in shear and moment capacity of weathering steel members due to corrosion process. The authors studied the uniform thickness loss of steel and its effect on reducing the service life of the structure, which is the point at which the resistance of the system drops to the target reliability index. Another type of corrosion that can reduce the service life of a member is pitting corrosion, which not only is more destructive than uniform corrosion, it can also cause stress corrosion cracking that can lead to premature failure of the whole system (Damgaard et al., 2010; Zhang et al., 2021).

In addition to corrosion, several studies (Fisher et al., 1974; Fisher, 1984; Kwon & Frangopol, 2010; Hurlebaus et al., 2018) investigated the potential failure of steel girders due to fatigue loading, particularly in fracture-critical member (FCM) welds and connections because fatigue-induced failure in these components can result in the collapse of the structural element.

Corrosion fatigue refers to material degradation because of alternating stress in a corrosive environment. When pitting corrosion initiates on a steel surface, it creates notches that can act as sites for crack initiation and propagation. As the localized corrosion grows, stress concentration beyond the notch increases, facilitating crack initiation under cyclic loading (Rokhlin et al., 1999; Cerit et al., 2009). These cracks then propagate and consequently cause the collapse of the structural member. Accelerating the corrosion process not only causes fatigue cracking, but it also accelerates the crack propagation, exacerbating the potential for catastrophic failure.

7.1.2 Corrosion Fatigue Deterioration in Weathering Steel

The service life of modern high-volume interstate steel bridges is usually controlled by fatigue loading because heavy trucks produce millions of stress cycles that result in fatigue failure over time (Russo et al., 2016). Stress life and strain life are two common fatigue life models that can be used to predict the fatigue life of a material. The stress life model is particularly useful in high cycle fatigue, where applied stresses occur at the tips of a crack, but it is not reliable at low cycles and can be scattered in the fatigue data. In contrast, the strain-life model is suited for high and low cycle fatigue because loading involves a combination of elastic and plastic behavior (Stephens et al., 2000; Dowling, 2009).

The American Association of State Highway and Transportation Officials (AASHTO) S-N curve is a common stress life model (Figure 7.1). According to this model, stress range can be defined as a function of fatigue categories and the number of cyclic loadings to failure (AASHTO, 2020):

$$\Delta\sigma = \left(\frac{A}{N_f}\right)^{\frac{1}{m}} \tag{7.1}$$

where N_f is the number of cyclic loads to failure; A is a constant, depending on the fatigue categories given in Table 7-1; $\Delta\sigma$ refers to the stress range; and m denotes the slope of the S-N curve (equal 3 for all kinds of fatigue categories) (AASHTO, 2020). In Figure 7.1, the dashed line refers to the constant amplitude fatigue threshold. If the stress range is below this threshold, the fatigue life of the member is assumed to be infinite, suggesting the failure is not happening due to fatigue loading.

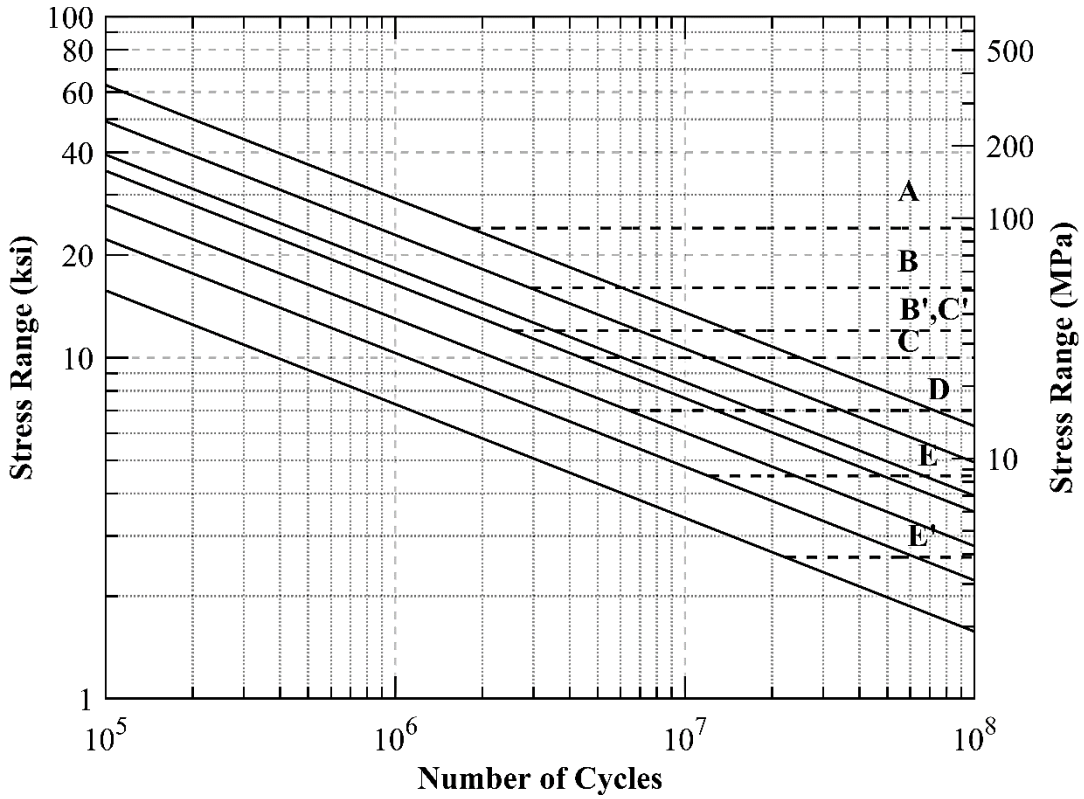


Figure 7.1. AASHTO S-N Curves for Various Fatigue Categories (AASHTO, 2020).

Table 7-1. Fatigue Category and Threshold (AASHTO, 2020).

Detail Category	Constant, A times 10^8 (ksi^3)	Threshold (ksi)
A	250.0	24.0
B	120.0	16.0
B′	61.0	12.0
C	44.0	10.0
C′	44.0	12.0
D	22.0	7.0
E	11.0	4.5
E′	3.9	2.6

The AASHTO stress life model is straightforward and considers a single stress component. It offers detailed guidance on fatigue category classification that helps engineers in the design process. Soliman et al. (2013) studied fatigue failures of structural elements and concluded that AASHTO overestimates fatigue damage on steel structures when the maximum stress range exceeds the constant amplitude fatigue threshold. To improve fatigue life prediction, the authors also proposed a bilinear S-N model that considers different exponential values in low and high cycles ranges.

The strain-life model is more complex than the stress life model and considers the effect of both elastic and plastic strain separately. Morrow (1965) introduced a strain-life model as the following:

$$\frac{\Delta\varepsilon}{2} = \frac{\sigma_f'}{E}(2N_f)^{\mathrm{b}} + \epsilon_f'(2N_f)^{\mathrm{c}} \tag{7.2}$$

where b is known as Basquin's exponent, representing the fatigue strength; c is known as the Coffin-Manson exponent, representing the fatigue ductility; $\Delta\varepsilon$ is strain range; σ_f is the fatigue strength coefficient; ϵ_f' is the fatigue ductility coefficient; E is the modulus of elasticity; and N_f is the number of cycles to failure. Equation (7.2) is composed of two separate parts: elastic strain and plastic components of the strain, as depicted in Figure 7.2.

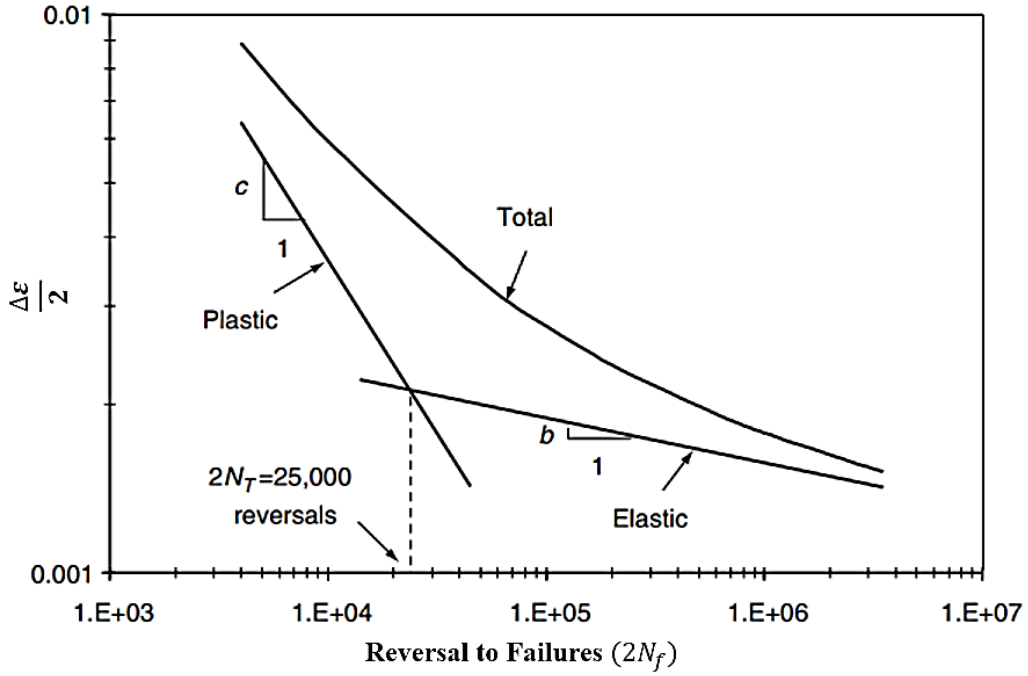


Figure 7.2. Strain Amplitude vs. Reversal to Failure.

Morrow's model does not factor in the effect of *mean stress*. Mean stress refers to the average stress level during cyclic loading, and it can be defined as negative and positive mean stress. Compressive mean stress is beneficial for fatigue life because it can effectively close and retard existing cracks, reducing their growth rate and extending the fatigue life. However, tensile mean stress accelerates crack growth and reduces fatigue life. Tensile mean stress promotes crack openings, making it easier for cracks to propagate (Stephens et al., 2000; Dowling, 2009; Ince &

Glinka, 2011). Smith (1970) proposed that the extent of damage from fatigue loading in a cycle can be modeled by the product of maximum tensile stress (σ_{max}) and strain amplitude (ε_a). Langlais and Vogel (1996) also suggested that the product of stain and stress amplitude for a fully reversed test is equal to the product of maximum stress and strain amplitude for a mean stress test:

$$\sigma_{max}\varepsilon_a = \sigma_{a,rev}\varepsilon_{a,rev} \tag{7.3}$$

where $\sigma_{a,rev}$ and $\varepsilon_{a,rev}$ are the fully reversed stress and strain amplitudes. Recall Marrow's model, maximum tensile stress can be defined as follows:

$$\sigma_{max} = \sigma_a = \sigma_f'(2N_f)^{\mathrm{b}} \tag{7.4}$$

By multiplying it with the strain-life equation, the Smith, Watson, and Topper (SWT) model (Smith, 1970) is:

$$\frac{\Delta\varepsilon}{2}\sigma_{max} = \frac{(\sigma_f')^2}{E}(2N_f)^{2\mathrm{b}} + \sigma_f'\epsilon_f'(2N_f)^{\mathrm{b+c}} \tag{7.5}$$

where σ_{max} is the maximum applied tensile stress; and E is the modulus of elasticity.El Aghoury and Galal (2014) modified the SWT model for weathering steel by considering the effect of corrosion. The authors proposed the following corrosion fatigue strain-life model:

$$\frac{\Delta\varepsilon}{2}\sigma_{max} = \frac{(\sigma_f')^2}{E}(2N_f)^{2b'} + \sigma_f'\epsilon_f'(2N_f)^{b'+c'} \tag{7.6}$$

where the factors b' and c' are modified exponents in corrosive environments:

$$b' = b(1 + \gamma_{corr}\alpha_b) \tag{7.7}$$

$$c' = c(1 + \gamma_{corr}\alpha_c) \tag{7.8}$$

where α_b and α_c are the correction constants. The effect of corrosion is introduced by the corrosion factor γ_{corr}:

$$\gamma_{corr} = 0.0776\,log(CR)^2 + 0.2121\,log(CR) + 0.2179 \tag{7.9}$$

where CR denotes the average annual thickness loss of metal.

7.1.3 Weldment and Their Effect on Fatigue

Welding of steel members introduces significant change to the material because of heating, cooling, and fusion processes, causing the formation of inhomogeneous crystal structures in steel. Imperfections such as inclusions and cavities are common in welds. The shape of the weld profile and the presence of nonwelded root gaps contribute to the creation of stress concentrations, which exhibit varying geometric properties. Residual stresses and distortions resulting from the welding process have a profound impact on the fatigue performance of welded joints (Stephens et al., 2000).

The potential failure of weathering steel girder bridges due to fatigue occurs at welds rather than in the base metal. One example is the fillet weld connecting the transverse stiffener to the flange or web. It is widely acknowledged that the geometrical discontinuity at the toe of the fillet weld poses a potential risk for fatigue crack initiation. Typically, these cracks initiate at the welded toe and subsequently propagate into the neighboring base metal. The stress concentration caused by the abrupt change in geometry at the weld toe can greatly contribute to the initiation and advancement of fatigue cracks (Fisher et al., 1974). One common approach to assessing the fatigue behavior of welded joints is introducing a stress concentration factor. Fisher (1984) suggested an empirical model to predict the stress concentration factor on the transverse weld on the cover plate:

$$k_w = -3.539 \ln \frac{z}{t_f} + 1.981 \ln \frac{t_{cp}}{t_f} + 5.798 \tag{7.10}$$

where z is the weld leg size; t_{cp} denotes the cover plate thickness; and t_f refers to the flange thickness. The stress concentration factor regarding the common weld connection is summarized in Table 7-2. More details about the stress concentration factor on welding and steel plate connections can be found in Pilkey et al. (2020).

Table 7-2. Stress Concentration Factor of Different Welds (Dimitrakis & Lawrence, 2001; Veritas, 2001; Spotts et al., 2004).

Type of Weld	Stress Concentration Factor k_w
Reinforced Butt Weld	1.2
Toe of the Transverse Fillet Weld or Normal Fillet Weld	1.5
End of Parallel Fillet Weld or Longitudinal Weld	2.7
T-butt Joint with Sharp Corners	2.0
Flange Connection with Soft Toe	2.2
Weld at the End of Local Stiffener	2.4
Weld Toe with a Radius (R) Greater Than 7.8 in.	$2.0 \times \left(\frac{2.36}{R}\right)^{0.05}$
Weldment with Longitudinal Attachment	2.64

7.1.4 Damage Indicator and Limit State Function

Based on the SWT model, a damage indicator called P_{SWT} that is the geometrical mean of maximum stress and stress range was introduced (Topper et al., 1969; Smith, 1970; Kujawski, 2014):

$$P_{SWT} = \sqrt{\sigma_{max}\varepsilon_a E} \tag{7.11}$$

The maximum tensile stress is denoted by σ_{max}; the strain amplitude that is half of the stress range is referred to as ε_a; and the modulus of elasticity is denoted by E. Figure 7.3 shows the critical parameters used in the fatigue model.

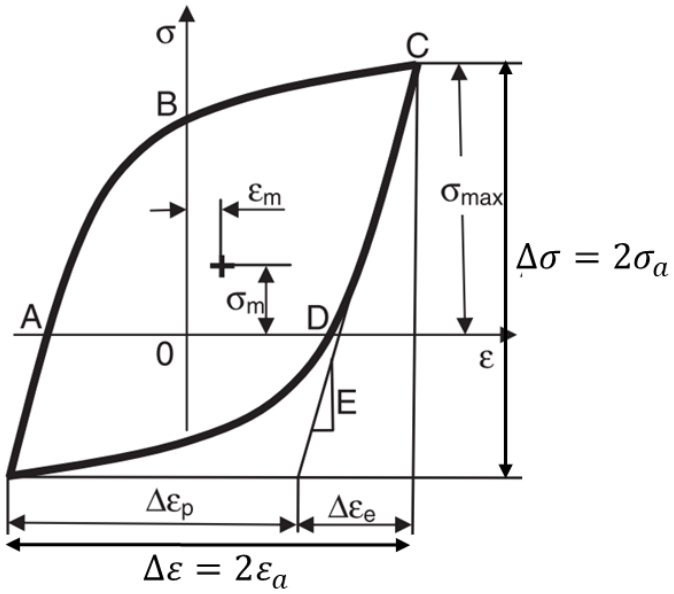


Figure 7.3. Fatigue Hysteresis Loop.

Figure 7.4 shows a steel plate with an edge crack subjected to a repeated cyclic load with the stress range σ_n. The maximum stress at the crack tip is:

$$\sigma_{max} = k_t \sigma_n \tag{7.12}$$

where k_t refers to the stress concentration factor; and σ_{max} is the local stress at the crack tip.

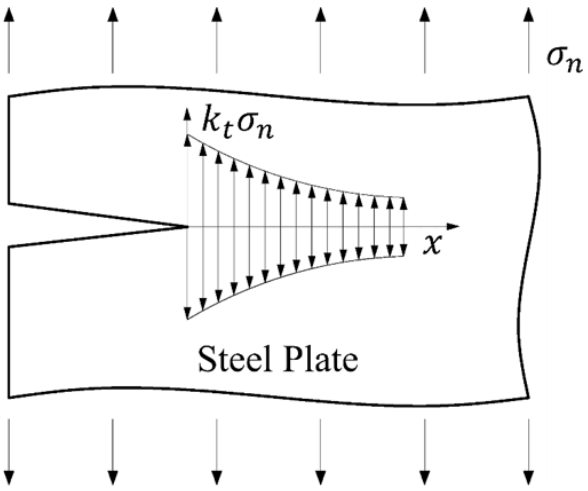


Figure 7.4. Steel Plate with Crack Subject to Cyclic Load.

In the plastic stage, the widely used Neuber's rule relates the stress concentration with the maximum stress by stating that the geometrical mean of the stress and strain concentration factors under plastic deformation conditions remains constant (Neuber, 1961; Topper et al., 1969):

$$\sigma_{max}\varepsilon_a = k_t \sigma_n \varepsilon_e \tag{7.13}$$

where:

$$\varepsilon_e = \frac{k_t \sigma_n}{E} \tag{7.14}$$

and:

$$\sqrt{\sigma_{max}\varepsilon_a E} = k_t \sigma_n \tag{7.15}$$

Figure 7.5 describes Neuber's rule about the strain energy in the elastic or elastoplastic stage remaining constant. In other words, the areas of the red and blue triangle are equal (Kujawski, 2014).

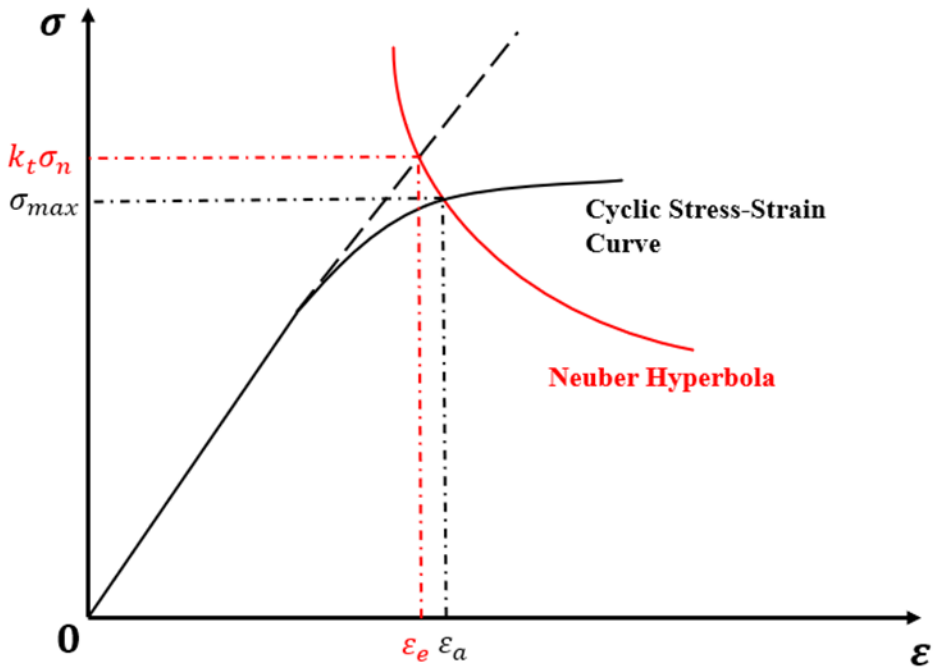


Figure 7.5. Energy Interpretation of Neuber's Rule.

The direct use of stress and strain-life models is not possible when a fatigue-sensitive element is subject to a variable-stress range. To address this, Miner (1945) proposed a linear damage accumulation hypothesis that is known as Miner's rule:

$$D = \sum_{i=1}^{k} \frac{n_i}{N_{c_i}} \tag{7.16}$$

where n_i is the number of stress cycles at level S_i; N_{c_i} is the total number of cycles to failures under the constant stress level S_i; and D refers to Miner's Damage Accumulation Index. The fatigue damage of weathering steel girder is assumed to result from truck loads. When trucks' daily traffic or the stress range is constant with time, the accumulated damage D is:

$$D = \frac{N_{year}}{N_{\Delta f}} \times t \tag{7.17}$$

where N_{year} is the yearly number of cycles at stress range Δf; $N_{\Delta f}$ is the number of cycles over bridge service life at stress range Δf; and t is the service life. Miner's rule is defined based on damage accumulation, wherein the cumulative damage caused by repeated loading cycles is compared to the fatigue strength of the material. This rule assumes that every loading cycle contributes a certain fraction of damage, and failure occurs when the accumulated damage exceeds a specified threshold. When D is larger than 1, fatigue failure will occur (Zhao et al., 1994) when:

$$D \geq \Delta \tag{7.18}$$

The fatigue damage threshold is denoted by Δ, and it is assumed to be 1.

7.1.5 Developed Framework to Predict Service Life of Weathering Steel

The service life of weathering steel subject to corrosion fatigue can be evaluated using a framework that considers both environmental and mechanical factors. Environmental factors include exposure to corrosive agents. The severity of exposure can be evaluated using the corrosion rate model and atmospheric corrosion classification defined by ISO 9223 and the corrosion risk assessment map provided in Chapter 3 of this report. Mechanical factors include the loading conditions and the mechanical properties of the steel. The modified SWT model proposed by El Aghoury and Galal (2014) effectively considers both environmental and mechanical factors when evaluating the fatigue resistance of weathering steel bridges. Fatigue analysis methods, such as the Miner's linear damage rule, can be further used to evaluate the fatigue life of weathering steel under cyclic loading. The proposed service life prediction framework is depicted in Figure 7.6.

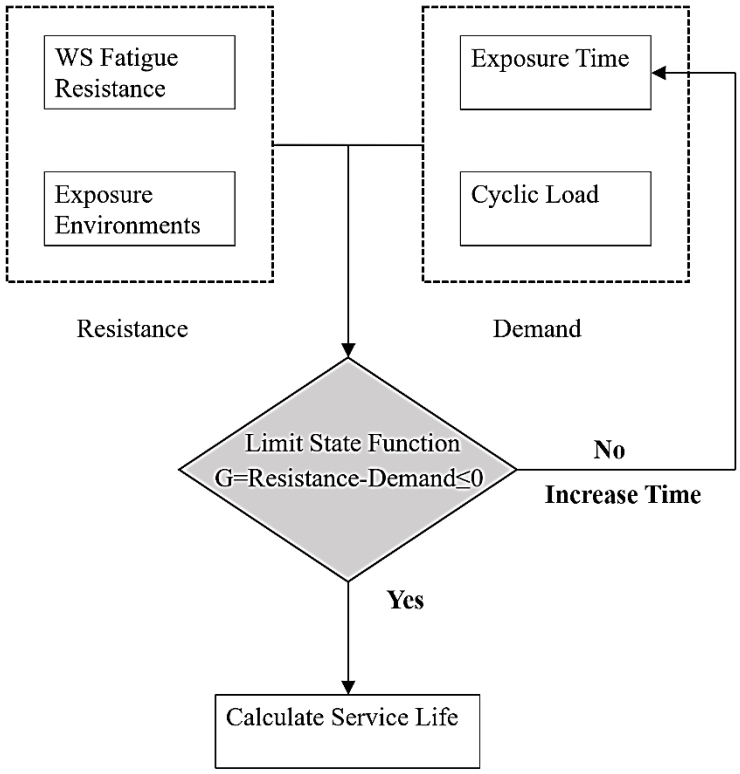


Figure 7.6. Developed Framework to Predict Service Life of Weathering Steel Bridges.

In this framework, the initial step is to determine the environmental and mechanical factors that include collecting data and conducting testing. The corrosion rate of steel should be predicted by considering the corrosivity of the environment and performing mechanical tests (such as tensile and fatigue tests) to determine the critical fatigue parameters used in the modified SWT model. The load conditions must also be determined. AASHTO recommends using truck loads for analyzing the fatigue damage of steel highway bridges. This step involves predicting the bridge's truck daily traffic and subsequently calculating the maximum tensile stress and stress amplitude applied to the steel girder. The final step is to use Miner's rule to calculate the accumulated damage due to the stress range and determine the corrosion fatigue resistance of weathering steel bridges. Therefore, the time when the accumulated damage exceeds the threshold, or the end of service life, can be estimated.

7.2 MODELING CORROSION FATIGUE DEGRADATION FOR WEATHERING STEEL

In this research, a deterministic model was proposed to assess the performance of the weathering steel bridges due to corrosion fatigue. This section focuses on the application of the corrosion fatigue model by comparing the simulation results and experimental data. The aim is to provide insights into the reliability and limitations of the proposed model by discussing a few case studies to facilitate the use of this framework for predicting the average service life of weathering steel girders in different corrosive environments.

7.2.1 Material Properties

ASTM A588 is the most common steel used in the United States for weathering steel bridges. It exhibits remarkable atmospheric corrosion resistance without the need of protective coatings. Moreover, high-strength low-alloy structural steel ASTM A588 can be found in a range of shapes, plates, and bars that are suitable for welded, riveted, or bolted construction (Albrecht & Naeemi, 1984). ASTM A588 Grade A/B and A709 Grade 50W are widely used in weathering steel structures and bridge construction, freight cars, telecommunication towers, and gusset plates. Mechanical parameters of the steel are given in Table 7-3.

Table 7-3. A588/A709W Mechanical Parameters.

Parameter	Notation	A588/A709W	Unit
Modulus of elasticity	E	29,000	ksi
Fatigue strength coefficient	σ_f'	126	ksi
Fatigue ductility coefficient	ϵ_f'	0.59	—
Basquin's exponent	b	−0.09	—
Coffin-manson exponent	c	−0.58	—
Cyclic strain hardening coefficient	K'	203	ksi
Cyclic strain hardening exponent	n'	0.15	—

7.2.2 Corrosion Fatigue Simulation Results and Comparative Analysis

The number of cycles to failure for different corrosion rates of weathering steel (A588 A/B and A709 50w) is shown in Figure 7.7. As shown in this figure, the constant amplitude fatigue limit only exists for a noncorrosive condition (CR = 0). When steel is placed in corrosive environments, the corrosive attack can create surface defects and microcracks. The stress concentration increases around these cracks, consequently causing crack growth under cyclic loading. Adasooriya et al. (2020) concluded that the endurance limit of high-strength steel will drop to 50 percent in air, while the limit will even reduce to 10 percent when steel is exposed to salt-laden water. Several studies (Albrecht & Naeemi, 1984; Albrecht, 1992; Albrecht & Shabshab, 1994; Albrecht & Lenwari, 2009) suggested an approach to waive a fatigue endurance limit for corroded weathering steel because under aggressive environments corrosion-induced cracking can initiate and propagate fatigue that leads to failure of the system.

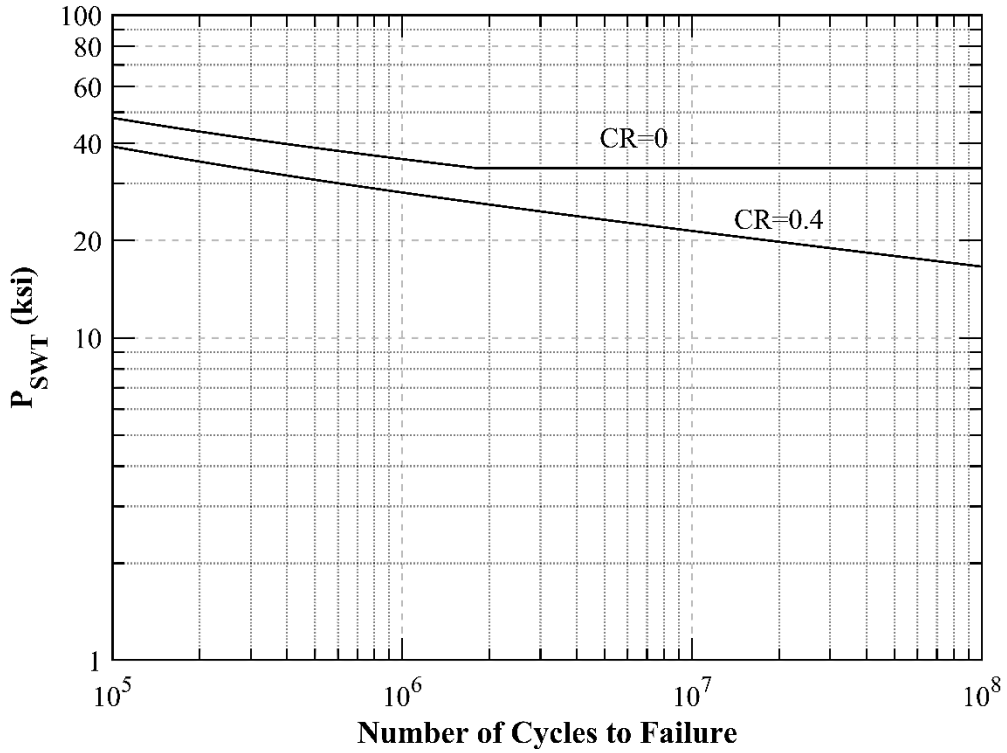


Figure 7.7. Number of Cycles to Failures vs. P_{SWT}.

The number of cycles to failure drops as the corrosive environments become more aggressive. In marine environments, the protective rust layer may break down more quickly, leading to accelerated corrosion and potentially reduced fatigue resistance. In freshwater environments, such as rivers or lakes, weathering steel has been found to have good fatigue resistance due to the absence of salts and other corrosive substances. However, it can be susceptible to corrosion and fatigue damage in saltwater environments due to the presence of chloride ions that accelerate the corrosion rate and also reduce the steel fatigue resistance (Albrecht & Shabshab, 1994).

Figure 7.8 shows the probable number of cycles to failure for weathering steel as the corrosion rate increases. The diagram illustrates the risk of the failure of weathering steel in different corrosive environments suggested by Morcillo et al. (2019b). P_{SWT} was calculated and shown in this diagram to facilitate the prediction of the average service life of weathering steel with different loading conditions.

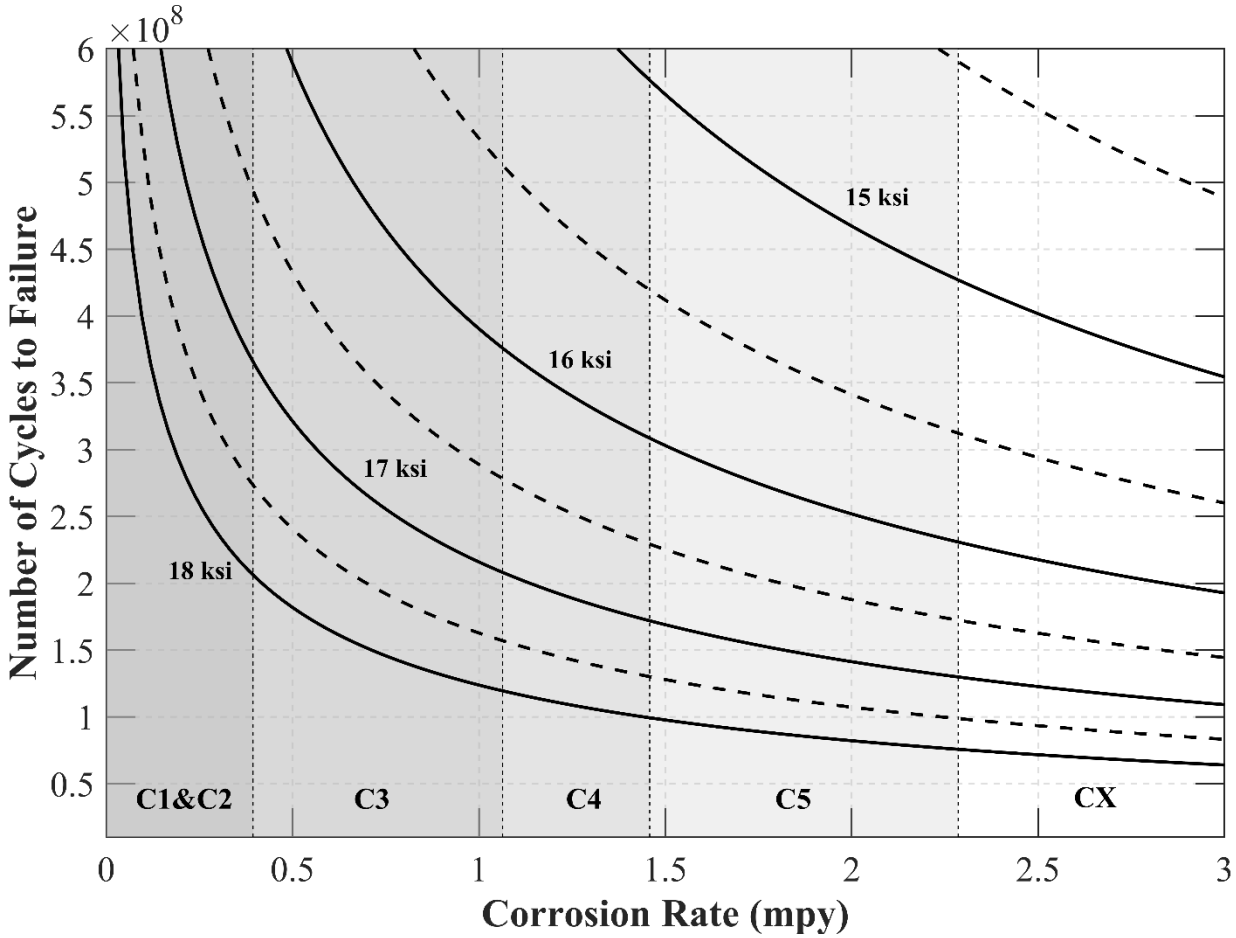


Figure 7.8. Number of Cycles to Failure in Different Corrosive Regions.

7.2.3 Corrosion Fatigue Limit State

Although the corrosion fatigue resistance model was developed in this research, it should be noted that there is still a gap between its design and the analysis of weathering steel structures. The AASHTO Load and Resistance Factor Design (LRFD) specification has not clearly defined the corrosion fatigue limit state; thus, further studies are needed to determine the proper load factors for the corrosion fatigue limit state and expected reliability index for weathering steel bridges. Kwon and Frangopol (2010) suggested a target reliability index of 1.65 that corresponds to the survival probability of 95 percent for fatigue assessment. However, other studies, such as Moses et al. (1987), suggested a target value of 2.0 for redundant members and 3.0 for nonredundant members. Most tension members or components subjected to fatigue loading are classified as FCMs whose failure will result in the collapse of the whole system. Thus, they should be considered the components with no redundancy. Therefore, the target reliability index for the

corrosion fatigue limit state in this research was set at 3.5, aligning with the target reliability indexes for strength limit states in AASHTO.

Nowak (1999) and (Kulicki, 2015) proposed an empirical model to estimate the load factors:

$$\gamma_i = \lambda_i(1 + K \times CoV_i) \tag{7.19}$$

where γ_i refers to the load factor for ith load; λ_i denotes the bias factor for load; K is a constant depending on target reliability limit; and $\mathrm{CoV_i}$ is the coefficient of variation of the ith load. Nowak (1999) recommended K = 2 to 2.5 when the target reliability index of the strength limit state of a structural member is selected as 3.5. The load factor for the corrosion fatigue limit state is summarized in Table 7-4. The recommended load factors are 1.25 for a dead load (except asphalt overlay, which is 1.5) and 1.50–1.70 for a fatigue live load and impact load.

Table 7-4. Load Factors for Corrosion Fatigue Limit State (Nowak, 1999; Kulicki, 2015).

Load	**Notation**	**Bias Factor λ_i**	**CoV V_i**	**Load Factor γ_i**
Deck Slab	$D1$	1.03	0.08	1.25
Wearing Surface	$D2$	1.00	0.25	1.50
Barriers	$D3$	1.05	0.10	1.25
Live Load and Impact Load	$F + IM$	1.10–1.20	0.18	1.50–1.75

7.2.4 Case Studies

Traditional fatigue design guidelines primarily focus on the applied cyclic stress and do not adequately account for the detrimental influence of corrosion. As a result, when the environment becomes corrosive, structures designed by using these specifications may have a shorter service life. The lack of explicit consideration for corrosion-induced fatigue effects can lead to the failure of steel bridges and increase safety concerns and maintenance costs. To ensure the long-term structural durability of weathering steel components, it is essential to factor in the corrosion effect in the design process and modify guidelines to account for the combined influence of corrosion and fatigue.

In all the following case studies, average daily traffic (ADT) is considered 20,000 vehicles per day, as stated in AASHTO LRFD C3.6.4.2. According to research findings, the typical daily traffic comprising cars and trucks is constrained to approximately 20,000 vehicles per lane per day

in regular circumstances. This limitation in traffic volume is a crucial factor to bear in mind when making estimations for the ADT volume.

Case 1 and Case 2 were developed based on guidelines recommended in the 5th edition of AASHTO's *LRFD Bridge Design Specifications* (AASHTO, 2010). However, other cases were developed in accordance with the 9th edition of AASHTO's *LRFD Bridge Design Specifications* (AASHTO, 2020). The recommended load factors assumed 1.25 for a dead load (except surface overlay, which was 1.5). The fatigue live load factors varied from 1.50 to 1.70: 1.50 was selected to calculate the upper bound of service life, 1.60 corresponded to the mean, and 1.70 was assumed for the lower bound of service life.

7.2.4.1 Simple-Span Noncomposite Rolled Steel Beam Bridge

A 35 ft simple-span noncomposite rolled steel beam bridge was designed for an HL-93 live load, as shown in Figure 7.9. The roadway width curb to curb was assumed to be 44 ft, and the compression strength of the concrete deck was 4 ksi. Uncoated AASHTO M270/M 270 (ASTM A709/A709M) Grade 50W steel was considered in this example and classified as Category B. The bridge was assumed to be part of a rural interstate highway with 20,000 vehicles per lane per day (Barker & Puckett, 2021). The maximum unfactored moment and shear for an interior and exterior girder are given in Table 7-5.

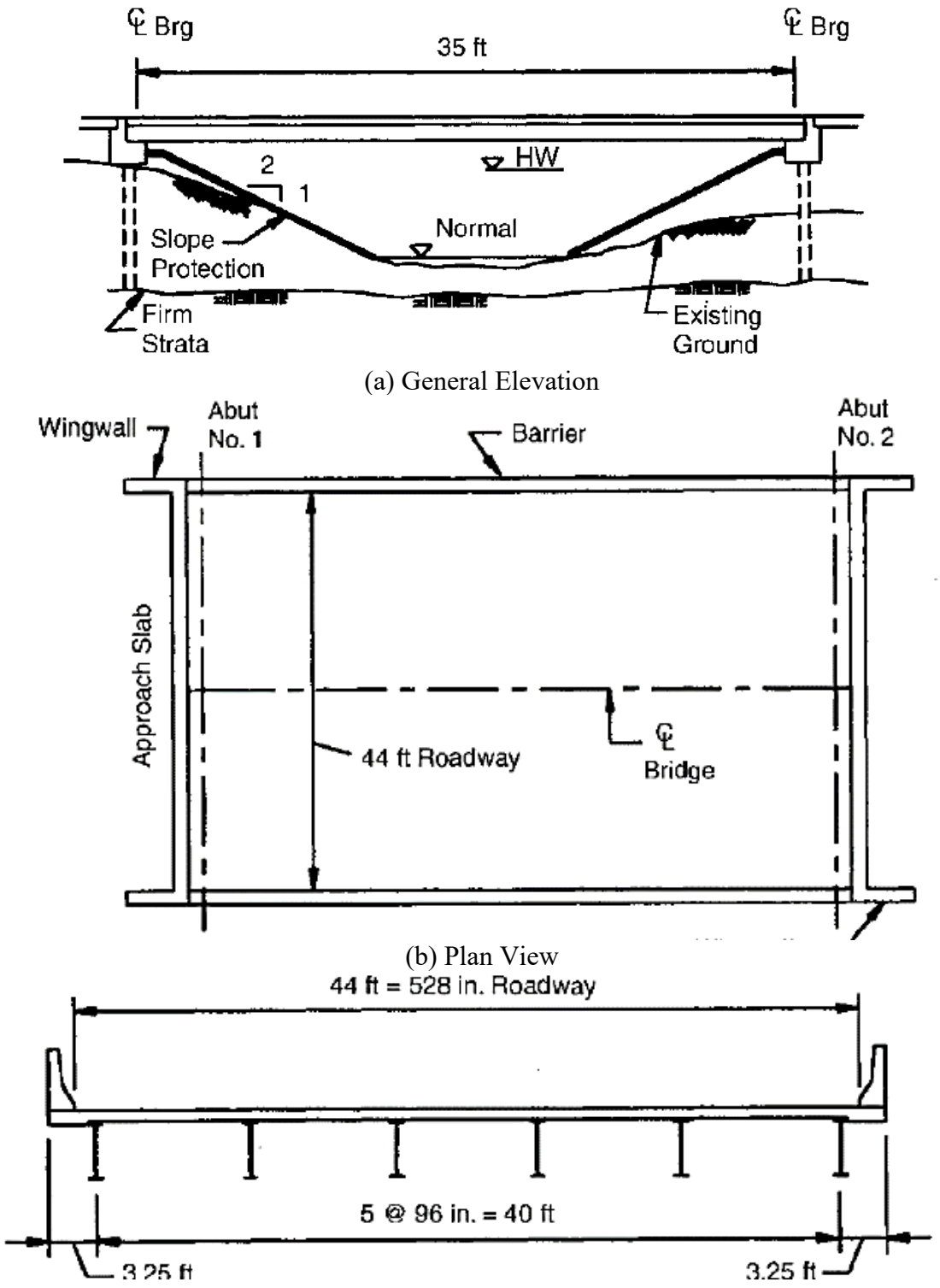


Figure 7.9. Noncomposite Steel Girder Layout (Barker & Puckett, 2021).

Table 7-5. Maximum Unfactored Moments and Shears (Barker & Puckett, 2021).

Load Type	Exterior Girder			Interior Girder		
	w (kip/ft)	Moment (kips ft)	Shear (kips)	w (kips/ft)	Moment (kips ft)	Shear (kips)
Deck Slab (D1)	1.33	203.7	23.3	0.90	137.8	15.75
Bituminous Paving (D2)	0.21	32.2	3.68	0.28	42.9	4.90
Live Load + Impact Load (LL+IM)	N/A	460.0	61.1	N/A	455.7	66.0
Fatigue + Impact Load (F)	N/A	211.3	26.5	N/A	161.4	24.0

Note:
N/A: Not Applicable

Barker and Puckett (2021) proposed a W30 × 90 section with 8.75 ft spacing lateral bracing to ensure the section was compact. The ADT was assumed to be 20,000. The fraction of trucks in traffic on the rural interstate highway bridge is 0.20, as shown in Table 7-6. And the fraction of truck traffic in a single lane is 0.85 for this 2-lane steel bridge based on Table 7-7.

Table 7-6. Fraction of Trucks in Traffic (AASHTO, 2020).

Class of Highway	Fraction of Trucks in Traffic
Rural Interstate	0.20
Urban Interstate	0.15
Other Rural	0.15
Other Urban	0.10

Table 7-7. Fraction of Single-Lane Truck Traffic (AASHTO, 2020).

Number of Lanes Available to Trucks	p
1	1.00
2	0.85
3 or more	0.80

The main cyclic load on the steel bridge is induced by the passage of vehicles, particularly heavy trucks. An HS-20 truck with axles spaced 14 ft apart followed by a tandem axle group of two 10-ton axles spaced 4 ft apart was used in this example.

The single-lane annual average daily truck traffic $ADTT_{SL}$ can be defined as:

$$ADTT_{SL} = p \times ADTT \tag{7.20}$$

where $ADTT$ is the number of trucks per day in one direction averaged over the design life and p is the fraction of traffic in a single lane. The average daily truck traffic is calculated according to AASHTO (2020):

$$ADTT = 0.20 \times ADT = 8000 \tag{7.21}$$

Thus, the average daily truck traffic in one single lane is:

$$ADTT_{SL} = p \times ADTT = 6800 \tag{7.22}$$

Since the base metal is unpainted weathering steel, the fatigue category is classified as B, which corresponds to stress threshold 16 ksi, as shown in Table 7-1.

The dynamic load allowance for fatigue is 15 percent of the live load. The load modifiers (η) are 1.0, and the section modulus (S) of W30 × 90 is 245 in^3. The maximum fatigue moment of the Fatigue-I limit state can be calculated as follows:

$$M_{Fatigue\,\mathrm{I}} = \eta\,[1.5(F)] = 317 \text{ kips ft} \tag{7.23}$$

and the load stress range is:

$$\Delta\sigma = \frac{M_{\text{Fatigue-I}}}{S} = 15.5 \text{ ksi} \leq 16 \text{ ksi} \tag{7.24}$$

Based on the AASHTO LRFD specifications—without considering the effects of corrosion—this bridge design meets infinite fatigue life and there is no need to check the finite fatigue life. However, the cyclic loading experienced by weathering steel in corrosive environments causes crack initiation and propagation, ultimately decreasing the fatigue resistance of the material. The modified SWT model was used to account for the mean stress and corrosion effect. The maximum tensile stress (σ_{max}) resulting from both dead and fatigue live loads was calculated by considering the ultimate limit state of the structure.

In this case, the maximum negative fatigue moment is 0. The ultimate moment and maximum tensile stress of this bridge are:

$$M_{max} = 1.25\,D_1 + 1.5\,D_2 + 1.6M_F^+ \tag{7.25}$$

and:

$$\sigma_{max} = \frac{M_{max}}{S} = 1.25\sigma_{D1} + 1.5\sigma_{D2} + 1.6\sigma_F^+ = 31.4\text{ksi} \tag{7.26}$$

The fatigue moment due to fatigue life and impact load is assumed:

$$\mathrm{M_{Fatigue}} = 1.6F \tag{7.27}$$

and the load stress amplitude can be calculated as:

$$\sigma_a = \frac{M_{\mathrm{Fatigue}}}{2 \times S} = 8.3 \text{ ksi} \tag{7.28}$$

Therefore, the corresponding fatigue damage indicator is:

$$\mathrm{P}_{SWT} = \sqrt{\sigma_{max}\sigma_a} = 16.15 \text{ ksi} \tag{7.29}$$

and the yearly number of fatigue cycles is calculated as:

$$\begin{aligned} N_{year} &= 365 \times n \times ADTT_{SL} \\ &= 365 \times 2 \times 6800 \\ &= 4.964 \times 10^7 \end{aligned} \tag{7.30}$$

The number of stress range cycles per truck passage (n) is taken from Table 7-8; it is 2.0 for the simple-span girders with a length shorter than 40.0 ft.

Table 7-8. Cycles Per Truck Passage for Simple Span and Continuous Girders (AASHTO, 2020).

Longitudinal Members	**Span Length**	
	>40.0 ft	<40.0 ft
Simple-Span Girders	1.0	2.0
Continuous Girders Near Interior Support	1.5	2.0
Continuous Girders Elsewhere	1.0	2.0

The upper bound, mean, and lower bound of service life of weathering steel in different environments subjected to 4.964×10^7 average yearly truck traffic per single lane is shown in Figure 7.10.

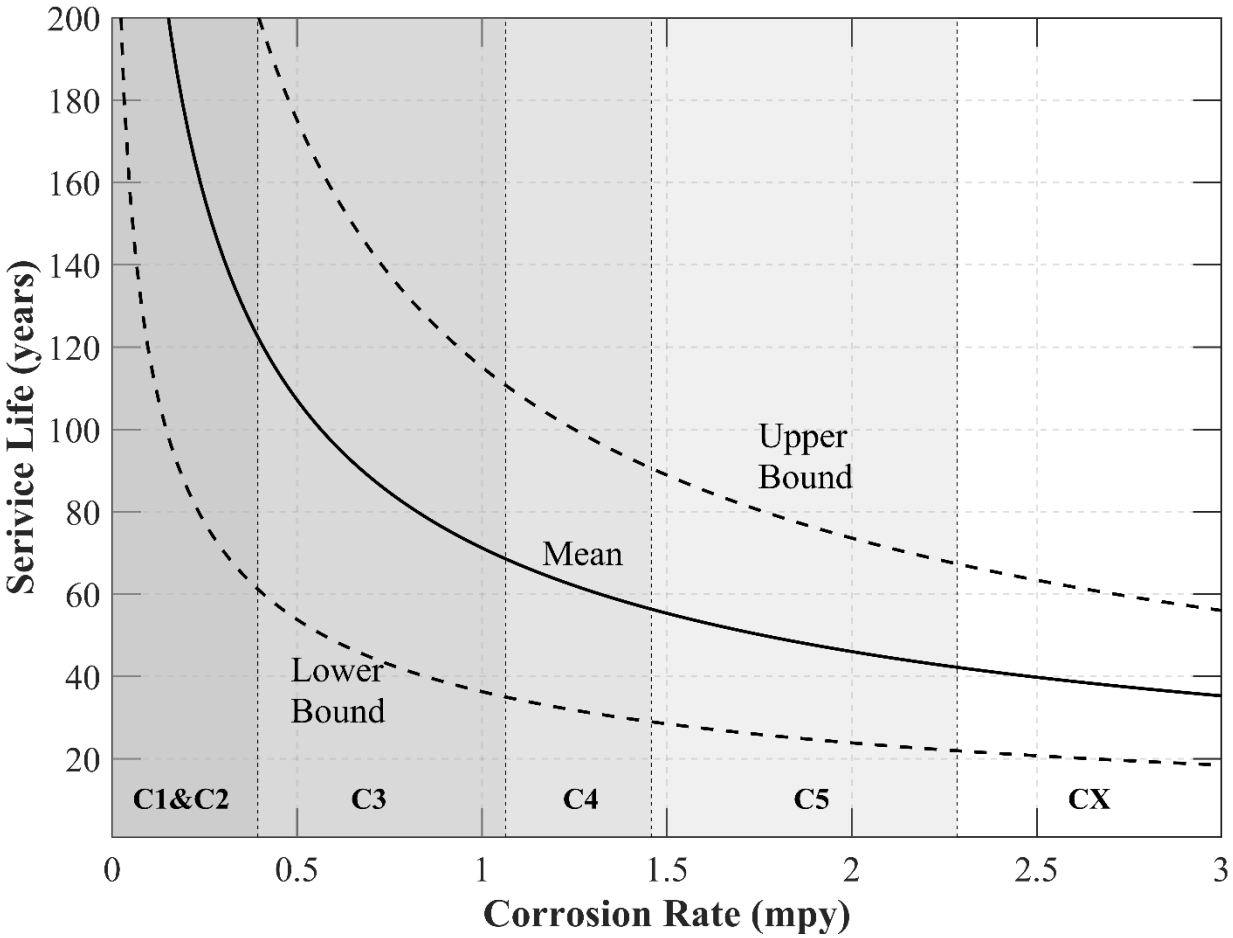


Figure 7.10. Service Life of Simple-Span Noncomposite Rolled Steel Beam Bridge in Different Corrosion Regions.

In C1 and C2 regions, where the corrosion rate is assumed to be relatively low, the average predicted average service life was 127 years, thereby exceeding the regular bridge lifespan. It also aligns closely with AASHTO infinite service life results, suggesting weathering steel structures in mildly corrosive environments have a comparable lifespan to what is traditionally expected. However, in highly corrosive environments such as highly polluted industry areas and coastal areas, the predicted service life significantly decreases in C5 and CX regions, falling significantly below the expected 75-year lifespan.

In designing noncomposite structures, the load is primarily carried by the steel girders without the active participation of the concrete deck, which results in uneven load distribution that leads to localized high stresses and increased fatigue damage. Noncomposite designs typically lack redundancy, meaning that failure or damage to one component can have a more significant impact

on the overall bridge performance. This flaw reduces the capability of the bridge to withstand fatigue-induced cracking and can lead to a shorter service life (Hurlebaus et al., 2018).

7.2.4.2 Simple-Span Composite Rolled Steel Beam Bridge

A simple-span composite rolled steel beam bridge with a 35 ft span was designed to accommodate an HL-93 live load, as illustrated in Figure 7.11. The curb-to-curb roadway width was assumed to be 44 ft. The concrete deck had a compression strength of 4 ksi. Uncoated AASHTO M270/M 270 (ASTM A709/A709M) Grade 50W steel was used, and the composite section had a haunch of 1 in., with a 7.5 in. net slab thickness and 96 in. effective width. Barker and Puckett (2021) proposed a W24 × 68 section with 105 in. spacing lateral bracing, as seen in Figure 7.11.

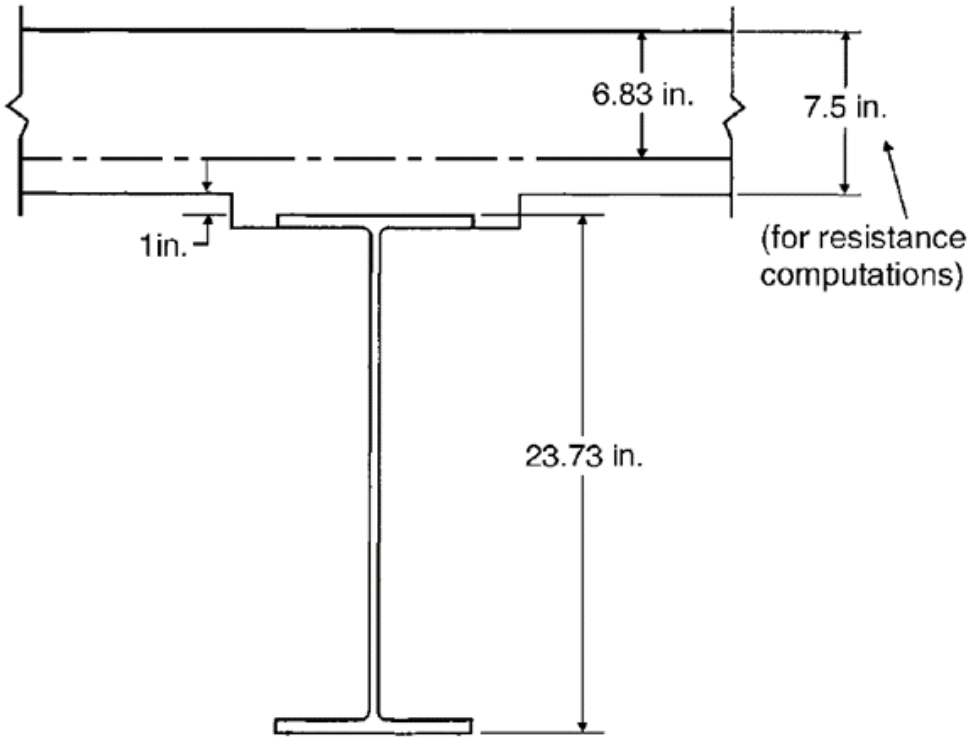


Figure 7.11. Composite Steel Section (Barker & Puckett, 2021).

Short-term and long-term composite section properties accounting for the effect of concrete creep are given in Table 7-9. The bridge was assumed to be a component of a rural interstate highway with a traffic volume of 20,000 vehicles per lane per day and meets the

required flexure and shear resistance, constructability, strength, and fatigue limit state recommended in standards (Barker & Puckett, 2021).

Table 7-9. Short-Term and Long-Term Composite Section Properties at Mid-span (Barker & Puckett, 2021).

Section Properties	Unit	Long-Term Value	Short-Term Value
Moment of Inertia I	in^4	5292	6785
Distance from Neutral Axis to Bottom Fiber c	in.	21.8	21.8
Distance from Neutral axis to Top Fiber y	in.	10.4	10.4
Composite Section Modulus (Bottom) S_{cb}	in^3	243	266
Composite Section Modulus (Top) S_{ct}	in^3	509	1001

The maximum unfactored moment and shear for an interior and exterior girder are provided in Table 7-10.

Table 7-10. Maximum Unfactored Moments and Shears (Barker & Puckett, 2021).

Load Type	Exterior Girder			Interior Girder		
	w (kip/ft)	Moment (kips ft)	Shear (kips)	w (kips/ft)	Moment (kips ft)	Shear (kips)
Deck Slab (D_1)	0.86	131.7	15.1	0.93	142.4	16.3
Bituminous Paving (D_2)	0.25	38.3	4.4	0.28	42.9	4.90
Barriers (D_3)	0.11	16.8	1.9	0.11	16.8	1.9
Live Load +Impact Load (LL+IM)	N/A	467.4	61.0	N/A	458.8	66.1
Fatigue +Impact Load (Fatigue+IM)	N/A	211.3	26.5	N/A	161.4	24.0

The average daily truck traffic per single lane $ADTT_{SL}$ is the same as the first case study. The maximum fatigue moment of the Fatigue-I limit state is:

$$M_{\text{Fatigue}-I} = \eta\left[1.50\left(L_{\text{Fatigue}} + IM\right)\right] = 317 \text{ kips ft} \tag{7.31}$$

The load stress range is smaller than the stress threshold:

$$\Delta\sigma = \frac{M_{\text{Fatigue}-I}}{S_{cb}} = \frac{317\times12}{266} = 14.3 \text{ ksi} \leq 16 \text{ ksi} \tag{7.32}$$

The design meets the AASHTO fatigue requirement and can achieve infinite fatigue life. In this case, the maximum negative fatigue moment is 0. The medium ultimate moment and maximum tensile stress of this bridge are:

$$M_{max} = 1.25\ D_1 + 1.5\ D_2 + 1.6M_F^+ \tag{7.33}$$

and:

$$\sigma_{max} = \frac{M_{max}}{S} = 1.25\sigma_{D1} + 1.5\sigma_{D2} + 1.6\sigma_F^+ = \ 31.22 \text{ ksi} \tag{7.34}$$

The medium fatigue moment due to the fatigue live and impact load is computed from:

$$\mathrm{M_{Fatigue}} = 1.6F \tag{7.35}$$

The load stress amplitude is:

$$\sigma_a = \frac{\mathrm{M_{Fatigue}}}{2\times S} = \ 7.62 \text{ ksi} \tag{7.36}$$

Then, the corresponding fatigue damage indicator is:

$$\mathrm{P}_{SWT} = \sqrt{\sigma_{max}\sigma_a} = 15.42 \text{ ksi} \tag{7.37}$$

The service life of weathering steel in different environments subjected to 4.964×10^7 yearly stress cycles per truck passage is shown in Figure 7.12.

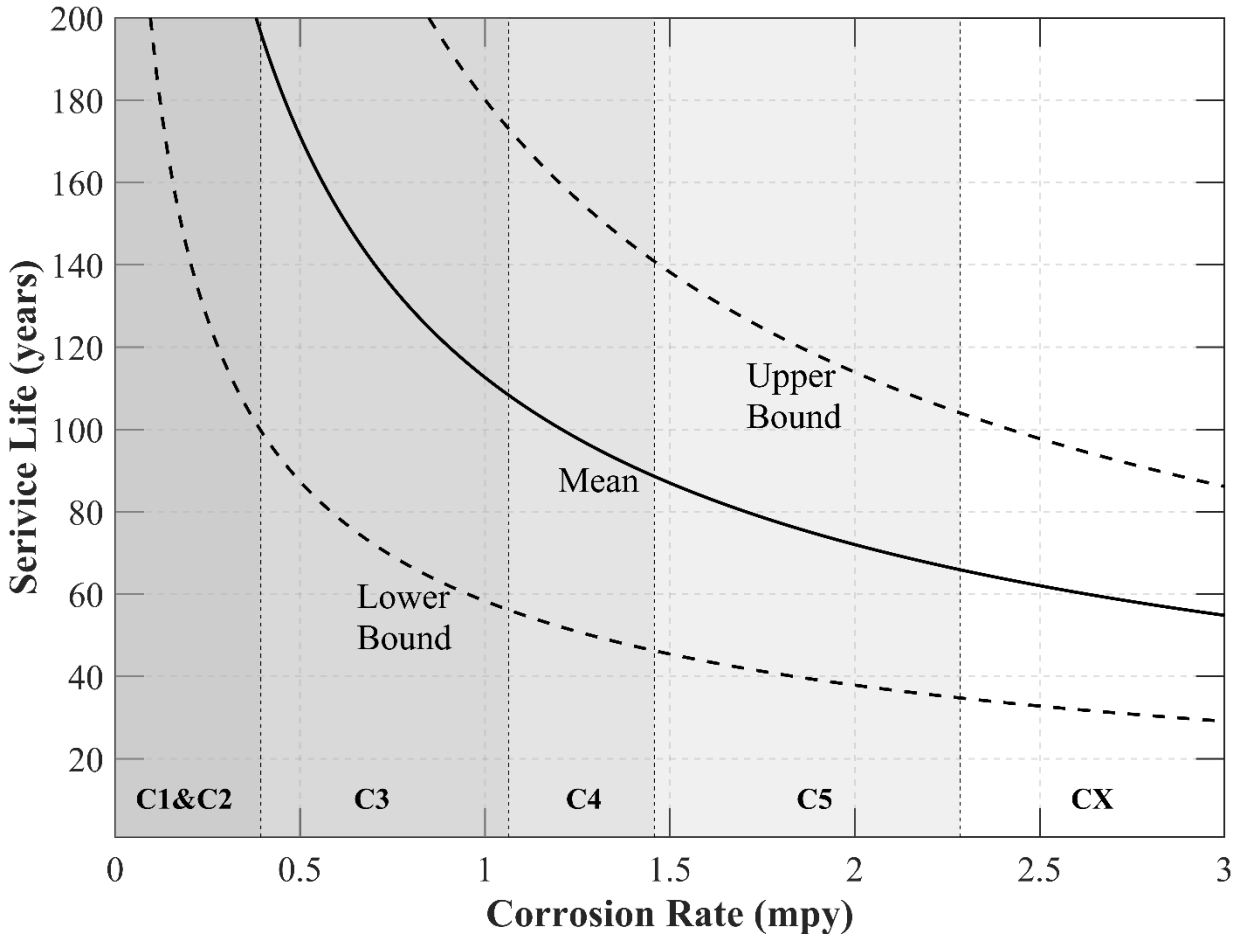


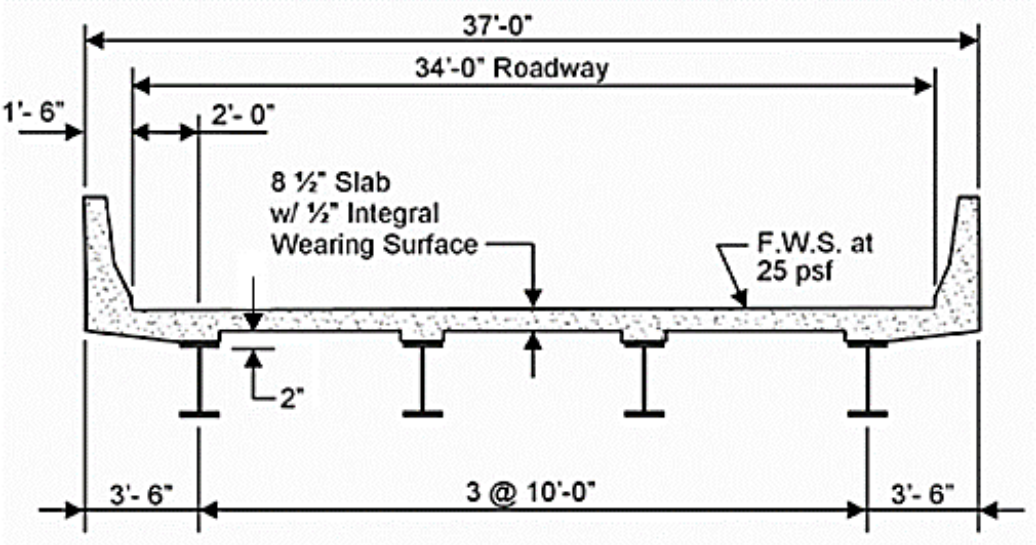
Figure 7.12. Service Life of Simple-Span Composite Rolled Steel Beam Bridge in Different Corrosion Regions.

This simple-span composite steel bridge in mildly corrosive environments can achieve remarkable service life comparable to traditional expectations. However, in regions characterized by high corrosion intensity, the service life diminishes significantly, thus emphasizing the need for careful consideration of corrosion protection measures in such areas. Additionally, the composite section design mitigates the high-stress concentrations at critical sections, increasing service life fatigue in comparison to the first noncomposite design.

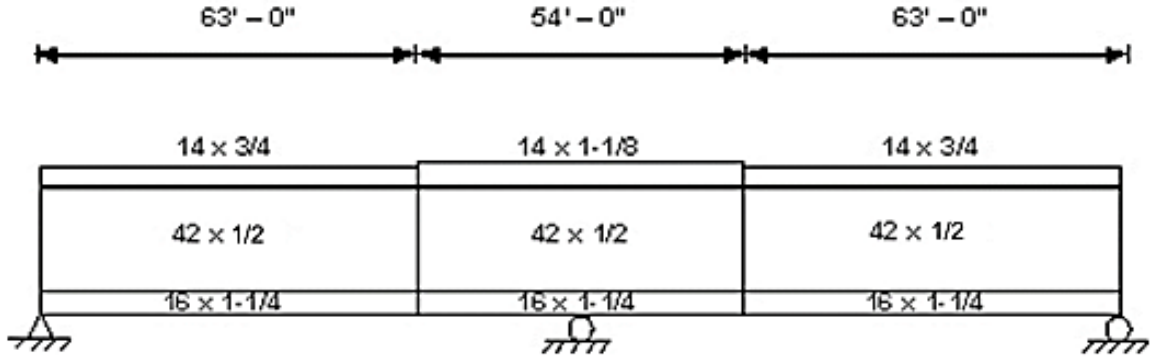
Additionally, the fatigue-induced fracture is more critical in simple-span bridges due to the lack of redundancy in their structural design. Redundancy refers to the presence of multiple load paths or alternative load-carrying elements within a structure. The absence of alternative load paths or additional load-carrying elements makes these bridges more vulnerable to the rapid propagation of fatigue cracks and increases the risk of catastrophic failure (Hurlebaus et al., 2018).

7.2.4.3 Two-Span Continuous Straight Composite Steel I-Girder Bridge

Another example is a continuous steel I-girder bridge with spans of 90 ft and intended to withstand an HL-93 live load, as illustrated in Figure 7.13. The roadway width was assumed to be 37 ft curb to curb, thereby accommodating an interstate highway. The concrete strength of the deck was assumed to be 4 ksi, and reinforcing bars with nominal Grade 60 and ASTM A709 Grade 50W steel with a yield strength of 50 ksi were considered for the steel girders. As shown in Figure 7.13(b), section transitions were implemented at 30 percent of the span length (27 ft) from the interior pier. A positive bending moment was considered for the middle girder 63 ft away from the abutments, while a negative bending moment was used for the girder near the interior pier (Barth, 2022).



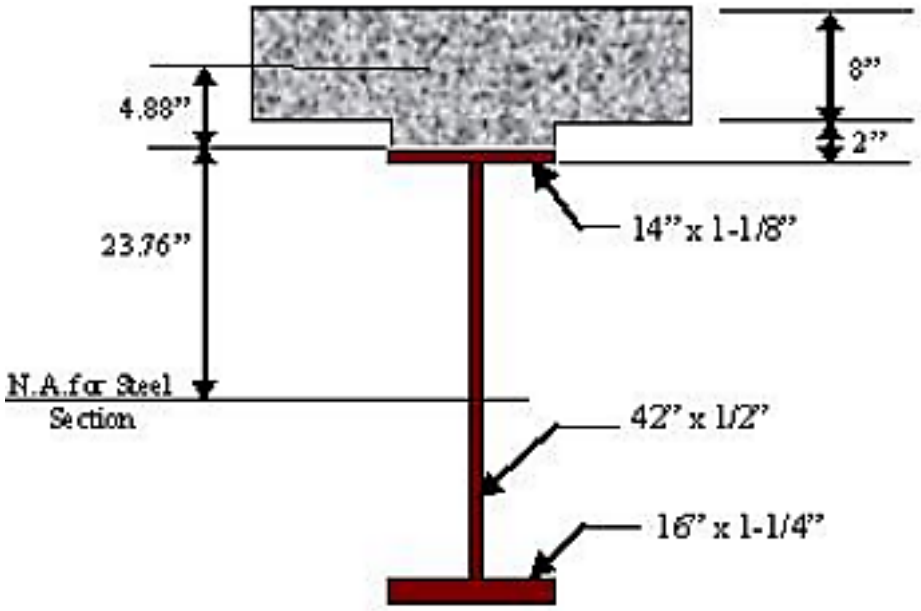
(a) Cross Section



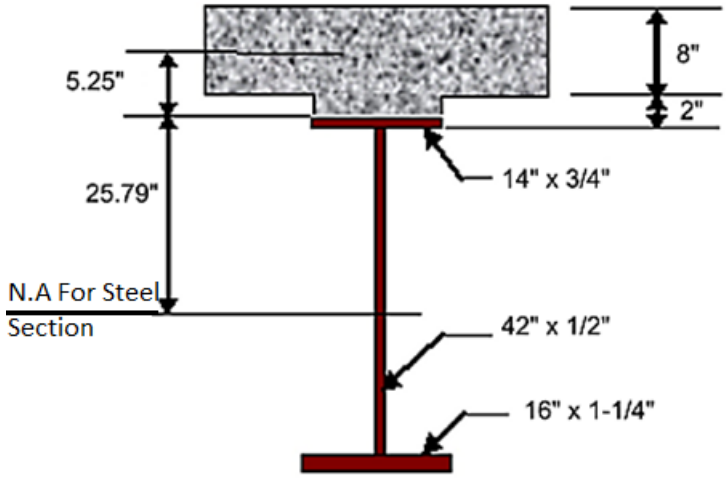
(b) Sketch of the Girder

Figure 7.13. Two-Span Composite Steel I-Girder Bridge Sketches (Barth, 2022).

In the negative moment region, the cross-sectional web was 0.5 × 42 in., and flanges were 1.125 × 14 in. and 1.25 × 16 in. The top layer of longitudinal reinforcement was #6 bars spaced at 6 in. intervals, and the bottom layer of reinforcement was #5 bars spaced at 8 in. intervals. Additionally, for transverse reinforcement, #5 bars spaced at 12 in. were used for the top and bottom layers. The concrete cover on the top was assumed to be 2 in. and was 1 in. on the bottom. The effective flange width was 120 in. for the interior girder and 102 in. for the exterior girder. The composite section had a haunch of 2 in., 8 in. net slab thickness, and 96 in. effective width, as shown in Figure 7.14(a). In the positive moment region, a selected steel section had a 0.625 × 12 in. top flange, a 0.4375 × 60 in. web, and a 1×16 in. bottom flange, as shown in Figure 7.14(b). The effective flange width was 120 in. and 102 in. for the interior and exterior girder, separately.



(a) Composite Section at Negative Moment Region



(b) Composite Section at Positive Moment Region

Figure 7.14. Multiple-Span Composite Steel Section (Barth, 2022).

The composite section properties in the negative region and in the positive moment region are given in Table 7-11 and Table 7-12. After calculating the short-term composite sections, the modular ratio was assumed to be 8. When calculating the long-term composite section, the reduction in strength due to creep effects was taken into consideration.

Table 7-11. Composite Section Properties at Negative Moment Region (Barth, 2022).

Section Properties	Unit	Long-Term Composite	Short-Term Composite
Moment of Inertia I	in^4	37222	50027
Distance from Neutral Axis to Bottom Fiber c	in.	31.35	39.02
Distance from Neutral Axis to Top Fiber y	in.	13.03	5.36
Composite Section Modulus (Bottom) S_{cb}	in^3	1187	1282
Composite Section Modulus (Top) S_{ct}	in^3	2857	9333
Steel Section Modulus (Bottom) S_{sb}	in^3	951.3	951.3
Steel Section Modulus (Top) S_{st}	in^3	825.6	825.6

Table 7-12. Composite Section Properties at Positive Moment Region (Barth, 2022).

Section Properties	Unit	Long-Term Value	Short-Term Value
Moment of Inertia I	in^4	36315	49905
Distance from Neutral Axis to Bottom Fiber c	in.	30.55	38.84
Distance from Neutral Axis to Top Fiber y	in.	13.45	5.16
Composite Section Modulus (Bottom) S_{cb}	in^3	1189	1285
Composite Section Modulus (Top) S_{ct}	in^3	2700	9672
Steel Section Modulus (Bottom) S_{sb}	in^3	900.7	900.7
Steel Section Modulus (Top) S_{st}	in^3	635.9	635.9

The AASHTO fatigue category for a structure depends on the number of load cycles and the specific connection details. Because the transverse stiffener was fillet welded to the flange, it falls under Category C', in which the 75-year equivalent of the average daily truck traffic per single lane is 975 trucks per day. In this design example, the assumed $ADTT_{SL}$ was 6800 trucks per day, which exceeds the limit of 975 trucks per day. Consequently, it was essential to assess the details for infinite fatigue life using the Fatigue-I load combination.

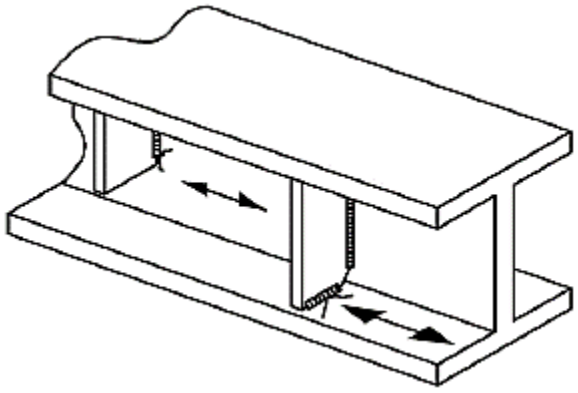


Figure 7.15. Welded Transverse Stiffener Connection (AASHTO, 2010).

In the negative moment region, the moment of inertia value of the exterior girder section is 50,027 in^4. The factored values for negative and positive moments, consisting of fatigue and the 15 percent dynamic load allowance, are 115 kips ft and –314 kips ft, respectively. The distance from the bottom of the top flange, where the weld is located, to the neural axis is 4.24 in. Consequently, the factored fatigue stress range can be expressed as follows:

$$\Delta\sigma = \eta \frac{[1.75(M_F^+ - M_F^-)]d_{\text{top of web}}}{I}$$

$$= \frac{1.75 \times (115 + |-314|) \times 12 \times 4.24}{50027}$$

$$= 0.77 \text{ ksi} \leq 12 \text{ ksi} \quad (7.38)$$

In the positive moment region, the factored maximum positive and negative moment at midspan due to fatigue and the 15 percent dynamic load allowance, are 588 kips ft and −157 kips ft, respectively. The distance from the top of bottom flange, where the weld is located, to the neural axis is 37.49 in. Thus, the factored stress range will be:

$$\Delta\sigma = \eta \frac{[1.75(M_F^+ - M_F^-)]d_{\text{bottom of web}}}{I}$$

$$= \frac{1.75 \times (588 + |-157|) \times 12 \times 37.59}{49905}$$

$$= 11.8 \text{ ksi} \leq 12 \text{ ksi} \quad (7.39)$$

The design meets the AASHTO fatigue requirements for infinite fatigue life. In the negative moment region, the medium maximum tensile stress is:

$$\sigma_{max} = -1.25\frac{M_{D_1}}{S_{\text{st}}} - 1.5\frac{M_{D_2}}{S_{\text{ct}}} - 1.25\frac{M_{D_3}}{S_{\text{ct}}} - 1.6\frac{(M_F^-)}{S_{\text{ct}}}$$

$$= -1.25\sigma_{D1} - 1.5\sigma_{D2} - 1.25\sigma_{D3} - 1.6\sigma_F^-$$

$$= 33.36 \text{ ksi} \quad (7.40)$$

In this example, a fillet weld joint was assumed, and therefore the steel is typically subjected to higher stress levels due to geometric irregularities and abrupt changes in the cross-sectional area. The stress concentration (k_w) needed to be considered in the calculation. The load stress amplitude is:

$$\sigma_a = 1.6\ \frac{(M_F^+ - M_F^-)d_{\text{top of web}}}{2\,I} = 0.35 \text{ ksi} \tag{7.41}$$

Therefore, the damage indicator P_{SWT}, considering the stress concentration at the fillet weld, is calculated from:

$$PSWT = k_w\sqrt{\sigma_{max}\sigma_a} = 1.5\sqrt{33.36 \times 0.35} = 5.14 \text{ ksi} \tag{7.42}$$

In positive moment region, the fatigue moment due to fatigue live and impact load is:

$$\sigma_{max} = 1.25\frac{M_{D_1}}{S_{\text{sb}}} + 1.5\frac{M_{D_2}}{S_{\text{cb}}} + 1.25\frac{M_{D_3}}{S_{\text{cb}}} + 1.6\frac{M_F^+}{S_{\text{cb}}}$$

$$= 24.75 \text{ ksi} \tag{7.43}$$

and the load stress amplitude, considering stress concentration due to the weld joint, is:

$$\sigma_a = 1.6\ \frac{(M_F^+ - M_F^-)d_{bottom\ of\ web}}{2\,I} = 5.39 \text{ ksi} \tag{7.44}$$

The damage indicator P_{SWT}, considering the stress concentration at the fillet weld, is calculated as:

$$P_{SWT} = k_w\sqrt{\sigma_{max}\sigma_a} = 1.5 \times \sqrt{24.75 \times 5.39} = 17.35 \text{ ksi} \tag{7.45}$$

The transverse welding at the bottom of the web on the exterior girder was the critical section. The number of stress range cycles per truck passage (n) is 1 for continuous bridges with less than 40 ft span length. The yearly number of fatigue cycles was calculated as:

$$N_{year} = 365 \times n \times ADTT_{SL}$$

$$= 365 \times 1 \times 6800$$

$$= 2.45 \times 10^7 \tag{7.46}$$

The service life of weathering steel in different environments subjected to 2.48×10^7 stress cycles per year is shown in Figure 7.16.

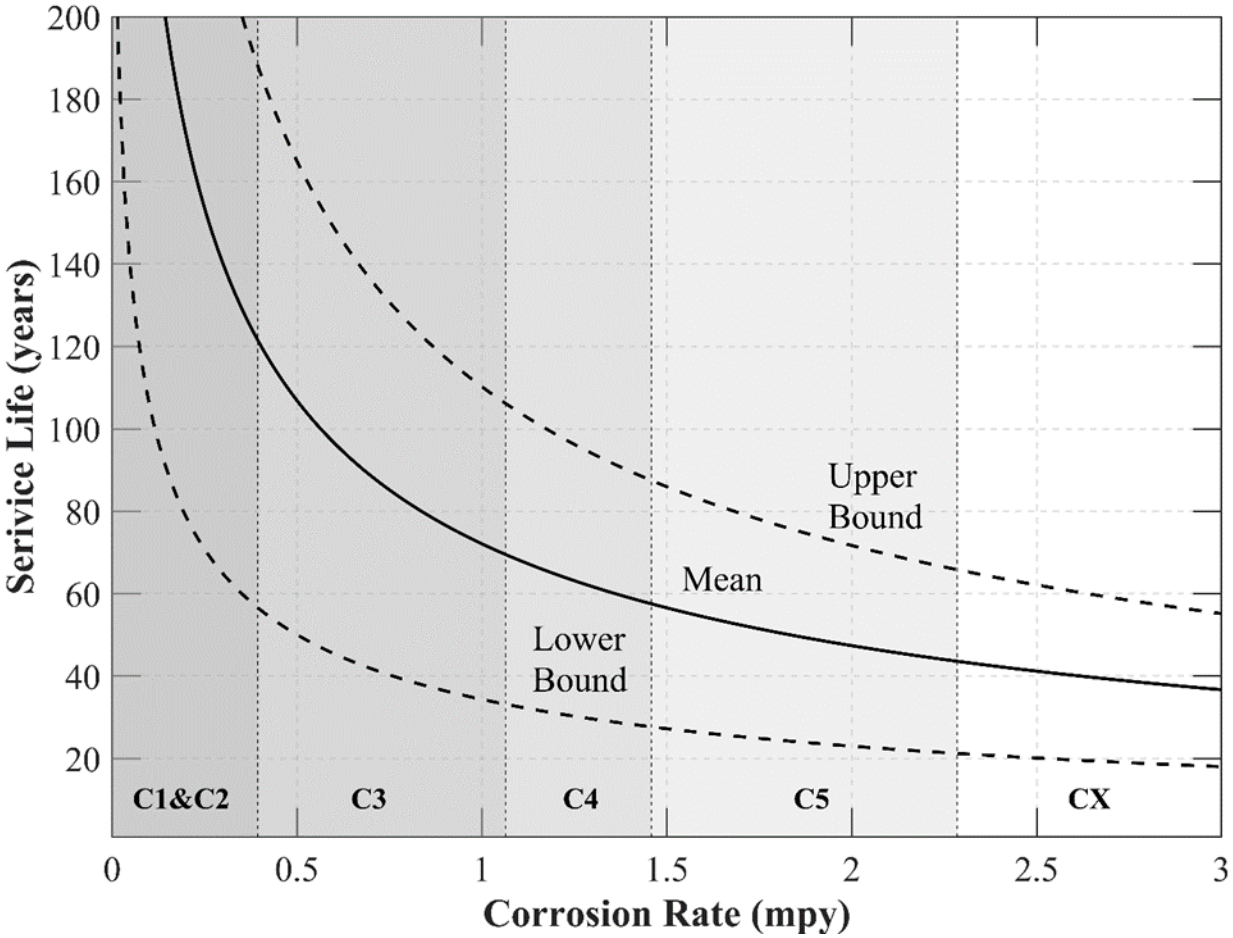


Figure 7.16. Service Life of Two-Span Continuous Straight Composite Steel I-Girder Bridge in Different Corrosion Regions.

In mildly corrosive environments, a simple-span composite steel bridge exhibits an average fatigue service life above 100 years. However, in regions CX, the service life of the bridge diminishes significantly. Although the stress range of this two-span continuous bridge is relatively lower than previous case studies, the presence of the transverse fillet weld results in the decrease of fatigue classification to Category C'. Additionally, in this example, as shown in Table 7-8, for the main fatigue critical member of continuous-span bridges not located near interior supports, the value of cycles per truck passage is 1.0 for spans above 40 ft. However, for the main longitudinal members in simple-span bridges, the design value is set at 1.0 for spans exceeding 40 ft (12 m) and 2.0 for shorter spans. The value of cycles per truck passage significantly affects the fatigue life (Schilling, 1984).

7.2.4.4 Three-Span Continuous Horizontally Curved Composite Steel I-Girder Bridge

This design pertains to a continuous curved, steel I-girder bridge comprising spans of 160, 210, and 160 ft designed to withstand an HL-93 live load. The bridge had a roadway width of 40–46 ft, measured from curb to curb, to accommodate an interstate highway. The maximum arc length of 214.95 ft occurred at the center span of the outside girder, G4. The construction materials included 4 ksi compression strength concrete, nominal Grade 60 reinforcing bars, and ASTM A709 Grade 50W steel with a yield strength of 50 ksi. The bridge cross section consisted of four I-girders spaced 11 ft apart in the center. Additionally, there were 3.75 ft deck overhangs, and the cross slope was assumed to be 5 percent with an angle of 2.862°, as presented in Figure 7.17(a). The girder elevation of the continuous curved composite is given in Figure 7.17(b). Each end span had a field splice, while the center span had two, resulting in a total of 20 sections for the entire bridge, with five sections in each girder line (Rivera & Chavel, 2022).

The critical section of this curved bridge was located on the exterior girder G4, as shown in Figure 7.18, because a significant fraction of loads will be transmitted to the outer, convex side of the bridge (Linzell et al., 2004). Lateral bending forces created by the horizontal curvature will push the bridge toward the outer side of the curve, causing the girder to experience the maximum bending moment. The eccentricity between the bridge deck centerline and the curved path will create torsional forces, twisting the bridge about its longitudinal axis and causing torsional moment on the exterior girder. The presence of deck overhangs also will introduce an eccentric load, with the G4 girder bearing the highest load intensity because of its proximity to the overhang extension. The wind load effect was also considered in the calculation.

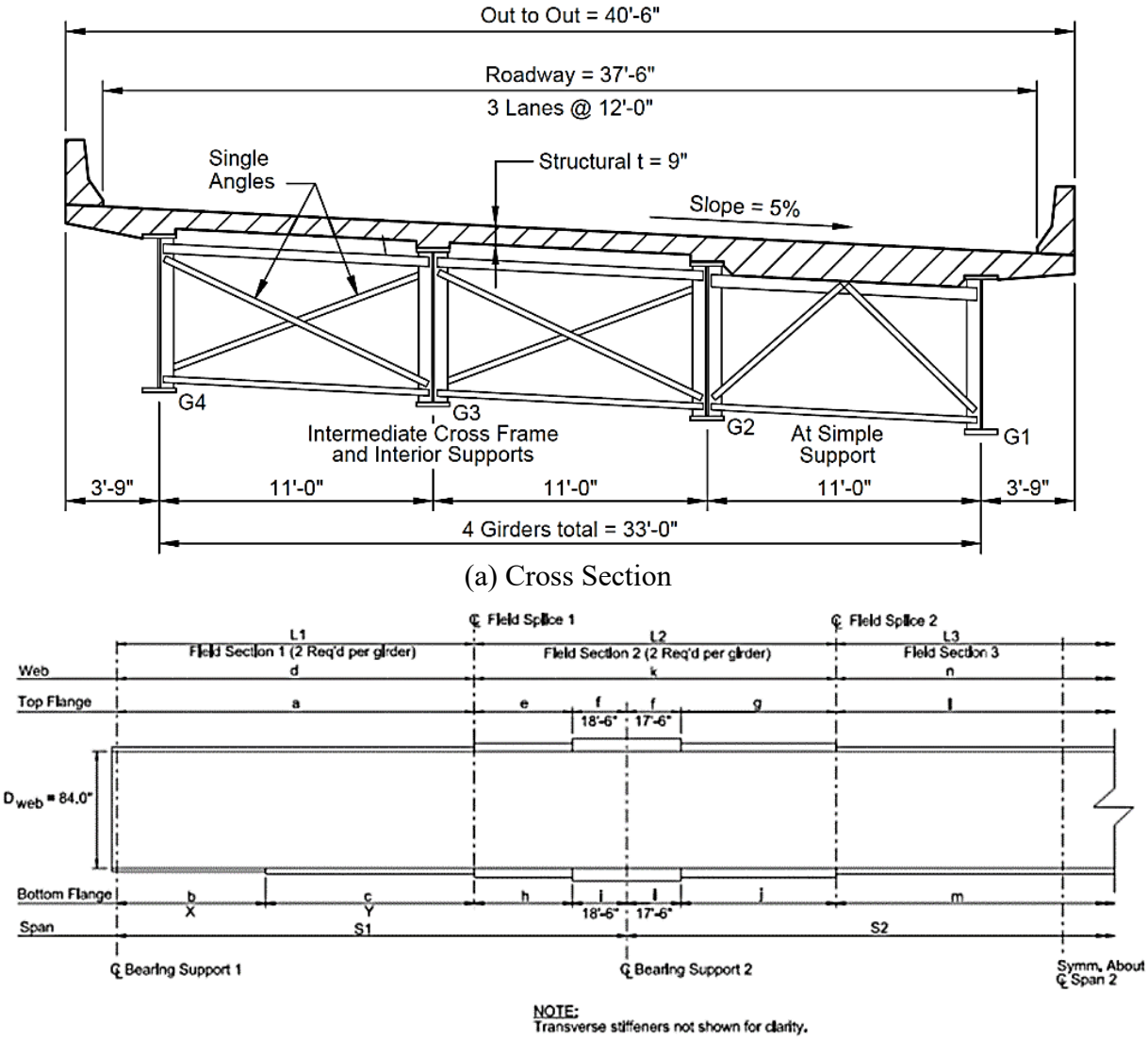
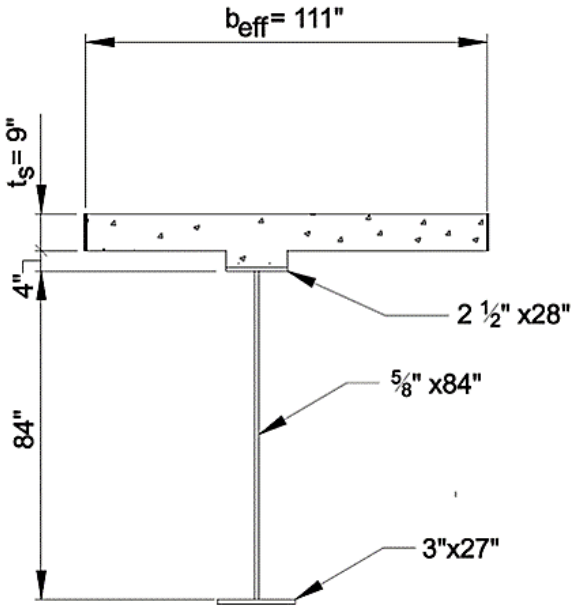


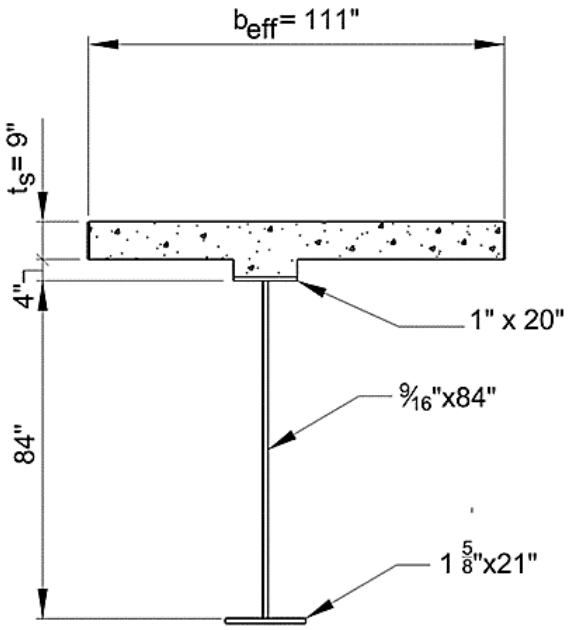
Figure 7.17. Three-Span Continuous Horizontally Curved Composite Steel I-girder Bridges Sketches (Rivera & Chavel, 2022).

In the negative moment region, the cross section of the bridge was assumed to be a 0.625 × 84 in. web, a 2.5 × 28 in. top flange, and 3 × 27 in. bottom flanges. The top layer of longitudinal reinforcement consisted of #6 bars spaced at 6 in. intervals, while the bottom layer consisted of #4 rebars spaced at 6 in. intervals. The composite section included a 4 in. haunch, 9 in. net slab thickness, and 111 in. effective width, as depicted in Figure 7.18(a). In the positive moment region, a steel section was employed consisting of a 1 × 20 in. top flange, a 0.5625 × 84 in. web, and a 1.625 × 21 in. bottom flange, as illustrated in Figure 7.18(b). The effective flange width was 111

in. The top flange was assumed to be smaller because the concrete provides additional strength. Table 7-13 provides the section properties at negative moment.



(a) Composite Section at Negative Moment Region



(b) Composite Section at Positive Moment Region

Figure 7.18. Critical Composite Steel Section at G4 (Rivera & Chavel, 2022).

Table 7-13. Composite Section Properties at Negative Moment Region (Rivera & Chavel, 2022).

Section Properties	Unit	Long-Term Composite	Short-Term Composite
Moment of Inertia I	in^4	415,746	539,403
Distance from Neutral Axis to Bottom Fiber c	in.	51.98	63.4
Distance from Neutral Axis to Top Fiber y	in.	37.52	26.1
Composite Section Modulus (Bottom) S_b	in^3	7377	8508
Composite Section Modulus (Top) S_t	in^3	1079	20,667
Steel Section Modulus (Bottom) S_{sb}	in^3	7377	7377
Steel Section Modulus (Top) S_{st}	in^3	6689	6689

The section properties in the positive moment region are reported in Table 7-14. When computing the short-term composite section, the modular ratio is assumed to be 7.56. In the calculation of the long-term composite section, the reduction in strength due to creep effects is taken into consideration.

Table 7-14. Composite Section Properties at Positive Moment Region (Rivera & Chavel, 2022).

Section Properties	Unit	Long-Term Value	Short-Term Value
Moment of Inertia I	in^4	221,188	306,979
Distance from Neutral Axis to Bottom Fiber c	in.	54.73	69.6
Distance from Neutral Axis to Top Fiber y	in.	31.90	17.0
Composite Section Modulus (Bottom) S_{cb}	in^3	4042	4412
Composite Section Modulus (Top) S_{ct}	in^3	6934	18,015
Steel Section Modulus (Bottom) S_{sb}	in^3	3266	3266
Steel Section Modulus (Top) S_{st}	in^3	2504	2504

The AASHTO fatigue category considers various factors, including load cycles and connection details such as the welding of interior cross-frames. In the specific case study under discussion, the transverse stiffener was fillet welded to the flange, and the interior cross-frame connection was welded too, which classifies it as Category C'. For this category, the fatigue threshold was defined as 12 ksi, and average daily truck traffic $ADTT_{SL}$ was assumed to be 6,800 trucks per day. However, the 75-year equivalent of ADT for a Category C' for infinite fatigue life was determined to be 975 trucks per day. Since the assumed $ADTT_{SL}$ exceeds this limit, it becomes necessary to evaluate the details for infinite fatigue life using the Fatigue-I load combination.

On the bottom flange at the positive moment region of G4, the unfactored negative and positive centrifugal force effects (accounting for fatigue), and the 15 percent dynamic load allowance were −603 kip-ft and 1,603 kip-ft, respectively. The distance from the bottom web $d_{\text{bot of web}}$, where the weld is located to the neutral axis was 67.96 in. Therefore, unfactored stress range due to vertical loads is:

$$\Delta\sigma_v = \frac{M_F^+ - M_F^-)d_{\text{bot of web}}}{I}$$

$$= \frac{(|-603| + 1603) \times 12 \times 67.96}{306{,}979}$$

$$= 5.86\ ksi \tag{7.47}$$

According to AASHTO (2020) Article C6.10.5.1, it is necessary to consider the flange lateral bending stress at the connection plate. In this case, the connection plates were assumed to have a width of 6 in. To calculate the flange lateral bending stress range at the top of the bottom flange caused by curvature, the flange lateral moment of inertia is:

$$\mathrm{I_{flg}} = \frac{bh^3}{12} = \frac{1.625 \times (21)^3}{12} = 1{,}254\ in.^4 \tag{7.48}$$

where b is the bottom flange depth in inches, and h is the bottom flange width in inches. The lateral moment at the connection plate is:

$$\mathrm{M_{lat}} = \frac{(M_F^+ - M_F^-)l^2}{NRD}$$

$$= \frac{(|-603| + 1{,}603) \times 20.47^3}{12 \times 716.5 \times 7}$$

$$= 15.36 \text{ kips ft} \tag{7.49}$$

where M is the major axis bending moment in kips ft; l is the unbraced length in ft; N is a constant and assumed to be 12; R is the girder radius in ft; and D is the web depth. The distance from the centerline of the web to the edge of the connection plate is:

$$c = 6 + \frac{0.5625}{2} = 6.3 \text{ in.} \tag{7.50}$$

The local stress range due to the lateral bending moment can be calculated as:

$$\Delta\sigma_l = \frac{M_{\text{lat}}c}{\text{I}_{\text{flg}}} = \frac{15.36\times12\times6.3}{1{,}254} = 0.93 \text{ ksi} \tag{7.51}$$

Design is the infinite fatigue life because the factored load stress range is smaller than the stress threshold:

$$\Delta\sigma = 1.75(\Delta\sigma_v + \Delta\sigma_l) = 11.88 \text{ ksi} \leq 12 \text{ ksi} \tag{7.52}$$

At the top flange of the negative moment region of G4, the unfactored negative and positive moments—considering fatigue, centrifugal force effects, and the 15 percent dynamic load allowance—are −1315 kip-ft and 351 kip-ft, respectively. In the calculation of major axis bending stresses for the fatigue limit state at this section, the concrete deck is considered effective. It can also be conservative in design and neglect the effect of concrete because cracks developed in concrete due to tensile stress reduce the structural functionality of deck. The distance from the top of the web, where the weld is located, to the neural axis is 23.60 in. Consequently, the unfactored stress range resulting from vertical loads can be determined as:

$$\Delta\sigma_v = \frac{(M_F^+ - M_F^-)d_{\text{top of web}}}{I}$$

$$= \frac{(|-1315| + 351) \times 12 \times 23.60}{539{,}403}$$

$$= 0.87 \text{ ksi} \tag{7.53}$$

The lateral bending stress range can be disregarded in this case because the top flange is continuously supported by the composite concrete deck, providing bracing against lateral bending. Table 7-15 shows the maximum unfactored moments due to deck slab, bituminous paving and barriers. The infinite fatigue life can be achieved because the factored load stress range is smaller than the stress threshold, as follows:

$$\Delta\sigma = 1.75(\Delta\sigma_v) = 1.53 \text{ ksi} \leq 12 \text{ ksi} \tag{7.54}$$

Table 7-15. Maximum Unfactored Dead Moments on Different Regions.

Load Type	Positive Moment (kips ft)	Negative Moment (kips ft)
Deck Slab (D1)	3343	−9189
Bituminous Paving (D2)	510	−1478
Barriers (D3)	583	−1537

The stress range in the positive region is much higher than that in the negative region. Therefore, the corrosion fatigue analysis is only needed at the negative moment critical section. In the positive moment region, the maximum vertical tensile stress due to dead load and maximum positive fatigue is as follows:

$$\sigma_v = 1.25\frac{M_{D_1}}{S_{\text{sb}}} + 1.5\frac{M_{D_2}}{S_{\text{cb}}} + 1.25\frac{M_{D_3}}{S_{\text{cb}}} + 1.6\frac{M_{\text{F}}^{+}}{S_{\text{cb}}}$$

$$= 1.25\sigma_{D1} + 1.5\sigma_{D2} + 1.25\sigma_{D3} + 1.6\sigma_F^{+}$$

$$= 25.93 \text{ ksi} \tag{7.55}$$

Curvature will also result in lateral bending stress on the bottom flange. The bottom flange lateral section modulus is:

$$S_{bf} = \frac{bh^2}{6} = \frac{1.625\times(21)^2}{6} = 119.4\ in.^3 \tag{7.56}$$

The unfactored lateral bending moment is calculated as:

$$M_{\text{lat_}D_1} = \frac{M_{D_1}l^2}{NRD} = \frac{3343\times20.47^2}{12\times716.5\times7} = 23.27 \text{ kips ft} \tag{7.57}$$

$$M_{\text{lat_}D_2} = \frac{M_{D_2}l^2}{NRD} = \frac{510\times20.47^2}{12\times716.5\times7} = 3.55 \text{ kips ft} \tag{7.58}$$

$$M_{\text{lat_}D_3} = \frac{M_{D_3}l^2}{NRD} = \frac{583\times20.47^2}{12\times716.5\times7} = 4.06 \text{ kips ft} \tag{7.59}$$

$$M_{\text{lat_F}}^{+} = \frac{M_{\text{F}}^{+}l^2}{NRD} = \frac{2398\times20.47^2}{12\times716.5\times7} = 16.69 \text{ kips ft} \tag{7.60}$$

where $M_{\text{lat_D}_1}$, $M_{\text{lat_D}_2}$, $M_{\text{lat_D}_3}$, and $M_{\text{lat_F+IM}}^{+}$ are lateral bending moments due to deck slab (D_1) 3 in. bituminous overlay (D_2), barrier loads (D_3), and maximum positive fatigue loads (F+IM) separately; l is the unbraced length in ft; N is a constant and assumed to be 12; R is the girder radius in ft; D is the web depth.

The maximum tensile stress of bottom steel fiber due to lateral bending is calculated as:

$$\sigma_l = \frac{1.25M_{lat_{D1}}}{S_{bf}} + \frac{1.5M_{lat_{D2}}}{S_{bf}} + \frac{1.25M_{lat_{D3}}}{S_{bf}} + \frac{1.60M_{lat_F}^{+}}{S_{bf}}$$

$$= 1.25\sigma_{lat_{D1}} + 1.5\sigma_{lat_{D2}} + 1.5\sigma_{lat_{D3}} + 1.6\sigma_F^{+}$$

$$= 6.66 \text{ ksi} \tag{7.61}$$

Based on the AASHTO LRFD 6.10.7.2.1-2, the ultimate tensile stress of the bottom fiber is the sum of the vertical part and one-third lateral part:

$$\sigma_{max} = \sigma_v + \frac{1}{3}\sigma_l = 47.66 \text{ ksi} \tag{7.62}$$

The load stress amplitude considering stress concentration due to the weld joint is:

$$\sigma_a = 1.6\left(\frac{\Delta\sigma_v + \Delta\sigma_l}{2}\right) = 28.15 \text{ ksi} \tag{7.63}$$

In this case, a fillet weld joint existed where the material was typically subjected to higher stress levels due to geometric irregularities and abrupt changes in the cross-sectional area. Therefore, the stress concentration (k_w) needed to be considered. The damage indicator P_{SWT}, considering the stress concentration at fillet weld, can be calculated from:

$$P_{SWT} = k_w\sqrt{\sigma_{max}\sigma_a} = 1.5\sqrt{28.15 \times 5.56} = 18.56 \text{ ksi} \tag{7.64}$$

The yearly number of fatigue cycles is calculated as 2.48×10^7. The service life of weathering steel in various environments subjected to 2.48×10^7 stress cycles per year is shown in Figure 7.19.

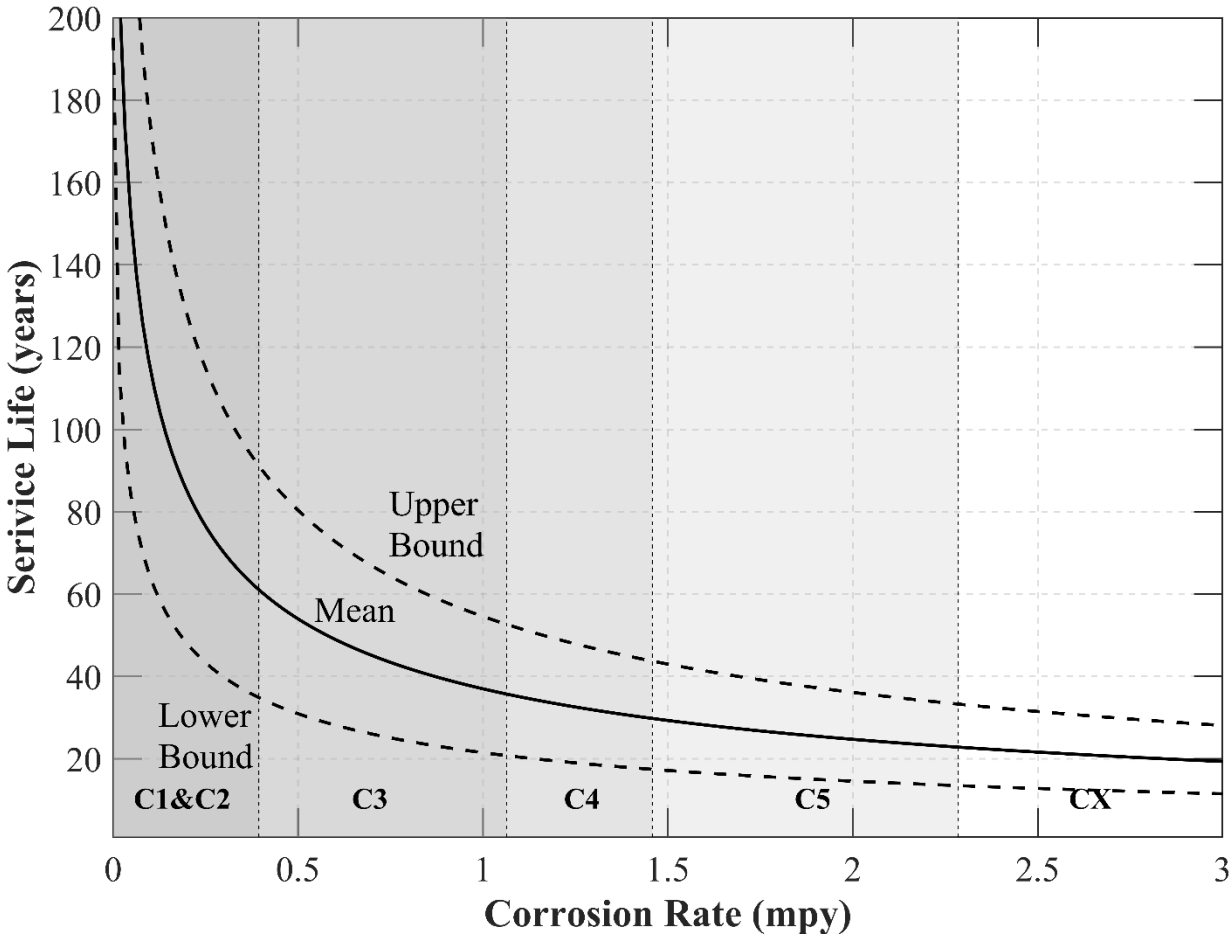


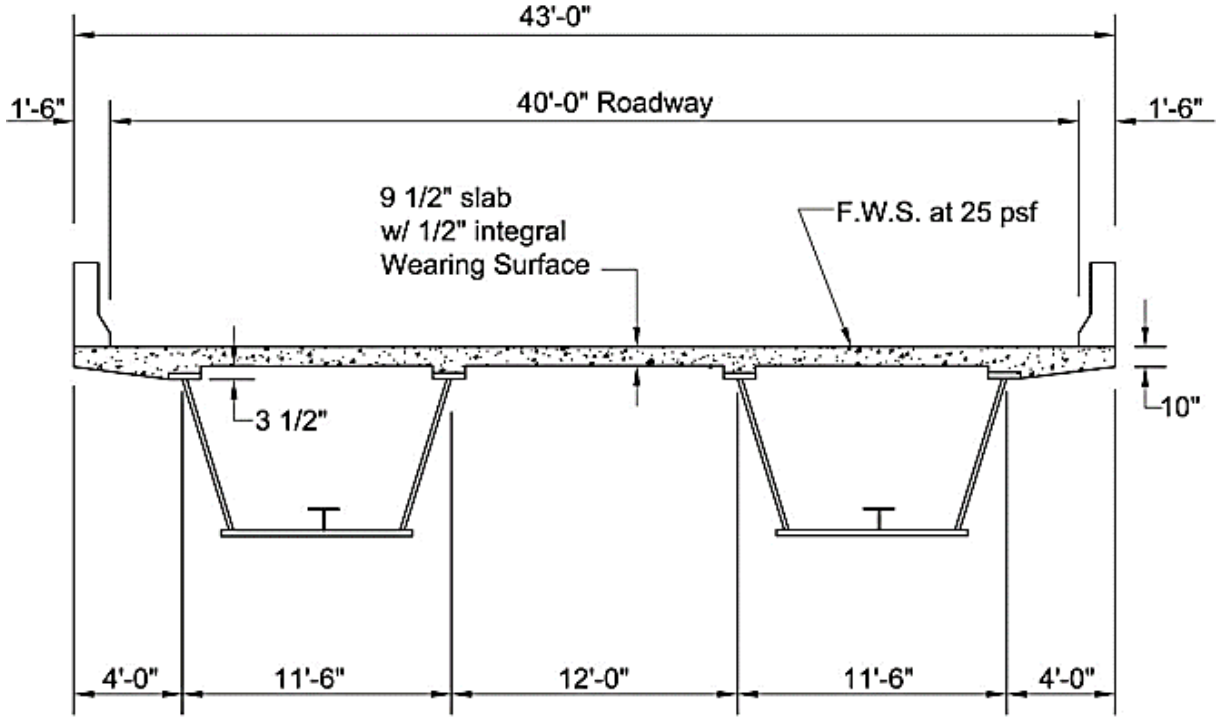
Figure 7.19. Service Life of Three-Span Continuous Horizontally Curved Composite Steel Bridge in Different Corrosion Regions.

In mildly corrosive environments, this curved bridge has a service life comparable to traditional expectations. However, in regions where the environment is aggressive, the service life of the bridge decreases significantly. The convex side is a focal point in the design of curved bridges primarily due to the influence of lateral bending moments. The lateral bending forces generated by the horizontal curvature increase the fatigue stress range by 16 percent.

7.2.4.5 Three-Span Continuous Straight Composite Steel Tub Girder Bridge

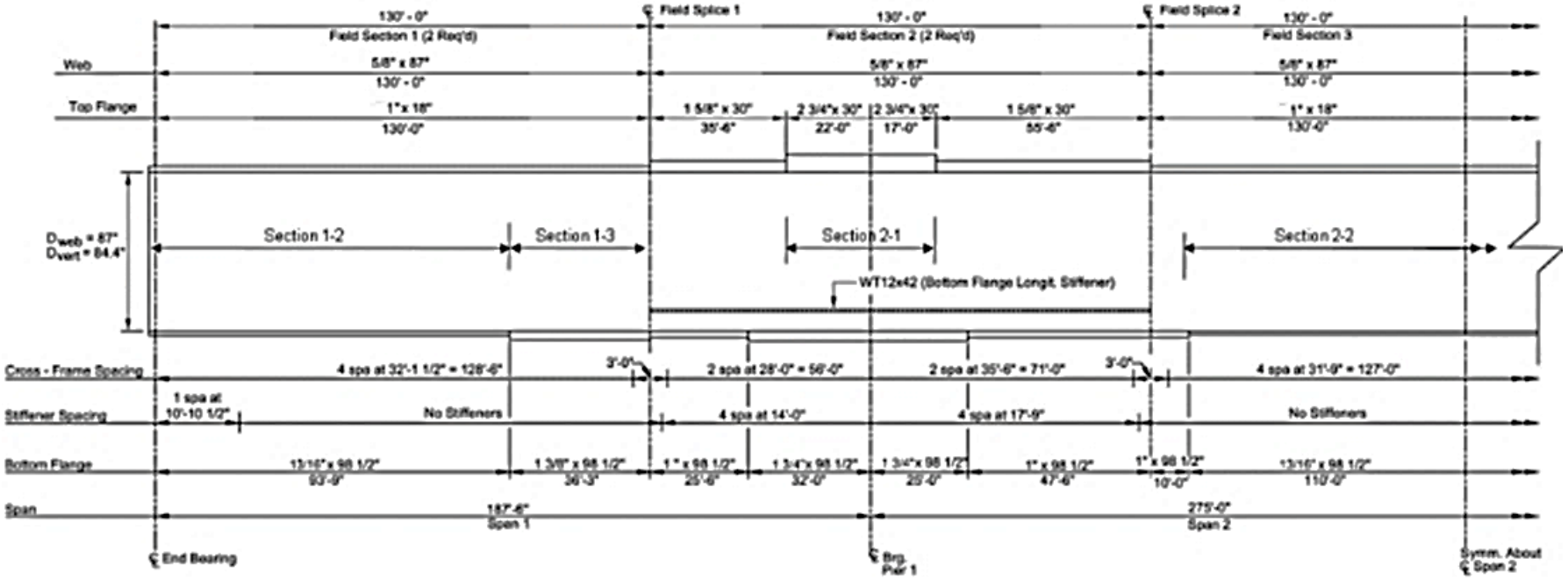
This design example focuses on a straight three-span continuous composite tub girder bridge with a span arrangement of 187.5 ft, 275.0 ft, and187.5 ft., as shown in Figure 7.20(a). The bridge cross-section features two trapezoidal tub girders with top flanges arranged at a spacing of 11.5 ft on centers. The distance between the centerlines of adjacent top tub flanges is 12.0 ft, allowing for proper alignment and support. Additionally, there are 4.0 ft overhangs on each side,

resulting in an overall deck width of 43.0 ft from outer edge to outer edge. This configuration provides the necessary structural support and deck width for the bridge. The construction materials selected for the bridge include 4 ksi compression strength concrete and nominal Grade 60 reinforcement steel. Additionally, ASTM A709 Grade 50W steel with a yield strength of 50 ksi is utilized. In Figure 7.20(b), the elevation view of the bridge shows the girder section and location in detail (Chavel & Carnahan, 2012).



(a) Cross Section

Figure 7.20. Three-Span Continuous Straight Composite Steel Tub Girder Bridge Sketches (Chavel & Carnahan, 2022).

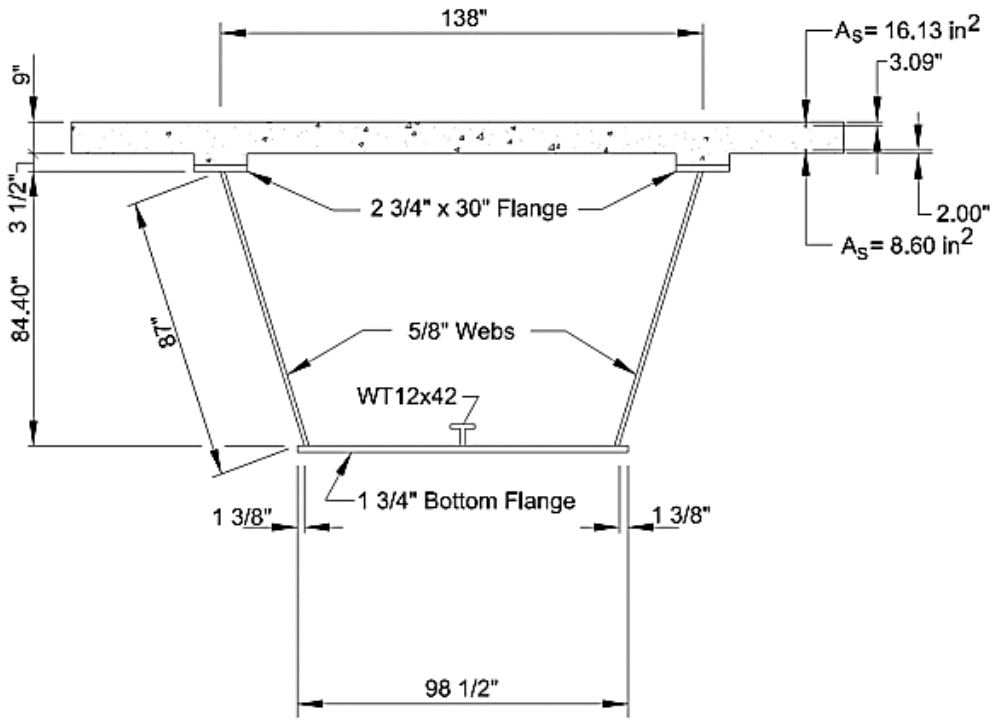


(b) Girder Elevation

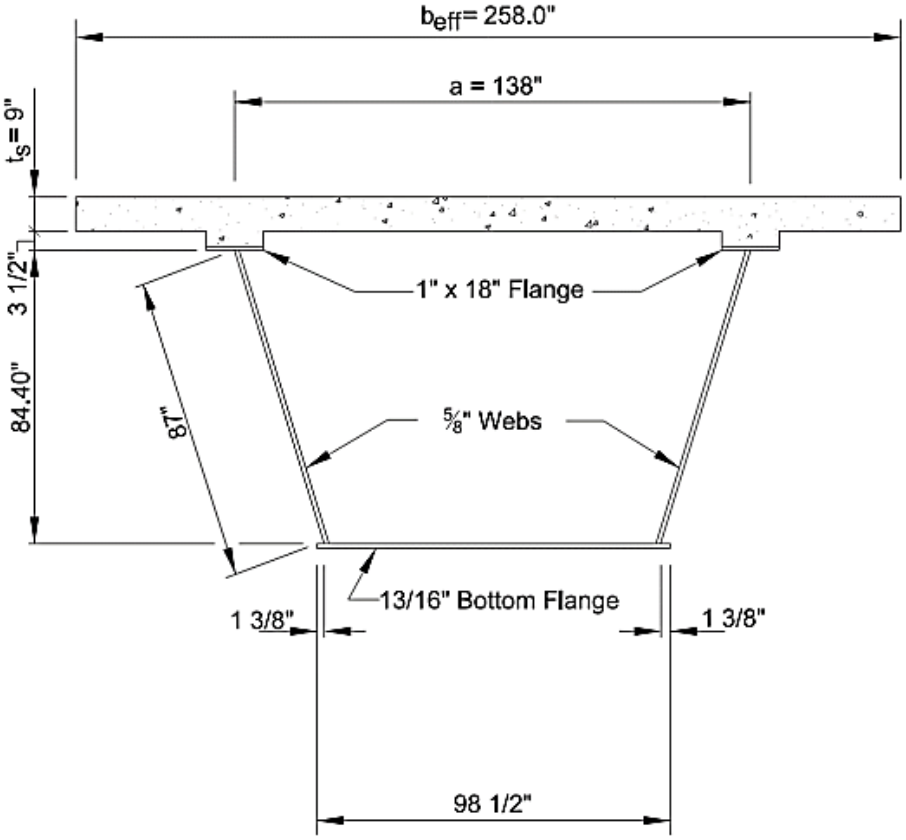
Figure 7-20. Three-Span Continuous Straight Composite Steel Tub Girder Bridge Sketches (Chavel & Carnahan, 2022) (Cont.).

In the negative moment region, the cross section 2-1 consists of a 0.625 in. × 84.4 in. web, two 2.75 in. × 30 in. top flanges and two 1.75 in. × 98.5 in. bottom flanges. The top layer of longitudinal reinforcement consists of #5 rebars spaced at 12 in. intervals and embedded at 2 in. from the cover. The bottom layer of reinforcement comprises #6 rebars spaced at 12-in. intervals and positioned. The composite section has a haunch of 3.5 in., a 9 in. net slab thickness, and a 138 in. effective width, as shown in Figure 7.21(a).

In the positive moment region at center span, a steel section 2-2 is utilized, which consists of two 1 in. × 18 in. top flanges, two 0.625 in. × 84.4 in. webs, and a 0.8125 in. × 98.5 in. bottom flange, as shown in Figure 7.21(b). The total effective flange width is 258 in.



(a) Section 2-1 at Negative Moment Region Around Interior Pier



(b) Section 2-2 at Maximum Positive Moment Region in the Center Span

Figure 7.21. Critical Composite Steel Section (Chavel & Carnahan, 2022).

The section properties in the positive and negative moment regions are summarized in Table 7-16 and Table 7-17, separately.

Table 7-16. Composite Section Properties at Negative Moment Region (Chavel & Carnahan, 2022).

Section Properties	Unit	Long-Term Composite	Short-Term Composite
Moment of Inertia I	in^4	924222	1186190
Distance from Neutral Axis to Bottom Fiber c	in.	51.54	63.55
Distance from Neutral Axis to Top Fiber y	in.	37.36	26.35
Composite Section Modulus (Bottom) S_b	in^3	17932	18964
Composite Section Modulus (Top) S_t	in^3	24738	45017
Steel Section Modulus (Bottom) S_{sb}	in^3	16709	16709
Steel Section Modulus (Top) S_{st}	in^3	15332	15332

Table 7-17. Composite Section Properties at Positive Moment Region (Chavel & Carnahan, 2022).

Section Properties	Unit	Long-Term Value	Short-Term Value
Moment of Inertia I	in^4	492283	695903
Distance from Neutral Axis to Bottom Fiber c	in.	52.29	67.66
Distance from Neutral Axis to Top Fiber y	in.	33.92	18.55
Composite Section Modulus (Bottom) S_{cb}	in^3	9414	10285
Composite Section Modulus (Top) S_{ct}	in^3	14513	37515
Steel Section Modulus (Bottom) S_{sb}	in^3	7494	7494
Steel Section Modulus (Top) S_{st}	in^3	5044	5044

The AASHTO fatigue category for a structure depends on the number of load cycles and the specific connection details. In this case study, the transverse stiffener was fillet welded to the flange. Therefore, it falls under Category C'. For Category C' fatigue detail, the 75-year equivalent of the average daily truck traffic per single lane is 975 trucks per day. In this design example, the assumed $ADTT_{SL}$ was 6800 trucks per day, which exceeds the limit of 975 trucks per day. Consequently, it is necessary to assess the details for infinite fatigue life using the Fatigue-I load combination.

In the negative moment region around Interior Pier 1, one WT 12 x 42 longitudinal stiffener was welded to the bottom flange and extended into the first span to prevent local bucking up to 93.75 ft from the end support, as shown in Figure 7.22. The transition radius at the stiffener

termination was 6 in., which is classified as Category C. The potential crack initialized from the point of tangency of the radius. For this category, the fatigue threshold is defined as 10 ksi. The assumed average daily truck traffic $ADTT_{SL}$ of 6,800 trucks per day exceeded the 75-year $ADTT_{SL}$ equivalent to the infinite life of 1,680 trucks per day for Category C. This stiffener weld termination was checked for infinite life. As shown in Figure 7.23(a), the unfactored values for negative and positive moments at the stiffener termination, consisting of fatigue and the 15 percent dynamic load allowance, are 2,398 kips ft and −1,121 kips ft, respectively. Consequently, the factored fatigue stress range can be computed as follows:

$$\Delta\sigma = \frac{\eta[1.75(M_F^+ - M_F^-)]}{S_{cb}}$$

$$= \frac{1.75 \times (2398 + |-1121|) * 12}{10285}$$

$$= 7.18 \text{ ksi} \leq 10 \text{ ksi} \qquad (7.65)$$

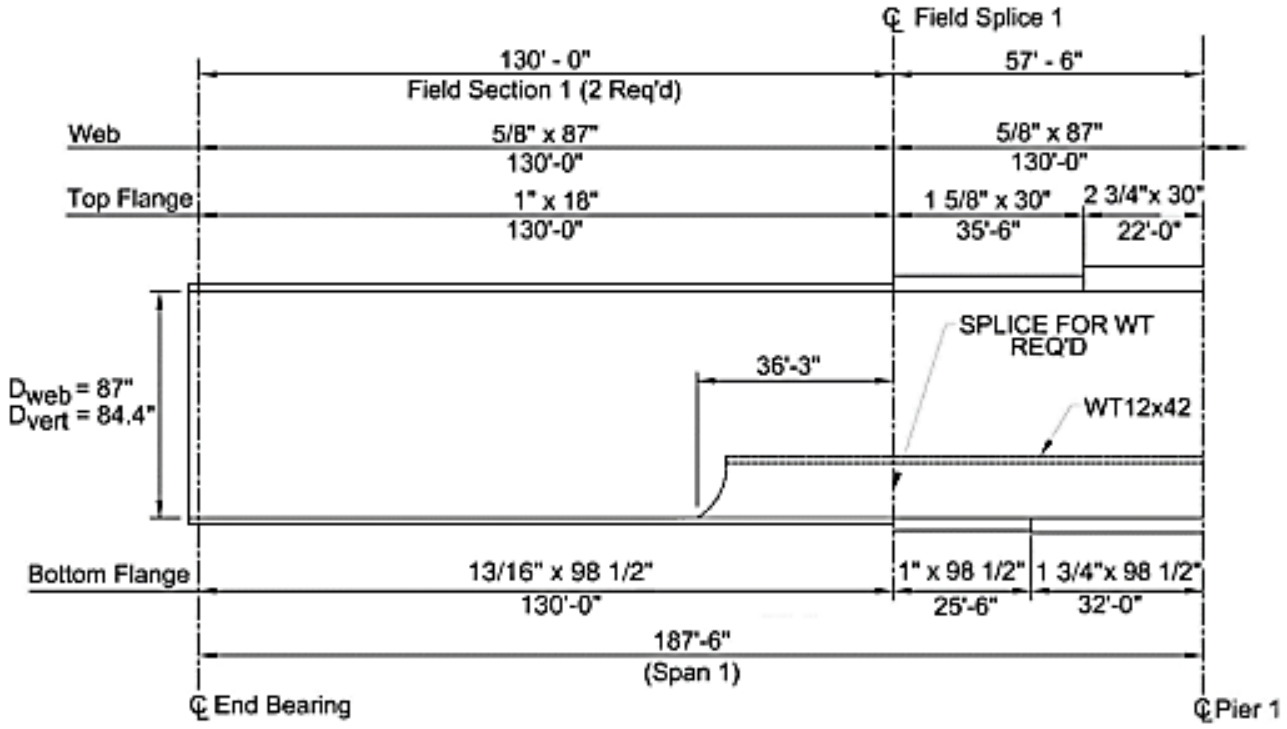
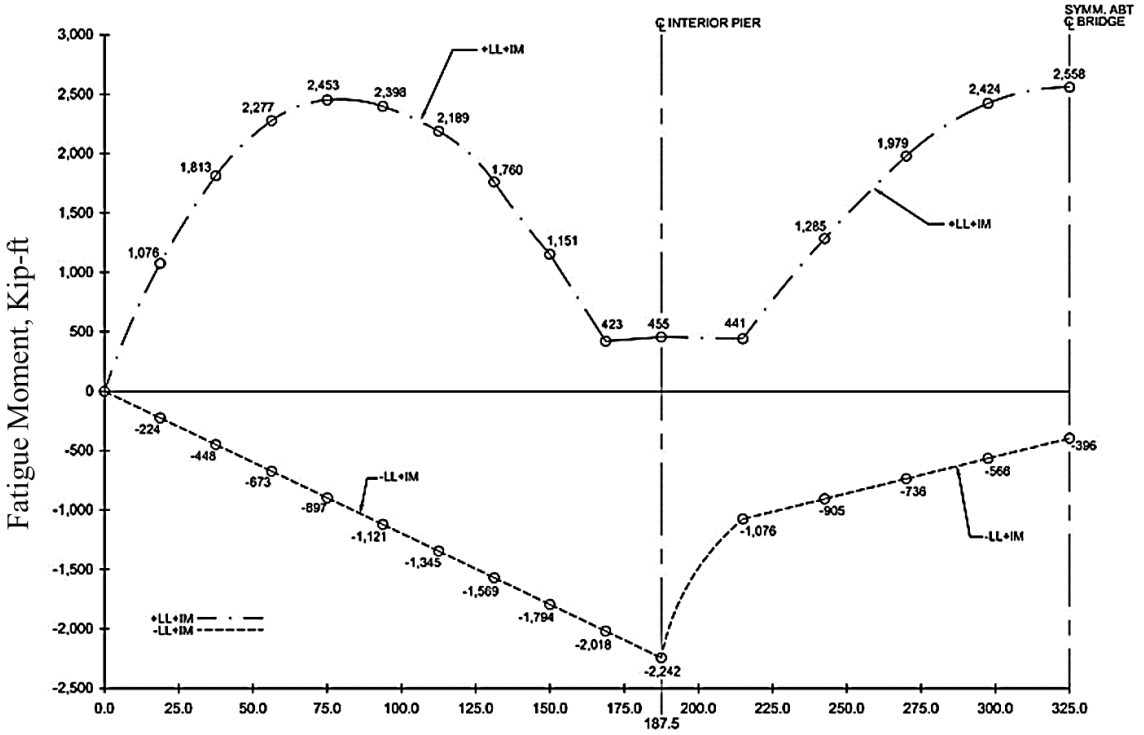
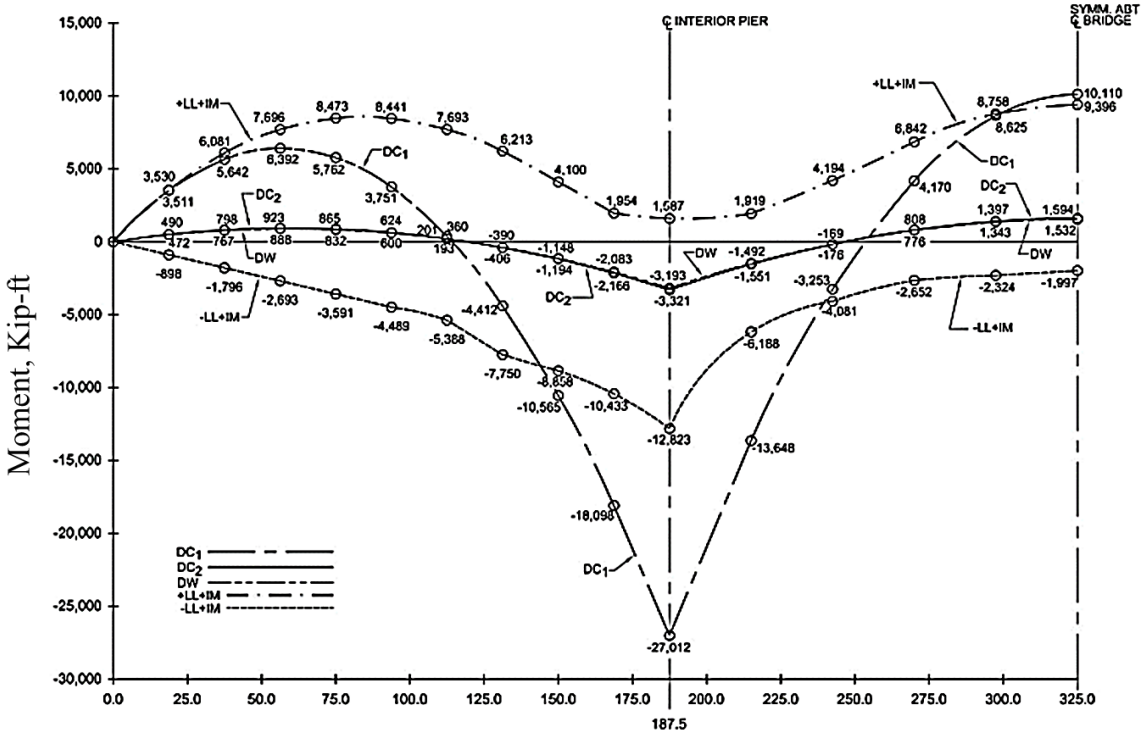


Figure 7.22. Longitudinal Stiffener on Bottom Flange (Chavel & Carnahan, 2022).



(a) Unfactored Fatigue Load Moments



(b) Unfactored Dead and Live Load Moment Envelopes

Figure 7.23. Unfactored Moment Envelope (Chavel & Carnahan, 2022).

The bottom flange of section 2-2 in the positive moment region, due to the transverse element welded connections, falls under Fatigue Category C'. The unfactored maximum positive and negative moment at midspan due to fatigue and the 15 percent dynamic load allowance are 2558 kips ft and −396 kips ft, respectively. The distance from the top of the web, where the weld in question is located, to the neural axis is 66.85 in. So, the factored stress range is:

$$\Delta\sigma = \frac{\eta[1.75(M_F^+ - M_F^-)]d_{top\ of\ web}}{I}$$

$$= \frac{1.75 \times (|-396| + 2558) \times 12 \times 66.85}{695903}$$

$$= 5.97 \text{ ksi} \leq 12 \text{ ksi} \tag{7.66}$$

These two critical sections both meet the AASHTO fatigue requirement and can achieve infinite fatigue life.

In the longitudinal stiffness weld termination, the steel girder with Section 1-3 alone is responsible for resisting the moment caused by the deck slab (DC1), while the composite section ignoring concrete, i.e., the section with only the steel section and longitudinal reinforcement, handles the moments resulting from the overlay load (D2), the barrier load (D3), and the fatigue and impact load (F + IM). At Section 1-3, the steel section modulus (bottom) S_{sb} is 8006 in.^{3}, and the composite section modulus (bottom) S_{cb} with longitudinal reinforcement is 8902 in.^{3} The maximum tensile stress at the stiffness weld termination is:

$$\sigma_{max} = 1.25\frac{M_{D1}}{S_{\text{sb}}} + 1.5\frac{M_{D2}}{S_{\text{cb}}} + 1.25\frac{M_{D3}}{S_{\text{cb}}} + 1.60\frac{M_F^+}{S_{\text{cb}}}$$

$$= 1.25\sigma_{D1} + 1.5\sigma_{D2} + 1.25\sigma_{D3} + 1.6\sigma_F^+$$

$$= 14.11 \text{ ksi} \tag{7.67}$$

The load stress amplitude is calculated as:

$$\sigma_a = 1.60\frac{(M_F^+ - M_F^-)}{2 \times S_{cb}} = 3.28 \text{ ksi} \tag{7.68}$$

In this case, the stress concentration k_w at the terminal of the local stiffener weld is 2.4. The corresponding damage indicator P_{SWT}, considering the stress concentration at the fillet weld, is:

$$P_{SWT} = k_w\sqrt{\sigma_{max}\sigma_a} = 2.4\sqrt{14.11 \times 3.28} = 16.33 \text{ ksi} \quad (7.69)$$

Another critical point is at the transverse weldment in the positive moment region; the maximum tensile stress is calculated from:

$$\begin{aligned}\sigma_{max} &= 1.25\frac{M_{D1}}{S_{sb}} + 1.5\frac{M_{D2}}{S_{cb}} + 1.25\frac{M_{D3}}{S_{cb}} + 1.6\frac{M_F^+}{S_{cb}} \\ &= 1.25\sigma_{D1} + 1.5\sigma_{D2} + 1.25\sigma_{D3} + 1.6\sigma_F^+ \\ &= 29.74\ ksi \end{aligned} \quad (7.70)$$

The load stress amplitude considering stress concentration due to the transverse stiffener weld joint is:

$$\sigma_a = 1.60\frac{(M_F^+ - M_F^-)d_{top\ of\ web}}{2 \times I} = 2.73 \text{ ksi} \quad (7.71)$$

Finally, the damage indicator P_{SWT}, considering the stress concentration at the fillet weld, can be obtained from:

$$P_{SWT} = k_w\sqrt{\sigma_{max}\sigma_a} = 1.5 \times \sqrt{29.74 \times 2.73} = 13.50 \text{ ksi} \quad (7.72)$$

The P_{SWT} value at the longitudinal stiffness weld termination is much higher, so this is the fatigue critical point. The yearly number of fatigue cycles is 2.48×10^7, the same as the third and fourth case. The service life of a tub bridge in various environments subject to 2.48×10^7 stress cycles per year is shown in Figure 7.24.

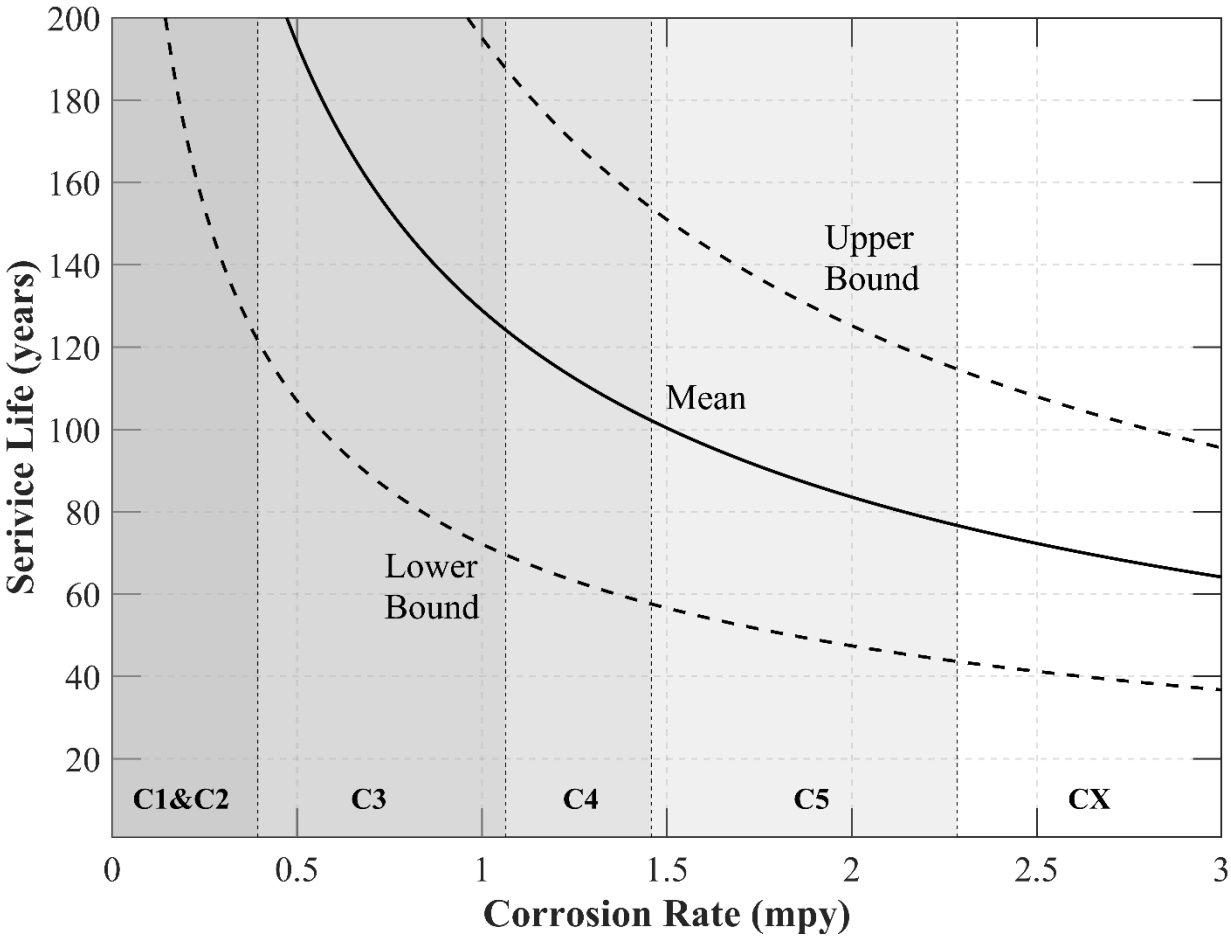


Figure 7.24. Service Life of Three-Span Continuous Straight Composite Steel Tub Girder Bridge in Different Corrosion Regions.

The tub bridge design has the best corrosion fatigue resistance among all five cases. Only when the corrosion rate is higher than 2.5 mpy does the service life of tub bridges drop below 70 years. This feature is partially because this design has the greatest safety margin. Its performance ratio, i.e., the ratio between the factored fatigue stress range and the nominal fatigue resistance, is 0.72. A lower performance ratio indicates a higher level of reliability in the design. This redundancy provides an additional safety margin and allows the structure to better withstand unexpected overloads and corrosion attacks.

7.2.5 Conclusion

The corresponding critical design parameters, including cycles per year, stress amplitude, stress concentration, and performance ratio, are summarized in Table 7-18. In low or medium corrosion regions, all the case studies meet an AASHTO infinite fatigue service life that is above

a 120-year service life. Popov (2015) suggested that metals and alloys do not impact the fatigue life in an air environment when the corrosion rate is low. Fatigue cracks initiate and grow over a specific number of cycles and only resume propagating when the material undergoes overload fracture, which occurs when the applied load surpasses the ultimate tensile stress.

Table 7-18. Summarized Results of Case Studies.

#	Bridge Type	$N_{year} \times 10^7$	σ_{max} (ksi)	σ_a (ksi)	k_w	$PSWT$ (ksi)	Performance Ratio
1	Simple-Span (Noncomposite I-Girder)	4.964	31.40	8.33	1	16.15	1.13*
2	Simple-Span (Composite I-Girder)	4.964	31.22	7.62	1	15.42	1.04*
3	Cont. (Composite I-Girder	2.482	24.75	5.39	1.5	17.35	0.98
4	Cont. (Composite I-Girder Curved)	2.482	28.15	5.56	1.5	18.56	0.99
5	Cont. (Composite Tub Girder)	2.482	14.11	3.28	2.4	16.32	0.72

* Results modified by AASHTO *LRFD* 2020.

The presence of corrosive agents accelerates the deterioration of weathering steel bridges, pushing them closer to the failure margin at a faster rate. In highly corrosive regions, all the case studies experienced a significant decline in service life. Note that none of these examples had 75 years expected service life in a high corrosion region (CX). Albrecht and Lenwari (2009) concluded that for sheltered girders with a corrosion rate between 3 and 4 mpy fabricated from A588 weathering steel and exposed to moist saltwater for 45 months, the fatigue strength decreases by 80 percent, and the fatigue classification degrades from Category B to Category D. Conversely, the same sample exposed to air with a corrosion rate around 0.3 mpy still maintained the relatively high fatigue resistance after 74 months and thus remains classified as a Category B. The results of the modified SWT model used in this study agrees with Albrecht and Lenwari (2009)'s results. The decline of service life of weathering steel in a corrosive environment depends on the performance ratio; a lower performance ratio corresponds to a lower rate of deterioration. A lower performance ratio in a structural design signifies a higher level of reliability that improves durability of the system and enables the structure to withstand unexpected overloading from degradation of components in corrosive environments. The steel tub girder allows for the

concealment of bracing, web stiffeners, utilities, and other structural or nonstructural components within the girder, thereby offering advantages over other superstructure types in terms of durability, corrosion protection, and future maintenance (Rivera & Chavel, 2022).

7.3 DECISION TOOL PROJECTING SERVICE LIFE OF WEATHERING STEEL

The Weathering Steel Service Life Projection Tool was developed in this work to estimate the average service life of weathering steel bridges in Texas. A spreadsheet file was created to enable the users predicting the average service life of weathering steel girders. This tool estimates service life of weathering steel bridges based on corrosion fatigue, which is one of the failure mechanisms in steel girder bridges. By considering essential factors such as stress levels, load factors, and average numbers of trucks passing bridges in Texas, the bridge engineers and maintenance personnel can make decisions at design level to optimize maintenance schedules and budget allocations.

7.3.1 Description of Decision Tool

Figure 7.25 shows that users should select the county in which the weathering steel bridge is located. The tool evaluates and responds to the associated corrosion risk within the county in addition to a potential range of corrosion rates specific to the county. By inputting the stress level and load factor data, the tool estimates the upper, mean, and lower values of the estimated service life. This approach leverages the county-specific corrosion risk map to predict the average service life of weathering steel bridges. Additionally, more description on symbols and equations can be found in Figure 7.27 and Table 7-19.

Input

Stress (ksi)			Load Factors			County	Truck	
DL	σ_{D1}	9.98	DL	γ_{D1}	1.25	Cass	$ADTT_{SL}$	6800
	σ_{D2}	1.58		γ_{D2}	1.50	Castro	n	2
	σ_{D3}	0.00		γ_{D3}	1.25	Chambers		
FL	σ_F^+	10.36	FL	γ_F	1.60	Cherokee		
	σ_F^-	0.00	SCF	k_w	1.00	Childress		

Output

Corrosion Risk Assessment Region	6
Corrosion Range (mpy)	> 2.285

σ_a (ksi)	8.29
σ_{max} (ksi)	31.42
P_{SWT} (ksi)	16.14

Number of Cycles to Failure ($\times 10^6$)	Lower Bound	1.32
	Average	1.62
	Upper Bound	2.15
Estimated Potential Service Life (year)	Lower Bound	27
	Average	33
	Upper Bound	43

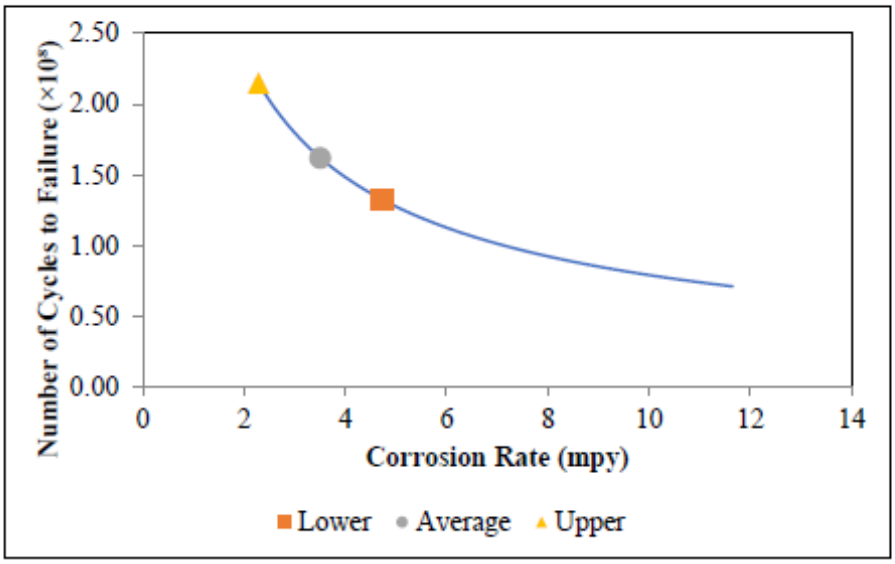


Figure 7.25. Countywide Service Life Prediction.

The second option allows users to input a custom corrosion rate, as depicted in Figure 7.27. There are several ways to estimate corrosion rate, including using portable potentiostat and measure corrosion rates of the steel member or estimating the rate based on phase analysis and ternary diagrams described in Chapter 5. Kamimura et al. (2006) conducted an experimental study on weathering steel girders and concluded that the corrosion rate of weathering steel will decrease

with the rust PAI, as shown in Figure 7.26. The relationship between the corrosion rate of weathering steel and the protective index can be expressed as:

$$\mathrm{CR} = \frac{0.4}{(\frac{\alpha}{\Gamma})^{\sqrt{2}}} \tag{7.73}$$

where CR refers to the corrosion rate of weathering steel in units of mpy; α refers to the mass fraction of goethite; and Γ is the sum of the mass fraction of lepidocrocite, akaganeite, and splines.

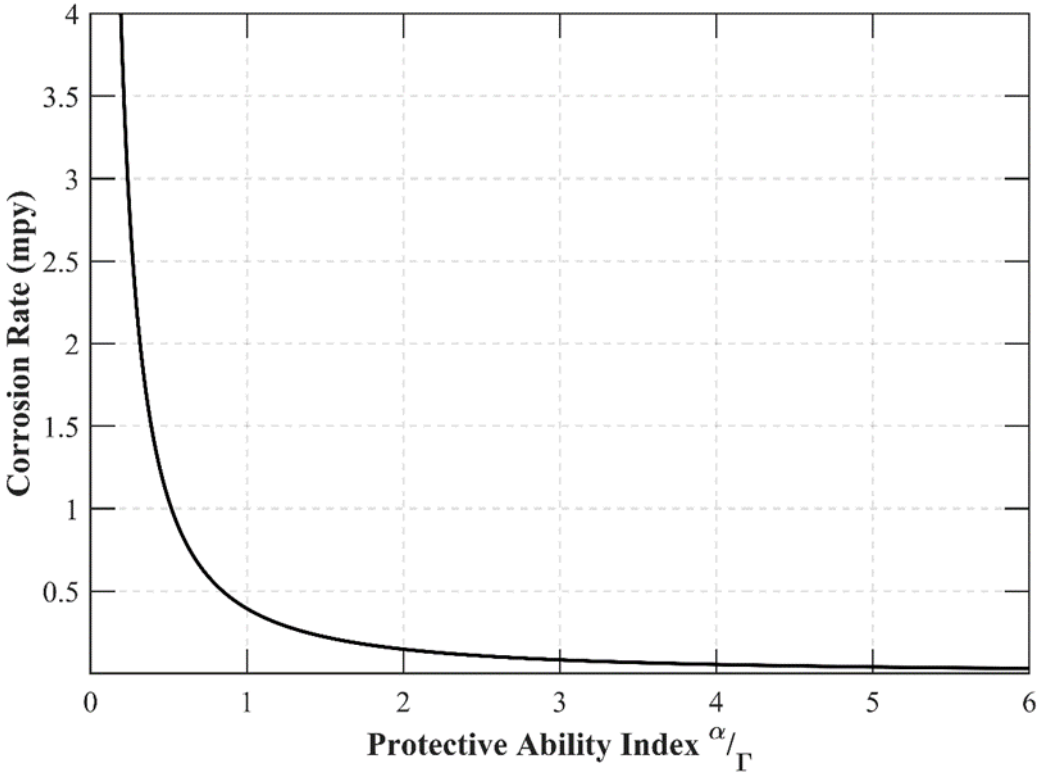


Figure 7.26. Corrosion Rate vs. Protective Ability Index α/Γ.

As the corrosion rate of the weathering steel is determined (from in-situ measurements or from the composition of the field rust sample), the tool estimates the average service life for a specific weathering steel girder.

Input

Stress (ksi)			Load Factors			Corrosion Rate		Truck	
DL	σ_{D1}	9.98	DL	γ_{D1}	1.25	2.28	mpy	$ADTT_{SL}$	6800
	σ_{D2}	1.58		γ_{D2}	1.50			n	2
	σ_{D3}	0.00		γ_{D3}	1.25				
FL	σ_F^+	10.36	FL	γ_F	1.60				
	σ_F^-	0.00	SCF	k_w	1.00				

Output

σ_a (ksi)	8.29
σ_{max} (ksi)	31.42
P_{SWT} (ksi)	16.14

Number of Cycles to Failure ($\times 10^5$)	2.14
Estimated Potential Service Life (year)	43

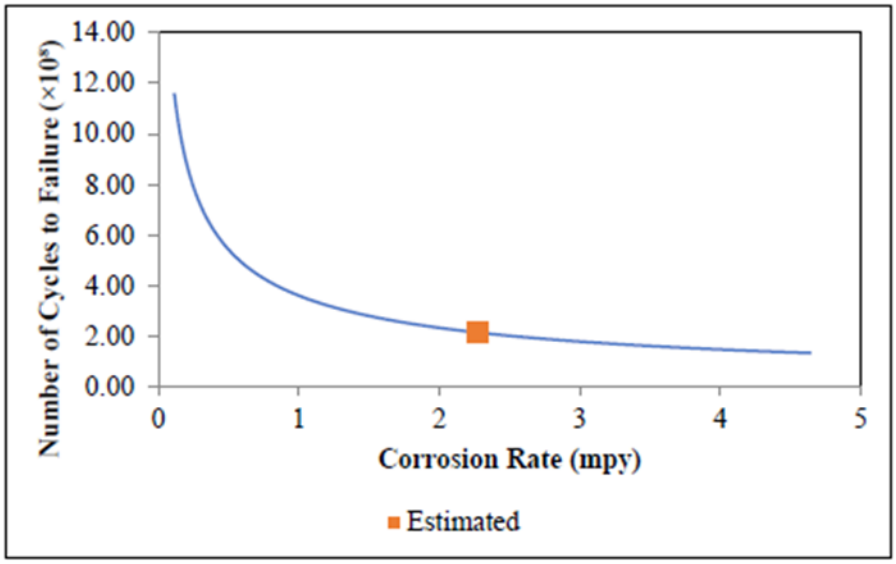


Figure 7.27. User-Defined Service Life Prediction.

Table 7-19 Provided Descriptions.

Input

$ADTT_{SL}$: Average Daily Truck Traffic per Single Lane

p: The fraction of trucks in traffic based on AASHTO Article Table C3.6.1.4.2-1 ($ADTT_{SL} = p \times ADTT$)

DL: Dead load

FL: Fatigue and Impact Load

SCF: Stress Concentration Factor

γ_{D1}: Load factor of deck slab

γ_{D2}: Load factor of wearing surface

γ_{D3}: Load factor of barrier

γ_F: Load factor of fatigue live load, ranging from 1.5 to 1.75

n: Cycles per truck passage, according to AASHTO Article Table 6.6.1.2.5.2

Output

σ_{max}: Maximum tensile stress in one load cycle

σ_a: Stress range

P_{SWT}: Damage Indicator

$$\sigma_{max} = \gamma_{D1\times}\sigma_{D1} + \gamma_{D2\times}\sigma_{D2} + \gamma_{D3\times}\sigma_{D3} + \gamma_{F\times}\sigma_F^+ \qquad \sigma_a = \gamma_{F\times}\frac{\sigma_F^+ - \sigma_F^-}{2}$$

$$P_{SWT} = \sqrt{\sigma_{max}\varepsilon_a E}$$

* Stress Concentration Factor, kw, of common welding can be taken from the table

Type of Weld	Stress Concentration Factor
Reinforced Butt Weld	1.2
Toe of the Transverse Fillet Weld or Normal Fillet Weld	1.5
End of Parallel Fillet Weld or Longitudinal Weld	2.7
T-butt Joint with Sharp Corners	2
Flange Connection with Soft Toe	2.2
Weld at the End of Local Stiffener	2.4
Weld Toe with a Radius (R) greater than 7.8 in.	$2.0 \times \left(\frac{2.36}{R}\right)^{0.05}$
Weldment with Longitudinal Attachment	2.64

Table 7-19 Provided Descriptions (Cont.).

At Positive Moment Region

$$\sigma_{D1} = \frac{M_{D1}}{S_{sb}} \qquad \sigma_{D2} = \frac{M_{D2}}{S_{cb}} \qquad \sigma_{D3} = \frac{M_{D3}}{S_{cb}} \qquad \sigma_F^+ = \frac{M_F^+}{S_{cb}} \qquad \sigma_F^- = \frac{M_F^-}{S_{cb}}$$

At Negative Moment Region

$$\sigma_{D1} = -\frac{M_{D1}}{S_{st}} \qquad \sigma_{D2} = -\frac{M_{D2}}{S_{ct}} \qquad \sigma_{D3} = -\frac{M_{D3}}{S_{ct}} \qquad \sigma_F^+ = -\frac{M_F^-}{S_{ct}} \qquad \sigma_F^- = -\frac{M_F^+}{S_{ct}}$$

At Welding Area of Interest on Positive Moment Region

$$\sigma_{D1} = \frac{M_{D1} \times d}{I_s} \qquad \sigma_{D2} = \frac{M_{D2} \times d}{I_c} \qquad \sigma_{D3} = \frac{M_{D3} \times d}{I_c}$$

$$\sigma_F^+ = \frac{M_F^+ \times d}{I_c} \qquad \sigma_F^- = \frac{M_F^- \times d}{I_c}$$

At Welding Area of Interest on Negative Moment Region

$$\sigma_{D1} = -\frac{M_{D1} \times d}{I_s} \qquad \sigma_{D2} = -\frac{M_{D2} \times d}{I_c} \qquad \sigma_{D3} = -\frac{M_{D3} \times d}{I_c}$$

$$\sigma_F^+ = -\frac{M_F^- \times d}{I_c} \qquad \sigma_F^- = -\frac{M_F^+ \times d}{I_c}$$

where,

σ_{D1}: Tensile stress due to deck slab
σ_{D2}: Tensile stress due to wearing surface
σ_{D3}: Tensile stress due to barrier
σ_F^+: Maximum tensile stress due to fatigue and impact load
σ_F^-: Maximum compression stress due to fatigue and impact load
S_{sb}: Steel Section modulus (Bottom)
S_{cb}: Short-term Composite Section modulus (Bottom)
I_s: Steel section moment of inertia
I_c: Short-term composite section moment of inertia
d: Distance from neural axis to the weld
M_{D1}: Moment due to deck slab
M_{D2}: Moment due to wearing surface
M_{D3}: Moment due to barrier
M_F^+: Maximum positive moment due to fatigue and impact load
M_F^-: Maximum negative moment due to fatigue and impact load

7.3.2 Application

The Weathering Steel Service Life Projection Tool can aid in planning for and management of weathering steel bridges across Texas. By integrating the Newton-Raphson method to solve the modified SWT model, the tool predicts the average fatigue life of steel girders by accounting for complexities of corrosion fatigue in weathering steel bridges. The tool was designed to be flexible and considers a wide range of scenarios, ensuring adaptability to the bridge locations and environmental conditions.

7.4 SUMMARY

A theoretical model introduced in this chapter can be used to predict the average service life of weathering steel girders. A modified SWT model was used to investigate the failure of steel girders due to corrosion fatigue. It was concluded that several factors can impact the service life, including surrounding environments, corrosivity, ADT, and applied loading. The service life of weathering steel generally decreases as the corrosion rate increases over 1.5 mpy, which represents a relatively high corrosion rate for weathering steel members. Note that the predicted service life of weathering steel reported in this work does not necessarily lead to the failure of the whole system. However, it can show the potential of localized failure of steel members. Therefore, routine maintenance and repair are required to maintain the functionality of steel structures.

8 SUMMARY AND CONCLUSIONS

Corrosion leads to the deterioration of steel components that can cause the failure of entire structures. To avoid the failure of steel components and prevent corrosion in structural members, using corrosion-resistant materials and coating steel girders are common protection systems in Texas. Weathering steel provides corrosion resistance in low to medium corrosive environments, and it is a cost-effective selection for bridge structures. However, there are some concerns regarding the performance of the mitigation technique in areas with heavy usage of deicing salt on the road and coastal areas with airborne salt deposition. Paint coating of steel girders is another option widely applied to mitigate corrosion activities on steel girders. Paint System I is used for repair and maintenance, and Paint System IV is shop-painting that is applied on girders of new structures. Among the coatings currently applied on state steel girders, Paint System III exhibits an acceptable resistance to corrosion in coastal areas and areas with a heavy usage of deicing salt, while Paint System II is frequently utilized in other regions of the state. A literature review conducted in this study showed certain attempts, particularly in the northern regions of Europe, to design and apply new coatings to protect steel members from corrosion. Although the new coating systems have shown greater corrosion resistance, they are more expensive than zinc coatings currently applied on TxDOT steel girders.

A corrosion risk assessment map developed in this research identifies the corrosivity of different regions in Texas. The map divides the state into six different risk regions from low to high corrosive environments. It was concluded that Region 5 and Region 6 are highly corrosive zones and include counties in the north of the state and along the Gulf of Mexico coastline. It was also determined that low corrosive environments are primarily located in the central region of the state and extend toward the western areas. This map also considers the risk of corrosion in industrial areas such as the Permian Basin, with high oil and gas activities.

Field test evaluations from this study showed that an increased volume of chloride contamination led to a surge in corrosion activities on the steel surface. For inspected bridges, the patina's color was found to range between an orange-brownish color and black. Defects such as poultice corrosion and localized delamination were sometimes detected on weathering steel girders, while stains were mostly found on bent caps. Overall, weathering steel girders exhibited satisfactory corrosion resistance when located in low to medium corrosive environments. Although minor rust spot and paint damage were detected on inspected paint-steel girders, on-system bridges

generally exhibited decent protection against corrosion. However, it was concluded that paint coatings applied on inspected off-system bridges underwent some degree of degradation, and repair and maintenance are recommended for these structures.

Laboratory examinations revealed the composition of the patina layer for every individual steel girder inspected in this research. After analyzing the crystalline rust components, a fraction of goethite, which is a dense and packed crystal structure, was calculated and demonstrated in ternary diagrams. The fraction of akaganeite, which is a chloride-based rust component, increased for the steel girders located in highly corrosive regions, indicating weathering steel girders are not suitable for bridge construction in such an environment. In addition, the laboratory testing helped to identify the paint system that was used on every inspected steel girder by differentiating between System II and System III paint systems. The results of examinations, along with the visual inspection documentation, revealed that Paint System III is more corrosion resistant than weathering steel in highly corrosive environments.

A metric was created in this study to assess the durability and performance of weathering and painted steel girders located in different corrosive environments in Texas. To this end, the results of visual inspections and laboratory examinations were used to evaluate the corrosion prevention and mitigation techniques employed on TxDOT bridges. A WSM was applied to combine variables of durability and cost scores. A decision tool was created based on field and laboratory testing to score the durability of corrosion protection systems, while a metric was developed to rank the mitigation techniques based on the cost analysis. It was concluded that weathering steel is suitable to employ on steel girders placed in low to medium corrosive regions. Paint System II can be an alternative to weathering steel in these regions, while Paint System III performs better protection as corrosivity increases.

The corrosion rate of weathering steel is expected to be more as the fraction of akaganeite and splines increases within patina layers. In an environment where the corrosion rate exceeds 1.5 mpy, repair and maintenance should be performed to prevent further deterioration. In such a corrosive environment, corrosion along with cyclic loading can lead to a significant reduction in the structural integrity of the material and decrease the service life of weathering steel girders. Pitting corrosion can form in the underlying steel due to a reduction in the volume of goethite within the patina layer, making it more susceptible to fatigue damage caused by cyclic loading. This process leads to the initiation and propagation of cracks on steel members, eventually

resulting in localized failure or even the collapse of the entire bridge structures. Corrosion can also accelerate the fatigue process by reducing the steel ductility and increasing the likelihood of brittle cracks. In this research, a modified SWT model based on Marrow's strain-life model was used to simulate the potential failure of weathering steel components due to the presence of corrosion pits and cyclic loading. To illustrate the application of the proposed method, five case studies were presented that predicted the service life of weathering steel structures subject to corrosion fatigue in different corrosive environments.

8.1 CONCLUSIONS

This section summarizes the main findings of this study evaluating corrosion prevention and mitigation methods applied to TxDOT steel girders. The outcomes of this research are divided into three categories. The conclusions drawn from field visits and laboratory testing of weathering steel bridges are followed by the outcomes of field inspections of painted steel structures. In addition, the conclusions drawn from mathematical calculations predicting the potential service life of weathering steel members are presented in this section.

8.2 WEATHERING STEEL

Conclusions were made regarding weathering steel as follows:

- The tape adhesion test exhibited reliable results among field testing conducted in this study. The documentation of the tape adhesion test can be used to assess patina ratings. From the field investigation, it was observed that the corrosion resistance of exterior surfaces of steel girders is greater than that of interior girders. A PRI was developed in this research that can be used in the field examination of weathering steel.
- A combination of XPS, XRD, and SEM/EDS can help identify the crystalline structure and evaluate the state of the patina (whether it is protective). This effect can be achieved by conducting a quantitative phase analysis in combination with ternary diagrams.
- A protective patina forms on weathering steel girders located in a low corrosive environment, while the rust layer that develops on the steel in a high corrosive environment such as Region 6 is not protective.

- A chloride field examination cannot provide reliable outcomes. The field measurements carried out on inspected weathering steel girders did not align with the expected outcomes from the visual inspections.
- A pH examination can help to determine the level of acidity of steel. Tests showed that the surface of inspected weathering steel girders was slightly acidic because a pH of 5 was recorded for these structures.

8.3 PAINT STEEL

Conclusions were made regarding paint steel as follows:

- Thermal imaging can aid in identifying surface defects, paint delamination, and rusting.
- Pull-off adhesion tests show that the examination can provide reliable results. Studying the results of the field testing revealed a strong bond between paint coats and steel substrate of on-system girders inspected across the state.
- Paint thickness measurements can be useful if the original thickness is known. The measurements are limited to small and micro sizes; hence, the exact original thickness of the steel plate is essential for precise measurement of the thickness loss. However, this information is rarely available unless measurements are initiated at the time of construction and repeated over years.

8.4 SERVICE LIFE OF WEATHERING STEEL

Findings to estimate the service life of weathering steel bridges as follows:

- Increased corrosion rates impact the service life of weathering steel, particularly in high corrosive environments where the rate of corrosion is greater than 1.5 mpy.
- Weathering steel should not be used when the structural members are likely to be exposed to high chloride deposition, which leads to a substantial volume of akaganeite within the patina layer.
- Corrosion activities at welds degrade the integrity of the joint, leading to reduced load-carrying capacity and increased susceptibility to fatigue cracking.
- Corrosion fatigue is more critical for nonredundant structural steel systems.

- A noncomposite design is discouraged due to its lower fatigue performance in comparison to composite design.
- The convex shape in the design of curved bridges increases the lateral bending moments. The convex portion experiences direct vehicular load effects, leading to stress concentrations and high-stress areas that increase the risk of corrosion fatigue damage.

8.5 RECOMMENDATIONS

The following recommendations are suggested based on the findings of this study:

- Routine maintenance and repair of steel girder bridges are required because corrosion activities can proceed even in low corrosive environments. Detecting corrosion-induced localized failure at an early stage can reduce the risk of structural member collapse.
- Corrosion-resistant materials such as weathering steel are suitable for the construction of bridge girders located in low to medium corrosive environments (Region 1 to Region 4).
- Paint System III is recommended for application on steel girders located in high corrosive environments (Region 5 and Region 6).
- The PRI developed in this study, along with visual inspections, can be used to assess the quality of the patina layer on weathering steel and determine whether it is protective. In the event the field evaluation shows a non-adherent patina, XRD and phase analysis should be used to determine the state of the patina.
- Among field examinations carried out in this study, the pull-off adhesion test is the best for investigating the quality of paint systems.
- The service life of weathering steel components reduces significantly with an increased rate of corrosion. Therefore, maintenance and repair are highly recommended for existing structures exposed to deicing salt and airborne chloride deposition.

REFERENCES

AASHTO. (2010). Lrfd bridge design specifications. American Association of State Highway and Transportation Officials.

AASHTO. (2020). Lrfd bridge design specifications. American Association of State Highway and Transportation Officials.

Adasooriya, N., Pavlou, D., & Hemmingsen, T. (2020). Fatigue strength degradation of corroded structural details: A formula for s-n curve. *Fatigue & Fracture of Engineering Materials & Structures, 43*(4), 721-733.

Albrecht, P. (1992). *Corrosion control of weathering steel bridges*: ASTM International.

Albrecht, P., Coburn, S., Wattar, F., Tinklenberg, G., & Gallagher, W. (1989). *Guidelines for the use of weathering steel in bridges* (NCHRP Report 314). Transportation Research Board.

Albrecht, P., & Lenwari, A. (2009). Fatigue strength of weathered a588 steel beams. *Journal of Bridge Engineering, 14*(6), 436-443.

Albrecht, P., & Naeemi, A. H. (1984). *Performance of weathering steel in bridges* (NCHRP Report 272). Transportation Research Board.

Albrecht, P., & Shabshab, C. (1994). Fatigue strength of weathered rolled beam made of a588 steel. *Journal of materials in civil engineering, 6*(3), 407-428.

Albrecht, P., & Sidani, M. (1989). Fatigue of eight-year weathered a588 steel stiffeners in salt water. *Journal of Structural Engineering, 115*(7), 1756-1767.

Alcántara, J., Chico, B., Díaz, I., De la Fuente, D., & Morcillo, M. (2015). Airborne chloride deposit and its effect on marine atmospheric corrosion of mild steel. *Corrosion Science, 97*, 74-88.

American Galvanizers Association. (2023). Retrieved from https://galvanizeit.org/

American Welding Society. (1974). *Corrosion tests of flame-sprayed coated steel; 19-year report*. American Welding Society. Miami, Fl.

American Welding Society. (1993). *Guide for the protection of steel with thermal sprayed coatings of aluminum and zinc and their alloys and composites*. American Welding Society. Miami, FL.

Ang, A. H.-S., & Tang, W. H. (1984). *Probability concepts in engineering planning and design, vol. 2: Decision, risk, and reliability*: John Wiley & Sons.

Appleman, B. R., Weaver, R., Bruno, J. A., & Council, S. S. P. (1995). *Maintenance coating of weathering steel: Field evaluation and guidelines*. Turner-Fairbank Highway Research Center.

Aramendia, J., Gomez-Nubla, L., Arrizabalaga, I., Prieto-Taboada, N., Castro, K., & Madariaga, J. M. (2013). Multianalytical approach to study the dissolution process of weathering steel: The role of urban pollution. *Corrosion Science, 76*, 154-162. doi:https://doi.org/10.1016/j.corsci.2013.06.038.

Asami, K., & Kikuchi, M. (2003). In-depth distribution of rusts on a plain carbon steel and weathering steels exposed to coastal–industrial atmosphere for 17 years. *Corrosion Science, 45*(11), 2671-2688. doi:https://doi.org/10.1016/S0010-938X(03)00070-2.

ASTM 7091. (2022). Standard practice for nondestructive measurement of dry film thickness of nonmagnetic coatings applied to ferrous metals and nonmagnetic, nonconductive coatings applied to non-ferrous metals. ASTM International. West Conshohocken, PA.

ASTM A123/A123M. (2017). Standard specification for zinc (hot-dip galvanized) coatings on iron and steel products. ASTM International. West Conshohocken, PA.

ASTM A242. (2018). Standard specification for high-strength low-alloy structural steel. ASTM International. West Conshohocken, PA.

ASTM A242/A242M. (2018). Standard specification for high-strength low-alloy structural steel. ASTM International. West Conshohocken, PA.

ASTM A588/A588M. (2019). Standard specification for high-strength low-alloy structural steel, up to 50 ksi [345 mpa] minimum yield point, with atmospheric corrosion resistance. ASTM International. West Conshohocken, PA.

ASTM A709/A709M. (2021). Standard specification for structural steel for bridges. ASTM International. West Conshohocken, PA.

ASTM D610. (2019). Standard practice for evaluating degree of rusting on painted steel surfaces. ASTM International. West Conshohocken, PA.

ASTM D660. (2019). Standard test method for evaluating degree of checking of exterior paints. ASTM International. West Conshohocken, PA.

ASTM D662. (2019). Standard test method for evaluating degree of erosion of exterior paints. ASTM International. West Conshohocken, PA.

ASTM D714. (2017). Standard test method for evaluating degree of blistering of paints. ASTM International. West Conshohocken, PA.

ASTM D3359. (2017). Standard test methods for rating adhesion by tape test. ASTM International. West Conshohocken, PA.

ASTM D4541. (2017). Standard test method for pull-off strength of coatings using portable adhesion. Astm international. ASTM International. West Conshohocken, PA.

ASTM D6386. (2022). Standard practice for preparation of zinc (hot-dip galvanized) coated iron and steel product and hardware surfaces for painting. ASTM International, West Conshohocken, PA.

ASTM E797/797M. (2021). Standard practice for measuring thickness by manual ultrasonic pulse-echo contact method. ASTM International, West Conshohocken, PA.

ASTM E1729. (2020). Standard practice for field collection of dried paint samples for subsequent lead determination. ASTM International. West Conshohocken, PA.

Ault, J. P., & Farschon, C. L. (2009). 20-year performance of bridge maintenance systems. *Journal of Protective Coatings & Linings, 26*.

Barker, R. M., & Puckett, J. A. (2021). *Design of highway bridges: An lrfd approach*: John Wiley & Sons.

Barth, K., Albrecht, P., & Righman, J. (2005). *Performance of weathering steel bridges in west virginia.* Paper presented at the Proceedings of 8th International Conference on Short and Medium Span Bridge Niagara Falls, Ontario, Canada.

Barth, K. E. (2022). *Steel bridge design handbook design example 2a: Two-span continuous straight composite steel i-girder bridge*. American Institute of Steel Construction.

Barton, K. (1980). Schutz gegan atmospherische korrosion, theorie und technik, verlag chemie. *Protection of metals, 16*, 387.

Bell, G. R. (2022). The decade of disaster. *Forensic Engineering 2022*, 1-11.

Biesinger, M. C., Payne, B. P., Grosvenor, A. P., Lau, L. W. M., Gerson, A. R., & Smart, R. S. C. (2011). Resolving surface chemical states in xps analysis of first row transition metals,

oxides and hydroxides: Cr, mn, fe, co and ni. *Applied Surface Science, 257*(7), 2717-2730.

Bock, A., Falcone, J., & Oelsner, G. (2018). Estimates of road salt application across the conterminous united states (1992–2015). *US Geological Survey data release*.

Boidot, A., Gheno, F., Bentiss, F., Jama, C., & Vogt, J.-B. (2022). Effect of aluminum flakes on corrosion protection behavior of water-based hybrid zinc-rich coatings for carbon steel substrate in nacl environment. *Coatings, 12*(10), 1390.

Bradski, G., & Kaehler, A. (2000). Opencv. *Dr. Dobb's journal of software tools, 3*(2).

Brevoort, B., Shields, G. H., MeLampy, K. R., & F, M. (1996). *Updated protective coating costs, products and service life.* Paper presented at the Corrosion 96.

Broomfield, J. P. (2023). *Corrosion of steel in concrete: Understanding, investigation and repair*: CRC Press.

Caddy, B. (2001). *Forensic examination of glass and paint: Analysis and interpretation*: CRC Press.

Cano, H., Díaz, I., de la Fuente, D., Chico, B., & Morcillo, M. (2018). Effect of cu, cr and ni alloying elements on mechanical properties and atmospheric corrosion resistance of weathering steels in marine atmospheres of different aggressivities. *Materials and Corrosion, 69*(1), 8-19. doi:https://doi.org/10.1002/maco.201709656.

Cano, H., Neff, D., Morcillo, M., Dillmann, P., Diaz, I., & de la Fuente, D. (2014). Characterization of corrosion products formed on ni 2.4 wt%–cu 0.5 wt%–cr 0.5 wt% weathering steel exposed in marine atmospheres. *Corrosion Science, 87*, 438-451. doi:https://doi.org/10.1016/j.corsci.2014.07.011.

Cao, Q., Qingge, L., & Yang, P. (2021). Performance analysis of otsu-based thresholding algorithms: A comparative study. *Journal of Sensors*. doi:https://doi.org/10.1155/2021/4896853.

Cerit, M., Genel, K., & Eksi, S. (2009). Numerical investigation on stress concentration of corrosion pit. *Engineering failure analysis, 16*(7), 2467-2472. doi:https://doi.org/10.1016/j.engfailanal.2009.04.004.

Chavan, N. M., Kiran, B., Jyothirmayi, A., Phani, P. S., & Sundararajan, G. (2013). The corrosion behavior of cold sprayed zinc coatings on mild steel substrate. *Journal of thermal spray technology, 22*, 463-470.

Chavel, B. W., & Carnahan, J. (2012). *Steel bridge design handbook design example 4: Three-span continuous straight composite steel tub girder bridge*. American Institute of Steel Construction.

Chavel, B. W., & Carnahan, J. (2022). *Steel bridge design handbook design example 4: Three-span continuous straight composite steel tub girder bridge*. American Institute of Steel Construction.

Chen, X.-p., Wang, X.-d., Liu, Q.-y., Mi, F.-y., Ying, C., & Li, Y.-s. (2010). Effect of micro-area ph value on formation of different rust phases of weathering steel in initial corrosion period. *Journal of Iron and Steel Research, International, 17*(9), 69-78.

Chen, Y. Y., Tzeng, H. J., Wei, L. I., Wang, L. H., Oung, J. C., & Shih, H. C. (2005). Corrosion resistance and mechanical properties of low-alloy steels under atmospheric conditions. *Corrosion Science, 47*(4), 1001-1021. doi:https://doi.org/10.1016/j.corsci.2004.04.009.

Cheng, X., Jin, Z., Liu, M., & Li, X. (2017). Optimizing the nickel content in weathering steels to enhance their corrosion resistance in acidic atmospheres. *Corrosion Science, 115*, 135-142. doi:https://doi.org/10.1016/j.corsci.2016.11.016.

Chico, B., De la Fuente, D., Díaz, I., Simancas, J., & Morcillo, M. (2017). Annual atmospheric corrosion of carbon steel worldwide. An integration of isocorrag, icp/unece and micat databases. *Materials, 10*(6), 601.

Cook, D. C. (2005). Spectroscopic identification of protective and non-protective corrosion coatings on steel structures in marine environments. *Corrosion Science, 47*(10), 2550-2570. doi:https://doi.org/10.1016/j.corsci.2004.10.018.

Corbun, S. K., & Kim 3rd, Y. W. (1990). *Asm metals handbook* (Vol. 1): ASM International.

Crampton, D. D., & Holloway, K. P. (2015). *Inspection and maintenance of weathering steel bridges.* Paper presented at the Structures Congress 2015.

Crampton, D. D., Holloway, K. P., & Fraczek, J. (2013). *Assessment of weathering steel bridge performance in iowa and development of inspection and maintenance techniques*. Iowa Department of Transportation, Office of Bridges and Structures (Research Office funds), 800 Lincoln Way, Ames, Iowa 50010

Cummings, B. (2017). Greenwichtime. *Then and now: I-95's Mianus River Bridge collapse.* Retrieved from https://www.greenwichtime.com/local/article/Then-and-now-I-95-s-Mianus-River-Bridge-11249964.php

Dallin, G., Gagné, M., Goodwin, F. E., & Pole, S. (2018). *Duplex zinc coatings for corrosion protection of steel structures.* Paper presented at the Proocedings of Conference: Transportation Research Board TRB 97th Annual Meeting.

Daly, C., Taylor, G., & Gibson, W. (1997). *The prism approach to mapping precipitation and temperature.* Paper presented at the Proc., 10th AMS Conf. on Applied Climatology.

Damgaard, N., & Walbridge, S. (2009). *Service life prediction for weathering steel highway structures.* Paper presented at the Structures Congress 2009: Don't Mess with Structural Engineers: Expanding Our Role.

Damgaard, N., Walbridge, S., Hansson, C., & Yeung, J. (2010). Corrosion protection and assessment of weathering steel highway structures. *Journal of Constructional Steel Research, 66*(10), 1174-1185.

Darden, W. (2016). *Toward a 100 year bridge coating system: Bridge topcoats in japan 2*.

de la Fuente, D., Díaz, I., Simancas, J., Chico, B., & Morcillo, M. (2011). Long-term atmospheric corrosion of mild steel. *Corrosion Science, 53*(2), 604-617. doi:https://doi.org/10.1016/j.corsci.2010.10.007.

Diaz, I., Cano, H., de la Fuente, D., Chico, B., Vega, J. M., & Morcillo, M. (2013). Atmospheric corrosion of ni-advanced weathering steels in marine atmospheres of moderate salinity. *Corrosion Science, 76*, 348-360. doi:https://doi.org/10.1016/j.corsci.2013.06.053.

Dimitrakis, S., & Lawrence, F. (2001). Improving the fatigue performance of fillet weld terminations. *Fatigue Fracture of Engineering Materials Structures, 24*(6), 429-438.

DMS 8100. (2004). Dms-8100, structural steel paints - formula. Departmental Material Specifications, Texas Department of Transportation.

DMS 8101. (2007). Structural steel paints — performance. Departmental Materials Specification, Texas Department of Transportation

Dowling, N. (2009). Mean stress effects in strain–life fatigue. *Fatigue Fracture of Engineering Materials Structures, 32*(12), 1004-1019.

El Aghoury, I. M., & Galal, K. (2014). Corrosion-fatigue strain-life model for steel bridge girders under various weathering conditions. *Journal of Structural Engineering, 140*(6), 04014026.

EPA. (2023). Enviroatlas interactive map. Retrieved from https://www.epa.gov/enviroatlas/enviroatlas-interactive-map

Eriksen, K. T., Ler, H. R., & Moe, K. R. (2020). *Comparative analysis of protective coating on scandinavian road bridges.* NTNU,

Faccini, M., Bautista, L., Soldi, L., Escobar, A. M., Altavilla, M., Calvet, M., Domènech, A., & Domínguez, E. (2021). Environmentally friendly anticorrosive polymeric coatings. *Applied Sciences, 11*(8), 3446.

Fishburn, P. C. (1967). Additive utilities with incomplete product sets: Application to priorities and assignments. *Operations Research, 15*(3), 537-542.

Fisher, J. W. (1984). *Fatigue and fracture in steel bridges. Case studies*. Newyork: John Wiley & Sons.

Fisher, J. W., Albrecht, P., Yen, B. T., Klingerman, D. J., & McNamee, B. (1974). *Fatigue strength of steel beams with welded stiffeners and attachments* (NCHRP Report 147). A. I. o. S. Construction.

Fontana, M. G., & Greene, N. D. (1967). *Corrosion engineering* (Third ed.): McGraw-Hill Book Company.

Galedari, S. A., Mahdavi, A., Azarmi, F., Huang, Y., & McDonald, A. (2019). A comprehensive review of corrosion resistance of thermally-sprayed and thermally-diffused protective coatings on steel structures. *Journal of thermal spray technology, 28*, 645-677.

Goodwin, F. E. (2018). Zinc and zinc alloys. *Springer handbook of materials data* (pp. 431-442): Springer.

Granata, R. D., Presuel-Moreno, F., Madani, M., & Tran, B. (2017). *Environmental suitability of weathering steel structures in florida - material selection, phase 2*. Florida Department of Transportation, 605 Suwannee Street, MS 30 Tallahassee, FL 32399

Grosvenor, A. P., Kobe, B. A., Biesinger, M. C., & McIntyre, N. S. (2004a). Investigation of multiplet splitting of fe 2p xps spectra and bonding in iron compounds. *Surface and Interface Analysis, 36*(12), 1564-1574.

Grosvenor, A. P., Kobe, B. A., Biesinger, M. C., & McIntyre, N. S. (2004b). Investigation of multiplet splitting of fe 2p xps spectra and bonding in iron compounds. *Surface and Interface Analysis: An International Journal devoted to the development and application of techniques for the analysis of surfaces, interfaces and thin films, 36*(12), 1564-1574.

Gupta, R. P., & Sen, S. K. (1975). Calculation of multiplet structure of core p-vacancy levels. Ii. *Physical Review B, 12*(1), 15.

Guttman, H., & Sereda, P. (1968). Metal corrosion in the atmosphere. *ASTM STP, 435*, 223.

Hakkarainen, T., & Yläsaari, S. (1982). Atmospheric corrosion testing in finland. *Atmospheric corrosion*: John Wiley & Sons.

Hamer, P. S. (1982). Pigment analysis in the forensic examination of paints. Iii. A guide to motor vehicle paint examination by transmitted light microscopy. *Journal of the Forensic Science Society, 22*(2), 187-192.

Hara, S., Kamimura, T., Miyuki, H., & Yamashita, M. (2007). Taxonomy for protective ability of rust layer using its composition formed on weathering steel bridge. *Corrosion Science, 49*(3), 1131-1142. doi:https://doi.org/10.1016/j.corsci.2006.06.016.

Hara, S., Uemura, T., Kadonaga, T., & Yuki, H. (2006). Wet environment evaluation based on measured dew condensation time at each part of bridge girder in mountainous area. *Zairyo-to-Kankyo, 55*(2), 75-81. doi:https://doi.org/10.3323/jcorr.55.75.

Harlow, D. G., & Wei, R. P. (1994). Probability approach for prediction of corrosion and corrosion fatigue life. *AIAA journal, 32*(10), 2073-2079.

Haynie, F., & Upham, J. (1974). *Correlation between corrosion behavior of steel and atmospheric pollution data*: ASTM International.

Hoang, N., Khoa, T. A., Nhung, L. T., Phuong, P. M., Binh, T. D., Hang, T. T. X., Chi, N. V., & Nguyen, T.-D. (2022). Flake znal alloy as an effective pigment in silicate coatings for the corrosion protection of steel. *Coatings, 12*(8), 1046.

Hou, W., & Liang, C. (1999). Eight-year atmospheric corrosion exposure of steels in china. *Corrosion, 55*(01).

Hurlebaus, S., Hueste, M. B. D., Karthik, M. M., & Terzioglu, T. (2017). *Inspection guidelines for bridge post-tensioning and stay cable systems using nde methods* (Project 14-28). Transportation Research Board.

Hurlebaus, S., Mander, J. B., Terzioglu, T., Boger, N. C., & Fatima, A. (2018). *Fracture critical steel twin tub girder bridges: Technical report*. Texas Department of Transportation.

Ince, A., & Glinka, G. (2011). A modification of morrow and smith–watson–topper mean stress correction models. *Fatigue Fracture of Engineering Materials Structures, 34*(11), 854-867.

ISO 9223. (2012). Corrosion of metals and alloys — corrosivity of atmospheres — classification, determination and estimation. International Organization for Standardization.

Jaén, J. A., Iglesias, J., & Adames, O. (2014). Indoor atmospheric corrosion of conventional weathering steels in the tropical atmosphere of panama. *Hyperfine Interactions, 224*, 279-288.

Jamali, S. S., & Mills, D. J. (2014). Steel surface preparation prior to painting and its impact on protective performance of organic coating. *Progress in Organic Coatings, 77*(12), 2091-2099.

Kain, R. M., & Baker, E. A. (1987). Marine atmospheric corrosion museum report on the performance of thermal spray coatings on steel. *Testing of Metallic and Inorganic Coatings, ASTM STP, 947*, 211-234.

Kakaei, M. N., Danaee, I., & Zaarei, D. (2013). Evaluation of cathodic protection behavior of waterborne inorganic zinc-rich silicates containing various contents of mio pigments. *Anti-Corrosion Methods and Materials, 60*(1), 37-44.

Kamimura, T., Hara, S., Miyuki, H., Yamashita, M., & Uchida, H. (2006). Composition and protective ability of rust layer formed on weathering steel exposed to various environments. *Corrosion Science, 48*(9), 2799-2812. doi:10.1016/j.corsci.2005.10.004.

Keiser, J. T., Brown, C. W., & Heidersbach, R. H. (1982). The electrochemical reduction of rust films on weathering steel surfaces. *Journal of the Electrochemical Society, 129*(12), 2686.

Kilbourn, J. H., & Marx, R. B. (1994). Polarized light microscopy of extenders in structural paints--forensic applications. *The microscope, 42*(4), 167-175.

Kim, K., Hwang, Y., & Yoo, J. (2002). Effect of silicon content on the corrosion properties of calcium-modified weathering steel in a chloride environment. *Corrosion, 58*(07).

Kline, E. S. (2008). Steel bridges: Corrosion protection for 100 years. *Journal of Protective Coatings & Linings*, 20.

Klinesmith, D. E., McCuen, R. H., & Albrecht, P. (2007). Effect of environmental conditions on corrosion rates. *Journal of Materials in Civil Engineering, 19*(2), 121-129.

Knotkova, D., Boschek, P., & Kreislova, K. (1995). Results of iso corrag program: Processing of one-year data in respect to corrosivity classification. *ASTM special technical publication, 1239*, 38-38.

Knotters, M., Brus, D., & Voshaar, J. O. (1995). A comparison of kriging, co-kriging and kriging combined with regression for spatial interpolation of horizon depth with censored observations. *Geoderma, 67*(3-4), 227-246.

Knudsen, O. Ø., Bjørgum, A., & Døssland, L. T. (2012). *Low maintenance coating systems for constructions with long lifetime.* Paper presented at the Nace Corrosion.

Knudsen, O. ø., Hasselø, J.-A., & Djuve, G. (2016). *Coating systems with long lifetime–paint on thermally sprayed zinc.* Paper presented at the Nace Corrosion.

Knudsen, O. Ø., Matre, H., Dahle, K. O., Gagné, M., Moe, K. R., Eriksen, K. T., & Ler, H. R. (2022). *Norwegian experience with zinc thermal spraying for bridges.* Paper presented at the Proceedings of the 1st Conference of the European Association on Quality Control of Bridges and Structures: Eurostruct 2021.

Knudsen, O. Ø., Matre, H., Dørum, C., & Gagné, M. (2019). Experiences with thermal spray zinc duplex coatings on road bridges. *Coatings, 9*(6), 371.

Kodumuri, P., & Lee, S.-K. (2011). Fhwa bridge coating study yields preliminary test results. *Journal of Protective Coatings & Linings, 28*(1), 38.

Kogler, R. (2015). *Steel bridge design handbook: Corrosion protection of steel bridges*. American Institute of Steel Construction.

Kogler, R., & Ocel, J. (2022). *Steel bridge design handbook*. American Institute of Steel Construction.

Kondo, Y. (1989). Prediction of fatigue crack initiation life based on pit growth. *Corrosion, 45*(1), 7-11.

Kubzova, M., Krivy, V., & Kreislova, K. (2017). Influence of chloride deposition on corrosion products. *Procedia Engineering, 192*, 504-509. doi:https://doi.org/10.1016/j.proeng.2017.06.087.

Kubzová, M., Křivý, V., Urban, V., & Kreislova, K. (2020). Corrosive environment factors and their influence on the development of weathering steel corrosion products. *Key Engineering Materials, 832*, 137-146.

Kujawski, D. (2014). A deviatoric version of the swt parameter. *International journal of fatigue, 67*, 95-102.

Kulicki, J. M. (2015). Bridges for service life beyond 100 years: Service limit state design.

Kumpulainen, S. (2006). Vulnerability concepts in hazard and risk assessment. *Special paper-geological survey of Finland, 42*, 65.

Kwon, K., & Frangopol, D. M. (2010). Bridge fatigue reliability assessment using probability density functions of equivalent stress range based on field monitoring data. *International journal of fatigue, 32*(8), 1221-1232.

Landolfo, R., Cascini, L., & Portioli, F. (2010). Modeling of metal structure corrosion damage: A state of the art report. *Sustainability, 2*(7), 2163-2175.

Langlais, T., & Vogel, J. (1996). Overcoming limitations of the conventional strain-life fatigue damage model. *Journal of Engineering Materials and Technology, 118*, 103-108. doi:https://doi.org/10.1115/1.2805921.

Lee, C. M. (2017). *Snow and ice control operations manual*. Texas Department of Transportation.

Leeco Steel, L. (2023). How much does steel plate cost: 2023? Retrieved from https://www.leecosteel.com/news/post/cost-of-steel-plate/

Leygraf, C., Wallinder, I. O., Tidblad, J., & Graedel, T. (2016). *Atmospheric corrosion*: John Wiley & Sons.

Leyland, D. S., Castler, L. B., & Chief, B. (2006). *Time tested performance of bridge coatings.* Paper presented at the The Society for Protective Coatings, Pittsburgh, PA.

Li, J., & Heap, A. D. (2008). *A review of spatial interpolation methods for environmental scientists*. Geoscience Australia.

Li, Q. X., Wang, Z. Y., Han, W., & Han, E. H. (2008). Characterization of the rust formed on weathering steel exposed to qinghai salt lake atmosphere. *Corrosion Science, 50*(2), 365-371. doi:https://doi.org/10.1016/j.corsci.2007.06.020.

Lichtenstein, A. G. (1993). The silver bridge collapse recounted. *Journal of performance of constructed facilities, 7*(4), 249-261.

Linke, W. F., & Seidell, A. (1958). *Solubilities, inorganic and metal-organic compounds: A compilation of solubility data from the periodical literature*: American Chemical Society.

Linzell, D., Hall, D., & White, D. (2004). Historical perspective on horizontally curved i girder bridge design in the united states. *Journal of Bridge Engineering, 9*(3), 218-229.

Liu, W., Liu, J., Pan, H., Cao, F., Wu, Z., Lv, H., & Xu, Z. (2020). Synergisic effect of mn, cu, p with cr content on the corrosion behavior of weathering steel as a train under the simulated industrial atmosphere. *Journal of Alloys and Compounds, 834*. doi:https://doi.org/10.1016/j.jallcom.2020.155095.

Liu, Z., Lian, X., Liu, T., Yang, Y., Zhu, J., & Dong, H. (2019). Effects of rare earth elements on corrosion behaviors of low-carbon steels and weathering steels. *Materials and Corrosion, 71*(2), 258-266. doi:https://doi.org/10.1002/maco.201911150.

Mateo, J. R. S. C. (2012). Weighted sum method and weighted product method. J. R. San Cristóbal Mateo (Ed.), *Multi criteria analysis in the renewable energy industry* (pp. 19-22). London: Springer.

McCuen, R. H., & Albrecht, P. (2005). Effect of alloy composition on atmospheric corrosion of weathering steel. *Journal of materials in civil engineering, 17*(2), 117-125.

McDad, B., Laffrey, D. C., Dammann, M., & Medlock, R. (2000). *Performance of weathering steel in txdot bridges*. Texas Department of Transportation.

McIntyre, N., & Zetaruk, D. (1977). X-ray photoelectron spectroscopic studies of iron oxides. *Analytical Chemistry, 49*(11), 1521-1529.

McKinney, W. (2011). Pandas: A foundational python library for data analysis and statistics. *Python for high performance and scientific computing, 14*(9), 1-9.

Miner, M. A. (1945). Cumulative damage in fatigue. *Journal of Applied Mechanics*.

Misawa, T., Asami, K., Hashimoto, K., & Shimodaira, S. (1974). The mechanism of atmospheric rusting and the protective amorphous rust on low alloy steel. *Corrosion Science, 14*(4), 279-289.

Mizoguchi, T., Ishii, Y., Okada, T., Kimura, M., & Kihira, H. (2005). Magnetic property based characterization of rust on weathering steels. *Corrosion Science, 47*(10), 2477-2491. doi:https://doi.org/10.1016/j.corsci.2004.10.017.

Momber, A., & Irmer, M. (2013). *Performance characteristics of surface protection coating systems for offshore structures under arctic conditions.* Paper presented at the Offshore Technology Conference.

Morcillo, M., Chico, B., Díaz, I., Cano, H., & de la Fuente, D. (2013). Atmospheric corrosion data of weathering steels. A review. *Corrosion Science, 77*, 6-24. doi:https://doi.org/10.1016/j.corsci.2013.08.021.

Morcillo, M., Díaz, I., Cano, H., Chico, B., & de la Fuente, D. (2019a). Atmospheric corrosion of weathering steels. Overview for engineers. Part i: Basic concepts. *Construction and Building Materials, 213*, 723-737. doi:https://doi.org/10.1016/j.conbuildmat.2019.03.334.

Morcillo, M., Díaz, I., Cano, H., Chico, B., & De La Fuente, D. (2019b). Atmospheric corrosion of weathering steels. Overview for engineers. Part ii: Testing, inspection, maintenance. *Construction Building and Materials, 222*, 750-765.

Morcillo, M., Díaz, I., Chico, B., Cano, H., & De la Fuente, D. (2014). Weathering steels: From empirical development to scientific design. A review. *Corrosion Science, 83*, 6-31.

Morrow, J. (1965). Cyclic plastic strain energy and fatigue of metals. *Internal friction, damping, and cyclic plasticity*: ASTM International.

Moses, F., Schilling, C. G., & Raju, K. (1987). *Fatigue evaluation procedures for steel bridges* (0309045681). Transportation Research Board.

Munger, C. G., Vincent, L., & Shifler, D. A. (2022). Marine coatings. *LaQue's Handbook of Marine Corrosion*, 527-571.

National Transportation Safety Board. (1986). *Collapse of u.S. 43 chickasawbogue creek bridge april 24, 1985*. Highway Accident Report.

National Transportation Safety Board. (2008). *Highway accident report - collapse of i-35w highway bridge, minneapolis, minnesota*. National Transportation Safety Board.

Neuber, H. (1961). Theory of stress concentration for shear-strained prismatical bodies with arbitrary nonlinear stress-strain law. *Journal of Applied Mechanics*.

Novak, S. R. (1983). *Corrosion-fatigue crack initiation behavior of four structural steels*: ASTM International.

Nowak, A. S. (1999). *Calibration of lrfd bridge design code* (0077-5614). Transportation Research Board.

Okada, H., Hosoi, Y., Yukawa, K., & Naito, H. (1969). Structure of the rust formed on low alloy steels in atmospheric corrosion. *Tetsu-to-Hagane, 55*(5), 355-365. doi:https://doi.org/10.2355/tetsutohagane1955.55.5_355.

Paglia, C., Antonietti, S., & Mosca, C. (2021). *The deterioration of 100 years old coated steel bridges.* Paper presented at the IOP Conference Series: Materials Science and Engineering.

Pickard, B. R., Daniel, J., Mehaffey, M., Jackson, L. E., & Neale, A. (2015). Enviroatlas: A new geospatial tool to foster ecosystem services science and resource management. *Ecosystem Services, 14*, 45-55.

Pilkey, W. D., Pilkey, D. F., & Bi, Z. (2020). *Peterson's stress concentration factors*: John Wiley & Sons.

Popov, B. N. (2015). *Corrosion engineering: Principles and solved problems*: Elsevier.

Porter, K. (2015). A beginner's guide to fragility, vulnerability, and risk. *Encyclopedia of earthquake engineering, 2015*, 235-260.

Pratt, A. R., Muir, I. J., & Nesbitt, H. W. (1994). X-ray photoelectron and auger electron spectroscopic studies of pyrrhotite and mechanism of air oxidation. *Geochimica et Cosmochimica Acta, 58*(2), 827-841.

Qian, Y., Ma, C., Niu, D., Xu, J., & Li, M. (2013). Influence of alloyed chromium on the atmospheric corrosion resistance of weathering steels. *Corrosion Science, 74*, 424-429. doi:https://doi.org/10.1016/j.corsci.2013.05.008.

Raja, V. K. B., Palanikumar, K., Rohith Renish, R., Ganesh Babu, A. N., Varma, J., & Gopal, P. (2021). Corrosion resistance of corten steel – a review. *Materials Today: Proceedings, 46*, 3572-3577. doi:https://doi.org/10.1016/j.matpr.2021.01.334.

Raman, A., Nasrazadani, S., & Sharma, L. (1989). Morphology of rust phases formed on weathering steels in various laboratory corrosion tests. *Metallography, 22*, 79-96.

Revie, R. W. (2011). *Uhlig's corrosion handbook* (Vol. 51): John Wiley & Sons.

Rivera, J., & Chavel, B. W. (2022). *Steel bridge design handbook design example 3: Three-span continuous horizontally curved composite steel i-girder bridge*. American Institute of Steel Construction.

Rodriguez, P., Ramirez, E., & Gonzalez, J. (1994). Methods for studying corrosion in reinforced concrete. *Magazine of Concrete Research, 46*(167), 81-90.

Rokhlin, S., Kim, J.-Y., Nagy, H., & Zoofan, B. (1999). Effect of pitting corrosion on fatigue crack initiation and fatigue life. *Engineering fracture mechanics, 62*(4-5), 425-444.

Russ, J. C. (2011). *The image processing handbook*. Boca Raton: CRC Press.

Russo, F. M., Mertz, D. R., Frank, K. H., & Wilson, K. E. (2016). *Design and evaluation of steel bridges for fatigue and fracture–reference manual*. U.S. Department of Transportation.

Saha, J. K. (2012). *Corrosion of constructional steels in marine and industrial environment: Frontier work in atmospheric corrosion*: Springer Science & Business Media.

Samanta, S., Pal, D. K., Lohar, D., & Pal, B. (2012). Interpolation of climate variables and temperature modeling. *Theoretical and Applied Climatology, 107*, 35-45.

Schilling, C. G. (1984). Stress cycles for fatigue design of steel bridges. *Journal of Structural Engineering, 110*(6), 1222-1234.

Schindelholz, E., Kelly, R. G., Cole, I. S., Ganther, W. D., & Muster, T. H. (2013). Comparability and accuracy of time of wetness sensing methods relevant for atmospheric corrosion. *Corrosion Science, 67*, 233-241.

Schindelholz, E., Risteen, B., & Kelly, R. (2014). Effect of relative humidity on corrosion of steel under sea salt aerosol proxies: Ii. Mgcl2, artificial seawater. *Journal of the Electrochemical Society, 161*(10), C460.

Schwertmann, U., & Cornell, R. M. (2000). *Iron oxides in the laboratory : Preparation and characterization*: John Wiley & Sons.

Scott, D. A., & Eggert, G. (2009). *Iron and steel in art: Corrosion, colorants, conservation*. London, UK: Archtype.

Sener, J. C., Stanley, A. F., Farrar, M. M., & Jobes, R. A. (1998). *Ultrasonic ndt of bridge steel and weathering steel bridge investigation in idaho.* Paper presented at the Structural Materials Technology III: An NDT Conference.

Seré, P. R., Deyá, C., Elsner, C. I., & Di Sarli, A. R. (2014). Behavior of two eco-compatible duplex systems used in the construction industry against corrosion. *International Journal of Adhesion and Adhesives, 50*, 1-6.

Sezgin, M., & Sankur, B. l. (2004). Survey over image thresholding techniques and quantitative performance evaluation. *Journal of Electronic imaging, 13*(1), 146-168.

Shi, P., & Mahadevan, S. (2001). Damage tolerance approach for probabilistic pitting corrosion fatigue life prediction. *Engineering fracture mechanics, 68*(13), 1493-1507.

Sidelev, A. (2014). *Subsurface imaging of corrosion in painted steel bridges*. University Transportation Reserch Center, The City College of New York https://www.utrc2.org/sites/default/files/pubs/Final-Subsurface-Imaging.pdf

Smith, K. (1970). A stress-strain function for the fatigue of metals. *Materials, 5*, 767-778.

Soille, P. (1999). *Morphological image analysis: Principles and applications* (Vol. 2): Springer.

Soliman, M., Frangopol, D. M., & Kown, K. (2013). Fatigue assessment and service life prediction of existing steel bridges by integrating shm into a probabilistic bilinear s-n approach. *Journal of Structural Engineering, 139*(10), 1728-1740.

Sørensen, P. A., Kiil, S., Dam-Johansen, K., & Weinell, C. E. (2009). Anticorrosive coatings: A review. *Journal of coatings technology and research, 6*, 135-176.

Spotts, M., Shoup, T., Hornberger, L., & Kazmer, D. O. (2004). Design of machine elements. Prentice-Hall Inc.

Stephens, M. T., Gleeson, B., Mash, J., & Li, B. (2019). *Steel bridge corrosion prevention and mitigation strategies : Literature review*. University of Pittsburgh

Stephens, R. I., Fatemi, A., Stephens, R. R., & Fuchs, H. O. (2000). *Metal fatigue in engineering*: John Wiley & Sons.

Stoecklein, W., & Tuente, J. (1994). Using the light microscope for analytical procedures–aids for solving cases involving hit-and-run offences. *Zeiss Information with Jena Review, 3*, 19-22.

Stojanović, I., Cindrić, I., Turkalj, L., Kurtela, M., & Rakela-Ristevski, D. (2022). Durability and corrosion properties of waterborne coating systems on mild steel dried under atmospheric conditions and by infrared radiation. *Materials, 15*(22), 8001.

Tempest, B., Whelan, M., Prah-Ennin, P. K., & Diep, T.-T. (2014). *Quantifying corrosive potential of de-icing and anti-icing solutions on bridge components* (Research Project No. FHWA/NC/2012-08). North Carolina Department of Transportation.

Texas Steel Quality Council. (2000). *Preferred practices for steel bridge design fabrication and erection*. Texas Department of Transportation.

Thee, C., Dong, J., & Ke, W. (2015). Corrosion monitoring of weathering steel in a simulated coastal-industrial environment. *International Journal of Environmental and Ecological Engineering, 9*(5), 587-593.

Topper, T., Wetzel, R., & Morrow, J. (1969). Neubers rule applied to fatigue of notched specimens. *Materials, 4*(1), 200-209.

Toubia, E. A., & Emami, S. (2016). *Performance comparison of structural steel coating systems*: Ohio Department of Transportation, Office of Statewide Planning & Research.

Townsend, H. (2001). Effects of alloying elements on the corrosion of steel in industrial atmospheres. *Corrosion, 57*(06).

Trejo, D., Hueste, M. B. D., & Gardoni, P. (2009). *Effect of voids in grouted, post-tensioned concrete bridge construction: Volume 1--electrochemical testing and reliability assessment*. Texas Department of Transportation.

Triantaphyllou, E. (2000). *Multi-criteria decision making methods*: Springer.

Triantaphyllou, E., & Mann, S. H. (1989). An examination of the effectiveness of multi-dimensional decision-making methods: A decision-making paradox. *Decision support systems, 5*(3), 303-312.

TxDOT. (1952). Item 446 field cleaning and painting steel. Texas Department of Transportation.

TxDOT. (1962). Item 446 field cleaning and painting steel. Texas Department of Transportation.

TxDOT. (1972). Item 446 field cleaning and painting steel. Texas Department of Transportation.

TxDOT. (1982). Item 446 field cleaning and painting steel. Texas Department of Transportation.

TxDOT. (1993). Item 446 field cleaning and painting steel. Texas Department of Transportation.

TxDOT. (2022). *Structure design corrosion protection guide*. Texas Department of Transportation.

TxDOT. (2023). Txdot bridges. *TxDOT Open Data Portal.* Retrieved from https://gis-txdot.opendata.arcgis.com/datasets/83af0d2957ca4c2eb340e4bd04a1046f/explore

Urban, V., Krivy, V., & Kreislova, K. (2015). The development of corrosion processes on weathering steel bridges. *Procedia Engineering, 114*, 546-554.

US Bureau of Labour Statistics. (2023). Us bureau of labour statistics (st. Louis federal reserve). Retrieved from https://www.bls.gov/.htm

Van der Walt, S., Schönberger, J. L., Nunez-Iglesias, J., Boulogne, F., Warner, J. D., Yager, N., Gouillart, E., & Yu, T. (2014). Scikit-image: Image processing in python. *PeerJ, 2*, e453.

Veritas, N. (2001). *Fatigue assessment of ship structures*: Det Norske Veritas.

Wagner, C. (1959). Reaktionstypen bei der oxydation von legierungen. *Zeitschrift für Elektrochemie, Berichte der Bunsengesellschaft für physikalische Chemie, 63*(7), 772-782.

Wang, X., & Triantaphyllou, E. (2008). Ranking irregularities when evaluating alternatives by using some electre methods. *Omega, 36*(1), 45-63.

Wang, Y., Mu, X., Chen, Z., Lin, Z., Dong, J., Daniel, E. F., Qi, J., & Ke, W. (2021). Understanding the role of alloyed cu and p in the initial rust composition of weathering steel formed in a simulated coastal-industrial atmosphere. *Corrosion Science, 193*. doi:https://doi.org/10.1016/j.corsci.2021.109912.

Waseda, Y., & Suzuki, S. (2006). *Advances in materials research; springer*. Berlin, Germany: Springer.

Webster, R., & Oliver, M. A. (2007). *Geostatistics for environmental scientists*: John Wiley & Sons.

Wilmot, R. (2007). Corrosion protection of reinforcement for concrete structures. *Journal of the Southern African Institute of Mining and Metallurgy, 107*(3), 139-146.

Wu, W., Cheng, X., Hou, H., Liu, B., & Li, X. (2018). Insight into the product film formed on ni-advanced weathering steel in a tropical marine atmosphere. *Applied Surface Science, 436*, 80-89. doi:https://doi.org/10.1016/j.apsusc.2017.12.018.

Wu, W., Cheng, X., Zhao, J., & Li, X. (2020). Benefit of the corrosion product film formed on a new weathering steel containing 3% nickel under marine atmosphere in maldives. *Corrosion Science, 165*. doi:https://doi.org/10.1016/j.corsci.2019.108416.

WVDOT. (2023). The byrd center blog. *The Legacy of the Collapse of the Silver Bridge.* Retrieved from https://www.herald-dispatch.com/multimedia/photo_galleries/photos_news/gallery-historical-photos-of-the-1967-collapse-of-the-silver-bridge/article_89262253-73c6-53d9-a1a9-9d027cdbd755.html

Yamashita, M., Miyuki, H., Matsuda, Y., Nagano, H., & Misawa, T. (1994). The long term growth of the protective rust layer formed on weathering steel by atmospheric corrosion during a quarter of a century. *Corrosion Science, 36*(2), 283-299. doi:https://doi.org/10.1016/0010-938X(94)90158-9.

Yamashita, M., Nagano, H., Misawa, T., & Townsend, H. E. (1998). Structure of protective rust layers formed on weathering steels by long-term exposure in the industrial atmospheres of japan and north america. *ISIJ Int., 38*(3), 285-290. doi:https://doi.org/10.2355/isijinternational.38.285.

Yen, J.-C., Chang, F.-J., & Chang, S. (1995). A new criterion for automatic multilevel thresholding. *IEEE Transactions on Image Processing, 4*(3), 370-378.

Zhang, Y., Zheng, K., Zhu, J., Lei, M., Feng, X. J. C., & Materials, B. (2021). Research on corrosion and fatigue performance of weathering steel and high-performance steel for bridges. *Construction Building Materials, 289*, 123108.

Zhao, Z., Haldar, A., & Breen Jr, F. L. (1994). Fatigue-reliability evaluation of steel bridges. *Journal of Structural Engineering, 120*(5), 1608-1623.

Zuraski, P. D., & Johnson, J. E. (1990). Fatigue strength of deteriorated steel highway bridges. *Journal of Structural Engineering, 116*(10), 2671-2690.

APPENDIX A

A.1. TYL-PS-02

- CR3100 over IH20
- Bridge ID 102120049506385, Coordinates (32.4375, -95.0996), Smith County
- Continuous steel I beam painted with System II type paint
- Built 2009
- Date of Inspection: January 25, 2021; girder inspection carried on southbound abutment and measurements are taken on girders within approximately four feet from the abutment.
- Revisited for pH test and scrape test
- No visual inspection on deck
- Location for Testing: A5-G1F1, A5-G2F1, A5-G3F2, A5-G4F2



Figure A.1. Typical Elevation of TYL-PS-02.

A.1.1. Observed Condition

The paint condition of this bridge is in very good condition. The appearance coat is also in good condition. Blistering, Erosion of paint, cracking in paint is not present. A slight discoloration is observed on edge of the bottom flange. Dirt is accumulated on the top face of the bottom flange. No checking and cracking of paint are observed. Joints are also in good condition.



(a) Overall Good Paint Condition on Girder 4 Face 2 with the dirt accumulated on BF Top



(b) Overall Good Paint Condition on Girder 1 Face 1 with Some Minor Patches of Rust And Dirt Collection Observed on BF Edge



(c) Interior Girder (G2F1) Exhibiting Good Paint Condition with Some Patches of Rust And Dirt Collected on Bottom Flange



(d) Paint on Stiffener and Joints in Good Condition



(e) Span Number 2 Observed from Ground



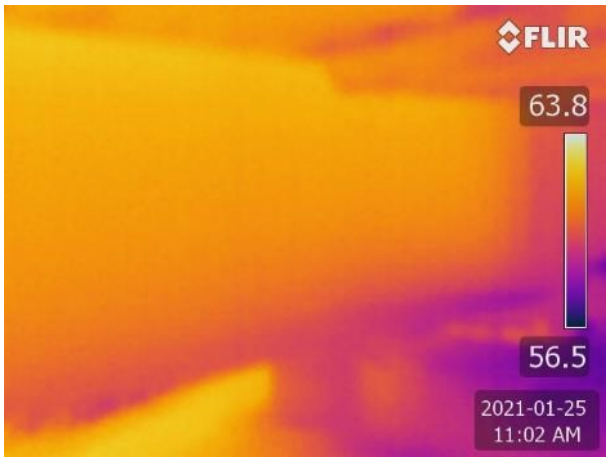
(f) Superstructure Showing No Paint Failure from the Ground

Figure A.2. Paint Condition on the Girder of TYL-PS-02.

A.1.2. NDT Results



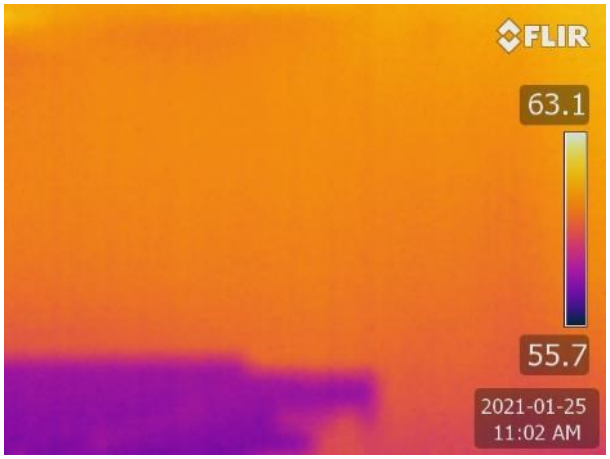
(a) Digital Image of Interior Face of I Beam



(b) Thermal Image of Interior Face of I Beam



(c) Digital Image of Connection



(d) Thermal Image of Connection



(e) Digital image of the exterior face of I beam (G1F1)



(f) Thermal image of the exterior of I beam (G1F1)

Figure A.3. Digital and Thermal Image of Painted Girder on TYL-PS-02.

Table A-1.Field Inspection Results for TYL-PS-02.

Location	Cl^- Conc. (ppm)	pH Test	Thickness (µm)	Thickness (inch)	Visual Inspection
A5-G1F1 TF Bot. Int.	-		Measured R1 114 R2 118 R3 147 Design Paint 140-381	Measured R1 0.986 R2 0.987 R3 0.988 R_Avg 0.987 Design	Rust Grade – 10 Blistering – Not Found Discoloration – Not Found Flaking – Not Found Delamination – Not Found
A5-G1F1 Web Int.	0		Measured R1 194 R2 164 R3 187 Design Paint 140-381	Measured R1 0.506 R2 0.507 R3 0.506 R_Avg 0.506 Design	Rust Grade – 10 Blistering – Not Found Discoloration – Not Found Flaking – Not Found Delamination – Not Found
A5-G1F1 BF Bot Int.	-		Measured R1 113 R2 73.7 R3 94.9 Design Paint 140-381	Measured R1 0.992 R2 0.991 R3 0.989 R_Avg 0.991 Design	Rust Grade – 10 Blistering – Not Found Discoloration – Not Found Flaking – Not Found Delamination – Not Found
A5-G2F1 TF Bot. Ext.	-		Measured R1 145 R2 136 R3 145 Design Paint 140-381	Measured R1 0.992 R2 0.994 R3 0.994 R_Avg 0.993 Design	Rust Grade – 10 Blistering – Not Found Discoloration – Not Found Flaking – Not Found Delamination – Not Found
A5-G2F1 Web. Ext.	0		Measured R1 177 R2 187 R3 158 Design Paint 140-381	Measured R1 0.505 R2 0.502 R3 0.506 R_Avg 0.504 Design	Rust Grade – 10 Blistering – Not Found Discoloration – Not Found Flaking – Not Found Delamination – Not Found
A5-G2F1 BF Bot. Ext.	-		Measured R1 127 R2 136 R3 124 Design Paint 140-381	Measured R1 0.990 R2 0.991 R3 0.990 R_Avg 0.990 Design	Rust Grade – 10 Blistering – Not Found Discoloration – Not Found Flaking – Not Found Delamination – Not Found

Table A-2. Field Inspection Results for TYL-PS-02.

Location	Cl^- Conc. (ppm)	pH Test	Thickness (µm)	Thickness (inch)	Visual Inspection
A5-G3F2 TF Bot. Int.	-		Measured R1 89.7 R2 110 R3 85.58 Design Paint 140-381	Measured R1 0.980 R2 0.979 R3 0.980 R_Avg 0.980 Design	Rust Grade – 10 Blistering – Not Found Discoloration – Not Found Flaking – Not Found Delamination – Not Found
A5-G3F2 Web Int.	0		Measured R1 123 R2 141 R3 110 Design Paint 140-381	Measured R1 0.502 R2 0.501 R3 0.501 R_Avg 0.501 Design	Rust Grade – 10 Blistering – Not Found Discoloration – Not Found Flaking – Not Found Delamination – Not Found
A5-G3F2 BF Bot Int.	-		Measured R1 78 R2 79.9 R3 92.4 Design Paint 140-381	Measured R1 0.988 R2 0.989 R3 0.988 R_Avg 0.988 Design	Rust Grade – 10 Blistering – Not Found Discoloration – Not Found Flaking – Not Found Delamination – Not Found
A5-G4F2 TF Bot. Ext.	-		Measured R1 64.3 R2 71.3 R3 61.9 Design Paint 140-381	Measured R1 0.980 R2 0.982 R3 0.979 R_Avg 0.980 Design	Rust Grade – 10 Blistering – Not Found Discoloration – Not Found Flaking – Not Found Delamination – Not Found
A5-G4F2 Web. Ext.	0		Measured R1 148 R2 143 R3 130 Design Paint 140-381	Measured R1 0.502 R2 0.504 R3 0.505 R_Avg 0.504 Design	Rust Grade – 10 Blistering – Not Found Discoloration – Not Found Flaking – Not Found Delamination – Not Found
A5-G4F2 BF Bot. Ext.	-		Measured R1 106 R2 112 R3 97.3 Design Paint 140-381	Measured R1 0.994 R2 0.993 R3 0.989 R_Avg 0.992 Design	Rust Grade – 10 Blistering – Not Found Discoloration – Not Found Flaking – Not Found Delamination – Not Found

A.1.3. Pull off Adhesion Results

Table A-3. Pull off Adhesion Results for TYL-PS-02.

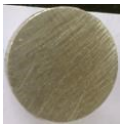
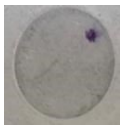
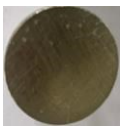
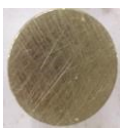
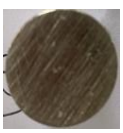
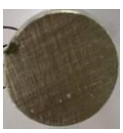
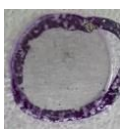
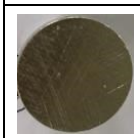
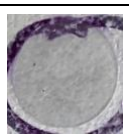
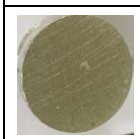
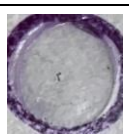
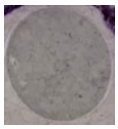
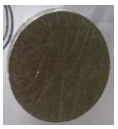
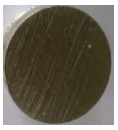
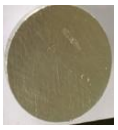
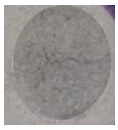
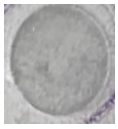
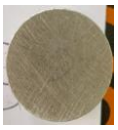
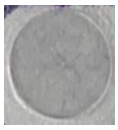
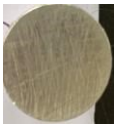
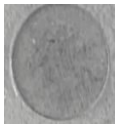
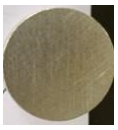
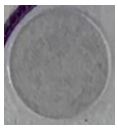
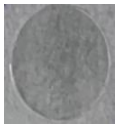
Location	Dolly Face	Substrate Face	Test Result(psi)	Attributes	Failure Type
A5-G1F1 Web			583	100% Y/Z	100% Glue Failure
			410	100% Y/Z	100% Glue Failure
			642	100% Y/Z	100% Glue Failure
			402	100% Y/Z	100% Glue Failure
			534	100% Y/Z	100% Glue Failure
A5-G2F1 Web			544	100% Y/Z	100% Glue Failure
			489	100% Y/Z	100% Glue Failure
			652	100% Y/Z	100% Glue Failure
			568	100% Y/Z	100% Glue Failure
			611	100% Y/Z	100% Glue Failure

Table A-4. Pull off Adhesion Results for TYL-PS-02.

Location	Dolly Face	Substrate Face	Test Result (psi)	Attributes	Failure Type
A5-G3F2 Web			430	100% Y/Z	100% Glue Failure
			369	100% Y/Z	100% Glue Failure
			549	100% Y/Z	100% Glue Failure
			551	100% Y/Z	100% Glue Failure
			519	100% Y/Z	100% Glue Failure
A5-G4F2 Web			567	100% Y/Z	100% Glue Failure
			606	100% Y/Z	100% Glue Failure
			393	100% Y/Z	100% Glue Failure
			598	100% Y/Z	100% Glue Failure
			708	100% Y/Z	100% Glue Failure

A.1.4. Optical Microscopy Results

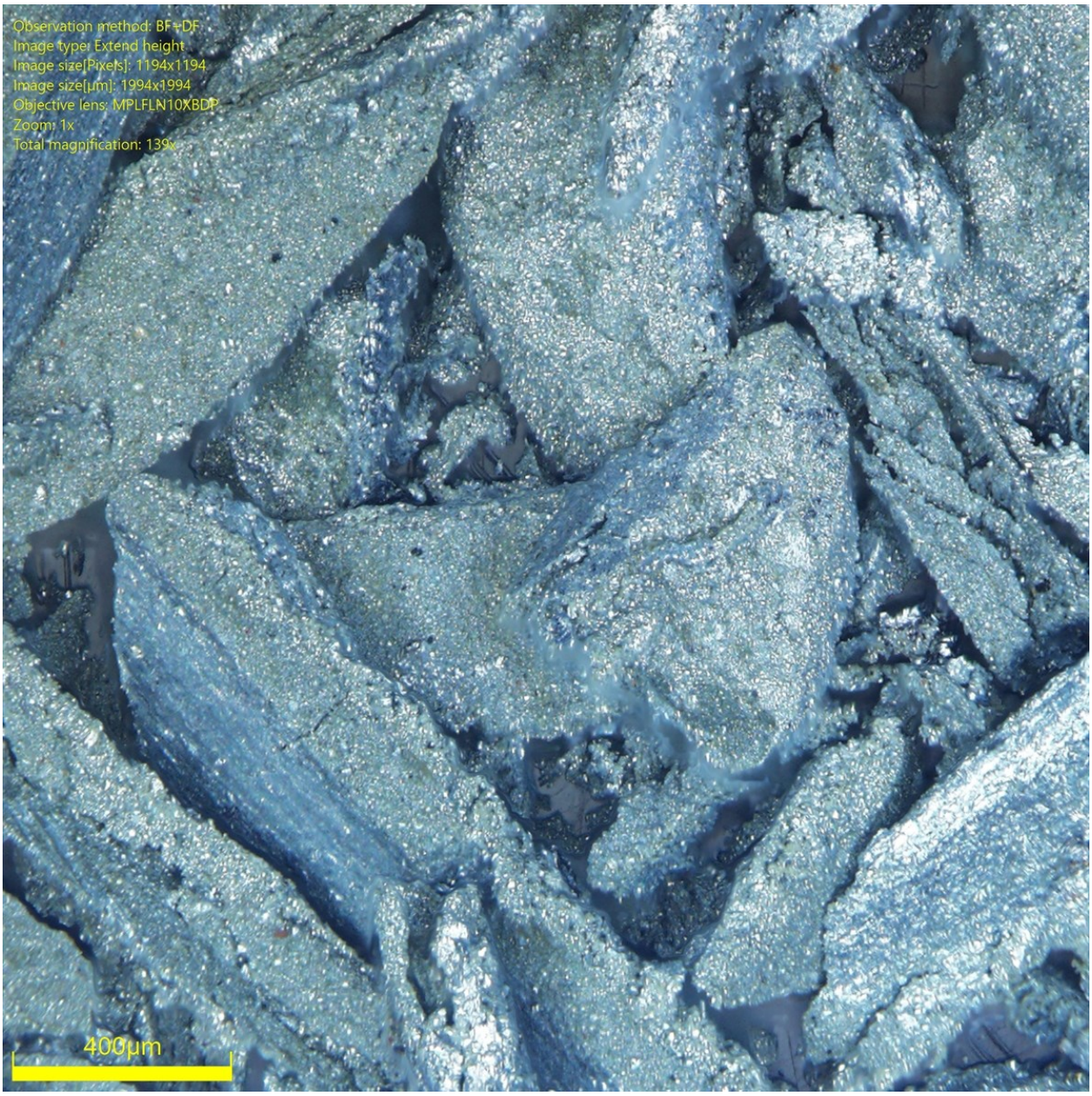


Figure A.4. Paint System Examined by Optical Microscope TYL–PS–02.

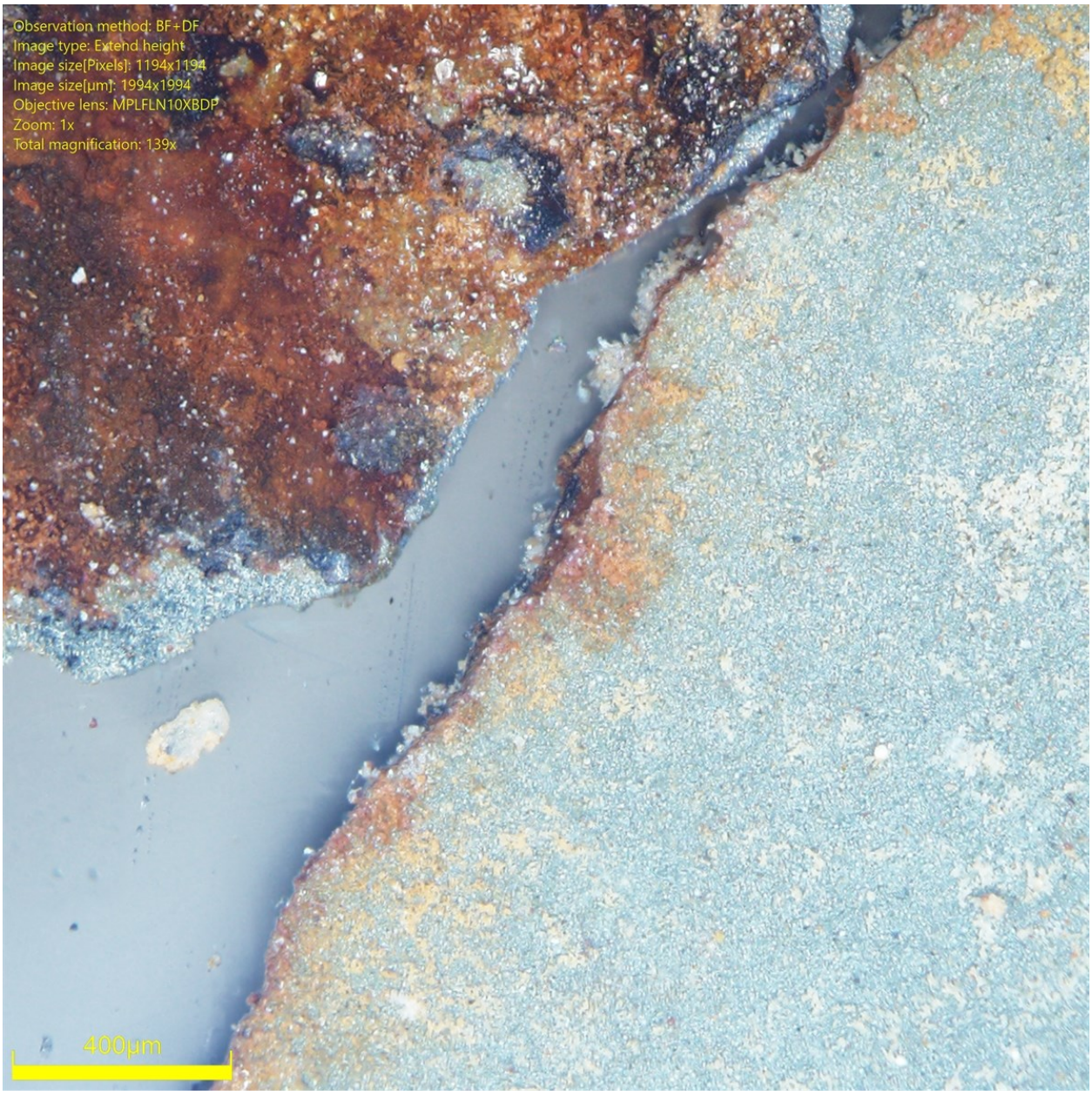
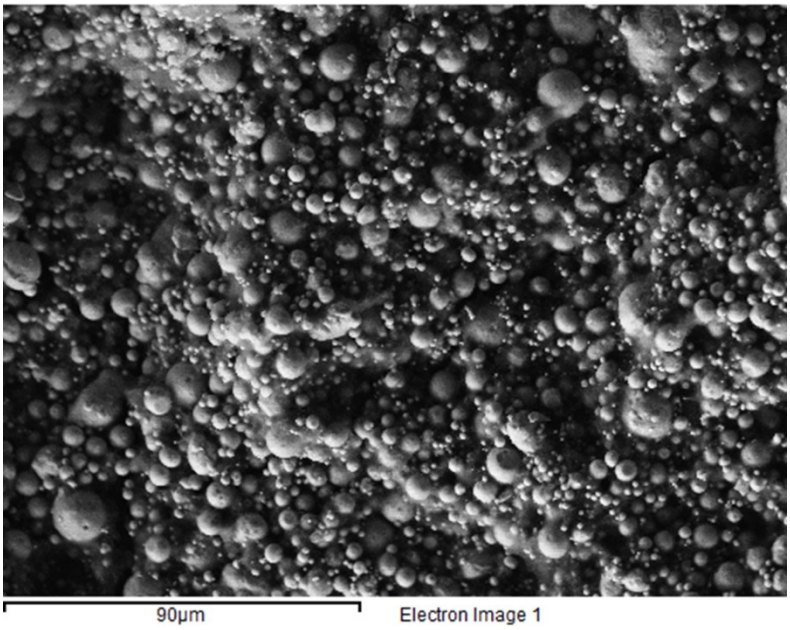


Figure A.5. Widespread Corrosion Observed Between Primer and Base Metal (G9F2).

A.1.5. SEM/EDS Results

Element	Weight %	Atomic %
C K	52.56	78.40
O K	9.89	11.08
Al K	0.23	0.15
Si K	0.23	0.15
Fe K	1.11	0.35
Zn K	35.99	9.86
Totals	100.00	



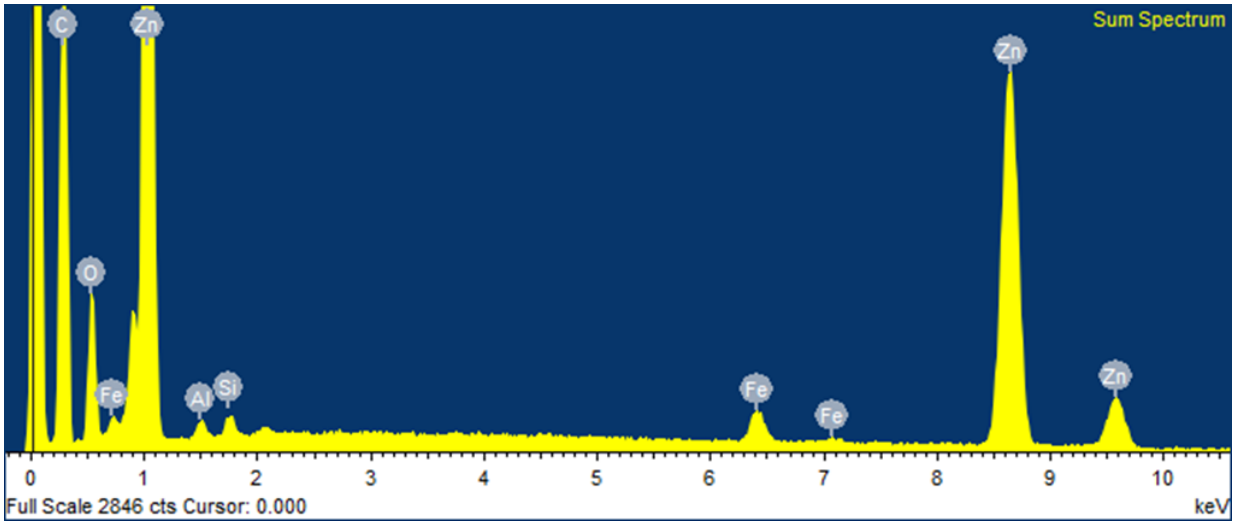


Figure A.6 SEM Image and EDS Spectrum of the Paint Collected from Exterior Web of the Girder.

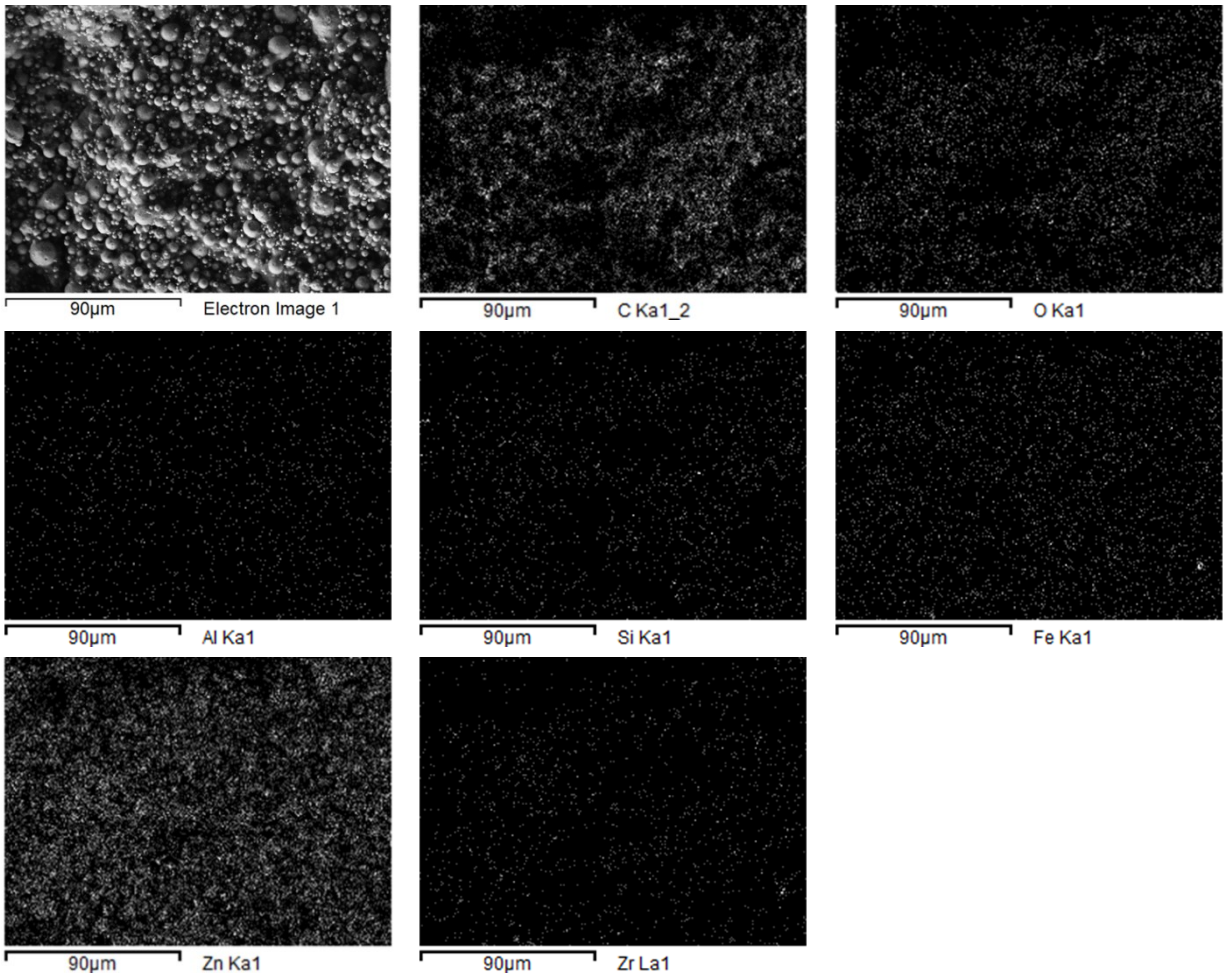
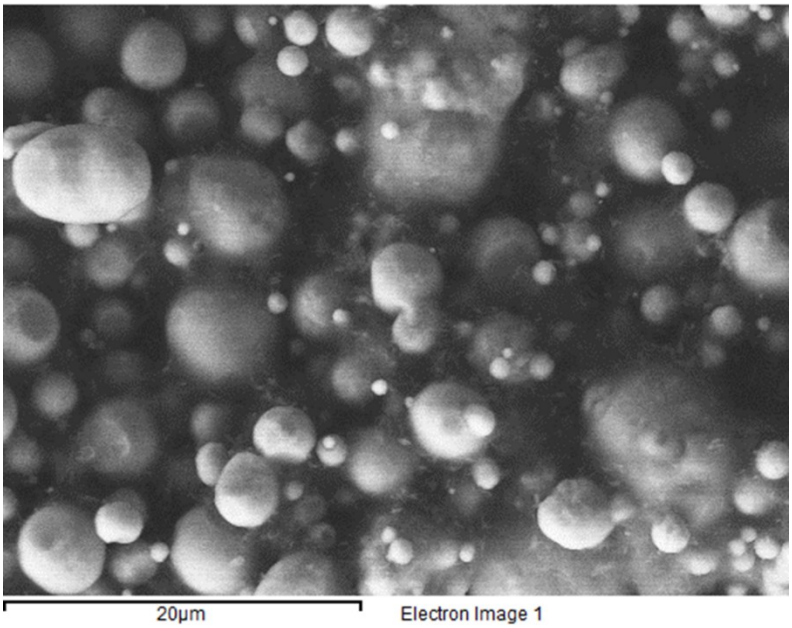
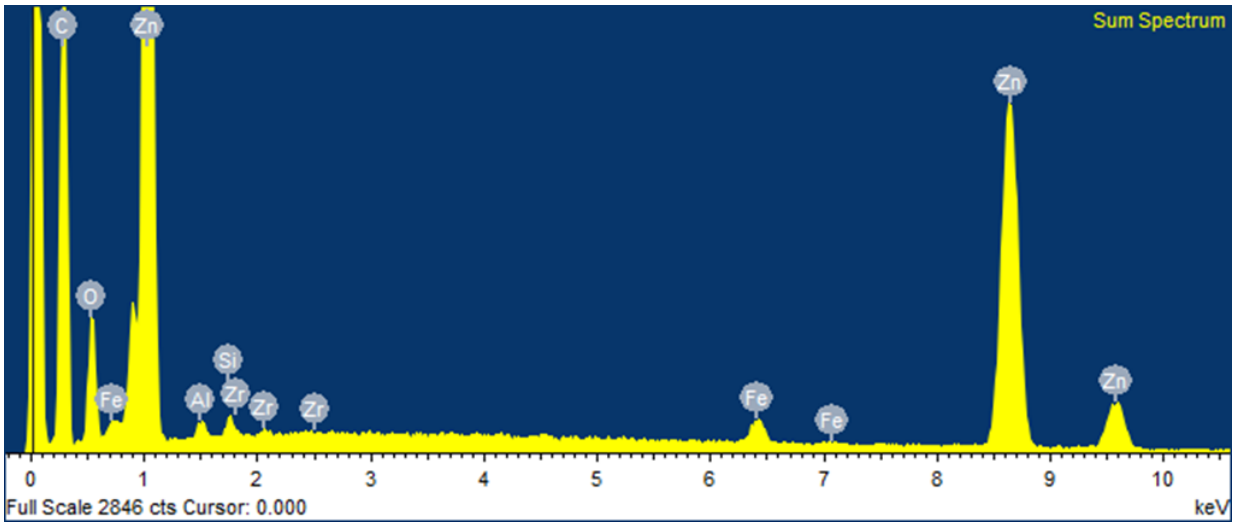


Figure A.7 EDS Elemental Mapping of Paint Collected from Exterior Web.

Element	Weight %	Atomic %
C K	53.50	79.44
O K	9.11	10.16
Al K	0.24	0.16
Si K	0.23	0.14
Fe K	0.88	0.28
Zn K	35.82	9.77
Zr L	0.22	0.04
Totals	100.00	





(a)

Figure A.8. SEM Image and EDS Spectrum of the Paint Collected from Exterior Web of the Girder.

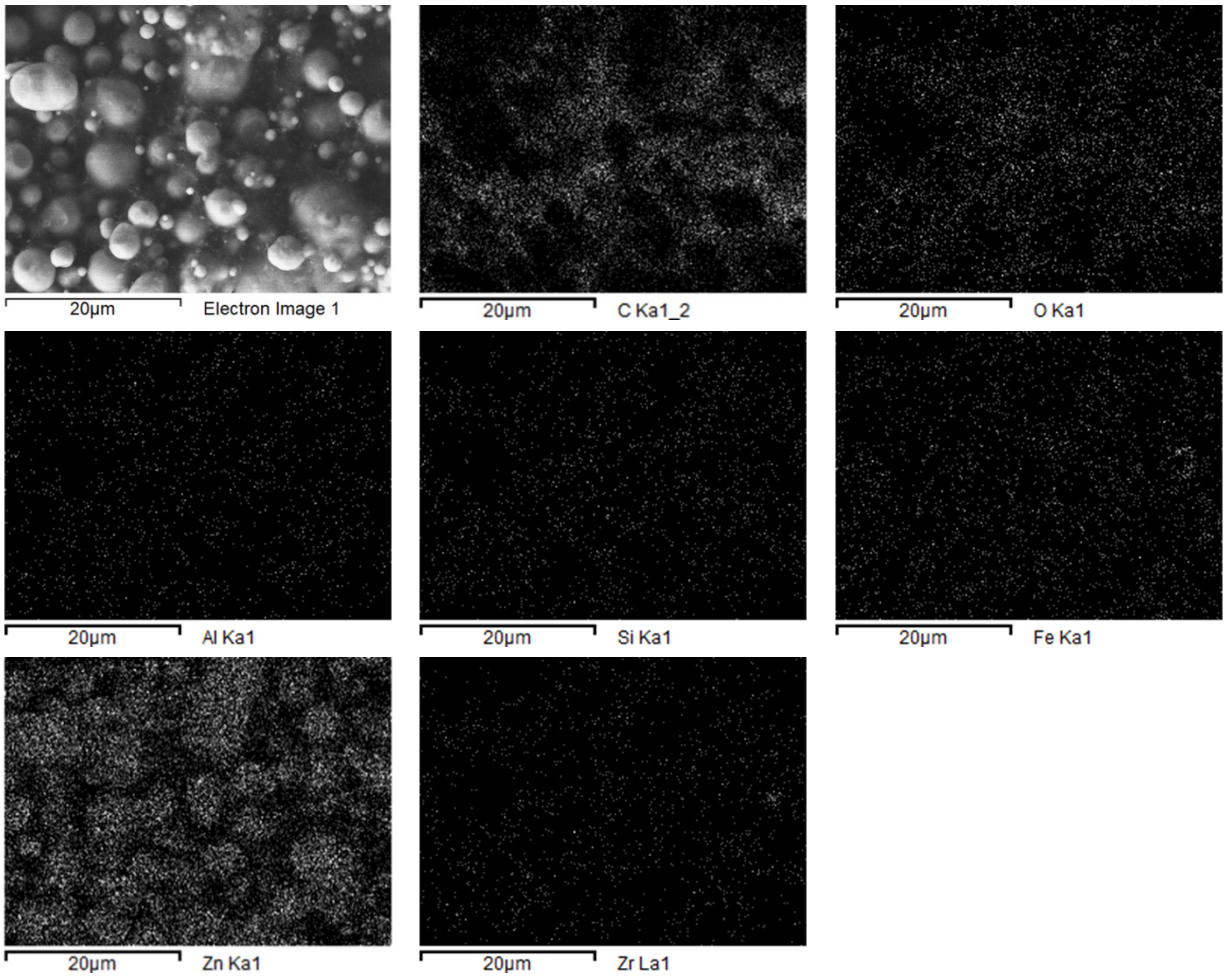
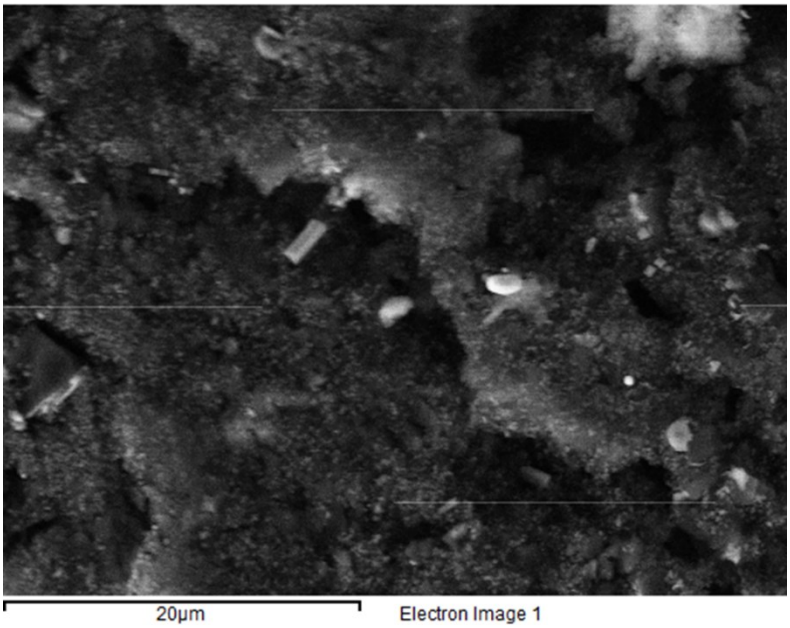


Figure A.9. EDS Elemental Mapping of Paint Collected from Exterior Web.

Element	Weight %	Atomic %
C K	31.66	43.06
O K	45.19	46.14
Al K	3.72	2.25
Si K	8.91	5.18
Ti K	7.89	2.69
Fe K	0.31	0.09
Zn K	2.32	0.58
Totals	100.00	



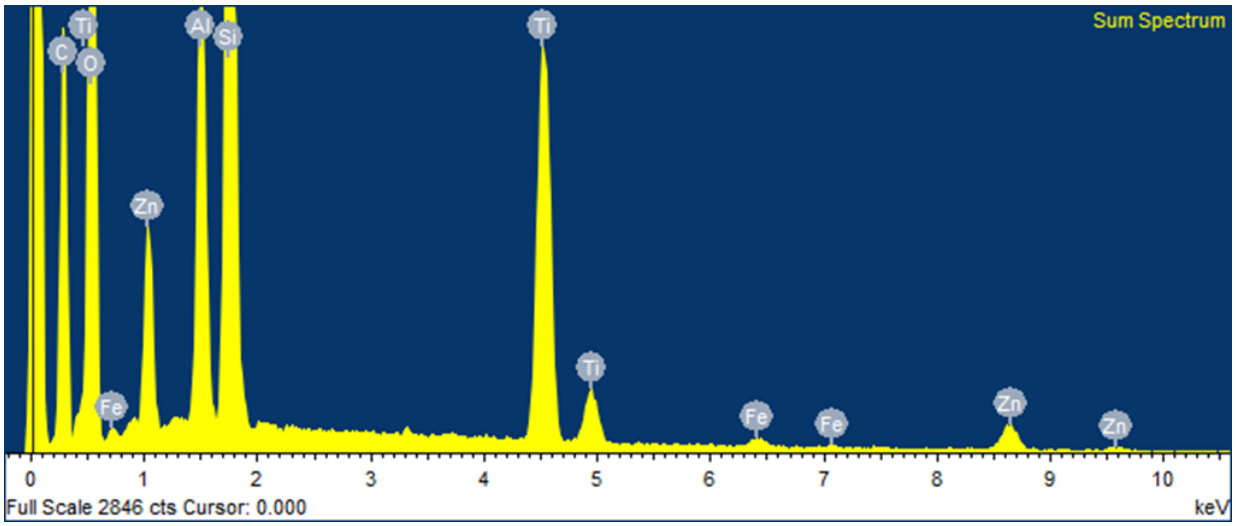


Figure A.10. SEM image and EDS Spectrum of the Paint Collected from Exterior Web of the Girder.

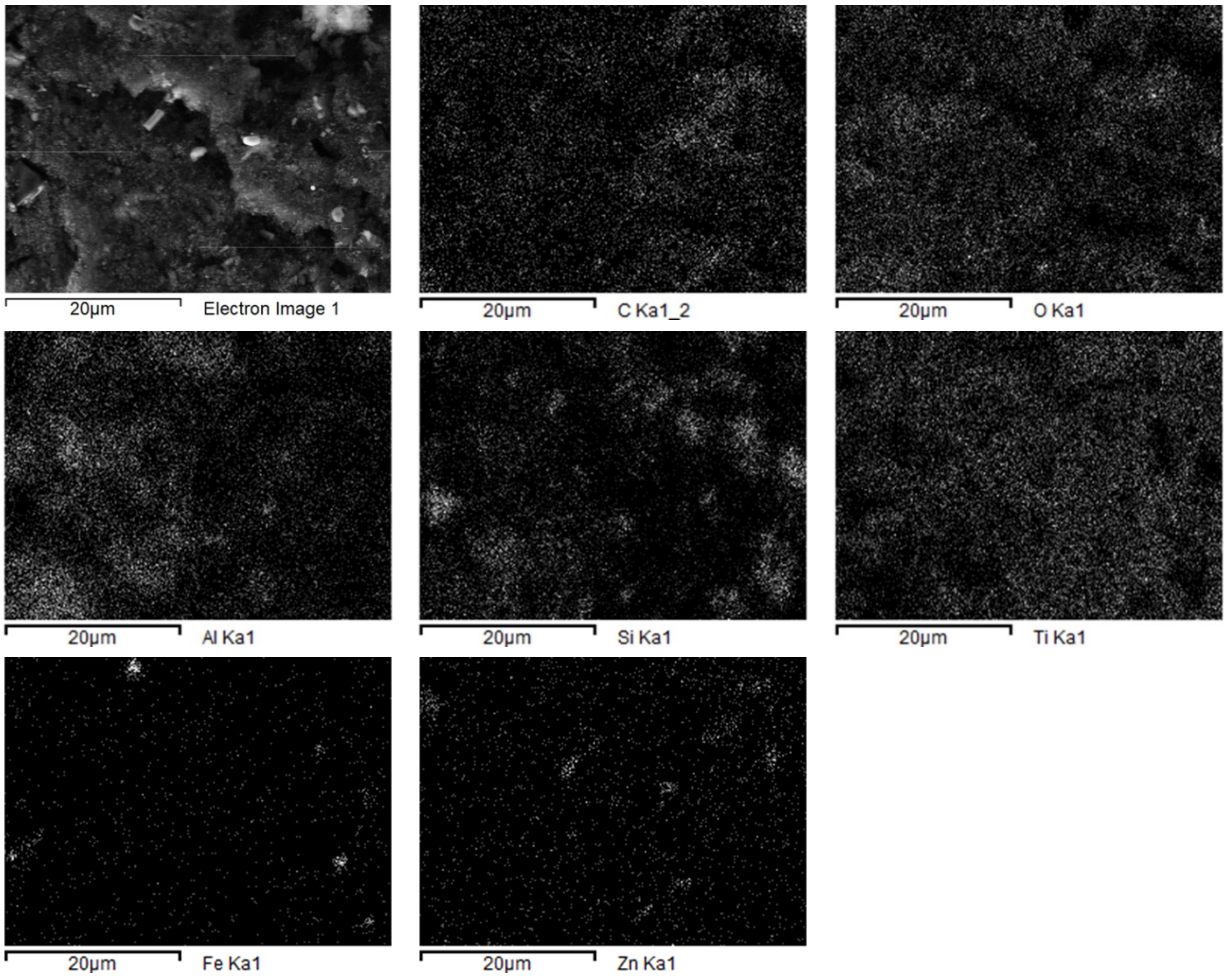
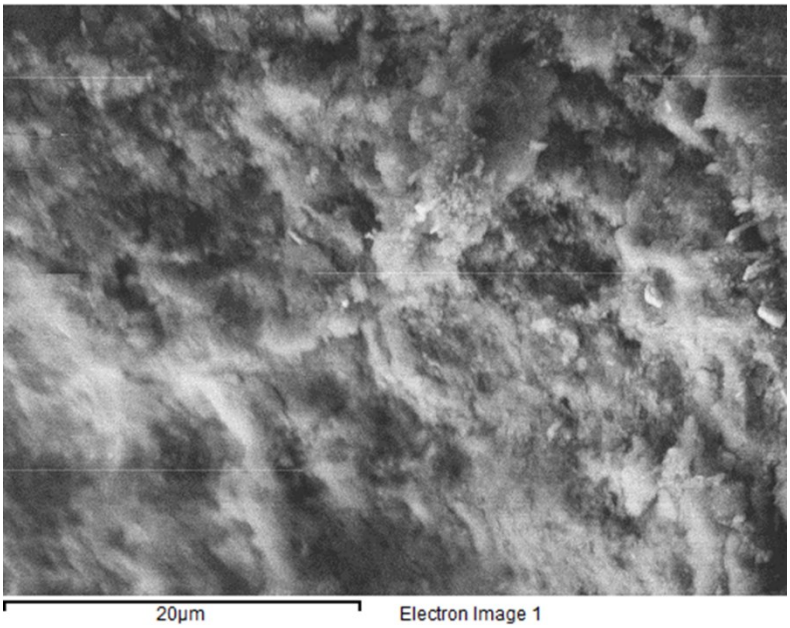


Figure A.11. EDS Elemental Mapping of Paint Collected from Exterior Web.

Element	Weight %	Atomic %
C K	31.43	42.77
O K	48.41	49.45
Al K	1.78	1.08
Si K	4.50	2.62
S K	0.32	0.16
Cl K	0.07	0.03
Ca K	0.06	0.02
Ti K	5.47	1.87
Fe K	0.13	0.04
Zn K	7.82	1.96
Totals	100.00	



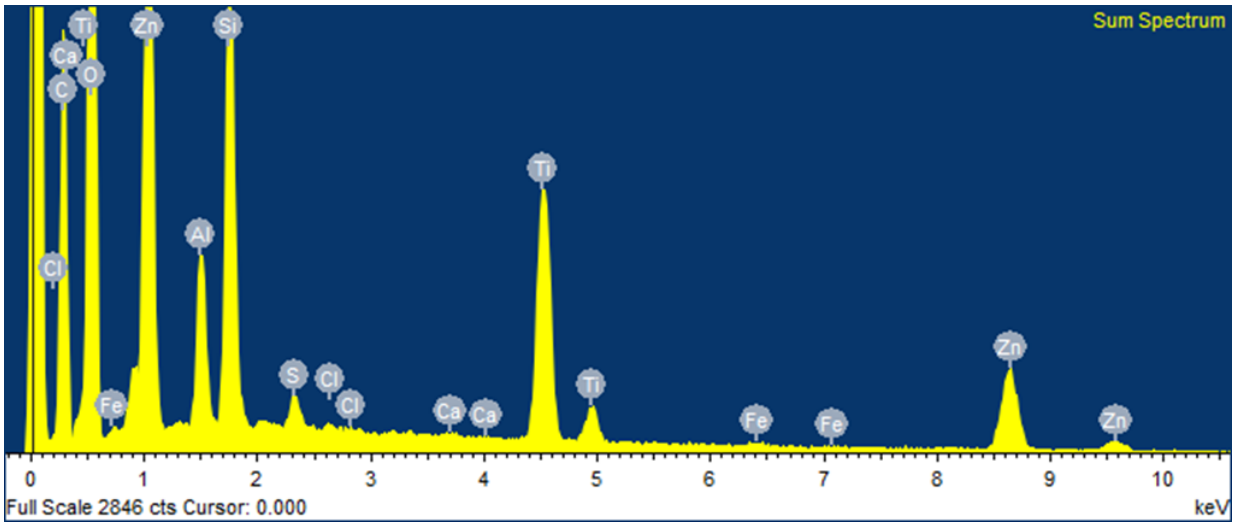


Figure A.12. SEM Image and EDS Spectrum of the Paint Collected from Interior Web of the Girder.

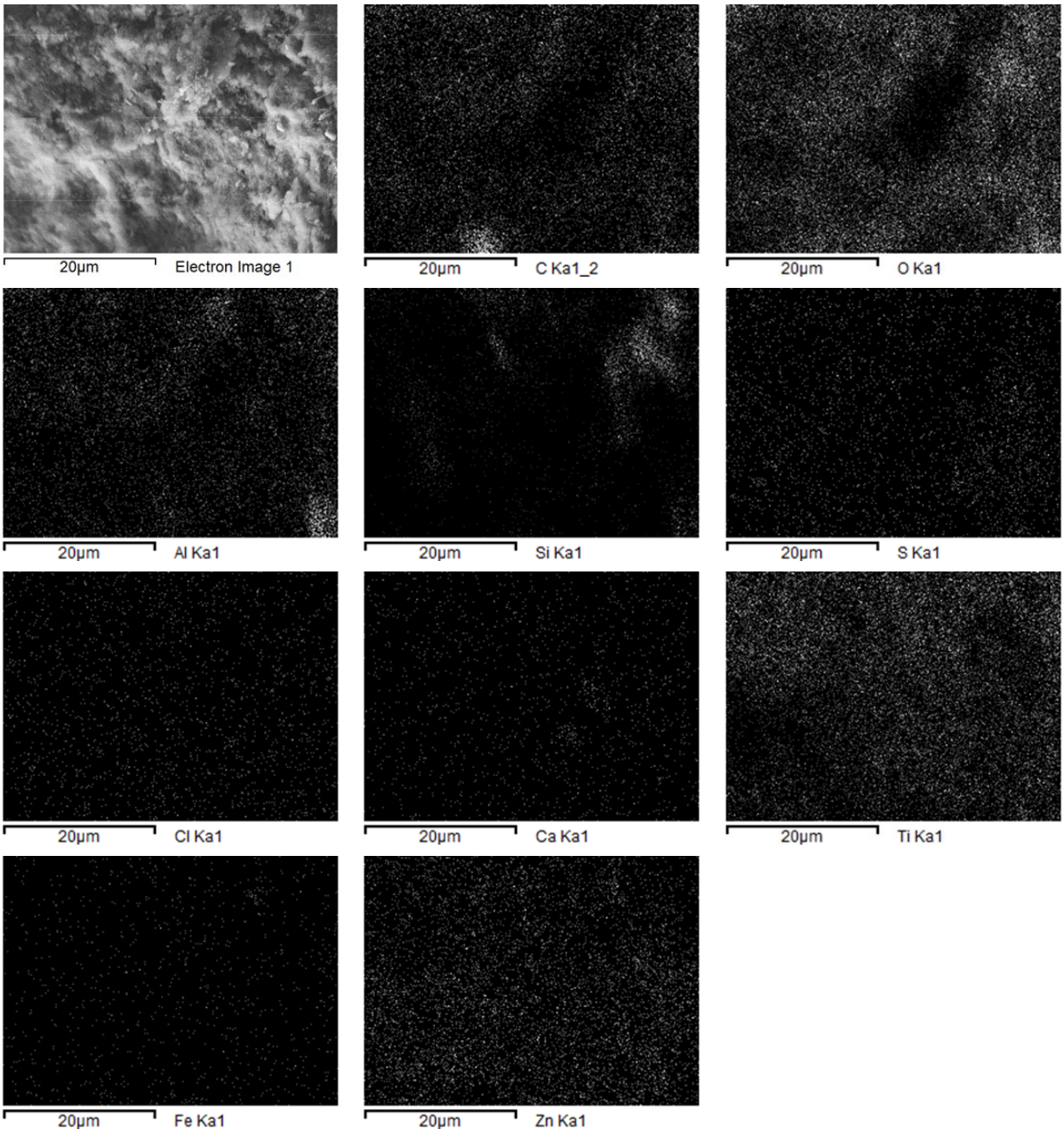
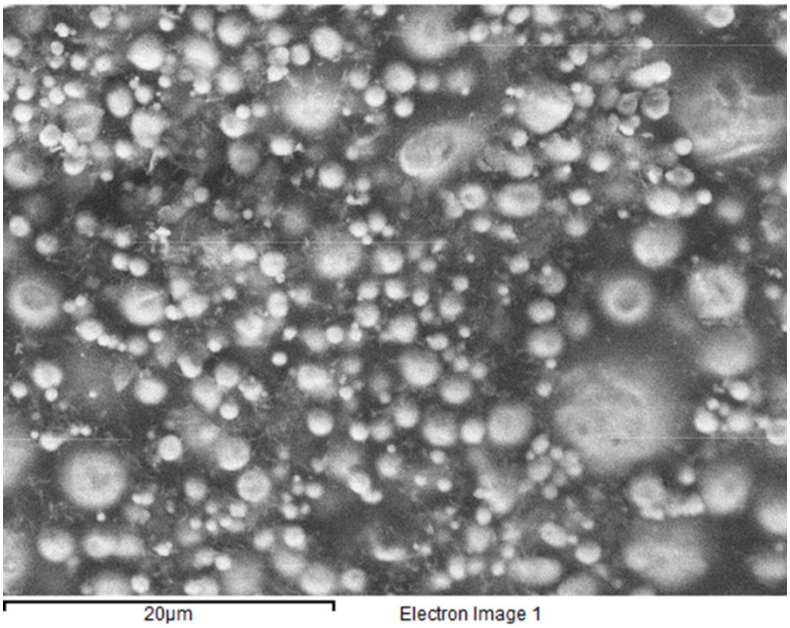


Figure A.13. EDS Elemental Mapping of Paint Collected from Interior Web.

Element	Weight %	Atomic %
C K	47.26	76.11
O K	8.65	10.45
Al K	0.44	0.31
Si K	0.30	0.20
Fe K	1.78	0.62
Zn K	41.58	12.30
Totals	100.00	



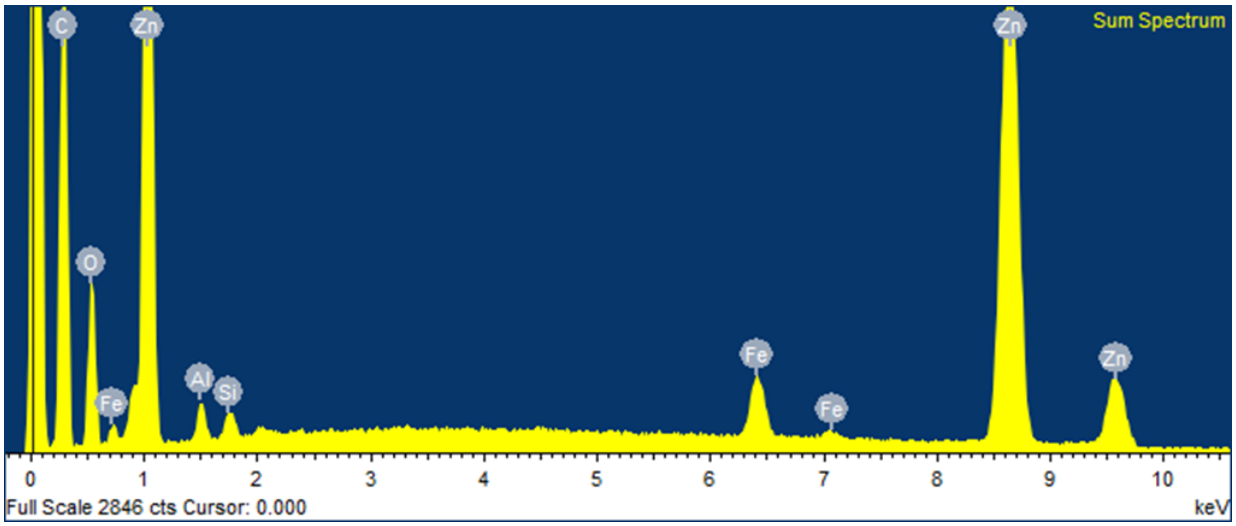


Figure A.14. SEM Image and EDS Spectrum of the Paint Collected from Interior Web of the Girder.

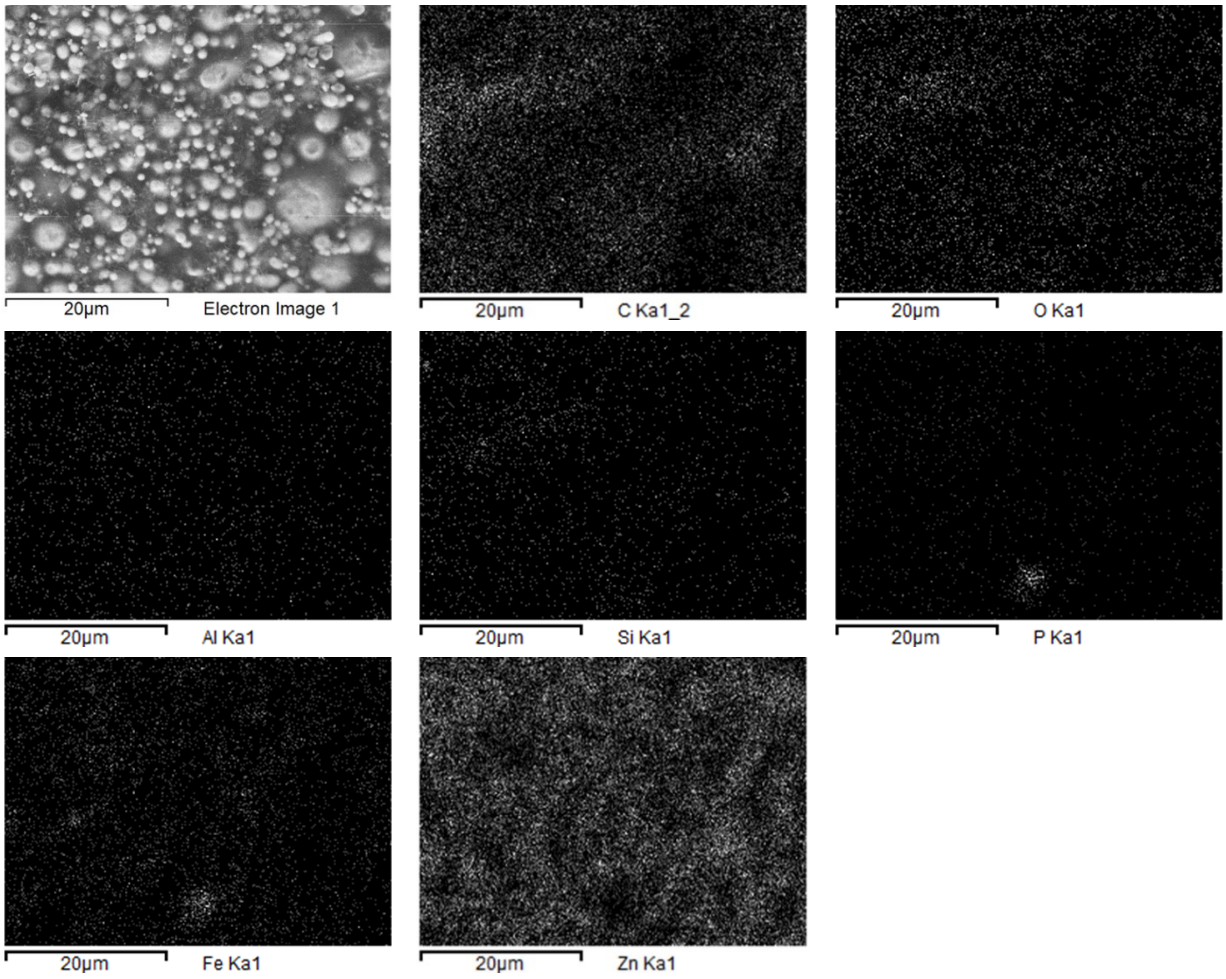


Figure A.15. EDS Elemental Mapping of Paint Collected from Interior Web.

A.2. BRY-PS-01

- Running River ln over Doe Run Creek
- Bridge ID 172390AA0291001, Coordinates (30.23199, -96.14536), Washington County
- Continuous steel I beam painted with System II type paint
- Built 2004
- Date of Inspection: October 20, 2020; girder inspection carried near abutment ends on girders within approximately four feet from the abutment
- Revisited for pH test and scrape test
- No visual inspection on deck
- Location for Testing: B1B2-G1, B1B2-G5, B1B2-G10, B5-G1, B5-G5, B5-G7, B5-G10



Figure A.16. Typical Elevation of BRY-PS-01

A.2.1. Observed Condition

Complete paint failure observed on all girders at northeast abutment. Painting failure and widespread rusting is also observed on steel bents and piles at several locations. There is an accumulation of debris underneath the middle span of the bridge. This bridge is an off-system bridge. From visual inspection it is observed that the spans of bridge have not been painted at the same time and the girders appear to be much older than the bridge-built year suggesting that it came from another TxDOT bridge that got replaced. Moreover, the inspection picture also suggests that the beams are older than the built year. Pitting is observed on webs and flanges at several locations near northeast abutment.



(a) Complete Paint Failure Observed on all Girders Near East Abutment



(b) Complete Paint Failure on Girder 8 Near East Abutment



(c) Exterior Girder in Good Condition Near West Abutment



(d) Paint on Stiffener and Joints in Good Condition



(e) Pile and Bent Cap



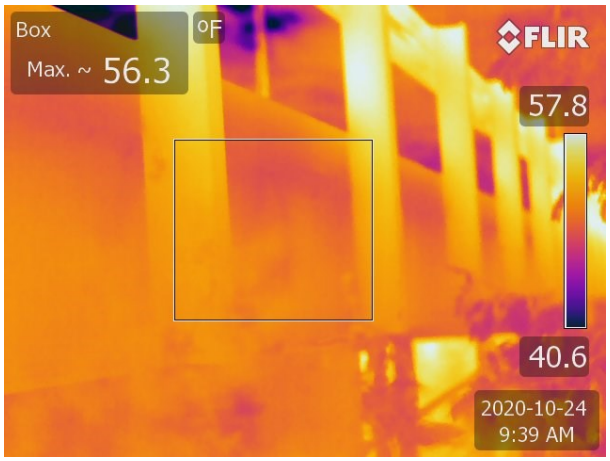
(f) Debris Collected on the Secondary

Figure A.17. Paint Condition on the Girder of BRY-PS-01.

A.2.2. NDT Results



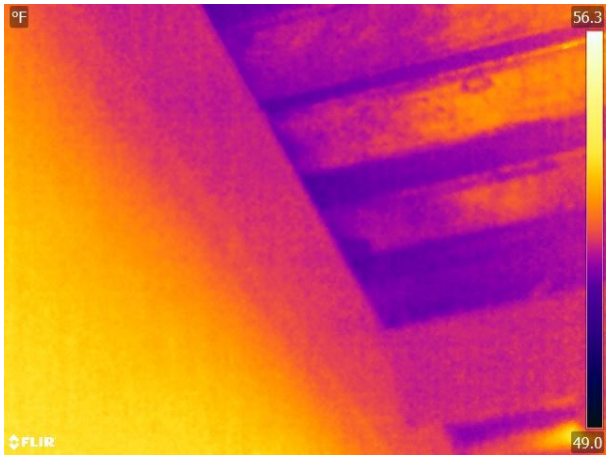
(a) Digital Image of Interior Face of I Beam



(b) Thermal Image of Interior Face of I Beam



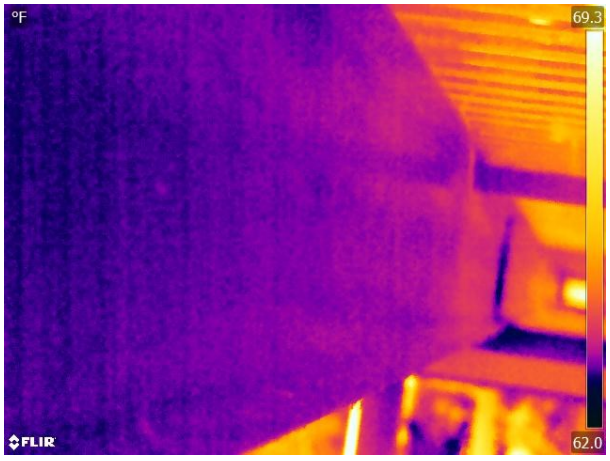
(c) Digital Image of Top Flange Showing Corrosion



(d) Thermal Image of Top Flange Showing Corrosion



(e) Digital image of the Interior Face of I Beam (G7F2)



(f) Thermal image of the exterior of I beam (G7F2)

Figure A.18. Digital and Thermal Image of Painted Girder on BRY-PS-01.

Table A-5. Field Inspection Results for BRY-PS-01.

Location	Cl^- Conc. (ppm)	pH Test	Thickness (µm)	Thickness (inch)	Visual Inspection
B5-G1F1 TF Bot. Int.	-		Measured R1 74.5 R2 89.2 R3 825.3 Design Paint 140-381	Measured R1 0.445 R2 0.442 R3 0.461 R_Avg 0. Design	Rust Grade– 10 Blistering– Not observed Discoloration– Not observed Flaking– Not observed Delamination– Not observed
B5-G1F1 Web Int.	1		Measured R1 113 R2 142 R3 129 Design Paint 140-381	Measured R1 0.355 R2 0.367 R3 0.369 R_Avg Design	Rust Grade– 10 Blistering– Not observed Discoloration– Not observed Flaking– Not observed Delamination– Not observed
B5-G1F1 BF Bot Int.	-		Measured R1 52.6 R2 53.1 R3 64.8 Design Paint 140-381	Measured R1 0.447 R2 0.449 R3 0.458 R_Avg 0 Design	Rust Grade– 10 Blistering– Not observed Discoloration– observed on top face of Bottom Flange Flaking– Not observed Delamination– Not observed
B5-G5F1 TF Bot. Ext.	-		Measured R1 69.2 R2 115 R3 99.2 Design Paint 140-381	Measured R1 0.445 R2 0.446 R3 0.448 R_Avg 0. Design	Rust Grade– 0 Blistering– Not observed Discoloration– Not observed Flaking– Not observed Delamination– Not observed
B5-G5F1 Web. Ext.	1		Measured R1 118 R2 141 R3 135 Design Paint 140-381	Measured R1 0.371 R2 0.371 R3 0.374 R_Avg 0 Design	Rust Grade– 0 Blistering–Not observed Discoloration– Not observed Flaking– Not observed Delamination– Not observed
B5-G5F1 BF Bot. Ext.	-		Measured R1 48.5 R2 54.6 R3 67.2 Design Paint 140-381	Measured R1 0.438 R2 0.439 R3 0.435 R_Avg Design	Rust Grade – 0 Blistering– Not observed Discoloration– observed on top face of Bottom Flange Flaking– Not observed Delamination– Not observed

Table A-6. Field Inspection Results for BRY-PS-01.

Location	Cl^- Conc. (ppm)	pH Test	Thickness (µm)	Thickness (inch)	Visual Inspection
B5-G7F2 TF Bot. Int.	-		Measured R1 72.5 R2 108 R3 103 Design Paint 140-381	Measured R1 0.450 R2 0.445 R3 0.443 R_Avg 0. Design	Rust Grade – 10 Blistering – Not observed Discoloration – Not observed Flaking – Not observed Delamination – Not observed
B5-G7F2 Web Int.	-		Measured R1 105 R2 151 R3 131 Design Paint 140-381	Measured R1 0.355 R2 0.358 R3 0.361 R_Avg 0. Design	Rust Grade– 10 Blistering– Not observed Discoloration– Not observed Flaking– Not observed Delamination– Not observed
B5-G7F2 BF Bot Int.	-		Measured R1 48.6 R2 57.2 R3 63.7 Design Paint 140-381	Measured R1 0.467 R2 0.470 R3 0.462 R_Avg 0. Design	Rust Grade– 10 Blistering– Not observed Discoloration– observed on top face of Bottom Flange Flaking– Not observed Delamination – Not observed
B5-G10F2 TF Bot. Ext.	-		Measured R1 82.3 R2 103 R3 95.5 Design Paint 140-381	Measured R1 0.444 R2 0.444 R3 0.443 R_Avg 0. Design	Rust Grade– 10 Blistering– Not observed Discoloration– Not observed Flaking– Not observed Delamination– Not observed
B5-G10F2 Web. Ext.	-		Measured R1 109 R2 147 R3 123 Design Paint 140-381	Measured R1 0.365 R2 0.368 R3 0.367 R_Avg 0. Design	Rust Grade– 10 Blistering– Not observed Discoloration– Not observed Flaking– Not observed Delamination– Not observed
B5-G10F2 BF Bot. Ext.	-		Measured R1 45.5 R2 65.3 R3 56.3 Design Paint 140-381	Measured R1 0.492 R2 0.468 R3 0.480 R_Avg 0. Design	Rust Grade– 0 Blistering– Not observed Discoloration– observed on top face of Bottom Flange Flaking– Not observed Delamination– Not observed

Table A-7. Field Inspection Results for BRY-PS-01

Location	Cl^- Conc. (ppm)	pH Test	Thickness (µm)	Thickness (inch)	Visual Inspection
B1B2-G1F1 TF Bot. Int.	-		Measured R1 124 R2 114 R3 140 Design Paint 140-381	Measured R1 0.467 R2 0.470 R3 0.471 R_Avg 0. Design	Rust Grade– 0 Blistering– Not observed Discoloration– Not observed Flaking– Not observed Delamination– Not observed
B1B2-G1F1 Web Int.	1		Measured R1 38.4 R2 43.4 R3 48.4 Design Paint 140-381	Measured R1 0.319 R2 0.318 R3 0.321 R_Avg 0. Design	Rust Grade– 0 Blistering– Not observed Discoloration– Not observed Flaking– Not observed Delamination– Not observed
B1B2-G1F1 BF Bot Int.	-		Measured R1 62.7 R2 64.2 R3 68.9 Design Paint 140-381	Measured R1 0.486 R2 0.479 R3 0.481 R_Avg 0. Design	Rust Grade– 0 Blistering– Not observed Discoloration– observed on top face of Bottom Flange Flaking– Not observed Delamination– Not observed
B1B2-G5F1 TF Bot. Ext.	-		Measured R1 30.6 R2 21.2 R3 39.5 Design Paint 140-381	Measured R1 0.475 R2 0.476 R3 0.475 R_Avg 0. Design	Rust Grade– 0 Blistering– Not observed Discoloration– Not observed Flaking– Not observed Delamination– Not observed
B1B2-G1F1 F1 Web. Ext.	-		Measured R1 73.6 R2 110 R3 98.8 Design Paint 140-381	Measured R1 0.320 R2 0.319 R3 0.319 R_Avg 0. Design	Rust Grade– 0 Blistering– Not observed Discoloration– Not observed Flaking– Not observed Delamination– Not observed
B1B2-G1F1 F2 BF Bot. Ext.	-		Measured R1 64.7 R2 38.1 R3 45.7 Design Paint 140-381	Measured R1 0.469 R2 0.465 R3 0.464 R_Avg 0. Design	Rust Grade– 0 Blistering– Not observed Discoloration– observed on top face of Bottom Flange Flaking– Not observed Delamination– Not observed

Table A-8. Field Inspection Results for BRY-PS-01

Location	Cl^- Conc. (ppm)	pH Test	Thickness (µm)	Thickness (inch)	Visual Inspection
B1B2-G10F2 TF Bot. Int.	-		Measured R1 33.5 R2 23.4 R3 35.2 Design Paint 140-381	Measured R1 0.467 R2 0.475 R3 0.474 R_Avg 0. Design	Rust Grade– 0 Blistering– Not observed Discoloration– Not observed Flaking– Not observed Delamination– Not observed
B1B2-G10F2 Web Int.	-		Measured R1 75.4 R2 106 R3 90.1 Design Paint 140-381	Measured R1 0.327 R2 0.333 R3 0.329 R_Avg 0. Design	Rust Grade– 0 Blistering– Not observed Discoloration– Not observed Flaking– Not observed Delamination– Not observed
B1B2-G10F2 BF Bot Int.	-		Measured R1 59.6 R2 36.2 R3 43.4 Design Paint 140-381	Measured R1 0.495 R2 0.494 R3 0.498 R_Avg 0. Design	Rust Grade – 0 Blistering – Not Found Discoloration – Not Found Flaking – Not Found Delamination – Not Found

Table A-9. Paint System Information

Cohesive Failure Layer		Adhesive Failure Layer	
Code	**Description**	**Code**	**Description**
A	Substrate	A/B	Substrate & Layer 1
B	Layer 1 (Gray)	B/Y	Layer 1 & Layer 2
Y	Glue	Y/Z	Glue & Dolly

A.2.3. Pull-off Adhesion Result

Table A-10. Pull-off Adhesion Results for BRY-PS-01

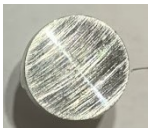
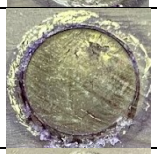
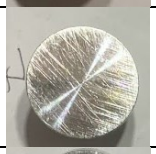
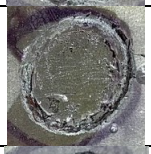
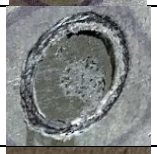
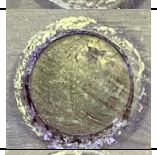
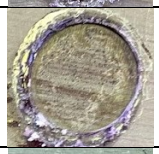
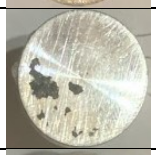
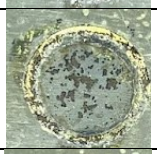
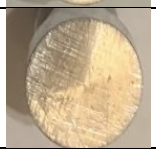
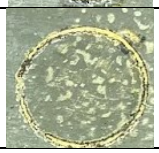
Location	Dolly Face	Substrate Face	Test Result (psi)	Attributes	Failure Type
B5-G1F1			140	100% Y/Z	100% Glue Failure
			870	100% Y/Z	100% Glue Failure
			646	100% Y/Z	100% Glue Failure
B5-G5F1			363	100% Y/Z	100% Glue Failure
			454	100% Y/Z	100% Glue Failure
			174	100% Y/Z	100% Glue Failure
B5-G7F2			702	100% Y/Z	100% Glue Failure
			966	100% Y/Z	100% Glue Failure
			860	100% Y/Z	100% Glue Failure

Table A-11. Pull-off Adhesion Results for BRY-PS-01

Location	Dolly Face	Substrate Face	Test Result (psi)	Attributes	Failure Type
B5-G10F2			**848**	100% Y/Z	100% Glue Failure
			**0**	100% Y/Z	100% Glue Failure
			**1703**	100% Y/Z	100% Glue Failure
B5-G3F1			**630**	100% Y/Z	100% Glue Failure
			**612**	100% Y/Z	100% Glue Failure
			**447**	100% Y/Z	100% Glue Failure
B1B2-G1F1			**585**	100% Y/Z	100% Glue Failure
			**518**	100% Y/Z	100% Glue Failure
			**746**	100% Y/Z	100% Glue Failure

A.2.4. Optical Microscopy Results

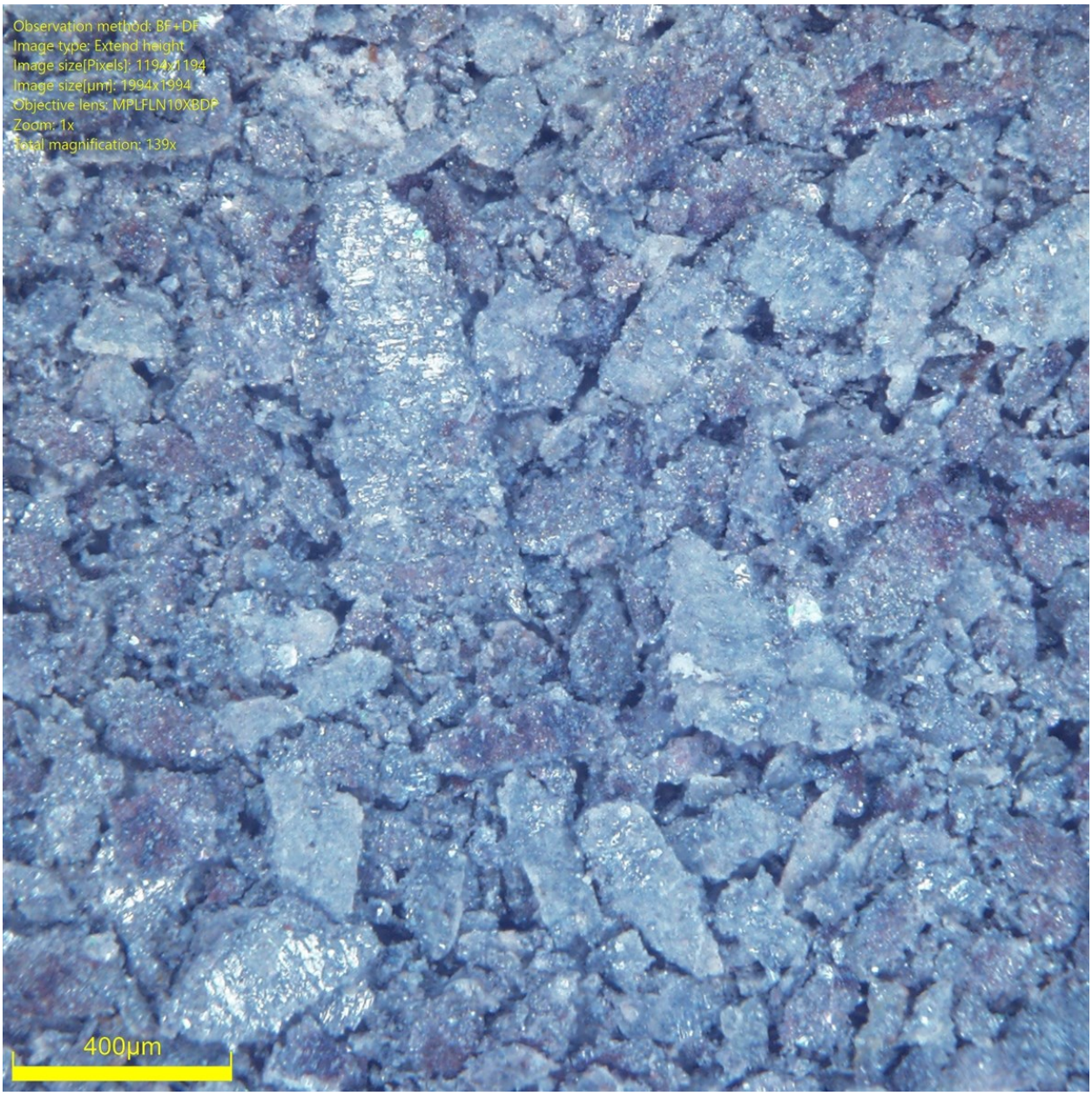


Figure A.19. Paint System Examined by Optical Microscope (BRY–PS–01 on Girder 1)

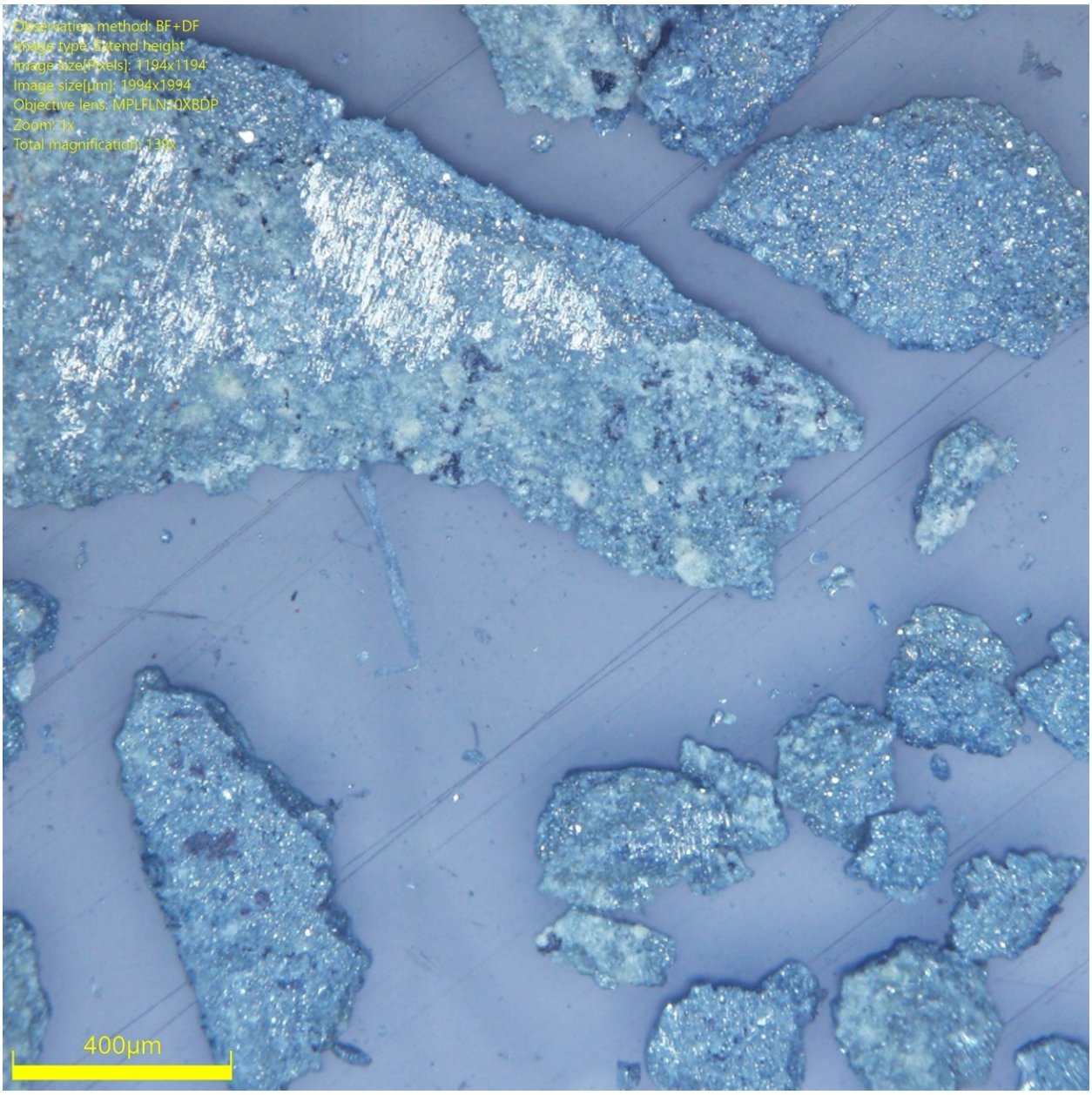


Figure A.20. Paint System Examined by Optical Microscope (A1G5F1)

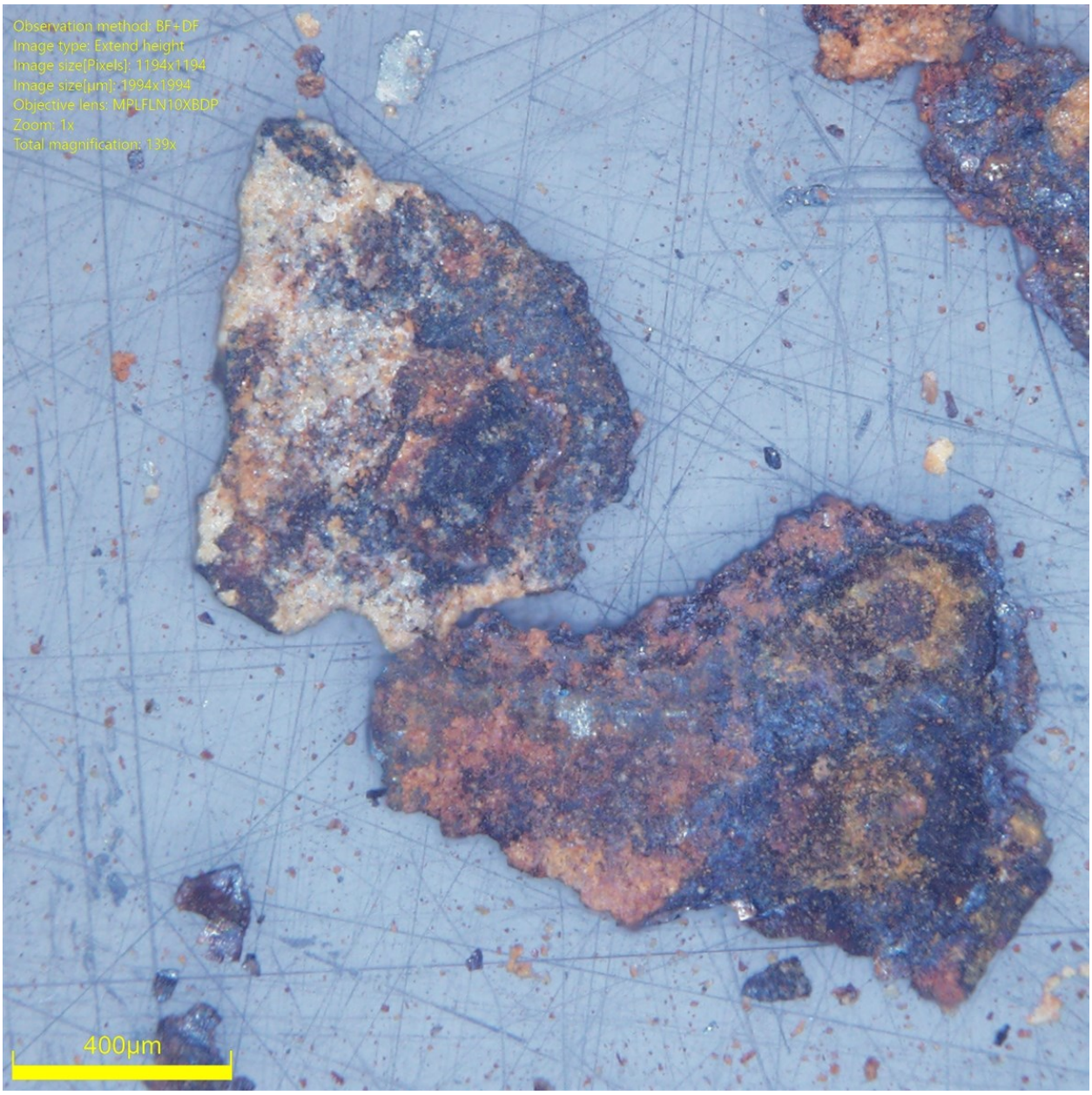
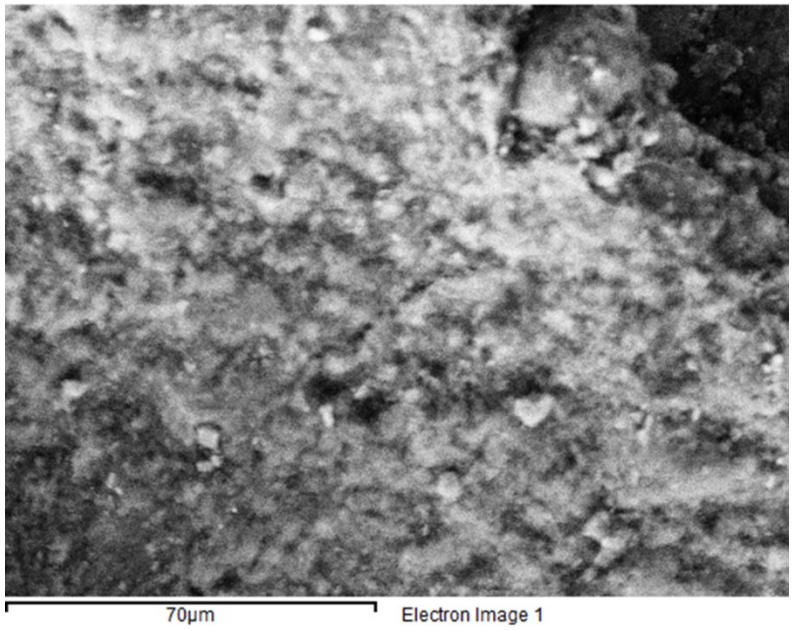


Figure A.21. Corroded Paint System Examined by Optical Microscope (A1G2F1)

A.2.5. SEM/EDS Results

Element	Weight %	Atomic %
C K	4.41	9.34
O K	36.58	58.13
Mg K	0.29	0.30
Al K	5.50	5.18
Si K	11.06	10.02
P K	0.14	0.12
S K	0.25	0.20
K K	0.36	0.23
Ca K	0.28	0.18
Ti K	0.26	0.14
Fe K	4.04	1.84
Zn K	36.83	14.32
Totals	100.00	



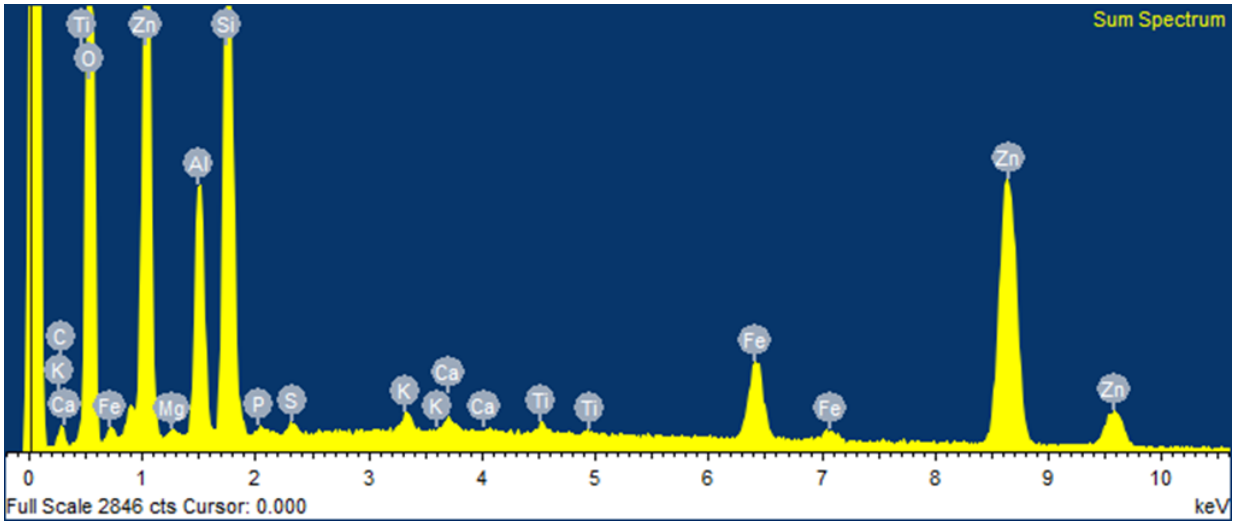


Figure A.22. SEM image of Paint and EDS Spectrum of the Paint Collected from Exterior Web of the Girder (A1G1F1)

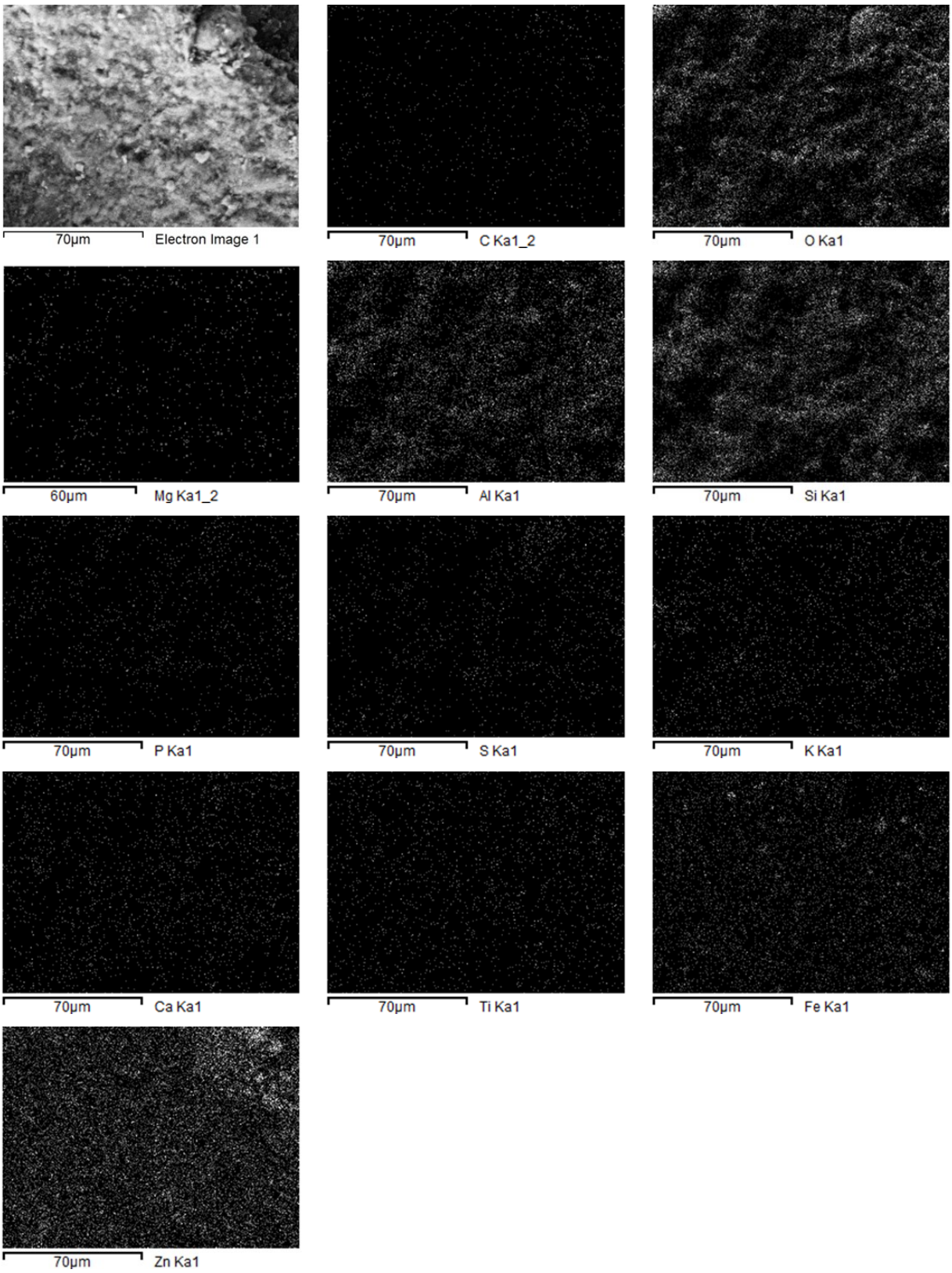
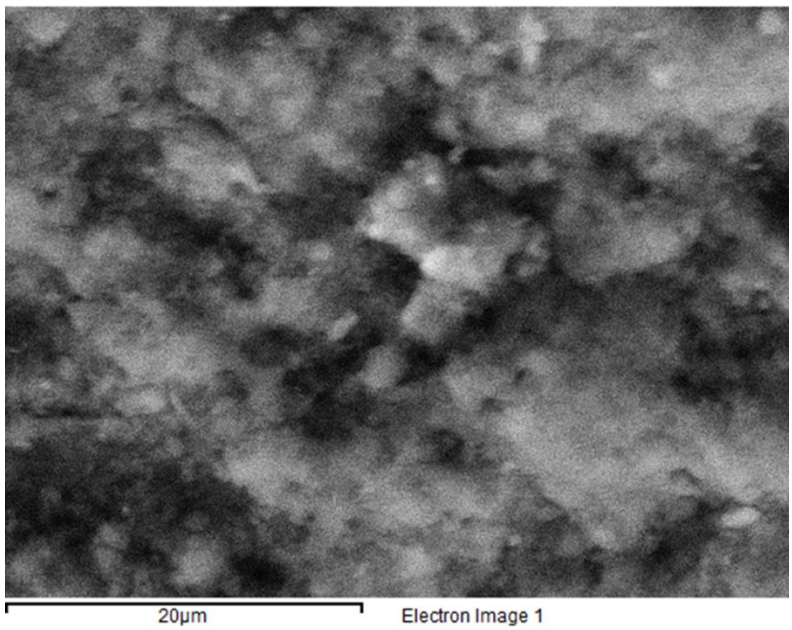
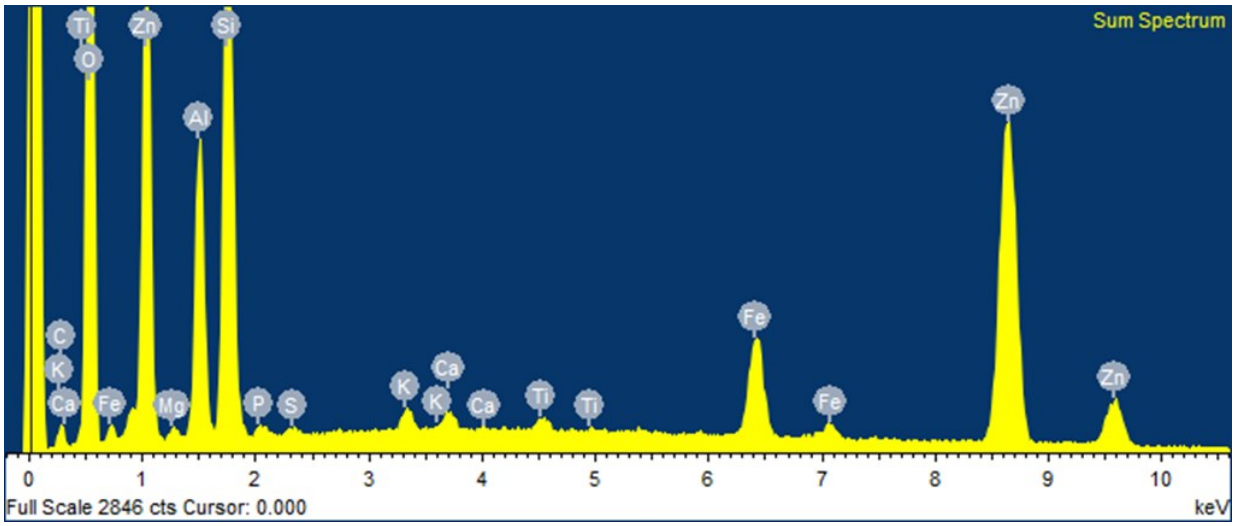


Figure A.23. EDS Elemental Mapping of Paint Collected from Exterior

Element	Weight %	Atomic %
C K	4.06	8.87
O K	34.33	56.37
Mg K	0.38	0.41
Al K	5.57	5.43
Si K	10.98	10.27
P K	0.18	0.16
S K	0.13	0.11
K K	0.38	0.26
Ca K	0.32	0.21
Ti K	0.35	0.19
Fe K	4.51	2.12
Zn K	38.81	15.60
Totals	100.00	



(a) SEM Image of Paint



(b) EDS Spectrum of Paint Showing Elemental Peaks

Figure A.24. SEM image of Paint and EDS Spectrum of the Paint Collected from Exterior Web of the Girder (A1G1F1)

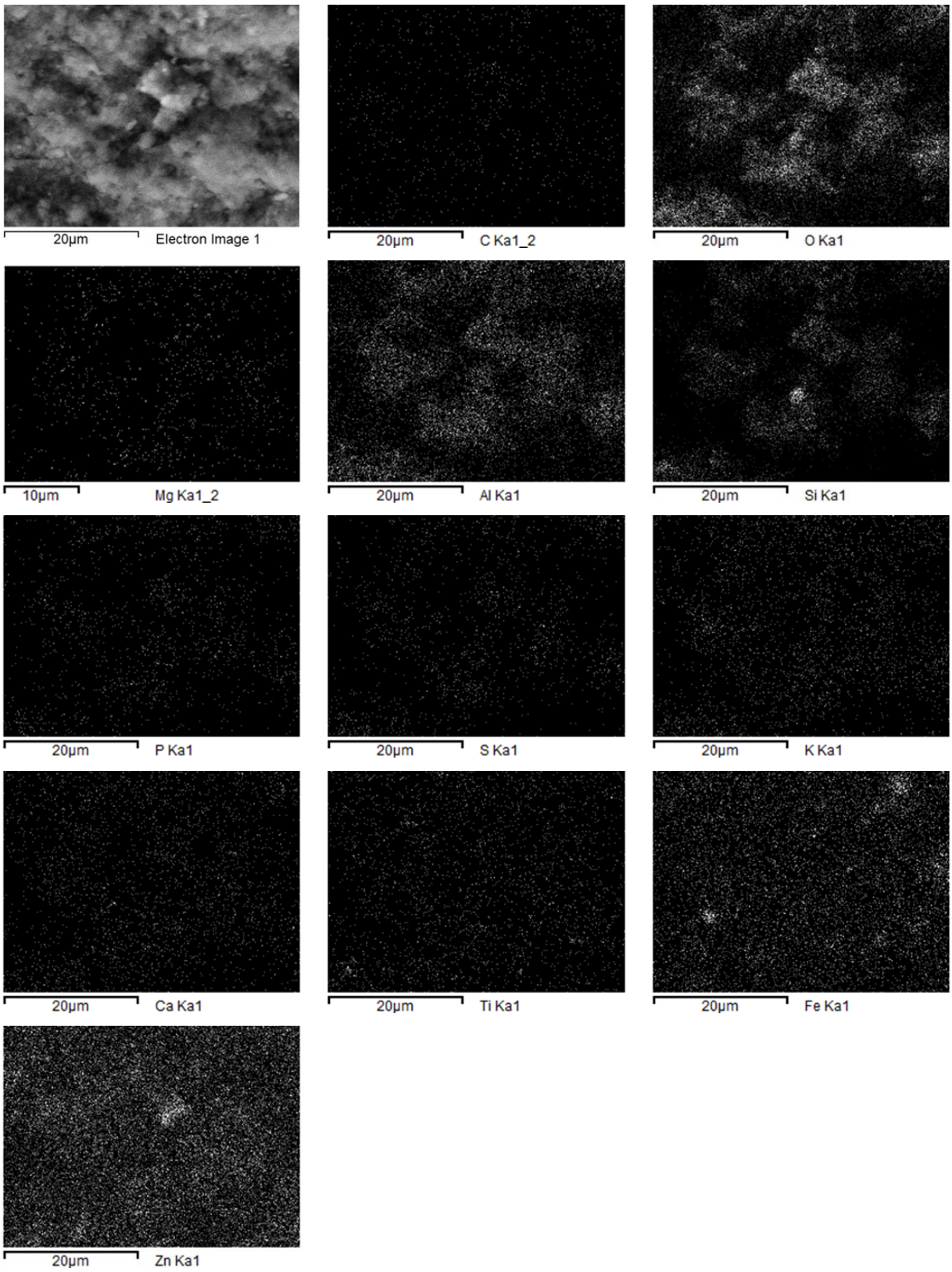
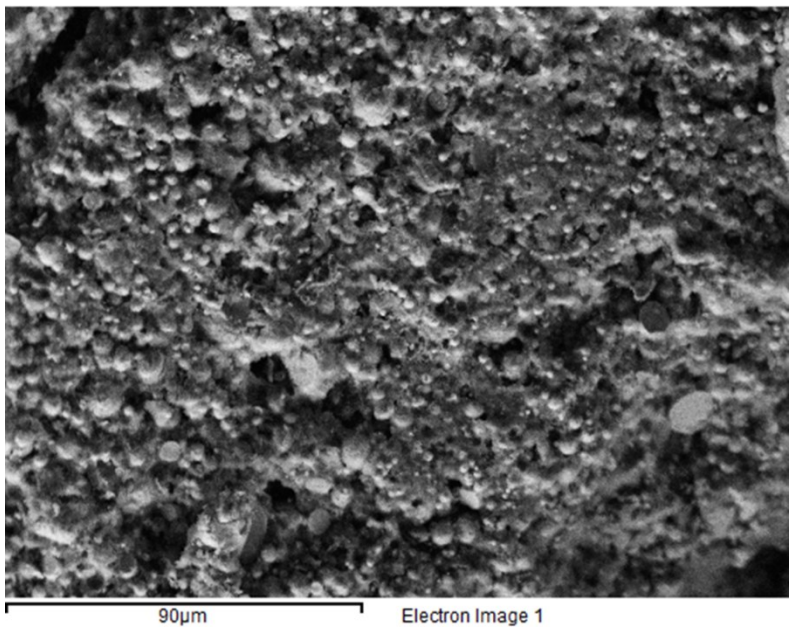


Figure A.25. EDS Elemental Mapping of Paint Collected from Exterior Girder (A1G1F1)

Element	Weight %	Atomic %
C K	5.21	14.32
O K	21.00	43.29
Al K	2.46	3.00
Si K	4.85	5.70
Ca K	0.33	0.27
Fe K	0.91	0.54
Zn K	64.89	32.74
Zr L	0.35	0.13
Totals	100.00	



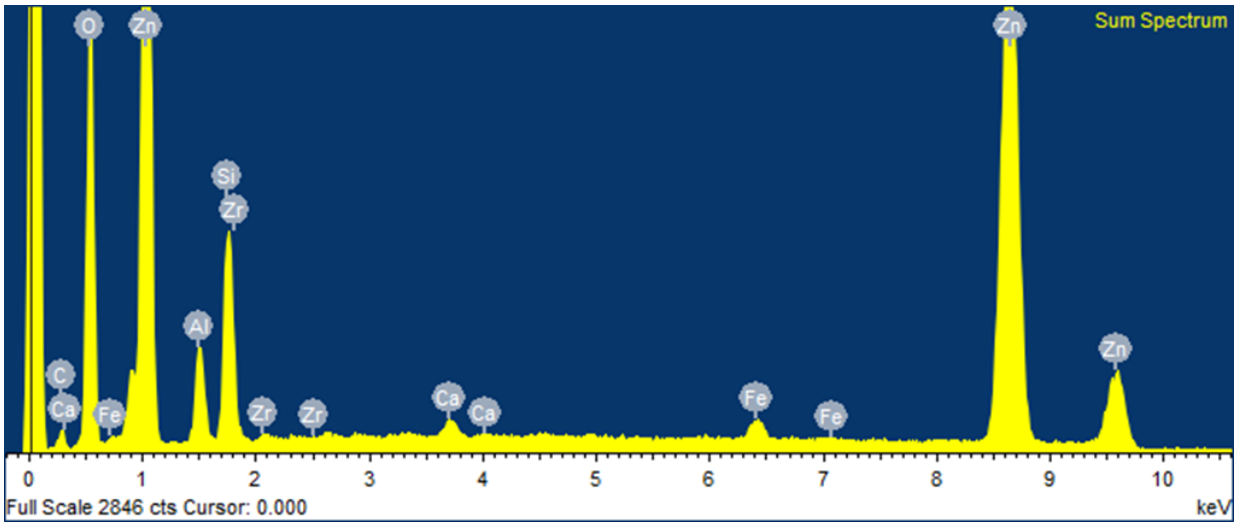


Figure A.26. SEM Image and EDS Spectrum of the Paint Collected from Exterior Web of the Girder (A1G5F1)

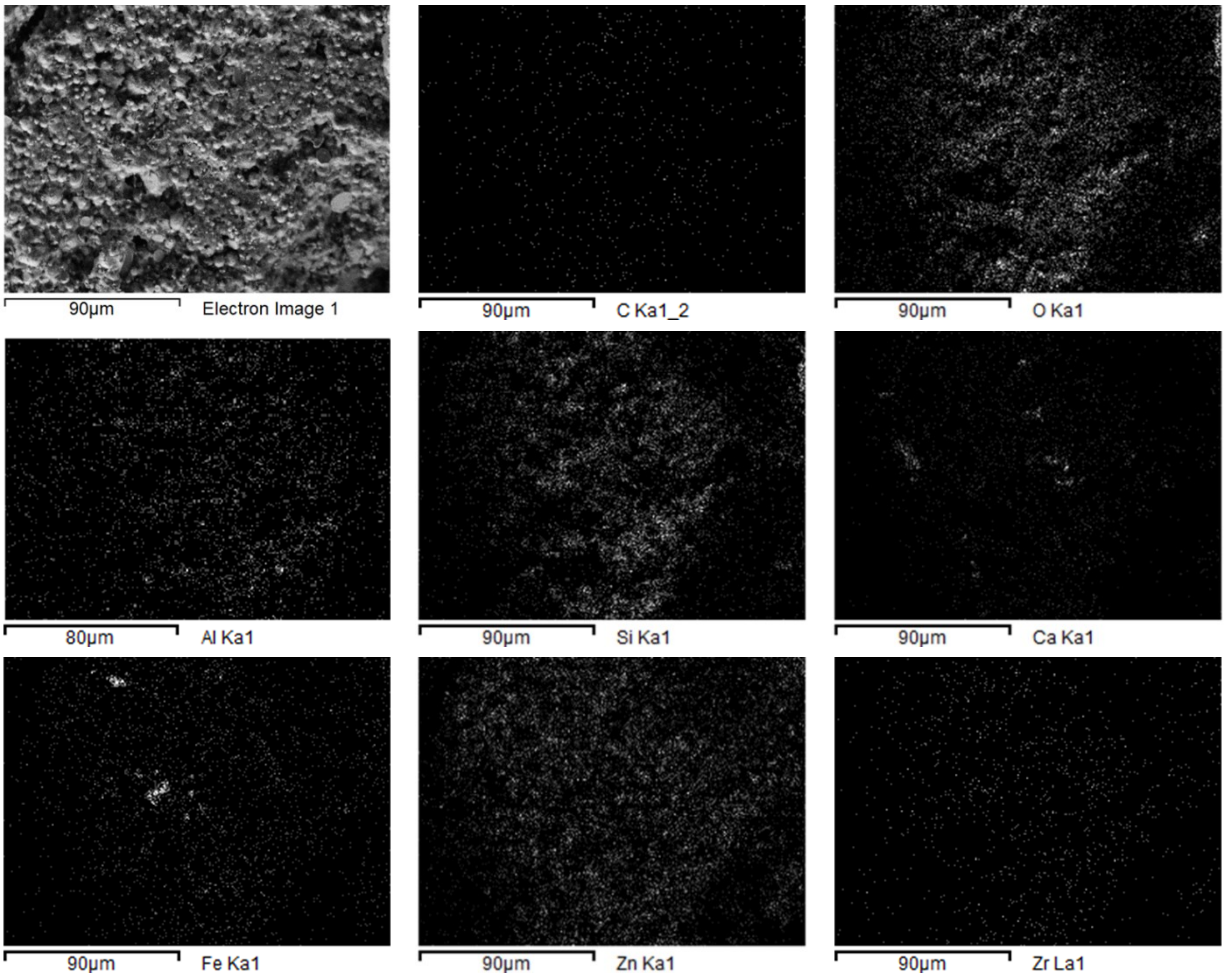
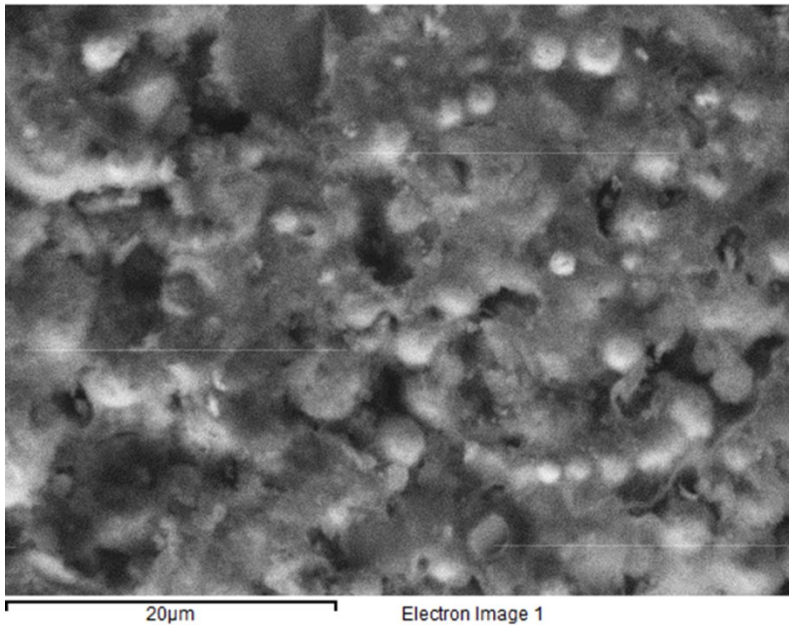


Figure A.27. EDS Elemental Mapping of Paint Collected from Exterior Girder (A1G5F1)

Element	Weight %	Atomic %
C K	4.44	11.32
O K	26.25	50.21
Al K	2.50	2.84
Si K	6.39	6.97
S K	0.10	0.10
Cl K	0.16	0.14
Ca K	0.71	0.54
Fe K	0.79	0.43
Zn K	58.65	27.45
Totals	100.00	



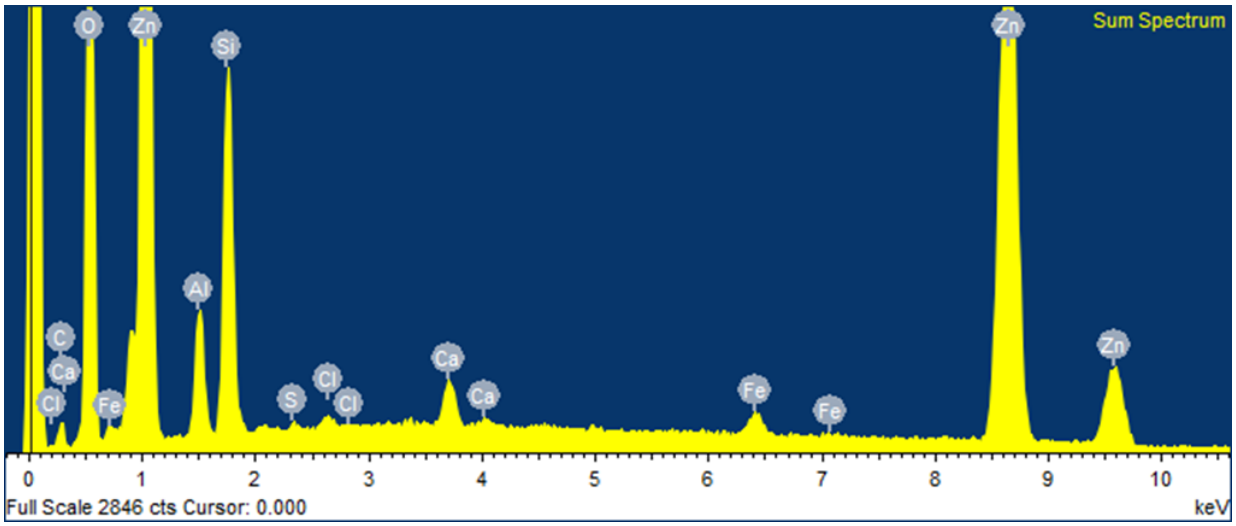


Figure A.28. SEM Image of Paint and EDS Spectrum of the Paint Collected from Exterior Web of the Girder (A1G5F1)

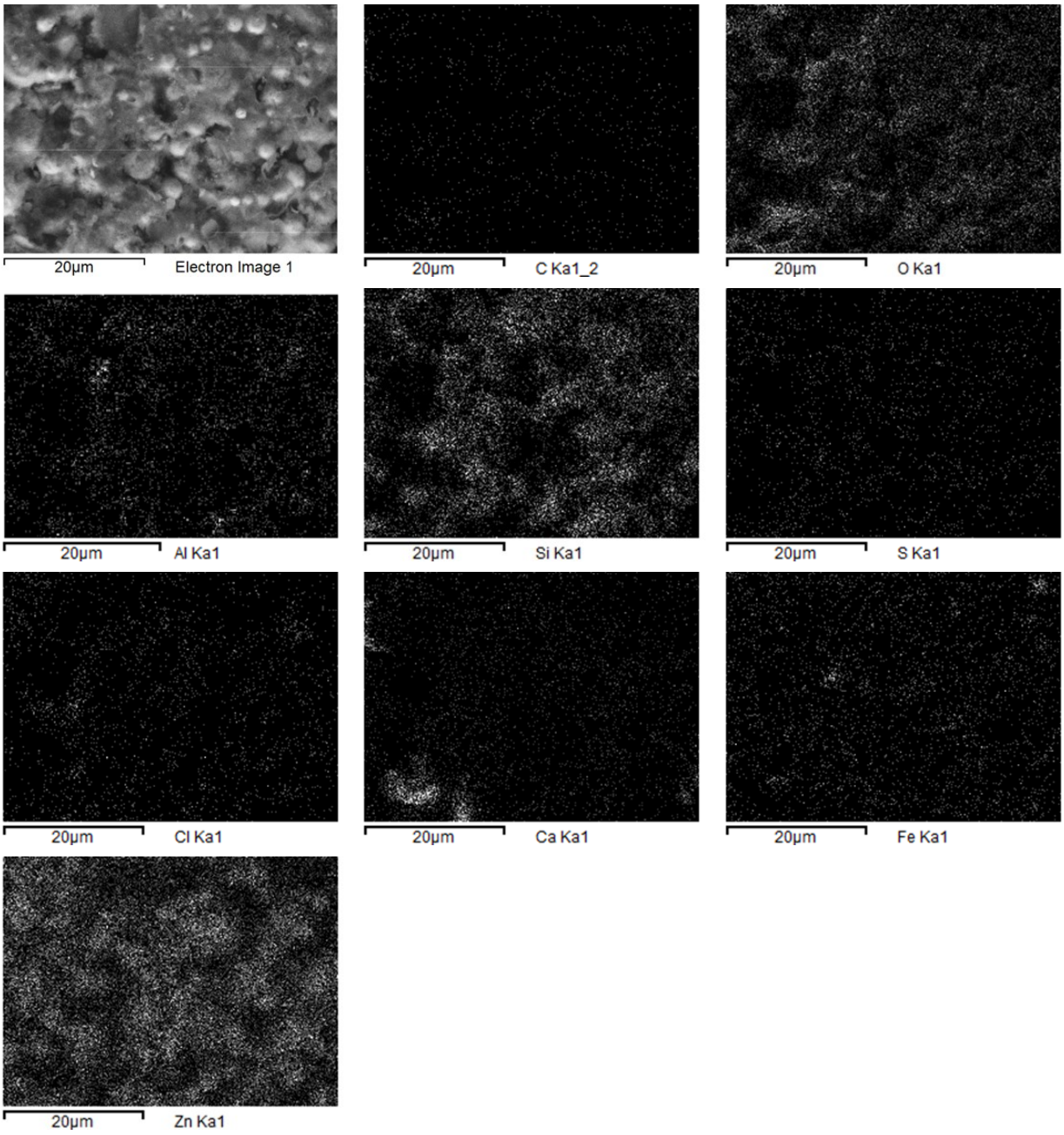


Figure A.29. EDS Elemental Mapping of Paint Collected from Exterior Girder (A5G1F1)

A.3. ATL-PS-01

- CR 4106 over Bear Creek
- Bridge ID 191030AA0109001, Coordinates (33.419281, -94.050253), Harrison County
- Continuous steel I beam painted with supposedly lead based paint, but the EDS analysis does not show presence of lead
- Built 2004

- Date of Inspection: October 24, 2020; girder inspection carried near abutment ends on girders within approximately four feet from the abutment
- Revisited for pH test and scrape test
- No visual inspection on deck
- Location for Testing: BN-G1, BN-G3, BN-G6



Figure A.30. Typical Elevation of ATL-PS-01.

A.3.1. Observed Condition

Complete paint failure over the top and bottom flanges. Painting failure and widespread rusting is also observed on webs at several locations. There is accumulation of debris on interior girders due to flooding that may have led to rapid paint deterioration and poultice corrosion. Pitting is also observed on webs and flanges at several locations.



(a) Widespread Paint Failure and Rusting on Web and Flange of Girder 1



(b) Widespread Paint Deterioration and Rusting on Web of Girder 1



(c) Interior Girder (G1F2 and G2F1) Exhibiting Good Paint Condition with Some Patches of Rust



(d) Widespread Paint Deterioration and Rusting on Girder 3



(e) Debris Collected on the Bottom Flange and Angles Connecting Girder



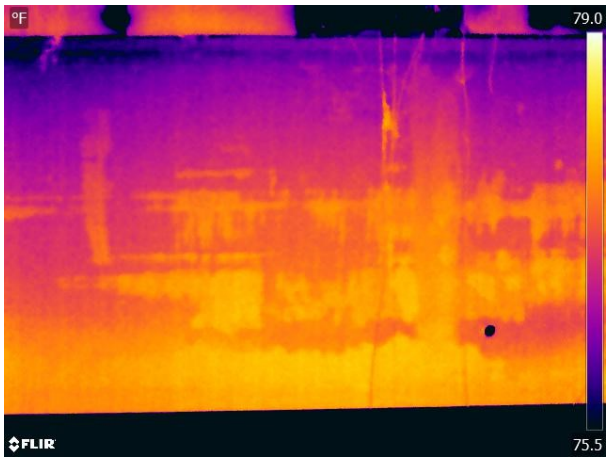
(f) Widespread Paint Deterioration and Rusting on Girder 5

Figure A.31. Paint Condition on the Girder of ATL-PS-01.

A.3.2. NDT Results



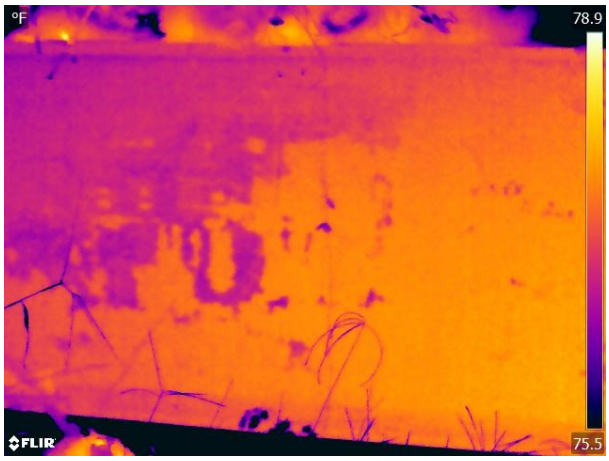
(c) Digital Image of I-Beam



(d) Thermal Image of I-Beam



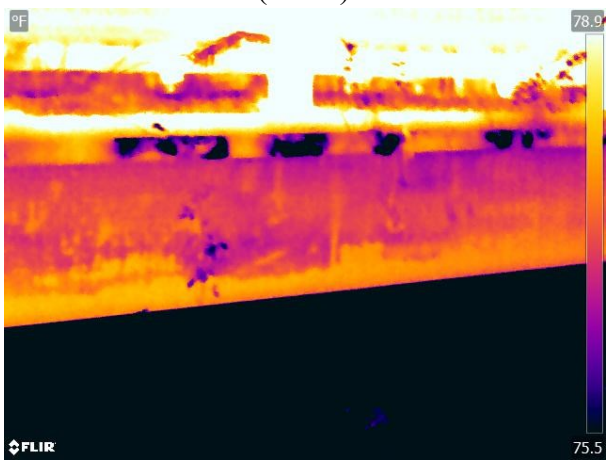
(e) Digital Image of the Exterior face of I Beam (G1F1)



(f) Thermal Image of the Exterior of I Beam (G1F1)



(g) Digital Image Showing Paint Failure and Widespread Rusting on Web and Flange



(h) Thermal Image Showing Paint Failure and Widespread Rusting on Web and Flange

Figure A.32. Digital and Thermal Image of Painted Girder on ATL-PS-01.

Table A-12. Field Inspection Results for ATL-PS-01.

Location	Cl^- Conc. (ppm)	pH Test	Thickness (µm)	Thickness (inch)	Visual Inspection
N-G1F1 TF Bot. Int.	-			Measured R1 0.897 R2 0.904 R3 0.896 R_Avg 0. Design	Rust Grade – 0 Blistering – observed Discoloration – observed Flaking – observed Delamination – observed
N-G1F1 Web Int.				Measured R1 0.581 R2 0.582 R3 0.579 R_Avg Design	Rust Grade – 5 Blistering – observed Discoloration – observed Flaking – observed Delamination – observed
N-G1F1 BF Bot Int.	-			Measured R1 0.902 R2 0.901 R3 0.887 R_Avg 0 Design	Rust Grade – 0 Blistering – observed Discoloration – observed Flaking – observed Delamination – observed
N-G3F1 TF Bot. Int.	-		Measured R1 115 R2 47.2 R3 47.9	Measured R1 0.872 R2 0.866 R3 0.863 R_Avg 0. Design	Rust Grade – 0 Blistering – observed Discoloration – observed Flaking – observed Delamination – observed
N-G3F1 Web. Int.	1		Measured R1 137 R2 131 R3 123	Measured R1 0.587 R2 0.590 R3 0.591 R_Avg 0 Design	Rust Grade – 3 Blistering – observed Discoloration – observed Flaking – observed Delamination – observed
N-G3F1 BF Bot. Int.	-		Measured R1 - R2 - R3 -	Measured R1 0.917 R2 0.892 R3 0.899 R_Avg 0. Design	Rust Grade – 0 Blistering – observed Discoloration – observed Flaking – observed Delamination – observed

Table A-13. Field Inspection Results for ATL-PS-01.

Location	Cl^- Conc. (ppm)	pH Test	Thickness (µm)	Thickness (inch)	Visual Inspection
N-G6F1 TF Bot. Int.	-		Measured R1 78.6 R2 66.9 R3 80.5	Measured R1 0.805 R2 0.809 R3 0.812 R_Avg 0. Design	Rust Grade – 0 Blistering – observed Discoloration – observed Flaking – observed Delamination – observed
N-G6F1 Web Int.	1		Measured R1 87.2 R2 114 R3 109	Measured R1 0.599 R2 0.603 R3 0.597 R_Avg Design	Rust Grade – 0 Blistering – observed Discoloration – observed Flaking – observed Delamination – observed
N-G6F1 BF Bot Int.	-		Measured R1 - R2 - R3 -	Measured R1 0.943 R2 0.936 R3 0.930 R_Avg 0 Design	Rust Grade – 0 Blistering – observed Discoloration – observed Flaking – observed Delamination – observed
S-G1F1 Web Ext. Corroded	-			Measured R1 0.567 R2 0.568 R3 0.569 R_Avg 0. Design	Rust Grade – 0 Blistering – observed Discoloration – observed Flaking – observed Delamination – observed
S-G1F1 Web. Int. Corroded	1			Measured R1 0.593 R2 0.597 R3 0.591 R_Avg 0 Design	Rust Grade – 0 Blistering – observed Discoloration – observed Flaking – observed Delamination – observed
S-G1F1 Web Int. Corroded	-			Measured R1 0.591 R2 0.594 R3 0.592 R_Avg Design	Rust Grade – 0 Blistering – observed Discoloration – observed Flaking – observed Delamination – observed

Table A-14. Paint System Information - 2-Layer System.

Cohesive Failure Layer		**Adhesive Failure Layer**	
Code	**Description**	**Code**	**Description**
A	Substrate	A/B	Substrate & Layer 1
B	Layer 1(Green)	B/C	Layer 1 & Layer 2
C	Layer 2 (White)	C/Y	Layer 2 & Glue
Y	Glue	Y/Z	Glue & Dolly

A.3.3. Pull-off Adhesion Results

Table A-15. Pull-off Adhesion Results for ATL-PS-01.

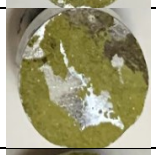
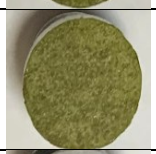
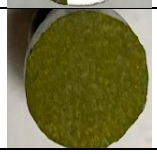
Location	Dolly Face	Substrate Face	Test Result (psi)	Attributes	Failure Type
N-G1F1		-	351	90% B 10%Y/Z	90% Cohesive Failure 10% Glue Failure
		-	511	100% B	100% Cohesive Failure
		-	472	100% B	100% Cohesive Failure
N-G3F1			29	20%B 80%Y/Z	20% Cohesive 80%Glue Failure
			33	20% B 80%Y/Z	Glue Failure
			302	70%B 30%Y/Z	Glue Failure
N-G6F1		-	234	90%B 10%Y/Z	Glue Failure
		-	No test	-	-
		-	No test	-	-

Table A-16. Pull-off Adhesion Results for ATL-PS-01.

Location	Dolly Face	Substrate Face	Test Result (psi)	Attributes	Failure Type
S-G1F1		-	108	90% B 10%Y/Z	90% Cohesive Failure 10% Glue Failure
		-	528	90%B 10%Y/Z	90% Cohesive Failure 10% Glue Failure
		-	543	100%B	100% Cohesive Failure
S-G6F2		-	No test	-	-
		-	76	80%B 20%Y/Z	80% Cohesive Failure 20% Glue Failure
		-	No test	-	-

A.3.4. Optical Microscopy Results

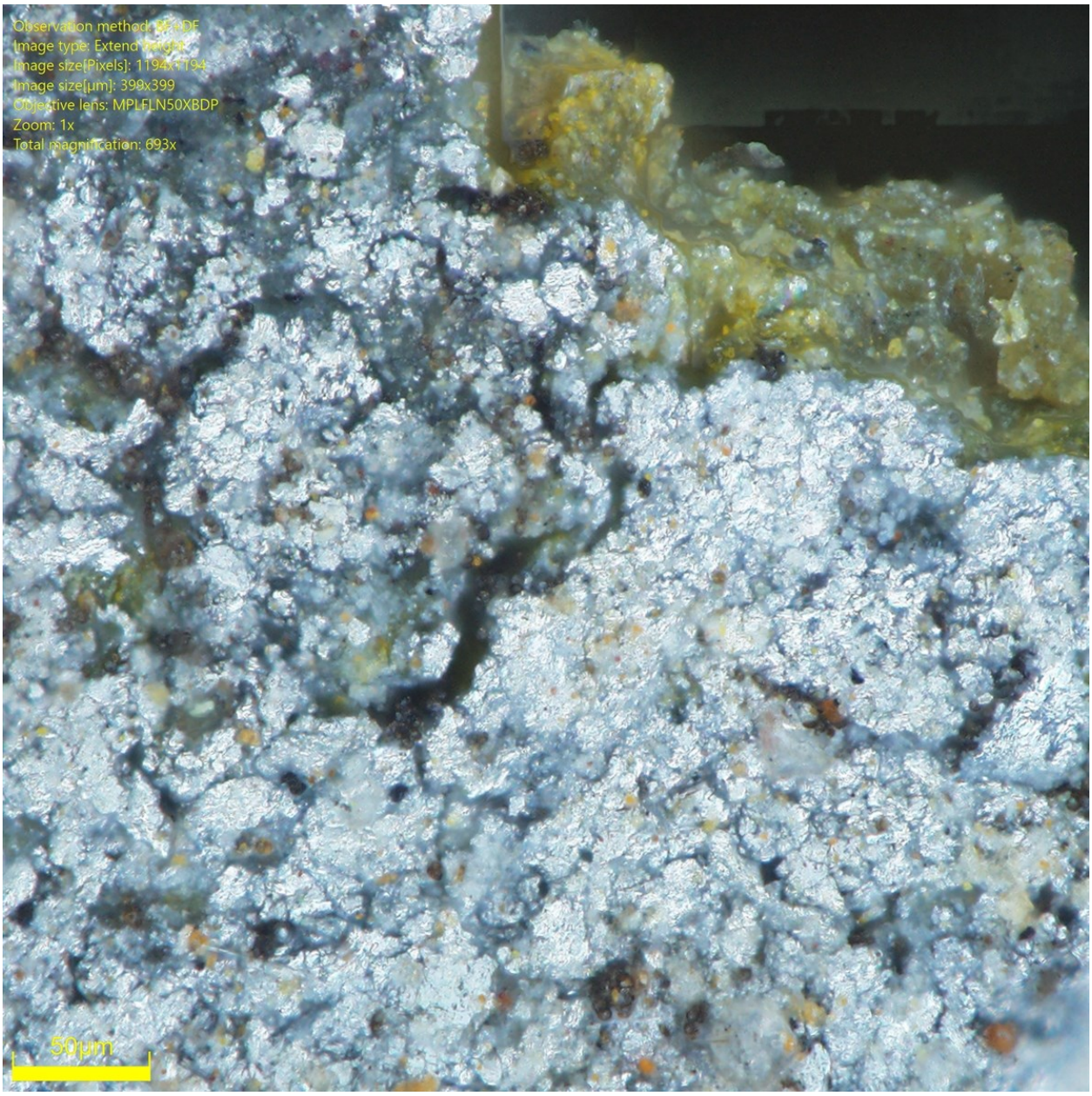


Figure A.33. Two Layer Paint System Examined by Optical Microscope ATL–PS–01.

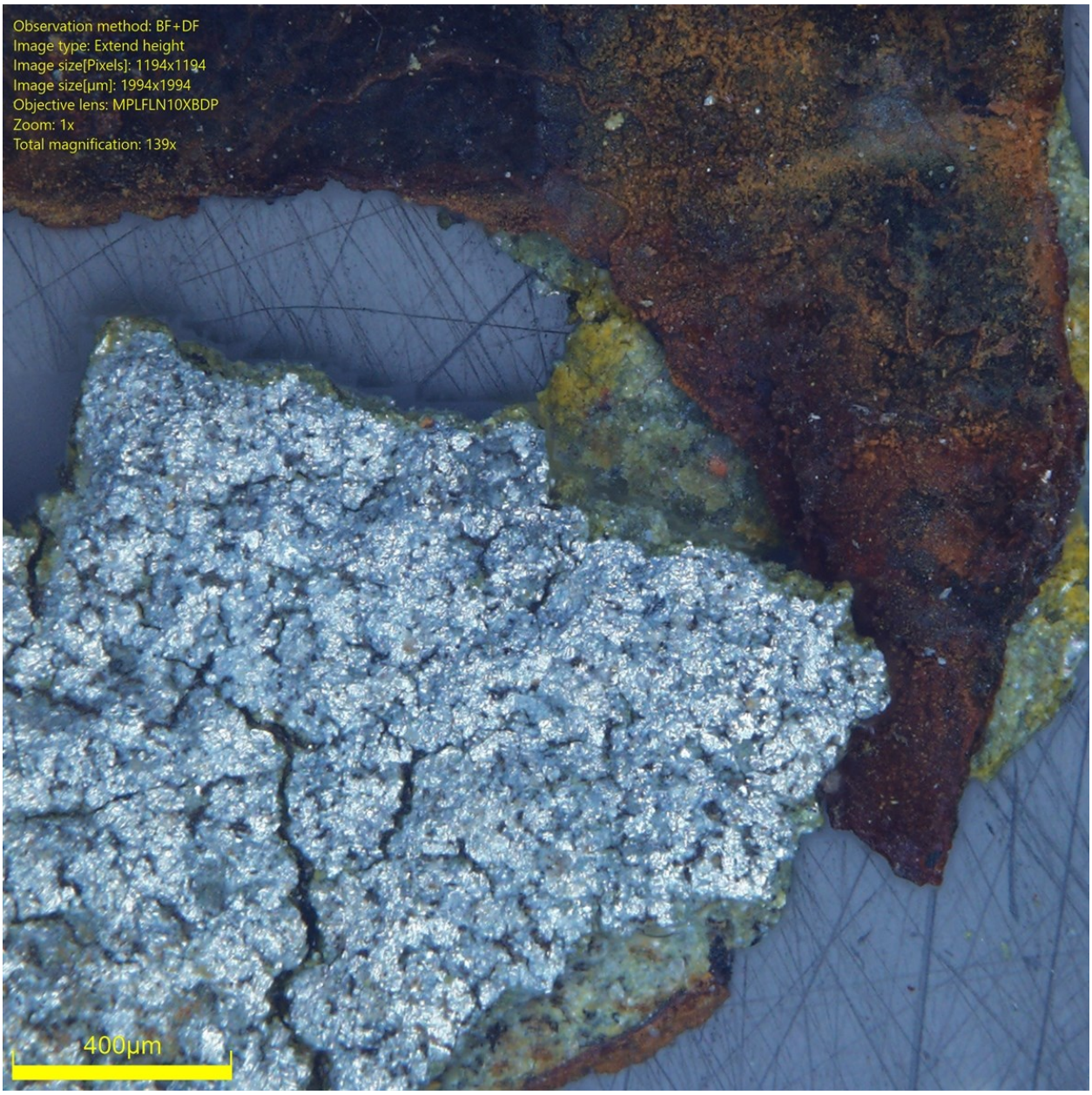
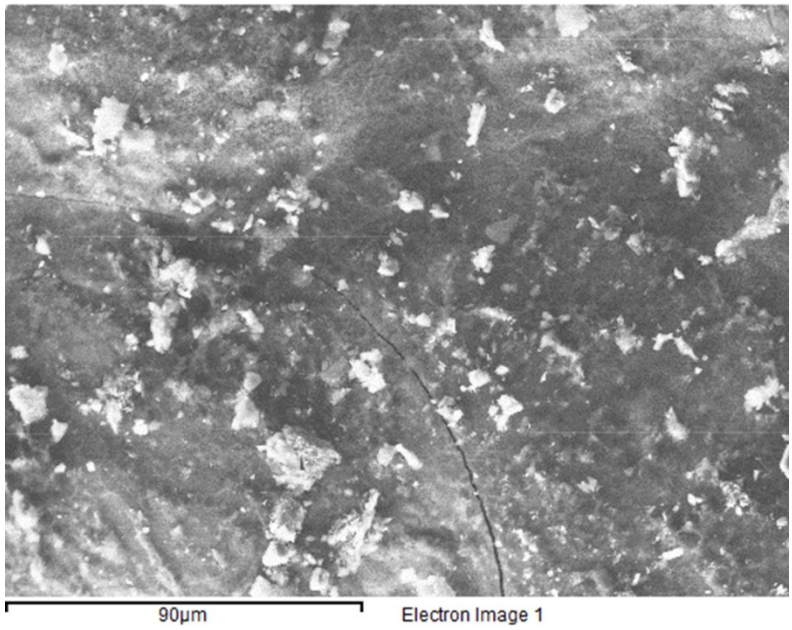


Figure A.34. Corrosion as Observed Between Primer and Base Metal by Optical Microscope ATL–PS–01.

A.3.5. SEM/EDS Results

Element	Weight %	Atomic %
C K	26.24	41.89
O K	36.93	44.26
Na K	0.16	0.13
Mg K	0.51	0.40
Al K	0.73	0.52
Si K	1.09	0.74
P K	0.14	0.09
S K	0.25	0.15
Cl K	0.27	0.14
K K	0.07	0.04
Ca K	0.67	0.32
Mn K	0.50	0.17
Fe K	32.45	11.14
Totals	100.00	



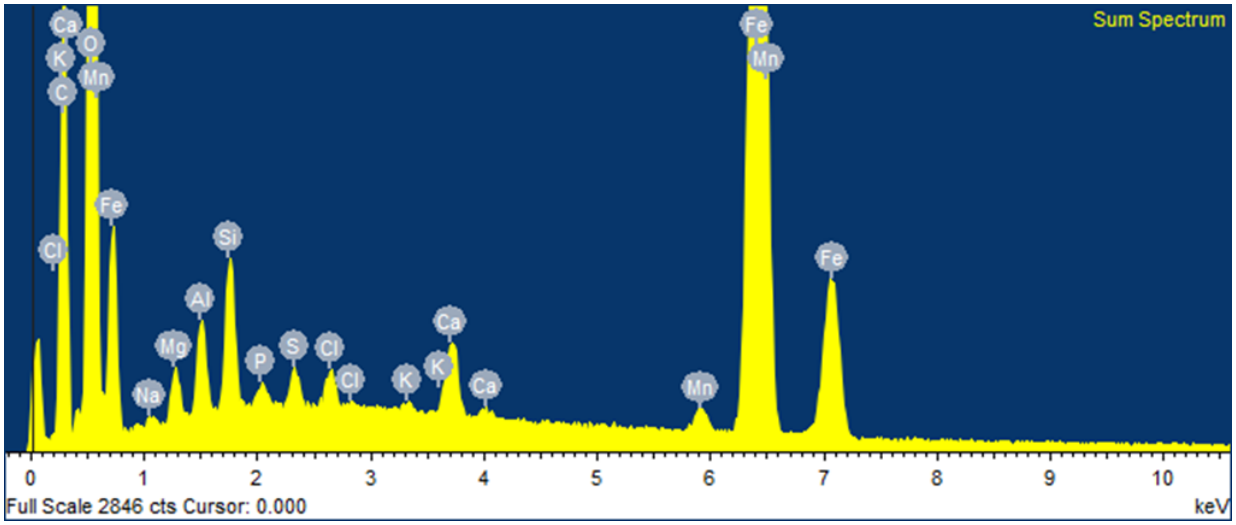


Figure A.35. SEM Image of Paint and EDS Spectrum of the Paint Collected from Exterior Web of the Girder.

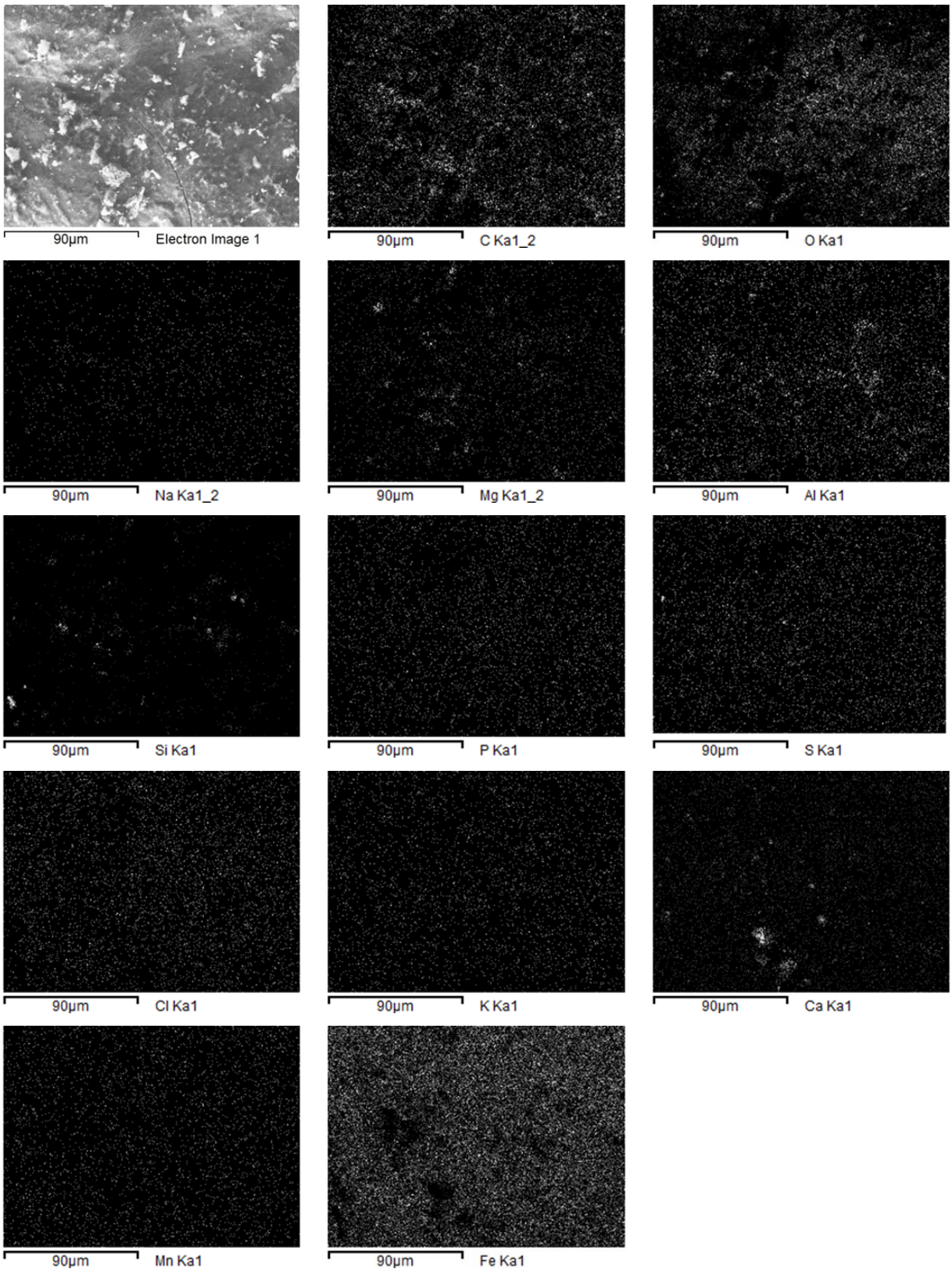
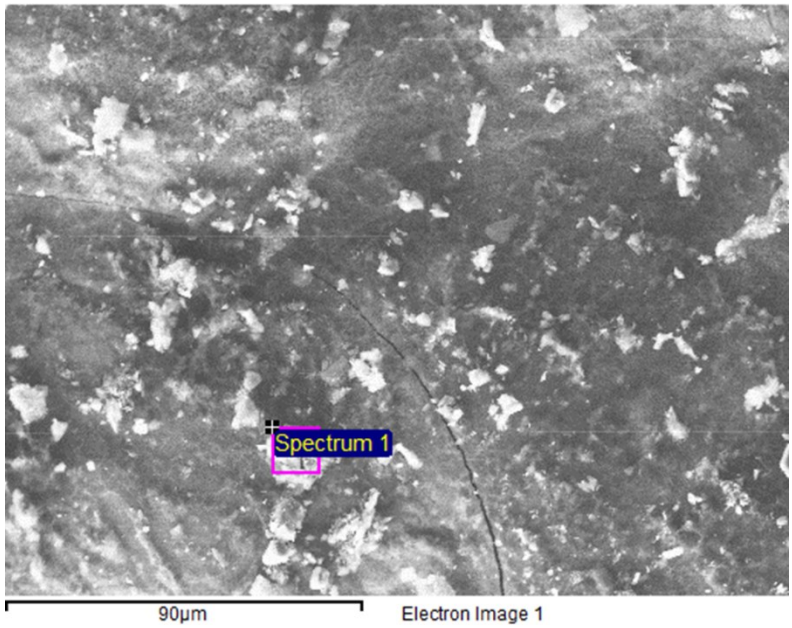
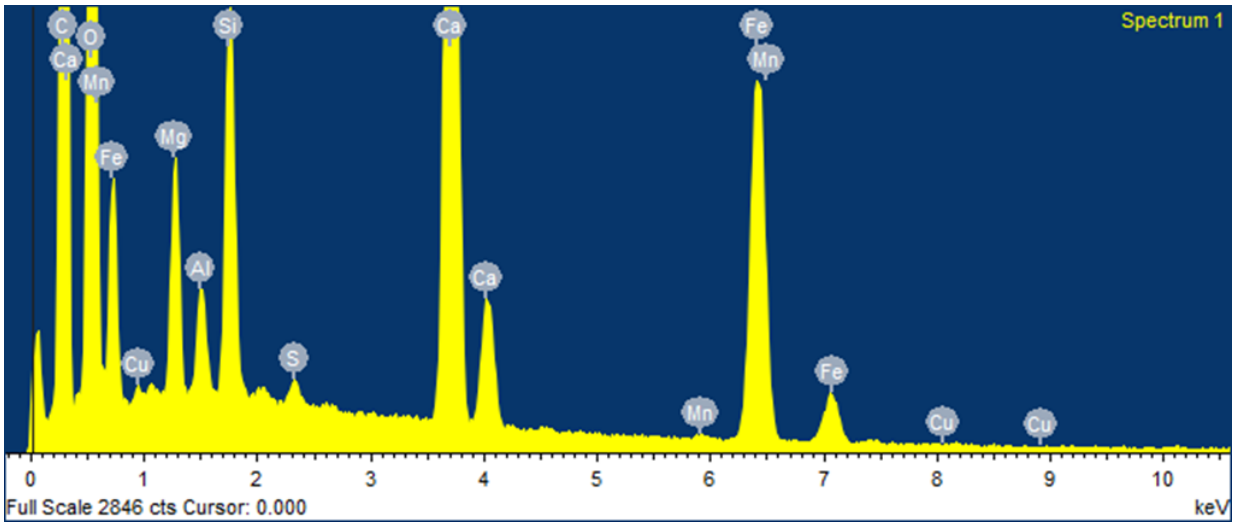


Figure A.36. EDS Elemental Mapping of Paint Collected from Exterior Web.

Element	Weight %	Atomic %
C K	36.18	46.99
O K	48.18	46.98
Mg K	1.18	0.76
Al K	0.40	0.23
Si K	1.48	0.82
S K	0.09	0.04
Ca K	6.21	2.42
Mn K	0.06	0.02
Fe K	6.23	1.74
Cu K	0.00	0.00
Totals	100.00	

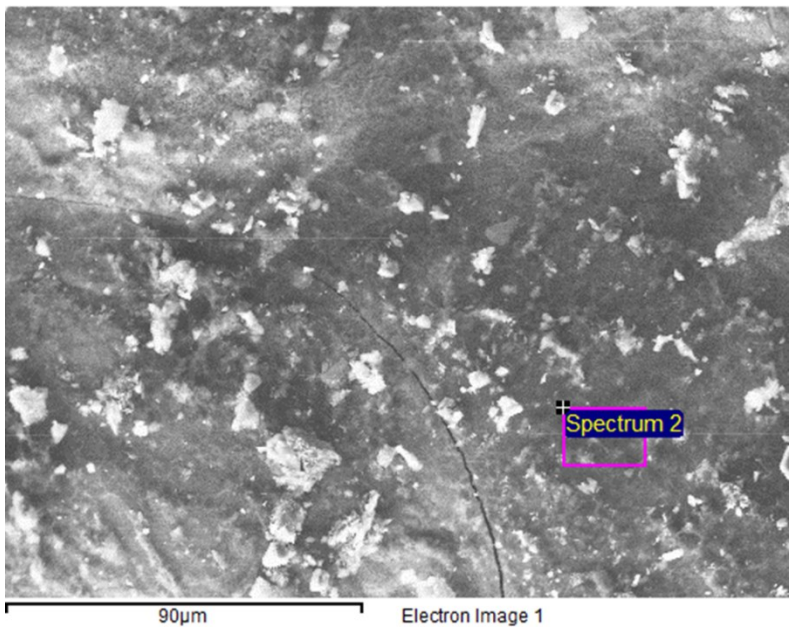




(a)

Figure A.37. SEM Image of Paint and EDS Spectrum of the Paint Collected from Exterior Web of the Girder.

Element	Weight %	Atomic %
C K	16.32	27.53
O K	45.01	57.02
Mg K	0.86	0.72
Al K	0.98	0.74
Si K	1.03	0.75
P K	0.12	0.08
S K	0.15	0.10
Cl K	0.39	0.22
K K	0.09	0.05
Ca K	0.63	0.32
Mn K	0.50	0.19
Fe K	33.92	12.31
Cu K	–0.02	–0.01
Totals	100.00	



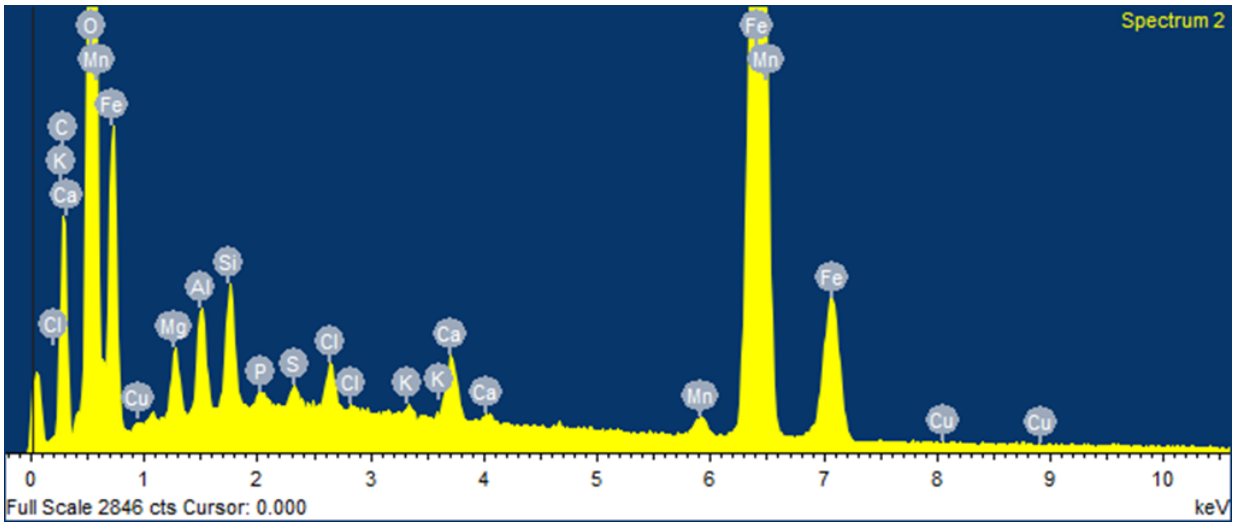
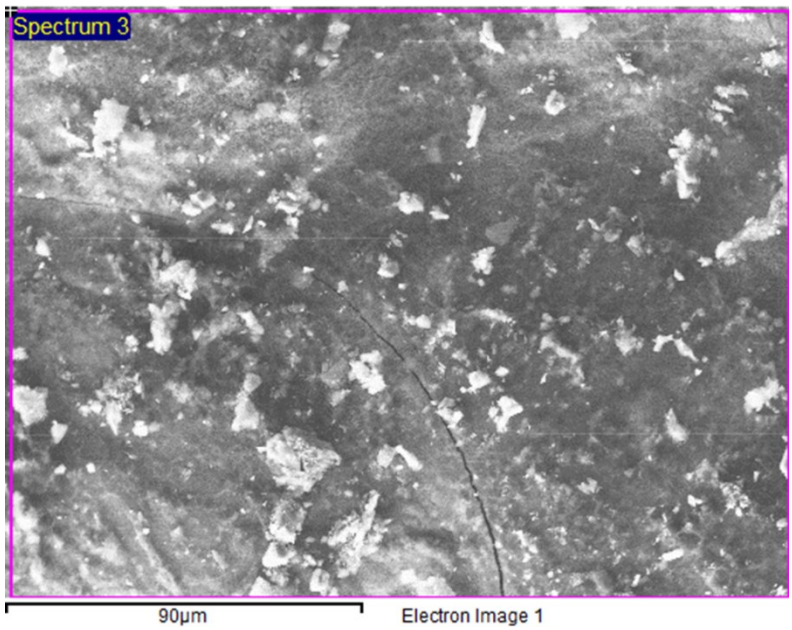
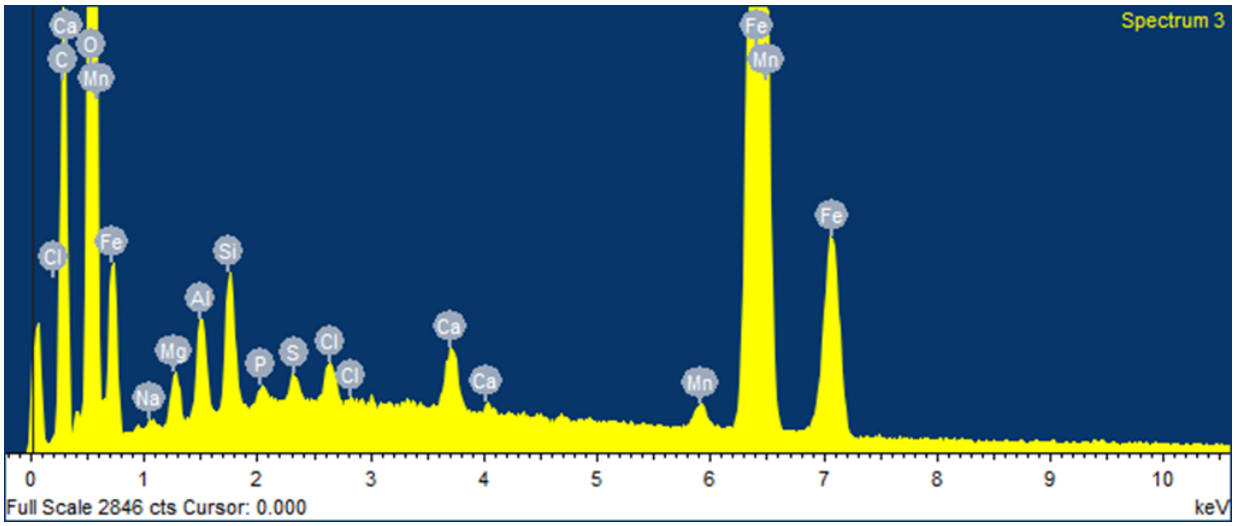


Figure A.38. SEM Image and EDS Spectrum of the Paint Collected from Exterior Web of the Girder.

Element	Weight %	Atomic %
C K	23.54	40.58
O K	32.22	41.70
Na K	0.16	0.15
Mg K	0.61	0.52
Al K	0.80	0.61
Si K	1.02	0.75
P K	0.14	0.09
S K	0.19	0.12
Cl K	0.31	0.18
Ca K	0.56	0.29
Mn K	0.52	0.19
Fe K	39.95	14.81
Totals	100.00	

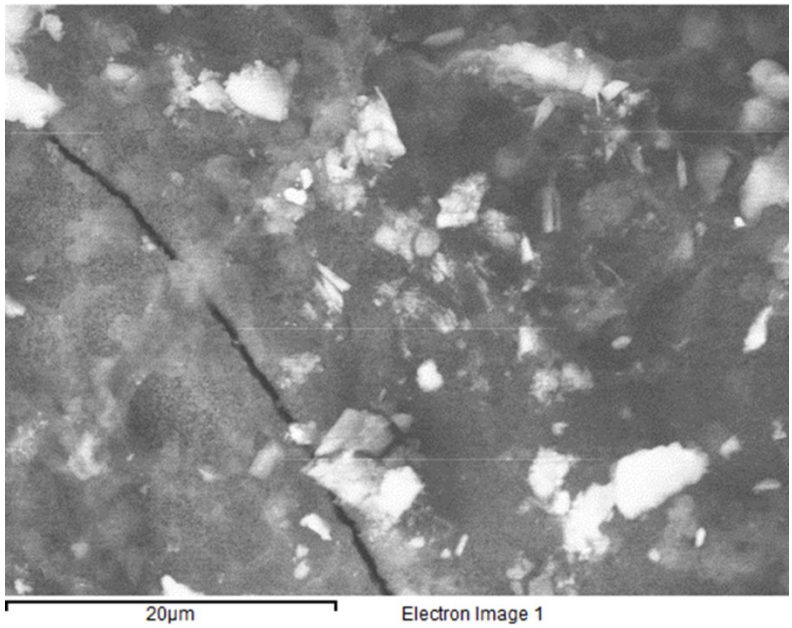




(a)

Figure A.39. SEM Image and EDS Spectrum of the Paint Collected from Exterior Web of the Girder.

Element	Weight %	Atomic %
C K	24.54	38.60
O K	41.19	48.65
Na K	0.18	0.14
Mg K	0.37	0.29
Al K	0.81	0.57
Si K	1.06	0.71
P K	0.13	0.08
S K	0.21	0.12
Cl K	0.28	0.15
K K	0.09	0.04
Ca K	0.77	0.36
Mn K	0.44	0.15
Fe K	29.93	10.13
Totals	100.00	



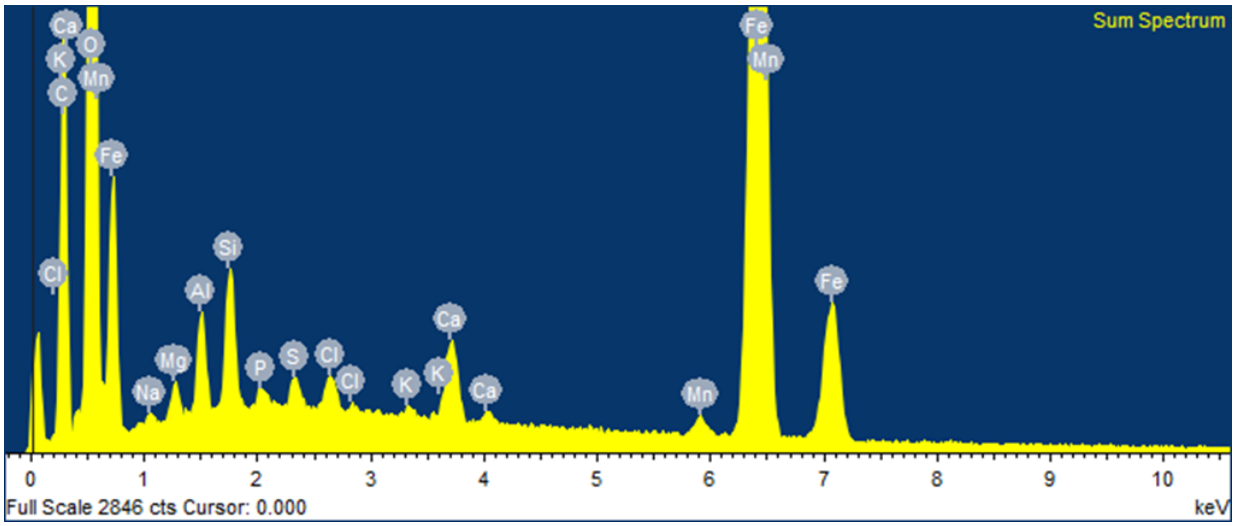


Figure A.40. SEM Image and EDS Spectrum of the Paint Collected from Interior Web of the Girder.

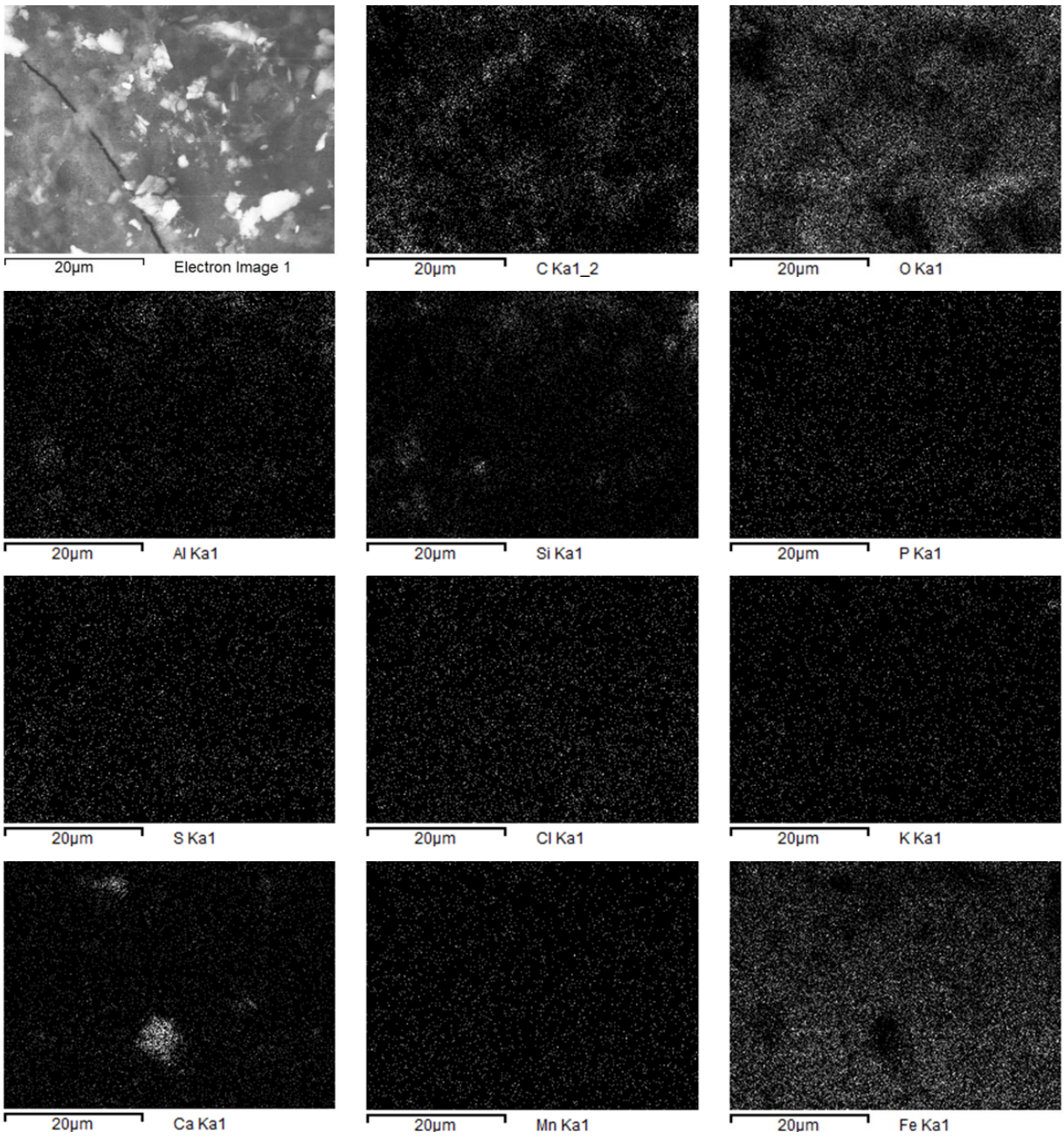
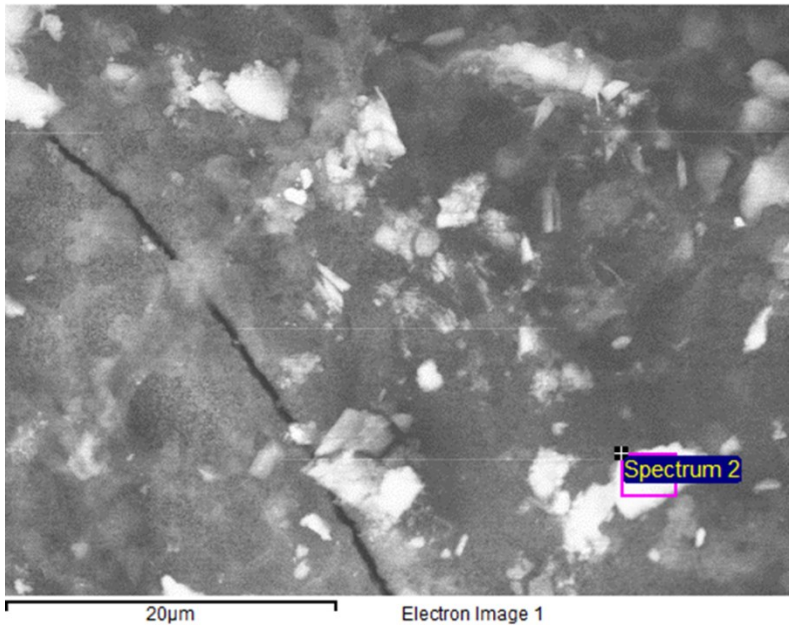


Figure A.41. EDS Elemental Mapping of Paint Collected from Interior Web.

Element	Weight %	Atomic %
C K	22.17	35.29
O K	43.41	51.89
Mg K	0.39	0.31
Al K	0.68	0.48
Si K	0.66	0.45
P K	0.17	0.11
S K	0.32	0.19
Cl K	0.50	0.27
Ca K	1.14	0.55
Mn K	0.27	0.10
Fe K	30.27	10.37
Totals	100.00	



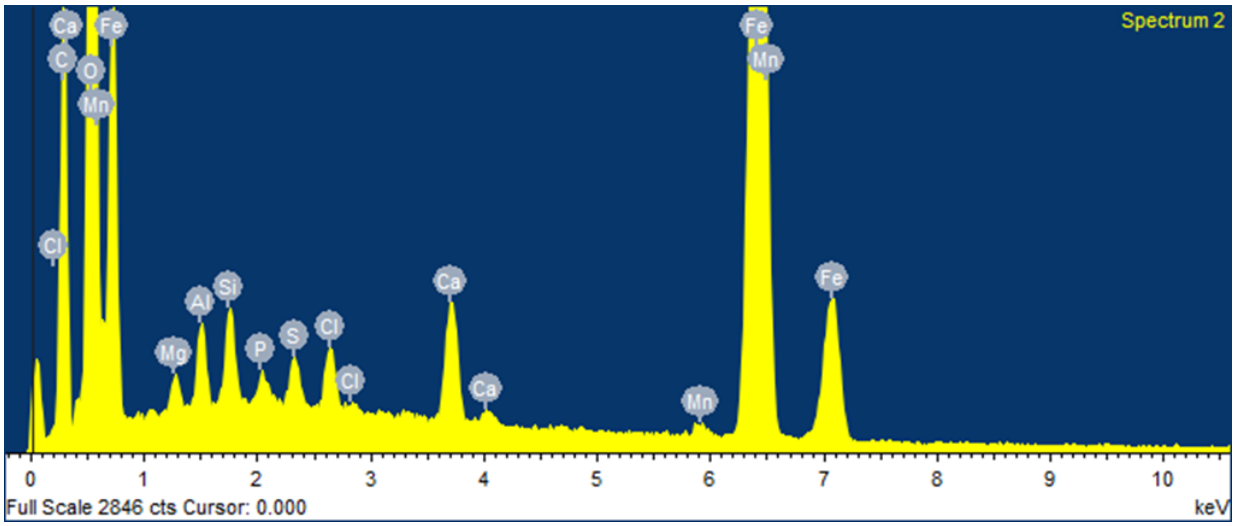


Figure A.42. SEM Image and EDS Spectrum of the Paint Collected from Interior Web of the Girder.

A.4. FTW-PS-01

- IH 820 Ramp K over SH 121
- Bridge ID 22200000813420, Coordinates (32.8264, -97.20478), Tarrant County
- Continuous Plate Girder with System II type paint

- Built 2002
- Date of Inspection: October 24, 2020; girder inspection carried near abutment ends on girders within approximately four feet from the abutment
- Revisited for pH test and scrape test
- No visual inspection on deck
- Location for Testing: A1-G1F1, A1-G2F1, A1G3F2, A1-G4F2



Figure A.43. Typical Elevation of FTW-PS-01.

A.4.1. Observed Condition

The paint condition of this bridge is in very good condition. The appearance coat is also in good condition. Blistering, Erosion of paint, cracking in paint is not present. A slight discoloration is observed on edge of the bottom flange. Dirt is accumulated on the top face of the bottom flange. No checking and cracking of paint are observed. Joints are also in good condition.



(a)Paint on Superstructure in Good Condition



(b) Paint on Superstructure in Good Condition



(c) Paint on Stiffener and Joints in Good Condition



(d) Dirt accumulated on Bottom Flange of Interior Girder



(e) Exterior Girder in Good Condition



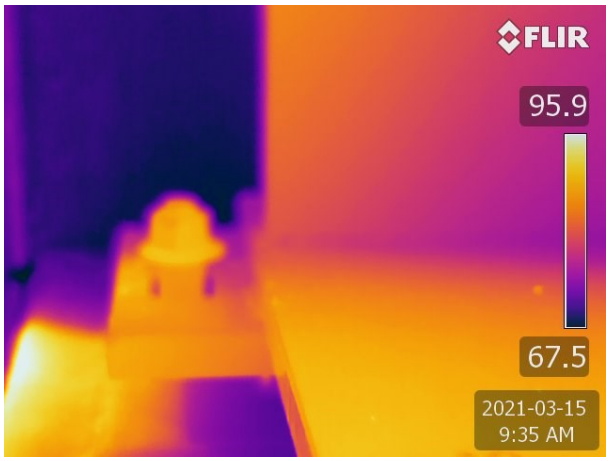
(f) Interior Girder in Good Condition

Figure A.44. Paint Condition on the Girder of FTW-PS-01.

A.4.2. NDT Results



(a) Digital Image of Exterior Face of Girder Near Abutment Ends



(b) Thermal Image of Exterior Face of Girder Near Abutment Ends



(c) Digital Image of Connection



(d) Thermal Image of Connection



(e) Digital image of the exterior face of Plate Girder (G1F1)



(f) Thermal image of the Exterior Face of Plate Girder (G1F1)

Figure A.45. Digital and Thermal Image of Painted Girder on FTW-PS-01.

Table A-17. Field Inspection Results for FTW-PS-01.

Location	Cl^- Conc. (ppm)	pH Test	Thickness (µm)	Thickness (inch)	Visual Inspection
A1-G1F1 TF Bot. Ext.	-		Measured R1 139 R2 143 R3 206 Design Paint 140-381	Measured R1 1.473 R2 1.471 R3 1.474 R_Avg 1.473 Design	Rust Grade – 10 Blistering – Not Found Discoloration – Not Found Flaking – Not Found Delamination – Not Found
A1-G1F1 Web. Ext.	1		Measured R1 214 R2 247 R3 219 Design Paint 140-381	Measured R1 0.761 R2 0.761 R3 0.762 R_Avg 0.761 Design	Rust Grade – 10 Blistering – Not Found Discoloration – Not Found Flaking – Not Found Delamination – Not Found
A1-G1F1 BF Top Ext.	-		Measured R1 218 R2 219 R3 197 Design Paint 140-381	Measured R1 1.504 R2 1.499 R3 1.501 R_Avg 1.501 Design	Rust Grade – 10 Blistering – Not Found Discoloration – Not Found Flaking – Not Found Delamination – Not Found
A1-G1F1 BF Bot. Ext.	-		Measured R1 135 R2 133 R3 110 Design Paint 140-381	Measured R1 - R2 - R3 - R_Avg - Design	Rust Grade – 10 Blistering – Not Found Discoloration – Not Found Flaking – Not Found Delamination – Not Found
A1-G2F1 TF Bot. Int.	-		Measured R1 155 R2 146 R3 157 Design Paint 140-381	Measured R1 1.468 R2 1.467 R3 1.469 R_Avg 1.468 Design	Rust Grade – 10 Blistering – Not Found Discoloration – Not Found Flaking – Not Found Delamination – Not Found
A1-G2F1 Web. Int.	1		Measured R1 195 R2 229 R3 193 Design Paint 140-381	Measured R1 0.740 R2 0.731 R3 0.741 R_Avg 0.737 Design	Rust Grade – 10 Blistering – Not Found Discoloration – Not Found Flaking – Not Found Delamination – Not Found

Table A-18. Field Inspection Results for FTW-PS-01.

Location	Cl^- Conc. (ppm)	pH Test	Thickness (µm)	Thickness (inch)	Visual Inspection
A1-G2F1 BF Top. Int.	-	-	Measured R1 294 R2 316 R3 271 Design Paint 140-381	Measured R1 1.509 R2 1.508 R3 1.507 R_Avg 1.508 Design	Rust Grade – 10 Blistering – Not Found Discoloration – Not Found Flaking – Not Found Delamination – Not Found
A1-G2F1 BF Bot. Int.	-	-	Measured R1 179 R2 186 R3 190 Design Paint 140-381	Measured R1 - R2 - R3 - R_Avg - Design	Rust Grade – 10 Blistering – Not Found Discoloration – Not Found Flaking – Not Found Delamination – Not Found
A1-G3F2 TF Bot. Int.	-	-	Measured R1 142 R2 154 R3 117 Design Paint 140-381	Measured R1 1.476 R2 1.476 R3 1.477 R_Avg 1.476 Design	Rust Grade – 10 Blistering – Not Found Discoloration – Not Found Flaking – Not Found Delamination – Not Found
A1-G3F2 Web. Int.	-		Measured R1 160 R2 158 R3 145 Design Paint 140-381	Measured R1 0.744 R2 0.748 R3 0.747 R_Avg 0.746 Design	Rust Grade – 10 Blistering – Not Found Discoloration – Not Found Flaking – Not Found Delamination – Not Found
A1-G3F2 BF Top. Int.	-		Measured R1 264 R2 253 R3 261 Design Paint 140-381	Measured R1 1.491 R2 1.492 R3 1.491 R_Avg 1.491 Design	Rust Grade – 10 Blistering – Not Found Discoloration – Not Found Flaking – Not Found Delamination – Not Found
A1-G3F2 BF Bot. Int.	-		Measured R1 192 R2 212 R3 177 Design Paint 140-381	Measured R1 - R2 - R3 - R_Avg - Design	Rust Grade – 10 Blistering – Not Found Discoloration – Not Found Flaking – Not Found Delamination – Not Found

Table A-19. Field Inspection Results for FTW-PS-01.

Location	Cl^- Conc. (ppm)	pH Test	Thickness (µm)	Thickness (inch)	Visual Inspection
A1-G4F2 TF Top. Ext.	-	-	Measured R1 251 R2 254 R3 259 Design Paint 140-381	Measured R1 1.476 R2 1.476 R3 1.478 R_Avg 1.477 Design	Rust Grade – 10 Blistering – Not Found Discoloration – Not Found Flaking – Not Found Delamination – Not Found
A1-G4F2 Web. Ext.	-	-	Measured R1 170 R2 171 R3 163 Design Paint 140-381	Measured R1 0.757 R2 0.760 R3 0.759 R_Avg 0.759 Design	Rust Grade – 10 Blistering – Not Found Discoloration – Not Found Flaking – Not Found Delamination – Not Found
A1-G4F2 BF Top. Ext.	-	-	Measured R1 266 R2 239 R3 225 Design Paint 140-381	Measured R1 1.481 R2 1.483 R3 1.485 R_Avg 1.483 Design	Rust Grade – 10 Blistering – Not Found Discoloration – Not Found Flaking – Not Found Delamination – Not Found
A1-G4F2 BF Bot. Ext.	-		Measured R1 180 R2 178 R3 208 Design Paint 140-381	Measured R1 - R2 - R3 - R_Avg - Design	Rust Grade – 10 Blistering – Not Found Discoloration – Not Found Flaking – Not Found Delamination – Not Found

Table A-20. Paint System Information: Exterior Girders (3-Layers).

Cohesive Failure Layer		Adhesive Failure Layer	
Code	**Description**	**Code**	**Description**
A	Substrate	A/B	Substrate & Layer 1
B	Layer 1 (Gray)	B/C	Layer 1 & Layer 2
C	Layer 2 (Burnt Sienna)	C/D	Layer 2 & Layer 3
D	Layer 3(Carrot)	D/Y	Layer 3 & Glue
Y	Glue	Y/Z	Glue & Dolly

Table A-21. Paint System Information: Interior Girders (2-Layer).

Cohesive Failure Layer		**Adhesive Failure Layer**	
Code	**Description**	**Code**	**Description**
A	Substrate	A/B	Substrate & Layer 1
B	Layer 1(Green)	B/C	Layer 1 & Layer 2
C	Layer 2 (White)	C/Y	Layer 2 & Glue
Y	Glue	Y/Z	Glue & Dolly

A.4.3. Pull-off Adhesion Results

Table A-22. Pull-off Adhesion Results for FTW-PS-01.

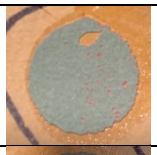
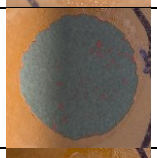
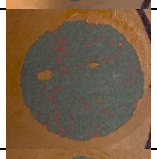
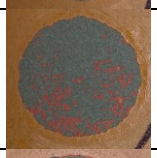
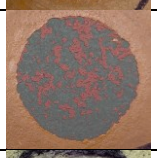
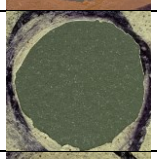
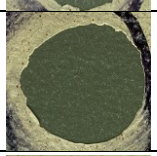
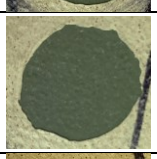
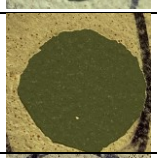
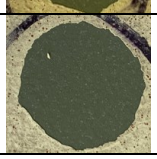
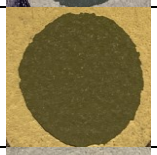
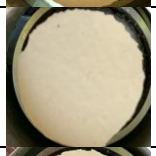
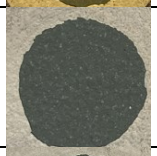
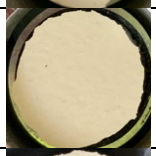
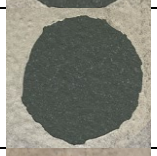
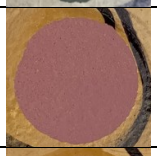
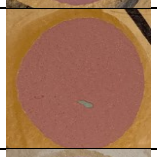
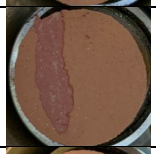
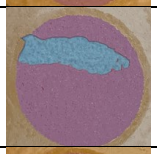
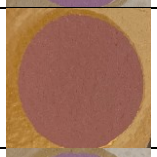
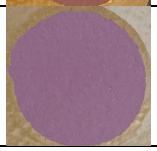
Location	Dolly Face	Substrate Face	Test Result (psi)	Attributes	Failure Type
A1-G4F2			792	90% B/C 10% Y/Z	90% Adhesive Failure 10% Glue Failure
			835	100% B/C	100%Adhesive Failure
			898	90% B/C 10% Y/Z	90% Adhesive Failure 10% Glue Failure
			925	20% C/D 80% B/C	80% Adhesive Failure
			913	30% C/D 70% B/C	70% Adhesive Failure
A1-G3F2			828	100% B/C	100% Adhesive Failure
			887	100% B/C	100% Adhesive Failure
			734	100% B/C	100% Adhesive Failure
			680	100% B/C	100% Adhesive Failure
			789	100% B/C	100% Adhesive Failure

Table A-23. Pull-off Adhesion Results for FTW-PS-01.

Location	Dolly Face	Substrate Face	Test Result (psi)	Attributes	Failure Type
A1-G2F2			630	100% B/C	100% Adhesive Failure
			663	100% B/C	100% Adhesive Failure
			705	100% B/C	100% Adhesive Failure
			718	100% B/C	100% Adhesive Failure
			802	100% B/C	100% Adhesive Failure
A1-G1F1			1051	100% B/C	100% Adhesive Failure
			1188	100% B	100% Cohesive Failure
			851	70% C/D 30% B/C	100% Adhesive Failure
			1118	100% B	100% Cohesive Failure
			1062	100% C/D	100% Adhesive Failure

A.4.4. Optical Microscopy Results

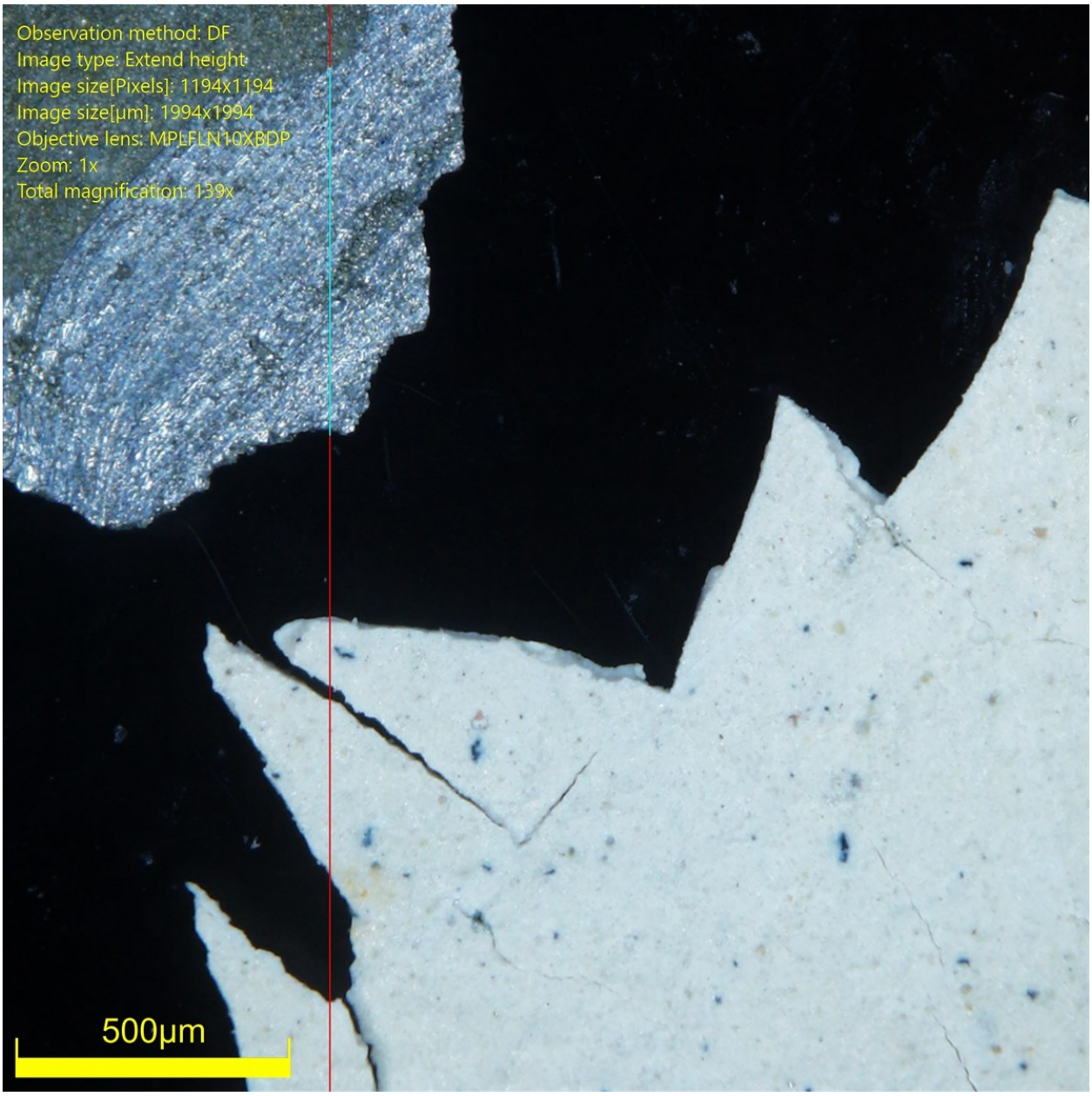


Figure A.46. Two Layer Paint System Examined by Optical Microscope FTW–PS–01 (Int.).

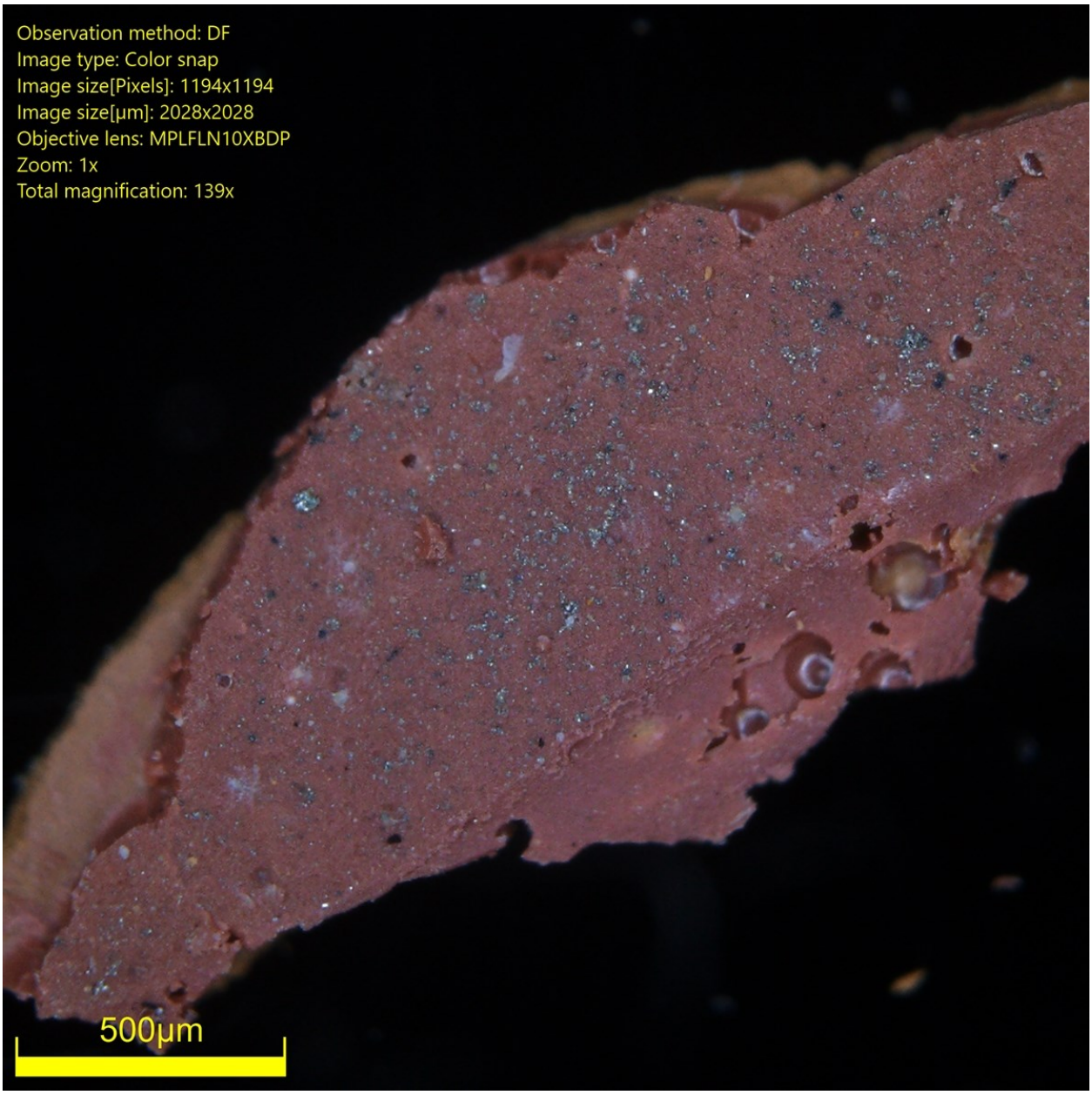
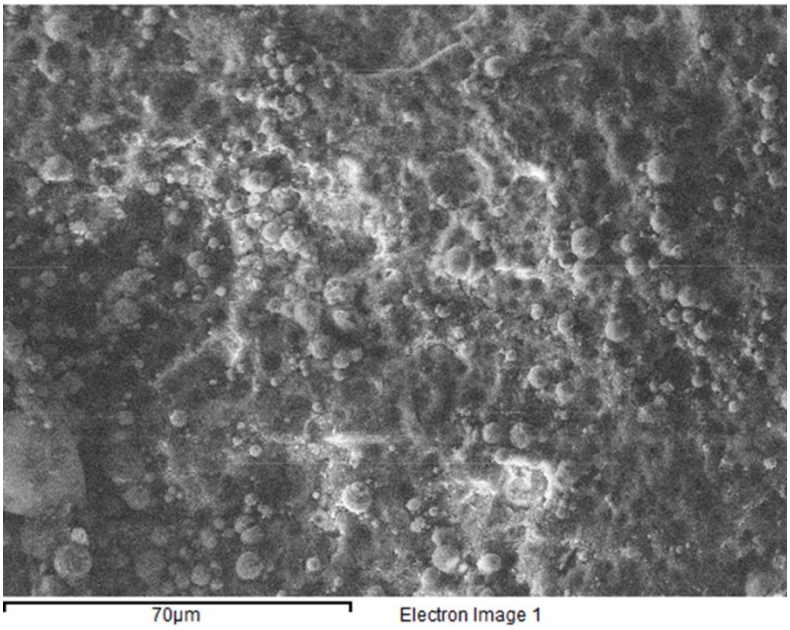


Figure A.47. Two Layer Paint System Examined by Optical Microscope FTW–PS–01 (Ext.).

A.4.5. SEM/EDS Results

Element	Weight %	Atomic %
C K	46.45	58.17
O K	40.81	38.37
Al K	0.65	0.36
Si K	0.23	0.12
S K	0.32	0.15
Cl K	0.07	0.03
Ca K	1.10	0.41
Ti K	0.18	0.06
Fe K	0.65	0.18
Zn K	8.84	2.03
Zr L	0.69	0.11
Totals	100.00	



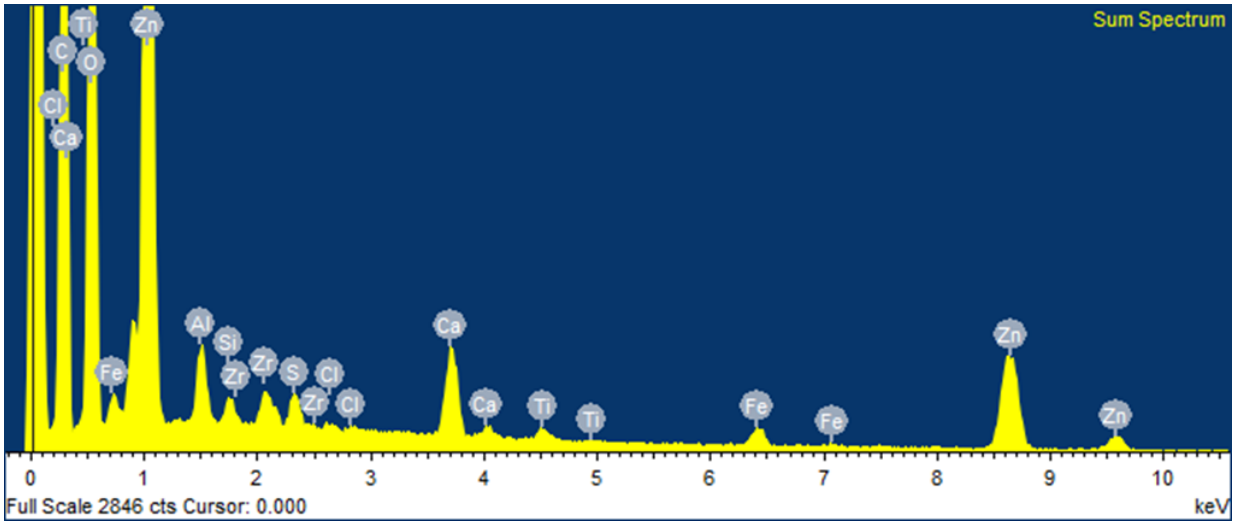


Figure A.48. SEM Image and EDS Spectrum of the Paint Collected from Exterior Web of the Girder.

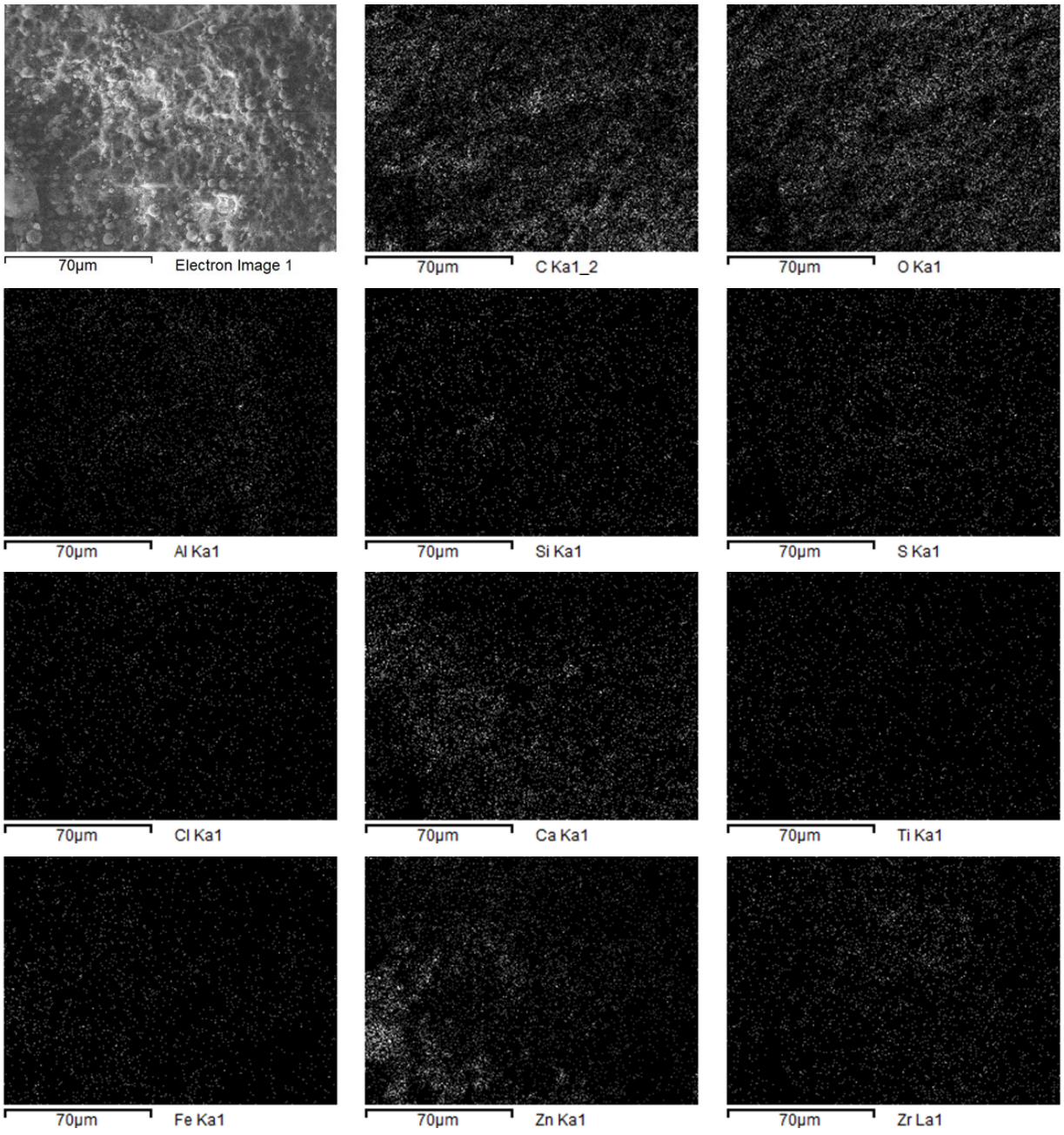
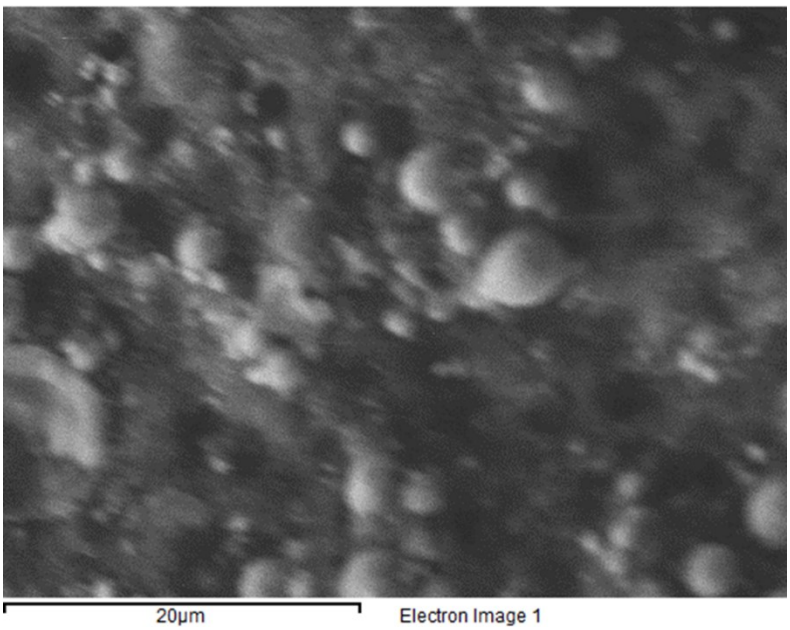


Figure A.49. EDS Elemental Mapping of Paint Collected from Exterior Web.

Element	Weight %	Atomic %
C K	53.44	66.20
O K	31.99	29.75
Al K	0.47	0.26
Si K	0.52	0.27
S K	0.12	0.06
Ca K	2.14	0.79
Ti K	0.44	0.14
Fe K	1.15	0.31
Zn K	9.73	2.22
Totals	100.00	



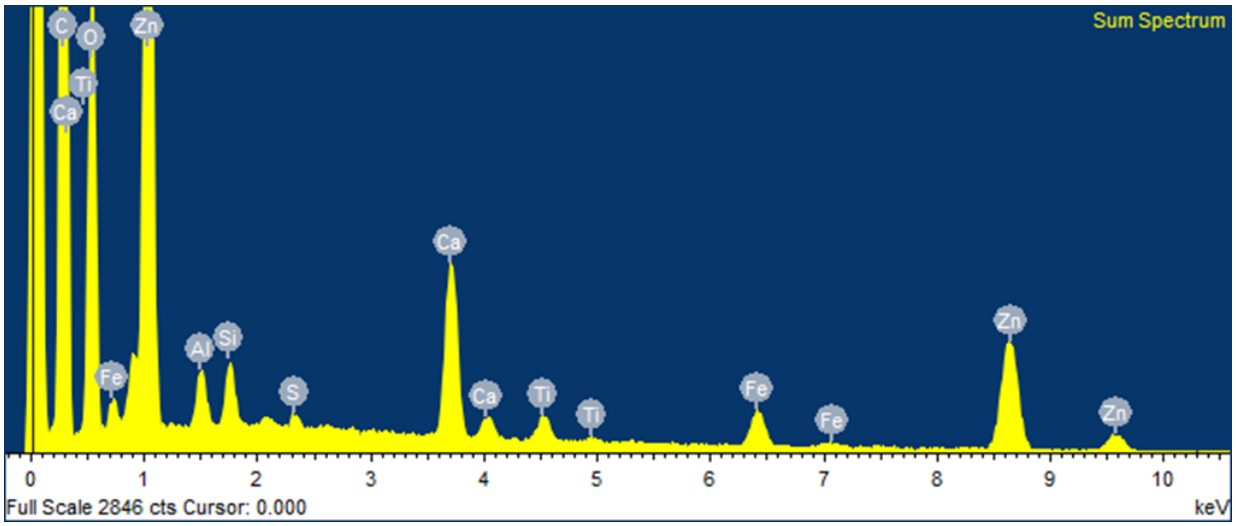


Figure A.50. SEM Image and EDS Spectrum of the Paint Collected from Exterior Web of the Girder.

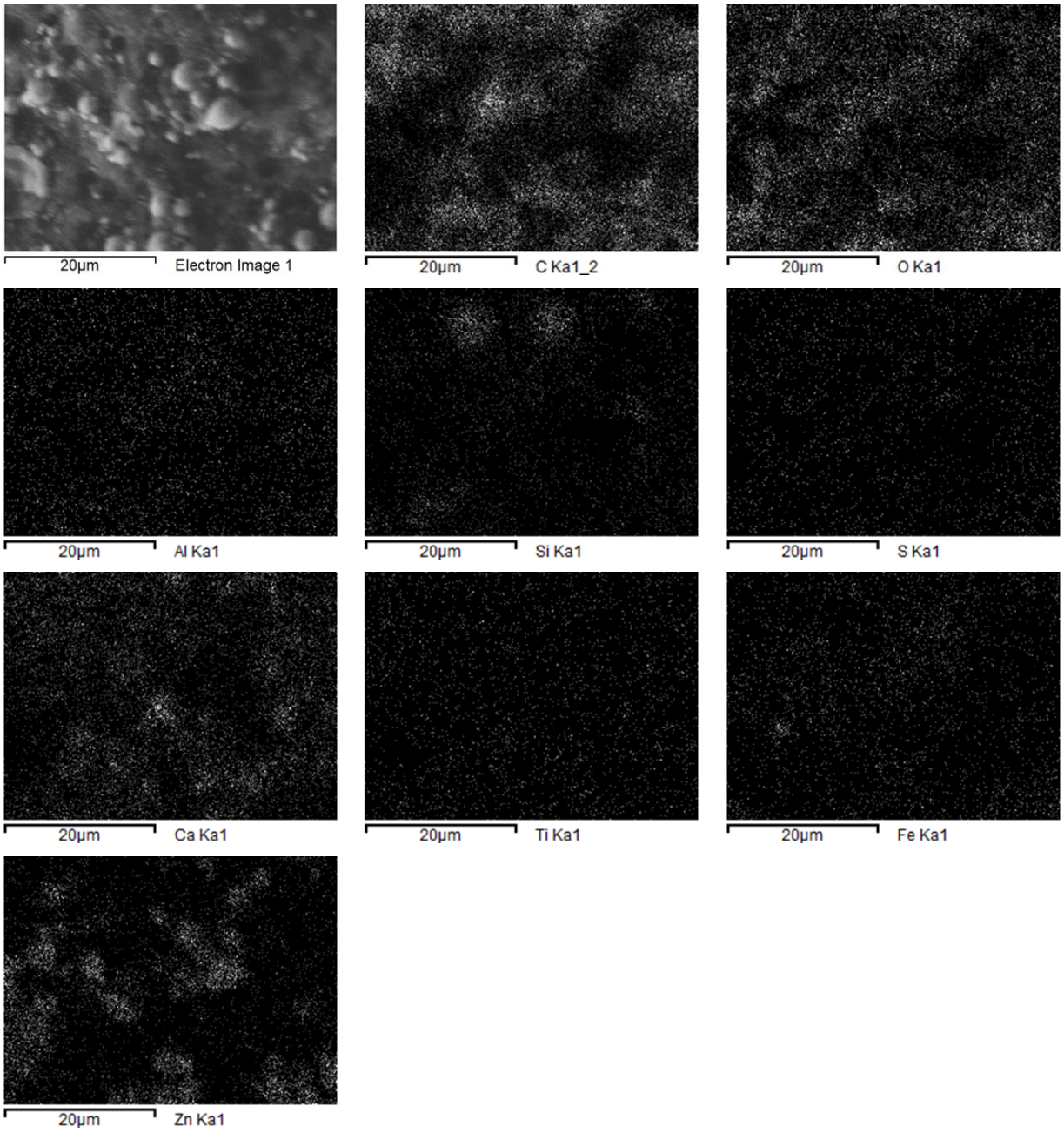
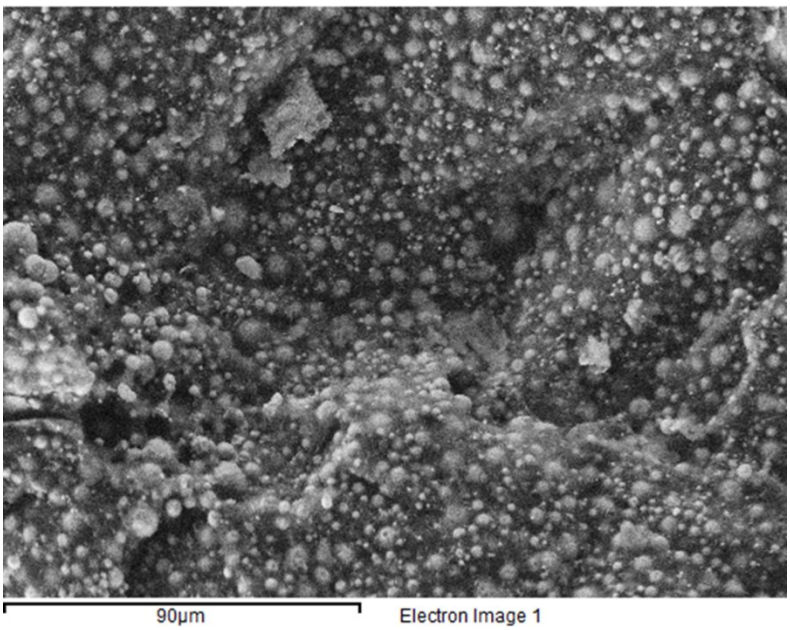


Figure A.51. EDS Elemental Mapping of Paint Collected from Exterior Web.

Element	Weight %	Atomic %
C K	57.61	76.70
O K	16.79	16.79
Al K	0.28	0.17
Si K	0.23	0.13
Fe K	1.80	0.52
Zn K	23.28	5.70
Totals	100.00	



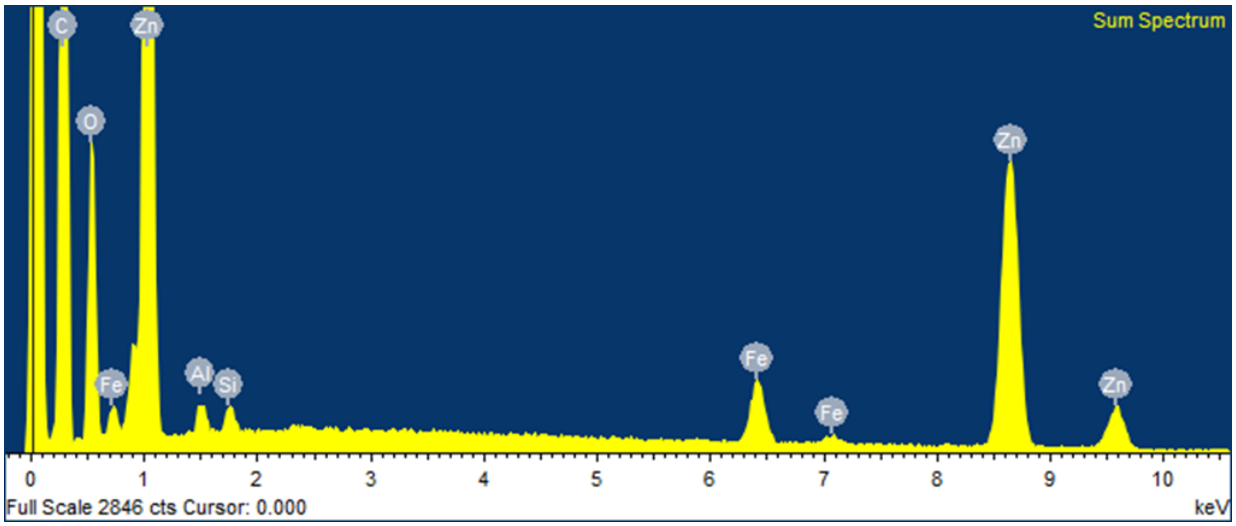


Figure A.52. SEM Image of Paint and EDS Spectrum of the Paint Collected from Interior Web of the Girder.

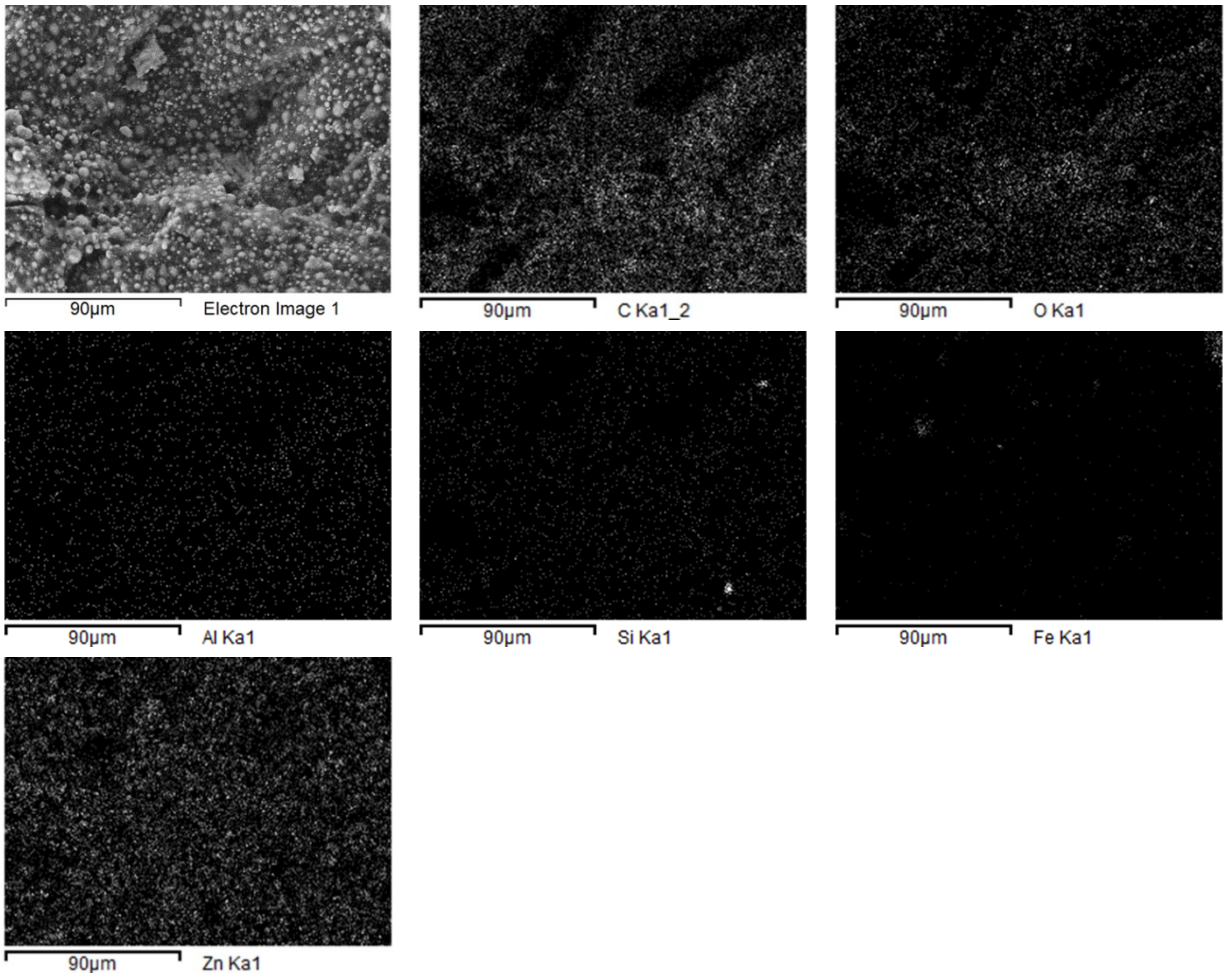
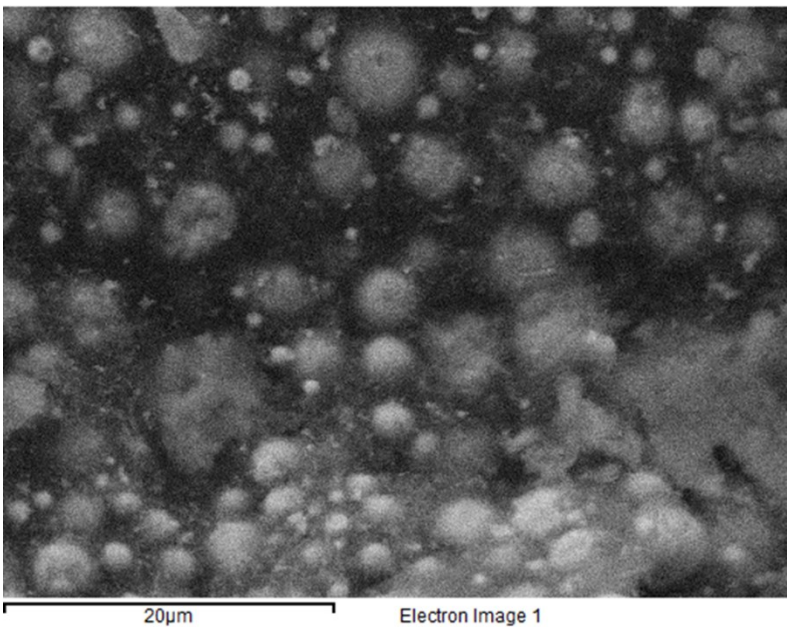


Figure A.53. EDS Elemental Mapping of Paint Collected from Interior Web.

Element	Weight %	Atomic %
C K	55.38	73.68
O K	20.16	20.14
Al K	0.24	0.14
Si K	0.20	0.11
Fe K	1.35	0.39
Zn K	22.68	5.54
Totals	100.00	



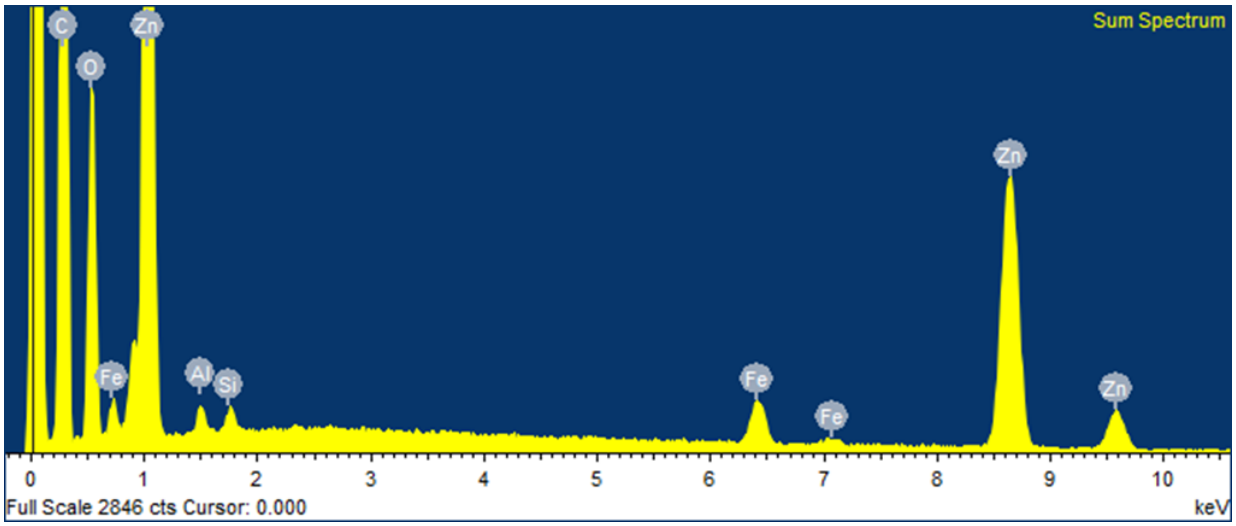


Figure A.54. SEM Image and EDS Spectrum of the Paint Collected from Interior Web of the Girder.

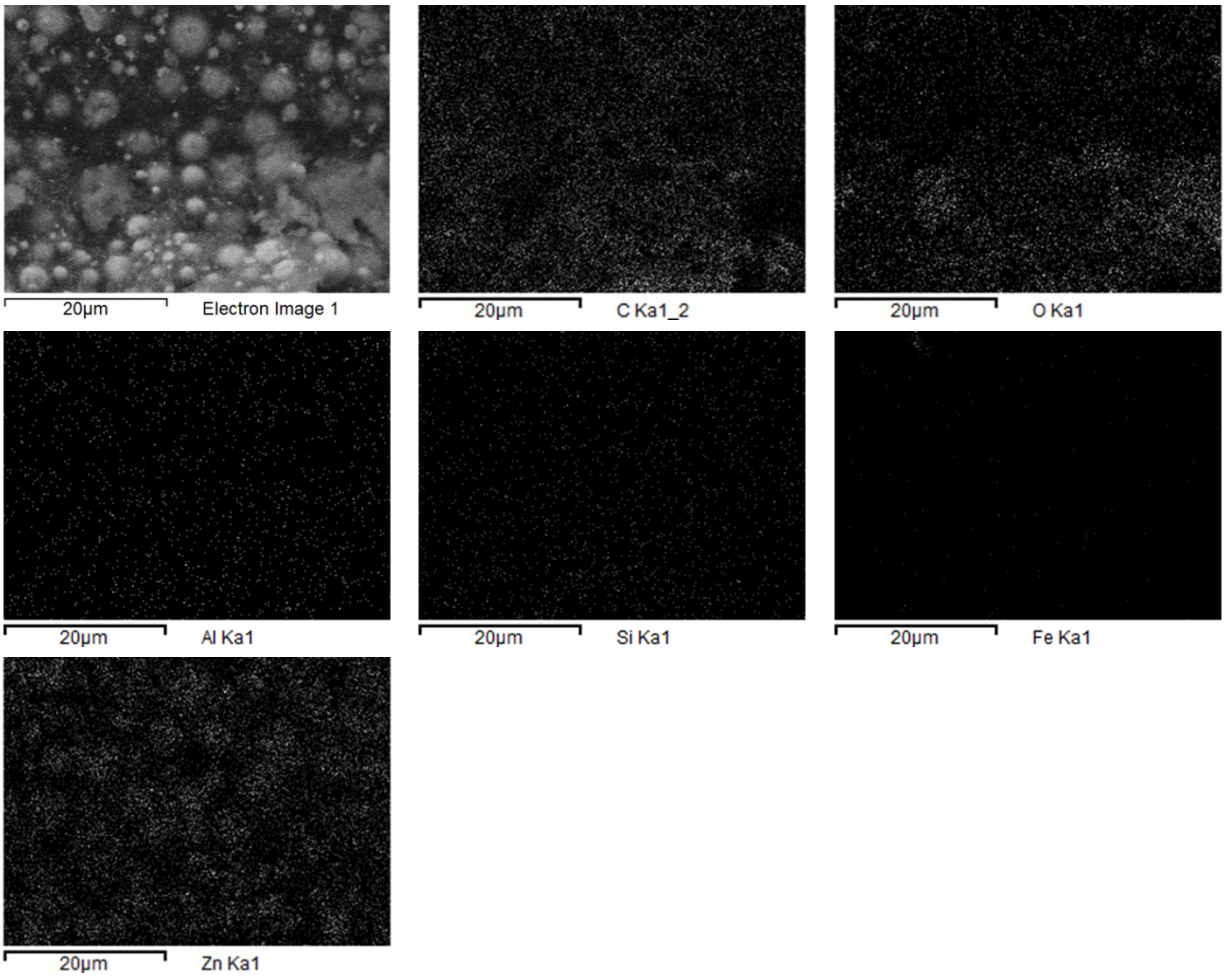
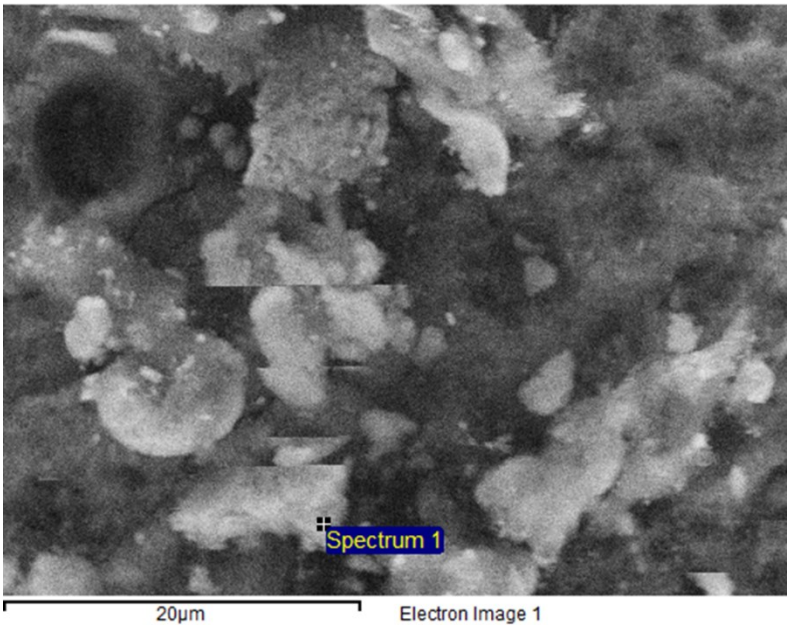


Figure A.55. EDS Elemental Mapping of Paint Collected from Interior Web.

Element	Weight %	Atomic %
C K	43.31	59.93
O K	31.77	33.00
Al K	0.57	0.35
Si K	0.40	0.23
S K	0.14	0.07
Cl K	0.13	0.06
Ca K	1.32	0.55
Ti K	1.05	0.36
Fe K	0.65	0.19
Zn K	20.66	5.25
Totals	100.00	



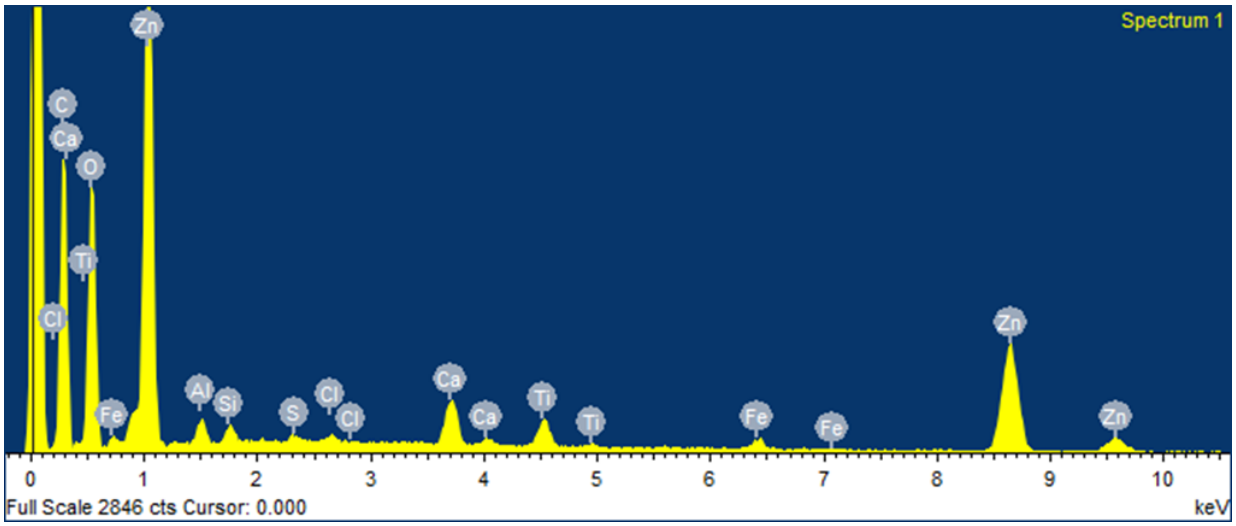


Figure A.56. SEM Image and EDS Spectrum of the Paint Collected from Interior Web of the Girder.

A.5. FTW-PS-02

- SH 199 EB over FM 730
- Bridge ID 22200017104049, Coordinates (32.8993, -97.5446), Tarrant County
- Continuous I-Beam with System II type paint

- Built 2007
- Date of Inspection: March 15, 2021; girder inspection carried near abutment ends on girders within approximately four feet from the abutment
- Revisited for pH test and scrape test
- No visual inspection on deck
- Location for Testing: G1F1, G3F1, G4F2, G6F2



Figure A.57. Typical Elevation of FTW-PS-02.

A.5.1. Observed Condition

While the external paint condition of this bridge seems to be in good shape, there are indications of localized rust spots within the organic zinc coating and metal substrate as observed on the pull-off adhesion paint surface. This may be attributed to inadequate surface preparation prior to painting. The appearance coat is also in good condition. Blistering, Erosion of paint, cracking in paint is not present. Dirt is accumulated on the top face of the bottom flange of interior girders. No checking and cracking of paint are observed. Joints are also in good condition.



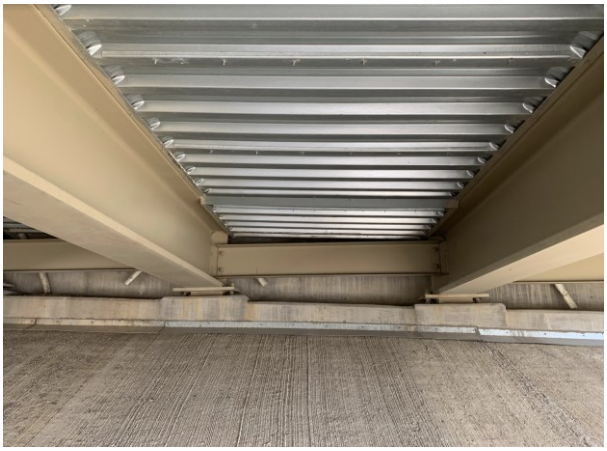
(a) Superstructure in Good Condition Near Abutment 1



(b) Superstructure in Good Condition



(c) Paint on Stiffener and Joints in Good Condition



(d) Paint on Stiffener and Joints in Good Condition Near Abutment 1



(e) Interior Girder in Good Condition Near Abutment 1



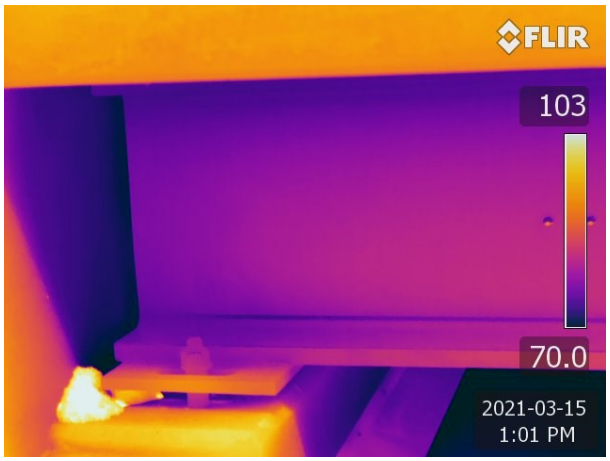
(f) Interior Girder in Good Condition Near Abutment 1

Figure A.58. Paint Condition on the Girder of FTW-PS-02.

A.5.2. NDT Results



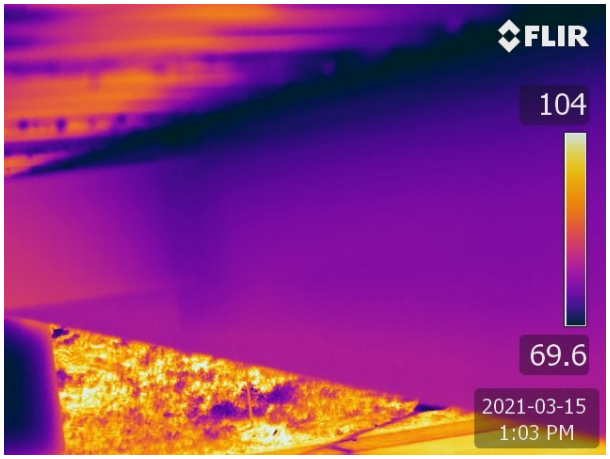
(a) Digital Image of Exterior Face of Girder Near Abutment Ends



(b) Thermal Image of Exterior Face of Girder Near Abutment Ends



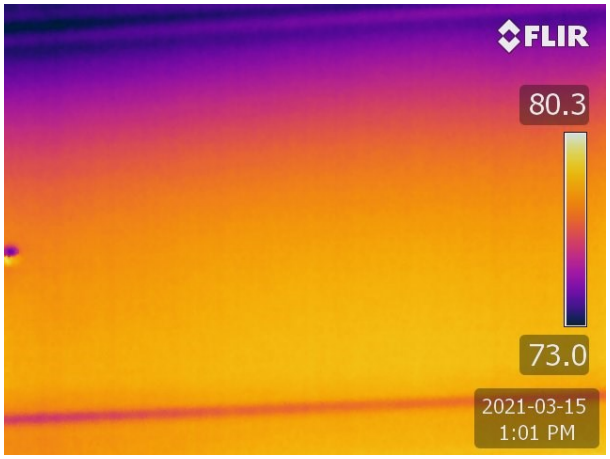
(c) Digital Image of Connection



(d) Thermal Image of Connection



(e) Digital image of the exterior face of Plate Girder (G1F1)



(f) Thermal image of the Exterior Face of Plate Girder (G1F1)

Figure A.59. Digital and Thermal Image of Painted Girder on FTW-PS-02.

Table A-24. Paint System Information: Interior Girders (2-Layer).

Cohesive Failure Layer		**Adhesive Failure Layer**	
Code	**Description**	**Code**	**Description**
A	Substrate	A/B	Substrate & Layer 1
B	Layer 1(Green)	B/C	Layer 1 & Layer 2
C	Layer 2 (White)	C/Y	Layer 2 & Glue
Y	Glue	Y/Z	Glue & Dolly

Table A-25. Field Inspection Results for FTW-PS-02.

Location	Cl^- Conc. (ppm)	pH Test	Thickness (µm)	Thickness (inch)	Visual Inspection
G1F1 TF Bot. Ext.	-	-	Measured R1 170 R2 135 R3 158 Design Paint 140-381	Measured R1 1.625 R2 1.623 R3 1.626 R_Avg 1.625 Design	Rust Grade – 10 Blistering – Not Found Discoloration – Not Found Flaking – Not Found Delamination – Not Found
G1F1 Web. Ext.	1		Measured R1 184 R2 162 R3 168 Design Paint 140-381	Measured R1 0.861 R2 0.862 R3 0.863 R_Avg 0.862 Design	Rust Grade – 10 Blistering – Not Found Discoloration – Not Found Flaking – Not Found Delamination – Not Found
G1F1 BF Top. Ext.	-	-	Measured R1 154 R2 163 R3 166 Design Paint 140-381	Measured R1 1.620 R2 1.621 R3 1.619 R_Avg 1.620 Design	Rust Grade – 10 Blistering – Not Found Discoloration – observed on the top of Bottom Flange Flaking – Not Found Delamination – Not Found
G1F1 BF Bot. Ext.	-	-	Measured R1 142 R2 129 R3 147 Design Paint 140-381	Measured R1 - R2 - R3 - R_Avg - Design	Rust Grade – 10 Blistering – Not Found Discoloration – Not Found Flaking – Not Found Delamination – Not Found
G3F1 TF Bot. Int.	-		Measured R1 189 R2 223 R3 185 Design Paint 140-381	Measured R1 1.595 R2 1.600 R3 1.596 R_Avg 1.597 Design	Rust Grade – 10 Blistering – Not Found Discoloration – Not Found Flaking – Not Found Delamination – Not Found
G3F1 Web. Int.	1	-	Measured R1 184 R2 203 R3 160 Design Paint 140-381	Measured R1 0.856 R2 0.859 R3 0.857 R_Avg 0.857 Design	Rust Grade – 10 Blistering – Not Found Discoloration – Not Found Flaking – Not Found Delamination – Not Found

Table A-26. Field Inspection Results for FTW-PS-02.

Location	Cl^- Conc. (ppm)	pH Test	Thickness (µm)	Thickness (inch)	Visual Inspection
G3F1 BF Top. Int.	-		Measured R1 229 R2 208 R3 224 Design Paint 140-381	Measured R1 1.643 R2 1.645 R3 1.645 R_Avg 1.644 Design	Rust Grade – 10 Blistering – Not Found Discoloration – Not Found Flaking – Not Found Delamination – Not Found
G3F1 BF Bot. Int.	-		Measured R1 139 R2 131 R3 156 Design Paint 140-381	Measured R1 - R2 - R3 - R_Avg - Design	Rust Grade – 10 Blistering – Not Found Discoloration – Not Found Flaking – Not Found Delamination – Not Found
G4F2 TF Bot. Int.	-		Measured R1 154 R2 170 R3 189 Design Paint 140-381	Measured R1 1.612 R2 1.614 R3 1.616 R_Avg 1.614 Design	Rust Grade – 10 Blistering – Not Found Discoloration – Not Found Flaking – Not Found Delamination – Not Found
G4F2 Web. Int.	1		Measured R1 196 R2 182 R3 179 Design Paint 140-381	Measured R1 0.857 R2 0.862 R3 0.857 R_Avg 0.859 Design	Rust Grade – 10 Blistering – Not Found Discoloration – Not Found Flaking – Not Found Delamination – Not Found
G4F2 BF Top. Int.	-		Measured R1 186 R2 151 R3 155 Design Paint 140-381	Measured R1 1.639 R2 1.638 R3 1.636 R_Avg 1.638 Design	Rust Grade – 10 Blistering – Not Found Discoloration – Not Found Flaking – Not Found Delamination – Not Found
G4F2 BF Bot. Int.	-		Measured R1 98.2 R2 114 R3 96.5 Design Paint 140-381	Measured R1 - R2 - R3 - R_Avg - Design	Rust Grade – 10 Blistering – Not Found Discoloration – Not Found Flaking – Not Found Delamination – Not Found

Table A-27. Field Inspection Results for FTW-PS-02.

Location	Cl^- Conc. (ppm)	pH Test	Thickness (µm)	Thickness (inch)	Visual Inspection
G6F2 TF Top. Ext.	-		Measured R1 177 R2 177 R3 148 Design Paint 140-381	Measured R1 1.582 R2 1.586 R3 1.587 R_Avg 1.585 Design	Rust Grade – 10 Blistering – Not Found Discoloration – Not Found Flaking – Not Found Delamination – Not Found
G6F2 Web. Ext.	1		Measured R1 183 R2 180 R3 256 Design Paint 140-381	Measured R1 0.852 R2 0.852 R3 0.852 R_Avg 0.852 Design	Rust Grade – 10 Blistering – Not Found Discoloration – Not Found Flaking – Not Found Delamination – Not Found
G6F2 BF Top. Ext.	-		Measured R1 166 R2 160 R3 143 Design Paint 140-381	Measured R1 1.577 R2 1.578 R3 1.580 R_Avg 1.578 Design	Rust Grade – 10 Blistering – Not Found Discoloration – observed on the top face of Bottom Flange Flaking – Not Found Delamination – Not Found
G6F2 BF Bot. Ext.	-		Measured R1 160 R2 166 R3 143 Design Paint 140-381	Measured R1 - R2 - R3 - R_Avg - Design	Rust Grade – 10 Blistering – Not Found Discoloration – Not Found Flaking – Not Found Delamination – Not Found

A.5.3. Pull-off Adhesion Results

Table A-28. Pull-off Adhesion Results for FTW-PS-02.

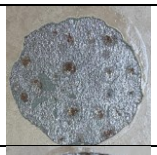
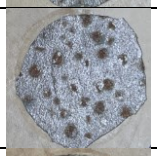
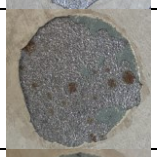
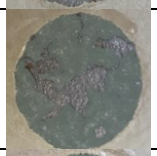
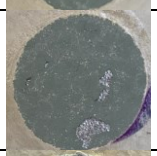
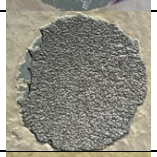
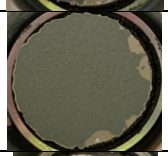
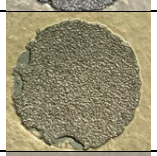
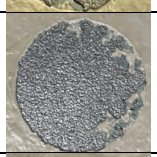
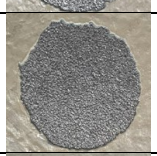
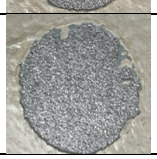
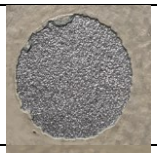
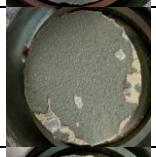
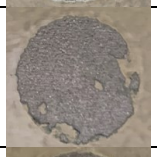
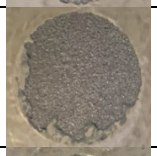
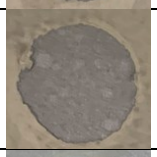
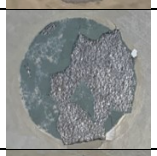
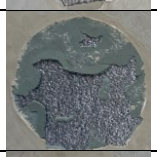
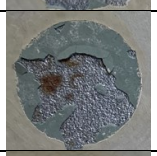
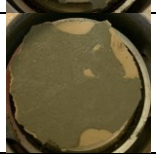
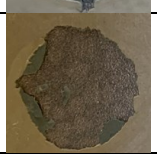
Location	Dolly Face	Substrate Face	Test Result (psi)	Attributes	Failure Type
A1-G6F2			629	100% A/B	100% Adhesive Failure
			572	100% A/B	100% Adhesive Failure
			858	10% B/C 90% A/B	100% Adhesive Failure
			1042	80% B/C 20% A/B	100% Adhesive Failure
			1123	90% B/C 10% A/B	100% Adhesive Failure
A1-G4F2			1398	10% B/C 90% A/B	100% Adhesive Failure
			1465	10% B/C 90% A/B	100% Adhesive Failure
			1820	20% B/C 80% A/B	100% Adhesive Failure
			1263	100% A/B	100% Adhesive Failure
			1616	10% B/C 90% A/B	100% Adhesive Failure

Table A-29. Pull-off Adhesion Results for FTW-PS-02.

Location	Dolly Face	Substrate Face	Test Result (psi)	Attributes	Failure Type
A1-G3F1			1705	100% A/B	100% Adhesive Failure
			1922	20% B/C 80% A/B	100% Adhesive Failure
			1837	20% B/C 80% A/B	100% Adhesive Failure
			1598	20% B/C 80% A/B	100% Adhesive Failure
			1245	100% A/B	100% Adhesive Failure
A1-G1F1			805	50% B/C 50% A/B	100% Adhesive Failure
			977	50% B/C 50% A/B	100% Adhesive Failure
			1057	60% B/C 40% A/B	100% Adhesive Failure
			702	20% B/C 80% A/B	100% Adhesive Failure
			512	20% B/C 80% A/B	100% Adhesive Failure

A.5.4. Optical Microscopy Results

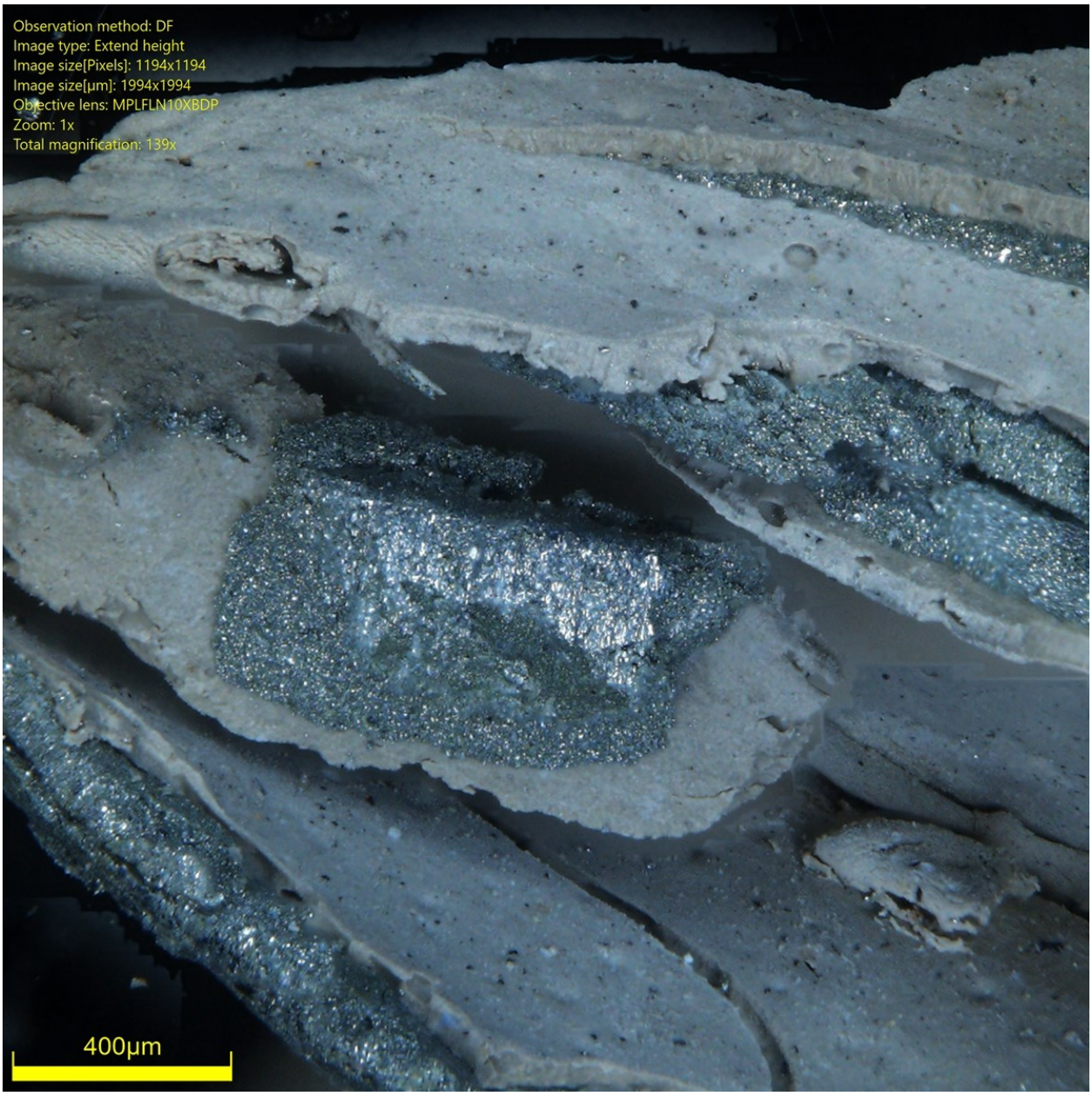


Figure A.60. Two Layer Paint System Examined by Optical Microscope FTW–PS–02.

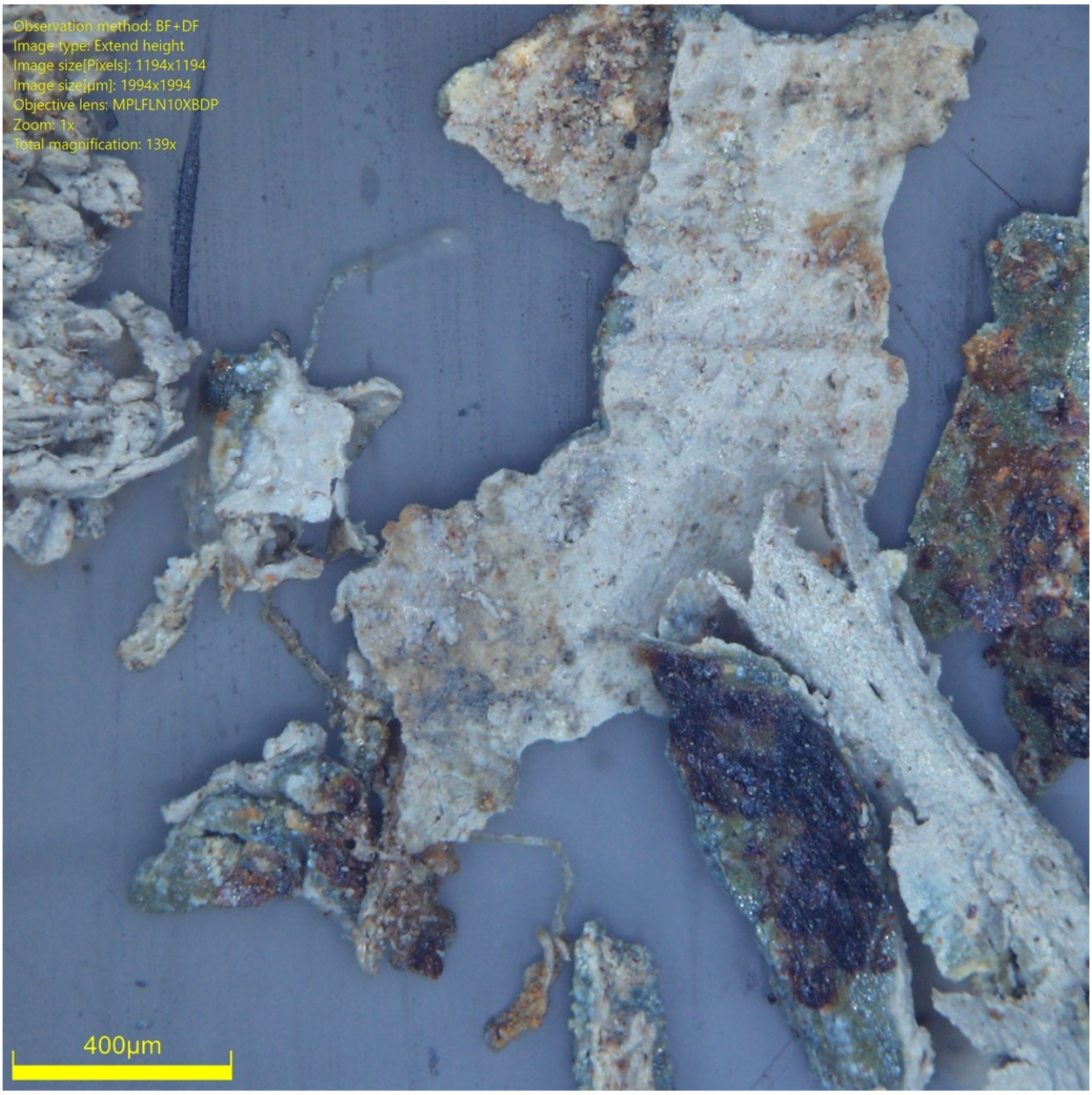
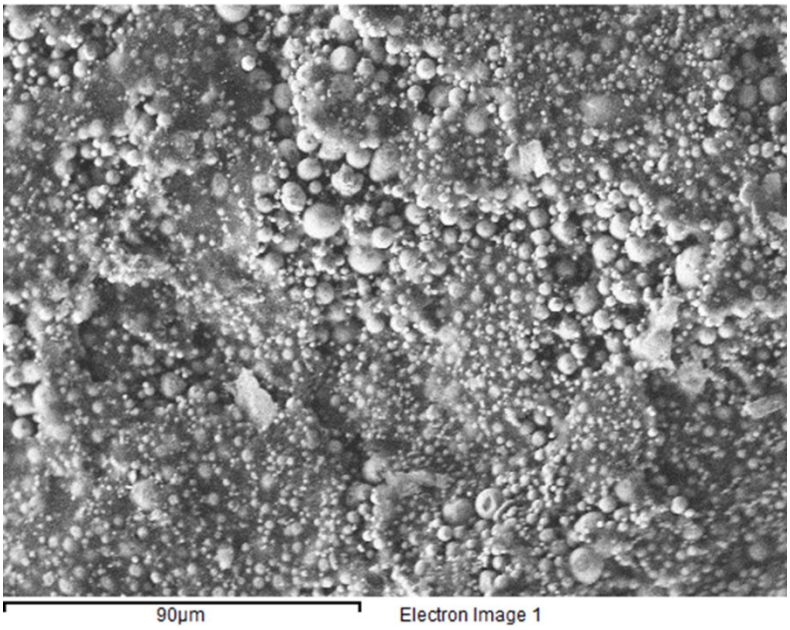


Figure A.61. Corrosion Underneath Paint Layer.

A.5.5. SEM/EDS Results

Element	Weight %	Atomic %
C K	55.93	77.05
O K	14.66	15.16
Al K	0.50	0.31
Si K	0.25	0.15
Fe K	2.15	0.64
Zn K	26.31	6.66
Zr L	0.20	0.04
Totals	100.00	



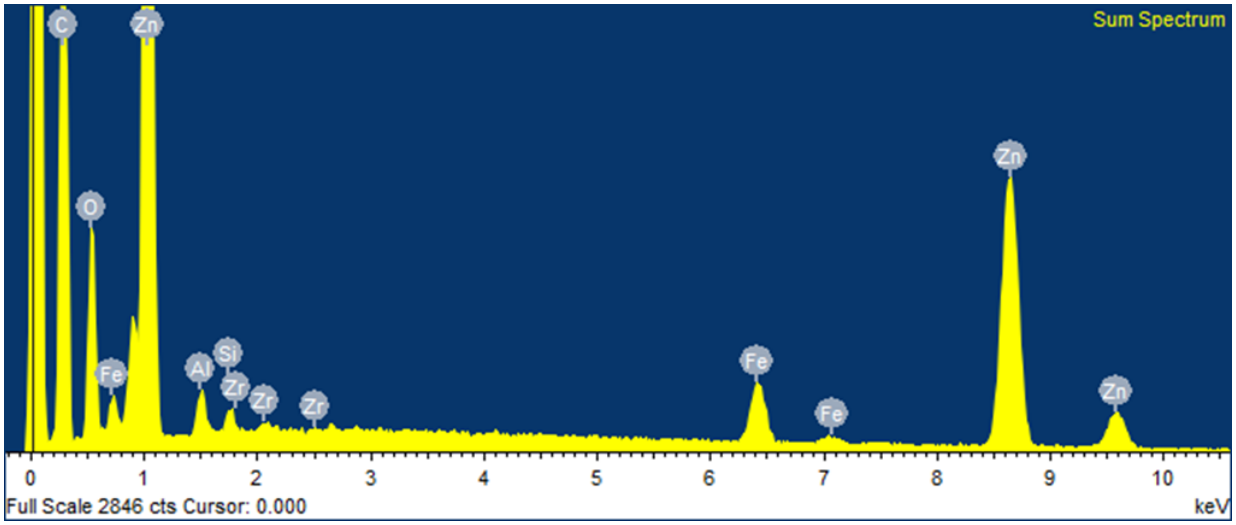


Figure A.62. SEM Image and EDS Spectrum of the Paint Collected from Exterior Web of the Girder.

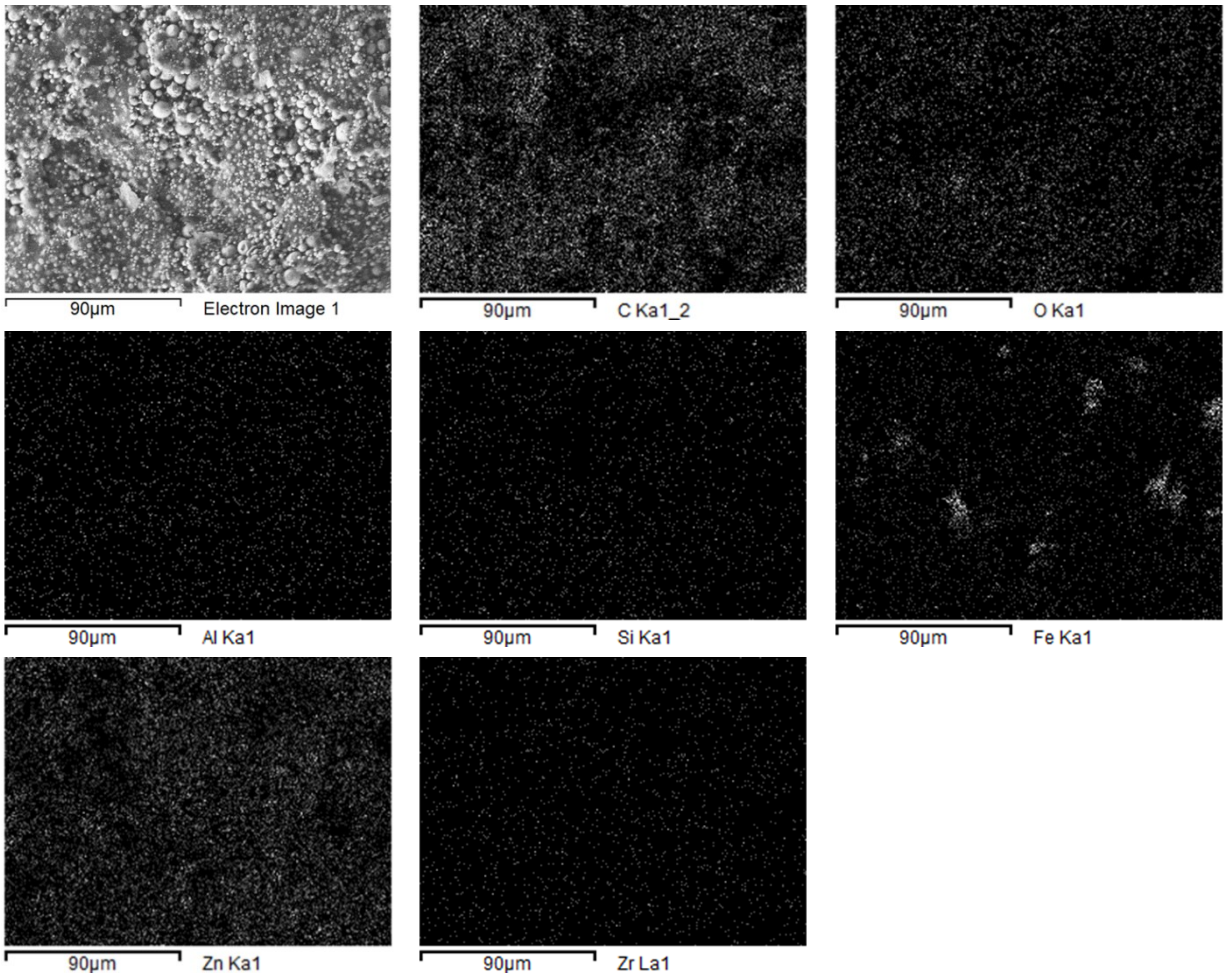
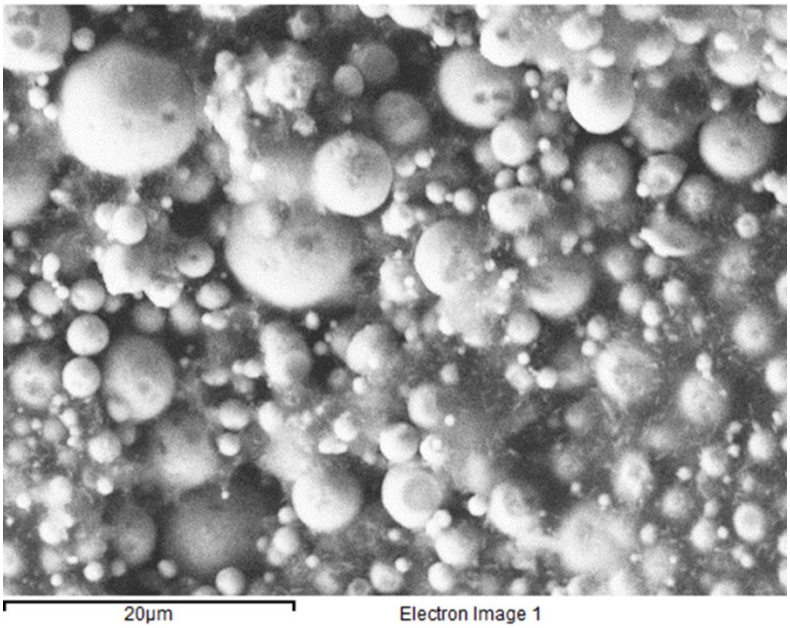


Figure A.63. SEM Image and EDS Spectrum of the Paint Collected from Exterior Web of the Girder.

Element	Weight %	Atomic %
C K	49.33	75.65
O K	11.15	12.83
Al K	0.65	0.44
Si K	0.23	0.15
Fe K	1.24	0.41
Ni K	0.12	0.04
Zn K	37.01	10.43
Zr L	0.28	0.06
Totals	100.00	



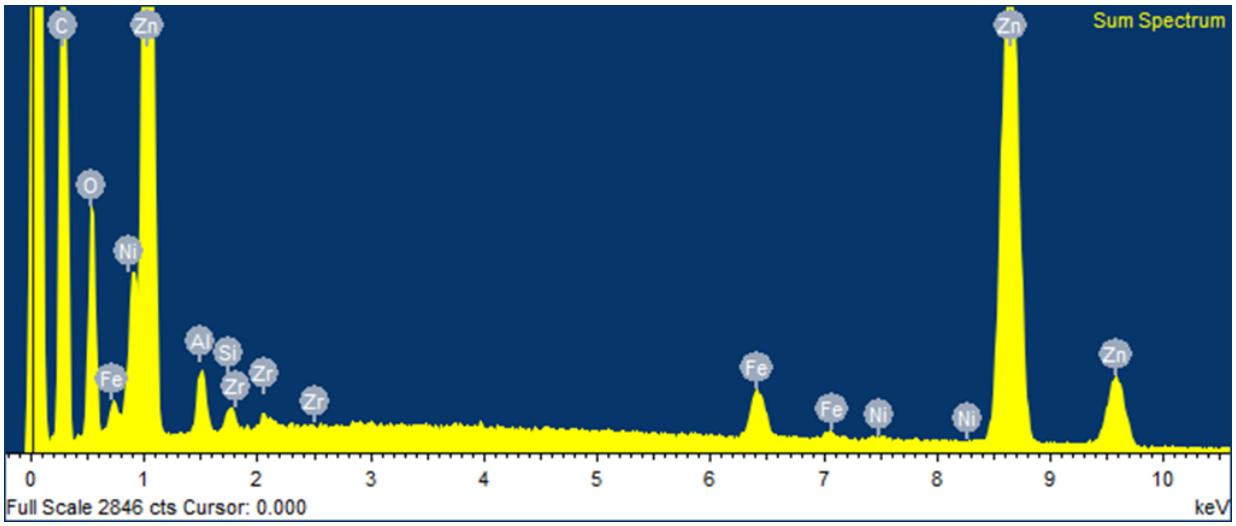


Figure A.64. SEM Image and EDS Spectrum of the Paint Collected from Exterior Web of the Girder.

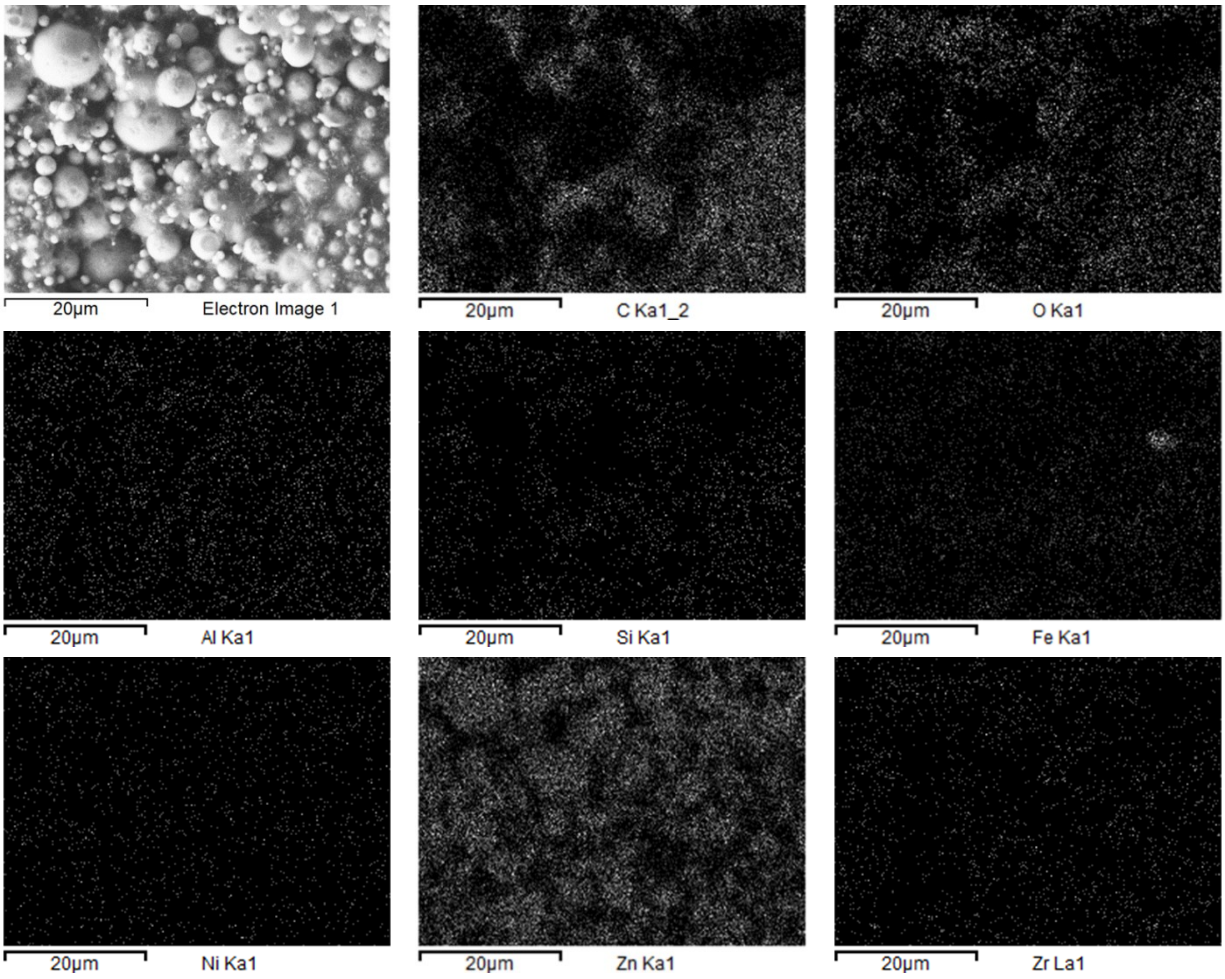
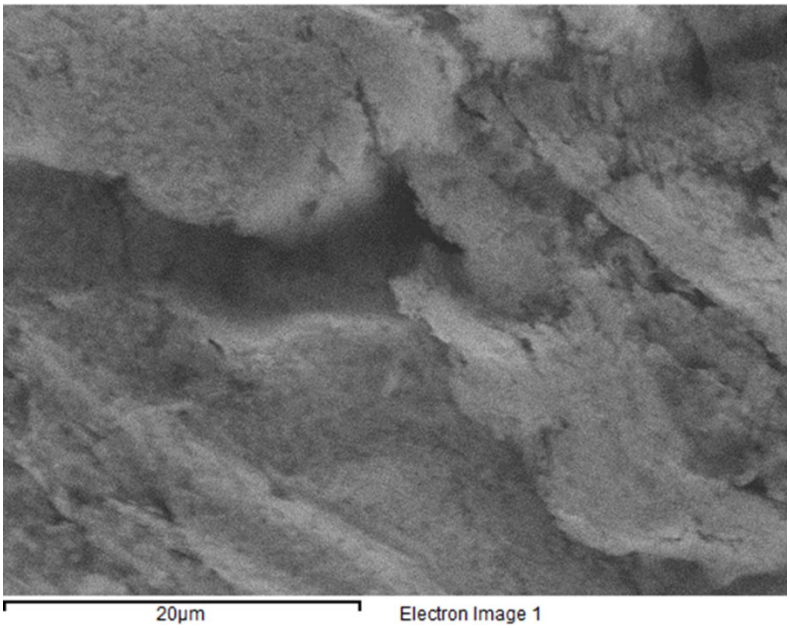


Figure A.65. EDS Elemental Mapping of Paint Collected from Exterior Web.

Element	Weight %	Atomic %
C K	27.68	59.59
O K	7.89	12.76
Al K	3.76	3.60
Fe K	0.66	0.31
Ni K	0.19	0.08
Zn K	59.82	23.66
Totals	100.00	



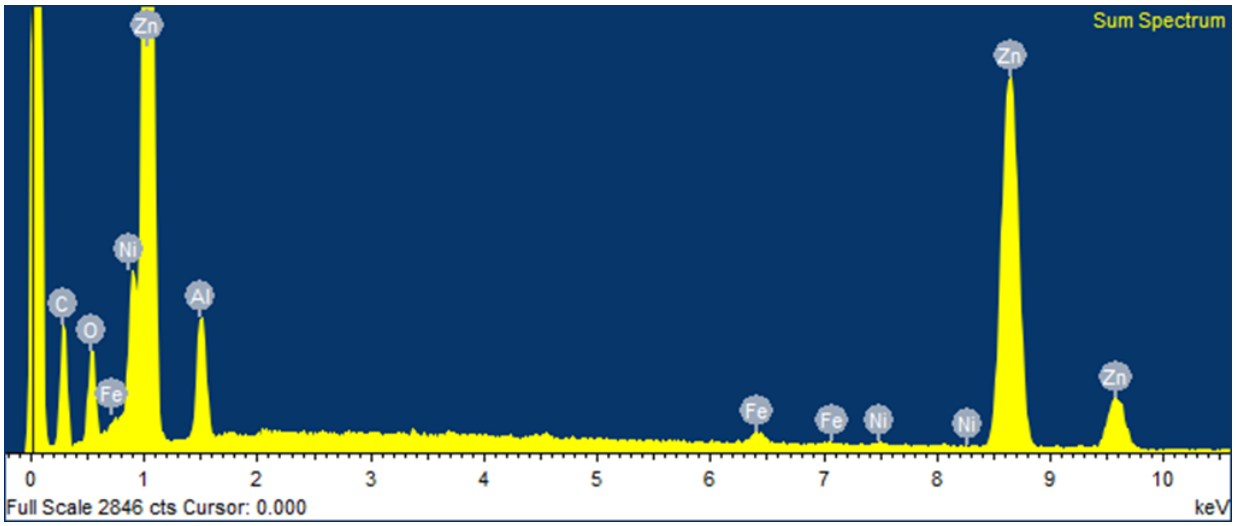


Figure A.66. SEM Image of Paint and EDS Spectrum of the Paint Collected from Exterior Web of the Girder.

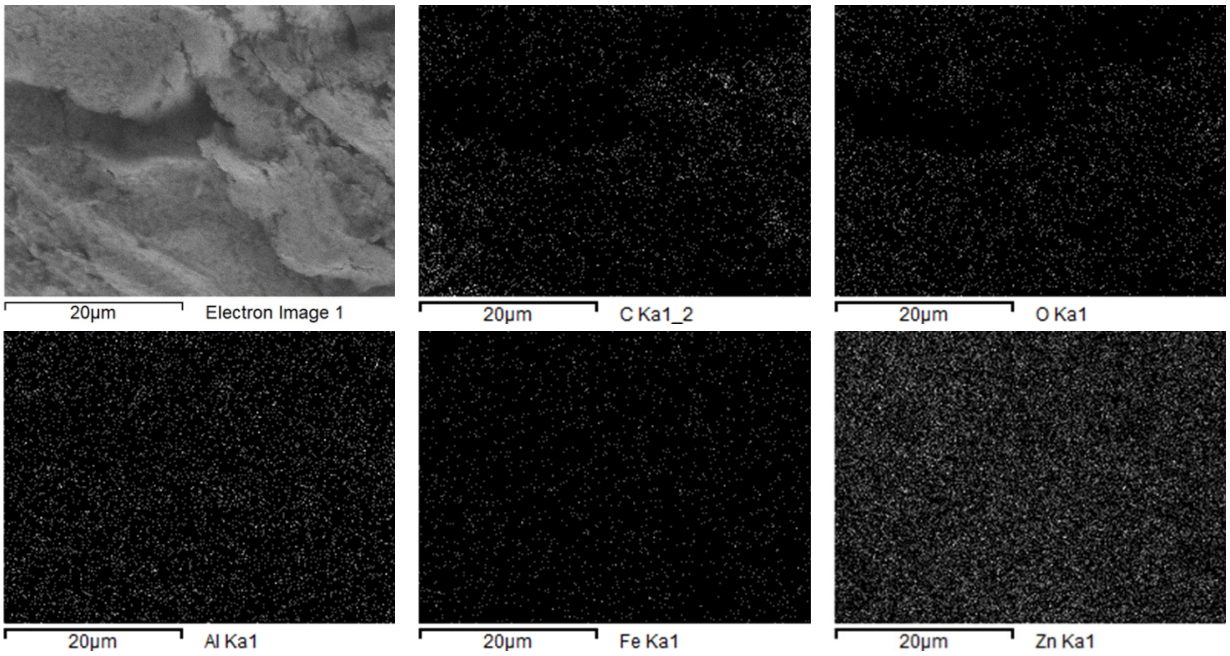
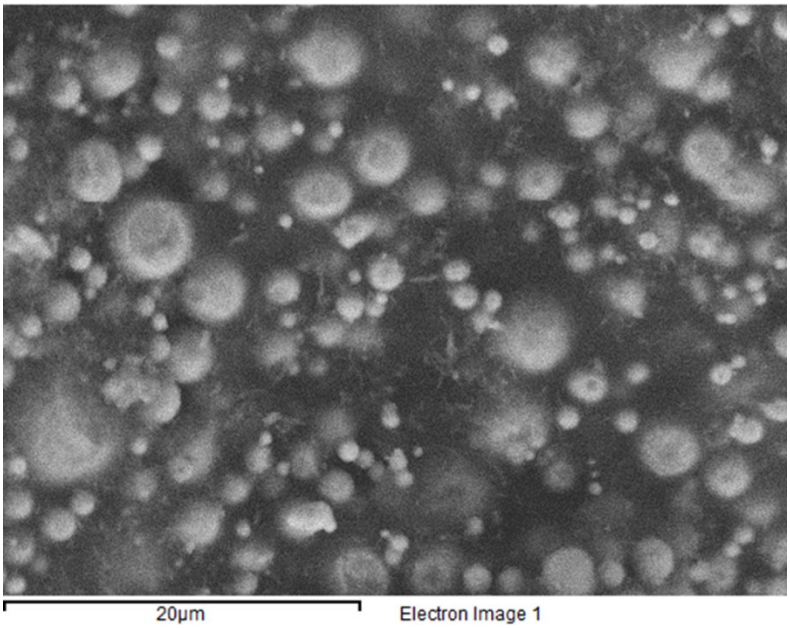


Figure A.67. EDS Elemental Mapping of Paint Collected from Exterior Web .

Element	Weight %	Atomic %
C K	51.86	80.15
O K	6.56	7.62
Al K	0.63	0.44
Si K	0.23	0.16
Fe K	1.69	0.56
Zn K	39.02	11.08
Totals	100.00	



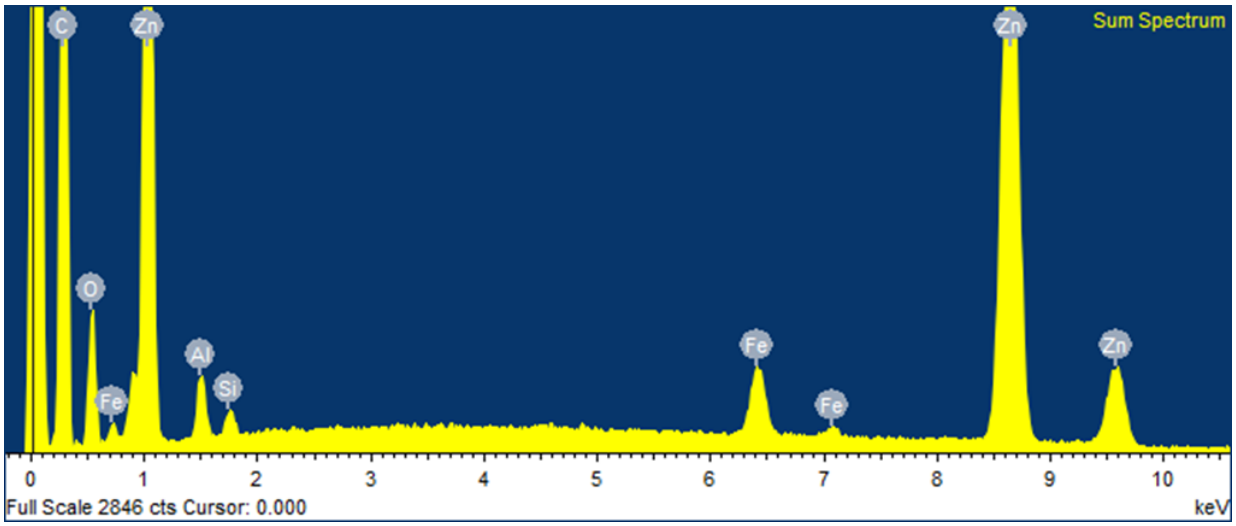


Figure A.68. SEM Image and EDS Spectrum of the Paint Collected from Interior Web of the Girder.

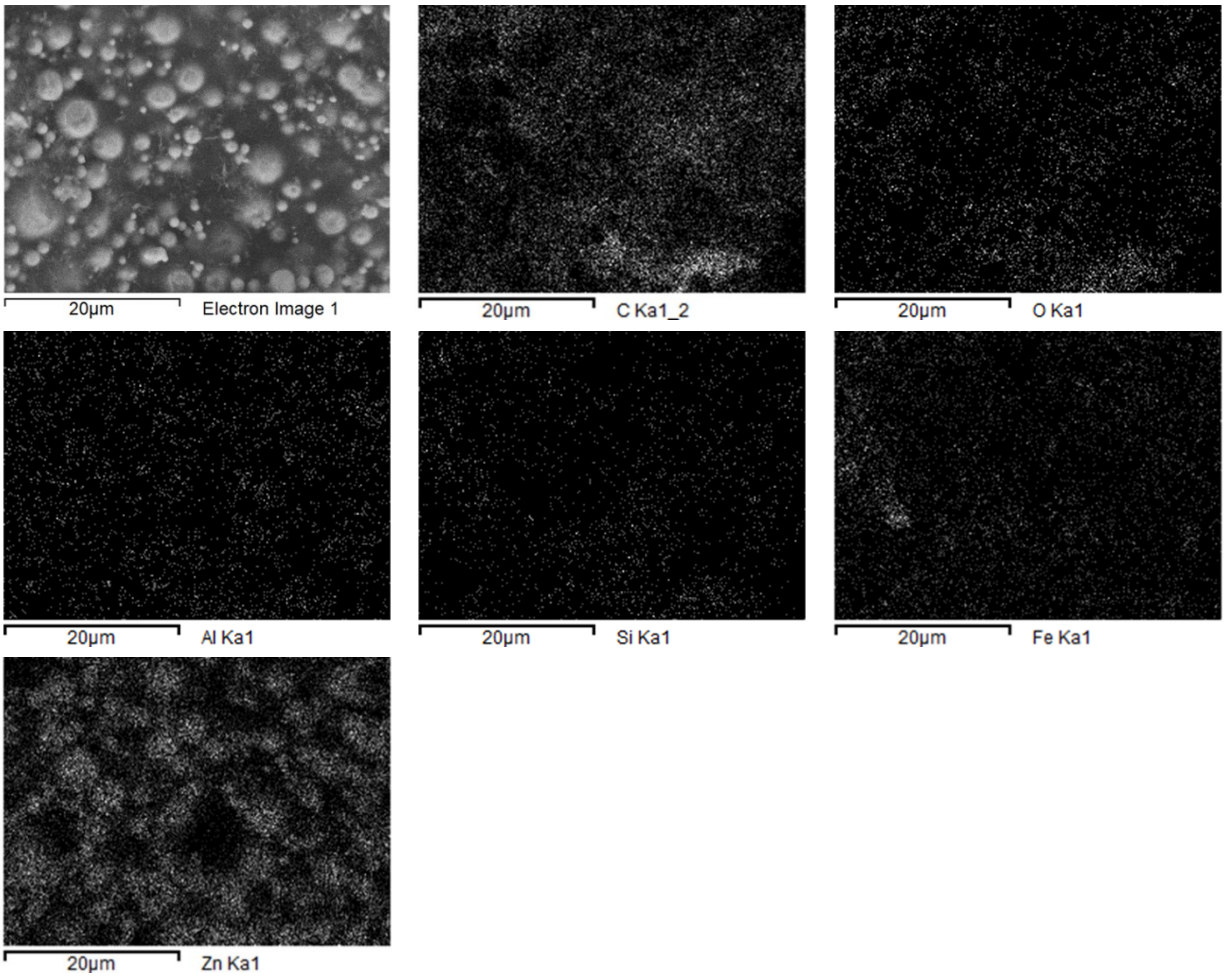
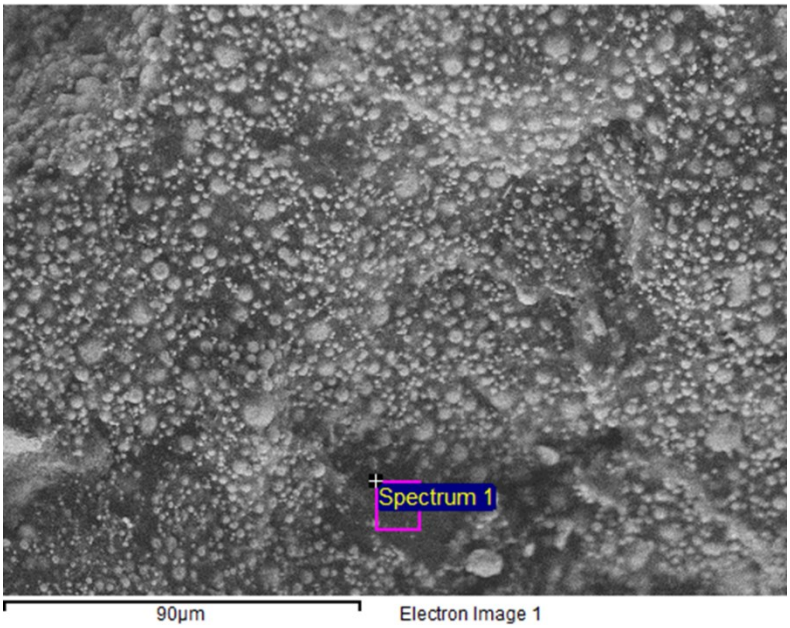


Figure A.69. EDS Elemental Mapping of Paint Collected from Interior Web.

Element	Weight %	Atomic %
C K	73.35	81.51
O K	20.49	17.09
Al K	0.18	0.09
Si K	0.20	0.09
Fe K	1.21	0.29
Zn K	4.58	0.93
Totals	100.00	



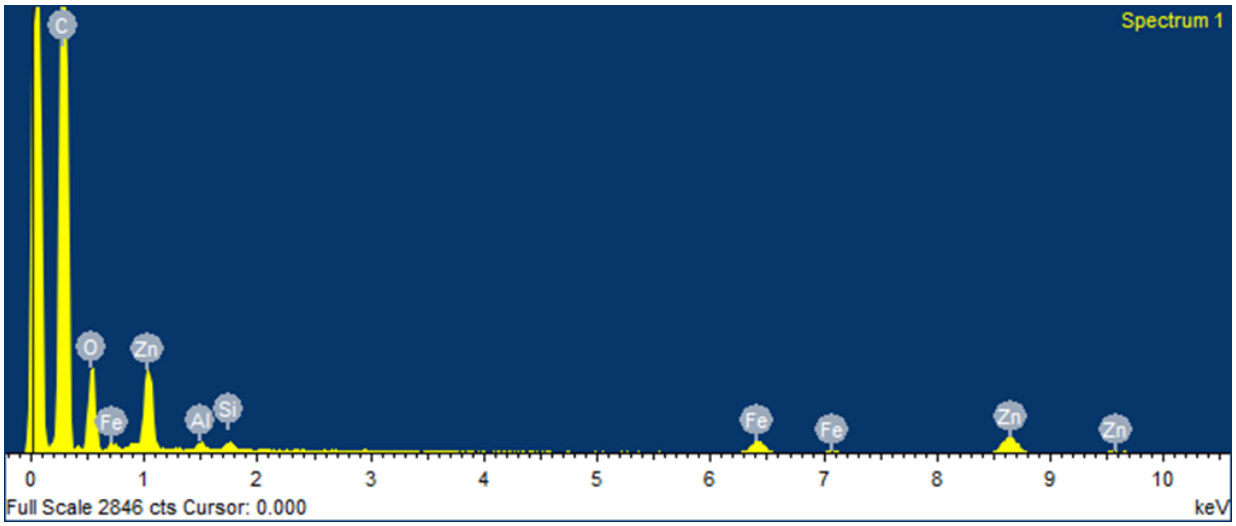


Figure A.70. SEM Image and EDS Spectrum of the Paint Collected from Interior Web of the Girder.

A.6. AMA-PS-01

- US 287 NB over Coldwater Creek
- Bridge ID 42110006603025, Coordinates (36.31385, -102.0553), Sherman County
- Steel pile with Aluminum appearance coat and lead based primer system

- Built 1986 but it is most likely that the bridge got repainted at some point in time
- Date of Inspection: June 14; 2021 pile inspection carried near Bent No.1 and measurements are taken on pile within approximately 3 feet above the ground
- Revisited for pH test and scrape test
- No visual inspection on deck
- Location for Testing: Pile 3, Pile 1



Figure A.71. Typical Elevation of AMA-PS-01.

A.6.1. Observed Condition

In summary, the paint condition of this bridge piles is generally good, with the appearance coat also remaining in good shape. There is no blistering observed, although some erosion of the appearance coat is noted on certain piles where they make contact with the ground, and there is no evidence of paint cracking. Corrosion is observed underneath the paint layer of some of the painted steel pile as observed from pull-off adhesion test. No checking and cracking of paint are observed. There are some patches of paint deterioration present at the bottom of piles.



(a) Painted Steel Pile in Good Condition at Bent 2



(b) Painted Steel Pile in Good Condition at Bent 3



(c) Painted Steel Pile in Good Condition at Bent 3



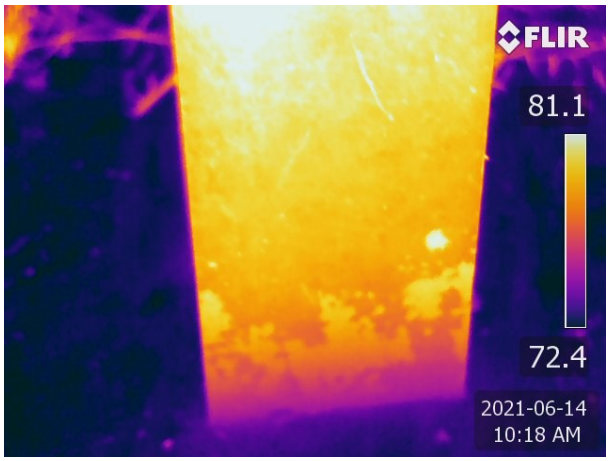
(d) Painted Steel Pile in Good Condition at Bent 3

Figure A.72. Paint Condition on the Girder of AMA-PS-01.

A.6.2. NDT Results



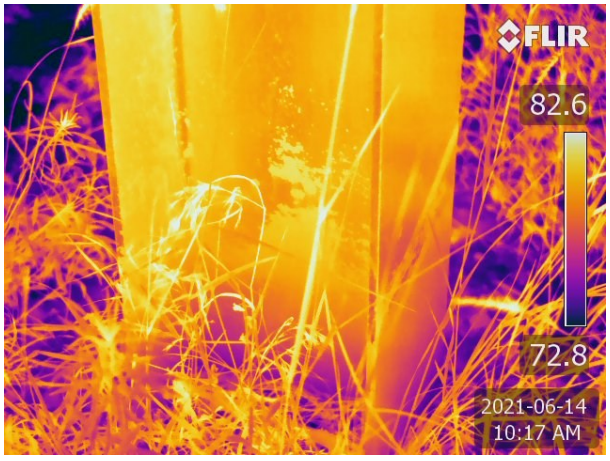
(a) Digital Image of Pile Showing Paint Deterioration



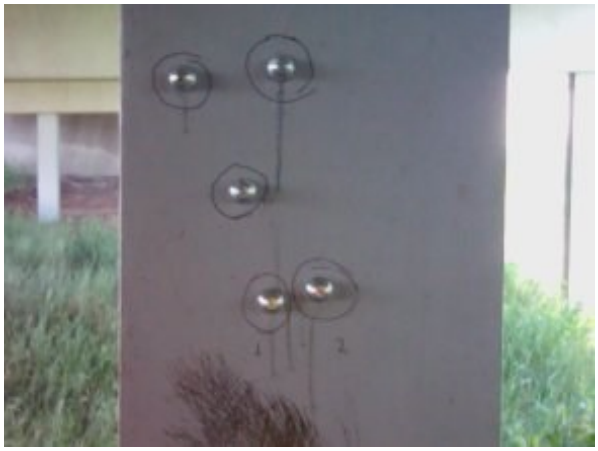
(b) Thermal Image of Pile Showing Paint Deterioration



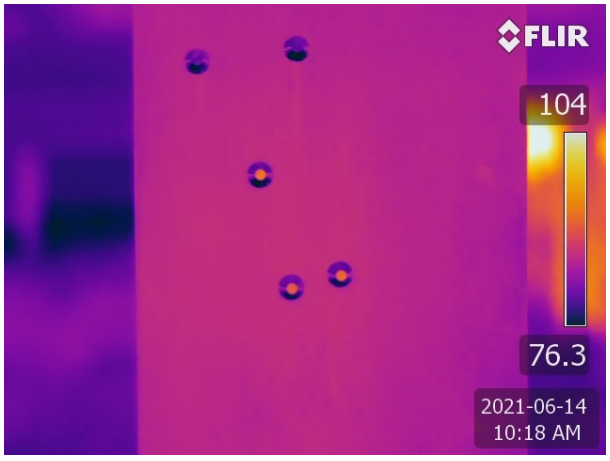
(c) Digital Image of Pile Showing Paint Deterioration



(d) Thermal Image of Pile Showing Paint Deterioration



(e) Digital Image of Pile



(f) Thermal Image of Pile

Figure A.73. Digital and Thermal Image of Painted Girder on AMA-PS-01.

Table A-30. Paint System Information: (2-Layer Lead-Based).

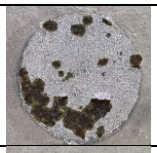
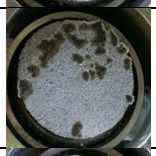
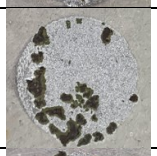
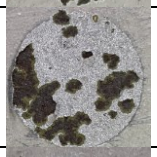
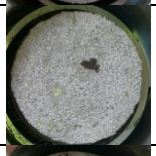
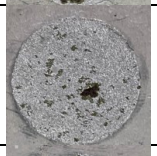
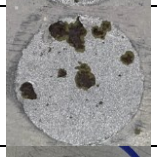
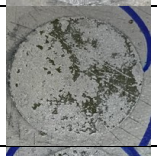
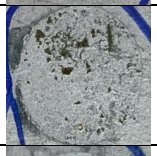
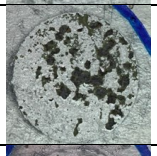
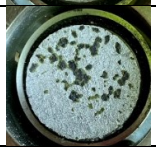
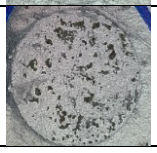
Cohesive Failure Layer		Adhesive Failure Layer	
Code	**Description**	**Code**	**Description**
A	Substrate	A/B	Substrate & Layer 1
B	Layer 1(Silver)	B/C	Layer 1 & Glue
C	Layer 2(Green)	C/Y	
Y	Glue	Y/Z	Glue & Dolly

Table A-31. Field Inspection Results for AMA-PS-01.

Location	Cl^- Conc. (ppm)	pH Test	Thickness (µm)	Thickness (inch)	Visual Inspection
Pile3 N FL. Int.	-	-	Measured R1 88.3 R2 106 R3 90.8	Measured R1 0.417 R2 0.418 R3 0.419 R_Avg 0.418 Design	Rust Grade – 10 Blistering – Not Found Discoloration – Not Found Flaking – Not Found Delamination – Not Found
Pile3 Web. Int.	1		Measured R1 116 R2 109 R3 92.3	Measured R1 0.431 R2 0.431 R3 0.430 R_Avg 0.431 Design	Rust Grade – 10 Blistering – Not Found Discoloration – Not Found Flaking – Not Found Delamination – Not Found
Pile3 S FL. Int.	-	-	Measured R1 109 R2 84.6 R3 115	Measured R1 0.424 R2 0.423 R3 0.415 R_Avg 0.421 Design	Rust Grade – 10 Blistering – Not Found Discoloration – Not Found Flaking – Not Found Delamination – Not Found
Pile1 N FL. Ext.	-	-	Measured R1 62.6 R2 67.4 R3 71.5	Measured R1 0.428 R2 0.426 R3 0.423 R_Avg 0.426 Design	Rust Grade – 10 Blistering – Not Found Discoloration – Not Found Flaking – Not Found Delamination – Not Found
Pile1 Web. Ext.	1		Measured R1 141 R2 128 R3 138	Measured R1 0.454 R2 0.452 R3 0.453 R_Avg 0.453 Design	Rust Grade – 10 Blistering – Not Found Discoloration – Not Found Flaking – Not Found Delamination – Not Found
Pile1 S FL. Ext.	-	-	Measured R1 92 R2 117 R3 72.7	Measured R1 0.431 R2 0.428 R3 0.431 R_Avg 0.430 Design	Rust Grade – 10 Blistering – Not Found Discoloration – Not Found Flaking – Not Found Delamination – Not Found

A.6.3. Pull-off Adhesion Results

Table A-32. Pull-off Adhesion Results for AMA-PS-01.

Location	Dolly Face	Substrate Face	Test Result (psi)	Attributes	Failure Type
PILE 3 Int.			498	70% C 30% A/B	70% Cohesive Failure 30% Adhesive Failure
			572	80% C 20% A/B	80% Cohesive 20% Adhesive Failure
			483	60% C 40% A/B	60% Cohesive 40% Adhesive Failure
			341	90% C 10% A/B	90% Cohesive 10% Adhesive Failure
			509	80% C 20% A/B	80% Cohesive 20% Adhesive Failure
PILE 1 Ext.			747	80% C 20% A/B	80% Cohesive 20% Adhesive Failure
			868	90% C 10% A/B	90% Cohesive 10% Adhesive Failure
			850	80% C 20% A/B	80% Cohesive 20% Adhesive Failure
			886	70% C 30% A/B	70% Cohesive 30% Adhesive Failure
			987	80% C 20% A/B	80% Cohesive 20% Adhesive Failure

A.6.4. Optical Microscopy Results

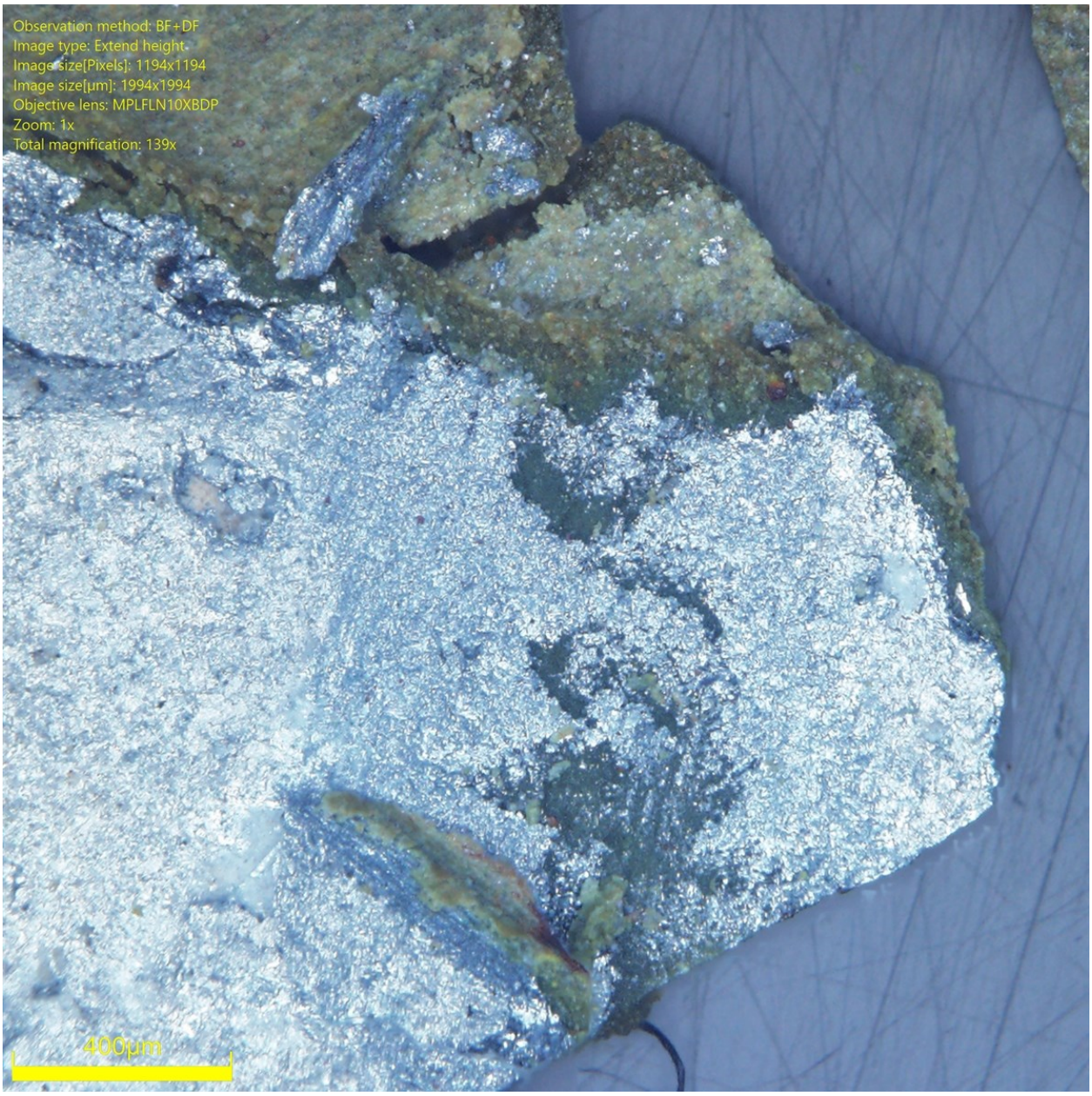


Figure A.74. Paint System Examined by Optical Microscope AMA–PS–01.

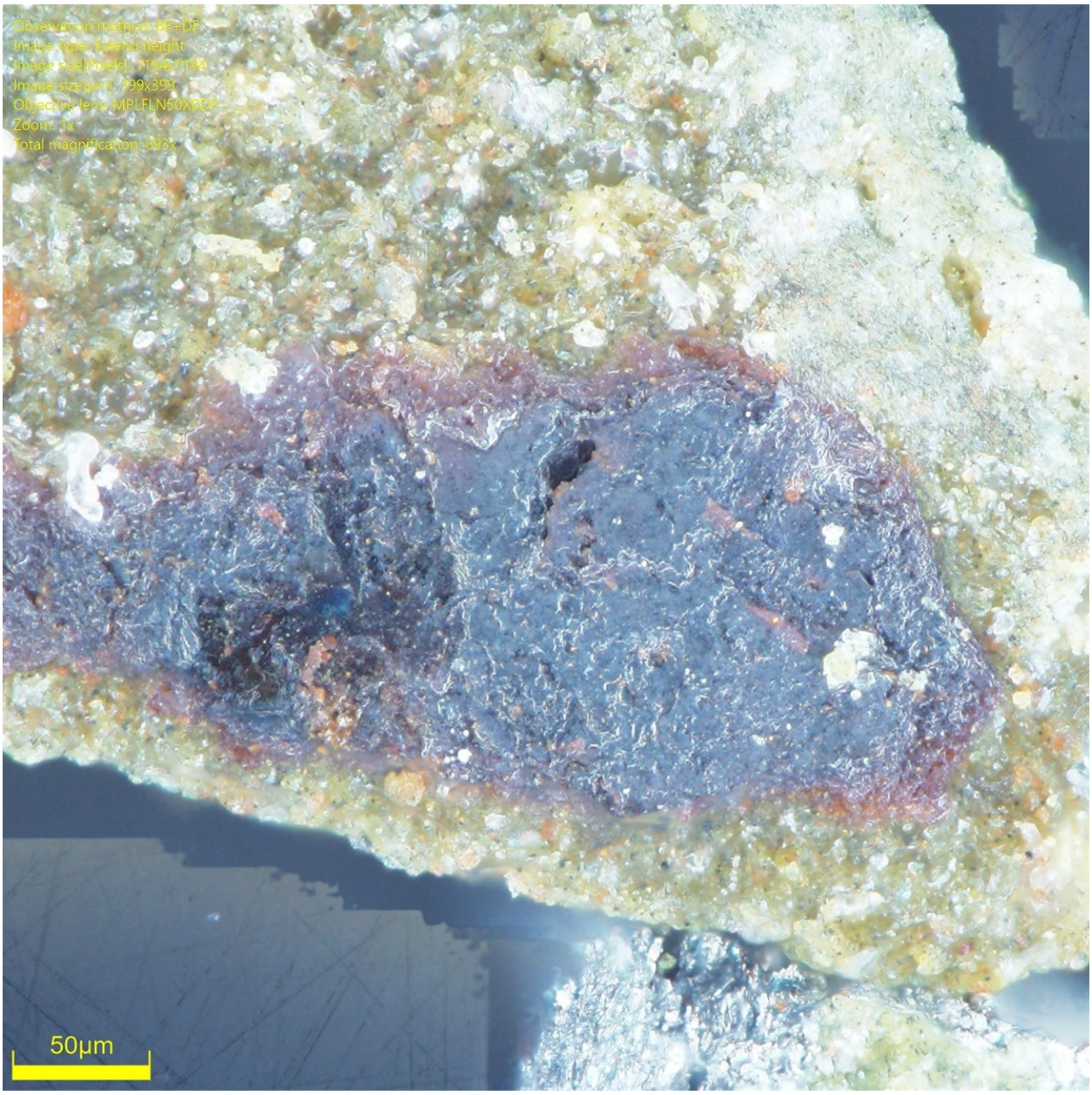
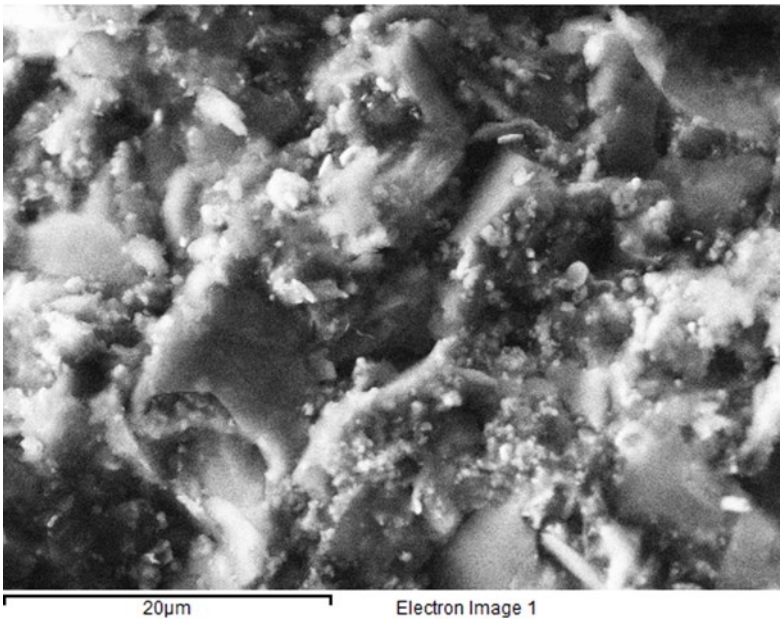


Figure A.75. Corrosion as Observed Between Primer and Base Metal on Exterior Pile.

A.6.5. SEM/EDS Results

Element	Weight %	Atomic %
C K	37.08	48.65
O K	43.69	43.04
Mg K	4.05	2.63
Al K	0.33	0.19
Si K	3.84	2.16
Cl K	4.15	1.84
K K	0.68	0.27
Ca K	0.18	0.07
Cr K	1.63	0.49
Fe K	0.34	0.10
Zn K	1.54	0.37
Pb M	2.49	0.19
Totals	100.00	



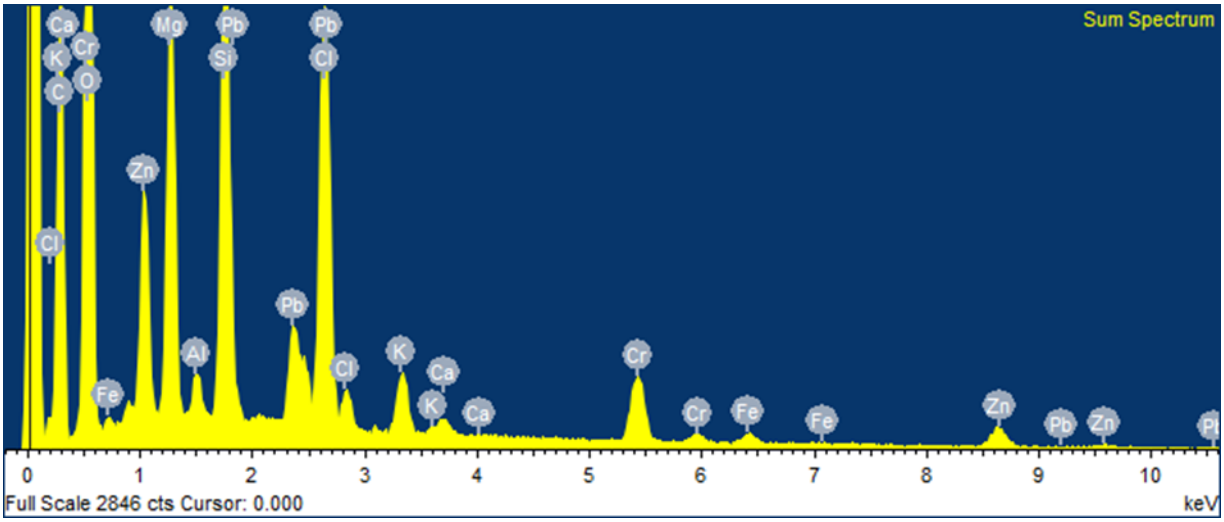


Figure A.76. SEM Image and EDS Spectrum of the Paint Collected from Exterior Web of the Girder.

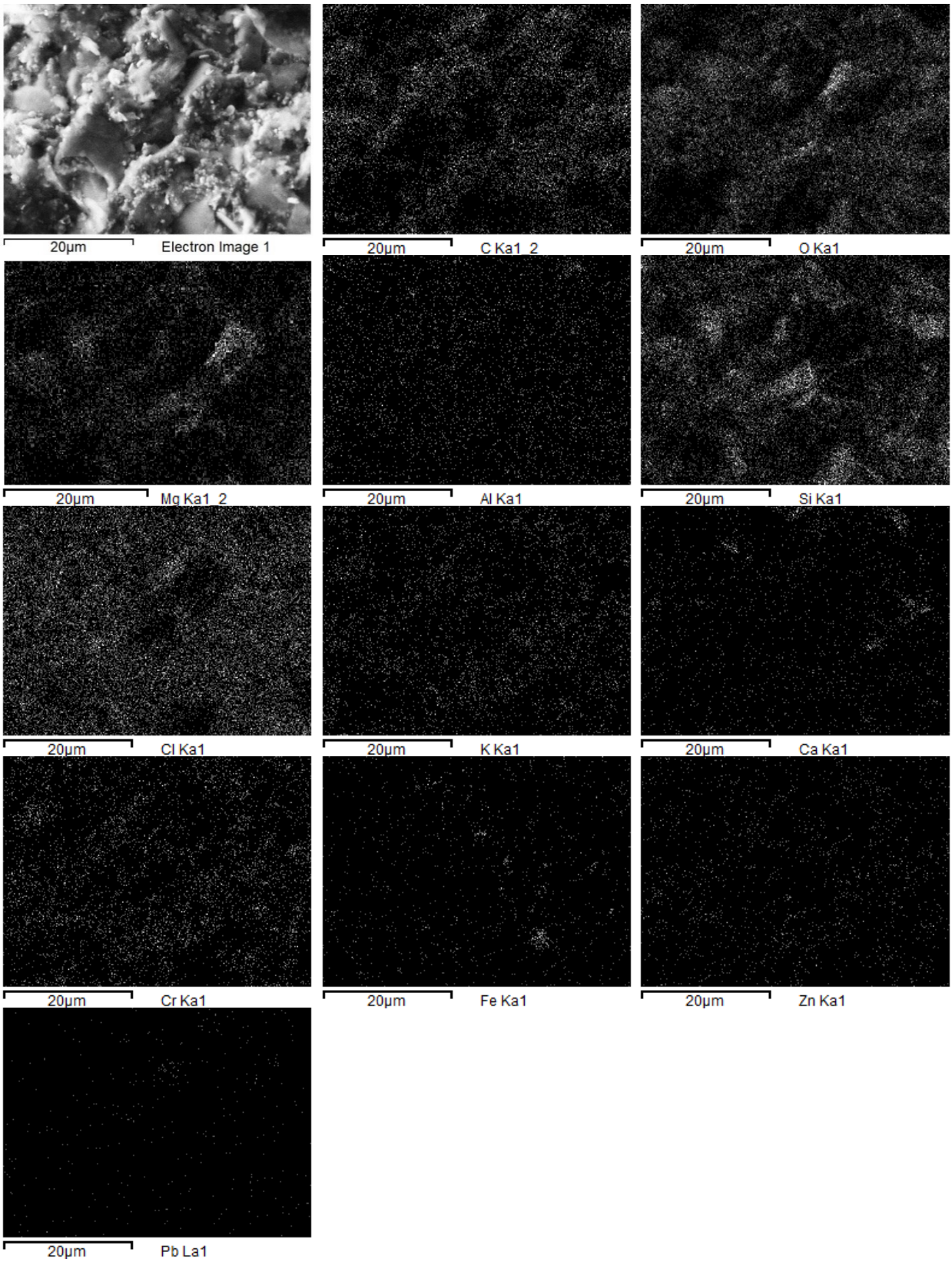
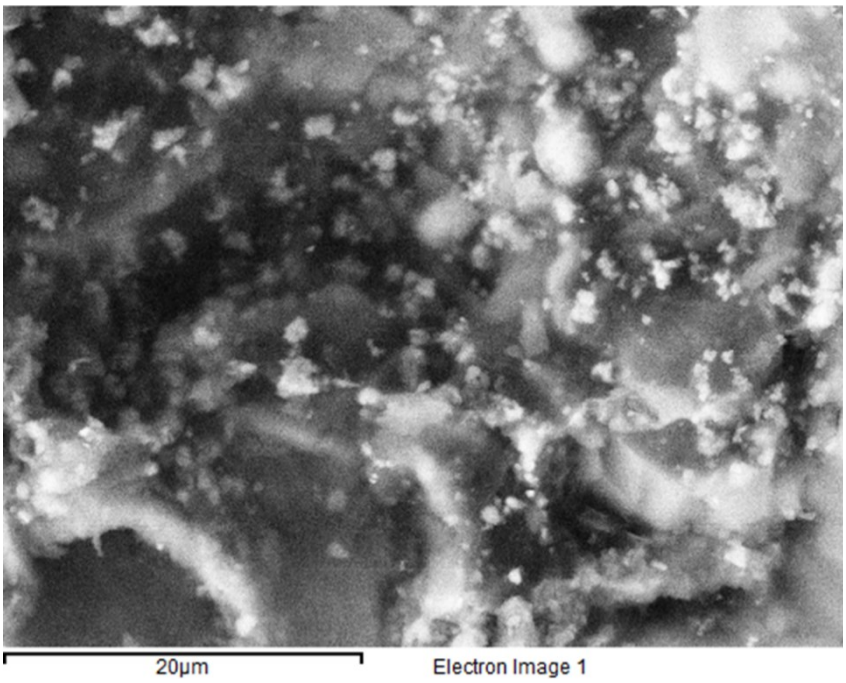


Figure A.77. EDS Elemental Mapping of Paint Collected from Exterior Web.

Element	Weight %	Atomic %
C K	34.49	48.16
O K	36.99	38.78
Mg K	5.29	3.65
Al K	0.51	0.31
Si K	6.11	3.65
Cl K	4.84	2.29
K K	1.24	0.53
Ca K	0.24	0.10
Cr K	3.24	1.05
Fe K	0.64	0.19
Zn K	4.35	1.12
Pb M	2.05	0.17
Totals	100.00	



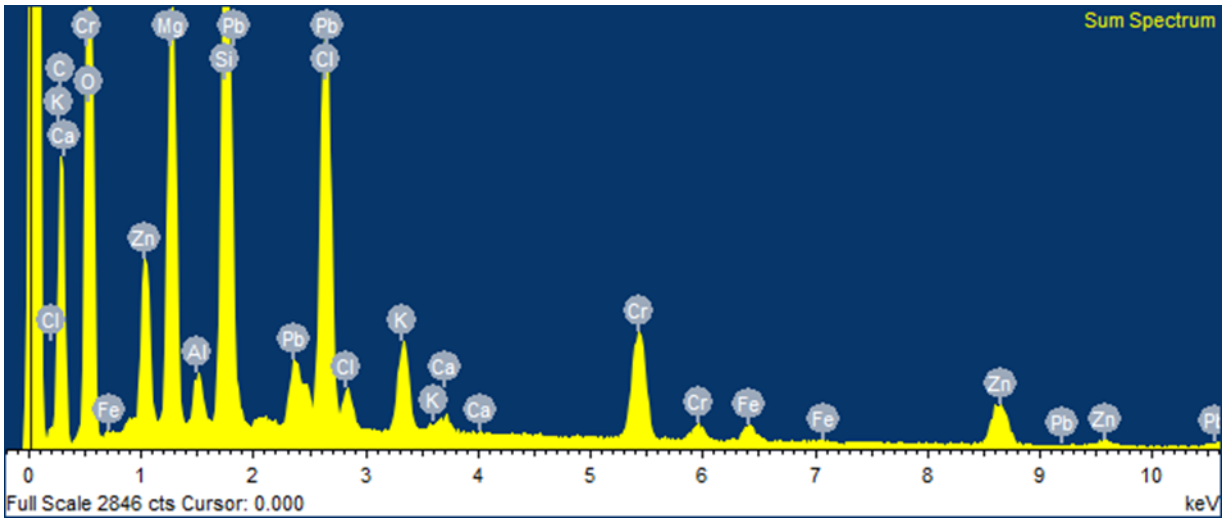


Figure A.78. SEM Image and EDS Spectrum of the Paint Collected from Interior Web of the Girder.

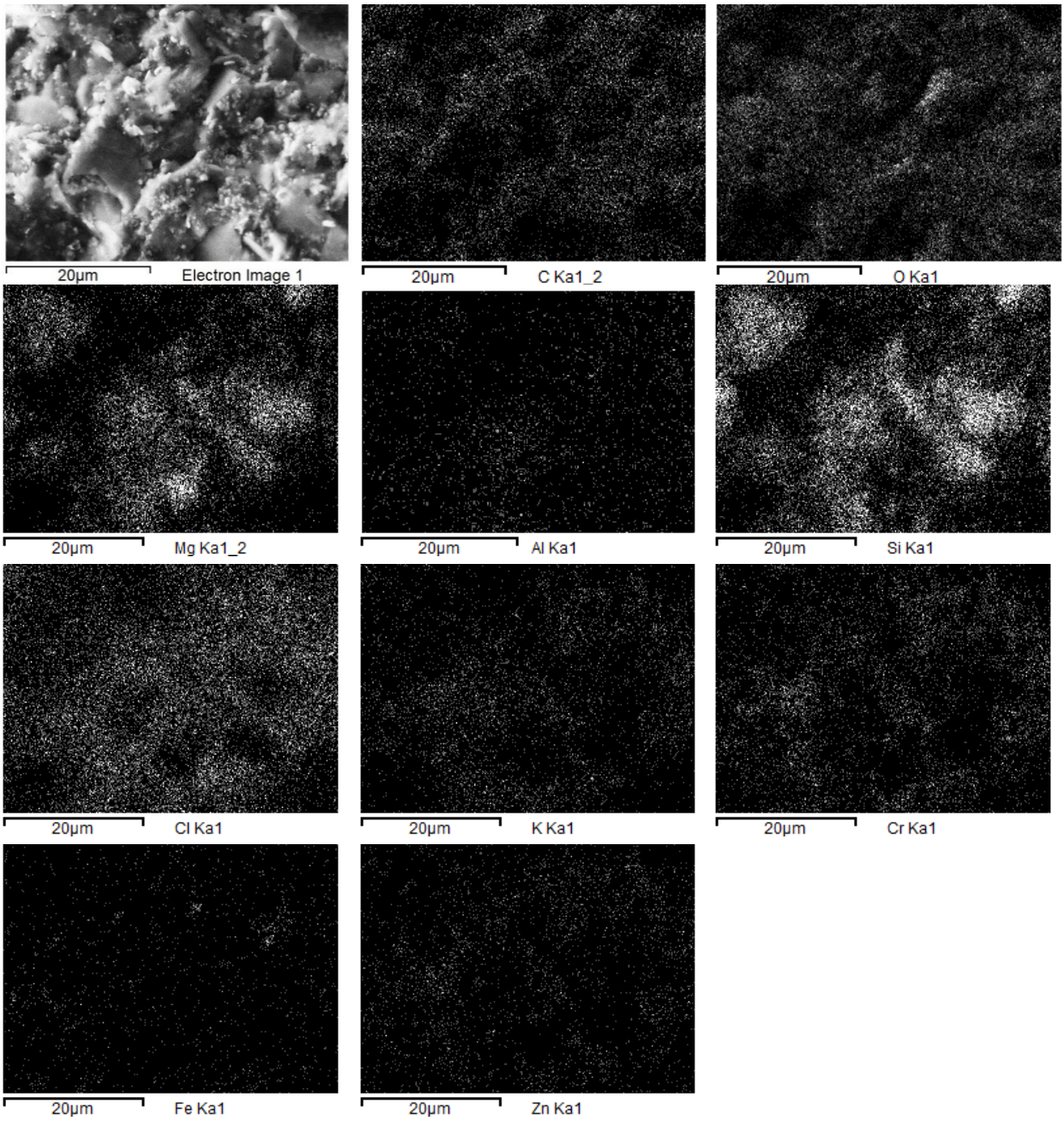
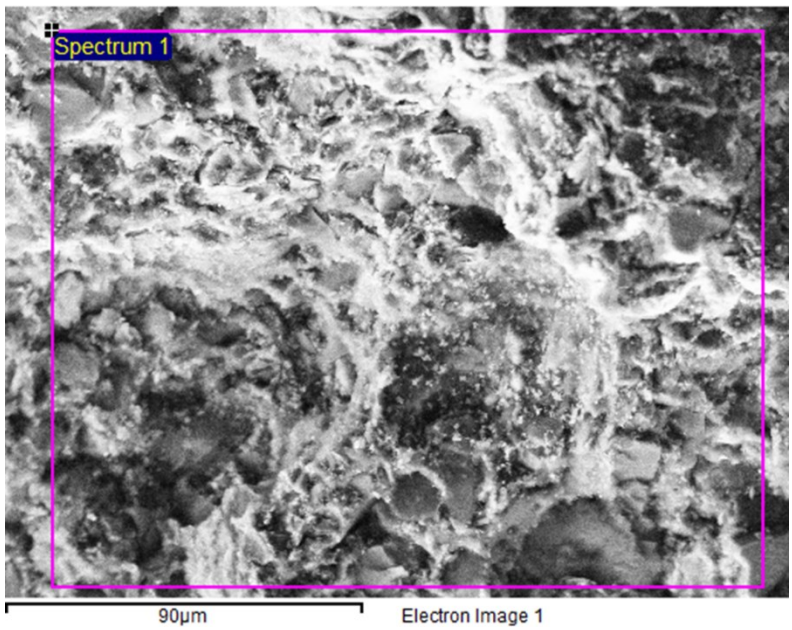


Figure A.79. EDS Elemental Mapping of Paint Collected from Exterior Web.

Element	Weight %	Atomic %
C K	35.02	48.28
O K	38.80	40.16
Mg K	4.31	2.94
Al K	0.87	0.53
Si K	4.95	2.92
Cl K	5.10	2.38
K K	0.79	0.34
Ca K	0.93	0.39
Cr K	2.51	0.80
Fe K	0.63	0.19
Zn K	3.48	0.88
Pb M	2.61	0.21
Totals	100.00	



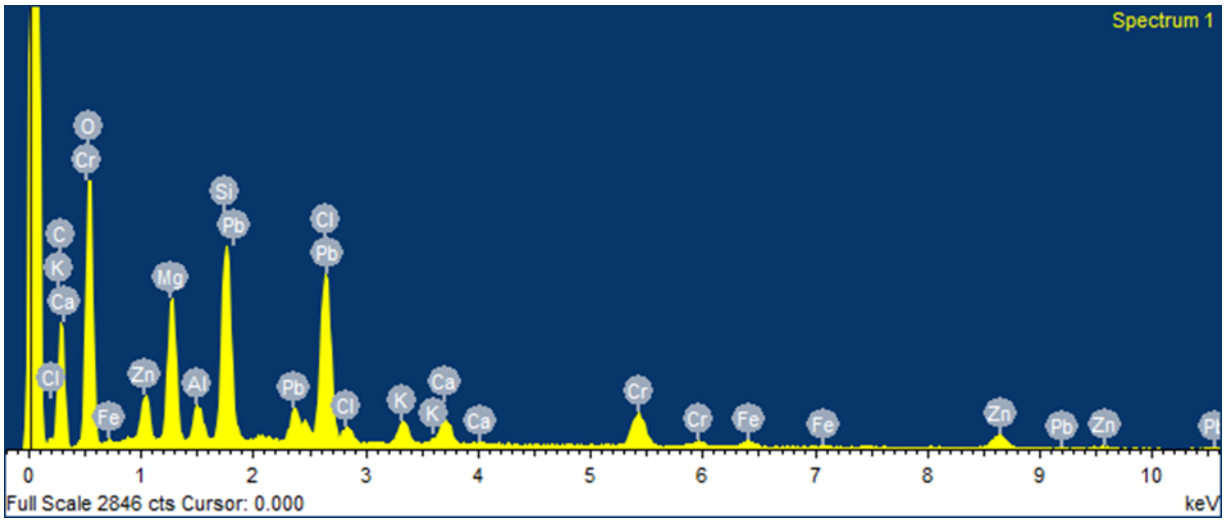


Figure A.80. SEM Image and EDS Spectrum of the Paint Collected from Exterior Web of the Girder.

A.7. AMA-PS-02

- US 287 NB over South Palo Duro Creek
- Bridge ID 41710006604020, Moore County
- Steel pile with System II type paint
- Built 1981
- Date of Inspection: June 14, 2021; pile inspection carried near Bent No. 3 and measurements are taken on piles within approximately 3 feet above the ground
- Revisited for pH test and scrape test
- No visual inspection on deck
- Location for Testing: Pile3, Pile1



Figure A.81. Typical Elevation of AMA-PS-02.

A.7.1. Observed Condition

Overall the paint condition of this bridge is in good condition. The appearance coat is also in good condition. Blistering, Erosion of paint, cracking in paint is not present. Corrosion is

observed on the bottom part of piles at locations where it touches the ground. No checking and cracking of paint are observed.



(a) Painted Steel Pile Showing Rusting and Paint Deterioration at Bottom



(b) Painted Steel Pile Showing Rusting and Paint Deterioration at Bottom



(c) Painted Steel Pile in Good Condition at Bent 3



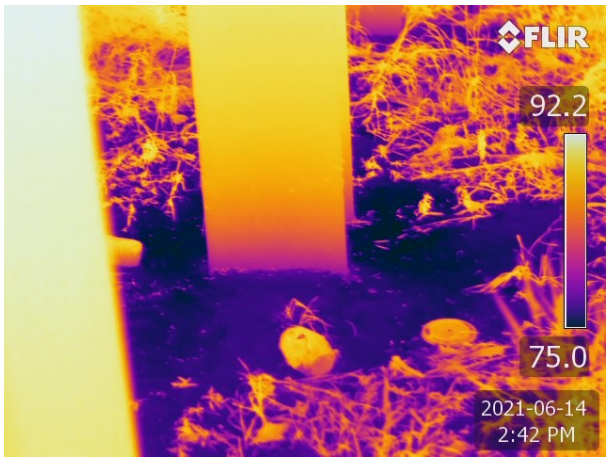
(d) Painted Steel Pile in Good Condition at Bent 2

Figure A.82. Paint Condition on the Girder of AMA-PS-02.

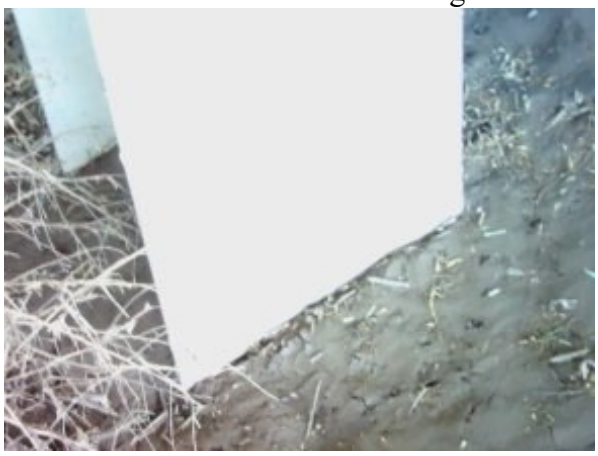
A.7.2. NDT Results



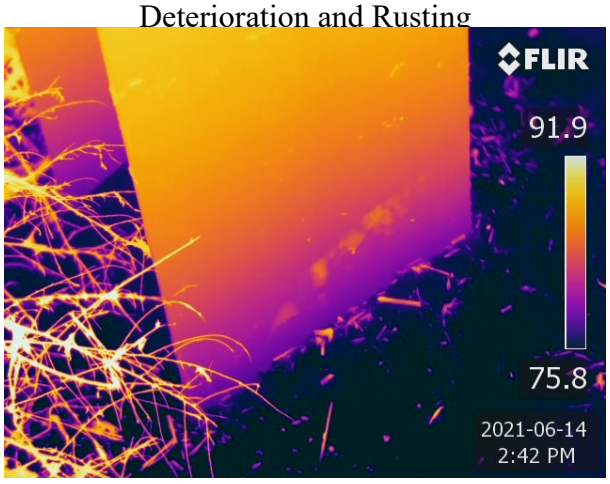
(a) Digital Image of Pile Showing Paint Deterioration and Rusting



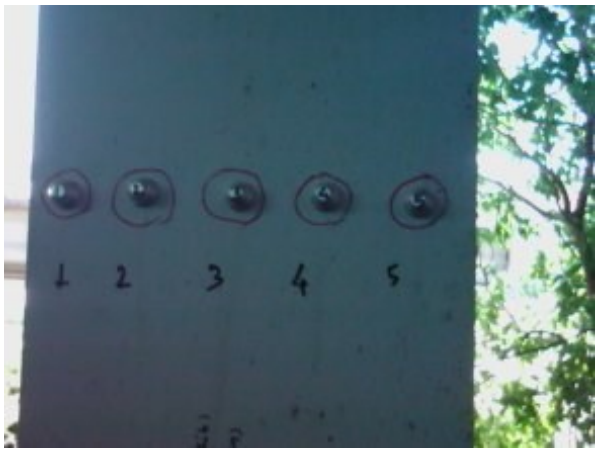
(b) Thermal Image of Pile Showing Paint Deterioration and Rusting



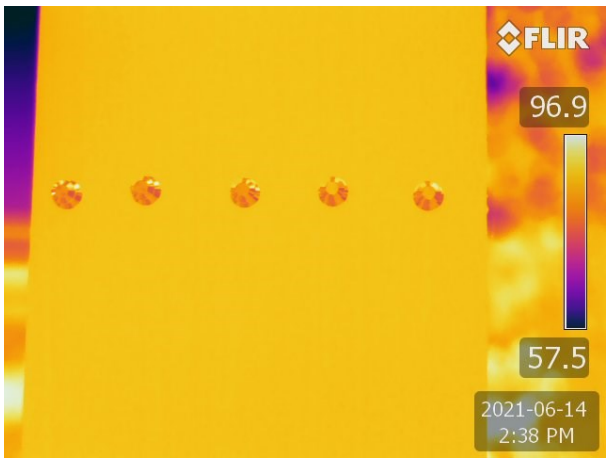
(c) Digital Image Showing Paint Deterioration on Interior Bridge Pile



(d) Thermal Image of Showing Paint Deterioration on Interior Bridge Pile



(e) Digital Image Showing Paint Condition on Exterior Bridge Pile



(f) Thermal Image Showing Paint Condition on Exterior Bridge Pile

Figure A.83. Digital and Thermal Image of Painted Girder on AMA-PS-02.

Table A-33. Paint System Information.

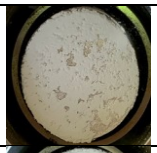
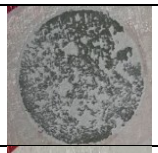
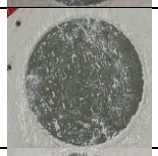
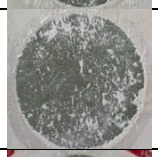
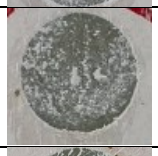
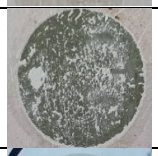
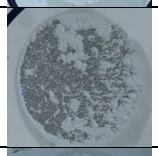
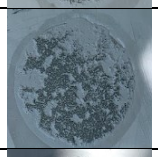
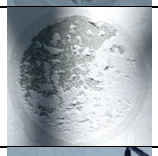
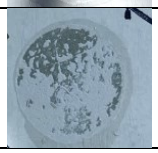
Cohesive Failure Layer		**Adhesive Failure Layer**	
Code	**Description**	**Code**	**Description**
A	Substrate	A/B	Substrate & Layer 1
B	Layer 1(Gray)	B/C	Layer 1 & Layer 2
C	Layer 2(White)	C/Y	Layer 2 & Glue
Y	Glue	Y/Z	Glue & Dolly

Table A-34. Field Inspection Results for AMA-PS-02.

Location	Cl^- Conc. (ppm)	pH Test	Thickness (µm)	Thickness (inch)	Visual Inspection
Pile3 E FL. Int.	-	-	Measured R1 128 R2 133 R3 122 Design Paint 140-381	Measured R1 0.434 R2 0.432 R3 0.434 R_Avg 0.433 Design	Rust Grade – 10 Blistering – Not Found Discoloration – Not Found Flaking – Not Found Delamination – Not Found
Pile3 Web. Int.	1		Measured R1 174 R2 152 R3 176 Design Paint 140-381	Measured R1 0.435 R2 0.436 R3 0.434 R_Avg 0.435 Design	Rust Grade – 10 Blistering – Not Found Discoloration – Not Found Flaking – Not Found Delamination – Not Found
Pile3 W FL. Int.	-	-	Measured R1 116 R2 109 R3 92.3 Design Paint 140-381	Measured R1 0.437 R2 0.439 R3 0.436 R_Avg 0.437 Design	Rust Grade – 10 Blistering – Not Found Discoloration – Not Found Flaking – Not Found Delamination – Not Found
Pile1 E FL. Ext.	-	-	Measured R1 207 R2 229 R3 202 Design Paint 140-381	Measured R1 0.440 R2 0.438 R3 0.441 R_Avg 0.440 Design	Rust Grade – 10 Blistering – Not Found Discoloration – Not Found Flaking – Not Found Delamination – Not Found
Pile1 Web. Ext.	1		Measured R1 231 R2 205 R3 196 Design Paint 140-381	Measured R1 0.437 R2 0.435 R3 0.436 R_Avg 0.436 Design	Rust Grade – 10 Blistering – Not Found Discoloration – Not Found Flaking – Not Found Delamination – Not Found
Pile1 W FL.Ext.	-	-	Measured R1 286 R2 288 R3 319 Design Paint 140-381	Measured R1 0.440 R2 0.440 R3 0.439 R_Avg 0.440 Design	Rust Grade – 10 Blistering – Not Found Discoloration – Not Found Flaking – Not Found Delamination – Not Found

A.7.3. Pull-off Adhesion Results

Table A-35. Pull-off Adhesion Results for AMA-PS-02.

Location	Dolly Face	Substrate Face	Test Result (psi)	Attributes	Failure Type
Pile 3 Int.			2096	50% C 50% B/C	50% Cohesive Failure 50% Adhesive Failure
			2481	90% C 10% B/C	90% Cohesive Failure 10% Adhesive Failure
			2379	70% C 30% B/C	70% Cohesive Failure 30% Adhesive Failure
			2473	70% C 30% B/C	70% Cohesive Failure 30% Adhesive Failure
			2432	60% C 40% B/C	60% Cohesive Failure 40% Adhesive Failure
Pile 1 Ext.			1537	30% C 70% B/C	30% Cohesive Failure 70% Adhesive Failure
			1587	40% C 60% B/C	40% Cohesive Failure 60% Adhesive Failure
			1564	40% C 60% B/C	40% Cohesive Failure 60% Adhesive Failure
			1644	70% C 30% B/C	70% Cohesive Failure 30% Adhesive Failure
			1877	70% C 30% B/C	70% Cohesive Failure 30% Adhesive Failure

A.7.4. Optical Microscopy Results

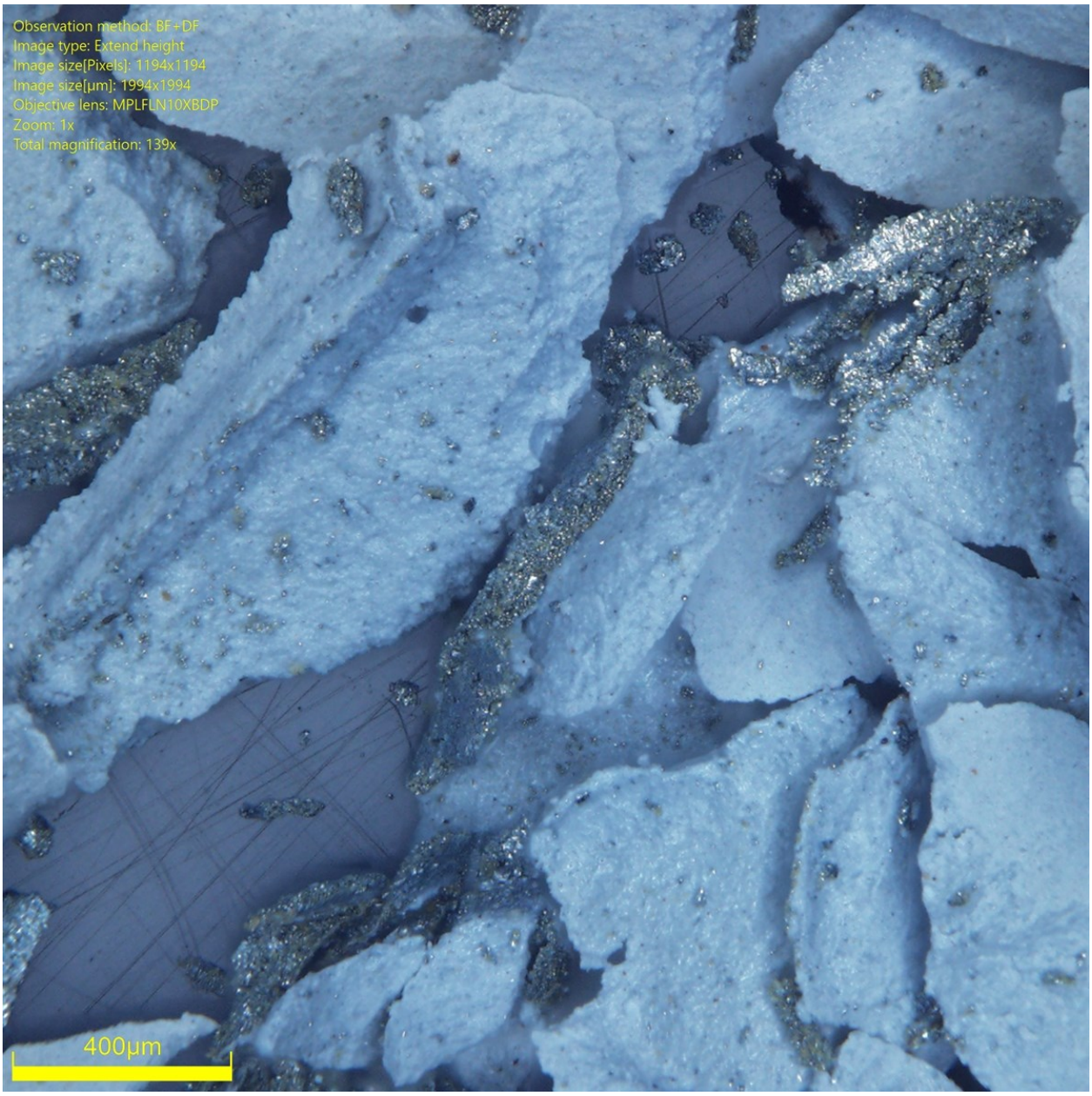
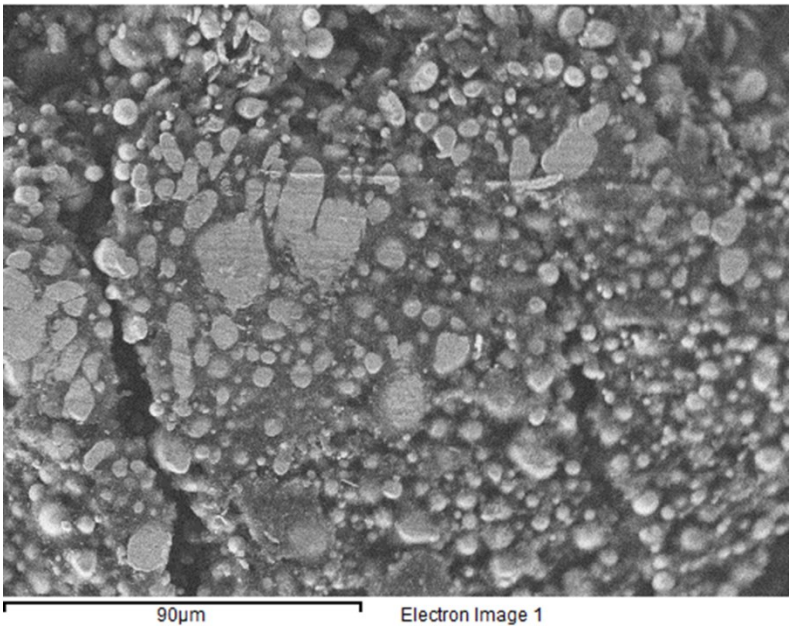


Figure A.84. Two Layer Paint System Examined by Optical Microscope AMA–PS–02.

A.7.5. SEM/EDS Results

Element	Weight %	Atomic %
C K	52.67	75.74
O K	13.29	14.35
Al K	0.52	0.34
Si K	0.66	0.41
Cl K	1.60	0.78
Ti K	0.82	0.30
Fe K	1.21	0.37
Zn K	29.22	7.72
Totals	100.00	



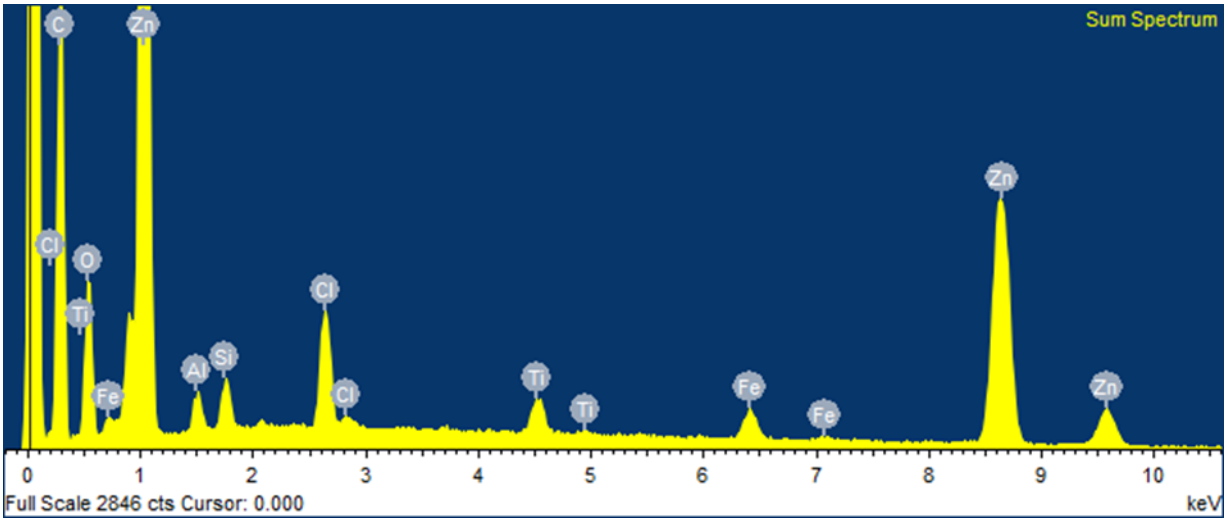


Figure A.85. SEM Image and EDS Spectrum of the Paint Collected from Exterior Web of the Girder.

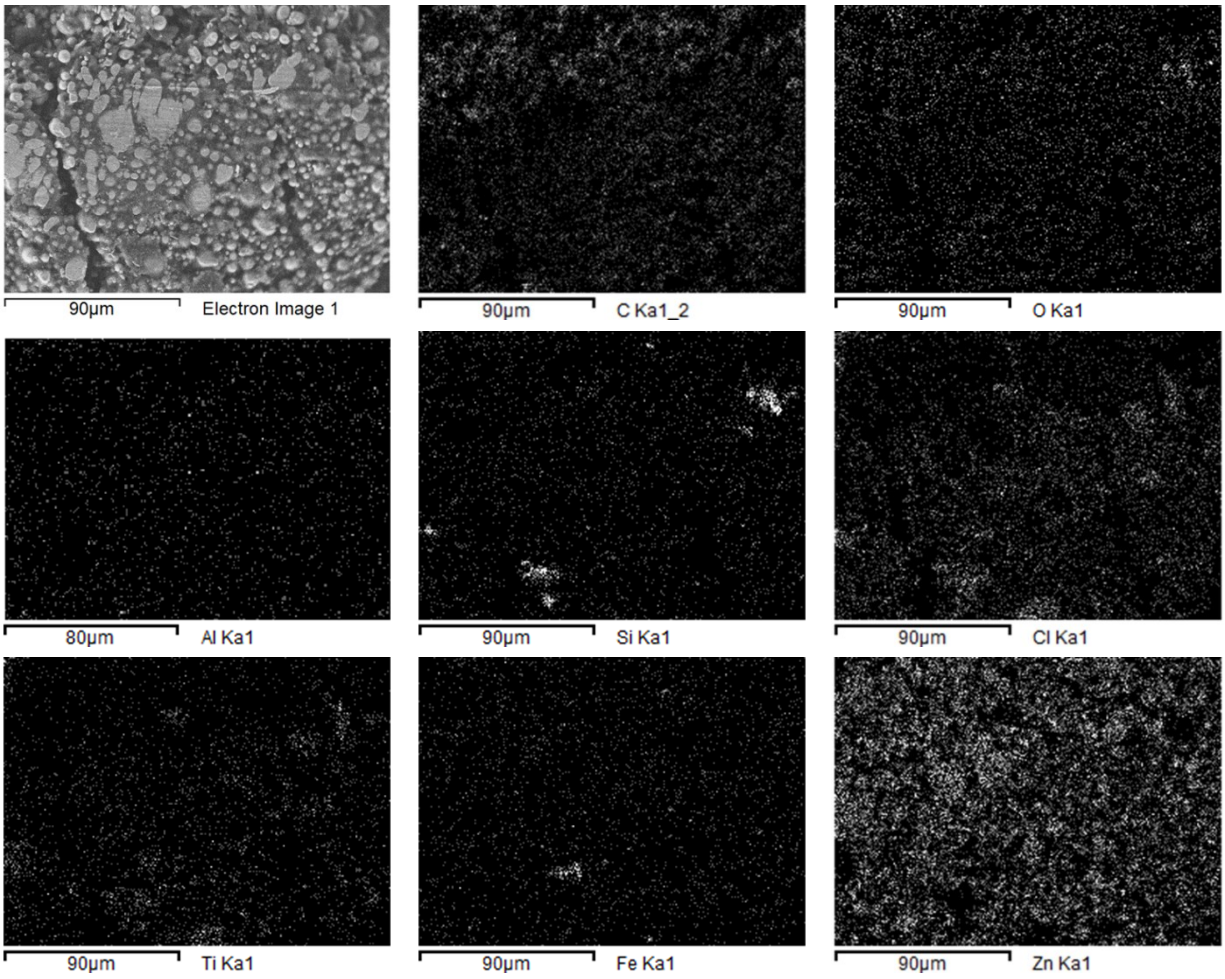
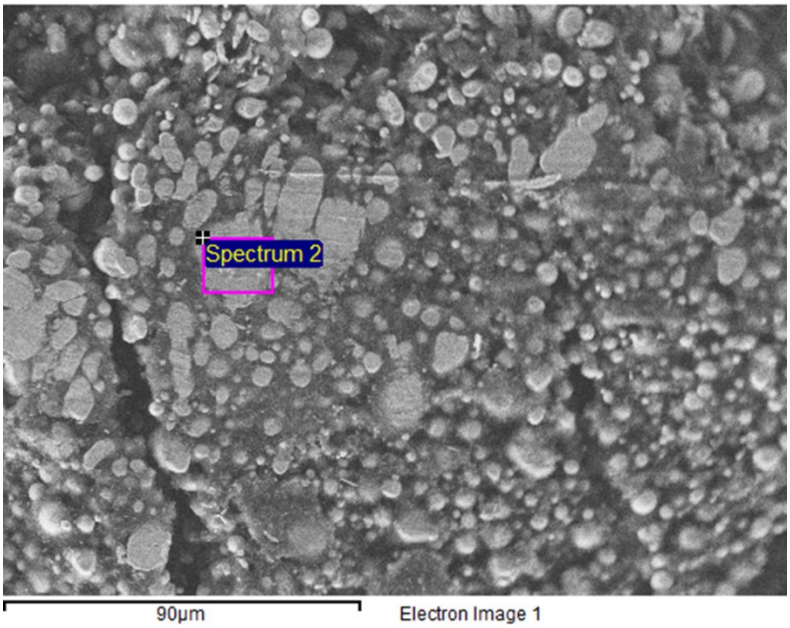


Figure A.86. EDS Elemental Mapping of Paint Collected from Exterior Web.

Element	Weight %	Atomic %
C K	28.76	60.59
O K	9.09	14.38
Al K	0.99	0.93
Si K	0.37	0.33
Cl K	0.52	0.37
Ti K	0.33	0.18
Fe K	0.27	0.12
Zn K	59.67	23.10
Totals	100.00	



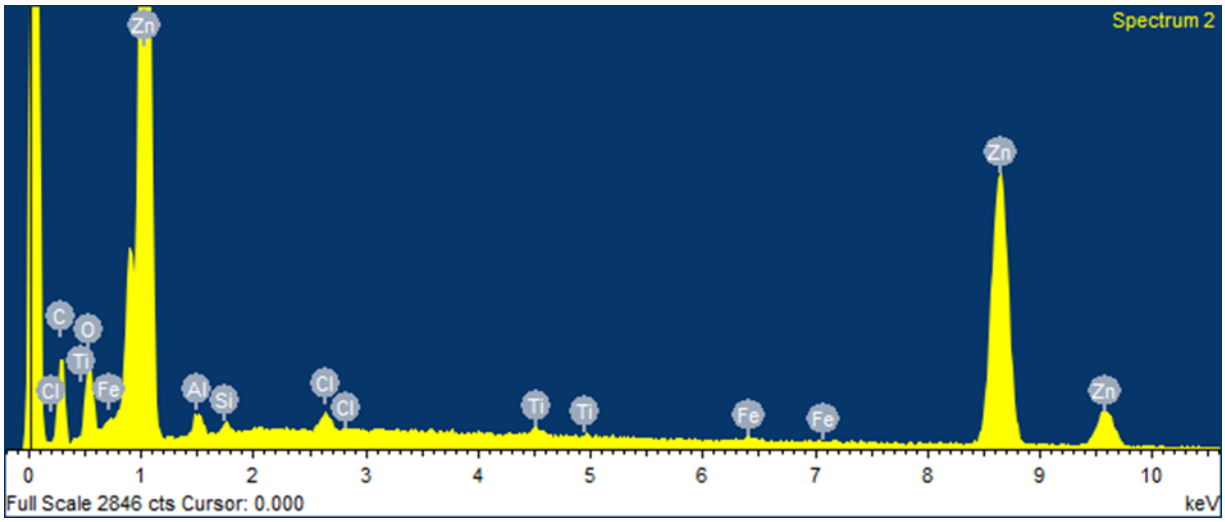
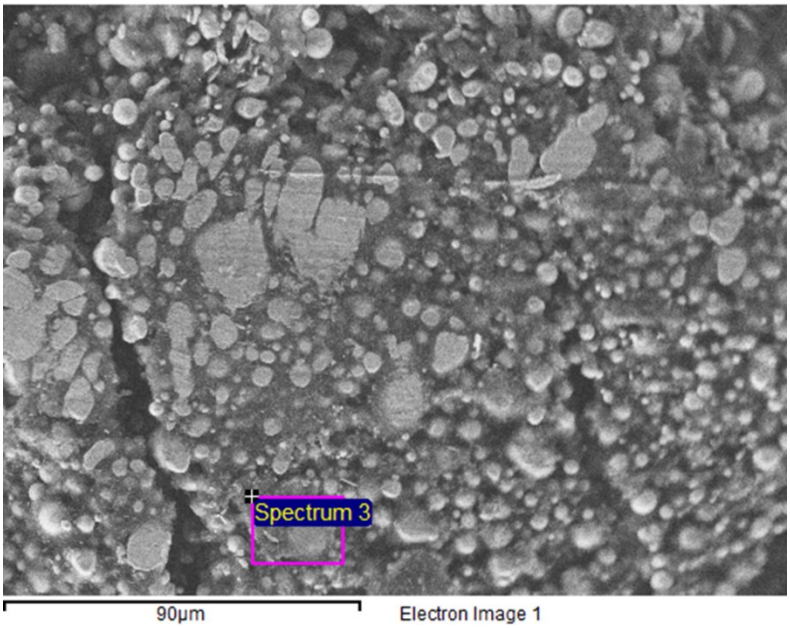


Figure A.87. SEM Image and EDS Spectrum of the Paint Collected from Interior Web of the Girder.

Element	Weight %	Atomic %
C K	53.14	73.41
O K	15.86	16.45
Al K	0.69	0.43
Si K	3.25	1.92
Cl K	2.94	1.38
Ti K	2.89	1.00
Fe K	0.72	0.21
Zn K	20.51	5.21
Totals	100.00	



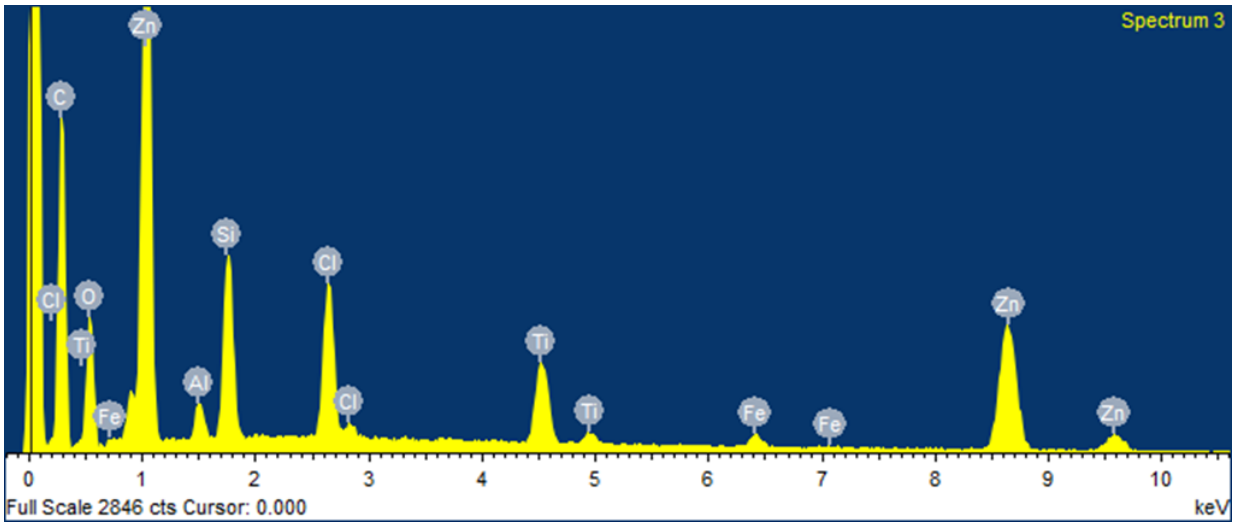


Figure A.88. SEM Image and EDS Spectrum of the Paint Collected from Exterior Web of the Girder.

A.8. AMA-PS-03

- IH 40 EB over Ivy rd
- Bridge ID 41800009002031, Coordinates (35.24947, -102.7874), Oldham County
- Steel Continuous I beam with System II type paint as EDS spectrum shows high percentage of zinc
- Built 1961
- Date of Inspection: June 15, 2021; girder inspection carried near abutment ends on girders within approximately four feet from the abutment
- Revisited for pH test and scrape test
- No visual inspection on deck
- Location for Testing: G1, G3



Figure A.89. Typical Elevation of AMA-PS-03

A.8.1. Observed Condition

Widespread paint failure over the top and bottom flanges. The paint failure and widespread rusting is also observed on webs at several locations. There is accumulation of debris on interior girders leading to poultice corrosion. Pitting is also observed on flanges of exterior girder. The paint condition is relatively good on interior girders as compared to exterior girder. A small area of paint deterioration is observed near the girder ends near abutment.



(a) Paint Deterioration and Section loss observed on Bearing



(b) Interior Girder in Good Condition



(c) Interior Girder Connection is in Good Condition



(d) Superstructure Showing Staining and Paint Deterioration Near Abutment 1



(e) Superstructure Showing Paint Deterioration Near Bent 3



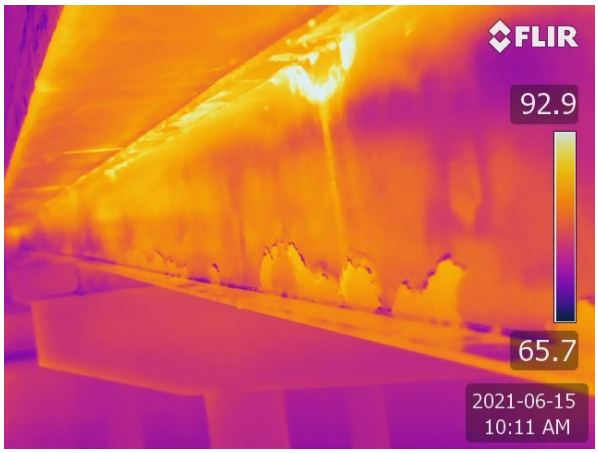
(f) Paint Deterioration and Rusting Observed on Exterior Girder

Figure A.90. Paint Condition on the Girder of AMA-PS-03

A.8.2. NDT Results



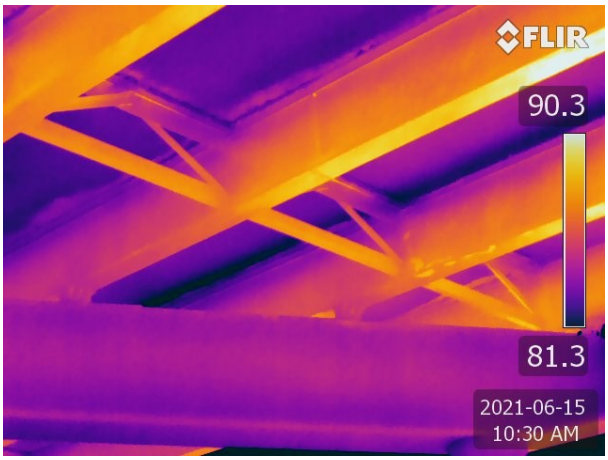
(a) Digital Image of Exterior Face of Girder Near Abutment Ends



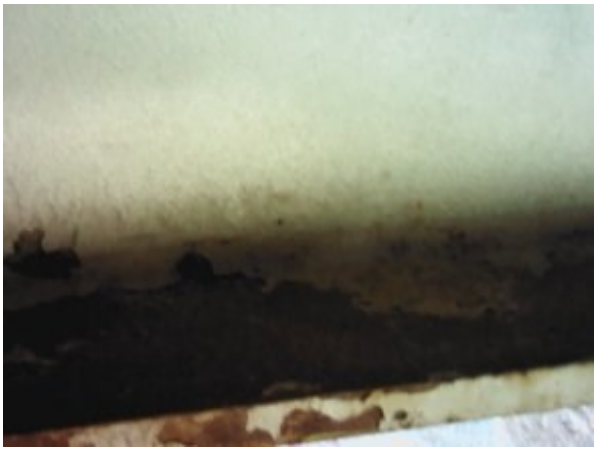
(b) Thermal Image of Exterior Face of Girder Near Abutment Ends



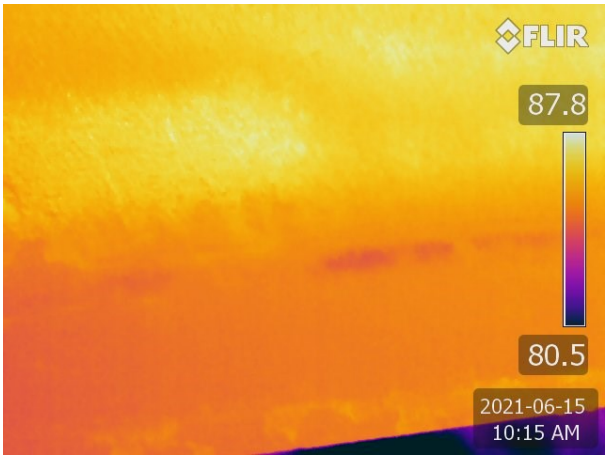
(c) Digital Image of Connection



(d) Thermal Image of Connection



(e) Digital Image Showing Rust on Bottom Flange of Interior Girder



(f) Thermal Image Showing Rust on Bottom Flange of Interior Girder

Figure A.91. Digital and Thermal Image of Painted Girder on AMA-PS-03.

Table A-36. Field Inspection Results for AMA-PS-03.

Location	Cl^- Conc. (ppm)	pH Test	Thickness (µm)	Thickness (inch)	Visual Inspection
G1F1 TF. Corroded	-	-	Measured R1 R2 R3 Design Paint 140-381	Measured R1 0.824 R2 0.822 R3 0.826 R_Avg 0.824 Design	Rust Grade – 0 Blistering – Not Found Discoloration – Not Found Flaking – Not Found Delamination – Not Found
G1F1 TF Bot.	-		Measured R1 155 R2 163 R3 172 Design Paint 140-381	Measured R1 0.834 R2 0.834 R3 0.836 R_Avg 0.835 Design	Rust Grade – 0 Blistering – Not Found Discoloration – Not Found Flaking – Not Found Delamination – Not Found
G1F1 Web Normal	1	-	Measured R1 158 R2 152 R3 182 Design Paint 140-381	Measured R1 0.591 R2 0.593 R3 0.599 R_Avg 0.594 Design	Rust Grade – 7 Blistering – Not Found Discoloration – Not Found Flaking – Not Found Delamination – Not Found
G1F1 Web Spot 1	-	-		Measured R1 0.584 R2 0.581 R3 0.582 R_Avg 0.582 Design	Rust Grade – 0 Blistering – Not Found Discoloration – Not Found Flaking – Not Found Delamination – Not Found
G1F1 Web Spot 2	-			Measured R1 0.587 R2 0.587 R3 0.586 R_Avg 0.587 Design	Rust Grade – 0 Blistering – Not Found Discoloration – Not Found Flaking – Not Found Delamination – Not Found
G1F1 BF Top.	-	-	Measured R1 350 R2 286 R3 236 Design Paint 140-381	Measured R1 0.913 R2 0.939 R3 0.935 R_Avg 0.940 Design	Rust Grade – 0 Blistering – Not Found Discoloration – Not Found Flaking – Not Found Delamination – Not Found

Table A-37. Field Inspection Results for AMA-PS-03.

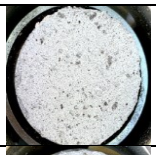
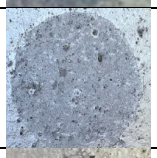
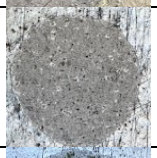
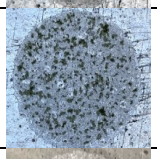
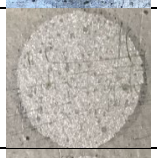
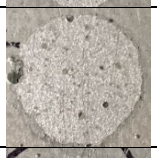
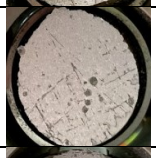
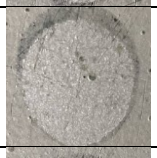
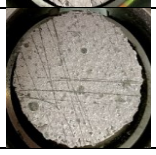
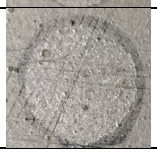
Location	Cl^- Conc. (ppm)	pH Test	Thickness (µm)	Thickness (inch)	Visual Inspection
G1F1 BF Bot.	-	-	Measured R1 202 R2 292 R3 150 Design Paint 140-381	Measured R1 0.946 R2 0.939 R3 0.935 R_Avg 0.940 Design	Rust Grade – 5 Blistering – Not Found Discoloration – Not Found Flaking – Not Found Delamination – Not Found
G3F1 TF Bot.	-		Measured R1 139 R2 121 R3 122 Design Paint 140-381	Measured R1 0.918 R2 0.918 R3 0.921 R_Avg 0.919 Design	Rust Grade – 7 Blistering – Not Found Discoloration – Not Found Flaking – Not Found Delamination – Not Found
G3F1 Web	1	-	Measured R1 160 R2 135 R3 128 Design Paint 140-381	Measured R1 0.597 R2 0.598 R3 0.600 R_Avg 0.598 Design	Rust Grade – 7 Blistering – Not Found Discoloration – Not Found Flaking – Not Found Delamination – Not Found
G3F1 BF Top.	-	-	Measured R1 230 R2 203 R3 207 Design Paint 140-381	Measured R1 0.937 R2 0.934 R3 0.932 R_Avg 0.934 Design	Rust Grade – 7 Blistering – Not Found Discoloration – observed on the top of Bottom Flange Flaking – Not Found Delamination – Not Found
G3F1 BF Bot.	-		Measured R1 178 R2 172 R3 168 Design Paint 140-381	Measured R1 0.928 R2 0.932 R3 0.931 R_Avg 0.930 Design	Rust Grade – 7 Blistering – Not Found Discoloration – Not Found Flaking – Not Found Delamination – Not Found

Table A-38. Paint System Information: (2-Layer Zinc-Based).

Cohesive Failure Layer		**Adhesive Failure Layer**	
Code	**Description**	**Code**	**Description**
A	Substrate	A/B	Substrate & Layer 1
B	Layer 1(Green)	B/C	Layer 1 & Layer 2
C	Layer 2(Silver)	C/Y	Layer 2 & Glue
Y	Glue	Y/Z	Glue & Dolly

A.8.3. Pull-off Adhesion Results

Table A-39. Pull-off Adhesion Results for AMA-PS-03.

Location	Dolly Face	Substrate Face	Test Result (psi)	Attributes	Failure Type
A1-G1F1			899	100% C	100% Cohesive Failure
			1028	100% C	100% Cohesive Failure
			985	100% C	100% Cohesive Failure
			1341	100% C	100% Cohesive Failure
			1283	80% C 20% A/B	80% Cohesive Failure 20% Adhesive Failure
A1-G2F1			643	100% C	100% Cohesive Failure
			582	100% C	100% Cohesive Failure
			660	100% C	100% Cohesive Failure
			629	100% C	100% Cohesive Failure
			682	100% C	100% Cohesive Failure

A.8.4. Optical Microscopy Results

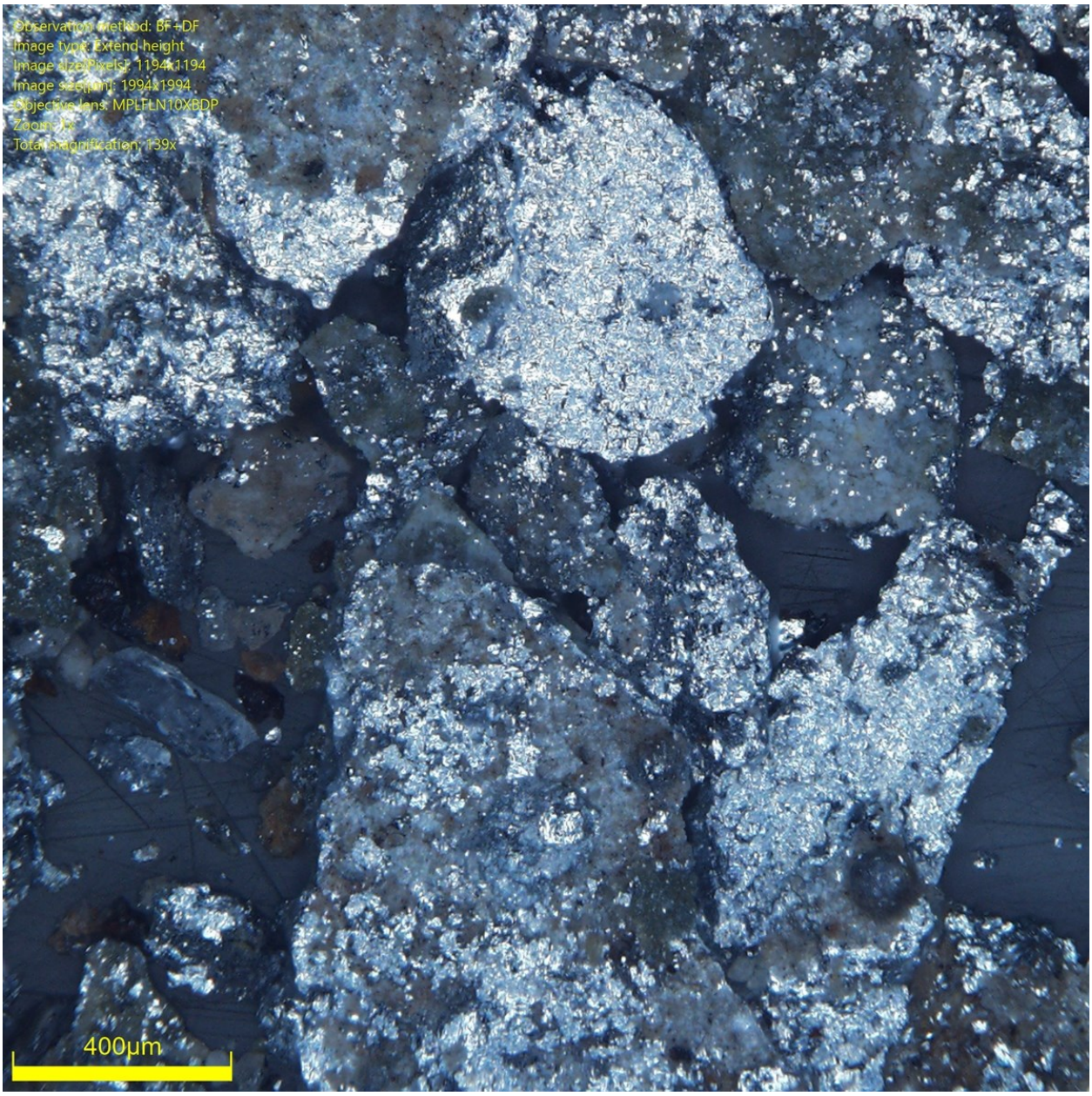


Figure A.92. Two Layer Paint System Examined by Optical Microscope AMA–PS–03.

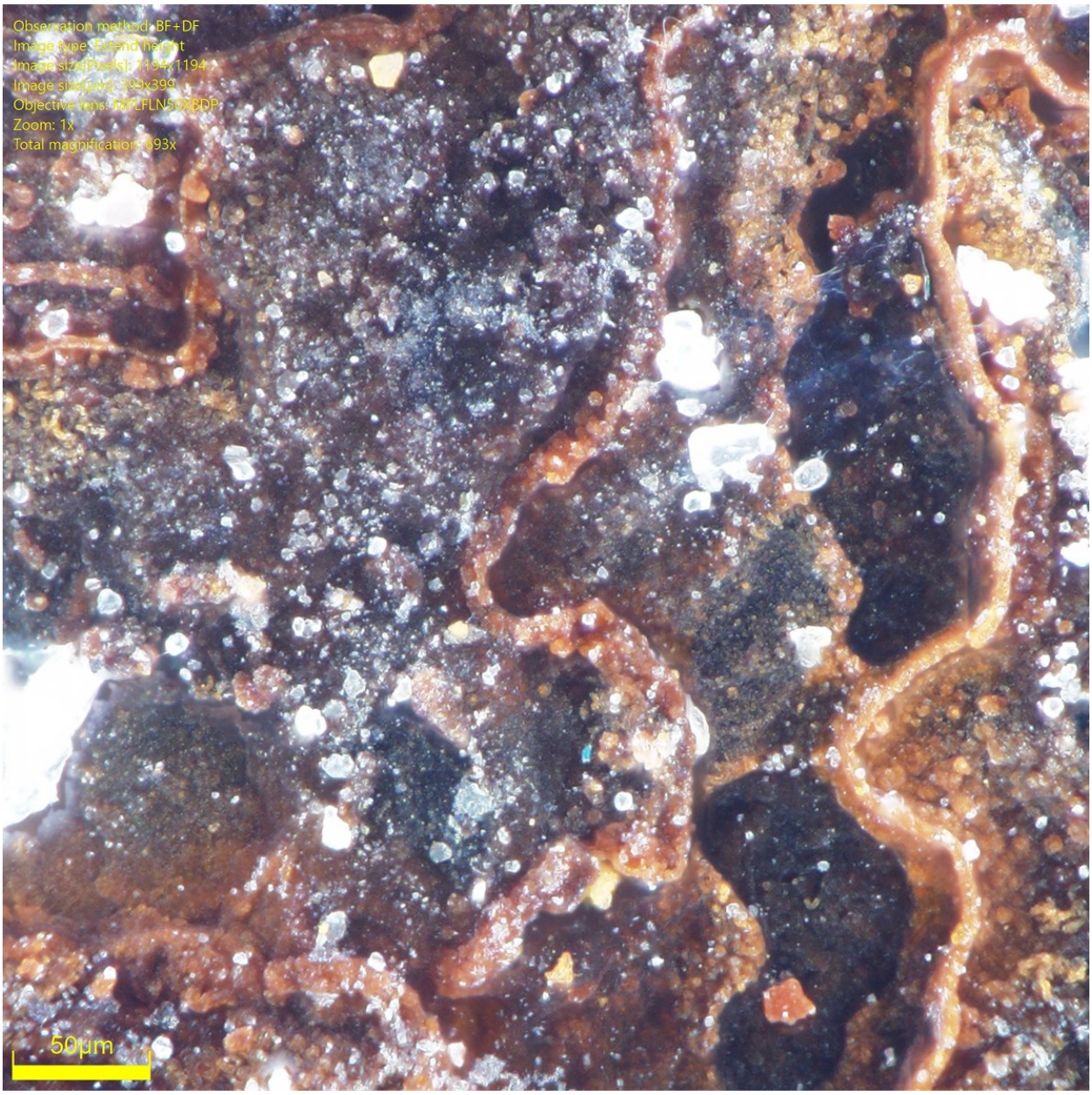
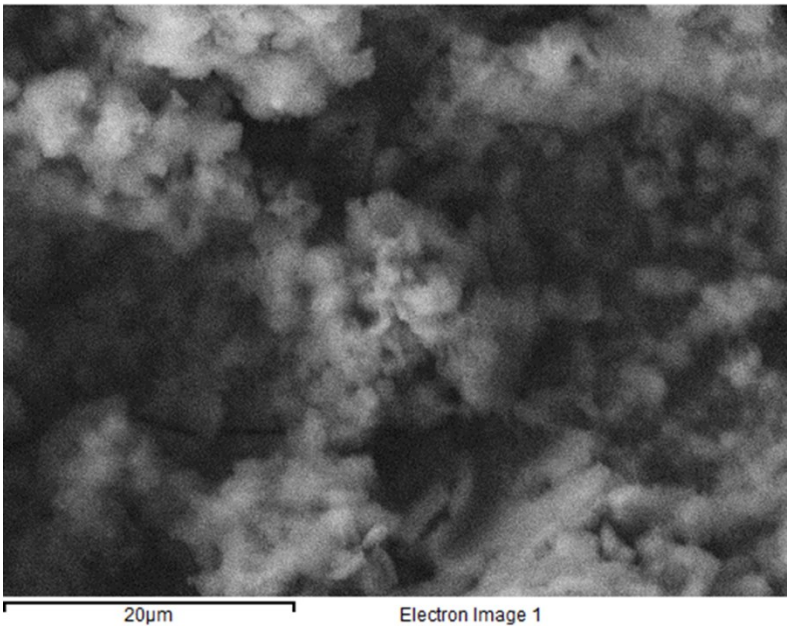


Figure A.93. Widespread corrosion and Complete Paint Failure.

A.8.5. SEM/EDS Results

Element	Weight %	Atomic %
C K	15.61	26.90
O K	42.99	55.62
Mg K	0.87	0.74
Al K	3.78	2.90
Si K	2.77	2.04
S K	0.58	0.37
Cl K	0.68	0.39
K K	0.23	0.12
Ca K	2.39	1.23
Cr K	0.70	0.28
Mn K	0.19	0.07
Fe K	1.32	0.49
Zn K	27.89	8.83
Totals	100.00	



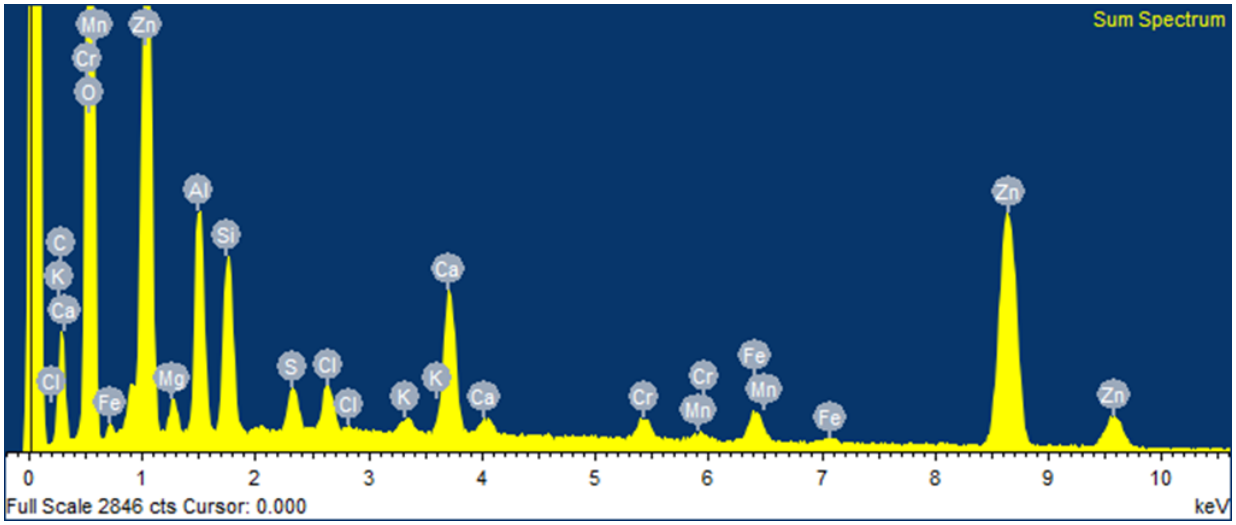


Figure A.94. SEM Image and EDS Spectrum of the Paint Collected from Exterior Web of the Girder.

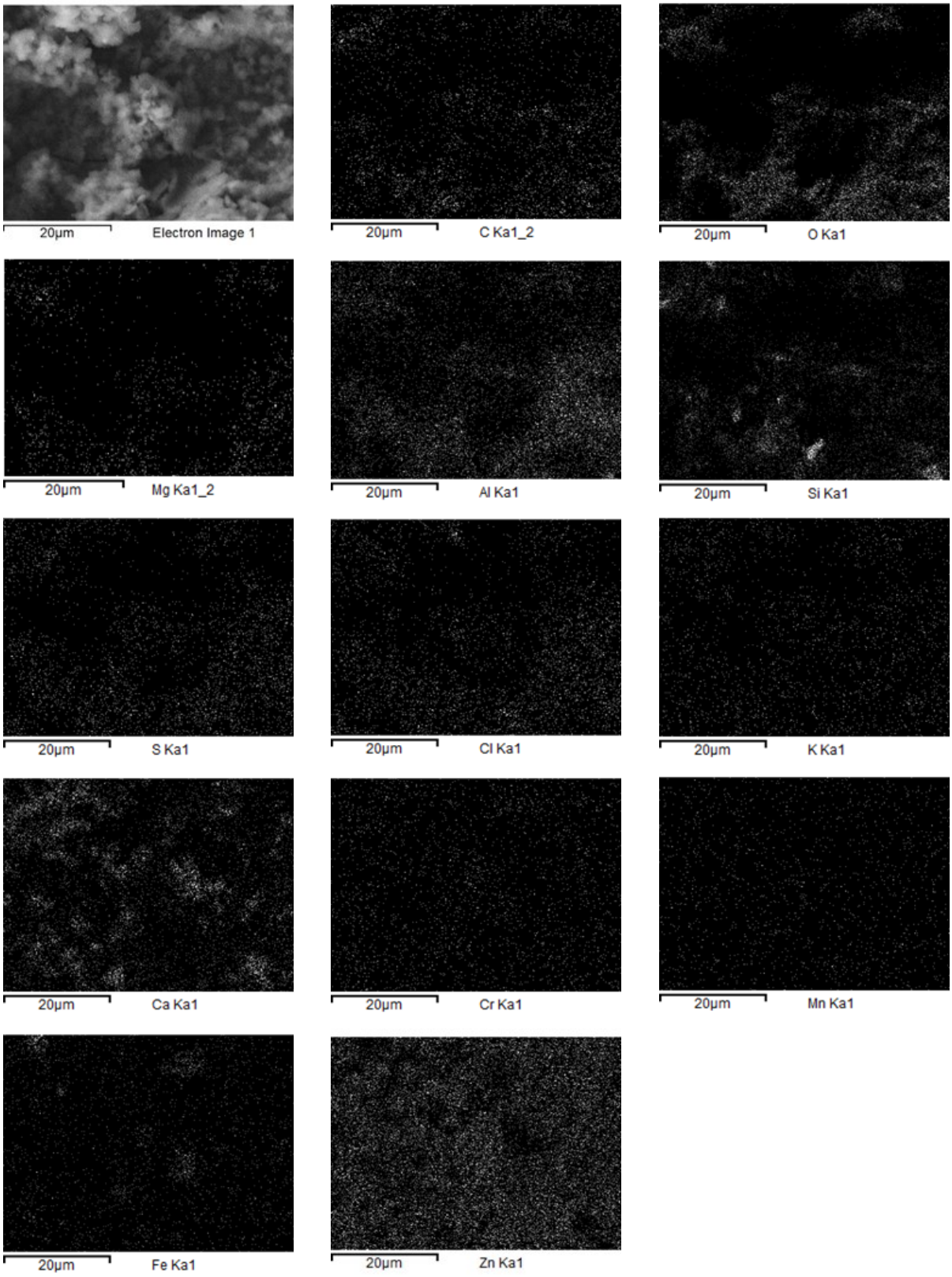
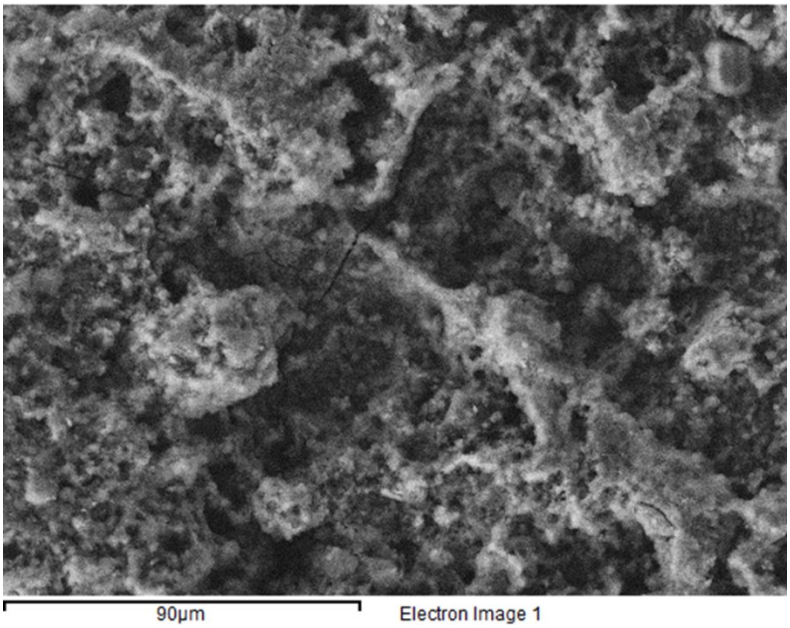


Figure A.95. EDS Elemental Mapping of Paint Collected from Exterior Web.

Element	Weight %	Atomic %
C K	17.39	28.93
O K	44.04	55.00
Mg K	0.90	0.74
Al K	2.88	2.13
Si K	3.24	2.30
P K	0.12	0.08
S K	0.55	0.34
Cl K	0.58	0.33
K K	0.30	0.16
Ca K	3.59	1.79
Cr K	0.85	0.33
Fe K	1.23	0.44
Zn K	24.33	7.44
Totals	100.00	



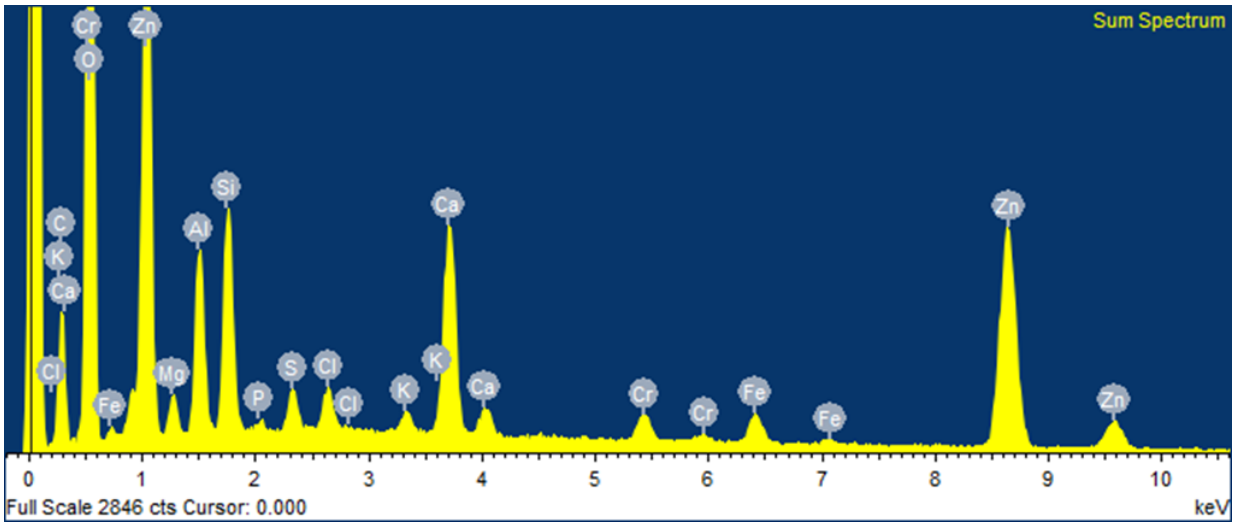


Figure A.96. SEM Image and EDS Spectrum of the Paint Collected from Exterior Web of the Girder.

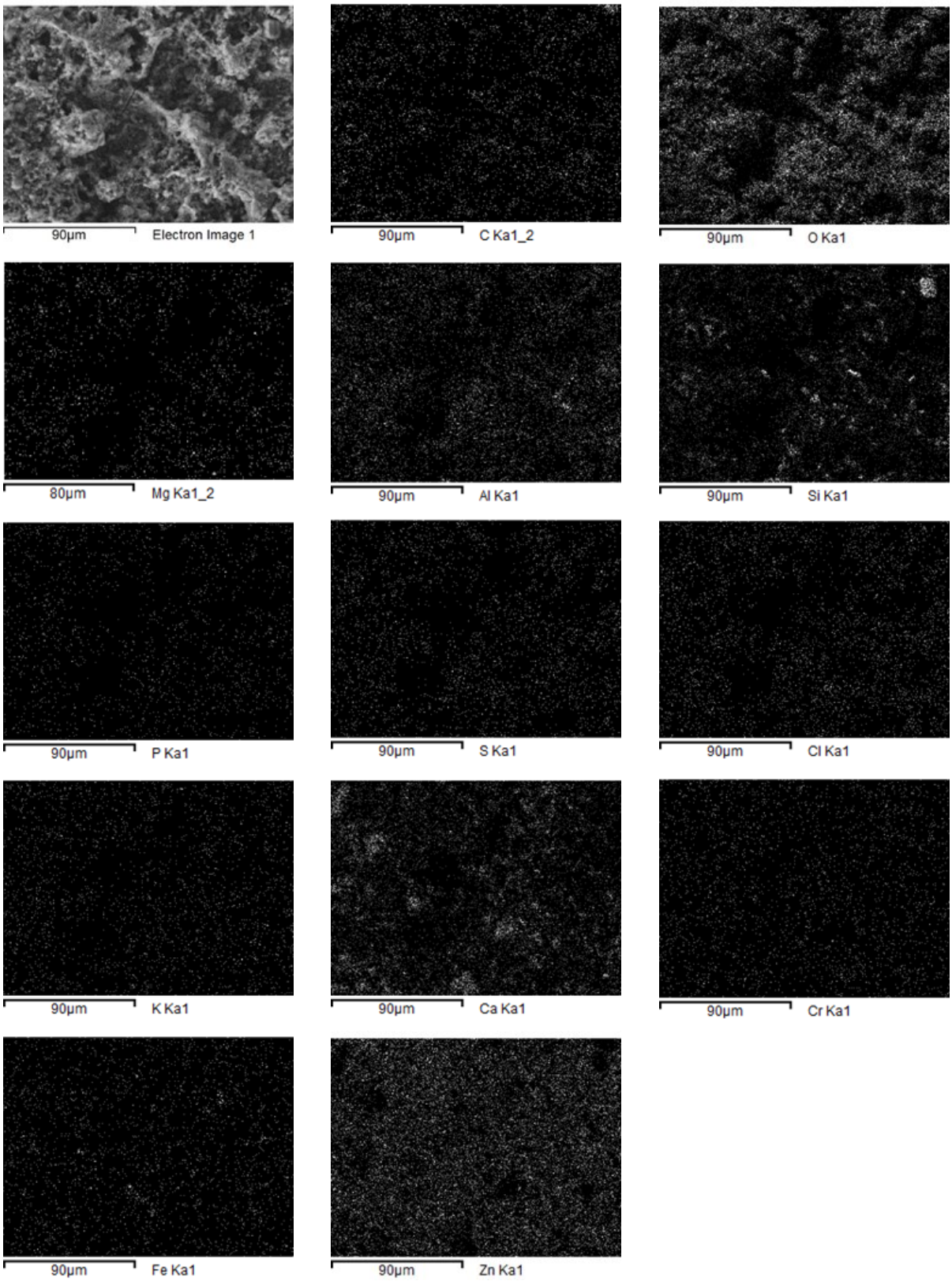
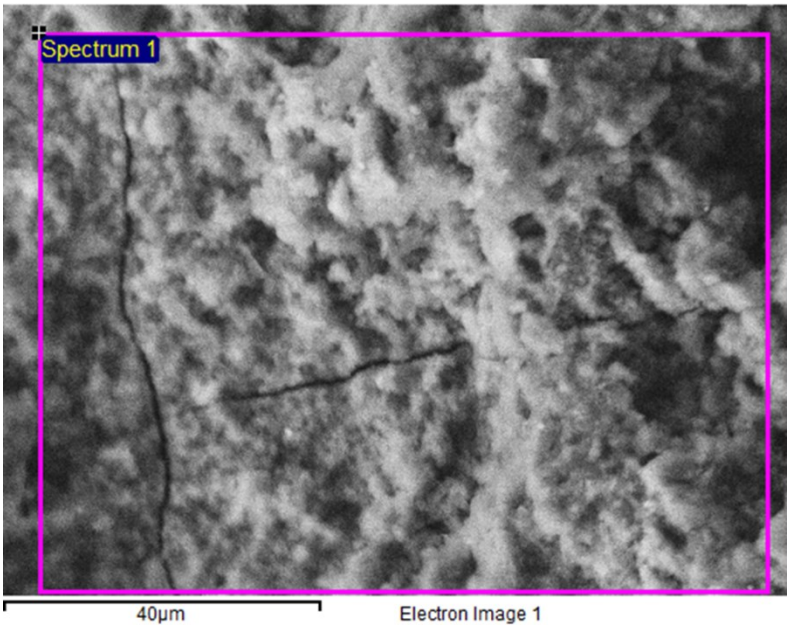


Figure A.97. EDS Elemental Mapping of Paint Collected from Exterior Web.

Element	Weight %	Atomic %
C K	18.12	29.78
O K	44.93	55.42
Mg K	0.60	0.48
Al K	2.35	1.72
Si K	3.13	2.20
P K	0.25	0.16
S K	0.42	0.26
Cl K	0.30	0.17
K K	0.27	0.14
Ca K	3.05	1.50
Cr K	0.95	0.36
Fe K	1.47	0.52
Zn K	24.16	7.29
Totals	100.00	



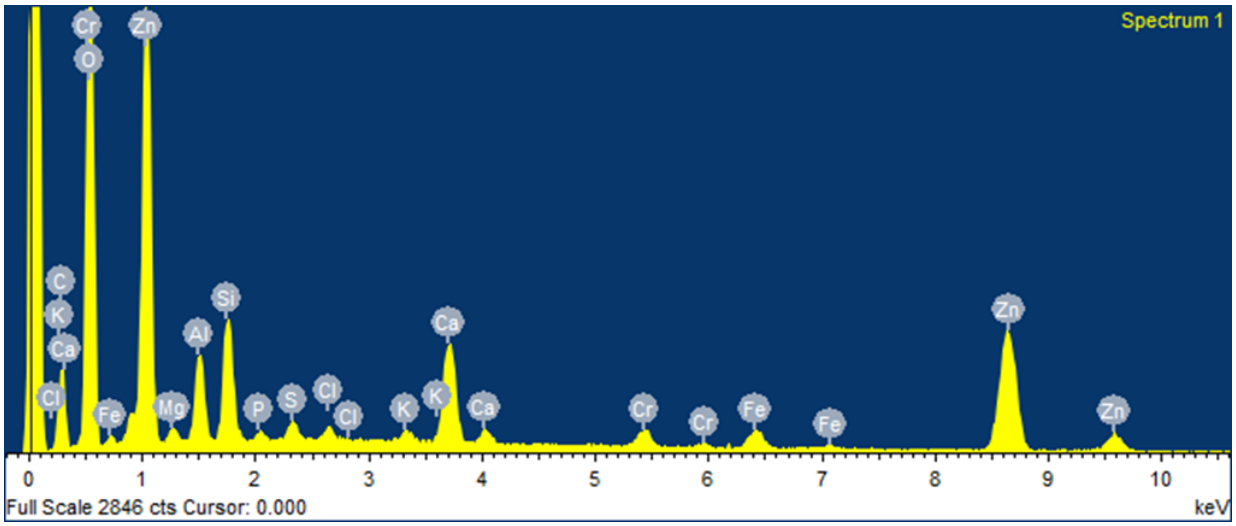
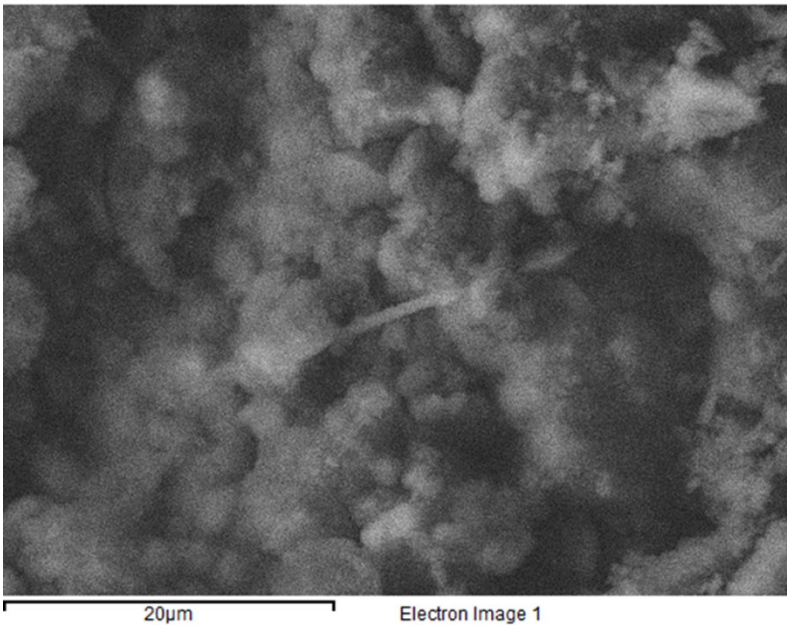


Figure A.98. SEM Image and EDS Spectrum of the Paint Collected from Exterior Web of the Girder.

Element	Weight %	Atomic %
C K	11.43	19.74
O K	45.97	59.58
Mg K	0.63	0.54
Al K	3.40	2.61
Si K	6.46	4.77
Cl K	0.10	0.06
K K	0.64	0.34
Ca K	5.91	3.06
Mn K	0.24	0.09
Fe K	22.71	8.43
Zn K	2.52	0.80
Totals	100.00	



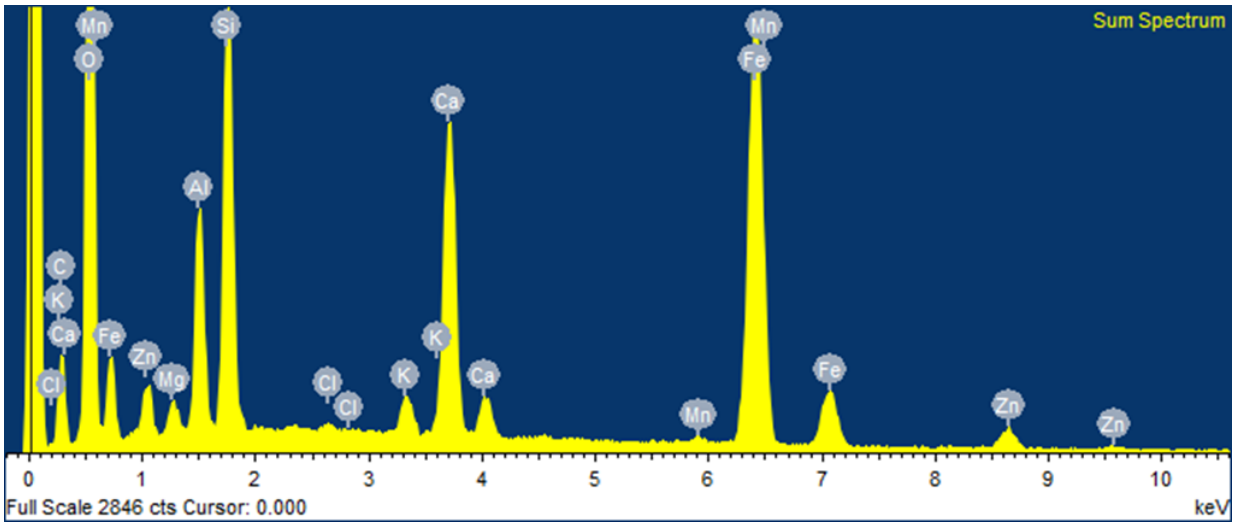


Figure A.99. SEM Image and EDS Spectrum of the Paint Collected from Exterior Web of the Girder.

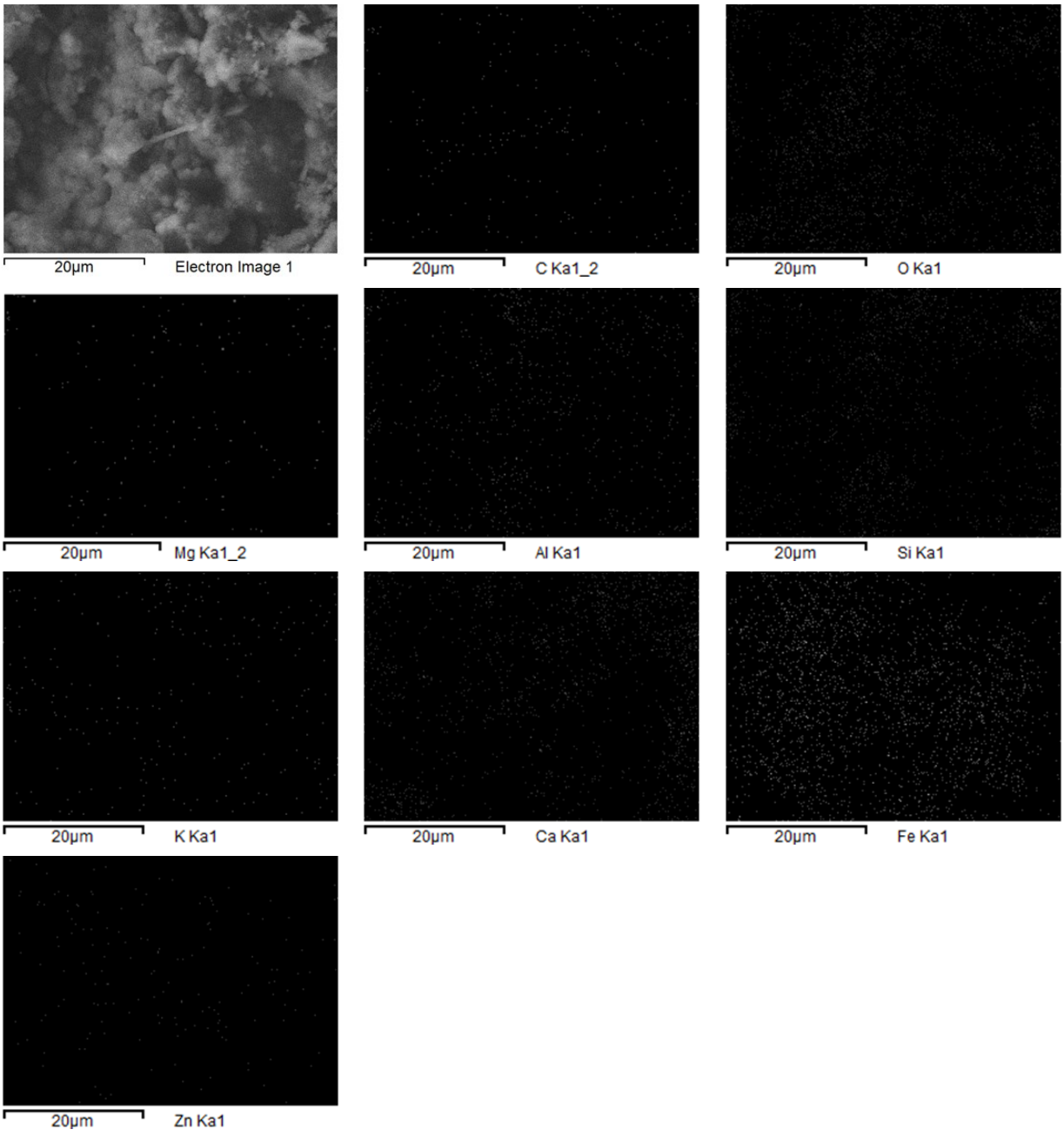


Figure A.100. EDS Elemental Mapping of Paint Collected from Exterior Web.

A.9. WFS-PS-01

- IH 44 SB over Maurine Street
- Bridge ID 32430004309191, Coordinates (33.936, -98.51859), Wichita County
- Steel Continuous I beam with System II type paint
- Built 2001
- Date of Inspection: June 1, 2021; girder inspection carried near abutment ends on girders within approximately four feet from the abutment
- Revisited for pH test and scrape test
- No visual inspection on deck
- Location for Testing: A1-G9, A1-G6, A1-G3, A1-G1



Figure A.101. Typical Elevation of WFS-PS-01.

A.9.1. Observed Condition

The paint condition of this bridge is in very good condition. The appearance coat is also in good condition. Blistering, Erosion of paint, cracking in paint is not present. Dirt is accumulated and paint failure is observed on the top face of the bottom flange near abutment on girder number 9. No checking and cracking of paint are observed. Joints are also in good condition.



(a) Staining observed on Bearing



(b) Interior Girder in Good Condition



(c) Interior Girder Connection is in Good Condition



(d) Staining and Paint Deterioration Observed on the Connector Plate



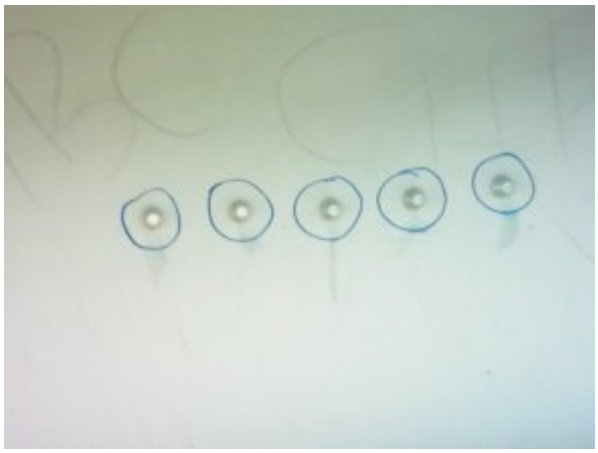
(e) Superstructure Showing Paint Deterioration Near Bent 3



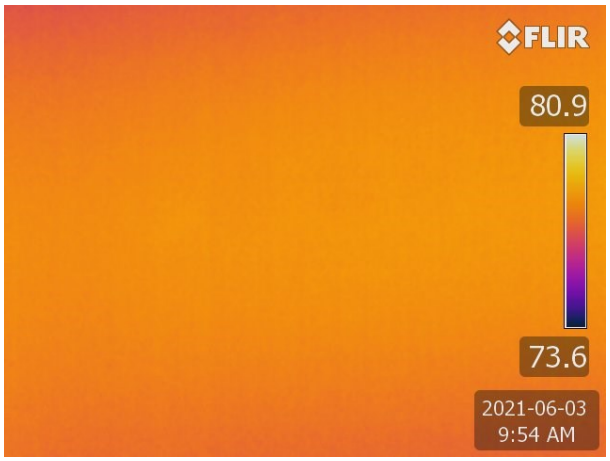
(f) Dirt Accumulation and Paint Deterioration on Interior Girder

Figure A.102. Paint Condition on the Girder of WFS-PS-01.

A.9.2. NDT Results



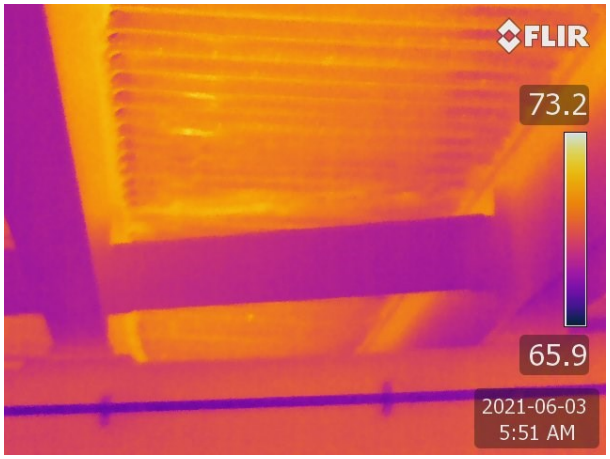
(a) Digital Image of Exterior Face of Girder Near Abutment Ends



(b) Thermal Image of Exterior Face of Girder Near Abutment Ends



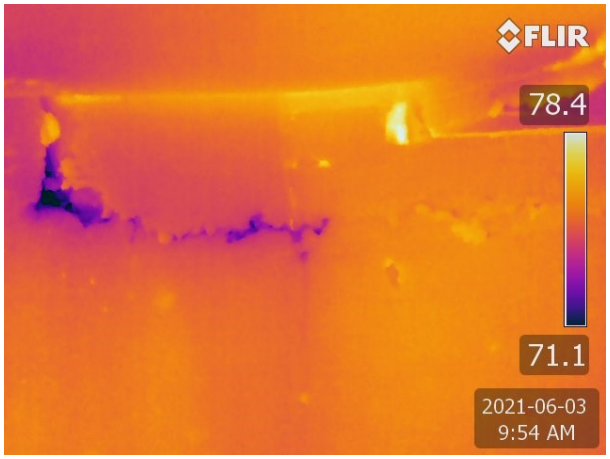
(c) Digital Image of Connection



(d) Thermal Image of Connection



(e) Digital Image of Crack Observed on Abutment Wall



(f) Thermal Image of Crack Observed on Abutment Wall

Figure A.103. Digital and Thermal Image of Painted Girder on WFS-PS-01.

Table A-40. Field Inspection Results for WFS-PS-01.

Location	Cl^- Conc. (ppm)	pH Test	Thickness (µm)	Thickness (inch)	Visual Inspection
A1-G9F2 TF Bot. Ext.	-	-	Measured R1 163 R2 168 R3 164 Design Paint 140-381	Measured R1 1.052 R2 1.043 R3 1.047 R_Avg 1.047 Design	Rust Grade – 10 Blistering – Not Found Discoloration – Not Found Flaking – Not Found Delamination – Not Found
A1-G9F2 Web. Ext.	0		Measured R1 176 R2 190 R3 190 Design Paint 140-381	Measured R1 0.634 R2 0.631 R3 0.633 R_Avg 0.633 Design	Rust Grade – 10 Blistering – Not Found Discoloration – Not Found Flaking – Not Found Delamination – Not Found
A1-G9F2 BF Top. Ext.	-	-	Measured R1 169 R2 176 R3 163 Design Paint 140-381	Measured R1 1.020 R2 1.020 R3 1.016 R_Avg 1.019 Design	Rust Grade – 10 Blistering – Not Found Discoloration – observed on the top face of Bottom Flange Flaking – Not Found Delamination – Not Found
A1-G9F2 BF Bot. Ext.	-	-	Measured R1 192 R2 172 R3 189 Design Paint 140-381	Measured R1 - R2 - R3 - R_Avg - Design	Rust Grade – 10 Blistering – Not Found Discoloration – Not Found Flaking – Not Found Delamination – Not Found
A1-G6F2 TF Bot. Int.	-		Measured R1 228 R2 219 R3 218 Design Paint 140-381	Measured R1 1.029 R2 1.031 R3 1.029 R_Avg 1.030 Design	Rust Grade – 10 Blistering – Not Found Discoloration – Not Found Flaking – Not Found Delamination – Not Found
A1-G6F2 Web. Int.	2	-	Measured R1 154 R2 141 R3 151 Design Paint 140-381	Measured R1 0.642 R2 0.640 R3 0.637 R_Avg 0.640 Design	Rust Grade – 10 Blistering – Not Found Discoloration – Not Found Flaking – Not Found Delamination – Not Found

Table A-41. Field Inspection Results for WFS-PS-01.

Location	Cl^- Conc. (ppm)	pH Test	Thickness (µm)	Thickness (inch)	Visual Inspection
A1-G6F2 BF Top. Int.	-	-	Measured R1 220 R2 245 R3 240 Design Paint 140-381	Measured R1 1.013 R2 1.016 R3 1.020 R_Avg 1.016 Design	Rust Grade – 2 Blistering – Not Found Discoloration – Not Found Flaking – Not Found Delamination – Not Found
A1-G6F2 BF Bot. Int.	-	-	Measured R1 188 R2 172 R3 177 Design Paint 140-381	Measured R1 - R2 - R3 - R_Avg - Design	Rust Grade – 10 Blistering – Not Found Discoloration – Not Found Flaking – Not Found Delamination – Not Found
A1-G3F1 TF Bot. Int.	-	-	Measured R1 187 R2 189 R3 207 Design Paint 140-381	Measured R1 1.020 R2 1.017 R3 1.019 R_Avg 1.019 Design	Rust Grade – 10 Blistering – Not Found Discoloration – Not Found Flaking – Not Found Delamination – Not Found
A1-G3F1 Web. Int.	1		Measured R1 217 R2 218 R3 226 Design Paint 140-381	Measured R1 0.641 R2 0.642 R3 0.641 R_Avg 0.641 Design	Rust Grade – 10 Blistering – Not Found Discoloration – Not Found Flaking – Not Found Delamination – Not Found
A1-G3F1 BF Top. Int.	-		Measured R1 184 R2 192 R3 175 Design Paint 140-381	Measured R1 1.050 R2 1.048 R3 1.046 R_Avg 1.048 Design	Rust Grade – 10 Blistering – Not Found Discoloration – observed on the top of Bottom Flange Flaking – Not Found Delamination – Not Found
A1-G3F1 BF Bot. Int.	-		Measured R1 199 R2 213 R3 201 Design Paint 140-381	Measured R1 - R2 - R3 - R_Avg - Design	Rust Grade – 10 Blistering – Not Found Discoloration – Not Found Flaking – Not Found Delamination – Not Found

\

Table A-42. Field Inspection Results for WFS-PS-01.

Location	Cl^- Conc. (ppm)	pH Test	Thickness (µm)	Thickness (inch)	Visual Inspection
A1-G1F1 TF Bot. Int.	-	-	Measured R1 208 R2 216 R3 211 Design Paint 140-381	Measured R1 1.010 R2 1.012 R3 1.016 R_Avg 1.013 Design	Rust Grade – 10 Blistering – Not Found Discoloration – Not Found Flaking – Not Found Delamination – Not Found
A1-G1F1 Web. Int.	1		Measured R1 238 R2 237 R3 242 Design Paint 140-381	Measured R1 0.649 R2 0.650 R3 0.649 R_Avg 0.649 Design	Rust Grade – 10 Blistering – Not Found Discoloration – Not Found Flaking – Not Found Delamination – Not Found
A1-G1F1 BF Top. Int.	-		Measured R1 157 R2 141 R3 148 Design Paint 140-381	Measured R1 1.044 R2 1.050 R3 1.050 R_Avg 1.048 Design	Rust Grade – 10 Blistering – Not Found Discoloration – observed on the top face of Bottom Flange Flaking – Not Found Delamination – Not Found
A1-G1F1 BF Bot. Int.	-		Measured R1 224 R2 202 R3 217 Design Paint 140-381	Measured R1 - R2 - R3 - R_Avg - Design	Rust Grade – 10 Blistering – Not Found Discoloration – Not Found Flaking – Not Found Delamination – Not Found

Table A-43. Paint System Information.

Cohesive Failure Layer		**Adhesive Failure Layer**	
Code	**Description**	**Code**	**Description**
A	Substrate	A/B	Substrate & Layer 1
B	Layer 1(Gray)	B/C	Layer 1 & Layer 2
C	Layer 2(White)	C/Y	Layer 2 & Glue
Y	Glue	Y/Z	Glue & Dolly

A.9.3. Pull-off Adhesion Results

Table A-44. Pull-off Adhesion Results for WFS-PS-01.

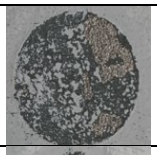
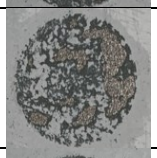
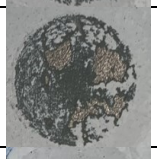
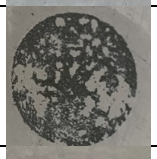
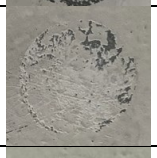
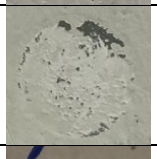
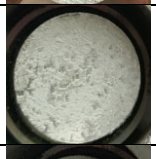
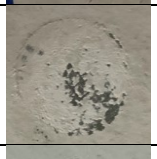
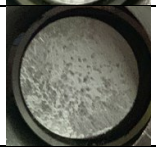
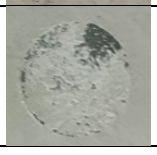
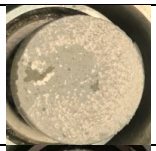
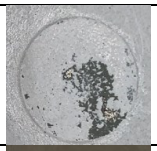
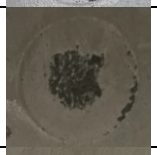
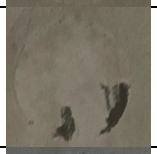
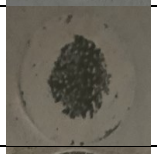
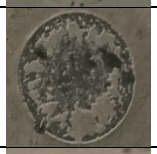
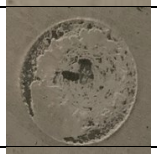
Location	Dolly Face	Substrate Face	Test Result (psi)	Attributes	Failure Type
A1-G9F2			1916	20% C 50% B/C 30% A/B	20% Cohesive Failure 80% Adhesive Failure
			1699	30% C 40% B/C 30% A/B	30% Cohesive Failure 70% Adhesive Failure
			2116	20% C 50% B/C 30% A/B	20% Cohesive Failure 80% Adhesive Failure
			2008	50% C 50% B/C	50% Cohesive Failure 50% Adhesive Failure
			1676	30% C 70% B/C	30% Cohesive Failure 70% Adhesive Failure
A1-G6F2			1726	90% C 10% B/C	90% Cohesive Failure 10% Adhesive Failure
			2285	90% C 10% B/C	90% Cohesive Failure 10% Adhesive Failure
			915	30% C/Y 50% C 10% B/C	30% Failure Glue 60% Cohesive Failure 10% Adhesive Failure
			2589	90% C 10% B/C	90% Cohesive Failure 10% Adhesive Failure
			2322	90% C 10% B/C	90% Cohesive Failure 10% Adhesive Failure

Table A-45. Pull-off Adhesion Results for WFS-PS-01.

Location	Dolly Face	Substrate Face	Test Result (psi)	Attributes	Failure Type
A1-G3F1			2597	70% C 30% B/C	70% Cohesive Failure 30% Adhesive Failure
			2536	80% C 20% B/C	80% Cohesive Failure 20% Adhesive Failure
			1408	20% C/Y 50% C 10% B/C	20% Glue Failure 50% Cohesive Failure 10% Adhesive Failure
			2532	50% C 50% B/C	50% Cohesive Failure 50% Adhesive Failure
			2301	80% C 20% B/C	80% Cohesive Failure 20% Adhesive Failure
A1-G1F1			2225	30% C/Y 70% B/C	100% Adhesive Failure
			2183	90% C 10% B/C	90% Cohesive Failure 10% Adhesive Failure
			2160	30% C/Y 70% B/C	100% Adhesive Failure
			2174	30% C/Y 70% B/C	100% Adhesive Failure
			2045	30% C/Y 70% B/C	100% Adhesive Failure

A.9.4. Optical Microscopy Results

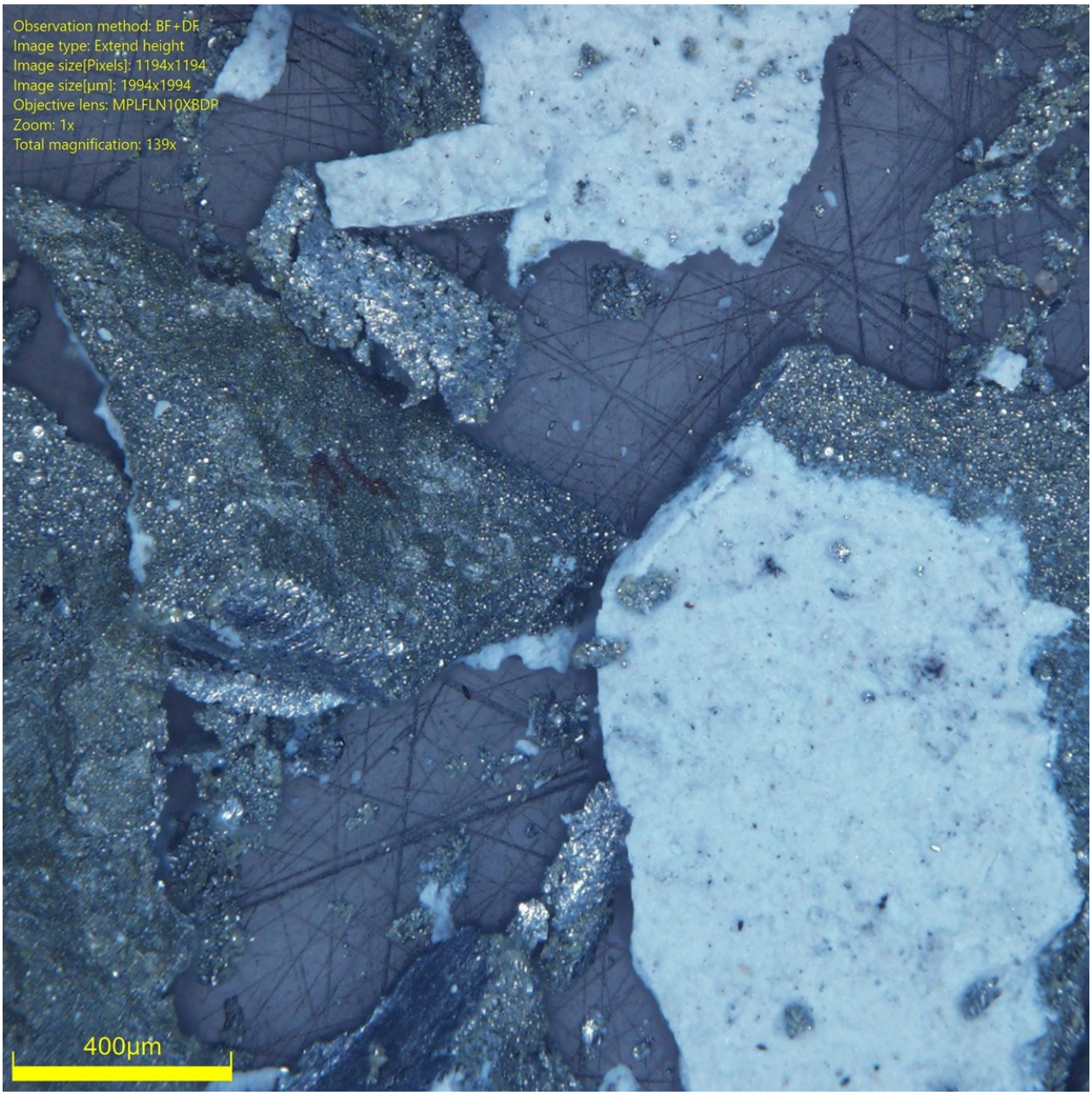
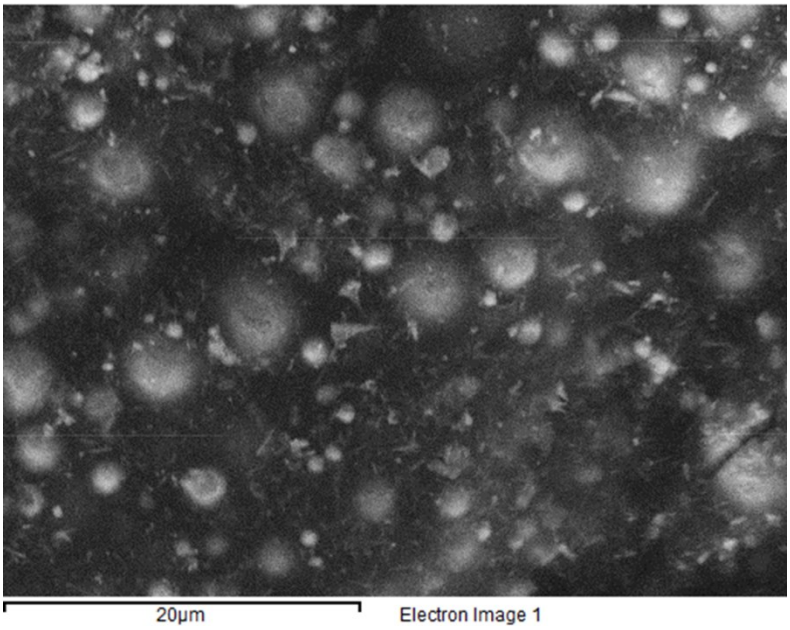


Figure A.104. Two Layer Paint System Examined by Optical Microscope WFS–PS–01.

A.9.5. SEM/EDS Results

Element	Weight %	Atomic %
C K	58.48	80.93
O K	10.47	10.88
Al K	0.37	0.23
Si K	0.24	0.14
Fe K	1.80	0.54
Zn K	28.63	7.28
Totals	100.00	



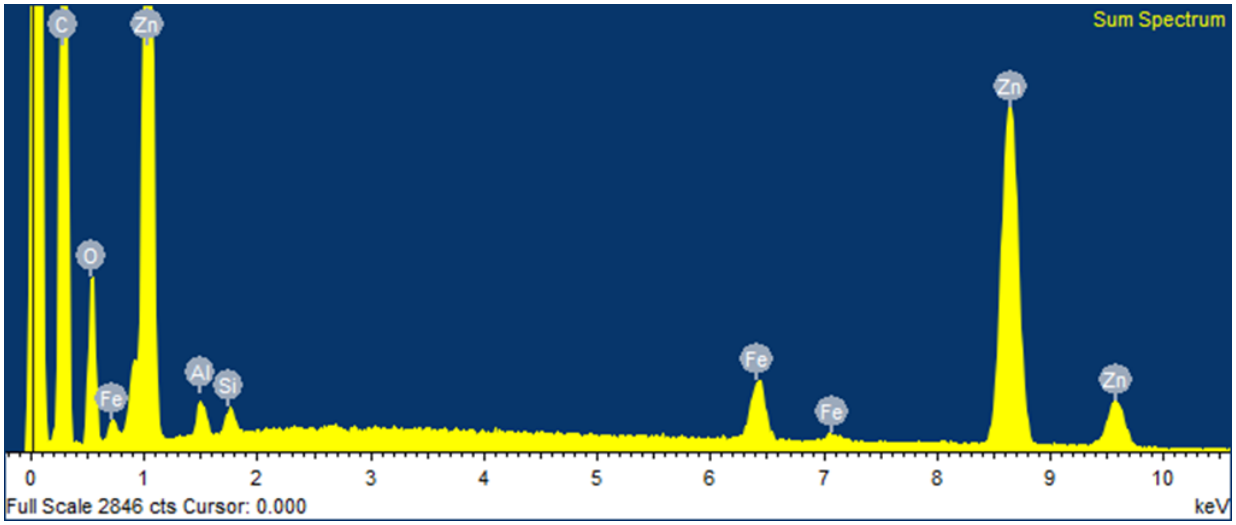


Figure A.105. SEM Image and EDS Spectrum of the Paint Collected from Exterior Web of the Girder.

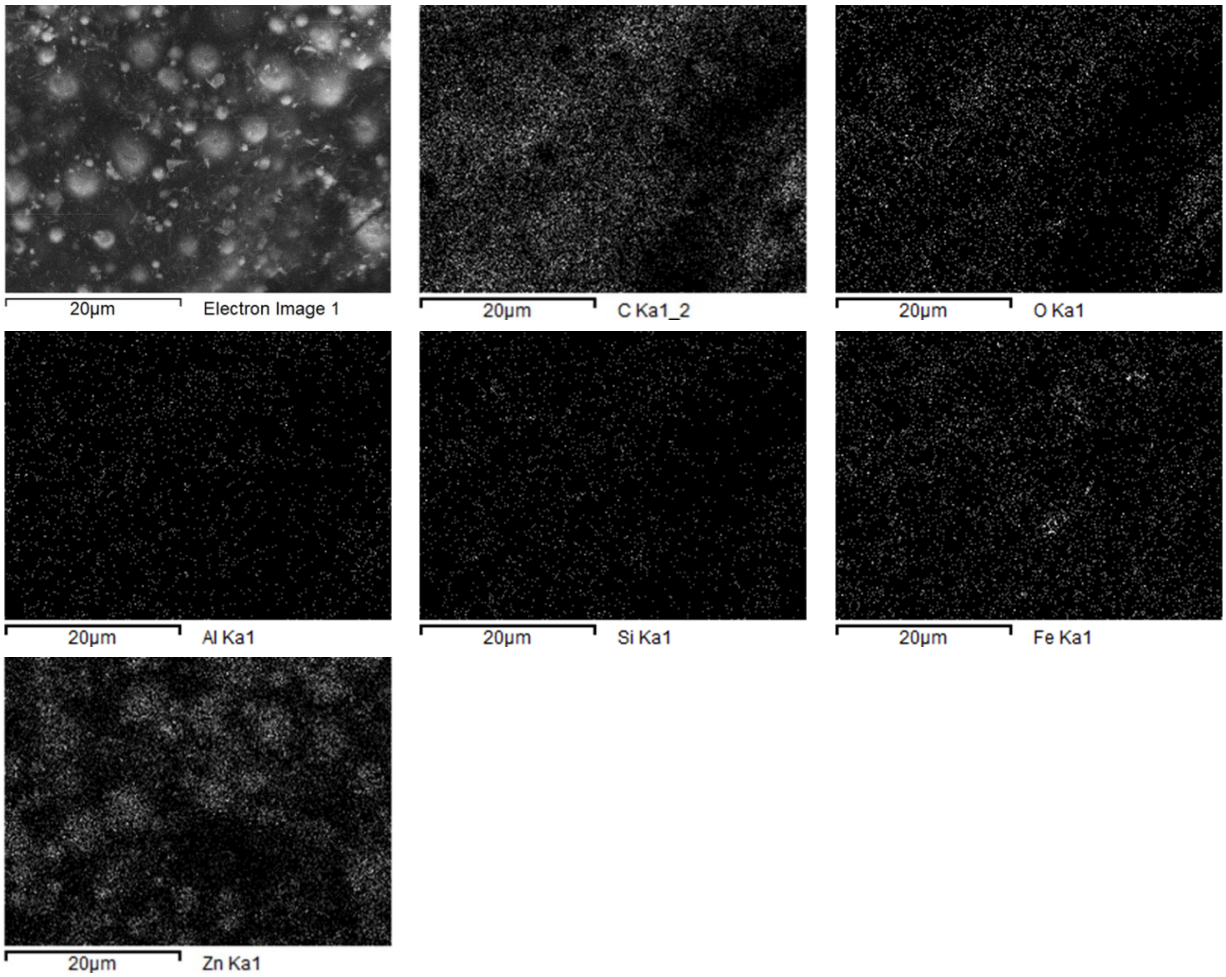


Figure A.106. EDS Elemental Mapping of Paint Collected from Exterior Web.

A.10. WFS-PS-02

- IH 44 SB over N 8th Street
- Bridge ID 32430004309193, Coordinates (33.92236, -98.51204), Wichita County
- Steel Continuous I beam with System II type paint
- Built 2001
- Date of Inspection: June 2, 2021; girder inspection carried near abutment ends on girders within approximately four feet from the abutment
- Revisited for pH test and scrape test
- No visual inspection on deck
- Location for Testing: G8, G6, G3, G1



Figure A.107. Typical Elevation of WFS-PS-02.

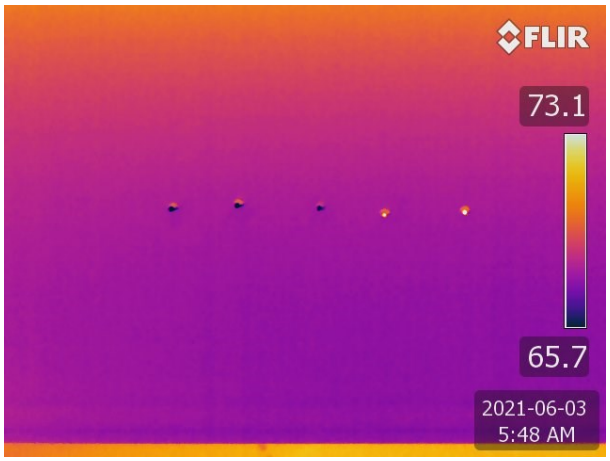
A.10.1. Observed Condition

The paint condition of this bridge is in very good condition. The appearance coat is also in good condition. Blistering, Erosion of paint, cracking in paint is not present. No checking and cracking of paint are observed. Joints are also in good condition.

A.10.2.NDT Results



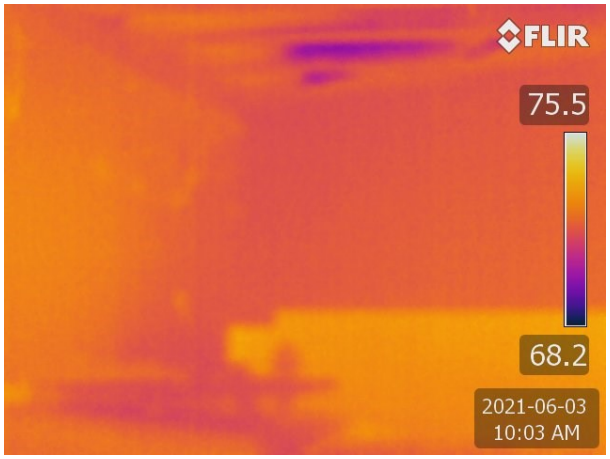
(a) Digital Image of Exterior Face of Girder Near Abutment Ends



(b) Thermal Image of Exterior Face of Girder Near Abutment Ends



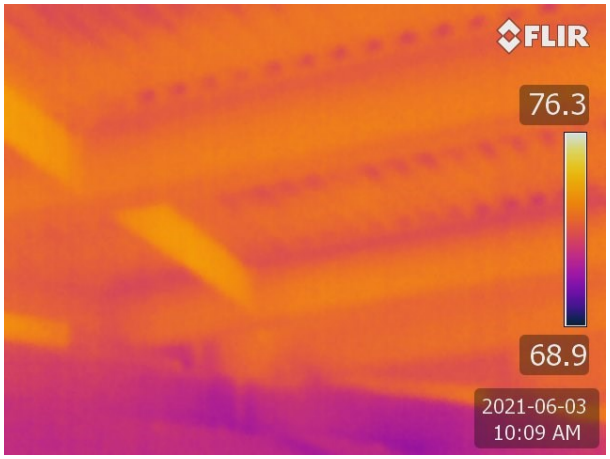
(c) Digital Image of Connection



(d) Thermal Image of Connection



(e) Digital image of the Superstructure



(f) Thermal image of the Superstructure

Figure A.108. Digital and Thermal Image of Painted Girder on WFS-PS-02.

Table A-46. Field Inspection Results for WFS-PS-02.

Location	Cl^- Conc. (ppm)	pH Test	Thickness (µm)	Thickness (inch)	Visual Inspection
G8F2 TF Bot. Ext.	-	-	Measured R1 202 R2 191 R3 205 Design Paint 140-381	Measured R1 0.746 R2 0.746 R3 0.742 R_Avg 0.745 Design	Rust Grade – 10 Blistering – Not Found Discoloration – Not Found Flaking – Not Found Delamination – Not Found
G8F2 Web. Ext.	0		Measured R1 231 R2 220 R3 214 Design Paint 140-381	Measured R1 0.502 R2 0.505 R3 0.502 R_Avg 0.503 Design	Rust Grade – 10 Blistering – Not Found Discoloration – Not Found Flaking – Not Found Delamination – Not Found
G8F2 BF Top. Ext.	-	-	Measured R1 224 R2 225 R3 233 Design Paint 140-381	Measured R1 0.743 R2 0.744 R3 0.754 R_Avg 0.747 Design	Rust Grade – 10 Blistering – Not Found Discoloration – observed on the top face of Bottom Flange Flaking – Not Found Delamination – Not Found
G8F2 BF Bot. Ext.	-	-	Measured R1 164 R2 180 R3 187 Design Paint 140-381	Measured R1 - R2 - R3 - R_Avg - Design	Rust Grade – 10 Blistering – Not Found Discoloration – Not Found Flaking – Not Found Delamination – Not Found
G6F2 TF Bot. Int.	-		Measured R1 186 R2 175 R3 174 Design Paint 140-381	Measured R1 0.762 R2 0.761 R3 0.767 R_Avg 0.763 Design	Rust Grade – 10 Blistering – Not Found Discoloration – Not Found Flaking – Not Found Delamination – Not Found
G6F2 Web. Int.	2	-	Measured R1 210 R2 218 R3 223 Design Paint 140-381	Measured R1 0.514 R2 0.517 R3 0.517 R_Avg 0.516 Design	Rust Grade – 10 Blistering – Not Found Discoloration – Not Found Flaking – Not Found Delamination – Not Found

Table A-47. Field Inspection Results for WFS-PS-02.

Location	Cl^- Conc. (ppm)	pH Test	Thickness (µm)	Thickness (inch)	Visual Inspection
G6F2 BF Top. Int.	-	-	Measured R1 221 R2 214 R3 222 Design Paint 140-381	Measured R1 0.730 R2 0.730 R3 0.734 R_Avg 0.731 Design	Rust Grade – 10 Blistering – Not Found Discoloration – Not Found Flaking – Not Found Delamination – Not Found
G6F2 BF Bot. Int.	-	-	Measured R1 209 R2 208 R3 209 Design Paint 140-381	Measured R1 - R2 - R3 - R_Avg - Design	Rust Grade – 10 Blistering – Not Found Discoloration – Not Found Flaking – Not Found Delamination – Not Found
G3F1 TF Bot. Int.	-	-	Measured R1 186 R2 182 R3 177 Design Paint 140-381	Measured R1 0.745 R2 0.744 R3 0.748 R_Avg 0.746 Design	Rust Grade – 10 Blistering – Not Found Discoloration – Not Found Flaking – Not Found Delamination – Not Found
G3F1 Web. Int.	1		Measured R1 227 R2 224 R3 236 Design Paint 140-381	Measured R1 0.505 R2 0.502 R3 0.503 R_Avg 0.503 Design	Rust Grade – 10 Blistering – Not Found Discoloration – Not Found Flaking – Not Found Delamination – Not Found
G3F1 BF Top. Int.	-		Measured R1 209 R2 221 R3 217 Design Paint 140-381	Measured R1 0.730 R2 0.736 R3 0.731 R_Avg 0.732 Design	Rust Grade – 10 Blistering – Not Found Discoloration – Not Found Flaking – Not Found Delamination – Not Found
G3F1 BF Bot. Int.	-		Measured R1 117 R2 125 R3 153 Design Paint 140-381	Measured R1 - R2 - R3 - R_Avg - Design	Rust Grade – 10 Blistering – Not Found Discoloration – observed on the top face of Bottom Flange Flaking – Not Found Delamination – Not Found

Table A-48. Field Inspection Results for WFS-PS-02.

Location	Cl^- Conc. (ppm)	pH Test	Thickness (µm)	Thickness (inch)	Visual Inspection
G1F1 TF Bot. Int.	-	-	Measured R1 158 R2 144 R3 173 Design Paint 140-381	Measured R1 0.758 R2 0.749 R3 0.752 R_Avg 0.753 Design	Rust Grade – 10 Blistering – Not Found Discoloration – Not Found Flaking – Not Found Delamination – Not Found
G1F1 Web. Int.	1		Measured R1 222 R2 191 R3 229 Design Paint 140-381	Measured R1 0.525 R2 0.527 R3 0.524 R_Avg 0.525 Design	Rust Grade – 10 Blistering – Not Found Discoloration – Not Found Flaking – Not Found Delamination – Not Found
G1F1 BF Top. Int.	-		Measured R1 182 R2 172 R3 171 Design Paint 140-381	Measured R1 0.785 R2 0.778 R3 0.782 R_Avg 0.782 Design	Rust Grade – 10 Blistering – Not Found Discoloration – observed on the top face of Bottom Flange Flaking – Not Found Delamination – Not Found
G1F1 BF Bot. Int.	-		Measured R1 200 R2 187 R3 201 Design Paint 140-381	Measured R1 - R2 - R3 - R_Avg - Design	Rust Grade – 10 Blistering – Not Found Discoloration – Not Found Flaking – Not Found Delamination – Not Found

Table A-49. Paint System Information.

Cohesive Failure Layer		Adhesive Failure Layer	
Code	**Description**	**Code**	**Description**
A	Substrate	A/B	Substrate & Layer 1
B	Layer 1(Gray)	B/C	Layer 1 & Layer 2
C	Layer 2(White)	C/Y	Layer 2 & Glue
Y	Glue	Y/Z	Glue & Dolly

A.10.3. Pull-off Adhesion Results

Table A-50. Pull-off Adhesion Results for WFS-PS-02.

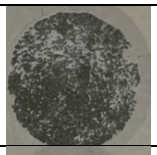
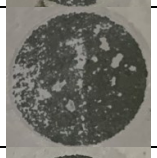
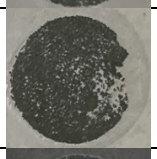
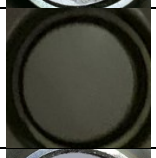
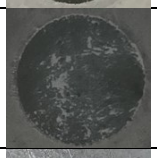
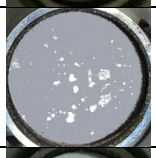
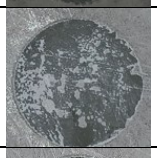
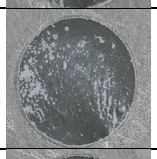
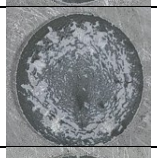
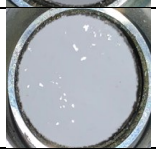
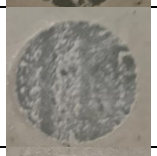
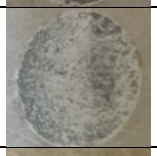
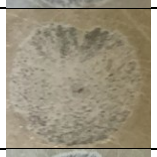
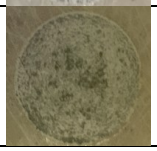
Location	Dolly Face	Substrate Face	Test Result (psi)	Attributes	Failure Type
A1-G8F2			1718	20% C 80% B/C	20% Cohesive Failure 80% Adhesive Failure
			1777	40% C 60% B/C	40% Cohesive Failure 60% Adhesive Failure
			2103	30% C 70% B/C	30% Cohesive Failure 70% Adhesive Failure
			1934	20% C 80% B/C	20% Cohesive Failure 80% Adhesive Failure
			1798	10% C 90% B/C	10% Cohesive Failure 90% Adhesive Failure
A1-G6F2			2140	20% C 80% B/C	20% Cohesive Failure 80% Adhesive Failure
			1922	10% C/Y 20% C 70% B/C	10% Glue Failure 20% Cohesive Failure 70% Adhesive Failure
			2059	10% C 90% B/C	10% Cohesive Failure 90% Adhesive Failure
			2333	30% C 70% B/C	30% Cohesive Failure 70% Adhesive Failure
			2339	10% C 90% B/C	10% Cohesive Failure 90% Adhesive Failure

Table A-51. Pull-off Adhesion Results for WFS-PS-02.

Location	Dolly Face	Substrate Face	Test Result (psi)	Attributes	Failure Type
A1-G3F1			2173	60% C 40% B/C	60% Cohesive Failure 40% Adhesive Failure
			1654	40% C 60% B/C	40% Cohesive Failure 60% Adhesive Failure
			2214	100% C	100% Cohesive Failure
			2090	100% C	100% Cohesive Failure
			2206	20%C/Y 80% B/C	100% Adhesive Failure
A1-G1F1			2295	100% C	100% Cohesive Failure
			2015	100% C	100% Cohesive Failure
			2125	100% C	100% Cohesive Failure
			2146	100% C	100% Cohesive Failure
			2153	100% C	100% Cohesive Failure

A.10.4.Optical Microscopy Results

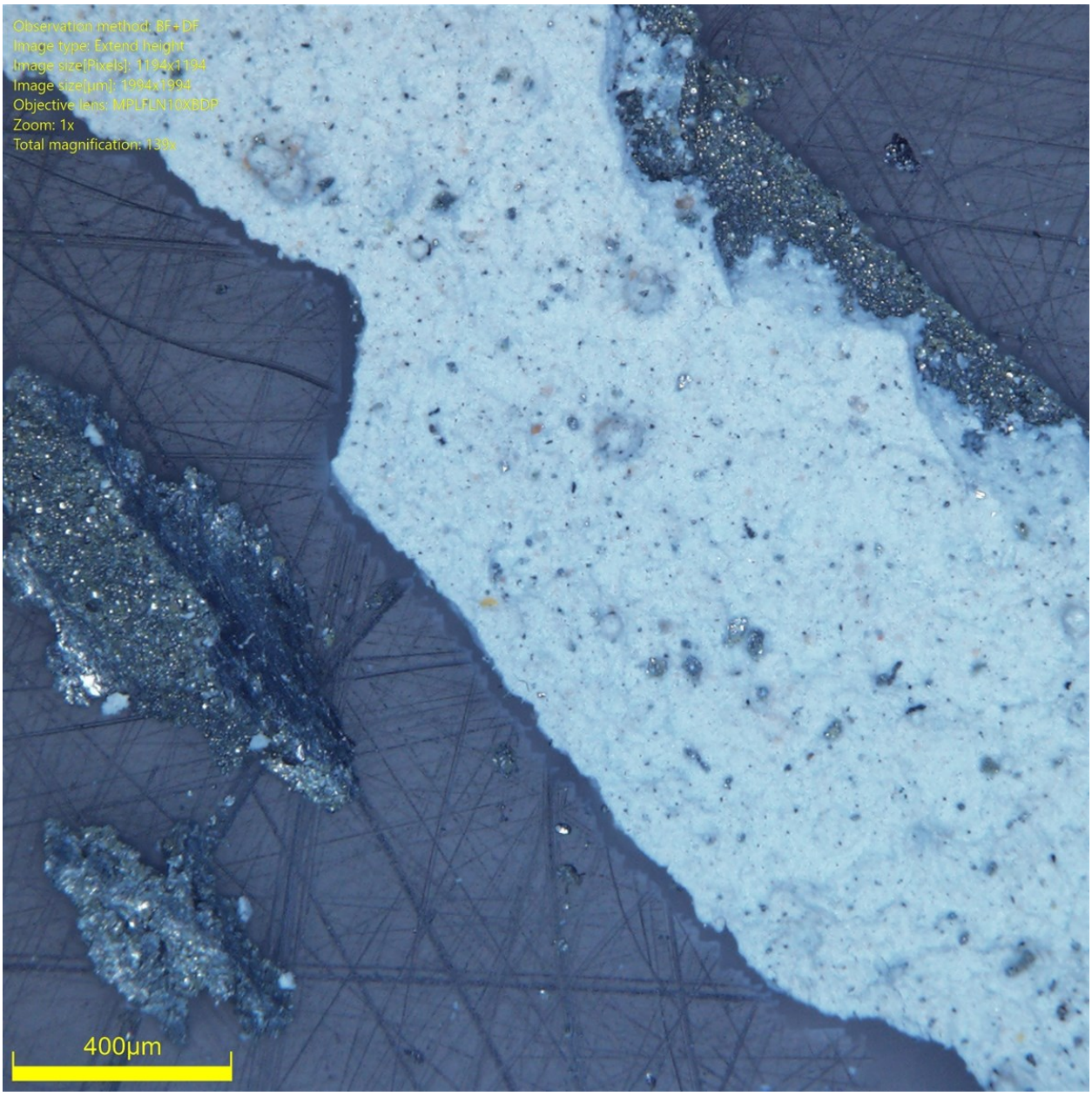
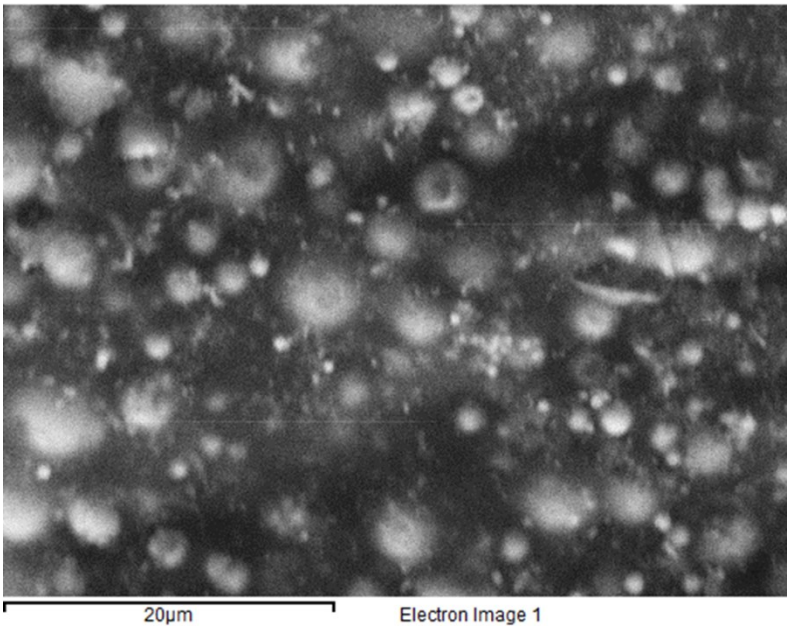


Figure A.109. Two Layer Paint System Examined by Optical Microscope WFS–PS–02.

A.10.5.SEM/EDS Results

Element	Weight %	Atomic %
C K	59.98	82.38
O K	9.25	9.54
Al K	0.43	0.26
Si K	0.26	0.15
Fe K	1.82	0.54
Zn K	28.26	7.13
Totals	100.00	



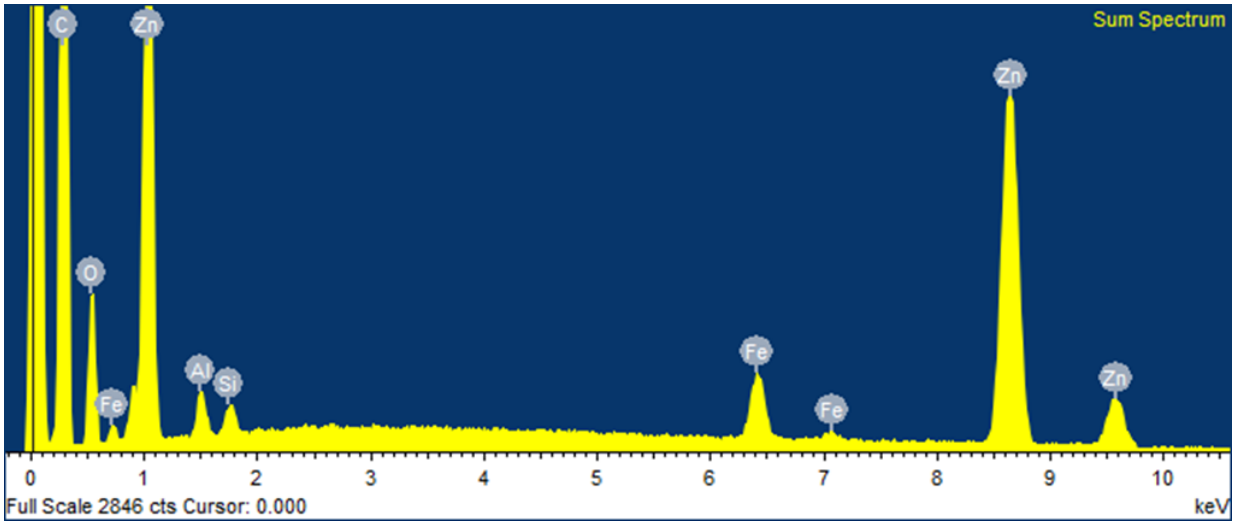


Figure A.110. SEM Image and EDS Spectrum of the Paint Collected from Exterior Web of the Girder.

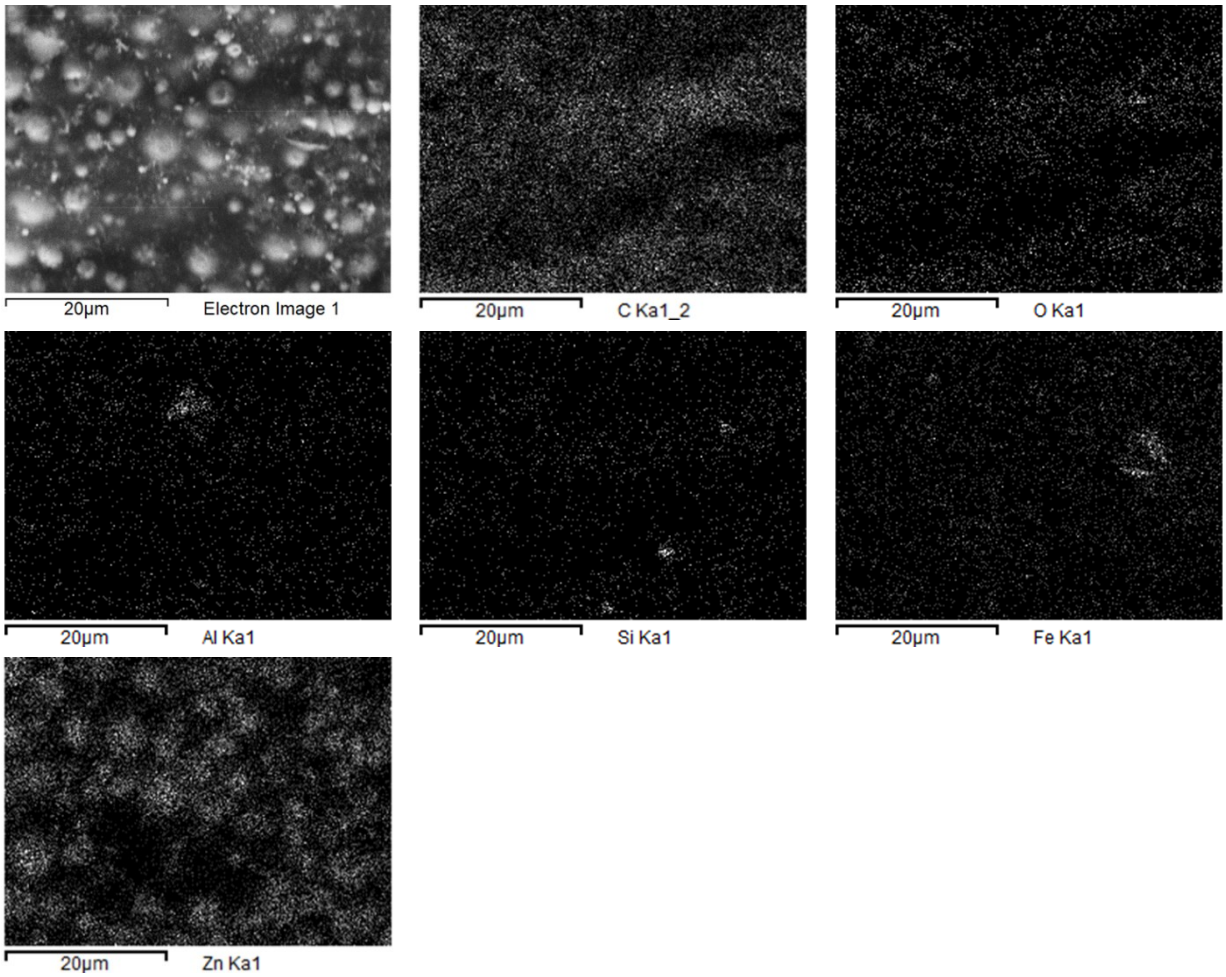
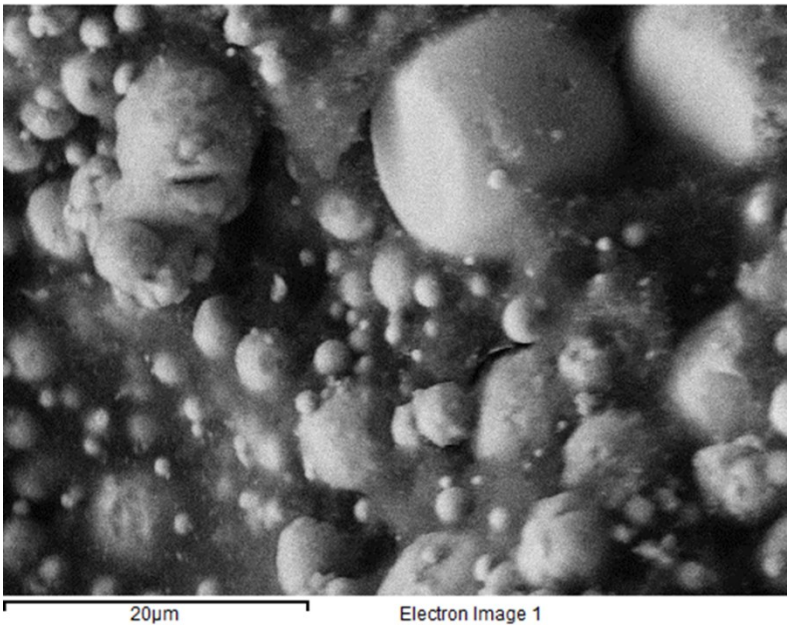


Figure A.111. EDS Elemental Mapping of Paint Collected from Exterior Web.

Element	Weight %	Atomic %
C K	53.96	77.49
O K	12.45	13.43
Al K	0.28	0.18
Si K	0.20	0.12
Cl K	0.07	0.03
Fe K	0.82	0.25
Zn K	32.22	8.50
Totals	100.00	



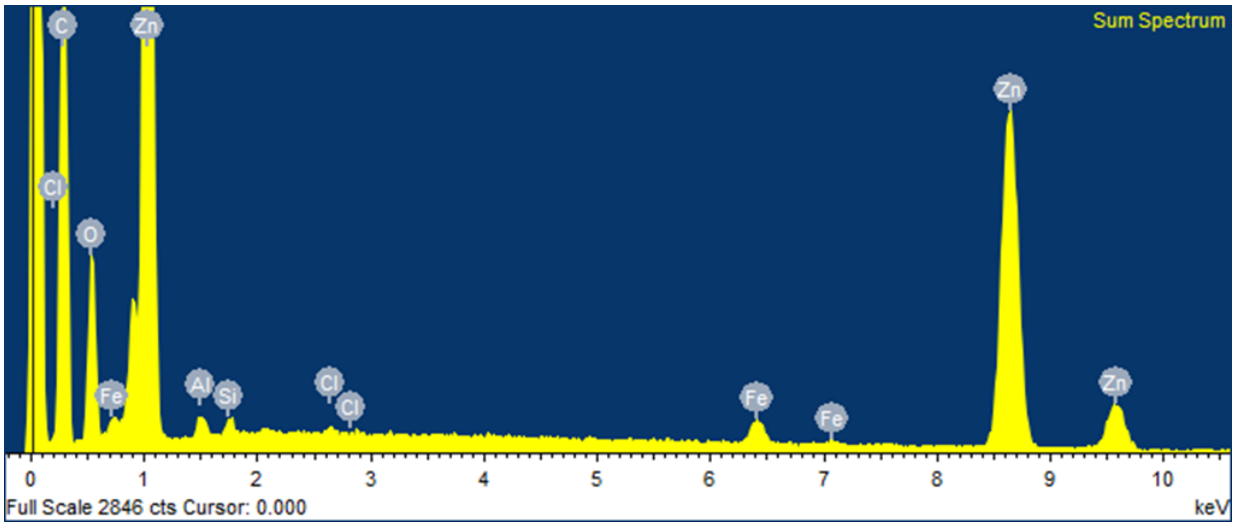


Figure A.112. SEM Image and EDS Spectrum of the Paint Collected from Interior Web of the Girder.

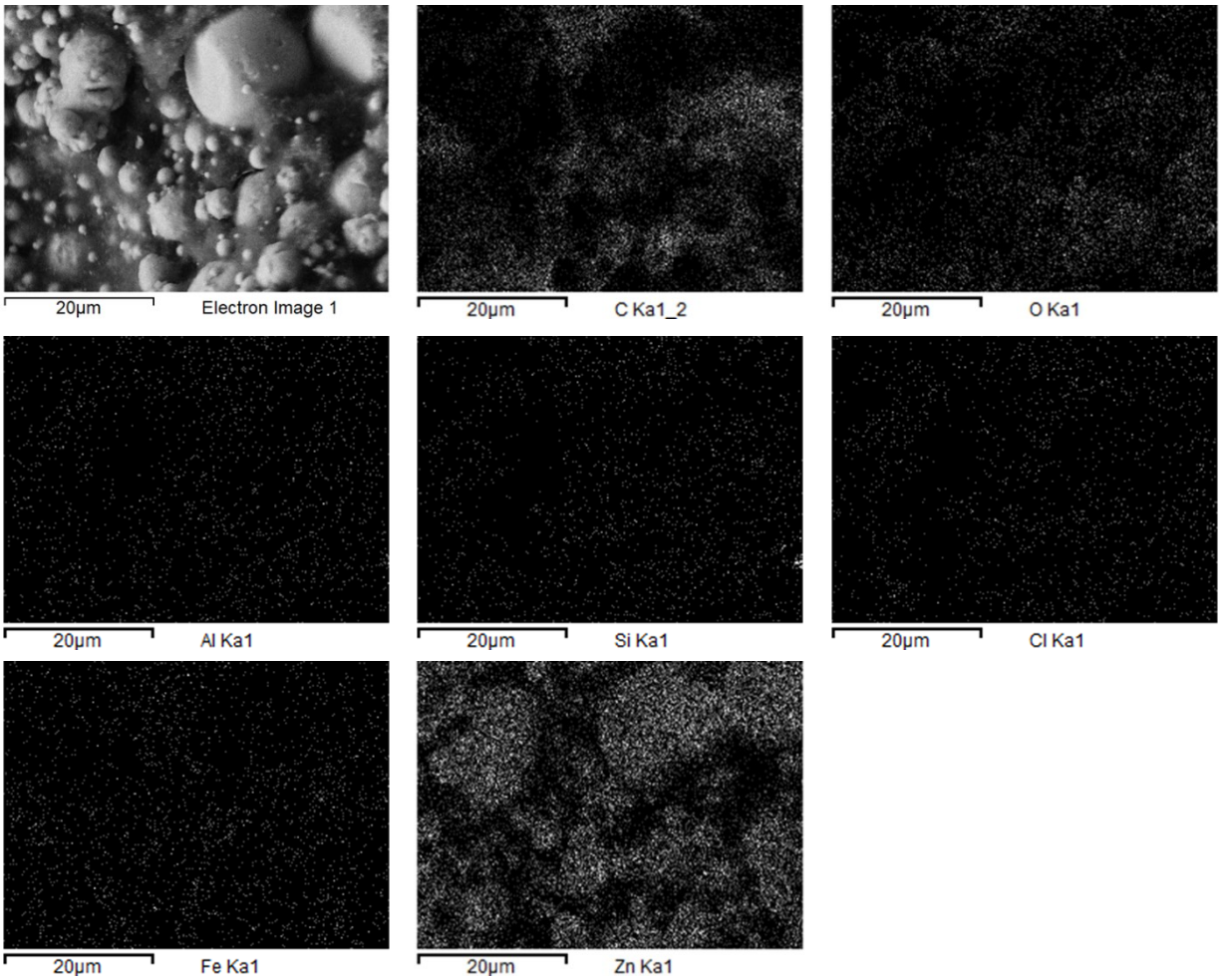
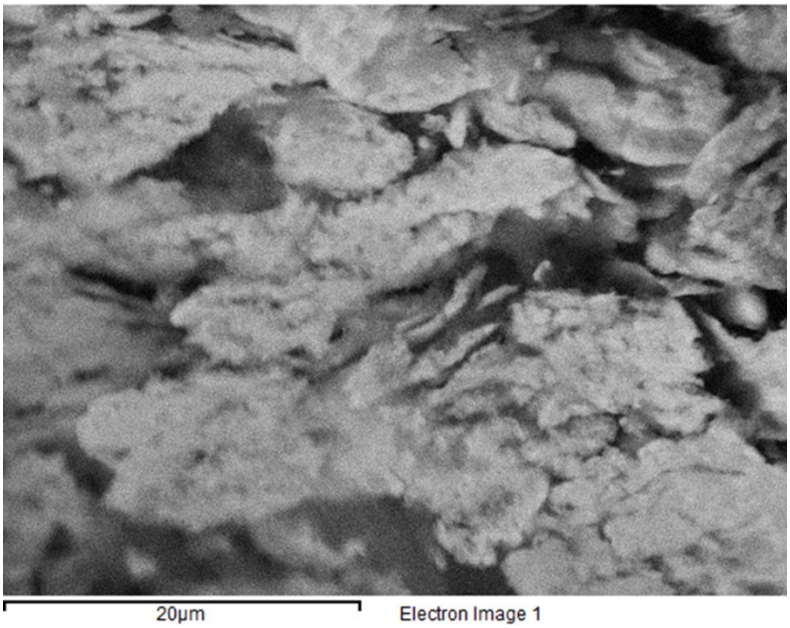


Figure A.113. EDS Elemental Mapping of Paint Collected from Interior Web.

Element	Weight %	Atomic %
C K	31.86	67.78
O K	4.07	6.51
Al K	0.87	0.83
Si K	0.21	0.19
Cl K	0.22	0.16
Ti K	0.18	0.09
Fe K	0.71	0.33
Ni K	0.21	0.09
Zn K	61.03	23.86
Zr L	0.46	0.13
Totals	100.00	



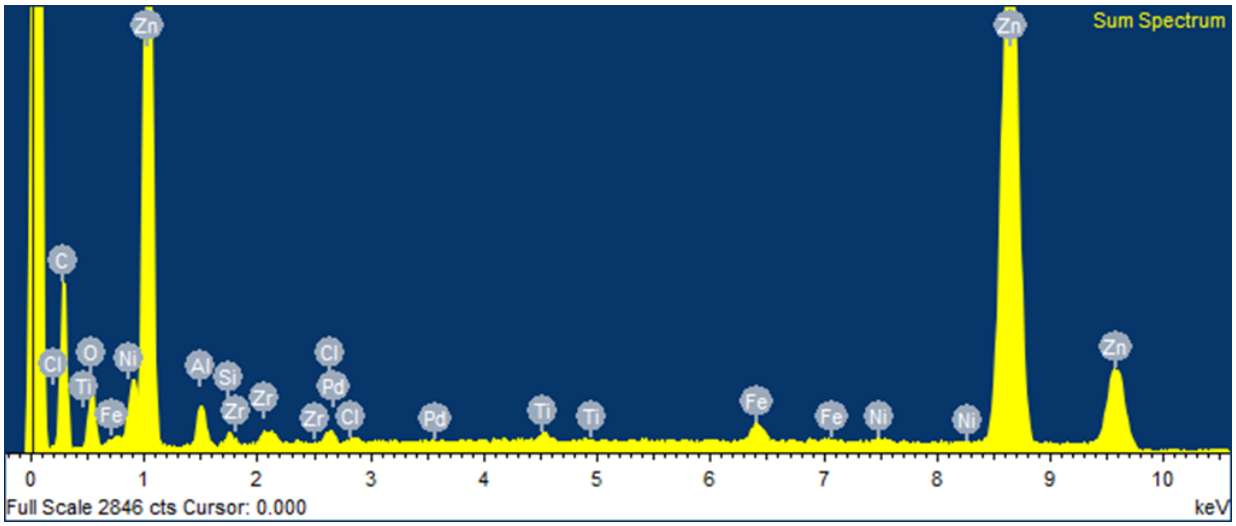


Figure A.114. SEM Image and EDS Spectrum of the Paint Collected from Interior Web of the Girder.

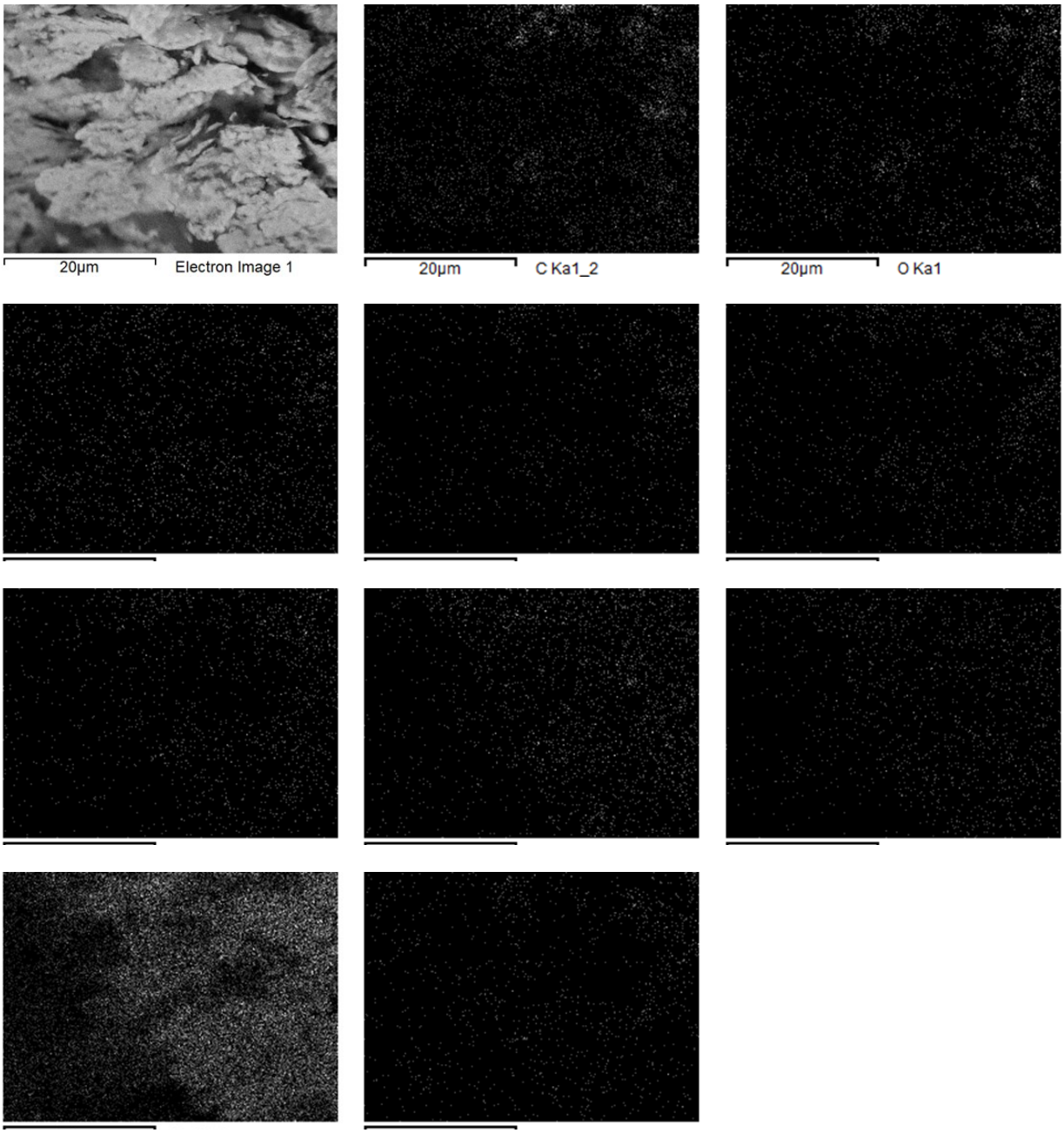


Figure A.115. EDS Elemental Mapping of Paint Collected from Interior Web.

A.11. WFS-RC-01

- IH 44 NB over 6th Street
- Bridge ID 32430004309188, Coordinates (33.90933, -98.5015), Wichita County
- Steel Continuous I beam with System I type paint
- Built 2001
- Date of Inspection: June 01, 2021; girder inspection carried near abutment ends on girders within approximately four feet from the abutment
- Revisited for pH test and scrape test
- No visual inspection on deck
- Location for Testing: G9, G5, G7, G1



Figure A.116. Typical Elevation of WFS-RC-01.

A.11.1. Observed Condition

The paint condition of this bridge is in good condition with paint discoloration and rusting observed on diaphragm and bottom flange near bearing plate. The reason behind rusting of end diaphragm near abutment seems to be leaking joint. Overall the appearance coat is also in good condition. Blistering, Erosion of paint, cracking in paint is not present. No checking and cracking of paint are observed. Joints are also in good condition.



(a) Staining observed on Bearing



(b) Interior Girder in Good Condition



(c) Interior Girder Connection is in Good Condition



(d) Superstructure in Good Condition



(e) Crack Observed on Abutment Wall



(f) Exterior Girder in Good Condition

Figure A.117. Paint Condition on the Girder of WFS-RC-01.

A.11.2.NDT Results



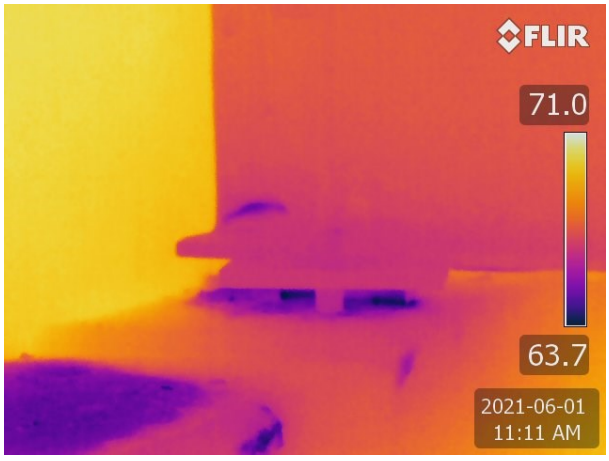
(a) Digital Image of Exterior Face of Girder Near Abutment Ends



(b) Thermal Image of Exterior Face of Girder Near Abutment Ends



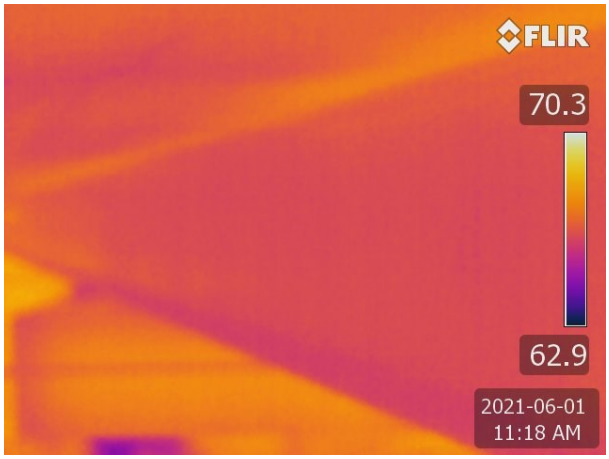
(c) Digital Image of Paint Deterioration and Rusting of Girder and Bearing



(d) Thermal Image of Paint Deterioration and Rusting of Girder and Bearing



(e) Digital image of the Interior Girder



(f) Thermal image of the Exterior Girder

Figure A.118. Digital and Thermal Image of Painted Girder on WFS-RC-01.

Table A-52. Field Inspection Results for WFS-RC-01.

Location	Cl^- Conc. (ppm)	pH Test	Thickness (µm)	Thickness (inch)	Visual Inspection
G9F2 TF Bot. Ext.	-	-	Measured R1 187 R2 191 R3 198 Design Paint 165-431	Measured R1 1.046 R2 1.043 R3 1.045 R_Avg 1.045 Design	Rust Grade – 10 Blistering – Not Found Discoloration – Not Found Flaking – Not Found Delamination – Not Found
G9F2 Web. Ext.	1		Measured R1 231 R2 229 R3 223 Design Paint 165-431	Measured R1 0.621 R2 0.617 R3 0.634 R_Avg 0.624 Design	Rust Grade – 10 Blistering – Not Found Discoloration – Not Found Flaking – Not Found Delamination – Not Found
G9F2 BF Top. Ext.	-	-	Measured R1 262 R2 289 R3 295 Design Paint 165-431	Measured R1 1.041 R2 1.035 R3 1.034 R_Avg 1.037 Design	Rust Grade – 10 Blistering – Not Found Discoloration – observed on the top of Bottom Flange Flaking – Not Found Delamination – Not Found
G9F2 BF Bot. Ext.	-	-	Measured R1 231 R2 259 R3 247 Design Paint 165-431	Measured R1 - R2 - R3 - R_Avg - Design	Rust Grade – 10 Blistering – Not Found Discoloration – Not Found Flaking – Not Found Delamination – Not Found
G5F1 TF Bot. Int.	-		Measured R1 252 R2 249 R3 232 Design Paint 165-431	Measured R1 1.041 R2 1.045 R3 1.047 R_Avg 1.044 Design	Rust Grade – 10 Blistering – Not Found Discoloration – Not Found Flaking – Not Found Delamination – Not Found
G5F1 Web. Int.	-	-	Measured R1 228 R2 211 R3 226 Design Paint 165-431	Measured R1 0.621 R2 0.621 R3 0.621 R_Avg 0.621 Design	Rust Grade – 10 Blistering – Not Found Discoloration – Not Found Flaking – Not Found Delamination – Not Found

Table A-53. Field Inspection Results for WFS-RC-01.

Location	Cl^- Conc. (ppm)	pH Test	Thickness (µm)	Thickness (inch)	Visual Inspection
G5F1 BF Top. Int.	-	-	Measured R1 255 R2 259 R3 241 Design Paint 165-431	Measured R1 1.018 R2 1.029 R3 1.018 R_Avg 1.022 Design	Rust Grade – 10 Blistering – Not Found Discoloration – observed on the top of Bottom Flange Flaking – Not Found Delamination – Not Found
G5F1 BF Bot. Int.	-	-	Measured R1 256 R2 240 R3 239 Design Paint 165-431	Measured R1 - R2 - R3 - R_Avg - Design	Rust Grade – 10 Blistering – Not Found Discoloration – Not Found Flaking – Not Found Delamination – Not Found
G7F2 TF Bot. Int.	-	-	Measured R1 199 R2 185 R3 200 Design Paint 165-431	Measured R1 1.061 R2 1.050 R3 1.062 R_Avg 1.058 Design	Rust Grade – 10 Blistering – Not Found Discoloration – Not Found Flaking – Not Found Delamination – Not Found
G7F2 Web. Int.	1		Measured R1 191 R2 176 R3 199 Design Paint 165-431	Measured R1 0.620 R2 0.621 R3 0.619 R_Avg 0.620 Design	Rust Grade – 10 Blistering – Not Found Discoloration – Not Found Flaking – Not Found Delamination – Not Found
G7F2 BF Top. Int.	-		Measured R1 241 R2 250 R3 240 Design Paint 165-431	Measured R1 1.018 R2 1.029 R3 1.018 R_Avg 1.022 Design	Rust Grade – 10 Blistering – Not Found Discoloration – observed on the top of Bottom Flange Flaking – Not Found Delamination – Not Found
G7F2 BF Bot. Int.	-		Measured R1 260 R2 244 R3 268 Design Paint 165-431	Measured R1 - R2 - R3 - R_Avg - Design	Rust Grade – 10 Blistering – Not Found Discoloration – Not Found Flaking – Not Found Delamination – Not Found

Table A-54. Field Inspection Results for WFS-RC-01.

Location	Cl^- Conc. (ppm)	pH Test	Thickness (µm)	Thickness (inch)	Visual Inspection
G1F1 TF Bot. Ext.	-	-	Measured R1 179 R2 192 R3 193 Design Paint 165-431	Measured R1 1.066 R2 1.070 R3 1.063 R_Avg 1.066 Design	Rust Grade – 10 Blistering – Not Found Discoloration – Not Found Flaking – Not Found Delamination – Not Found
G1F1 Web. Ext.	1		Measured R1 144 R2 163 R3 162 Design Paint 165-431	Measured R1 0.623 R2 0.623 R3 0.622 R_Avg 0.623 Design	Rust Grade – 10 Blistering – Not Found Discoloration – Not Found Flaking – Not Found Delamination – Not Found
G1F1 BF Top. Ext.	-		Measured R1 225 R2 216 R3 212 Design Paint 165-431	Measured R1 1.008 R2 1.002 R3 1.002 R_Avg 1.004 Design	Rust Grade – 10 Blistering – Not Found Discoloration – observed on the top face of Bottom Flange Flaking – Not Found Delamination – Not Found
G1F1 BF Bot. Ext.	-		Measured R1 252 R2 249 R3 272 Design Paint 165-431	Measured R1 - R2 - R3 - R_Avg - Design	Rust Grade – 10 Blistering – Not Found Discoloration – Not Found Flaking – Not Found Delamination – Not Found

Table A-55. Paint System Information.

Cohesive Failure Layer		Adhesive Failure Layer	
Code	**Description**	**Code**	**Description**
A	Substrate	A/B	Substrate & Layer 1
B	Layer 1(Carrot)	B/C	Layer 1 & Layer 2
C	Layer 2(White)	C/Y	Layer 2 & Glue
Y	Glue	Y/Z	Glue & Dolly

A.11.3.Pull-off Adhesion Results

Table A-56. Pull-off Adhesion Results for WFS-RC-01.

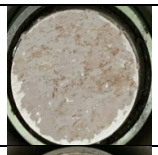
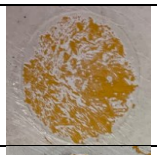
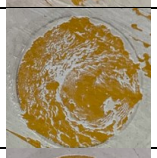
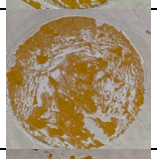
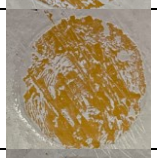
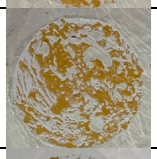
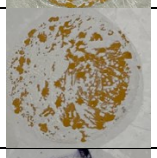
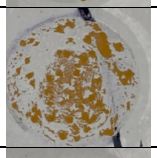
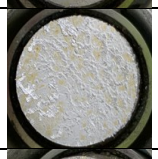
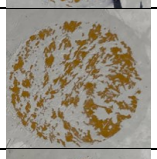
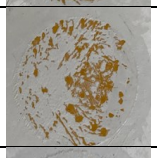
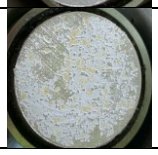
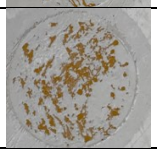
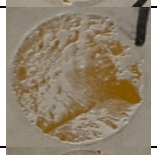
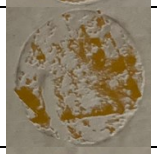
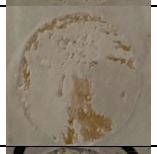
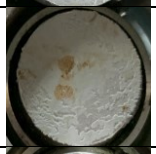
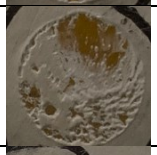
Location	Dolly Face	Substrate Face	Test Result (psi)	Attributes	Failure Type
A1-G1F1			1199	10% Y/Z 30% C 60% B/C	10% Glue Failure 30% Cohesive Failure 60% Adhesive Failure
			1386	20% C 80% B/C	20% Cohesive Failure 80% Adhesive Failure
			1413	20% C 80% B/C	20% Cohesive Failure 80% Adhesive Failure
			1496	20% C 80% B/C	20% Cohesive Failure 80% Adhesive Failure
			1072	40% C 60% B/C	40% Cohesive Failure 60% Adhesive Failure
A1-G9F2			1479	50% C 50% B/C	50% Cohesive Failure 50% Adhesive Failure
			1658	50% C 50% B/C	50% Cohesive Failure 50% Adhesive Failure
			1662	50% C 50% B/C	50% Cohesive Failure 50% Adhesive Failure
			1323	70% C 30% B/C	70% Cohesive Failure 30% Adhesive Failure
			1027	70% C 30% B/C	70% Cohesive Failure 30% Adhesive Failure

Table A-57. Pull-off Adhesion Results for WFS-RC-01.

Location	Dolly Face	Substrate Face	Test Result (psi)	Attributes	Failure Type
A1-G5F1			1117	20% C/Y 50% C 30% B/C	20% Glue Failure 50% Cohesive Failure 30% Adhesive Failure
			1378	50% C 50% B/C	50% Cohesive Failure 50% Adhesive Failure
			1297	70% C 30% B/C	70% Cohesive Failure 30% Adhesive Failure
			2197	60% C 40% B/C	60% Cohesive Failure 40% Adhesive Failure
			1262	80% C 20% B/C	80% Cohesive Failure 20% Adhesive Failure
A1-G7F2			869	80% C 20% B/C	80% Cohesive Failure 20% Adhesive Failure
			1560	60% C 40% B/C	60% Cohesive Failure 40% Adhesive Failure
			1408	60% C 30% B/C 10% B	70% Cohesive Failure 40% Adhesive Failure
			1399	70% C 30% B/C	70% Cohesive Failure 30% Adhesive Failure
			1458	70% C 30% B/C	70% Cohesive Failure 30% Adhesive Failure

A.11.4.Optical Microscopy Results

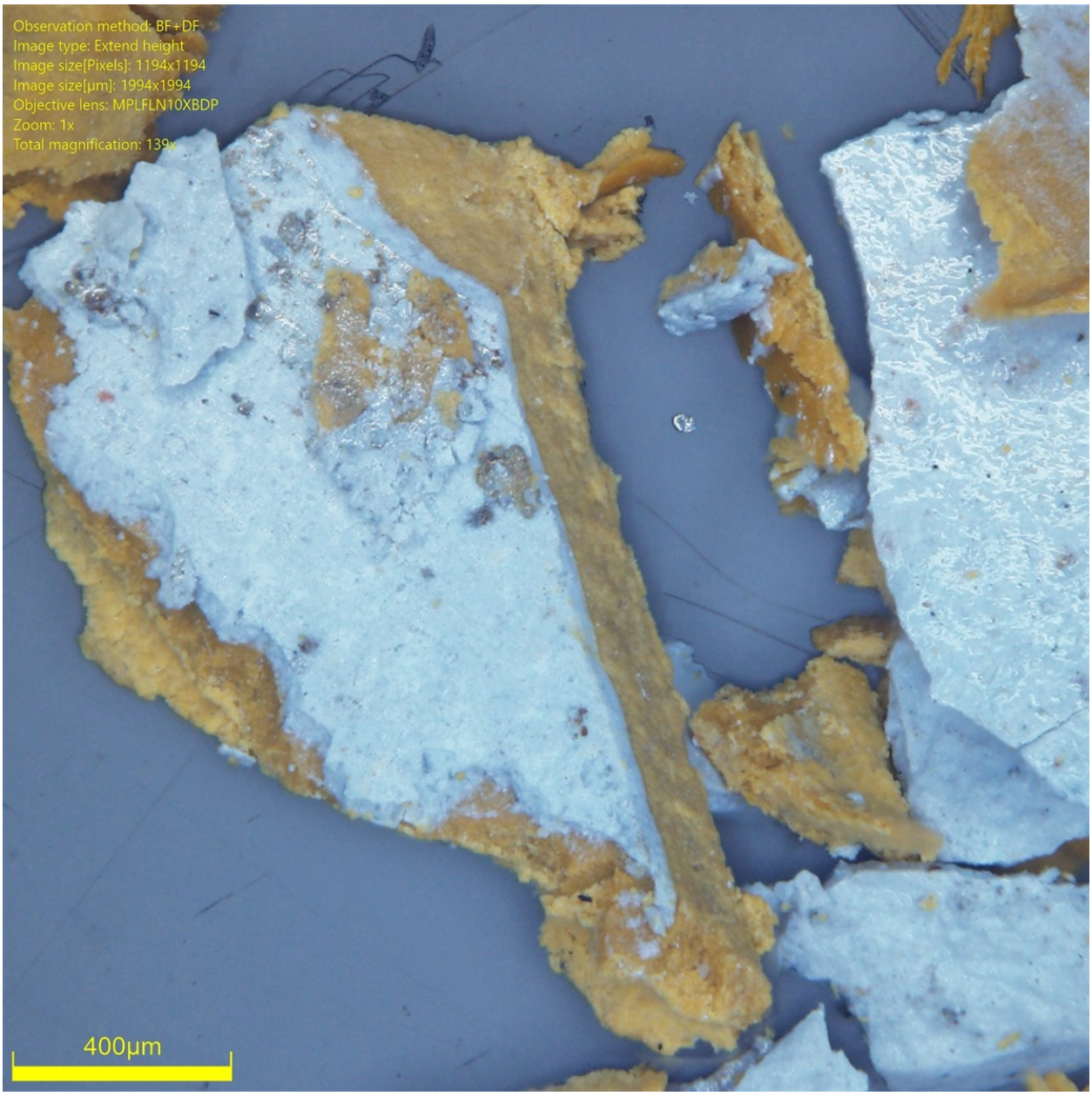


Figure A.119. Two Layer Paint System Examined by Optical Microscope WFS–RC–01.

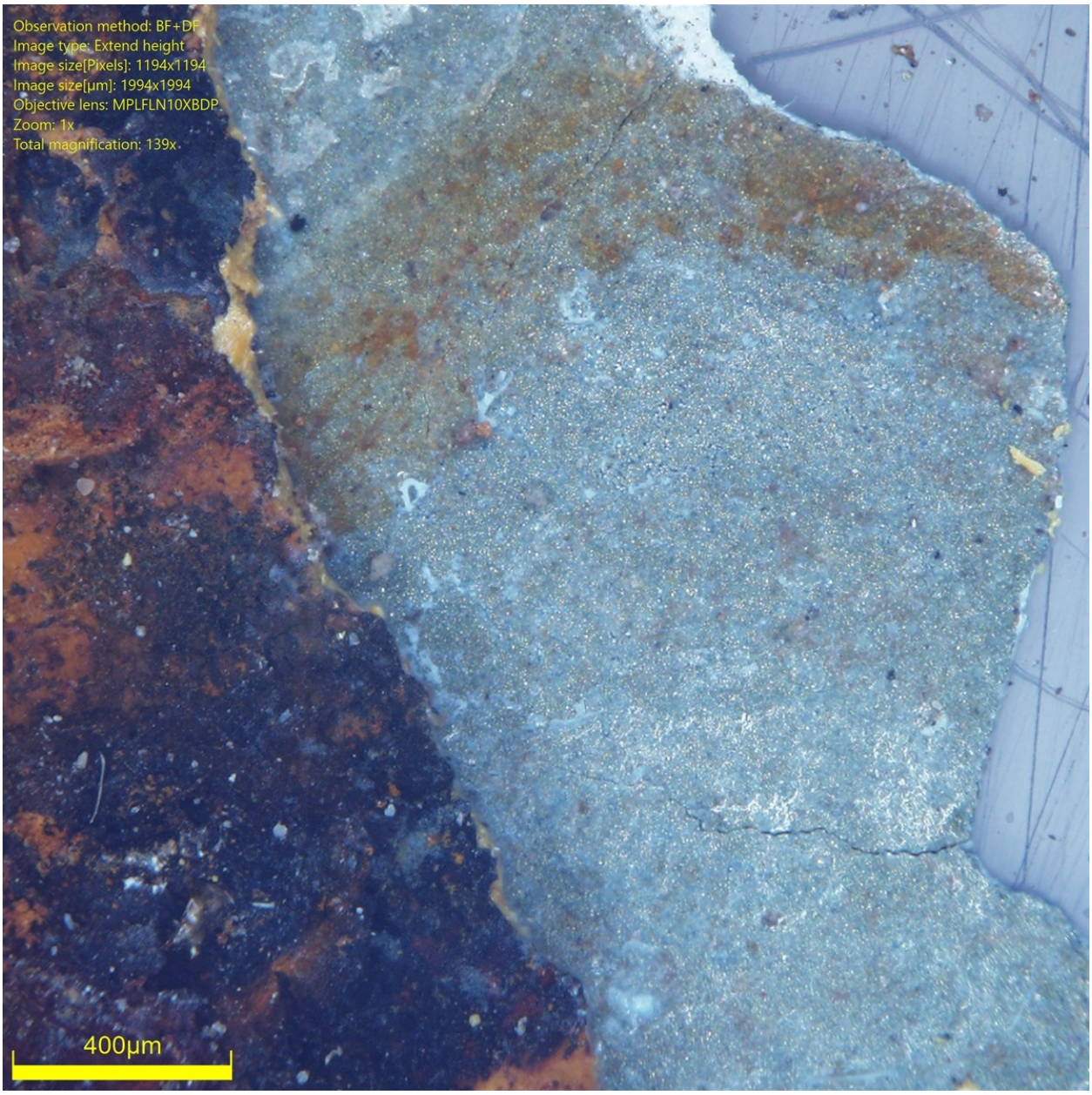
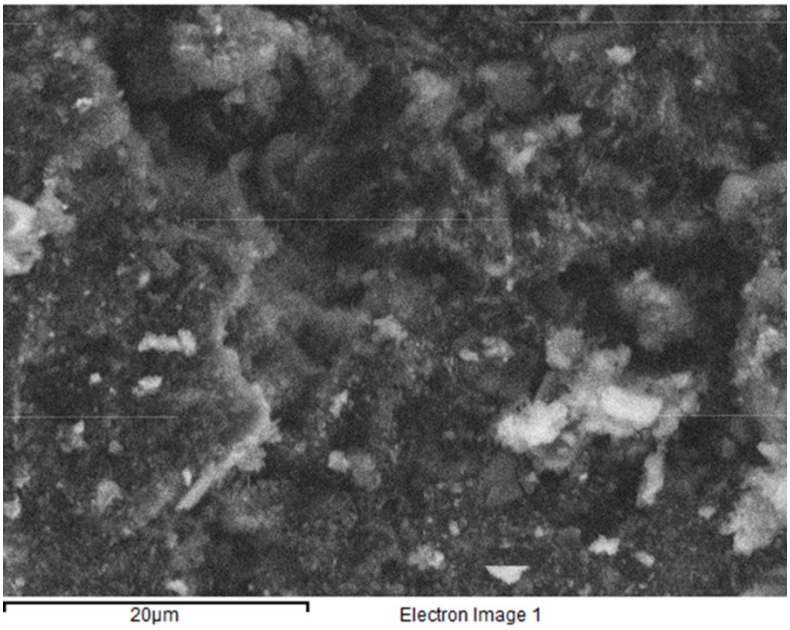


Figure A.120. Widespread Corrosion Observed Between Primer and Base Metal.

A.11.5.SEM/EDS Results

Element	Weight %	Atomic %
C K	51.72	61.13
O K	39.98	35.48
Al K	0.34	0.18
Si K	3.89	1.97
P K	0.37	0.17
Cl K	0.07	0.03
Ca K	1.33	0.47
Ti K	0.16	0.05
Fe K	1.70	0.43
Zn K	0.44	0.09
Totals	100.00	



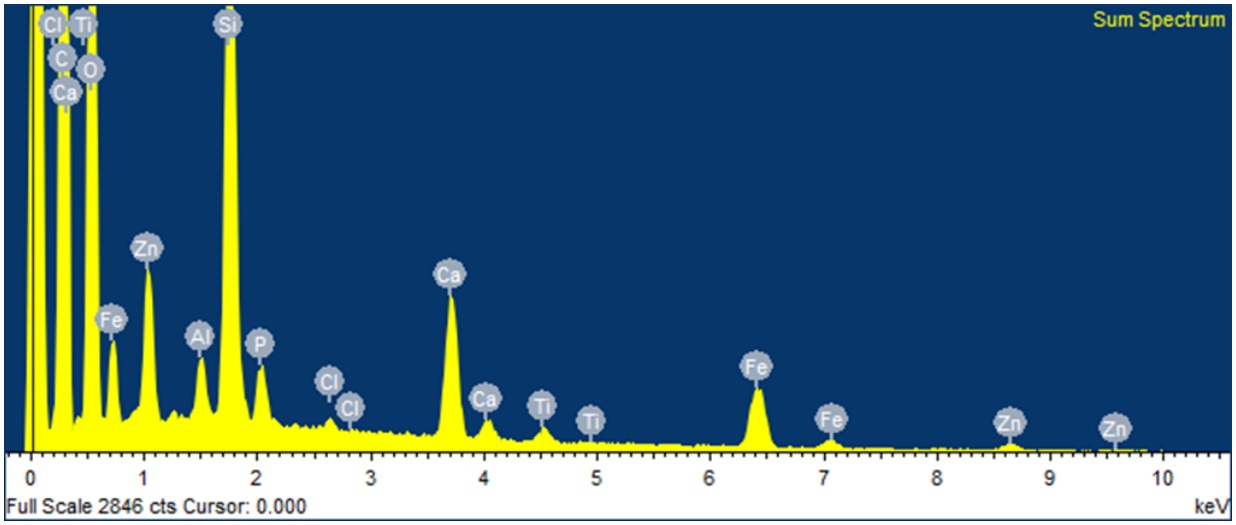


Figure A.121. SEM Image and EDS Spectrum of the Paint Collected from Exterior Web of the Girder.

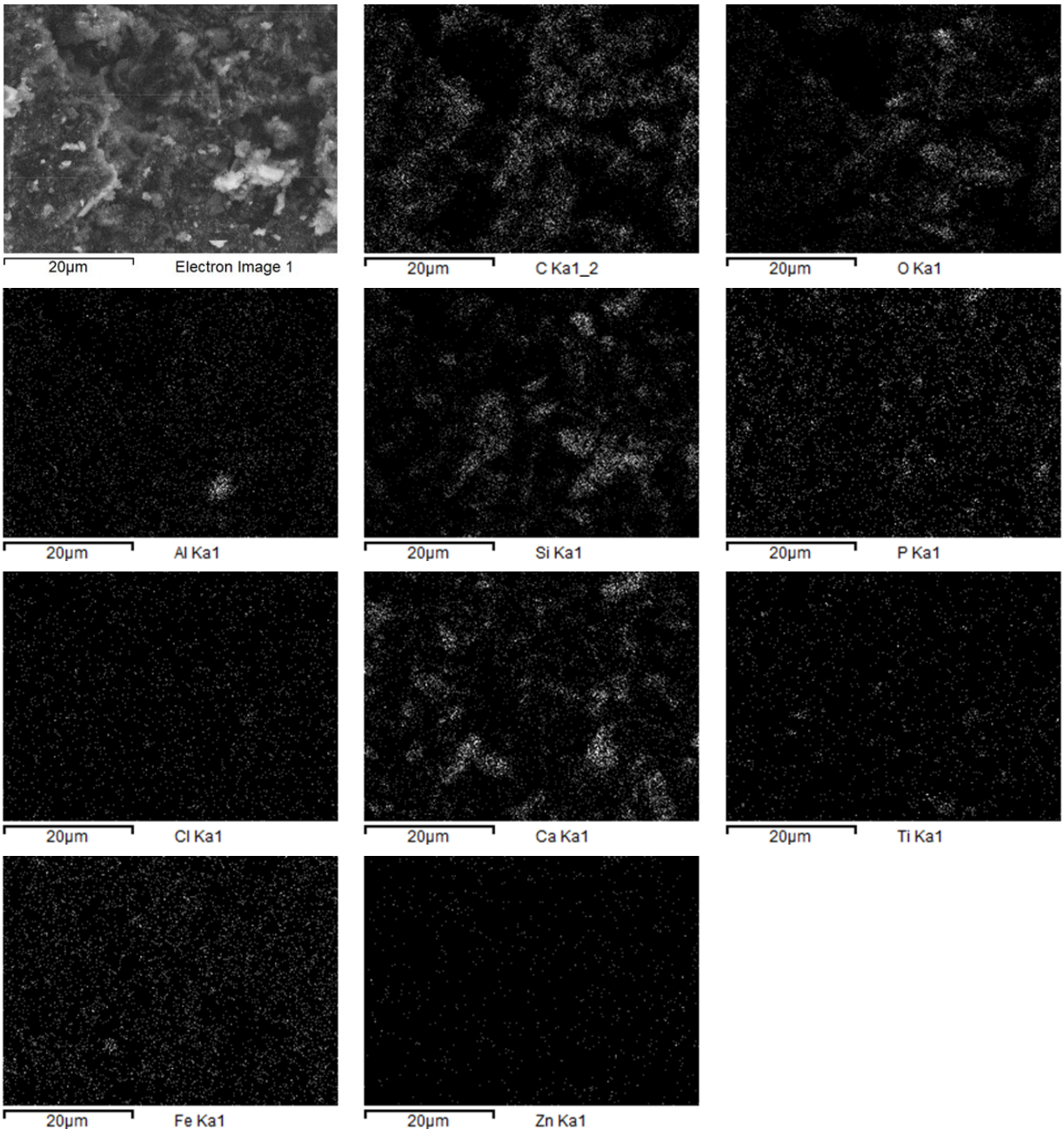
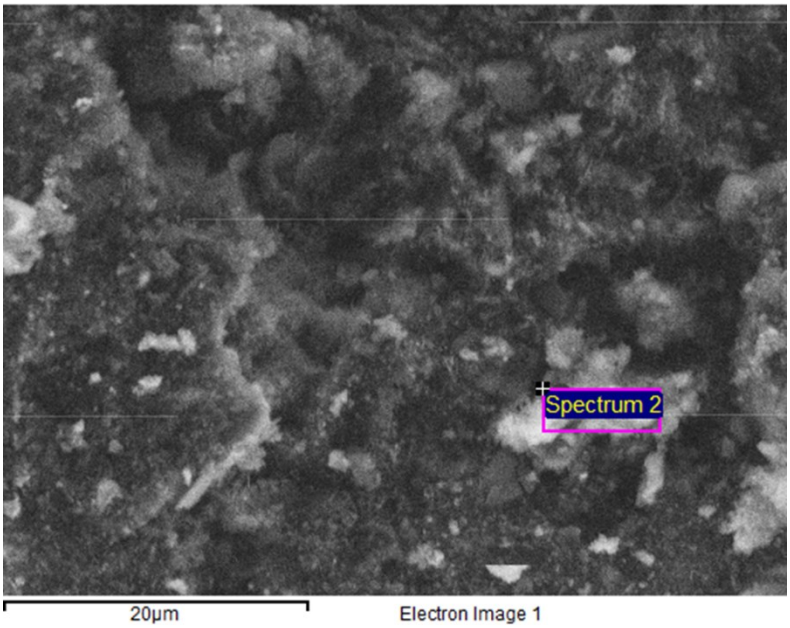


Figure A.122. EDS Elemental Mapping of Paint Collected from Exterior Web.

Element	Weight %	Atomic %
C K	34.57	44.43
O K	49.72	47.97
Al K	0.41	0.24
Si K	9.86	5.42
P K	0.10	0.05
Cl K	0.07	0.03
Ca K	3.84	1.48
Ti K	0.15	0.05
Fe K	1.10	0.30
Zn K	0.19	0.04
Totals	100.00	



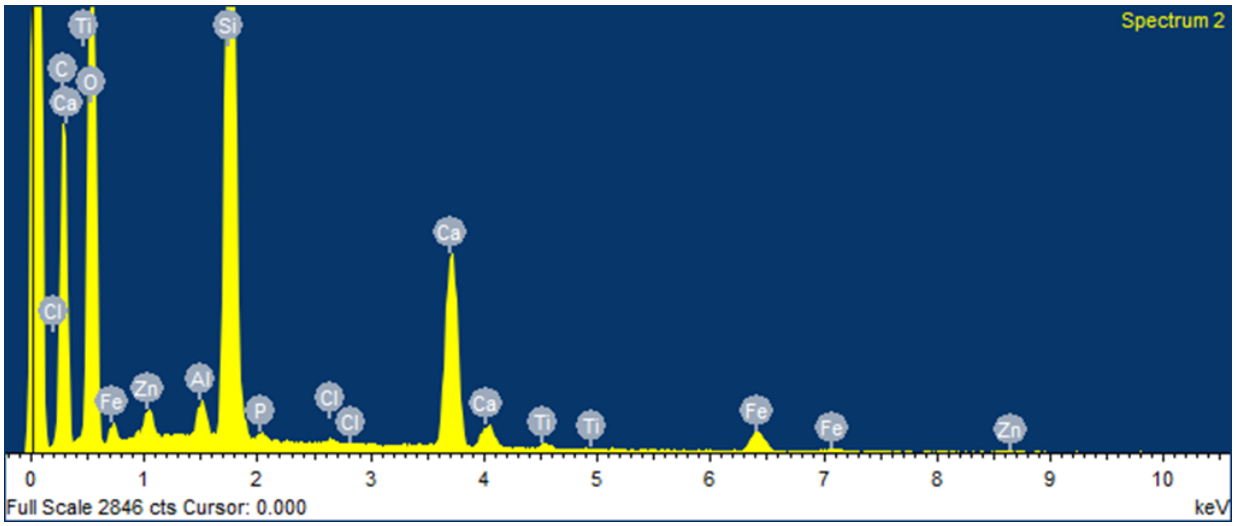
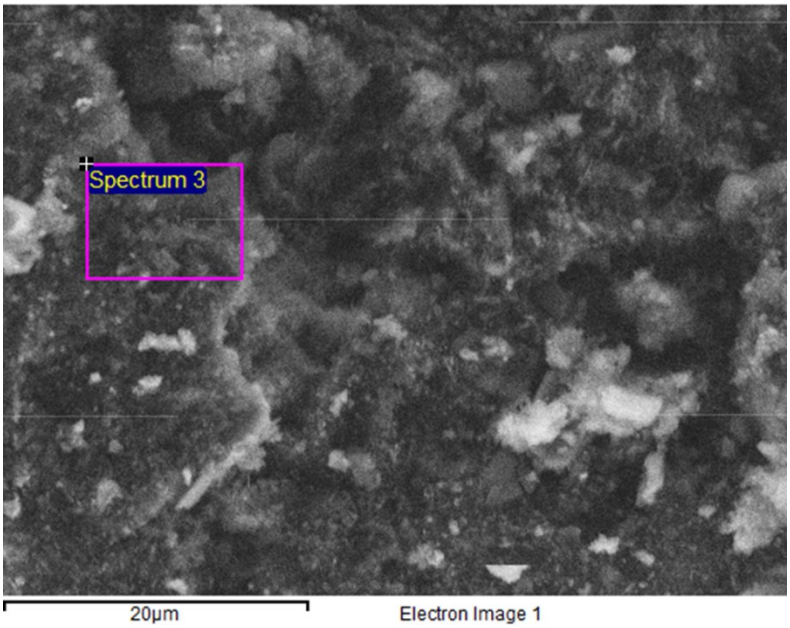


Figure A.123. SEM Image and EDS Spectrum of the Paint Collected from Exterior Web of the Girder.

Element	Weight %	Atomic %
C K	55.10	65.19
O K	35.00	31.09
Al K	0.20	0.10
Si K	3.49	1.76
P K	0.32	0.15
Cl K	0.07	0.03
Ca K	2.23	0.79
Ti K	0.15	0.04
Fe K	2.67	0.68
Zn K	0.77	0.17
Totals	100.00	



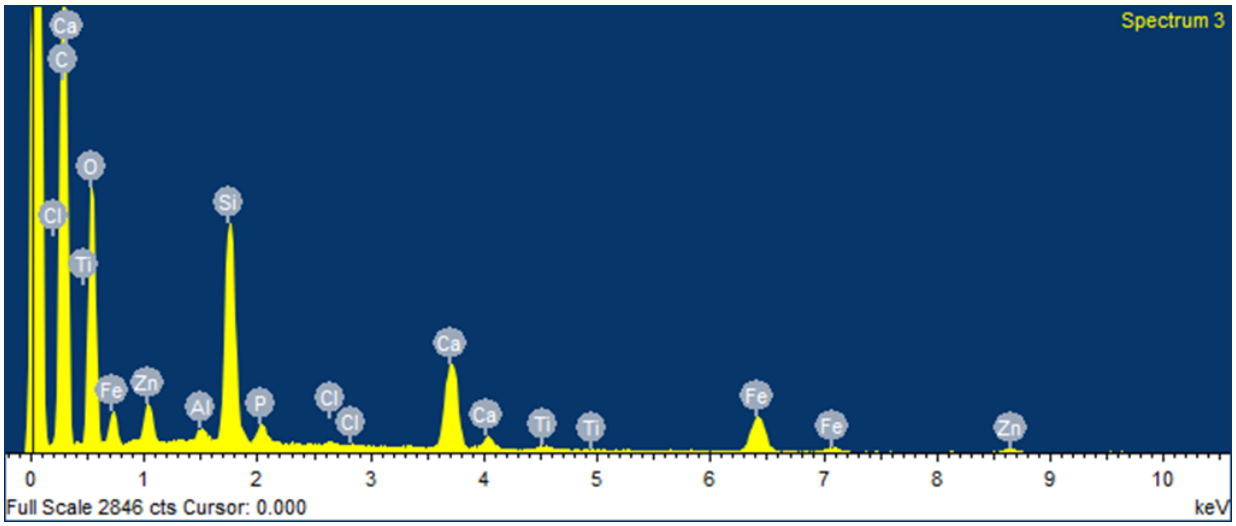
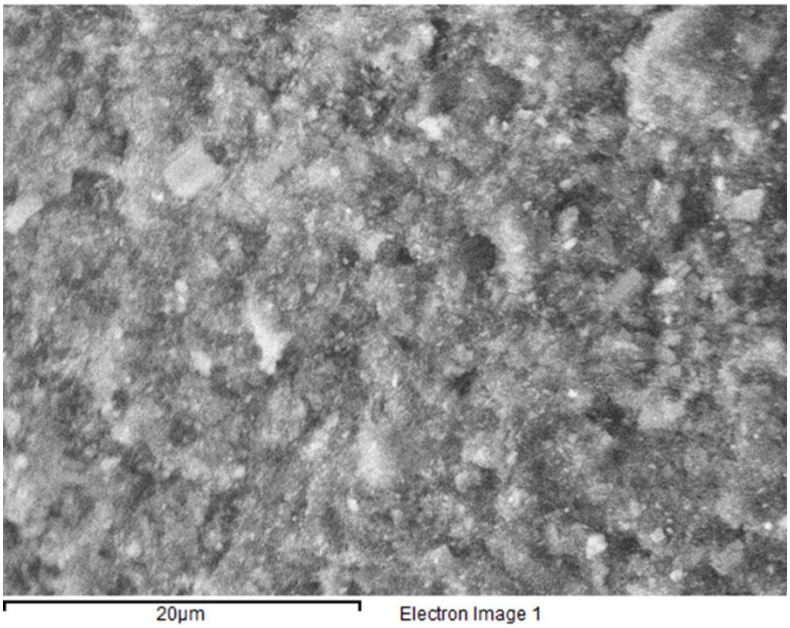


Figure A.124. SEM Image of Paint and EDS Spectrum of the Paint Collected from Exterior Web of the Girder.

Element	Weight %	Atomic %
C K	49.25	59.68
O K	39.43	35.87
Al K	0.42	0.22
Si K	4.45	2.30
P K	0.50	0.24
Cl K	0.30	0.12
Ca K	1.28	0.46
Ti K	0.12	0.04
Fe K	3.02	0.79
Cu K	0.33	0.08
Zn K	0.90	0.20
Totals	100.00	



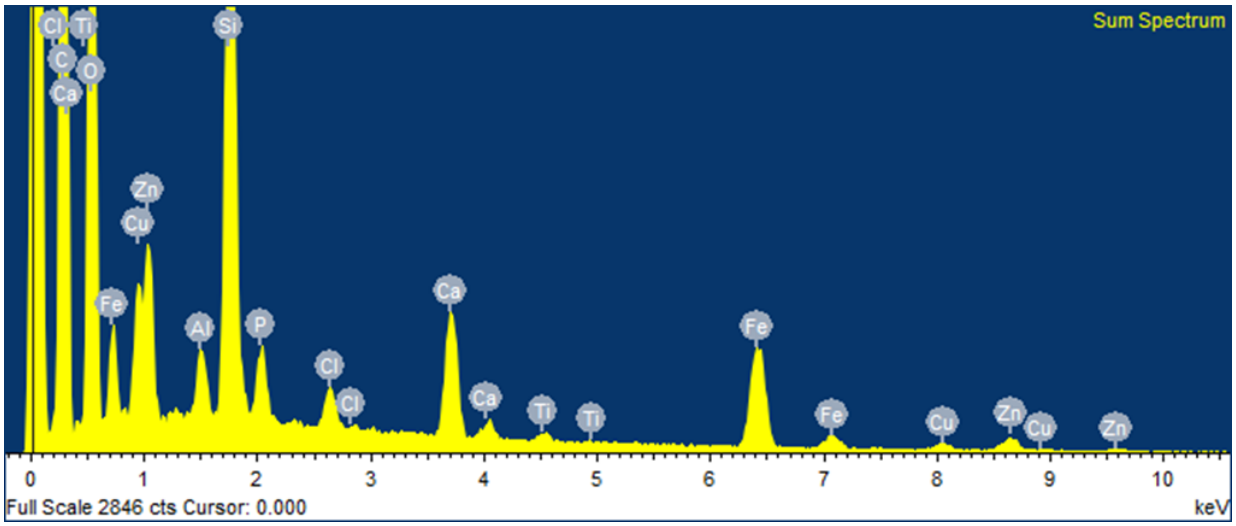


Figure A.125. SEM Image and EDS Spectrum of the Paint Collected from Interior Web of the Girder.

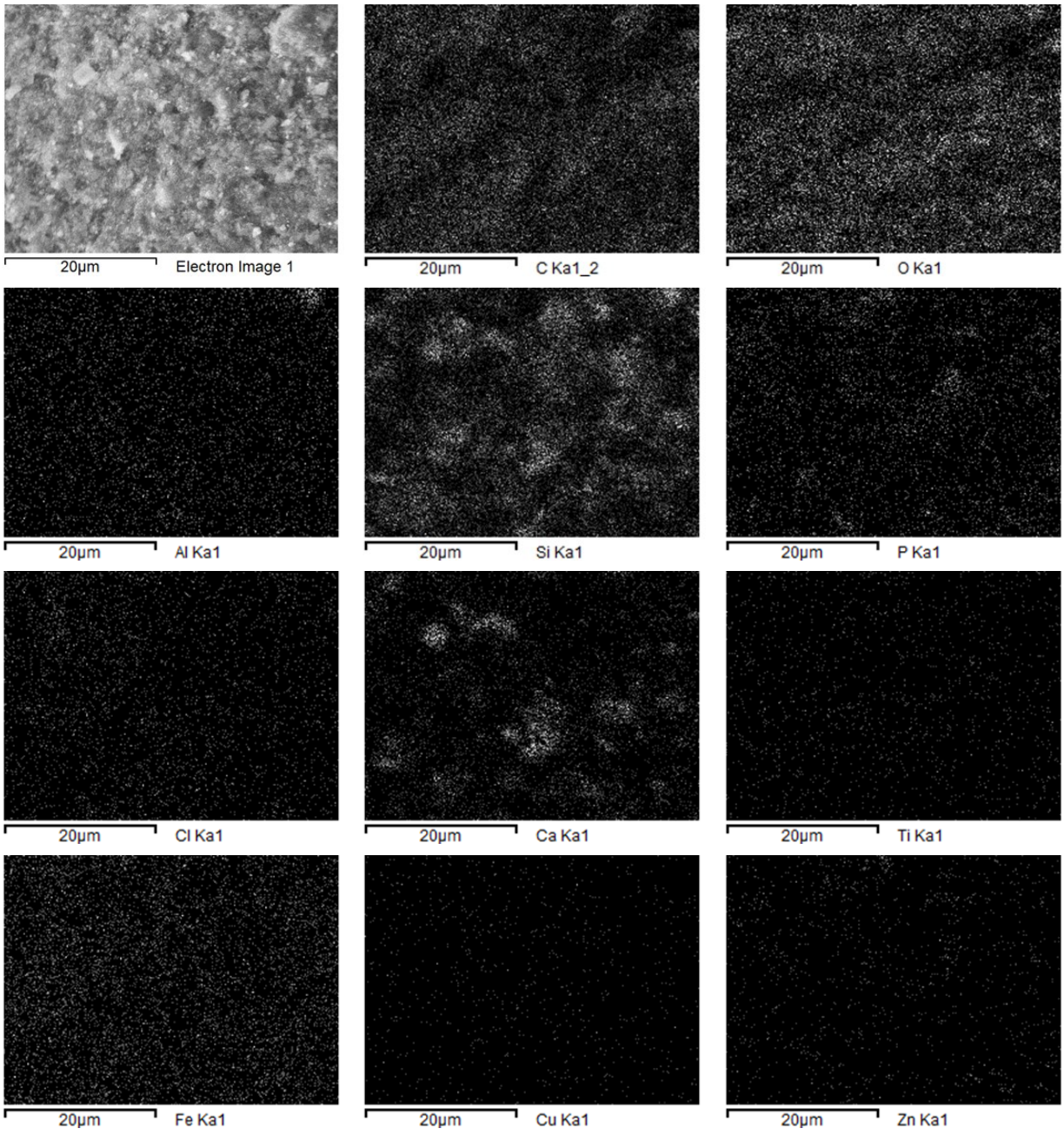


Figure A.126. EDS Elemental Mapping of Paint Collected from Interior Web.

A.12. WFS-RC-02

- IH 44 IH 44 SB
- Bridge ID 32430004309202, Coordinates (33.9137, -98.50605), Wichita County
- Steel Continuous I beam with System I type paint
- Built 2001
- Date of Inspection: June 3, 2021; girder inspection carried near abutment ends on girders within approximately four feet from the abutment
- Revisited for pH test and scrape test
- No visual inspection on deck
- Location for Testing: G9, G6, G3, G1



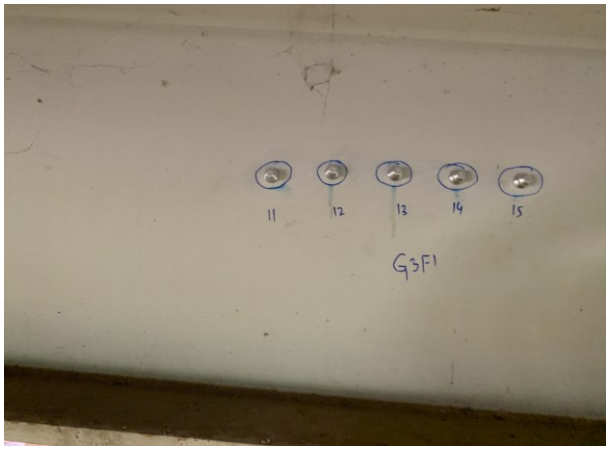
Figure A.127. Typical Elevation of WFS-RC-02.

A.12.1. Observed Condition

The paint condition of the bridge good condition with minor spot rusting observed on bearing plate and top face of bottom flange near abutment. Rusting and widespread paint deterioration is observed on two interior girders. Blistering, Erosion of paint, cracking in paint is not present. No checking and cracking of paint are observed. Joints are also in good condition.



(a) Staining observed on Bearing



(b) Interior Girder in Good Condition



(c) Interior Girder Connection is in Good Condition



(d) Paint Deterioration and Rusting Observed Interior Girders



(e) Crack Observed on Abutment Wall



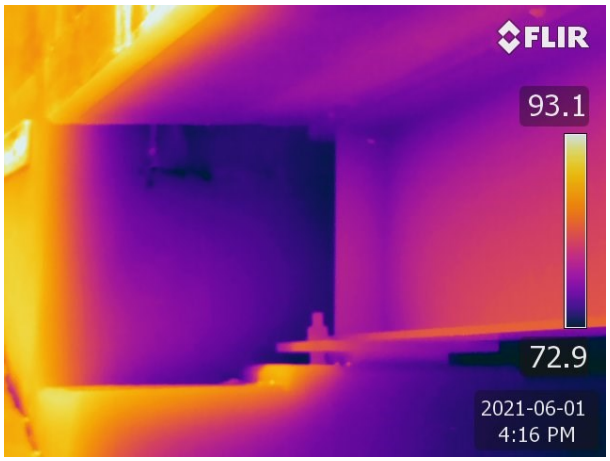
(f) Exterior Girder in Good Condition

Figure A.128. Paint Condition on the Girder of WFS-RC-02.

A.12.2.NDT Results



(a) Digital Image of Exterior Face of Girder Near Abutment Ends



(b) Thermal Image of Exterior Face of Girder Near Abutment Ends



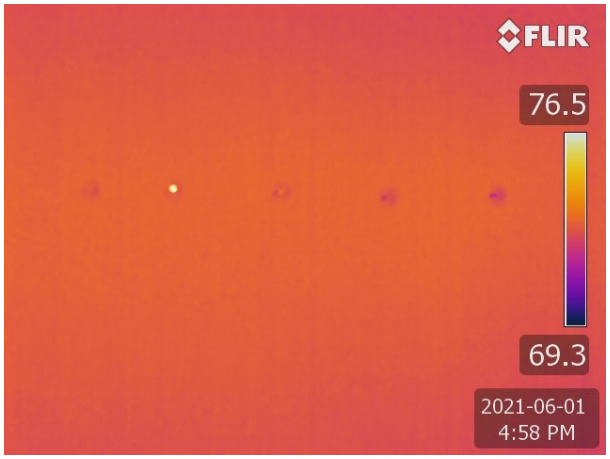
(c) Digital Image of Paint Deterioration and Rusting of Girder and Bearing



(d) Thermal Image of Paint Deterioration and Rusting of Girder and Bearing



(e) Digital image of the Interior Girder



(f) Thermal image of the Exterior Girder

Figure A.129. Digital and Thermal Image of Painted Girder on WFS-RC-02.

Table A-58. Field Inspection Results for WFS-RC-02.

Location	Cl^- Conc. (ppm)	pH Test	Thickness (µm)	Thickness (inch)	Visual Inspection
G9 TF Bot. Ext.	-	-	Measured R1 209 R2 234 R3 240 Design Paint 165-431	Measured R1 0.826 R2 0.832 R3 0.828 R_Avg 0.829 Design	Rust Grade – 10 Blistering – Not Found Discoloration – Not Found Flaking – Not Found Delamination – Not Found
G9 Web. Ext.	-		Measured R1 181 R2 195 R3 198 Design Paint 165-431	Measured R1 0.532 R2 0.534 R3 0.534 R_Avg 0.533 Design	Rust Grade – 10 Blistering – Not Found Discoloration – Not Found Flaking – Not Found Delamination – Not Found
G9 BF Top. Ext.	-	-	Measured R1 159 R2 141 R3 139 Design Paint 165-431	Measured R1 0.816 R2 0.814 R3 0.815 R_Avg 0.815 Design	Rust Grade – 10 Blistering – Not Found Discoloration – observed on the top of Bottom Flange Flaking – Not Found Delamination – Not Found
G9 BF Bot. Ext.	-	-	Measured R1 260 R2 276 R3 280 Design Paint 165-431	Measured R1 - R2 - R3 - R_Avg - Design	Rust Grade – 10 Blistering – Not Found Discoloration – Not Found Flaking – Not Found Delamination – Not Found
G6 TF Bot. Int.	-		Measured R1 163 R2 145 R3 143 Design Paint 165-431	Measured R1 0.828 R2 0.827 R3 0.831 R_Avg 0.829 Design	Rust Grade – 10 Blistering – Not Found Discoloration – Not Found Flaking – Not Found Delamination – Not Found
G6 Web. Int.	-	-	Measured R1 152 R2 186 R3 158 Design Paint 165-431	Measured R1 0.533 R2 0.536 R3 0.538 R_Avg 0.536 Design	Rust Grade – 10 Blistering – Not Found Discoloration – Not Found Flaking – Not Found Delamination – Found

Table A-59. Field Inspection Results for WFS-RC-02.

Location	Cl^- Conc. (ppm)	pH Test	Thickness (µm)	Thickness (inch)	Visual Inspection
G6 BF Top. Int.	-	-	Measured R1 185 R2 191 R3 201 Design Paint 165-431	Measured R1 0.814 R2 0.811 R3 0.810 R_Avg 0.812 Design	Rust Grade – 10 Blistering – Not Found Discoloration – Not Found Flaking – Not Found Delamination – Not Found
G6 BF Bot. Int.	-	-	Measured R1 186 R2 196 R3 185 Design Paint 165-431	Measured R1 - R2 - R3 - R_Avg - Design	Rust Grade – 10 Blistering – Not Found Discoloration – Not Found Flaking – Not Found Delamination – Not Found
G3 TF Bot. Int.	-	-	Measured R1 133 R2 130 R3 156 Design Paint 165-431	Measured R1 0.829 R2 0.831 R3 0.826 R_Avg 0.829 Design	Rust Grade – 10 Blistering – Not Found Discoloration – Not Found Flaking – Not Found Delamination – Found
G3 Web. Int.	1		Measured R1 183 R2 157 R3 158 Design Paint 165-431	Measured R1 0.532 R2 0.536 R3 0.535 R_Avg 0.534 Design	Rust Grade – 10 Blistering – Not Found Discoloration – Not Found Flaking – Not Found Delamination – Not Found
G3 BF Top. Int.	-		Measured R1 218 R2 217 R3 200 Design Paint 165-431	Measured R1 0.807 R2 0.812 R3 0.808 R_Avg 0.809 Design	Rust Grade – 10 Blistering – Not Found Discoloration – observed on the top of Bottom Flange Flaking – Not Found Delamination – Not Found
G3 BF Bot. Int.	-		Measured R1 175 R2 187 R3 163 Design Paint 165-431	Measured R1 - R2 - R3 - R_Avg - Design	Rust Grade – 10 Blistering – Not Found Discoloration – Not Found Flaking – Not Found Delamination – Not Found

Table A-60. Field Inspection Results for WFS-RC-02.

Location	Cl^- Conc. (ppm)	pH Test	Thickness (µm)	Thickness (inch)	Visual Inspection
G1 TF Bot. Ext.	-	-	Measured R1 196 R2 187 R3 170 Design Paint 165-431	Measured R1 0.826 R2 0.829 R3 0.835 R_Avg 0.830 Design	Rust Grade – 10 Blistering – Not Found Discoloration – Not Found Flaking – Not Found Delamination – Not Found
G1 Web. Ext.	-		Measured R1 170 R2 145 R3 162 Design Paint 165-431	Measured R1 0.537 R2 0.542 R3 0.542 R_Avg 0.540 Design	Rust Grade – 10 Blistering – Not Found Discoloration – Not Found Flaking – Not Found Delamination – Not Found
G1 BF Top. Ext.	-		Measured R1 203 R2 225 R3 213 Design Paint 165-431	Measured R1 0.820 R2 0.824 R3 0.828 R_Avg 0.824 Design	Rust Grade – 10 Blistering – Not Found Discoloration – observed on the top face of Bottom Flange Flaking – Not Found Delamination – Not Found
G1 BF Bot. Ext.	-		Measured R1 170 R2 186 R3 161 Design Paint 165-431	Measured R1 - R2 - R3 - R_Avg - Design	Rust Grade – 10 Blistering – Not Found Discoloration – Not Found Flaking – Not Found Delamination – Not Found

A.12.3. Pull-off Adhesion Results

Table A-61. Pull-off Adhesion Results for WFS-RC-02.

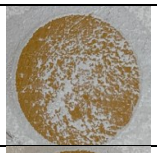
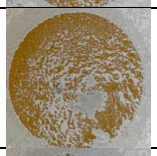
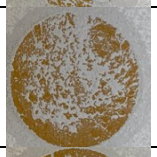
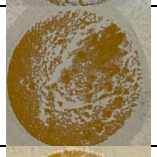
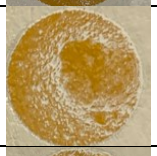
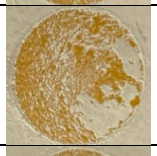
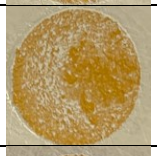
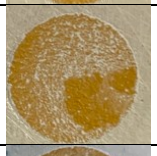
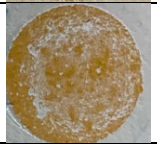
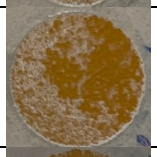
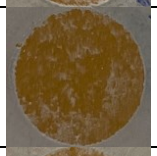
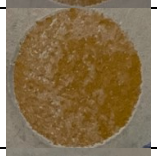
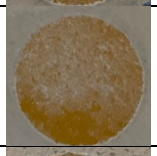
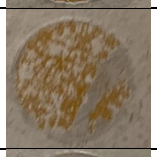
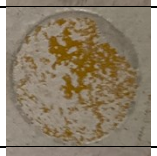
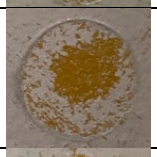
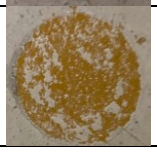
Location	Dolly Face	Substrate Face	Test Result (psi)	Attributes	Failure Type
A1-G9F2			2506	60% C 40% B/C	60% Cohesive Failure 40% Adhesive Failure
			2263	40% C 60% B/C	40% Cohesive Failure 40% Adhesive Failure
			2466	60% C 40% B/C	60% Cohesive Failure 40% Adhesive Failure
			2102	40% C 60% B/C	40% Cohesive Failure 60% Adhesive Failure
			2284	30% C 70% B/C	30% Cohesive Failure 70% Adhesive Failure
A1-G6F2			1485	20% C 80% B/C	20% Cohesive Failure 80% Adhesive Failure
			1471	40% C 60% B/C	40% Cohesive Failure 60% Adhesive Failure
			1544	20% C 80% B/C	20% Cohesive Failure 80% Adhesive Failure
			1346	70% C 30% B/C	70% Cohesive Failure 30% Adhesive Failure
			1717	100% C 30% B/C	100% Cohesive Failure

Table A-62. Pull-off Adhesion Results for WFS-RC-02.

Location	Dolly Face	Substrate Face	Test Result (psi)	Attributes	Failure Type
A1-G3F1			681	70% C 30% B/C	70% Cohesive Failure 30% Adhesive Failure
			1095	50% C 50% B/C	50% Cohesive Failure 50% Adhesive Failure
			1256	80% C 20% B/C	80% Cohesive Failure 20% Adhesive Failure
			1146	60% C 40% B/C	60% Cohesive Failure 40% Adhesive Failure
			941	80% C 20% B/C	80% Cohesive Failure 20% Adhesive Failure
A1-G1F1			906	40% C/Y 60% C	40% Glue Failure 60% Cohesive Failure
			1688	50% C 50% B/C	50% Cohesive Failure 50% Adhesive Failure
			1819	70% C 30% B/C	70% Cohesive Failure 30% Adhesive Failure
			1922	70% C 30% B/C	70% Cohesive Failure 30% Adhesive Failure
			1779	30% C 70% B/C	30% Cohesive Failure 70% Adhesive Failure

A.12.4. Optical Microscopy Results

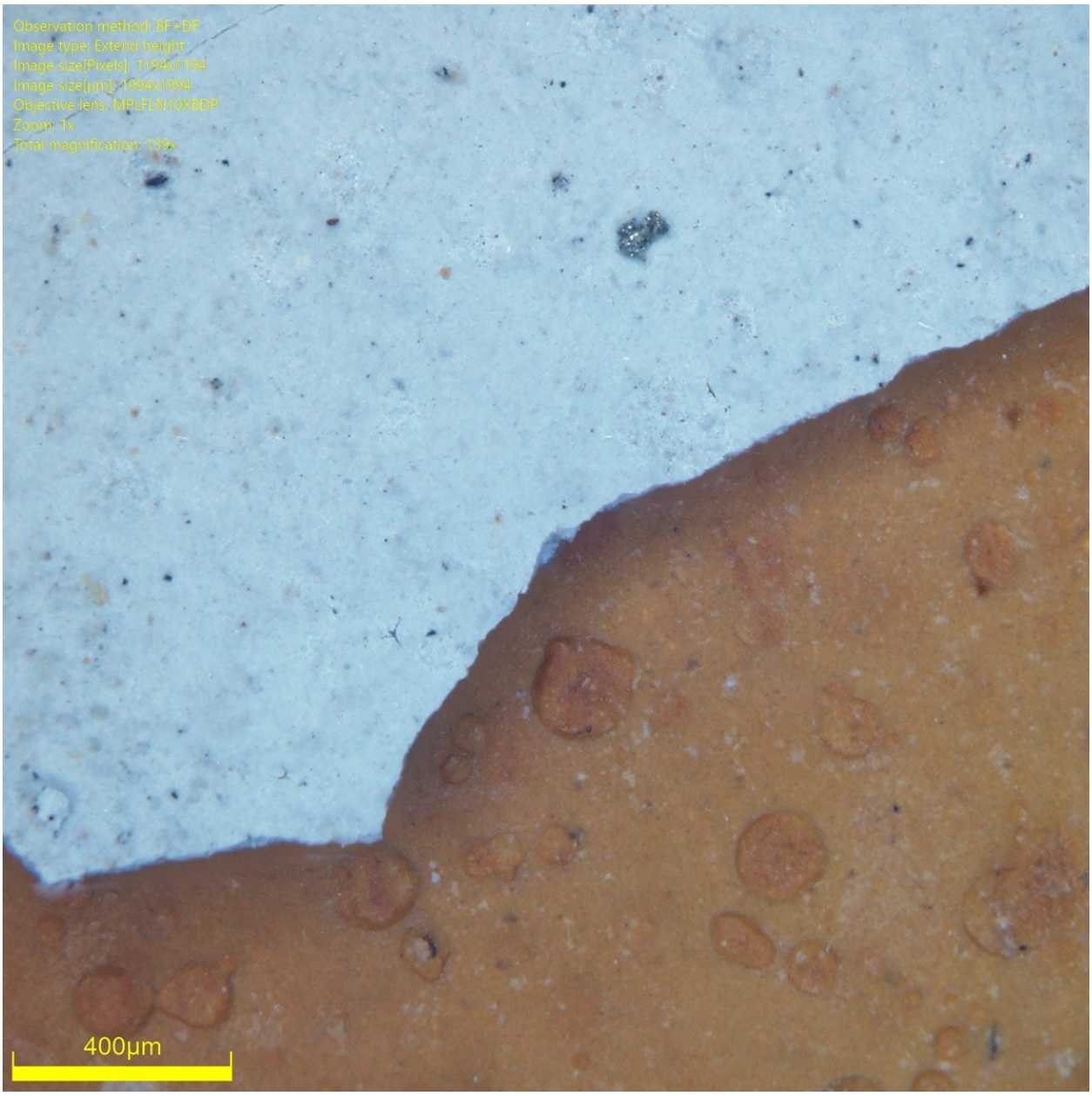


Figure A.130. Two Layer Paint System Examined by Optical Microscope WFS–RC–02.

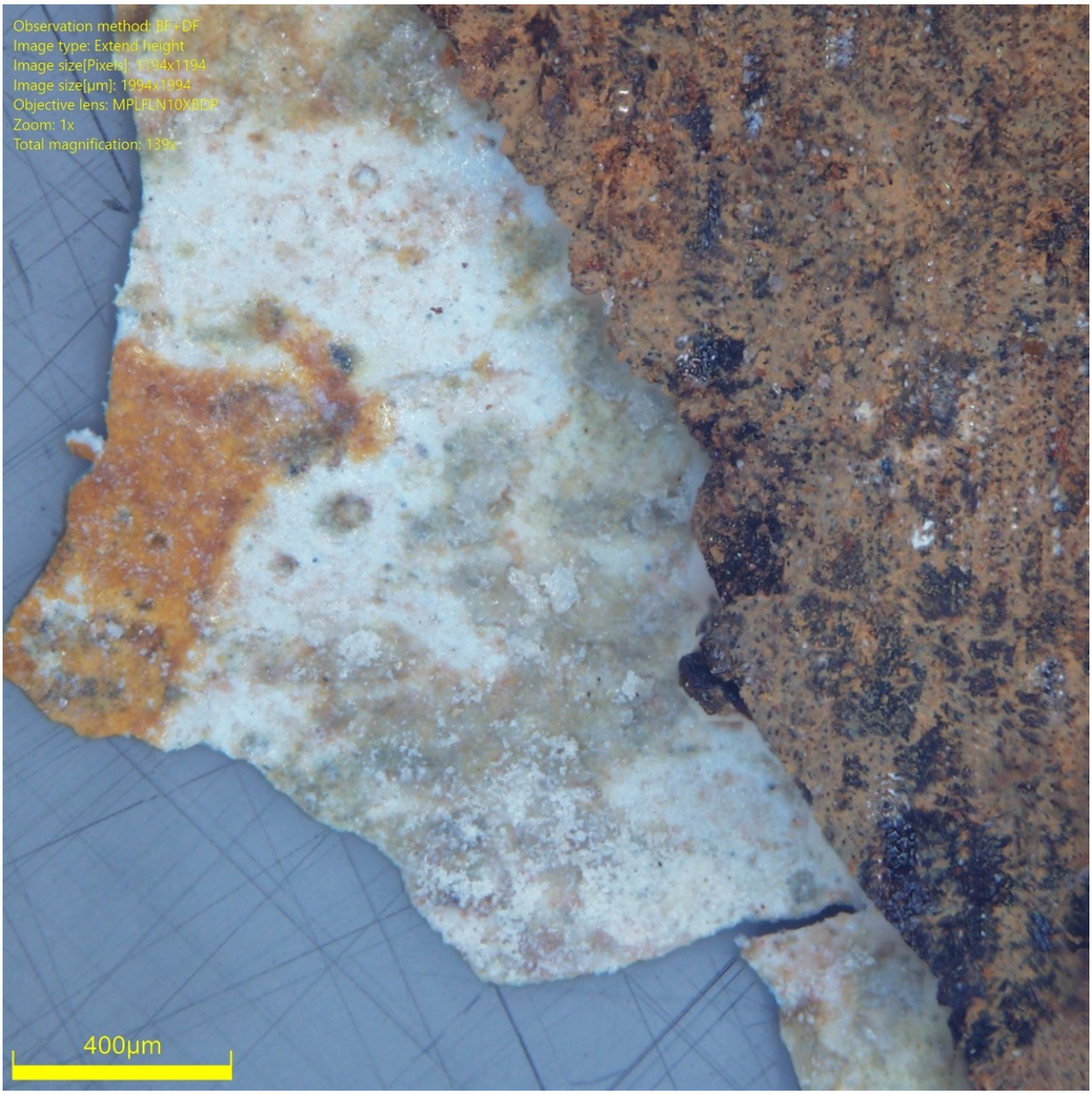
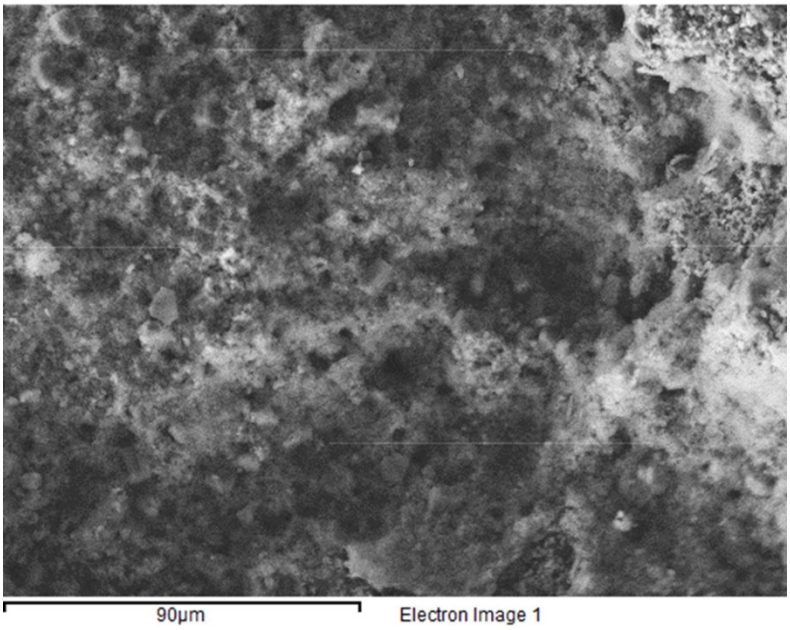


Figure A.131. Widespread Corrosion Observed under Paint.

A.12.5.SEM/EDS Results

Element	Weight %	Atomic %
C K	16.35	28.13
O K	41.70	53.87
Na K	2.00	1.80
Mg K	0.16	0.13
Al K	0.73	0.56
Si K	1.22	0.90
S K	0.16	0.10
Cl K	1.70	0.99
K K	0.24	0.13
Ca K	1.80	0.93
Mn K	0.95	0.36
Fe K	31.19	11.54
Zn K	1.81	0.57
Totals	100.00	



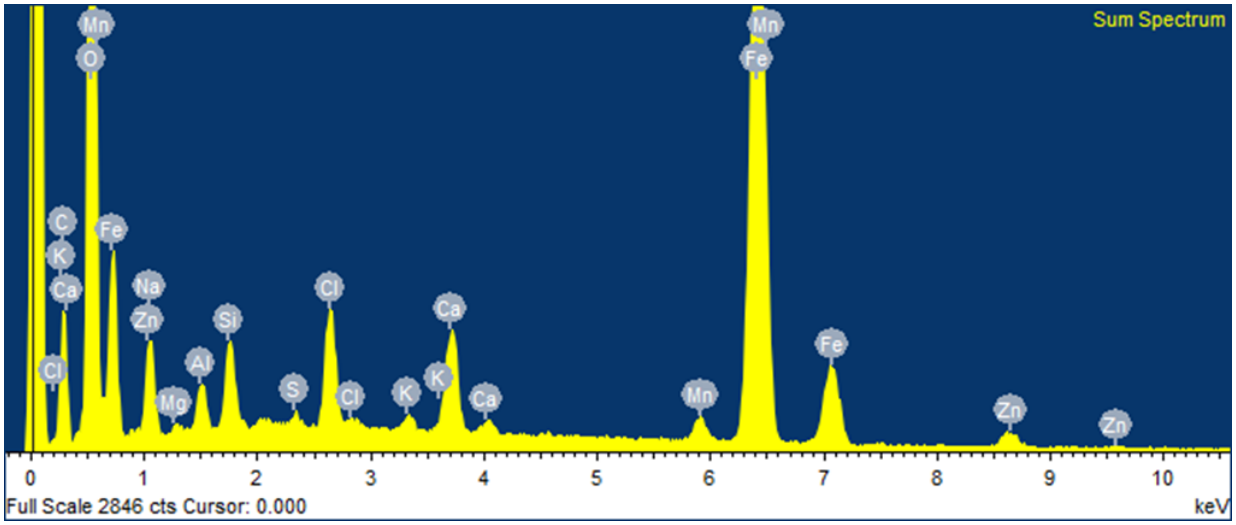


Figure A.132. SEM Image and EDS Spectrum of the Paint Collected from Exterior Web of the Girder.

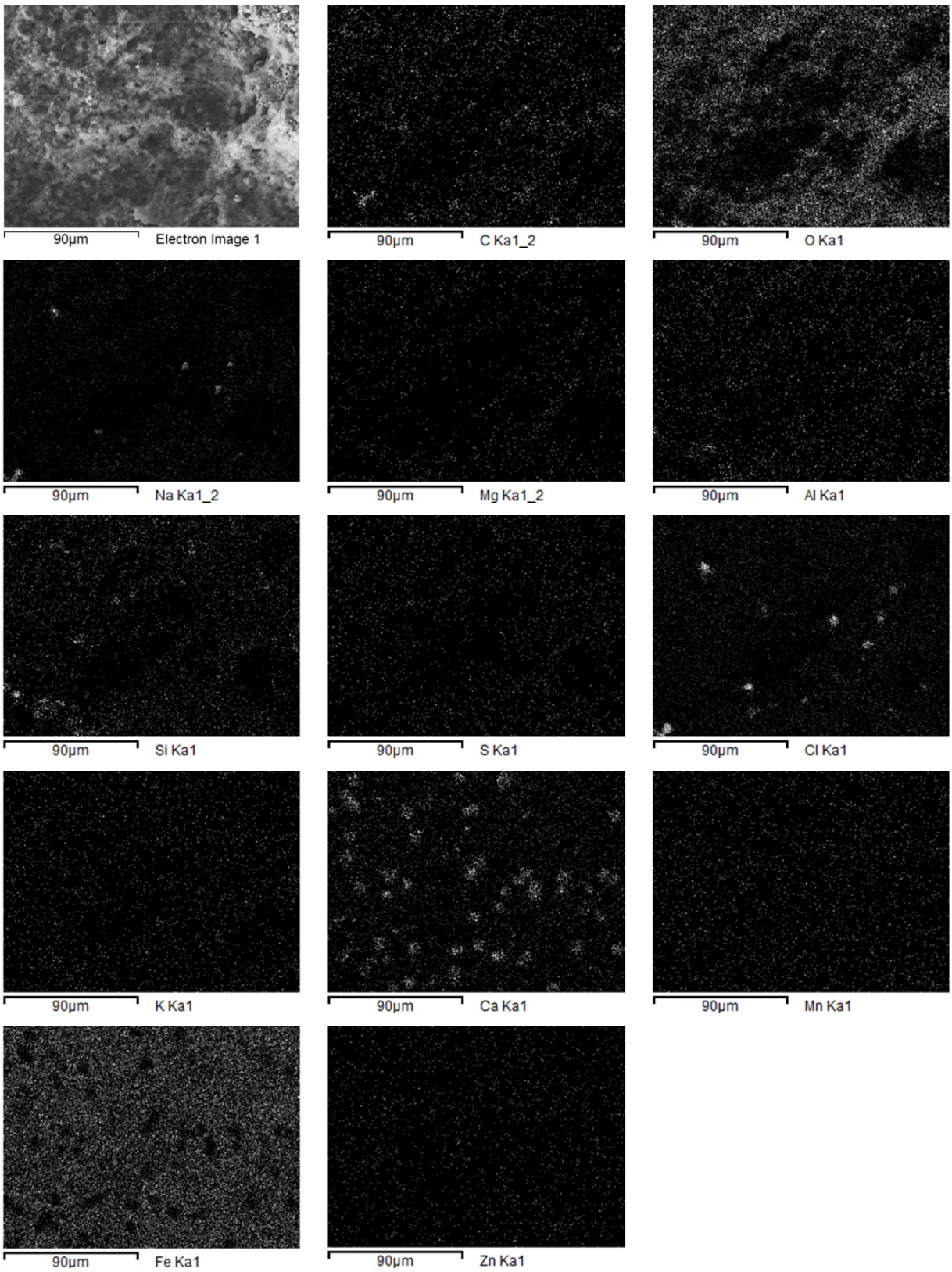
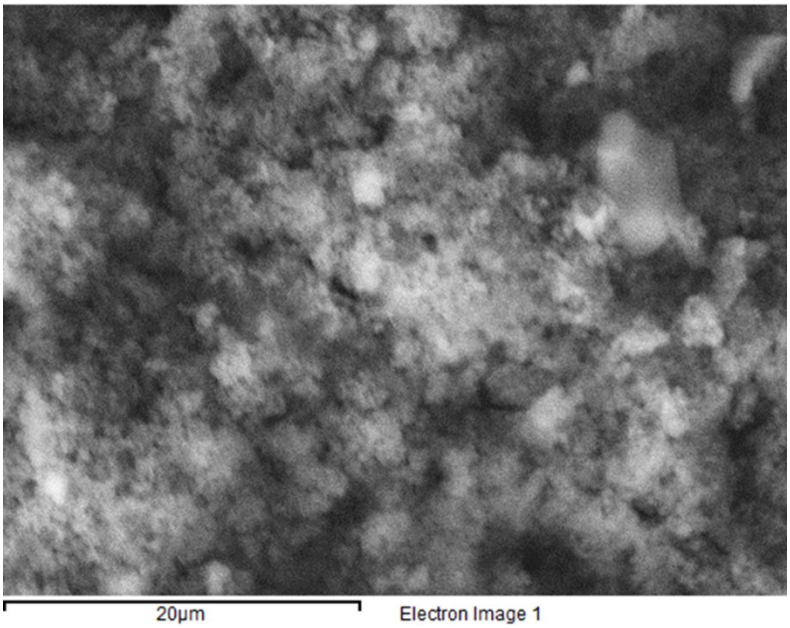


Figure A.133. EDS Elemental Mapping of Paint Collected from Exterior Web.

Element	Weight %	Atomic %
C K	16.06	27.23
O K	42.83	54.54
Na K	3.45	3.06
Al K	0.60	0.45
Si K	1.13	0.82
P K	0.12	0.08
S K	0.17	0.11
Cl K	2.56	1.47
K K	0.24	0.12
Ca K	1.60	0.81
Mn K	0.99	0.37
Fe K	28.26	10.31
Zn K	1.99	0.62
Totals	100.00	



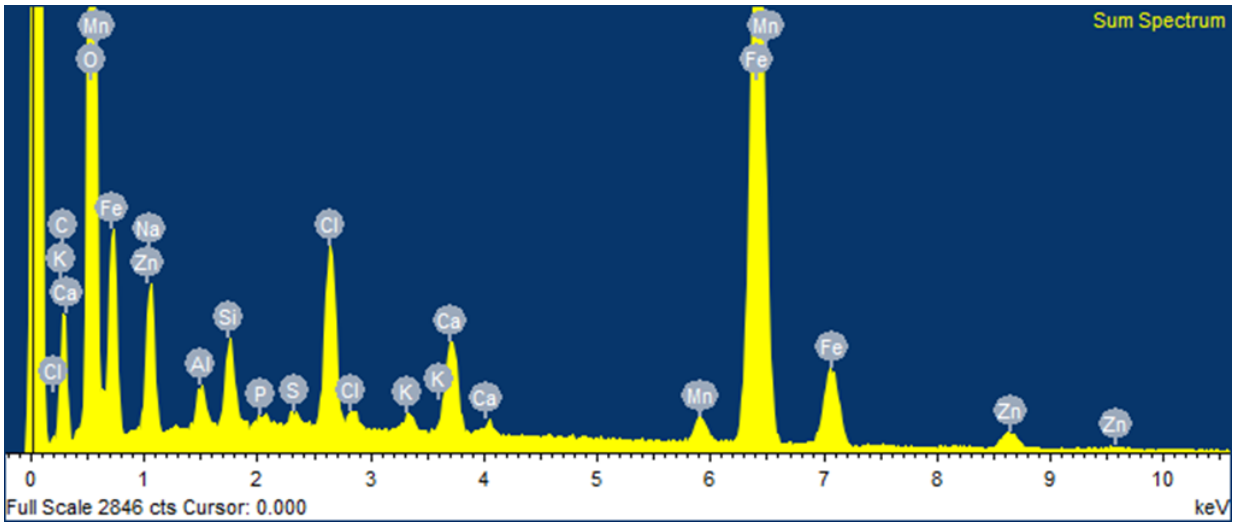


Figure A.134. SEM Image and EDS Spectrum of the Paint Collected from Exterior Web of the Girder.

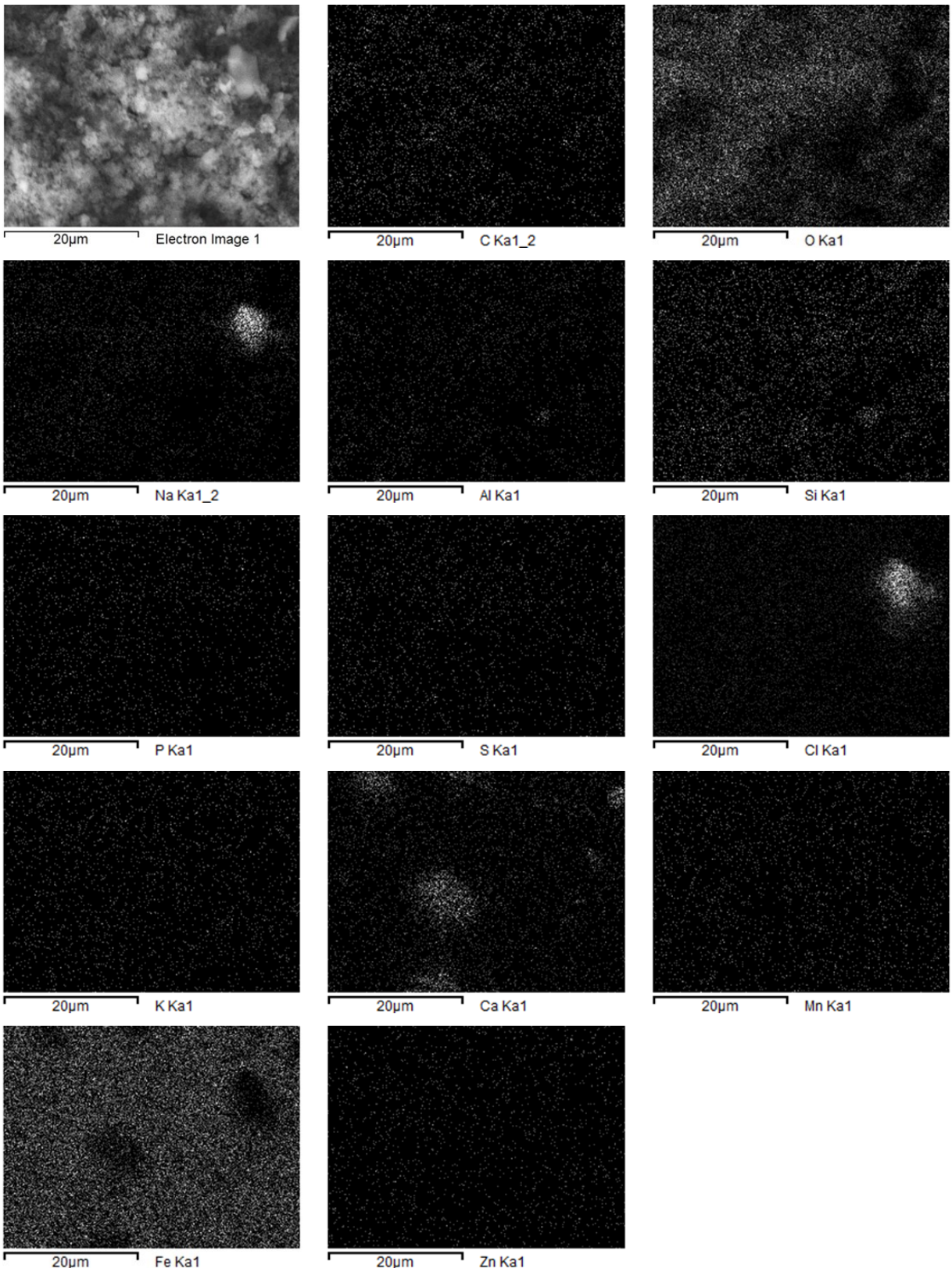


Figure A.135. EDS Elemental Mapping of Paint Collected from Exterior Web.

A.13. DAL-PS-01

- Ramp L (to US 67 NB) over US 287 BUS
- Bridge ID 180710026101225, Coordinates (32.48177, -97.00948), Ellis County
- Steel Continuous I beam with System I type paint
- Built 2007
- Date of Inspection: December 8, 2021; girder inspection carried near abutment ends on girders within approximately four feet from the abutment
- Revisited for pH test and scrape test
- No visual inspection on deck
- Location for Testing: A4-G5, A4-G3, A4-G2, A4-G1



Figure A.136. Typical Elevation of DAL-PS-01

A.13.1. Observed Condition

The paint condition of this bridge is in very good condition. The appearance coat is also in good condition. Blistering, Erosion of paint, cracking in paint is not present. A slight discoloration is observed on edge of the bottom flange. Dirt is accumulated on the top face of the bottom flange. No checking and cracking of paint are observed. Joints are also in good condition.



(a) Staining observed on Bearing



(b) Interior Girder in Good Condition



(c) Interior Girder Connection is in Good Condition



(d) Connection in Good Condition



(e) Dirt Accumulated on Bottom Flange of Interior Girder



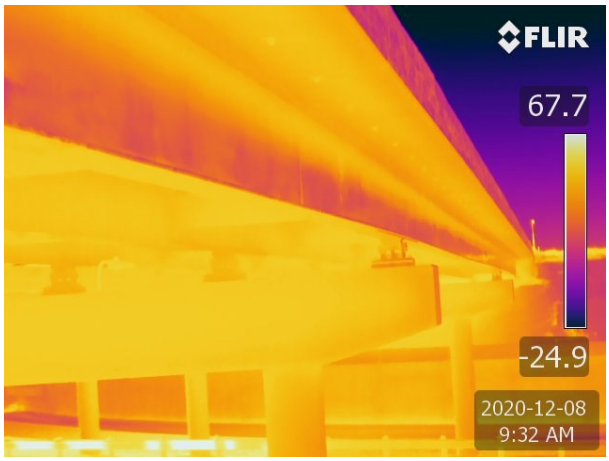
(f) Exterior Girder in Good Condition

Figure A.137. Paint Condition on the Girder of DAL-PS-01.

A.13.2.NDT Results



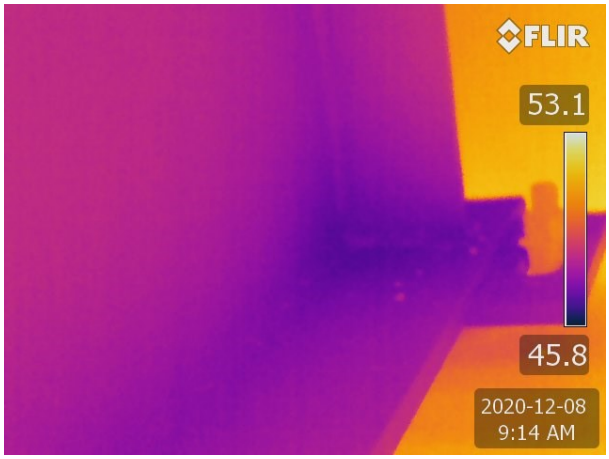
(a) Digital Image of Exterior Face of Girder



(b) Thermal Image of Exterior Face of Girder



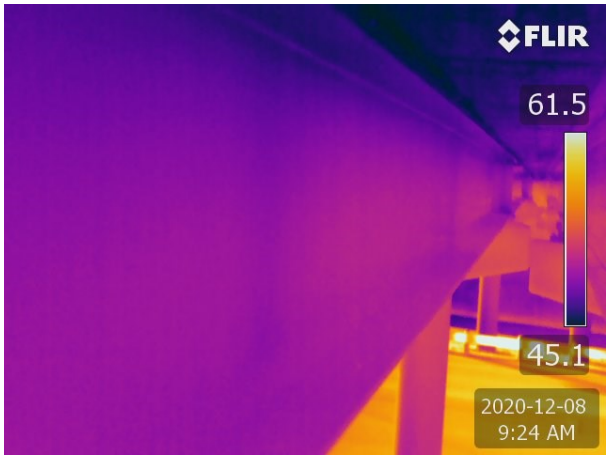
(c) Digital Image of Bearing



(d) Thermal Image of Bearing



(e) Digital image of the Interior Girder



(f) Thermal image of the Exterior Girder

Figure A.138. Digital and Thermal Image of Painted Girder on DAL-PS-01.

Table A-63. Field Inspection Results for DAL-PS-01.

Location	Cl^- Conc. (ppm)	pH Test	Thickness (µm)	Thickness (inch)	Visual Inspection
A4-G4F2 TF Bot. Ext.	-	-	Measured R1 194 R2 196 R3 209 Design Paint 165-431	Measured R1 1.096 R2 1.095 R3 1.096 R_Avg 1.096 Design	Rust Grade – 10 Blistering – Not Found Discoloration – Not Found Flaking – Not Found Delamination – Not Found
A4-G4F2 Web. Ext.	2		Measured R1 195 R2 215 R3 214 Design Paint 165-431	Measured R1 0.727 R2 0.726 R3 0.726 R_Avg 0.726 Design	Rust Grade – 10 Blistering – Not Found Discoloration – Not Found Flaking – Not Found Delamination – Not Found
A4-G4F2 BF Top. Ext.	-	-	Measured R1 228 R2 228 R3 221 Design Paint 165-431	Measured R1 1.268 R2 1.264 R3 1.264 R_Avg 1.265 Design	Rust Grade – 10 Blistering – Not Found Discoloration – observed on the top face of Bottom Flange Flaking – Not Found Delamination – Not Found
A4-G4F2 BF Bot. Ext.	-	-	Measured R1 2314 R2 240 R3 239 Design Paint 165-431	Measured R1 - R2 - R3 - R_Avg - Design	Rust Grade – 10 Blistering – Not Found Discoloration – Not Found Flaking – Not Found Delamination – Not Found
A4-G3F2 TF Bot. Int.	-		Measured R1 215 R2 200 R3 211 Design Paint 165-431	Measured R1 1.122 R2 1.122 R3 1.118 R_Avg 1.121 Design	Rust Grade – 10 Blistering – Not Found Discoloration – Not Found Flaking – Not Found Delamination – Not Found
A4-G3F2 Web. Int.	-0	-	Measured R1 270 R2 218 R3 282 Design Paint 165-431	Measured R1 0.726 R2 0.727 R3 0.726 R_Avg 0.726 Design	Rust Grade – 10 Blistering – Not Found Discoloration – Not Found Flaking – Not Found Delamination – Found

Table A-64. Field Inspection Results for DAL-PS-01.

Location	Cl^- Conc. (ppm)	pH Test	Thickness (µm)	Thickness (inch)	Visual Inspection
A4-G3F2 BF Top. Int.	-	-	Measured R1 258 R2 264 R3 264 Design Paint 165-431	Measured R1 1.050 R2 1.055 R3 1.051 R_Avg 1.052 Design	Rust Grade – 10 Blistering – Not Found Discoloration – Not Found Flaking – Not Found Delamination – Not Found
A4-G3F2 BF Bot. Int.	-	-	Measured R1 145 R2 162 R3 188 Design Paint 165-431	Measured R1 - R2 - R3 - R_Avg - Design	Rust Grade – 10 Blistering – Not Found Discoloration – Not Found Flaking – Not Found Delamination – Not Found
A4-G2F1 TF Bot. Int.	-	-	Measured R1 259 R2 274 R3 237 Design Paint 165-431	Measured R1 1.082 R2 1.083 R3 1.080 R_Avg 1.082 Design	Rust Grade – 10 Blistering – Not Found Discoloration – Not Found Flaking – Not Found Delamination – Found
A4-G2F1 Web. Int.	-		Measured R1 211 R2 211 R3 242 Design Paint 165-431	Measured R1 0.731 R2 0.732 R3 0.731 R_Avg 0.731 Design	Rust Grade – 10 Blistering – Not Found Discoloration – Not Found Flaking – Not Found Delamination – Not Found
A4-G2F1 BF Top. Int.	-		Measured R1 265 R2 271 R3 249 Design Paint 165-431	Measured R1 1.272 R2 1.271 R3 1.278 R_Avg 1.274 Design	Rust Grade – 10 Blistering – Not Found Discoloration – Not Found Flaking – Not Found Delamination – Not Found
A4-G2F1 BF Bot. Int.	-		Measured R1 254 R2 208 R3 238 Design Paint 165-431	Measured R1 - R2 - R3 - R_Avg - Design	Rust Grade – 10 Blistering – Not Found Discoloration – Not Found Flaking – Not Found Delamination – Found

Table A-65. Field Inspection Results for DAL-PS-01.

Location	Cl^- Conc. (ppm)	pH Test	Thickness (µm)	Thickness (inch)	Visual Inspection
A4-G1F1 Web. Ext.		-	Measured R1 185 R2 206 R3 177 Design Paint 165-431	Measured R1 1.122 R2 1.118 R3 1.118 R_Avg 1.119 Design	Rust Grade – 10 Blistering – Not Found Discoloration – Not Found Flaking – Not Found Delamination – Not Found
A4-G1F1 Web. Ext.	0	-	Measured R1 216 R2 205 R3 201 Design Paint 165-431	Measured R1 0.727 R2 0.727 R3 0.726 R_Avg 0.727 Design	Rust Grade – 10 Blistering – Not Found Discoloration – Not Found Flaking – Not Found Delamination – Not Found
A4-G1F1 BF Top. Ext.	-	-	Measured R1 262 R2 276 R3 271 Design Paint 165-431	Measured R1 1.052 R2 1.049 R3 1.051 R_Avg 1.051 Design	Rust Grade – 10 Blistering – Not Found Discoloration – observed on the top face of BF Flaking – Not Found Delamination – Not Found
A4-G1F1 BF Bot. Ext.	-		Measured R1 156 R2 181 R3 205 Design Paint 165-431	Measured R1 - R2 - R3 - R_Avg - Design	Rust Grade – 10 Blistering – Not Found Discoloration – Not Found Flaking – Not Found Delamination – Not Found

A.13.3. Pull-off Adhesion Results

Table A-66. Pull-off Adhesion Results for DAL-PS-01.

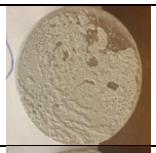
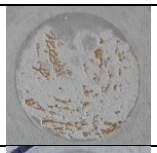
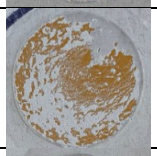
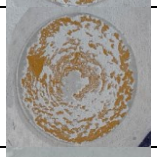
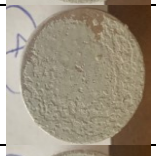
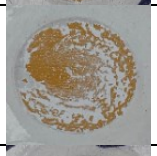
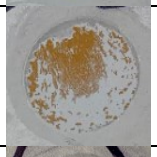
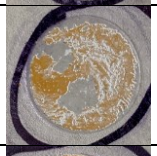
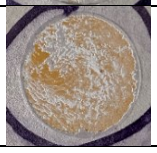
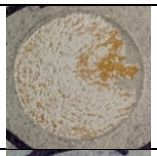
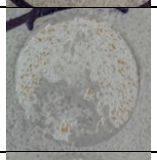
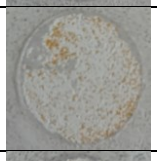
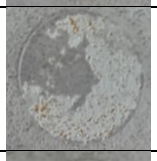
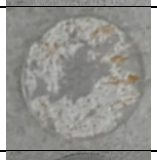
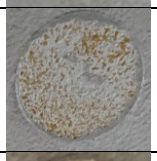
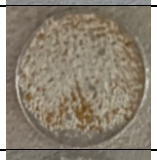
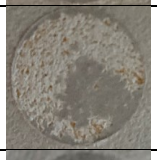
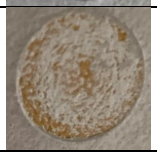
Location	Dolly Face	Substrate Face	Test Result (psi)	Attributes	Failure Type
A4-G4F2			1393	90% C 10% B/C	90% Cohesive Failure 10% Adhesive Failure
			1750	70% C 30% B/C	70% Cohesive Failure 30% Adhesive Failure
			1974	70% C 30% B/C	70% Cohesive Failure 30% Adhesive Failure
			1841	60% C 40% B/C	60% Cohesive Failure 40% Adhesive Failure
			1742	60% C 40% B/C	60% Cohesive Failure 40% Adhesive Failure
A4-G3F2			1083	30% C/Y 70% C	30% Glue Failure 70% Cohesive Failure
			1617	20% C/Y 20% C 60% B/C	20% Glue Failure 20% Cohesive Failure 60% Adhesive Failure
			1996	10% C/Y 10% C 80% B/C	10% Glue Failure 10% Cohesive Failure 80% Adhesive Failure
			985	50% C/Y 20% C 30% B/C	50% Glue Failure 20% Cohesive Failure 30% Adhesive Failure
			2055	80% C 20% B/C	80% Cohesive Failure 20% Adhesive Failure

Table A-67. Pull-off Adhesion Results for DAL-PS-01.

Location	Dolly Face	Substrate Face	Test Result (psi)	Attributes	Failure Type
A4-G2F1			1711	90% C 10% B/C	90% Cohesive Failure 10% Adhesive
			1185	30% C/Y 70% C	30% Glue Failure 70% Cohesive Failure
			2170	10% C/Y 90% C	10% Glue Failure 90% Cohesive Failure
			1218	30% C/Y 70% C	30% Glue Failure 70% Cohesive Failure
			1464	30% C/Y 70% C	30% Glue Failure 70% Cohesive Failure
A4-G1F1			2119	10% C/Y 70% C 20% B/C	10% Glue Failure 70% Cohesive Failure 20% Adhesive Failure
			1805	80% C 20% B/C	80% Cohesive Failure 20% Adhesive Failure
			1486	30% C/Y 70% C	30% Glue Failure 70% Cohesive Failure
			1292	20% C/Y 80% C	20% Glue Failure 80% Cohesive Failure
			2097	80% C 20% B/C	80% Cohesive Failure 20% Adhesive Failure

A.13.4. Optical Microscopy Results

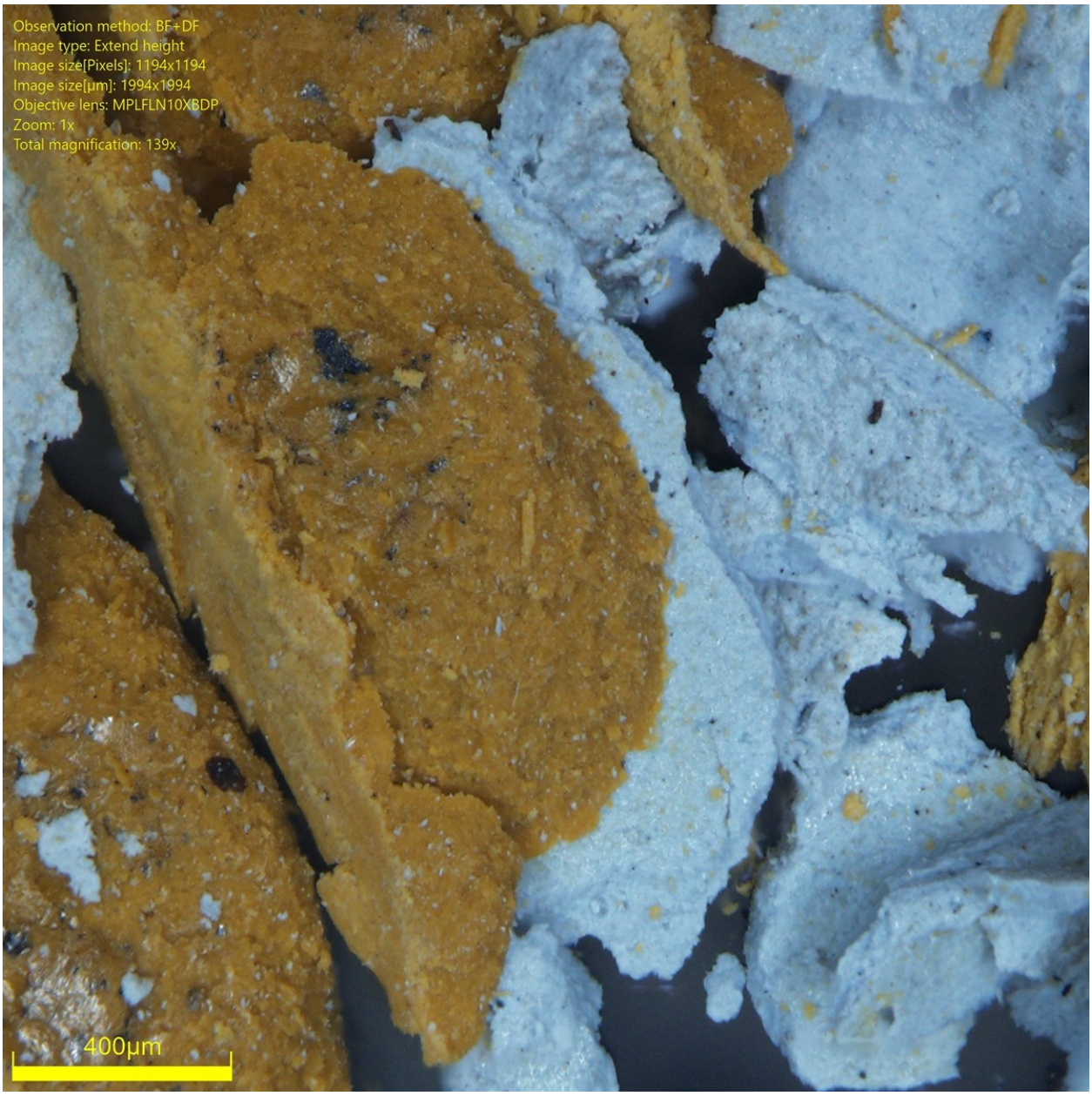
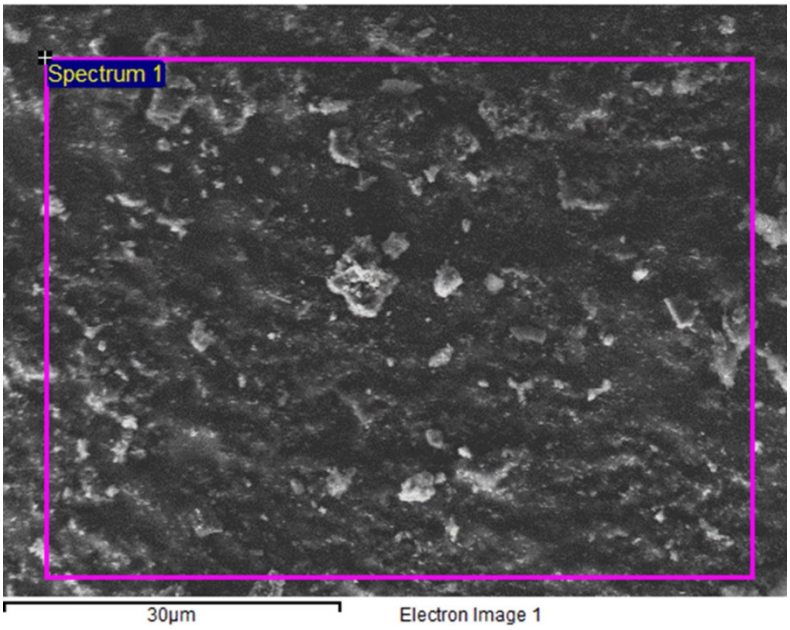


Figure A.139. Two Layer Paint System Examined by Optical Microscope DAL–PS–02.

A.13.5.SEM/EDS Results

Element	Weight %	Atomic %
C K	54.46	63.02
O K	39.84	34.60
Al K	0.49	0.25
Si K	1.96	0.97
Cl K	1.96	0.77
Ca K	0.28	0.10
Ti K	0.90	0.26
Zn K	0.10	0.02
Totals	100.00	



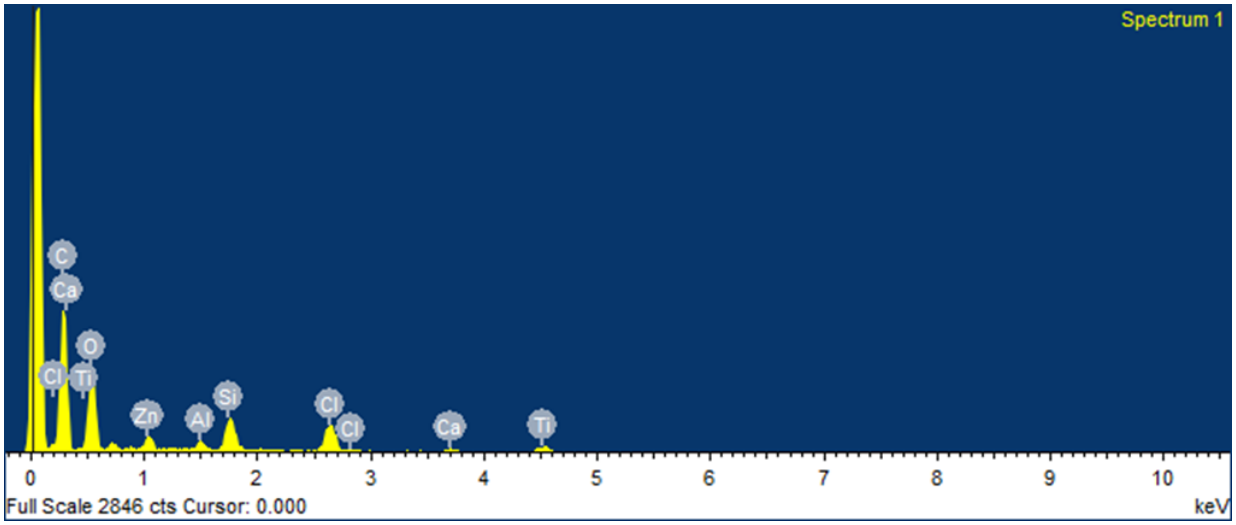
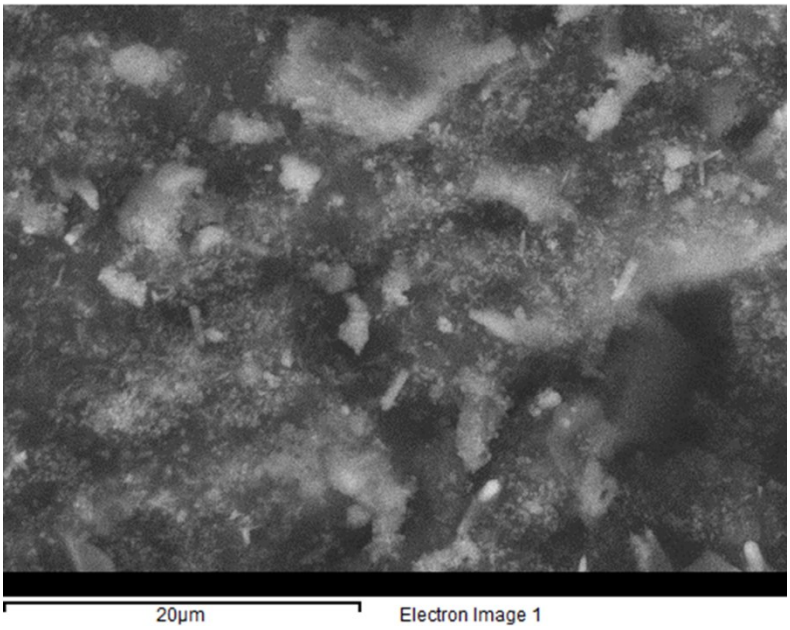


Figure A.140. SEM Image of Paint and EDS Spectrum of the Paint Collected from Exterior Web of the Girder.

Element	Weight %	Atomic %
C K	45.35	60.67
O K	29.33	29.46
Al K	0.63	0.38
Si K	4.03	2.31
Cl K	5.06	2.29
Ca K	0.78	0.31
Ti K	10.16	3.41
Fe K	0.62	0.18
Zn K	4.03	0.99
Totals	100.00	



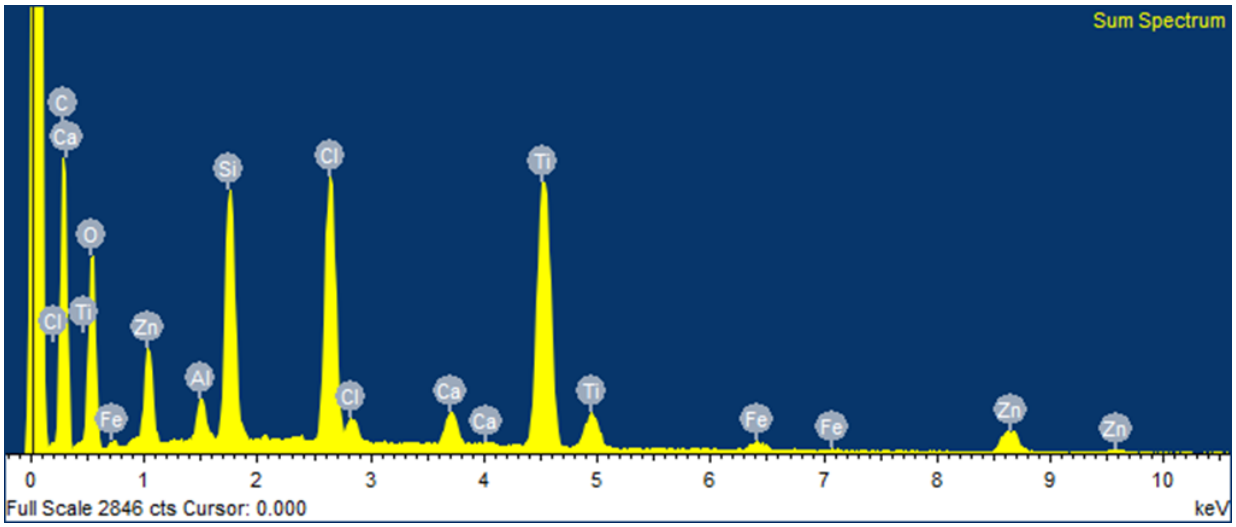


Figure A.141. SEM Image of Paint and EDS Spectrum of the Paint Collected from Exterior Web of the Girder.

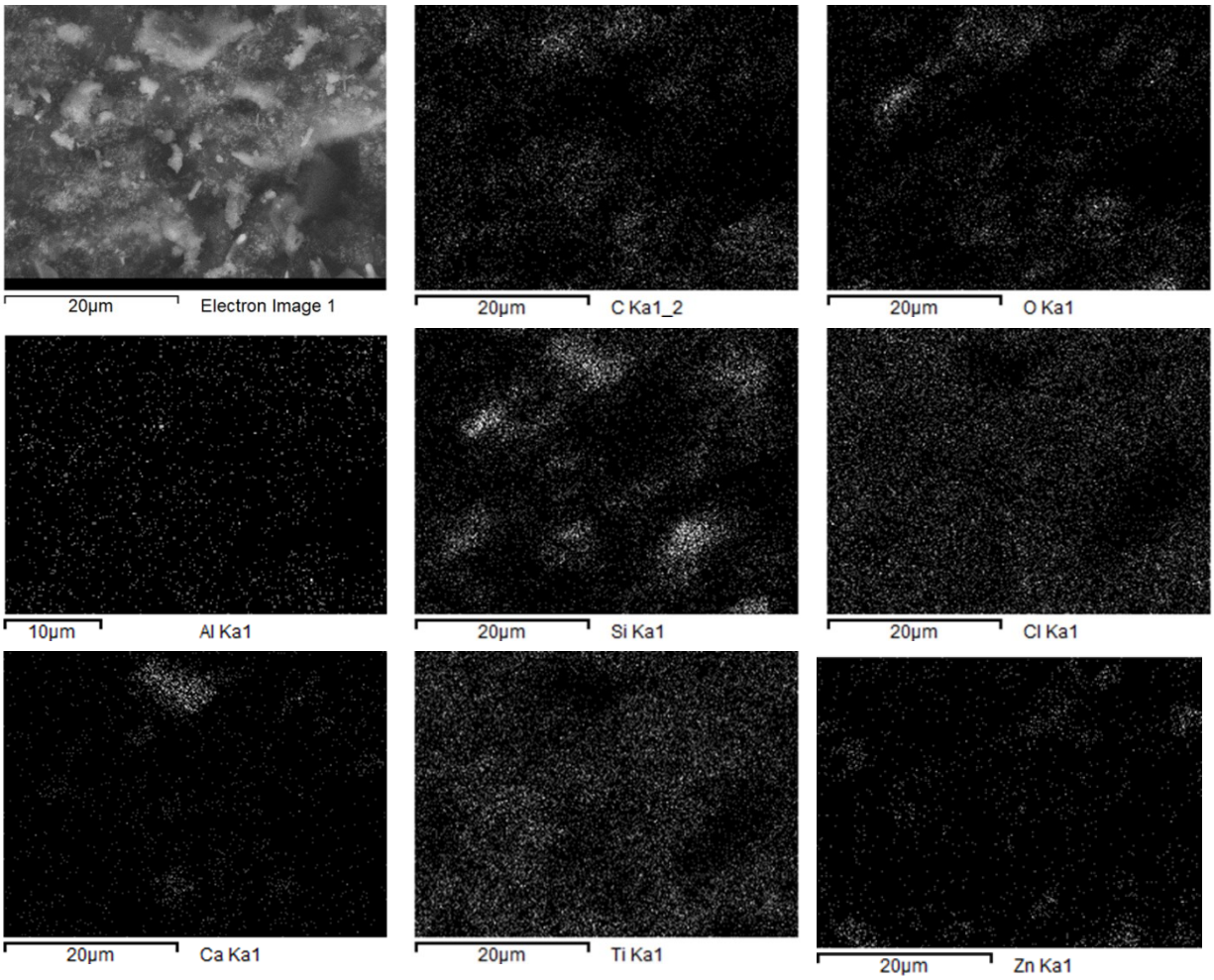
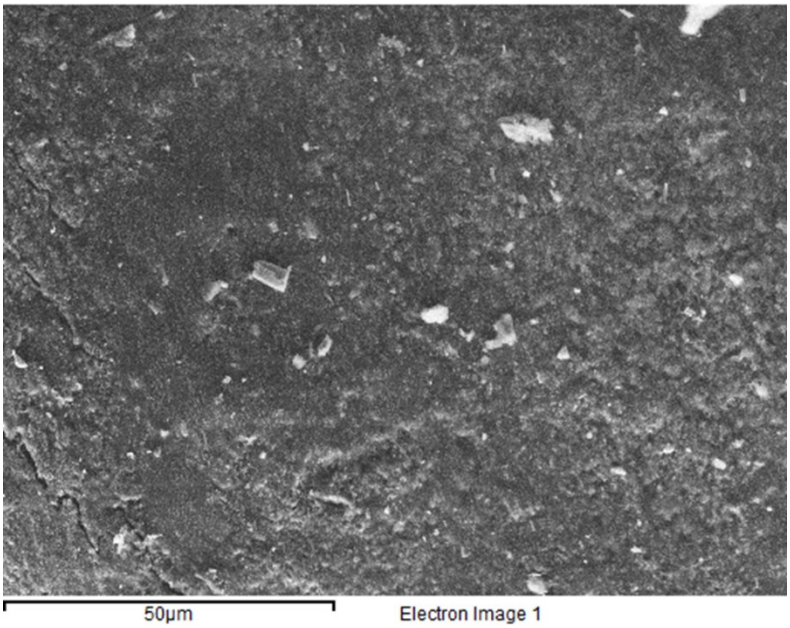


Figure A.142. EDS Elemental Mapping of Paint Collected from Exterior Web.

Element	Weight %	Atomic %
O K	62.84	79.66
Al K	1.48	1.11
Si K	8.40	6.07
P K	1.18	0.77
Cl K	10.47	5.99
Ca K	3.16	1.60
Ti K	5.73	2.43
Fe K	5.44	1.98
Zn K	1.29	0.40
Totals	100.00	



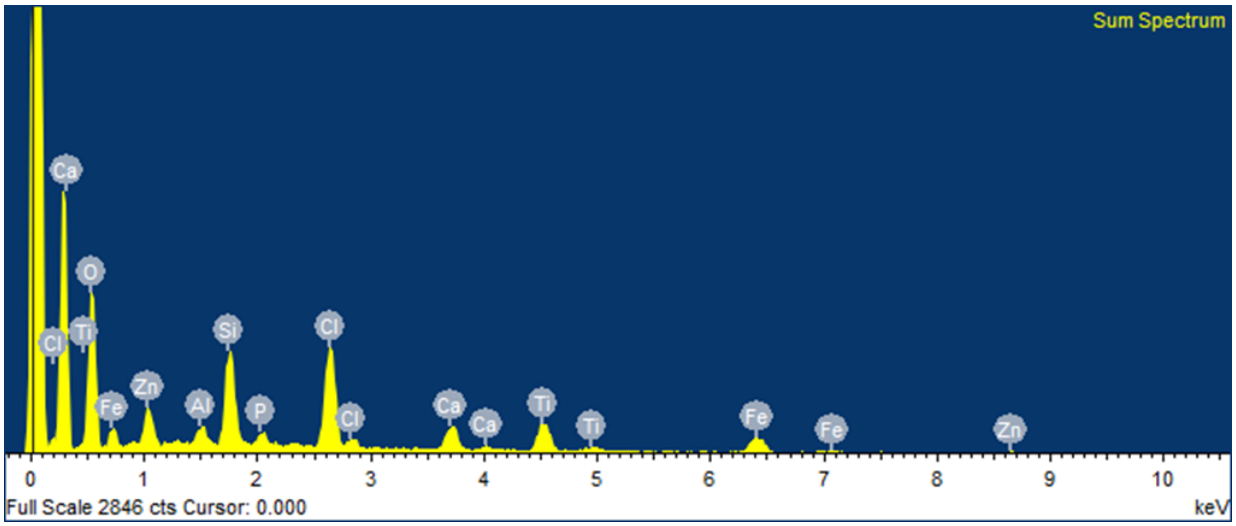


Figure A.143. SEM Image of Paint and EDS Spectrum of the Paint Collected from Interior Web of the Girder.

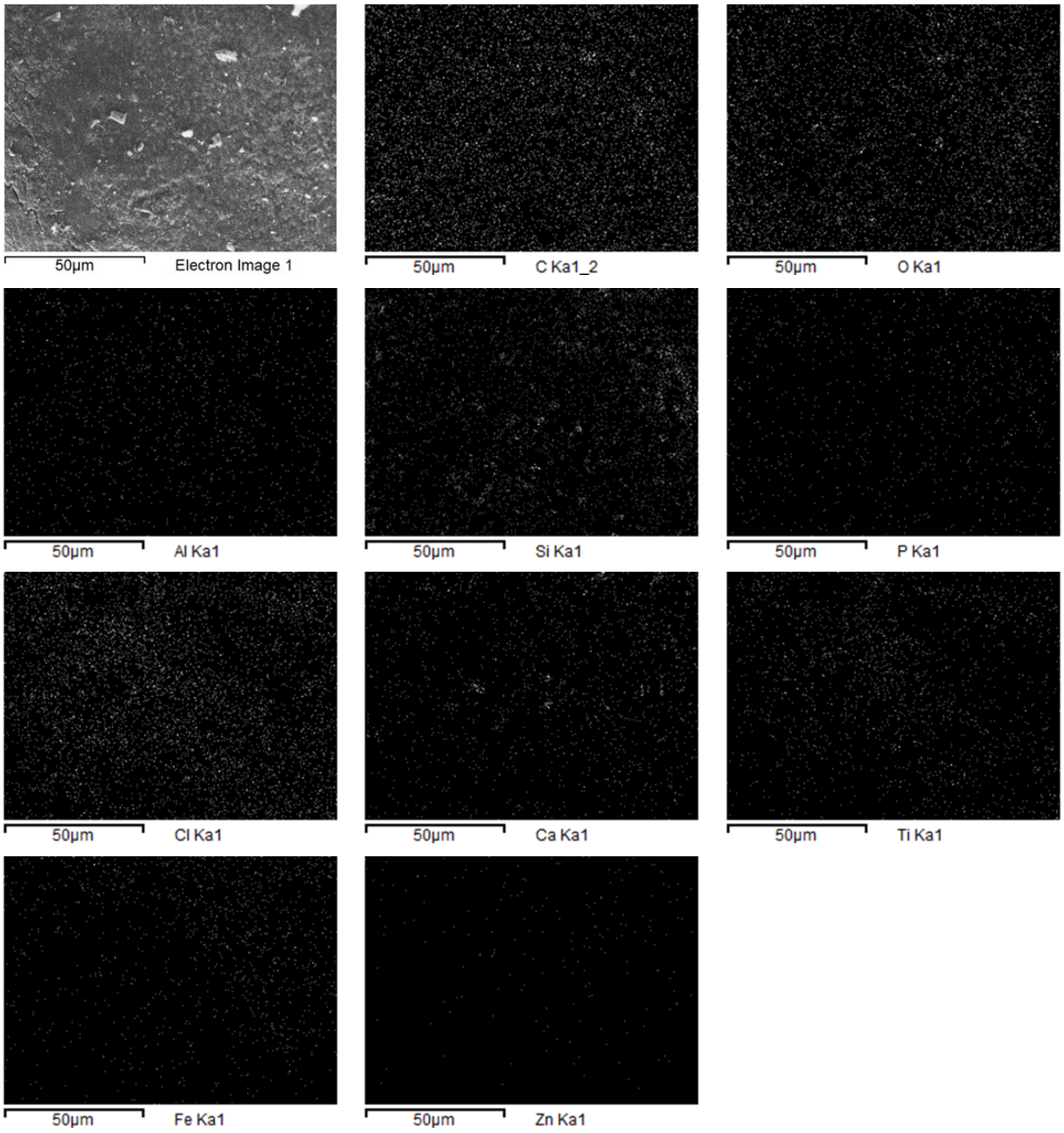
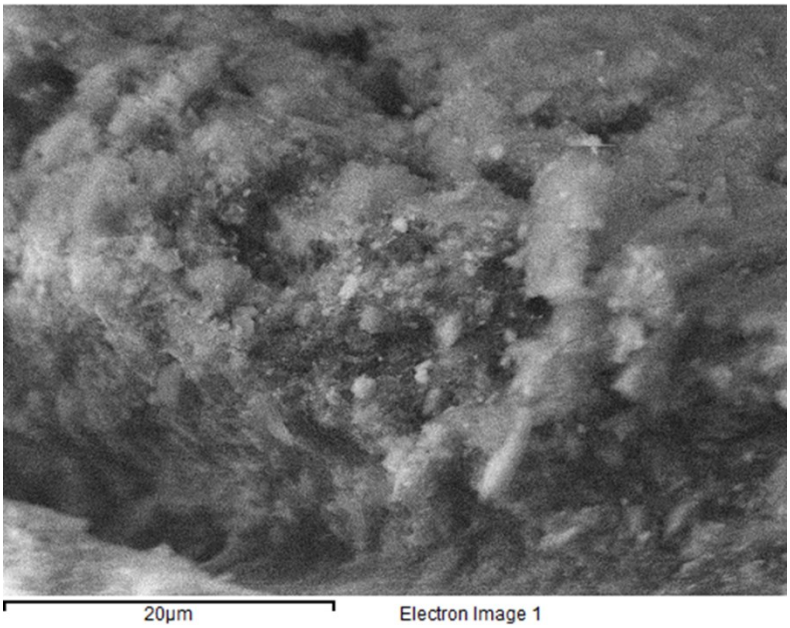


Figure A.144. EDS Elemental Mapping of Paint Collected from Exterior Web.

Element	Weight %	Atomic %
C K	51.69	61.89
O K	38.28	34.41
Al K	0.22	0.12
Si K	2.98	1.53
P K	0.47	0.22
Cl K	0.76	0.31
Ca K	1.22	0.44
Ti K	0.57	0.17
Fe K	2.53	0.65
Zn K	1.28	0.28
Totals	100.00	



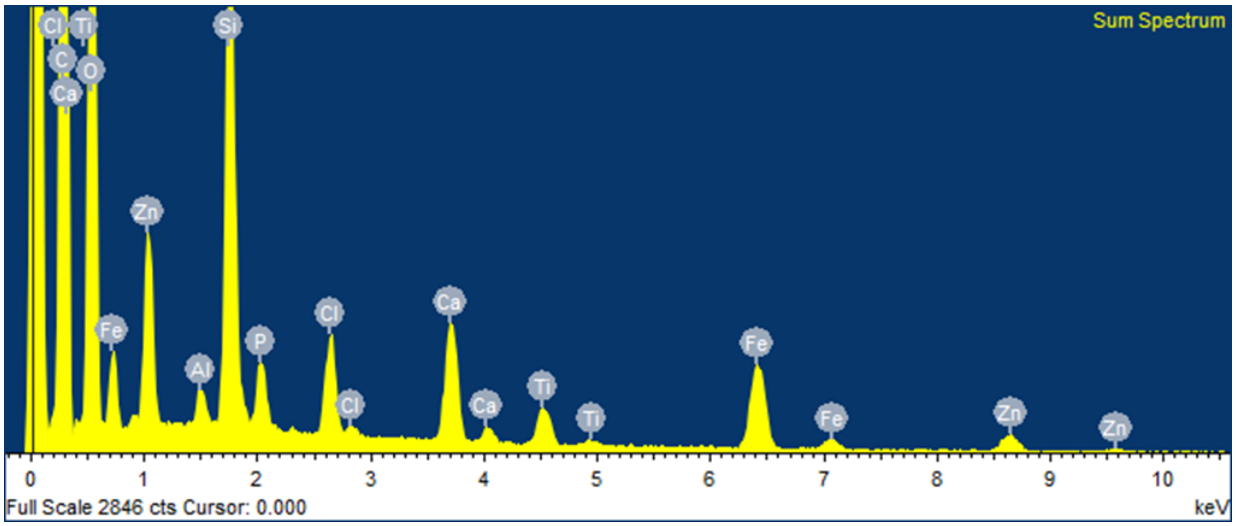


Figure A.145. SEM image of Paint and EDS Spectrum of the Paint Collected from Interior Web of the Girder.

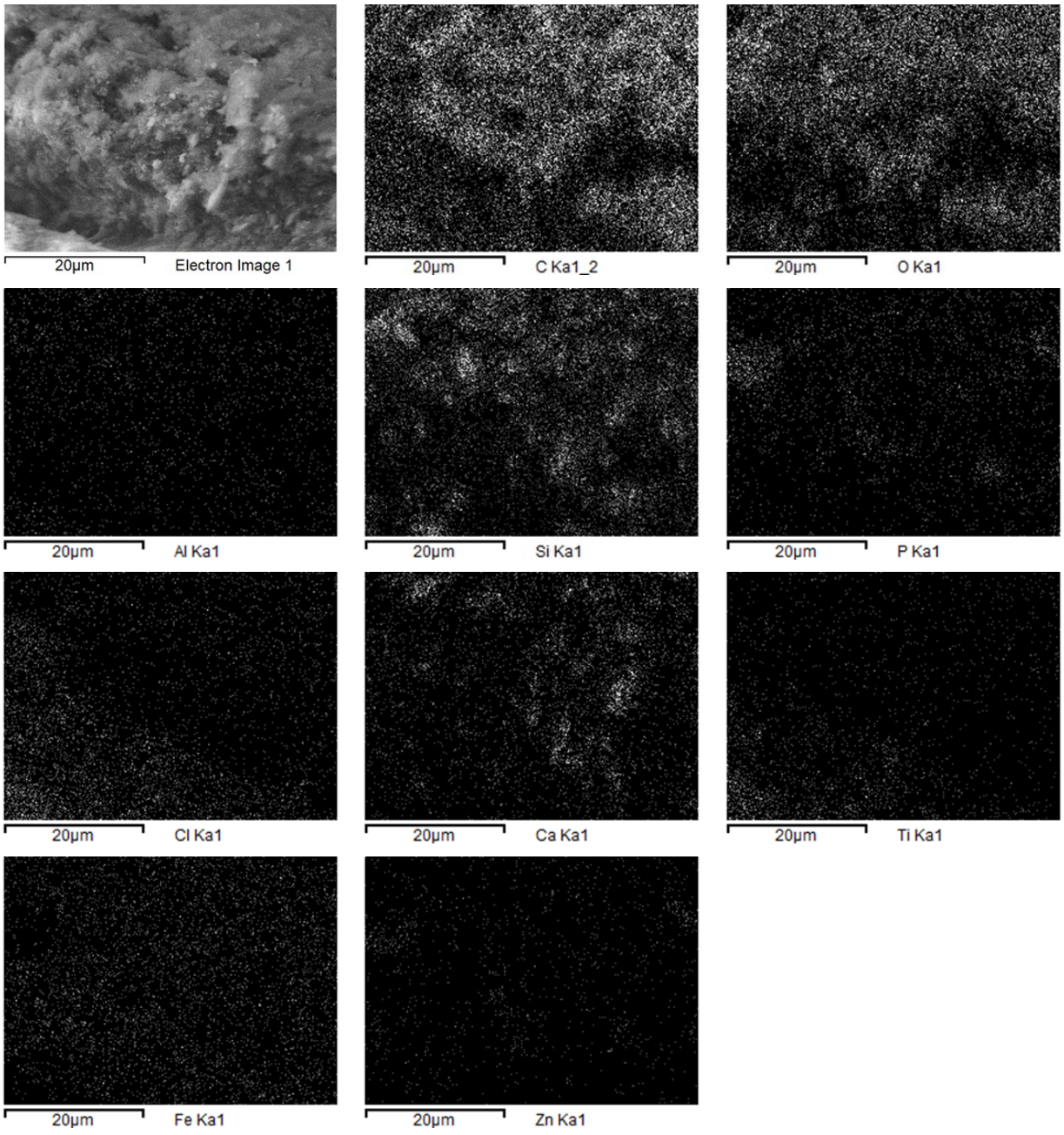


Figure A.146. EDS Elemental Mapping of Paint Collected from Interior Web.

A.14. YKM-PS-01

- N Gulf RD/CR 244 over Little Boggy Creek
- Bridge ID 131580AA0220001, Coordinates (28.75717, -95.93349), Matagorda County
- Steel Continuous I beam with multiple Lead-based paint system
- Built 2004
- Date of Inspection: November 24, 2020; girder inspection carried near abutment ends on girders within approximately four feet from the abutment
- Revisited for pH test and scrape test
- No visual inspection on deck
- Location for Testing: A2-Bent, A2-G1F1, A2-G4F1, A2-G7F2, A2-G10F1



Figure A.147. Typical Elevation of YKM-PS-01.

A.14.1. Observed Condition

Complete paint failure over the top and bottom flanges. Painting failure and widespread rusting is also observed on webs at several locations. There is accumulation of debris on interior

girders due to flooding that may have led to rapid paint deterioration and poultice corrosion. Pitting is also observed on webs and flanges at several locations. More than one type of paint system has been used in some bridges. This bridge is categorized as an off-system bridge, with beams sourced from other bridge structures. It is noteworthy that despite the complete failure of the coatings, indicating that they may be 50 years old or older, there is minimal section loss. Additionally, an EDS analysis confirmed the presence of lead in the paint sample collected from this bridge.



(a) Widespread Paint Failure and Rusting on Web and Flange of Girder 1



(b) Different Type of Paint System Observed



(c) Interior Girder (G2F1) Exhibiting Rusting and Widespread Paint Failure



(d) Paint Failure and Rusting Throughout Flange of G1F2



(e) Complete Paint Failure and Rusting Observed on Bottom Flange (G3F1)



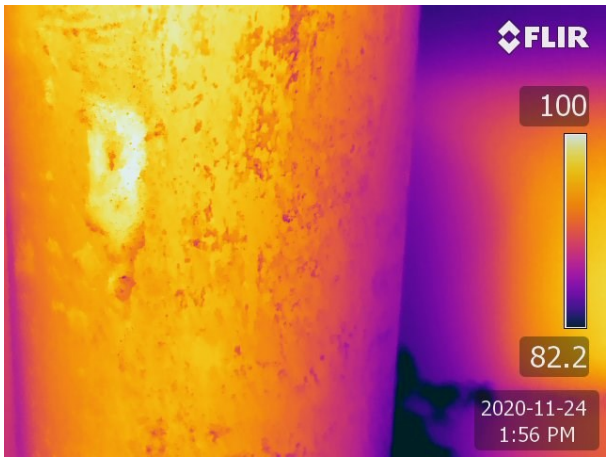
(f) Debris Accumulated on the Bottom Flange of G7f1 and G6F2

Figure A.148. Paint Condition on the Girder of YKM-PS-01.

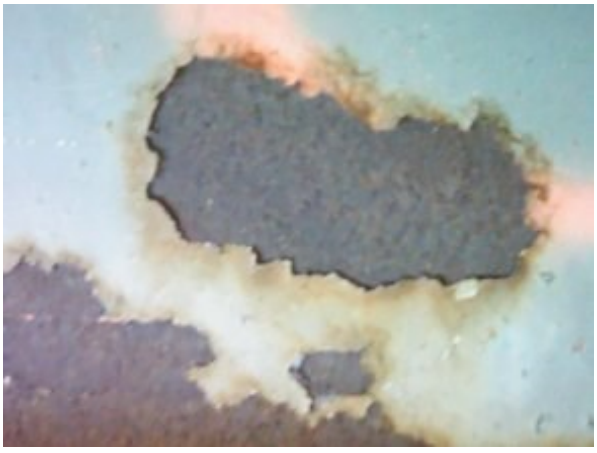
A.14.2.NDT Results



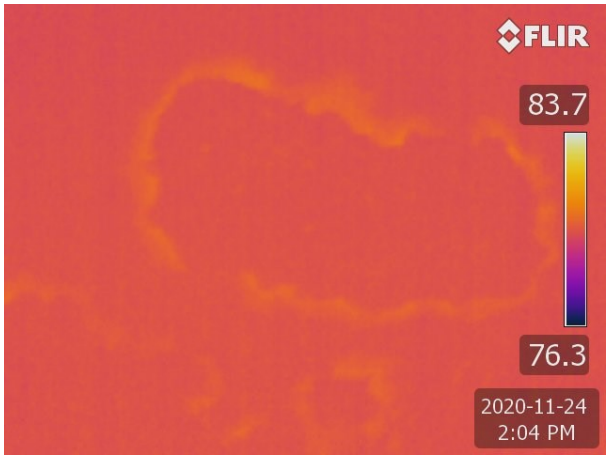
(a) Digital Image of the Pile



(b) Thermal image of the Pile



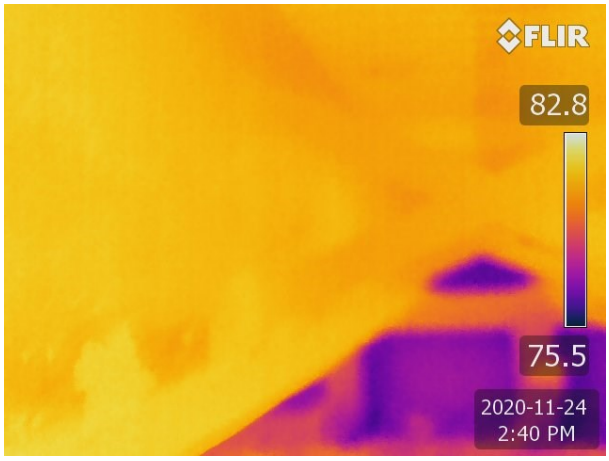
(c) Digital Image Showing Rusting



(d) Thermal Image Showing Rusting



(e) Digital Image Showing Widespread Paint Deterioration and Rusting on Girders



(f) Thermal Image Showing Widespread Paint Deterioration and Rusting on Girders

Figure A.149. Digital and Thermal Image of Painted Girder on YKM-PS-01.

Table A-68. Field Inspection Results for YKM-PS-01.

Location	Cl^- Conc. (ppm)	pH Test	Thickness (µm)	Thickness (inch)	Visual Inspection
A2-Bent TF Bot. Ext.	-	-	-	Measured R1 0.490 R2 0.488 R3 0.489 R_Avg 0.489 Design	Rust Grade – 0 Blistering – Not Found Discoloration – Not Found Flaking – Not Found Delamination – Yes
A2-Bent Web. Ext.	-		-	Measured R1 0.519 R2 0.517 R3 0.515 R_Avg 0.517 Design	Rust Grade – 0 Blistering – Not Found Discoloration – Not Found Flaking – Not Found Delamination – Yes
A2-Bent BF Top. Ext.	-	-	--	Measured R1 0.512 R2 0.515 R3 0.511 R_Avg 0.513 Design	Rust Grade – 0 Blistering – Not Found Discoloration – Not Found Flaking – Not Found Delamination – Yes
A2-Bent BF Bot. Ext.	-	-	-	Measured R1 - R2 - R3 - R_Avg - Design	Rust Grade – 0 Blistering – Not Found Discoloration – Not Found Flaking – Not Found Delamination – Yes
A2-G1F1 TF Bot. Ext.	-		Measured R1 64.1 R2 73.6 R3 72.1	Measured R1 0.707 R2 0.709 R3 0.707 R_Avg 0.708 Design 0.700	Rust Grade – 0 Blistering – Not Found Discoloration – Not Found Flaking – Not Found Delamination – Yes
A2-G1F1 Web. Ext.	1	-	Measured R1 41.6 R2 56 R3 45.9	Measured R1 0.505 R2 0.506 R3 0.506 R_Avg 0.506 Design 0.500	Rust Grade – 0 Blistering – Not Found Discoloration – Not Found Flaking – Not Found Delamination – Yes

Table A-69. Field Inspection Results for YKM-PS-01.

Location	Cl^- Conc. (ppm)	pH Test	Thickness (µm)	Thickness (inch)	Visual Inspection
A2-G1F1 BF Top Ext.	-	-	Measured R1 61.3 R2 58 R3 63.8	Measured R1 0.782 R2 0.786 R3 0.779 R_Avg 0.782 Design 0.700	Rust Grade – 0 Blistering – Not Found Discoloration – Not Found Flaking – Not Found Delamination – Yes
A2-G1F1 BF Bot. Ext.	-	-	Measured R1 - R2 - R3 -	Measured R1 - R2 - R3 - R_Avg - Design	Rust Grade – 0 Blistering – Not Found Discoloration – Not Found Flaking – Not Found Delamination – Yes
A2-G4F1 TF Bot. Int.	-	-	Measured R1 161 R2 163 R3 166	Measured R1 0.681 R2 0.684 R3 0.678 R_Avg 0.681 Design 0.680	Rust Grade – 0 Blistering – Not Found Discoloration – Not Found Flaking – Not Found Delamination – Yes
A2-G4F1 Web. Int.	0		Measured R1 134 R2 135 R3 138	Measured R1 0.462 R2 0.461 R3 0.464 R_Avg 0.462 Design 0.440	Rust Grade – 0 Blistering – Not Found Discoloration – Not Found Flaking – Not Found Delamination – Yes
A2-G4F1 BF Top. Int.	-		Measured R1 203 R2 200 R3 193	Measured R1 0.690 R2 0.690 R3 0.694 R_Avg 0.691 Design	Rust Grade – 0 Blistering – Not Found Discoloration – Not Found Flaking – Not Found Delamination – Yes
A2-G4F1 BF Bot. Int.	-		Measured R1 - R2 - R3 -	Measured R1 - R2 - R3 - R_Avg - Design	Rust Grade – 0 Blistering – Not Found Discoloration – Not Found Flaking – Not Found Delamination – Yes

Table A-70. Field Inspection Results for YKM-PS-01.

Location	Cl^- Conc. (ppm)	pH Test	Thickness (µm)	Thickness (inch)	Visual Inspection
A2-G7F2 TF Bot. Int.	-	-	Measured R1 46.4 R2 57 R3 55.3	Measured R1 0.760 R2 0.757 R3 0.760 R_Avg 0.759 Design 0.750	Rust Grade – 0 Blistering – Not Found Discoloration – Not Found Flaking – Not Found Delamination – Yes
A2-G7F2 Web. Int.	0		Measured R1 43.5 R2 44.6 R3 59.7	Measured R1 0.454 R2 0.456 R3 0.457 R_Avg 0.456 Design 0.440	Rust Grade – 0 Blistering – Not Found Discoloration – Not Found Flaking – Not Found Delamination – Yes
A2-G7F2 BF Top. Int.	-		Measured R1 71.3 R2 74.2 R3 72.6	Measured R1 0.740 R2 0.748 R3 0.747 R_Avg 0.745 Design	Rust Grade – 0 Blistering – Not Found Discoloration – Not Found Flaking – Not Found Delamination – Yes
A2-G7F2 BF Bot. Int.	-		Measured R1 - R2 - R3 -	Measured R1 - R2 - R3 - R_Avg - Design	Rust Grade – 0 Blistering – Not Found Discoloration – Not Found Flaking – Not Found Delamination – Yes
A2-G10F1 TF Bot. Int.	-	-	-	Measured R1 0.740 R2 0.731 R3 0.739 R_Avg 0.737 Design 0.700	Rust Grade – 0 Blistering – Not Found Discoloration – Not Found Flaking – Not Found Delamination – Yes
A2-G10F1 Web. Int.	-		-	Measured R1 0.511 R2 0.506 R3 0.507 R_Avg 0.508 Design 0.500	Rust Grade – 0 Blistering – Not Found Discoloration – Not Found Flaking – Not Found Delamination – Yes

Table A-71. Field Inspection Results for YKM-PS-01.

Location	Cl^- Conc. (ppm)	pH Test	Thickness (µm)	Thickness (inch)	Visual Inspection
A2-G10F1 BF Top. Int.	-	-	--	Measured R1 0.680 R2 0.678 R3 0.675 R_Avg 0.678 Design 0.700	Rust Grade – 0 Blistering – Not Found Discoloration – Not Found Flaking – Not Found Delamination – Yes
A2-G10F1 BF Bot. Int.	-		-	Measured R1 - R2 - R3 - R_Avg - Design	Rust Grade – 0 Blistering – Not Found Discoloration – Not Found Flaking – Not Found Delamination – Yes

A.14.3. Pull-off Adhesion Results

Table A-72. Pull-off Adhesion Results for YKM-PS-01.

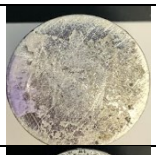
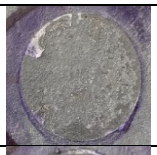
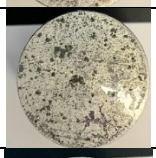
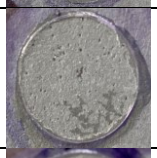
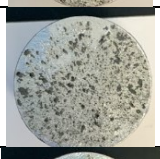
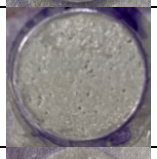
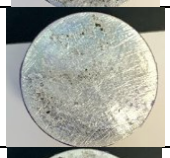
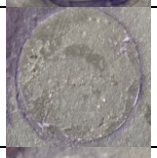
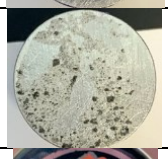
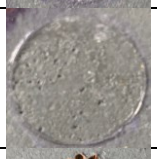
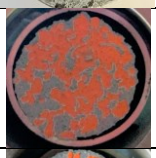
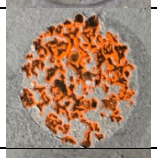
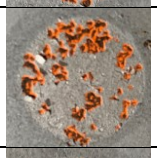
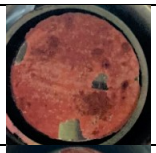
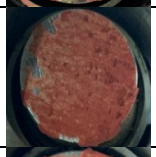
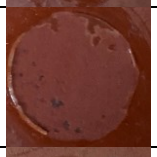
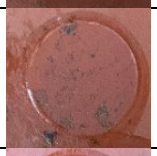
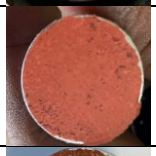
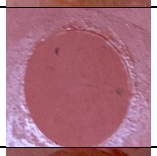
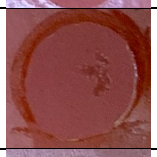
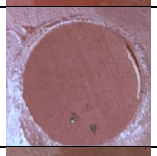
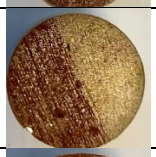
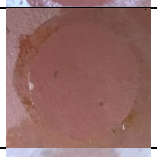
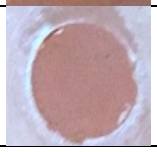
Location	Dolly Face	Substrate Face	Test Result (psi)	Attributes	Failure Type
A2-G1F1			272	80% C/Y 20% C	80% Glue Failure 20% Cohesive Failure
			1625	80% C 20% B/C	80% Cohesive Failure 20% Adhesive Failure
			2307	80% C 20% B/C	80% Cohesive Failure 20% Adhesive Failure
			380	80% C/Y 20% C	80% Glue Failure 20% Cohesive Failure
			1254	30% C/Y 60% C 10% B/C	30% Glue Failure 60% Cohesive Failure 10% Adhesive Failure
A2-G4F1			494	30% C 70% B	30% Cohesive Failure 70% Cohesive Failure
			465	70% C 30% B/C	70% Cohesive Failure 20% Cohesive Failure
			421	90% C 10% B	90% Cohesive Failure 10% Cohesive Failure
			491	80% C 20% B	80% Cohesive Failure 20% Cohesive Failure
			429	70% C 30% B	70% Cohesive Failure 30% Cohesive Failure

Table A-73. Pull-off Adhesion Results for YKM-PS-01.

Location	Dolly Face	Substrate Face	Test Result (psi)	Attributes	Failure Type
A2-G6F1			635	10% B/Y 90% B	10% Glue Failure 90% Cohesive Failure
			892	10% B/Y 90% B	10% Glue Failure 90% Cohesive Failure
			1035	20% B/Y 80% B	20% Glue Failure 80% Cohesive Failure
			1565	100% B	100% Cohesive Failure
			1554	100% B	100% Cohesive Failure
A2-G8F1			1329	100% B	100% Cohesive Failure
			1111	20% B/Y 80% B	20% Glue Failure 80% Cohesive Failure
			1184	100% B	100% Cohesive Failure
			955	50% B/Y 50% B	50% Glue Failure 50% Cohesive Failure
			1286	100% B	100% Cohesive Failure

A.14.4.Optical Microscopy Results

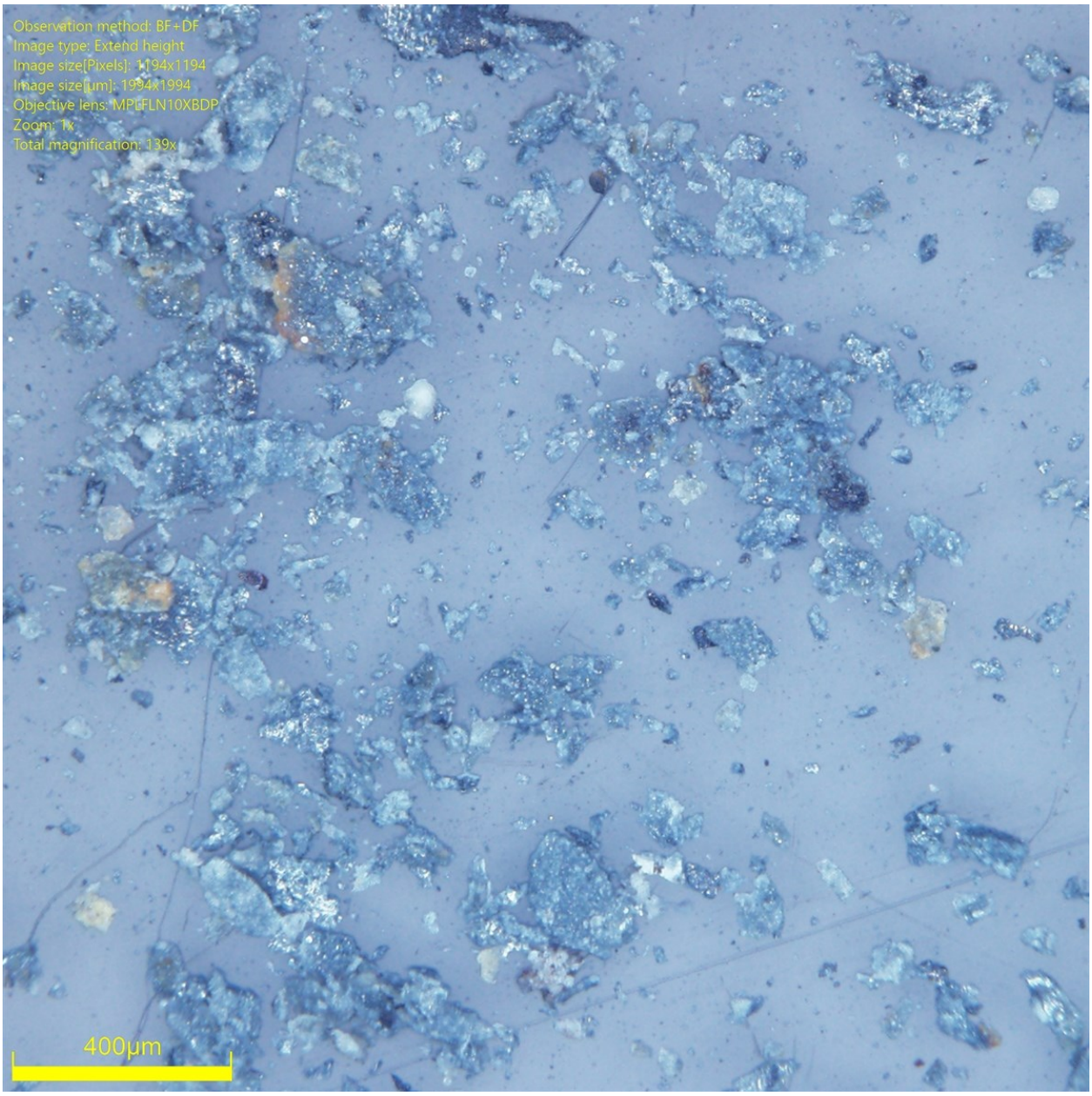


Figure A.150. Two Layer Paint System Examined by Optical Microscope YKM–PS–01 (G1F1).

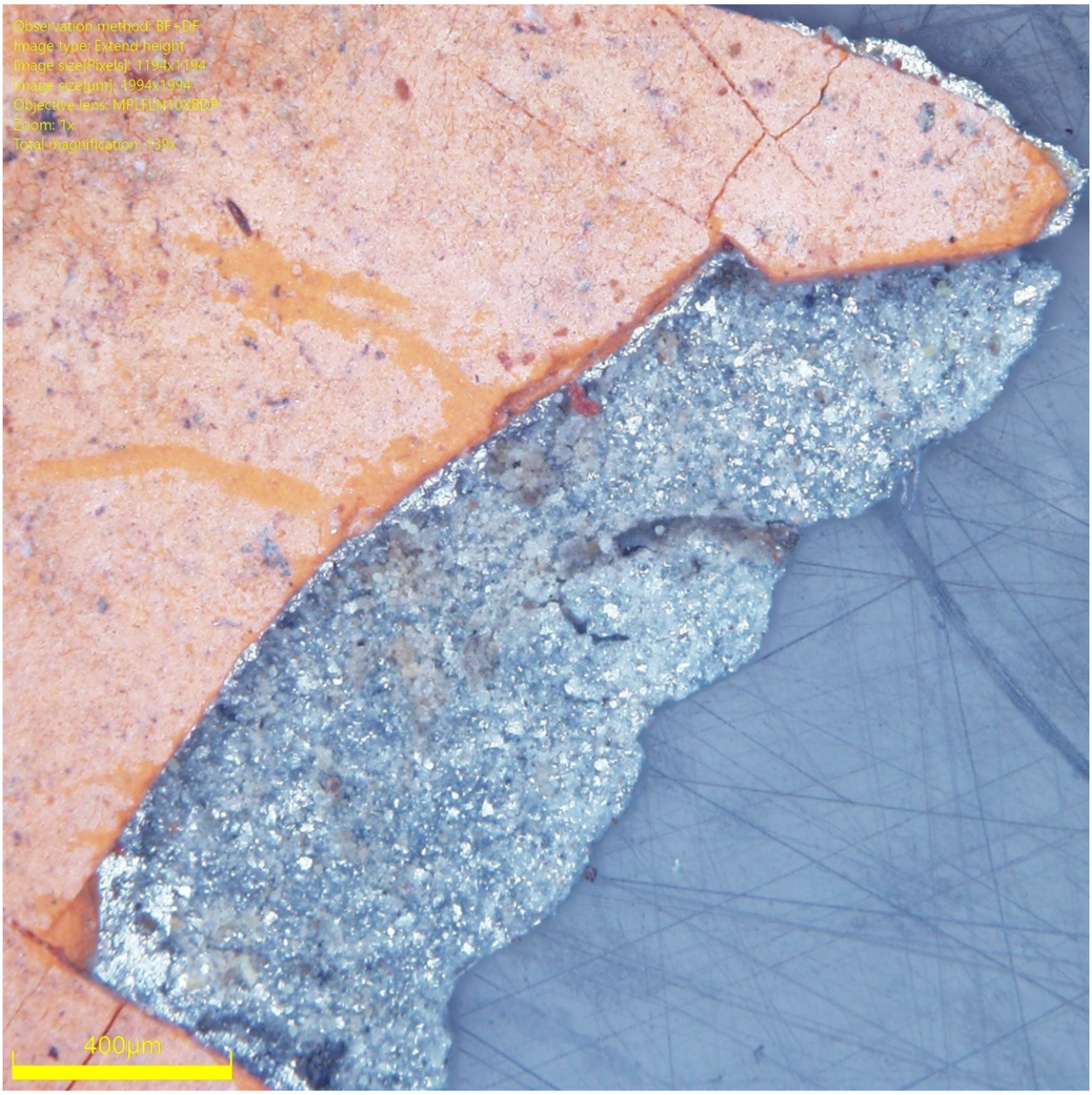


Figure A.151. Two Layer Paint System Examined by Optical Microscope YKM–PS–01 (G3F1).

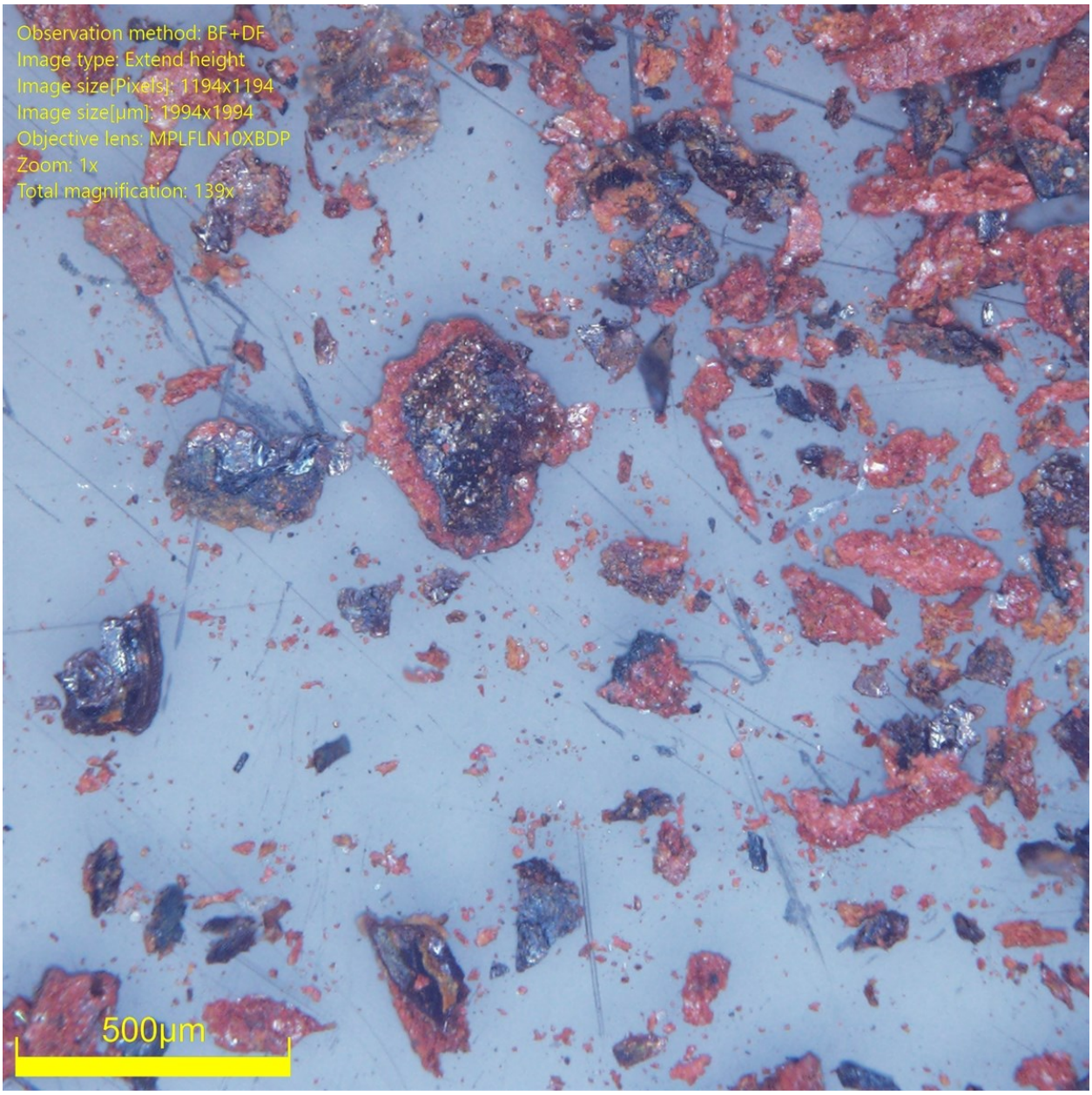
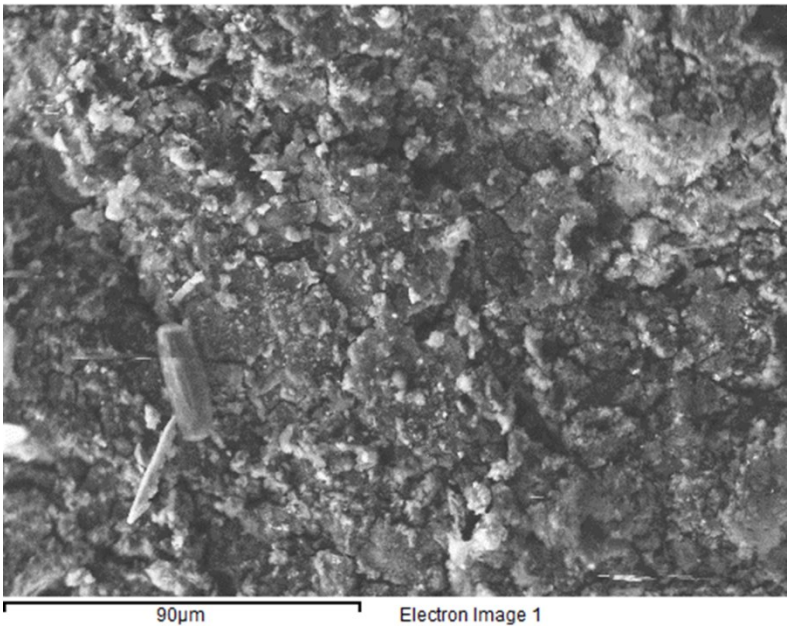


Figure A.152. Paint System Examined by Optical Microscope YKM–PS–01 (G6F1).

A.14.5.SEM/EDS Results

Element	Weight %	Atomic %
C K	21.21	30.95
O K	47.36	51.90
Mg K	0.10	0.07
Al K	18.43	11.97
Si K	2.88	1.80
P K	0.79	0.45
S K	1.61	0.88
K K	0.56	0.25
Cr K	2.54	0.86
Fe K	1.02	0.32
Cu K	0.18	0.05
Zn K	1.22	0.33
Pb M	2.10	0.18
Totals	100.00	



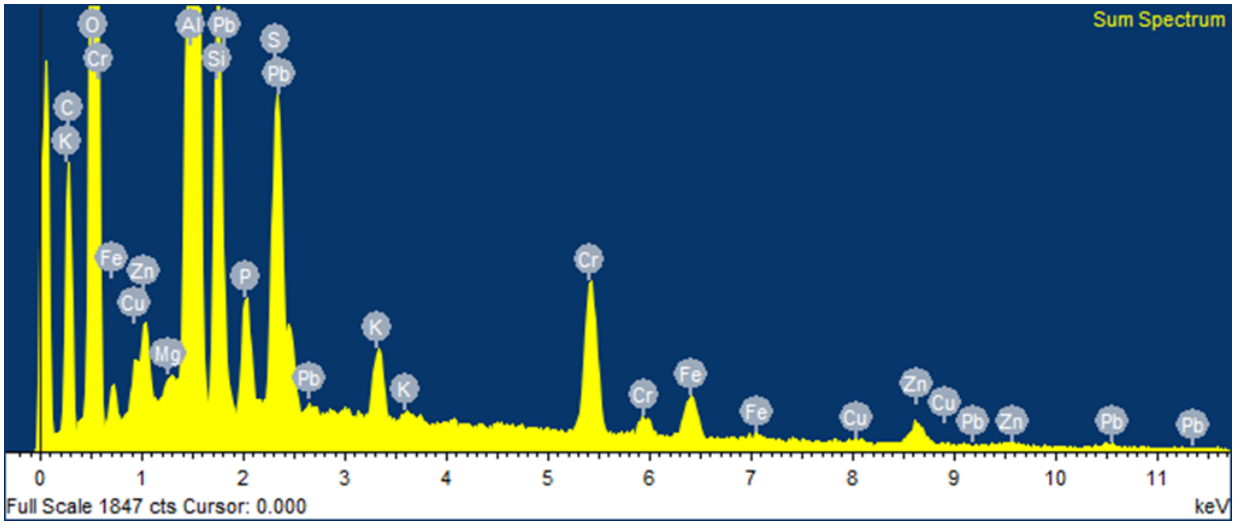


Figure A.153. SEM Image and EDS Spectrum of the Paint Collected from Exterior Web of the Girder.

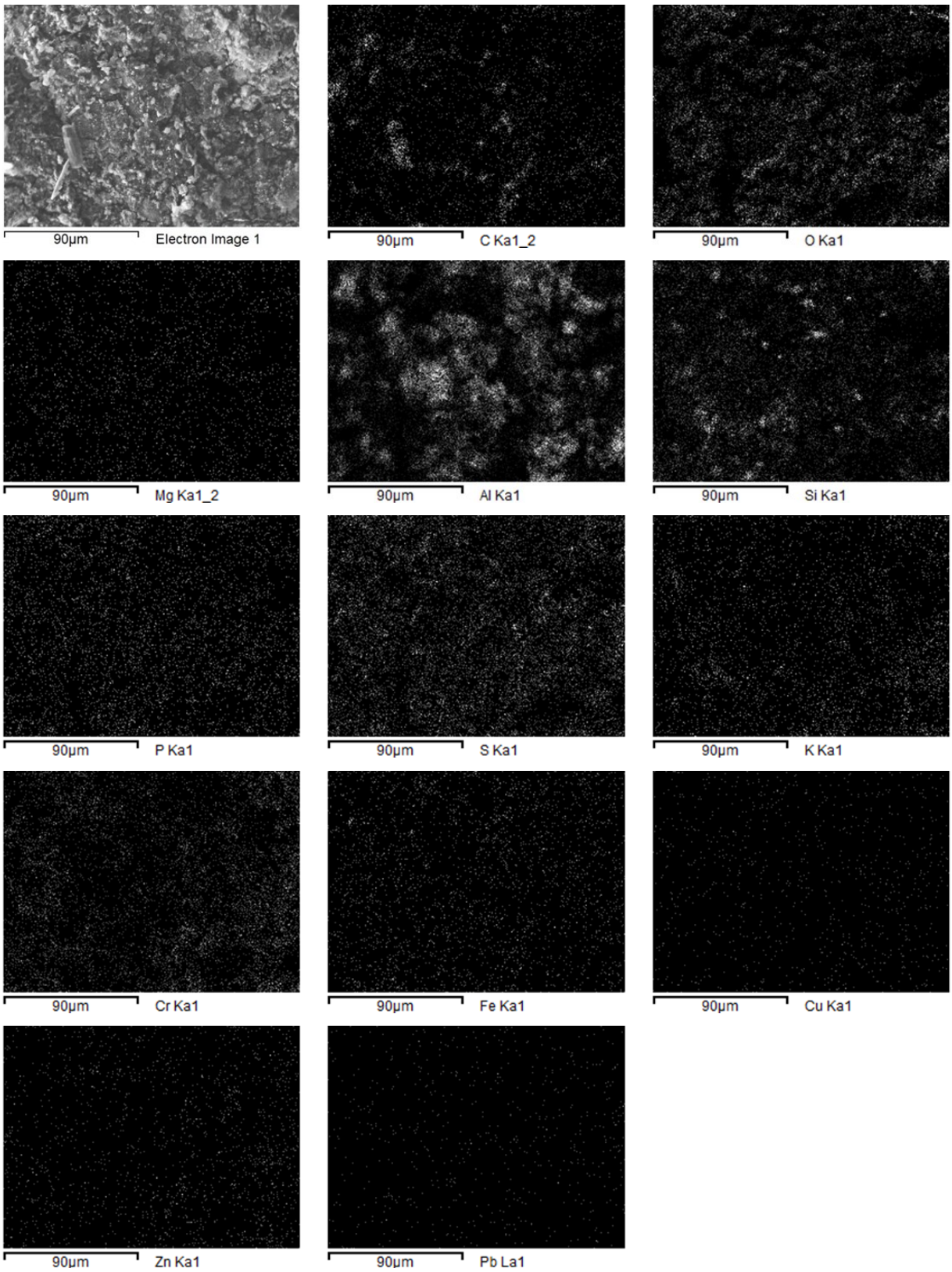
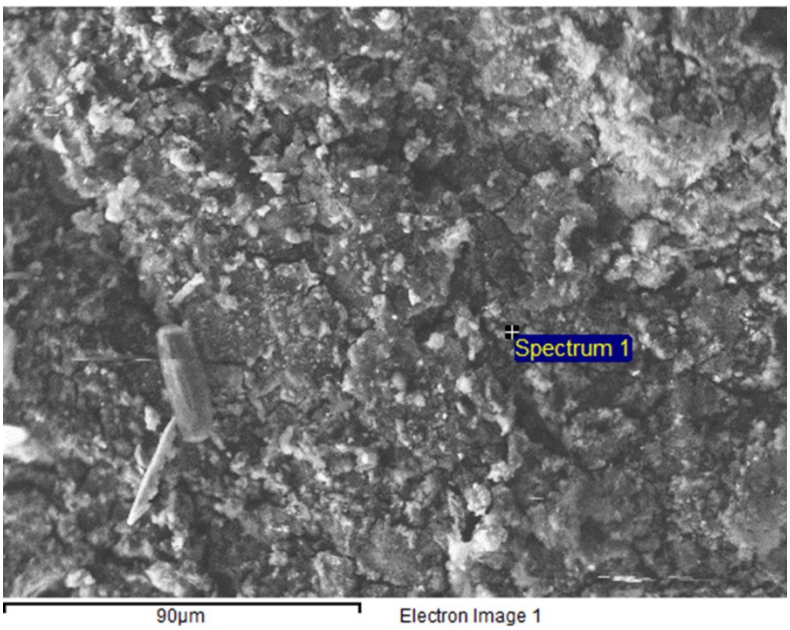


Figure A.154. EDS Elemental Mapping of Paint Collected from Exterior Web (G1F1).

Element	Weight %	Atomic %
C K	15.05	24.05
O K	45.84	55.00
Mg K	0.13	0.10
Al K	14.87	10.58
Si K	5.13	3.51
P K	1.03	0.64
S K	2.57	1.54
K K	2.39	1.17
Cr K	4.98	1.84
Fe K	1.34	0.46
Cu K	0.16	0.05
Zn K	2.33	0.68
Pb M	4.19	0.39
Totals	100.00	



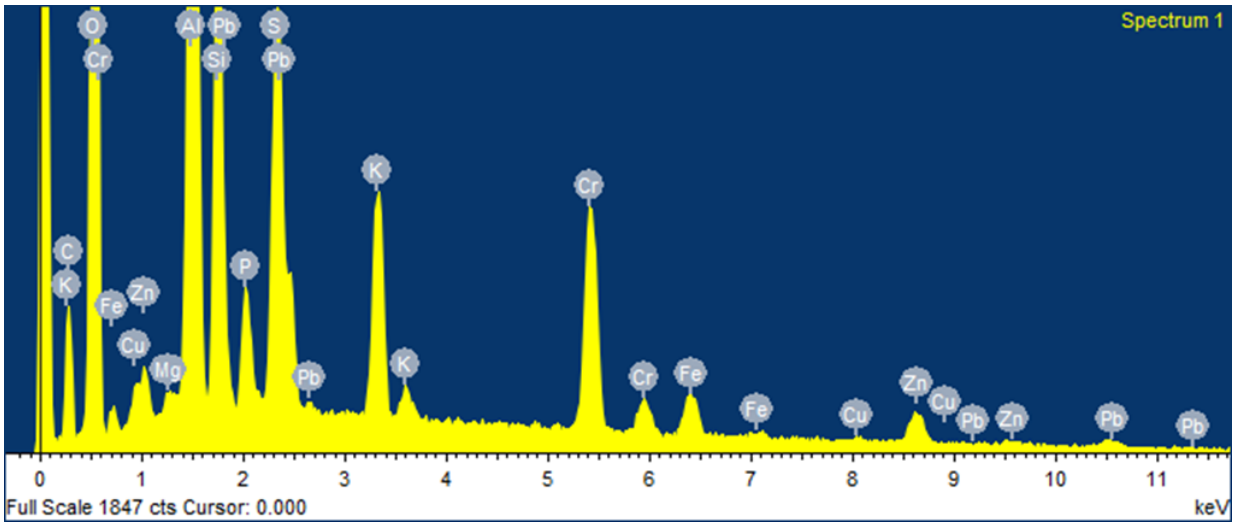
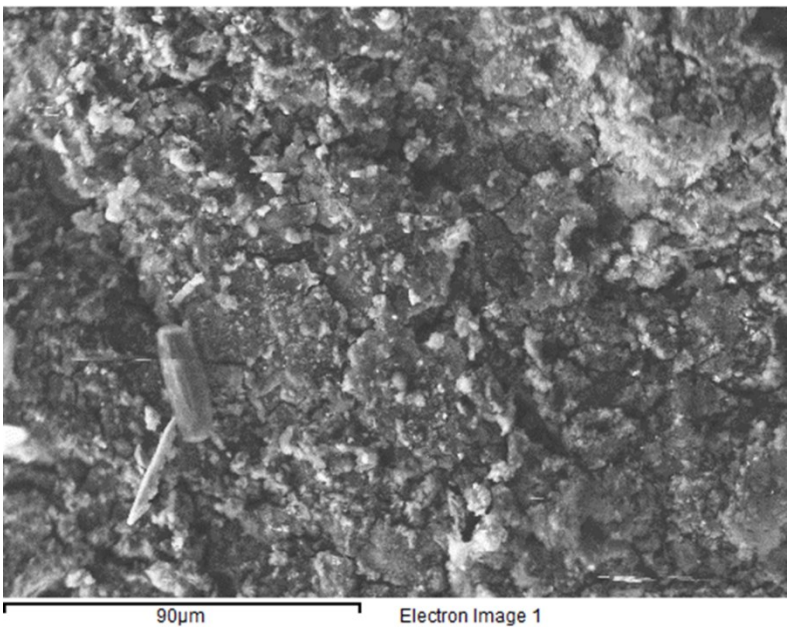


Figure A.155. SEM Image and EDS Spectrum of the Paint Collected from Exterior Web of the Girder.

Element	Weight %	Atomic %
C K	21.21	30.95
O K	47.36	51.90
Mg K	0.10	0.07
Al K	18.43	11.97
Si K	2.88	1.80
P K	0.79	0.45
S K	1.61	0.88
K K	0.56	0.25
Cr K	2.54	0.86
Fe K	1.02	0.32
Cu K	0.18	0.05
Zn K	1.22	0.33
Pb M	2.10	0.18
Totals	100.00	



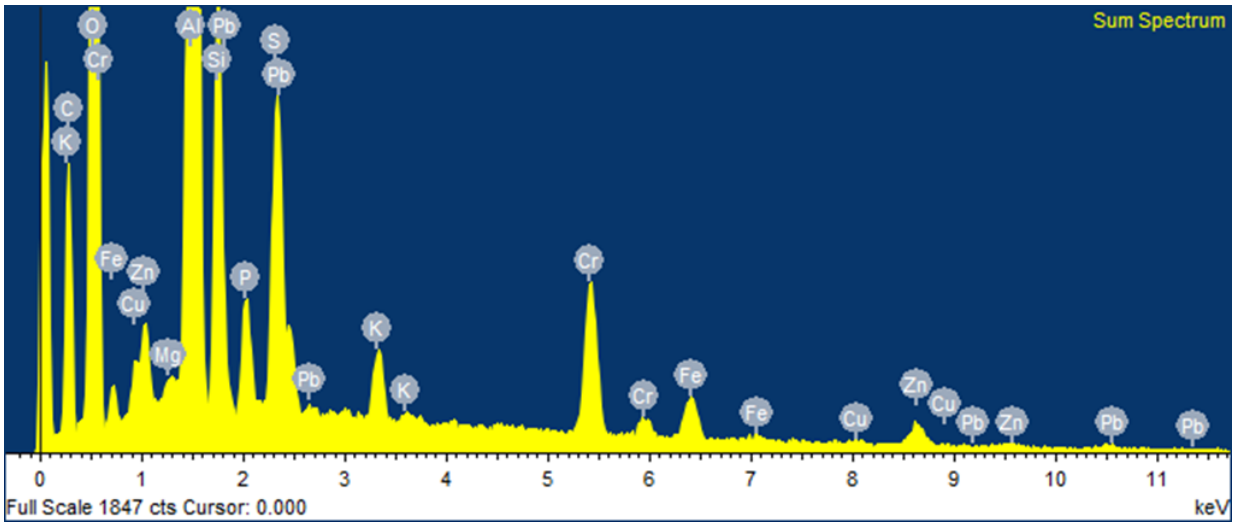


Figure A.156. SEM Image and EDS Spectrum of the Paint Collected from Exterior Web of the Girder.

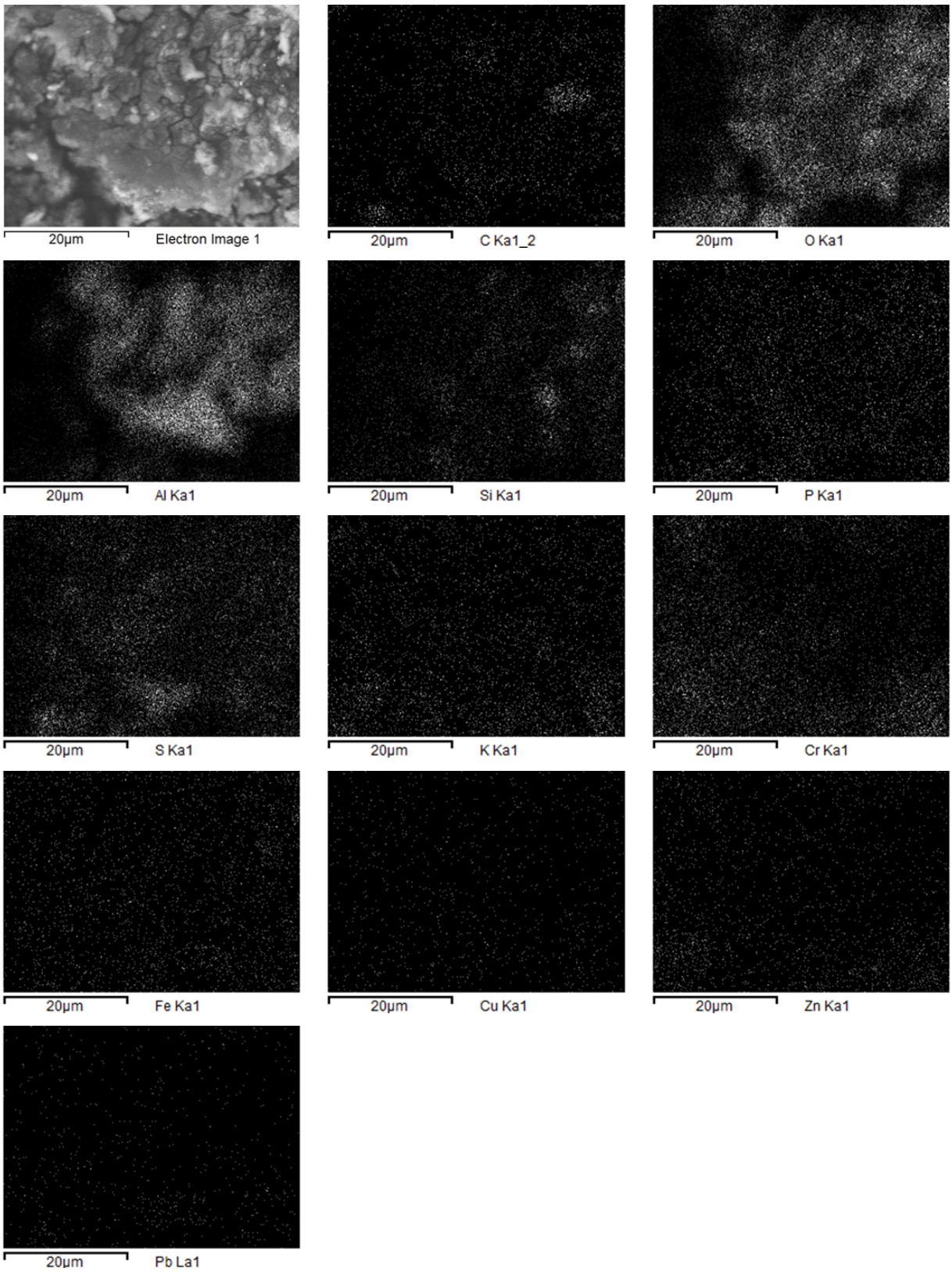
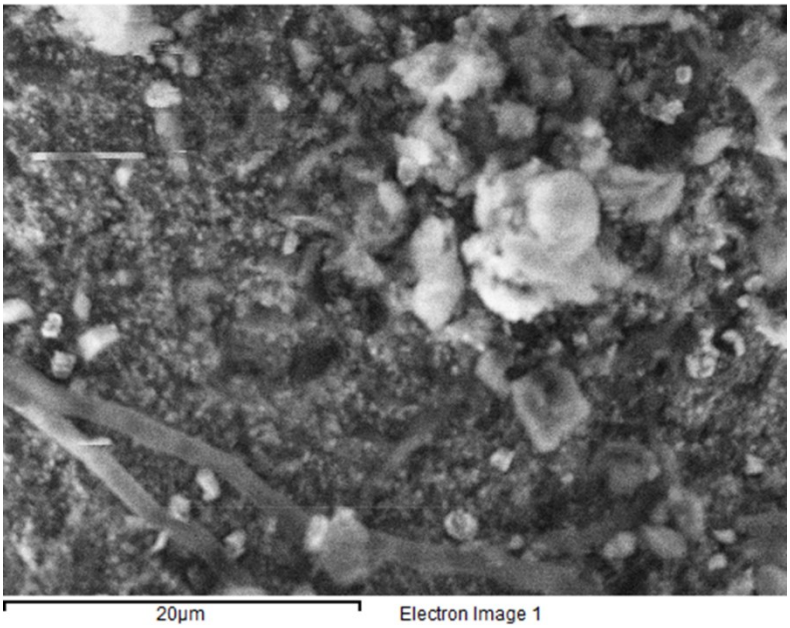


Figure A.157. EDS Elemental Mapping of Paint Collected from Exterior Web.

Element	Weight %	Atomic %
C K	43.46	55.44
O K	42.92	41.11
Al K	1.53	0.87
Si K	2.10	1.15
S K	0.81	0.39
K K	0.40	0.16
Cr K	0.61	0.18
Fe K	0.14	0.04
Ni K	0.19	0.05
Zn K	0.10	0.02
Zr L	0.30	0.05
Pb M	7.44	0.55
Totals	100.00	



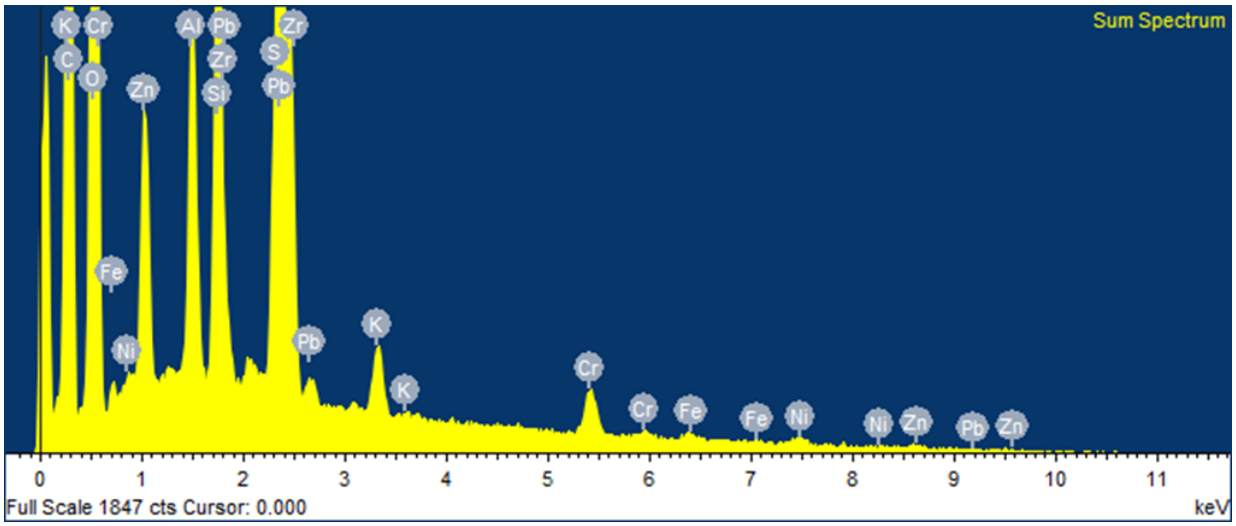


Figure A.158. SEM Image and EDS Spectrum of the Paint Collected from Exterior Web of the Girder.

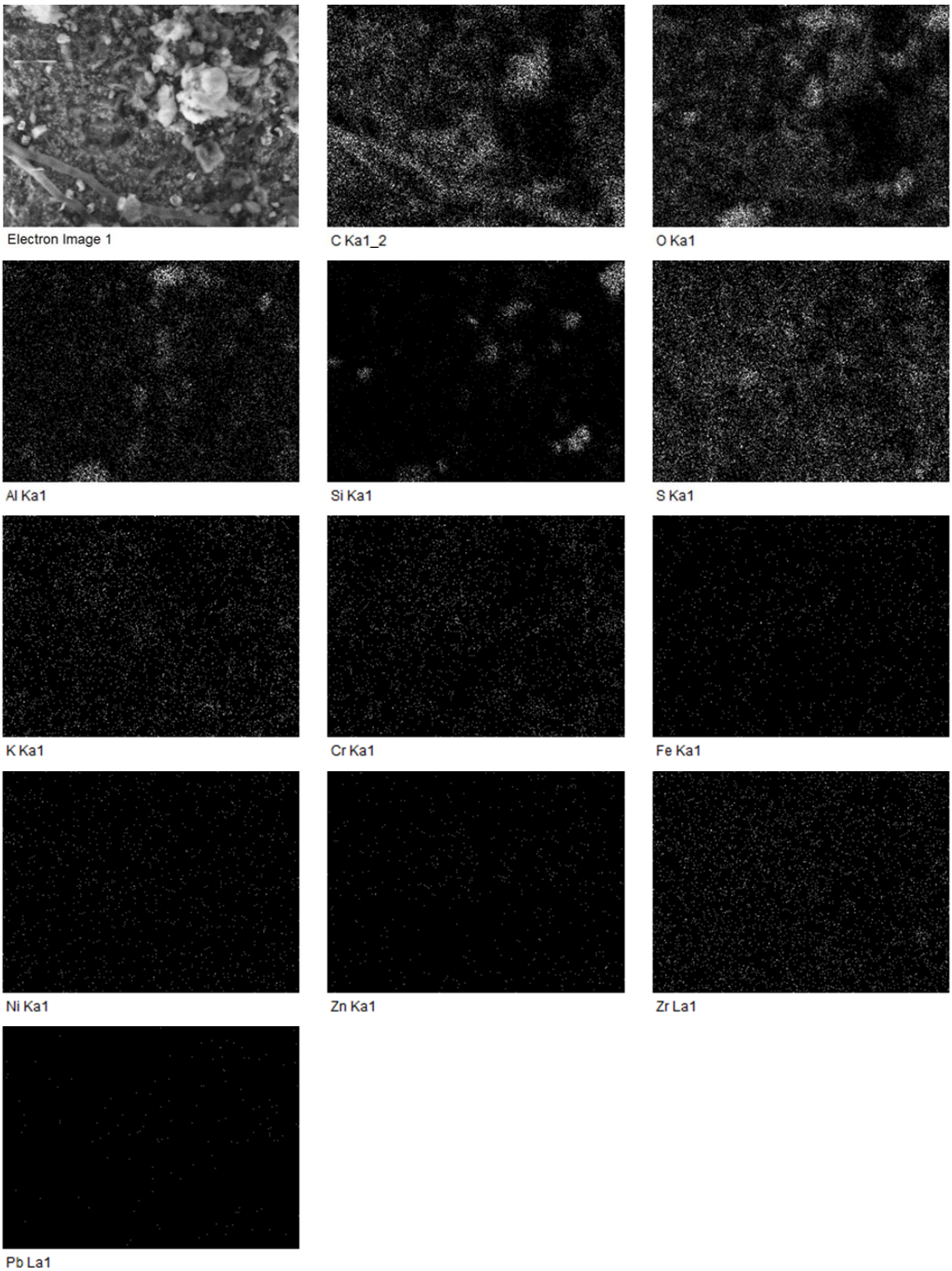
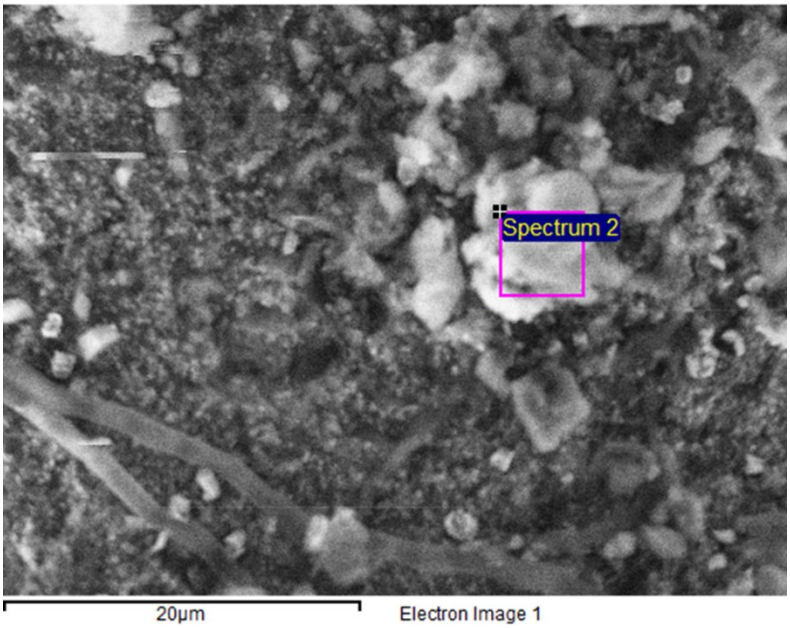


Figure A.159. EDS Elemental Mapping of Paint Collected from Exterior Web.

Element	Weight %	Atomic %
C K	52.53	64.31
O K	35.60	32.71
Al K	0.94	0.51
Si K	2.48	1.30
S K	0.75	0.35
K K	0.17	0.06
Cr K	0.27	0.08
Fe K	0.22	0.06
Ni K	0.12	0.03
Zn K	0.55	0.12
Zr L	0.27	0.04
Pb M	6.11	0.43
Totals	100.00	



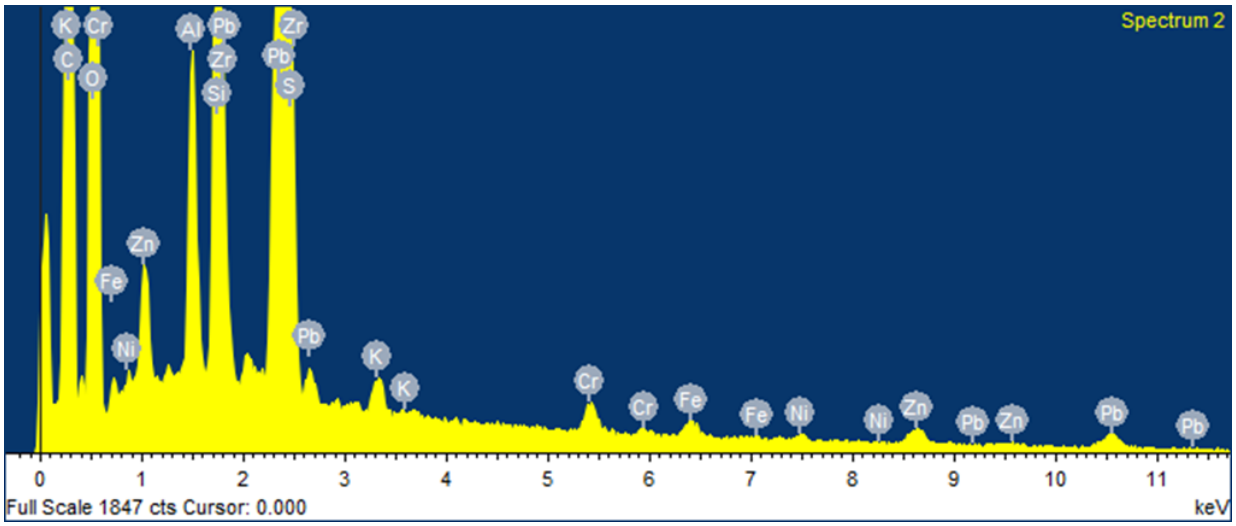
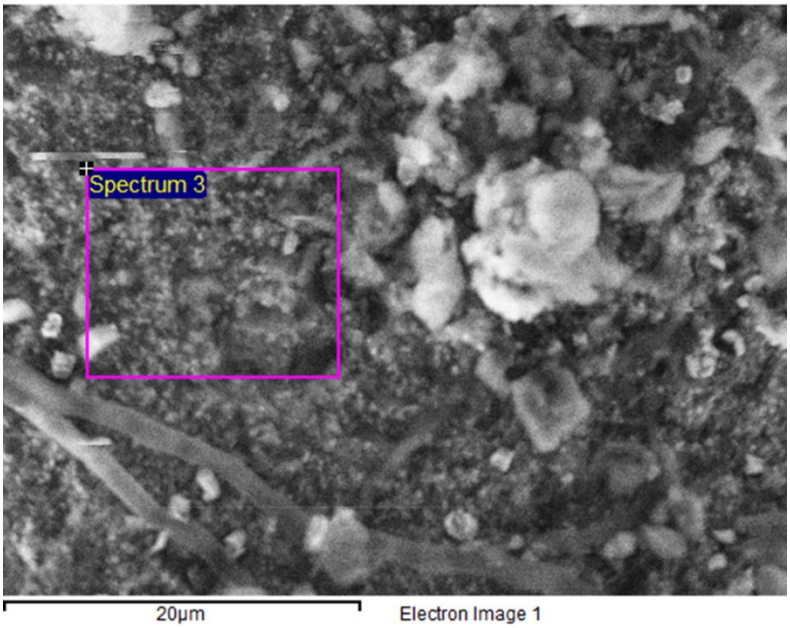


Figure A.160. SEM Image and EDS Spectrum of the Paint Collected from Exterior Web of the Girder.

Element	Weight %	Atomic %
C K	47.24	61.82
O K	35.99	35.36
Al K	0.93	0.54
Si K	0.42	0.23
S K	1.00	0.49
K K	0.54	0.22
Cr K	0.81	0.24
Ni K	0.30	0.08
Zn K	0.08	0.02
Zr L	0.35	0.06
Pb M	12.35	0.94
Totals	100.00	



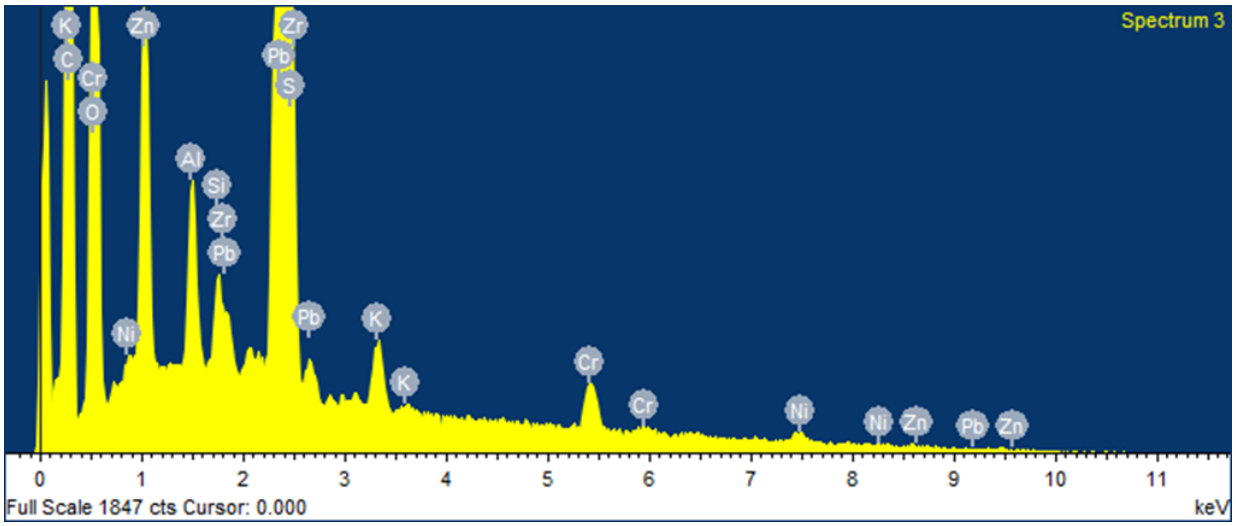
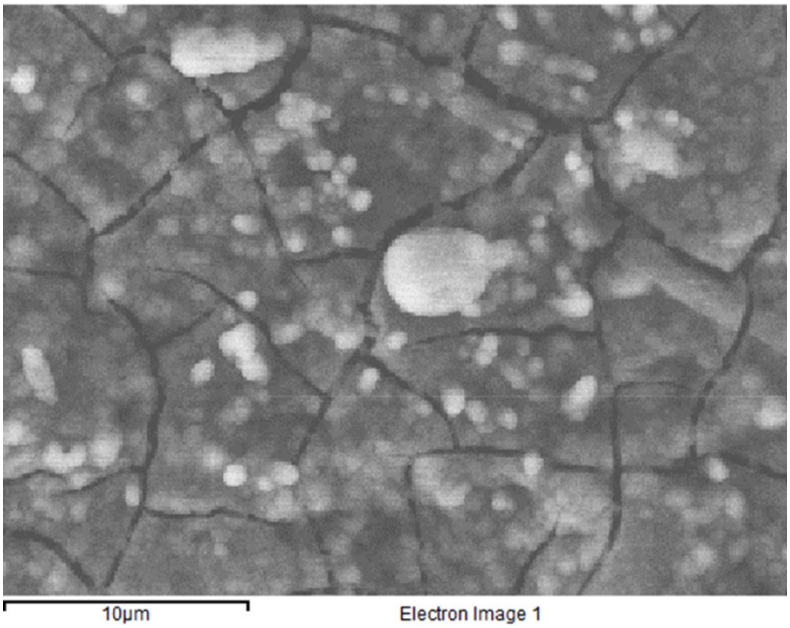


Figure A.161. SEM Image and EDS Spectrum of the Paint Collected from Exterior Web of the Girder.

Element	Weight %	Atomic %
C K	29.19	51.41
O K	32.30	42.71
Al K	0.56	0.44
Cl K	0.44	0.26
Ca K	0.27	0.14
Fe K	4.19	1.59
Ni K	0.22	0.08
Zn K	0.07	0.02
Pb M	32.76	3.35
Totals	100.00	



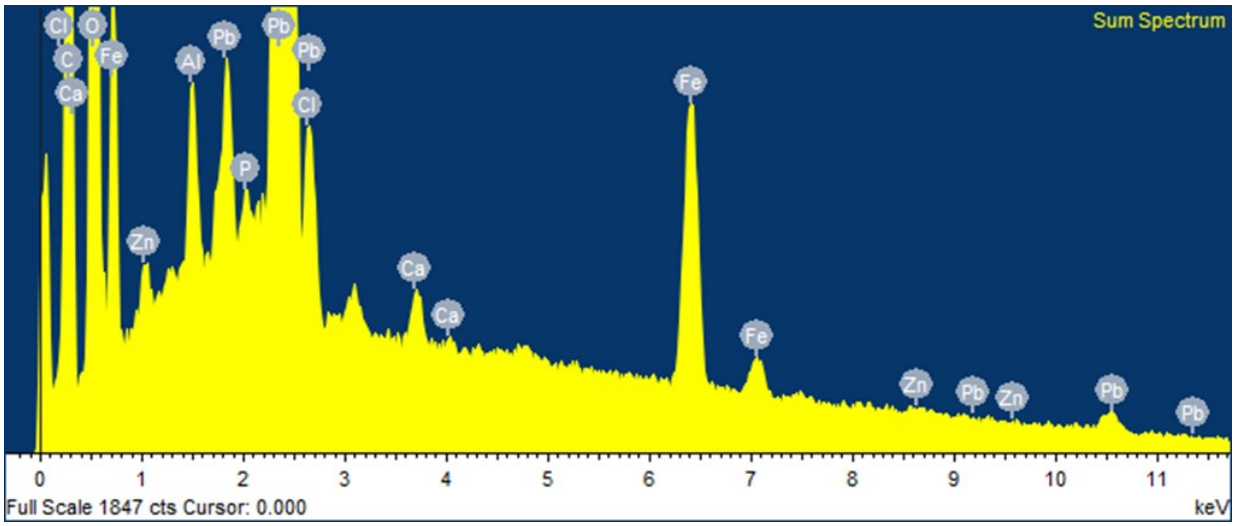
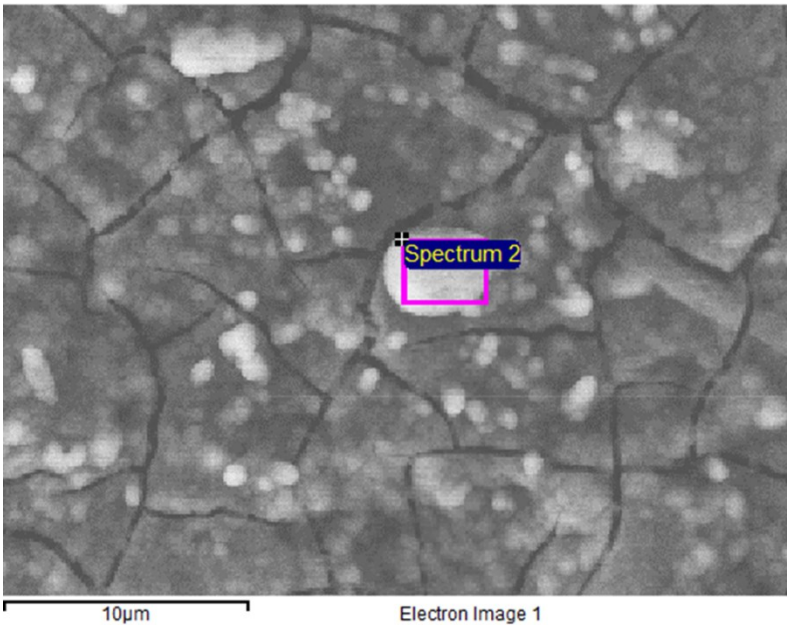


Figure A.162. SEM Image and EDS Spectrum of the Paint Collected from Interior Web of the Girder (G3F1).

Element	Weight %	Atomic %
C K	30.57	53.46
O K	29.44	38.64
Al K	0.98	0.76
Si K	0.43	0.32
P K	0.24	0.17
Cl K	0.47	0.28
Ca K	0.87	0.46
Fe K	7.61	2.86
Zn K	0.37	0.12
Pb M	29.03	2.94
Totals	100.00	



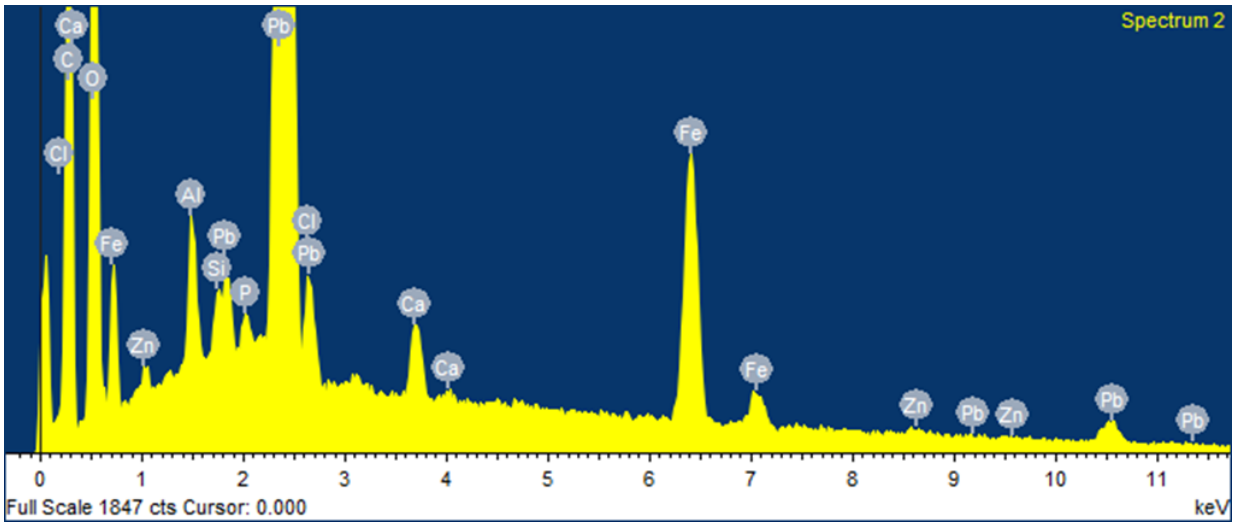


Figure A.163. SEM Image and EDS Spectrum of the Paint Collected from Interior Web of the Girder (G3F1).

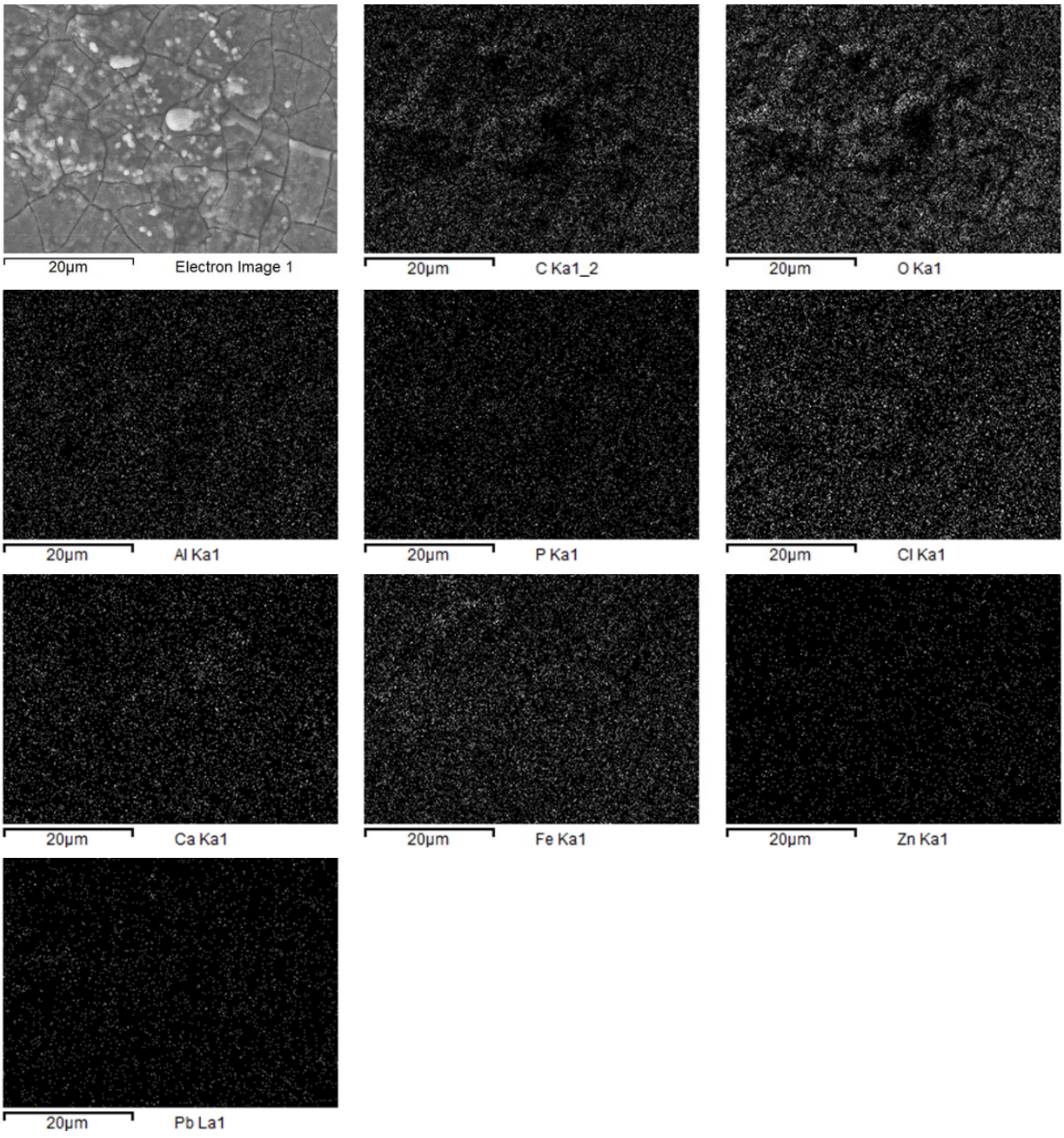
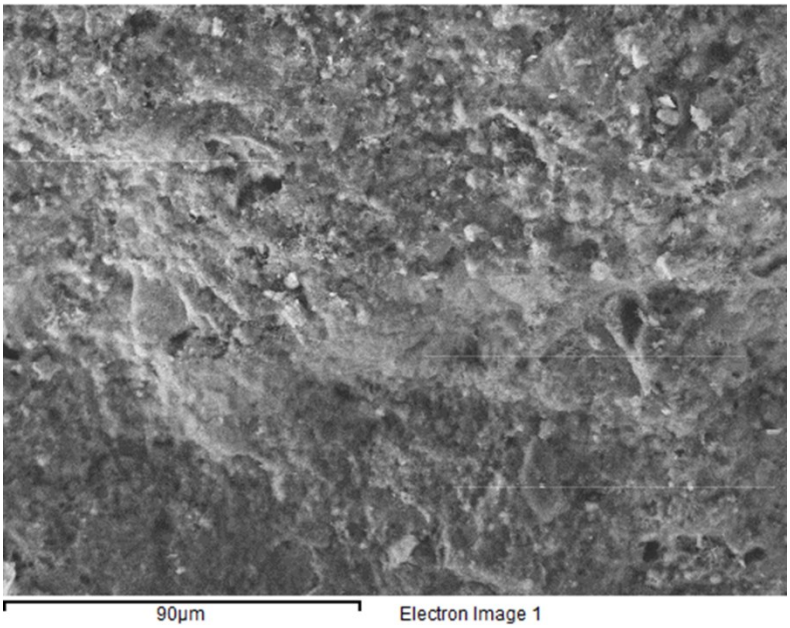


Figure A.164. EDS Elemental Mapping of Paint Collected from Interior Web (G3F1).

Element	Weight %	Atomic %
C K	6.60	16.02
O K	27.40	49.95
Al K	1.76	1.90
Si K	4.29	4.45
S K	0.17	0.15
Cl K	1.71	1.41
K K	0.10	0.08
Fe K	3.08	1.61
Ni K	0.13	0.06
Zn K	54.28	24.21
Zr L	0.49	0.16
Totals	100.00	



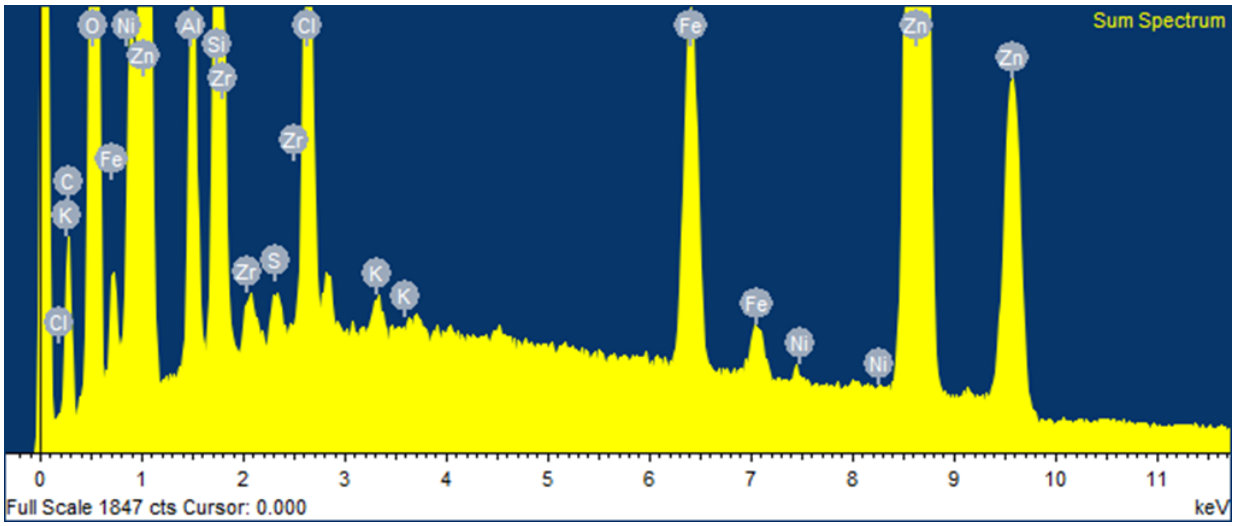


Figure A.165. SEM Image and EDS Spectrum of the Paint Collected from Interior Web of the Girder (G6F1).

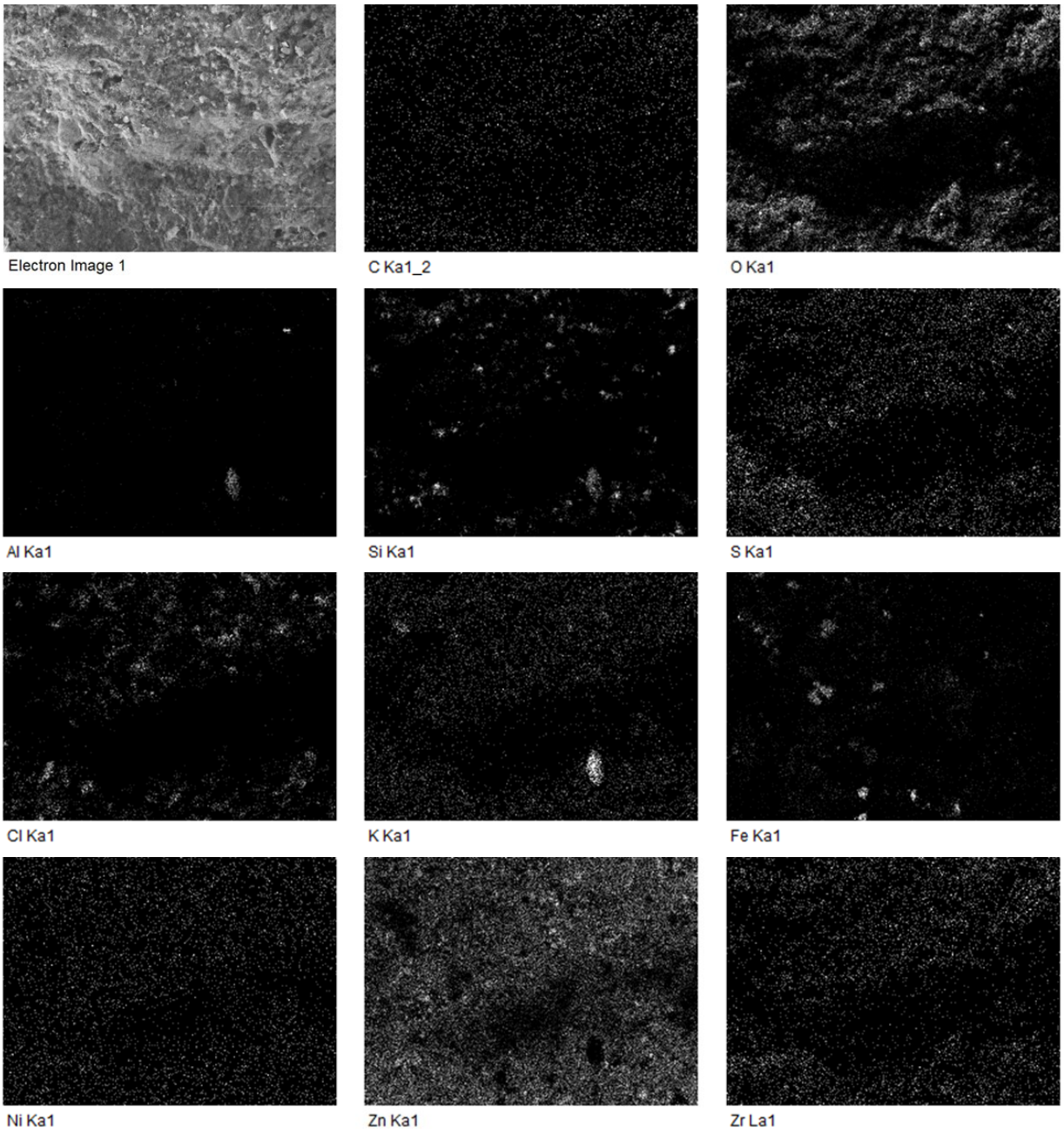
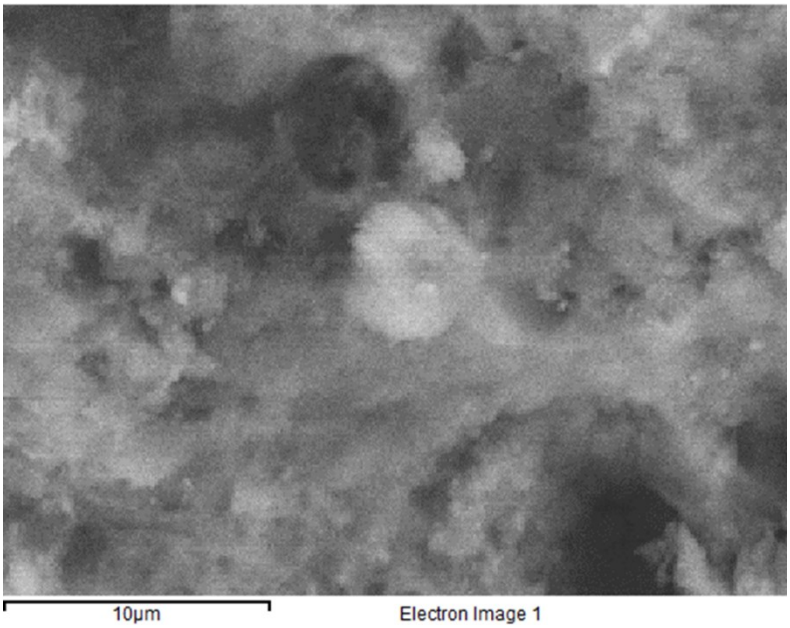


Figure A.166. EDS Elemental Mapping of Paint Collected from Interior Web (G6F1).

Element	Weight %	Atomic %
C K	8.01	20.95
O K	20.76	40.78
Al K	1.82	2.12
Si K	3.34	3.73
S K	0.16	0.16
Cl K	0.67	0.60
Fe K	4.59	2.58
Zn K	60.20	28.94
Zr L	0.44	0.15
Totals	100.00	



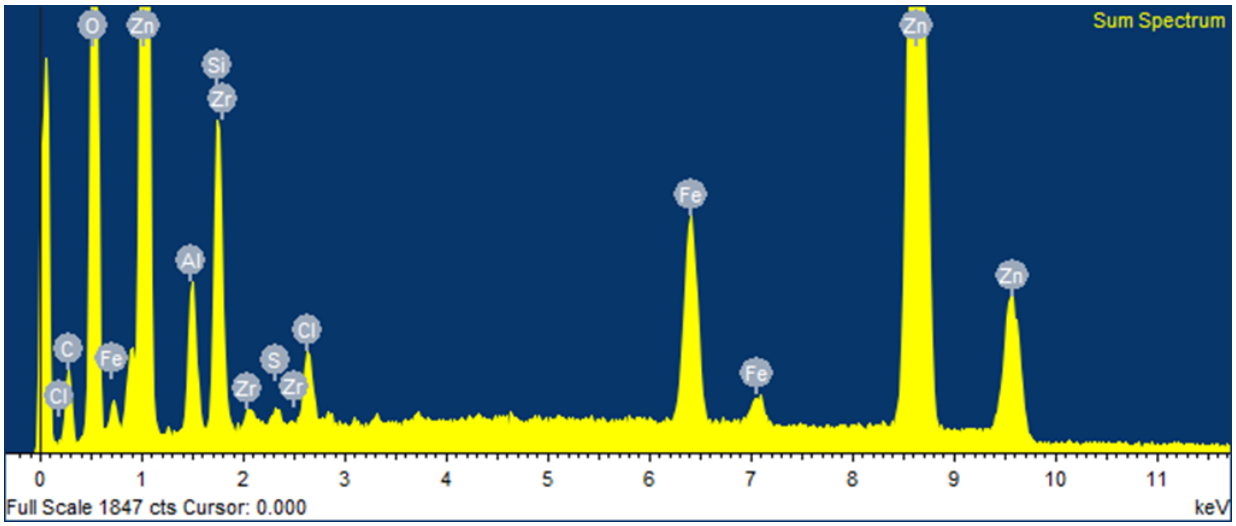


Figure A.167. SEM Image of Paint and EDS Spectrum of the Paint Collected from Interior Web of the Girder (G6F1).

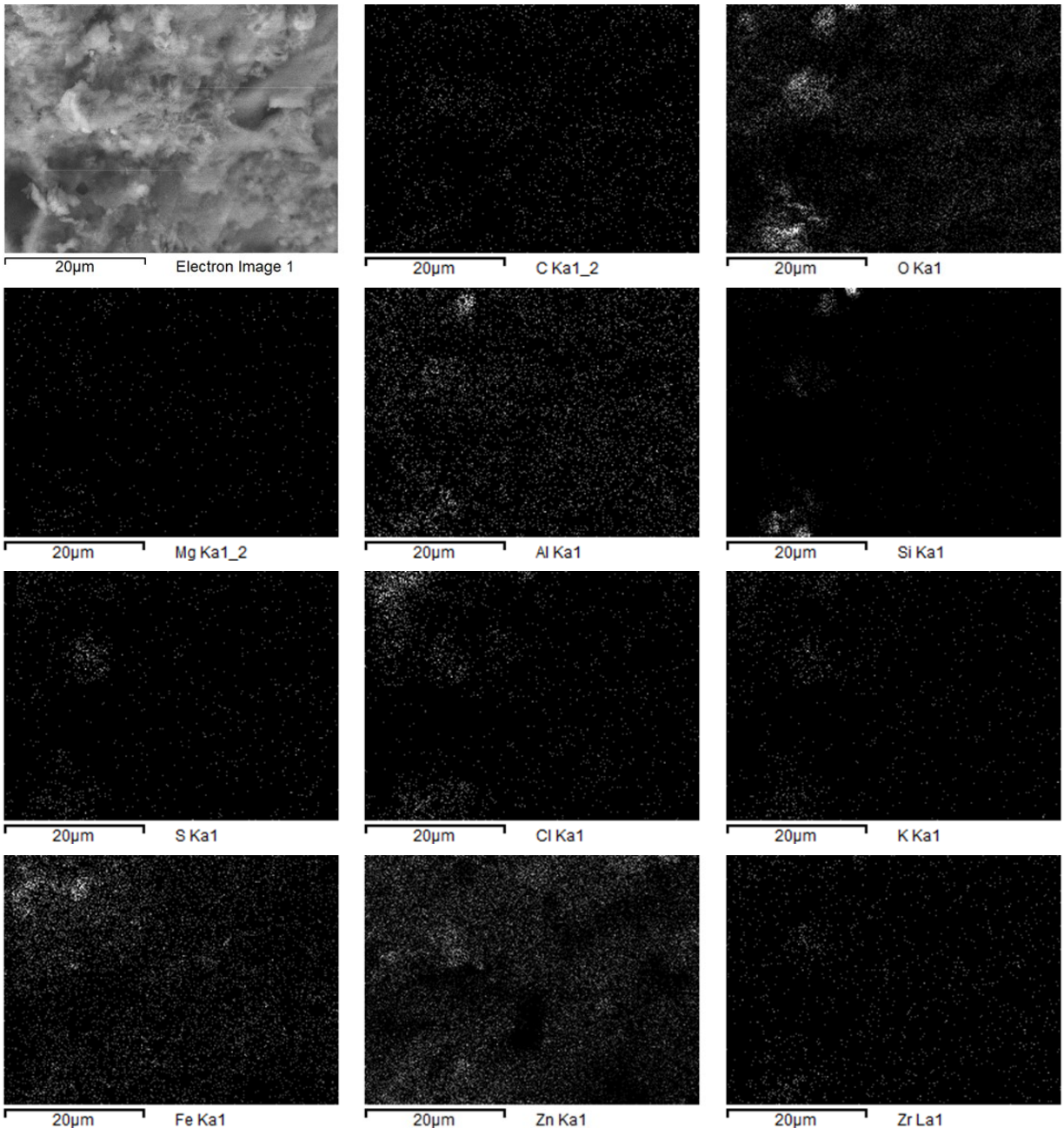


Figure A.168. SEM Image of Paint and EDS Spectrum of the Paint Collected from Interior Web of the Girder (G6F1).

A.15. CRP-PS-01

- US 181 over C C Ship Channel
- Bridge ID 161780010106041, Coordinates (27.81248, -97.39529), Nueces County
- Steel Truss bridge with System III type paint
- Built 1959(2005**)
- Date of Inspection: October 24, 2020; bearing and connector plate inspection
- Revisited for pH test and scrape test
- No visual inspection on deck
- Location for Testing: F4 Conn. Plate, F1 Conn. Plate, F2 Channel Member., Channel Member., F3 Connector Plate



Figure A.169. Typical Elevation of CRP-PS-01

A.15.1. Observed Condition

The paint of this bridge is in overall fair condition with some areas in excellent condition and some areas with complete paint failure and rusting. corrosion is observed on the joints of girders, diaphragm of the span that is over the Corpus Christi ship channel (water body). Overall the appearance coat is in good condition. Blistering, Erosion of paint, and cracking in paint is not present. This bridge has undergone multiple repainting cycles, with the most recent paint application dating back approximately 15 to 20 years ago.

** Year reconstructed



(a) Bearing



(b) Superstructure



(c) Bearing



(d) Connector Plate



(e) Bearing



(f) Bearing

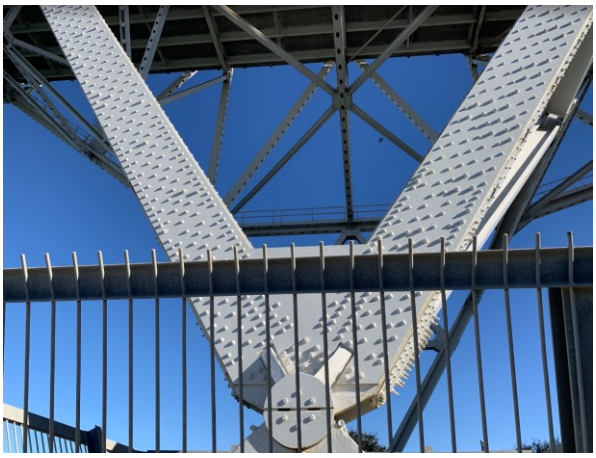
Figure A.170. Paint Condition of Bearing, Superstructure, and Truss Members of CRP-PS-01.



(a) Bearing



(b) Bearing



(c) Truss Member



(d) Truss Member



(e) Superstructure



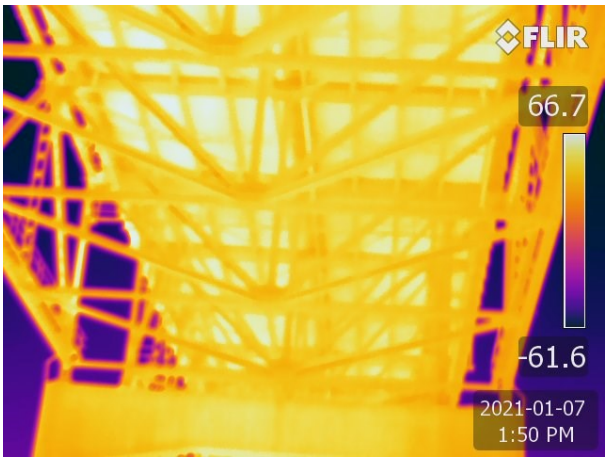
(f) Superstructure

Figure A.171. Paint Condition of Bearing, Superstructure, and Truss Members of CRP-PS-01.

A.15.2.NDT Results



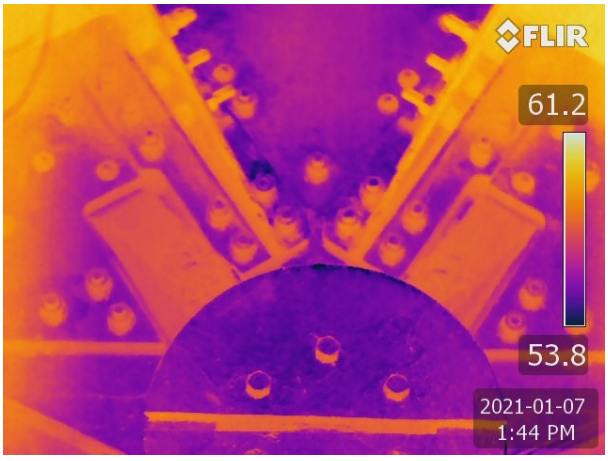
(a) Digital Image of Superstructure



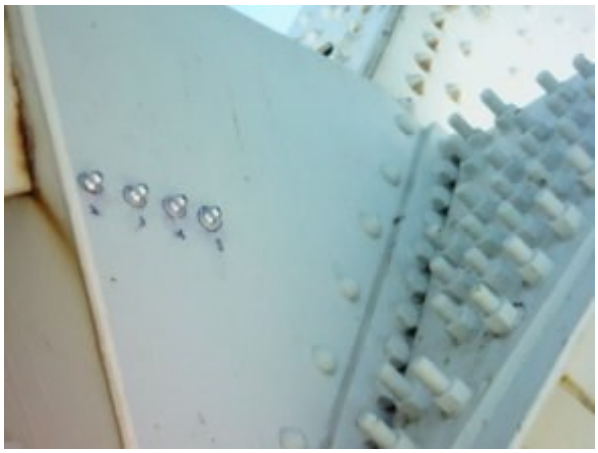
(b) Thermal Image of Superstructure



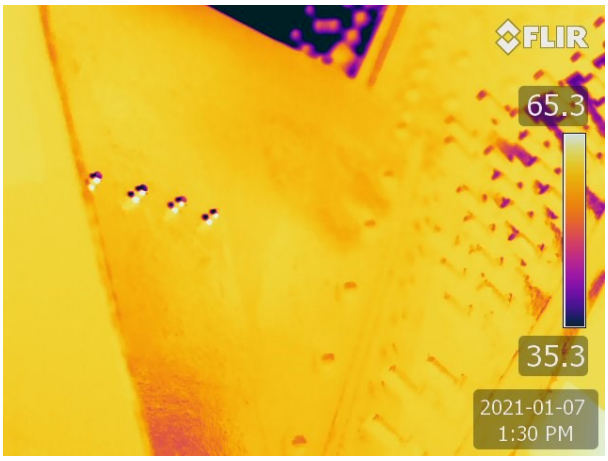
(c) Digital Image of Connector Plate



(d) Thermal Image of Connector Plate



(e) Digital Image of the Truss Member with Connector Plate



(f) Thermal image of the Truss Member with Connector Plate

Figure A.172. Digital and Thermal Image of Connector Plate and Truss Member on CRP-PS-01.

Table A-74. Field Inspection Results for CRP-PS-01.

Location	Cl^- Conc. (ppm)	pH Test	Thickness (µm)	Thickness (inch)	Visual Inspection
F4 Conn. Plate Ext.	1	-	Measured R1 270 R2 260 R3 358 Design Paint >= 190.5	Measured R1 0.571 R2 0.565 R3 0.567 R_Avg 0.568 Design	Rust Grade – 10 Blistering – Not Found Discoloration – Not Found Flaking – Not Found Delamination – Not Found
F1 Conn. Plate Ext.	1		Measured R1 330 R2 370 R3 332 Design Paint >= 190.5	Measured R1 0.797 R2 0.797 R3 0.795 R_Avg 0.796 Design	Rust Grade – 10 Blistering – Not Found Discoloration – Not Found Flaking – Not Found Delamination – Not Found
F2 Channel Memb Ext.	1	-	Measured R1 419 R2 427 R3 393 Design Paint >= 190.5	Measured R1 0.522 R2 0.526 R3 0.528 R_Avg 0.525 Design	Rust Grade – 10 Blistering – Not Found Discoloration – Not Found Flaking – Not Found Delamination – Found
Channel Memb Ext.	-	-	Measured R1 R2 R3	Measured R1 0.573 R2 0.573 R3 0.574 R_Avg 0.573 Design	Rust Grade – 10 Blistering – Not Found Discoloration – Not Found Flaking – Not Found Delamination – Not Found
F3 Conn. Plate Ext.	-		Measured R1 286 R2 322 R3 377 Design Paint >= 190.5	Measured R1 0.791 R2 0.790 R3 0.789 R_Avg 0.790 Design	Rust Grade – 10 Blistering – Not Found Discoloration – Not Found Flaking – Not Found Delamination – Not Found

A.15.3. Pull-off Adhesion Results

Table A-75. Pull-off Adhesion Results for CRP-PS-01.

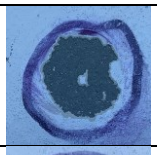
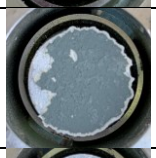
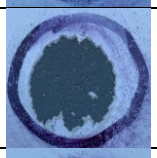
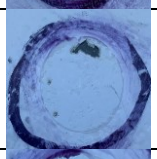
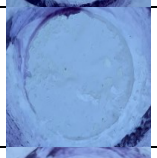
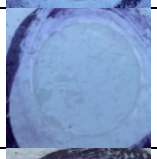
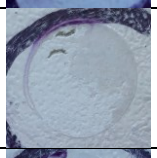
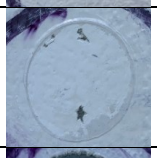
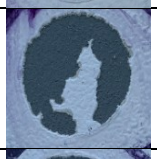
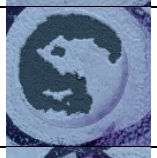
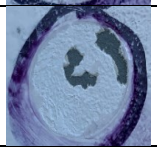
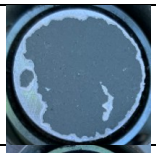
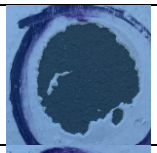
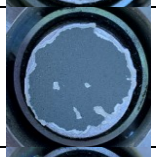
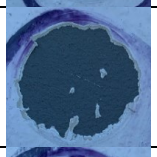
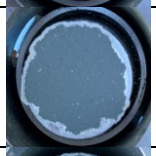
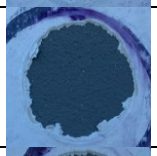
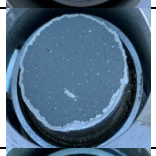
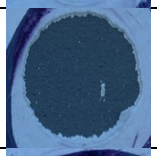
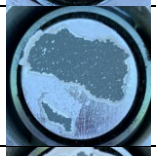
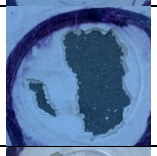
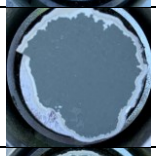
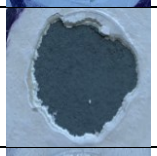
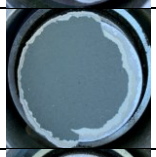
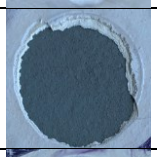
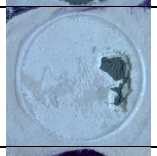
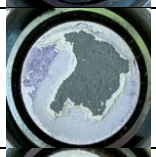
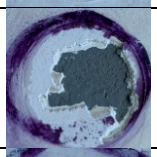
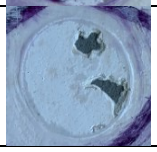
Location	Dolly Face	Substrate Face	Test Result (psi)	Attributes	Failure Type
F1			1777	10% C 90% A/B	10% Cohesive Failure 90% Adhesive Failure
			2326	20% C 80% A/B	20% Cohesive Failure 80% Adhesive Failure
			1966	90% C 10% A/B	90% Cohesive Failure 10% Adhesive Failure
			1393	10% C/Y 90% C	10% Glue Failure 90% Cohesive Failure
			1603	100% C	100% Cohesive Failure
F2			1094	30% C/Y 70% C	30% Glue Failure 70% Cohesive Failure
			1618	90% C 10% A/B	90% Cohesive Failure 10% Adhesive Failure
			2321	30% C 70% A/B	30% Cohesive Failure 70% Adhesive Failure
			1247	20% C/Y 20% C 60% A/B	20% Glue Failure 20% Cohesive Failure 60% Adhesive Failure
			2067	20% C 80% A/B	20% Cohesive Failure 80% Adhesive Failure

Table A-76. Pull-off Adhesion Results for CRP-PS-01.

Location	**Dolly Face**	**Substrate Face**	Test Result (psi)	Attributes	Failure Type
F3			2218	20% C 80% A/B	20% Cohesive Failure 80% Adhesive Failure
			2313	10% C 90% A/B	10% Cohesive Failure 90% Adhesive Failure
			2464	10% C 90% A/B	10% Cohesive Failure 90% Adhesive Failure
			2547	10% C 90% A/B	10% Cohesive Failure 90% Adhesive Failure
			1739	50% C 50% A/B	50% Cohesive Failure 50% Adhesive Failure
F4			1883	20% C 80% A/B	20% Cohesive Failure 80% Adhesive Failure
			2068	20% C 80% A/B	20% Cohesive Failure 80% Adhesive Failure
			2024	90% C 10% A/B	90% Cohesive Failure 10% Adhesive Failure
			2314	60% C 40% A/B	60% Cohesive Failure 40% Adhesive Failure
			2062	80% C 20% A/B	80% Cohesive Failure 20% Adhesive Failure

A.15.4. Optical Microscopy Results

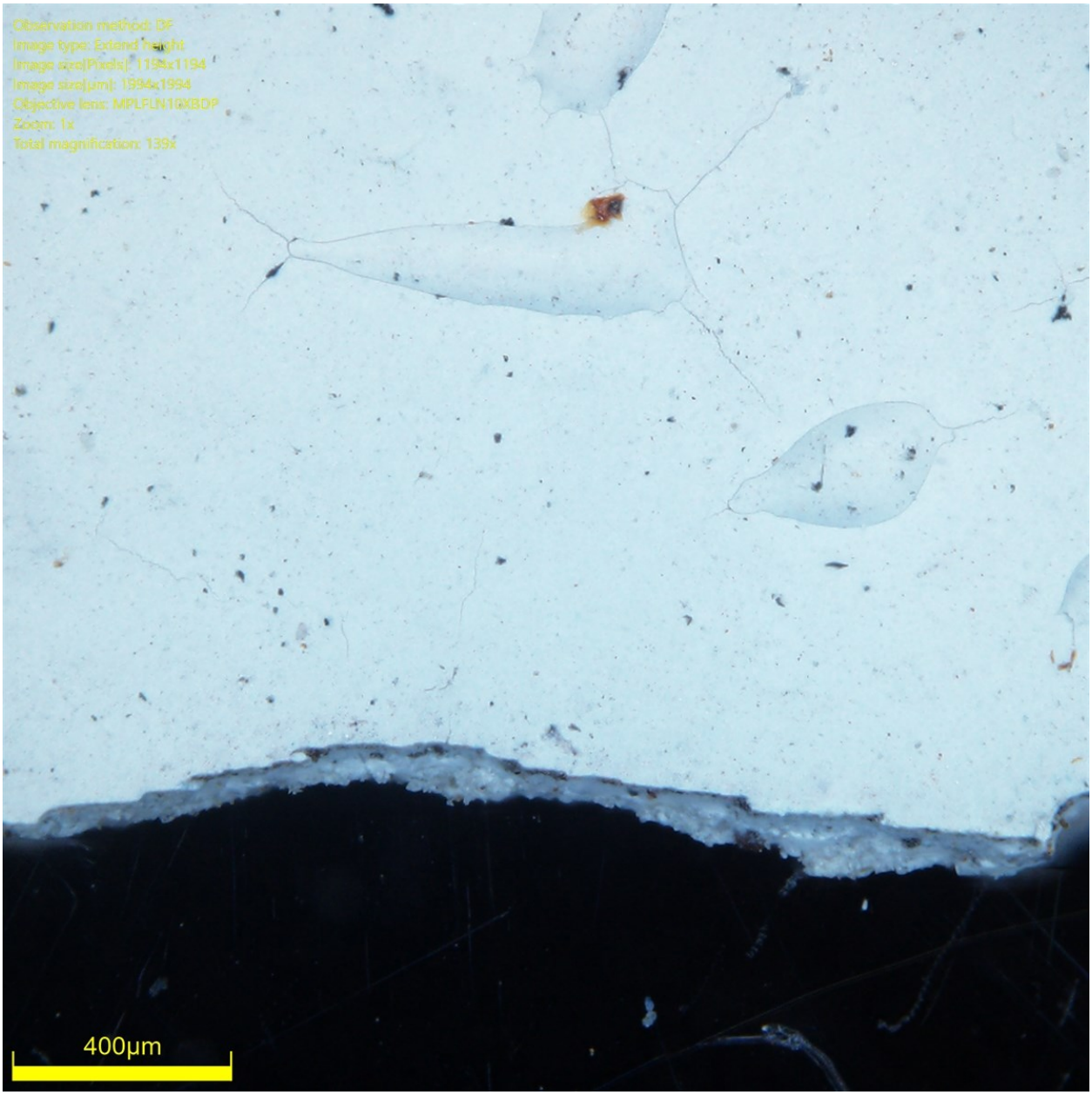


Figure A.173. Two Layer Paint System Examined by Optical Microscope CRP–PS–01.

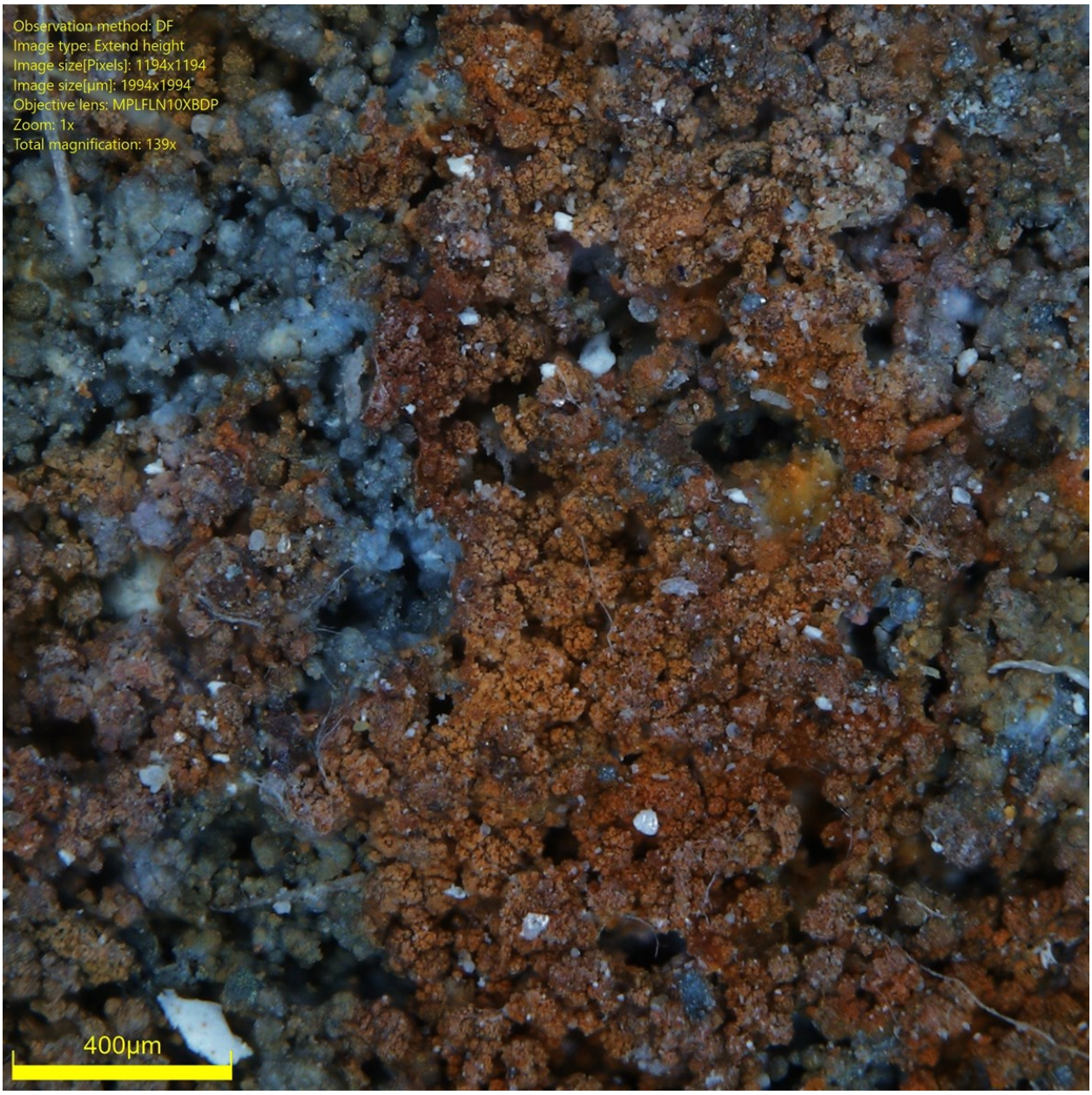
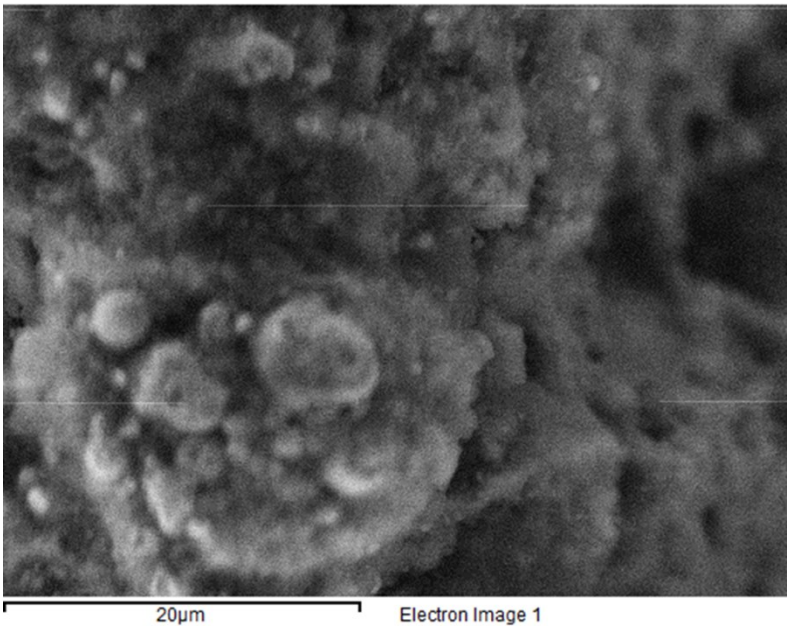


Figure A.174. Corrosion as Observed Between Primer and Base Metal.

A.15.5.SEM/EDS Results

Element	Weight %	Atomic %
C K	33.61	51.99
O K	31.11	36.14
Mg K	0.19	0.14
Al K	1.73	1.19
Si K	1.42	0.94
P K	0.29	0.17
S K	0.18	0.11
Cl K	0.54	0.28
K K	0.10	0.05
Ca K	0.35	0.16
Ti K	0.38	0.15
Fe K	2.43	0.81
Cu K	0.26	0.08
Zn K	27.41	7.79
Totals	100.00	



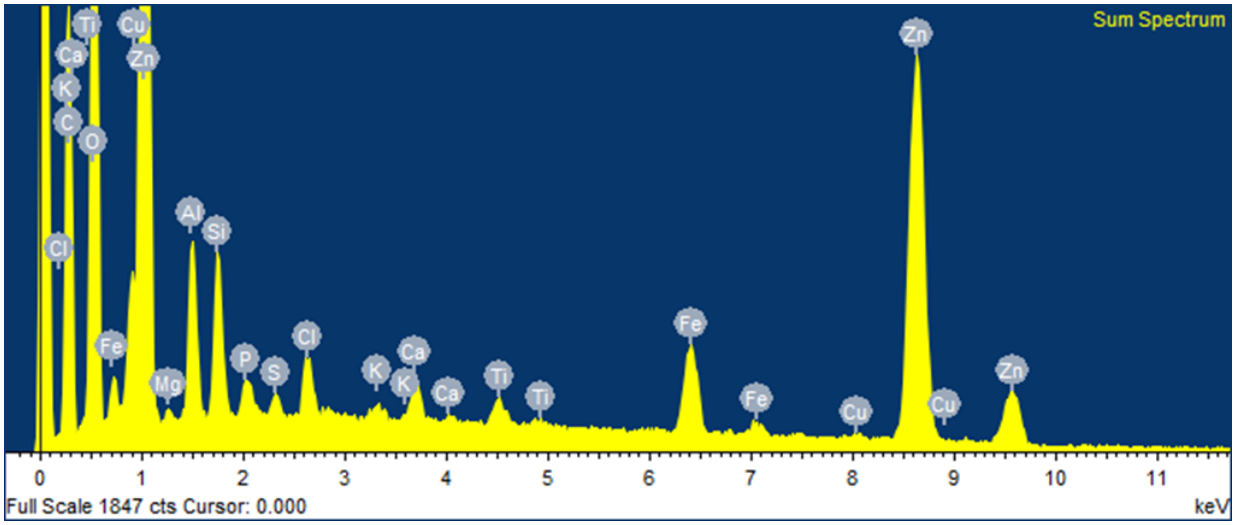


Figure A.175. SEM Image and EDS Spectrum of the Paint Collected from Exterior Web of the Girder.

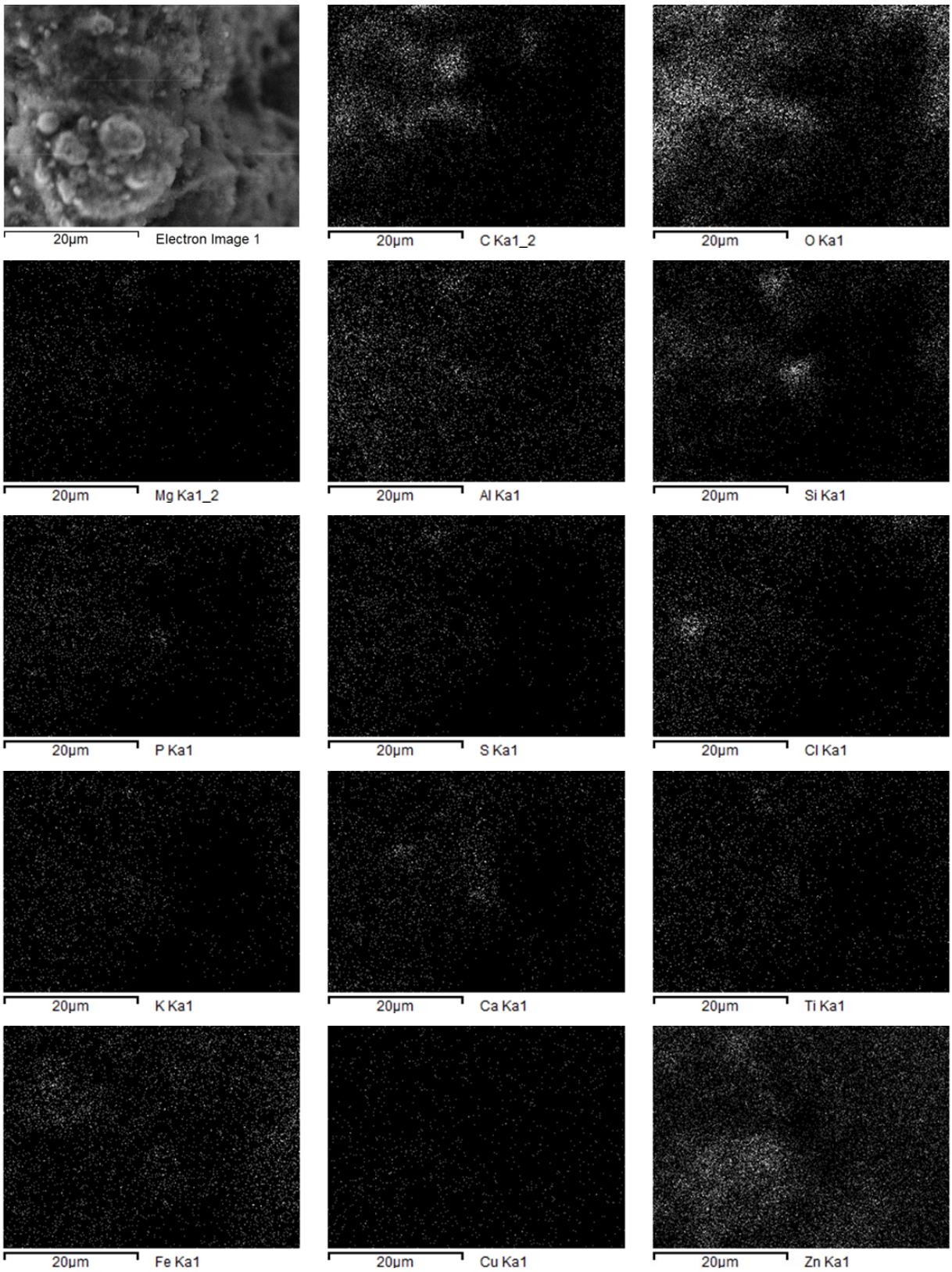
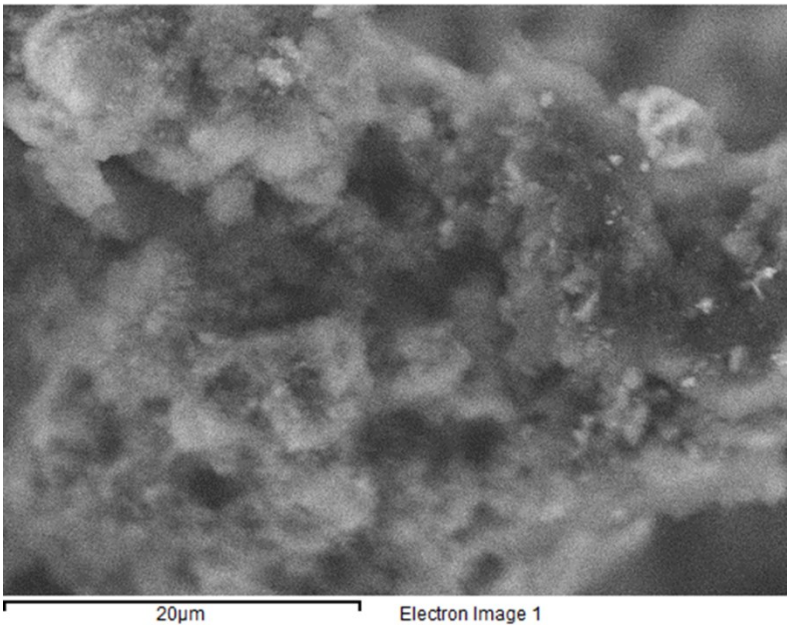


Figure A.176. EDS Elemental Mapping of Paint Collected from Exterior Web.

Element	Weight %	Atomic %
C K	36.28	50.47
O K	39.21	40.96
Mg K	0.32	0.22
Al K	1.59	0.98
Si K	2.11	1.25
P K	0.34	0.18
S K	0.28	0.14
Cl K	0.97	0.46
K K	0.89	0.38
Ca K	1.04	0.44
Ti K	0.69	0.24
Fe K	2.51	0.75
Zn K	13.78	3.52
Totals	100.00	



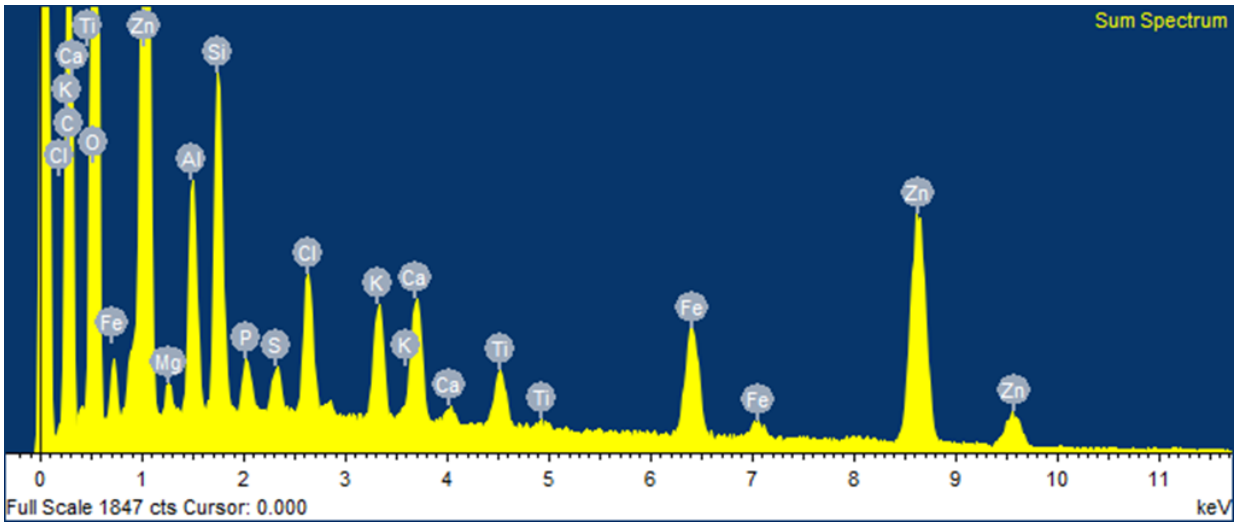


Figure A.177. SEM Image and EDS Spectrum of the Paint Collected from Exterior Web of the Girder.

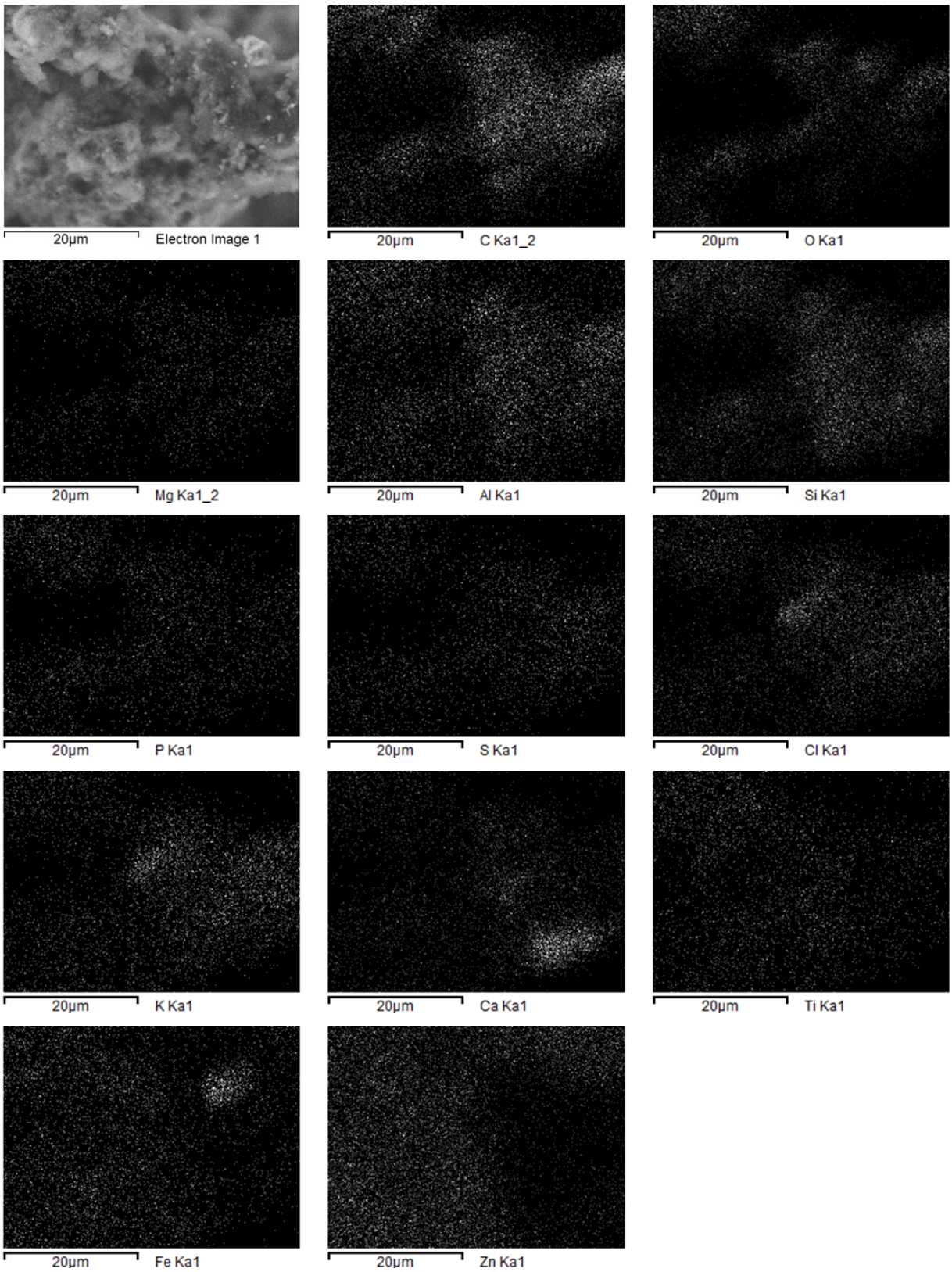
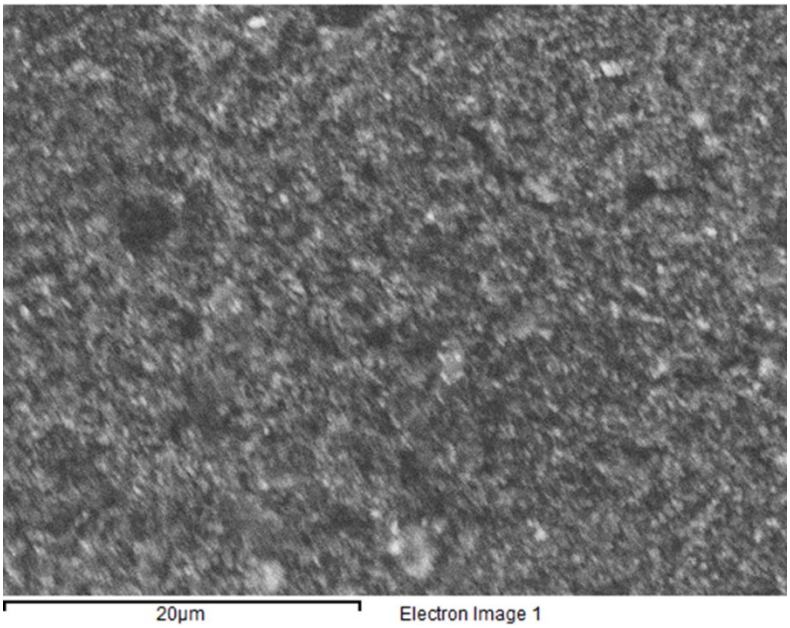


Figure A.178. EDS Elemental Mapping of Paint Collected from Exterior Web.

Element	Weight %	Atomic %
C K	32.28	42.51
O K	51.28	50.70
Na K	0.47	0.32
Mg K	0.21	0.14
Al K	2.41	1.42
Si K	2.04	1.15
P K	0.11	0.06
Cl K	0.29	0.13
K K	0.09	0.04
Ca K	0.10	0.04
Ti K	10.30	3.40
Fe K	0.25	0.07
Zn K	0.15	0.04
Totals	100.00	



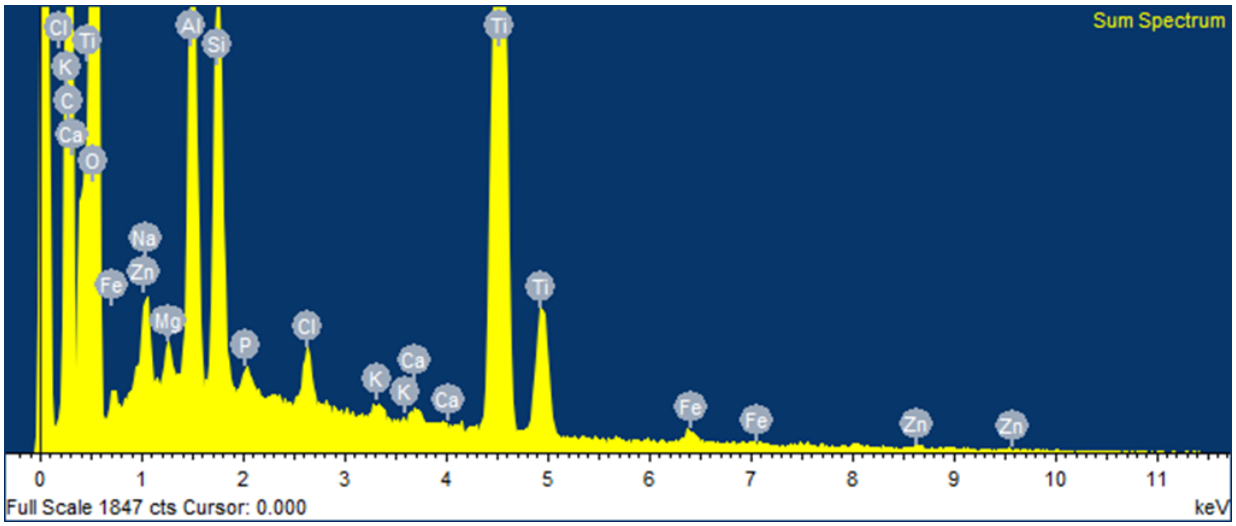


Figure A.179. SEM Image and EDS Spectrum of the Paint Collected from Exterior Web of the Girder.

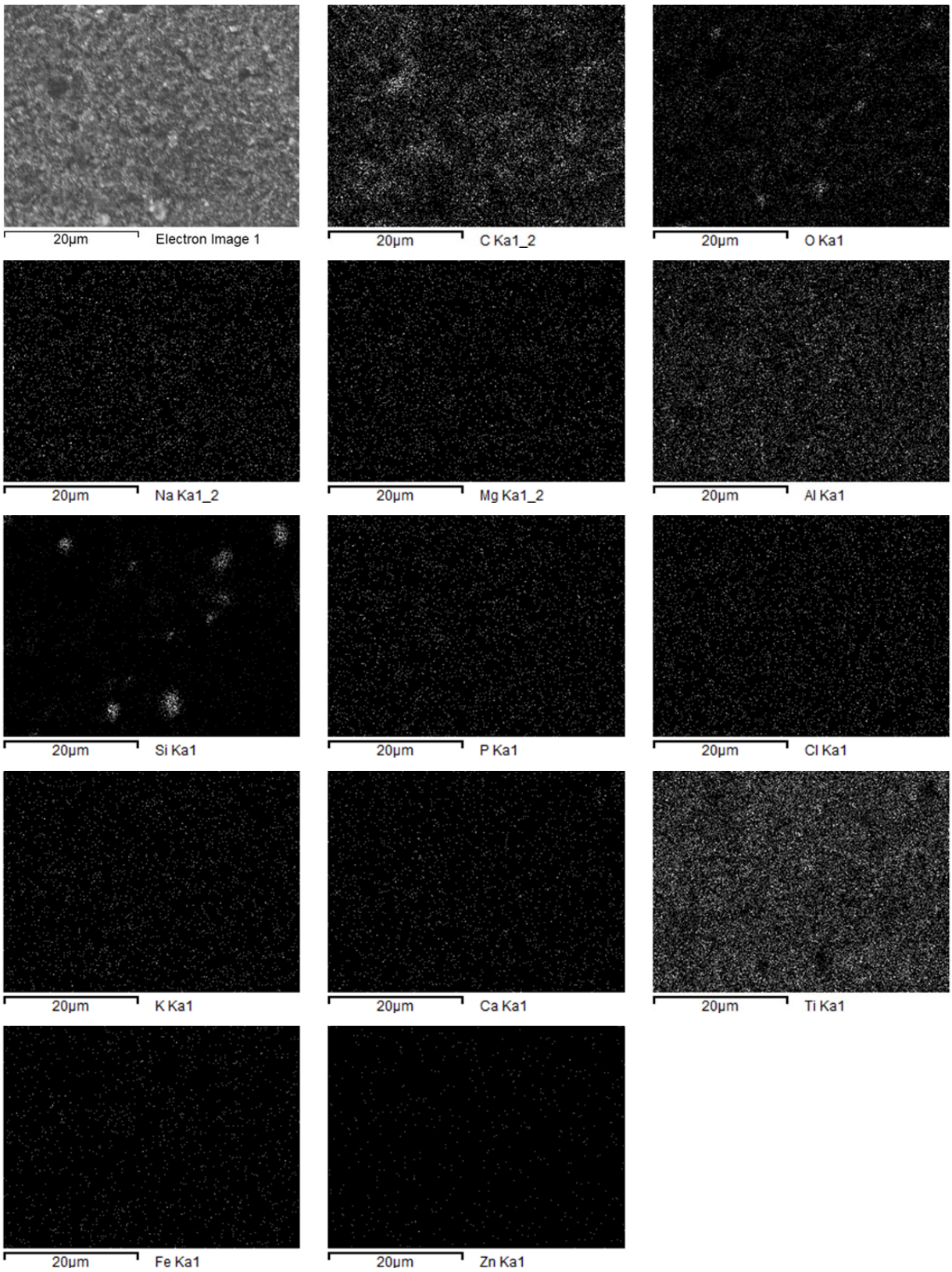


Figure A.180. EDS Elemental Mapping of Paint Collected from Exterior Web.

A.16. TYL-PS-01

- SH 64 over SH 135
- Bridge ID 102120024507306, Coordinates (32.2349, -95.0427), Smith County
- Continuous steel I beam painted with System II type paint
- Built 2009
- Date of Inspection: January 25, 2021; girder inspection carried near abutment ends on girders within approximately four feet from the abutment
- Revisited for pH test and scrape test
- No visual inspection on deck
- Location for Testing: A4-G1F1, A4-G3F1, A4-G5F2, A4-G9F2



Figure A.181. Typical Elevation of TYL-PS-01.

A.16.1. Observed Condition

Overall the paint condition of this bridge is good with minor rusting on the bearing plate and edge of bottom flange near the abutment . Blistering, Erosion of paint, cracking in paint is not present. A slight discoloration is observed on edge of the bottom flange. Dirt is accumulated on the top face of the bottom flange. No checking and cracking of paint are observed. Joints are also in good condition. TYL-PS-01 paint system should be 2 layer paint system but the appearance coat is not present at any location of girder. It's important to highlight that both TYL-PS-01 and TYL-PS-02 were constructed in the same year (2009). The lack of an appearance coat suggests rapid paint deterioration, which could be attributed to either subpar paint quality or deficiencies in the painting quality control process.



(a) Minor rusting on Edge of Bottom Flange on Exterior Girder Near Abutment



(b) Interior Girder Connnection is in Good Condition



(c) Exterior Girder in Good Condition



(d) Staining Observed on Edge of Bottom Flange of Interior Girder Near Abutment



(e) Superstructure in Good Condition



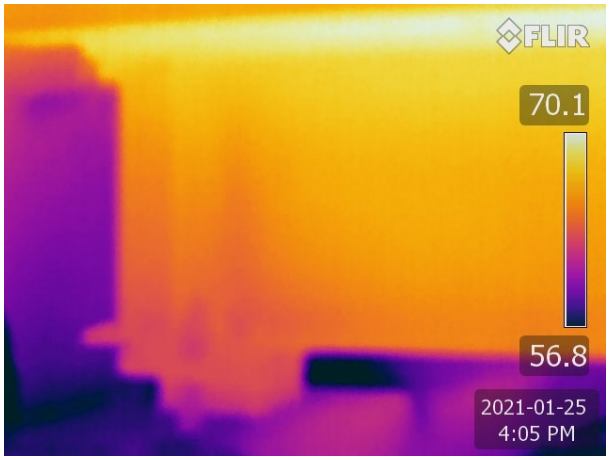
(f) Edge of Interior Girder Showing Signs of Corrosion and Rusting

Figure A.182. Paint Condition on the Girder of TYL-PS-01.

A.16.2.NDT Results



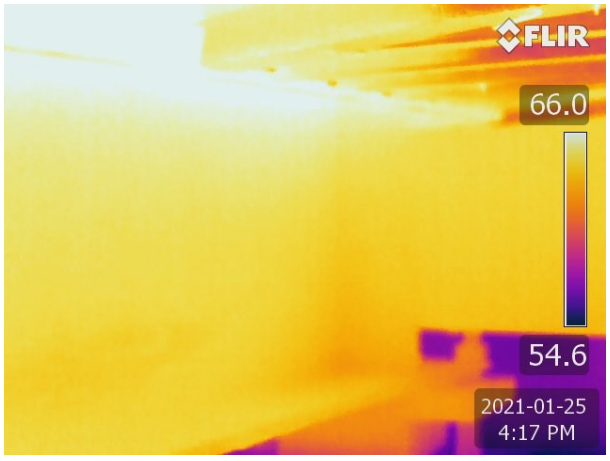
(a) Digital Image of Exterior Face of I Beam(G1F1)



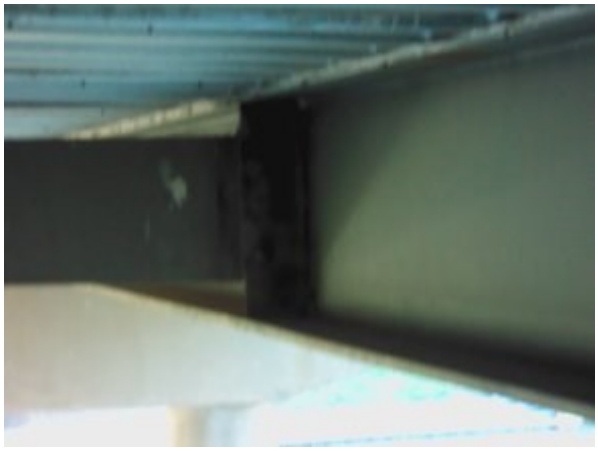
(b) Thermal Image of Exterior Face of I Beam (G1F1)



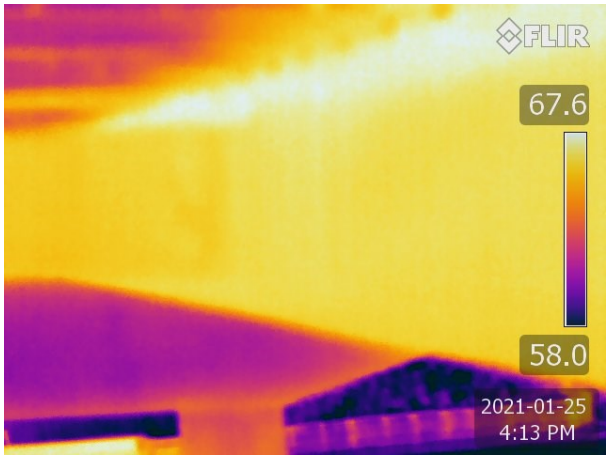
(c) Digital Image of Connection showing Rusting



(d) Thermal Image of Connection showing Rusting



(e) Digital image of the Interior face of I Beam



(f) Thermal image of the Interior of I Beam

Figure A.183. Digital and Thermal Image of Painted Girder on TYL-PS-01.

Table A-77. Field Inspection Results for TYL-PS-01.

Location	Cl^- Conc. (ppm)	pH Test	Thickness (µm)	Thickness (inch)	Visual Inspection
A4-G1F1 TF Bot. Ext.	-	-	Measured R1 -150 R2 -148 R3 -156 Design Paint 140-381	Measured R1 0.998 R2 0.998 R3 0.998 R_Avg 0.998 Design	Rust Grade – 10 Blistering – Not Found Discoloration – Not Found Flaking – Not Found Delamination – Not Found
A4-G1F1 Web Ext.	1		Measured R1 -201 R2 -186 R3 -198 Design Paint 140-381	Measured R1 0.506 R2 0.506 R3 0.506 R_Avg 0.506 Design	Rust Grade – 10 Blistering – Not Found Discoloration – Not Found Flaking – Not Found Delamination – Not Found
A4-G1F1 BF Top Ext.	-	-	Measured R1 -205 R2 -187 R3 -190 Design Paint 140-381	Measured R1 1.001 R2 1.001 R3 1.004 R_Avg 1.002 Design	Rust Grade – 10 Blistering – Not Found Discoloration – observed on the top of Bottom Flange Flaking – Not Found Delamination – Not Found
A4-G1F1 BF Bot. Ext.	-	-	Measured R1 -184 R2 -188 R3 -163 Design Paint 140-381	Measured R1 - R2 - R3 - R_Avg - Design	Rust Grade – 10 Blistering – Not Found Discoloration – Not Found Flaking – Not Found Delamination – Not Found
A4-G3F1 TF Bot. Int.	-		Measured R1 -112 R2 -105 R3 -101 Design Paint 140-381	Measured R1 1.002 R2 1.003 R3 1.001 R_Avg 1.002 Design	Rust Grade – 10 Blistering – Not Found Discoloration – Not Found Flaking – Not Found Delamination – Not Found
A4-G3F1 Web Int.	1	-	Measured R1 -168 R2 -144 R3 -141 Design Paint 140-381	Measured R1 0.500 R2 0.500 R3 0.499 R_Avg 0.500 Design	Rust Grade – 10 Blistering – Not Found Discoloration – observed on the top face of Bottom Flange Flaking – Not Found Delamination – Not Found

Table A-78. Field Inspection Results for TYL-PS-01.

Location	Cl^- Conc. (ppm)	pH Test	Thickness (µm)	Thickness (inch)	Visual Inspection
A4-G3F1 BF Top. Int.	-	-	Measured R1 -140 R2 -141 R3 -179 Design Paint 140-381	Measured R1 0.991 R2 0.990 R3 0.993 R_Avg 0.991 Design	Rust Grade – 10 Blistering – Not Found Discoloration – Not Found Flaking – Not Found Delamination – Not Found
A4-G3F1 BF Bot. Int.	-	-	Measured R1 -101 R2 -104 R3 -117 Design Paint 140-381	Measured R1 - R2 - R3 - R_Avg - Design	Rust Grade – 10 Blistering – Not Found Discoloration – Not Found Flaking – Not Found Delamination – Not Found
A4-G5F2 TF Bot Int.	-	-	Measured R1 -69.8 R2 -80.8 R3 -99.6 Design Paint 140-381	Measured R1 0.993 R2 0.993 R3 0.992 R_Avg 0.993 Design	Rust Grade – 10 Blistering – Not Found Discoloration – Not Found Flaking – Not Found Delamination – Found
A4-G5F2 Web Int.	1	-	Measured R1 -141 R2 -133 R3 -118 Design Paint 140-381	Measured R1 0.507 R2 0.507 R3 0.508 R_Avg 0.507 Design	Rust Grade – 10 Blistering – Not Found Discoloration – Not Found Flaking – Not Found Delamination – Not Found
A4-G5F2 BF Top. Int.	-		Measured R1 -121 R2 -112 R3 -114 Design Paint 140-381	Measured R1 1.003 R2 1.002 R3 1.004 R_Avg 1.003 Design	Rust Grade – 10 Blistering – Not Found Discoloration – Not Found Flaking – Not Found Delamination – Not Found
A4-G5F2 BF Bot. Int.	-	-	Measured R1 -98.1 R2 -90.1 R3 -98.8 Design Paint 140-381	Measured R1 - R2 - R3 - R_Avg - Design	Rust Grade – 10 Blistering – Not Found Discoloration – Not Found Flaking – Not Found Delamination – Found

Table A-79. Field Inspection Results for TYL-PS-01.

Location	Cl^- Conc. (ppm)	pH Test	Thickness (µm)	Thickness (inch)	Visual Inspection
A4-G9F2 TF Bot Int.	-	-	Measured R1 -84.2 R2 -68 R3 -69.6 Design Paint 140-381	Measured R1 0.994 R2 0.996 R3 0.995 R_Avg 0.995 Design	Rust Grade – 10 Blistering – Not Found Discoloration – Not Found Flaking – Not Found Delamination – Not Found
A4-G9F2 Web Int.	0	-	Measured R1 -69.7 R2 -90.2 R3 -105 Design Paint 140-381	Measured R1 0.508 R2 0.507 R3 0.507 R_Avg 0.507 Design	Rust Grade – 10 Blistering – Not Found Discoloration – Not Found Flaking – Not Found Delamination – Not Found
A4-G9F2 BF Top. Int.	-	-	Measured R1 -106 R2 -110 R3 -117 Design Paint 140-381	Measured R1 0.993 R2 0.995 R3 0.993 R_Avg 0.994 Design	Rust Grade – 10 Blistering – Not Found Discoloration – observed on the top of Bottom Flange Flaking – Not Found Delamination – Not Found
A4-G9F2 BF Bot. Int.	-	-	Measured R1 -73.1 R2 -79.2 R3 -85.2 Design Paint 140-381	Measured R1 - R2 - R3 - R_Avg - Design	Rust Grade – 10 Blistering – Not Found Discoloration – Not Found Flaking – Not Found Delamination – Not Found

A.16.3.Pull-off Adhesion Results

Table A-80. Pull-off Adhesion Results for TYL-PS-01.

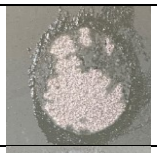
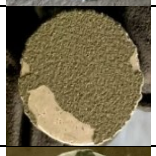
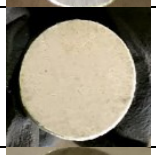
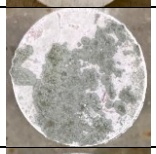
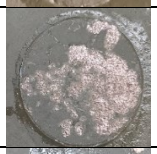
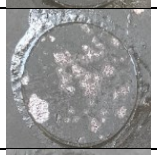
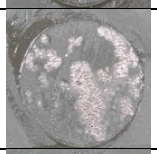
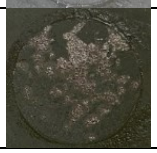
Location	Dolly Face	Substrate Face	Test Result (psi)	Attributes	Failure Type
A4-G1F1			1856	30% B 70% A/B	30% Cohesive Failure 70% Adhesive Failure
			2181	10% B 90% A/B	10% Cohesive Failure 90% Adhesive Failure
			2415	100% A/B	100% Adhesive Failure
			2676	20% B 80% A/B	20% Cohesive Failure 80% Adhesive Failure
			2117	10% B 90% A/B	10% Cohesive Failure 90% Adhesive Failure
A4-G3F1			1786	20% B 80% A/B	20% Cohesive Failure 80% Adhesive Failure
			2174	20% B 80% A/B	20% Cohesive Failure 80% Adhesive Failure
			1652	20% B 80% A/B	20% Cohesive Failure 80% Adhesive Failure
			2181	20% B 80% A/B	20% Cohesive Failure 80% Adhesive Failure
			2054	20% B 80% A/B	20% Cohesive Failure 80% Adhesive Failure

Table A-81. Pull-off Adhesion Results for TYL-PS-01.

Location	Dolly Face	Substrate Face	Test Result (psi)	Attributes	Failure Type
A4-G5F2			1854	100% B/Y	100% Glue Failure
			1604	100% B/Y	100% Glue Failure
			1923	100% B/Y	100% Glue Failure
			1820	100% B/Y	100% Glue Failure
			1682	100% B/Y	100% Glue Failure
A4-G9F2			2502	50% B/Y 50% A/B	50% Adhesive Failure 50% Adhesive Failure
			2320	60% B/Y 30% B 10% A/B	60% Glue Failure 30% Cohesive Failure 10% Adhesive Failure
			2241	50% B/Y 50% A/B	50% Adhesive Failure 50% Adhesive Failure
			2918	80% B 20% A/B	80% Cohesive Failure 20% Adhesive Failure
			2233	10% B/Y 10% B 80% A/B	10% Glue Failure 10% Cohesive Failure 80% Adhesive Failure

A.16.4.Optical Microscopy Results

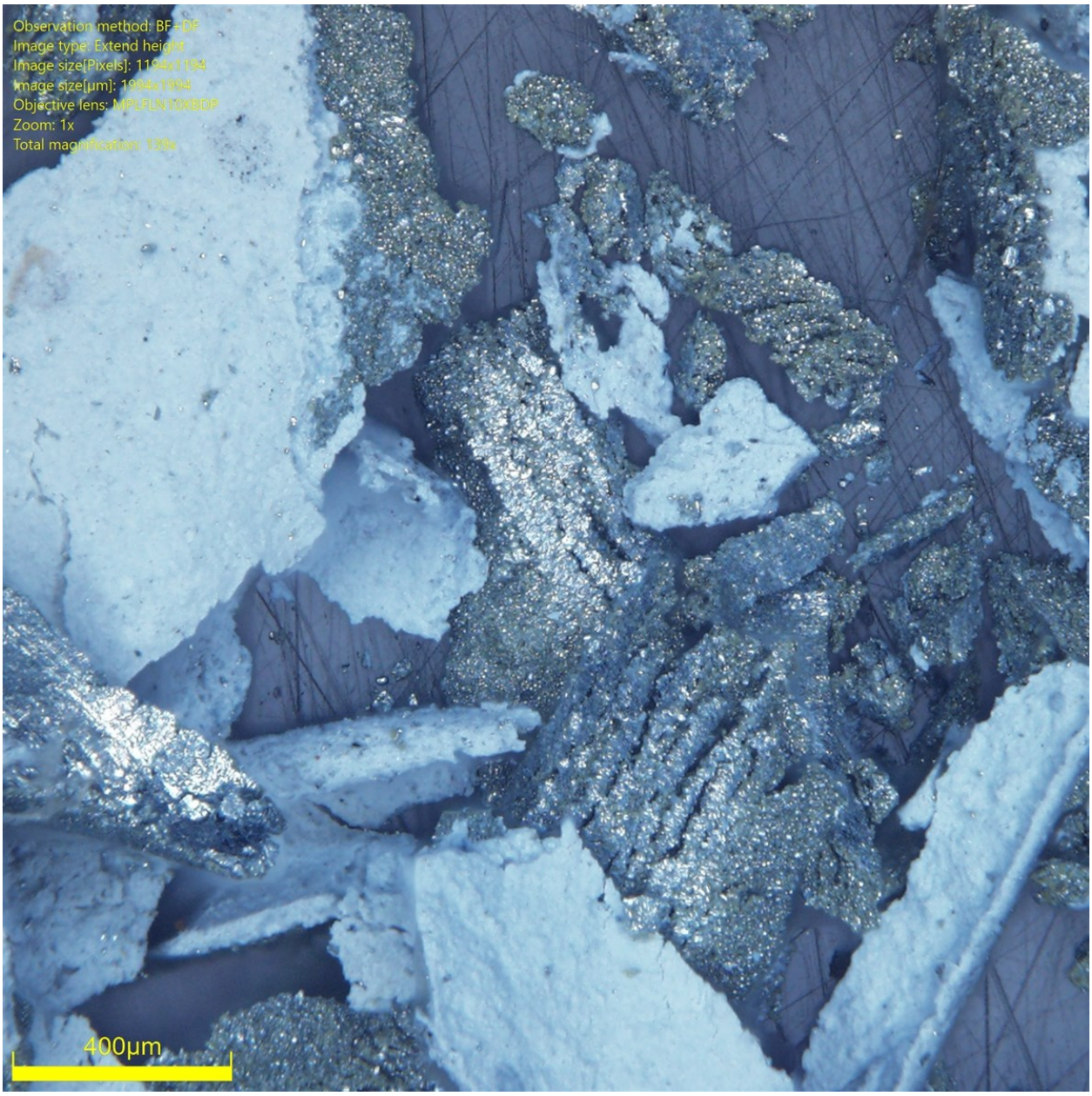


Figure A.184. Two Layer Paint System Examined by Optical Microscope TYL–PS–01.

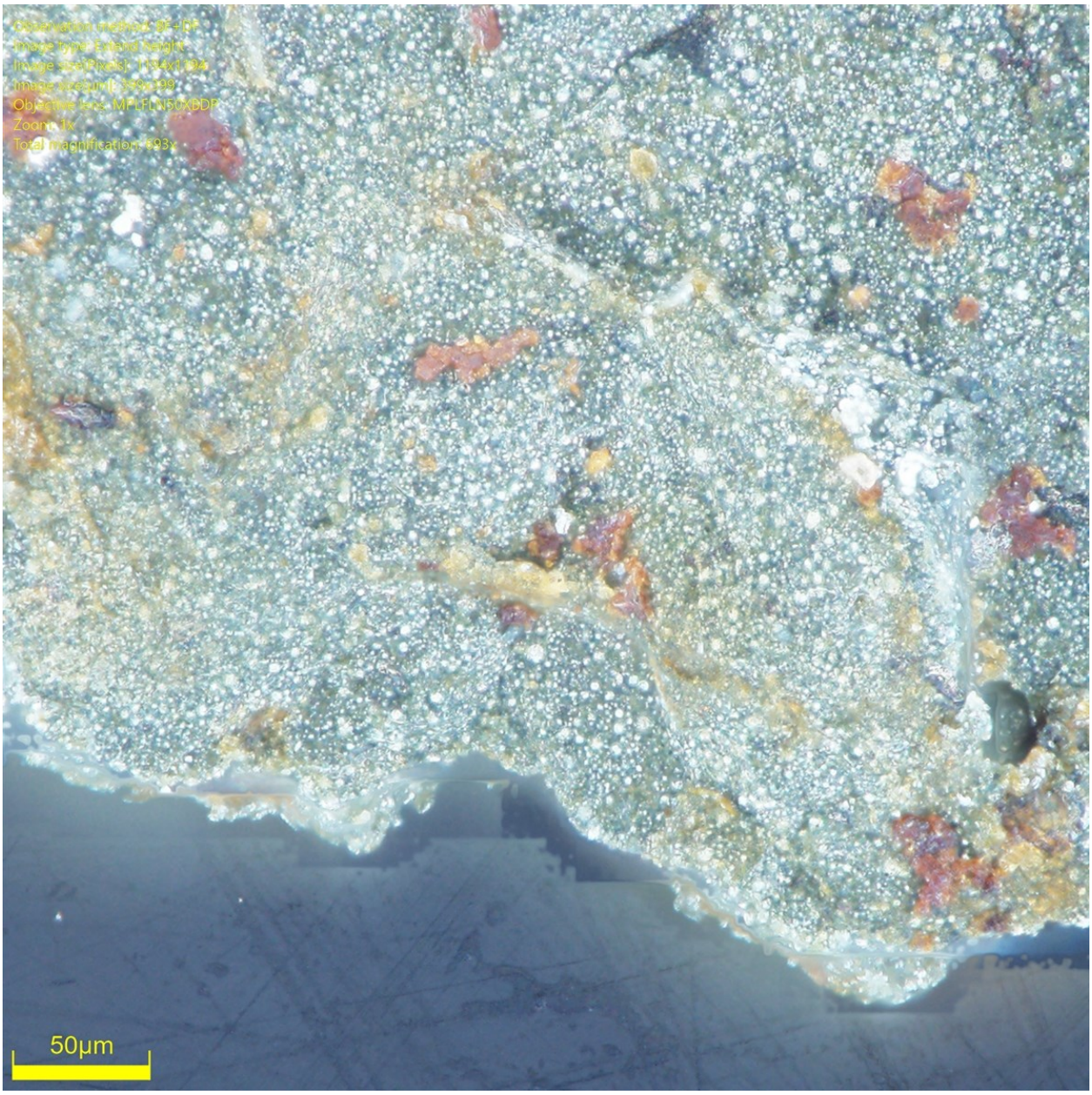
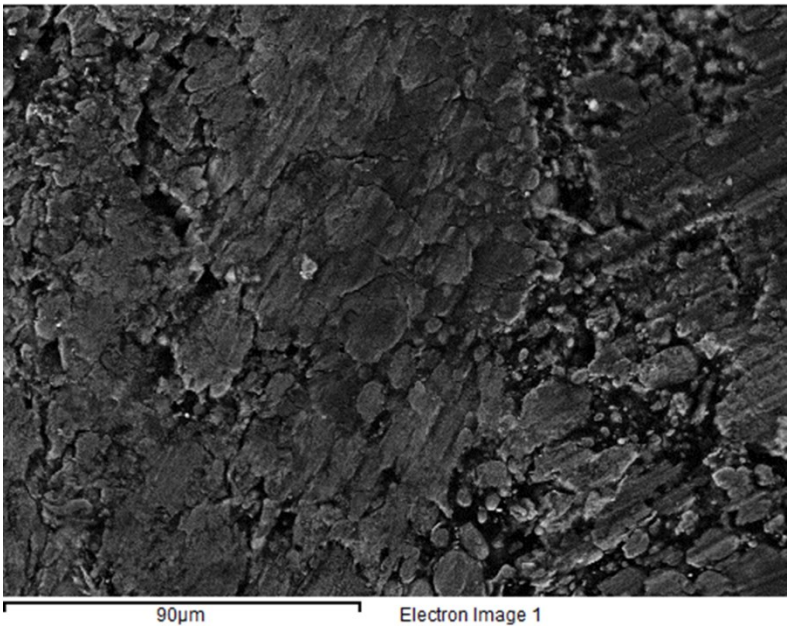


Figure A.185. Spot Rust Observed Between Primer and Base Metal.

A.16.5.SEM/EDS Results

Element	Weight %	Atomic %
C K	23.78	47.95
O K	20.27	30.68
Al K	0.25	0.23
Si K	0.30	0.26
S K	0.56	0.42
Cl K	0.26	0.18
Fe K	0.81	0.35
Ni K	0.09	0.04
Zn K	53.67	19.89
Totals	100.00	



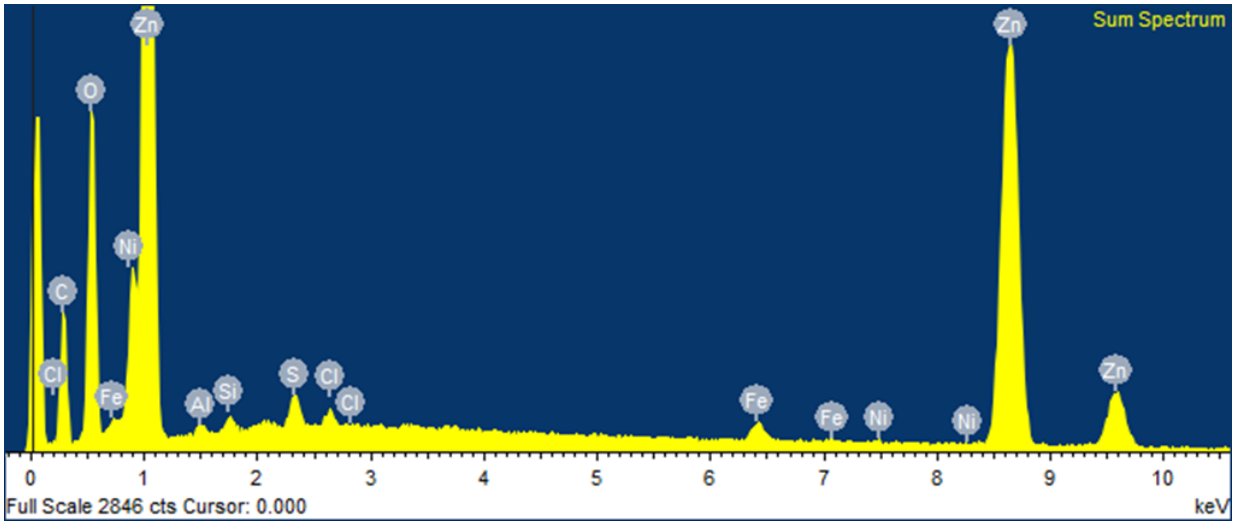


Figure A.186. SEM Image and EDS Spectrum of the Paint Collected from Exterior Web of the Girder.

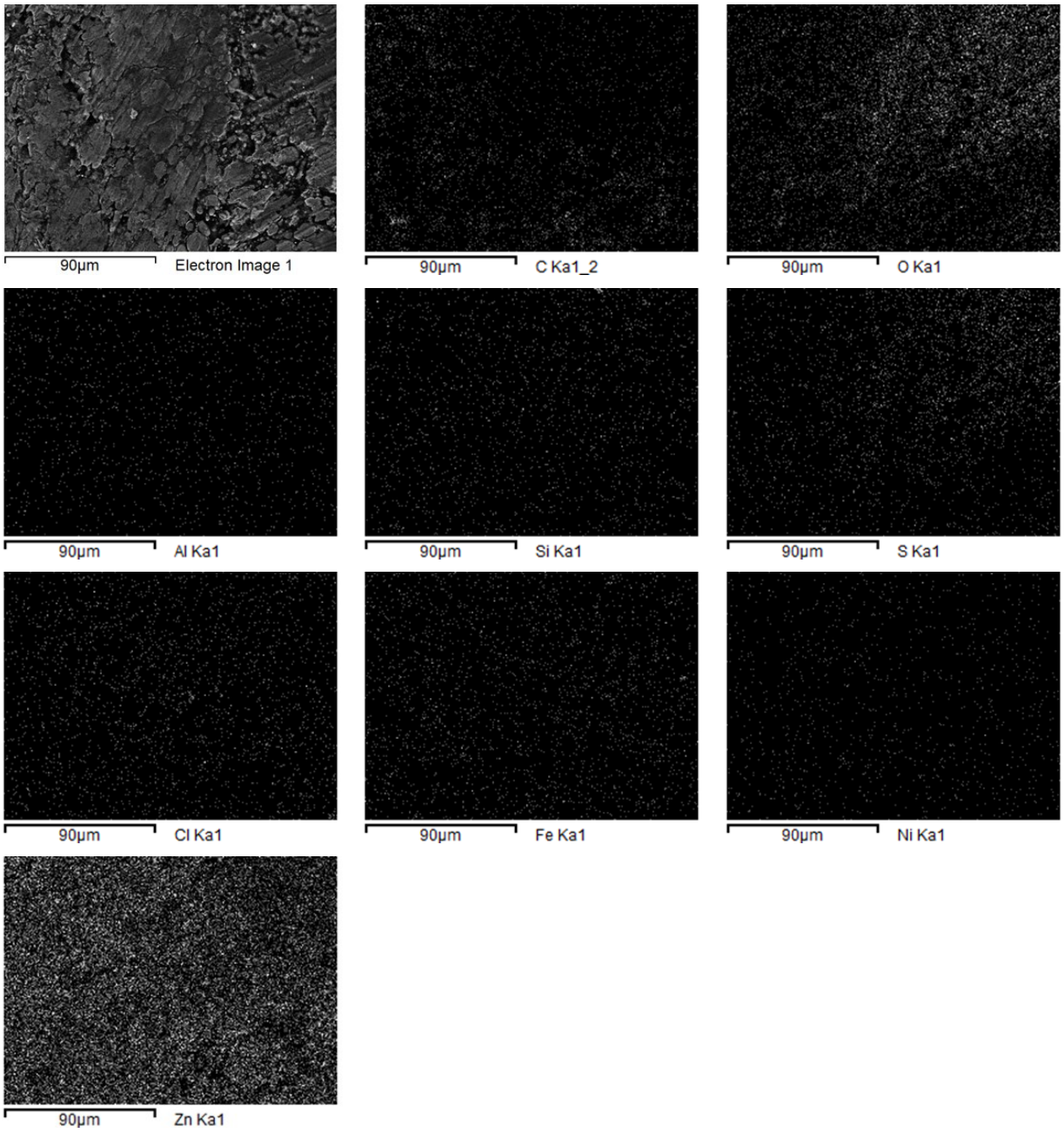
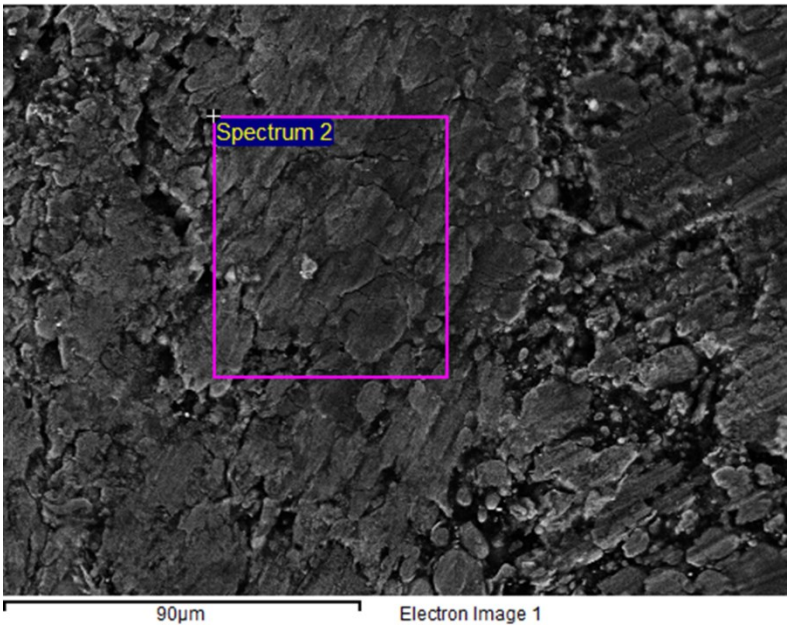


Figure A.187. EDS Elemental Mapping of Paint Collected from Exterior Web.

Element	Weight %	Atomic %
C K	16.50	36.33
O K	23.21	38.37
Al K	0.31	0.30
Si K	0.37	0.35
S K	0.81	0.67
Cl K	0.36	0.27
Fe K	0.99	0.47
Zn K	57.45	23.25
Totals	100.00	



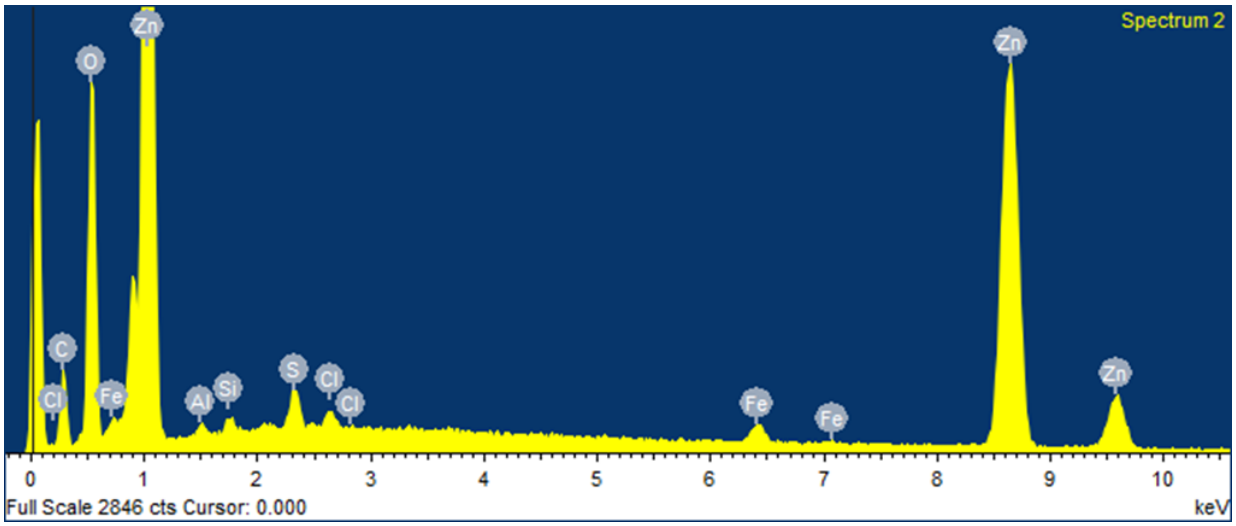
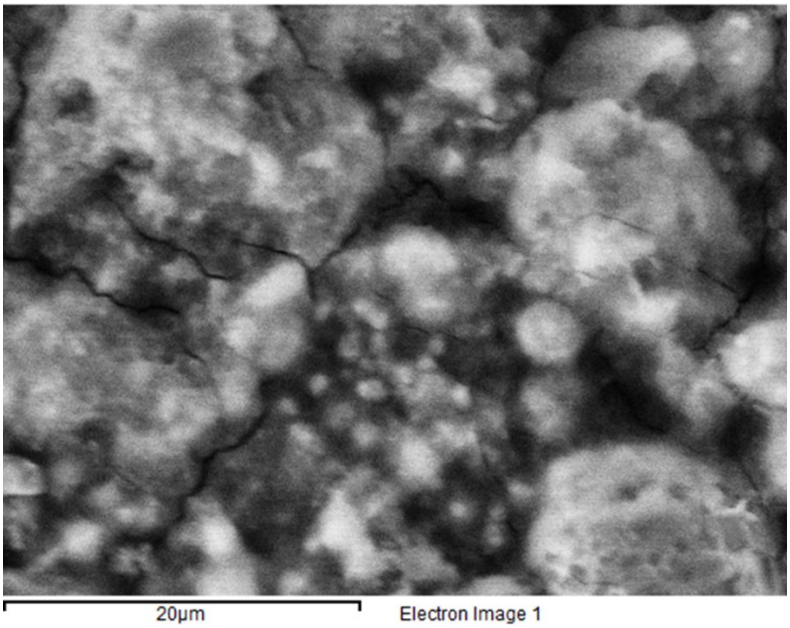


Figure A.188. SEM Image and EDS Spectrum of the Paint Collected from Exterior Web of the Girder.

Element	Weight %	Atomic %
C K	10.19	21.29
O K	36.00	56.47
Al K	0.46	0.43
Si K	0.79	0.71
S K	1.87	1.46
Cl K	0.24	0.17
K K	0.15	0.10
Fe K	1.10	0.50
Zn K	49.20	18.89
Totals	100.00	



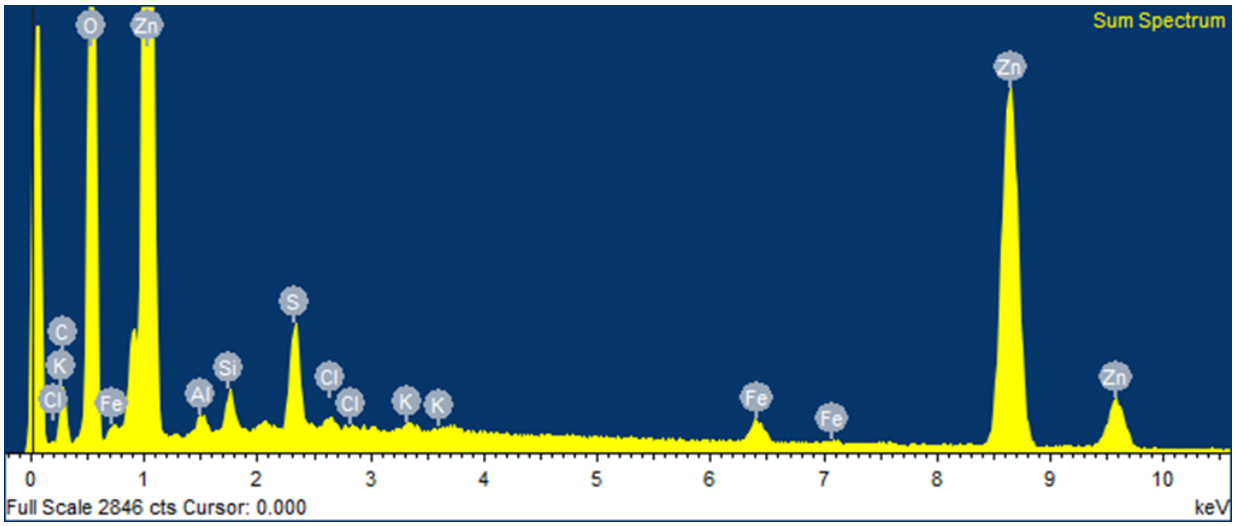


Figure A.189. SEM Image and EDS Spectrum of the Paint Collected from Exterior Web of the Girder.

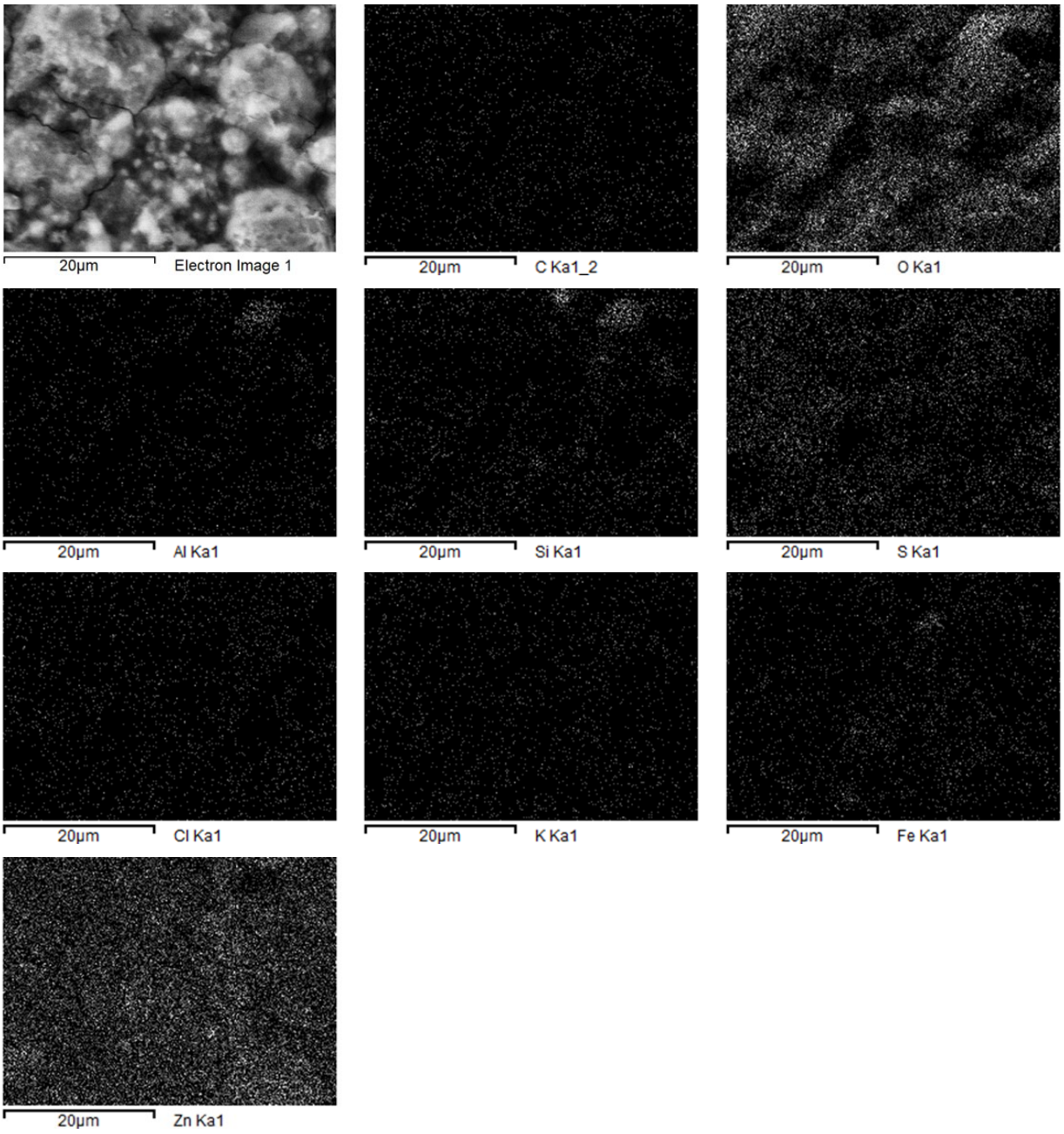
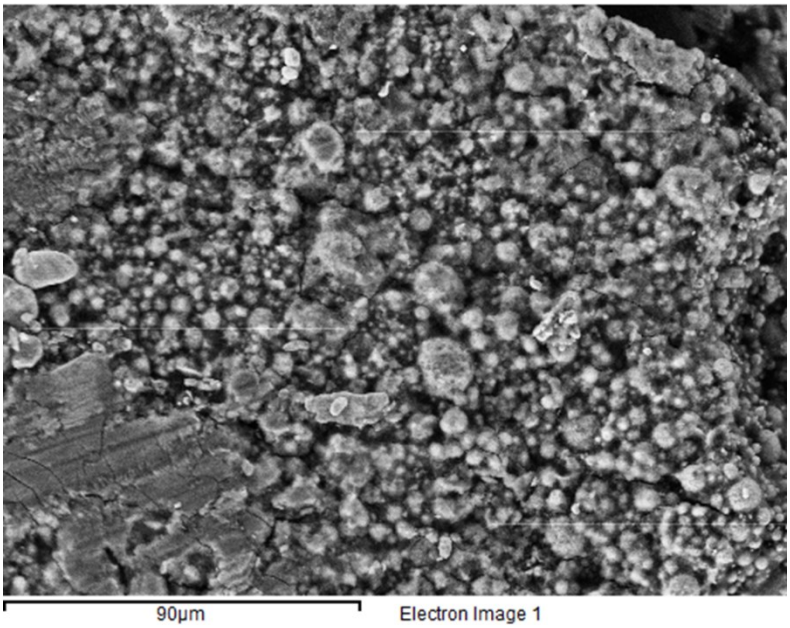


Figure A.190. EDS Elemental Mapping of Paint Collected from Exterior Web.

Element	Weight %	Atomic %
C K	14.95	29.48
O K	34.26	50.72
Al K	0.35	0.31
Si K	0.60	0.51
P K	0.17	0.13
S K	1.66	1.23
Cl K	0.31	0.21
K K	0.12	0.07
Ca K	0.17	0.10
Fe K	0.96	0.41
Ni K	0.19	0.08
Zn K	46.27	16.77
Totals	100.00	



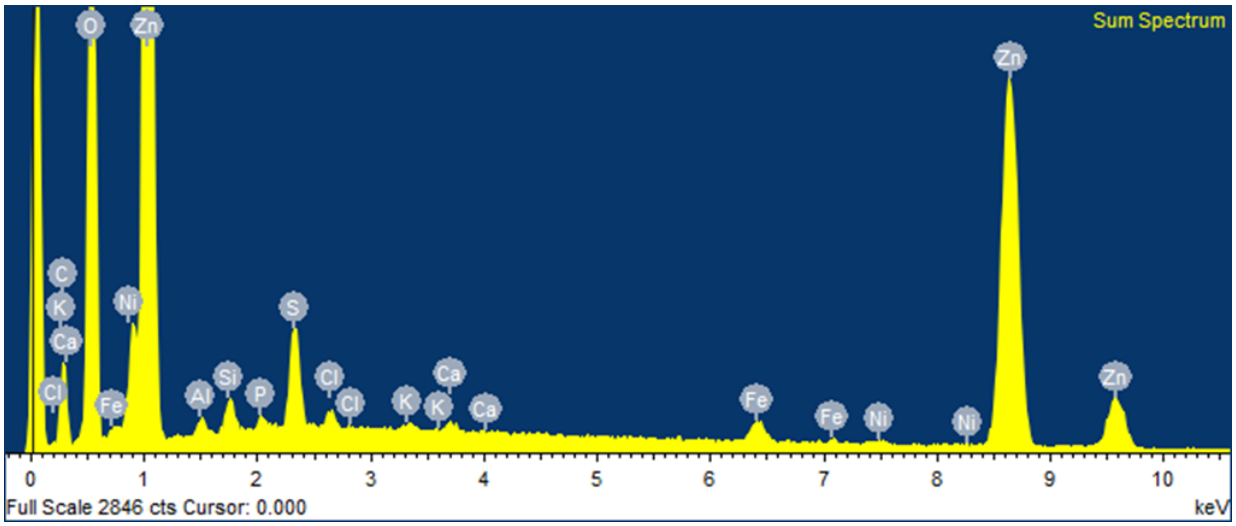


Figure A.191. SEM Image and EDS Spectrum of the Paint Collected from Exterior Web of the Girder.

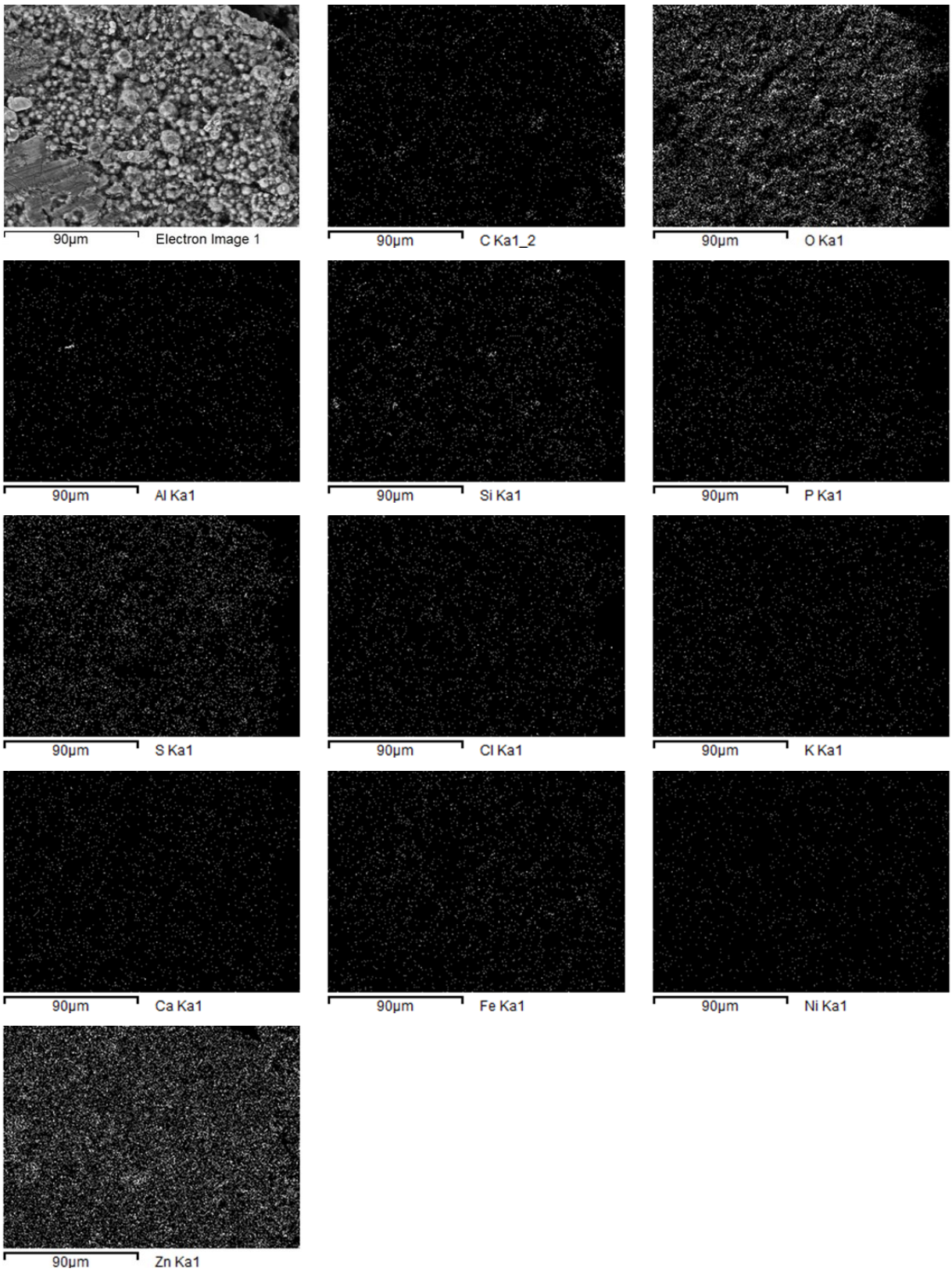
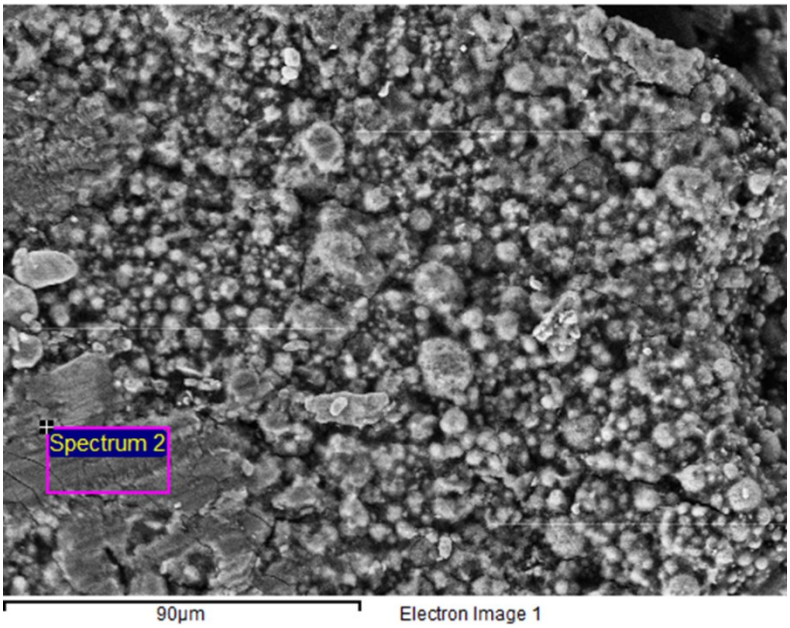


Figure A.192. EDS Elemental Mapping of Paint Collected from Exterior Web.

Element	Weight %	Atomic %
C K	14.98	28.81
O K	36.35	52.48
Al K	0.24	0.20
Si K	0.36	0.30
P K	0.41	0.30
S K	2.30	1.65
Cl K	0.27	0.17
K K	0.36	0.21
Ca K	0.16	0.09
Fe K	0.48	0.20
Zn K	44.08	15.57
Totals	100.00	



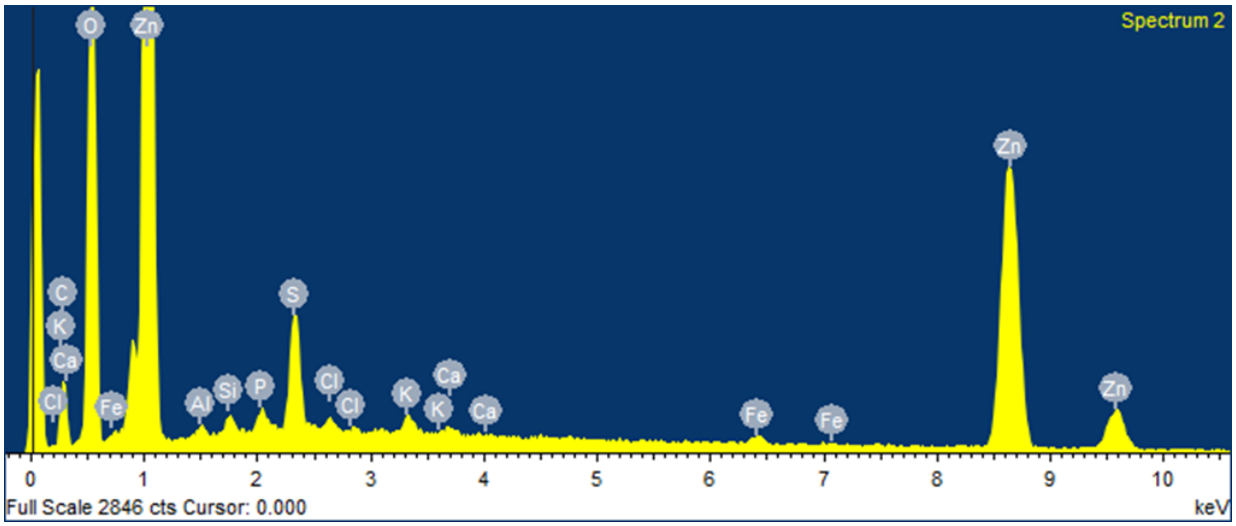


Figure A.193. SEM Image and EDS Spectrum of the Paint Collected from Exterior Web of the Girder.

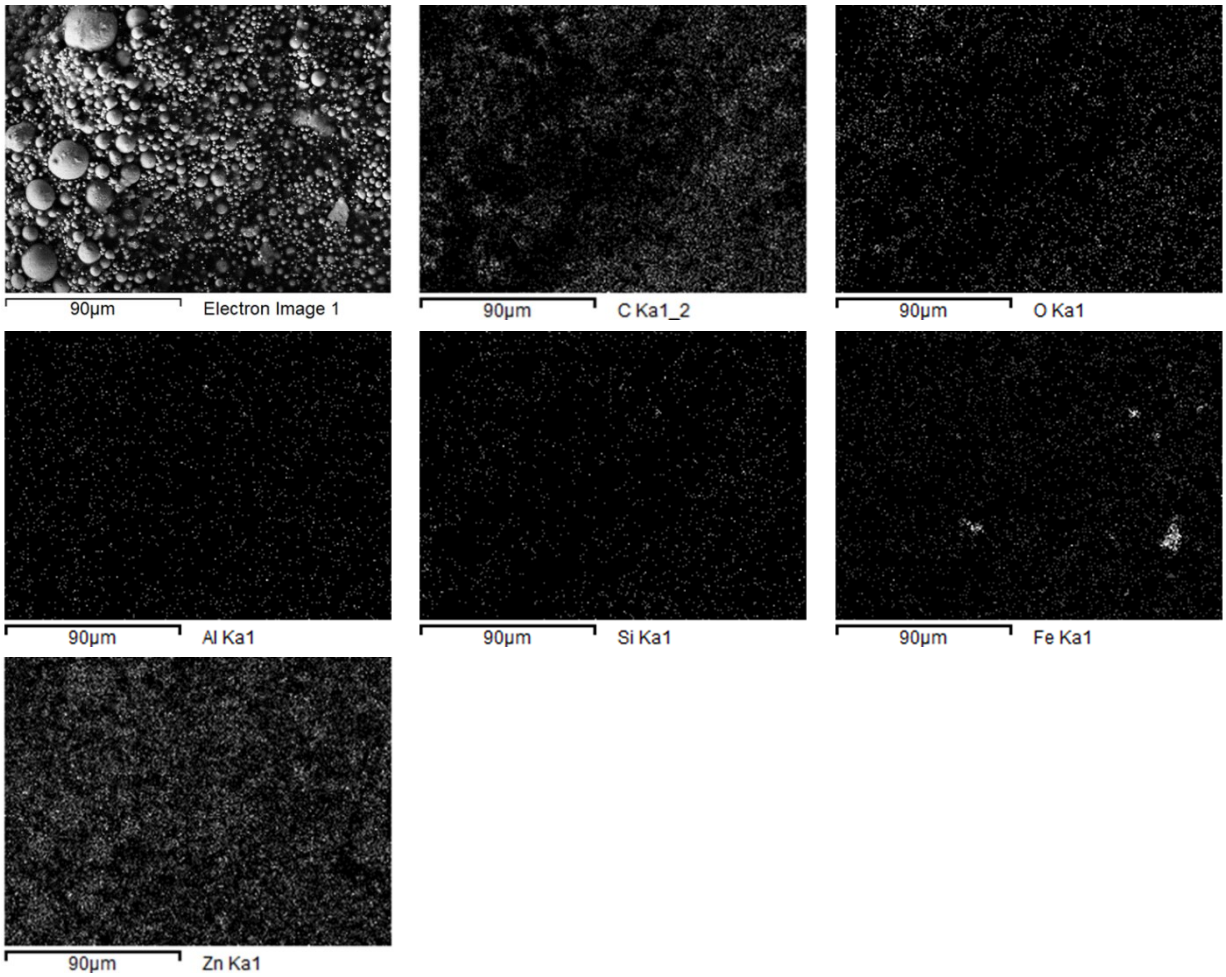
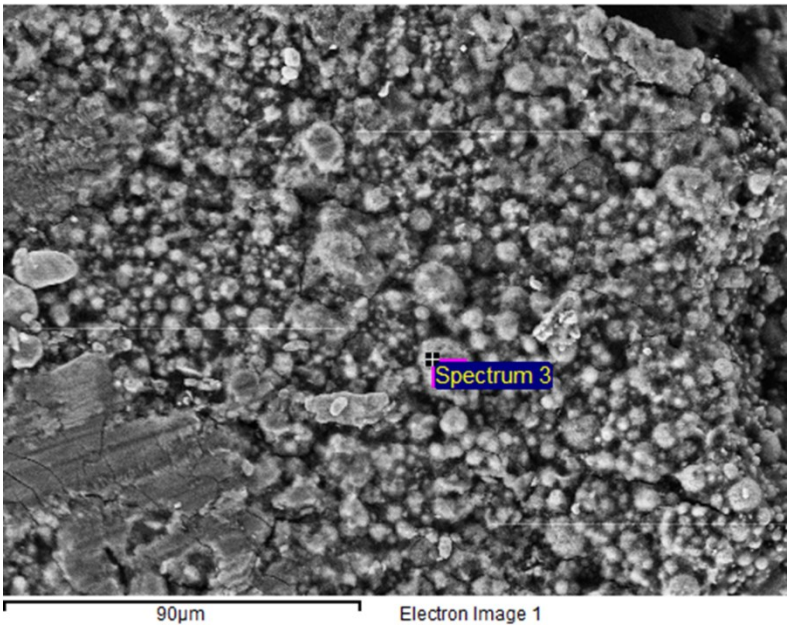


Figure A.194. EDS Elemental Mapping of Paint Collected from Exterior Web.

Element	Weight %	Atomic %
C K	9.66	24.43
O K	23.04	43.75
Al K	0.23	0.26
S K	0.64	0.61
Cl K	0.17	0.15
Ni K	0.20	0.10
Zn K	66.06	30.71
Totals	100.00	



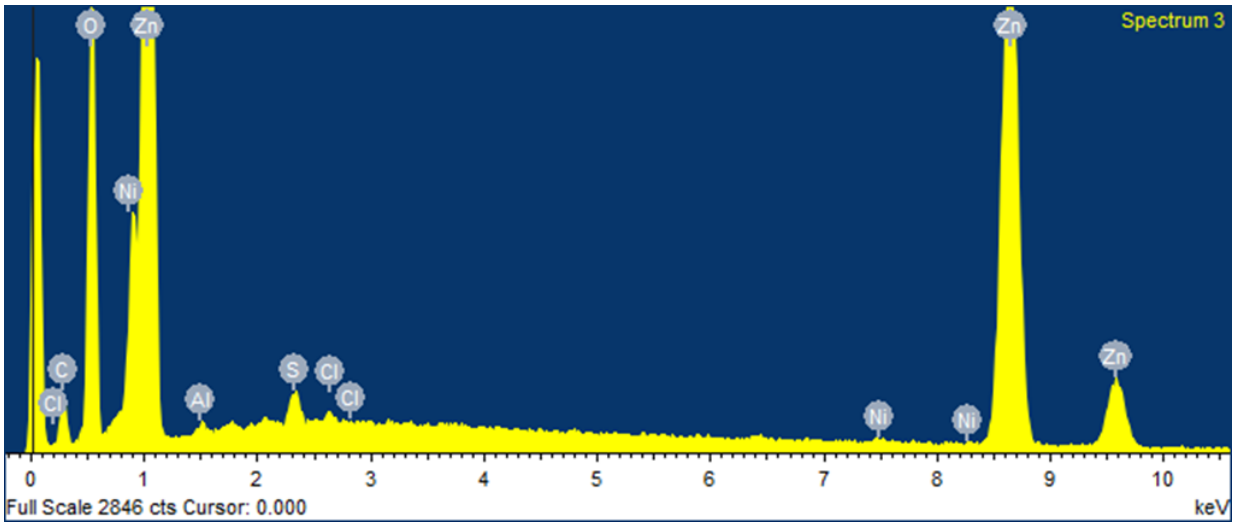
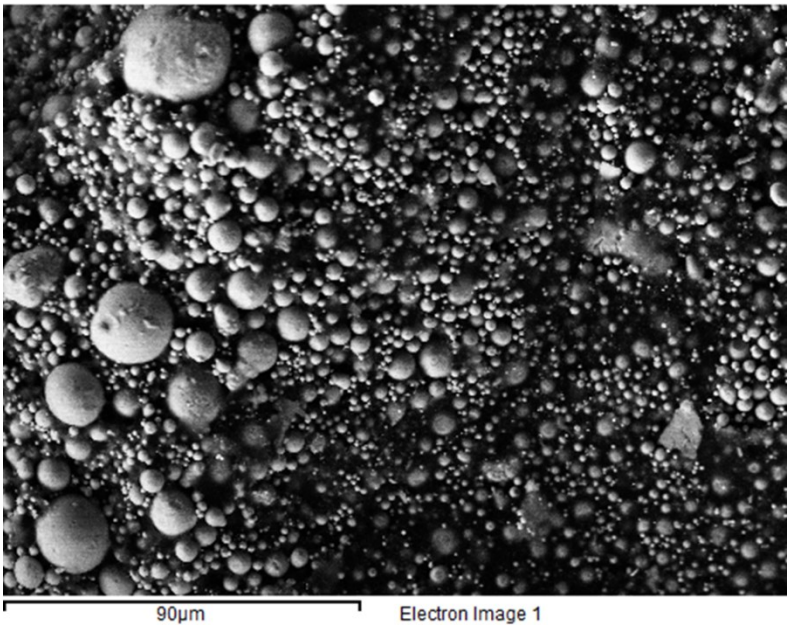


Figure A.195. SEM Image and EDS Spectrum of the Paint Collected from Exterior Web of the Girder.

Element	Weight %	Atomic %
C K	51.48	79.20
O K	7.77	8.97
Al K	0.39	0.27
Si K	0.21	0.14
Fe K	1.46	0.48
Zn K	38.69	10.94
Totals	100.00	



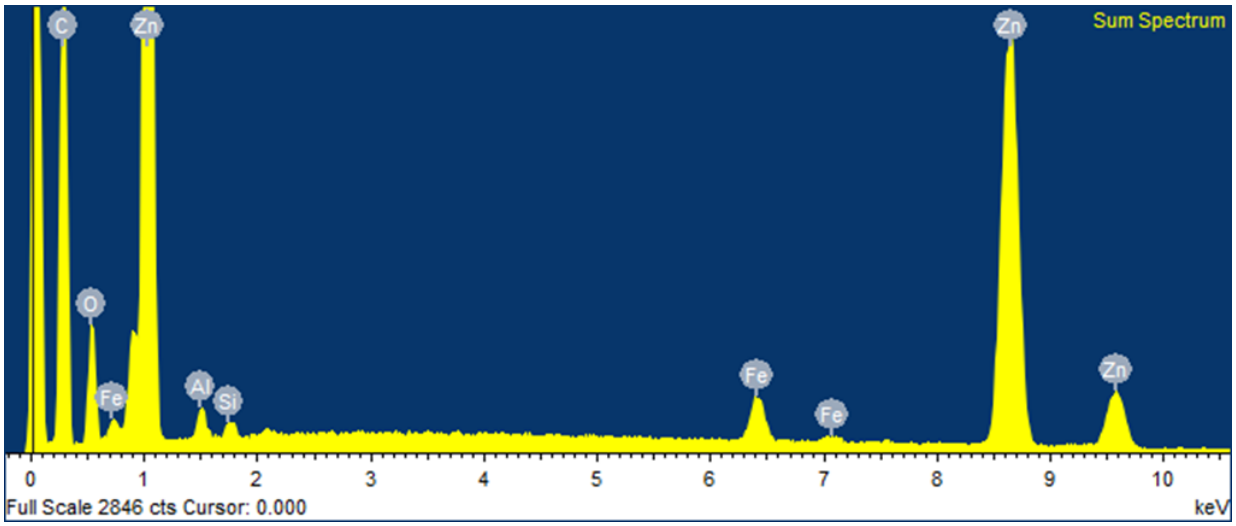
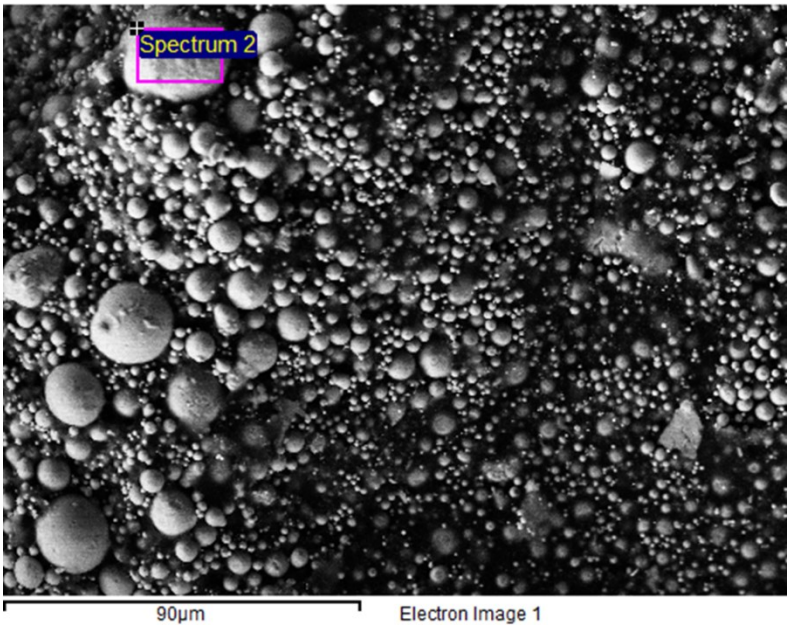


Figure A.196. SEM Image of Paint and EDS Spectrum of the Paint Collected from Interior Web of the Girder.

Element	Weight %	Atomic %
C K	17.59	45.01
O K	10.78	20.71
Al K	0.91	1.04
Zn K	70.72	33.24
Totals	100.00	



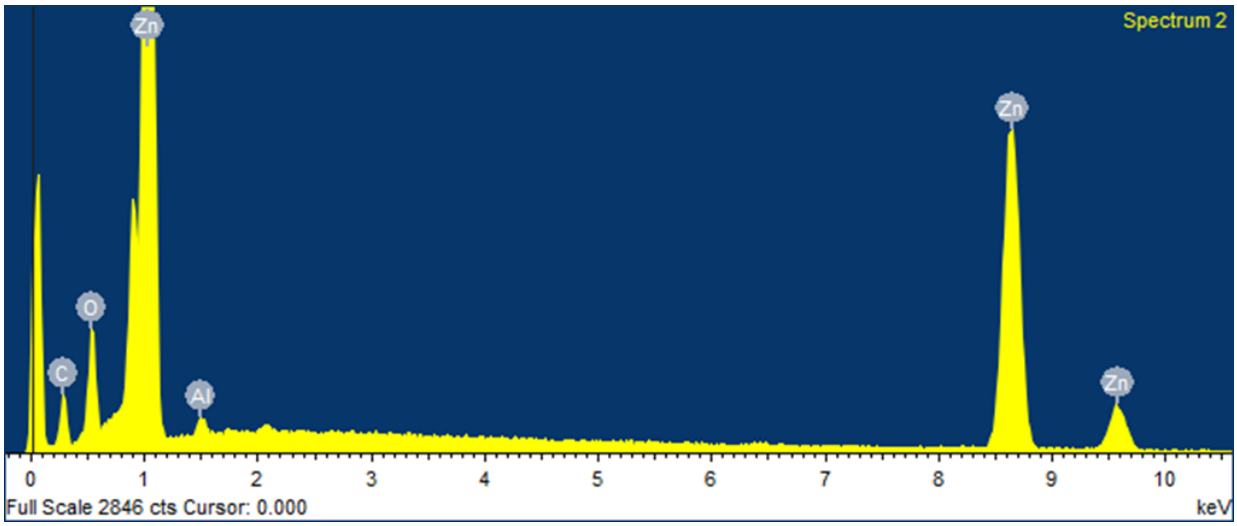
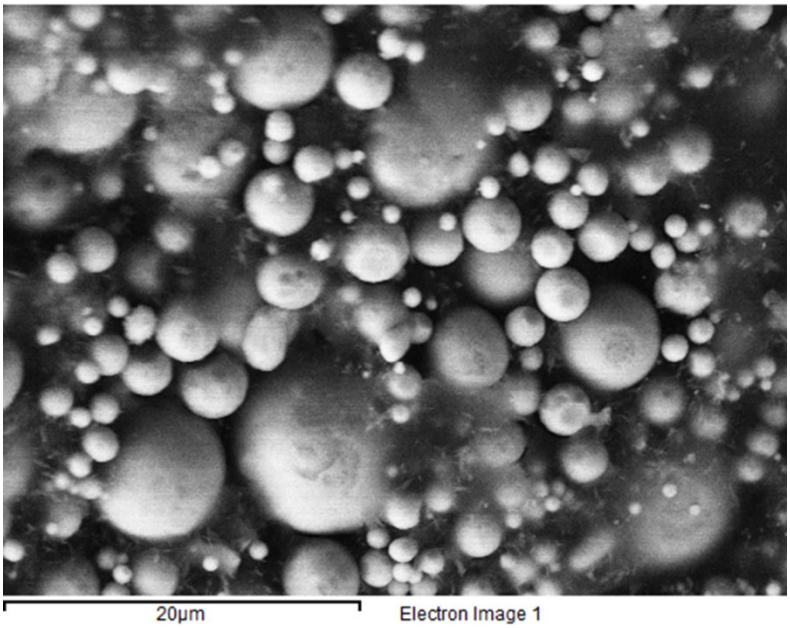


Figure A.197. SEM Image of Paint and EDS Spectrum of the Paint Collected from Interior Web of the Girder.

Element	Weight %	Atomic %
C K	40.47	74.90
O K	4.23	5.87
Al K	0.62	0.51
Si K	0.11	0.09
Fe K	1.30	0.52
Zn K	53.27	18.11
Totals	100.00	



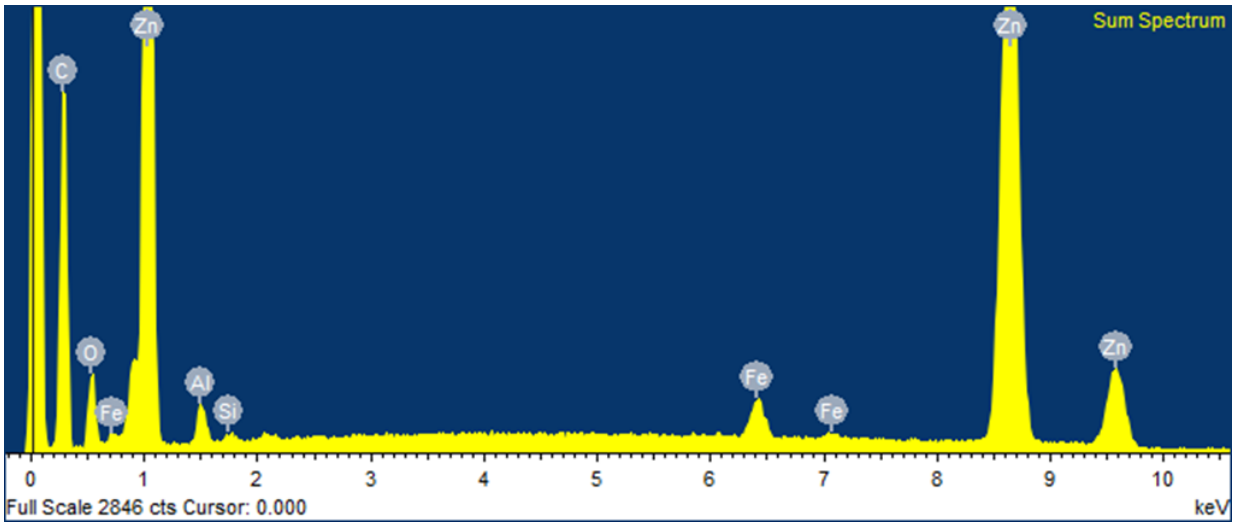


Figure A.198. SEM Image and EDS Spectrum of the Paint Collected from Interior Web of the Girder.

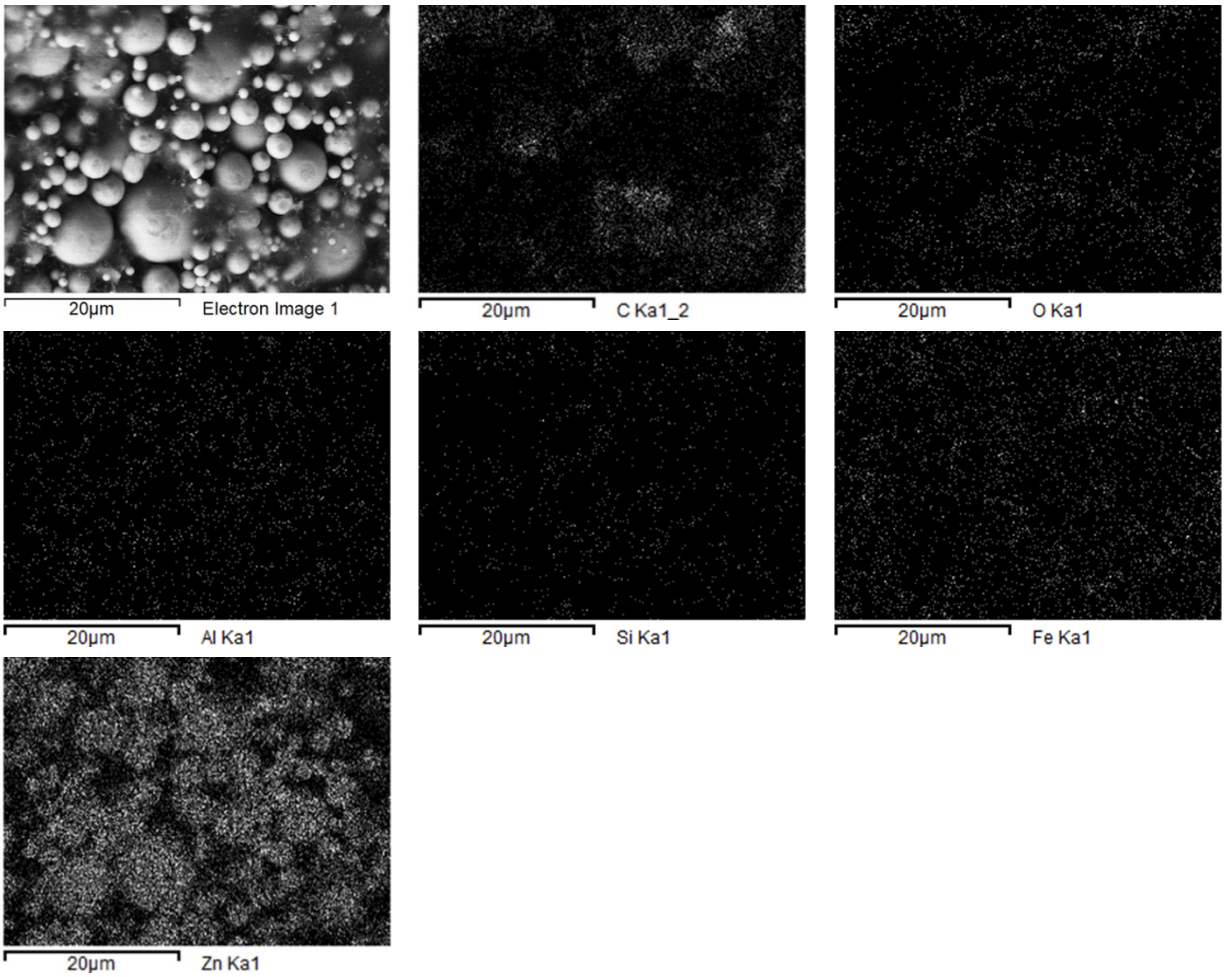
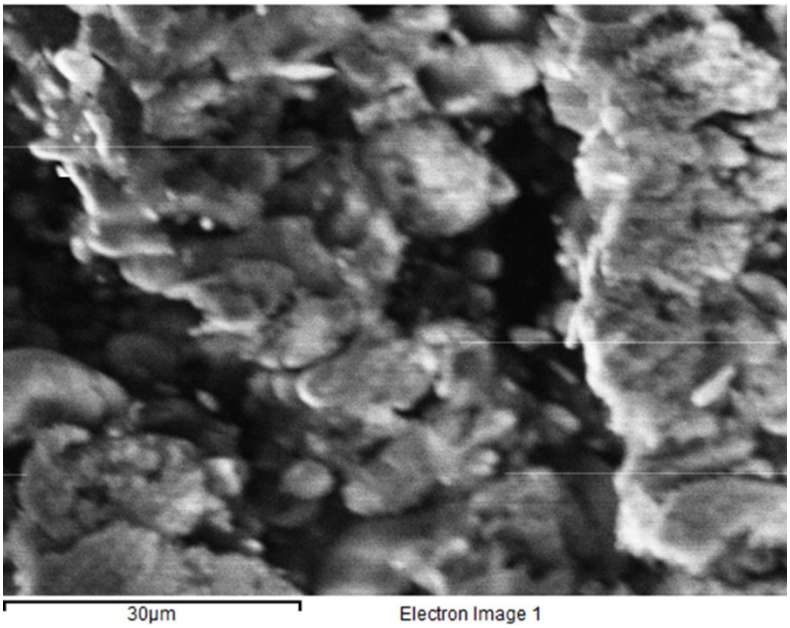


Figure A.199. EDS Elemental Mapping of Paint Collected from Interior Web.

Element	Weight %	Atomic %
C K	38.55	71.39
O K	6.90	9.59
Al K	0.67	0.55
Si K	0.18	0.14
Fe K	0.80	0.32
Zn K	52.90	18.00
Totals	100.00	



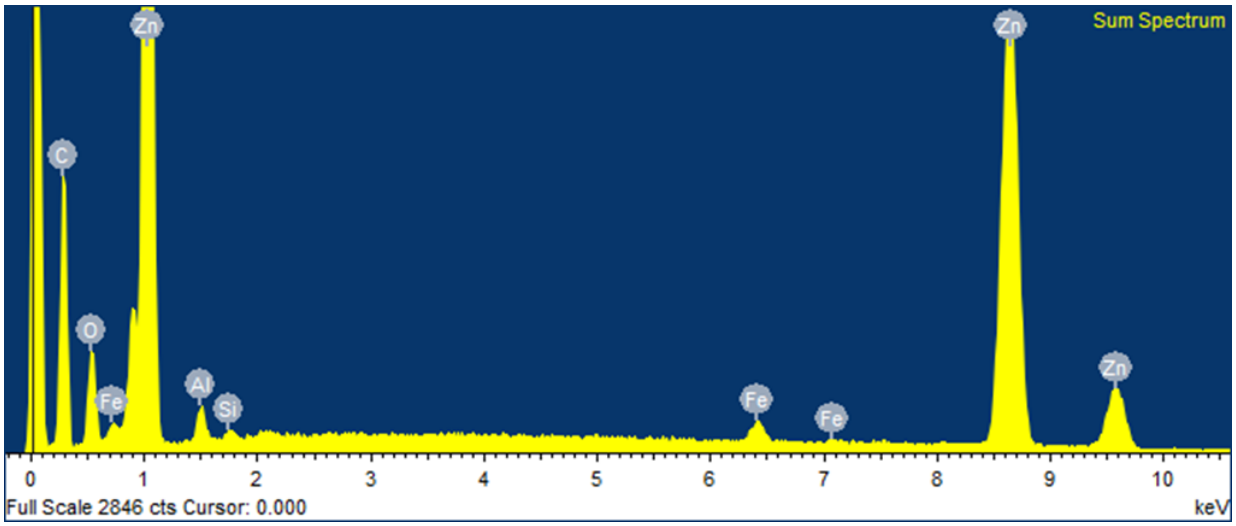


Figure A.200. SEM Image of Paint and EDS Spectrum of the Paint Collected from Interior Web of the Girder.

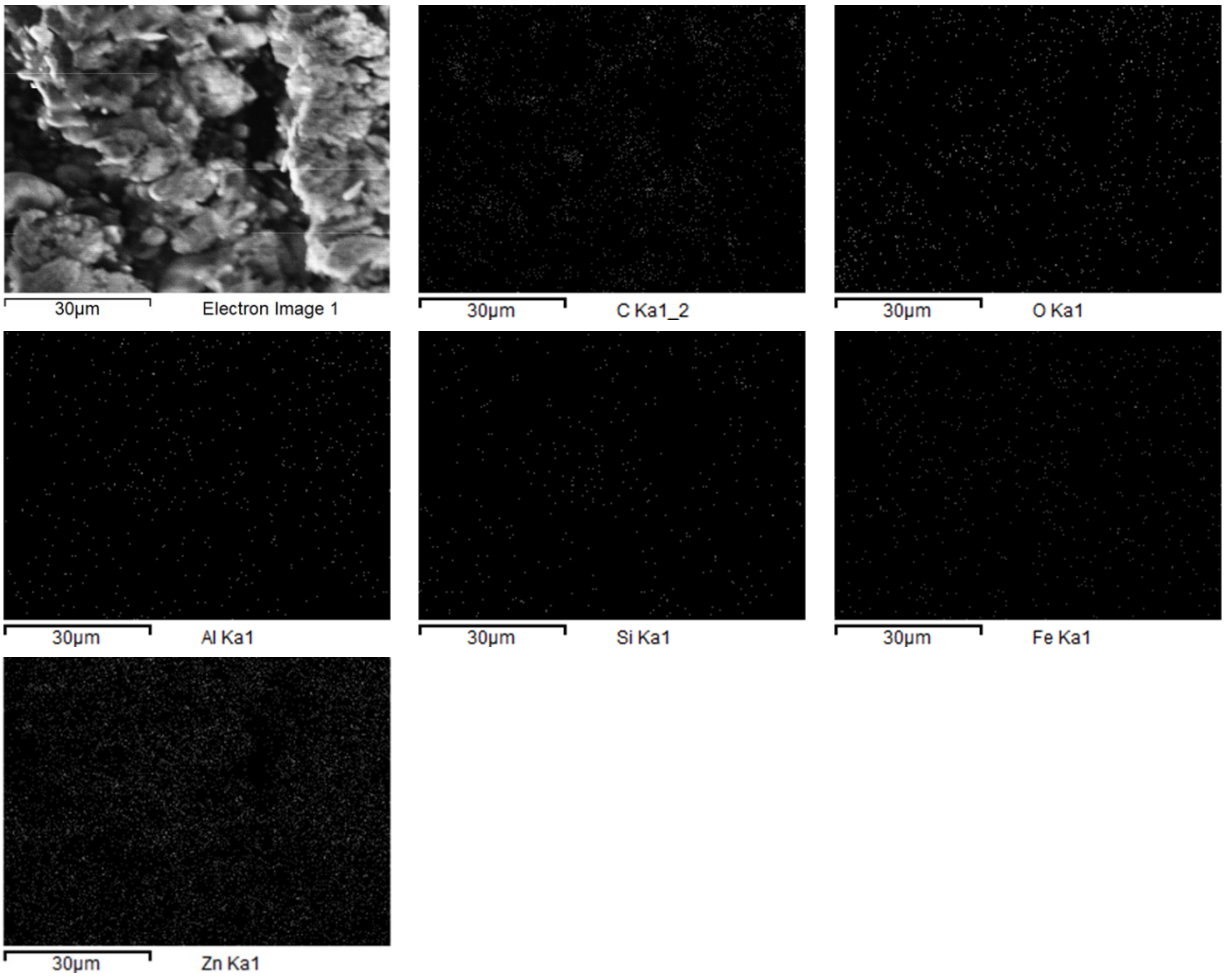


Figure A.201. EDS Elemental Mapping of Paint Collected from Interior Web.

A.17. ELP-PS-01

- Carrington Rd over Spur 601
- Bridge ID 240720104603116, Coordinates (31.82634, -106.41311), El Paso County
- Steel Plate Girder with System I type paint
- Built 2000
- Date of Inspection: June 2021; girder inspection carried near abutment ends on girders within approximately four feet from the abutment
- No visual inspection on deck
- Location for Testing: A1-G1, A1-G2, A1-G4, A1-G5



Figure A.202. Typical Elevation of ELP-PS-01

A.17.1. Observed Condition

The paint condition of this bridge is in very good condition. The appearance coat is also in good condition. Blistering, Erosion of paint, cracking in paint is not present. No checking and cracking of paint are observed. Joints are also in good condition. This bridge was coated by the Core of Engineers. Since EDS analysis confirmed that there is absence of zinc based primer it should be System I type paint.



(a) External Bearing in Good Condition



(b) Interior Girder Connnection is in Good Condition



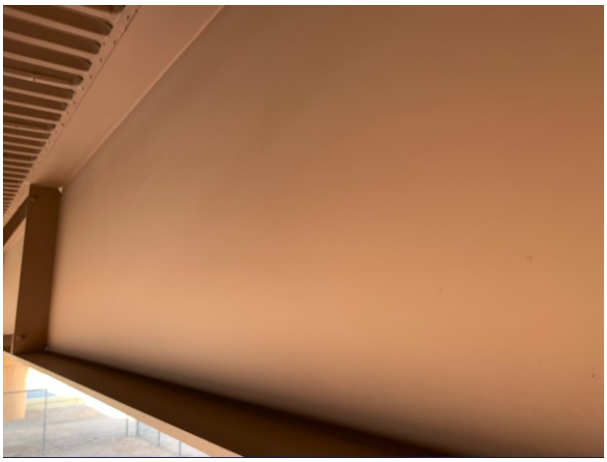
(c) Exterior Girder in Good Condition



(d) Internal Bearing in Good Condition



(e) Superstructure in Good Condition



(f) Interior Girder in Good Condition

Figure A.203. Paint Condition on the Girder of ELP-PS-01.

A.17.2.NDT Results



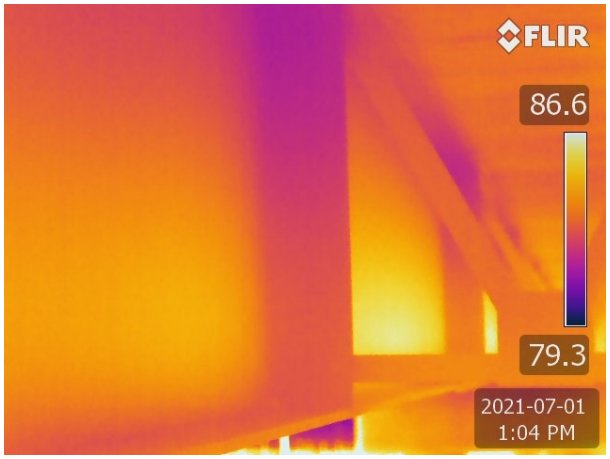
(a) Digital Image of Exterior Face of I Beam



(b) Thermal Image of Interior Face of I Beam



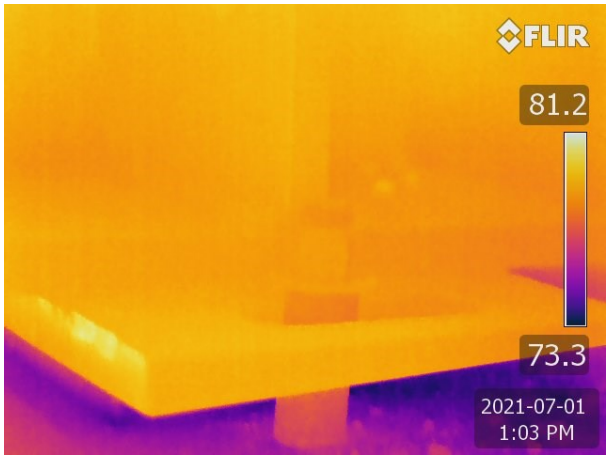
(c) Digital Image of Connection



(d) Thermal Image of Connection



(e) Digital image of the exterior face of I beam (G1F1)



(f) Thermal image of the exterior of I beam (G1F1)

Figure A.204. Digital and Thermal Image of Painted Girder on ELP-PS-01.

Table A-82. Field Inspection Results for ELP-PS-01.

Location	Cl^- Conc. (ppm)	pH Test	Thickness (µm)	Thickness (inch)	Visual Inspection
A1-G1F1 TF Bot. Ext.	-	-	Measured R1 R2 R3 R_Avg	Measured R1 0.784 R2 0.782 R3 0.782 R_Avg 0.783 Design	Rust Grade – 10 Blistering – Not Found Discoloration – Not Found Flaking – Not Found Delamination – Not Found
A1-G1F1 Web Ext.	1		Measured R1 R2 R3 R_Avg	Measured R1 0.623 R2 0.623 R3 0.622 R_Avg 0.623 Design	Rust Grade – 10 Blistering – Not Found Discoloration – Not Found Flaking – Not Found Delamination – Not Found
A1-G1F1 BF Top Ext.	-	-	Measured R1 R2 R3 R_Avg	Measured R1 1.232 R2 1.232 R3 1.231 R_Avg 1.232 Design	Rust Grade – 10 Blistering – Not Found Discoloration – Not Found Flaking – Not Found Delamination – Found
A1-G1F1 BF Bot. Ext.	-	-	Measured R1 R2 R3 R_Avg	Measured R1 - R2 - R3 - R_Avg - Design	Rust Grade – 10 Blistering – Not Found Discoloration – Not Found Flaking – Not Found Delamination – Not Found
A1-G2F1 TF Bot. Int.	-		Measured R1 R2 R3 R_Avg	Measured R1 0.783 R2 0.788 R3 0.782 R_Avg 0.784 Design	Rust Grade – 10 Blistering – Not Found Discoloration – Not Found Flaking – Not Found Delamination – Not Found
A1-G2F1 Web Int.	1	-	Measured R1 R2 R3 R_Avg	Measured R1 0.627 R2 0.627 R3 0.627 R_Avg 0.627 Design	Rust Grade – 10 Blistering – Not Found Discoloration – Not Found Flaking – Not Found Delamination – Found

Table A-83. Field Inspection Results for ELP-PS-01.

Location	Cl^- Conc. (ppm)	pH Test	Thickness (µm)	Thickness (inch)	Visual Inspection
A1-G2F1 BF Top. Int.	-	-	Measured R1 R2 R3 R_Avg	Measured R1 1.239 R2 1.240 R3 1.242 R_Avg 1.240 Design	Rust Grade – 10 Blistering – Not Found Discoloration – Not Found Flaking – Not Found Delamination – Not Found
A1-G2F1 BF Bot. Int.	-	-	Measured R1 R2 R3 R_Avg	Measured R1 - R2 - R3 - R_Avg - Design	Rust Grade – 10 Blistering – Not Found Discoloration – Not Found Flaking – Not Found Delamination – Not Found
A1-G4F2 TF Bot Int.	-	-	Measured R1 R2 R3 R_Avg	Measured R1 0.782 R2 0.783 R3 0.783 R_Avg 0.783 Design	Rust Grade – 10 Blistering – Not Found Discoloration – Not Found Flaking – Not Found Delamination – Found
A1-G4F2 Web Int.	5	-	Measured R1 R2 R3 R_Avg	Measured R1 0.630 R2 0.633 R3 0.630 R_Avg 0.631 Design	Rust Grade – 10 Blistering – Not Found Discoloration – Not Found Flaking – Not Found Delamination – Not Found
A1-G4F2 BF Top. Int.	-		Measured R1 R2 R3 R_Avg	Measured R1 1.236 R2 1.235 R3 1.234 R_Avg 1.235 Design	Rust Grade – 10 Blistering – Not Found Discoloration – Not Found Flaking – Not Found Delamination – Not Found
A1-G4F2 BF Bot. Int.	-	-	Measured R1 R2 R3 R_Avg	Measured R1 - R2 - R3 - R_Avg - Design	Rust Grade – 10 Blistering – Not Found Discoloration – Not Found Flaking – Not Found Delamination – Found

Table A-84. Field Inspection Results for ELP-PS-01.

Location	Cl^- Conc. (ppm)	pH Test	Thickness (µm)	Thickness (inch)	Visual Inspection
A1-G5 TF Bot Int.	-	-	Measured R1 R2 R3 R_Avg	Measured R1 0.778 R2 0.780 R3 0.779 R_Avg 0.779 Design	Rust Grade – 10 Blistering – Not Found Discoloration – Not Found Flaking – Not Found Delamination – Not Found
A1-G5 Web Int.	2	-	Measured R1 R2 R3 R_Avg	Measured R1 0.630 R2 0.629 R3 0.629 R_Avg 0.629 Design	Rust Grade – 10 Blistering – Not Found Discoloration – Not Found Flaking – Not Found Delamination – Not Found
A1-G5 BF Top. Int.	-	-	Measured R1 R2 R3 R_Avg	Measured R1 1.232 R2 1.230 R3 1.227 R_Avg 1.230 Design	Rust Grade – 10 Blistering – Not Found Discoloration – Not Found Flaking – Not Found Delamination – Found
A1-G5 BF Bot. Int.	-	-	Measured R1 R2 R3 R_Avg	Measured R1 - R2 - R3 - R_Avg - Design	Rust Grade – 10 Blistering – Not Found Discoloration – Not Found Flaking – Not Found Delamination – Not Found

A.17.3.Pull-off Adhesion Results

Table A-85. Pull-off Adhesion Results for ELP-PS-01.

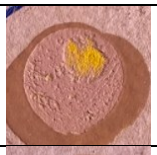
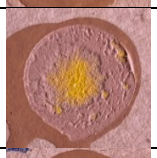
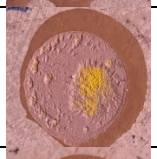
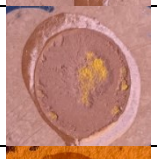
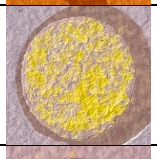
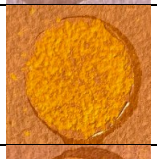
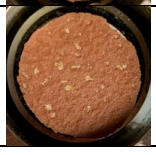
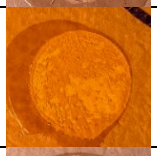
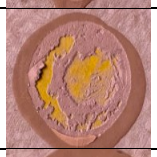
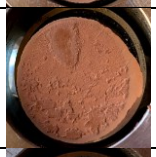
Location	Dolly Face	Substrate Face	Test Result (psi)	Attributes	Failure Type
A1-G1F1			1709	30% B 70% A/B	30% Cohesive Failure 70% Adhesive Failure
			1655	10% B 90% A/B	10% Cohesive Failure 90% Adhesive Failure
			1807	100% A/B	100% Adhesive Failure
			1843	20% B 80% A/B	20% Cohesive Failure 80% Adhesive Failure
			2054	10% B 90% A/B	10% Cohesive Failure 90% Adhesive Failure
A1-G3F1			1624	20% B 80% A/B	20% Cohesive Failure 80% Adhesive Failure
			1148	20% B 80% A/B	20% Cohesive Failure 80% Adhesive Failure
			1269	20% B 80% A/B	20% Cohesive Failure 80% Adhesive Failure
			1124	30% B 70% A/B	30% Cohesive Failure 70% Adhesive Failure
			1253	20% B 80% A/B	20% Cohesive Failure 80% Adhesive Failure

Table A-86. Pull-off Adhesion Results for ELP-PS-01.

Location	Dolly Face	Substrate Face	Test Result (psi)	Attributes	Failure Type
A1-G1F1			1259	30% B 70% A/B	30% Cohesive Failure 70% Adhesive Failure
			1467	10% B 90% A/B	10% Cohesive Failure 90% Adhesive Failure
			1637	100% A/B	100% Adhesive Failure
			2204	20% B 80% A/B	20% Cohesive Failure 80% Adhesive Failure
			2011	10% B 90% A/B	10% Cohesive Failure 90% Adhesive Failure
A1-G3F1			1510	20% B 80% A/B	20% Cohesive Failure 80% Adhesive Failure
			1674	20% B 80% A/B	20% Cohesive Failure 80% Adhesive Failure
			1587	20% B 80% A/B	20% Cohesive Failure 80% Adhesive Failure
			1784	30% B 70% A/B	30% Cohesive Failure 70% Adhesive Failure
			1224	20% B 80% A/B	20% Cohesive Failure 80% Adhesive Failure

A.17.4. Optical Microscopy Results

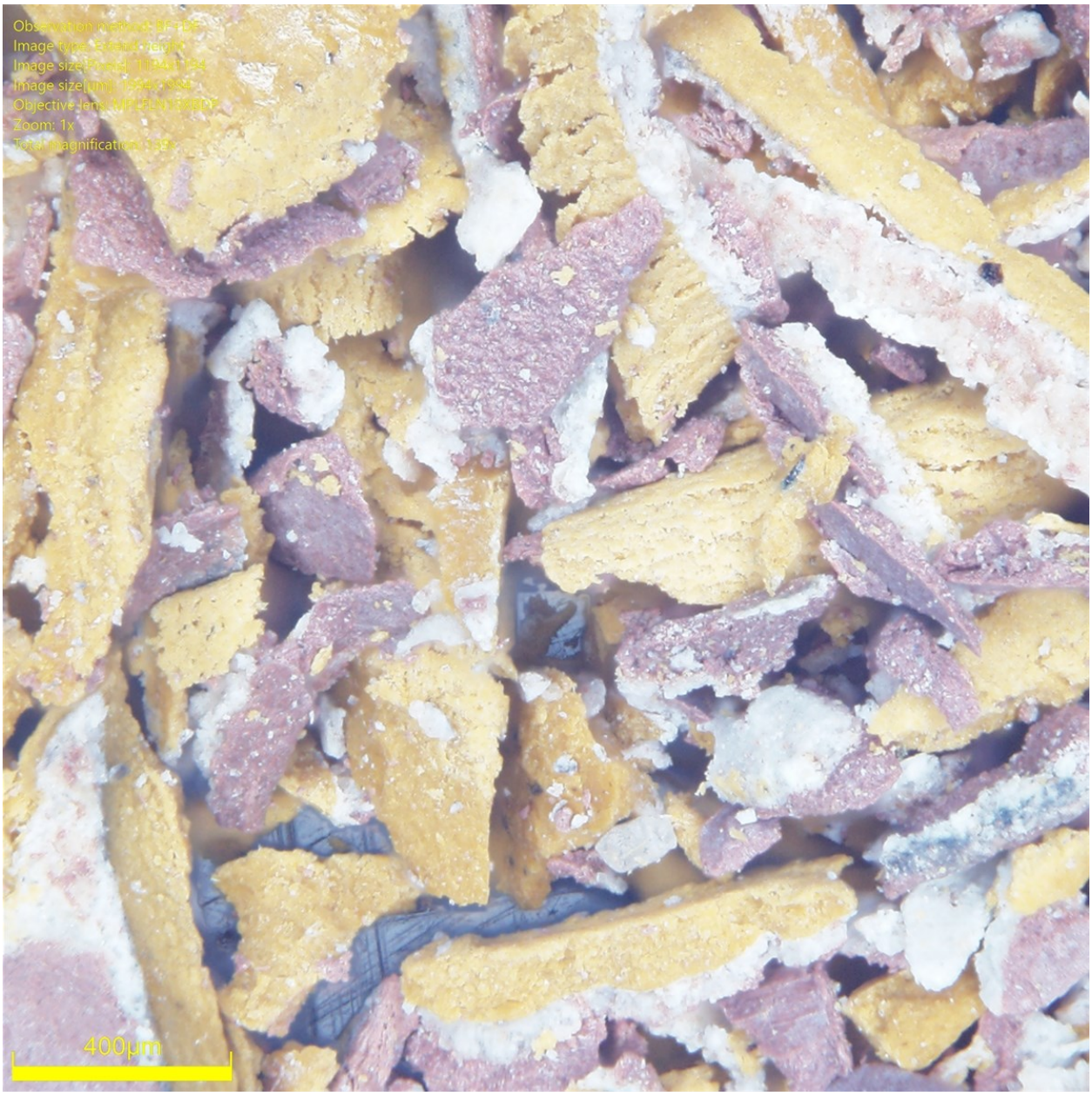
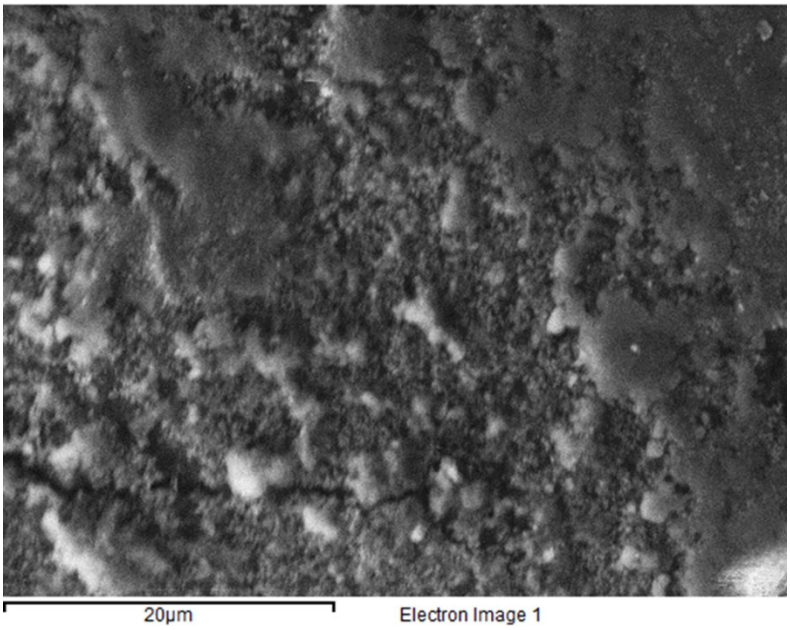


Figure A.205. Two Layer Paint System Examined by Optical Microscope ELP-WS-01.

A.17.5.SEM/EDS Results

Element	Weight %	Atomic %
C K	27.53	37.15
O K	53.38	54.08
Na K	1.34	0.94
Mg K	0.35	0.23
Al K	1.57	0.95
Si K	4.33	2.50
Cl K	2.92	1.33
K K	0.13	0.05
Ca K	0.88	0.36
Ti K	5.54	1.88
Fe K	1.15	0.33
Ni K	0.29	0.08
Zn K	0.19	0.05
Zr L	0.40	0.07
Totals	100.00	



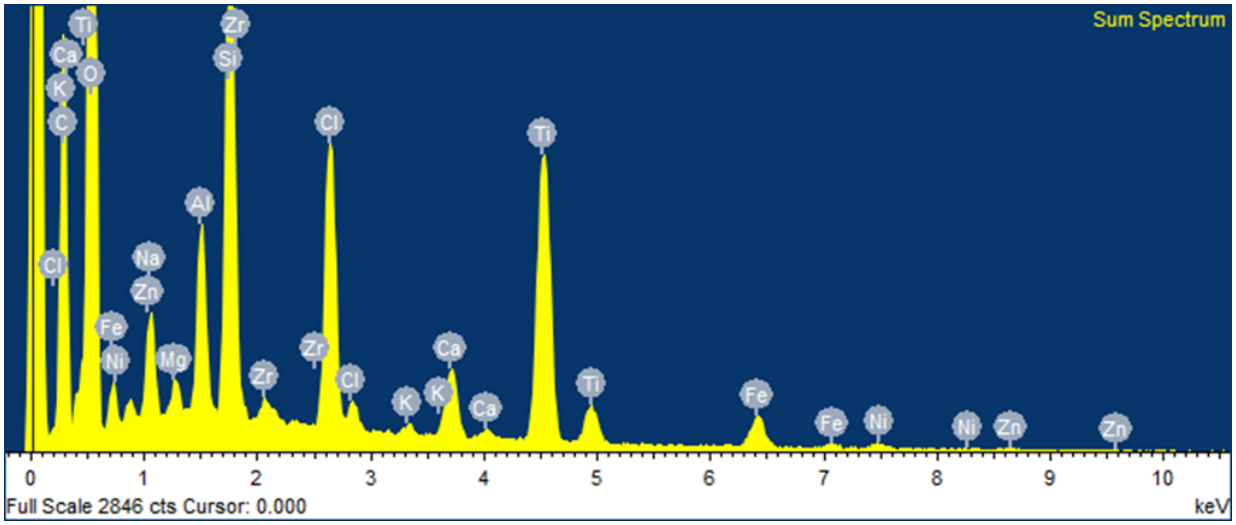


Figure A.206. SEM Image and EDS Spectrum of the Paint Collected from Exterior Web of the Girder.

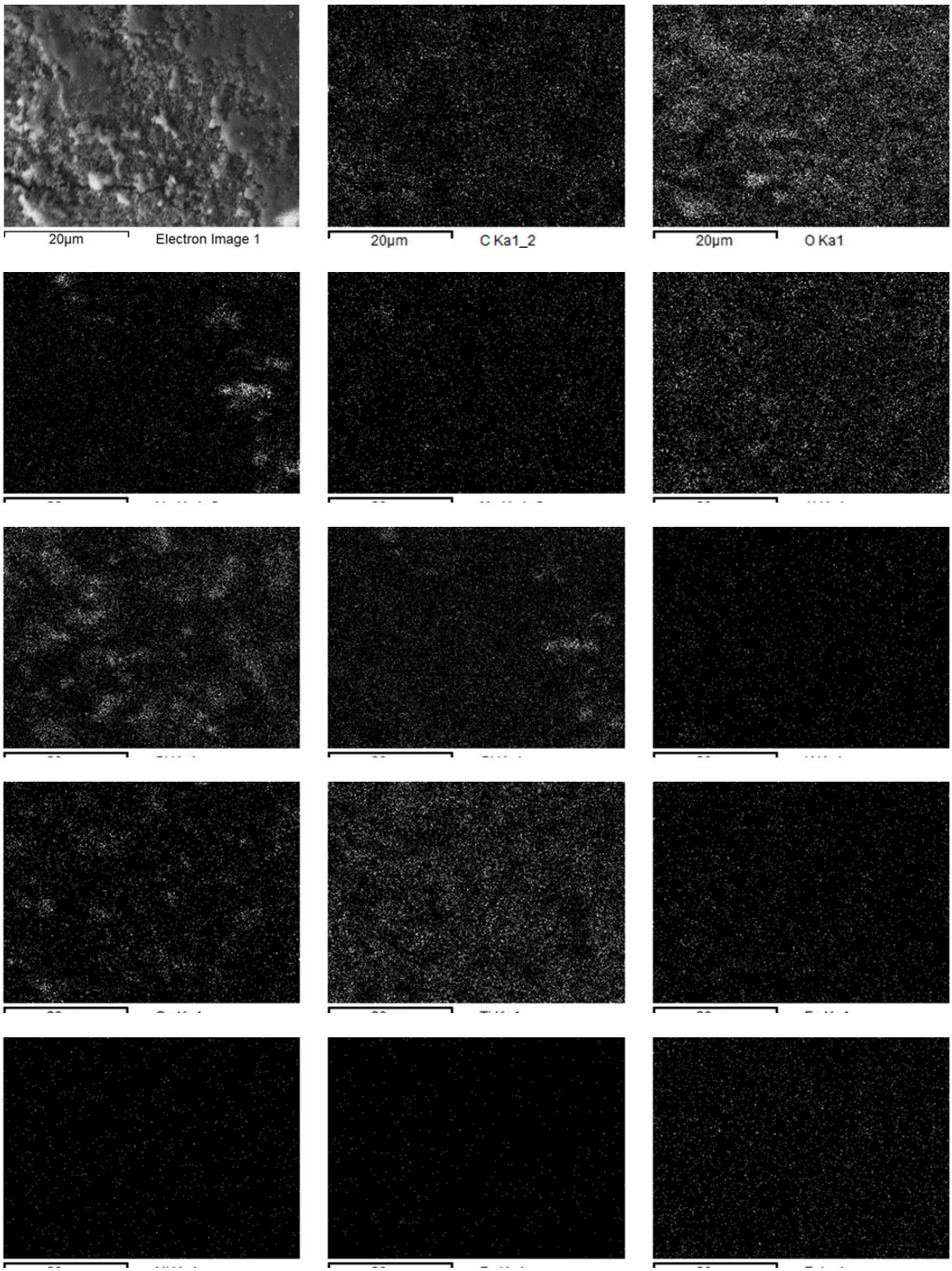
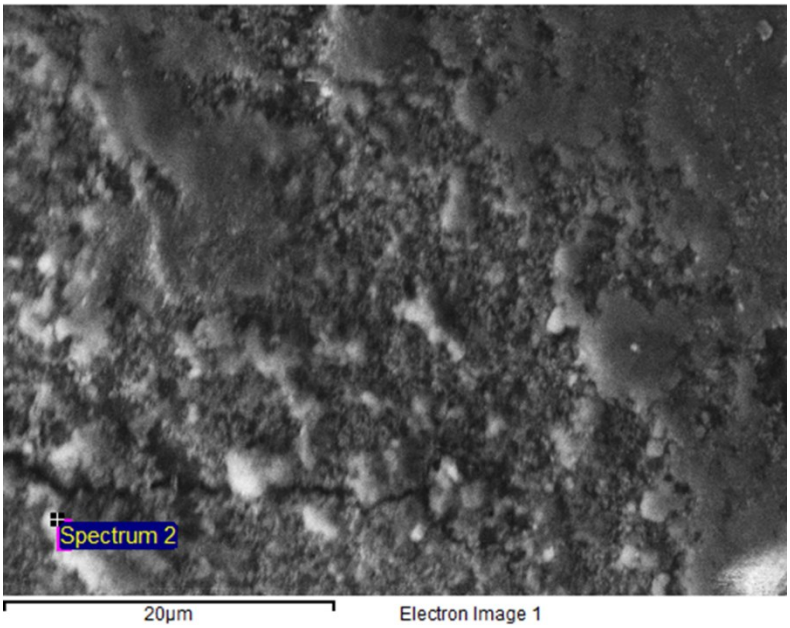


Figure A.207. EDS Elemental Mapping of Paint Collected from Exterior Web.

Element	Weight %	Atomic %
C K	43.81	56.55
O K	37.68	36.51
Mg K	0.21	0.14
Al K	1.29	0.74
Si K	2.25	1.24
Cl K	2.10	0.92
Ca K	0.78	0.30
Ti K	7.70	2.49
Fe K	3.27	0.91
Ni K	0.13	0.04
Zn K	0.34	0.08
Zr L	0.45	0.08
Totals	100.00	



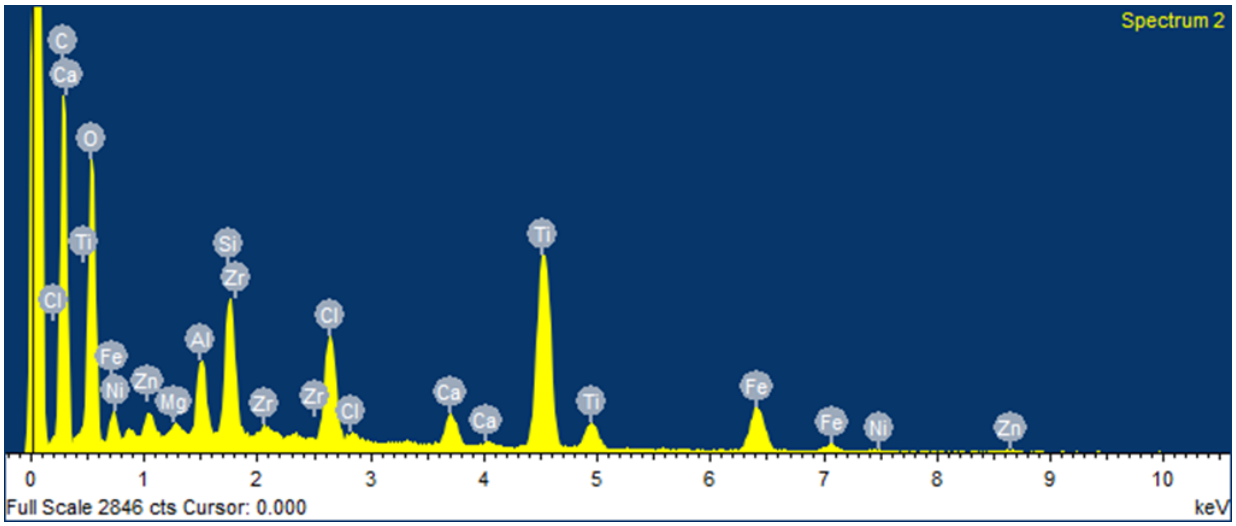
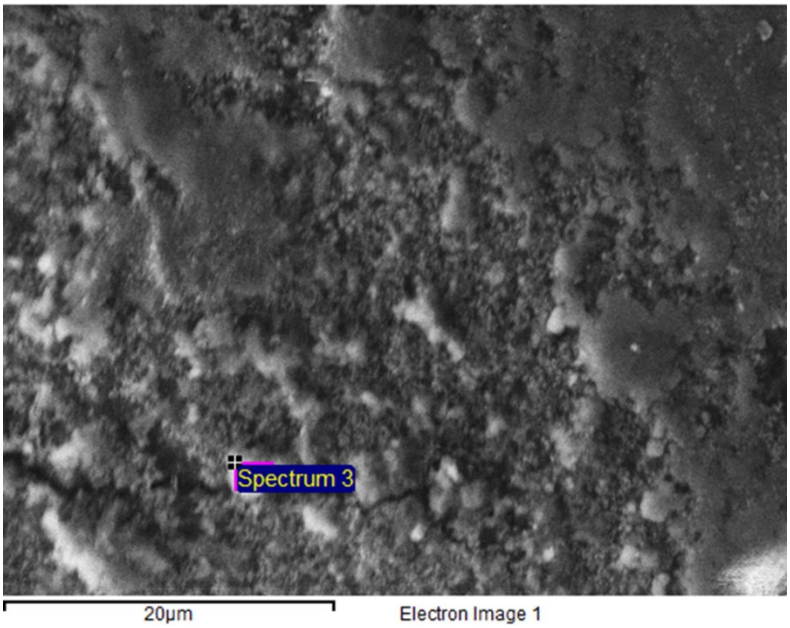


Figure A.208. SEM Image and EDS Spectrum of the Paint Collected from Exterior Web of the Girder.

Element	Weight %	Atomic %
C K	30.23	40.31
O K	52.42	52.47
Mg K	0.51	0.34
Al K	1.49	0.89
Si K	3.64	2.07
Cl K	2.12	0.96
Ca K	0.38	0.15
Ti K	5.33	1.78
Fe K	2.44	0.70
Ni K	0.33	0.09
Zn K	0.73	0.18
Zr L	0.39	0.07
Totals	100.00	



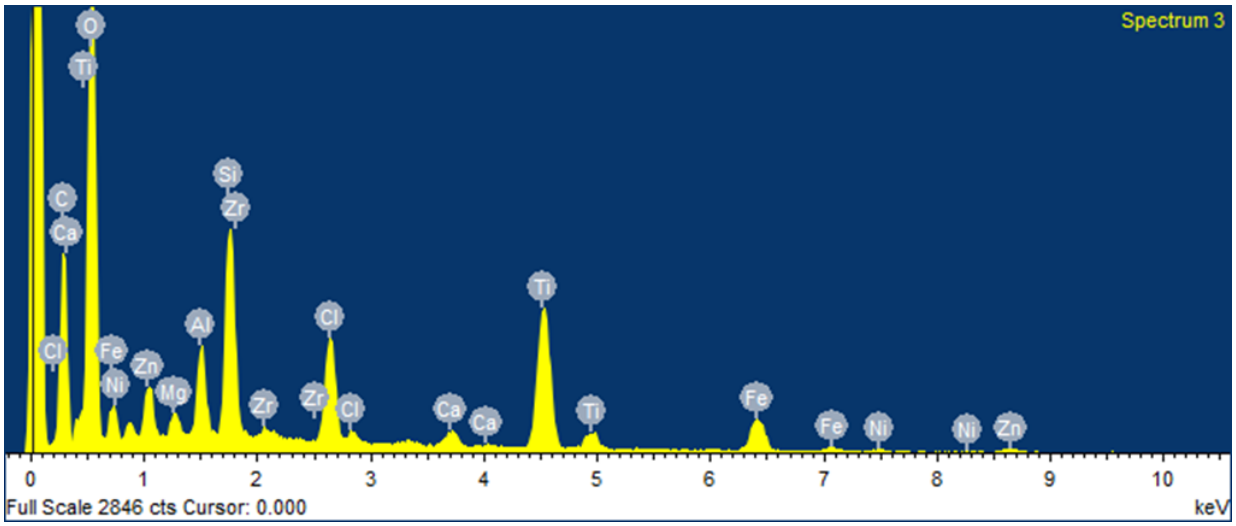
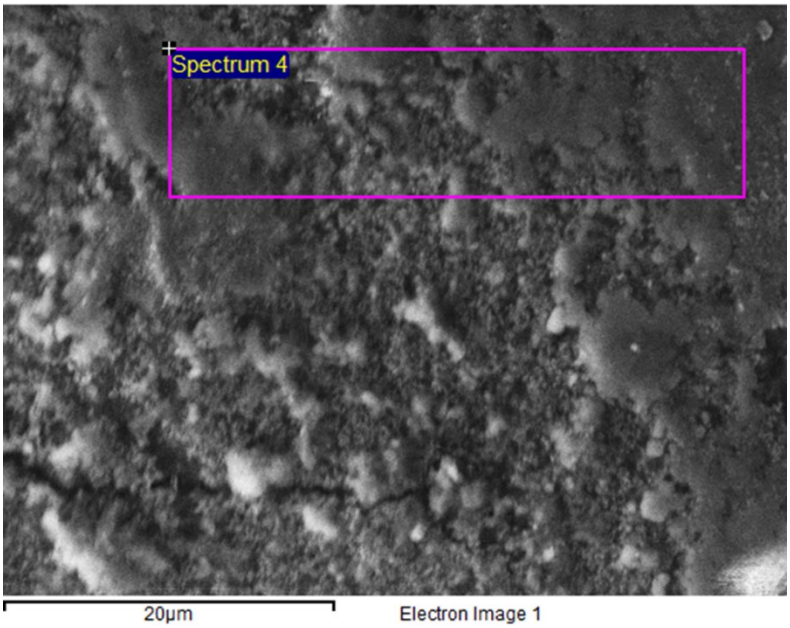


Figure A.209. SEM Image and EDS Spectrum of the Paint Collected from Exterior Web of the Girder.

Element	Weight %	Atomic %
C K	27.71	37.16
O K	53.97	54.34
Na K	1.34	0.94
Mg K	0.40	0.26
Al K	1.74	1.04
Si K	4.71	2.70
Cl K	2.07	0.94
K K	0.12	0.05
Ca K	0.90	0.36
Ti K	5.22	1.75
Fe K	0.99	0.29
Ni K	0.22	0.06
Zr L	0.62	0.11
Totals	100.00	



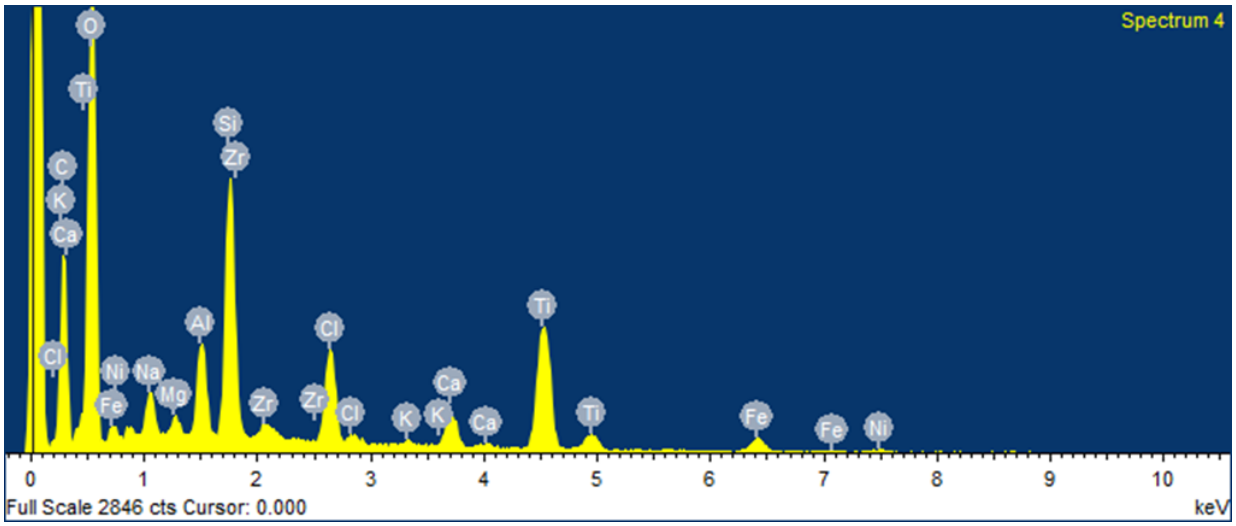
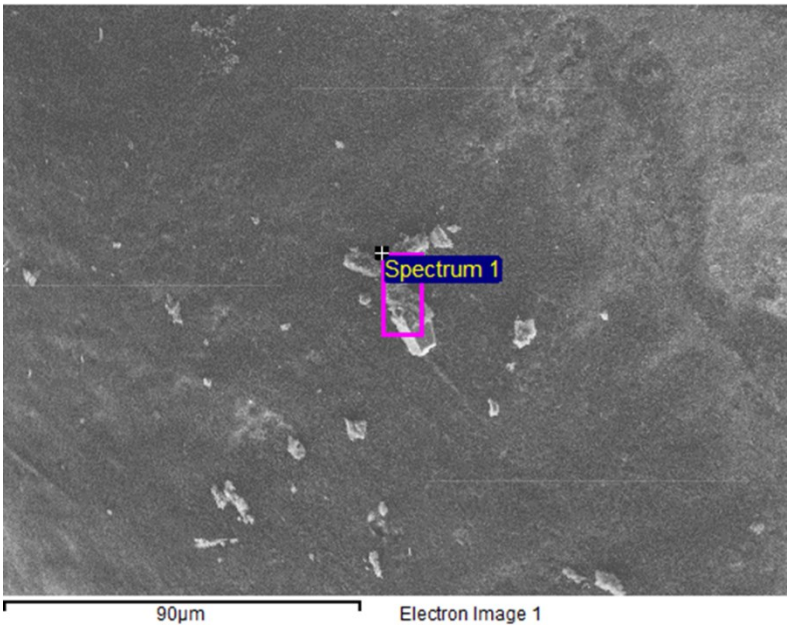


Figure A.210. SEM Image and EDS Spectrum of the Paint Collected from Exterior Web of the Girder.

Element	Weigh t%	Atomic %
C K	63.08	70.91
O K	32.61	27.52
Al K	0.62	0.31
Si K	0.93	0.45
Cl K	1.02	0.39
Ca K	0.24	0.08
Ti K	0.57	0.16
Fe K	0.44	0.11
Zn K	0.11	0.02
Zr L	0.39	0.06
Totals	100.00	



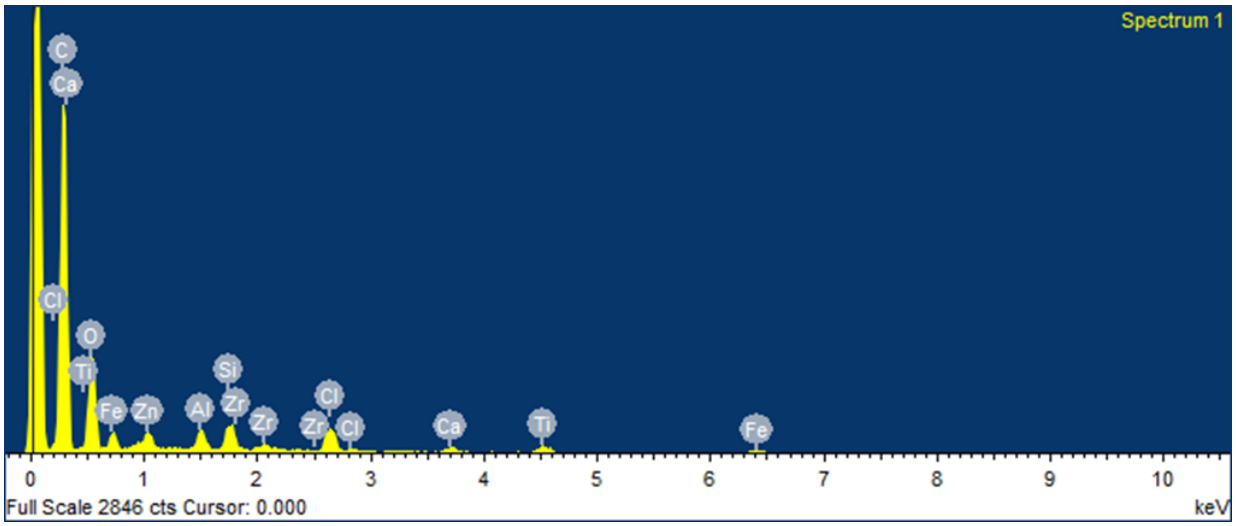
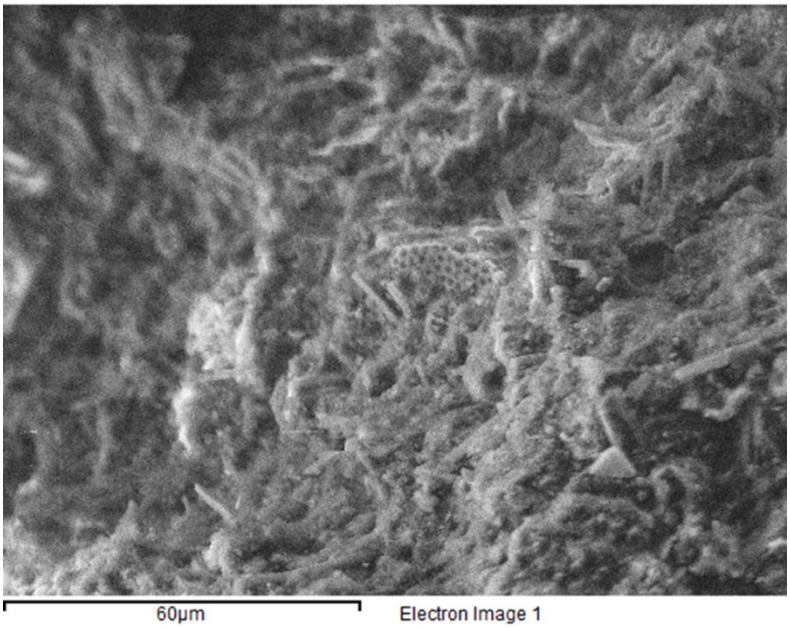


Figure A.211. SEM Image and EDS Spectrum of the Paint Collected from Exterior Web of the Girder.

Element	Weight %	Atomic %
C K	51.82	61.25
O K	40.01	35.50
Al K	0.40	0.21
Si K	3.65	1.85
P K	0.31	0.14
Ca K	1.11	0.39
Fe K	1.94	0.49
Zn K	0.75	0.16
Totals	100.00	



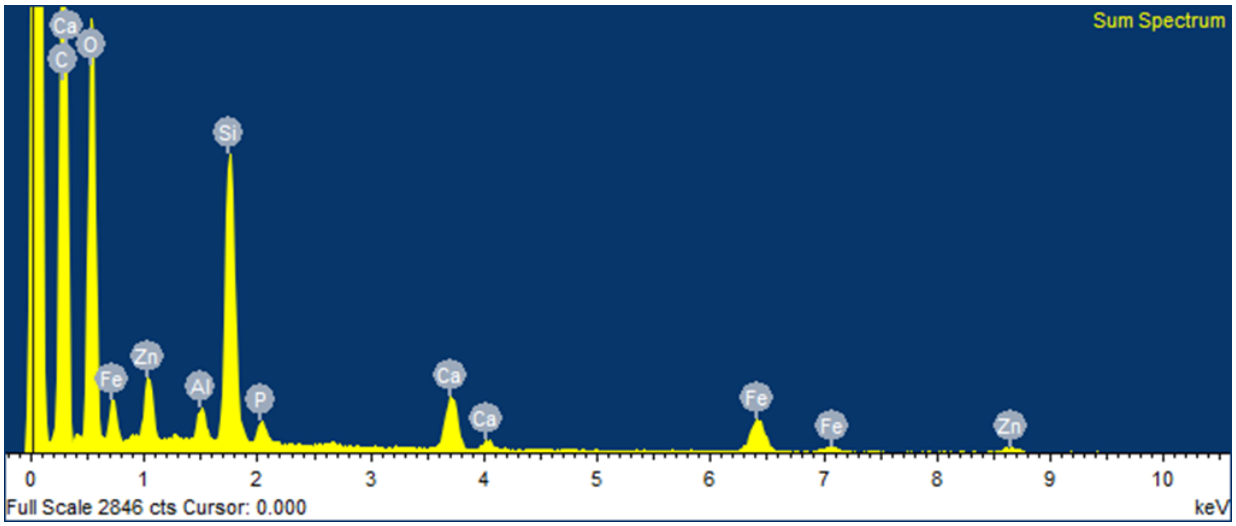


Figure A.212. SEM Image and EDS Spectrum of the Paint Collected from Interior Web of the Girder.

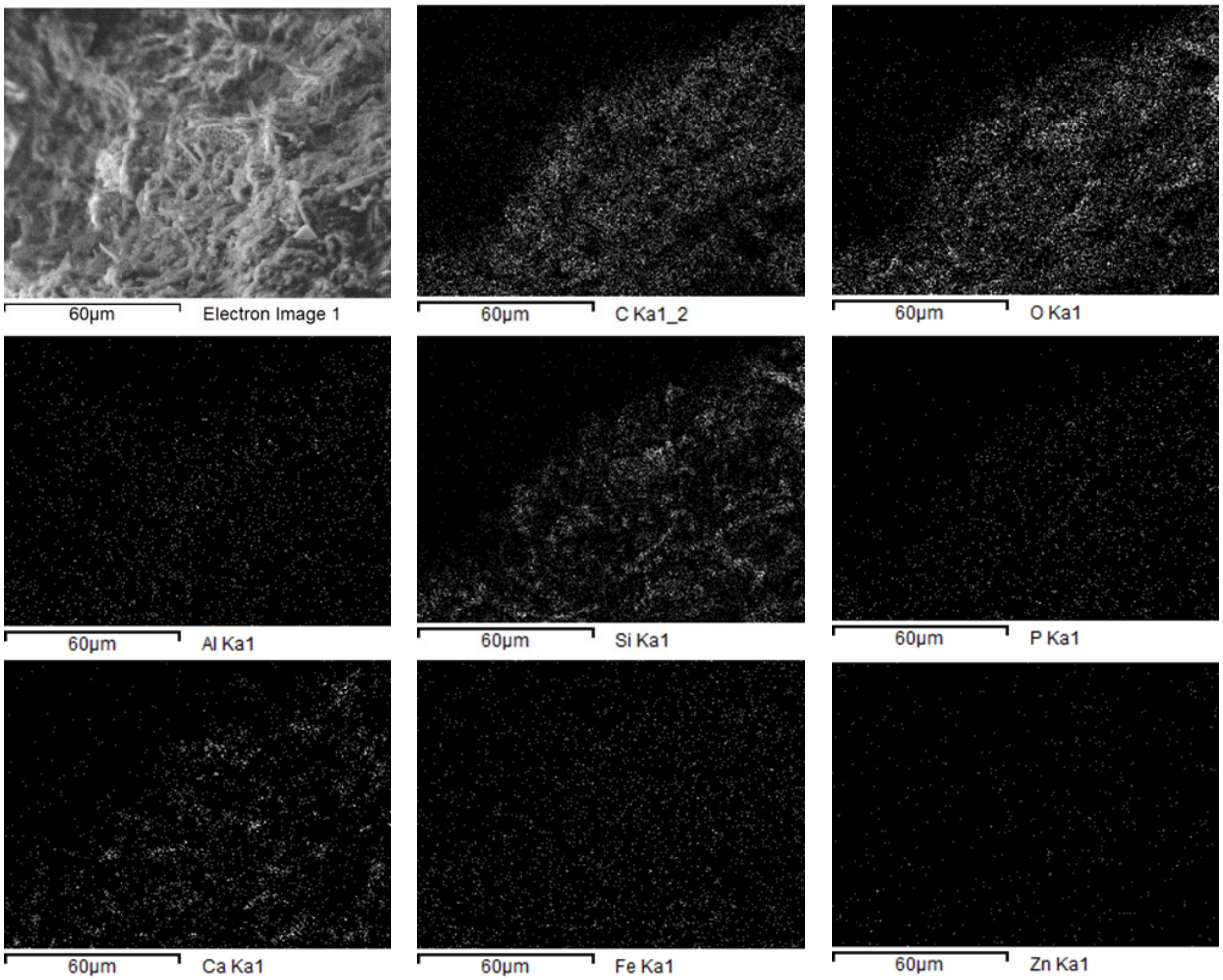
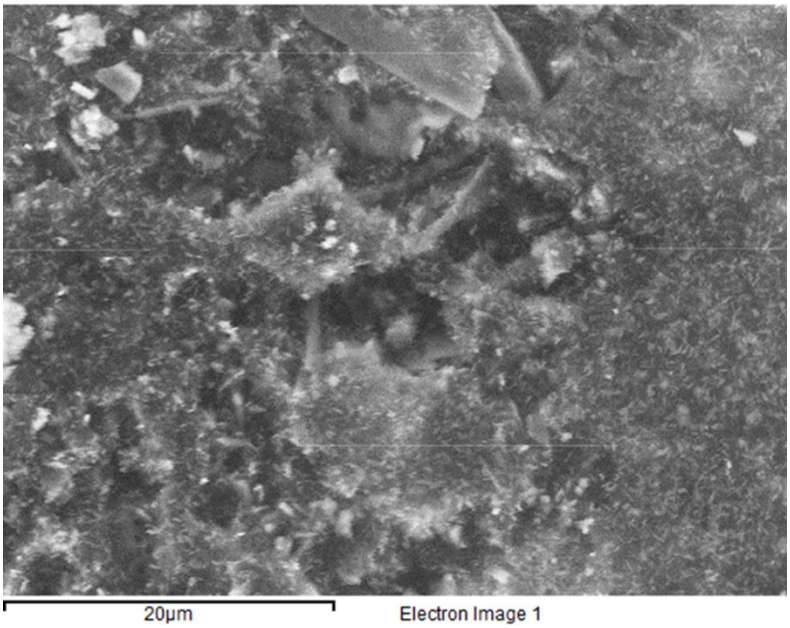


Figure A.213. SEM Image and EDS Spectrum of the Paint Collected from Interior Web of the Girder.

Element	Weight %	Atomic %
C K	57.10	66.30
O K	35.30	30.77
Al K	0.29	0.15
Si K	3.00	1.49
P K	0.49	0.22
Cl K	0.06	0.02
Ca K	1.30	0.45
Fe K	1.98	0.49
Zn K	0.47	0.10
Totals	100.00	



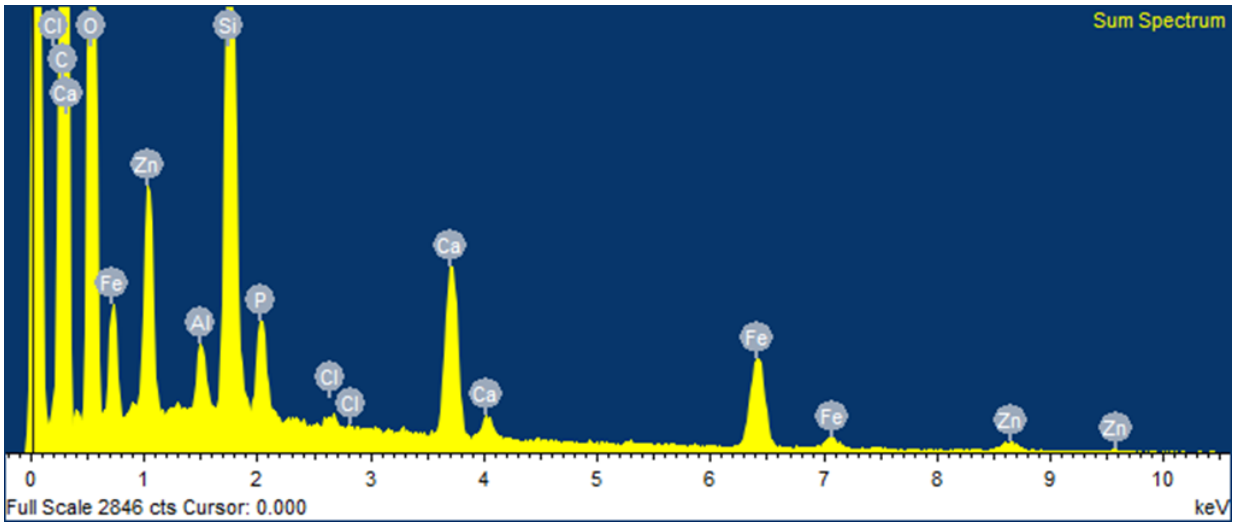


Figure A.214. SEM Image of Paint and EDS Spectrum of the Paint Collected from Interior Web of the Girder.

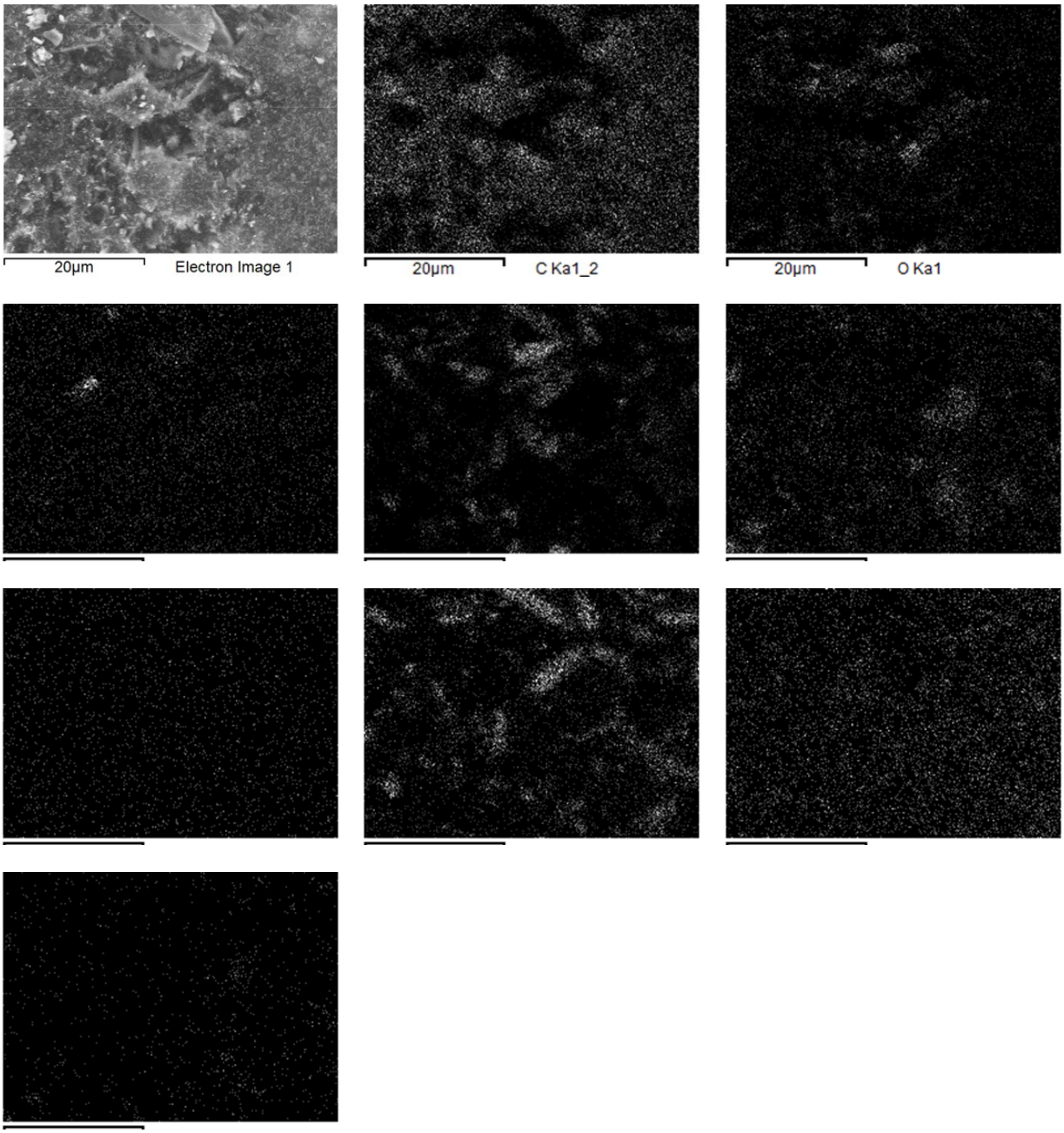
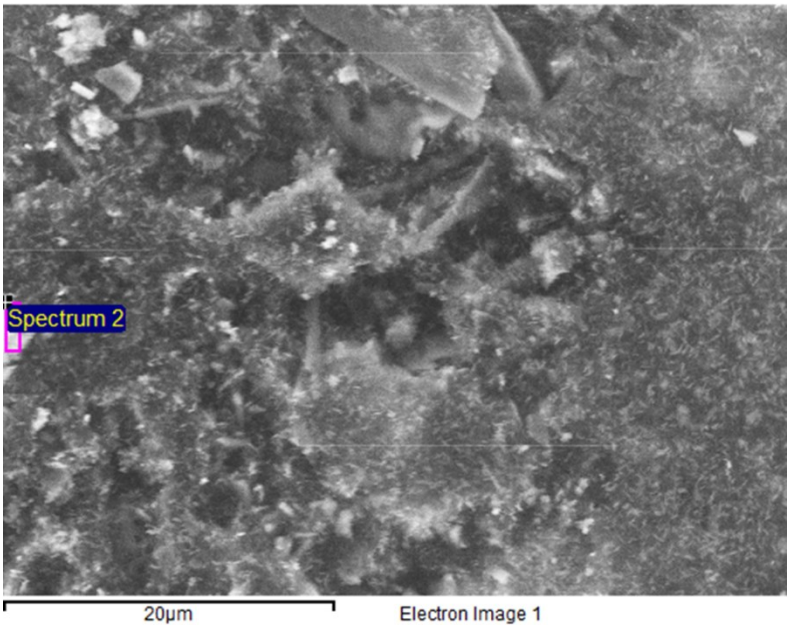


Figure A.215. EDS Elemental Mapping of Paint Collected from Interior Web.

Element	Weight %	Atomic %
C K	65.32	73.97
O K	28.22	23.99
Al K	0.16	0.08
Si K	0.98	0.47
P K	0.96	0.42
Cl K	0.04	0.02
Ca K	0.54	0.18
Fe K	2.20	0.54
Zn K	1.59	0.33
Totals	100.00	



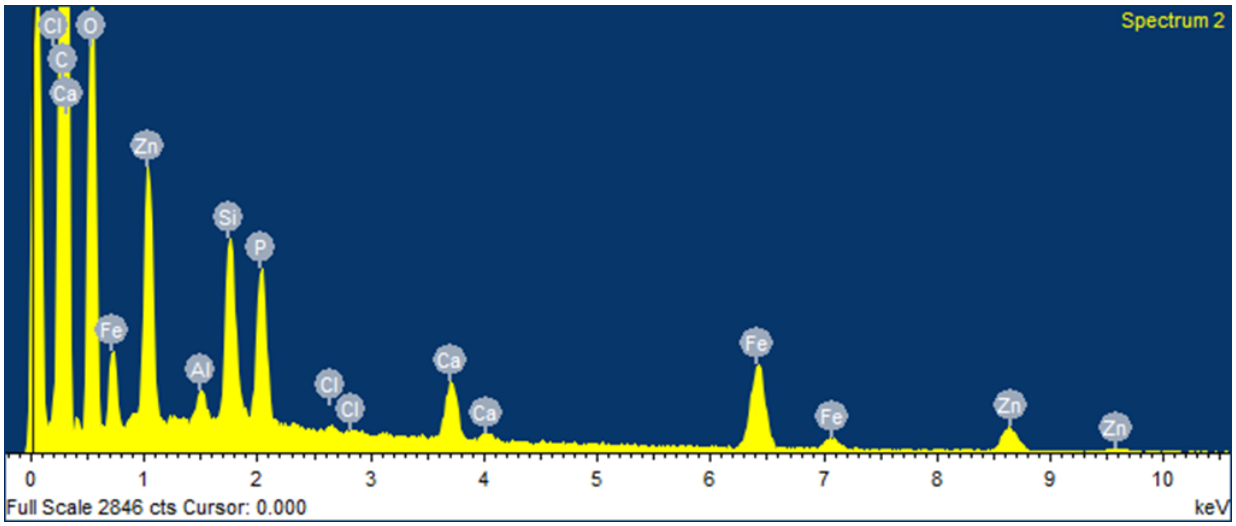
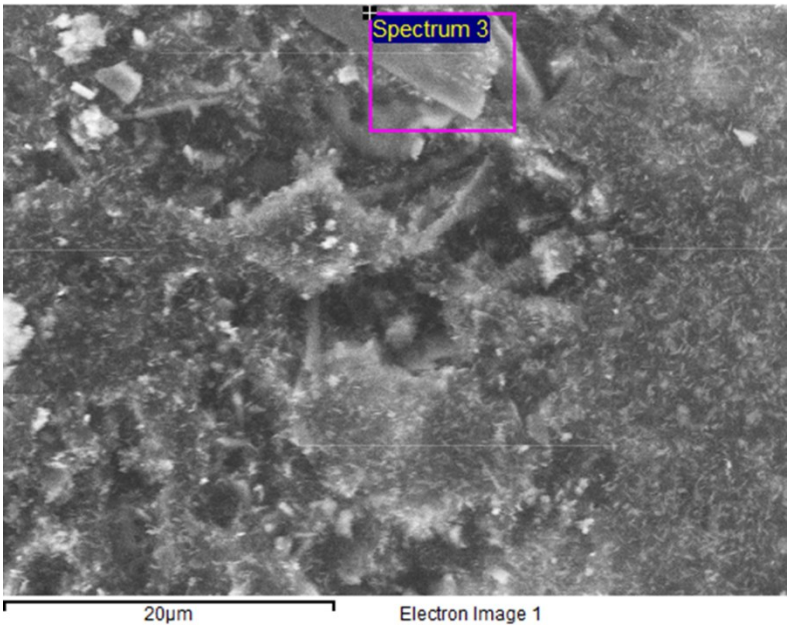


Figure A.216. SEM Image and EDS Spectrum of the Paint Collected from Interior Web of the Girder.

Element	Weight %	Atomic %
C K	45.79	56.77
O K	39.73	36.98
Al K	0.29	0.16
Si K	6.46	3.42
P K	0.43	0.21
Ca K	5.10	1.89
Fe K	1.68	0.45
Zn K	0.51	0.12
Totals	100.00	



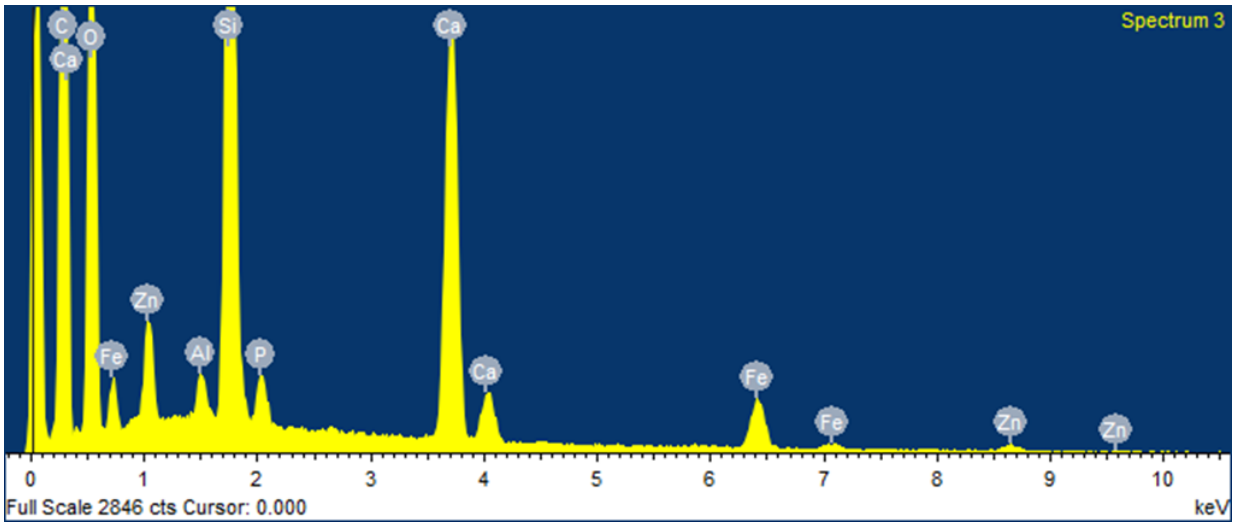
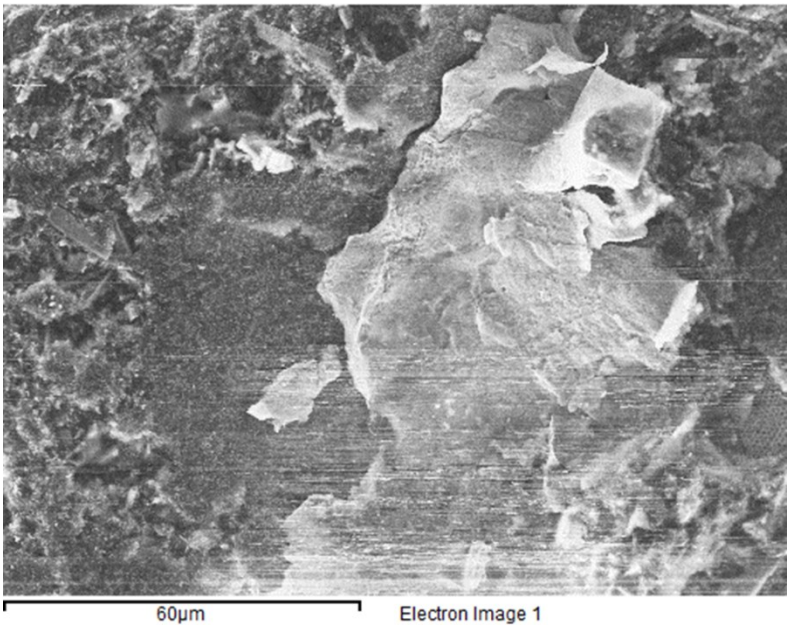


Figure A.217. SEM Image and EDS Spectrum of the Paint Collected from Interior Web of the Girder.

Element	Weight %	Atomic %
C K	52.72	66.90
O K	28.14	26.80
Al K	0.34	0.19
Si K	3.01	1.63
P K	0.33	0.16
Ca K	1.08	0.41
Mn K	0.17	0.05
Fe K	13.50	3.69
Zn K	0.71	0.17
Totals	100.00	



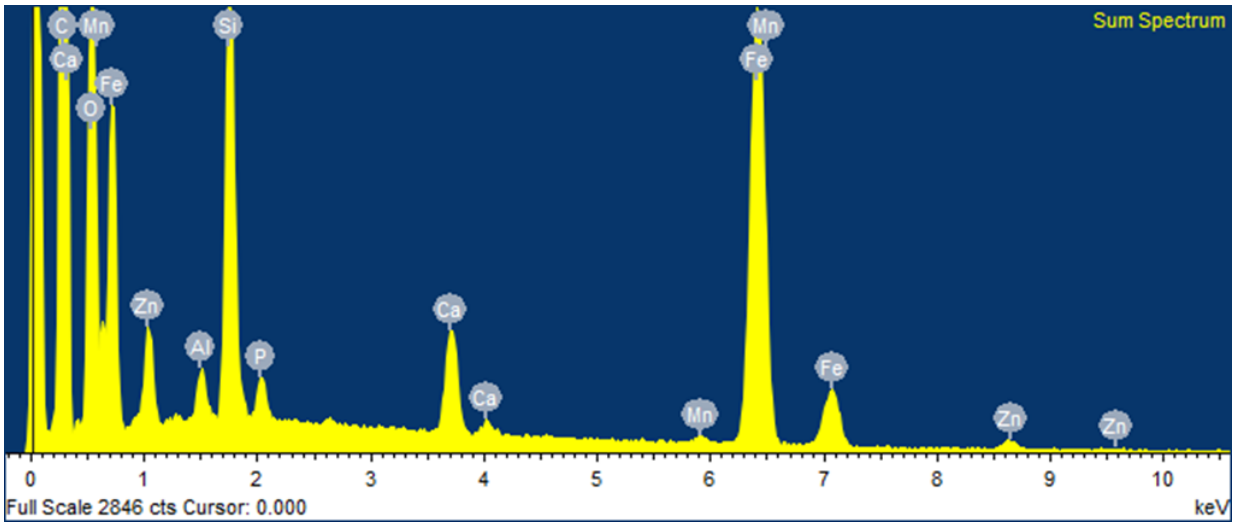


Figure A.218. SEM Image and EDS Spectrum of the Paint Collected from Interior Web of the Girder.

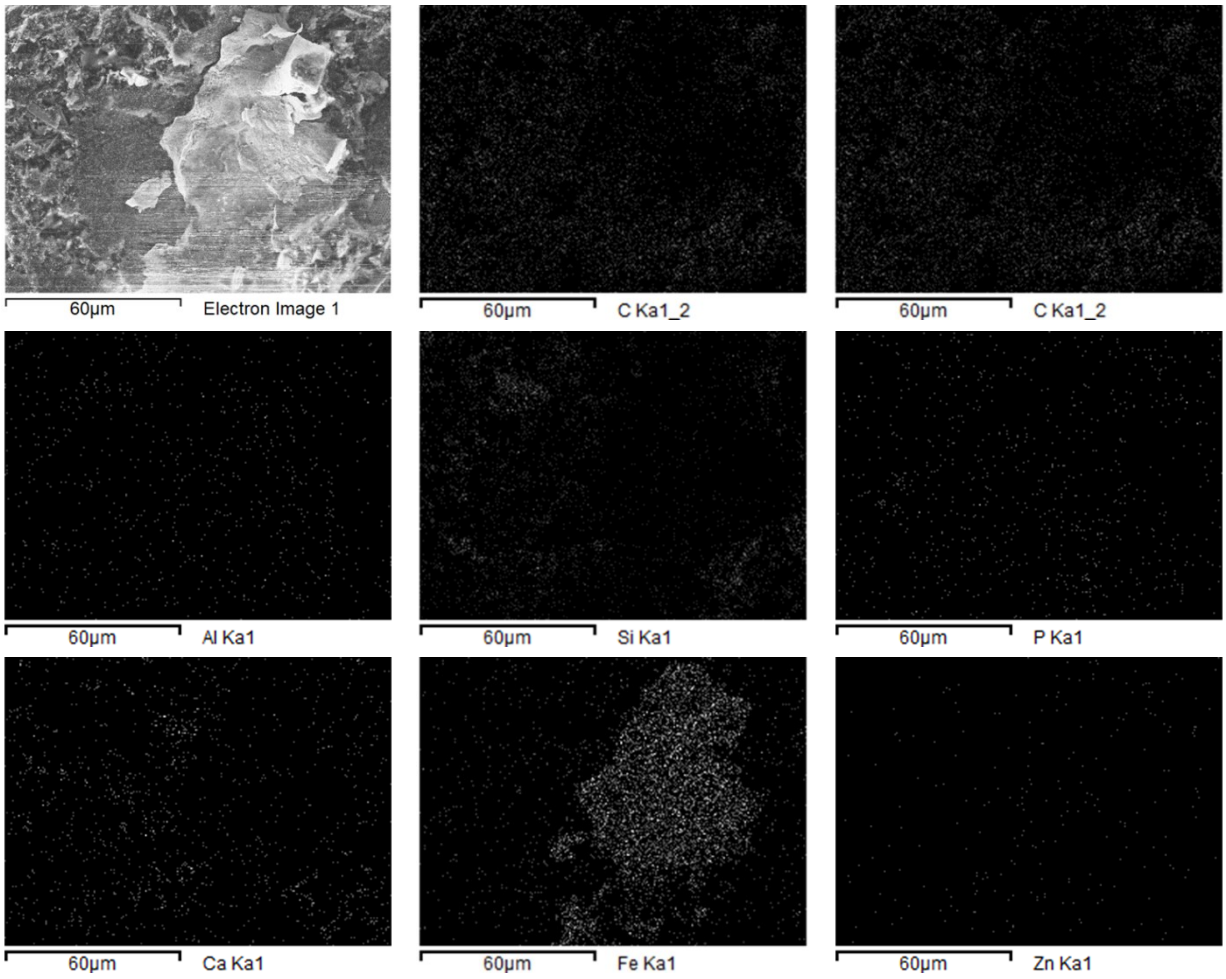
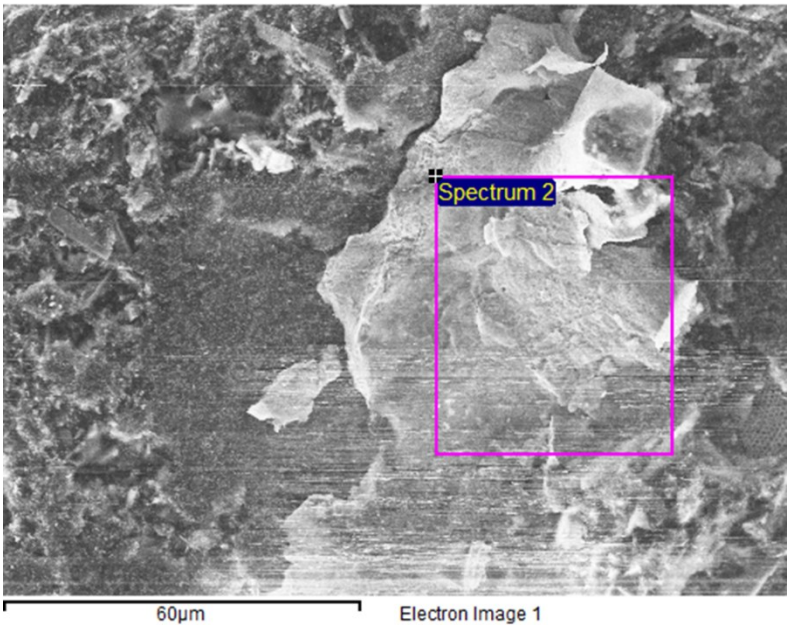


Figure A.219. EDS Elemental Mapping of Paint Collected from Interior Web.

Element	Weight %	Atomic %
C K	29.58	59.34
O K	6.56	9.88
F K	3.01	3.82
Al K	0.97	0.86
Si K	0.54	0.46
Ca K	0.34	0.20
Mn K	0.78	0.34
Fe K	57.74	24.91
Zn K	0.49	0.18
Totals	100.00	



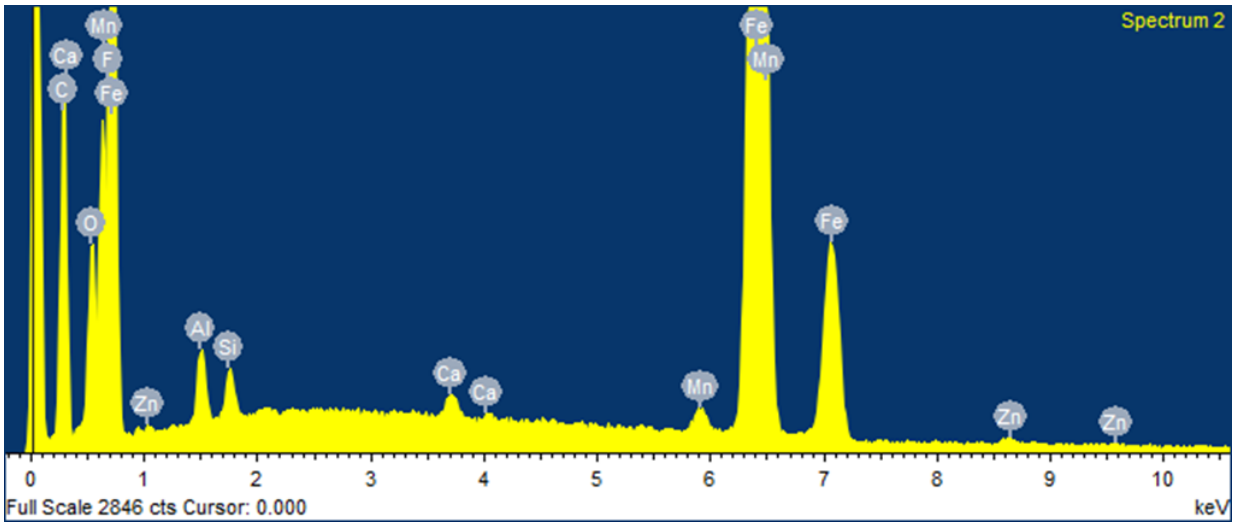


Figure A.220. SEM Image and EDS Spectrum of the Paint Collected from Interior Web of the Girder.

A.18. HOU-PS-01

- Carrington Rd over Spur 601
- Bridge ID 121020038905356, Coordinates (29.6038, -95.0282), Harris County
- Steel Plate Girder with System II type paint as it has two layer of paint that is an appearance coat and zinc rich primer coat
- Built 2016
- Date of Inspection: March 9, 2021; girder inspection carried near Bent No. 4 ends on girders within approximately four feet from the abutment
- No visual inspection on deck
- Location for Testing: A31-G1F1, A31-G2F1, A31-G3F2, A31-G4F2



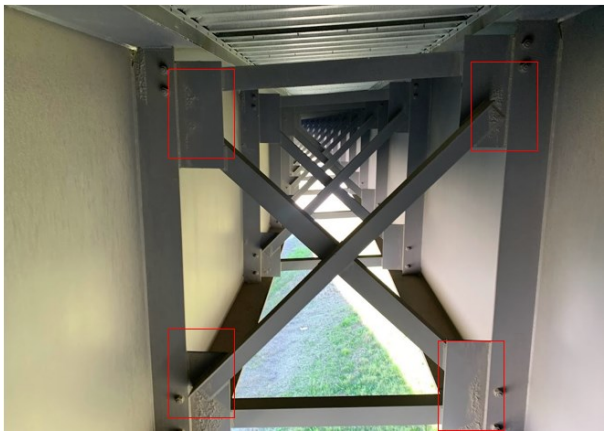
Figure A.221. Typical Elevation of HOU-PS-01.

A.18.1. Observed Condition

The paint condition of this bridge appears to be in good condition. The appearance coat is also in good condition except at top of bottom flange near the bents but corrosion is observed under the paint layer evident from scraping and after pull-off adhesion test. Blistering is observed near the bents on the stiffener and top of bottom flange. Erosion of paint and cracking in paint is not present. Spot rust is observed on the connection of girder and stiffener. No checking and cracking of paint are observed.



(a) Blistering and Dirt accumulation on Top of Bottom Flange of Interior Girder



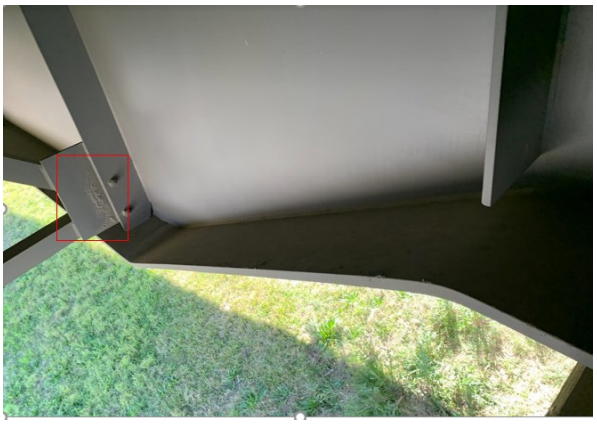
(b) Blisters observed on Interior Girder Connnection



c) Corrosion Observed Near the Bolted Connection



(d) Internal Bearing in Good Condition with Corrosion Observed Near the Bolted Connection



(e) Blistering observed on Gusset Plate of Interior Girder

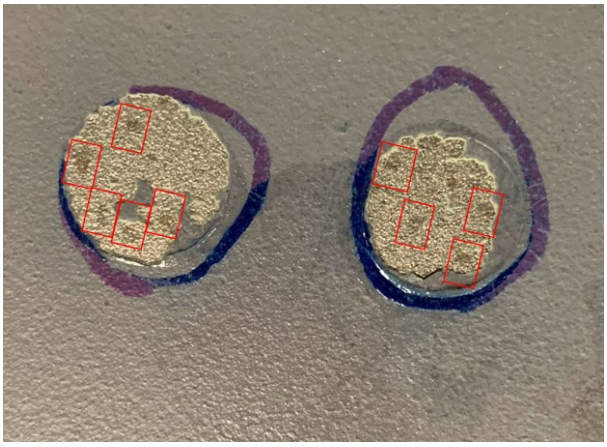


(f) Interior Girder in Good Condition

Figure A.222. Paint Condition on the Girder of HOU-PS-01.



(a) Blistering and Dirt accumulation on Top of Bottom Flange of Exterior Girder



(b) Spot Rust Observed Underneath Paint Layer



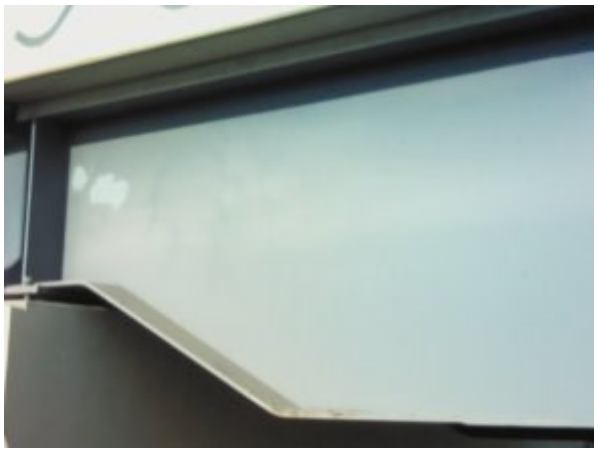
(c) Paint Deterioration and RustingObseved on Flange of Exterior Girder



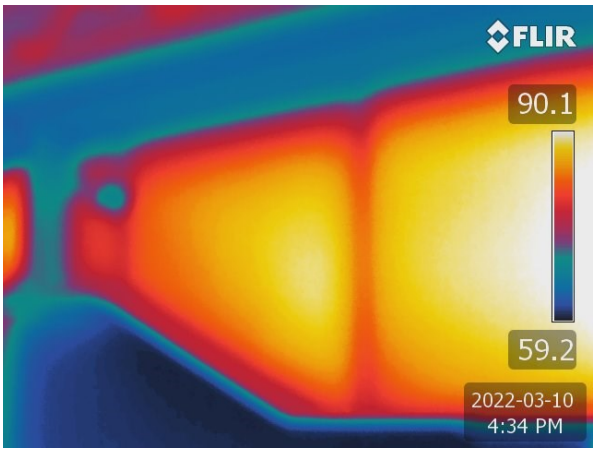
(d) Overall Exterior Girder in Good Condition

Figure A.223. Paint Condition on the Girder of HOU-PS-01.

A.18.2.NDT Results



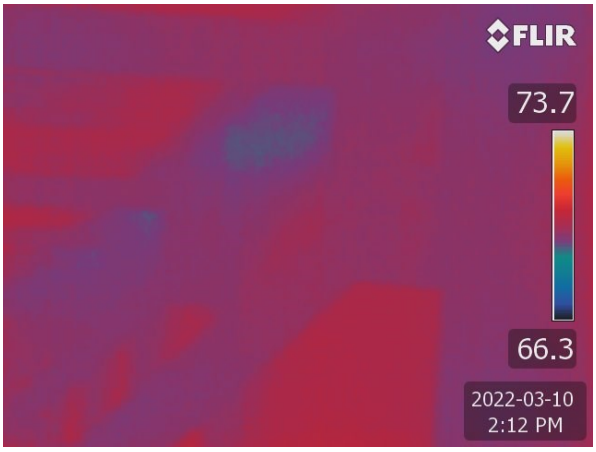
(a) Digital Image of Exterior Face of I Beam(G1F1)



(b) Thermal Image of Exterior Face of I Beam (G1F1)



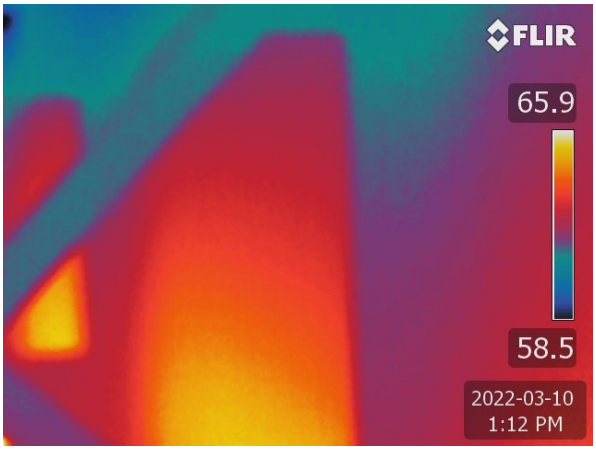
(c) Digital Image of Connection



(d) Thermal Image of Connection



(e) Digital image of the Interior face of I Beam



(f) Thermal image of the Interior of I Beam

Figure A.224. Digital and Thermal Image of Painted Girder on HOU-PS-01.

Table A-87. Paint System Information.

Cohesive Failure Layer		**Adhesive Failure Layer**	
Code	**Description**	**Code**	**Description**
A	Substrate	A/B	Substrate & Layer 1
B	Layer 1 (Metallic Green)	B/C	Layer 1 & Glue
C	Layer 2 (Blue)	C/Y	
Y	Glue	Y/Z	Glue & Dolly

Table A-88. Field Inspection Results for HOU-PS-01.

Location	Cl^- Conc. (ppm)	pH Test	Thickness (µm)	Thickness (inch)	Visual Inspection
B4-G1F2 TF Bot.		-	Measured R1 147 R2 177 R3 167 Design Paint 140-381	Measured R1 1.232 R2 1.233 R3 1.232 R_Avg Design	Rust Grade – 10 Blistering – Not Found Discoloration – Not Found Flaking – Not Found Delamination – Not Found
B4-G1F2 Web	1		Measured R1 241 R2 223 R3 253 Design Paint 140-381	Measured R1 0.694 R2 0.694 R3 0.694 R_Avg Design	Rust Grade – 10 Blistering – Not Found Discoloration – Not Found Flaking – Not Found Delamination – Not Found
B4-G1F2 BF Top		-	Measured R1 288 R2 230 R3 246 Design Paint 140-381	Measured R1 1.236 R2 1.239 R3 1.233 R_Avg Design	Rust Grade – 10 Blistering – Not Found Discoloration – Not Found Flaking – Not Found Delamination – Found
B4-G1F2 BF Bot.	-	-	Measured R1 225 R2 213 R3 229 Design Paint 140-381	Measured R1 R2 R3 R_Avg Design	Rust Grade – 10 Blistering – Not Found Discoloration – Not Found Flaking – Not Found Delamination – Not Found
B4-G2F2 TF Bot.	-		Measured R1 249 R2 309 R3 275 Design Paint 140-381	Measured R1 1.232 R2 1.232 R3 1.233 R_Avg Design	Rust Grade – 10 Blistering – Not Found Discoloration – Not Found Flaking – Not Found Delamination – Not Found
B4-G2F2 Web	1		Measured R1 249 R2 309 R3 275 Design Paint 140-381	Measured R1 0.705 R2 0.701 R3 0.704 R_Avg Design	Rust Grade – 10 Blistering – Not Found Discoloration – Not Found Flaking – Not Found Delamination – Not Found

Table A-89. Field Inspection Results for HOU-PS-01.

Location	Cl^- Conc. (ppm)	pH Test	Thickness (µm)	Thickness (inch)	Visual Inspection
B4-G2F2 BF Top		-	Measured R1 249 R2 309 R3 275 Design Paint 140-381	Measured R1 1.237 R2 1.239 R3 1.239 R_Avg Design	Rust Grade – 10 Blistering – Not Found Discoloration – Not Found Flaking – Not Found Delamination – Not Found
B4-G2F2 BF Bot.			Measured R1 216 R2 239 R3 203 Design Paint 140-381	Measured R1 R2 R3 R_Avg Design	Rust Grade – 10 Blistering – Not Found Discoloration – Not Found Flaking – Not Found Delamination – Not Found
B4-G3F1 TF BOT		-	Measured R1 225 R2 234 R3 247 Design Paint 140-381	Measured R1 1.233 R2 1.237 R3 1.237 R_Avg Design	Rust Grade – 10 Blistering – Not Found Discoloration – Not Found Flaking – Not Found Delamination – Found
B4-G3F1 Web	1	-	Measured R1 206 R2 195 R3 212 Design Paint 140-381	Measured R1 0.694 R2 0.699 R3 0.699 R_Avg Design	Rust Grade – 10 Blistering – Not Found Discoloration – Not Found Flaking – Not Found Delamination – Not Found
B4-G3F1 BF Top	-		Measured R1 183 R2 192 R3 180 Design Paint 140-381	Measured R1 1.236 R2 1.240 R3 1.240 R_Avg Design	Rust Grade – 10 Blistering – Not Found Discoloration – Not Found Flaking – Not Found Delamination – Not Found
B4-G3F1 BF Bot.			Measured R1 232 R2 239 R3 228 Design Paint 140-381	Measured R1 R2 R3 R_Avg Design	Rust Grade – 10 Blistering – Not Found Discoloration – Not Found Flaking – Not Found Delamination – Not Found

Table A-90. Field Inspection Results for HOU-PS-01.

Location	Cl^- Conc. (ppm)	pH Test	Thickness (µm)	Thickness (inch)	Visual Inspection
B4-G4F2 TF Bot.		-	Measured R1 281 R2 288 R3 233 Design Paint 140-381	Measured R1 1.235 R2 1.237 R3 1.238 R_Avg Design	Rust Grade – 10 Blistering – Not Found Discoloration – Not Found Flaking – Not Found Delamination – Not Found
B4-G4F2 Web	1		Measured R1 288 R2 264 R3 290 Design Paint 140-381	Measured R1 0.704 R2 0.704 R3 0.699 R_Avg Design	Rust Grade – 10 Blistering – Not Found Discoloration – Not Found Flaking – Not Found Delamination – Not Found
B4-G4F2 BF Top		-	Measured R1 236 R2 231 R3 227 Design Paint 140-381	Measured R1 1.245 R2 1.245 R3 1.243 R_Avg Design	Rust Grade – 10 Blistering – Not Found Discoloration – Not Found Flaking – Not Found Delamination – Found
B4-G4F2 BF Bot.	-	-	Measured R1 252 R2 235 R3 271 Design Paint 140-381	Measured R1 R2 R3 R_Avg Design	Rust Grade – 10 Blistering – Not Found Discoloration – Not Found Flaking – Not Found Delamination – Not Found

A.18.3. Pull-off Adhesion Results

Table A-91. Pull-off Adhesion Results for HOU-PS-01.

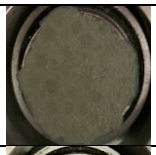
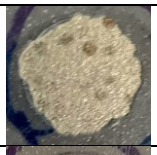
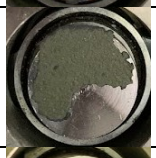
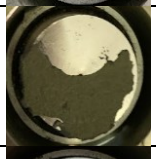
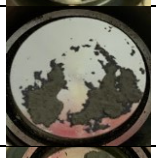
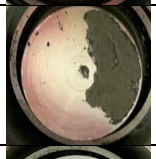
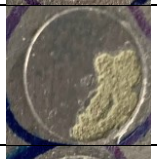
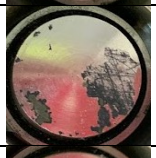
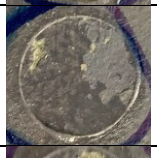
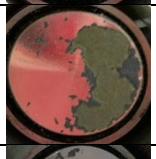
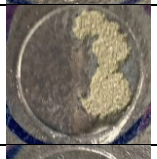
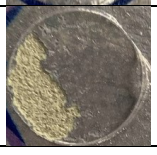
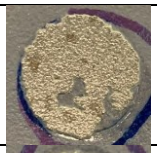
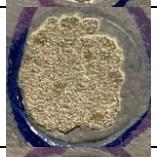
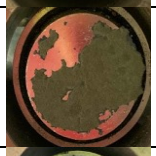
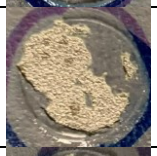
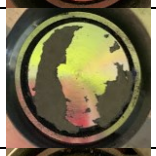
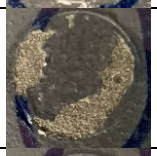
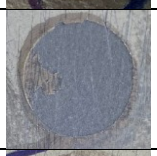
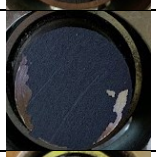
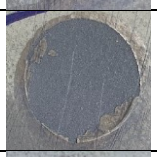
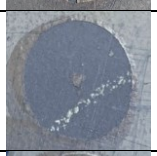
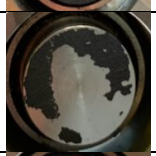
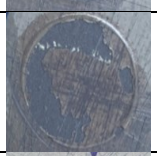
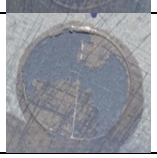
Location	Dolly Face	Substrate Face	Test Result (psi)	Attributes	Failure Type
B4-G1F2			952	100% A/B	100% Adhesive Failure
			780	80% A/B 20% Y/Z	80% Adhesive Failure 20% Adhesive Failure
			754	70% A/B 30% Y/Z	70% Adhesive Failure 30% Adhesive Failure
			555	70% A/B 30% Y/Z	70% Adhesive Failure 30% Adhesive Failure
			861	70% A/B 30% Y/Z	70% Adhesive Failure 30% Adhesive Failure
B4-G2F2			759	40% B 60% Y/Z	30% Cohesive Failure 70% Adhesive Failure
			615	40% B 60% Y/Z	30% Cohesive Failure 70% Adhesive Failure
			717	30% C 10%A/B 60% Y/Z	30% Cohesive Failure 10% Adhesive Failure 60% Adhesive Failure
			827	30% B 10% C 60% Y/Z	30% Cohesive Failure 10% Cohesive Failure 60% Adhesive Failure
			783	30% B 10% C 70% A/B	30% Cohesive Failure 10% Cohesive Failure 60% Adhesive Failure

Table A-92. Pull-off Adhesion Results for HOU-PS-01.

Location	Dolly Face	Substrate Face	Test Result (psi)	Attributes	Failure Type
B4-G3F1			924	90% A/B 10%Y/Z	90% Adhesive Failure 10% Adhesive Failure
			638	80% A/B 20%Y/Z	80% Adhesive Failure 10% Adhesive Failure
			798	70% A/B 30%Y/Z	70% Adhesive Failure 30% Adhesive Failure
			517	50% A/B 50%Y/Z	50% Adhesive Failure 50% Adhesive Failure
			733	30% A/B 70%Y/Z	30% Adhesive Failure 70% Adhesive Failure
B4-G4F2			853	90% C 10% Y/Z	90% Cohesive Failure 10% Adhesive Failure
			902	90% C 10% Y/Z	90% Cohesive Failure 10% Adhesive Failure
			930	90% C 10% Y/Z	90% Cohesive Failure 10% Adhesive Failure
			497	40% C 60% Y/Z	40% Cohesive Failure 60% Adhesive Failure
			617	50% C 50% Y/Z	50% Cohesive Failure 50% Adhesive Failure

A.18.4. Optical Microscopy Results

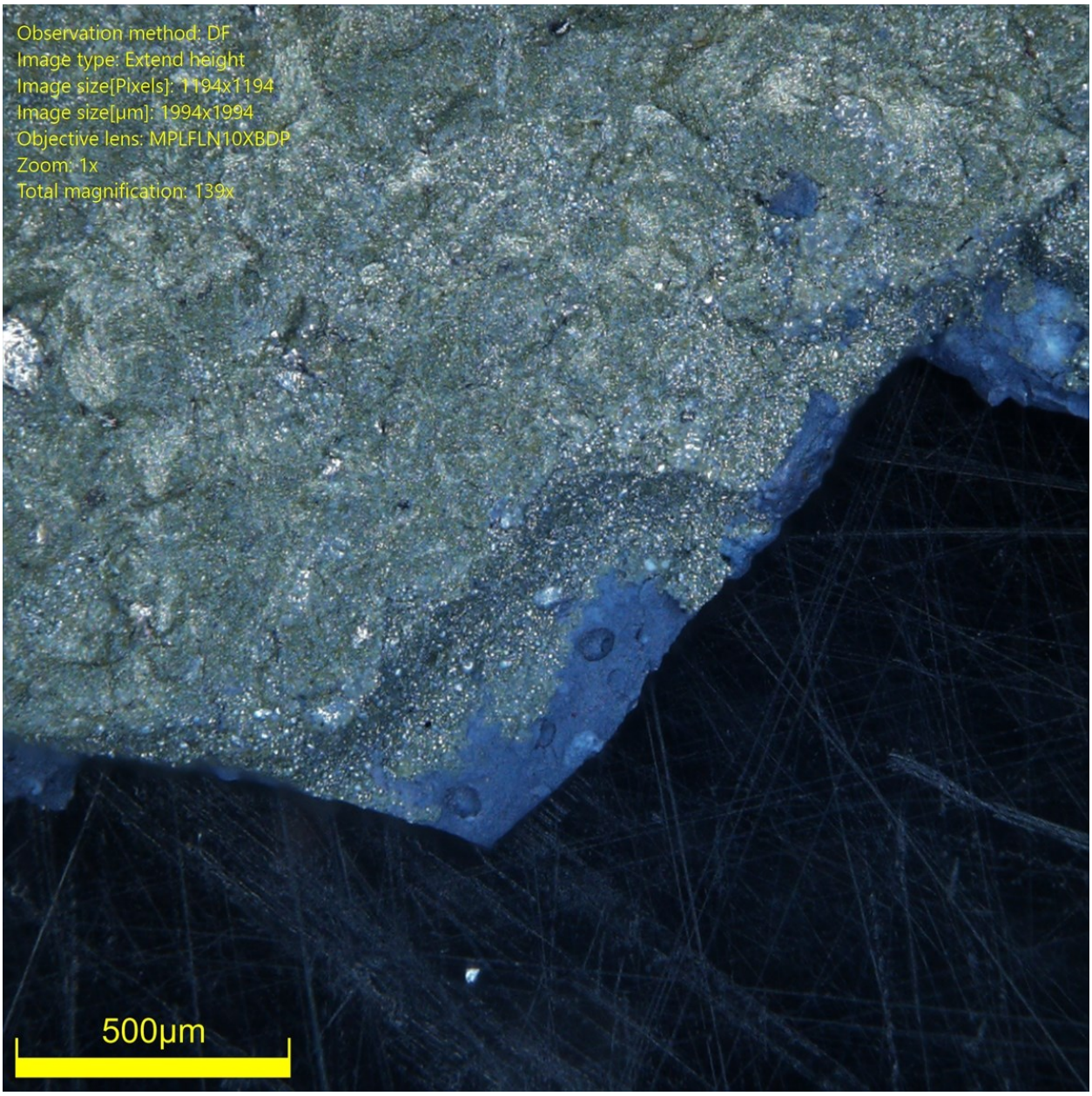


Figure A.225. Two Layer Paint System Examined by Optical Microscope HOU–PS–01.

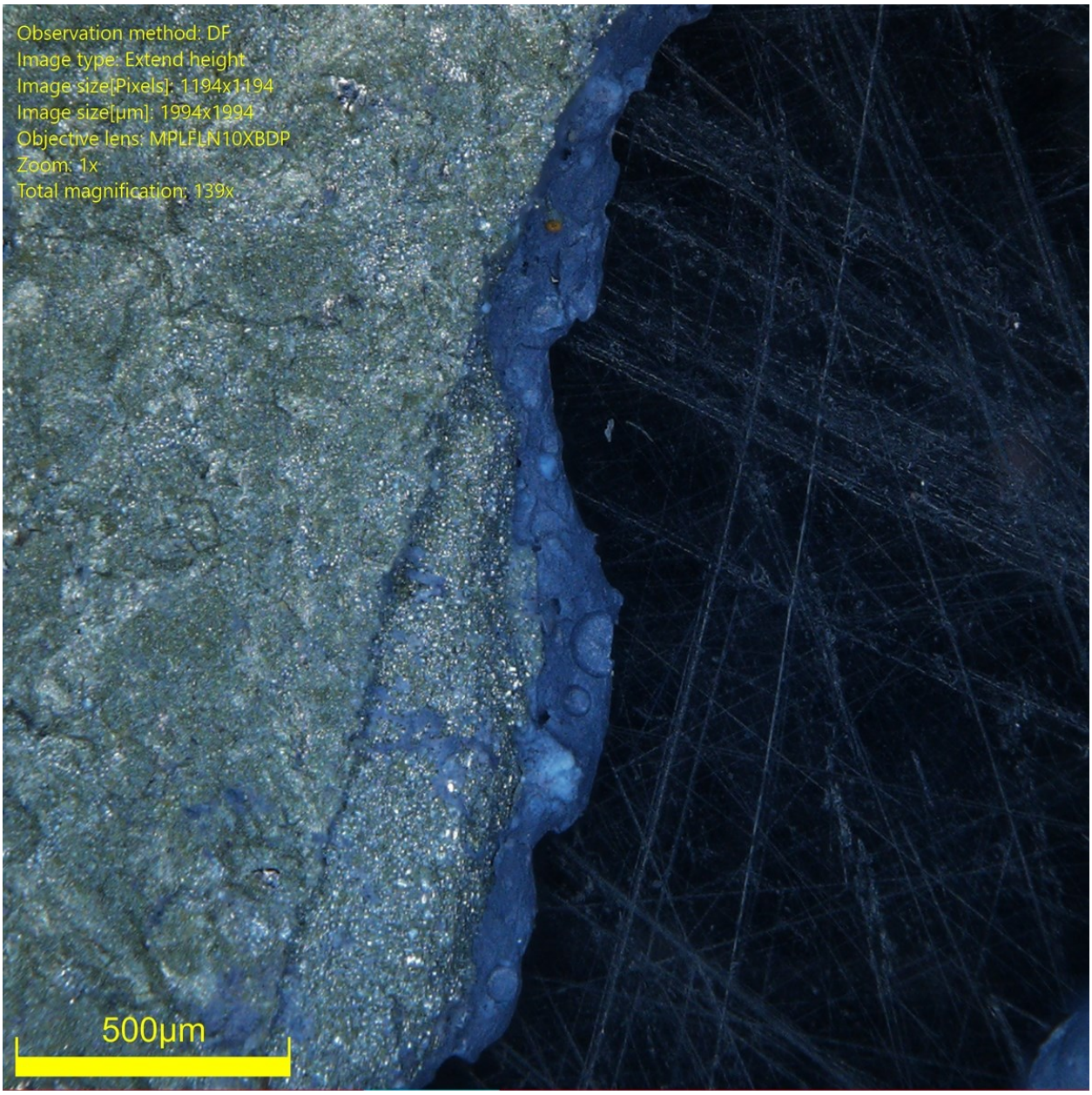
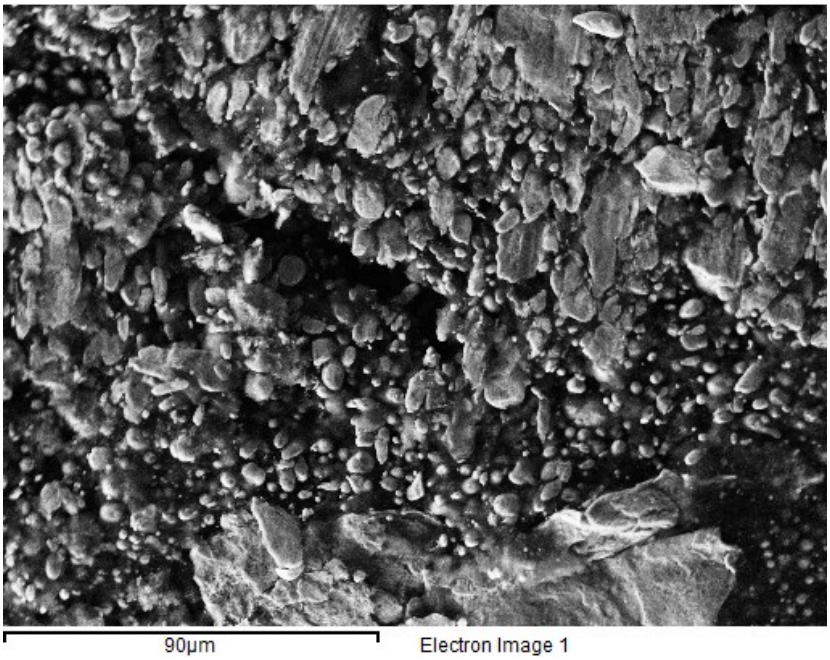


Figure A.226. Two Layer Paint System Examined by Optical Microscope HOU–PS–01.

A.18.5.SEM/EDS Results

Element	Weight %	Atomic %
C K	46.64	73.91
O K	10.91	12.98
Al K	0.67	0.48
Si K	0.25	0.17
Ca K	0.12	0.06
Fe K	7.11	2.42
Zn K	34.30	9.99
Totals	100.00	



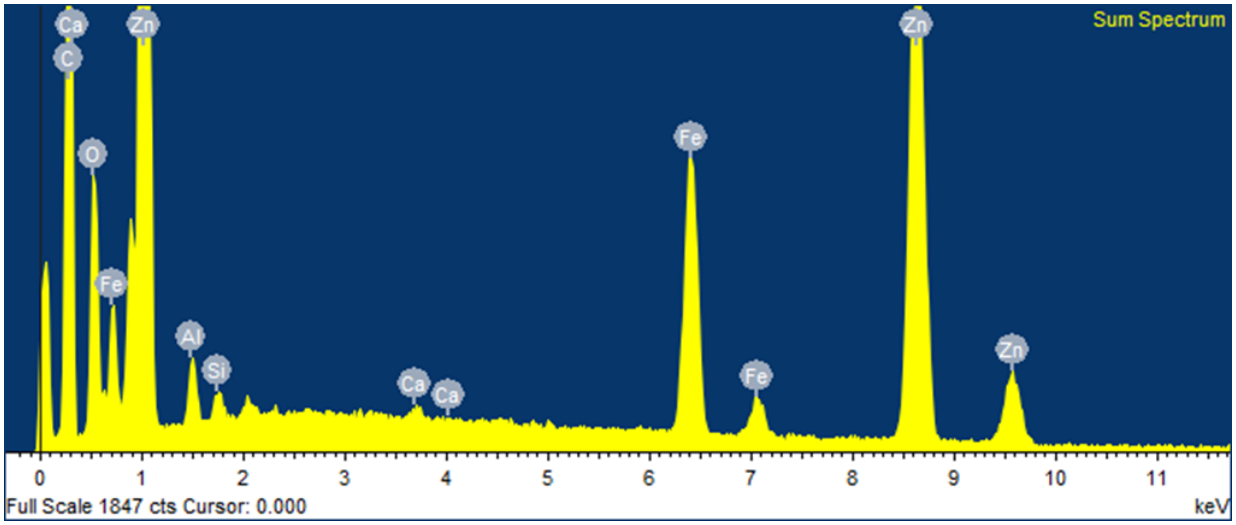
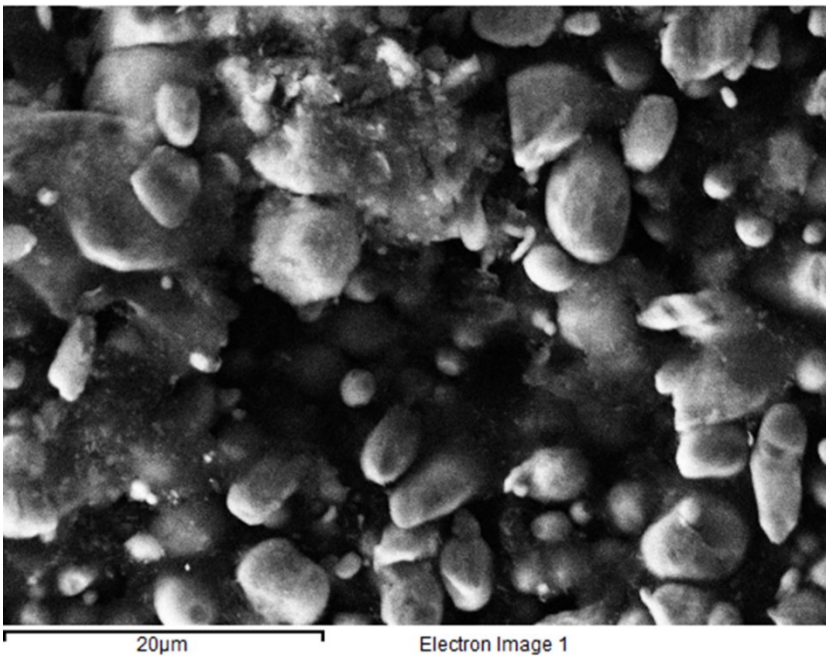


Figure A.227. SEM Image and EDS Spectrum of the Paint Collected from Exterior Web of the Girder.

Element	Weight %	Atomic %
C K	50.37	75.41
O K	12.48	14.02
Al K	0.51	0.34
Si K	0.26	0.17
Ca K	0.11	0.05
Fe K	1.12	0.36
Zn K	34.87	9.59
Zr L	0.28	0.05
Totals	100.00	



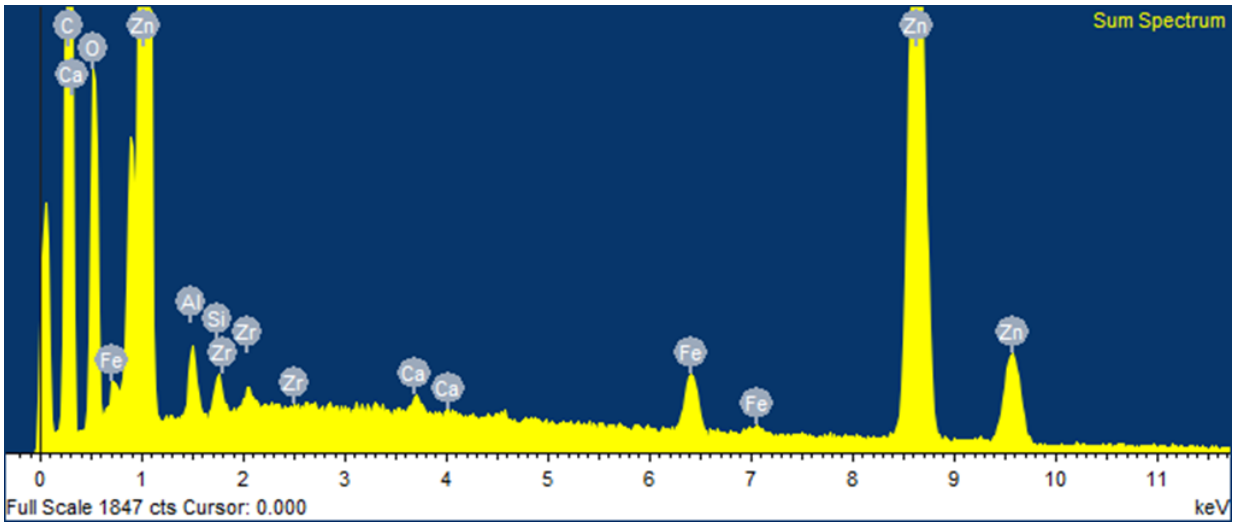
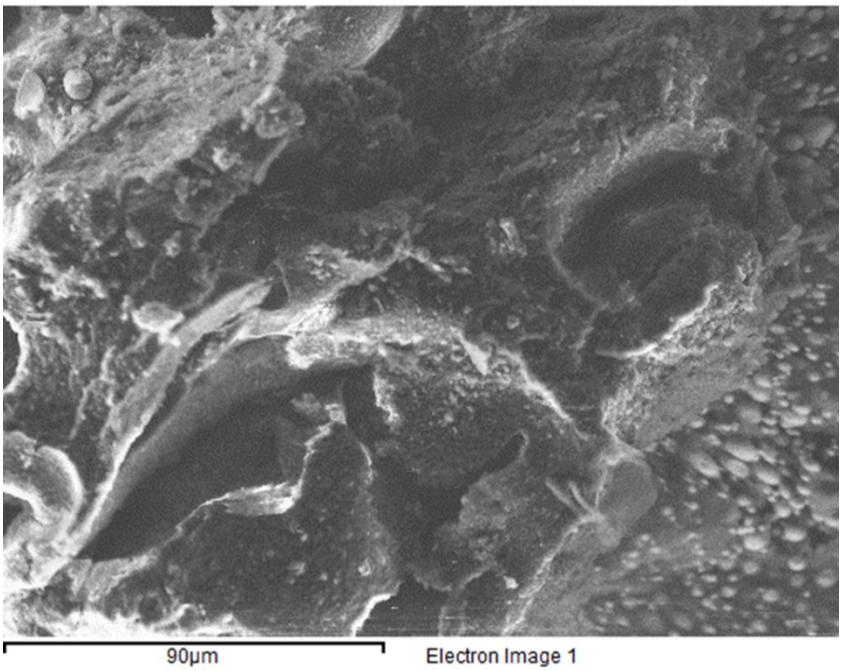


Figure A.228. SEM Image and EDS Spectrum of the Paint Collected from Exterior Web of the Girder.

Element	Weight %	Atomic %
C K	57.69	69.07
O K	30.73	27.62
Mg K	0.06	0.04
Al K	0.63	0.33
Si K	0.29	0.15
S K	0.05	0.02
Ca K	1.59	0.57
Ti K	2.46	0.74
Fe K	0.97	0.25
Zn K	5.36	1.18
Zr L	0.18	0.03
Totals	100.00	



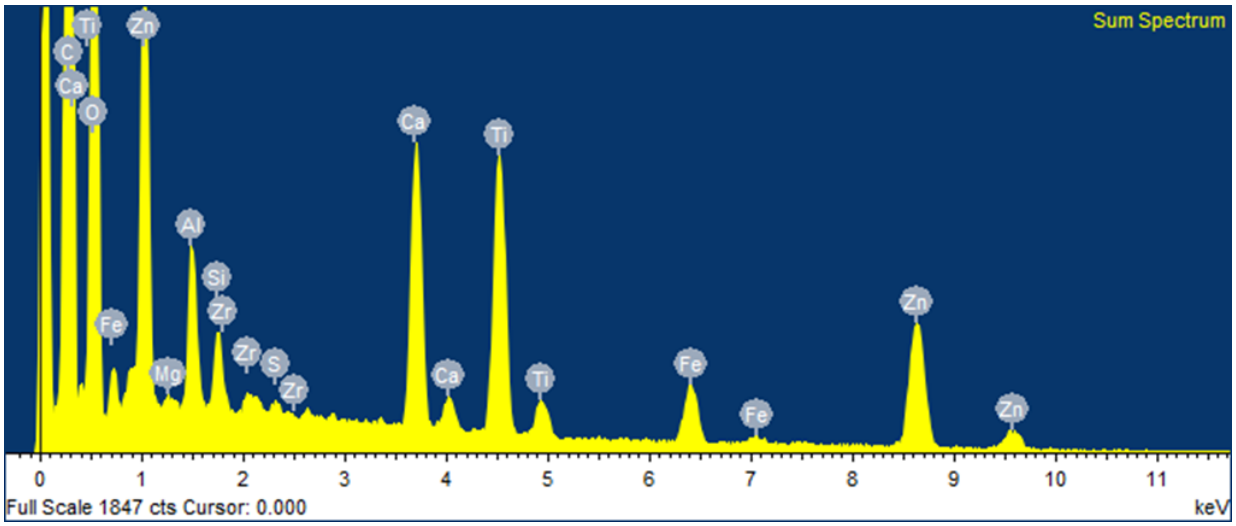


Figure A.229. SEM Image and EDS Spectrum of the Paint Collected from Exterior Web of the Girder.

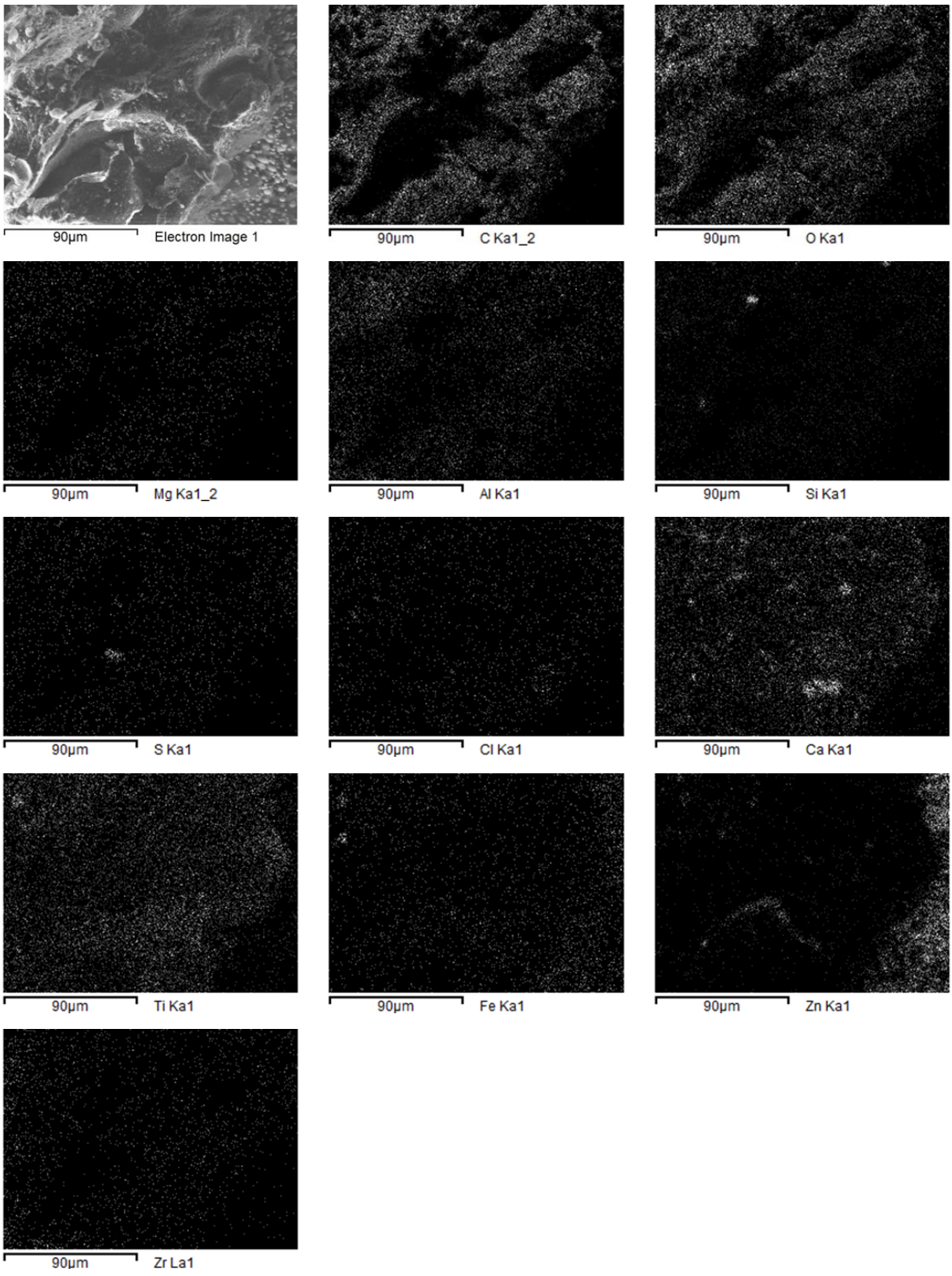


Figure A.230. EDS Elemental Mapping of Paint Collected from Exterior Web.

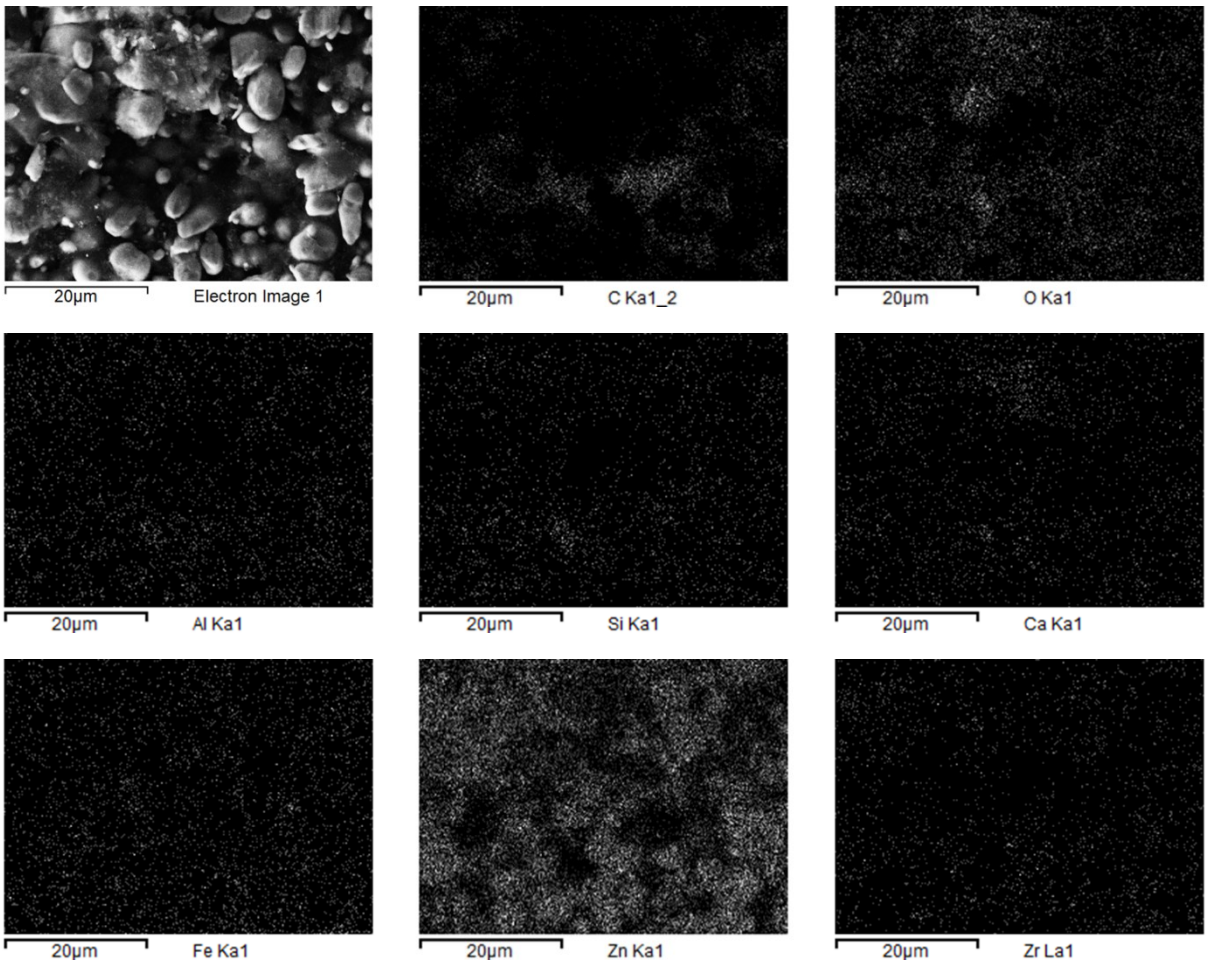


Figure A.231. EDS Elemental Mapping of Paint Collected from Exterior Web.

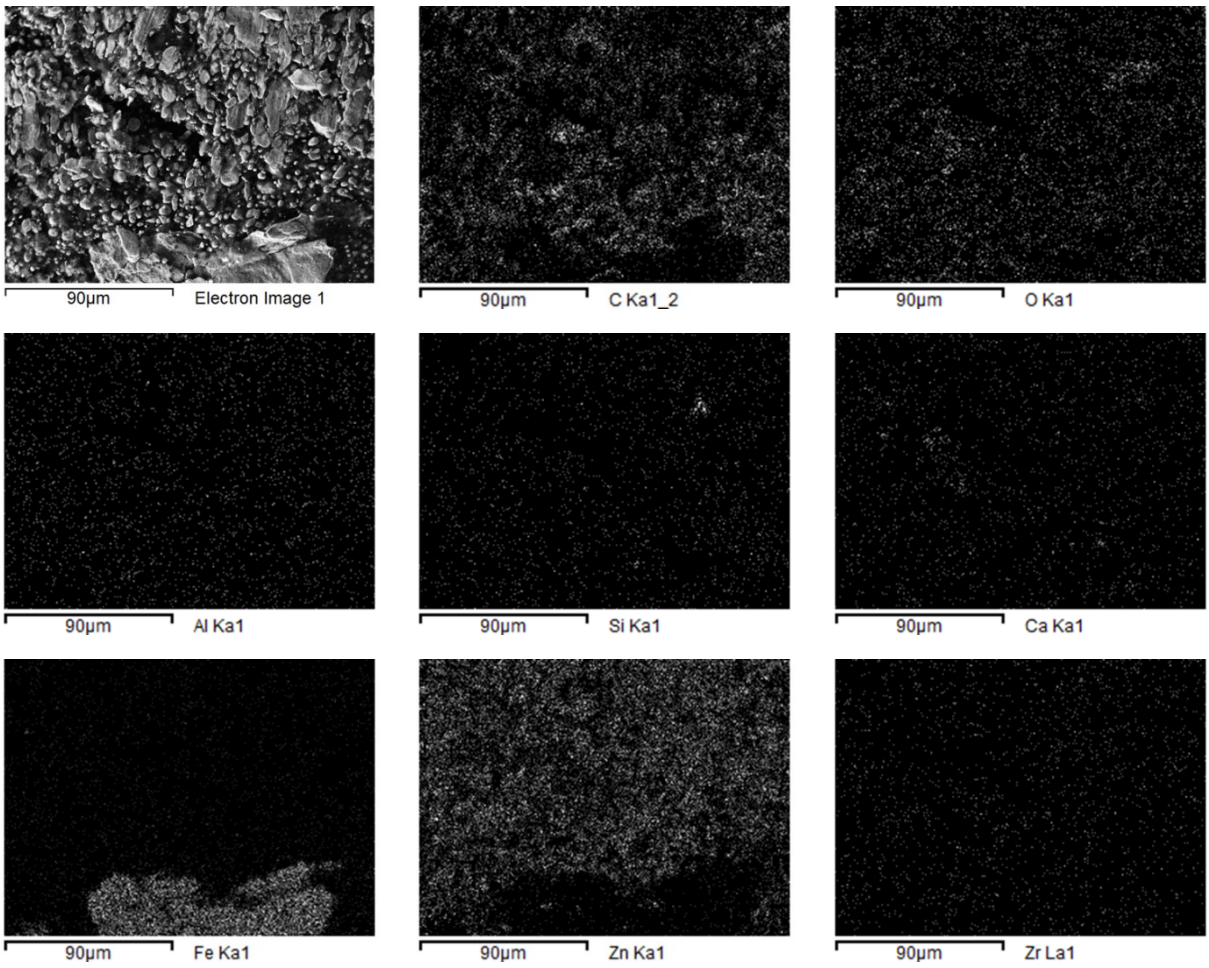


Figure A.232. EDS Elemental Mapping of Paint Collected from Exterior Web.

A.19. BMT-PS-01

- US 69-96 287 NB over US 69 SB CONN TO IH 10
- Bridge ID 201240020011132, Coordinates (30.09663, -94.13594), Jefferson County
- Steel Plate Girder with System II type paint
- Built 1966
- Date of Inspection: April 14, 2021; girder inspection carried out on south abutment (Abutment number 1) and measurements are taken on girders within approximately four feet from the abutment.
- No visual inspection on deck
- Location for Testing: A1-G1F1, A1-G2F1, A1-G3F2, A1-G6F2



Figure A.233. Typical Elevation of BMT-PS-01.

A.19.1. Observed Condition

The overall paint condition of this bridge is in very good condition. The appearance coat is also in good condition. Blistering is observed in a small area of web of exterior girder. Erosion of paint, cracking in paint is not present. No checking and cracking of paint are observed. Joints are also in good condition.



(a) Superstructure in Good Condition over Roadway



(b) Superstructure in Good Condition Near Abutments



(c) Blistering observed on web of Exterior Girder



(d) External Girder in Good Condition



(e) Internal Bearing in Good Condition



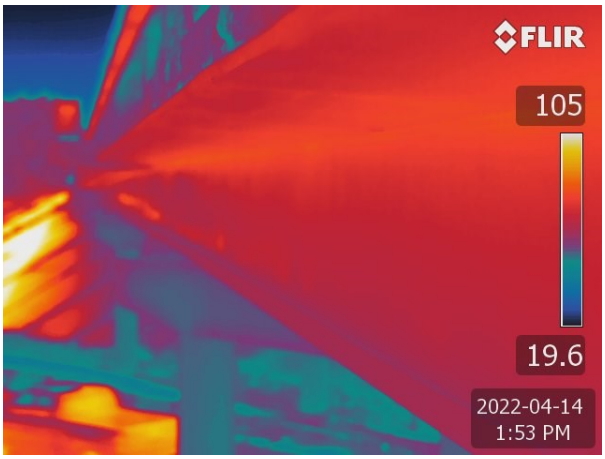
(f) Interior Girder in Good Condition

Figure A.234. Paint Condition on the Girder of BMT-PS-01.

A.19.2.NDT Results



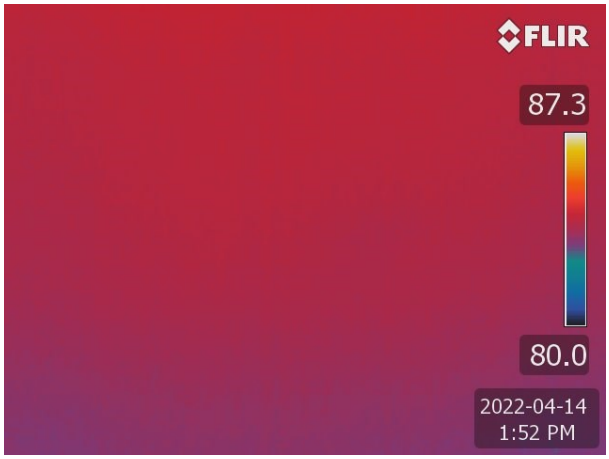
(a) Digital Image of Exterior Face of I Beam(G1F1)



(b) Thermal Image of Exterior Face of I Beam (G1F1)



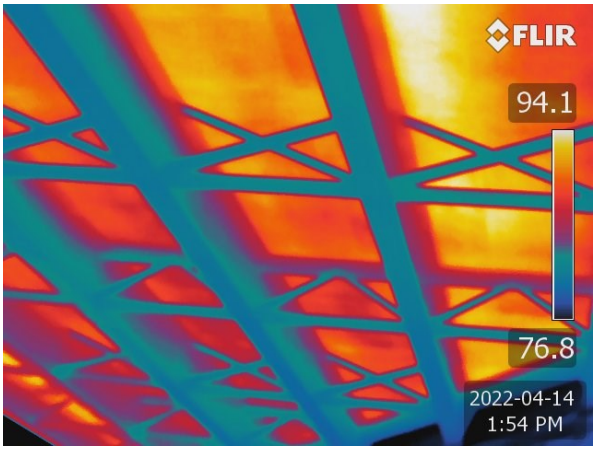
(c) Digital Image of Connection showing Rusting



(d) Thermal Image of Connection showing Rusting



(g) Digital Image of Superstructure



(h) Thermal Image of Superstructure

Figure A.235. Digital and Thermal Image of Painted Girder on BMT-PS-01.

Table A-93. Paint System Information.

Cohesive Failure Layer		**Adhesive Failure Layer**	
Code	**Description**	**Code**	**Description**
A	Substrate	A/B	Substrate & Layer 1
B	Layer 1 (Metallic Green)	B/C	Layer 1 & Glue
C	Layer 2 (White)	C/Y	
Y	Glue	Y/Z	Glue & Dolly

Table A-94. Field Inspection Results for BMT-PS-01.

Location	Cl^- Conc. (ppm)	pH Test	Thickness (µm)	Thickness (inch)	Visual Inspection
A1-G1F1 TF Bot.		-	Measured R1 126 R2 127 R3 124 Design Paint 140-381	Measured R1 0.768 R2 0.777 R3 0.774 R_Avg Design	Rust Grade – 10 Blistering – Found in small area Discoloration – Not Found Flaking – Not Found Delamination – Not Found
A1-G1F1 Web	1		Measured R1 118 R2 136 R3 144 Design Paint 140-381	Measured R1 0.615 R2 0.617 R3 0.619 R_Avg Design	Rust Grade – 10 Blistering – Not Found Discoloration – Not Found Flaking – Not Found Delamination – Not Found
A1-G1F1 BF Top		-	Measured R1 121 R2 129 R3 119 Design Paint 140-381	Measured R1 0.784 R2 0.798 R3 0.776 R_Avg Design	Rust Grade – 10 Blistering – Not Found Discoloration – observed on the top face of Bottom Flange Flaking – Not Found Delamination – Found
A1-G1F1 BF Bot.	-	-	Measured R1 220 R2 225 R3 180 Design Paint 140-381	Measured R1 R2 R3 R_Avg Design	Rust Grade – 10 Blistering – Not Found Discoloration – Not Found Flaking – Not Found Delamination – Not Found
A1-G2F1 TF Bot.	-		Measured R1 214 R2 197 R3 212 Design Paint 140-381	Measured R1 0.766 R2 0.768 R3 0.762 R_Avg Design	Rust Grade – 10 Blistering – Not Found Discoloration – Not Found Flaking – Not Found Delamination – Not Found
A1-G2F1 Web	1		Measured R1 198 R2 182 R3 169 Design Paint 140-381	Measured R1 0.62 R2 0.619 R3 0.622 R_Avg Design	Rust Grade – 10 Blistering – Not Found Discoloration – Not Found Flaking – Not Found Delamination – Not Found

Table A-95. Field Inspection Results for BMT-PS-01.

Location	Cl^- Conc. (ppm)	pH Test	Thickness (µm)	Thickness (inch)	Visual Inspection
A1-G2F1 BF Top		-	Measured R1 165 R2 174 R3 160 Design Paint 140-381	Measured R1 0.732 R2 0.735 R3 0.735 R_Avg	Rust Grade – 10 Blistering – Not Found Discoloration – Not Found Flaking – Not Found Delamination – Not Found
A1-G2F1 BF Bot.			Measured R1 171 R2 189 R3 157 Design Paint 140-381	Measured R1 R2 R3 R_Avg	Rust Grade – 10 Blistering – Not Found Discoloration – Not Found Flaking – Not Found Delamination – Not Found
A1-G3F2 TF BOT		-	Measured R1 161 R2 169 R3 162 Design Paint 140-381	Measured R1 0.739 R2 0.738 R3 0.739 R_Avg	Rust Grade – 10 Blistering – Not Found Discoloration – Not Found Flaking – Not Found Delamination – Not Found
A1-G3F2 Web	1	-	Measured R1 212 R2 209 R3 191 Design Paint 140-381	Measured R1 0.616 R2 0.620 R3 0.619 R_Avg	Rust Grade – 10 Blistering – Not Found Discoloration – Not Found Flaking – Not Found Delamination – Not Found
A1-G3F2 BF Top	-		Measured R1 201 R2 188 R3 195 Design Paint 140-381	Measured R1 0.757 R2 0.755 R3 0.739 R_Avg	Rust Grade – 10 Blistering – Not Found Discoloration – Not Found Flaking – Not Found Delamination – Not Found
A1-G3F2 BF Bot.			Measured R1 212 R2 198 R3 197 Design Paint 140-381	Measured R1 R2 R3 R_Avg	Rust Grade – 10 Blistering – Not Found Discoloration – Not Found Flaking – Not Found Delamination – Not Found

Table A-96. Field Inspection Results for BMT-PS-01.

Location	Cl^- Conc. (ppm)	pH Test	Thickness (µm)	Thickness (inch)	Visual Inspection
A1-G6F2 TF Bot.		-	Measured R1 242 R2 252 R3 296 Design Paint 140-381	Measured R1 0.744 R2 0.742 R3 0.747 R_Avg	Rust Grade – 10 Blistering – Not Found Discoloration – Not Found Flaking – Not Found Delamination – Not Found
A1-G6F2 Web	1		Measured R1 149 R2 162 R3 157 Design Paint 140-381	Measured R1 0.610 R2 0.612 R3 0.613 R_Avg	Rust Grade – 10 Blistering – Not Found Discoloration – Not Found Flaking – Not Found Delamination – Not Found
A1-G6F2 BF Top		-	Measured R1 148 R2 153 R3 171 Design Paint 140-381	Measured R1 0.761 R2 0.760 R3 0.739 R_Avg	Rust Grade – 10 Blistering – Not Found Discoloration – Not Found Flaking – Not Found Delamination – Not Found
A1-G6F2 BF Bot.	-	-	Measured R1 277 R2 258 R3 323 Design Paint 140-381	Measured R1 R2 R3 R_Avg	Rust Grade – 10 Blistering – Not Found Discoloration – Not Found Flaking – Not Found Delamination – Not Found

A.19.3. Pull-off Adhesion Results

Table A-97. Pull-off Adhesion Results for BMT-PS-01.

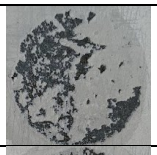
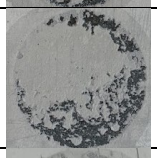
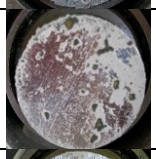
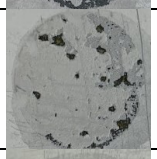
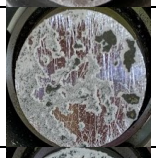
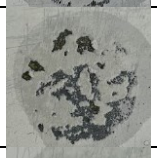
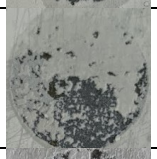
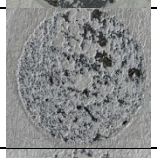
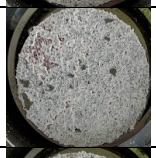
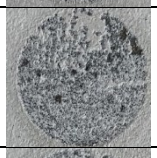
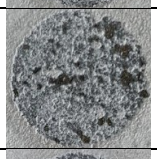
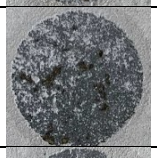
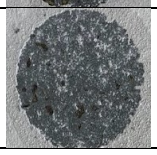
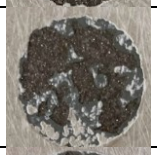
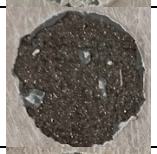
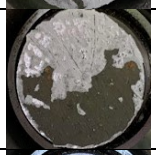
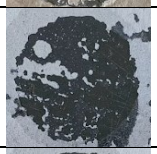
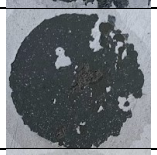
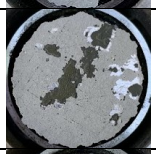
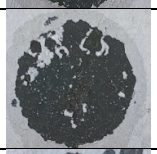
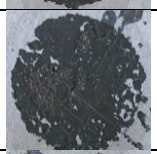
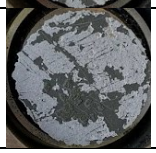
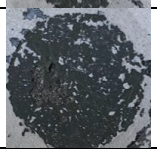
Location	Dolly Face	Substrate Face	Test Result (psi)	Attributes	Failure Type
A1-G1F1			1134	50% B 50% B/C	50%Cohesive Failure 50% Adhesive Failure
			1415	70% B 30% B/C	50%Cohesive Failure 50% Adhesive Failure
			1166	80% B 20% B/C	80% Cohesive Failure 20% Adhesive Failure
			1091	70% B 30% B/C	70% Cohesive Failure 30% Adhesive Failure
			1188	70% B 30% B/C	70% Cohesive Failure 30% Adhesive Failure
A1-G2F1			1987	80% B 20% B/C	80% Cohesive Failure 20% Adhesive Failure
			2038	90% B 10% B/C	90% Cohesive Failure 10% Adhesive Failure
			1886	70% C 30%B/C	30% Cohesive Failure 70% Adhesive Failure
			1717	30% C 50% B/C 20% A/B	30% Cohesive Failure 50% Cohesive Failure 20% Adhesive Failure
			1522	10% B 80% B/C 10% A/B	10% Cohesive Failure 80% Cohesive Failure 10% Adhesive Failure

Table A-98. Pull-off Adhesion Results for BMT-PS-01.

Location	Dolly Face	Substrate Face	Test Result (psi)	Attributes	Failure Type
A1-G3F2			1460	10% B 40% B/C 50% A/B	10% Cohesive Failure 40% Adhesive Failure 50% Adhesive Failure
			1653	80% A/B 20% Y/Z	80% Adhesive Failure 10% Adhesive Failure
			1353	80% A/B 20% B/C	80% Adhesive Failure 20% Adhesive Failure
			1674	60% B/C 40% A/B	60% Adhesive Failure 40% Adhesive Failure
			1493	20% C 30% B/C 50% A/B	20% Cohesive Failure 30% Adhesive Failure 50% Adhesive Failure
A1-G6F2			925	20% C 80% B/C	20% Cohesive Failure 80% Adhesive Failure
			718	20% C 80% B/C	20% Cohesive Failure 80% Adhesive Failure
			700	70% B/C 30% A/B	70% Cohesive Failure 30% Adhesive Failure
			1354	30% A/B 50% B/C 20% B	30% Adhesive Failure 50% Adhesive Failure 20% Cohesive Failure
			1278	20% A/B 70% B/C 10% B	20% Adhesive Failure 70% Adhesive Failure 10% Cohesive Failure

A.19.4.Optical Microscopy Results

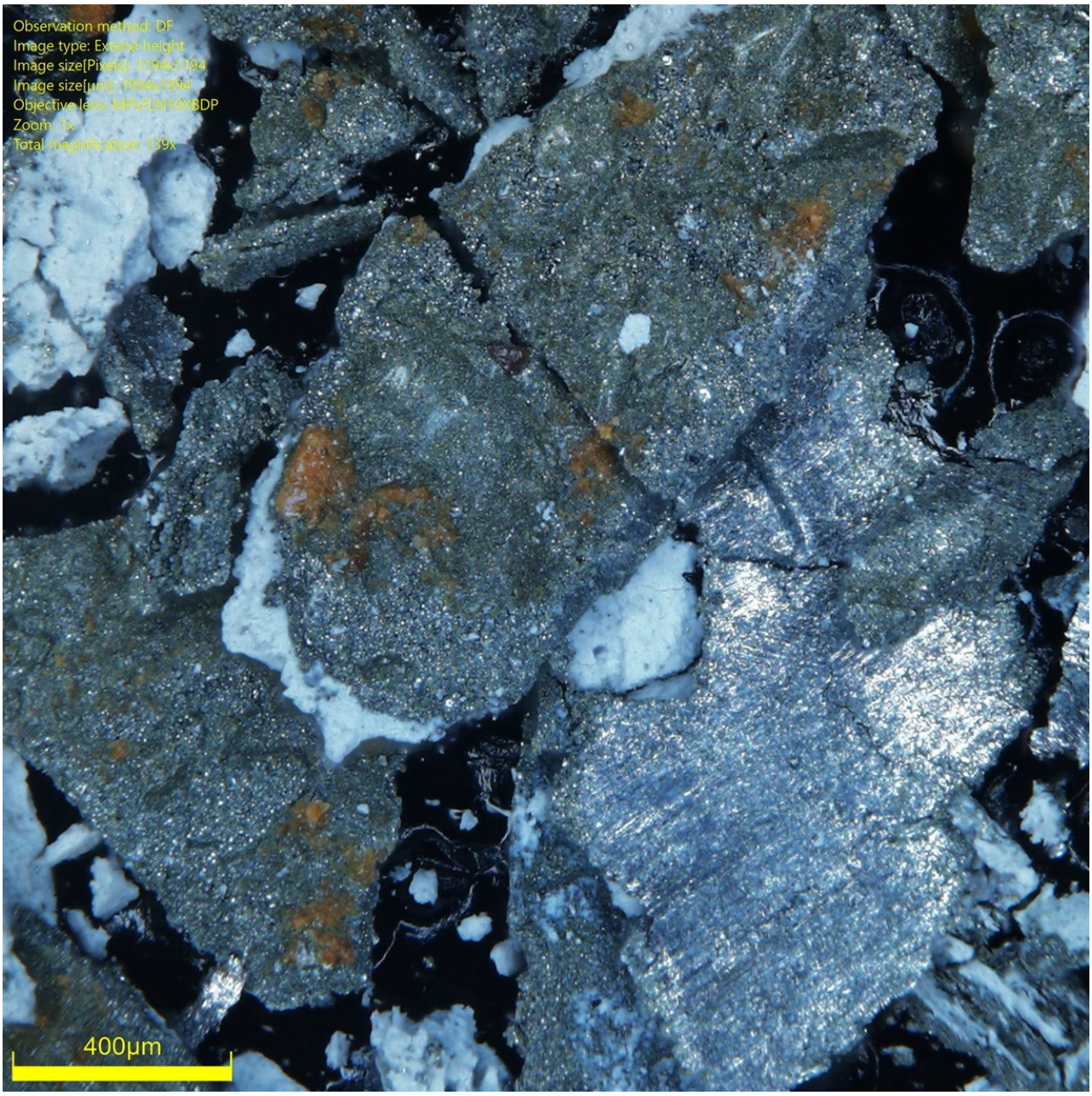


Figure A.236. Two Layer Paint System Examined by Optical Microscope BMT–PS–01.

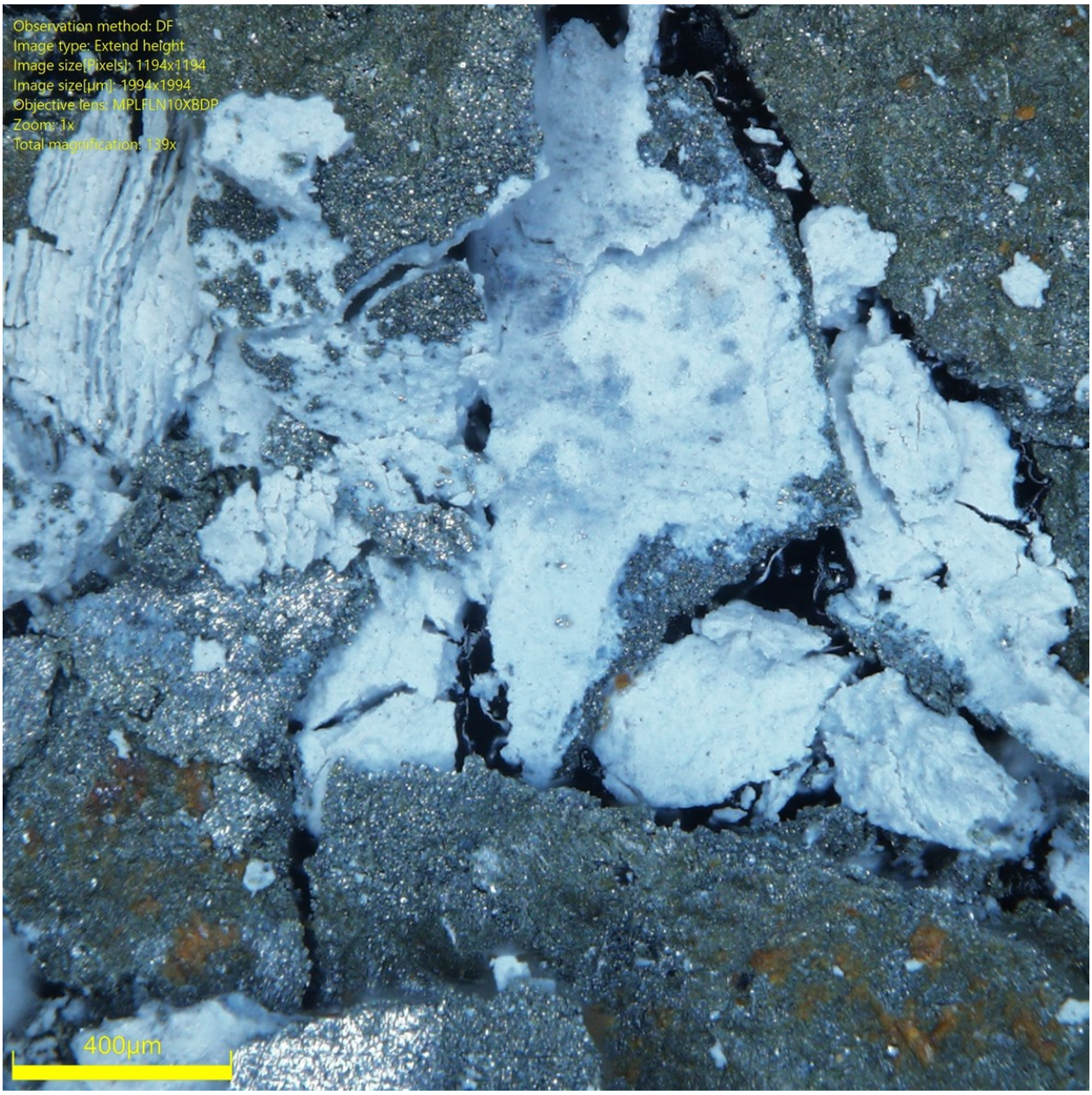
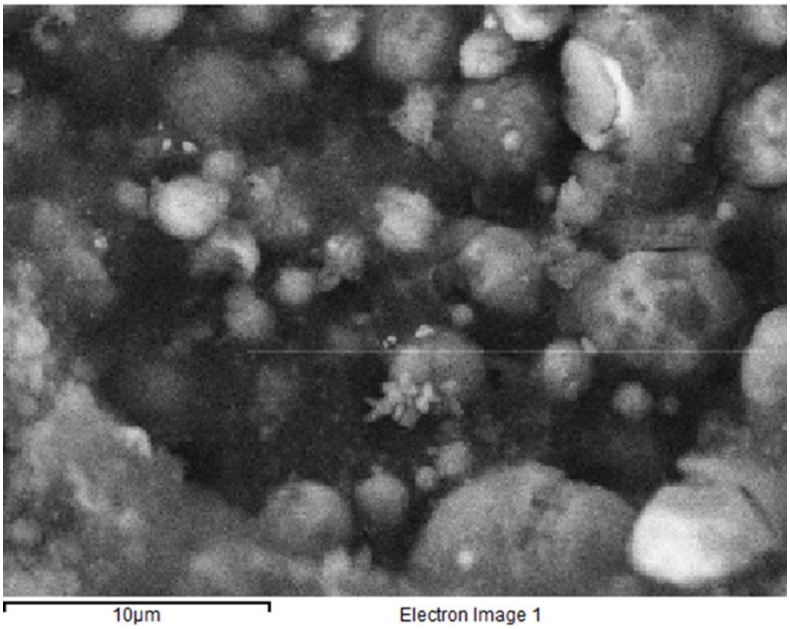


Figure A.237. Two Layer Paint System Examined by Optical Microscope BMT–PS–01.

A.19.5.SEM/EDS Results

Element	Weight %	Atomic %
C K	46.83	67.52
O K	21.92	23.73
Al K	0.39	0.25
Si K	0.83	0.51
Cl K	0.39	0.19
K K	0.09	0.04
Ti K	0.14	0.05
Cr K	0.22	0.07
Fe K	2.19	0.68
Zn K	25.92	6.87
Pb M	1.08	0.09
Totals	100.00	



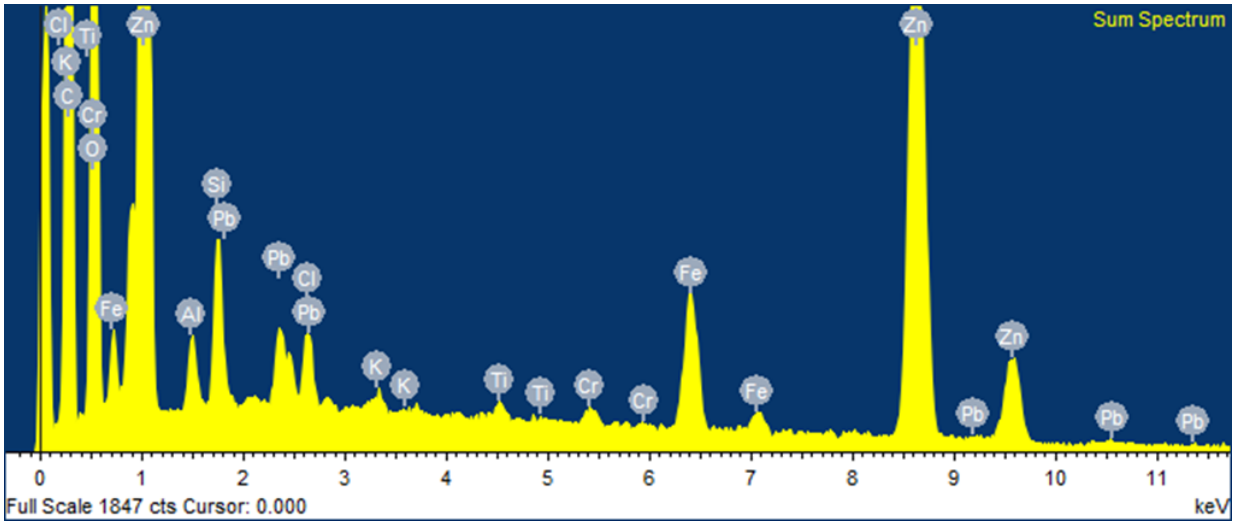


Figure A.238. SEM Image and EDS Spectrum of the Paint Collected from Exterior Web of the Girder.

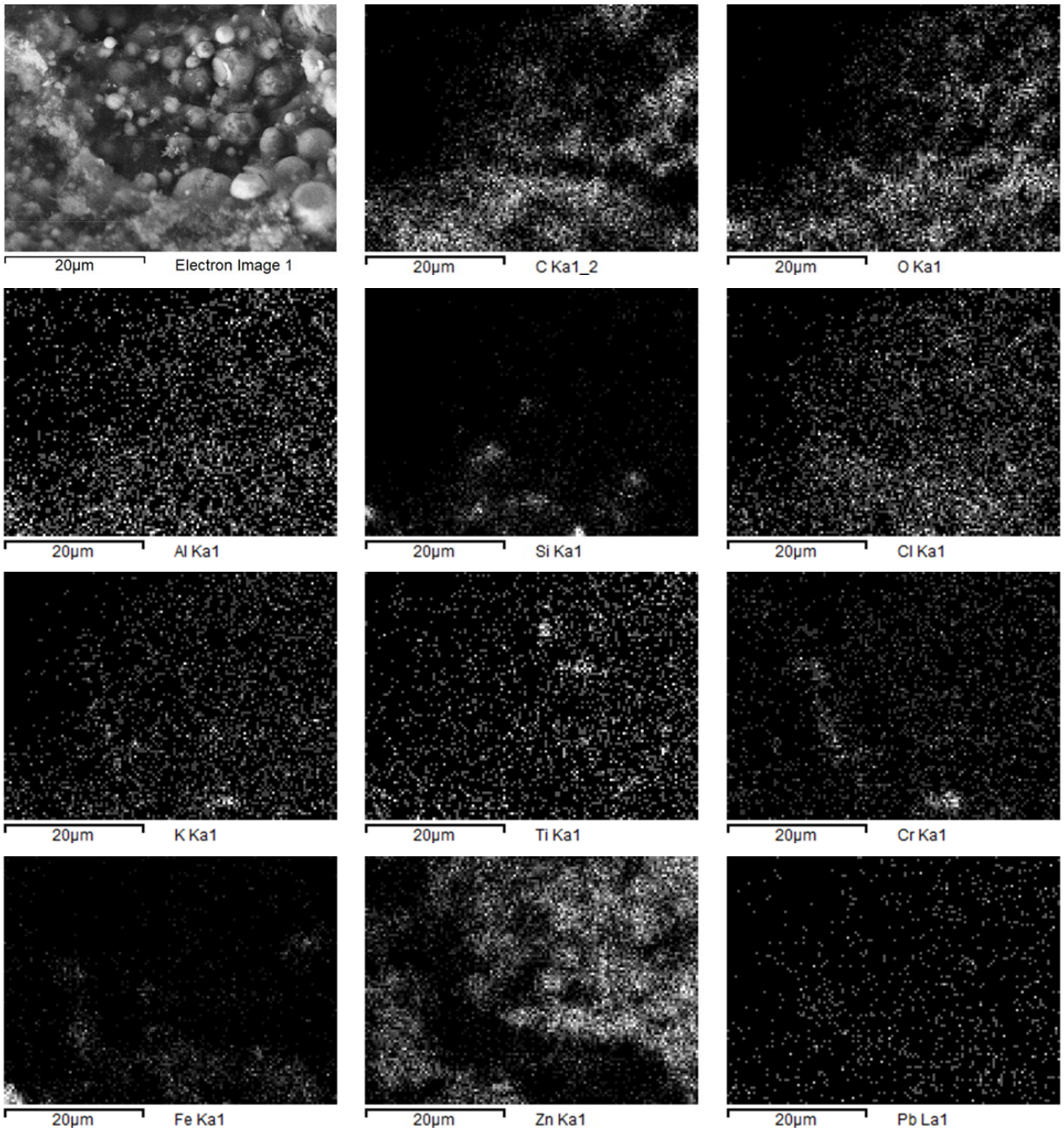
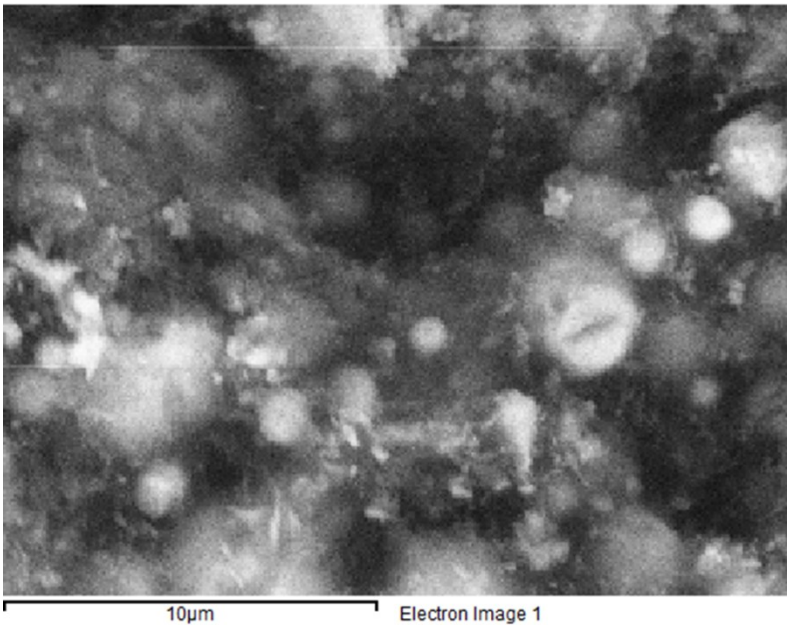


Figure A.239. EDS Elemental Mapping of Paint Collected from Exterior Web.

Element	Weight %	Atomic %
C K	52.21	71.61
O K	19.97	20.57
Al K	0.49	0.30
Si K	1.61	0.94
P K	0.05	0.02
Cl K	0.32	0.15
K K	0.05	0.02
Ti K	0.12	0.04
Fe K	2.27	0.67
Zn K	22.33	5.63
Pb M	0.59	0.05
Totals	100.00	



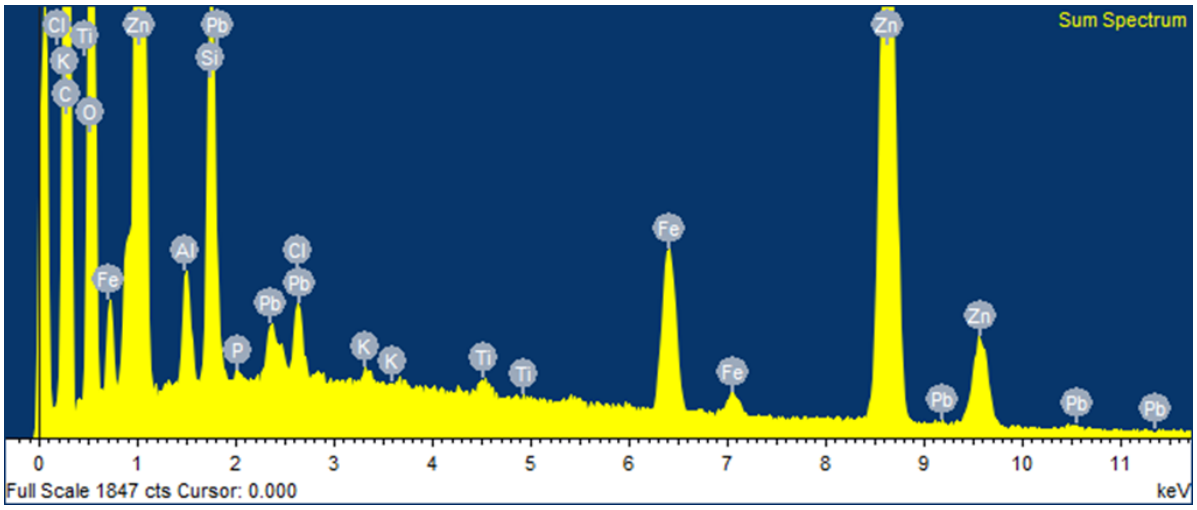


Figure A.240. SEM Image and EDS Spectrum of the Paint Collected from Exterior Web of the Girder.

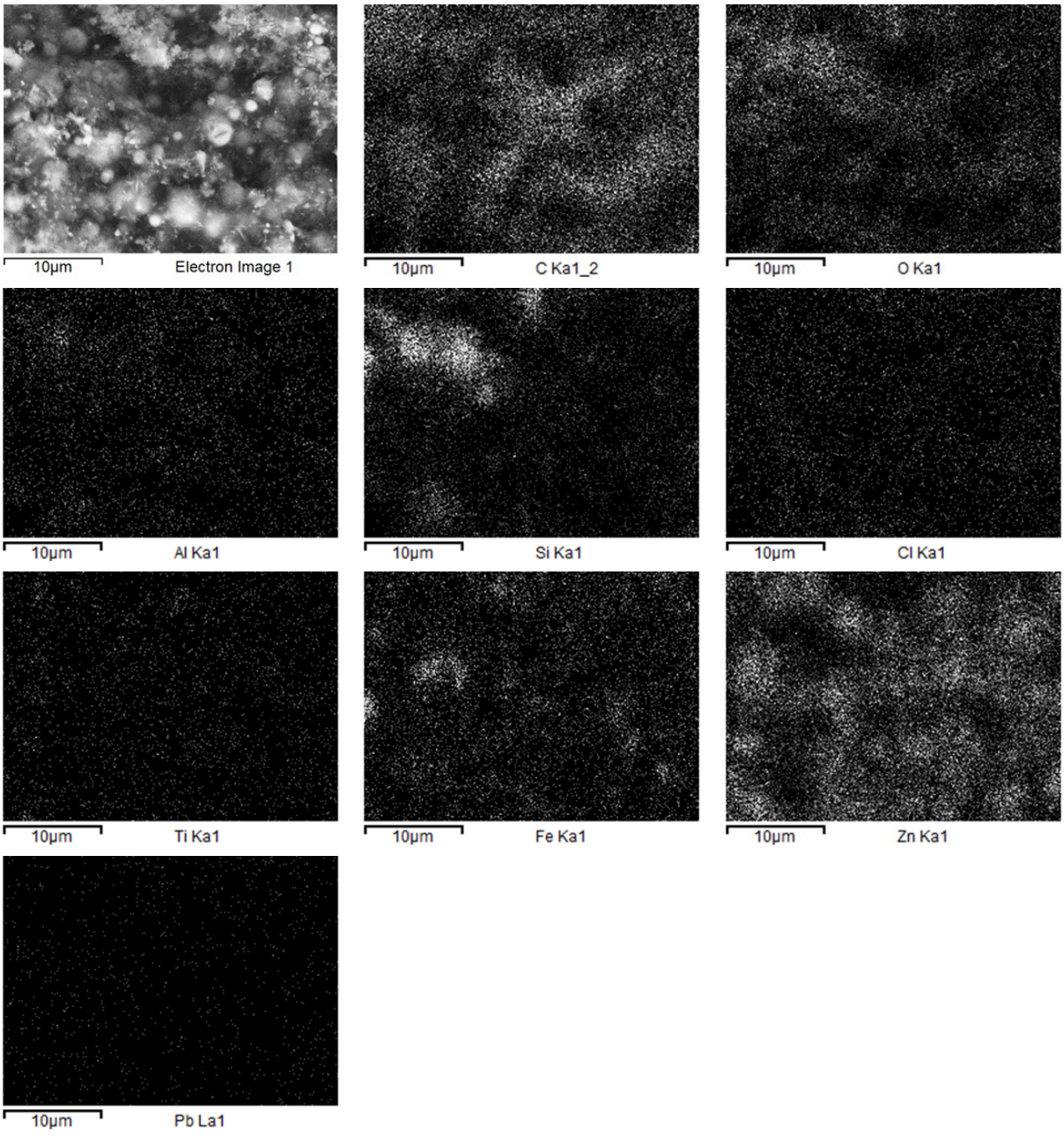
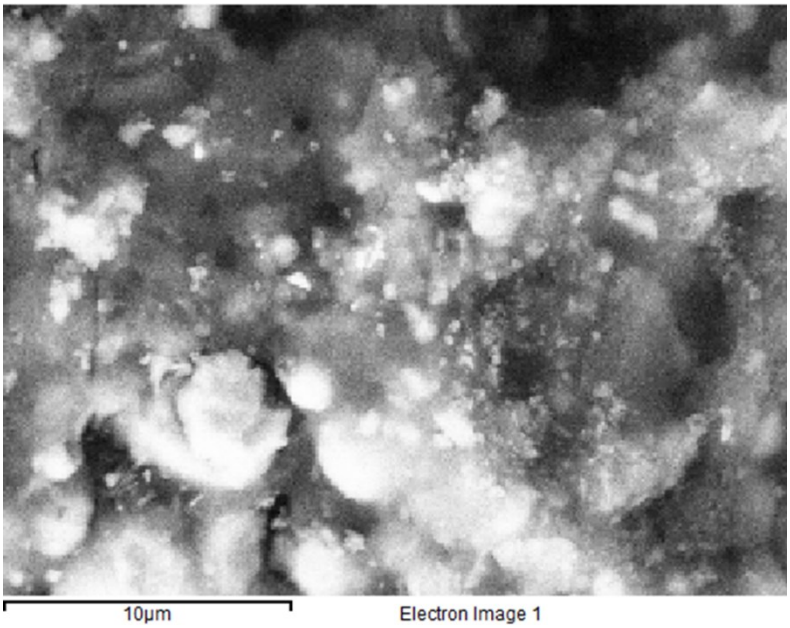


Figure A.241. EDS Elemental Mapping of Paint Collected from Exterior Web .

Element	Weight %	Atomic %
C K	48.57	71.64
O K	16.29	18.04
Al K	0.55	0.36
Si K	1.64	1.03
Cl K	0.74	0.37
K K	0.37	0.17
Ti K	0.22	0.08
Cr K	0.92	0.31
Fe K	1.23	0.39
Zn K	27.38	7.42
Pb M	2.09	0.18
Totals	100.00	



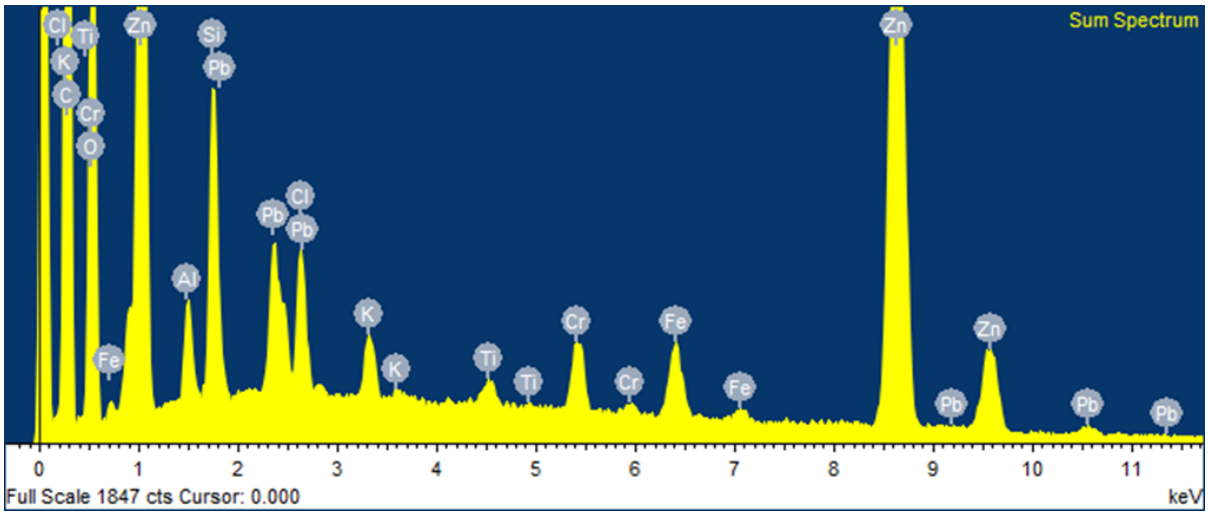
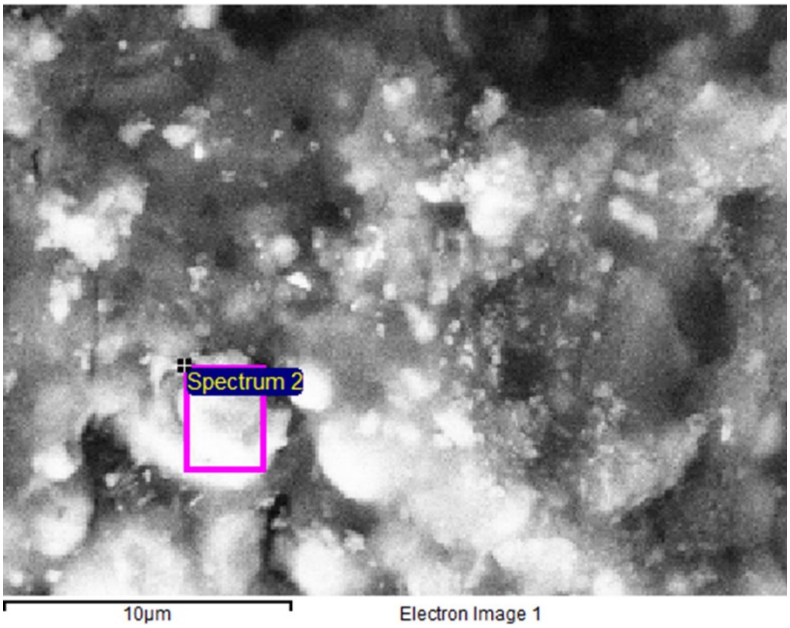


Figure A.242. SEM Image and EDS Spectrum of the Paint Collected from Exterior Web of the Girder.

Element	Weight %	Atomic %
C K	23.69	51.33
O K	14.18	23.07
Al K	0.72	0.69
Si K	0.44	0.40
Cl K	0.42	0.31
Ti K	0.30	0.16
Fe K	0.50	0.23
Zn K	59.76	23.79
Totals	100.00	



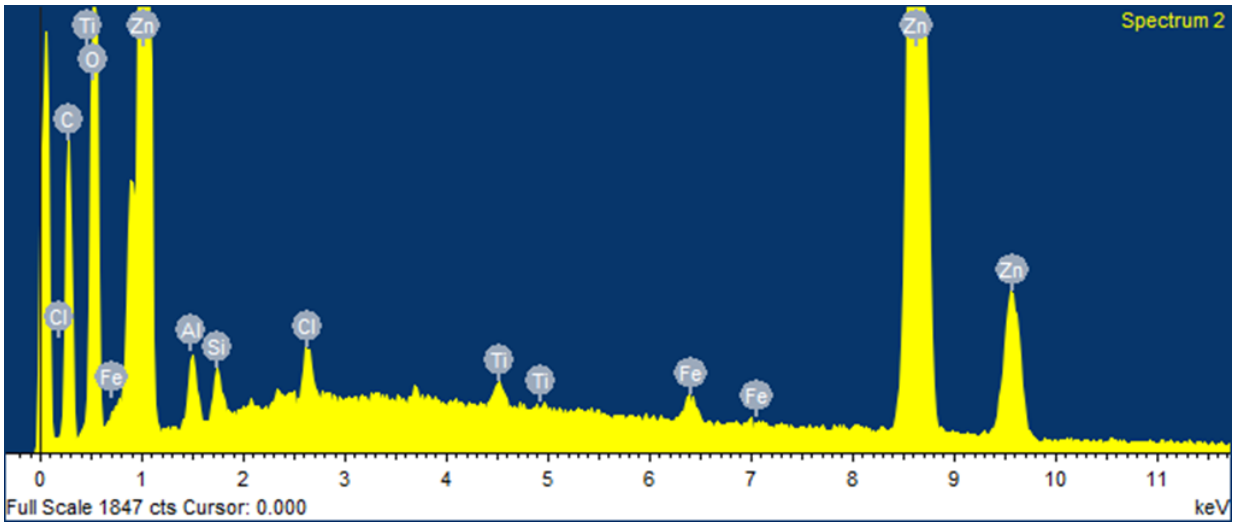
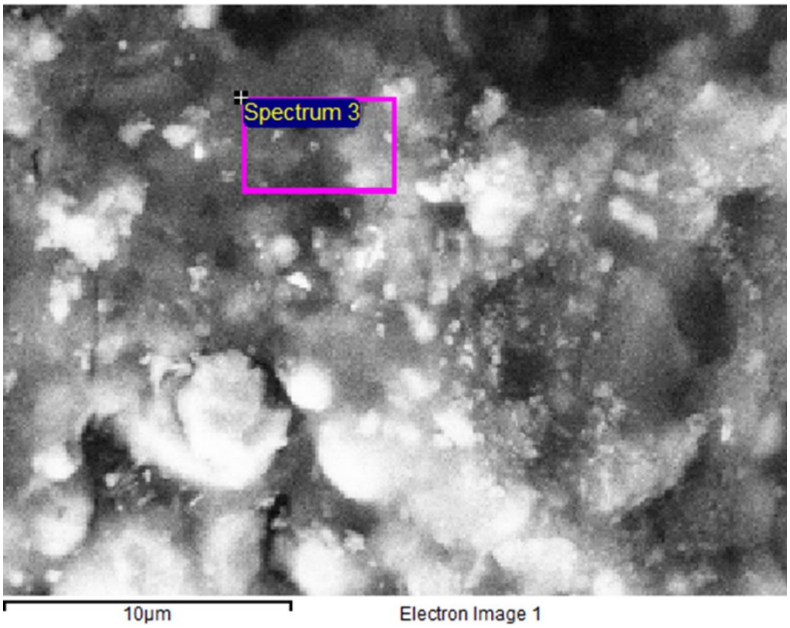


Figure A.243. SEM Image and EDS Spectrum of the Paint Collected from Exterior Web of the Girder.

Element	Weight %	Atomic %
C K	62.67	79.89
O K	14.68	14.05
Al K	0.48	0.27
Si K	1.86	1.01
Cl K	1.92	0.83
K K	0.59	0.23
Ti K	0.13	0.04
Cr K	1.56	0.46
Fe K	0.56	0.15
Zn K	11.89	2.78
Pb M	3.66	0.27
Totals	100.00	



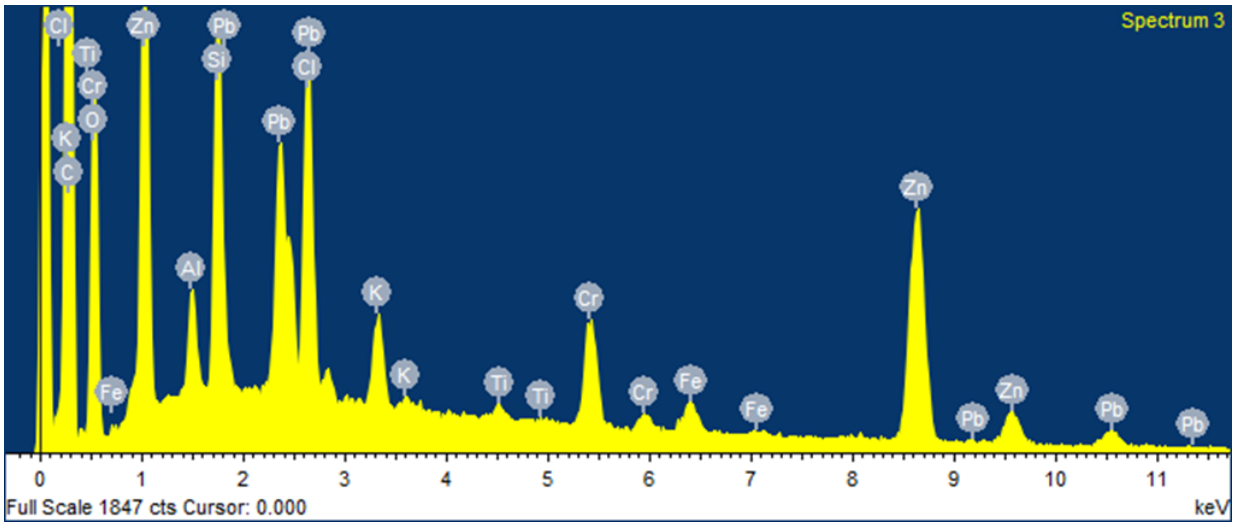


Figure A.244. SEM Image and EDS Spectrum of the Paint Collected from Exterior Web of the Girder.

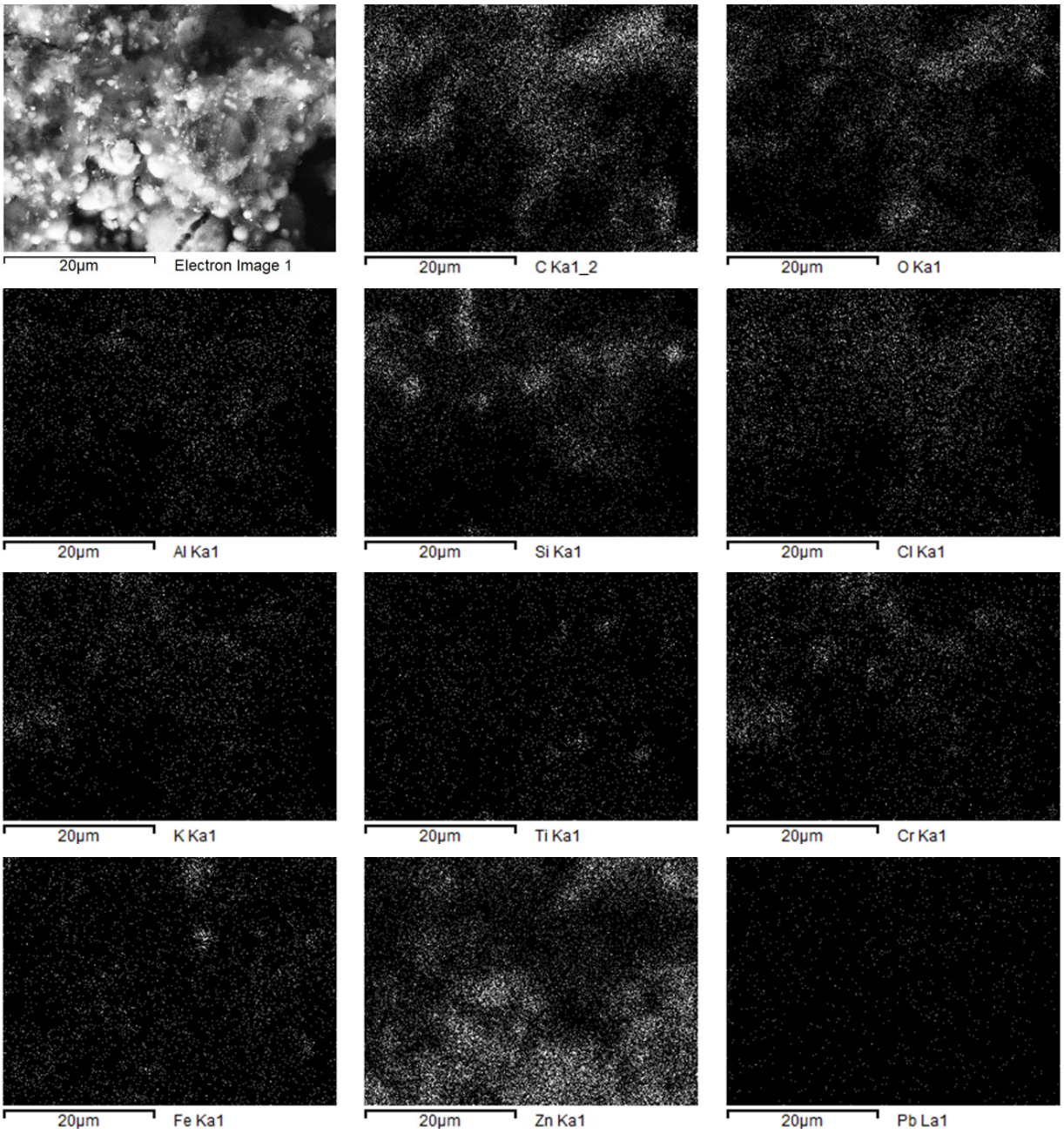
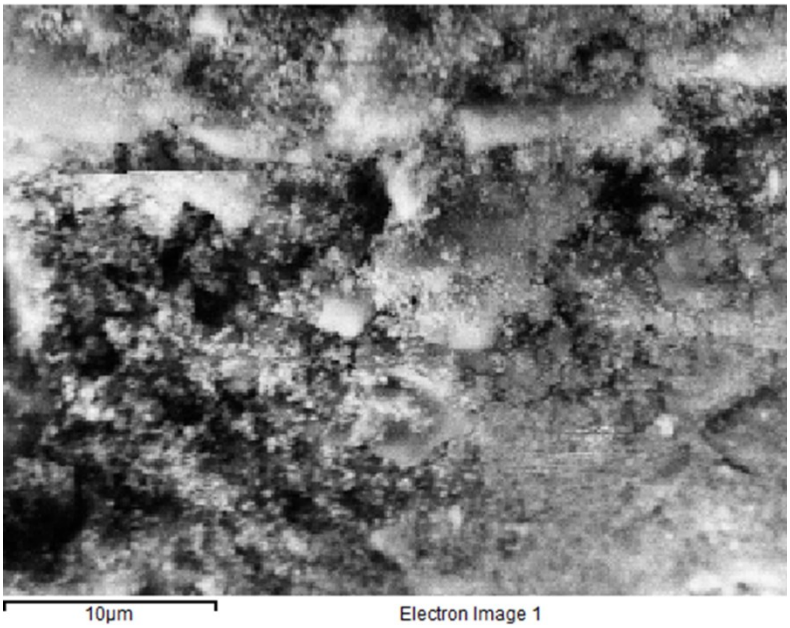


Figure A.245. EDS Elemental Mapping of Paint Collected from Exterior Web.

Element	Weight %	Atomic %
C K	37.54	52.92
O K	33.42	35.37
Al K	1.11	0.70
Si K	4.46	2.69
Cl K	2.03	0.97
Ca K	0.81	0.34
Ti K	17.40	6.15
Fe K	0.63	0.19
Zn K	2.60	0.67
Totals	100.00	



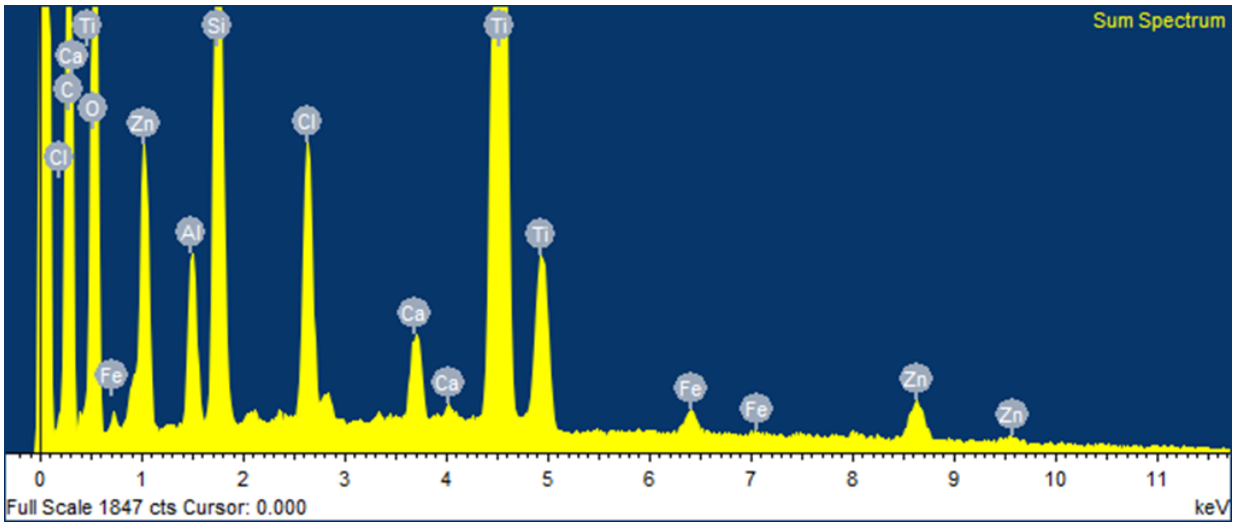
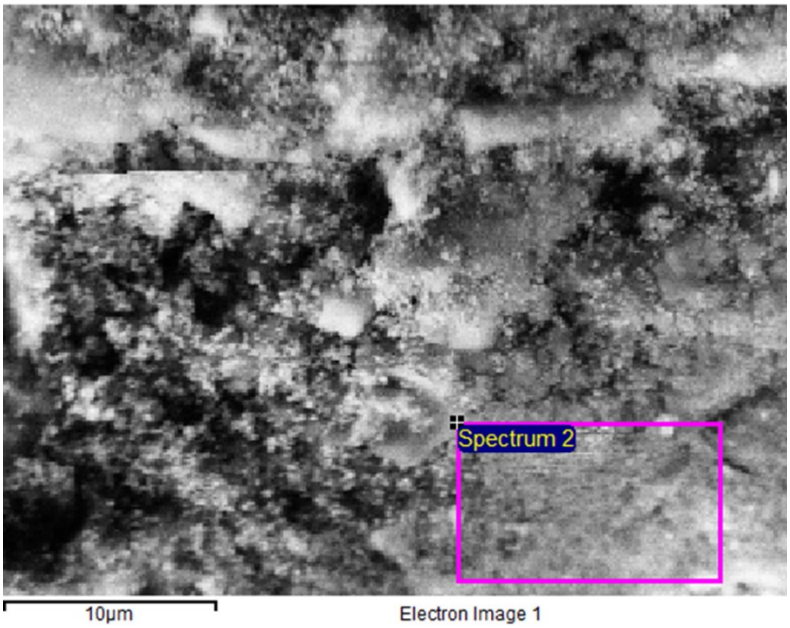


Figure A.246. SEM Image and EDS Spectrum of the Paint Collected from Exterior Web of the Girder.

Element	Weight %	Atomic %
C K	42.53	56.50
O K	35.29	35.20
Al K	1.58	0.93
Si K	2.49	1.41
Cl K	0.92	0.41
Ca K	0.71	0.28
Ti K	13.82	4.60
Fe K	0.57	0.16
Zn K	1.82	0.44
Zr L	0.27	0.05
Totals	100.00	



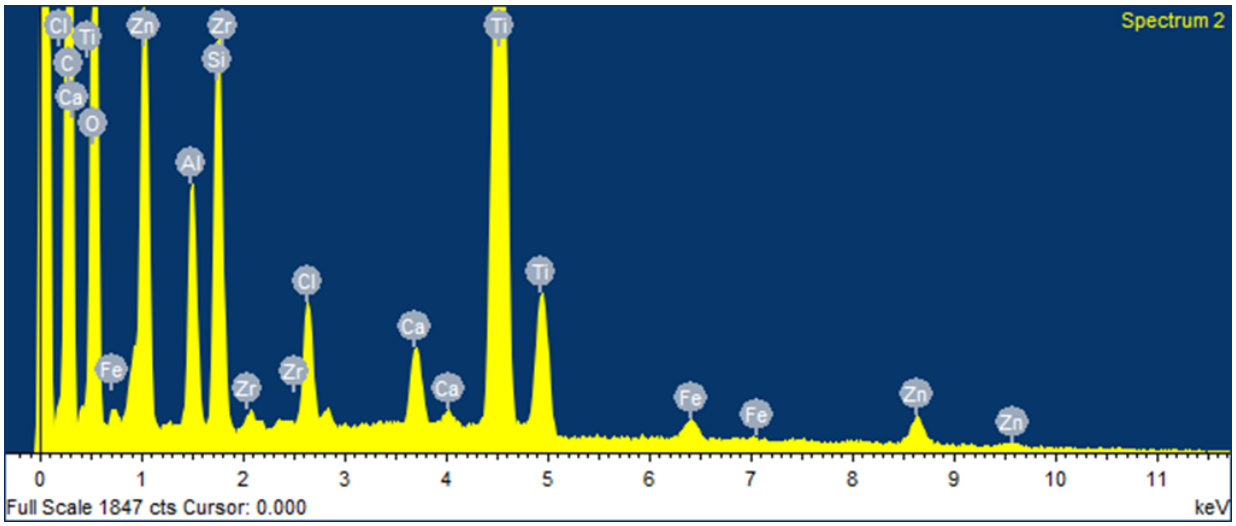


Figure A.247. SEM Image and EDS Spectrum of the Paint Collected from Exterior Web of the Girder.

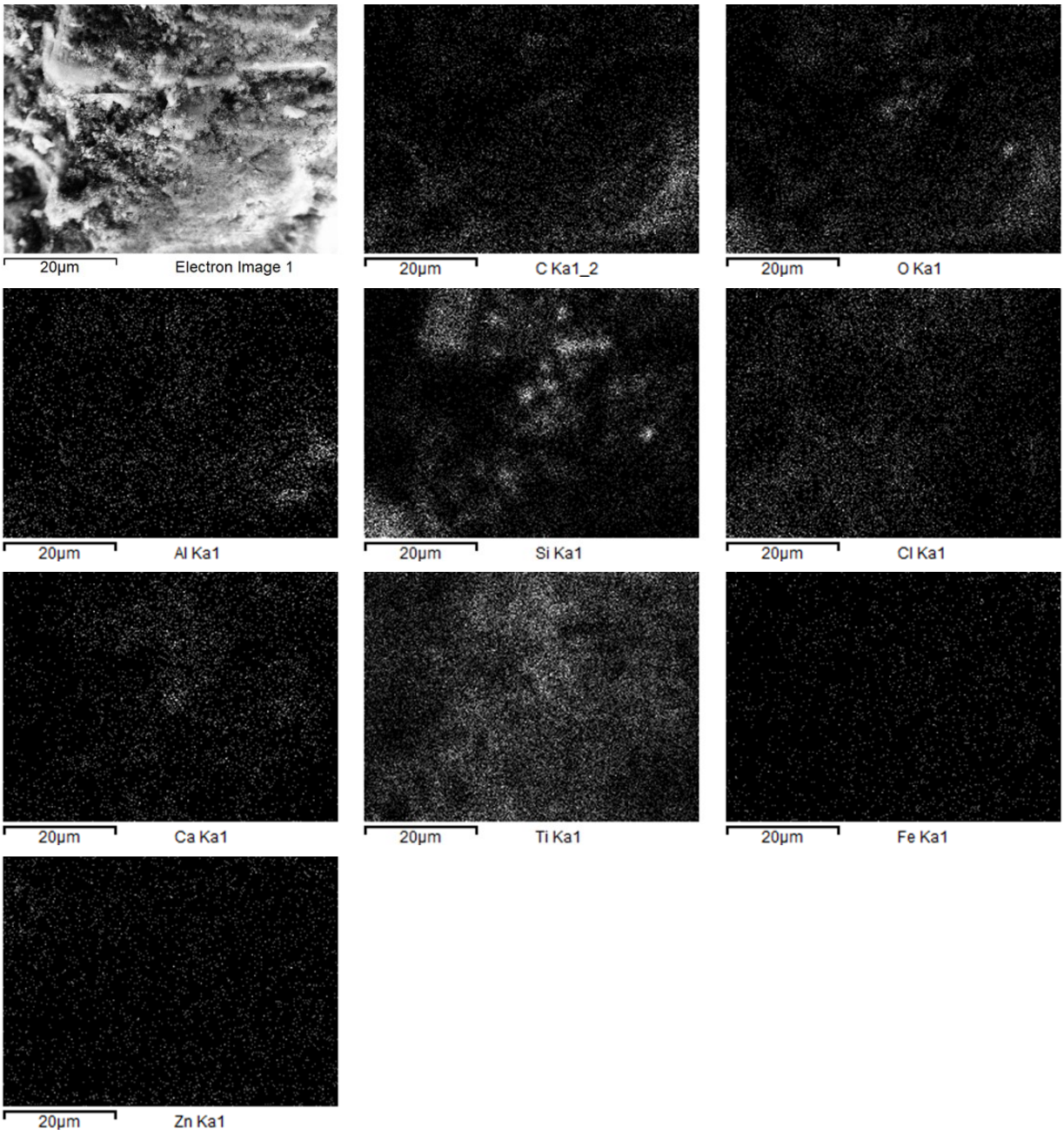
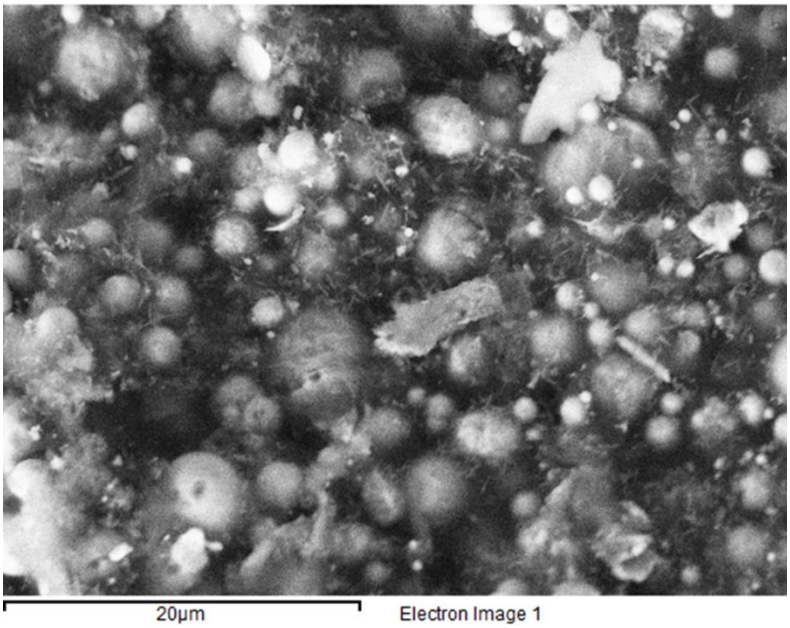


Figure A.248. EDS Elemental Mapping of Paint Collected from Exterior Web.

Element	Weight %	Atomic %
C K	56.05	74.84
O K	18.37	18.41
Al K	0.38	0.22
Si K	0.79	0.45
Cl K	0.05	0.02
Fe K	2.54	0.73
Zn K	21.58	5.29
Pb M	0.24	0.02
Totals	100.00	



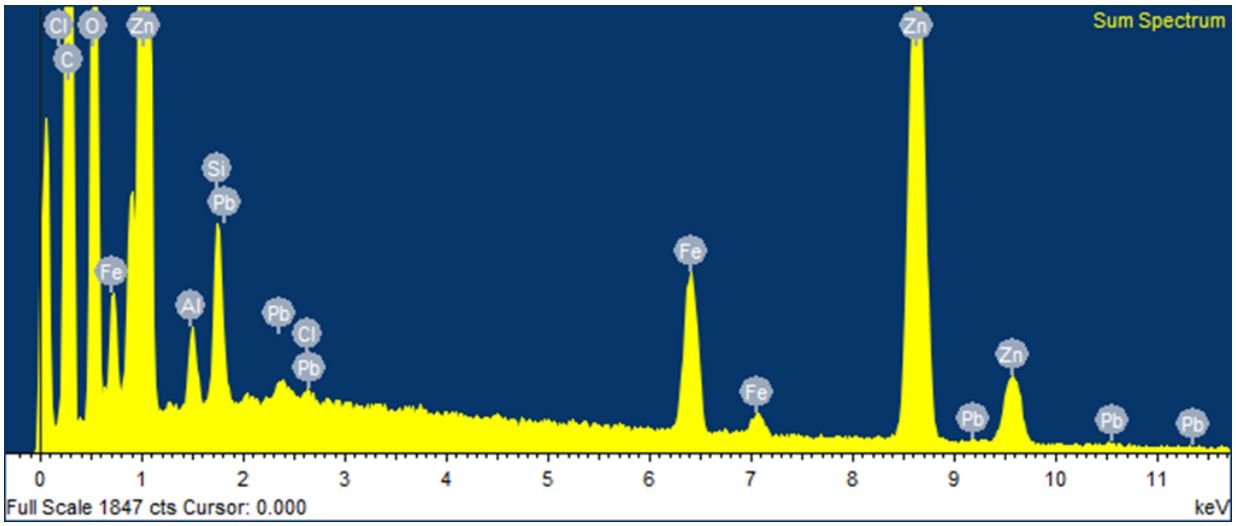


Figure A.249. SEM Image and EDS Spectrum of the Paint Collected from Interior Web of the Girder.

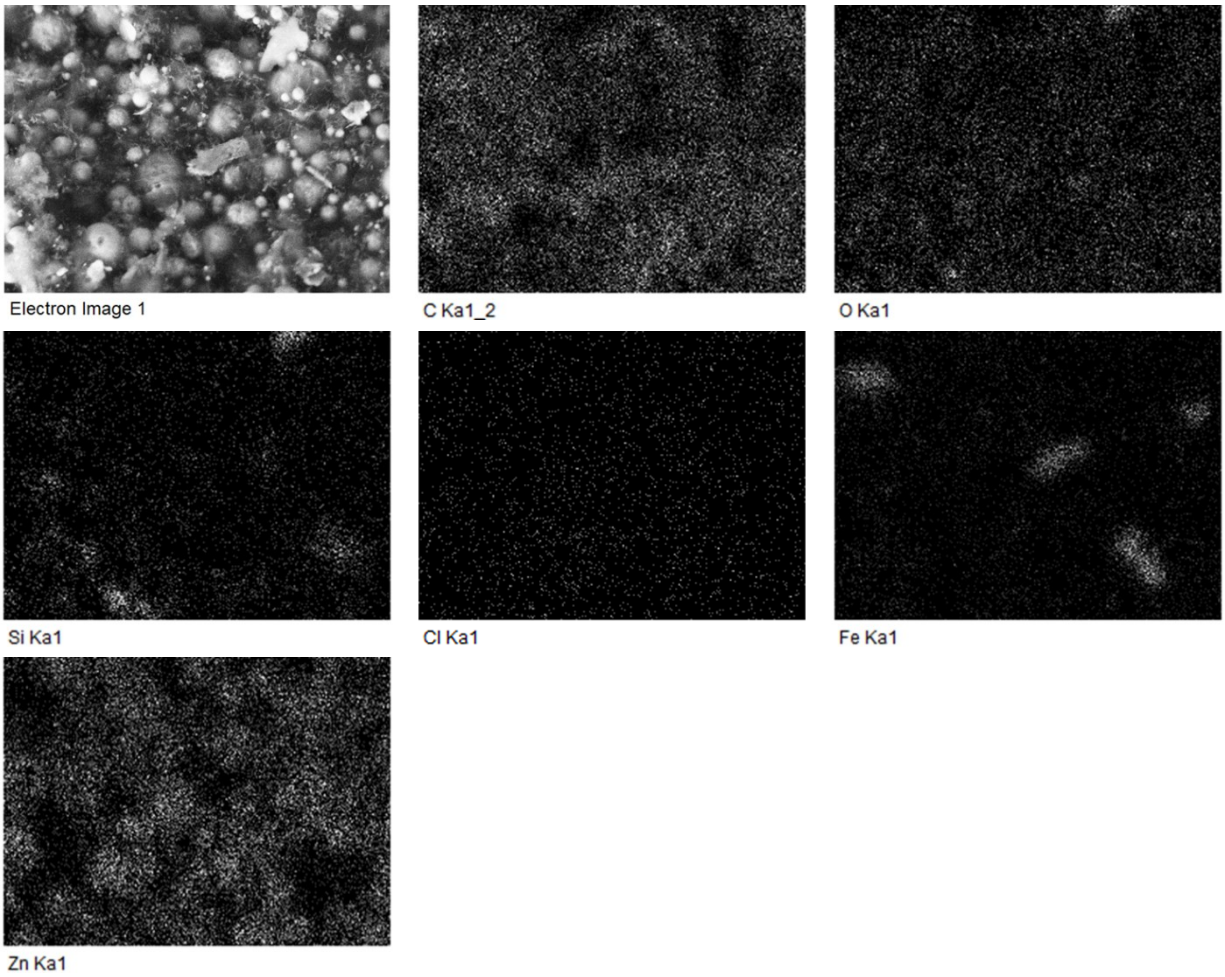
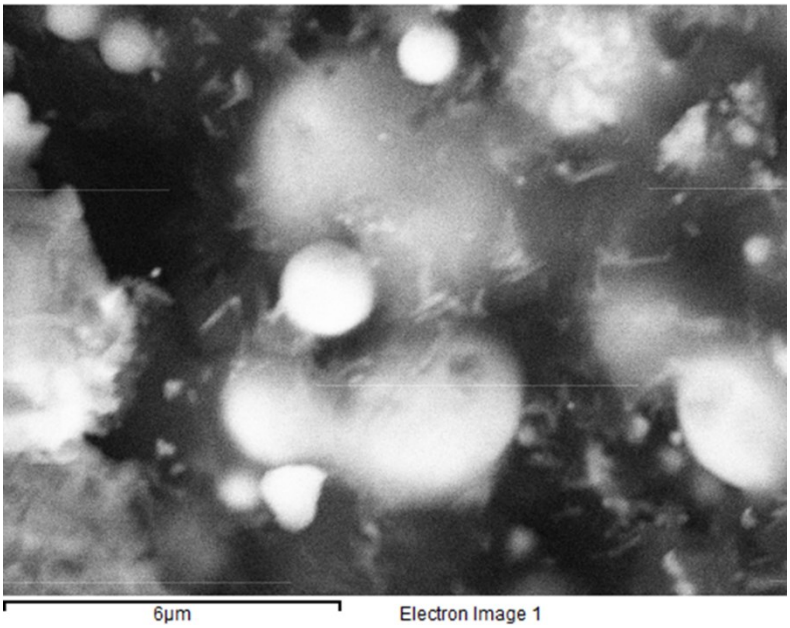


Figure A.250. EDS Elemental Mapping of Paint Collected from Interior Web.

Element	Weight %	Atomic %
C K	50.54	75.87
O K	10.57	11.91
F K	0.74	0.70
Al K	0.44	0.30
Si K	0.61	0.39
Fe K	12.61	4.07
Zn K	24.48	6.75
Totals	100.00	



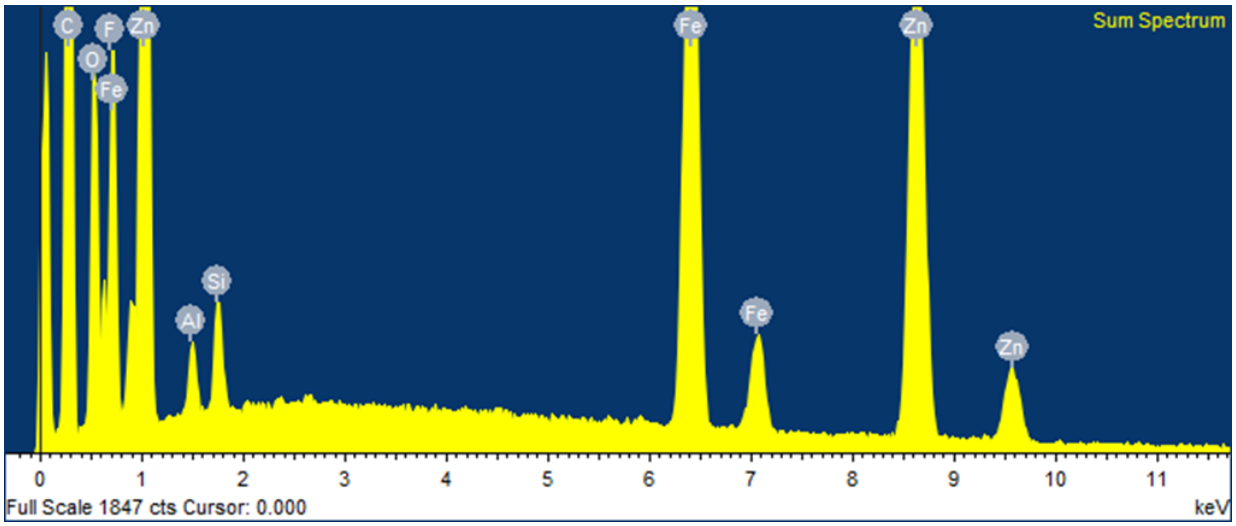


Figure A.251. SEM Image of Paint and EDS Spectrum of the Paint Collected from Interior Web of the Girder.

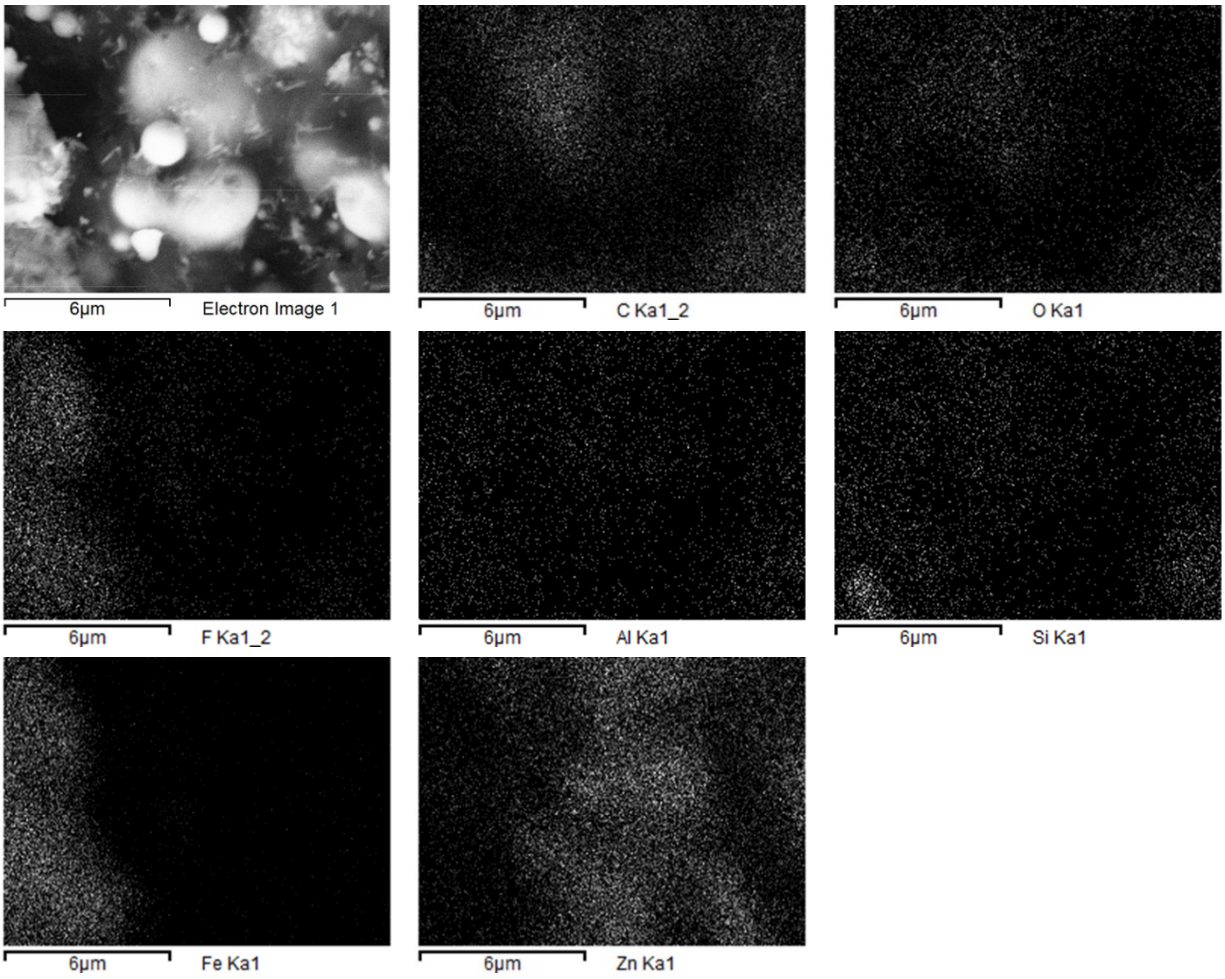
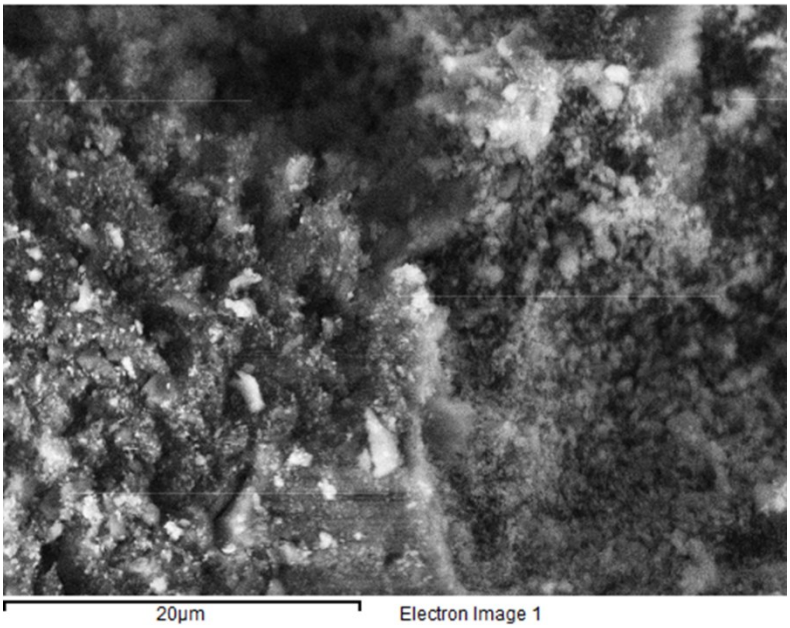


Figure A.252. EDS Elemental Mapping of Paint Collected from Interior Web.

Element	Weight %	Atomic %
C K	33.63	44.80
O K	46.85	46.85
Al K	0.83	0.49
Si K	6.73	3.84
Cl K	2.13	0.96
Ca K	0.06	0.02
Ti K	7.12	2.38
Fe K	0.28	0.08
Cu K	0.13	0.03
Zn K	2.24	0.55
Totals	100.00	



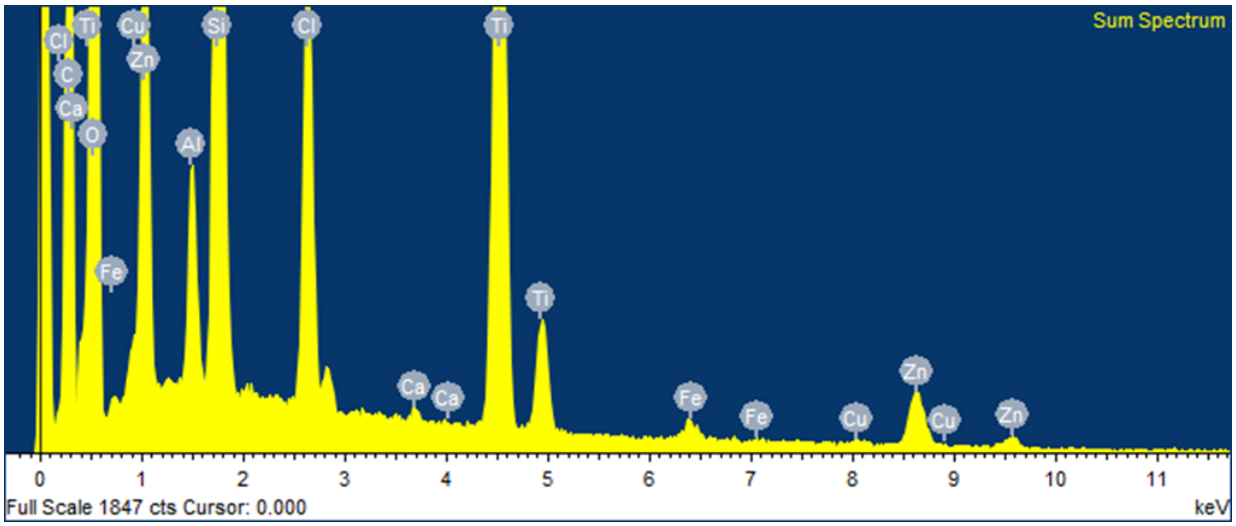
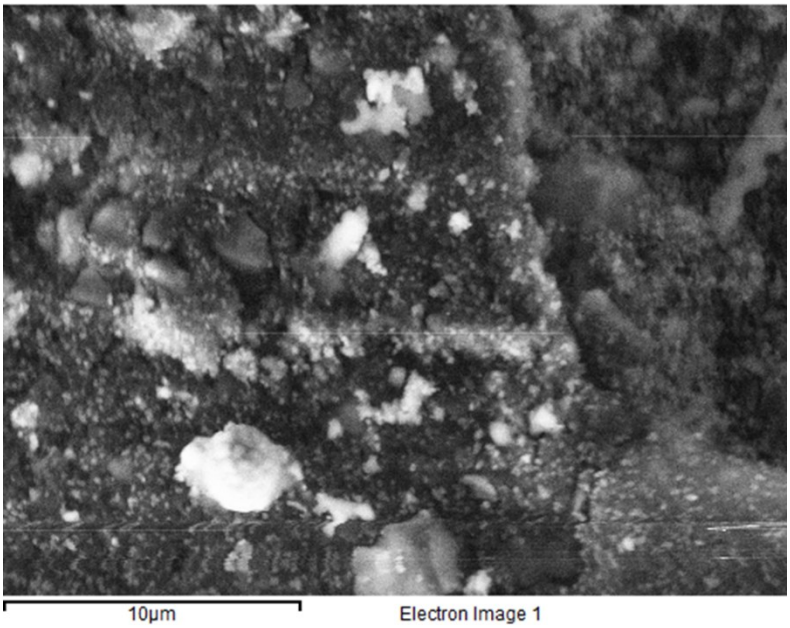
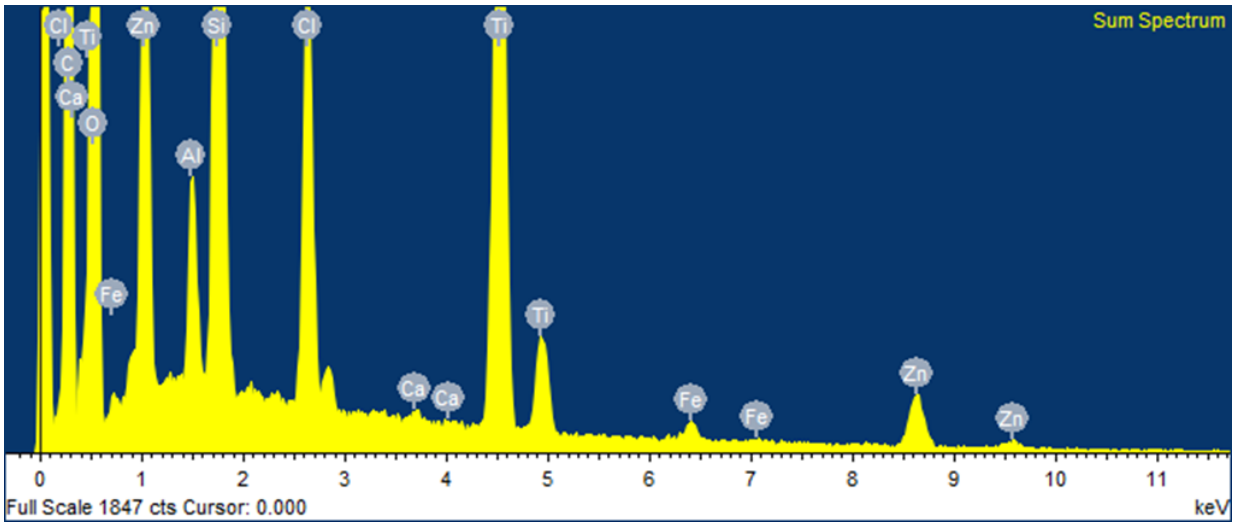


Figure A.253. SEM Image and EDS Spectrum of the Paint Collected from Interior Web of the Girder.

Element	Weight %	Atomic %
C K	37.48	49.12
O K	43.56	42.86
Al K	0.79	0.46
Si K	6.65	3.73
Cl K	2.14	0.95
Ca K	0.06	0.03
Ti K	6.83	2.24
Fe K	0.31	0.09
Zn K	2.17	0.52
Totals	100.00	



(a) SEM Image of Paint



(b) EDS Spectrum of Paint Showing Elemental Peaks

Figure A.254. SEM Image and EDS Spectrum of the Paint Collected from Interior Web of the Girder.

A.20. BMT-PS-02

- IH 10 WB over Walden Road,
- Bridge ID 201240073902013, Coordinates (30.03822, -94.15693), Jefferson County
- Steel Plate Girder with System II type paint
- Built 1961 repainted with System II in 2004
- Date of Inspection: April 14, 2021; girder inspection carried out on North East abutment (Abutment number 1) and measurements are taken on girders within approximately four feet from the abutment.
- No visual inspection on deck
- Location for Testing: A1-G1F1, A1-G2F2, A1-G4F1, A1-G6F2



Figure A.255. Typical Elevation of BMT-PS-02.

A.20.1. Observed Condition

The paint condition of this bridge is in very good condition. The appearance coat is also in good condition except on the top flange of diaphragm which shows rusting. Blistering, Erosion of paint, cracking in paint is not present. No checking and cracking of paint are observed. Joints are also in good condition.



(a) Crack Observed Deck



(b) Paint Deterioration and Rusting on the Exterior Bearing



c) Corrosion Observed on top Flange of Diaphragm



(d) Internal Bearing in Good Condition



(e) External Girder in Good Condition



(f) Interior Girder in Good Condition

Figure A.256. Paint Condition on the Girder of BMT-PS-02.

A.20.2.NDT Results



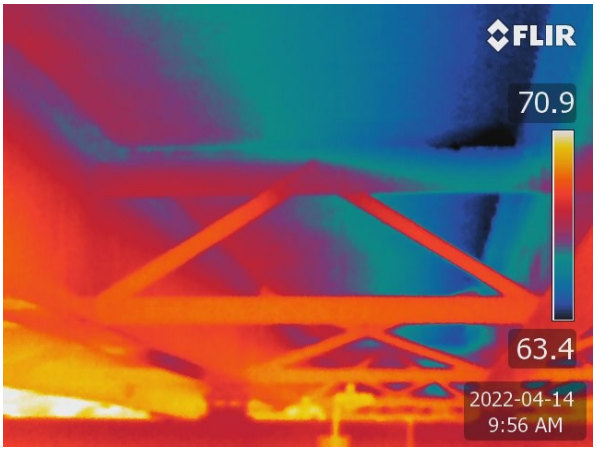
(a) Digital Image of Exterior Face of I Beam(G1F1)



(b) Thermal Image of Exterior Face of I Beam (G1F1)



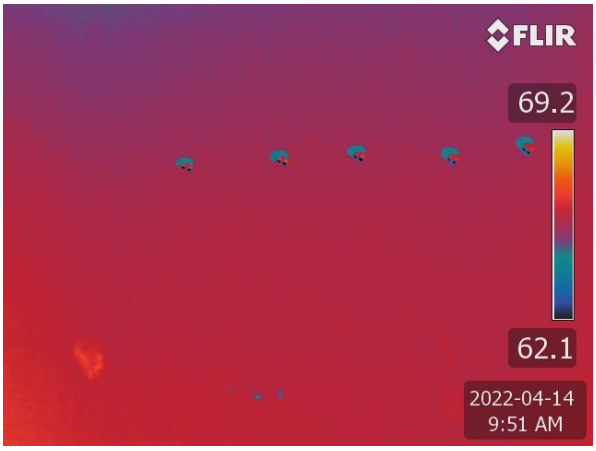
(c) Digital Image of Connection



(d) Thermal Image of Connection



(e) Digital image of the Interior face of I Beam



(f) Thermal image of the Interior of I Beam

Figure A.257. Digital and Thermal Image of Painted Girder on BMT-PS-02.

Table A-99. Paint System Information.

Cohesive Failure Layer		**Adhesive Failure Layer**	
Code	**Description**	**Code**	**Description**
A	Substrate	A/B	Substrate & Layer 1
B	Layer 1 (Metallic Green)	B/C	Layer 1 & Glue
C	Layer 2 (Blue)	C/Y	
Y	Glue	Y/Z	Glue & Dolly

Table A-100. Field Inspection Results for BMT-PS-02.

Location	Cl^- Conc. (ppm)	pH Test	Thickness (µm)	Thickness (inch)	Visual Inspection
A1-G1F1 TF Bot.		-	Measured R1 58.7 R2 78.5 R3 75.1 Design Paint 140-381	Measured R1 0.939 R2 0.953 R3 0.936 R_Avg Design	Rust Grade – 10 Blistering – Not Found Discoloration – Not Found Flaking – Not Found Delamination – Not Found
A1-G1F1 Web	1		Measured R1 149 R2 156 R3 130 Design Paint 140-381	Measured R1 0.639 R2 0.637 R3 0.638 R_Avg Design	Rust Grade – 10 Blistering – Not Found Discoloration – Not Found Flaking – Not Found Delamination – Not Found
A1-G1F1 BF Top		-	Measured R1 152 R2 155 R3 143 Design Paint 140-381	Measured R1 . R2 R3 R_Avg Design	Rust Grade – 10 Blistering – Not Found Discoloration – Not Found Flaking – Not Found Delamination – Found
A1-G1F1 BF Bot.	-	-	Measured R1 263 R2 262 R3 284 Design Paint 140-381	Measured R1 0.881 R2 0.878 R3 0.882 R_Avg Design	Rust Grade – 10 Blistering – Not Found Discoloration – Not Found Flaking – Not Found Delamination – Not Found
A1-G2F2 TF Bot.	-		Measured R1 66.7 R2 58.7 R3 86.5 Design Paint 140-381	Measured R1 0.897 R2 0.898 R3 0.897 R_Avg Design	Rust Grade – 10 Blistering – Not Found Discoloration – Not Found Flaking – Not Found Delamination – Not Found
A1-G2F2 Web	1		Measured R1 144 R2 121 R3 114 Design Paint 140-381	Measured R1 0.639 R2 0.639 R3 0.637 R_Avg Design	Rust Grade – 10 Blistering – Not Found Discoloration – Not Found Flaking – Not Found Delamination – Not Found

Table A-101. Field Inspection Results for BMT-PS-02.

Location	Cl^- Conc. (ppm)	pH Test	Thickness (µm)	Thickness (inch)	Visual Inspection
A1-G2F2 BF Top.		-	Measured R1 165 R2 144 R3 155 Design Paint 140-381	Measured R1 R2 R3 R_Avg Design	Rust Grade – 10 Blistering – Not Found Discoloration – Not Found Flaking – Not Found Delamination – Not Found
A1-G2F2 BF Bot	1		Measured R1 271 R2 272 R3 249 Design Paint 140-381	Measured R1 0.930 R2 0.936 R3 0.932 R_Avg Design	Rust Grade – 10 Blistering – Not Found Discoloration – Not Found Flaking – Not Found Delamination – Not Found
A1-G4F1 TF Bot.	-		Measured R1 70.7 R2 68.6 R3 71.8 Design Paint 140-381	Measured R1 0.929 R2 0.929 R3 0.925 R_Avg Design	Rust Grade – 10 Blistering – Not Found Discoloration – Not Found Flaking – Not Found Delamination – Not Found
A1-G4F1 Web	1		Measured R1 126 R2 106 R3 114 R_Avg Design Paint 140-381	Measured R1 0.610 R2 0.609 R3 0.614 R_Avg Design	Rust Grade – 10 Blistering – Not Found Discoloration – Not Found Flaking – Not Found Delamination – Not Found
A1-G4F1 BF Top		-	Measured R1 171 R2 135 R3 129 Design Paint 140-381	Measured R1 R2 R3 R_Avg Design	Rust Grade – 10 Blistering – Not Found Discoloration – Not Found Flaking – Not Found Delamination – Not Found
A1-G4F1 BF Bot.	1		Measured R1 406 R2 403 R3 350 Design Paint 140-381	Measured R1 0.927 R2 0.918 R3 0.918 R_Avg Design	Rust Grade – 10 Blistering – Not Found Discoloration – Not Found Flaking – Not Found Delamination – Not Found

Table A-102. Field Inspection Results for BMT-PS-02.

Location	Cl^- Conc. (ppm)	pH Test	Thickness (µm)	Thickness (inch)	Visual Inspection
A1-G6F2 TF Bot.		-	Measured R1 83.2 R2 81.8 R3 76.7 Design Paint 140-381	Measured R1 0.896 R2 0.898 R3 0.896 R_Avg Design	Rust Grade – 10 Blistering – Not Found Discoloration – Not Found Flaking – Not Found Delamination – Found
A1-G6F2 Web.	-	-	Measured R1 188 R2 161 R3 162 Design Paint 140-381	Measured R1 0.591 R2 0.633 R3 0.633 R_Avg Design	Rust Grade – 10 Blistering – Not Found Discoloration – Not Found Flaking – Not Found Delamination – Not Found
A1-G6F2 BF Top	-		Measured R1 163 R2 155 R3 148 Design Paint 140-381	Measured R1 R2 R3 R_Avg Design	Rust Grade – 10 Blistering – Not Found Discoloration – Not Found Flaking – Not Found Delamination – Not Found
A1-G6F2 BF Bot.	1		Measured R1 161 R2 172 R3 170 Design Paint 140-381	Measured R1 0.913 R2 0.913 R3 0.923 R_Avg Design	Rust Grade – 10 Blistering – Not Found Discoloration – Not Found Flaking – Not Found Delamination – Not Found

A.20.3. Pull-off Adhesion Results

Table A-103. Pull-off Adhesion Results for BMT-PS-02.

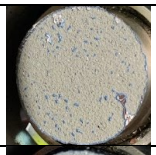
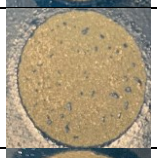
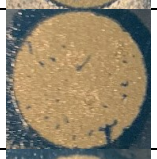
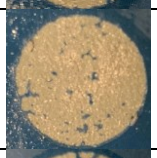
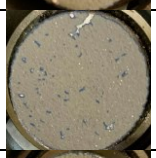
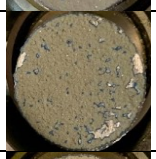
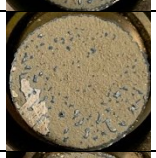
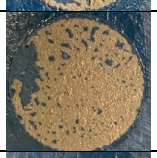
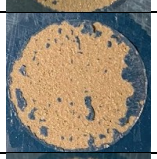
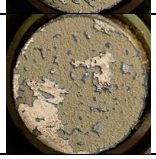
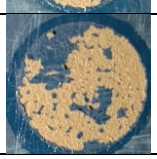
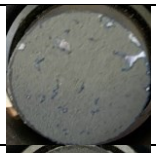
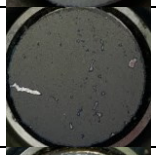
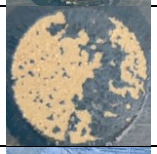
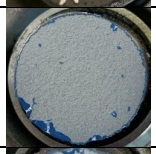
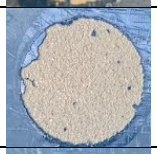
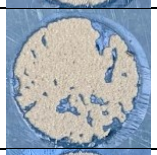
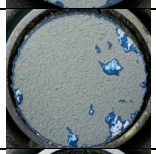
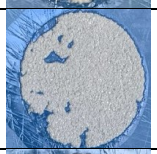
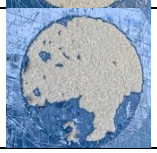
Location	Dolly Face	Substrate Face	Test Result (psi)	Attributes	Failure Type
A1-G1F1			2301	100% A/B	100% Adhesive Failure
			2422	100% A/B	100% Adhesive Failure
			2333	100% A/B	100% Adhesive Failure
			1951	100% A/B	100% Adhesive Failure
			2429	100% A/B	100% Adhesive Failure
A1-G2F2			2478	30% B 70% A/B	30% Cohesive Failure 70% Adhesive Failure
			2320	30% B 70% A/B	30% Cohesive Failure 70% Adhesive Failure
			2474	30% B 70% A/B	30% Cohesive Failure 70% Adhesive Failure
			2363	50% B 50% C/Y	50% Cohesive Failure 50% Adhesive Failure
			2523	40% B 60% C/Y	40% Cohesive Failure 60% Adhesive Failure

Table A-104. Pull-off Adhesion Results for BMT-PS-02.

Location	Dolly Face	Substrate Face	Test Result (psi)	Attributes	Failure Type
A1-G4F1			2363	10% B 90% C/Y	10% Cohesive Failure 10% Adhesive Failure
			2091	100% A/B	100% Adhesive Failure
			2552	70% A/B 30% C/Y	70% Adhesive Failure 30% Adhesive Failure
			2518	90% A/B 10%B	90% Adhesive Failure 10% Adhesive Failure
			2552	70% A/B 30% C/Y	30% Adhesive Failure 70% Adhesive Failure
A1-G6F2			2493	100% A/B	100% Adhesive Failure
			2414	70% A/B 20% B 10% C/Y	70% Cohesive Failure 20% Adhesive Failure 10% Adhesive Failure
			2481	80% A/B 20% B	80% Cohesive Failure 20% Adhesive Failure
			2298	90% A/B 10% B	90% Cohesive Failure 10% Adhesive Failure
			2545	70% A/B 30% B	70% Adhesive Failure 30% Cohesive Failure

A.20.4. Optical Microscopy Results

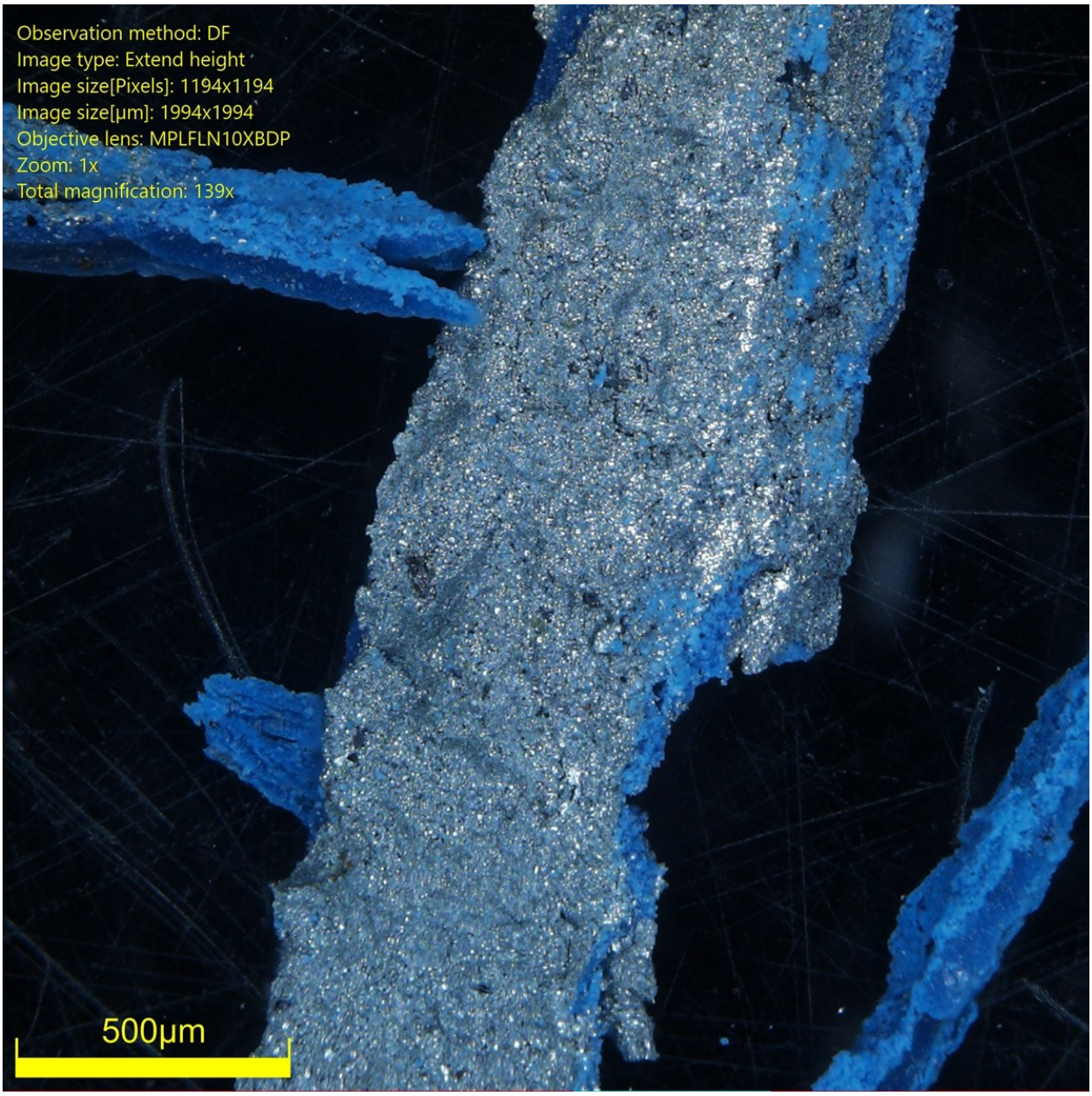


Figure A.258. Two Layer Paint System Examined by Optical Microscope BMT–PS–02.

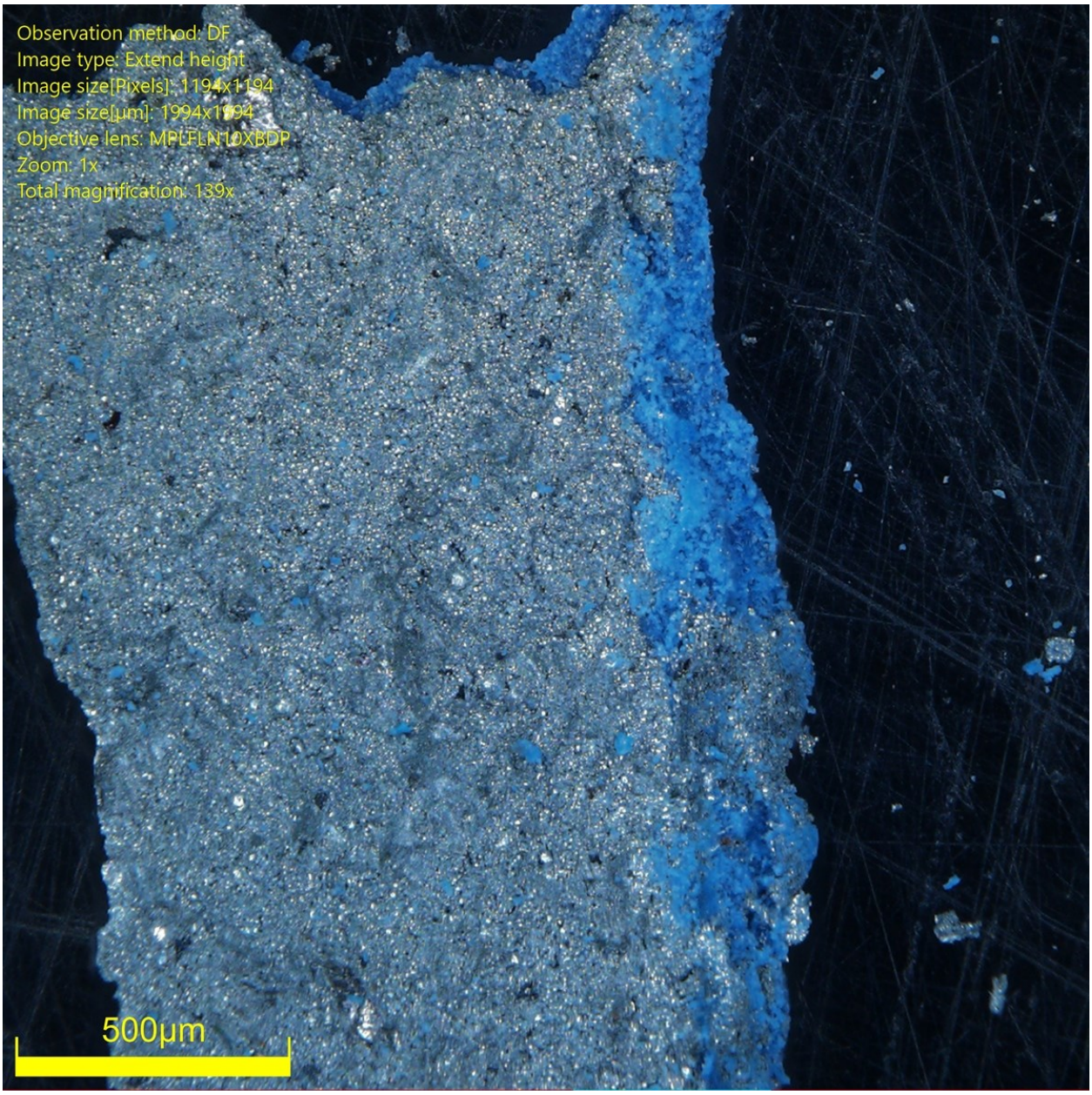
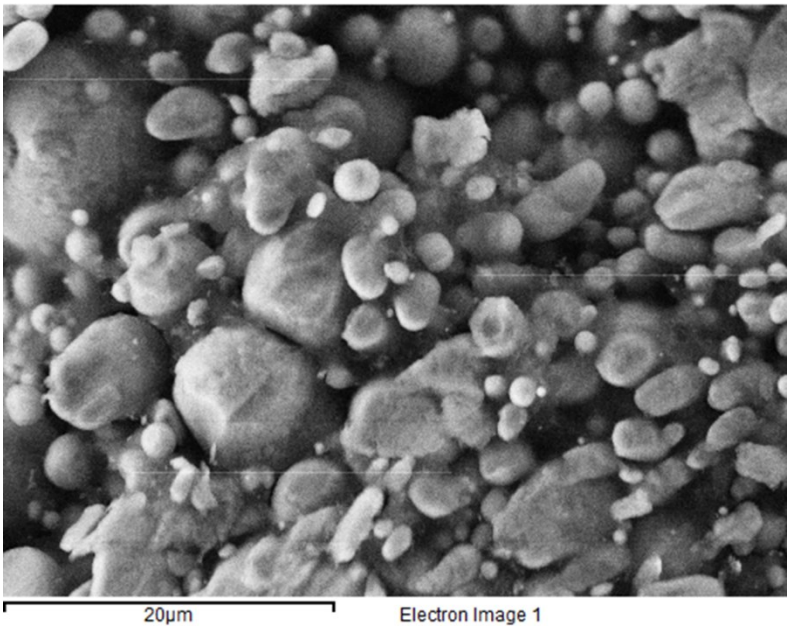


Figure A.259. Two Layer Paint System Examined by Optical Microscope BMT–PS–02.

A.20.5.SEM/EDS Results

Element	Weight %	Atomic %
C K	44.88	75.27
O K	7.79	9.81
Al K	0.55	0.41
Si K	0.19	0.13
Fe K	0.40	0.15
Zn K	46.19	14.23
Totals	100.00	



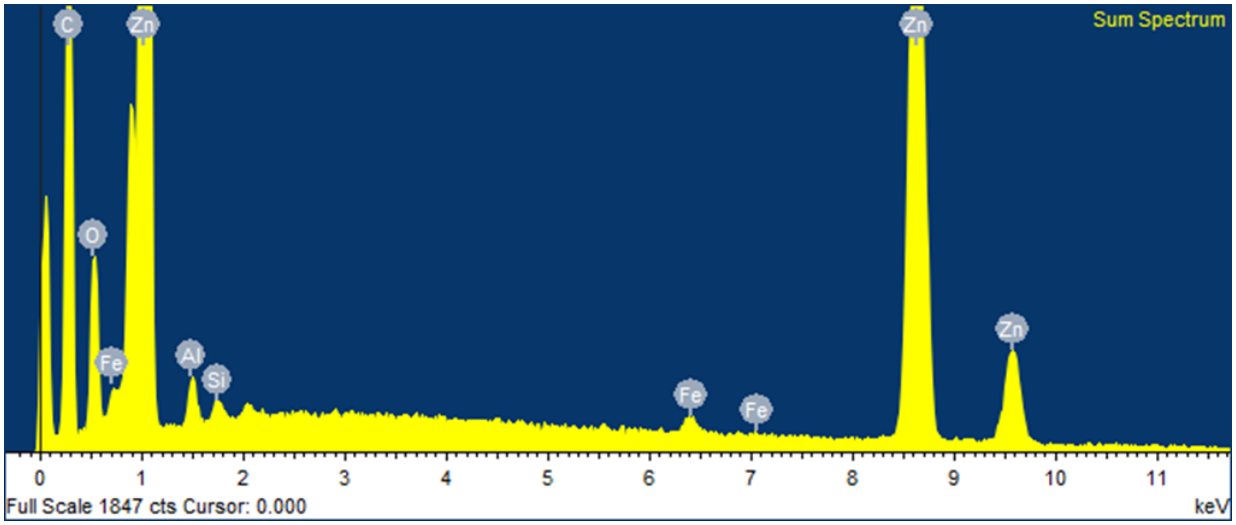


Figure A.260. SEM Image and EDS Spectrum of the Paint Collected from Exterior Web of the Girder.

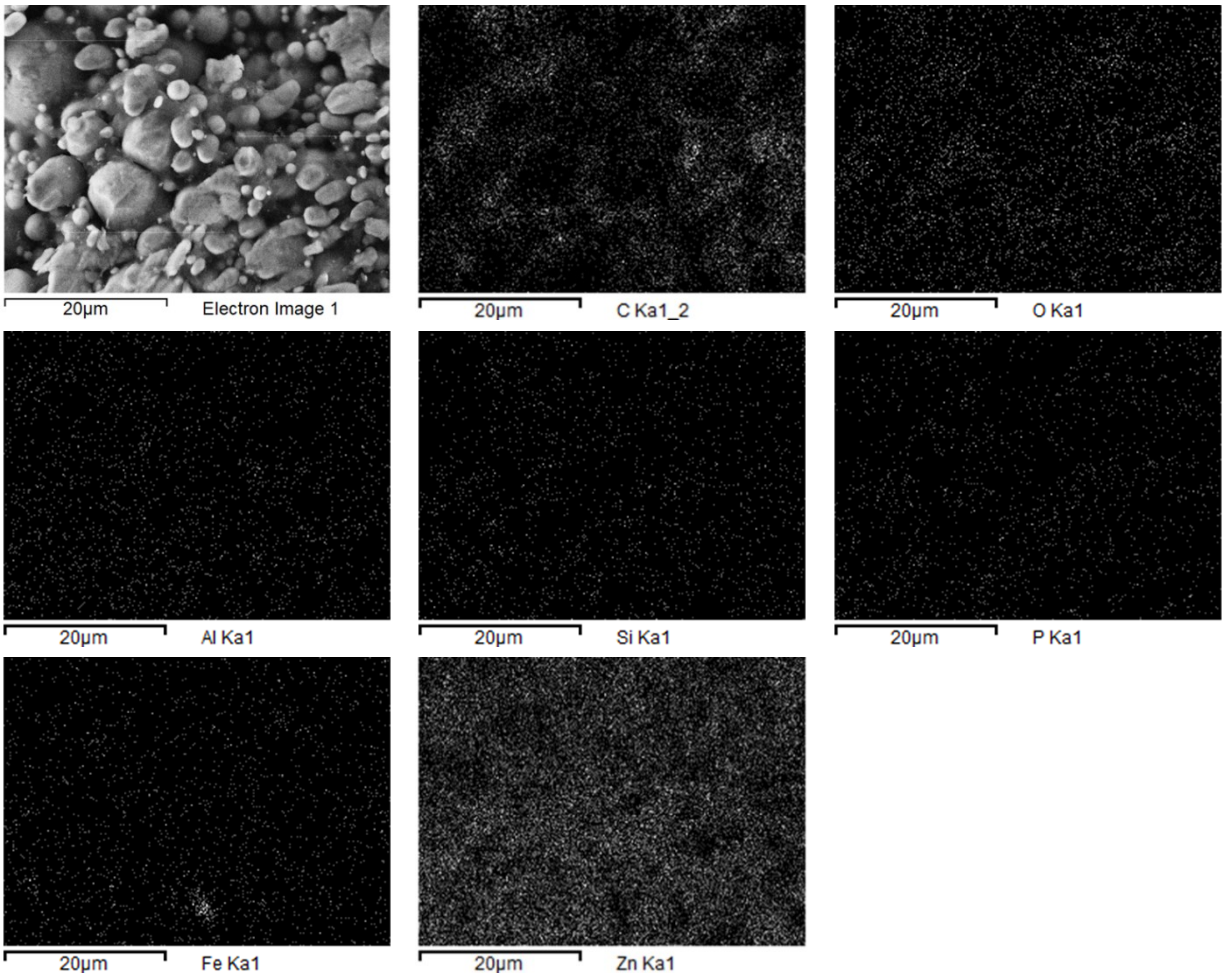
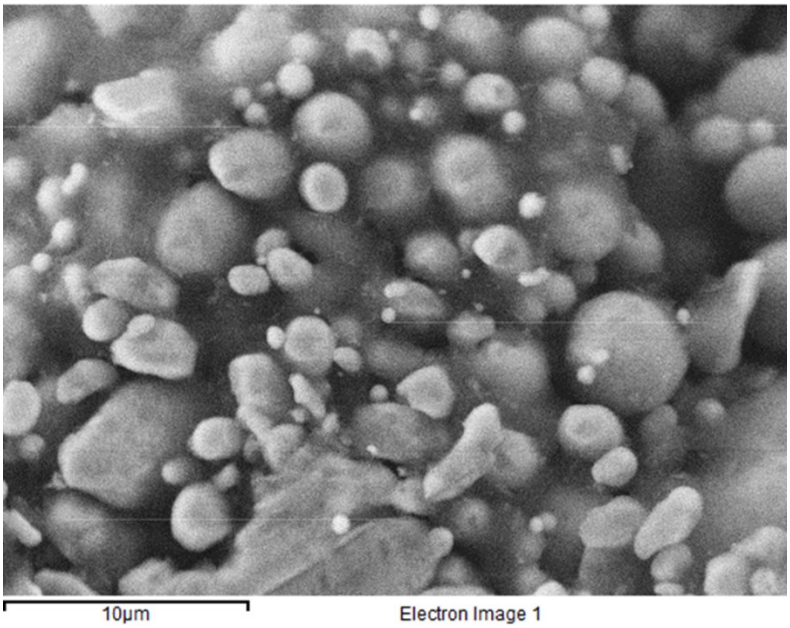


Figure A.261. EDS Elemental Mapping of Paint Collected from Exterior Web.

Element	Weight %	Atomic %
C K	52.43	79.17
O K	8.62	9.77
Al K	0.33	0.22
Si K	0.28	0.18
Fe K	0.51	0.17
Zn K	37.83	10.50
Totals	100.00	



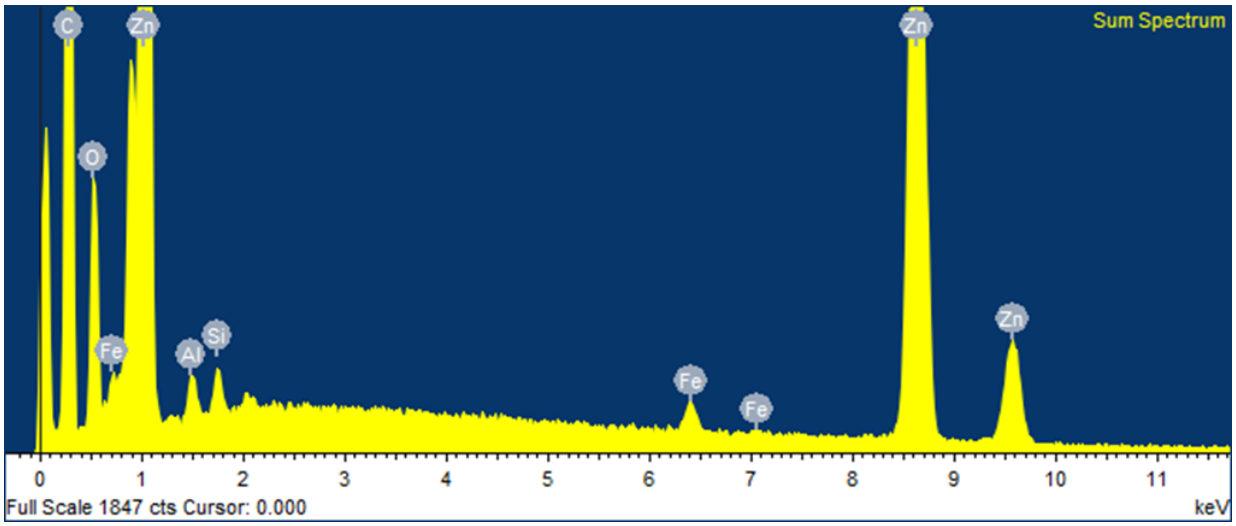


Figure A.262. SEM Image and EDS Spectrum of the Paint Collected from Exterior Web of the Girder.

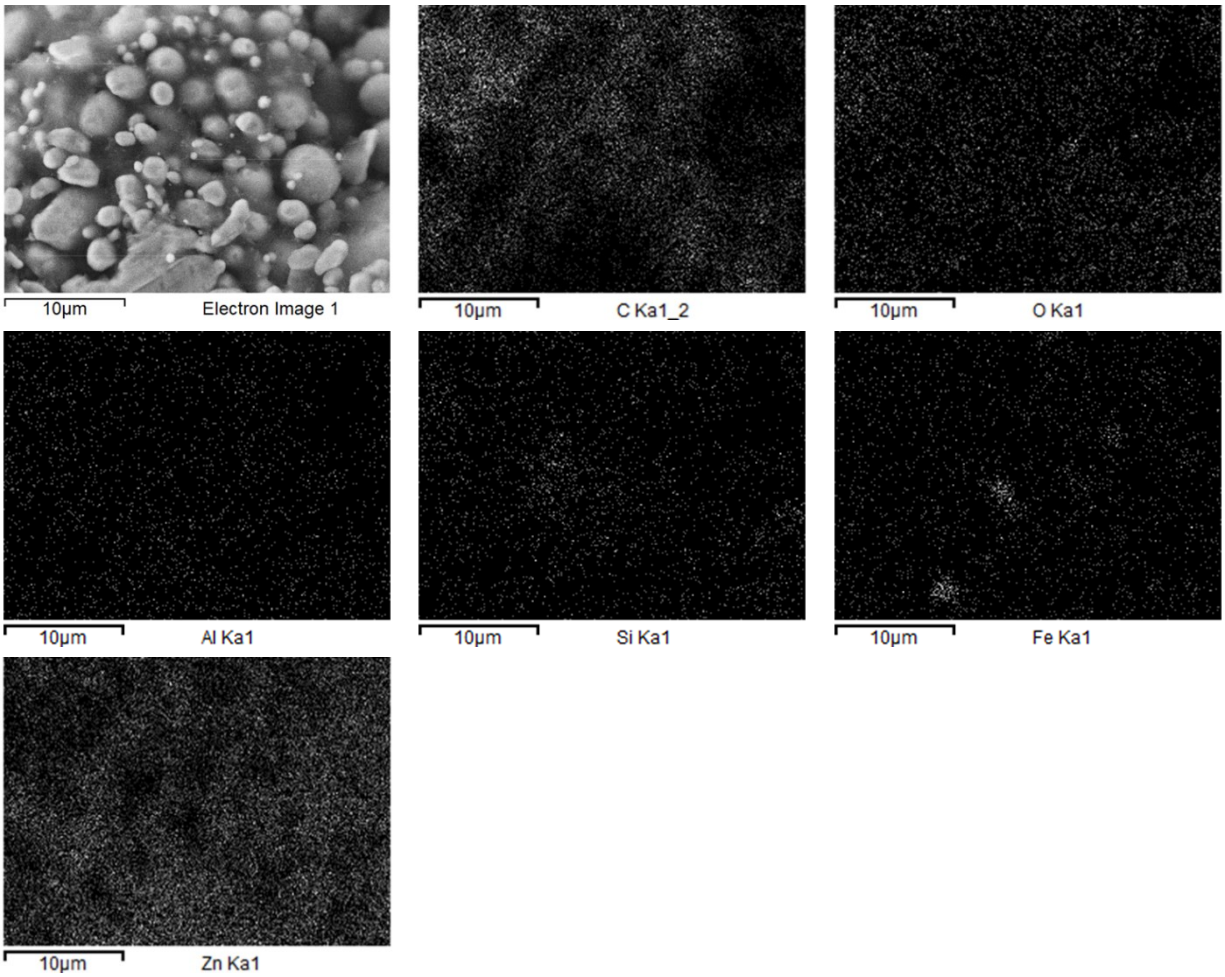
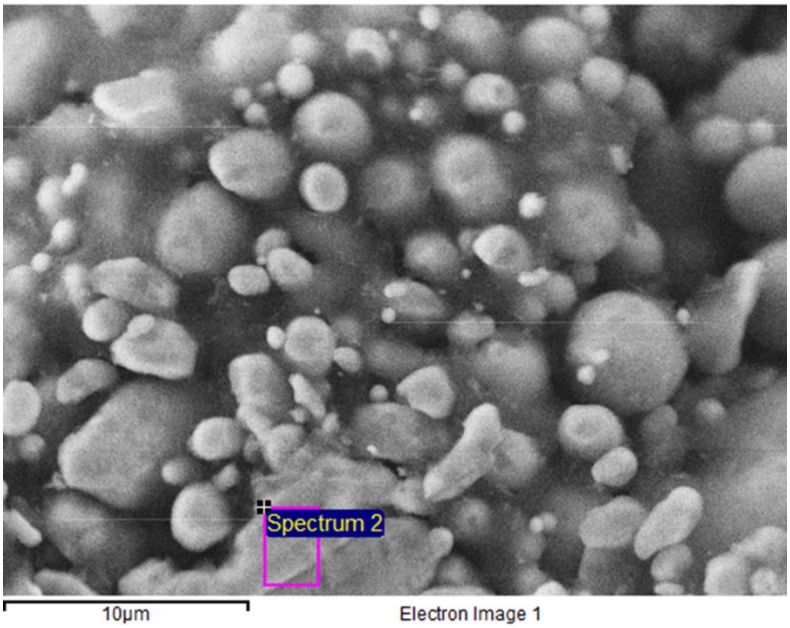


Figure A.263. EDS Elemental Mapping of Paint Collected from Exterior Web.

Element	Weight %	Atomic %
C K	21.65	56.33
O K	3.80	7.42
Al K	0.83	0.97
Fe K	0.56	0.31
Zn K	73.16	34.98
Totals	100.00	



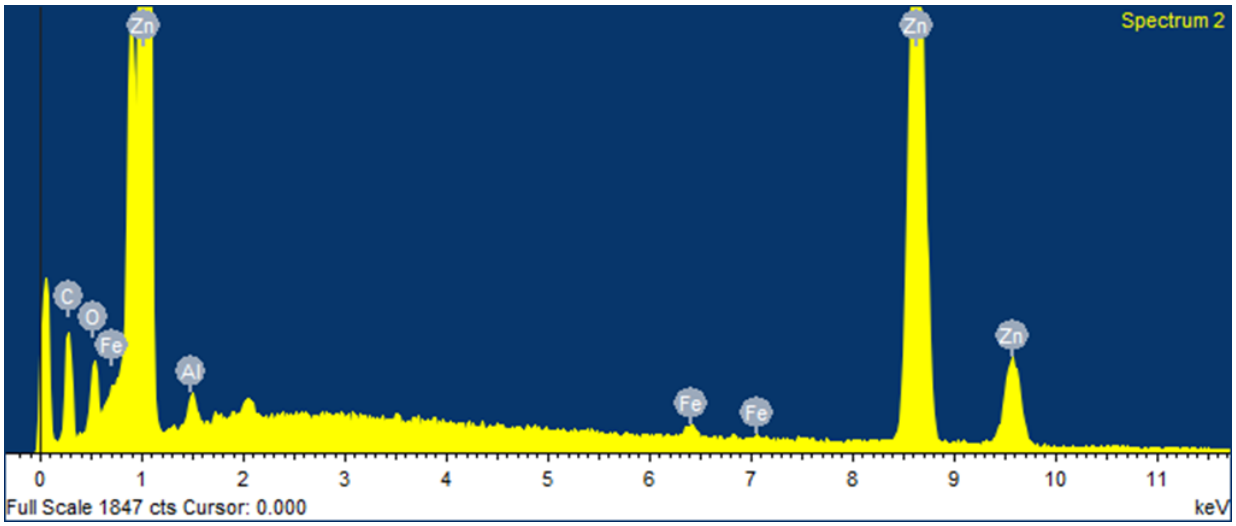
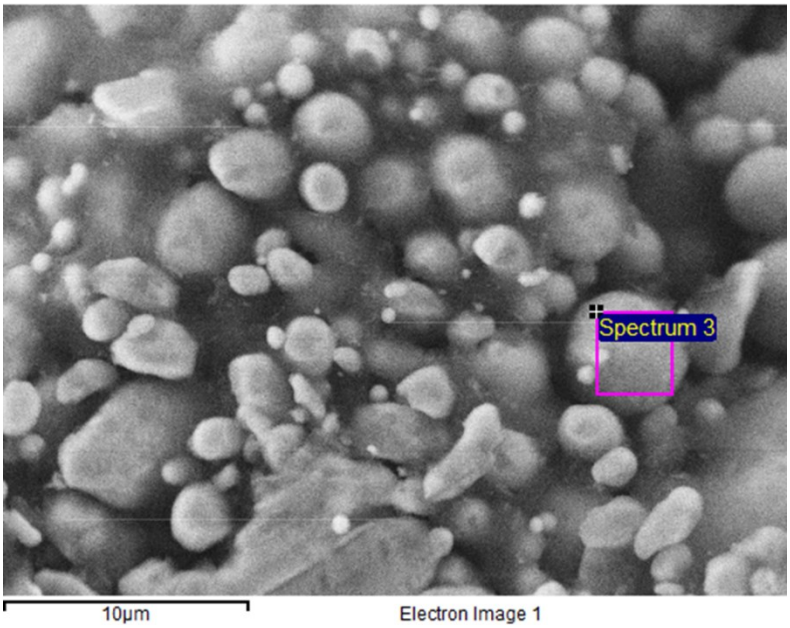


Figure A.264. SEM Image and EDS Spectrum of the Paint Collected from Exterior Web of the Girder.

Element	Weight %	Atomic %
C K	28.26	63.41
O K	5.22	8.78
Al K	0.50	0.50
Si K	0.14	0.14
Fe K	0.26	0.13
Zn K	65.62	27.05
Totals	100.00	



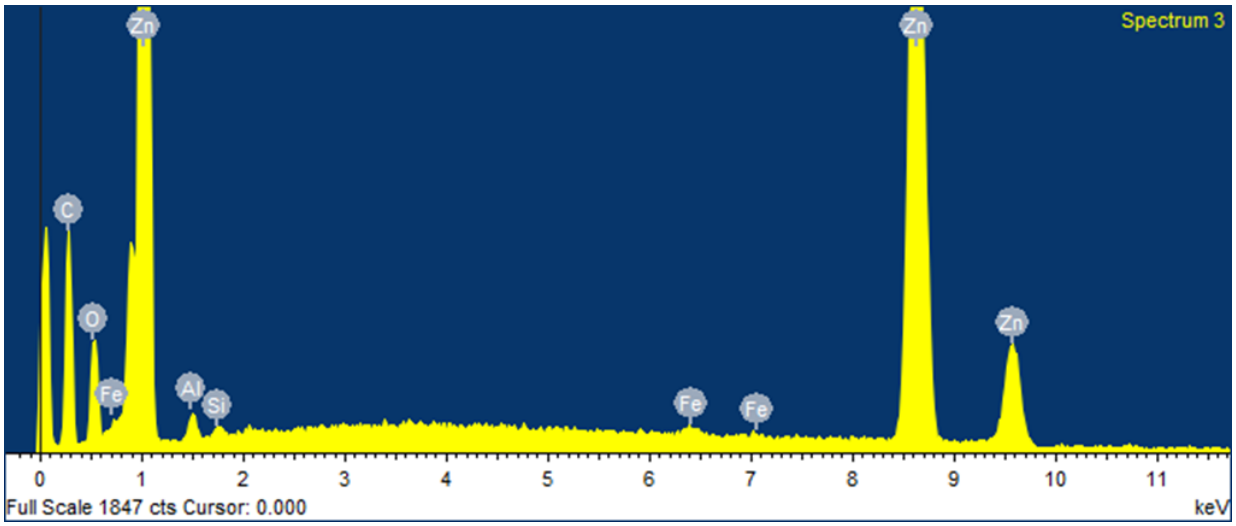
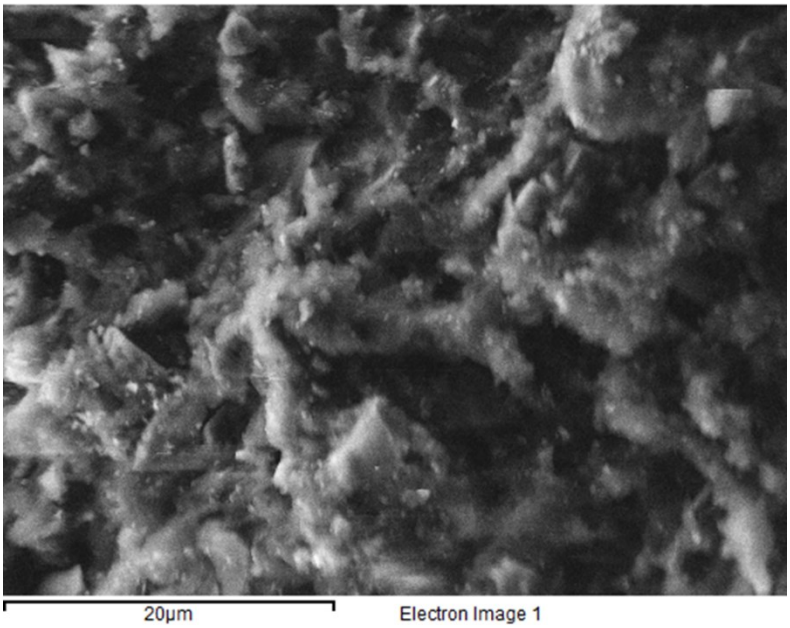


Figure A.265. SEM Image and EDS Spectrum of the Paint Collected from Exterior Web of the Girder.

Element	Weight %	Atomic %
C K	68.71	75.71
O K	26.92	22.27
Na K	0.83	0.48
Al K	1.10	0.54
Si K	1.76	0.83
K K	0.17	0.06
Ca K	0.03	0.01
Ti K	0.20	0.05
Fe K	0.04	0.01
Zn K	0.11	0.02
Zr L	0.12	0.02
Totals	100.00	



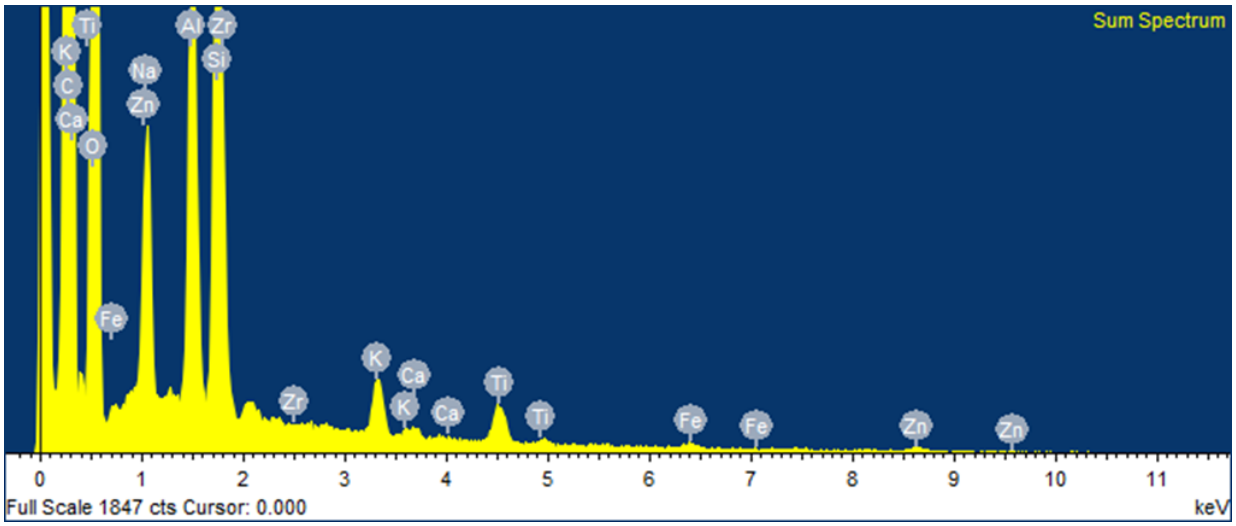


Figure A.266. SEM Image and EDS Spectrum of the Paint Collected from Exterior Web of the Girder.

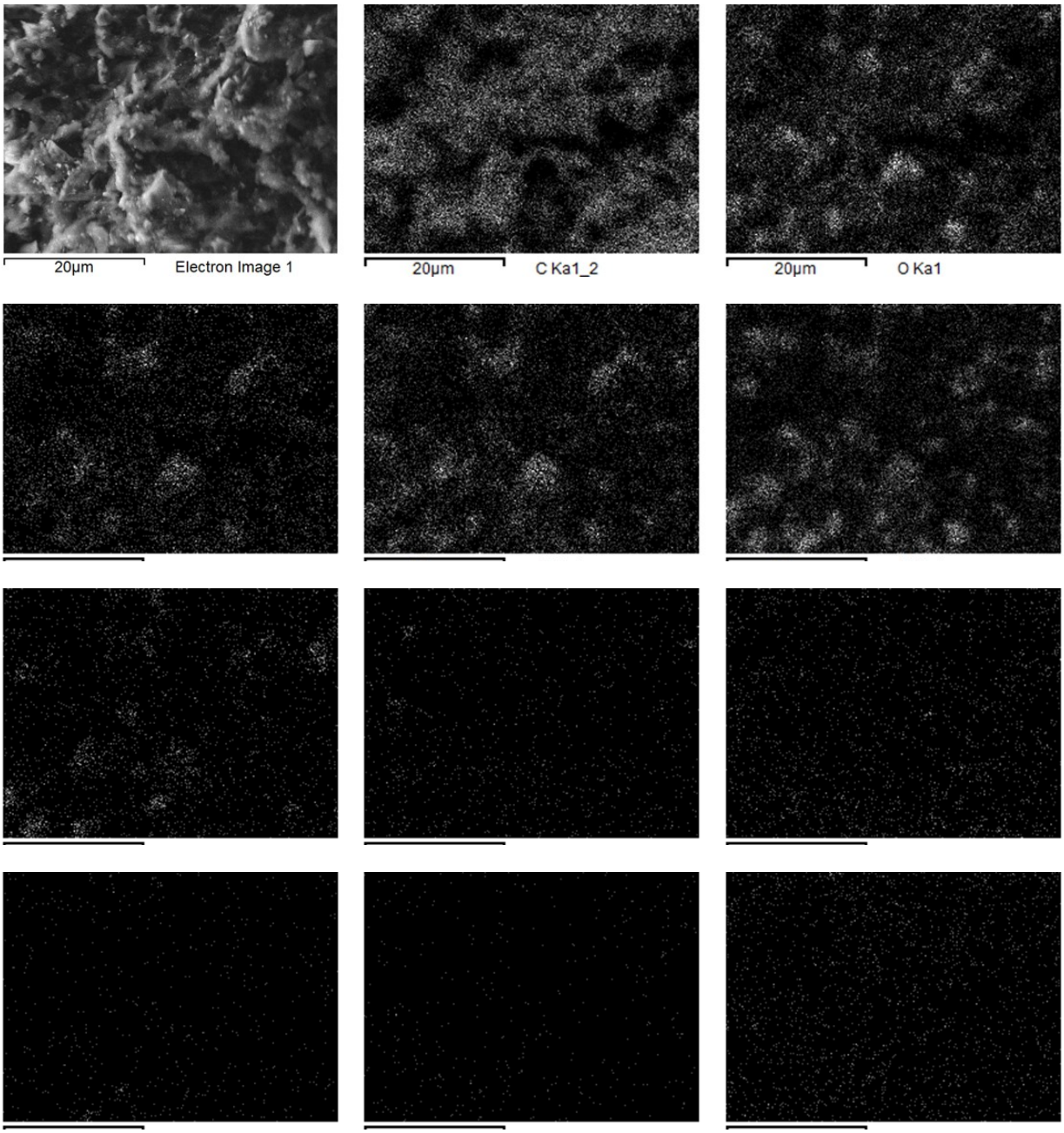
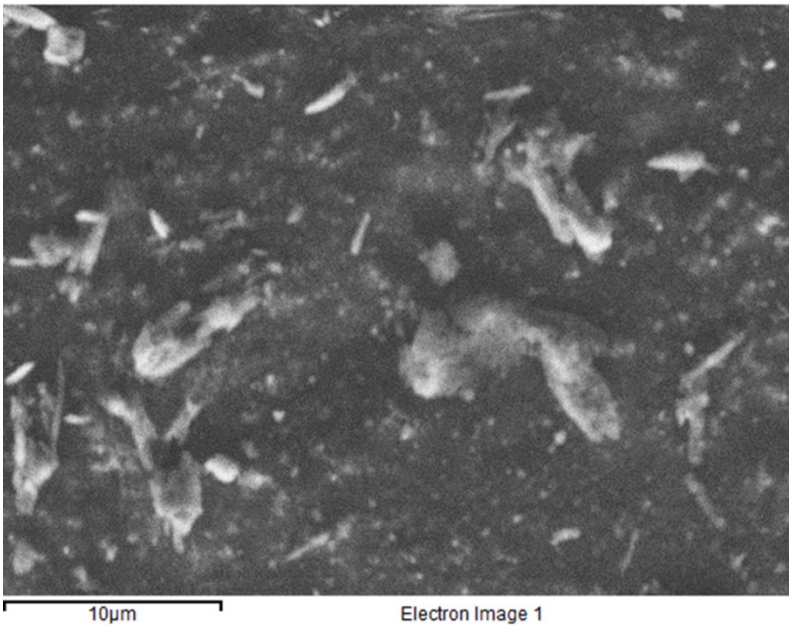


Figure A.267. EDS Elemental Mapping of Paint Collected from Exterior Web.

Element	Weight %	Atomic %
C K	64.48	71.61
O K	32.52	27.11
Al K	0.87	0.43
Si K	1.16	0.55
S K	0.11	0.05
Cl K	0.09	0.03
K K	0.06	0.02
Ca K	0.31	0.10
Ti K	0.10	0.03
Fe K	0.06	0.01
Cu K	0.14	0.03
Zn K	0.10	0.02
Totals	100.00	



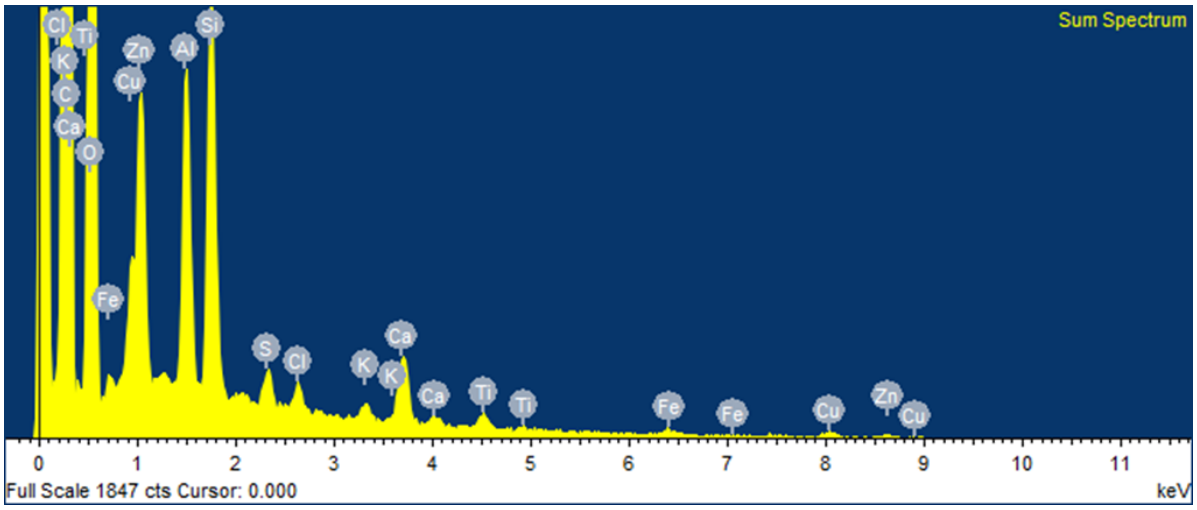


Figure A.268. SEM Image and EDS Spectrum of the Paint Collected from Interior Web of the Girder.

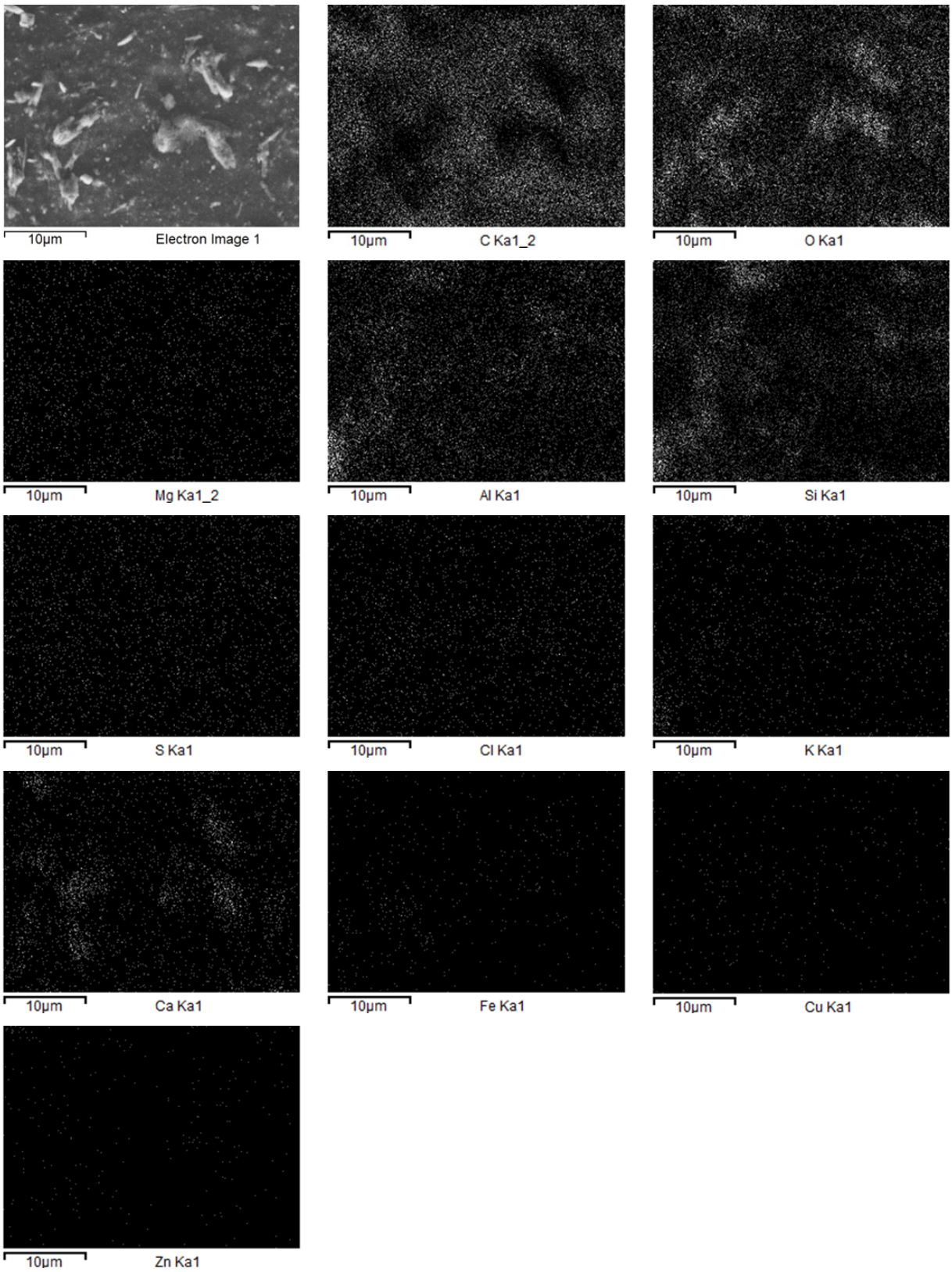
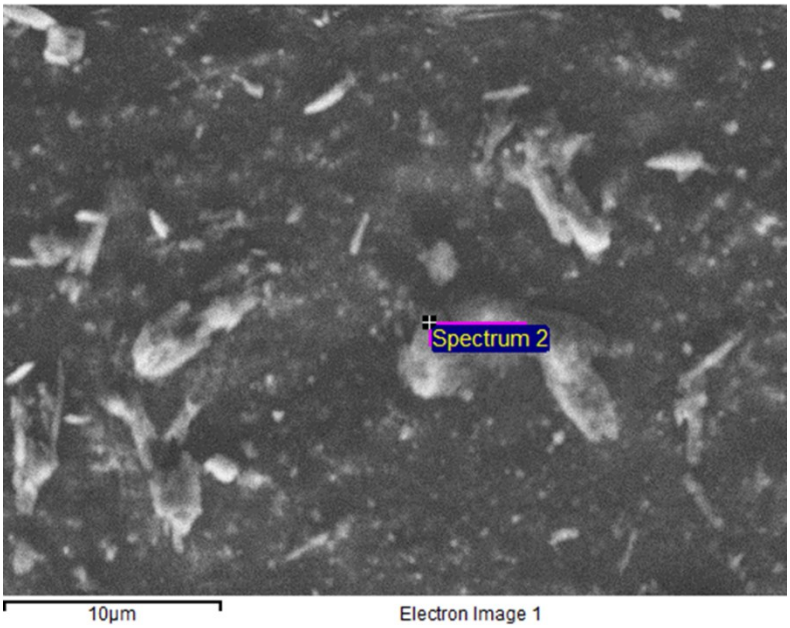


Figure A.269. EDS Elemental Mapping of Paint Collected from Interior Web.

Element	Weight %	Atomic %
C K	70.98	78.11
O K	24.32	20.09
Al K	0.97	0.48
Si K	1.44	0.68
S K	0.13	0.06
Cl K	0.17	0.06
K K	0.17	0.06
Ca K	0.42	0.14
Ti K	0.58	0.16
Fe K	0.09	0.02
Cu K	0.17	0.04
Zn K	0.56	0.11
Totals	100.00	



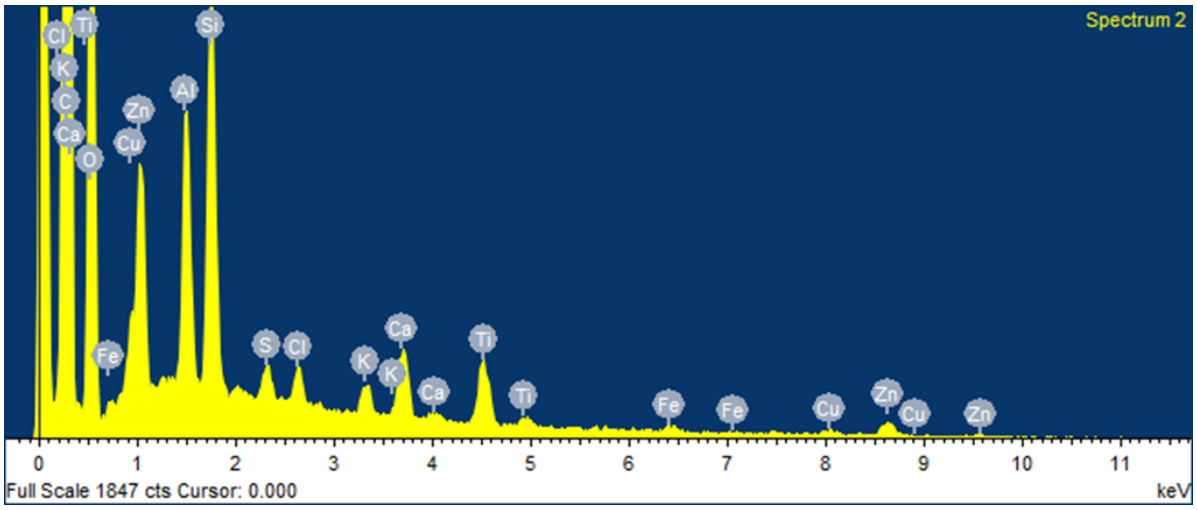
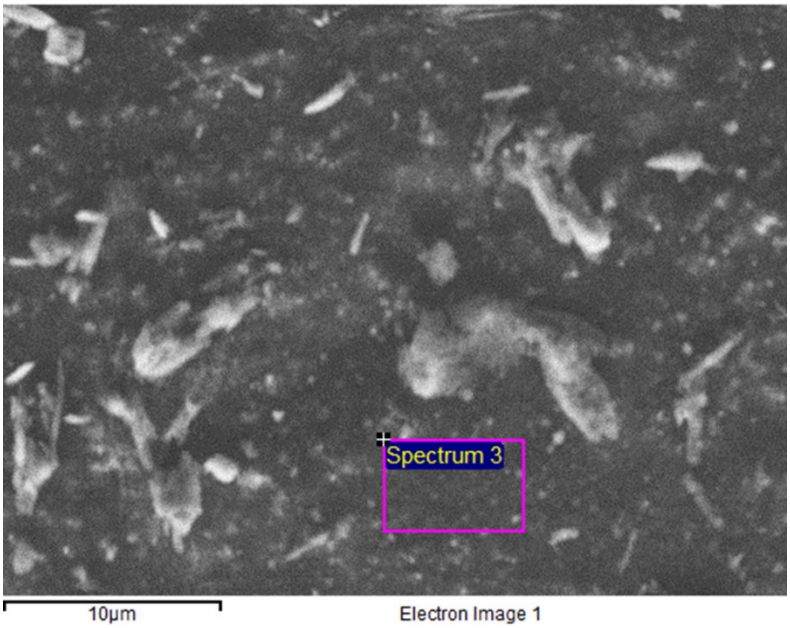


Figure A.270. SEM Image and EDS Spectrum of the Paint Collected from Interior Web of the Girder.

Element	Weight %	Atomic %
C K	67.69	75.46
O K	25.46	21.31
Na K	1.22	0.71
Al K	1.48	0.73
Si K	3.06	1.46
S K	0.11	0.04
Cl K	0.13	0.05
K K	0.12	0.04
Ca K	0.17	0.06
Ti K	0.28	0.08
Cu K	0.12	0.02
Zn K	0.17	0.03
Totals	100.00	



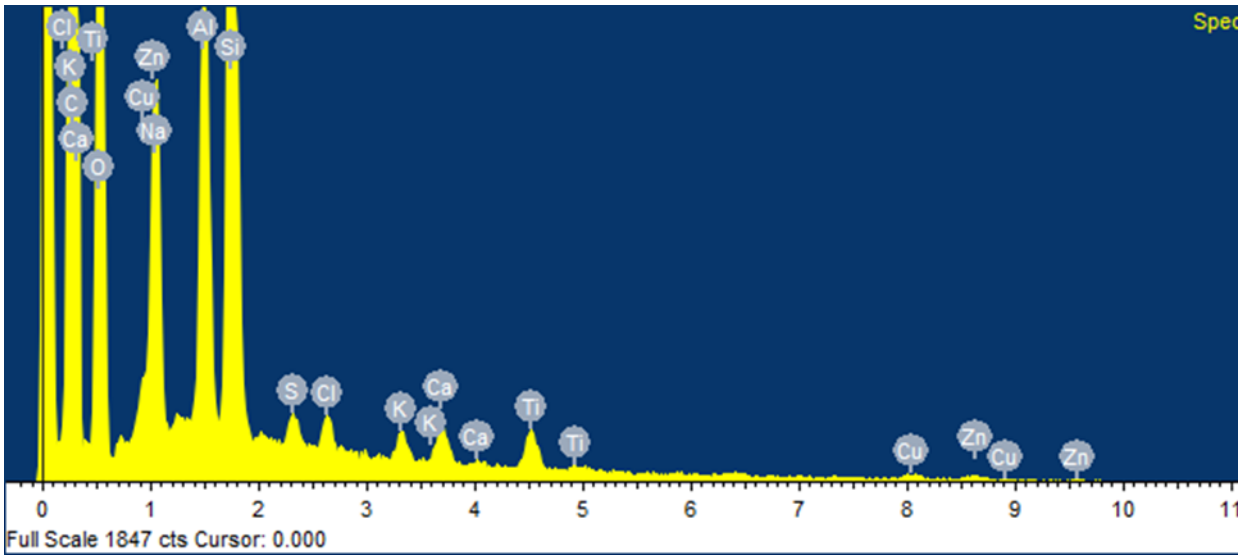
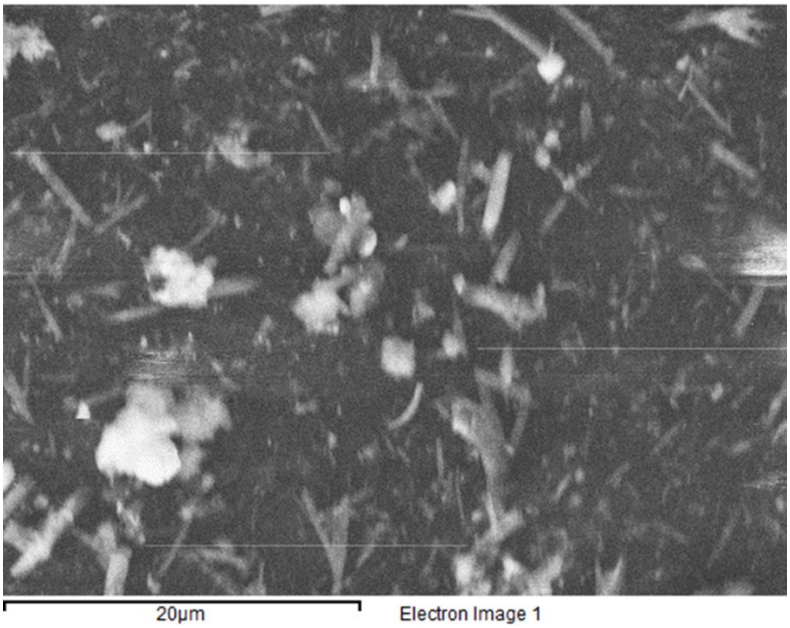


Figure A.271. SEM Image and EDS Spectrum of the Paint Collected from Interior Web of the Girder.

Element	Weight %	Atomic %
C K	65.86	72.65
O K	32.04	26.54
Al K	0.49	0.24
Si K	0.60	0.28
S K	0.12	0.05
Cl K	0.06	0.02
K K	0.03	0.01
Ca K	0.33	0.11
Ti K	0.08	0.02
Fe K	0.04	0.01
Ni K	0.13	0.03
Zn K	0.08	0.02
Zr L	0.14	0.02
Totals	100.00	



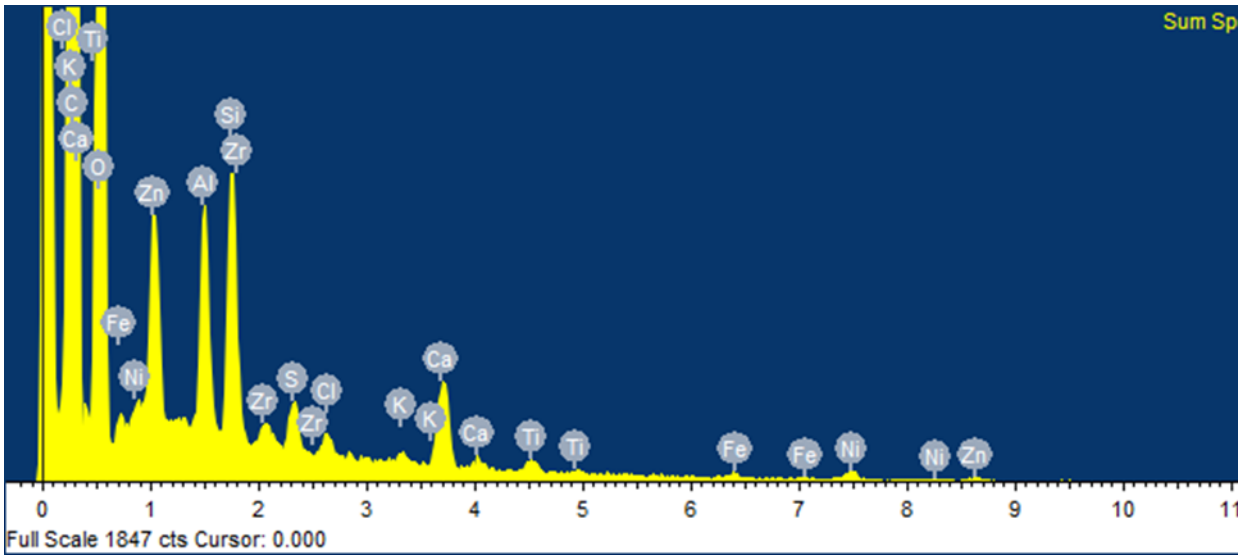


Figure A.272. SEM Image and EDS Spectrum of the Paint Collected from Interior Web of the Girder.

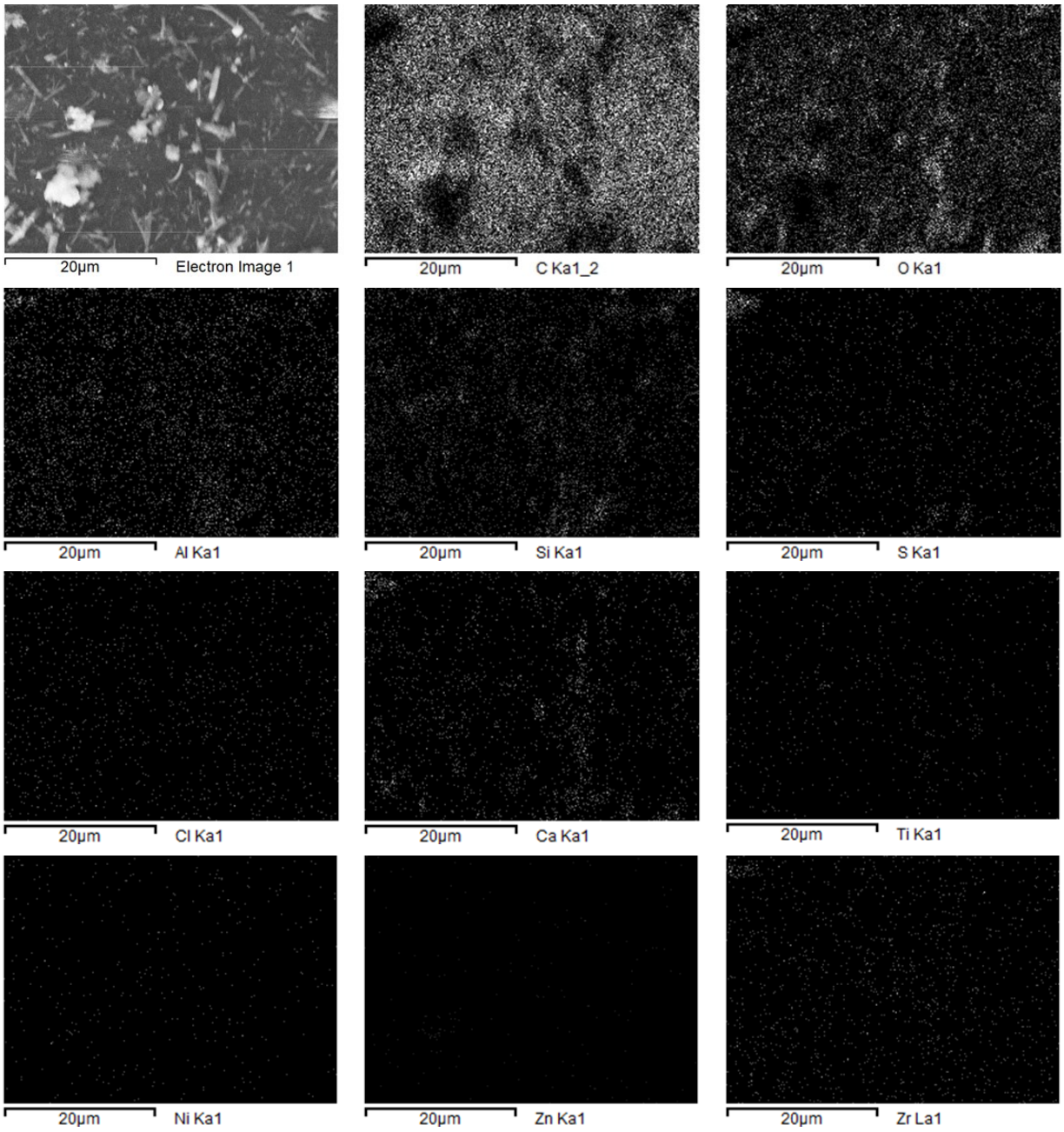
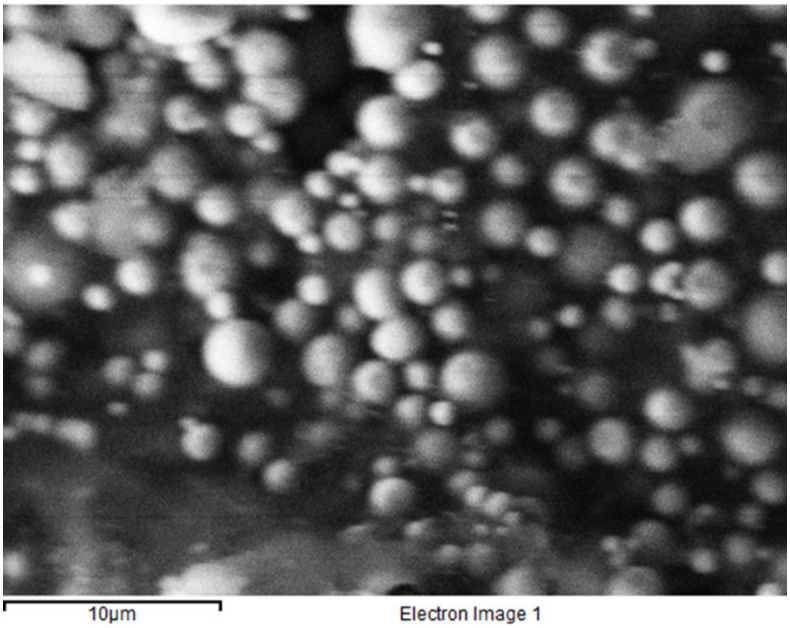


Figure A.273. EDS Elemental Mapping of Paint Collected from Interior Web.

Element	Weight %	Atomic %
C K	56.87	79.83
O K	10.68	11.26
Mg K	0.26	0.18
Al K	0.26	0.16
Si K	0.49	0.30
Ca K	0.11	0.05
Fe K	3.31	1.00
Zn K	28.01	7.23
Totals	100.00	



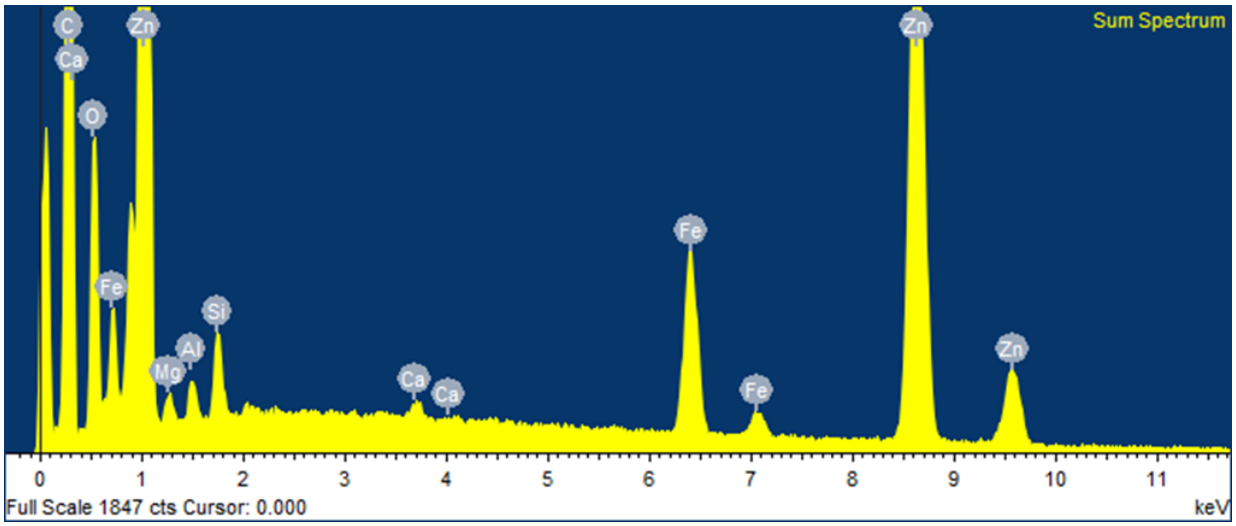
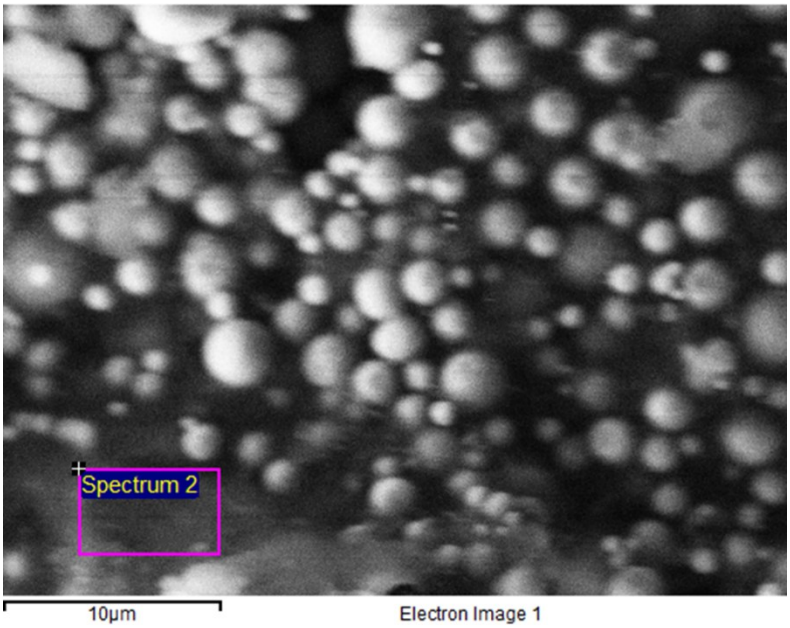
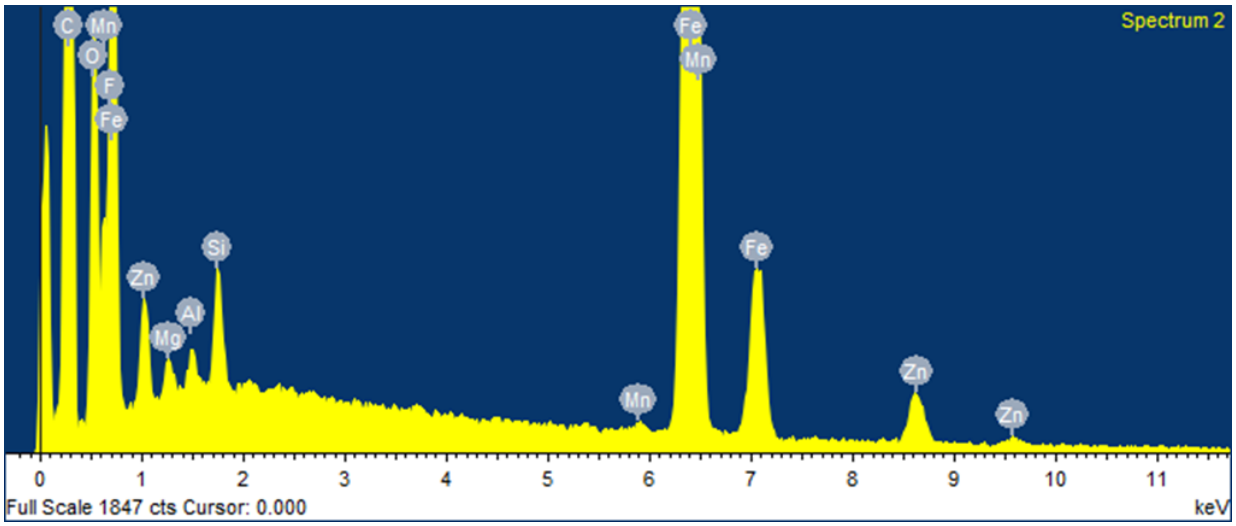


Figure A.274. SEM Image and EDS Spectrum of the Paint Collected from Interior Web of the Girder.

Element	Weight %	Atomic %
C K	59.63	78.82
O K	11.39	11.31
F K	2.67	2.23
Mg K	0.20	0.13
Al K	0.15	0.09
Si K	0.46	0.26
Mn K	0.14	0.04
Fe K	23.26	6.61
Zn K	2.10	0.51
Totals	100.00	

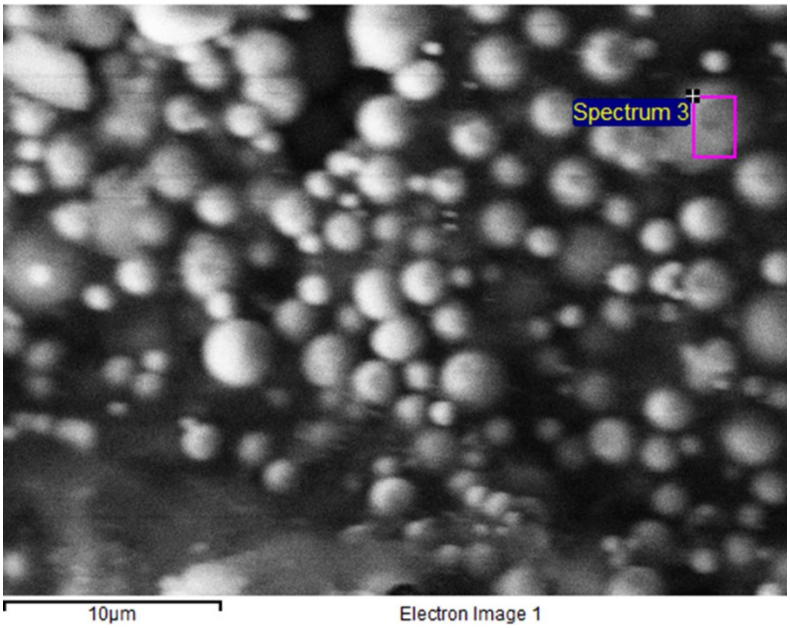




(a)

Figure A.275. SEM Image and EDS Spectrum of the Paint Collected from Interior Web of the Girder.

Element	Weight %	Atomic %
C K	62.40	85.44
O K	6.37	6.55
Al K	0.19	0.11
Si K	0.19	0.11
Fe K	0.53	0.16
Zn K	30.32	7.63
Totals	100.00	



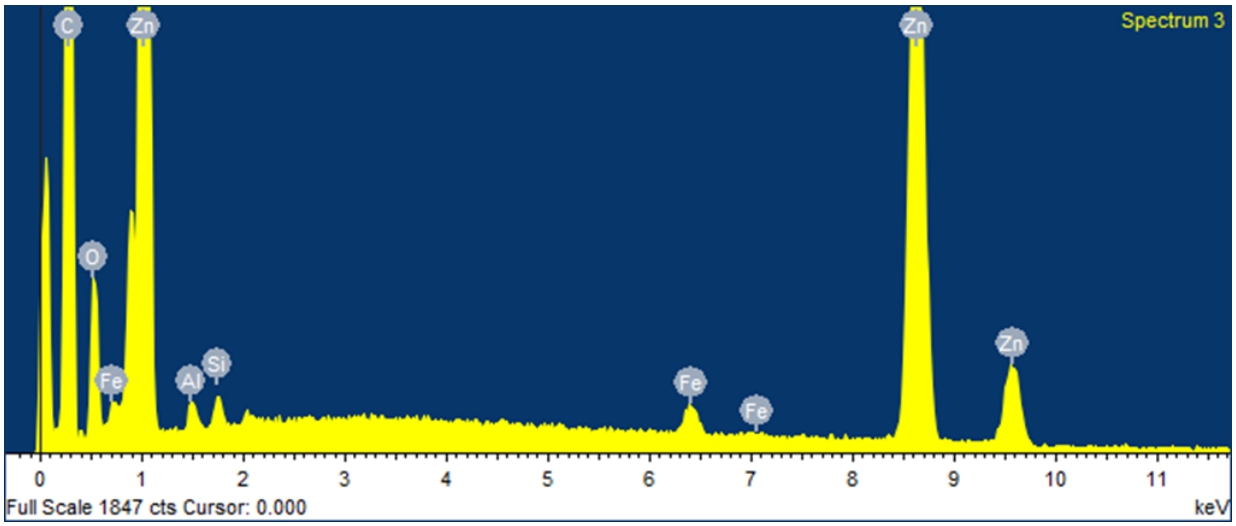


Figure A.276. SEM Image and EDS Spectrum of the Paint Collected from Interior Web of the Girder.

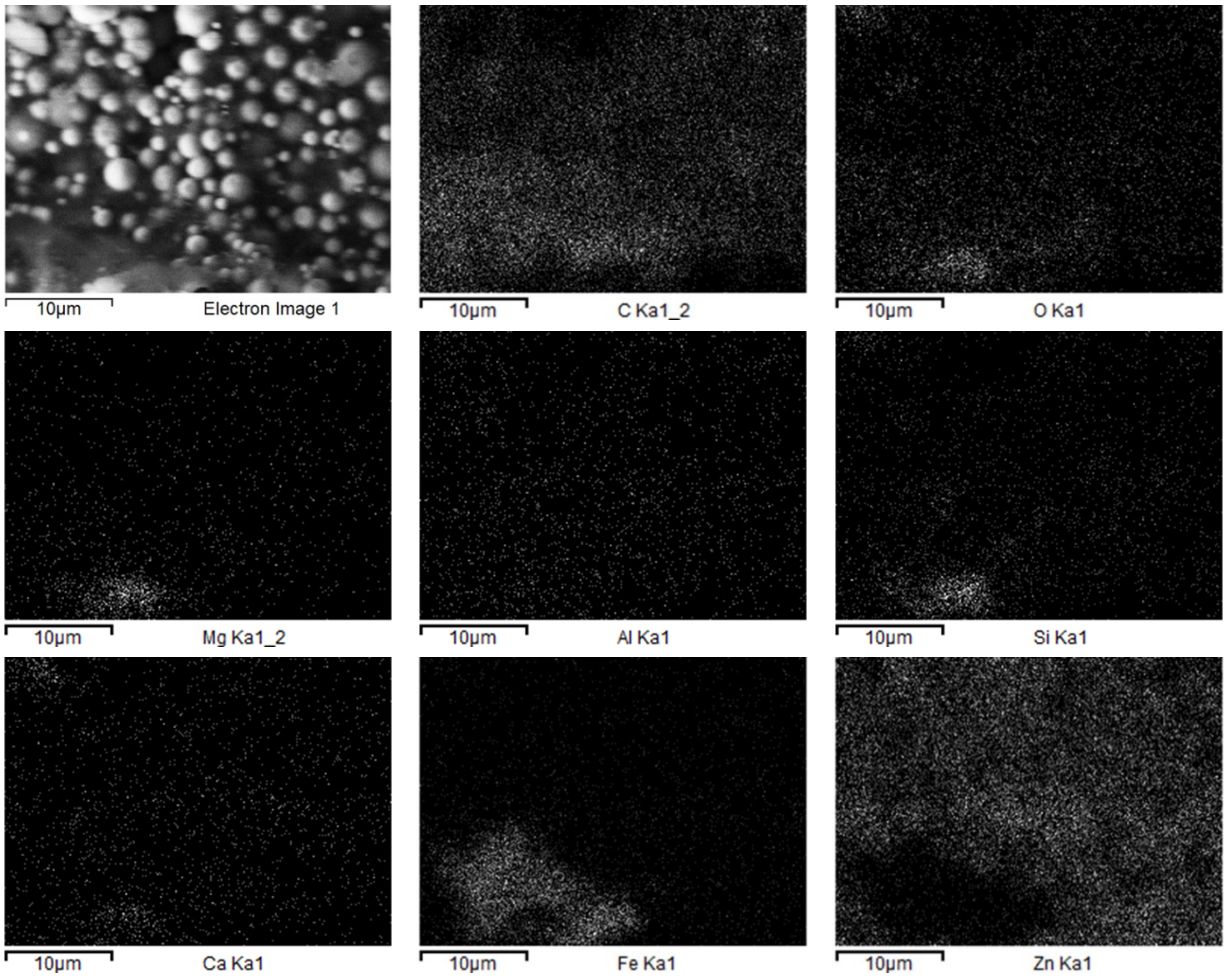
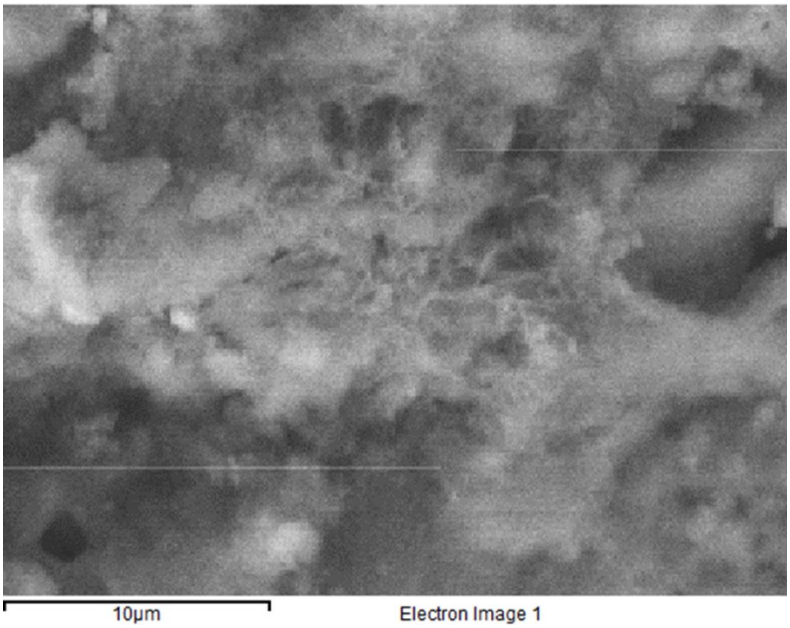


Figure A.277. EDS Elemental Mapping of Paint Collected from Interior Web.

Element	Weight %	Atomic %
C K	10.05	27.63
O K	14.95	30.86
Al K	2.16	2.65
Si K	2.39	2.81
S K	0.12	0.13
Cl K	0.38	0.35
K K	0.05	0.04
Fe K	3.19	1.89
Zn K	66.21	33.46
Zr L	0.50	0.18
Totals	100.00	



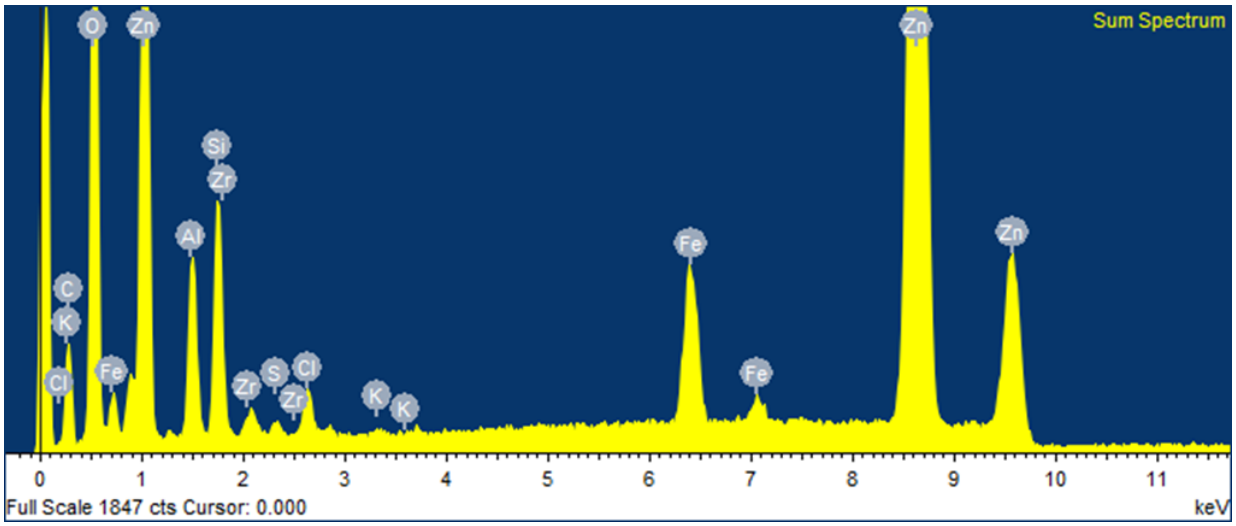


Figure A.278. SEM Image of Paint and EDS Spectrum of the Paint Collected from Interior Web of the Girder (G6F1).

A.21. AUS-WS-01

- IH 35 N T/A @ 51st over IH 35
- Bridge ID 142270001513363, Coordinates (30.30992, -97.710012), Travis County
- Continuous weathering steel plate girder (ASTM A588 HS 50)
- Built 1977
- Date of Inspection: November 25, 2020 girder inspection carried on east end abutment and bent 3, and measurements are taken on girder within three feet from the abutment or bent.
- No visual inspection on deck
- Location for Testing: A1-G4F2, A1-G3F2, B3-G1F1, B3-G2F2, B3-G4F2



Figure A.279. Typical Elevation of AUS-WS-01

A.21.1. Observed Condition

Delaminated areas of the patina are visible on the bottom face of the top flange. The web has a uniform patina formation with a patina rating of 7. The interior girders have significant poultice corrosion on the top face of the bottom flange due to the accumulation of dirt Index 5 to 4 whereas exterior girders have less accumulation of dirt.



(a) Delamination and Color Variation on Girder Number 1



(b) Patina Condition on Exterior Girder Number 4



(c) Widespread Rust Flakes



(d) Drip Plates Installed on Bottom Flange of Girder Number 4



(e) No Poultice Corrosion on Exterior Girder



(f) Poultice Corrosion on BF Top of Interior Girder

Figure A.280. Patina Condition on Girder of AUS-WS-01.

A.21.2.Field Testing Results and Tape Adhesion Test Results

Table A-105. Field Inspection Results for AUS-WS-01.

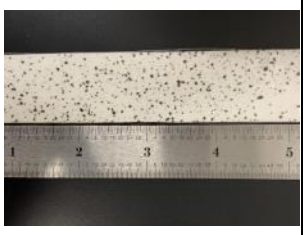
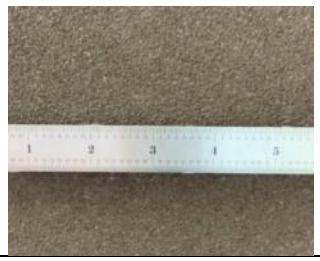
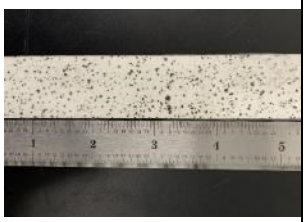
Location	Patina Rating	Thickness (inch)	Cl^- Conc. (ppm)	Field Condition	Tape Test
A1-G3F2 TF Bot. Int.	6	Measured R1 0.994 R2 0.995 R3 0.996 R_Avg 0.995 Design	-		
A1-G3F2 Web Int.	7	Measured R1 0.324 R2 0.325 R3 0.326 R_Avg 0.325 Design	1		
A1-G3F2 BF Top Int.	4	Measured R1 0.990 R2 0.991 R3 0.990 R_Avg 0.990 Design	-		
A1-G3F2 BF Bot. Int.	7	Measured R1 0.990 R2 0.991 R3 0.990 R_Avg 0.990 Design	-		
A1-G4F2 TF Bot. Ext.	6	Measured R1 1.032 R2 1.026 R3 1.027 R_Avg1.028 Design	-		

Table A-106. Field Inspection Results for AUS-WS-01.

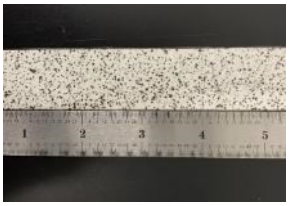
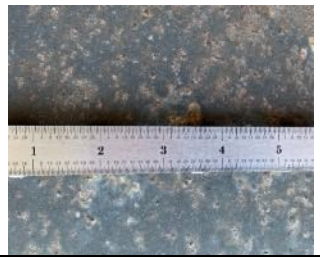
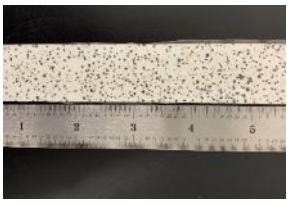
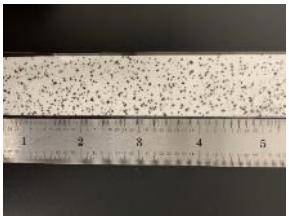
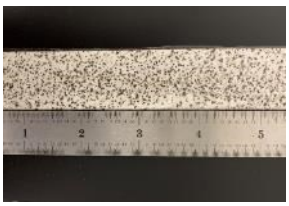
Location	Patina Rating	Thickness (inch)	Cl^- Conc. (ppm)	Field Condition	Tape Test
A1-G4F2 Web Ext.	7	Measured R1 0.320 R2 0.320 R3 0.319 R_Avg 0.320 Design	1		
A1-G4F2 BF Top Ext.	4	Measured R1 1.014 R2 1.014 R3 1.015 R_Avg 1.014 Design	-		
A1-G4F2 BF Bot. Ext.	5	Measured R1 1.014 R2 1.014 R3 1.015 R_Avg 1.014 Design	-		
B3-G1F1 TF Bot. Ext.	6	Measured R1 1.977 R2 1.972 R3 1.974 R_Avg 1.974 Design	-		
B3-G1F1 Web Ext.	7	Measured R1 0.329 R2 0.331 R3 0.332 R_Avg 0.331 Design	-		

Table A-107. Field Inspection Results for AUS-WS-01.

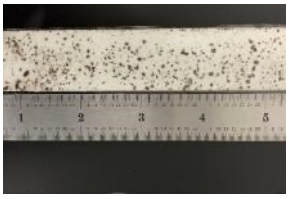
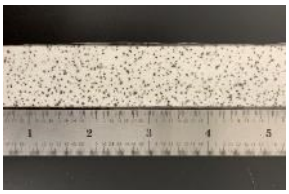
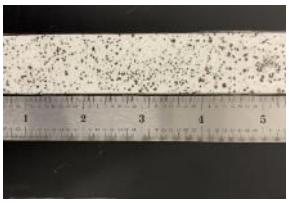
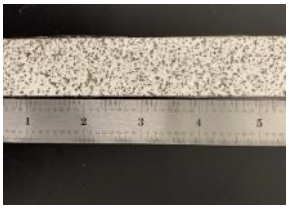
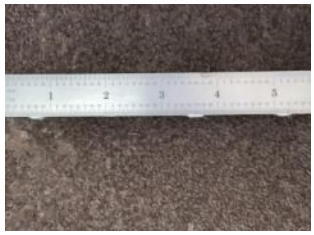
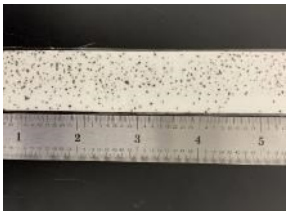
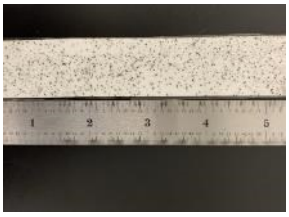
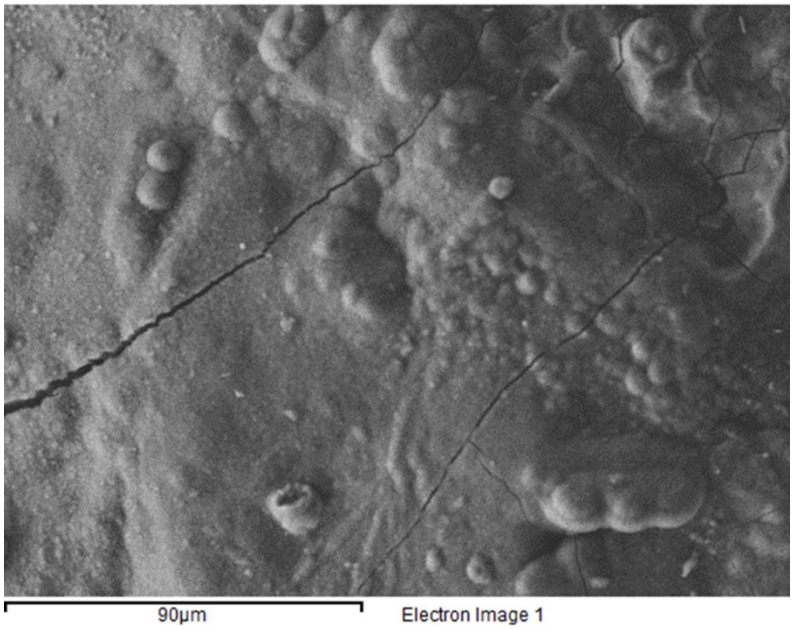
Location	Patina Rating	Thickness (inch)	Cl^- Conc. (ppm)	Field Condition	Tape Test
B3-G1F1 BF Top Ext.	4	Measured R1 1.985 R2 1.982 R3 1.982 R_Avg 1.982 Design	-		
B3-G1F1 BF Bot. Ext.	7	Measured R1 1.985 R2 1.982 R3 1.982 R_Avg 1.982 Design	-		
B3-G2F2 TF Bot. Int.	5	Measured R1 1.989 R2 1.990 R3 1.994 R_Avg 1.991 Design	-		
B3-G2F2 Web Int.	7	Measured R1 0.320 R2 0.319 R3 0.319 R_Avg 0.319 Design			
B3-G2F2 BF Top Int.	4	Measured R1 1.987 R2 1.986 R3 1.984 R_Avg 1.986 Design	-		

Table A-108. Field Inspection Results for AUS-WS-01.

Location	Patina Rating	Thickness (inch)	Cl^- Conc. (ppm)	Field Condition	Tape Test
B3-G2F2 BF Bot. Int.	5	Measured R1 1.987 R2 1.986 R3 1.984 R_Avg 1.986 Design	-		
B3-G4F2 TF Bot. Ext.	5	Measured R1 1.994 R2 1.989 R3 1.993 R_Avg 1.991 Design	-		
B3-G4F2 Web Ext.	8	Measured R1 0.313 R2 0.315 R3 0.314 R_Avg 0.314 Design	2		
B3-G4F2 BF Top Ext.	4	Measured R1 1.983 R2 1.982 R3 1.982 R_Avg 1.982 Design	-		
B3-G4F2 BF Bot. Ext.	5	Measured R1 1.983 R2 1.982 R3 1.982 R_Avg 1.982 Design	-		

A.21.3.SEM/EDS Results: Exterior Web Girder

Element	Weight %	Atomic %
O K	50.05	76.61
Na K	0.33	0.35
Al K	0.73	0.66
Si K	0.48	0.42
S K	1.27	0.97
Cl K	1.18	0.81
Ca K	0.17	0.10
Mn K	0.38	0.17
Fe K	45.15	19.80
Ni K	0.26	0.11
Totals	100.00	



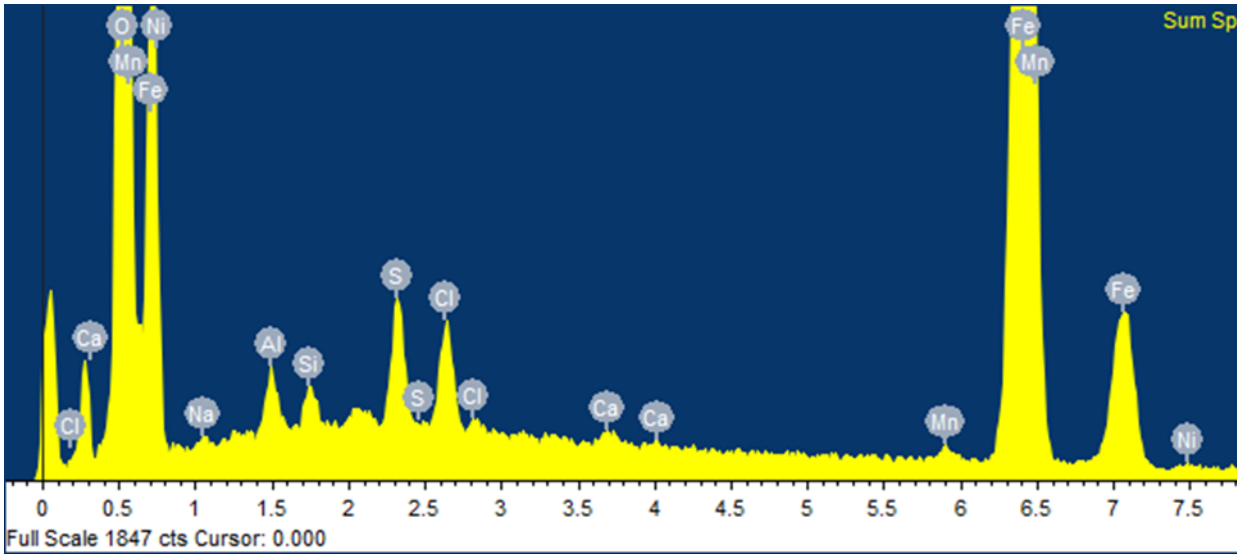
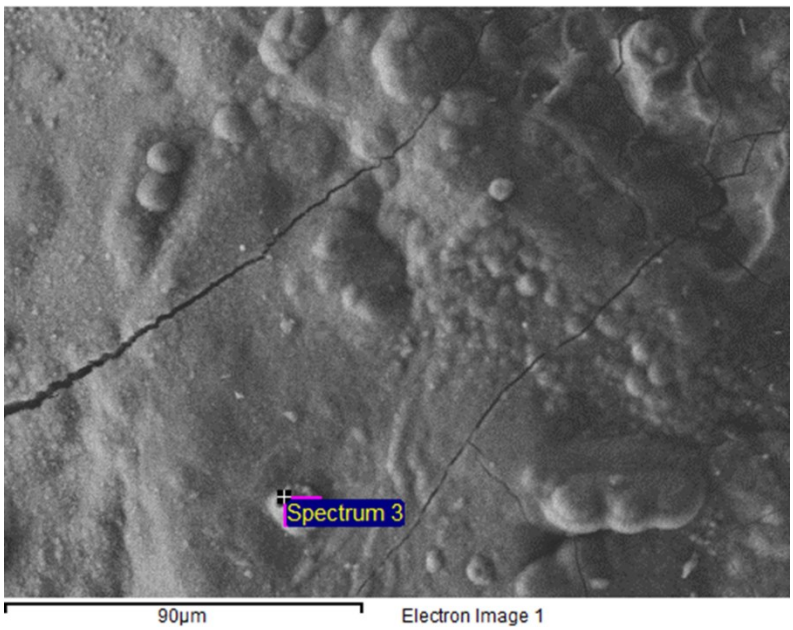


Figure A.281. SEM Image and EDS Spectrum of the Rust Collected from Exterior Web of the Girder.

Element	Weight %	Atomic %
O K	53.24	77.84
Mg K	0.35	0.34
Al K	1.13	0.98
Si K	2.95	2.46
S K	1.09	0.80
Cl K	1.07	0.71
Ca K	0.36	0.21
Mn K	0.26	0.11
Fe K	39.54	16.56
Totals	100.00	



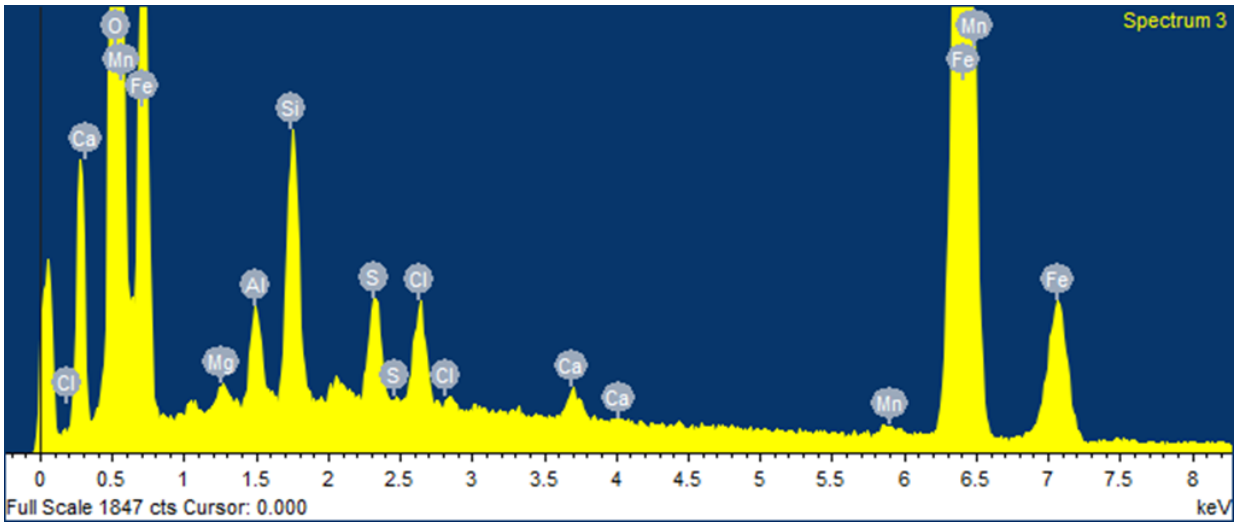
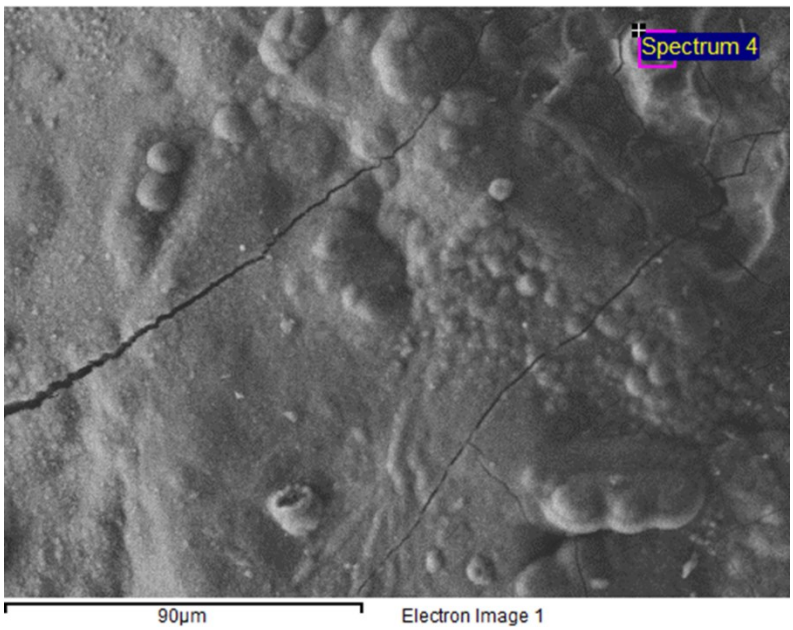


Figure A.282. SEM Image and EDS Spectrum of the Rust Collected from Exterior Web of the Girder.

Element	Weight %	Atomic %
O K	54.33	79.39
Al K	0.93	0.81
Si K	0.88	0.73
S K	1.47	1.07
Cl K	0.79	0.52
Ca K	0.38	0.22
Mn K	0.25	0.11
Fe K	40.97	17.15
Totals	100.00	



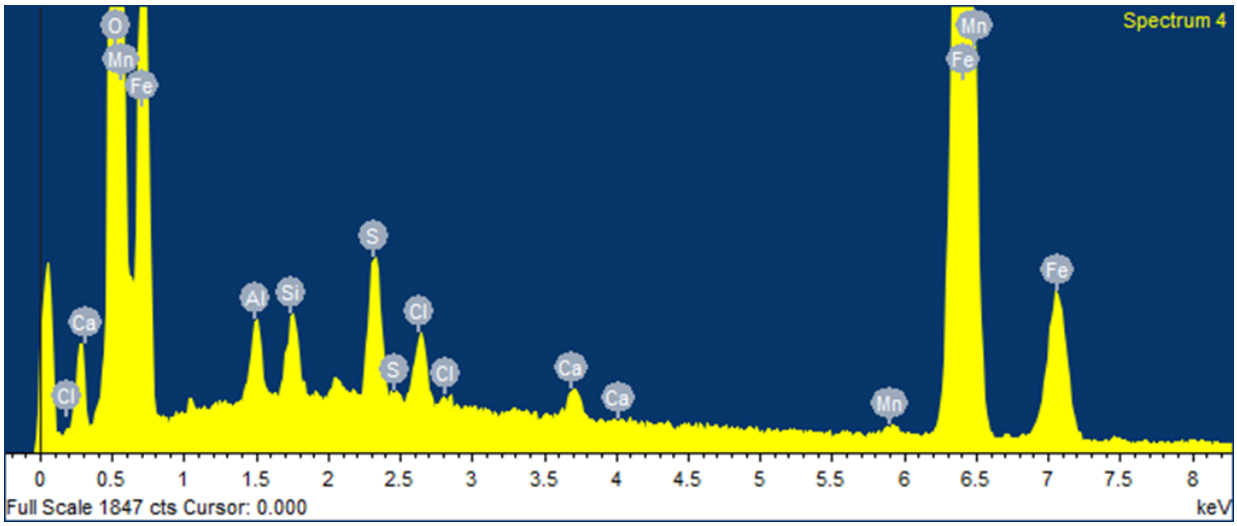
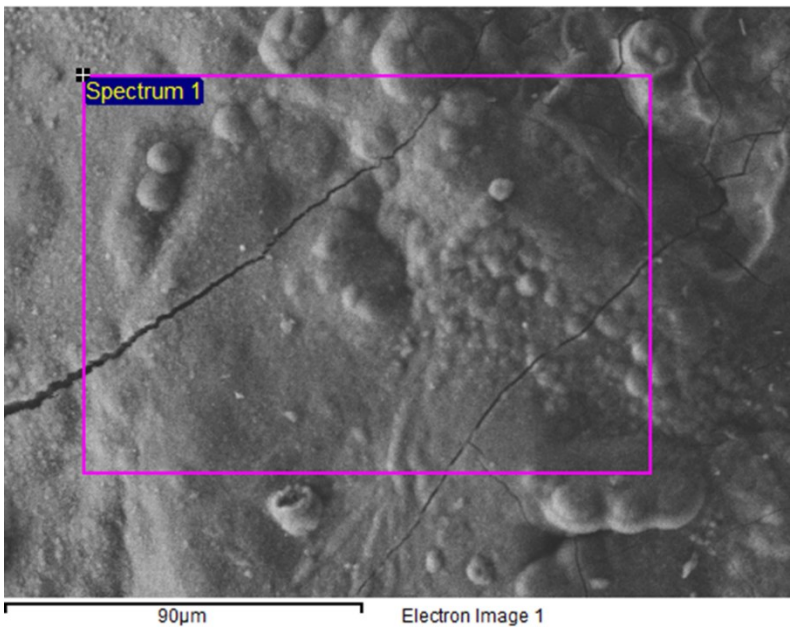


Figure A.283. SEM Image and EDS Spectrum of the Rust Collected from Exterior Web of the Girder.

Element	Weight %	Atomic %
O K	52.94	78.72
Al K	0.81	0.71
Si K	0.35	0.30
S K	1.35	1.00
Cl K	1.13	0.76
Ca K	0.12	0.07
Mn K	0.43	0.18
Fe K	42.63	18.16
Ni K	0.24	0.10
Totals	100.00	



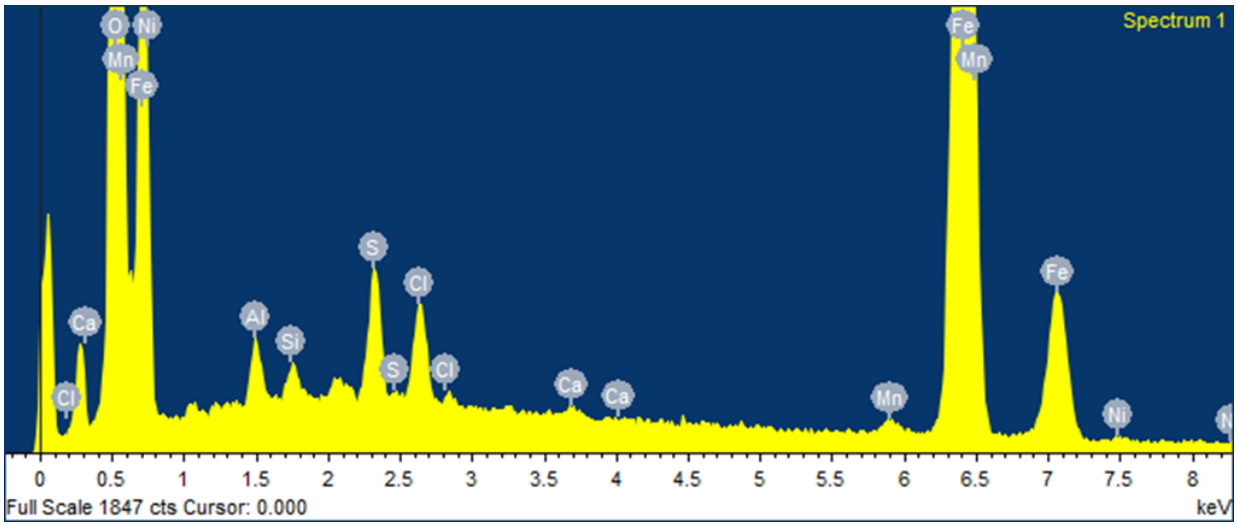


Figure A.284. SEM Image and EDS Spectrum of the Rust Collected from Exterior Web of the Girder.

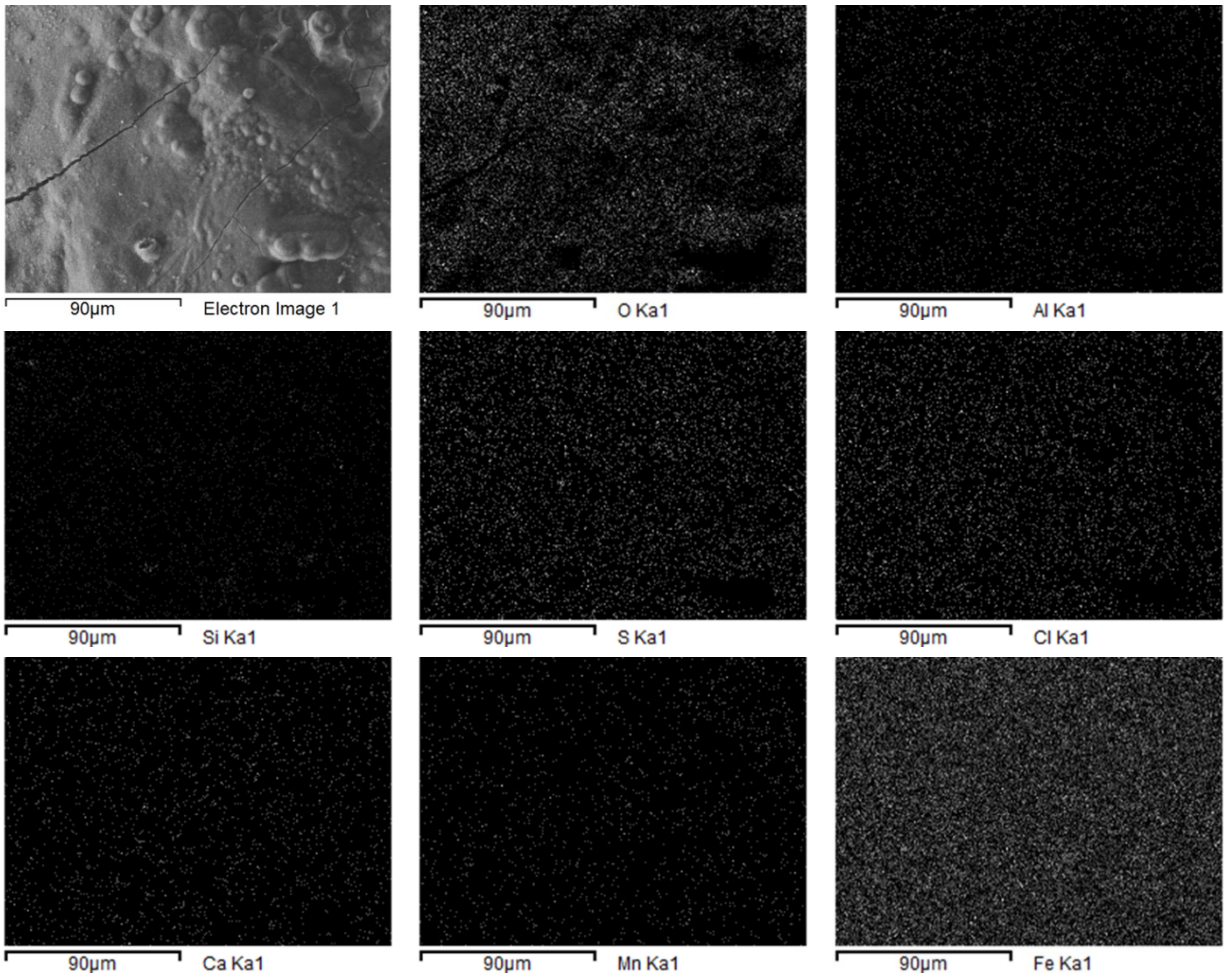
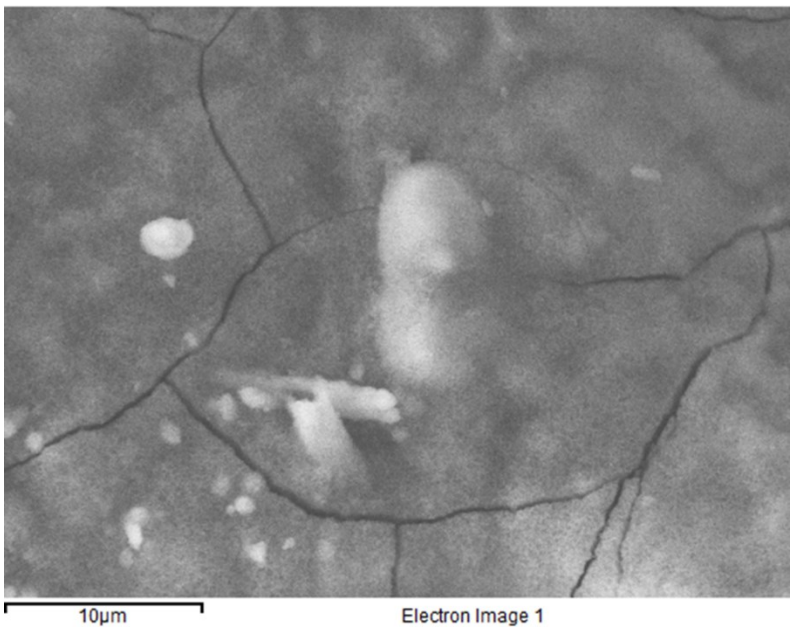


Figure A.285. EDS Elemental Mapping of Rust Collected from Exterior Web.

Element	Weight %	Atomic %
O K	50.36	77.11
Al K	0.61	0.56
Si K	0.40	0.35
S K	1.34	1.02
Cl K	0.75	0.52
Ca K	0.14	0.09
Mn K	0.32	0.14
Fe K	46.09	20.22
Totals	100.00	



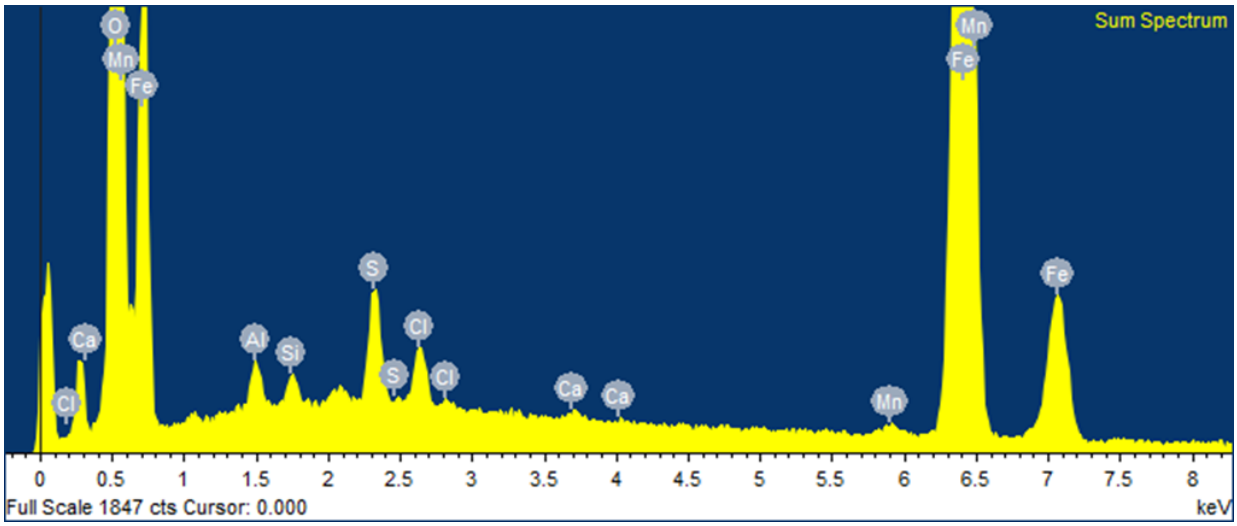
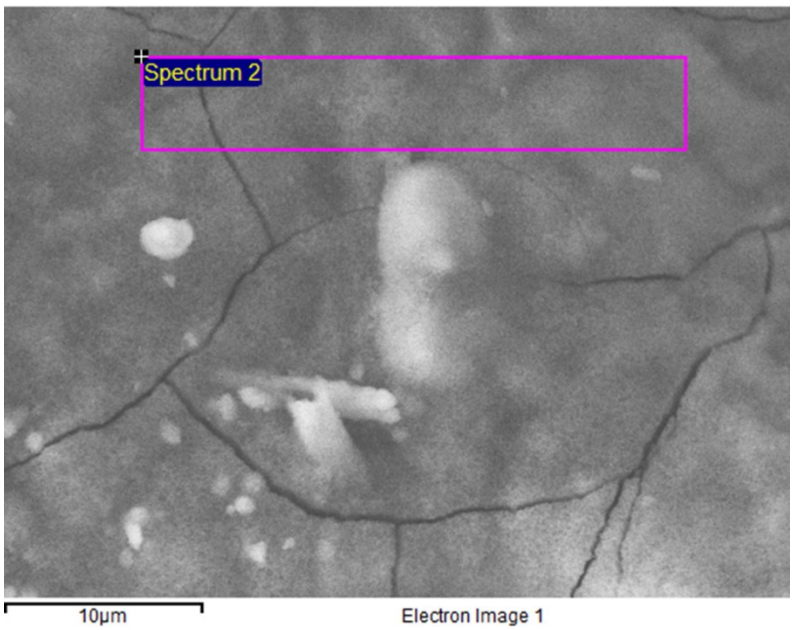


Figure A.286. SEM Image and EDS Spectrum of the Rust Collected from Exterior Web of the Girder.

Element	Weight %	Atomic %
O K	53.22	79.11
Al K	0.51	0.45
Si K	0.23	0.19
S K	1.42	1.06
Cl K	0.79	0.53
Mn K	0.44	0.19
Fe K	43.39	18.47
Totals	100.00	



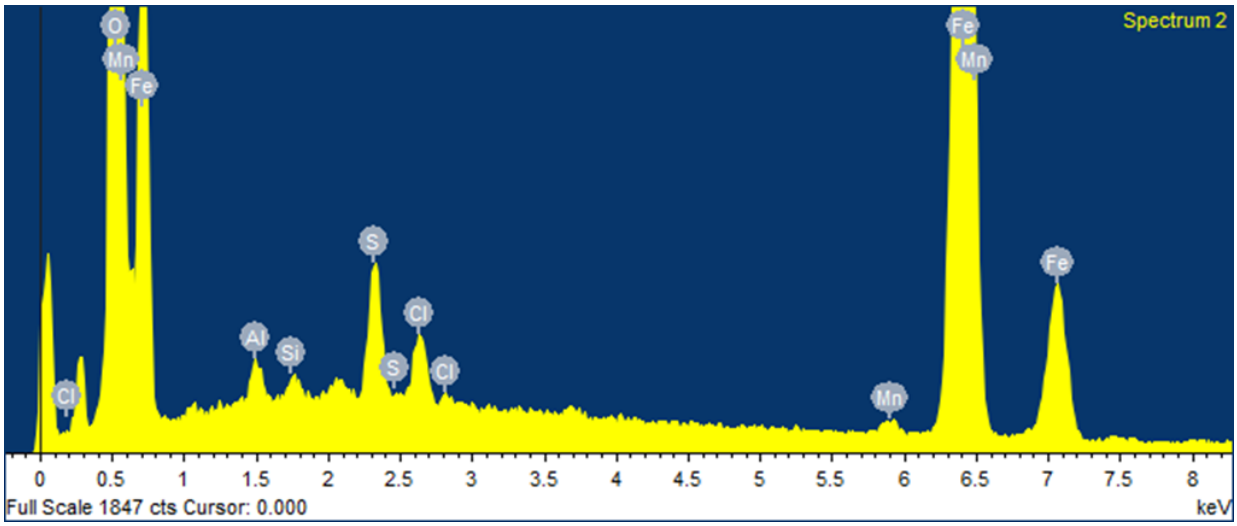
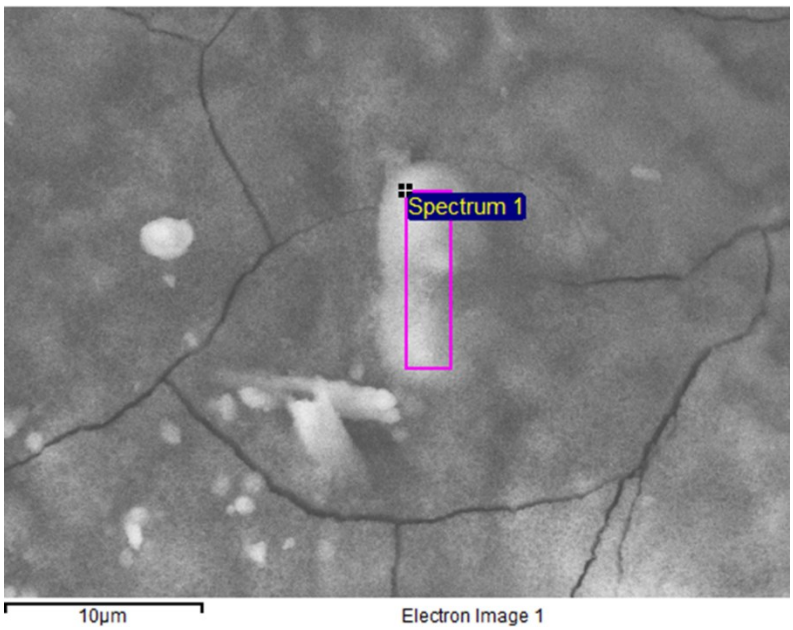


Figure A.287. SEM Image and EDS Spectrum of the Rust Collected from Exterior Web of the Girder.

Element	Weight %	Atomic %
O K	56.20	80.78
Al K	0.93	0.80
Si K	0.39	0.32
S K	1.41	1.01
Cl K	0.79	0.51
Mn K	0.27	0.11
Fe K	39.61	16.31
Ni K	0.40	0.16
Totals	100.00	



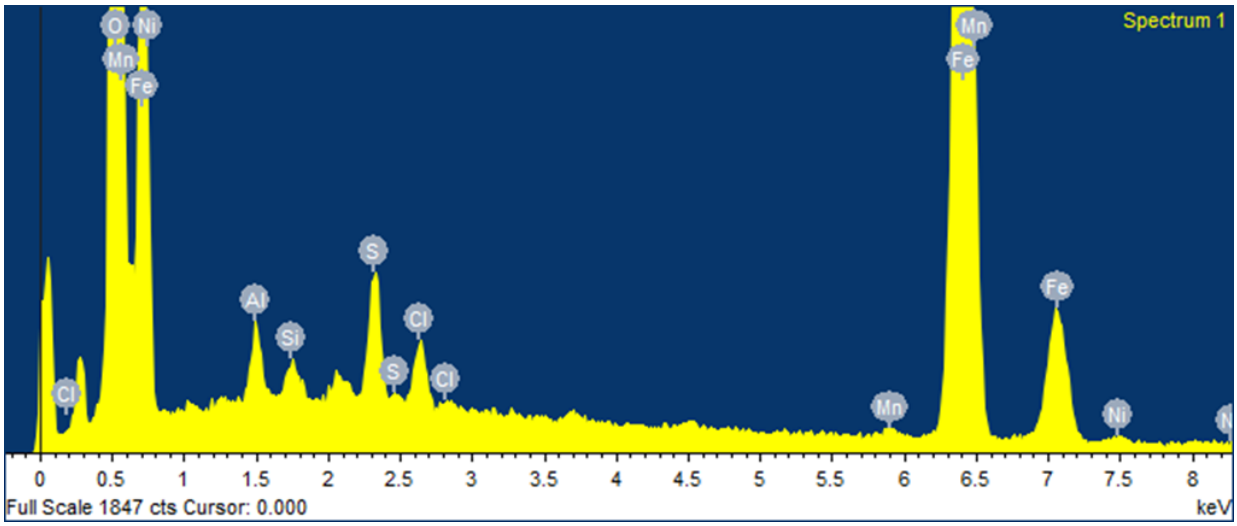


Figure A.288. SEM Image and EDS Spectrum of the Rust Collected from Exterior Web of the Girder.

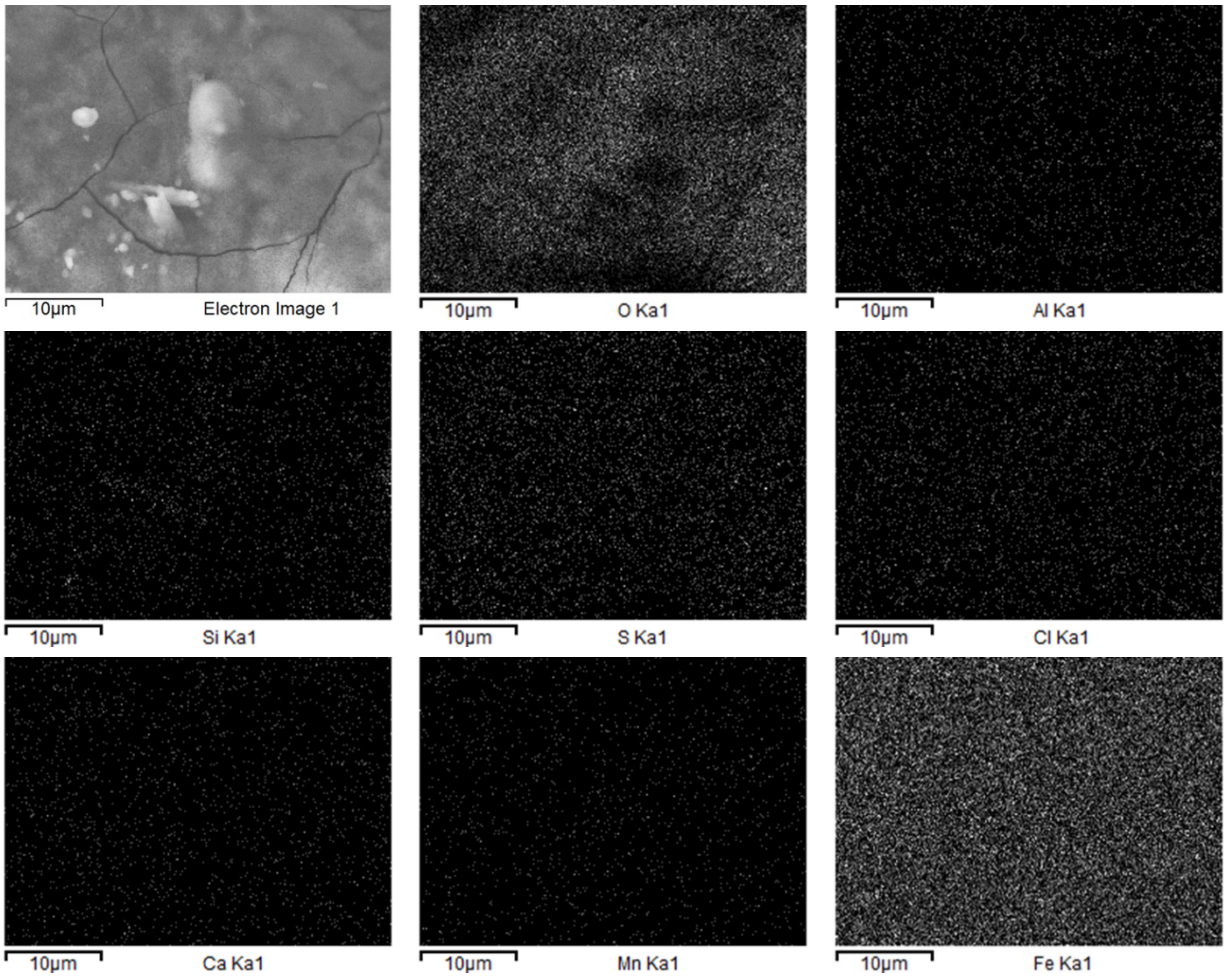
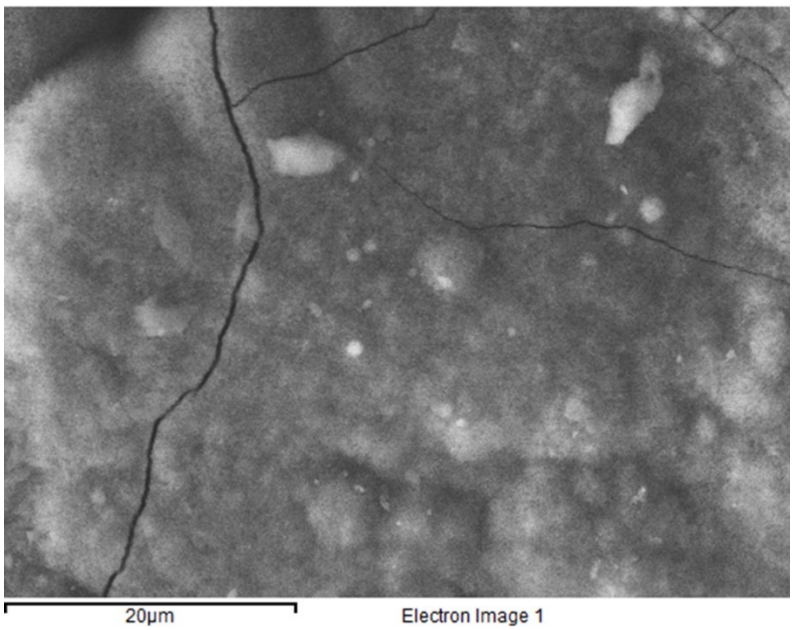


Figure A.289. EDS Elemental Mapping of Rust Collected from Exterior Web.

Element	Weight %	Atomic %
O K	41.93	70.53
Al K	1.00	1.00
Si K	0.41	0.39
S K	1.34	1.13
Cl K	0.88	0.67
Ca K	0.27	0.18
Mn K	0.49	0.24
Fe K	53.68	25.86
Totals	100.00	



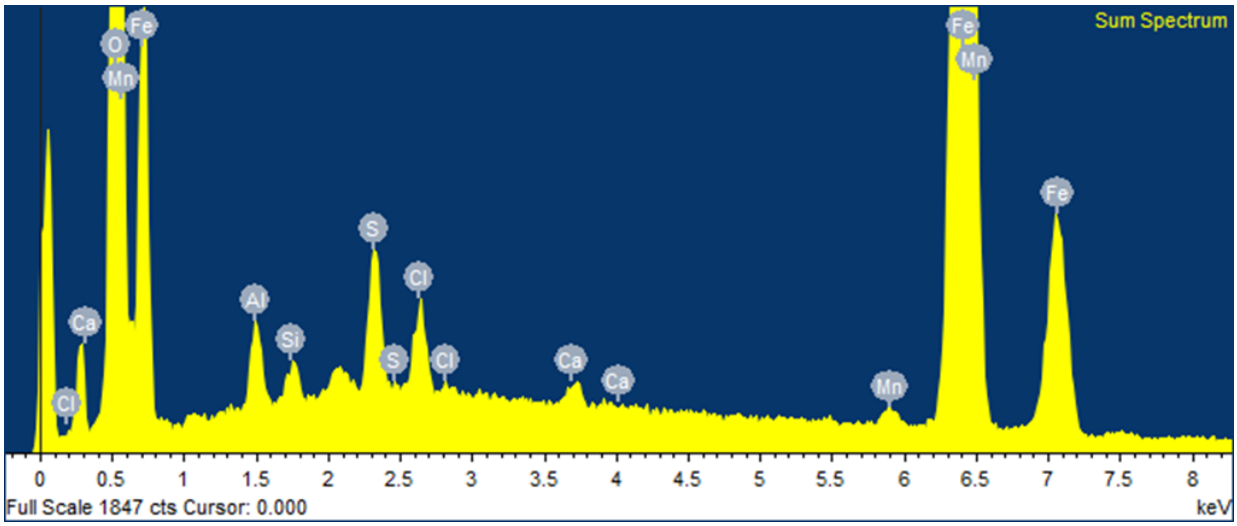


Figure A.290. SEM Image and EDS Spectrum of the Rust Collected from Exterior Web of the Girder.

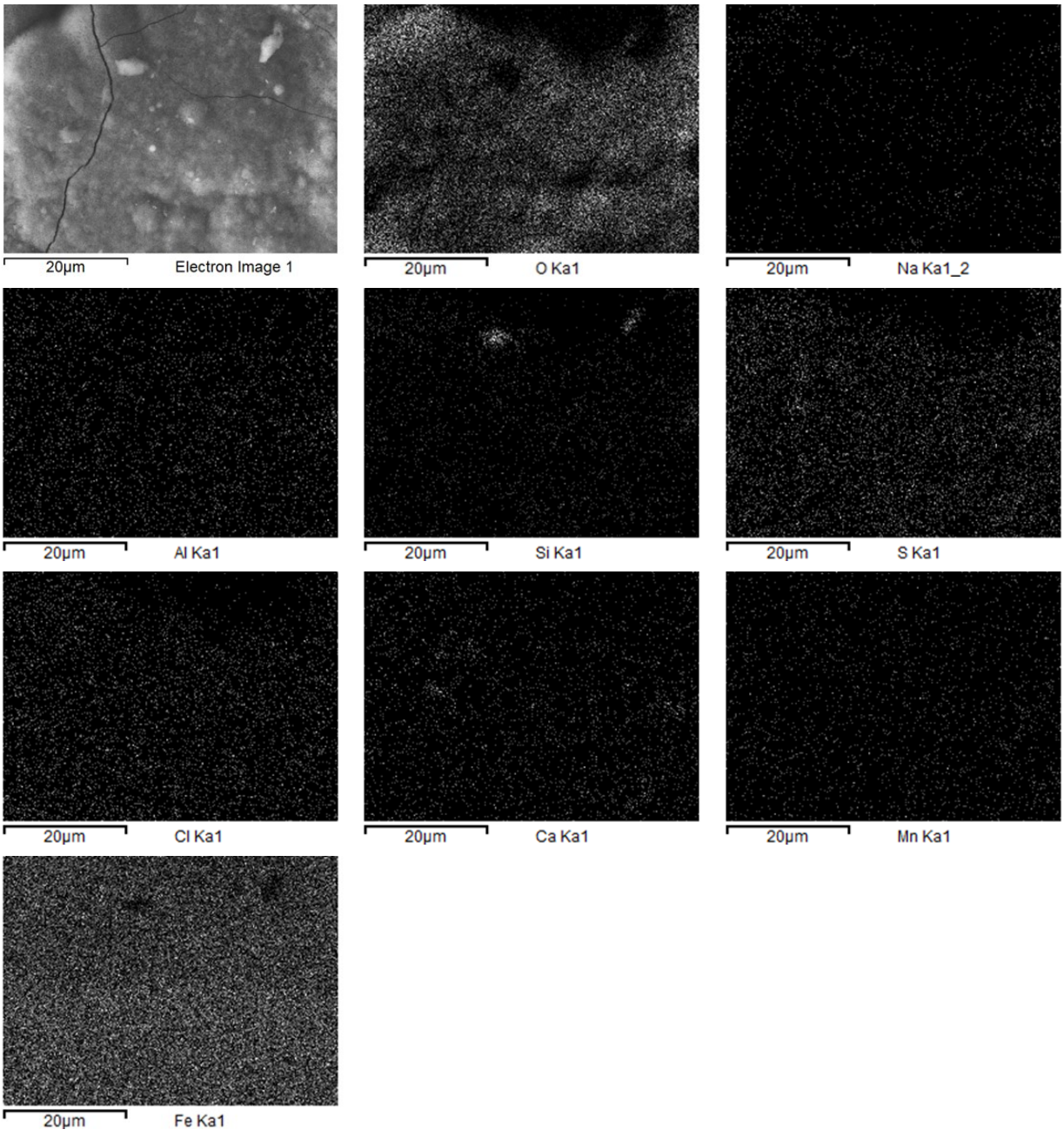
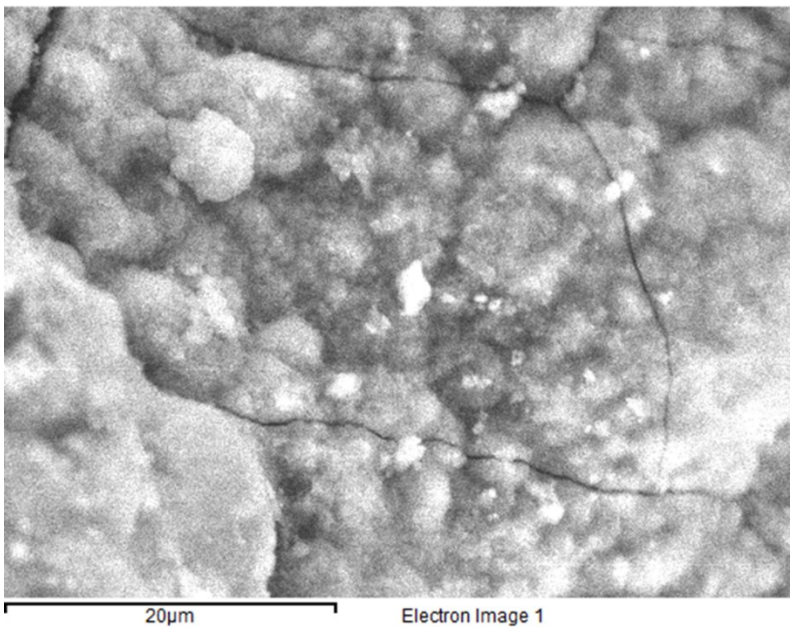


Figure A.291. EDS Elemental Mapping of Rust Collected from Exterior Web.

Element	Weight %	Atomic %
O K	46.97	73.60
Mg K	0.41	0.42
Al K	1.53	1.42
Si K	2.29	2.05
P K	0.26	0.21
S K	0.99	0.78
Cl K	0.30	0.21
K K	0.12	0.07
Ca K	0.45	0.28
Mn K	0.55	0.25
Fe K	46.12	20.70
Totals	100.00	



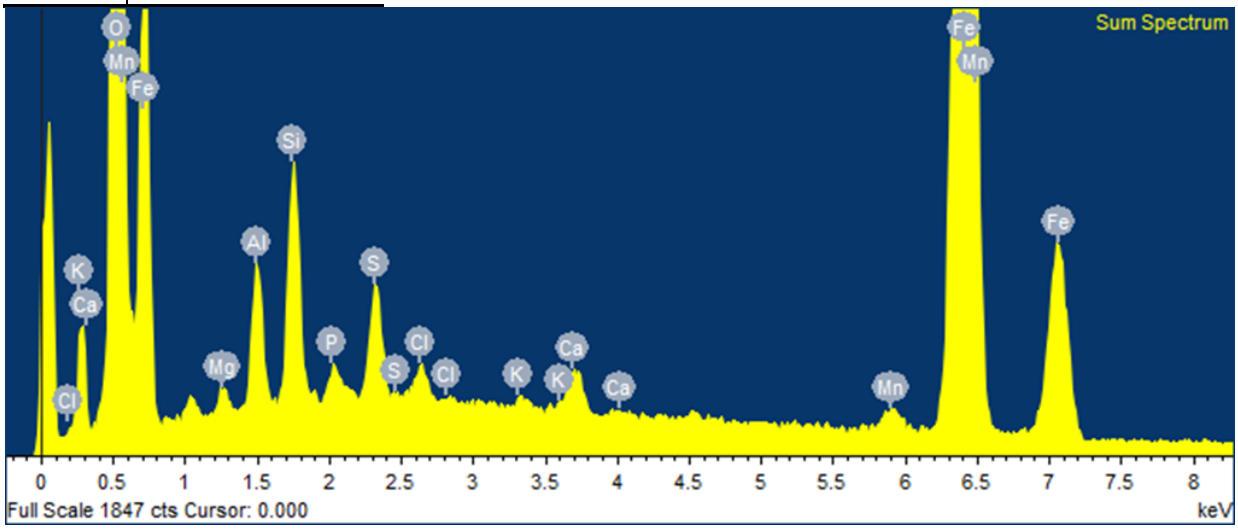


Figure A.292. SEM Image and EDS Spectrum of the Rust Collected from Exterior Web of the Girder.

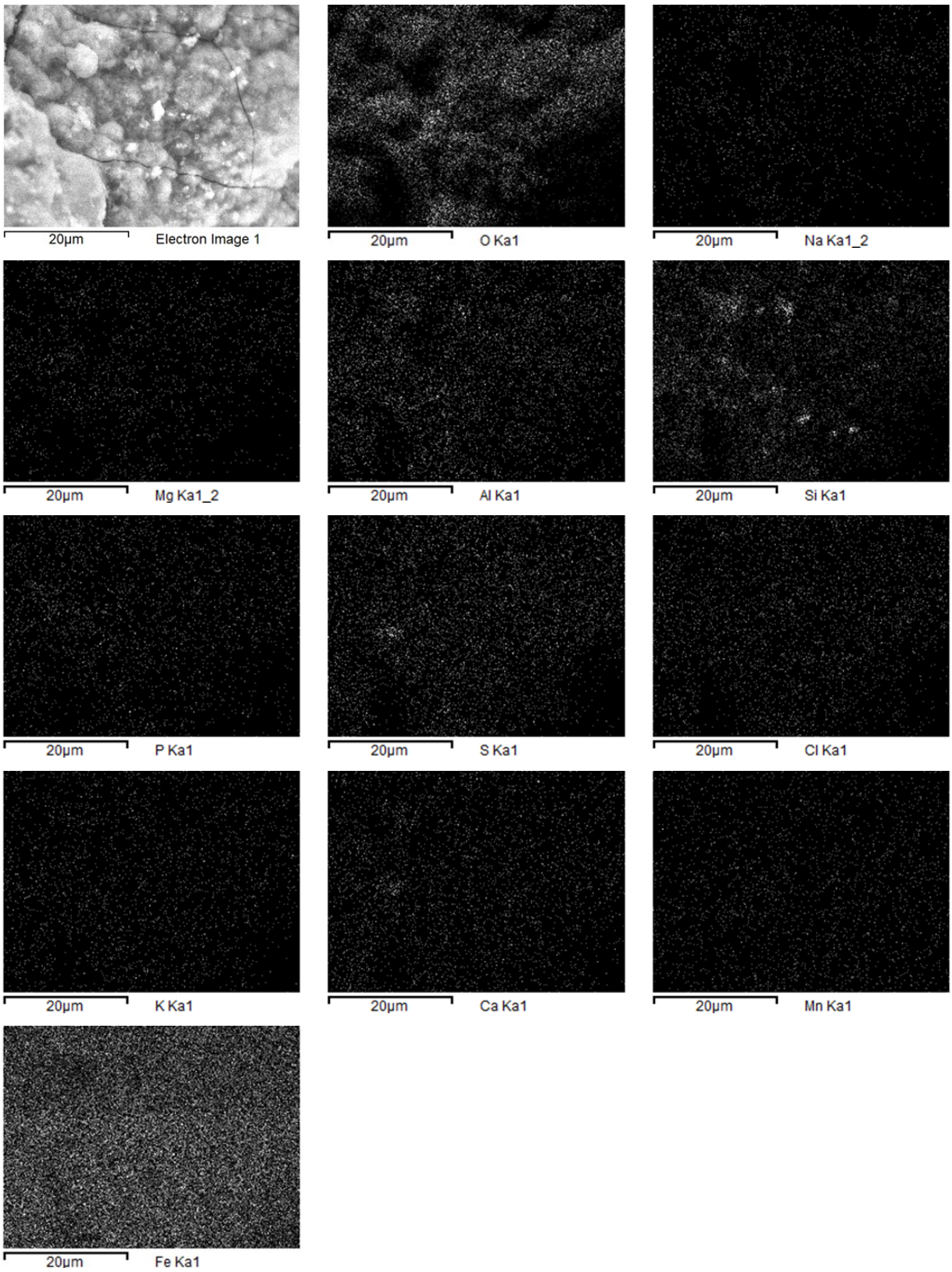
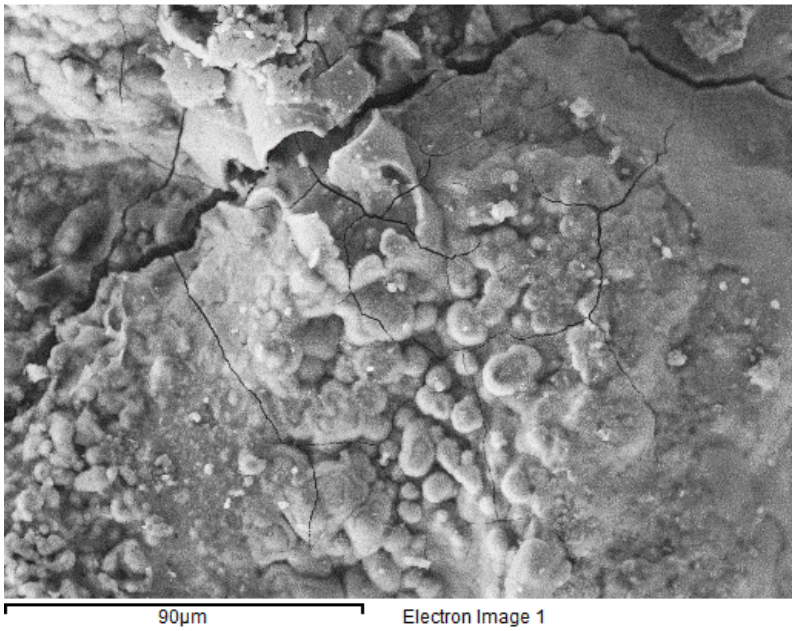


Figure A.293. EDS Elemental Mapping of Rust Collected from Exterior Web.

A.21.4.SEM/EDS Results: Interior Web Girder

Element	Weight %	Atomic %
O K	43.85	72.19
Al K	0.98	0.95
Si K	0.72	0.68
S K	1.09	0.90
Cl K	0.41	0.30
Ca K	0.10	0.06
Mn K	0.76	0.36
Fe K	51.67	24.37
Cu K	0.42	0.17
Totals	100.00	



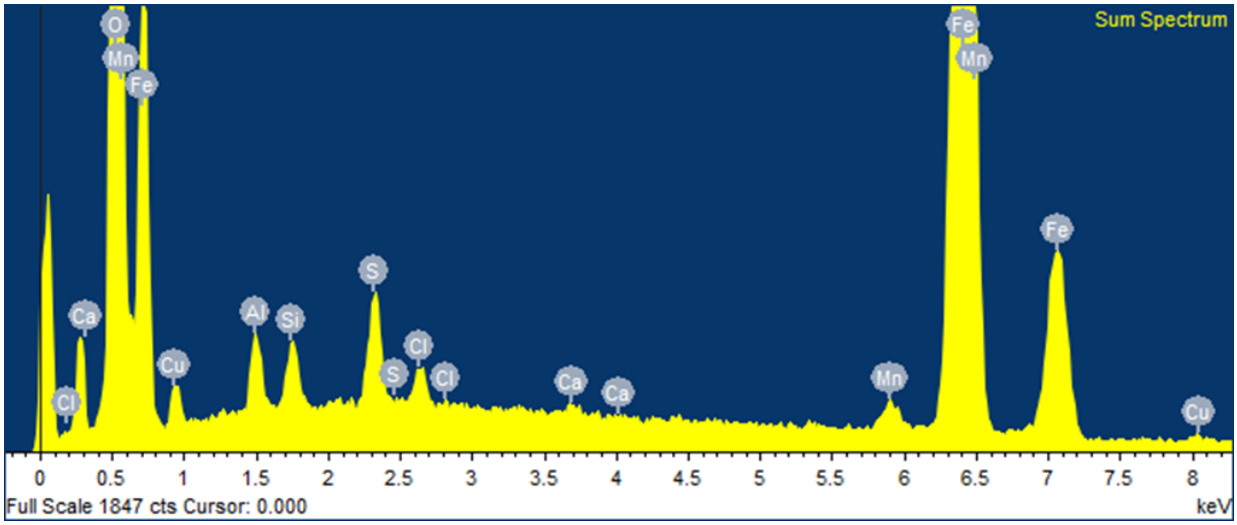
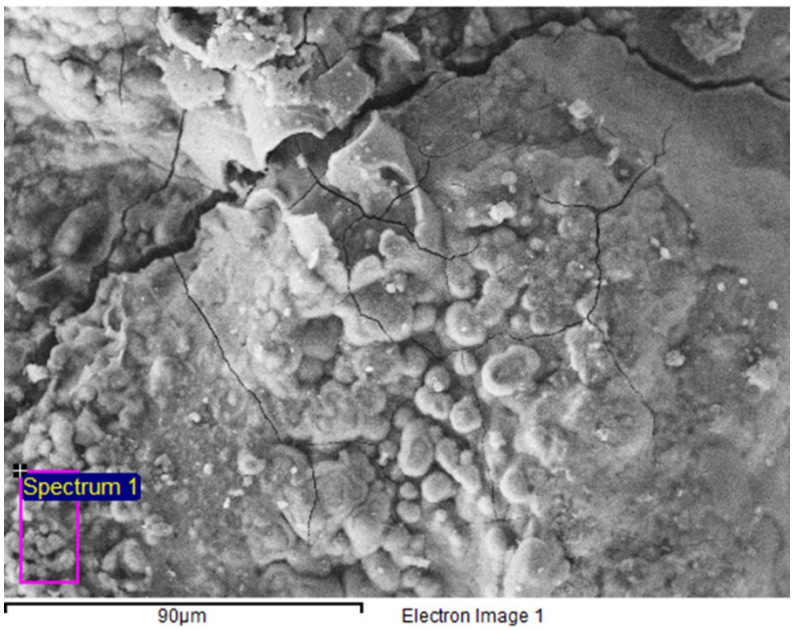


Figure A.294. SEM Image and EDS Spectrum of the Rust Collected from Interior Web of the Girder.

Element	Weight %	Atomic %
O K	48.99	75.62
Al K	1.34	1.23
Si K	1.93	1.69
S K	0.73	0.56
Cl K	0.15	0.10
K K	0.39	0.24
Mn K	1.06	0.48
Fe K	45.19	19.99
Cu K	0.23	0.09
Totals	100.00	



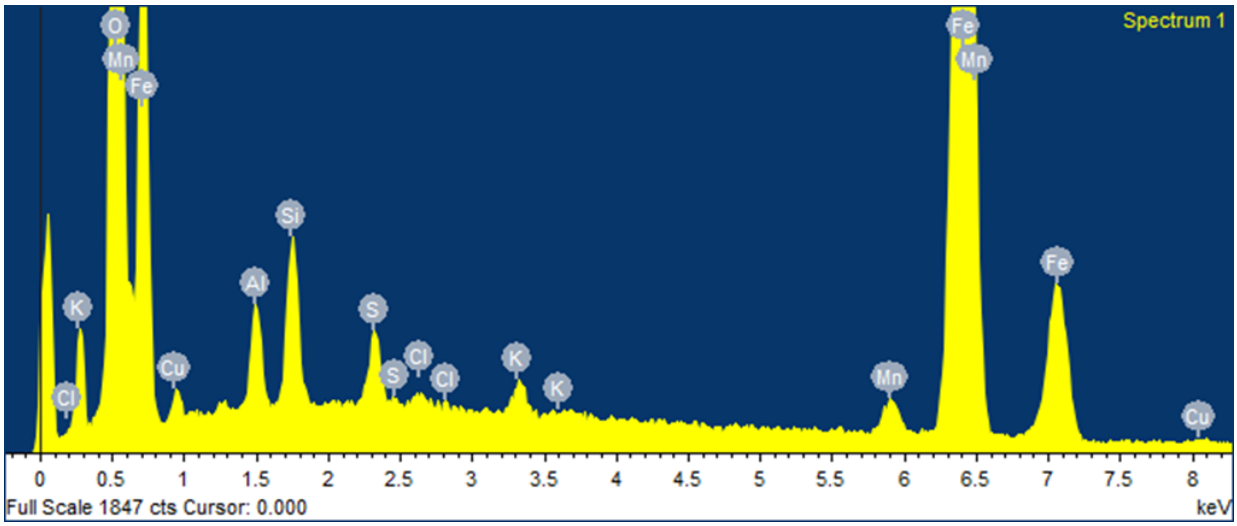
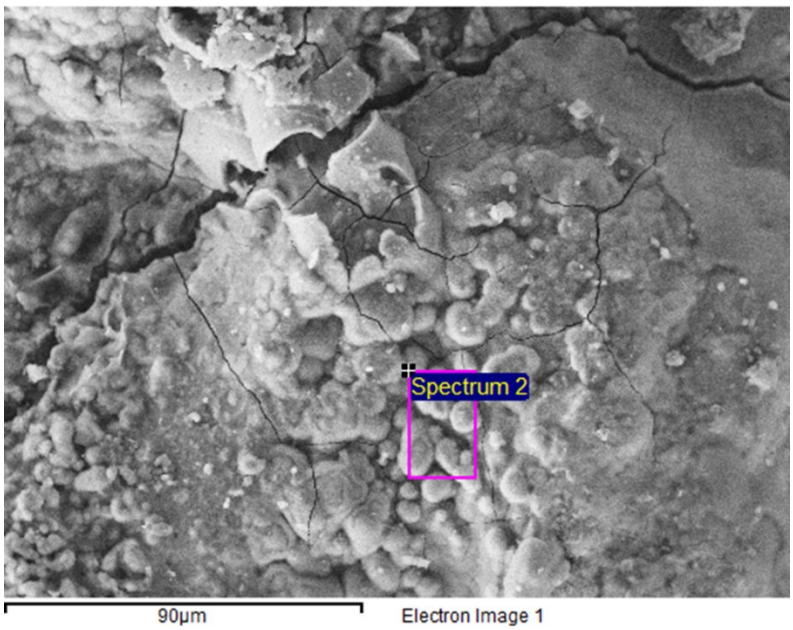


Figure A.295. SEM Image and EDS Spectrum of the Rust Collected from Interior Web of the Girder.

Element	Weight %	Atomic %
O K	45.61	73.68
Al K	0.93	0.89
Si K	0.15	0.14
S K	1.22	0.98
Cl K	0.46	0.34
Ca K	0.48	0.31
Mn K	0.85	0.40
Fe K	49.92	23.11
Cu K	0.37	0.15
Totals	100.00	



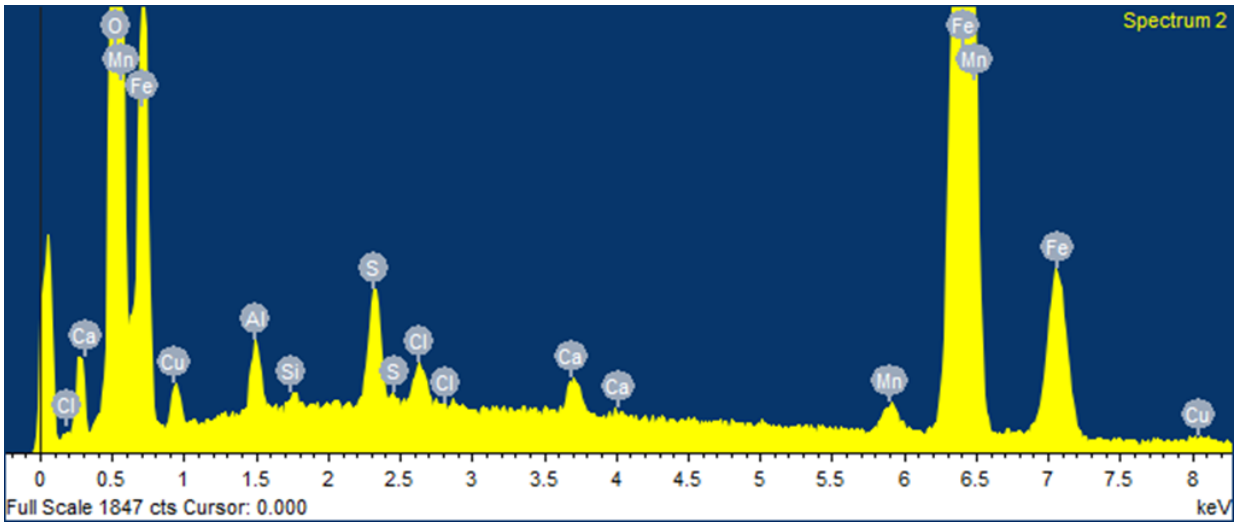
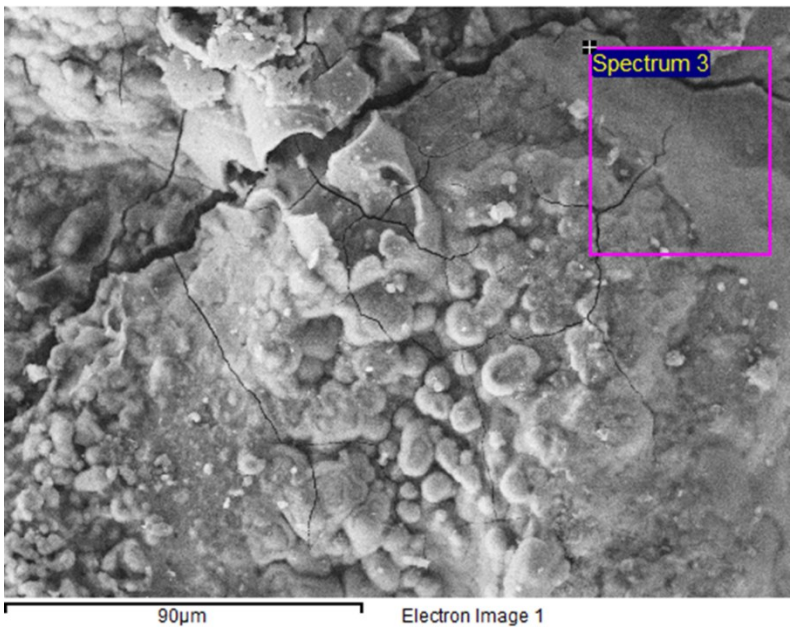


Figure A.296. SEM Image and EDS Spectrum of the Rust Collected from Interior Web of the Girder.

Element	Weight %	Atomic %
O K	35.46	64.97
Al K	1.09	1.18
Si K	0.12	0.13
S K	1.02	0.94
Cl K	0.30	0.25
Mn K	0.80	0.43
Fe K	60.97	32.00
Cu K	0.23	0.11
Totals	100.00	



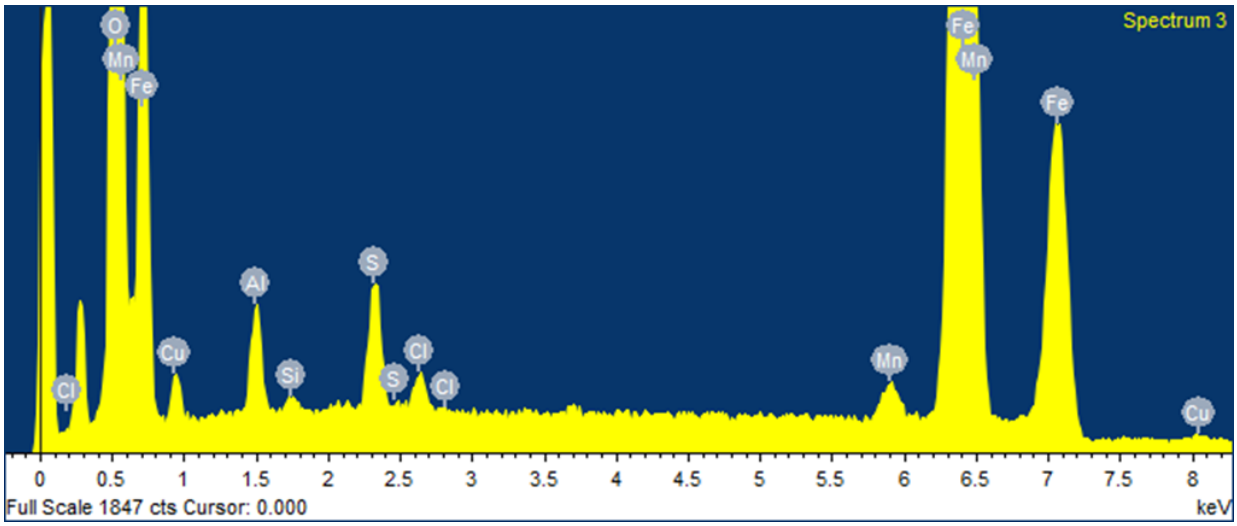


Figure A.297. SEM Image and EDS Spectrum of the Rust Collected from Interior Web of the Girder.

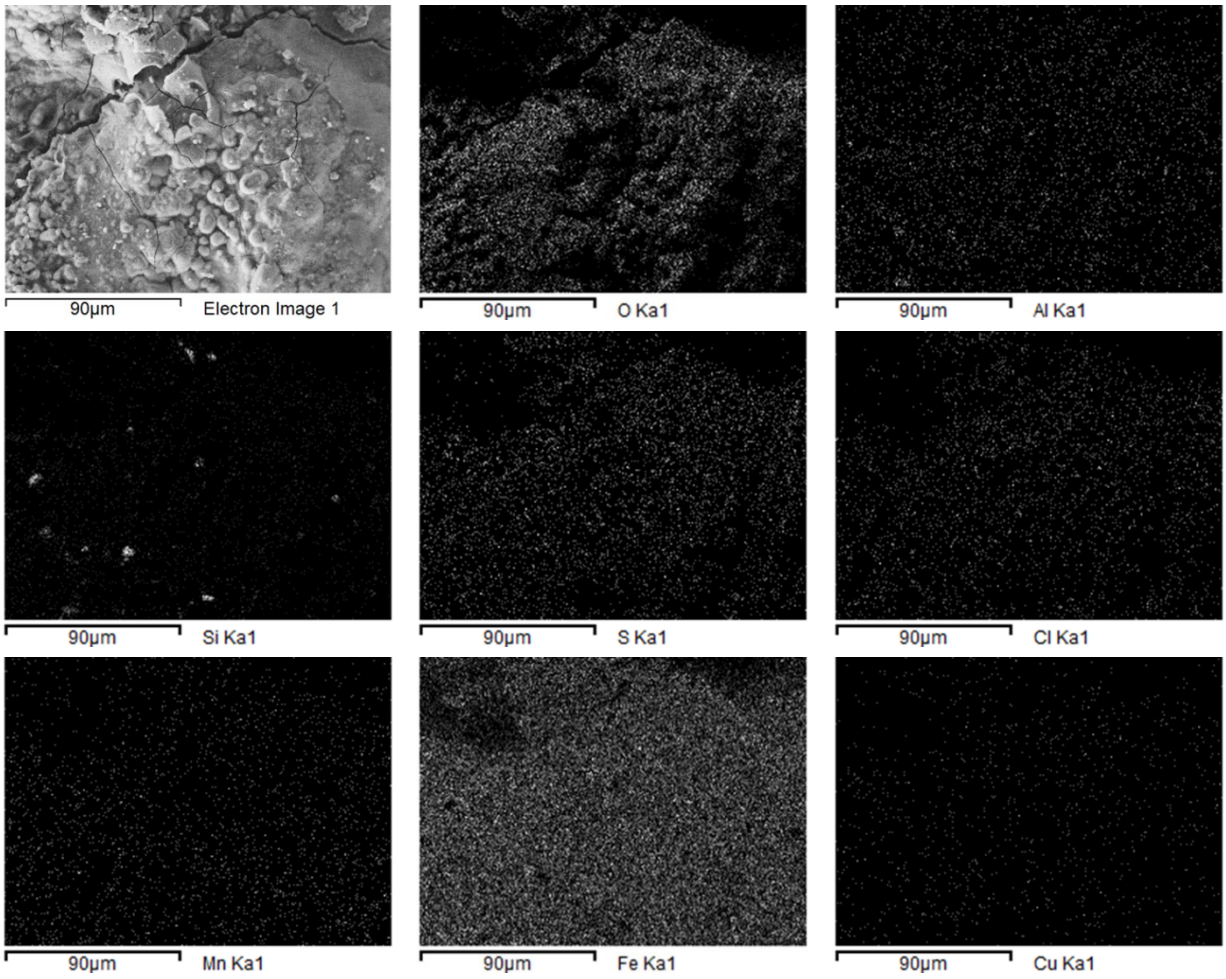
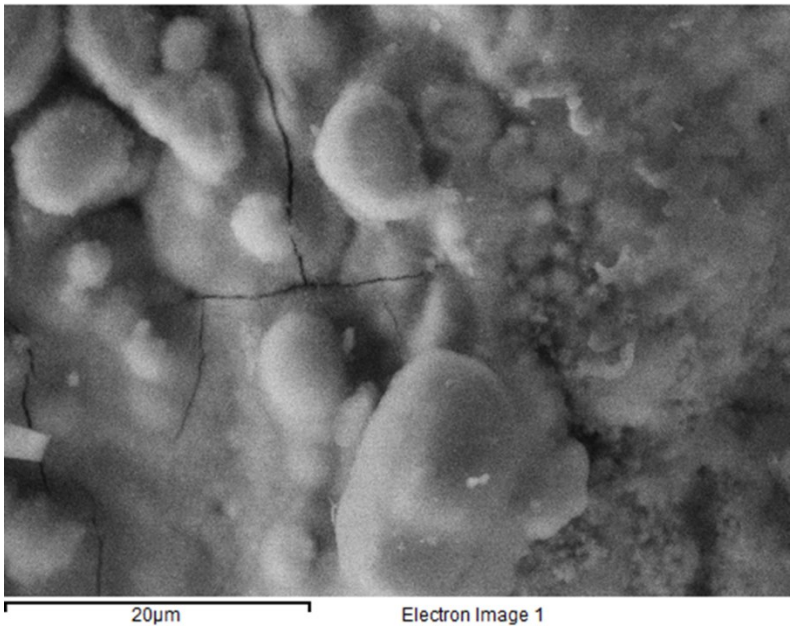


Figure A.298. EDS Elemental Mapping of Rust Collected from Interior Web.

A.21.5.SEM/EDS Results: Interior Web Girder

Element	Weight %	Atomic %
O K	38.04	67.26
Al K	1.39	1.45
Si K	0.57	0.58
S K	0.77	0.68
Cl K	0.20	0.16
Mn K	0.87	0.45
Fe K	57.67	29.21
Cu K	0.48	0.22
Totals	100.00	



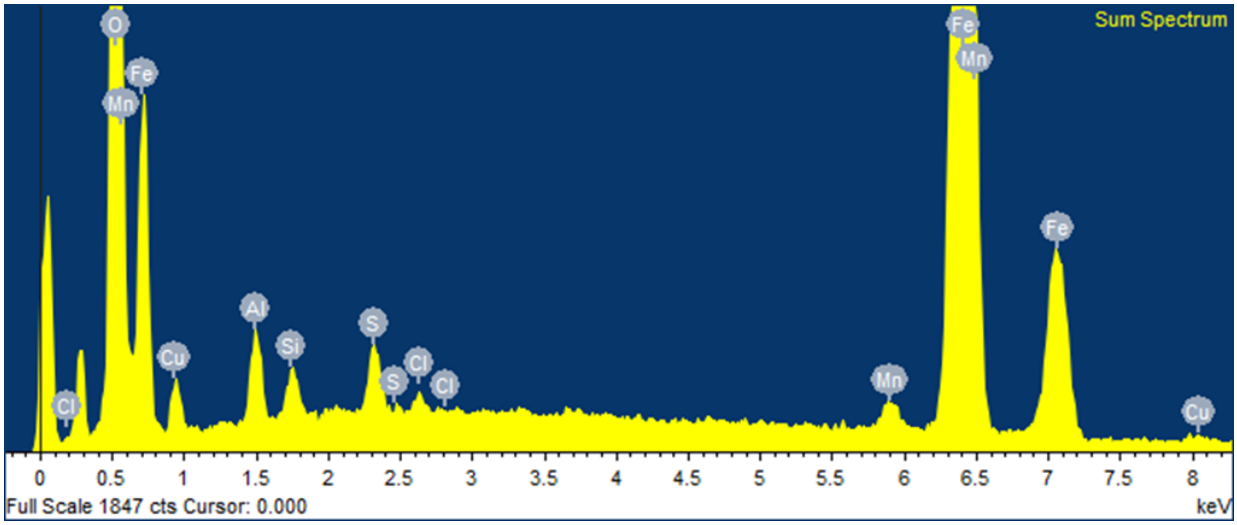


Figure A.299. SEM Image and EDS Spectrum of the Rust Collected from Interior Web of the Girder.

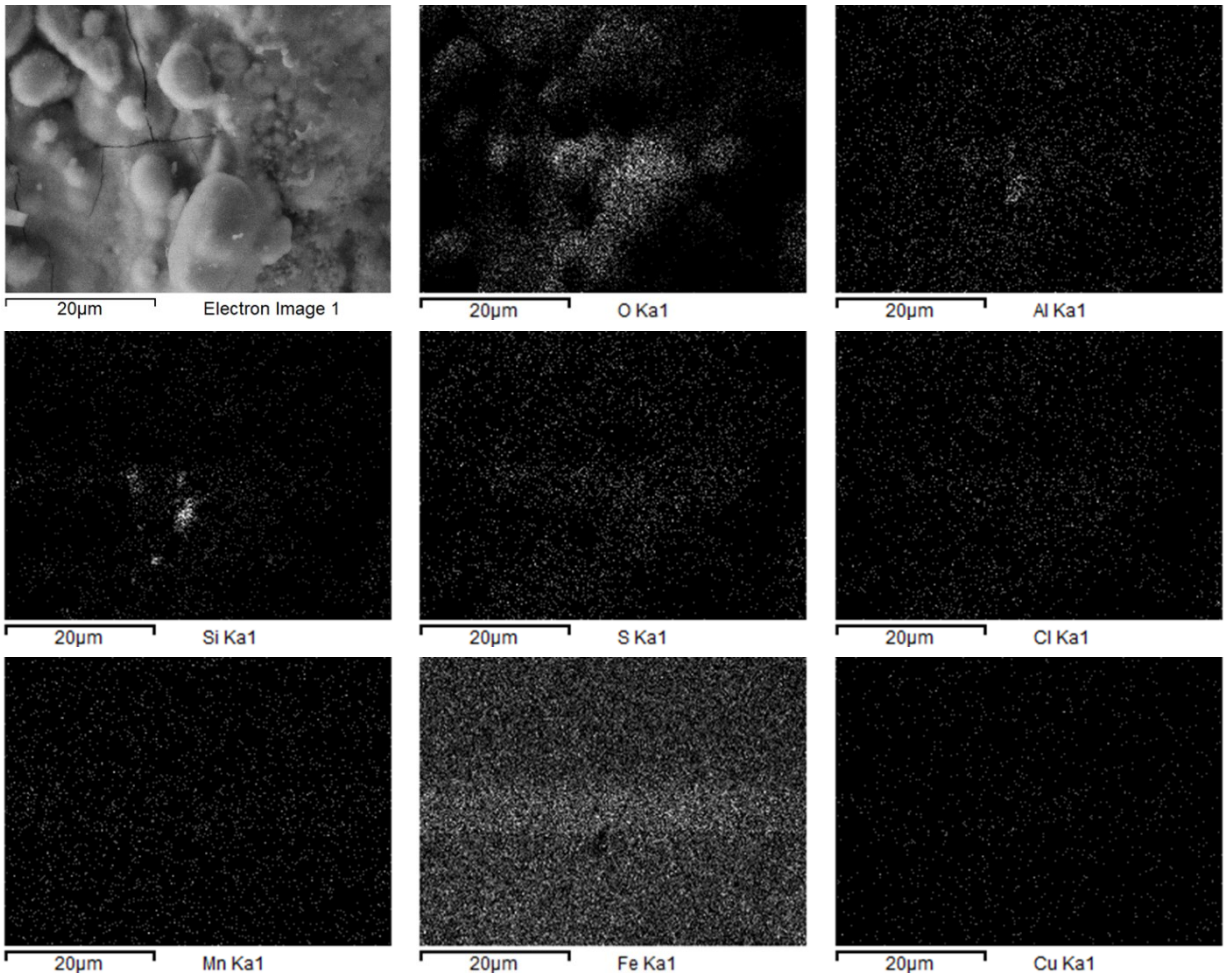
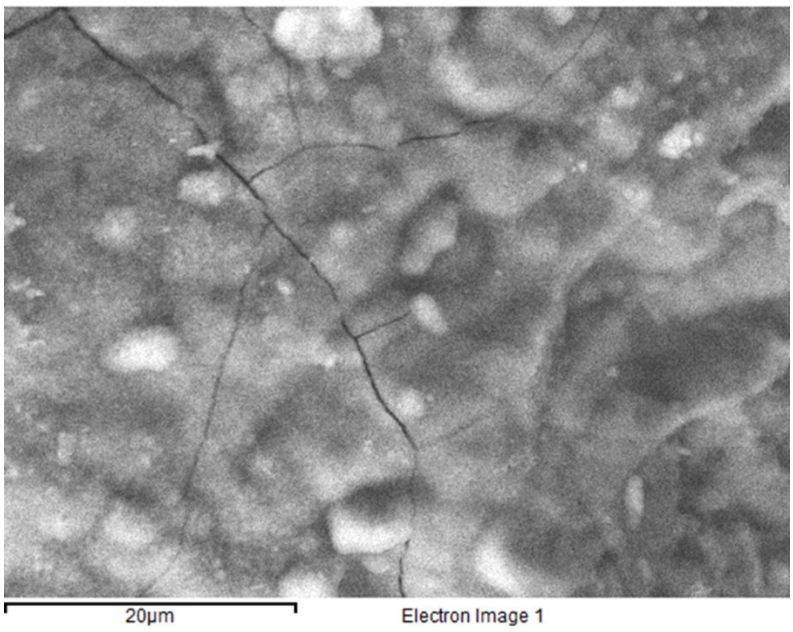


Figure A.300. EDS Elemental Mapping of Rust Collected from Interior Web.

Element	Weight %	Atomic %
O K	26.98	55.41
Al K	1.04	1.27
Si K	0.57	0.66
S K	0.95	0.98
Cl K	0.60	0.55
Ca K	0.22	0.18
Mn K	1.33	0.80
Fe K	67.86	39.92
Cu K	0.45	0.23
Totals	100.00	



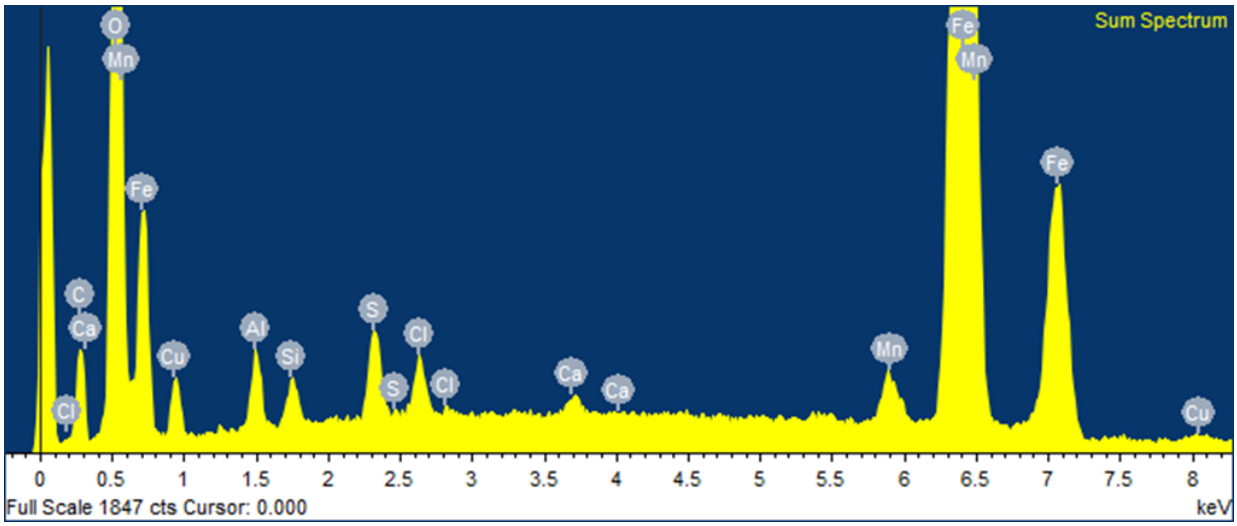


Figure A.301. SEM Image and EDS Spectrum of the Rust Collected from Interior Web of the Girder.

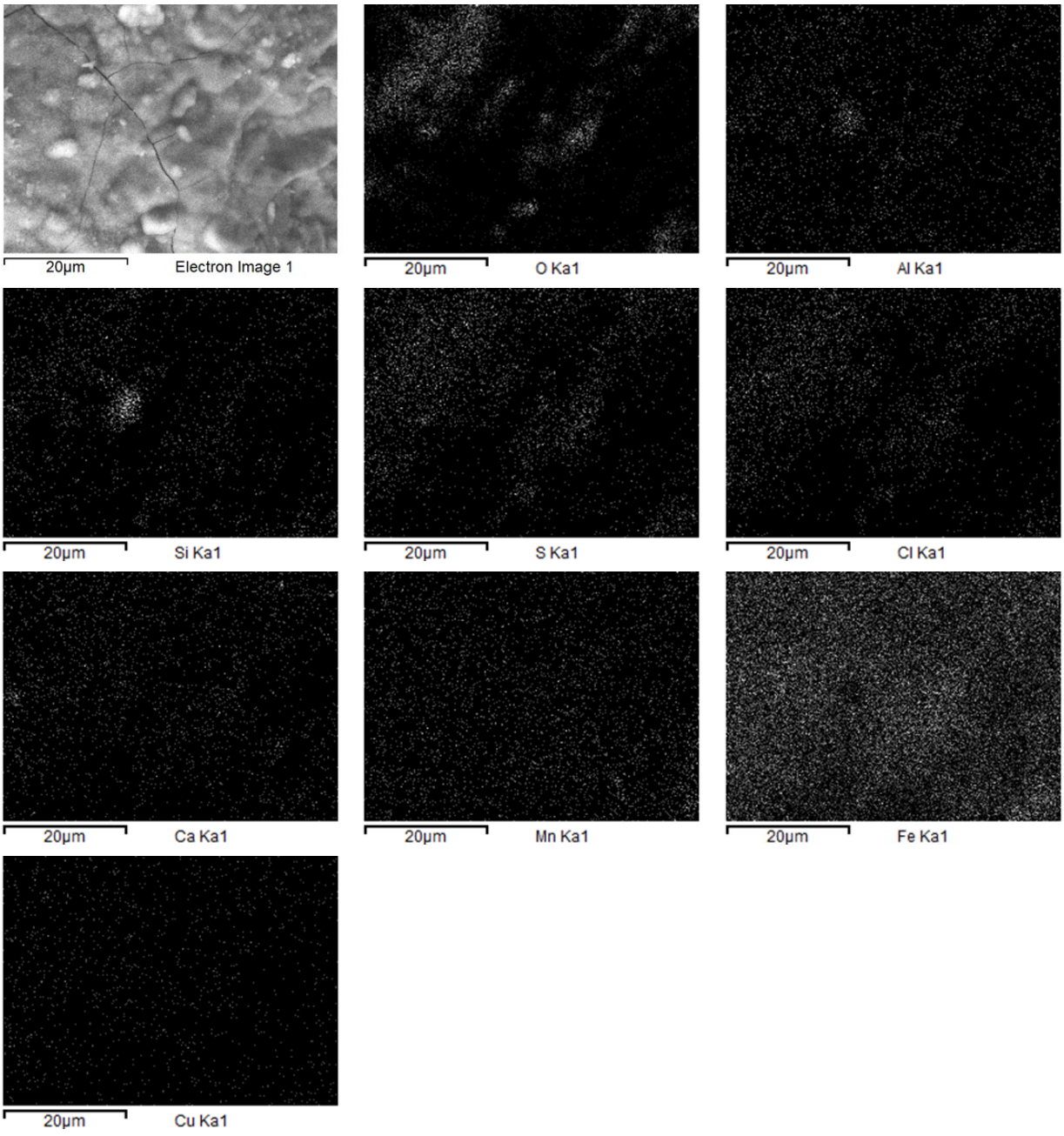


Figure A.302. EDS Elemental Mapping of Rust Collected from Interior Web.

A.21.6.XPS Result: Exterior Girder

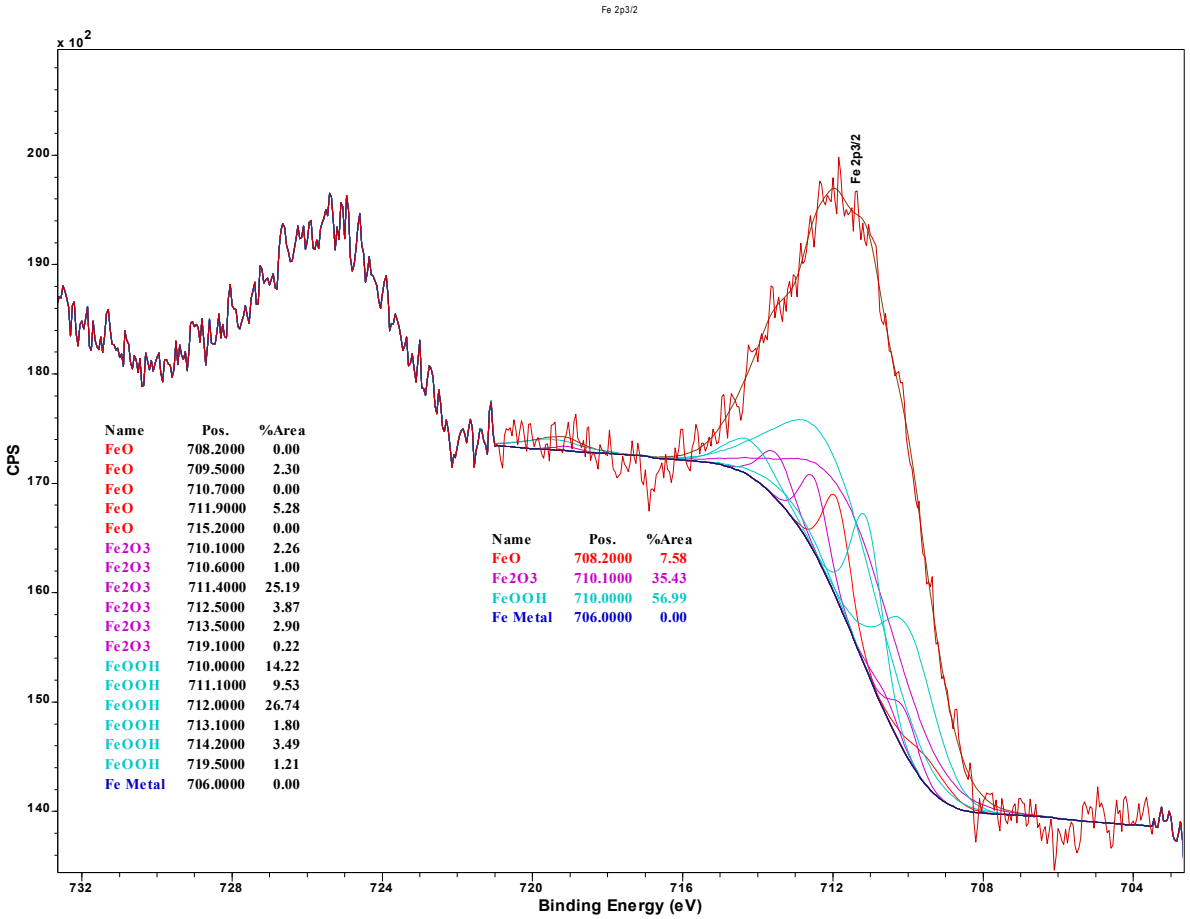


Figure A.303. XPS Spectrum of the Rust Collected from Exterior Web of the Girder.

A.21.7.XPS Result: Interior Girder

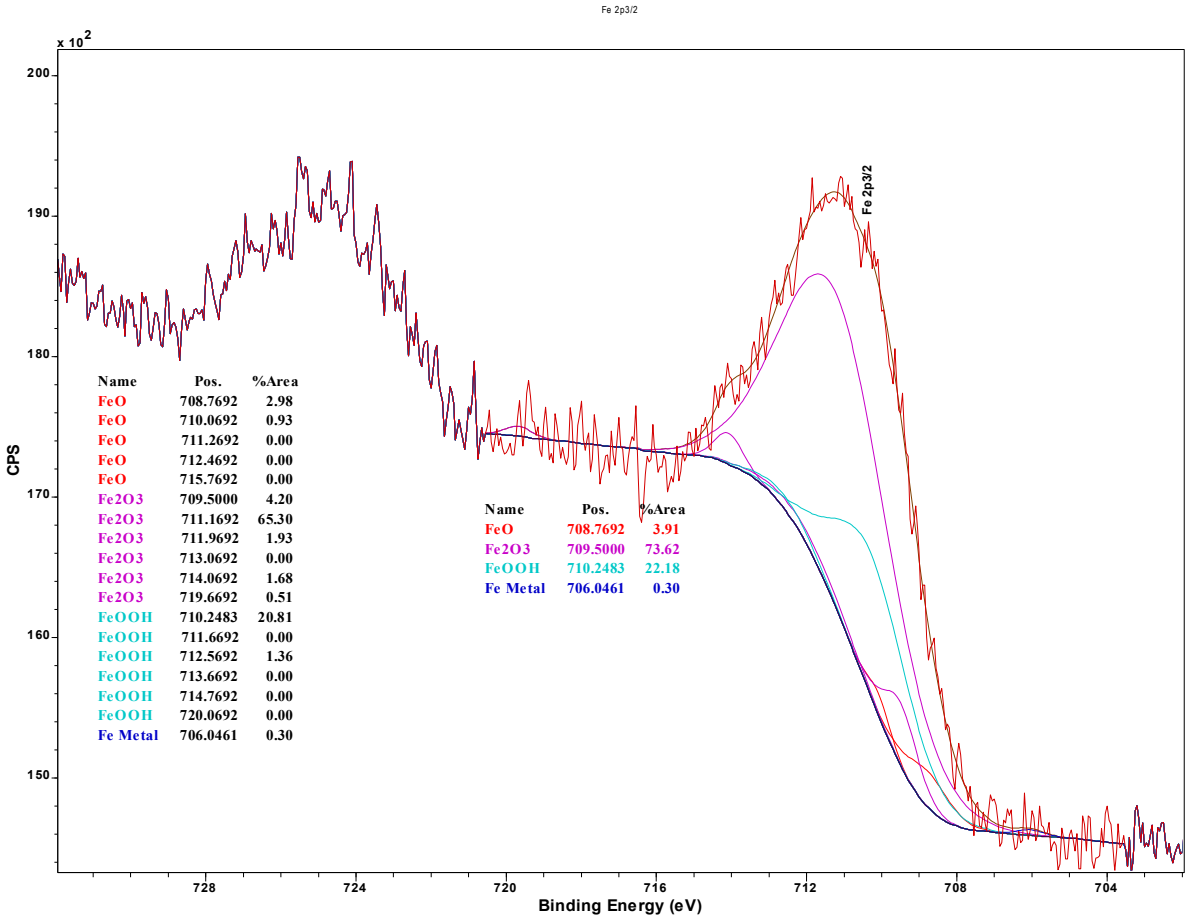


Figure A.304. XPS Spectrum of the Rust Collected from Interior Web of the Girder.

A.21.8.XRD Result: Exterior and Interior Girder

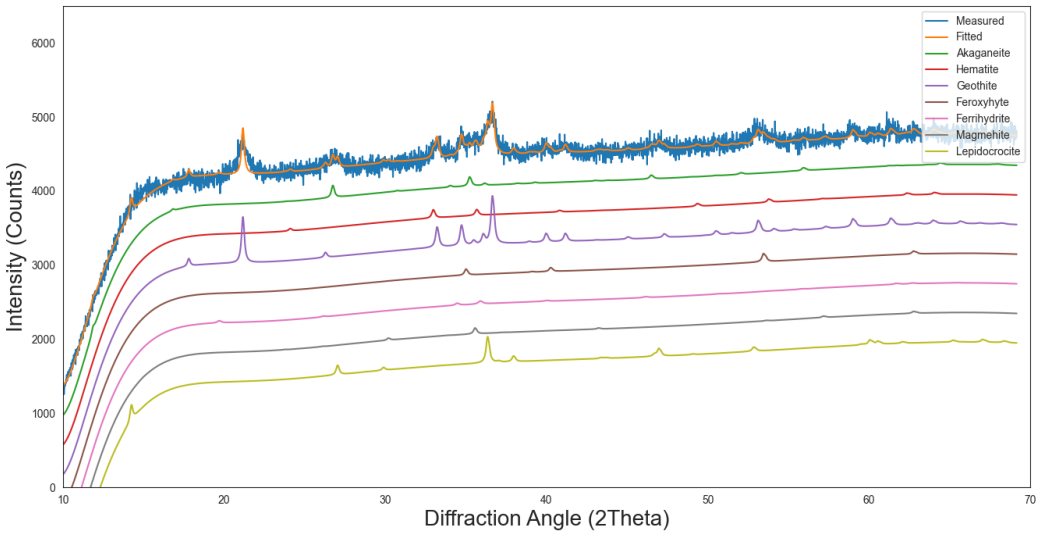


Figure A.305. XRD Pattern of Powdered Rust Collected from Exterior Web of the Girder.

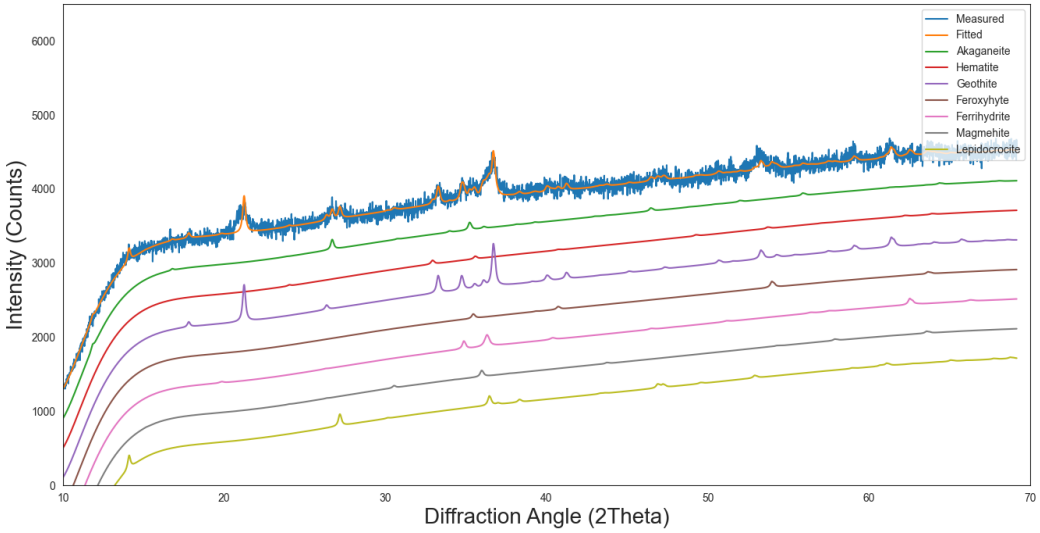


Figure A.306. XRD Pattern of Powdered Rust Collected from Interior Web of the Girder.

A.21.9.Particle Size Analysis: Tape Adhesion Results

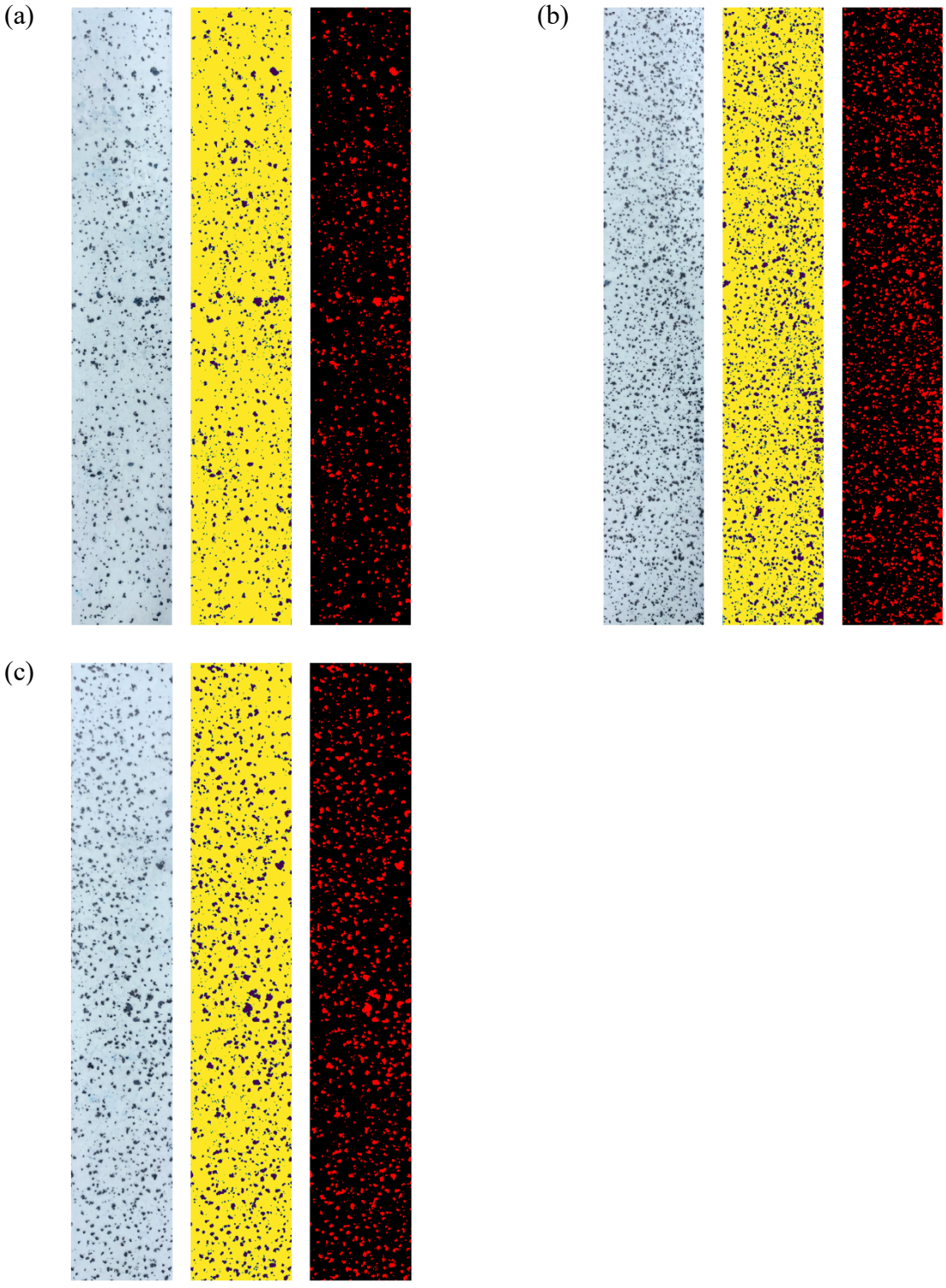


Figure A.307. Particle Size Analysis Results at A1G4F2 (a) Top Flange Bottom, (b) Web, (c) Bottom Flange Bottom.

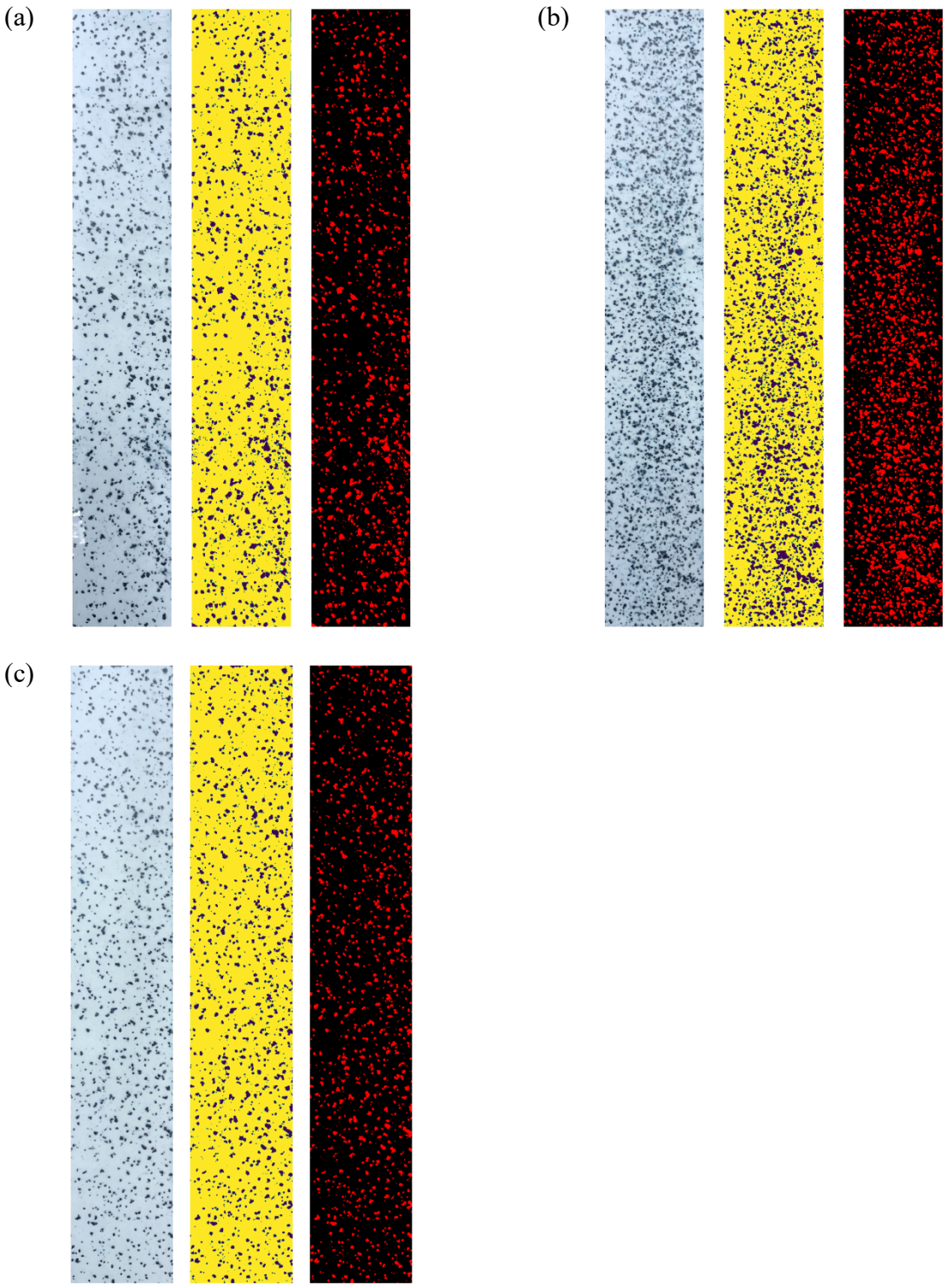


Figure A.308. Particle Size Analysis Results at B3G1F1 (a) Top Flange Bottom, (b) Web, (c) Bottom Flange Bottom.

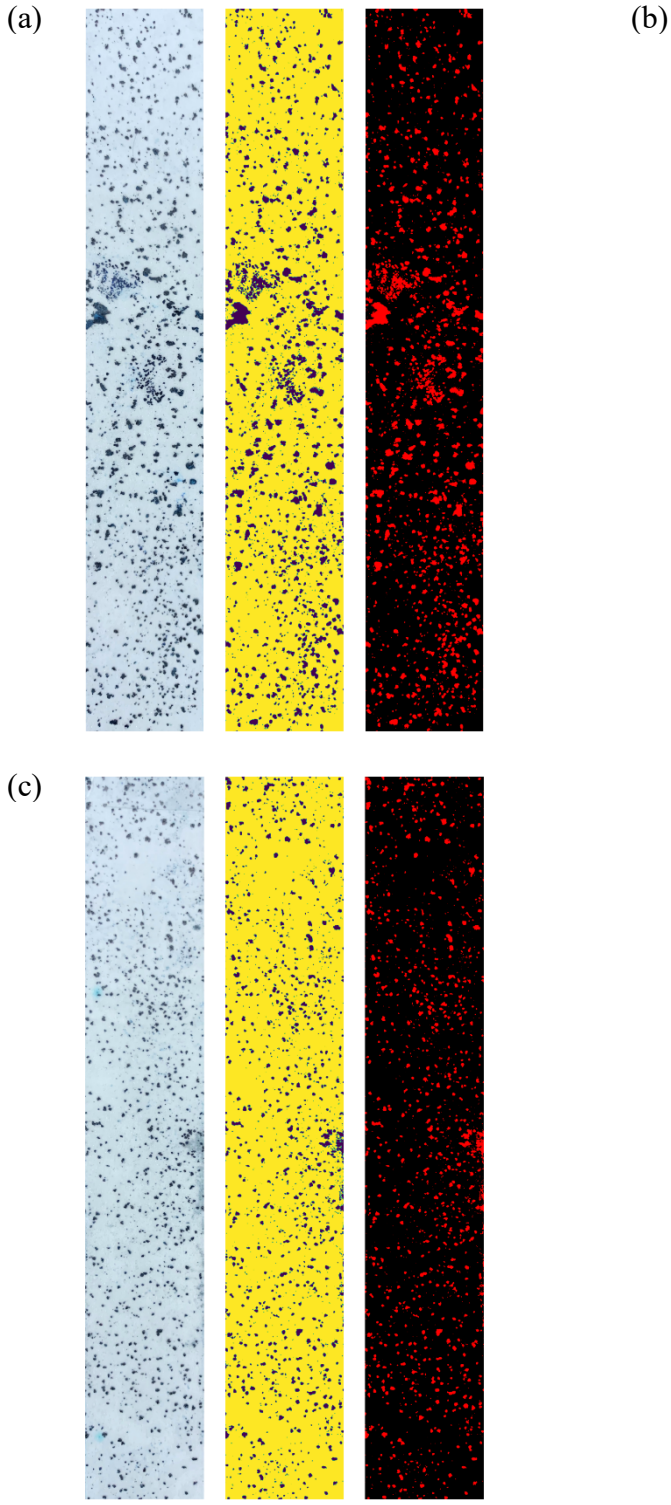


Figure A.309. Particle Size Analysis Results at B3G2F2 (a) Top Flange Bottom, (b) Web, (c) Bottom Flange Bottom.

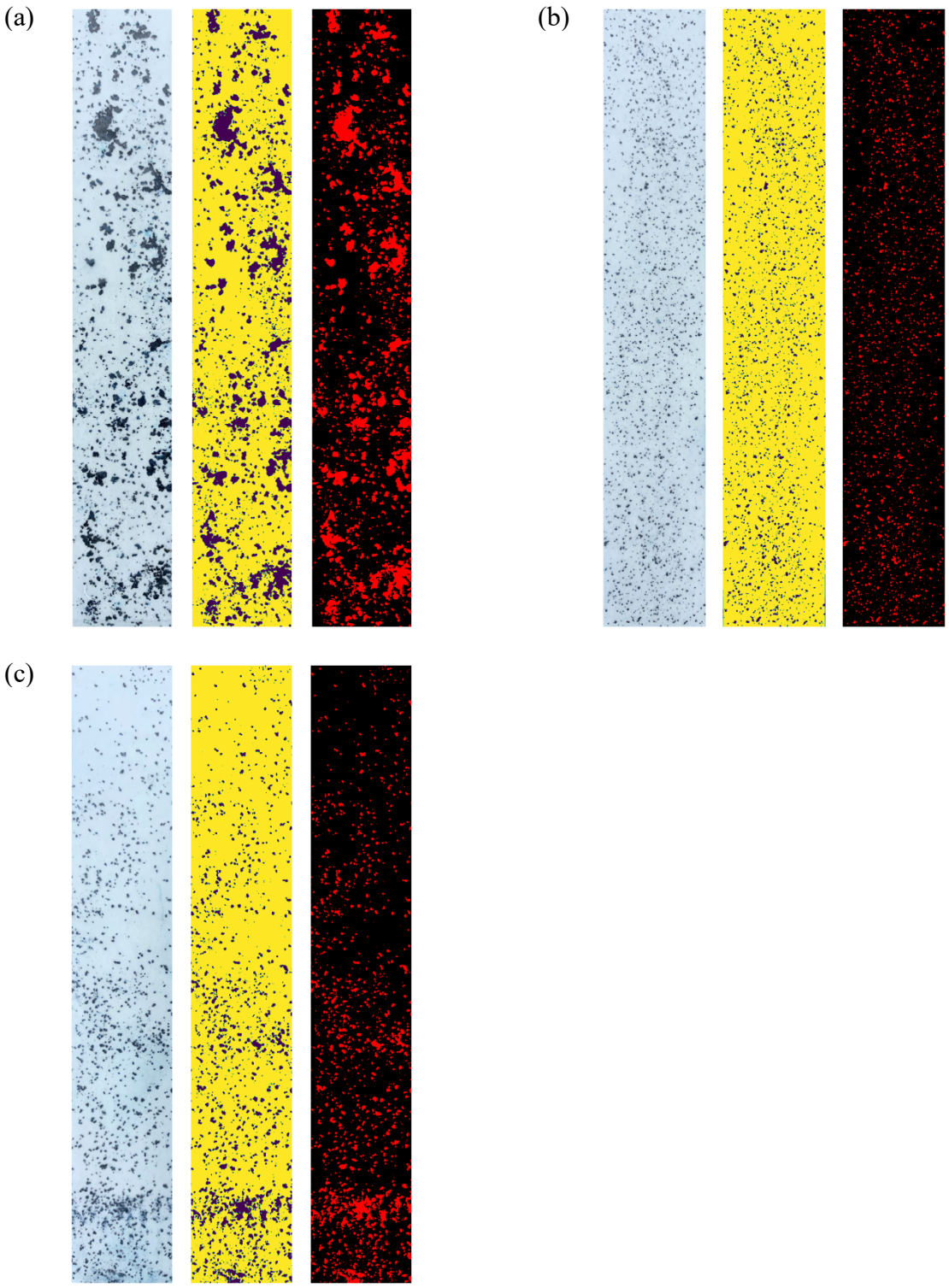


Figure A.310. Particle Size Analysis Results at B3G4F2 (a) Top Flange Bottom, (b) Web, (c) Bottom Flange Bottom.

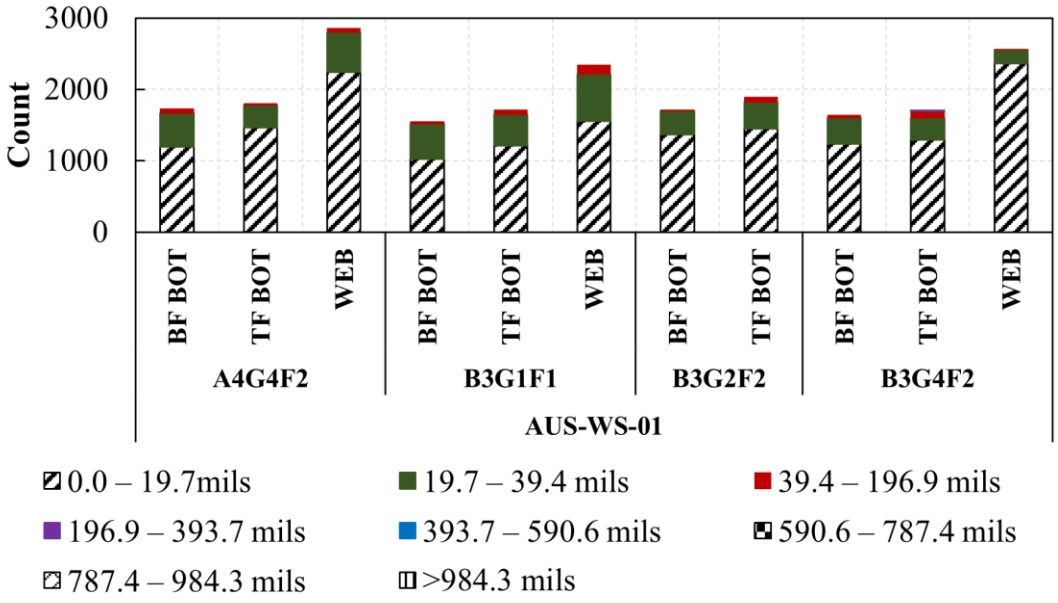


Figure A.311. Particle Size Analysis Showing Different Locations Examined.

A.22. AUS-WS-03

- Heatherwilde Blvd over SH 45
- Bridge ID 142270068307073, Coordinates (30.48421552, -97.613130), Travis County
- Continuous weathering steel plate girder (ASTM A588 HS 50)
- Built 2006
- Date of Inspection: December 8, 2020 girder inspection carried on east end abutment and bent 3, and measurements are taken on girder within three feet from the abutment or bent.
- No visual inspection on deck
- Location for Testing: A1-G4F2, A1-G3F2, B3-G1F1, B3-G2F2, B3-G4F2



Figure A.312. Typical Picture of AUS-WS-03.

A.22.1. Observed Condition

Overall patina condition on web, top flange and bottom flange of trapezoidal box girder is in good condition. Patina Rating web – 8, Patina Rating Top Flange – 7, Patina Rating Bottom Flange – 7, Poultice corrosion with localized pitting is observed throughout the girder on top of bottom flange. Patina Rating – 4.

A.22.2.Field Testing and Tape Adhesion Results

Table A-109. Field Inspection Results for AUS-WS-03.

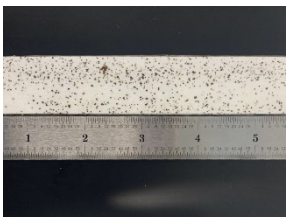
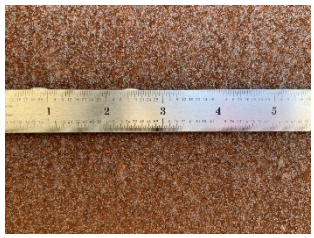
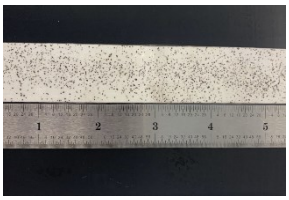
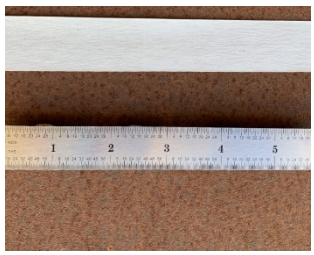
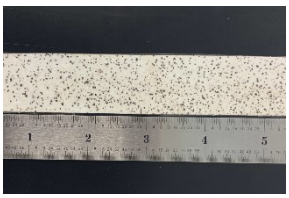
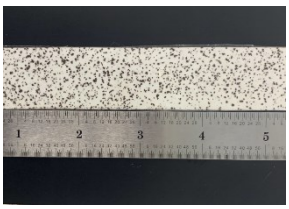
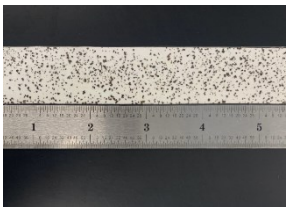
Location	Patina Rating	Thickness (inch)	Cl^- Conc. (ppm)	Field Condition	Tape Test
A1-G1F1 TF Bot. Ext.	7	Measured R1 1.017 R2 1.015 R3 1.017 R_Avg 1.016 Design			
A1-G1F1 Web Ext.	8	Measured R1 0.624 R2 0.624 R3 0.622 R_Avg 0.623 Design	1		
A1-G1F1 BF Top Ext.	7	Measured R1 1.013 R2 1.015 R3 1.015 R_Avg 1.014 Design			
A1-G1F1 BF Bot. Ext.	7	Measured R1 1.013 R2 1.015 R3 1.015 R_Avg 1.014 Design			
A1-G5F2 TF Bot. Int.	7	Measured R1 1.004 R2 1.002 R3 1.002 R_Avg 1.003 Design			

Table A-110. Field Inspection Results for AUS-WS-03.

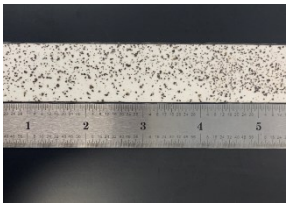
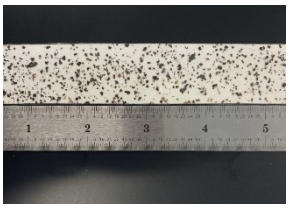
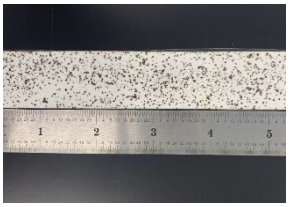
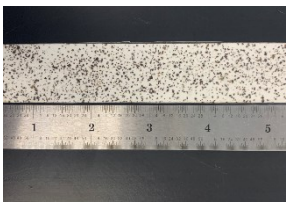
Location	Patina Rating	Thickness (inch)	Cl^- Conc. (ppm)	Field Condition	Tape Test
A1-G5F2 Web Int.	7	Measured R1 0.634 R2 0.635 R3 0.637 R_Avg 0.635 Design			
A1-G5F2 BF Top Int.	4	Measured R1 1.018 R2 1.021 R3 1.014 R_Avg 1.018 Design			
A1-G5F2 BF Bot. Int.	7	Measured R1 1.018 R2 1.021 R3 1.014 R_Avg 1.018 Design			
A1-G6F1 TF Bot. Int.	7	Measured R1 1.005 R2 1.005 R3 1.005 R_Avg 1.005 Design			
A1-G6F1 Web Int.	7	Measured R1 0.632 R2 0.631 R3 0.631 R_Avg 0.631 Design	1		

Table A-111. Field Inspection Results for AUS-WS-03.

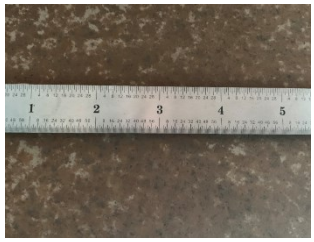
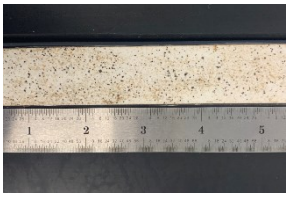
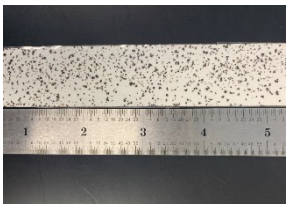
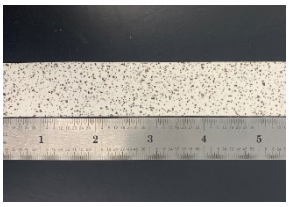
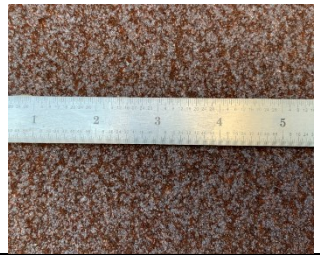
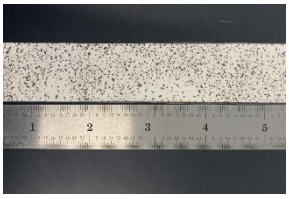
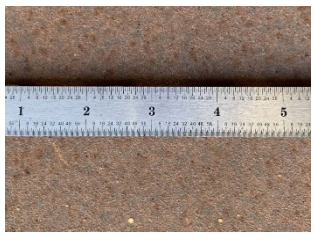
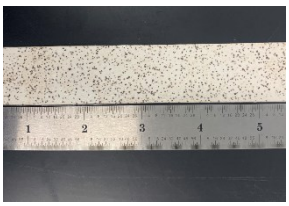
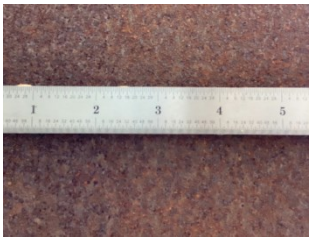
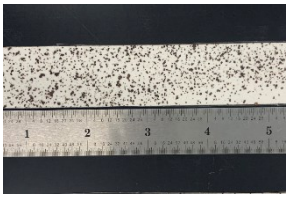
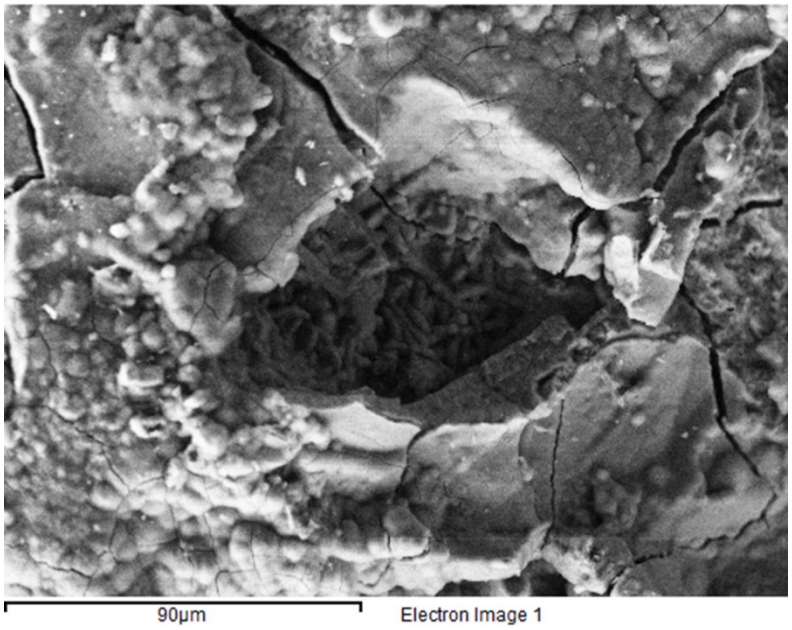
Location	Patina Rating	Thickness (inch)	Cl^- Conc. (ppm)	Field Condition	Tape Test
A1-G6F1 BF Top Int.	4	Measured R1 1.016 R2 1.014 R3 1.015 R_Avg 1.015 Design			
A1-G6F1 BF Bot. Int.	7	Measured R1 1.016 R2 1.014 R3 1.015 R_Avg 1.015 Design			
A1-G12F2 TF Bot. Ext.	7	Measured R1 1.006 R2 1.006 R3 1.006 R_Avg 1.006 Design			
A1-G12F2 Web Ext.	7	Measured R1 0.623 R2 0.624 R3 0.624 R_Avg 0.624 Design	0		
A1-G12F2 BF Top Ext.	5	Measured R1 0.997 R2 0.998 R3 0.997 R_Avg 0.997 Design			

Table A-112. Field Inspection Results for AUS-WS-03.

Location	Patina Rating	Thickness (inch)	Cl^- Conc. (ppm)	Field Condition	Tape Test
A1-G12F2 BF Bot. Ext.	7	Measured R1 0.997 R2 0.998 R3 0.997 R_Avg 0.997 Design			

A.22.3.SEM/EDS Results: Exterior Web Girder

Element	Weight %	Atomic %
O K	37.10	66.49
Al K	0.96	1.02
Si K	0.71	0.73
S K	0.56	0.50
Cl K	0.16	0.13
Ca K	0.26	0.18
Mn K	0.58	0.31
Fe K	59.55	30.58
Cu K	0.11	0.05
Totals	100.00	



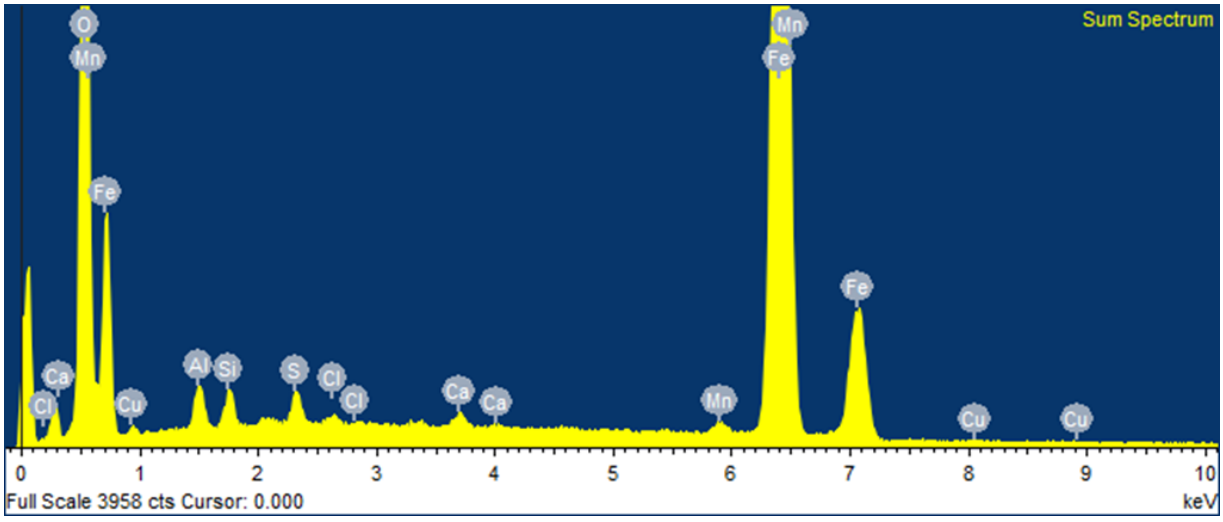
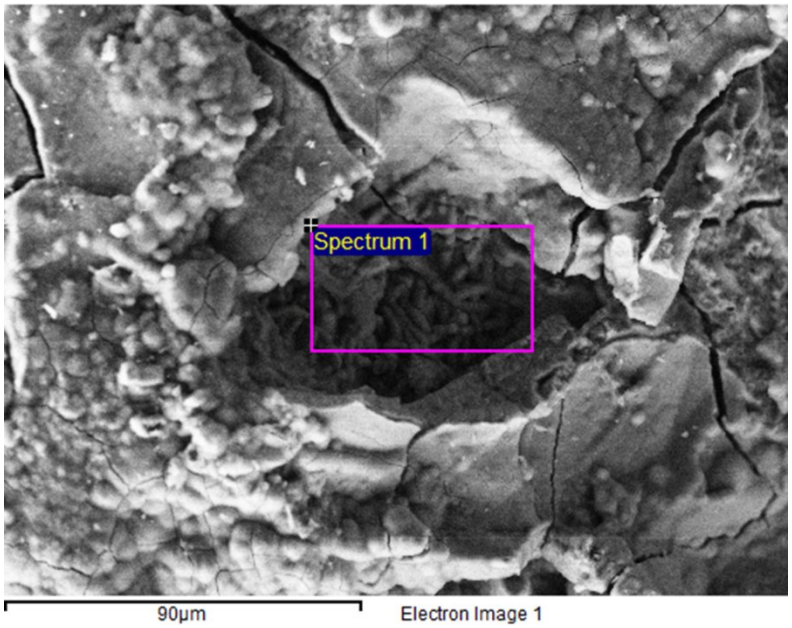


Figure A.313. SEM Image and EDS Spectrum of the Rust Collected from Exterior Web of the Girder.

Element	Weight %	Atomic %
O K	12.83	32.81
Al K	2.00	3.04
Si K	0.10	0.15
S K	0.08	0.10
Ca K	5.74	5.86
Mn K	0.92	0.68
Fe K	77.83	57.03
Ni K	0.22	0.15
Cu K	0.29	0.18
Totals	100.00	



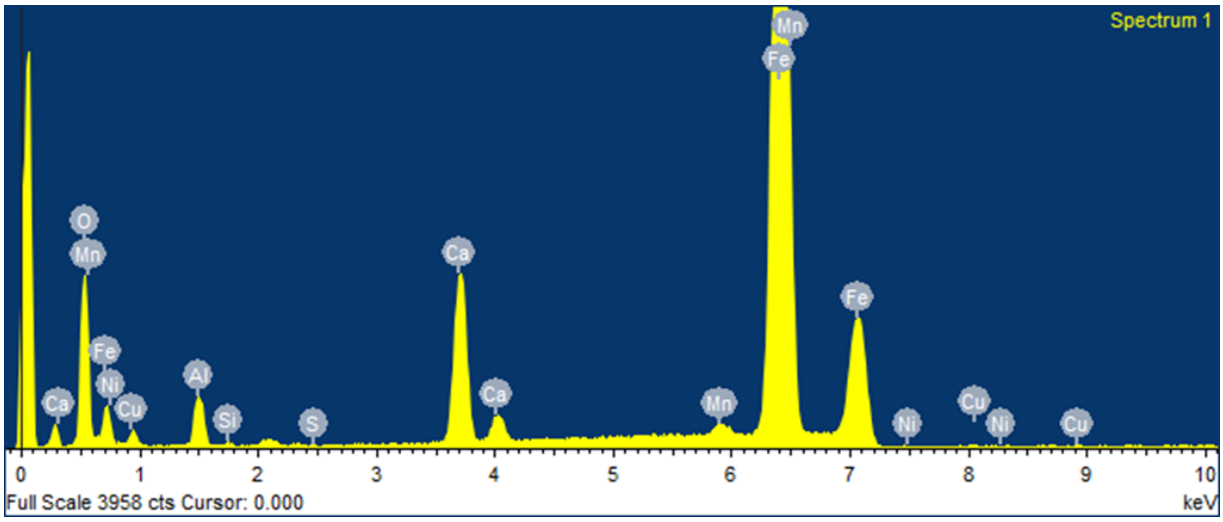
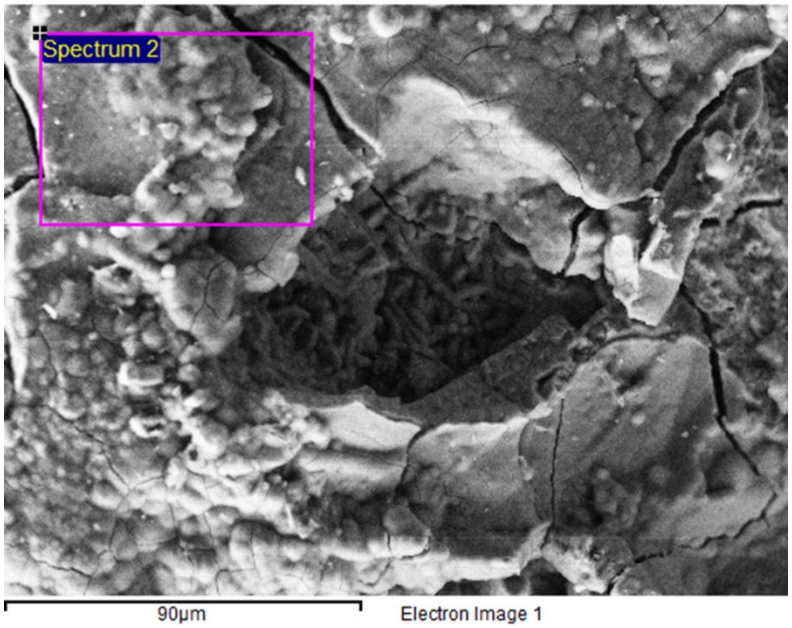


Figure A.314. SEM Image and EDS Spectrum of the Rust Collected from Exterior Web of the Girder.

Element	Weight %	Atomic %
O K	50.48	77.39
Al K	0.73	0.66
Si K	0.49	0.43
S K	0.76	0.58
Cl K	0.17	0.12
Ca K	0.14	0.09
Mn K	0.28	0.13
Fe K	46.80	20.55
Cu K	0.15	0.06
Totals	100.00	



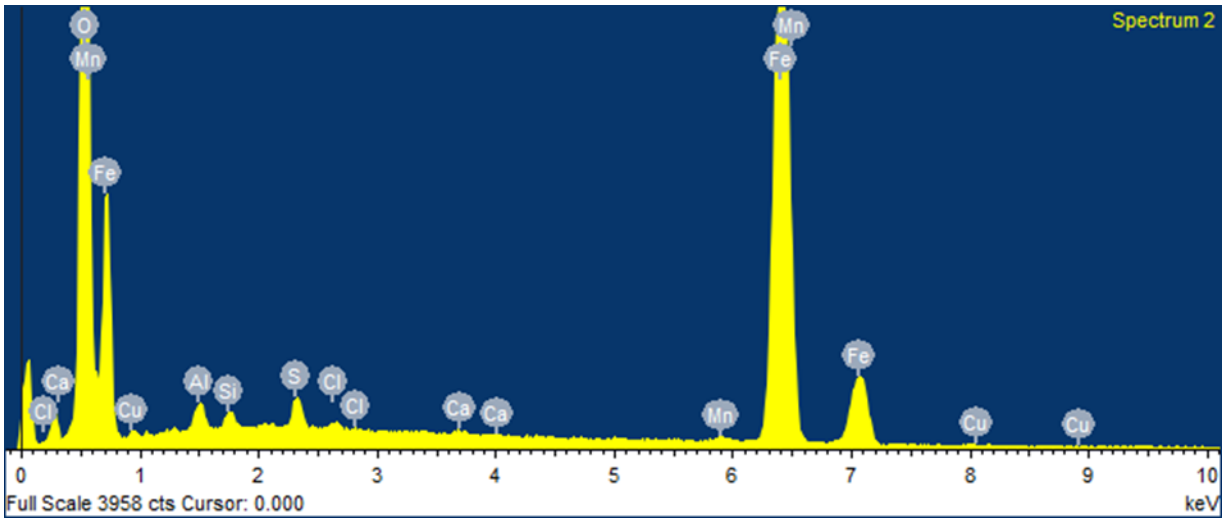


Figure A.315. SEM Image and EDS Spectrum of the Rust Collected from Exterior Web of the Girder.

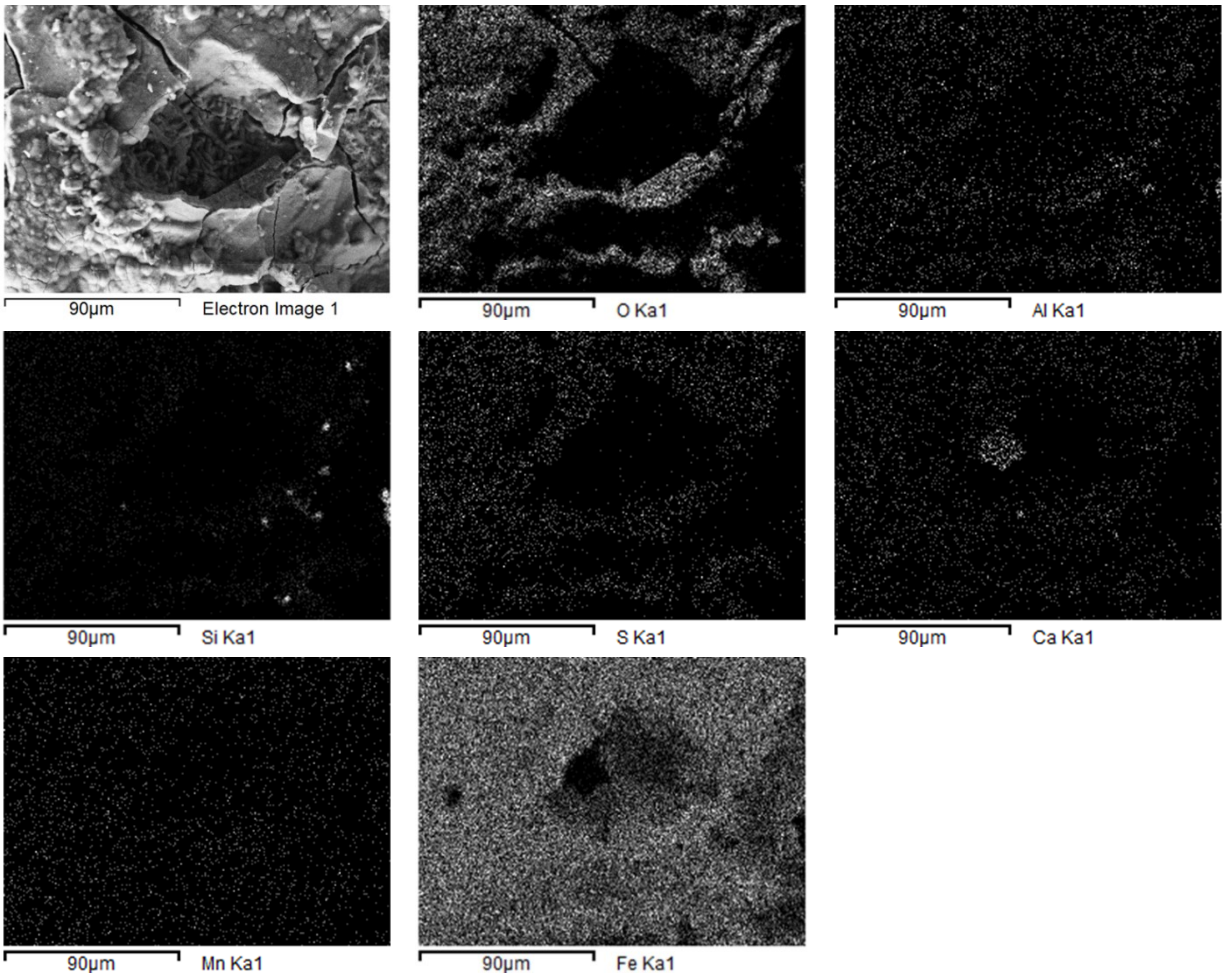
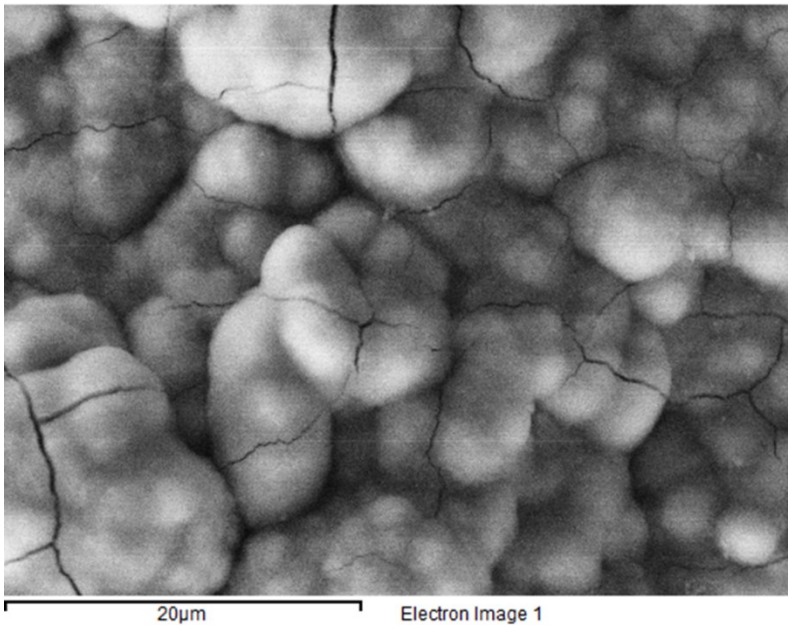


Figure A.316. EDS Elemental Mapping of Rust Collected from Exterior Web.

Element	Weight %	Atomic %
O K	46.65	74.74
Al K	0.74	0.70
Si K	0.17	0.15
S K	0.73	0.58
Cl K	0.22	0.16
Ca K	0.17	0.11
Mn K	0.50	0.23
Fe K	50.74	23.29
Cu K	0.09	0.03
Totals	100.00	



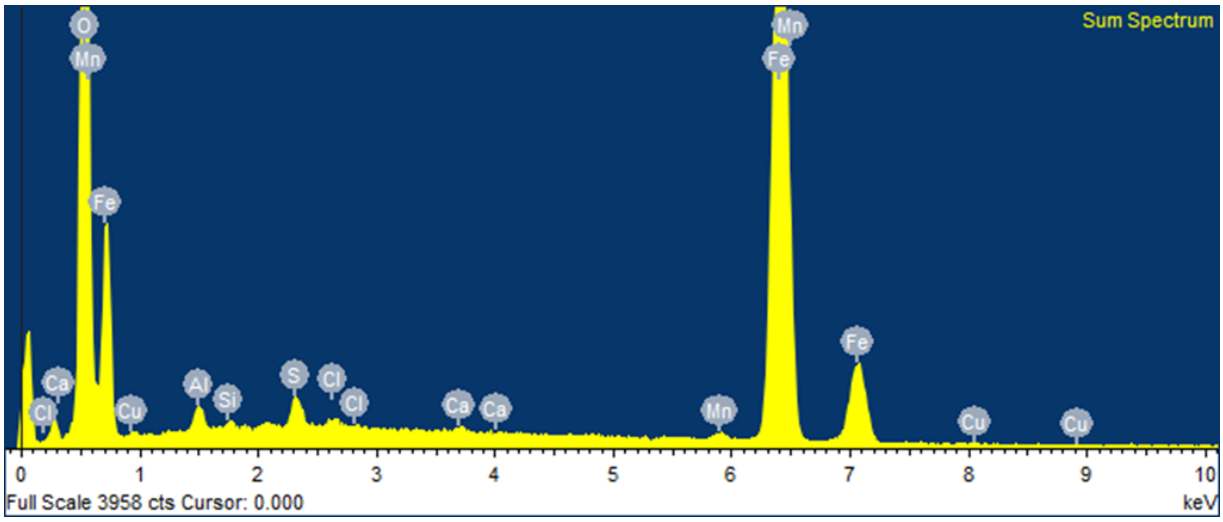


Figure A.317. SEM Image and EDS Spectrum of the Rust Collected from Exterior Web of the Girder.

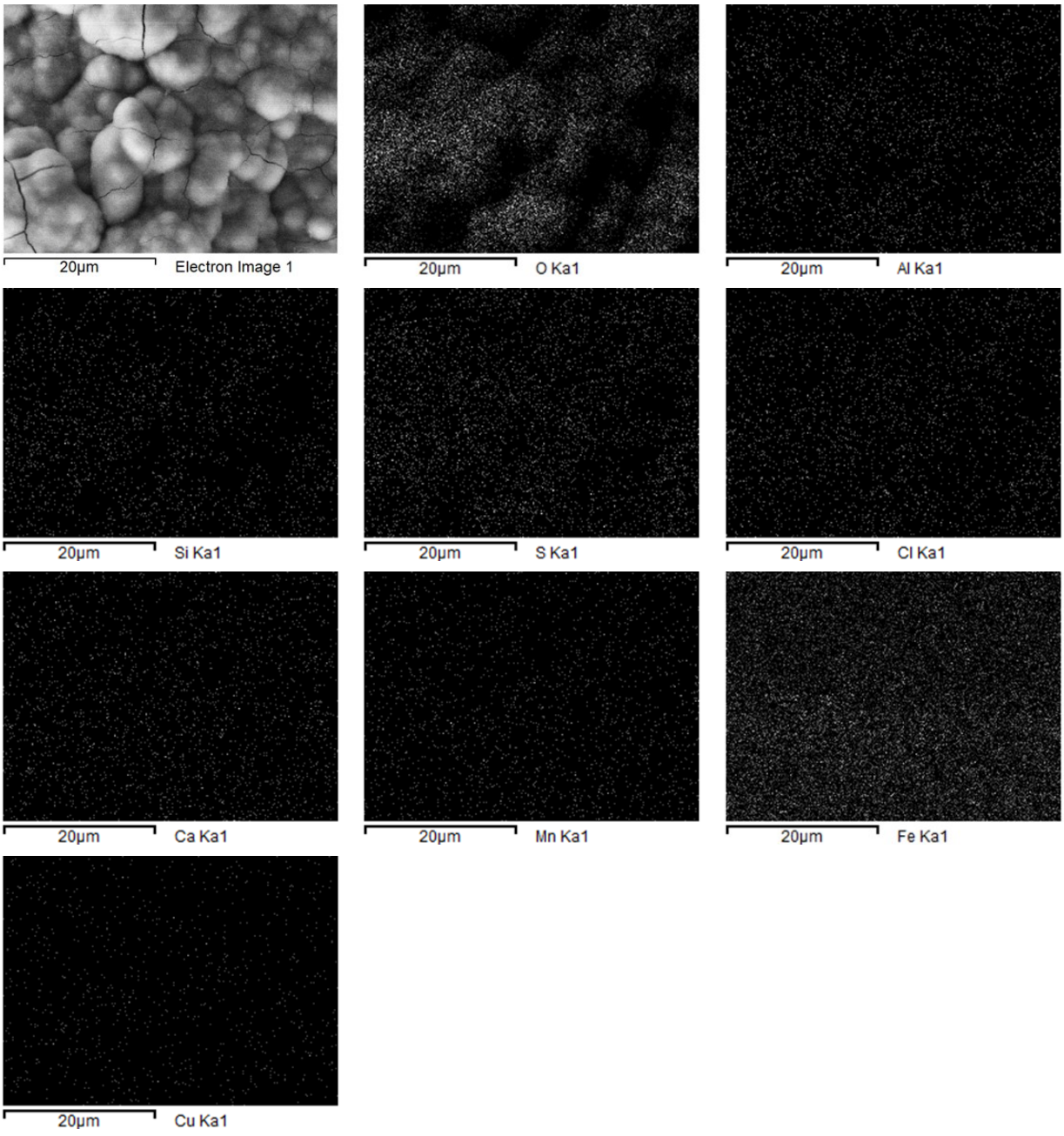
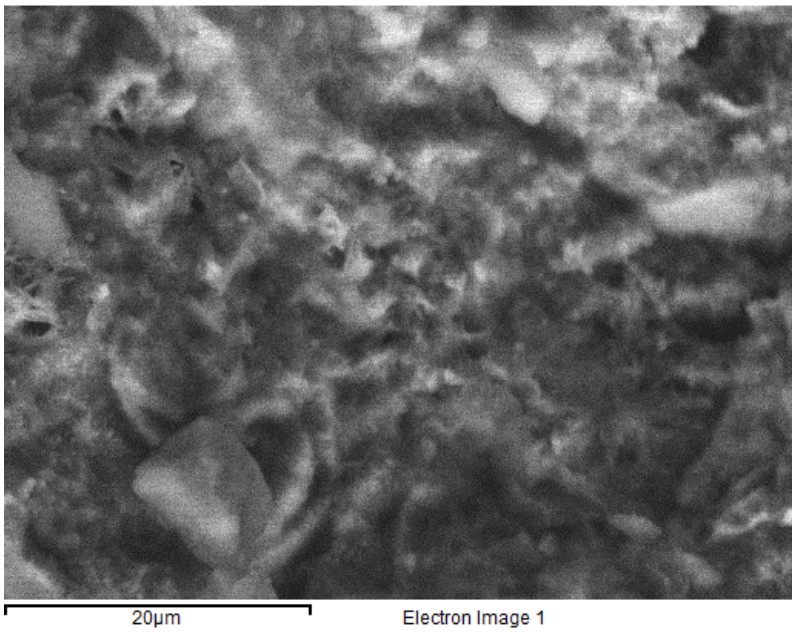


Figure A.318. EDS Elemental Mapping of Rust Collected from Exterior Web.

Element	Weight %	Atomic %
O K	30.85	59.61
Al K	1.31	1.50
Si K	2.06	2.27
S K	0.24	0.23
Cl K	0.11	0.10
K K	0.13	0.10
Ca K	0.18	0.14
Mn K	0.92	0.52
Fe K	64.11	35.49
Cu K	0.09	0.04
Totals	100.00	



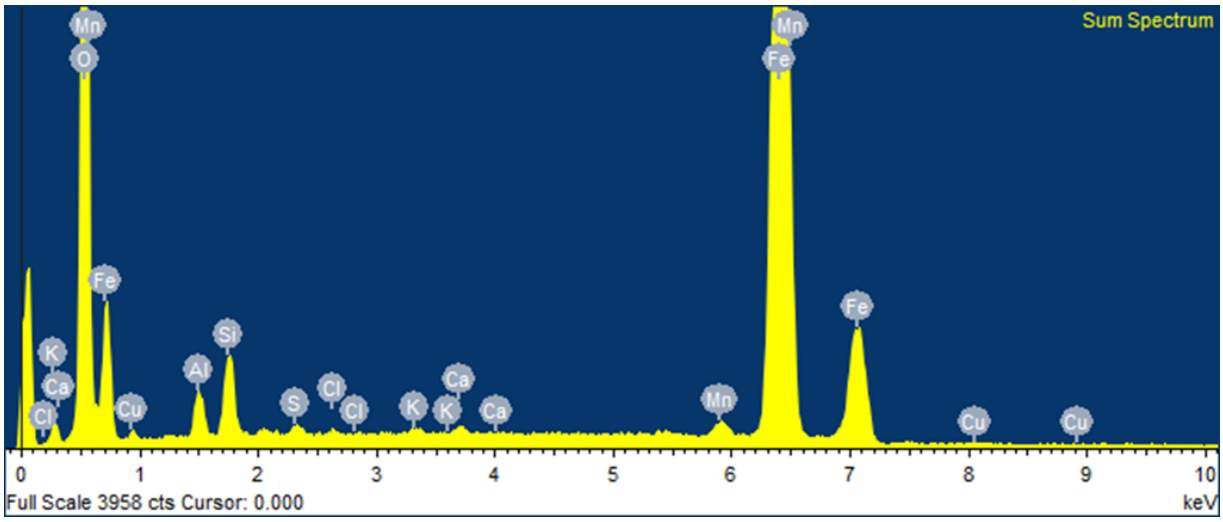


Figure A.319. SEM Image and EDS Spectrum of the Rust Collected from Exterior Web of the Girder.

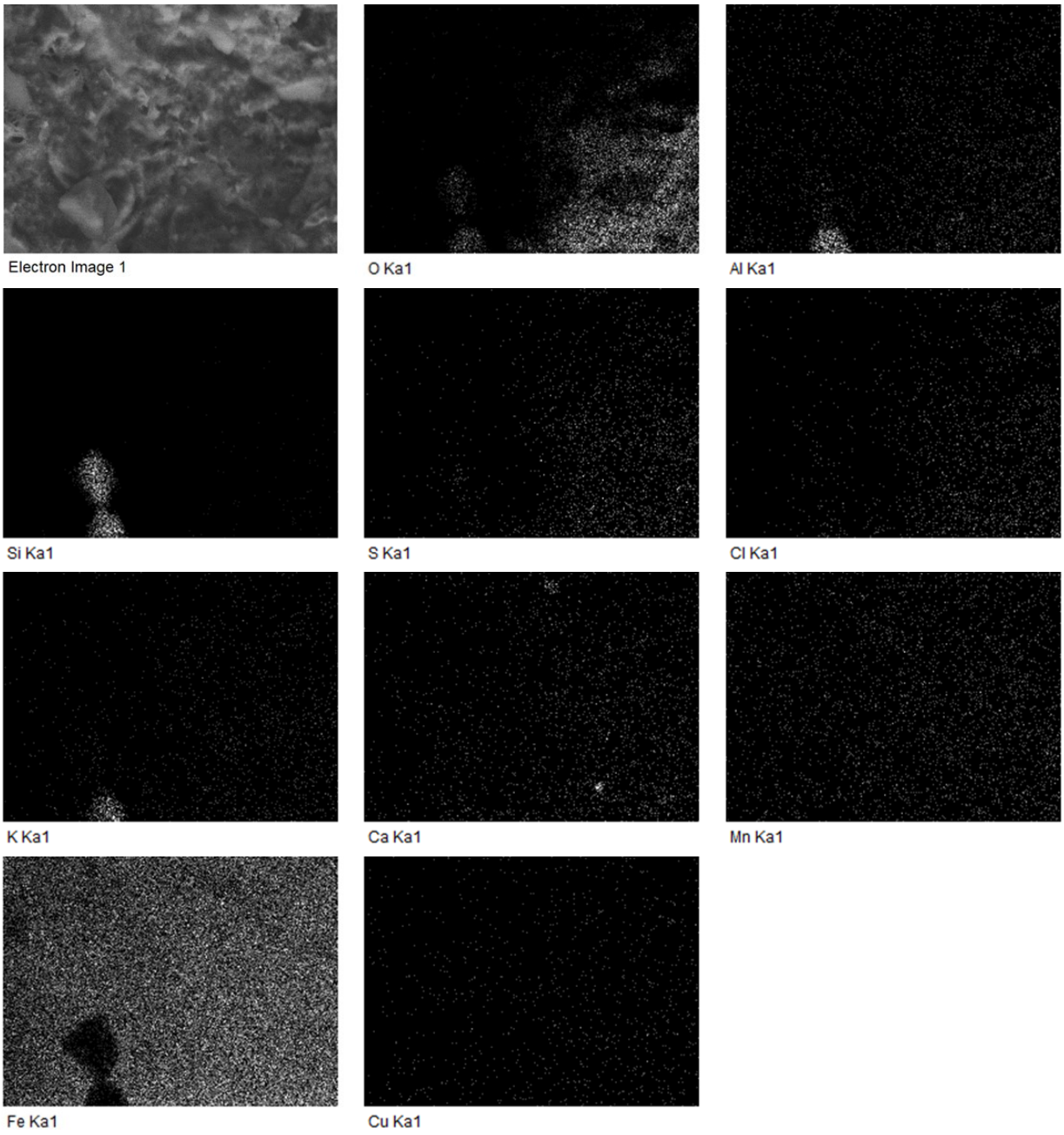
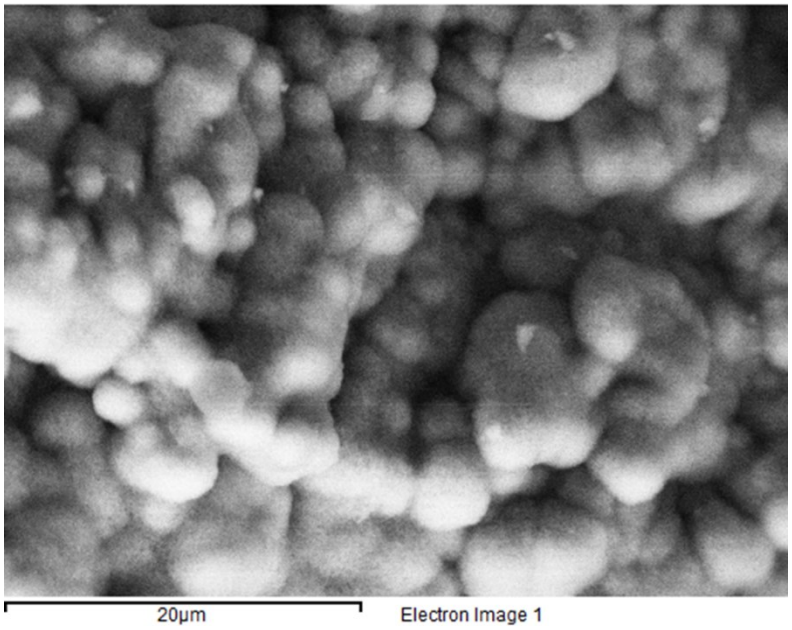


Figure A.320. EDS Elemental Mapping of Rust Collected from Exterior Web.

A.22.4.SEM/EDS Results: Interior Web Girder

Element	Weight %	Atomic %
O K	34.52	64.08
Al K	0.81	0.89
Si K	0.32	0.34
S K	0.66	0.61
Cl K	0.26	0.22
Ca K	0.46	0.34
Mn K	2.49	1.35
Fe K	60.47	32.16
Totals	100.00	



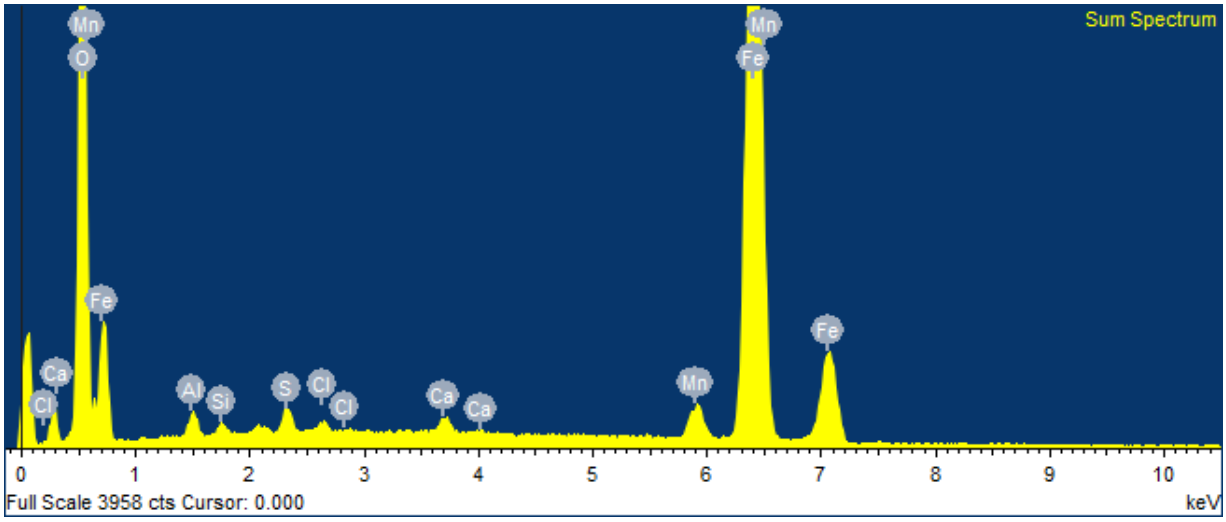
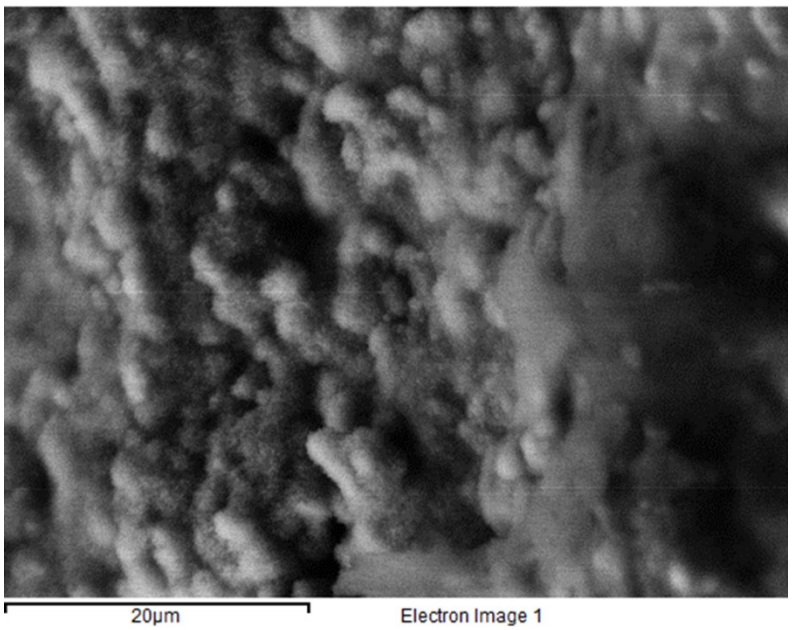


Figure A.321. SEM Image and EDS Spectrum of the Rust Collected from Interior Web of the Girder.

Element	Weight %	Atomic %
O K	46.34	73.39
Na K	1.81	1.99
Al K	0.57	0.54
Si K	0.53	0.47
S K	0.80	0.63
Cl K	0.63	0.45
K K	0.34	0.22
Ca K	0.42	0.27
Mn K	1.42	0.65
Fe K	46.61	21.15
Ni K	0.54	0.23
Totals	100.00	



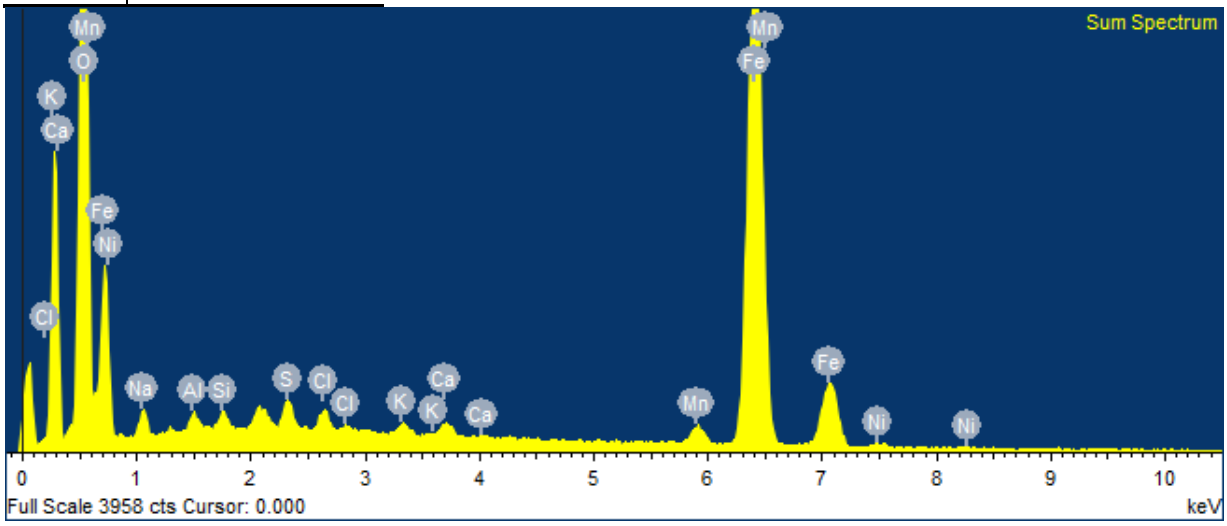
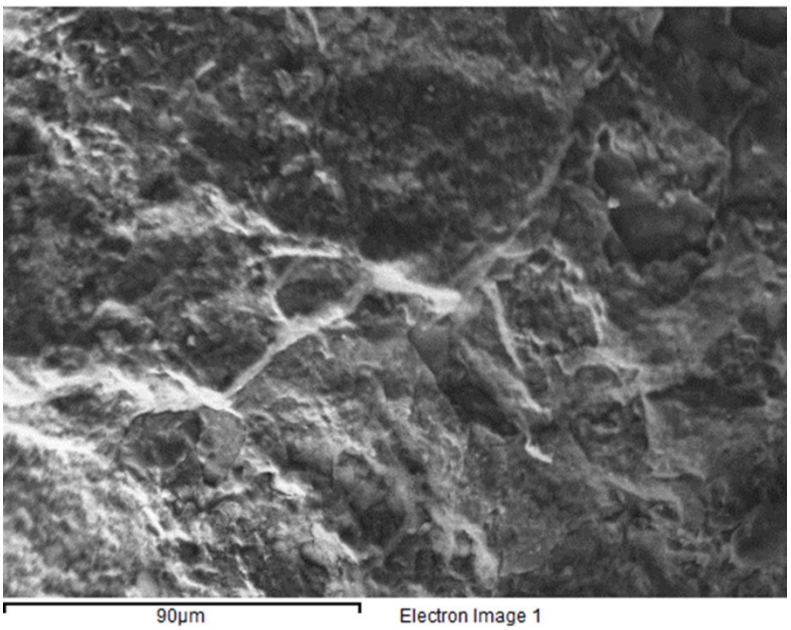


Figure A.322. SEM Image and EDS Spectrum of the Rust Collected from Interior Web of the Girder.

Element	Weight %	Atomic %
O K	32.16	61.52
Al K	0.82	0.93
Si K	0.99	1.08
S K	0.49	0.47
Cl K	0.18	0.16
Ca K	0.22	0.17
Cr K	0.40	0.24
Mn K	0.92	0.51
Fe K	62.91	34.48
Ni K	0.47	0.24
Cu K	0.45	0.21
Totals	100.00	



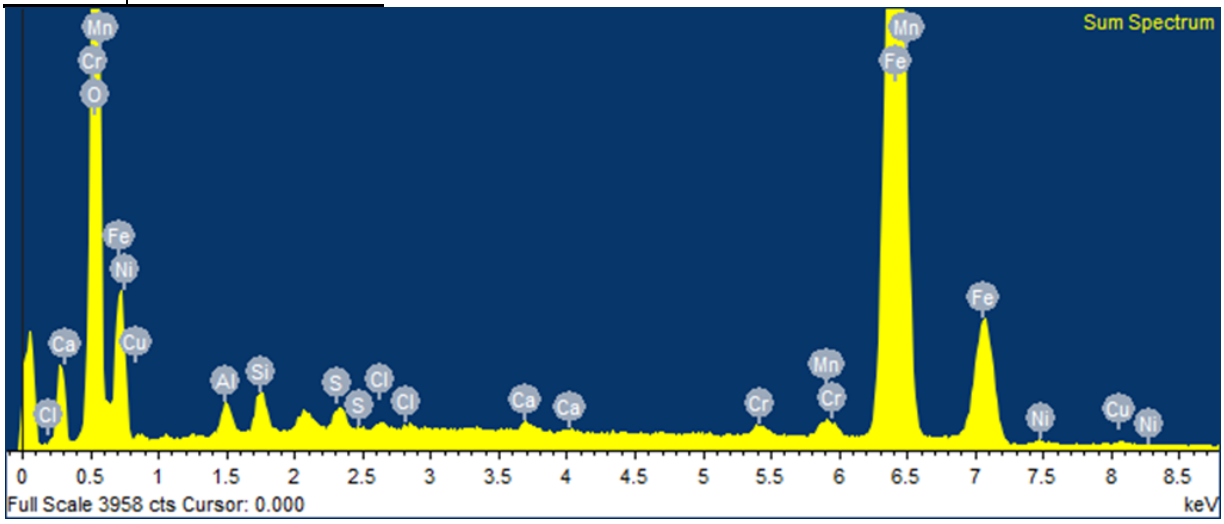


Figure A.323. SEM Image and EDS Spectrum of the Rust Collected from Interior Web of the Girder.

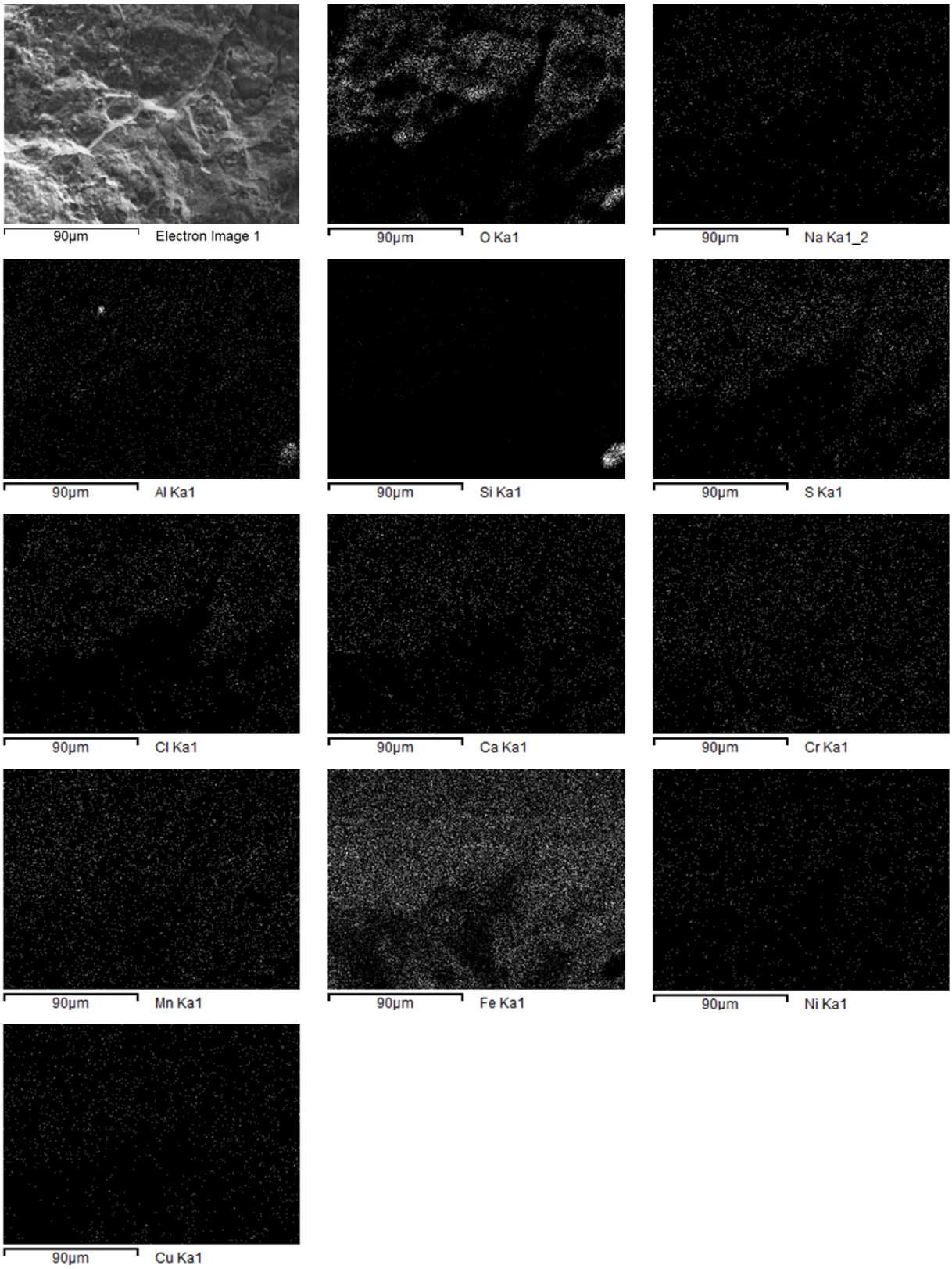
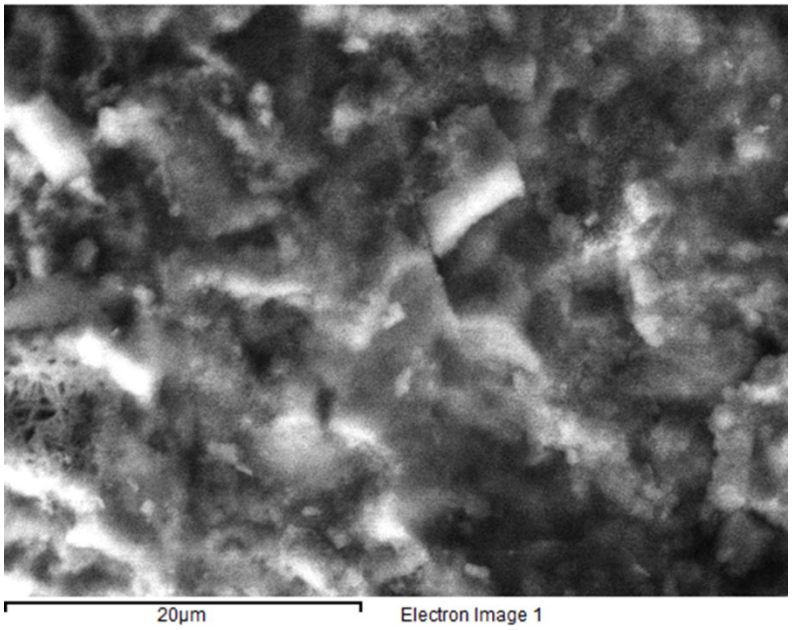


Figure A.324. EDS Elemental Mapping of Rust Collected from Interior Web.

A.22.5.SEM/EDS Results: Interior Web Girder

Element	Weight %	Atomic %
O K	39.29	68.18
Na K	0.40	0.49
Mg K	0.23	0.26
Al K	1.13	1.16
Si K	0.48	0.48
S K	0.68	0.59
Cl K	0.13	0.10
Ca K	0.46	0.32
Cr K	0.36	0.19
Mn K	1.47	0.74
Fe K	54.44	27.06
Ni K	0.44	0.21
Cu K	0.49	0.22
Totals	100.00	



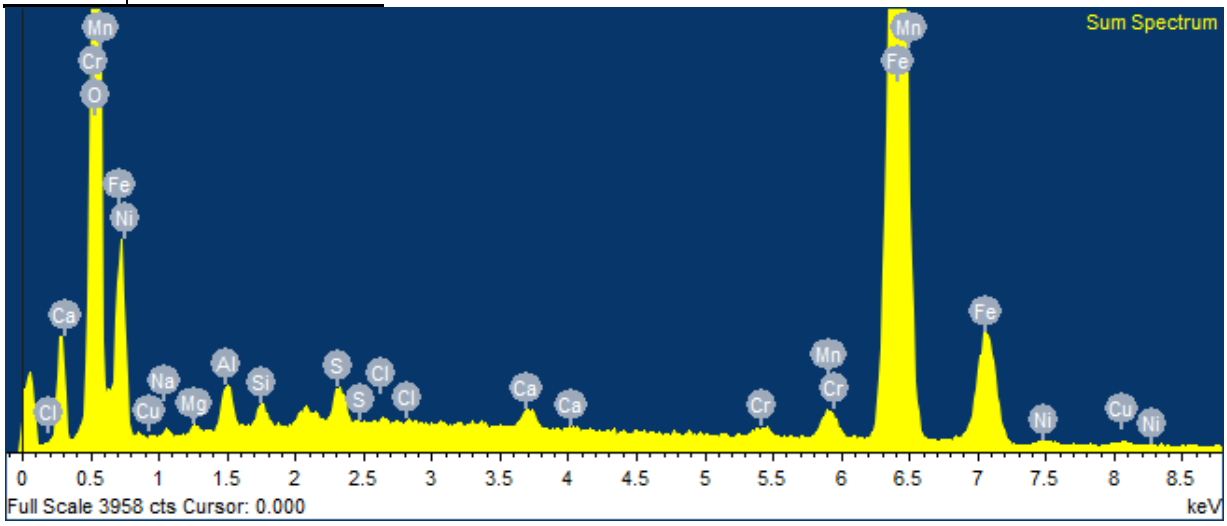


Figure A.325. SEM Image and EDS Spectrum of the Rust Collected from Interior Web of the Girder.

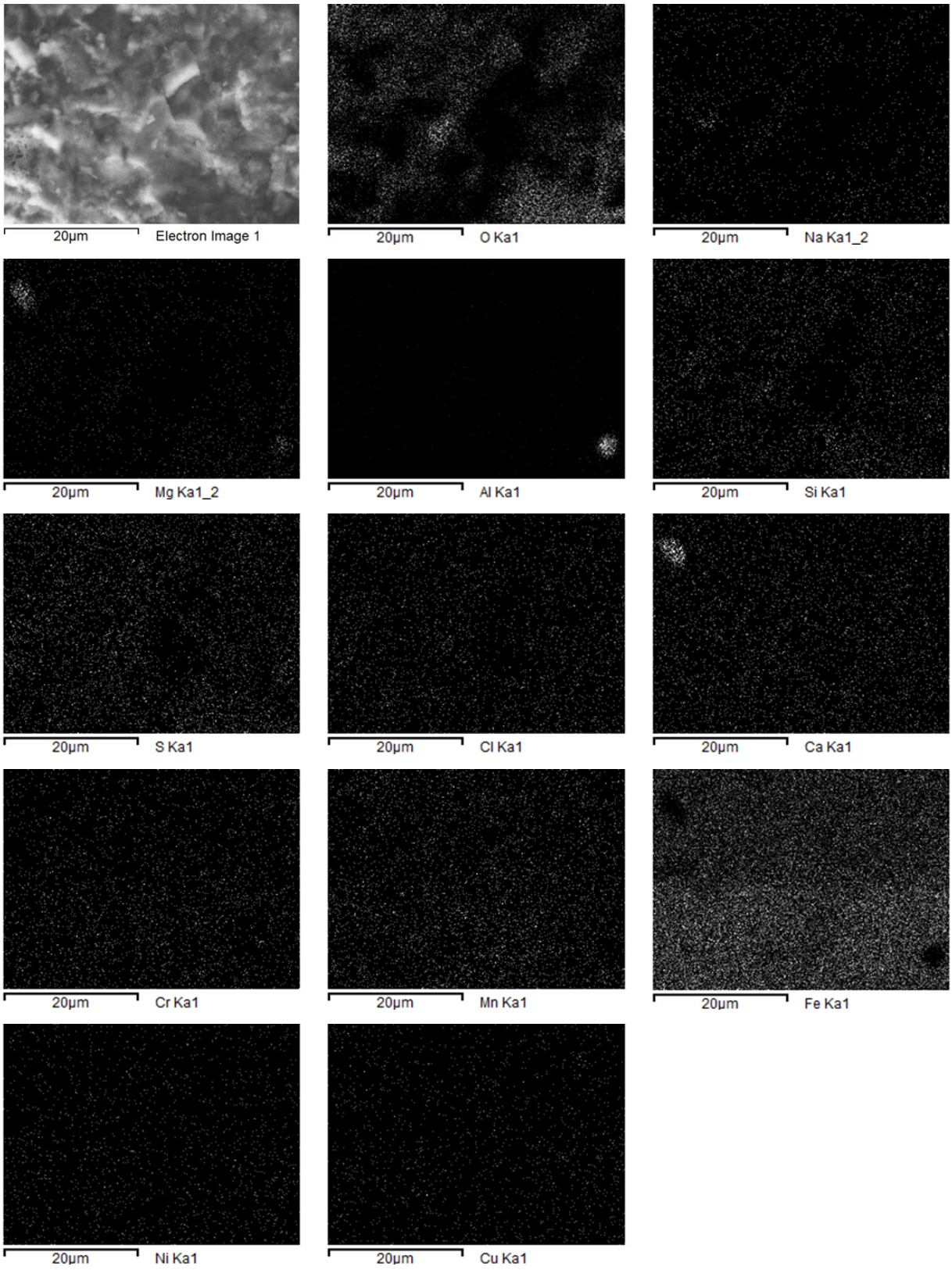
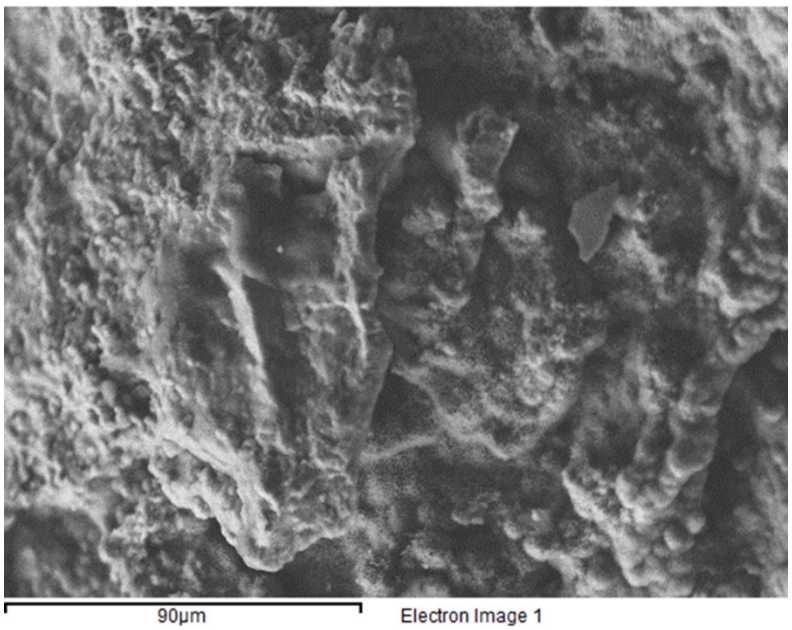


Figure A.326. EDS Elemental Mapping of Rust Collected from Interior Web.

Element	Weight %	Atomic %
O K	39.24	68.39
Na K	0.65	0.79
Al K	0.53	0.55
Si K	0.27	0.27
S K	0.58	0.50
Cl K	0.27	0.21
K K	0.11	0.08
Ca K	0.34	0.24
Mn K	1.49	0.76
Fe K	56.10	28.01
Ni K	0.42	0.20
Totals	100.00	



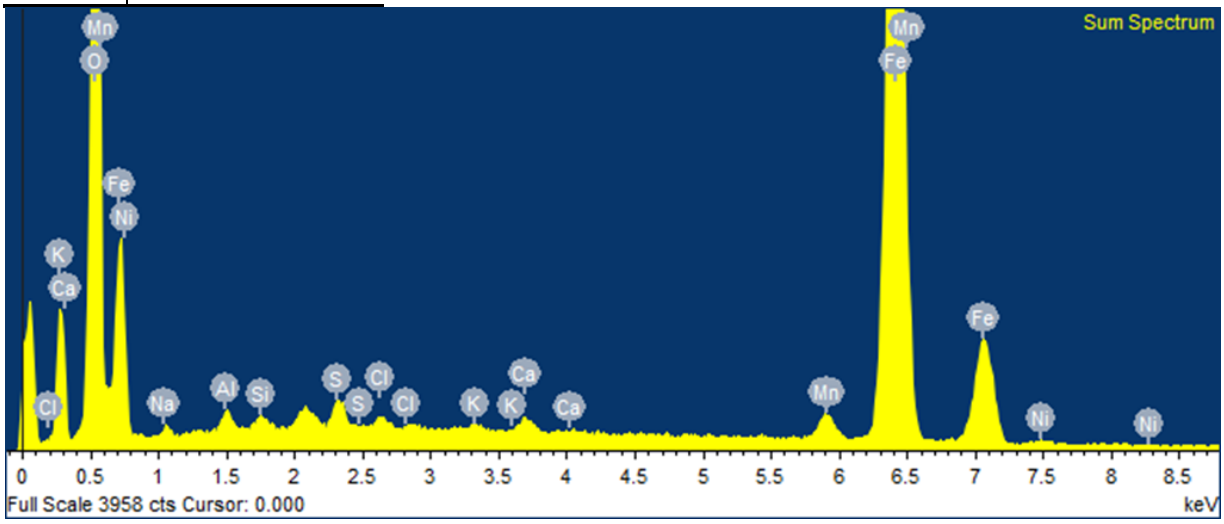


Figure A.327. SEM Image and EDS Spectrum of the Rust Collected from Interior Web of the Girder.

A.22.6.XPS Result: Exterior Girder

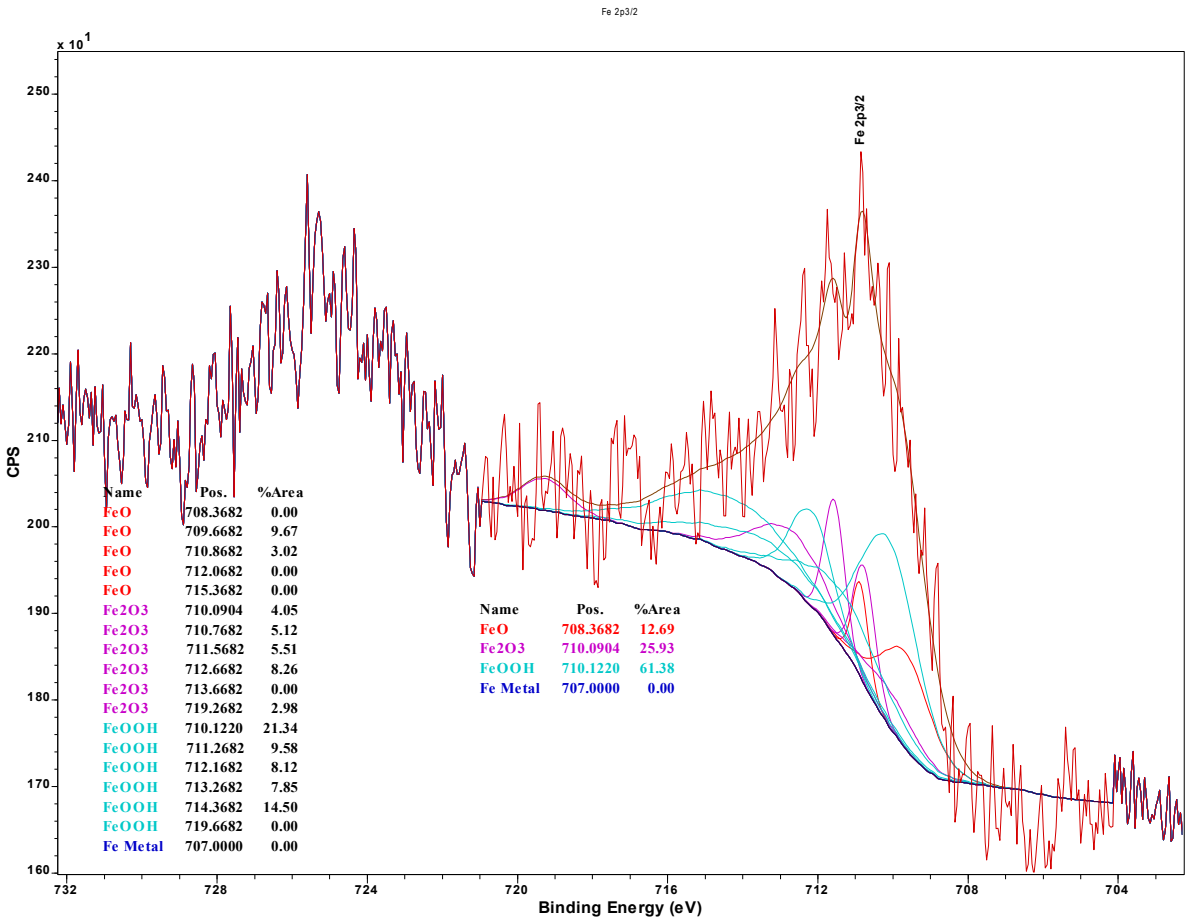


Figure A.328. XPS Spectrum of the Rust Collected from Exterior Web of the Girder.

A.22.7.XPS Result: Interior Girder

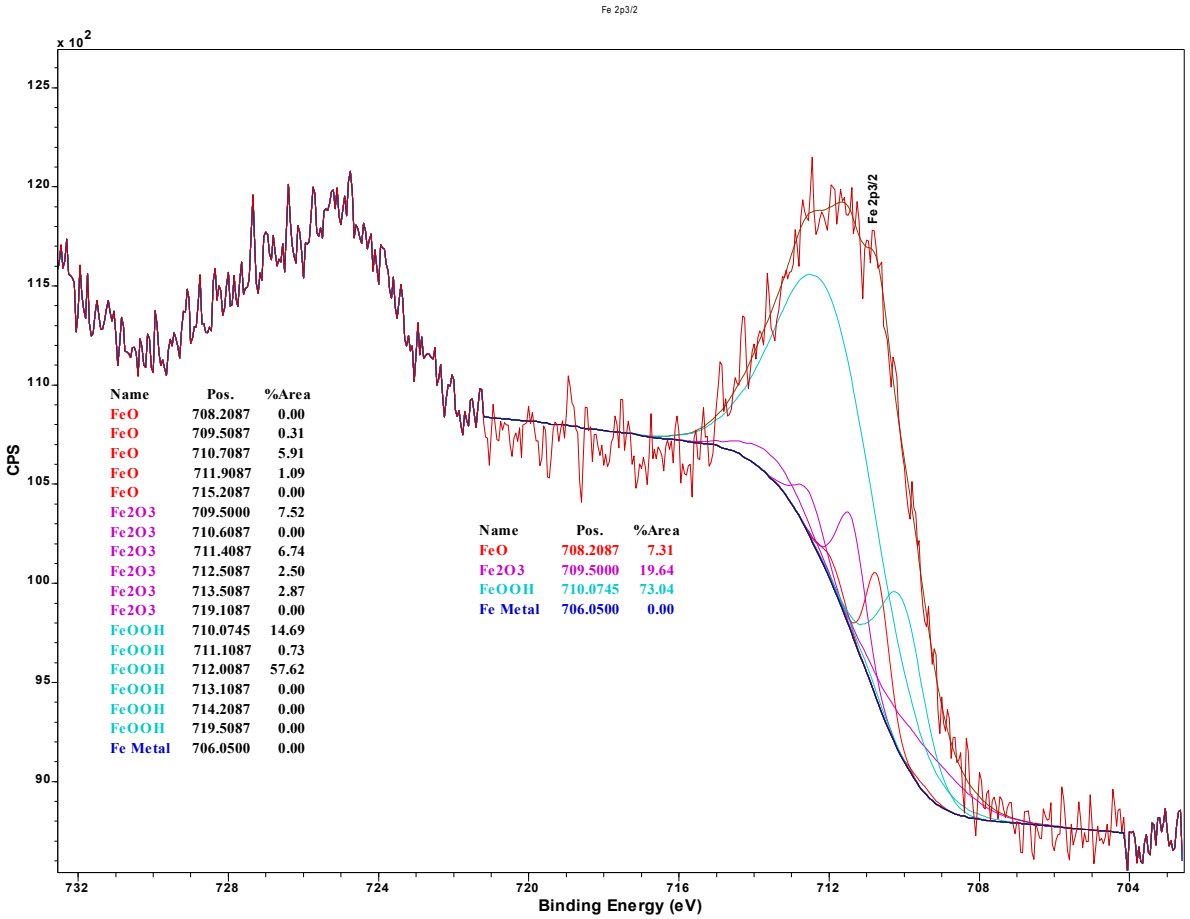


Figure A.329. XPS Spectrum of the Rust Collected from Interior Web of the Girder.

A.22.8.XRD Result: Exterior and Interior Girder

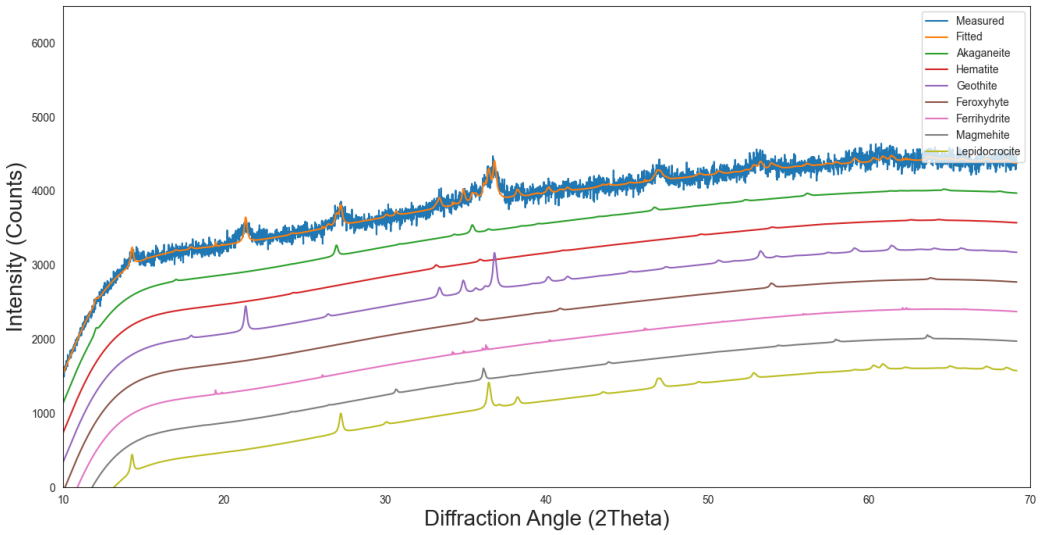


Figure A.330. XRD Pattern of Powdered Rust Collected from Exterior Web of the Girder.

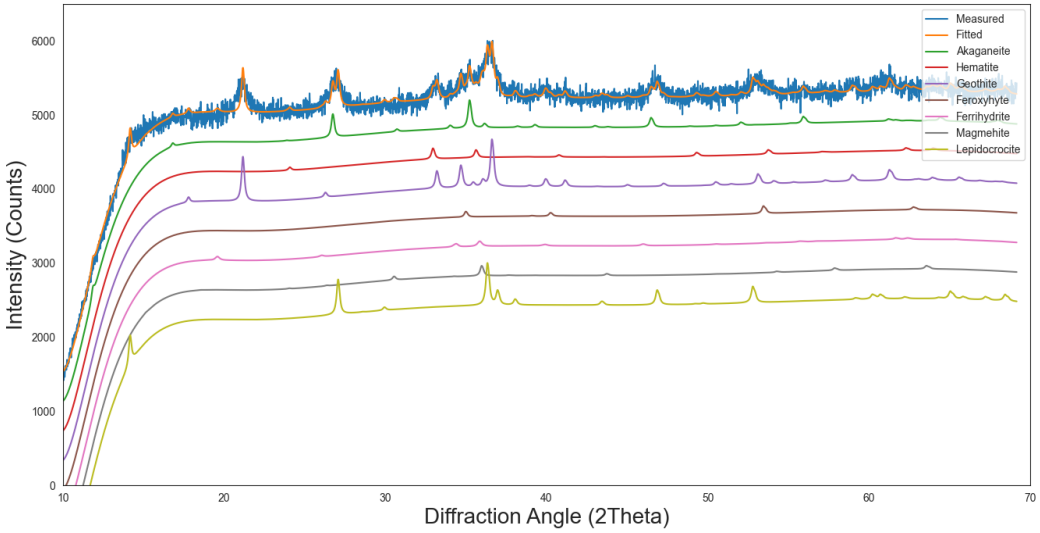


Figure A.331. XRD Pattern of Powdered Rust Collected from Interior Web of the Girder.

A.22.9. Particle Size Analysis: Tape Adhesion Results

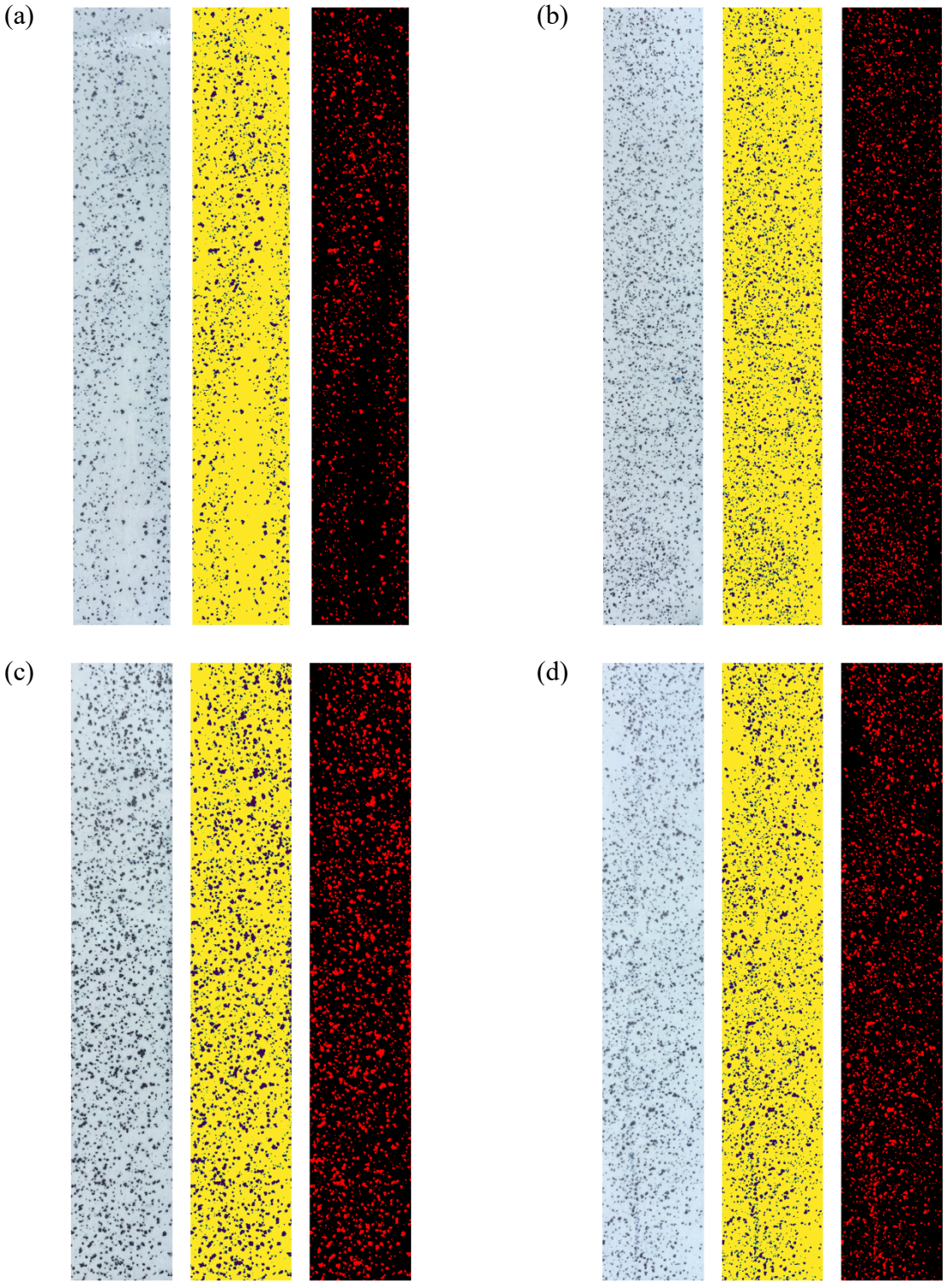


Figure A.332. Particle Size Analysis Results at A1G1F1 (a) Top Flange Bottom, (b) Web, (c) Bottom Flange Bottom.

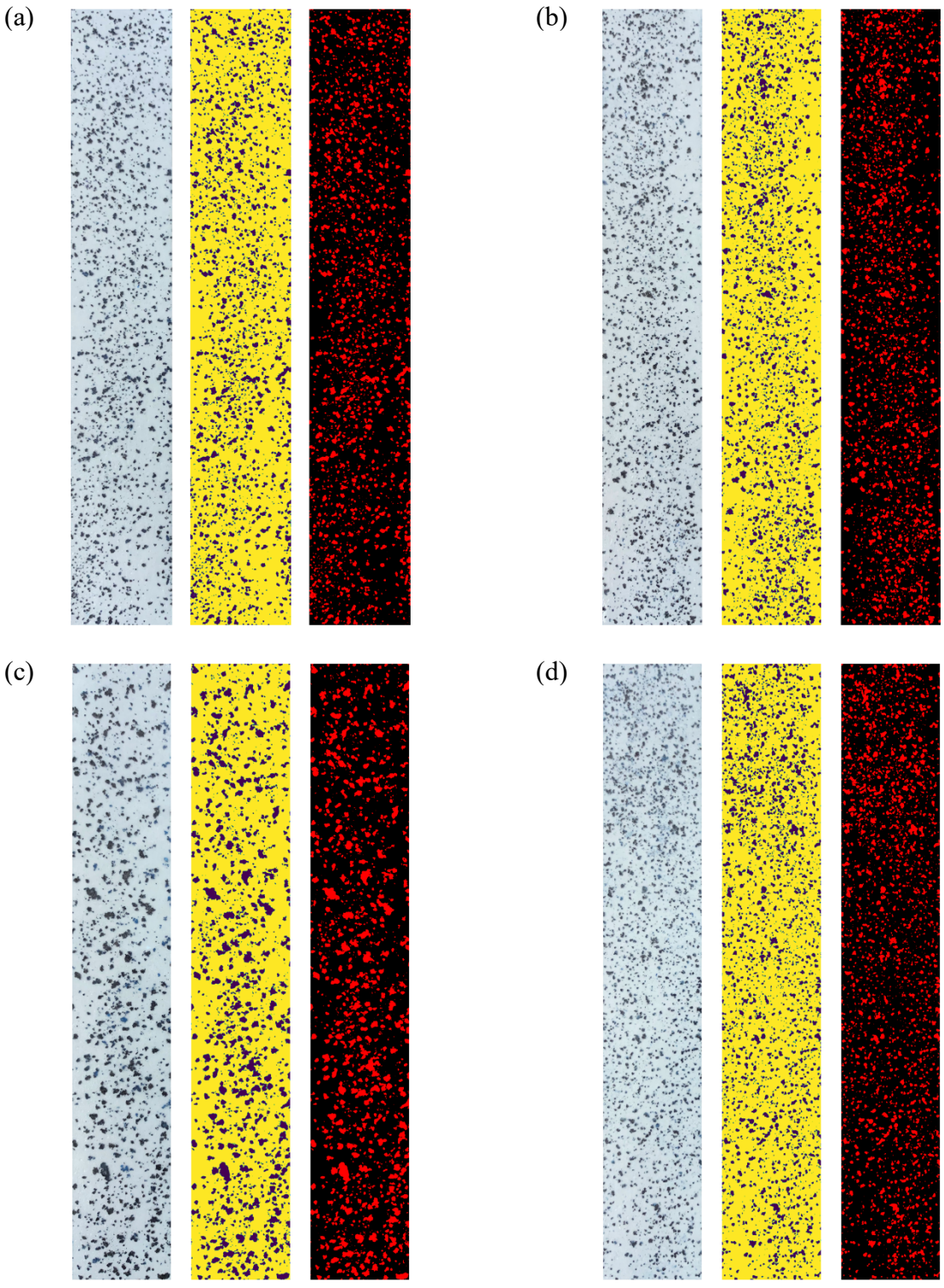


Figure A.333. Particle Size Analysis Results at A1G5F2 (a) Top Flange Bottom, (b) Web, (c) Bottom Flange Bottom.

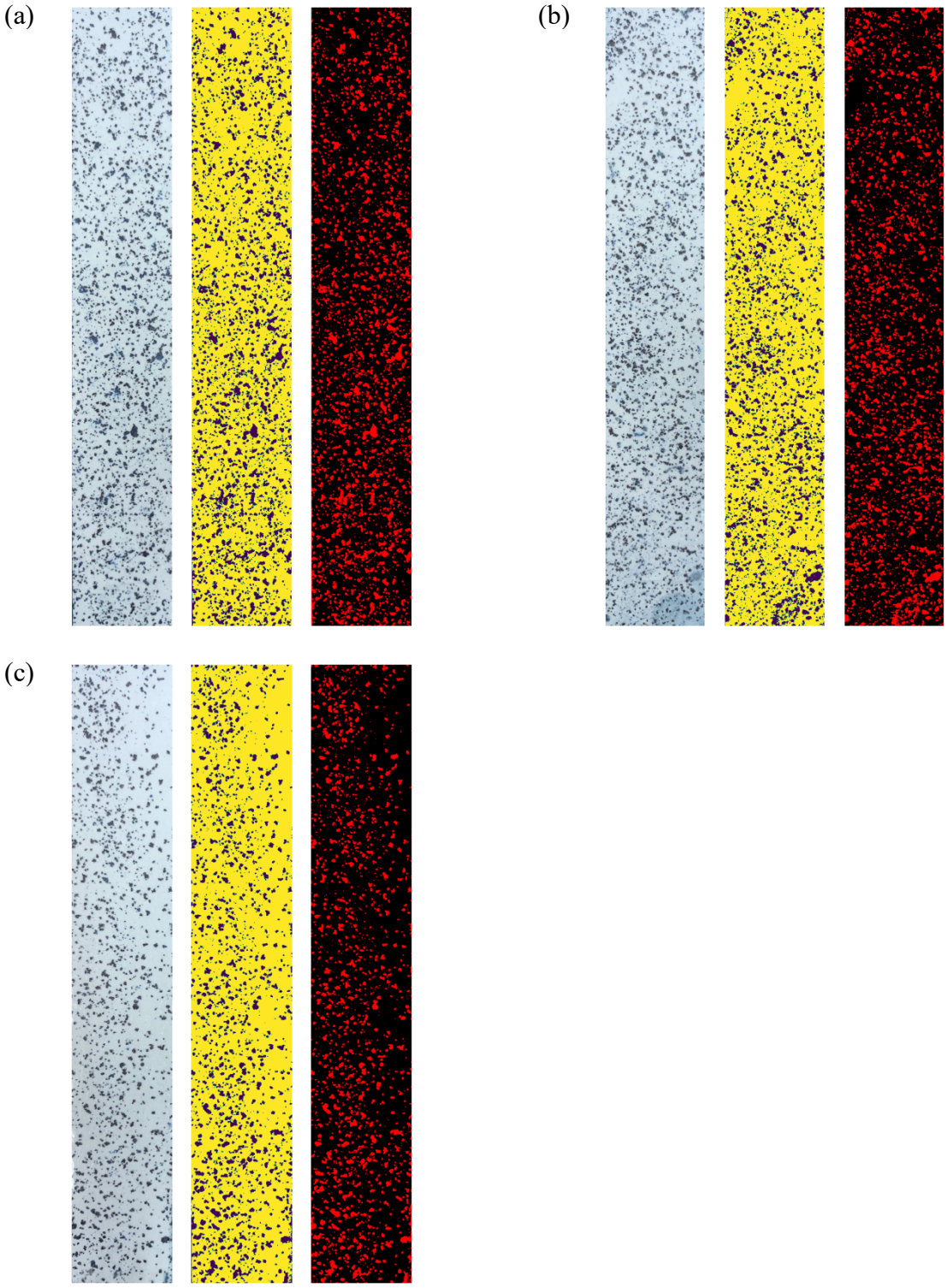


Figure A.334. Particle Size Analysis Results at A1G6F1 (a) Top Flange Bottom, (b) Web, (c) Bottom Flange Bottom.

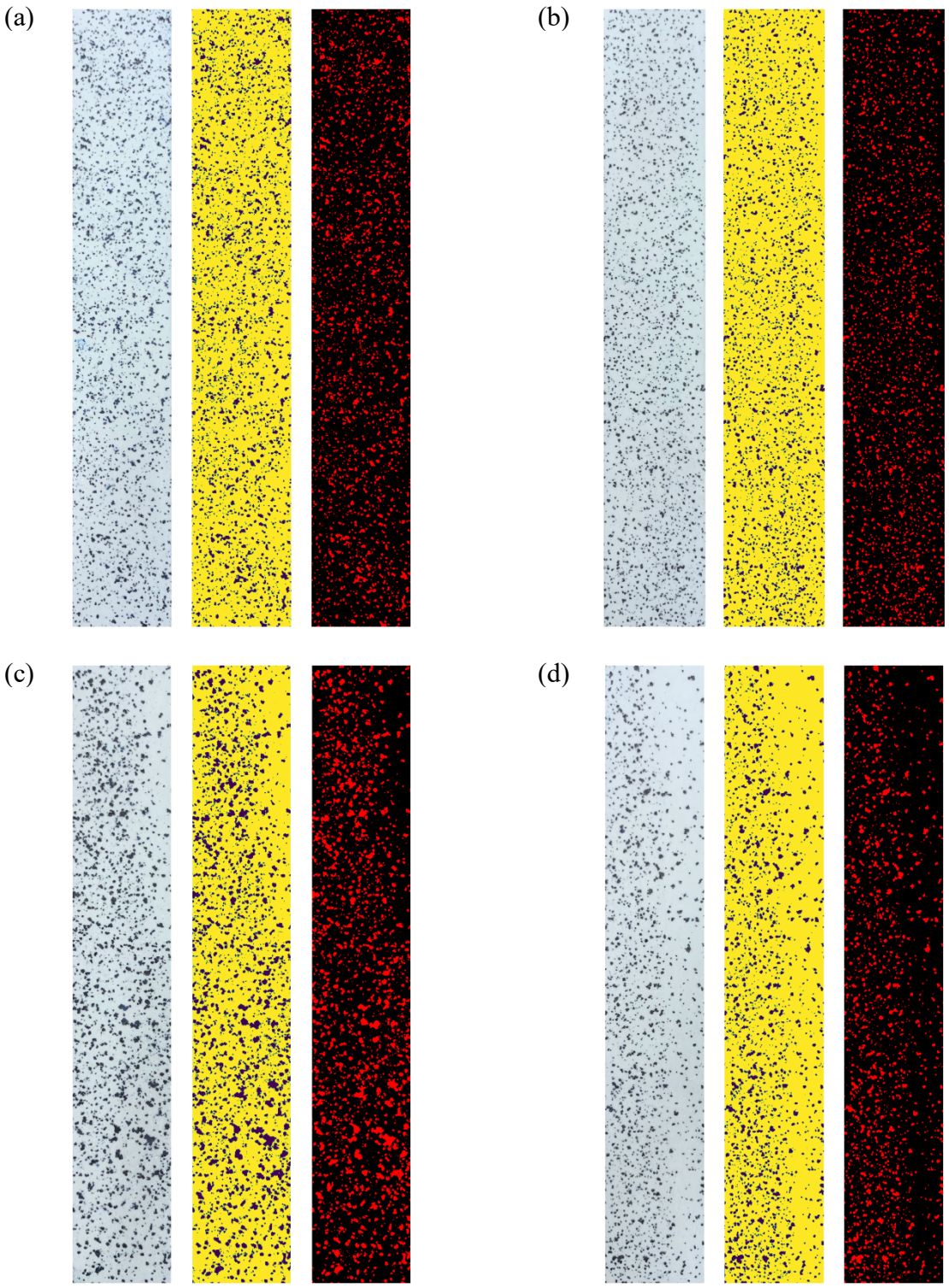


Figure A.335. Particle Size Analysis Results at A1G12F2 (a) Top Flange Bottom, (b) Web, (c) Bottom Flange Bottom (d) Stiffener.

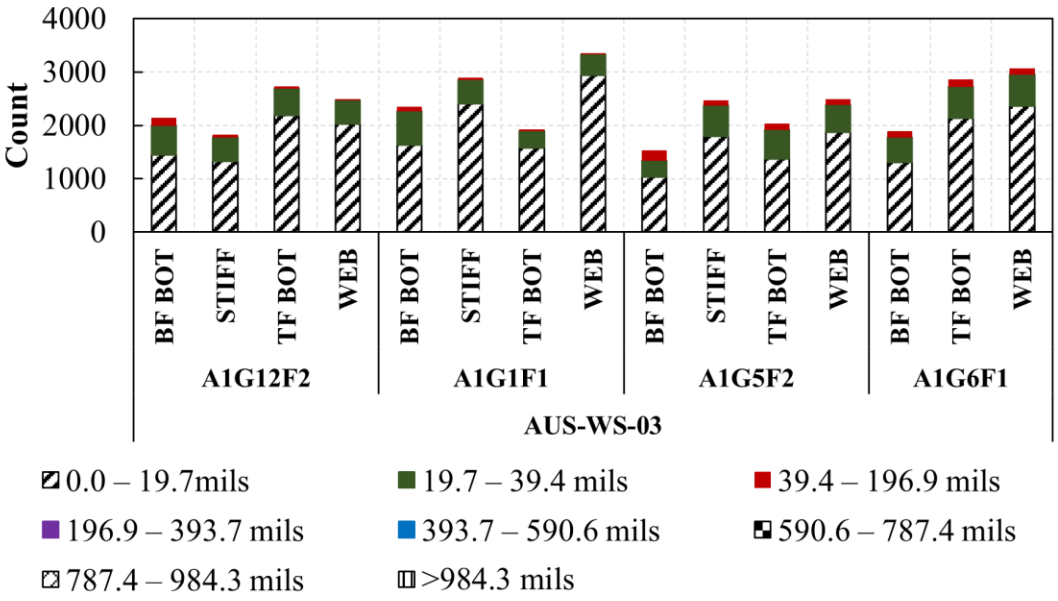


Figure A.336. Particle Size Analysis Showing Different Locations Examined.

A.23. AUS-WS-04

- IH 35 NB to US 290 EB over IH 35 NB FR
- Bridge ID 142270001513451, Coordinates (30.3202, -97.7067), Travis County
- Continuous weathering steel box girder (ASTM A588 HS 50)
- Built 2002
- Date of Inspection: November 25, 2020 girder inspection carried on east end abutment and bent 3, and measurements are taken on girder within three feet from the abutment or bent.
- No visual inspection on deck
- Location for Testing: A1-G1F1, A1-G1F2, A1-G2F1, A1-G2F2



Figure A.337. Typical Elevation of AUS-WS-04

A.23.1. Observed Condition

Overall patina condition on web, top flange and bottom flange of trapezoidal box girder is in good condition. Overall patina rating of web is 8. For top flange bottom, the patina ating is 7, the patina rating for bottom flange bottom is 7. The steel bent cap is inspected visually from ground. Overall bent cap has a patina rating between 6 and 7.



(a) Patina Condition Observed on Girder 1 and Girder 2 for Span 1



(c) Patina Condition observed on Girders for Span 2



(e) Patina Condition of Bent



(f) Poultice Corrosion on BF Top of Interior Girder

Figure A.338. Patina Condition on Girders and Bent Cap of AUS-WS-04

A.23.2.Field Testing and Tape Adhesion Results

Table A-113. Field Inspection Results for AUS-WS-04.

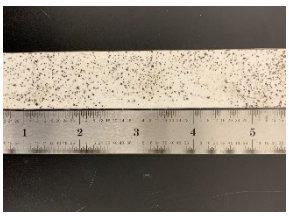
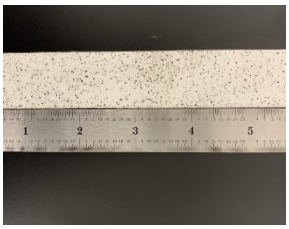
Location	Patina Rating	Thickness (inch)	Cl^- Conc. (ppm)	Field Condition	Tape Test
A1-G1F1 TF Bot. Ext.	7	Measured R1 0.996 R2 0.996 R3 0.995 R_Avg 0.996 Design 1.000			
A1-G1F1 Web Ext.	8	Measured R1 0.629 R2 0.631 R3 0.630 R_Avg 0.630 Design 0.625	3		
A1-G1F1 BF Bot. Ext.	7	Measured R1 0.748 R2 0.748 R3 0.748 R_Avg 0.748 Design 1.000			
A1-G1F2 TF Bot. Int.	7	Measured R1 0.999 R2 0.996 R3 0.997 R_Avg 0.997 Design 1.000			
A1-G1F2 Web Int.	8	Measured R1 0.625 R2 0.626 R3 0.628 R_Avg 0.626 Design 0.625	1		

Table A-114. Field Inspection Results for AUS-WS-04.

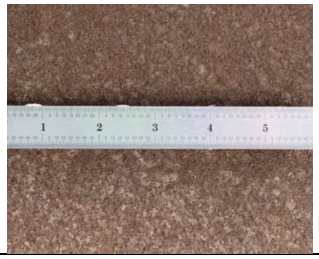
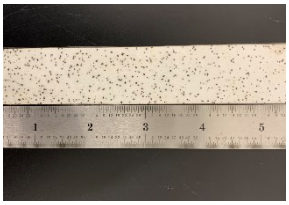
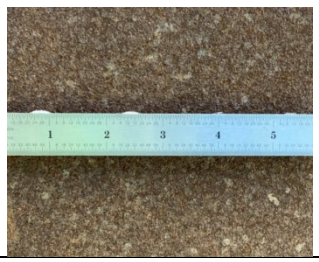
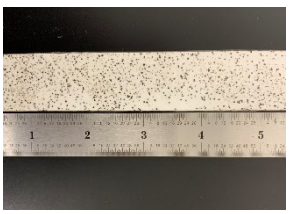
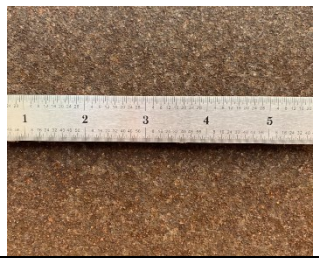
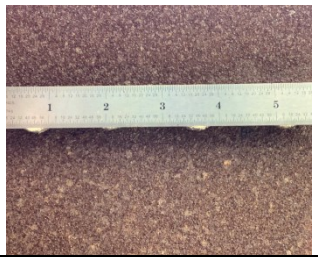
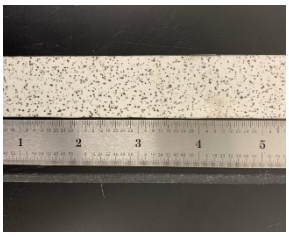
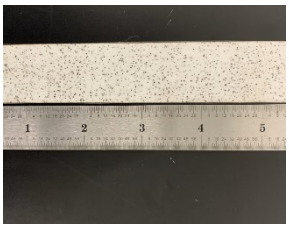
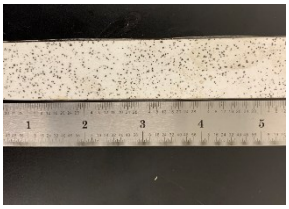
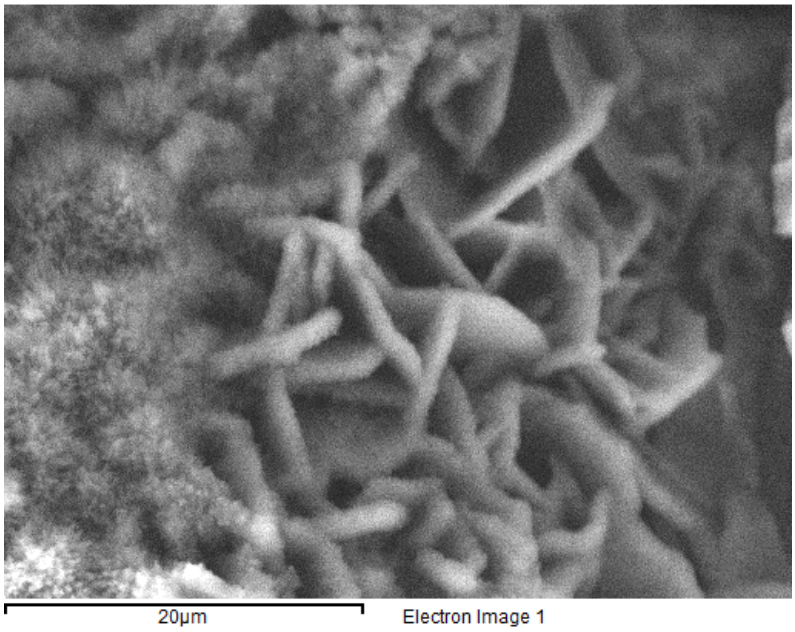
Location	Patina Rating	Thickness (inch)	Cl^- Conc. (ppm)	Field Condition	Tape Test
A1-G1F2 BF Bot. Int.	7	Measured R1 0.748 R2 0.746 R3 0.751 R_Avg 0.748 Design 0.750			
A1-G2F1 TF Bot. Int.	7	Measured R1 0.994 R2 0.993 R3 0.991 R_Avg 0.993 Design 1.000			
A1-G2F1 Web Int.	8	Measured R1 0.627 R2 0.627 R3 0.625 R_Avg 0.626 Design 0.625			
A1-G2F1 BF Bot. Int.	7	Measured R1 0.752 R2 0.750 R3 0.753 R_Avg 0.752 Design 0.750			
A1-G2F2 TF Bot. Ext.	7	Measured R1 0.997 R2 0.994 R3 0.992 R_Avg 0.994 Design 1.000	3		

Table A-115. Field Inspection Results for AUS-WS-04.

Location	Patina Rating	Thickness (inch)	Cl^- Conc. (ppm)	Field Condition	Tape Test
A1-G2F2 Web Ext.	8	Measured R1 0.634 R2 0.632 R3 0.629 R_Avg 0.632 Design 0.625			
A1-G2F2 BF Bot. Ext.	7	Measured R1 0.751 R2 0.751 R3 0.750 R_Avg 0.751 Design 0.750			
B2-G1F1 Web Ext.	8	Measured R1 0.750 R2 0.752 R3 0.753 R_Avg 0.752 Design 0.750			
B2-G1F1 BF Bot. Ext.	7	Measured R1 2.224 R2 2.227 R3 2.226 R_Avg 2.226 Design 2.225			

A.23.3.SEM/EDS Results: Exterior Web Girder

Element	Weight %	Atomic %
O K	47.51	75.50
Al K	0.26	0.25
S K	1.02	0.81
Cl K	0.48	0.34
Mn K	0.57	0.26
Fe K	49.92	22.73
Ni K	0.25	0.11
Totals	100.00	



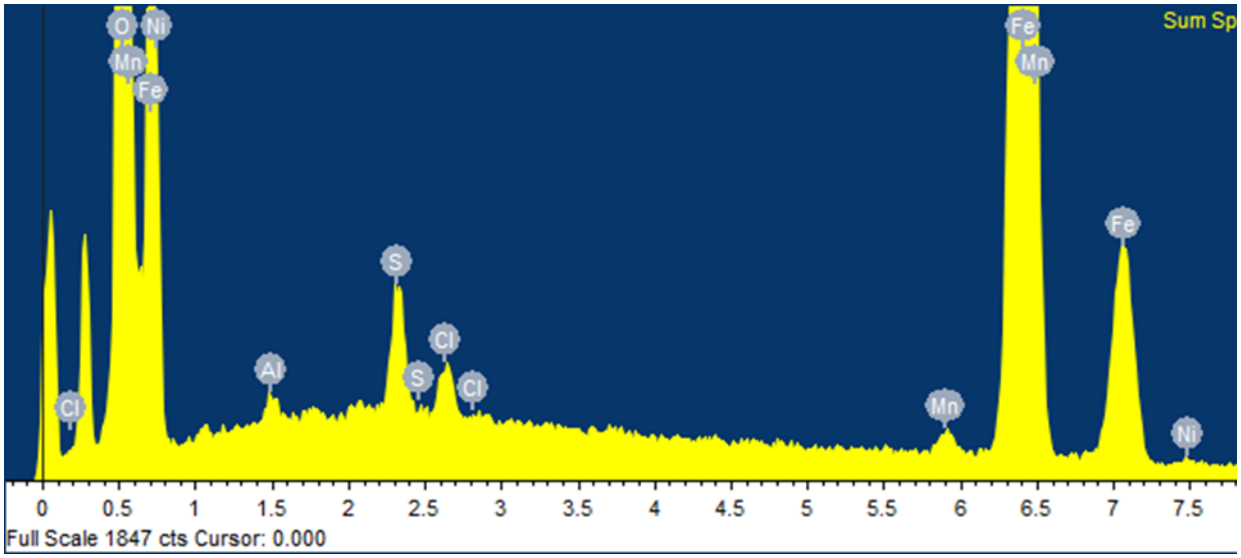


Figure A.339. SEM Image and EDS Spectrum of the Rust Collected from Exterior Web of the Girder.

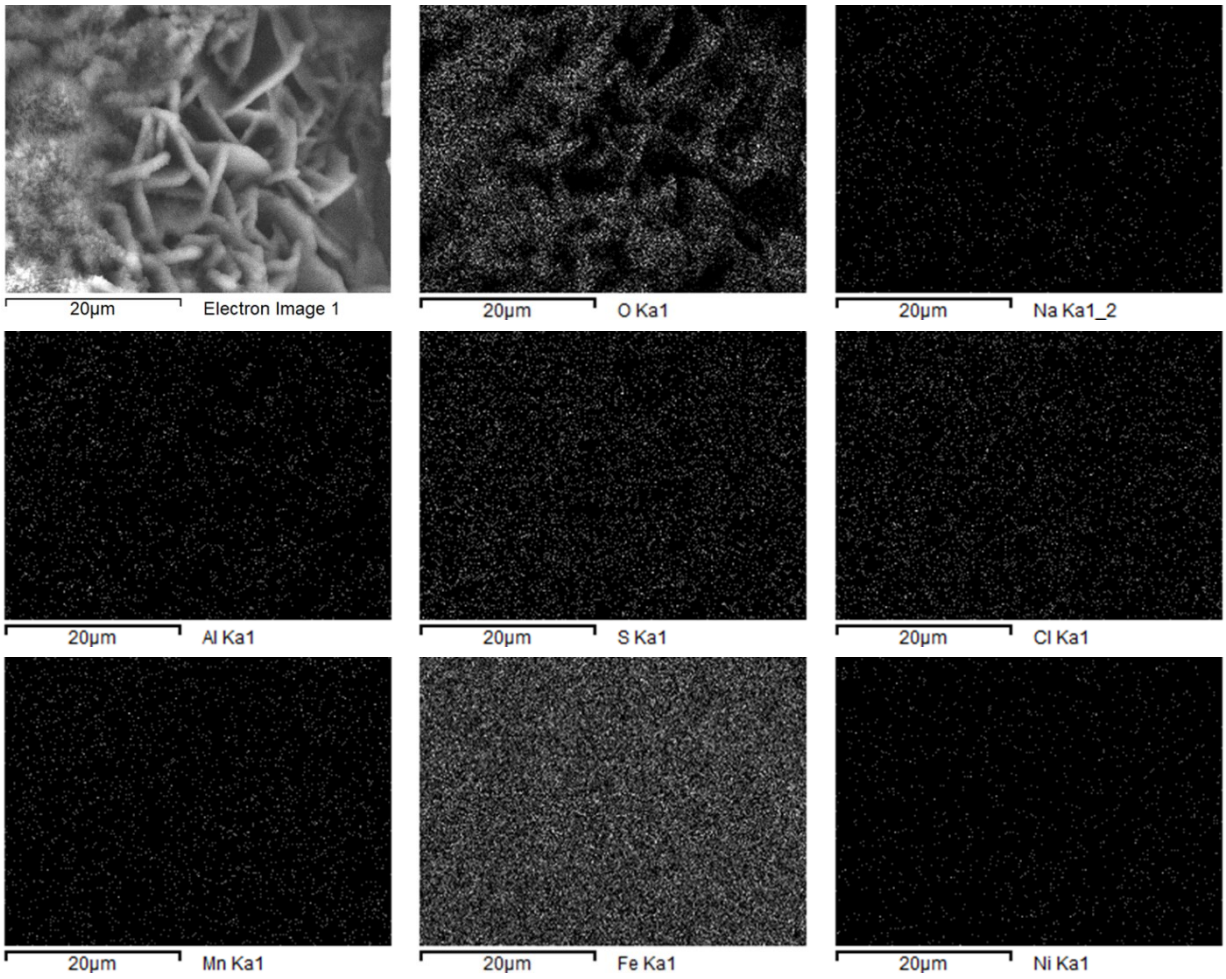
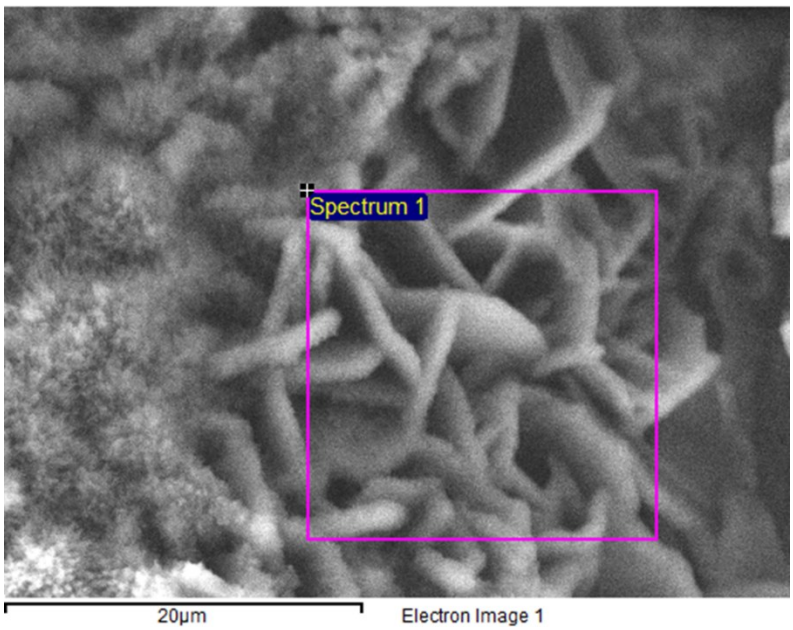


Figure A.340. EDS Elemental Mapping of Rust Collected from Exterior Web.

Element	Weight %	Atomic %
O K	45.12	73.44
Na K	0.47	0.53
Al K	0.31	0.30
S K	1.17	0.95
Cl K	0.38	0.28
Mn K	0.61	0.29
Fe K	51.68	24.10
Ni K	0.26	0.11
Totals	100.00	



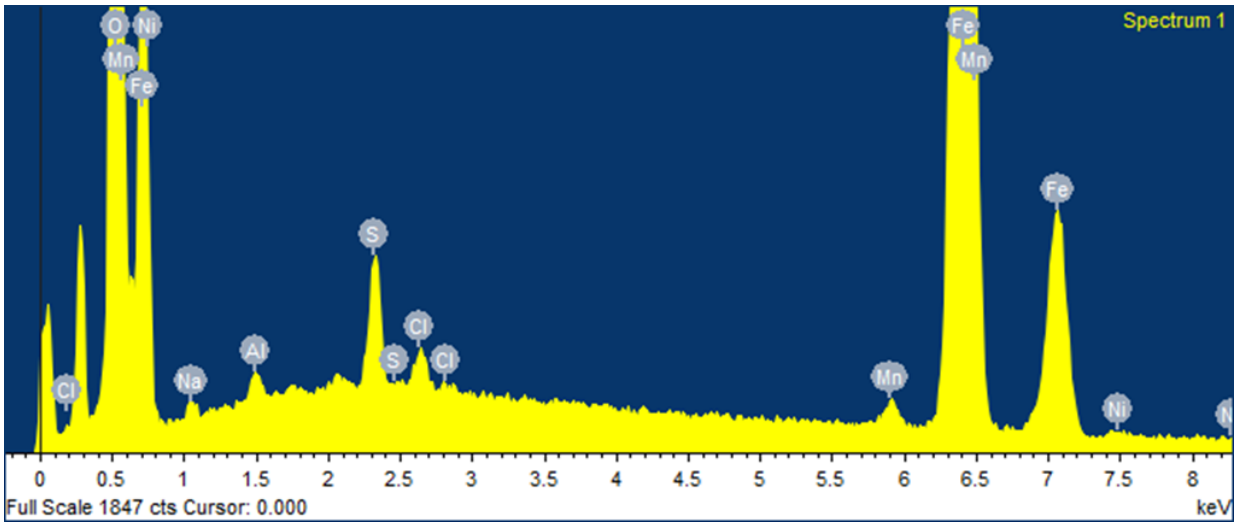
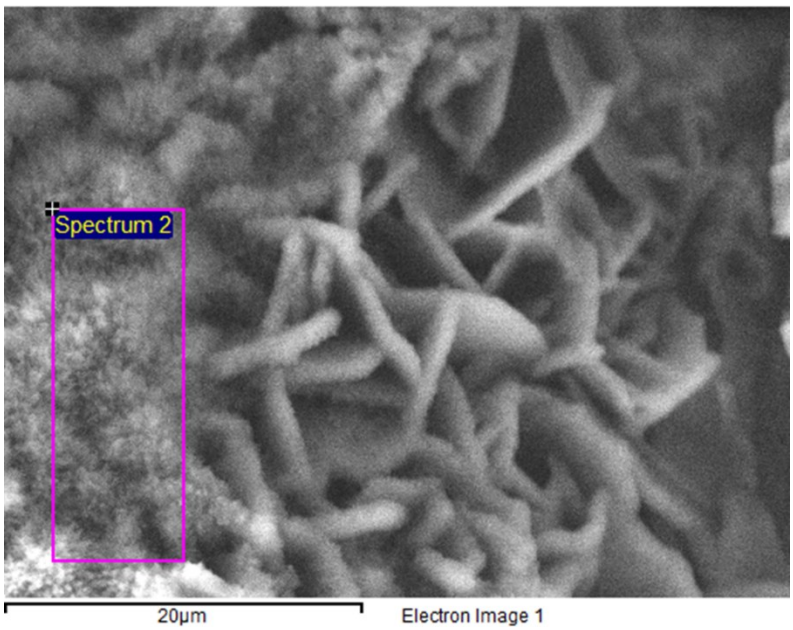


Figure A.341. SEM Image and EDS Spectrum of the Rust Collected from Exterior Web of the Girder.

Element	Weight %	Atomic %
O K	54.16	80.06
Al K	0.27	0.24
S K	0.99	0.73
Cl K	0.40	0.27
Mn K	0.46	0.20
Fe K	43.71	18.51
Totals	100.00	



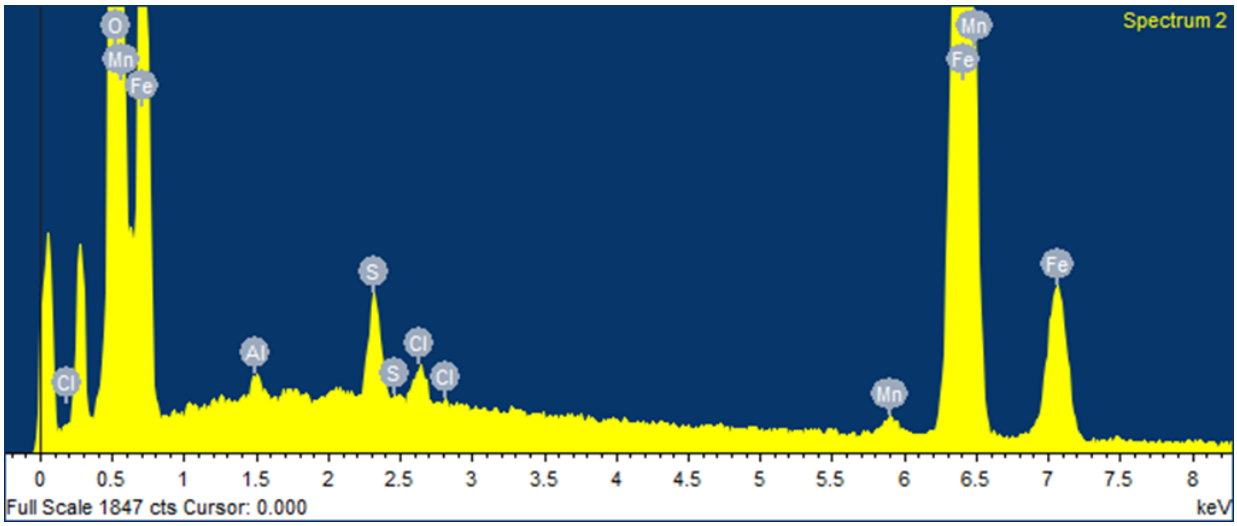


Figure A.342. SEM Image and EDS Spectrum of the Rust Collected from Exterior Web of the Girder.

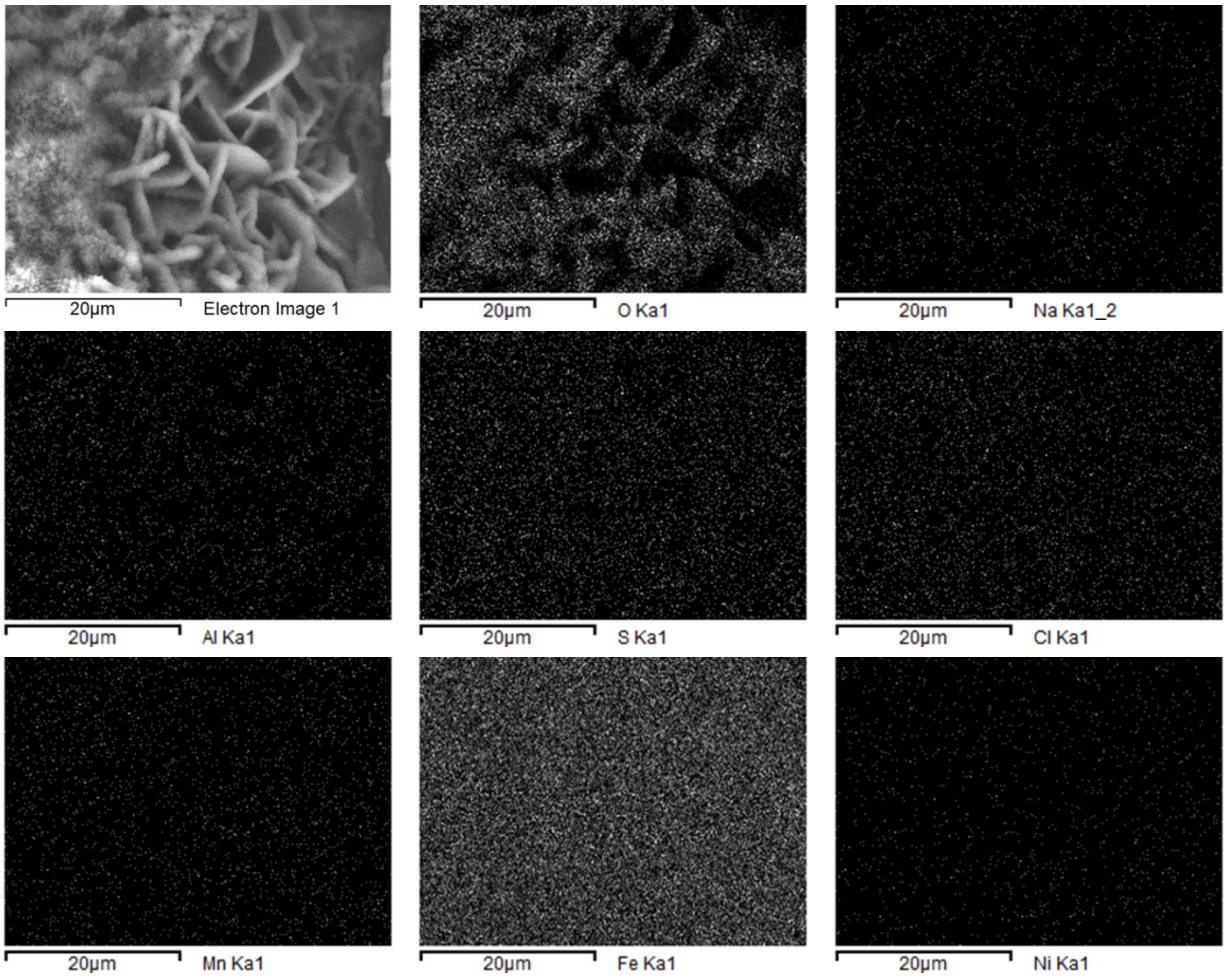
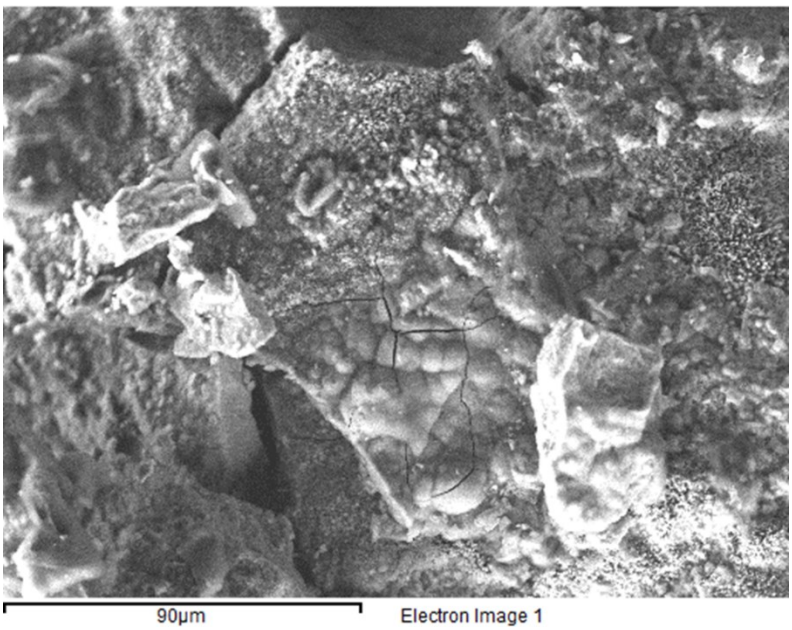


Figure A.343. EDS Elemental Mapping of Rust Collected from Exterior Web.

Element	Weight %	Atomic %
O K	41.18	69.09
Na K	2.02	2.36
Al K	0.54	0.54
Si K	0.30	0.29
S K	1.20	1.00
Cl K	1.03	0.78
K K	0.40	0.27
Ca K	0.20	0.13
Cr K	0.12	0.06
Mn K	0.77	0.38
Fe K	51.93	24.96
Ni K	0.31	0.14
Totals	100.00	



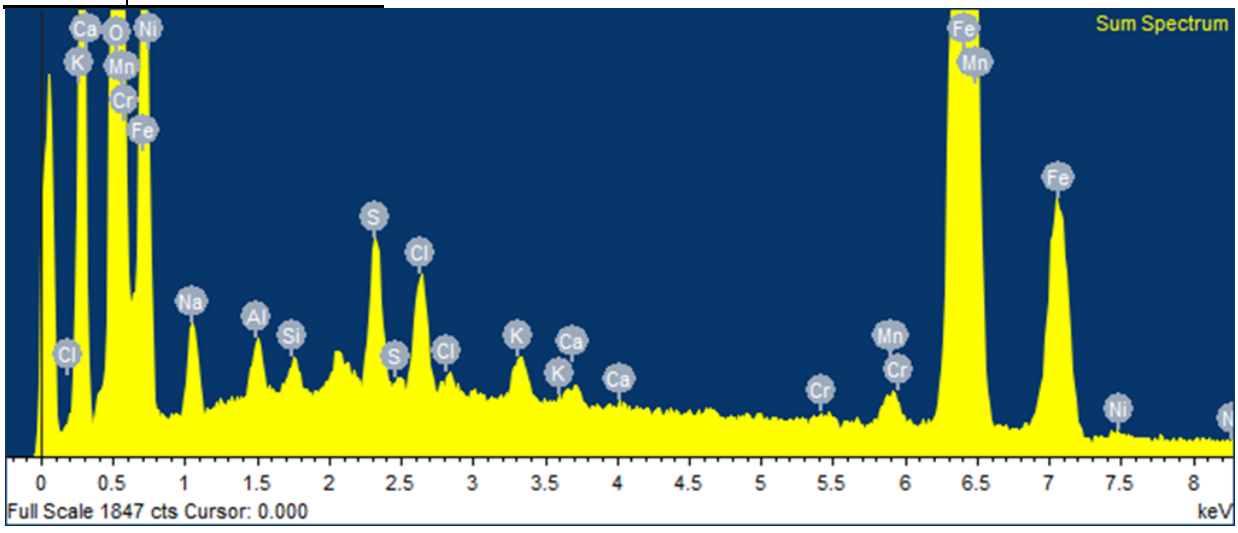
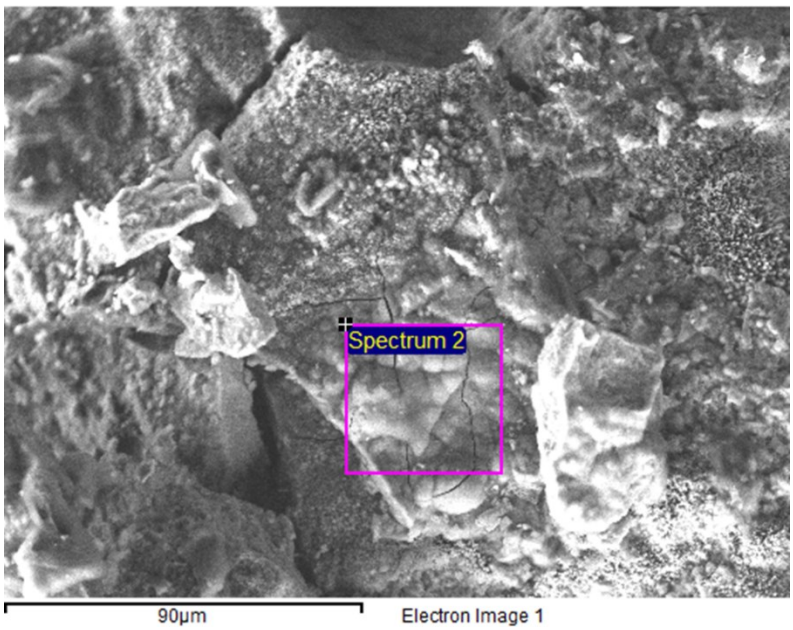


Figure A.344. SEM Image and EDS Spectrum of the Rust Collected from Exterior Web of the Girder.

Element	Weight %	Atomic %
O K	45.68	73.74
Na K	0.38	0.43
Al K	0.50	0.47
S K	1.63	1.31
Cl K	0.34	0.24
Mn K	0.56	0.26
Fe K	50.64	23.42
Ni K	0.27	0.12
Totals	100.00	



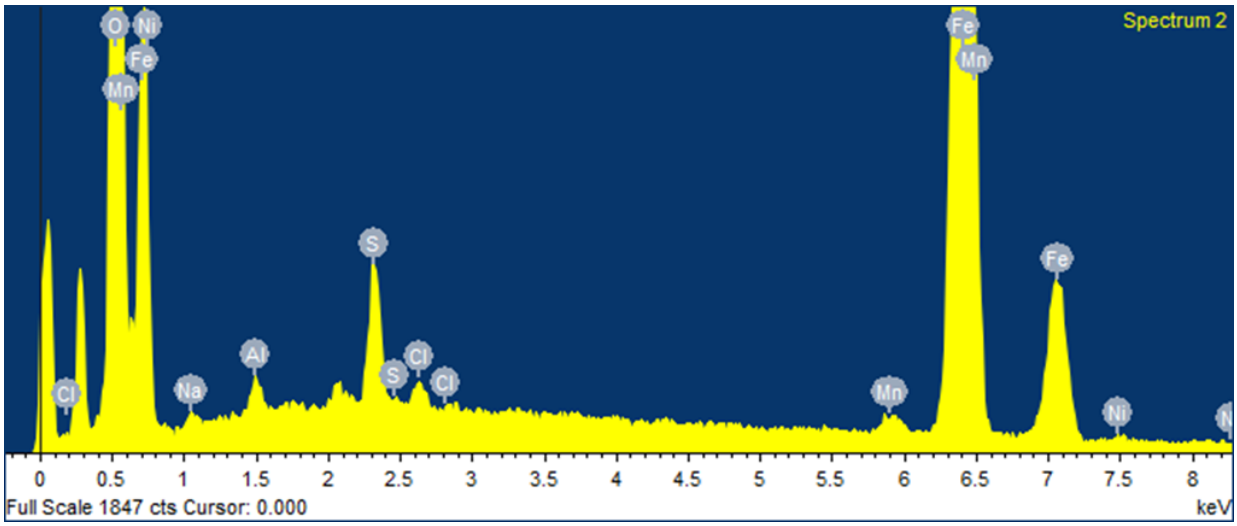
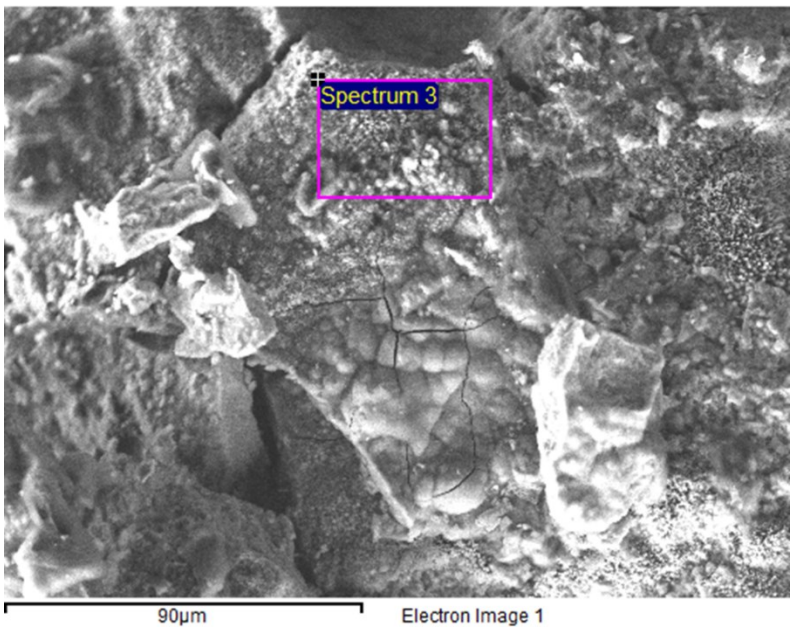


Figure A.345. SEM Image and EDS Spectrum of the Rust Collected from Exterior Web of the Girder.

Element	Weight %	Atomic %
O K	39.62	67.74
Na K	1.94	2.30
Al K	0.71	0.72
Si K	0.25	0.25
S K	1.29	1.10
Cl K	0.91	0.70
K K	0.43	0.30
Ca K	0.16	0.11
Mn K	1.18	0.59
Fe K	53.16	26.03
Ni K	0.35	0.16
Totals	100.00	



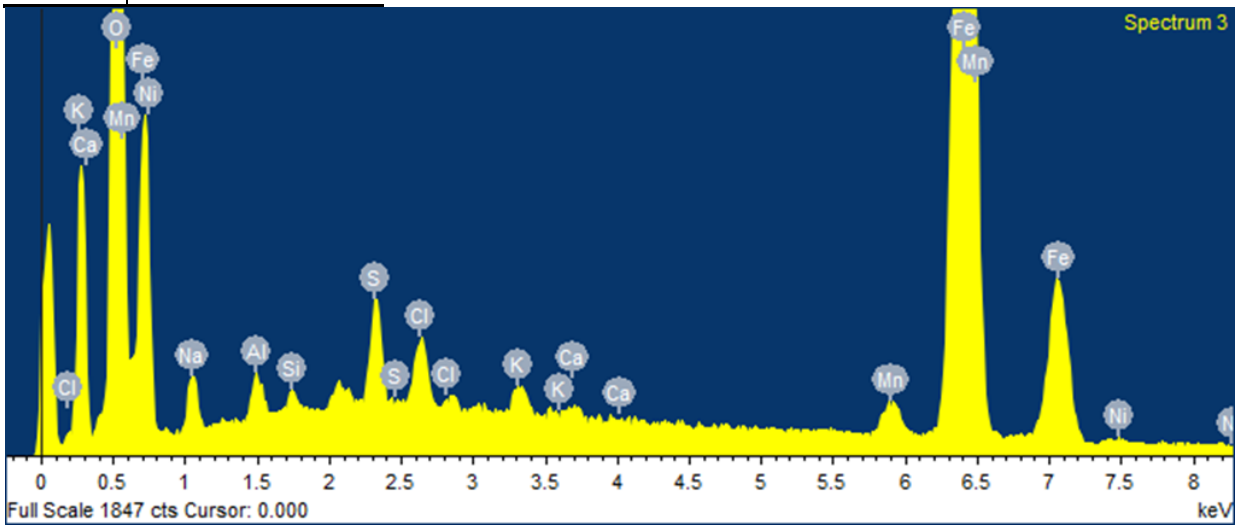


Figure A.346. SEM Image and EDS Spectrum of the Rust Collected from Exterior Web of the Girder.

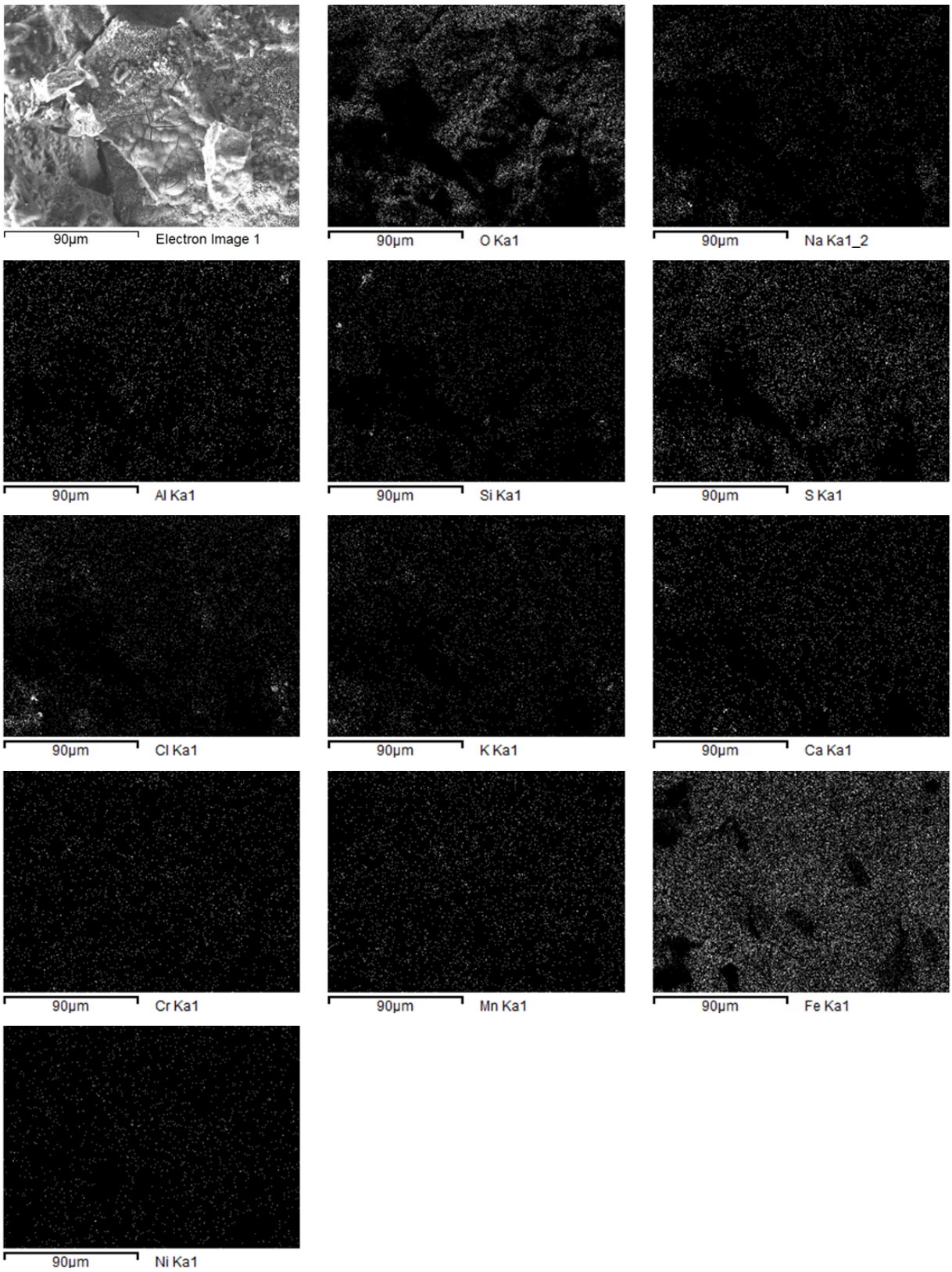
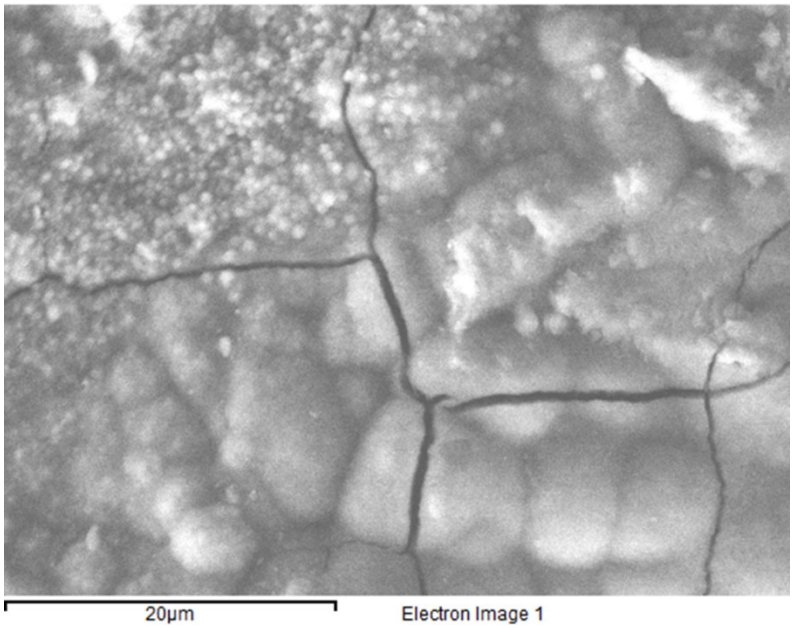


Figure A.347. EDS Elemental Mapping of Rust Collected from Exterior Web.

Element	Weight %	Atomic %
O K	45.04	73.00
Na K	0.71	0.81
Al K	0.46	0.44
Si K	0.18	0.17
S K	1.64	1.33
Cl K	0.46	0.34
Mn K	0.77	0.36
Fe K	50.45	23.43
Ni K	0.28	0.12
Totals	100.00	



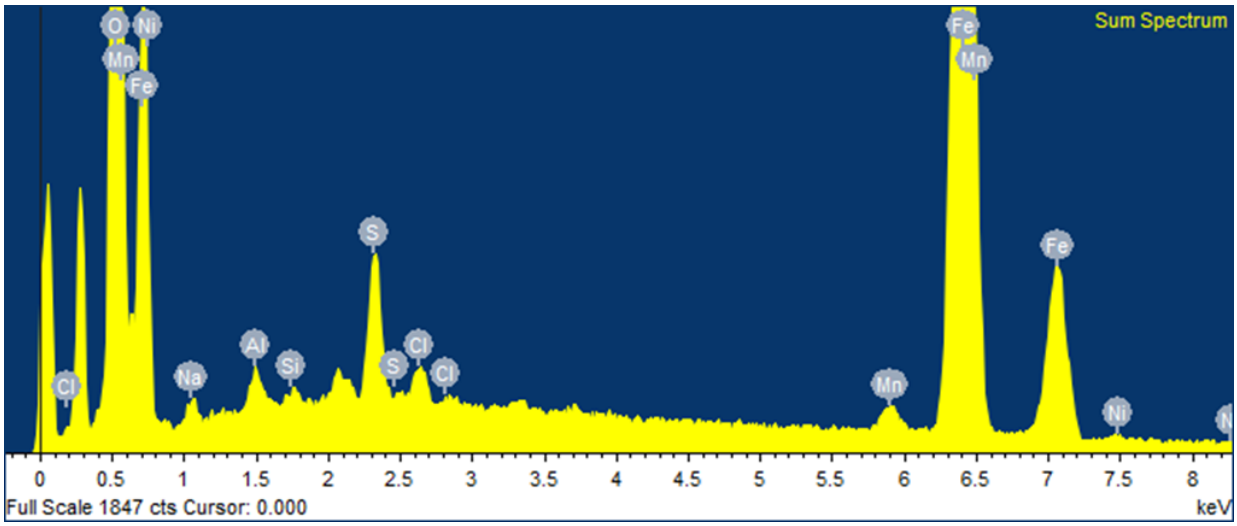
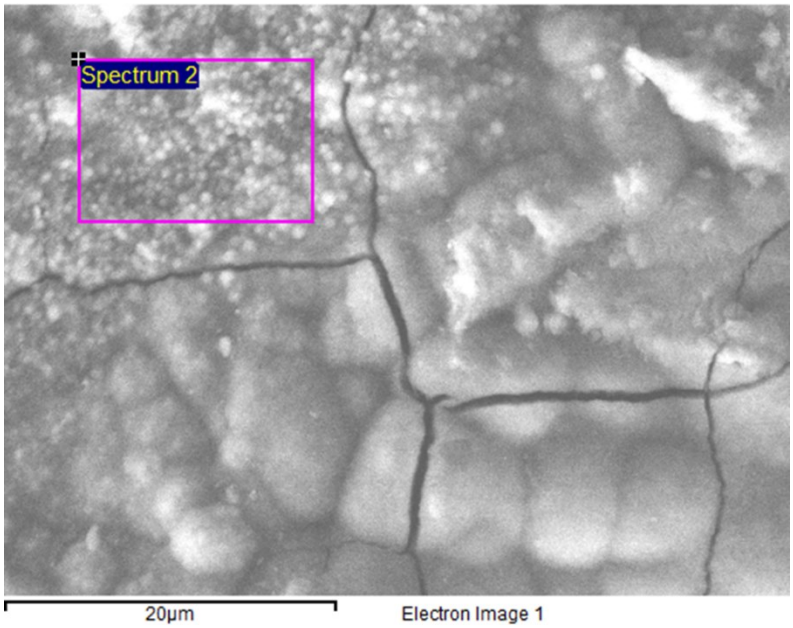


Figure A.348. SEM Image and EDS Spectrum of the Rust Collected from Exterior Web of the Girder.

Element	Weight %	Atomic %
O K	44.86	72.87
Na K	0.77	0.87
Al K	0.64	0.62
S K	1.44	1.17
Cl K	0.43	0.32
Ca K	0.12	0.08
Mn K	1.08	0.51
Fe K	50.23	23.37
Ni K	0.43	0.19
Totals	100.00	



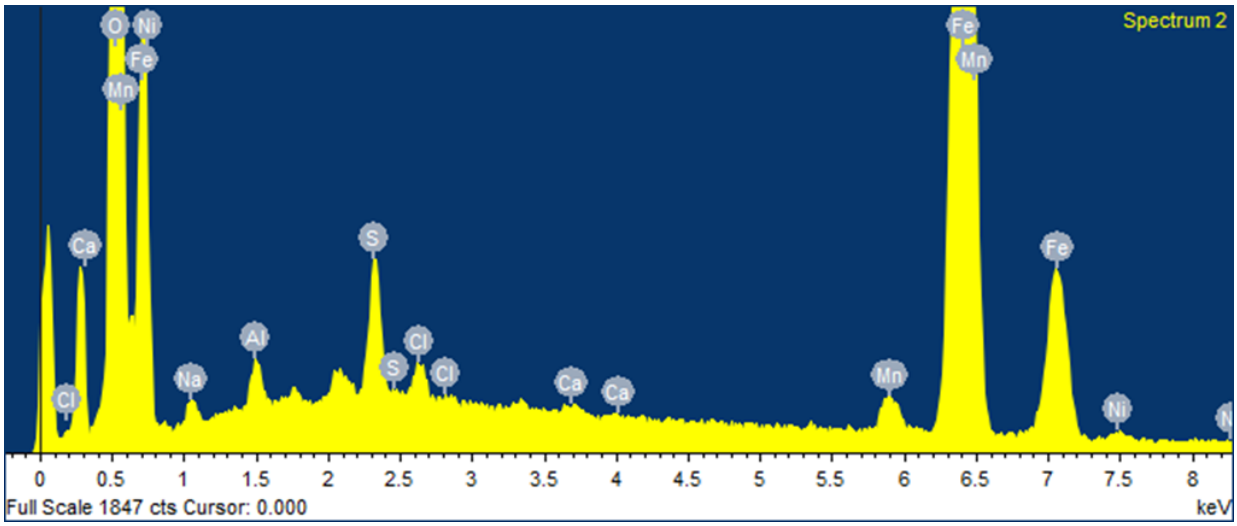
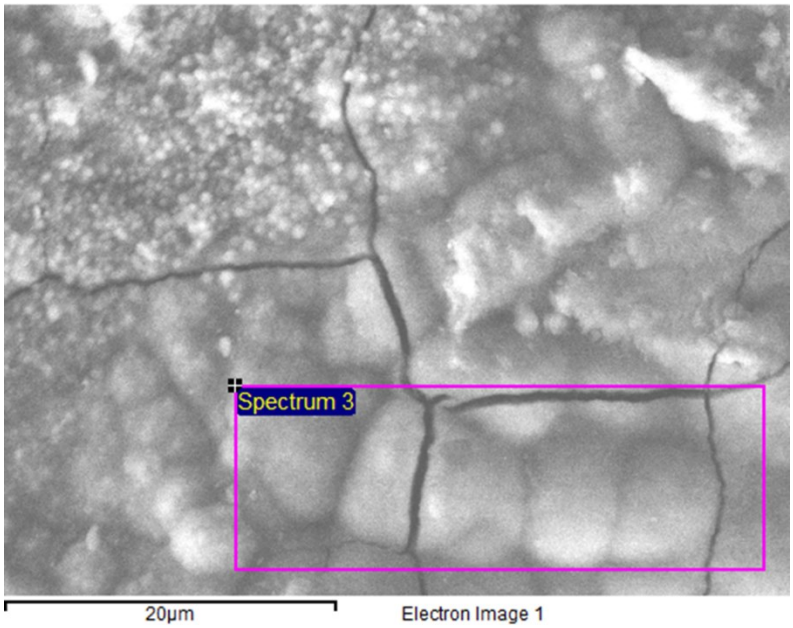


Figure A.349. SEM Image and EDS Spectrum of the Rust Collected from Exterior Web of the Girder.

Element	Weight %	Atomic %
O K	46.72	74.69
Al K	0.47	0.44
S K	1.68	1.34
Cl K	0.34	0.24
Ca K	0.12	0.08
Mn K	0.71	0.33
Fe K	49.54	22.69
Ni K	0.42	0.18
Totals	100.00	



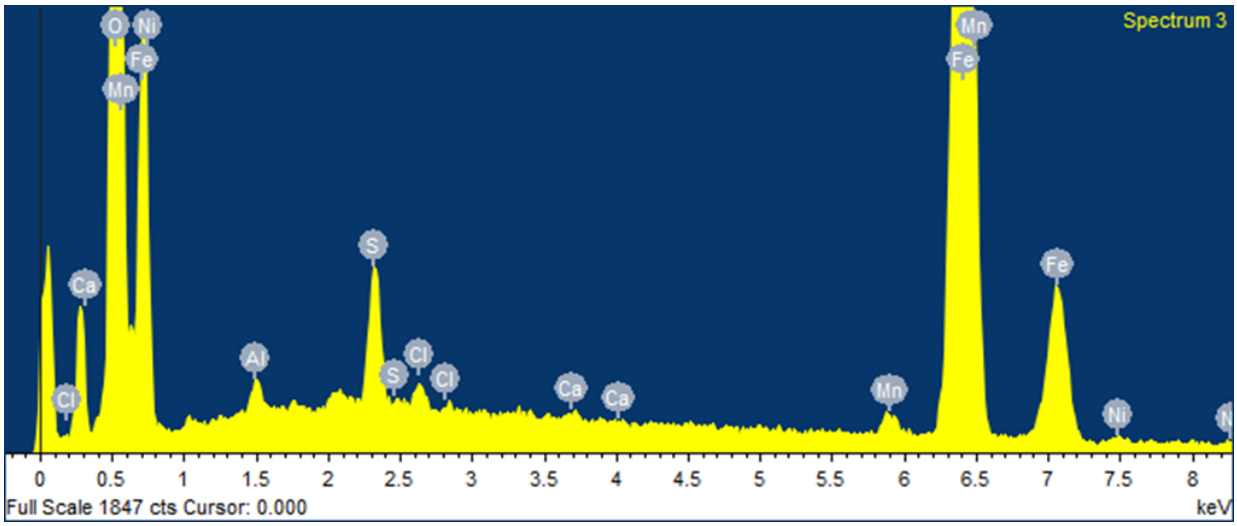


Figure A.350. SEM Image and EDS Spectrum of the Rust Collected from Exterior Web of the Girder.

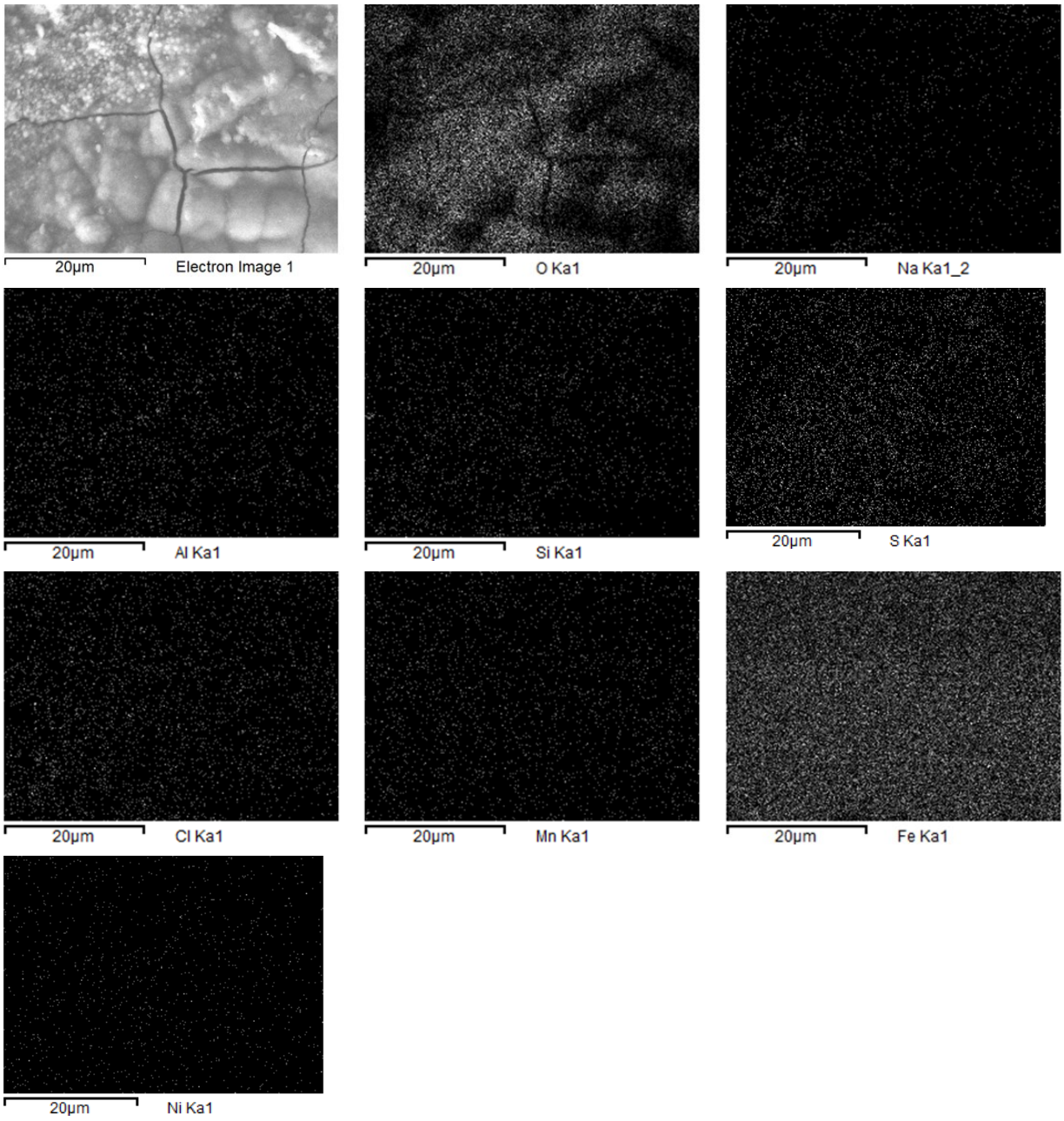
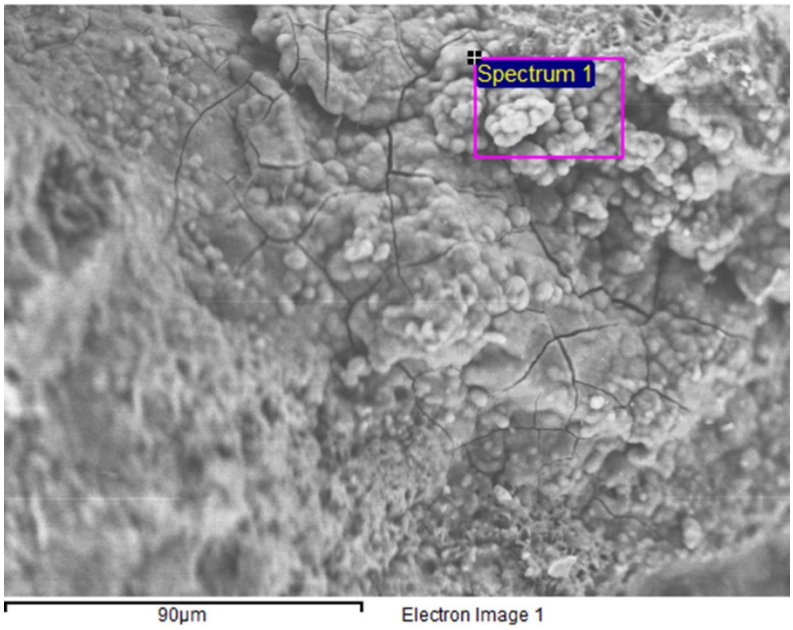


Figure A.351. EDS Elemental Mapping of Rust Collected from Exterior Web.

A.23.4.SEM/EDS Results: Interior Web Girder

Element	Weight %	Atomic %
O K	49.16	76.19
Al K	0.50	0.46
S K	2.01	1.55
Cl K	1.39	0.98
Fe K	46.19	20.51
Ni K	0.76	0.32
Totals	100.00	



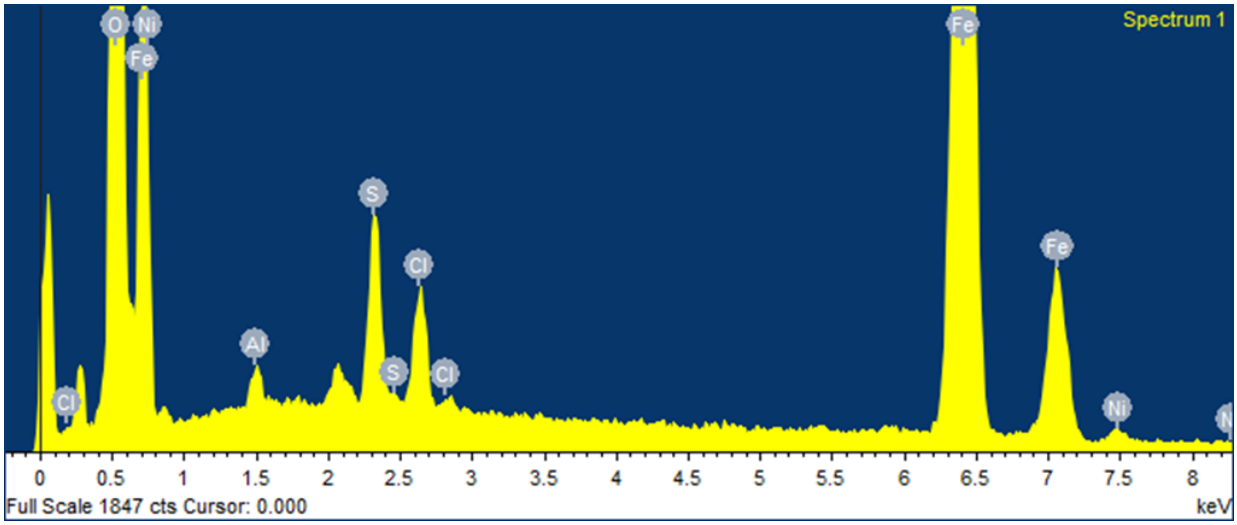
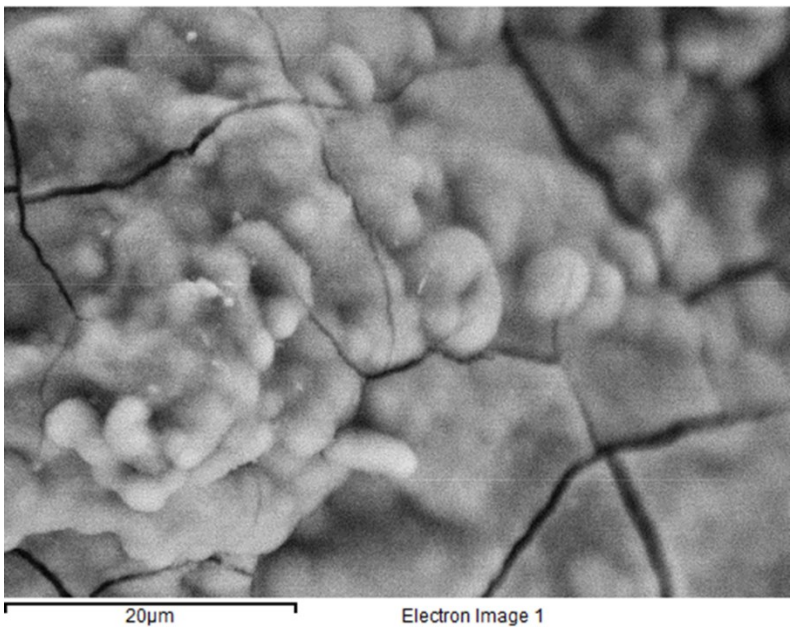


Figure A.352. SEM Image and EDS Spectrum of the Rust Collected from Interior Web of the Girder.

Element	Weight %	Atomic %
O K	12.53	32.49
Al K	2.63	4.04
Si K	0.12	0.17
S K	0.65	0.84
Cl K	0.28	0.33
Cr K	0.17	0.13
Mn K	0.27	0.21
Fe K	80.38	59.70
Ni K	2.97	2.10
Totals	100.00	



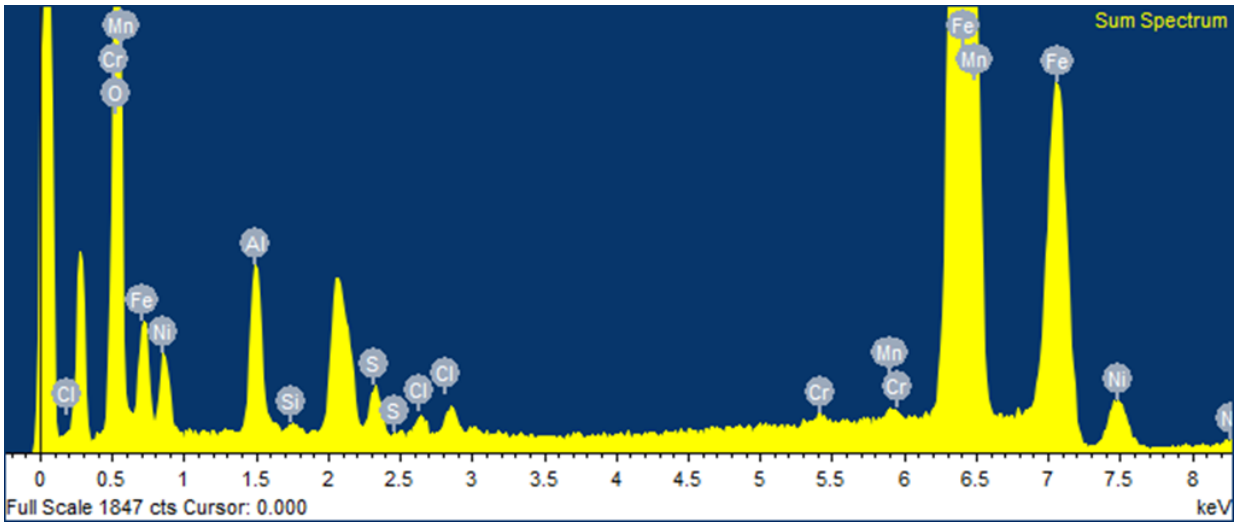


Figure A.353. SEM Image and EDS Spectrum of the Rust Collected from Interior Web of the Girder.

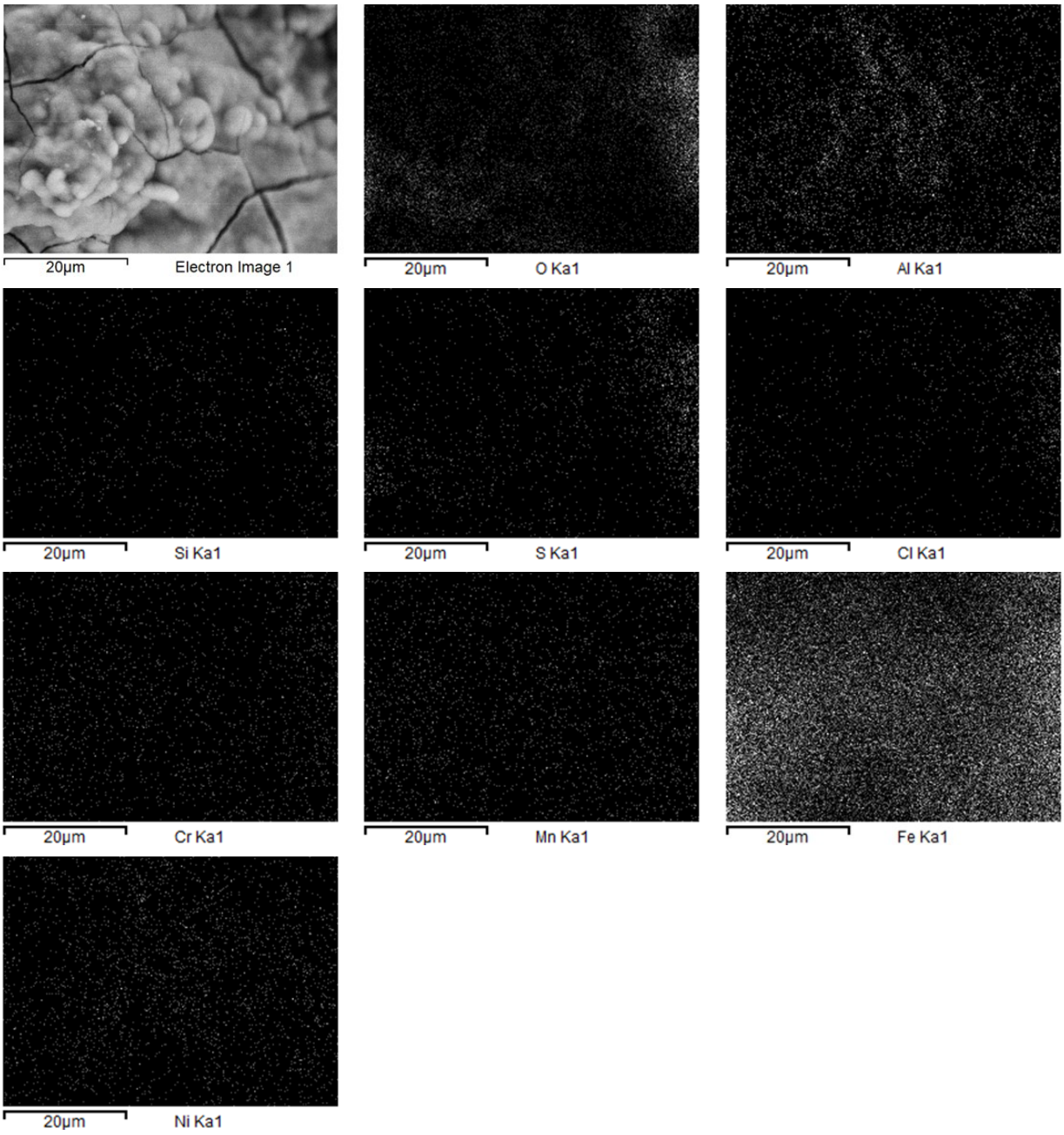
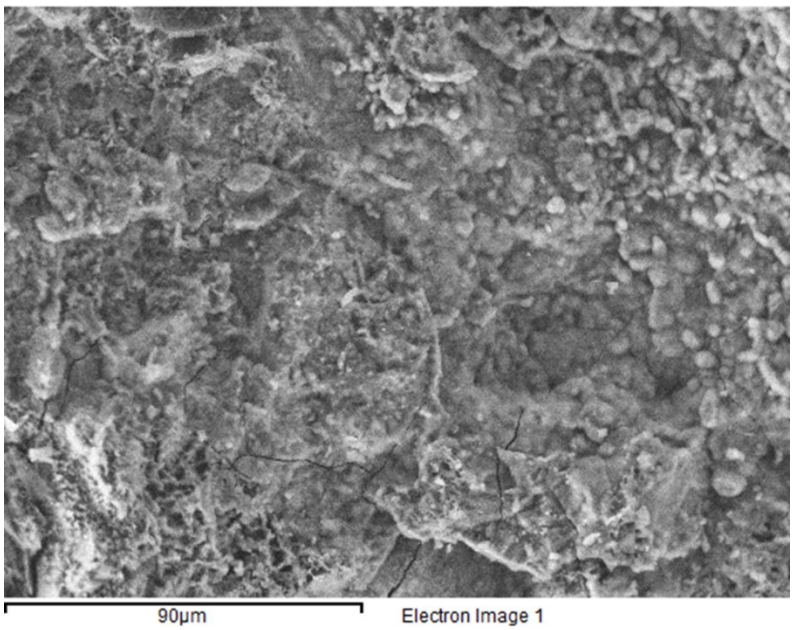


Figure A.354. EDS Elemental Mapping of Rust Collected from Interior Web.

Element	Weight %	Atomic %
O K	39.91	69.27
Al K	0.38	0.39
Si K	0.29	0.28
S K	1.08	0.94
Cl K	0.40	0.31
Cr K	0.19	0.10
Mn K	0.76	0.39
Fe K	56.52	28.10
Ni K	0.46	0.22
Totals	100.00	



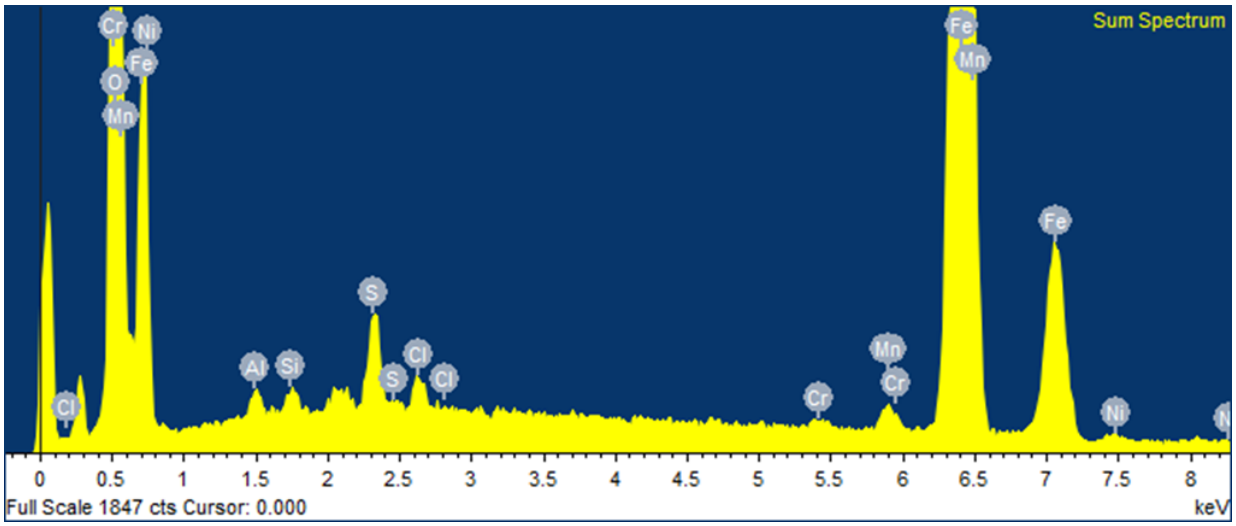
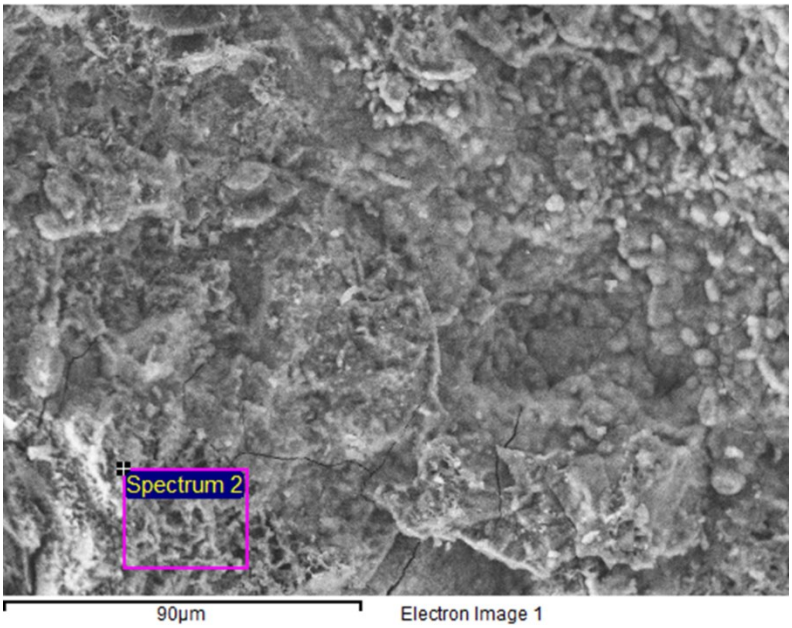


Figure A.355. SEM Image and EDS Spectrum of the Rust Collected from Interior Web of the Girder.

Element	Weight %	Atomic %
O K	40.14	69.61
Al K	0.26	0.27
Si K	0.15	0.15
S K	1.01	0.87
Cl K	0.27	0.21
Mn K	0.46	0.23
Fe K	57.39	28.51
Ni K	0.32	0.15
Totals	100.00	



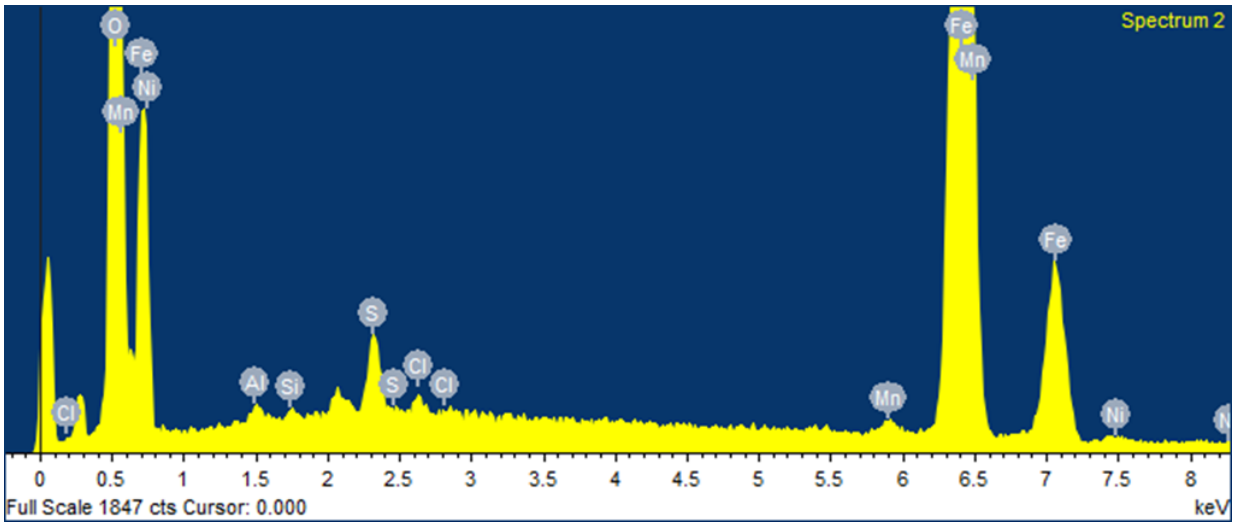
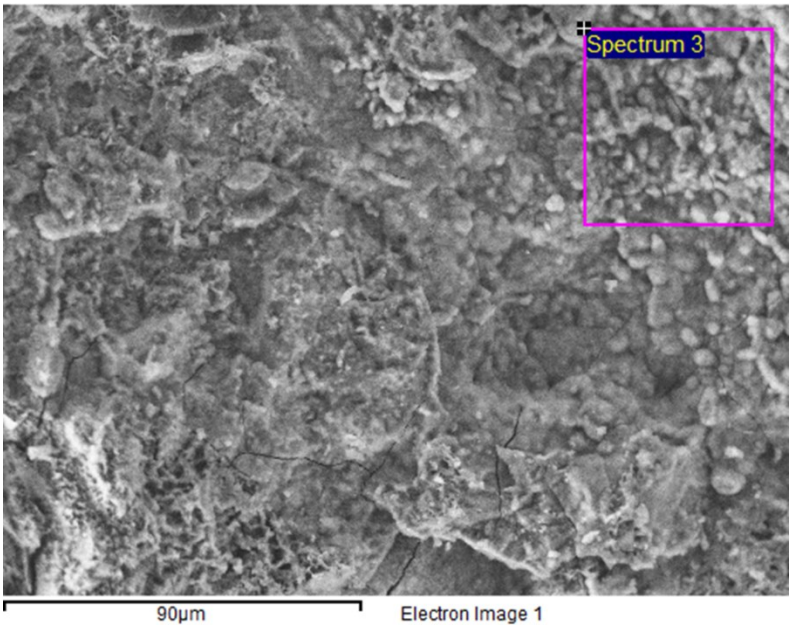


Figure A.356. SEM Image and EDS Spectrum of the Rust Collected from Interior Web of the Girder.

Element	Weight %	Atomic %
O K	44.60	73.09
Al K	0.36	0.35
Si K	0.23	0.21
S K	1.39	1.14
Cl K	0.46	0.34
Mn K	0.70	0.33
Fe K	51.91	24.37
Ni K	0.35	0.16
Totals	100.00	



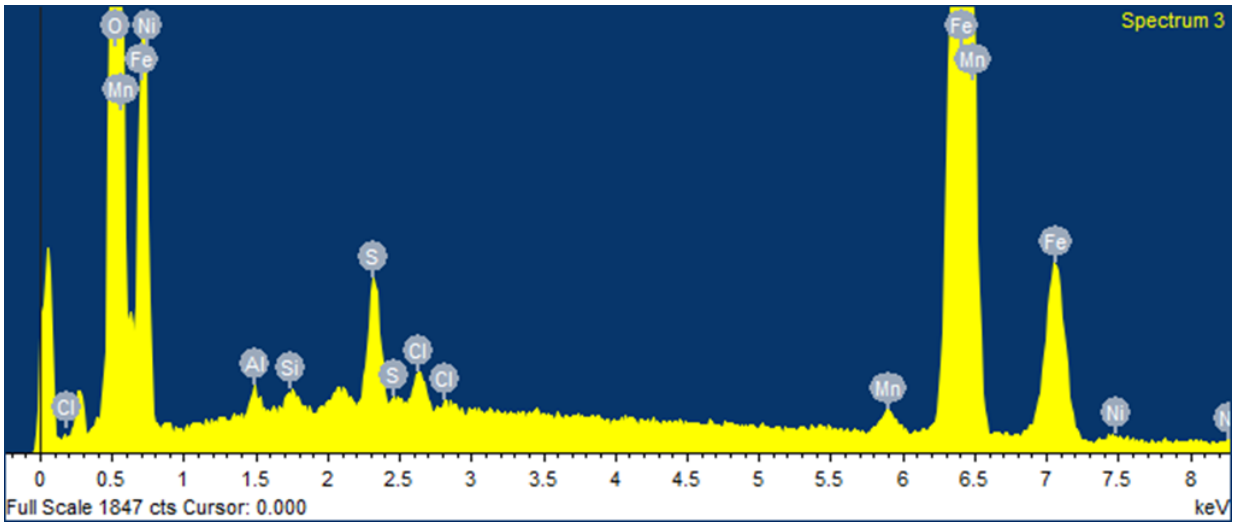


Figure A.357. SEM Image and EDS Spectrum of the Rust Collected from Interior Web of the Girder.

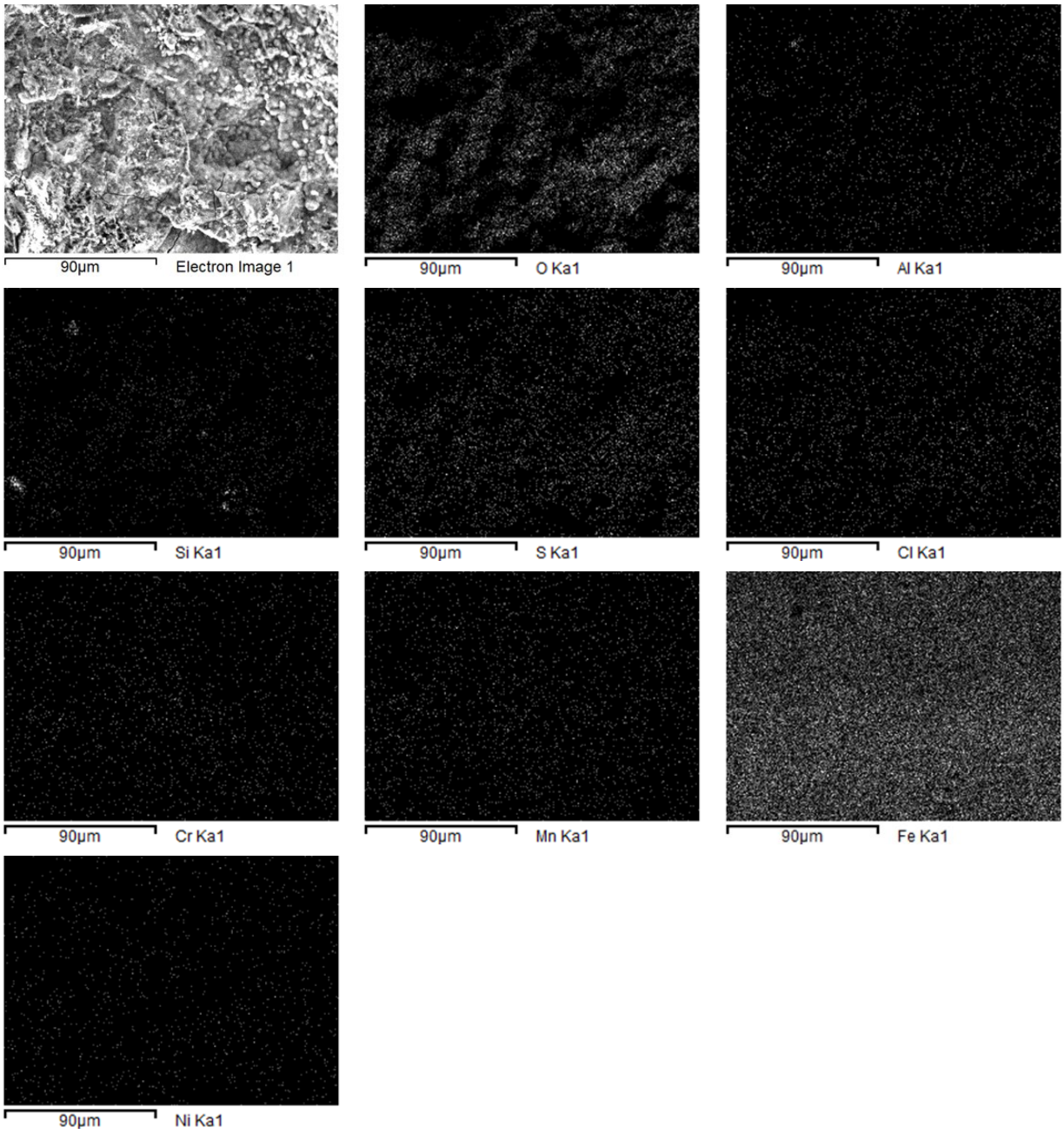
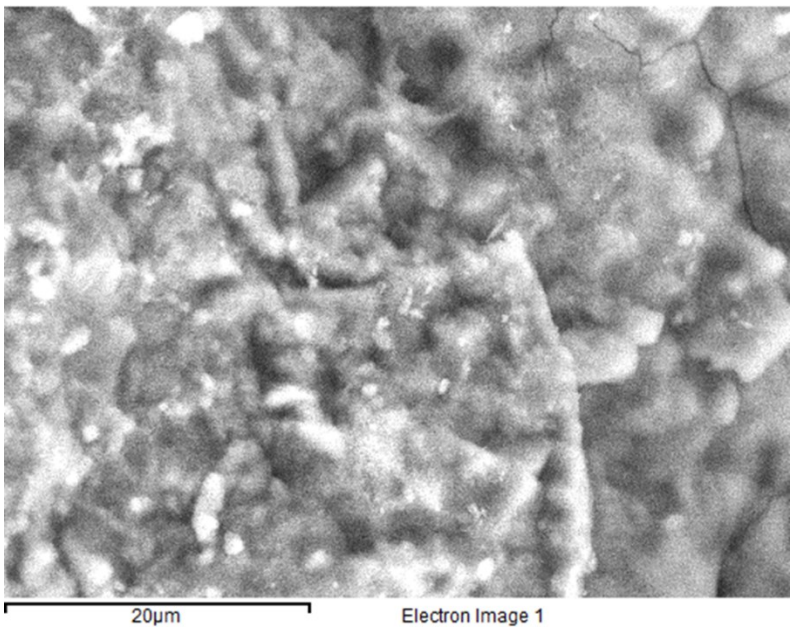


Figure A.358. EDS Elemental Mapping of Rust Collected from Interior Web.

Element	Weight %	Atomic %
O K	41.34	70.41
Al K	0.43	0.44
Si K	0.69	0.67
S K	0.86	0.73
Cl K	0.29	0.22
Cr K	0.64	0.34
Mn K	0.87	0.43
Fe K	54.40	26.54
Ni K	0.49	0.23
Totals	100.00	



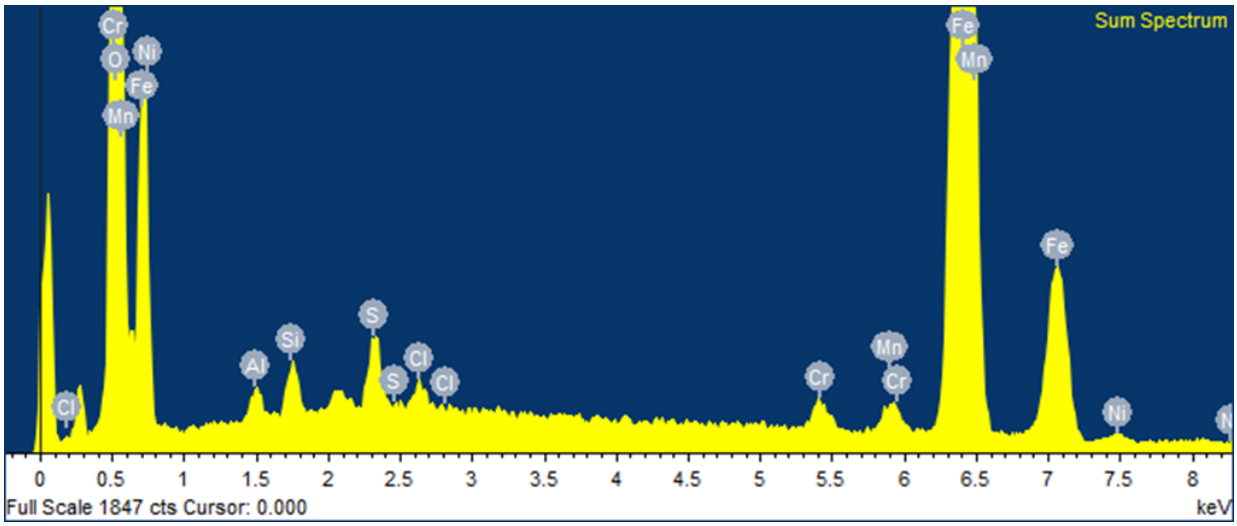


Figure A.359. SEM Image and EDS Spectrum of the Rust Collected from Interior Web of the Girder.

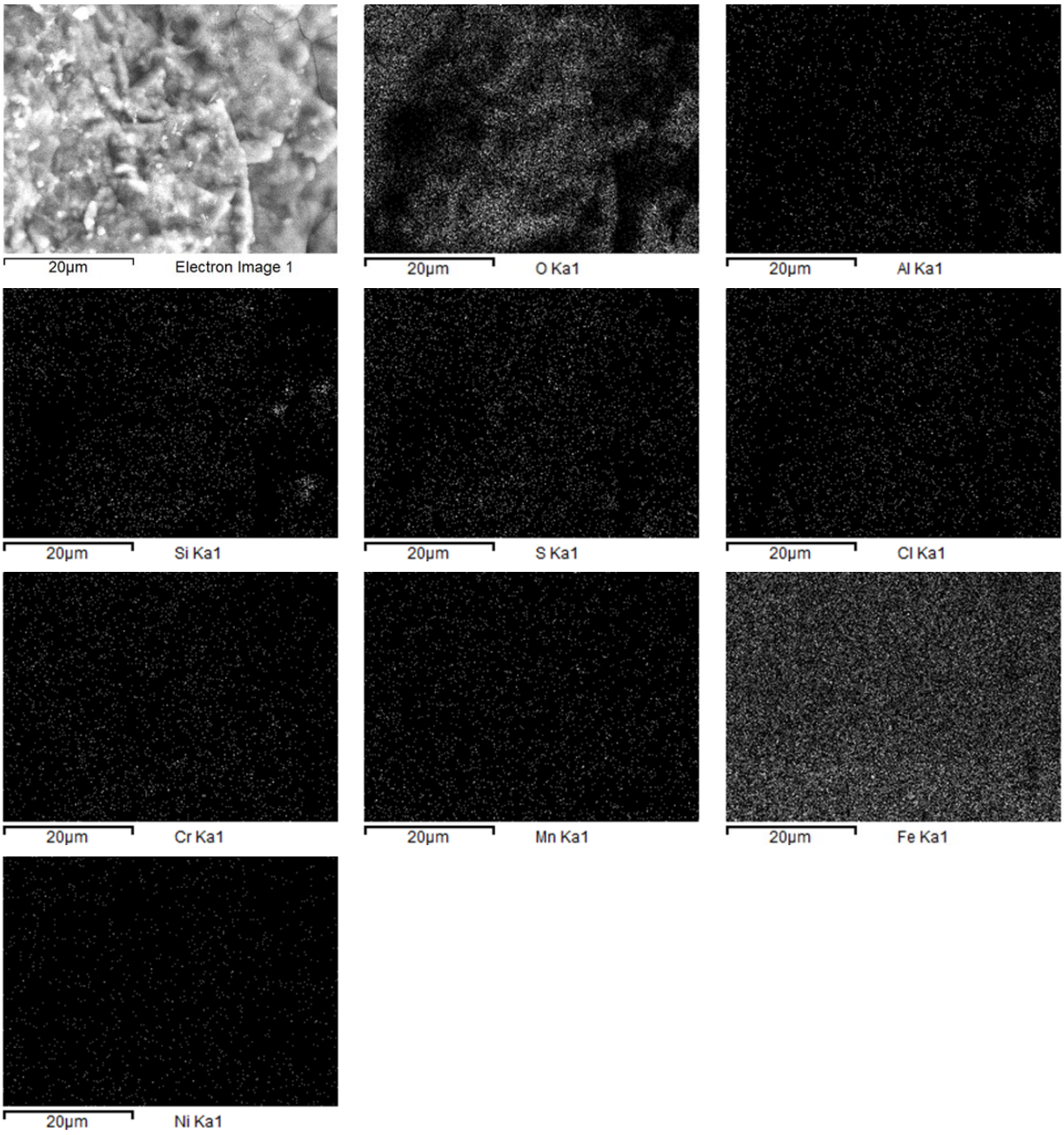


Figure A.360. EDS Elemental Mapping of Rust Collected from Interior.

A.23.5.XPS Result: Exterior Girder

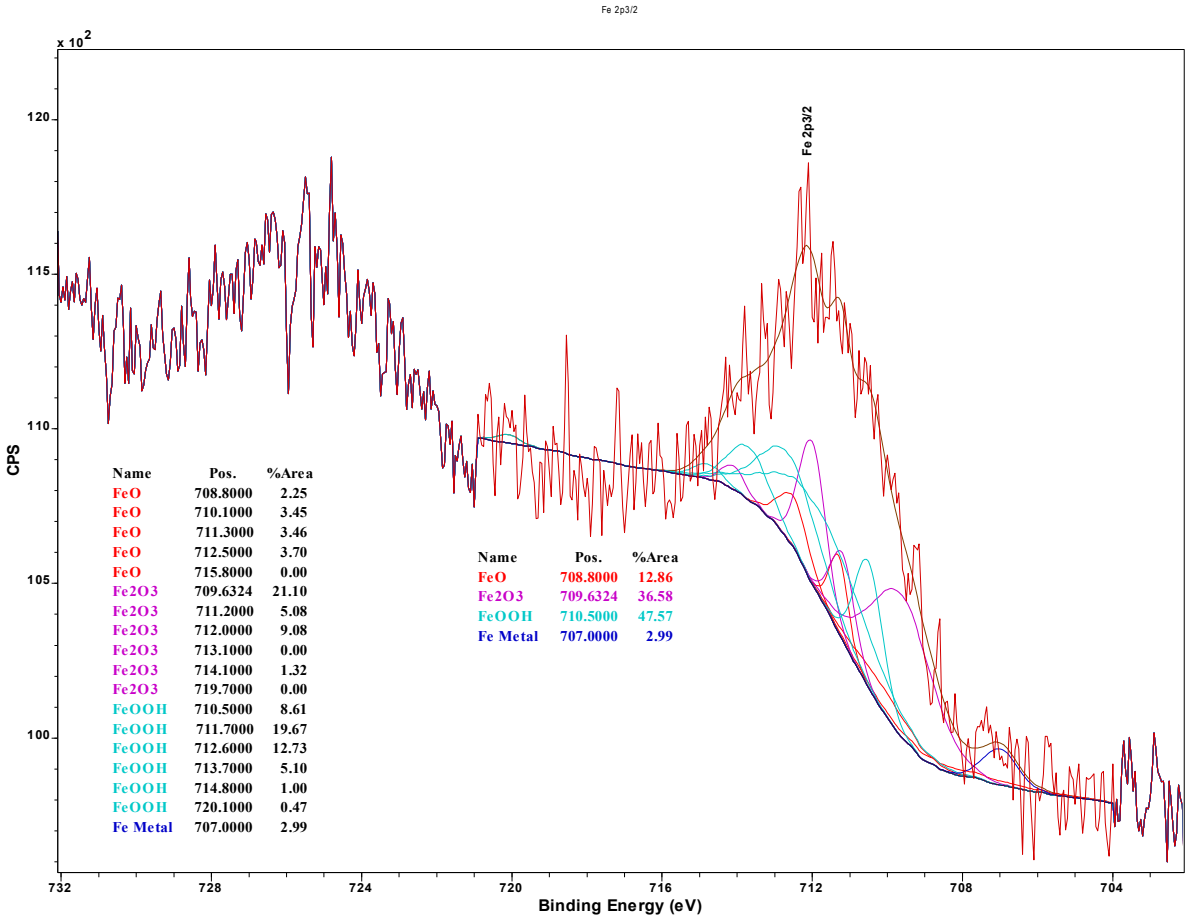


Figure A.361. XPS Spectrum of the Rust Collected from Exterior Web of the Girder.

A.23.6.XPS Result: Interior Girder

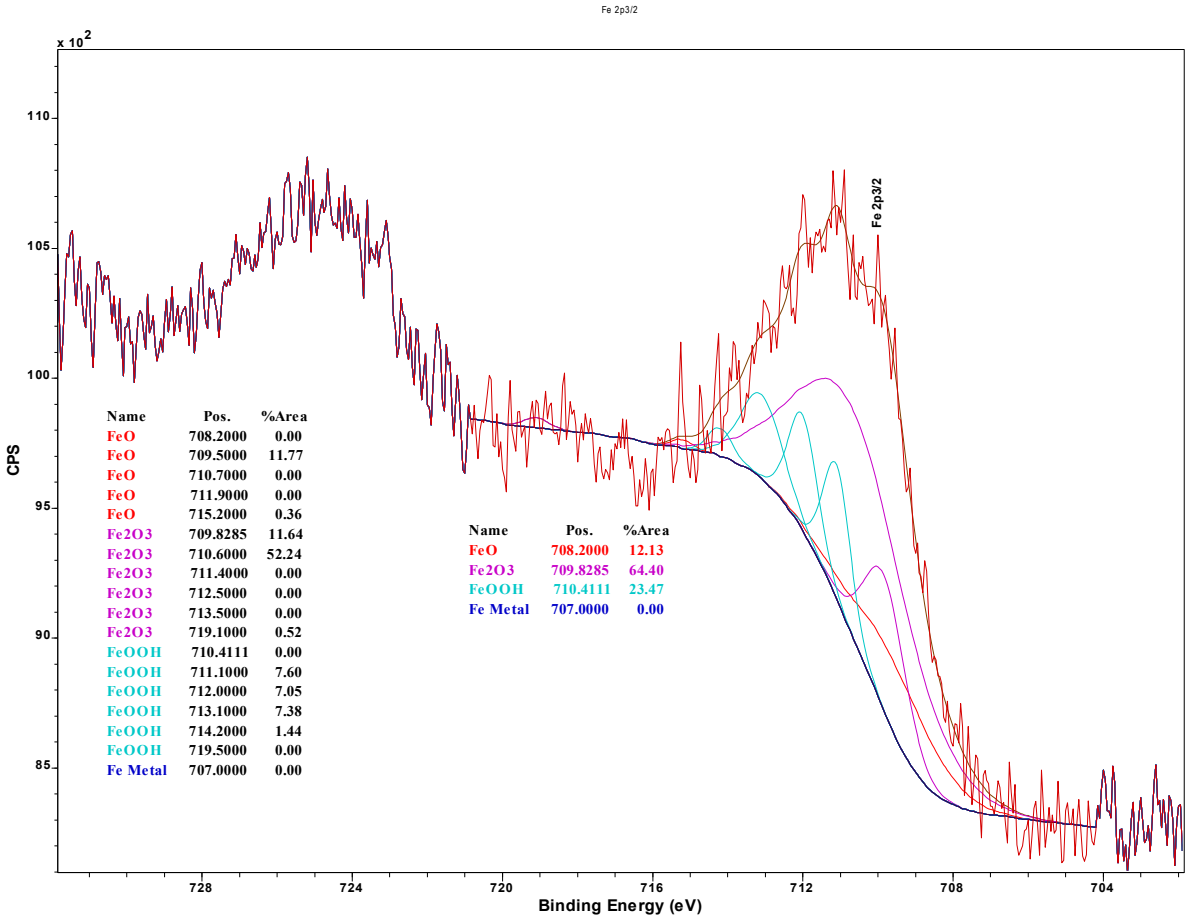


Figure A.362. XPS Spectrum of the Rust Collected from Interior Web of the Girder.

A.23.7.XRD Result: Exterior and Interior Girder

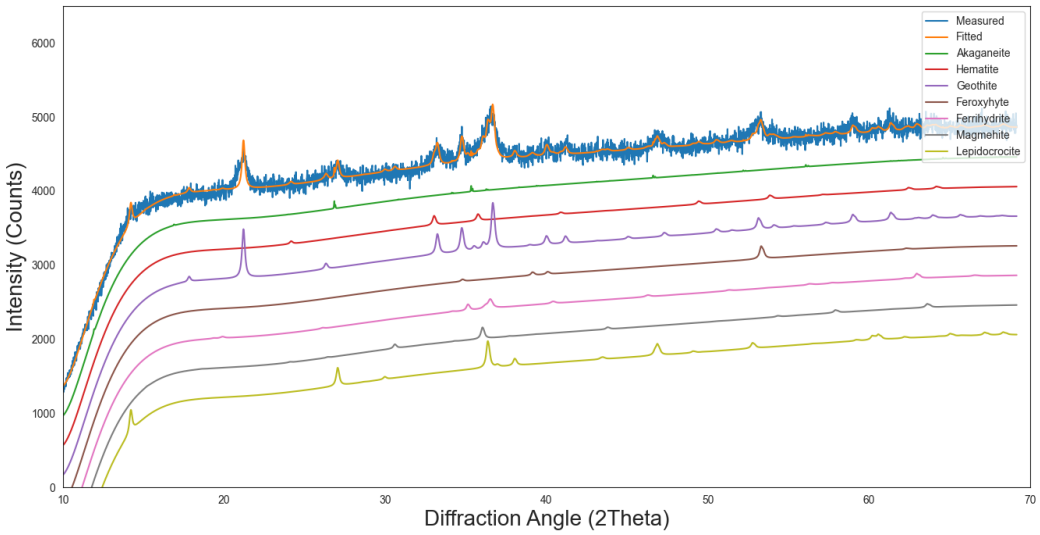


Figure A.363. XRD Pattern of Powdered Rust Collected from Exterior Web of the Girder.

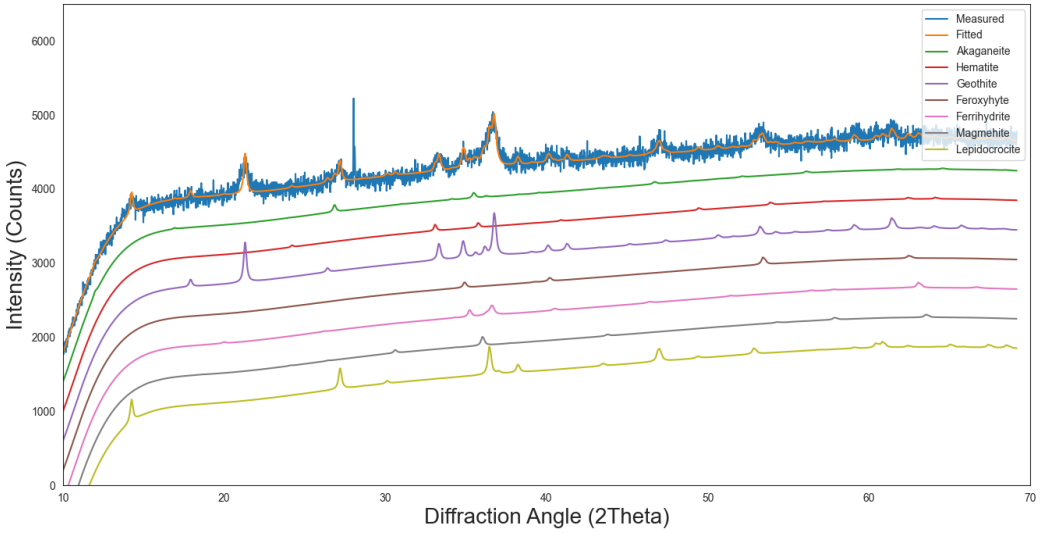


Figure A.364. XRD Pattern of Powdered Rust Collected from Interior Web of the Girder.

A.23.8. Particle Size Analysis: Tape Adhesion Results

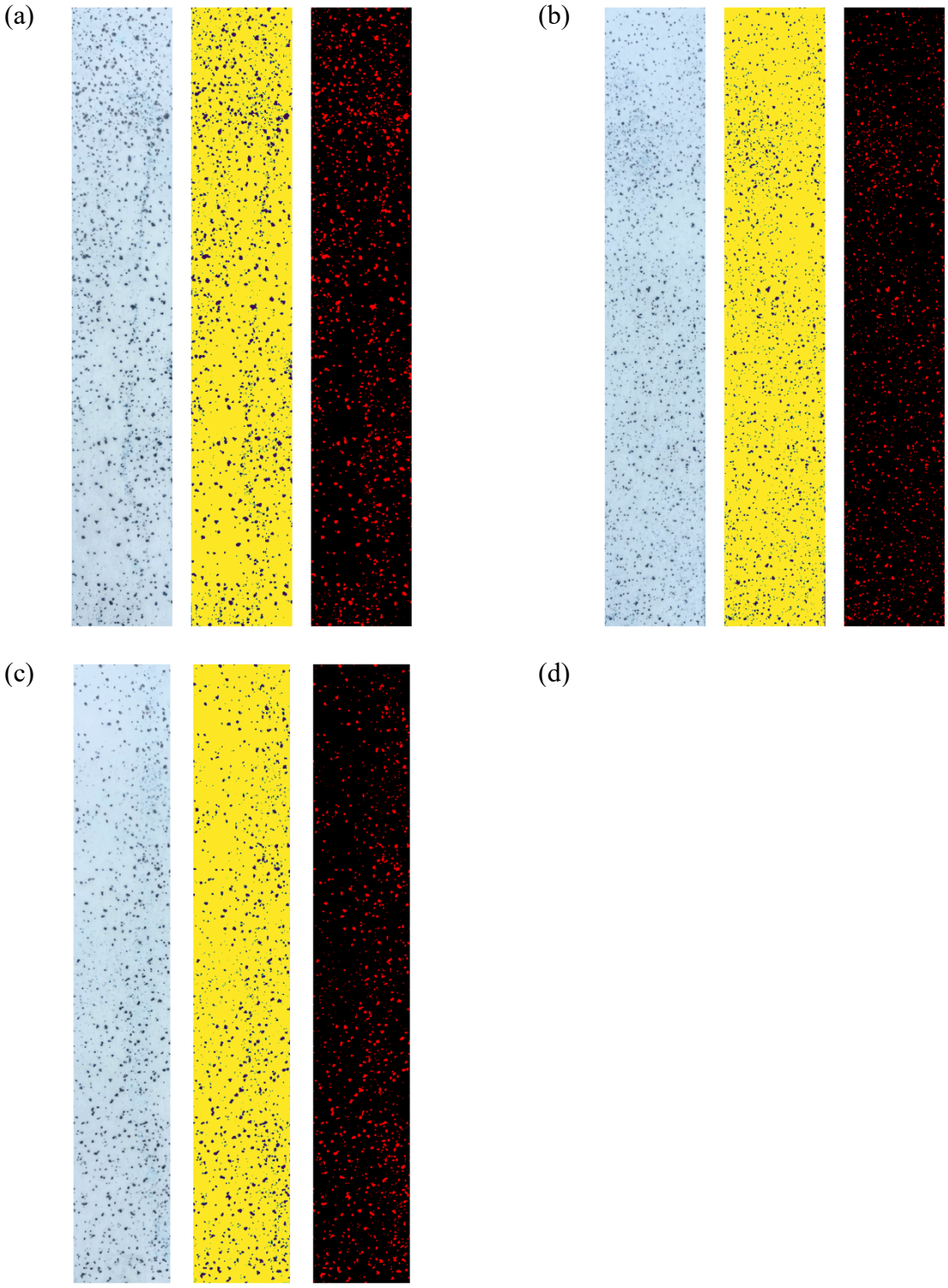


Figure A.365. Particle Size Analysis Results at A1G1F1 (a) Top Flange Bottom, (b) Web, (c) Bottom Flange Bottom (d) Stiffener.

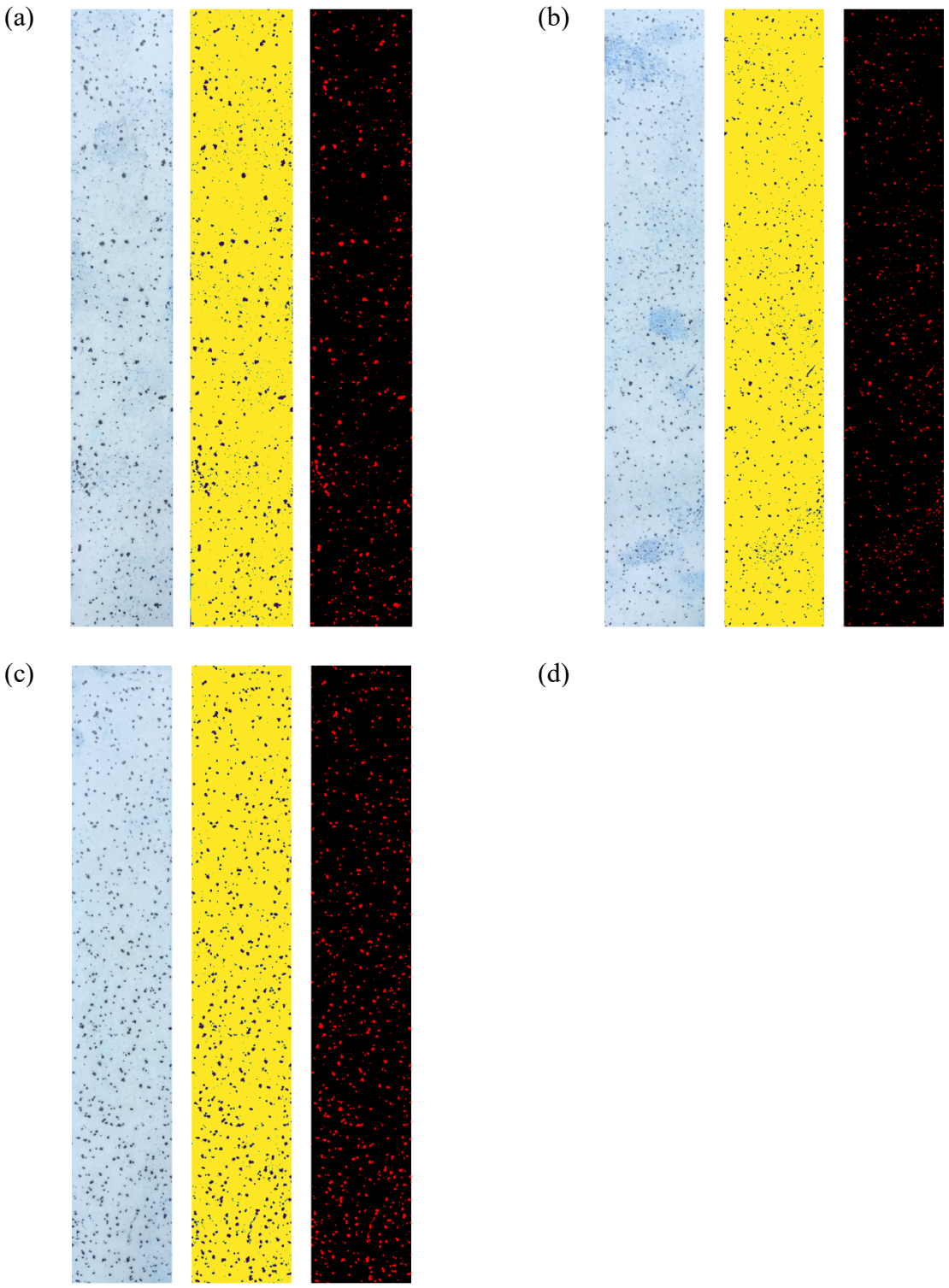


Figure A.366. Particle Size Analysis Results at A1G1F2 (a) Top Flange Bottom, (b) Web, (c) Bottom Flange Bottom (d) Stiffener.

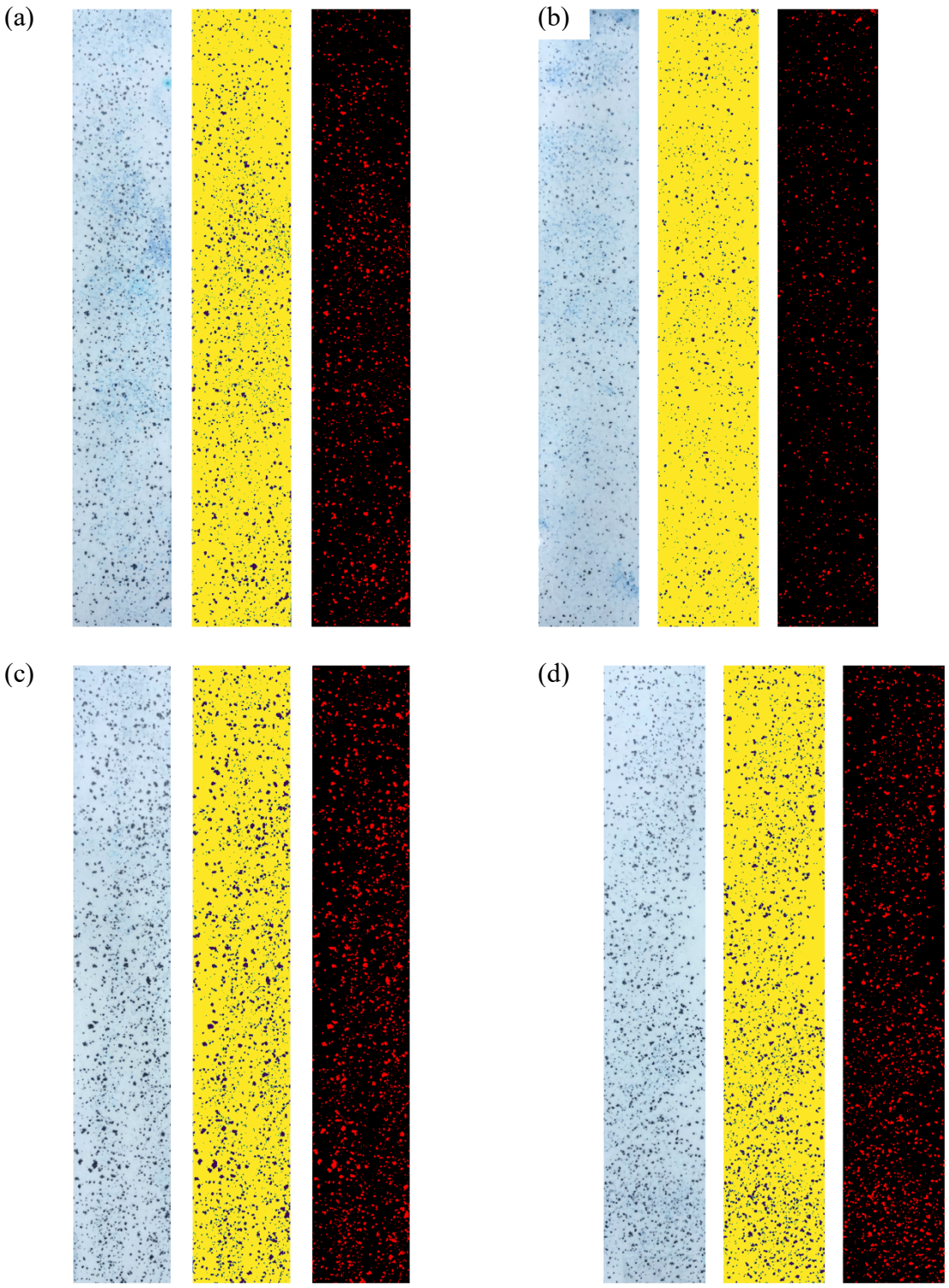


Figure A.367. Particle Size Analysis Results at A1G2F1 (a) Top Flange Bottom, (b) Web, (c) Bottom Flange Bottom (d) Stiffener.

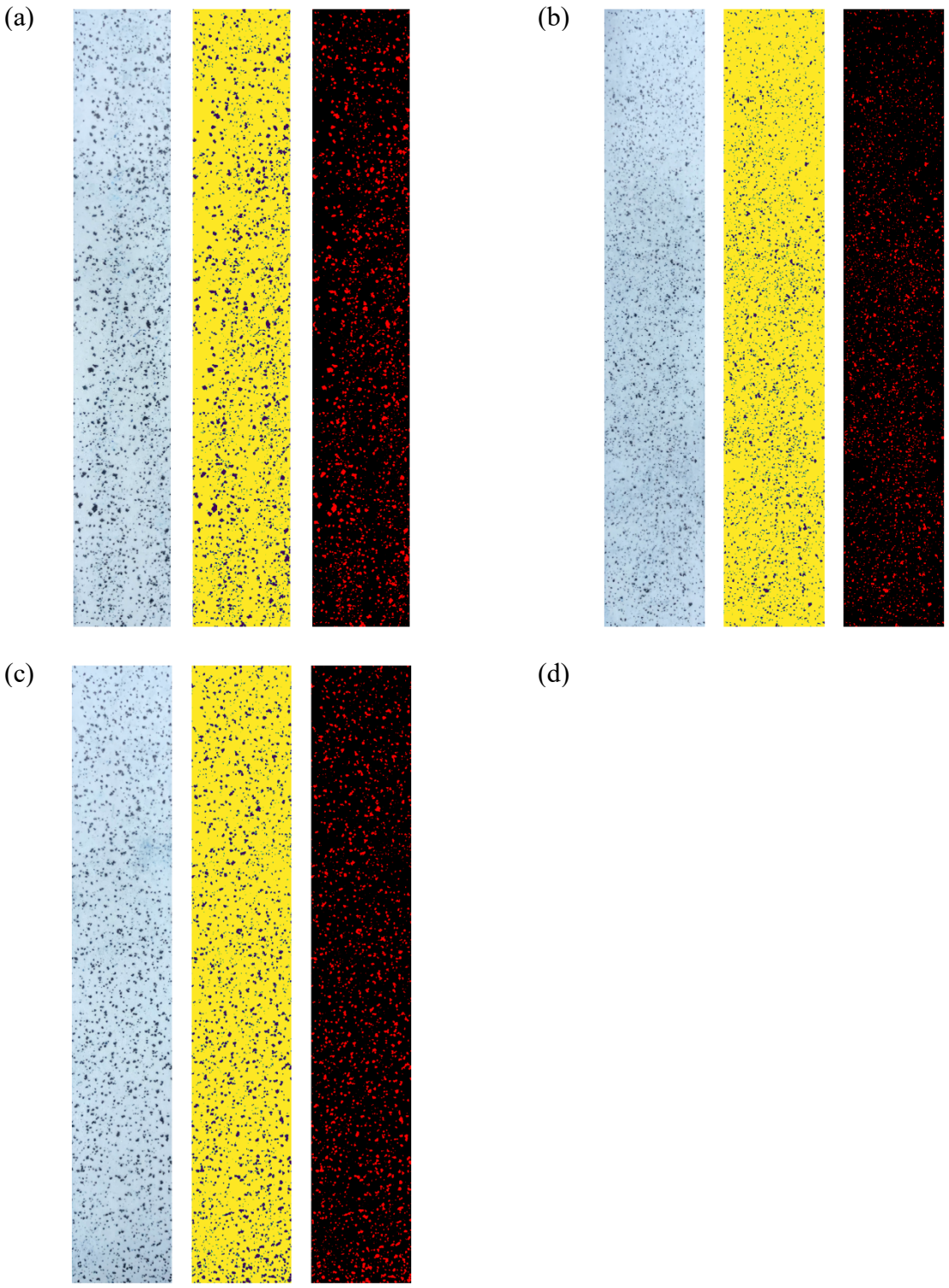
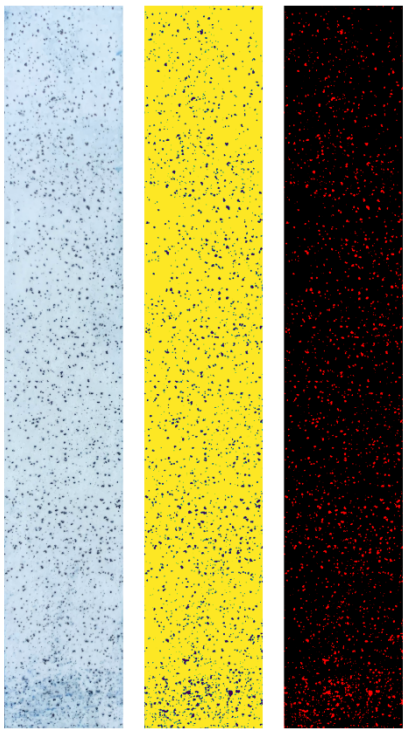


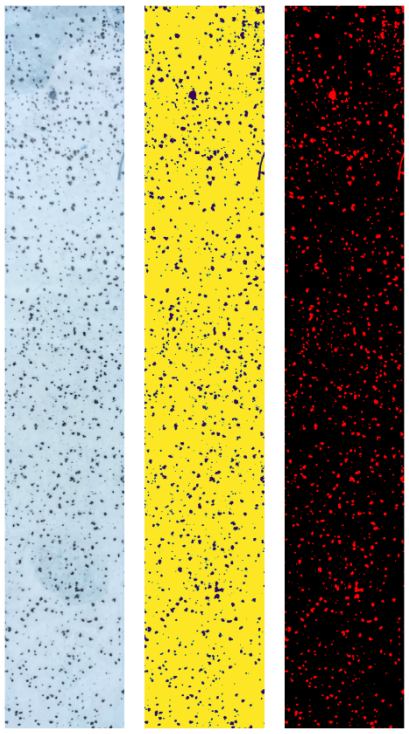
Figure A.368. Particle Size Analysis Results at A1G2F2 (a) Top Flange Bottom, (b) Web, (c) Bottom Flange Bottom (d) Stiffener.

(a)

(b)



(c)



(d)

Figure A.369. Particle Size Analysis Results at B2G2F1 (a) Top Flange Bottom, (b) Web, (c) Bottom Flange Bottom (d) Stiffener.

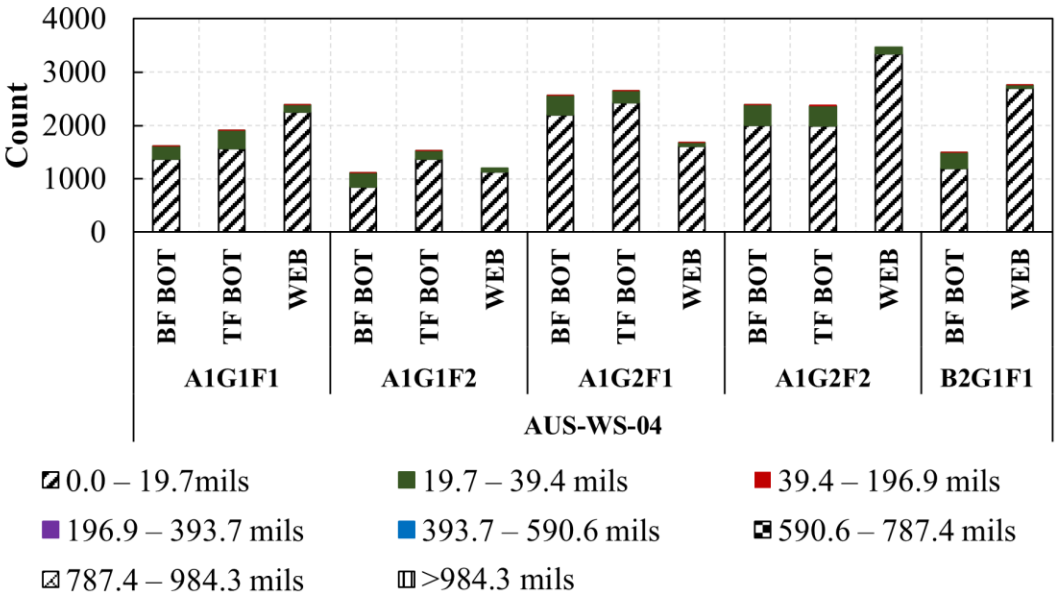


Figure A.370. Particle Size Analysis Showing Different Locations Examined.

A.24. HOU-WS-01

- Westpark DR
- Bridge ID 121020125803209, Coordinates (29.72187, -95.49358), Harris County
- Continuous weathering steel plate girder
- Built 1993
- Girder inspection carried on bent 8, and measurements are taken on girder within four feet from the abutment or bent.
- No visual inspection on deck
- Location for Testing: B8-G1F1, B8-G4F1



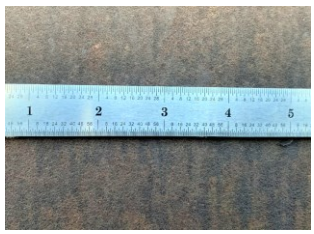
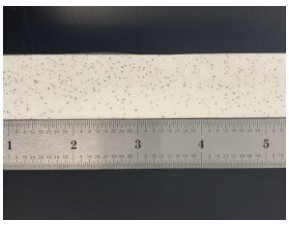
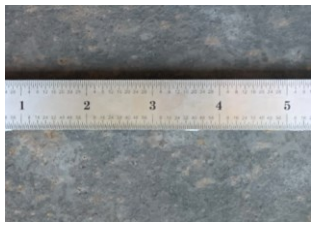
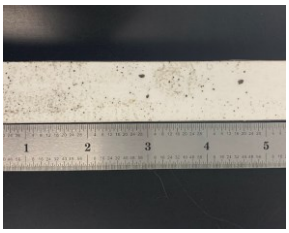
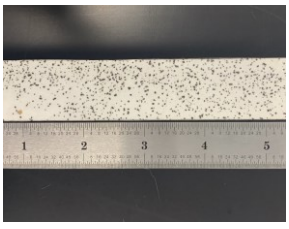
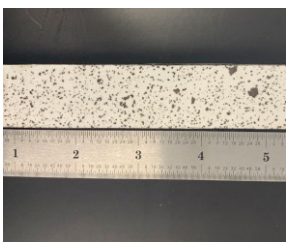
Figure A.371. Typical Picture of HOU-WS-01

A.24.1. Observed Condition

Delaminated areas of the patina are visible on the bottom face of the top flange. The web has a uniform patina formation with a patina rating of 7. The interior girders have significant poultice corrosion on the top face of the bottom flange due to the accumulation of dirt Index 5 whereas exterior girders have less accumulation of dirt.

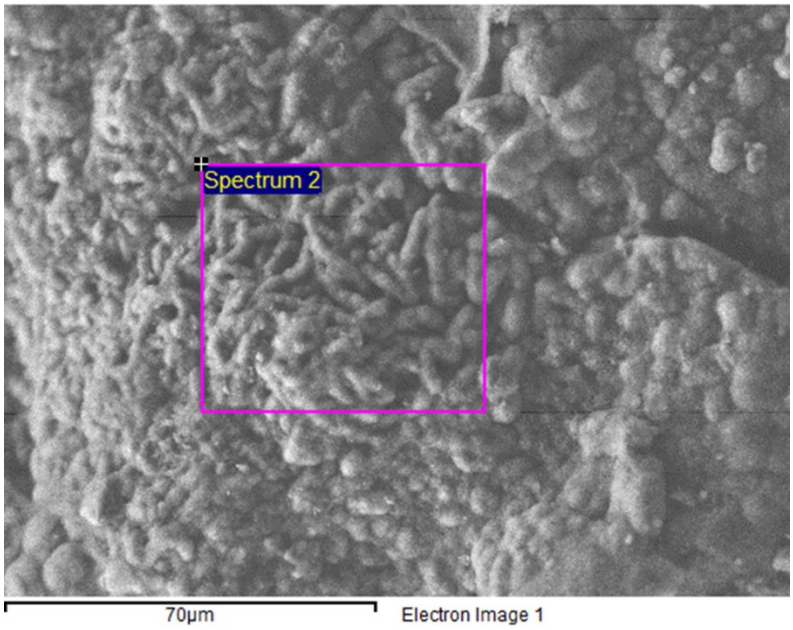
A.24.2.Field Inspection Results

Table A-116. Field Inspection Results for HOU-WS-01.

Location	Patina Rating	Thickness (inch)	Cl^- Conc. (ppm)	Field Condition	Tape Test
B8-G1F1 TF Bot. Ext.	6	-			
B8-G1F1 Web Ext.	7	Measured R1 0.488 R2 0.489 R3 0.491 R_Avg 0.489 Design			
B8-G1F1 BF Top Ext.	5	Measured R1 1.366 R2 1.361 R3 1.359 R_Avg 1.362 Design			
B8-G1F1 BF Bot. Ext.	7	-			
B8-G4F1 BF Bot. Int.	6	Measured R1 1.367 R2 1.365 R3 1.365 R_Avg 1.365 Design			

A.24.3.SEM/EDS Results: Exterior Web Girder

Element	Weight %	Atomic %
O K	46.87	74.16
Al K	2.19	2.05
Si K	0.71	0.64
S K	0.77	0.61
Cl K	0.29	0.21
K K	0.16	0.11
Ca K	0.18	0.12
Mn K	0.67	0.31
Fe K	47.61	21.58
Cu K	0.55	0.22
Totals	100.00	



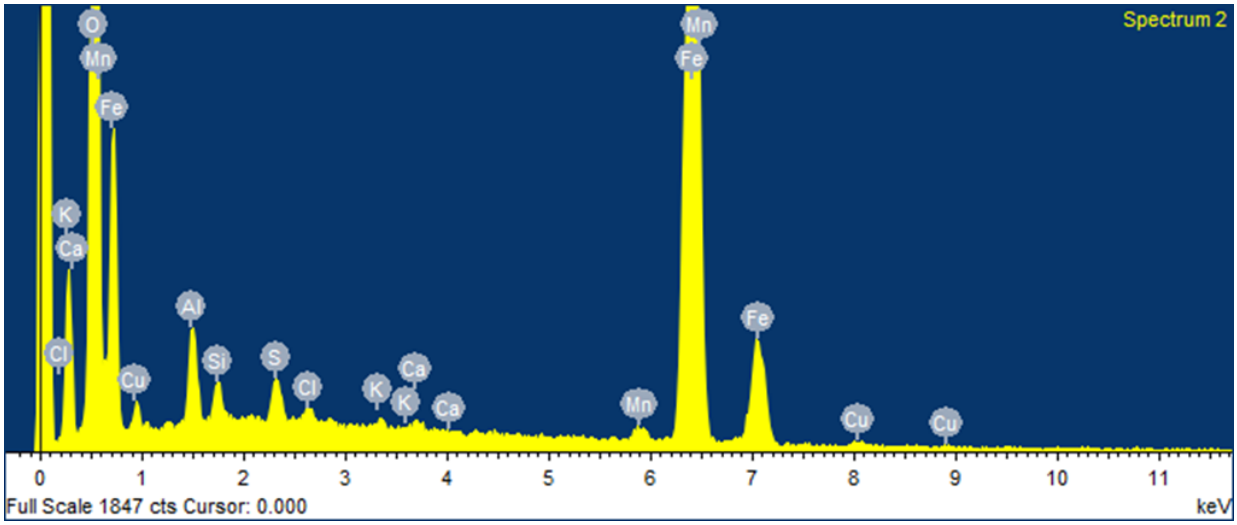
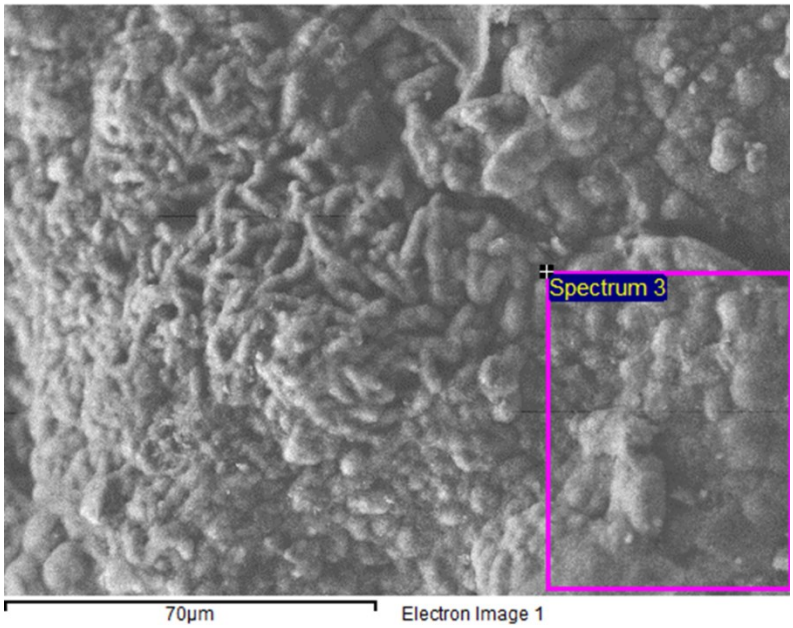


Figure A.372. SEM Image and EDS Spectrum of the Rust Collected from Exterior Web of the Girder.

Element	Weight %	Atomic %
O K	49.69	76.41
Al K	1.75	1.59
Si K	0.80	0.70
S K	0.61	0.47
Cl K	0.17	0.12
Ca K	0.14	0.08
Mn K	0.68	0.30
Fe K	45.94	20.24
Cu K	0.23	0.09
Totals	100.00	



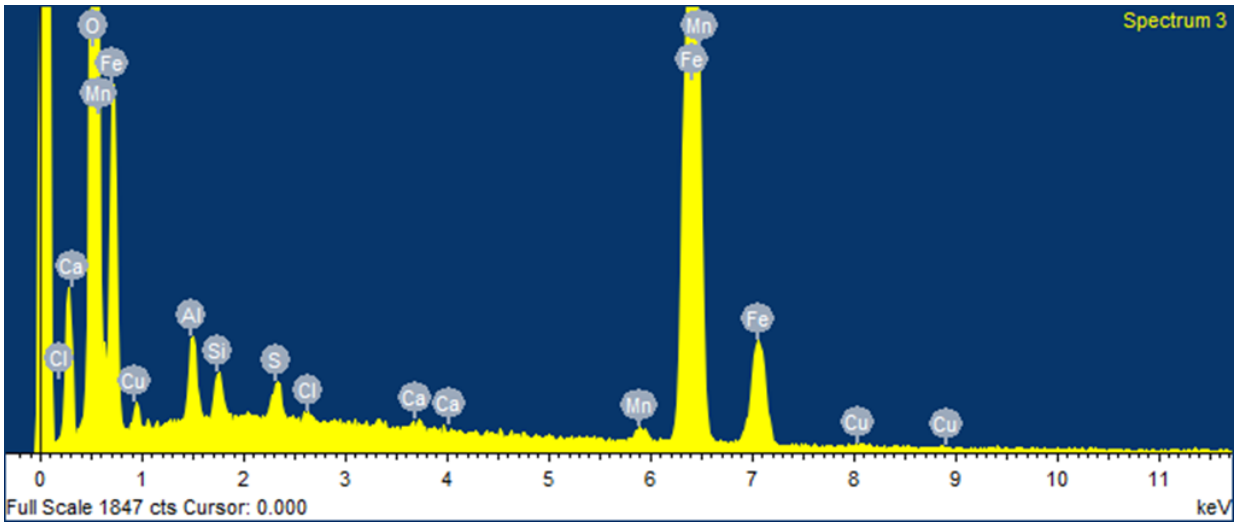
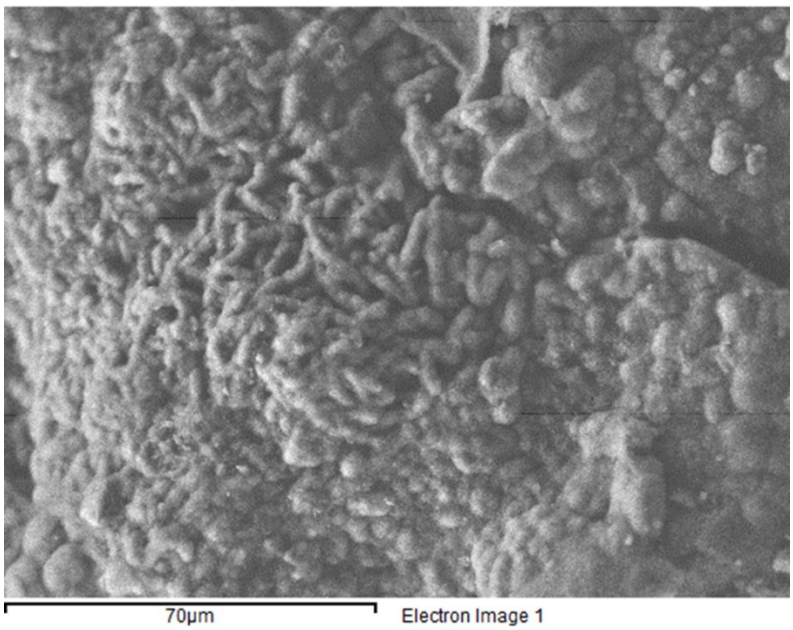


Figure A.373. SEM Image and EDS Spectrum of the Rust Collected from Exterior Web of the Girder.

Element	Weight %	Atomic %
O K	46.00	73.53
Al K	2.18	2.06
Si K	0.79	0.72
S K	0.72	0.58
Cl K	0.24	0.17
Ca K	0.17	0.11
Mn K	0.80	0.37
Fe K	48.58	22.25
Cu K	0.53	0.21
Totals	100.00	



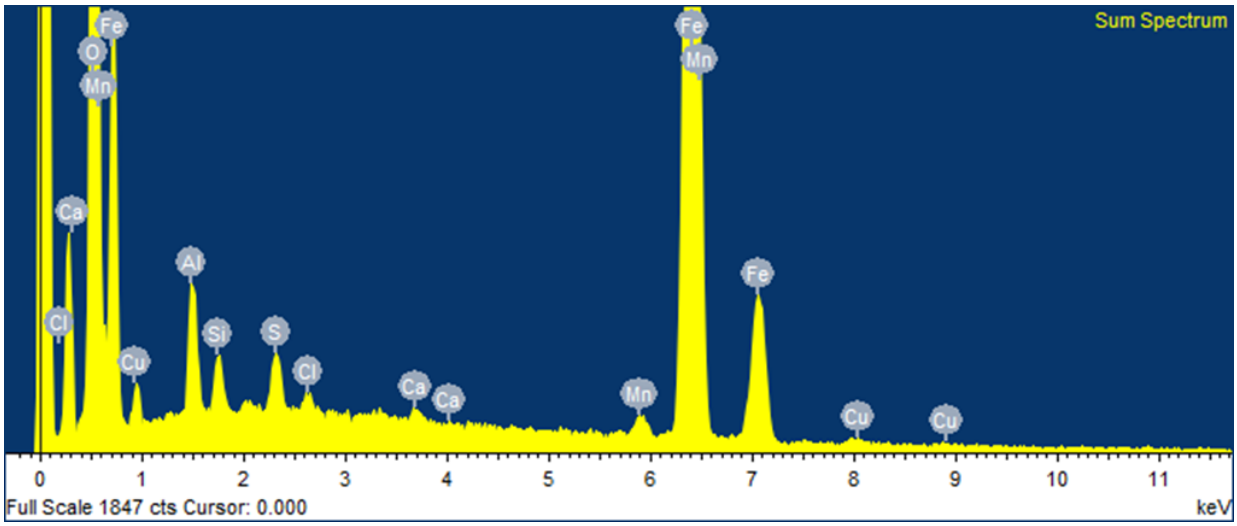


Figure A.374. SEM Image and EDS Spectrum of the Rust Collected from Exterior Web of the Girder.

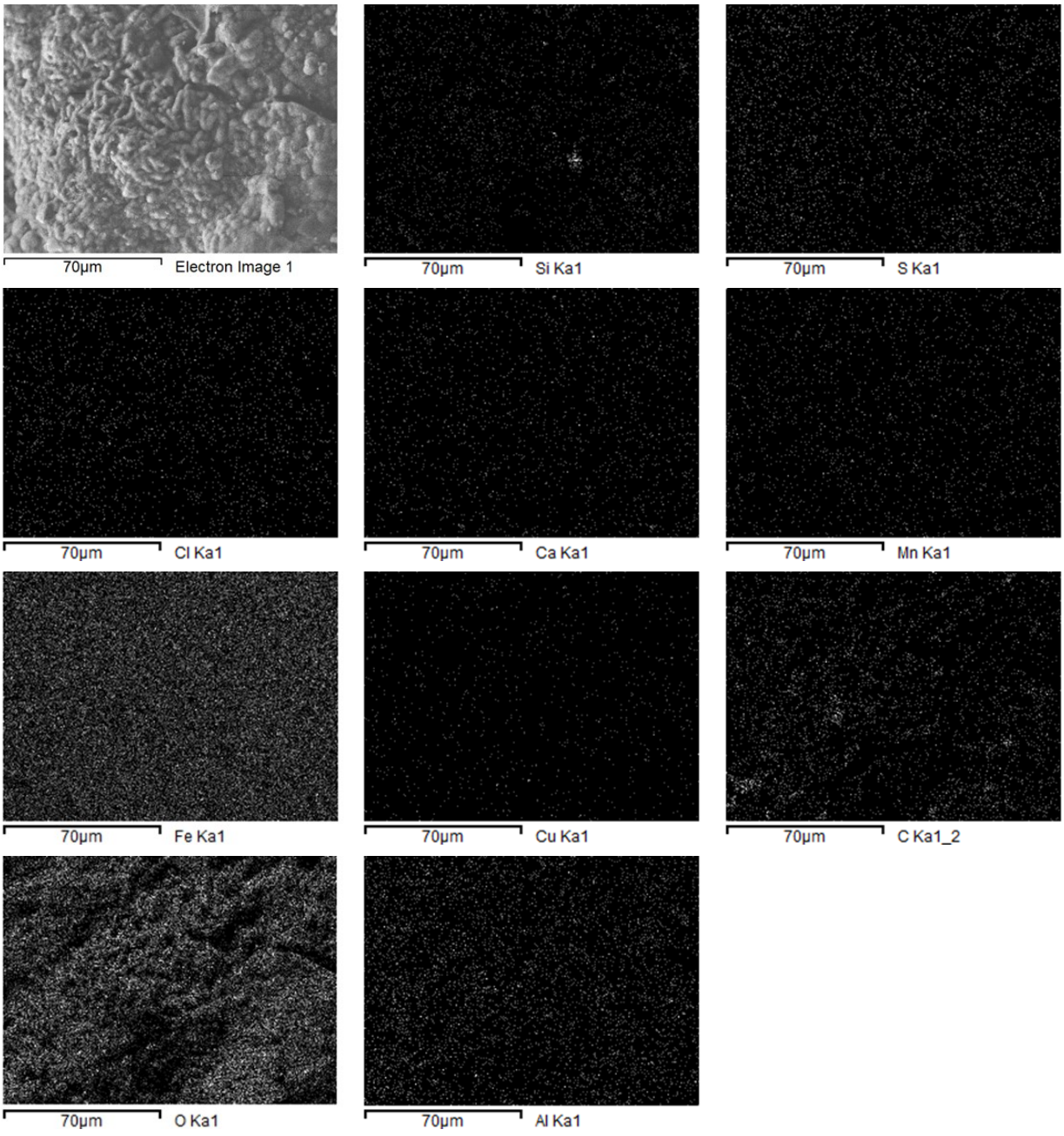
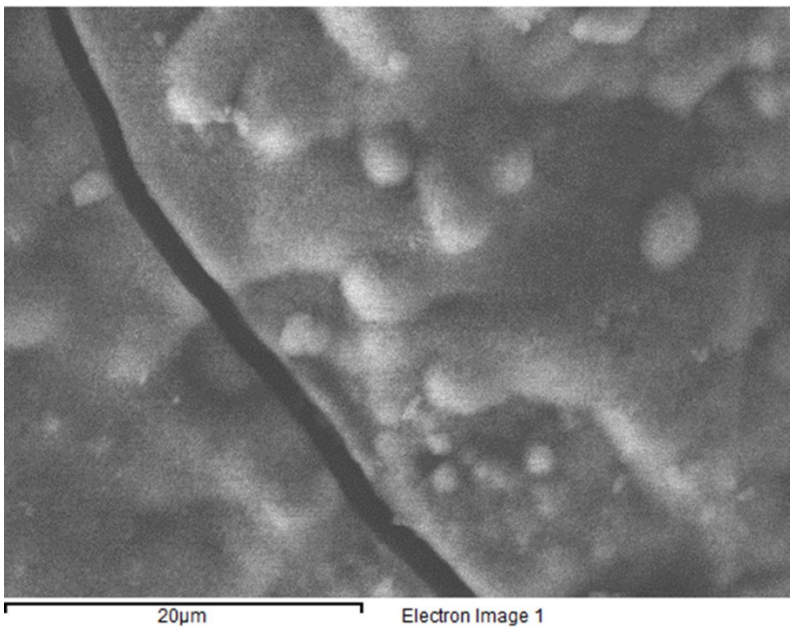


Figure A.375. EDS Elemental Mapping of Rust Collected from Exterior Web.

Element	Weight %	Atomic %
O K	26.34	54.58
Al K	1.68	2.06
Si K	0.53	0.63
S K	0.66	0.68
Ca K	0.15	0.12
Mn K	1.21	0.73
Fe K	69.19	41.07
Cu K	0.25	0.13
Totals	100.00	



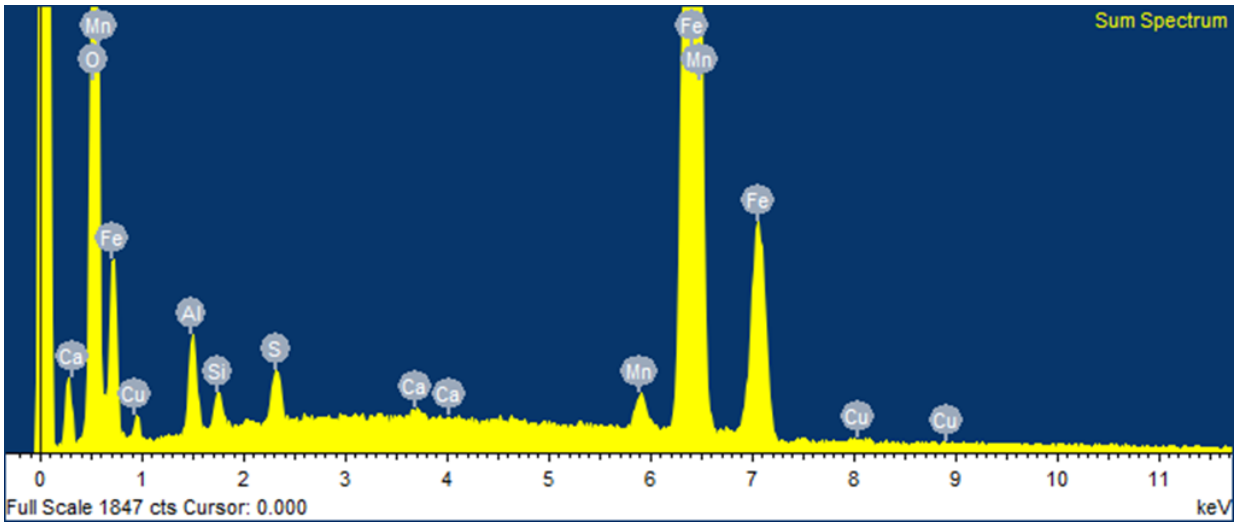
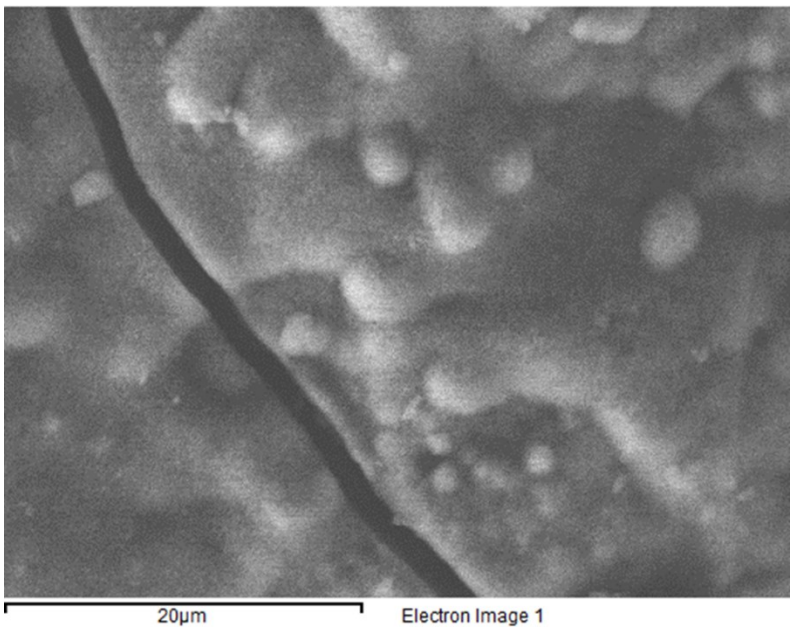


Figure A.376. SEM Image and EDS Spectrum of the Rust Collected from Exterior Web of the Girder.

Element	Weight %	Atomic %
O K	23.09	50.30
Al K	1.70	2.19
Si K	0.51	0.63
S K	0.57	0.62
Mn K	1.25	0.79
Fe K	72.66	45.34
Cu K	0.23	0.13
Totals	100.00	



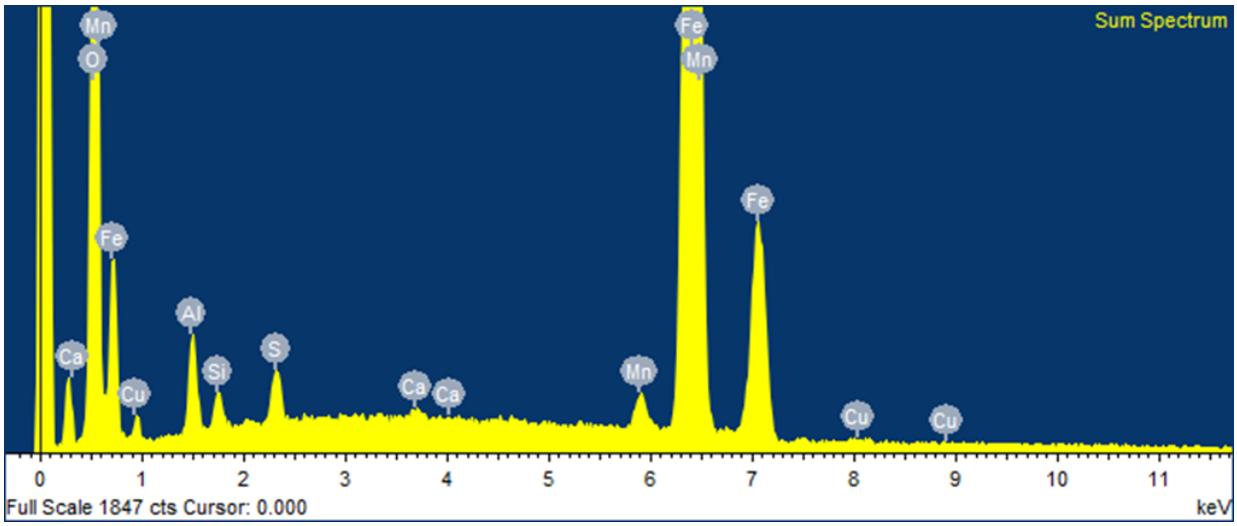


Figure A.377. SEM Image and EDS Spectrum of the Rust Collected from Exterior Web of the Girder.

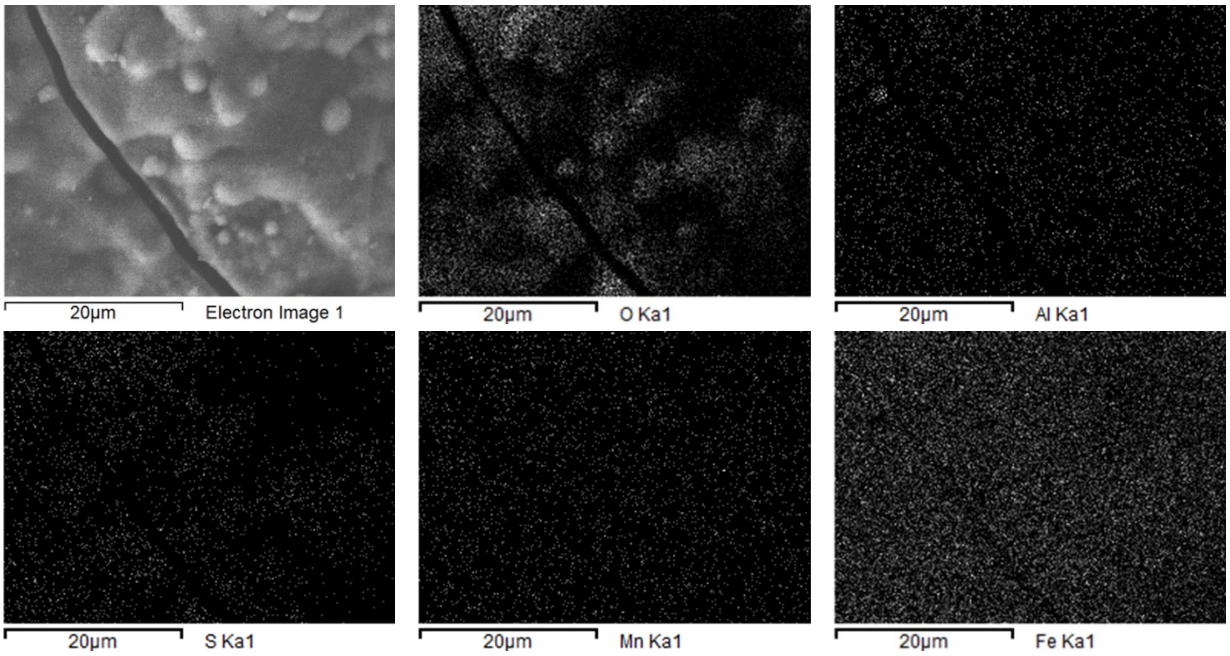


Figure A.378. EDS Elemental Mapping of Rust Collected from Exterior Web.

A.24.4.XPS Results: Exterior Web Girder

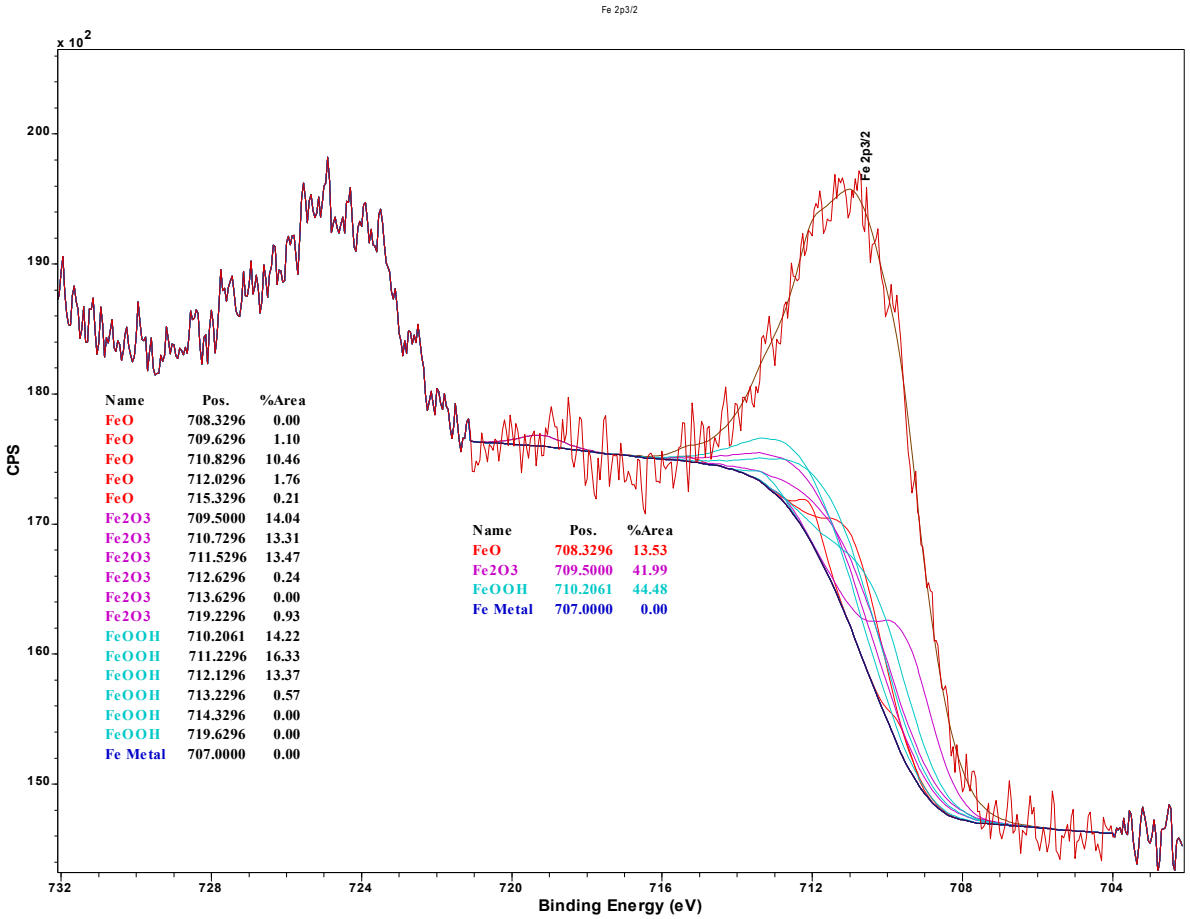


Figure A.379. XPS Spectrum of the Rust Collected from Exterior Web of the Girder.

A.24.5.XRD Result: Exterior and Interior Girder

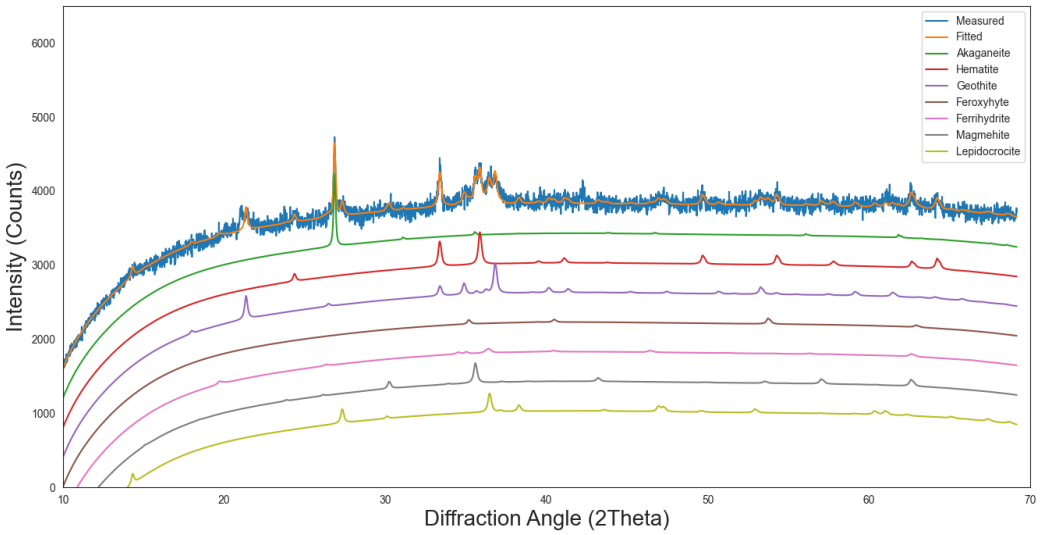
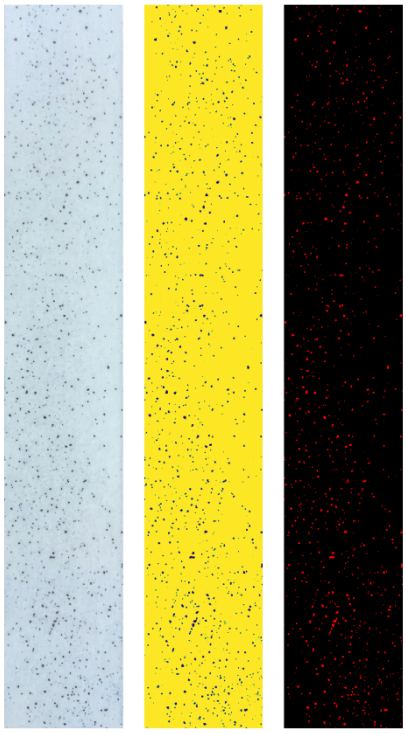


Figure A.380. XRD Pattern of Powdered Rust Collected from Exterior Web of the Girder.

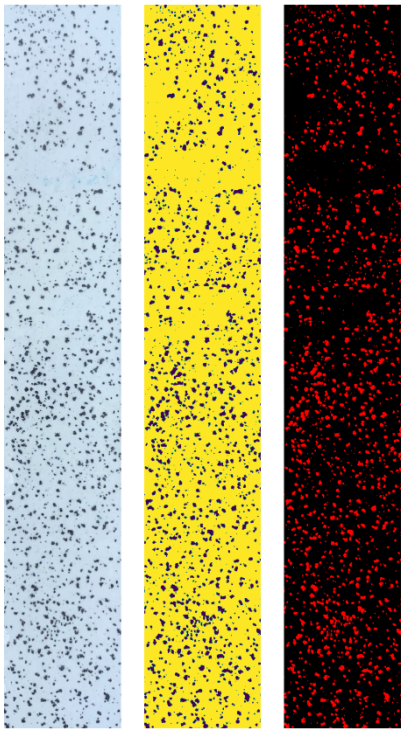
A.24.6.Particle Size Analysis: Tape Adhesion Results

(a)

(b)



(c)



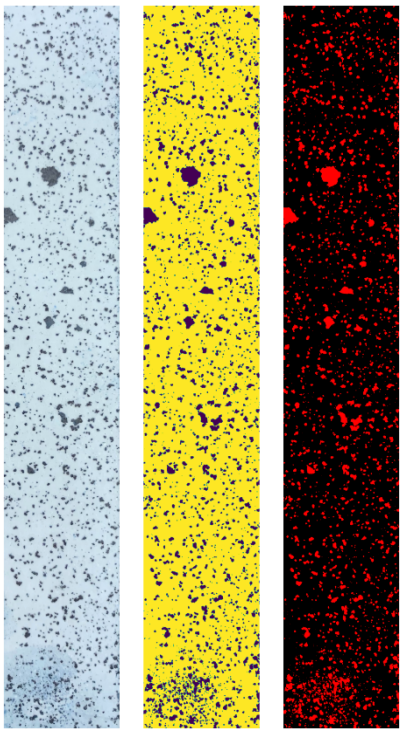
(d)

Figure A.381. Particle Size Analysis Results at B8G1F1 (a) Top Flange Bottom, (b) Web, (c) Bottom Flange Bottom (d) Stiffener.

(a)

(b)

(c)



(d)

Figure A.382. Particle Size Analysis Results at B6G4F1 (a) Top Flange Bottom, (b) Web, (c) Bottom Flange Bottom (d) Stiffener.

A.25. HOU-WS-02

- FM 1902B
- Bridge ID 121020TOL010109, Coordinates (29.9532, -95.9532), Brazoria County
- Continuous weathering steel box girder
- Built 2006
- Date of Inspection: January 29, 2021 Girder inspection carried on girder 1, 3, 4 and 6, and measurements are taken on girder within four feet from the abutment or bent.
- No visual inspection on deck
- Location for Testing: A1G1F1, A1G1F2, A1G2F1, A1G3F2



Figure A.383. Typical Picture of HOU-WS-02

A.25.1. Observed Condition

Overall bridge is in very good condition with development of uniform patina throughout the girder. Stiffener connecting interior girder has non adhering loosely attached patina on top and bottom flange.

A.25.2.Field Inspection Results

Table A-117. Field Inspection Results for HOU-WS-02.

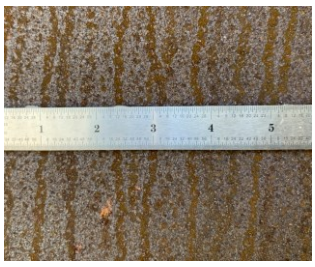
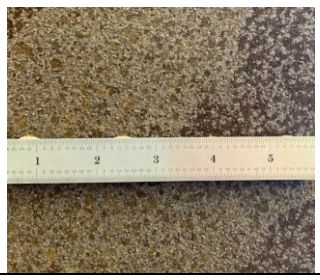
Location	Patina Rating	Thickness (inch)	Cl^- Conc. (ppm)	Field Condition	Tape Test
A1-G1F1 TF Bot. Ext.	7	Measured R1 0.746 R2 0.745 R3 0.746 R_Avg 0.746 Design			
A1-G1F1 Web Ext.	8	Measured R1 0.621 R2 0.622 R3 0.622 R_Avg 0.622 Design			
A1-G1F1 BF Bot. Ext.	8	Measured R1 0.751 R2 0.747 R3 0.747 R_Avg 0.748 Design			
A1-G1F2 TF Bot. Int.	8	Measured R1 0.743 R2 0.743 R3 0.743 R_Avg 0.743 Design			
A1-G1F2 Web Int.	8	Measured R1 0.625 R2 0.625 R3 0.625 R_Avg 0.625 Design			

Table A-118. Field Inspection Results for HOU-WS-02.

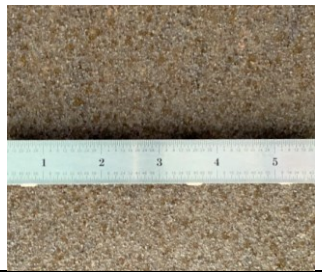
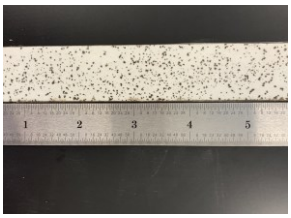
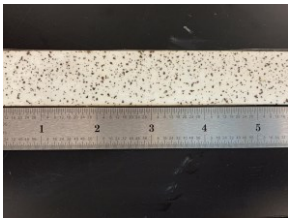
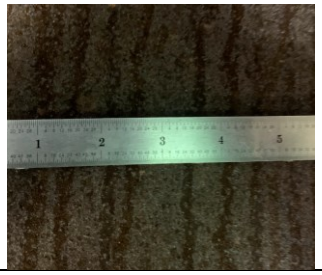
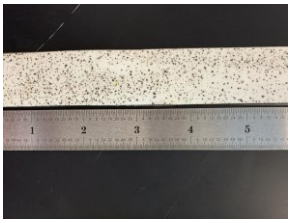
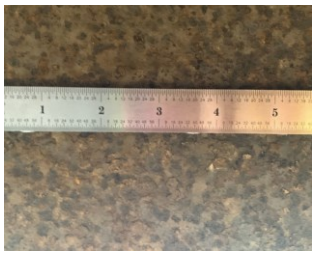
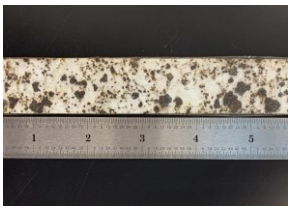
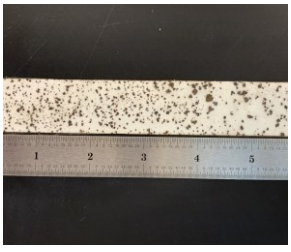
Location	Patina Rating	Thickness (inch)	Cl^- Conc. (ppm)	Field Condition	Tape Test
A1-G1F2 BF Bot. Int.	8	Measured R1 0.744 R2 0.745 R3 0.743 R_Avg 0.744 Design			
A1-G1G2 TF Bot. Stiff. Int.	7	Measured R1 0.985 R2 0.987 R3 0.988 R_Avg 0.987 Design			
A1-G1G2 Web Stiff. Int.	8	Measured R1 0.623 R2 0.623 R3 0.623 R_Avg 0.623 Design			
A1-G1G2 BF Top. Stiff. Int.	5	Measured R1 R2 R3 R_Avg Design			
A1-G1G2 BF Bot. Stiff. Int.	6	Measured R1 0.995 R2 0.997 R3 0.993 R_Avg Design			

Table A-119. Field Inspection Results for HOU-WS-02.

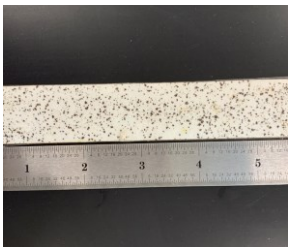
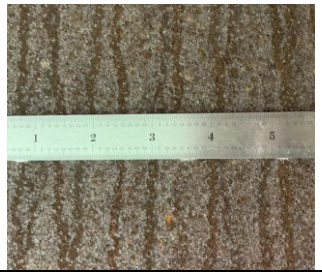
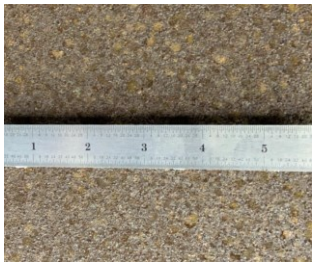
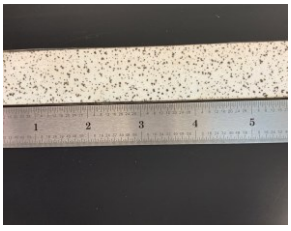
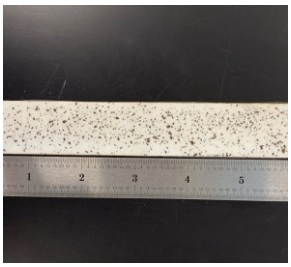
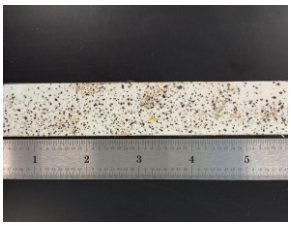
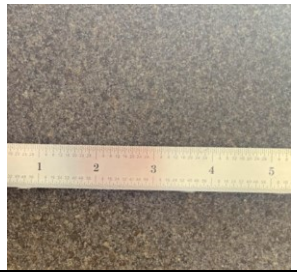
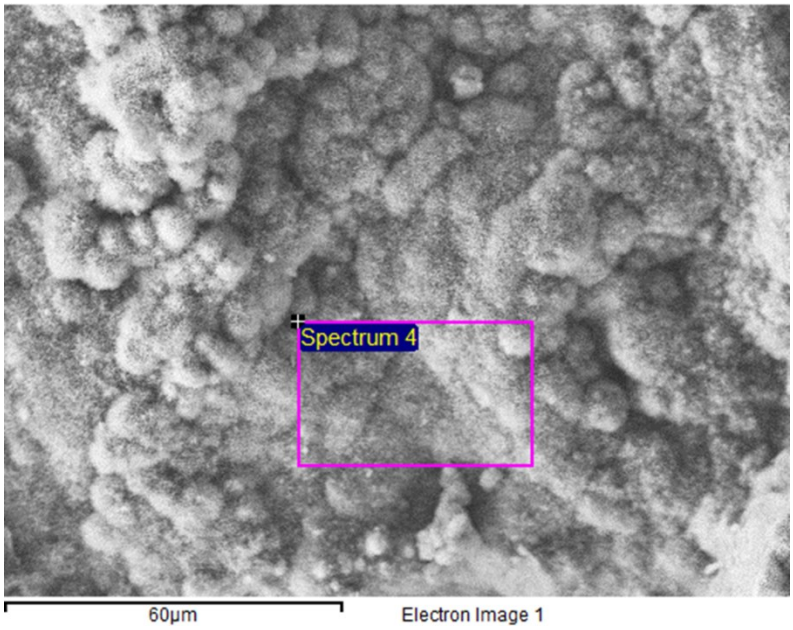
Location	Patina Rating	Thickness (inch)	Cl^- Conc. (ppm)	Field Condition	Tape Test
A1-G2F1 TF Bot. Int.	7	Measured R1 0.743 R2 0.743 R3 0.743 R_Avg 0.743 Design			
A1-G2F1 Web Int.	8	Measured R1 0.625 R2 0.625 R3 0.625 R_Avg 0.625 Design			
A1-G2F1 BF Bot. Int.	7	Measured R1 0.744 R2 0.745 R3 0.743 R_Avg 0.744 Design			
A1-G3F2 TF Bot. Ext.	7	Measured R1 0.751 R2 0.752 R3 0.751 R_Avg 0.751 Design			
A1-G3F2 Web 1 Ext.	8	Measured R1 0.623 R2 0.624 R3 0.623 R_Avg 0.623 Design			

Table A-120. Field Inspection Results for HOU-WS-02.

Location	Patina Rating	Thickness (inch)	Cl^- Conc. (ppm)	Field Condition	Tape Test
A1-G3F2 Web 2 Ext.	7	Measured R1 0.613 R2 0.613 R3 0.613 R_Avg 0.613 Design			
A1-G3F2 BF Bot. Ext.	6	Measured R1 0.741 R2 0.743 R3 0.743 R_Avg 0.742 Design			

A.25.3.SEM/EDS Results: Exterior Web Girder

Element	Weight %	Atomic %
O K	32.16	61.59
Al K	1.58	1.79
Si K	0.25	0.27
S K	0.30	0.28
Mn K	1.22	0.68
Fe K	64.12	35.18
Ni K	0.37	0.19
Totals	100.00	



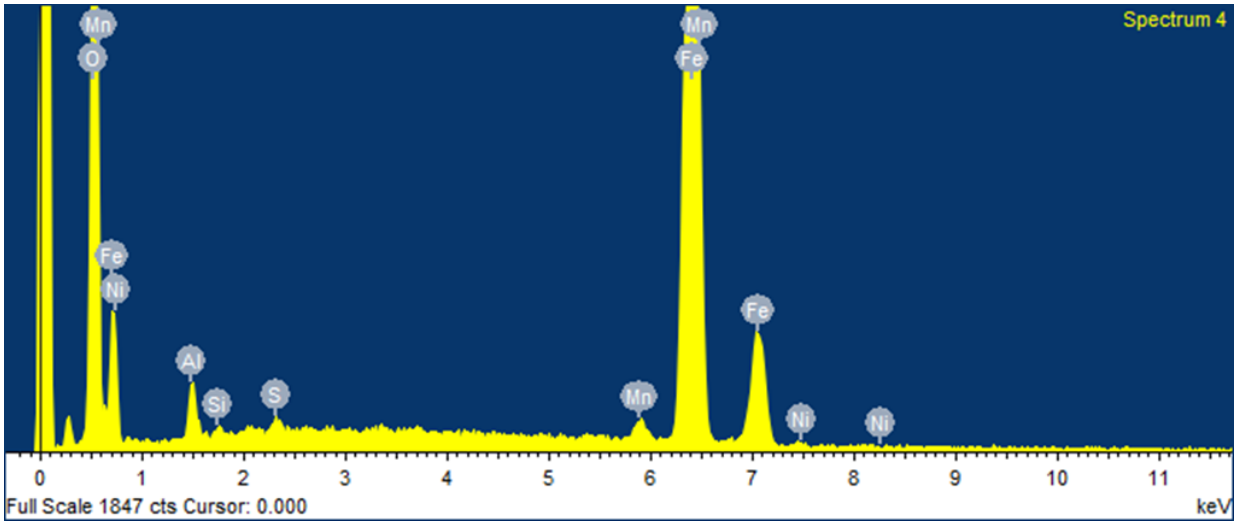
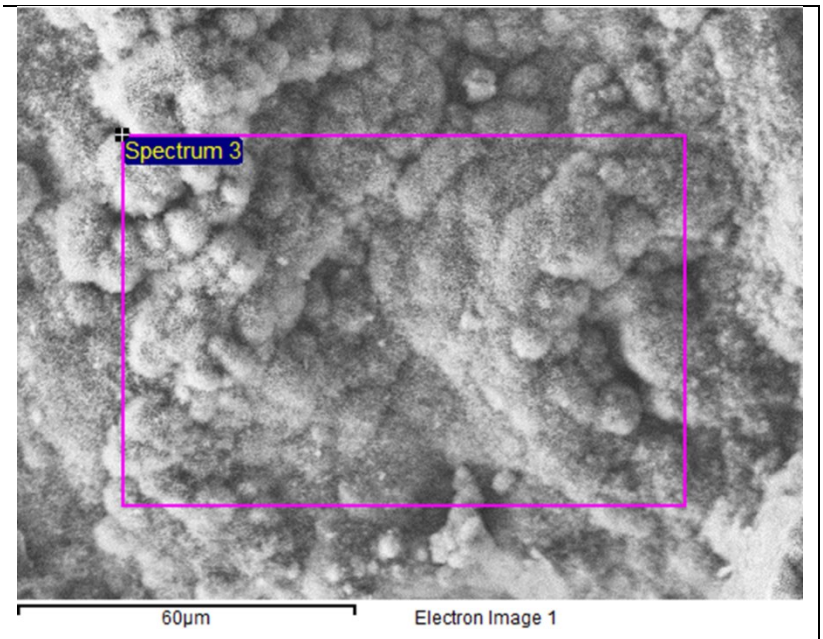


Figure A.384. SEM Image and EDS Spectrum of the Rust Collected from Exterior Web of the Girder.

Element	Weight %	Atomic %
O K	35.24	64.81
Al K	1.42	1.55
Si K	0.27	0.28
S K	0.31	0.28
Mn K	1.18	0.63
Fe K	61.59	32.45
Totals	100.00	



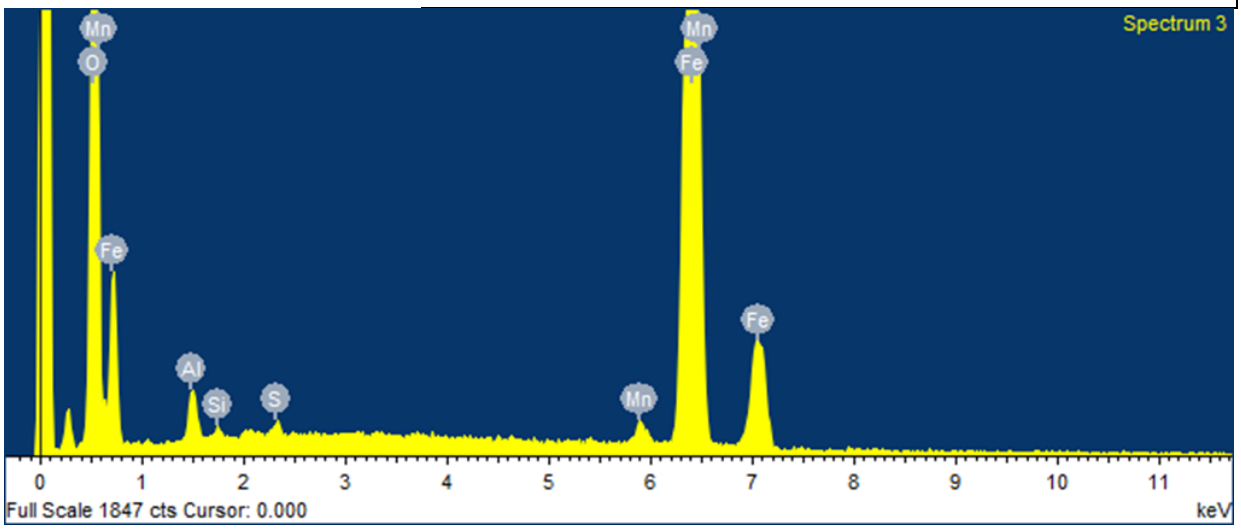
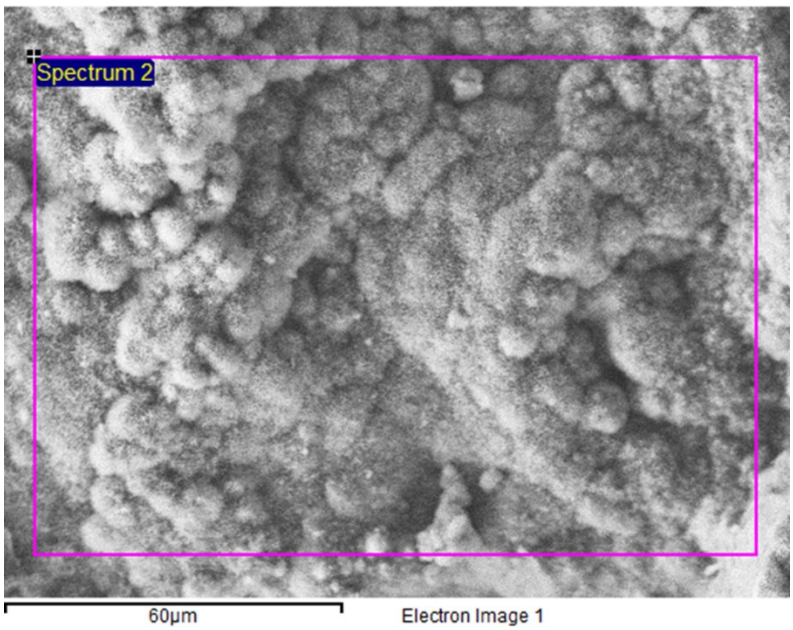


Figure A.385. SEM Image and EDS Spectrum of the Rust Collected from Exterior Web of the Girder.

Element	Weight %	Atomic %
O K	37.76	67.15
Al K	1.44	1.51
Si K	0.38	0.38
S K	0.31	0.28
K K	0.16	0.12
Mn K	1.07	0.56
Fe K	58.87	29.99
Totals	100.00	



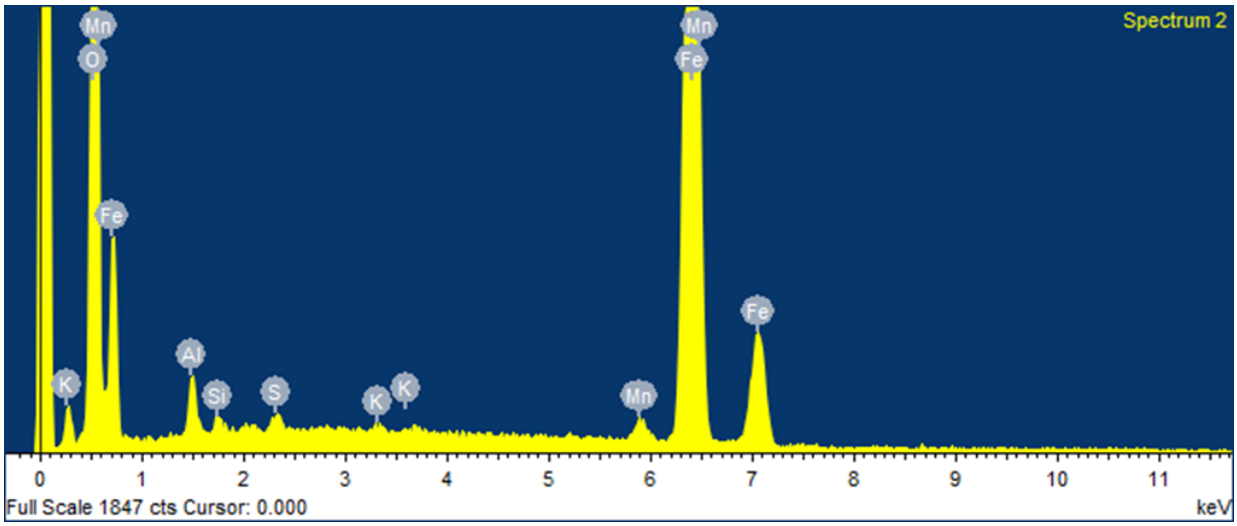
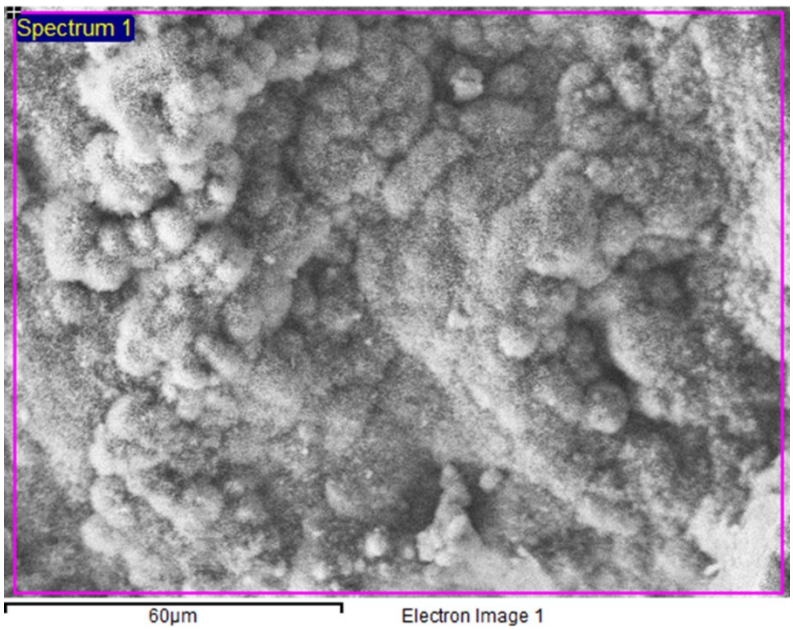


Figure A.386. SEM Image and EDS Spectrum of the Rust Collected from Exterior Web of the Girder.

Element	Weight %	Atomic %
O K	37.74	67.21
Al K	1.34	1.42
Si K	0.36	0.37
S K	0.26	0.23
Mn K	1.13	0.59
Fe K	59.16	30.18
Totals	100.00	



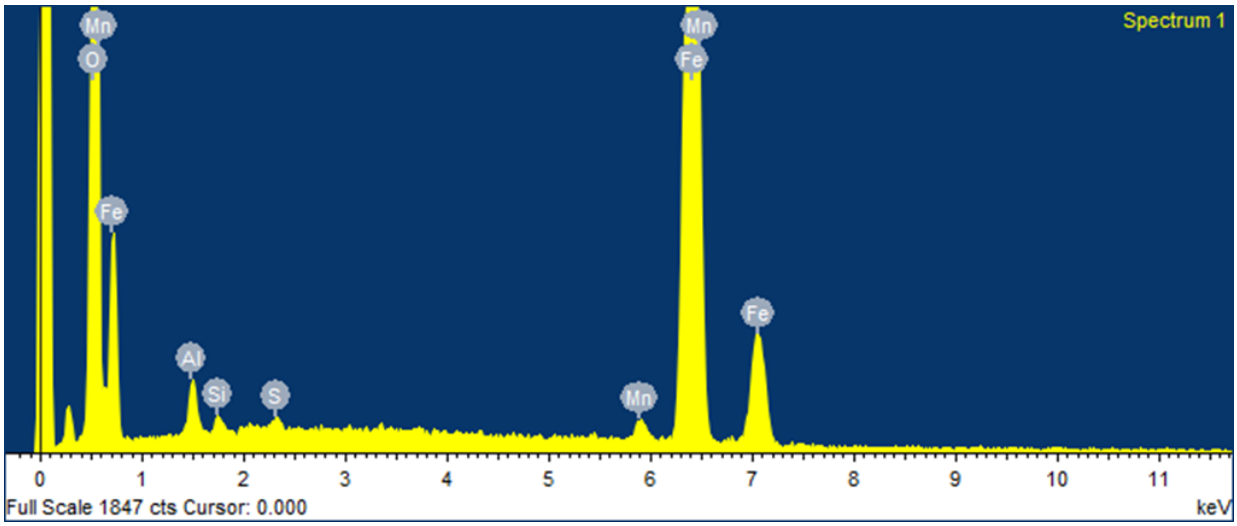
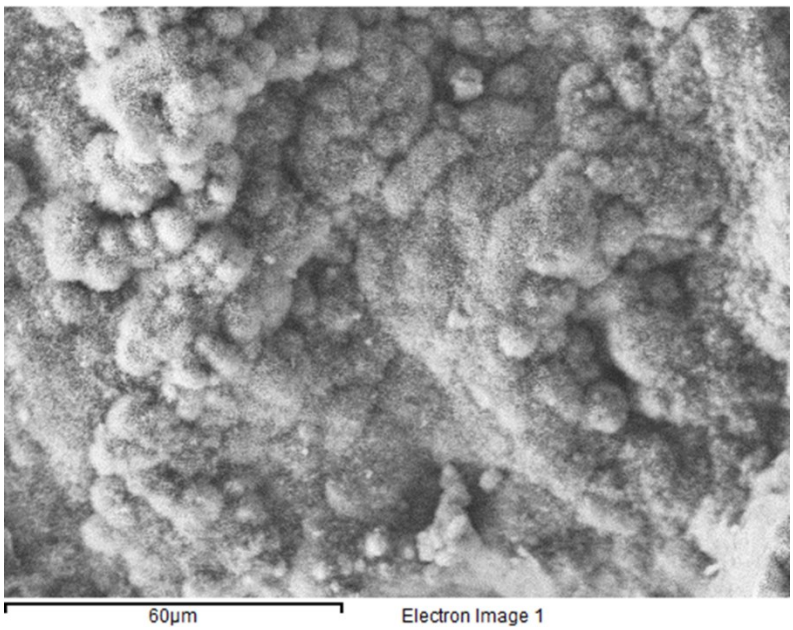


Figure A.387. SEM Image and EDS Spectrum of the Rust Collected from Exterior Web of the Girder.

Element	Weight %	Atomic %
O K	37.77	67.22
Al K	1.38	1.45
Si K	0.34	0.34
S K	0.34	0.30
Mn K	1.11	0.58
Fe K	59.06	30.11
Totals	100.00	



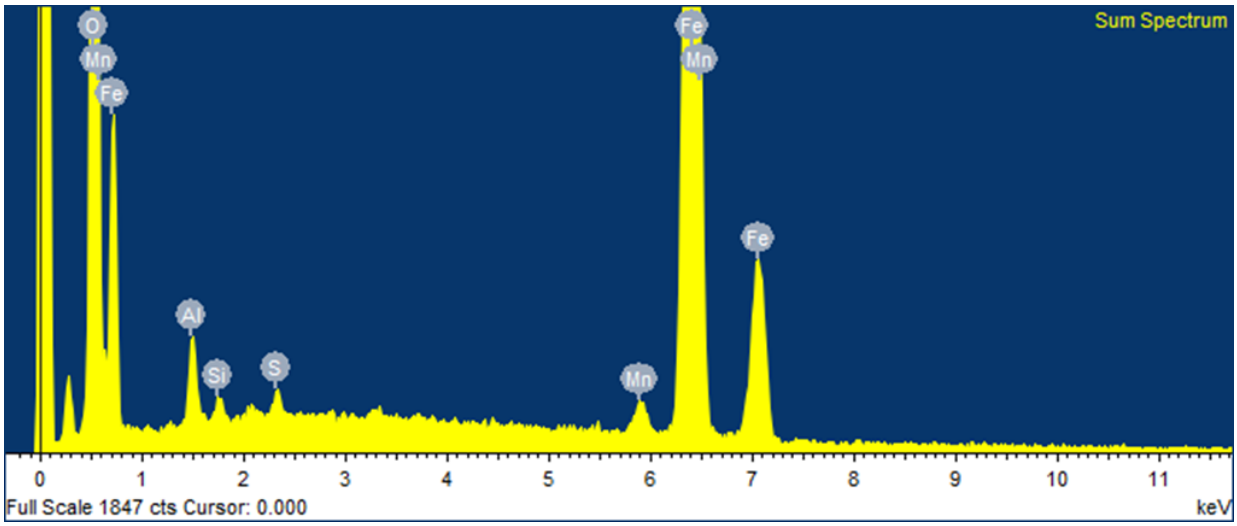


Figure A.388. SEM Image and EDS Spectrum of the Rust Collected from Exterior Web of the Girder.

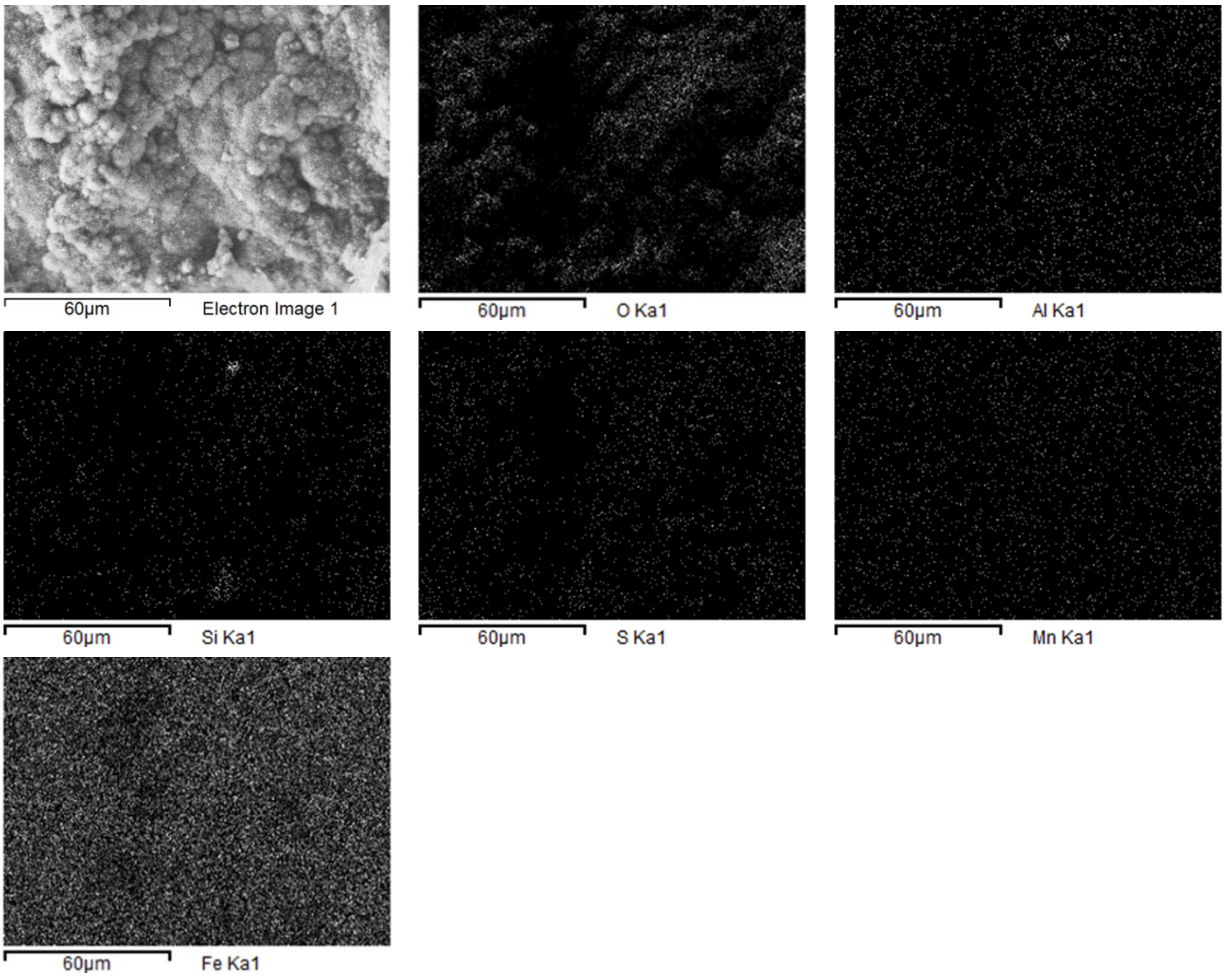
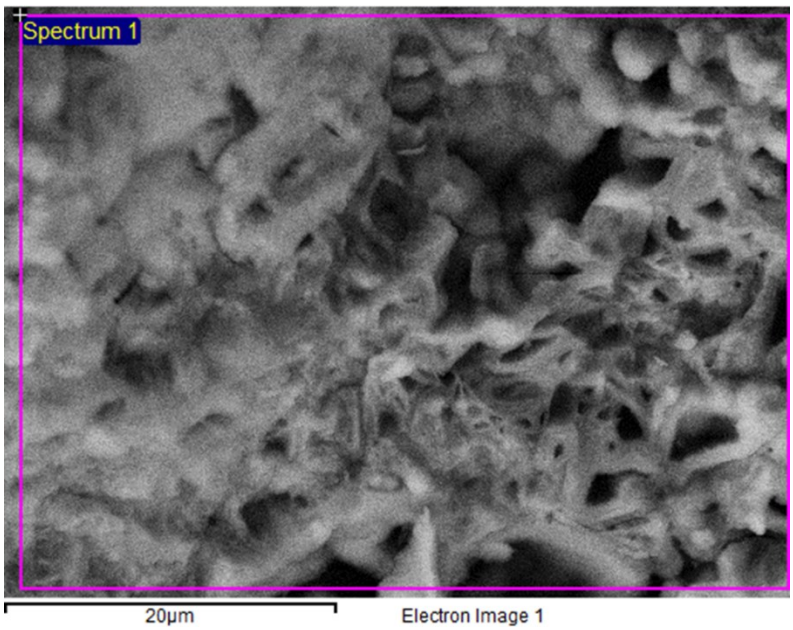


Figure A.389. EDS Elemental Mapping of Rust Collected from Exterior Web.

Element	Weight %	Atomic %
O K	21.28	46.55
Al K	5.43	7.04
Si K	0.52	0.64
S K	0.33	0.36
Cr K	0.65	0.43
Mn K	1.46	0.93
Fe K	69.63	43.63
Ni K	0.70	0.42
Totals	100.00	



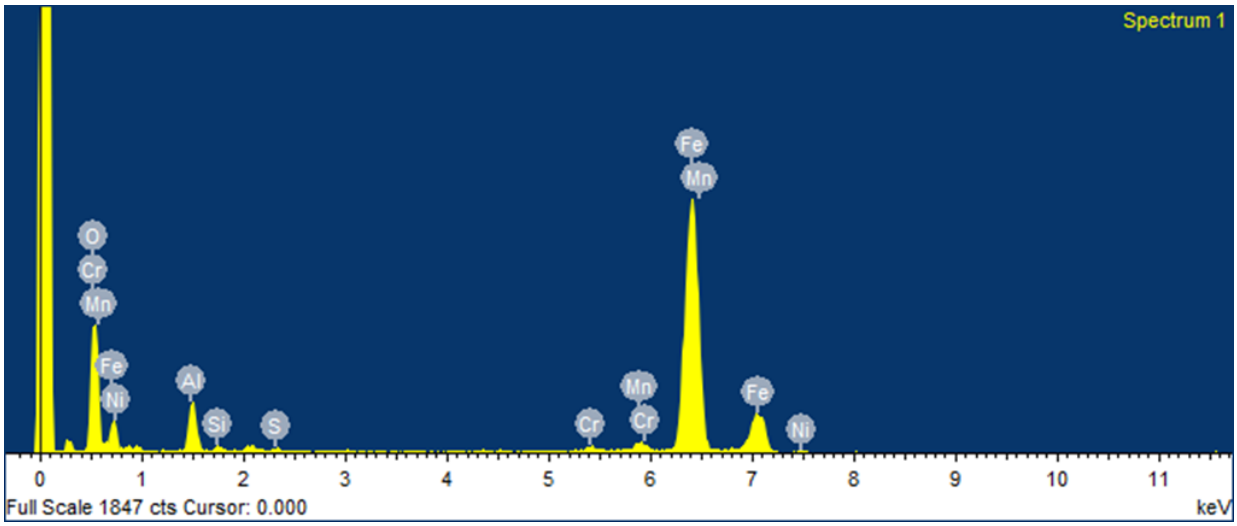
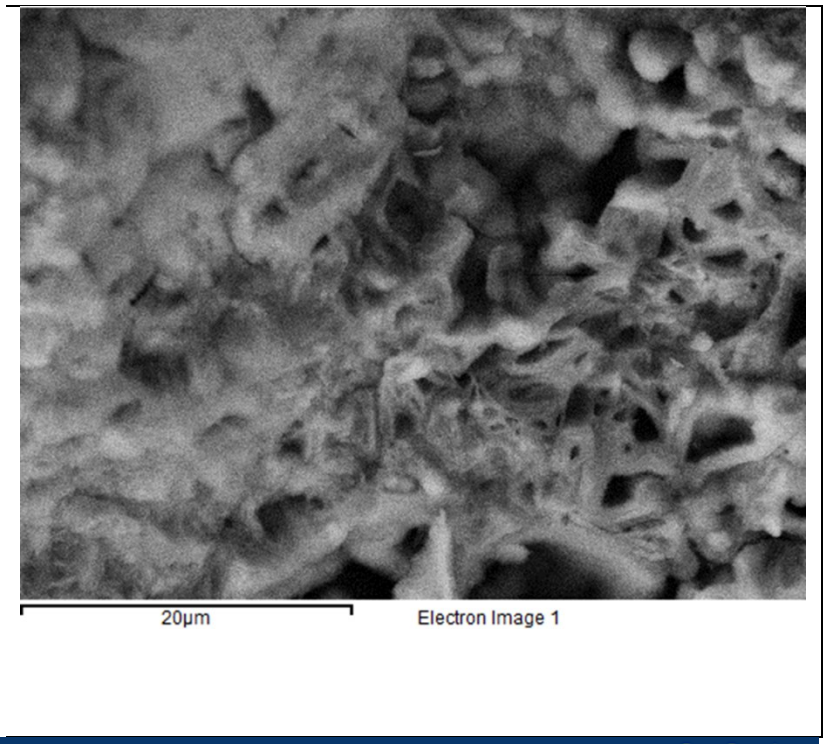


Figure A.390. SEM Image and EDS Spectrum of the Rust Collected from Exterior Web of the Girder.

Element	Weight %	Atomic %
O K	20.96	46.34
Al K	5.28	6.92
Fe K	73.77	46.73
Totals	100.00	



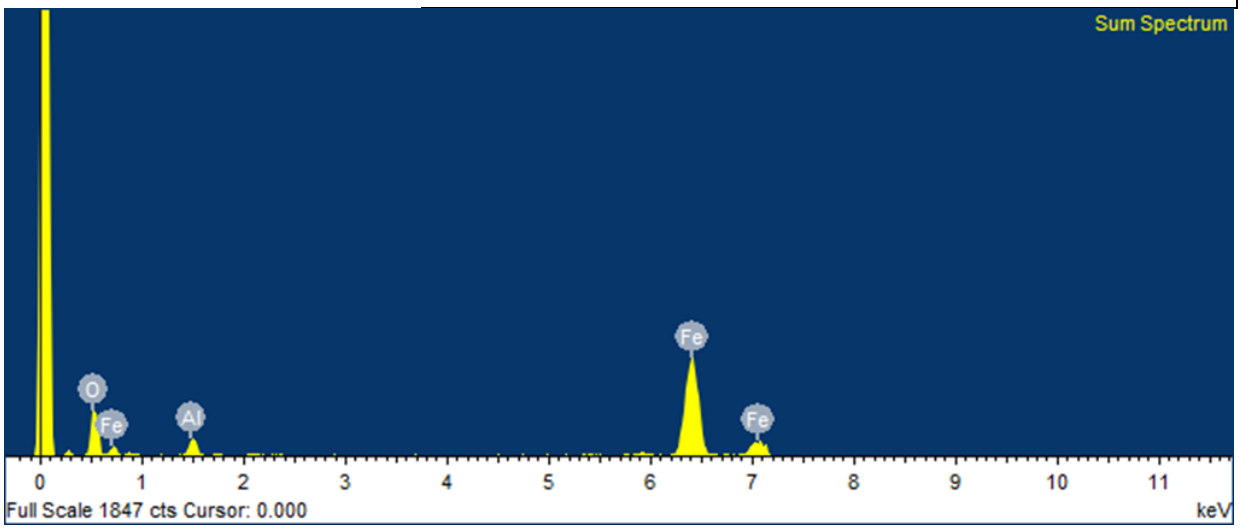


Figure A.391. SEM Image and EDS Spectrum of the Rust Collected from Exterior Web of the Girder.

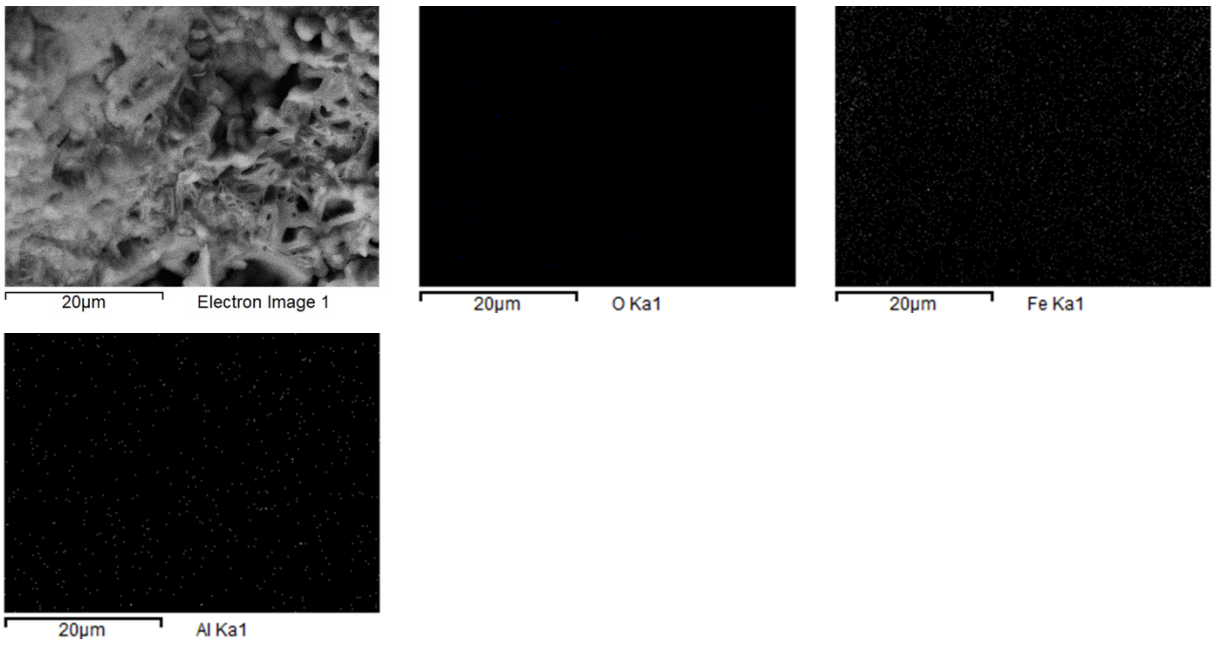
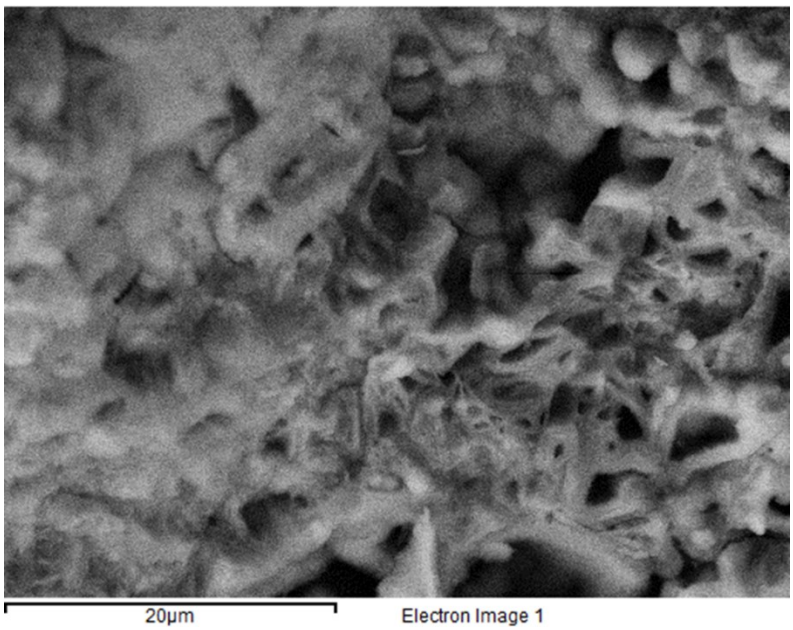


Figure A.392. EDS Elemental Mapping of Rust Collected from Exterior Web.

Element	Weight %	Atomic %
O K	20.96	46.34
Al K	5.28	6.92
Fe K	73.77	46.73
Totals	100.00	



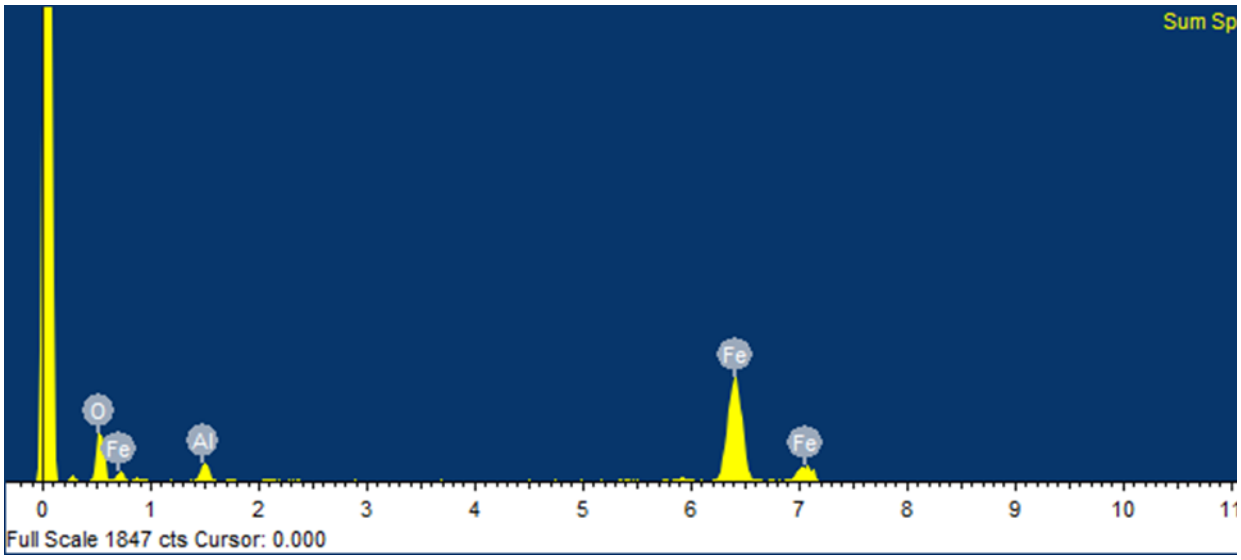
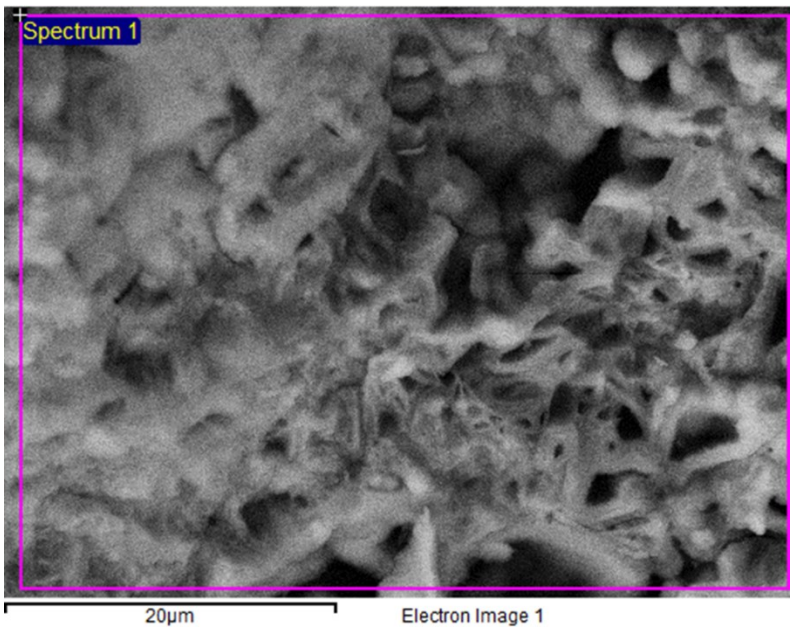


Figure A.393. SEM Image and EDS Spectrum of the Rust Collected from Exterior Web of the Girder.

Element	Weight %	Atomic %
O K	21.28	46.55
Al K	5.43	7.04
Si K	0.52	0.64
S K	0.33	0.36
Cr K	0.65	0.43
Mn K	1.46	0.93
Fe K	69.63	43.63
Ni K	0.70	0.42
Totals	100.00	



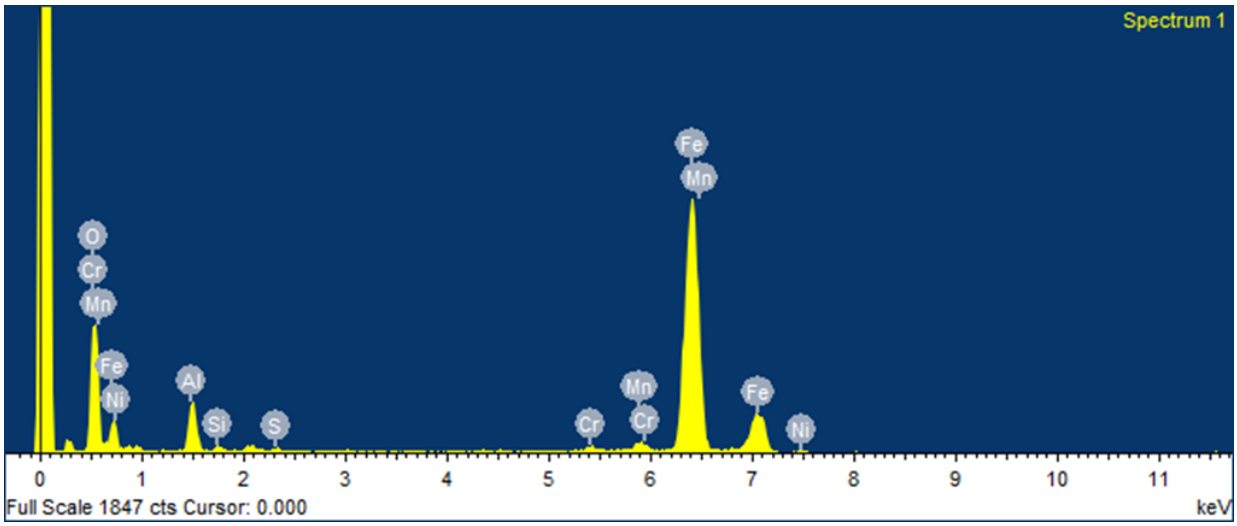
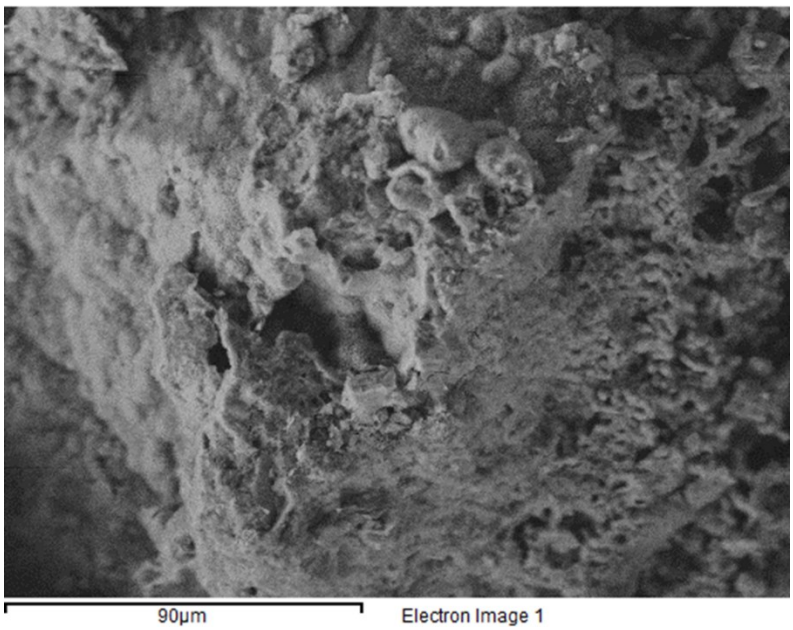


Figure A.394. SEM Image and EDS Spectrum of the Rust Collected from Exterior Web of the Girder.

Element	Weight %	Atomic %
O K	39.42	68.07
Al K	1.63	1.66
Si K	1.25	1.23
S K	0.99	0.86
Ca K	0.60	0.41
Cr K	0.20	0.11
Mn K	1.02	0.52
Fe K	54.61	27.01
Ni K	0.27	0.13
Totals	100.00	



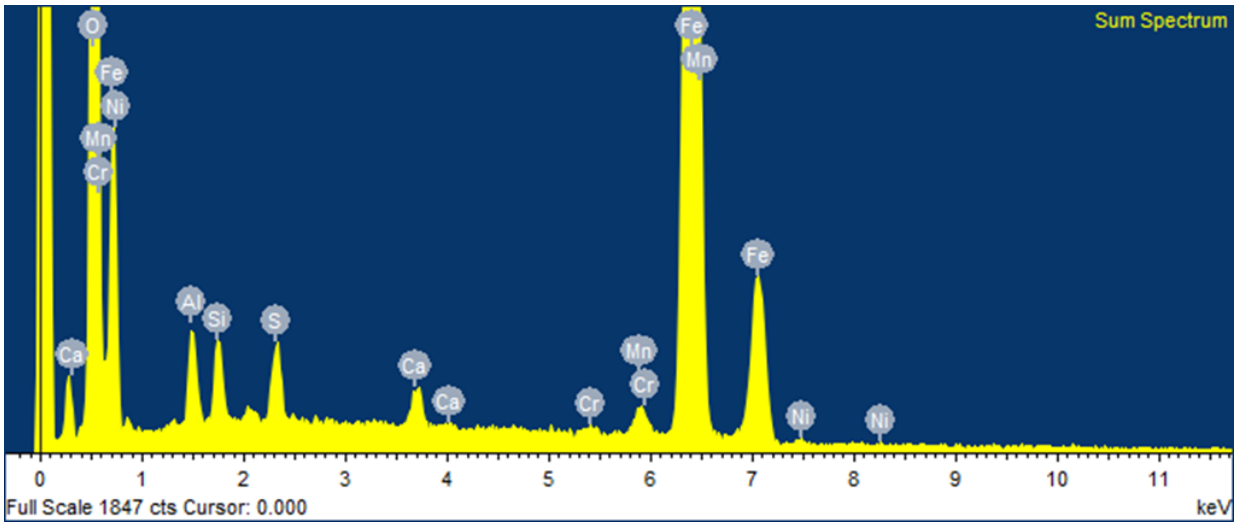
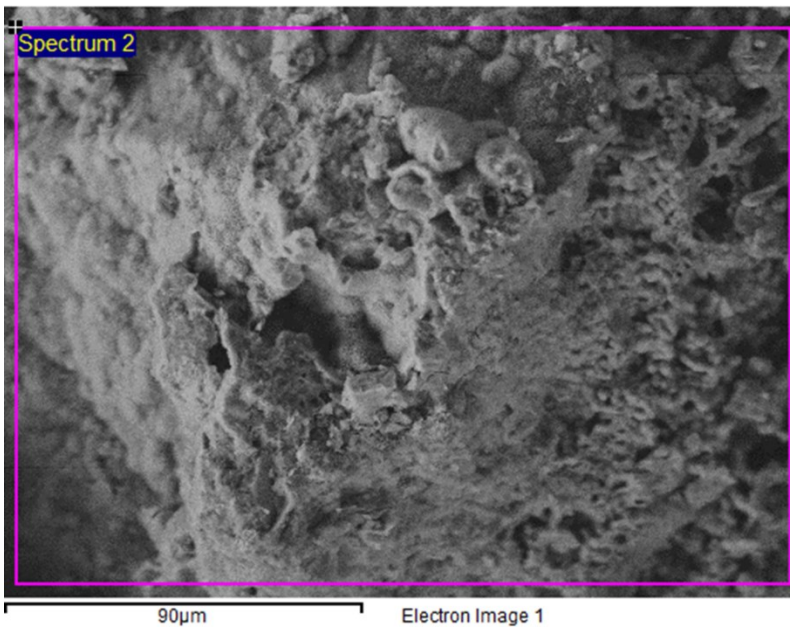


Figure A.395. SEM Image and EDS Spectrum of the Rust Collected from Exterior Web of the Girder.

Element	Weight %	Atomic %
O K	39.17	67.82
Al K	1.74	1.78
Si K	1.24	1.22
S K	0.97	0.84
Ca K	0.57	0.40
Mn K	1.07	0.54
Fe K	55.24	27.40
Totals	100.00	



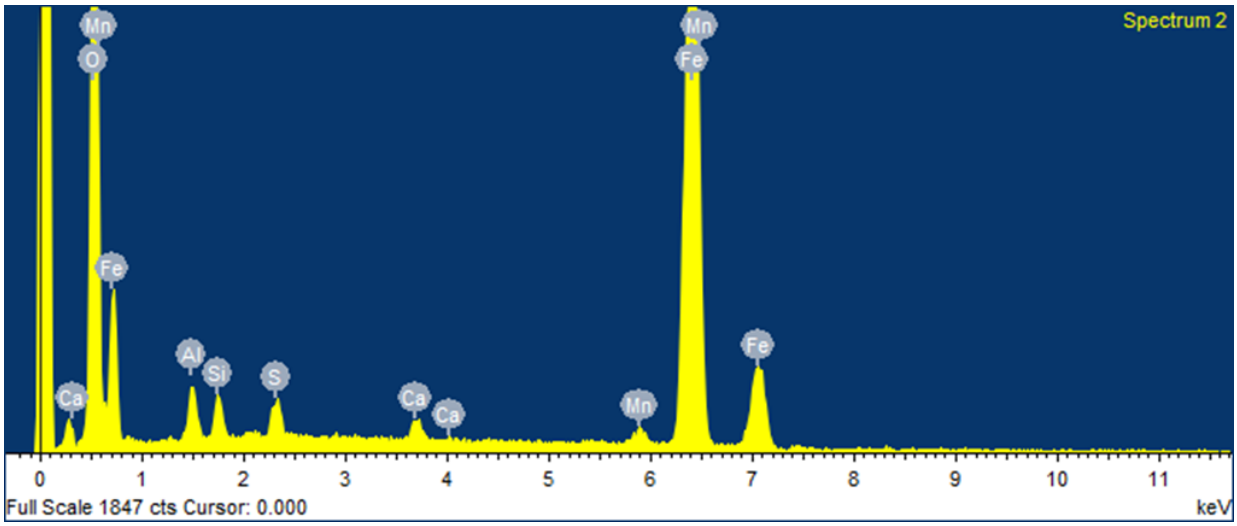


Figure A.396. SEM Image and EDS Spectrum of the Rust Collected from Exterior Web of the Girder.

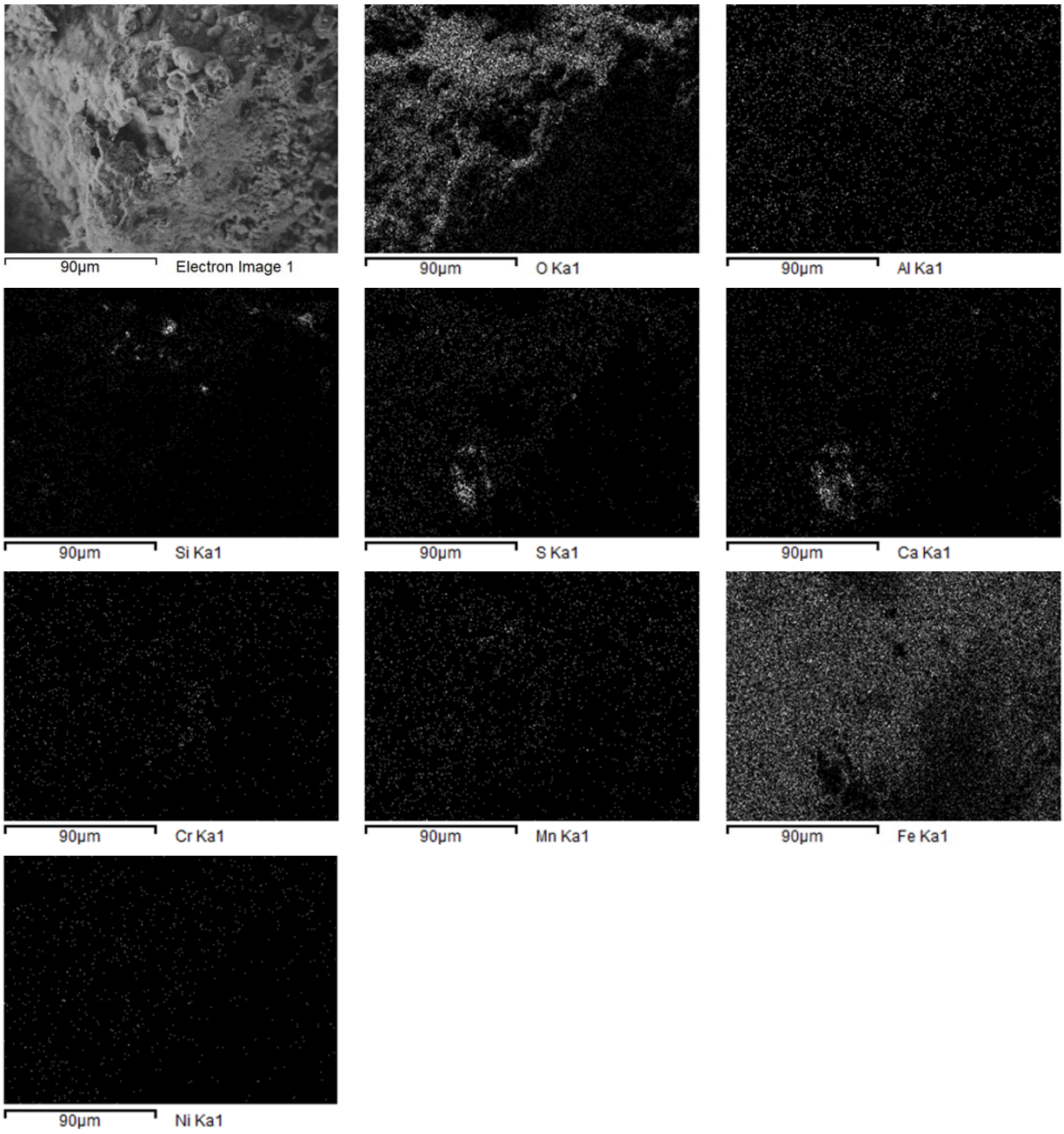
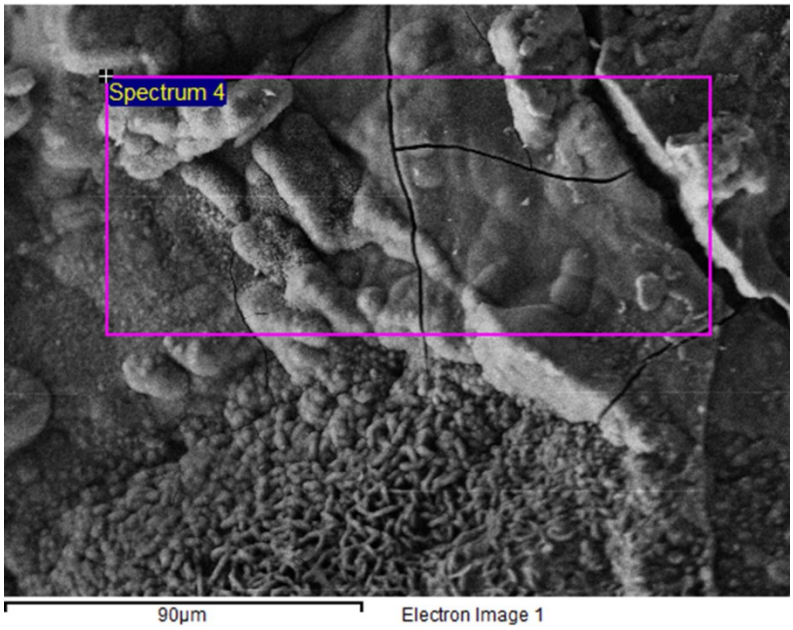


Figure A.397. EDS Elemental Mapping of Rust Collected from Exterior Web.

A.25.4.SEM/EDS Results: Interior Web

Element	Weight %	Atomic %
O K	52.44	78.74
Al K	0.62	0.56
S K	1.44	1.08
Cl K	0.18	0.12
Mn K	0.65	0.28
Fe K	44.67	19.22
Totals	100.00	



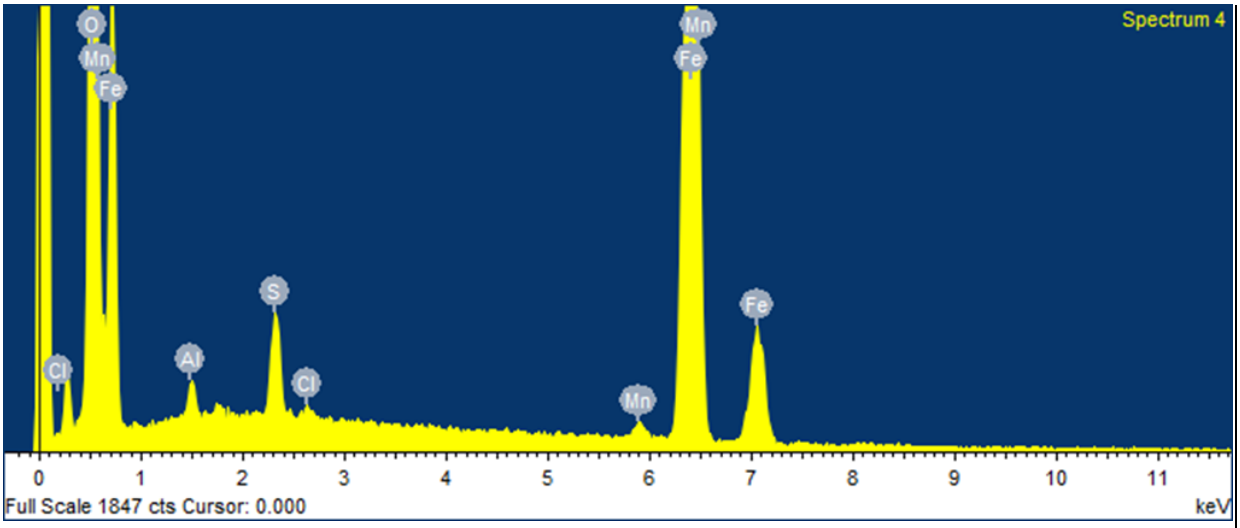
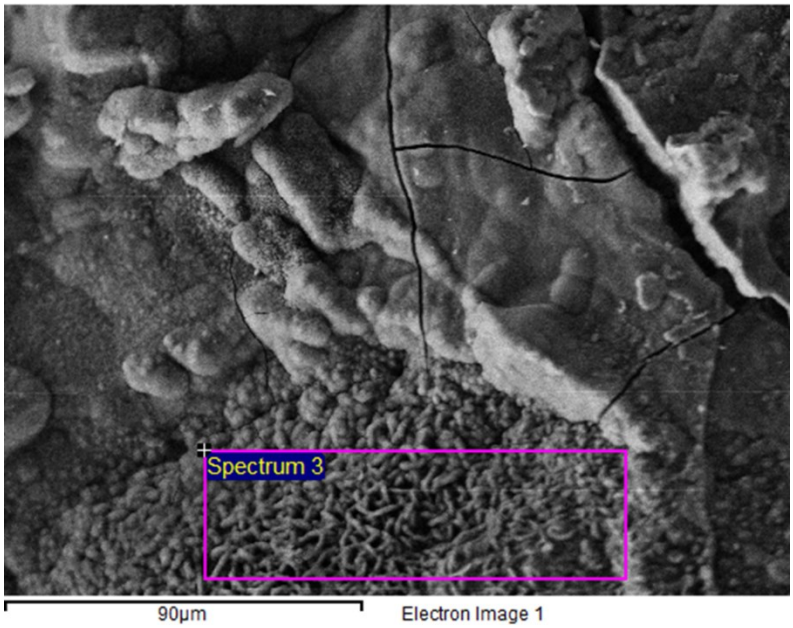


Figure A.398. SEM Image and EDS Spectrum of the Rust Collected from Interior Web of the Girder.

Element	Weight %	Atomic %
O K	54.63	80.28
Al K	0.55	0.48
S K	1.15	0.84
Mn K	0.89	0.38
Fe K	42.78	18.01
Totals	100.00	



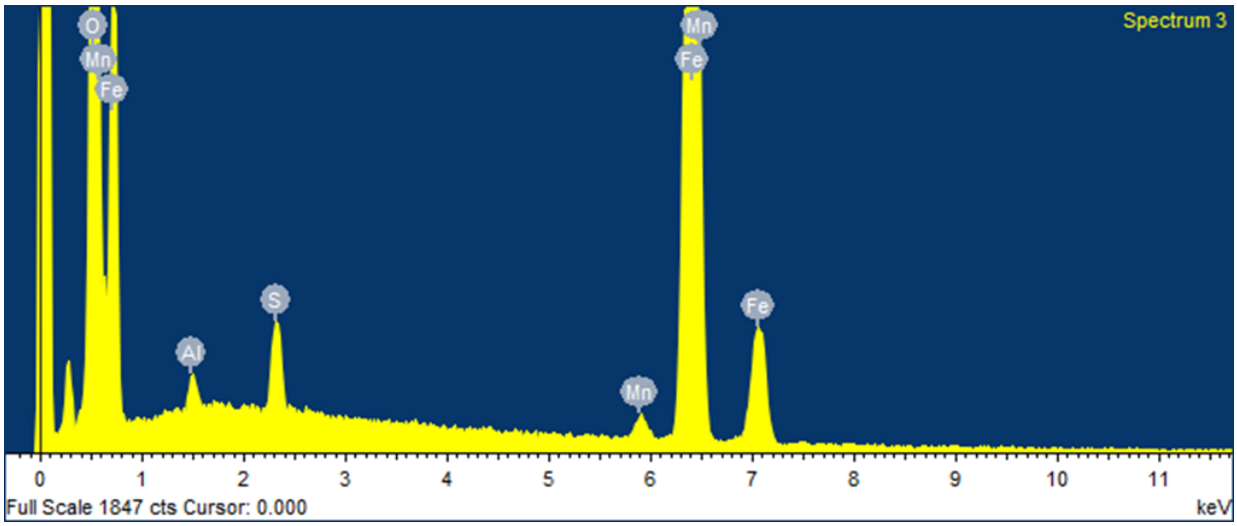
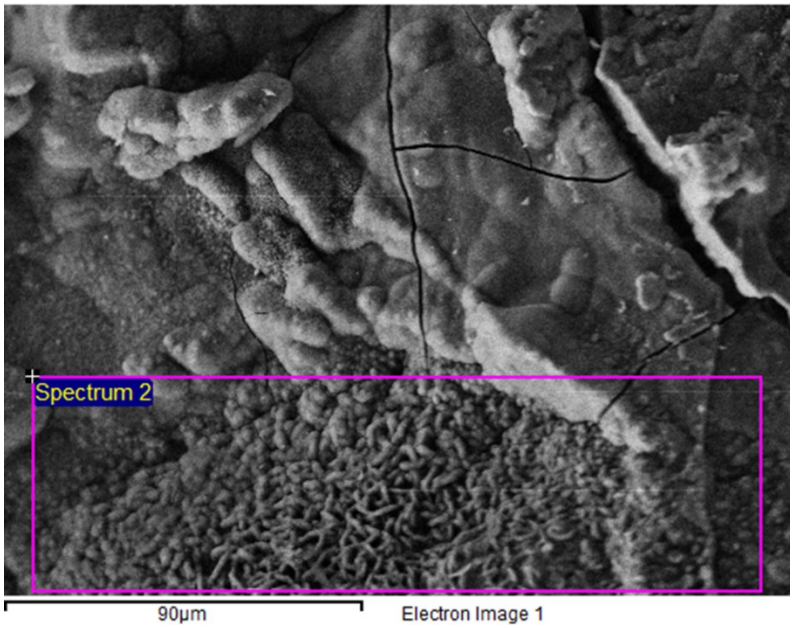


Figure A.399. SEM Image and EDS Spectrum of the Rust Collected from Interior Web of the Girder.

Element	Weight %	Atomic %
O K	52.82	79.06
Al K	0.56	0.50
S K	1.26	0.94
Cl K	0.17	0.12
Mn K	0.97	0.42
Fe K	44.21	18.96
Totals	100.00	



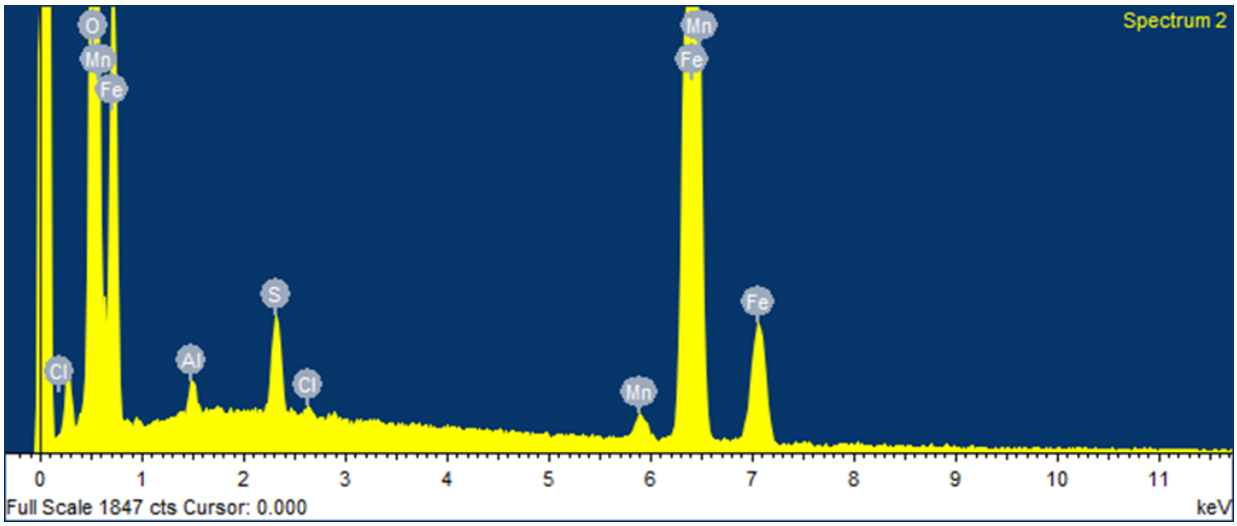
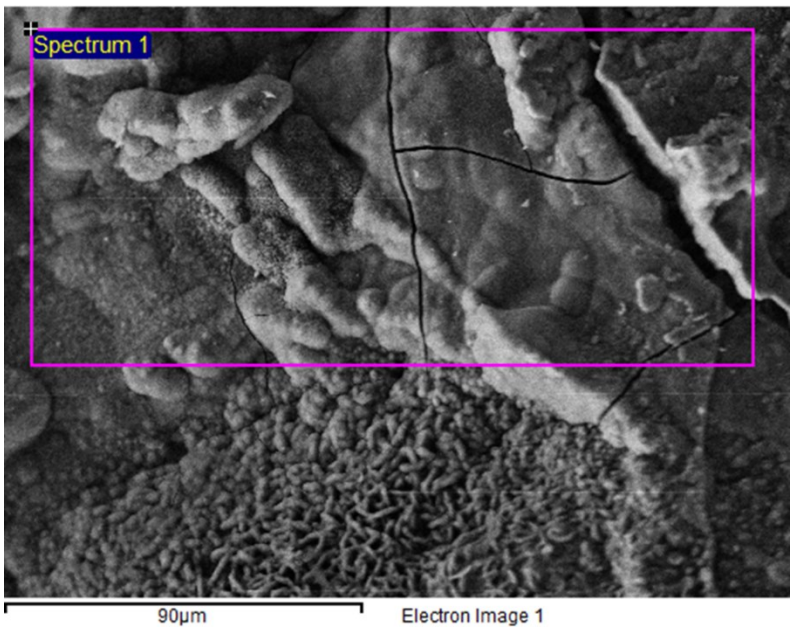


Figure A.400. SEM Image and EDS Spectrum of the Rust Collected from Interior Web of the Girder.

Element	Weight %	Atomic %
O K	51.72	78.29
Al K	0.58	0.52
S K	1.42	1.07
Cl K	0.19	0.13
Mn K	0.61	0.27
Fe K	45.20	19.60
Ni K	0.28	0.12
Totals	100.00	



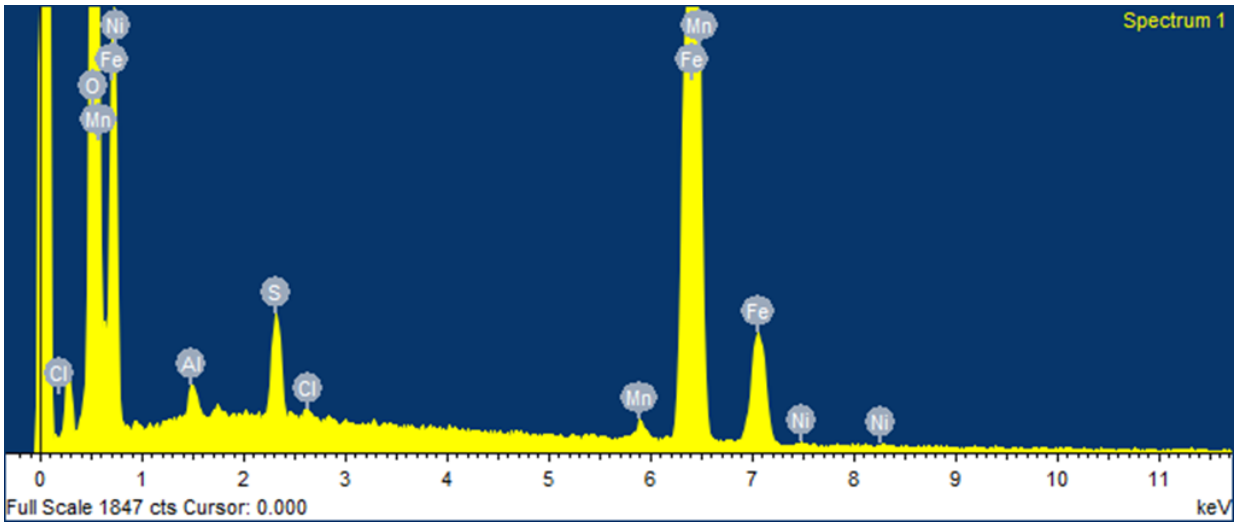
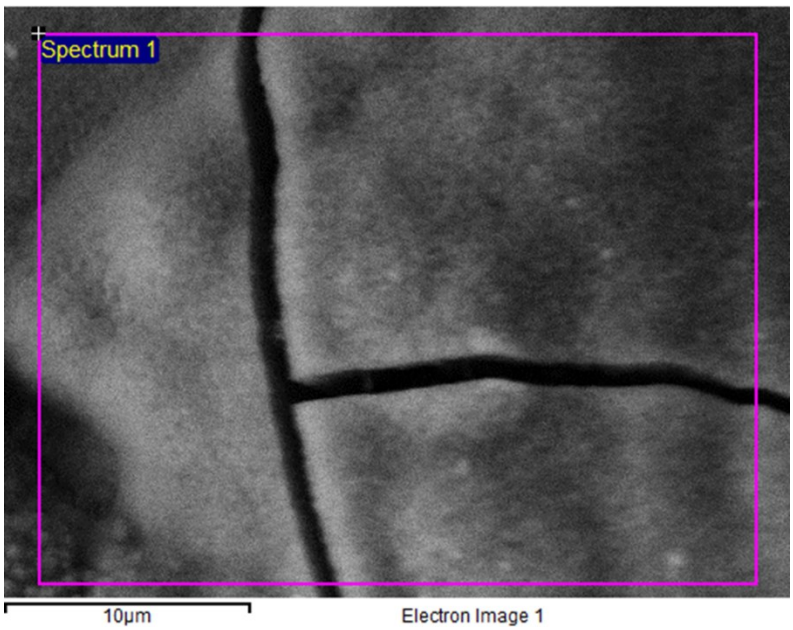


Figure A.401. SEM Image and EDS Spectrum of the Rust Collected from Interior Web of the Girder.

Element	Weight %	Atomic %
O K	55.29	80.53
Al K	0.51	0.44
S K	1.74	1.26
Cl K	0.21	0.14
Mn K	0.91	0.39
Fe K	41.35	17.25
Totals	100.00	



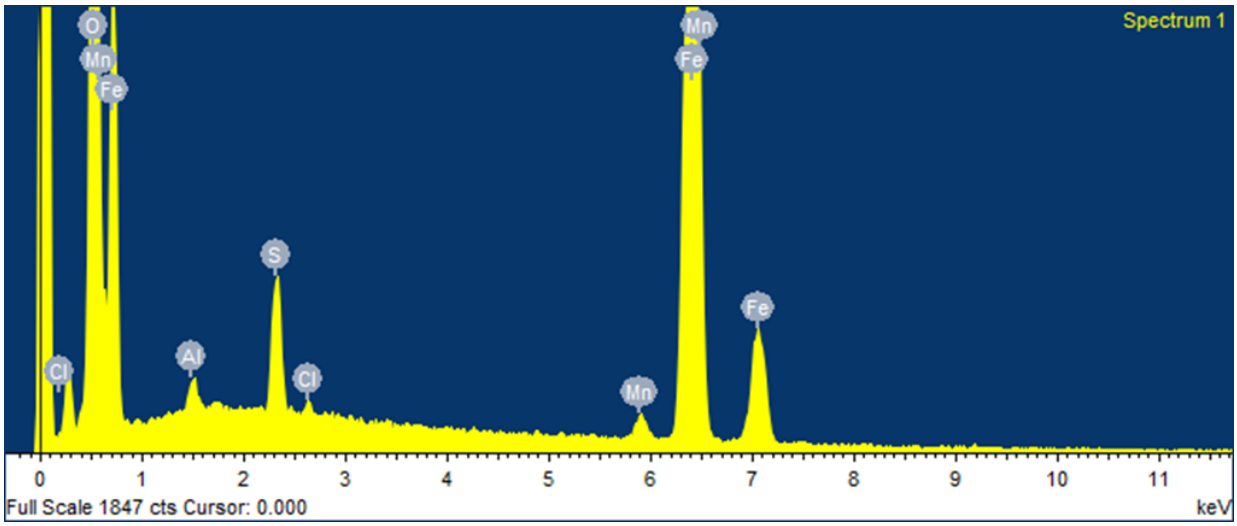
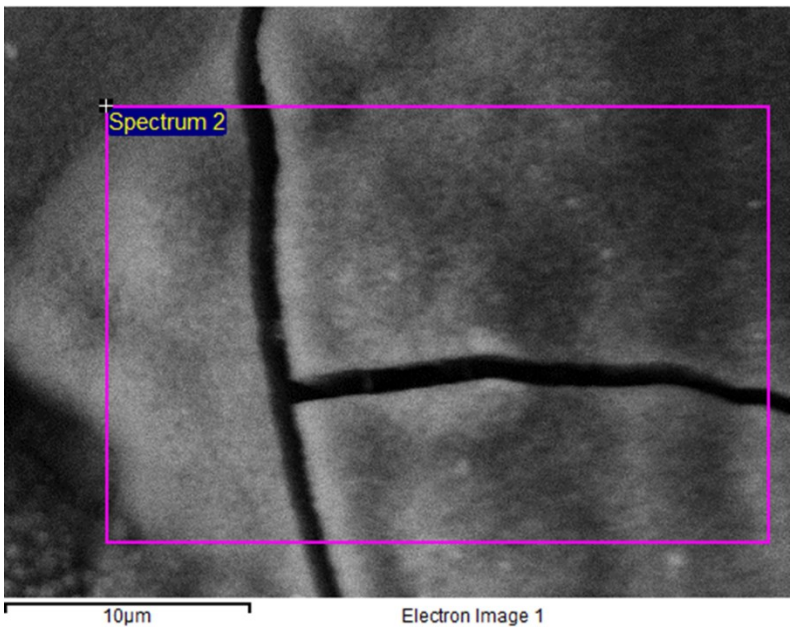


Figure A.402. SEM Image and EDS Spectrum of the Rust Collected from Interior Web of the Girder.

Element	Weight %	Atomic %
O K	54.68	80.12
Al K	0.55	0.48
S K	1.74	1.28
Cl K	0.22	0.15
Mn K	0.94	0.40
Fe K	41.86	17.57
Totals	100.00	



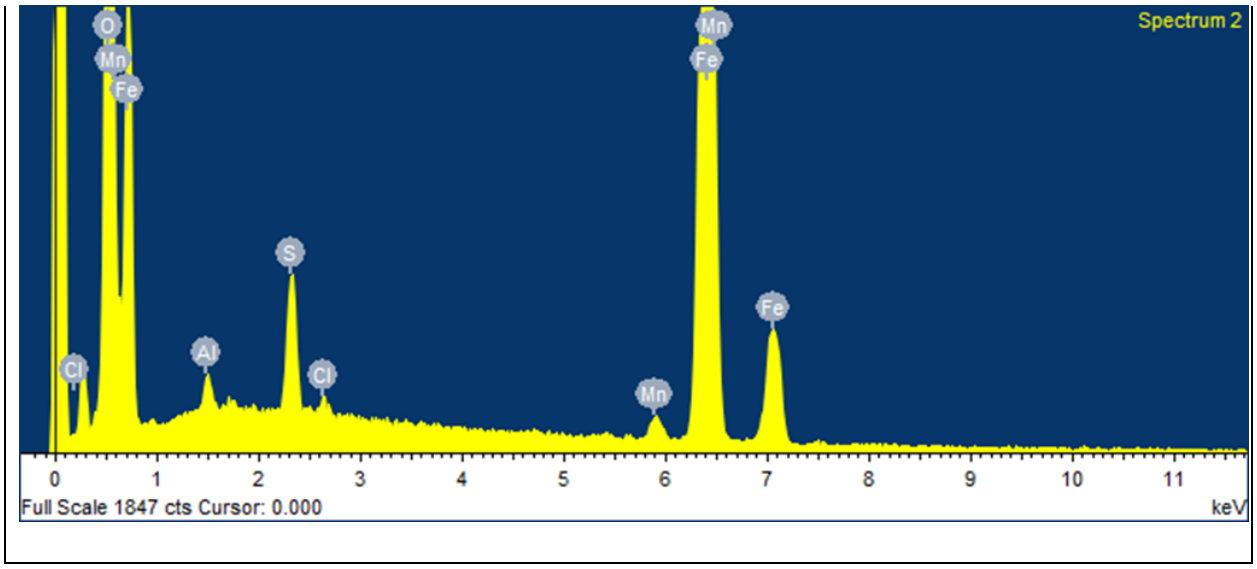
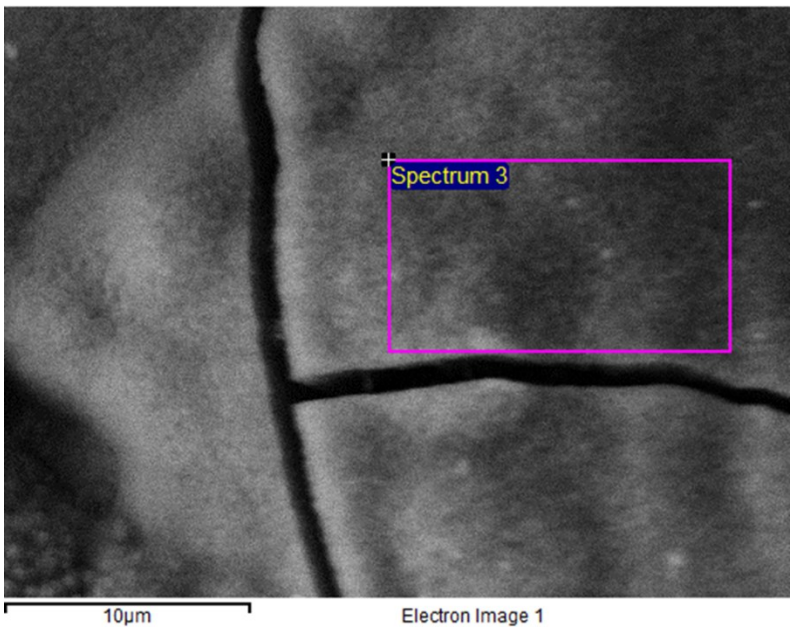


Figure A.403. SEM Image and EDS Spectrum of the Rust Collected from Interior Web of the Girder.

Element	Weight %	Atomic %
O K	55.95	80.82
Al K	0.57	0.49
Si K	0.17	0.14
S K	1.89	1.36
Cl K	0.21	0.14
Mn K	0.31	0.13
Fe K	40.83	16.90
Cu K	0.06	0.02
Totals	100.00	



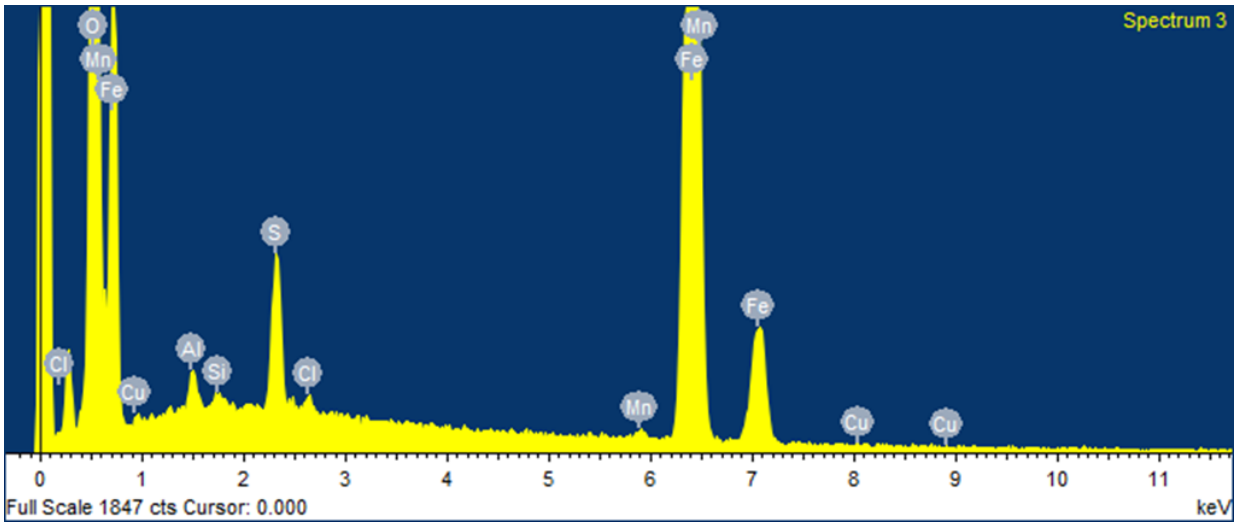
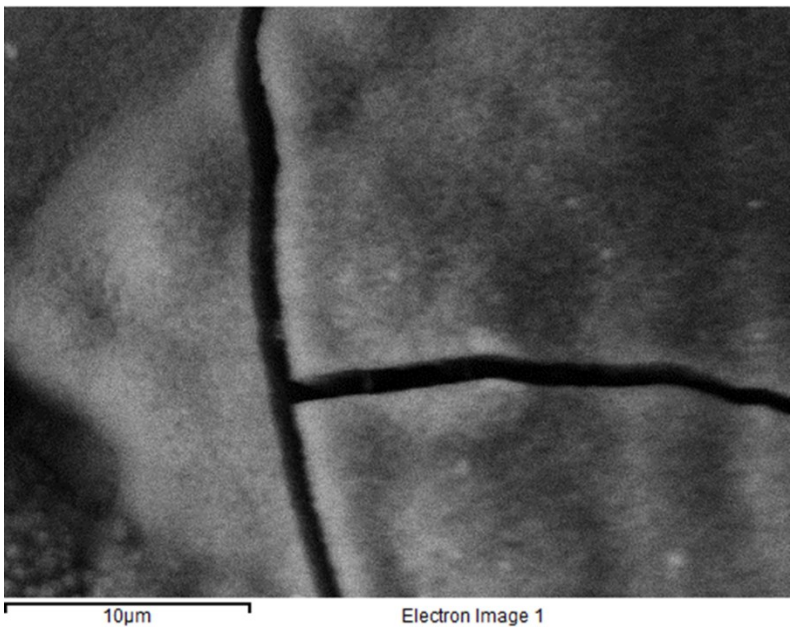


Figure A.404. SEM Image and EDS Spectrum of the Rust Collected from Interior Web of the Girder.

Element	Weight %	Atomic %
O K	54.85	80.23
Al K	0.58	0.51
S K	1.72	1.26
Cl K	0.18	0.12
Mn K	0.92	0.39
Fe K	41.75	17.50
Totals	100.00	



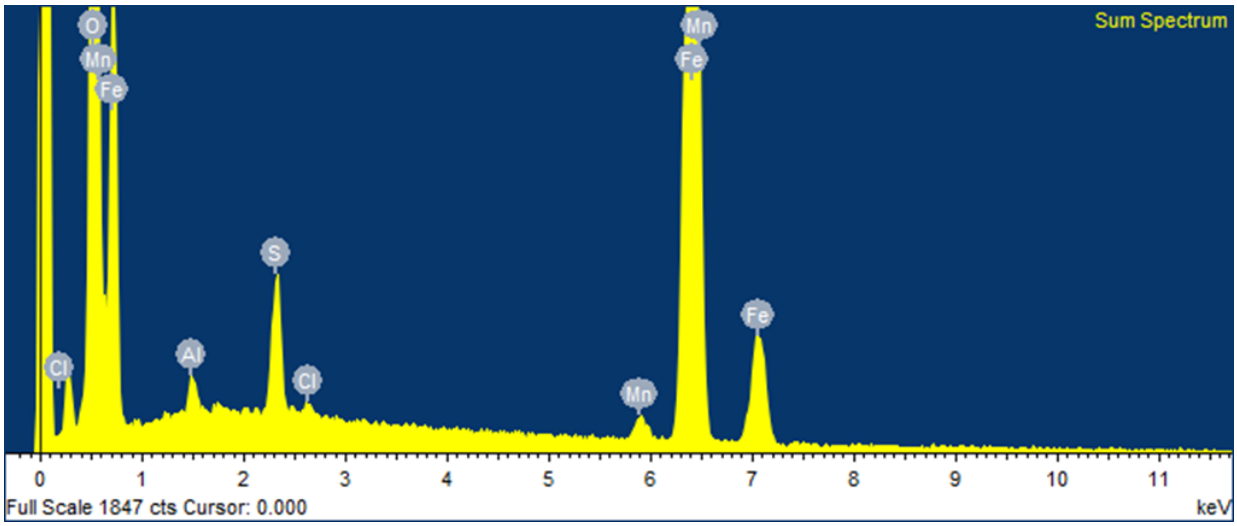


Figure A.405. SEM Image and EDS Spectrum of the Rust Collected from Interior Web of the Girder.

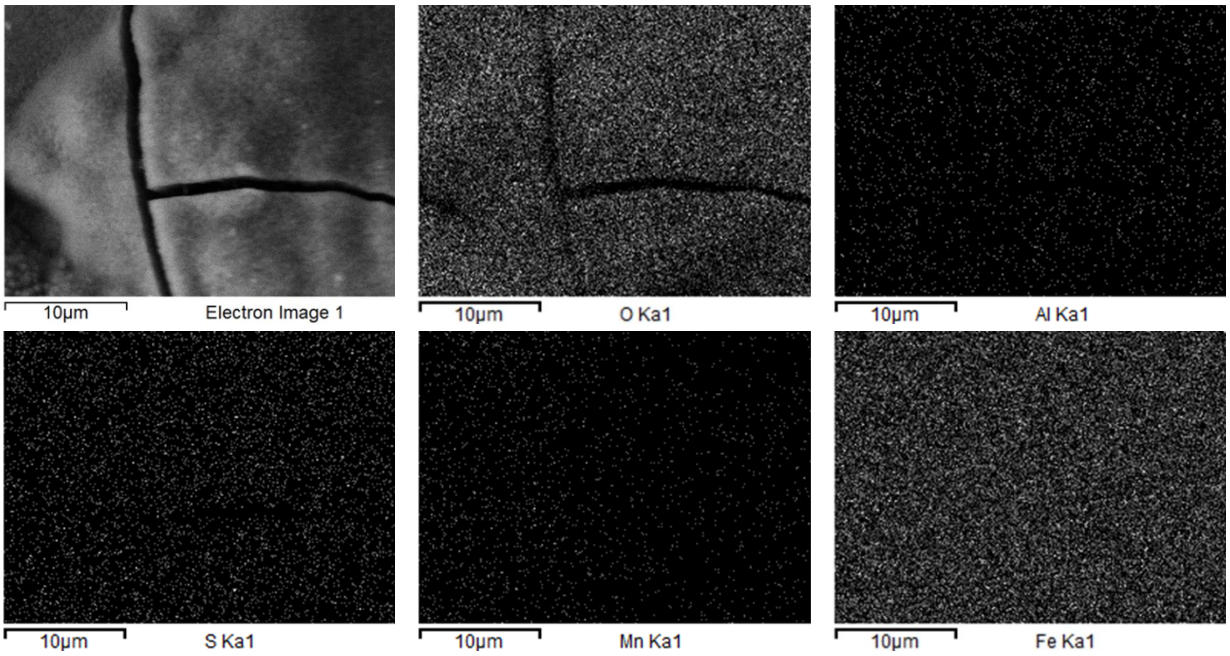
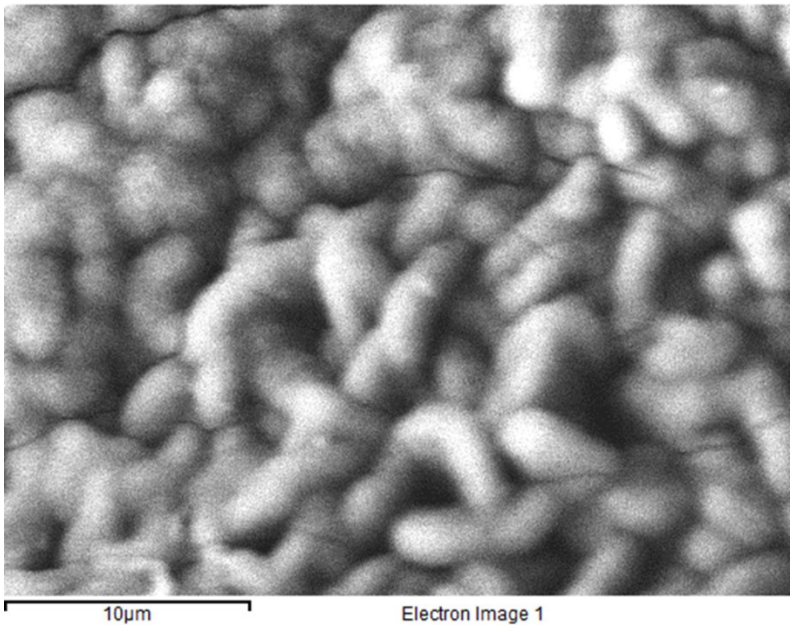


Figure A.406. EDS Elemental Mapping of Rust Collected from Interior Web.

Element	Weight %	Atomic %
O K	53.29	79.34
Al K	0.51	0.45
S K	1.40	1.04
Cl K	0.18	0.12
Cr K	0.14	0.07
Mn K	0.70	0.30
Fe K	43.78	18.68
Totals	100.00	



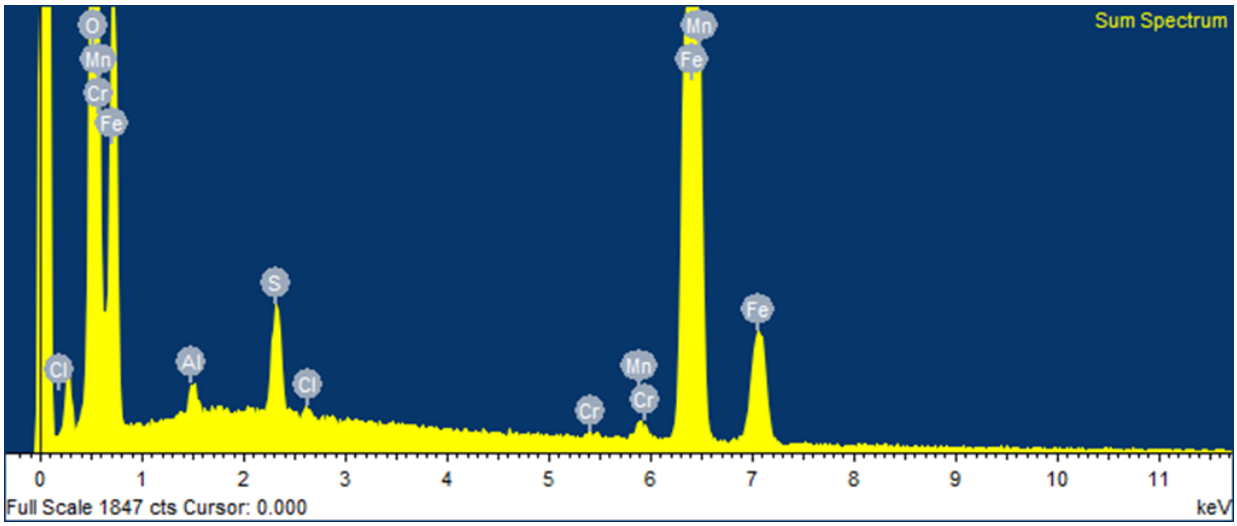


Figure A.407. SEM Image and EDS Spectrum of the Rust Collected from Interior Web of the Girder.

A.25.5.XPS Results: Exterior Web Girder

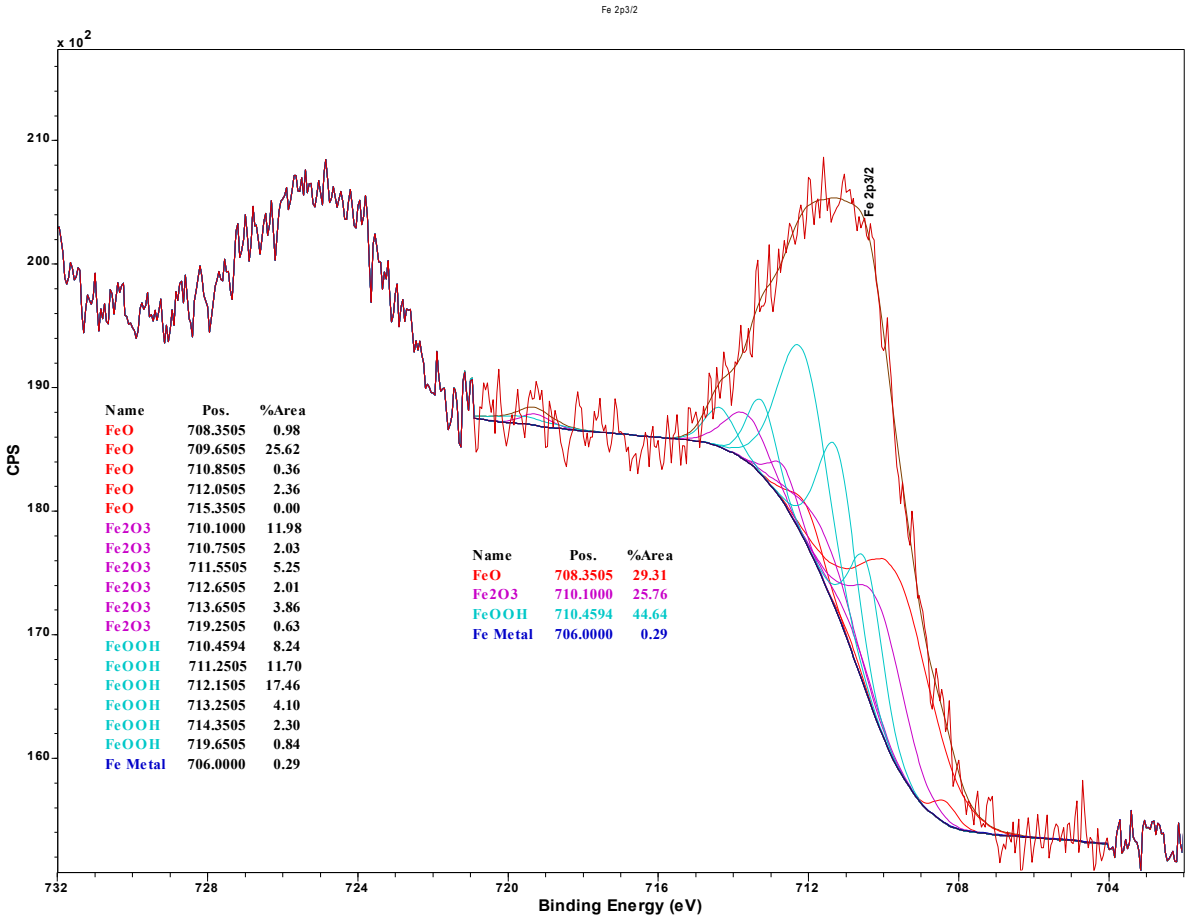


Figure A.408. XPS Spectrum of the Rust Collected from Exterior Web of the Girder.

A.25.6.XPS Results: Interior Web Girder

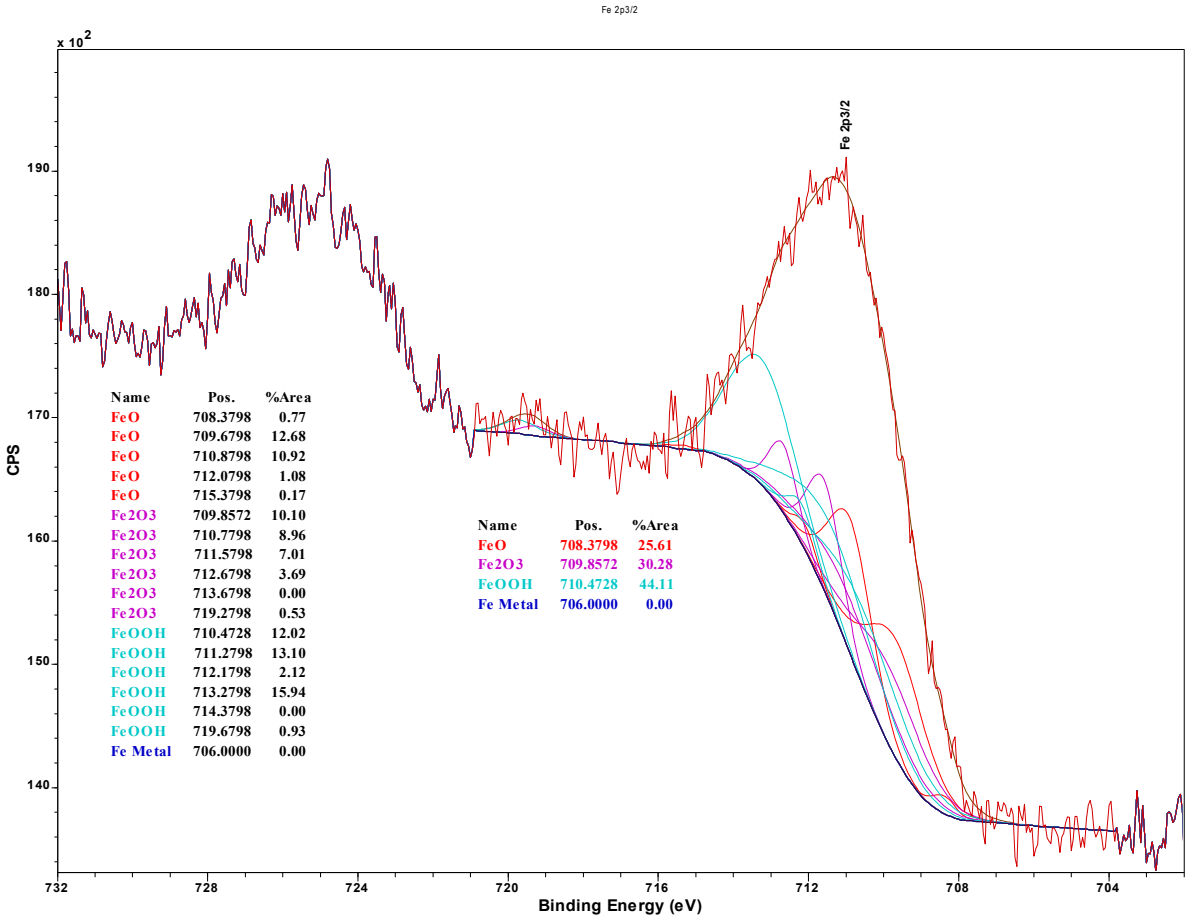


Figure A.409. XPS Spectrum of the Rust Collected from Interior Web of the Girder.

A.25.7.XRD Result: Exterior and Interior Girder

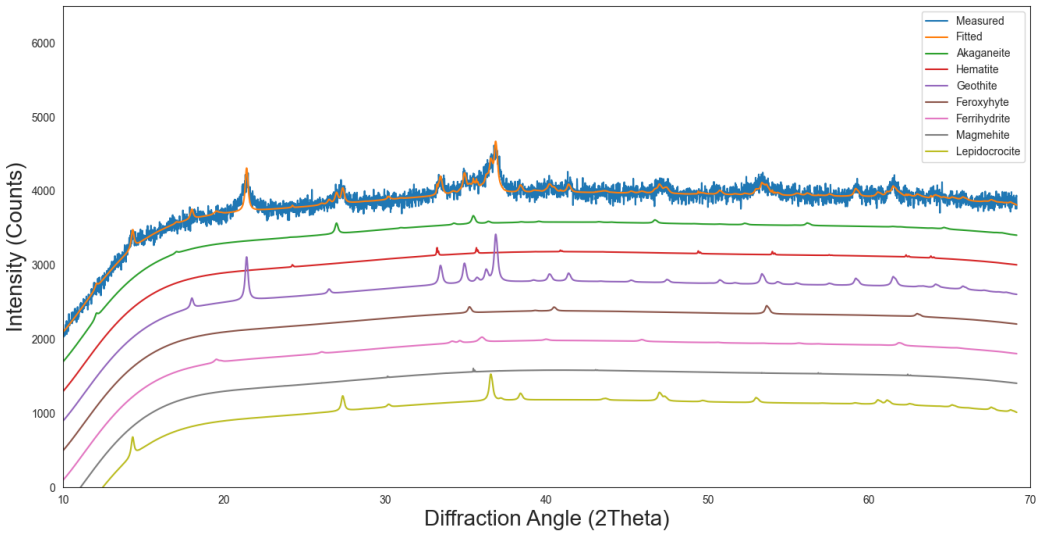


Figure A.410. XRD Pattern of Powdered Rust Collected from Exterior Web of the Girder.

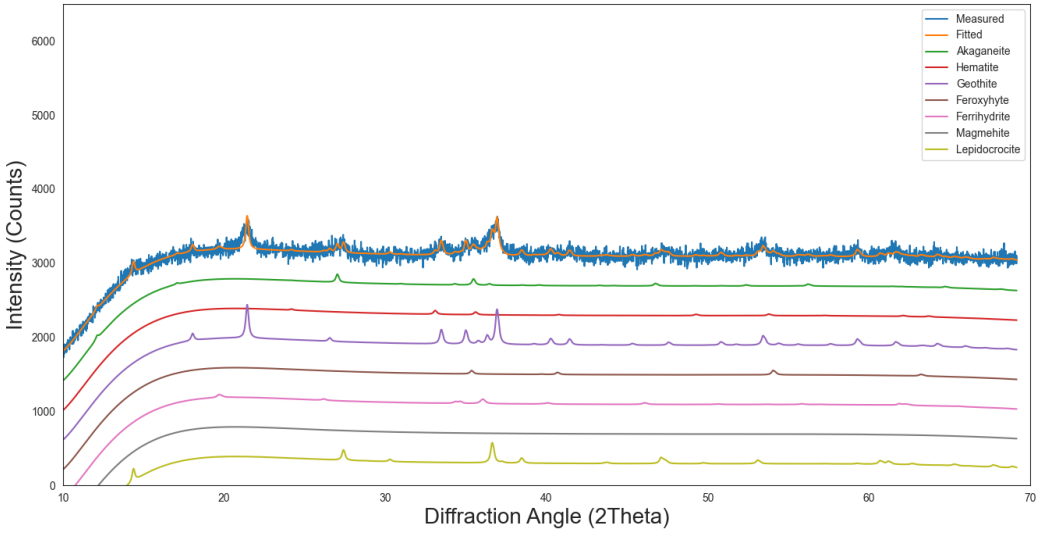


Figure A.411. XRD Pattern of Powdered Rust Collected from Interior Web of the Girder.

A.25.8. Particle Size Analysis: Tape Adhesion Results

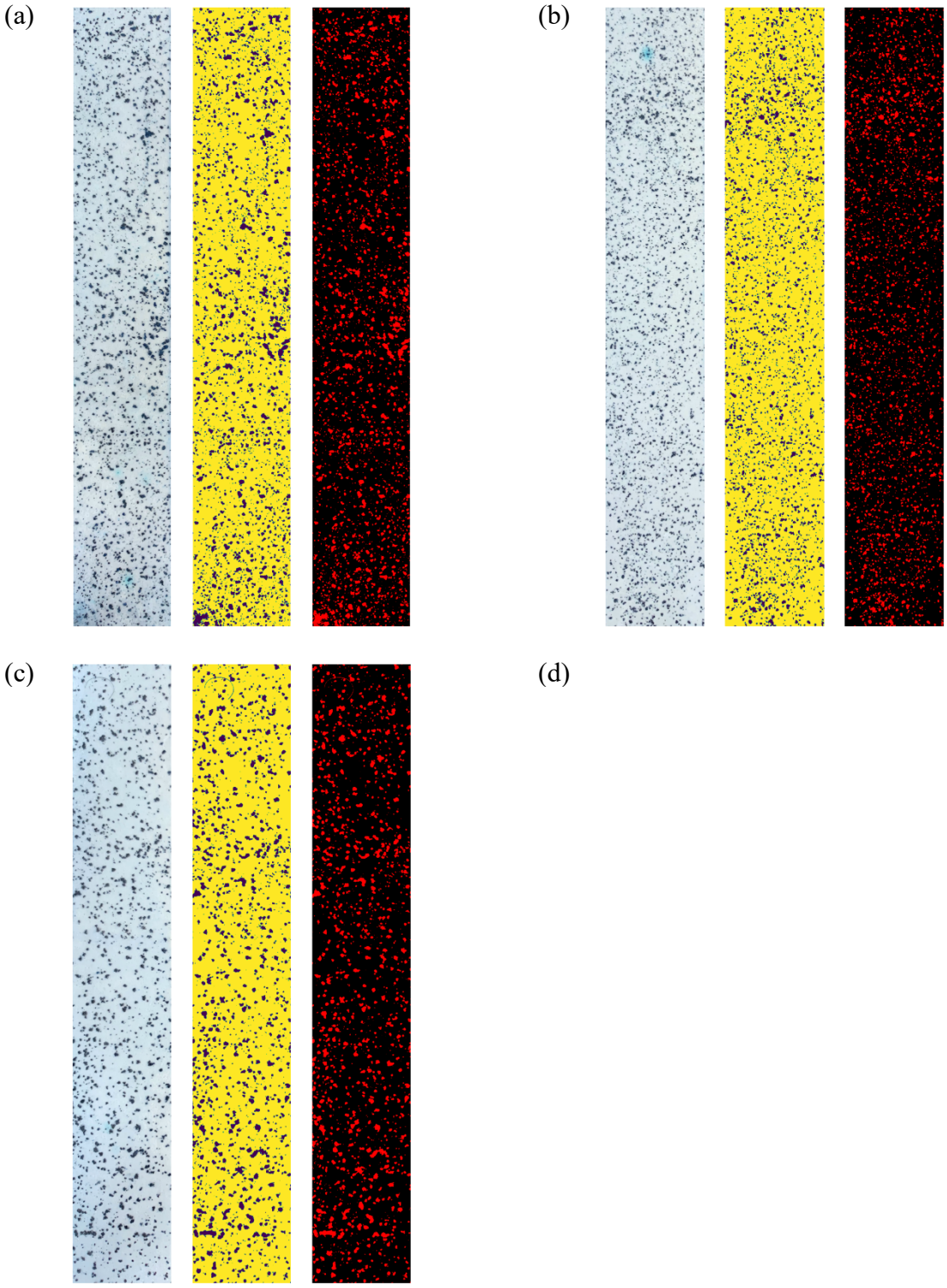


Figure A.412. Particle Size Analysis Results at A1G1F1 (a) Top Flange Bottom, (b) Web, (c) Bottom Flange Bottom.

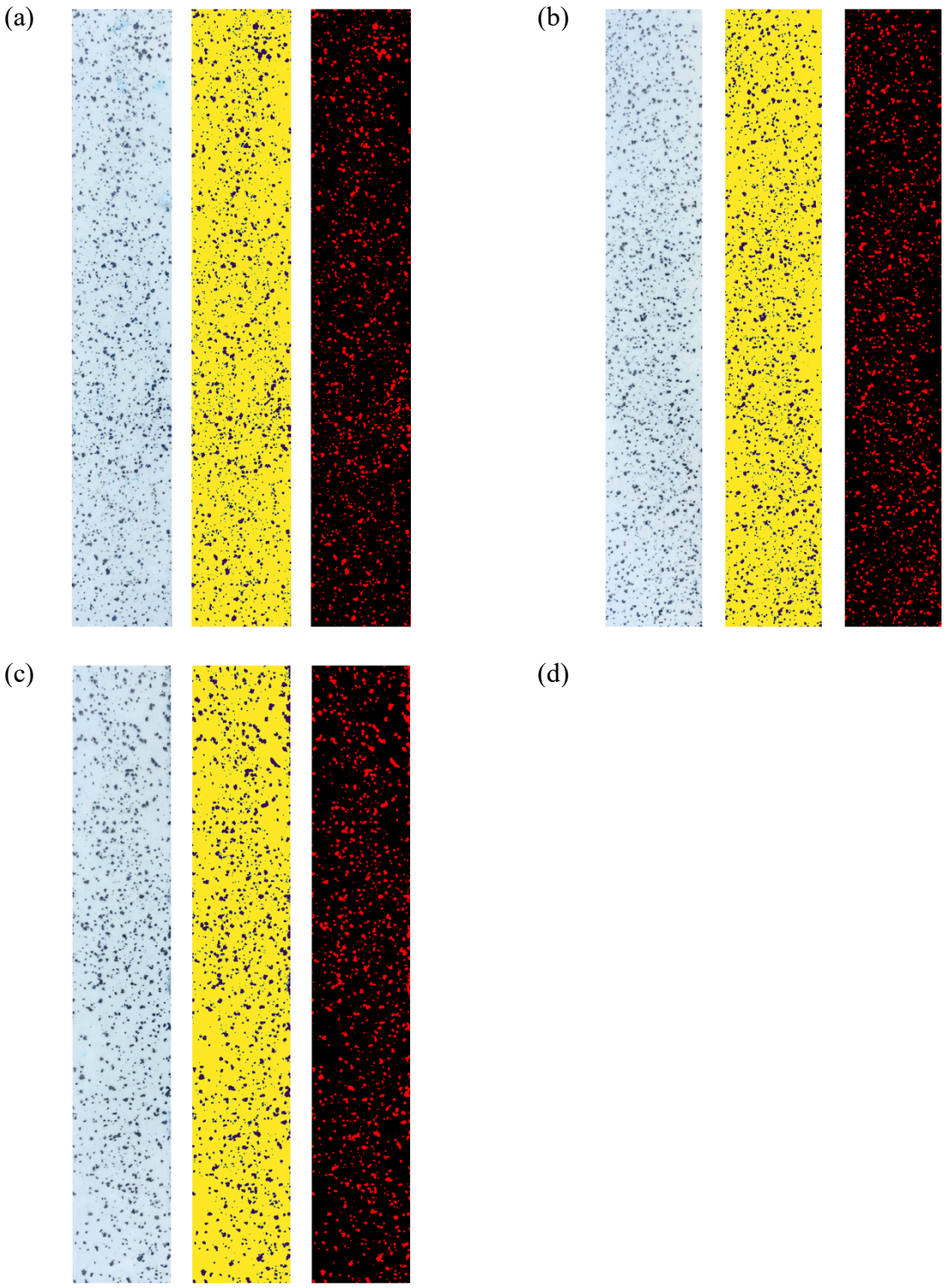


Figure A.413. Particle Size Analysis Results at A1G1F2 (a) Top Flange Bottom, (b) Web, (c) Bottom Flange Bottom

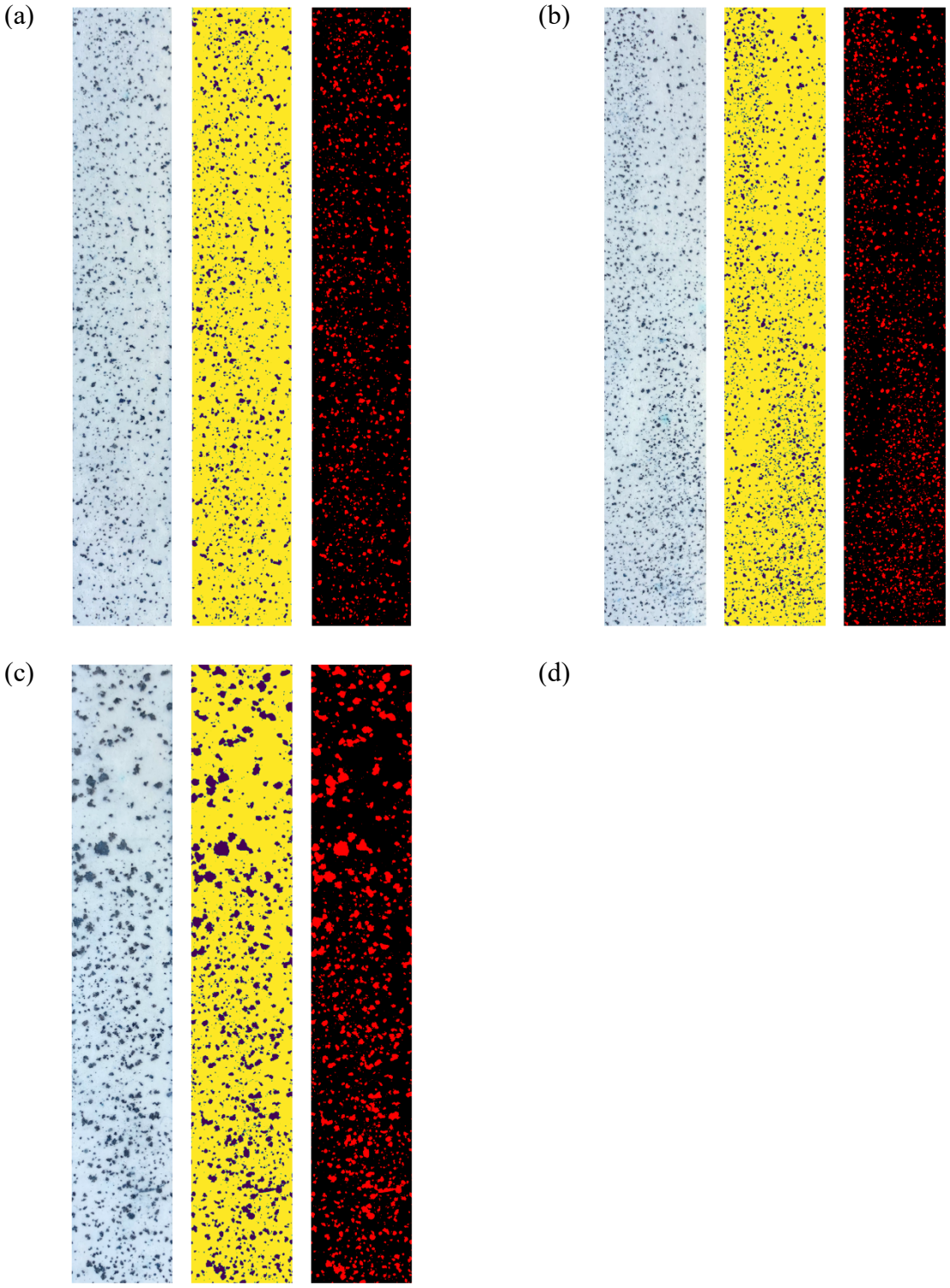
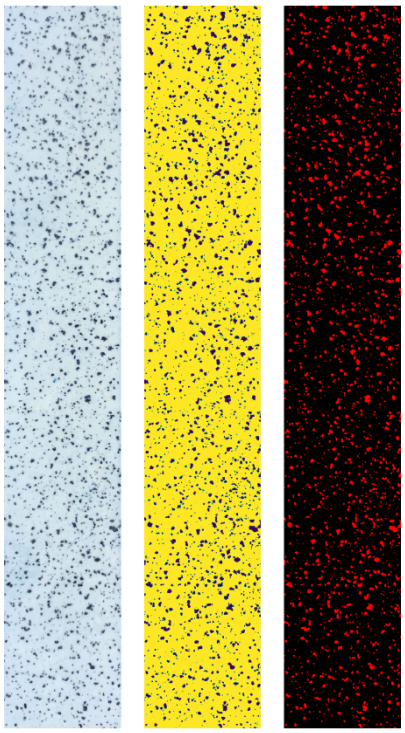


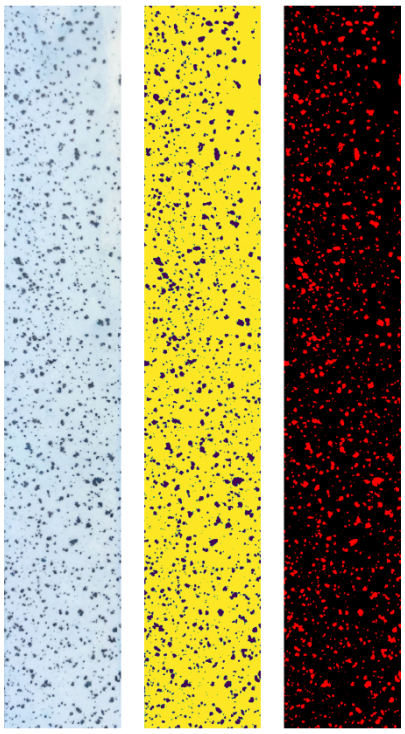
Figure A.414. Particle Size Analysis Results at A1G1G2 STIFFENER (a) Top Flange Bottom, (b) Web, (c) Bottom Flange Bottom.

(a)

(b)



(c)



(d)

Figure A.415. Particle Size Analysis Results at A1G2F1 (a) Top Flange Bottom, (b) Web, (c) Bottom Flange Bottom.

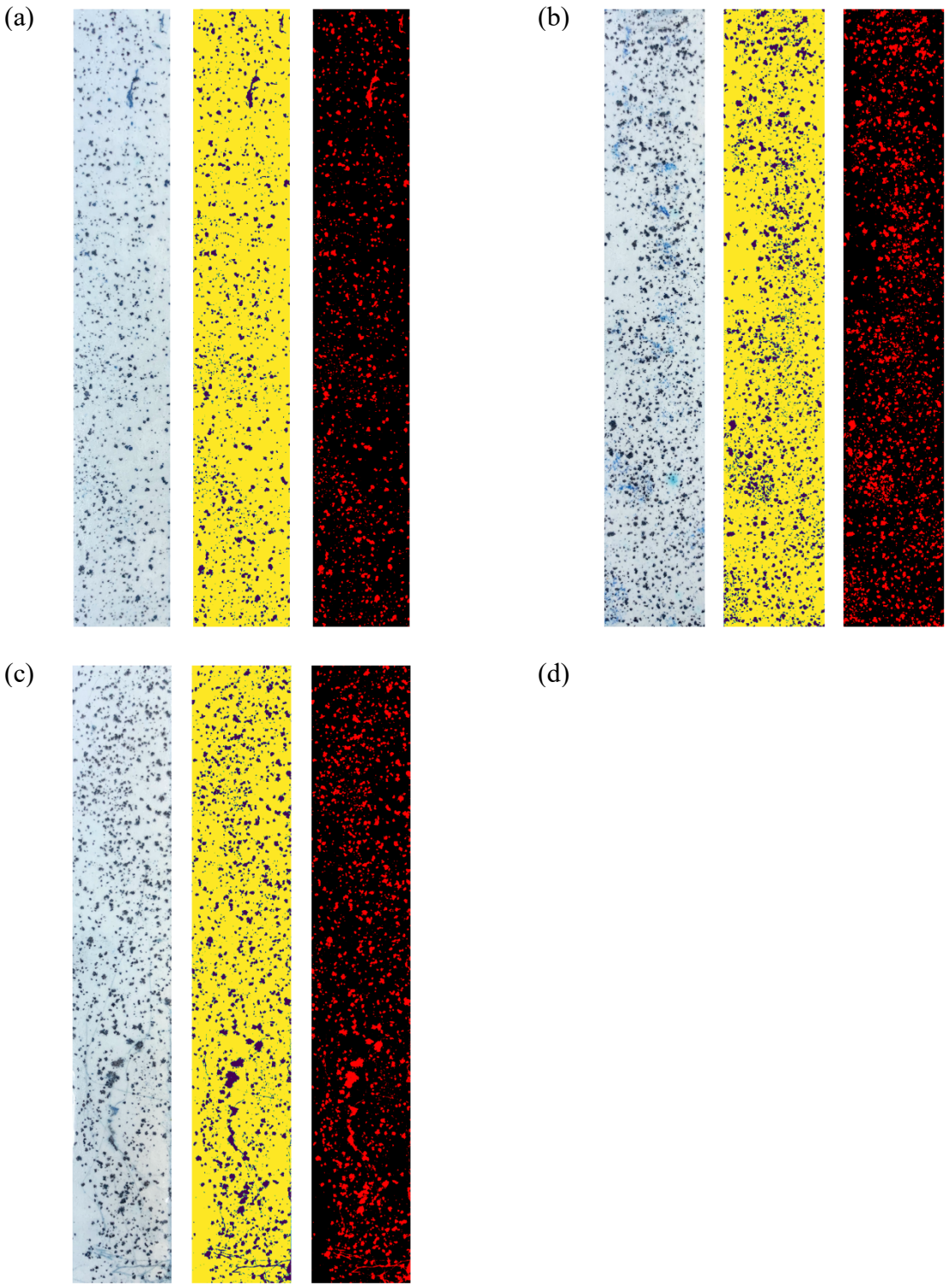


Figure A.416. Particle Size Analysis Results at A1G3F2 (a) Top Flange Bottom, (b) Web, (c) Bottom Flange Bottom.

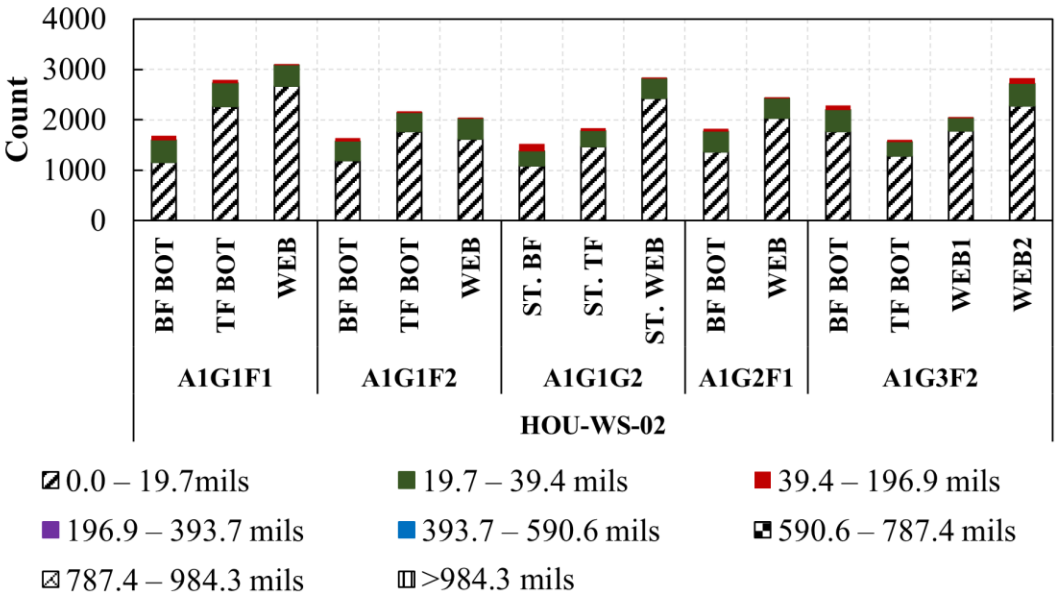


Figure A.417. Particle Size Analysis Showing Different Locations Examined.

A.26. HOU-WS-03

- BW 8 NB over West Road
- Bridge ID 121020325601192, Coordinates (29.90281, -95.55183), Harris County
- Continuous weathering steel plate girder
- Built 1990
- Girder inspection carried on end abutment, and measurements are taken on girder within four feet from the abutment or bent.
- No visual inspection on deck
- Location for Testing: A1-G1F1, A1-G3F1, A1-G5F1, A1-G7F2, A1-G9F2



Figure A.418. Typical Picture of HOU-WS-03.

A.26.1. Observed Condition

Delaminated areas of the patina are visible on the bottom face of the top flange. The web has a uniform patina formation with a patina rating of 7. The interior girders have significant poultice corrosion on the top face of the bottom flange due to the accumulation of dirt Index 5 whereas exterior girders have less accumulation of dirt.

A.26.2.Field Inspection Results

Table A-121. Field Inspection Results for HOU-WS-03.

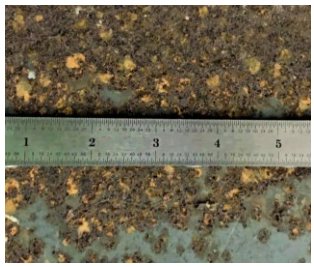
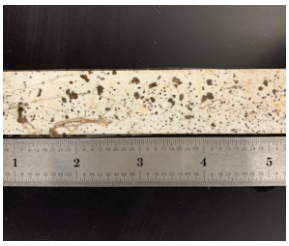
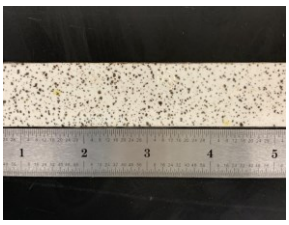
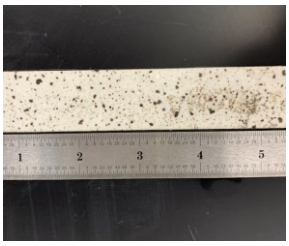
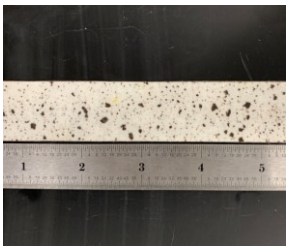
Location	Patina Rating	Thickness (inch)	Cl^- Conc. (ppm)	Field Condition	Tape Test
A1-G1F1 TF Bot. Ext.	6	Measured R1 0.776 R2 0.777 R3 0.777 R_Avg 0.777 Design			
A1-G1F1 Web Ext.	7	Measured R1 0.457 R2 0.457 R3 0.457 R_Avg 0.457 Design			
A1-G1F1 BF Top Ext.	6	Measured R1 0.899 R2 0.900 R3 0.901 R_Avg 0.900 Design			
A1-G1F1 BF Bot. Ext.	6	-			
A1-G3F1 TF Bot. Int.	5	Measured R1 0.782 R2 0.782 R3 0.782 R_Avg 0.782 Design			

Table A-122. Field Inspection Results for HOU-WS-03.

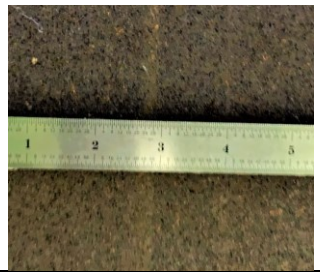
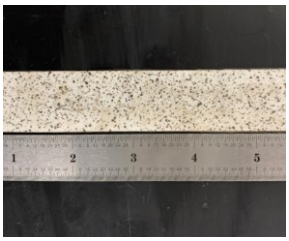
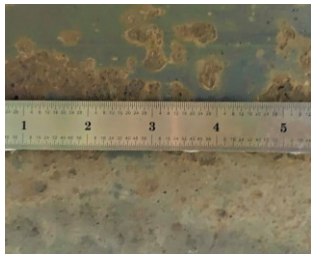
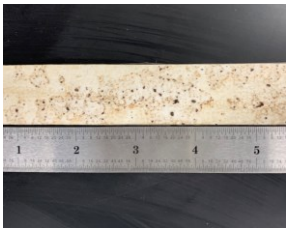
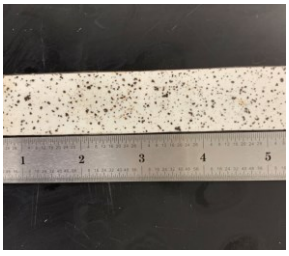
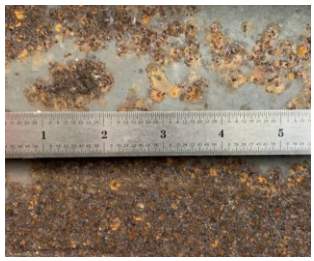
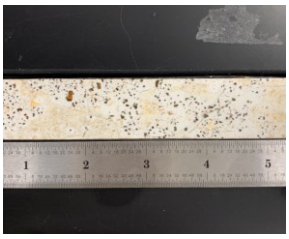
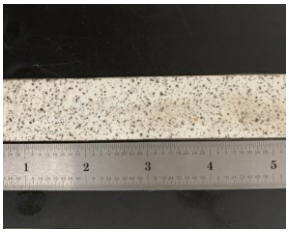
Location	Patina Rating	Thickness (inch)	Cl^- Conc. (ppm)	Field Condition	Tape Test
A1-G3F1 Web Int.	7	Measured R1 0.459 R2 0.460 R3 0.460 R_Avg 0.460 Design			
A1-G3F1 BF Top Int.	5	Measured R1 0.897 R2 0.899 R3 0.896 R_Avg 0.897 Design			
A1-G3F1 BF Bot. Int.	6	-			
A1-G5F1 TF Bot. Int.	5	Measured R1 0.780 R2 0.780 R3 0.782 R_Avg 0.781 Design			
A1-G5F1 Web Int.	7	Measured R1 0.442 R2 0.440 R3 0.440 R_Avg 0.441 Design			

Table A-123. Field Inspection Results for HOU-WS-03.

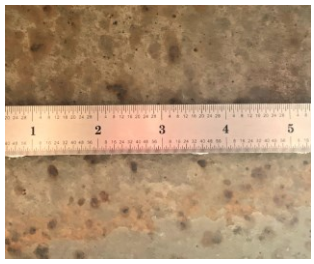
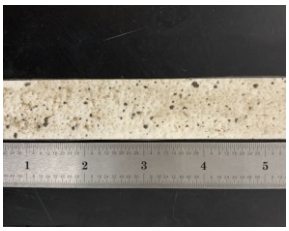
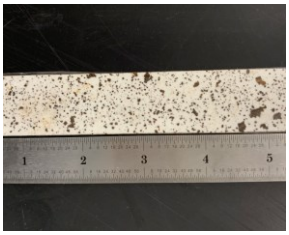
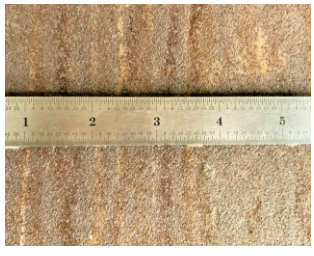
Location	Patina Rating	Thickness (inch)	Cl^- Conc. (ppm)	Field Condition	Tape Test
A1-G5F1 BF Top Int.	6	Measured R1 0.906 R2 0.907 R3 0.903 R_Avg 0.905 Design			
A1-G5F1 BF Bot. Int.	6	-			
A1-G5F1 Stiffener Int.	5	Measured R1 0.882 R2 0.878 R3 0.880 R_Avg 0.880			
A1-G7F2 TF Bot. Int.		Measured R1 0.786 R2 0.791 R3 0.792 R_Avg 0.790 Design		-	
A1-G7F2 Web Int.	8	Measured R1 0.443 R2 0.443 R3 0.443 R_Avg 0.443 Design			

Table A-124. Field Inspection Results for HOU-WS-03.

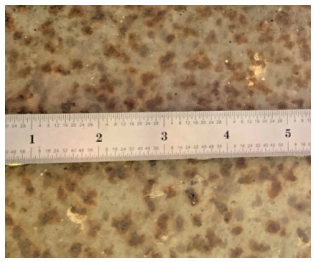
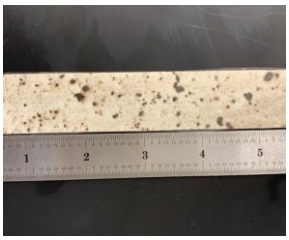
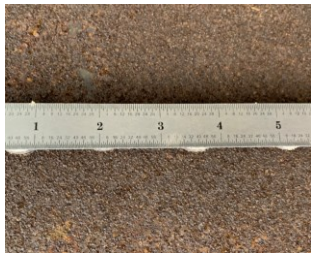
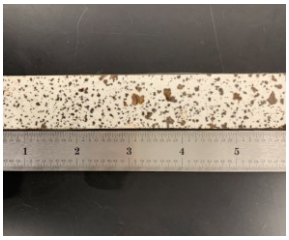
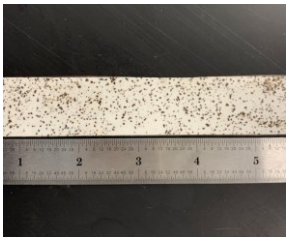
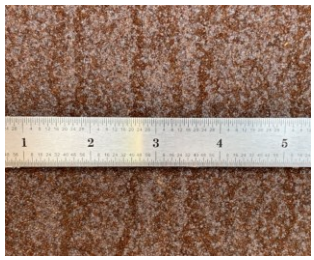
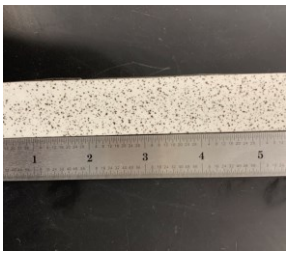
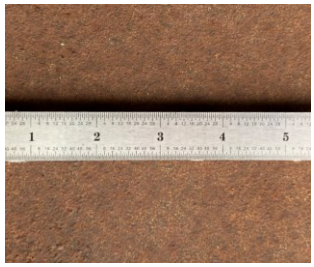
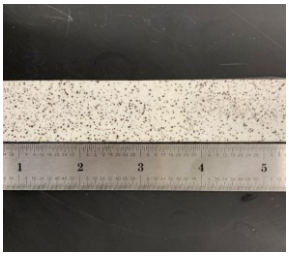
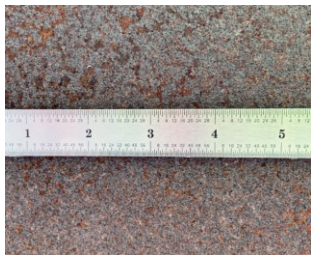
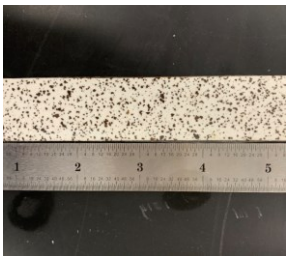
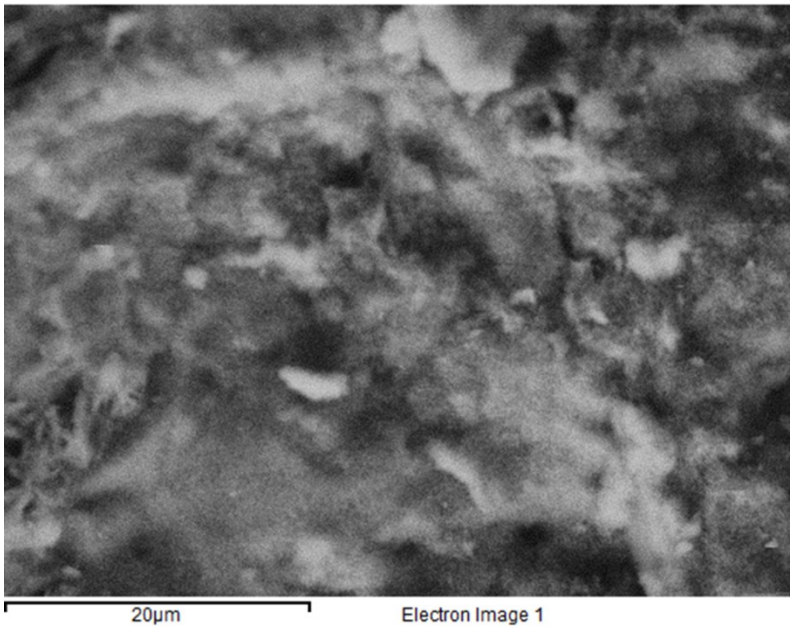
Location	Patina Rating	Thickness (inch)	Cl^- Conc. (ppm)	Field Condition	Tape Test
A1-G7F2 BF Top Int.	6	Measured R1 0.913 R2 0.915 R3 0.919 R_Avg 0.916 Design			
A1-G7F2 BF Bot. Int.	6	-			
A1-G9F2 TF Bot. Ext.	7	Measured R1 0.736 R2 0.736 R3 0.736 R_Avg 0.736 Design			
A1-G9F2 Web Ext.	8	Measured R1 0.493 R2 0.493 R3 0.492 R_Avg 0.493 Design			
A1-G9F2 BF Top Ext.	8	Measured R1 0.746 R2 0.745 R3 0.747 R_Avg 0.746 Design			

Table A-125. Field Inspection Results for HOU-WS-03.

Location	Patina Rating	Thickness (inch)	Cl^- Conc. (ppm)	Field Condition	Tape Test
A1-G9F2 BF Bot. Ext.	7	-			

A.26.3.SEM/EDS Results: Exterior Web Girder

Element	Weight %	Atomic %
O K	27.77	56.55
Al K	1.39	1.68
Si K	0.34	0.39
S K	0.52	0.53
Ca K	0.14	0.12
Cr K	0.60	0.38
Mn K	0.63	0.37
Fe K	67.77	39.54
Ni K	0.29	0.16
Cu K	0.55	0.28
Totals	100.00	



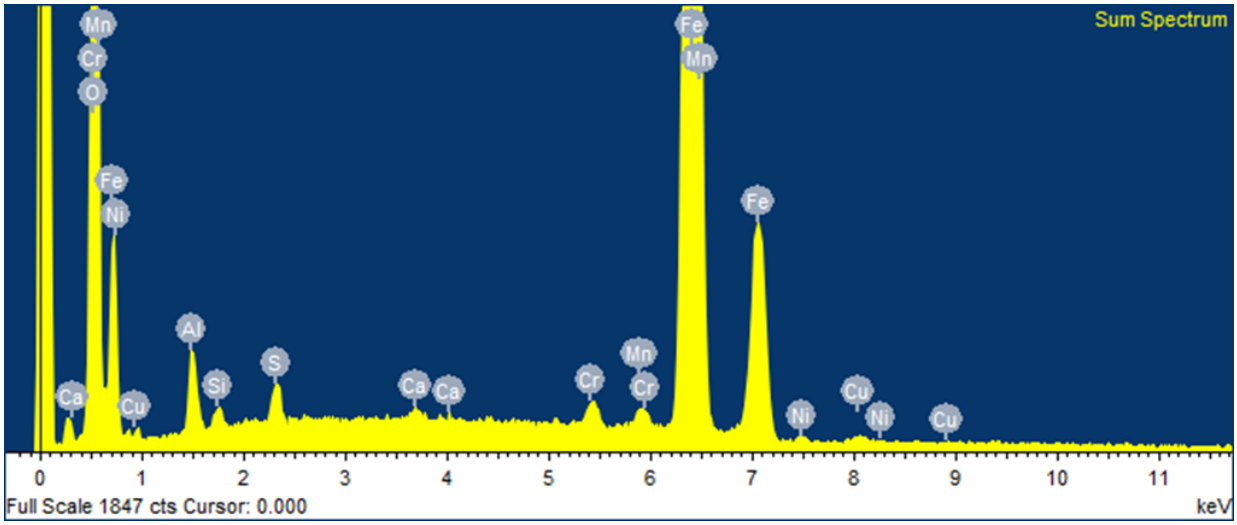


Figure A.419. SEM Image and EDS Spectrum of the Rust Collected from Exterior Web of the Girder.

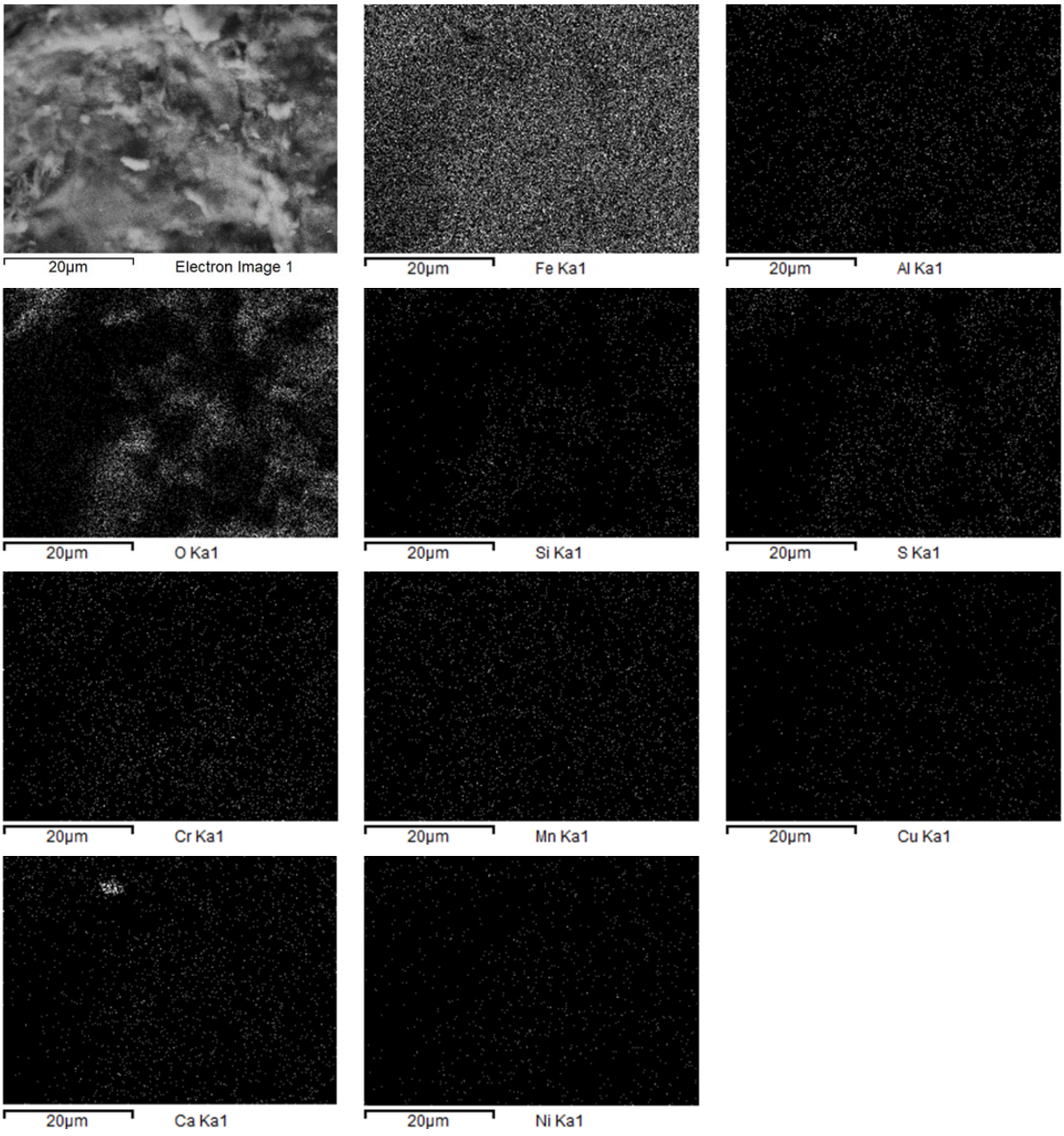
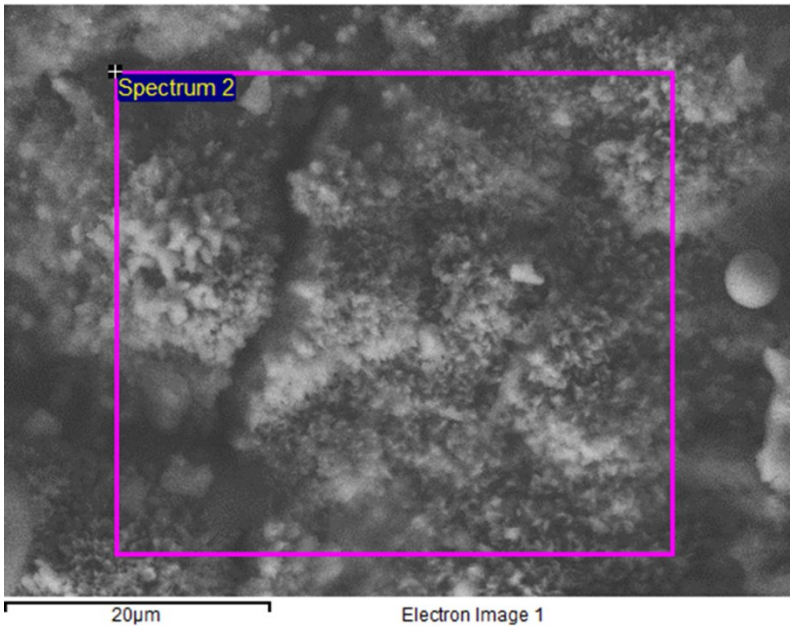


Figure A.420. EDS Elemental Mapping of Rust Collected from Exterior Web.

A.26.4.SEM/EDS Results: Interior Web

Element	Weight %	Atomic %
O K	39.76	68.81
Al K	1.23	1.26
Si K	0.42	0.41
S K	1.05	0.91
Cl K	0.23	0.18
Mn K	1.85	0.93
Fe K	55.46	27.50
Totals	100.00	



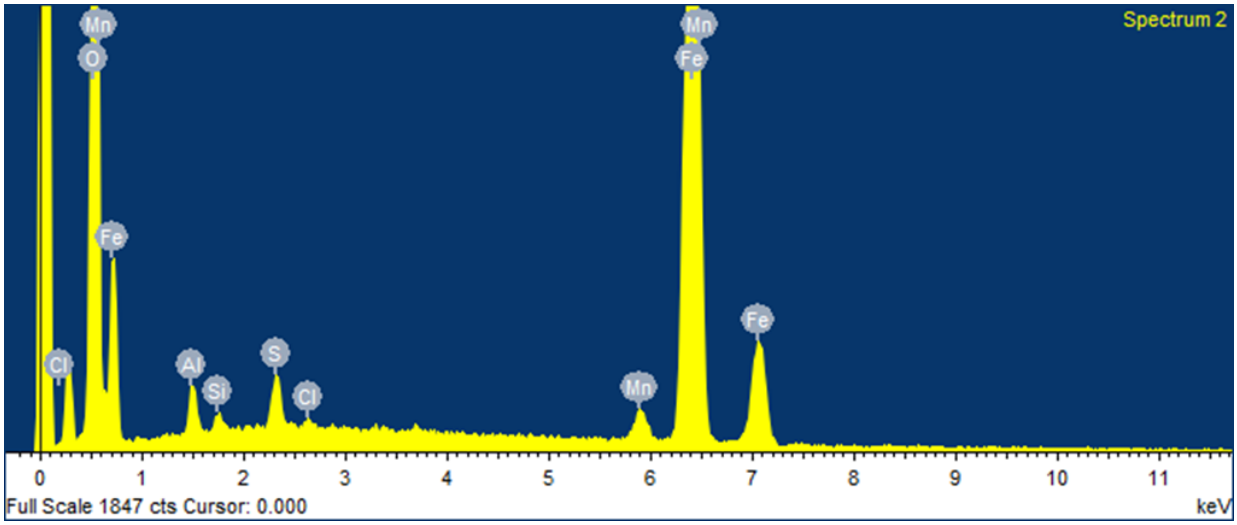
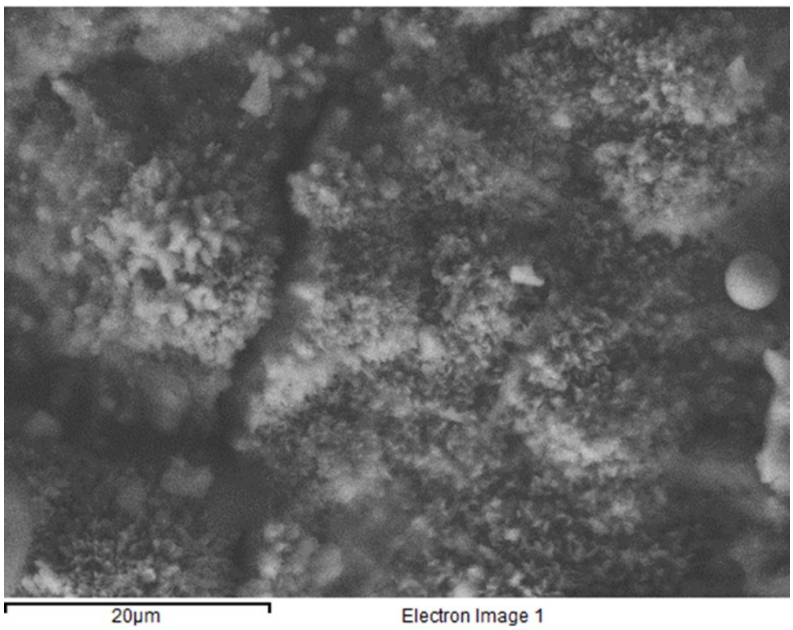


Figure A.421. SEM Image and EDS Spectrum of the Rust Collected from Interior Web of the Girder.

Element	Weight %	Atomic %
O K	40.25	69.20
Al K	1.25	1.27
Si K	0.54	0.53
S K	1.07	0.92
Cl K	0.18	0.14
Mn K	1.81	0.90
Fe K	54.65	26.92
Ni K	0.25	0.12
Totals	100.00	



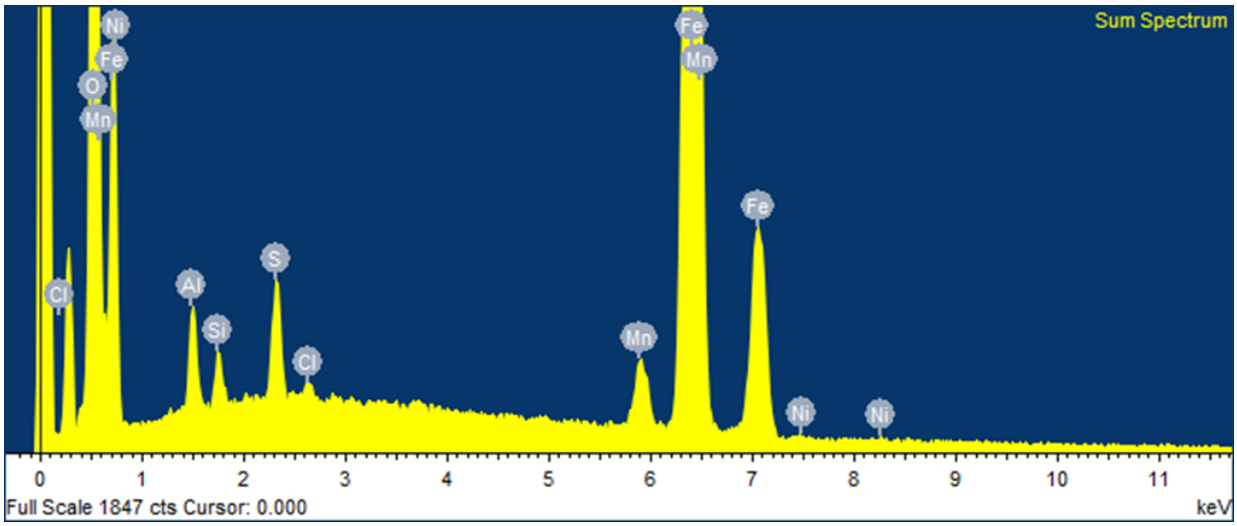


Figure A.422. SEM Image and EDS Spectrum of the Rust Collected from Interior Web of the Girder (G3F1).

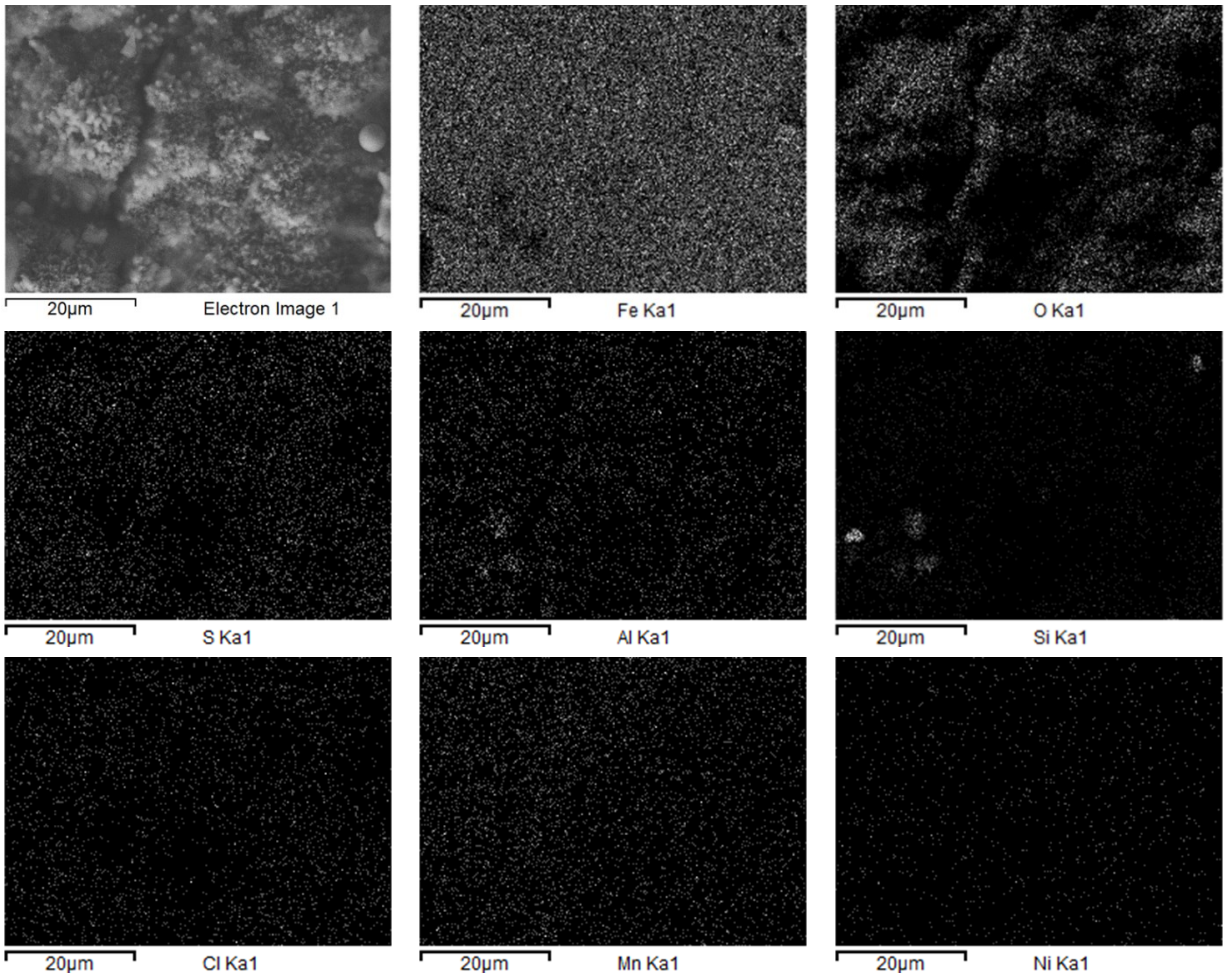
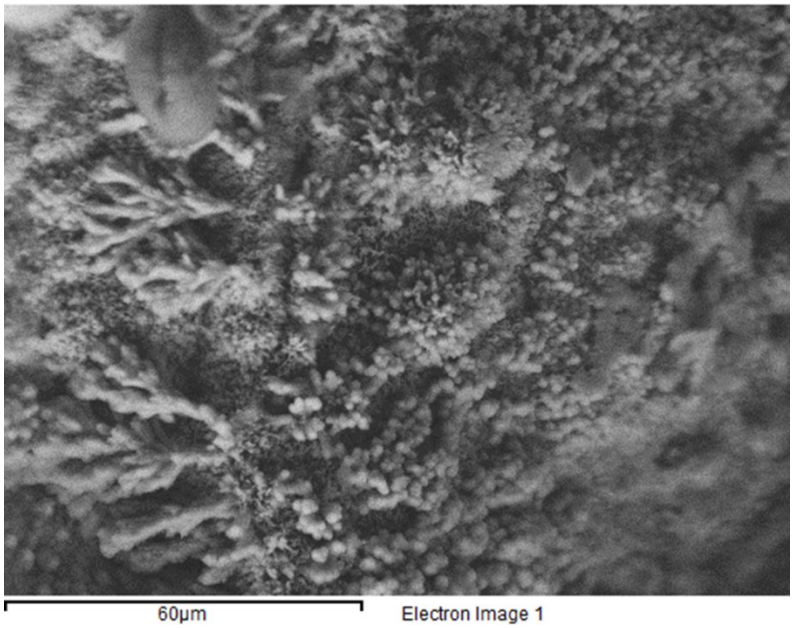


Figure A.423. EDS Elemental Mapping of Rust Collected from Interior Web (G3F1).

Element	Weight %	Atomic %
O K	24.06	51.39
Al K	2.06	2.60
Si K	0.50	0.61
S K	0.78	0.83
Cl K	0.16	0.16
Ca K	0.20	0.17
Mn K	1.68	1.04
Fe K	70.56	43.19
Totals	100.00	



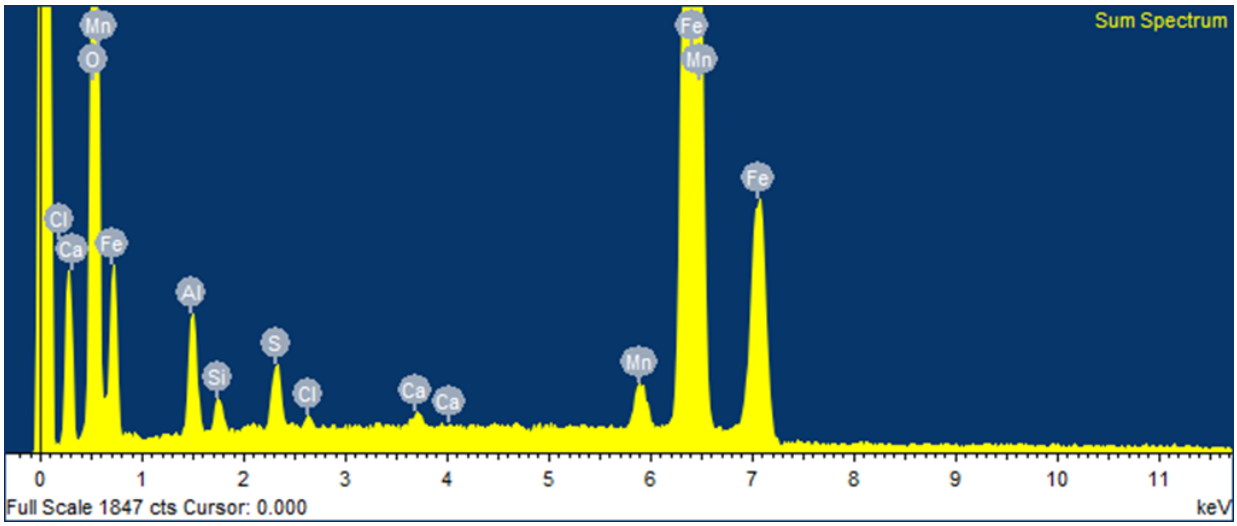


Figure A.424. SEM Image and EDS Spectrum of the Rust Collected from Interior Web of the Girder (G3F1).

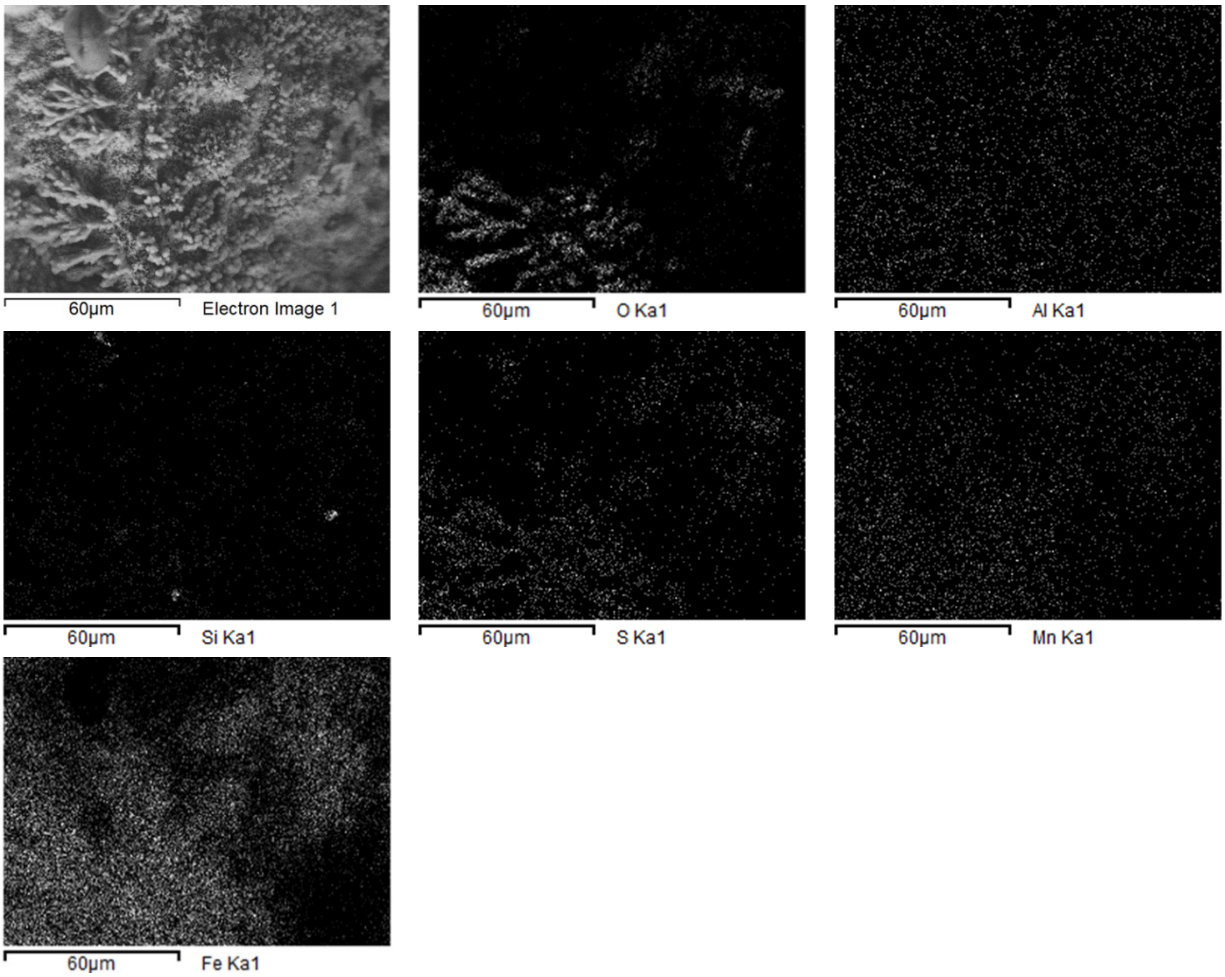
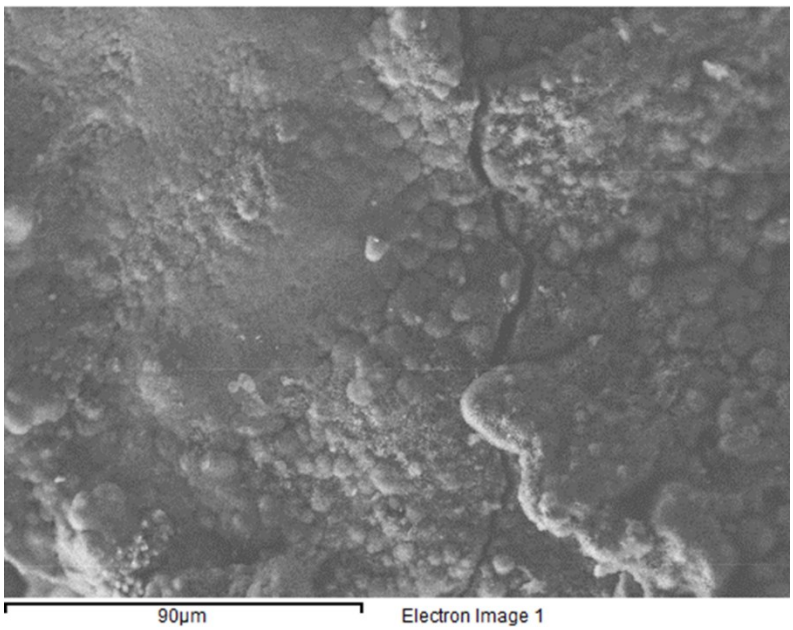


Figure A.425. EDS Elemental Mapping of Rust Collected from Interior Web (G3F1).

Element	Weight %	Atomic %
O K	41.02	70.41
Al K	0.60	0.61
S K	0.72	0.61
Mn K	2.12	1.06
Fe K	55.23	27.16
Ni K	0.31	0.15
Totals	100.00	



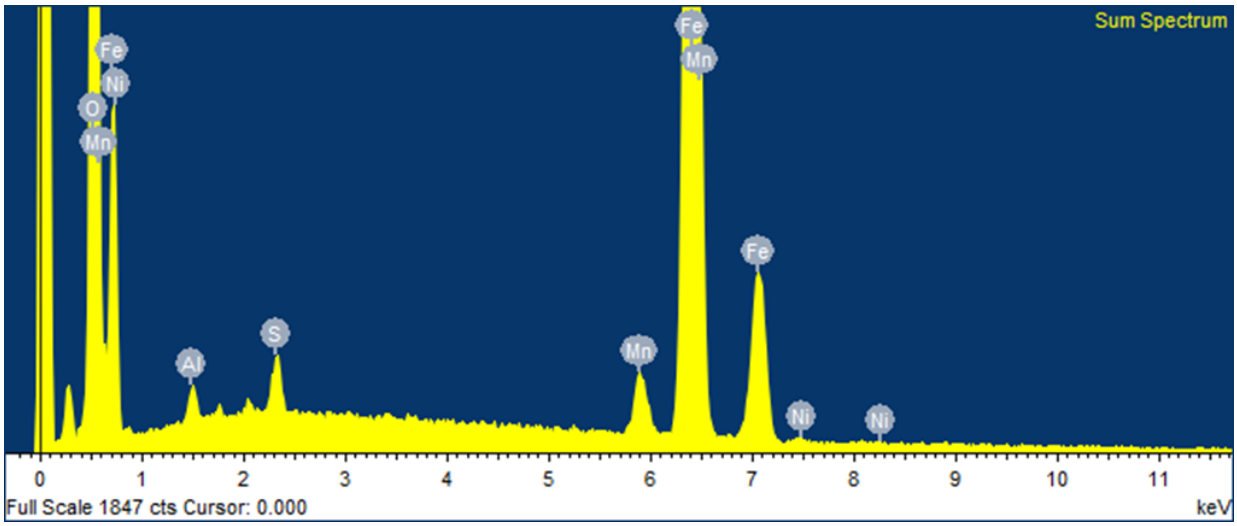


Figure A.426. SEM Image and EDS Spectrum of the Rust Collected from Interior Web of the Girder.

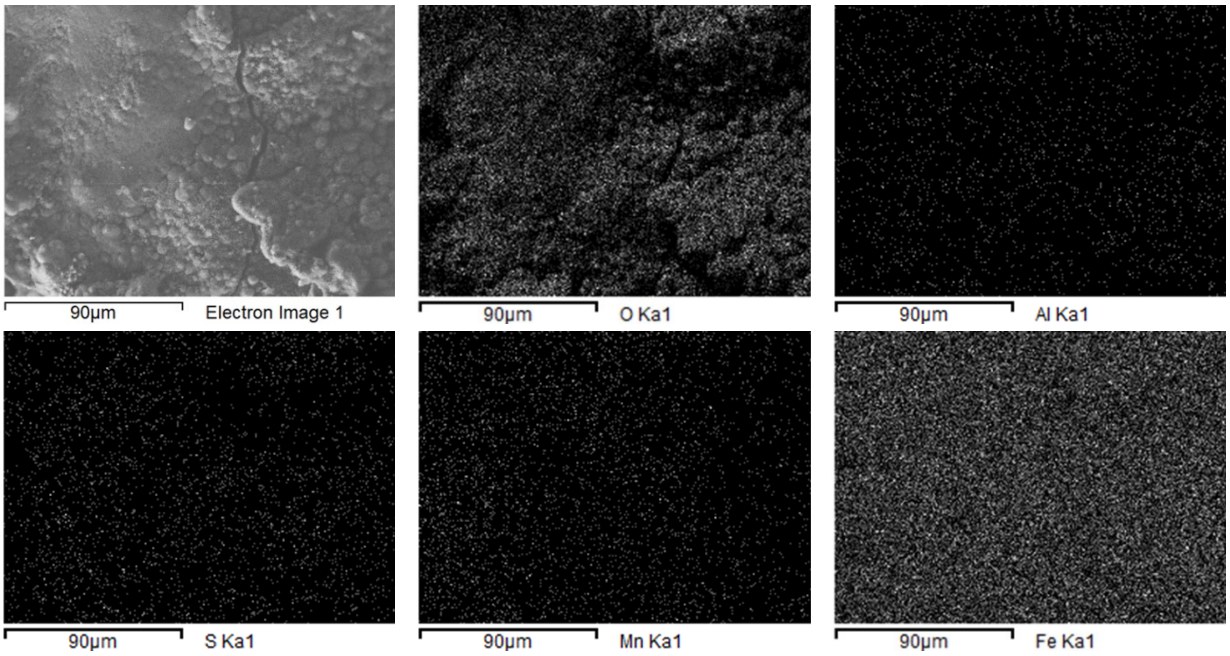
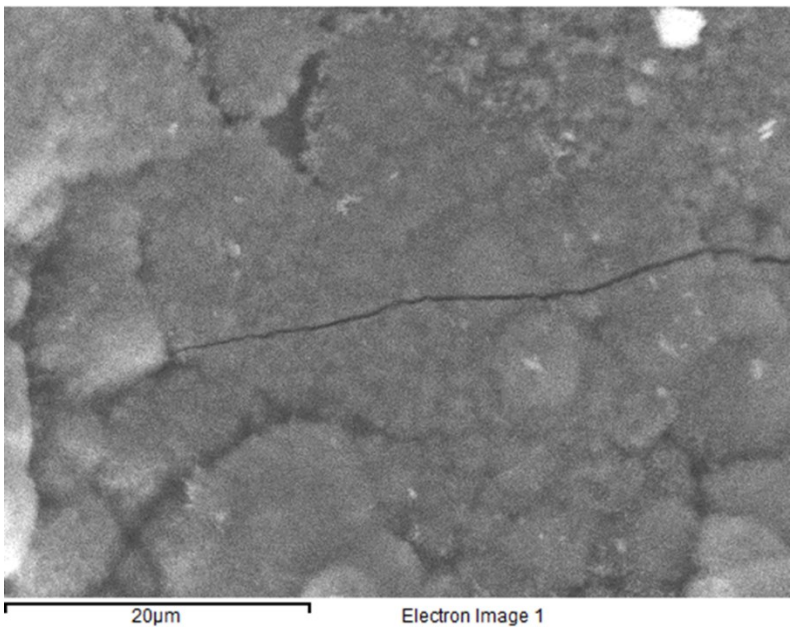


Figure A.427. EDS Elemental Mapping of Rust Collected from Interior Web (G6F1).

Element	Weight %	Atomic %
O K	45.32	73.90
Al K	0.63	0.61
S K	0.64	0.52
Mn K	3.24	1.54
Fe K	50.17	23.44
Totals	100.00	



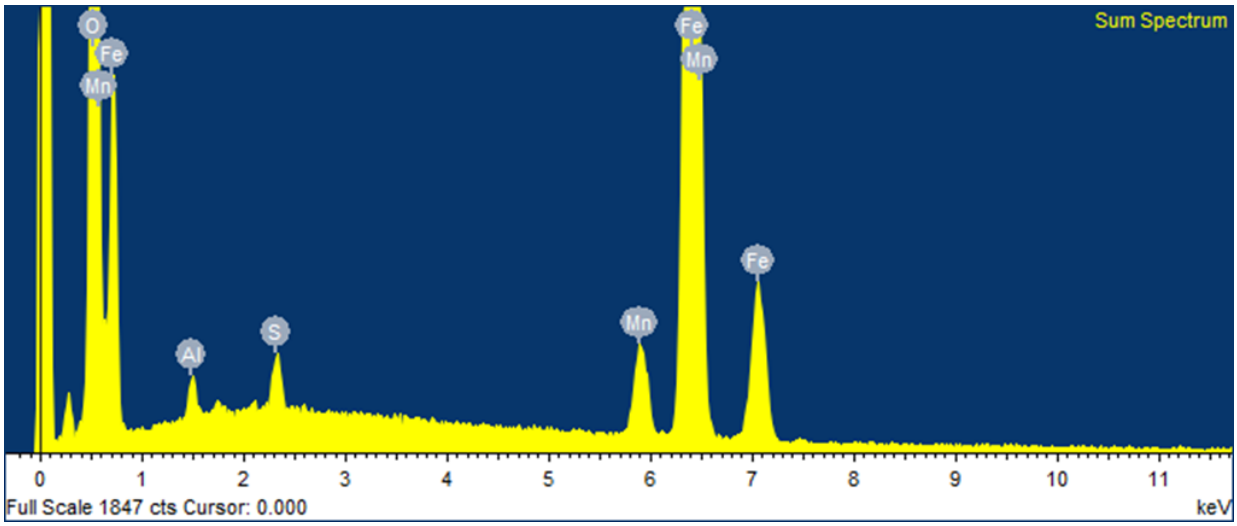
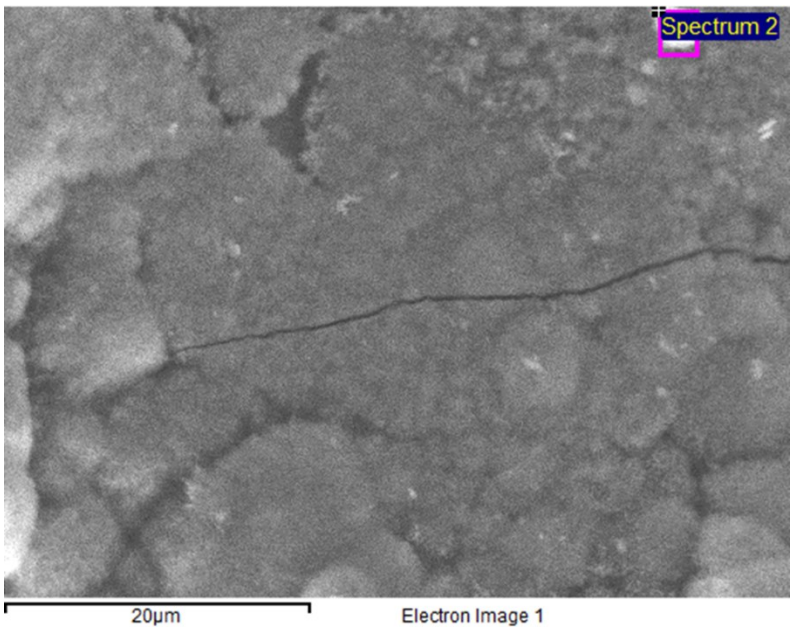


Figure A.428. SEM Image and EDS Spectrum of the Rust Collected from Interior Web of the Girder.

Element	Weight %	Atomic %
O K	44.34	73.14
Al K	0.59	0.57
S K	0.68	0.56
Mn K	3.54	1.70
Fe K	50.85	24.03
Totals	100.00	



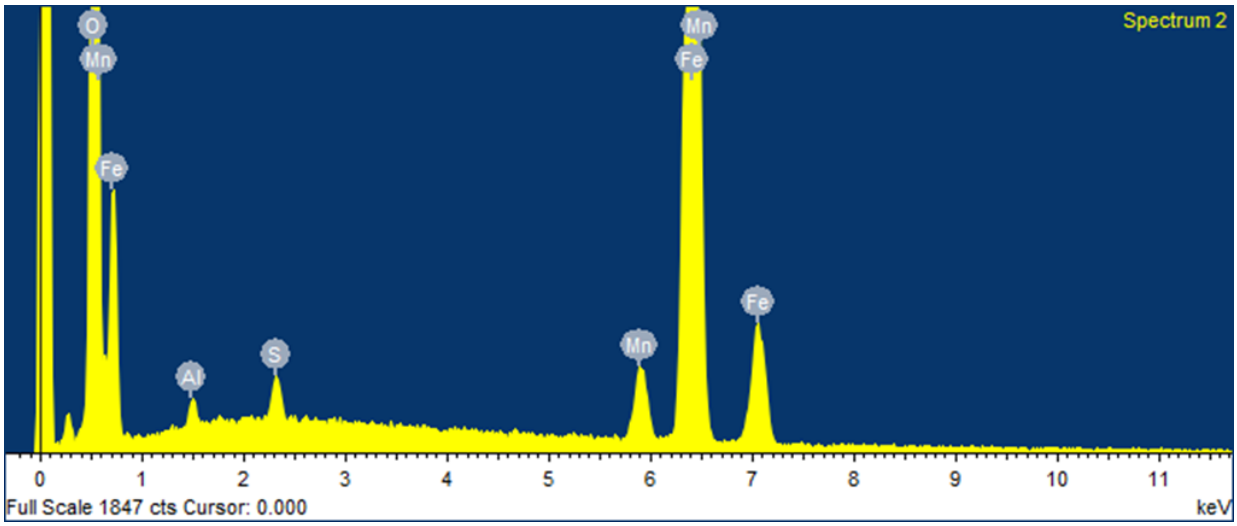


Figure A.429. SEM Image and EDS Spectrum of the Rust Collected from Interior Web of the Girder.

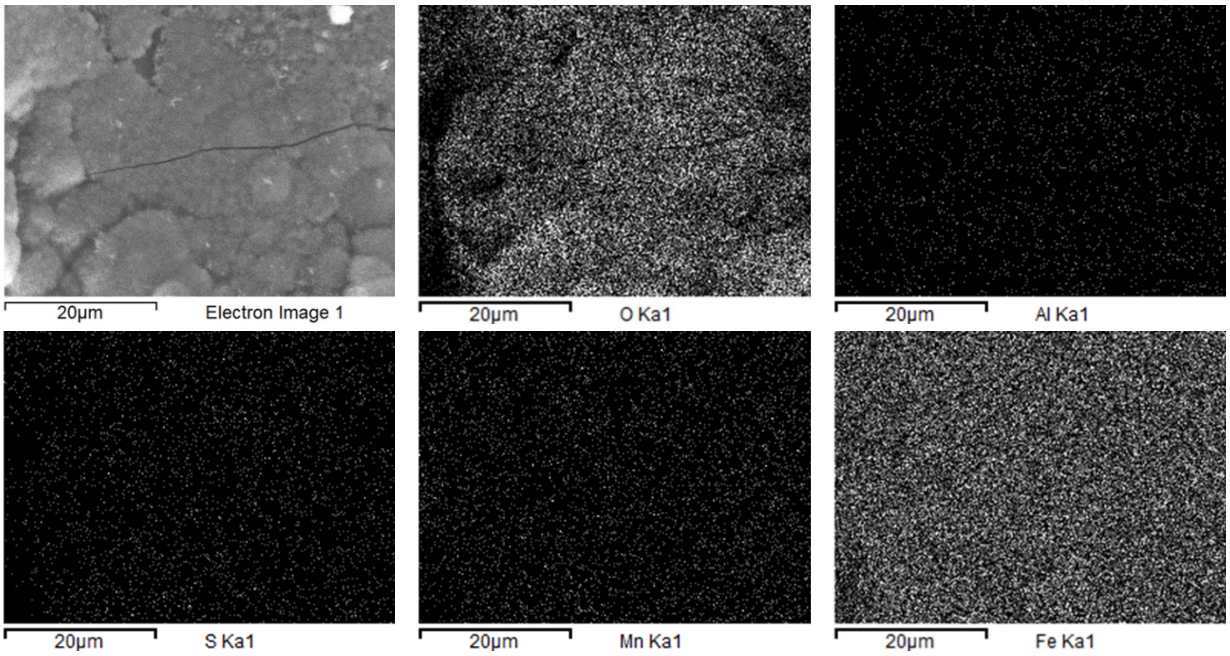


Figure A.430. EDS Elemental Mapping of Rust Collected from Interior Web (G6F1).

A.26.5.XPS Results: Exterior Web Girder

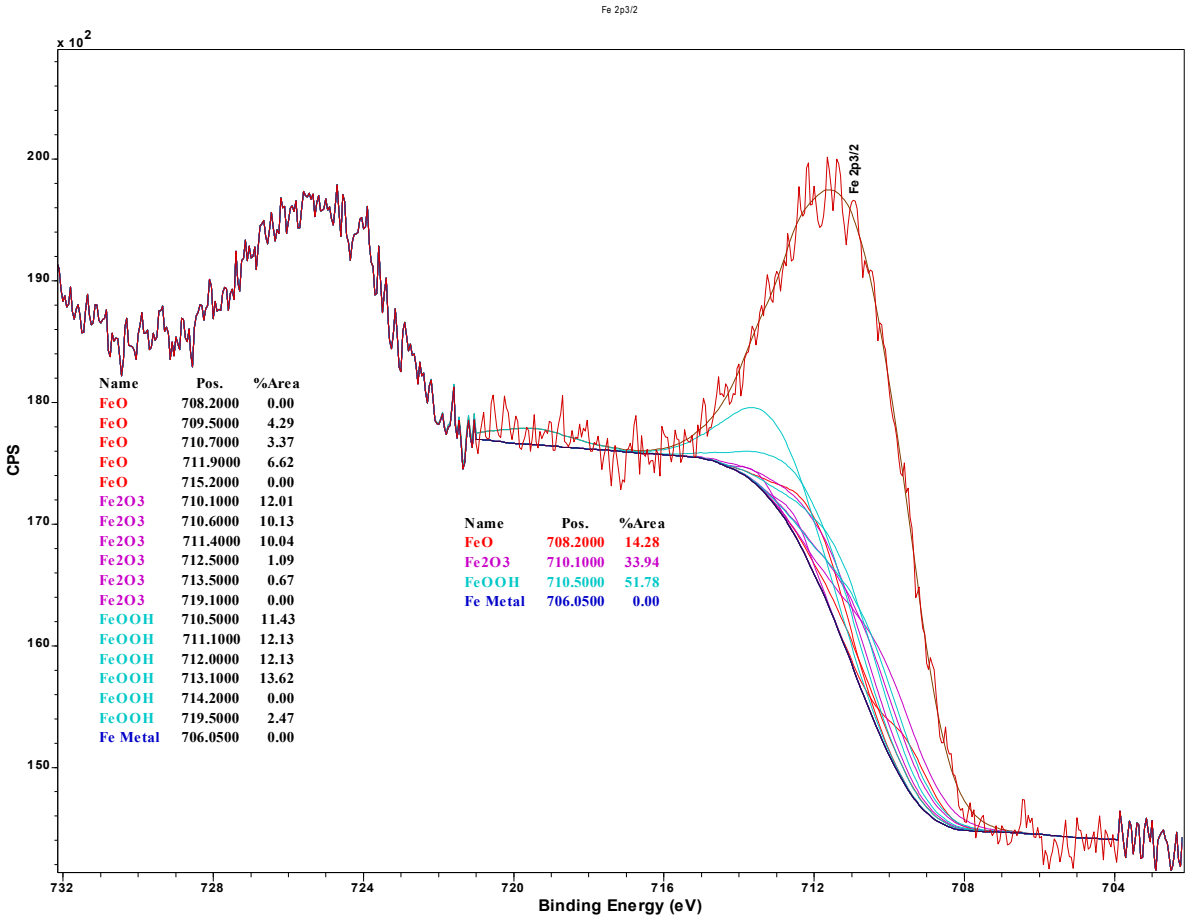


Figure A.431. XPS Spectrum of the Rust Collected from Exterior Web of the Girder.

A.26.6.XPS Results: Interior Web Girder

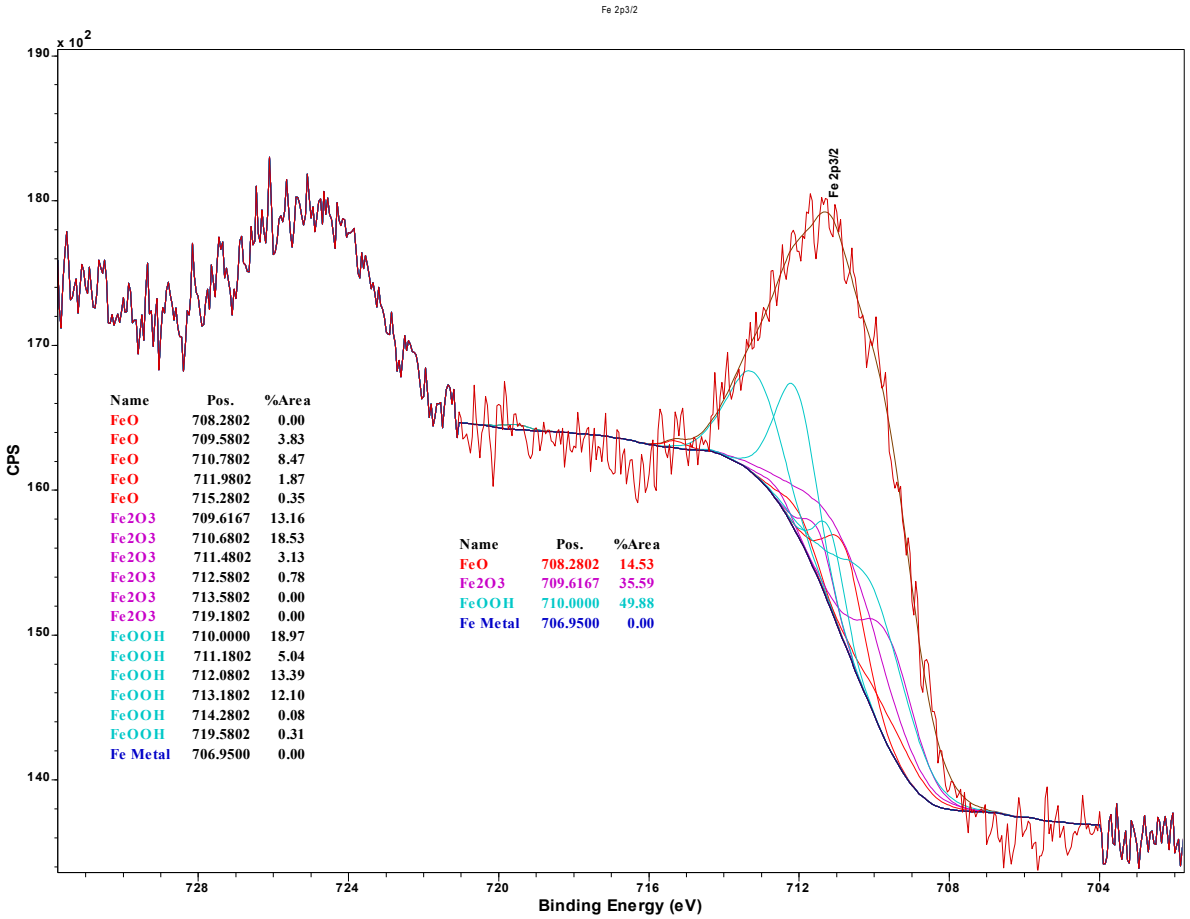


Figure A.432. XPS Spectrum of the Rust Collected from Interior Web of the Girder.

A.26.7.XRD Result: Exterior and Interior Girder

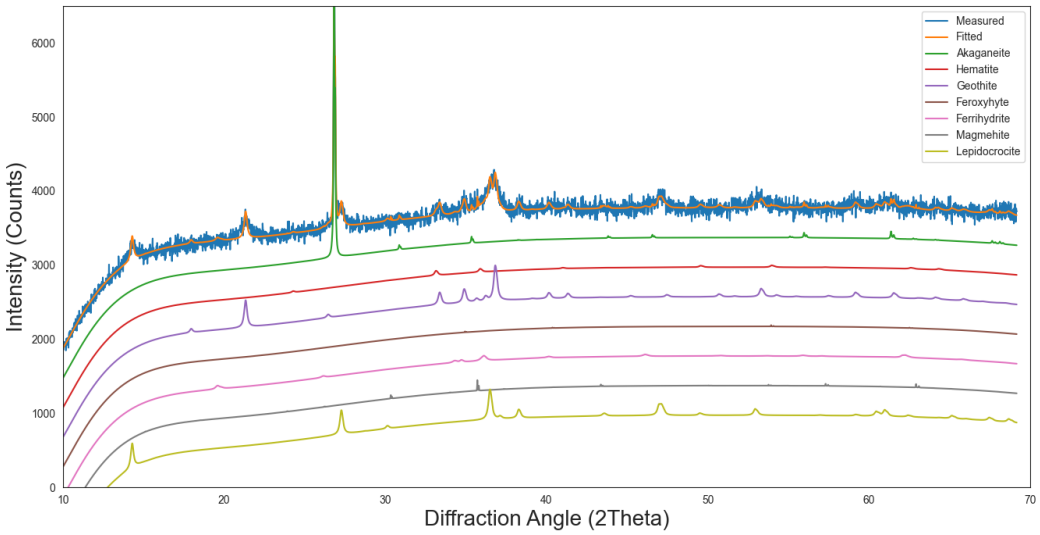


Figure A.433. XRD Pattern of Powdered Rust Collected from Exterior Web of the Girder (G1F1).

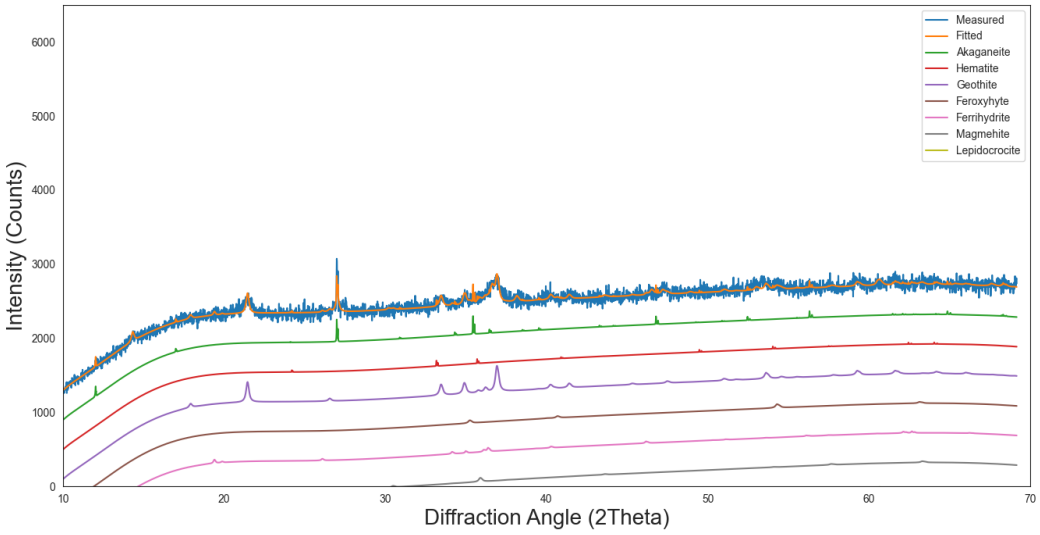


Figure A.434. XRD Pattern of Powdered Rust Collected from Interior Web of the Girder (G6F1).

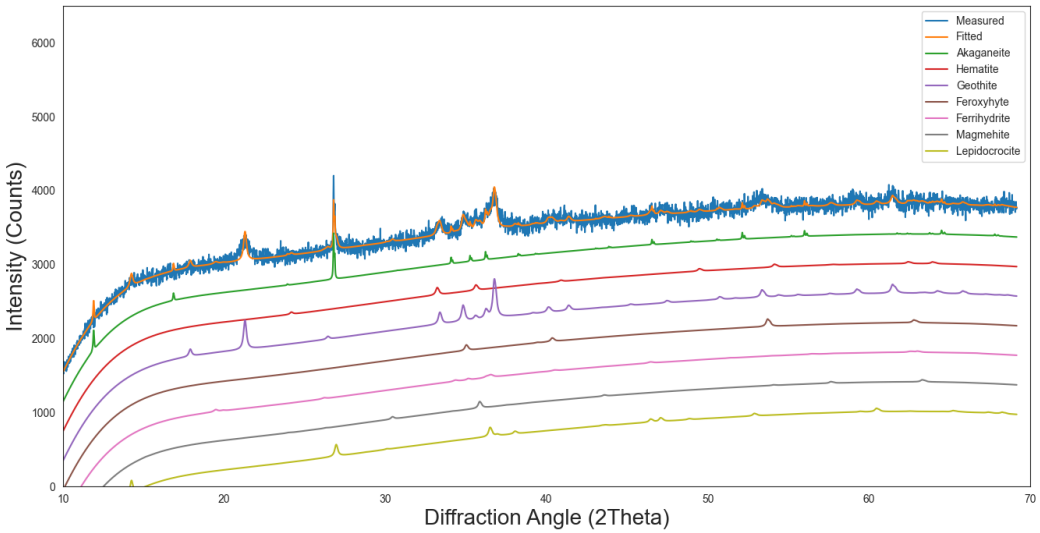


Figure A.435. XRD Pattern of Powdered Rust Collected from Interior Web of the Girder (G3F1).

A.26.8.Particle Size Analysis: Tape Adhesion Results

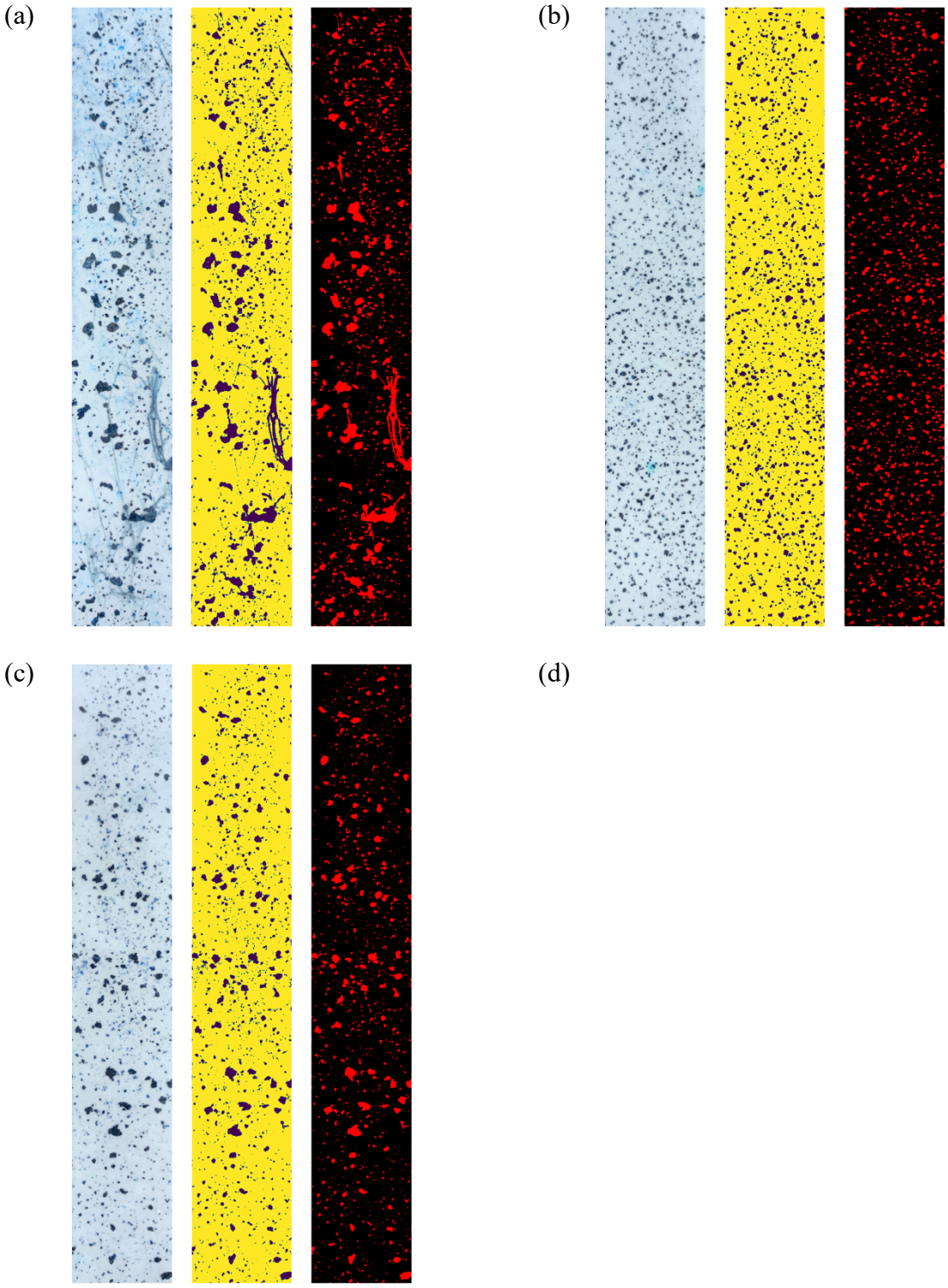


Figure A.436. Particle Size Analysis Results at A1G1F1 (a) Top Flange Bottom, (b) Web, (c) Bottom Flange Bottom (d) StiffenerA1G1F1.

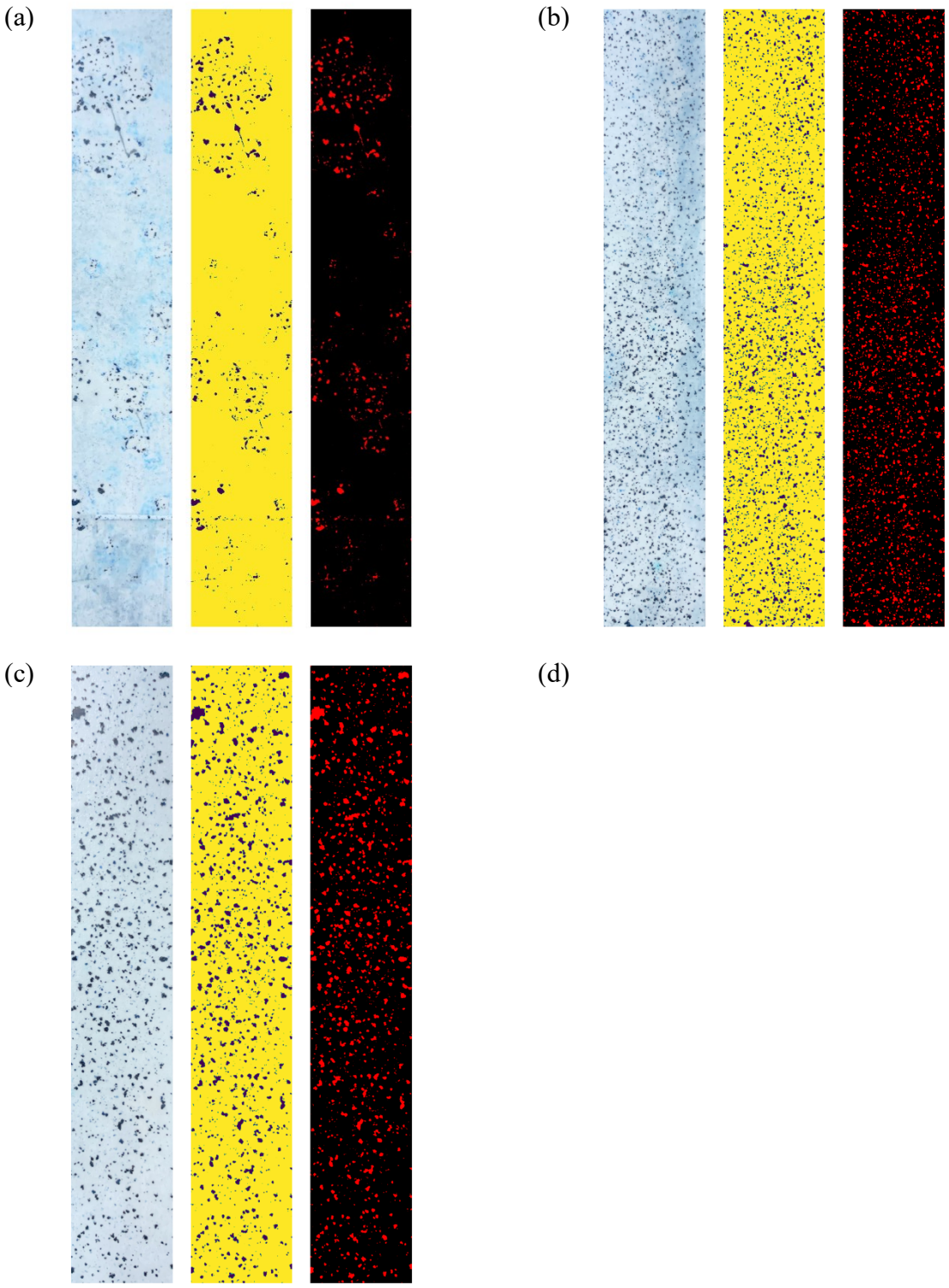


Figure A.437. Particle Size Analysis Results at A1G3F1 (a) Top Flange Bottom, (b) Web, (c) Bottom Flange Bottom (d) Stiffener.

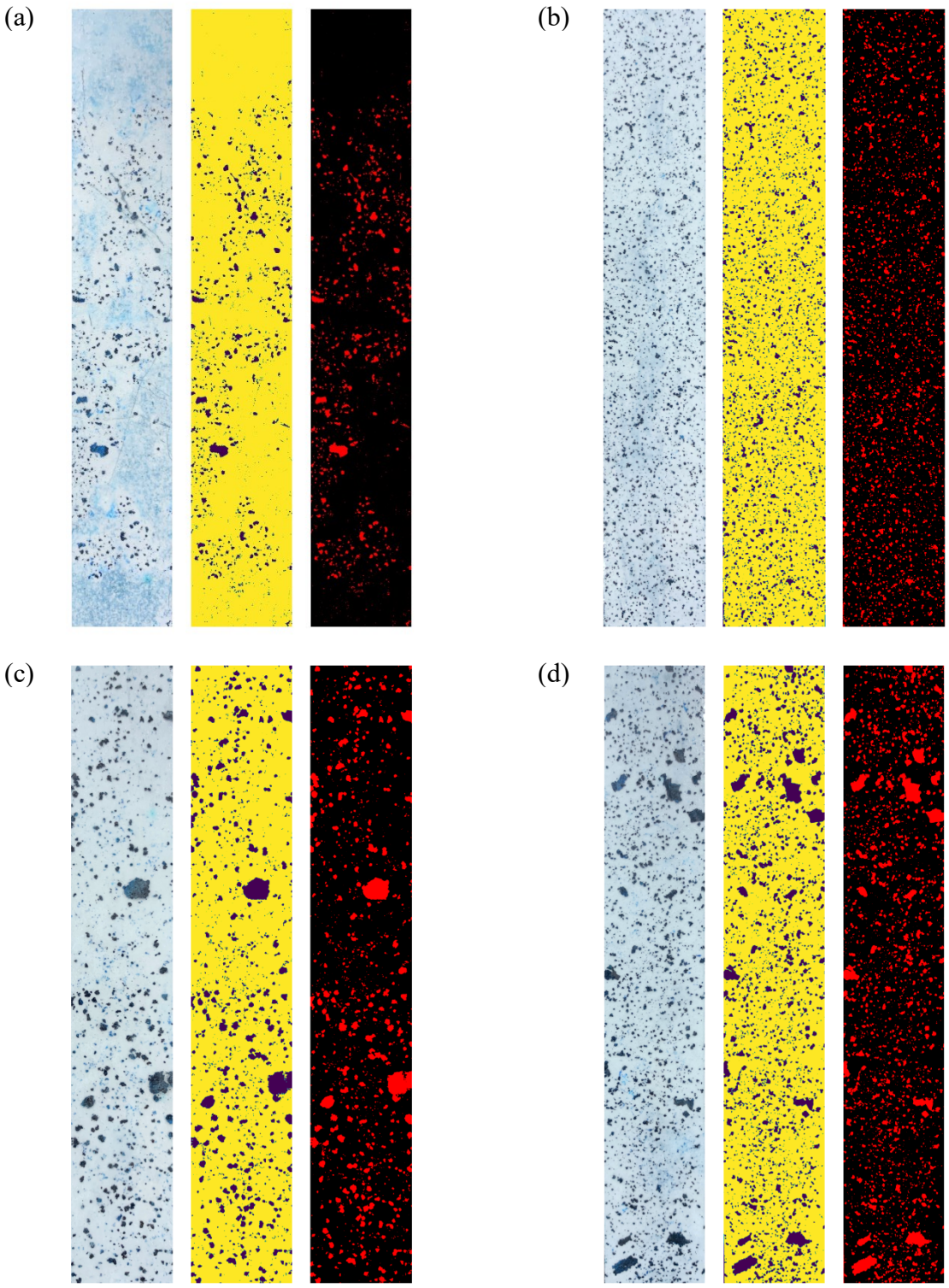
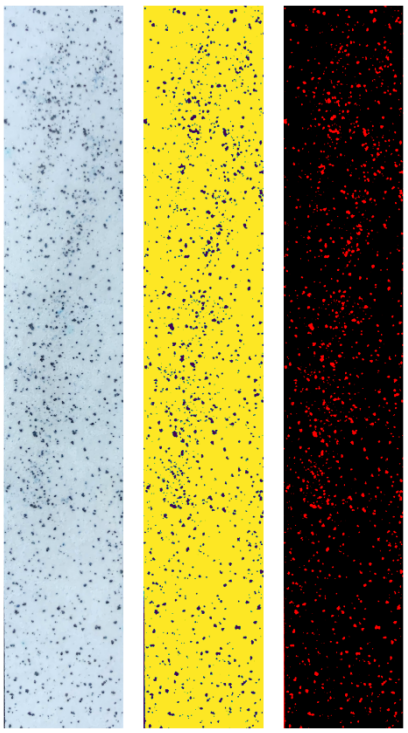


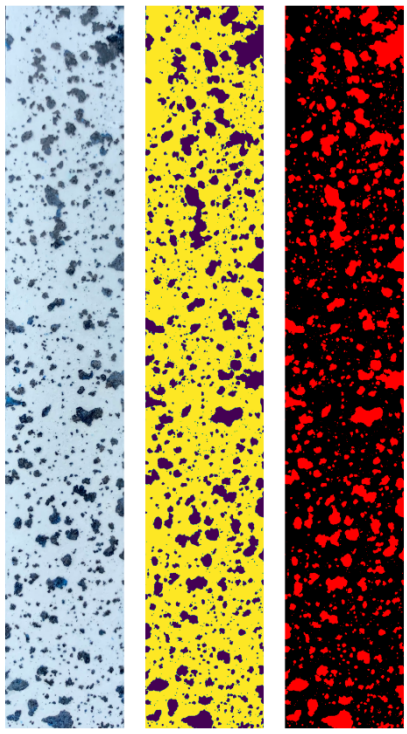
Figure A.438. Particle Size Analysis Results at A1G5F2 (a) Top Flange Bottom, (b) Web, (c) Bottom Flange Bottom (d) Stiffener.

(a)

(b)



(c)



(d)

Figure A.439. Particle Size Analysis Results at A1G7F2 (a) Top Flange Bottom, (b) Web, (c) Bottom Flange Bottom (d) Stiffener.

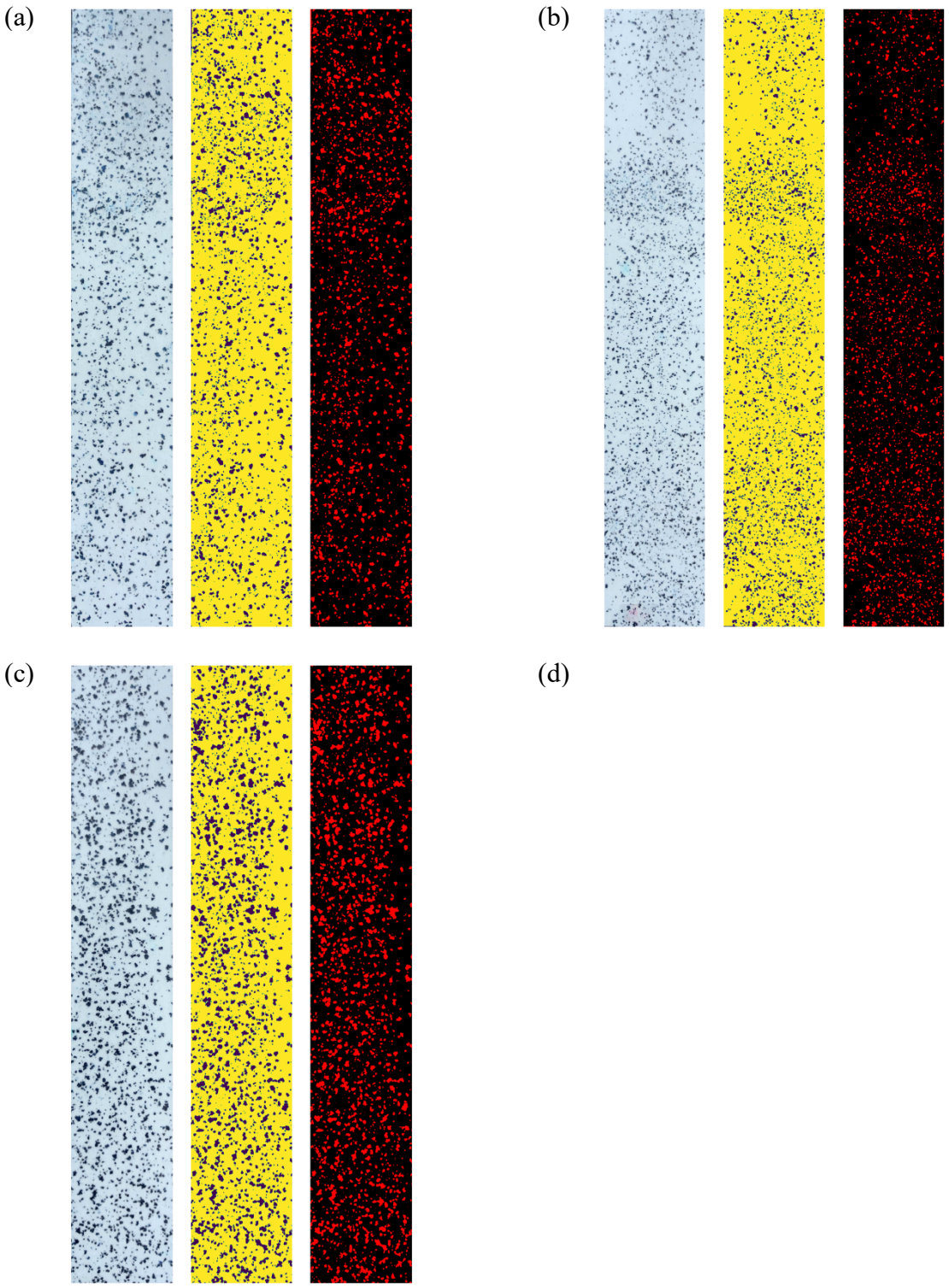


Figure A.440. Particle Size Analysis Results at A1G9F2 (a) Top Flange Bottom, (b) Web, (c) Bottom Flange Bottom (d) Stiffener.

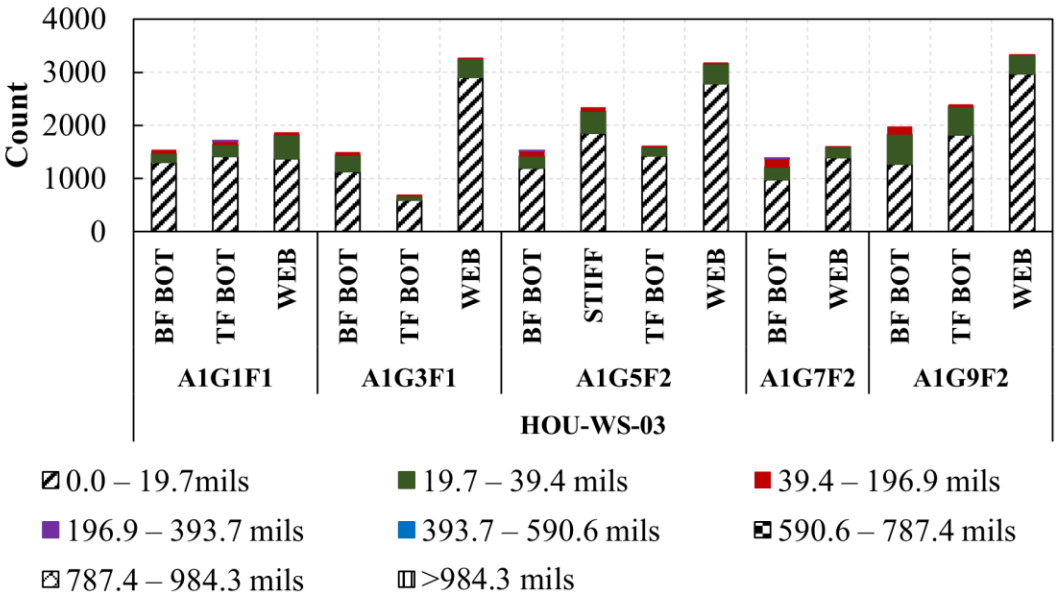


Figure A.441. Particle Size Analysis Showing Different Locations Examined.

A.27. HOU-WS-04

- Westheimer Pkwy (FM 1093)
- Bridge ID 121020125804124, Coordinates (29.73735, -95.55783), Harris County
- Continuous weathering steel plate girder
- Built 1987
- Girder inspection carried on east end abutment, and measurements are taken on girder within four feet from the abutment or bent.
- No visual inspection on deck
- Location for Testing: A1-G1F1, A1-G3F1, A1-G5F1, A1-G7F2, A1-G10F2



Figure A.442. Typical Picture of HOU-WS-04

A.27.1. Observed Condition

Delaminated areas of the patina are visible on the bottom face of the top flange and bottom flange. The web has a uniform patina formation with a patina rating of 7 to 8. The interior girders have significant poultice corrosion on the top face of the bottom flange due to the accumulation of dirt. (Patina Index 5) whereas exterior girders have less accumulation of dirt. Pitting corrosion is observed on the top face of bottom flange.

A.27.2.Field Testing and Tape Adhesion Results

Table A-126. Field Inspection Results for HOU-WS-04.

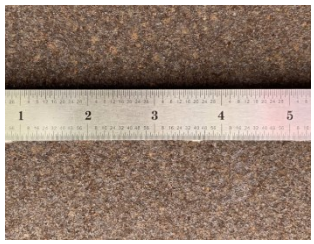
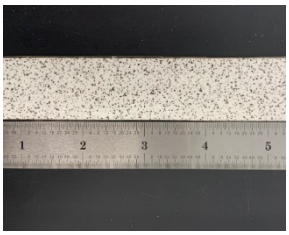
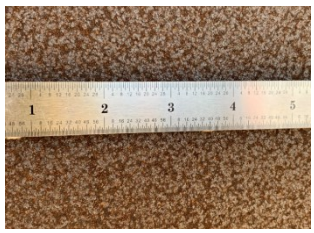
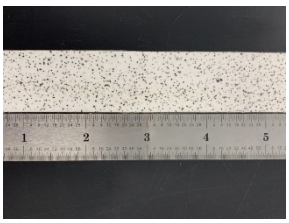
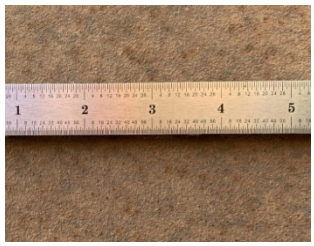
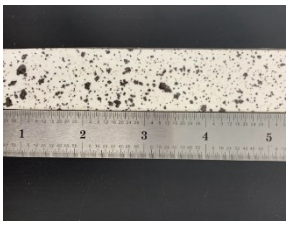
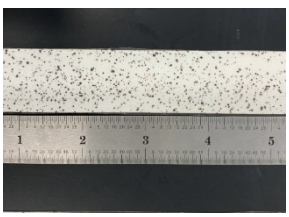
Location	Patina Rating	Thickness (inch)	Cl^- Conc. (ppm)	Field Condition	Tape Test
A1-G1F1 TF Bot. Ext.	8	Measured R1 0.745 R2 0.744 R3 0.746 R_Avg 0.745 Design 0.750			
A1-G1F1 Web Ext.	8	Measured R1 0.502 R2 0.504 R3 0.503 R_Avg 0.503 Design 0.500			
A1-G1F1 BF Top Ext.	7	Measured R1 0.989 R2 0.989 R3 0.992 R_Avg 0.990 Design 1.000			
A1-G1F1 BF Bot. Ext.	6	-			
A1-G3F1 TF Bot. Int.	8	Measured R1 0.769 R2 0.764 R3 0.765 R_Avg 0.766 Design 0.750			

Table A-127. Field Inspection Results for HOU-WS-04.

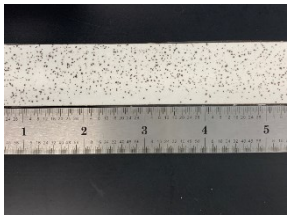
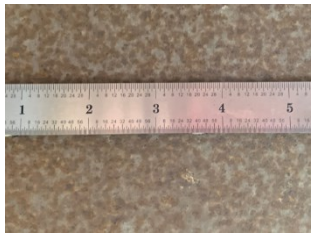
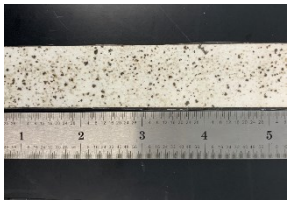
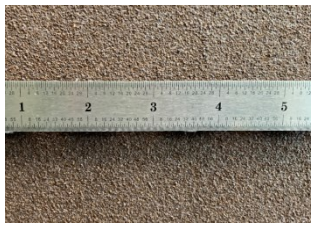
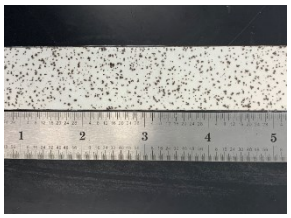
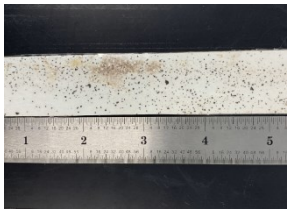
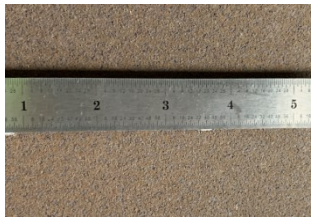
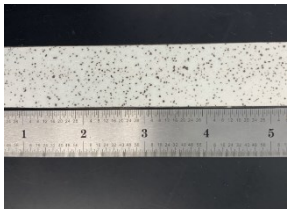
Location	Patina Rating	Thickness (inch)	Cl^- Conc. (ppm)	Field Condition	Tape Test
A1-G3F1 Web Int.	8	Measured R1 0.371 R2 0.373 R3 0.373 R_Avg 0.372 Design 0.375			
A1-G3F1 BF Top Int.	7	Measured R1 1.017 R2 1.017 R3 1.018 R_Avg 1.017 Design 1.000			
A1-G3F1 BF Bot. Int.	7	-			
A1-G5F1 TF Bot. Int.	7	Measured R1 0.770 R2 0.771 R3 0.768 R_Avg 0.770 Design 0.750			
A1-G5F1 Web Int.	8	Measured R1 0.367 R2 0.365 R3 0.366 R_Avg 0.366 Design 0.375			

Table A-128. Field Inspection Results for HOU-WS-04.

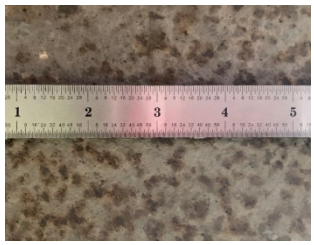
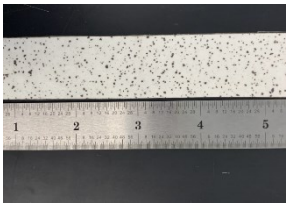
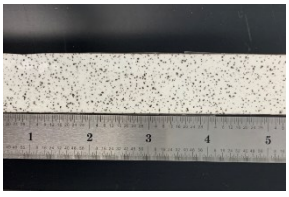
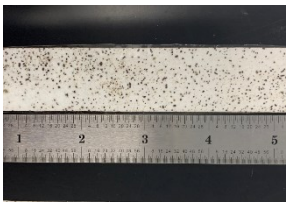
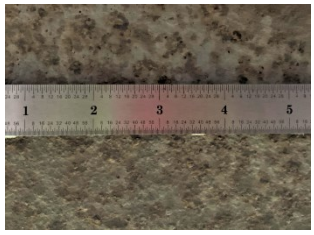
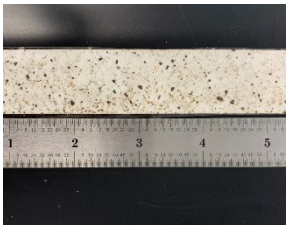
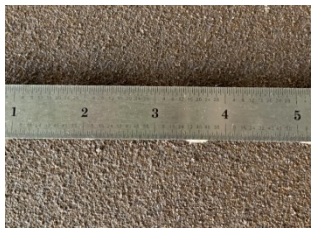
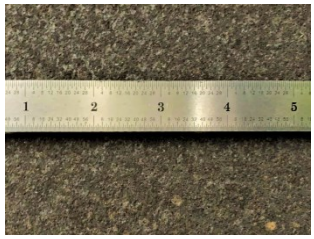
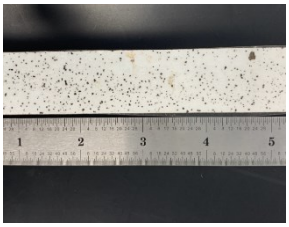
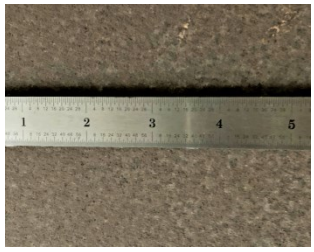
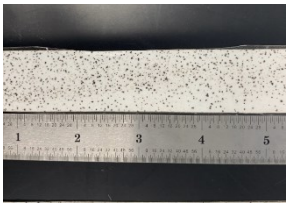
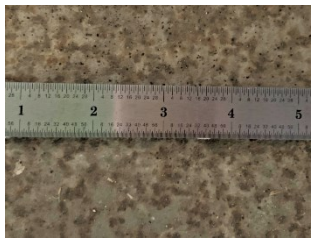
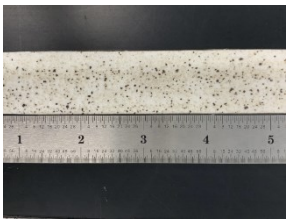
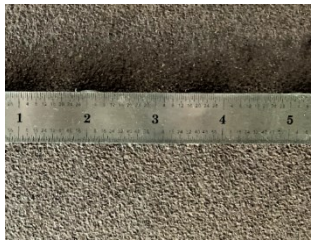
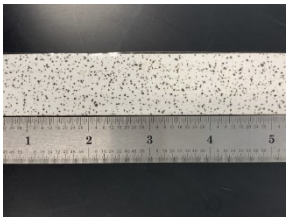
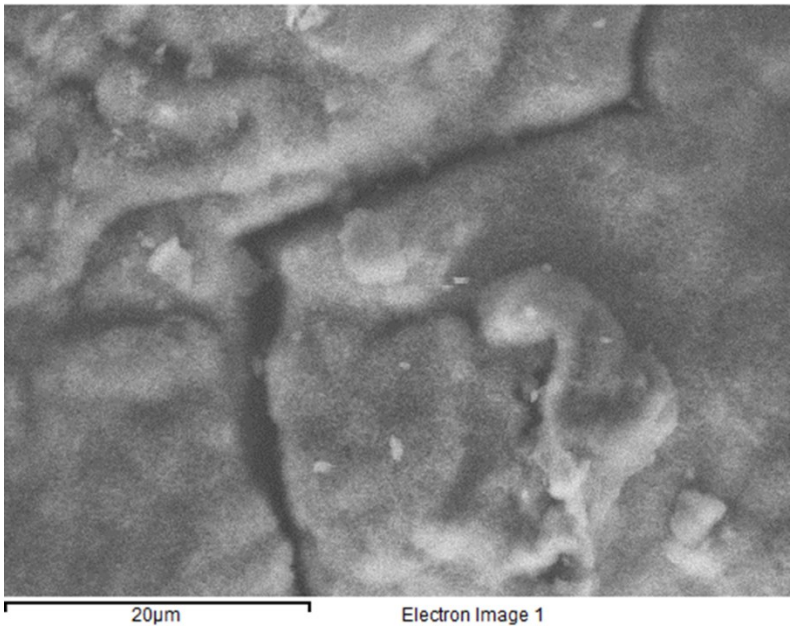
Location	Patina Rating	Thickness (inch)	Cl^- Conc. (ppm)	Field Condition	Tape Test
A1-G5F1 BF Top Int.	5	Measured R1 1.021 R2 1.028 R3 1.019 R_Avg 1.023 Design 1.000			
A1-G5F1 BF Bot. Int.	7	-			
A1-G7F2 TF Bot. Int.	8	Measured R1 0.752 R2 0.754 R3 0.754 R_Avg 0.753 Design 0.750			
A1-G7F2 Web Int.	7	Measured R1 0.365 R2 0.364 R3 0.362 R_Avg 0.364 Design 0.375			
A1-G7F2 BF Top Int.	5	Measured R1 0.992 R2 0.988 R3 1.003 R_Avg 0.994 Design 1.000			

Table A-129. Field Inspection Results for HOU-WS-04.

Location	Patina Rating	Thickness (inch)	Cl^- Conc. (ppm)	Field Condition	Tape Test
A1-G7F2 BF Bot. Int.	6	-			
A1-G10F2 TF Bot. Ext.	7	Measured R1 0.765 R2 0.769 R3 0.771 R_Avg 0.768 Design 0.750			
A1-G10F2 Web Ext.	8	Measured R1 0.369 R2 0.370 R3 0.370 R_Avg 0.370 Design 0.375			
A1-G10F2 BF Top Ext.	5	Measured R1 1.014 R2 1.015 R3 1.017 R_Avg 1.015 Design 1.000			
A1-G10F2 BF Bot. Ext.	7	-			

A.27.3.SEM/EDS Results: Exterior Web Girder

Element	Weight %	Atomic %
O K	40.08	69.17
Al K	1.08	1.10
Si K	0.80	0.78
S K	0.54	0.46
Ca K	0.24	0.16
Mn K	1.51	0.76
Fe K	55.37	27.37
Ni K	0.39	0.18
Totals	100.00	



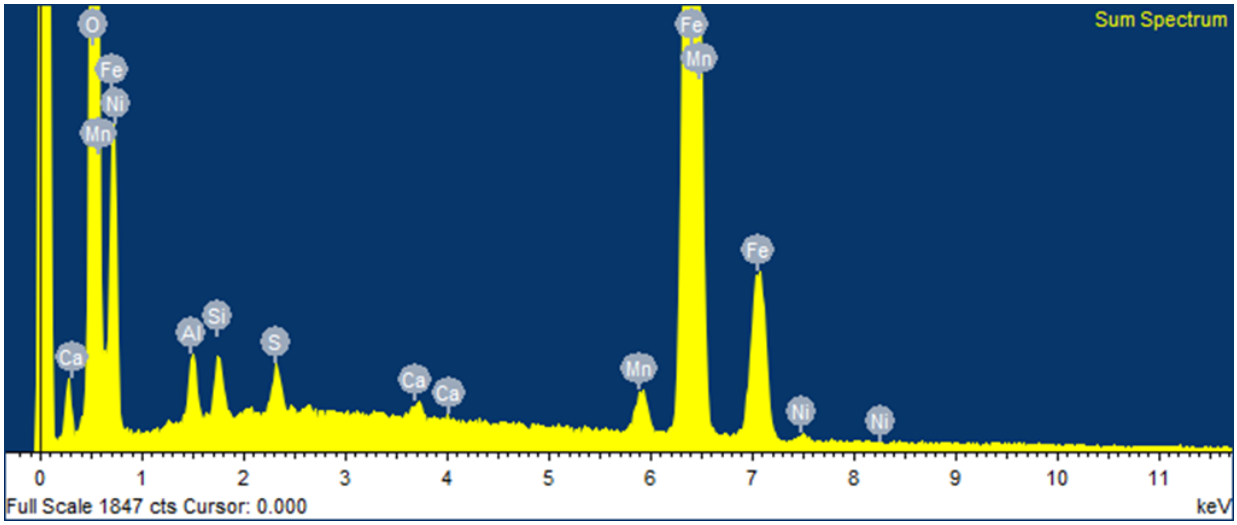


Figure A.443. SEM Image and EDS Spectrum of the Rust Collected from Exterior Web of the Girder.

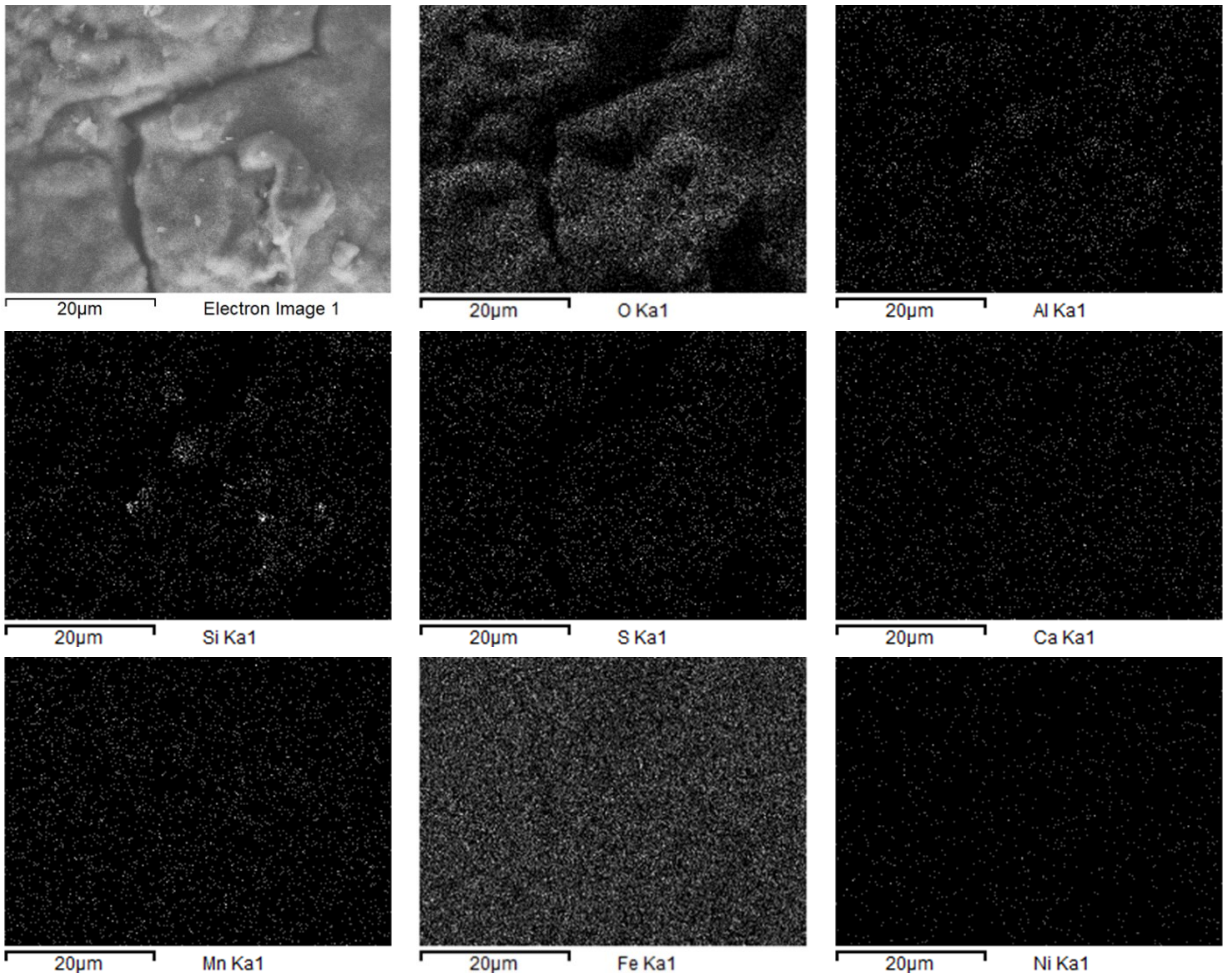
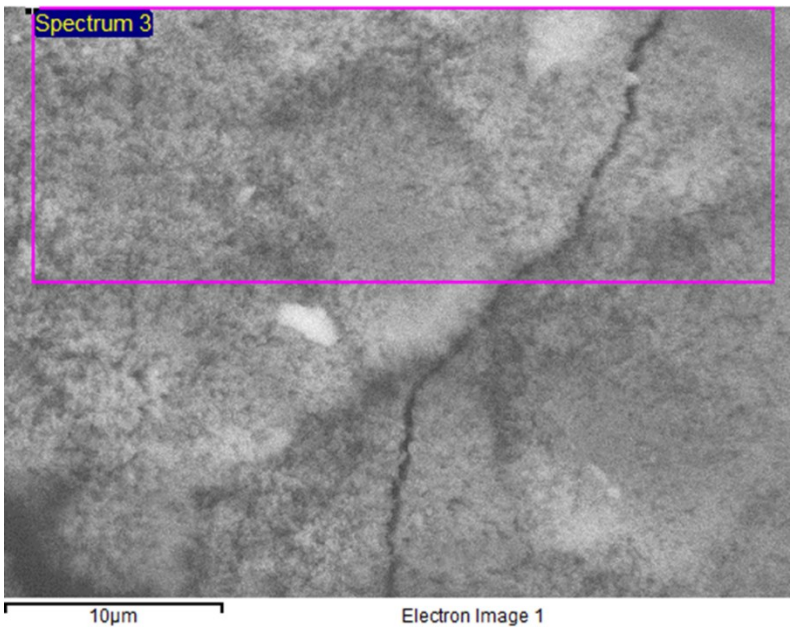


Figure A.444. EDS Elemental Mapping of Rust Collected from Exterior Web.

Element	Weight %	Atomic %
O K	23.46	51.05
Al K	1.93	2.50
Si K	0.25	0.31
Mn K	2.61	1.65
Fe K	70.87	44.18
Mo L	0.88	0.32
Totals	100.00	



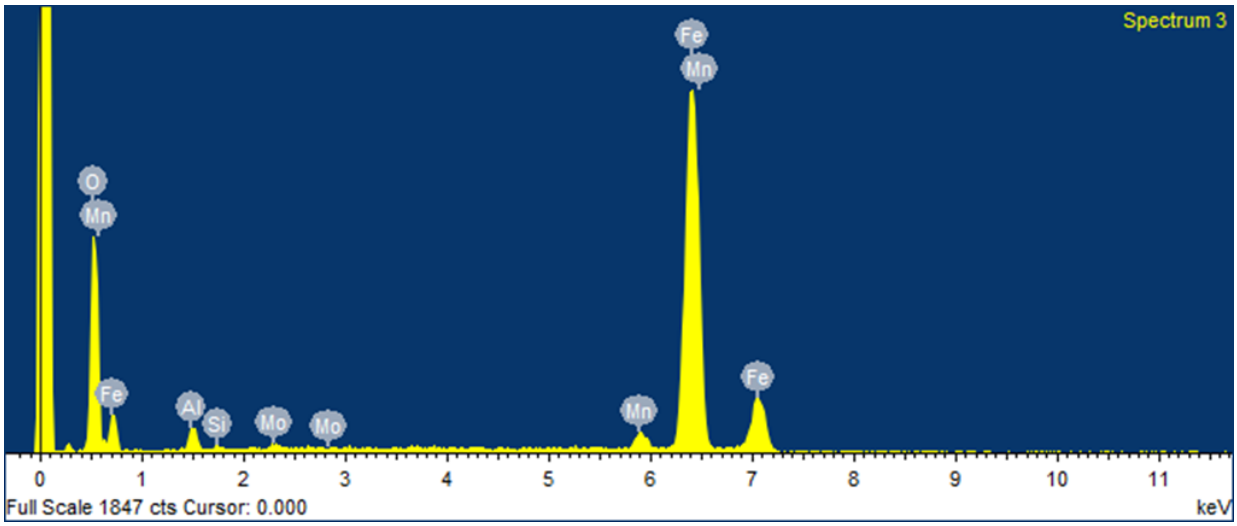
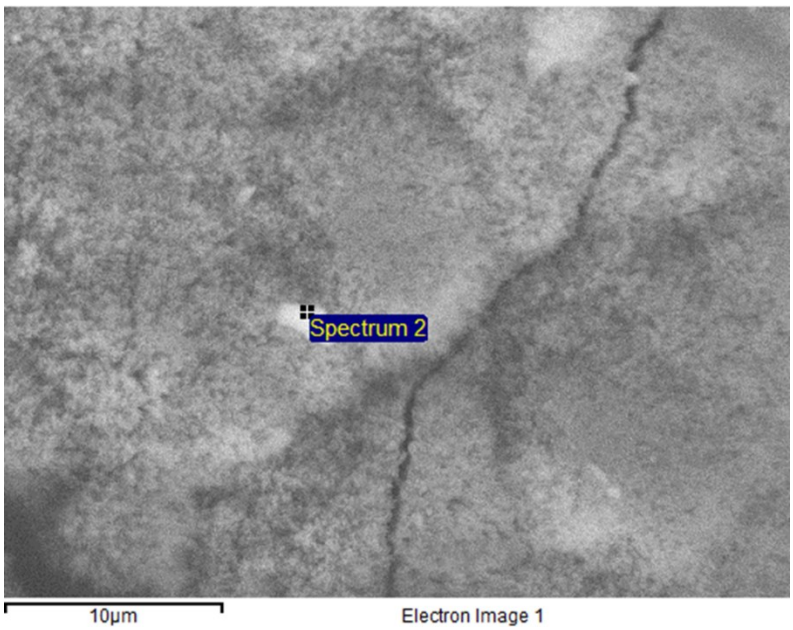


Figure A.445. SEM Image and EDS Spectrum of the Rust Collected from Exterior Web of the Girder.

Element	Weight %	Atomic %
O K	24.24	51.18
Al K	4.05	5.07
Si K	0.42	0.51
S K	0.29	0.31
Mn K	1.31	0.81
Fe K	69.20	41.86
Cu K	0.50	0.26
Totals	100.00	



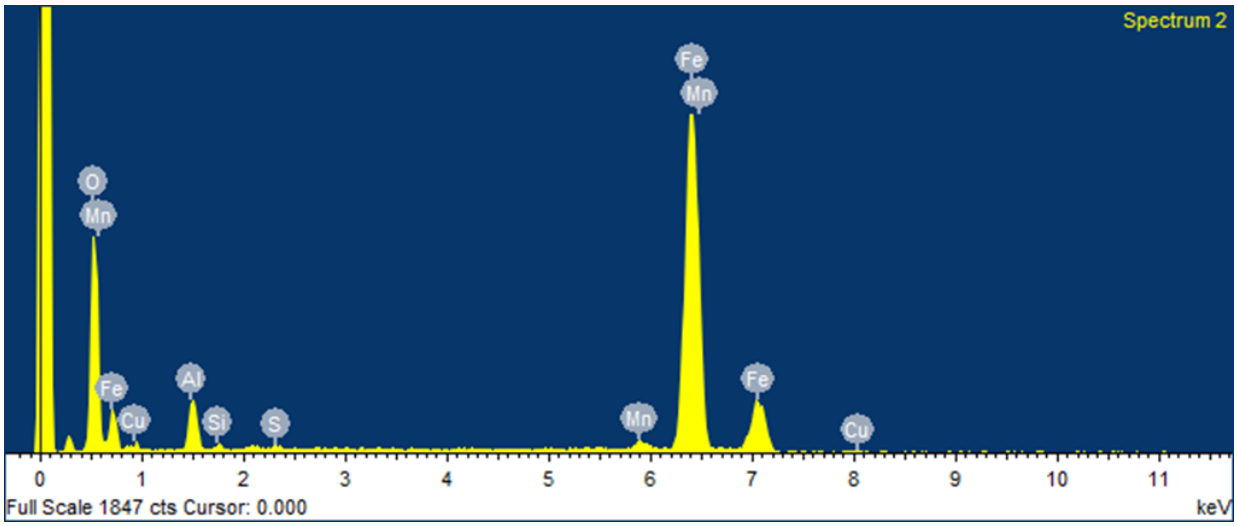
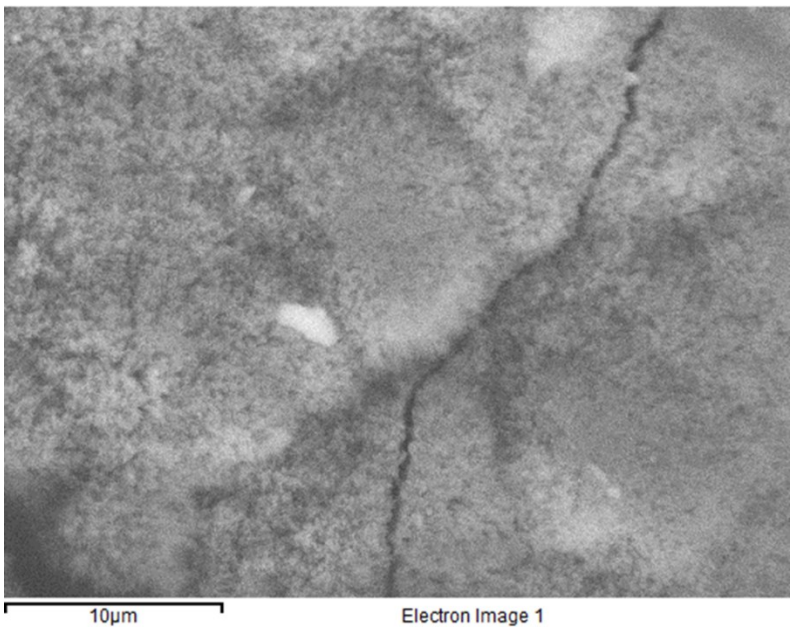


Figure A.446. SEM Image and EDS Spectrum of the Rust Collected from Exterior Web of the Girder.

Element	Weight %	Atomic %
O K	23.55	50.96
Al K	1.98	2.53
Si K	0.34	0.42
S K	0.29	0.31
Mn K	2.16	1.36
Fe K	71.26	44.16
Ni K	0.42	0.25
Totals	100.00	



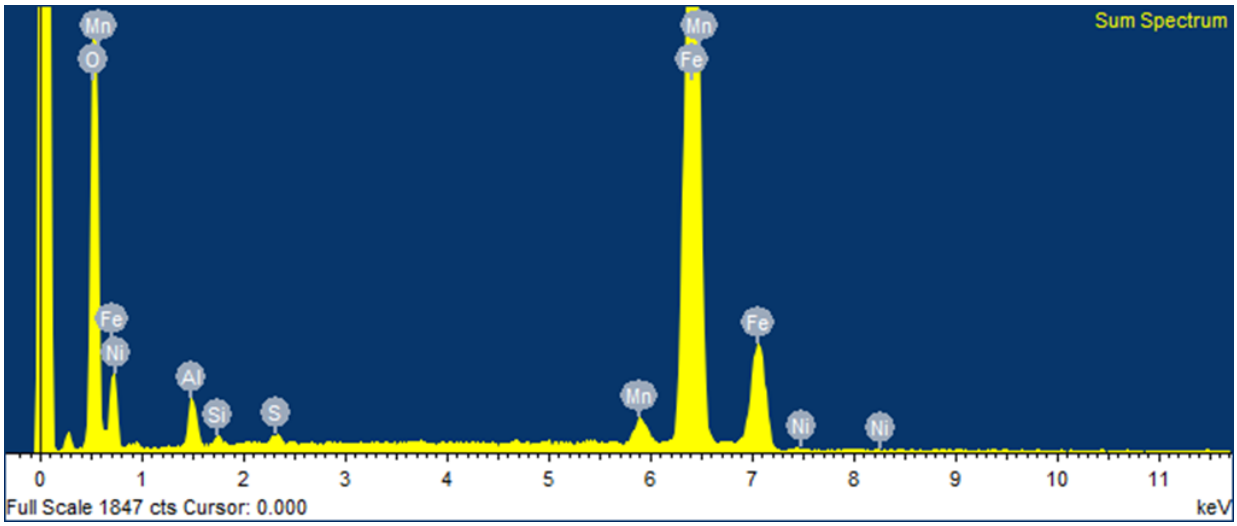


Figure A.447. SEM Image and EDS Spectrum of the Rust Collected from Exterior Web of the Girder.

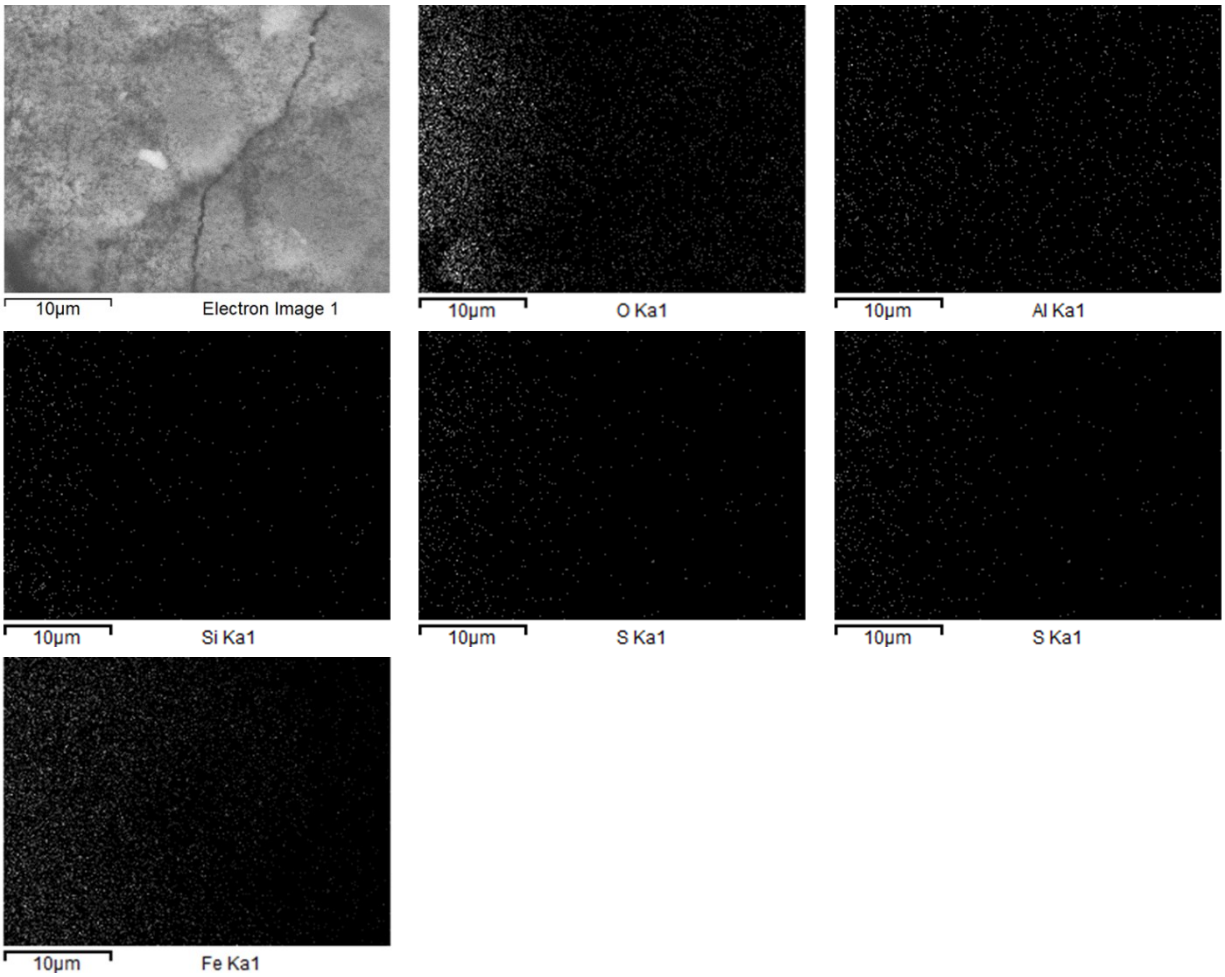
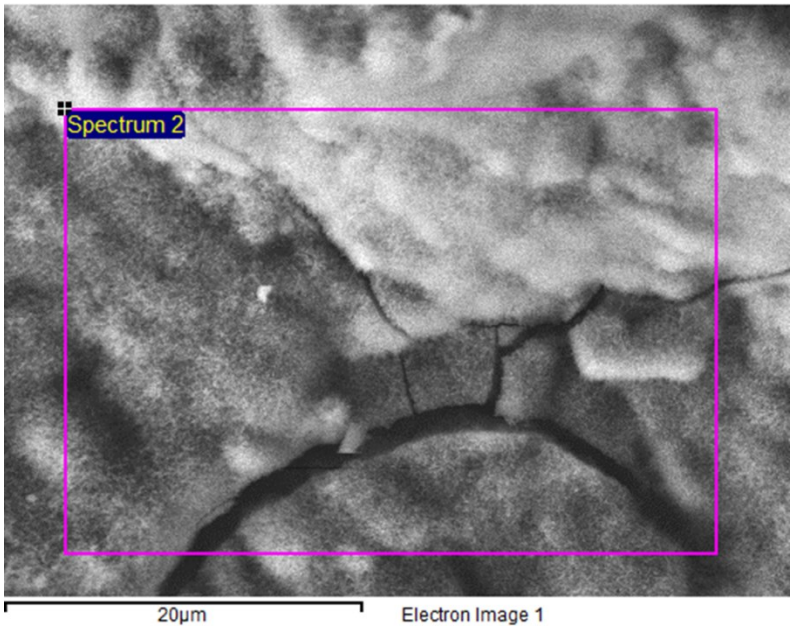


Figure A.448. EDS Elemental Mapping of Rust Collected from Exterior Web.

A.27.4.SEM/EDS Results: Interior Web

Element	Weight %	Atomic %
O K	27.04	55.82
Al K	0.95	1.17
Si K	0.21	0.25
S K	0.65	0.67
Cr K	0.27	0.17
Mn K	0.98	0.59
Fe K	69.53	41.13
Ni K	0.36	0.20
Totals	100.00	



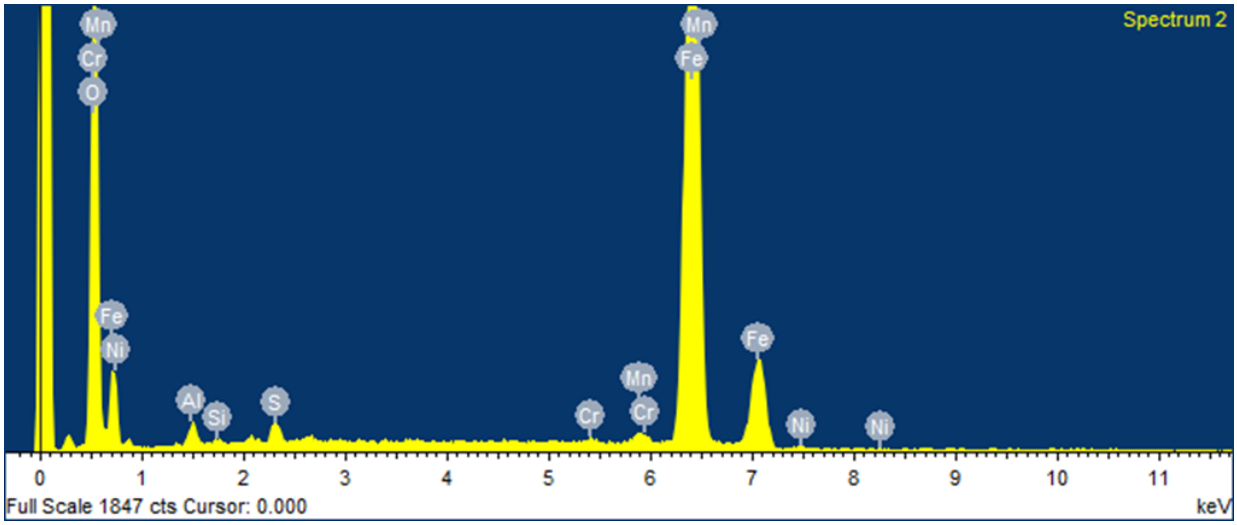
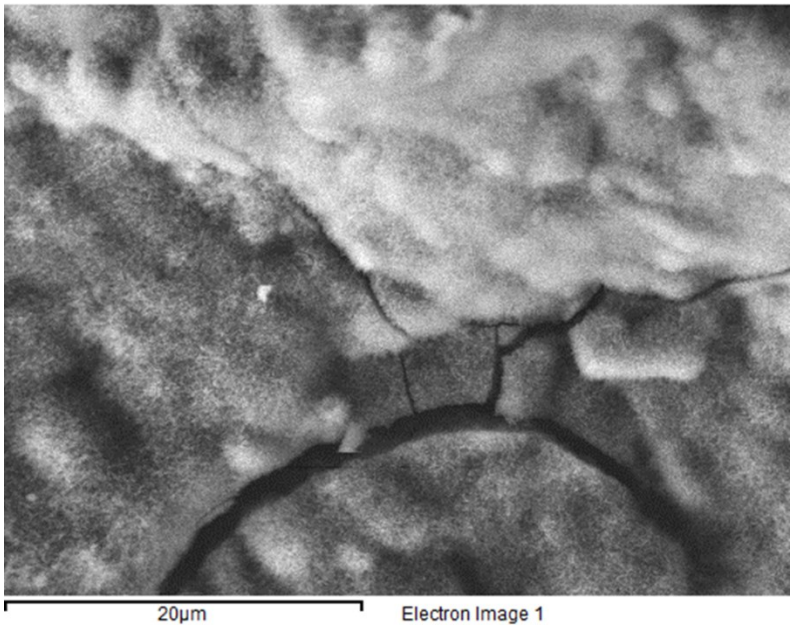


Figure A.449. SEM Image and EDS Spectrum of the Rust Collected from Interior Web of the Girder.

Element	Weight %	Atomic %
O K	29.34	58.58
Al K	0.90	1.07
Si K	0.20	0.23
S K	0.67	0.67
Cl K	0.18	0.17
Cr K	0.14	0.08
Mn K	1.11	0.65
Fe K	67.04	38.34
Ni K	0.41	0.22
Totals	100.00	



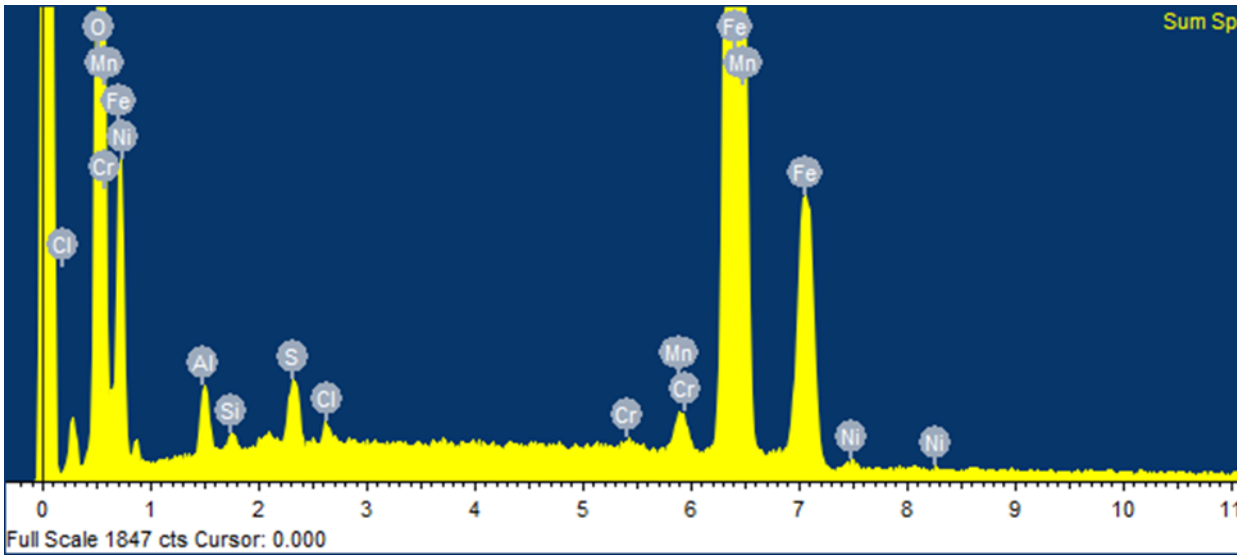


Figure A.450. SEM Image and EDS Spectrum of the Rust Collected from Interior Web of the Girder.

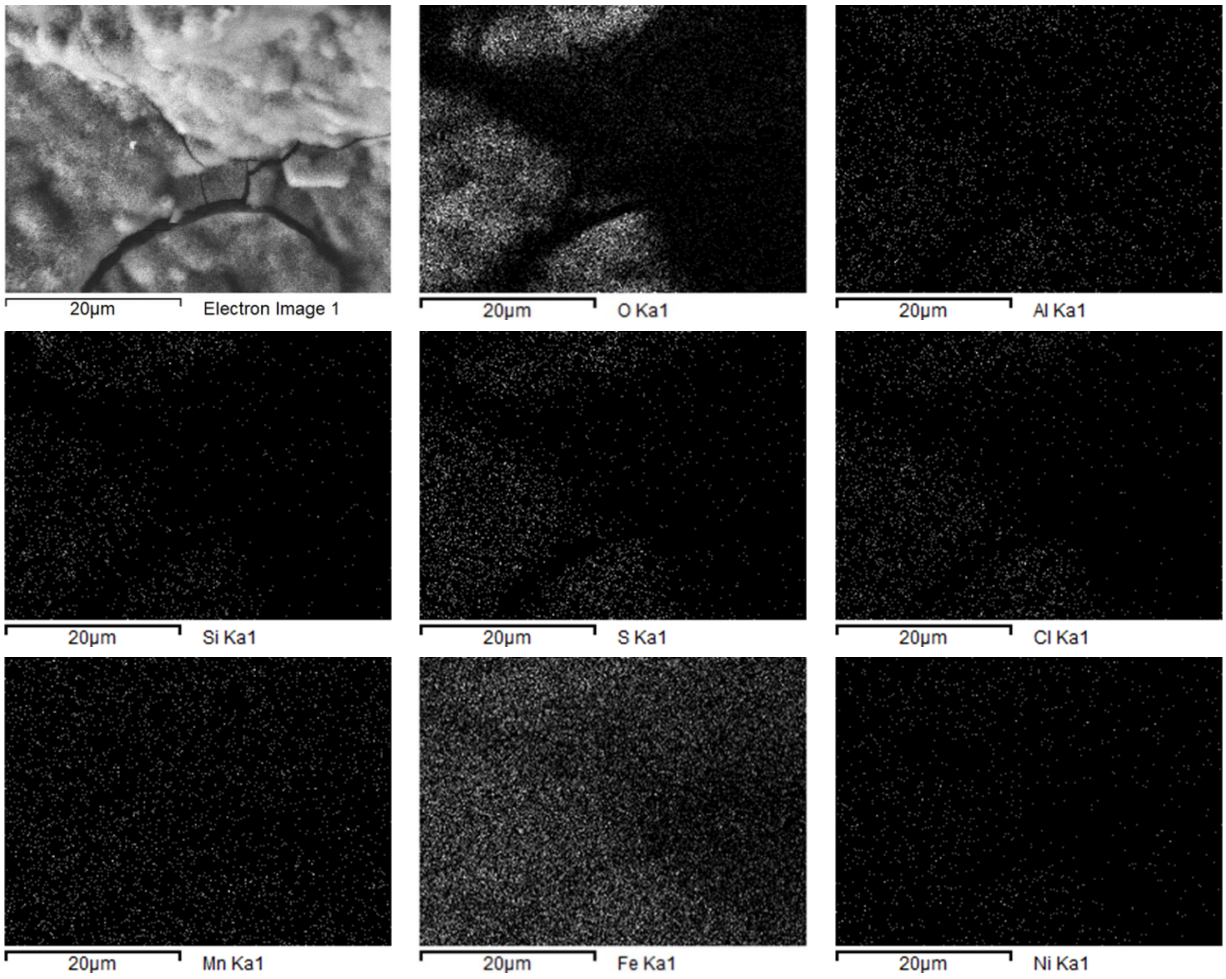
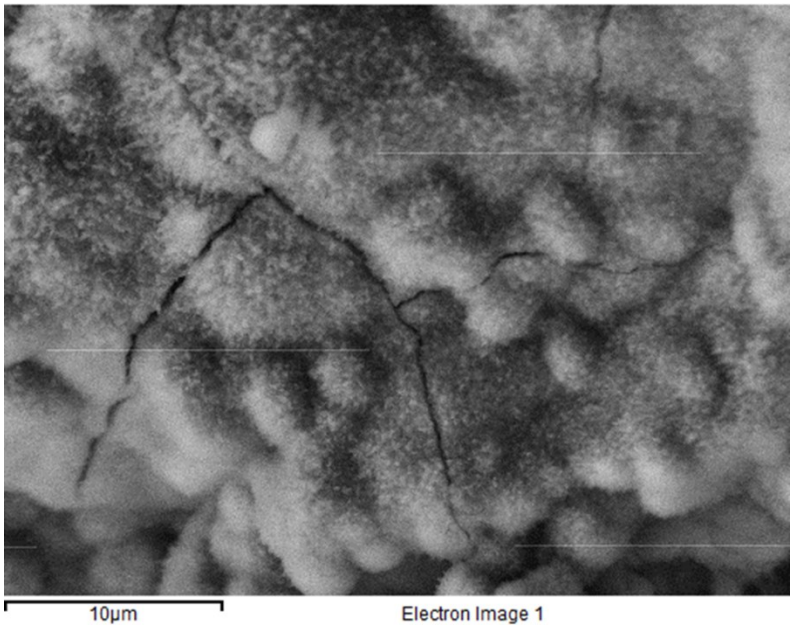


Figure A.451. EDS Elemental Mapping of Rust Collected from Interior Web.

Element	Weight %	Atomic %
O K	34.28	63.95
Al K	0.73	0.81
Si K	0.15	0.16
S K	0.84	0.78
Cl K	0.32	0.27
Mn K	1.01	0.55
Fe K	62.36	33.33
Ni K	0.30	0.15
Totals	100.00	



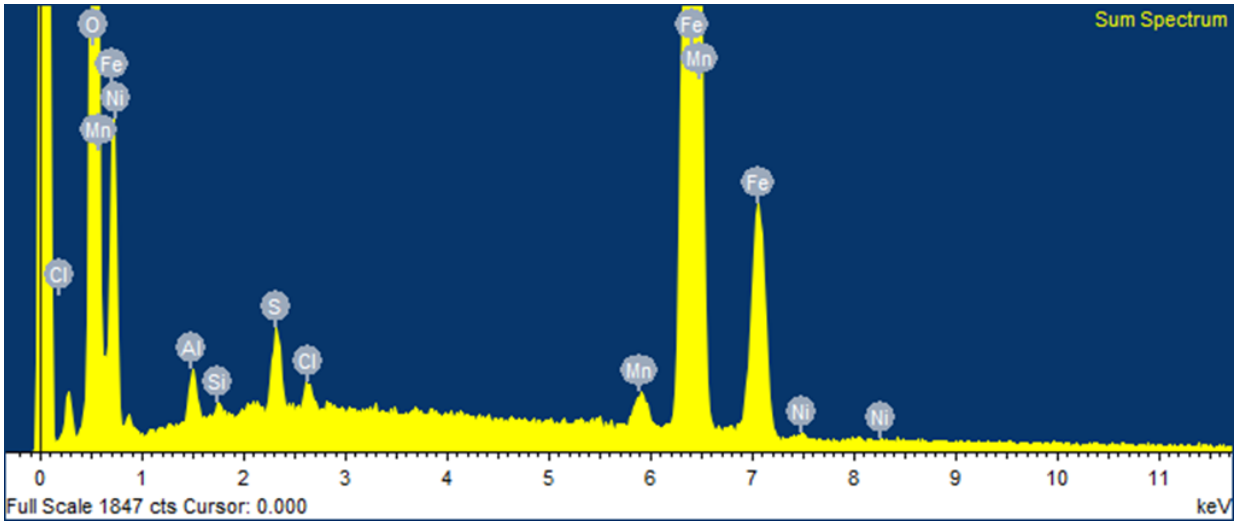


Figure A.452. SEM Image and EDS Spectrum of the Rust Collected from Interior Web of the Girder.

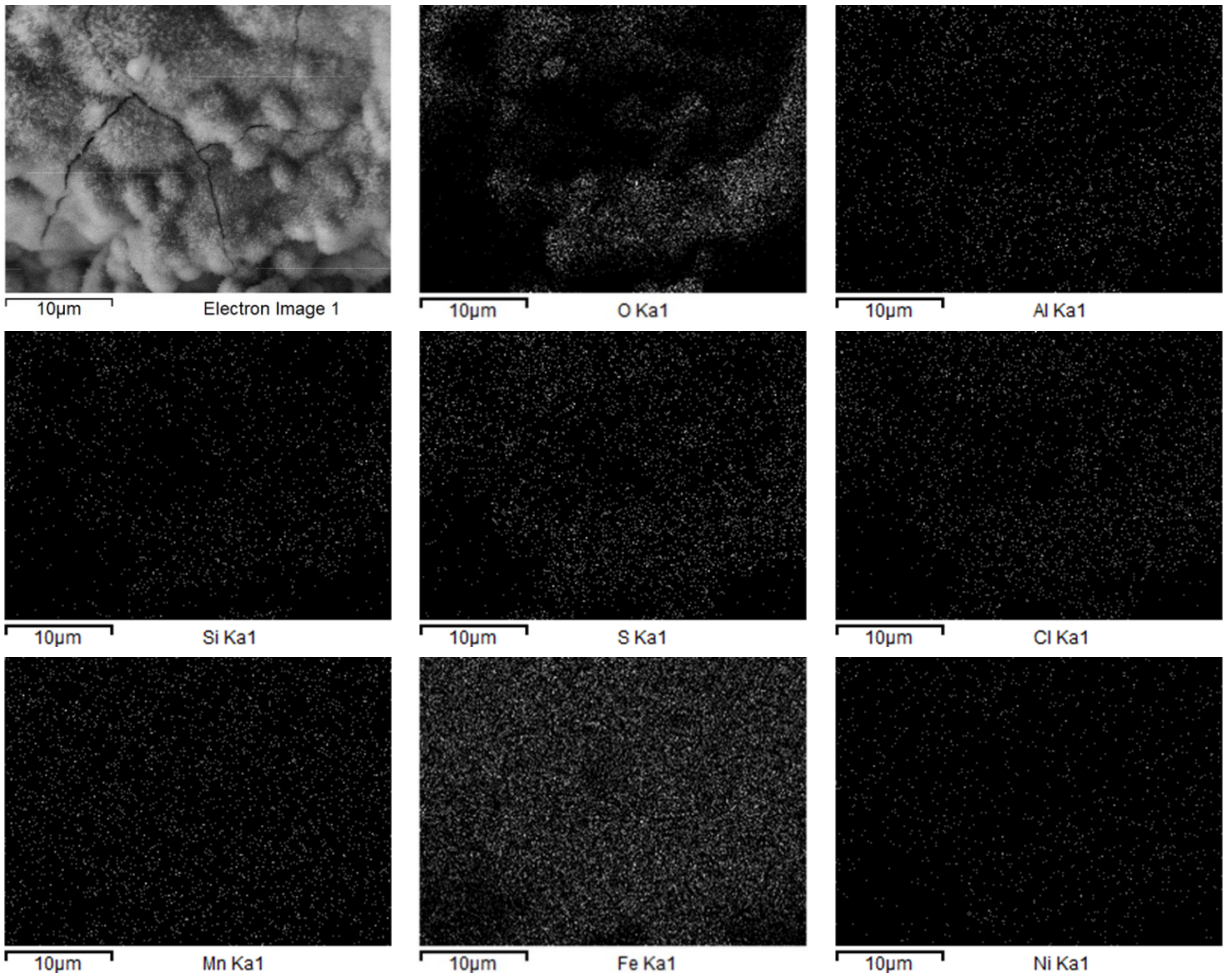


Figure A.453. EDS Elemental Mapping of Rust Collected from Interior Web.

A.27.5.XPS Results: Exterior Web Girder

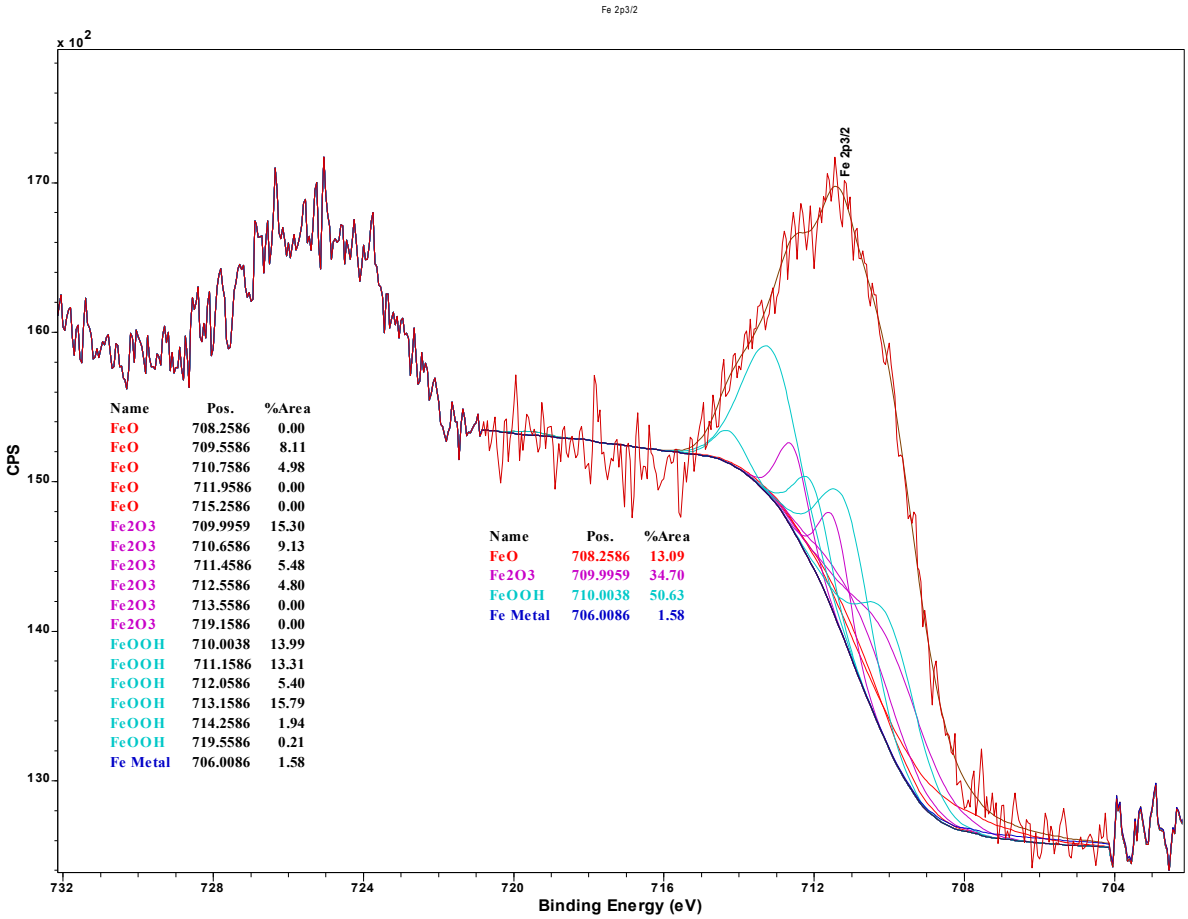


Figure A.454. XPS Spectrum of the Rust Collected from Exterior Web of the Girder.

A.27.6.XPS Results: Interior Web Girder

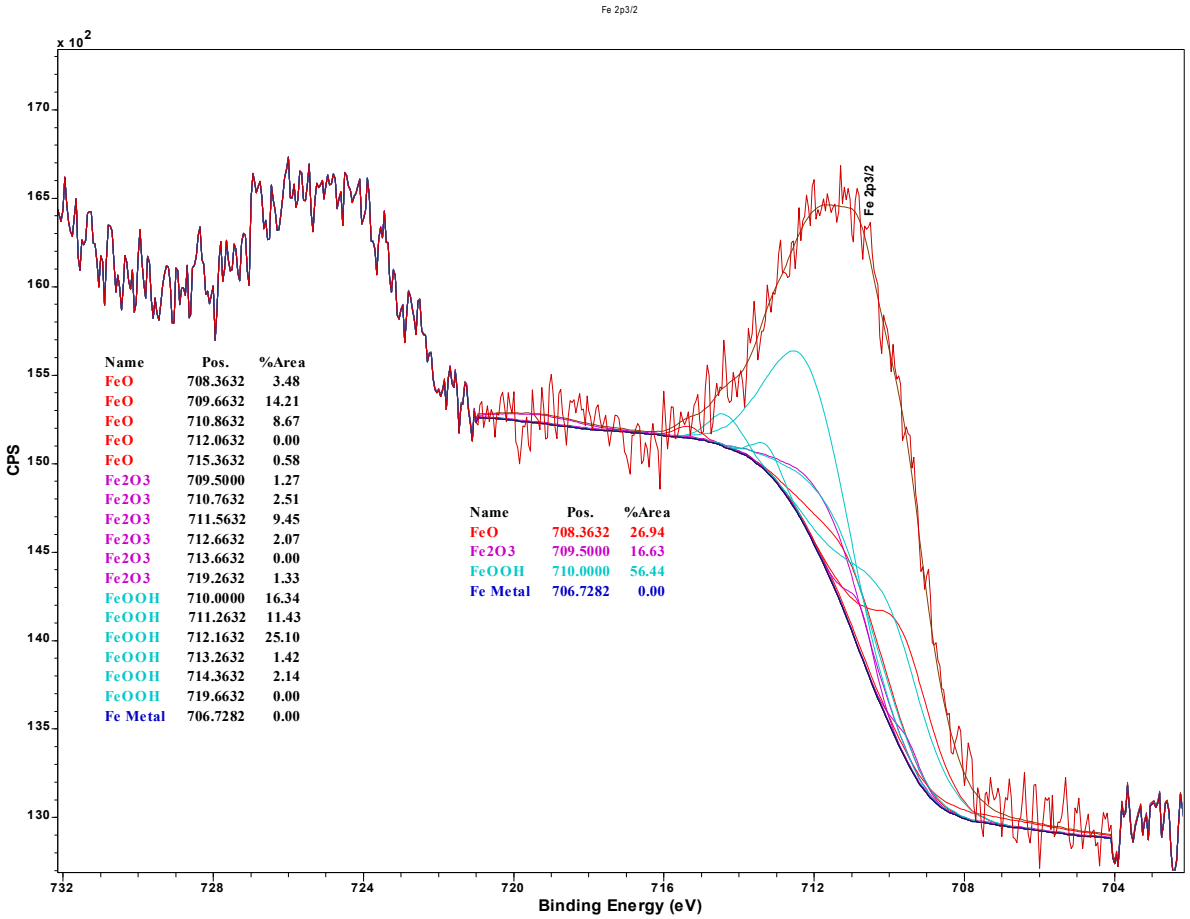


Figure A.455. XPS Spectrum of the Rust Collected from Interior Web of the Girder.

A.27.7.XRD Result: Exterior and Interior Girder

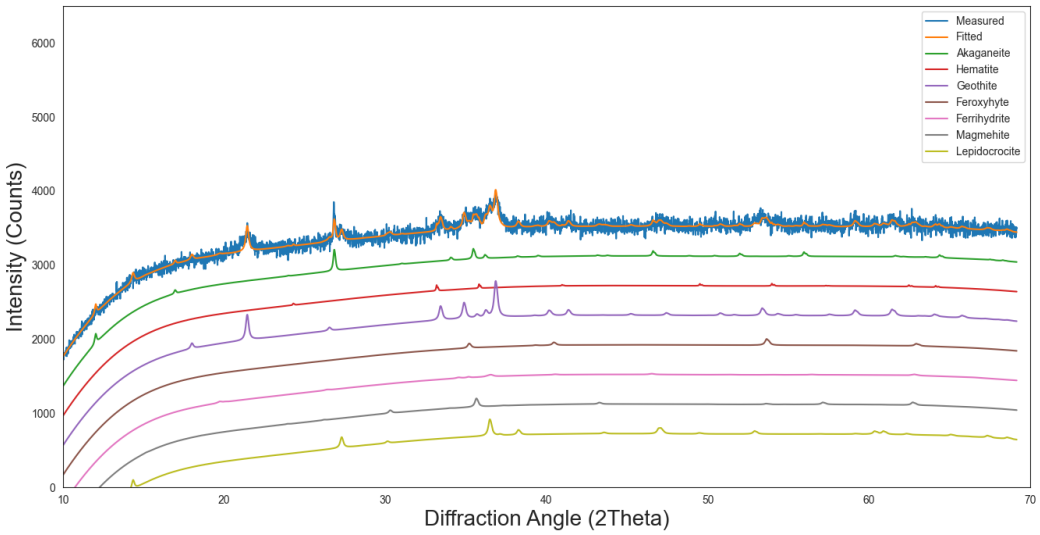


Figure A.456. XRD Pattern of Powdered Rust Collected from Exterior Web of the Girder (G10F2).

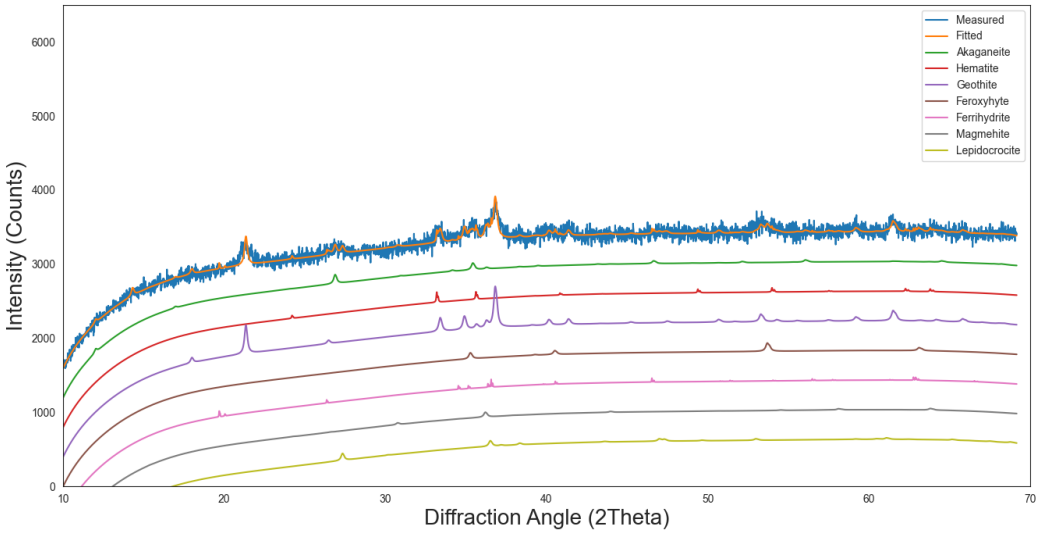


Figure A.457. XRD Pattern of Powdered Rust Collected from Interior Web of the Girder (G8F2).

A.27.8.Particle Size Analysis: Tape Adhesion Results

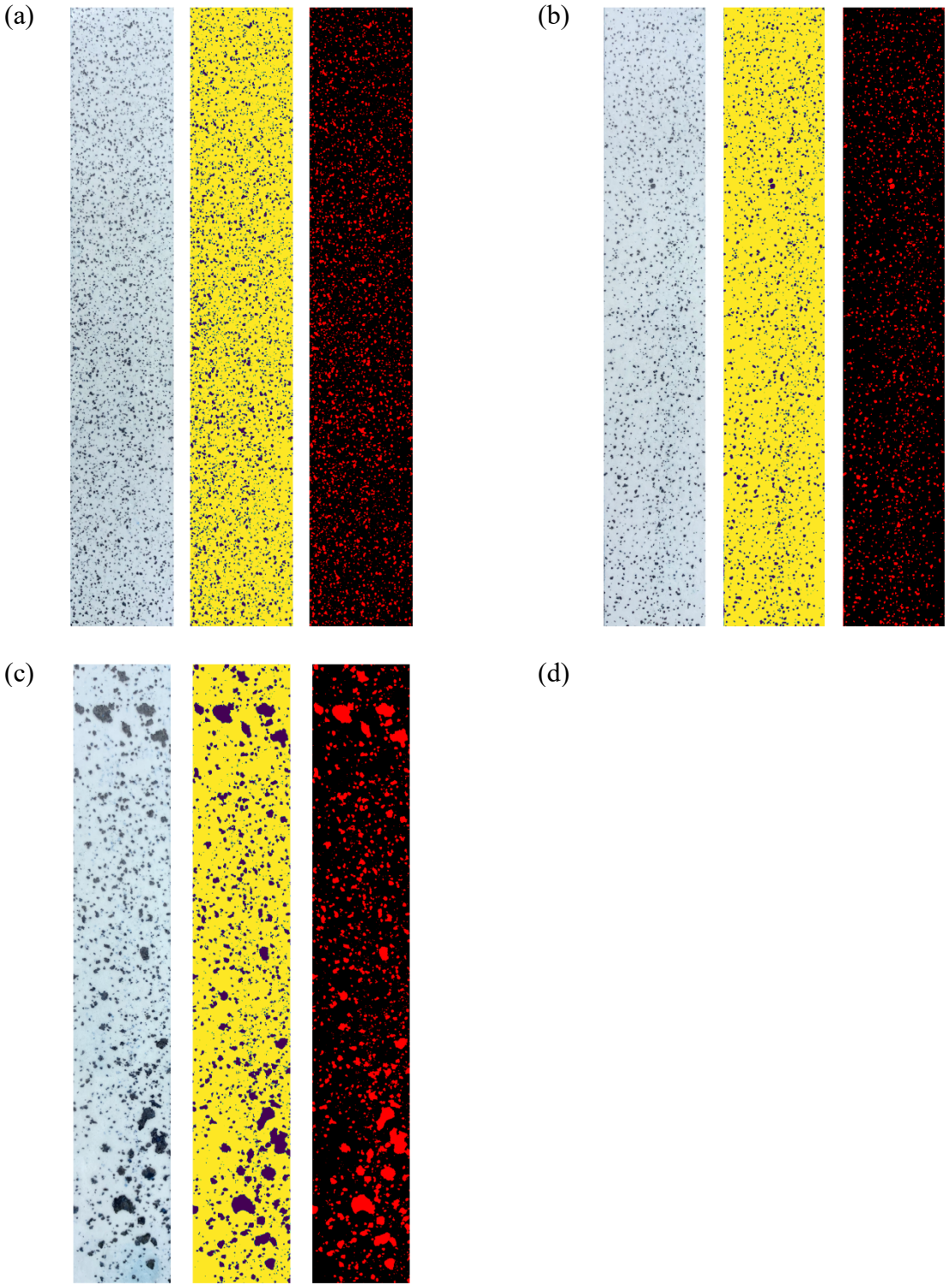


Figure A.458. Particle Size Analysis Results at A1G1F1 (a) Top Flange Bottom, (b) Web, (c) Bottom Flange Bottom (d) Stiffener.

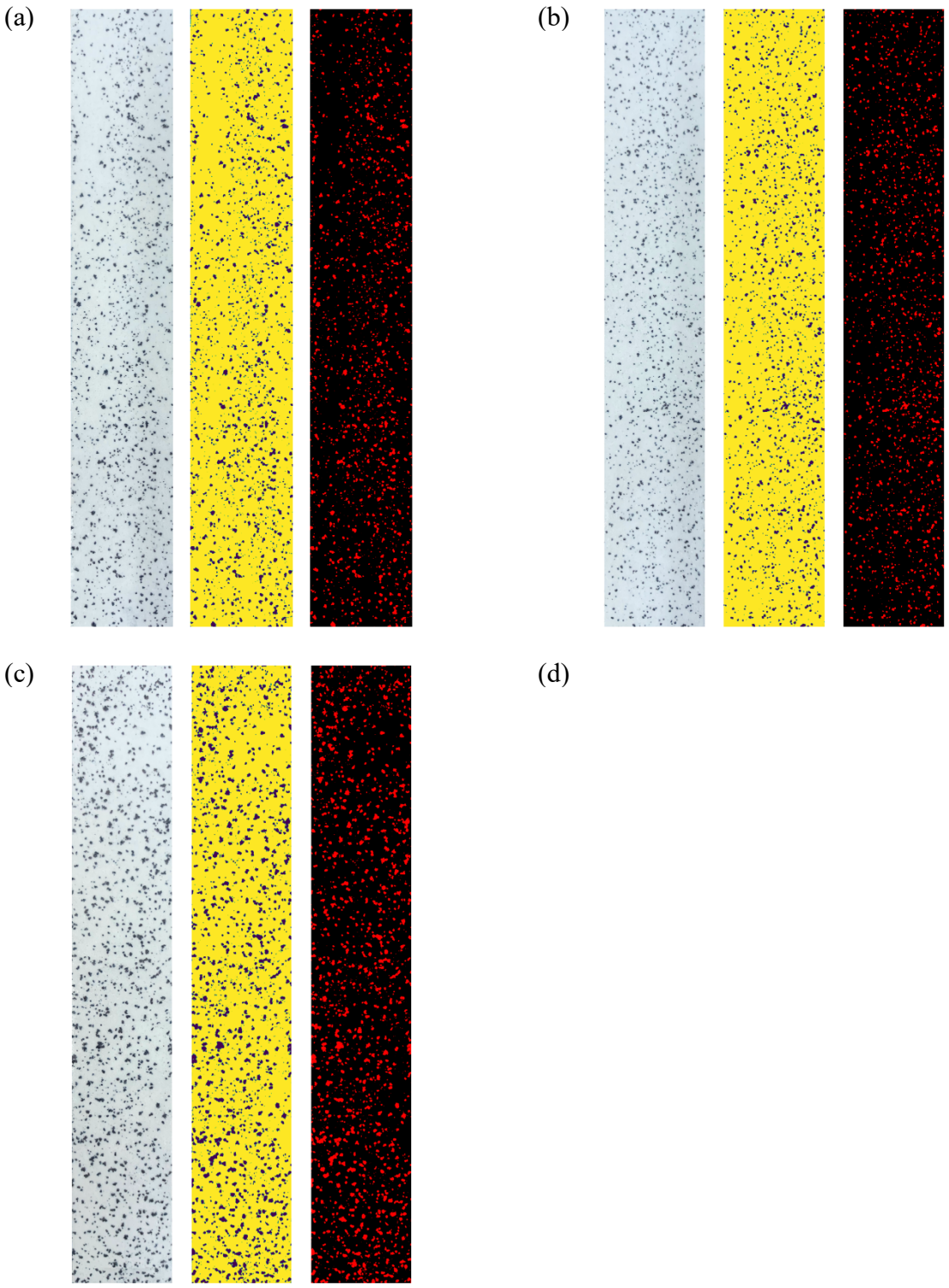


Figure A.459. Particle Size Analysis Results at A1G3F1 (a) Top Flange Bottom, (b) Web, (c) Bottom Flange Bottom (d) Stiffener.

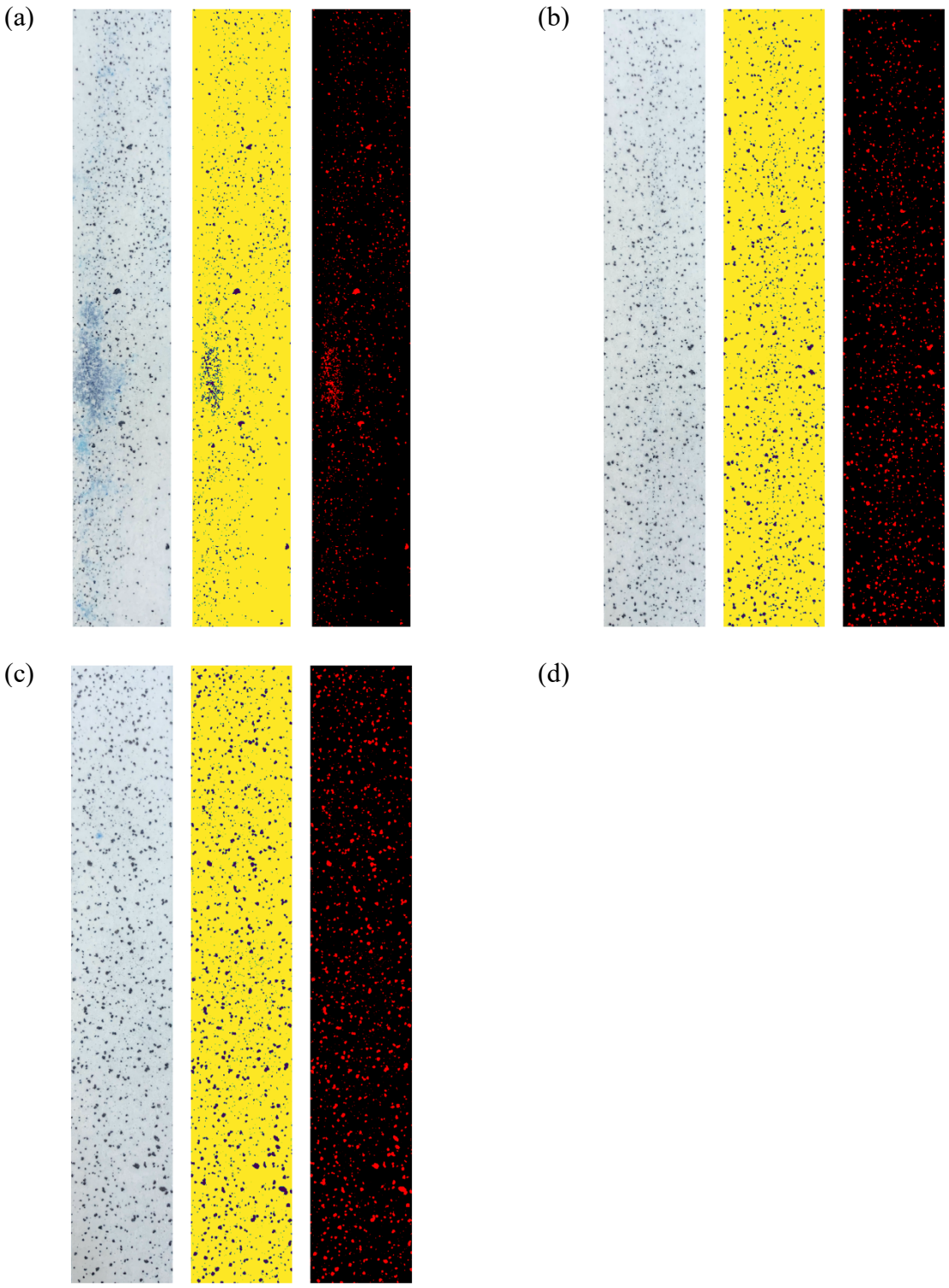


Figure A.460. Particle Size Analysis Results at A1G5F1 (a) Top Flange Bottom, (b) Web, (c) Bottom Flange Bottom (d) Stiffener.

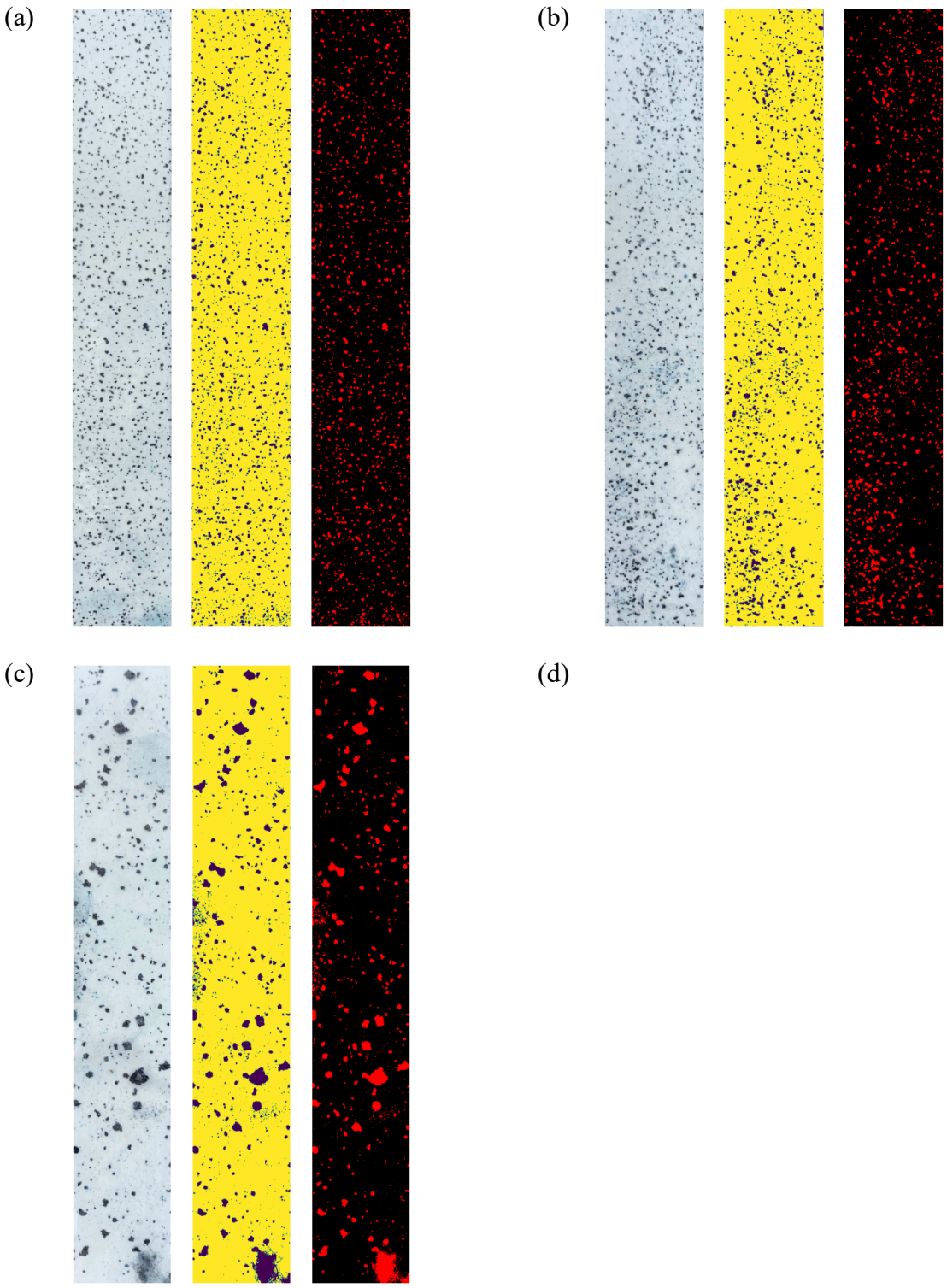


Figure A.461. Particle Size Analysis Results at A1G7F2 (a) Top Flange Bottom, (b) Web, (c) Bottom Flange Bottom (d) Stiffener.

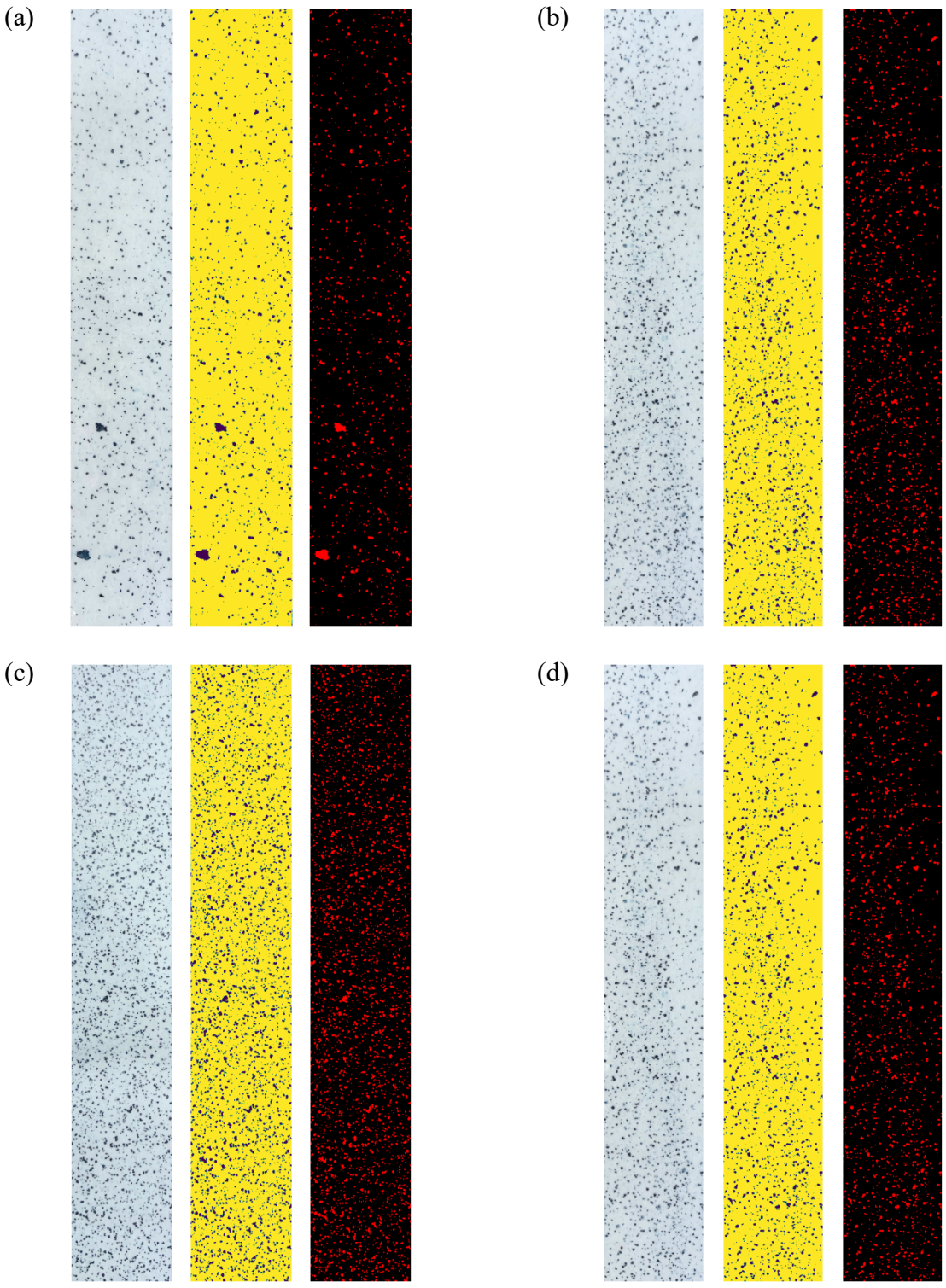


Figure A.462. Particle Size Analysis Results at A1G10F2 (a) Top Flange Bottom, (b) Web, (c) Bottom Flange Bottom (d) Stiffener.

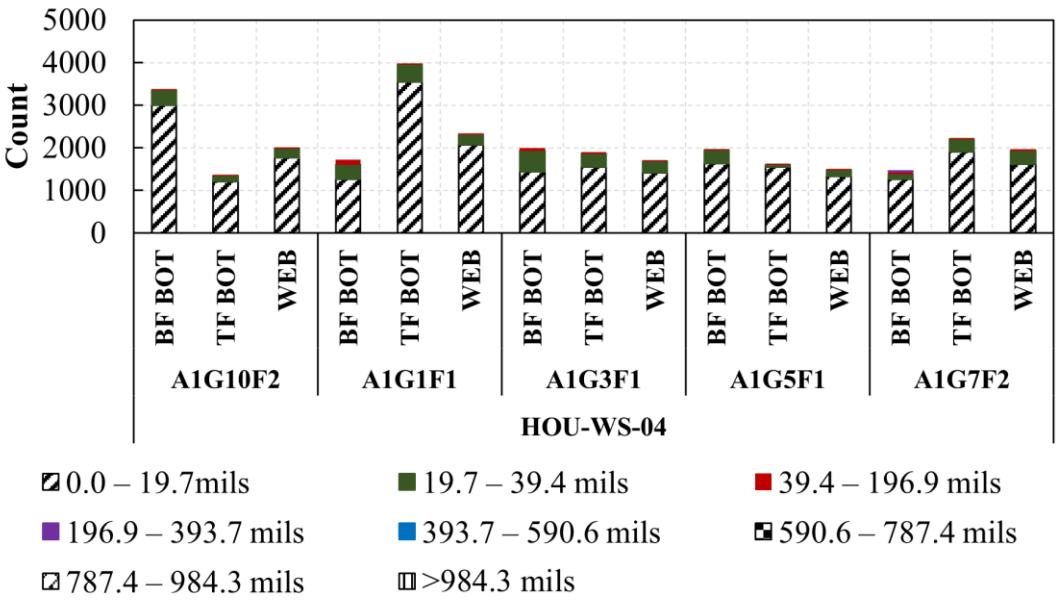


Figure A.463. Particle Size Analysis Showing Different Locations Examined.

A.28. HOU-WS-05

- HB&T RR
- Bridge ID 121020B40177001, Coordinates (29.81554, -95.31726), Harris County
- Continuous weathering steel plate girder
- Built 1989
- Girder inspection carried on End abutment, and measurements are taken on girder within four feet from the abutment or bent.
- No visual inspection on deck
- Location for Testing: A1-G1F1, A1-G3F1, A1-G2F2, A1-G5F2



Figure A.464. Typical Picture of HOU-WS-05.

A.28.1. Observed Condition

Delaminated areas of the patina are visible on the bottom face of the top flange. The web has a uniform patina formation with a patina rating of 7. The interior girders have significant poultice corrosion on the top face of the bottom flange due to the accumulation of dirt Index 5 whereas exterior girders have less accumulation of dirt.

A.28.2.Field Inspection Results

Table A-130. Field Inspection Results for HOU-WS-05.

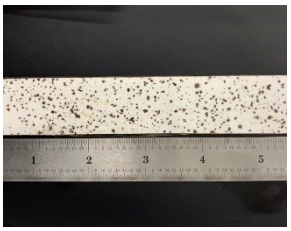
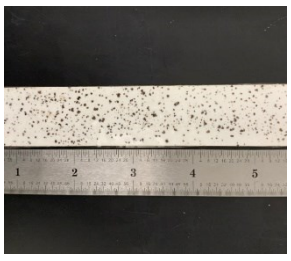
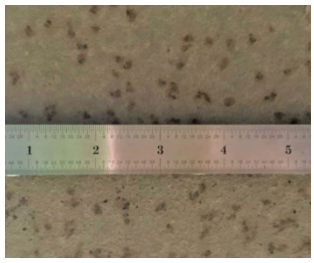
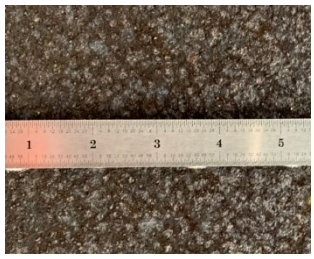
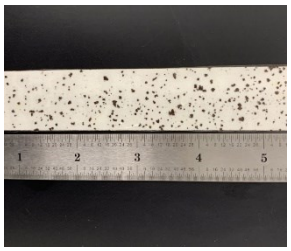
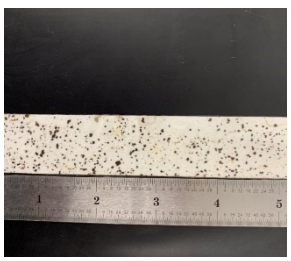
Location	Patina Rating	Thickness (inch)	Cl^- Conc. (ppm)	Field Condition	Tape Test
A1-G1F1 TF Bot. Ext.	7	Measured R1 1.008 R2 1.009 R3 1.009 R_Avg 1.008 Design			
A1-G1F1 Web Ext.	8	Measured R1 0.640 R2 0.639 R3 0.641 R_Avg 0.640 Design			
A1-G1F1 BF Top Ext.	5	Measured R1 1.490 R2 1.490 R3 1.489 R_Avg 1.490 Design			
A1-G1F1 BF Bot. Ext.	7	-			
A1-G3F1 TF Bot. Int.	7	Measured R1 0.996 R2 0.996 R3 0.997 R_Avg 0.996 Design			

Table A-131. Field Inspection Results for HOU-WS-05.

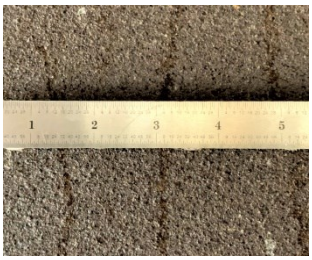
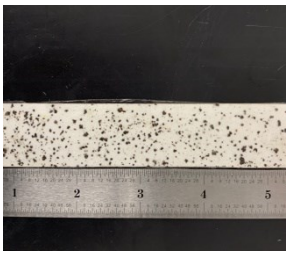
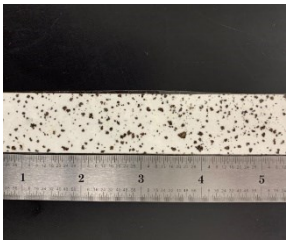
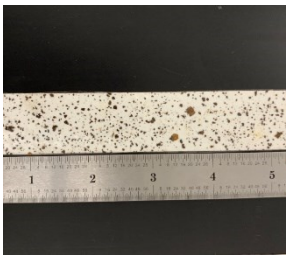
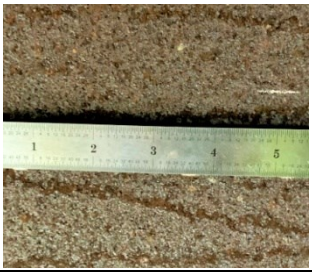
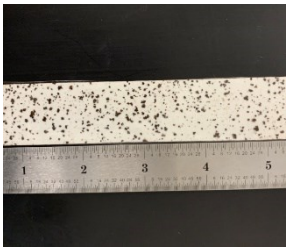
Location	Patina Rating	Thickness (inch)	Cl^- Conc. (ppm)	Field Condition	Tape Test
A1-G3F1 Web Int.	7	Measured R1 0.625 R2 0.625 R3 0.623 R_Avg 0.624 Design			
A1-G3F1 BF Top Int.	7	Measured R1 1.492 R2 1.493 R3 1.492 R_Avg 1.492 Design			
A1-G3F1 BF Bot. Int.	6	-			
A1-G2F2 TF Bot. Int.	7	Measured R1 1.006 R2 1.008 R3 1.009 R_Avg 1.008 Design			
A1-G2F2 Web Int.	7	Measured R1 0.636 R2 0.639 R3 0.638 R_Avg 0.638 Design			

Table A-132. Field Inspection Results for HOU-WS-05.

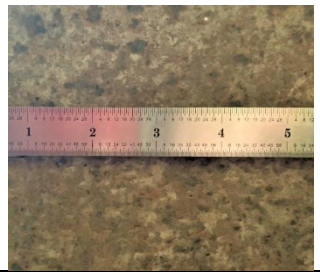
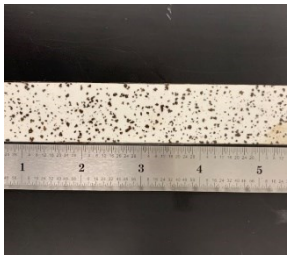
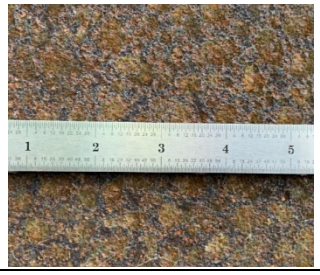
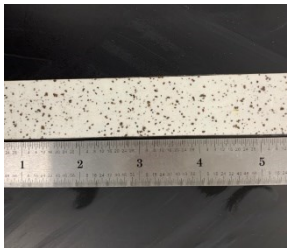
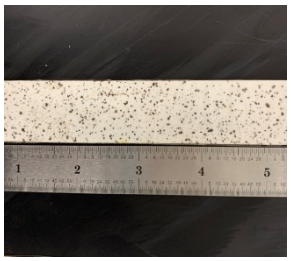
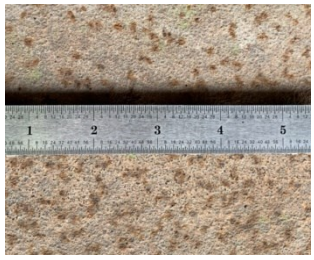
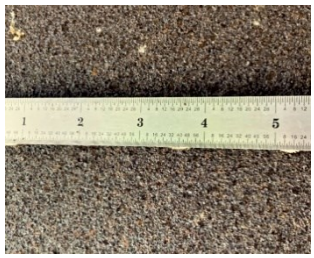
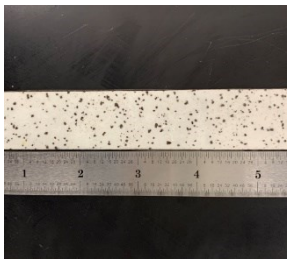
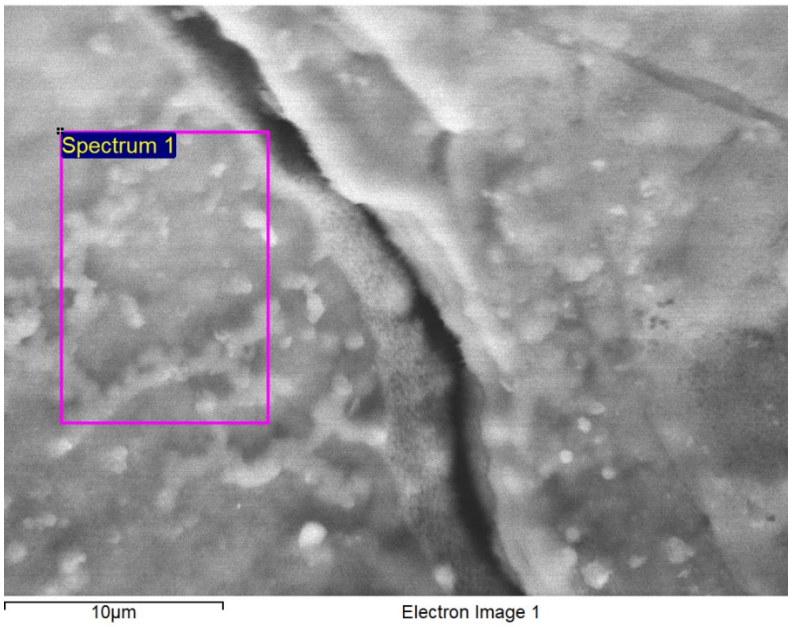
Location	Patina Rating	Thickness (inch)	Cl^- Conc. (ppm)	Field Condition	Tape Test
A1-G2F2 BF Top Int.	6	Measured R1 1.491 R2 1.485 R3 1.487 R_Avg 1.488 Design			
A1-G2F2 BF Bot. Int.	7	-			
A1-G5F2 TF Bot. Ext.	8	Measured R1 0.996 R2 0.996 R3 0.993 R_Avg 0.995 Design			
A1-G5F2 Web Ext.	8	Measured R1 0.625 R2 0.626 R3 0.626 R_Avg 0.626 Design			
A1-G5F2 BF Top Ext.	7	Measured R1 1.484 R2 1.484 R3 1.488 R_Avg 1.485 Design			

Table A-133. Field Inspection Results for HOU-WS-05.

Location	Patina Rating	Thickness (inch)	Cl^- Conc. (ppm)	Field Condition	Tape Test
A1-G5F2 BF Bot. Ext.	7	-			

A.28.3.SEM/EDS Results: Exterior Web Girder

Element	Weight %	Atomic %
O K	35.75	61.27
Al K	13.98	14.20
Fe K	44.11	21.65
Ni K	6.16	2.88
Totals	100.00	



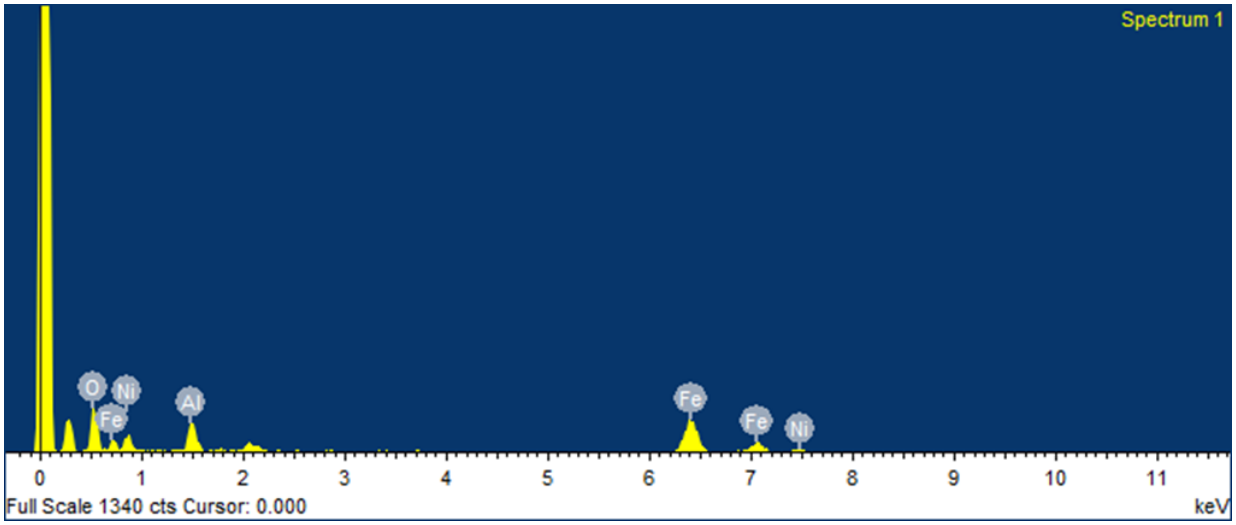
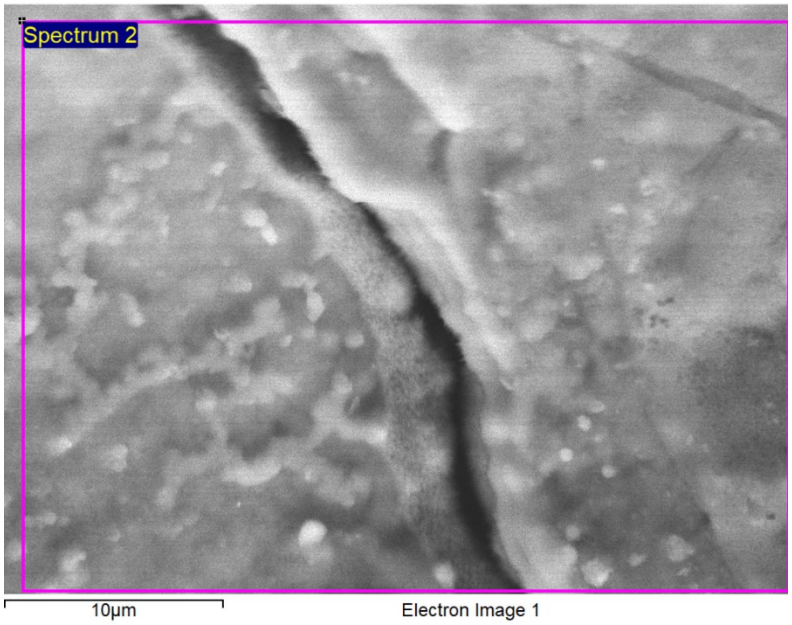


Figure A.465. SEM Image and EDS Spectrum of the Rust Collected from Exterior Web of the Girder.

Element	Weight %	Atomic %
O K	34.80	59.97
Al K	13.96	14.26
Si K	1.34	1.32
Fe K	42.26	20.86
Ni K	7.63	3.58
Totals	100.00	



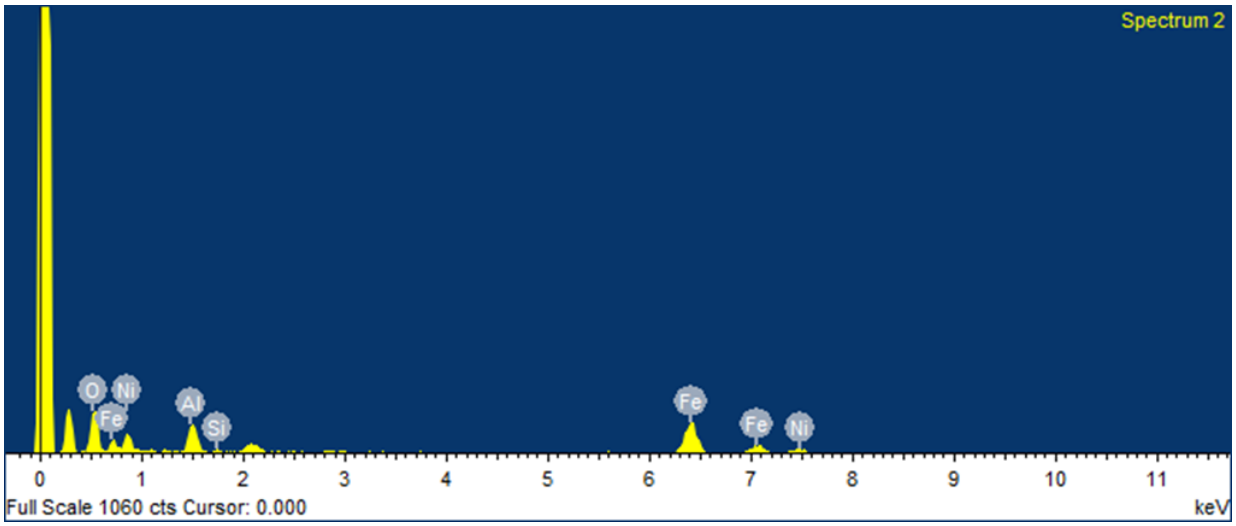
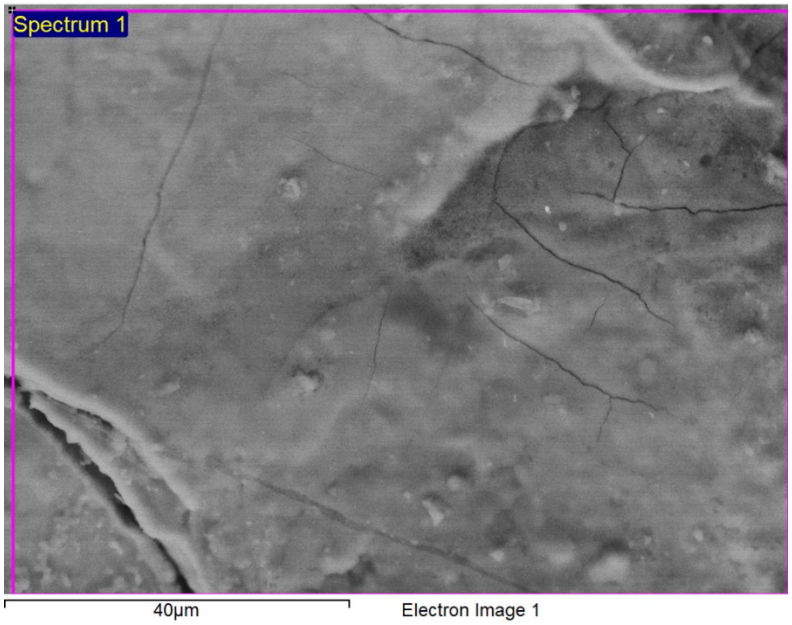


Figure A.466. SEM Image and EDS Spectrum of the Rust Collected from Exterior Web of the Girder.

Element	Weight %	Atomic %
O K	39.54	64.61
Al K	14.41	13.96
Fe K	40.31	18.87
Ni K	5.74	2.56
Totals	100.00	



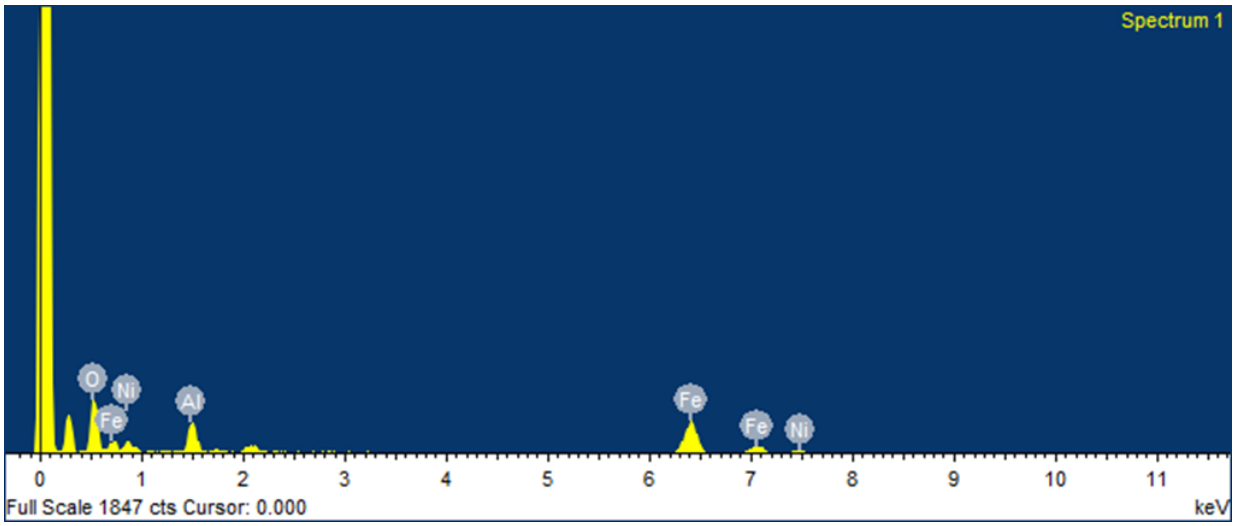
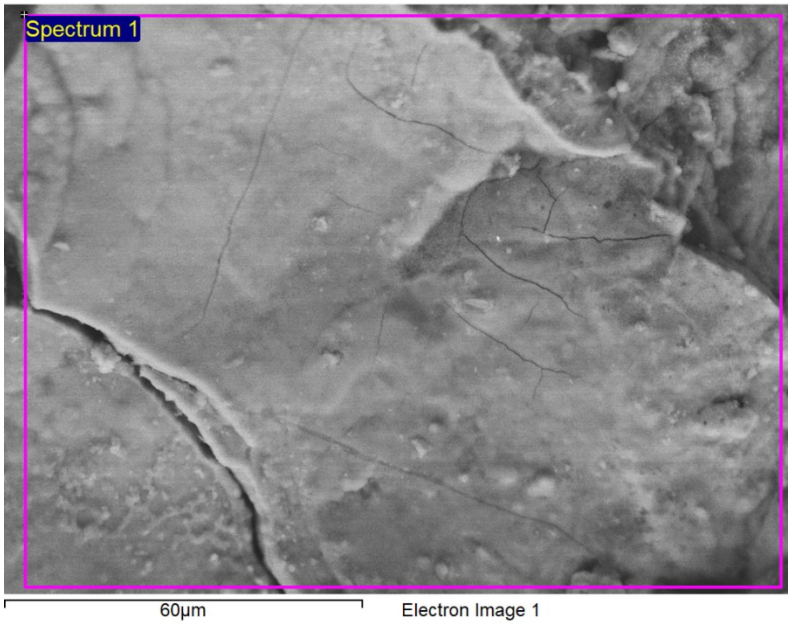


Figure A.467. SEM Image and EDS Spectrum of the Rust Collected from Exterior Web of the Girder.

Element	Weight %	Atomic %
O K	35.82	61.57
Al K	12.24	12.48
Si K	1.01	0.99
Fe K	46.15	22.72
Ni K	4.77	2.24
Totals	100.00	



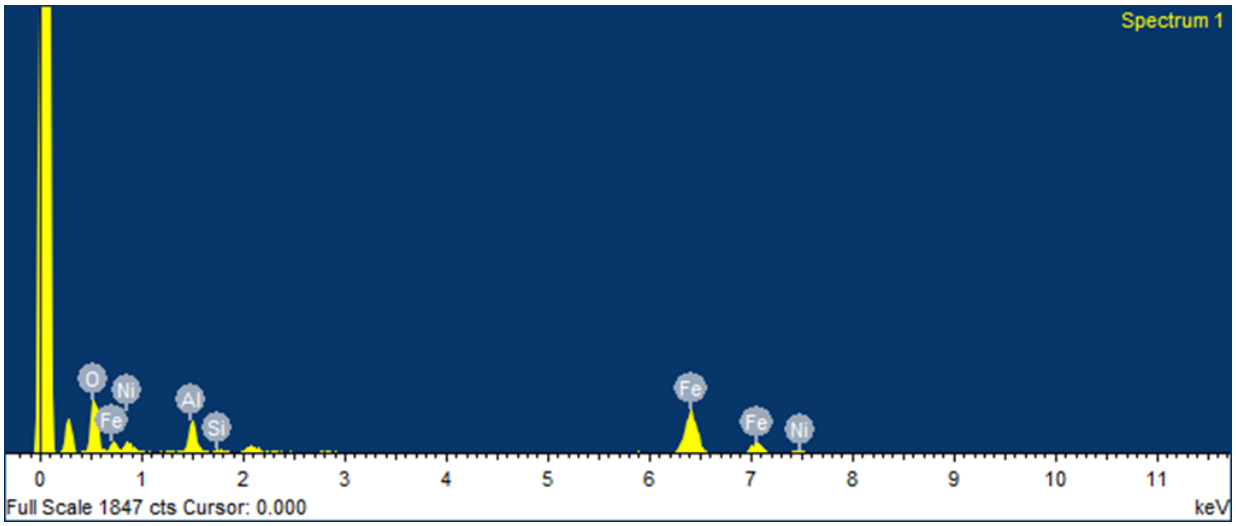
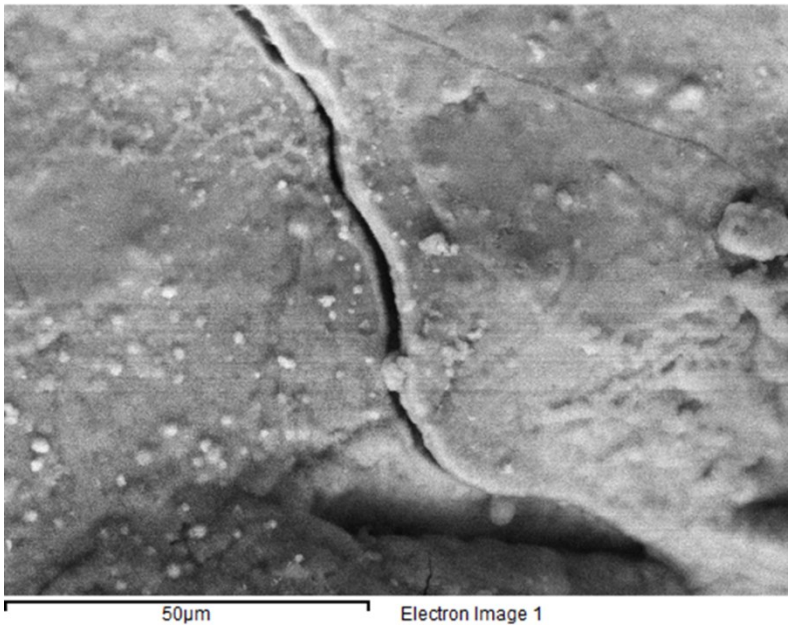


Figure A.468. SEM Image and EDS Spectrum of the Rust Collected from Exterior Web of the Girder.

Element	Weight %	Atomic %
O K	21.24	44.92
Al K	11.53	14.46
Fe K	62.89	38.11
Ni K	4.34	2.50
Totals	100.00	



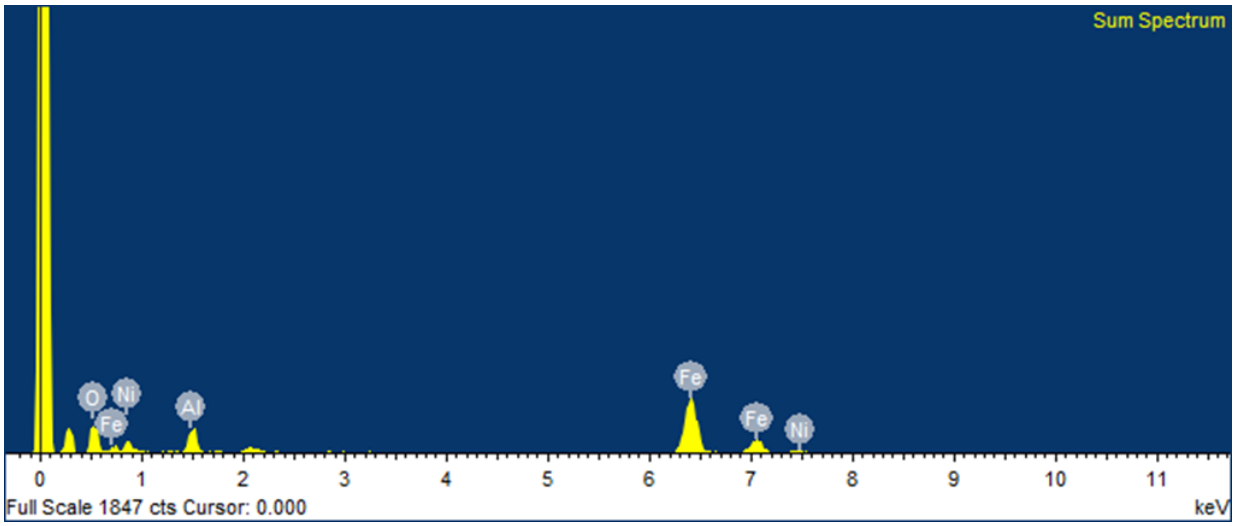


Figure A.469. SEM Image and EDS Spectrum of the Rust Collected from Exterior Web of the Girder.

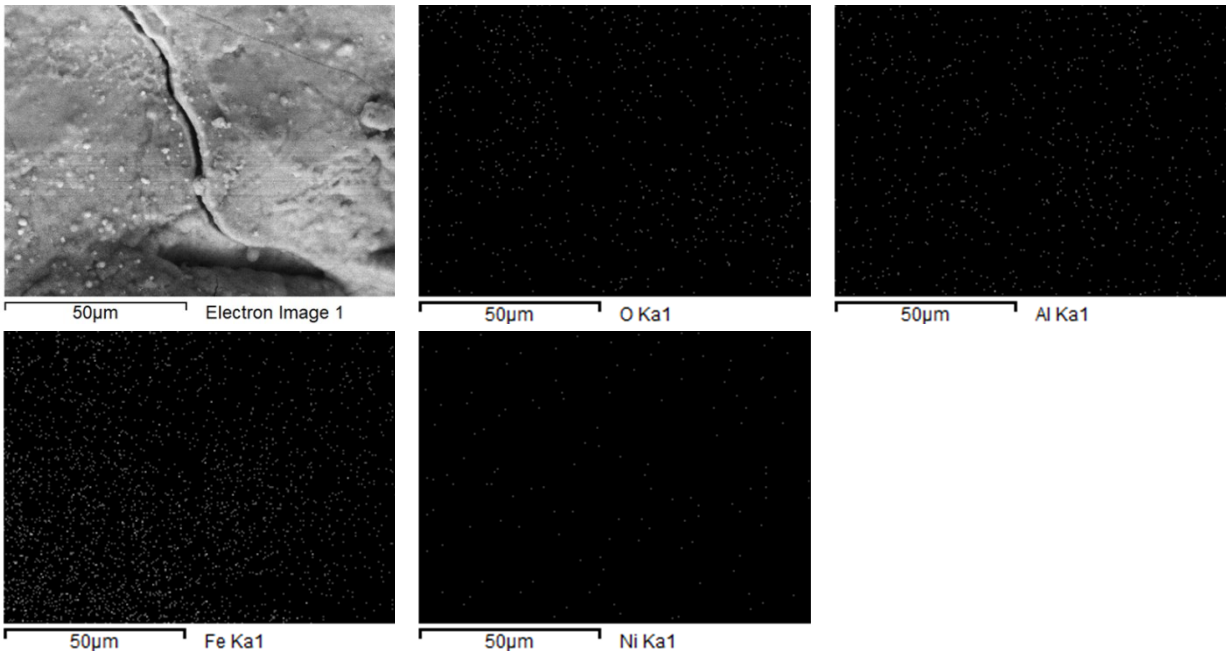
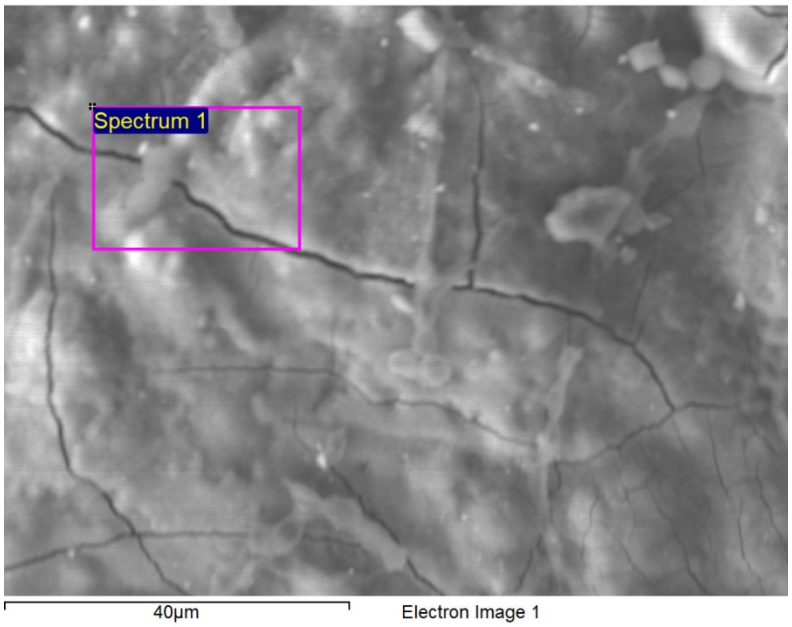


Figure A.470. EDS Elemental Mapping of Rust Collected from Exterior Web.

A.28.4.SEM/EDS Results: Interior Web

Element	Weight %	Atomic %
O K	49.20	76.50
Al K	0.34	0.31
Si K	0.17	0.15
S K	0.85	0.66
Cl K	1.18	0.83
Ca K	0.25	0.16
Mn K	0.19	0.09
Fe K	47.82	21.30
Totals	100.00	



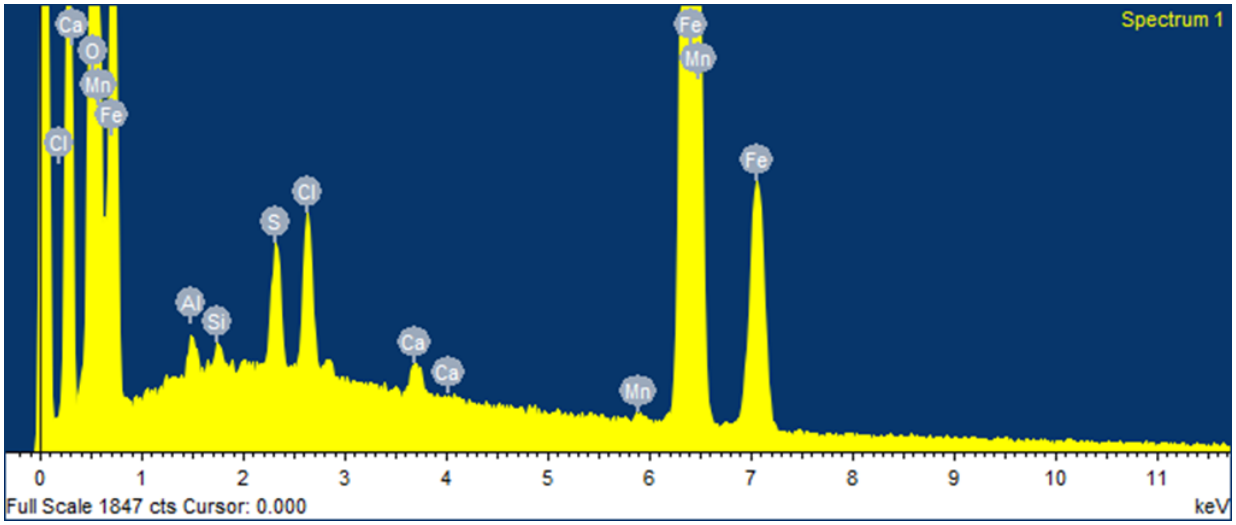
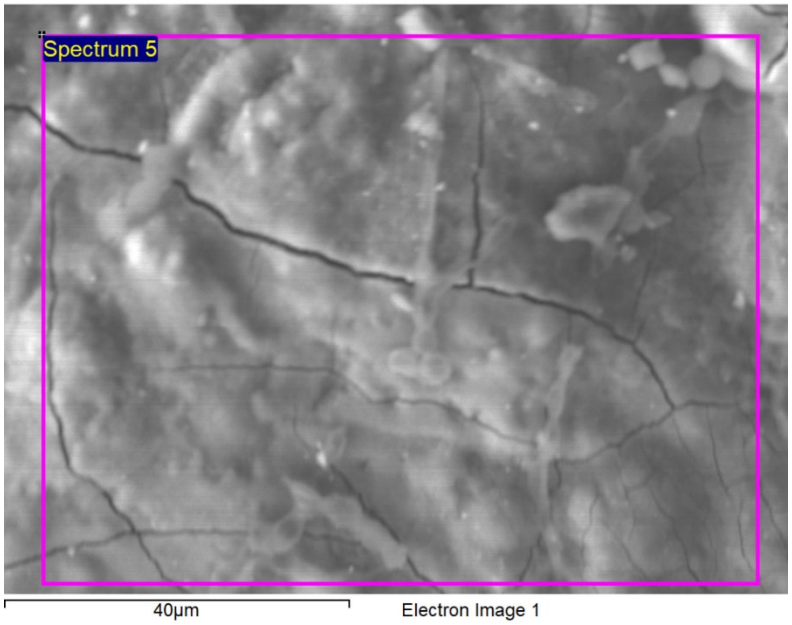


Figure A.471. SEM Image and EDS Spectrum of the Rust Collected from Interior Web of the Girder.

Element	Weight %	Atomic %
O K	37.91	67.01
Al K	0.51	0.53
Si K	1.20	1.20
S K	0.84	0.74
Cl K	1.02	0.81
Ca K	0.37	0.26
Mn K	0.31	0.16
Fe K	57.84	29.29
Totals	100.00	



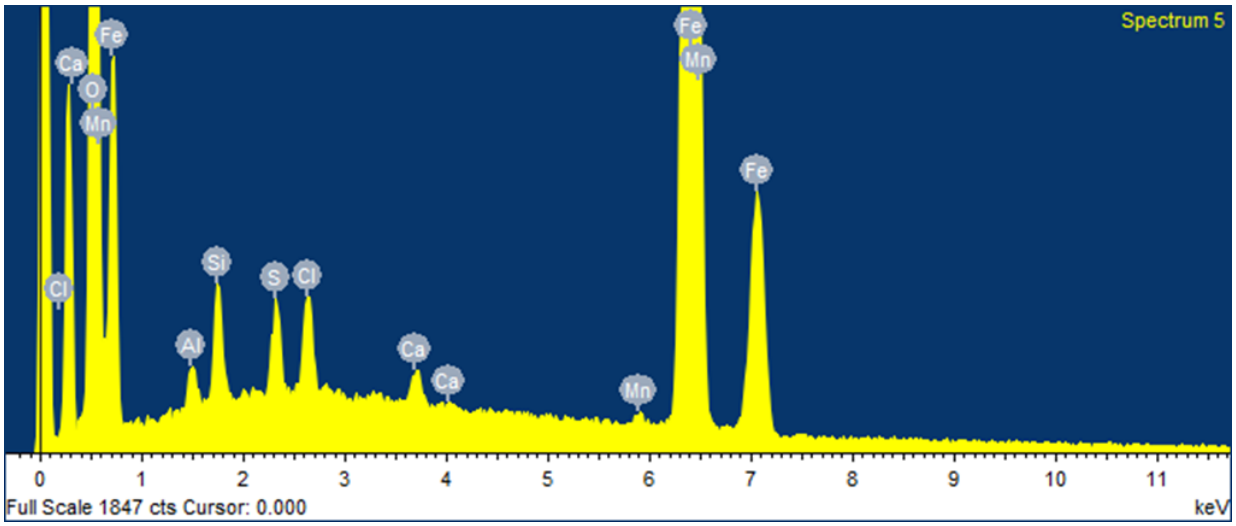
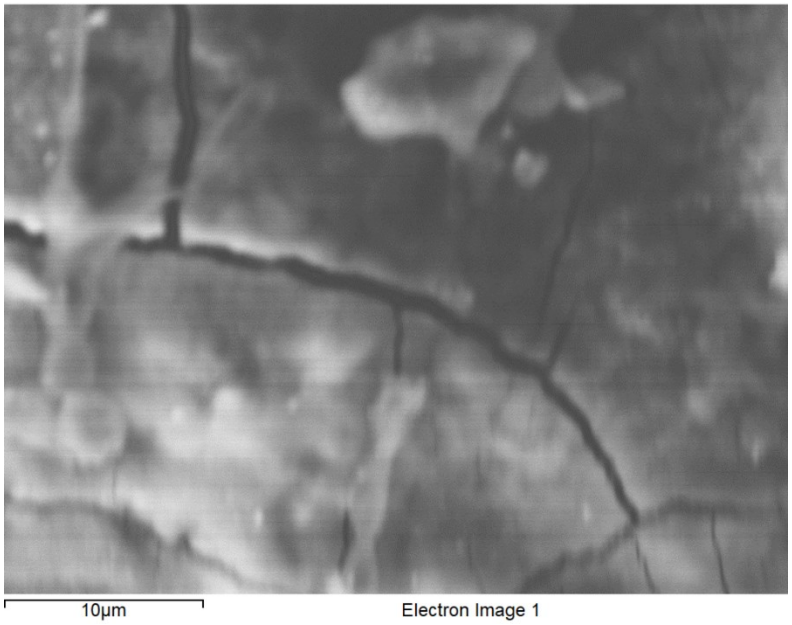


Figure A.472. SEM Image and EDS Spectrum of the Rust Collected from Interior Web of the Girder.

Element	Weight %	Atomic %
O K	32.09	60.26
Al K	0.70	0.77
Si K	3.82	4.09
S K	0.91	0.85
Cl K	0.87	0.74
Ca K	0.65	0.49
Fe K	60.97	32.81
Totals	100.00	



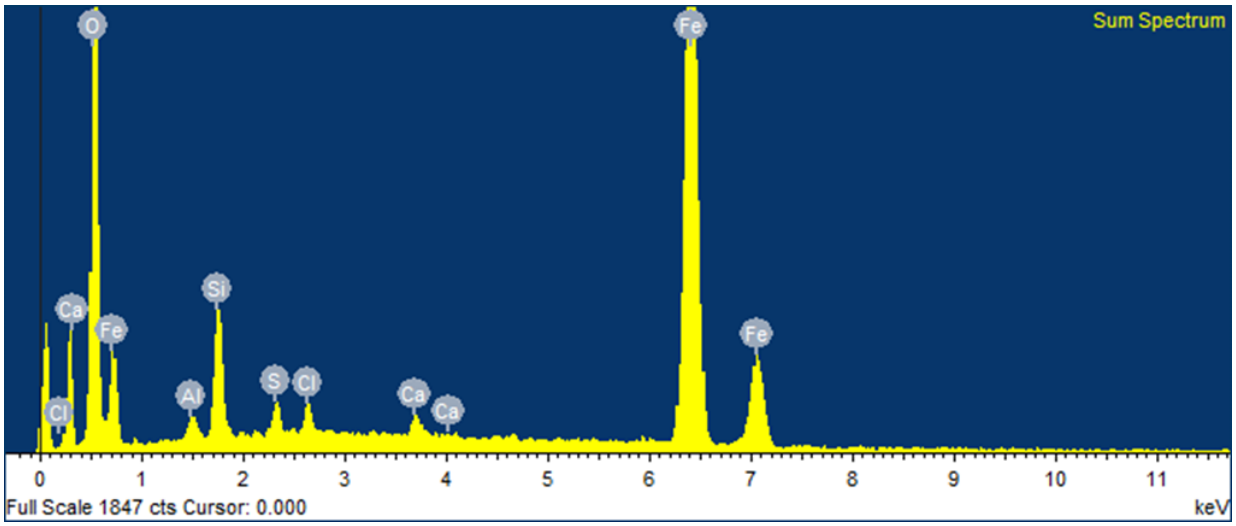


Figure A.473. SEM Image and EDS Spectrum of the Rust Collected from Interior Web of the Girder.

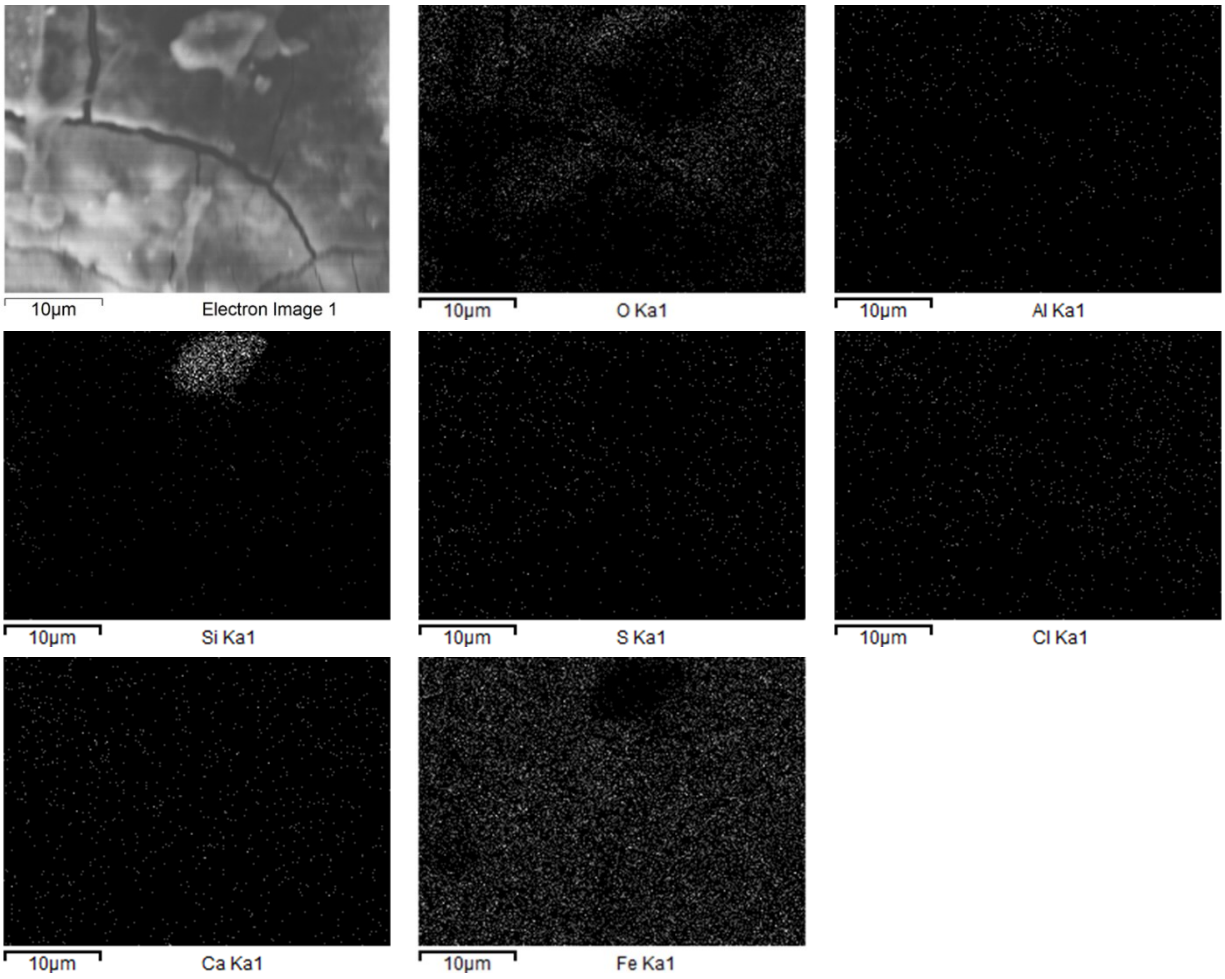


Figure A.474. EDS Elemental Mapping of Rust Collected from Interior Web.

A.28.5.XPS Results: Exterior Web Girder

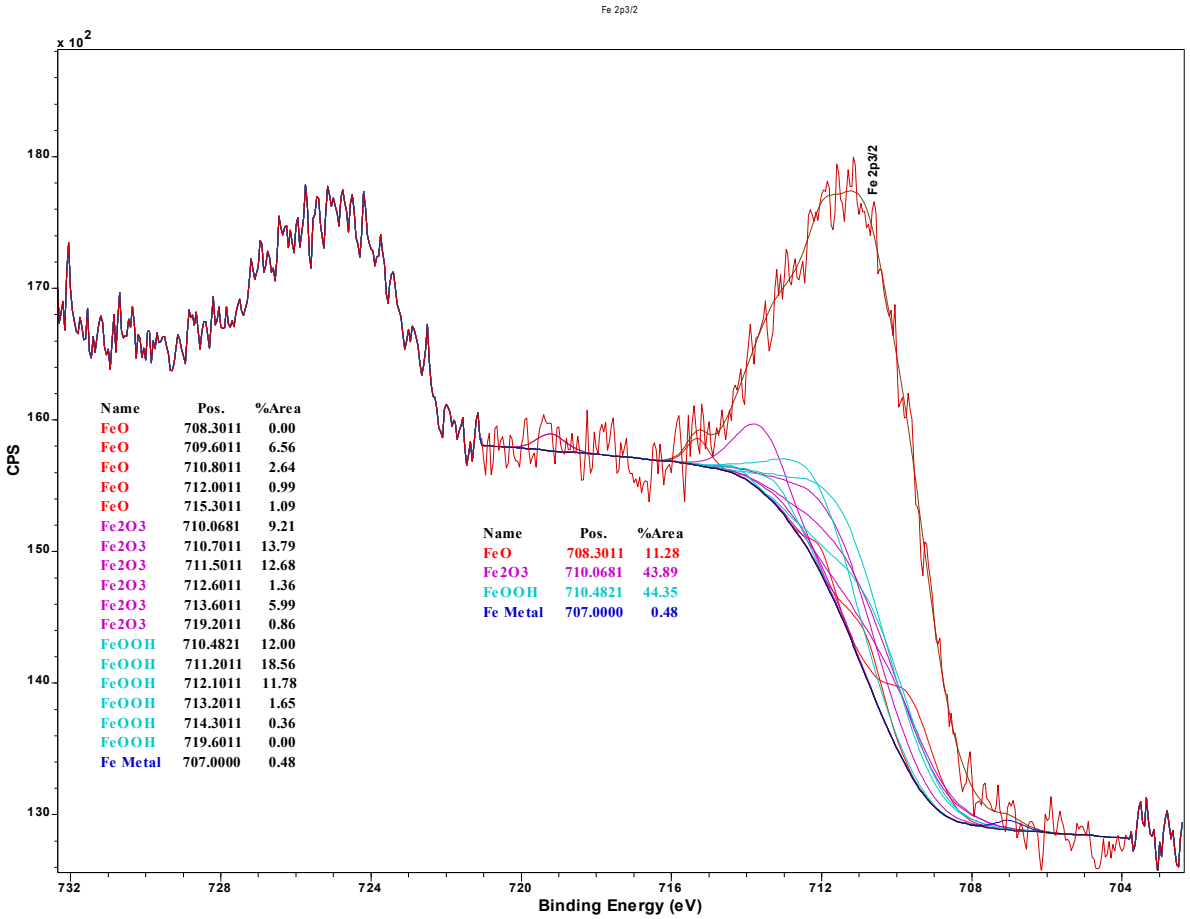


Figure A.475. XPS Spectrum of the Rust Collected from Exterior Web of the Girder.

A.28.6.XPS Results: Interior Web Girder

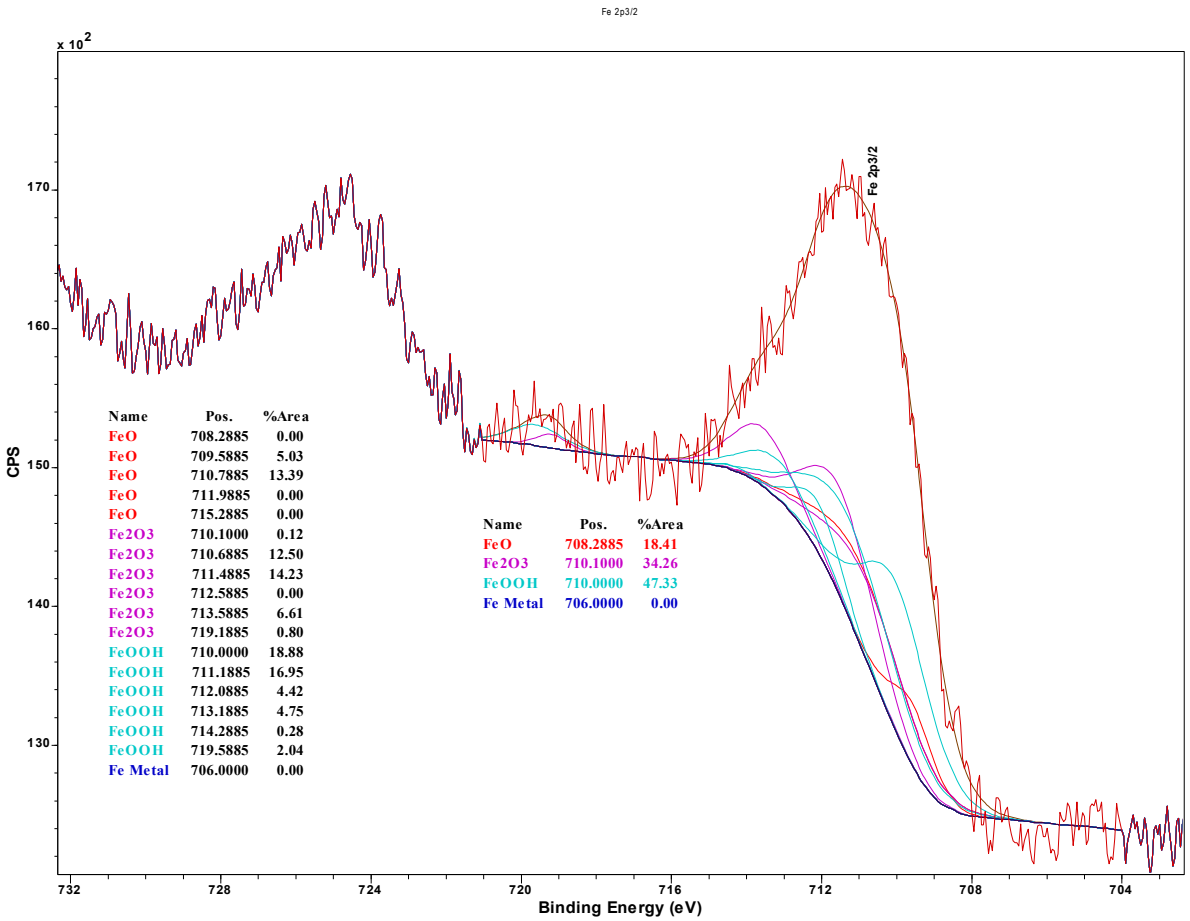


Figure A.476. XPS Spectrum of the Rust Collected from Interior Web of the Girder.

A.28.7.XRD Result: Exterior and Interior Girder

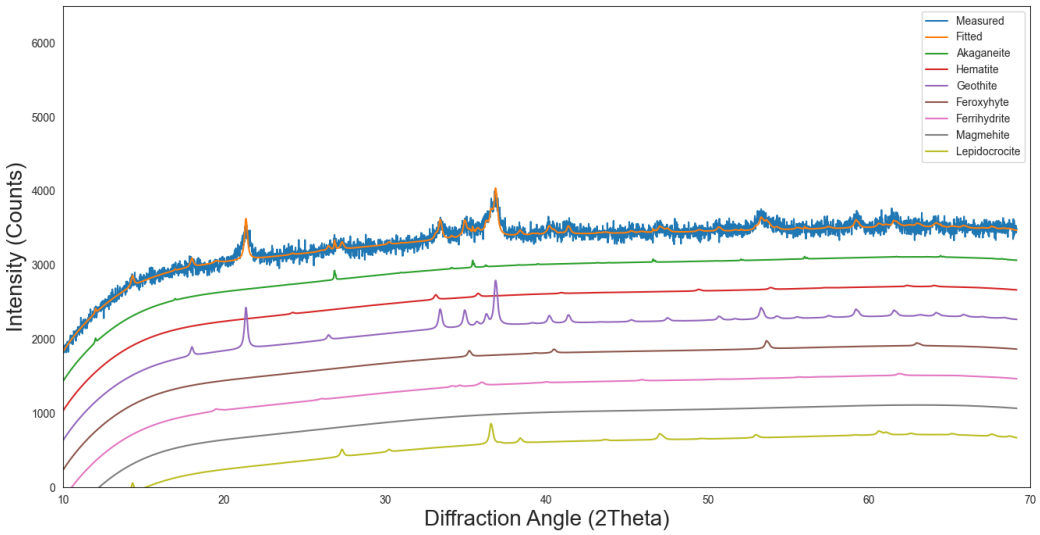


Figure A.477. XRD Pattern of Powdered Rust Collected from Exterior Web of the Girder.

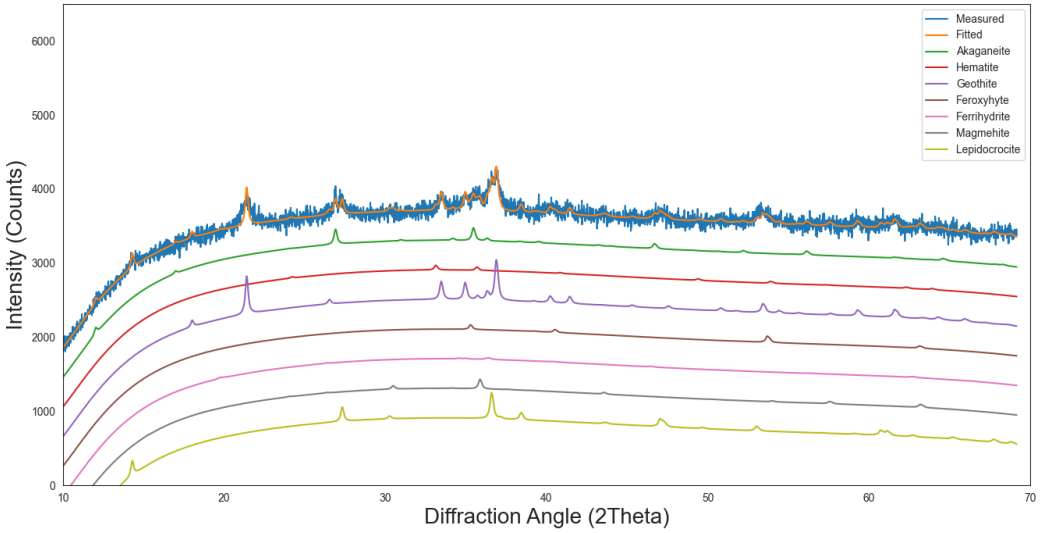


Figure A.478. XRD Pattern of Powdered Rust Collected from Interior Web of the Girder.

A.28.8. Particle Size Analysis: Tape Adhesion Results

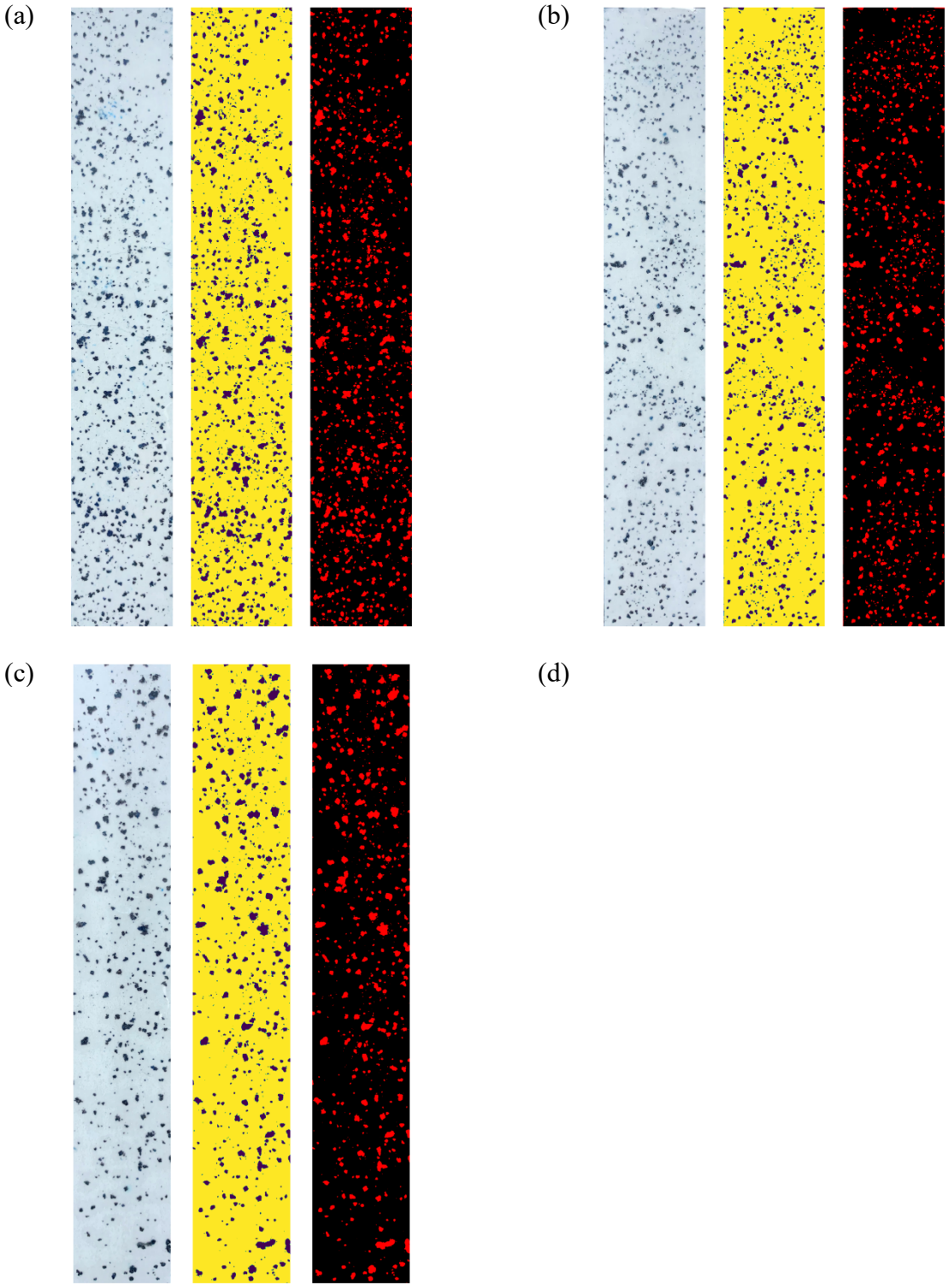


Figure A.479. Particle Size Analysis Results at A1G1F1 (a) Top Flange Bottom, (b) Web, (c) Bottom Flange Bottom (d) Stiffener.

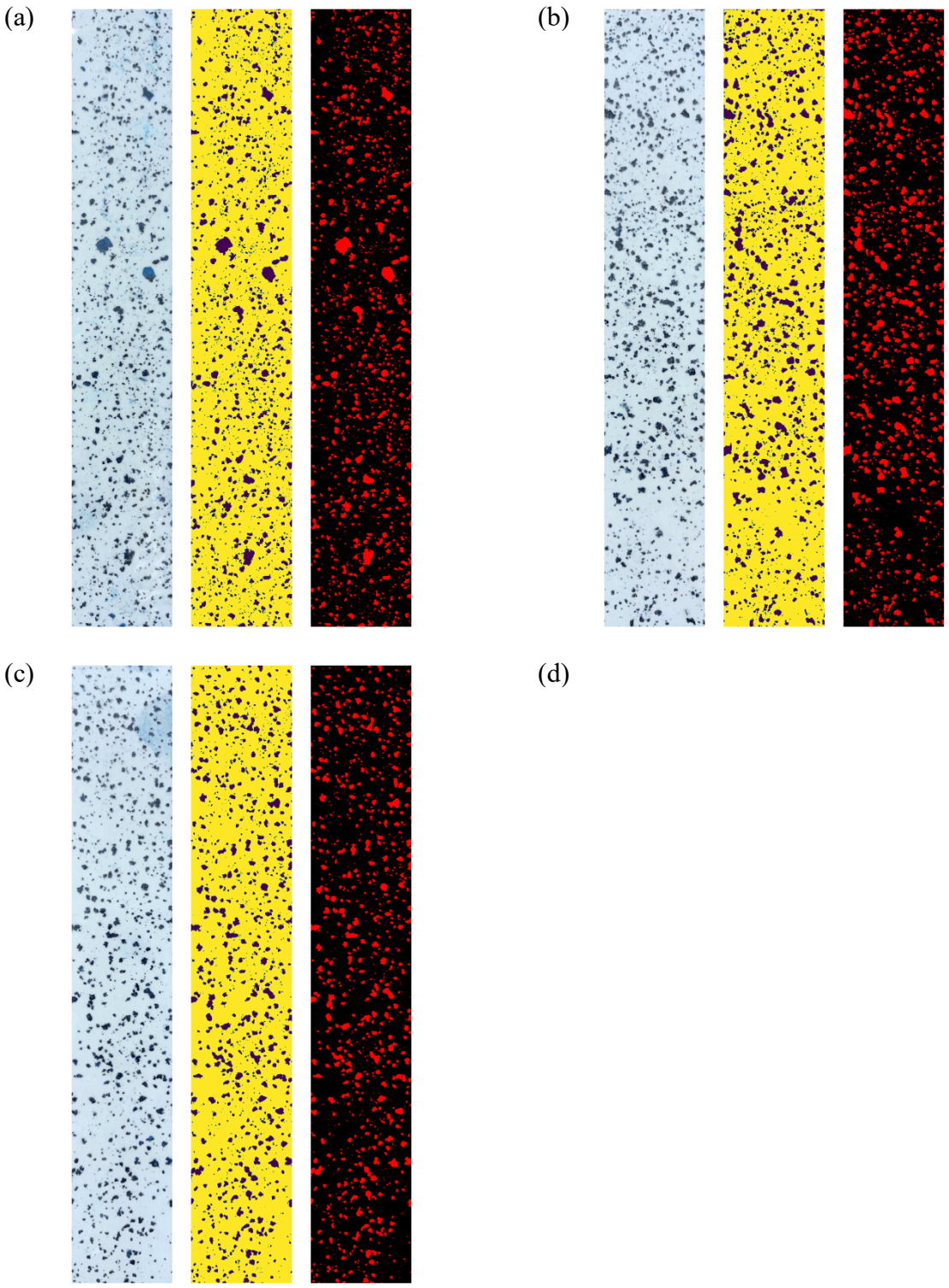


Figure A.480. Particle Size Analysis Results at A1G2F2 (a) Top Flange Bottom, (b) Web, (c) Bottom Flange Bottom (d) Stiffener.

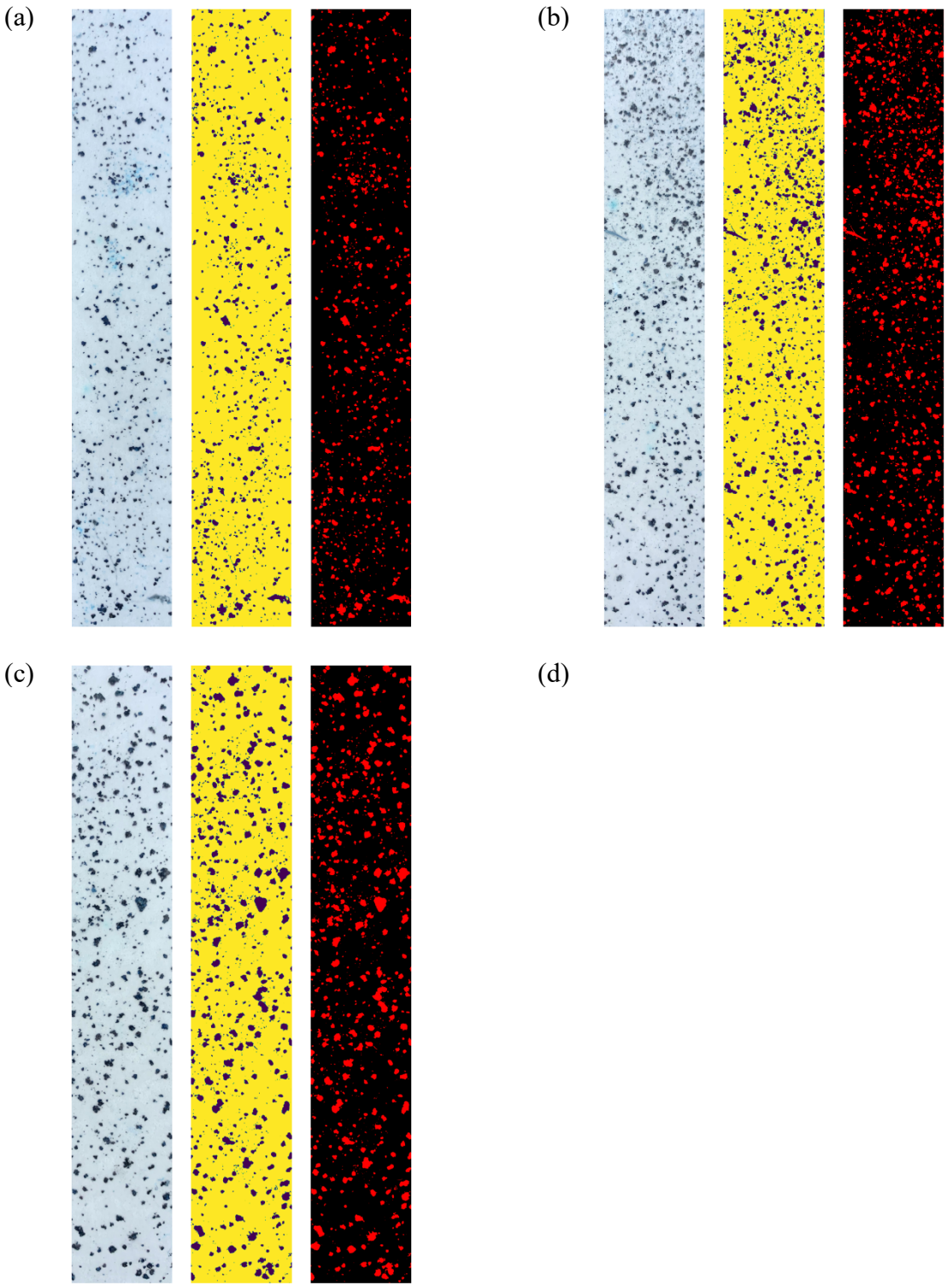


Figure A.481. Particle Size Analysis Results at A1G3F1 (a) Top Flange Bottom, (b) Web, (c) Bottom Flange Bottom (d) Stiffener.

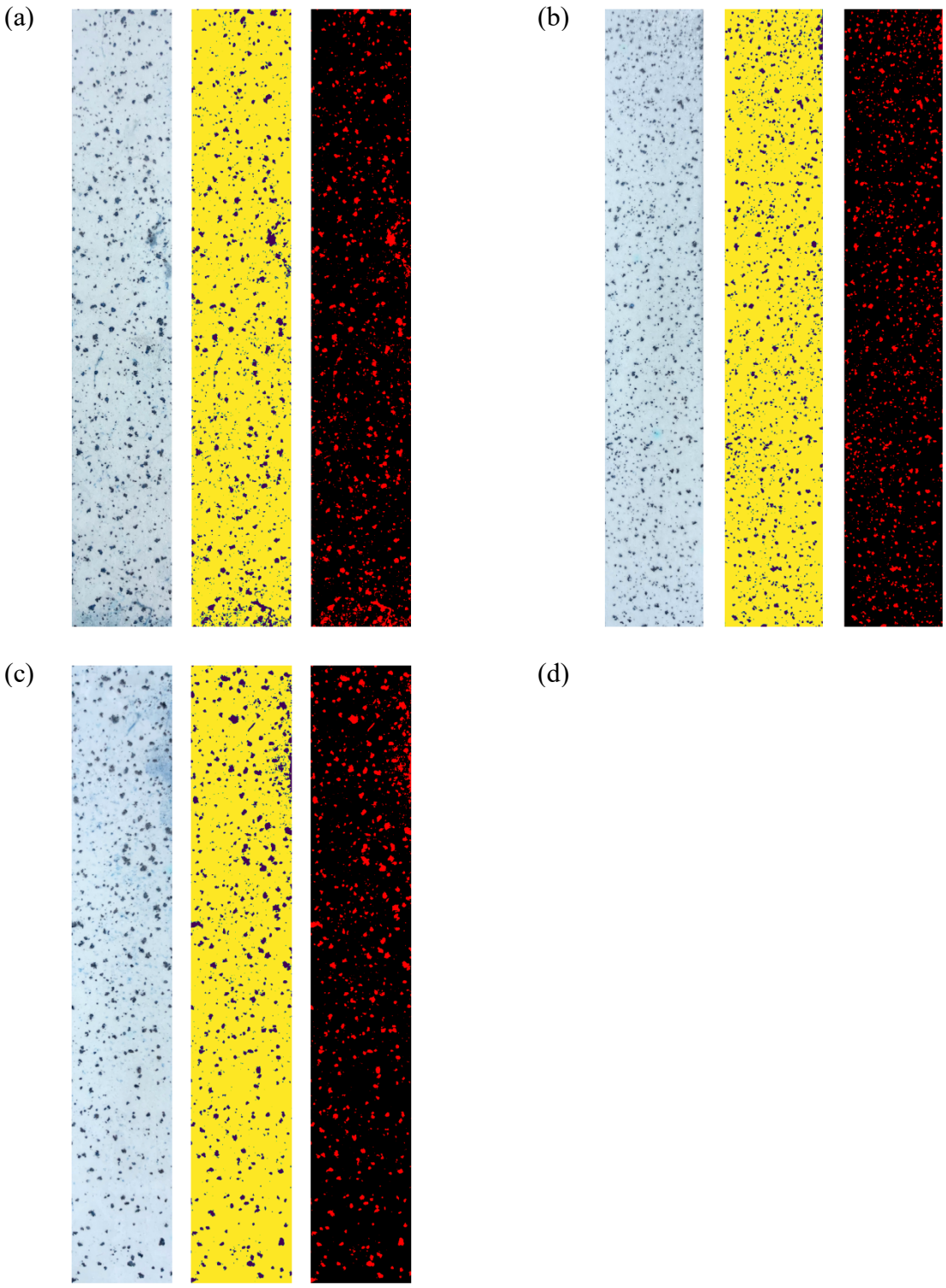


Figure A.482. Particle Size Analysis Results at A1G5F2 (a) Top Flange Bottom, (b) Web, (c) Bottom Flange Bottom (d) Stiffener.

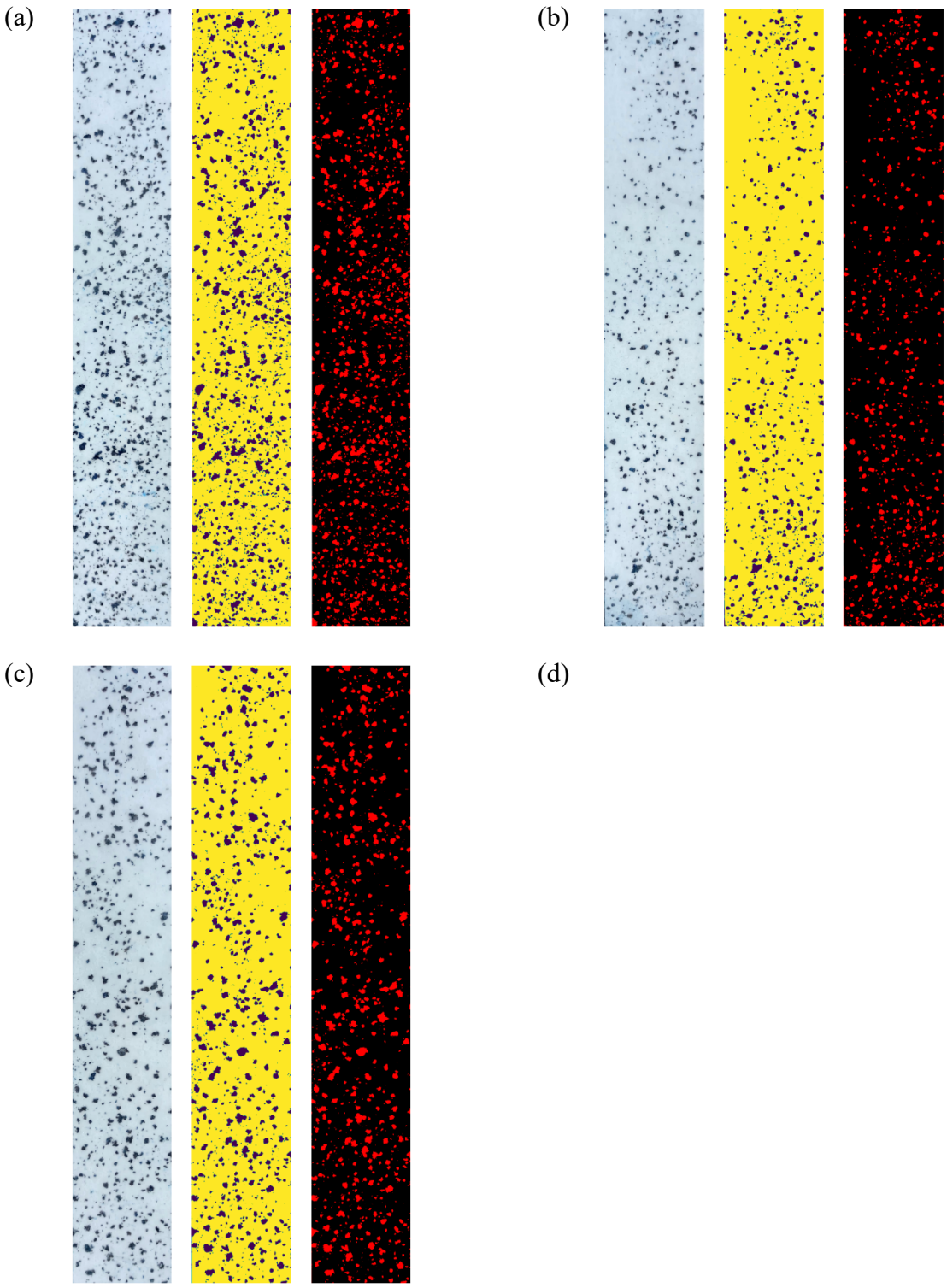


Figure A.483. Particle Size Analysis Results at A1G1F1 (77002) (a) Top Flange Bottom, (b) Web, (c) Bottom Flange Bottom (d) Stiffener.

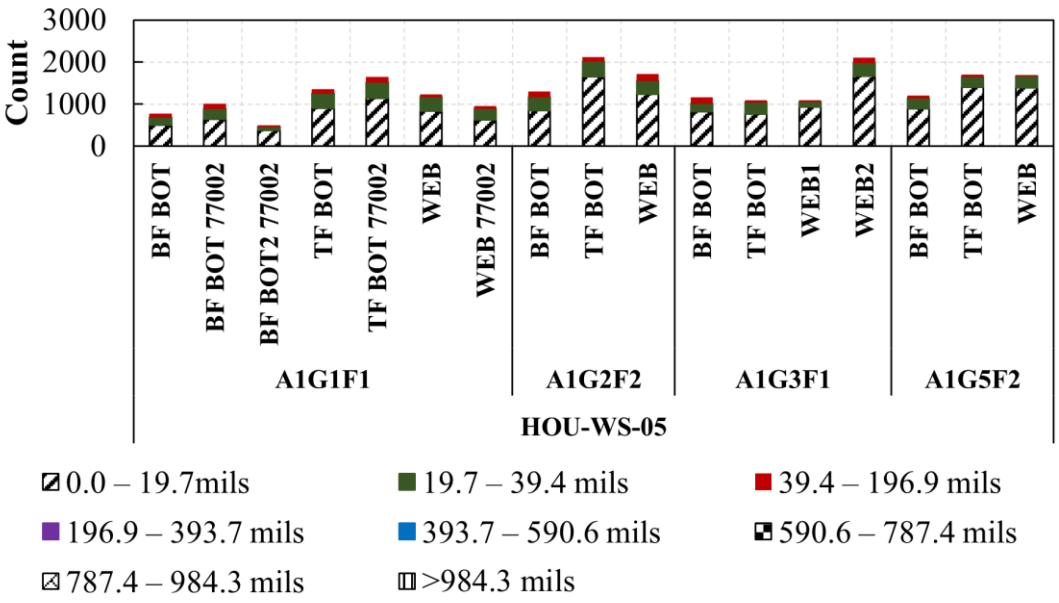


Figure A.484. Particle Size Analysis Showing Different Locations Examined.

A.29. HOU-WS-05*

- HB&T RR
- Bridge ID 121020B40177002, Coordinates (29.81554, -95.31726), Harris County
- Continuous weathering steel plate girder
- Built 1989
- Girder inspection carried on end abutment, and measurements are taken on girder within four feet from the abutment or bent.
- No visual inspection on deck
- Location for Testing: A1-G1F1



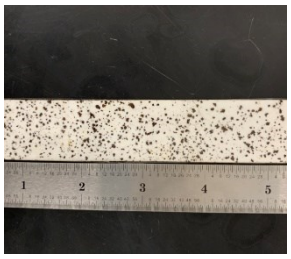
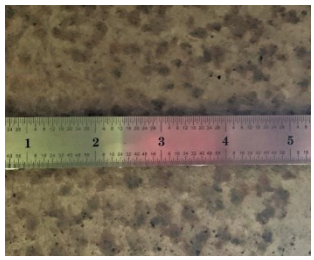
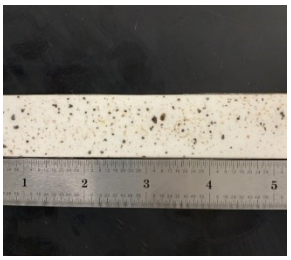
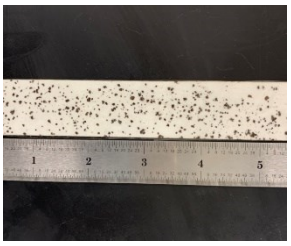
Figure A.485. Typical Picture of HOU-WS-05*

A.29.1. Observed Condition

Delaminated areas of the patina are visible on the bottom face of the top flange. The web has a uniform patina formation with a patina rating of 7. The interior girders have significant poultice corrosion on the top face of the bottom flange due to the accumulation of dirt Index 5 whereas exterior girders have less accumulation of dirt.

A.29.2.Field Inspection Results

Table A-134. Field Inspection Results for HOU-WS-05*.

Location	Patina Rating	Thickness (inch)	Cl^- Conc. (ppm)	Field Condition	Tape Test
A1-G1F1 TF Bot. Ext.	7	Measured R1 1.039 R2 1.027 R3 1.031 R_Avg 1.032 Design			
A1-G1F1 Web Ext.	8	Measured R1 0.647 R2 0.643 R3 0.648 R_Avg 0.646 Design			
A1-G1F1 BF Top Ext.	5	Measured R1 1.498 R2 1.501 R3 1.497 R_Avg 1.499 Design			
A1-G1F1 BF Bot. Ext.	7	-			

A.30. HOU-WS-06

- Bellaire Blvd over IH 69
- Bridge ID 121020002713240, Coordinates (29.70436, -95.51306), Harris County
- Continuous weathering steel plate girder
- Built 1992
- girder inspection carried on end abutment, and measurements are taken on girder within four feet from the abutment or bent.
- No visual inspection on deck
- Location for Testing: A1-G1F1, A1-G3F2, A1-G4F1, A1-G8F2, A1-G9F1, A1-G12F2



Figure A.486. Typical Picture of AUS-WS-06.

A.30.1. Observed Condition

Delaminated areas of the patina are visible on the bottom face of the top flange. The web has a uniform patina formation with a patina rating of 7. The interior girders have significant poultice corrosion on the top face of the bottom flange due to the accumulation of dirt Index 5 to 4 whereas exterior girders have less accumulation of dirt.

A.30.2.Field Testing and Tape Adhesion Results

Table A-135. Field Inspection Results for HOU-WS-06.

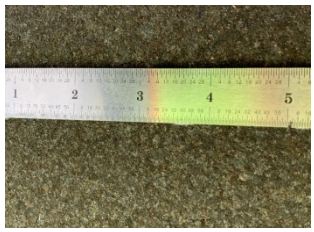
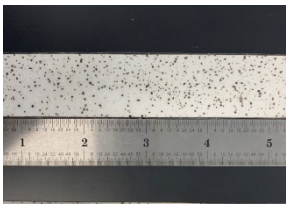
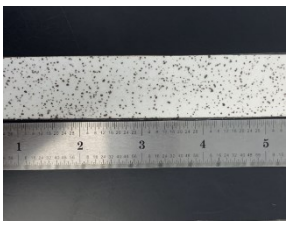
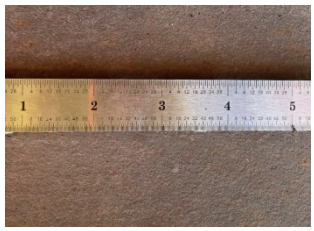
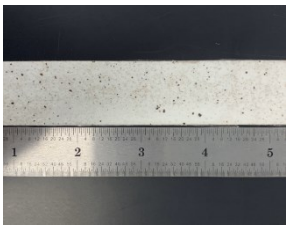
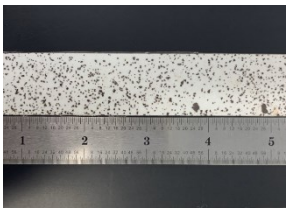
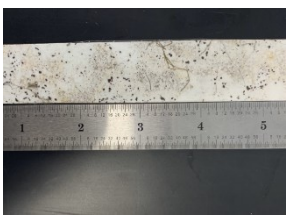
Location	Patina Rating	Thickness (inch)	Cl^- Conc. (ppm)	Field Condition	Tape Test
A1-G1F1 TF Bot. Ext.	7	Measured R1 1.040 R2 1.040 R3 1.038 R_Avg 1.039 Design 1.000			
A1-G1F1 Web Ext.	7	Measured R1 0.540 R2 0.538 R3 0.538 R_Avg 0.539 Design 0.500			
A1-G1F1 BF Top Ext.	4-	Measured R1 1.000 R2 0.999 R3 0.997 R_Avg 0.999 Design 1.000			
A1-G1F1 BF Bot. Ext.	6	-			
A1-G3F2 TF Bot. Int.	5	Measured R1 1.006 R2 1.006 R3 1.009 R_Avg 1.007 Design 1.000			

Table A-136. Field Inspection Results for HOU-WS-06.

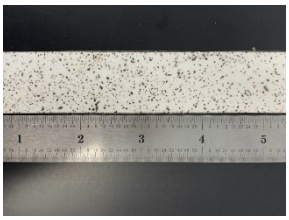
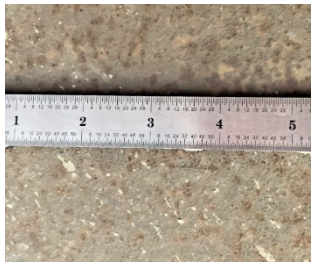
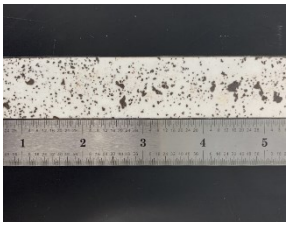
Location	Patina Rating	Thickness (inch)	Cl^- Conc. (ppm)	Field Condition	Tape Test
A1-G3F2 Web Int.	7	Measured R1 0.523 R2 0.532 R3 0.534 R_Avg 0.530 Design 0.500			
A1-G3F2 BF Top Int.	4	Measured R1 1.016 R2 1.015 R3 1.016 R_Avg 1.016 Design 1.000			
A1-G3F2 BF Bot. Int.	5	-			
A1-G4F1 TF Bot. Int.	4	Measured R1 1.017 R2 1.019 R3 1.019 R_Avg 1.018 Design 1.000			
A1-G4F1 Web Int.	7	Measured R1 0.537 R2 0.538 R3 0.537 R_Avg 0.537 Design 0.500			

Table A-137. Field Inspection Results for HOU-WS-06.

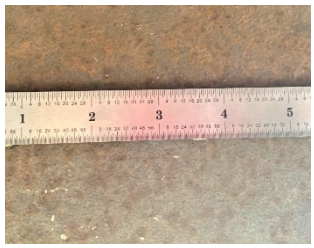
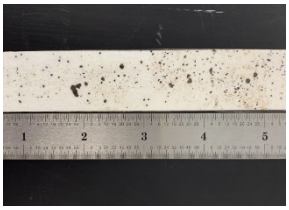
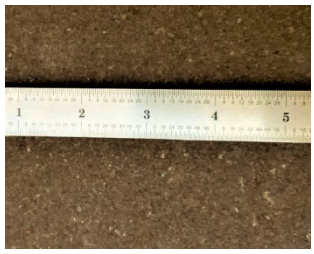
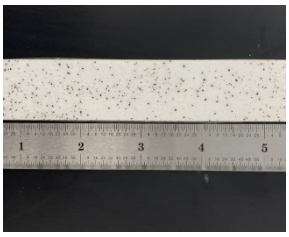
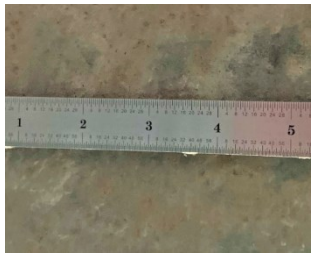
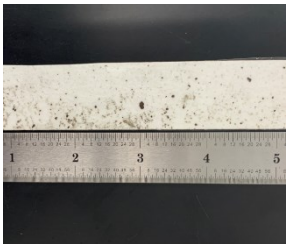
Location	Patina Rating	Thickness (inch)	Cl^- Conc. (ppm)	Field Condition	Tape Test
A1-G4F1 BF Top Int.	4	Measured R1 1.019 R2 1.019 R3 1.020 R_Avg 1.020 Design 1.000			
A1-G4F1 BF Bot. Int.	4	-			
A1-G8F2 TF Bot. Int.	5	Measured R1 1.004 R2 1.005 R3 1.002 R_Avg 1.004 Design 1.000			
A1-G8F2 Web Int.	7	Measured R1 0.499 R2 0.501 R3 0.501 R_Avg 0.500 Design 0.500			
A1-G8F2 BF Top Int.	4	Measured R1 0.997 R2 0.999 R3 0.990 R_Avg 0.995 Design 1.000			

Table A-138. Field Inspection Results for HOU-WS-06.

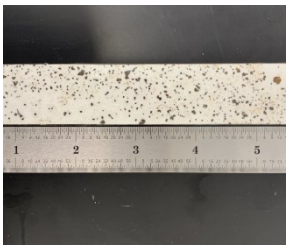
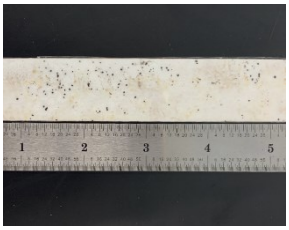
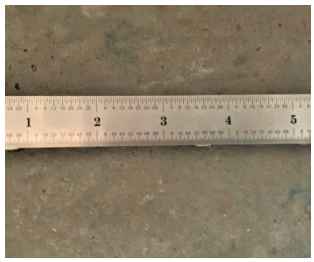
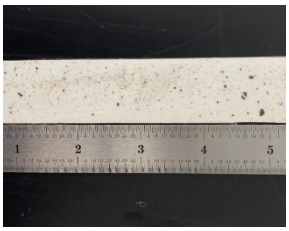
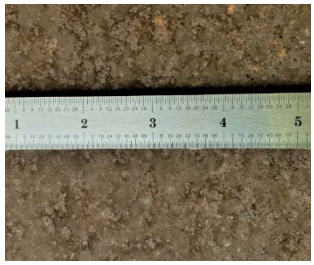
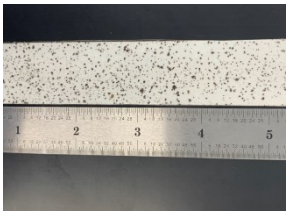
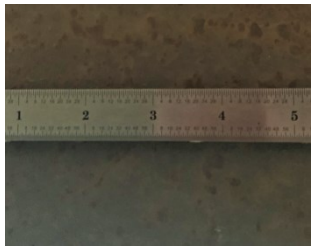
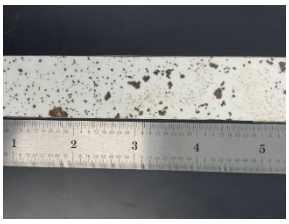
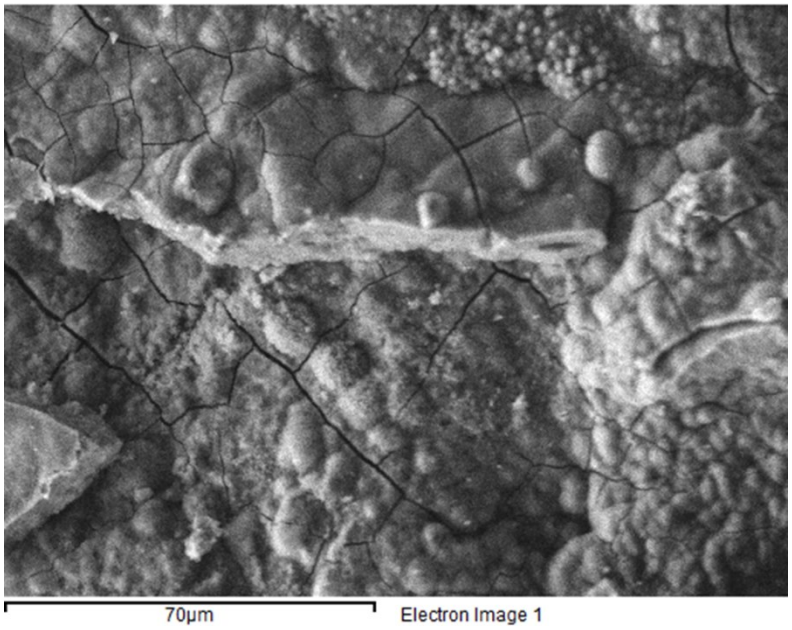
Location	Patina Rating	Thickness (inch)	Cl^- Conc. (ppm)	Field Condition	Tape Test
A1-G8F2 BF Bot. Int.	5	-			
A1-G9F1 TF Bot. Int.	4	Measured R1 0.999 R2 0.997 R3 0.998 R_Avg 0.998 Design 1.000			
A1-G9F1 Web Int.	5	Measured R1 0.504 R2 0.504 R3 0.506 R_Avg 0.505 Design 0.500			
A1-G9F1 BF Top Int.	4	Measured R1 1.003 R2 1.001 R3 0.999 R_Avg 1.001 Design 1.000			
A1-G9F1 BF Bot. Int.	4	-			

Table A-139. Field Inspection Results for HOU-WS-06.

Location	Patina Rating	Thickness (inch)	Cl^- Conc. (ppm)	Field Condition	Tape Test
A1-G12F2 TF Bot. Ext.	6	Measured R1 1.000 R2 1.001 R3 1.002 R_Avg 1.001 Design 1.000			
A1-G12F2 Web Ext.	7	Measured R1 0.505 R2 0.504 R3 0.505 R_Avg 0.505 Design 0.500			
A1-G12F2 BF Top Ext.	4	Measured R1 0.994 R2 0.996 R3 0.998 R_Avg 0.996 Design 1.000			
A1-G12F2 BF Bot. Ext.	4	-			

A.30.3.SEM/EDS Results: Exterior Web Girder

Element	Weight %	Atomic %
O K	44.76	73.19
Al K	0.74	0.72
S K	1.42	1.16
Cl K	0.21	0.15
Mn K	0.47	0.22
Fe K	52.41	24.55
Totals	100.00	



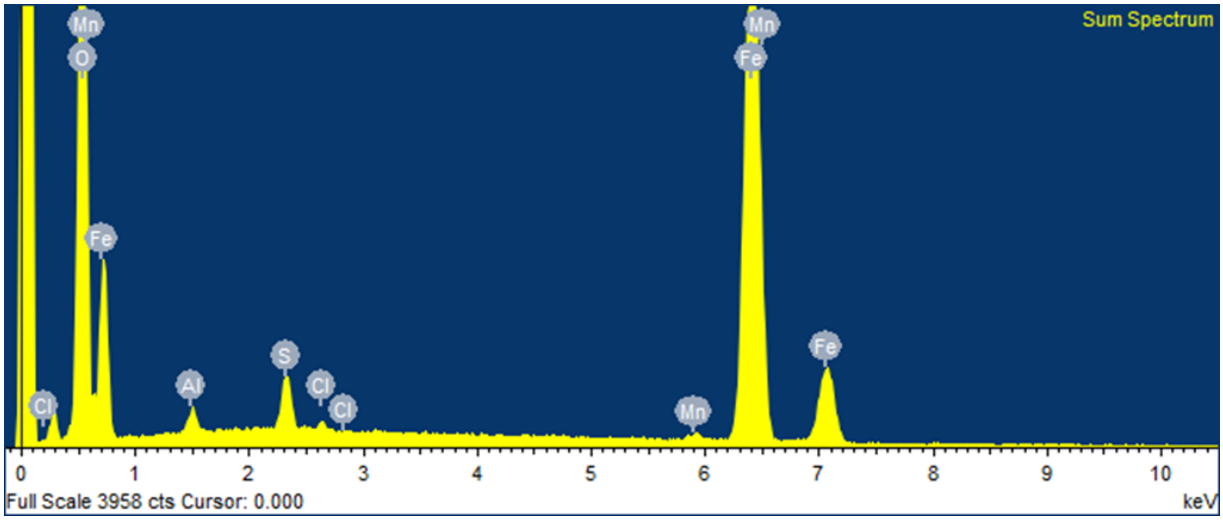


Figure A.487. SEM Image and EDS Spectrum of the Rust Collected from Exterior Web of the Girder.

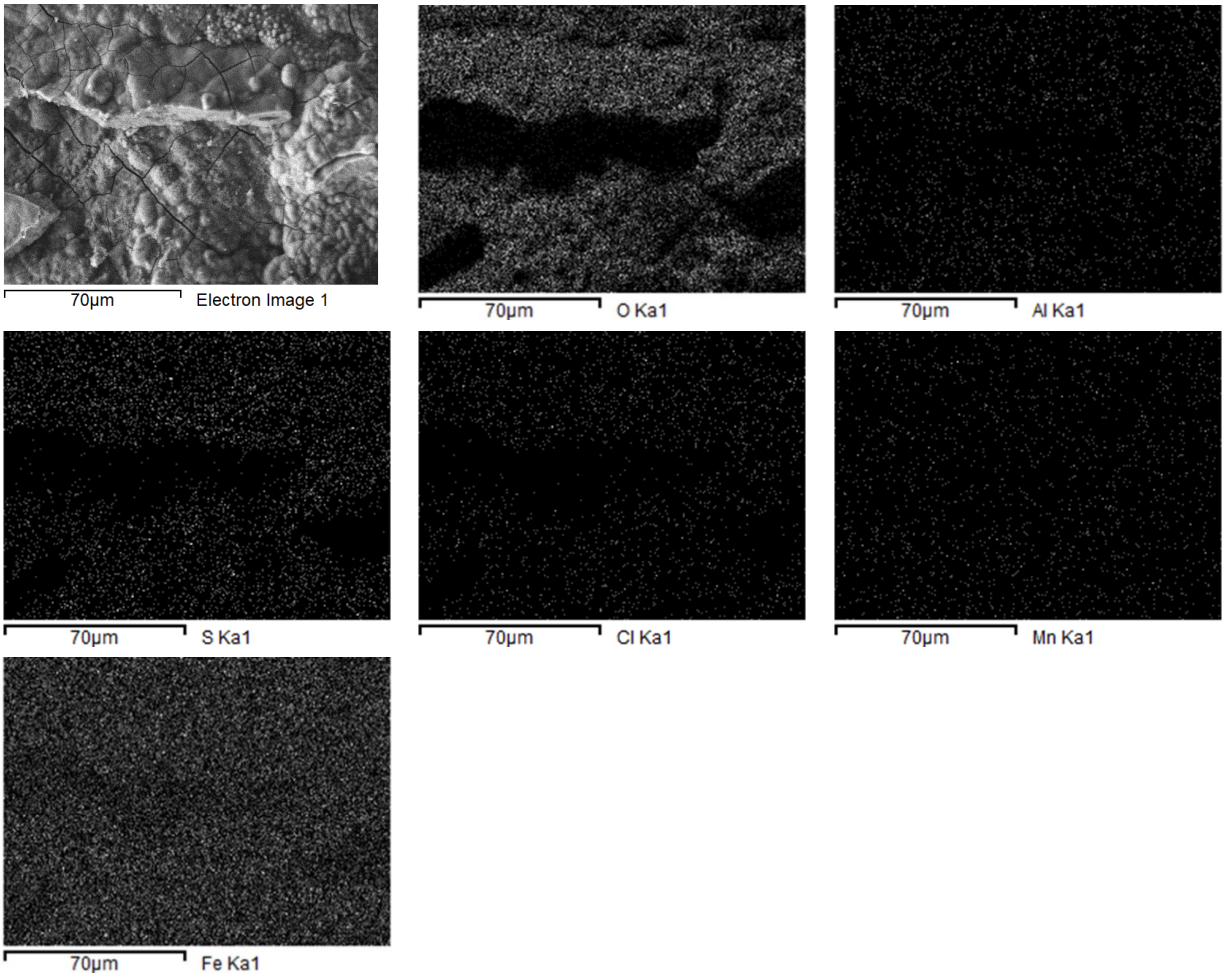
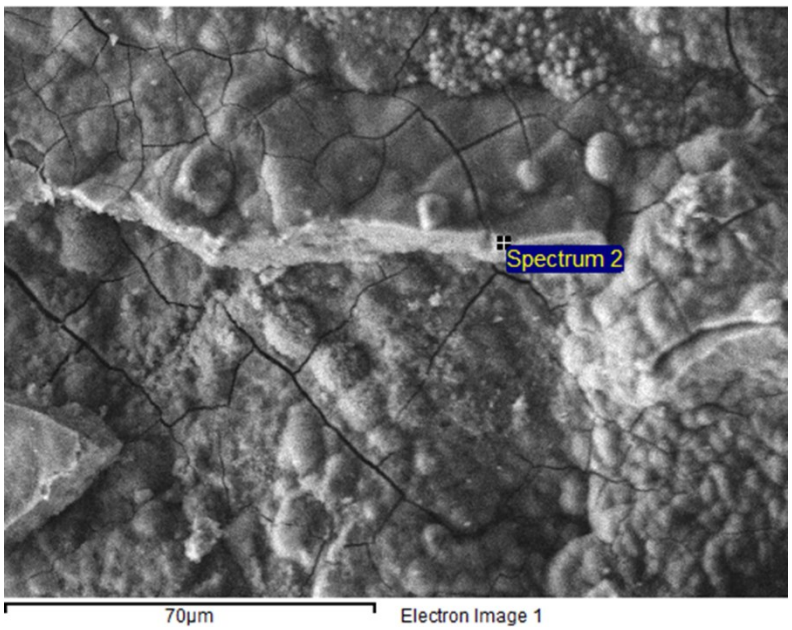


Figure A.488. EDS Elemental Mapping of Rust Collected from Exterior Web.

Element	Weight %	Atomic %
O K	52.69	78.80
Al K	0.96	0.85
S K	1.28	0.95
Cl K	0.36	0.24
Mn K	0.55	0.24
Fe K	44.16	18.92
Totals	100.00	



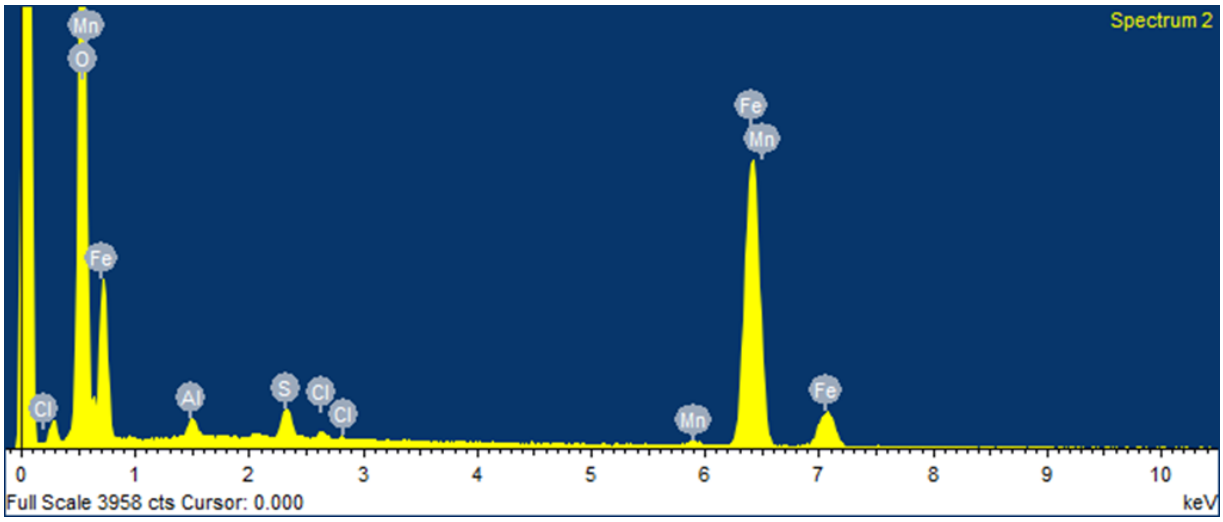
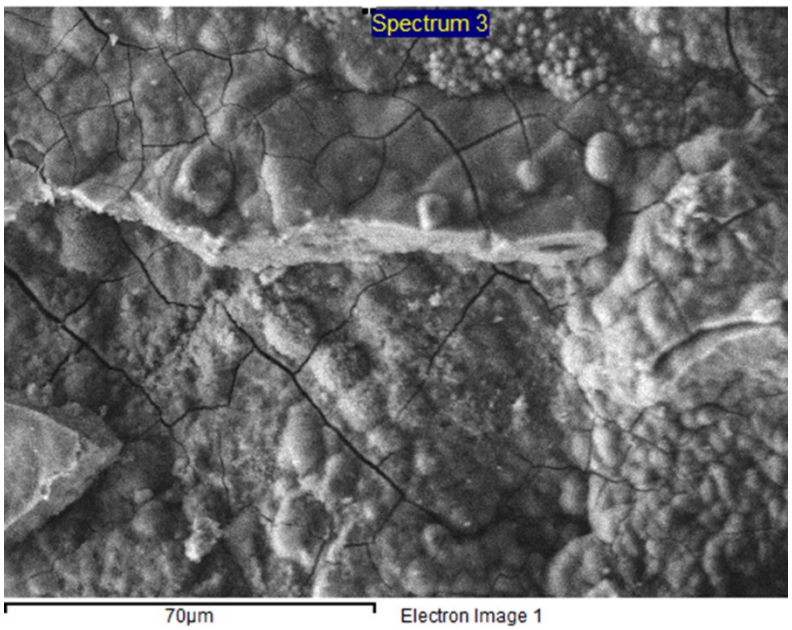


Figure A.489. SEM Image and EDS Spectrum of the Rust Collected from Exterior Web of the Girder.

Element	Weight %	Atomic %
O K	44.62	73.01
Al K	0.63	0.61
S K	1.65	1.34
Cl K	0.53	0.39
Mn K	0.31	0.15
Fe K	52.27	24.50
Totals	100.00	



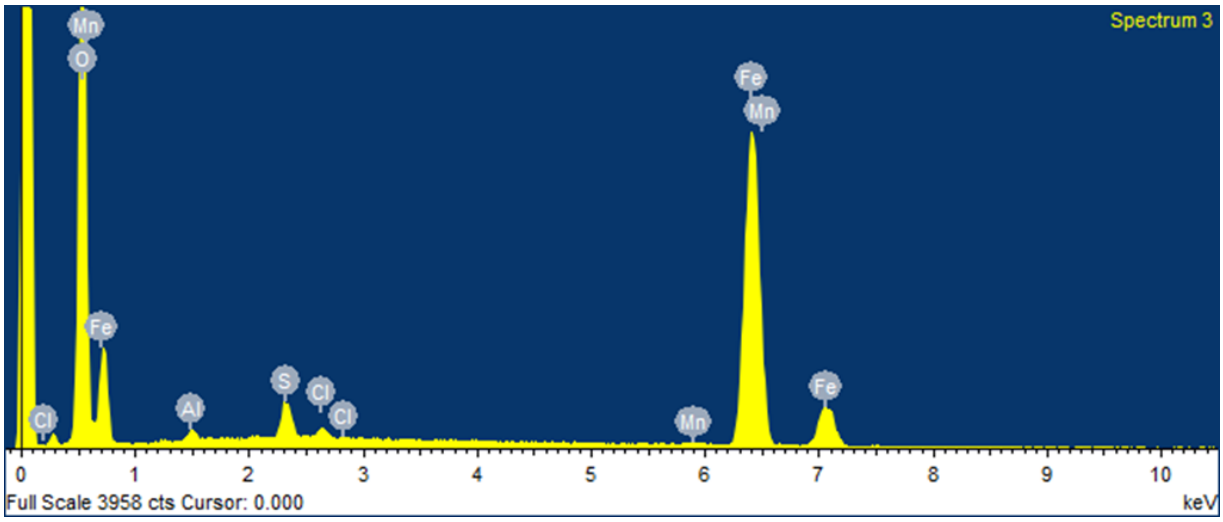
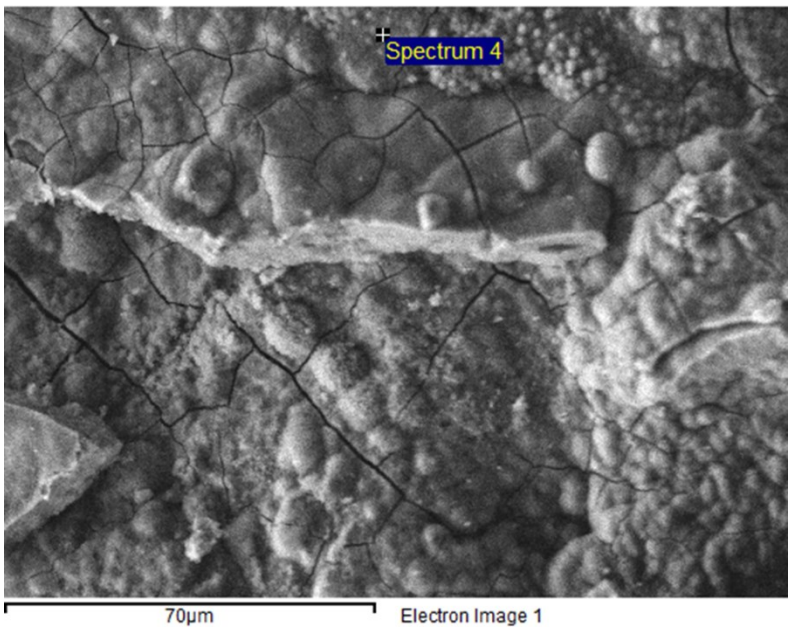


Figure A.490. SEM Image and EDS Spectrum of the Rust Collected from Exterior Web of the Girder.

Element	Weight %	Atomic %
O K	41.71	70.51
Al K	0.93	0.93
S K	1.72	1.45
Cl K	0.54	0.42
Mn K	0.56	0.28
Fe K	54.53	26.41
Totals	100.00	



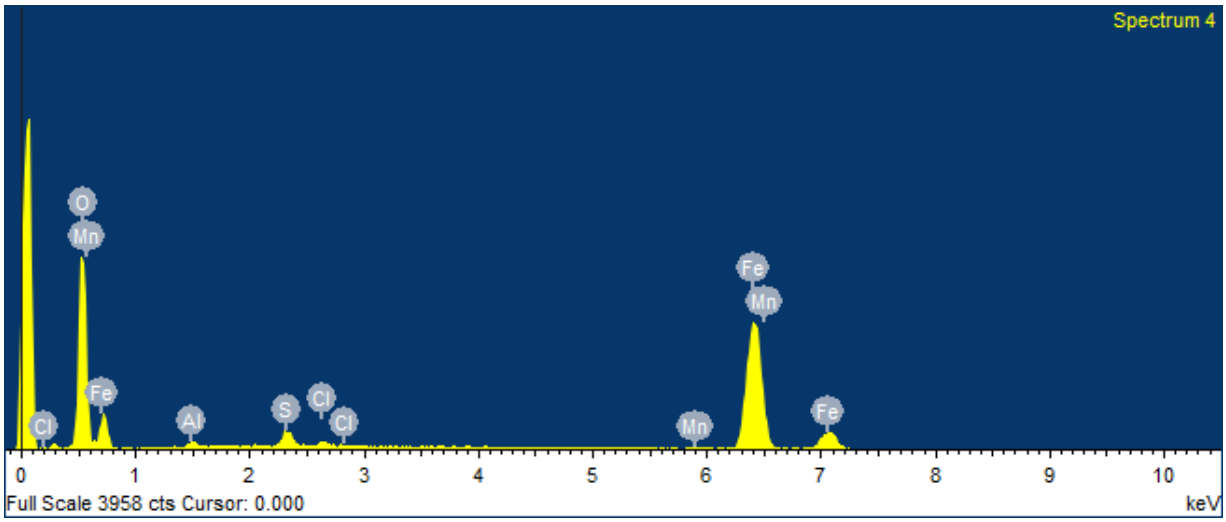
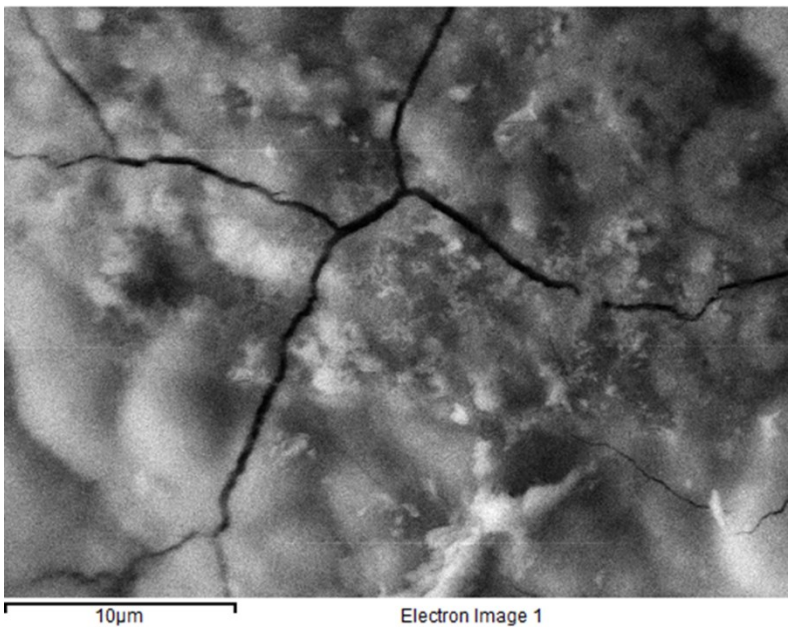


Figure A.491. SEM Image and EDS Spectrum of the Rust Collected from Exterior Web of the Girder.

Element	Weight %	Atomic %
O K	45.90	74.13
Al K	0.79	0.76
S K	1.22	0.99
Cl K	0.13	0.10
Mn K	0.98	0.46
Fe K	50.56	23.39
Ni K	0.23	0.10
Cu K	0.19	0.08
Totals	100.00	



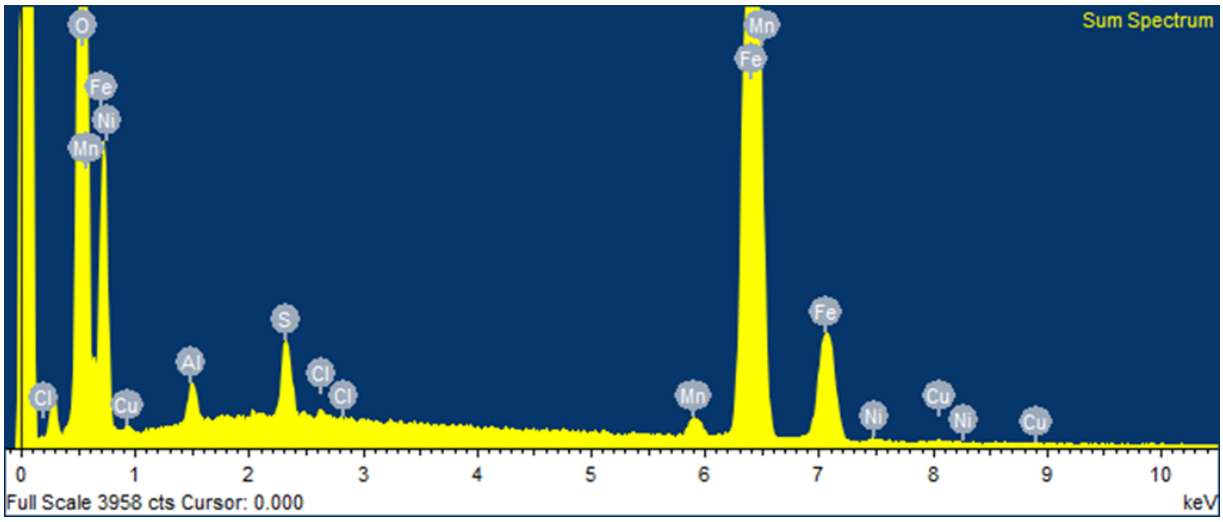


Figure A.492. SEM Image and EDS Spectrum of the Rust Collected from Exterior Web of the Girder.

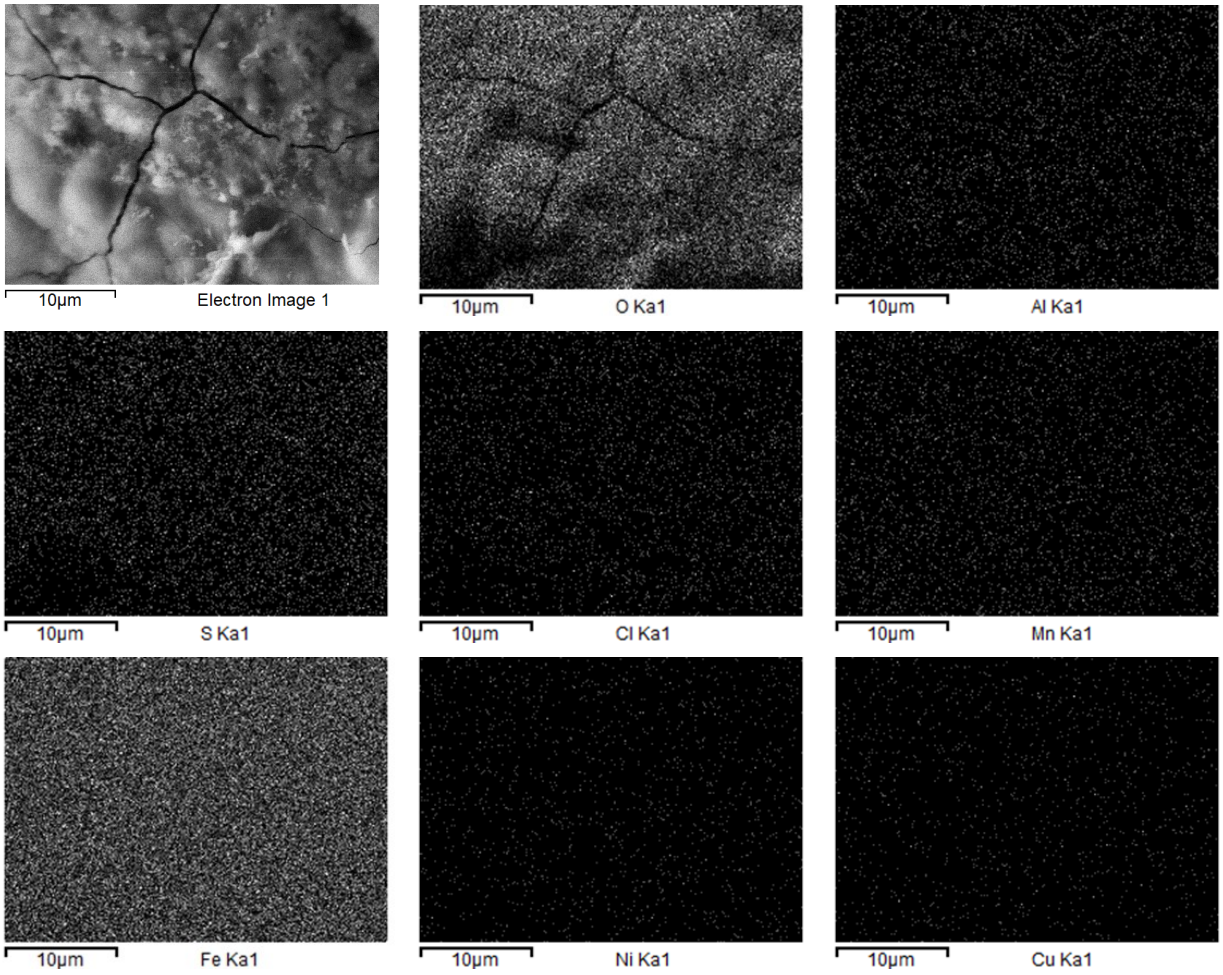
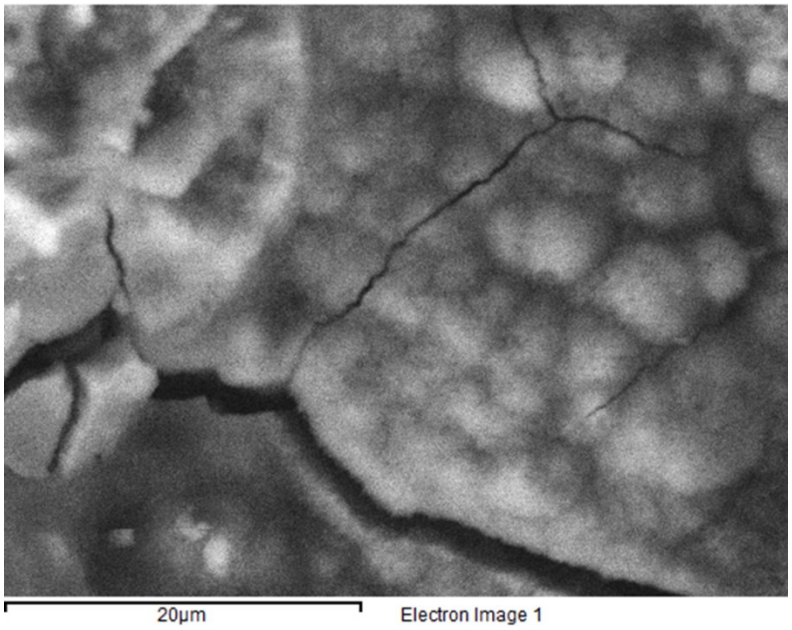


Figure A.493. EDS Elemental Mapping of Rust Collected from Exterior Web.

A.30.4.SEM/EDS Results: Interior Web Girder

Element	Weight %	Atomic %
O K	30.56	59.71
Al K	2.27	2.63
Si K	0.15	0.16
Cr K	0.18	0.11
Mn K	0.85	0.48
Fe K	65.33	36.57
Ni K	0.30	0.16
Cu K	0.35	0.17
Totals	100.00	



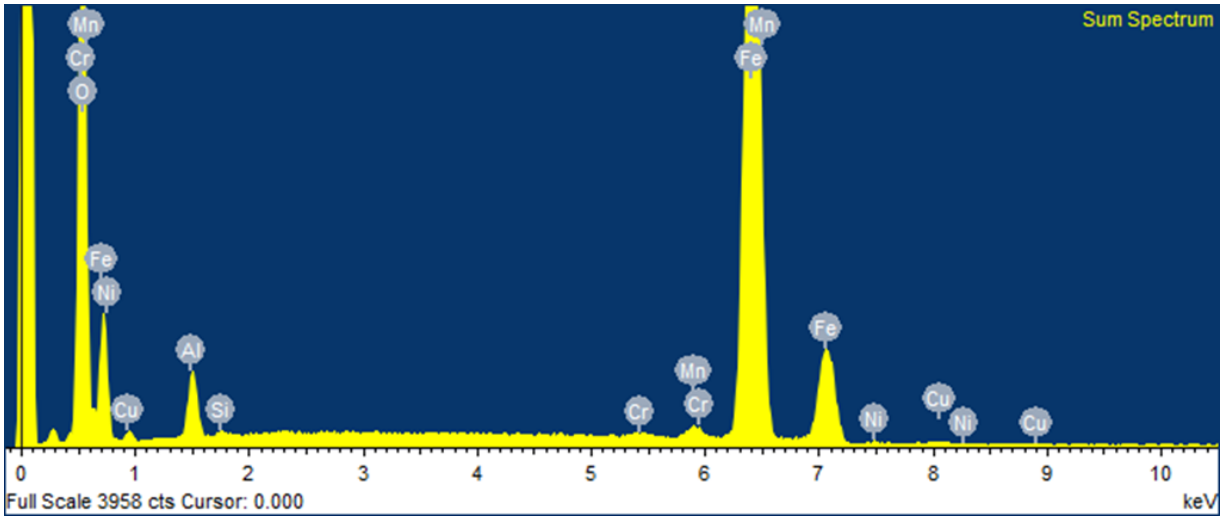


Figure A.494. SEM Image and EDS Spectrum of the Rust Collected from Interior Web of the Girder.

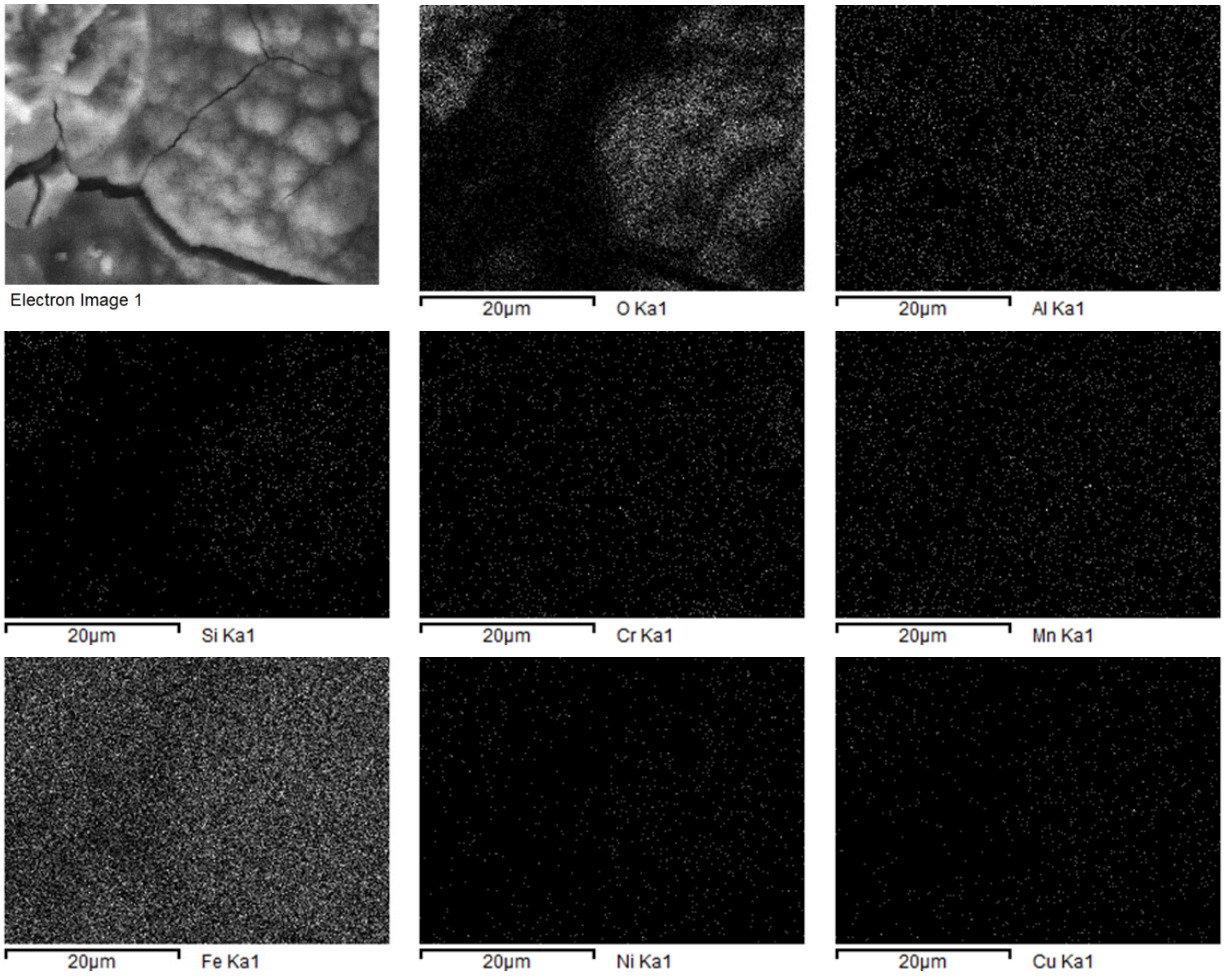
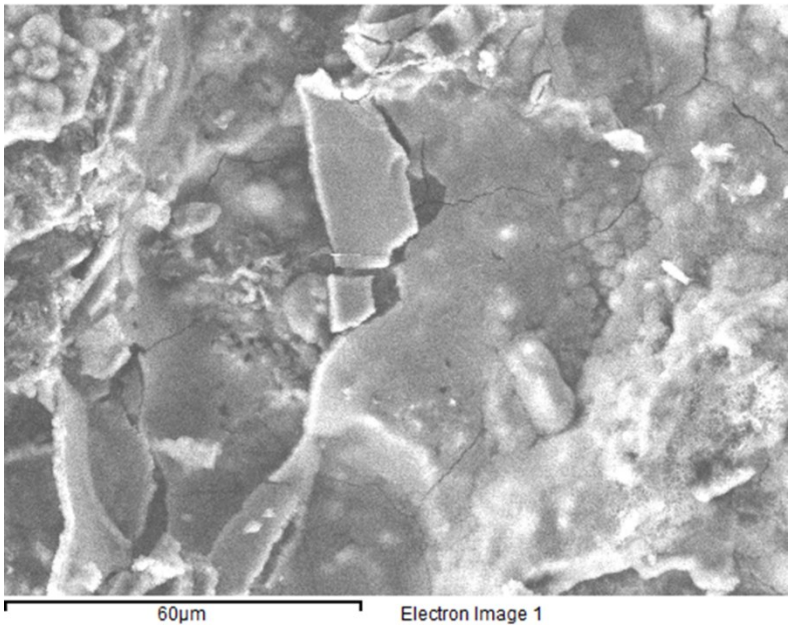


Figure A.495. EDS Elemental Mapping of Rust Collected from Interior Web.

Element	Weight %	Atomic %
O K	38.85	68.29
Al K	1.52	1.58
Si K	0.14	0.14
S K	0.13	0.11
Cr K	0.34	0.18
Mn K	0.70	0.36
Fe K	57.58	29.00
Cu K	0.75	0.33
Totals	100.00	



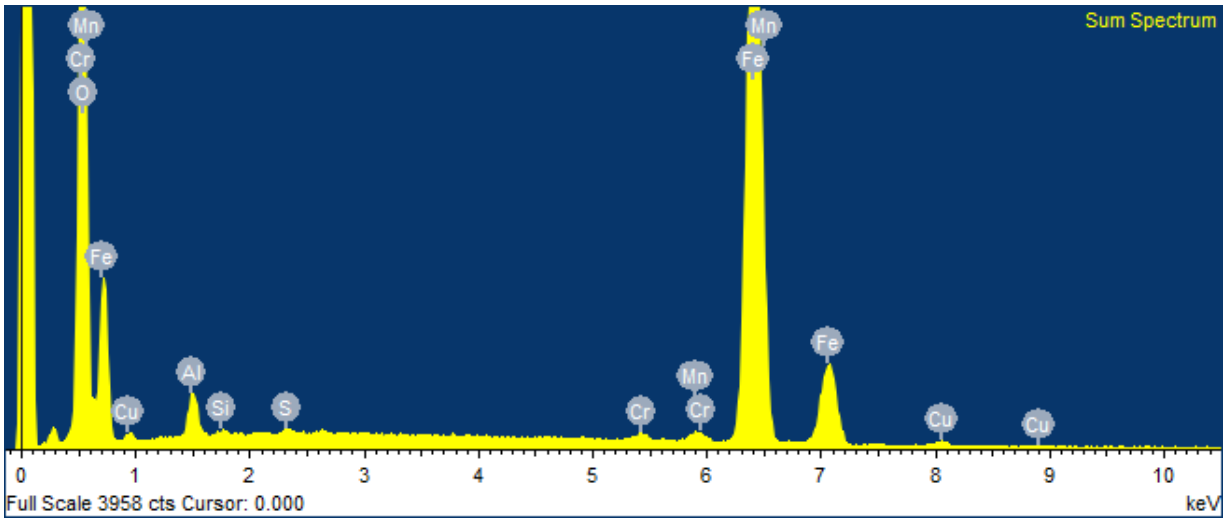


Figure A.496. SEM Image and EDS Spectrum of the Rust Collected from Interior Web of the Girder.

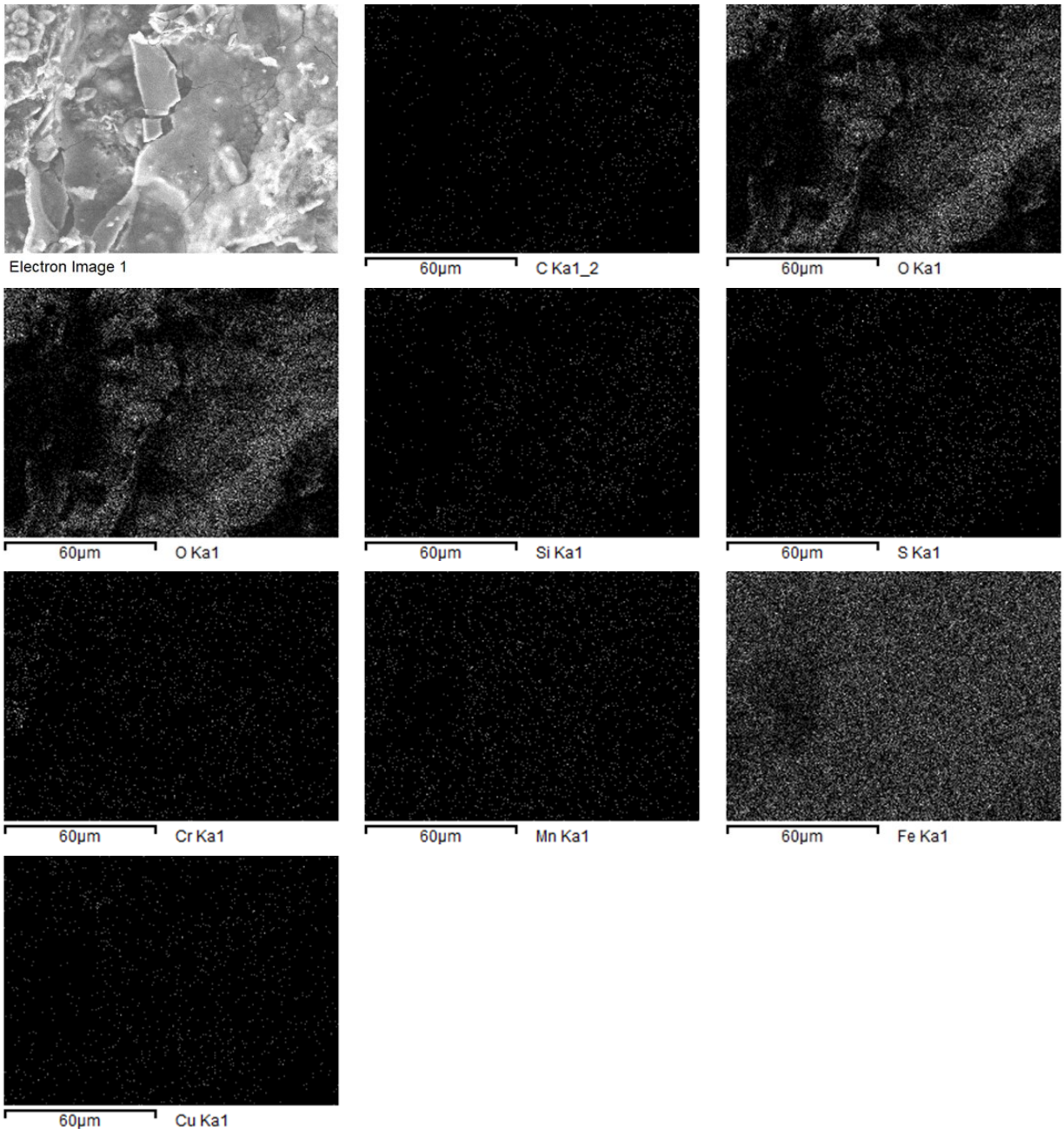


Figure A.497. EDS Elemental Mapping of Rust Collected from Interior Web.

A.30.5.XPS Results: Exterior Web Girder

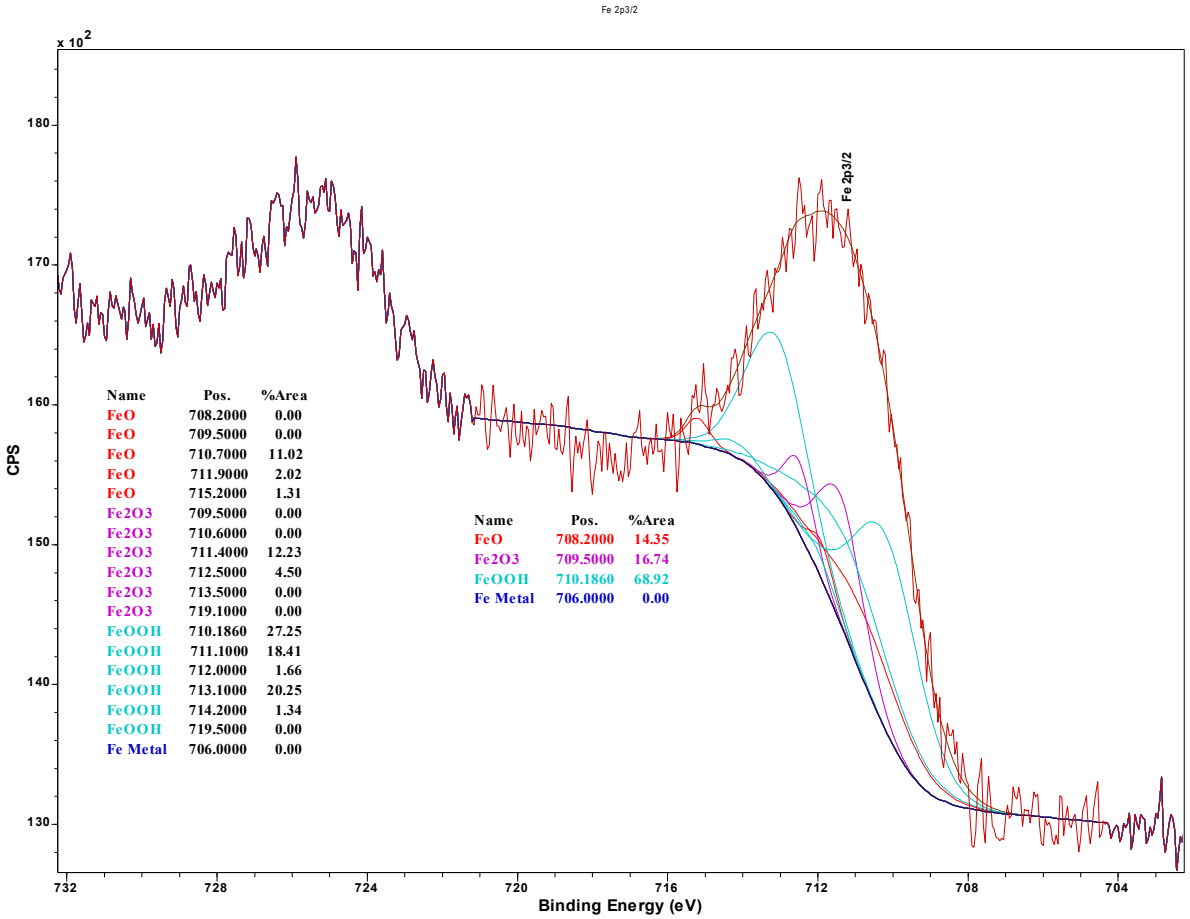


Figure A.498. XPS Spectrum of the Rust Collected from Exterior Web of the Girder.

A.30.6.XPS Results: Interior Web Girder

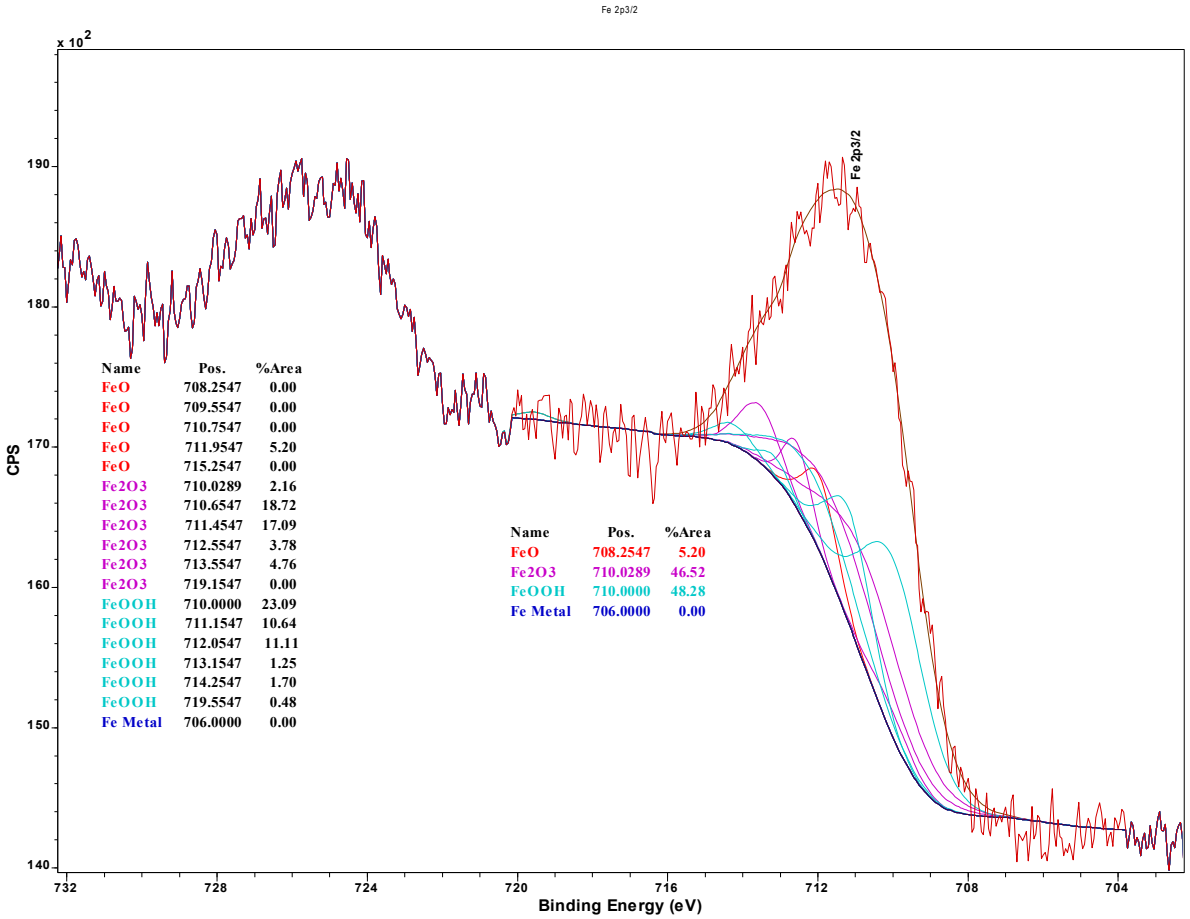


Figure A.499. XPS Spectrum of the Rust Collected from Exterior Web of the Girder.

A.30.7.XRD Result: Exterior and Interior Girder

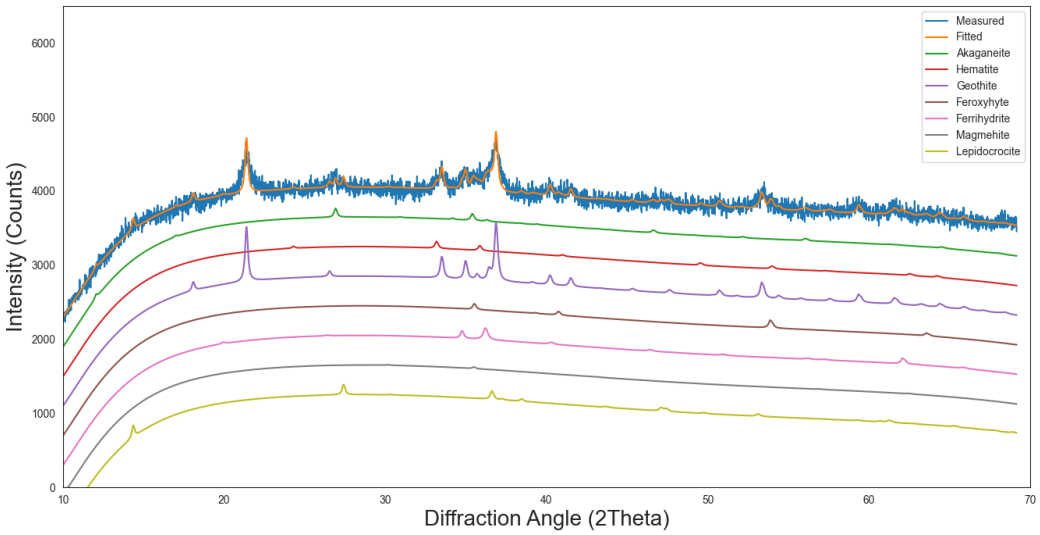


Figure A.500. XRD Pattern of Powdered Rust Collected from Exterior Web of the Girder.

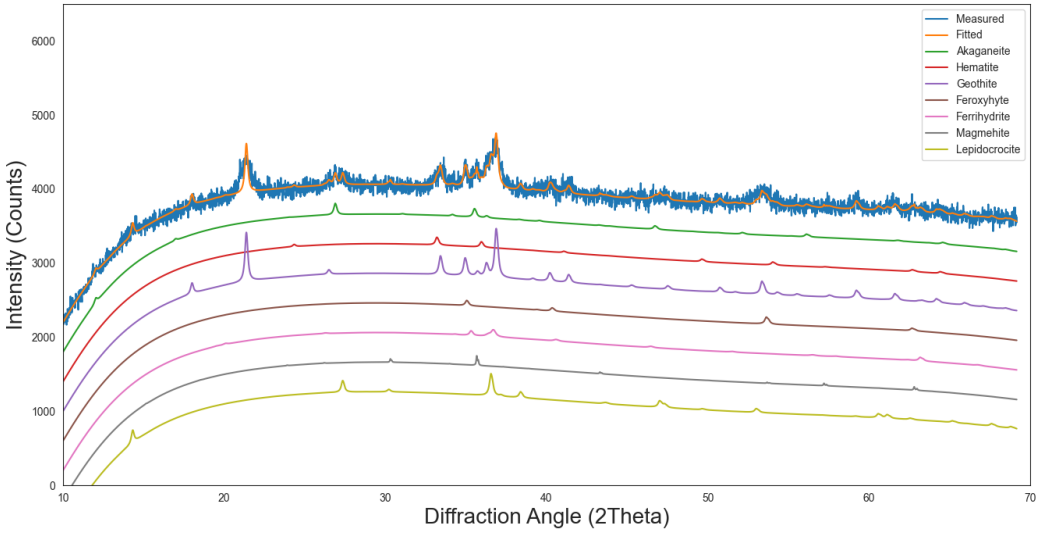


Figure A.501. XRD Pattern of Powdered Rust Collected from Interior Web of the Girder.

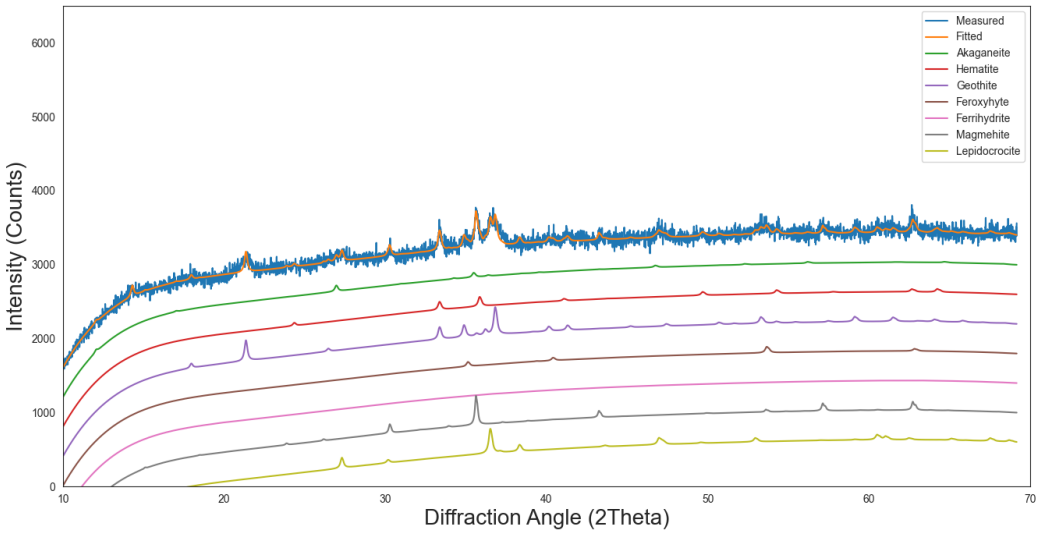


Figure A.502. XRD Pattern of Powdered Rust Collected from Bottom face of Top Flange of the Interior Girder.

A.30.8. Particle Size Analysis: Tape Adhesion Results

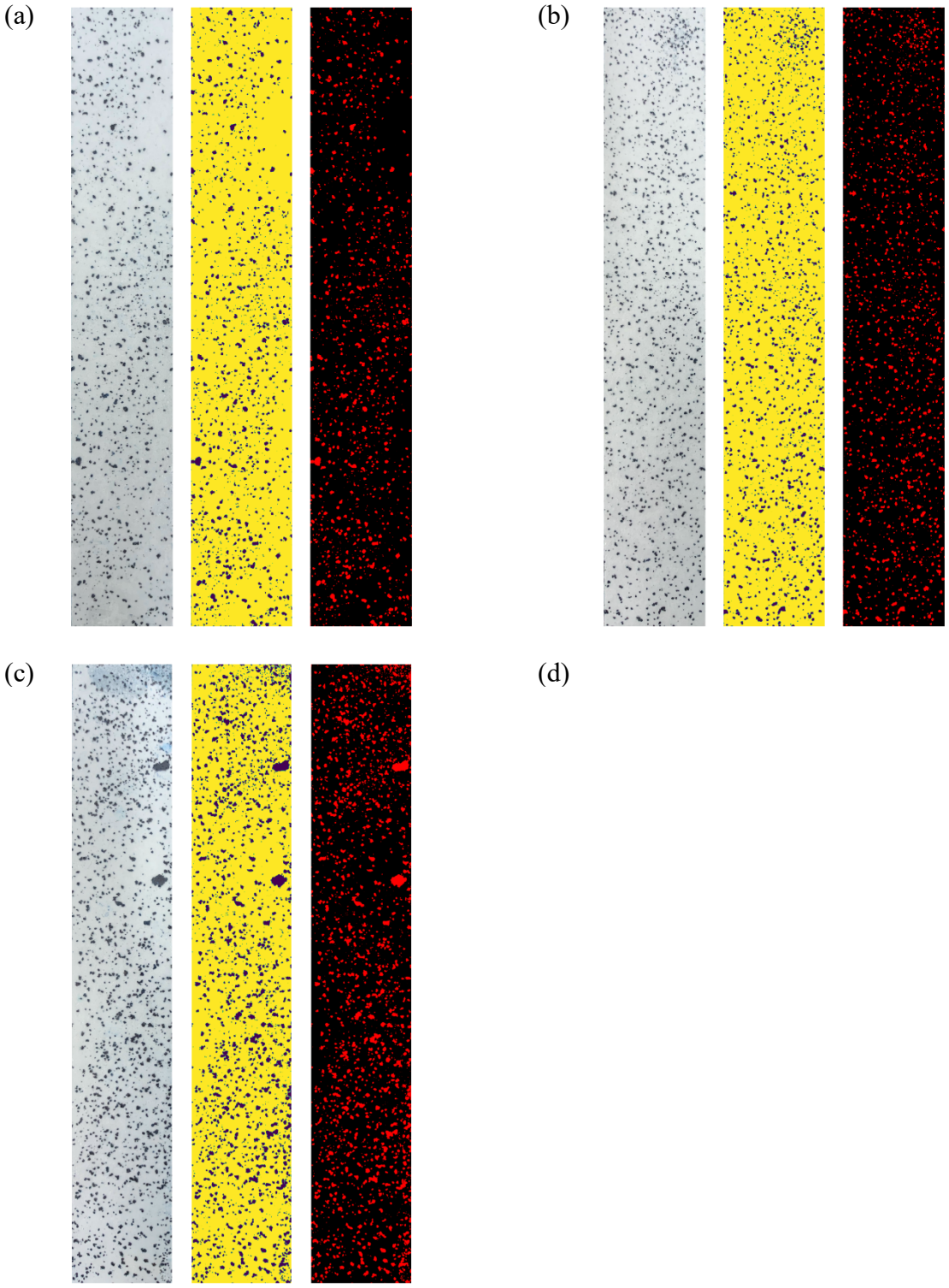


Figure A.503. Particle Size Analysis Results at A1G1F1 (a) Top Flange Bottom, (b) Web, (c) Bottom Flange Bottom (d) Stiffener.

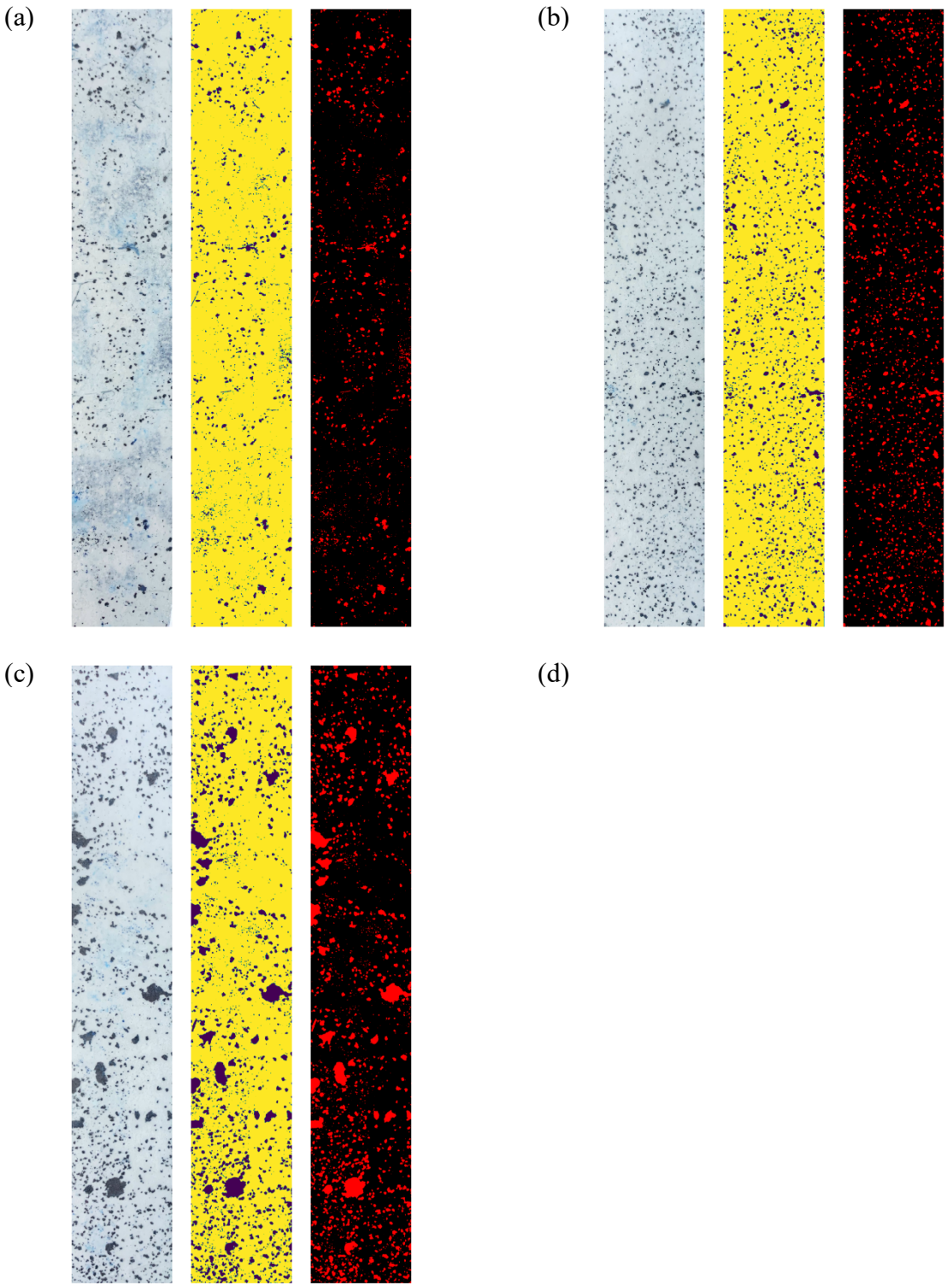


Figure A.504. Particle Size Analysis Results at A1G3F2 (a) Top Flange Bottom, (b) Web, (c) Bottom Flange Bottom (d) Stiffener.

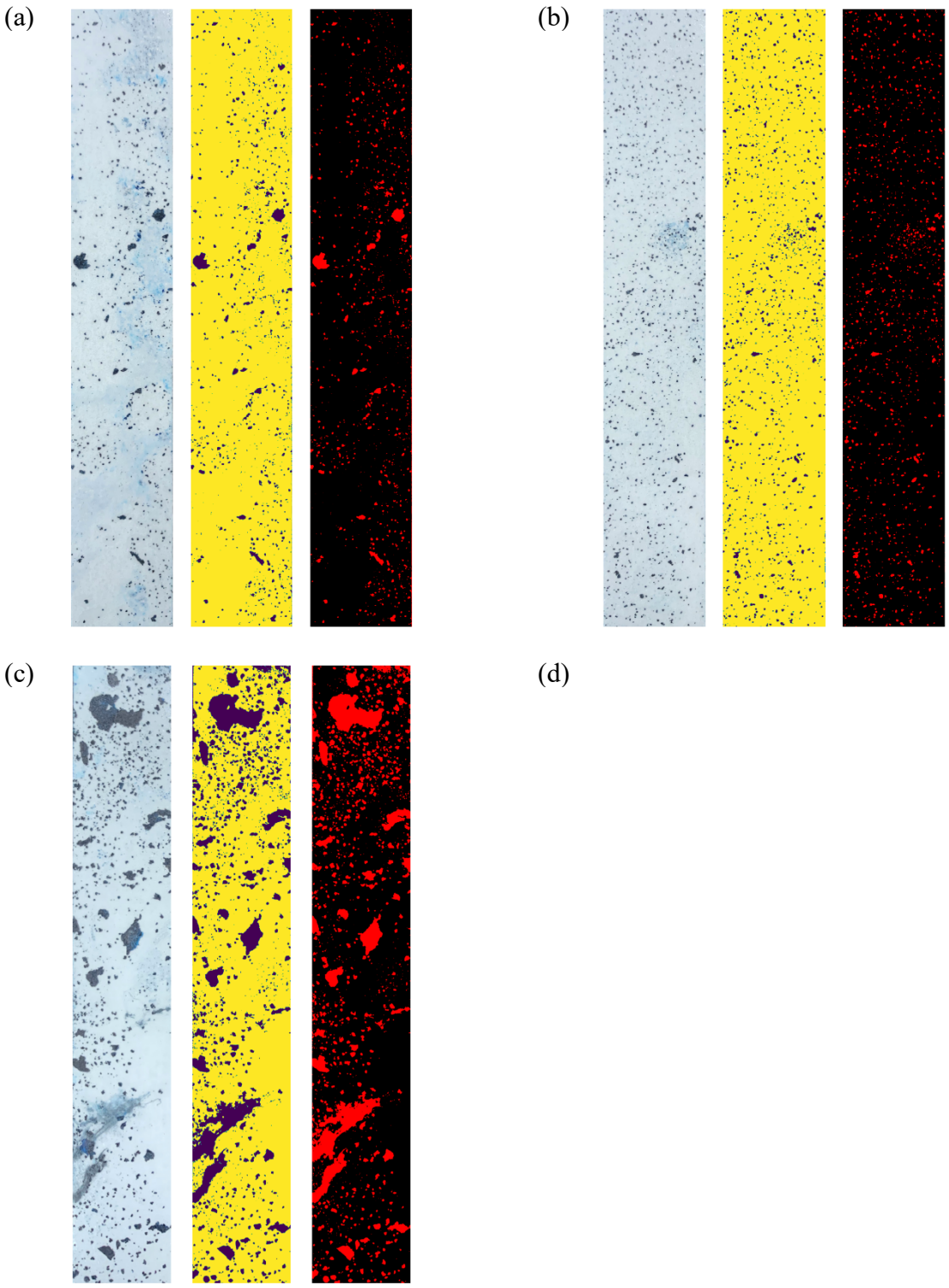


Figure A.505. Particle Size Analysis Results at A1G4F1 (a) Top Flange Bottom, (b) Web, (c) Bottom Flange Bottom (d) Stiffener.

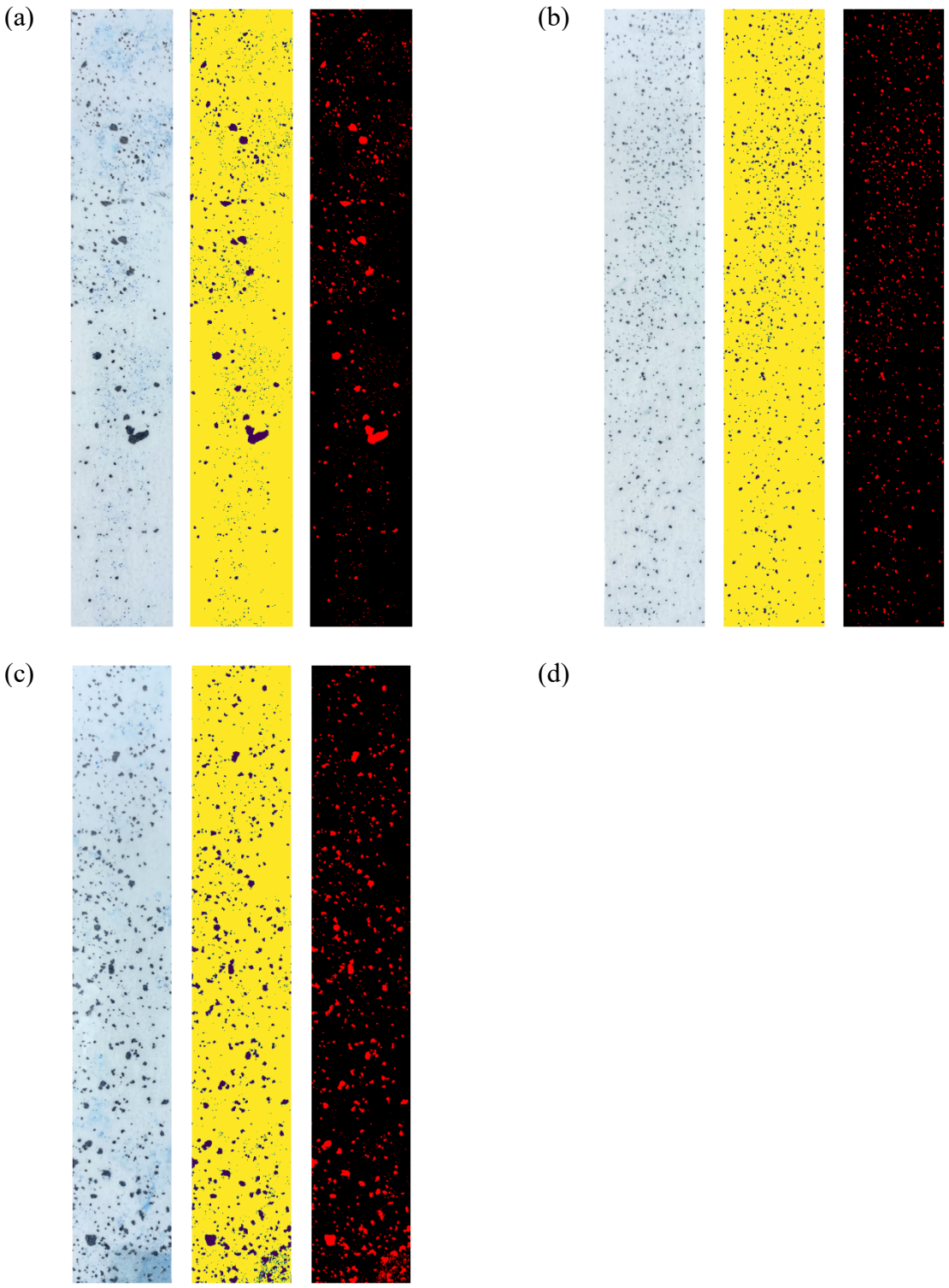


Figure A.506. Particle Size Analysis Results at A1G8F2 (a) Top Flange Bottom, (b) Web, (c) Bottom Flange Bottom (d) Stiffener.

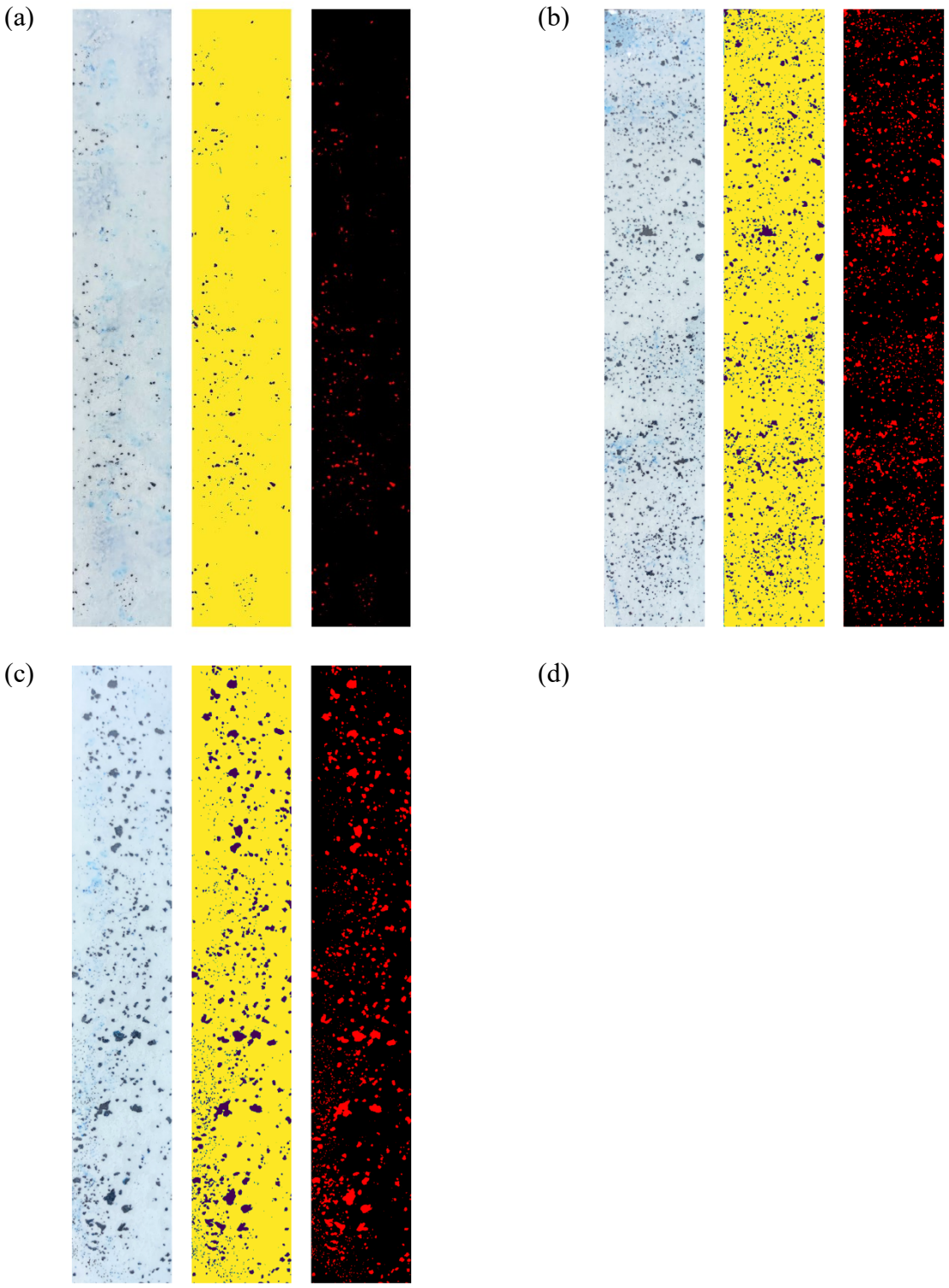


Figure A.507. Particle Size Analysis Results at A1G9F1 (a) Top Flange Bottom, (b) Web, (c) Bottom Flange Bottom (d) Stiffener.

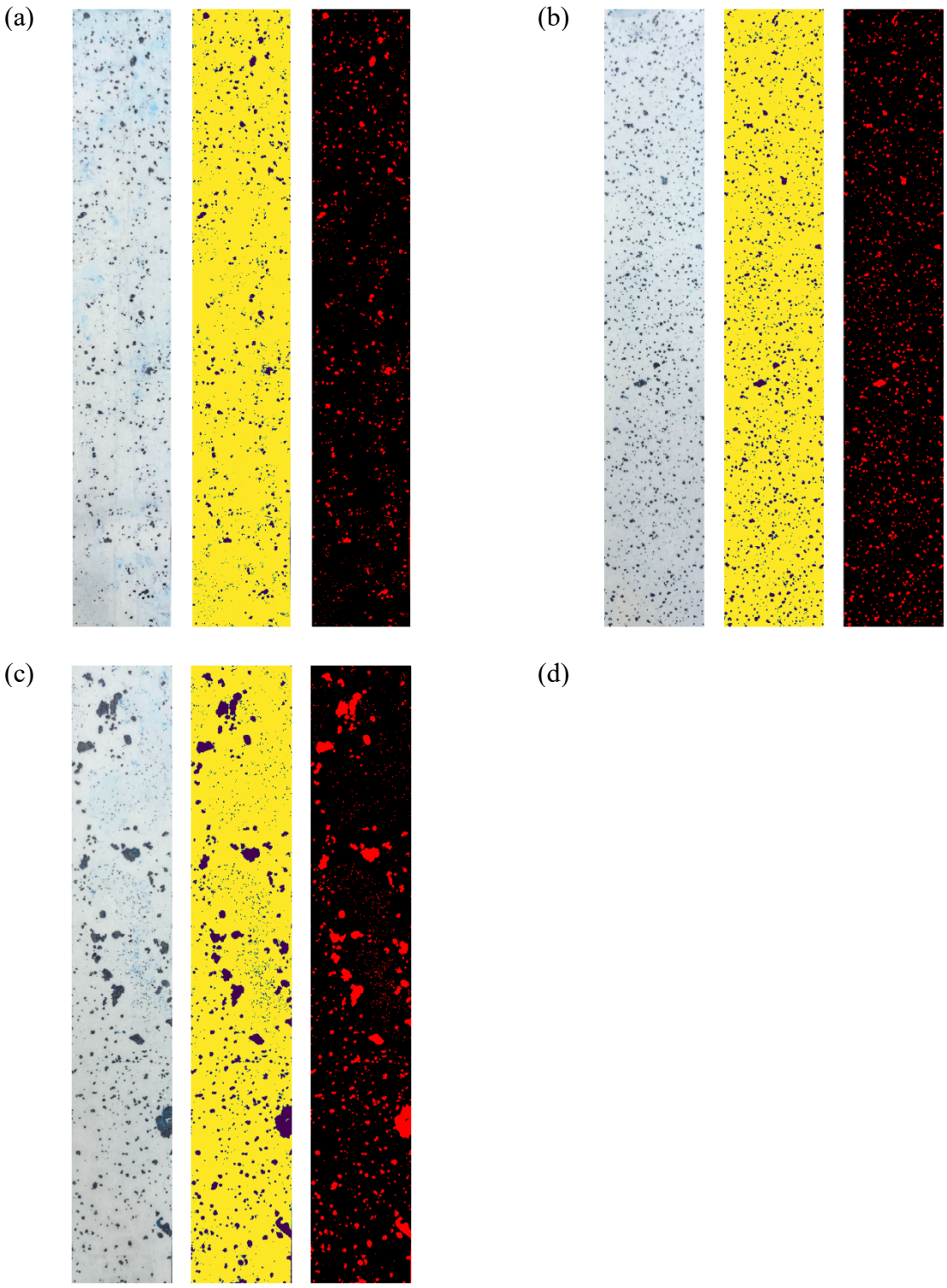


Figure A.508. Particle Size Analysis Results at A1G12F2 (a) Top Flange Bottom, (b) Web, (c) Bottom Flange Bottom (d) Stiffener.

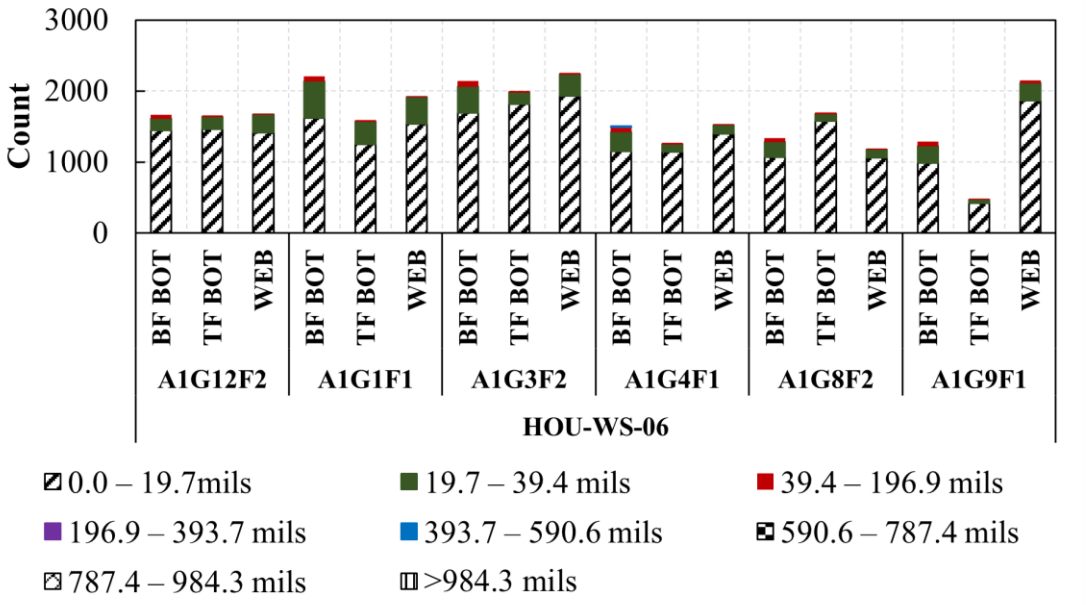


Figure A.509. Particle Size Analysis Showing Different Locations Examined.

A.31. HOU-WS-07

- CON IH10 EB-BW8 SB over IH10 EBFR/BW8 SBFR/UP RR
- Bridge ID 121020050801447, Coordinates (29.7718, -95.1509), Harris County, Houston
- Continuous weathering steel plate girder
- Built 1994
- Girder inspection carried on girder 1, 2, 3 and 4, and measurements are taken on girder within four feet from the abutment or bent.
- Datalogger installed at bent 30 on girder number 2 for continuous monitoring of temperature, humidity, and time of wetness (TOW)
- Location for Testing: A31G1F1, A31G3F1, A31G3F2, A31G4F2



Figure A.510. Typical Picture of HOU-WS-07.

A.31.1. Observed Condition

Overall bridge is in good condition with development of uniform patina throughout the girder with a patina index rating ranging between 7 and 6.

A.31.2.Field Inspection Results

Table A-140. Field Inspection Results for HOU-WS-07.

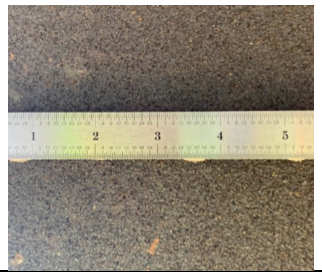
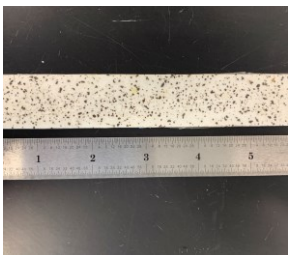
Location	Patina Rating	Thickness (inch)	Cl^- Conc. (ppm)	Field Condition	Tape Test
A31-G1F1 TF Bot. Ext.	7	Measured R1 1.016 R2 1.017 R3 1.017 R_Avg Design			
A31-G1F1 Web Ext.	7	Measured R1 0.512 R2 0.511 R3 0.510 R_Avg Design			
A31-G1F1 BF Top Ext.	7	Measured R1 0.988 R2 0.988 R3 0.991 R_Avg Design			
A31-G1F1 BF Bot. Ext.	6	Measured R1 R2 R3 R_Avg Design			
A31-G1F1 Stiff. Ext.	7	Measured R1 0.744 R2 0.744 R3 0.746 R_Avg Design			

Table A-141. Field Inspection Results for HOU-WS-07.

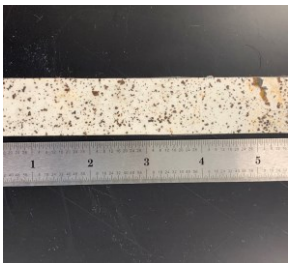
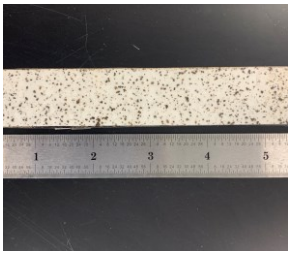
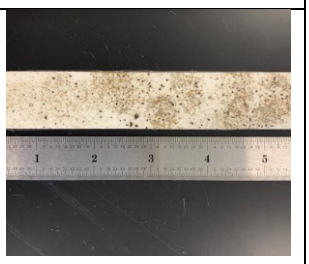
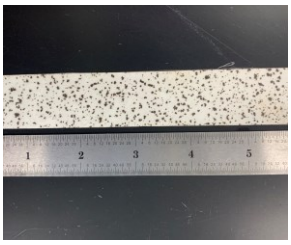
Location	Patina Rating	Thickness (inch)	Cl^- Conc. (ppm)	Field Condition	Tape Test
A31-G2F1 TF Bot. Int.	7	Measured R1 1.015 R2 1.016 R3 1.015 R_Avg Design			
A31-G2F1 Web Int.	7	Measured R1 0.507 R2 0.501 R3 0.520 R_Avg Design			
A31-G2F1 BF Top Int.	7	Measured R1 0.993 R2 0.997 R3 0.996 R_Avg Design			
A31-G2F1 BF Bot. Int.	6	Measured R1 R2 R3 R_Avg Design			
A31-G2F1 Stiff. Int.	7	Measured R1 0.743 R2 0.742 R3 0.765 R_Avg Design			

Table A-142. Field Inspection Results for HOU-WS-07.

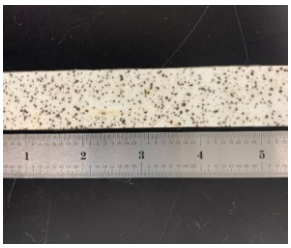
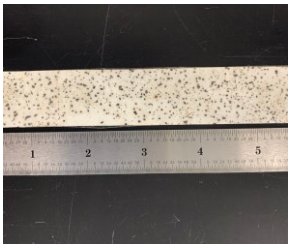
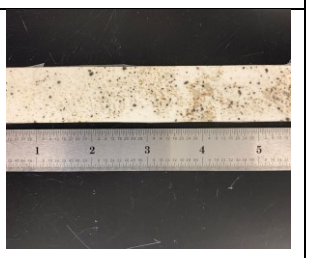
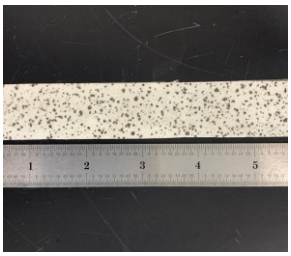
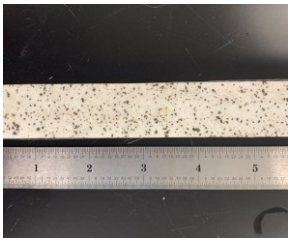
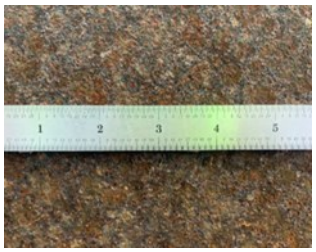
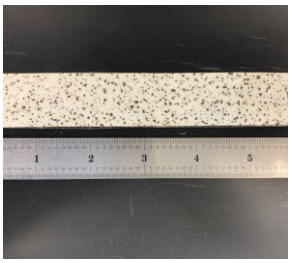
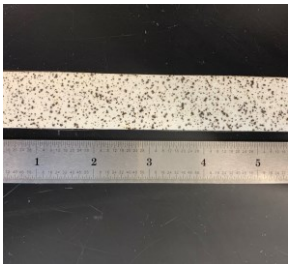
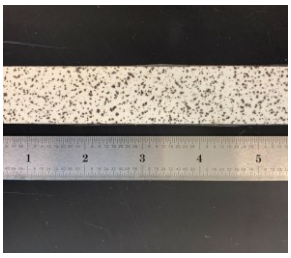
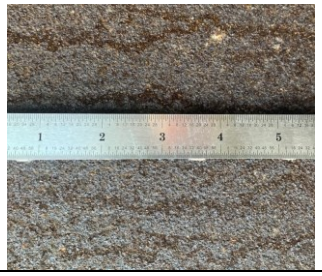
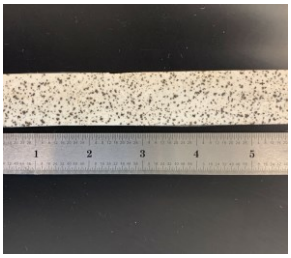
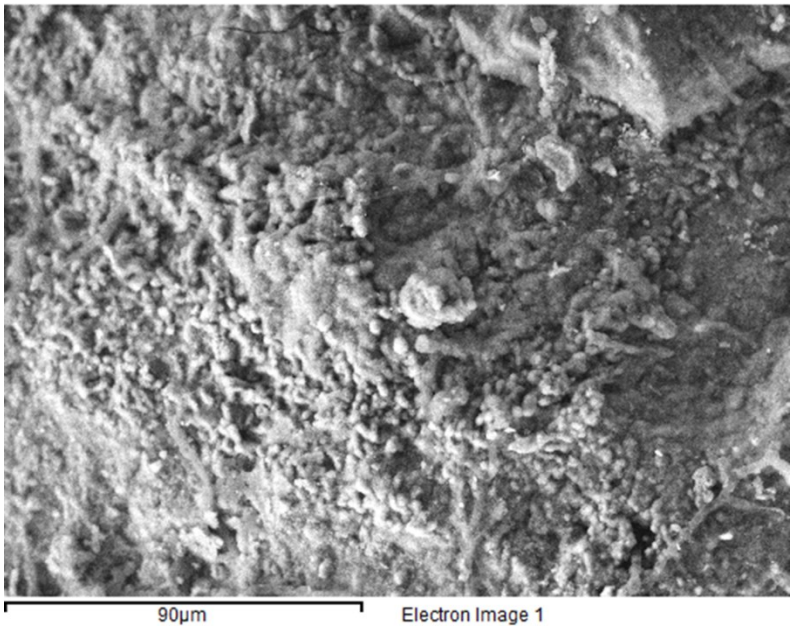
Location	Patina Rating	Thickness (inch)	Cl^- Conc. (ppm)	Field Condition	Tape Test
A31-G3F2 TF Bot. Int.	7	Measured R1 0.982 R2 0.998 R3 0.982 R_Avg Design			
A31-G3F2 Web Int.	7	Measured R1 0.510 R2 0.513 R3 0.508 R_Avg Design			
A31-G3F2 BF Top Int.	7	Measured R1 0.987 R2 0.985 R3 0.990 R_Avg Design			
A31-G3F2 BF Bot. Int.	6	Measured R1 R2 R3 R_Avg Design			
A31-G3F2 Stiff. Int.	7	Measured R1 0.742 R2 0.738 R3 0.740 R_Avg Design			

Table A-143. Field Inspection Results for HOU-WS-07.

Location	Patina Rating	Thickness (inch)	Cl^- Conc. (ppm)	Field Condition	Tape Test
A31-G4F2 TF Bot. Ext.	7	Measured R1 0.983 R2 0.986 R3 0.982 R_Avg Design			
A31-G4F2 Web Ext.	7	Measured R1 0.508 R2 0.510 R3 0.516 R_Avg Design			
A31-G4F2 BF Top Ext.	7	Measured R1 0.985 R2 0.983 R3 0.984 R_Avg Design			
A31-G4F2 BF Bot. Ext.	6	Measured R1 R2 R3 R_Avg Design			
A31-G4F2 Stiff. Ext.	7	Measured R1 0.740 R2 0.741 R3 0.738 R_Avg Design			

A.31.3.SEM/EDS Results: Exterior Web Girder

Element	Weight %	Atomic %
C K	12.34	20.84
O K	51.29	65.03
Al K	0.93	0.70
Si K	1.04	0.75
P K	0.09	0.06
S K	0.52	0.33
Ca K	0.12	0.06
Cr K	0.12	0.05
Mn K	0.83	0.31
Fe K	32.53	11.82
Cu K	0.20	0.06
Totals	100.00	



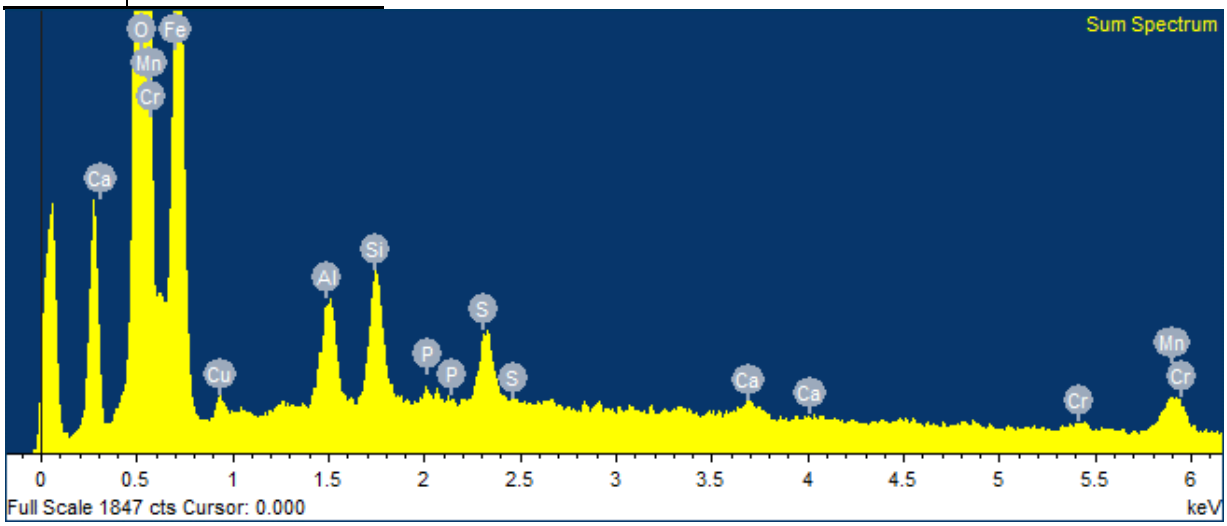
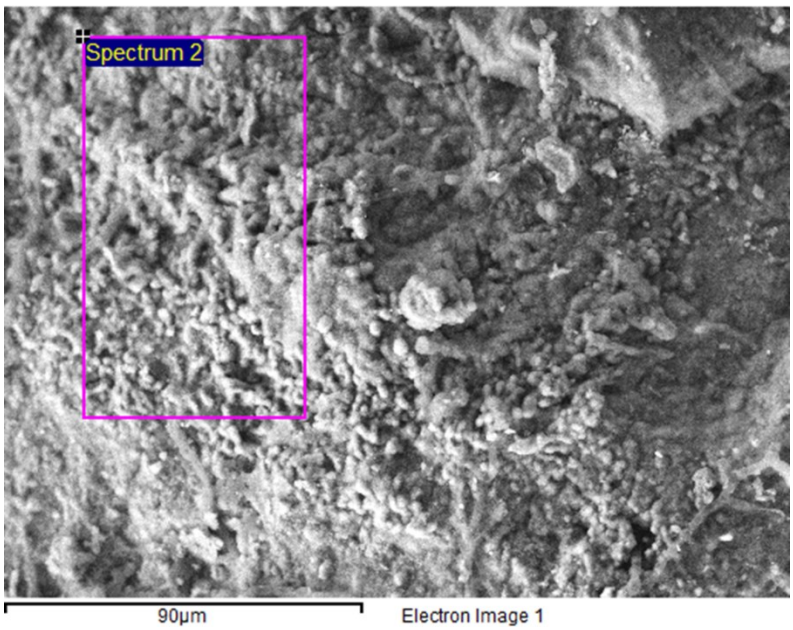


Figure A.511. SEM Image and EDS Spectrum of the Rust Collected from Exterior Web of the Girder.

Element	Weight %	Atomic %
O K	54.39	79.11
Al K	1.77	1.53
Si K	2.12	1.75
S K	0.70	0.51
Ca K	0.11	0.06
Mn K	0.88	0.37
Fe K	39.77	16.57
Cu K	0.26	0.09
Totals	100.00	



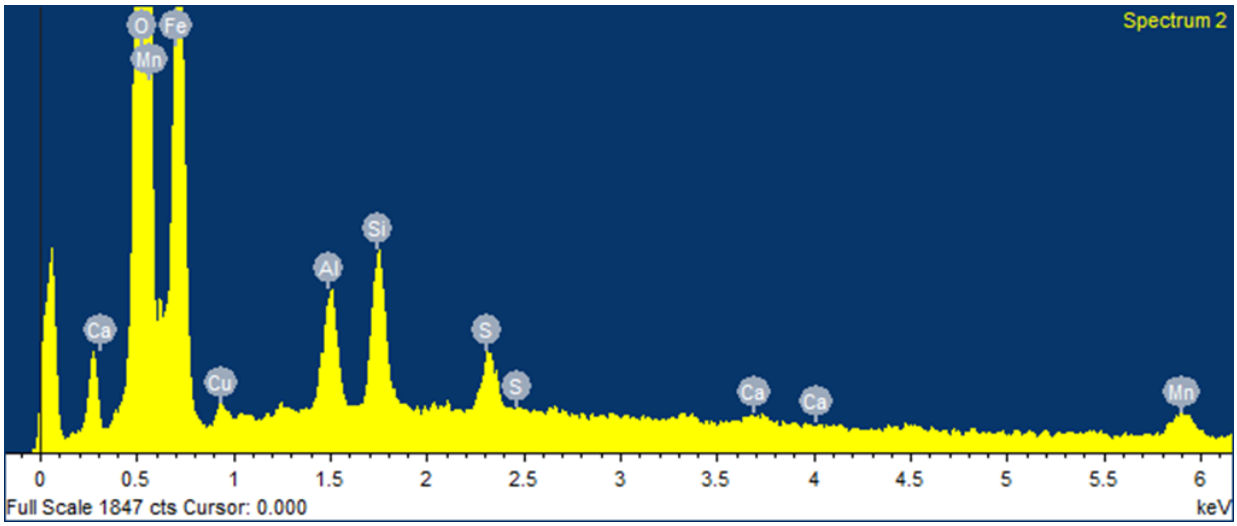
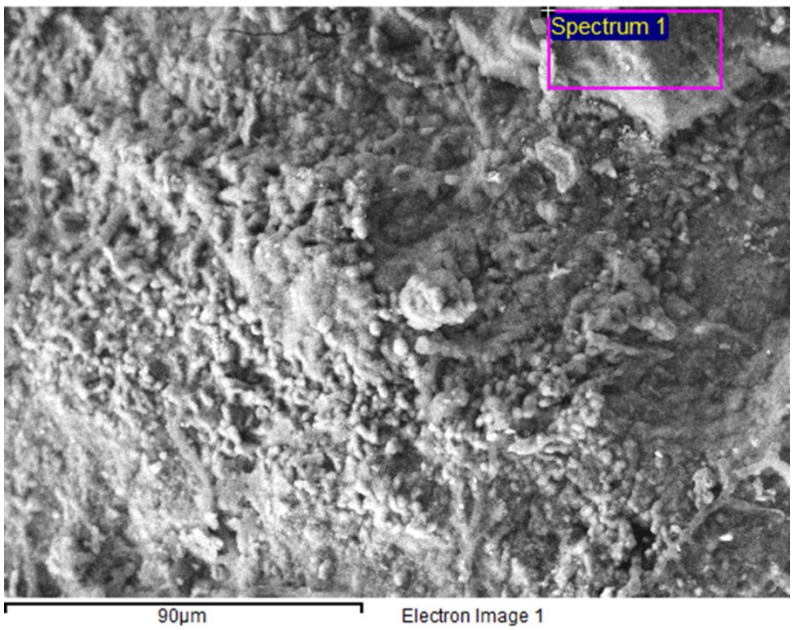


Figure A.512. SEM Image and EDS Spectrum of the Rust Collected from Exterior Web of the Girder.

Element	Weight %	Atomic %
O K	43.64	71.29
Al K	1.92	1.86
Si K	2.19	2.03
S K	0.75	0.61
Cl K	0.18	0.13
Ca K	0.29	0.19
Cr K	0.17	0.09
Mn K	1.34	0.64
Fe K	49.33	23.09
Cu K	0.20	0.08
Totals	100.00	



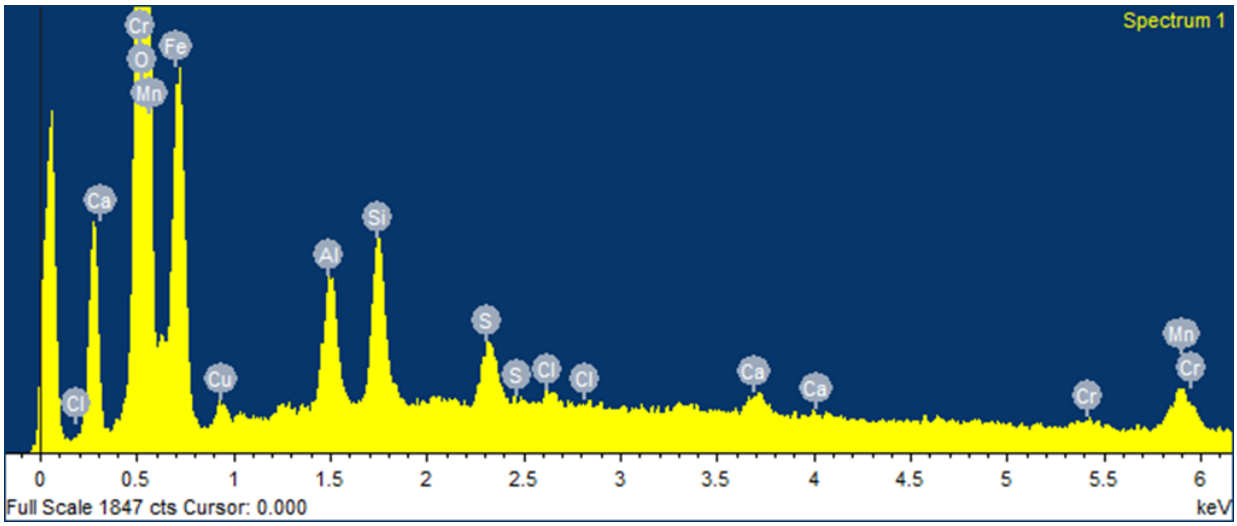


Figure A.513. SEM Image and EDS Spectrum of the Rust Collected from Exterior Web of the Girder.

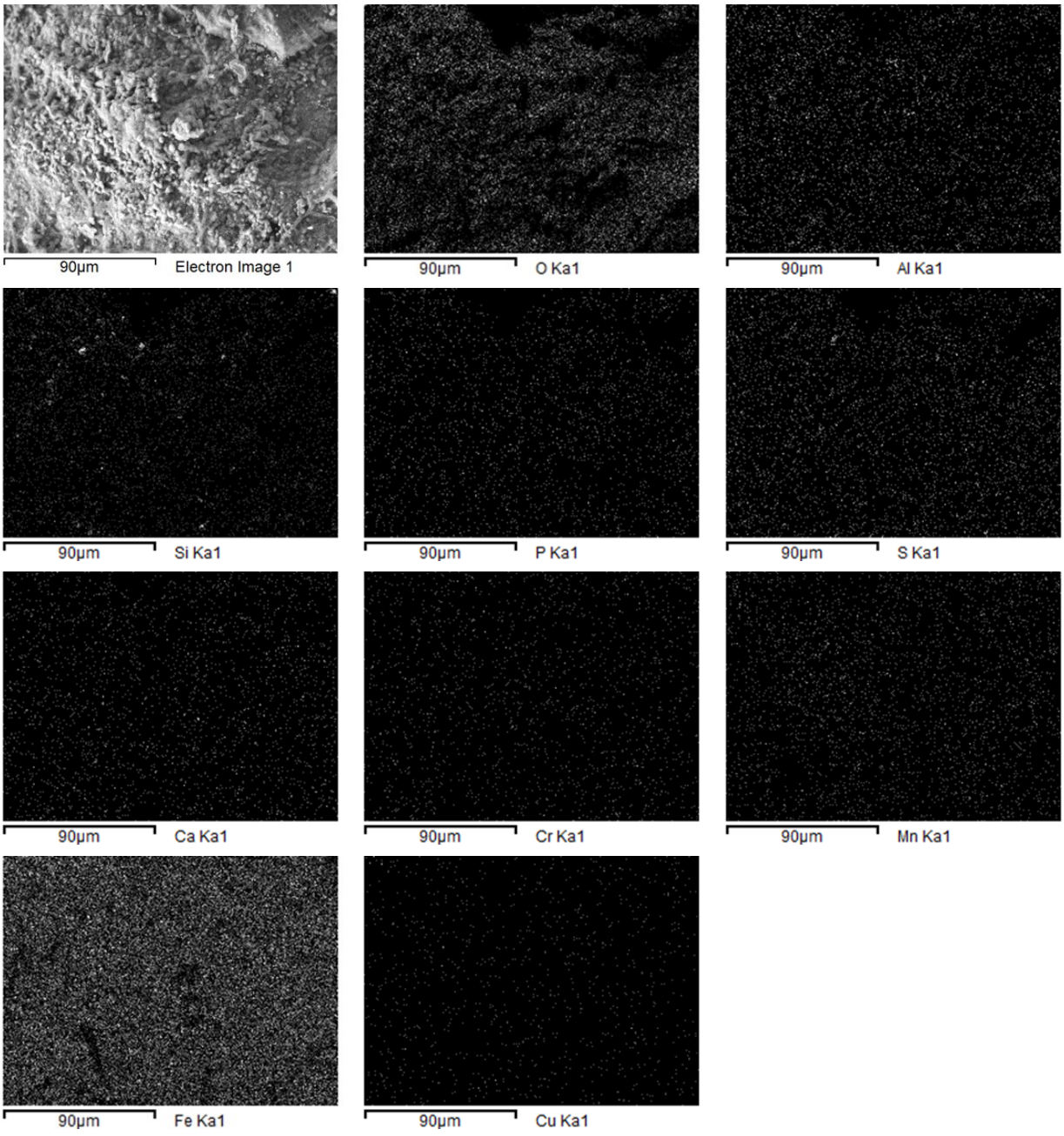
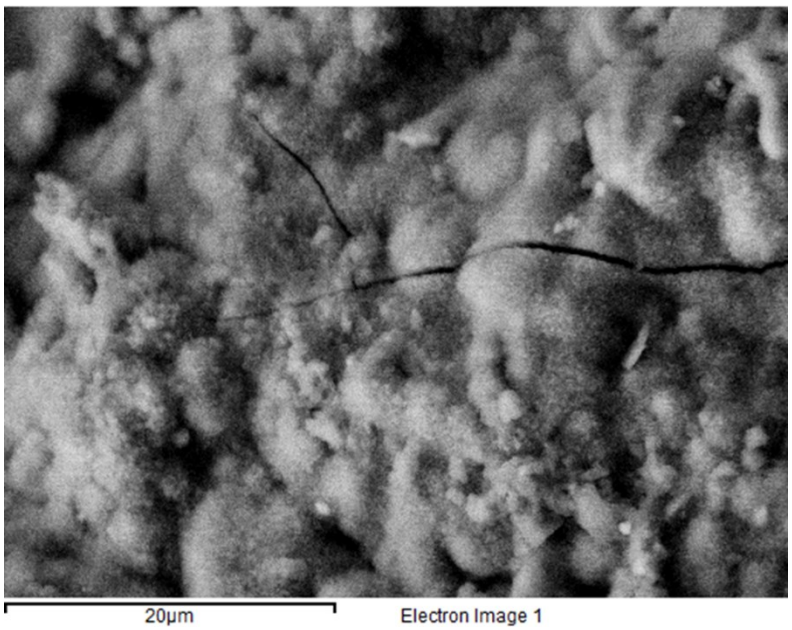


Figure A.514. EDS Elemental Mapping of Rust Collected from Exterior Web.

Element	Weight %	Atomic %
O K	54.09	78.94
Al K	1.72	1.49
Si K	2.07	1.72
S K	0.71	0.52
Ca K	0.16	0.09
Mn K	0.87	0.37
Fe K	40.10	16.77
Cu K	0.27	0.10
Totals	100.00	



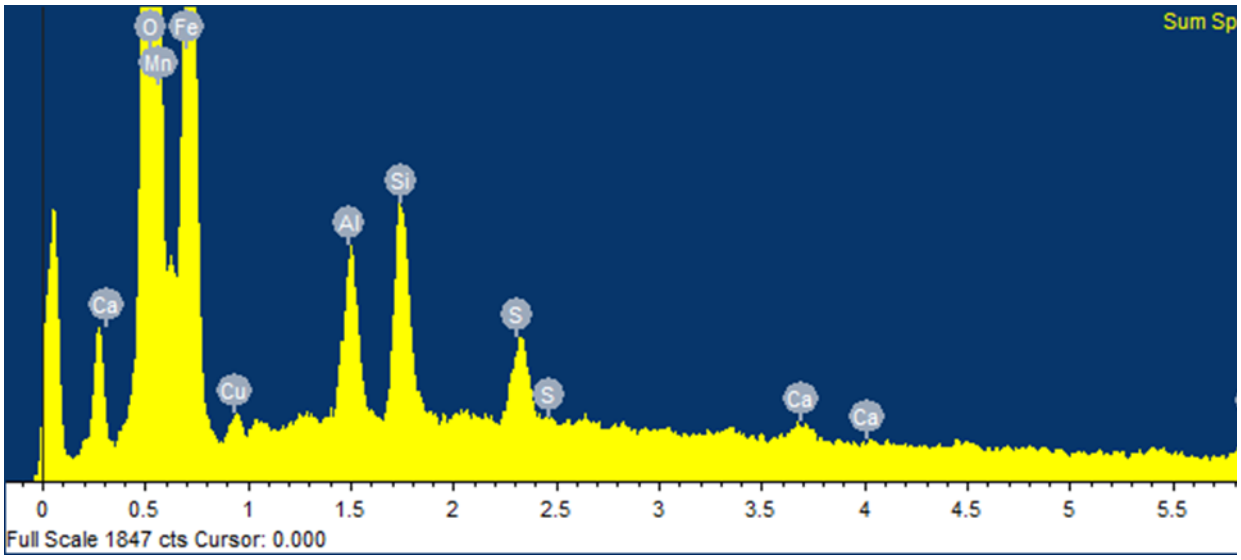


Figure A.515. SEM Image and EDS Spectrum of the Rust Collected from Exterior Web of the Girder.

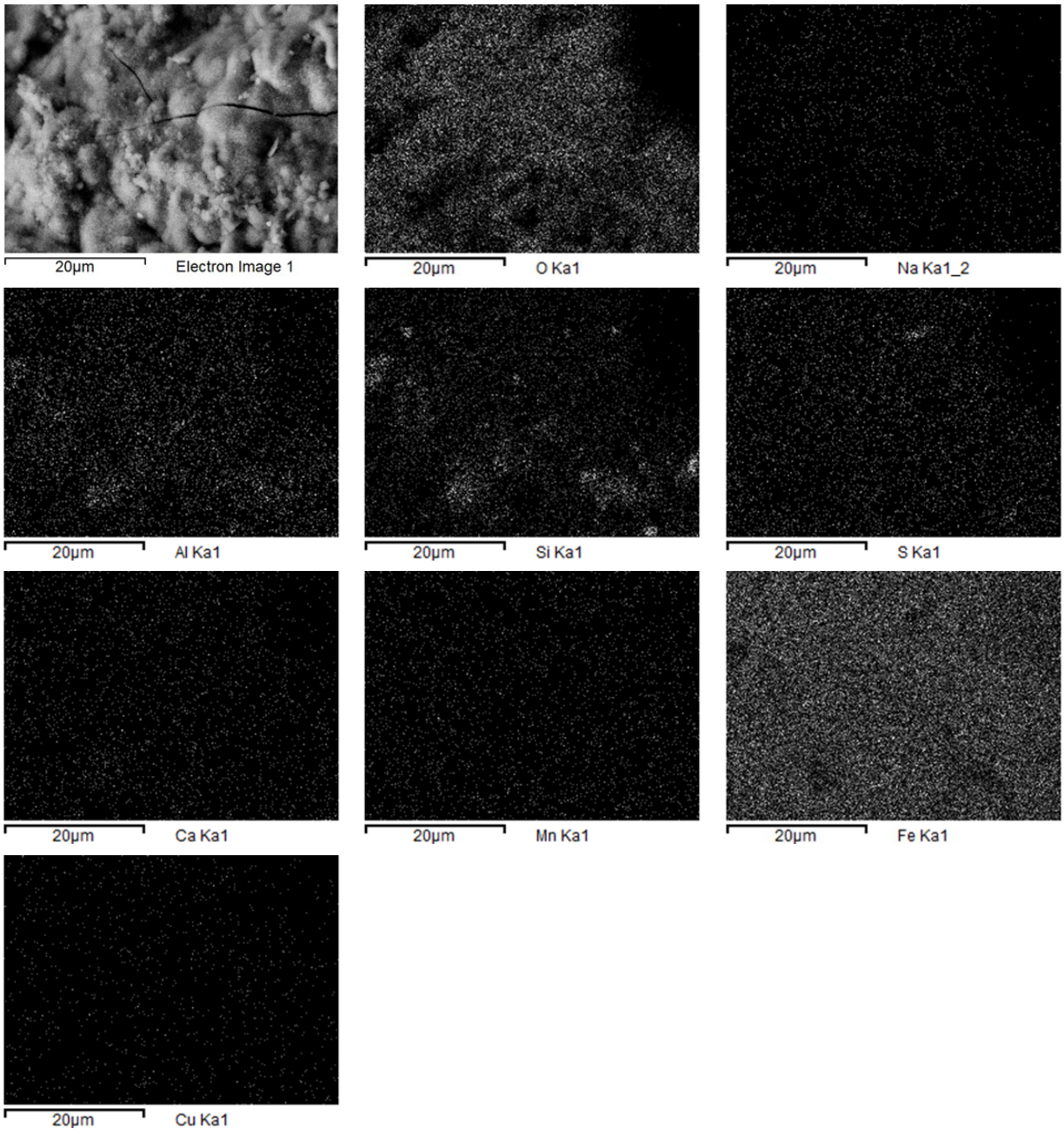
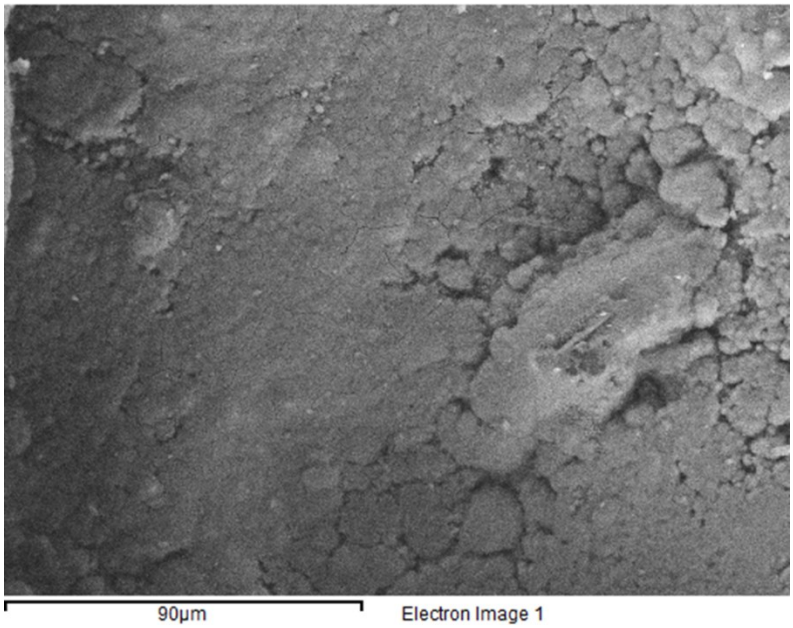


Figure A.516. EDS Elemental Mapping of Rust Collected from Exterior Web.

Element	Weight %	Atomic %
O K	39.90	69.11
Al K	0.92	0.95
Si K	0.59	0.58
S K	0.72	0.62
Ca K	0.19	0.13
Mn K	1.57	0.79
Fe K	55.68	27.63
Cu K	0.43	0.19
Totals	100.00	



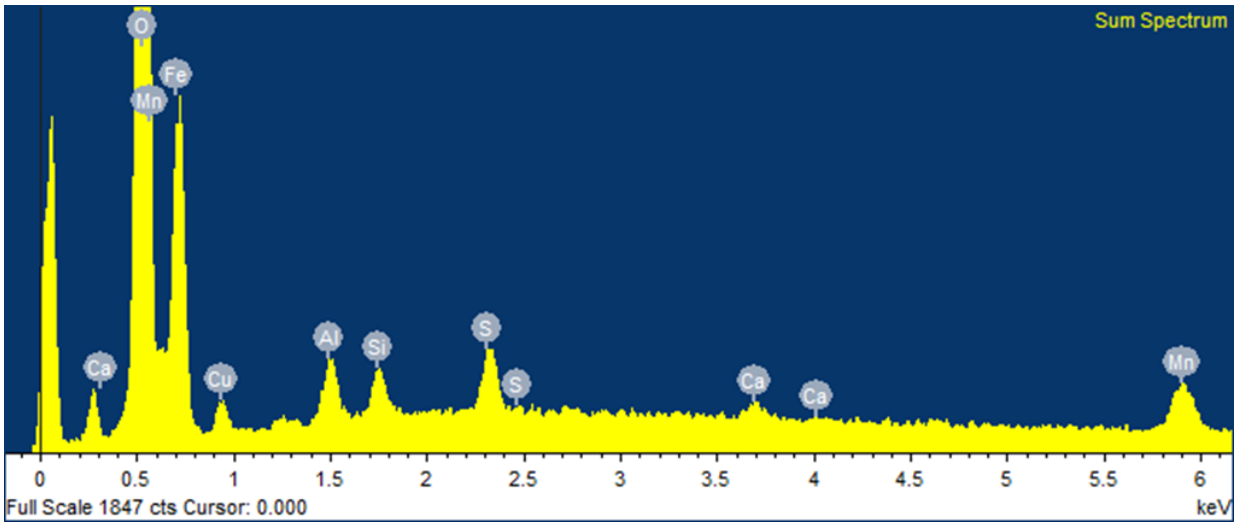


Figure A.517. SEM Image and EDS Spectrum of the Rust Collected from Exterior Web of the Girder.

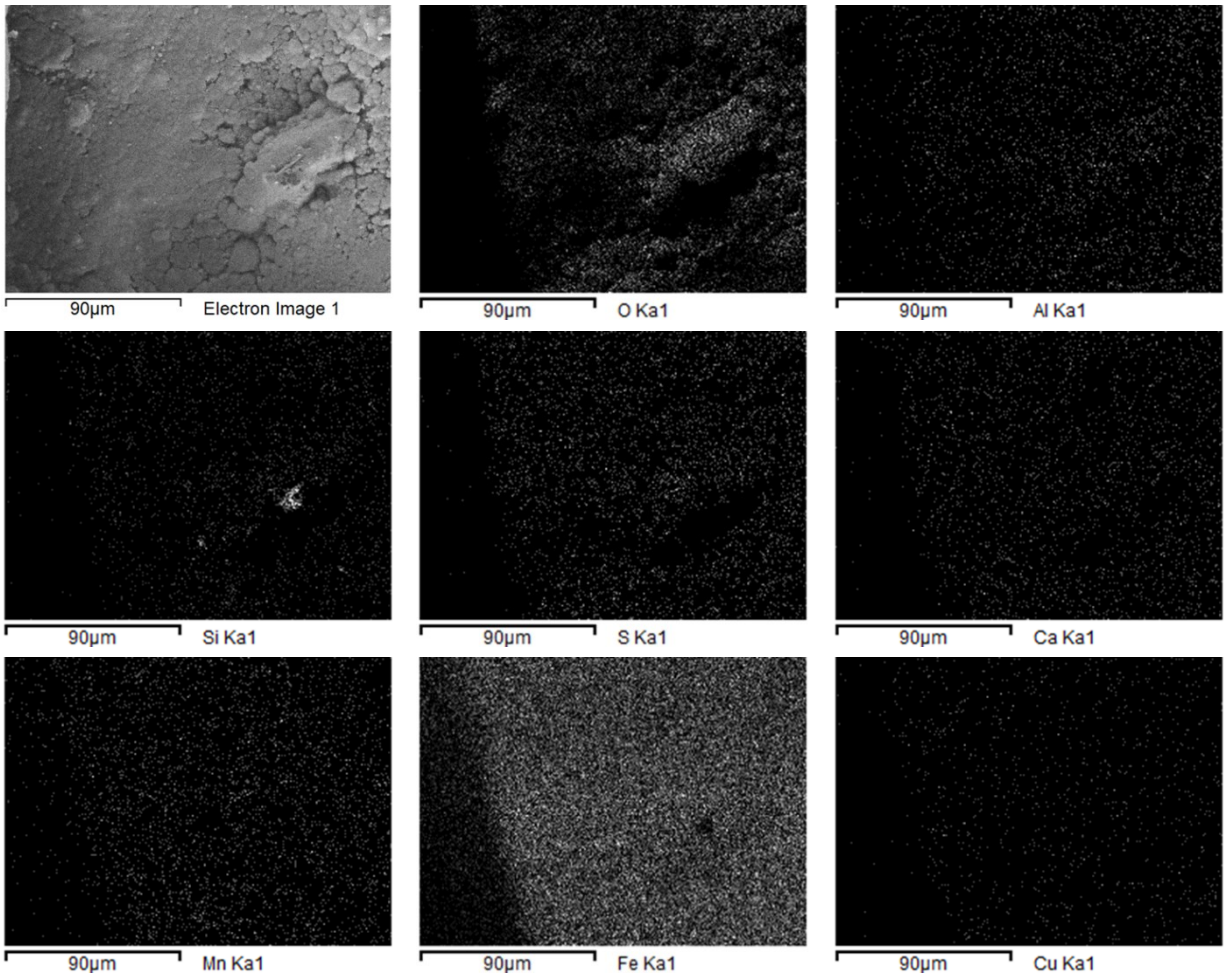
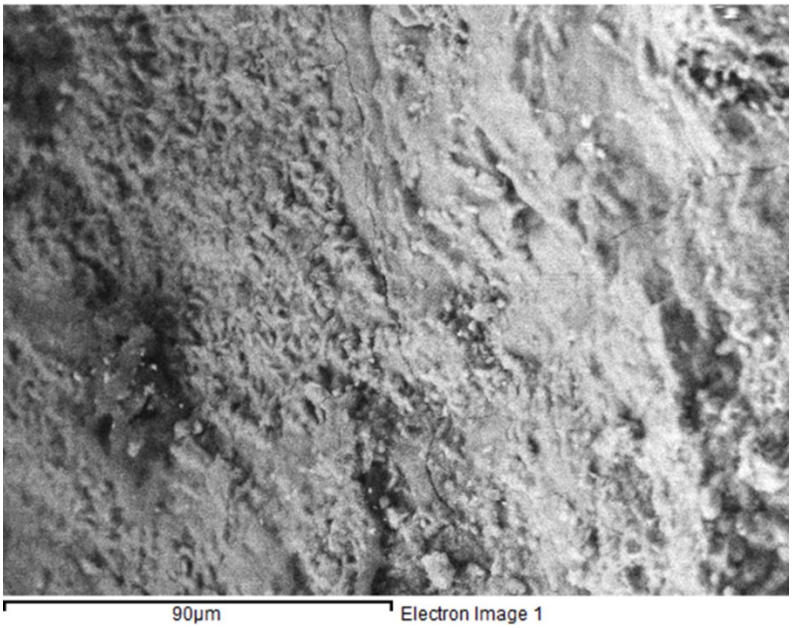


Figure A.518. EDS Elemental Mapping of Rust Collected from Exterior Web.

Element	Weight %	Atomic %
O K	42.31	71.07
Al K	1.22	1.21
Si K	0.61	0.58
S K	0.53	0.45
Cl K	0.13	0.10
Ca K	0.20	0.14
Cr K	0.18	0.10
Mn K	1.30	0.64
Fe K	53.14	25.57
Cu K	0.37	0.16
Totals	100.00	



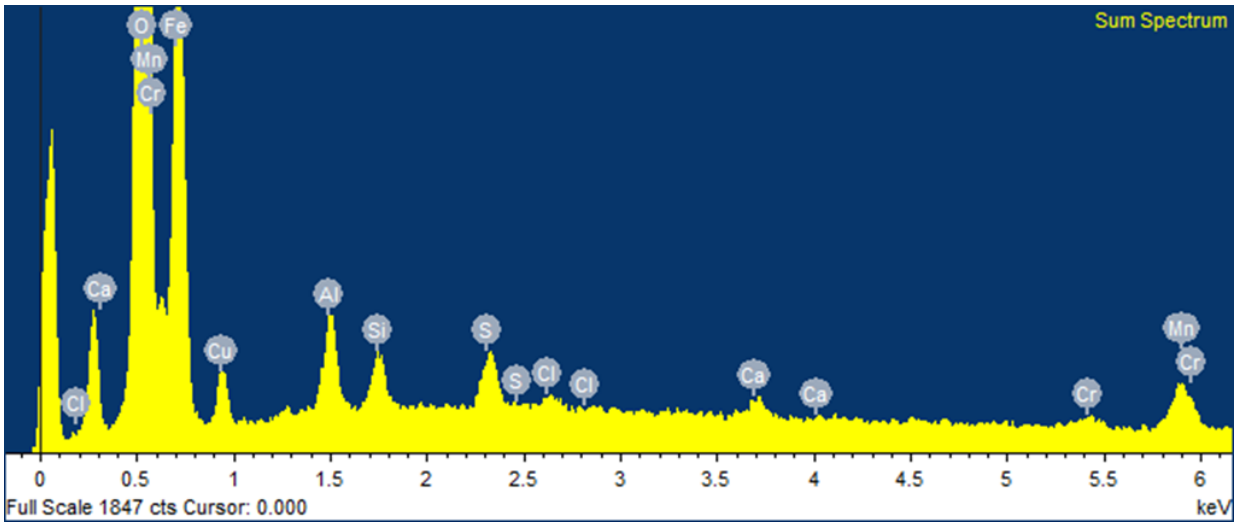


Figure A.519. SEM Image and EDS Spectrum of the Rust Collected from Exterior Web of the Girder.

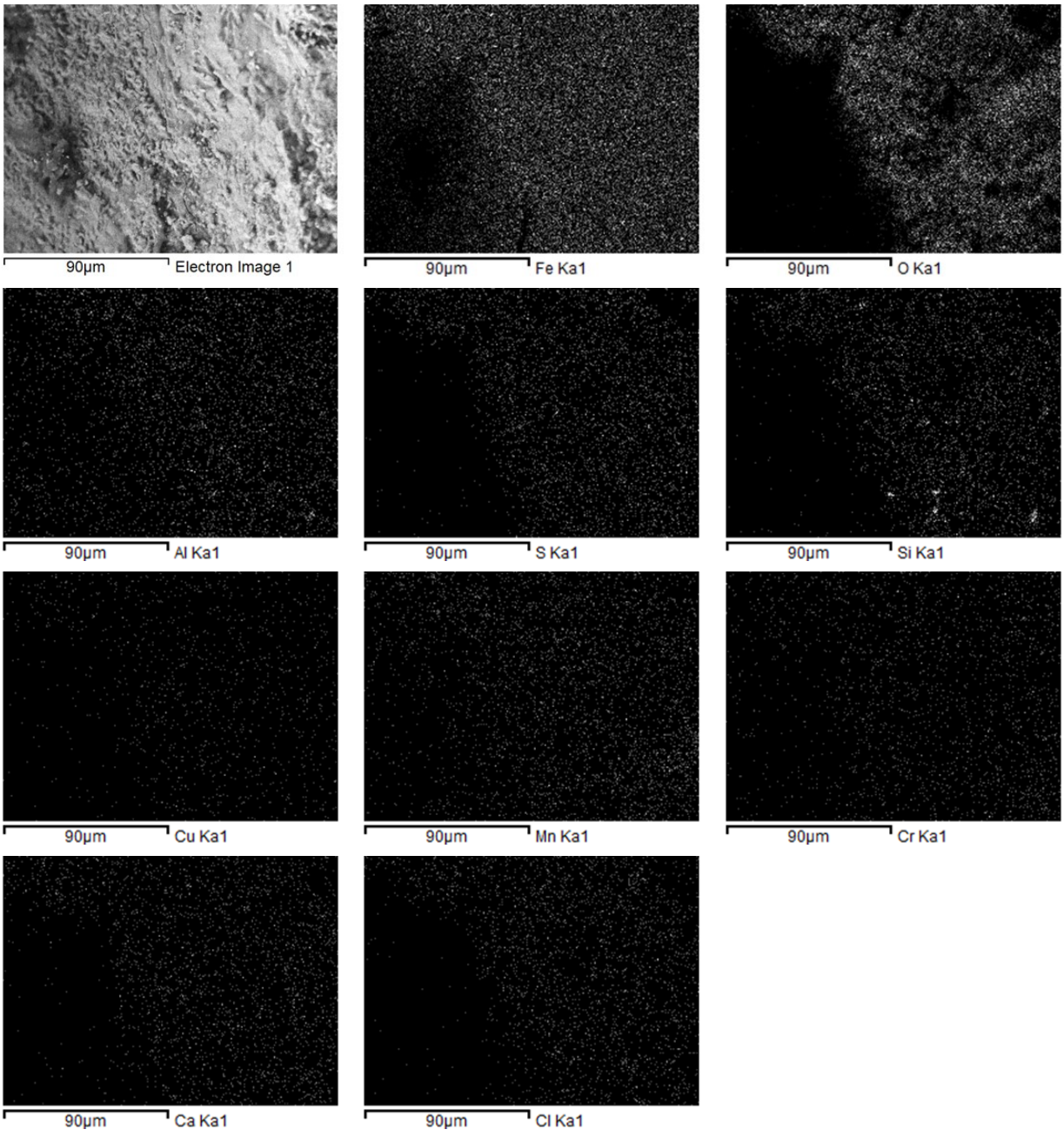
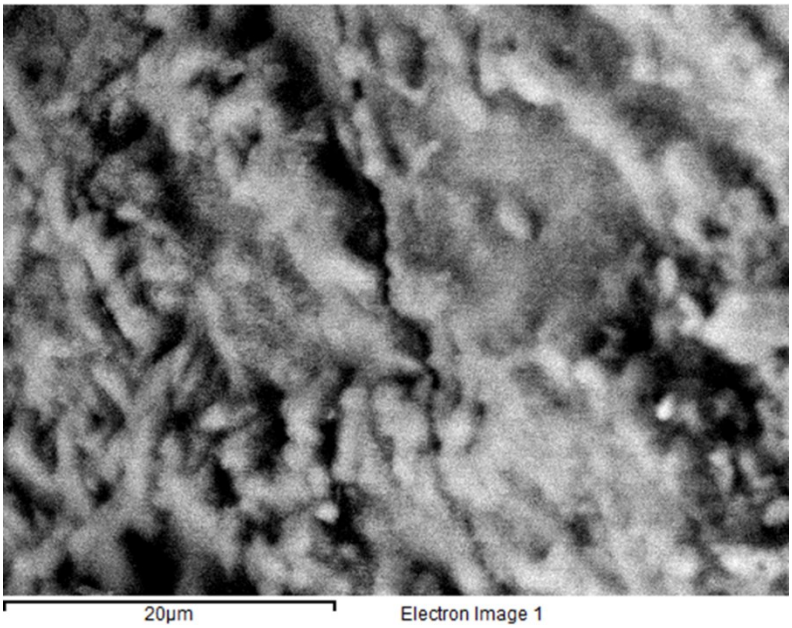


Figure A.520. EDS Elemental Mapping of Rust Collected from Exterior Web.

Element	Weight %	Atomic %
O K	45.63	73.78
Al K	1.04	1.00
Si K	0.57	0.52
S K	0.57	0.46
Cl K	0.15	0.11
Ca K	0.21	0.14
Cr K	0.10	0.05
Mn K	0.99	0.46
Fe K	50.39	23.34
Cu K	0.36	0.15
Totals	100.00	



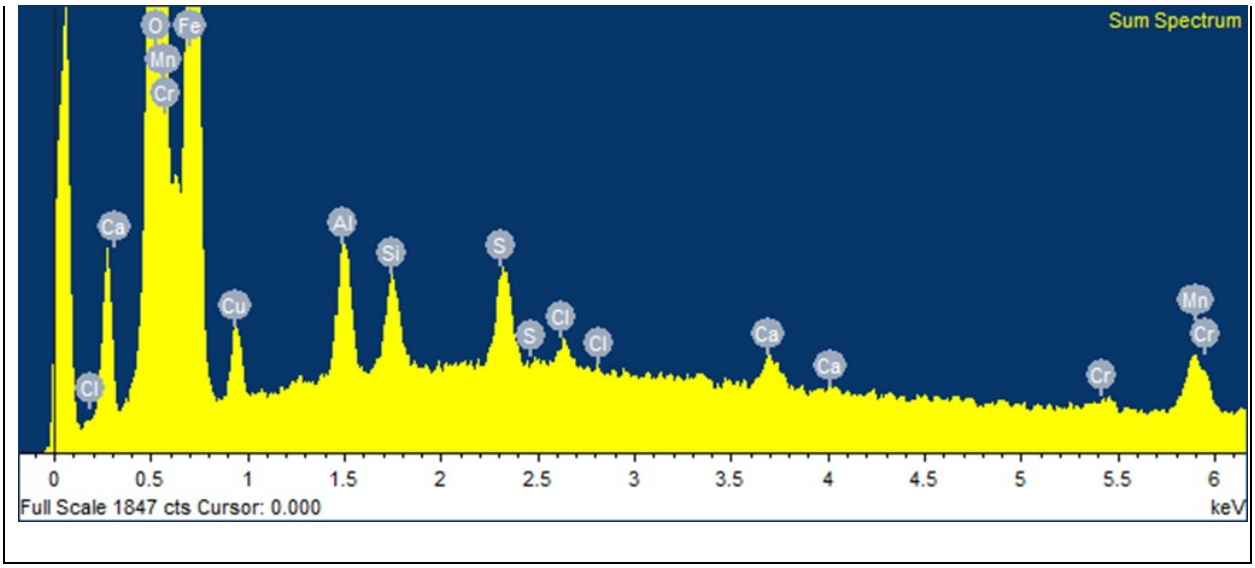


Figure A.521. SEM Image and EDS Spectrum of the Rust Collected from Exterior Web of the Girder.

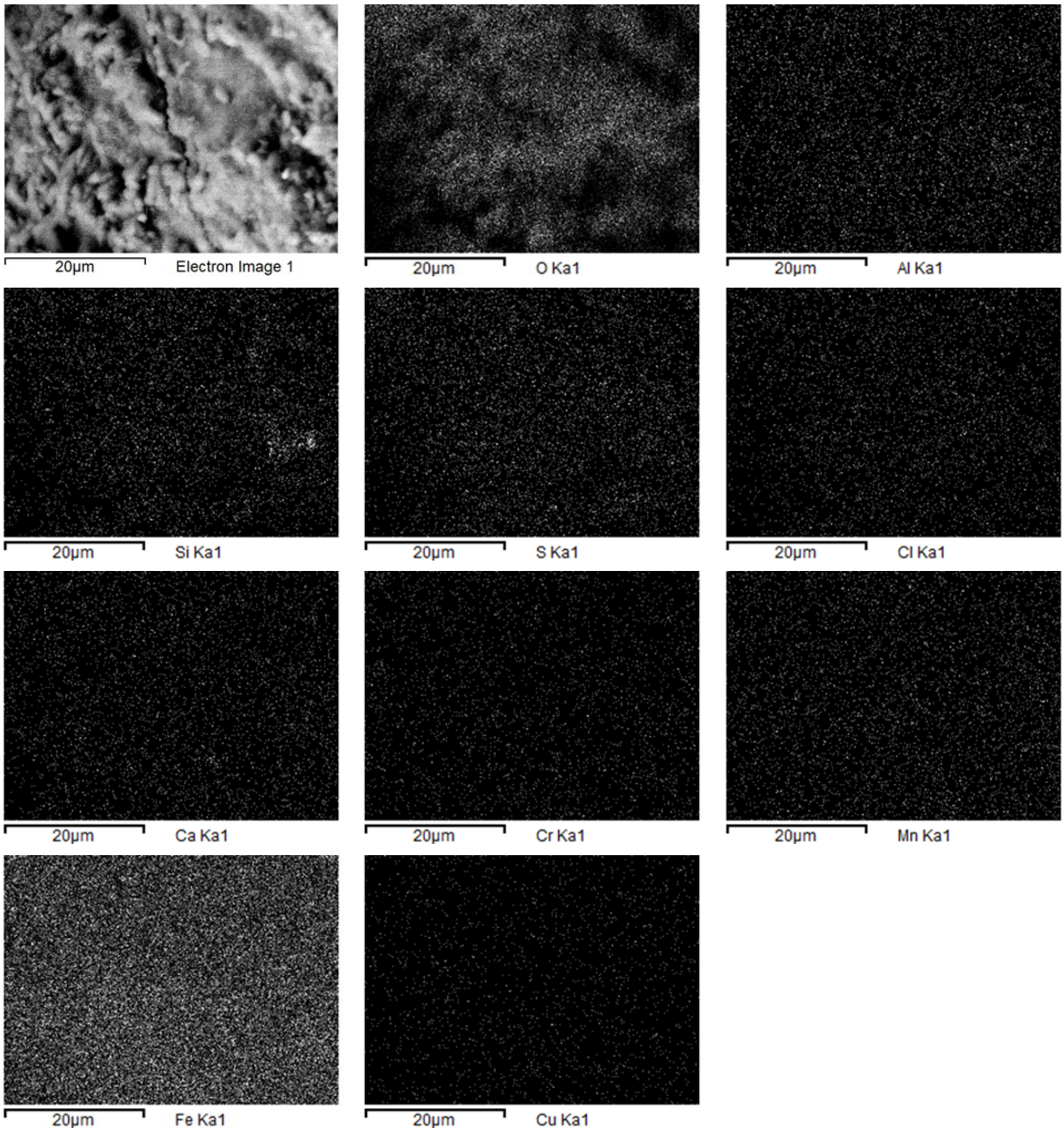
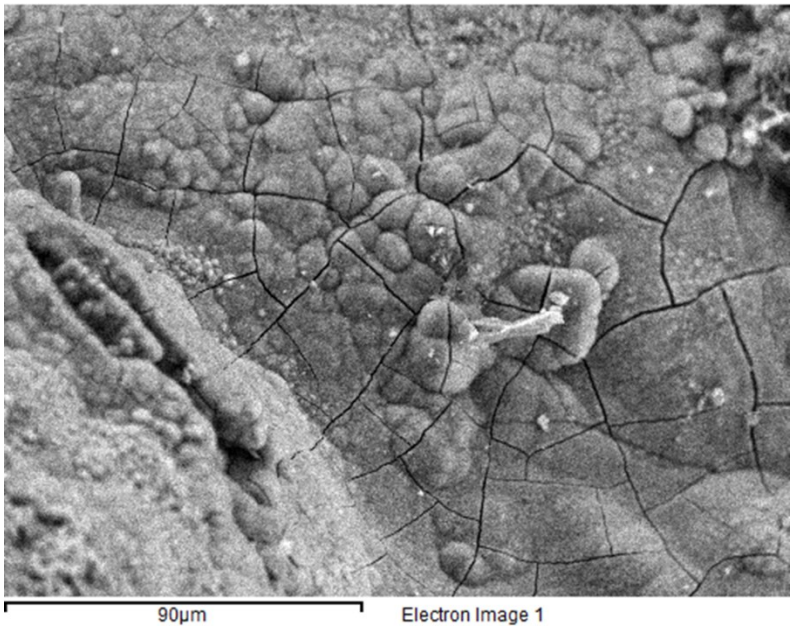


Figure A.522. EDS Elemental Mapping of Rust Collected from Exterior Web.

A.31.4.SEM/EDS Results: Interior Web Girder

Element	Weight %	Atomic %
O K	51.37	78.25
Si K	0.17	0.15
S K	1.25	0.95
Cl K	0.18	0.12
Mn K	1.04	0.46
Fe K	45.99	20.07
Totals	100.00	



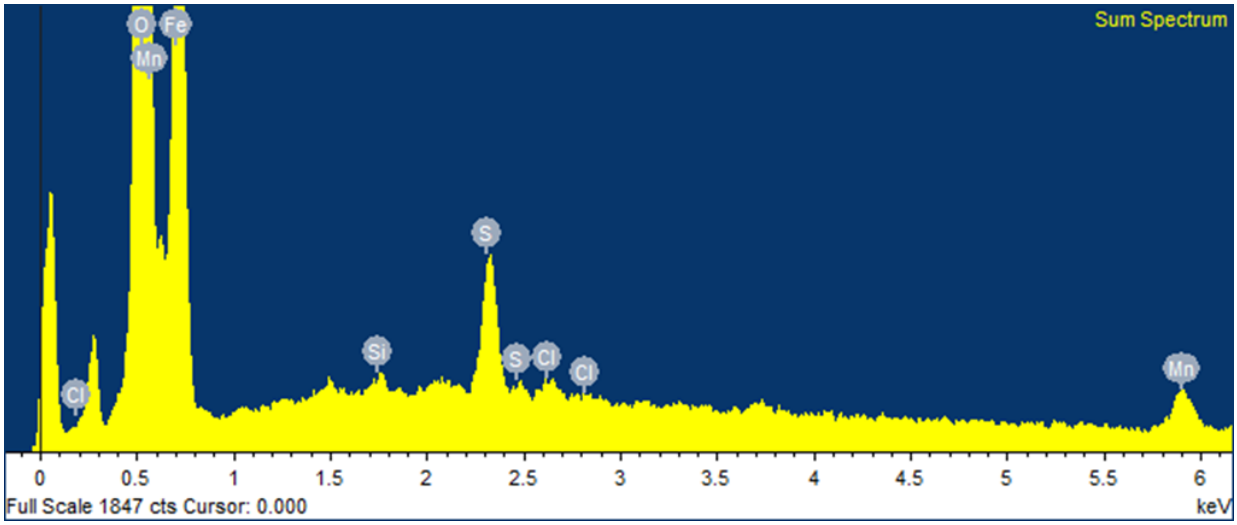
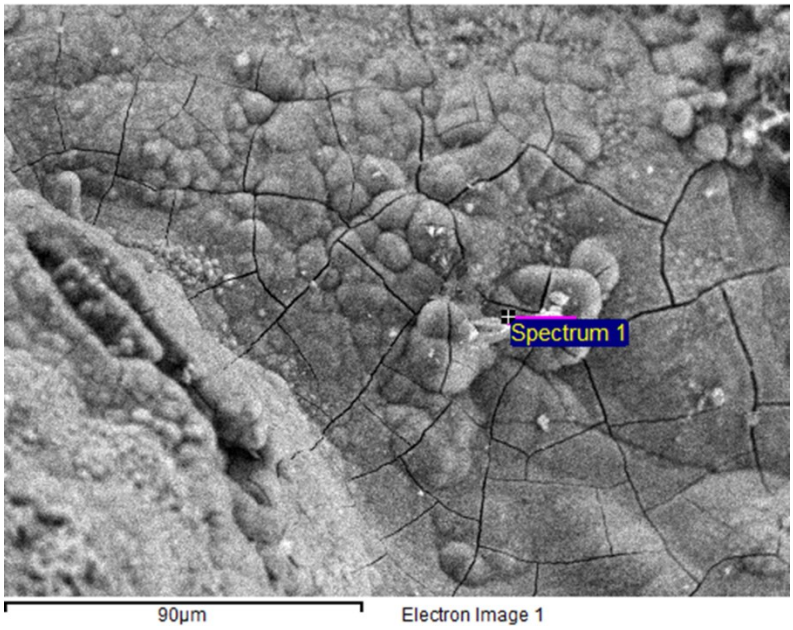


Figure A.523. SEM Image and EDS Spectrum of the Rust Collected from Interior Web of the Girder.

A.31.5.SEM/EDS Results: Interior Web Girder

Element	Weight %	Atomic %
O K	46.18	74.55
Al K	0.24	0.23
Si K	0.27	0.25
S K	0.76	0.62
Ca K	0.21	0.13
Mn K	1.29	0.60
Fe K	51.05	23.61
Totals	100.00	



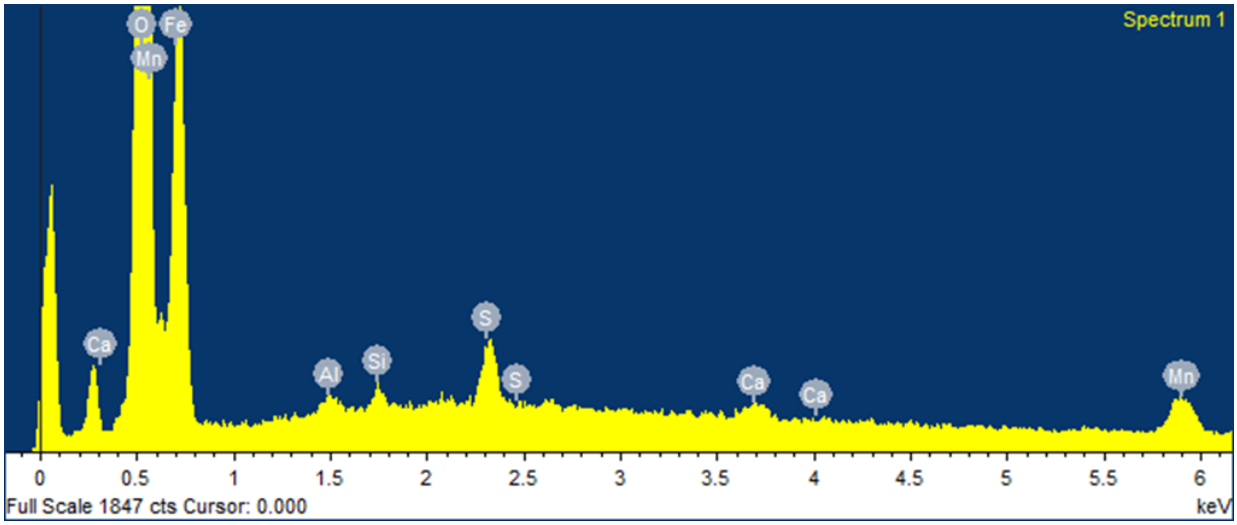
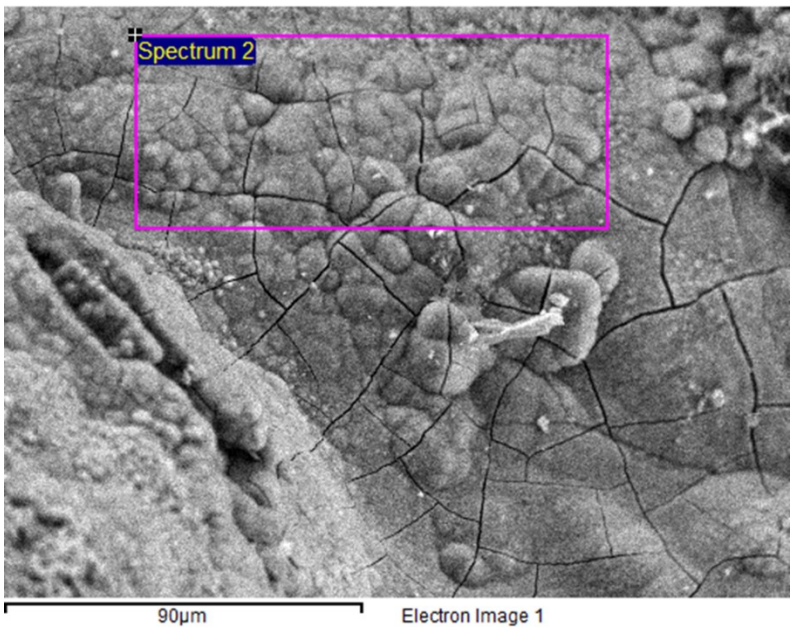


Figure A.524. SEM Image and EDS Spectrum of the Rust Collected from Interior Web of the Girder.

Element	Weight %	Atomic %
O K	56.43	81.37
Si K	0.42	0.35
S K	1.21	0.87
Cl K	0.24	0.15
Ca K	0.12	0.07
Mn K	1.15	0.48
Fe K	40.43	16.70
Totals	100.00	



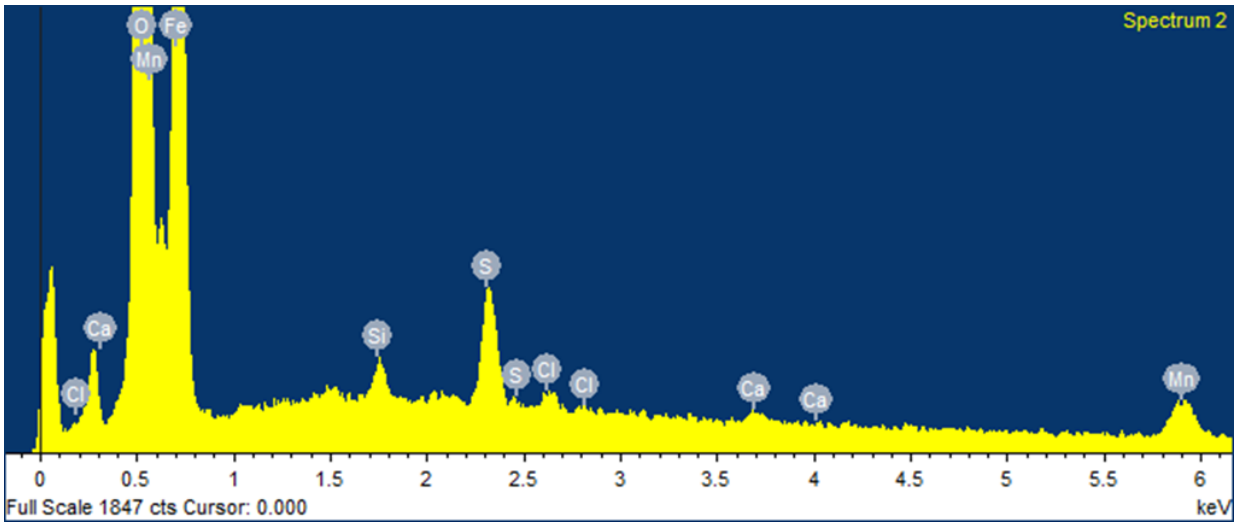


Figure A.525. SEM Image and EDS Spectrum of the Rust Collected from Interior Web of the Girder.

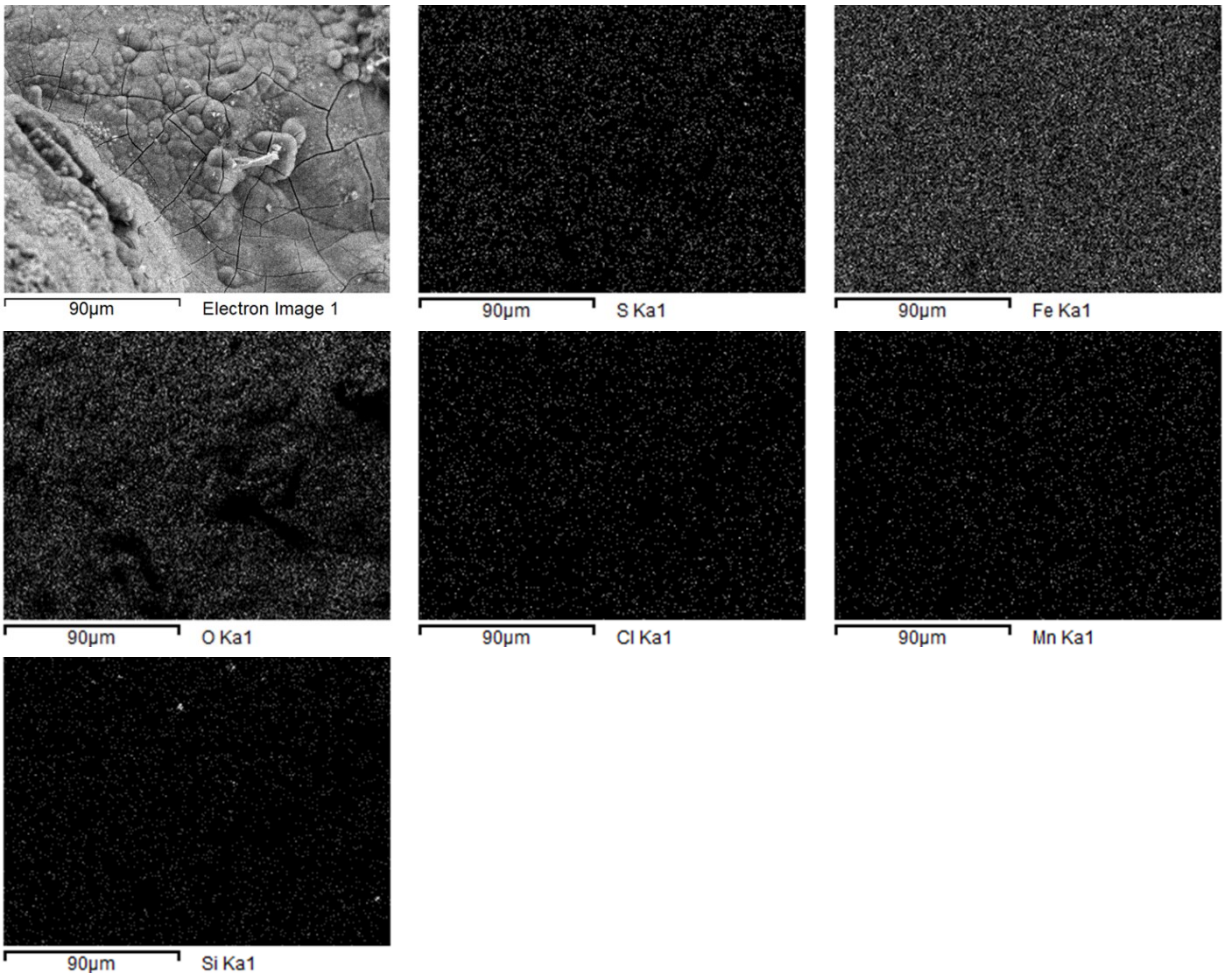
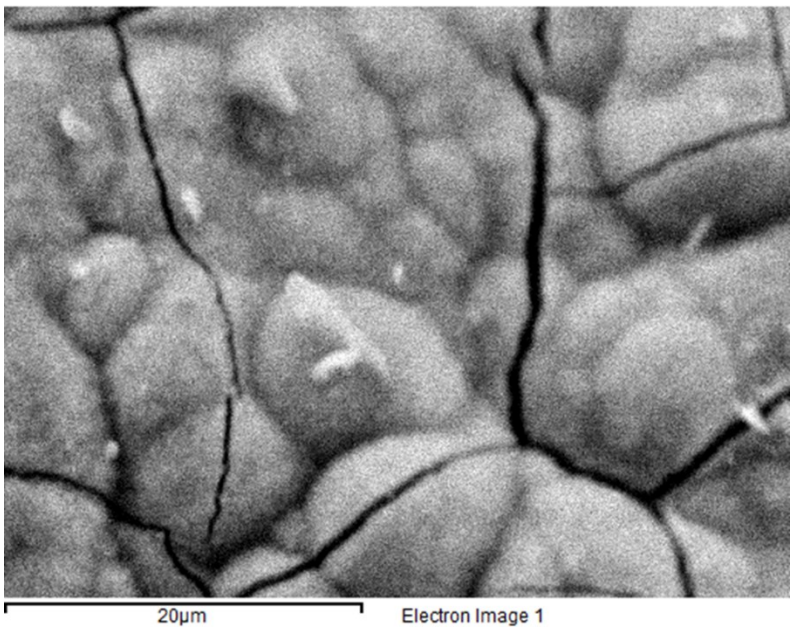


Figure A.526. EDS Elemental Mapping of Rust Collected from Interior Web.

Element	Weight %	Atomic %
O K	56.41	81.30
Na K	0.26	0.26
Al K	0.18	0.15
Si K	0.16	0.13
S K	1.23	0.89
Cl K	0.13	0.08
Mn K	1.11	0.47
Fe K	40.24	16.61
Ni K	0.28	0.11
Totals	100.00	



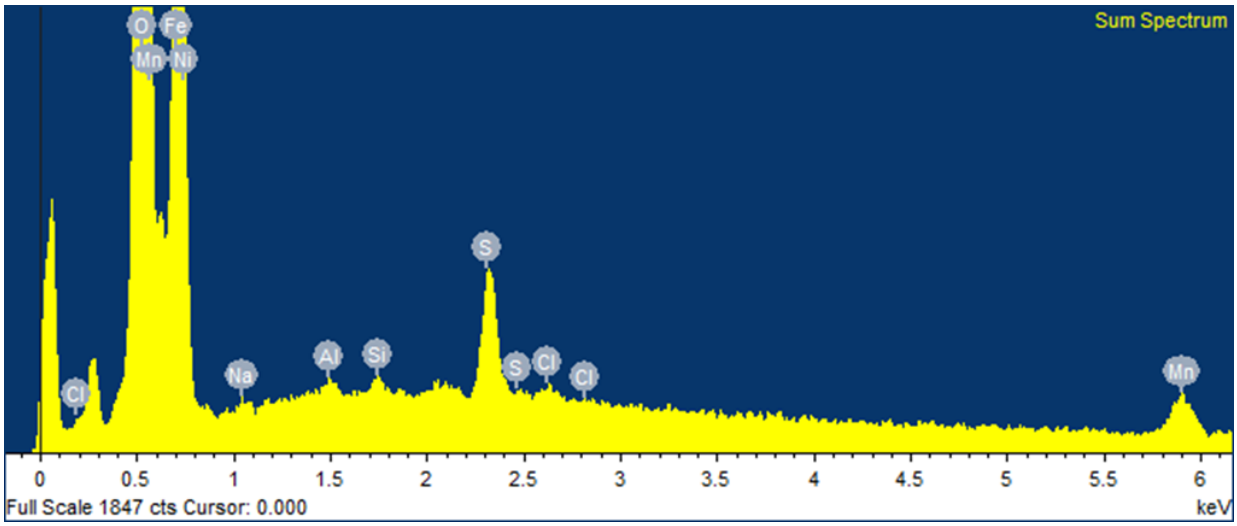


Figure A.527. SEM Image and EDS Spectrum of the Rust Collected from Interior Web of the Girder.

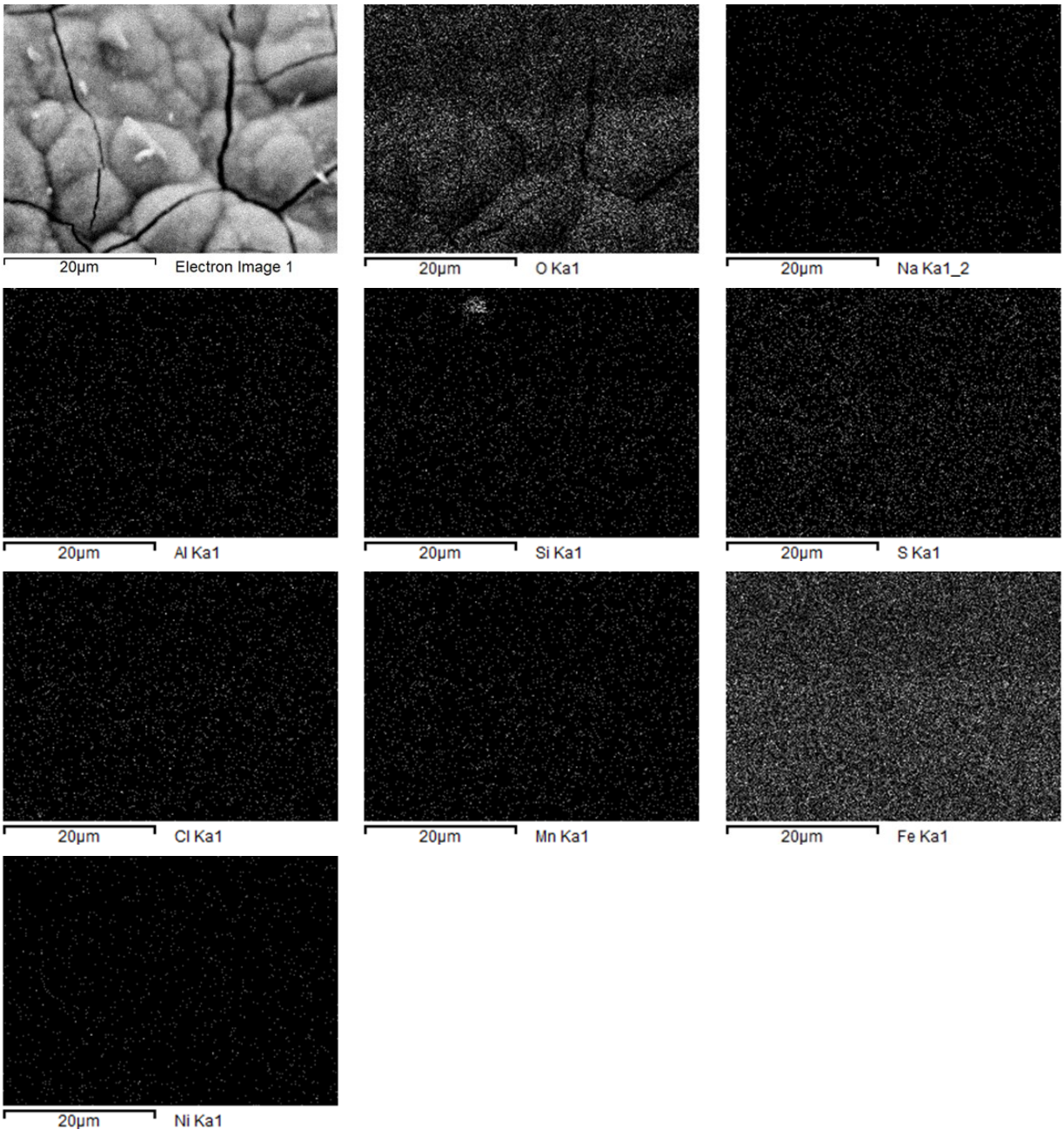
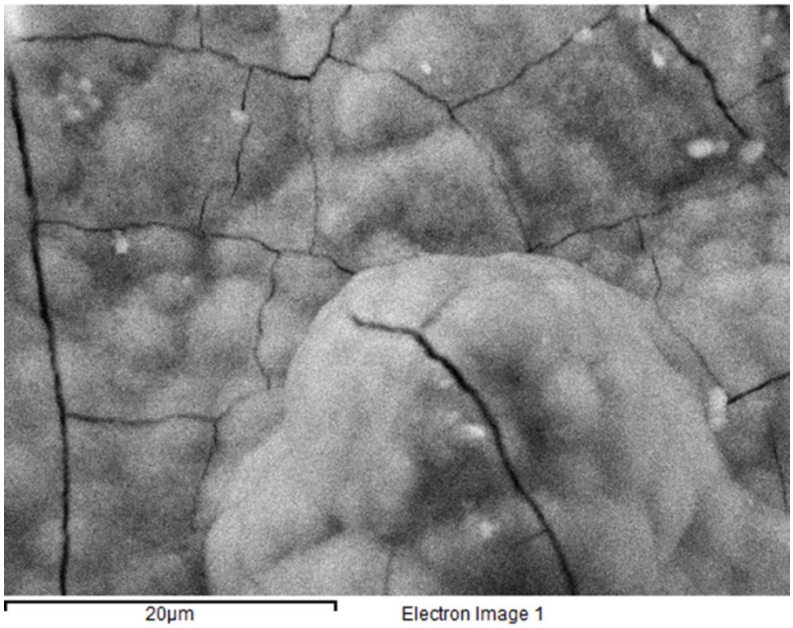


Figure A.528. EDS Elemental Mapping of Rust Collected from Interior Web.

Element	Weight %	Atomic %
O K	53.74	79.78
Al K	0.19	0.17
S K	1.29	0.96
Cl K	0.20	0.13
Mn K	0.71	0.31
Fe K	43.64	18.56
Ni K	0.23	0.09
Totals	100.00	



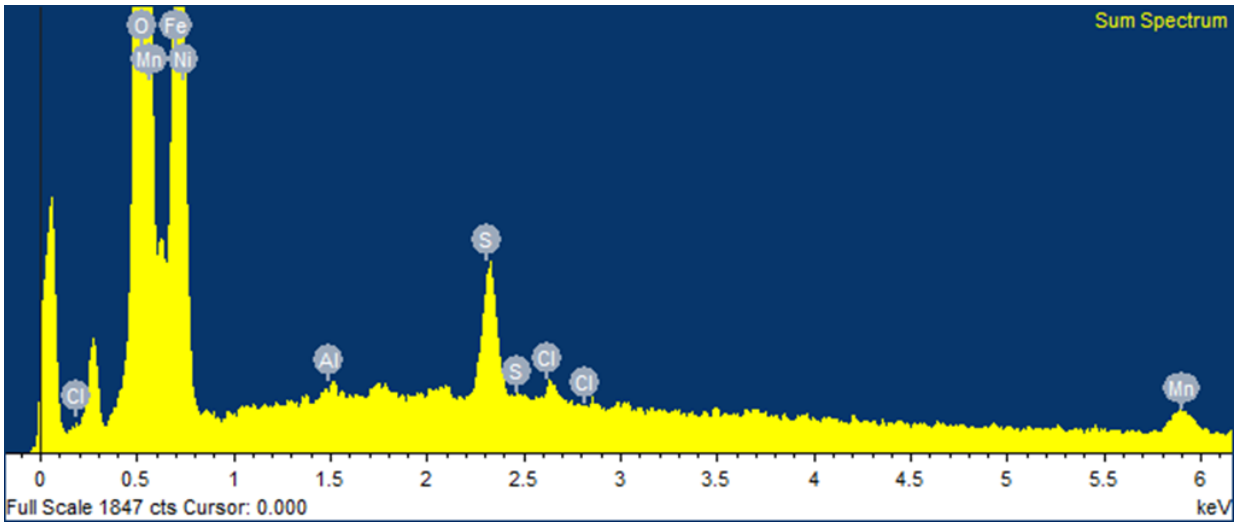


Figure A.529. SEM Image and EDS Spectrum of the Rust Collected from Interior Web of the Girder.

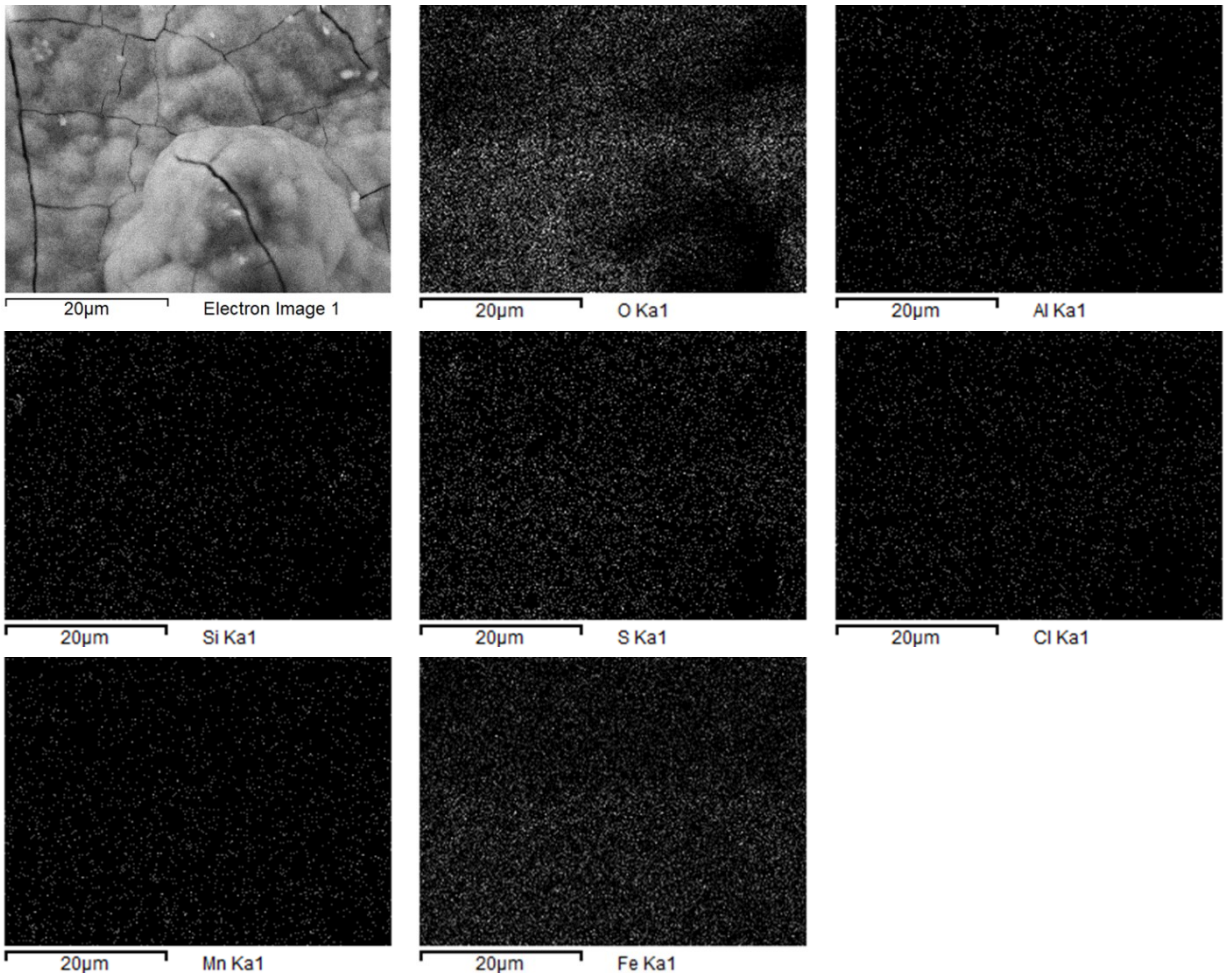


Figure A.530. EDS Elemental Mapping of Rust Collected from Interior Web.

A.31.6.XPS Results: Exterior Web Girder

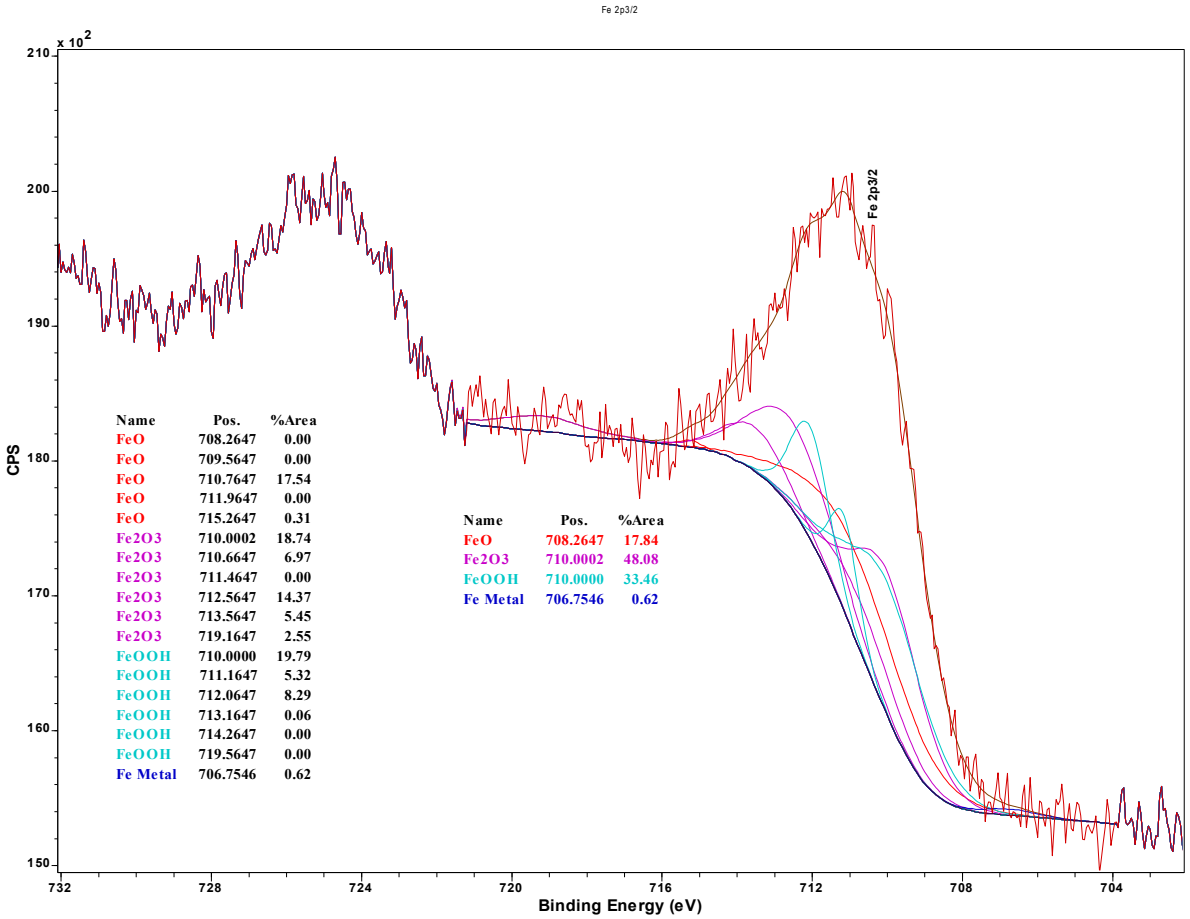


Figure A.531. XPS Spectrum of the Rust Collected from Exterior Web of the Girder.

A.31.7.XPS Results: Interior Web Girder

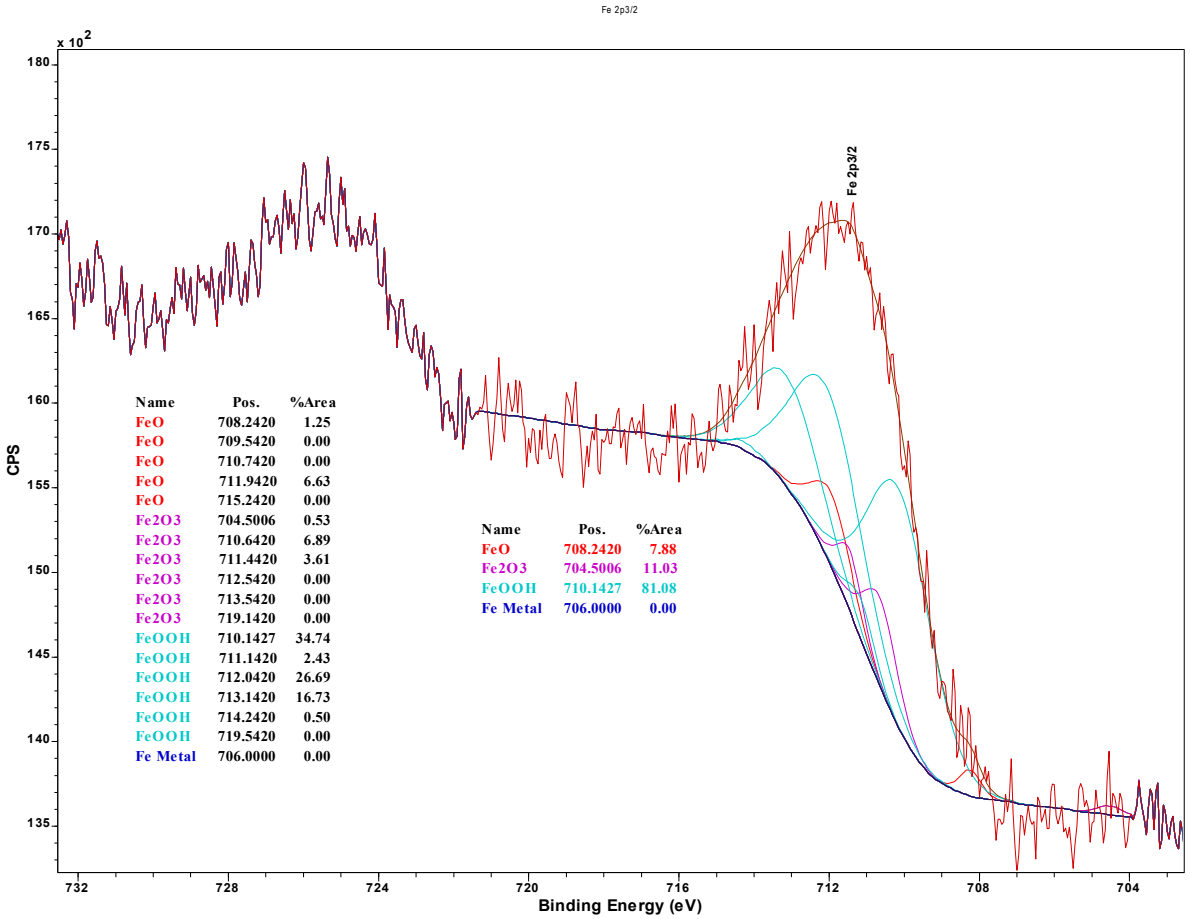


Figure A.532. XPS Spectrum of the Rust Collected from Interior Web of the Girder.

A.31.8.XRD Result: Exterior and Interior Girder

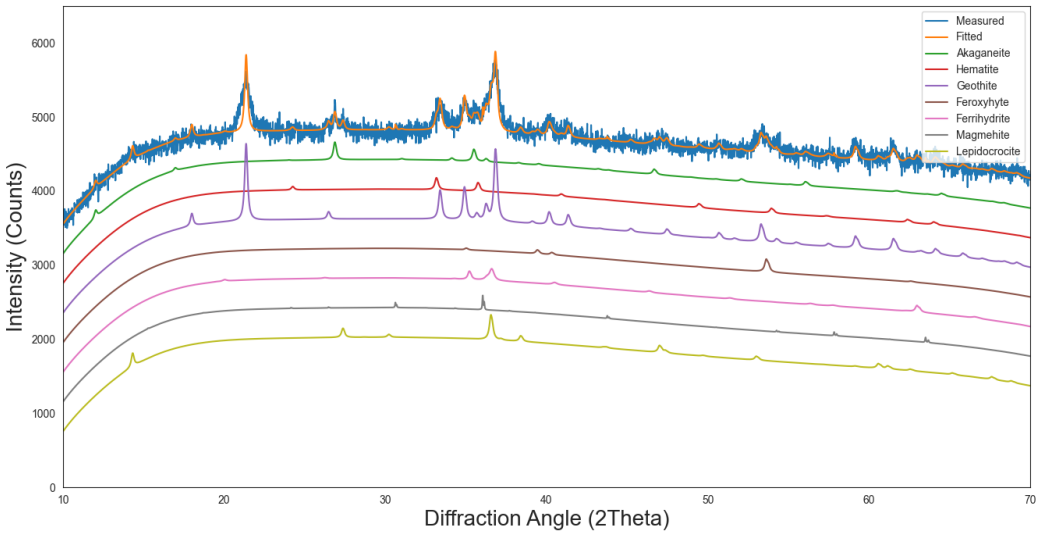


Figure A.533. XRD Pattern of Powdered Rust Collected from Exterior Web of the Girder.

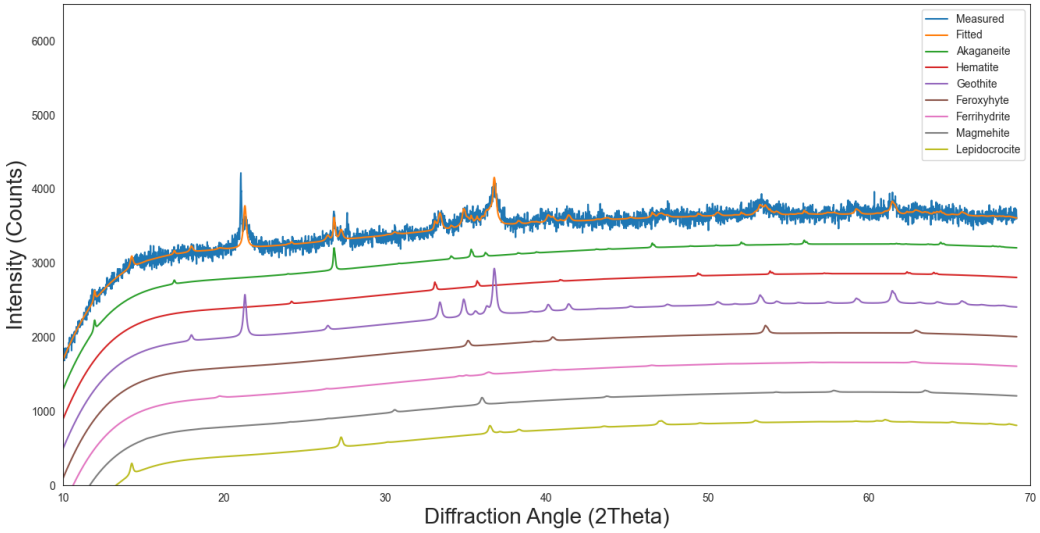


Figure A.534. XRD Pattern of Powdered Rust Collected from Interior Web of the Girder.

A.31.9. Particle Size Analysis: Tape Adhesion Results

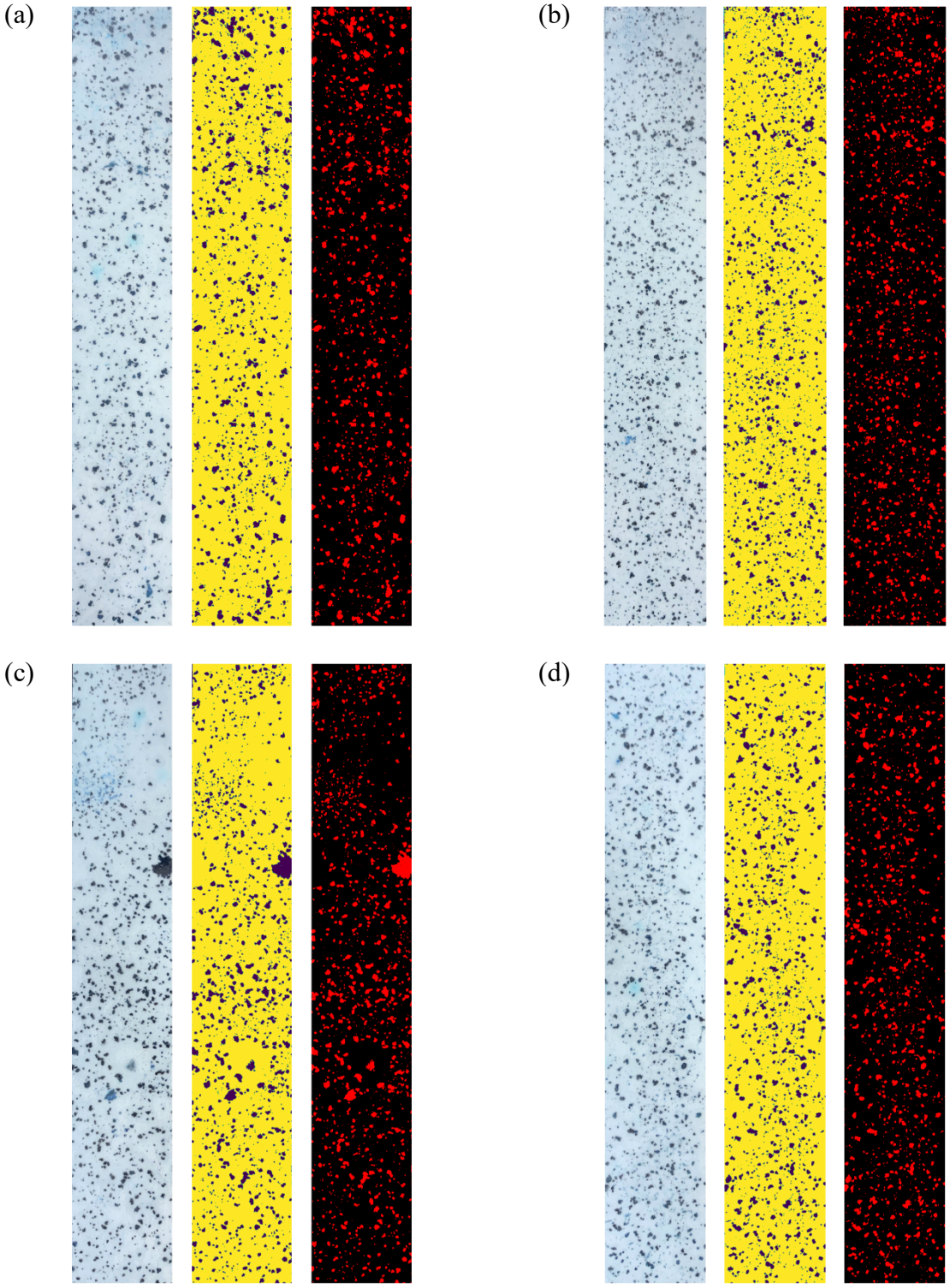


Figure A.535. Particle Size Analysis Results at A31G1F1 (a) Top Flange Bottom, (b) Web, (c) Bottom Flange Bottom (d) Stiffener.

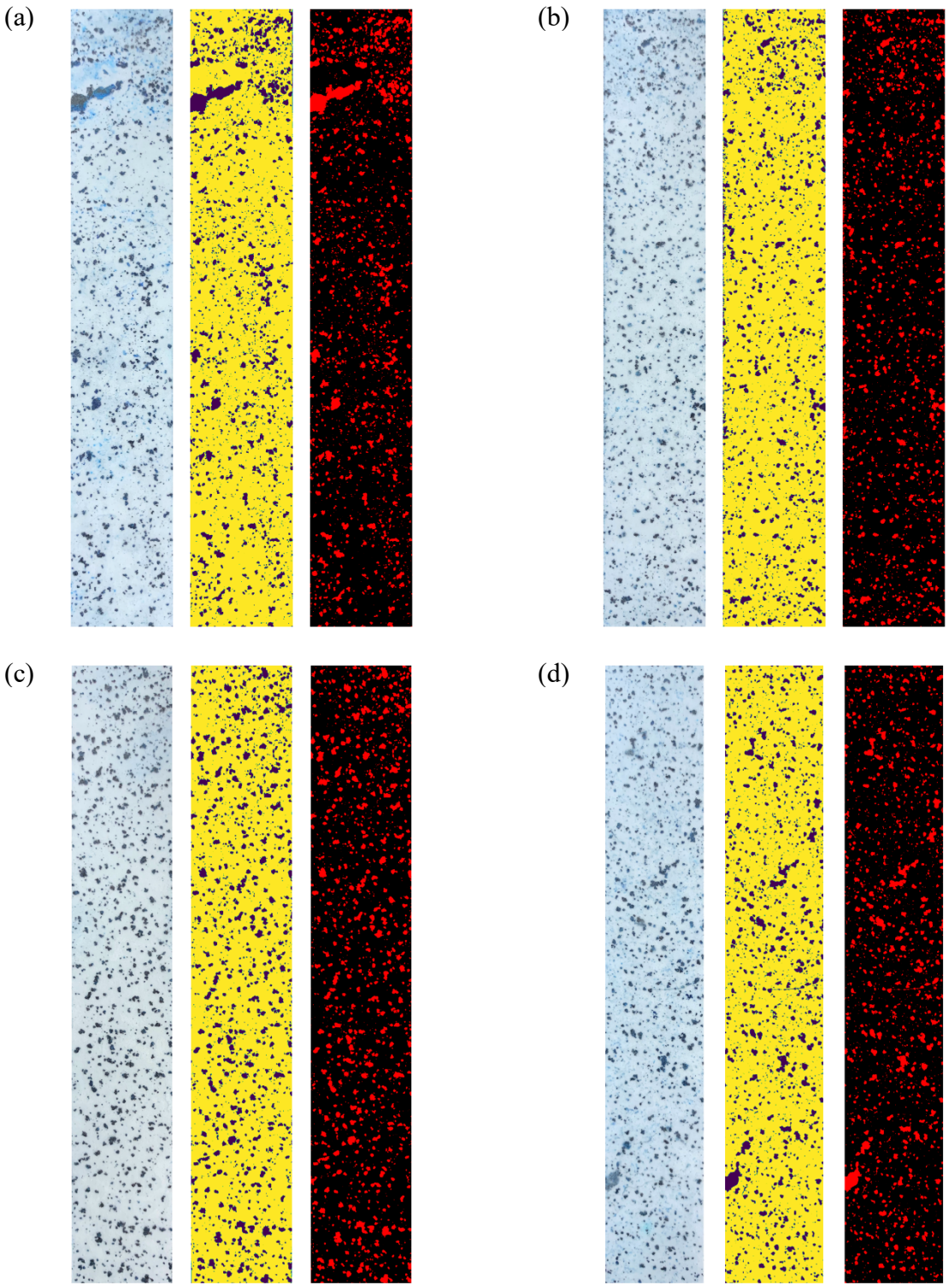


Figure A.536. Particle Size Analysis Results at A31G2F1 (a) Top Flange Bottom, (b) Web, (c) Bottom Flange Bottom (d) Stiffener.

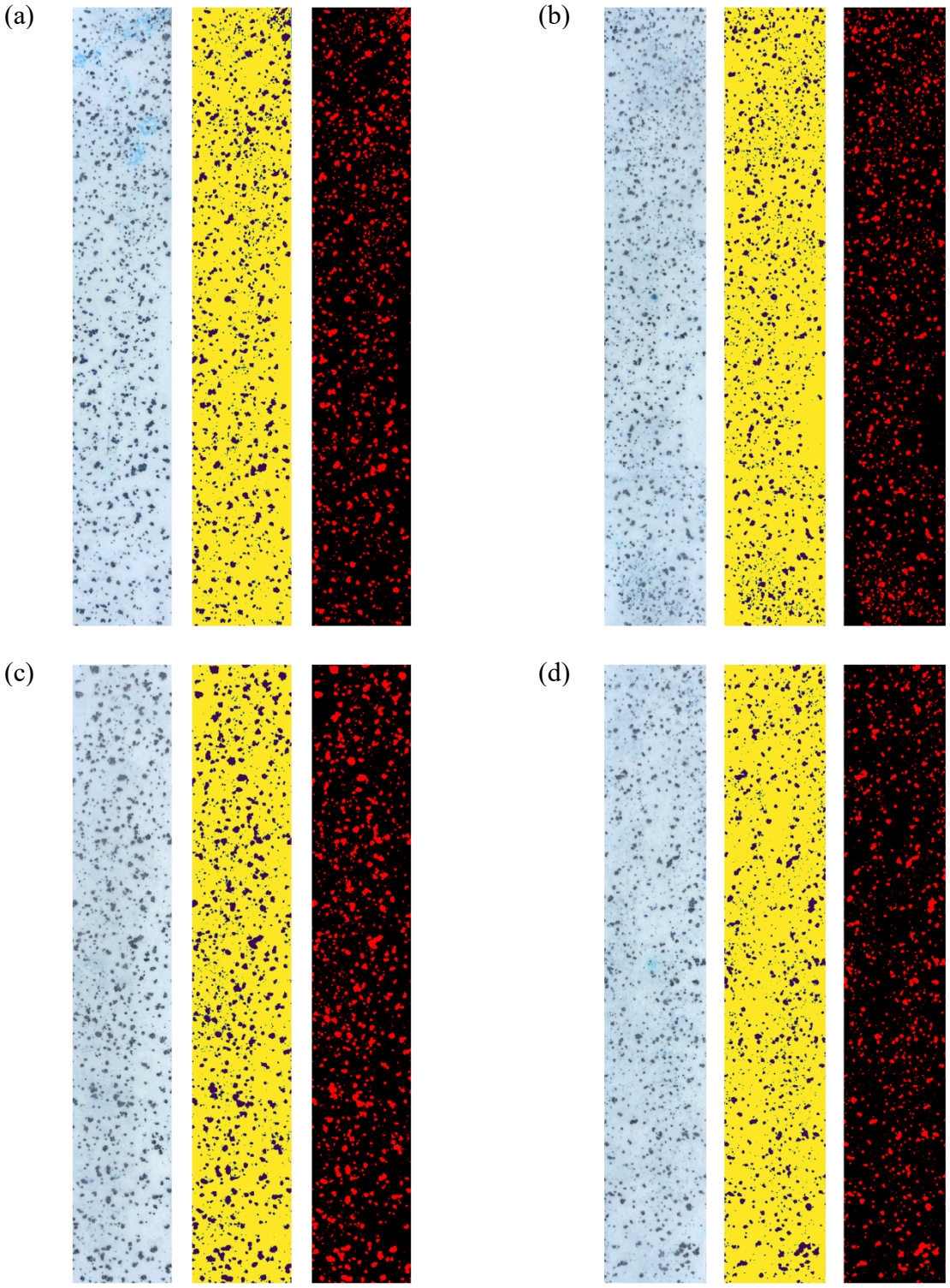


Figure A.537. Particle Size Analysis Results at A31G3F2 (a) Top Flange Bottom, (b) Web, (c) Bottom Flange Bottom (d) Stiffener.

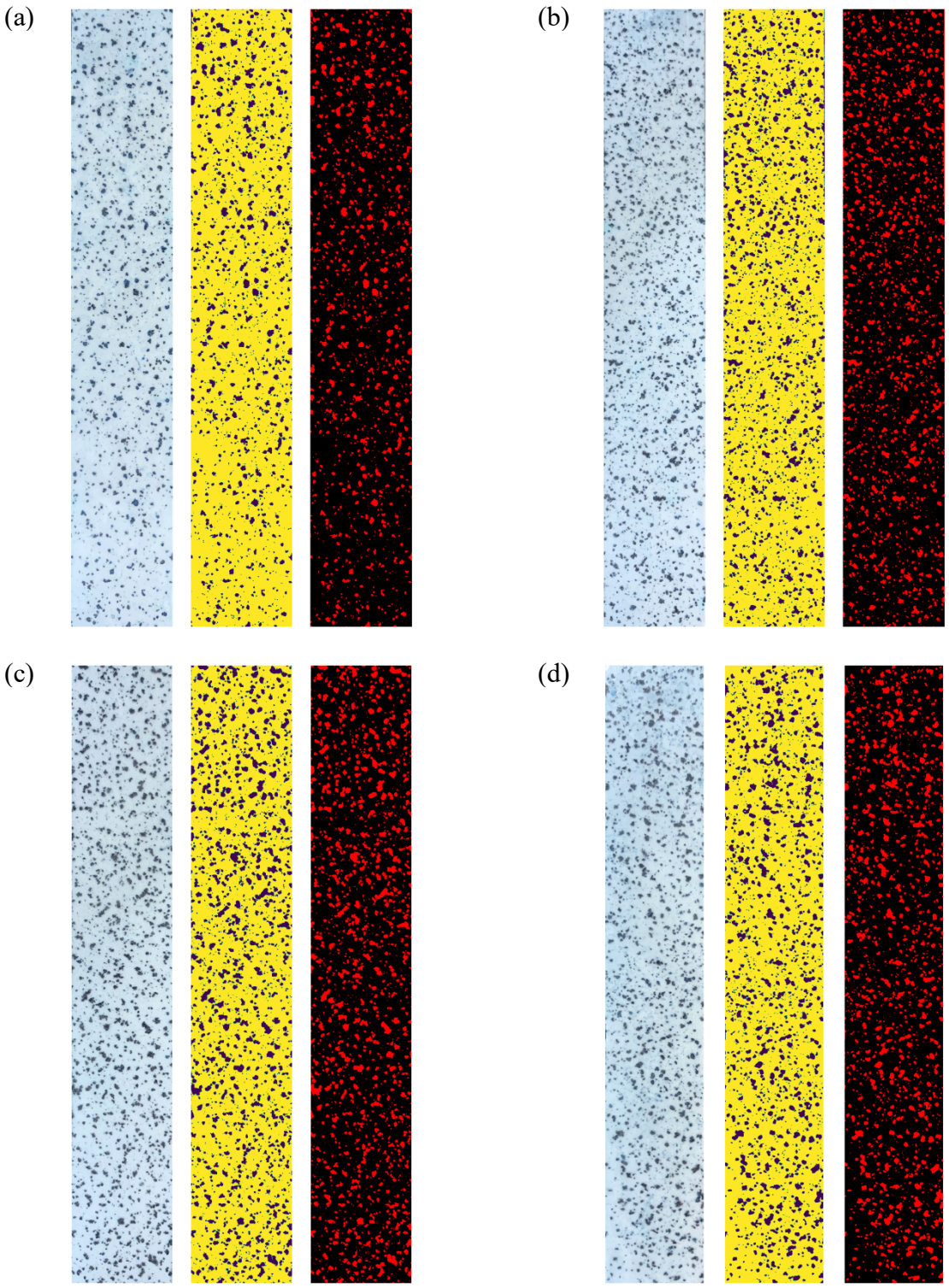


Figure A.538. Particle Size Analysis Results at A31G4F2 (a) Top Flange Bottom, (b) Web, (c) Bottom Flange Bottom (d) Stiffener.

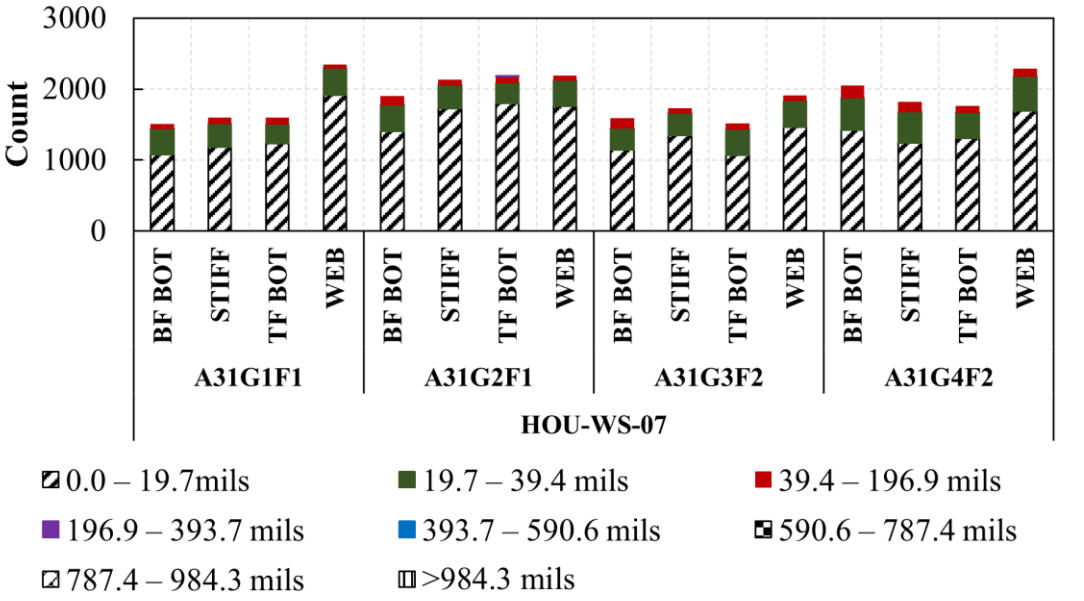


Figure A.539. Particle Size Analysis Showing Different Locations Examined.

A.32. CRP-WS-01

- FM 624 CONN over US 77 SB
- Bridge ID 161780037301038, Coordinates (27.86335, -97.62398), Nueces County
- Continuous weathering steel plate girder
- Built 2007
- Girder inspection carried on end abutment and bent , and measurements are taken on girder within four feet from the abutment or bent.
- No visual inspection on deck
- Location for Testing: A9-G1F1, A9-G2F1, A9-G3F2, A9-G4F2, Bent



Figure A.540. Typical Picture of CRP-WS-01.

A.32.1. Observed Condition

Delaminated areas of the patina are visible on the bottom face of the top flange with a patina rating of 7 on exterior girder. The web has a uniform patina formation with a patina rating of 6. The interior girders have significant poultice corrosion on the top face of the bottom flange due to the accumulation of dirt Index 5 whereas exterior girders have less accumulation of dirt.

A.32.2.Field Inspection Results

Table A-144. Field Inspection Results for CRP-WS-01.

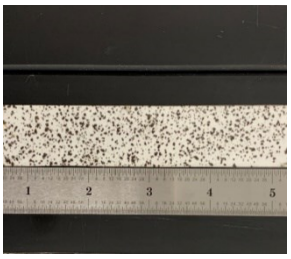
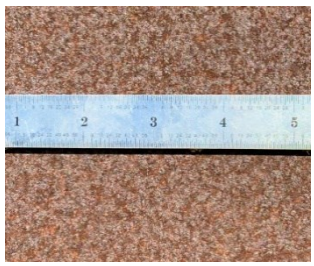
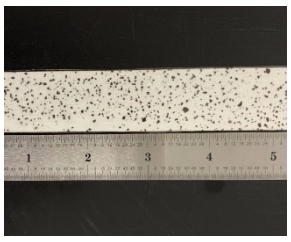
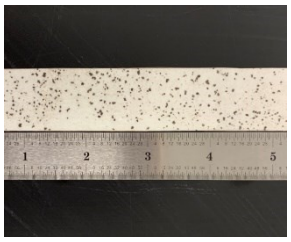
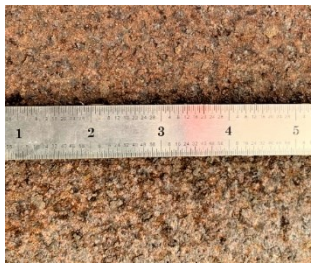
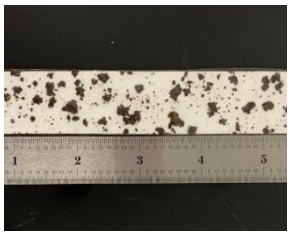
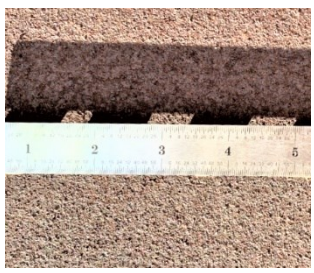
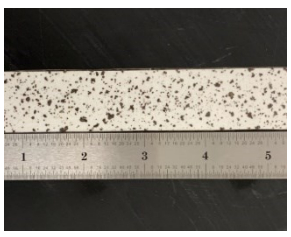
Location	Patina Rating	Thickness (inch)	Cl^- Conc. (ppm)	Field Condition	Tape Test
A9-G1F1 TF Bot. Ext.	7	Measured R1 0.999 R2 0.998 R3 0.997 R_Avg 0.998 Design			
A9-G1F1 Web Ext.	7	Measured R1 0.747 R2 0.747 R3 0.749 R_Avg 0.748 Design			
A9-G1F1 BF Top Ext.	7	Measured R1 1.236 R2 1.237 R3 1.237 R_Avg 1.237 Design			
A9-G1F1 BF Bot. Ext.	5	-			
A9-G1F1 Stiffener Ext.	7	Measured R1 0.871 R2 0.874 R3 0.872 R_Avg 0.872 Design			

Table A-145. Field Inspection Results for CRP-WS-01.

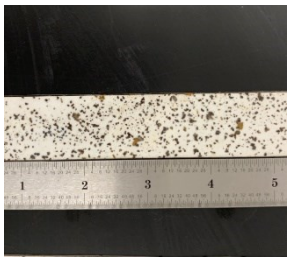
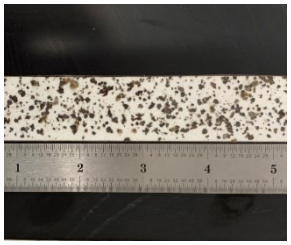
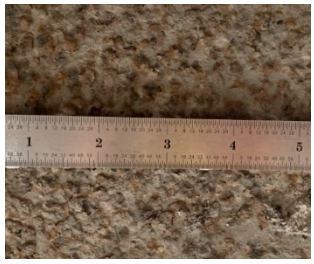
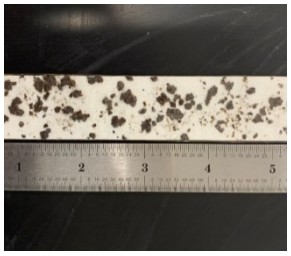
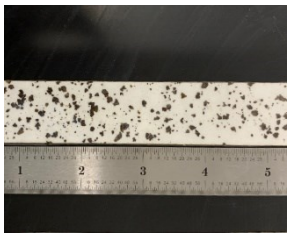
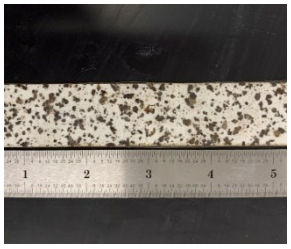
Location	Patina Rating	Thickness (inch)	Cl^- Conc. (ppm)	Field Condition	Tape Test
A9-G2F1 TF Bot. Int.	7	Measured R1 0.999 R2 0.998 R3 0.998 R_Avg 0.998 Design			
A9-G2F1 Web Int.	5	Measured R1 0.752 R2 0.752 R3 0.750 R_Avg 0.751 Design			
A9-G2F1 BF Top Int.	5	Measured R1 1.250 R2 1.247 R3 1.249 R_Avg 1.249 Design			
A9-G2F1 BF Bot. Int.	6	-			
A9-G2F1 Stiffener Ext.	6	Measured R1 0.873 R2 0.880 R3 0.877 R_Avg 0.877 Design			

Table A-146. Field Inspection Results for CRP-WS-01.

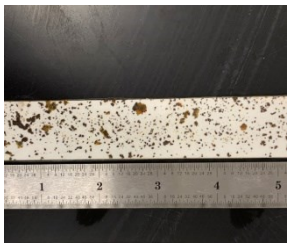
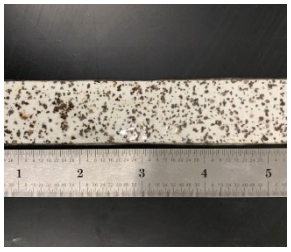
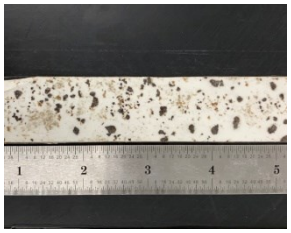
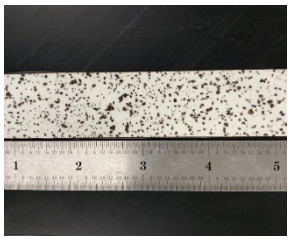
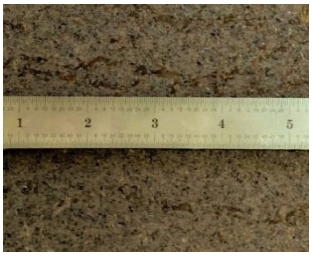
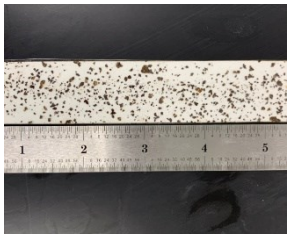
Location	Patina Rating	Thickness (inch)	Cl^- Conc. (ppm)	Field Condition	Tape Test
A9-G3F2 TF Bot. Int.	6	Measured R1 0.993 R2 0.992 R3 0.994 R_Avg 0.993			
A9-G3F2 Web Int.	6	Measured R1 0.745 R2 0.747 R3 0.746 R_Avg 0.746 Design			
A9-G3F2 BF Top Int.	5	Measured R1 1.243 R2 1.245 R3 1.245 R_Avg 1.244 Design			
A9-G3F2 BF Bot. Int.	6	-			
A9-G3F2 Stiffener Int.	6	Measured R1 0.865 R2 0.868 R3 0.868 R_Avg 0.867 Design			

Table A-147. Field Inspection Results for CRP-WS-01.

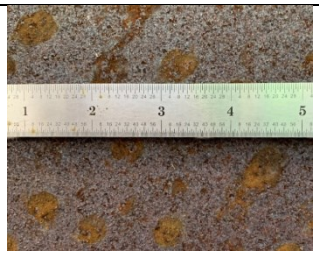
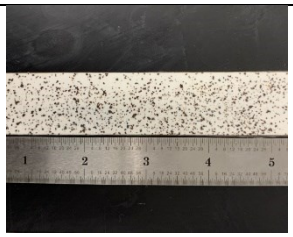
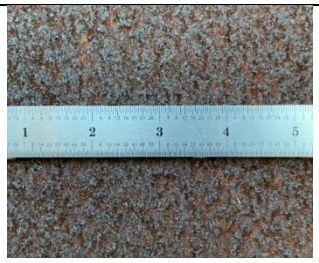
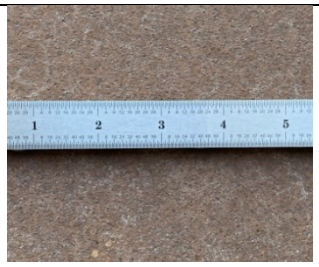
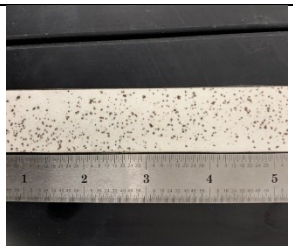
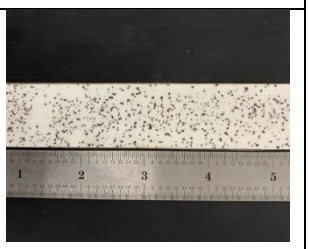
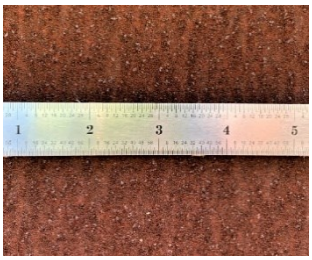
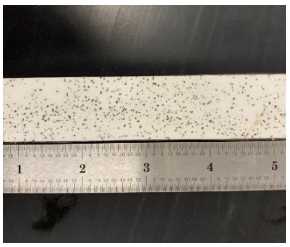
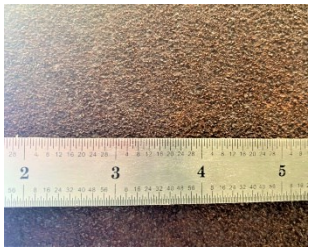
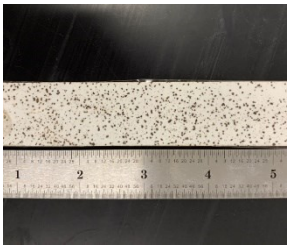
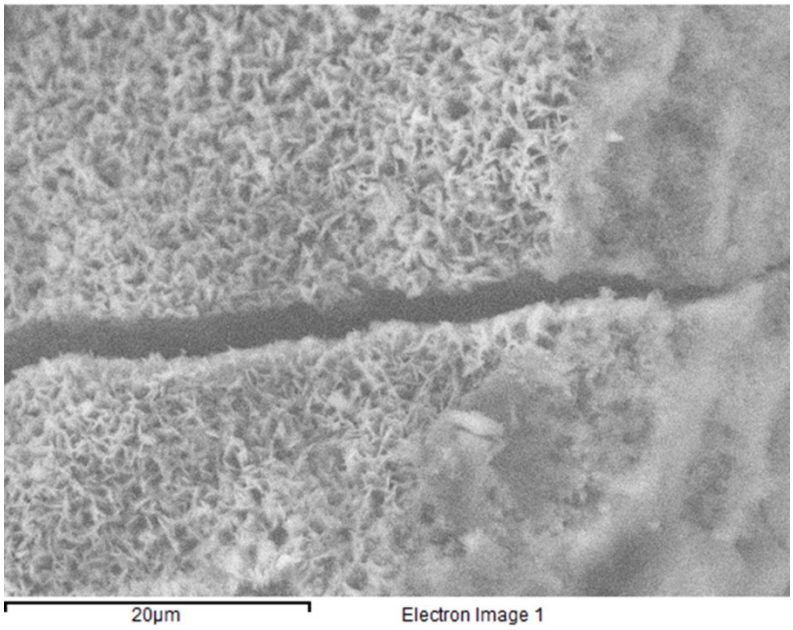
Location	Patina Rating	Thickness (inch)	Cl^- Conc. (ppm)	Field Condition	Tape Test
A9-G4F2 TF Bot. Ext.	7	Measured R1 0.993 R2 0.994 R3 0.995 R_Avg 0.994 Design			
A9-G4F2 Web Ext.	8	Measured R1 0.746 R2 0.747 R3 0.747 R_Avg 0.747 Design			
A9-G4F2 BF Top Ext.	7	Measured R1 1.240 R2 1.240 R3 1.240 R_Avg 1.240 Design			
A9-G4F2 BF Bot. Ext.	6				
A9-G4F2 Stiffener Ext.	7	Measured R1 0.867 R2 0.867 R3 0.867 R_Avg 0.867 Design			

Table A-148. Field Inspection Results for CRP-WS-01.

Location	Patina Rating	Thickness (inch)	Cl^- Conc. (ppm)	Field Condition	Tape Test
Bent Web Ext.	8	Measured R1 0.623 R2 0.624 R3 0.624 R_Avg 0.624 Design			
Bent BF Bot. Ext.	8	Measured R1 2.003 R2 2.008 R3 2.008 R_Avg 2.006 Design			

A.32.3.SEM/EDS Results: Exterior Web Girder

Element	Weight %	Atomic %
O K	45.59	73.60
Al K	0.92	0.88
Si K	1.02	0.94
S K	0.41	0.33
Cl K	0.57	0.41
Ca K	0.11	0.07
Mn K	0.41	0.19
Fe K	50.97	23.57
Totals	100.00	



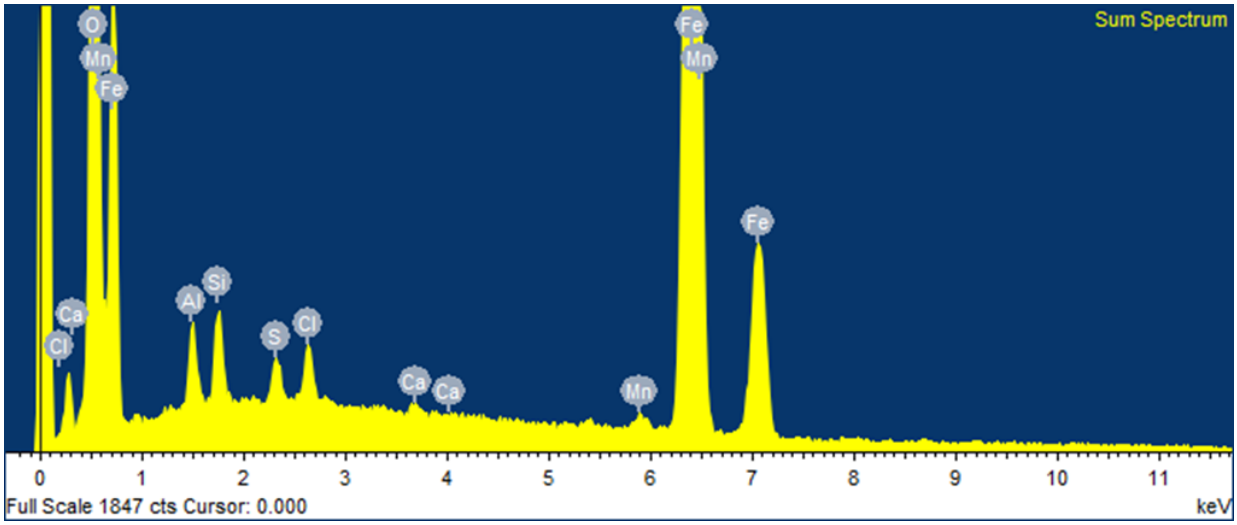
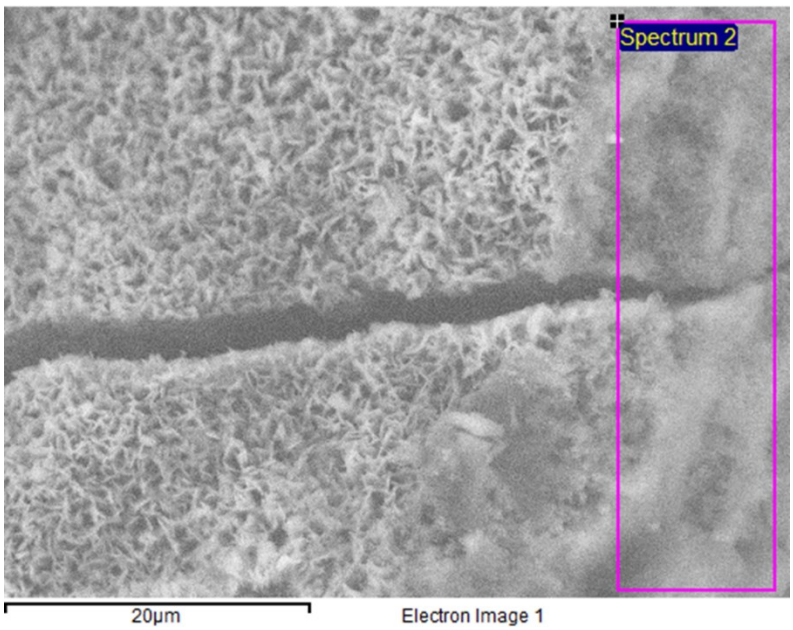


Figure A.541. SEM Image and EDS Spectrum of the Rust Collected from Exterior Web of the Girder.

Element	Weight %	Atomic %
O K	27.78	56.07
Al K	1.39	1.66
Si K	1.73	1.99
S K	0.31	0.31
Cl K	0.52	0.47
Cr K	0.27	0.17
Mn K	0.58	0.34
Fe K	67.33	38.94
Cu K	0.10	0.05
Totals	100.00	



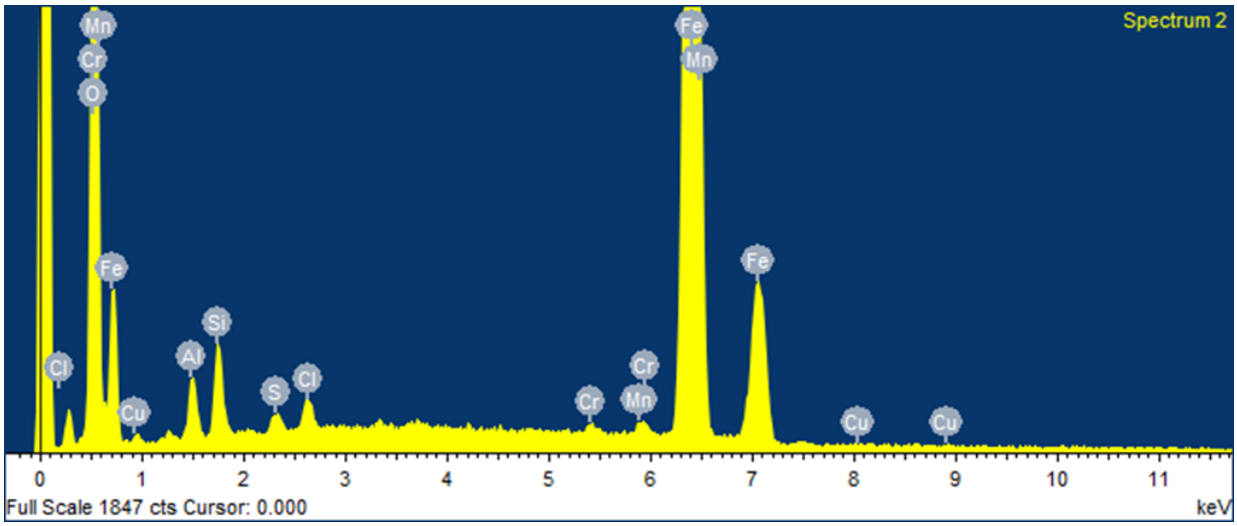
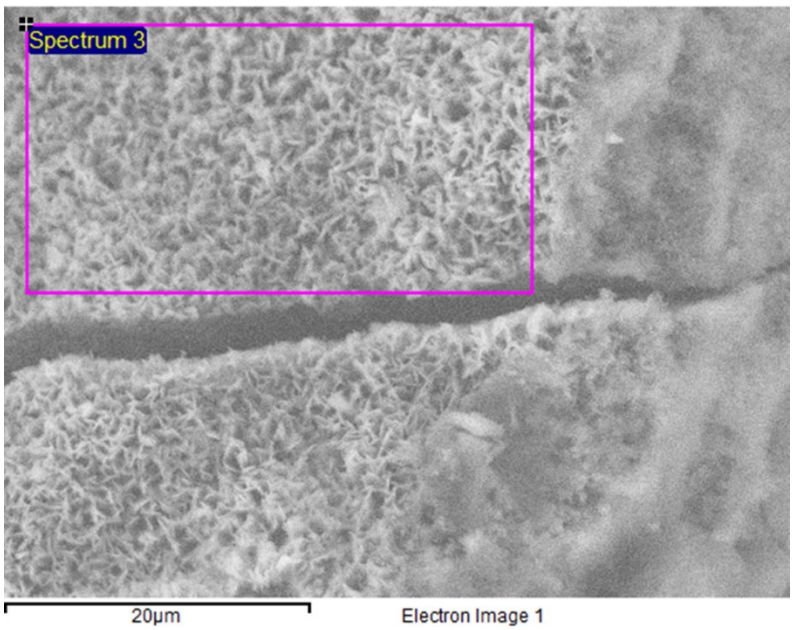


Figure A.542. SEM Image and EDS Spectrum of the Rust Collected from Exterior Web of the Girder.

Element	Weight %	Atomic %
O K	49.74	76.97
Al K	0.72	0.66
Si K	0.31	0.28
S K	0.39	0.30
Cl K	0.55	0.38
Mn K	0.34	0.15
Fe K	47.96	21.26
Totals	100.00	



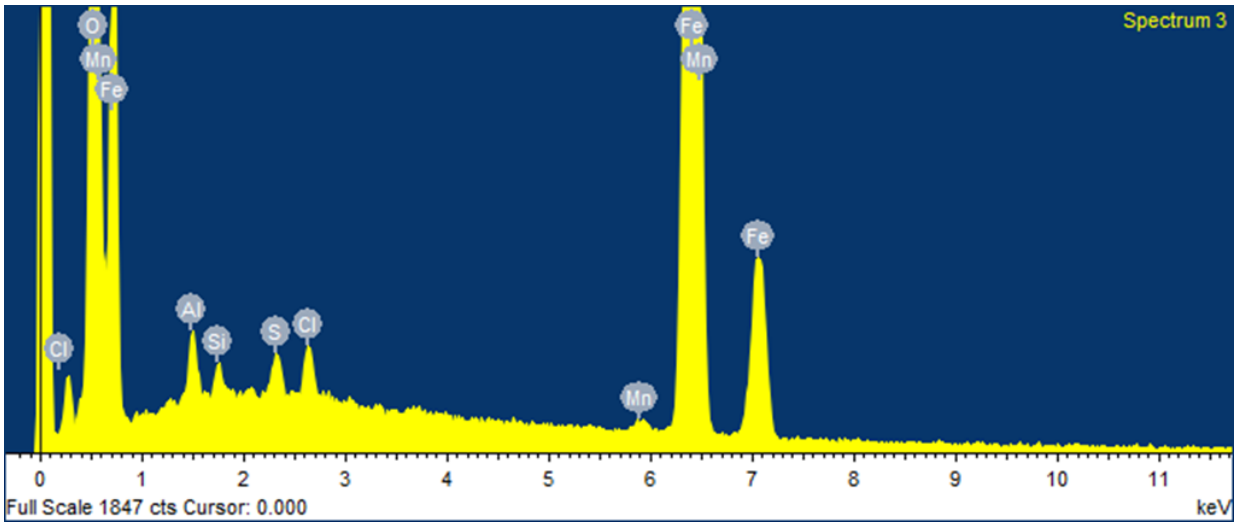


Figure A.543. SEM Image and EDS Spectrum of the Rust Collected from Exterior Web of the Girder.

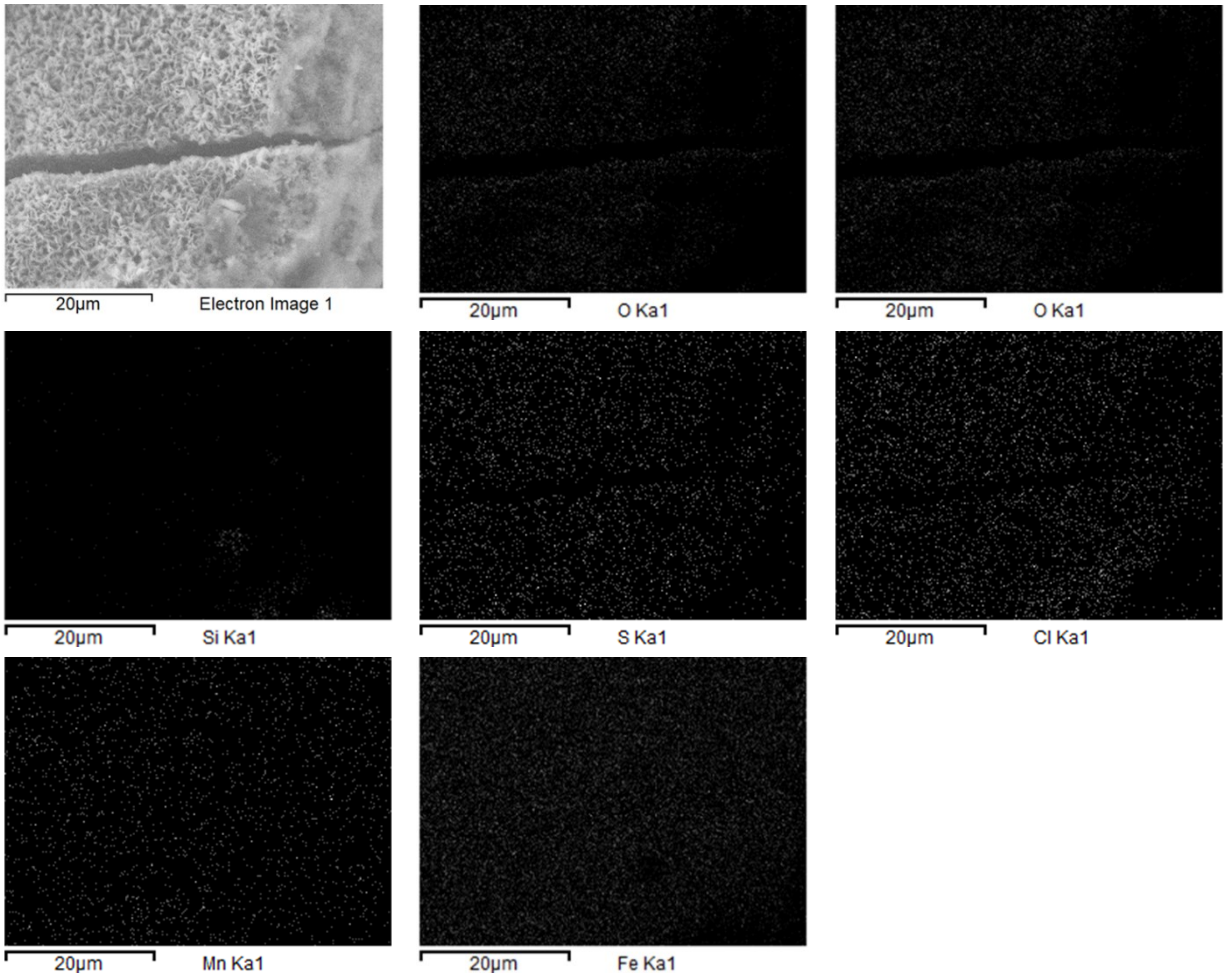
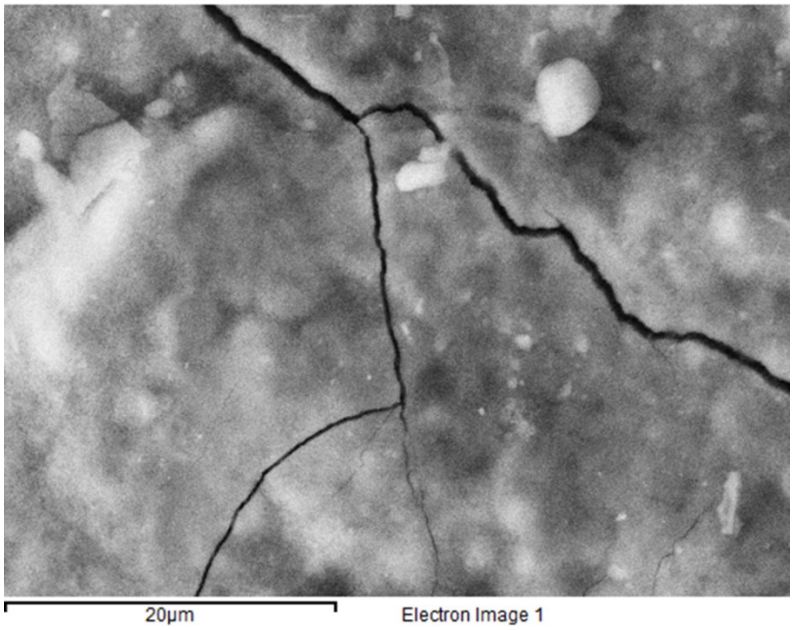


Figure A.544. EDS Elemental Mapping of Rust Collected from Exterior Web.

A.32.4.SEM/EDS Results: Interior Web Girder

Element	Weight %	Atomic %
O K	43.50	71.15
Al K	1.44	1.39
Si K	2.36	2.20
S K	0.86	0.70
Cl K	0.76	0.56
K K	0.19	0.12
Ca K	0.15	0.10
Mn K	1.11	0.53
Fe K	49.37	23.13
Cu K	0.26	0.11
Totals	100.00	



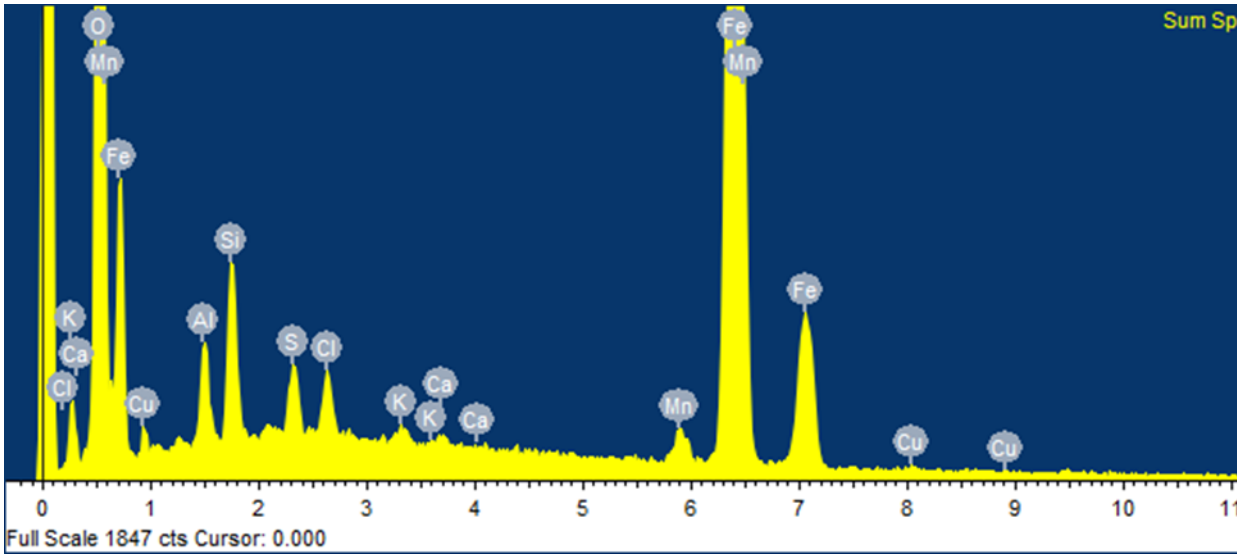


Figure A.545. SEM Image and EDS Spectrum of the Rust Collected from Interior Web of the Girder.

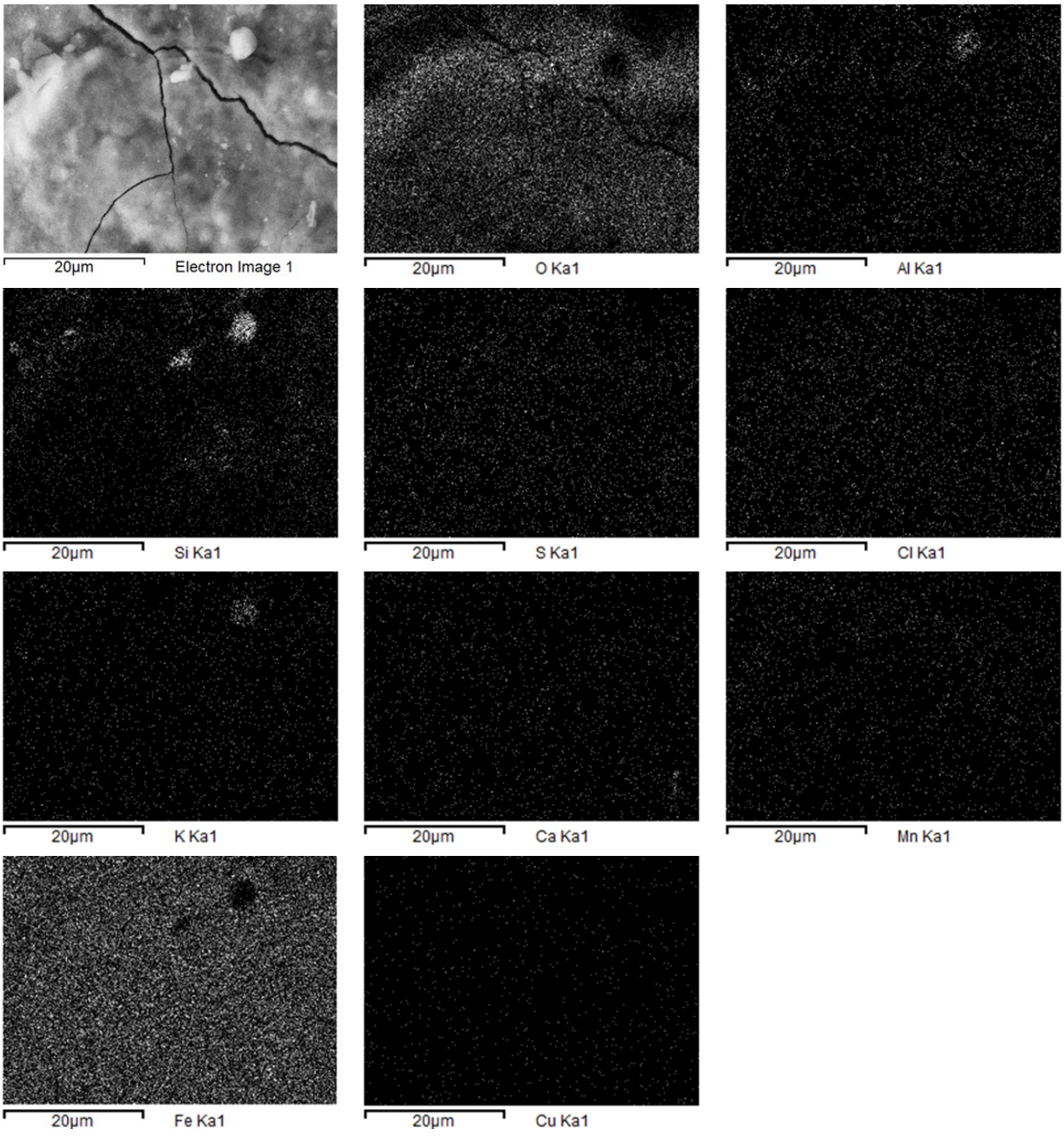


Figure A.546. EDS Elemental Mapping of Rust Collected from Interior Web.

A.32.5.XPS Result: Exterior Girder

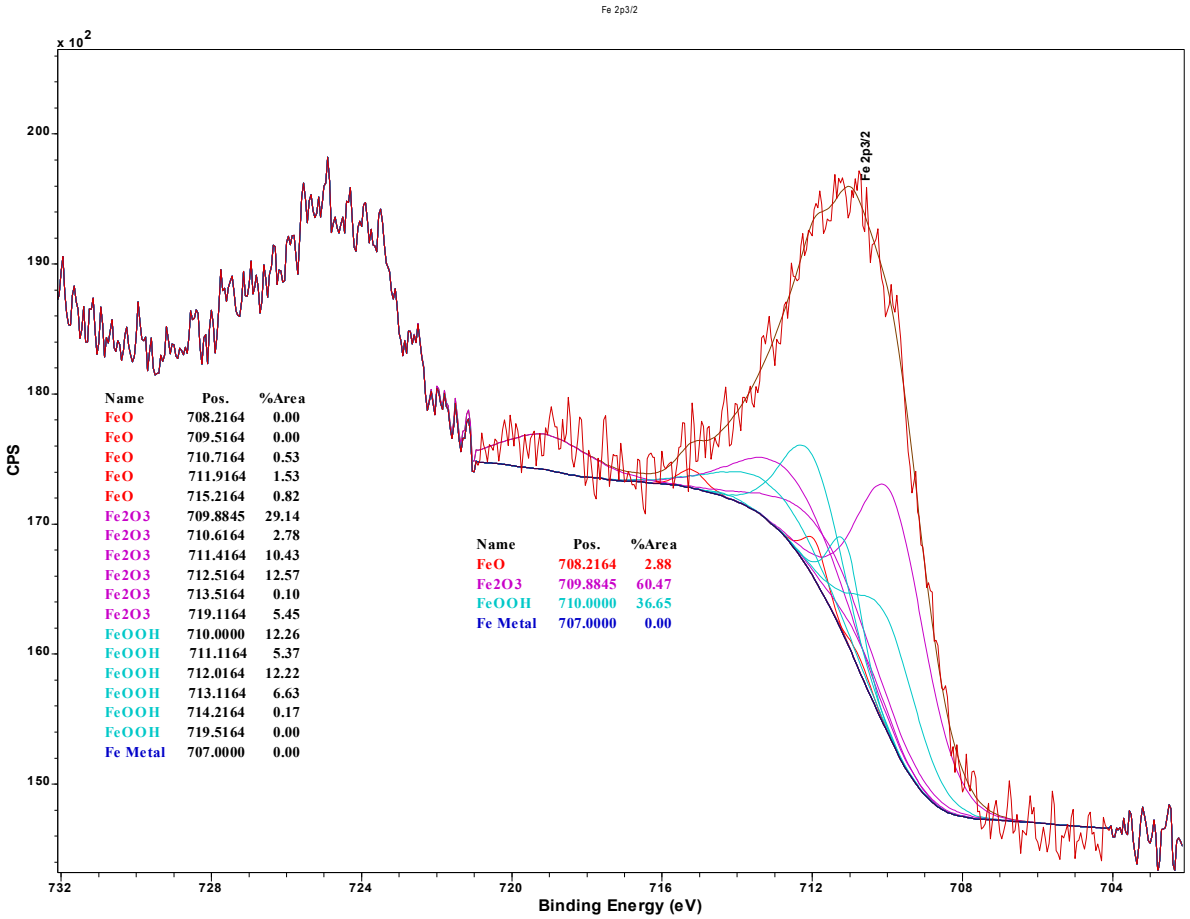


Figure A.547. XPS Spectrum of the Rust Collected from Exterior Web of the Girder.

A.32.6.XPS Result: Interior Girder

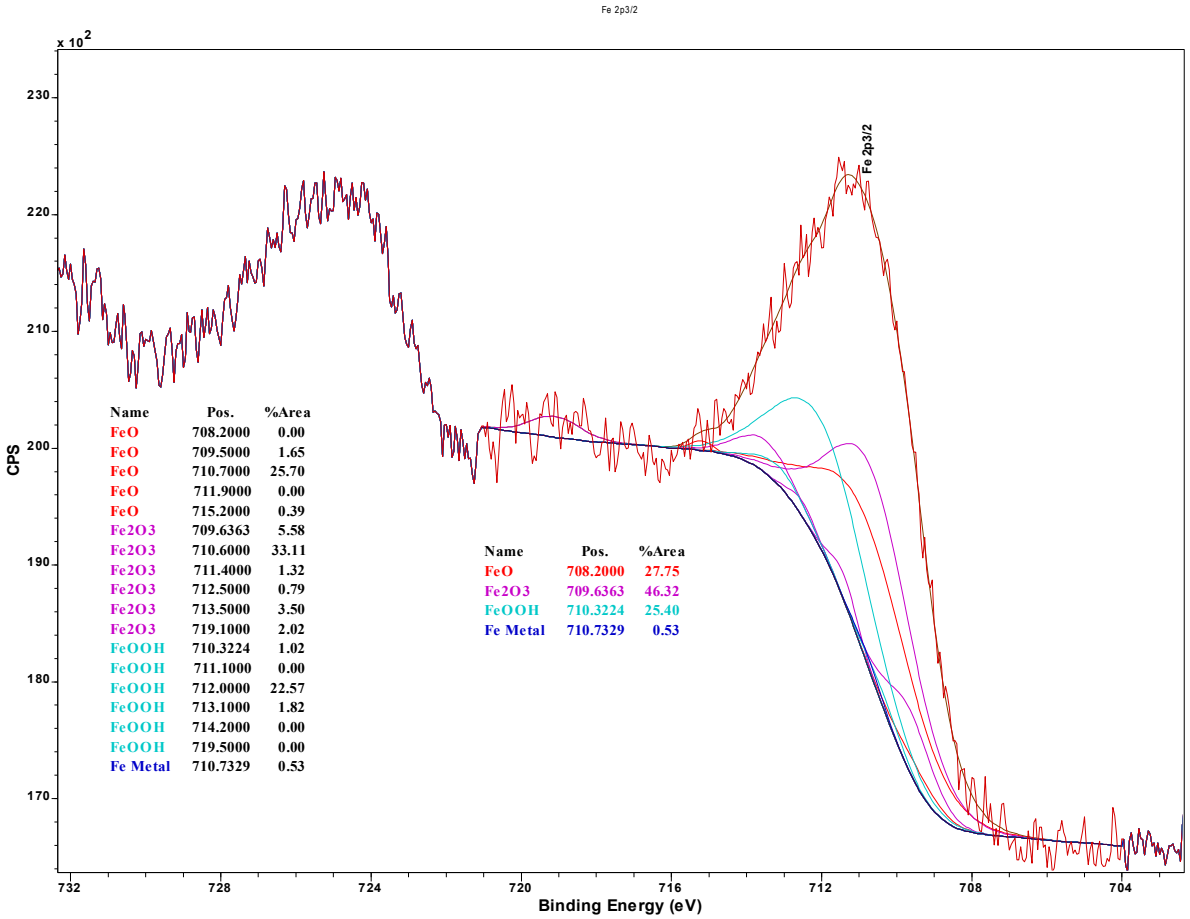


Figure A.548. XPS Spectrum of the Rust Collected from Interior Web of the Girder.

A.32.7.XRD Result: Exterior and Interior Girder

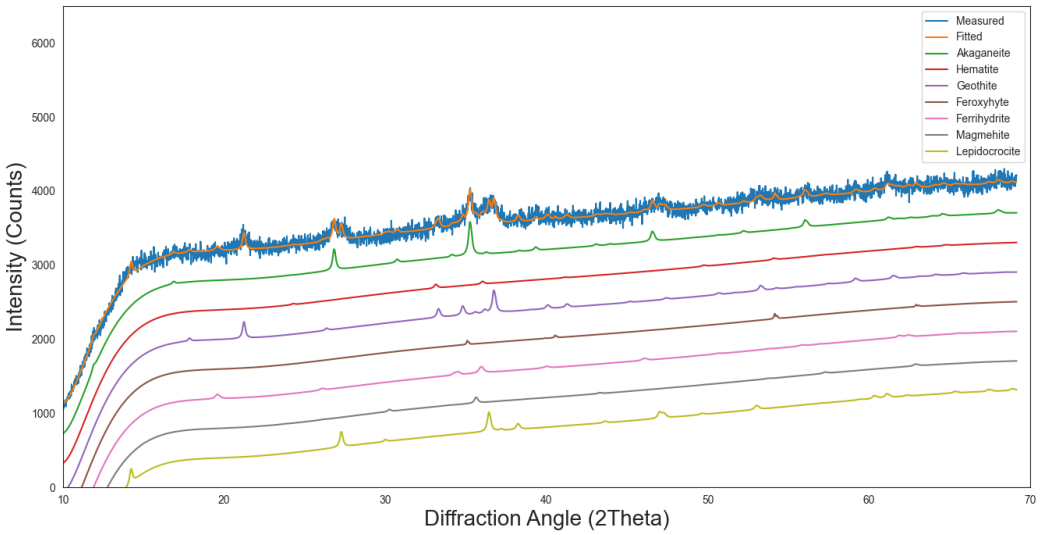


Figure A.549 XRD Pattern of Powdered Rust Collected from Exterior Web of the Girder (G1F1).

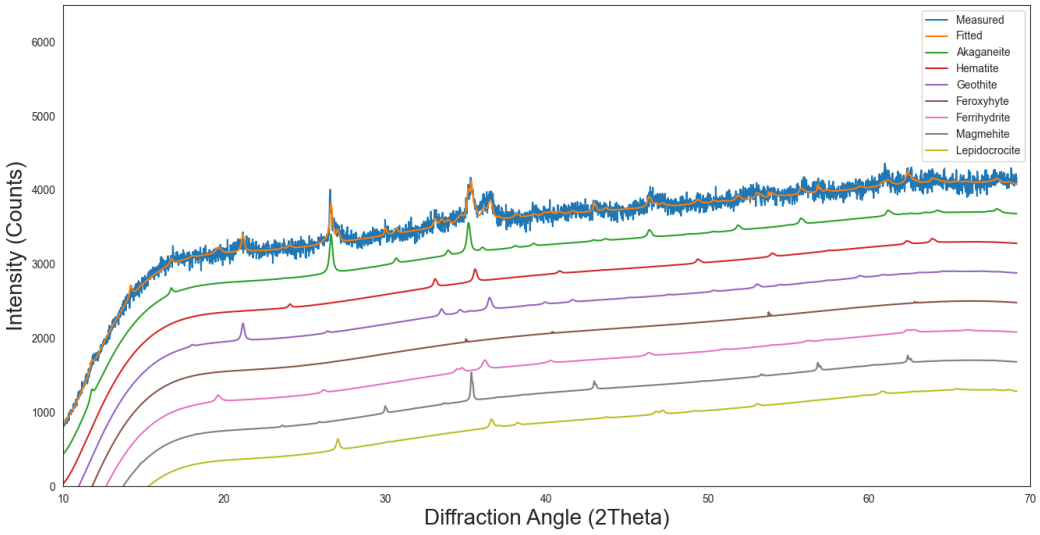


Figure A.550 XRD Pattern of Powdered Rust Collected from Interior Web of the Girder (G2F1).

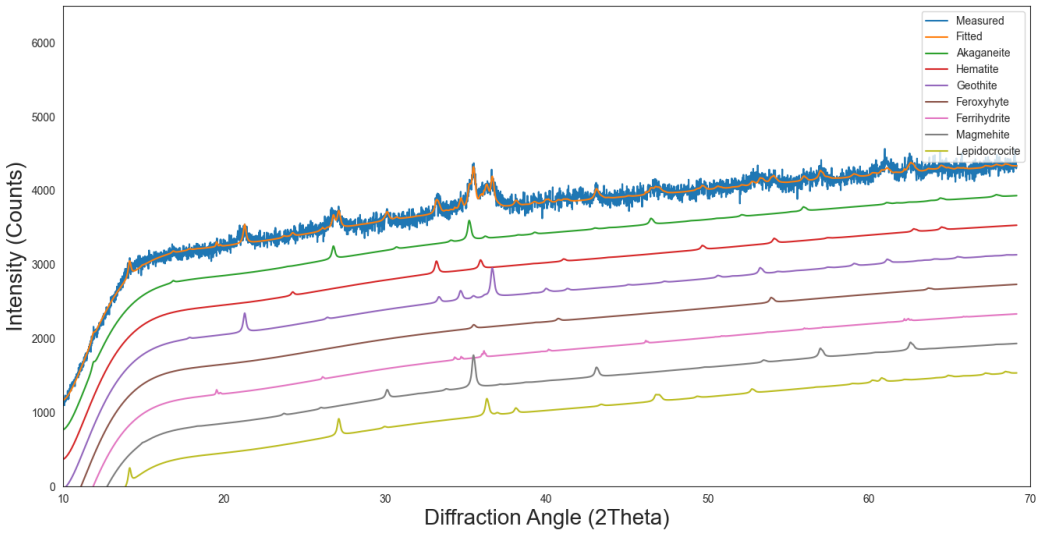


Figure A.551. XRD Pattern of Powdered Rust Collected from Interior Web of the Girder (G3F2).

A.32.8. Particle Size Analysis: Tape Adhesion Results

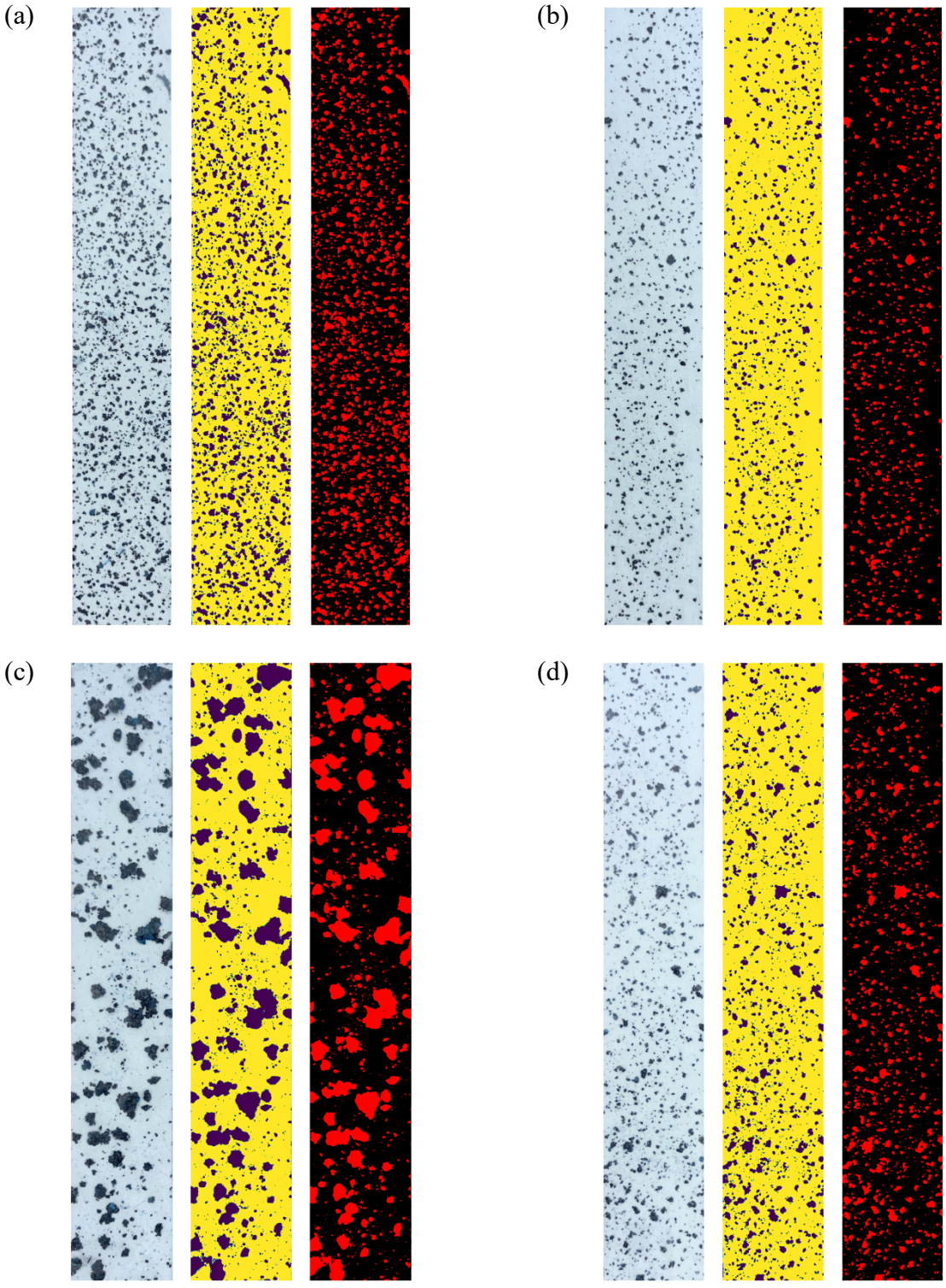


Figure A.552. Particle Size Analysis Results at A9G1F1 (a) Top Flange Bottom, (b) Web, (c) Bottom Flange Bottom (d) Stiffener.

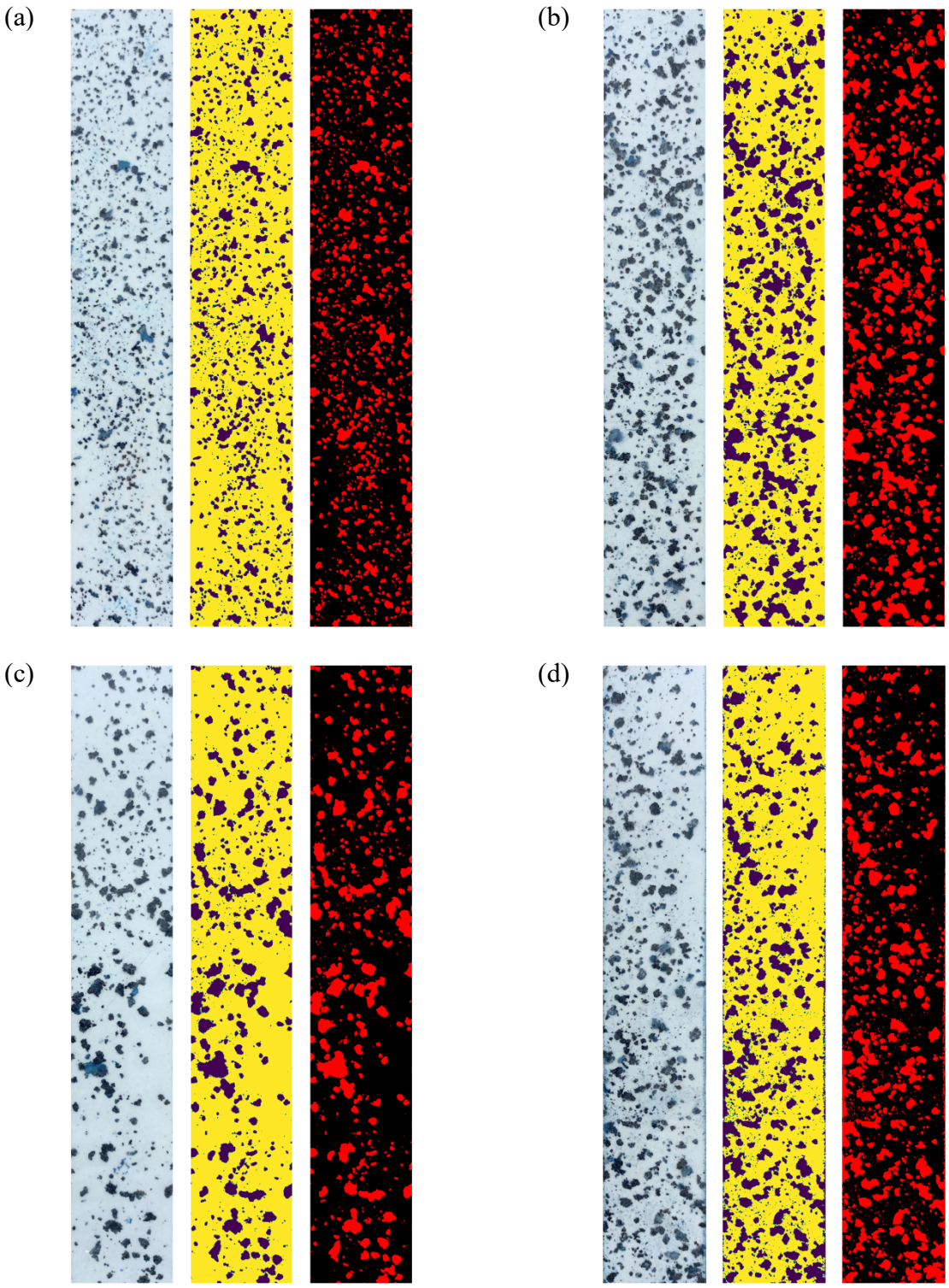


Figure A.553. Particle Size Analysis Results at A9G2F1 (a) Top Flange Bottom, (b) Web, (c) Bottom Flange Bottom (d) Stiffener.

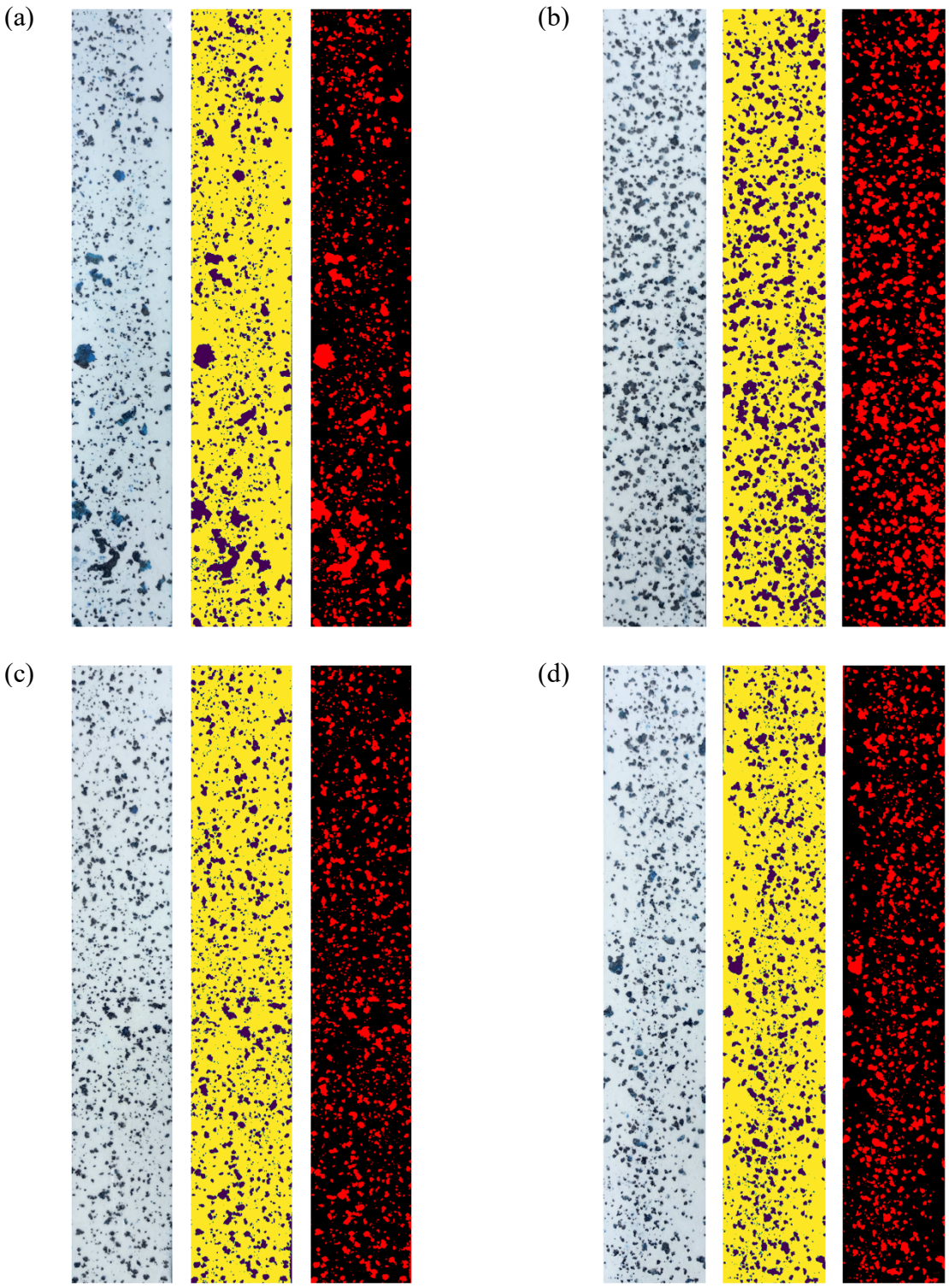


Figure A.554. Particle Size Analysis Results at A9G3F2 (a) Top Flange Bottom, (b) Web, (c) Bottom Flange Bottom (d) Stiffener.

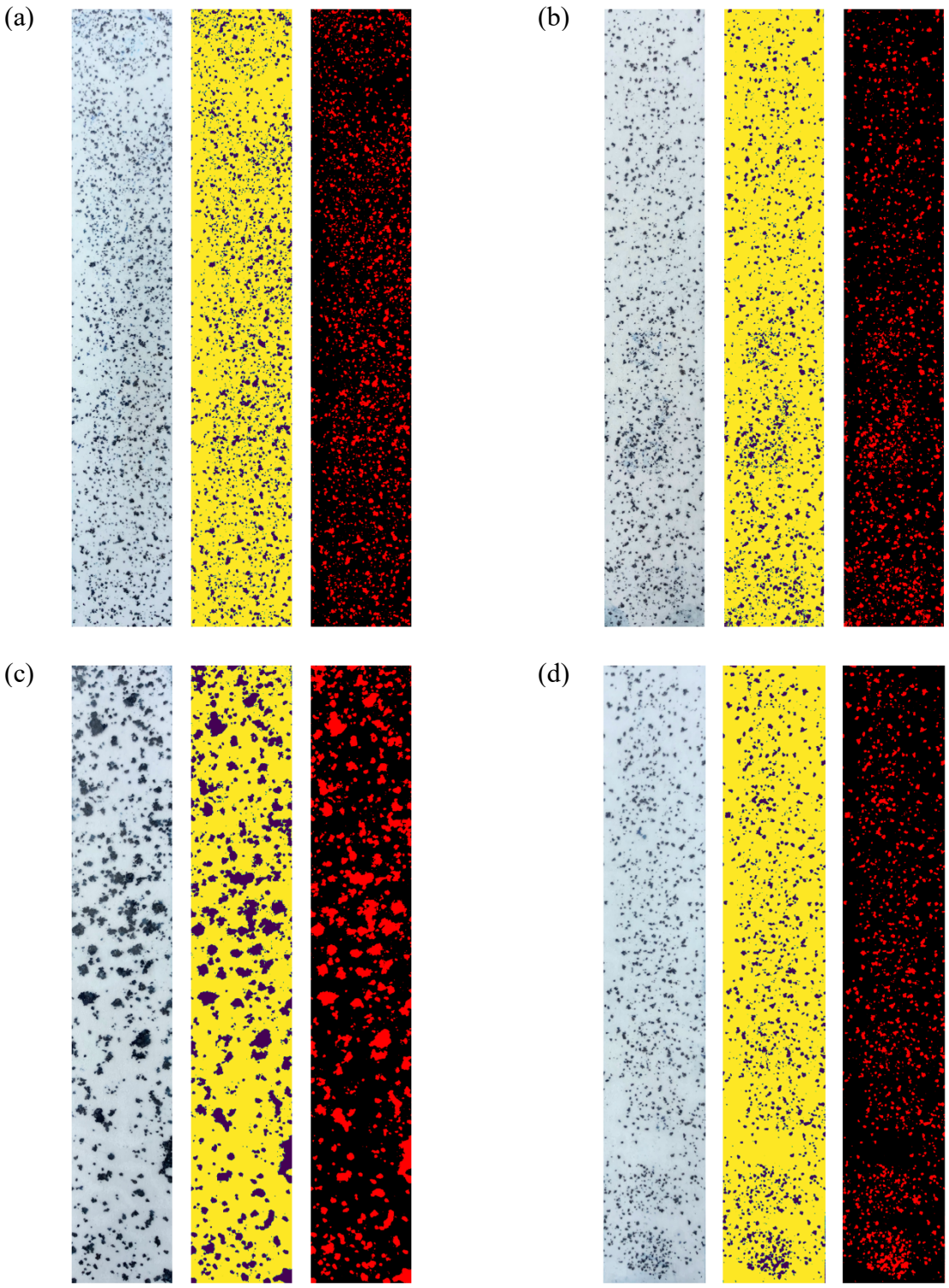


Figure A.555. Particle Size Analysis Results at A9G4F2 (a) Top Flange Bottom, (b) Web, (c) Bottom Flange Bottom (d) Stiffener.

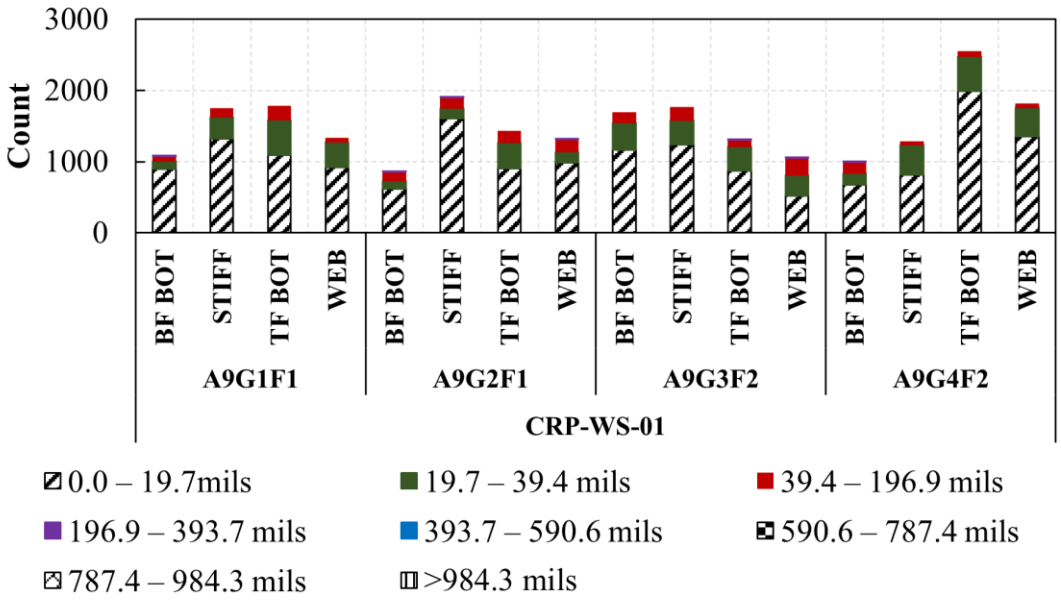


Figure A.556. Particle Size Analysis Showing Different Locations Examined.

A.33. SAT-WS-01

- IH 410 Conn & Randolph
- Bridge ID 150150001710329, Coordinates (29.52328, -98.39419), Bexar County
- Continuous weathering steel plate girder
- Built 1983
- Girder inspection carried on bent 6 and bent 5, and measurements are taken on girder within four feet from the abutment or bent.
- No visual inspection on deck
- Location for Testing: B6-G1F1, B6-G4F1, B6-G7F2, B5-G1F1, B5-G4F1, B5-G7F2



Figure A.557. Typical Picture of SAT-WS-01.

A.33.1. Observed Condition

Delaminated areas of the patina are visible on the bottom face of the top flange with a patina rating of 7. The web has a uniform patina formation with a patina rating of 7. The interior girders have significant poultice corrosion on the top face of the bottom flange due to the accumulation of dirt Index 7 whereas exterior girders have less accumulation of dirt. Delamination observed on bottom face of bottom flange.

A.33.2.Field Inspection Results

Table A-149. Field Inspection Results for SAT-WS-01.

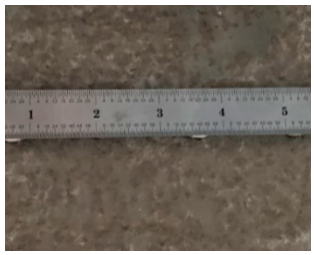
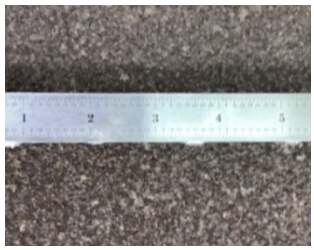
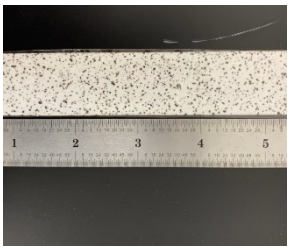
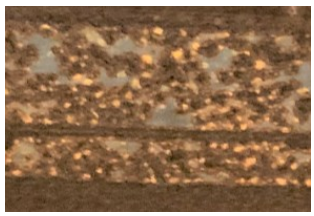
Location	Patina Rating	Thickness (inch)	Cl^- Conc. (ppm)	Field Condition	Tape Test
B6-G1F1 TF Bot. Ext.	7	-			
B6-G1F1 Web Ext.	7	Measured R1 0.576 R2 0.574 R3 0.575 R_Avg 0.575 Design	1		
B6-G1F1 BF Top Ext.	6	Measured R1 2.099 R2 2.098 R3 2.101 R_Avg 2.099 Design	-		
B6-G1F1 BF Bot. Ext.	8	-	-		
B6-G4F1 TF Bot. Int.	7				

Table A-150. Field Inspection Results for SAT-WS-01.

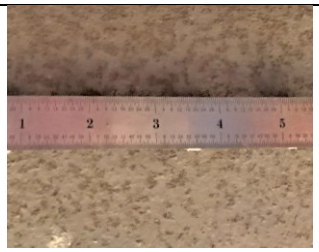
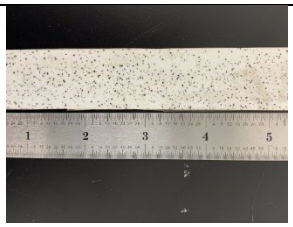
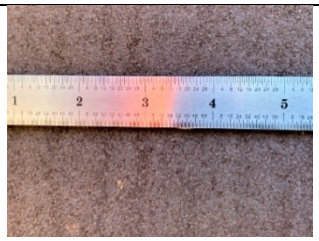
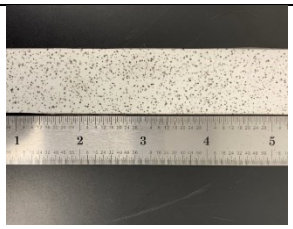
Location	Patina Rating	Thickness (inch)	Cl^- Conc. (ppm)	Field Condition	Tape Test
B6-G4F1 Web Int.	8	Measured R1 0.576 R2 0.577 R3 0.577 R_Avg 0.577 Design	1		
B6-G4F1 BF Top Int.	5	Measured R1 2.065 R2 2.063 R3 2.063 R_Avg 2.064 Design	-		
B6-G4F1 BF Bot. Int.	8	-	-		
B6-G7F2 TF Bot. Ext.	7				
B6-G7F2 Web Ext.	8	Measured R1 0.594 R2 0.595 R3 0.592 R_Avg 0.594 Design	-		

Table A-151. Field Inspection Results for SAT-WS-01.

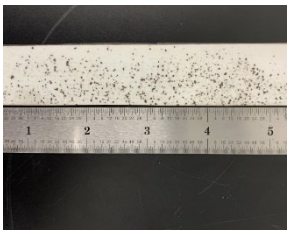
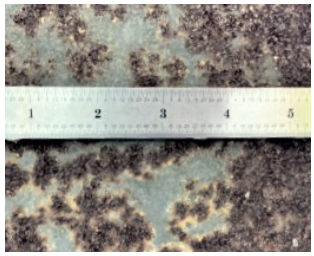
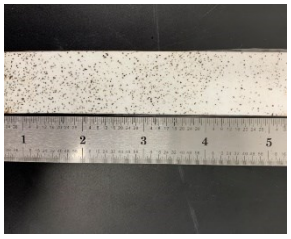
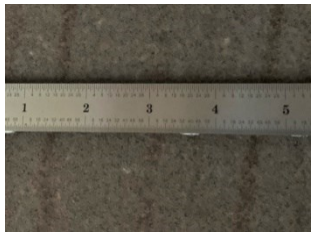
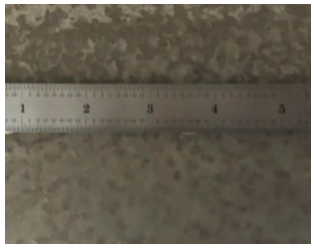
Location	Patina Rating	Thickness (inch)	Cl^- Conc. (ppm)	Field Condition	Tape Test
B6-G7F2 BF Top Ext.	7	Measured R1 2.035 R2 2.037 R3 2.039 R_Avg 2.037 Design	-		
B6-G7F2 BF Bot. Ext.	5	-	-		
B5-G1F1 TF Bot. Ext.	7				
B5-G1F1 Web Ext.	8	Measured R1 0.563 R2 0.562 R3 0.564 R_Avg 0.563 Design			
B5-G1F1 BF Top Ext.	5	Measured R1 1.037 R2 1.037 R3 1.039 R_Avg 1.038 Design	-		

Table A-152. Field Inspection Results for SAT-WS-01.

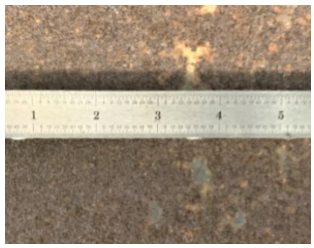
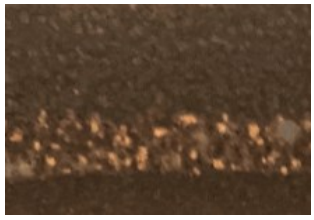
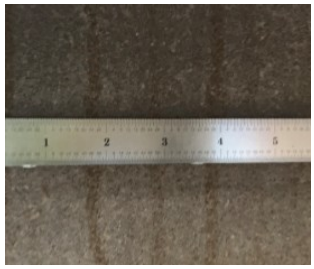
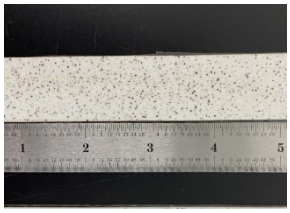
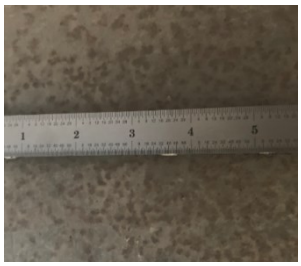
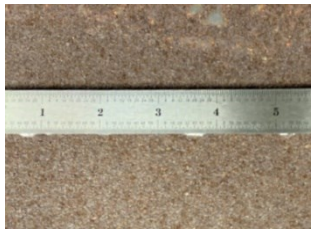
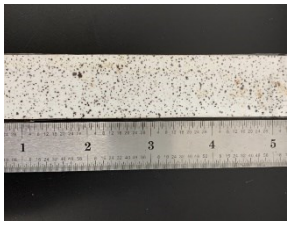
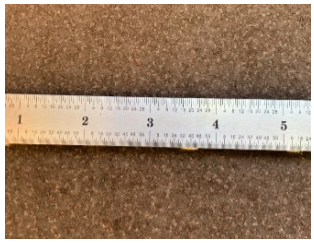
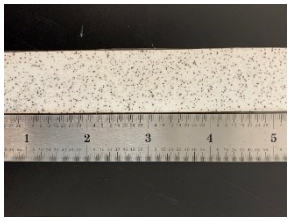
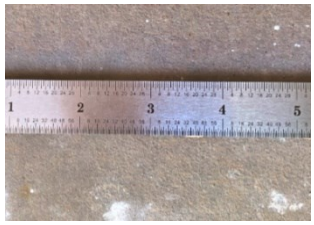
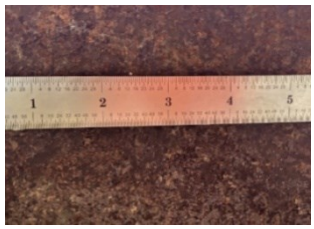
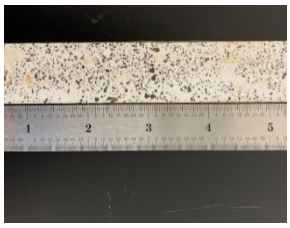
Location	Patina Rating	Thickness (inch)	Cl^- Conc. (ppm)	Field Condition	Tape Test
B5-G1F1 BF Bot. Ext.	8	-	-		
B5-G4F1 TF Bot. Ext.	7				
B5-G4F1 Web Int.	8	Measured R1 0.583 R2 0.582 R3 0.580 R_Avg 0.582 Design	2		
B5-G4F1 BF Top Int.	5	Measured R1 1.035 R2 1.032 R3 1.031 R_Avg 1.033 Design	-		
B5-G4F1 BF Bot. Int.	7	-	-		

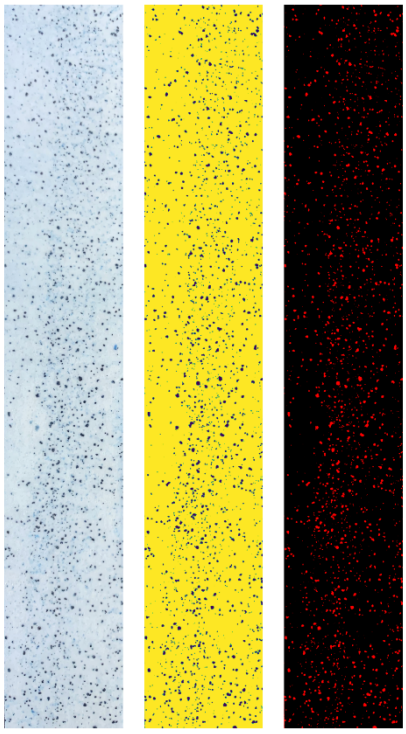
Table A-153. Field Inspection Results for SAT-WS-01.

Location	Patina Rating	Thickness (inch)	Cl^- Conc. (ppm)	Field Condition	Tape Test
B5-G7F2 TF Bot. Ext.	7				
B5-G7F2 Web Ext.	8	Measured R1 0.563 R2 0.562 R3 0.564 R_Avg 0.563 Design	2		
B5-G7F2 BF Top Ext.	5	Measured R1 1.020 R2 1.022 R3 1.028 R_Avg 1.023 Design	-		
B5-G7F2 BF Bot. Ext.	7	-	-		

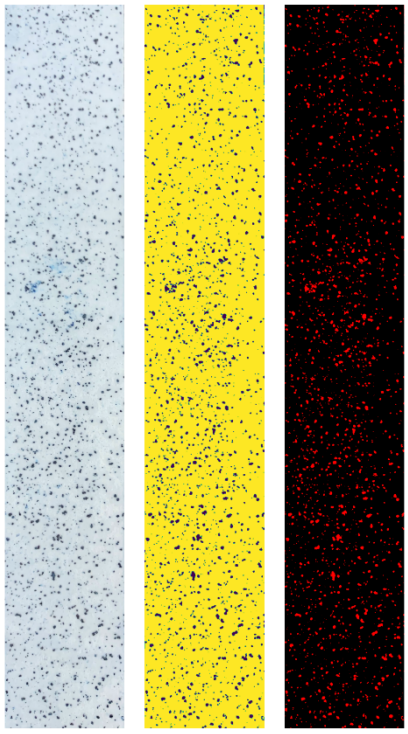
A.33.3.Particle Size Analysis: Tape Adhesion Results

(a)

(b)



(c)

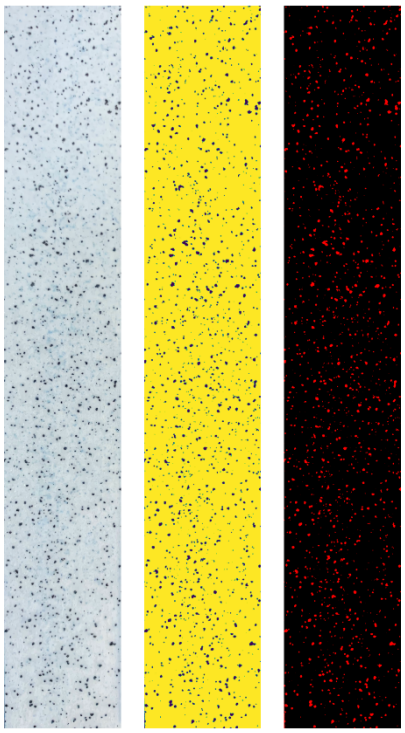


(d)

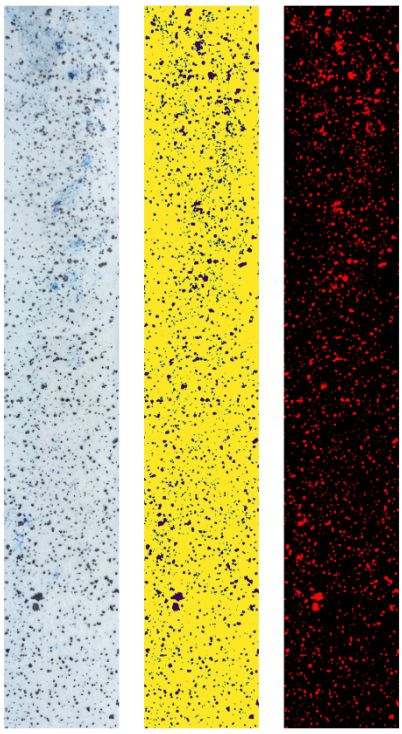
Figure A.558. Particle Size Analysis Results at B5G1F1 (a) Top Flange Bottom, (b) Web, (c) Bottom Flange Bottom (d) Stiffener.

(a)

(b)



(c)

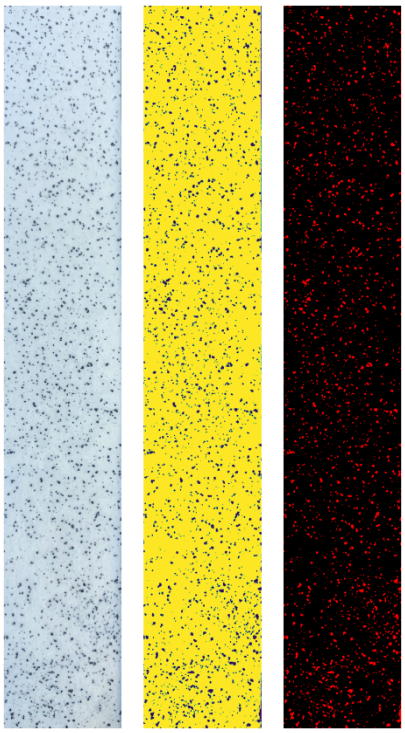


(d)

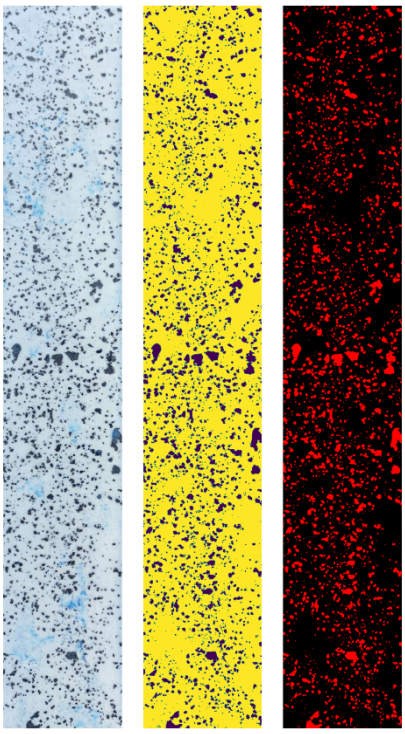
Figure A.559. Particle Size Analysis Results at B5G4F1 (a) Top Flange Bottom, (b) Web, (c) Bottom Flange Bottom (d) Stiffener.

(a)

(b)



(c)

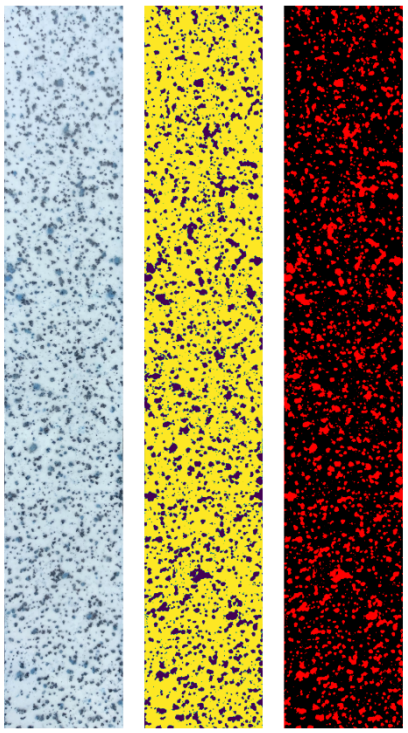


(d)

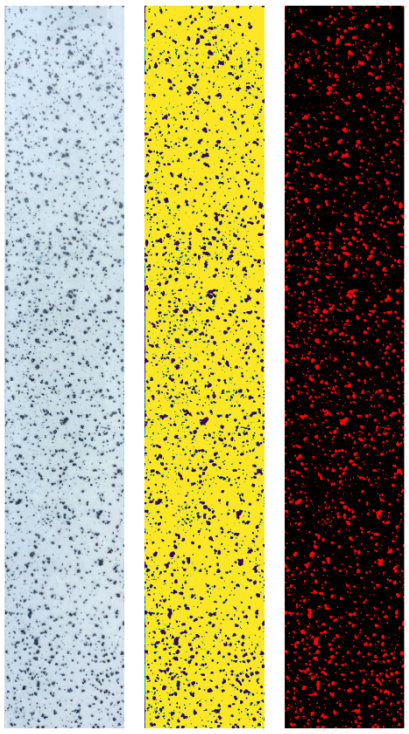
Figure A.560. Particle Size Analysis Results at B5G7F2 (a) Top Flange Bottom, (b) Web, (c) Bottom Flange Bottom (d) Stiffener.

(a)

(b)



(c)

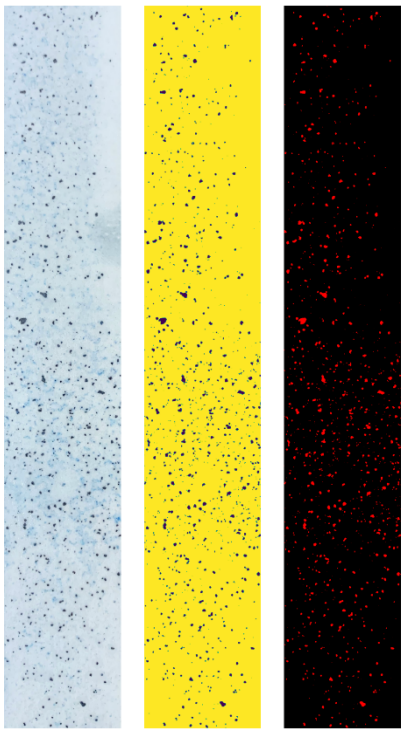


(d)

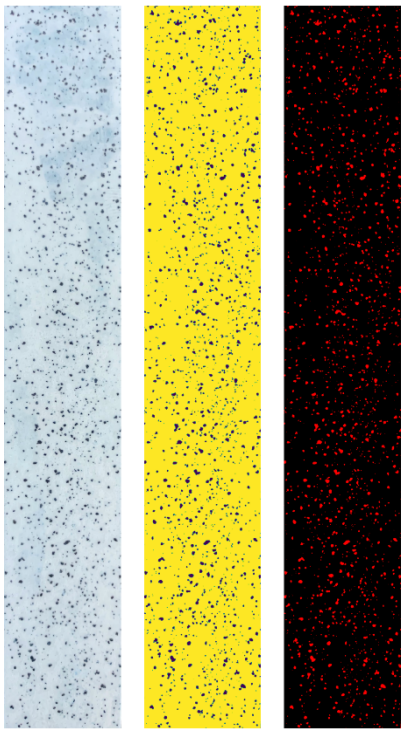
Figure A.561. Particle Size Analysis Results at B6G1F1 (a) Top Flange Bottom, (b) Web, (c) Bottom Flange Bottom (d) Stiffener.

(a)

(b)



(c)

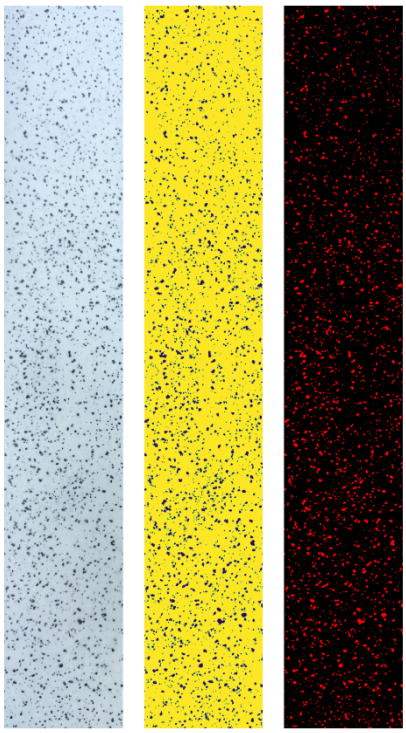


(d)

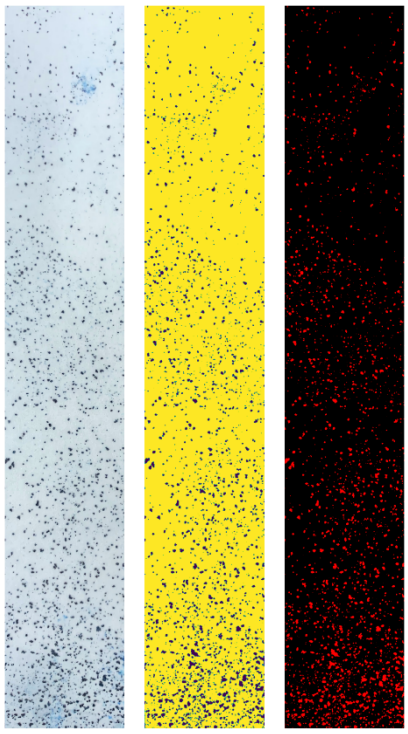
Figure A.562. Particle Size Analysis Results at B6G4F1 (a) Top Flange Bottom, (b) Web, (c) Bottom Flange Bottom (d) Stiffener.

(a)

(b)



(c)



(d)

Figure A.563. Particle Size Analysis Results at B6G7F2 (a) Top Flange Bottom, (b) Web, (c) Bottom Flange Bottom (d) Stiffener.

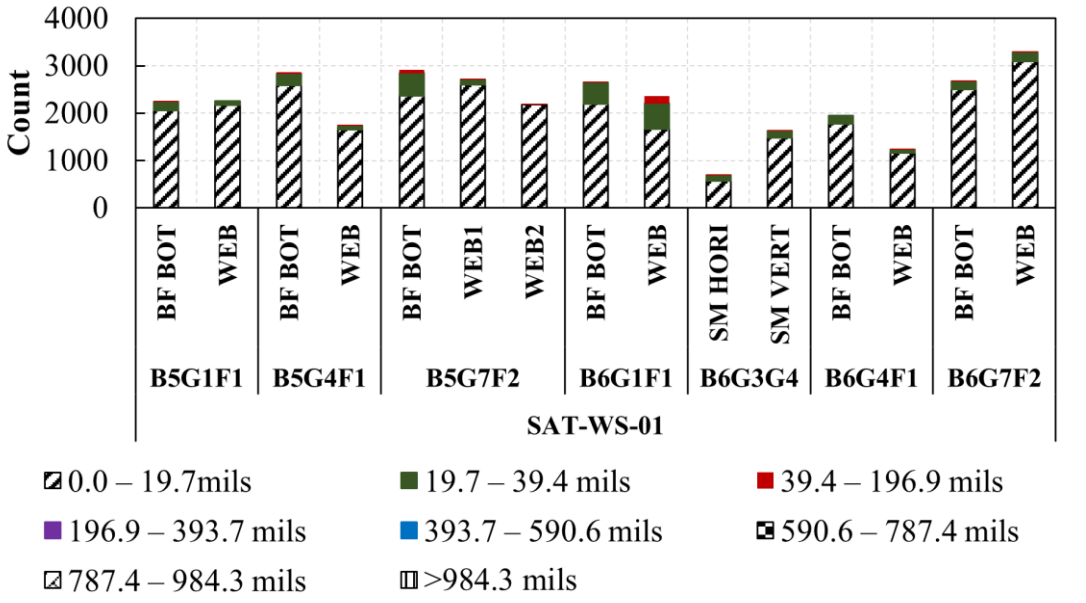


Figure A.564. Particle Size Analysis Showing Different Locations Examined.

A.34. ATL-WS-01

- SH 93 overpass over US71
- Bridge ID 190190021701007, Coordinates (33.3954808, -94. 0981214), Harris County
- Continuous weathering steel plate girder
- Built 2004
- Girder inspection carried on End abutment, and measurements are taken on girder within four feet from the abutment or bent.
- No visual inspection on deck
- Location for Testing: A1-G1F1, A1-G3F2, A1-G2F1, B2-G1F1, B2-G2F1, B3-G3F1



Figure A.565. Typical Picture of ATL-WS-01.

A.34.1. Observed Condition

Overall all the patina is well formed over the girder surface and is in very good condition with no delamination or poultice corrosion observed on top face of bottom flange. The average patina rating is 8 consideringt all the inspected locations.

A.34.2.Field Inspection Results

Table A-154. Field Inspection Results for ATL-WS-01.

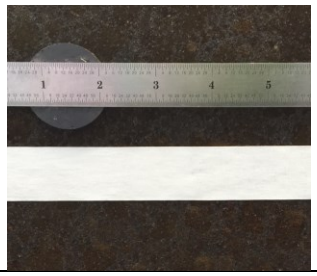
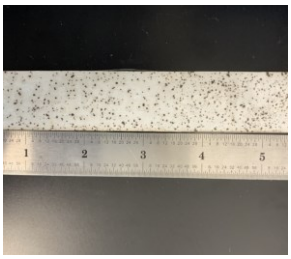
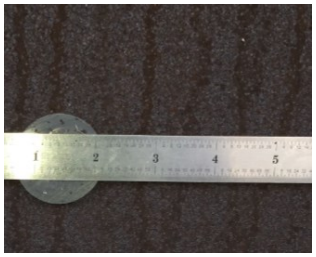
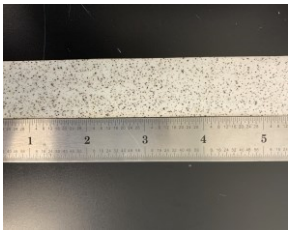
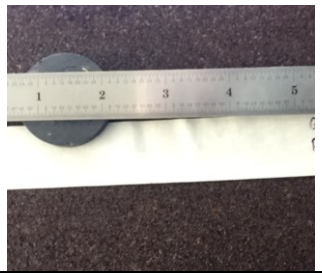
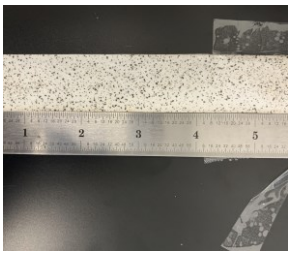
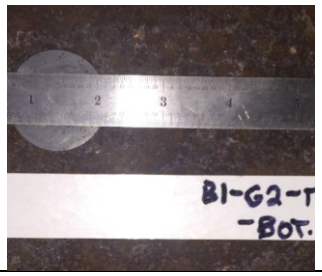
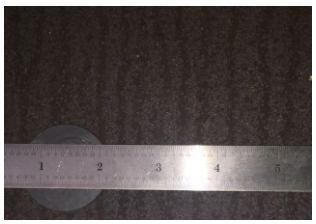
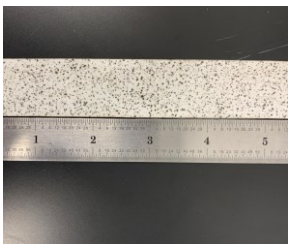
Location	Patina Rating	Thickness (inch)	Cl^- Conc. (ppm)	Field Condition	Tape Test
A1-G1F1 TF Bot. Ext.	8	Measured 0.793 Design			
A1-G1F1 Web Ext.	8	Measured 0.473 Design	4		
A1-G1F1 BF Bot. Ext.	8	Measured 0.486 Design			
A1-G2F1 TF Bot. Ext.	8	Measured 0.795 Design			
A1-G2F1 Web Ext.	8	Measured 0.473 Design	9		

Table A-155. Field Inspection Results for ATL-WS-01.

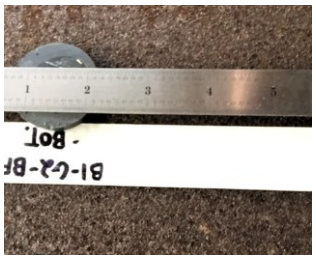
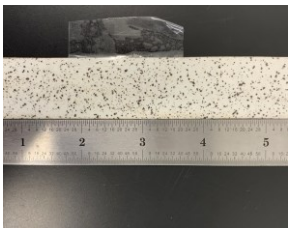
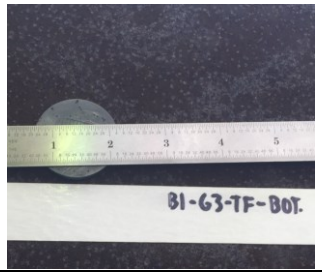
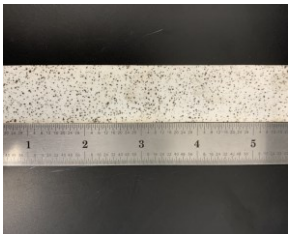
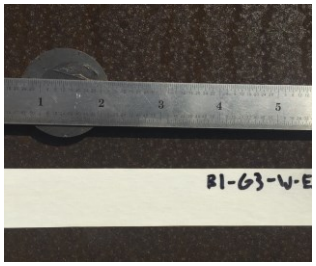
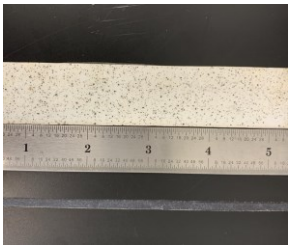
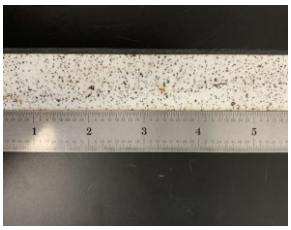
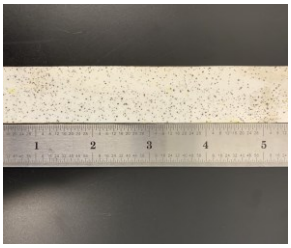
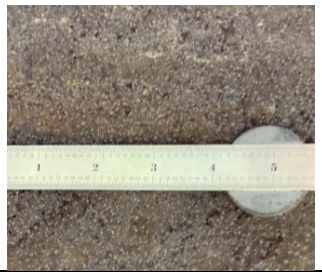
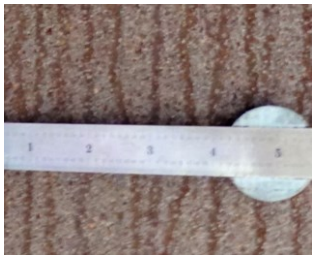
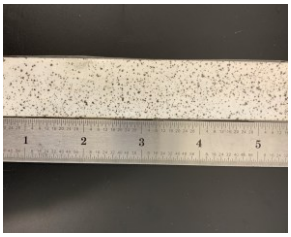
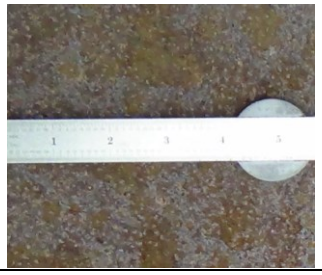
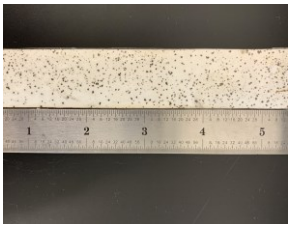
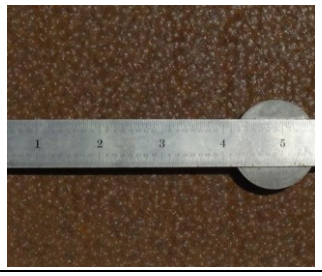
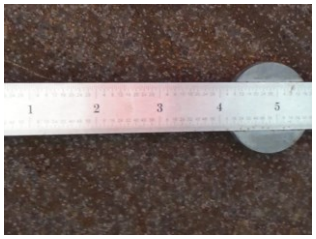
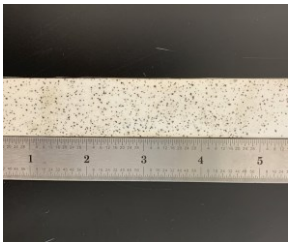
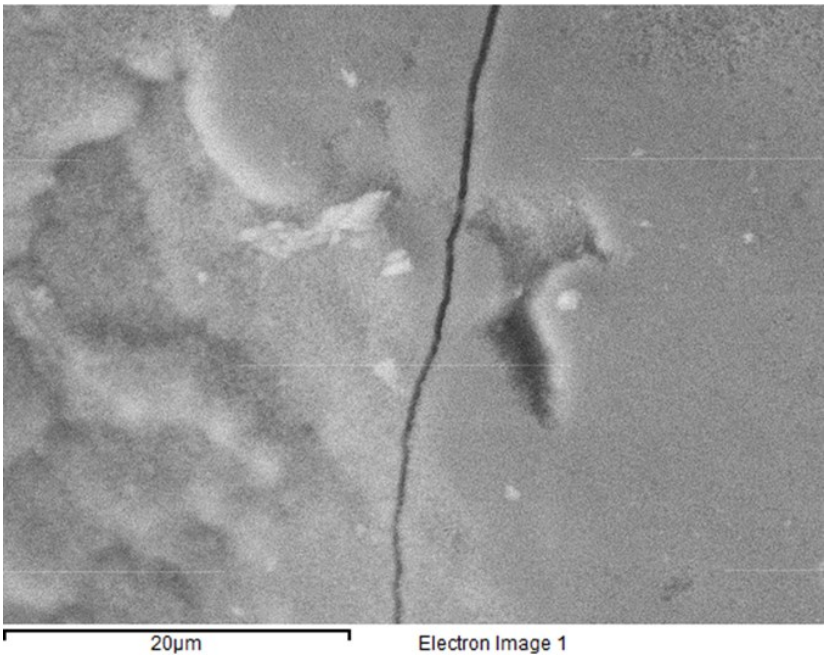
Location	Patina Rating	Thickness (inch)	Cl^- Conc. (ppm)	Field Condition	Tape Test
A1-G2F1 BF Bot. Ext.	8	Measured 0.472 Design			
A1-G3F2 TF Bot. Ext.	8	Measured 0.790 Design			
A1-G3F2 Web Ext.	8	Measured 0.471 Design			
A1-G3F2 BF Bot. Ext.	8	Measured 0.478 Design			
B2-G1F1 Web Ext.	8	Measured 0.478 Design	1		

Table A-156. Field Inspection Results for ATL-WS-01.

Location	Patina Rating	Thickness (inch)	Cl^- Conc. (ppm)	Field Condition	Tape Test
B2-G1F1 BF Bot Ext.	8	Measured 1.571 Design			
B2-G2F1 Web Ext.	8	Measured 0.476 Design	1		
B2-G2F1 BF Bot Ext.	8	Measured 1.589 Design			
B2-G3F1 Web Ext.	8	Measured 0.473 Design			
B2-G3F1 BF Bot Ext.	8	Measured 1.571 Design			

A.34.3.SEM/EDS Results: Exterior Girder

Element	Weight %	Atomic %
O K	30.87	60.17
Al K	1.46	1.69
Si K	0.21	0.23
S K	0.63	0.61
Mn K	2.35	1.33
Fe K	63.81	35.63
Ni K	0.38	0.20
Cu K	0.29	0.14
Totals	100.00	



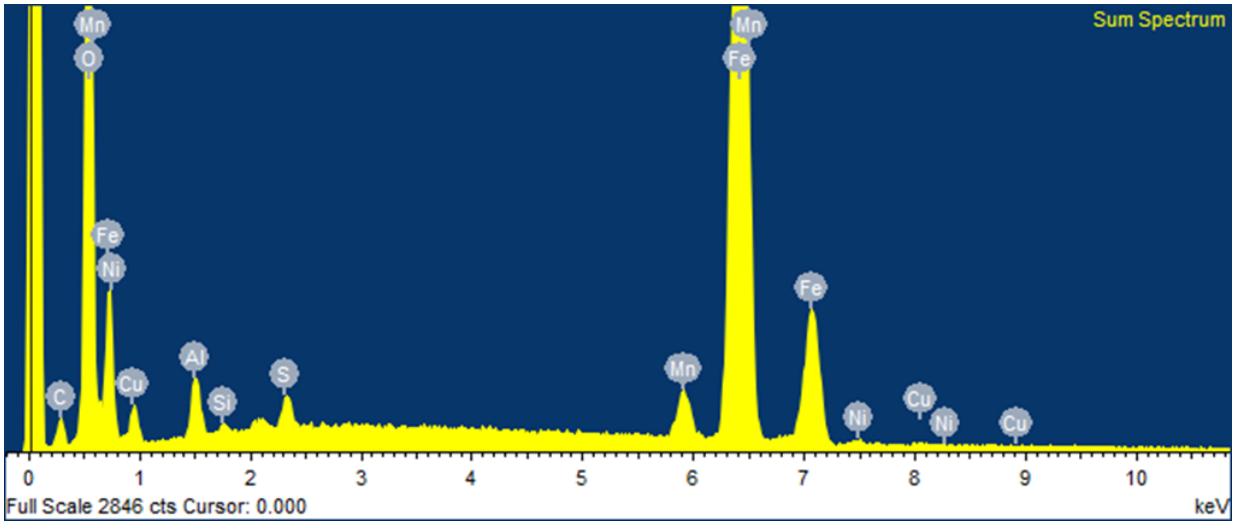


Figure A.566. SEM image of Rust and EDS Spectrum of the Rust Collected from Exterior Web of the Girder.

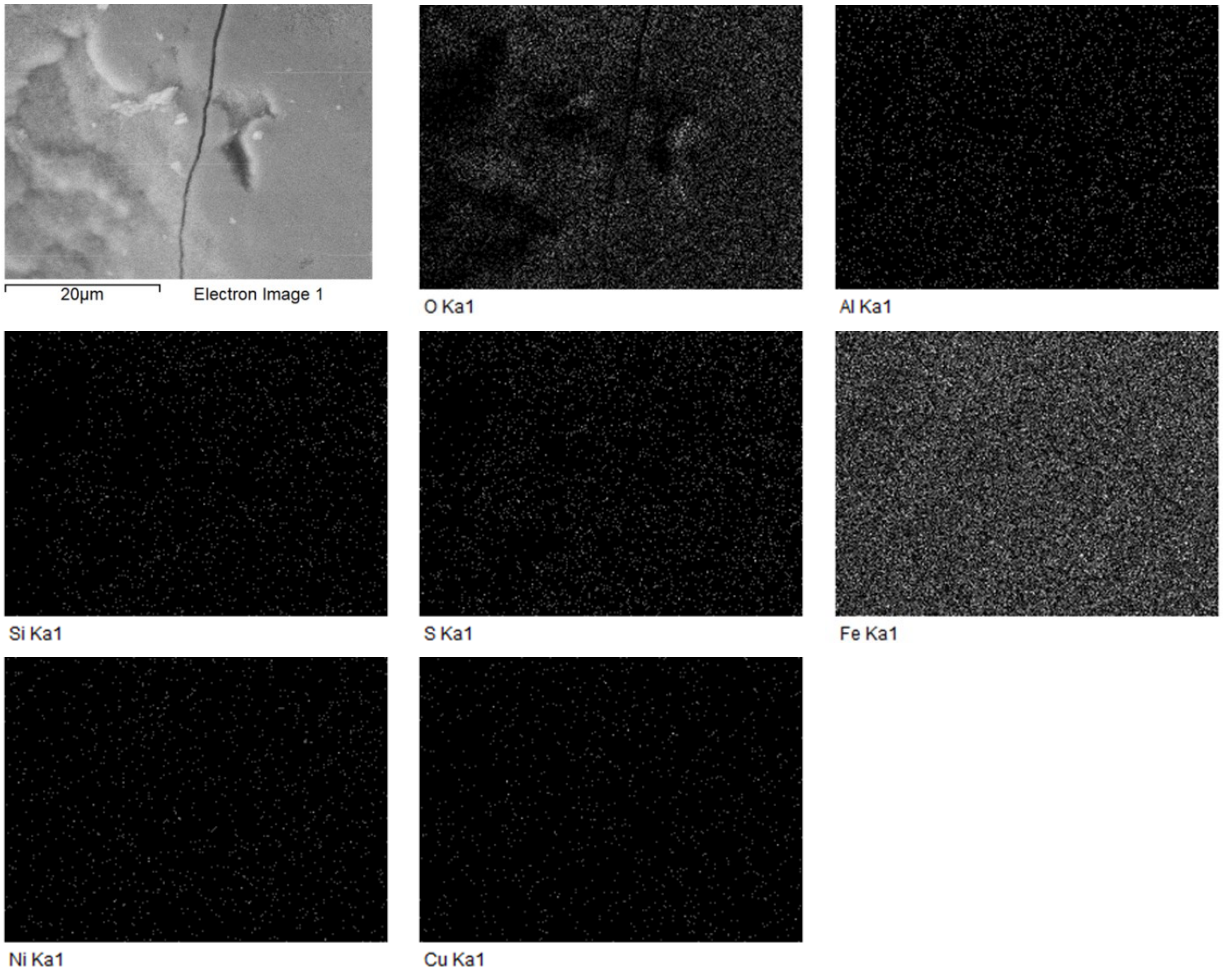
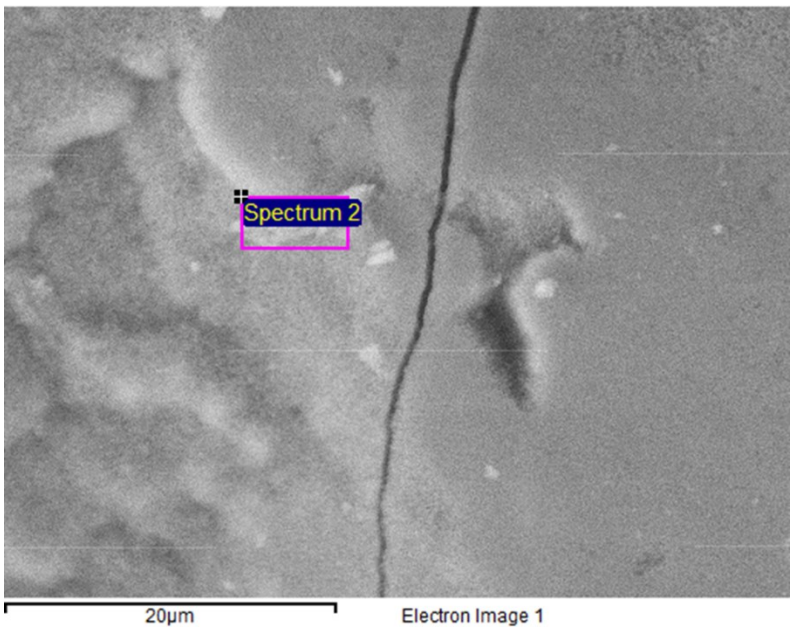


Figure A.567. EDS Elemental Mapping of Rust Collected from Exterior Web.

Element	Weight %	Atomic %
O K	25.73	53.95
Al K	1.79	2.23
S K	0.70	0.73
Mn K	2.26	1.38
Fe K	69.04	41.47
Cu K	0.48	0.25
Totals	100.00	



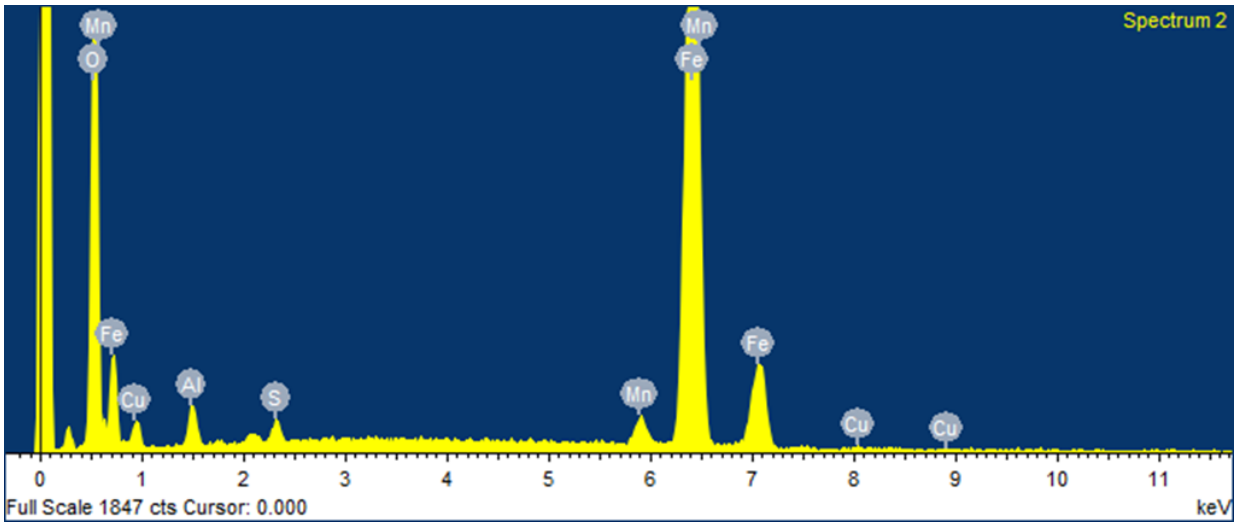
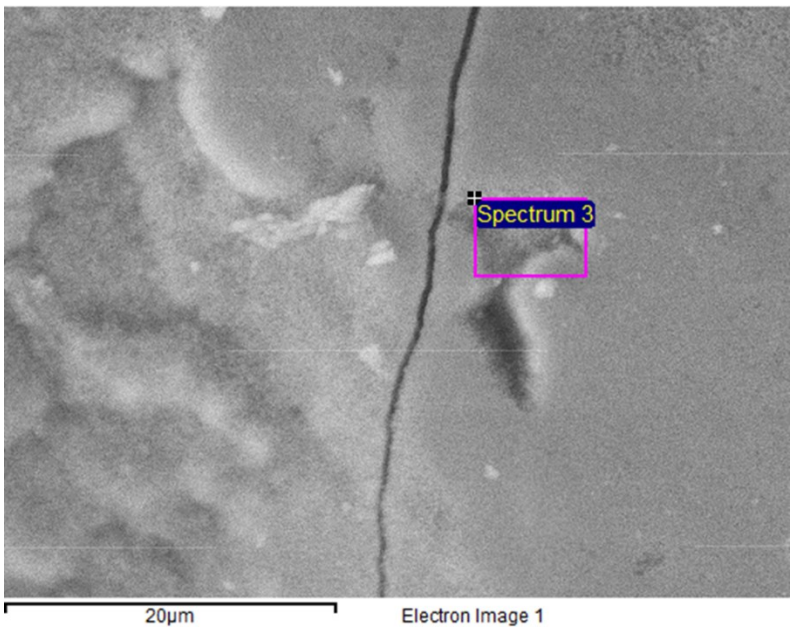


Figure A.568. SEM Image and EDS Spectrum of the Rust Collected from Exterior Web of the Girder.

Element	Weight %	Atomic %
O K	23.02	50.23
Al K	2.00	2.58
S K	0.72	0.78
Mn K	3.00	1.90
Fe K	70.83	44.27
Cu K	0.44	0.24
Totals	100.00	



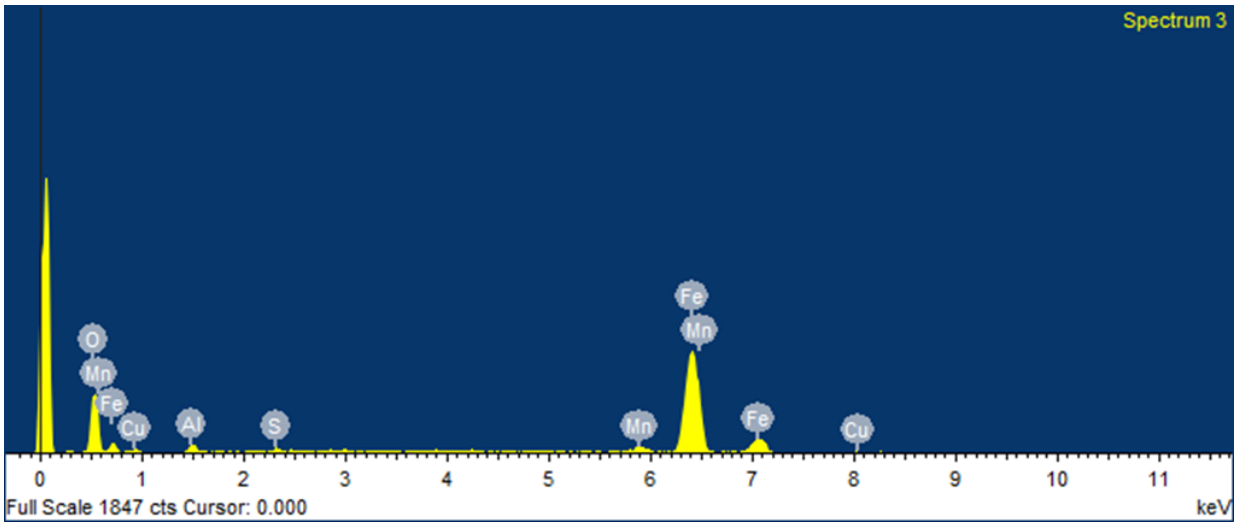
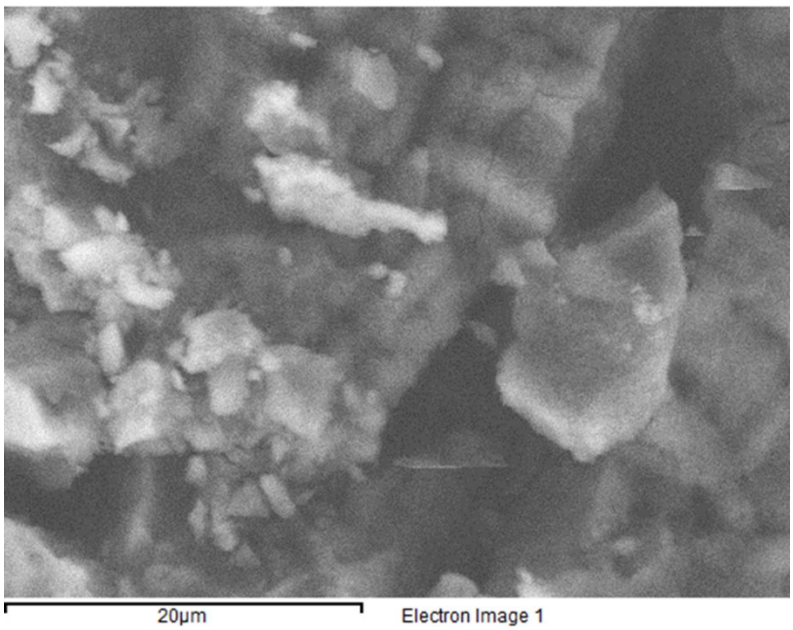


Figure A.569. SEM Image and EDS Spectrum of the Rust Collected from Exterior Web of the Girder.

Element	Weight %	Atomic %
O K	38.32	67.53
Al K	1.44	1.51
Si K	0.62	0.62
S K	0.71	0.63
Mn K	0.57	0.29
Fe K	57.68	29.12
Ni K	0.27	0.13
Cu K	0.38	0.17
Totals	100.00	



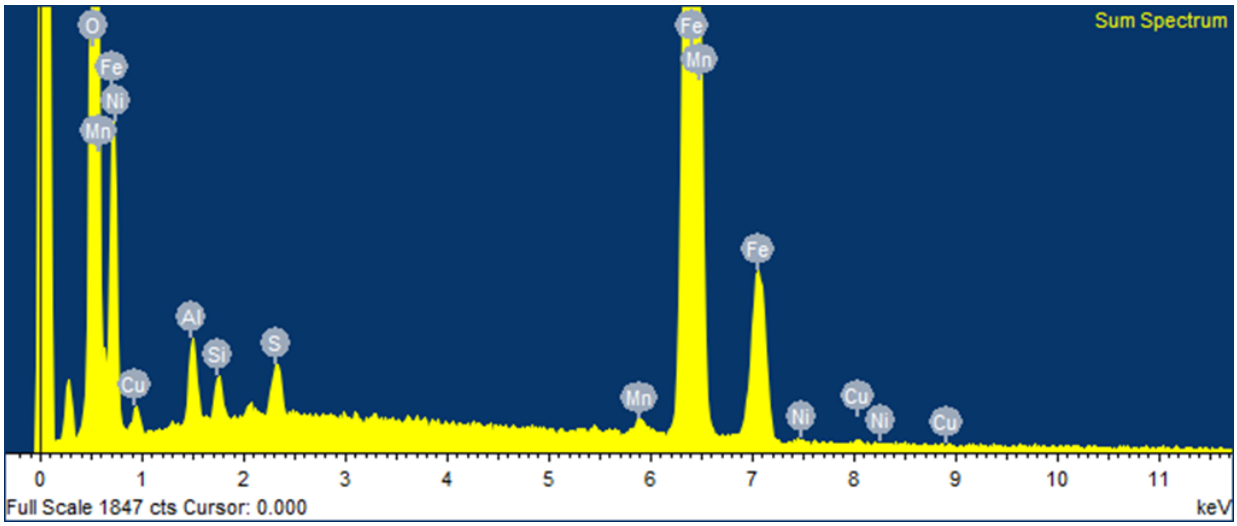


Figure A.570. SEM Image and EDS Spectrum of the Rust Collected from Exterior Web of the Girder.

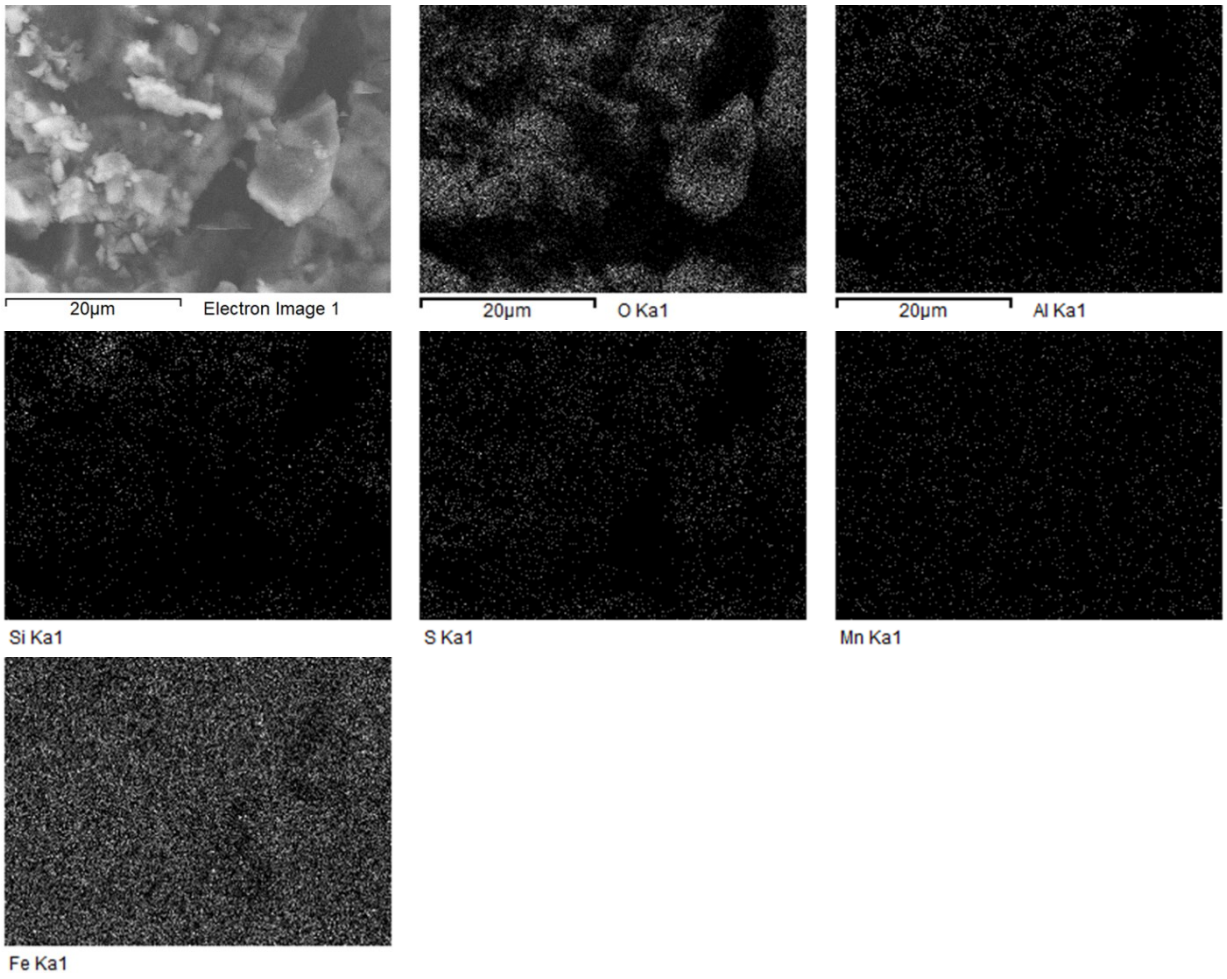
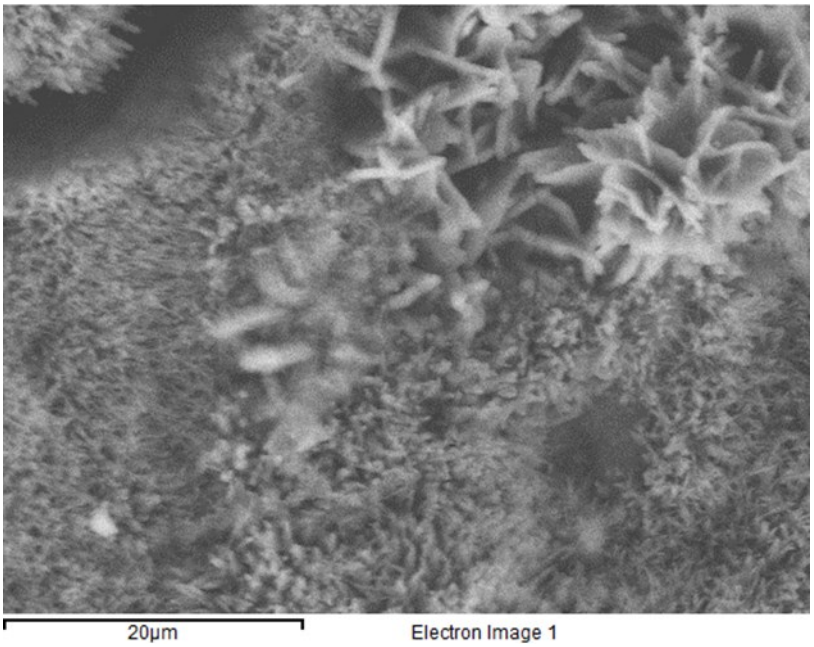


Figure A.571. EDS Elemental Mapping of Rust Collected from Exterior Web.

A.34.4.SEM/EDS: Interior Girder

Element	Weight %	Atomic %
O K	36.85	66.46
Al K	0.65	0.70
Si K	0.55	0.56
S K	0.69	0.62
Mn K	2.73	1.44
Fe K	58.03	29.98
Ni K	0.49	0.24
Totals	100.00	



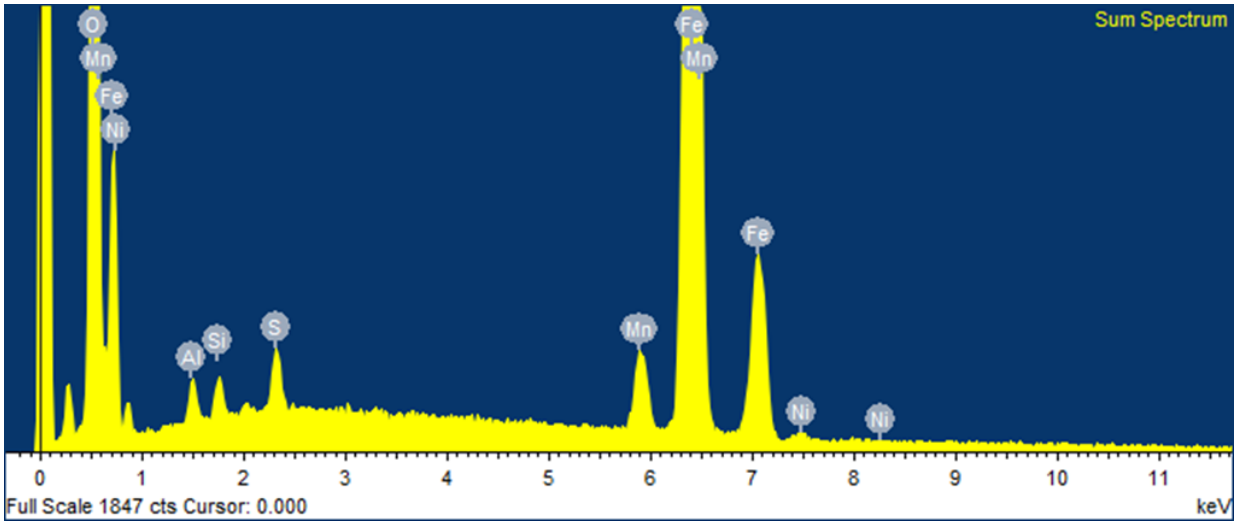


Figure A.572. SEM Image and EDS Spectrum of the Rust Collected from Interior Web of the Girder.

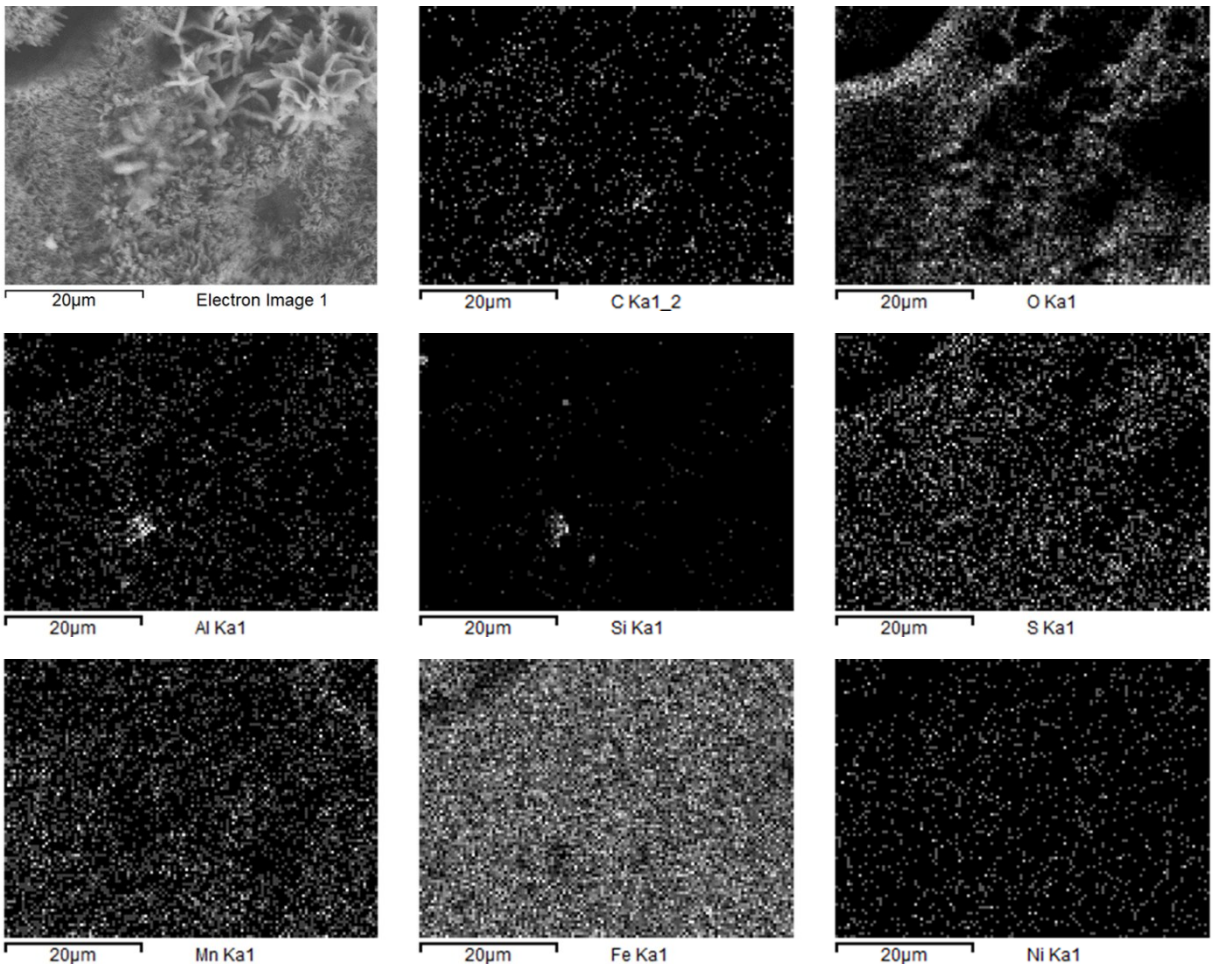
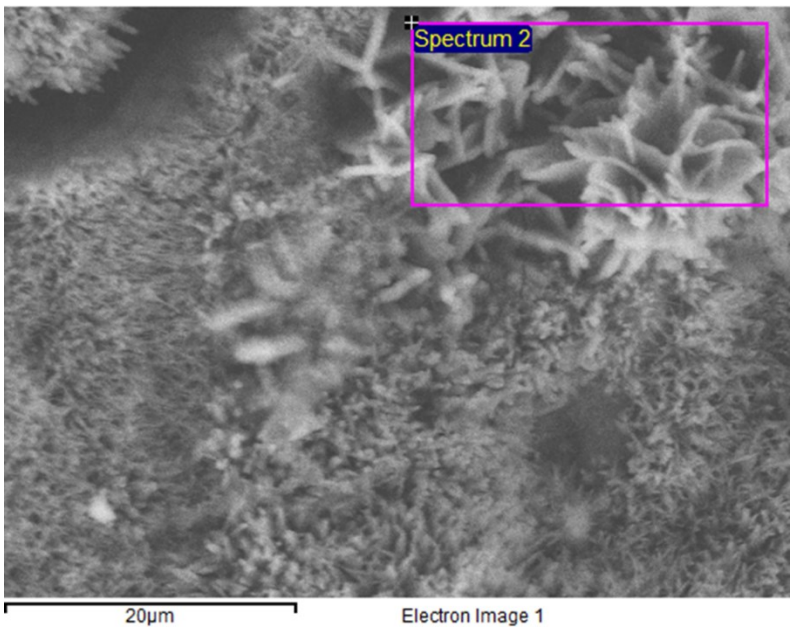


Figure A.573. EDS Elemental Mapping of Rust Collected from Interior Web.

Element	Weight %	Atomic %
O K	33.52	63.32
Al K	0.43	0.48
Si K	0.30	0.33
S K	0.71	0.67
Mn K	2.35	1.29
Fe K	62.28	33.70
Ni K	0.41	0.21
Totals	100.00	



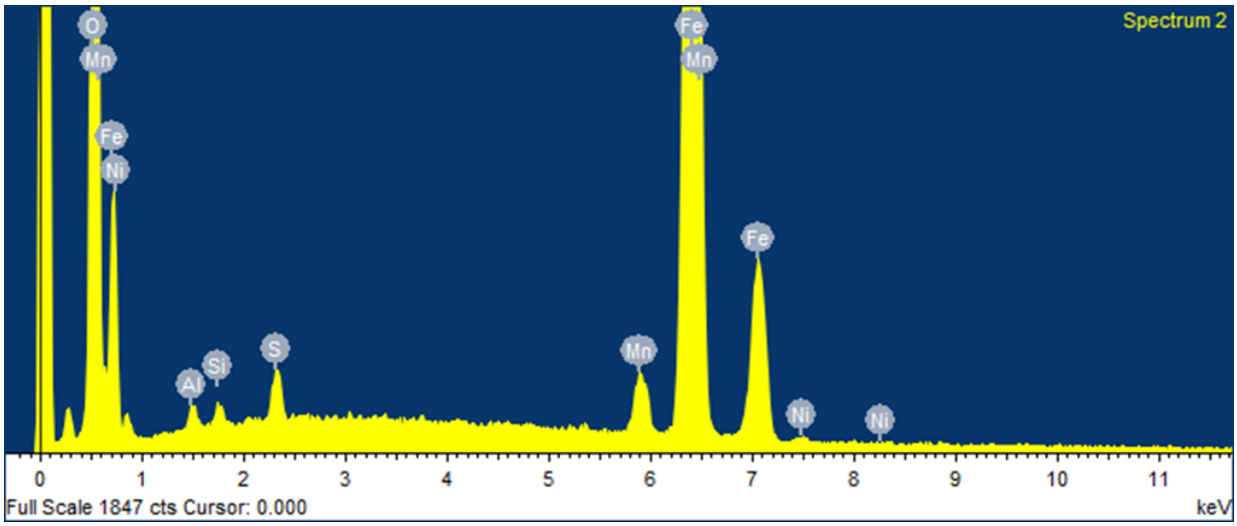
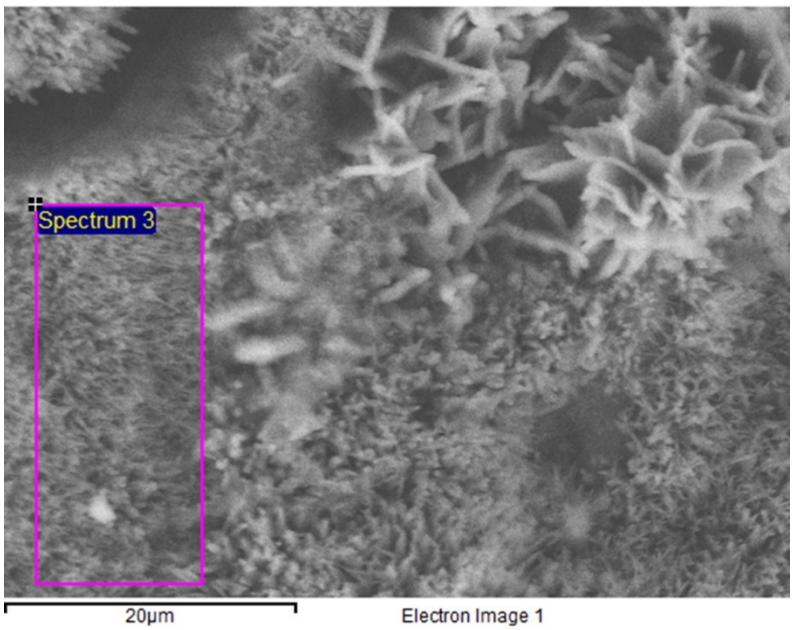


Figure A.574. SEM Image and EDS Spectrum of the Rust Collected from Interior Web of the Girder.

Element	Weight %	Atomic %
O K	35.17	64.95
Al K	0.54	0.59
Si K	0.33	0.34
S K	0.64	0.59
Mn K	3.77	2.03
Fe K	58.84	31.14
Ni K	0.71	0.36
Totals	100.00	



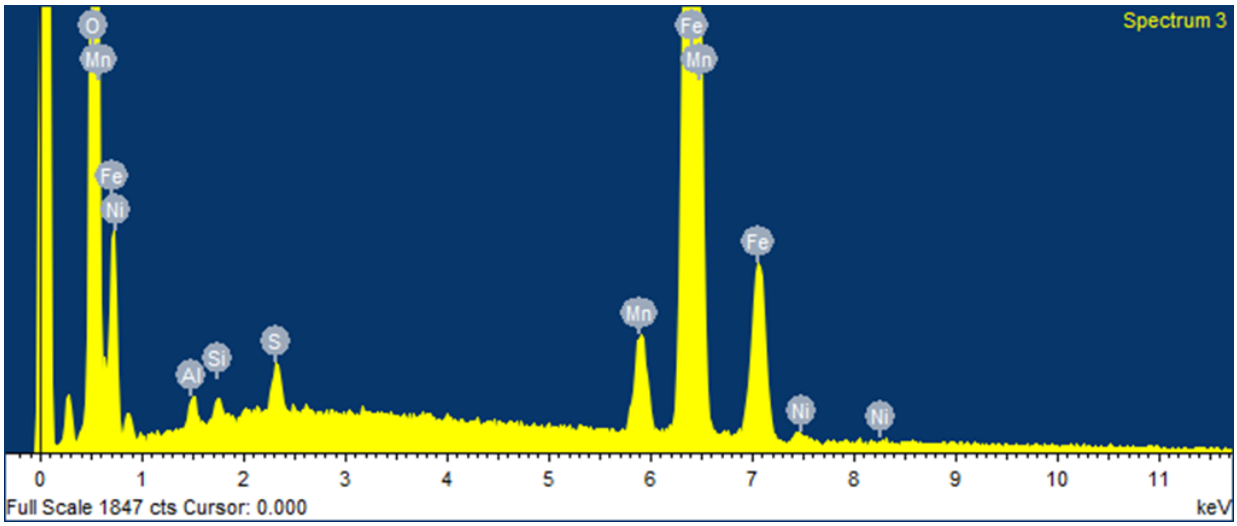


Figure A.575. SEM Image and EDS Spectrum of the Rust Collected from Interior Web of the Girder.

A.34.5.XPS Result: Exterior Girder

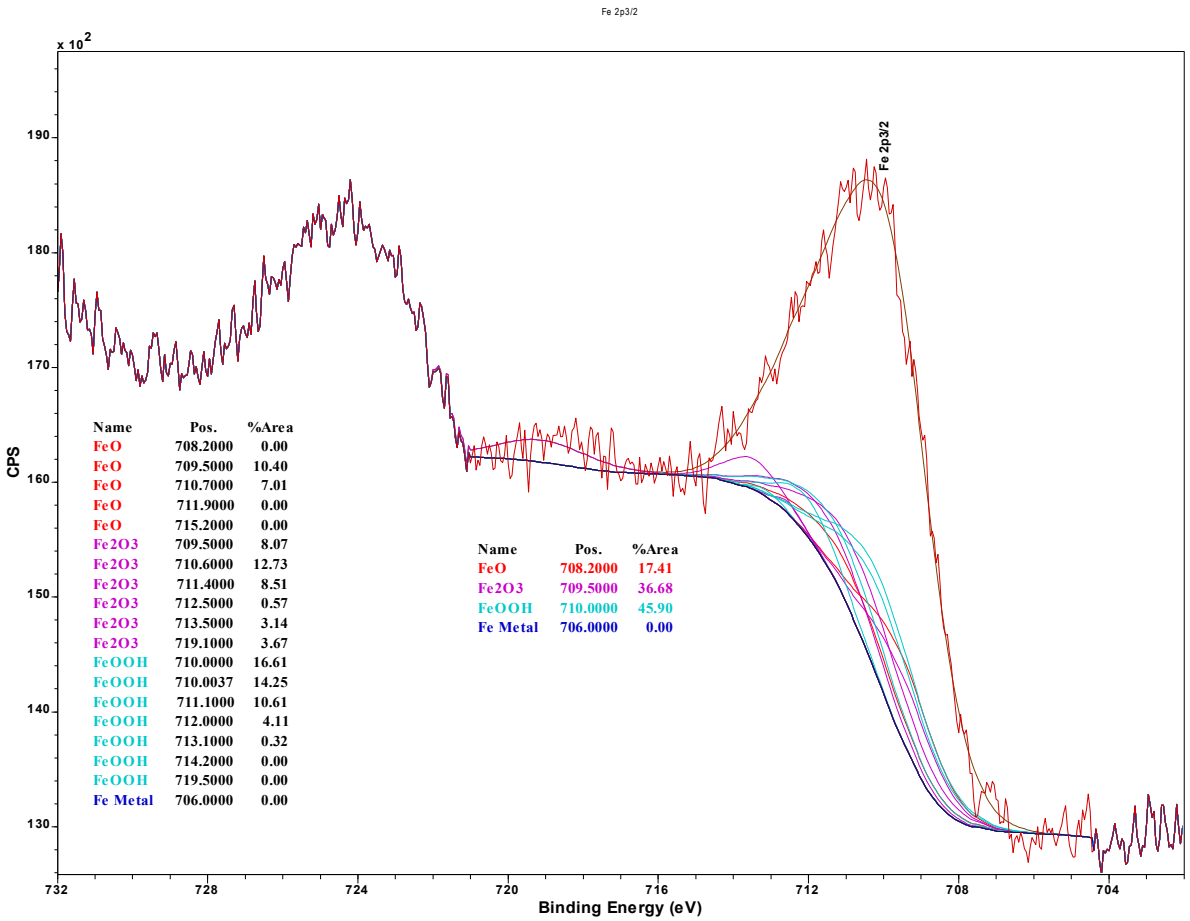


Figure A.576. XPS Spectrum of the Rust Collected from Exterior Web of the Girder.

A.34.6.XPS Result: Interior Girder

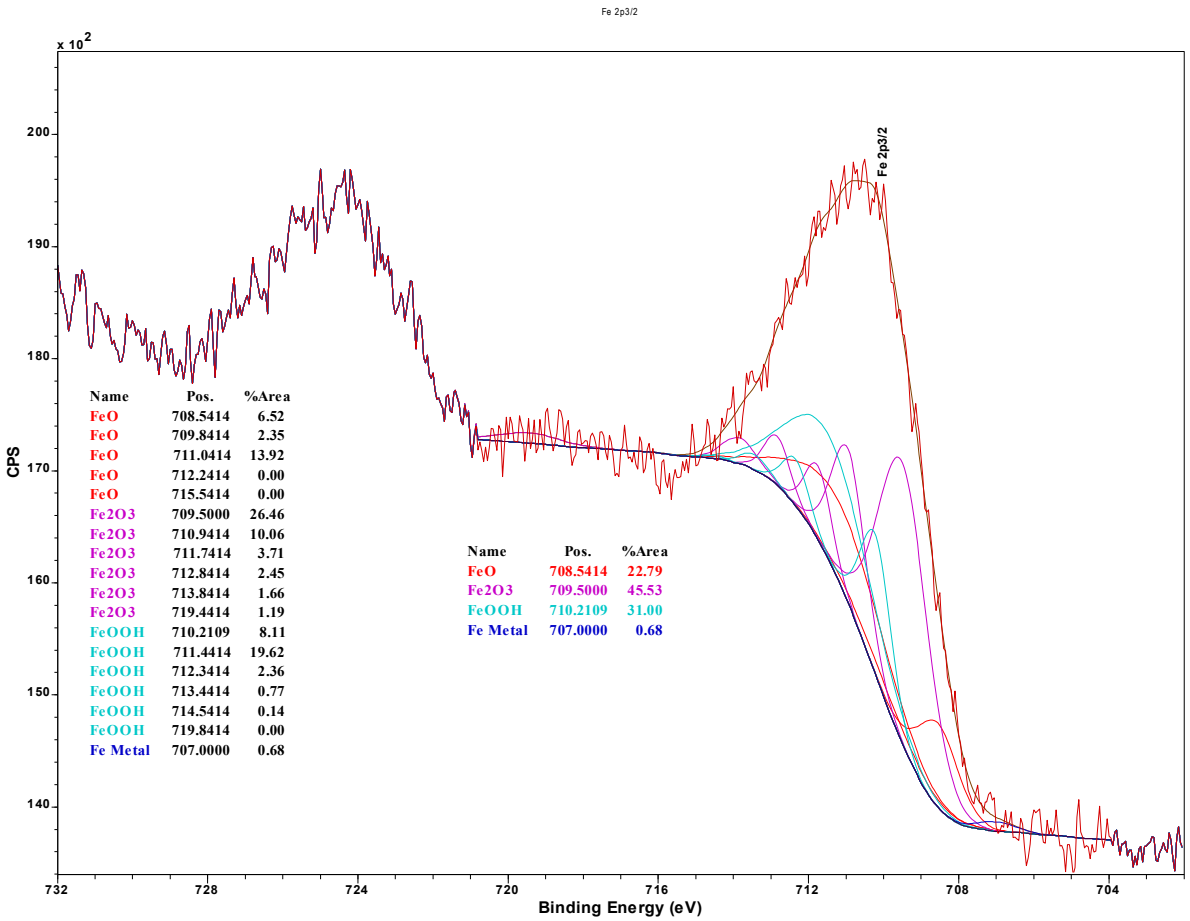


Figure A.577. XPS spectra of the Rust Collected from Interior Web of the Girder.

A.34.7.XRD Result: Exterior, Interior, and Bottom Flange of Girder

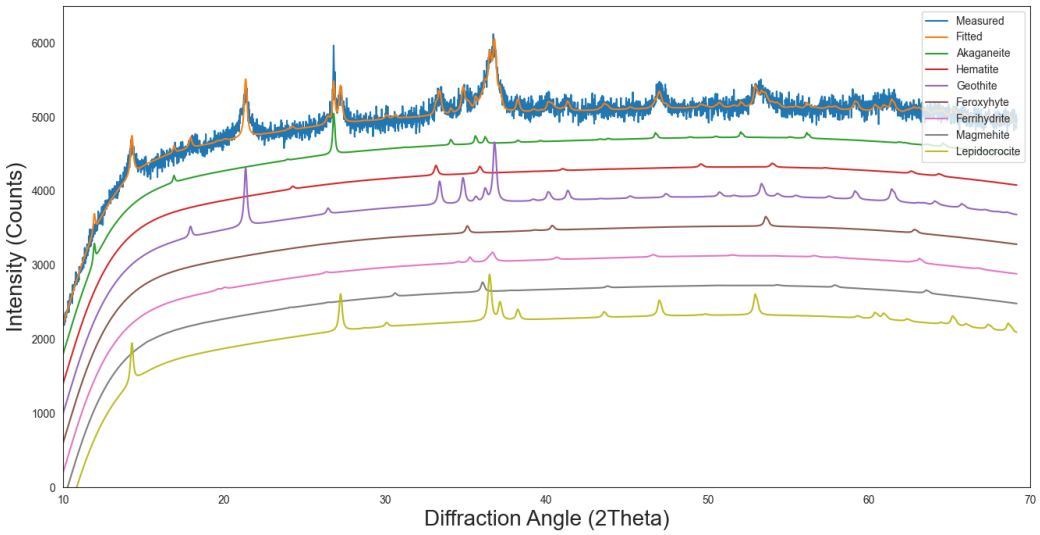


Figure A.578. XRD Pattern of Powdered Rust Collected from Exterior Web of the Girder.

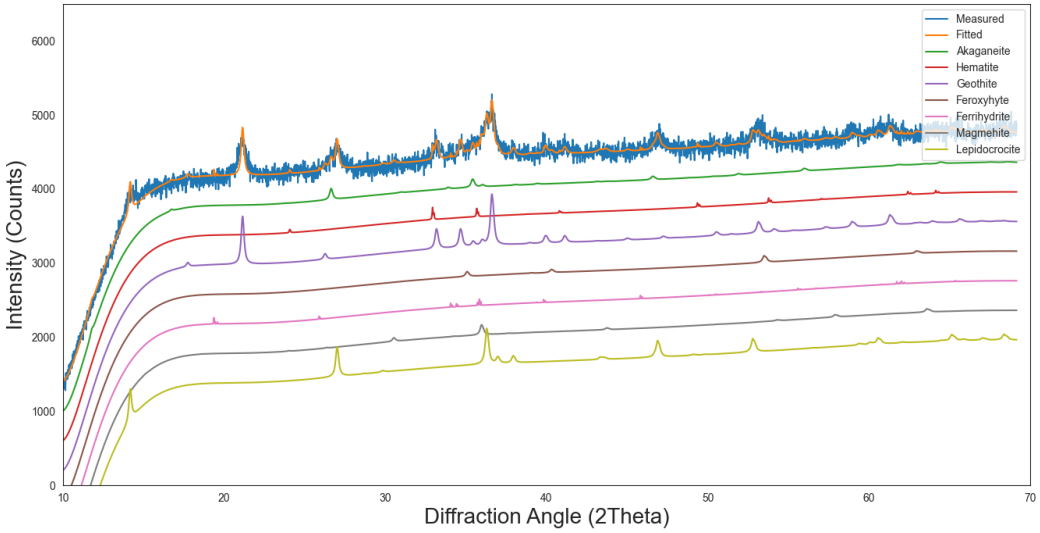


Figure A.579. XRD Pattern of Powdered Rust Collected from Interior Web of the Girder.

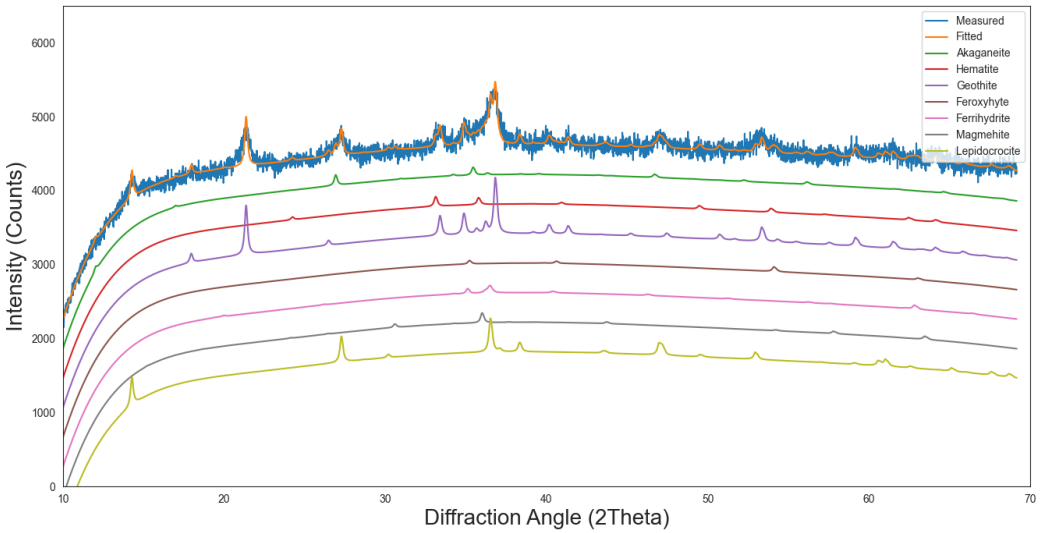


Figure A.580. XRD Pattern of Powdered Rust Collected from Bottom face of Bottom Flange of the Interior Girder.

A.34.8.Particle Size Analysis: Tape Adhesion Results

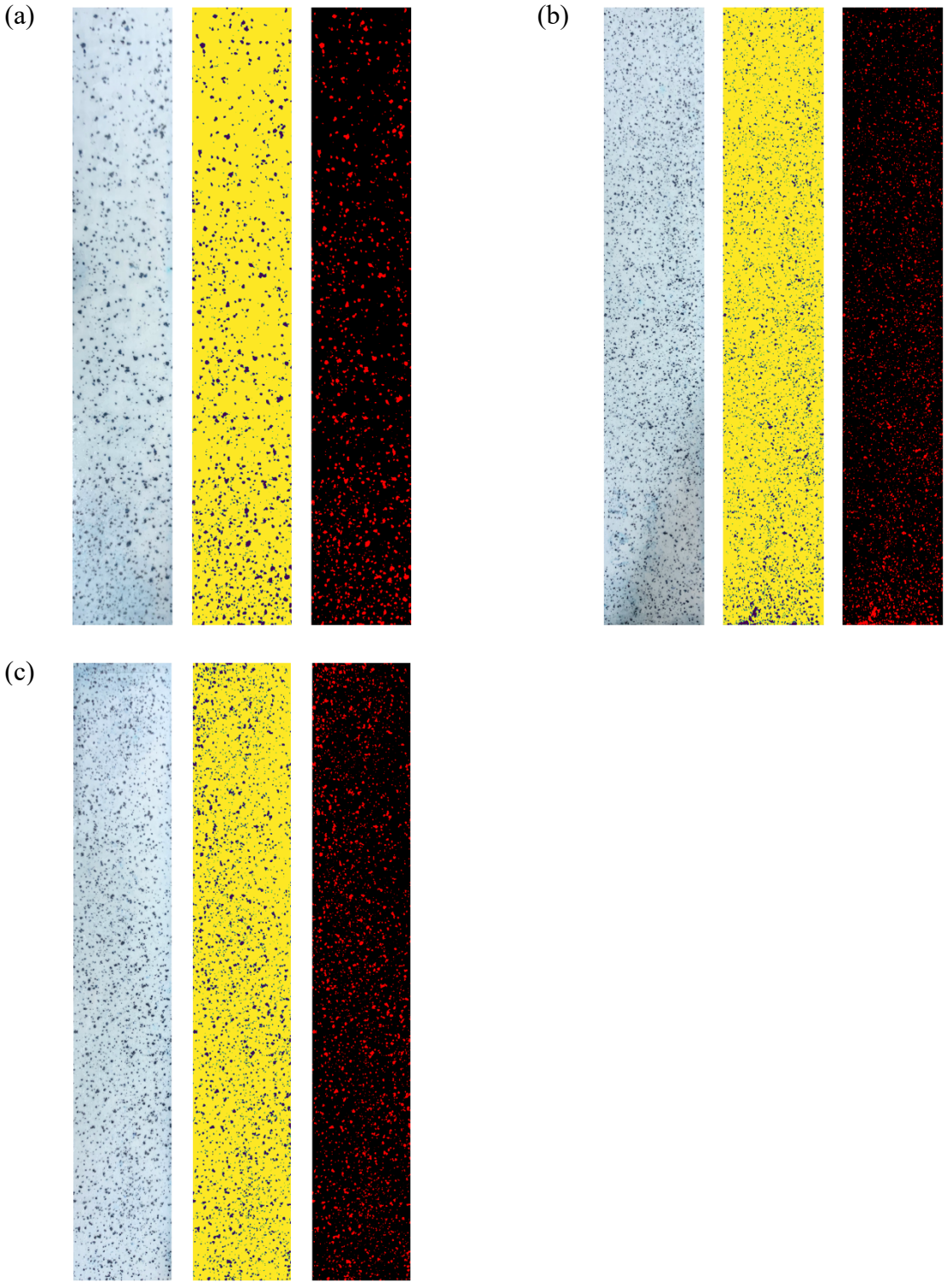


Figure A.581. Particle Size Analysis Results at A1G1F1 (a) Top Flange Bottom, (b) Web, (c) Bottom Flange Bottom.

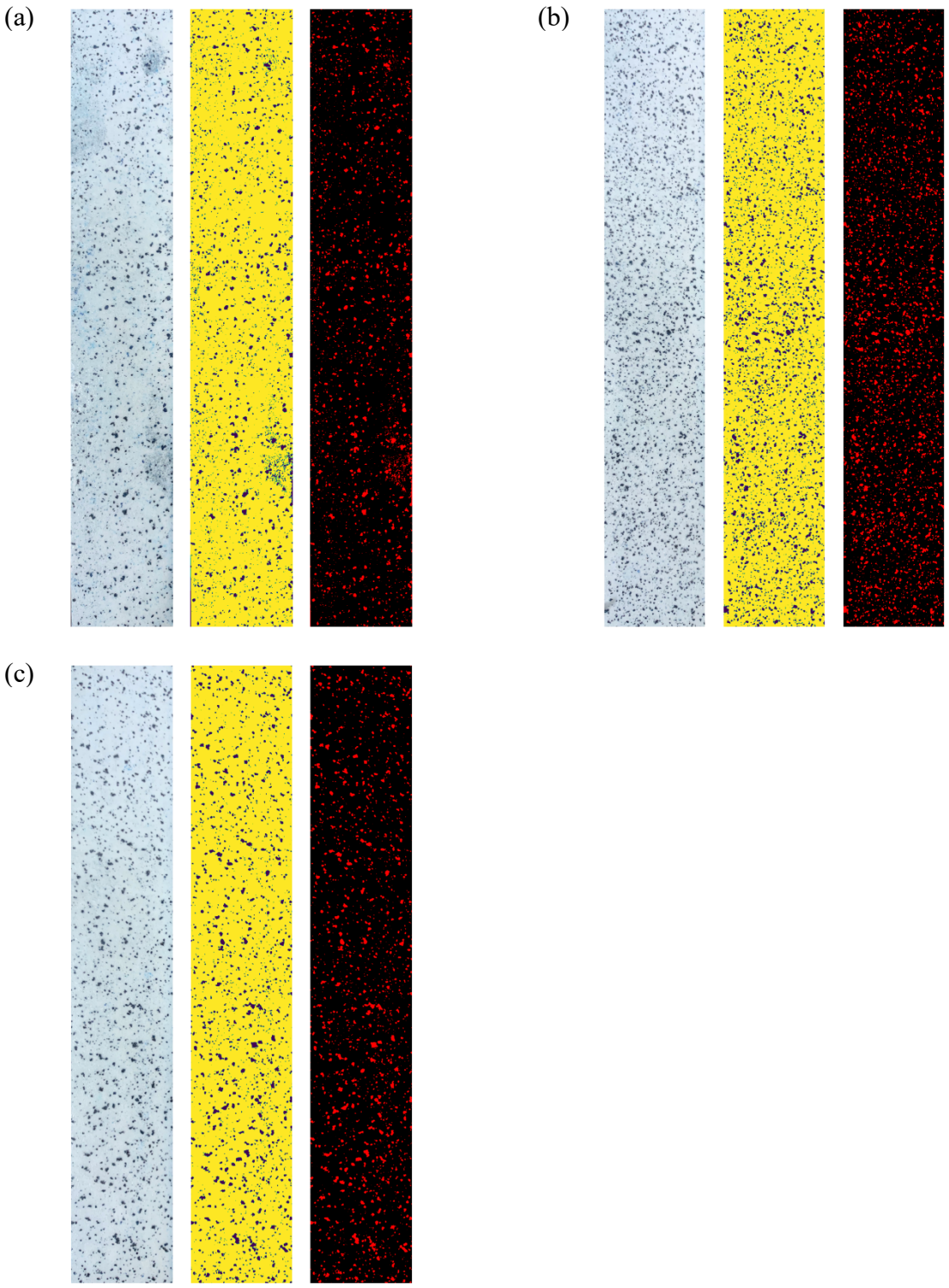


Figure A.582. Particle Size Analysis Results at A1G2F1 (a) Top Flange Bottom, (b) Web, (c) Bottom Flange Bottom.

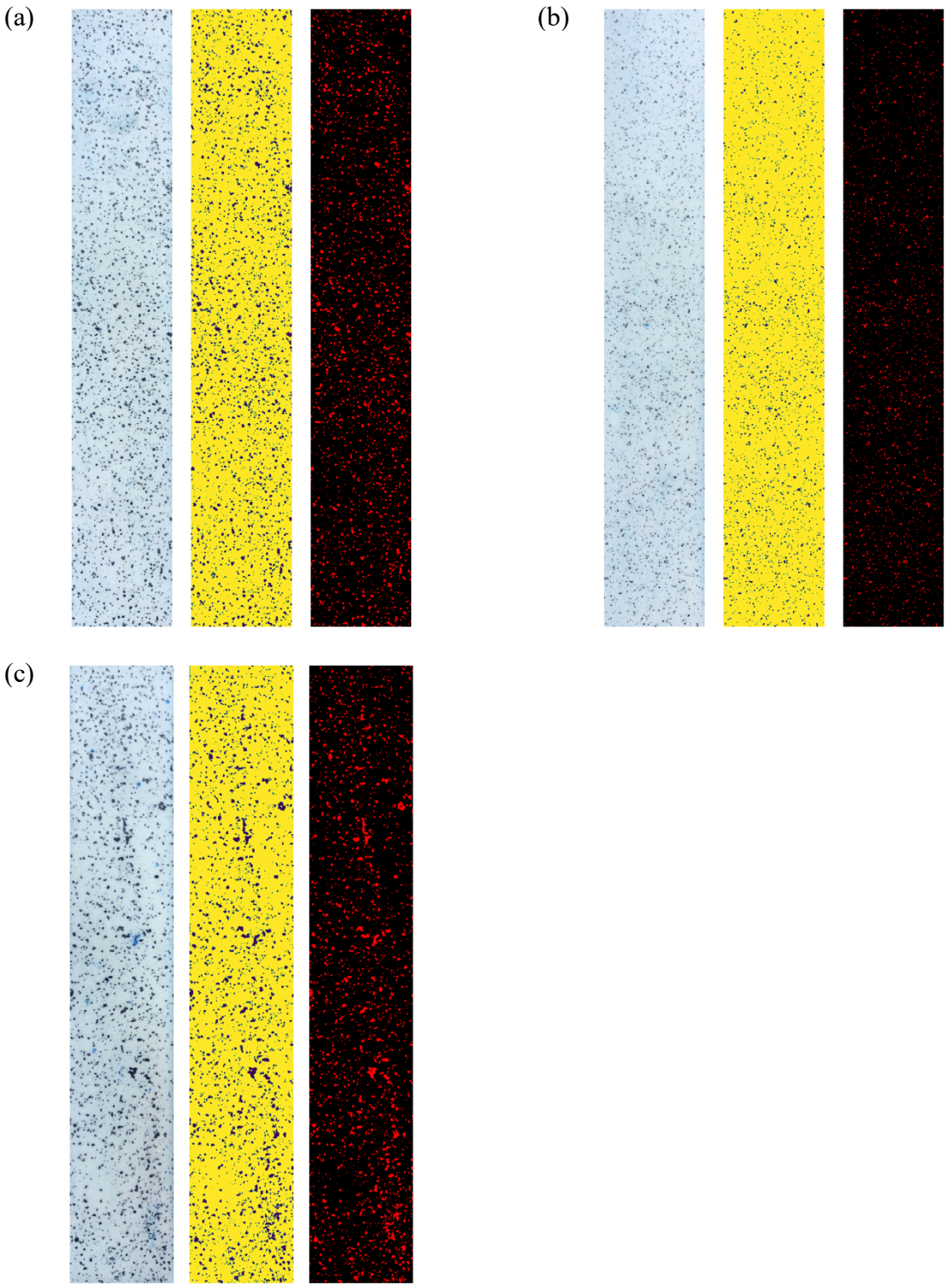
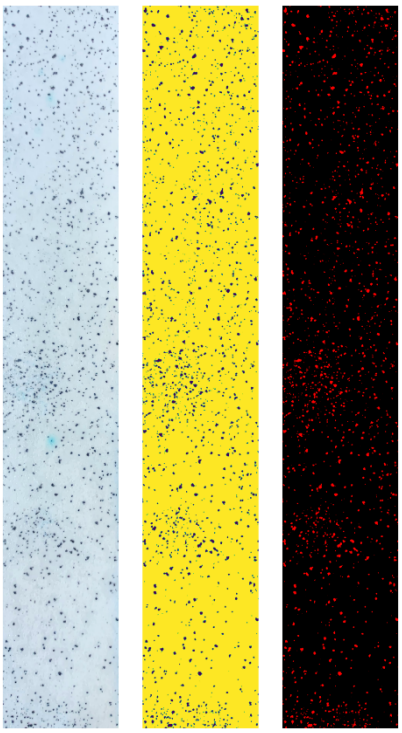


Figure A.583. Particle Size Analysis Results at A1G3F2 (a) Top Flange Bottom, (b) Web, (c) Bottom Flange Bottom.

(a)

(b)



(c)

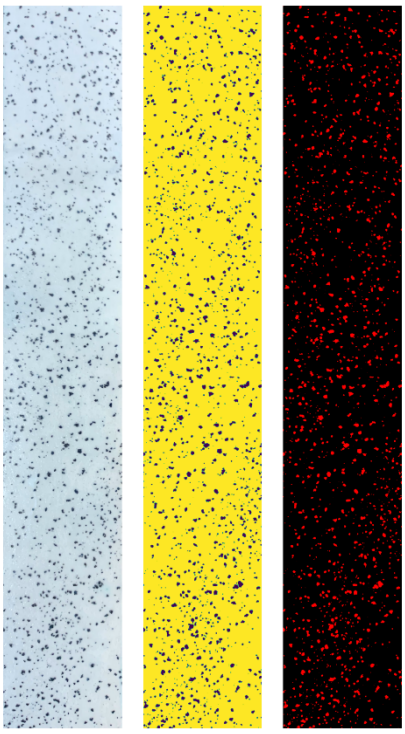
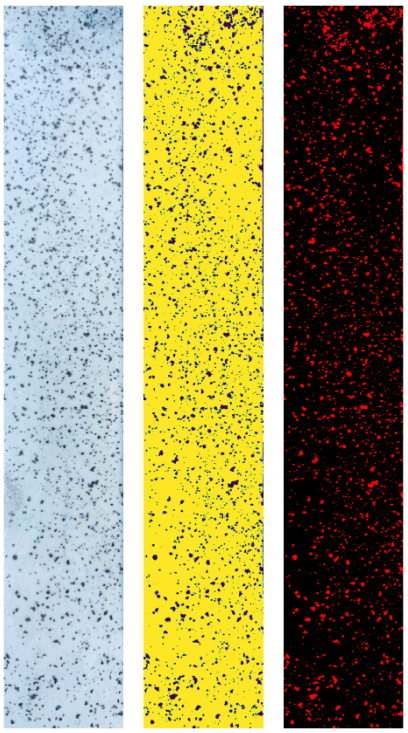


Figure A.584. Particle Size Analysis Results at A2G1F1 (a) Top Flange Bottom, (b) Web, (c) Bottom Flange Bottom.

(a)

(b)



(c)

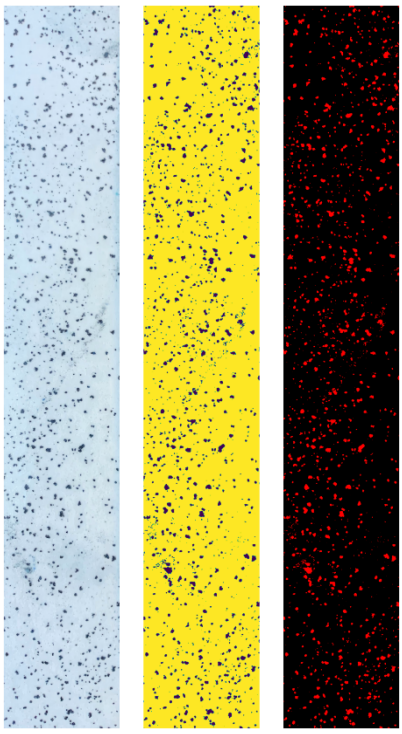
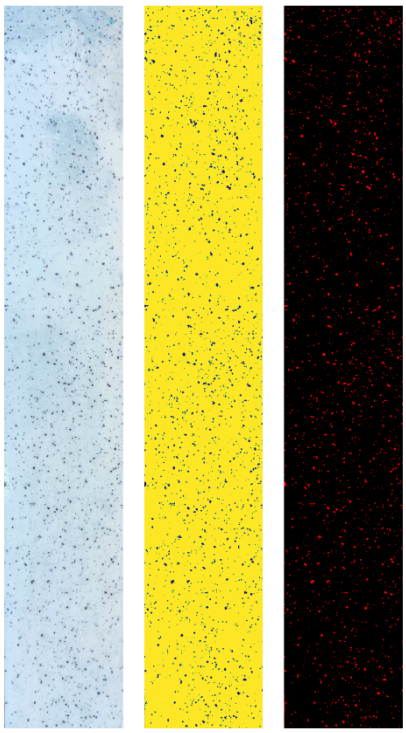


Figure A.585. Particle Size Analysis Results at A3G2F1 (a) Top Flange Bottom, (b) Web, (c) Bottom Flange Bottom.

(a)

(b)



(c)

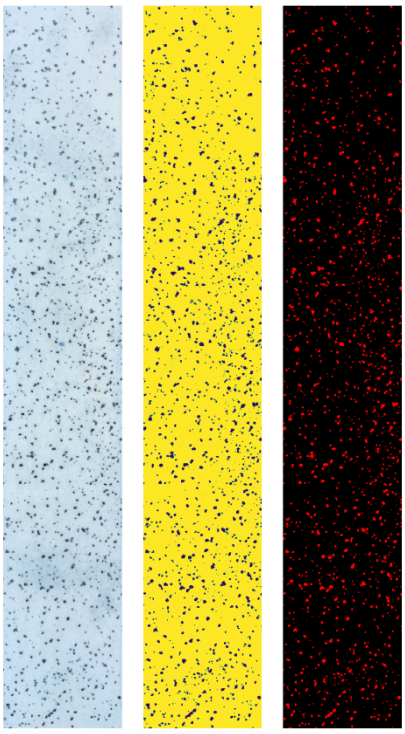


Figure A.586. Particle Size Analysis Results at A3G2F2 (a) Top Flange Bottom, (b) Web, (c) Bottom Flange Bottom.

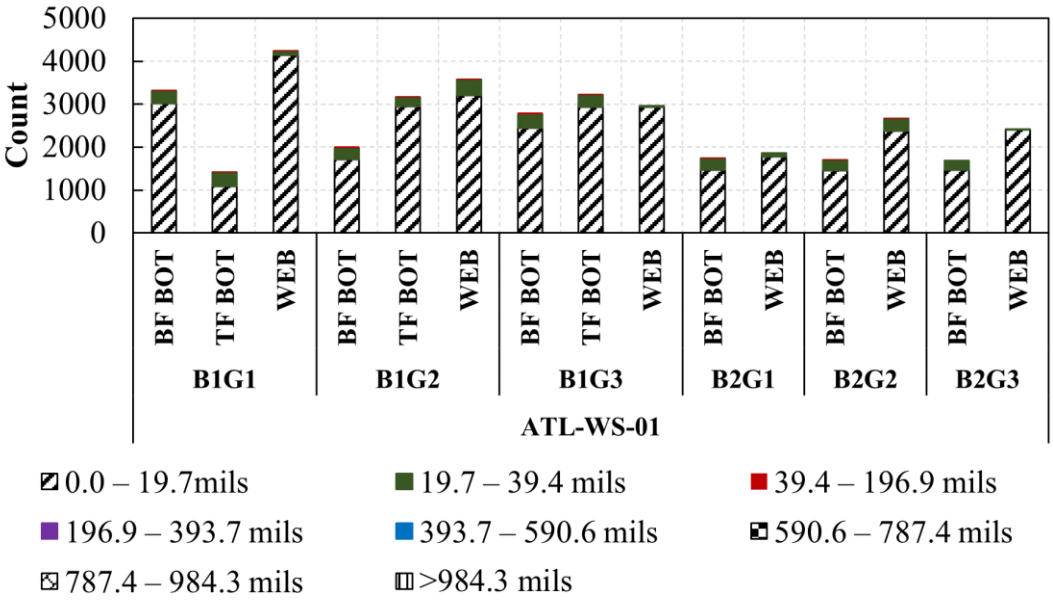


Figure A.587. Particle Size Analysis Showing Different Locations Examined.

A.35. ATL-WS-02

- LP151 SB over SH 93
- Bridge ID 1901900205003072, Coordinates (33.3954808, -94. 0981214), Harris County
- Continuous weathering steel plate girder
- Built 2004
- Girder inspection carried on End abutment, and measurements are taken on girder within four feet from the abutment or bent.
- No visual inspection on deck
- Location for Testing: B10-G1F1, B11-G3F2, B10-G2F1, B11-G1F1, B11-G2F1



Figure A.588. Typical Picture of ATL-WS-02.

A.35.1. Observed Condition

Uniform patina are visible on the bottom face of the top flange with a patina rating of 8. The web has a uniform patina formation with a patina rating of 8. The interior girders also have patina rating of 8 while the bottom flange has patina rating of 7. Overall the bridge has uniform patina and is in very good condition because of formation of uniform patina.

A.35.2.Field Inspection Results

Table A-157. Field Inspection Results for ATL-WS-02.

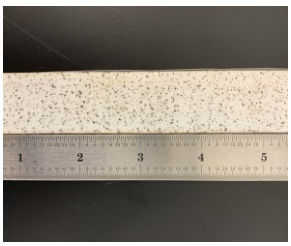
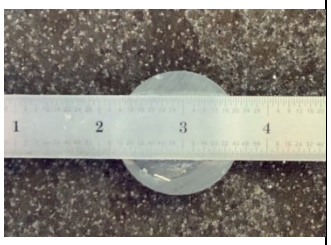
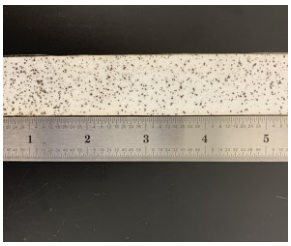
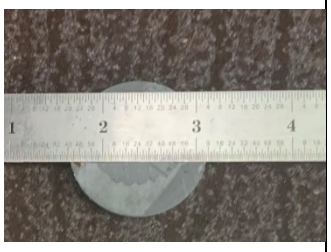
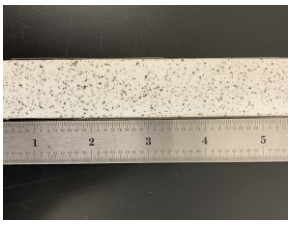
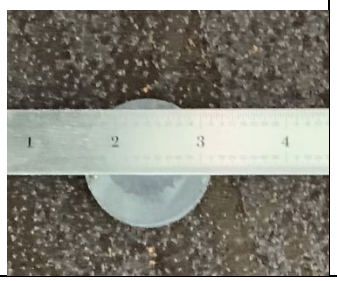
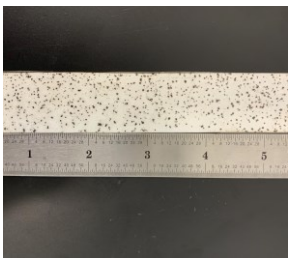
Location	Patina Rating	Thickness (inch)	Cl^- Conc. (ppm)	Field Condition	Tape Test
B10-G1F1 TF Bot. Ext.	8	Measured - Design			
B10-G1F1 Web Ext.	8	Measured 0.474 Design	6		
B10-G1F1 BF Bot. Ext.	8	Measured 1.233 Design			
B10-G2F1 Web Ext.	8	Measured 0.476 Design	5		
B10-G2F1 BF Bot. Ext.	8	Measured 1.284 Design			

Table A-158. Field Inspection Results for ATL-WS-02.

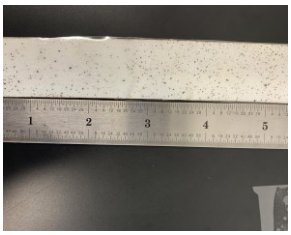
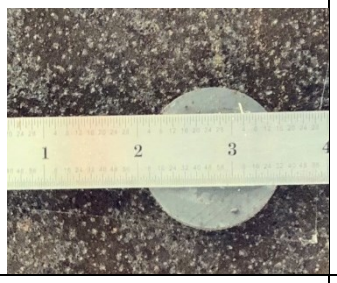
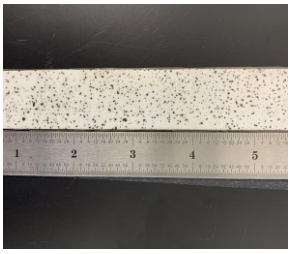
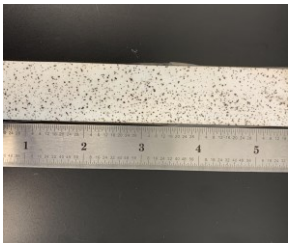
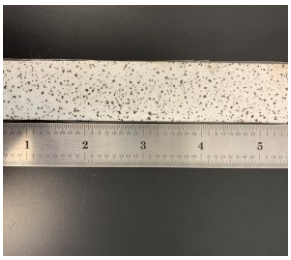
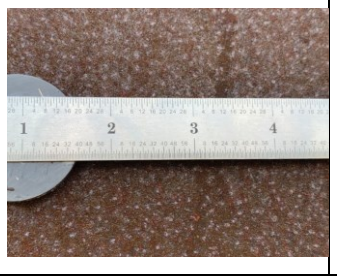
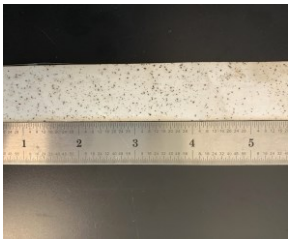
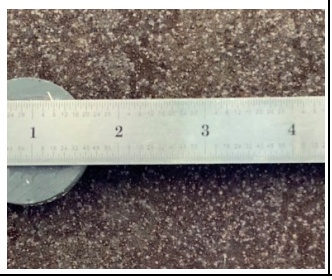
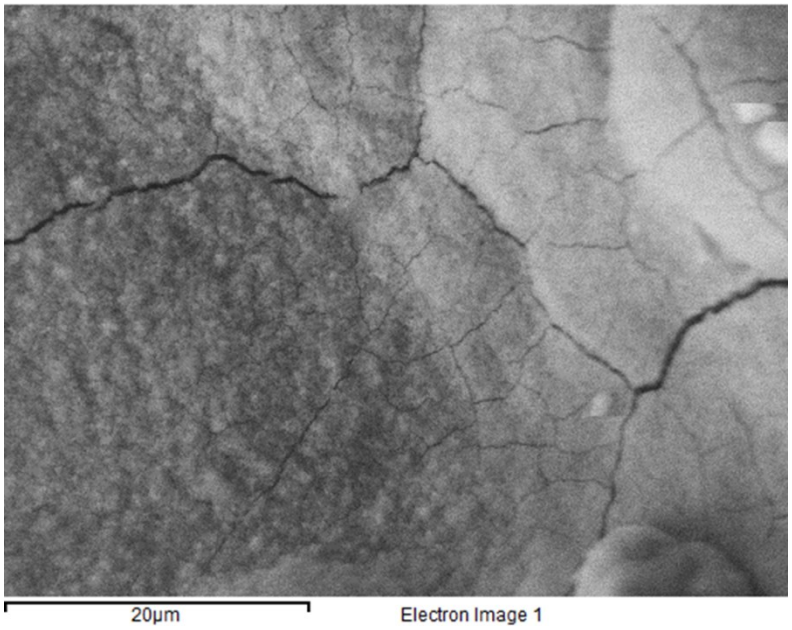
Location	Patina Rating	Thickness (inch)	Cl^- Conc. (ppm)	Field Condition	Tape Test
B11-G1F1 Web Ext.	8	Measured 0.474 Design	4		
B11-G1F1 BF Bot. Ext.	7	Measured 1.610 Design			
B11-G2F1 Web Ext.	8	Measured 0.476 Design	10		
B11-G2F1 BF Top Ext.	7	Measured 1.612 Design			
B11-G3F2 Web Ext.	7	Measured 0.470 Design			

Table A-159. Field Inspection Results for ATL-WS-02.

Location	Patina Rating	Thickness (inch)	Cl^- Conc. (ppm)	Field Condition	Tape Test
B11-G3F2 BF Bot. Ext.	7	Measured 1.589 Design			

A.35.3.SEM/EDS Results: Exterior Girder Web

Element	Weight %	Atomic %
O K	49.11	76.43
Al K	1.15	1.06
S K	1.01	0.79
Mn K	0.58	0.26
Fe K	48.08	21.43
Cu K	0.06	0.02
Totals	100.00	



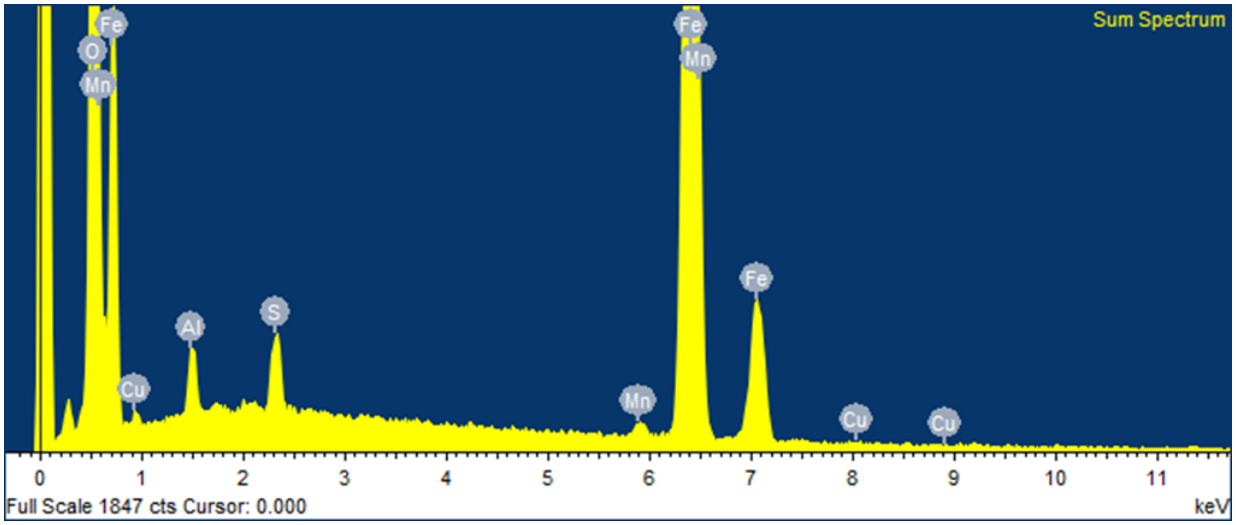


Figure A.589. SEM Image and EDS Spectrum of the Rust Collected from Exterior Web of the Girder.

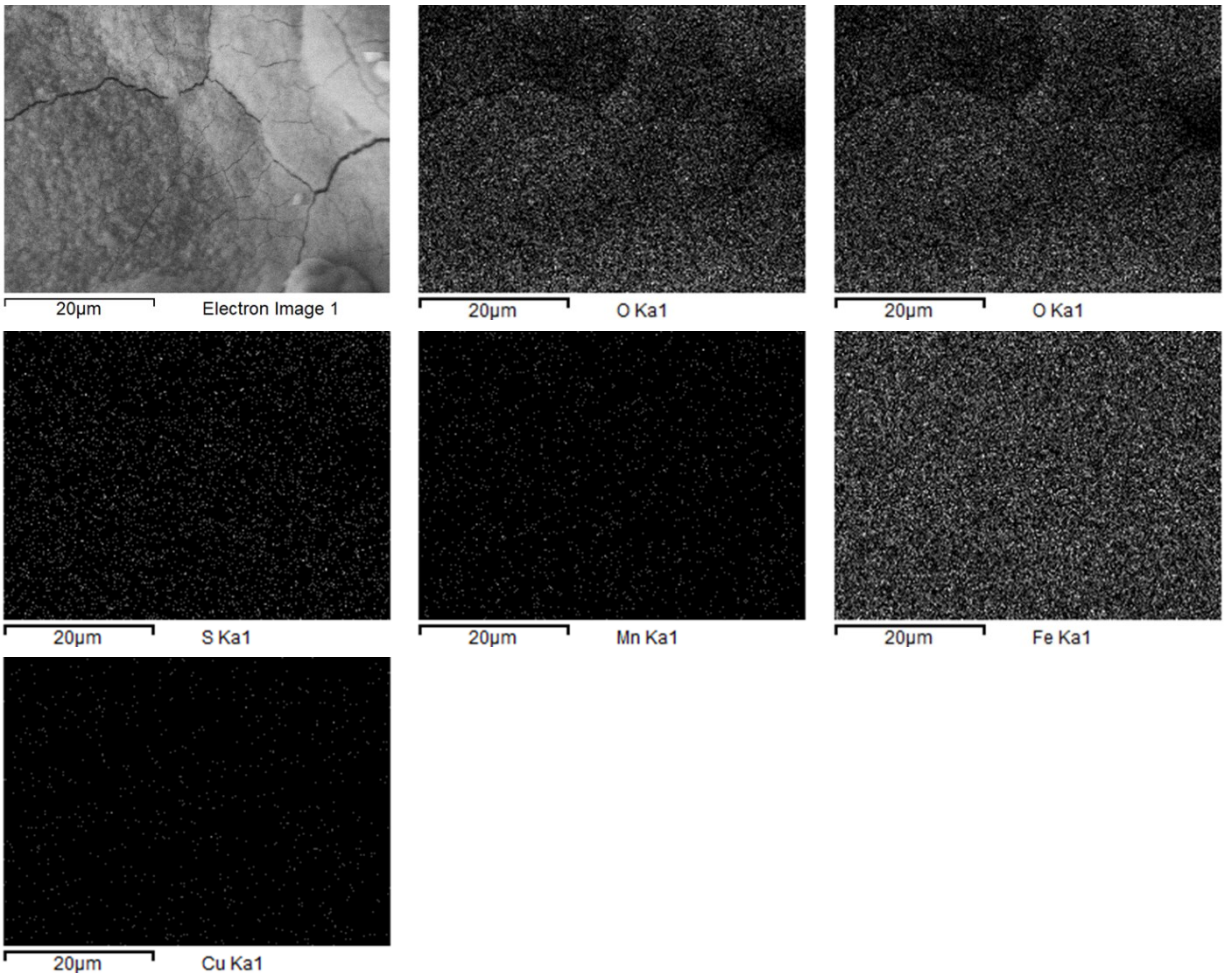
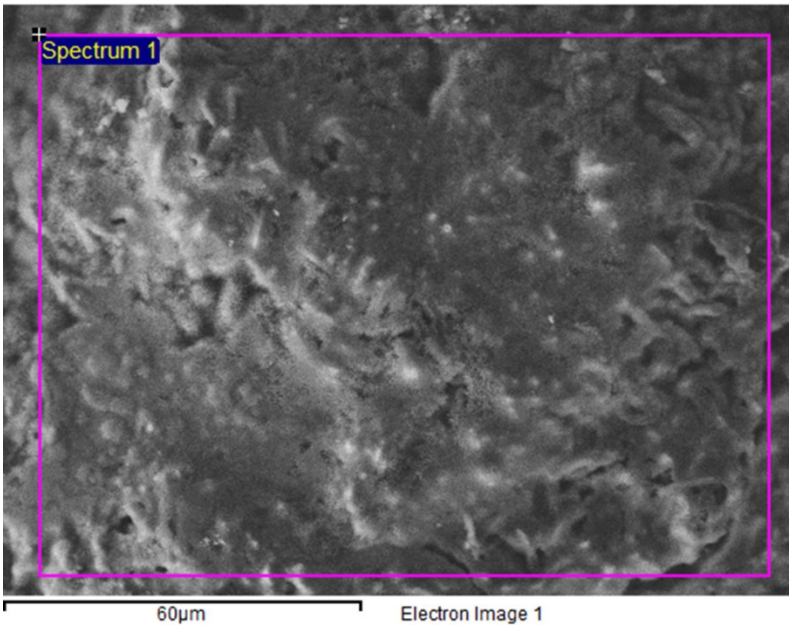


Figure A.590. EDS Elemental Mapping of Rust Collected from Exterior Web.

Element	Weight %	Atomic %
O K	44.39	72.97
Al K	0.89	0.87
Si K	0.27	0.25
S K	0.74	0.61
Mn K	0.57	0.27
Fe K	53.09	25.00
Cu K	0.05	0.02
Totals	100.00	



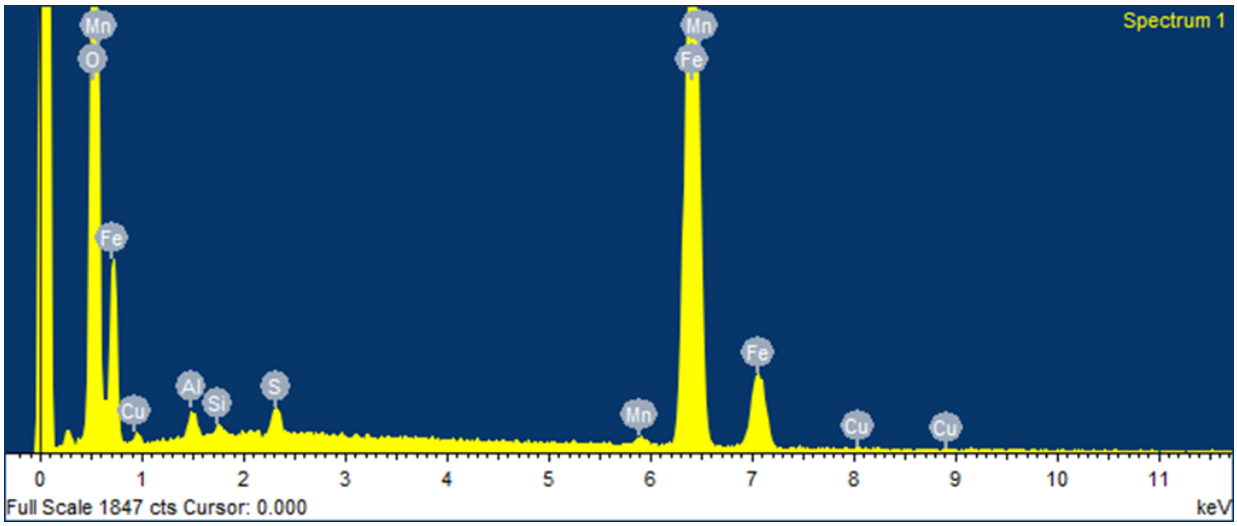
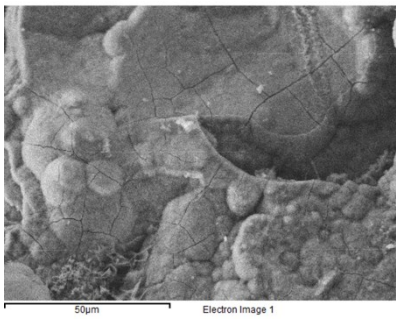
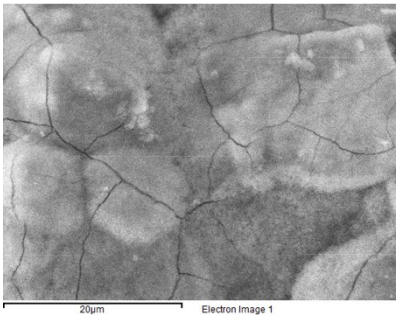
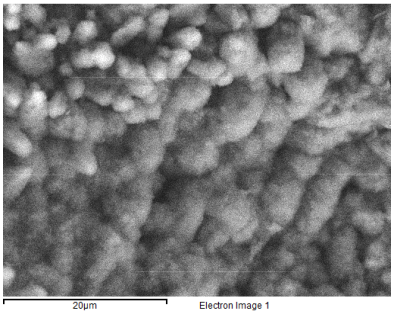


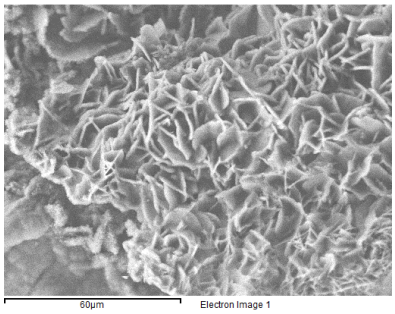
Figure A.591. SEM Image and EDS Spectrum of the Rust Collected from Exterior Web of the Girder.

A.35.4.SEM/EDS Results: Interior Girder Web

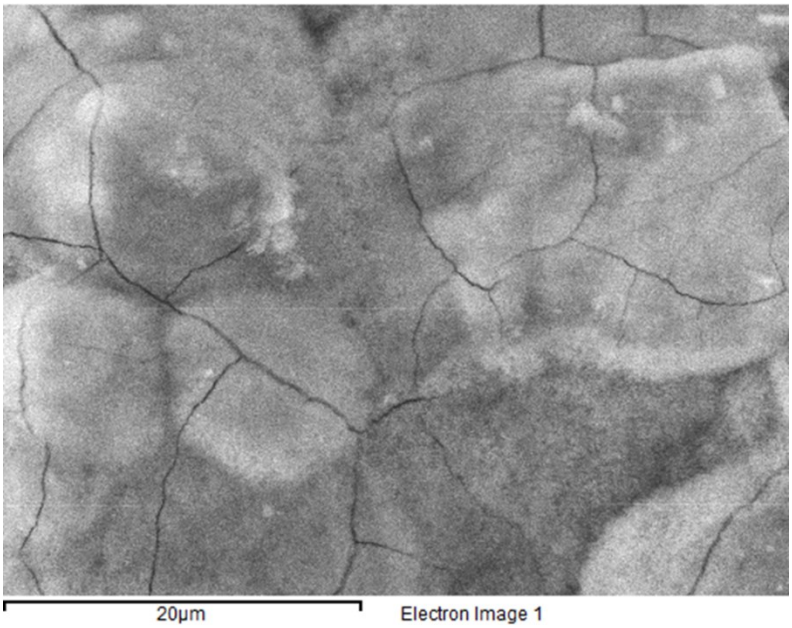








Element	Weight %	Atomic %
O K	49.02	76.52
Al K	0.69	0.64
Si K	0.26	0.23
S K	0.74	0.58
Mn K	0.78	0.35
Fe K	48.36	21.62
Cu K	0.15	0.06
Totals	100.00	



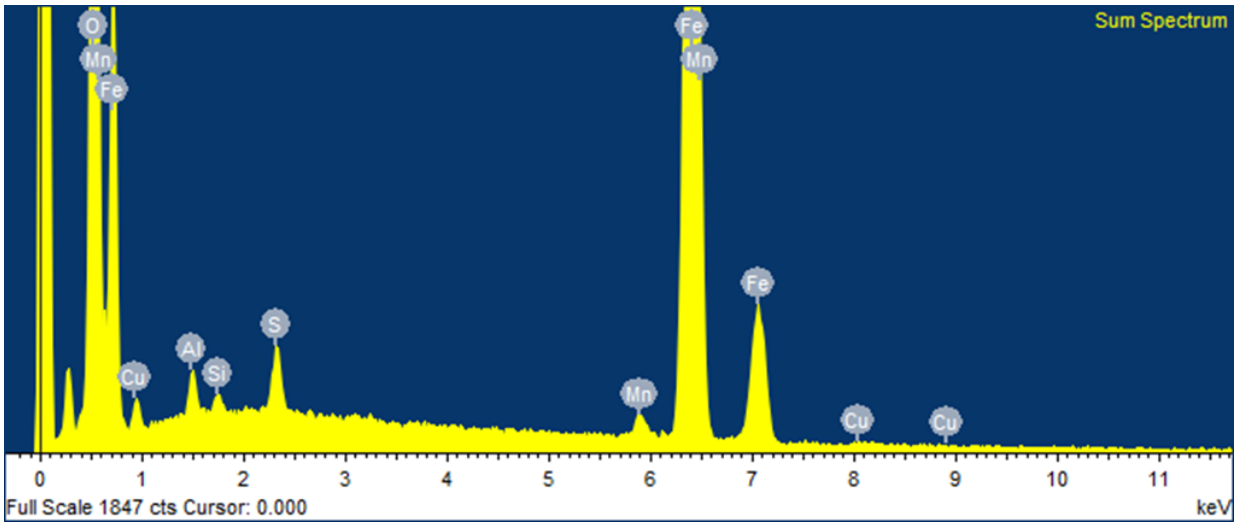


Figure A.592. SEM Image and EDS Spectrum of the Rust Collected from Interior Web of the Girder.

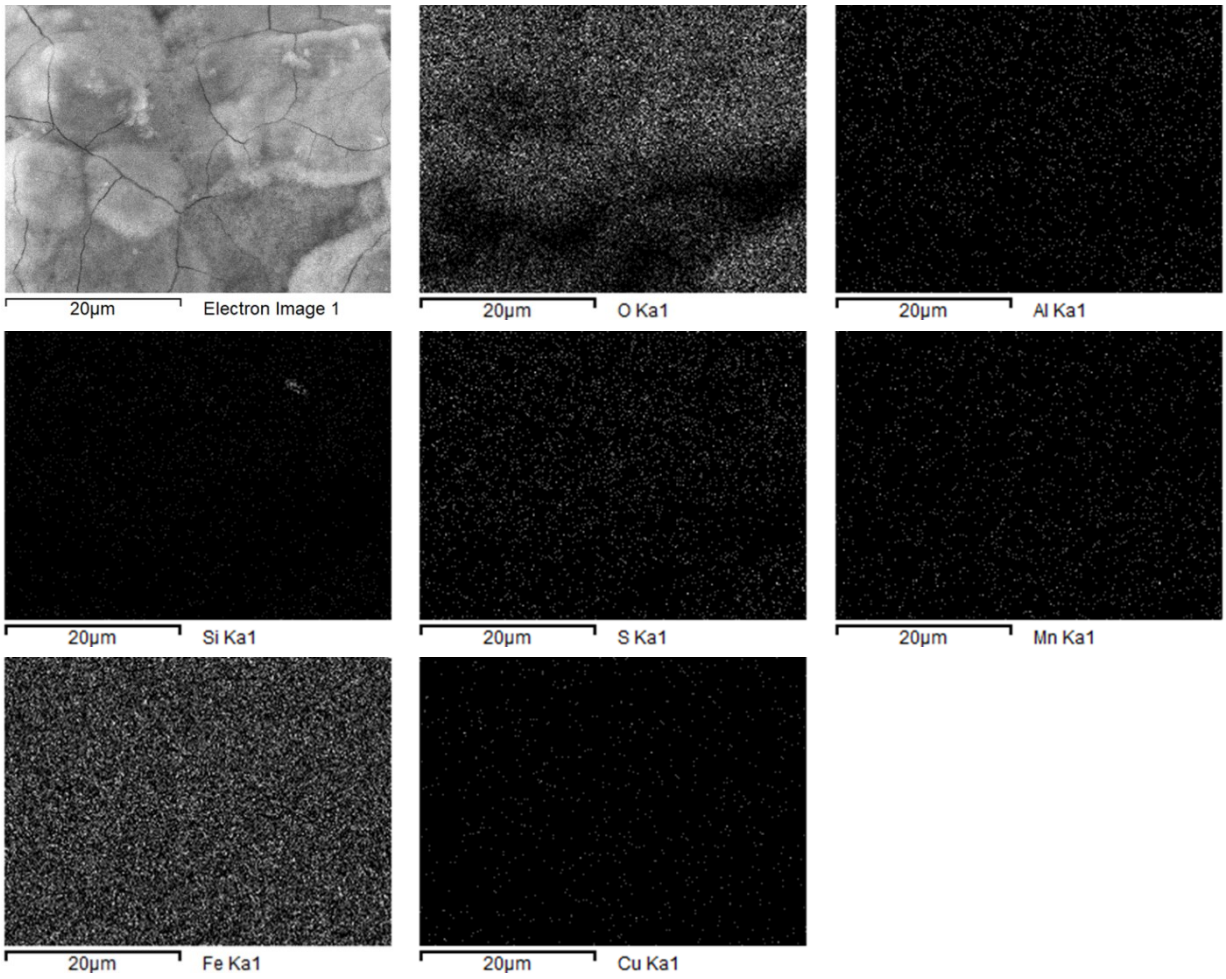
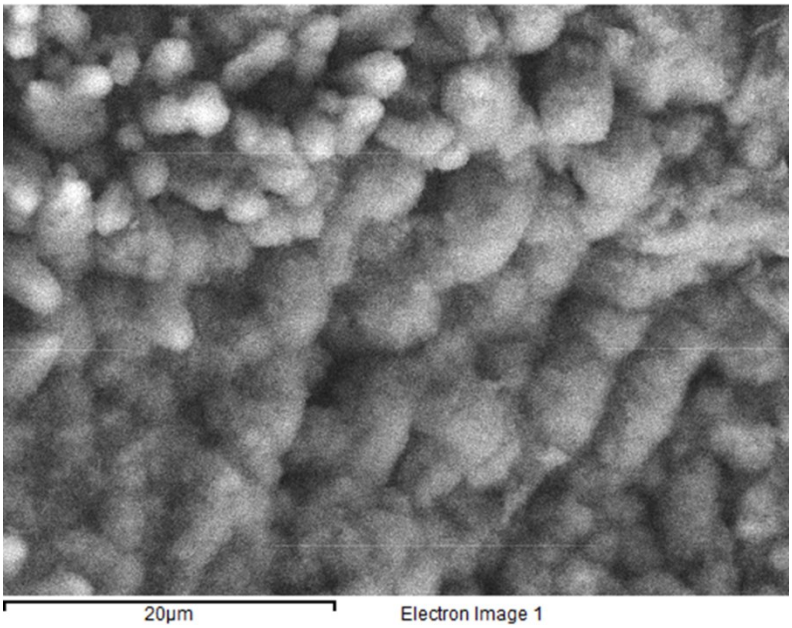


Figure A.593. EDS Elemental Mapping of Rust Collected from Interior Web.

Element	Weight %	Atomic %
O K	30.33	59.79
Al K	0.90	1.05
Si K	0.16	0.18
S K	0.55	0.54
Mn K	1.18	0.68
Fe K	66.75	37.70
Cu K	0.12	0.06
Totals	100.00	



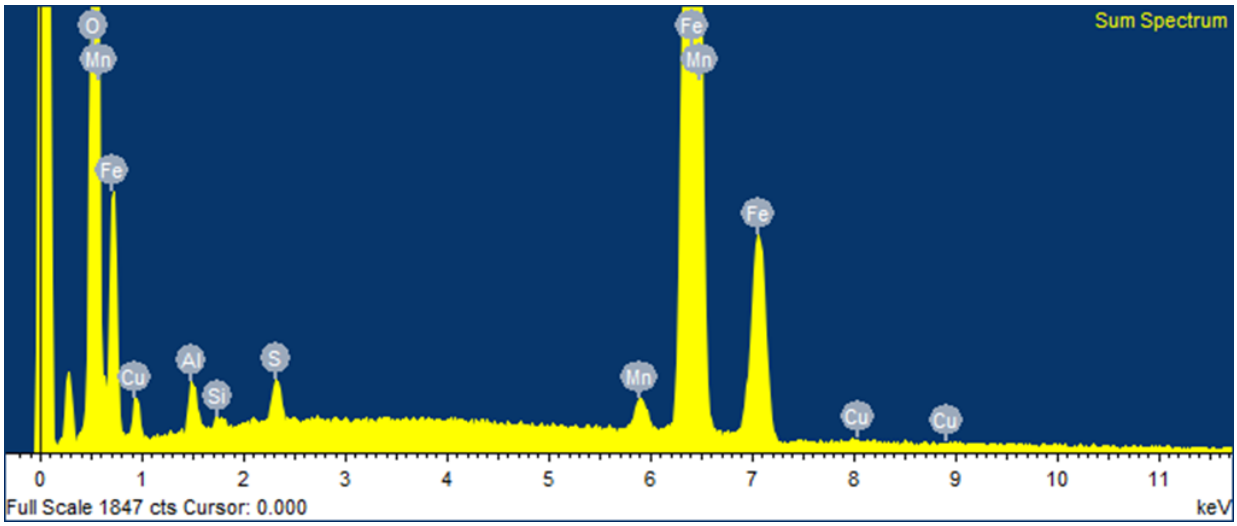


Figure A.594. SEM Image and EDS Spectrum of the Rust Collected from Interior Web of the Girder.

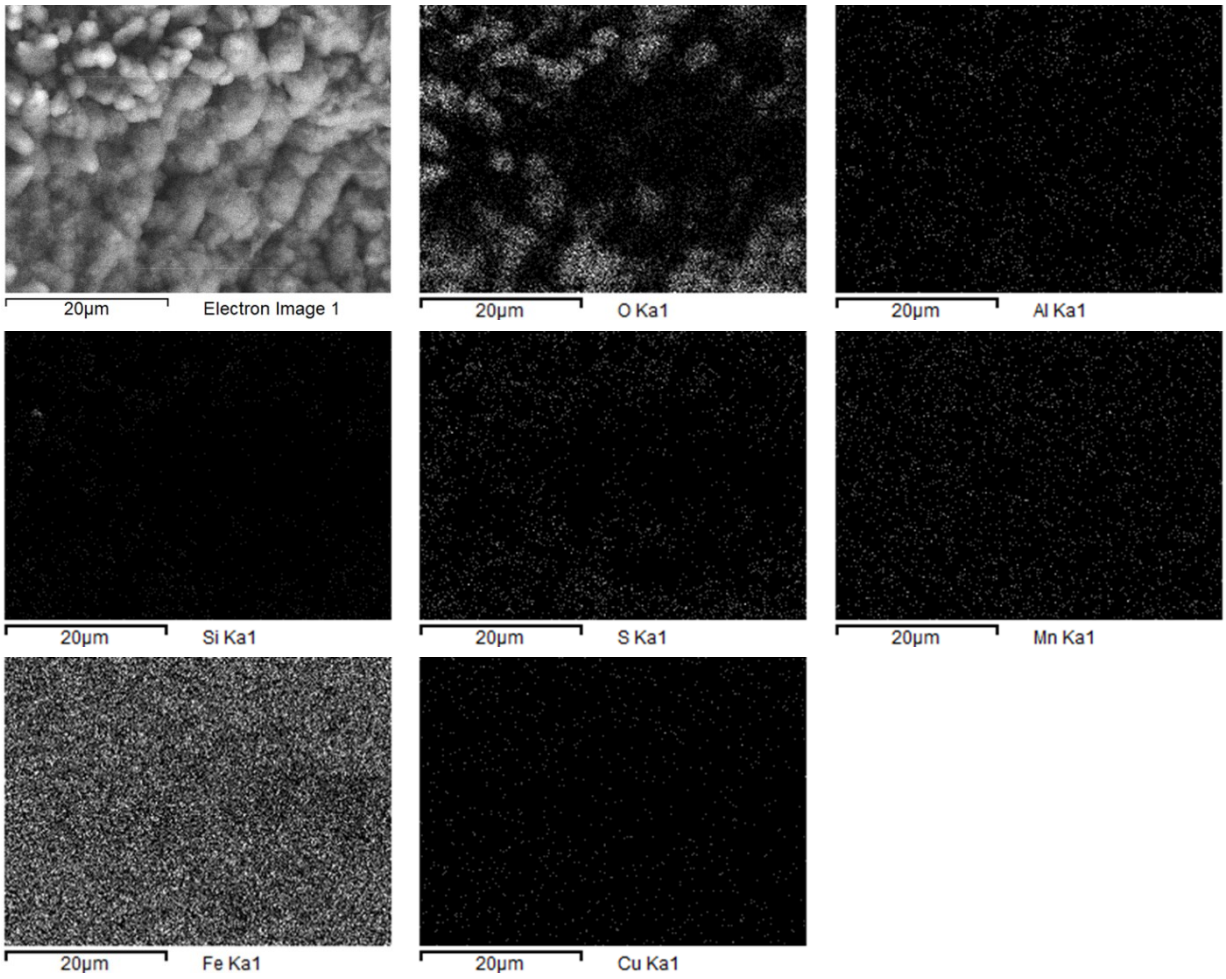
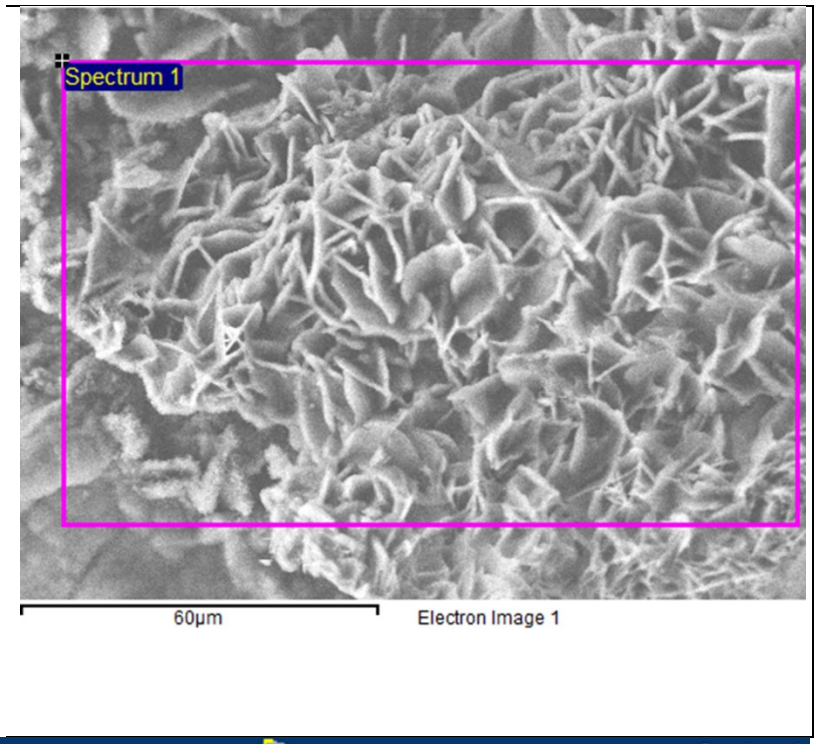


Figure A.595. EDS Elemental Mapping of Rust Collected from Interior Web.

Element	Weight %	Atomic %
O K	45.77	74.19
Al K	0.66	0.63
S K	0.99	0.80
Mn K	0.64	0.30
Fe K	51.12	23.74
Cu K	0.83	0.34
Totals	100.00	



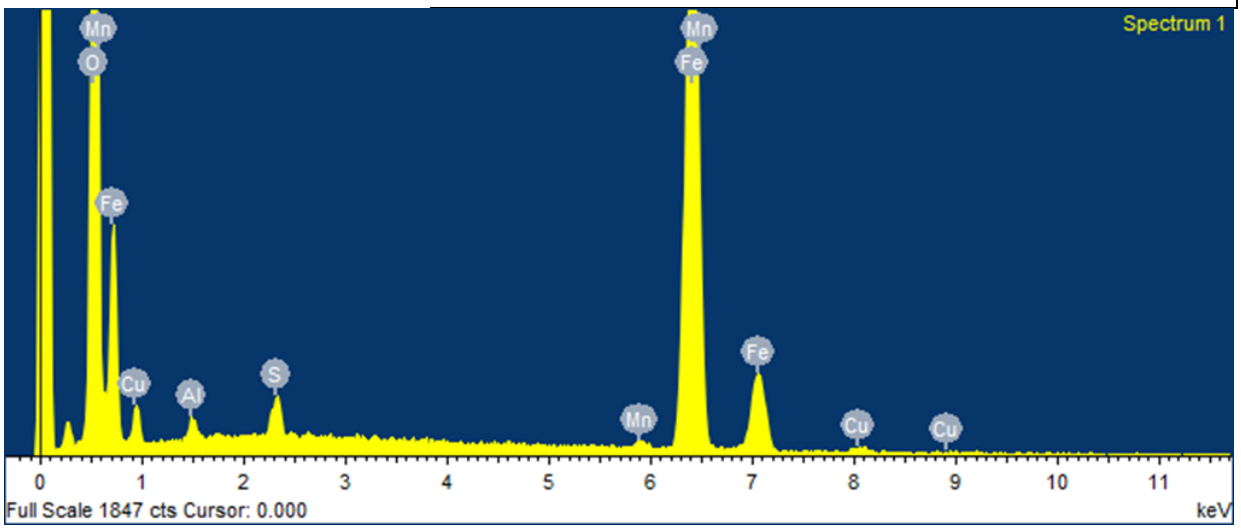


Figure A.596. SEM Image and EDS Spectrum of the Rust Collected from Interior Web of the Girder.

A.35.5.XPS Result: Exterior Girder

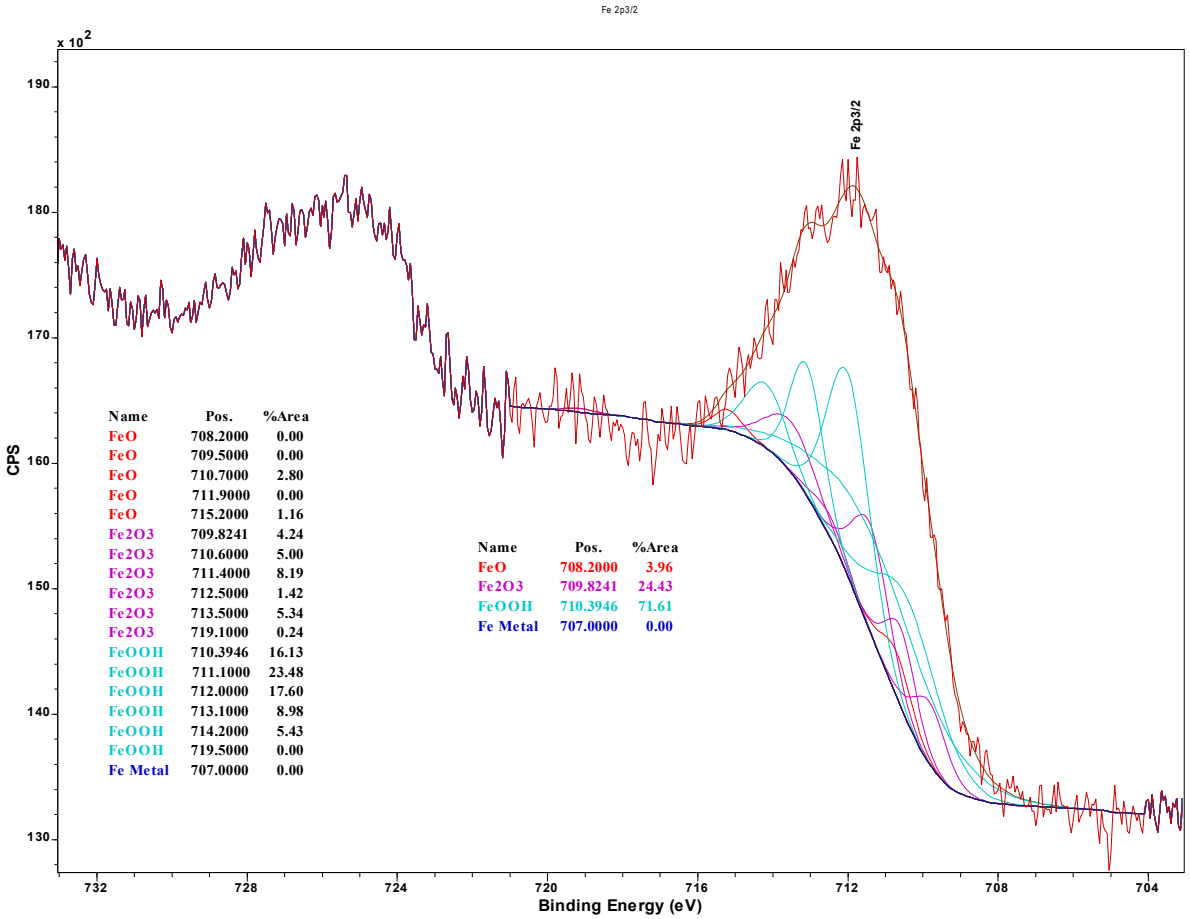


Figure A.597. XPS Spectrum of the Rust Collected from Exterior Web of the Girder.

A.35.6.XPS Result: Interior Girder

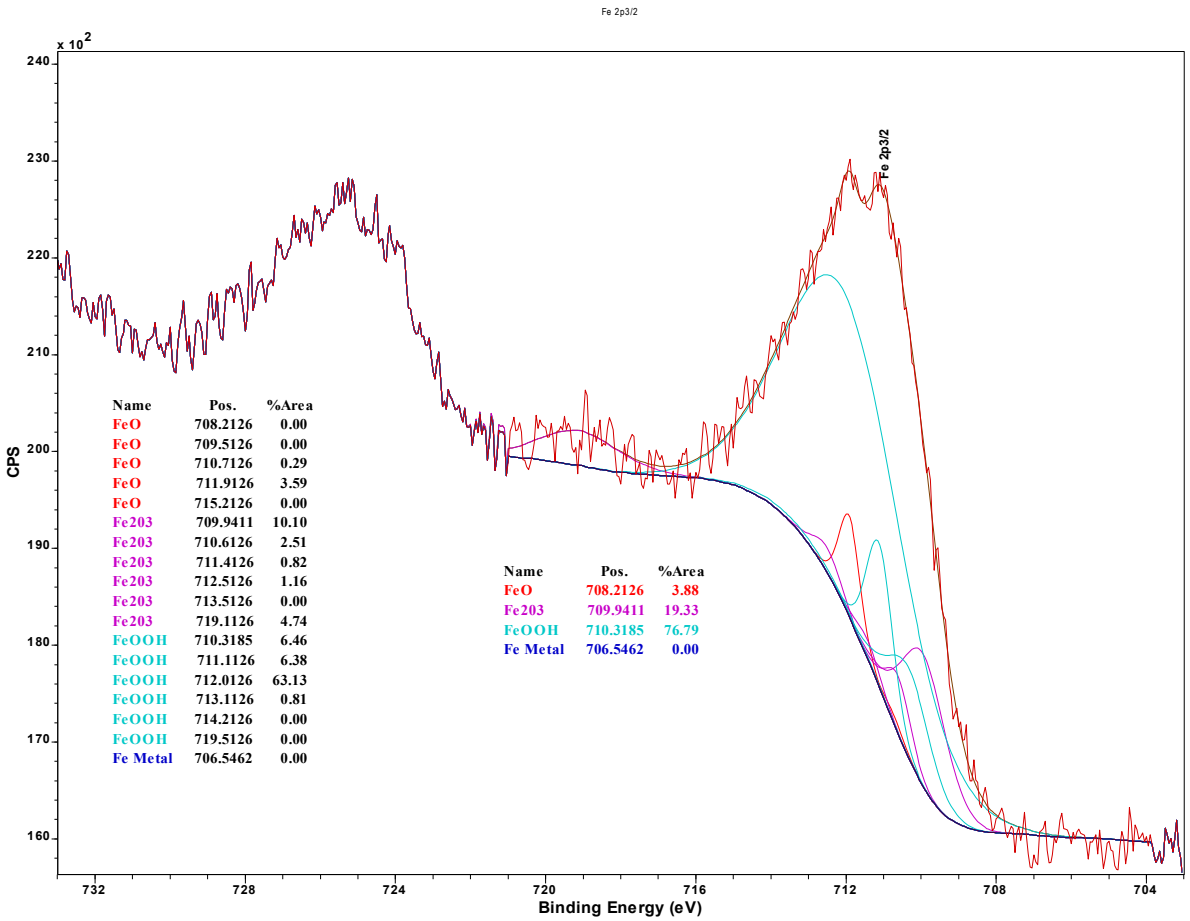


Figure A.598. XPS spectra of the Rust Collected from Interior Web of the Girder.

A.35.7.XRD Result: Exterior, Interior, and Bottom Flange of Girder

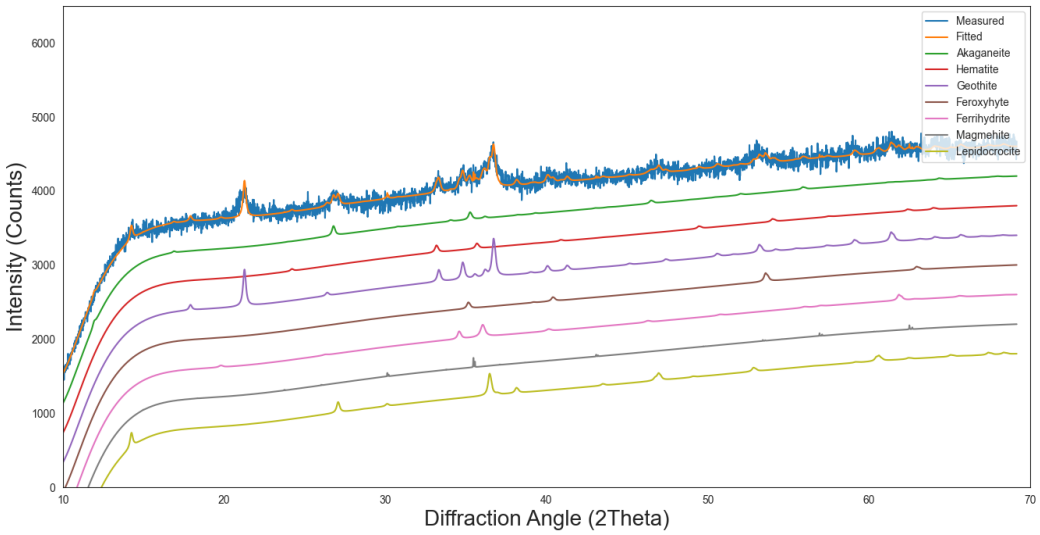


Figure A.599 XRD Pattern of Powdered Rust Collected from Exterior Web of the Girder.

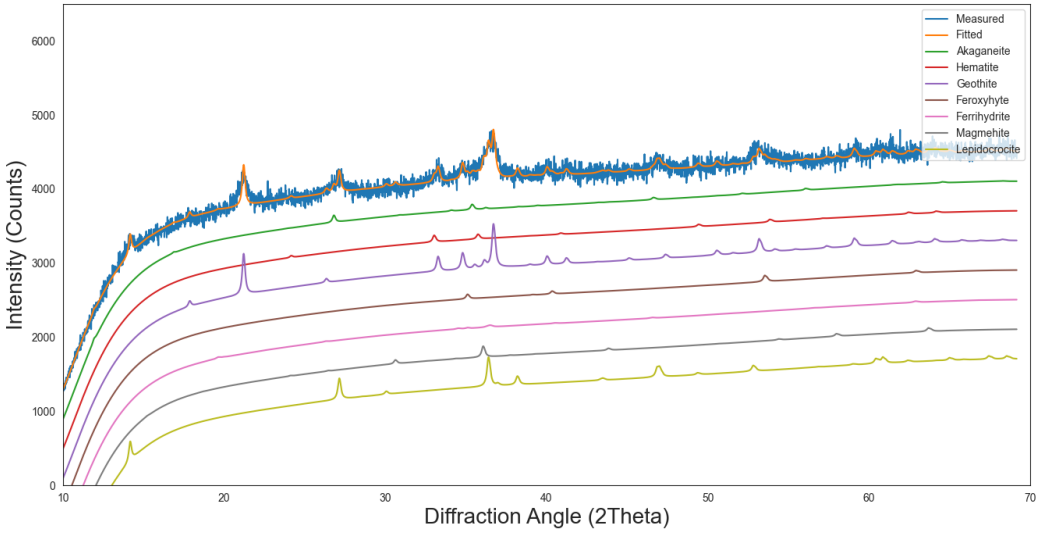


Figure A.600 XRD Pattern of Powdered Rust Collected from Interior Web of the Girder.

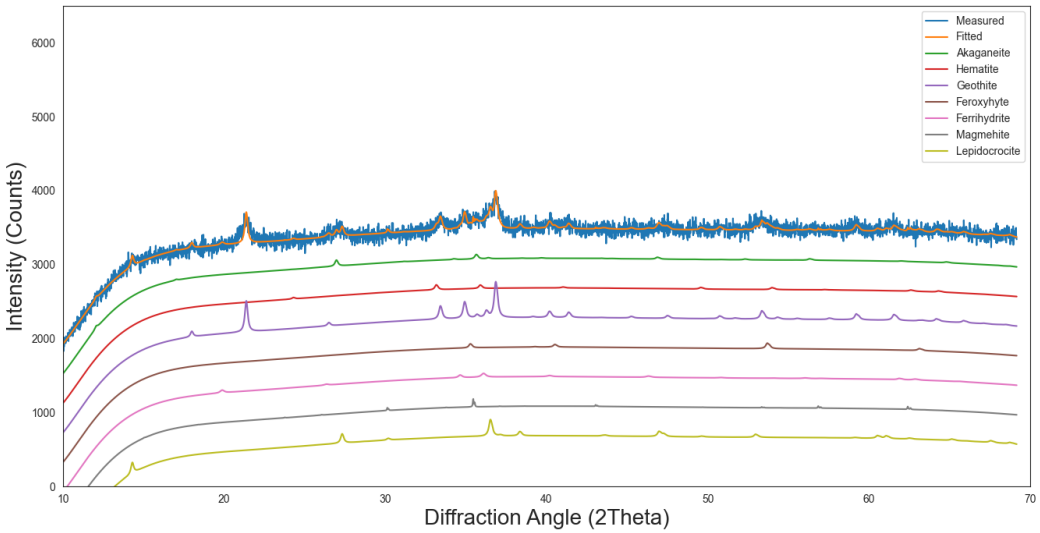
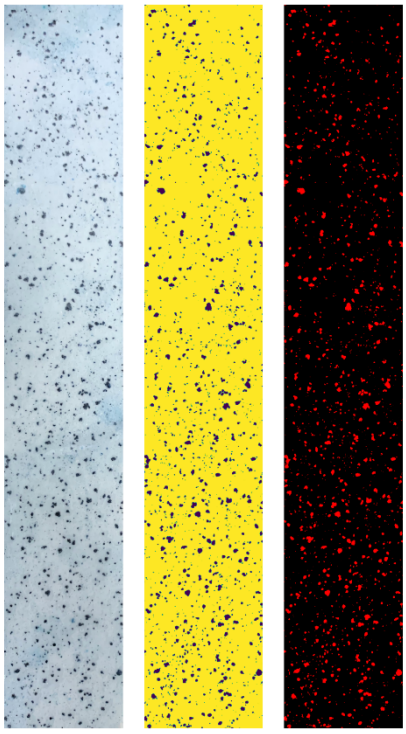


Figure A.601. XRD Pattern of Powdered Rust Collected from Bottom face of Bottom Flange of the Interior Girder.

A.35.8. Particle Size Analysis: Tape Adhesion Results

(a)

(b)



(c)

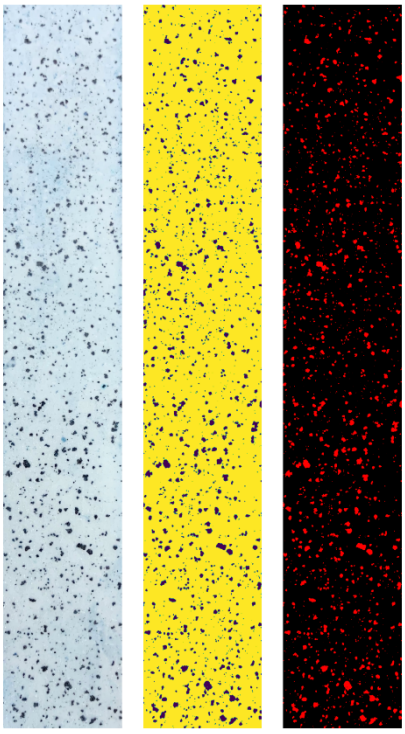
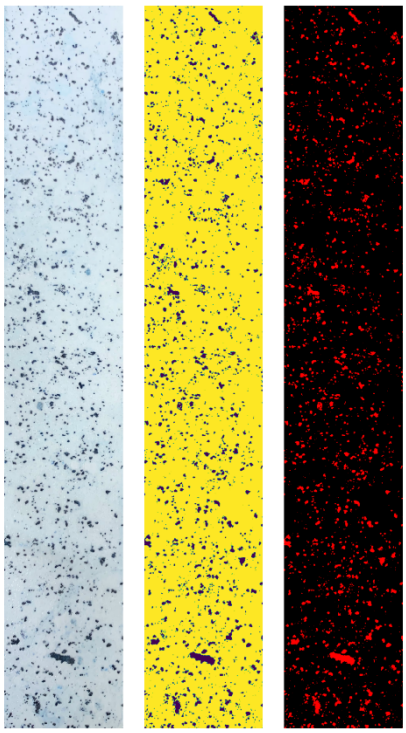


Figure A.602. Particle Size Analysis Results at B14G1F1 (a) Top Flange Bottom, (b) Web, (c) Bottom Flange Bottom.

(a)

(b)



(c)

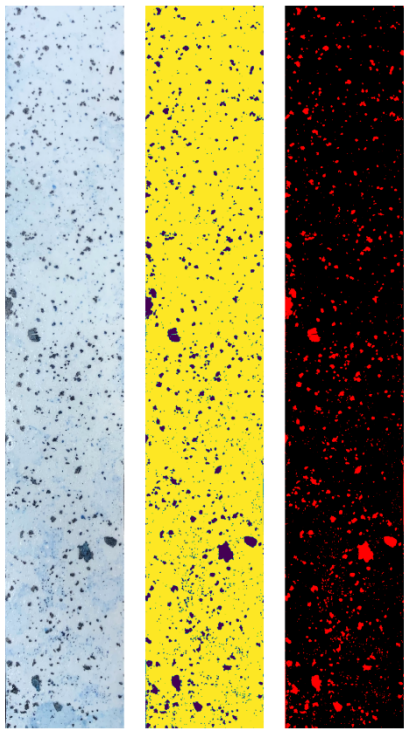


Figure A.603. Particle Size Analysis Results at B14G3F2 (a) Top Flange Bottom, (b) Web, (c) Bottom Flange Bottom.

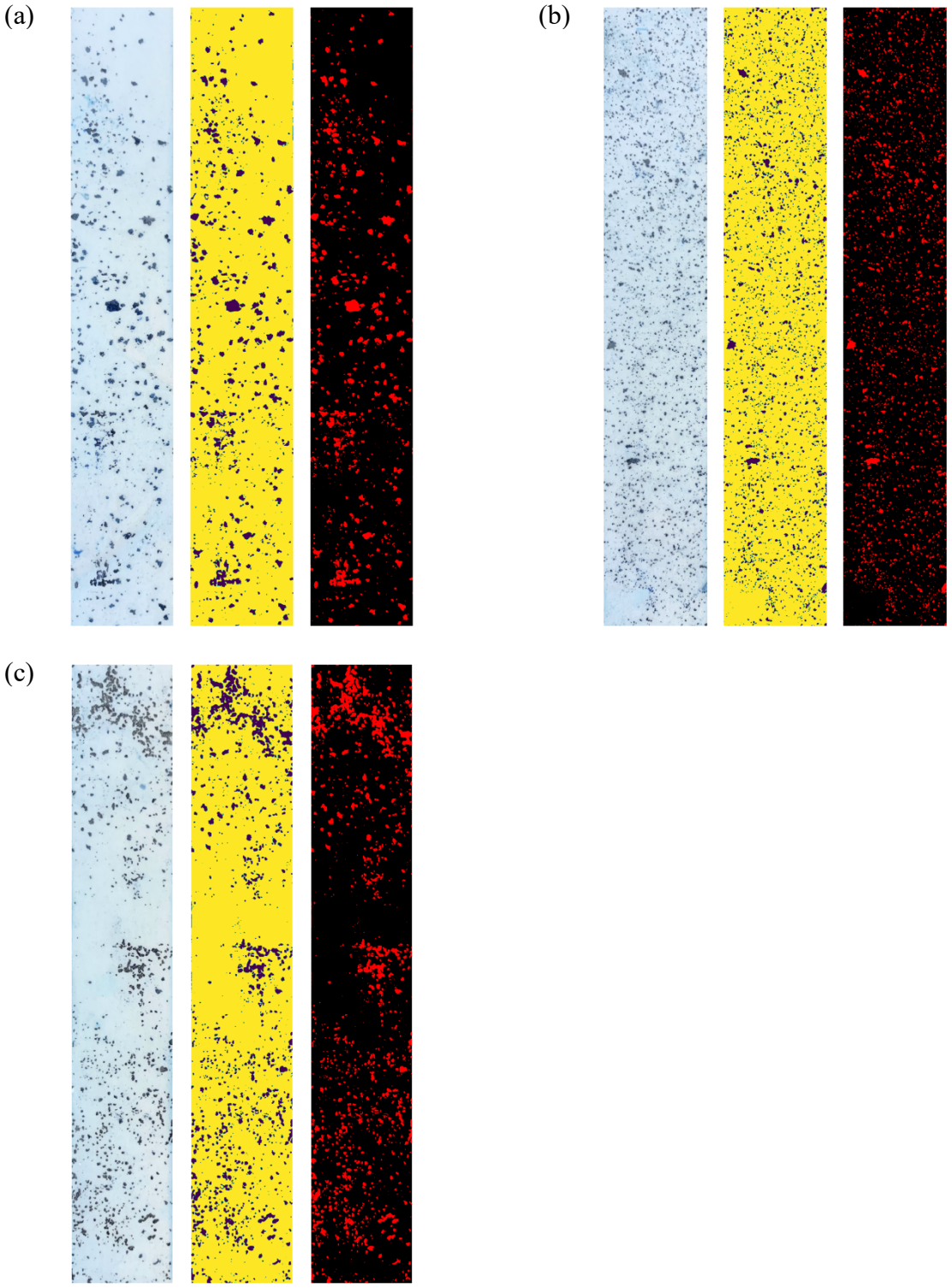


Figure A.604. Particle Size Analysis Results at B15G1F1 (a) Top Flange Bottom, (b) Web, (c) Bottom Flange Bottom.

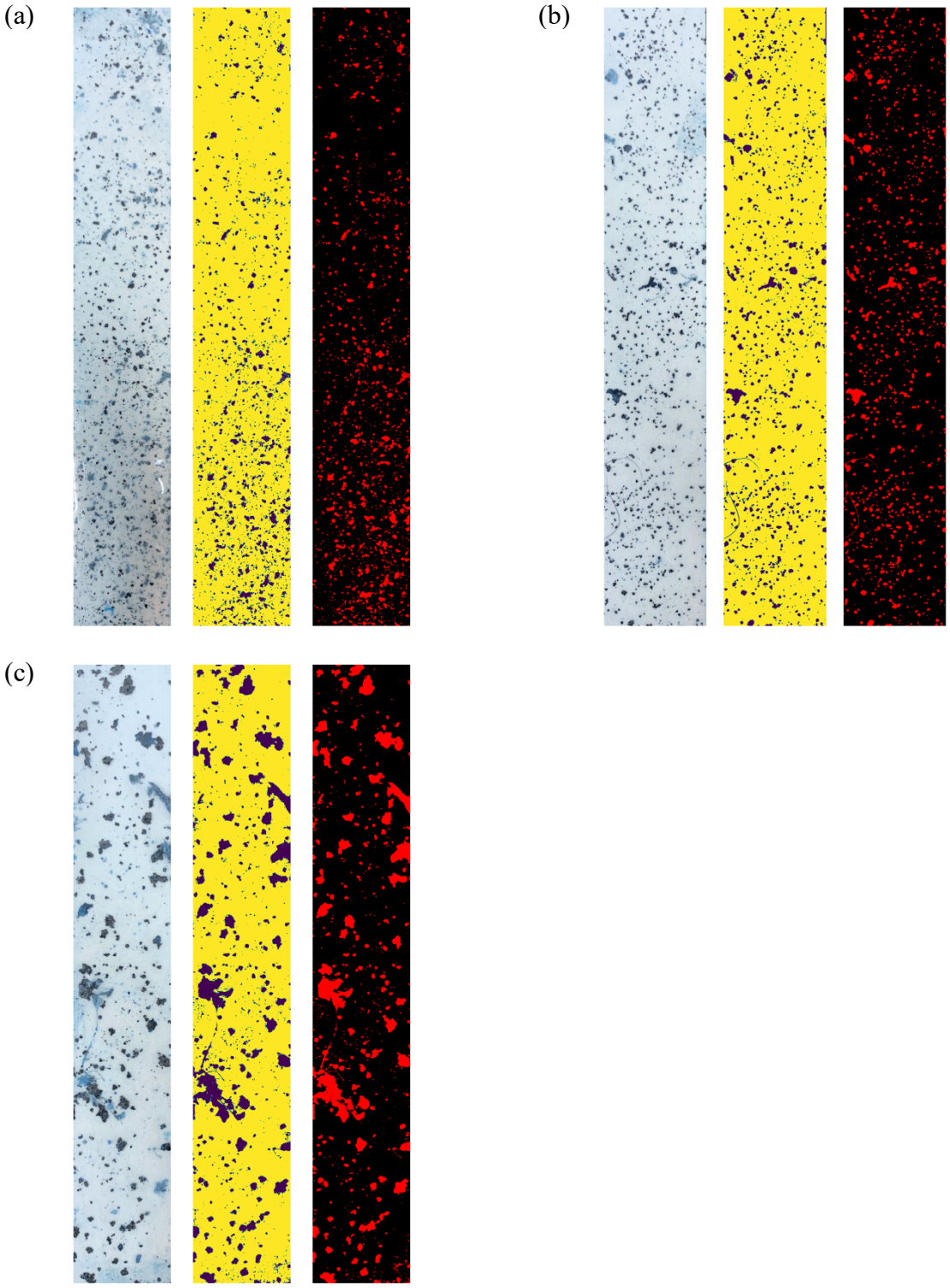


Figure A.605. Particle Size Analysis Results at B15G3F2 (a) Top Flange Bottom, (b) Web, (c) Bottom Flange Bottom.

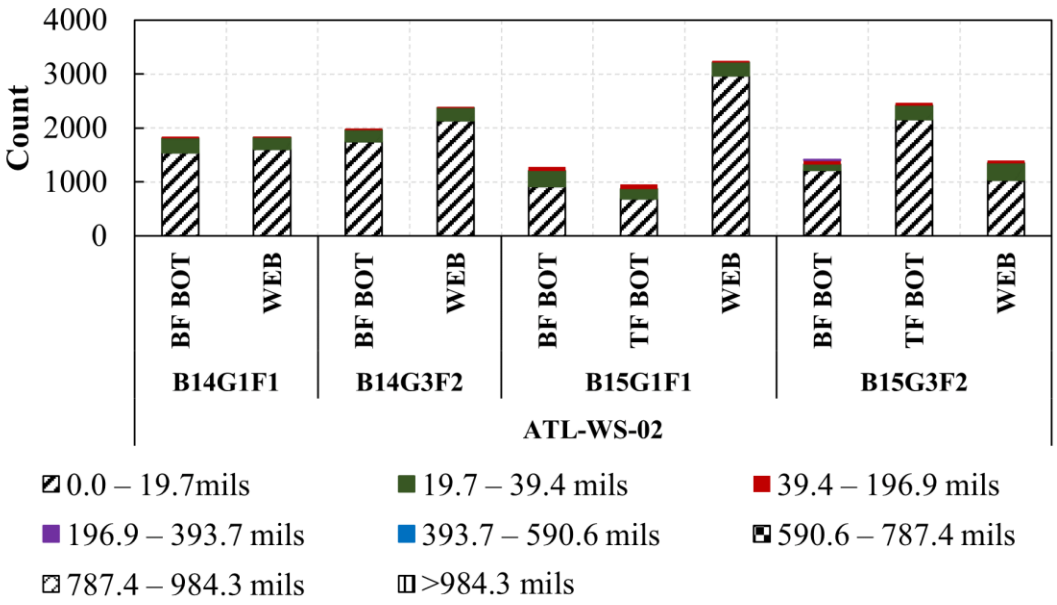


Figure A.606. Particle Size Analysis Showing Different Locations Examined.

A.36. ATL-WS-03

- US 59/71 SB over Red River
- Bridge ID 190190021701007, Coordinates (33.5494928, -94.0436889), Harris County
- Continuous weathering steel plate girder
- Built 1974
- Girder inspection carried on End abutment, and measurements are taken on girder within four feet from the abutment or bent.
- No visual inspection on deck
- Location for Testing: B15-G1F1, B15-G2F1, B15-G3F2, B15-G4F2, B14-G1F1, B14-G3F1



Figure A.607. Typical Picture of ATL-WS-03.

A.36.1. Observed Condition

Delaminated areas of patina visible on the exterior face of web and flange of girder 1 and girder 3 near bent 15. Patina condition of girder 3 (Index = 6 for flange and Index = 7 for web) near bent 14, which is relatively better than that observed on all the girders near bent 15 because of dirt accumulation and leaking joint near bent 15.Top face of bottom flange has significant poultice corrosion due to accumulation of dirt Index 5 to 4. Joint material beneath finger joint is torn at several location near bent 15 that results in collection of debris on the horizontal members.



(a) Heavy delamination and discoloration on bottom face of top flange of girder 1 (bent 15) Index = 5 to 4



(b) Widespread delamination and discoloration observed on web of girder 1 (bent 15) Index = 6 to 5



(c) Widespread delamination and discoloration observed on top of bottom flange of girder 1 (bent 15) Index = 6



(d) Close up of widespread discoloration and pitting observed on bottom of bottom flange girder 1 (bent 15) Index = 6 to 5



(e) Widespread delamination and discoloration observed on web and flange of girder 1 (bent 15) Index = 6 to 5



(f) Widespread pitting and discoloration observed on bottom of bottom flange of girder 1 (bent 15) Index = 6 to 5

Figure A.608. Fiels Inspection Picture of ATL-WS-03.

A.36.2.Field Inspection Results

Table A-160. Field Inspection Results for ATL-WS-03.

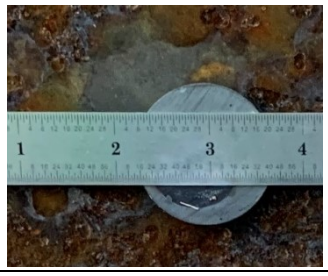
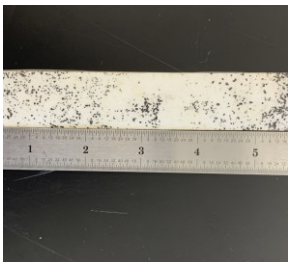
Location	Patina Rating	Thickness (inch)	Cl^- Conc. (ppm)	Field Condition	Tape Test
B15-G1F1 TF Bot. Ext.	6	Measured 2.028 Design			
B15-G1F1 Web Ext.	7	Measured 0.515 Design	1		
B15-G1F1 BF Top Ext.	7	Measured 2.015 Design			
B15-G1F1 BF Bot. Ext.	6	Measured - Design			
B15-G2F1 TF Bot. Ext.	6	Measured 2.056 Design			

Table A-161. Field Inspection Results for ATL-WS-03.

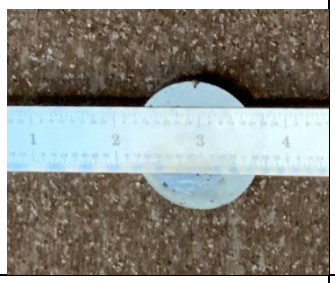
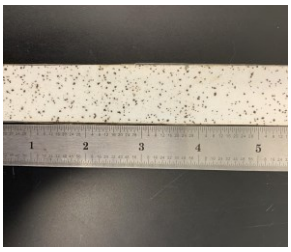
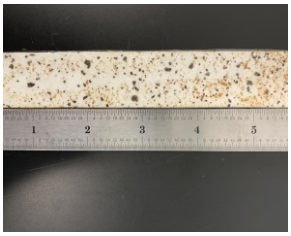
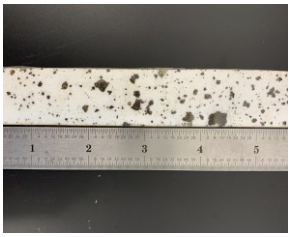
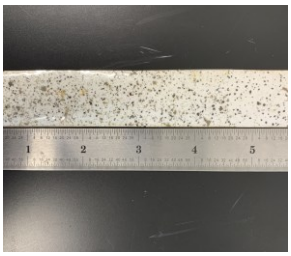
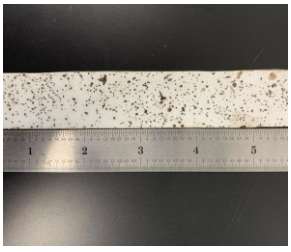
Location	Patina Rating	Thickness (inch)	Cl^- Conc. (ppm)	Field Condition	Tape Test
B15-G2F1 Web Ext.	8	Measured 0.524 Design	1		
B15-G2F1 BF Top Ext.	6	Measured 2.033 Design			
B15-G2F1 BF Bot. Ext.	5	Measured - Design			
B15-G3F2 TF Bot. Ext.	8	Measured 2.008 Design			
B15-G3F2 Web Ext.	7	Measured 0.515 Design			

Table A-162. Field Inspection Results for ATL-WS-03.

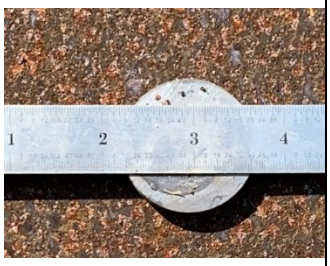
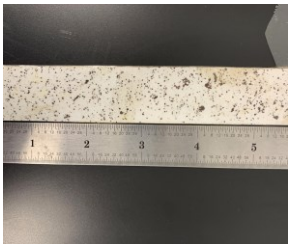
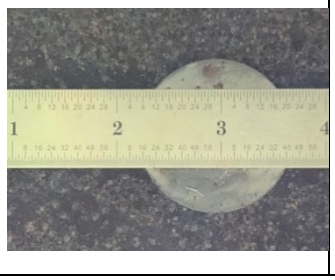
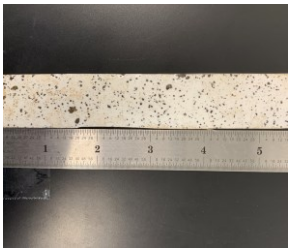
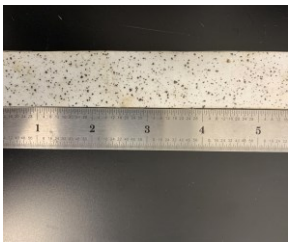
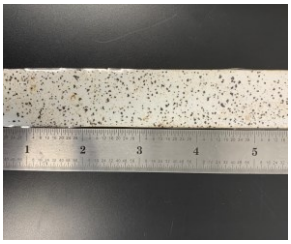
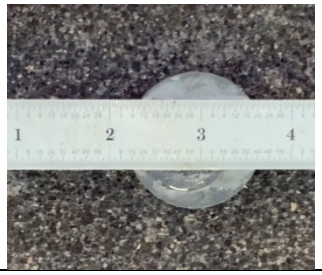
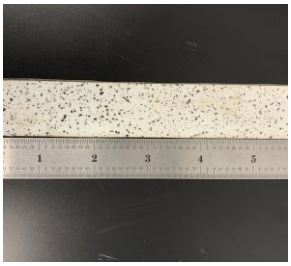
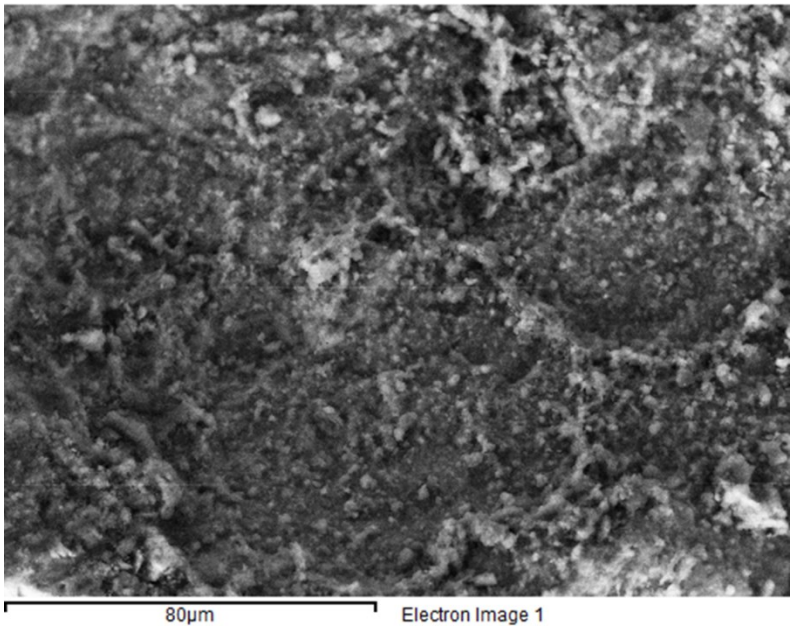
Location	Patina Rating	Thickness (inch)	Cl^- Conc. (ppm)	Field Condition	Tape Test
B15-G3F2 BF Top Ext.	7	Measured 2.033 Design			
B15-G3F2 BF Bot. Ext.	6	Measured - Design			
B14-G3F2 Web Ext.	7	Measured 0.797 Design	2		
B14-G3F2 BF Top Ext.	7	Measured 2.574 Design			
B14-G3F2 BF Bot. Ext.	7	Measured - Design			

Table A-163. Field Inspection Results for ATL-WS-03.

Location	Patina Rating	Thickness (inch)	Cl^- Conc. (ppm)	Field Condition	Tape Test
B14-G1F1 Web Ext.	8	Measured 0.534 Design			
B14-G1F1 BF Top Ext.	7	Measured 2.016 Design			
B14-G1F1 BF Bot. Ext.	7	Measured - Design			

A.36.3.SEM/EDS Results: Exterior Girder Web

Element	Weight %	Atomic %
O K	49.73	74.16
Na K	0.47	0.49
Mg K	0.54	0.53
Al K	2.47	2.19
Si K	5.34	4.54
S K	0.27	0.20
Cl K	0.82	0.55
K K	0.45	0.27
Ca K	0.12	0.07
Cr K	0.15	0.07
Mn K	0.23	0.10
Fe K	39.22	16.76
Ni K	0.17	0.07
Totals	100.00	



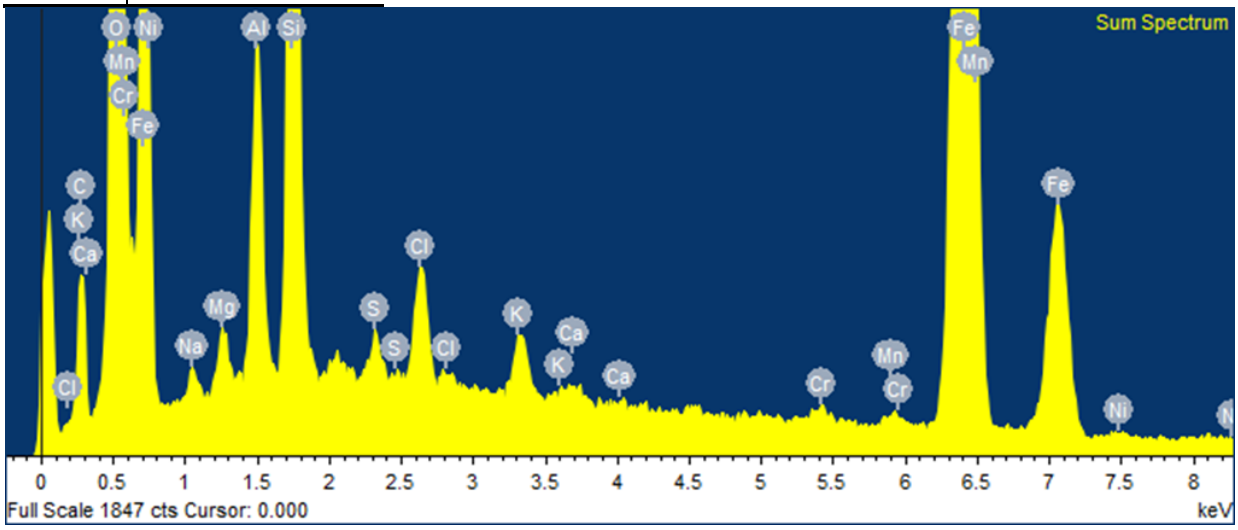
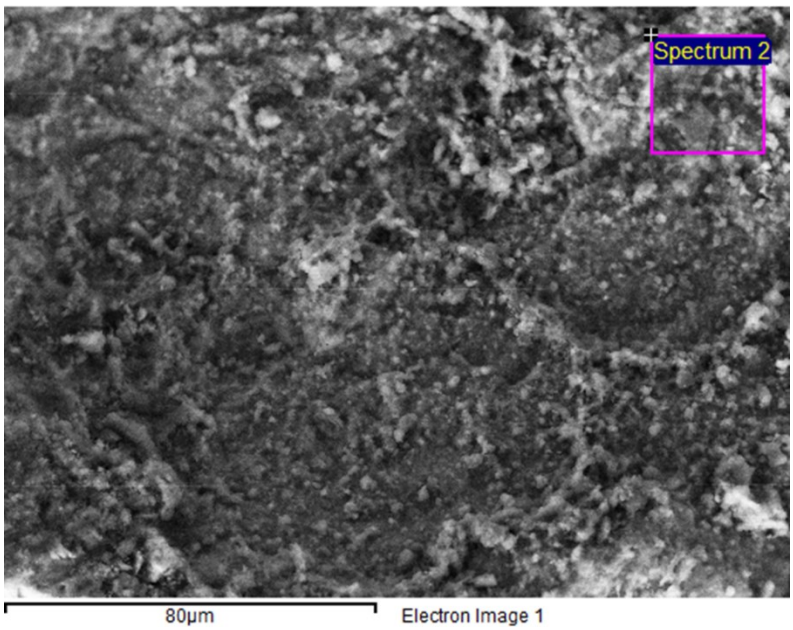


Figure A.609. SEM Image and EDS Spectrum of the Rust Collected from Exterior Web of the Girder.

Element	Weight %	Atomic %
O K	43.25	70.04
Na K	0.37	0.42
Mg K	0.43	0.46
Al K	2.11	2.02
Si K	3.41	3.14
S K	0.29	0.24
Cl K	1.23	0.90
K K	0.29	0.19
Ca K	0.14	0.09
Mn K	0.29	0.14
Fe K	48.20	22.36
Totals	100.00	



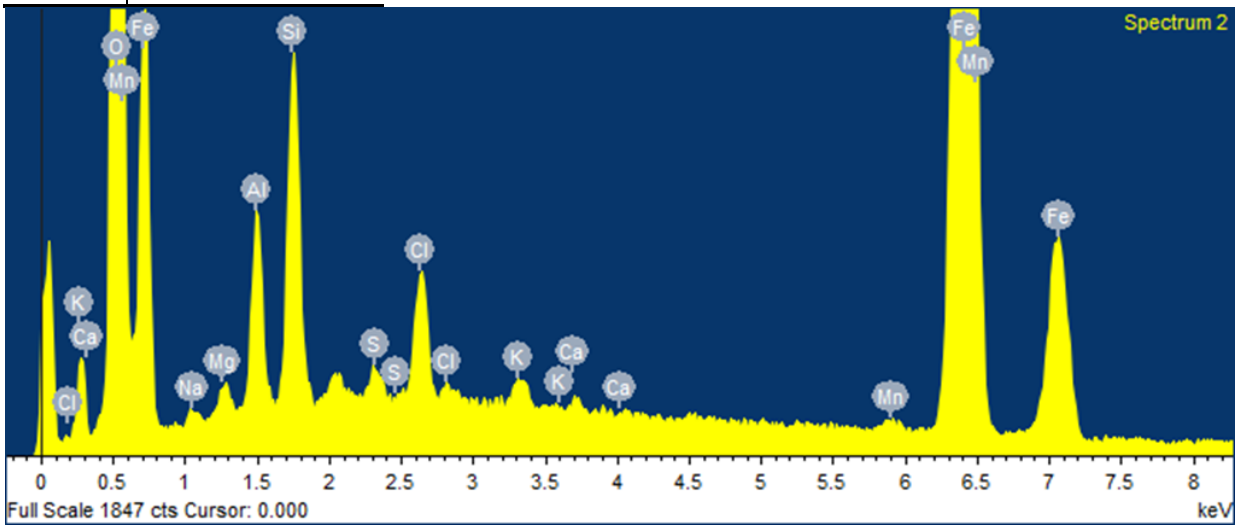
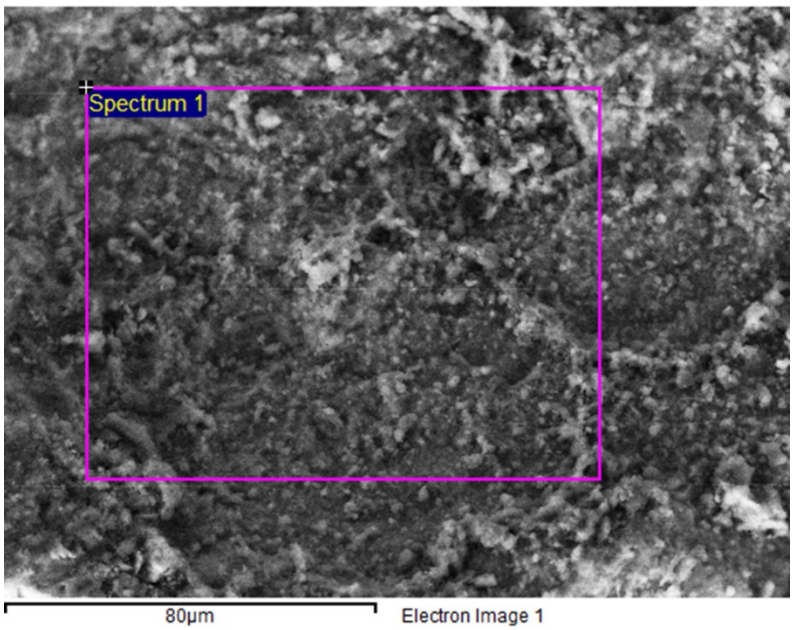


Figure A.610. SEM Image and EDS Spectrum of the Rust Collected from Exterior Web of the Girder.

Element	Weight %	Atomic %
O K	47.19	72.19
Na K	0.46	0.49
Mg K	0.52	0.53
Al K	2.45	2.23
Si K	5.71	4.98
P K	0.16	0.13
S K	0.25	0.19
Cl K	0.76	0.52
K K	0.46	0.29
Ca K	0.19	0.12
Cr K	0.22	0.10
Mn K	0.27	0.12
Fe K	41.35	18.12
Totals	100.00	



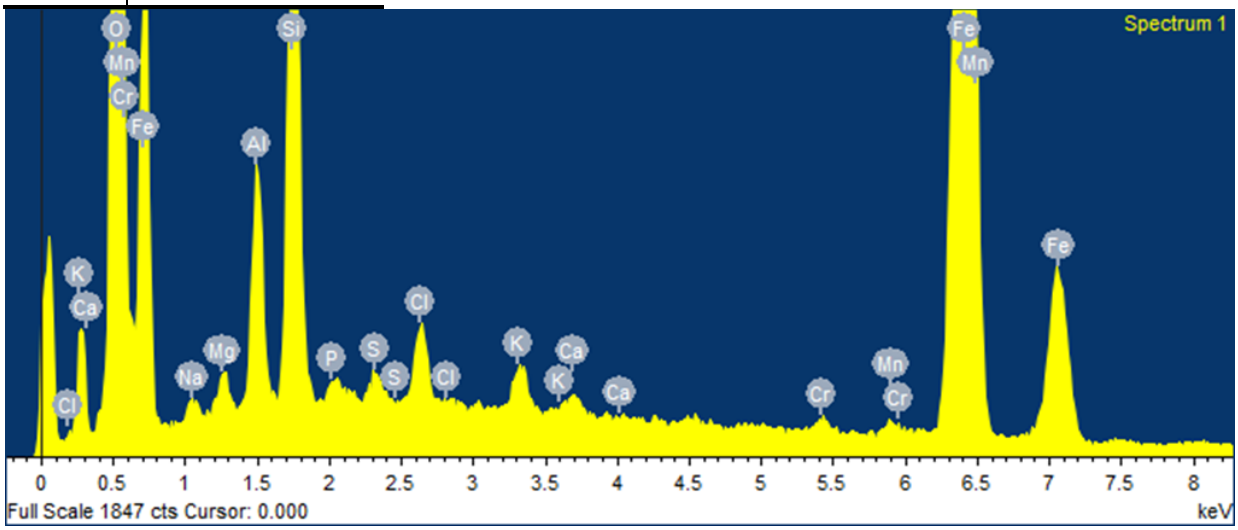


Figure A.611. SEM Image and EDS Spectrum of the Rust Collected from Exterior Web of the Girder.

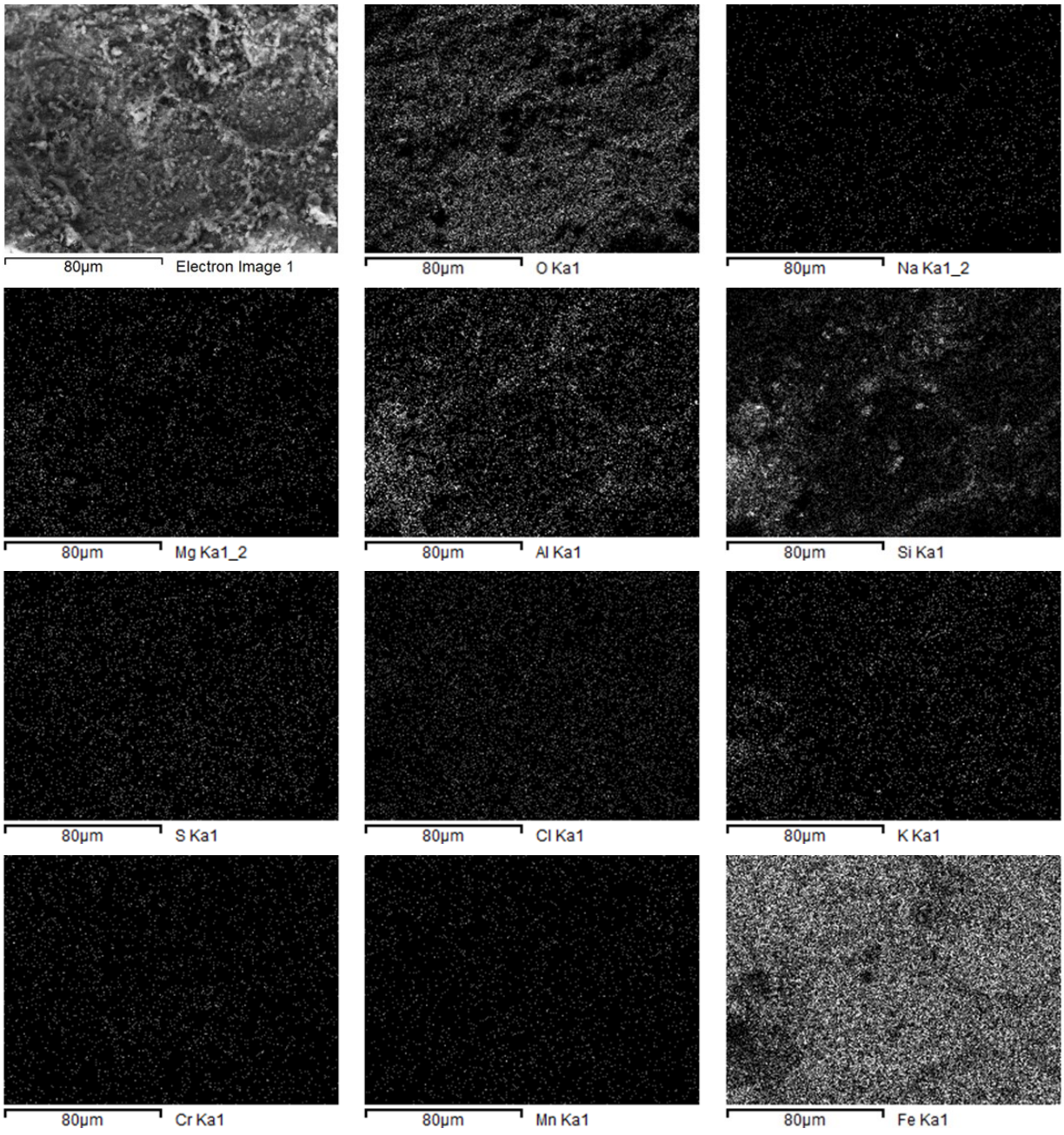
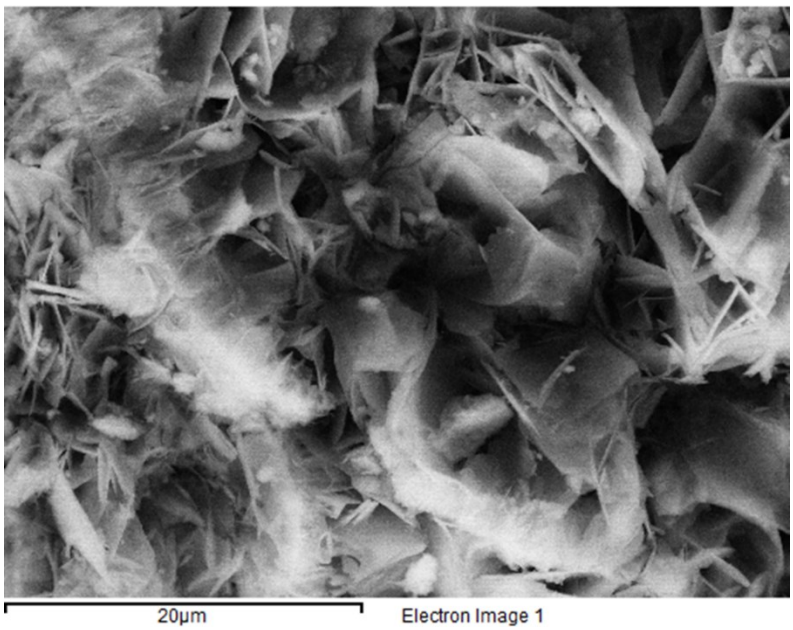


Figure A.612. EDS Elemental Mapping of Rust Collected from Exterior Web.

Element	Weight %	Atomic %
O K	37.01	66.16
Al K	0.97	1.03
Si K	0.32	0.33
S K	1.37	1.22
Cl K	1.24	1.00
Mn K	0.42	0.22
Fe K	58.66	30.04
Totals	100.00	



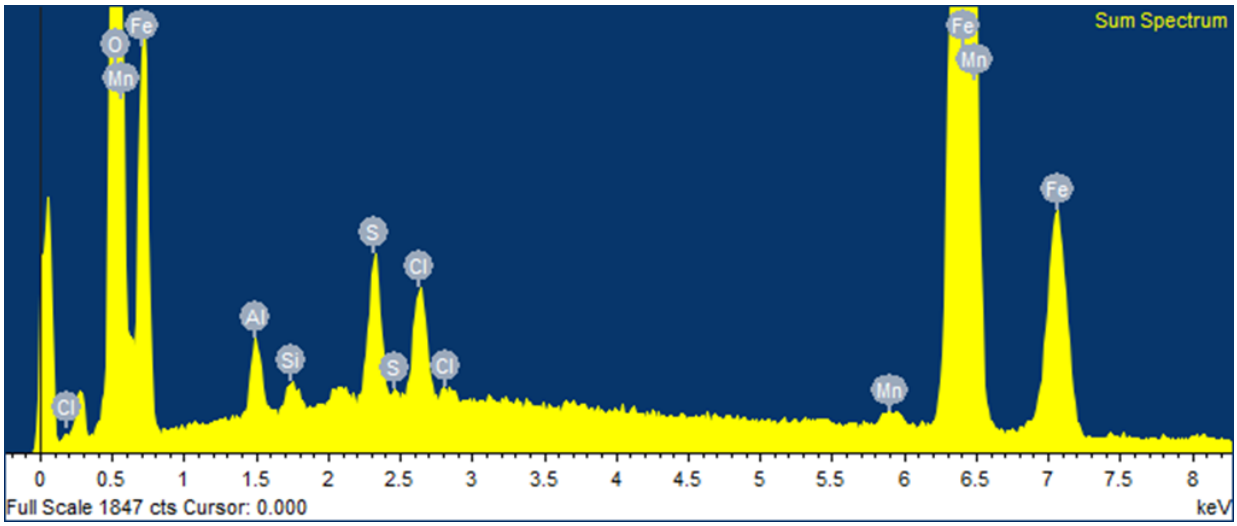


Figure A.613. SEM Image and EDS Spectrum of the Rust Collected from Exterior Web of the Girder.

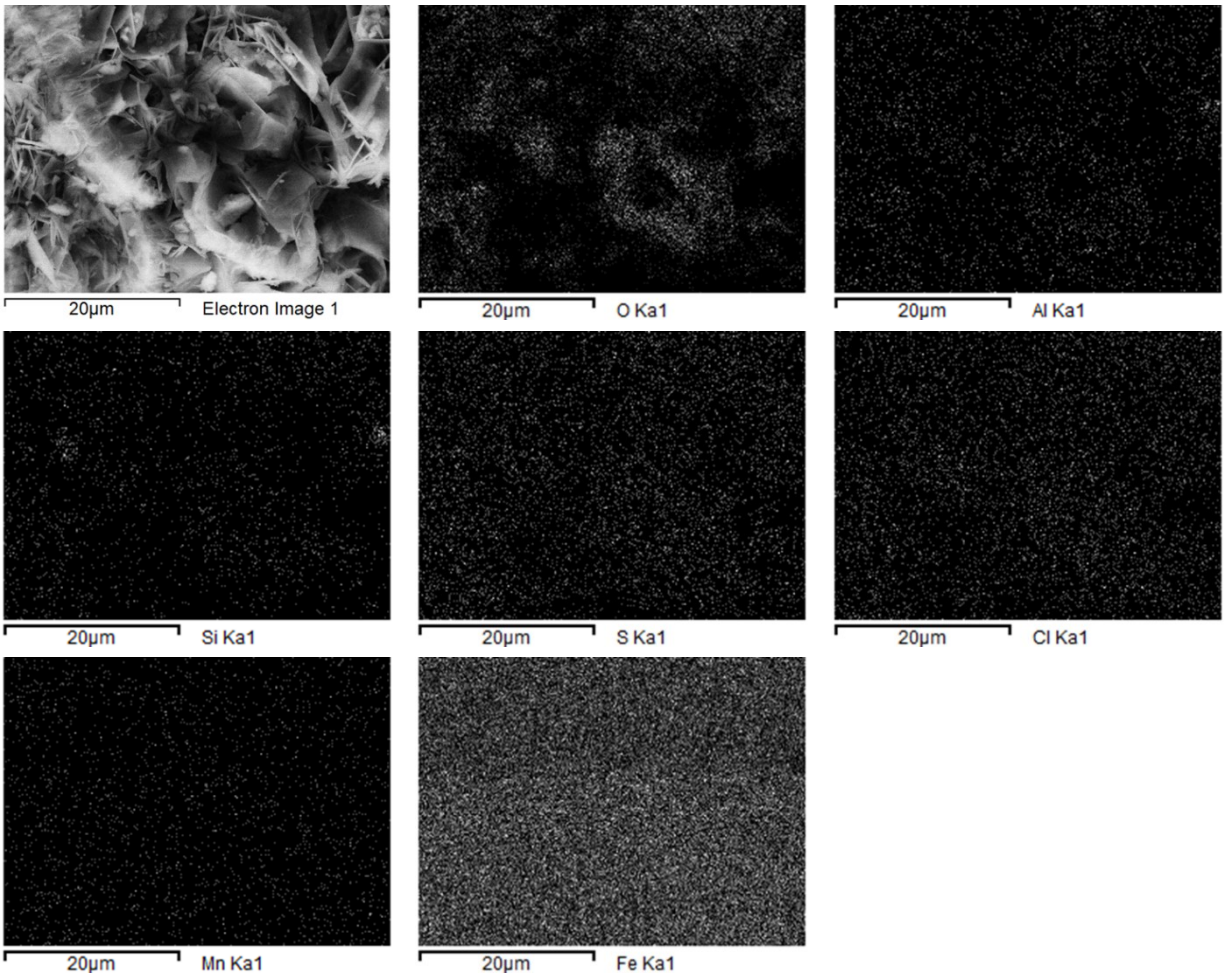
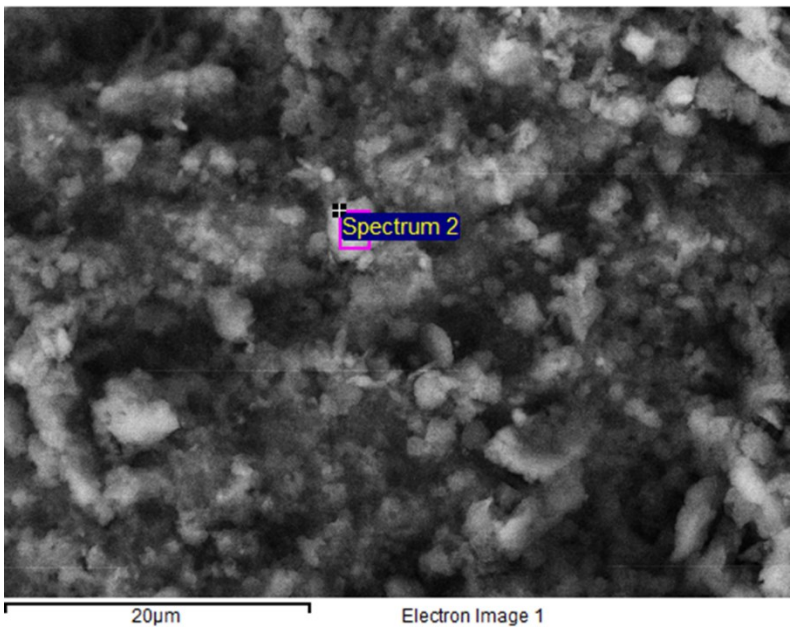


Figure A.614. EDS Elemental Mapping of Rust Collected from Exterior Web.

Element	Weight %	Atomic %
O K	45.25	70.00
Na K	0.45	0.49
Mg K	0.83	0.85
Al K	3.26	2.99
Si K	6.47	5.70
P K	0.35	0.28
S K	0.23	0.18
Cl K	0.94	0.66
K K	0.59	0.37
Ca K	0.21	0.13
Mn K	0.29	0.13
Fe K	41.12	18.22
Totals	100.00	



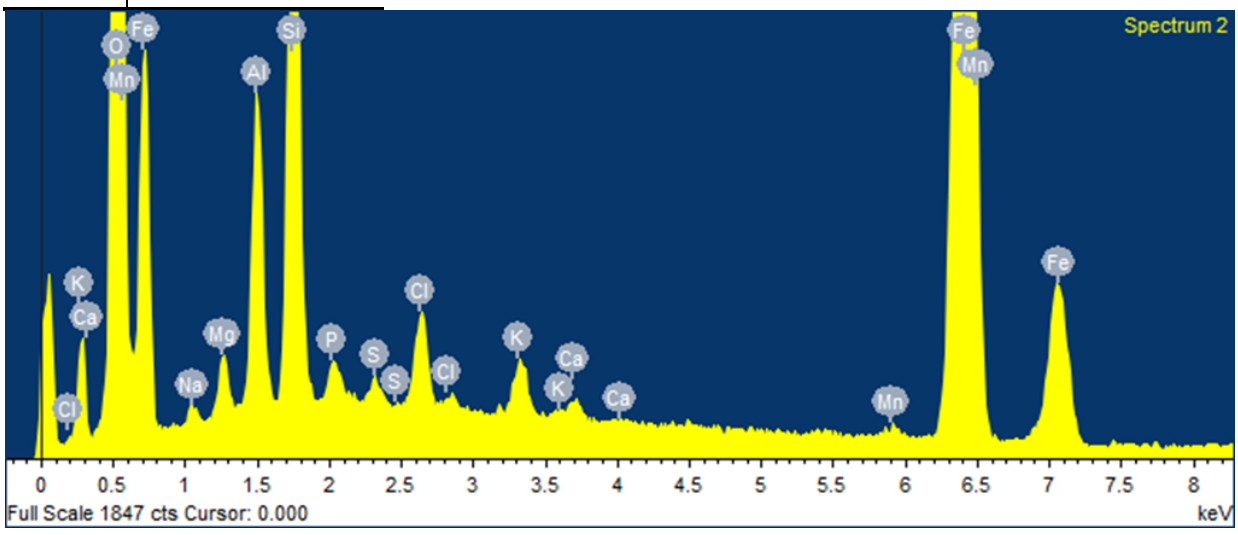
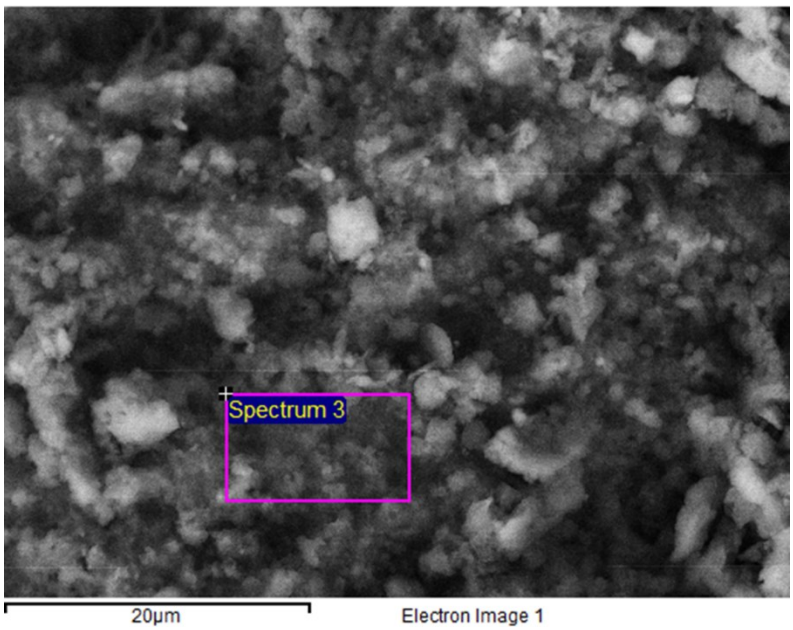


Figure A.615. SEM Image and EDS Spectrum of the Rust Collected from Exterior Web of the Girder.

Element	Weight %	Atomic %
O K	43.21	71.23
Al K	1.38	1.35
Si K	2.07	1.94
S K	0.26	0.22
Cl K	0.63	0.47
K K	0.16	0.11
Cr K	0.16	0.08
Mn K	0.50	0.24
Fe K	51.30	24.23
Cu K	0.33	0.14
Totals	100.00	



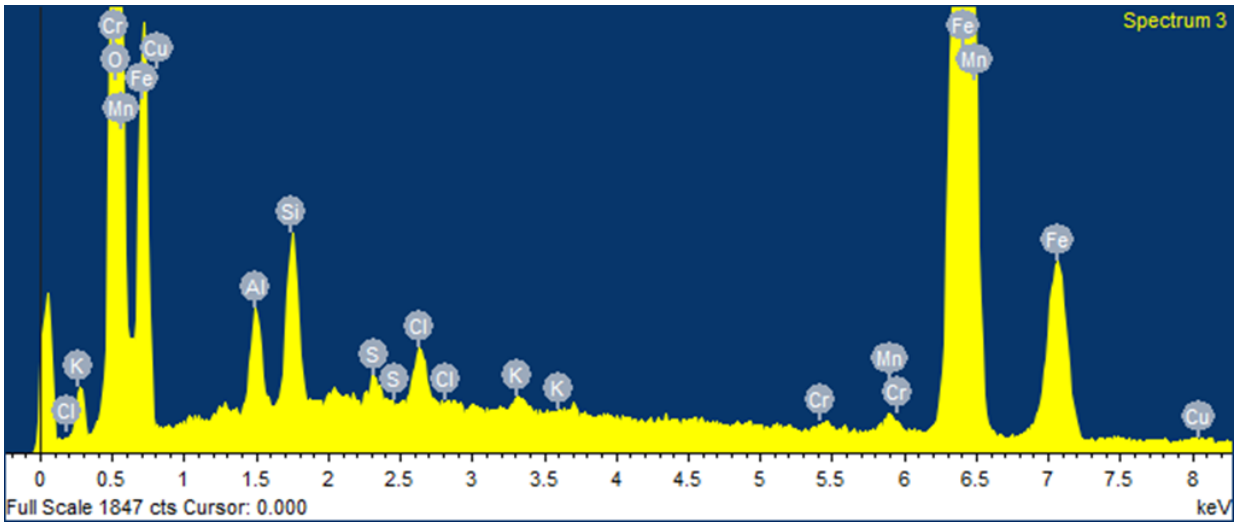
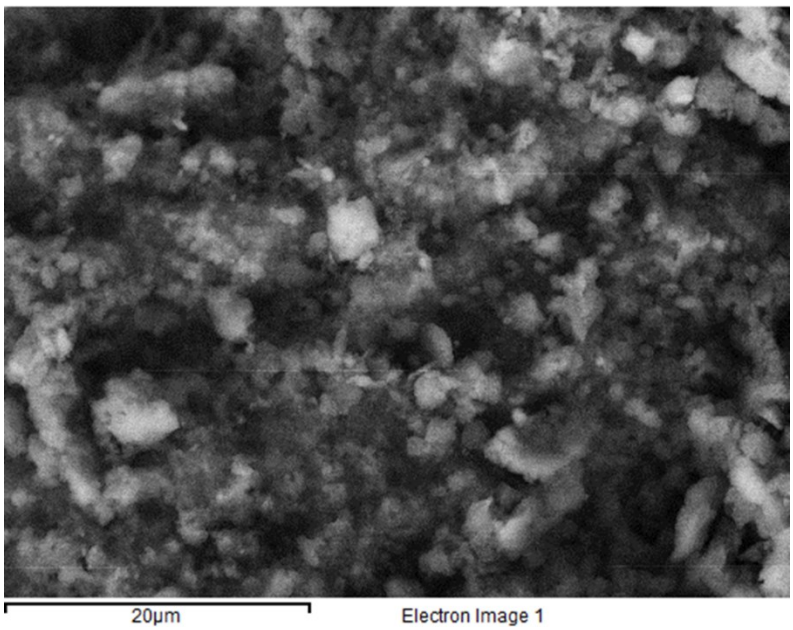


Figure A.616. SEM Image and EDS Spectrum of the Rust Collected from Exterior Web of the Girder.

Element	Weight %	Atomic %
O K	46.33	71.63
Na K	0.50	0.53
Mg K	0.59	0.60
Al K	2.60	2.38
Si K	5.25	4.63
P K	0.18	0.15
S K	0.21	0.16
Cl K	0.72	0.50
K K	0.46	0.29
Cr K	0.23	0.11
Mn K	0.27	0.12
Fe K	42.67	18.90
Totals	100.00	



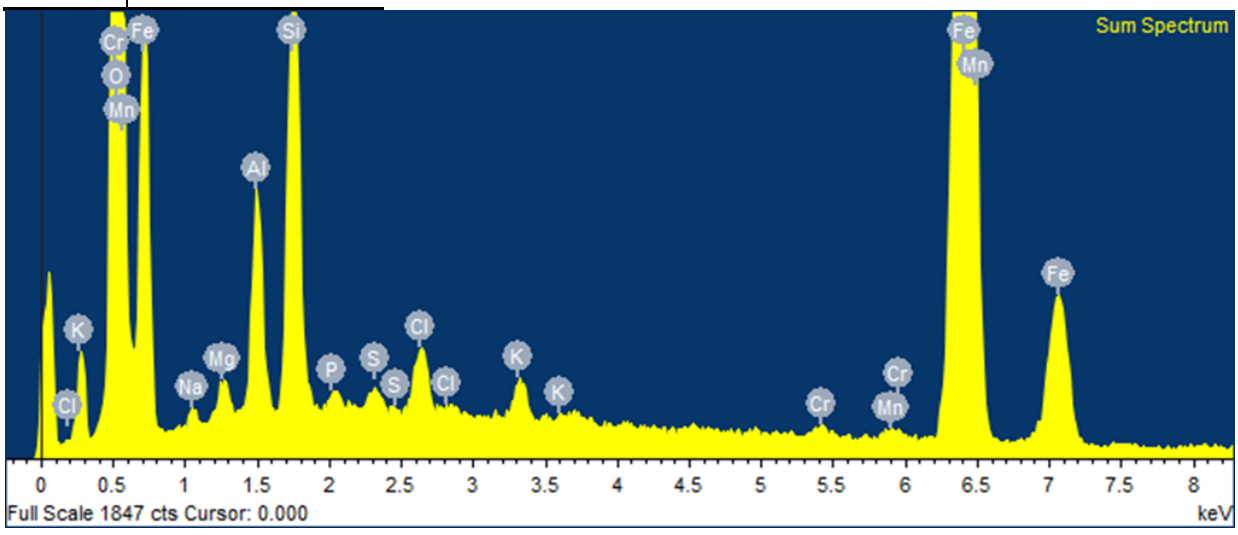


Figure A.617. SEM Image and EDS Spectrum of the Rust Collected from Exterior Web of the Girder.

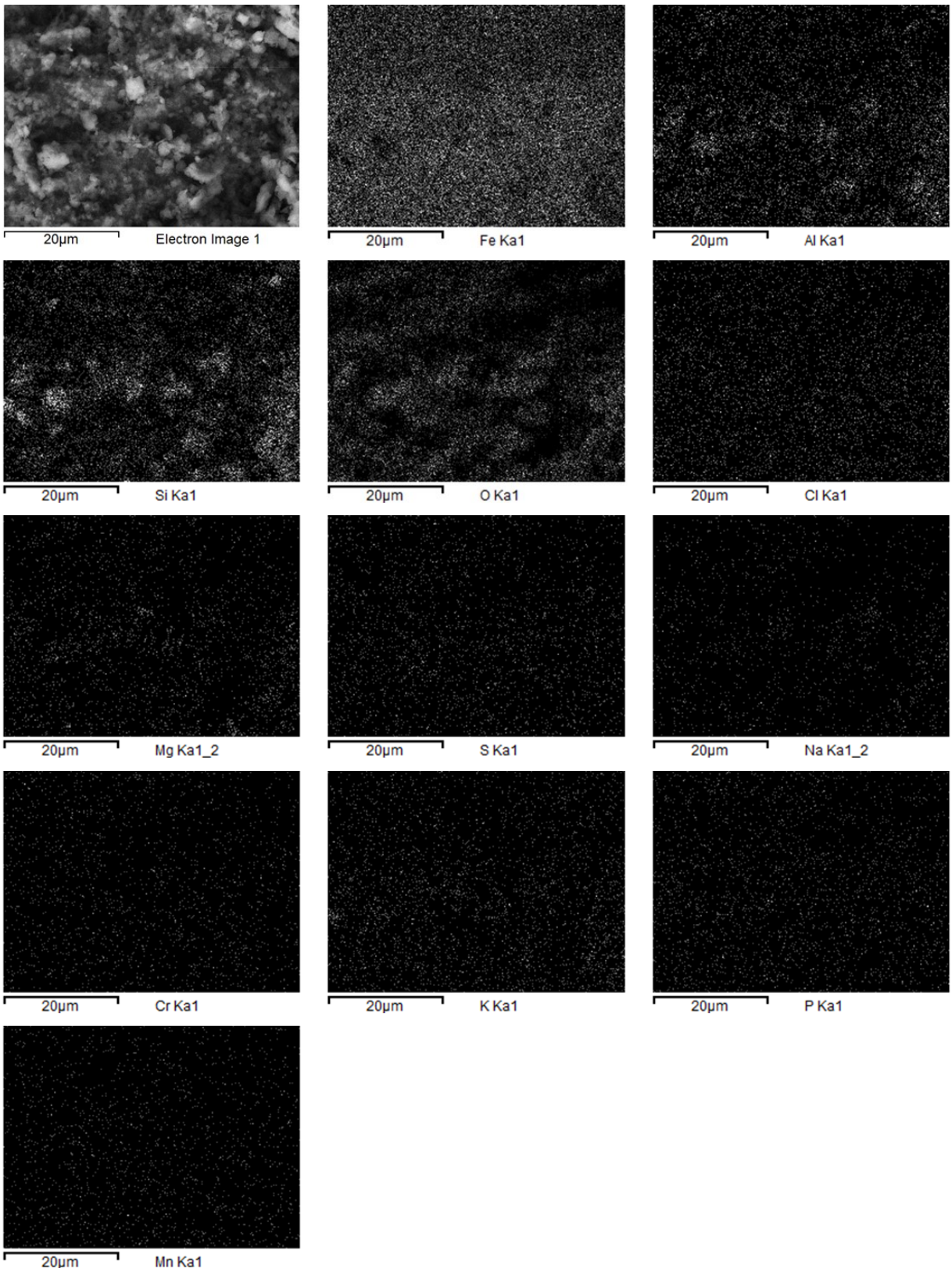
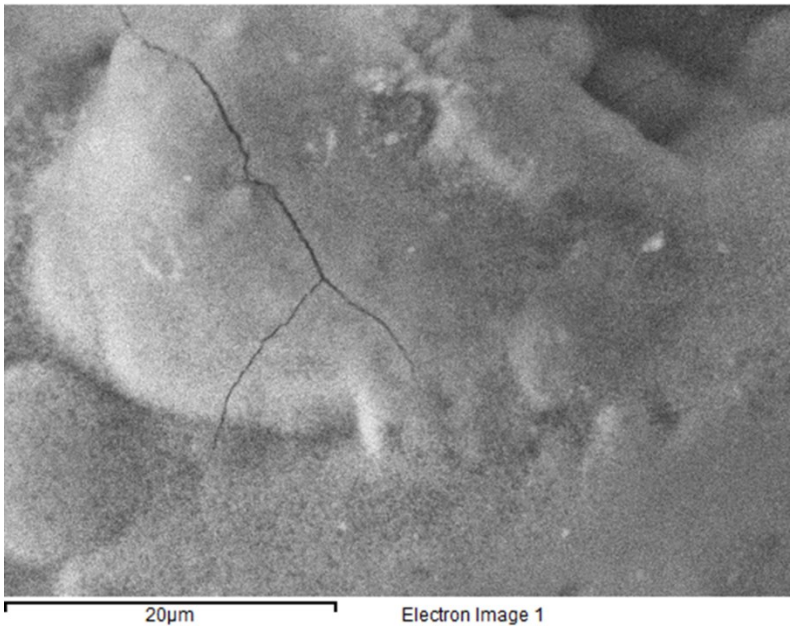


Figure A.618. EDS Elemental Mapping of Rust Collected from Exterior Web.

A.36.4.SEM/EDS Results: Interior Girder

Element	Weight %	Atomic %
O K	50.32	76.63
Al K	1.62	1.46
Si K	1.56	1.35
S K	0.73	0.55
Cl K	0.13	0.09
Mn K	0.47	0.21
Fe K	44.98	19.62
Cu K	0.20	0.08
Totals	100.00	



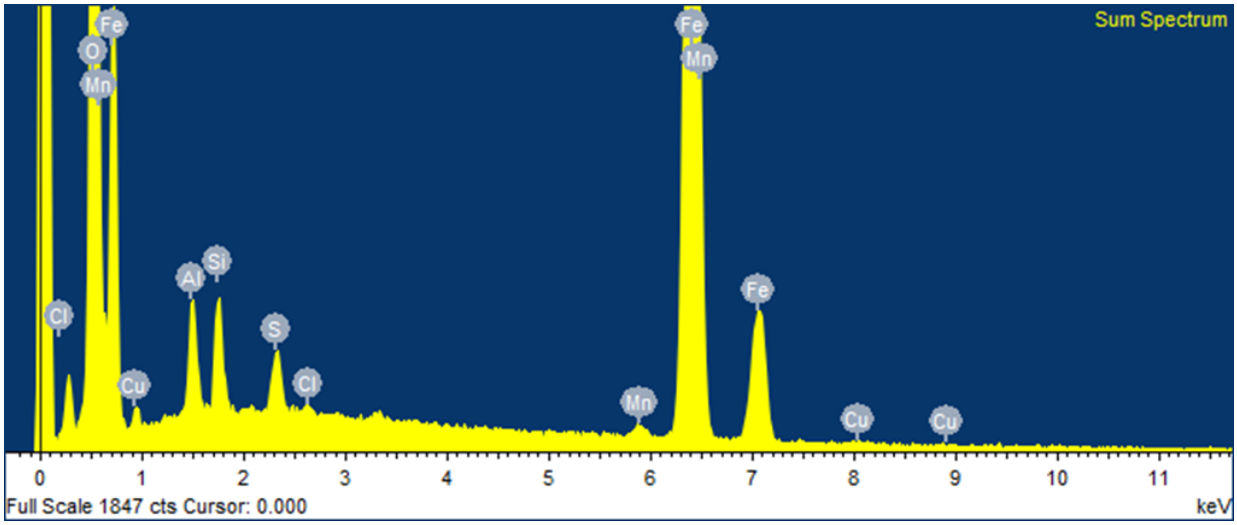


Figure A.619. SEM Image and EDS Spectrum of the Rust Collected from Interior Web of the Girder.

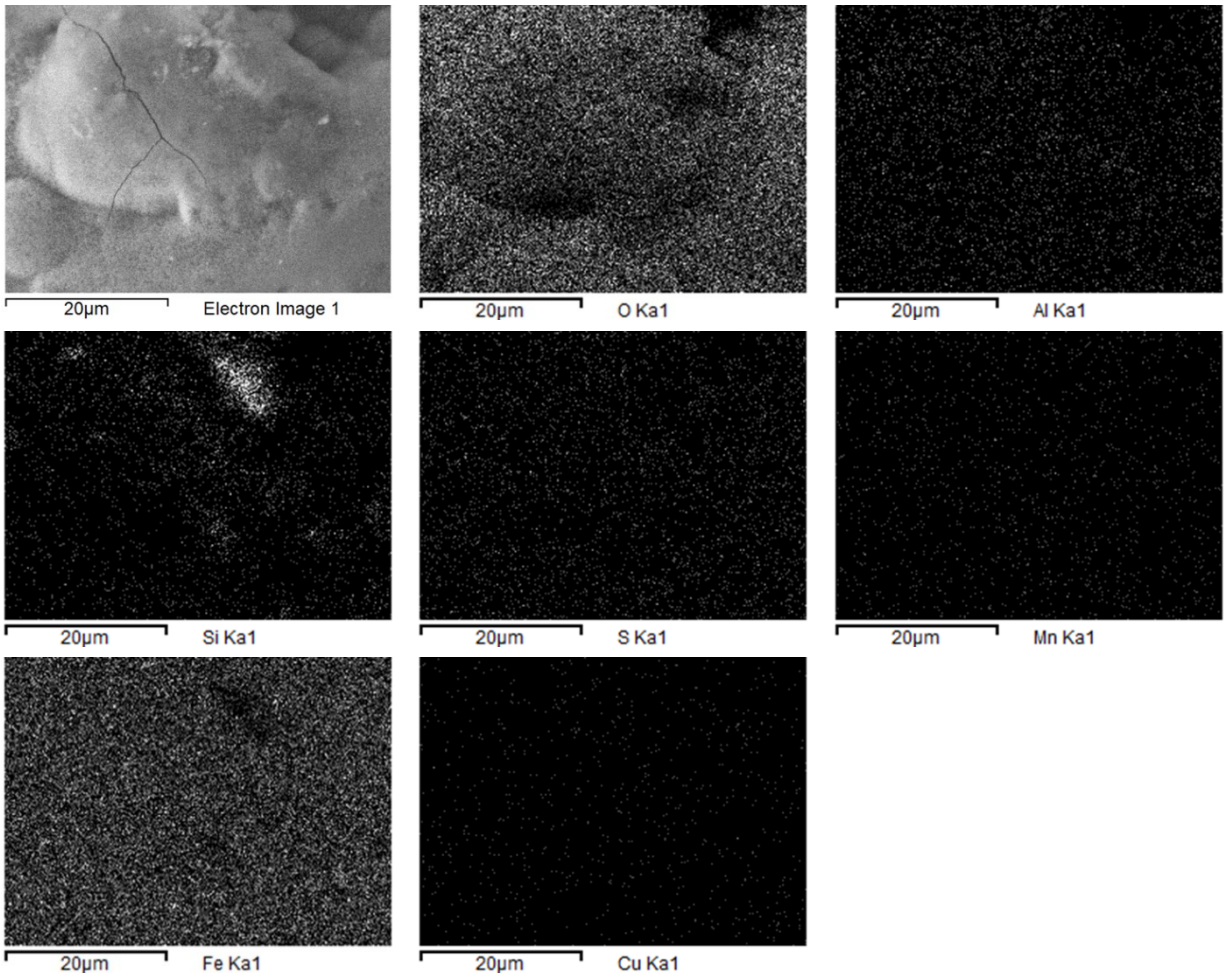
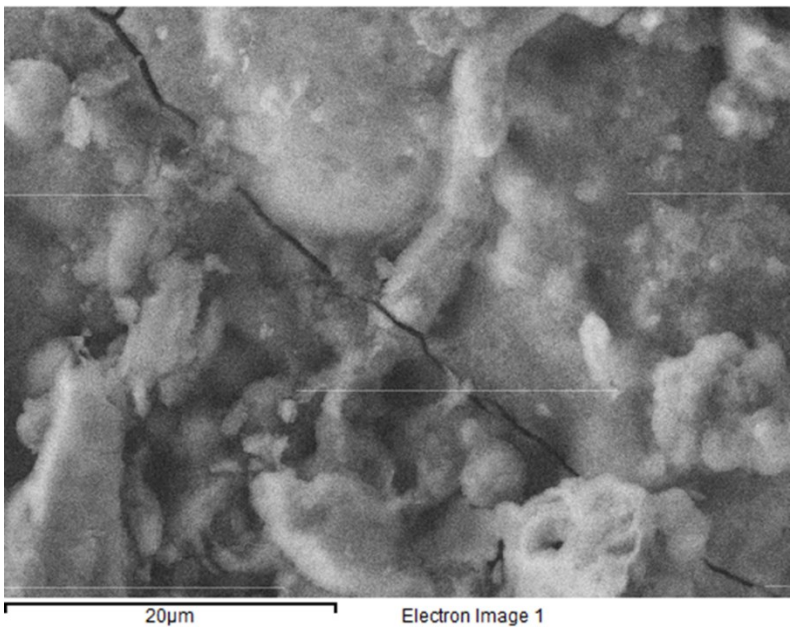


Figure A.620. EDS Elemental Mapping of Rust Collected from Interior Web.

Element	Weight %	Atomic %
O K	42.35	69.08
Mg K	0.21	0.22
Al K	3.04	2.94
Si K	4.47	4.15
S K	0.66	0.54
K K	0.27	0.18
Mn K	0.63	0.30
Fe K	48.07	22.46
Cu K	0.31	0.13
Totals	100.00	



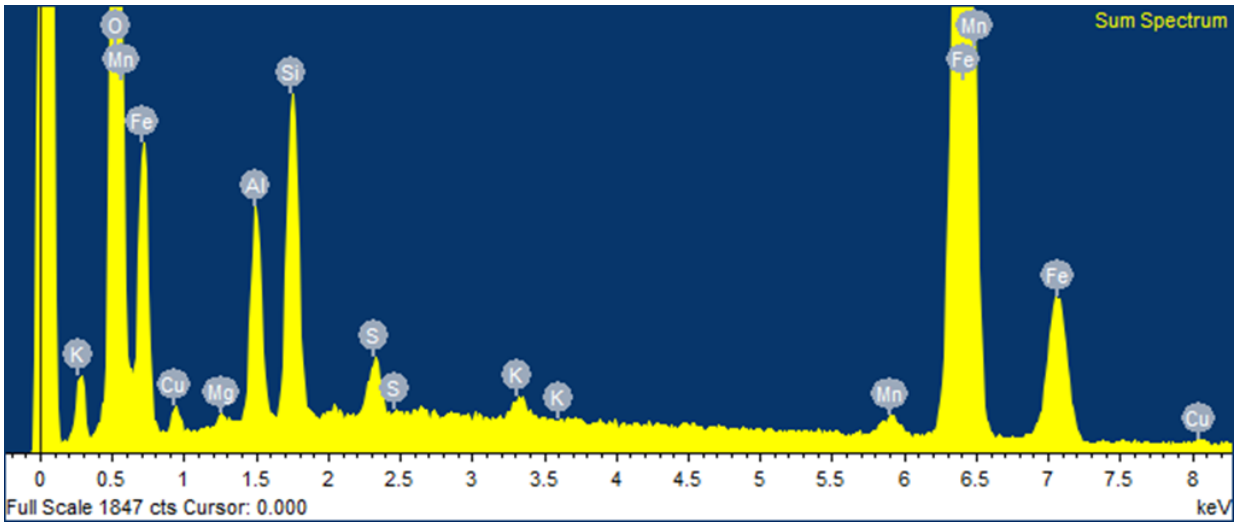


Figure A.621. SEM Image and EDS Spectrum of the Rust Collected from Interior Web of the Girder.

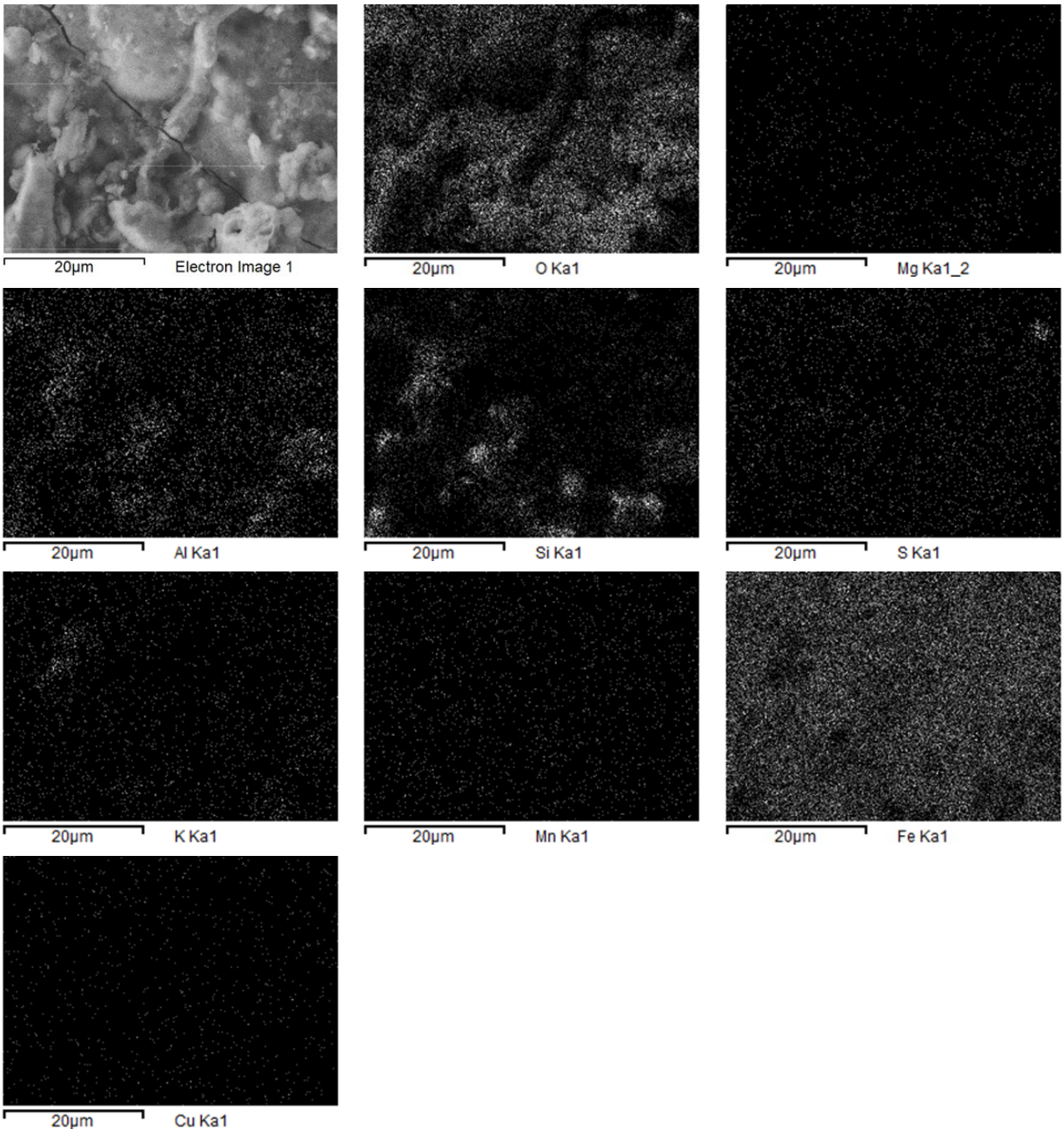
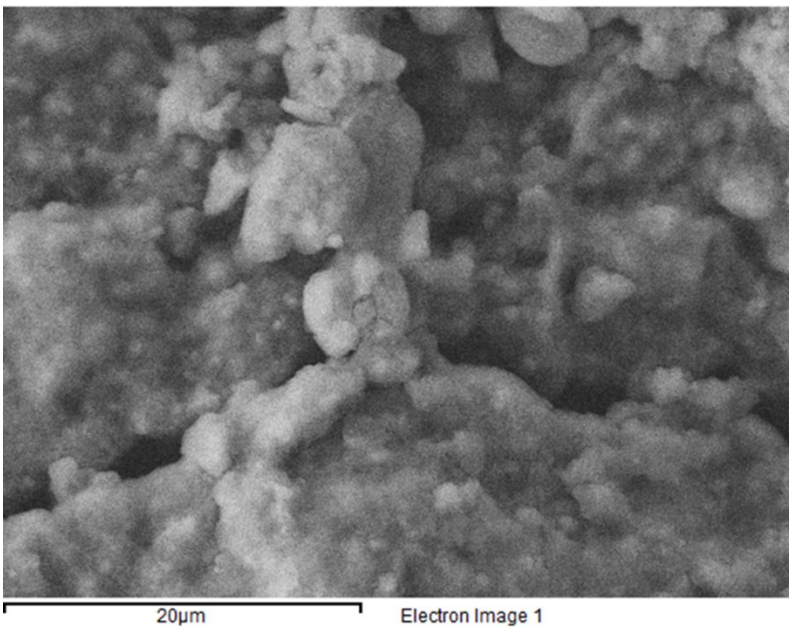


Figure A.622. EDS Elemental Mapping of Rust Collected from Interior Web.

Element	Weight %	Atomic %
O K	49.11	74.65
Al K	2.51	2.27
Si K	4.09	3.54
S K	0.65	0.49
Cl K	0.13	0.09
K K	0.16	0.10
Mn K	0.38	0.17
Fe K	42.76	18.62
Cu K	0.21	0.08
Totals	100.00	



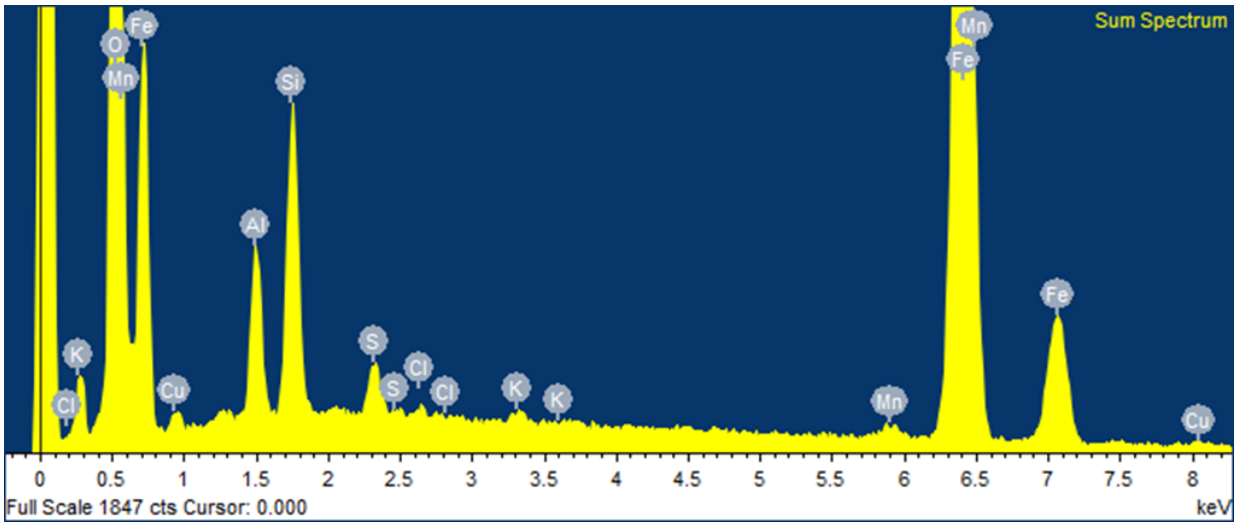


Figure A.623. SEM Image and EDS Spectrum of the Rust Collected from Interior Web of the Girder.

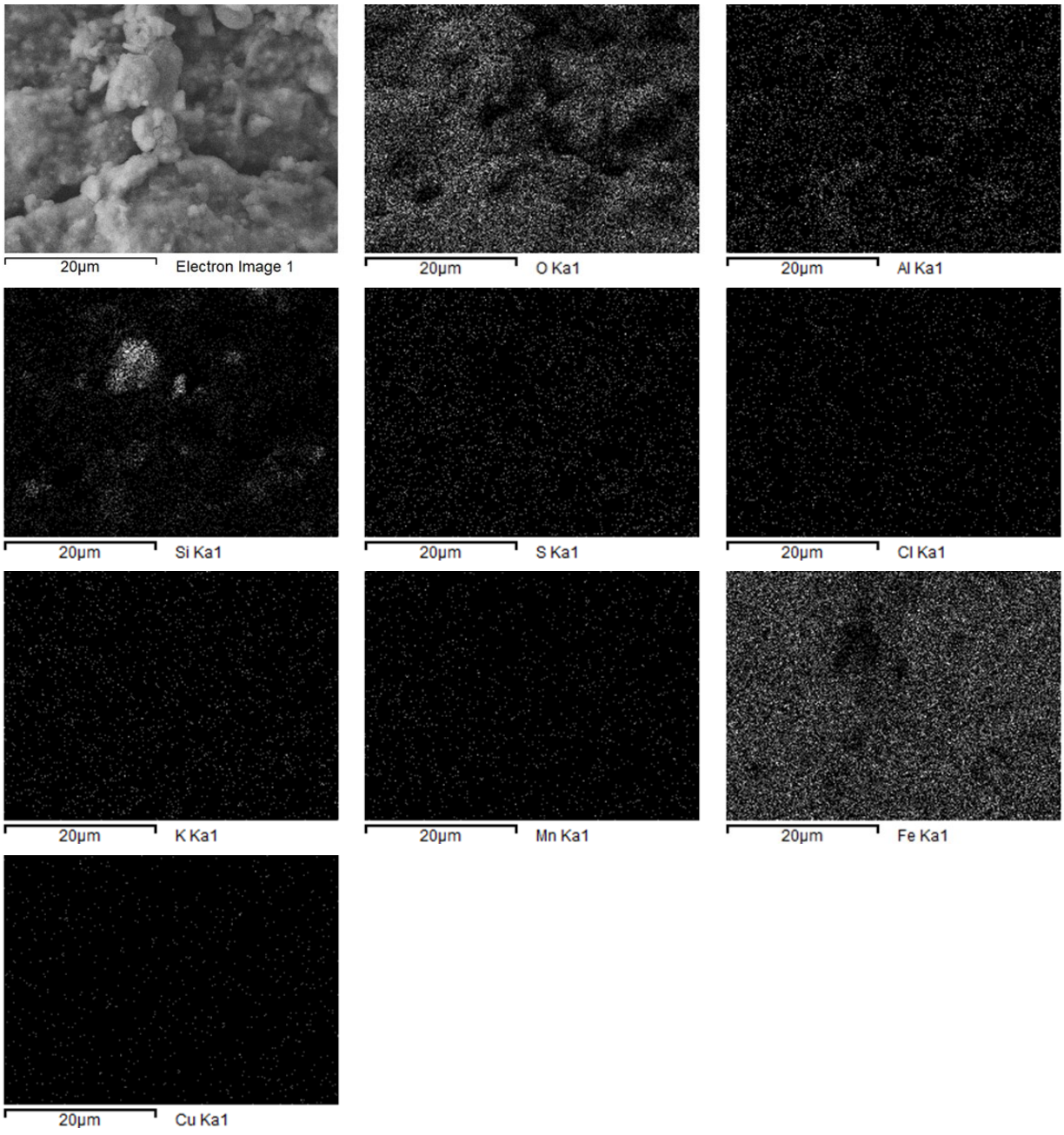
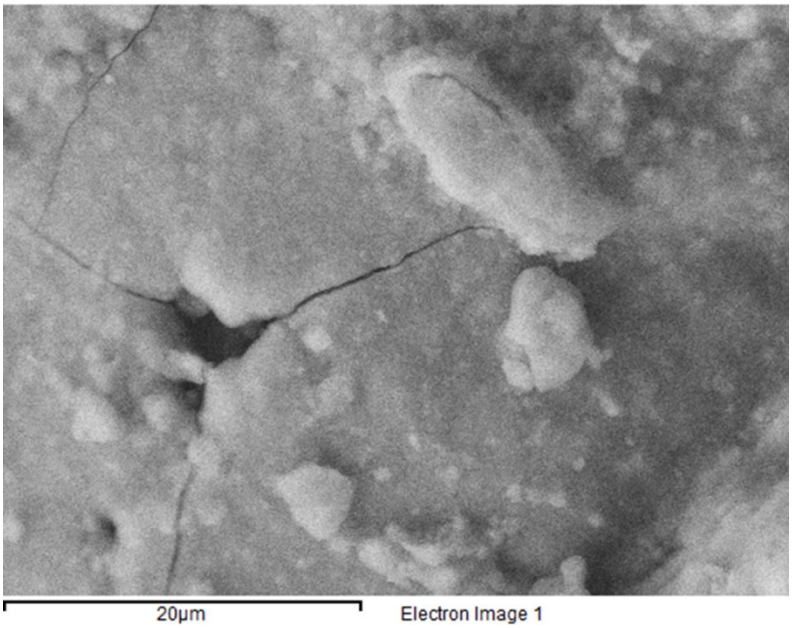


Figure A.624. EDS Elemental Mapping of Rust Collected from Interior Web.

Element	Weight %	Atomic %
O K	36.79	65.07
Al K	2.71	2.84
Si K	1.93	1.94
S K	0.69	0.61
Cl K	0.65	0.52
K K	0.12	0.09
Mn K	0.33	0.17
Fe K	56.54	28.65
Cu K	0.24	0.10
Totals	100.00	



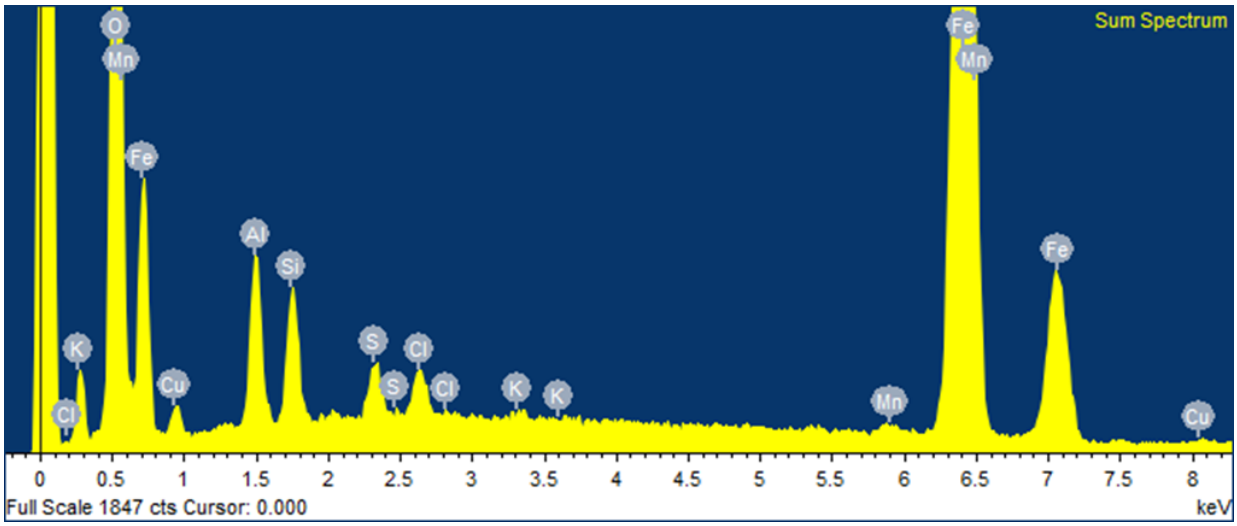


Figure A.625. SEM Image and EDS Spectrum of the Rust Collected from Interior Web of the Girder.

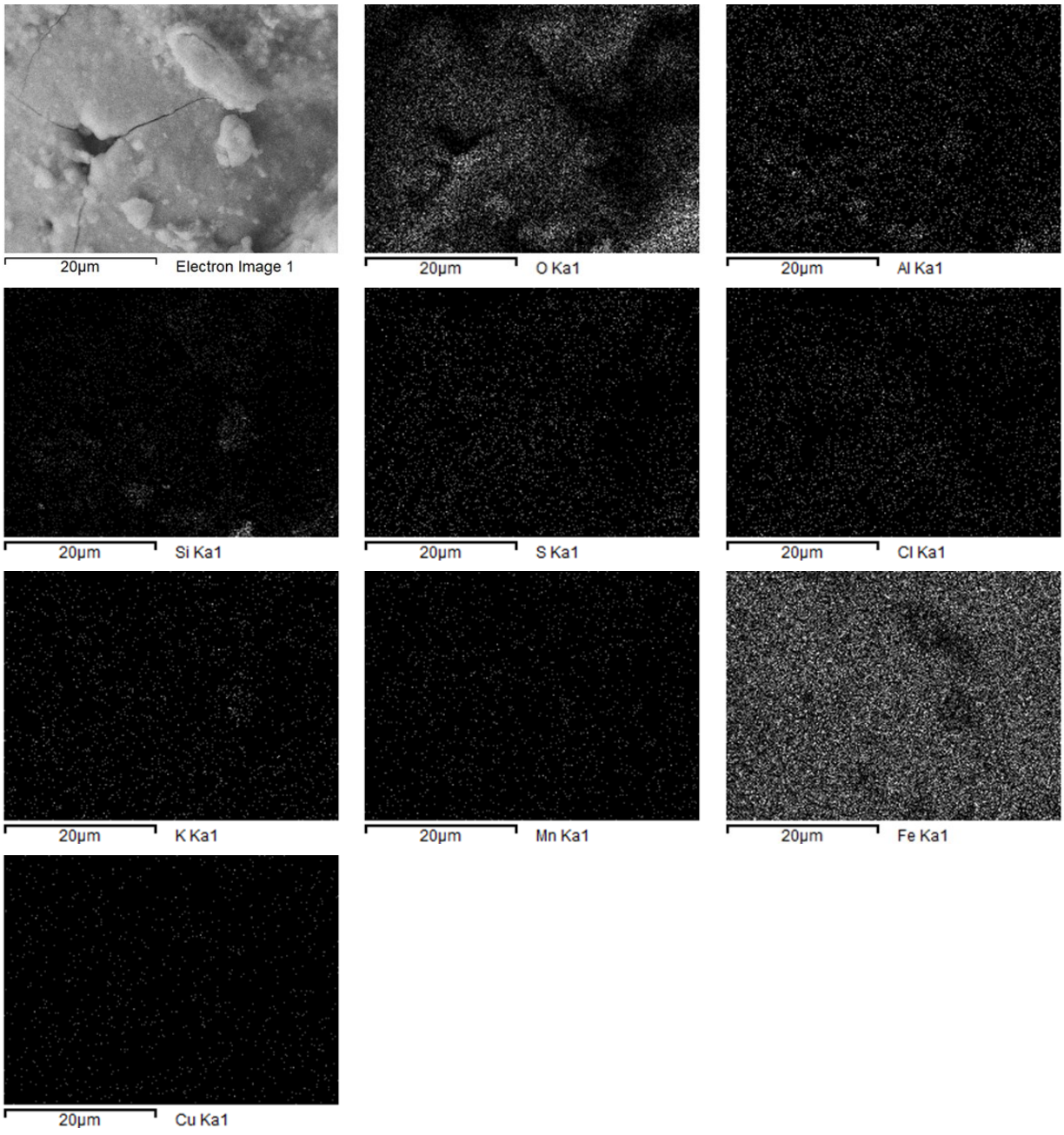


Figure A.626. EDS Elemental Mapping of Rust Collected from Interior Web.

A.36.5.XPS Result: Exterior Girder

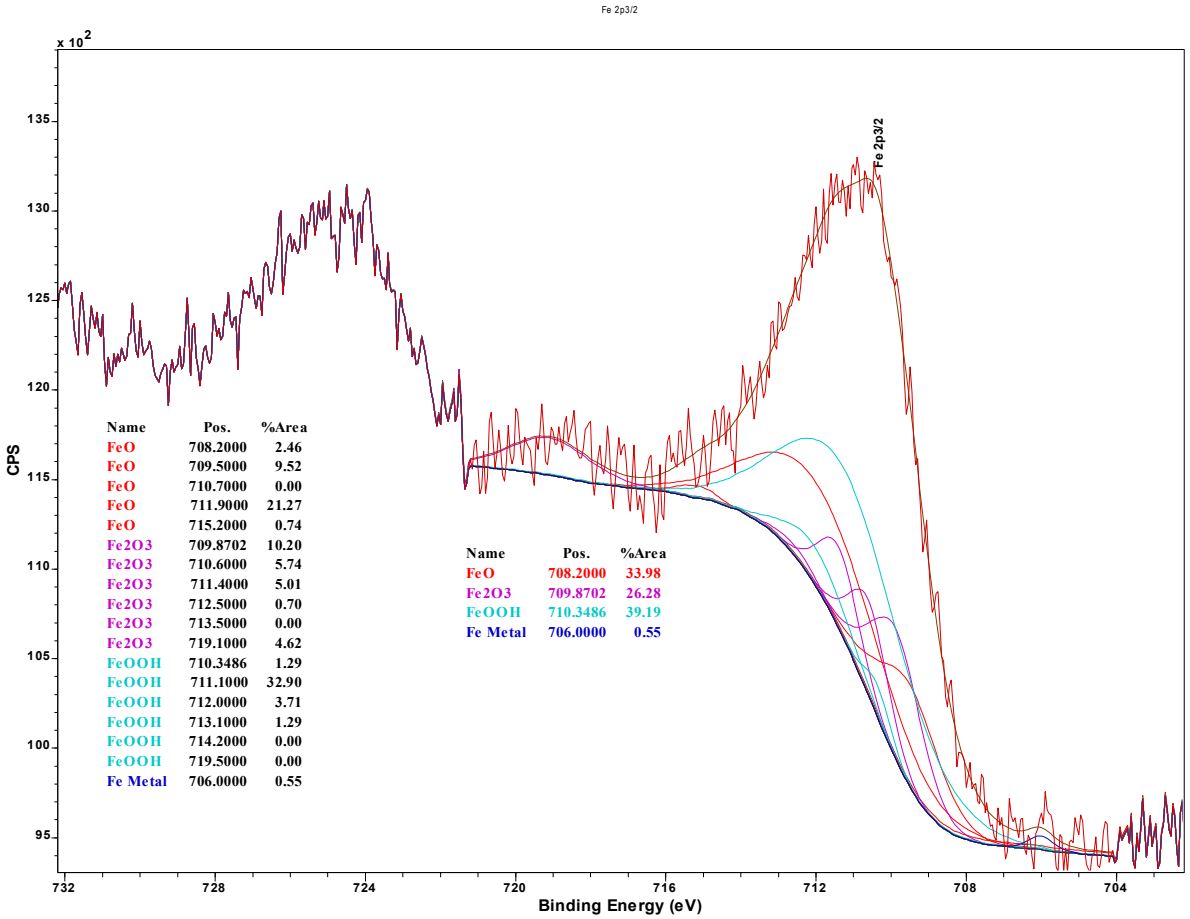


Figure A.627. XPS Spectrum of the Rust Collected from Exterior Web of the Girder.

A.36.6.XPS Result: Interior Girder

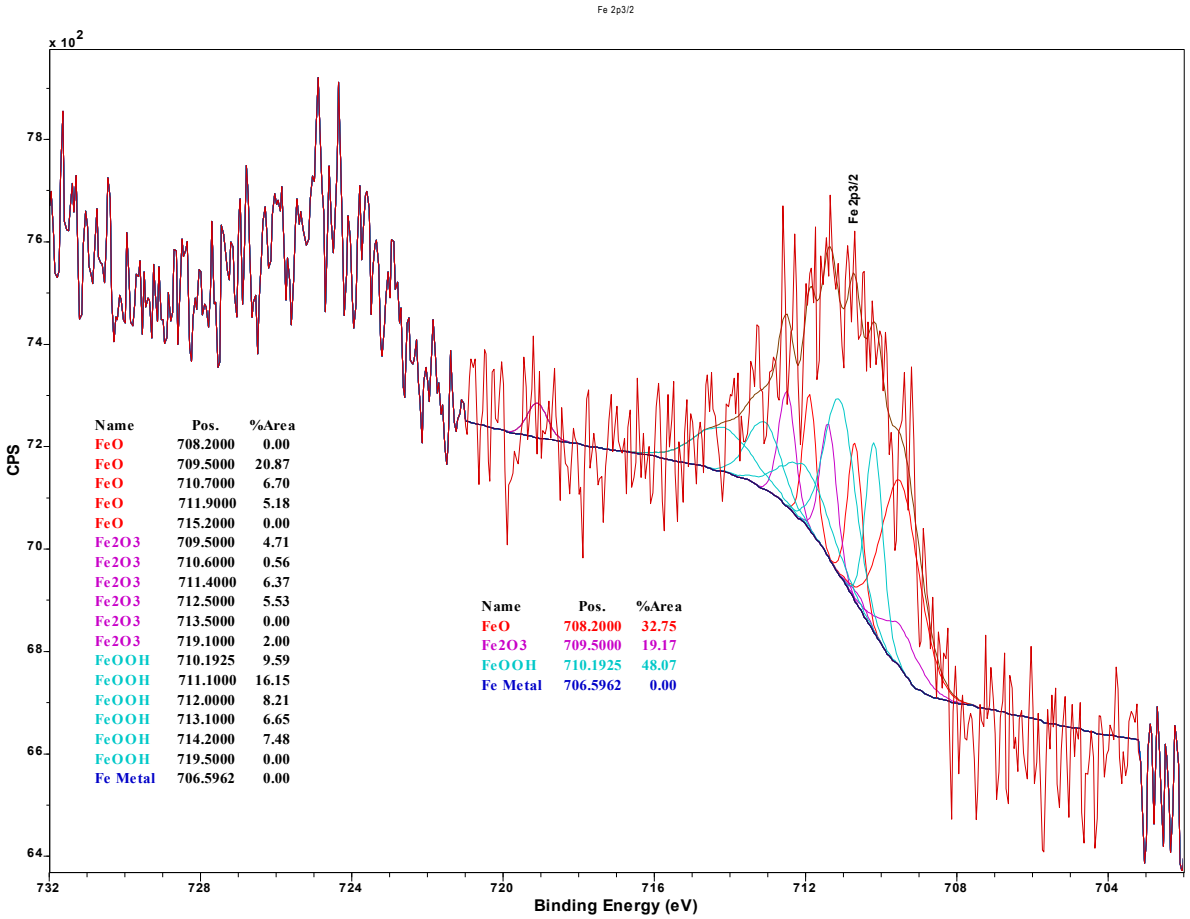


Figure A.628. XPS Spectrum of the Rust Collected from Interior Web of the Girder.

A.36.7.XRD Result: Exterior and Interior Girder

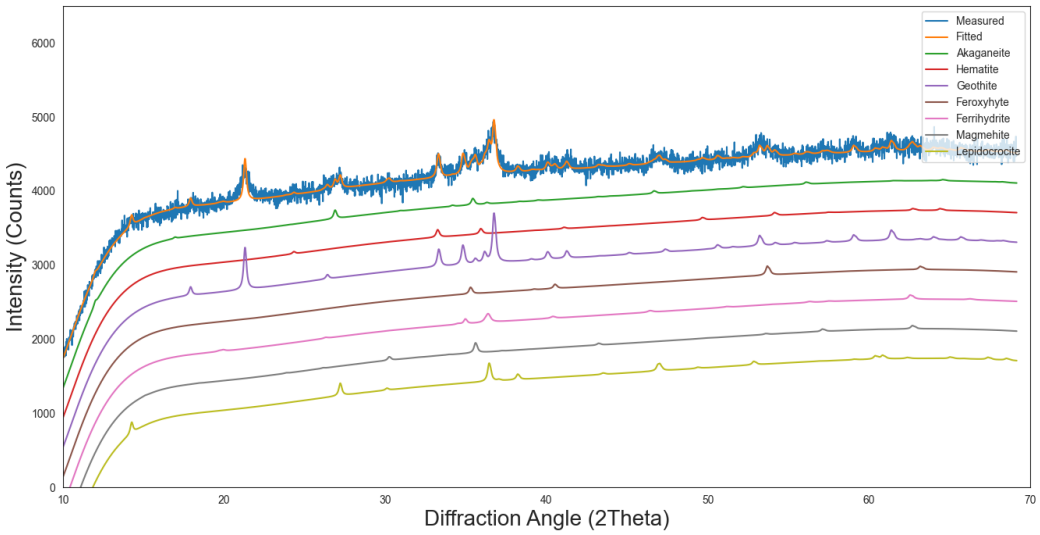


Figure A.629. XRD Pattern of Powdered Rust Collected from Exterior Web of the Girder.

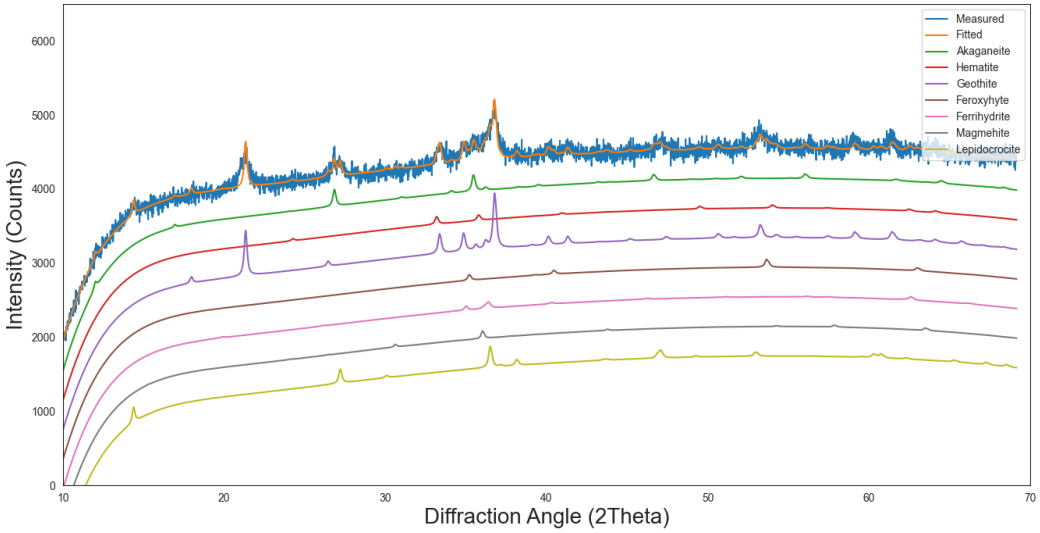
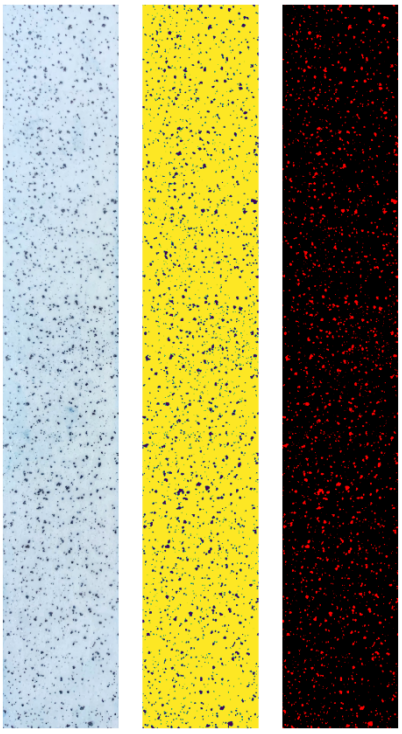


Figure A.630. XRD Pattern of Powdered Rust Collected from Interior Web of the Girder.

A.36.8.Particle Size Analysis: Tape Adhesion Results

(a)

(b)



(c)

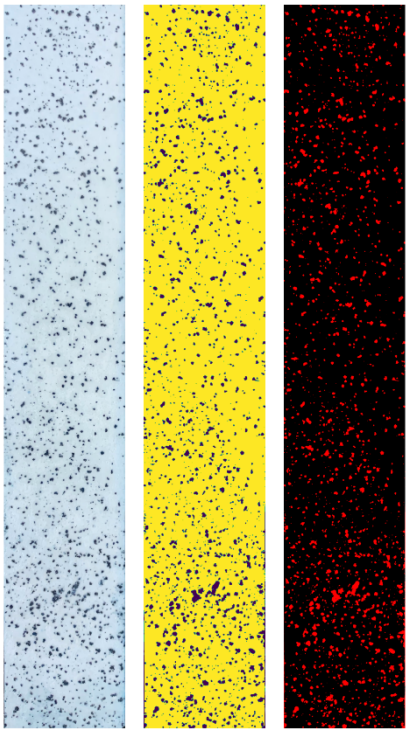
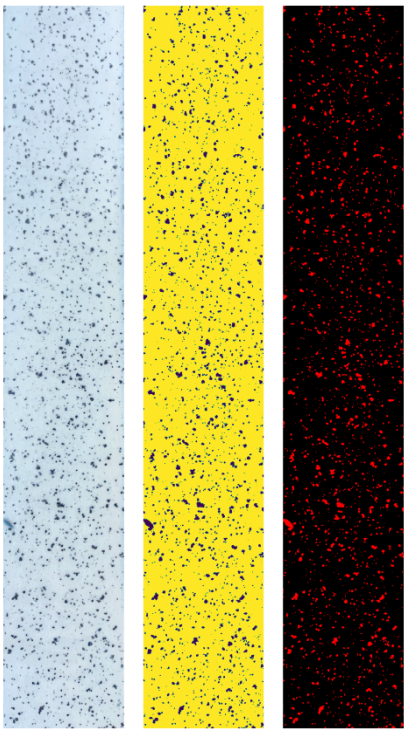


Figure A.631. Particle Size Analysis Results at B10G1F1 (a) Top Flange Bottom, (b) Web, (c) Bottom Flange Bottom.

(a)

(b)



(c)

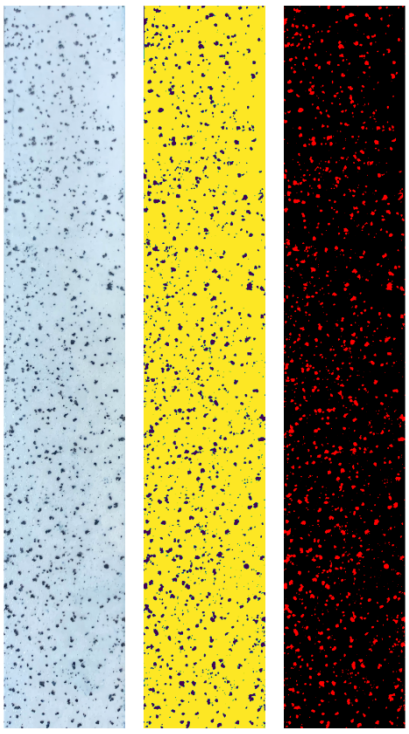
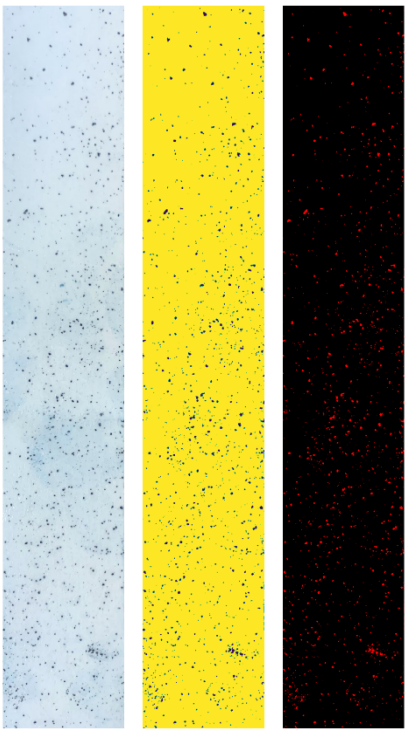


Figure A.632. Particle Size Analysis Results at B10G2F1 (a) Top Flange Bottom, (b) Web, (c) Bottom Flange Bottom.

(a)

(b)



(c)

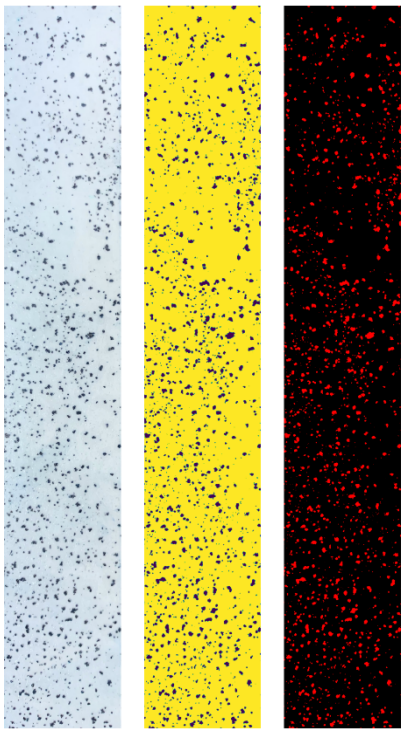
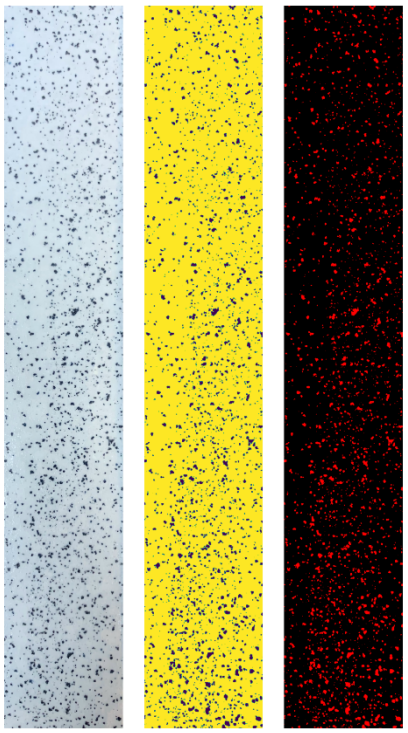


Figure A.633. Particle Size Analysis Results at B11G1F1 (a) Top Flange Bottom, (b) Web, (c) Bottom Flange Bottom.

(a)

(b)



(c)

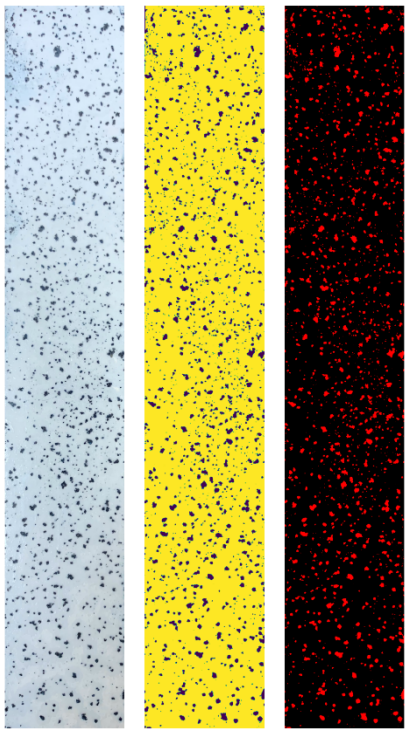
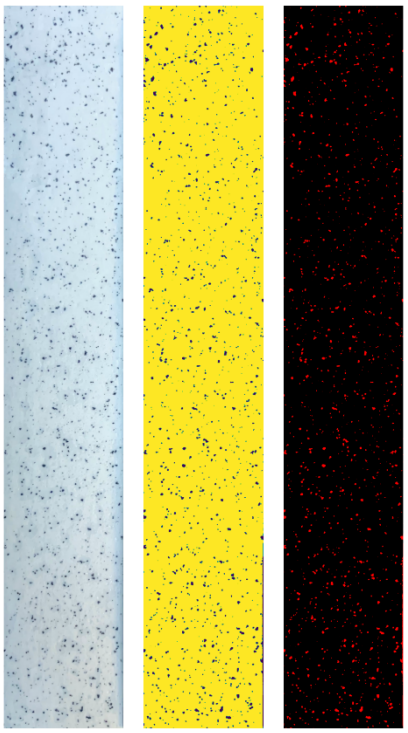


Figure A.634. Particle Size Analysis Results at B11G2F1 (a) Top Flange Bottom, (b) Web, (c) Bottom Flange Bottom.

(a)

(b)



(c)

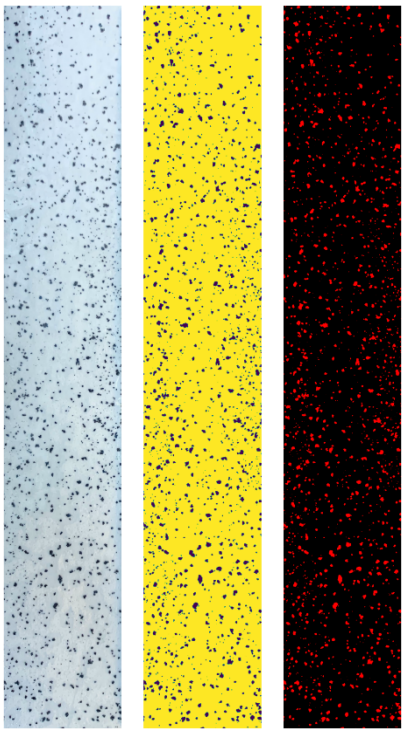


Figure A.635. Particle Size Analysis Results at B11G3F2 (a) Top Flange Bottom, (b) Web, (c) Bottom Flange Bottom.

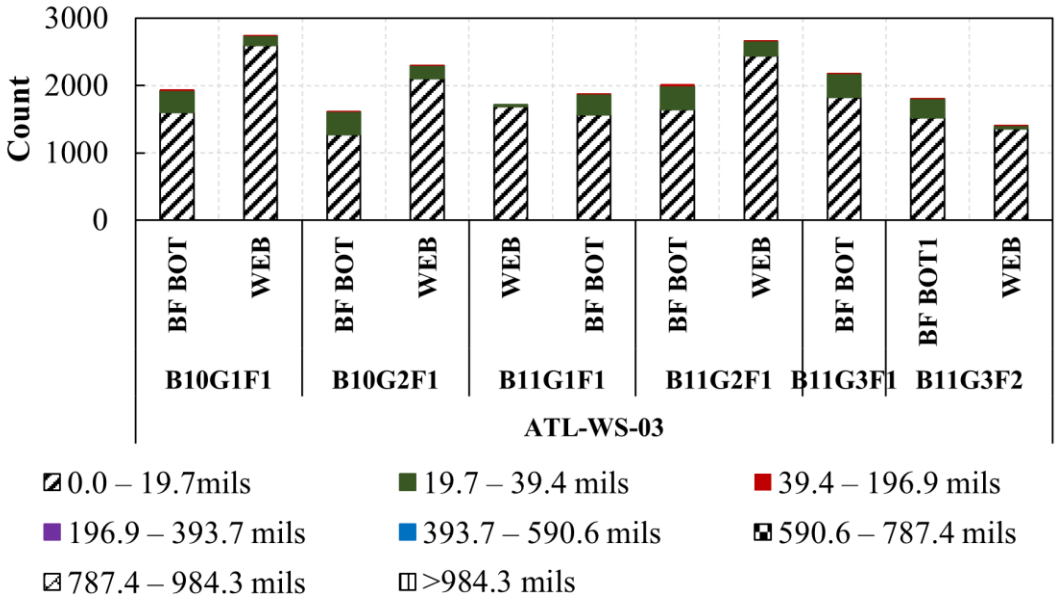


Figure A.636. Particle Size Analysis Showing Different Locations Examined.

A.37. LBB-WS-01

- US 82 EB DIR CONN
- Bridge ID 51520038001002, Coordinates (33.55028174, -101.9379612), Lubbock County
- Continuous weathering plate girder
- Built 2009
- Girder inspection carried on bent 3 and bent 4, and measurements are taken on girder within four feet from the abutment or bent.
- No visual inspection on deck
- Location for Testing: B3-G2F2, B3-G4F2, B4-G1F1, B4-G3F1, B4-G4F2



Figure A.637. Typical Picture of LBB-WS-01

A.37.1. Observed Condition

Unifrom patina are visible on the bottom face of the top flange with a rating of 8. The web has a uniform patina formation with a patina rating of 8. The interior girders have a patina rating of 7.

A.37.2.Field Inspection Results

Table A-164. Field Inspection Results for LBB-WS-01.

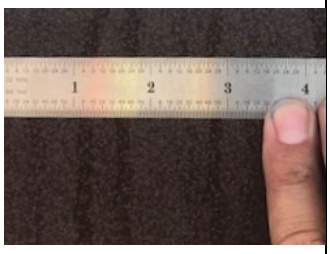
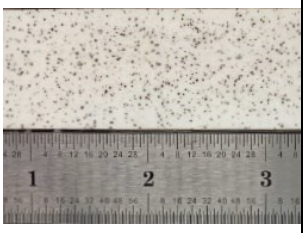
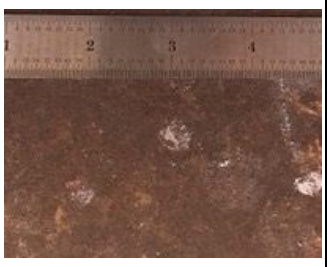
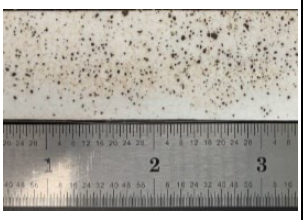
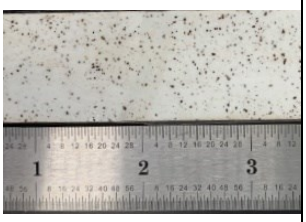
Location	Patina Rating	Thickness (inch)	Cl^- Conc. (ppm)	Field Condition	Tape Test
B3-G4F2 TF Bot. Ext.	8	Measured 0.996 Design			
B3-G4F2 Web Ext.	8	Measured 0.635 Design			
B3-G4F2 BF Top Ext.	7	Measured 0.996 Design			
B3-G4F2 BF Bot. Ext.	8	Measured - Design			
B3-G2F2 TF Bot. Int.	8	Measured 1.004 Design			

Table A-165. Field Inspection Results for LBB-WS-01.

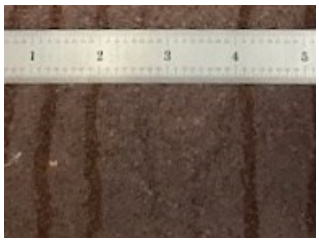
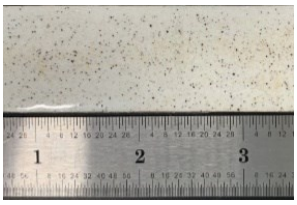
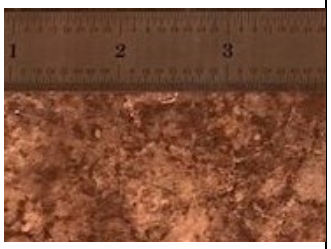
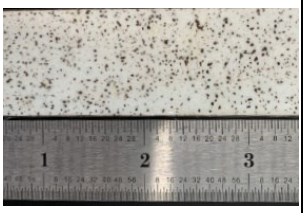
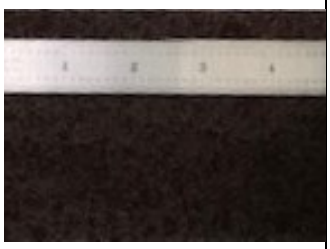
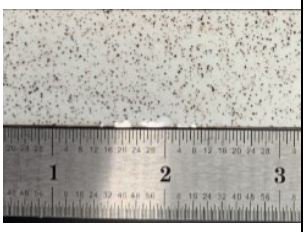
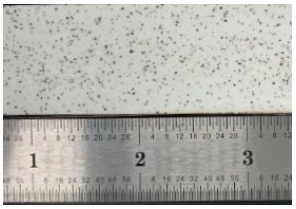
Location	Patina Rating	Thickness (inch)	Cl^- Conc. (ppm)	Field Condition	Tape Test
B3-G2F2 Web Int.	8	Measured 0.627 Design	6		
B3-G2F2 BF Top Int.	8	Measured 1.003 Design			
B3-G2F2 BF Bot. Int.	7	Measured - Design			
B4-G4F2 TF Bot. Ext.	8	Measured 2.498 Design			
B4-G4F2 Web Ext.	8	Measured 0.636 Design	9		

Table A-166. Field Inspection Results for LBB-WS-01.

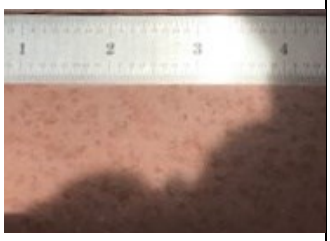
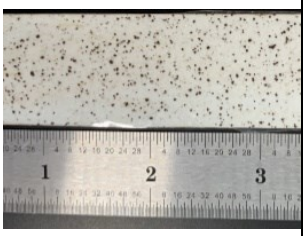
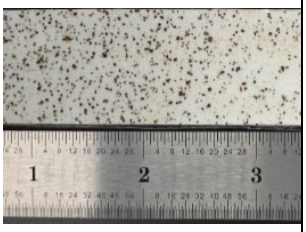
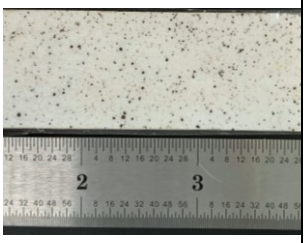
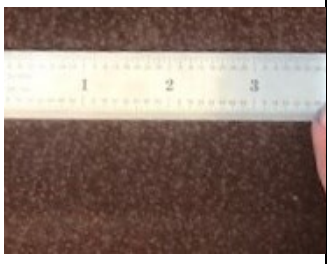
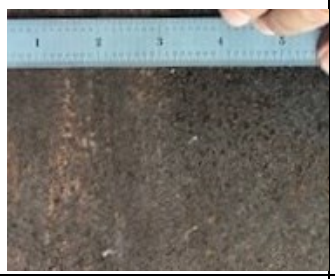
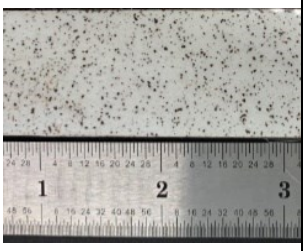
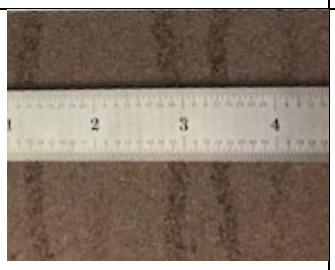
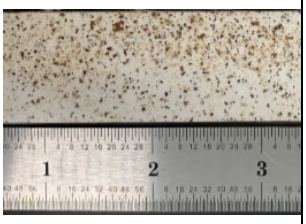
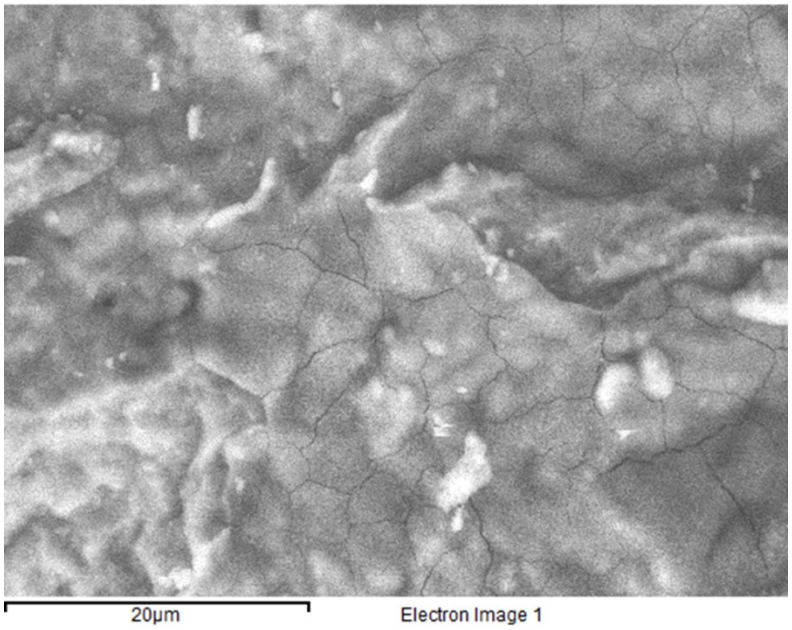
Location	Patina Rating	Thickness (inch)	Cl^- Conc. (ppm)	Field Condition	Tape Test
B4-G4F2 BF Top Ext.	7	Measured 2.511 Design			
B4-G4F2 BF Bot. Ext.	8	Measured - Design			
B3-G1F1 TF Bot. Ext.	8	Measured 1.000 Design			
B3-G1F1 Web Ext.	8	Measured 0.626 Design	11		
B3-G1F1 BF Top Ext.	7	Measured 0.999 Design			

Table A-167. Field Inspection Results for LBB-WS-01.

Location	Patina Rating	Thickness (inch)	Cl^- Conc. (ppm)	Field Condition	Tape Test
B3-G1F1 BF Bot. Ext.	6	Measured - Design			
B4-G3F1 TF Bot. Int.	8	Measured 0.980 Design			
B4-G3F1 Web Int.	8	Measured 0.630 Design	13		
B4-G3F1 BF Top Int.	8	Measured 1.069 Design			
B4-G3F1 BF Bot. Int.	8	Measured - Design			

A.37.3.SEM/EDS Results: Exterior Web Girder

Element	Weight %	Atomic %
O K	38.06	67.18
Al K	1.10	1.15
Si K	0.27	0.27
S K	1.65	1.45
Cl K	0.48	0.38
Cr K	0.34	0.19
Mn K	1.05	0.54
Fe K	56.73	28.69
Cu K	0.31	0.14
Totals	100.00	



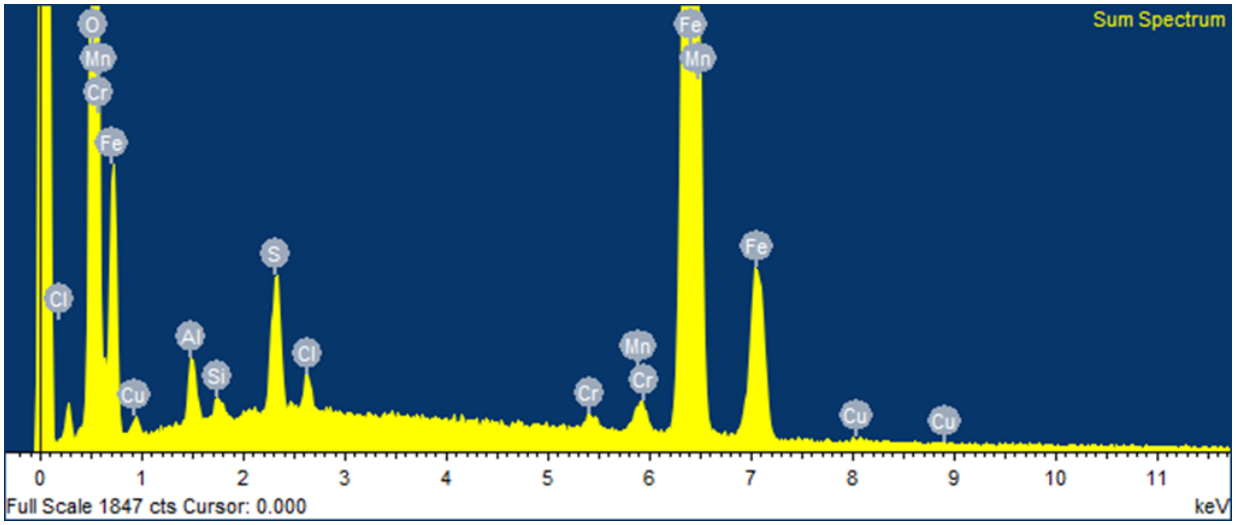


Figure A.638. SEM Image and EDS Spectrum of the Rust Collected from Exterior Web of the Girder.

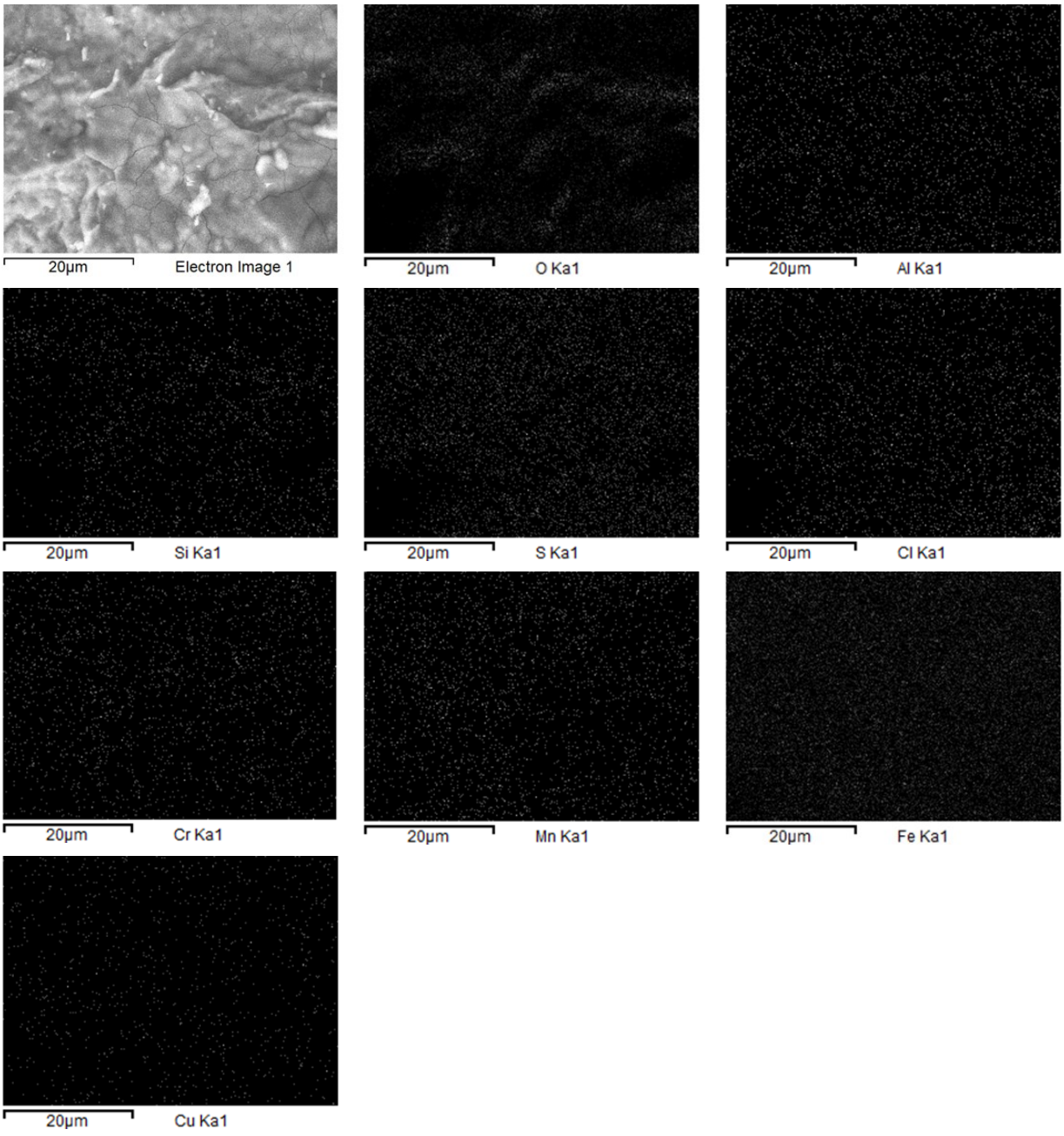
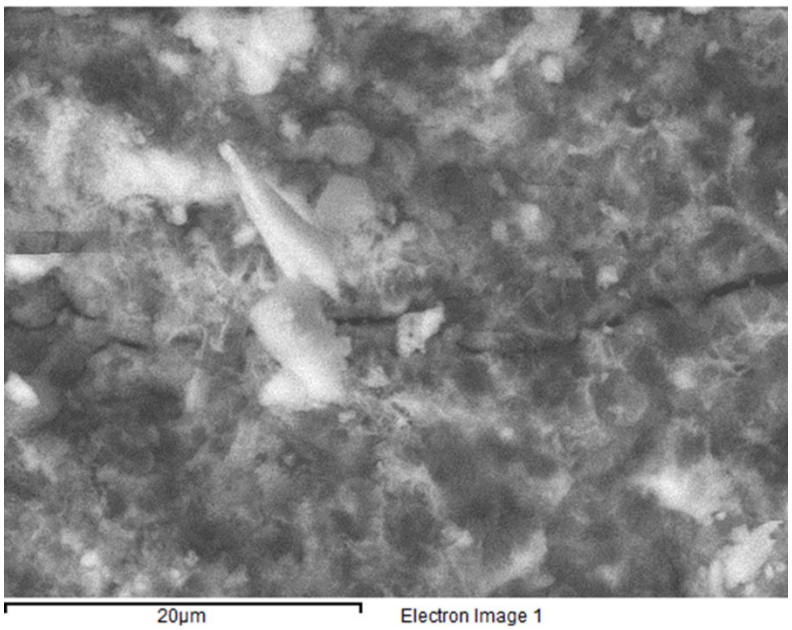


Figure A.639. EDS Elemental Mapping of Rust Collected from Exterior Web.

Element	Weight%	Atomic%
O K	37.08	66.13
Na K	0.53	0.66
Al K	0.93	0.99
Si K	0.48	0.48
S K	1.18	1.05
K K	0.12	0.09
Ca K	0.83	0.59
Cr K	0.33	0.18
Mn K	0.88	0.46
Fe K	56.24	28.73
Ni K	0.37	0.18
Cu K	1.02	0.46
Totals	100.00	



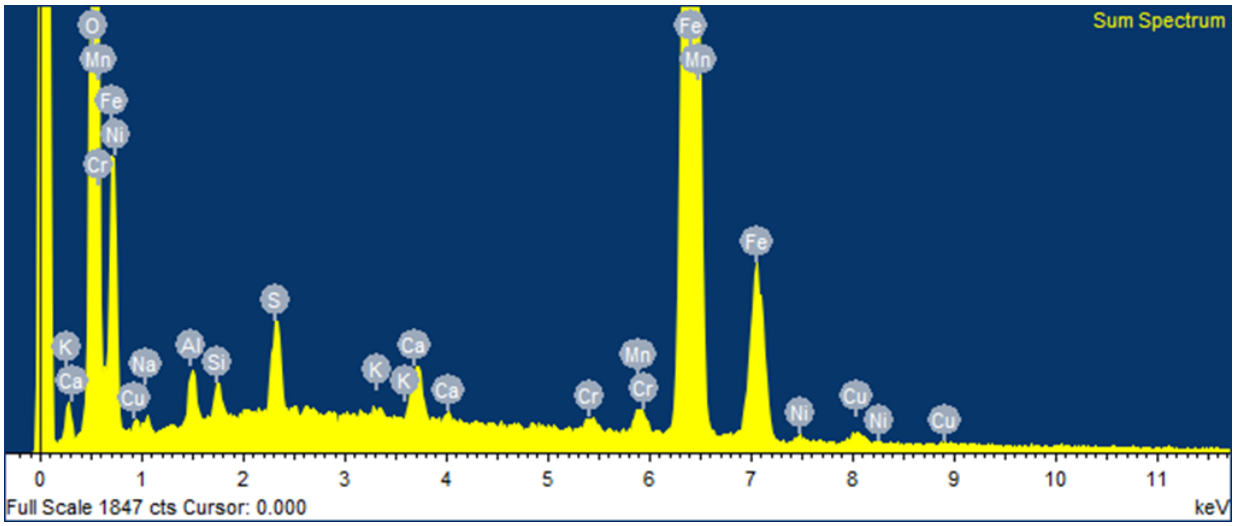
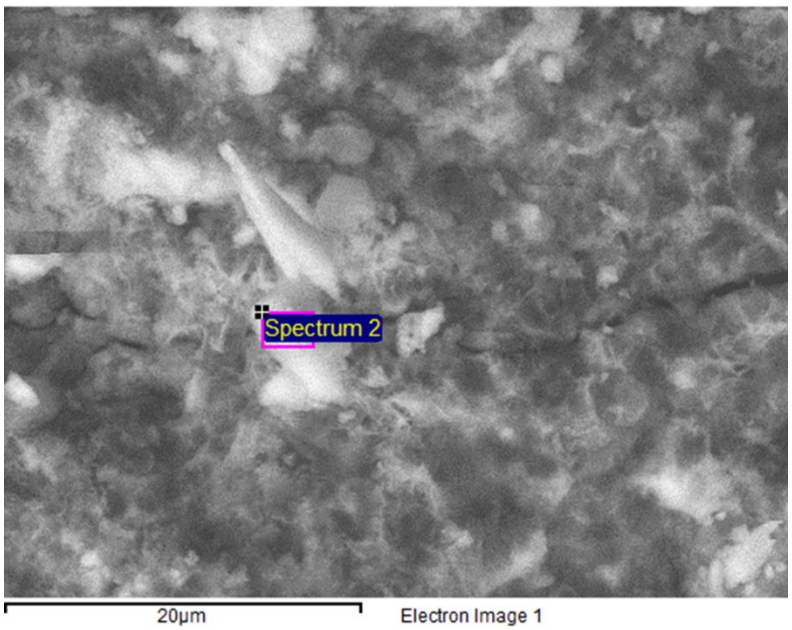


Figure A.640. SEM Image and EDS Spectrum of the Rust Collected from Interior BF Bottom of the Girder.

Element	Weight %	Atomic %
O K	62.02	80.35
Al K	0.71	0.55
Si K	0.41	0.30
S K	11.49	7.43
Ca K	13.39	6.93
Fe K	11.97	4.44
Totals	100.00	



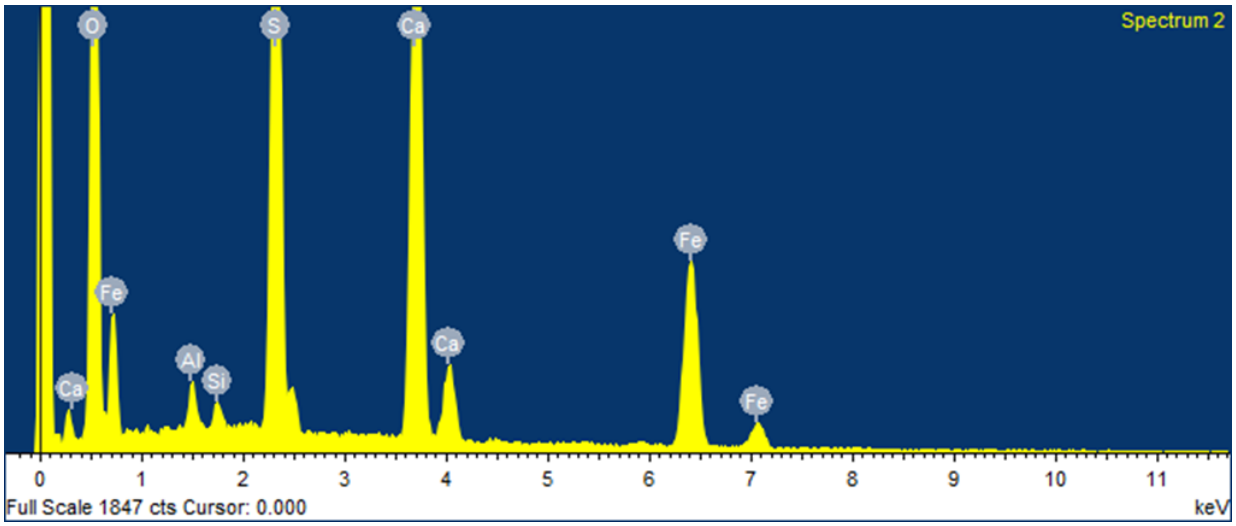


Figure A.641. SEM Image and EDS Spectrum of the Rust Collected from Interior BF Bottom of the Girder.

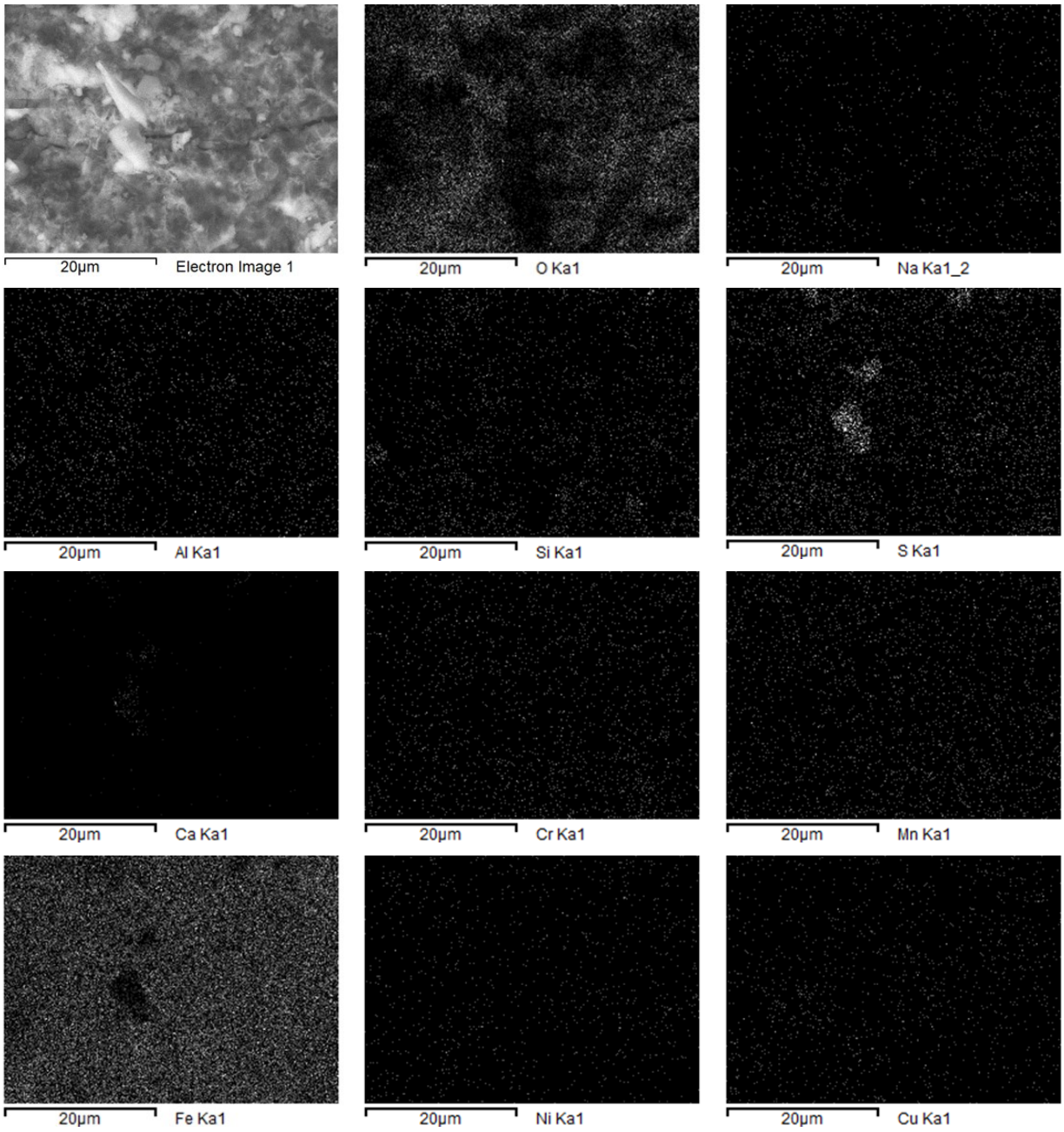
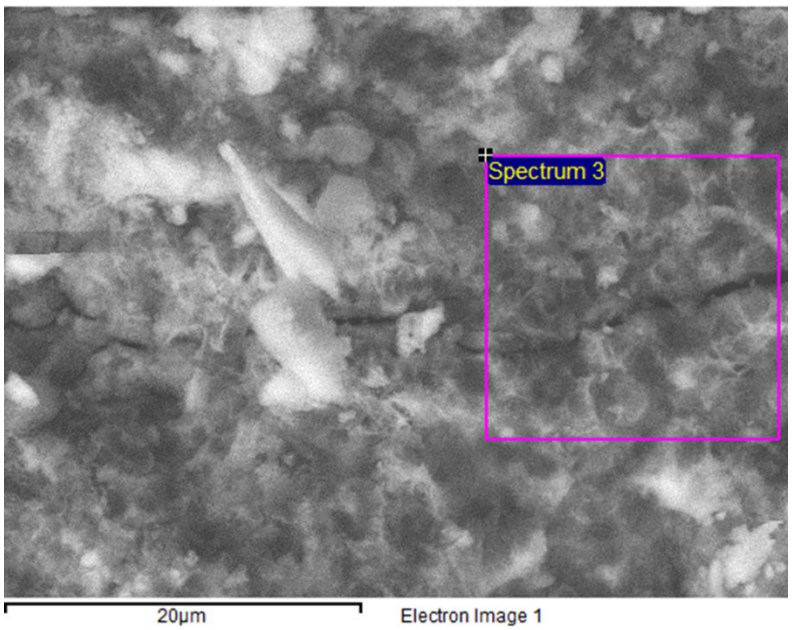


Figure A.642. EDS Elemental Mapping of Rust Collected from Interior BF Bottom.

Element	Weight%	Atomic%
O K	39.67	68.72
Na K	0.78	0.94
Al K	0.84	0.87
S K	0.88	0.76
Ca K	0.42	0.29
Cr K	0.27	0.14
Mn K	0.56	0.28
Fe K	55.03	27.31
Ni K	0.48	0.23
Cu K	1.07	0.47
Totals	100.00	



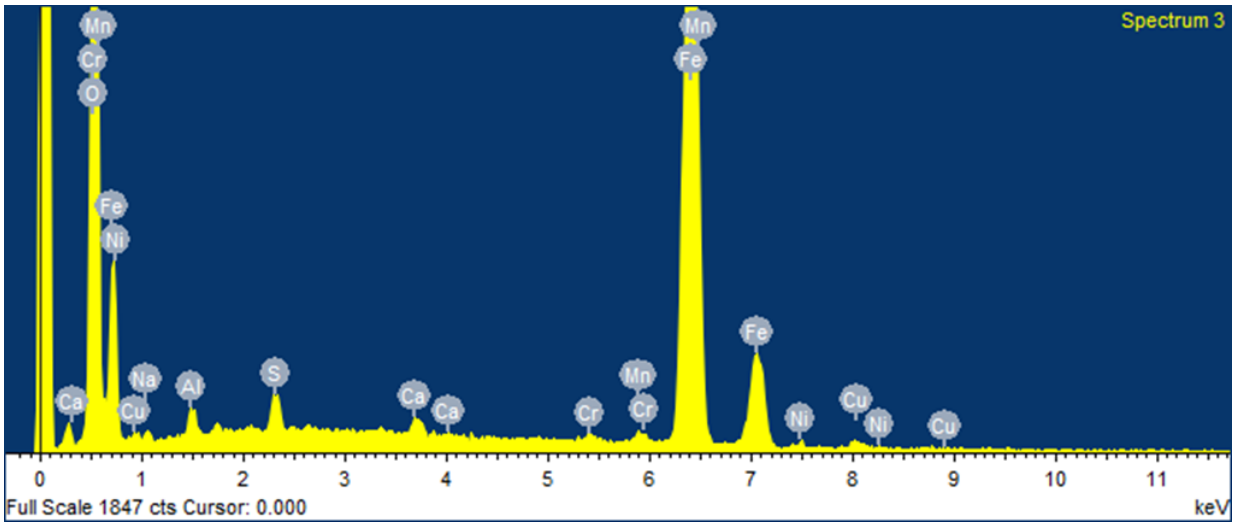
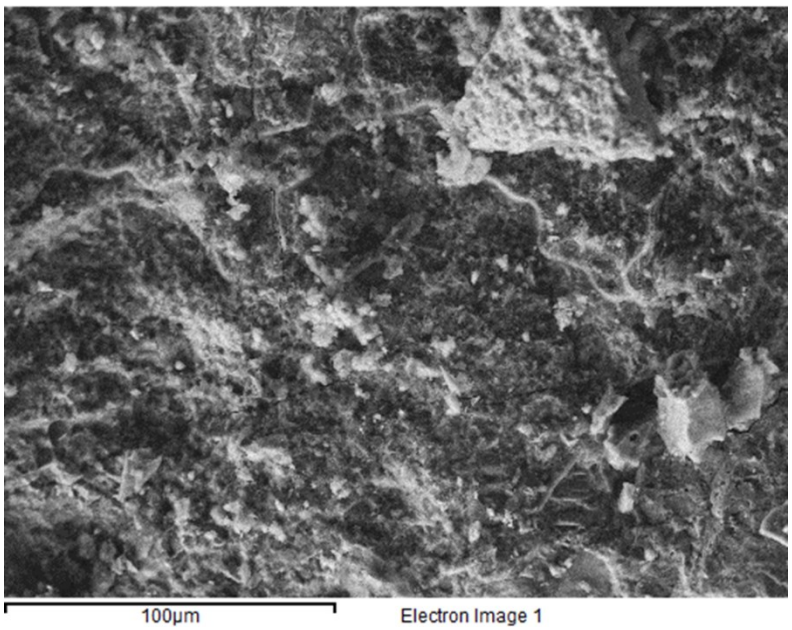


Figure A.643. SEM Image and EDS Spectrum of the Rust Collected from Interior BF Bottom of the Girder.

Element	Weight%	Atomic%
O K	32.60	61.73
Na K	0.32	0.43
Al K	1.14	1.28
Si K	0.64	0.69
S K	0.85	0.80
Ca K	0.70	0.53
Cr K	0.38	0.22
Mn K	0.97	0.53
Fe K	61.37	33.29
Ni K	0.37	0.19
Cu K	0.66	0.31
Totals	100.00	



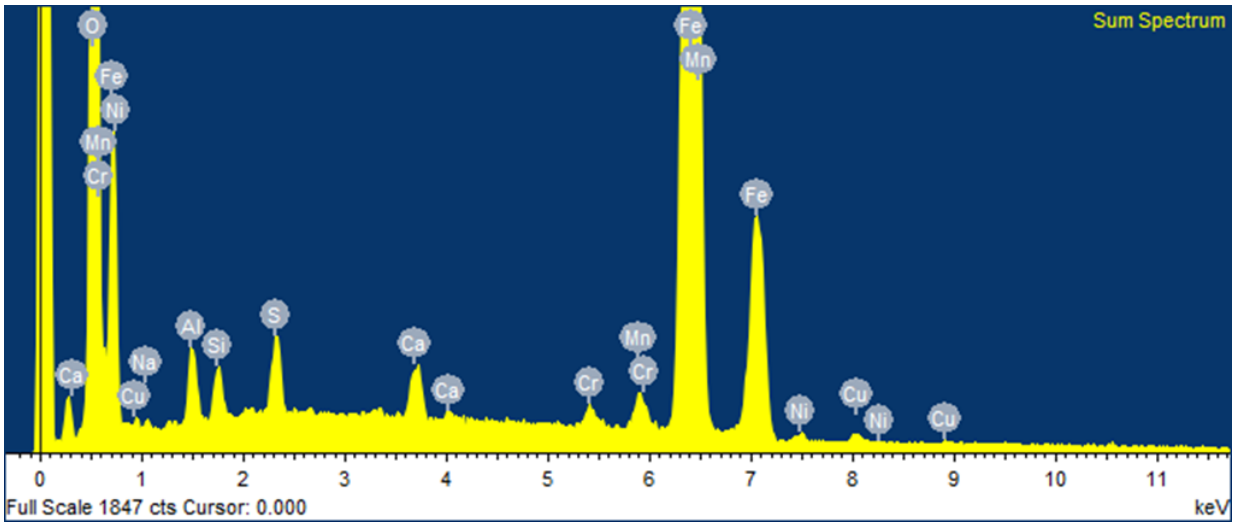


Figure A.644. SEM Image and EDS Spectrum of the Rust Collected from Interior BF Bottom of the Girder.

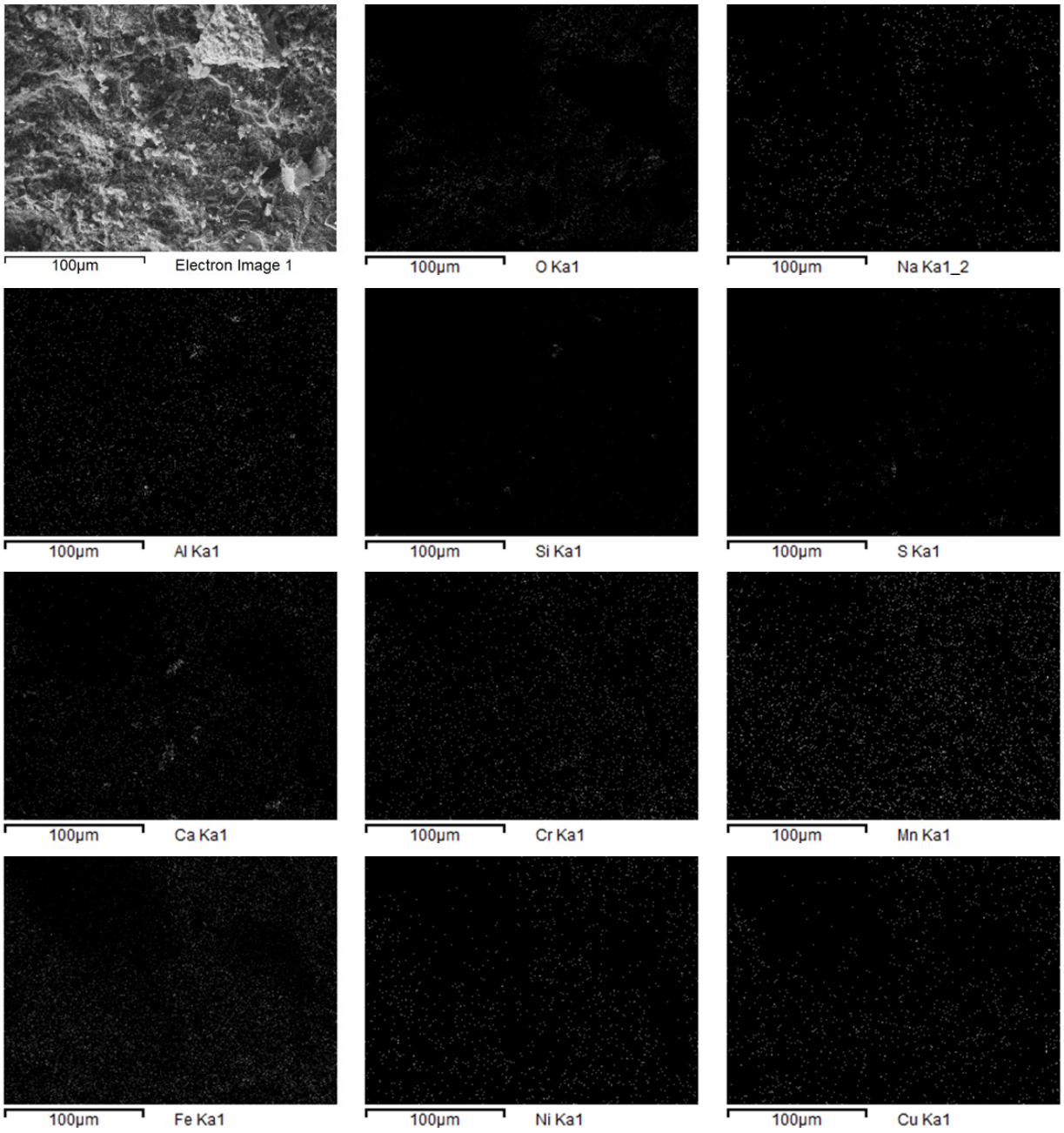
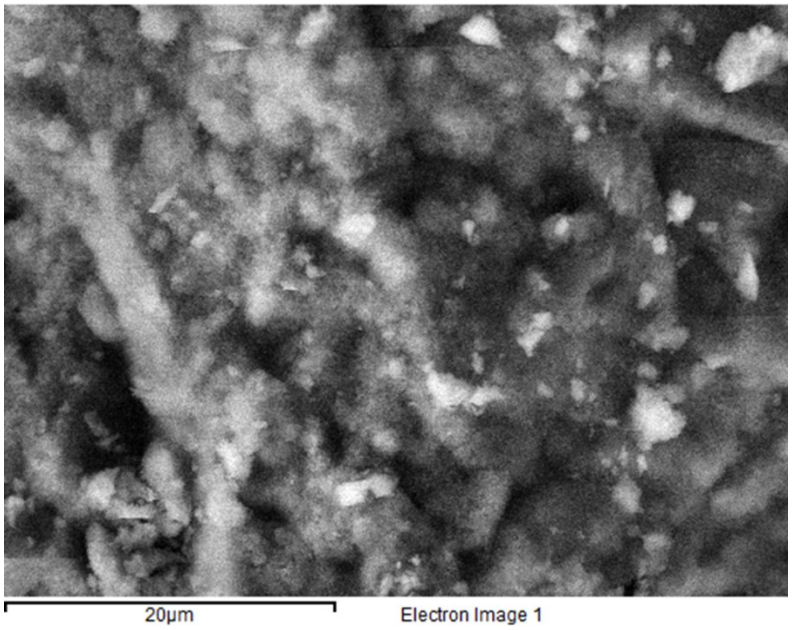


Figure A.645. EDS Elemental Mapping of Rust Collected from Interior BF Bottom.

A.37.4.SEM/EDS Results: Interior Web Girder

Element	Weight%	Atomic%
O K	37.52	66.43
Al K	1.73	1.81
Si K	1.16	1.17
S K	0.80	0.71
Ca K	0.34	0.24
Mn K	0.66	0.34
Fe K	57.50	29.17
Cu K	0.30	0.13
Totals	100.00	



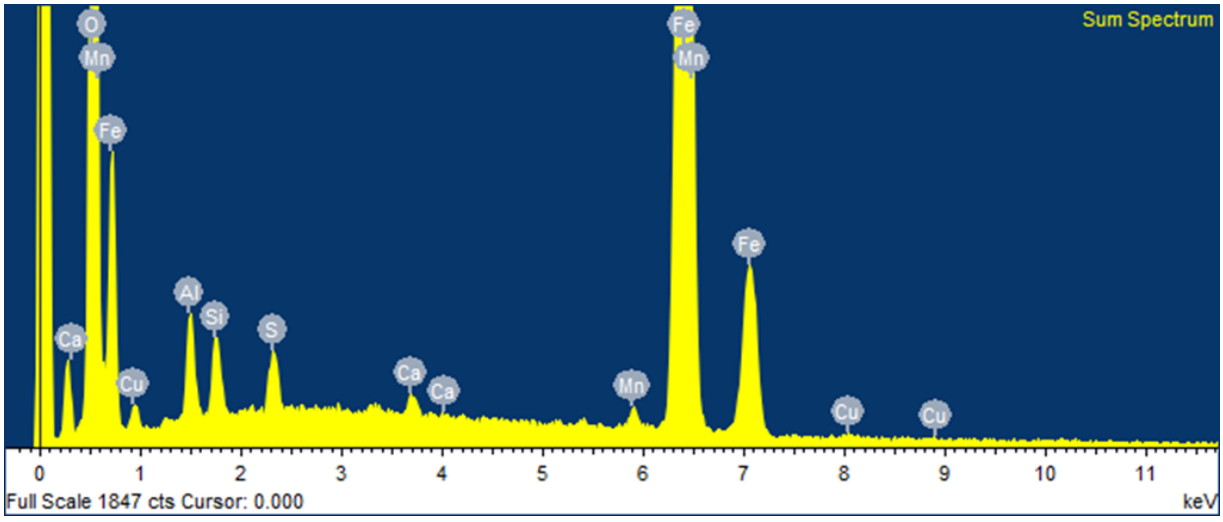
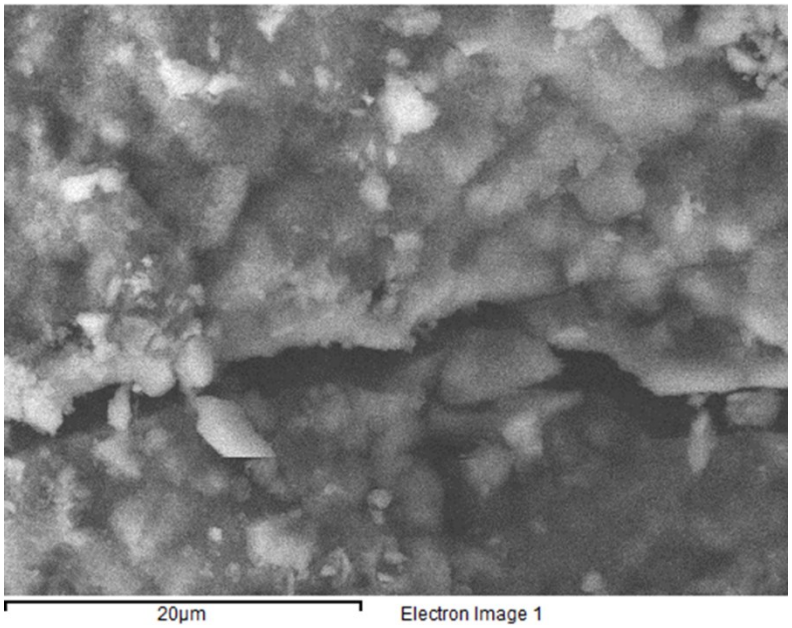


Figure A.646. SEM Image and EDS Spectrum of the Rust Collected from Interior Web of the Girder.

Element	Weight%	Atomic%
O K	31.16	59.90
Al K	1.89	2.16
Si K	1.27	1.39
S K	0.81	0.77
Ca K	0.35	0.27
Mn K	0.56	0.31
Fe K	63.58	35.01
Cu K	0.37	0.18
Totals	100.00	



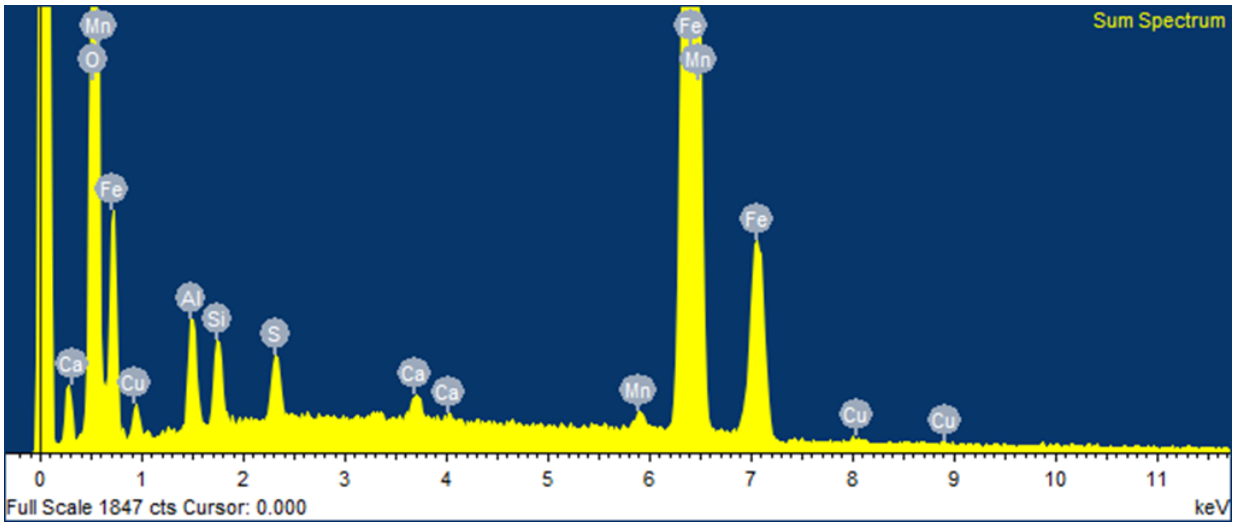


Figure A.647. SEM Image and EDS Spectrum of the Rust Collected from Interior Web of the Girder.

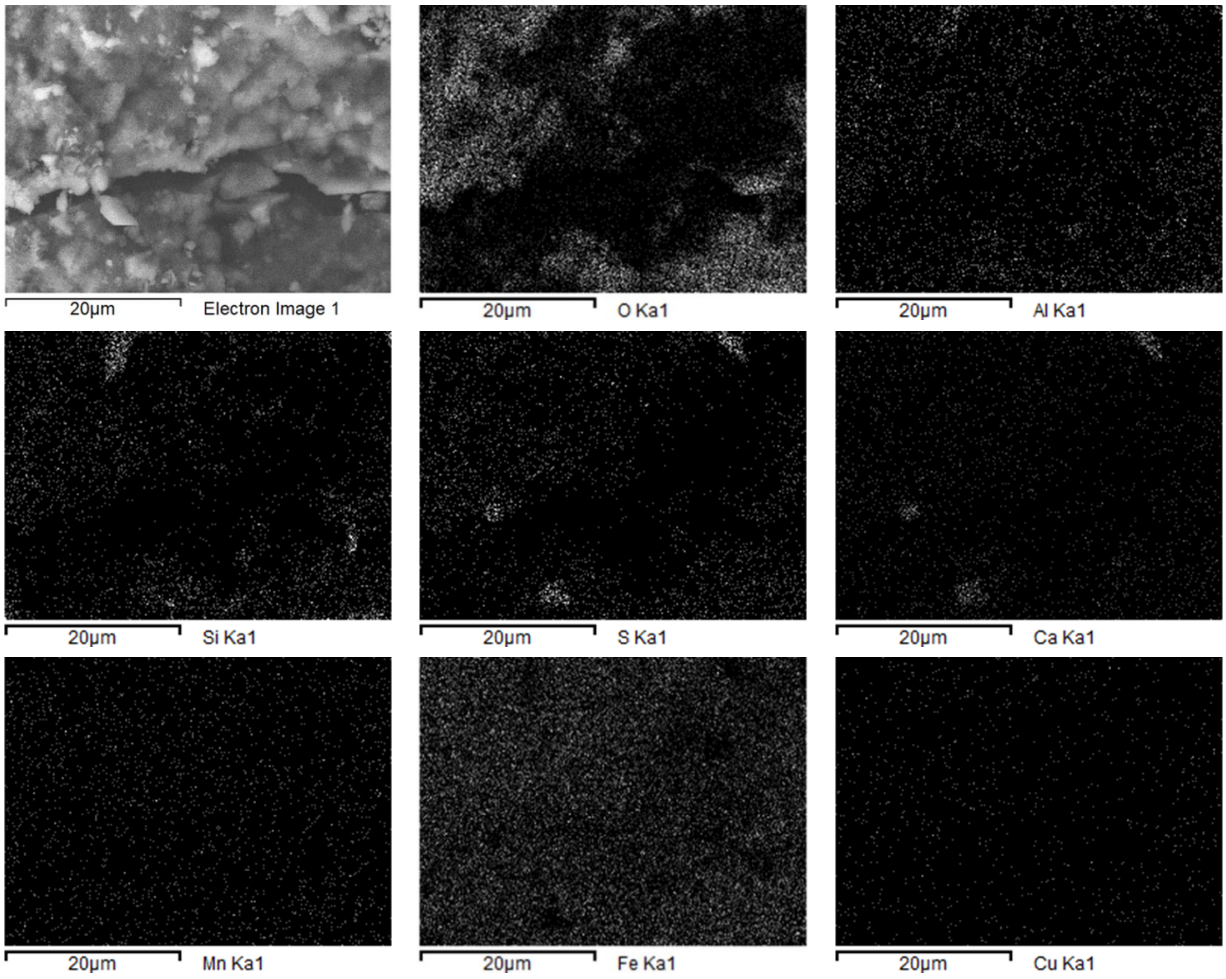


Figure A.648. EDS Elemental Mapping of Rust Collected from Interior Web.

A.37.5.XPS Result: Exterior Girder

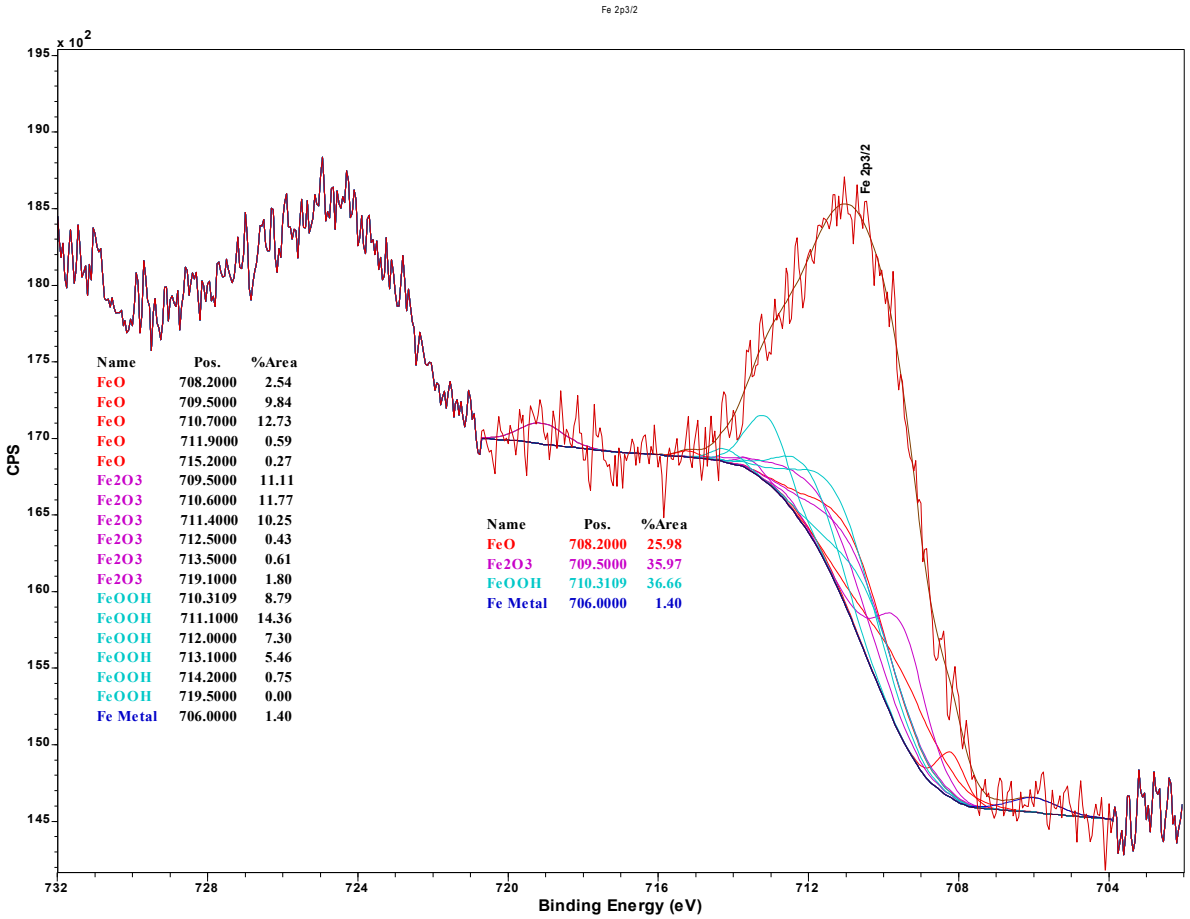


Figure A.649. XPS Spectrum of the Rust Collected from Exterior Web of the Girder.

A.37.6.XPS Result: Interior Girder

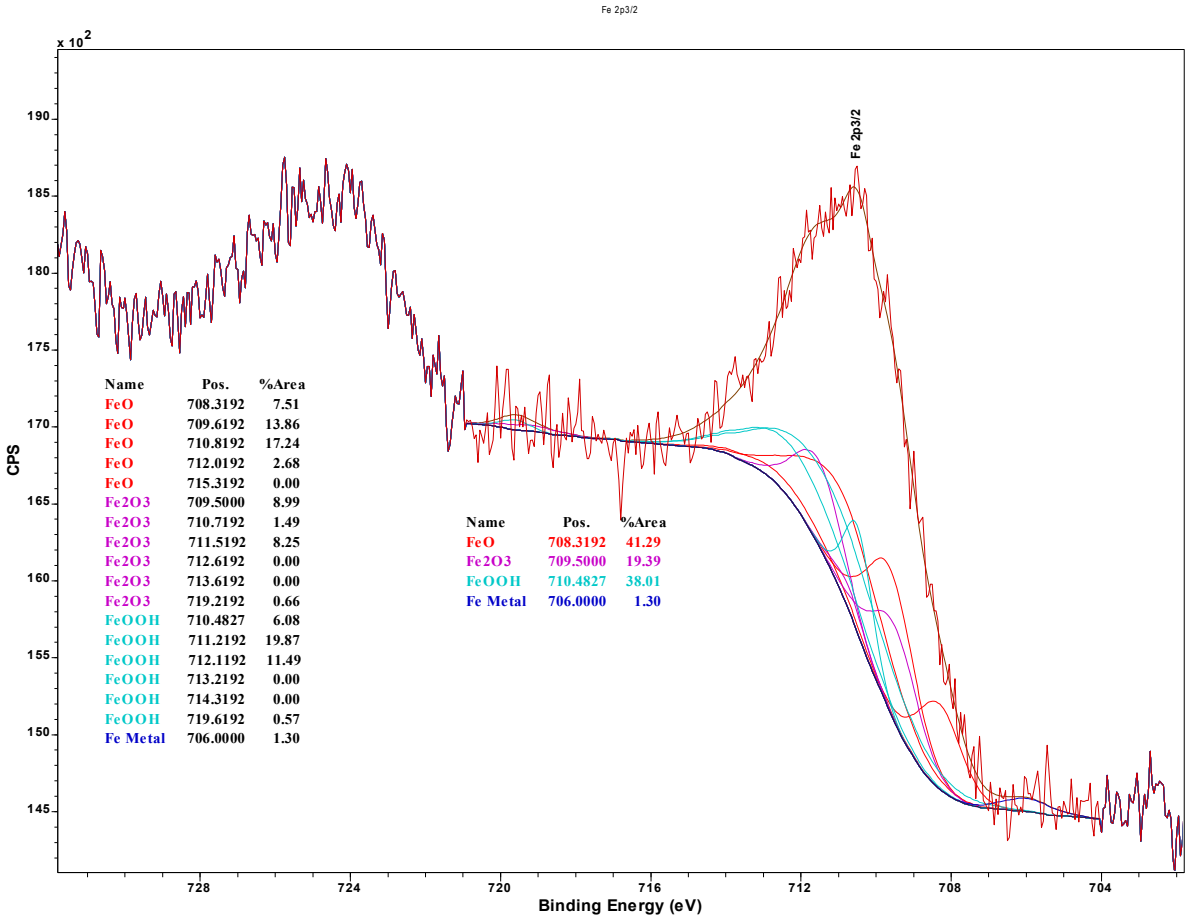


Figure A.650. XPS Spectrum of the Rust Collected from Interior Web of the Girder.

A.37.7.XRD Result: Exterior and Interior Girder

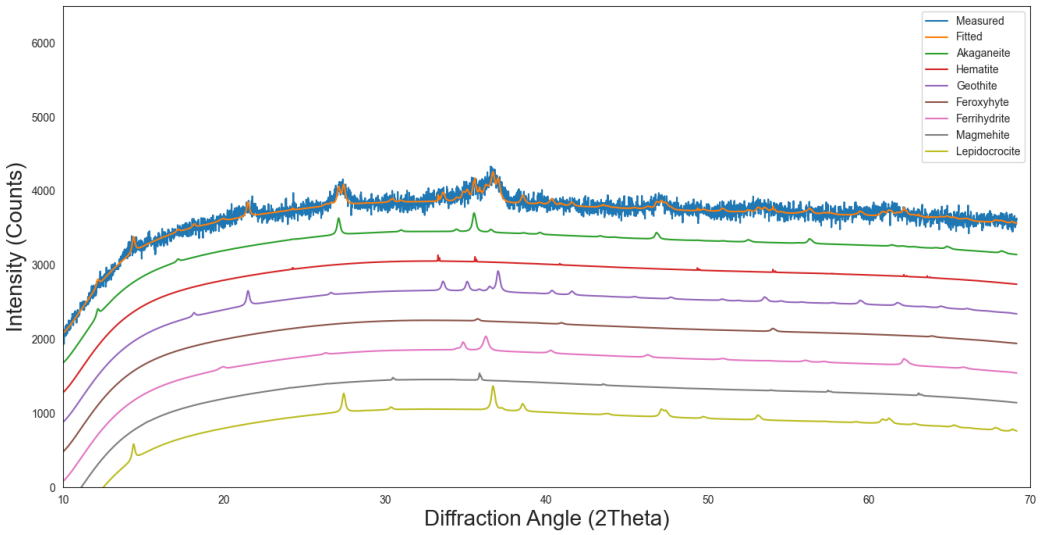


Figure A.651. XRD Pattern of Powdered Rust Collected from Exterior Web of the Girder.

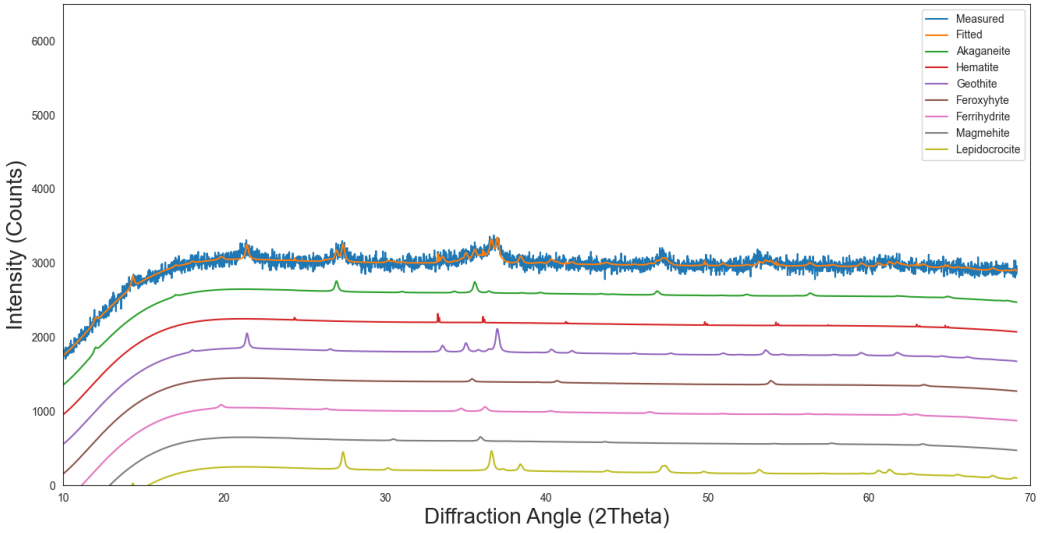


Figure A.652. XRD Pattern of Powdered Rust Collected from Interior Web of the Girder.

A.37.8. Particle Size Analysis: Tape Adhesion Results

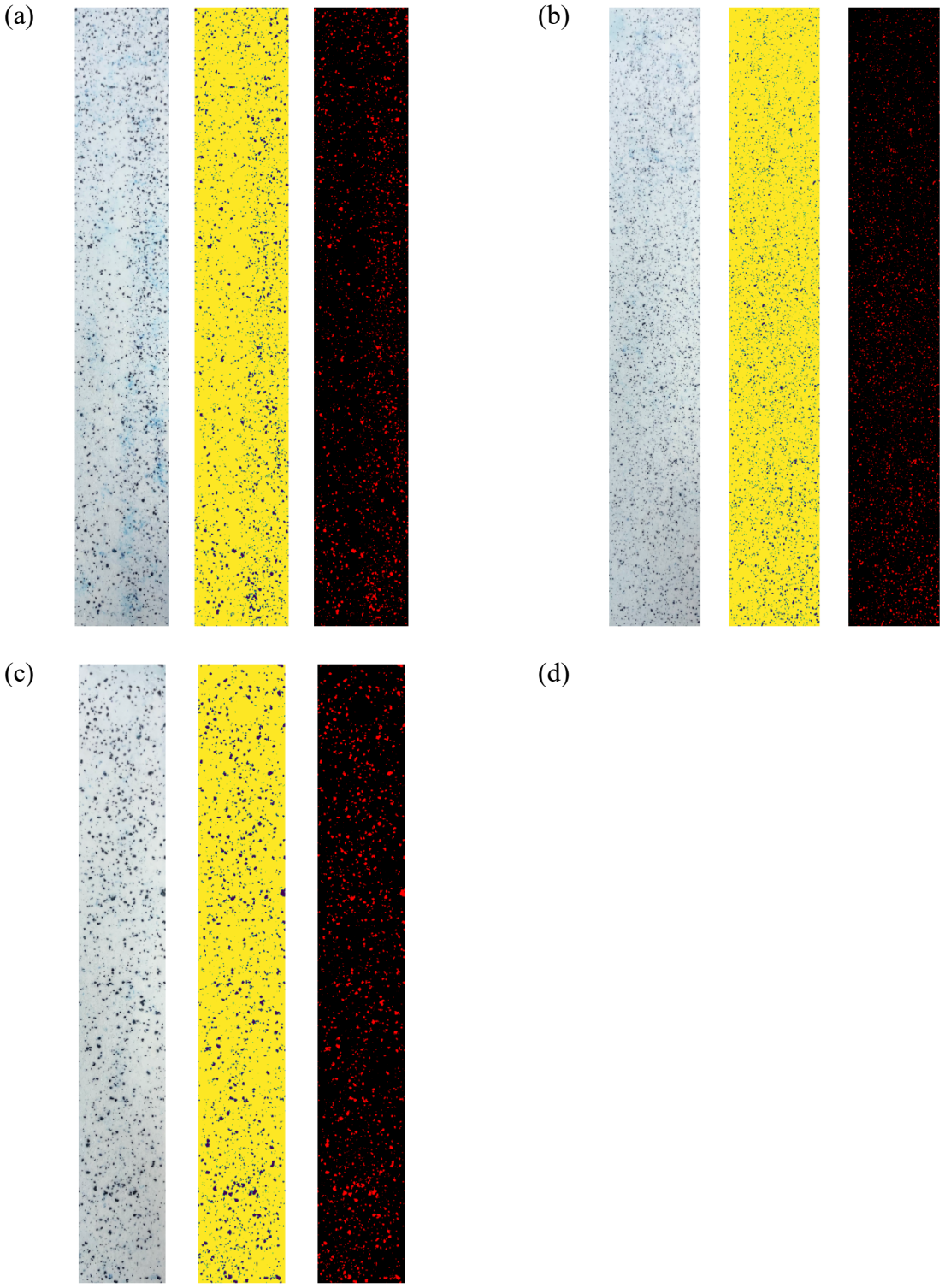


Figure A.653. Particle Size Analysis Results at B5G1F1 (a) Top Flange Bottom, (b) Web, (c) Bottom Flange Bottom (d) Stiffener.

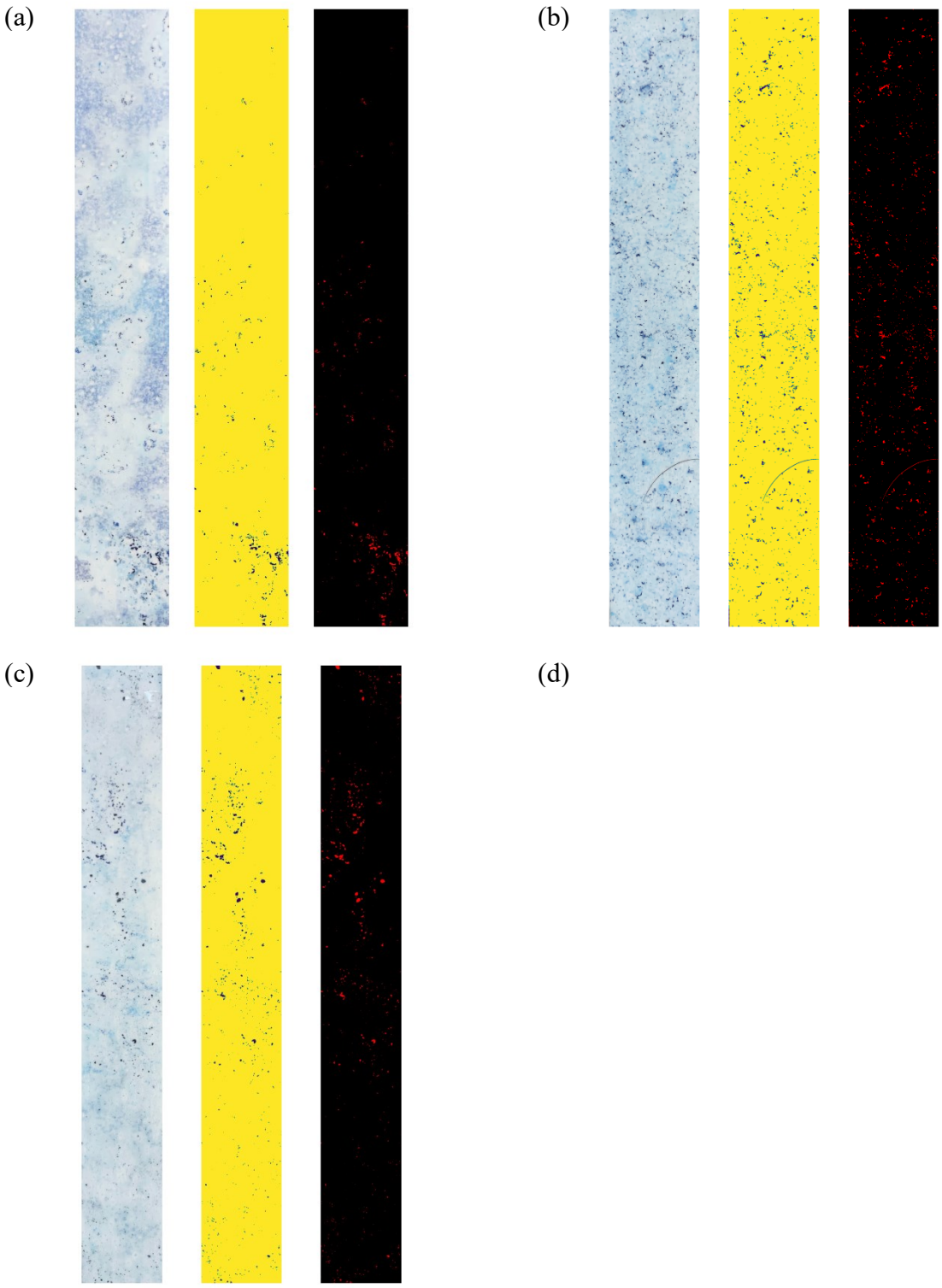


Figure A.654. Particle Size Analysis Results at B5G2F1 (a) Top Flange Bottom, (b) Web, (c) Bottom Flange Bottom (d) Stiffener.

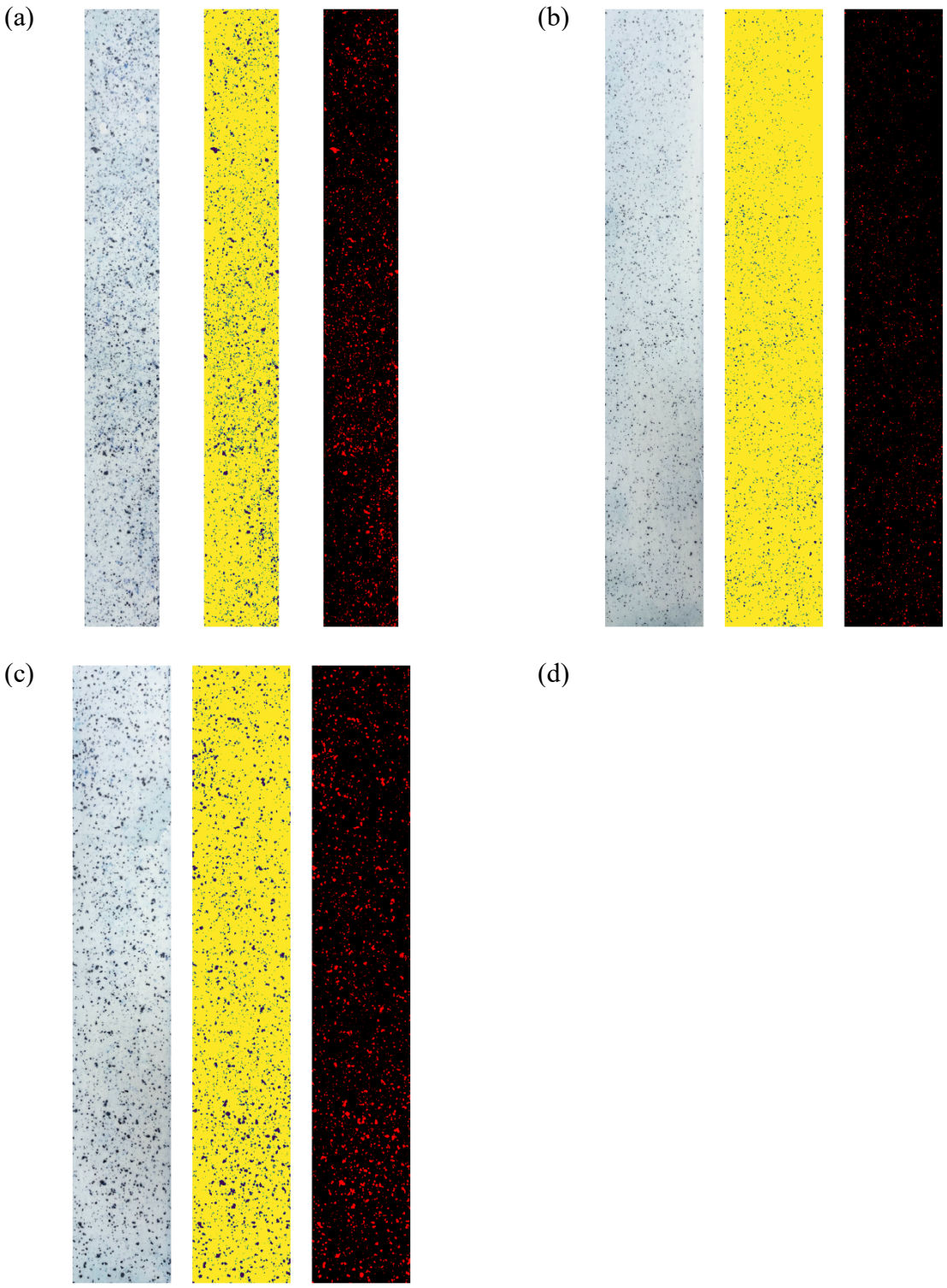


Figure A.655. Particle Size Analysis Results at B5G4F2 (a) Top Flange Bottom, (b) Web, (c) Bottom Flange Bottom (d) Stiffener.

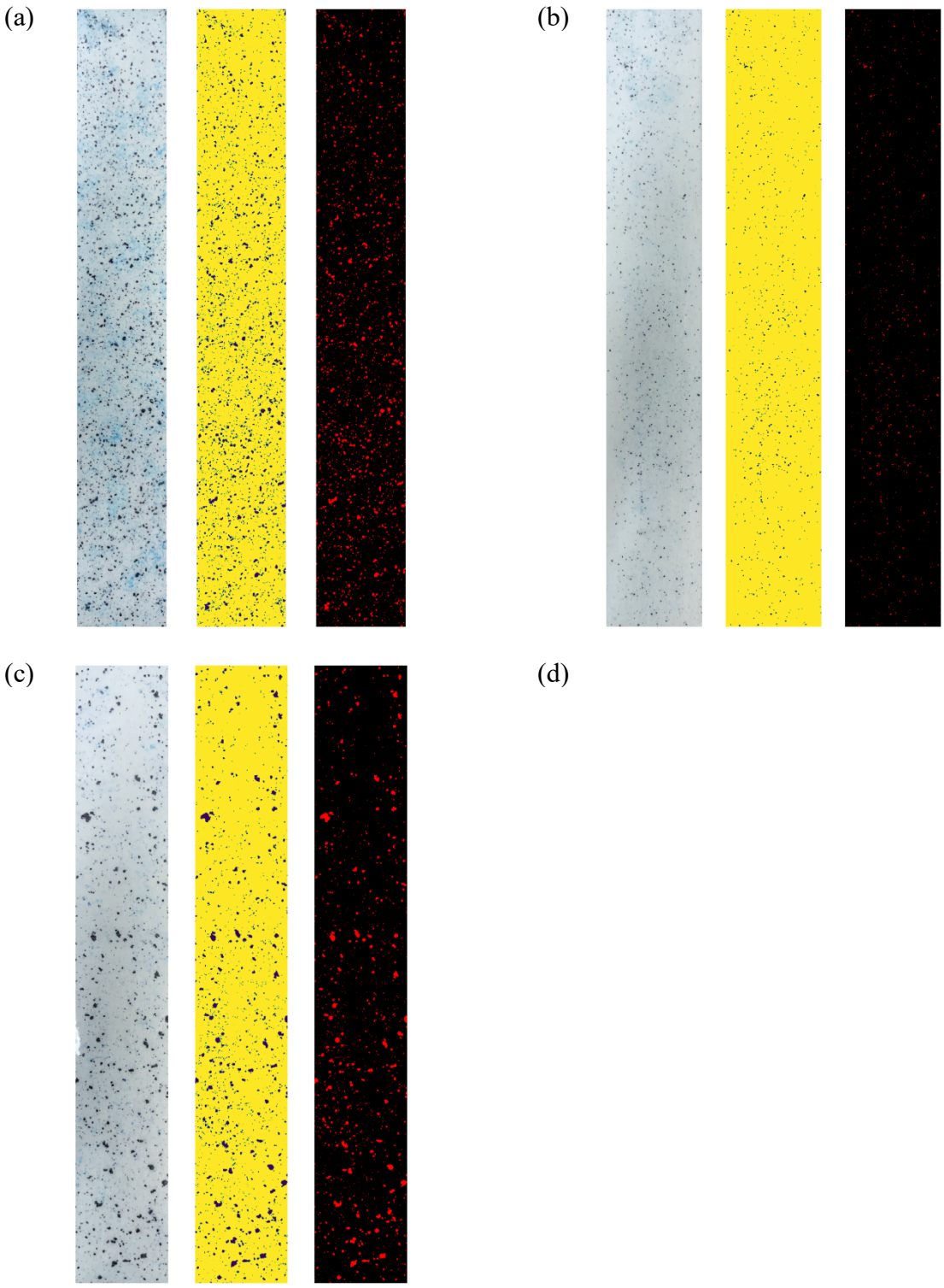
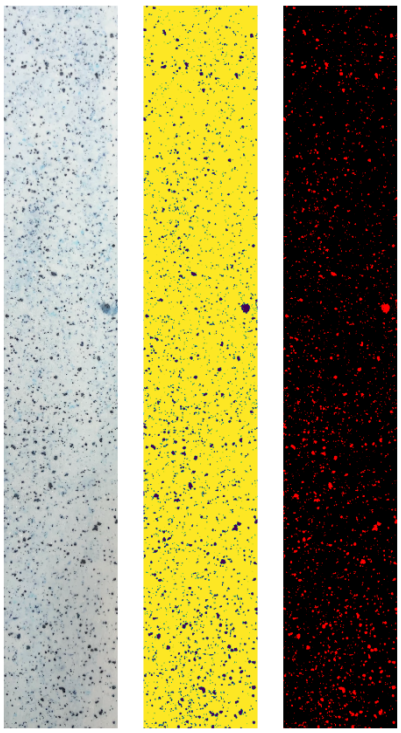


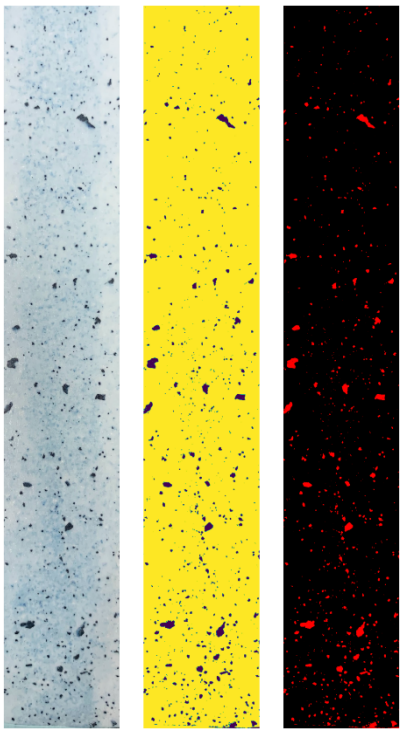
Figure A.656. Particle Size Analysis Results at B6G1F1 (a) Top Flange Bottom, (b) Web, (c) Bottom Flange Bottom (d) Stiffener.

(a)

(b)



(c)



(d)

Figure A.657. Particle Size Analysis Results at B6G2F1 (a) Top Flange Bottom, (b) Web, (c) Bottom Flange Bottom (d) Stiffener.

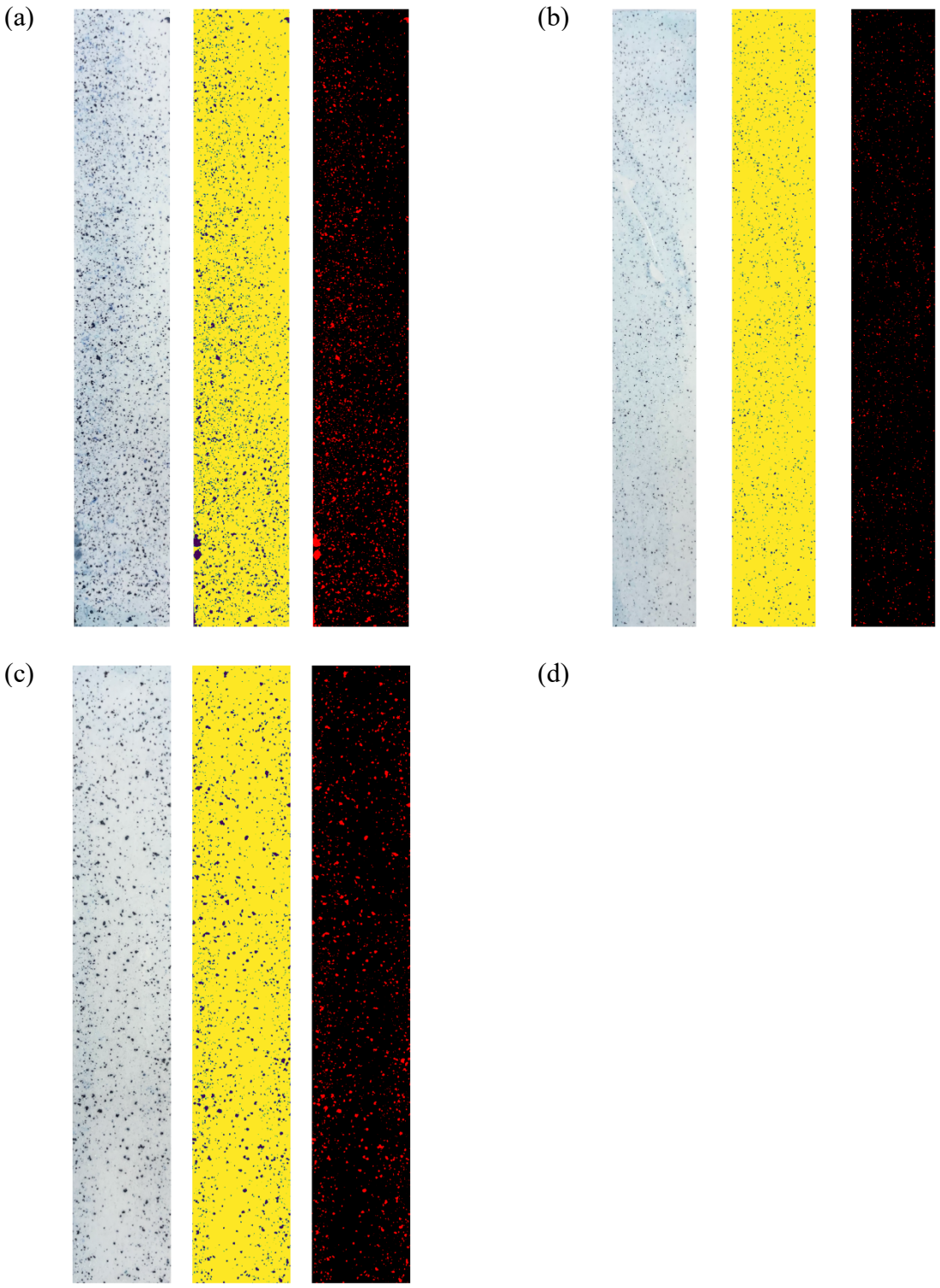


Figure A.658. Particle Size Analysis Results at B6G4F2 (a) Top Flange Bottom, (b) Web, (c) Bottom Flange Bottom (d) Stiffener.

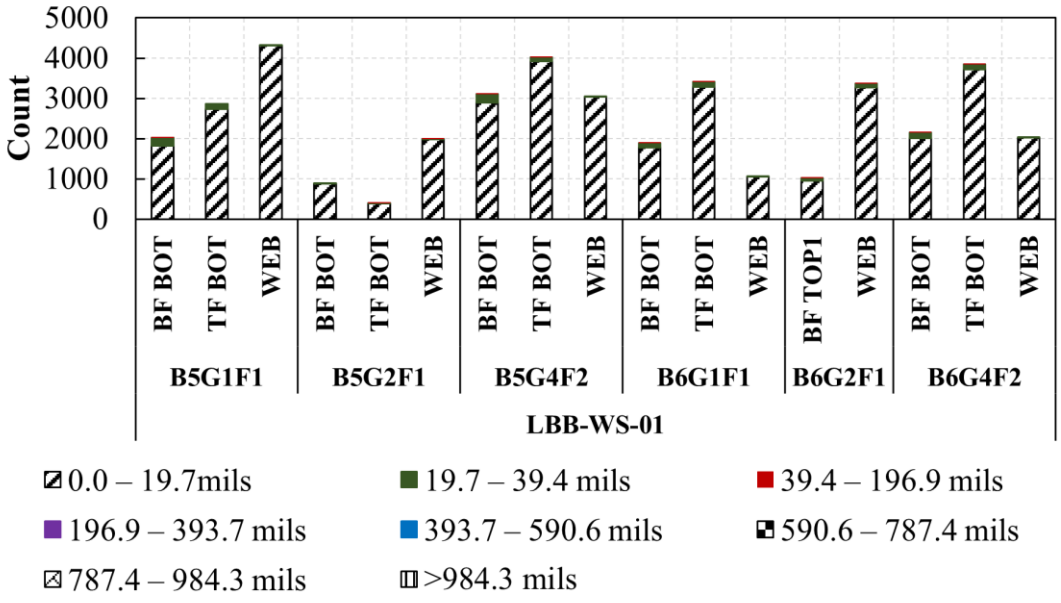


Figure A.659. Particle Size Analysis Showing Different Locations Examined.

A.38. LBB-WS-02

- 4TH EAST RAMP
- Bridge ID 51520038001038, Coordinates (33.5919511, -101.8783759), Lubbock County
- Continuous weathering plate girder
- Built 2009
- Girder inspection carried on bent 6 and bent 5, and measurements are taken on girder within four feet from the abutment or bent.
- No visual inspection on deck
- Location for Testing: B5-G1F1, B5-G4F2, B5-G2F1, B5-G1F1, B6-G1F1, B6-G2F1, B6-G4F2



Figure A.660. Typical Picture of LBB-WS-02

A.38.1. Observed Condition

Uniform patina are visible on the bottom face of the top flange with a rating of 8. The web has a uniform patina formation with a patina rating of 8. For the interior girders, the patina rating ranges between 8 and 7 showing that a protective adhesive patina is formed on the girders surface. Overall, the bridge is in good condition.

A.38.2.Field Inspection Results

Table A-168. Field Inspection Results for LBB-WS-02.

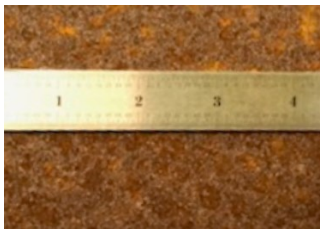
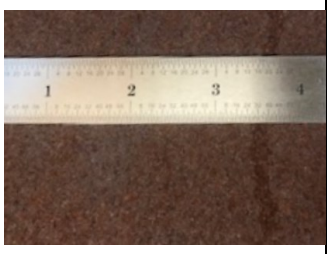
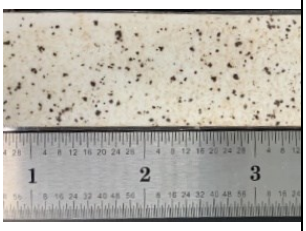
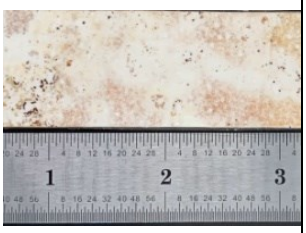
Location	Patina Rating	Thickness (inch)	Cl^- Conc. (ppm)	Field Condition	Tape Test
B5-G1F1 TF Bot. Ext.	8	Measured 1.252 Design 1.250			
B5-G1F1 Web Ext.	8	Measured 0.552 Design 0.500	6		
B5-G1F1 BF Top Ext.	7	Measured - Design 1.250			
B5-G1F1 BF Bot. Ext.	7	Measured - Design			
B5-G2F1 TF Bot. Int.	6	Measured 1.249 Design 1.250			

Table A-169. Field Inspection Results for LBB-WS-02.

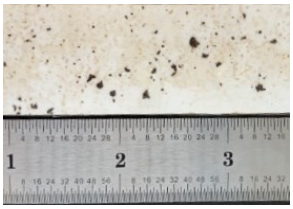
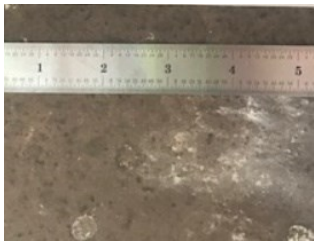
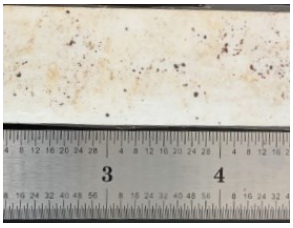
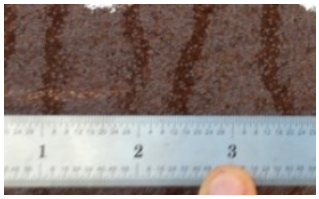
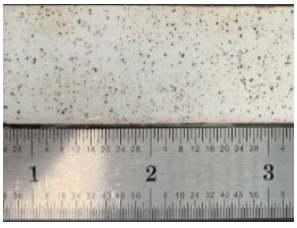
Location	Patina Rating	Thickness (inch)	Cl^- Conc. (ppm)	Field Condition	Tape Test
B5-G2F1 Web Int.	8	Measured 0.493 Design 0.500	1		
B5-G2F1 BF Top Int.	7	Measured 1.265 Design 1.250			
B5-G2F1 BF Bot. Int.	7	Measured - Design			
B5-G4F2 TF Bot. Ext.	8	Measured 1.250 Design 1.250			
B5-G4F2 Web Ext.	8	Measured 0.507 Design 0.500	1		

Table A-170. Field Inspection Results for LBB-WS-02.

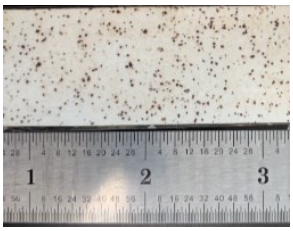
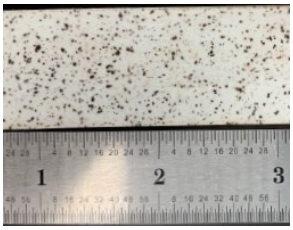
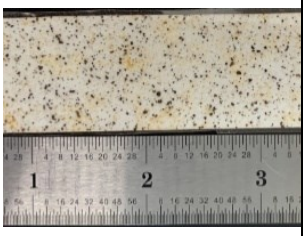
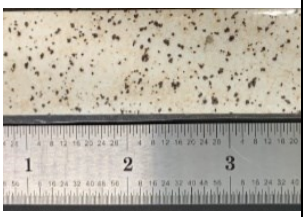
Location	Patina Rating	Thickness (inch)	Cl^- Conc. (ppm)	Field Condition	Tape Test
B5-G4F2 BF Top Ext.	7	Measured 1.259 Design 1.250			
B5-G4F2 BF Bot. Ext.	7	Measured - Design			
B6-G1F1 TF Bot. Ext.	7	Measured 1.237 Design 1.250			
B6-G1F1 Web Ext.	8	Measured 0.495 Design 0.500	2		
B6-G1F1 BF Top Ext.	7	Measured 1.264 Design 1.250			

Table A-171.Field Inspection Results for LBB-WS-02.

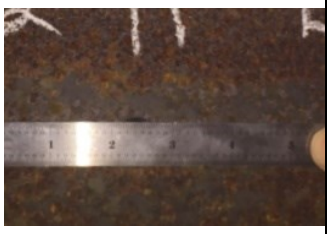
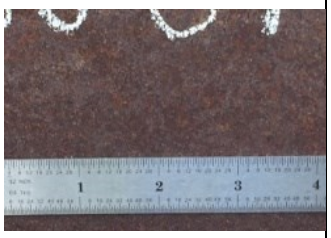
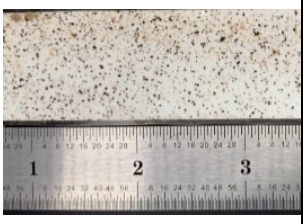
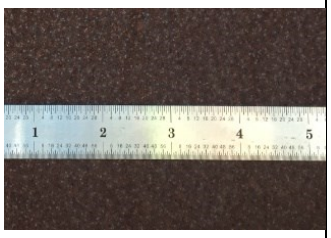
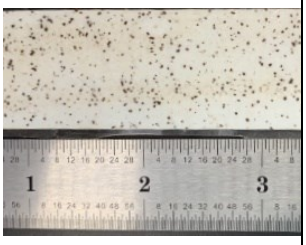
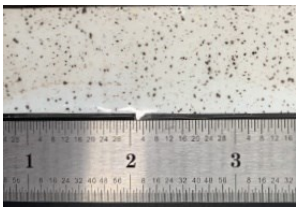
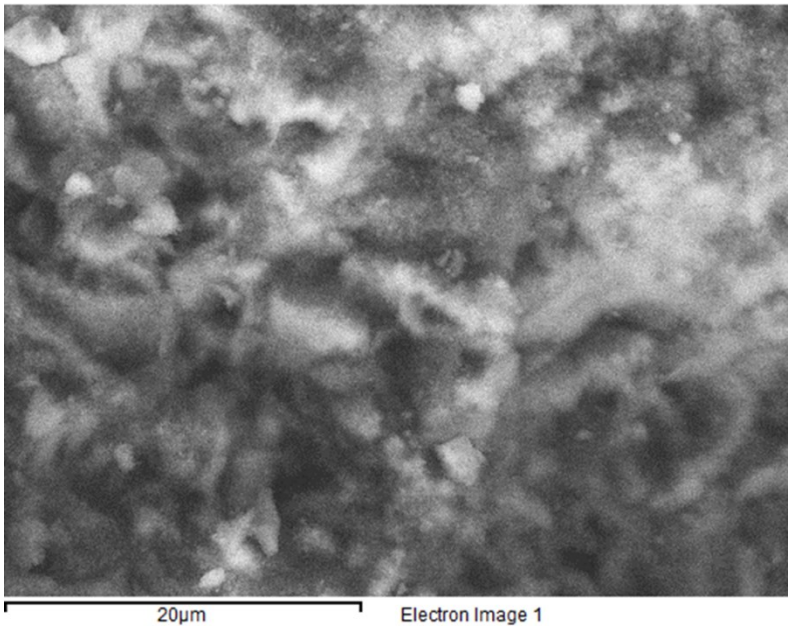
Location	Patina Rating	Thickness (inch)	Cl^- Conc. (ppm)	Field Condition	Tape Test
B6-G1F1 BF Bot. Ext.	7	Measured - Design			
B6-G2F1 TF Bot. Int.	5	Measured 1.258 Design 1.250			
B6-G2F1 Web Int.	8	Measured 0.494 Design 0.500			
B6-G2F1 BF Top Int.	7	Measured 1.256 Design 1.250			
B6-G2F1 BF Bot. Int.	6	Measured - Design			

Table A-172. Field Inspection Results for LBB-WS-02.

Location	Patina Rating	Thickness (inch)	Cl^- Conc. (ppm)	Field Condition	Tape Test
B6-G4F2 TF Bot. Ext.	8	Measured 1.251 Design 1.250			
B6-G4F2 Web Ext.	8	Measured 0.497 Design 0.500			
B6-G4F2 BF Top Ext.	7	Measured 1.252 Design 1.250			
B6-G4F2 BF Bot. Ext.	8	Measured - Design			

A.38.3.SEM/EDS Results: Exterior Web Girder

Element	Weight %	Atomic %
O K	31.92	61.30
Al K	0.84	0.96
Si K	0.97	1.06
S K	0.45	0.43
Ca K	0.17	0.13
Mn K	1.34	0.75
Fe K	63.87	35.13
Ni K	0.43	0.23
Totals	100.00	



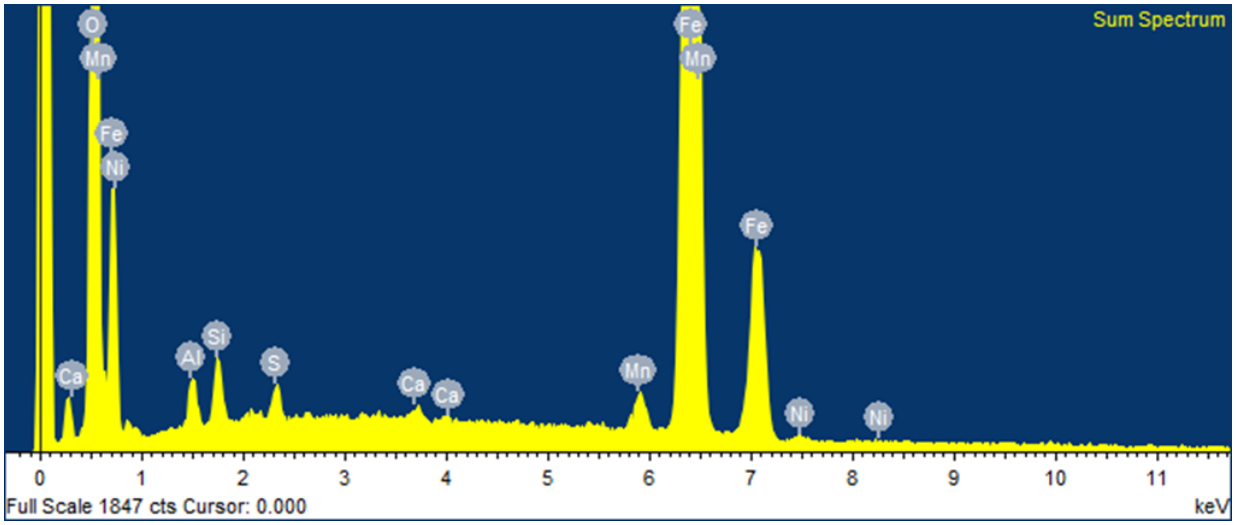


Figure A.661. SEM Image and EDS Spectrum of the Rust Collected from Exterior Web of the Girder.

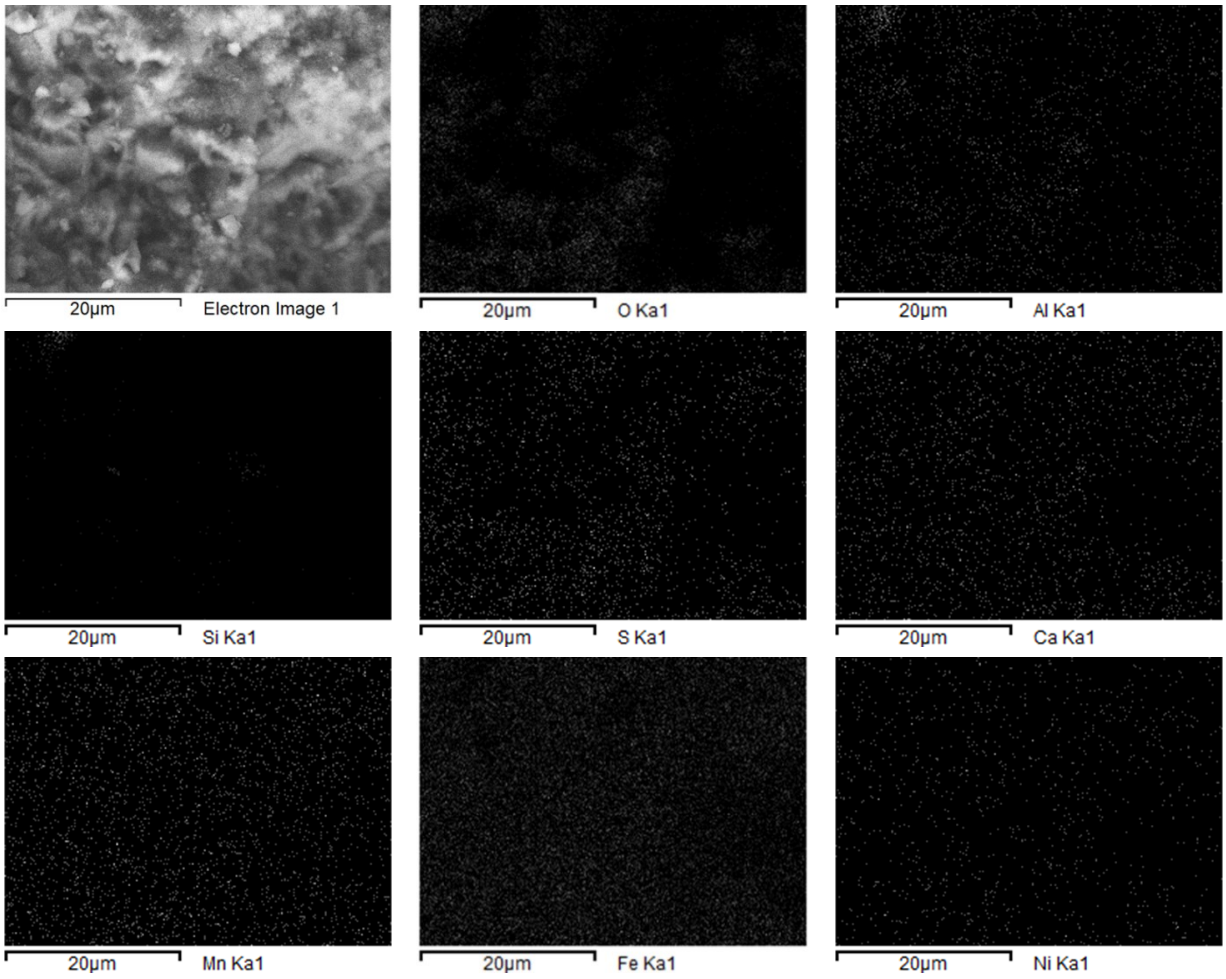
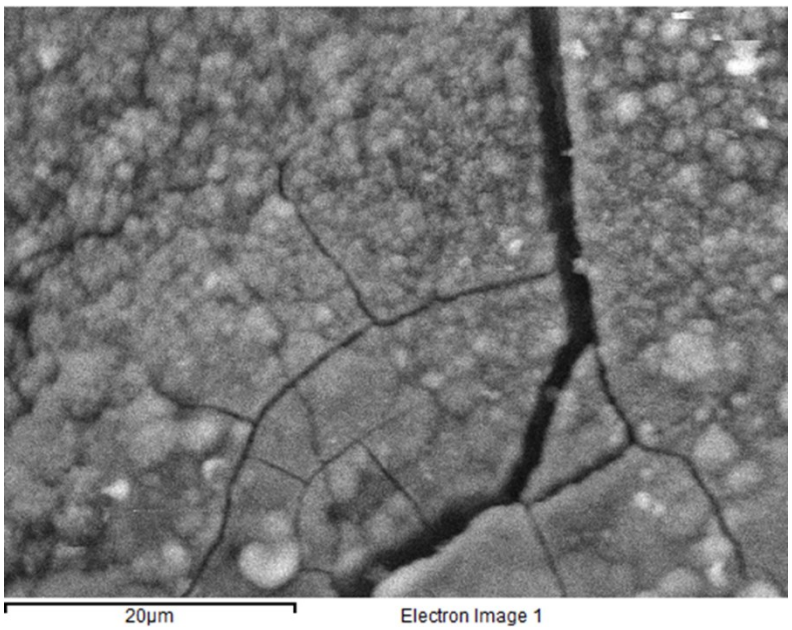


Figure A.662. EDS Elemental Mapping of Rust Collected from Exterior Web.

Element	Weight %	Atomic %
O K	54.96	80.07
Al K	0.45	0.39
Si K	0.16	0.13
S K	2.34	1.70
Cl K	0.63	0.41
Mn K	0.65	0.27
Fe K	40.70	16.99
Cu K	0.12	0.04
Totals	100.00	



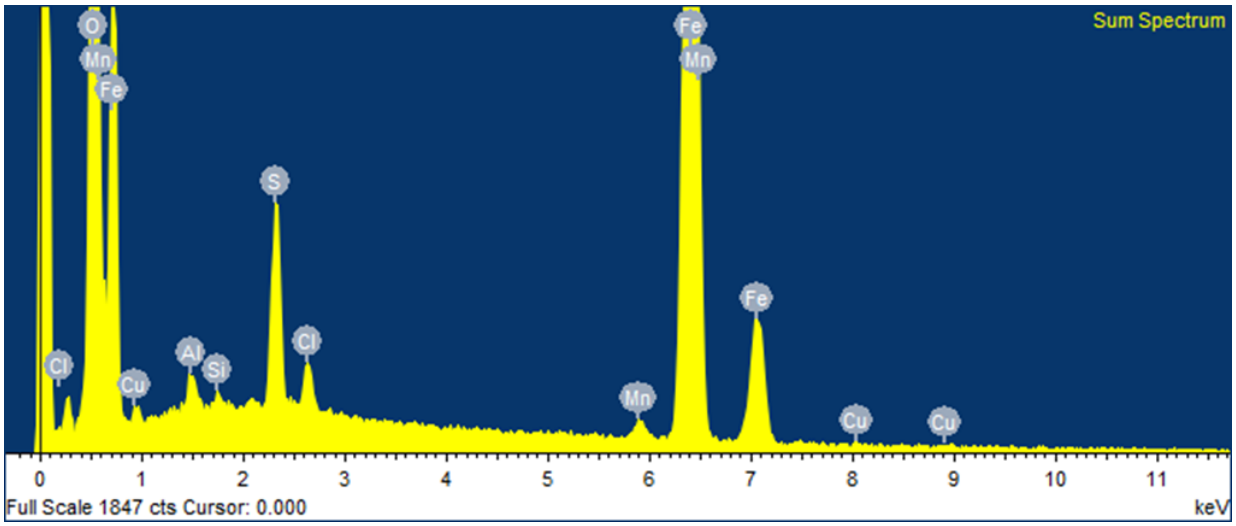


Figure A.663. SEM Image and EDS Spectrum of the Rust Collected from Exterior Web of the Girder.

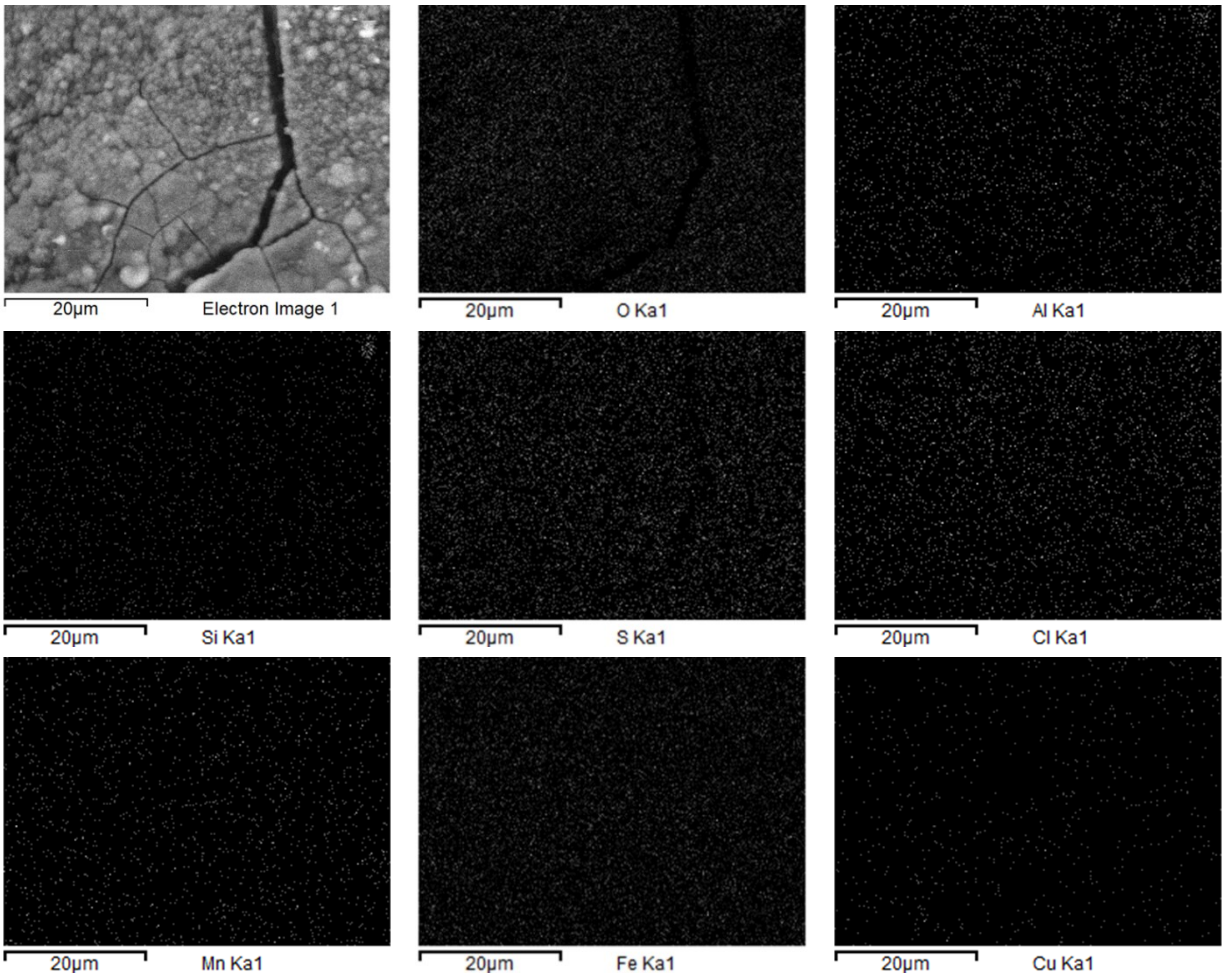
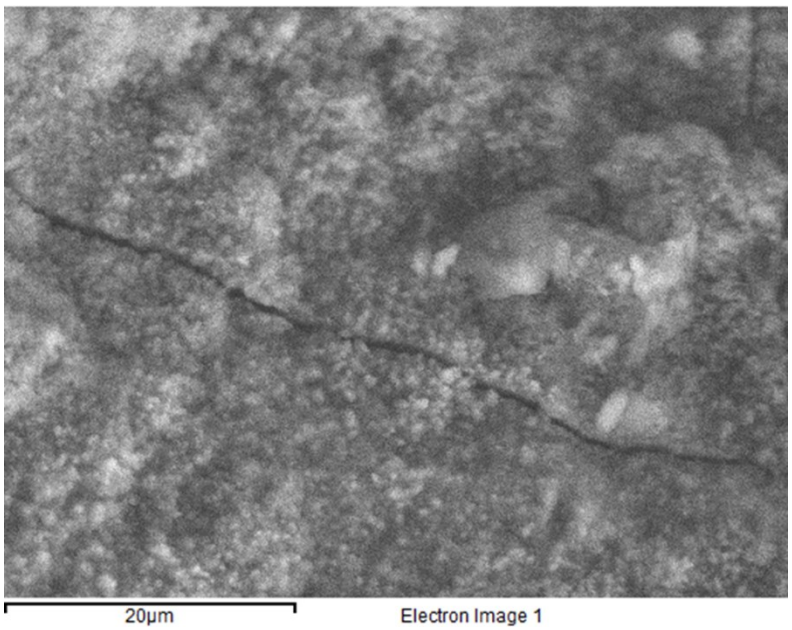


Figure A.664. EDS Elemental Mapping of Rust Collected from Exterior Web.

Element	Weight %	Atomic %
O K	43.98	72.63
Al K	0.85	0.83
Si K	0.18	0.17
S K	0.71	0.59
Ca K	0.57	0.37
Mn K	1.29	0.62
Fe K	52.29	24.73
Cu K	0.14	0.06
Totals	100.00	



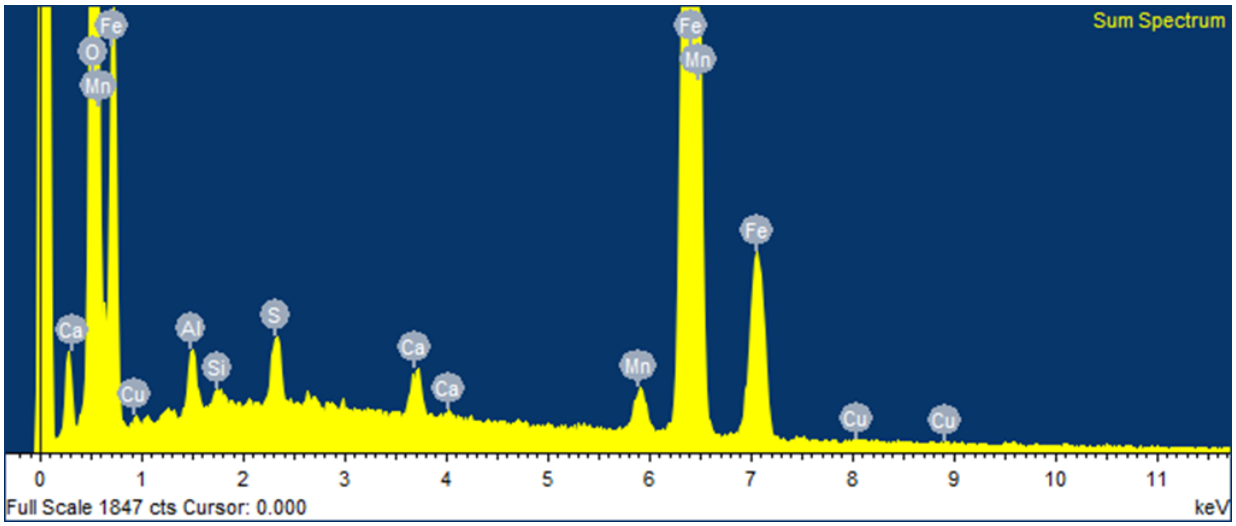


Figure A.665. SEM Image and EDS Spectrum of the Rust Collected from Exterior BF Bottom of the Girder.

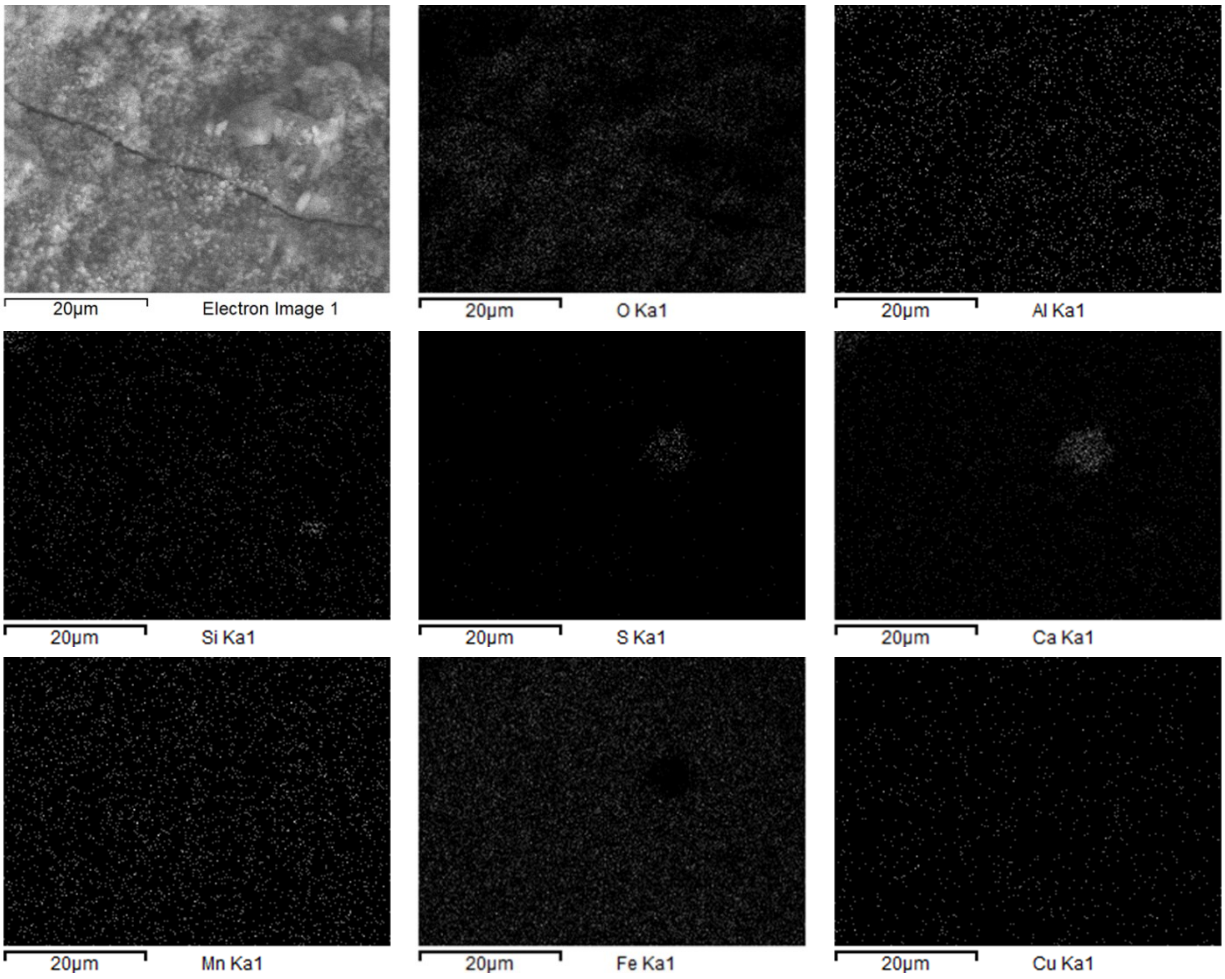
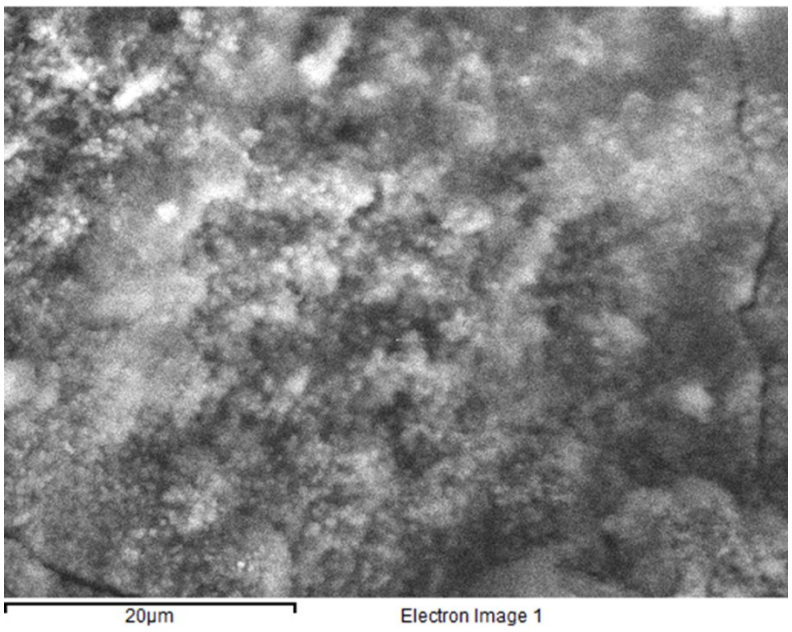


Figure A.666. EDS Elemental Mapping of Rust Collected from Exterior BF Bottom.

Element	Weight %	Atomic %
O K	37.85	67.12
Na K	0.28	0.35
Mg K	0.19	0.22
Al K	1.00	1.05
Si K	0.20	0.20
S K	0.62	0.55
Ca K	0.45	0.32
Mn K	1.37	0.71
Fe K	58.01	29.47
Cu K	0.03	0.01
Totals	100.00	



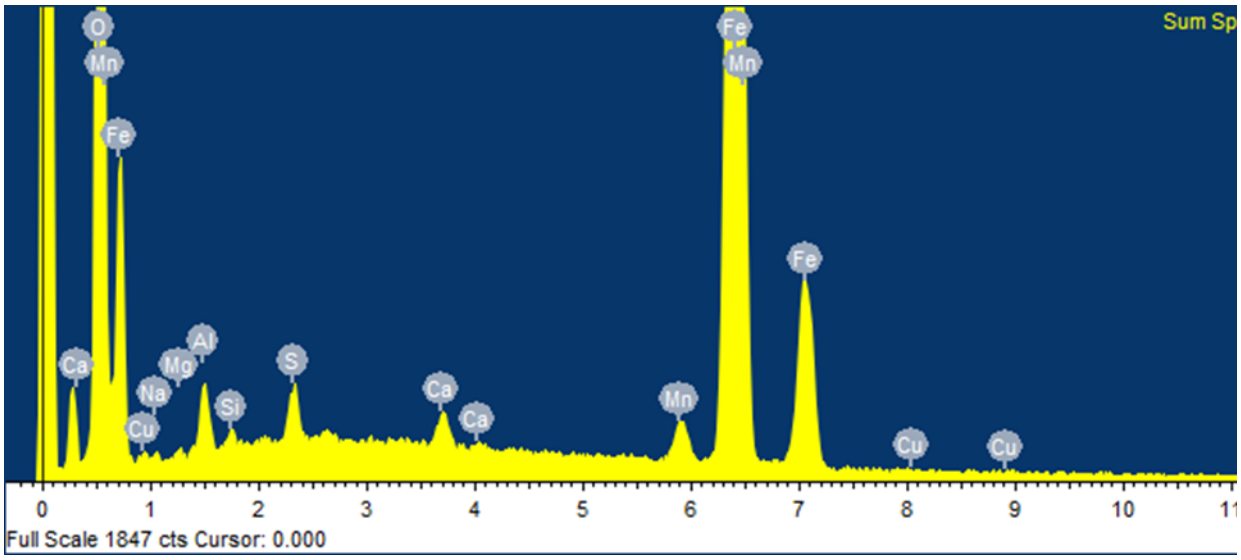


Figure A.667. SEM Image and EDS Spectrum of the Rust Collected from Exterior BF Bottom of the Girder.

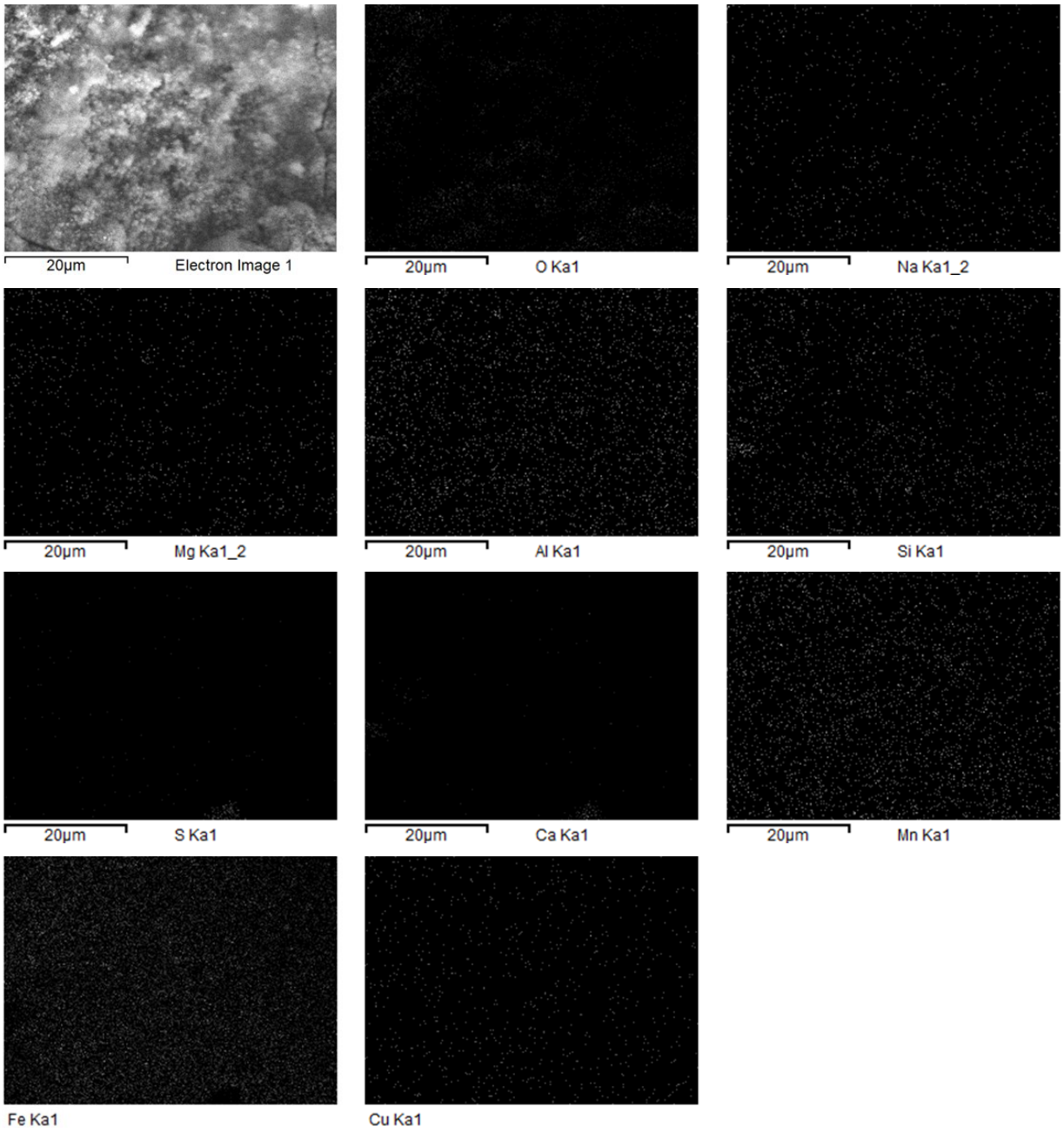
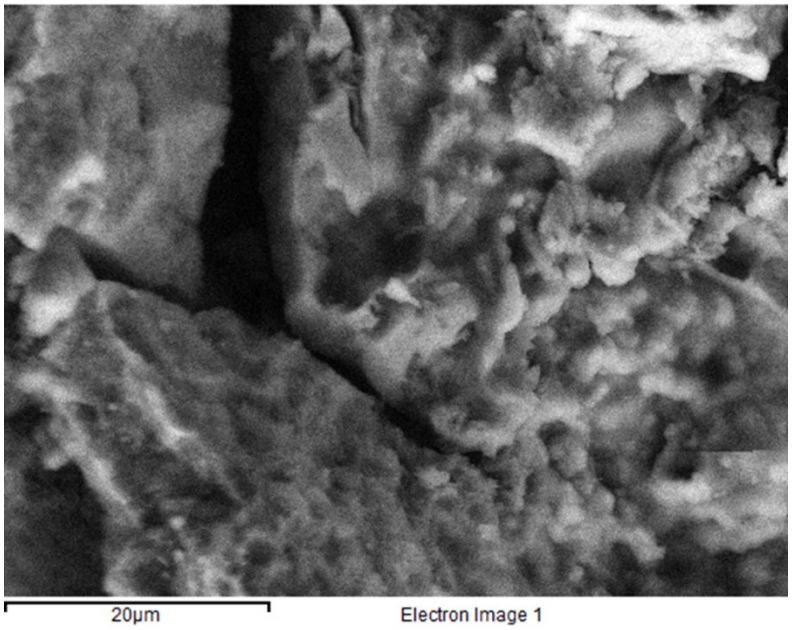


Figure A.668. EDS Elemental Mapping of Rust Collected from Exterior BF Bottom.

A.38.4.SEM/EDS Results: Interior Web Girder

Element	Weight %	Atomic %
O K	32.86	62.15
Al K	0.71	0.79
Si K	0.34	0.37
S K	1.52	1.44
Cl K	0.49	0.42
Ca K	0.62	0.47
Cr K	0.42	0.24
Mn K	0.98	0.54
Fe K	61.08	33.09
Ni K	0.61	0.32
Cu K	0.37	0.18
Totals	100.00	



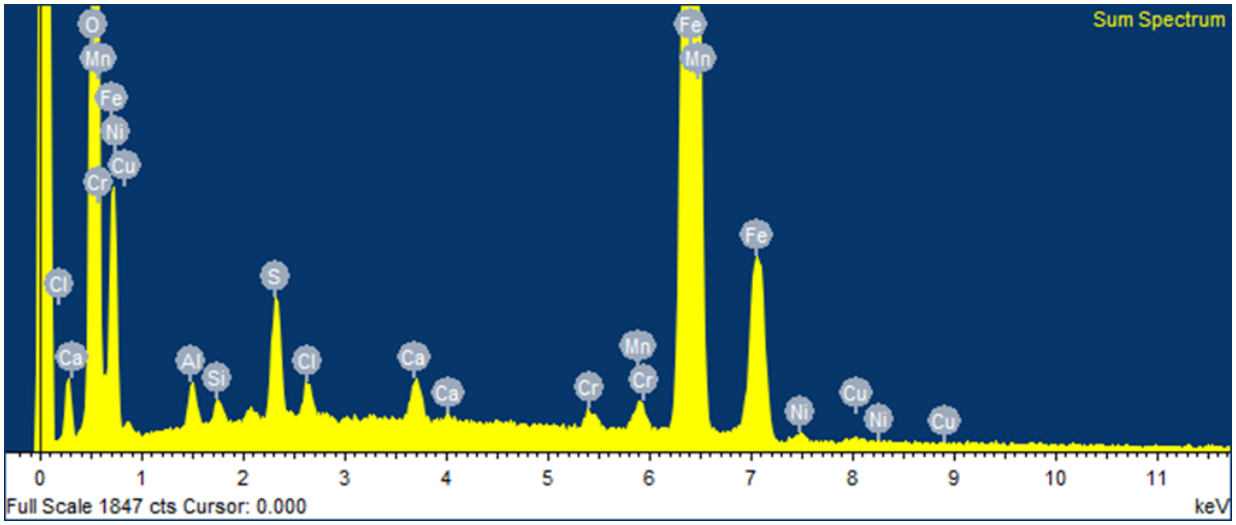


Figure A.669. SEM Image and EDS Spectrum of the Rust Collected from Interior Web of the Girder.

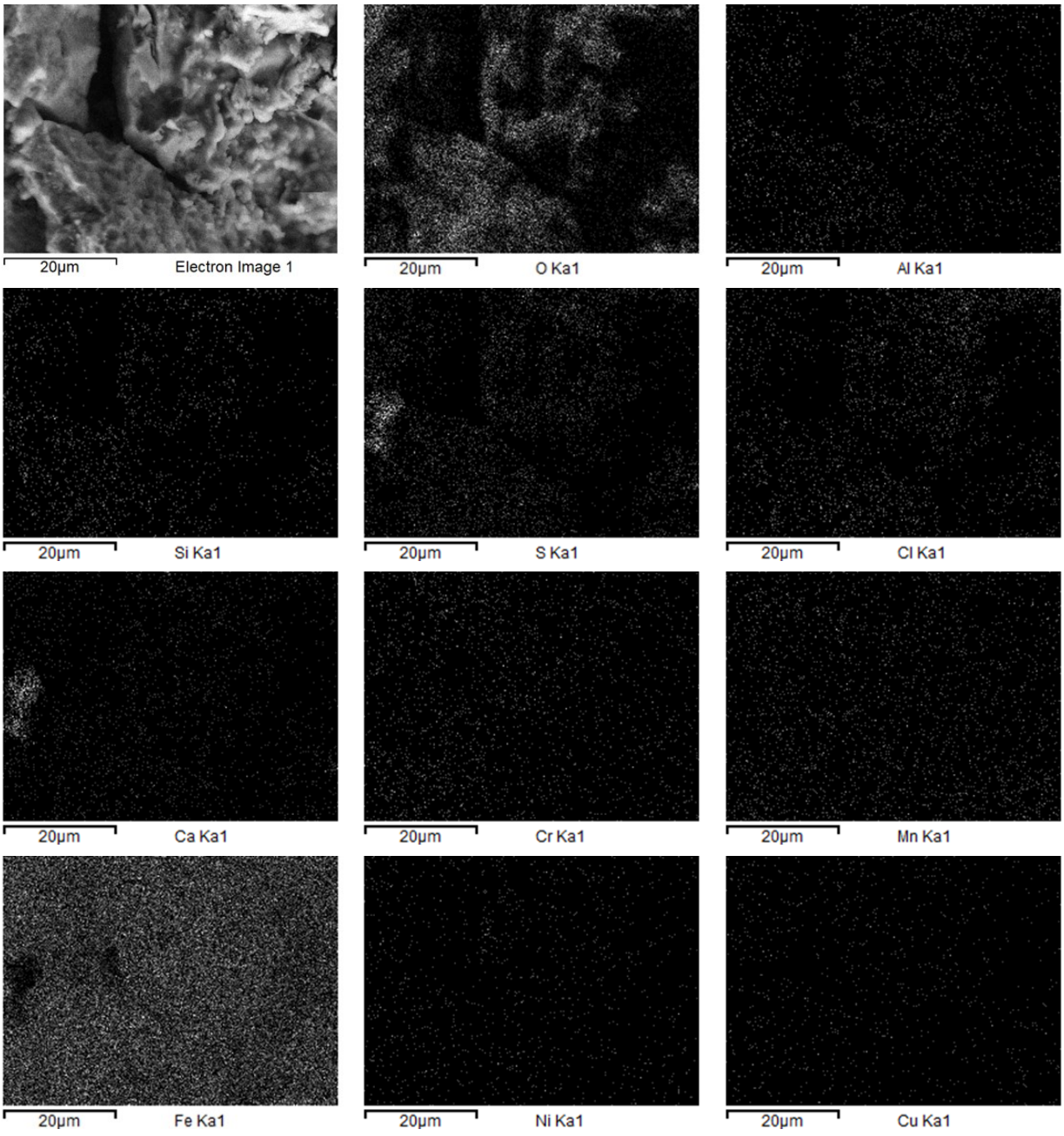
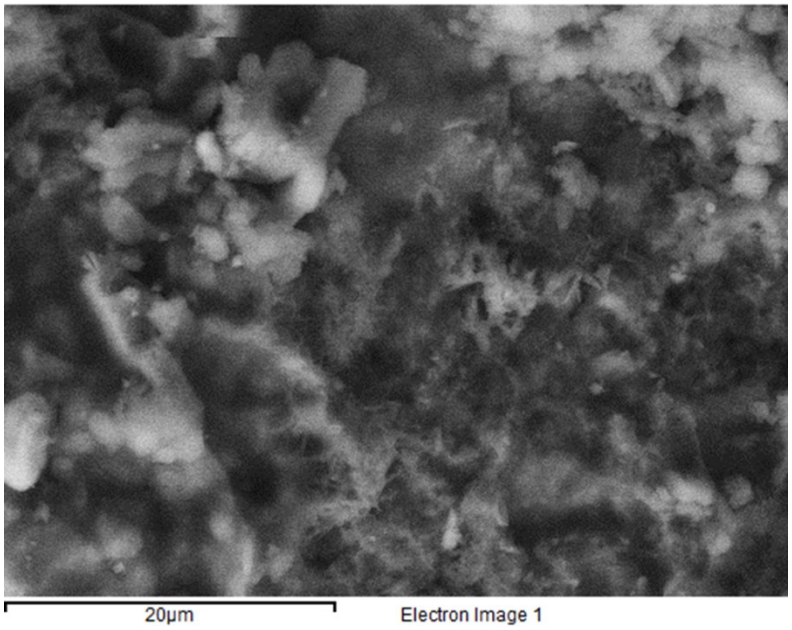


Figure A.670. EDS Elemental Mapping of Rust Collected from Interior Web.

A.38.5.SEM/EDS Results: Interior Web Girder

Element	Weight %	Atomic %
O K	34.44	62.95
Al K	0.87	0.94
Si K	0.91	0.95
S K	3.06	2.79
Ca K	2.88	2.10
Cr K	0.73	0.41
Mn K	0.93	0.49
Fe K	54.73	28.66
Ni K	0.65	0.32
Cu K	0.81	0.37
Totals	100.00	



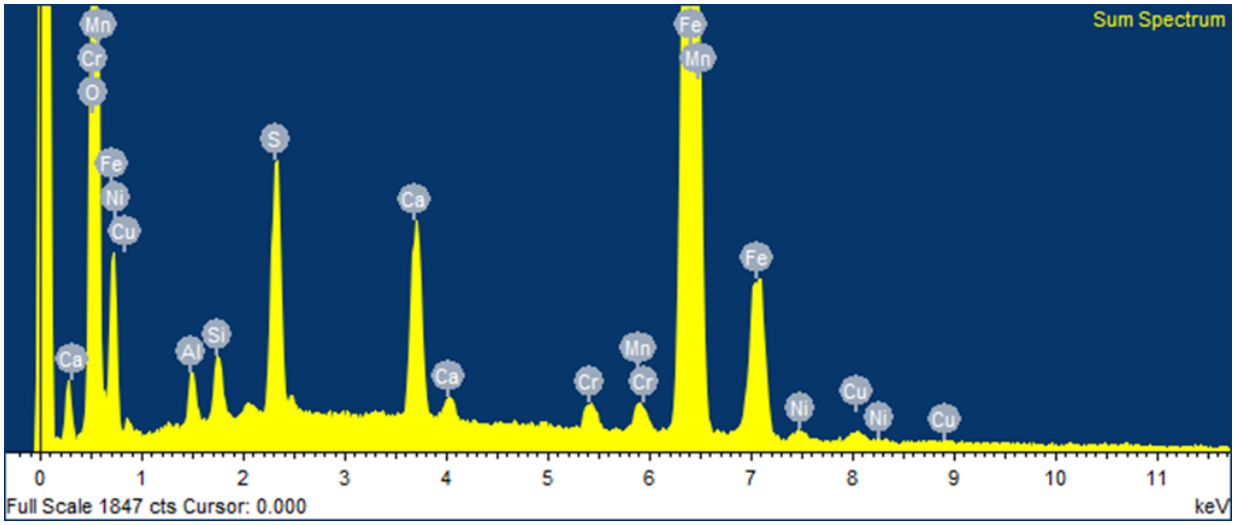


Figure A.671. SEM Image and EDS Spectrum of the Rust Collected from Interior Web of the Girder.

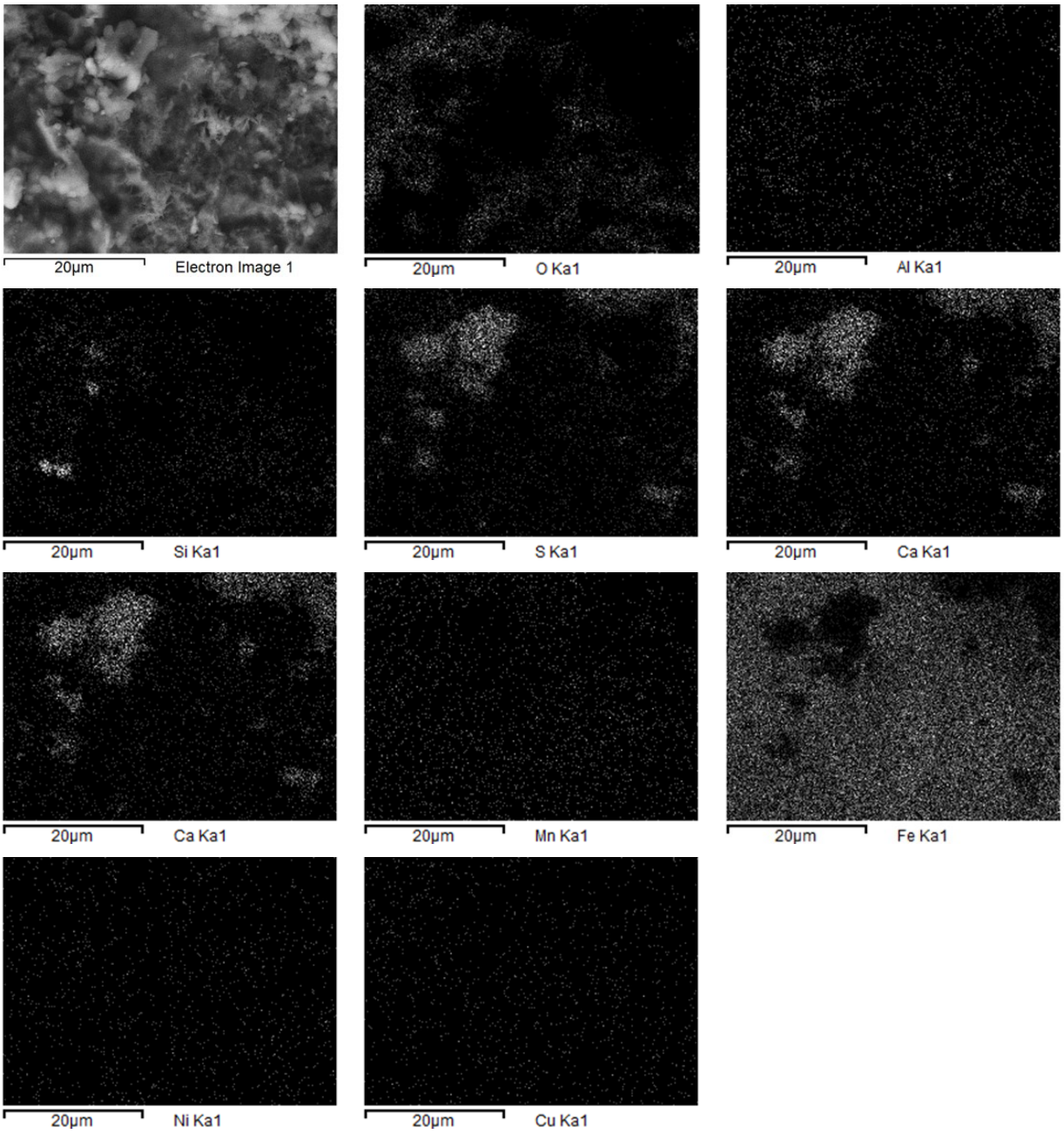


Figure A.672. EDS Elemental Mapping of Rust Collected from Interior Web.

A.38.6.XPS Result: Exterior Girder

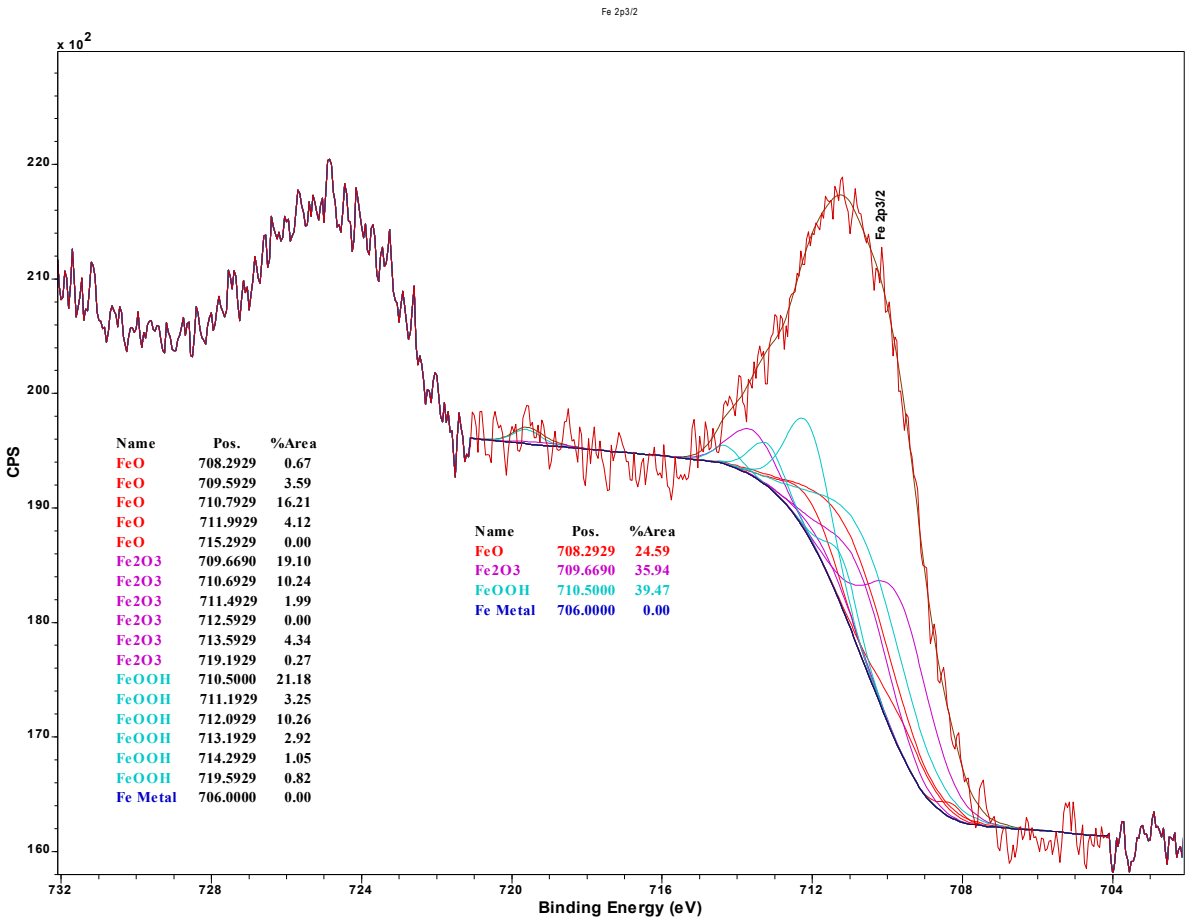


Figure A.673. XPS Spectrum of the Rust Collected from Exterior Web of the Girder.

A.38.7.XPS Result: Interior Girder

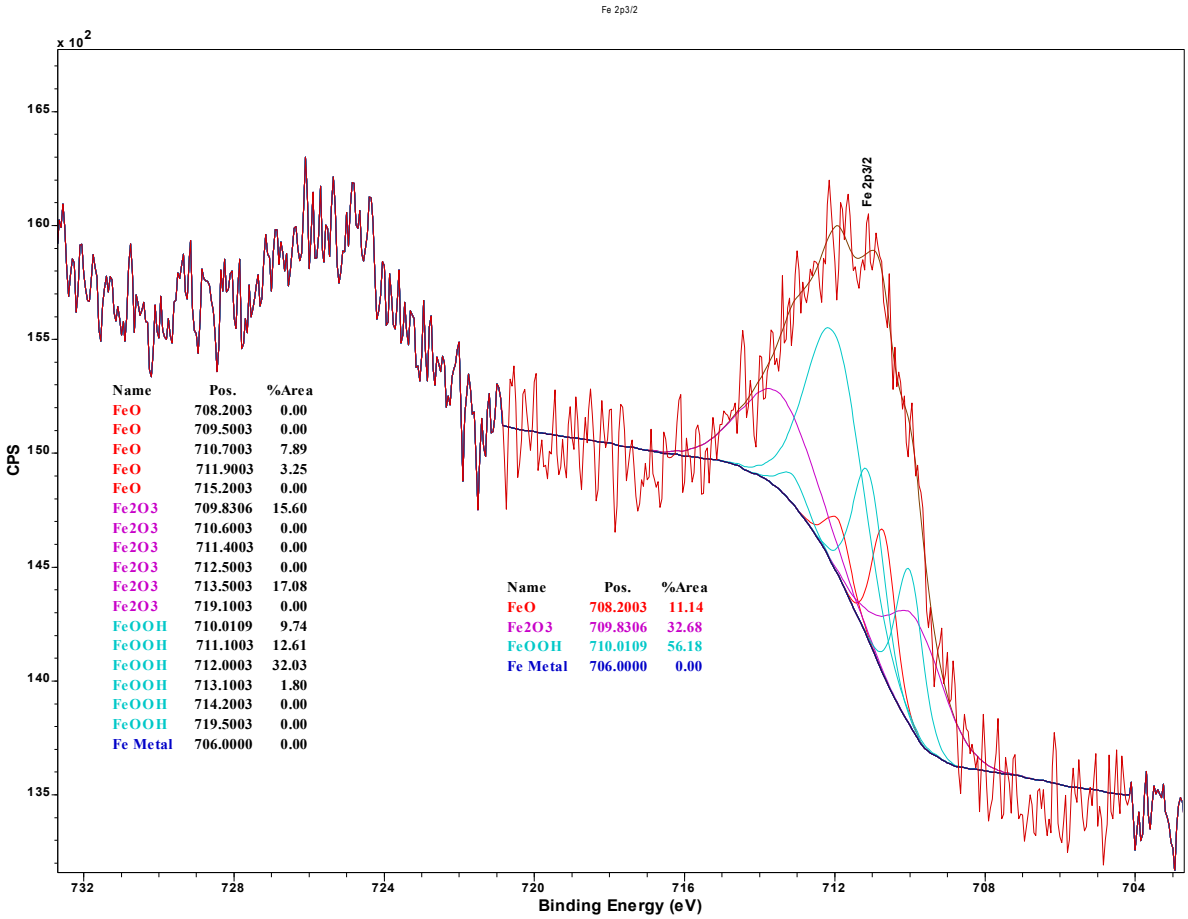


Figure A.674. XPS Spectrum of the Rust Collected from Interior Web of the Girder.

A.38.8.XRD Result: Exterior and Interior Girder

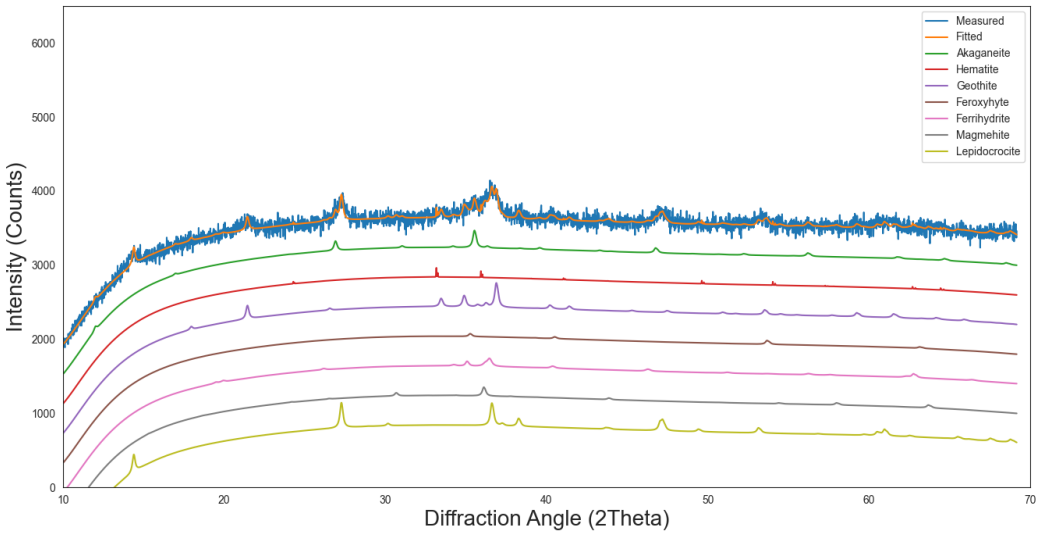


Figure A.675. XRD Pattern of Powdered Rust Collected from Exterior Web of the Girder.

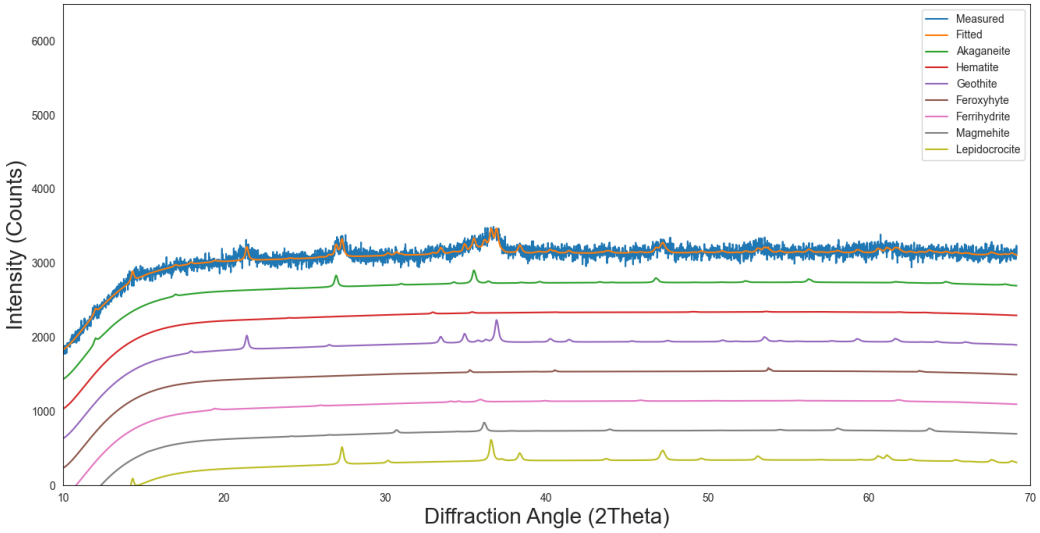
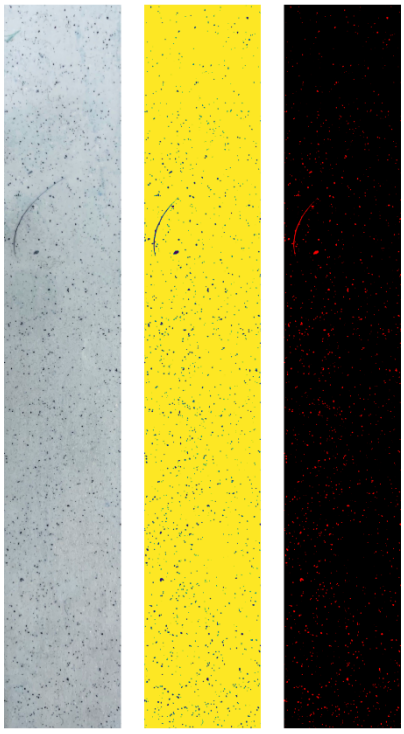


Figure A.676. XRD Pattern of Powdered Rust Collected from Interior Web of the Girder.

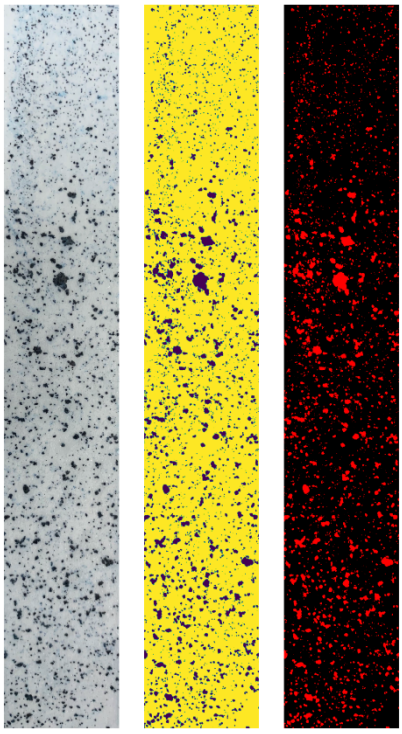
A.38.9.Particle Size Analysis: Tape Adhesion Results

(a)

(b)



(c)



(d)

Figure A.677. Particle Size Analysis Results at B3G1F1 (a) Top Flange Bottom, (b) Web, (c) Bottom Flange Bottom (d) Stiffener.

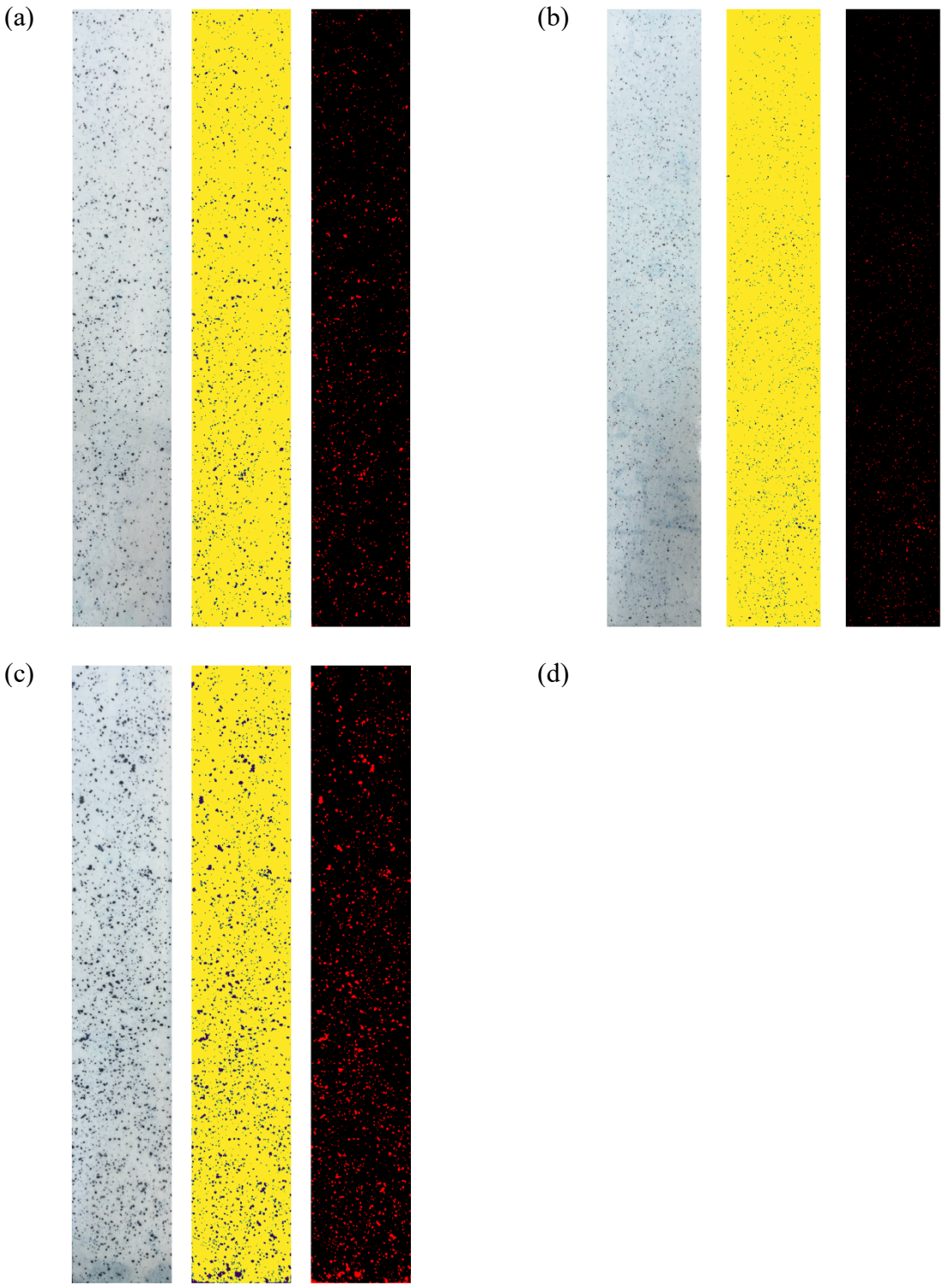


Figure A.678. Particle Size Analysis Results at B3G2F2 (a) Top Flange Bottom, (b) Web, (c) Bottom Flange Bottom (d) Stiffener.

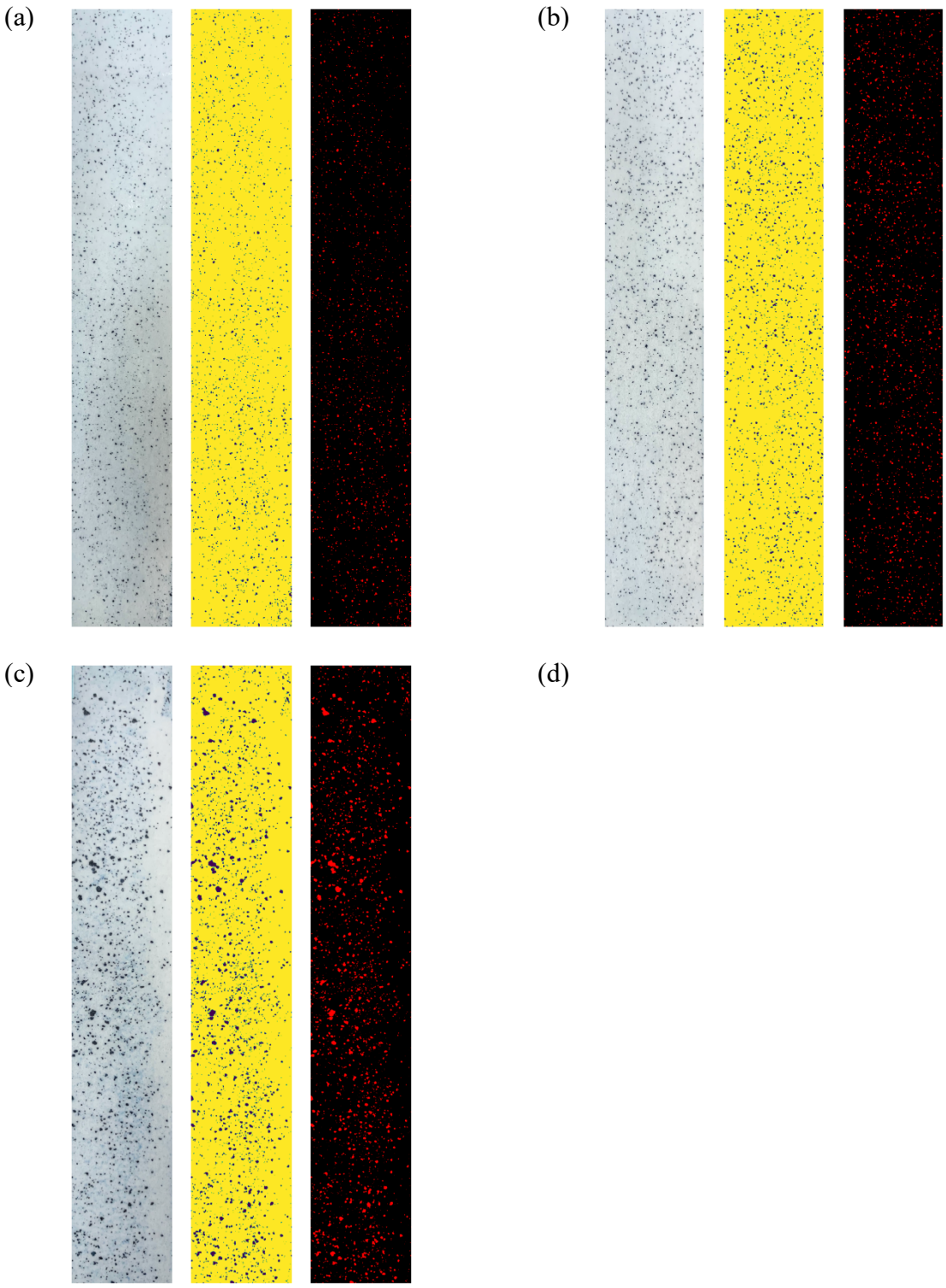


Figure A.679. Particle Size Analysis Results at B3G4F2 (a) Top Flange Bottom, (b) Web, (c) Bottom Flange Bottom (d) Stiffener.

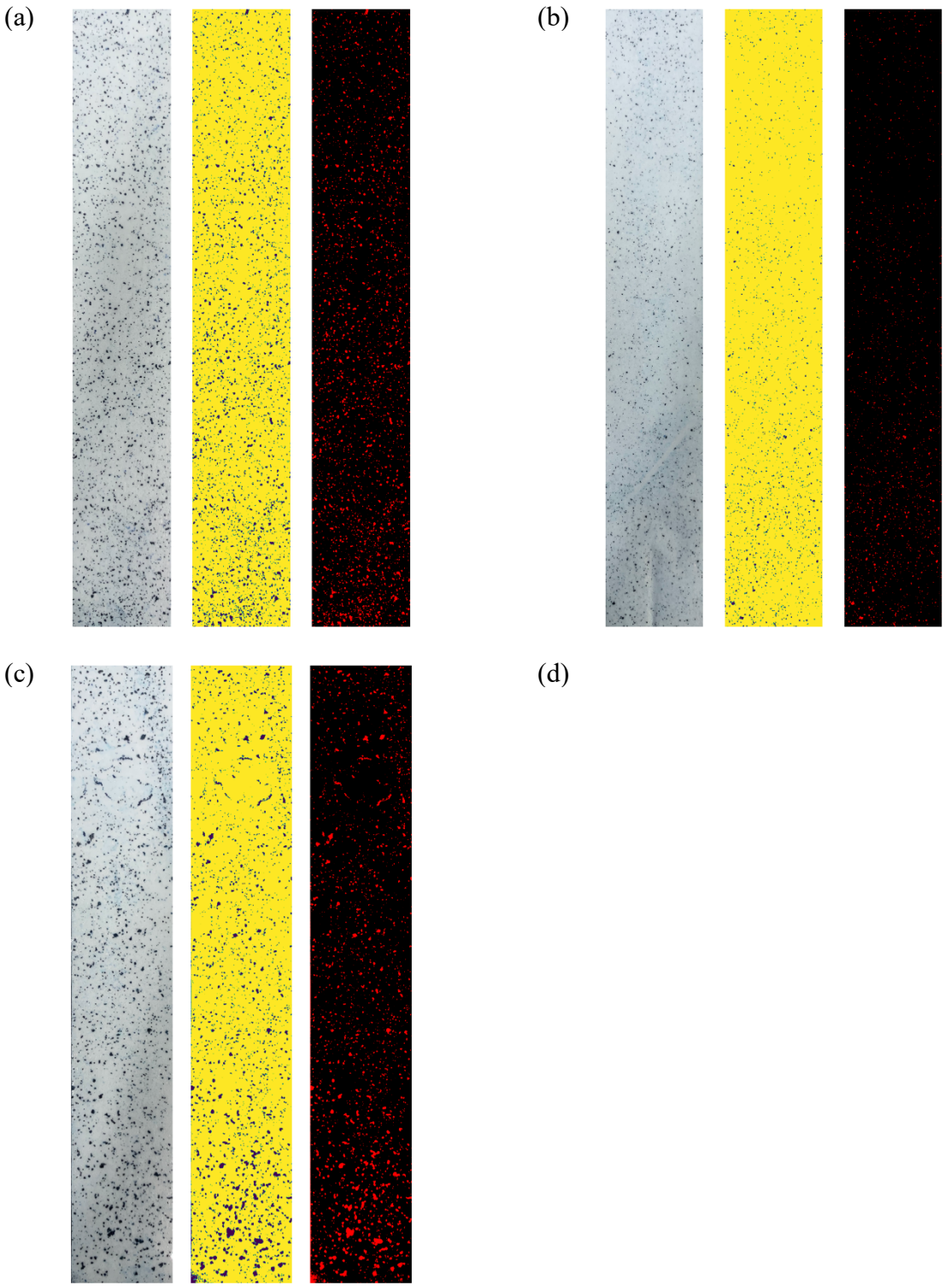


Figure A.680. Particle Size Analysis Results at B4G3F1 (a) Top Flange Bottom, (b) Web, (c) Bottom Flange Bottom (d) Stiffener.

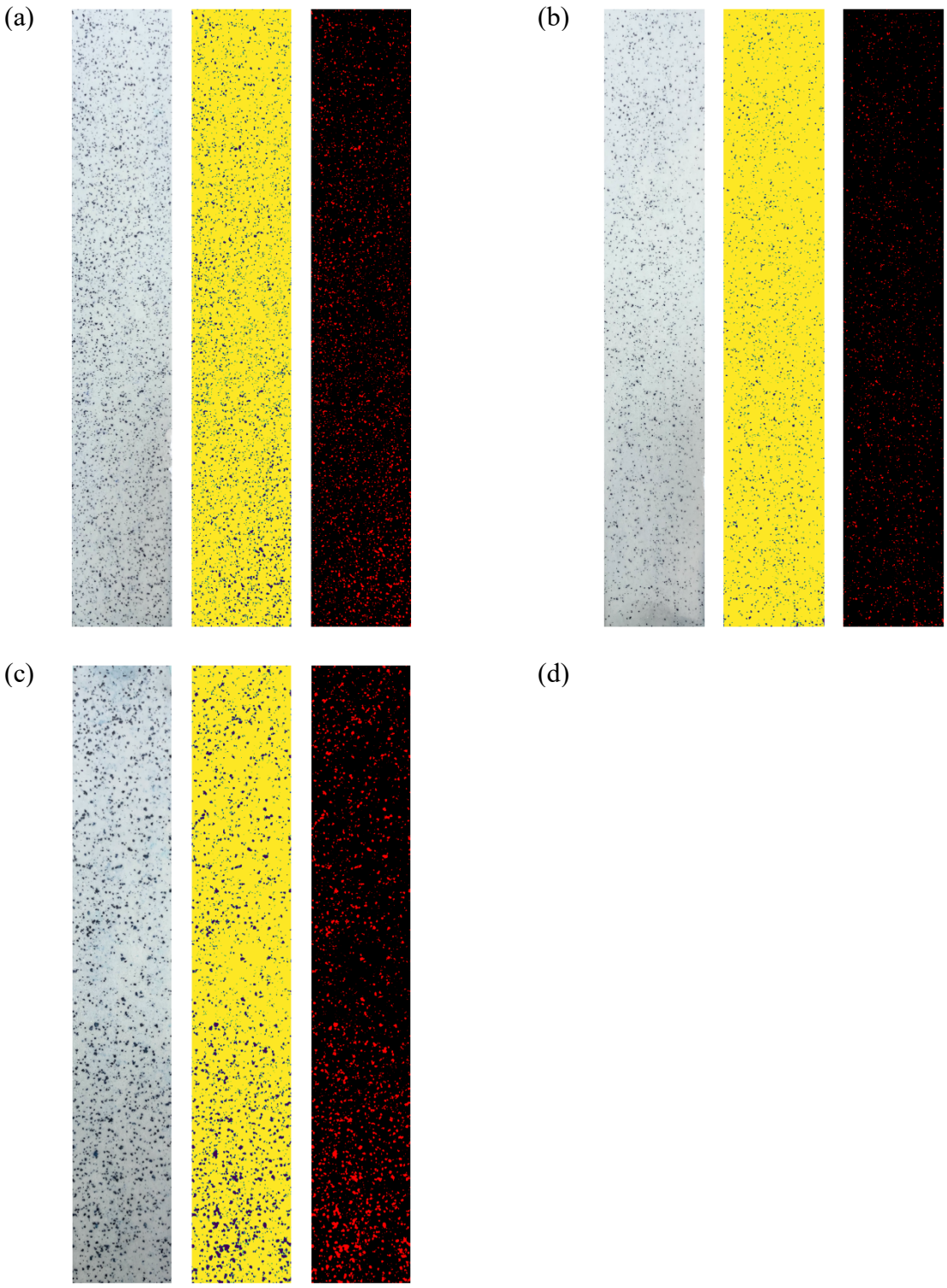


Figure A.681. Particle Size Analysis Results at B4G4F2 (a) Top Flange Bottom, (b) Web, (c) Bottom Flange Bottom (d) Stiffener.

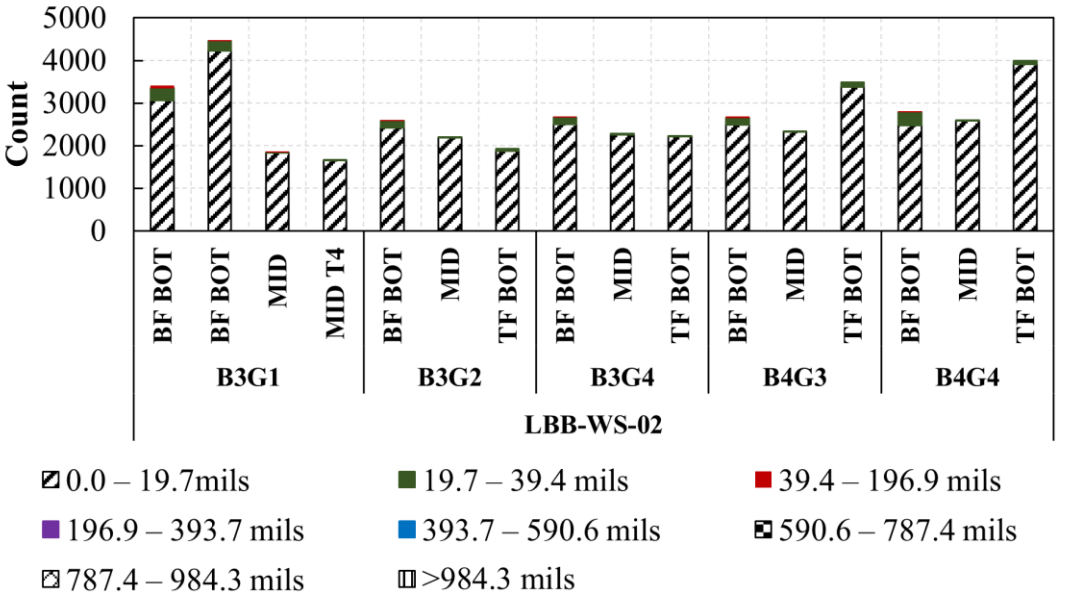


Figure A.682. Particle Size Analysis Showing Different Locations Examined.

A.39. ELP-WS-01

- LP 375 over US 62 (Montana Ave)
- Bridge ID 240720037402084, Coordinates (31.8071, -106.268), El Paso County
- Continuous weathering plate girder
- Built 2003
- Girder inspection carried on bent 6 and bent 5, and measurements are taken on girder within four feet from the abutment or bent.
- No visual inspection on deck
- Location for Testing: B5-G1F1, B5-G4F2, B5-G2F1, B5-G1F1, B6-G1F1, B6-G2F1, B6-G4F2



Figure A.683. Typical Picture of ELP-WS-01.

A.39.1. Observed Condition

Overall, patina is in very good condition. Uniform patina are visible on the bottom face of the top flange with a rating of 8. The web has a uniform patina formation with a patina rating of 8. The interior girders have a patina rating ranging between 7 and 8 for different locations. A rating of 7 is observed at top face of bottom flange.

A.39.2.Field Inspection Results

Table A-173. Field Inspection Results for ELP-WS-01.

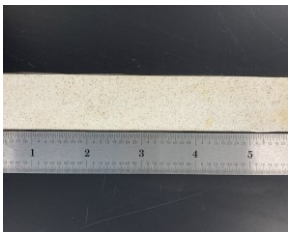
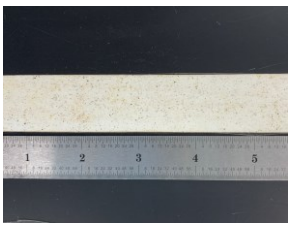
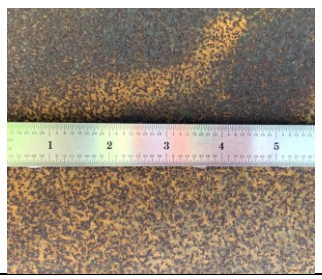
Location	Patina Rating	Thickness (inch)	Cl^- Conc. (ppm)	Field Condition	Tape Test
A1-G1F1 TF Bot. Ext.	8	Measured R1 0.977 R2 0.979 R3 0.977 Avg. 0.978 Design			
A1-G1F1 Web1 Ext.	8	Measured R1 0.492 R2 0.493 R3 0.493 Avg. 0.493 Design	5		
A1-G1F1 Web2 Ext.	8	Measured R1 0.496 R2 0.494 R3 0.495 Avg. 0.495 Design			
A1-G1F1 BF Top Ext.	7	Measured R1 1.223 R2 1.224 R3 1.224 Avg. 1.224			
A1-G1F1 BF Bot. Ext.	8				

Table A-174. Field Inspection Results for ELP-WS-01.

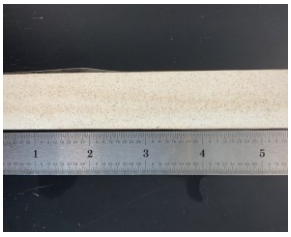
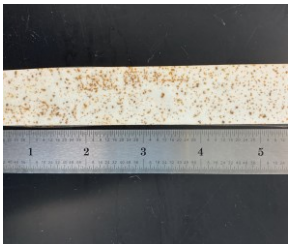
Location	Patina Rating	Thickness (inch)	Cl^- Conc. (ppm)	Field Condition	Tape Test
A1-G1F1 Stiffness. Ext.	8	Measured R1 0.978 R2 0.977 R3 0.976 Avg. 0.977-			
A1-G3F1 TF Bot. Ext.	8	Measured R1 0.983 R2 0.983 R3 0.984 Avg. 0.983 Design			
A1-G3F1 Web Ext.	8	Measured R1 0.491 R2 0.492 R3 0.492 Avg. 0.492 Design			
A1-G3F1 BF Top Ext.	8	Measured R1 1.227 R2 1.227 R3 1.226 Avg. 1.227			
A1-G3F1 BF Bot. Ext.	7				

Table A-175. Field Inspection Results for ELP-WS-01.

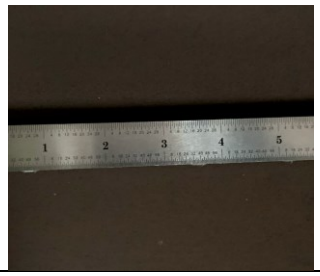
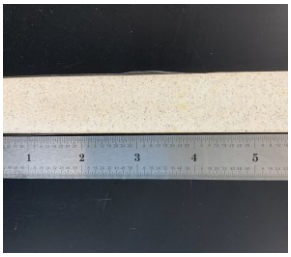
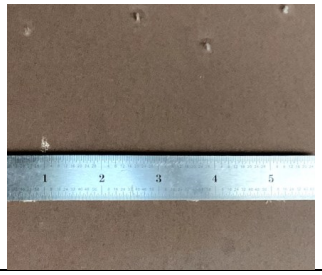
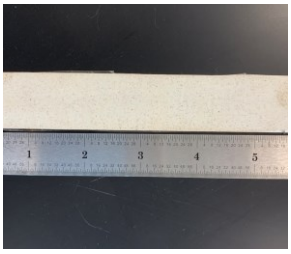
Location	Patina Rating	Thickness (inch)	Cl^- Conc. (ppm)	Field Condition	Tape Test
A1-G3F1 Stiff. Ext.	7	Measured R1 0.994 R2 0.974 R3 0.972 Avg. 0.980.			
A1-G5F2 TF Bot. Ext.	8	Measured R1 0.971 R2 0.972 R3 0.972 Avg. 0.972- Design			
A1-G5F2 Web Ext.	8	Measured R1 0.486 R2 0.486 R3 0.488 Avg. 0.487- Design			
A1-G5F2 BF Top Ext.	7	Measured R1 1.222 R2 1.217 R3 1.220 Avg. 1.220 Design			
A1-G5F2 BF Bot. Ext.	8	Measured - Design			

Table A-176. Field Inspection Results for ELP-WS-01.

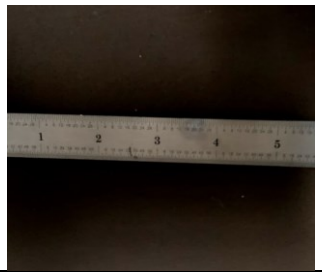
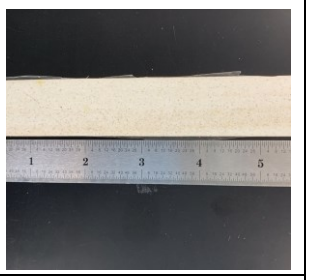
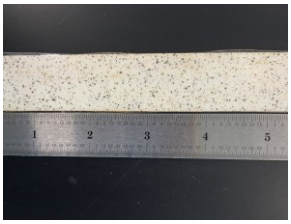
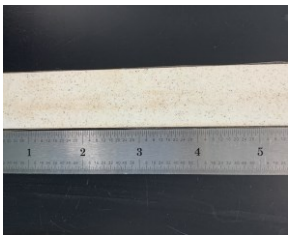
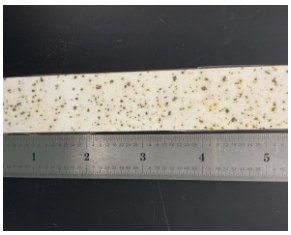
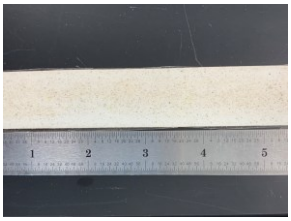
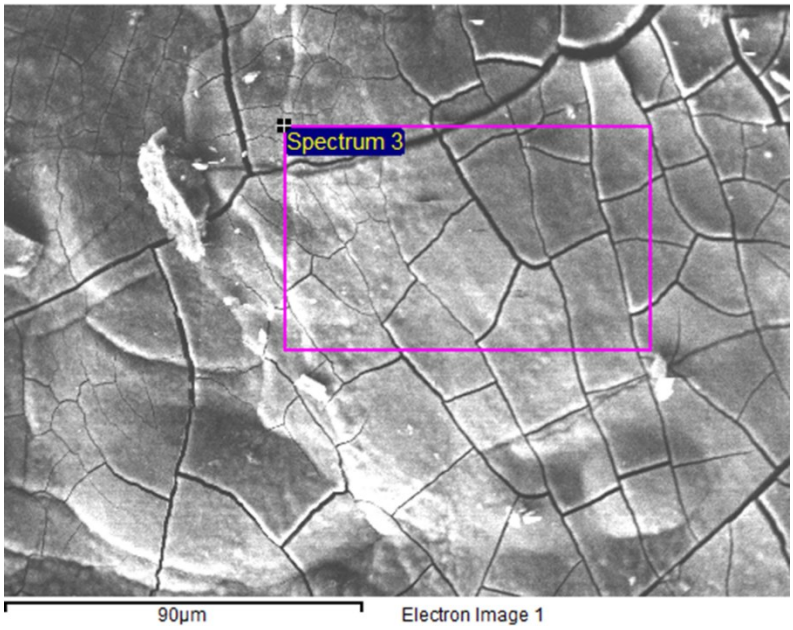
Location	Patina Rating	Thickness (inch)	Cl^- Conc. (ppm)	Field Condition	Tape Test
A1-G5F2 Stiff. Ext.	7	Measured R1 0.975 R2 0.975 R3 0.975 Avg. 0.975			
A1-GLast F1 TF Bot. Ext.	8	Measured R1 0.972 R2 0.974 R3 0.972 Avg. 0.973 Design			
A1-GLast F1 Web1 Ext.	8	Measured R1 0.493 R2 0.494 R3 0.492 Avg. 0.493 Design	11		
A1-GLast F1 Web2 Ext.	8	Measured R1 0.500 R2 0.499 R3 0.499 Avg. 0.499			
A1-GLast F1 BF Top Ext.	7	Measured R1 1.228 R2 1.232 R3 1.230 Avg. 1.230			

Table A-177. Field Inspection Results for ELP-WS-01.

Location	Patina Rating	Thickness (inch)	Cl^- Conc. (ppm)	Field Condition	Tape Test
A1-GLast F1 BF Bot. Ext.	8				
A1-GLast F1 Stiff. Ext.	8	Measured R1 0.975 R2 0.975 R3 0.975 Avg. 0.975 Design			

A.39.3.SEM/EDS Results: Exterior Web Girder

Element	Weight %	Atomic %
O K	48.52	75.86
Al K	0.68	0.63
S K	1.86	1.45
Cl K	0.57	0.40
Mn K	0.21	0.10
Fe K	47.91	21.46
Cu K	0.25	0.10
Totals	100.00	



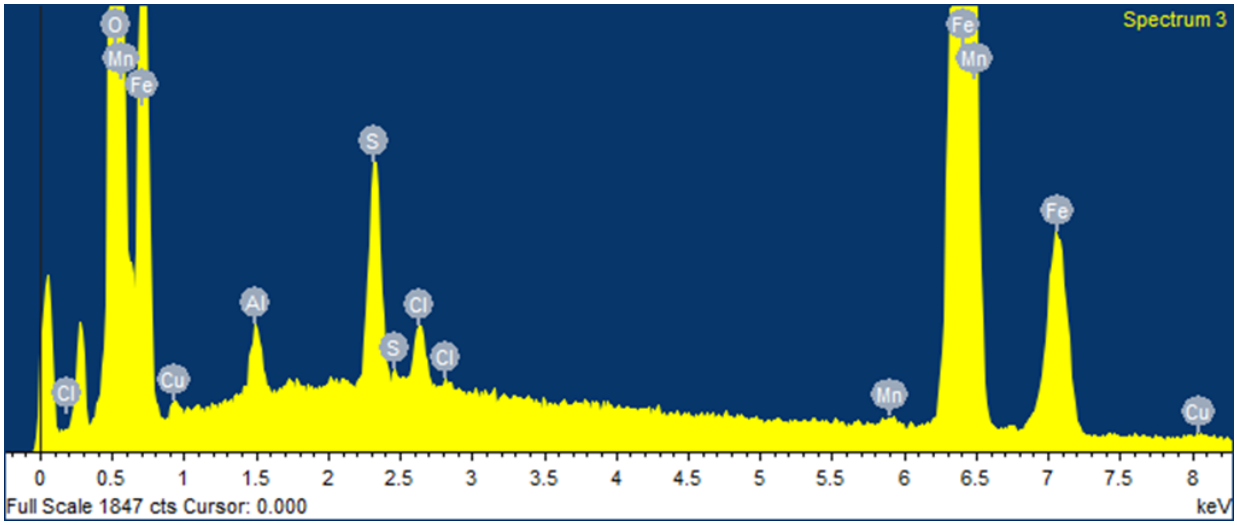
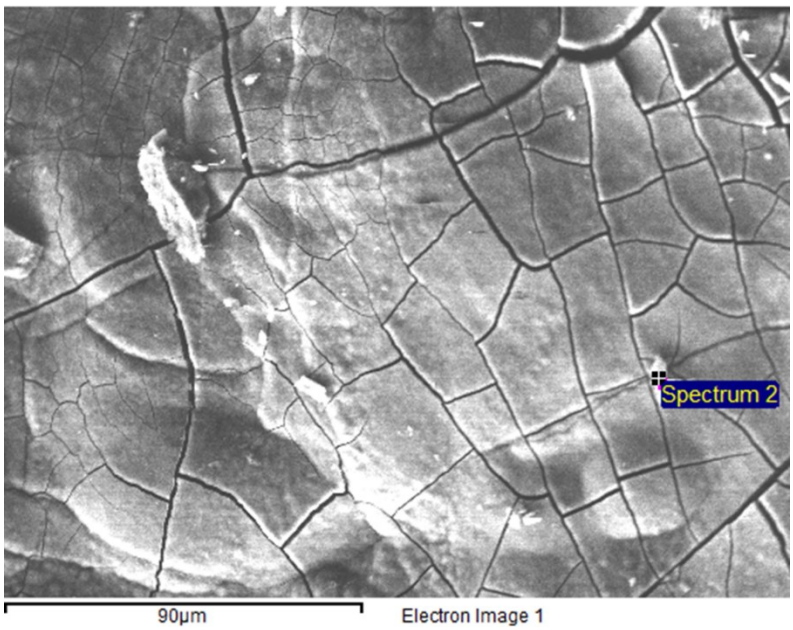


Figure A.684. SEM Image and EDS Spectrum of the Rust Collected from Exterior Web of the Girder.

Element	Weight %	Atomic %
O K	40.92	69.77
Al K	0.96	0.97
S K	1.96	1.67
Cl K	0.61	0.47
Mn K	0.21	0.10
Fe K	55.14	26.93
Cu K	0.20	0.09
Totals	100.00	



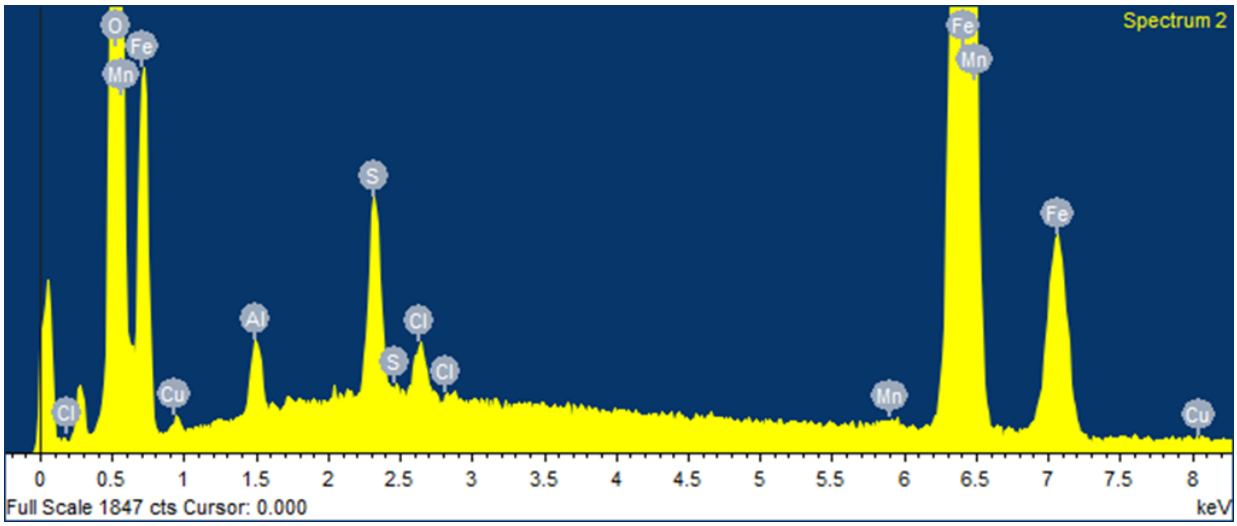
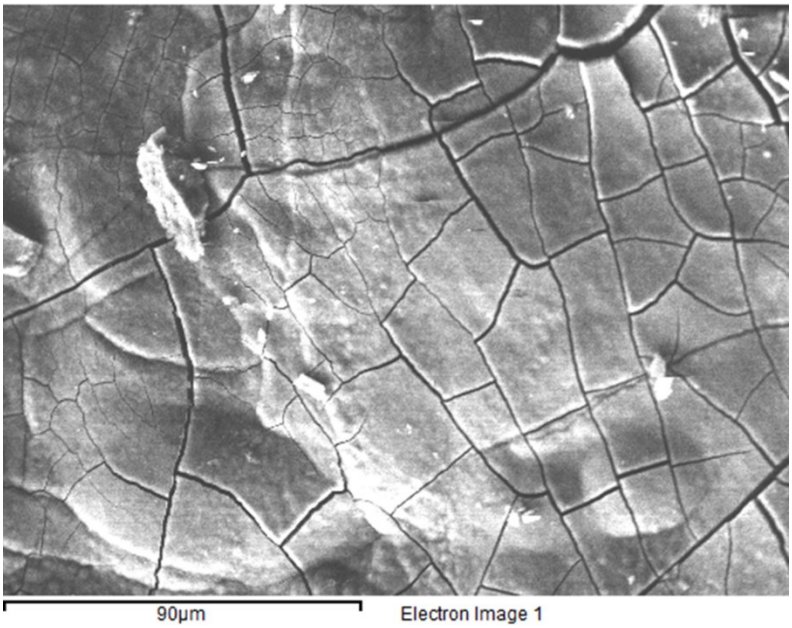


Figure A.685. SEM Image and EDS Spectrum of the Rust Collected from Exterior Web of the Girder.

Element	Weight %	Atomic %
O K	45.63	73.74
Al K	0.78	0.75
S K	1.70	1.37
Cl K	0.43	0.31
Mn K	0.36	0.17
Fe K	50.94	23.59
Cu K	0.15	0.06
Totals	100.00	



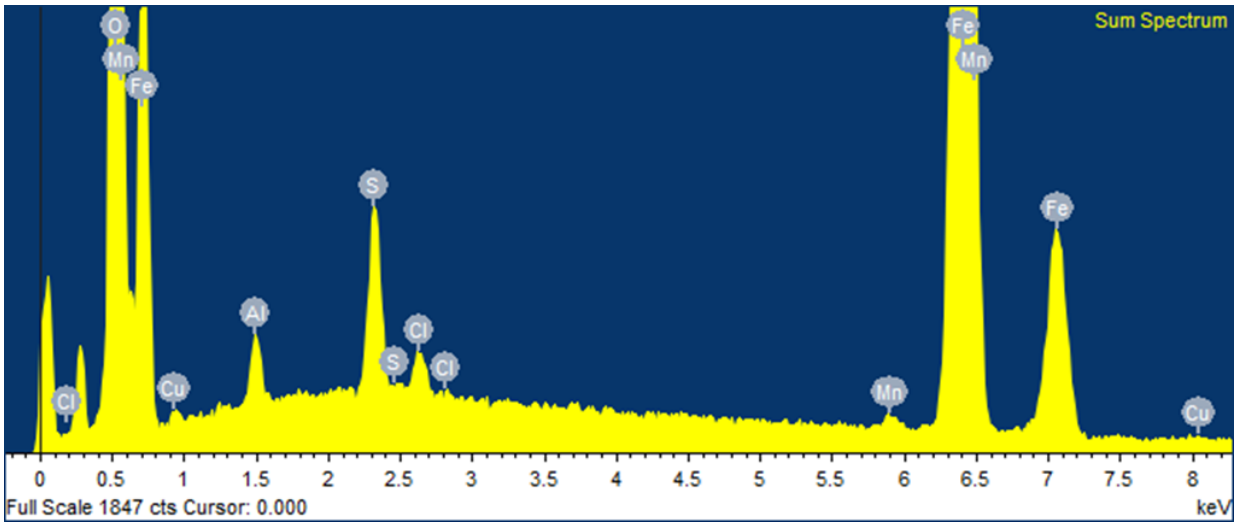


Figure A.686. SEM Image and EDS Spectrum of the Rust Collected from Exterior Web of the Girder.

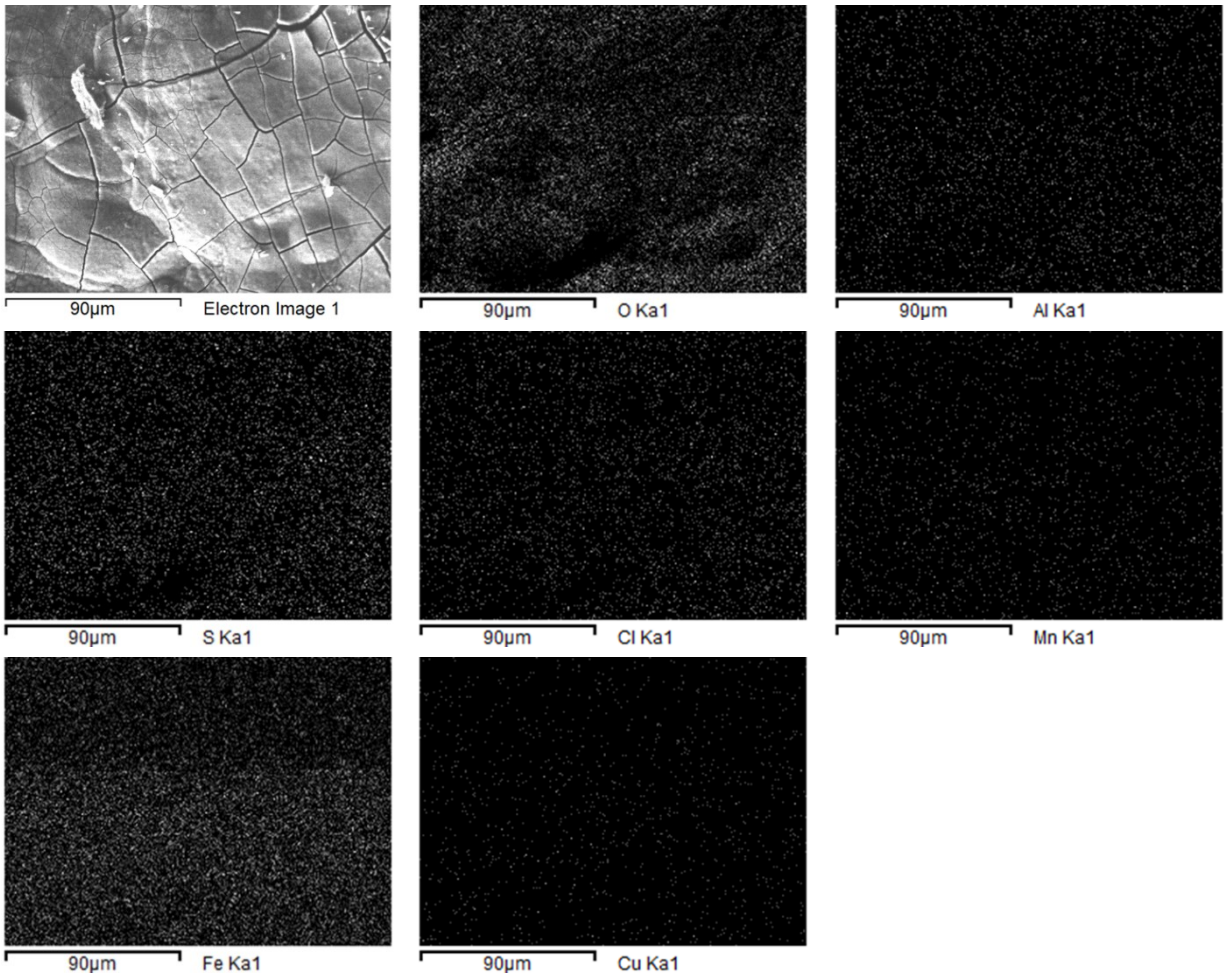
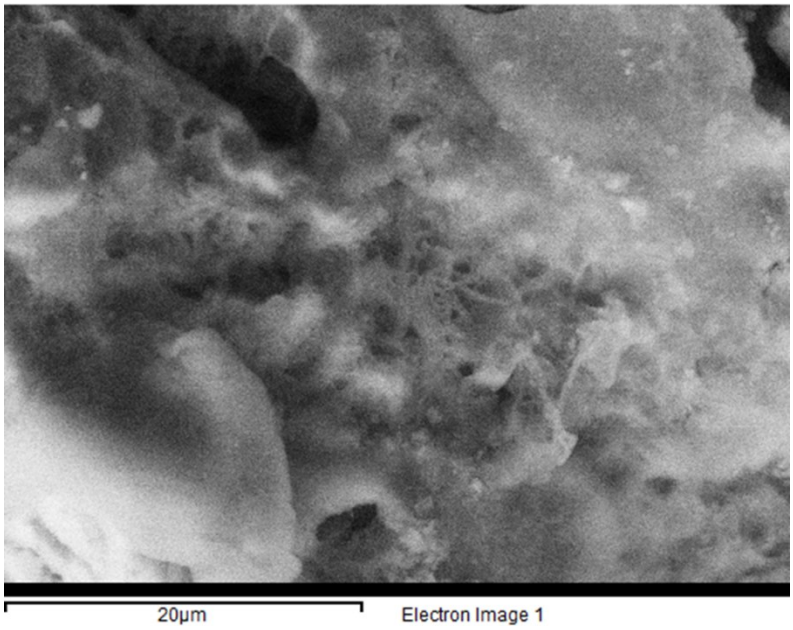


Figure A.687. EDS Elemental Mapping of Rust Collected from Exterior Web.

A.39.4.SEM/EDS Results: Interior Web Girder

Element	Weight %	Atomic %
O K	31.57	59.61
Na K	1.25	1.65
Al K	1.83	2.05
Si K	0.90	0.97
S K	1.15	1.09
Cl K	0.56	0.48
K K	0.20	0.16
Ca K	0.79	0.59
Mn K	0.37	0.20
Fe K	61.37	33.20
Totals	100.00	



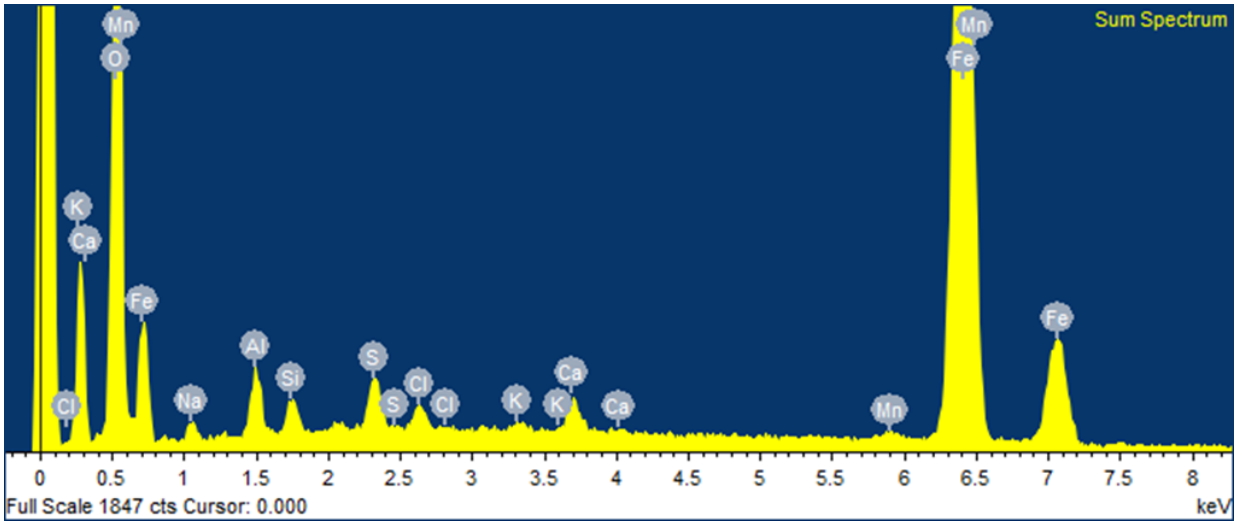


Figure A.688. SEM Image and EDS Spectrum of the Rust Collected from Interior Web of the Girder.

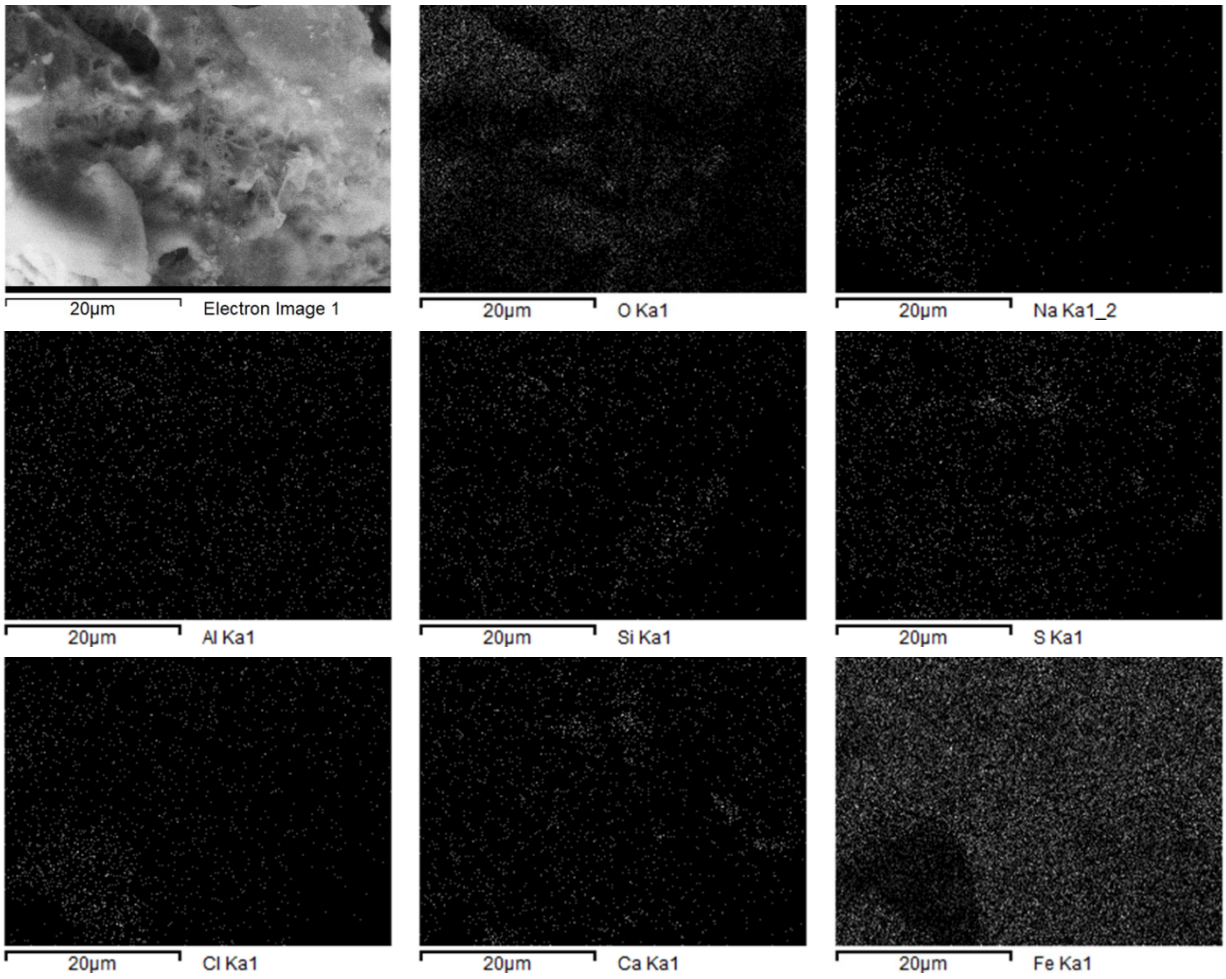
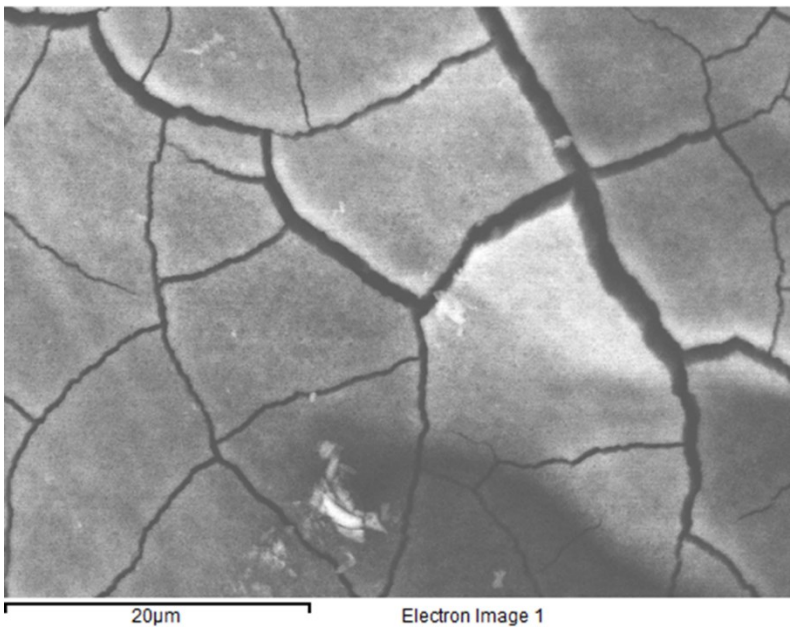


Figure A.689. EDS Elemental Mapping of Rust Collected from Interior Web.

Element	Weight %	Atomic %
O K	43.60	72.00
Al K	0.87	0.85
S K	1.99	1.64
Cl K	0.67	0.50
Mn K	0.25	0.12
Fe K	52.46	24.82
Cu K	0.17	0.07
Totals	100.00	



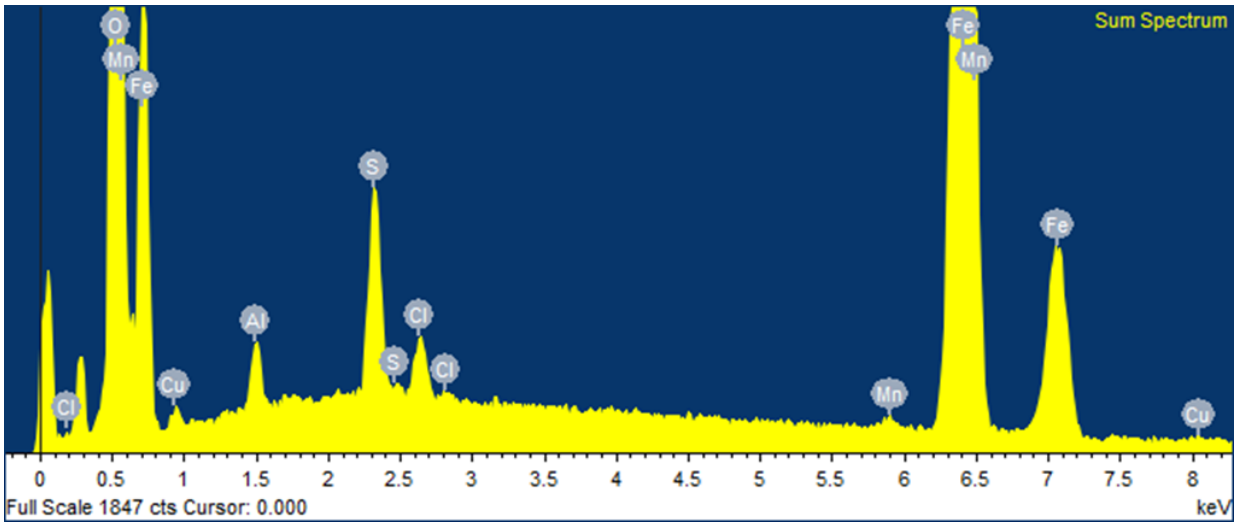
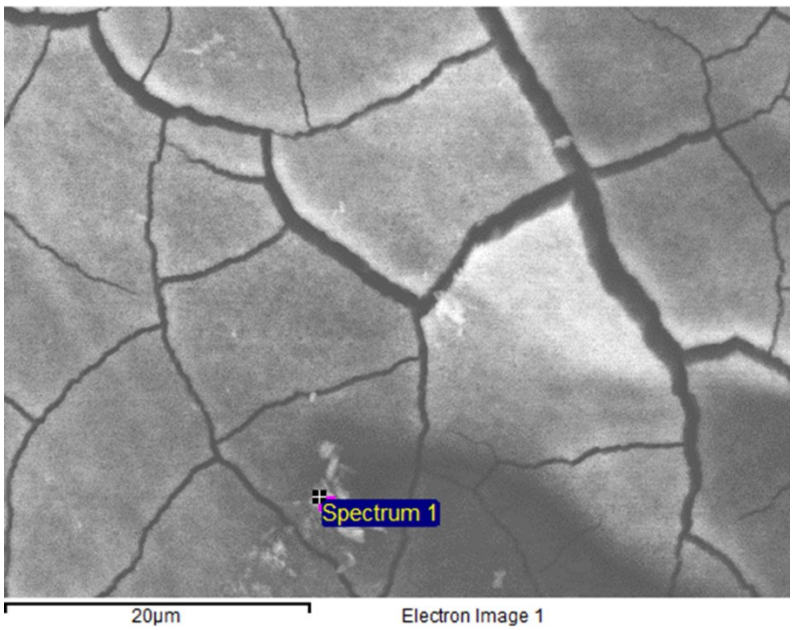


Figure A.690. SEM Image and EDS Spectrum of the Rust Collected from Exterior Web of the Girder.

Element	Weight %	Atomic %
O K	50.38	77.10
Al K	0.70	0.64
S K	2.06	1.57
Cl K	0.61	0.42
Mn K	0.26	0.12
Fe K	45.80	20.08
Cu K	0.18	0.07
Totals	100.00	



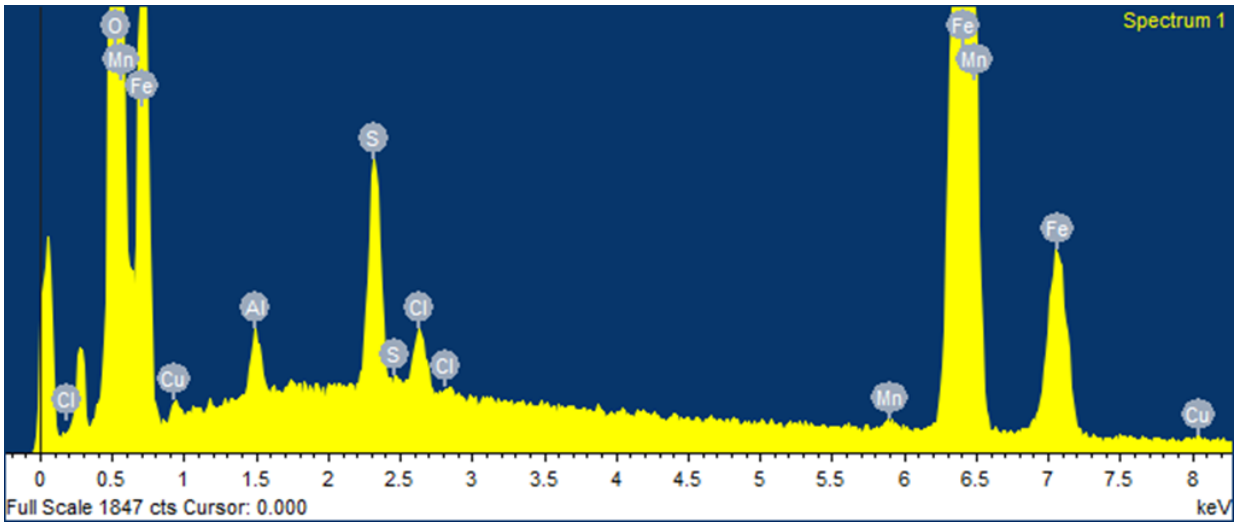
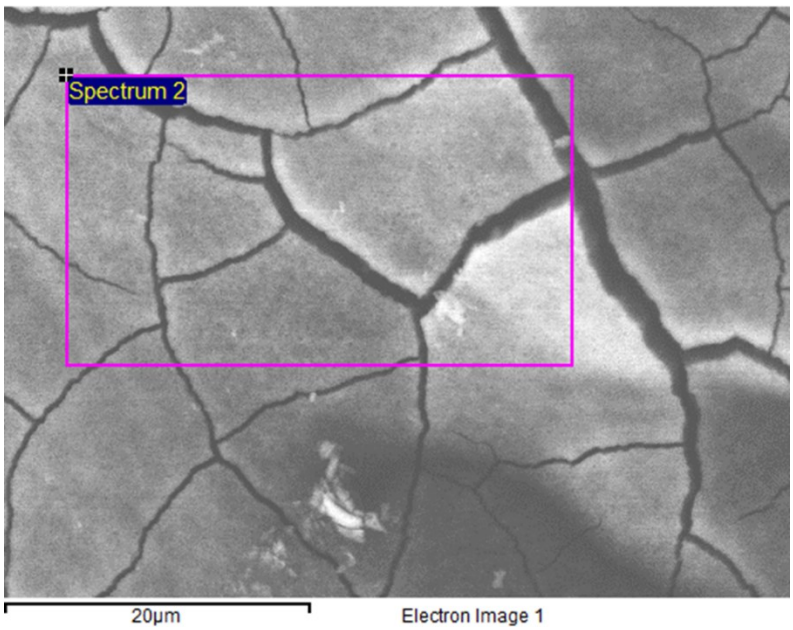


Figure A.691. SEM Image and EDS Spectrum of the Rust Collected from Exterior Web of the Girder.

Element	Weight %	Atomic %
O K	50.38	77.10
Al K	0.70	0.64
S K	2.06	1.57
Cl K	0.61	0.42
Mn K	0.26	0.12
Fe K	45.80	20.08
Cu K	0.18	0.07
Totals	100.00	



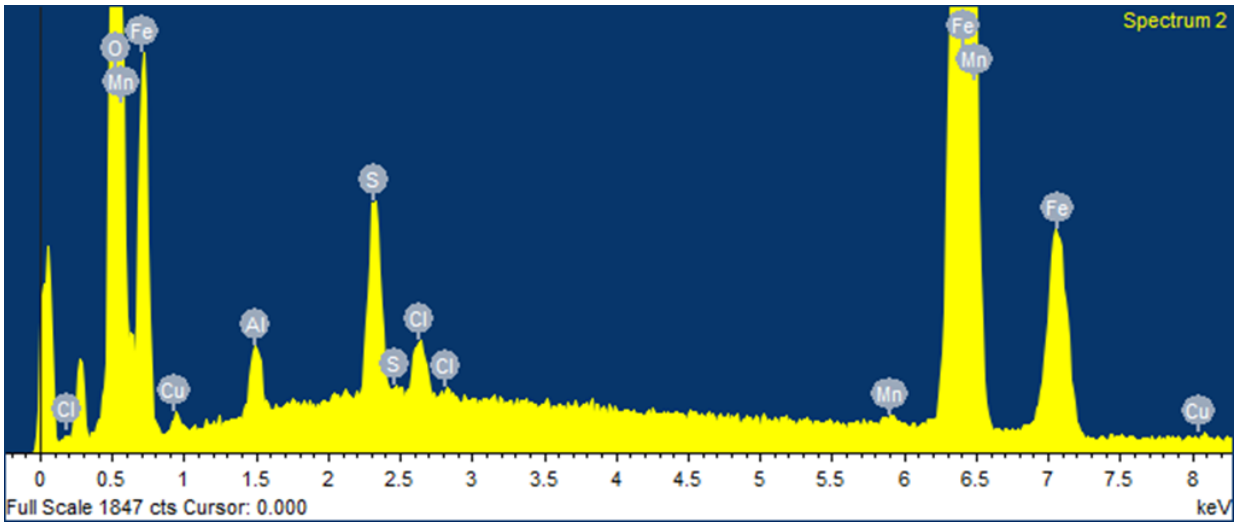


Figure A.692. SEM Image and EDS Spectrum of the Rust Collected from Exterior Web of the Girder.

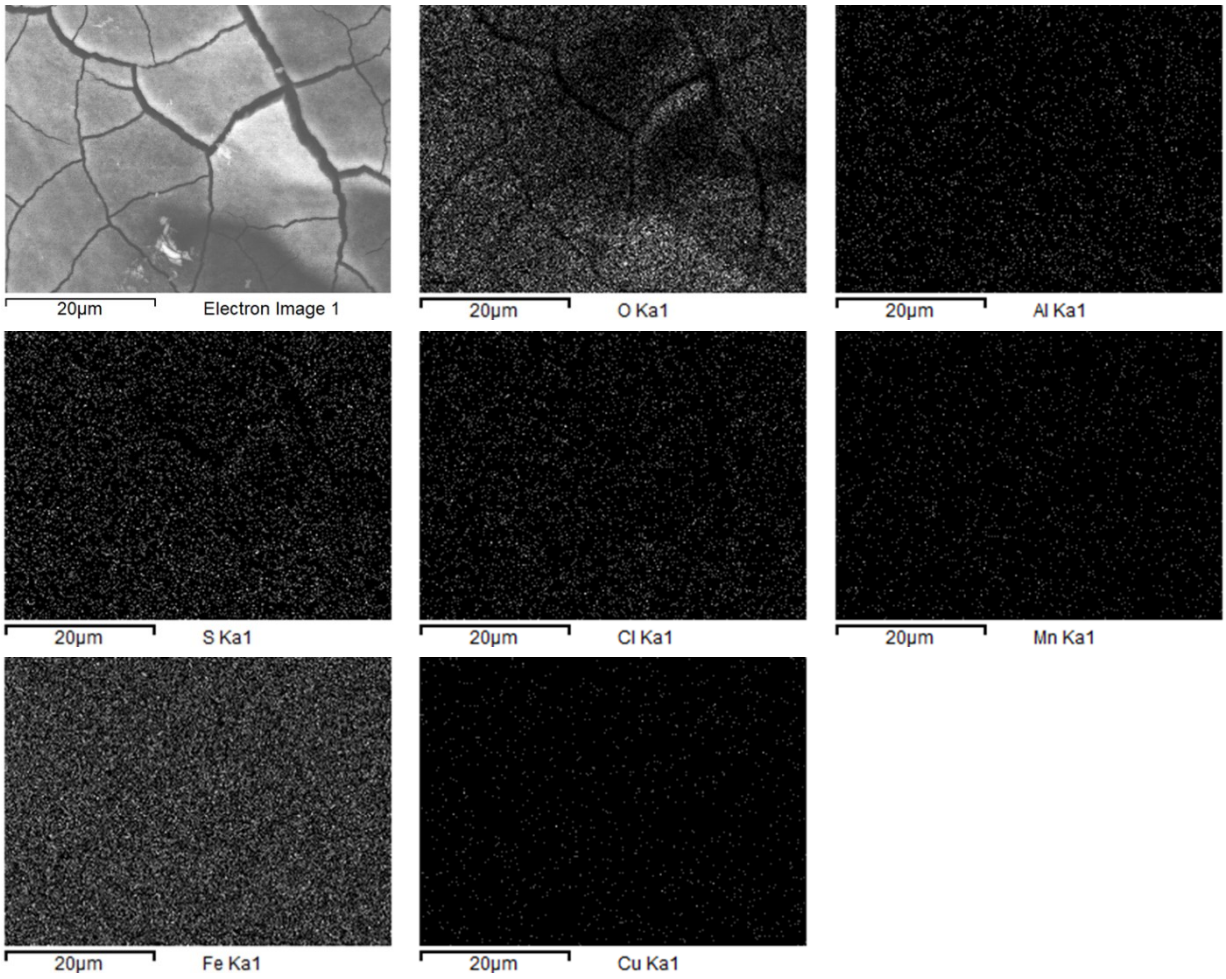
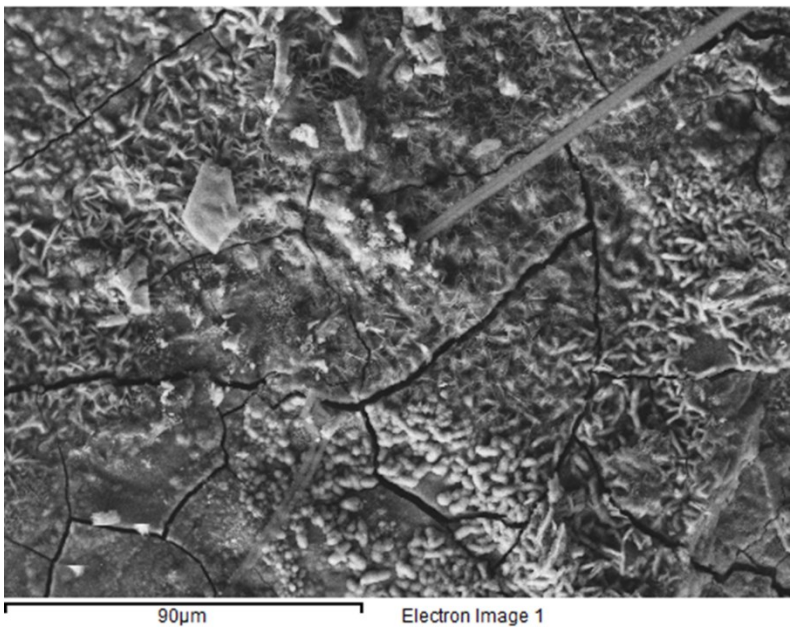


Figure A.693. EDS Elemental Mapping of Rust Collected from Exterior Web.

Element	Weight %	Atomic %
O K	35.54	65.40
Al K	0.82	0.90
S K	0.33	0.30
Mn K	2.14	1.15
Fe K	61.12	32.23
Cu K	0.05	0.02
Totals	100.00	



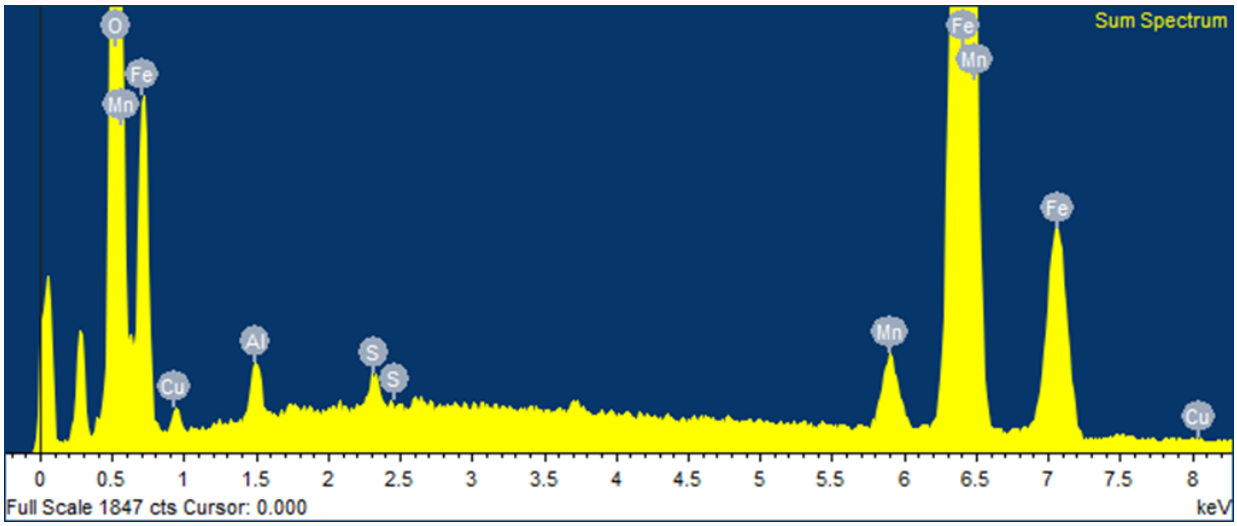


Figure A.694. SEM Image and EDS Spectrum of the Rust Collected from Exterior Web of the Girder.

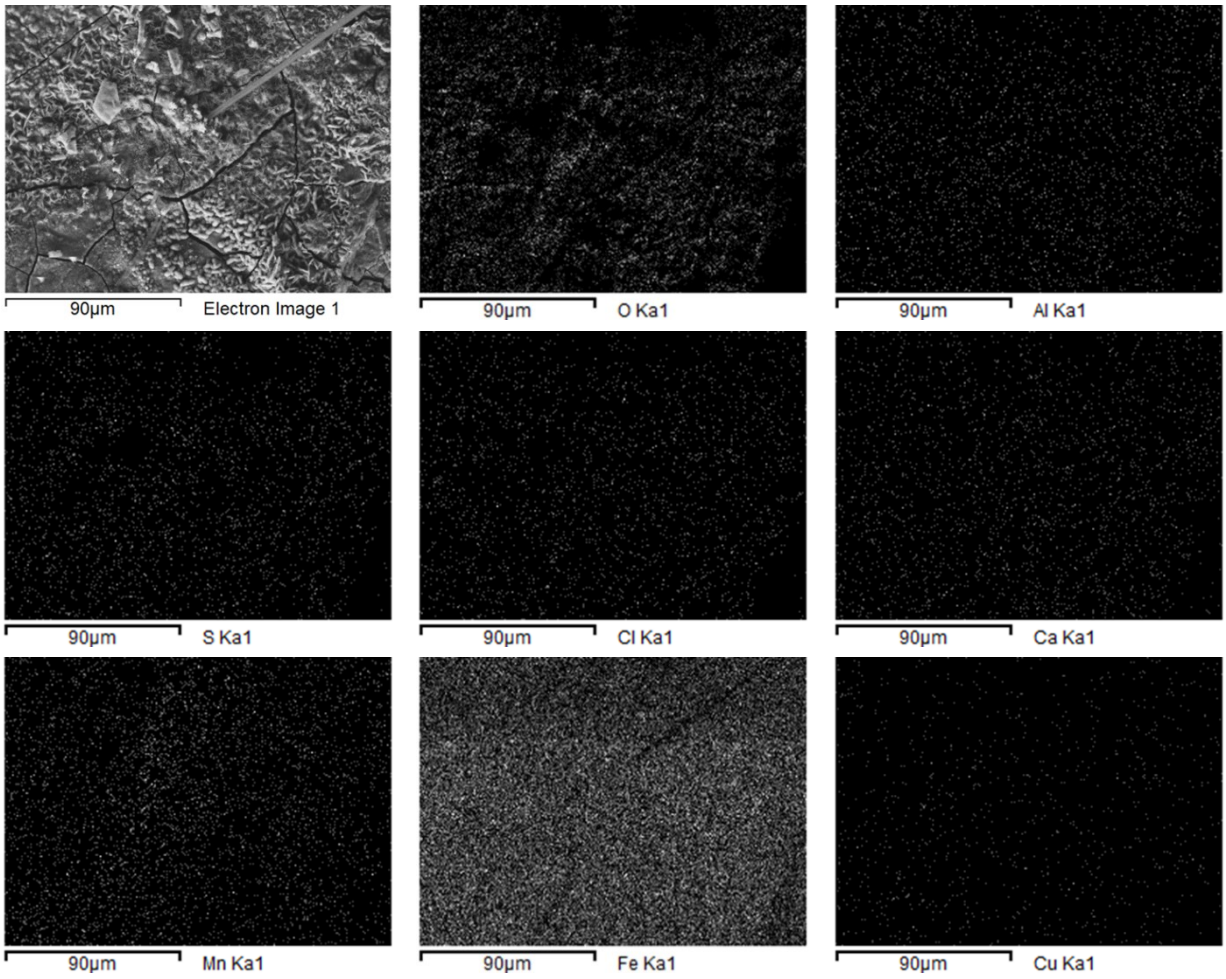
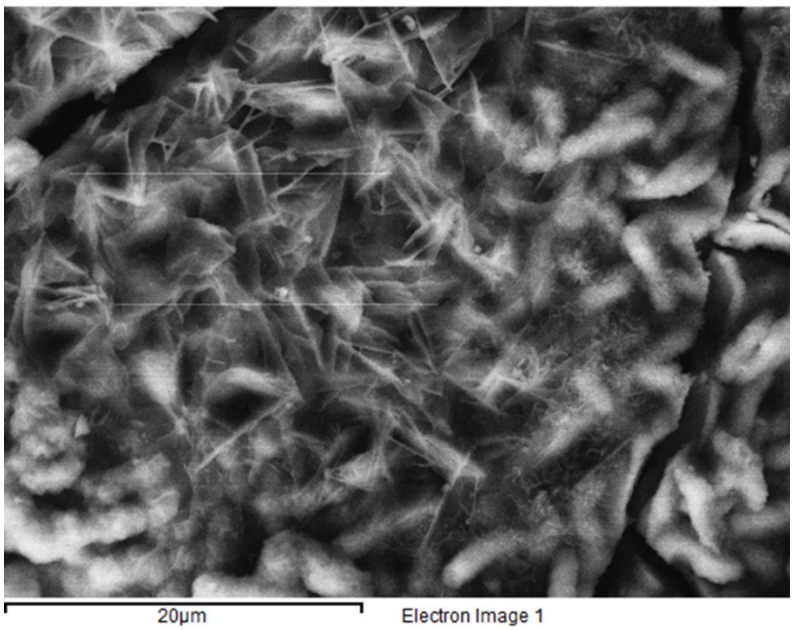


Figure A.695. EDS Elemental Mapping of Rust Collected from Exterior Web.

Element	Weight %	Atomic %
O K	38.70	68.41
Al K	0.82	0.86
S K	0.27	0.24
Mn K	1.59	0.82
Fe K	58.45	29.60
Cu K	0.17	0.08
Totals	100.00	



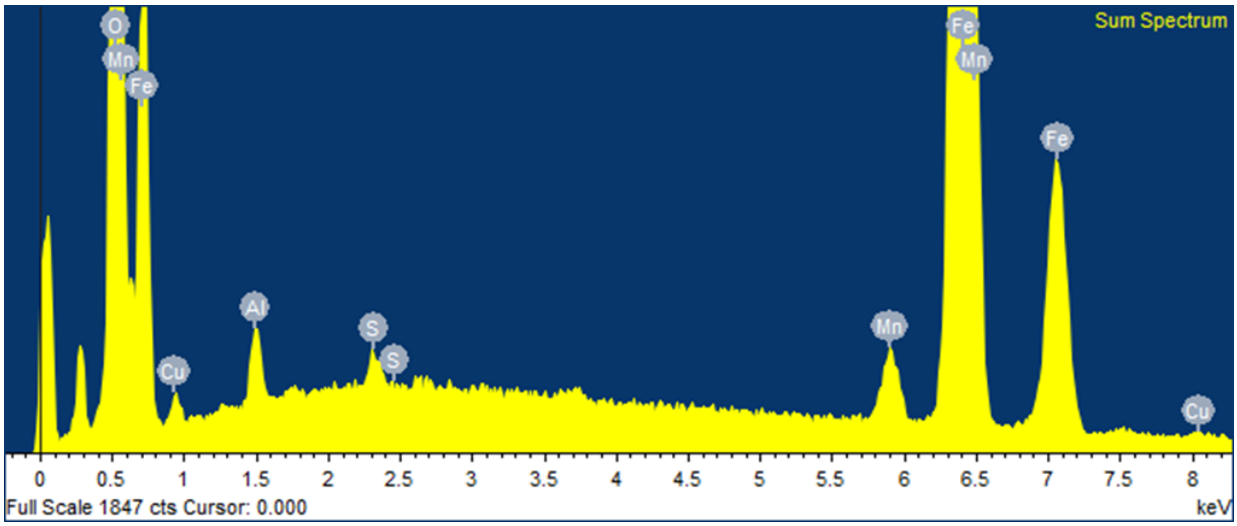


Figure A.696. SEM Image and EDS Spectrum of the Rust Collected from Exterior Web of the Girder.

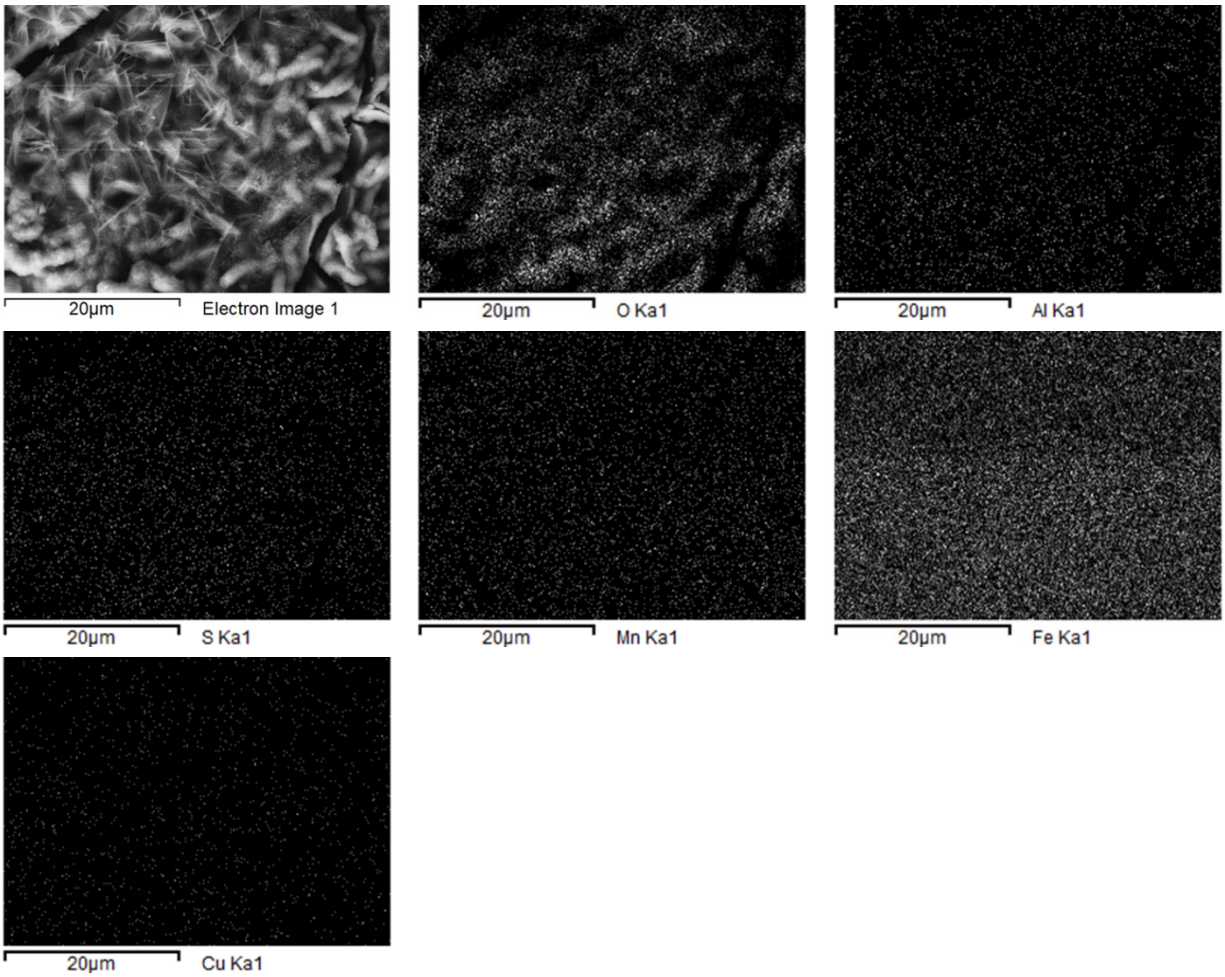


Figure A.697. EDS Elemental Mapping of Rust Collected from Exterior Web.

A.39.5.XPS Result: Exterior Girder

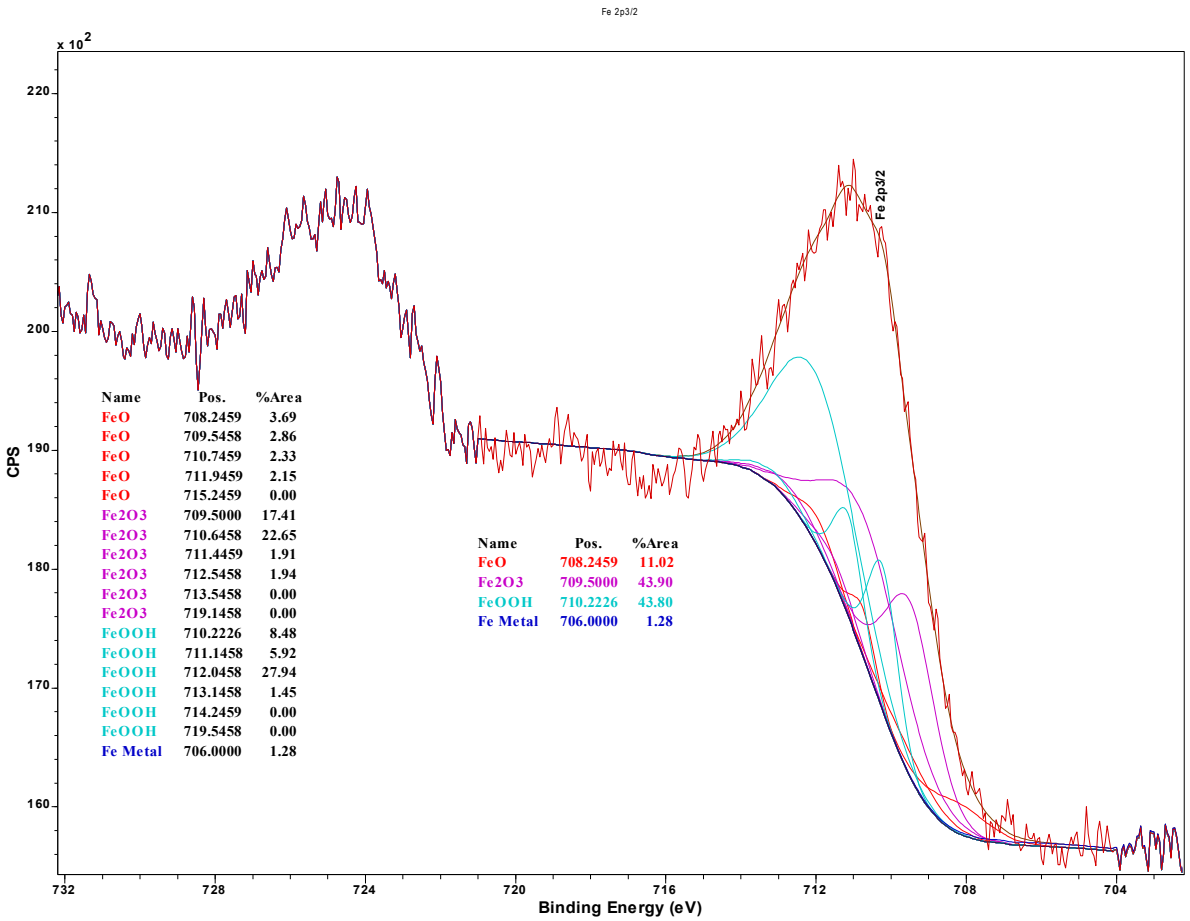


Figure A.698. XPS Spectrum of the Rust Collected from Exterior Web of the Girder.

A.39.6.XPS Result: Interior Girder

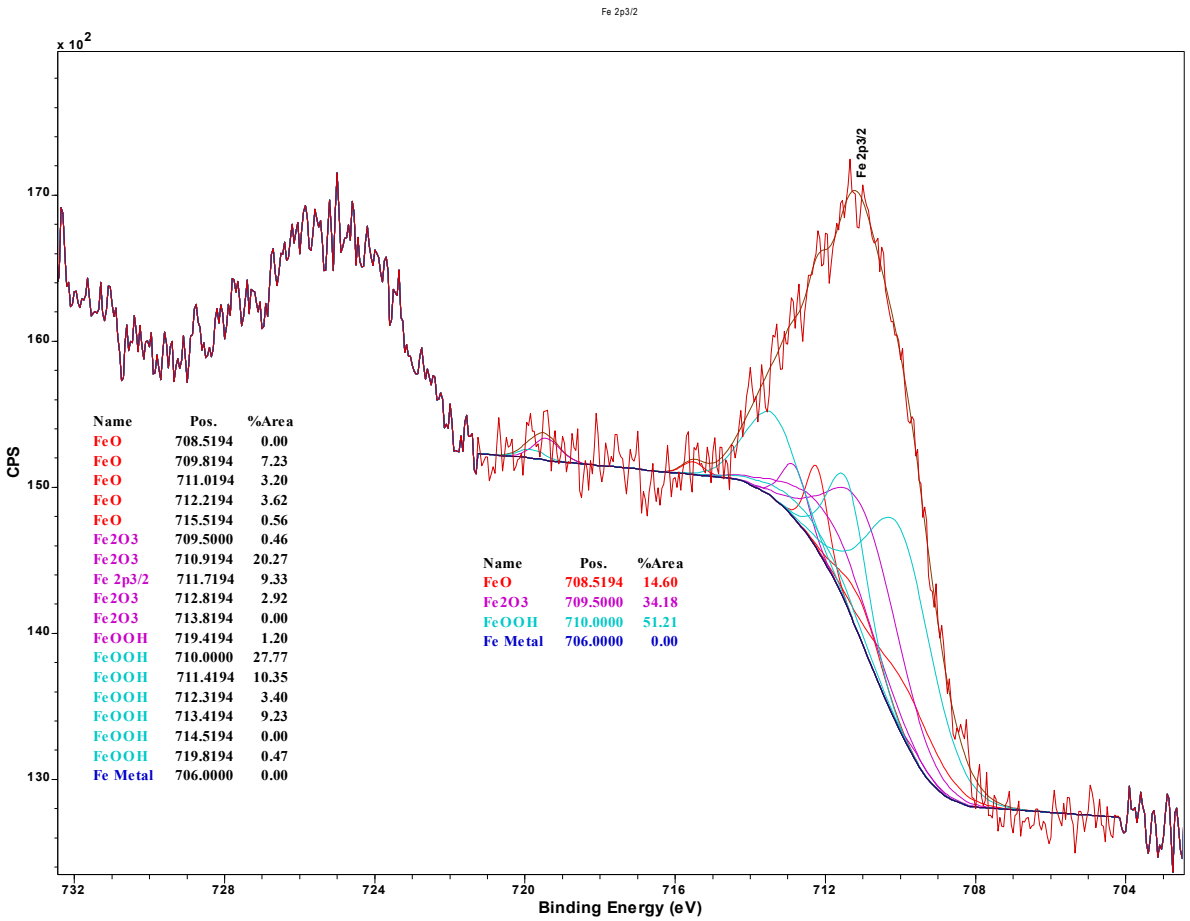


Figure A.699. XPS Spectrum of the Rust Collected from Interior Web of the Girder.

A.39.7.XRD Result: Exterior and Interior Girder

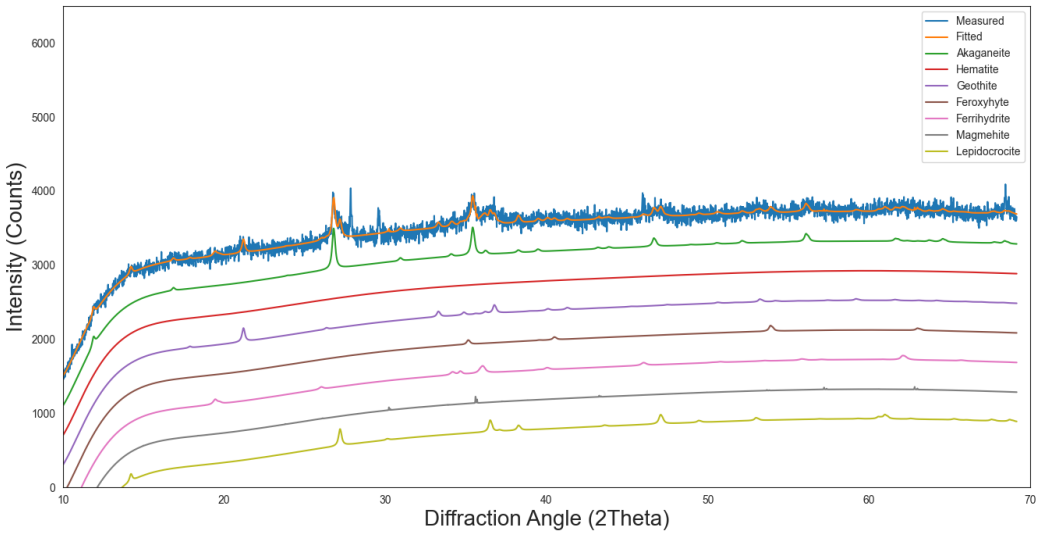


Figure A.700. XRD Pattern of Powdered Rust Collected from Exterior Web of the Girder.

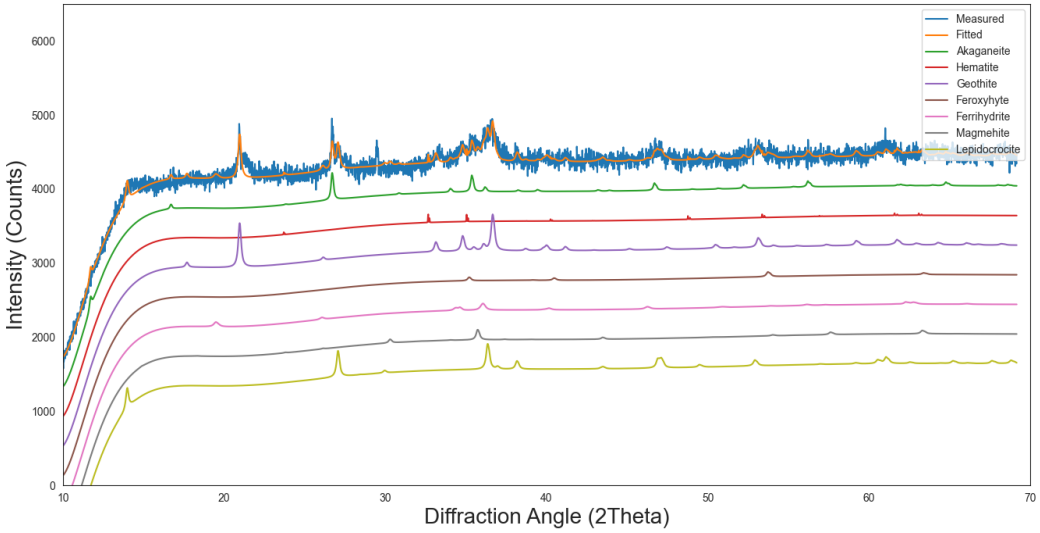


Figure A.701. XRD Pattern of Powdered Rust Collected from Interior Web of the Girder.

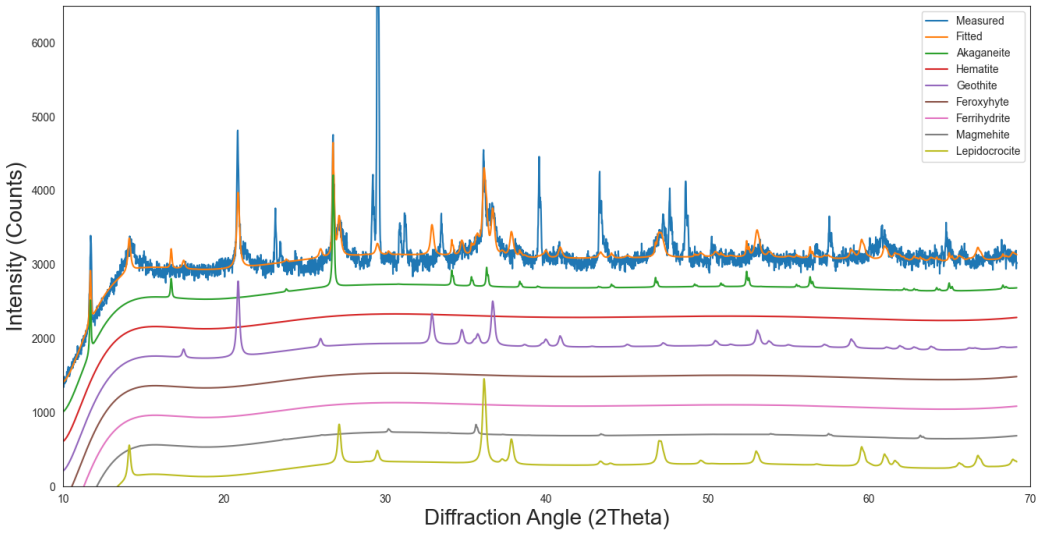


Figure A.702. XRD Pattern of Powdered Rust Collected from Bottom face of Bottom Flange of the Interior Girder.

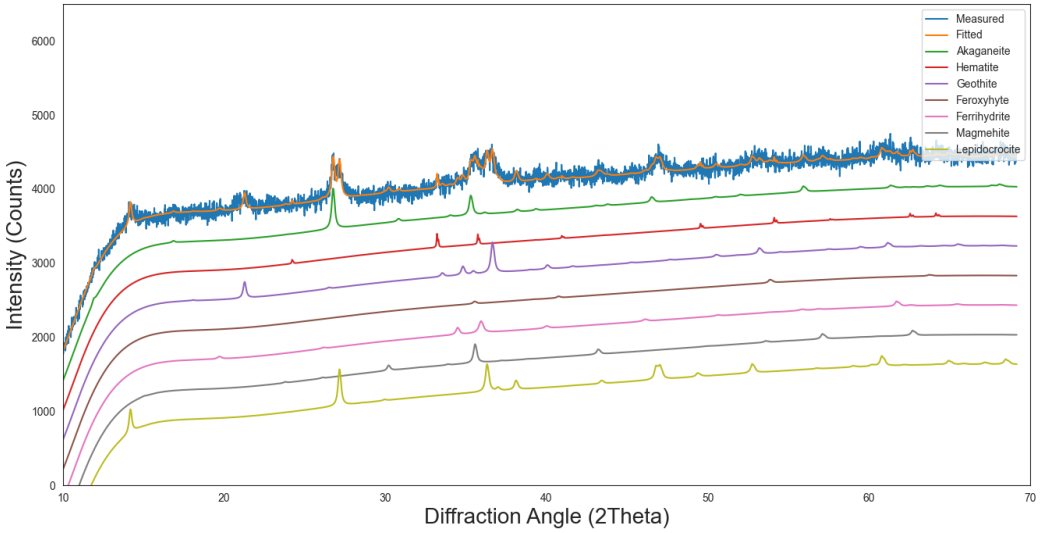


Figure A.703. XRD Pattern of Powdered Rust Collected from Bottom face of Bottom Flange of the Exterior Girder.

A.39.8. Particle Size Analysis: Tape Adhesion Results

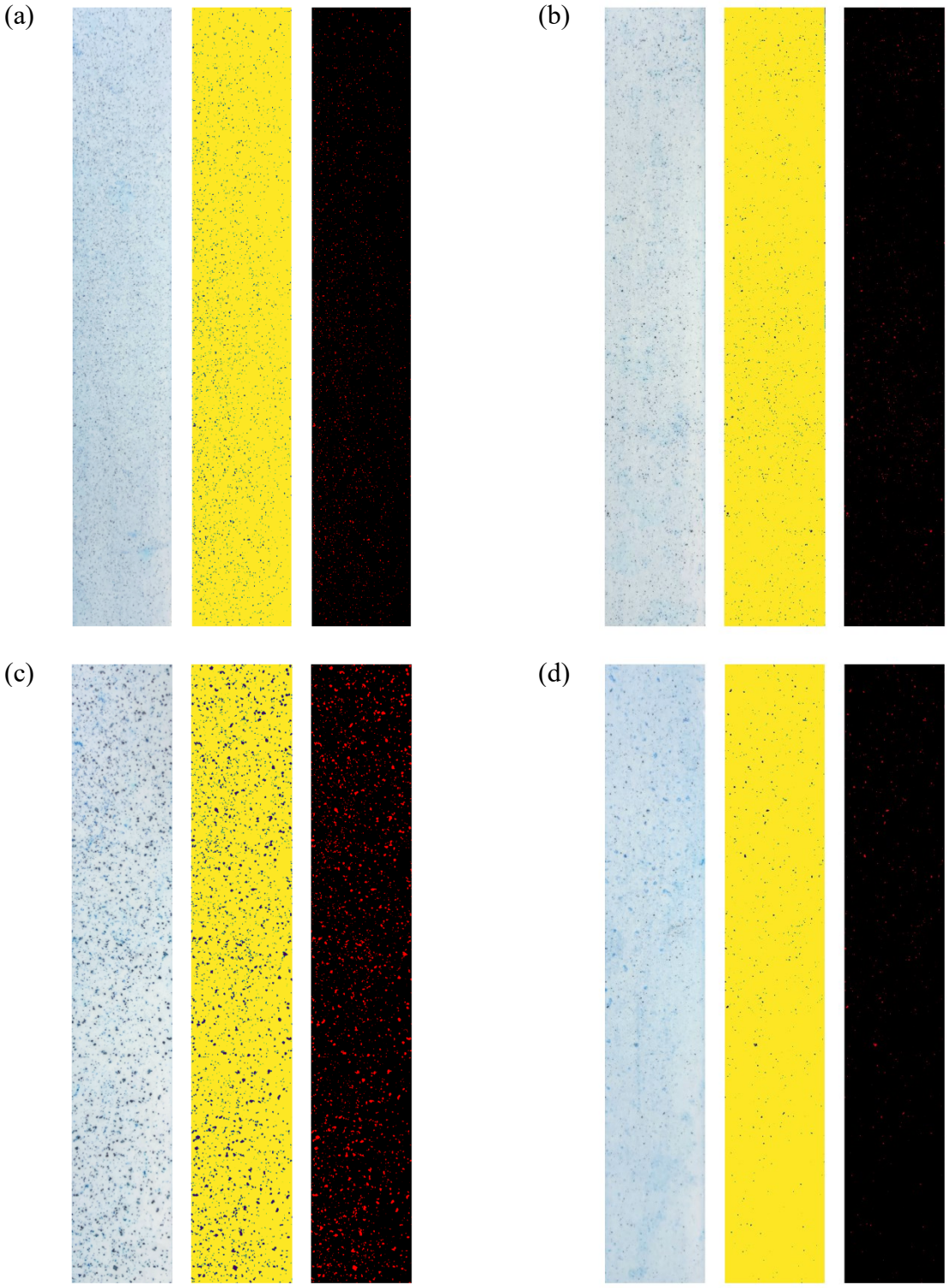


Figure A.704. Particle Size Analysis Results at A1G1F1 (a) Top Flange Bottom, (b) Web, (c) Bottom Flange Bottom (d) Stiffener.

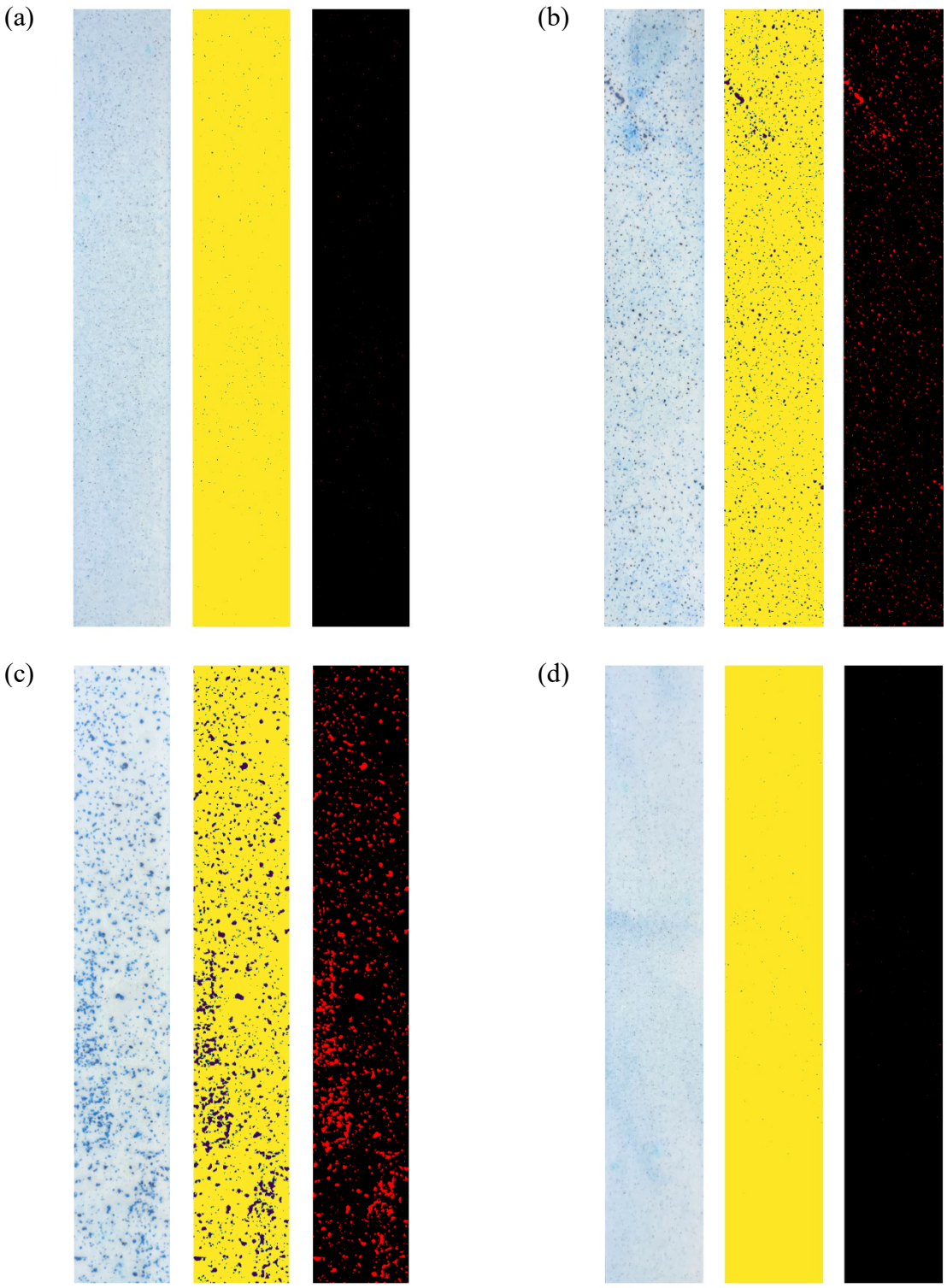


Figure A.705. Particle Size Analysis Results at A1G3F1 (a) Top Flange Bottom, (b) Web, (c) Bottom Flange Bottom (d) Stiffener.

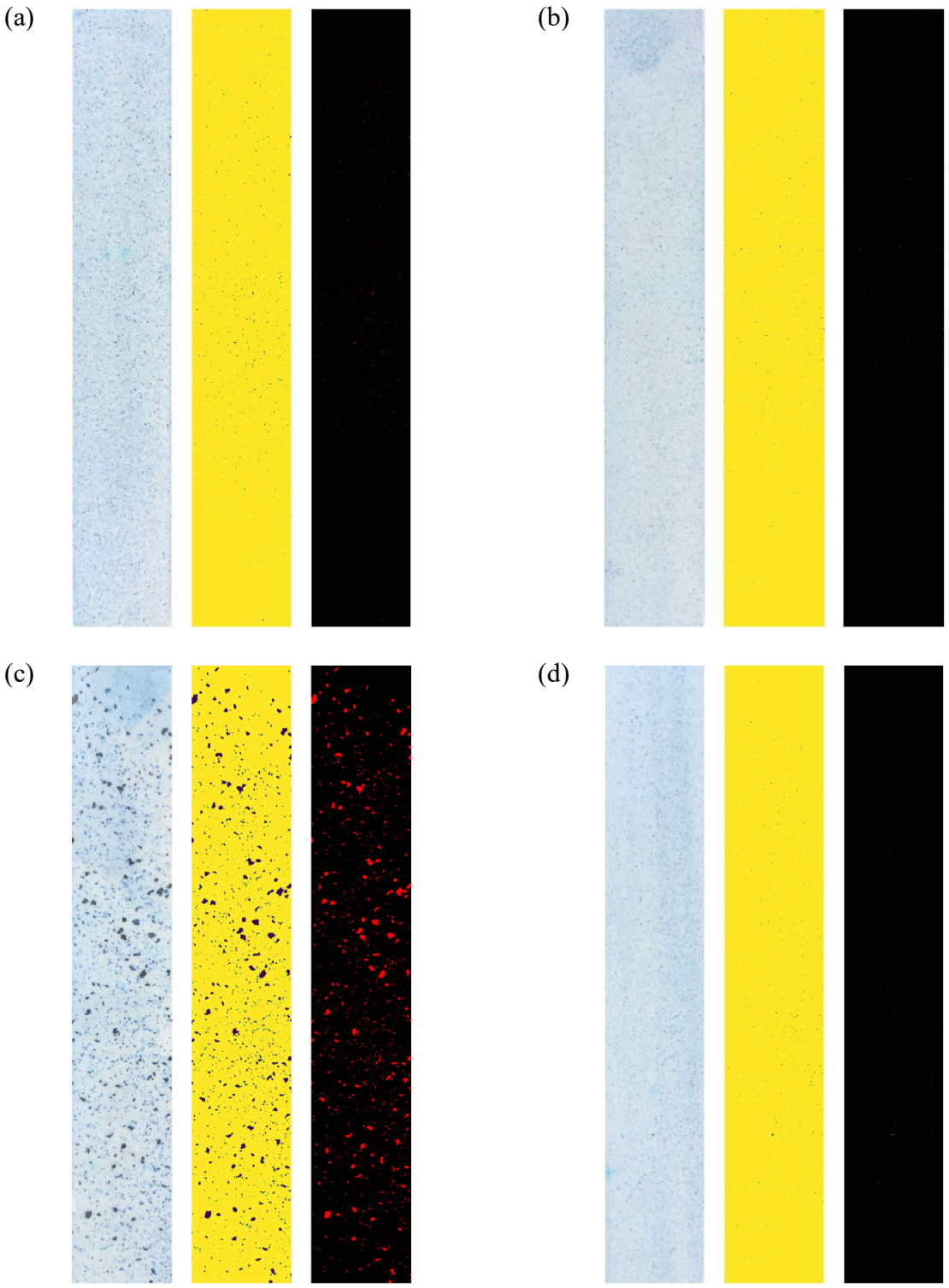


Figure A.706. Particle Size Analysis Results at A1G5F2 (a) Top Flange Bottom, (b) Web, (c) Bottom Flange Bottom (d) Stiffener.

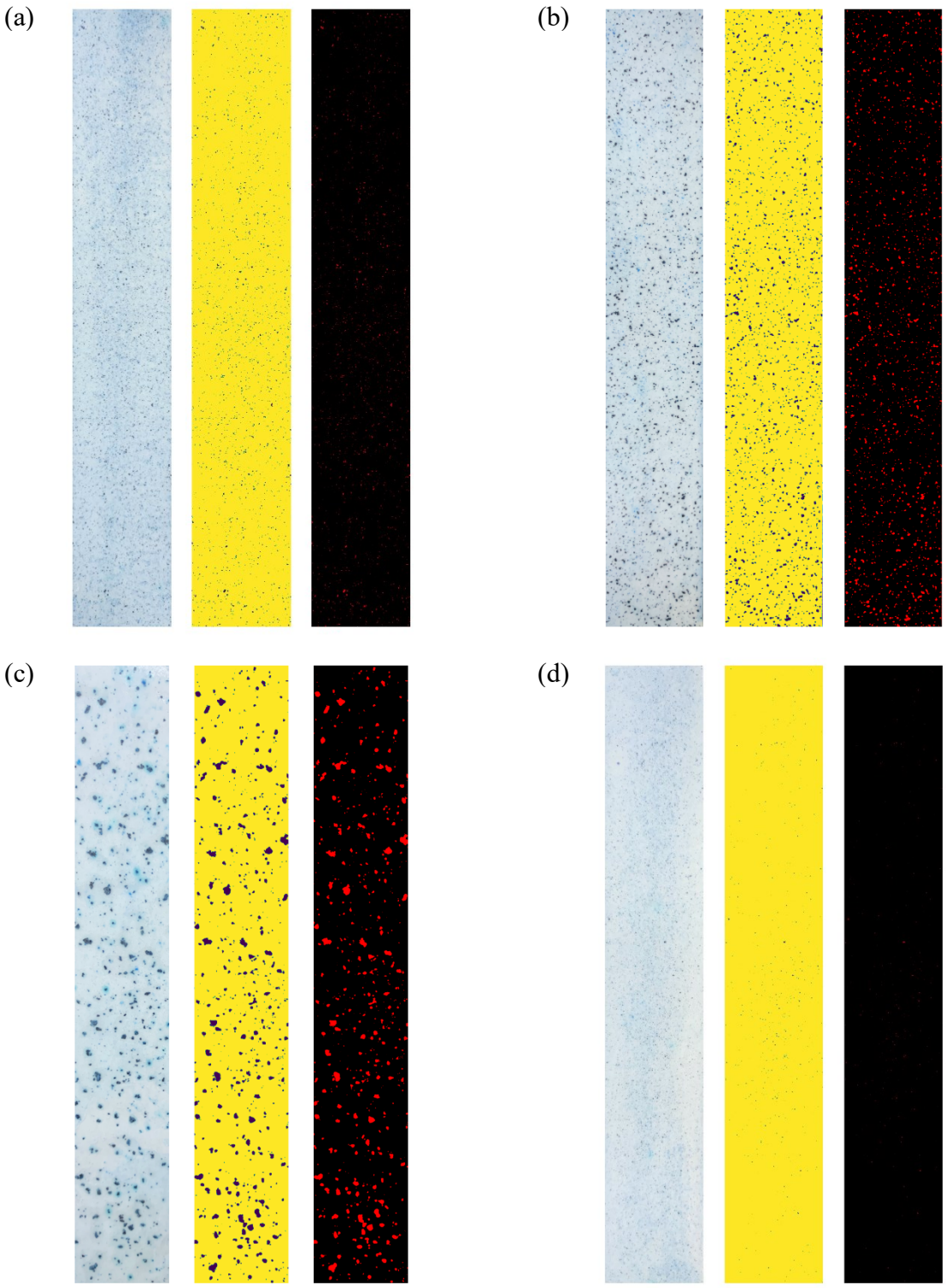


Figure A.707. Particle Size Analysis Results at A1G12F1 (a) Top Flange Bottom, (b) Web, (c) Bottom Flange Bottom (d) Stiffener.

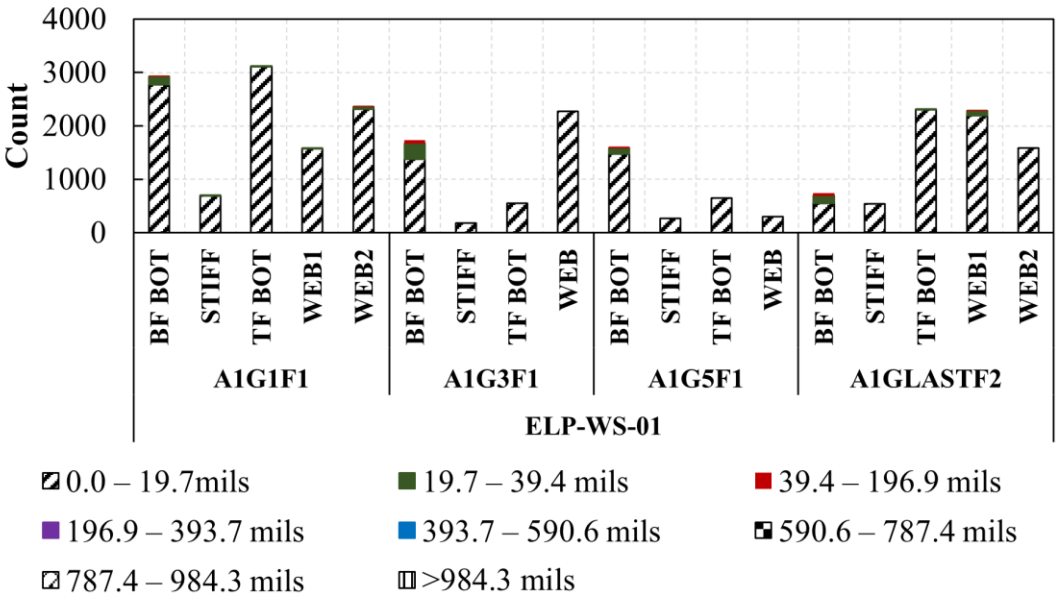


Figure A.708. Particle Size Analysis Showing Different Locations Examined.

A.40. AUS-WS-02

- US 290 EB over Manchaca/Westgate Blvd
- Bridge ID 142270011313114, Coordinates (30.23207, -97.80089), Travis County
- Continuous weathering steel plate girder
- Built 1997
- Inspection carried on girder 4, and measurements are taken on girder within four feet from the abutment or bent.
- No visual inspection on deck
- Location for Testing: B16 G7F2, B15-G4F1, B16-G5F1



Figure A.709. Typical Picture of AUS-WS-02.

A.40.1. Observed Condition

Delaminated areas of the patina are visible on the bottom face of the top flange with a patina rating of 6. The exterior web has a uniform patina formation with a patina rating of 8 wheras interior web has delaminated patina with a patina rating of 6. The interior girders has accumulation of bird feces and dirt leading to poultice corrosion on the top face of the bottom

flange with a patina rating of 6 whereas exterior girders have less accumulation of dirt. Patina delamination is also observed on bottom face of bottom flange.

A.40.2.Field Inspection Results

Table A-178. Field Inspection Results for AUS-WS-02.

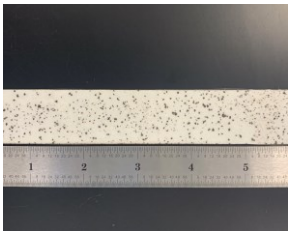
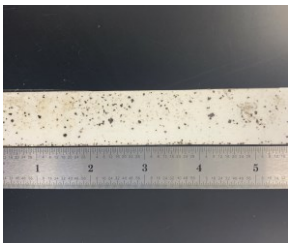
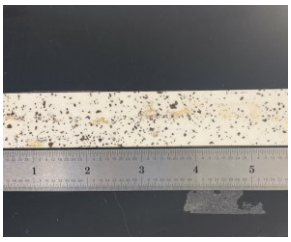
Location	Patina Rating	Thickness (inch)	Cl^- Conc. (ppm)	Field Condition	Tape Test
B15-G4F1 TF Bot.		-	-		-
B15-G4F1 Web	8	Measured R1 0.510 R2 0.512 R3 0.513 R_Avg 0.512 Design 0.500	0		
B15-G4F1 BF Top	6	Measured R1 1.019 R2 1.018 R3 1.015 R_Avg 1.017 Design 1.000	-		
B15-G4F1 BF Bot	6	-	-		
B16-G5F1 TF Bot		-	-		

Table A-179. Field Inspection Results for AUS-WS-02.

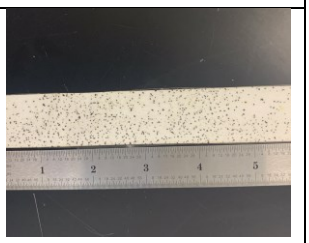
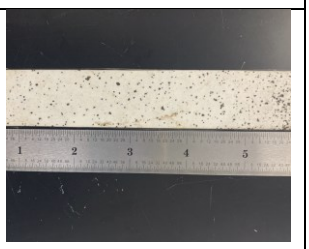
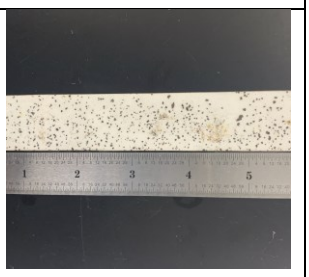
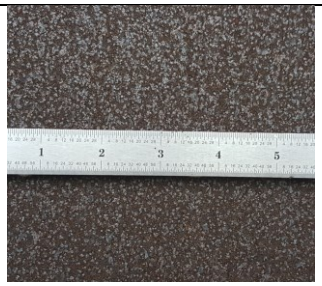
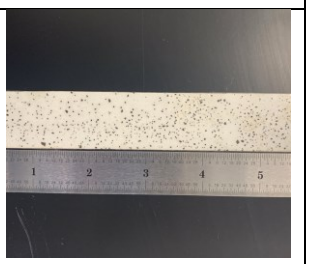
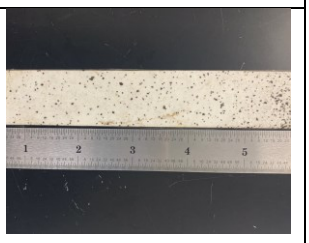
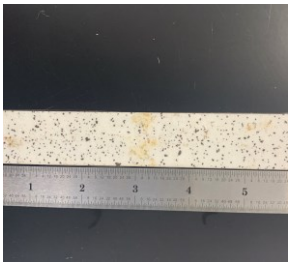
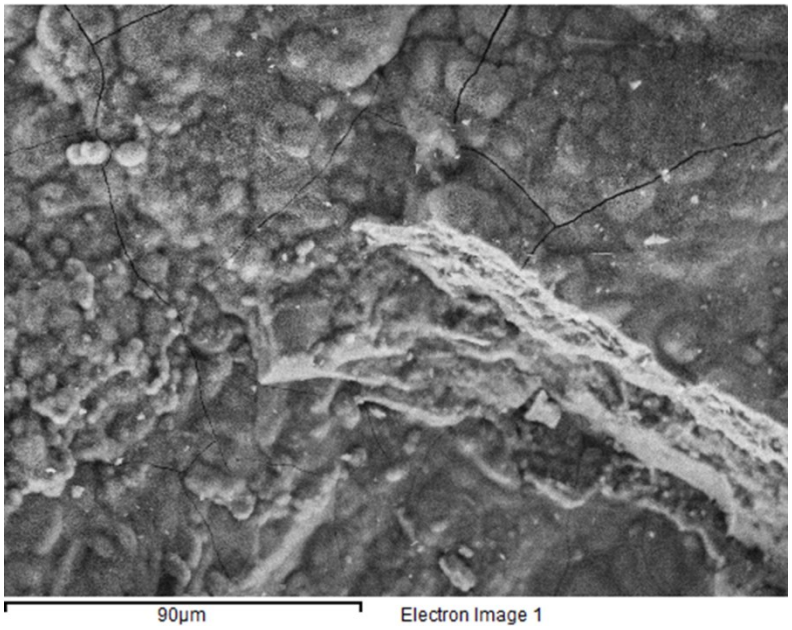
Location	Patina Rating	Thickness (inch)	Cl^- Conc. (ppm)	Field Condition	Tape Test
B16-G5F1 Web	8	Measured R1 0.508 R2 0.511 R3 0.509 R_Avg 0.509 Design 0.500	1		
B16-G5F1 BF Top	6	Measured R1 1.014 R2 1.016 R3 1.015 R_Avg 1.015 Design 1.000	-		
B16-G5F1 BF Bot	7	-	-		
B16-G7F2 TF Bot		-	-		
B16-G7F2 Web	7	Measured R1 0.499 R2 0.498 R3 0.499 R_Avg 0.499 Design 0.500			

Table A-180. Field Inspection Results for AUS-WS-02.

Location	Patina Rating	Thickness (inch)	Cl^- Conc. (ppm)	Field Condition	Tape Test
B16-G7F2 BF Top	6	Measured R1 1.013 R2 1.012 R3 1.015 R_Avg 1.013 Design 1.000	-		
B16-G7F2 BF Bot	6	-	-		

A.40.3.SEM/EDS Results: Interior Web Girder

Element	Weight %	Atomic %
O K	41.52	70.69
Al K	0.55	0.56
Si K	0.35	0.34
S K	0.68	0.58
Cl K	0.15	0.11
Ca K	0.25	0.17
Mn K	2.41	1.20
Fe K	53.49	26.09
Ni K	0.31	0.14
Cu K	0.29	0.13
Totals	100.00	



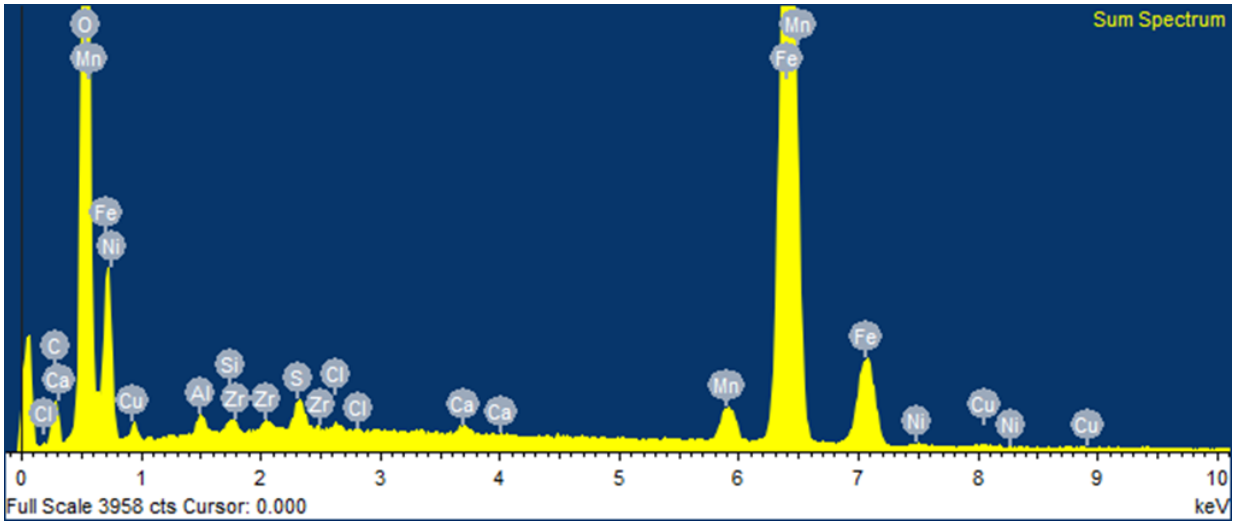


Figure A.710. SEM Image and EDS Spectrum of the Rust Collected from Interior Web of the Girder.

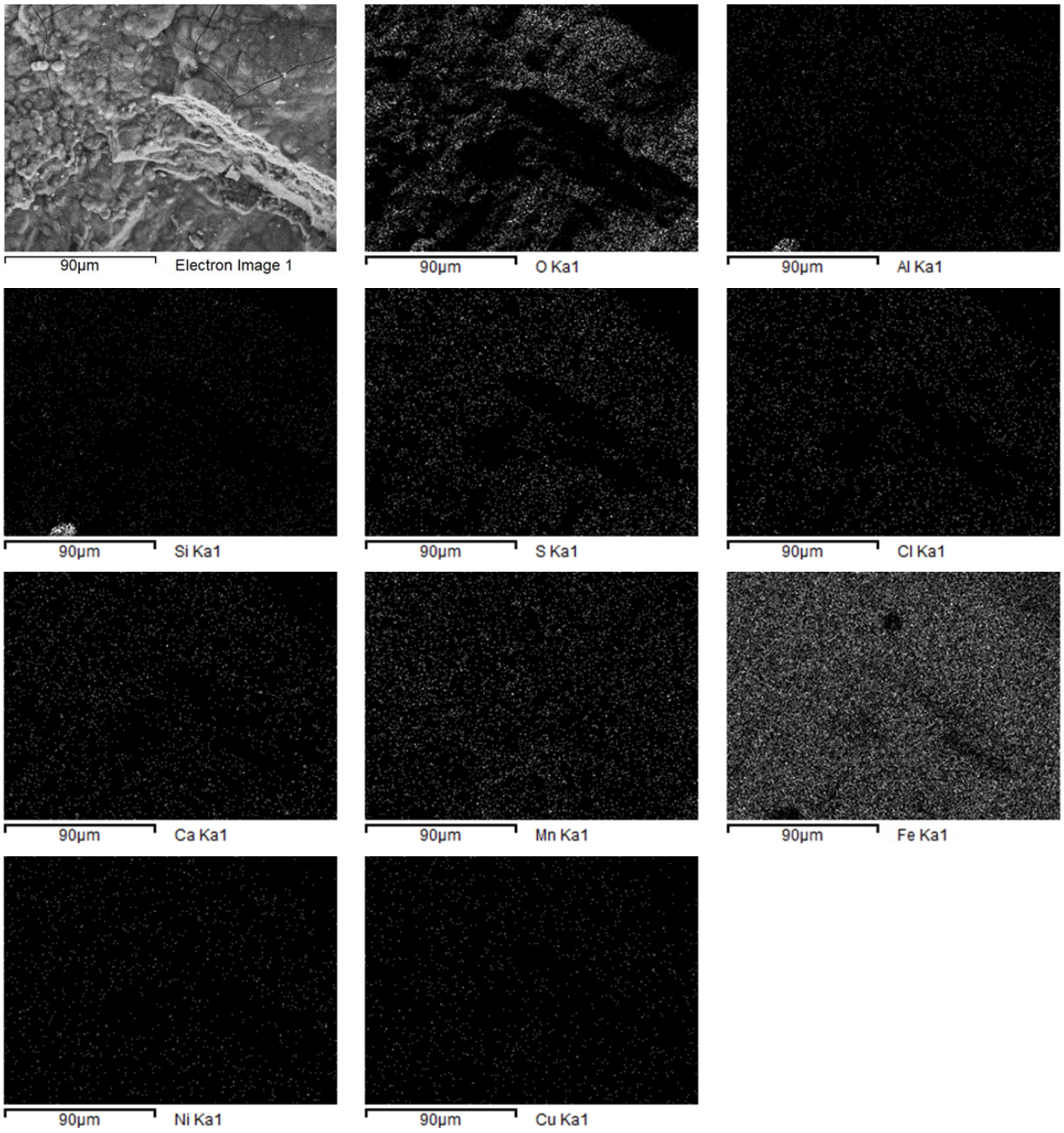
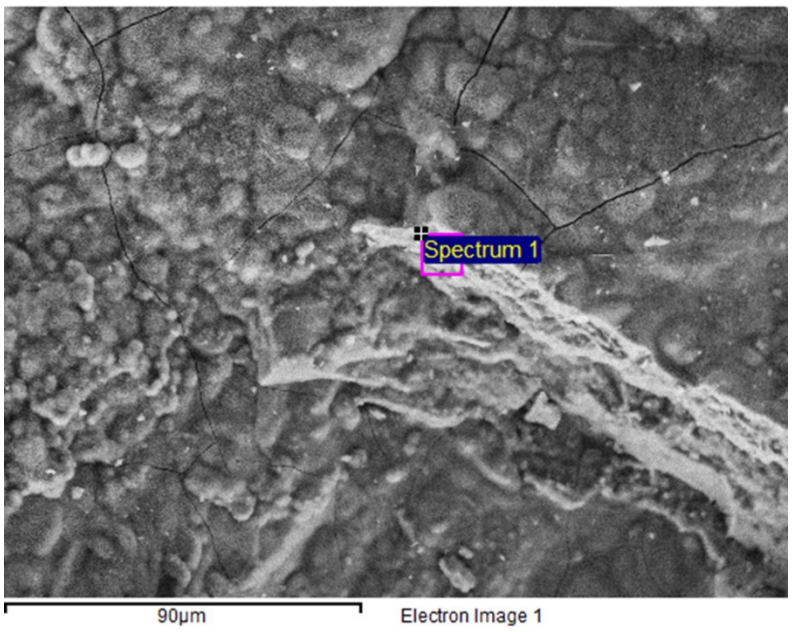


Figure A.711. EDS Elemental Mapping of Rust Collected from Interior Web.

Element	Weight %	Atomic %
O K	15.30	38.13
Al K	1.21	1.79
Si K	0.28	0.40
S K	0.42	0.53
Cl K	0.12	0.14
Ca K	0.18	0.18
Mn K	2.09	1.52
Fe K	79.66	56.86
Cu K	0.73	0.46
Totals	100.00	



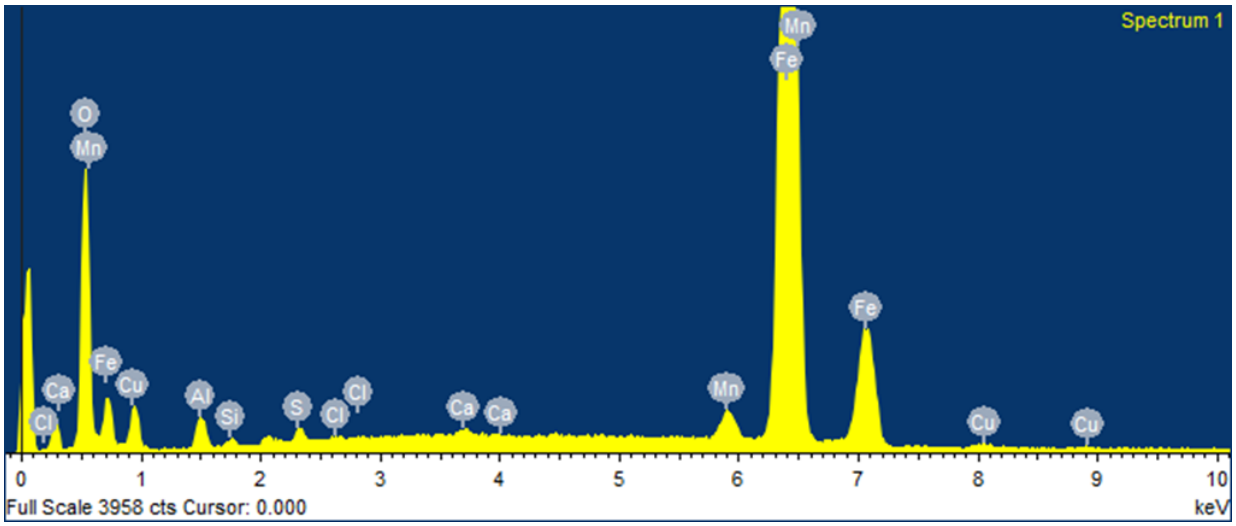
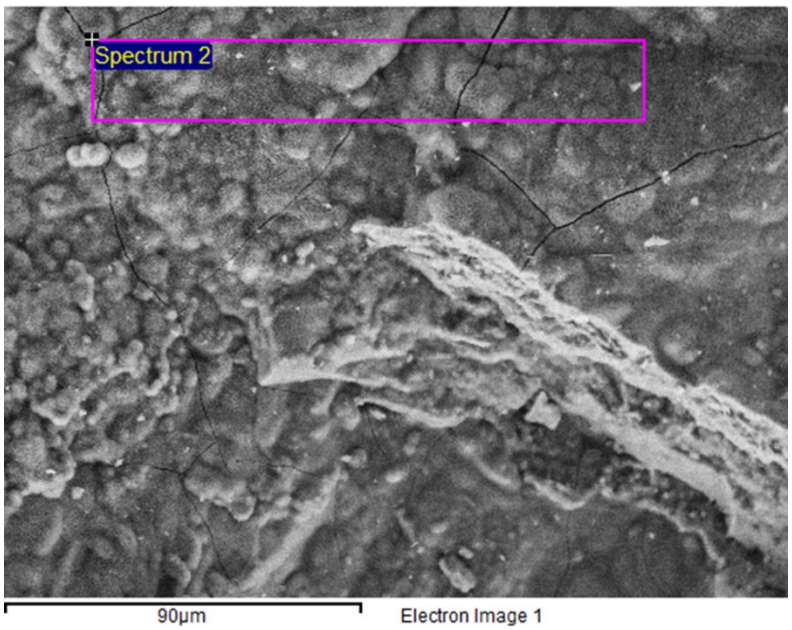


Figure A.712. SEM Image and EDS Spectrum of the Rust Collected from Interior Web of the Girder.

Element	Weight %	Atomic %
O K	48.30	75.84
Al K	0.59	0.55
Si K	0.76	0.68
S K	0.75	0.59
Ca K	0.17	0.11
Mn K	1.80	0.82
Fe K	47.08	21.18
Ni K	0.31	0.13
Cu K	0.24	0.10
Totals	100.00	



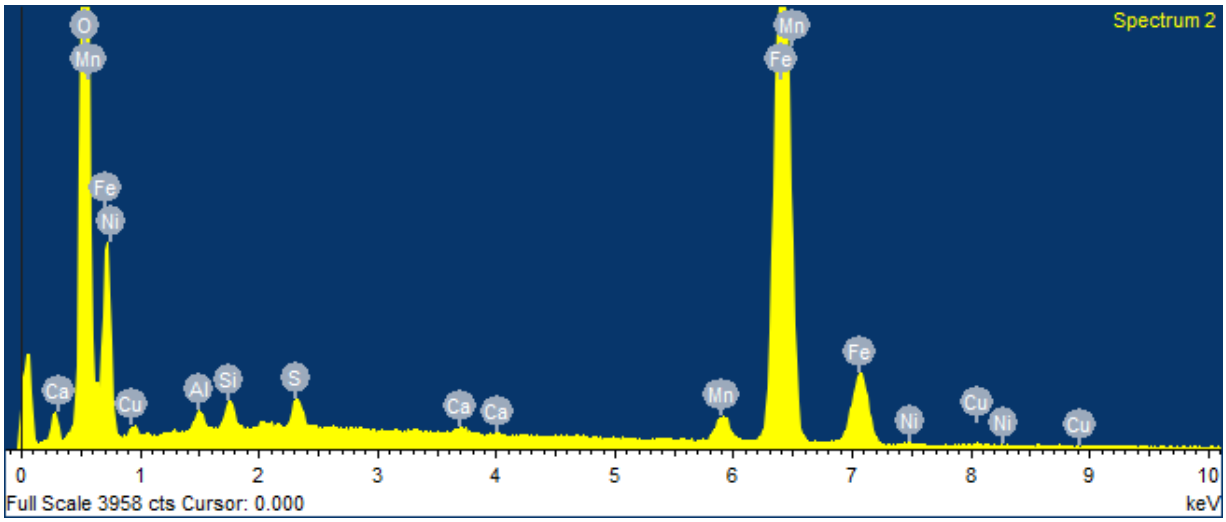
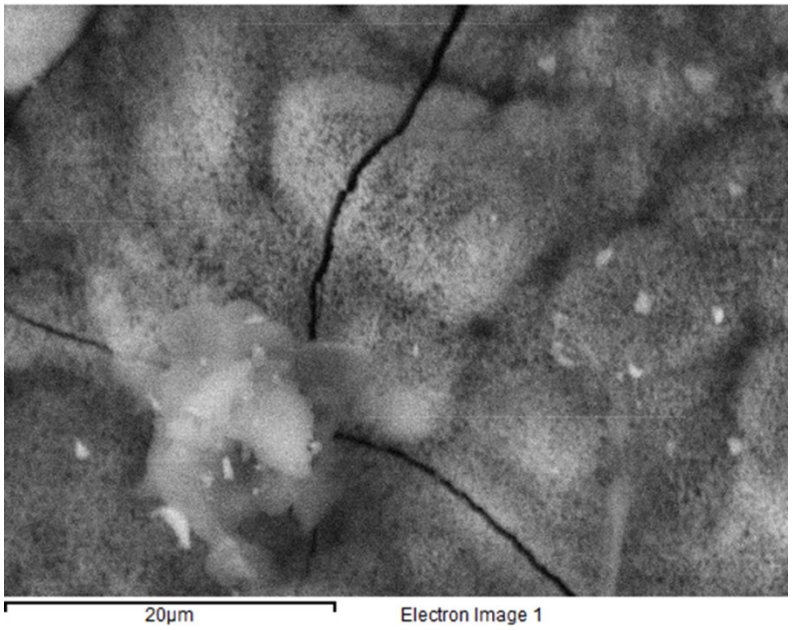


Figure A.713. SEM Image and EDS Spectrum of the Rust Collected from Interior Web of the Girder.

A.40.4.SEM/EDS Results: Interior Web Girder

Element	Weight %	Atomic %
O K	51.70	78.44
Al K	0.40	0.36
Si K	0.16	0.14
S K	0.85	0.65
Ca K	0.26	0.16
Mn K	1.74	0.77
Fe K	44.29	19.25
Ni K	0.27	0.11
Cu K	0.31	0.12
Totals	100.00	



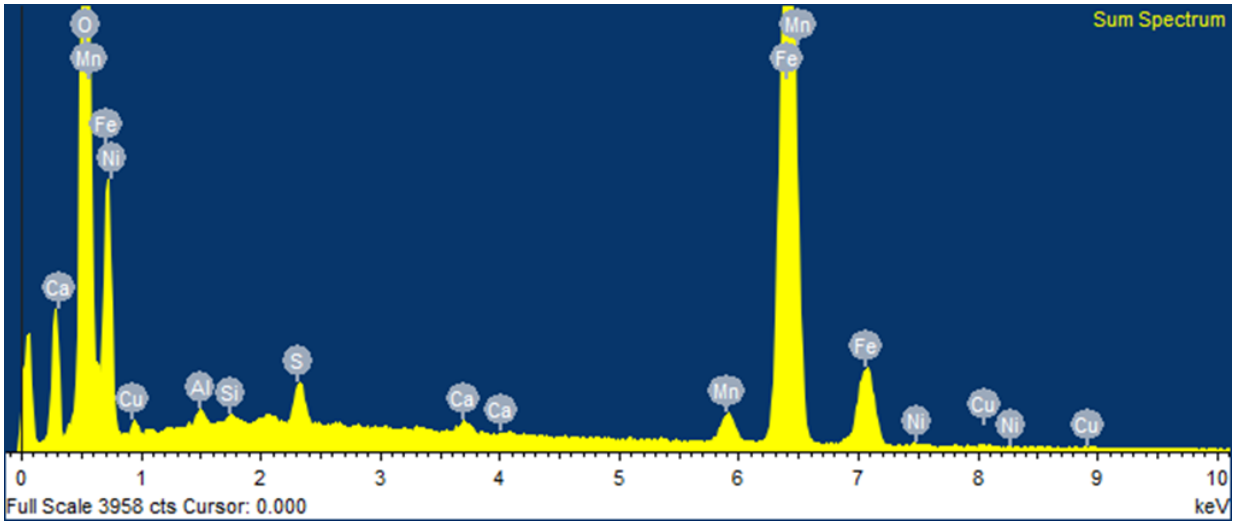


Figure A.714. SEM Image and EDS Spectrum of the Rust Collected from Interior Web of the Girder.

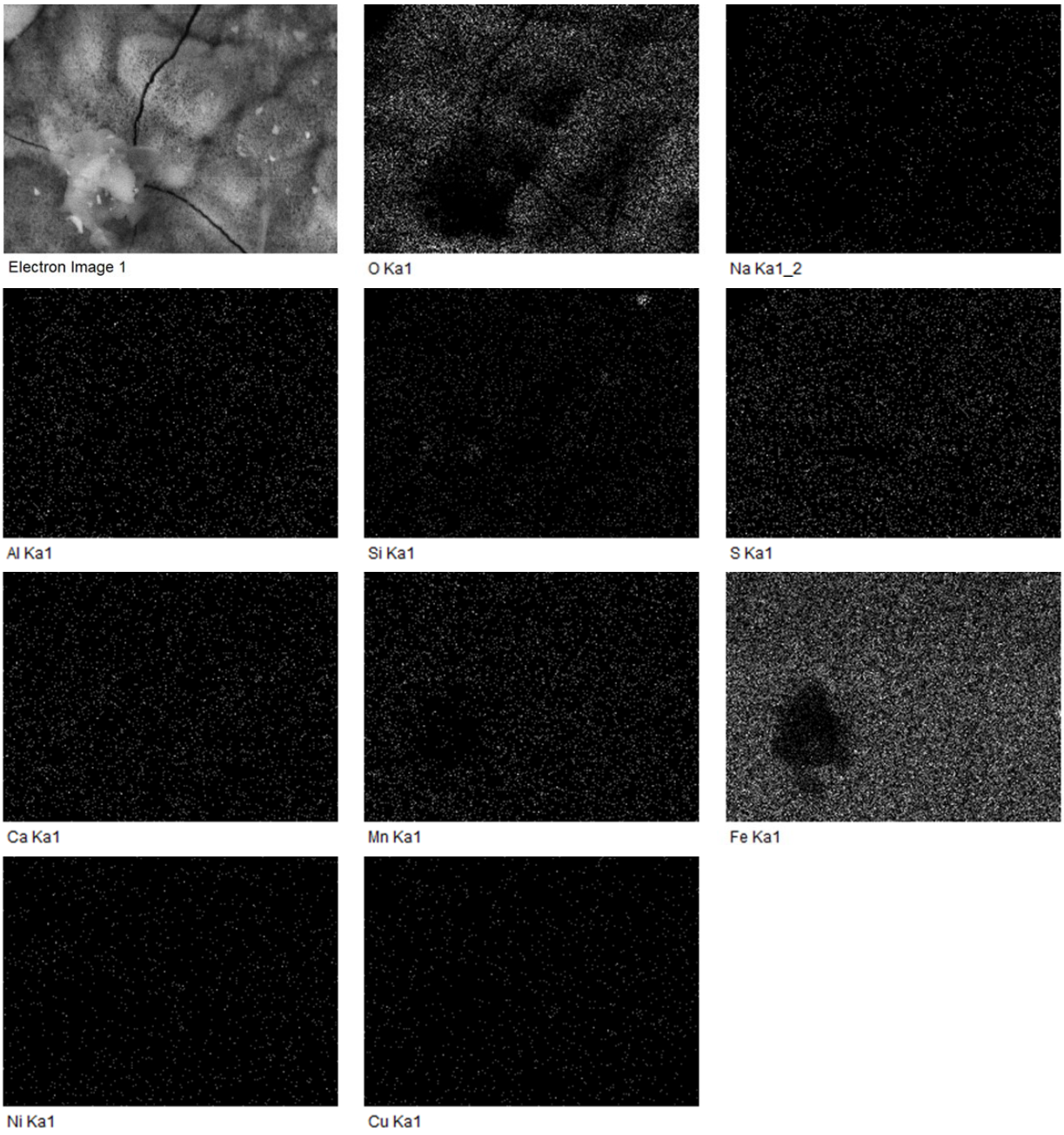
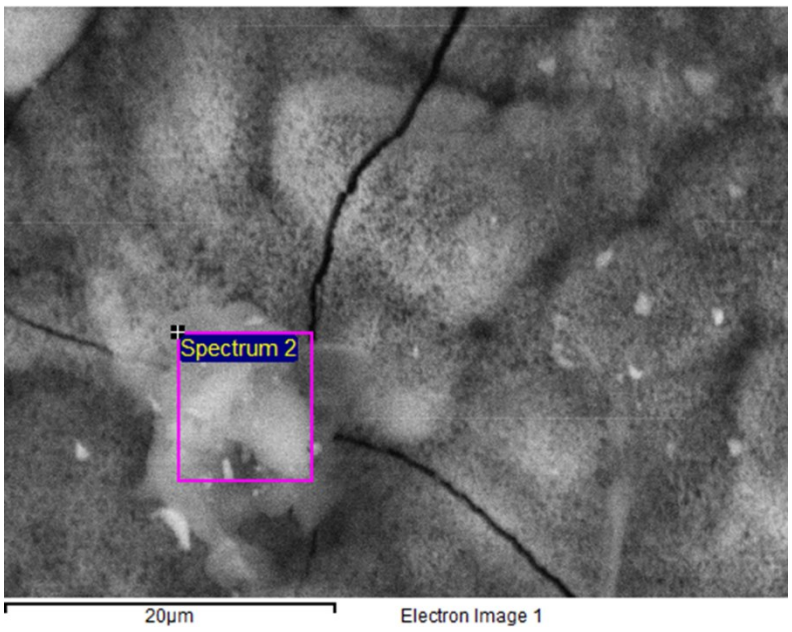


Figure A.715. EDS Elemental Mapping of Rust Collected from Interior Web.

Element	Weight %	Atomic %
N K	20.03	26.17
O K	57.43	65.70
Na K	0.37	0.30
Al K	0.25	0.17
Si K	0.19	0.13
P K	0.38	0.22
S K	0.74	0.42
K K	0.40	0.19
Ca K	0.57	0.26
Mn K	0.74	0.25
Fe K	18.78	6.15
Cu K	0.12	0.03
Totals	100.00	



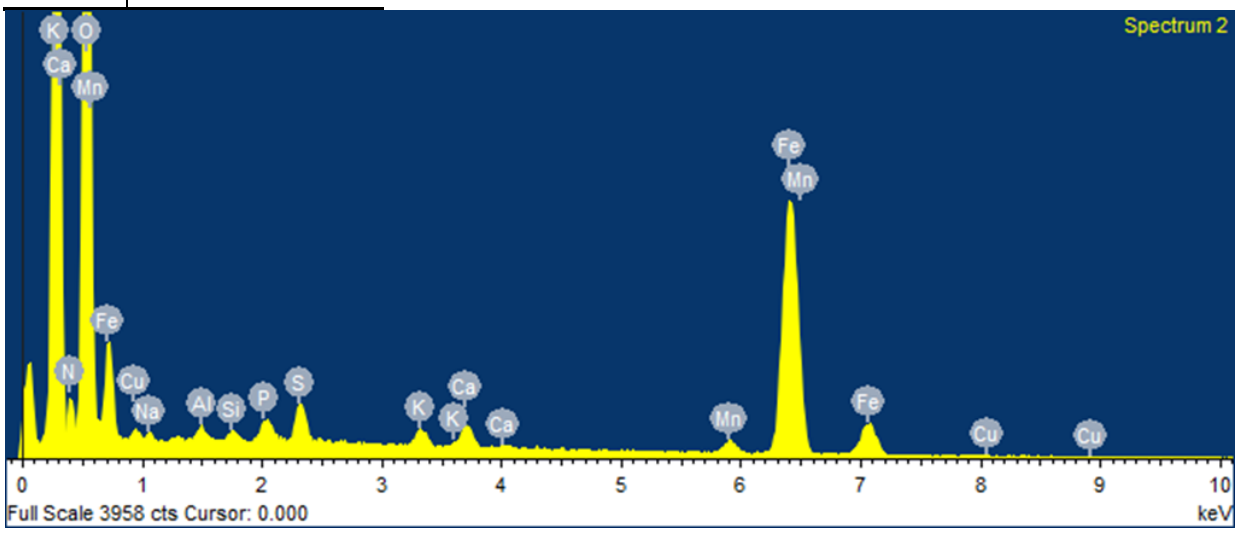
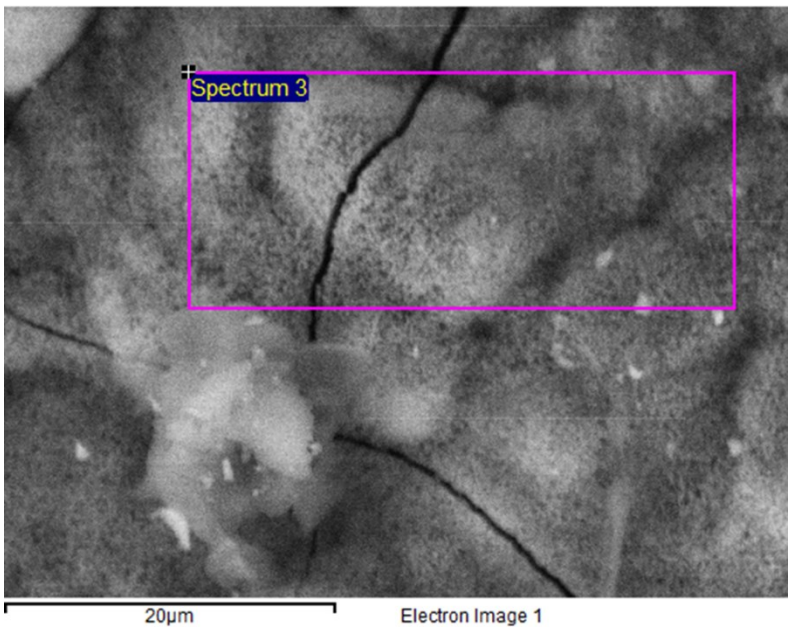


Figure A.716. SEM Image and EDS Spectrum of the Rust Collected from Interior Web of the Girder.

Element	Weight %	Atomic %
O K	55.02	80.66
Al K	0.31	0.27
S K	0.91	0.66
Ca K	0.14	0.08
Mn K	1.79	0.76
Fe K	41.62	17.48
Cu K	0.21	0.08
Totals	100.00	



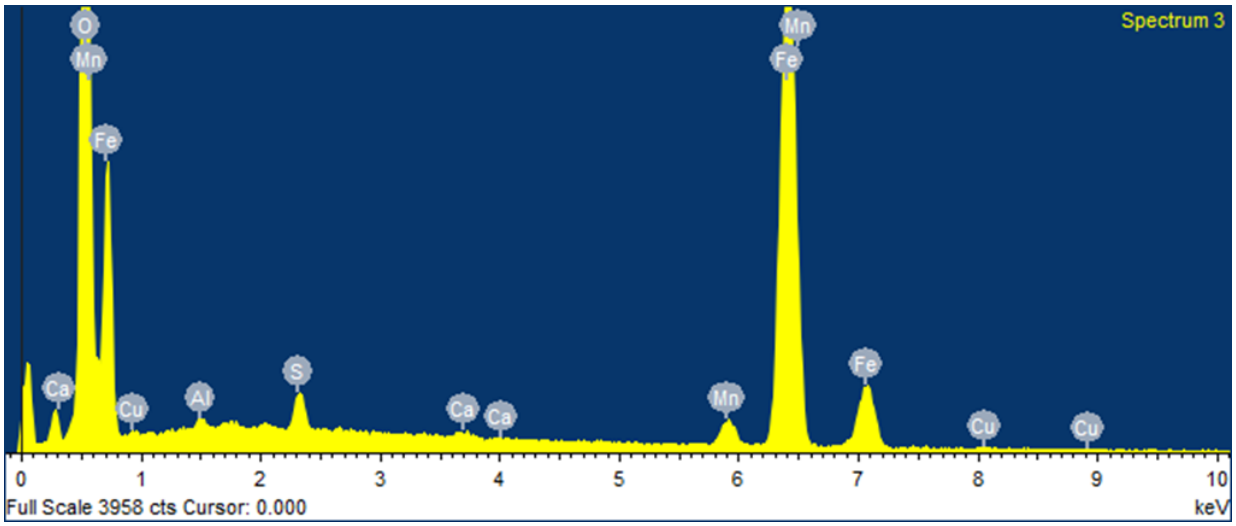
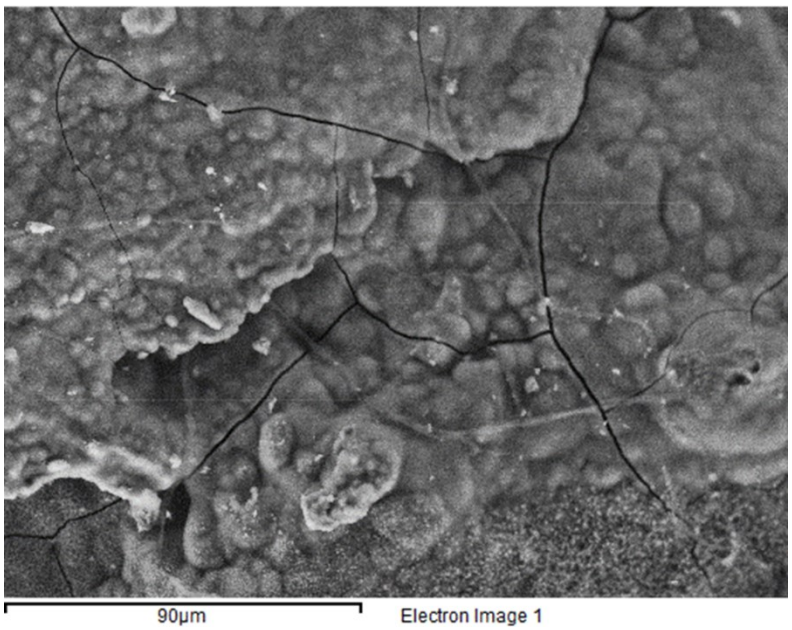


Figure A.717. SEM Image and EDS Spectrum of the Rust Collected from Interior Web of the Girder.

Element	Weight %	Atomic %
O K	46.82	74.91
Al K	0.37	0.35
S K	1.24	0.99
Cl K	0.22	0.16
Ca K	0.25	0.16
Mn K	1.44	0.67
Fe K	49.48	22.68
Cu K	0.19	0.08
Totals	100.00	



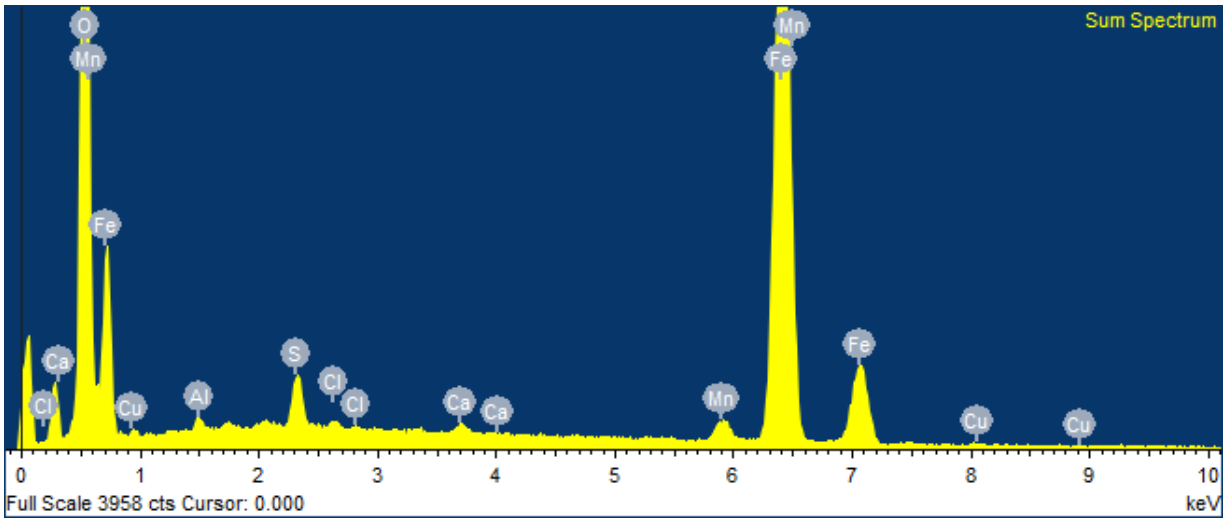


Figure A.718. SEM Image and EDS Spectrum of the Rust Collected from Interior Web of the Girder.

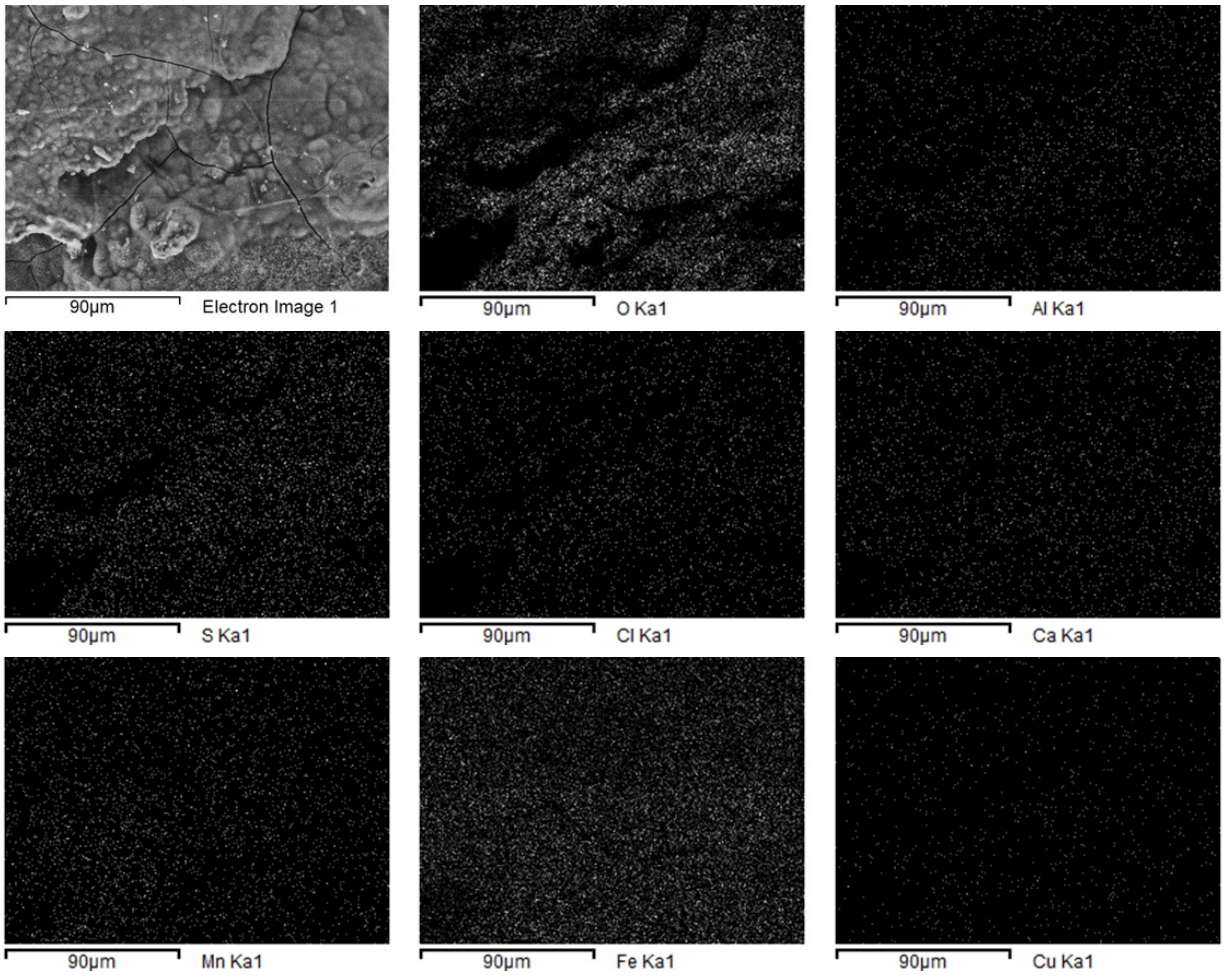
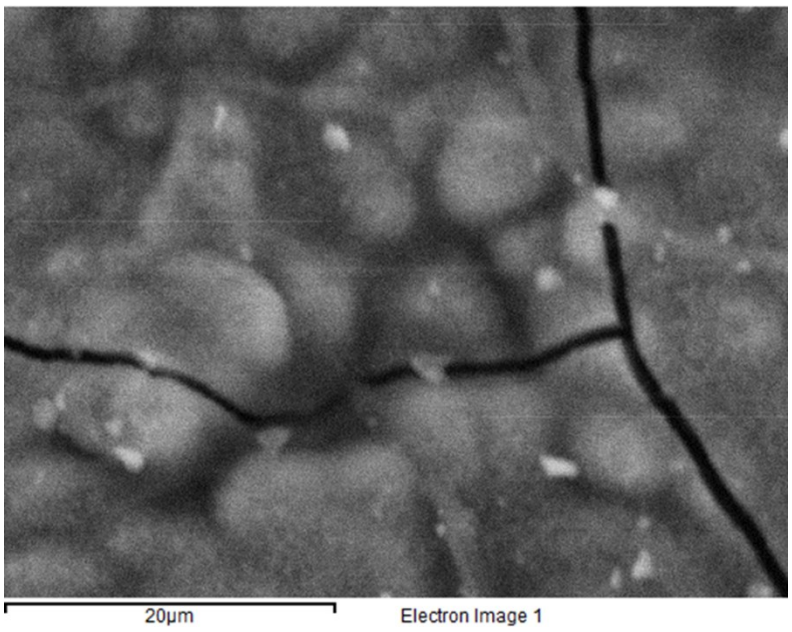


Figure A.719. EDS Elemental Mapping of Rust Collected from Interior Web.

Element	Weight %	Atomic %
O K	51.73	78.16
Na K	0.34	0.36
Al K	0.26	0.23
Si K	0.17	0.15
P K	0.17	0.13
S K	1.23	0.92
Cl K	0.19	0.13
Ca K	0.22	0.13
Mn K	1.22	0.54
Fe K	44.40	19.22
Cu K	0.07	0.03
Totals	100.00	



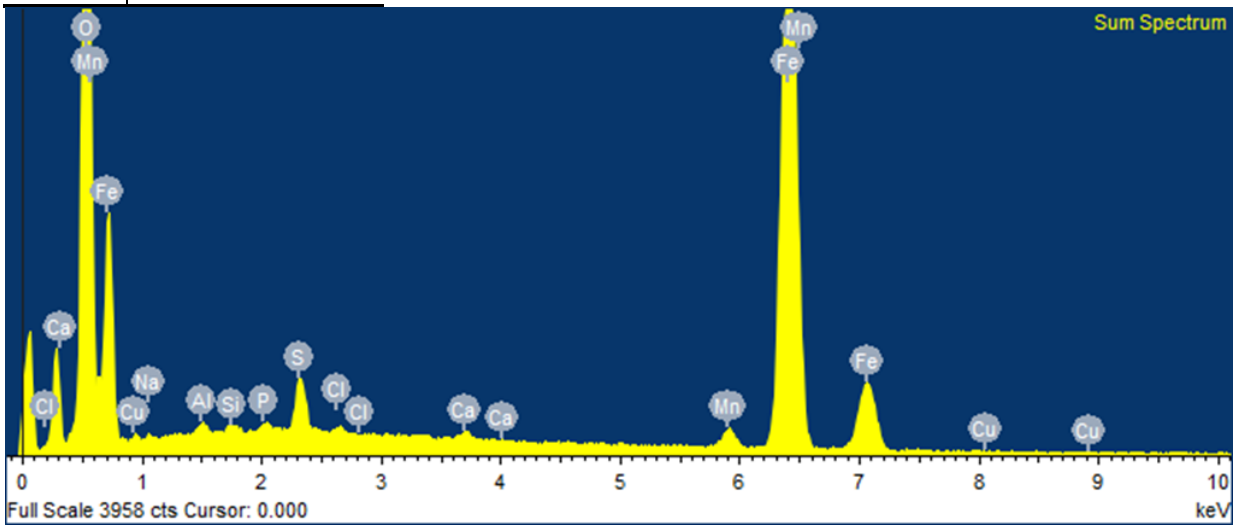


Figure A.720. SEM Image and EDS Spectrum of the Rust Collected from Interior Web of the Girder.

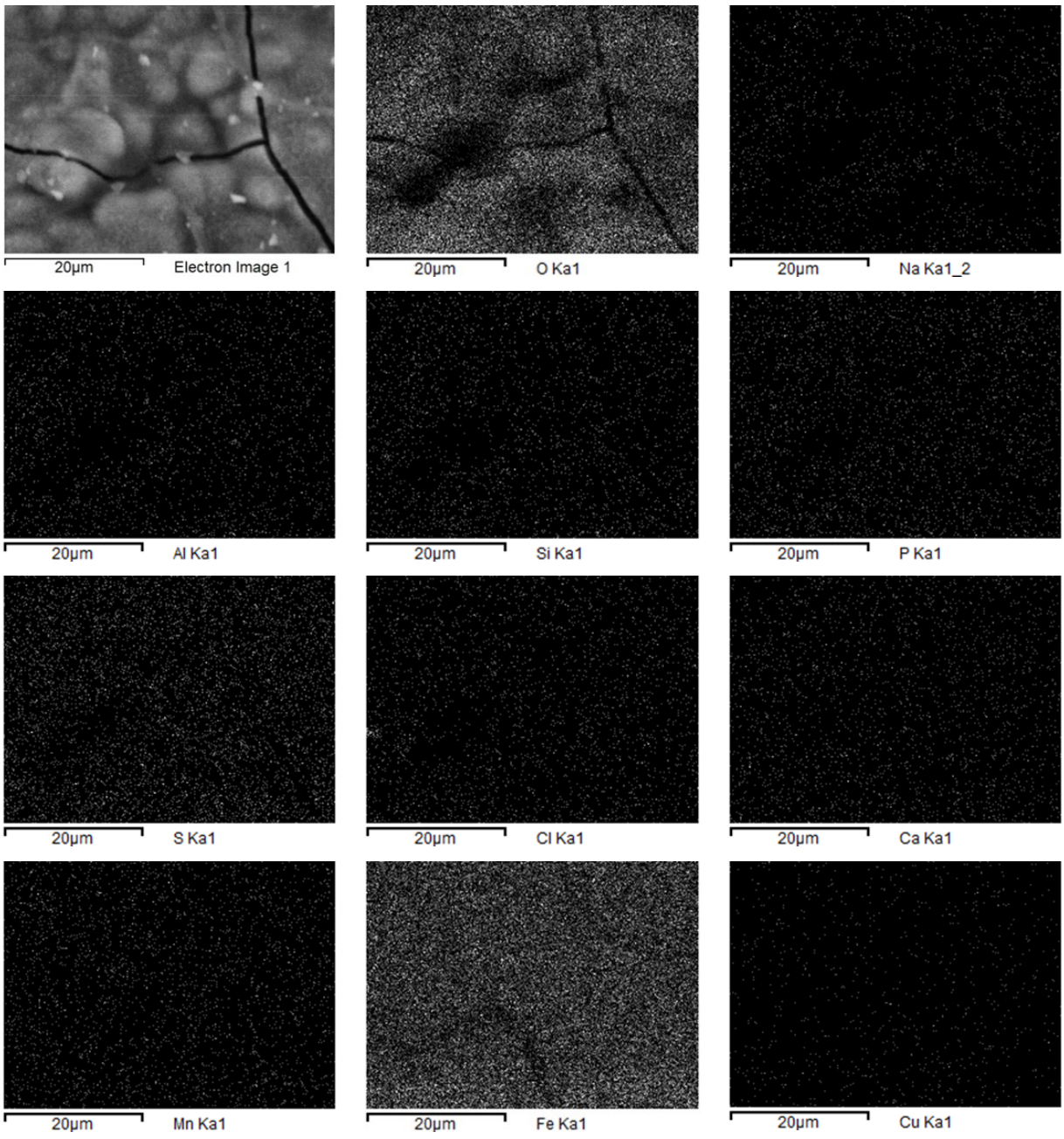


Figure A.721. EDS Elemental Mapping of Rust Collected from Interior Web.

A.40.5.XPS Result: Interior Girder

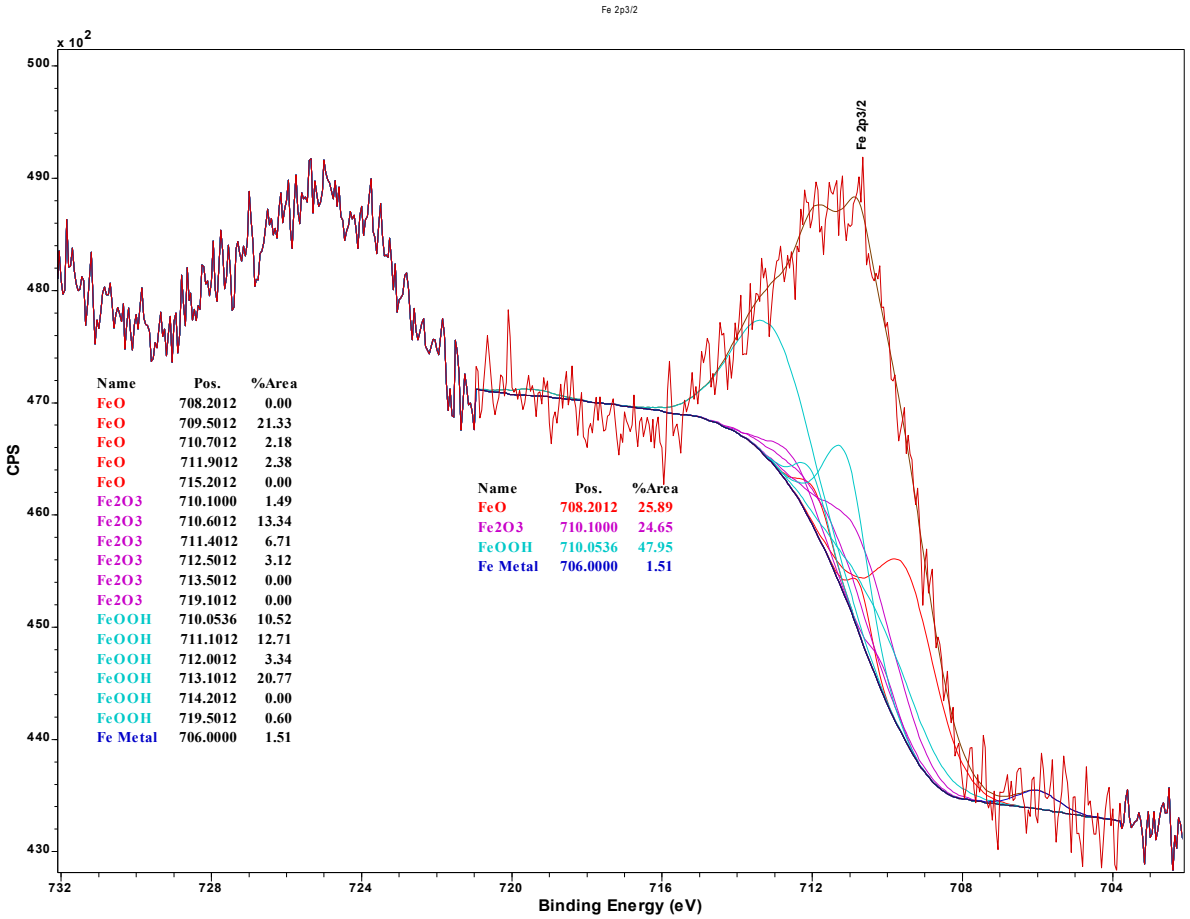


Figure A.722. XPS Spectrum of the Rust Collected from Interior Web of the Girder.

A.40.6.XRD Result: Exterior and Interior Girder

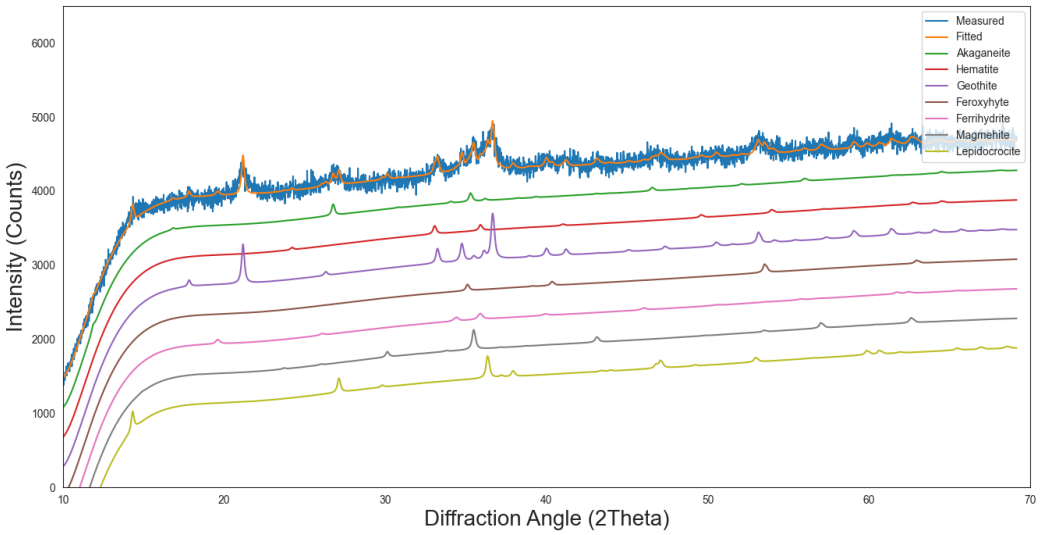
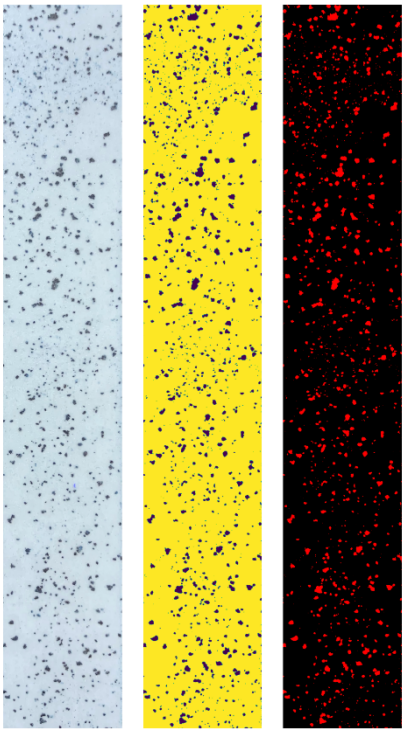


Figure A.723. XRD Pattern of Powdered Rust Collected from Interior Web of the Girder.

A.40.7.Particle Size Analysis: Tape Adhesion Results

(a)

(b)



(c)

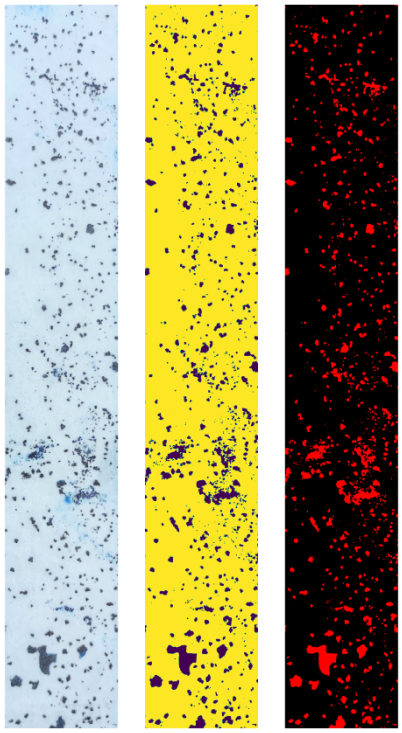
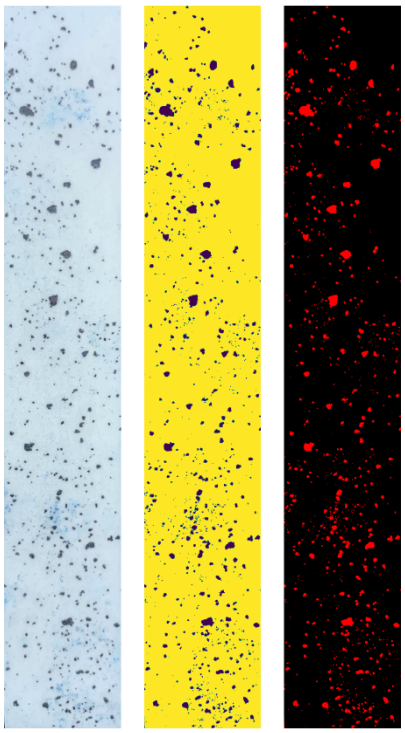


Figure A.724. Particle Size Analysis Results at B16G4F1 (a) Top Flange Bottom, (b) Web, (c) Bottom Flange Bottom.

(a)

(b)



(c)

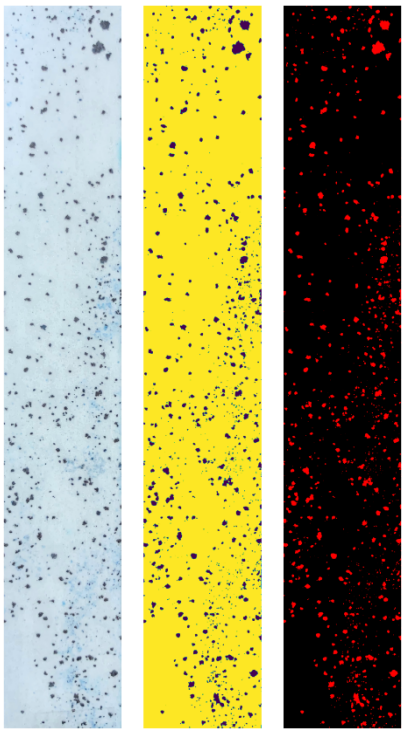
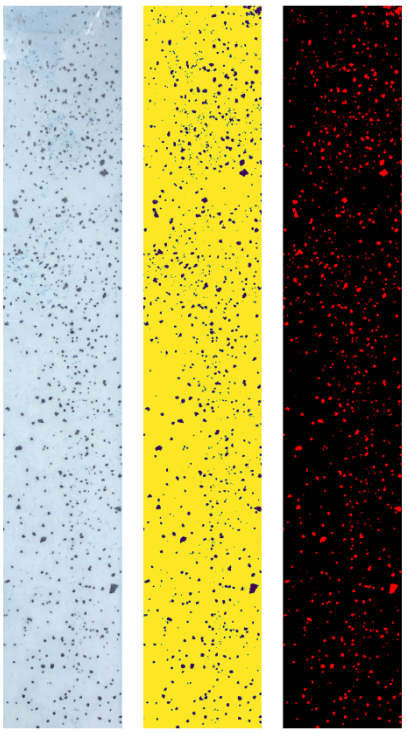


Figure A.725. Particle Size Analysis Results at B16G5F1 (a) Top Flange Bottom, (b) Web, (c) Bottom Flange Bottom.

(a)

(b)



(c)

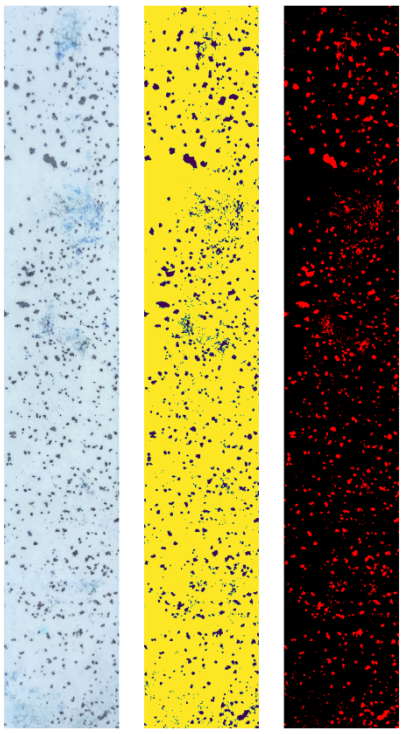


Figure A.726. Particle Size Analysis Results at B16G7F2 (a) Top Flange Bottom, (b) Web, (c) Bottom Flange Bottom.

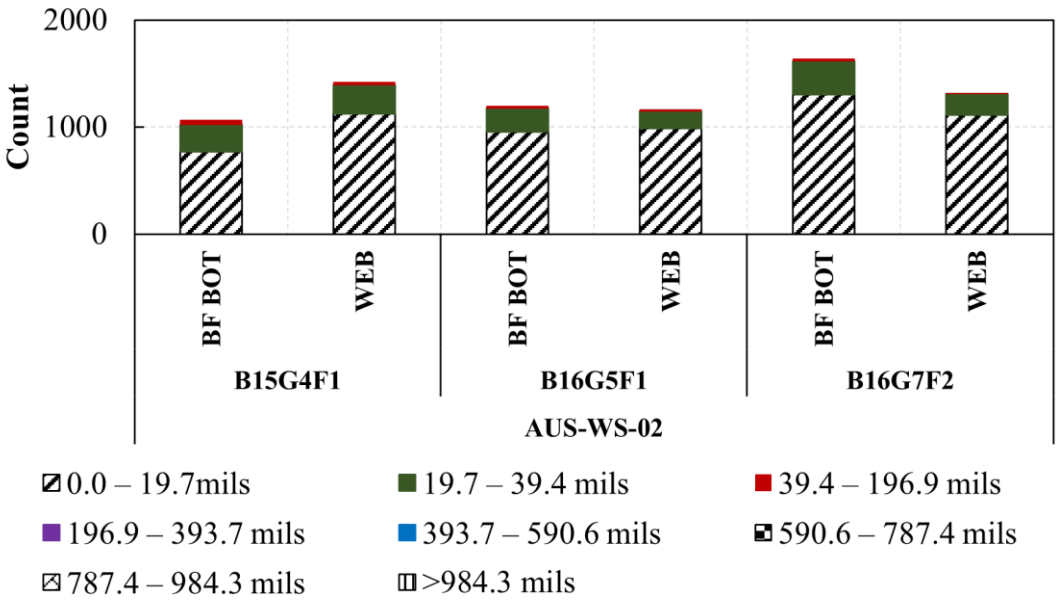


Figure A.727. Particle Size Analysis Showing Different Locations Examined.

A.41. FTW-WS-01

- RAMPS C-1S C-1N
- Bridge ID 022200BB0985007, Coordinates (32.91424, -97.03961), Tarrant County
- Continuous weathering steel plate girder
- Built 1974
- Girder inspection carried on abutment, and measurements are taken on girder within four feet from the abutment or bent.
- No visual inspection on deck
- Location for Testing: A1-G1F1, A1-G1F2, A1-G2F1, A3-G2F1, A3-G1F1



Figure A.728. Typical Picture of FTW-WS-01.

A.41.1. Observed Condition

Overall bridge is in very good condition with development of uniform patina throughout the girder. Delamination and pitting corrosion are observed in some areas of the bottom and top face of bottom flange. A patina rating ranging between 7 and 8 is observed showing good corrosion protection provided by developed patina.

A.41.2.Field Inspection Results

Table A-181. Field Inspection Results for FTW-WS-01.

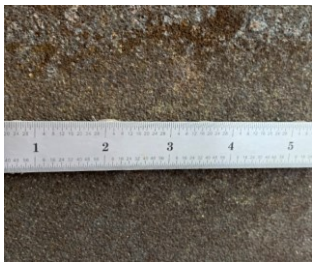
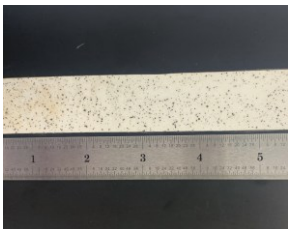
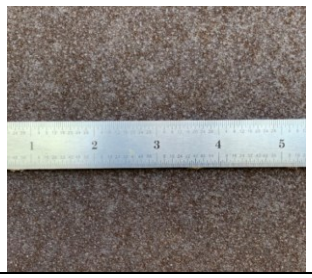
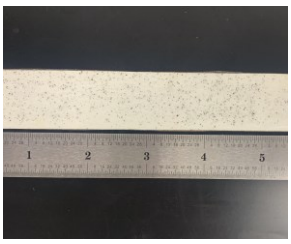
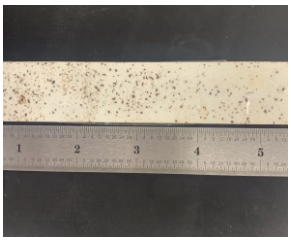
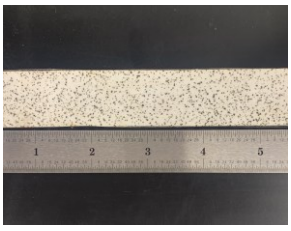
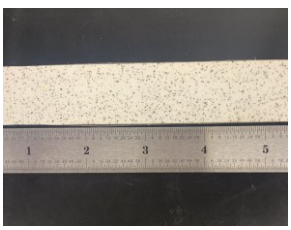
Location	Patina Rating	Thickness (inch)	Cl^- Conc. (ppm)	Field Condition	Tape Test
A1-G1F1 TF Bot. Ext.	8	Measured R1 0.627 R2 0.627 R3 0.626 R_Avg 0.627 Design	-		
A1-G1F1 Web Ext.	8	Measured R1 0.438 R2 0.440 R3 0.439 R_Avg 0.439 Design	1		
A1-G1F1 BF Top Ext.	7	Measured R1 0.746 R2 0.745 R3 0.747 R_Avg 0.746 Design	-		
A1-G1F1 BF Bot Ext.	8	-	-		
A1-G1F1 Stiffener Ext.	8	Measured R1 0.855 R2 0.858 R3 0.856 R_Avg 0.856 Design			

Table A-182. Field Inspection Results for FTW-WS-01.

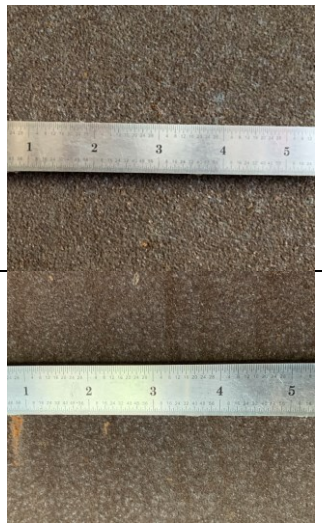
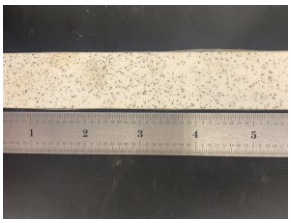
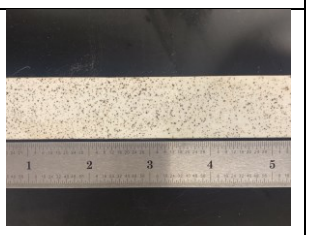
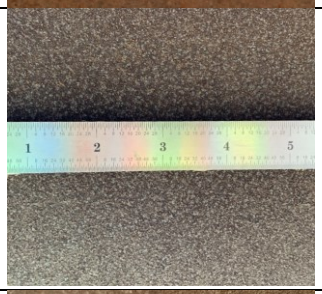
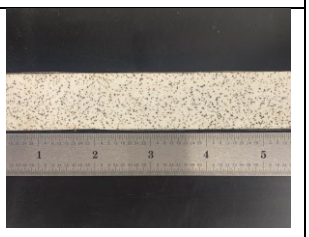
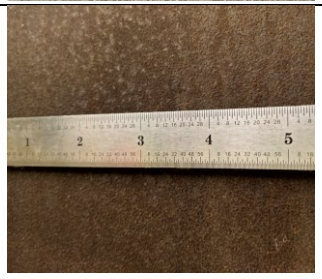
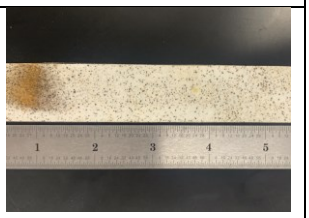
Location	Patina Rating	Thickness (inch)	Cl^- Conc. (ppm)	Field Condition	Tape Test
A1-G1F2 TF Bot Int.	8	Measured R1 0.625 R2 0.626 R3 0.627 R_Avg 0.626 Design			
A1-G1F2 Web Int.	8	Measured R1 0.441 R2 0.441 R3 0.441 R_Avg 0.441 Design	1		
A1-G1F2 BF Top Int.	7	Measured R1 0.746 R2 0.745 R3 0.741 R_Avg 0.744 Design	-		
A1-G1F2 BF Bot Int.	8	-			
A1-G1F2 Stiffener Int.	8	Measured R1 0.971 R2 0.871 R3 0.874 R_Avg 0.905 Design			

Table A-183. Field Inspection Results for FWA-WS-01.

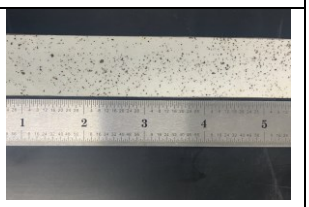
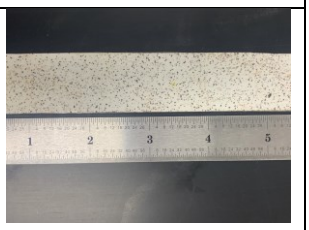
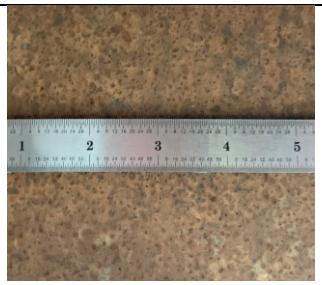
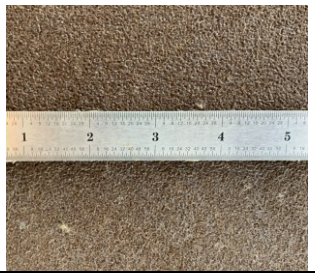
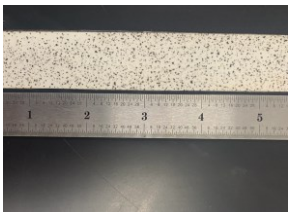
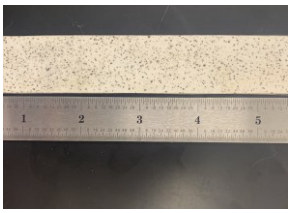
Location	Patina Rating	Thickness (inch)	Cl^- Conc. (ppm)	Field Condition	Tape Test
A1-G2F1 TF Bot Int.	8	Measured R1 0.637 R2 0.638 R3 0.636 R_Avg 0.637 Design	-		
A1-G2F1 Web Int.	8	Measured R1 0.431 R2 0.431 R3 0.434 R_Avg 0.432 Design	-		
A1-G2F1 BF Top Int.	8	-	-		
A1-G2F1 BF Bot Int.	8	Measured R1 0.751 R2 0.752 R3 0.751 R_Avg 0.751 Design	-		
A1-G2F1 Stiffener Int.	8	Measured R1 0.850 R2 0.850 R3 0.848 R_Avg 0.849 Design			

Table A-184. Field Inspection Results for FWA-WS-01.

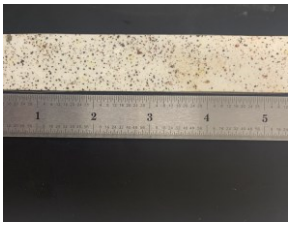
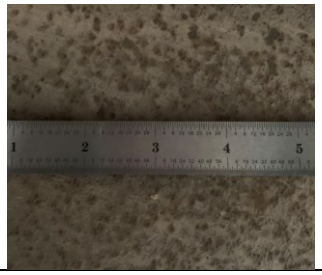
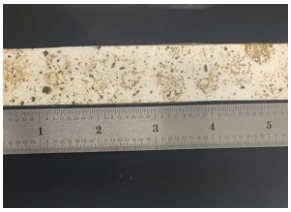
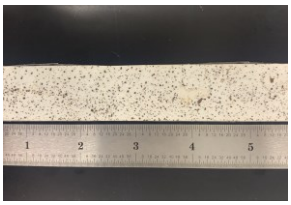
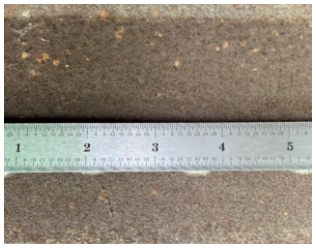
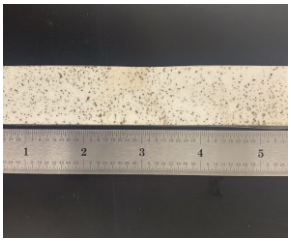
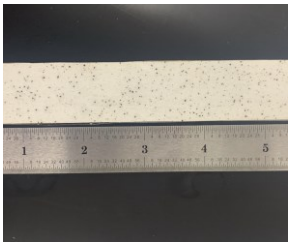
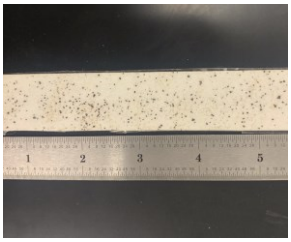
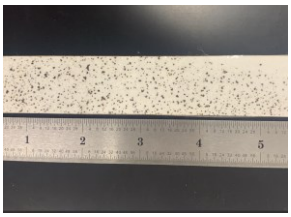
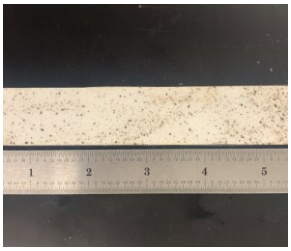
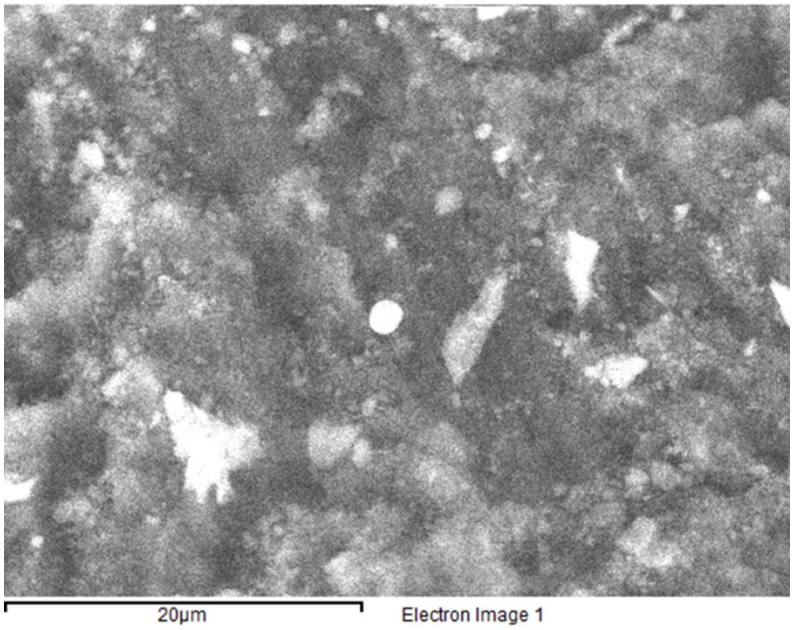
Location	Patina Rating	Thickness (inch)	Cl^- Conc. (ppm)	Field Condition	Tape Test
A3-G2F1 TF Bot. Int.		-	-		
A3-G2F1 Web. Int.	8	Measured R1 0.453 R2 0.450 R3 0.445 R_Avg 0.449 Design	1		
A3-G2F1 BF Top. Int.	6	-	-		
A3-G2F1 BF Bot. Int.	6	Measured R1 0.743 R2 0.742 R3 0.743 R_Avg 0.743 Design			
A3-G2F1 Stiffener Int.	8	Measured R1 0.319 R2 0.320 R3 0.319 R_Avg 0.319 Design			

Table A-185. Field Inspection Results for FWA-WS-01.

Location	Patina Rating	Thickness (inch)	Cl^- Conc. (ppm)	Field Condition	Tape Test
A3-G1F1 TF Bot. Ext.		-			
A3-G1F1 Web Ext.	8	Measured R1 0.438 R2 0.440 R3 0.439 R_Avg 0.439 Design	0		
A3-G1F1 BF Top. Int.	8	-	-		
A3-G1F1 BF Bot. Int.	8	Measured R1 0.764 R2 0.761 R3 0.760 R_Avg 0.762 Design			
A3-G1F1 End Stiffener	7	Measured R1 0.730 R2 0.732 R3 0.729 R_Avg 0.730 Design			

A.41.3.SEM/EDS Results: Exterior Web Girder

Element	Weight %	Atomic %
O K	50.99	75.70
Mg K	0.28	0.27
Al K	2.36	2.08
Si K	4.30	3.63
P K	0.70	0.53
Cl K	0.20	0.13
K K	0.26	0.16
Ca K	0.55	0.32
Mn K	0.40	0.17
Fe K	39.92	16.98
Cu K	0.05	0.02
Totals	100.00	



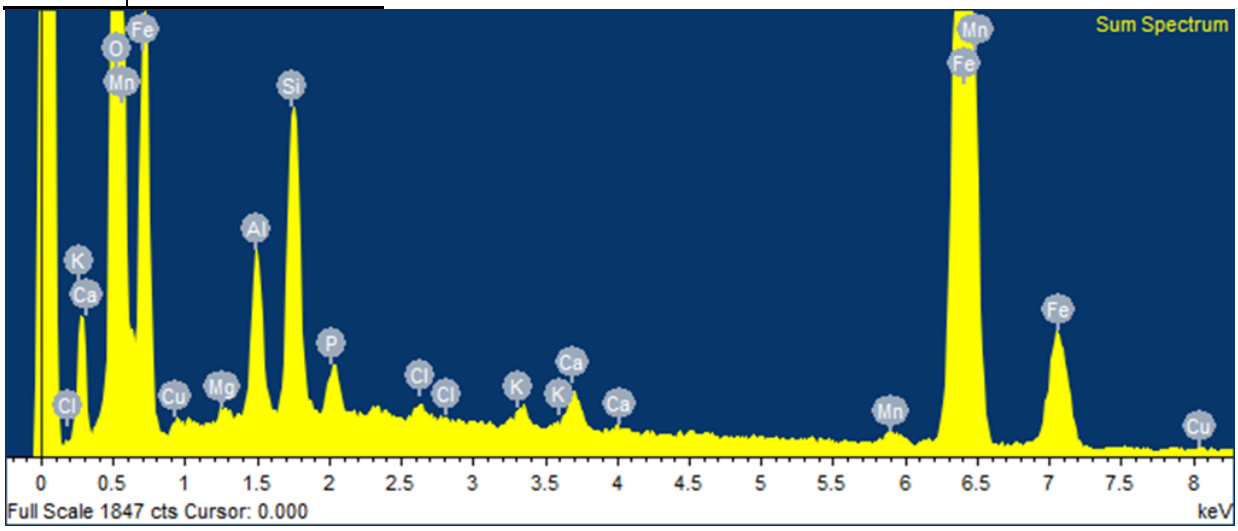
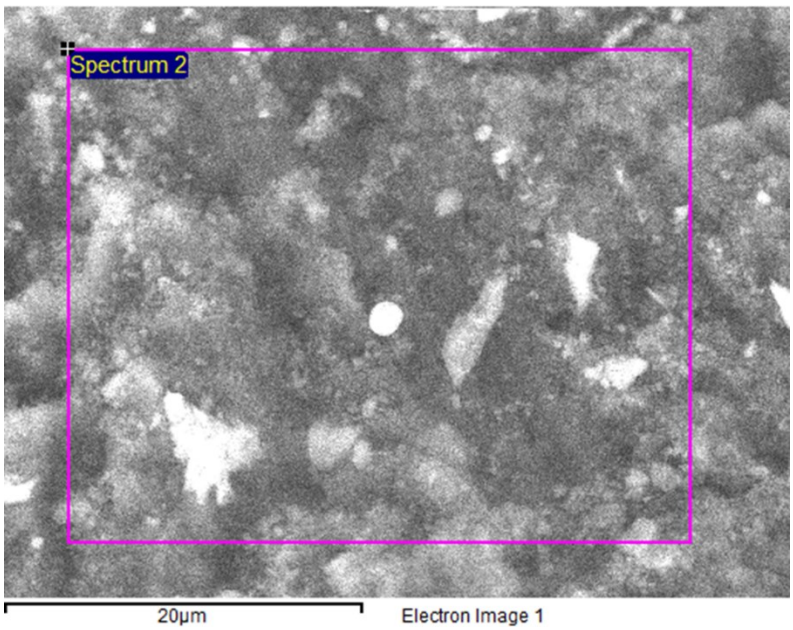


Figure A.729. SEM Image and EDS Spectrum of the Rust Collected from Exterior Web of the Girder.

Element	Weight %	Atomic %
O K	51.23	75.90
Al K	2.42	2.13
Si K	4.55	3.84
P K	0.79	0.60
K K	0.18	0.11
Ca K	0.54	0.32
Mn K	0.29	0.13
Fe K	39.99	16.97
Totals	100.00	



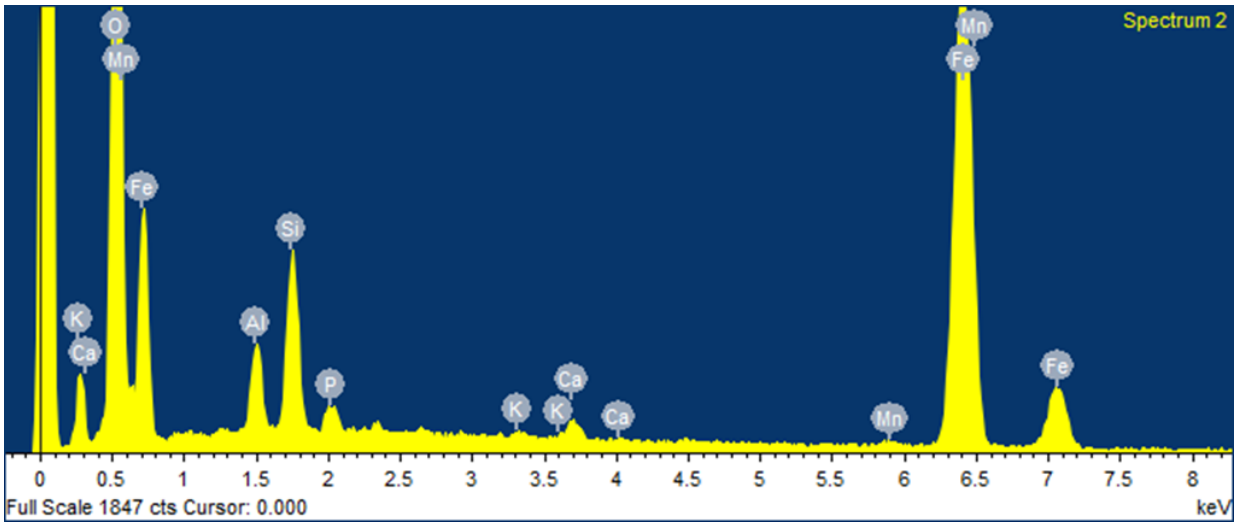
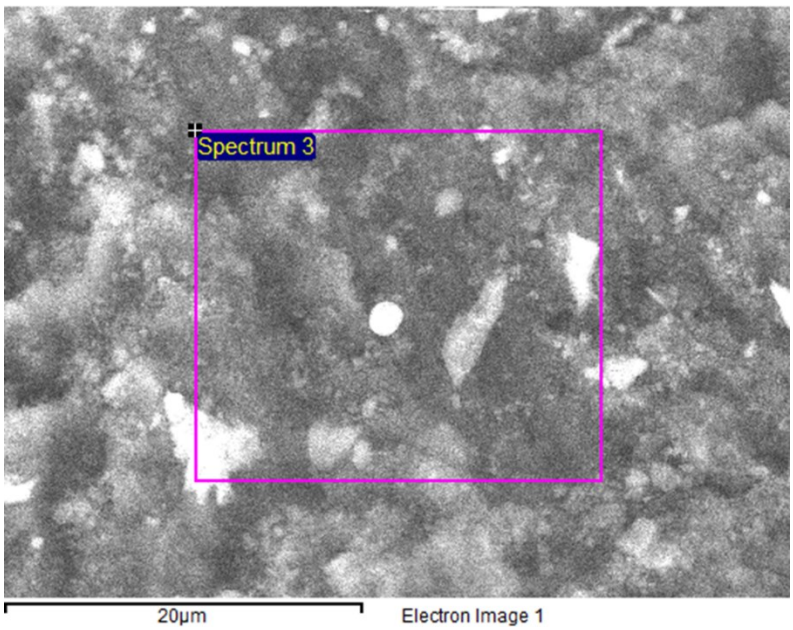


Figure A.730. SEM Image and EDS Spectrum of the Rust Collected from Exterior Web of the Girder.

Element	Weight %	Atomic %
O K	50.99	75.61
Al K	2.57	2.26
Si K	4.53	3.83
P K	0.77	0.59
S K	0.24	0.18
K K	0.29	0.18
Ca K	0.58	0.34
Mn K	0.39	0.17
Fe K	39.64	16.84
Totals	100.00	



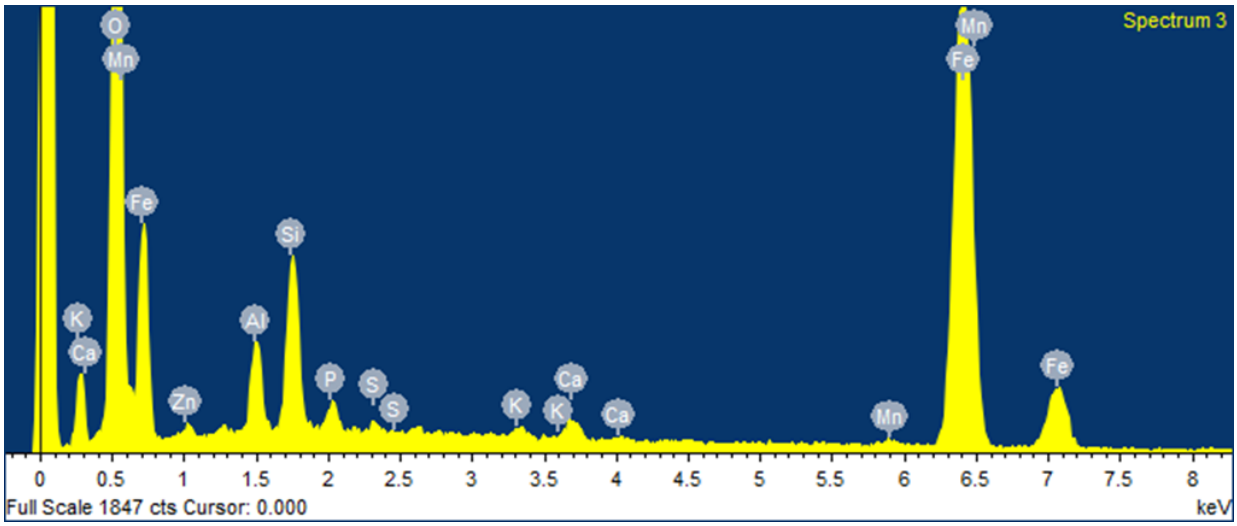
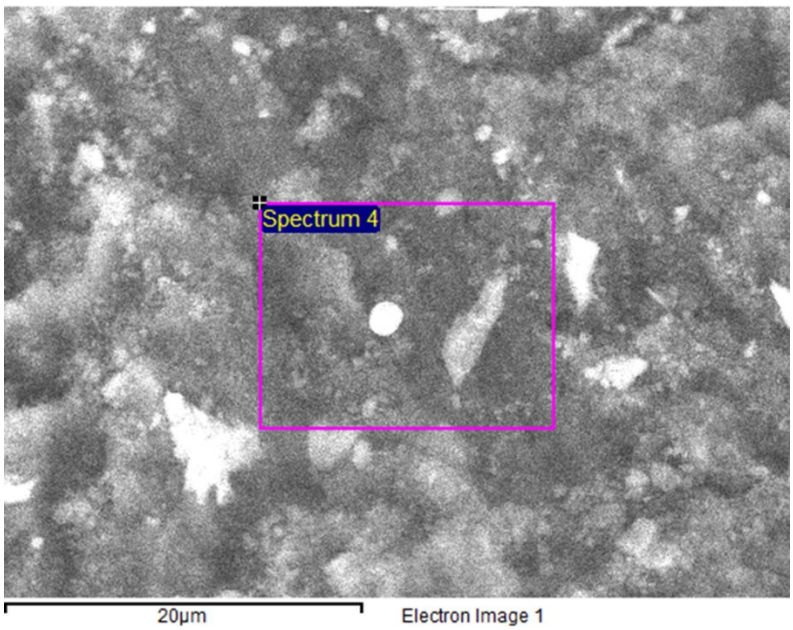


Figure A.731. SEM Image and EDS Spectrum of the Rust Collected from Exterior Web of the Girder.

Element	Weight %	Atomic %
O K	50.48	75.15
Al K	2.75	2.43
Si K	5.02	4.25
P K	0.61	0.47
K K	0.27	0.16
Ca K	0.59	0.35
Mn K	0.49	0.21
Fe K	39.79	16.97
Totals	100.00	



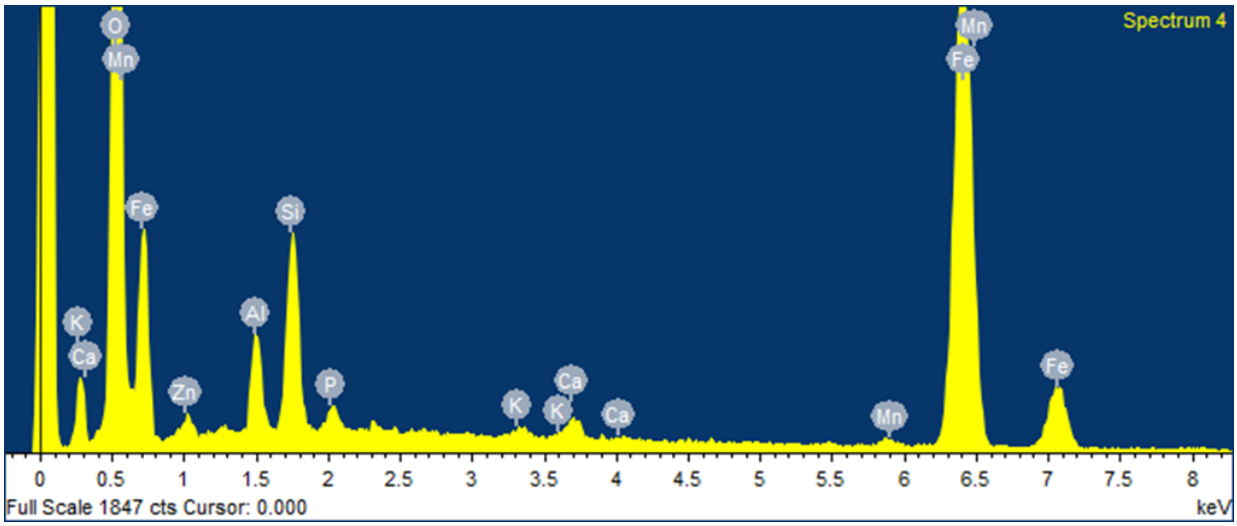
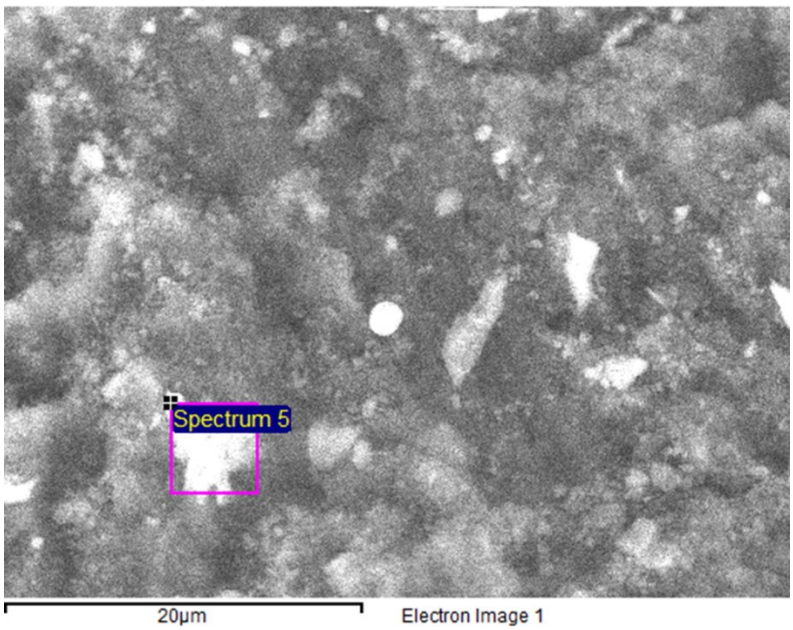


Figure A.732. SEM Image and EDS Spectrum of the Rust Collected from Exterior Web of the Girder.

Element	Weight %	Atomic %
O K	50.09	75.70
Al K	1.92	1.72
Si K	3.37	2.90
P K	0.47	0.37
Cl K	0.38	0.26
K K	0.20	0.12
Ca K	0.36	0.22
Mn K	0.25	0.11
Fe K	42.96	18.60
Totals	100.00	



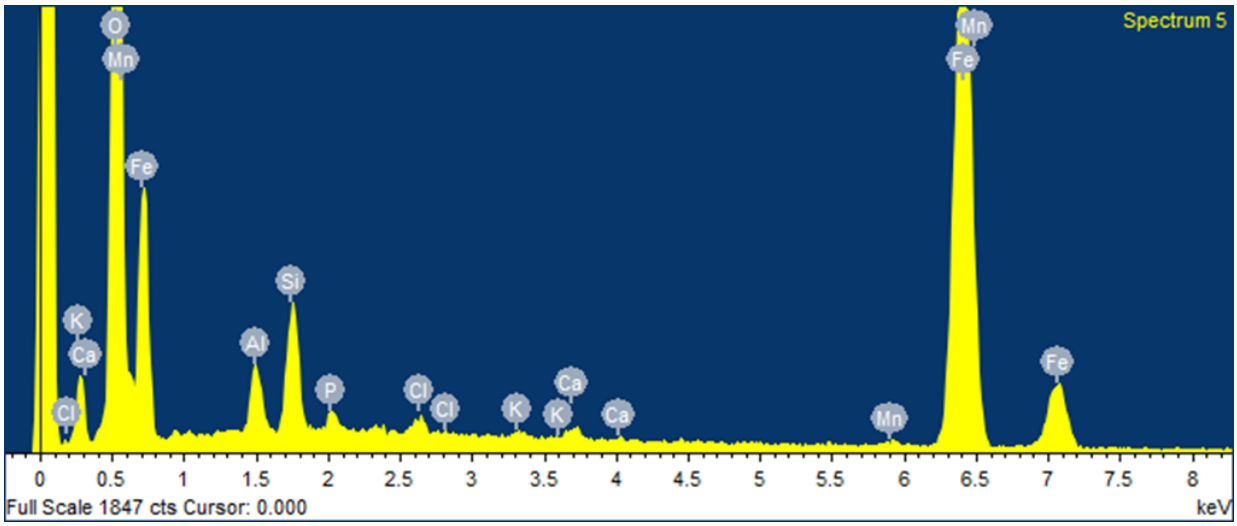


Figure A.733. SEM Image and EDS Spectrum of the Rust Collected from Exterior Web of the Girder.

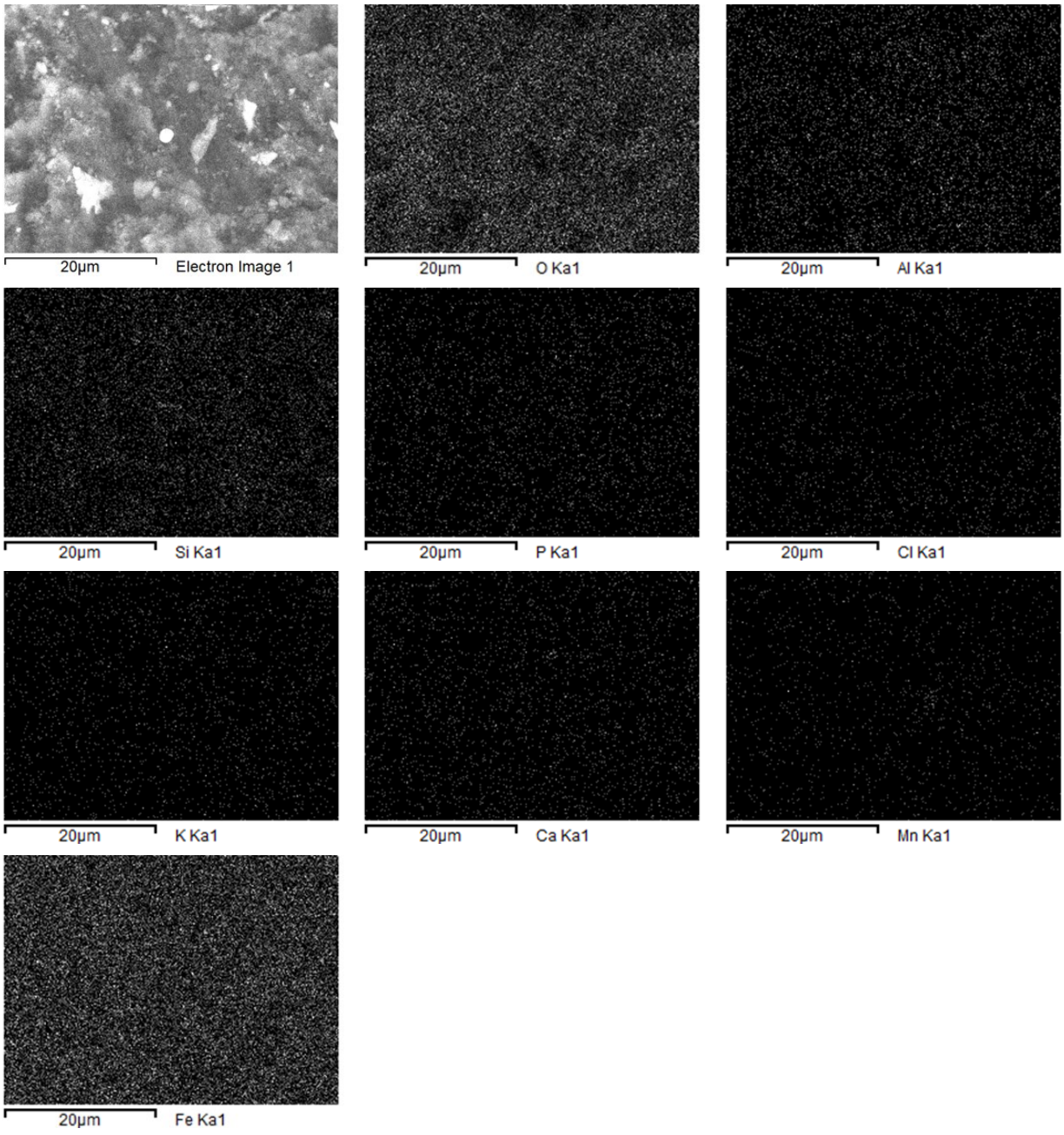
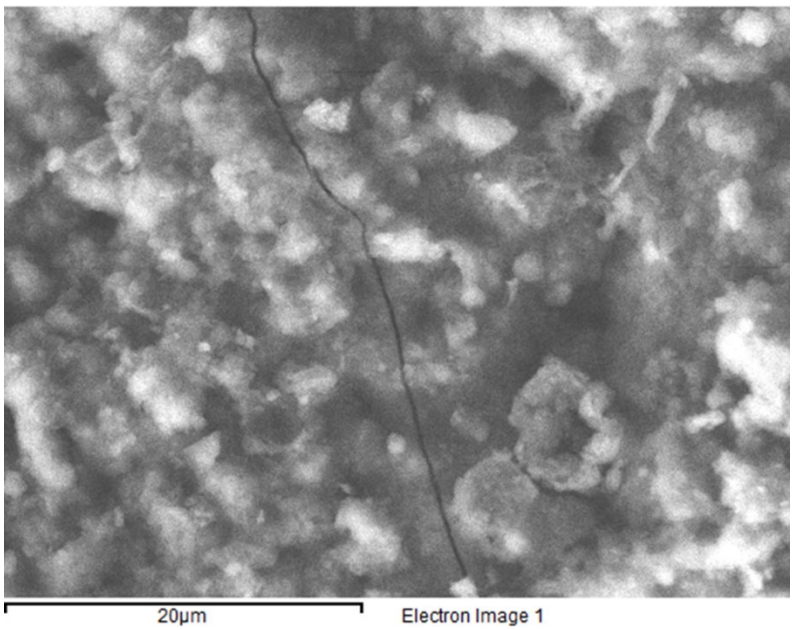


Figure A.734. EDS Elemental Mapping of Rust Collected from Exterior Web.

Element	Weight%	Atomic%
O K	46.76	72.29
Mg K	0.37	0.37
Al K	2.78	2.55
Si K	4.47	3.94
P K	1.19	0.95
Cl K	0.22	0.15
K K	0.21	0.14
Ca K	0.74	0.45
Mn K	0.23	0.10
Fe K	43.04	19.06
Totals	100.00	



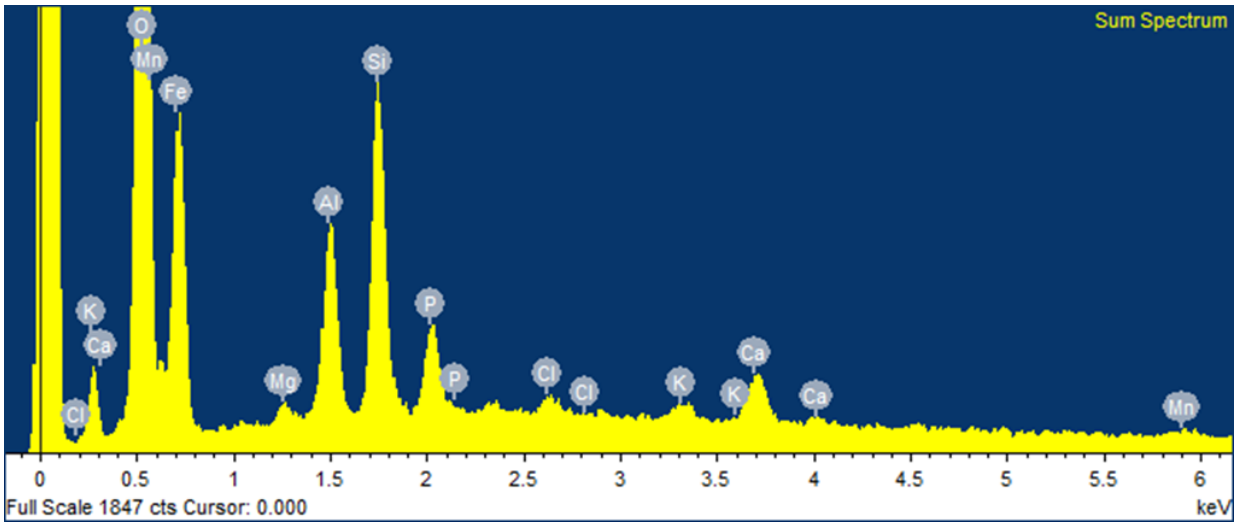


Figure A.735. SEM Image and EDS Spectrum of the Rust Collected from Exterior Web of the Girder.

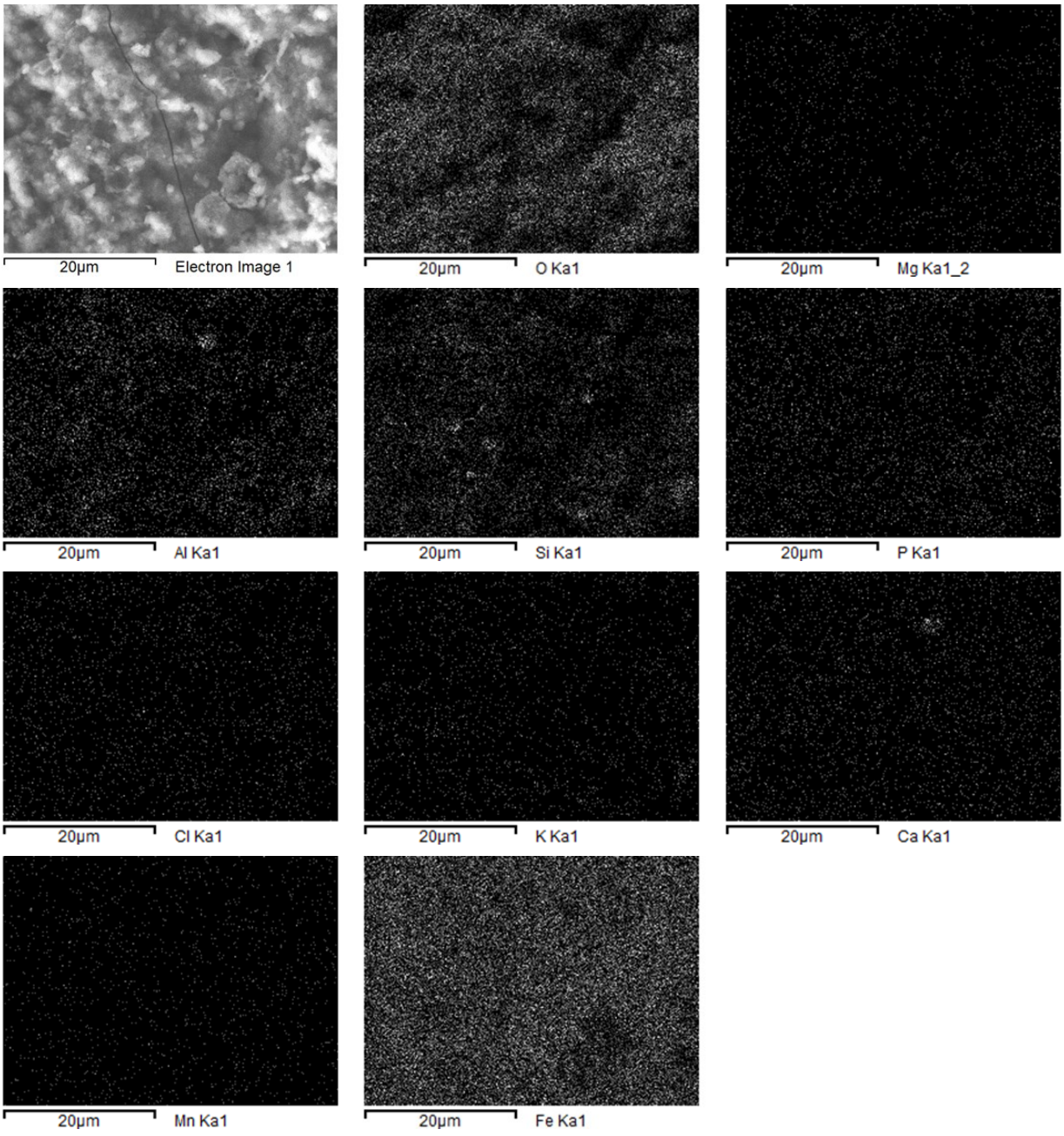
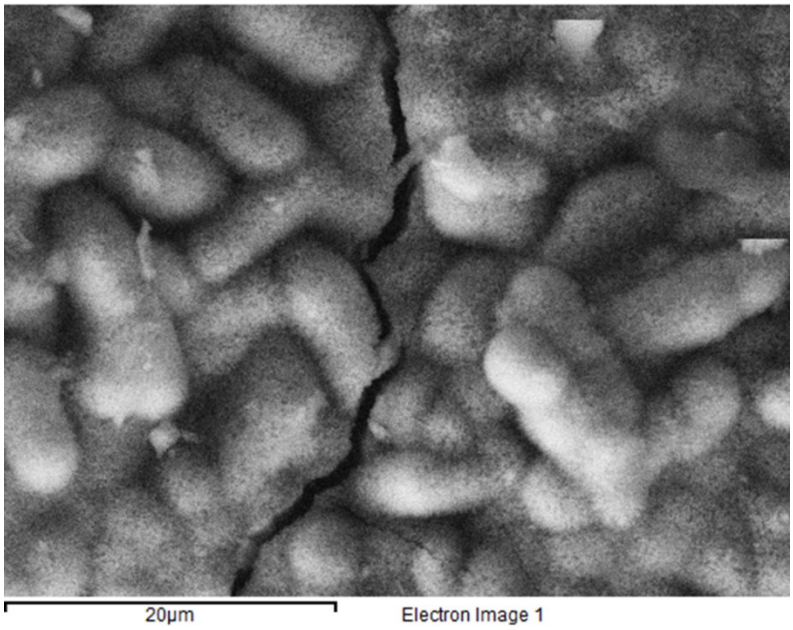


Figure A.736. EDS Elemental Mapping of Rust Collected from Exterior Web.

A.41.4.SEM/EDS Results: Interior Web Girder

Element	Weight %	Atomic %
O K	43.44	71.45
Na K	0.16	0.19
Al K	1.24	1.21
Si K	0.82	0.77
S K	0.71	0.58
Cl K	1.88	1.39
Ca K	0.17	0.11
Fe K	51.58	24.30
Totals	100.00	



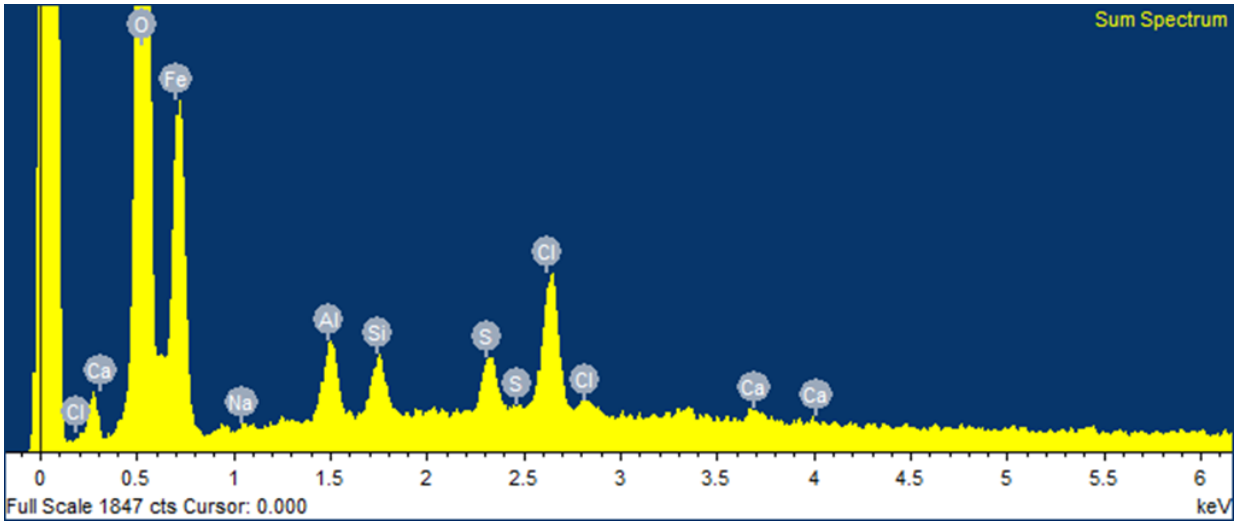


Figure A.737. SEM Image and EDS Spectrum of the Rust Collected from Interior Web of the Girder.

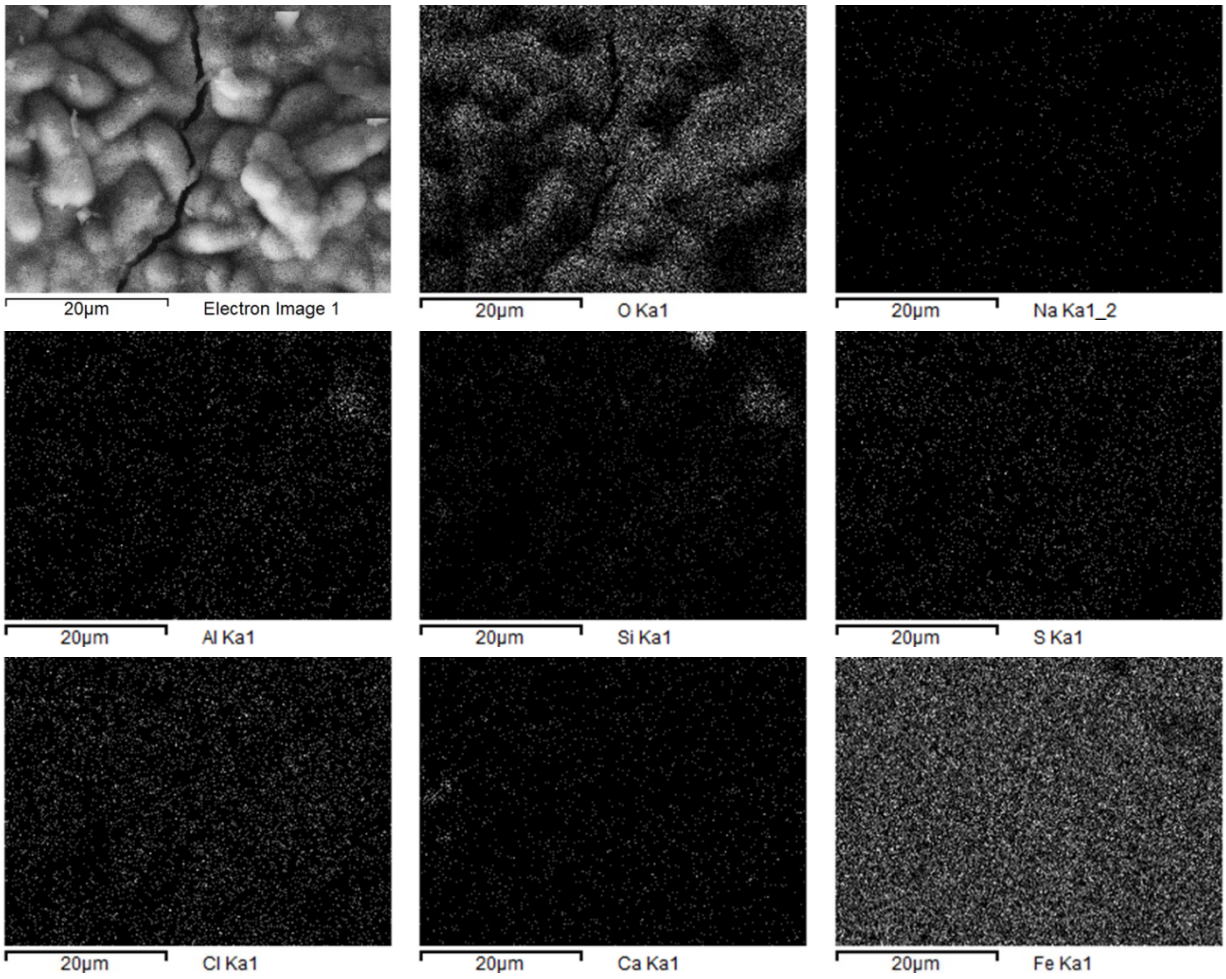


Figure A.738. EDS Elemental Mapping of Rust Collected from Interior Web.

A.41.5.XPS Results: Exterior Web Girder

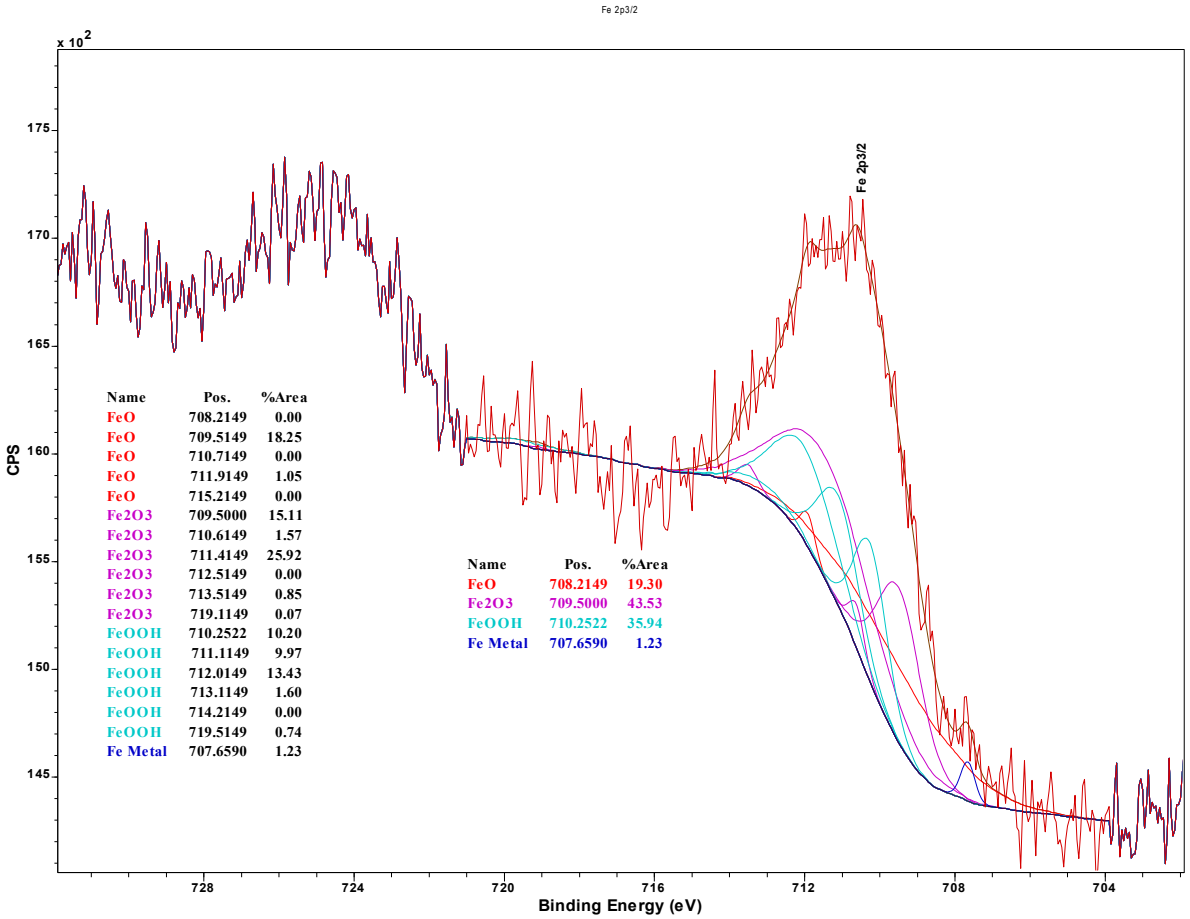


Figure A.739. XPS Spectrum of the Rust Collected from Exterior Web of the Girder.

A.41.6.XPS Results: Interior Web Girder

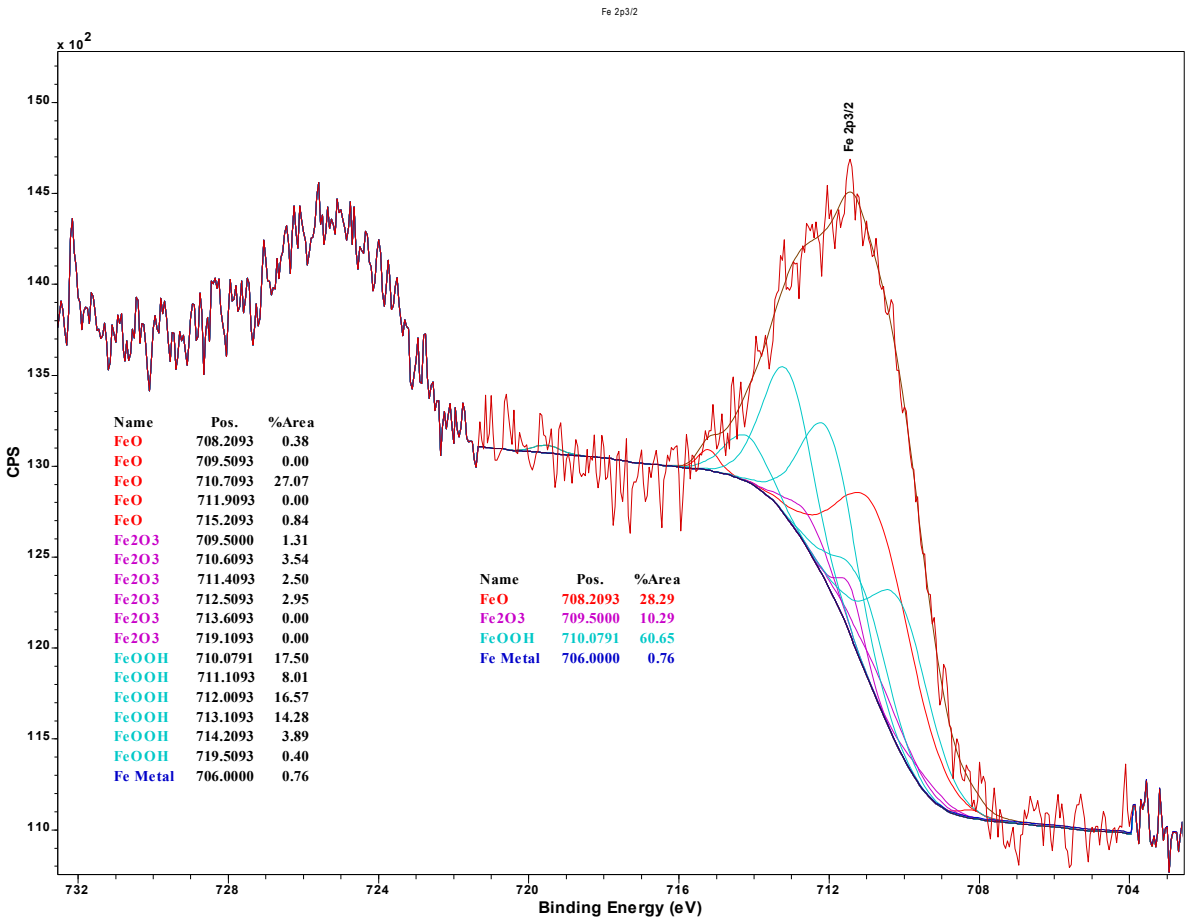


Figure A.740. XPS Spectrum of the Rust Collected from Interior Web of the Girder.

A.41.7.XRD Result: Exterior and Interior Girder

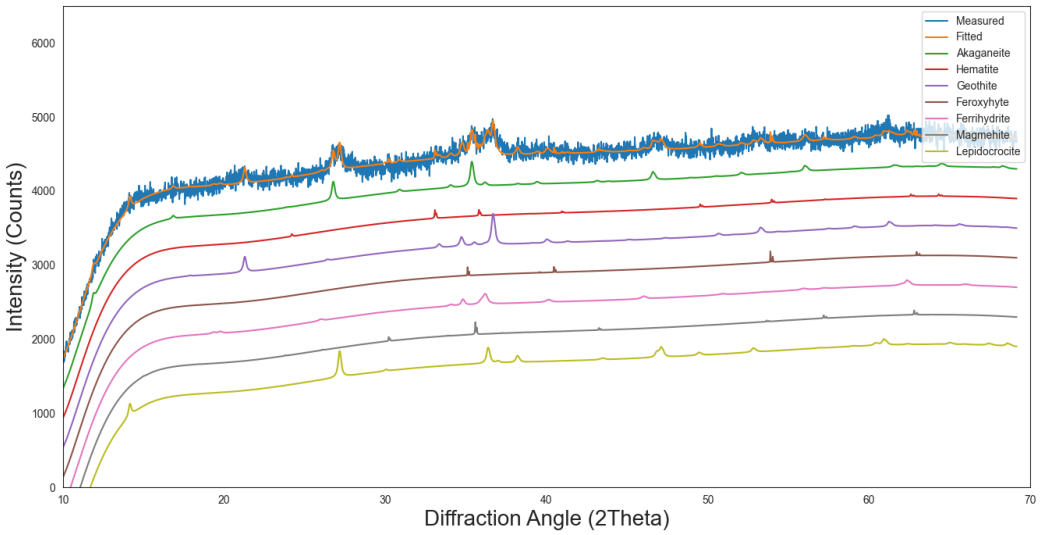


Figure A.741. XRD Pattern of Powdered Rust Collected from Exterior Web of the Girder.

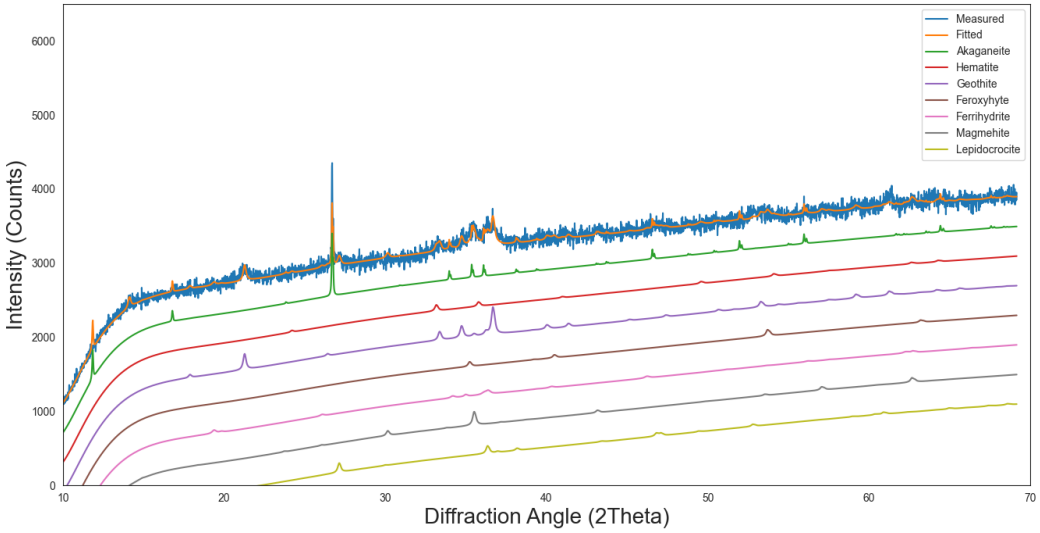


Figure A.742. XRD Pattern of Powdered Rust Collected from Interior Web of the Girder.

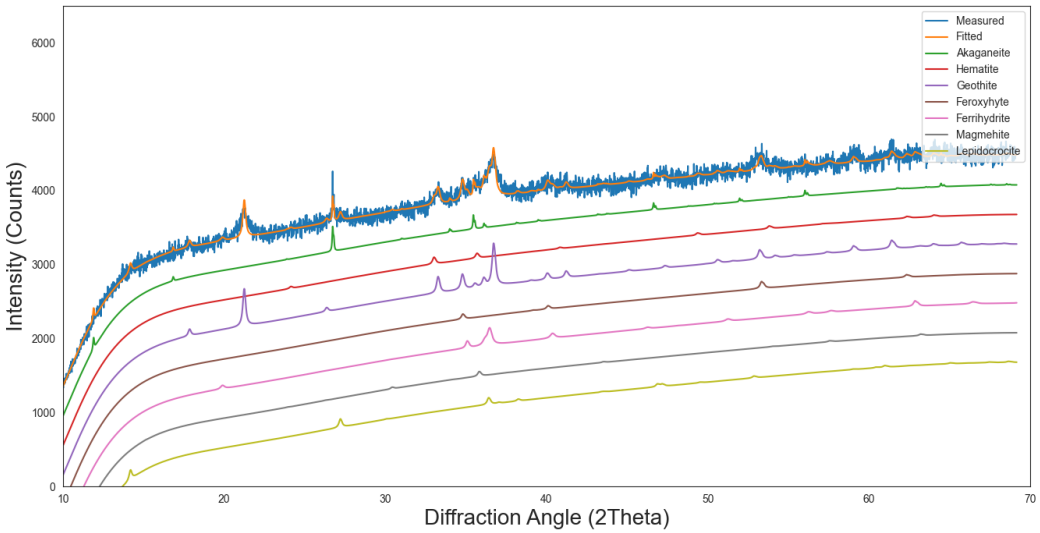


Figure A.743. XRD Pattern of Powdered Rust Collected from Bottom face of Bottom Flange of the Interior Girder.

A.41.8.Particle Size Analysis: Tape Adhesion Results

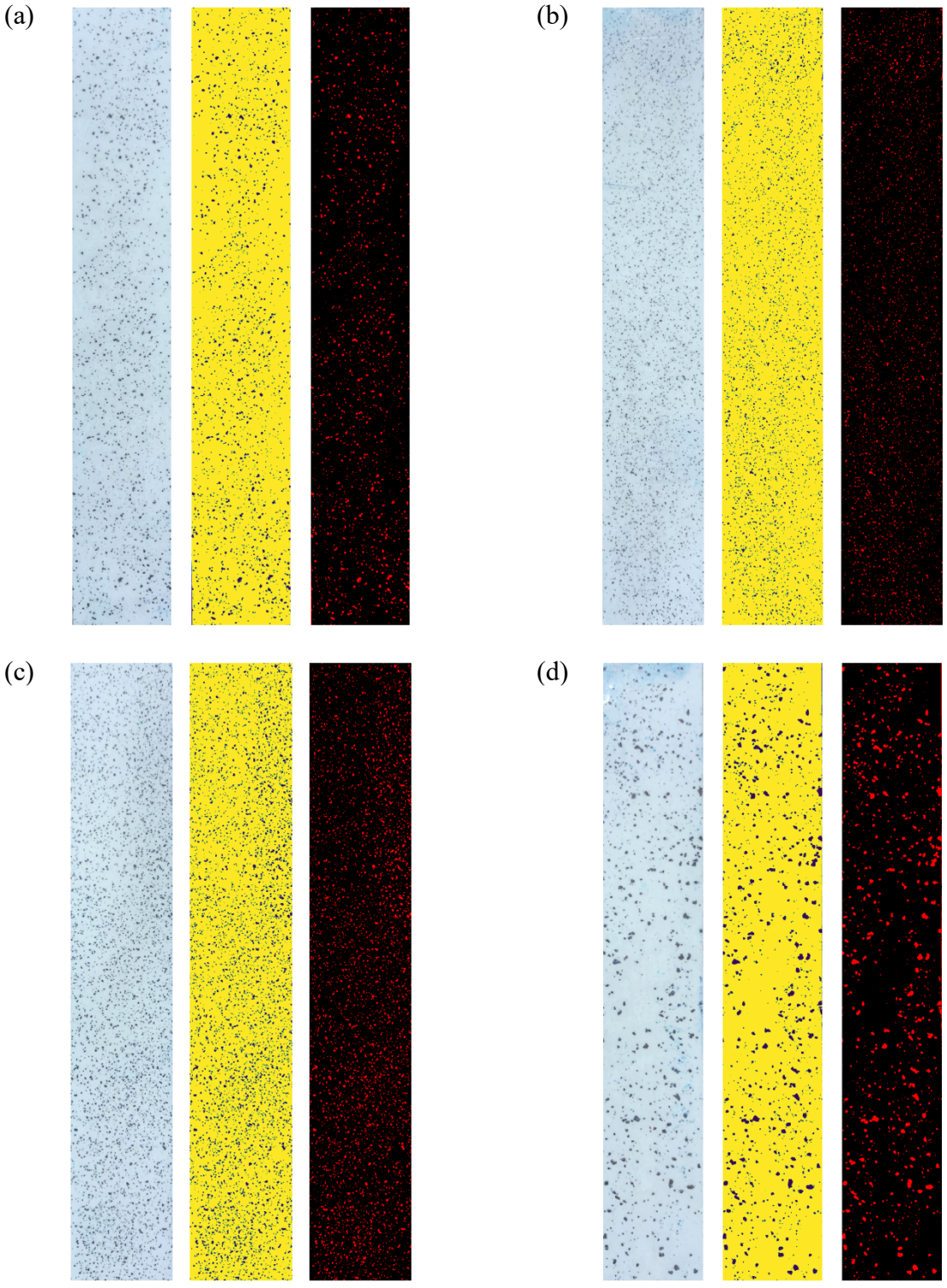


Figure A.744. Particle Size Analysis Results at A1G1F1 (a) Top Flange Bottom, (b) Web, (c) Bottom Flange Bottom (d) Stiffener.

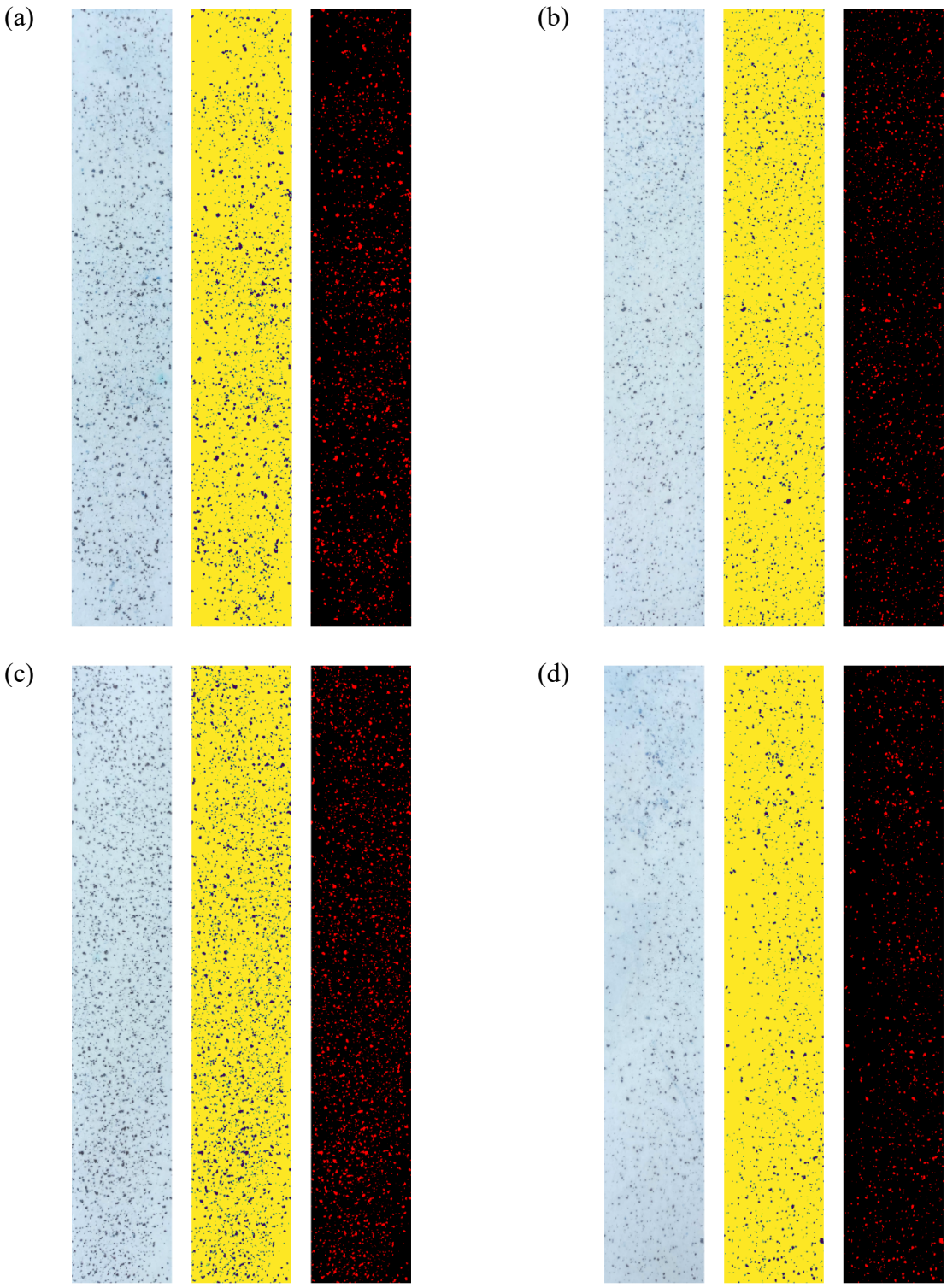


Figure A.745. Particle Size Analysis Results at A3G7F1 (a) Top Flange Bottom, (b) Web, (c) Bottom Flange Bottom (d) Stiffener.

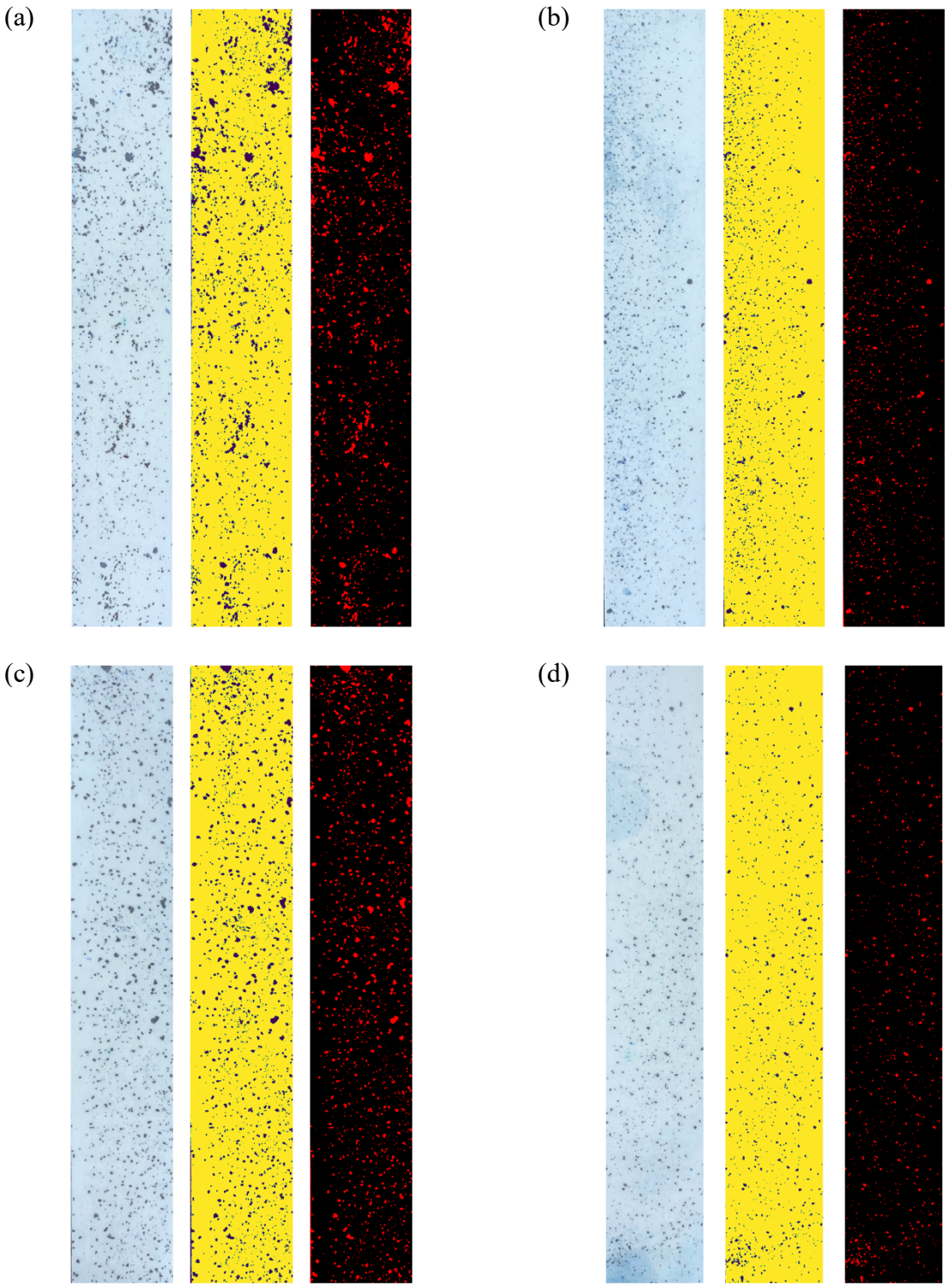


Figure A.746. Particle Size Analysis Results at A3G9F2 (a) Top Flange Bottom, (b) Web, (c) Bottom Flange Bottom (d) Stiffener.

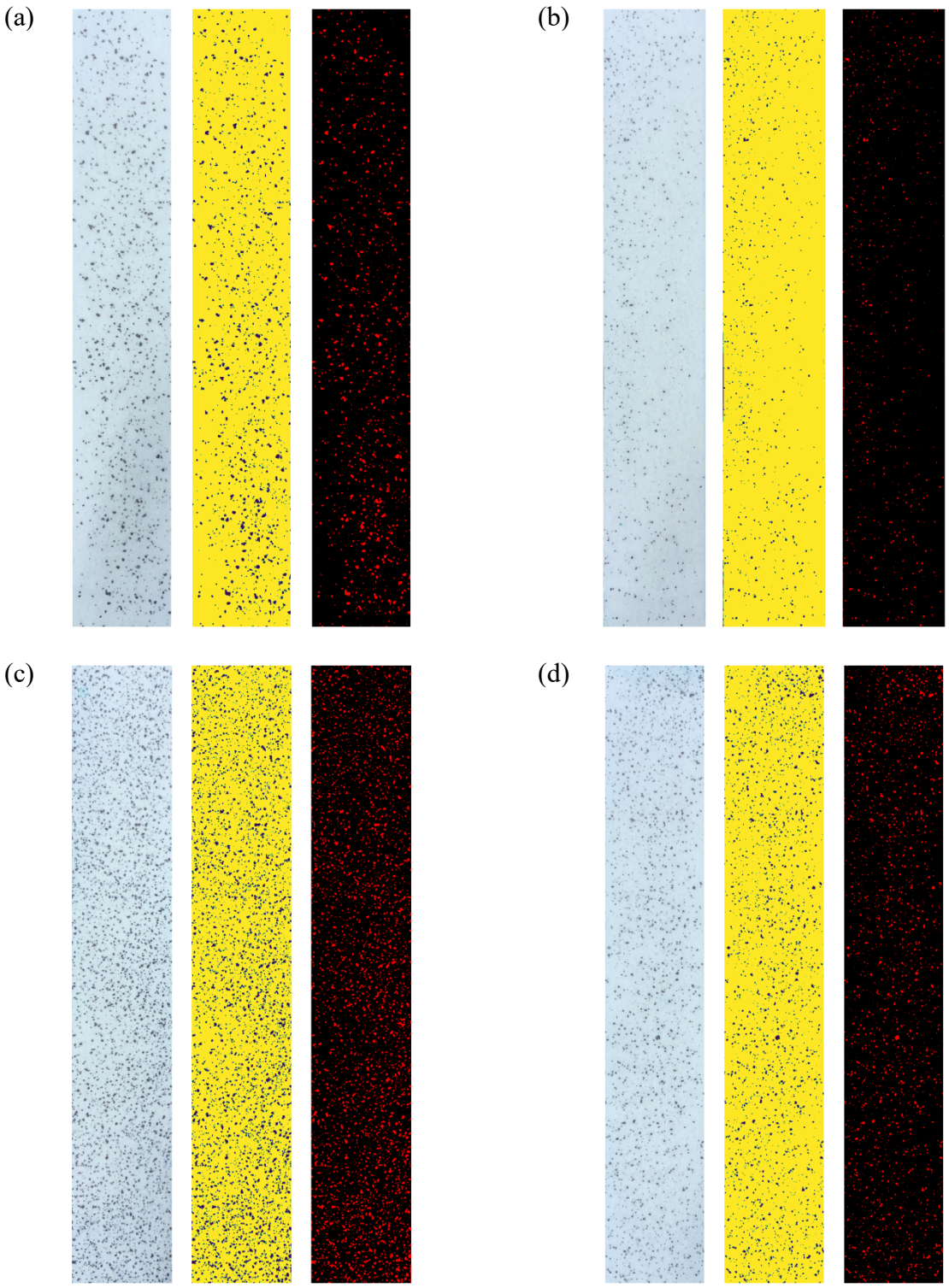


Figure A.747. Particle Size Analysis Results at A3G11F2 (a) Top Flange Bottom, (b) Web, (c) Bottom Flange Bottom (d) Stiffener.

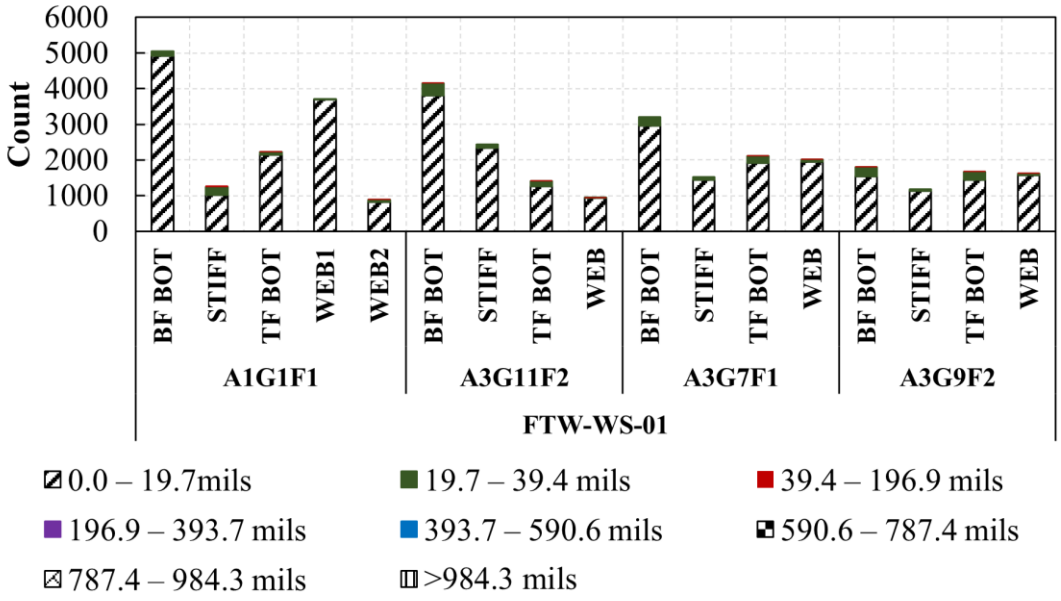


Figure A.748. Particle Size Analysis Showing Different Locations Examined.

A.42. FTW-WS-02

- Cross under #6 RD
- Bridge ID 022200F00189003, Coordinates (32.87667, -97.03976), Tarrant County
- Continuous weathering steel plate girder
- Built 1974
- Girder inspection carried on abutment, and measurements are taken on girder within four feet from the abutment or bent.
- No visual inspection on deck
- Location for Testing: A3-G1F1, A3-G7F1, A3-G9F2, A1-G11F2



Figure A.749. Typical Picture of FTW-WS-02.

A.42.1. Observed Condition

Overall bridge is in very good condition with development of uniform patina throughout the girder with a patina rating ranging between 7 and 8 showing good protection and adherence of patina to the steel surface.

A.42.2.Field Inspection Results

Table A-186. Field Inspection Results for FTW-WS-02.

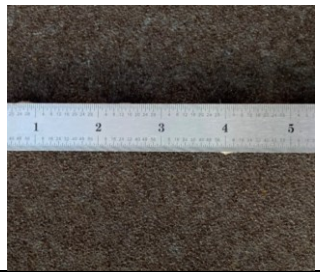
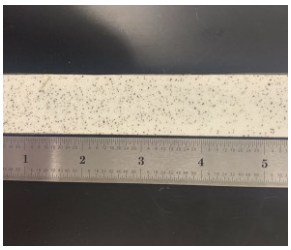
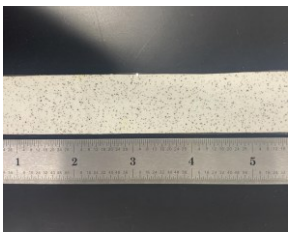
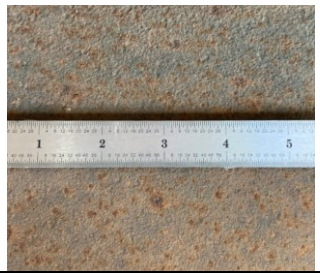
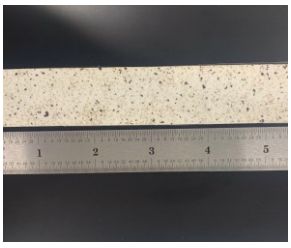
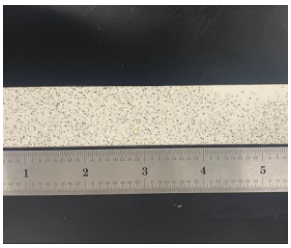
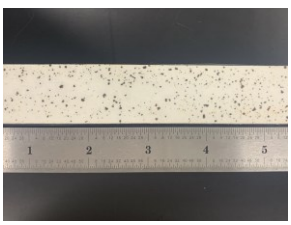
Location	Patina Rating	Thickness (inch)	Cl^- Conc. (ppm)	Field Condition	Tape Test
A3-G1F1 TF Bot. Ext.	8	Measured R1 0.630 R2 0.631 R3 0.634 R_Avg 0.632 Design	-		
A3-G1F1 Web Ext.	8	Measured R1 0.439 R2 0.439 R3 0.439 R_Avg 0.439 Design	1		
A3-G1F1 BF Top Ext.	8	Measured R1 0.746 R2 0.747 R3 0.745 R_Avg 0.746 Design	-		
A3-G1F1 BF Bot Ext.	8	-	-		
A3-G1F1 Stiffener Ext.	7	Measured R1 0.730 R2 0.728 R3 0.731 R_Avg 0.730 Design			

Table A-187. Field Inspection Results for FTW-WS-02.

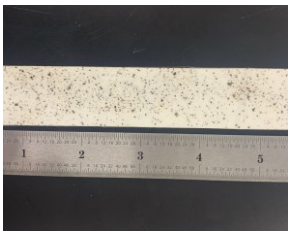
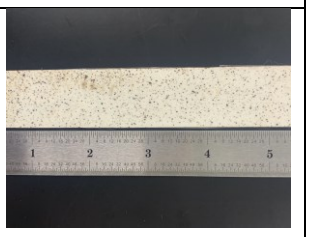
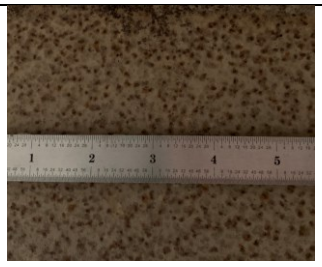
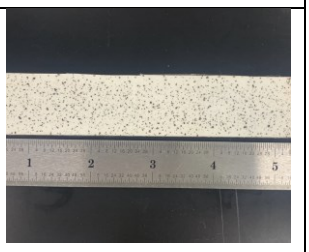
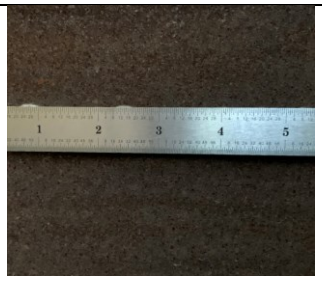
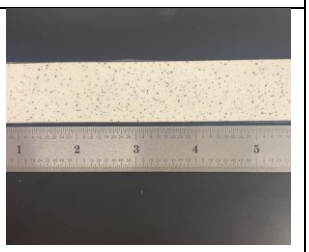
Location	Patina Rating	Thickness (inch)	Cl^- Conc. (ppm)	Field Condition	Tape Test
A3-G7F1 TF Bot Int.	7	Measured R1 0.633 R2 0.634 R3 0.637 R_Avg 0.635 Design	-		
A3-G7F1 Web Int.	8	Measured R1 0.431 R2 0.431 R3 0.433 R_Avg 0.432 Design	1		
A3-G7F1 BF Top Int.	7	Measured R1 0.631 R2 0.634 R3 0.636 R_Avg 0.634 Design	-		
A3-G7F1 BF Bot Int.	8	-			
A3-G7F1 Stiffener Int.	8	Measured R1 0.620 R2 0.622 R3 0.623 R_Avg 0.622 Design			

Table A-188. Field Inspection Results for FWA-WS-02.

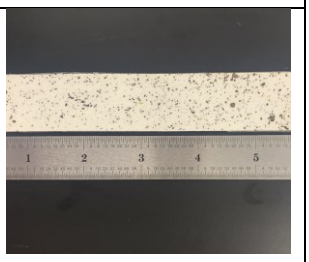
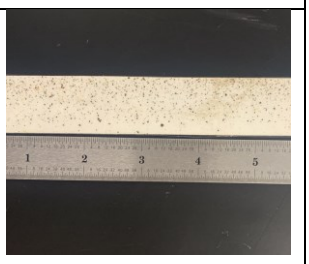
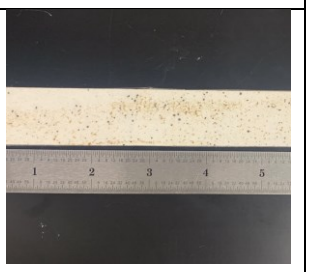
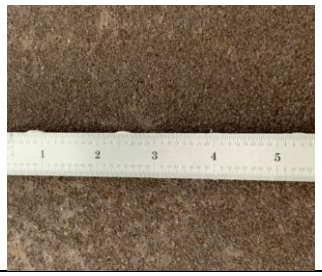
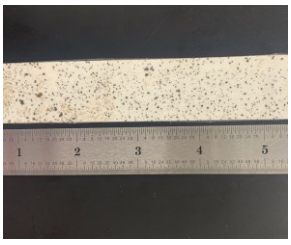
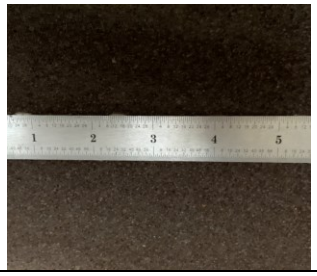
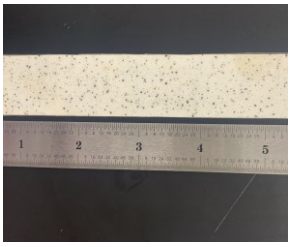
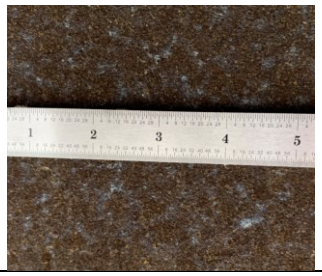
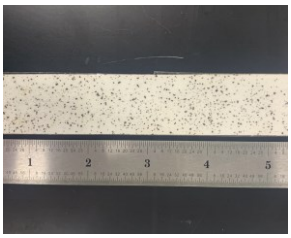
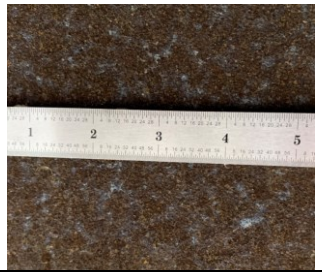
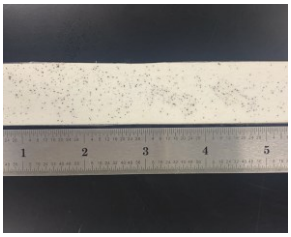
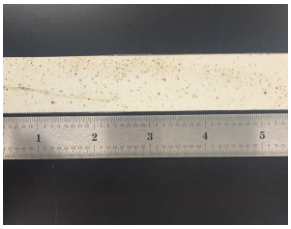
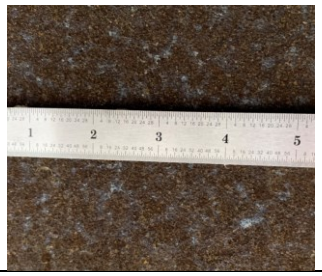
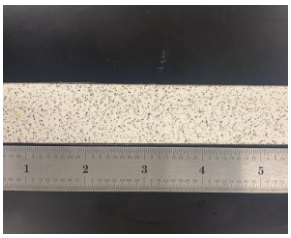
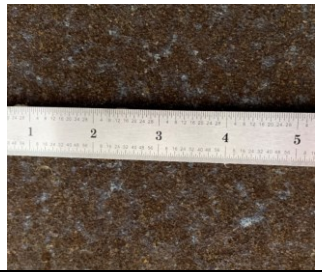
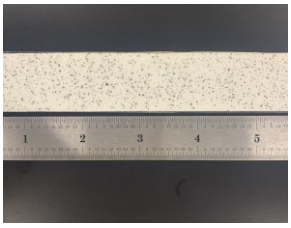
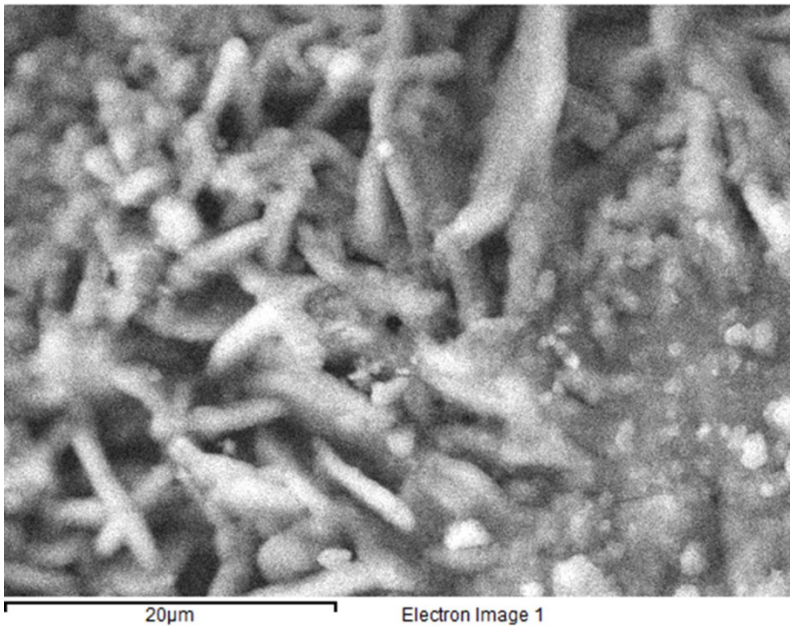
Location	Patina Rating	Thickness (inch)	Cl^- Conc. (ppm)	Field Condition	Tape Test
A3-G9F2 TF Bot Int.	7	Measured R1 0.605 R2 0.603 R3 0.605 R_Avg 0.604 Design	-		
A3-G9F2 Web Int.	8	Measured R1 0.440 R2 0.439 R3 0.441 R_Avg 0.440 Design	0		
A3-G9F2 BF Top Int.	6	Measured R1 0.609 R2 0.604 R3 0.607 R_Avg 0.607 Design	-		
A3-G9F2 BF Bot Int.	7	-	-		
A3-G9F2 Stiffener Int.	8	Measured R1 0.615 R2 0.613 R3 0.616 R_Avg 0.615 Design			

Table A-189. Field Inspection Results for FTW-WS-02.

Location	Patina Rating	Thickness (inch)	Cl^- Conc. (ppm)	Field Condition	Tape Test
A1-G11F2 TF Bot. Ext.	8	Measured R1 0.626 R2 0.627 R3 0.627 R_Avg 0.627 Design	-		
A1-G11F2 Web. Ext.	8	Measured R1 0.439 R2 0.440 R3 0.440 R_Avg 0.440 Design	0		
A1-G11F2 BF Top. Ext.	7	Measured R1 0.615 R2 0.616 R3 0.616 R_Avg 0.616 Design			
A1-G11F2 BF Bot. Ext.	8	-	-		
A1-G11F2 Stiffener Ext.	8	Measured R1 0.611 R2 0.615 R3 0.613 R_Avg 0.613 Design			

A.42.3.SEM/EDS Results: Exterior Web Girder

Element	Weight %	Atomic %
O K	48.34	75.35
Mg K	0.22	0.23
Al K	1.23	1.14
Si K	1.13	1.00
S K	1.10	0.86
Mn K	0.56	0.25
Fe K	47.42	21.18
Totals	100.00	



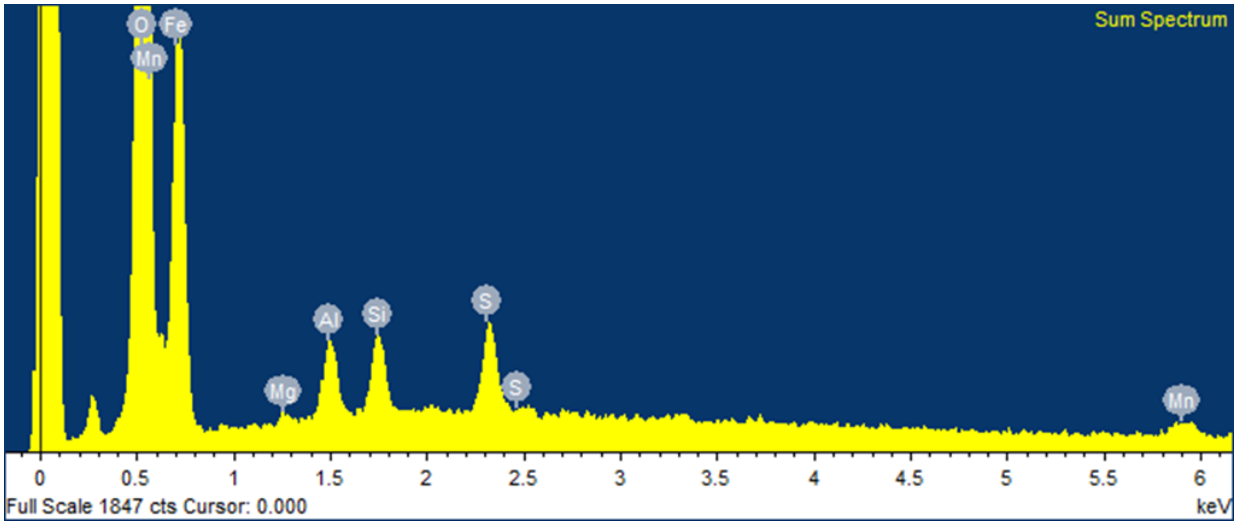


Figure A.750. SEM Image and EDS Spectrum of the Rust Collected from Exterior Web of the Girder.

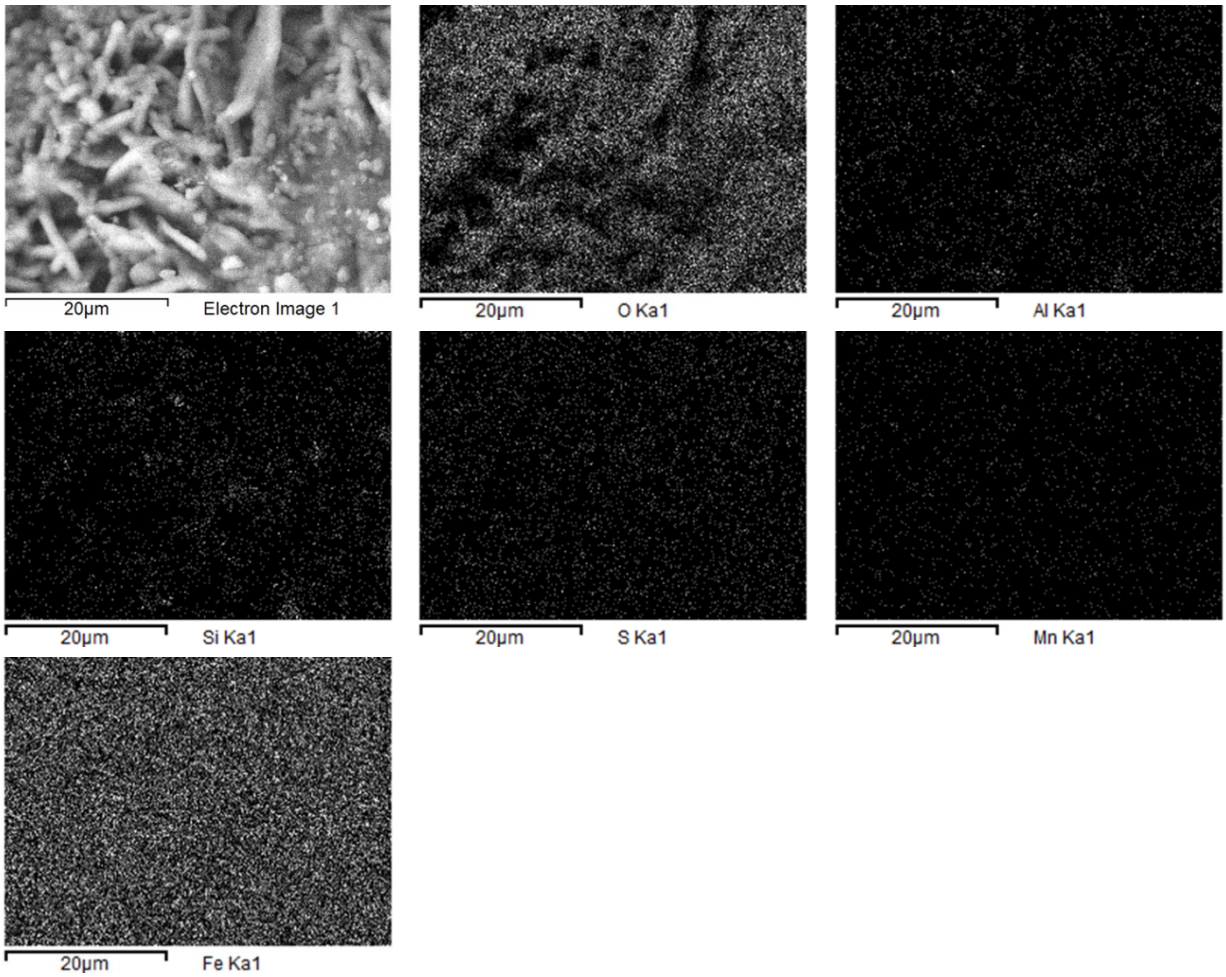
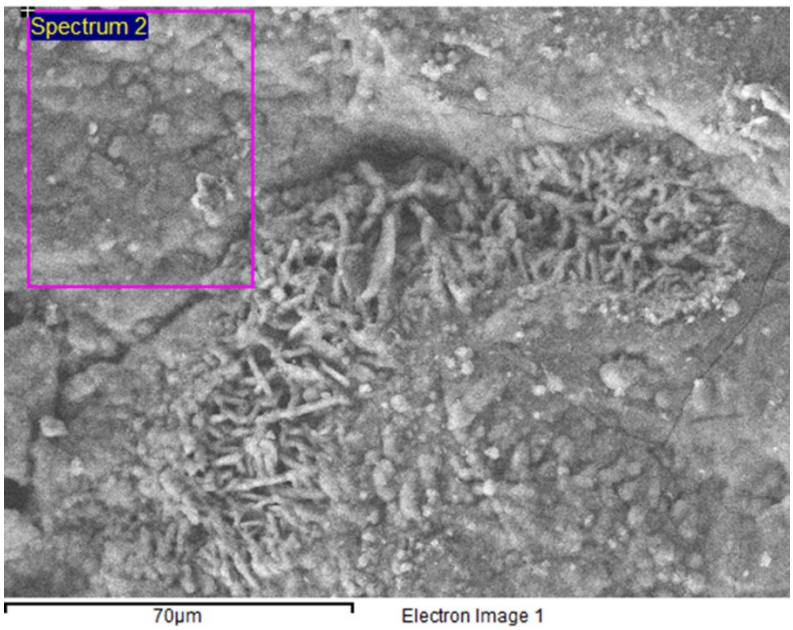


Figure A.751. EDS Elemental Mapping of Rust Collected from Exterior Web.

Element	Weight %	Atomic %
O K	41.38	70.08
Al K	1.16	1.16
Si K	0.99	0.95
S K	1.11	0.94
Mn K	0.71	0.35
Fe K	54.65	26.52
Totals	100.00	



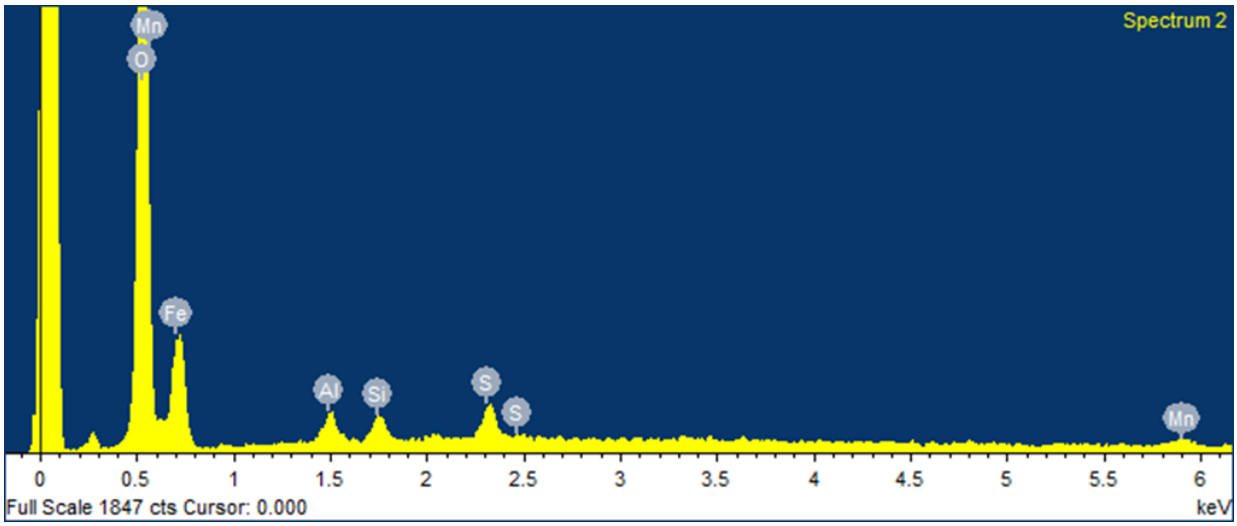
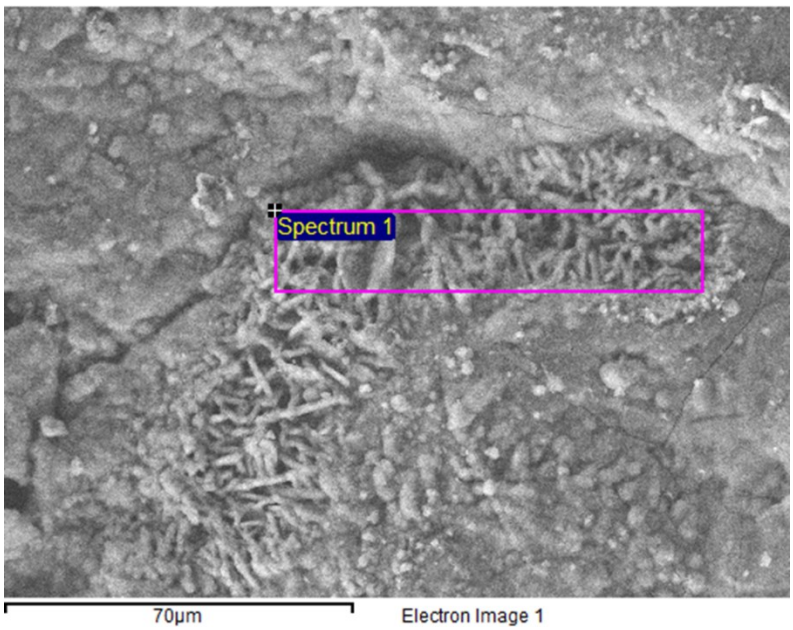


Figure A.752. SEM Image and EDS Spectrum of the Rust Collected from Exterior Web of the Girder.

Element	Weight %	Atomic %
O K	50.28	77.00
Al K	0.83	0.75
Si K	0.99	0.86
S K	1.13	0.86
Mn K	0.43	0.19
Fe K	46.35	20.34
Totals	100.00	



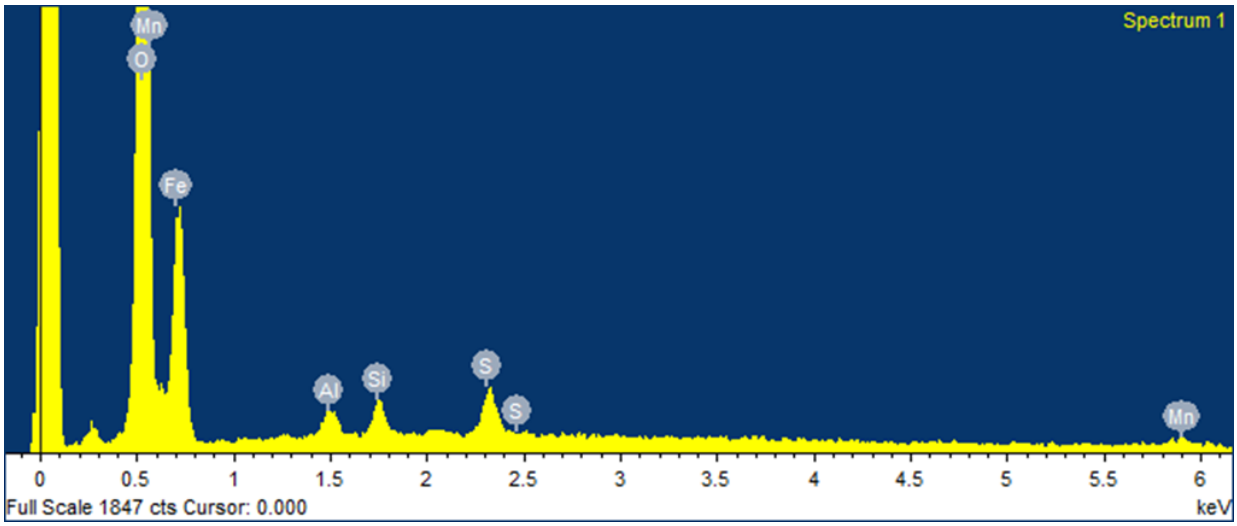
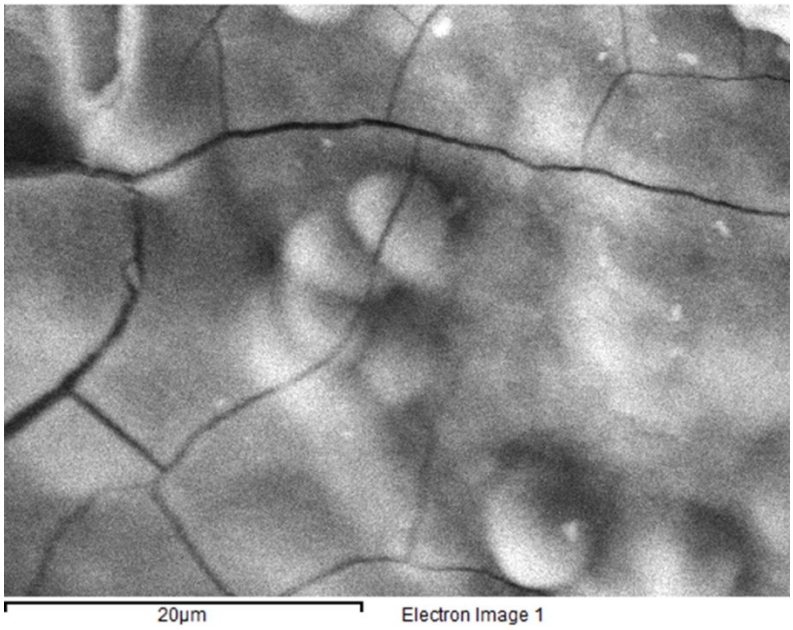


Figure A.753. SEM Image and EDS Spectrum of the Rust Collected from Exterior Web of the Girder.

A.42.4.SEM/EDS Results: Interior Web Girder

Element	Weight %	Atomic %
O K	31.87	61.21
Al K	0.96	1.10
S K	1.45	1.39
Cl K	0.48	0.41
Mn K	1.38	0.77
Fe K	63.42	34.89
Ni K	0.43	0.22
Totals	100.00	



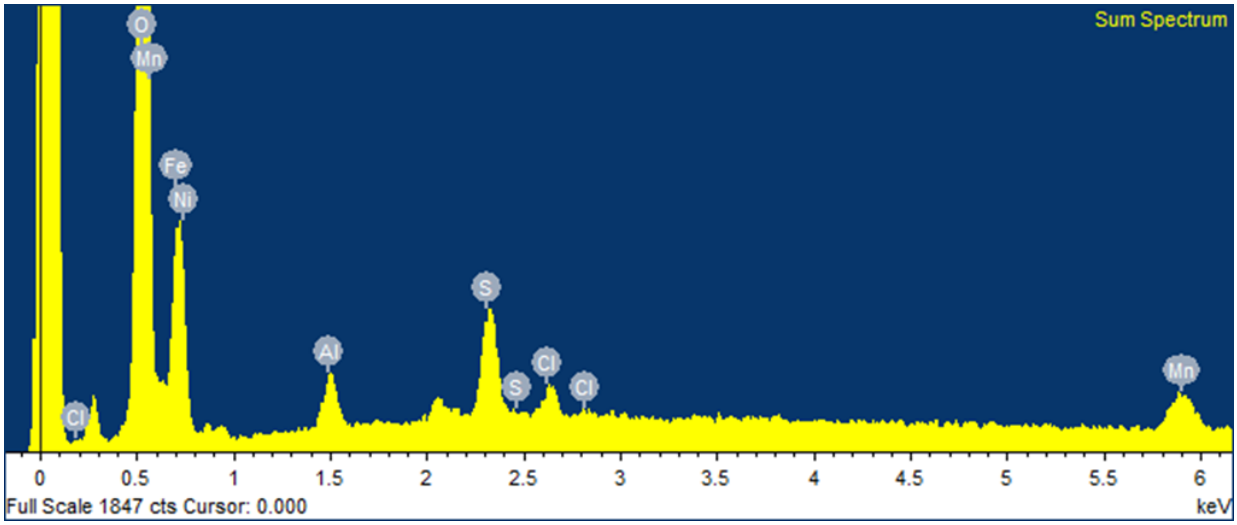


Figure A.754. SEM Image and EDS Spectrum of the Rust Collected from Interior Web of the Girder.

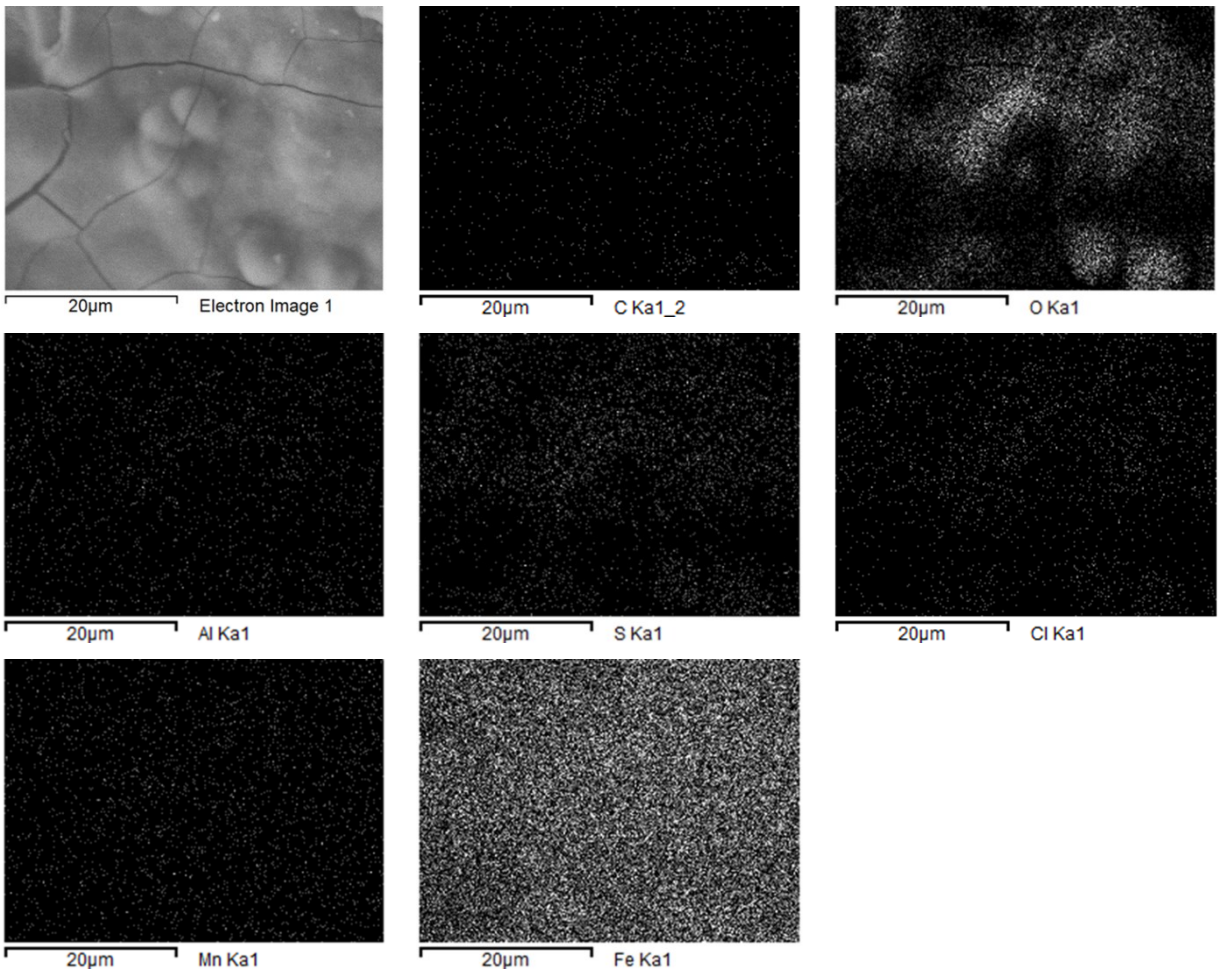


Figure A.755. EDS Elemental Mapping of Rust Collected from Interior Web.

A.42.5.XPS Results: Exterior Web Girder

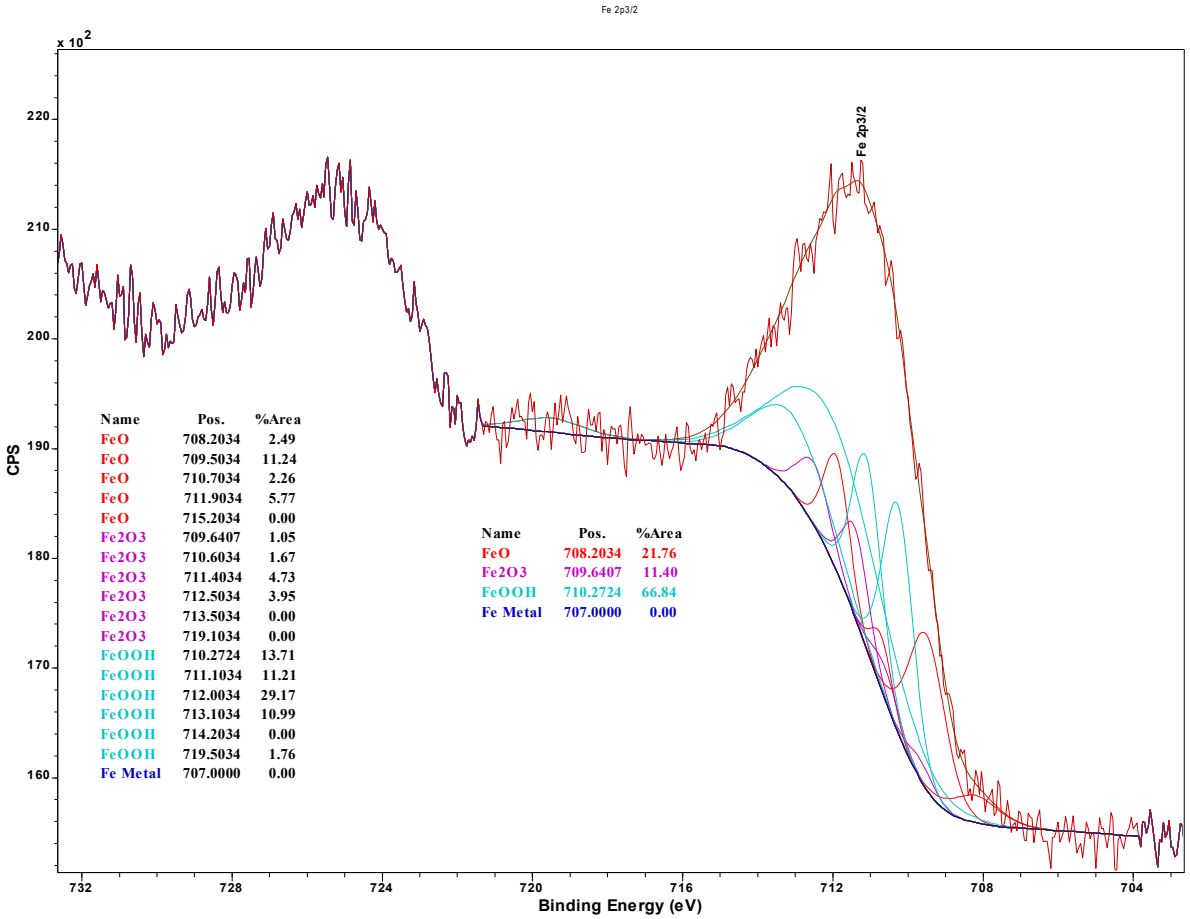


Figure A.756. XPS Spectrum of the Rust Collected from Exterior Web of the Girder.

A.42.6.XPS Results: Interior Web Girder

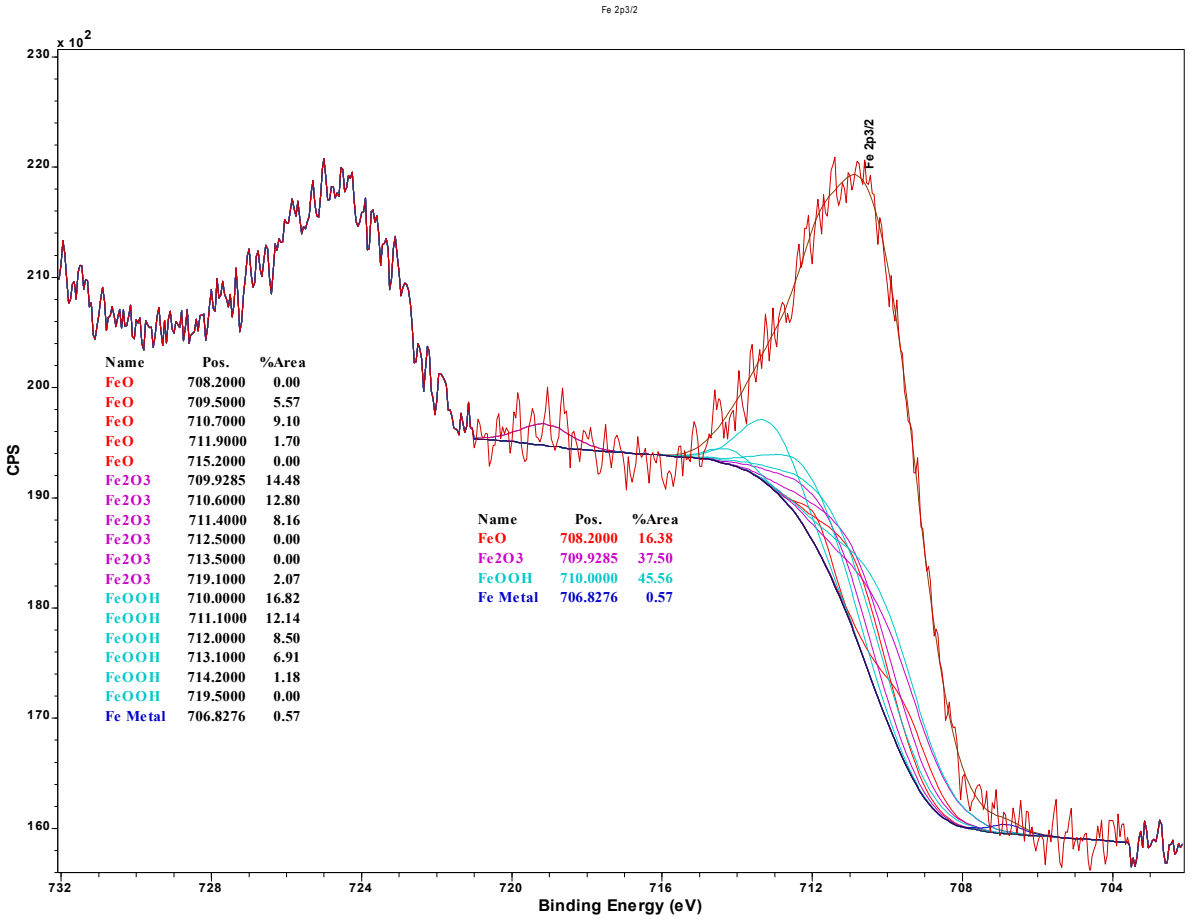


Figure A.757. XPS Spectrum of the Rust Collected from Interior Web of the Girder.

A.42.7.XRD Result: Exterior and Interior Girder

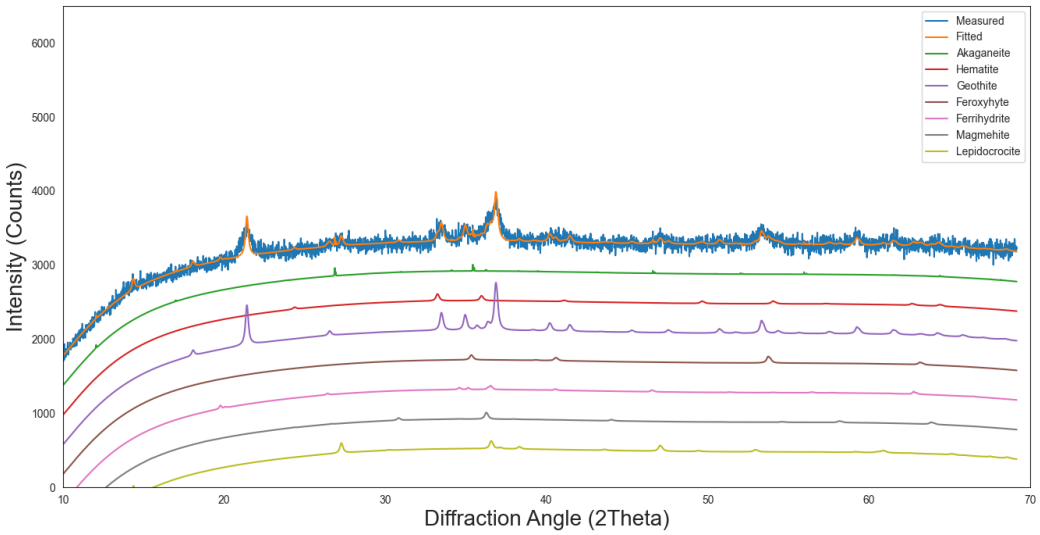


Figure A.758. XRD Pattern of Powdered Rust Collected from Exterior Web of the Girder.

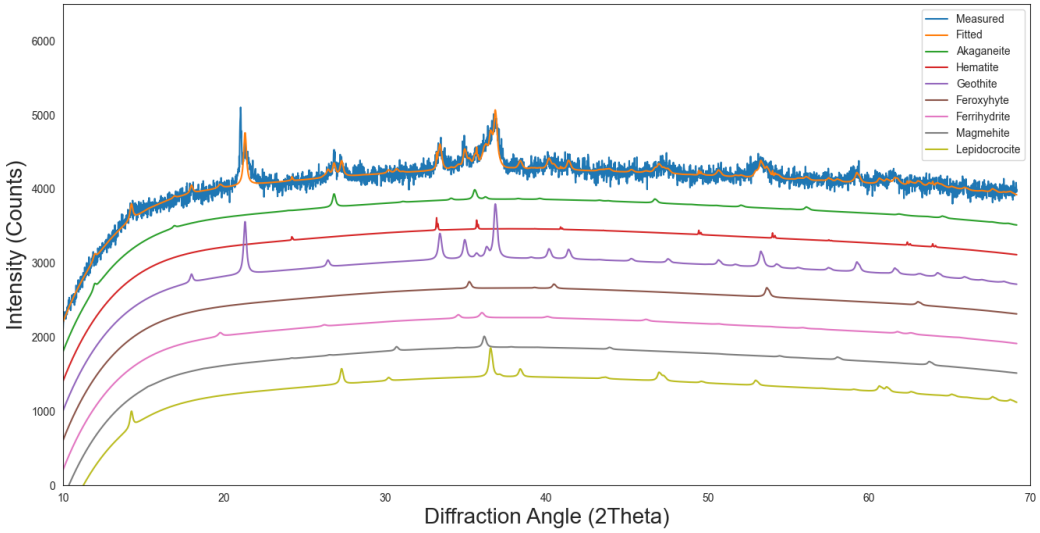


Figure A.759. XRD Pattern of Powdered Rust Collected from Interior Web of the Girder.

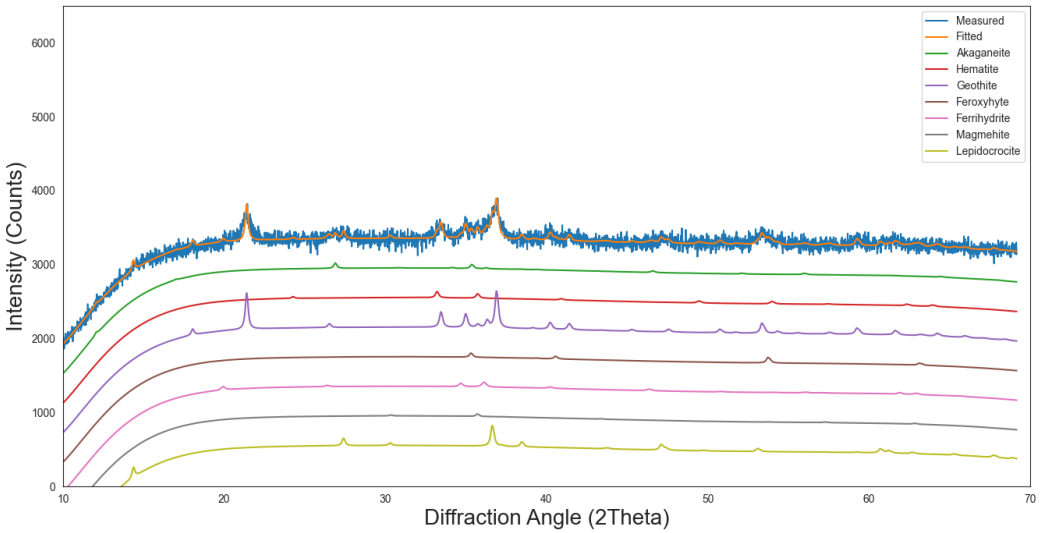


Figure A.760. XRD Pattern of Powdered Rust Collected from Bottom face of Bottom Flange of the Interior Girder.

A.42.8.Particle Size Analysis: Tape Adhesion Results

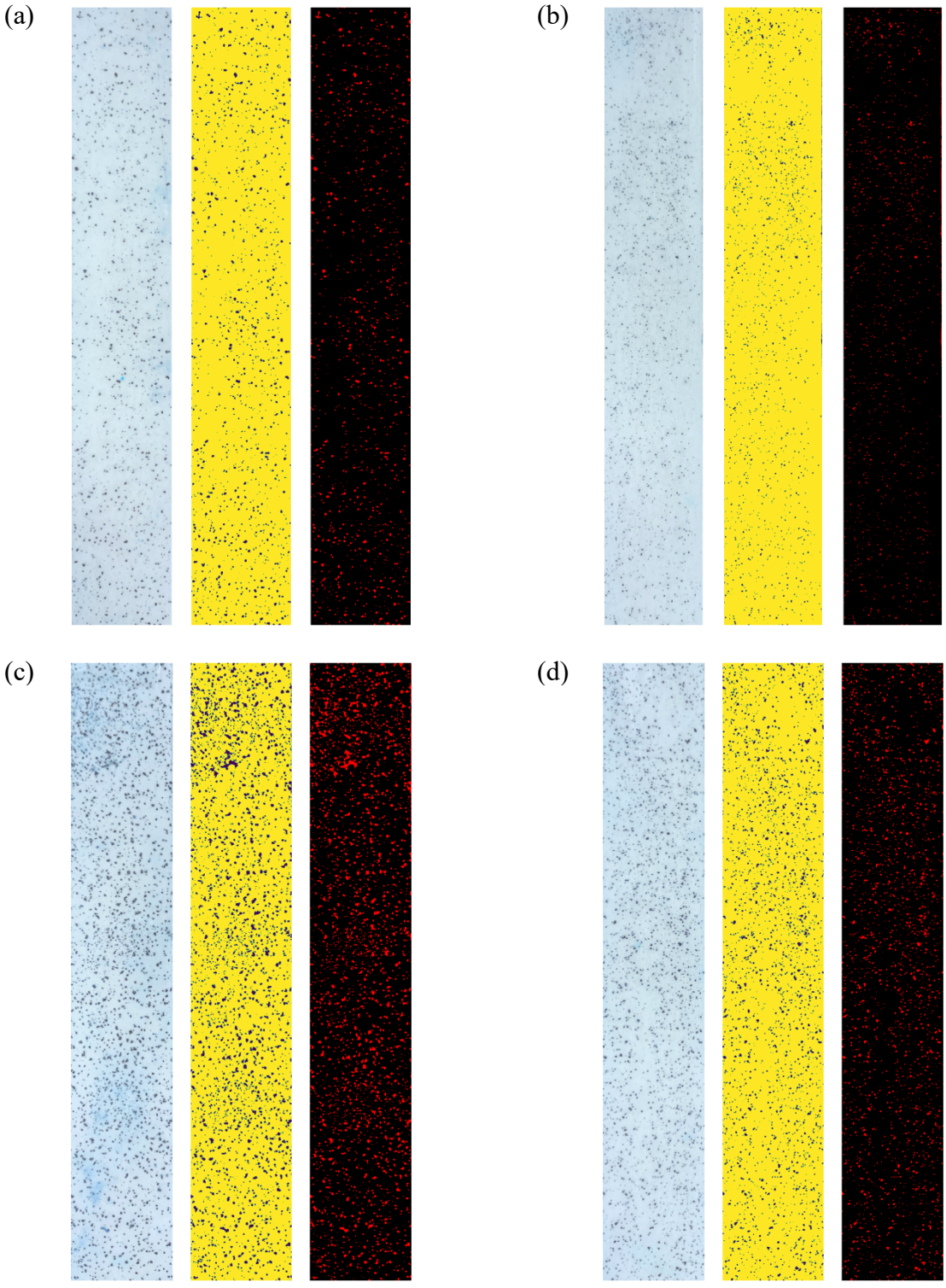


Figure A.761. Particle Size Analysis Results at A1G1F1 (a) Top Flange Bottom, (b) Web, (c) Bottom Flange Bottom (d) Stiffener.

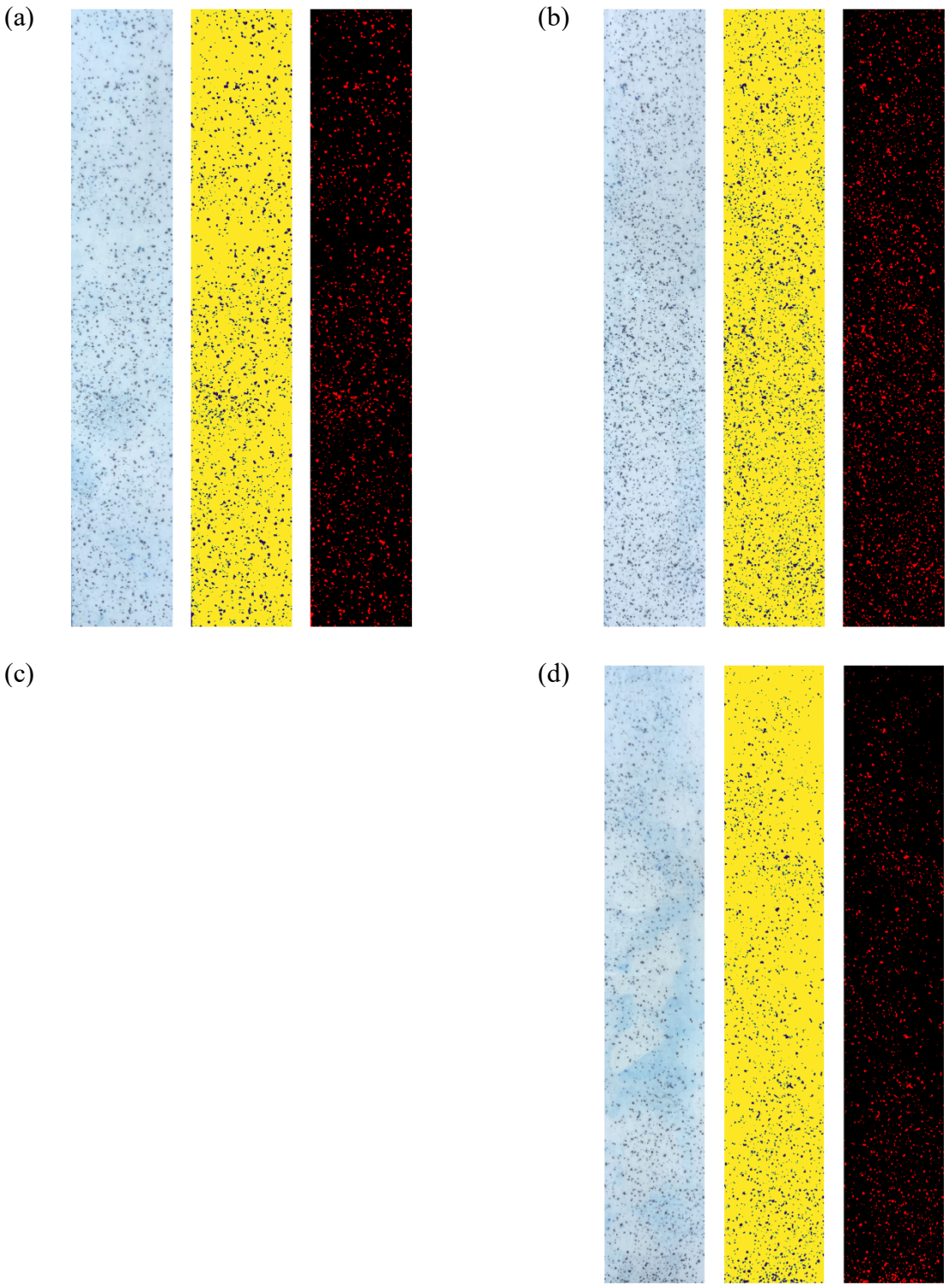


Figure A.762. Particle Size Analysis Results at A1G1F2 (a) Top Flange Bottom, (b) Web, (c) Bottom Flange Bottom (d) Stiffener.

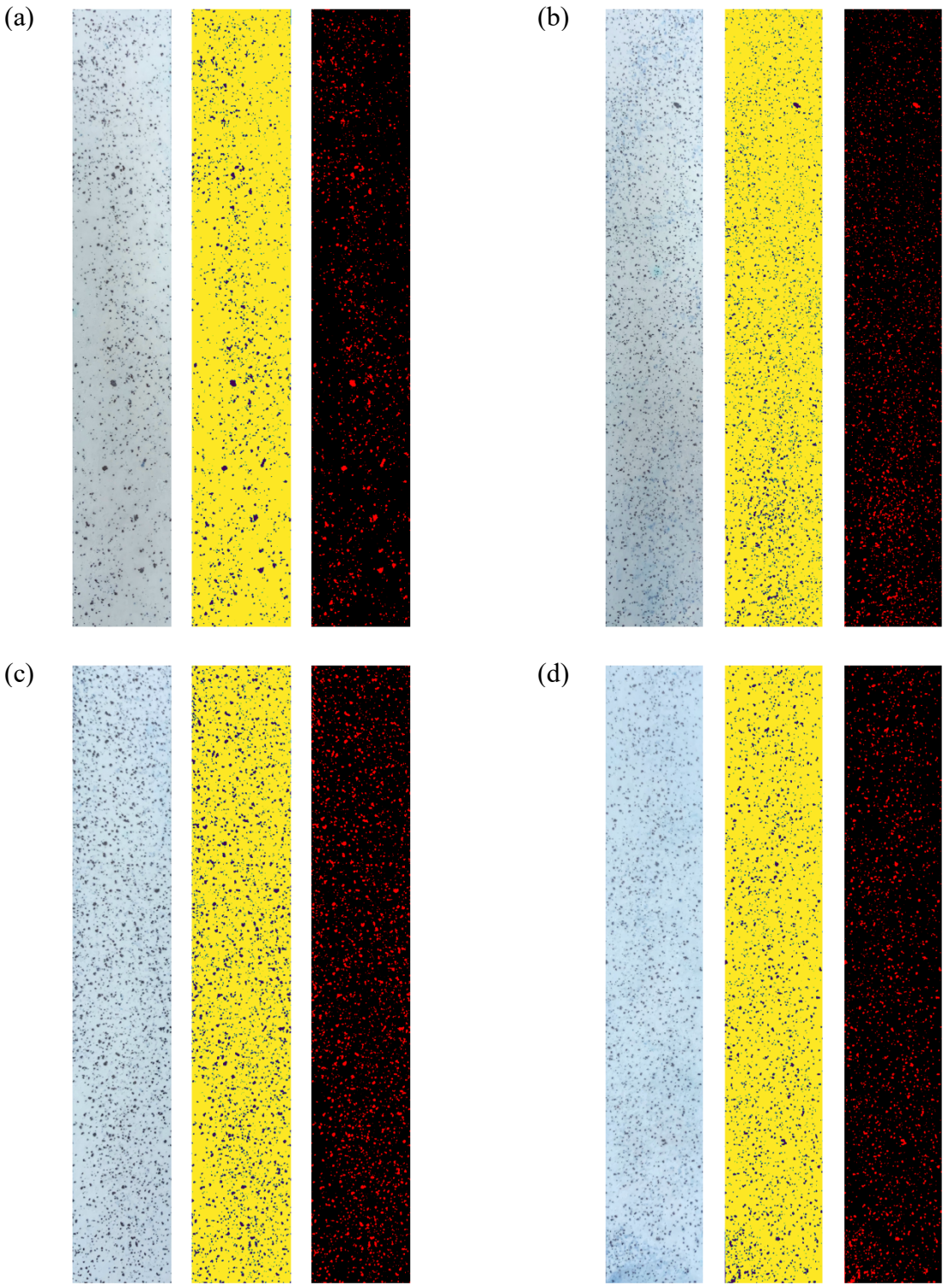


Figure A.763. Particle Size Analysis Results at A1G2F1 (a) Top Flange Bottom, (b) Web, (c) Bottom Flange Bottom (d) Stiffener.

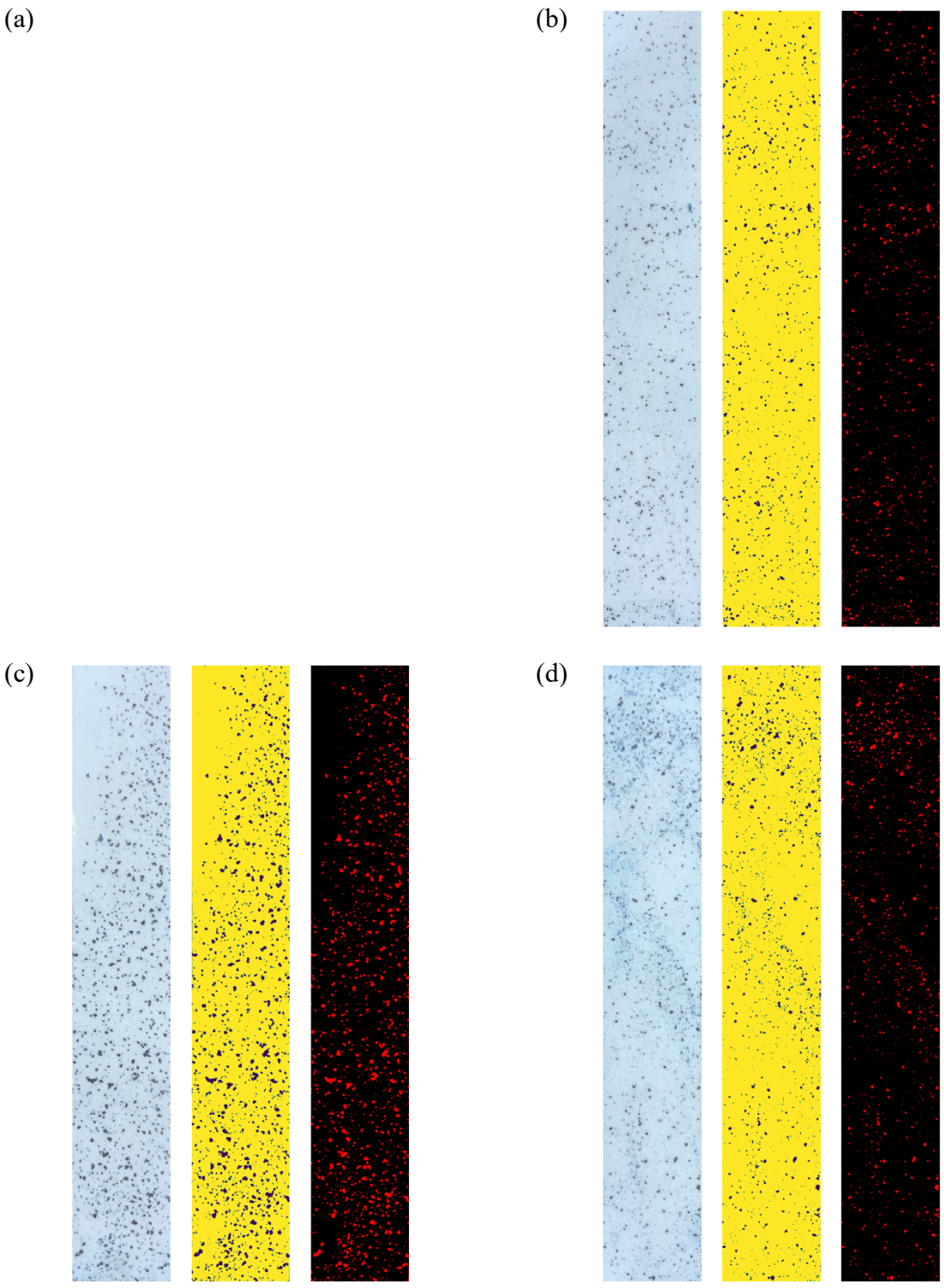


Figure A.764. Particle Size Analysis Results at A3G1F1 (a) Top Flange Bottom, (b) Web, (c) Bottom Flange Bottom (d) Stiffener.

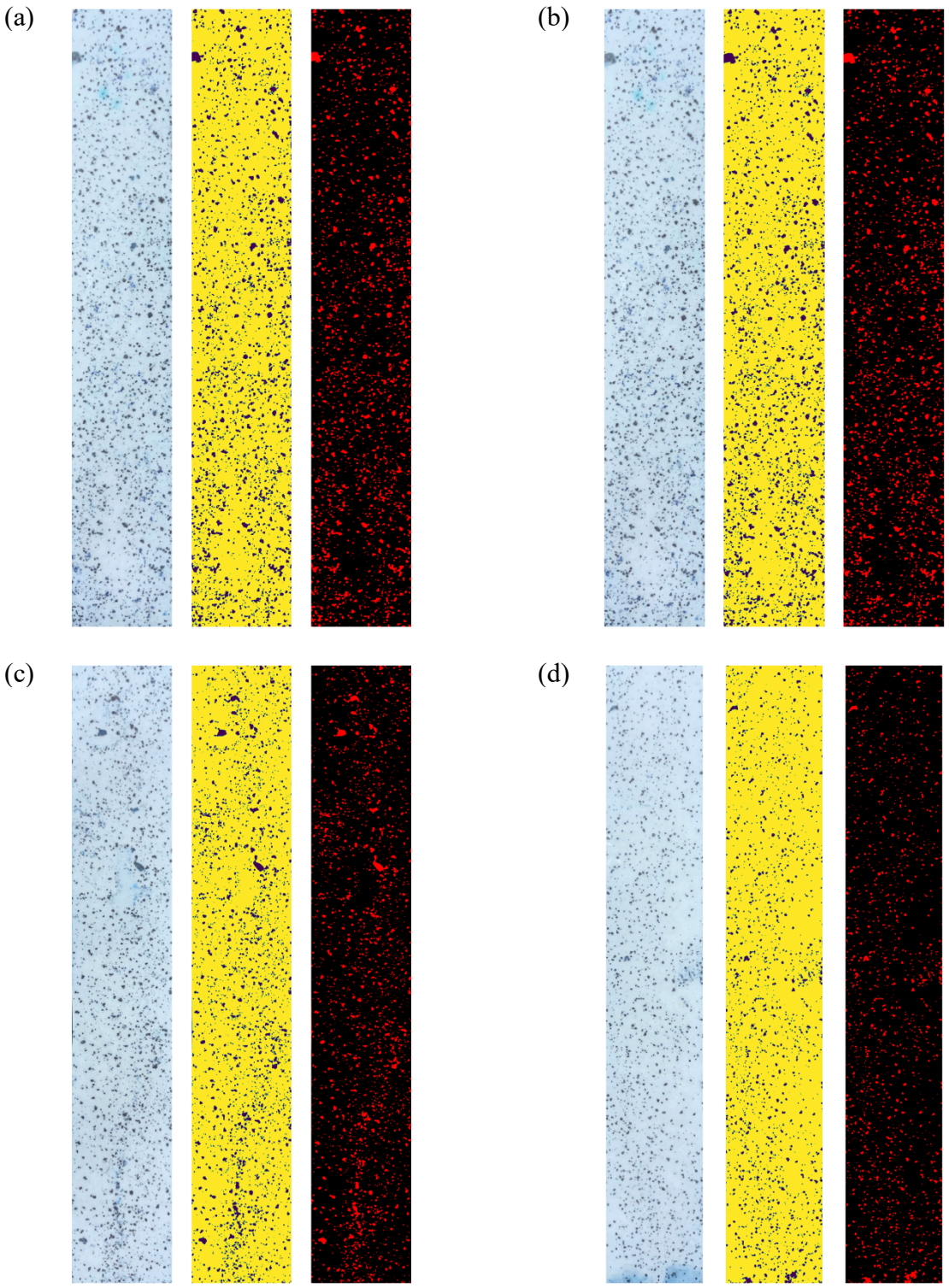


Figure A.765. Particle Size Analysis Results at A3G2F1 (a) Top Flange Bottom, (b) Web, (c) Bottom Flange Bottom (d) Stiffener.

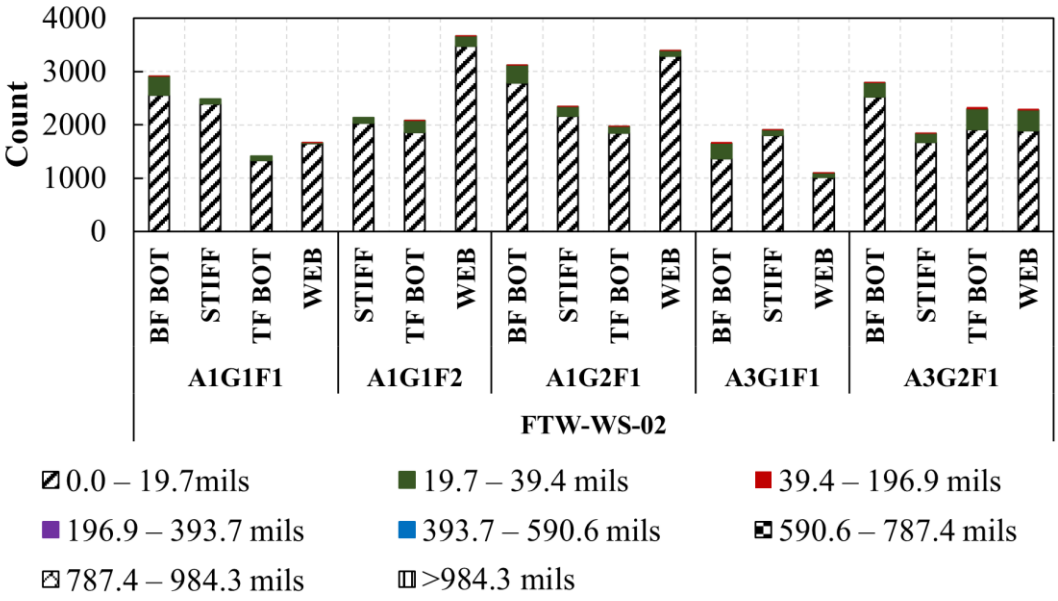


Figure A.766. Particle Size Analysis Showing Different Locations Examined.

A.43. FTW-WS-03

- FM 1902B
- Bridge ID 21270050405501, Coordinates (32.4944, -97.42291), Johnson County
- Continuous weathering steel plate girder
- Built 2014
- Girder inspection carried on girder 1, 3, 4 and 6, and measurements are taken on girder within four feet from the abutment or bent.
- No visual inspection on deck
- Location for Testing: G1F1, G3F1, G4F2, G6F2



Figure A.767. Typical Picture of FTW-WS-03.

A.43.1. Observed Condition

Overall bridge is in very good condition with development of uniform patina throughout the girder. The patina rating varied between 7 and 8 showing good protection and adherence to the steel surface.

A.43.2.Field Inspection Results

Table A-190. Field Inspection Results for FTW-WS-03.

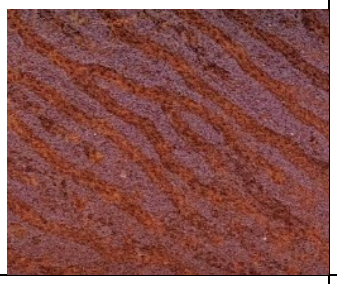
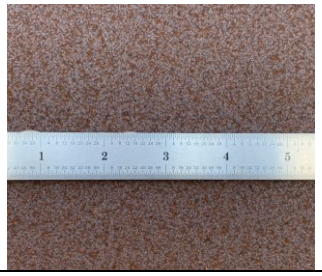
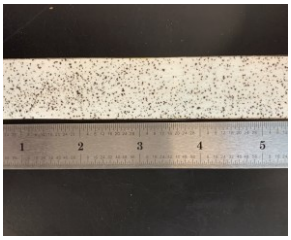
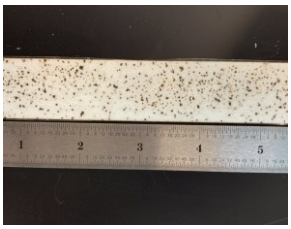
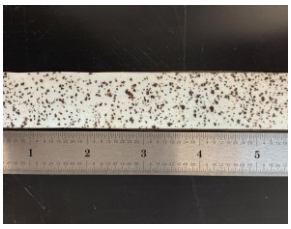
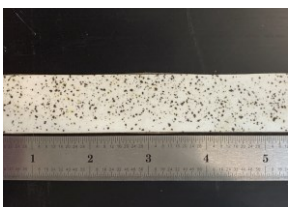
Location	Patina Rating	Thickness (inch)	Cl^- Conc. (ppm)	Field Condition	Tape Test
G1F1 TF Bot. Ext.	8	Measured R1 1.514 R2 1.515 R3 1.517 R_Avg 1.515 Design	-		
G1F1 Web Ext.	8	Measured R1 0.637 R2 0.636 R3 0.633 R_Avg 0.635 Design	6		
G1F1 BF Top Ext.	8	Measured R1 1.494 R2 1.493 R3 1.494 R_Avg 1.494 Design	-		
G1F1 BF Bot Ext.	7	-	-		
G1F1 Stiffener Ext.	7	Measured R1 1.252 R2 1.252 R3 1.250 R_Avg 1.251 Design	-		

Table A-191. Field Inspection Results for FTW-WS-03.

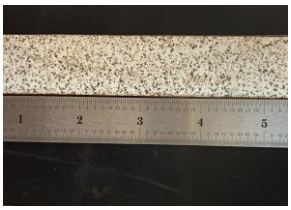
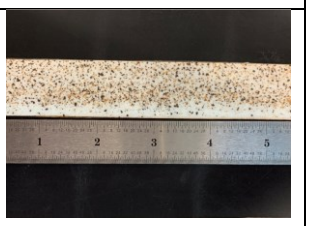
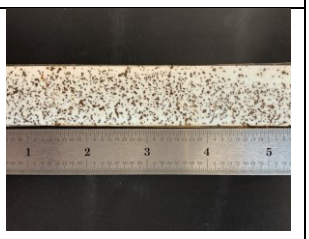
Location	Patina Rating	Thickness (inch)	Cl^- Conc. (ppm)	Field Condition	Tape Test
G3F1 TF Bot Int.	7	Measured R1 1.244 R2 1.246 R3 1.244 R_Avg 1.245 Design	-		
G3F1 Web Int.	7	Measured R1 0.630 R2 0.631 R3 0.630 R_Avg 0.630 Design	0		
G3F1 BF Top Int.	7	Measured R1 1.513 R2 1.514 R3 1.516 R_Avg 1.514 Design	-		
G3F1 BF Bot Int.	7	-	-		
G3F1 Stiffener Int.	7	Measured R1 1.496 R2 1.497 R3 1.496 R_Avg 1.496 Design	-		

Table A-192. Field Inspection Results for FTW-WS-03 .

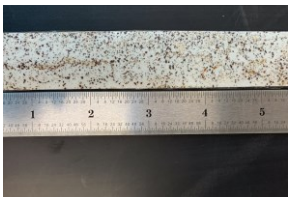
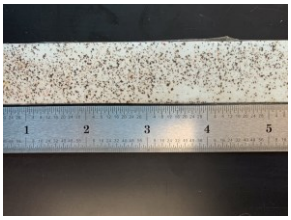
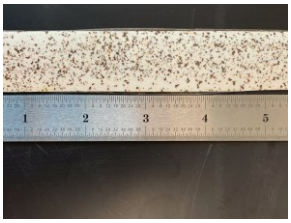
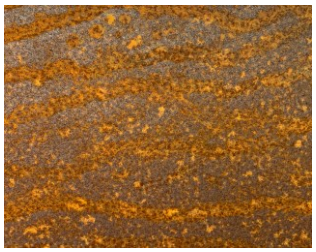
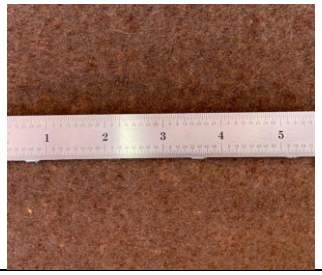
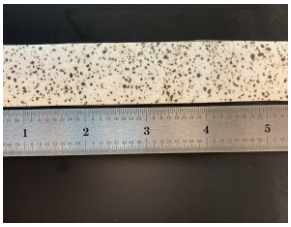
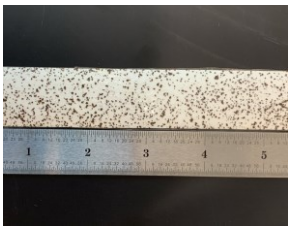
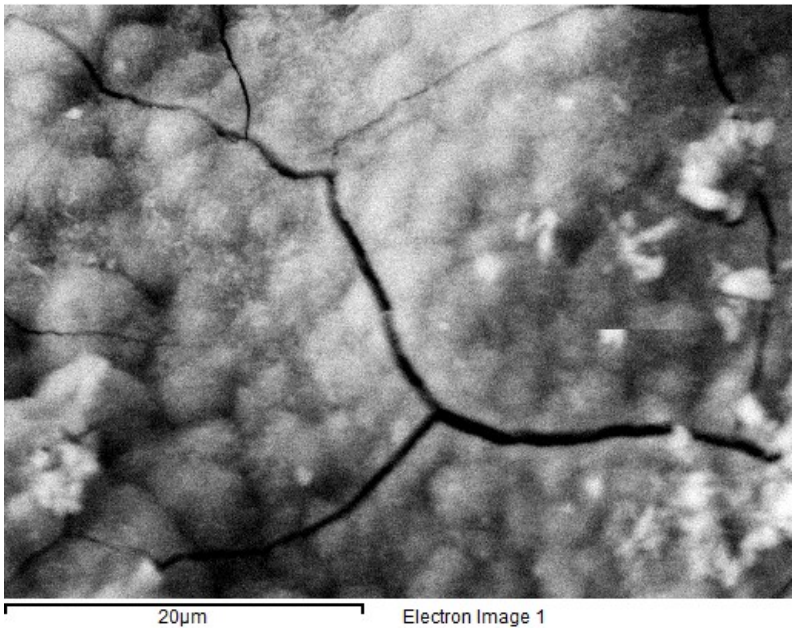
Location	Patina Rating	Thickness (inch)	Cl^- Conc. (ppm)	Field Condition	Tape Test
G4F2 TF Bot Int.	7	Measured R1 1.516 R2 1.513 R3 1.519 R_Avg 1.516 Design	-		
G4F2 Web Int.	8	Measured R1 0.638 R2 0.637 R3 0.639 R_Avg 0.638 Design	-		
G4F2 BF Top Int.	8	Measured R1 1.519 R2 1.522 R3 1.520 R_Avg 1.520	-		
G4F2 BF Bot Int.	7	-	-		
G4F2 Stiffener Int.	8	Measured R1 1.265 R2 1.264 R3 1.266 R_Avg 1.265 Design			

Table A-193. Field Inspection Results for FTW-WS-03 .

Location	Patina Rating	Thickness (inch)	Cl^- Conc. (ppm)	Field Condition	Tape Test
G6F2 TF Bot. Ext.	7	Measured R1 1.522 R2 1.520 R3 1.520 R_Avg 1.521 Design	-		
G6F2 Web Ext.	8	Measured R1 0.637 R2 0.641 R3 0.640 R_Avg 0.639 Design	4		
G6F2 BF Top. Ext.	7	Measured R1 1.524 R2 1.524 R3 1.520 R_Avg 1.523 Design	-		
G6F2 BF Bot. Ext.	7	-			
G6F2 Stiffener Ext.	8	Measured R1 1.246 R2 1.246 R3 1.247 R_Avg 1.246 Design			

A.43.3.SEM/EDS Results: Exterior Web Girder

Element	Weight %	Atomic %
O K	52.59	77.93
Al K	3.42	3.00
S K	1.06	0.78
Cl K	0.28	0.19
Mn K	0.35	0.15
Fe K	41.76	17.73
Ni K	0.54	0.22
Totals	100.00	



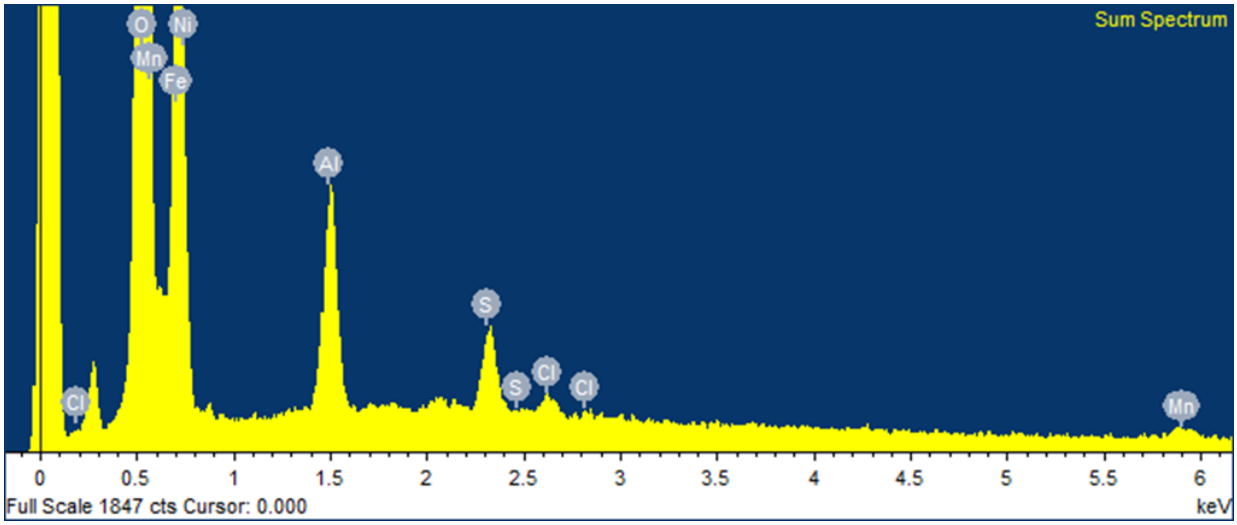


Figure A.768. SEM Image and EDS Spectrum of the Rust Collected from Exterior Web of the Girder.

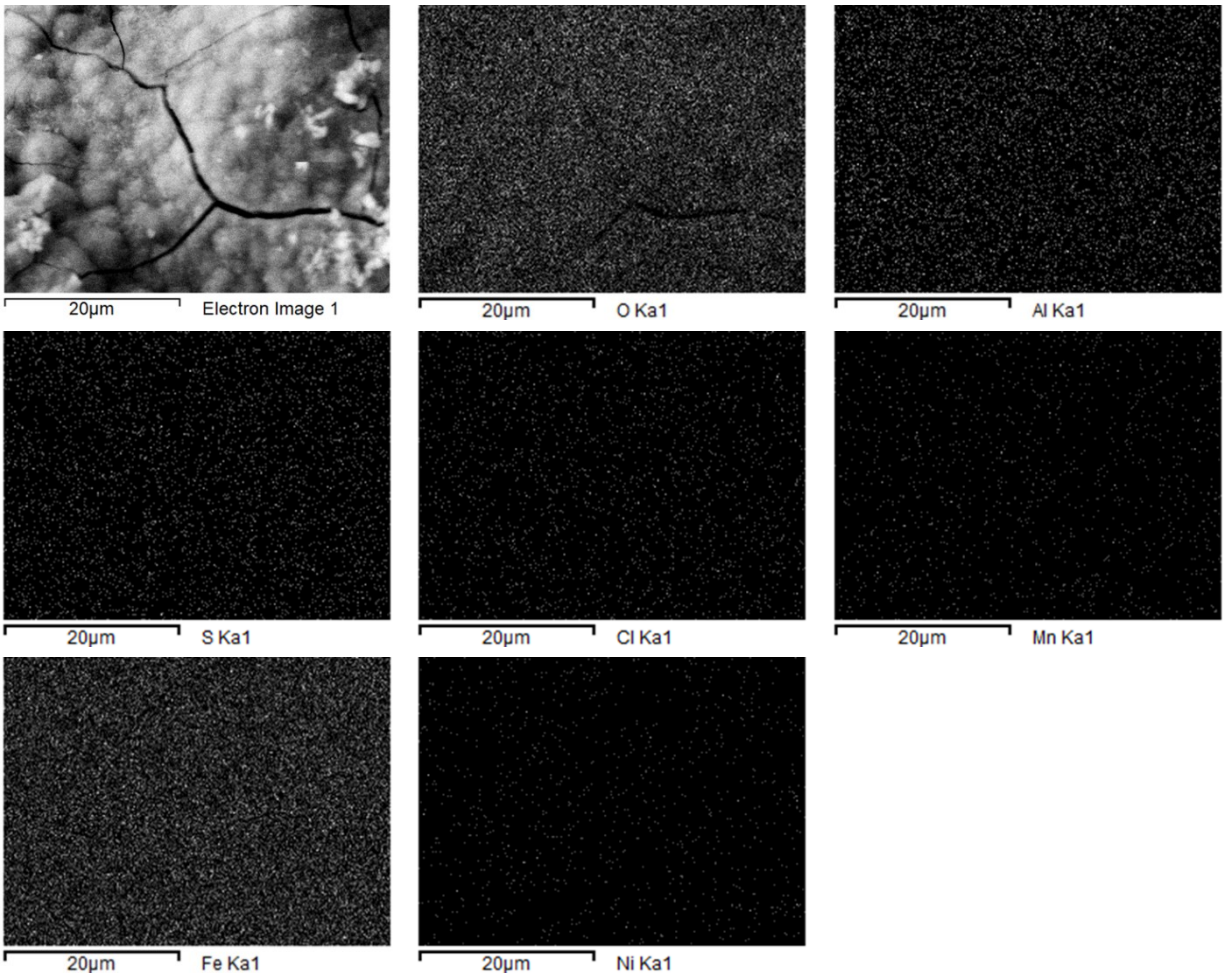
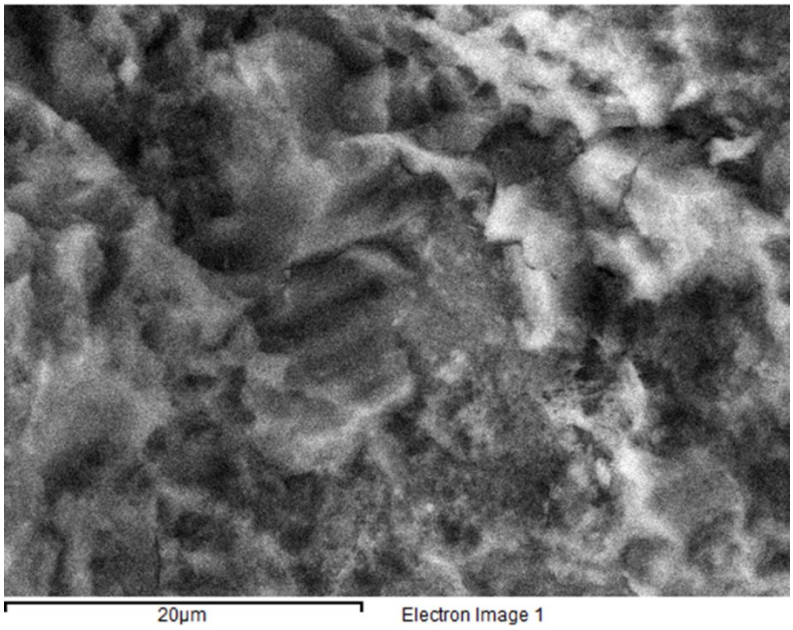


Figure A.769. EDS Elemental Mapping of Rust Collected from Exterior Web.

A.43.4.SEM/EDS Results: Interior Web Girder

Element	Weight %	Atomic %
O K	41.96	70.94
Al K	1.19	1.19
Si K	0.34	0.32
S K	0.23	0.20
Cl K	0.29	0.22
Ca K	0.18	0.12
Cr K	0.28	0.14
Mn K	1.55	0.76
Fe K	53.23	25.78
Cu K	0.75	0.32
Totals	100.00	



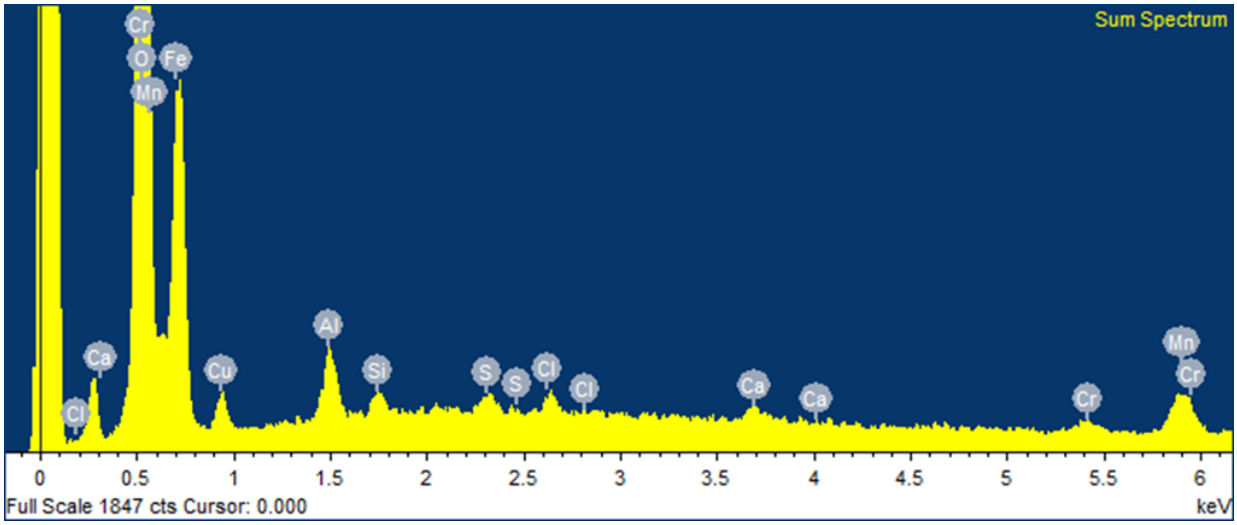


Figure A.770. SEM Image and EDS Spectrum of the Rust Collected from Interior Web of the Girder.

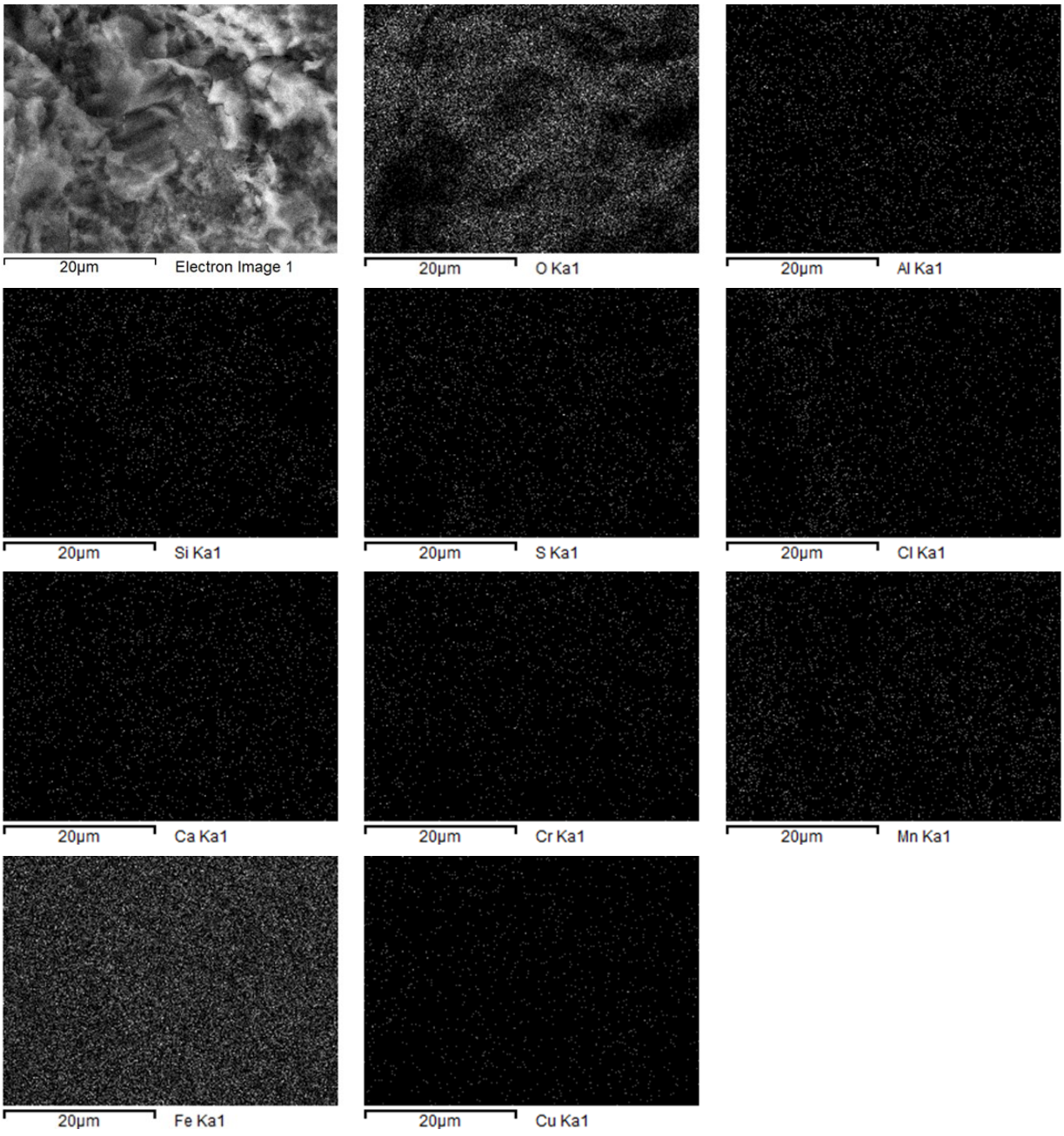


Figure A.771. EDS Elemental Mapping of Rust Collected from Interior Web.

A.43.5.XPS Results: Exterior Web Girder

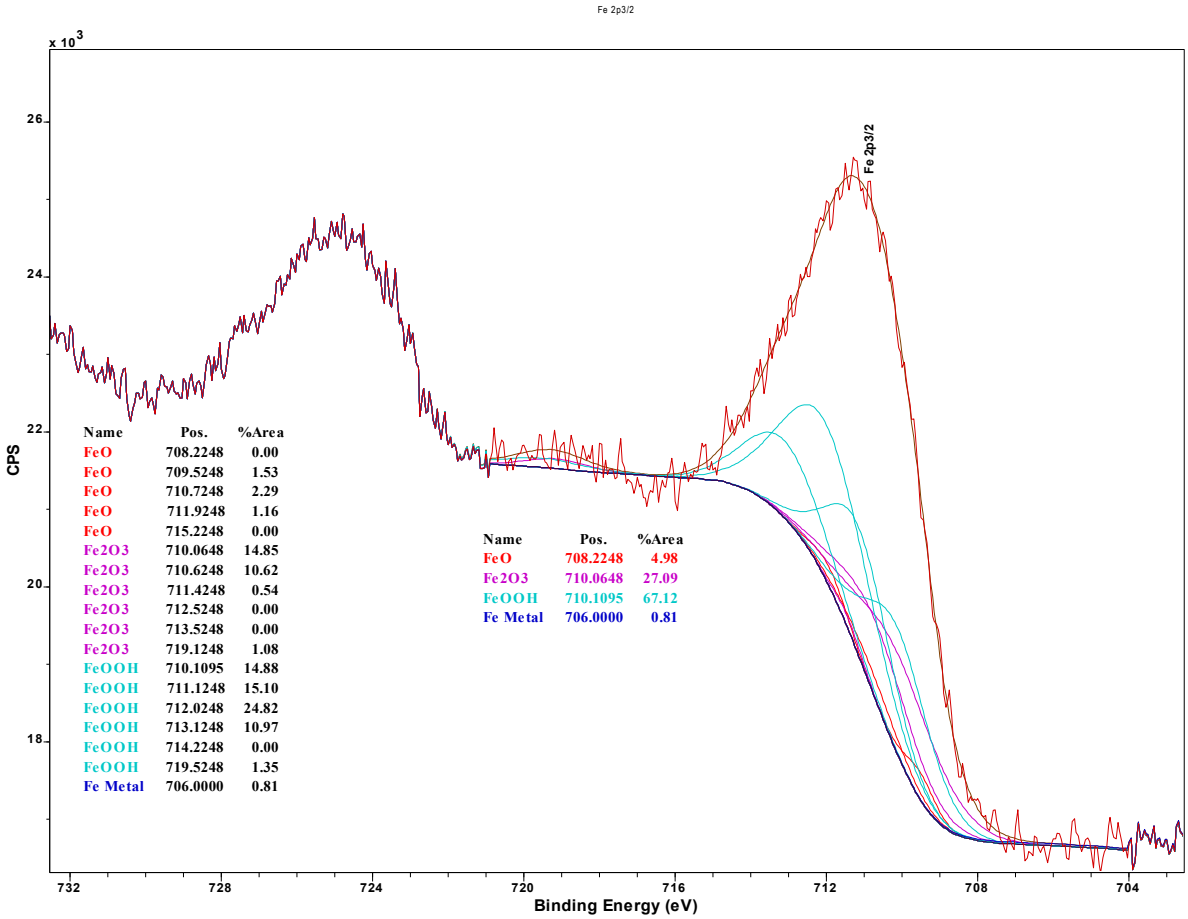


Figure A.772. XPS Spectrum of the Rust Collected from Exterior Web of the Girder.

A.43.6.XPS Results: Interior Web Girder

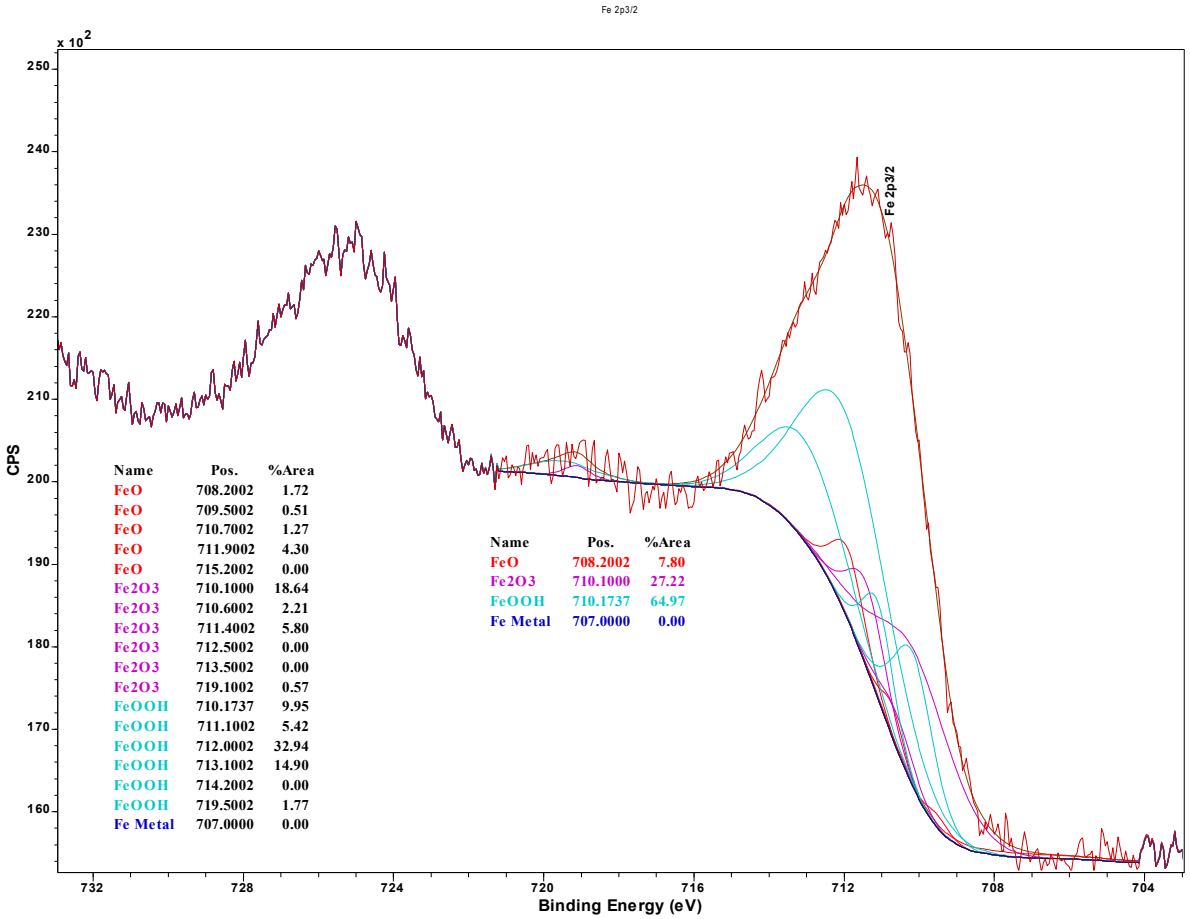


Figure A.773. XPS Spectrum of the Rust Collected from Interior Web of the Girder.

A.43.7.XRD Result: Exterior and Interior Girder

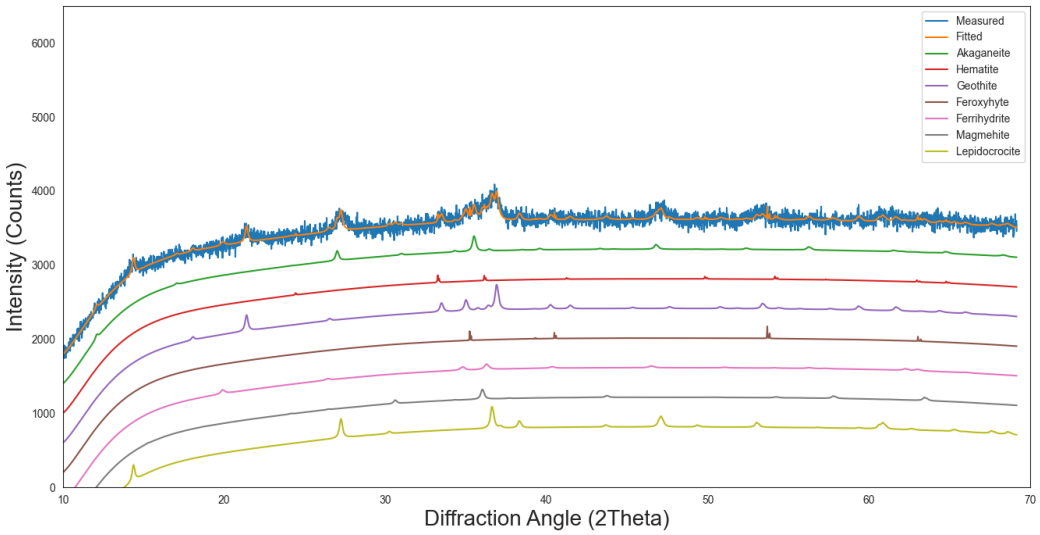


Figure A.774. XRD Pattern of Powdered Rust Collected from Exterior Web of the Girder.

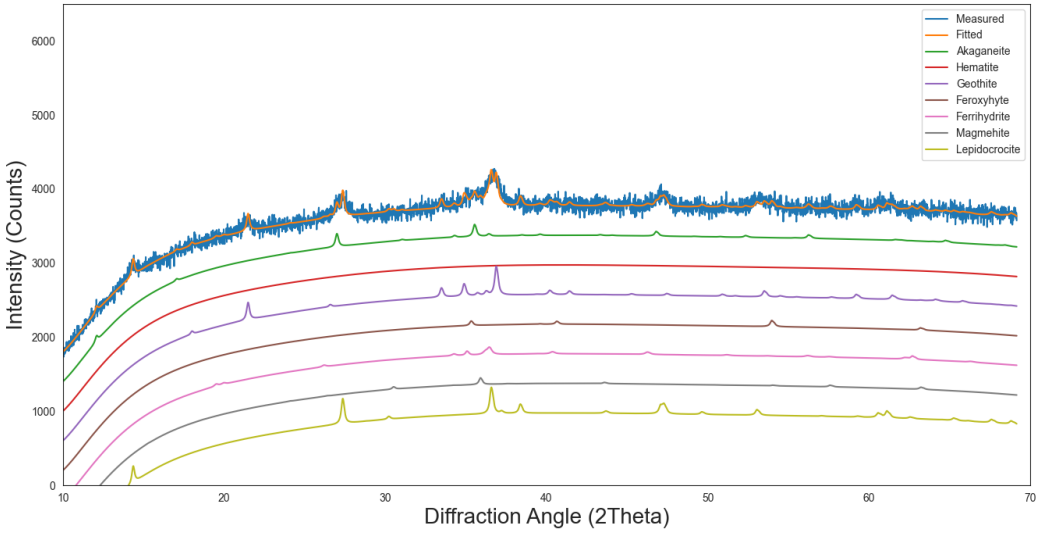


Figure A.775. XRD Pattern of Powdered Rust Collected from Interior Web of the Girder.

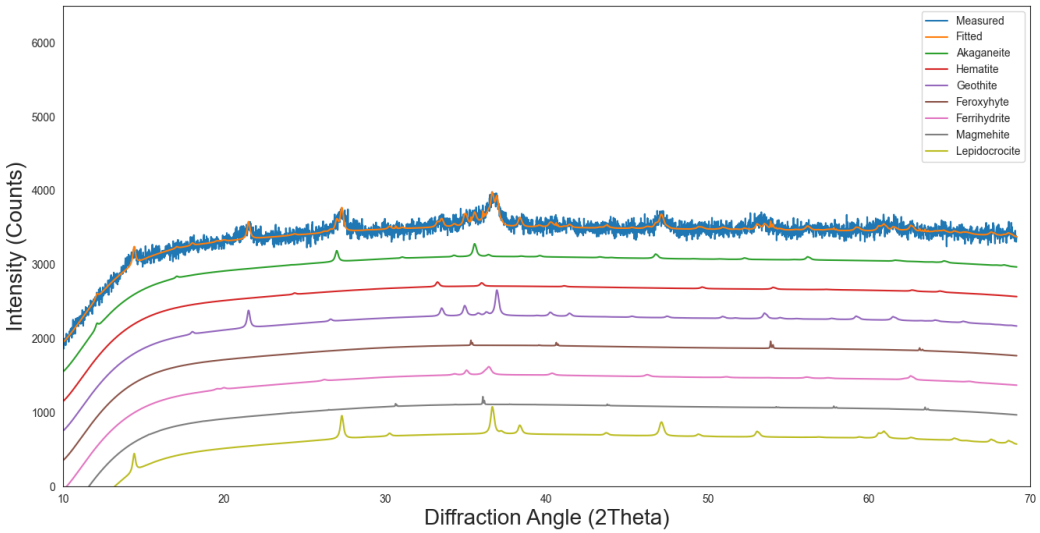


Figure A.776. XRD Pattern of Powdered Rust Collected from Bottom face of Bottom Flange of the Interior Girder.

A.43.8.Particle Size Analysis: Tape Adhesion Results

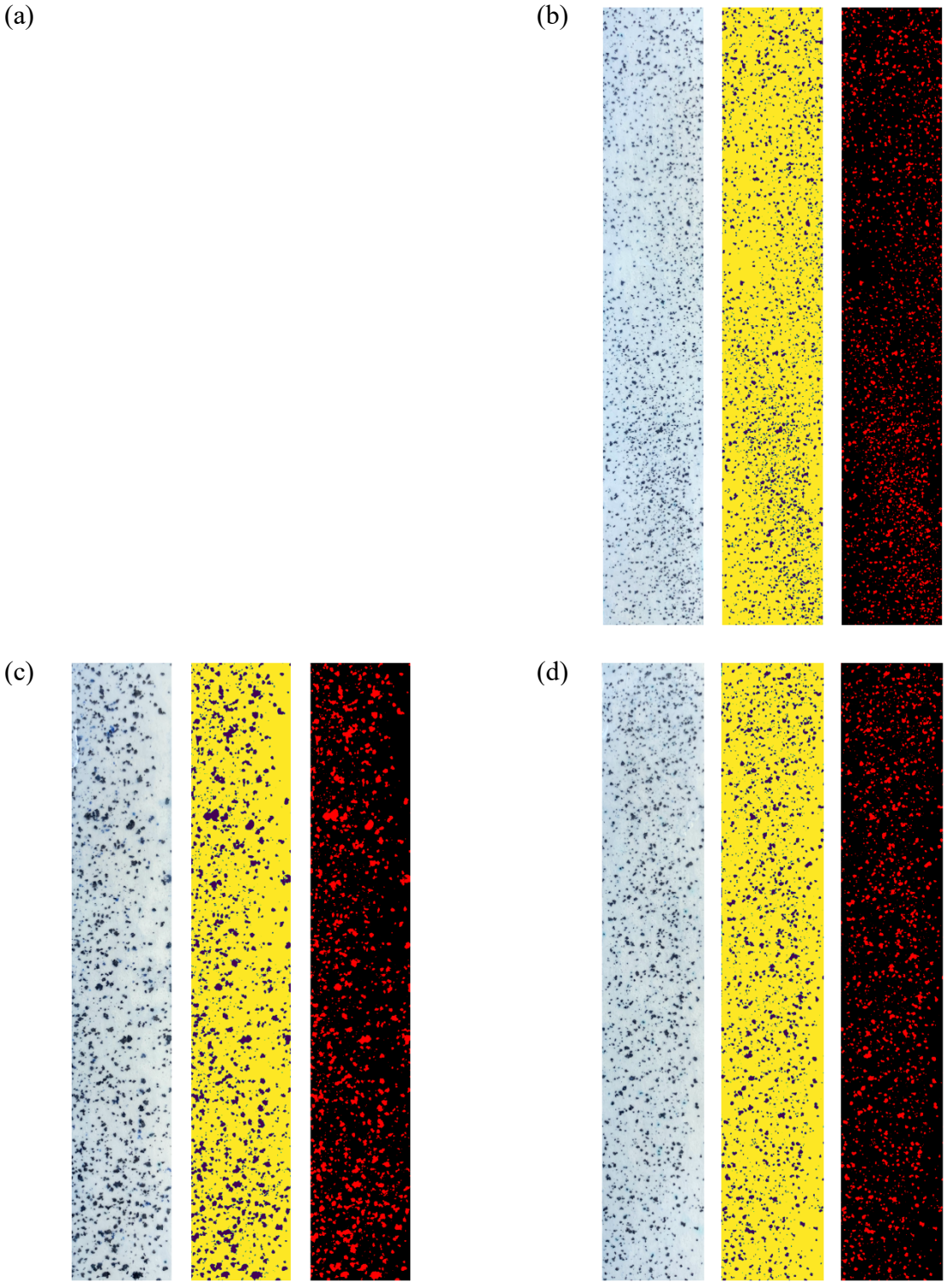


Figure A.777. Particle Size Analysis Results at A1G1F1 (a) Top Flange Bottom, (b) Web, (c) Bottom Flange Bottom (d) Stiffener.

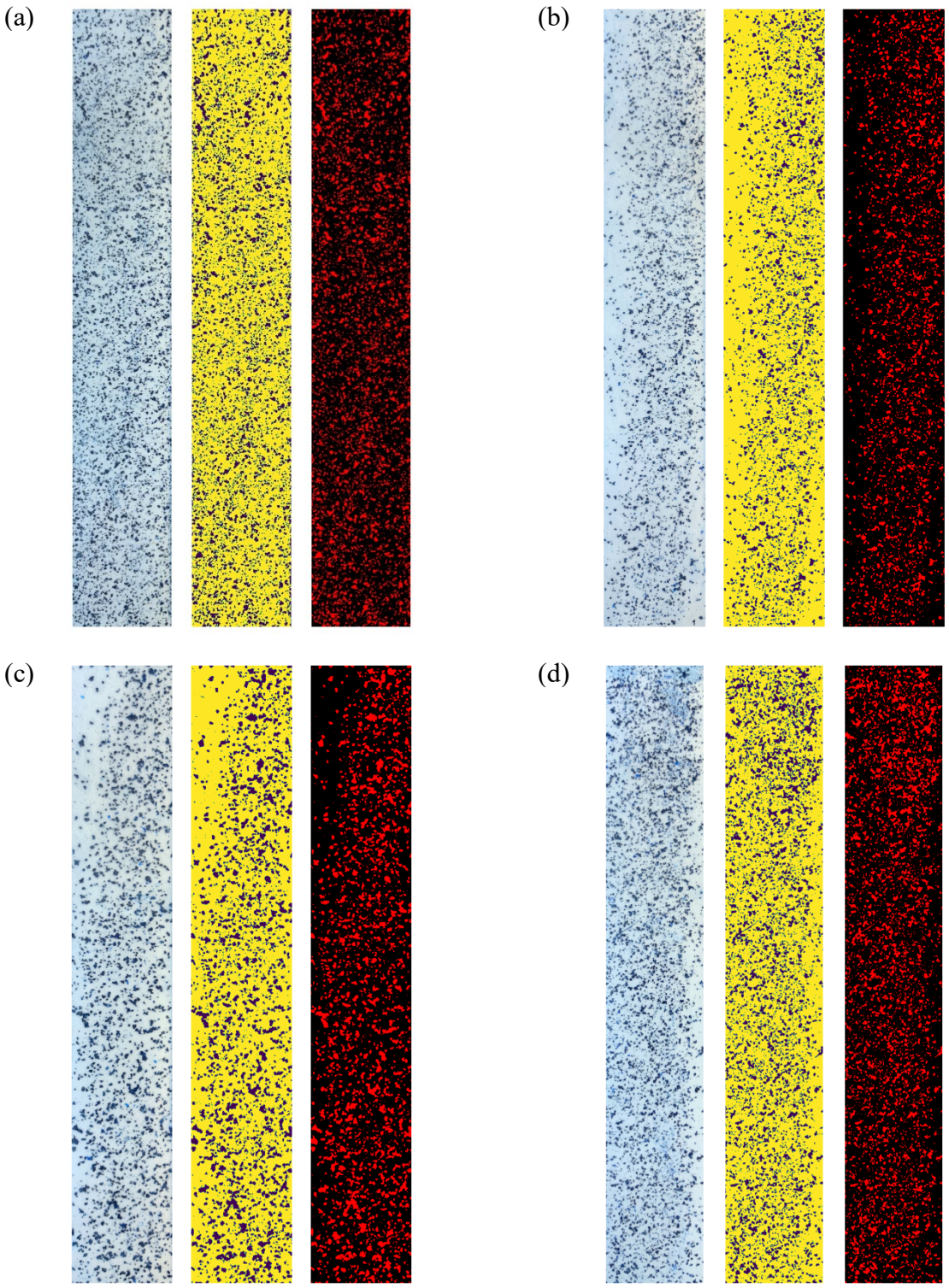


Figure A.778. Particle Size Analysis Results at A1G3F1 (a) Top Flange Bottom, (b) Web, (c) Bottom Flange Bottom (d) Stiffener.

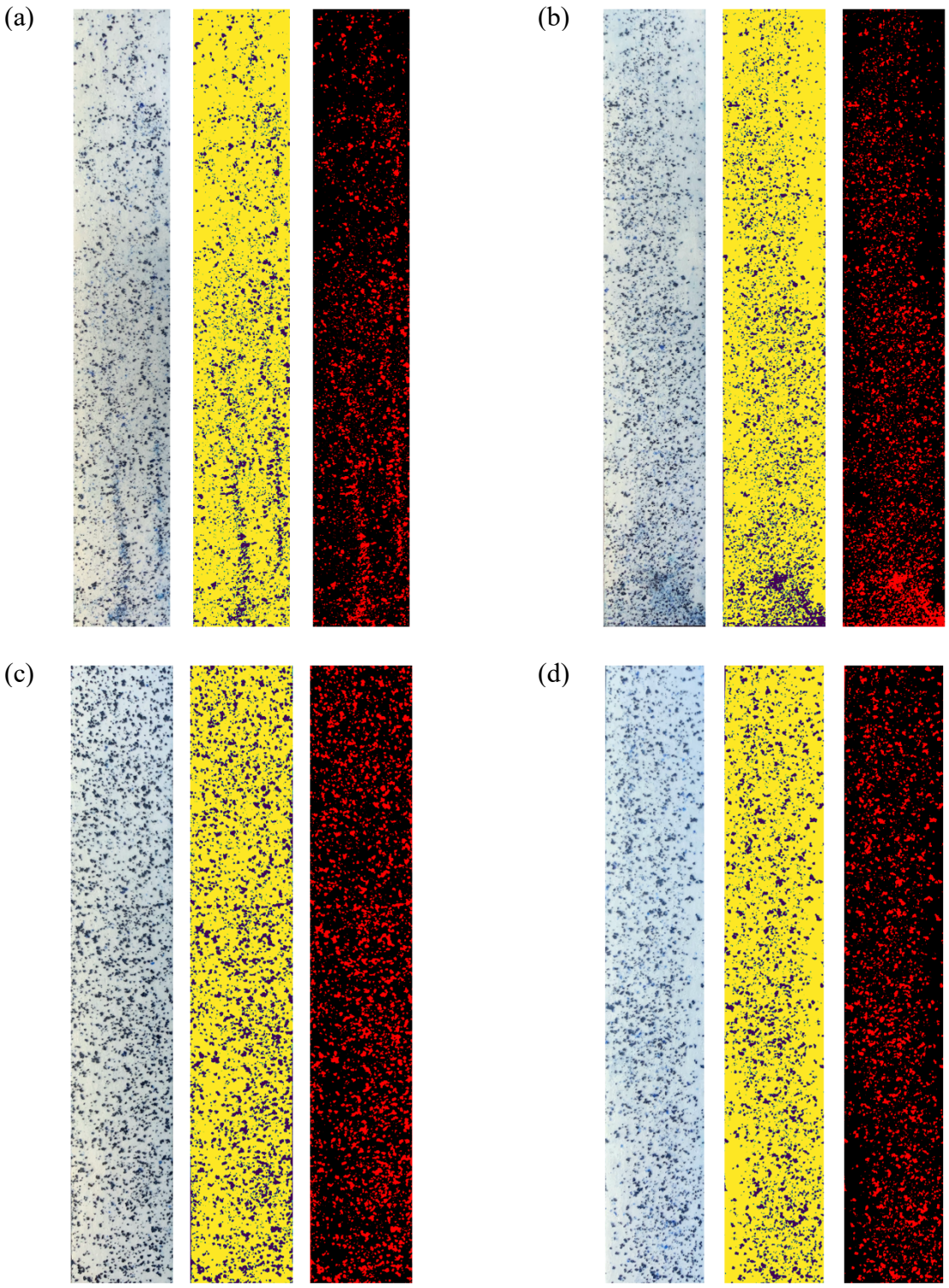


Figure A.779. Particle Size Analysis Results at A1G4F2 (a) Top Flange Bottom, (b) Web, (c) Bottom Flange Bottom (d) Stiffener.

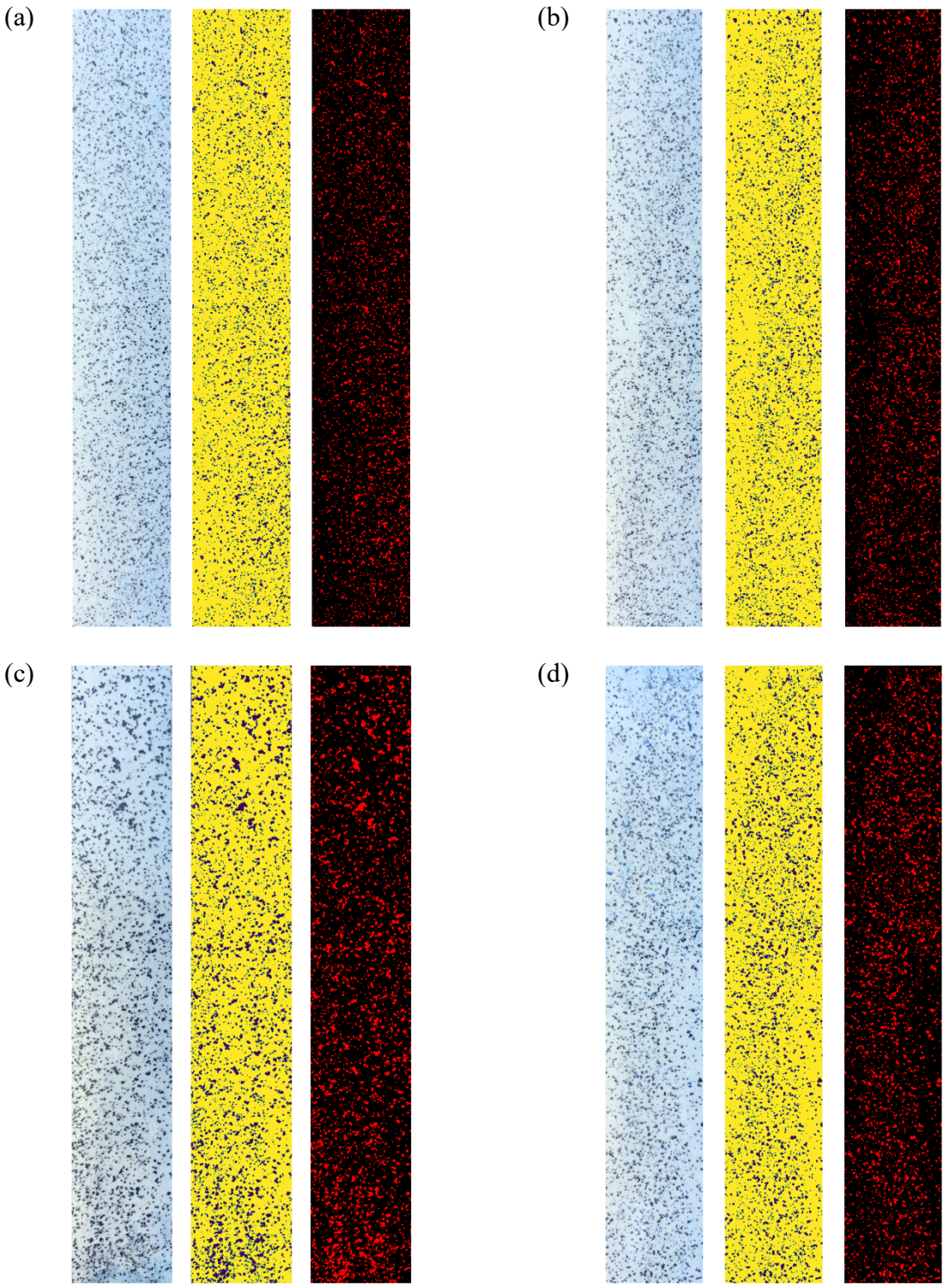


Figure A.780. Particle Size Analysis Results at A1G6F2 (a) Top Flange Bottom, (b) Web, (c) Bottom Flange Bottom (d) Stiffener.

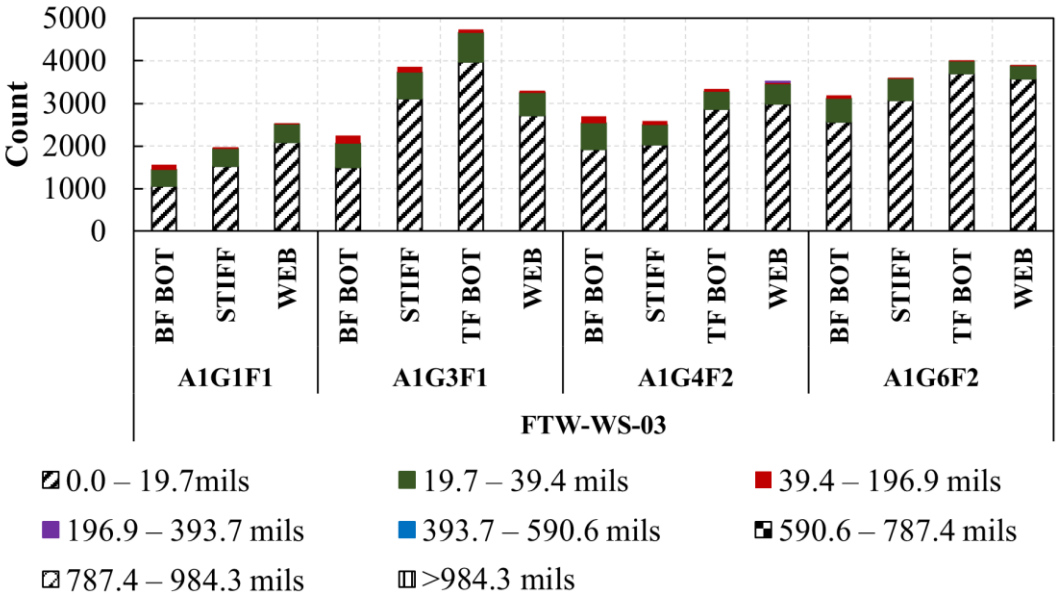


Figure A.781. Particle Size Analysis Showing Different Locations Examined.

A.44. DAL-WS-01

- S Fitzhugh Ave SB over UP Railroad
- Bridge ID , 1805709F4360012, Dallas County, Dallas
- Simply supported weathering steel box girder
- Built 1973
- Girder inspection carried on girder number 1, 3, 4, and 6. Measurements are taken on girder within four feet from the abutment or bent.
- Location for Testing: A1G1F1, A1G3F2, A1G4F1, A1G6F2



Figure A.782. Typical Picture of DAL-WS-01.

A.44.1. Observed Condition

There was accumulation of water and debris inside the box girders which led to severe deterioration of bottom flange of the girder. The water got accumulated inside the girder from the unsealed manhole and the dirt mostly consisted of bird feces which led to aggravated corrosion and section loss of the bottom flange. Therefore, a portion of the bottom flange was replaced, and manhole was sealed. Overall bridge is in good condition with development of uniform patina throughout the girder.

A.44.2.Field Inspection Results

Table A-194. Field Inspection Results for DAL-WS-01.

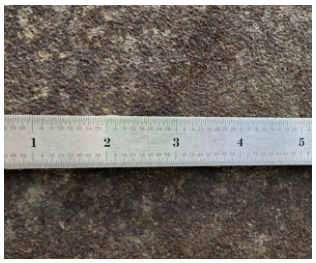
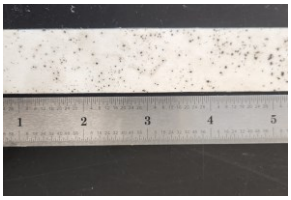
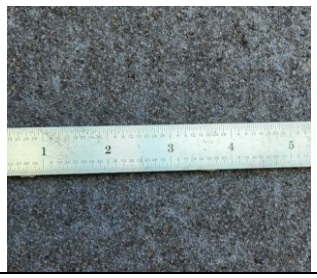
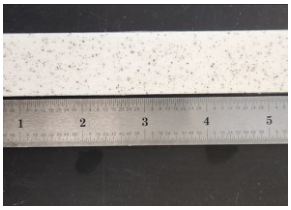
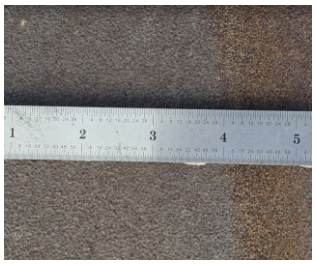
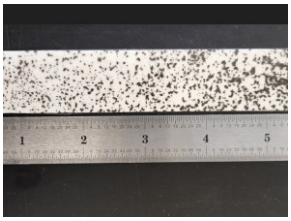
Location	Patina Rating	Thickness (inch)	Cl^- Conc. (ppm)	Field Condition	Tape Test
A1-G1F1 TF Bot. Ext.	8	Measured R1 0.860 R2 0.875 R3 0.881 R_Avg Design			
A1-G1F1 Web Ext.	8	Measured R1 0.382 R2 0.382 R3 0.380 R_Avg Design	1		
A1-G1F1 BF Top Ext.		Measured R1 R2 R3 R_Avg Design			
A1-G1F1 BF Bot. Ext.	6	Measured R1 .0.336 R2 0.337 R3 0.340 R_Avg Design			

Table A-195. Field Inspection Results for DAL-WS-01.

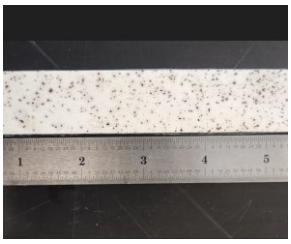
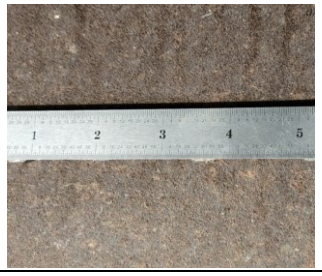
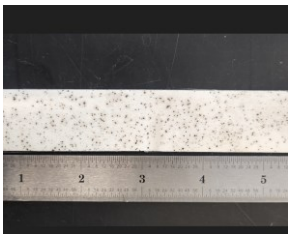
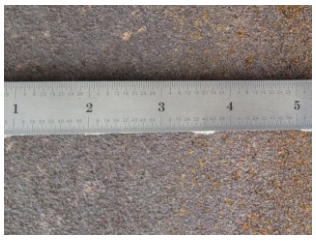
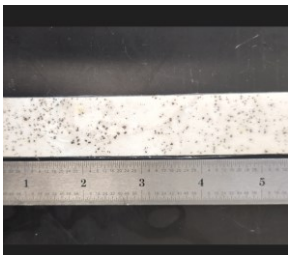
Location	Patina Rating	Thickness (inch)	Cl^- Conc. (ppm)	Field Condition	Tape Test
A1-G3F2 TF Bot. Int.	8	Measured R1 .0.874 R2 0.875 R3 0.879 R_Avg Design			
A1-G3F2 Web Int.	8	Measured R1 0.401 R2 0.402 R3 0.399 R_Avg Design	1		
A1-G3F2 BF Top Int.		Measured R1 0.375 R2 0.374 R3 0.374 R_Avg Design			
A1-G3F2 BF Bot. Int.	8	Measured R1 0.374 R2 0.375 R3 0.375 R_Avg Design			

Table A-196. Field Inspection Results for DAL-WS-01.

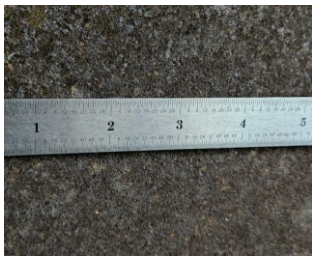
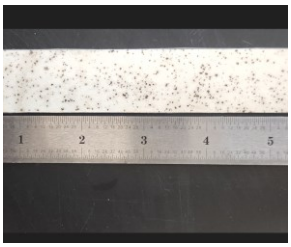
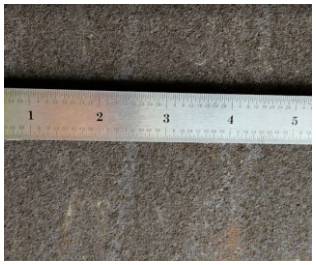
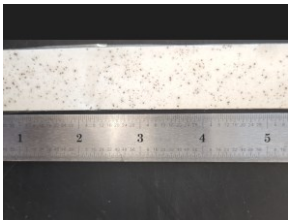
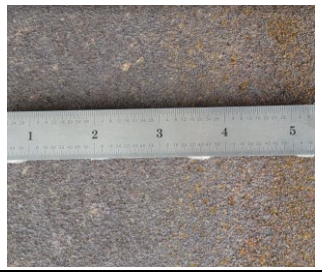
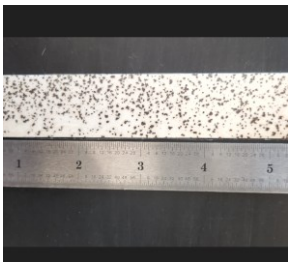
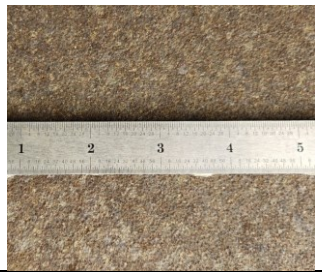
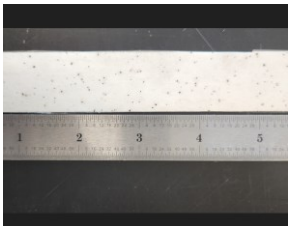
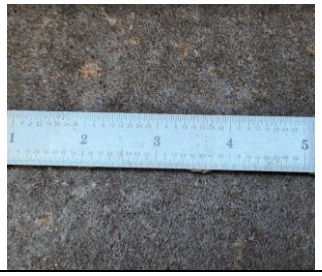
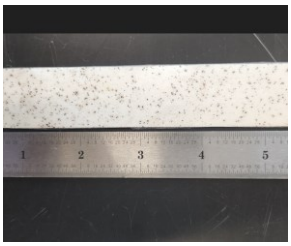
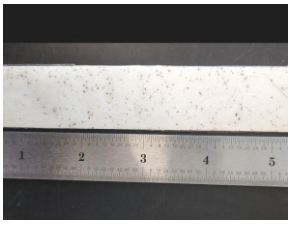
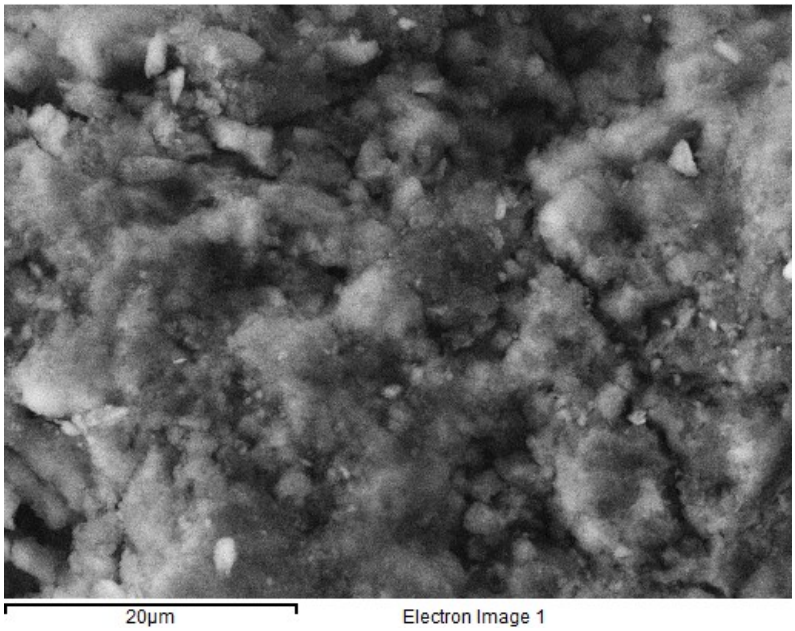
Location	Patina Rating	Thickness (inch)	Cl^- Conc. (ppm)	Field Condition	Tape Test
A1-G4F1 TF Bot. Int.	8	Measured R1 0.878 R2 0.879 R3 0.881 R_Avg Design			
A1-G4F1 Web Int.	8	Measured R1 0.394 R2 0.394 R3 0.393 R_Avg Design	1		
A1-G4F1 BF Top Int.		Measured R1 R2 R3 R_Avg Design			
A1-G4F1 BF Bot. Int.	6	Measured R1 0.365 R2 0.366 R3 0.365 R_Avg Design			

Table A-197. Field Inspection Results for DAL-WS-01.

Location	Patina Rating	Thickness (inch)	Cl^- Conc. (ppm)	Field Condition	Tape Test
A1-G6F2 TF Bot. Ext.	8	Measured R1 0.873 R2 0.871 R3 0.875 R_Avg Design			
A1-G6F2 Web Ext.	8	Measured R1 0.385 R2 0.385 R3 0.386 R_Avg Design	1		
A1-G6F2 BF Top Ext.		Measured R1 0.381 R2 0.382 R3 0.382 R_Avg Design			
A31-G4F2 BF Bot. Ext.	8	Measured R1 0.383 R2 0.384 R3 0.382 R_Avg Design			

A.44.3.SEM/EDS Results: Exterior Web Girder

Element	Weight %	Atomic %
O K	55.15	76.67
Na K	0.22	0.21
Mg K	0.44	0.40
Al K	2.69	2.22
Si K	6.69	5.30
P K	0.30	0.21
S K	0.71	0.50
K K	0.59	0.34
Ca K	5.82	3.23
Ti K	0.11	0.05
Mn K	0.24	0.10
Fe K	27.05	10.77
Totals	100.00	



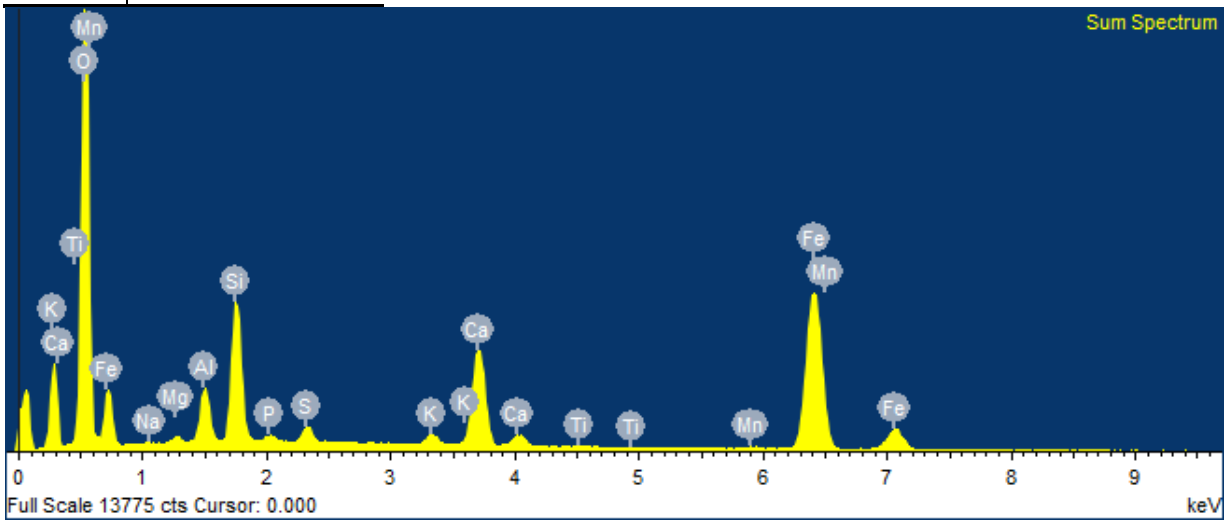
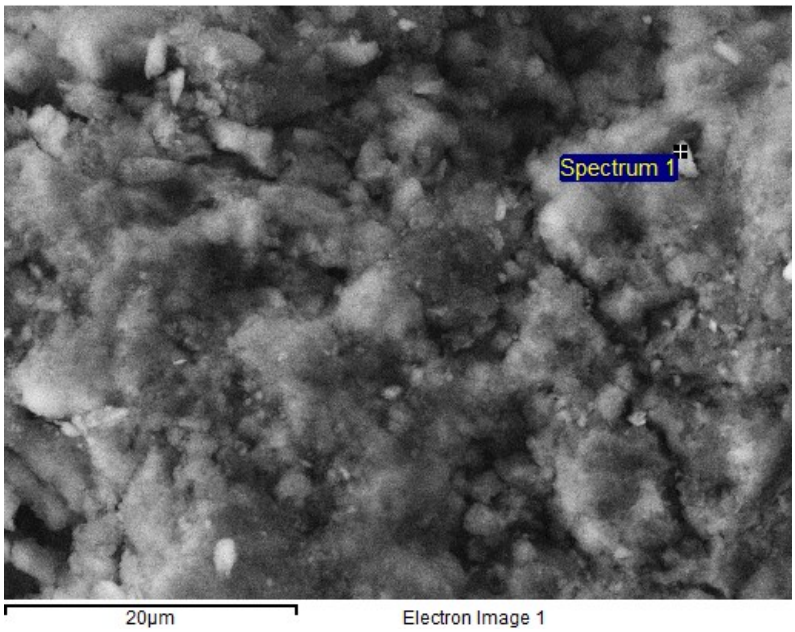


Figure A.783. SEM Image and EDS Spectrum of the Rust Collected from Exterior Web of the Girder.

Element	Weight %	Atomic %
O K	58.26	79.83
Mg K	0.25	0.22
Al K	2.37	1.92
Si K	4.58	3.57
P K	0.19	0.13
S K	0.94	0.64
Cl K	0.29	0.18
K K	0.43	0.24
Ca K	2.69	1.47
Mn K	0.22	0.09
Fe K	29.79	11.69
Totals	100.00	



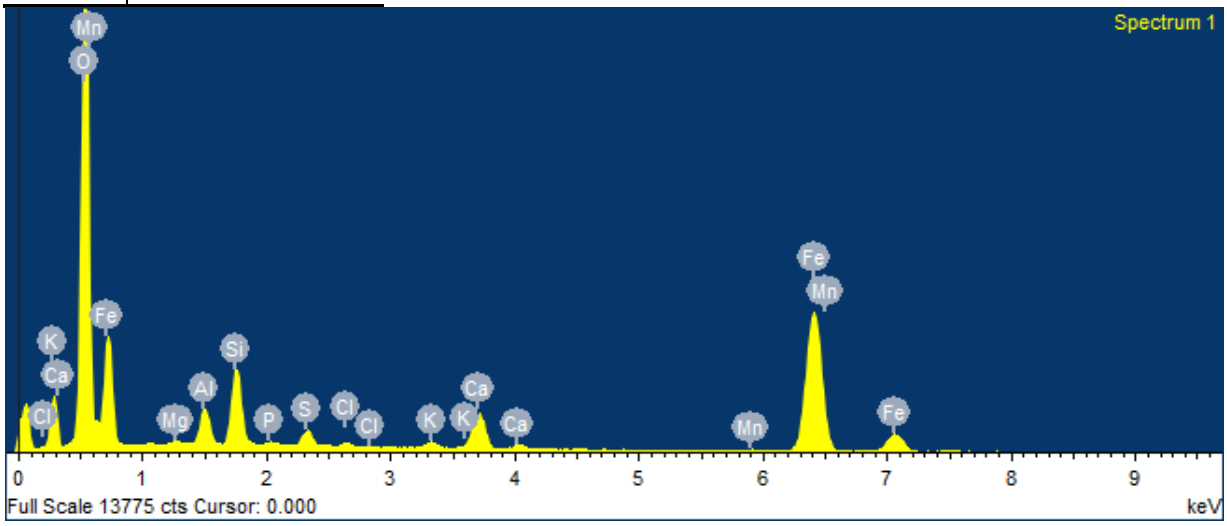
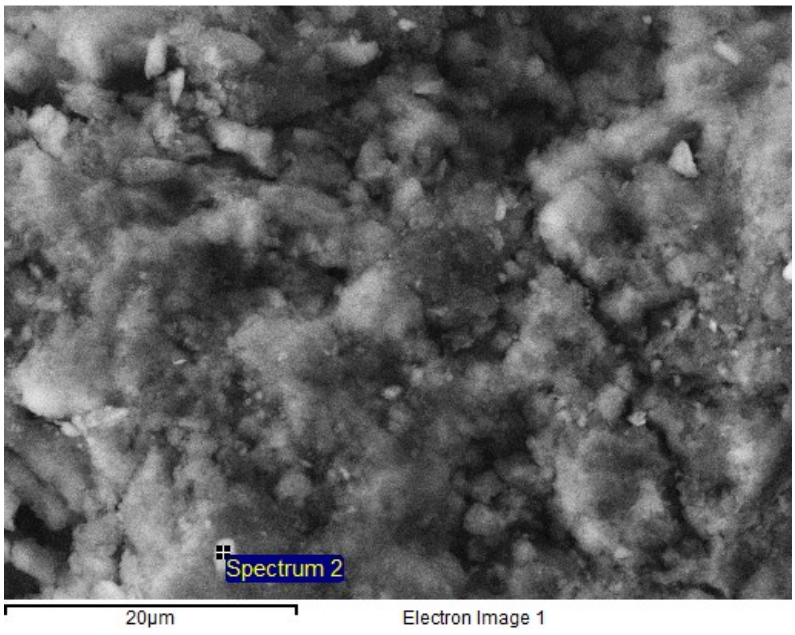


Figure A.784. SEM Image and EDS Spectrum of the Rust Collected from Exterior Web of the Girder.

Element	Weight %	Atomic %
O K	59.95	78.29
Mg K	0.85	0.73
Al K	5.11	3.96
Si K	8.98	6.68
P K	0.37	0.25
S K	0.60	0.39
K K	0.81	0.43
Ca K	3.68	1.92
Fe K	19.49	7.29
Ni K	0.18	0.06
Totals	100.00	



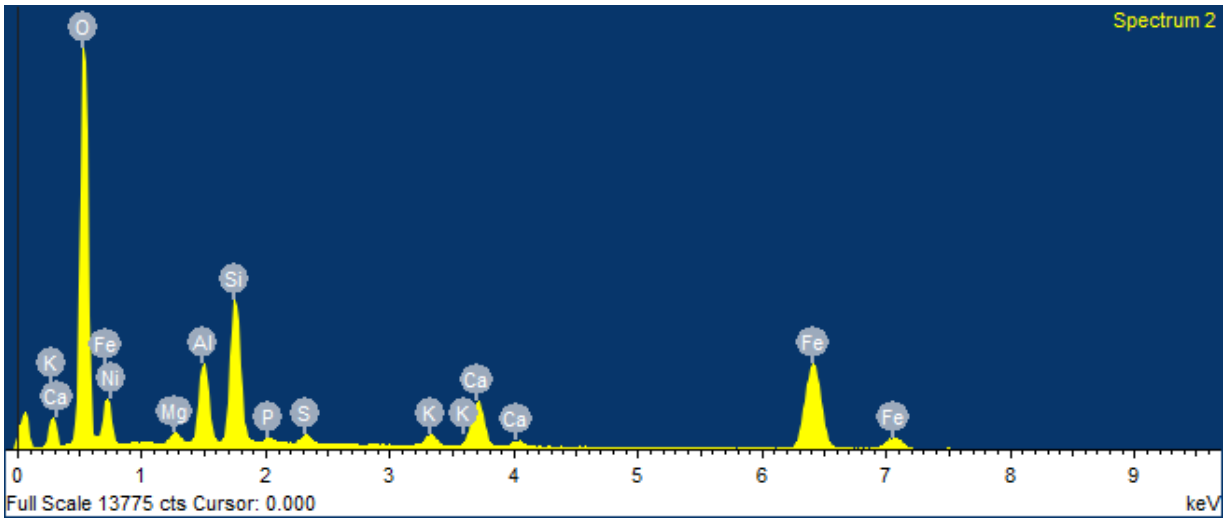
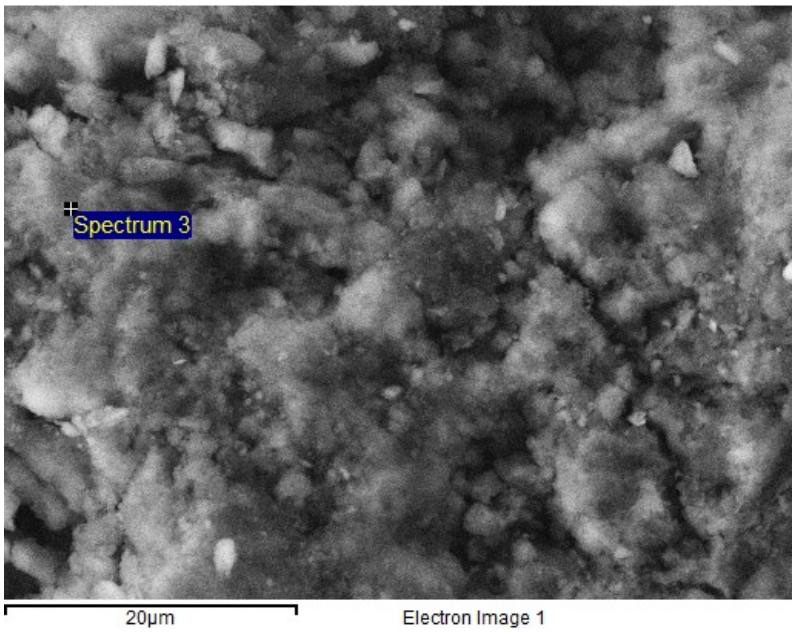


Figure A.785. SEM Image and EDS Spectrum of the Rust Collected from Exterior Web of the Girder.

Element	Weight %	Atomic %
O K	58.35	79.30
Na K	0.33	0.32
Mg K	0.24	0.21
Al K	2.15	1.74
Si K	5.73	4.44
P K	0.24	0.17
S K	0.62	0.42
K K	0.34	0.19
Ca K	4.97	2.70
Mn K	0.16	0.06
Fe K	26.86	10.46
Totals	100.00	



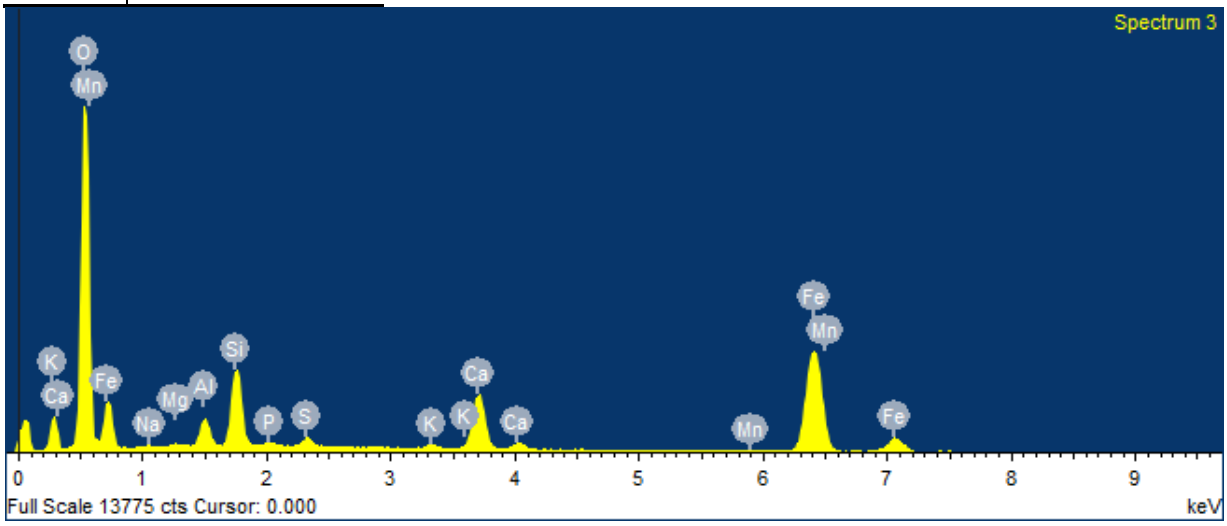


Figure A.786. SEM Image and EDS Spectrum of the Rust Collected from Exterior Web of the Girder.

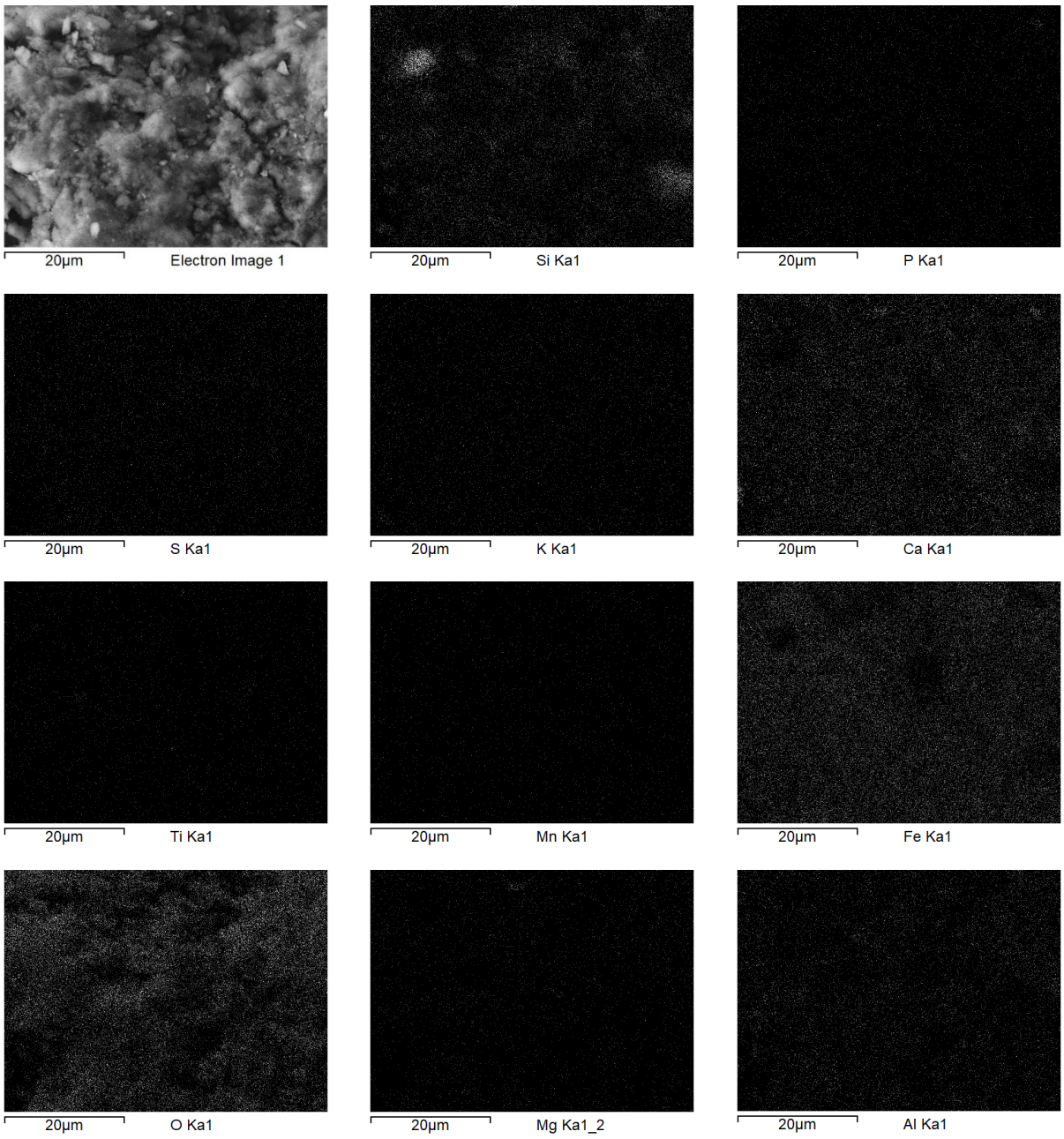
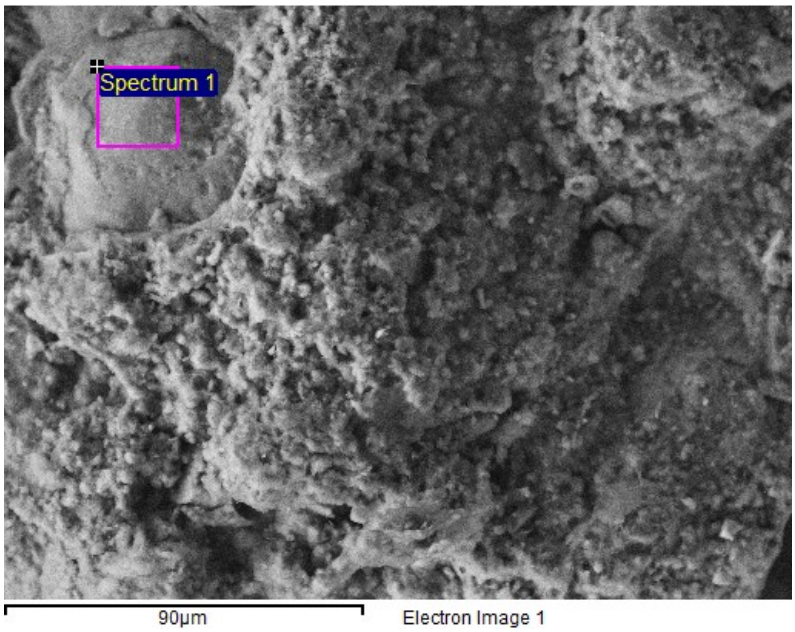


Figure A.787. EDS Elemental Mapping of Rust Collected from Exterior Web.

Element	Weight %	Atomic %
O K	54.84	80.47
Al K	0.53	0.46
Si K	0.41	0.34
S K	0.35	0.25
Ca K	0.25	0.15
Mn K	0.31	0.13
Fe K	42.99	18.07
Ni K	0.33	0.13
Totals	100.00	



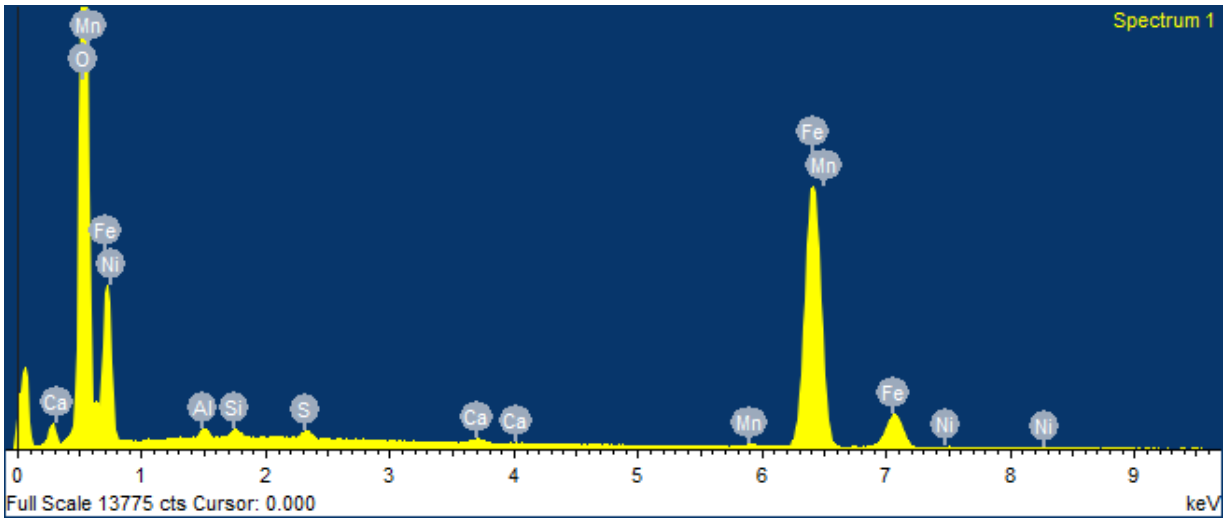
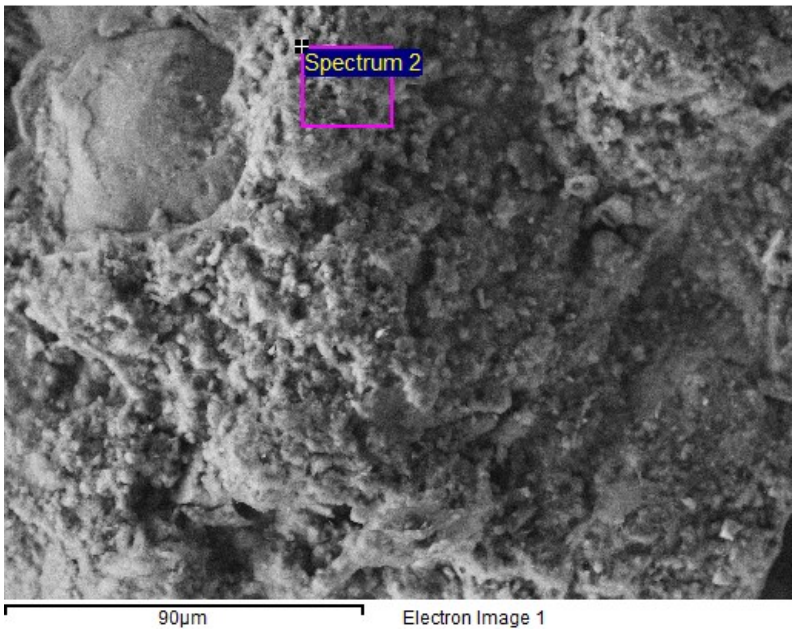


Figure A.788. SEM Image and EDS Spectrum of the Rust Collected from Exterior Web of the Girder.

Element	Weight %	Atomic %
O K	52.48	75.69
Mg K	0.31	0.29
Al K	2.69	2.30
Si K	4.94	4.06
S K	0.99	0.71
K K	0.55	0.32
Ca K	5.47	3.15
Mn K	0.25	0.11
Fe K	32.31	13.35
Totals	100.00	



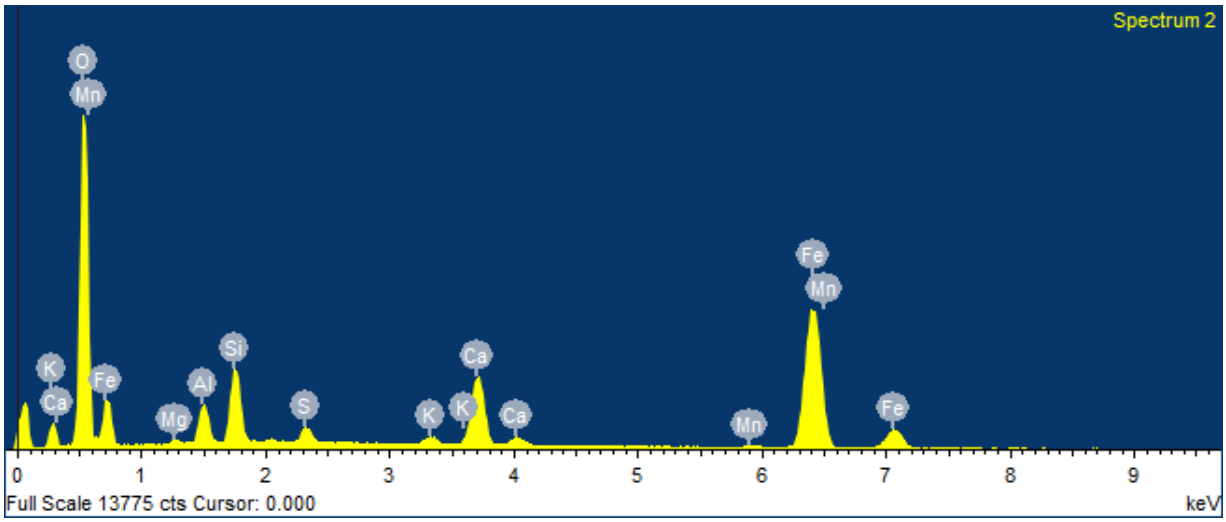
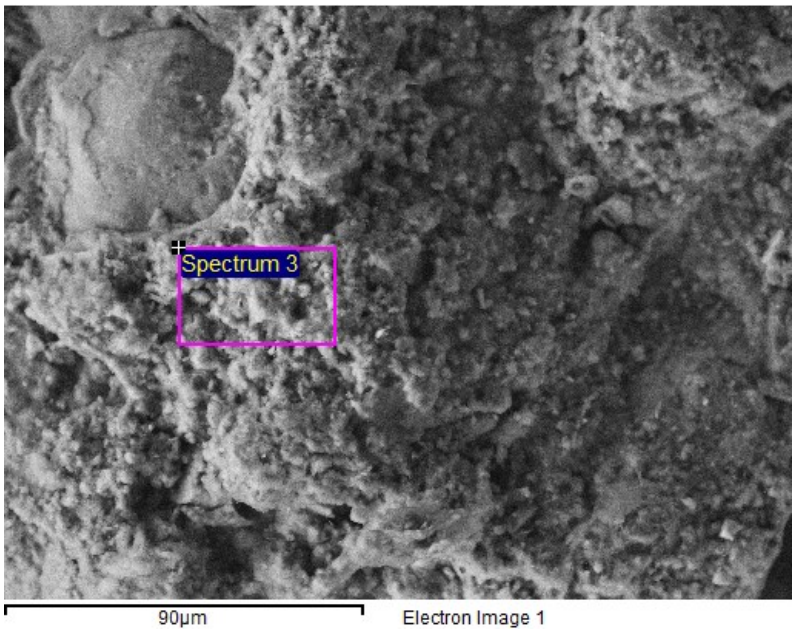


Figure A.789. SEM Image and EDS Spectrum of the Rust Collected from Exterior Web of the Girder.

Element	Weight %	Atomic %
O K	47.99	73.41
Mg K	0.19	0.19
Al K	1.96	1.78
Si K	3.76	3.27
S K	0.87	0.66
K K	0.40	0.25
Ca K	4.57	2.79
Mn K	0.32	0.14
Fe K	39.72	17.41
Ni K	0.23	0.10
Totals	100.00	



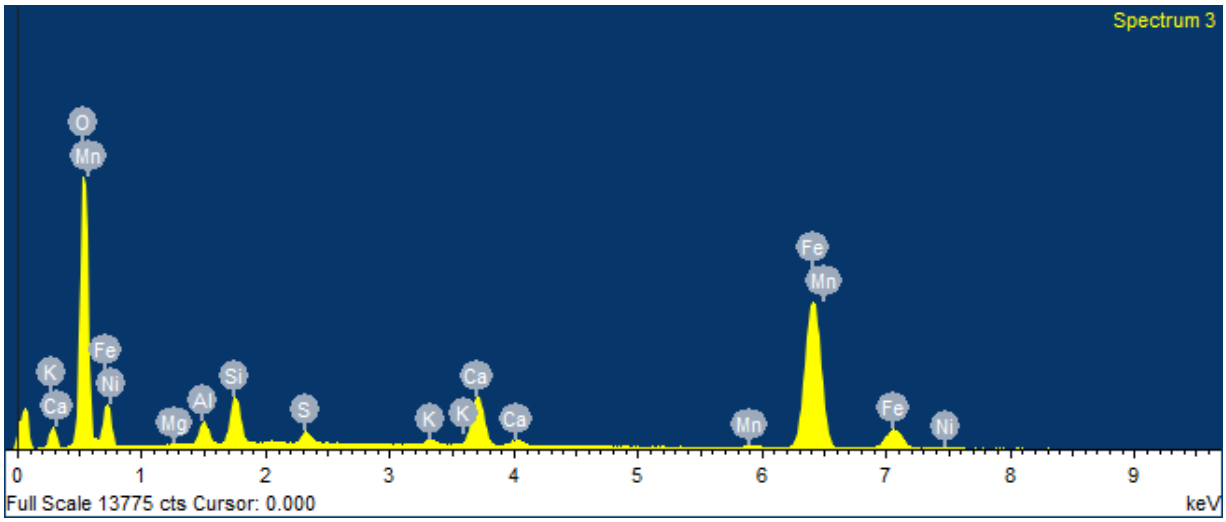
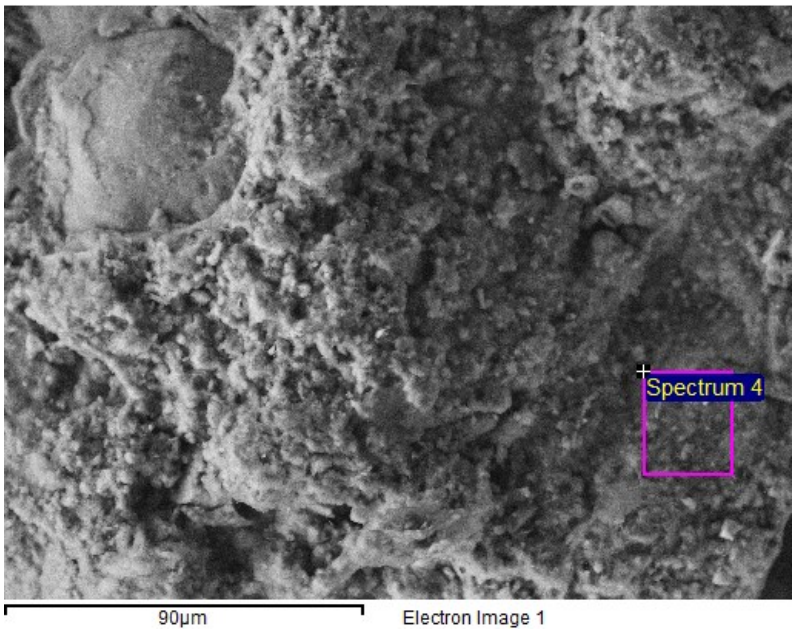


Figure A.790. SEM Image and EDS Spectrum of the Rust Collected from Exterior Web of the Girder.

Element	Weight %	Atomic %
O K	57.79	81.00
Al K	1.30	1.08
Si K	2.07	1.65
P K	0.17	0.12
S K	0.56	0.39
Ca K	2.87	1.61
Mn K	0.42	0.17
Fe K	34.82	13.98
Totals	100.00	



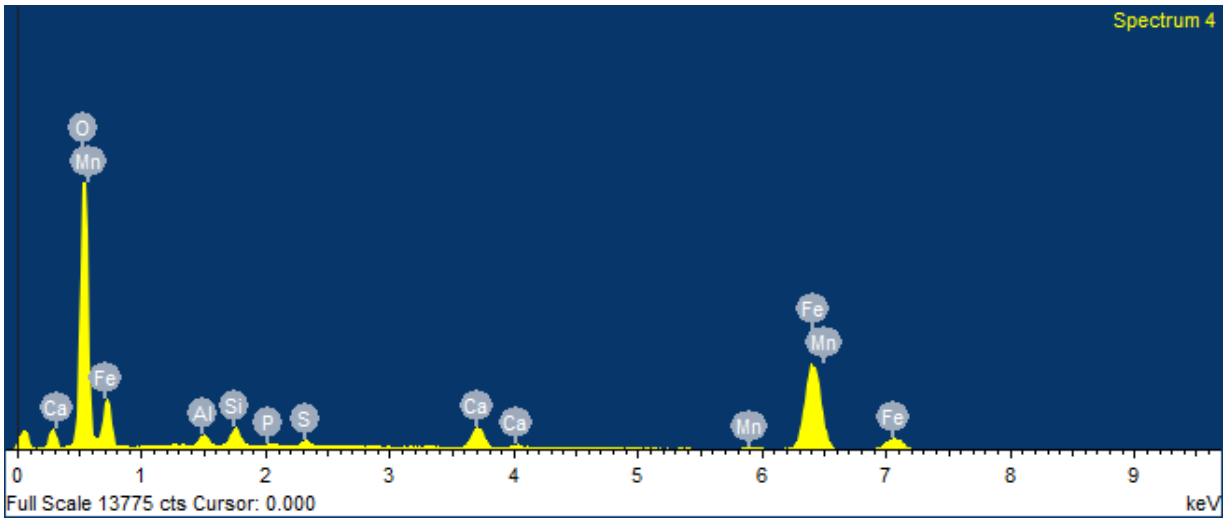
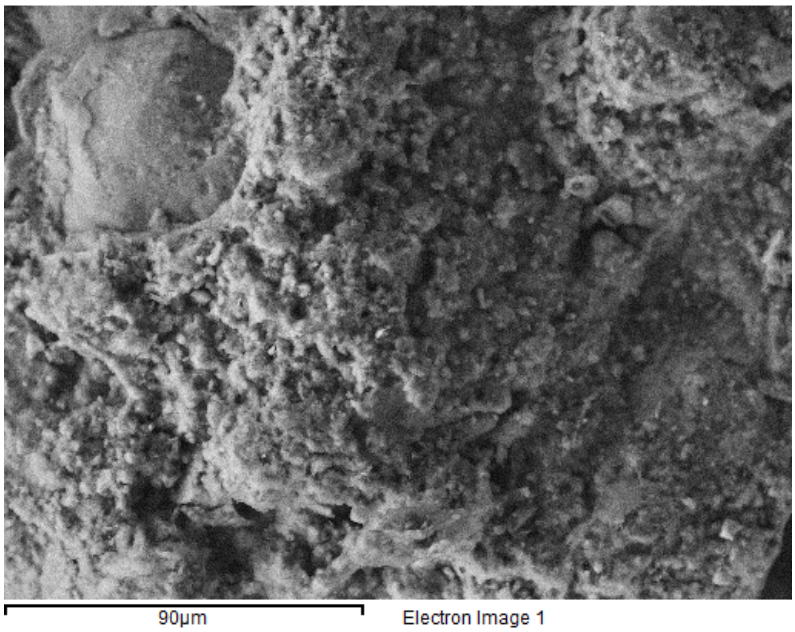


Figure A.791. SEM Image and EDS Spectrum of the Rust Collected from Exterior Web of the Girder.

Element	Weight %	Atomic %
C K	11.77	20.59
O K	47.03	61.77
Mg K	0.17	0.15
Al K	1.28	1.00
Si K	2.19	1.64
P K	0.10	0.07
S K	0.72	0.47
K K	0.23	0.12
Ca K	3.05	1.60
Mn K	0.35	0.13
Fe K	33.10	12.45
Totals	100.00	



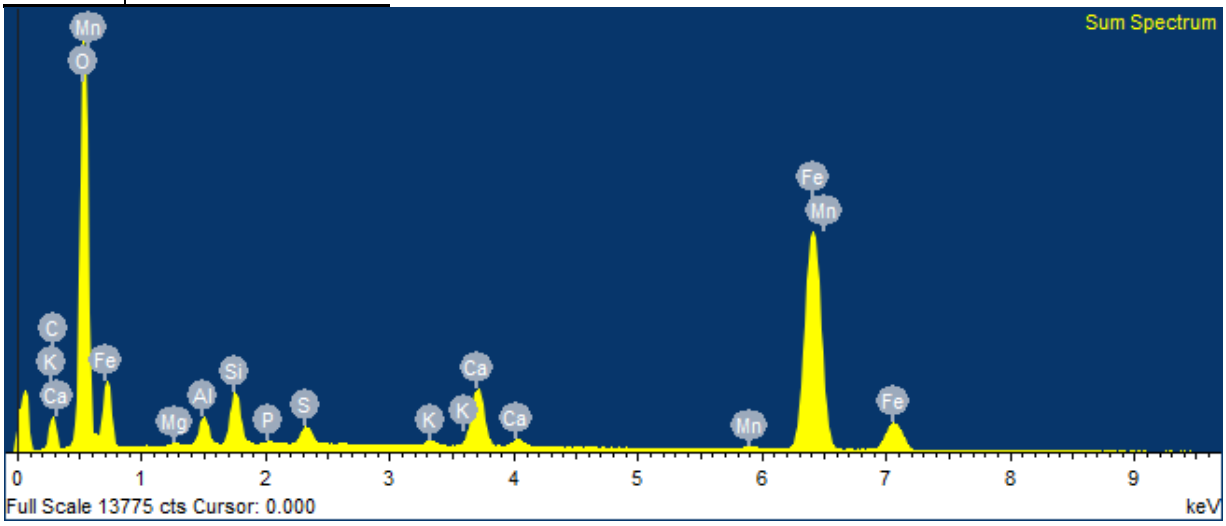


Figure A.792. SEM Image and EDS Spectrum of the Rust Collected from Exterior Web of the Girder.

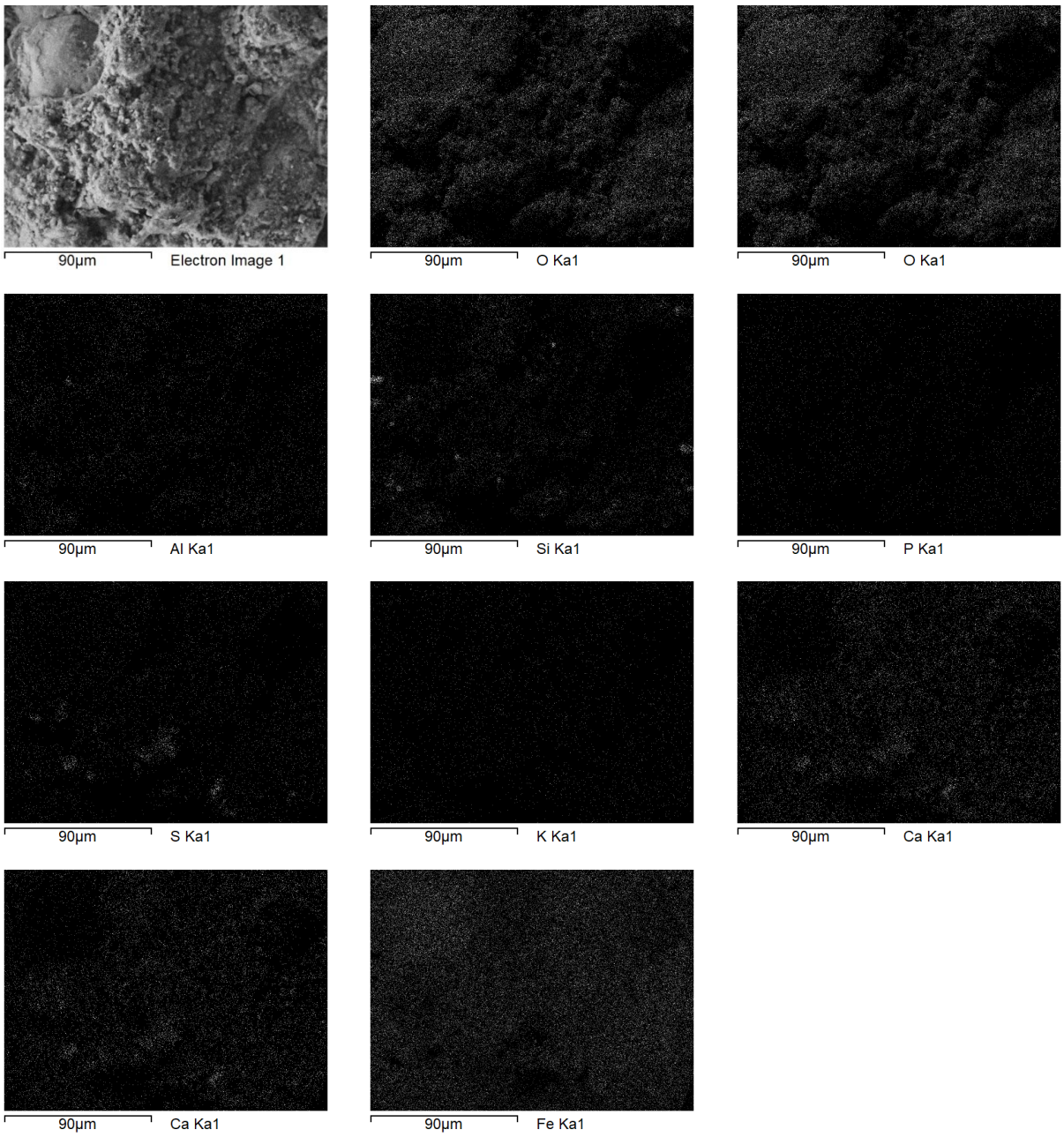
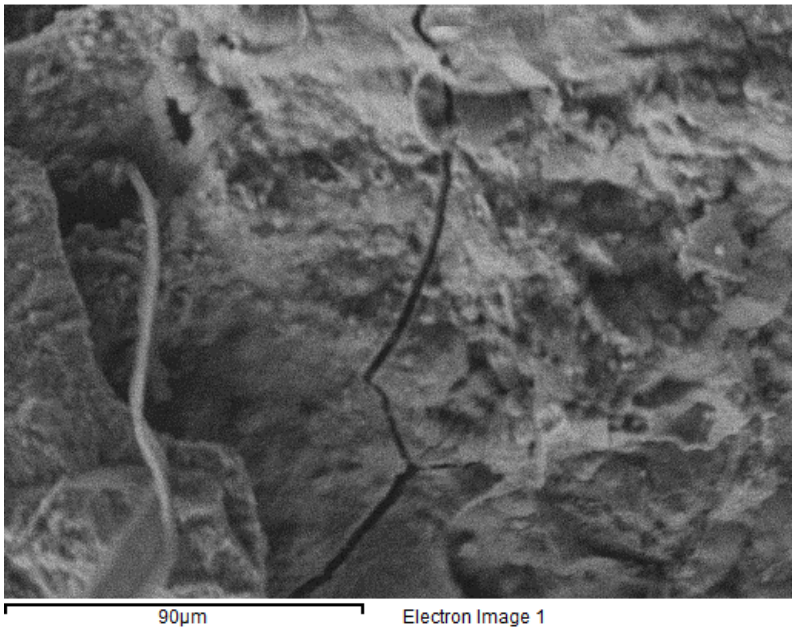


Figure A.793. EDS Elemental Mapping of Rust Collected from Exterior Web.

A.44.4.SEM/EDS Results: Interior Web Girder

Element	Weight %	Atomic %
O K	33.13	61.44
Al K	3.52	3.87
Si K	0.99	1.05
S K	0.62	0.57
Cl K	0.26	0.22
K K	0.11	0.09
Ca K	0.82	0.60
Mn K	0.58	0.31
Fe K	59.80	31.77
Cu K	0.18	0.08
Totals	100.00	



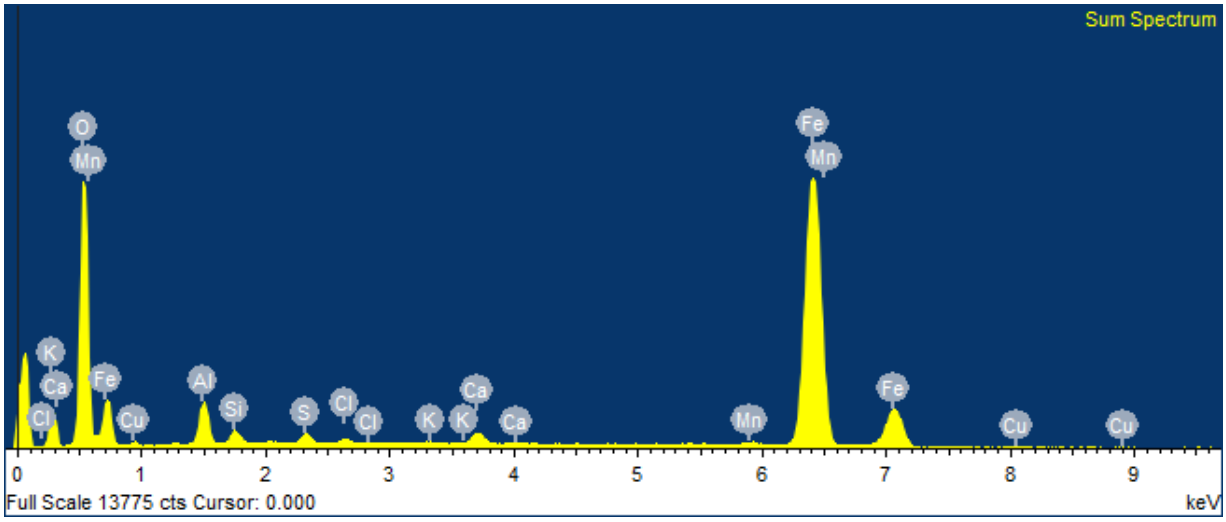


Figure A.794. SEM Image and EDS Spectrum of the Rust Collected from Interior Web of the Girder.

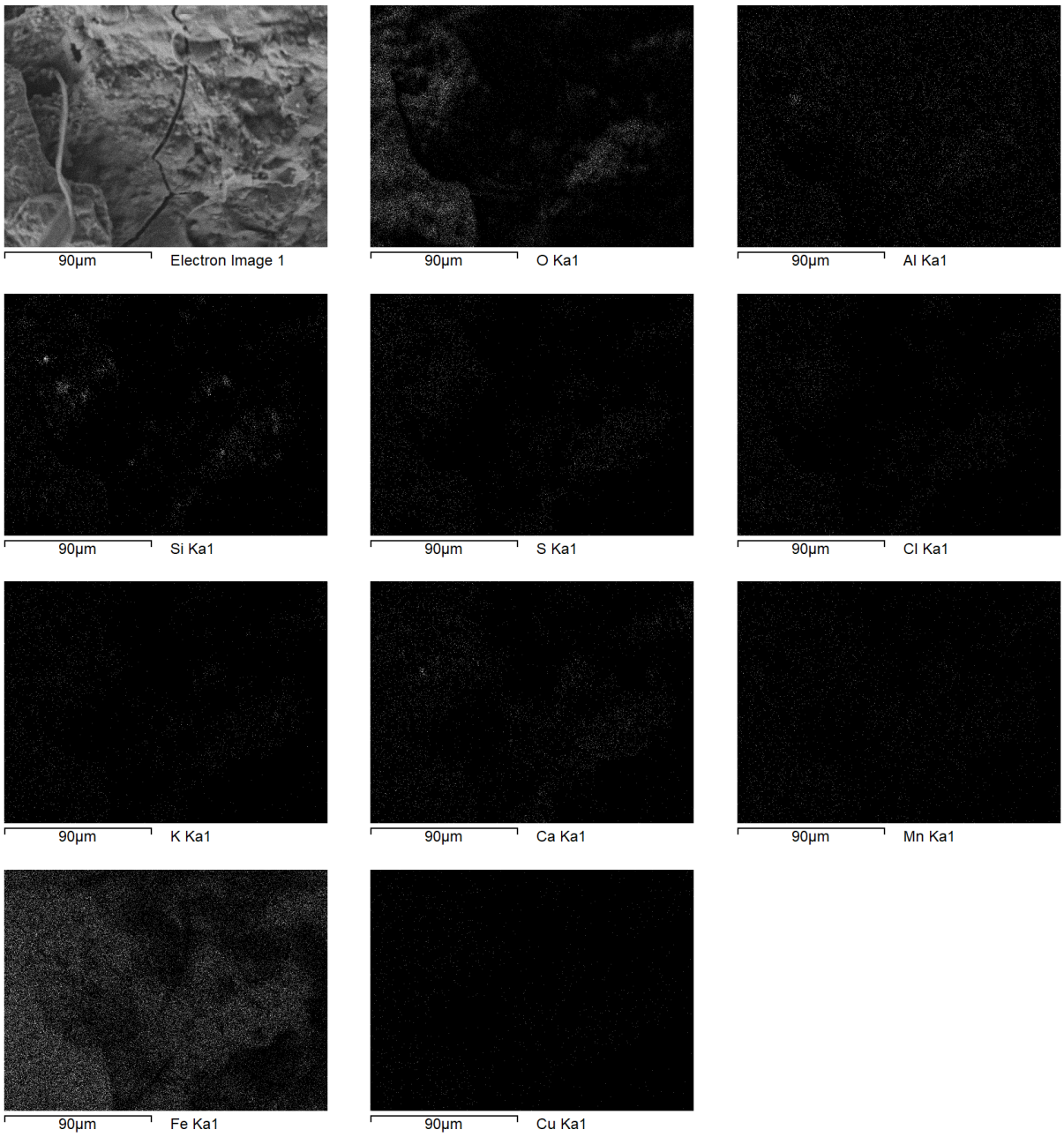
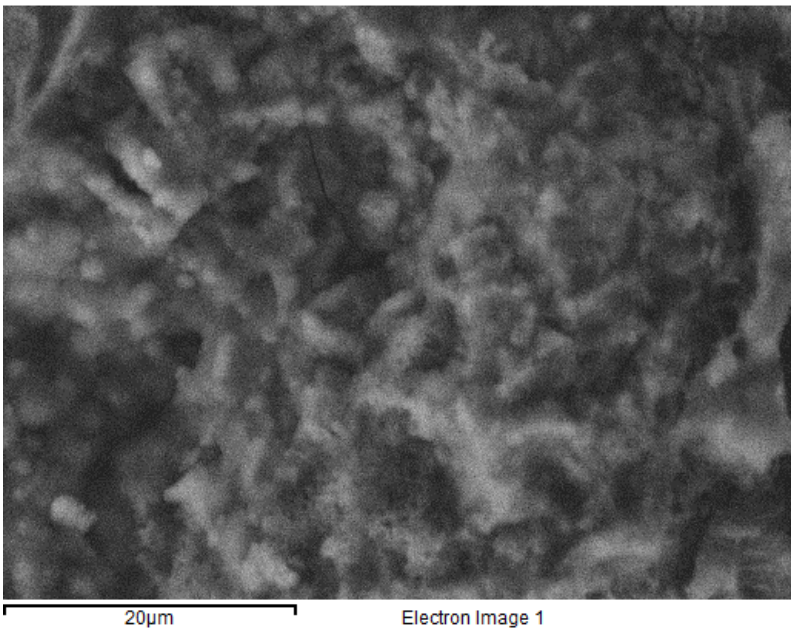


Figure A.795. EDS Elemental Mapping **of Rust Collected from Interior Web.**

Element	Weight %	Atomic %
O K	45.95	73.70
Al K	1.72	1.63
Si K	0.26	0.23
S K	0.91	0.73
Cl K	0.53	0.38
Ca K	0.33	0.21
Mn K	1.22	0.57
Fe K	48.76	22.40
Ni K	0.32	0.14
Totals	100.00	



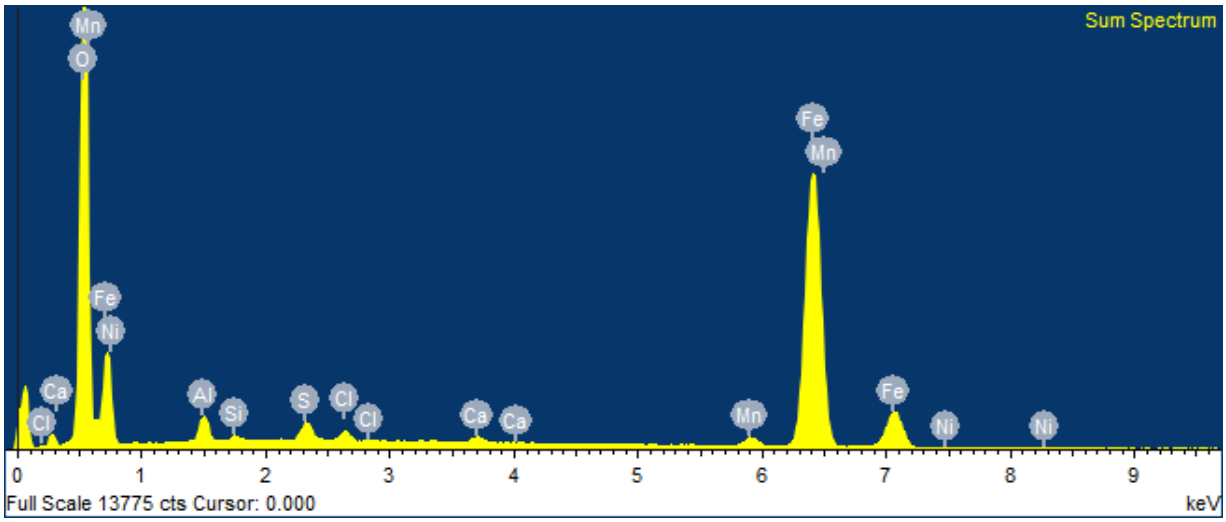


Figure A.796. SEM Image and EDS Spectrum of the Rust Collected from Interior Web of the Girder.

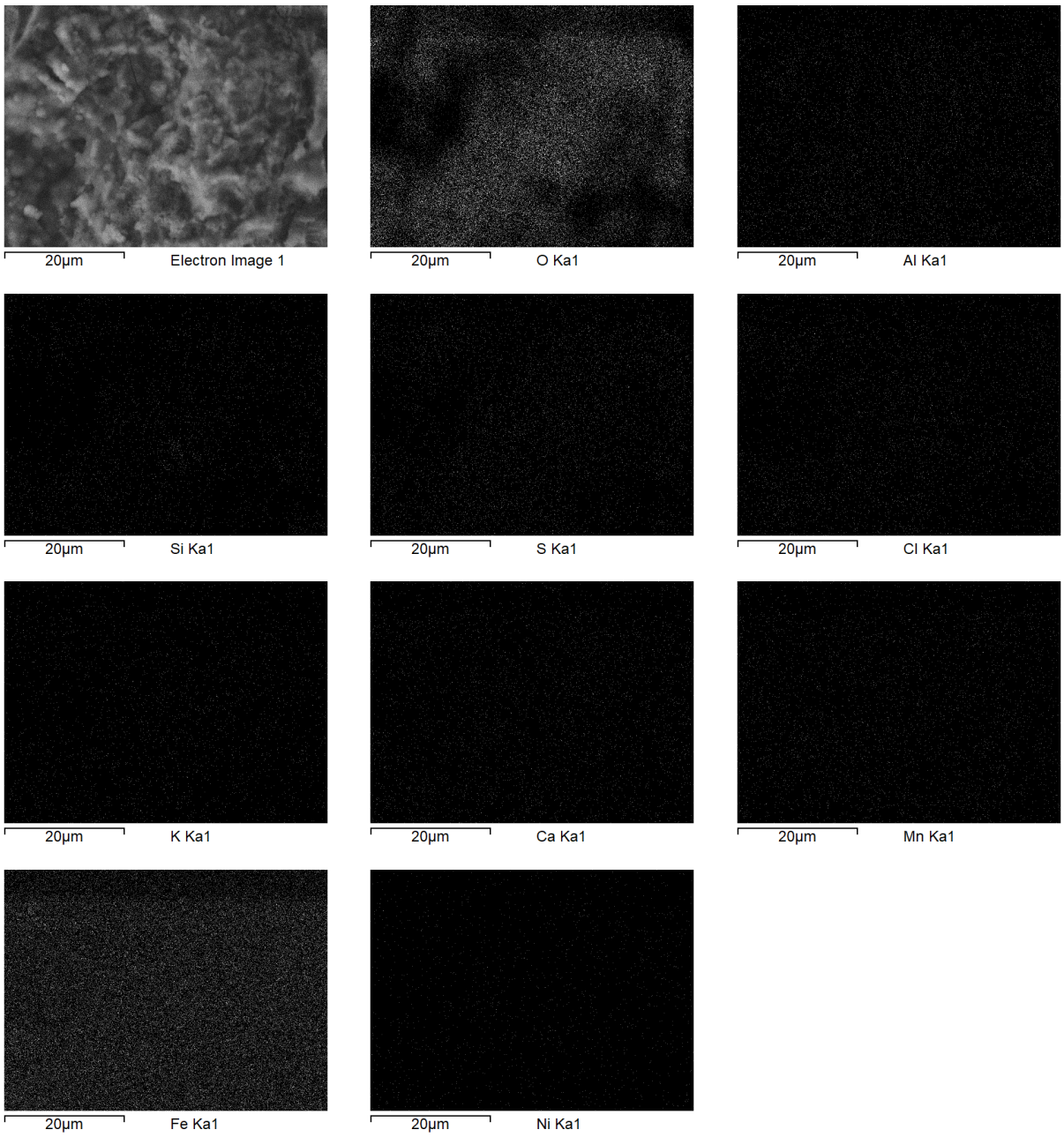
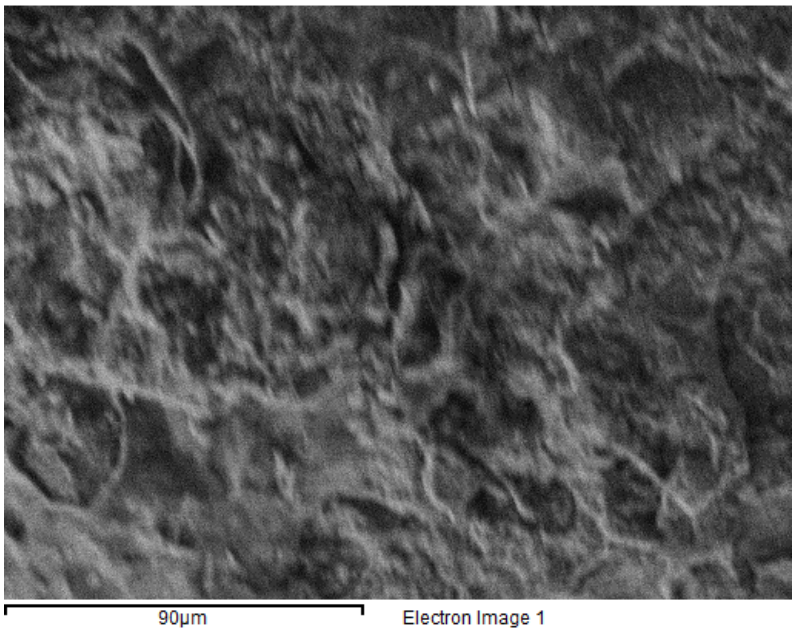


Figure A.797. EDS Elemental Mapping of Rust Collected from Interior Web.

Element	Weight %	Atomic %
O K	39.06	67.91
Al K	2.25	2.32
Si K	0.18	0.18
S K	0.67	0.58
Cl K	0.54	0.42
Ca K	0.26	0.18
Cr K	0.19	0.10
Mn K	1.00	0.51
Fe K	55.38	27.58
Ni K	0.27	0.13
Cu K	0.21	0.09
Totals	100.00	



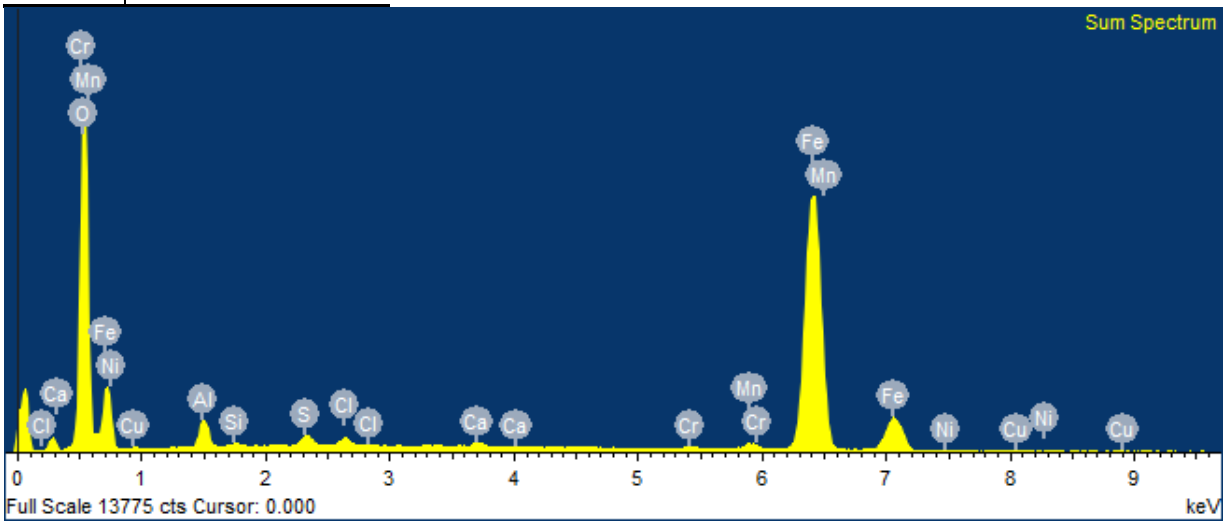


Figure A.798. SEM Image and EDS Spectrum of the Rust Collected from Interior Web of the Girder.

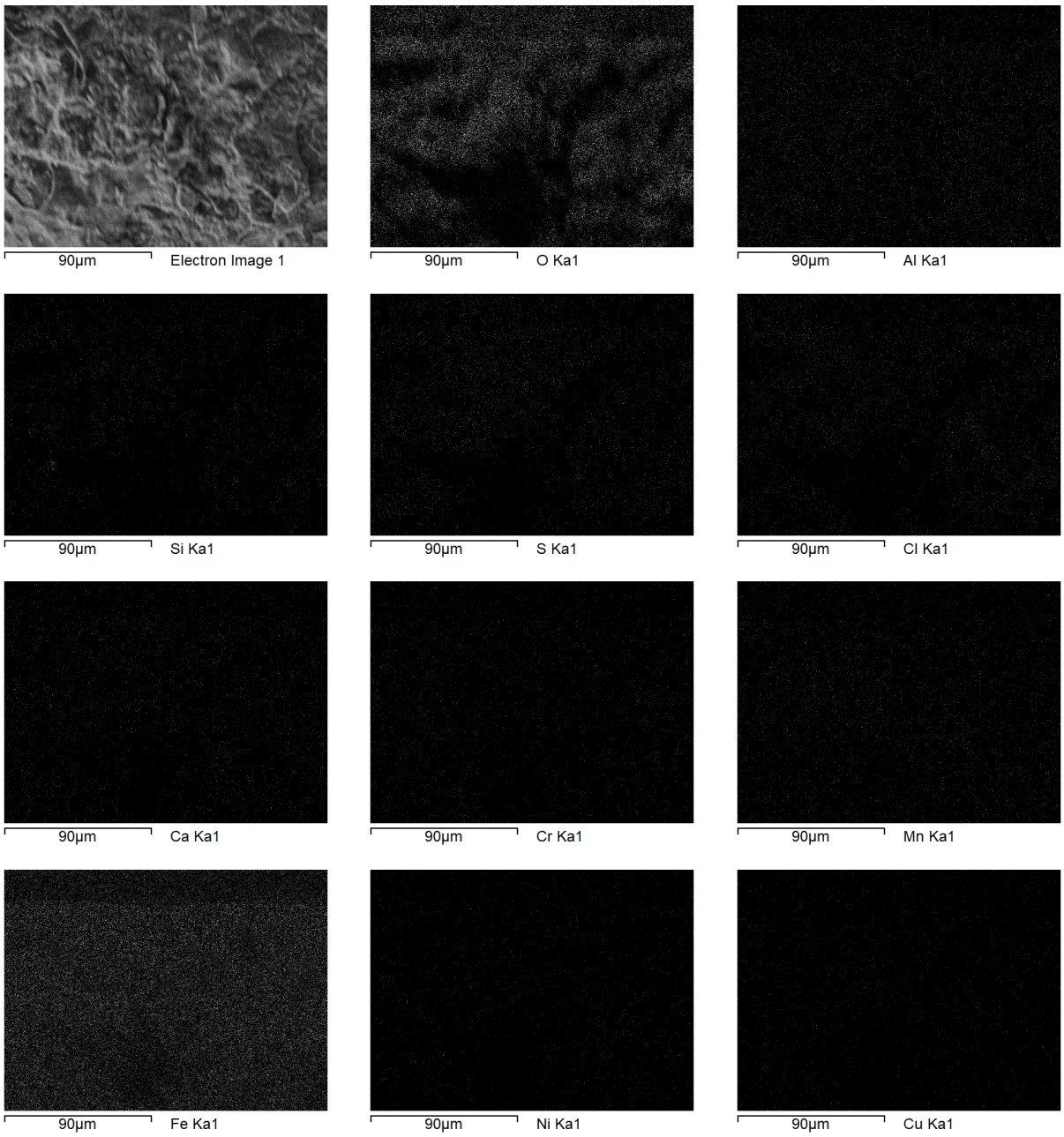


Figure A.799. EDS Elemental Mapping of Rust Collected from Interior Web.

A.44.5.XPS Result: Exterior Girder

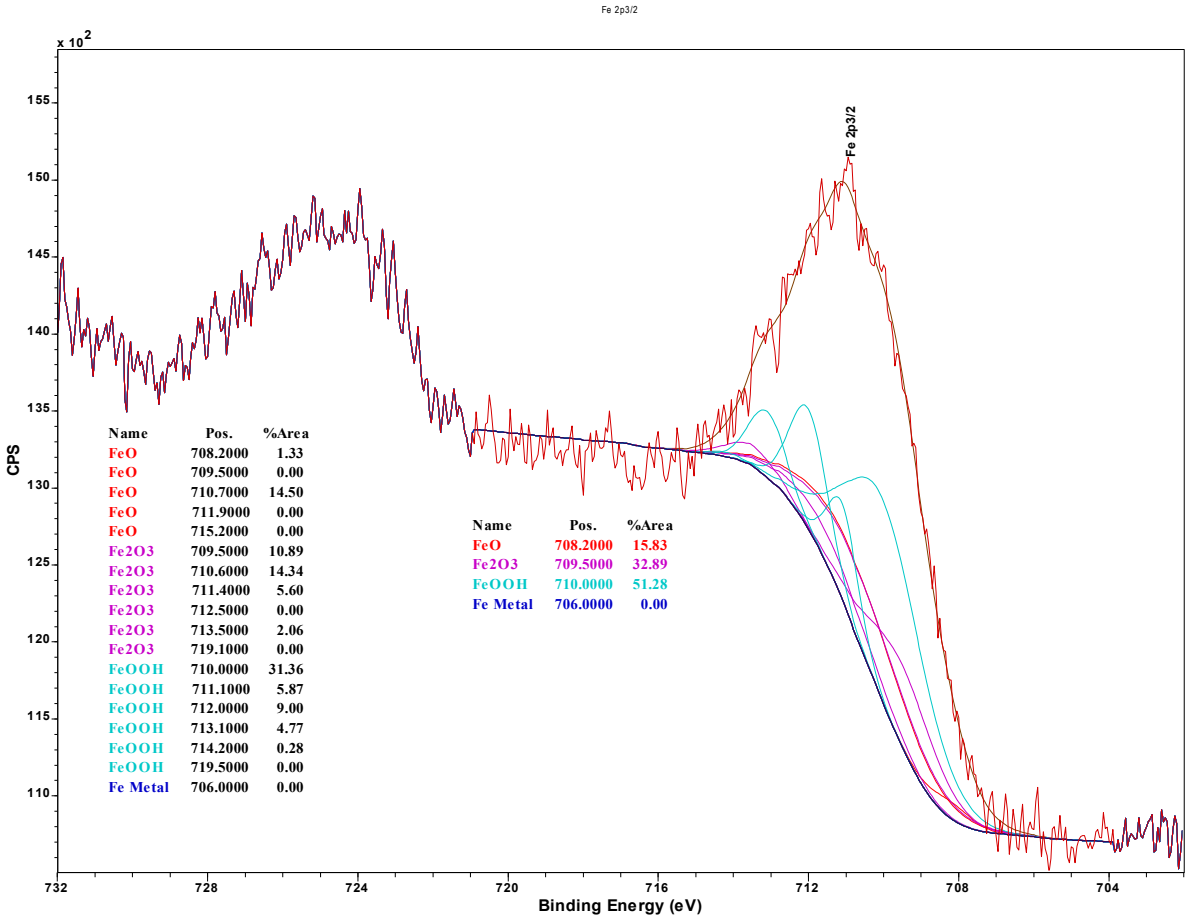


Figure A.800. XPS Spectrum of the Rust Collected from Exterior Web of the Girder.

A.44.6.XPS Result: Interior Girder

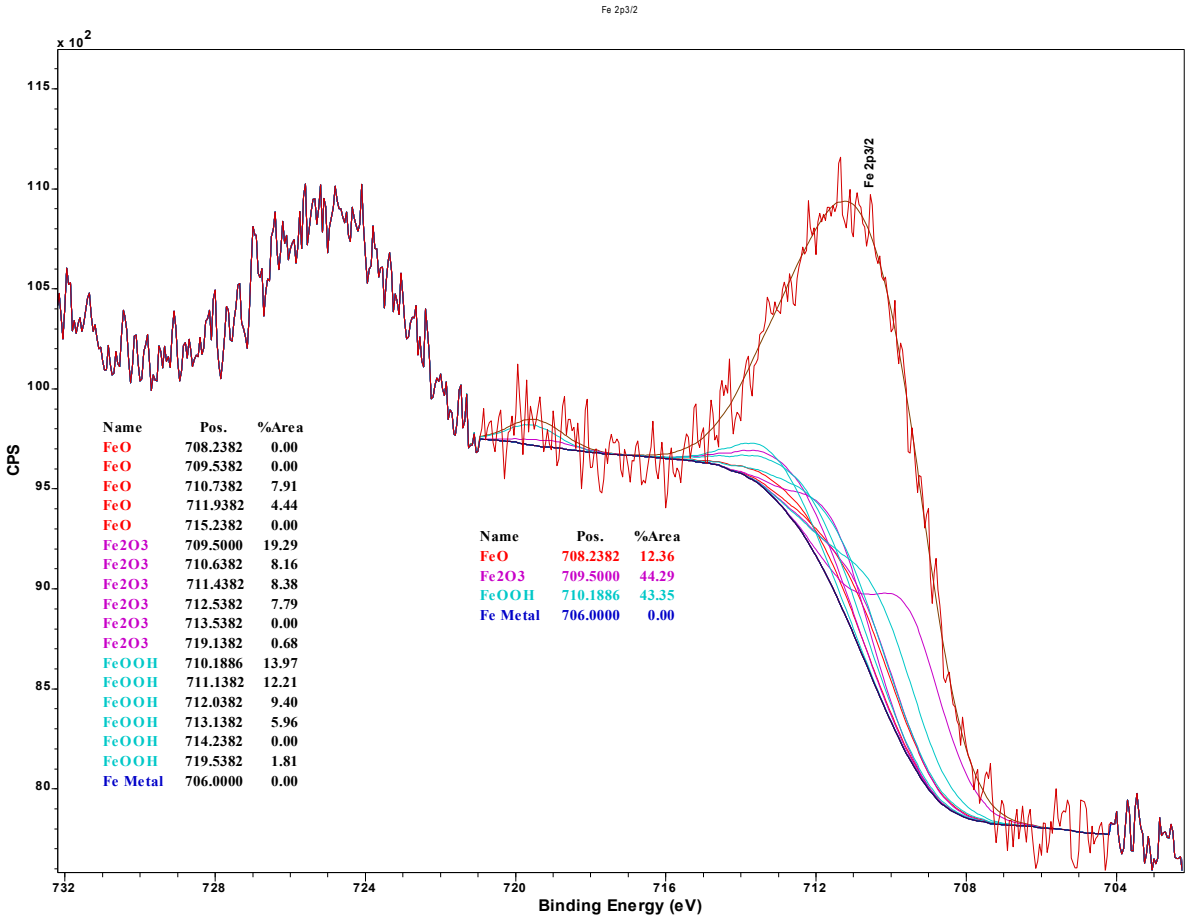


Figure A.801. XPS Spectrum of the Rust Collected from Interior Web of the Girder.

A.44.7.XRD Result: Exterior and Interior Girder

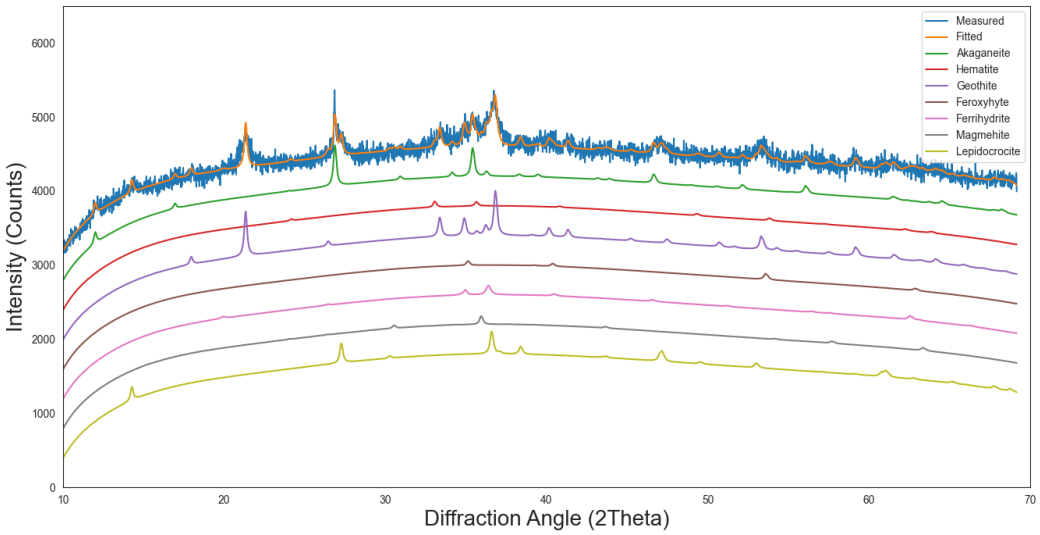


Figure A.802. XRD Pattern of Powdered Rust Collected from Exterior Web of the Girder.

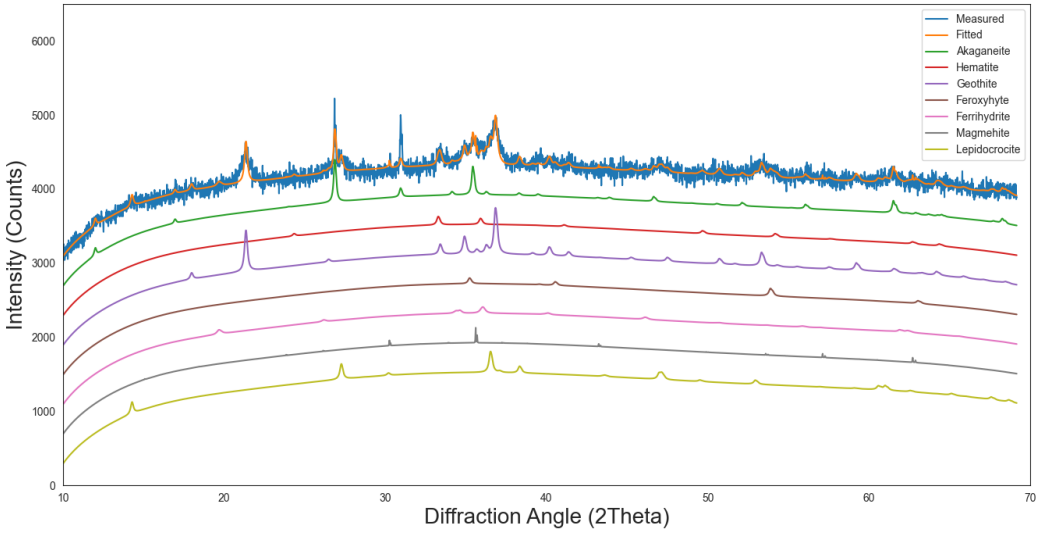


Figure A.803. XRD Pattern of Powdered Rust Collected from Interior Web of the Girder.

A.44.8.Particle Size Analysis: Tape Adhesion Results

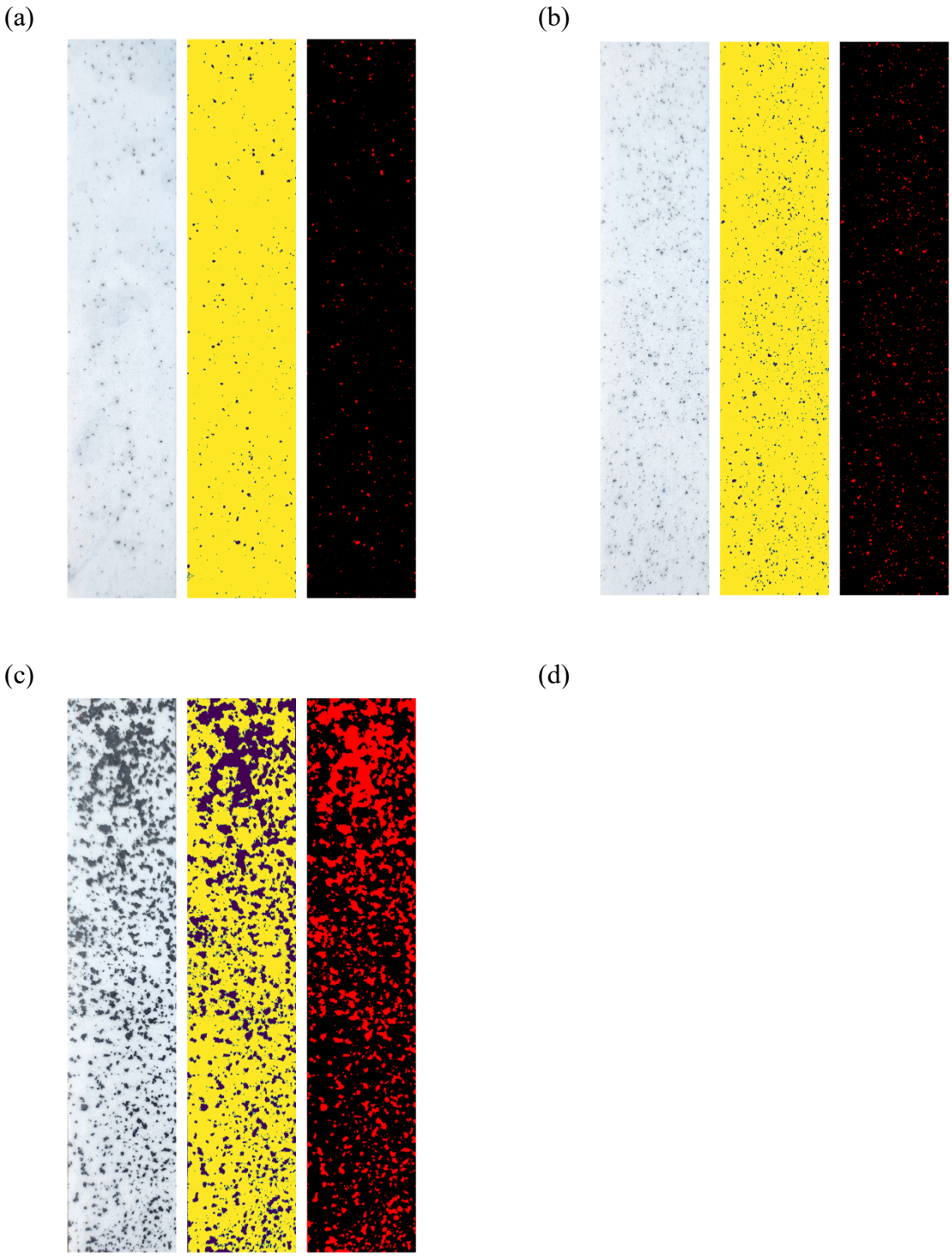
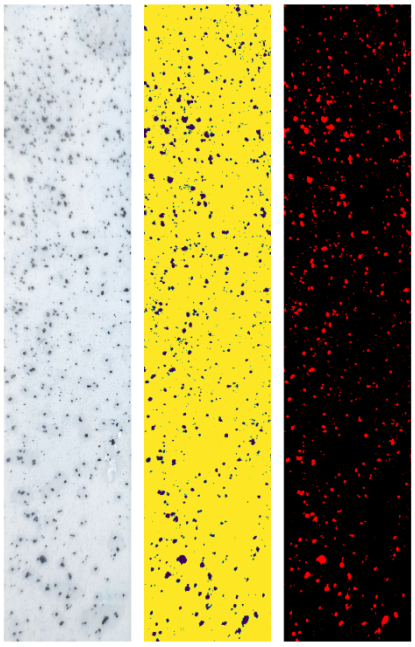
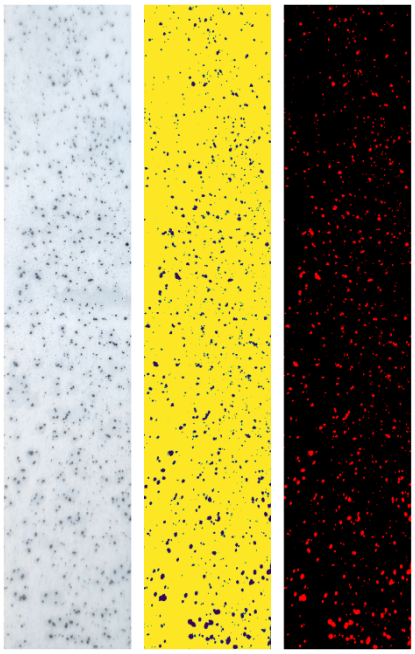


Figure A.804. Particle Size Analysis Results at A1G1F1 (a) Top Flange Bottom, (b) Web, (c) Bottom Flange Bottom (d) Stiffener.

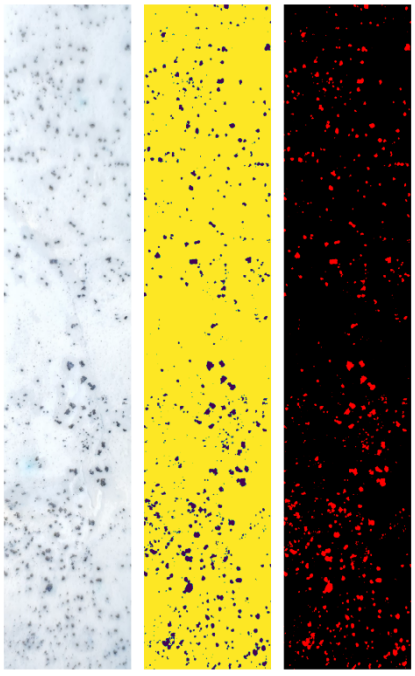
(a)



(b)



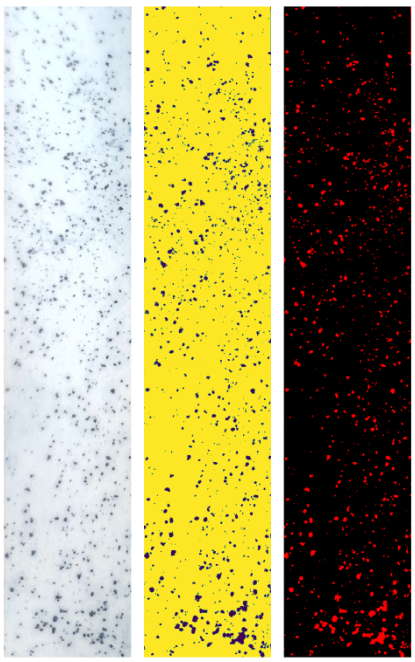
(c)



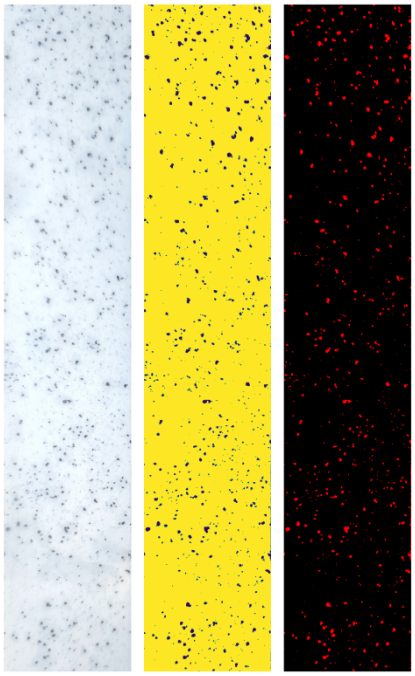
(d)

Figure A.805. Particle Size Analysis Results at A1G3F1 (a) Top Flange Bottom, (b) Web, (c) Bottom Flange Bottom (d) Stiffener.

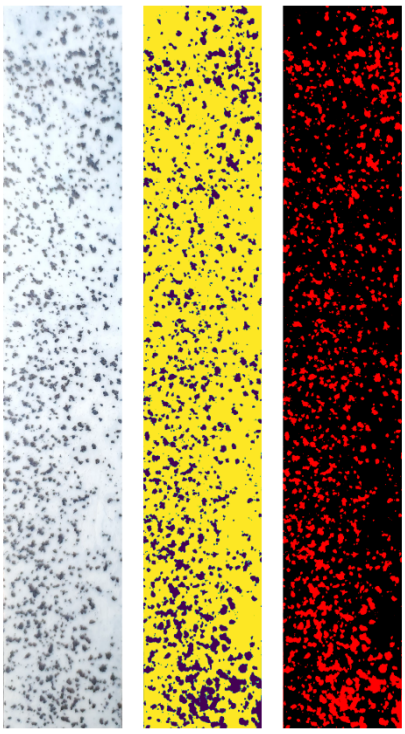
(a)



(b)



(c)



(d)

Figure A.806. Particle Size Analysis Results at A1G4F2 (a) Top Flange Bottom, (b) Web, (c) Bottom Flange Bottom (d) Stiffener.

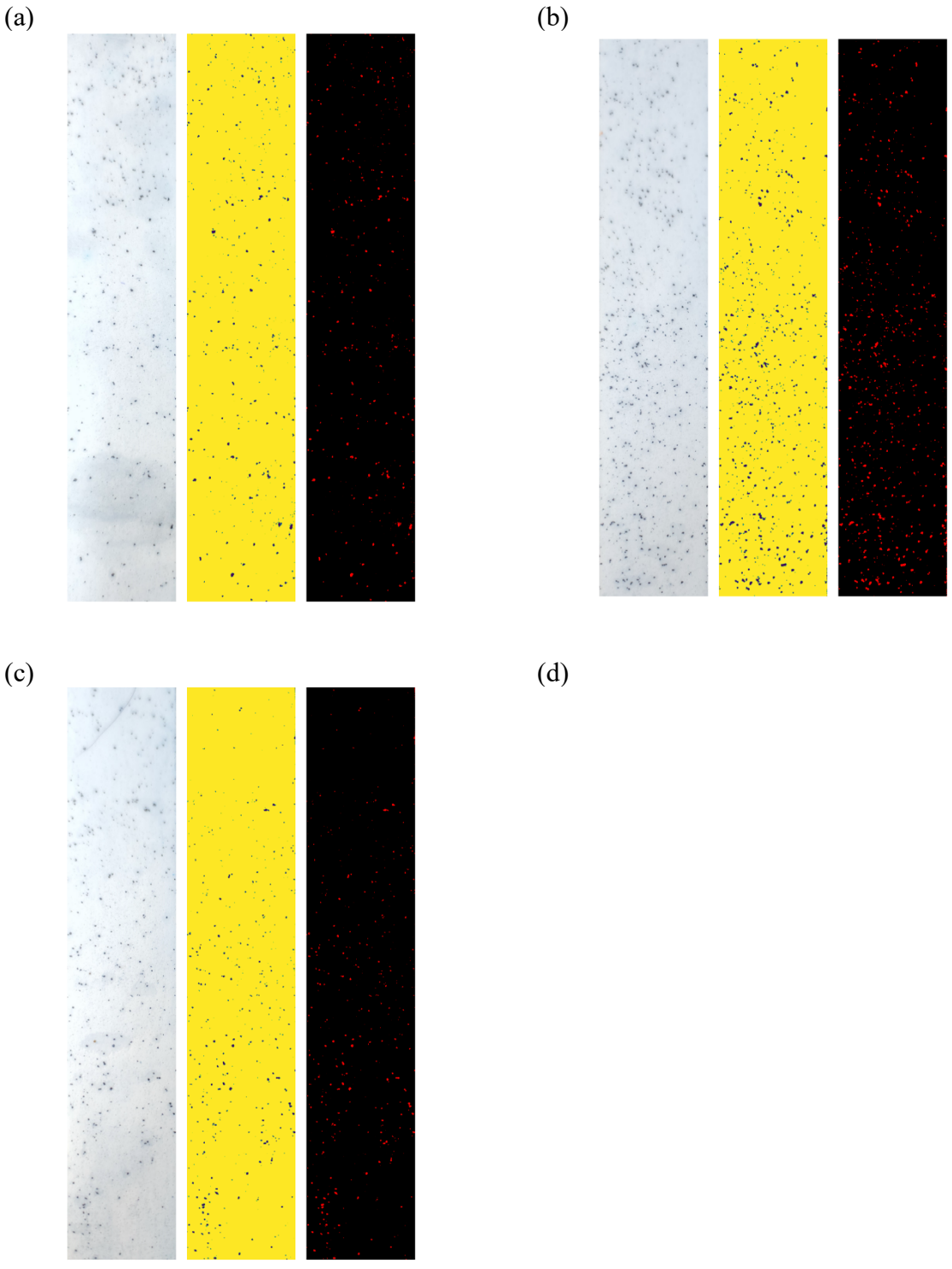


Figure A.807. Particle Size Analysis Results at A1G6F2 (a) Top Flange Bottom, (b) Web, (c) Bottom Flange Bottom (d) Stiffener.

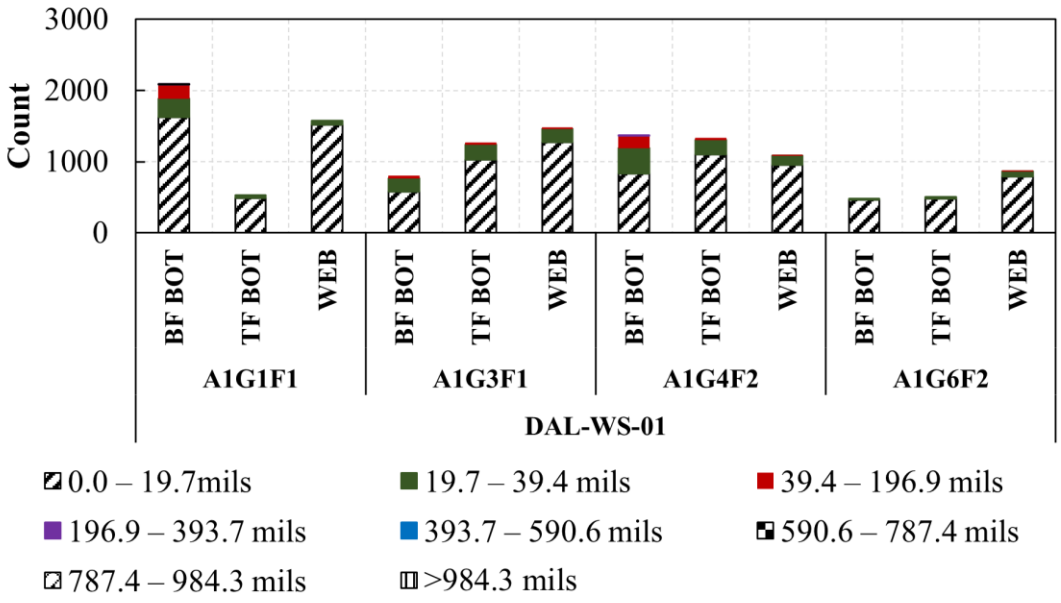


Figure A.808. Particle Size Analysis Showing Different Locations Examined.

A.45. DAL-WS-02

- CON IH10 EB-BW8 SB over IH10 EBFR/BW8 SBFR/UP RR
- Bridge ID 180570296406467, Dallas County, Dallas
- Continuous weathering steel plate girder
- Built 2011
- Girder inspection carried on girder 1, 2, 3 and 4, and measurements are taken on girder within four feet from the abutment or bent.
- Datalogger installed at abutment 1 on girder number 4 for continuous monitoring of temperature, humidity, and time of wetness (TOW)
- Location for Testing: A1G1F1, A1G2F2, A1G3F1, A1G4F2



Figure A.809. Typical Picture of DAL-WS-02.

A.45.1. Observed Condition

Overall bridge is in good condition with development of uniform patina throughout the girder with a patina rating ranging between 6 and 8.

A.45.2.Field Inspection Results

Table A-198. Field Inspection Results for DAL-WS-02.

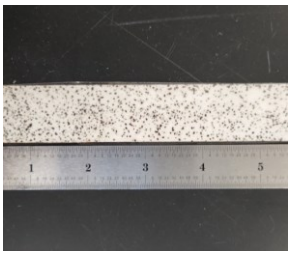
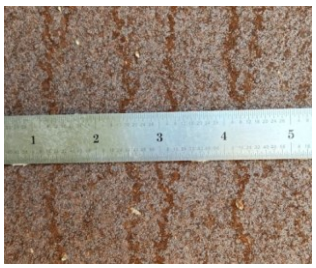
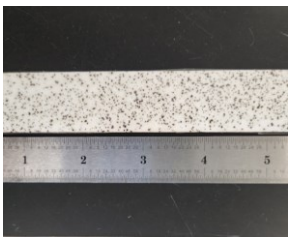
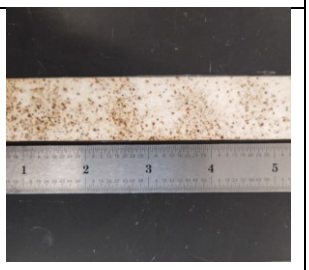
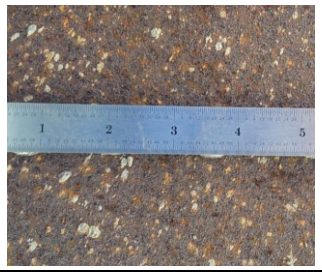
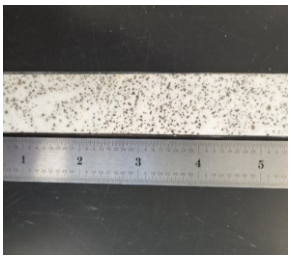
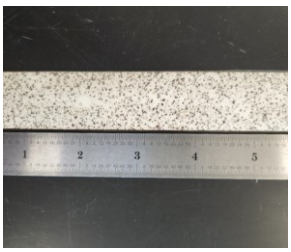
Location	Patina Rating	Thickness (inch)	Cl^- Conc. (ppm)	Field Condition	Tape Test
A1-G1F1 TF Bot. Ext.	8	Measured R1 .1.226 R2 1.224 R3 1.224 R_Avg Design			
A1-G1F1 Web Ext.	8	Measured R1 0.687 R2 0.686 R3 0.684 R_Avg Design			
A1-G1F1 BF Top Ext.	7	Measured R1 R2 R3 R_Avg Design			
A1-G1F1 BF Bot. Ext.	7	Measured R1 1.232 R2 1.233 R3 1.230 R_Avg Design			
A1-G1F1 Stiff. Ext.	8	Measured R1 1.225 R2 1.225 R3 1.225 R_Avg Design			

Table A-199. Field Inspection Results for DAL-WS-02.

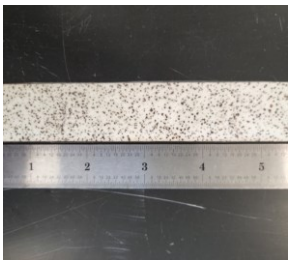
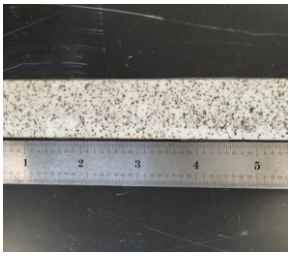
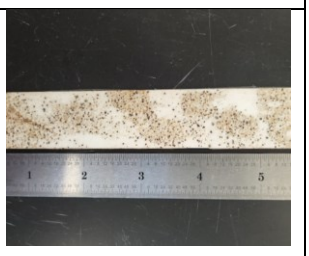
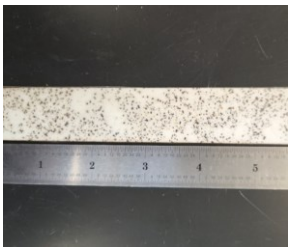
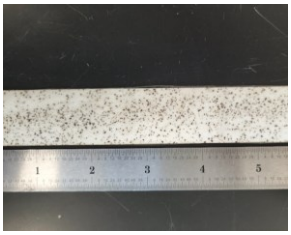
Location	Patina Rating	Thickness (inch)	Cl^- Conc. (ppm)	Field Condition	Tape Test
A1-G2F2 TF Bot. Int.	8	Measured R1 .1.224 R2 1.223 R3 1.225 R_Avg Design			
A1-G2F2 Web Int.	8	Measured R1 0.683 R2 0.685 R3 0.682 R_Avg Design			
A1-G2F2 BF Top Int.	7	Measured R1 R2 R3 R_Avg Design			
A1-G2F2 BF Bot. Int.	7	Measured R1 1.245 R2 1.246 R3 1.245 R_Avg Design			
A1-G2F2 Stiff. Int.	8	Measured R1 1.224 R2 1.224 R3 1.223 R_Avg Design			

Table A-200. Field Inspection Results for DAL-WS-02.

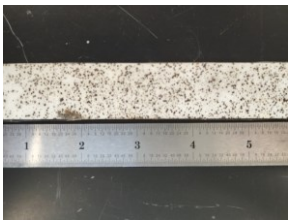
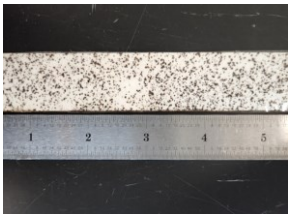
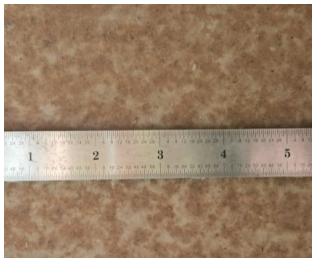
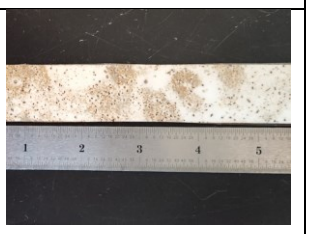
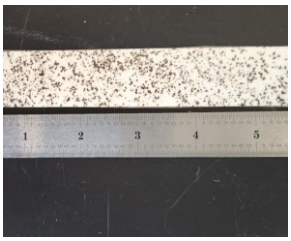
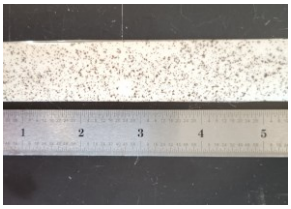
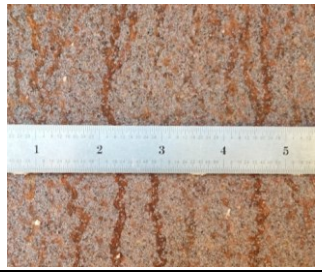
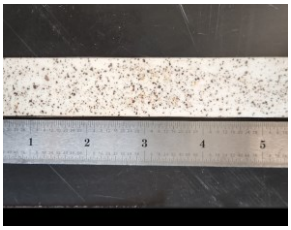
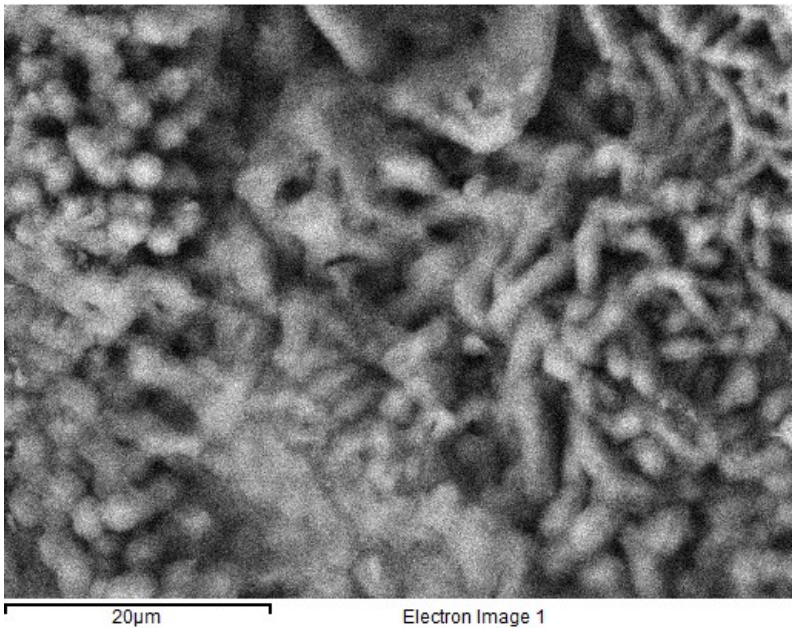
Location	Patina Rating	Thickness (inch)	Cl^- Conc. (ppm)	Field Condition	Tape Test
A1-G3F1 TF Bot. Int.	7	Measured R1 1.226 R2 1.226 R3 1.227 R_Avg Design			
A1-G3F1 Web Int.	7	Measured R1 0.681 R2 0.682 R3 0.682 R_Avg Design			
A1-G3F1 BF Top Int.	7	Measured R1 R2 R3 R_Avg Design			
A1-G3F1 BF Bot. Int.	7	Measured R1 1.234 R2 1.236 R3 1.239 R_Avg Design			
A1-G3F1 Stiff. Int.	7	Measured R1 1.231 R2 1.231 R3 1.228 R_Avg Design			

Table A-201. Field Inspection Results for DAL-WS-02.

Location	Patina Rating	Thickness (inch)	Cl^- Conc. (ppm)	Field Condition	Tape Test
A1-G4F2 TF Bot. Ext.	8	Measured R1 .1.226 R2 1.222 R3 1.224 R_Avg Design			
A1-G4F2 Web Ext.	8	Measured R1 0.687 R2 0.686 R3 0.684 R_Avg Design			
A1-G4F2 BF Top Ext.	7	Measured R1 R2 R3 R_Avg Design			
A1-G4F2 BF Bot. Ext.	6	Measured R1 1.232 R2 1.233 R3 1.230 R_Avg Design			
A1-G4F2 Stiff. Ext.	7	Measured R1 1.225 R2 1.225 R3 1.225 R_Avg Design			

A.45.3.SEM/EDS Results: Exterior Web Girder

Element	Weight %	Atomic %
O K	44.55	73.26
Al K	0.48	0.47
Si K	0.28	0.26
S K	0.65	0.53
Mn K	1.08	0.52
Fe K	52.97	24.96
Totals	100.00	



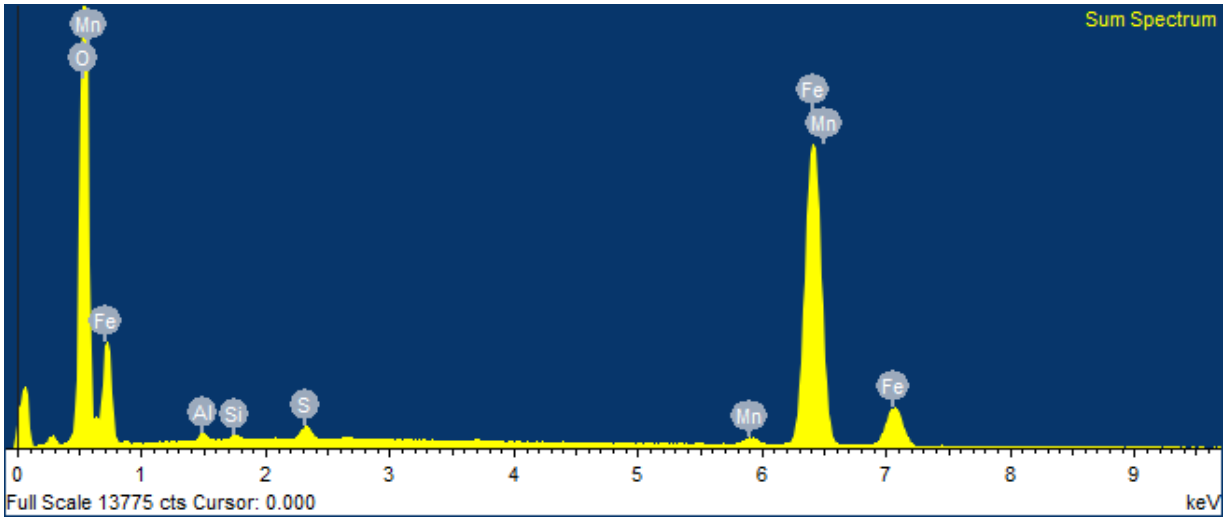
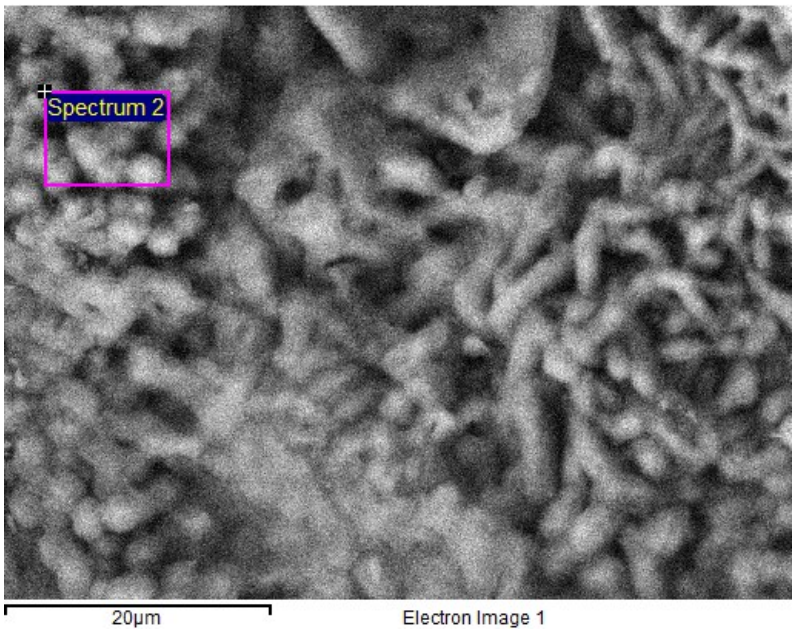


Figure A.810. SEM Image and EDS Spectrum of the Rust Collected from Exterior Web of the Girder.

Element	Weight %	Atomic %
O K	49.24	76.78
Al K	0.33	0.31
Si K	0.27	0.24
S K	0.72	0.56
Cl K	0.11	0.08
Mn K	0.99	0.45
Fe K	48.10	21.49
Ni K	0.24	0.10
Totals	100.00	



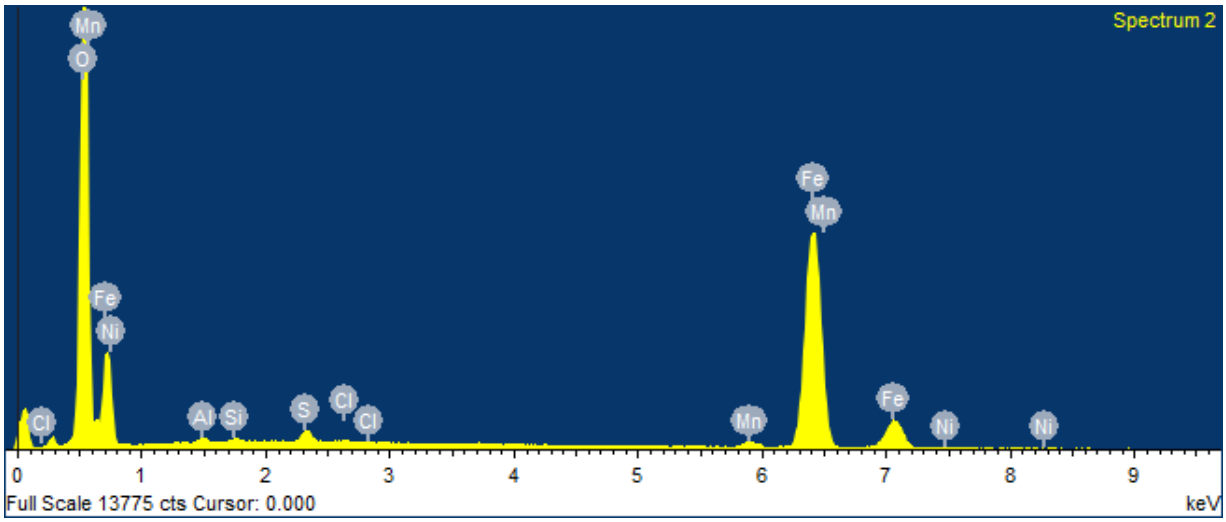
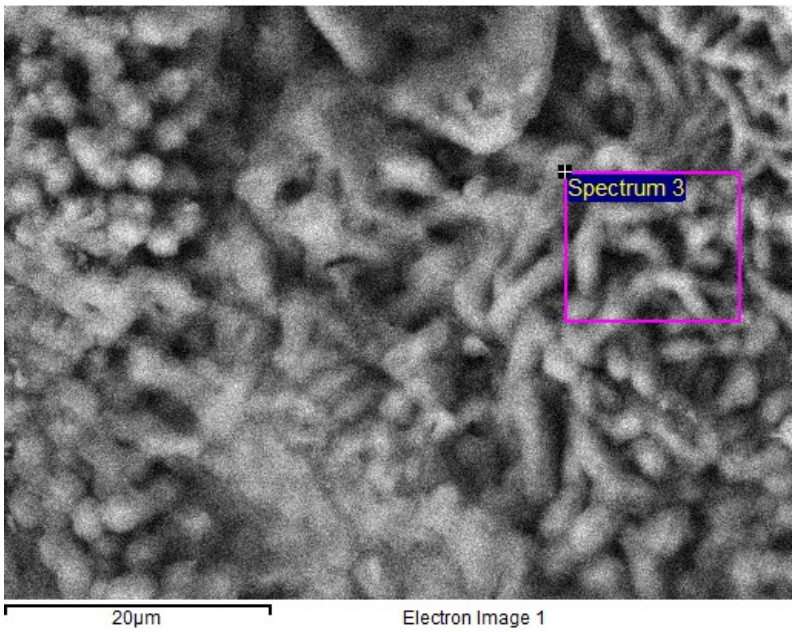


Figure A.811. SEM Image and EDS Spectrum of the Rust Collected from Exterior Web of the Girder.

Element	Weight %	Atomic %
O K	48.20	76.18
Al K	0.30	0.28
S K	0.68	0.54
Mn K	0.79	0.36
Fe K	49.77	22.53
Ni K	0.25	0.11
Totals	100.00	



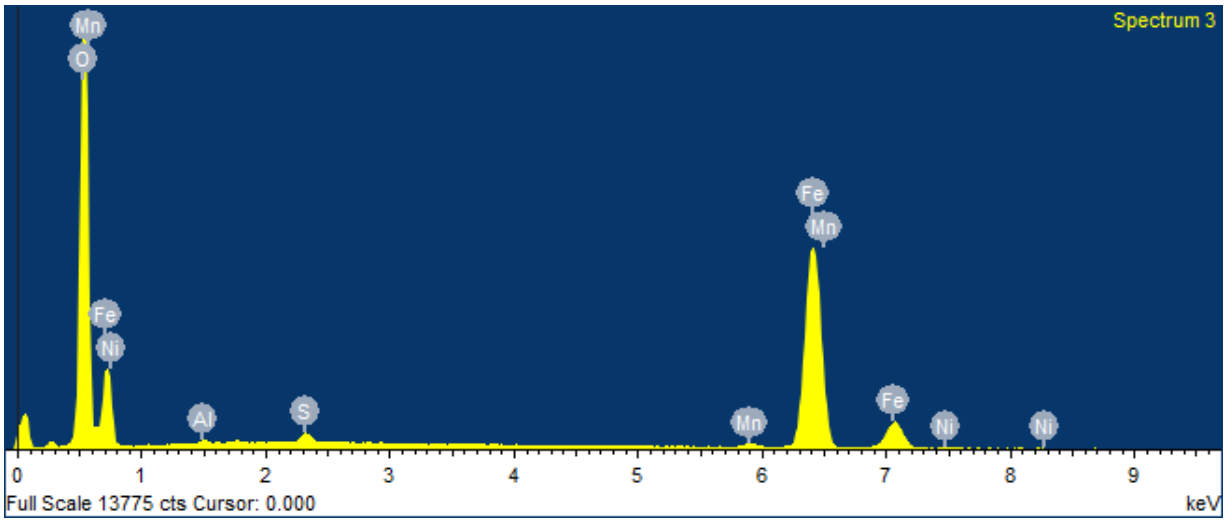
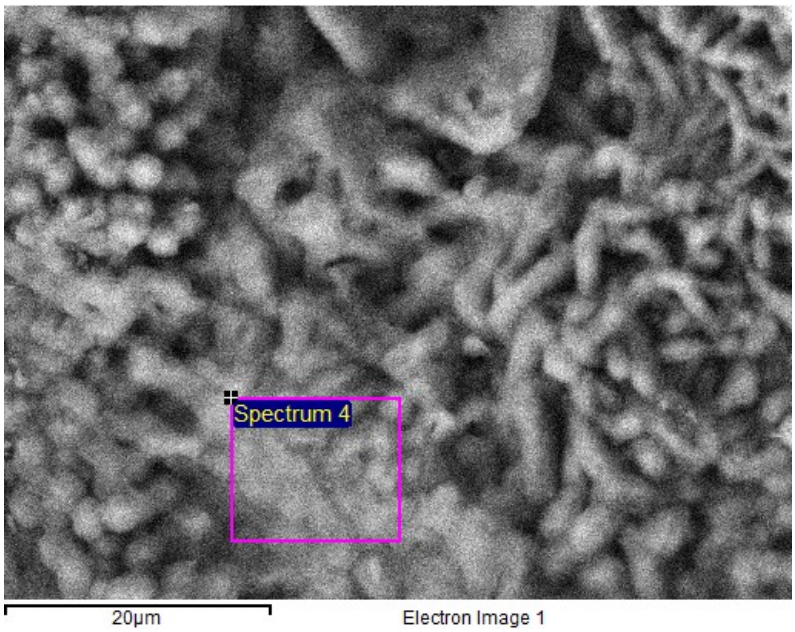


Figure A.812. SEM Image and EDS Spectrum of the Rust Collected from Exterior Web of the Girder.

Element	Weight %	Atomic %
O K	43.41	72.16
Al K	0.72	0.70
Si K	0.35	0.33
S K	0.89	0.74
Cl K	0.16	0.12
Mn K	0.61	0.30
Fe K	53.86	25.65
Totals	100.00	



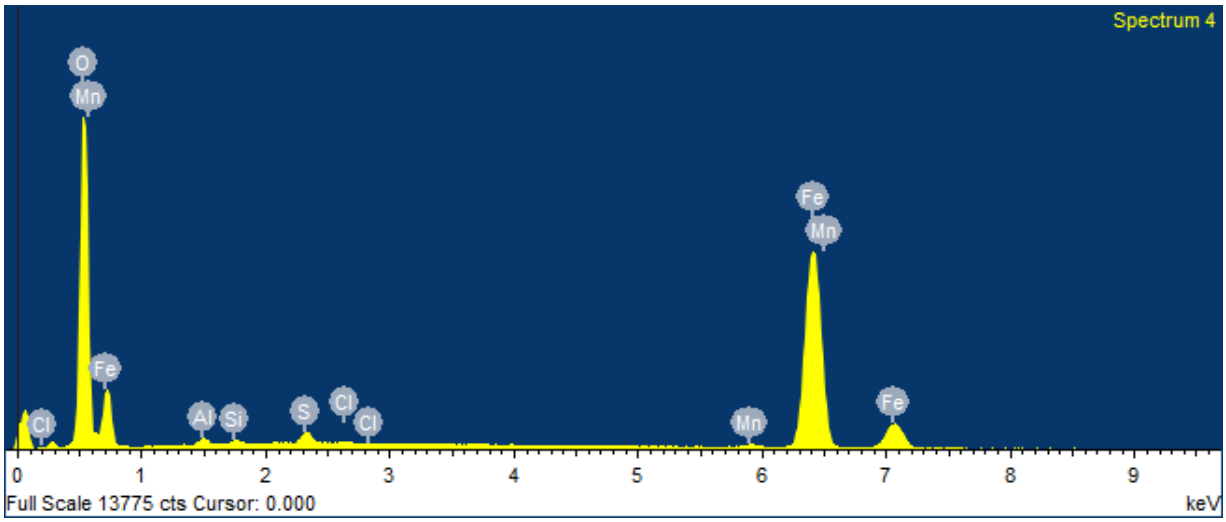
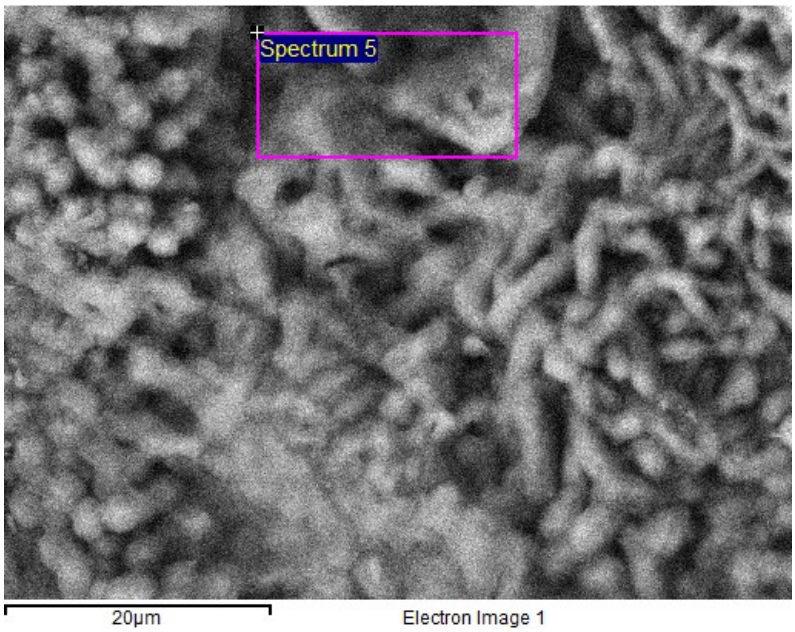


Figure A.813. SEM Image and EDS Spectrum of the Rust Collected from Exterior Web of the Girder.

Element	Weight %	Atomic %
O K	44.20	73.09
Al K	0.33	0.32
Si K	0.23	0.22
S K	0.55	0.45
Mn K	1.60	0.77
Fe K	52.76	24.99
Ni K	0.33	0.15
Totals	100.00	



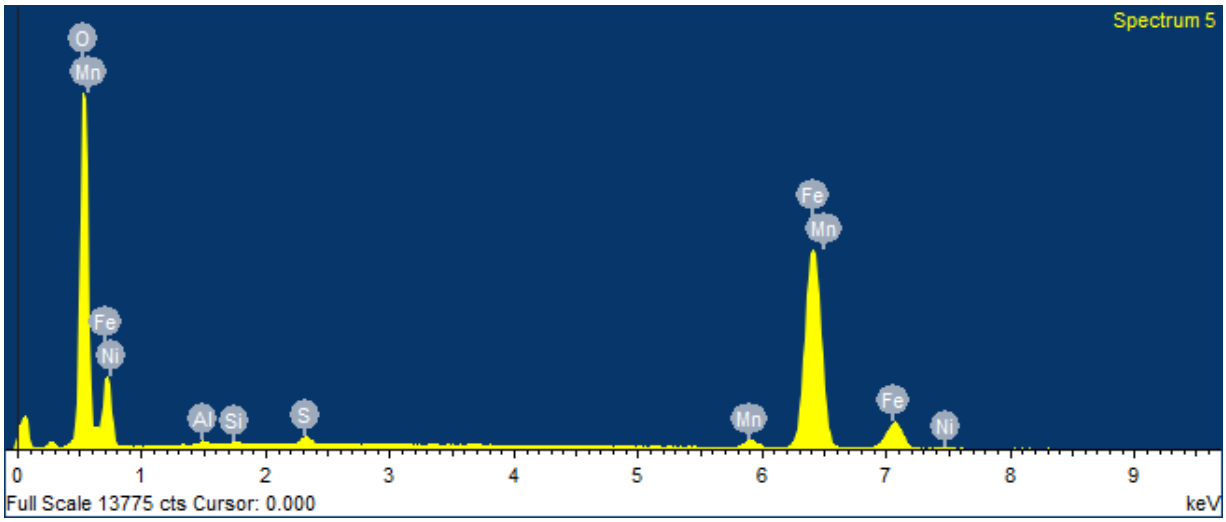


Figure A.814. SEM Image and EDS Spectrum of the Rust Collected from Exterior Web of the Girder.

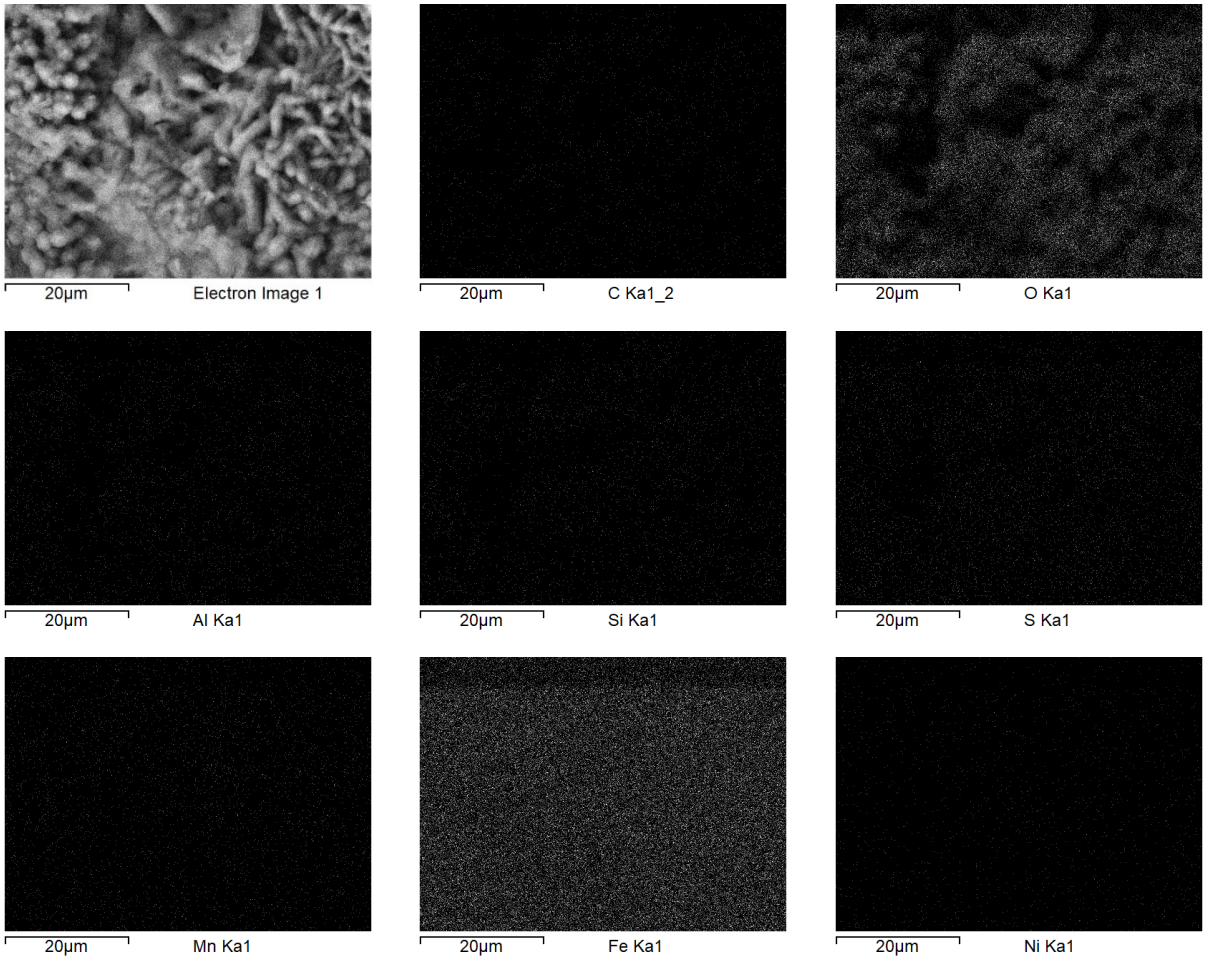
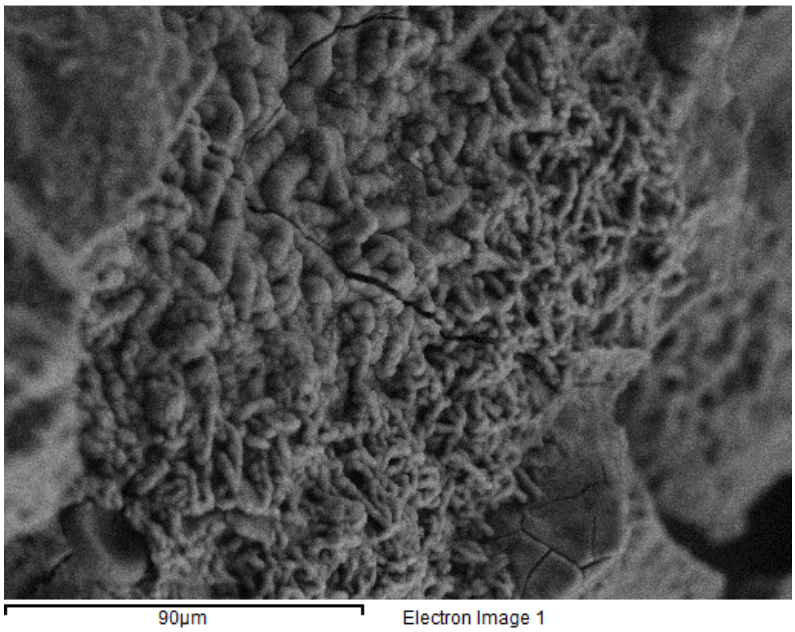


Figure A.815. EDS Elemental Mapping of Rust Collected from Exterior Web.

Element	Weight %	Atomic %
O K	30.42	59.88
Al K	0.38	0.44
Si K	0.24	0.27
P K	0.22	0.22
S K	0.81	0.80
Cl K	0.35	0.31
Ca K	0.11	0.09
Mn K	0.81	0.47
Fe K	64.06	36.13
Ni K	2.60	1.39
Totals	100.00	



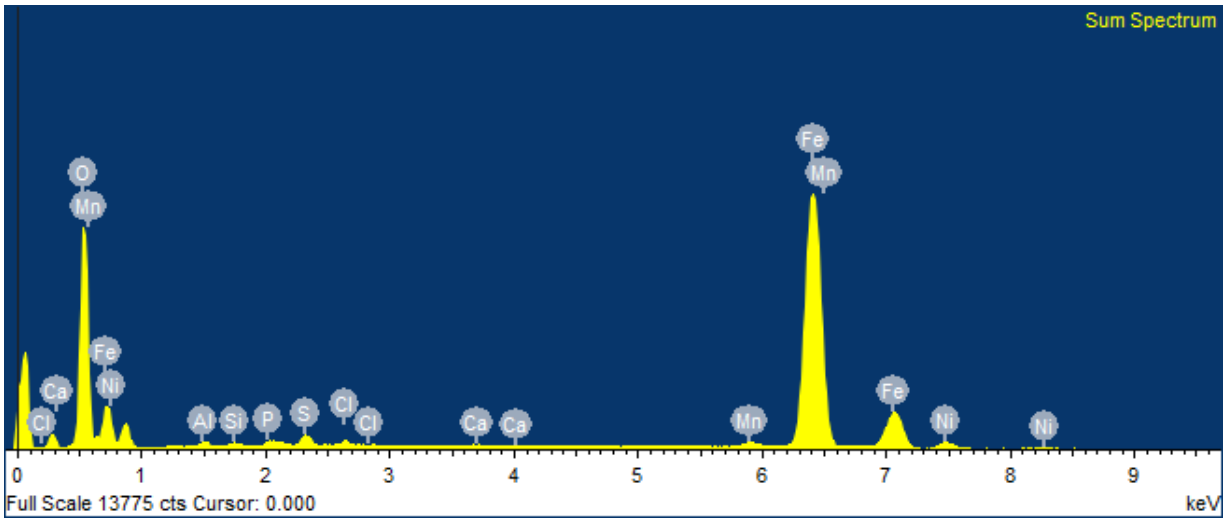
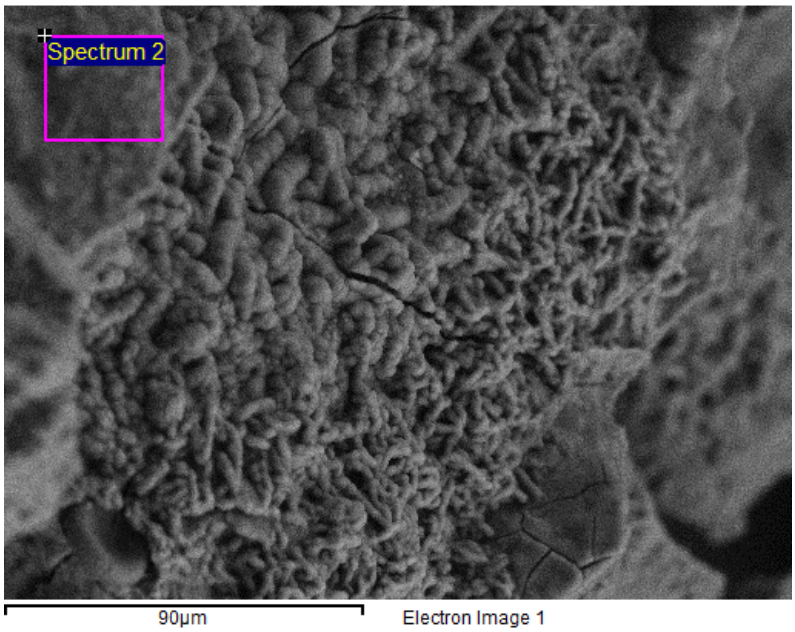


Figure A.816. SEM Image and EDS Spectrum of the Rust Collected from Exterior Web of the Girder.

Element	Weight %	Atomic %
O K	48.52	76.36
Al K	0.20	0.18
Si K	0.27	0.24
S K	0.73	0.58
Cr K	0.29	0.14
Mn K	1.57	0.72
Fe K	47.06	21.22
Ni K	1.04	0.44
Cu K	0.32	0.13
Totals	100.00	



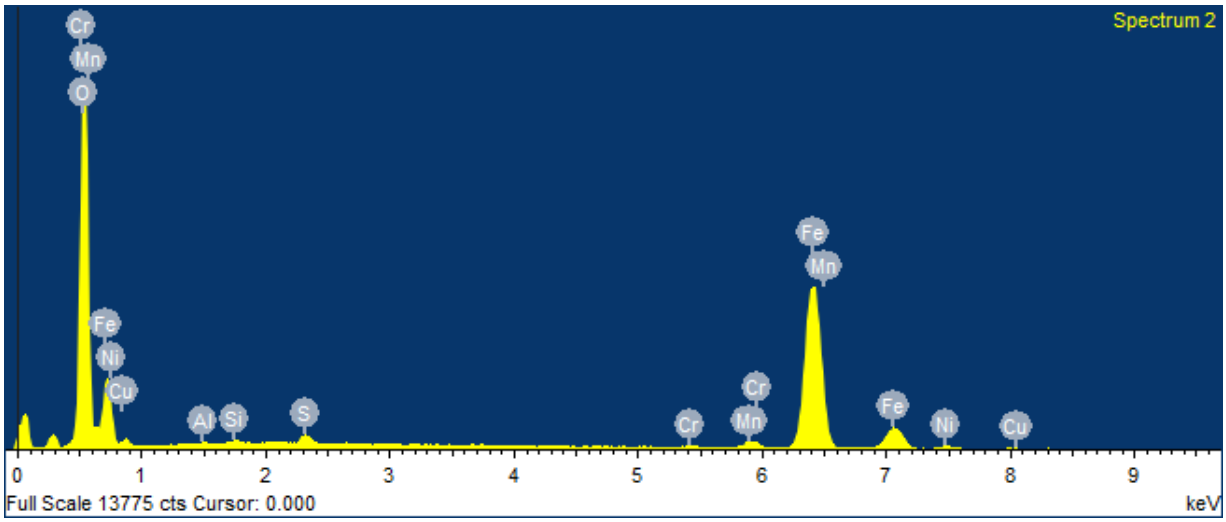
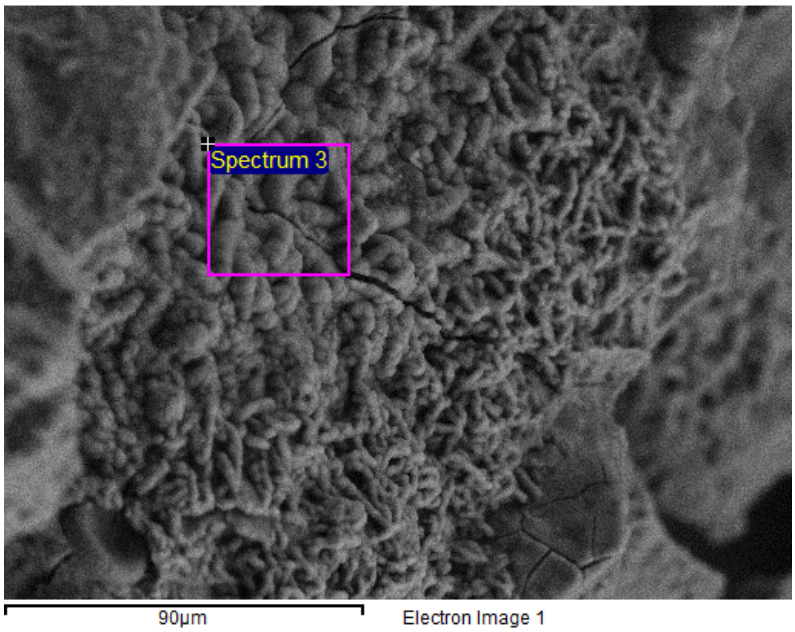


Figure A.817. SEM Image and EDS Spectrum of the Rust Collected from Exterior Web of the Girder.

Element	Weight%	Atomic%
O K	26.48	55.25
Al K	0.35	0.44
Si K	0.16	0.19
S K	0.79	0.82
Cl K	0.57	0.53
Mn K	0.76	0.46
Fe K	68.28	40.82
Ni K	2.61	1.48
Totals	100.00	



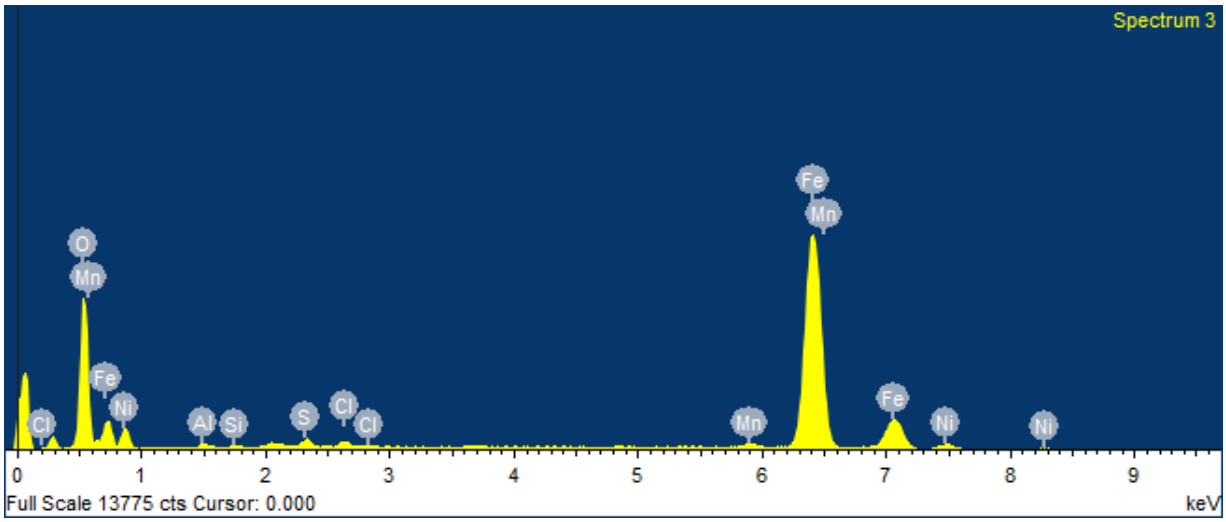


Figure A.818. SEM Image and EDS Spectrum of the Rust Collected from Exterior Web of the Girder.

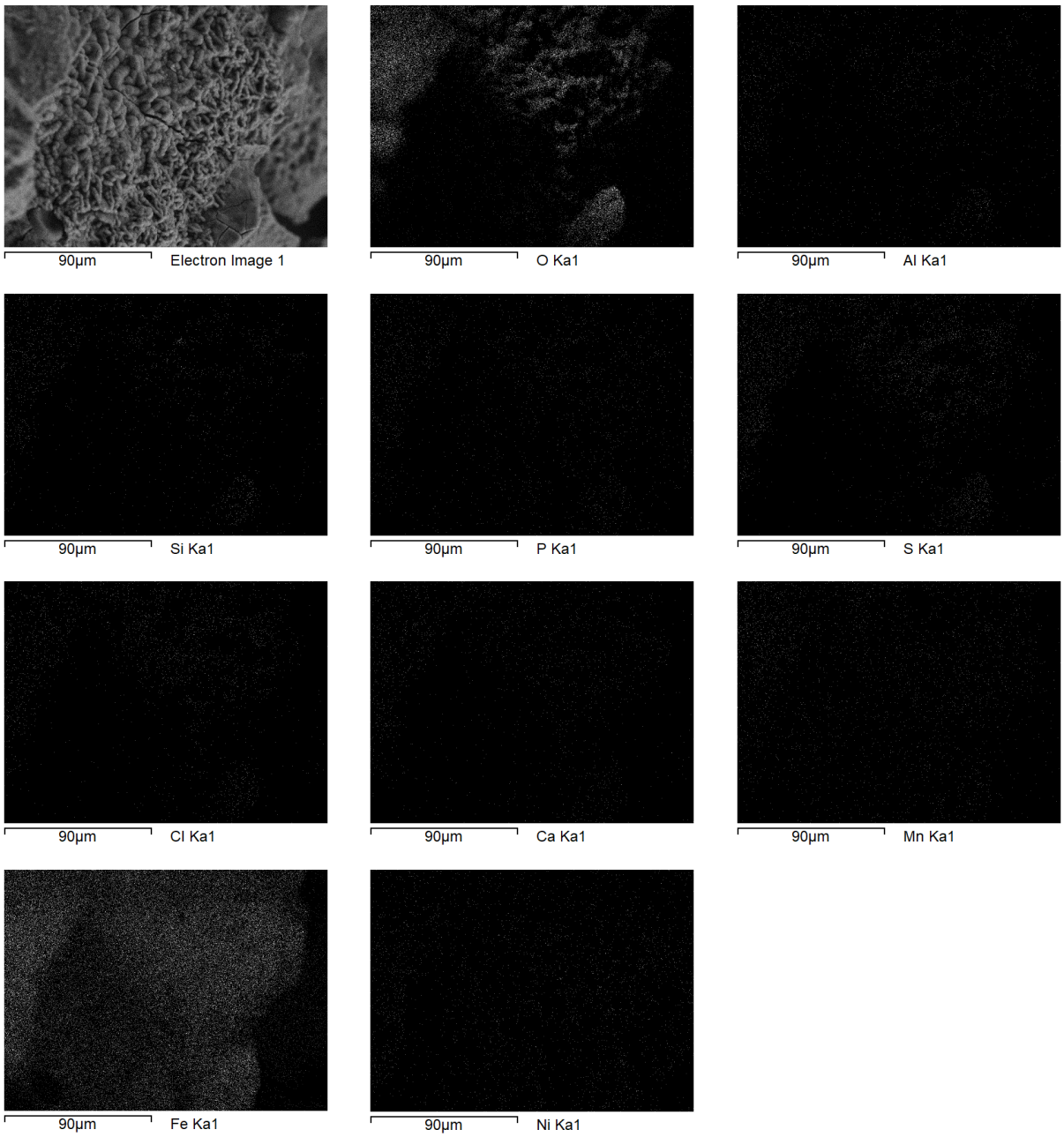
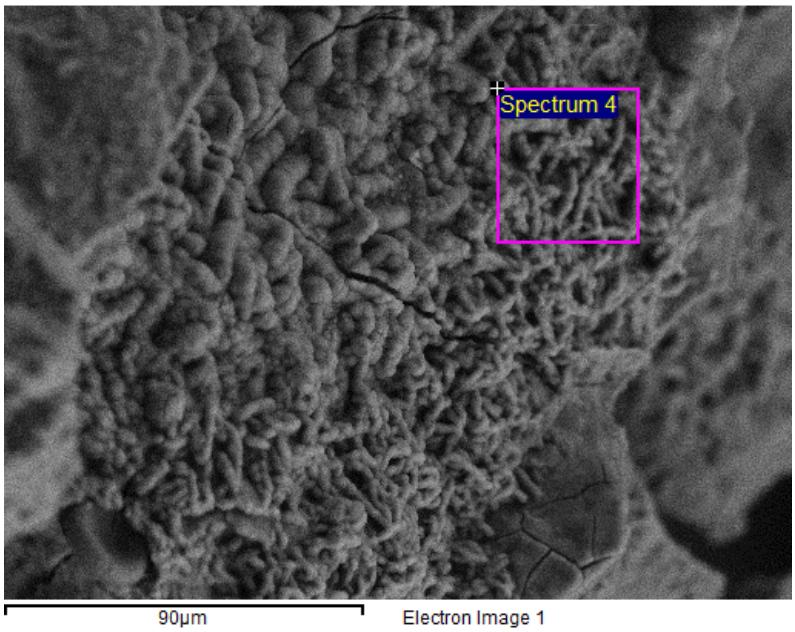


Figure A.819. EDS Elemental Mapping of Rust Collected from Exterior Web.

Element	Weight %	Atomic %
O K	45.25	73.78
S K	1.29	1.05
Cl K	0.85	0.62
Mn K	0.25	0.12
Fe K	51.20	23.91
Ni K	1.16	0.52
Totals	100.00	



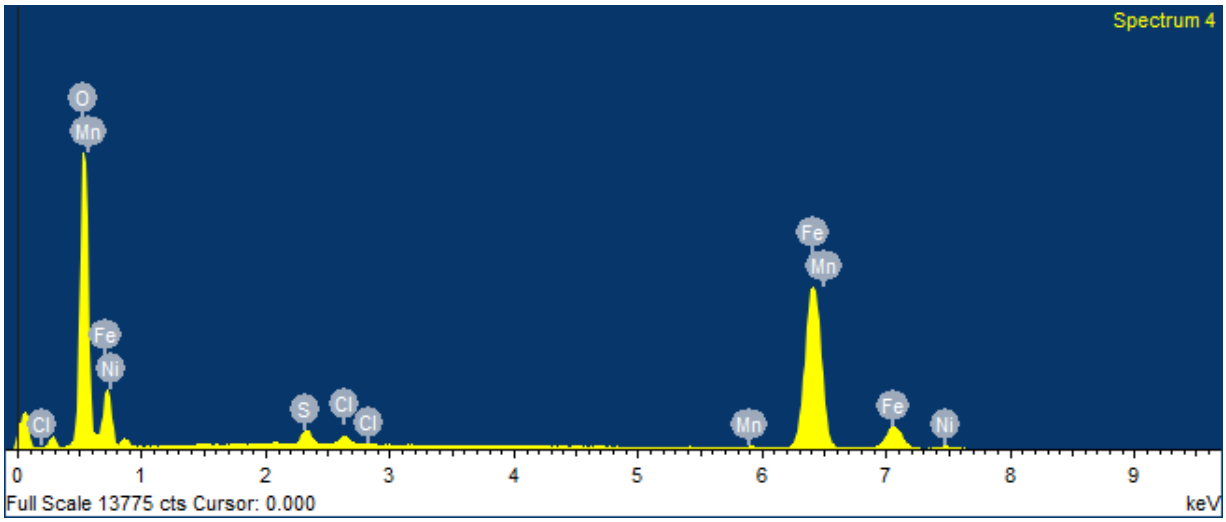
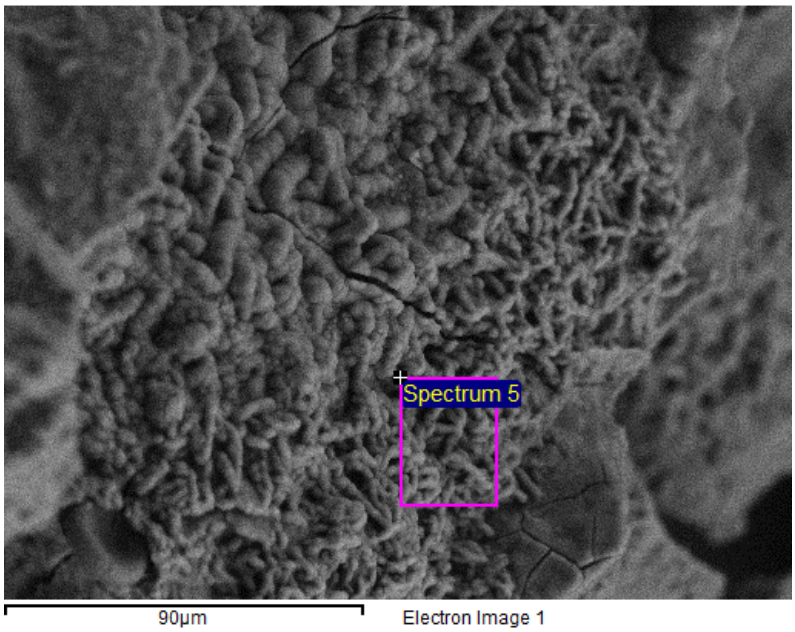


Figure A.820. SEM Image and EDS Spectrum of the Rust Collected from Exterior Web of the Girder.

Element	Weight %	Atomic %
O K	12.95	33.83
Al K	0.52	0.81
Si K	0.12	0.18
P K	0.32	0.43
S K	0.56	0.73
Cl K	0.25	0.30
Mn K	0.48	0.37
Fe K	81.80	61.23
Ni K	2.99	2.13
Totals	100.00	



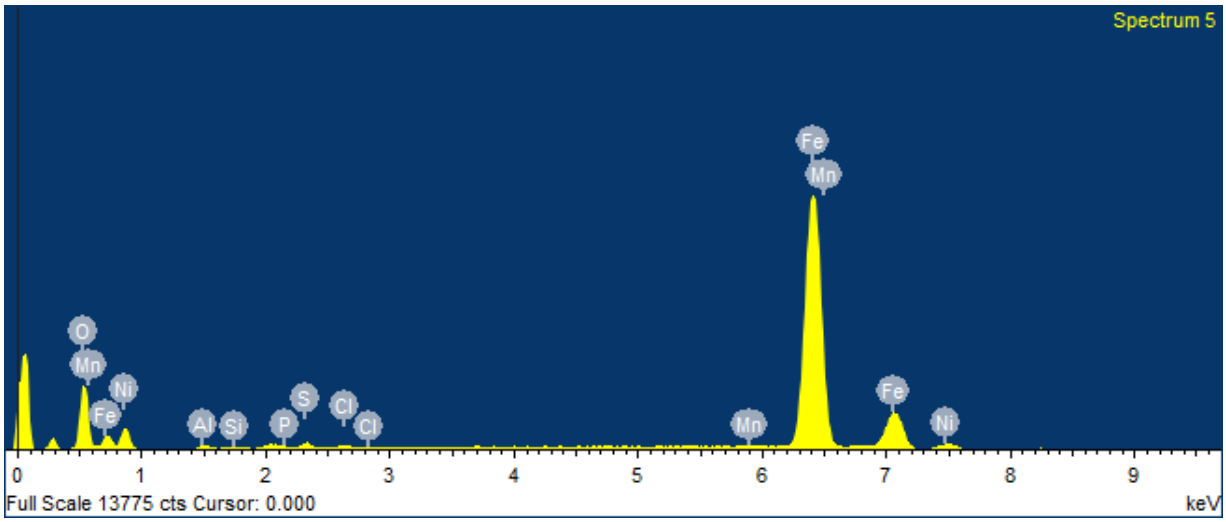
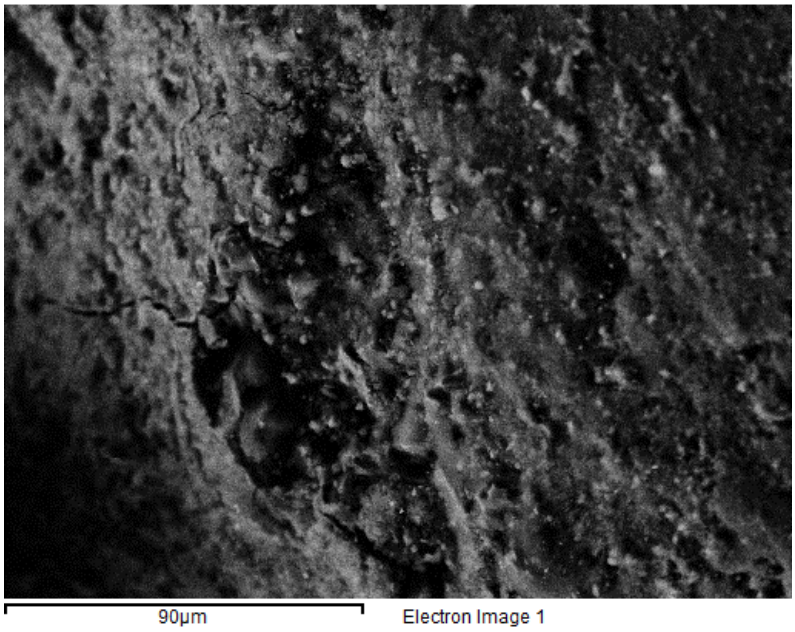


Figure A.821. SEM Image and EDS Spectrum of the Rust Collected from Exterior Web of the Girder.

A.45.4.SEM/EDS Results: Interior Web Girder

Element	Weight %	Atomic %
O K	57.55	77.21
Mg K	0.42	0.37
Al K	2.37	1.88
Si K	6.81	5.20
P K	0.16	0.11
S K	0.45	0.30
K K	0.20	0.11
Ca K	16.25	8.70
Mn K	5.97	2.33
Fe K	9.22	3.54
Ni K	0.59	0.22
Totals	100.00	



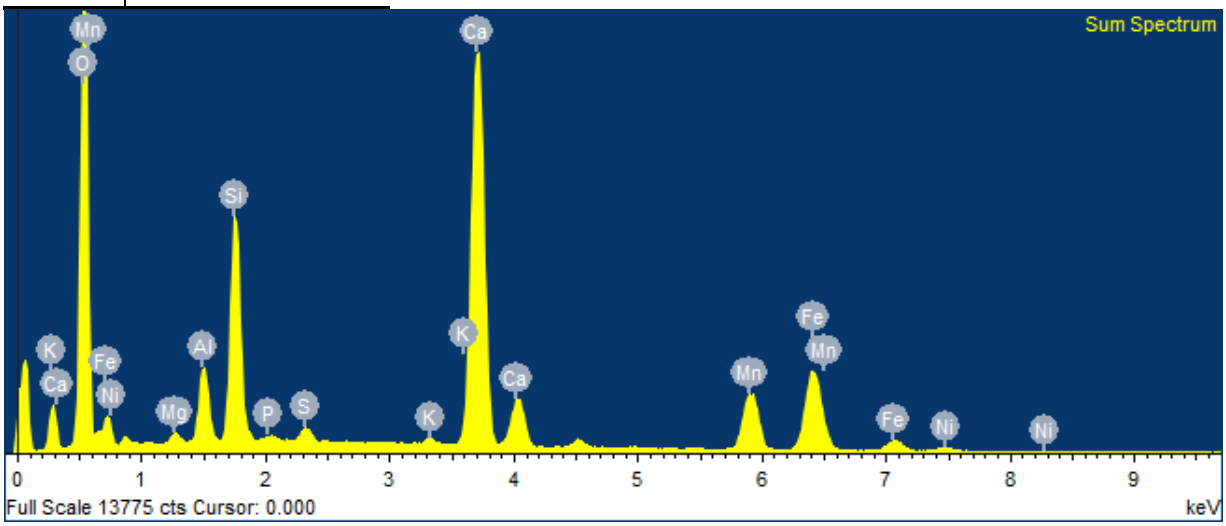


Figure A.822. SEM Image and EDS Spectrum of the Rust Collected from Interior Web of the Girder.

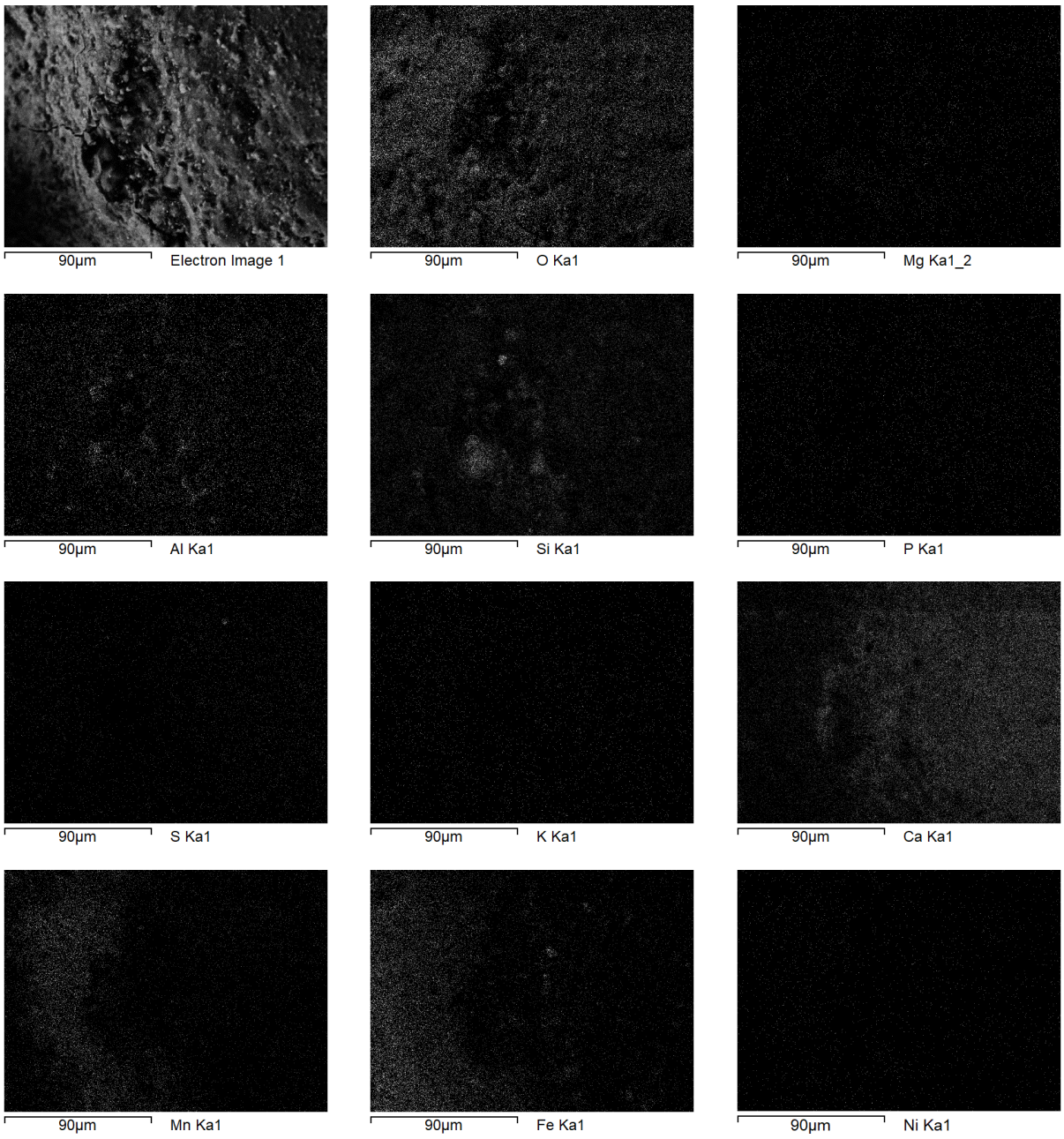
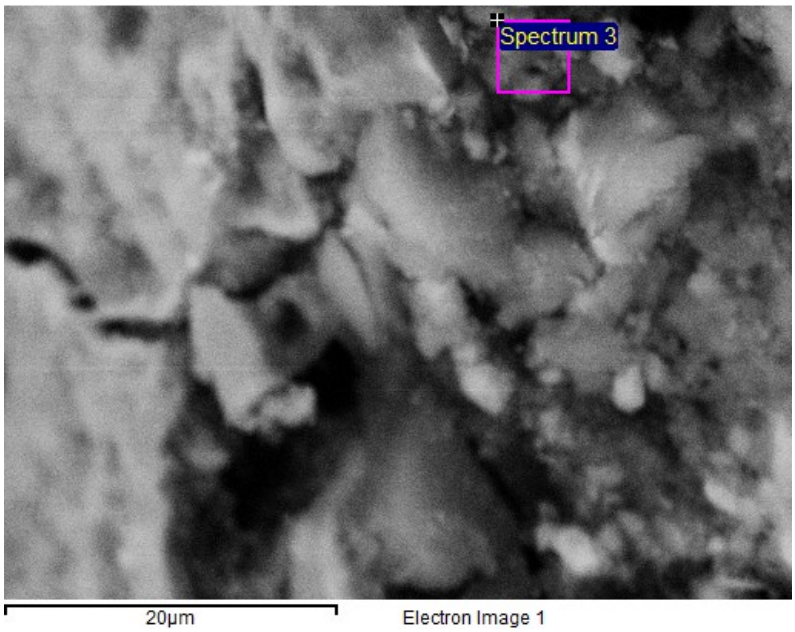


Figure A.823. EDS Elemental Mapping of Rust Collected from Interior Web.

Element	Weight %	Atomic %
O K	39.39	62.24
Mg K	0.39	0.40
Al K	2.73	2.56
Si K	6.07	5.47
P K	0.17	0.14
S K	0.25	0.20
K K	0.39	0.25
Ca K	32.48	20.49
Mn K	10.54	4.85
Fe K	6.40	2.90
Ni K	1.18	0.51
Totals	100.00	



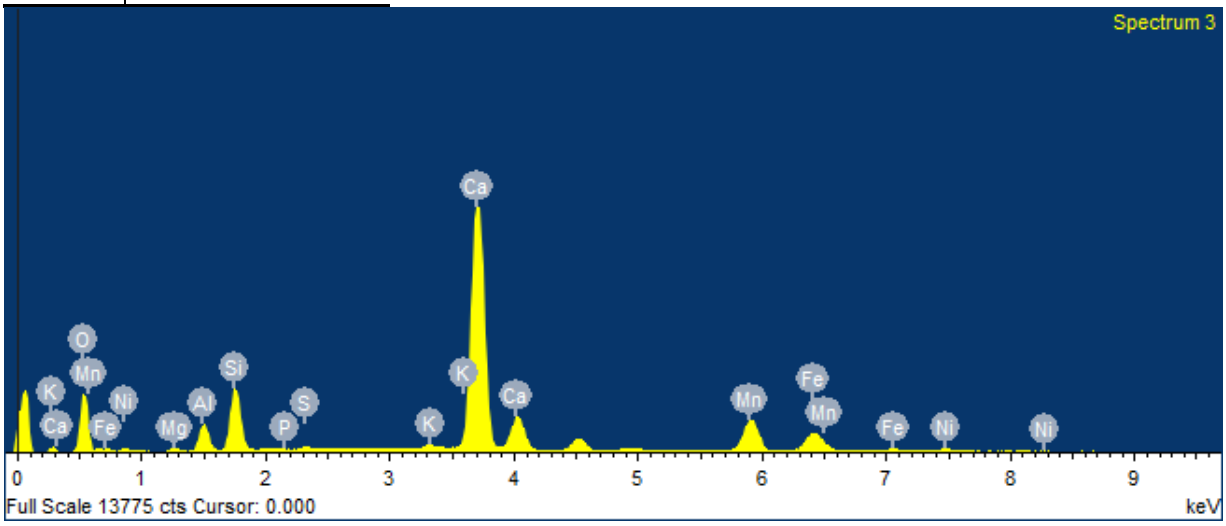
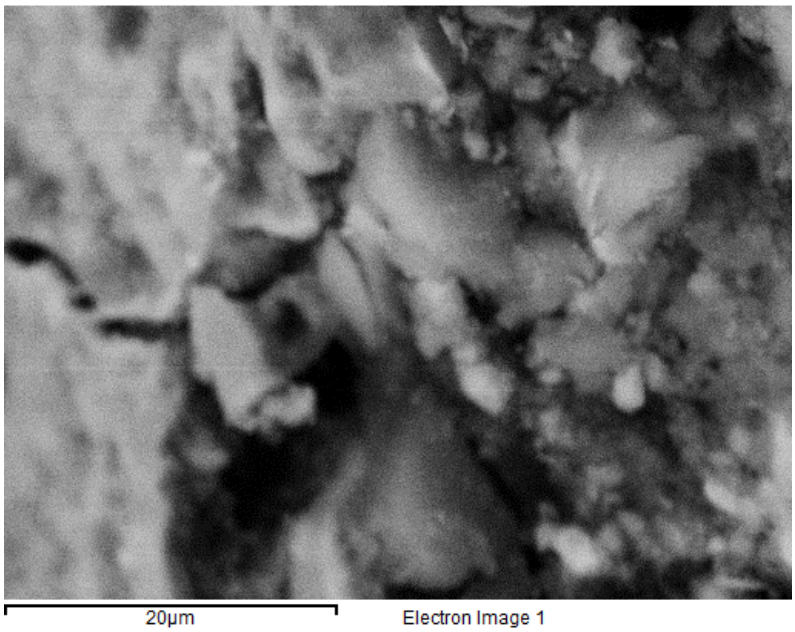


Figure A.824. SEM Image and EDS Spectrum of the Rust Collected from Interior Web of the Girder.

Element	Weight %	Atomic %
O K	52.92	73.52
Mg K	0.61	0.55
Al K	3.19	2.63
Si K	8.88	7.03
P K	0.19	0.13
S K	0.16	0.11
K K	0.23	0.13
Ca K	15.26	8.46
Mn K	8.92	3.61
Fe K	8.74	3.48
Ni K	0.90	0.34
Totals	100.00	



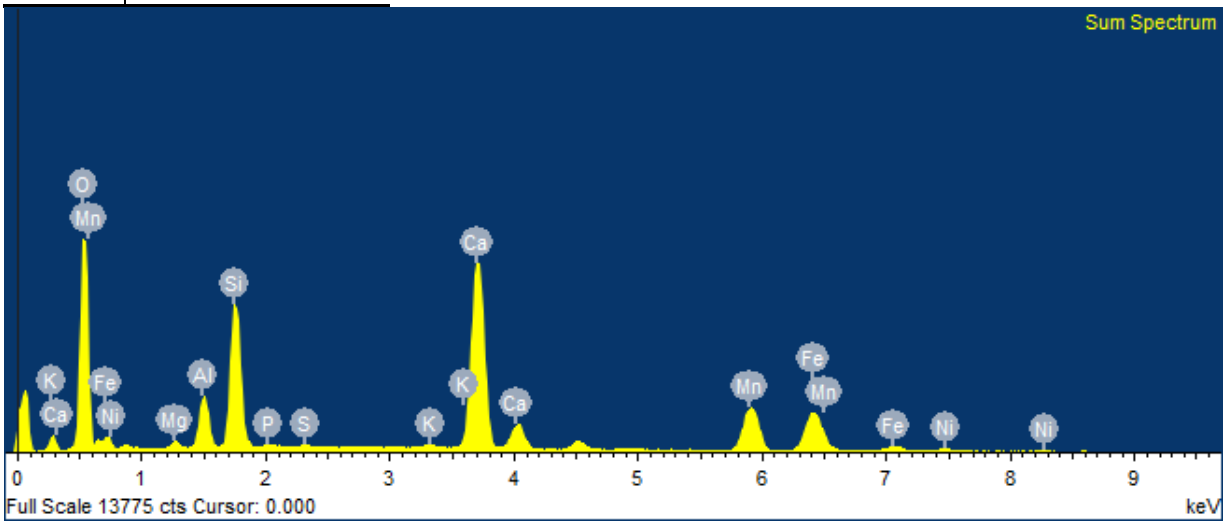


Figure A.825. SEM Image and EDS Spectrum of the Rust Collected from Interior Web of the Girder.

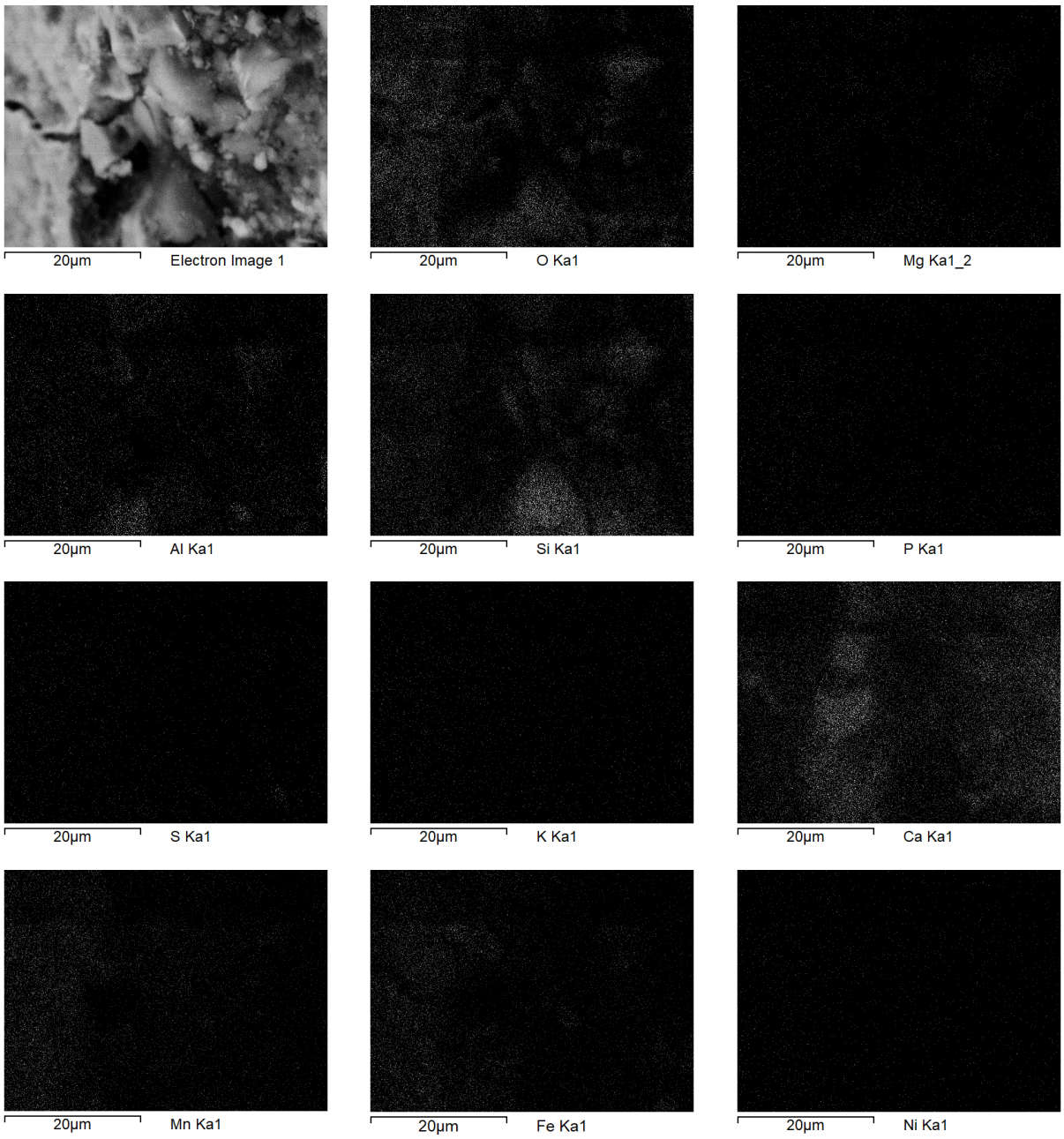
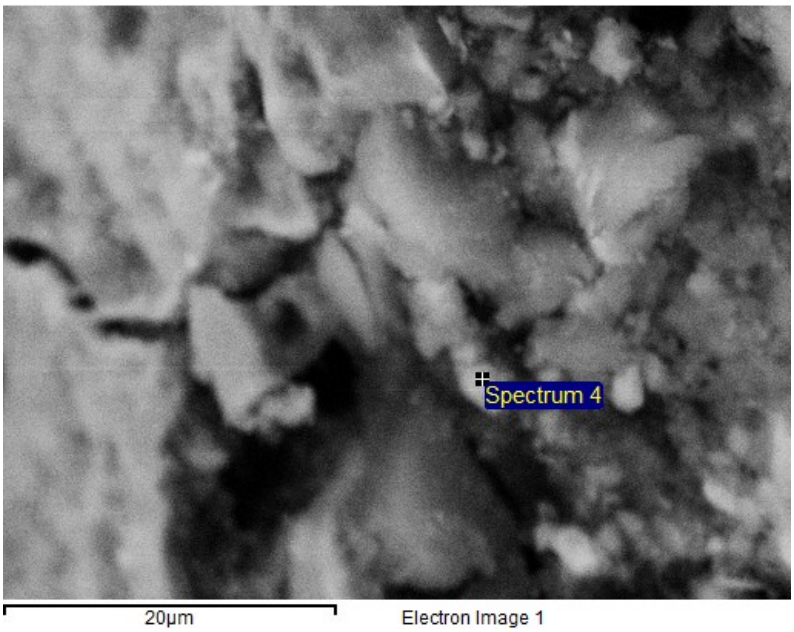


Figure A.826. EDS Elemental Mapping of Rust Collected from Interior Web.

Element	Weight %	Atomic %
O K	47.85	70.07
Mg K	0.63	0.60
Al K	3.19	2.77
Si K	11.50	9.59
P K	0.26	0.20
S K	0.19	0.14
K K	0.17	0.10
Ca K	7.81	4.57
Mn K	11.69	4.99
Fe K	15.32	6.43
Ni K	1.39	0.55
Totals	100.00	



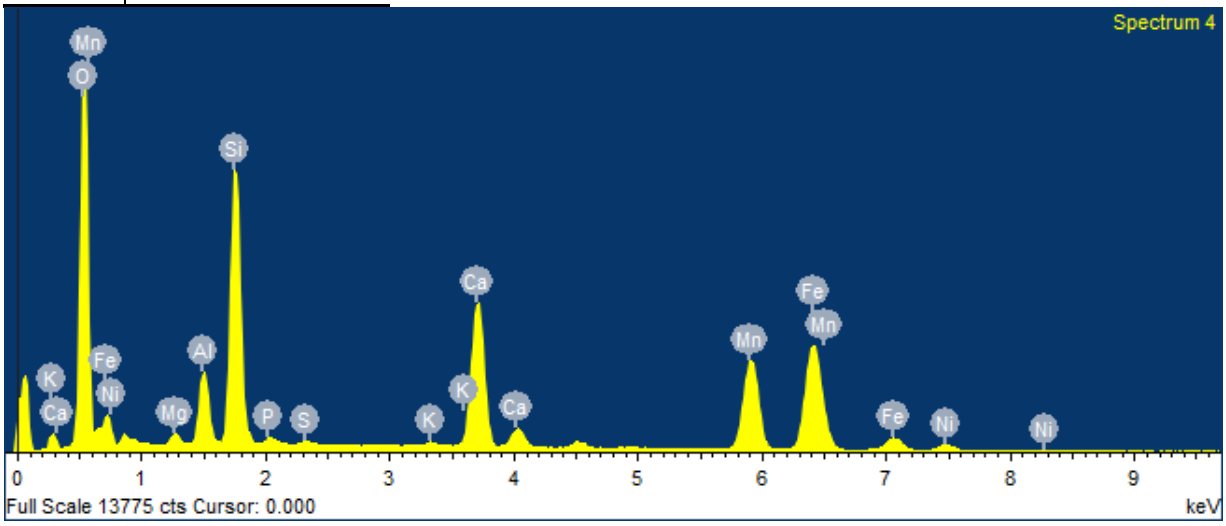


Figure A.827. SEM Image and EDS Spectrum of the Rust Collected from Interior Web of the Girder.

A.45.5.XPS Result: Exterior Girder

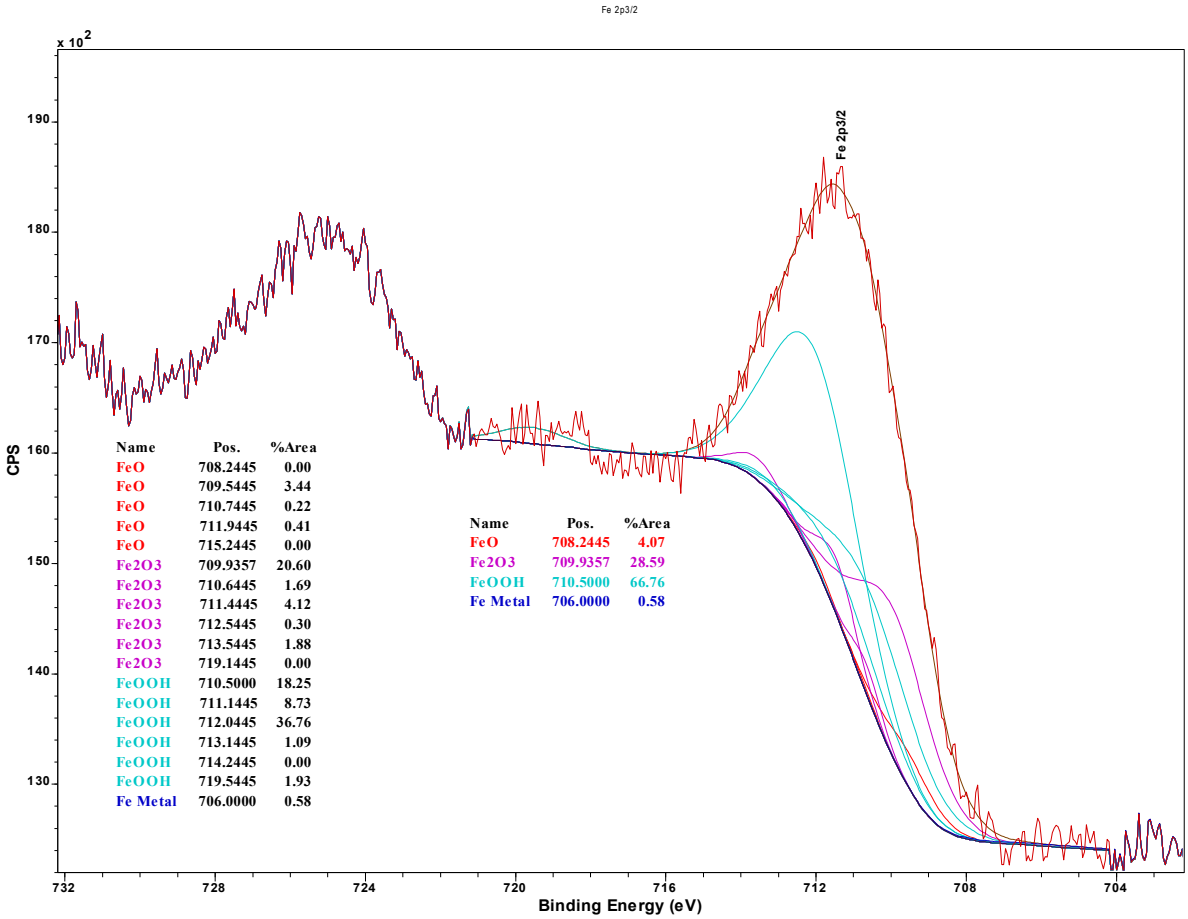


Figure A.828. XPS Spectrum of the Rust Collected from Exterior Web of the Girder.

A.45.6.XPS Result: Interior Girder

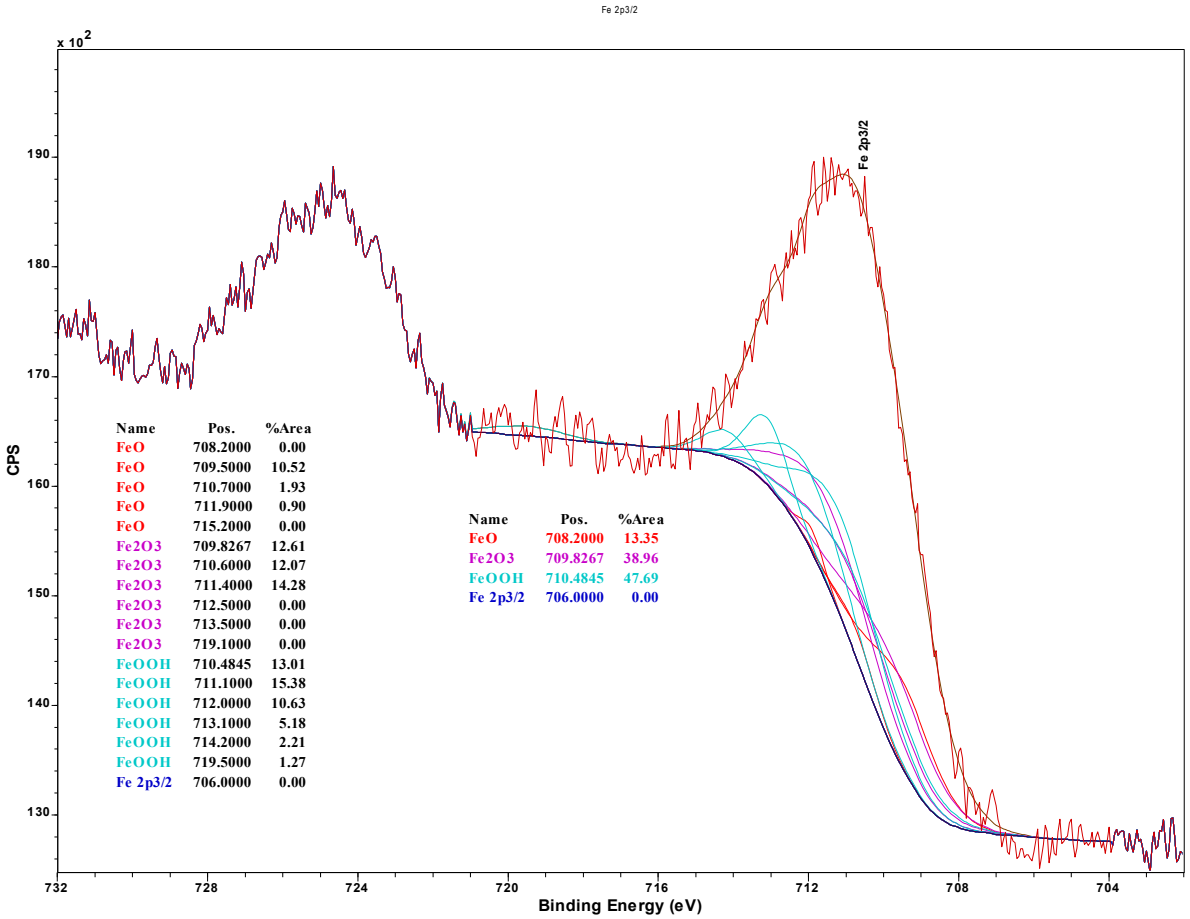


Figure A.829. XPS Spectrum of the Rust Collected from Interior Web of the Girder.

A.45.7.XRD Result: Exterior and Interior Girder

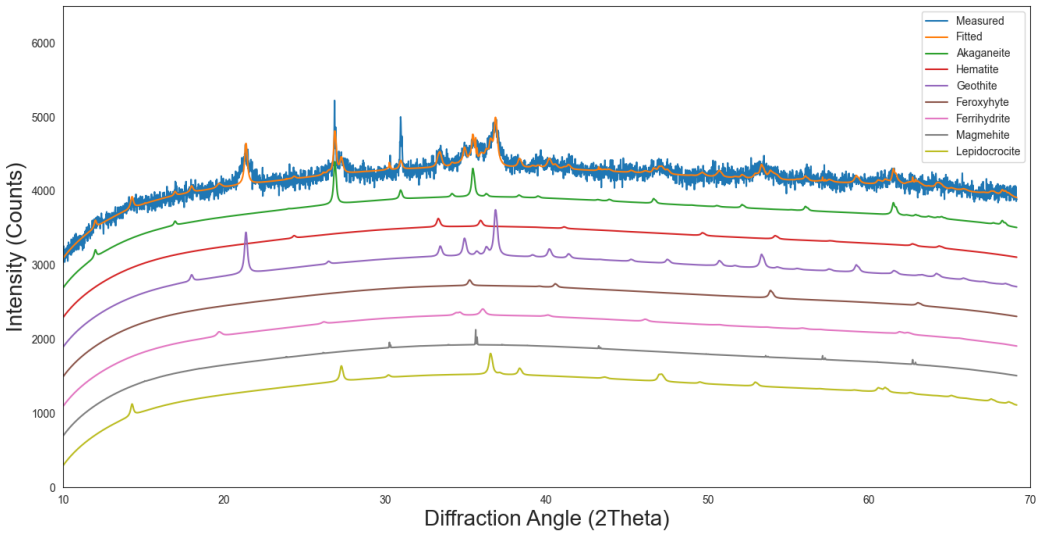


Figure A.830. XRD Pattern of Powdered Rust Collected from Exterior Web of the Girder.

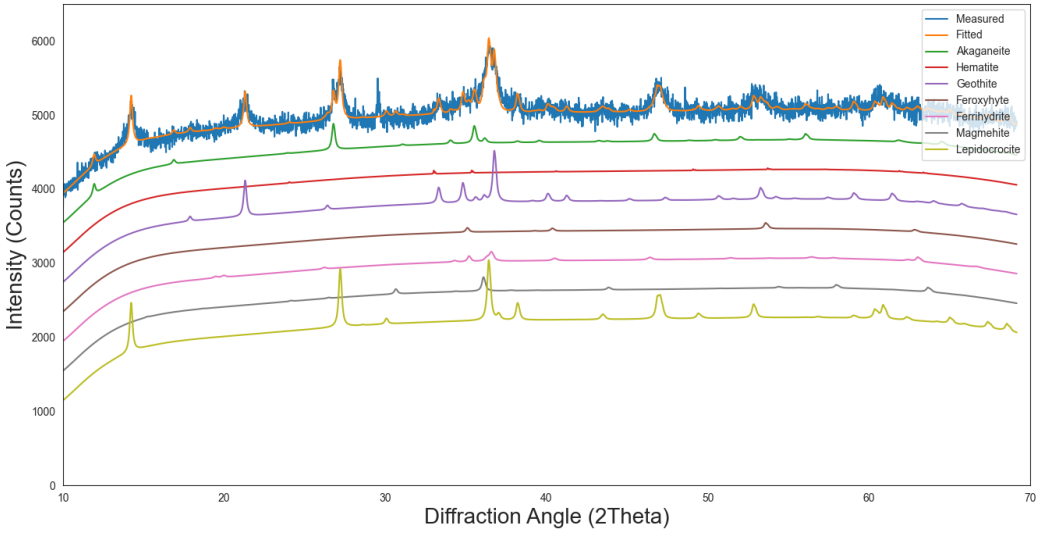


Figure A.831. XRD Pattern of Powdered Rust Collected from Interior Web of the Girder.

A.45.8.Particle Size Analysis: Tape Adhesion Results

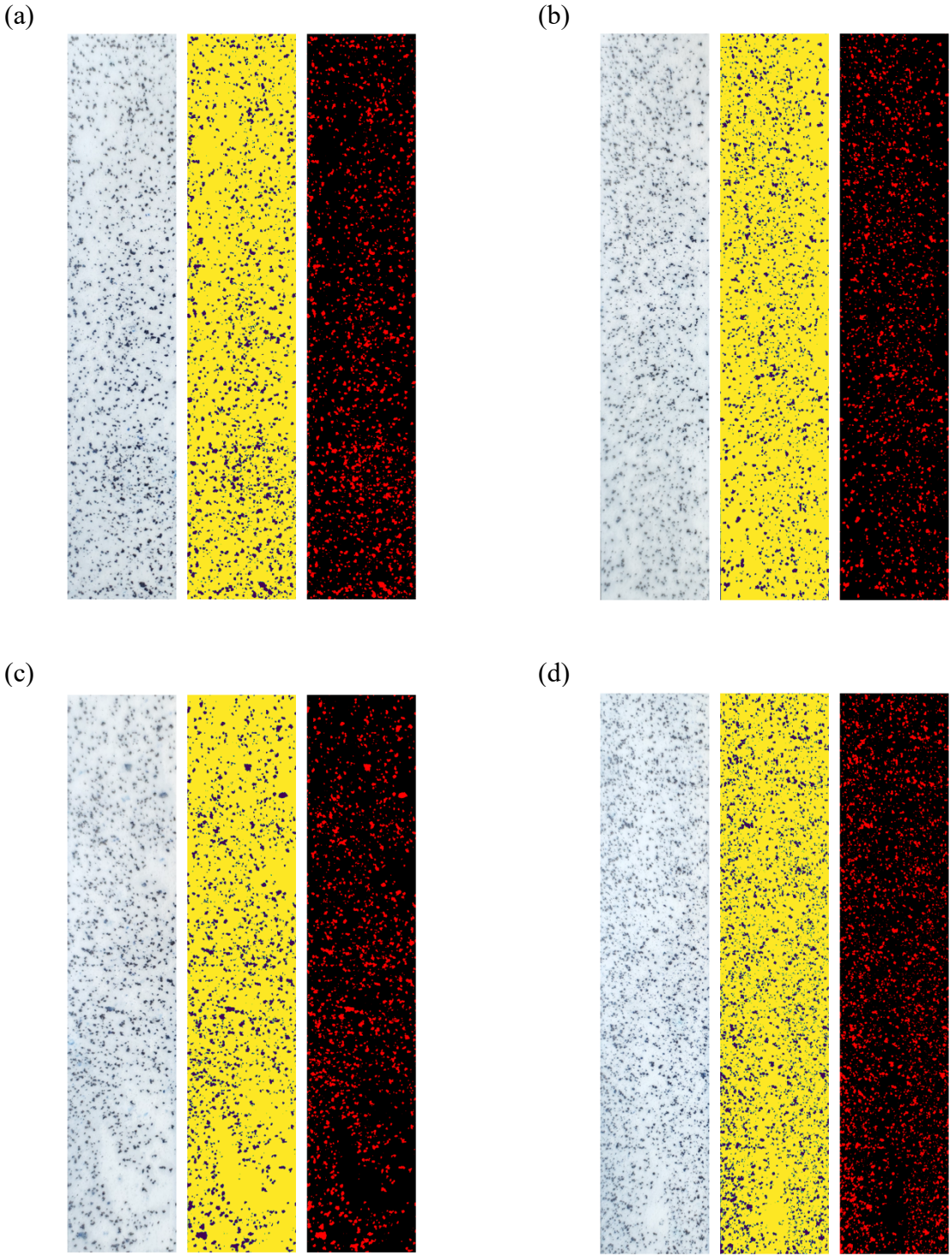


Figure A.832. Particle Size Analysis Results at A1G1F1 (a) Top Flange Bottom, (b) Web, (c) Bottom Flange Bottom (d) StiffenerA1G1F1.

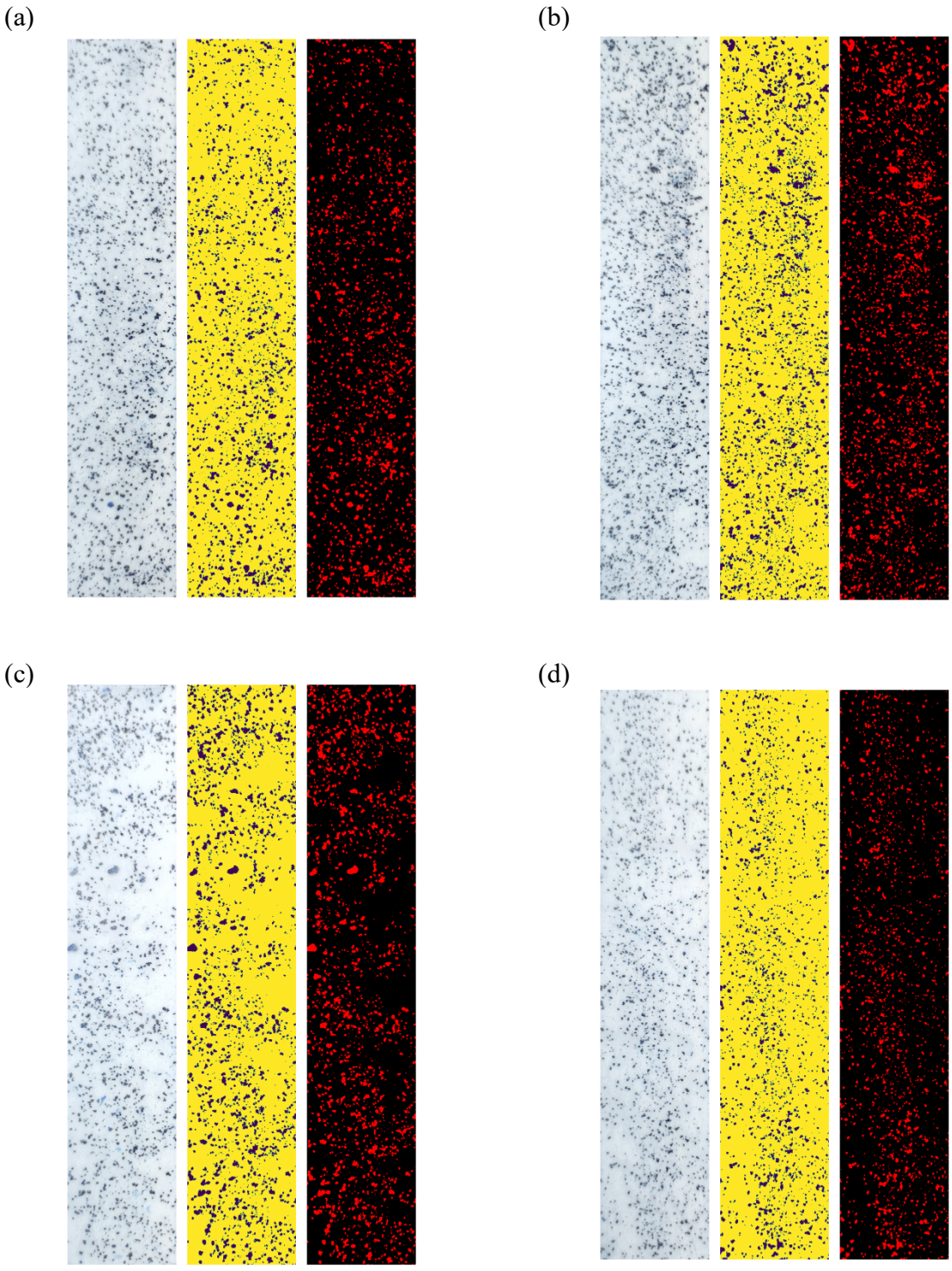


Figure A.833. Particle Size Analysis Results at A1G2F1 (a) Top Flange Bottom, (b) Web, (c) Bottom Flange Bottom (d) Stiffener.

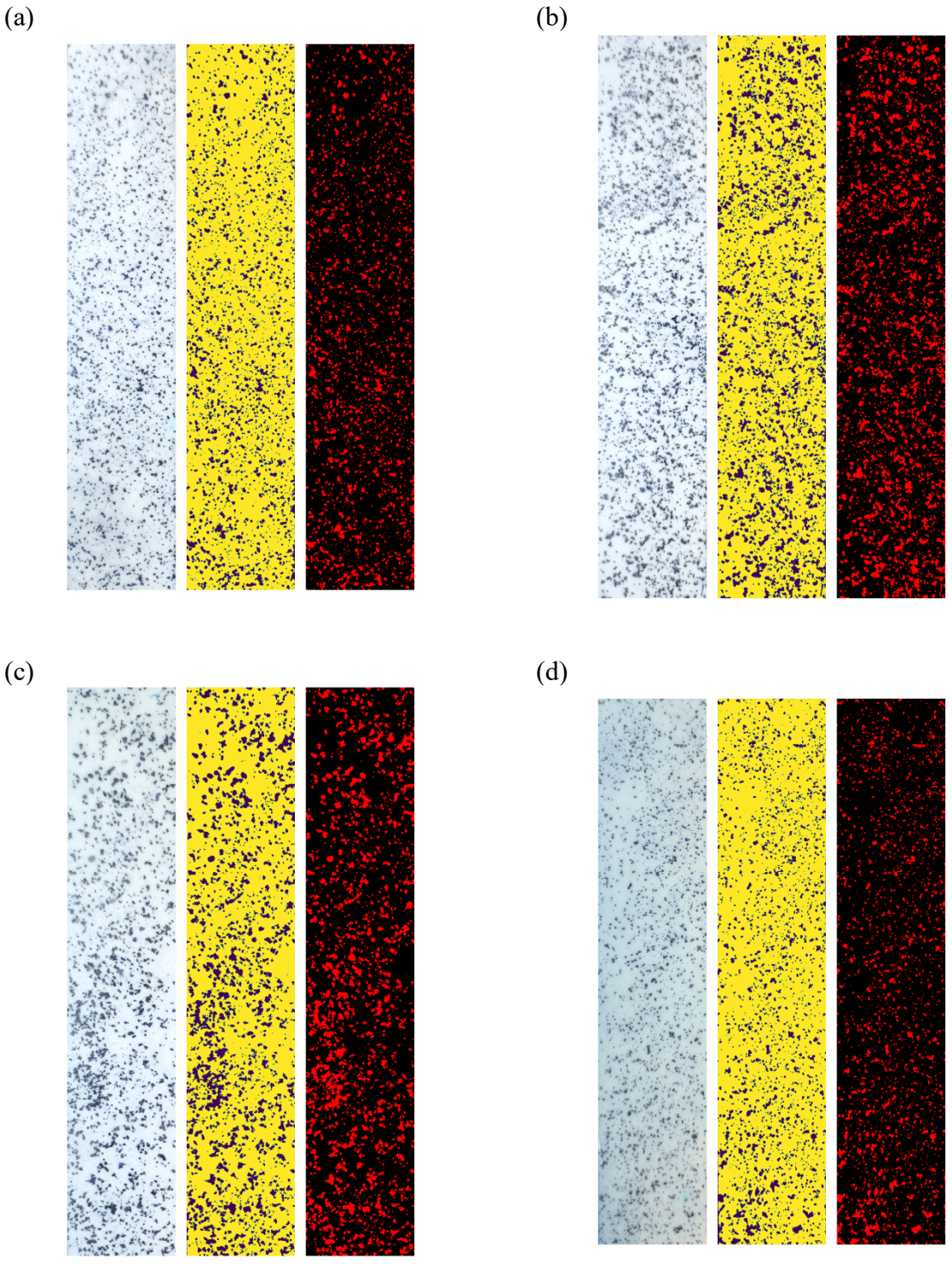


Figure A.834. Particle Size Analysis Results at A1G3F2 (a) Top Flange Bottom, (b) Web, (c) Bottom Flange Bottom (d) Stiffener.

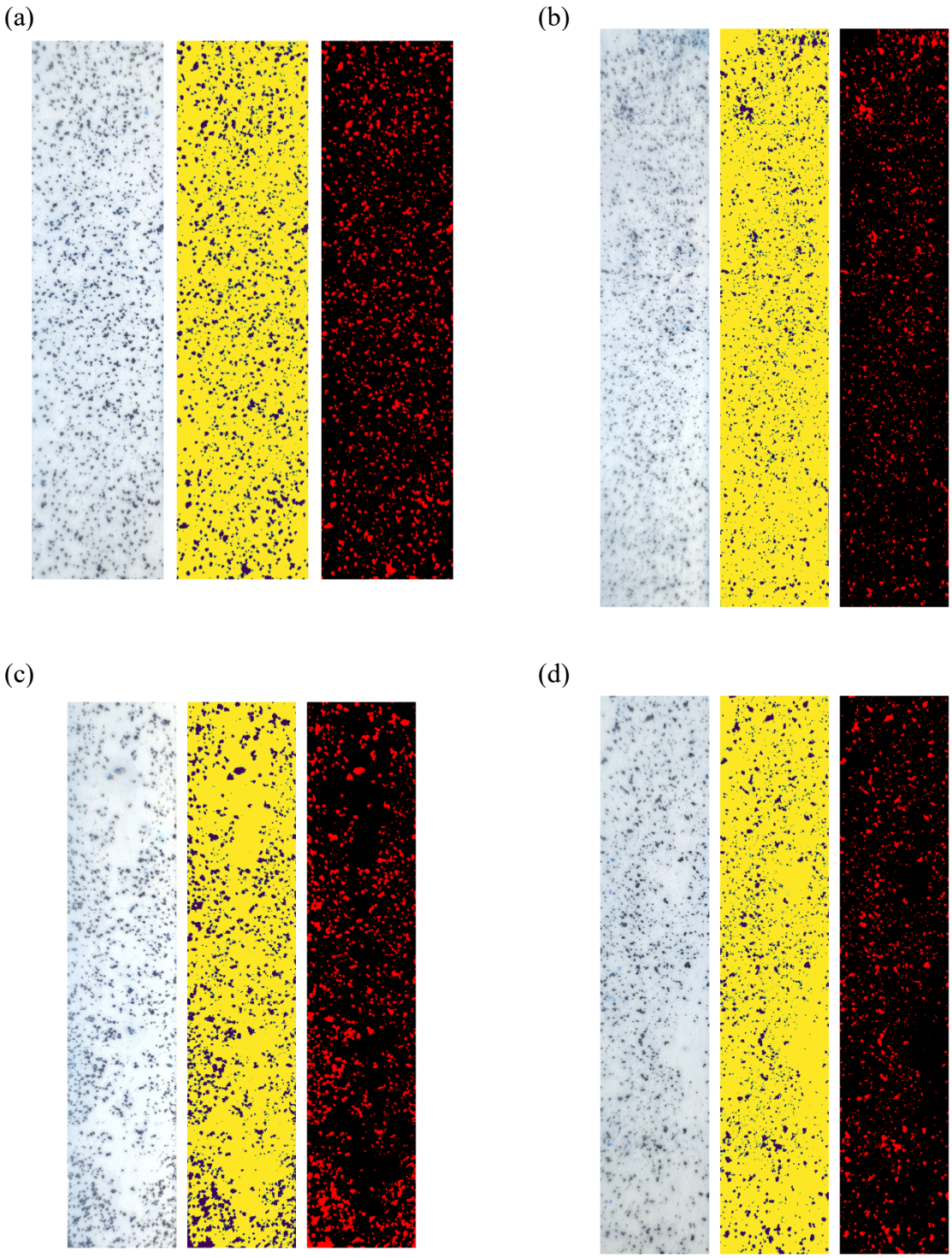


Figure A.835. Particle Size Analysis Results at A1G4F2 (a) Top Flange Bottom, (b) Web, (c) Bottom Flange Bottom (d) Stiffener.

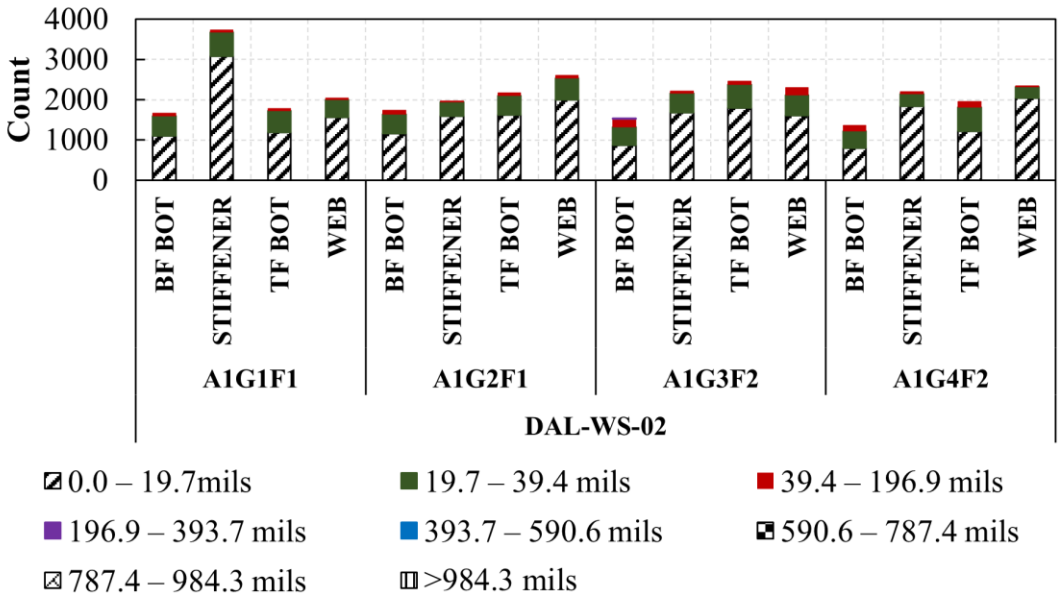


Figure A.836. Particle Size Analysis Showing Different Locations Examined.

A.46. DAL-WS-03

- CON IH10 EB-BW8 SB over IH10 EBFR/BW8 SBFR/UP RR
- Bridge ID 180570000911373, Dallas County, Dallas
- Continuous weathering steel I beam
- Built 1960
- Girder inspection carried on girder 1, 2, 3 and 4, and measurements are taken on girder within four feet from the abutment or bent.
- Location for Testing: A6G1F1, A6G3F1, A6G5F2, A6G8F2



Figure A.837. Typical Picture of DAL-WS-03.

A.46.1. Observed Condition

Overall bridge is in good condition with development of uniform patina throughout the girder with a patina rating between 6 and 8.

A.46.2.Field Inspection Results

Table A-202. Field Inspection Results for DAL-WS-03.

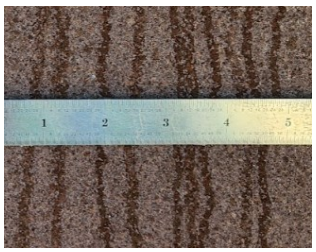
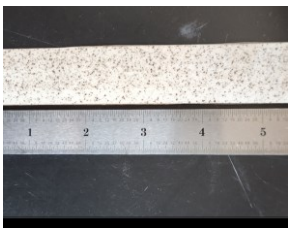
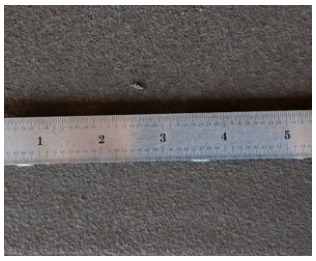
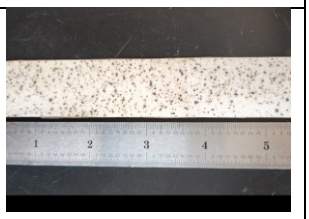
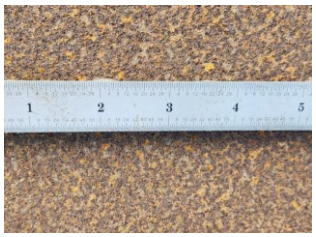
Location	Patina Rating	Thickness (inch)	Cl^- Conc. (ppm)	Field Condition	Tape Test
A6-G1F1 TF Bot. Ext.	8	Measured R1 .0.749 R2 0.748 R3 0.746 R_Avg Design			
A6-G1F1 Web Ext.	8	Measured R1 0.572 R2 0.573 R3 0.574 R_Avg Design			
A6-G1F1 BF Top Ext.	8	Measured R1 R2 R3 R_Avg Design			
A6-G1F1 BF Bot. Ext.	7	Measured R1 0.805 R2 0.806 R3 0.807 R_Avg Design			
A6-G3F1 TF Bot. Int.	7	Measured R1 .0.791 R2 0.790 R3 0.792 R_Avg Design			

Table A-203. Field Inspection Results for DAL-WS-03.

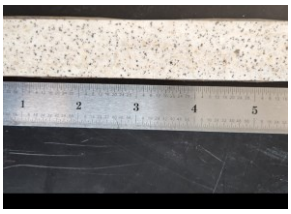
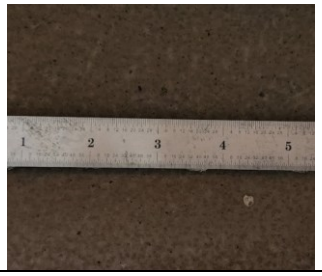
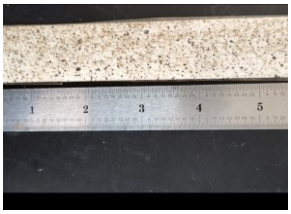
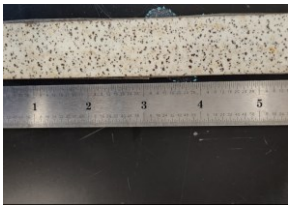
Location	Patina Rating	Thickness (inch)	Cl^- Conc. (ppm)	Field Condition	Tape Test
A6-G3F1 Web Int.	8	Measured R1 0.575 R2 0.575 R3 0.575 R_Avg Design			
A6-G3F1 BF Top Int.	8	Measured R1 R2 R3 R_Avg Design			
A6-G3F1 BF Bot. Int.	7	Measured R1 0.806 R2 0.803 R3 0.805 R_Avg Design			
A6-G5F2 TF Bot. Int.	6	Measured R1 0.750 R2 0.749 R3 0.750 R_Avg Design			
A6-G5F2 Web Int.	7	Measured R1 0.569 R2 0.570 R3 0.571 R_Avg Design			

Table A-204. Field Inspection Results for DAL-WS-03.

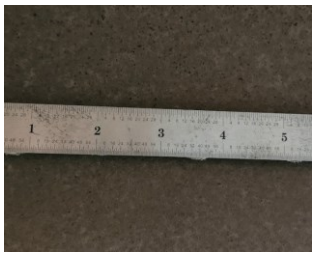
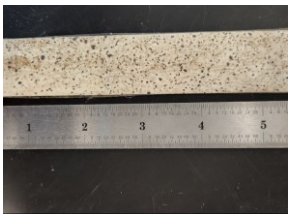
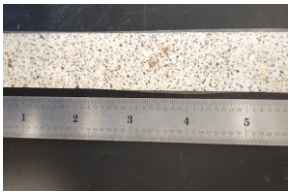
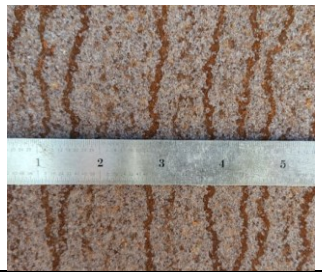
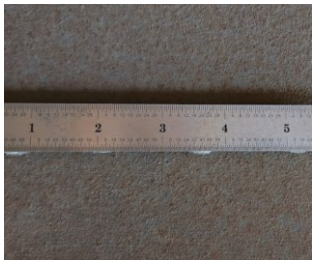
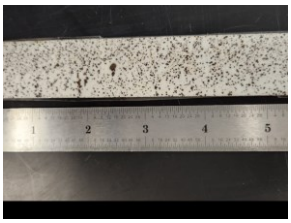
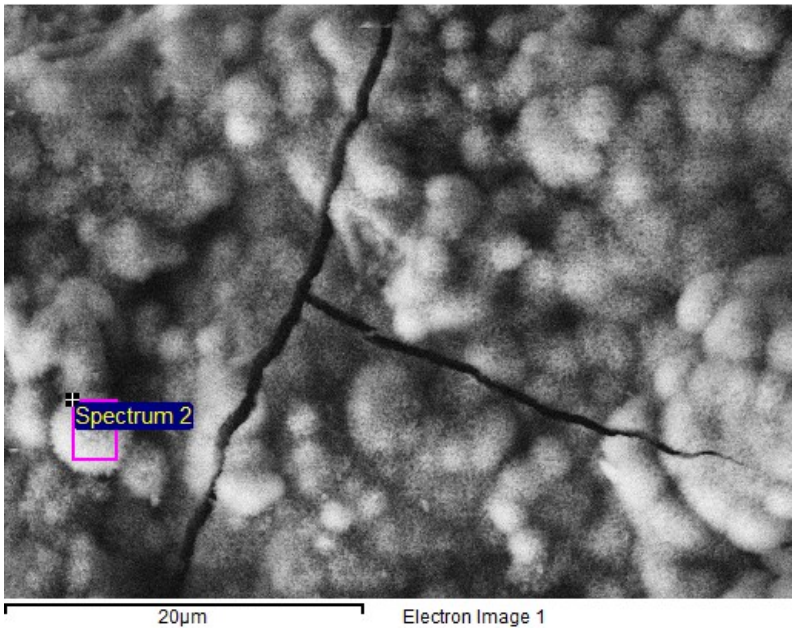
Location	Patina Rating	Thickness (inch)	Cl^- Conc. (ppm)	Field Condition	Tape Test
A6-G5F2 BF Top Int.	7	Measured R1 R2 R3 R_Avg Design			
A6-G5F2 BF Bot. Int.	7	Measured R1 0.791 R2 0.791 R3 0.791 R_Avg Design			
A6-G8F2 TF Bot Ext.	7	Measured R1 0.780 R2 0.781 R3 0.781 R_Avg Design			
A6-G8F2 Web Ext.	7	Measured R1 0.580 R2 0.577 R3 0.581 R_Avg Design			
A6-G8F2 BF Top Ext.	7	Measured R1 R2 R3 R_Avg Design			

Table A-205. Field Inspection Results for DAL-WS-03.

Location	Patina Rating	Thickness (inch)	Cl^- Conc. (ppm)	Field Condition	Tape Test
A6-G8F2 BF Bot. Ext.	6	Measured R1 0.784 R2 0.783 R3 0.786 R_Avg Design			

A.46.3.SEM/EDS Results: Exterior Web Girder

Element	Weight %	Atomic %
O K	66.59	85.52
Al K	2.06	1.57
Si K	1.35	0.99
S K	0.41	0.26
K K	0.11	0.06
Ti K	12.56	5.39
Mn K	0.25	0.09
Fe K	16.58	6.10
Cu K	0.09	0.03
Totals	100.00	



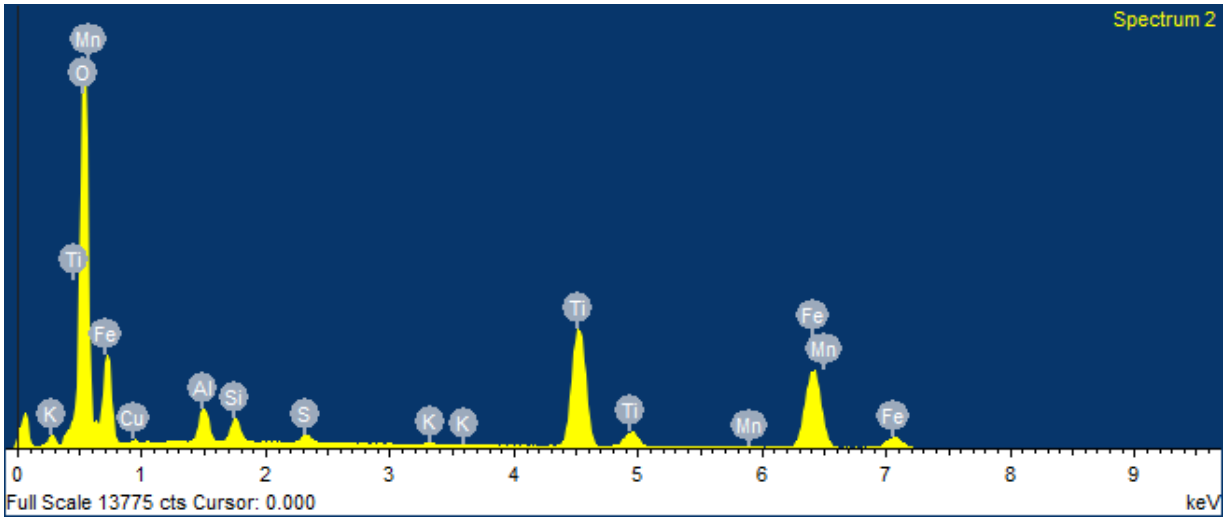
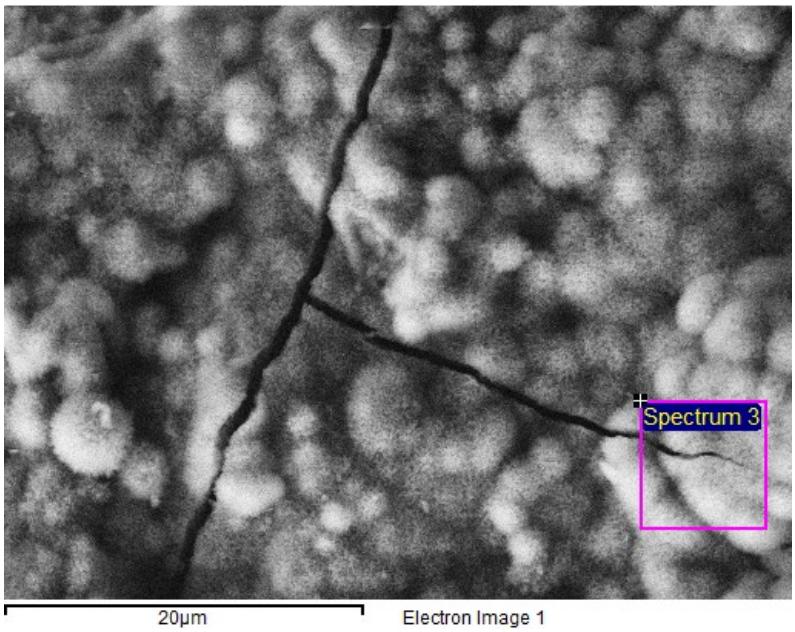


Figure A.838. SEM Image and EDS Spectrum of the Rust Collected from Exterior Web of the Girder.

Element	Weight %	Atomic %
O K	55.33	80.25
Al K	1.61	1.38
Si K	0.16	0.13
S K	1.11	0.81
Cl K	0.25	0.16
Mn K	1.43	0.61
Fe K	40.09	16.66
Cu K	0.00	0.00
Totals	100.00	



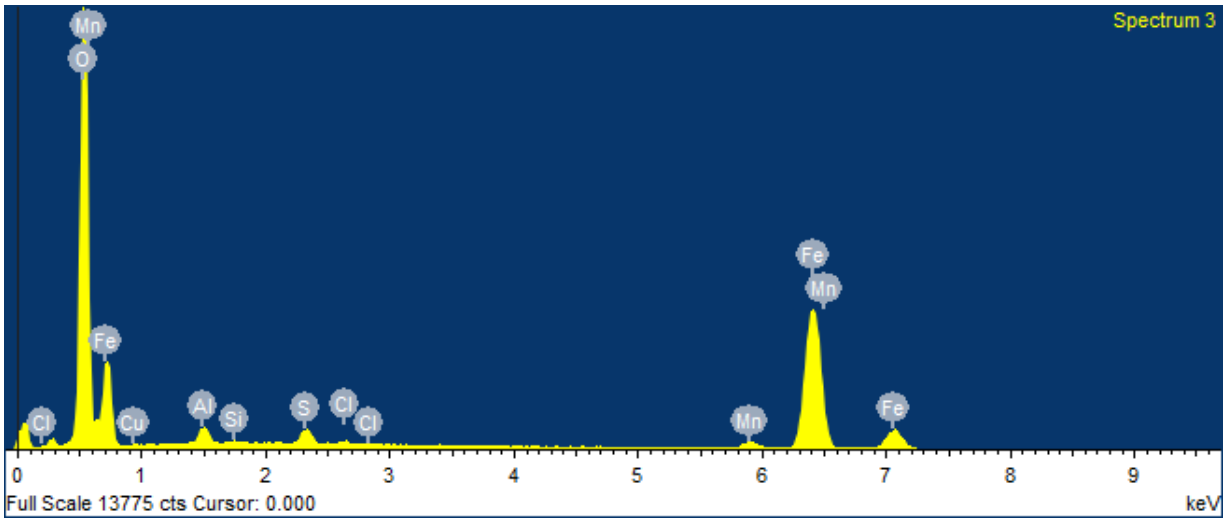
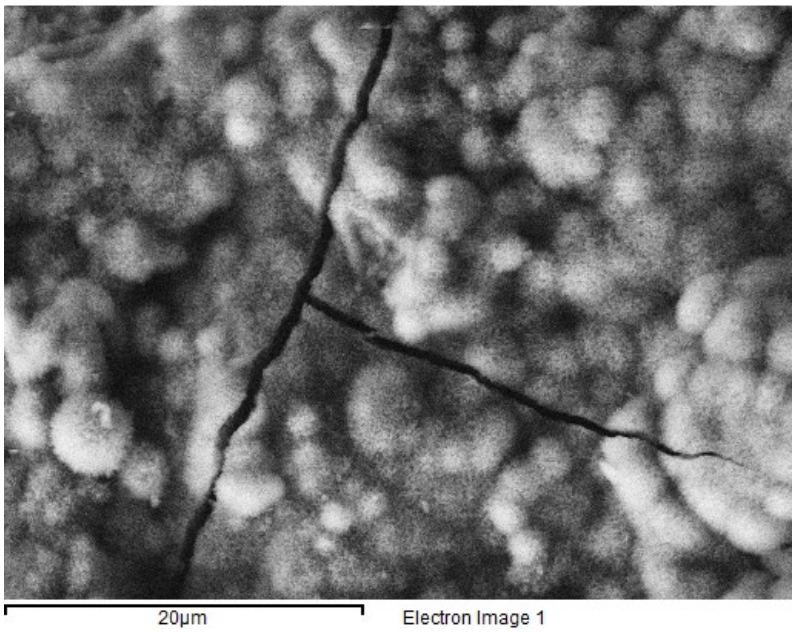


Figure A.839. SEM Image and EDS Spectrum of the Rust Collected from Exterior Web of the Girder.

Element	Weight %	Atomic %
O K	52.68	78.45
Al K	1.77	1.56
Si K	0.30	0.25
S K	1.12	0.83
Cl K	0.26	0.17
Ti K	0.14	0.07
Mn K	1.07	0.47
Fe K	42.47	18.12
Cu K	0.19	0.07
Totals	100.00	



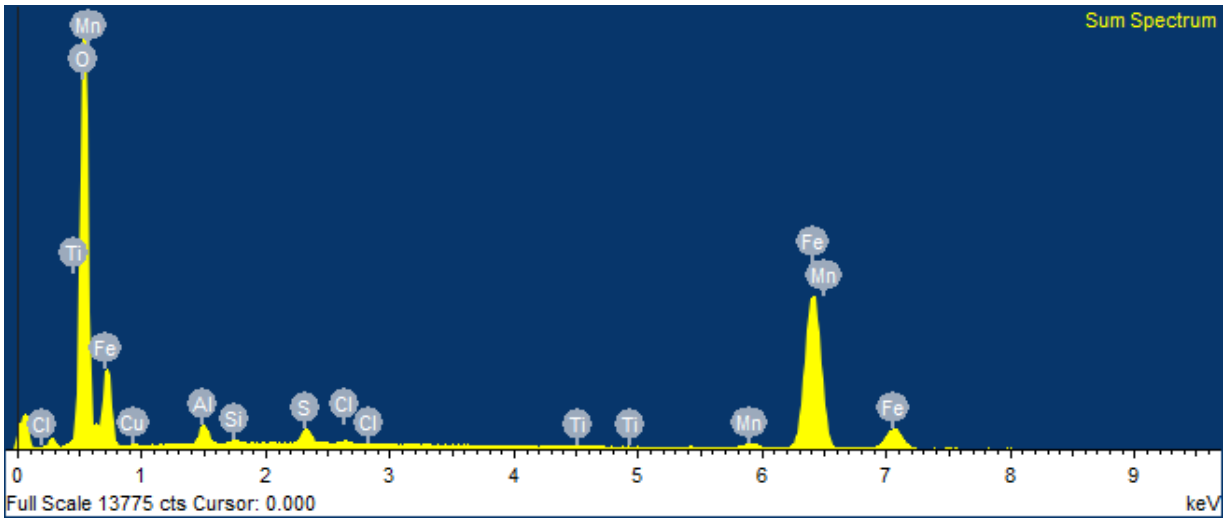


Figure A.840. SEM Image and EDS Spectrum of the Rust Collected from Exterior Web of the Girder.

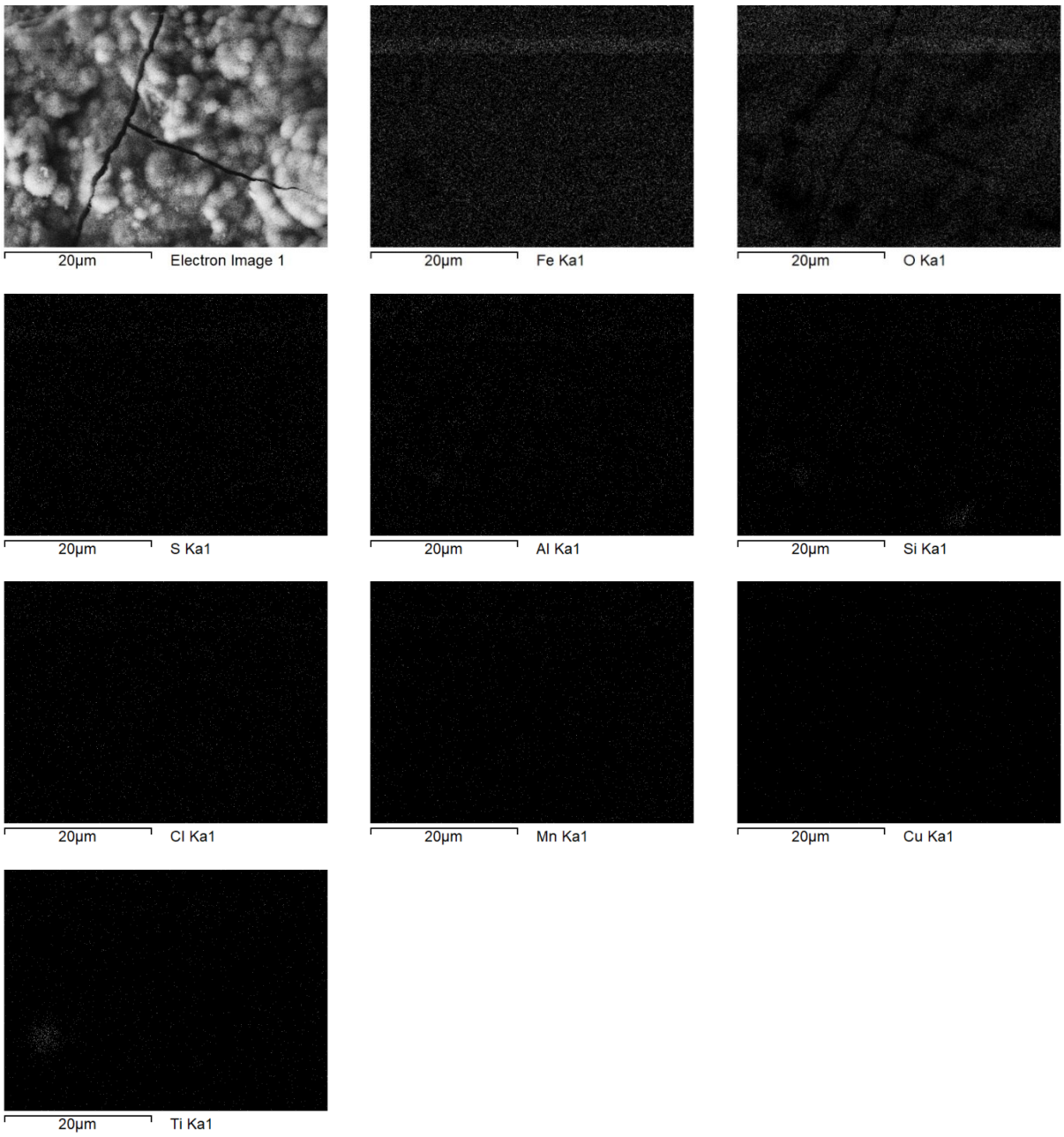
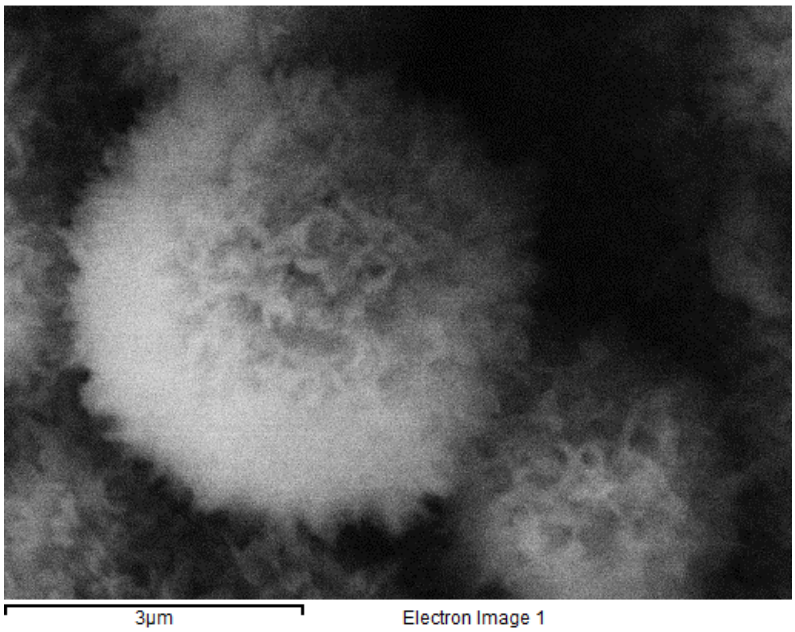


Figure A.841. EDS Elemental Mapping of Rust Collected from Exterior Web.

Element	Weight %	Atomic %
O K	55.06	79.04
Al K	2.62	2.23
Si K	1.57	1.28
S K	0.77	0.55
Cl K	0.14	0.09
K K	0.12	0.07
Ca K	0.09	0.05
Ti K	5.70	2.73
Mn K	0.53	0.22
Fe K	33.28	13.69
Cu K	0.10	0.03
Totals	100.00	



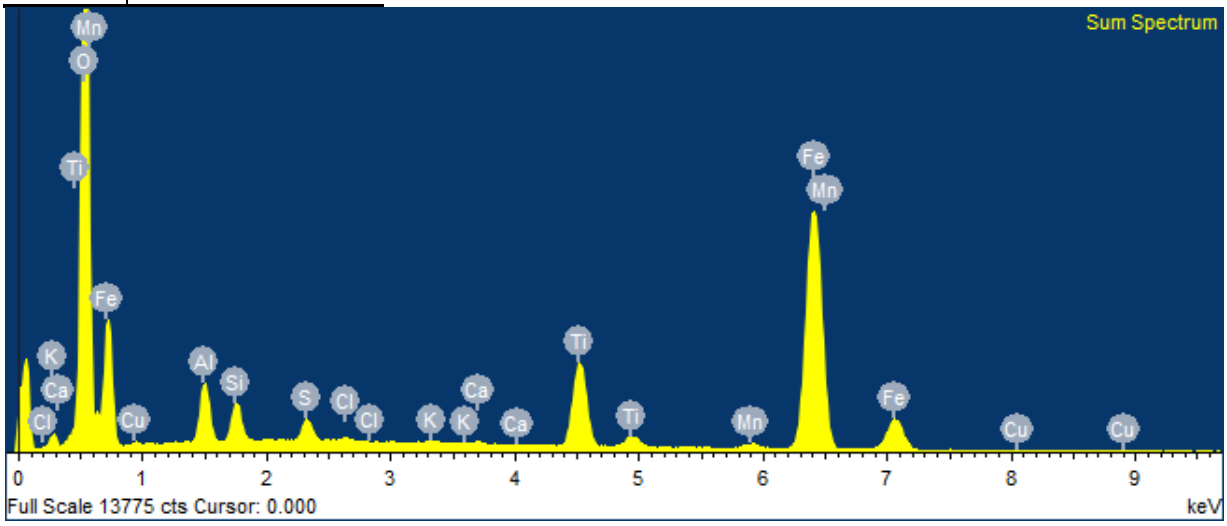


Figure A.842. SEM Image and EDS Spectrum of the Rust Collected from Exterior Web of the Girder.

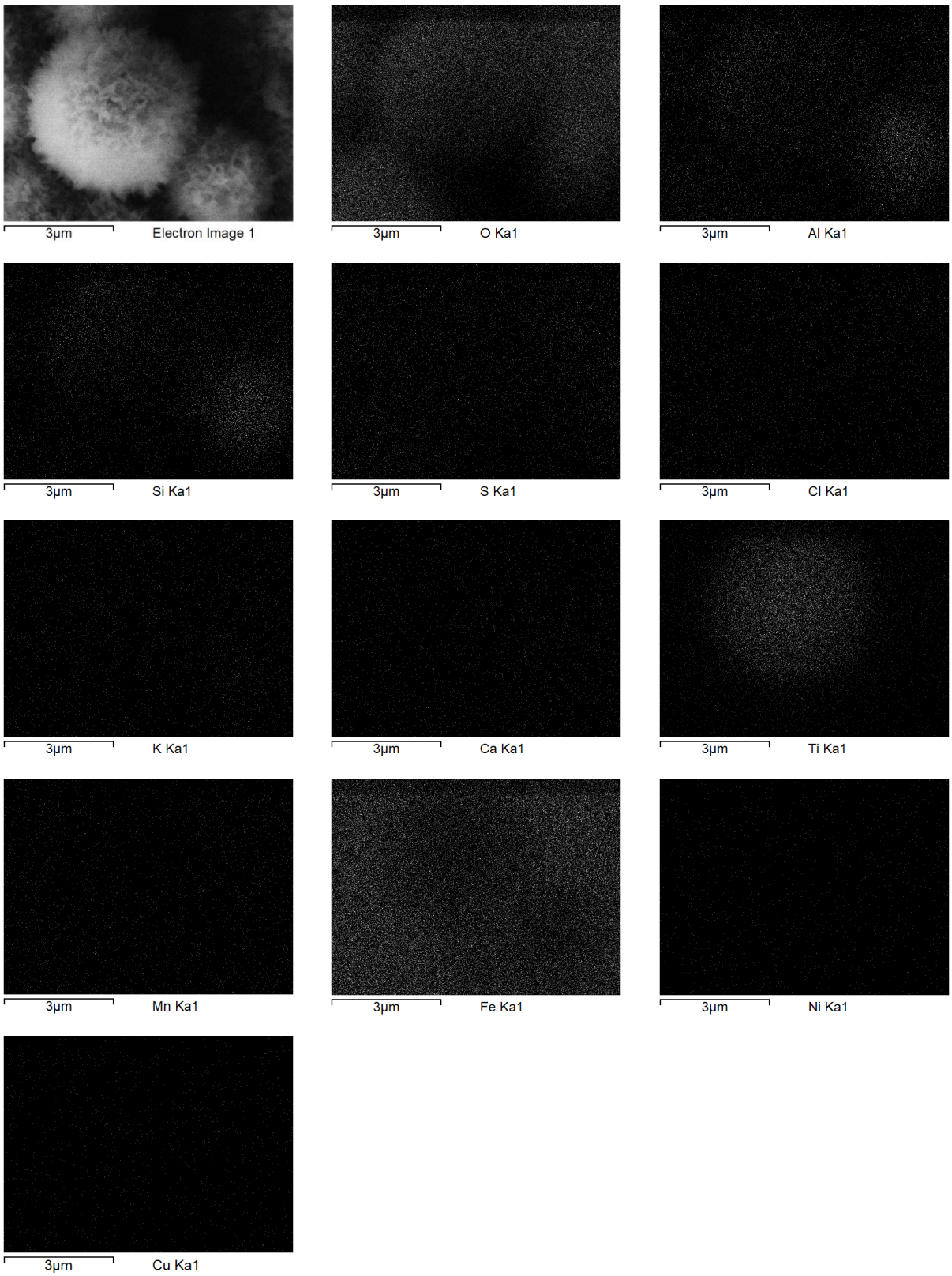
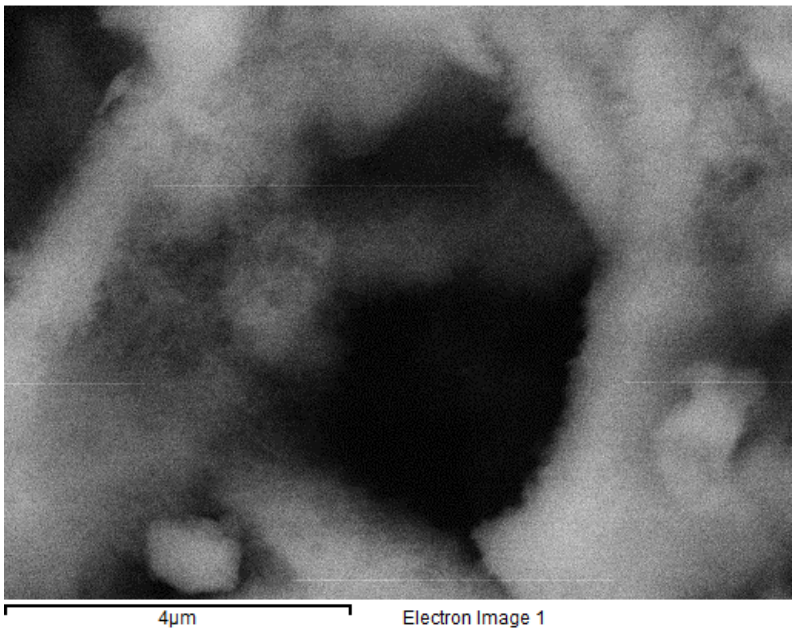


Figure A.843. EDS Elemental Mapping of Rust Collected from Exterior Web.

Element	Weight %	Atomic %
O K	39.57	68.16
Al K	2.13	2.18
Si K	1.49	1.46
S K	0.40	0.35
Mn K	0.79	0.40
Fe K	55.61	27.45
Totals	100.00	



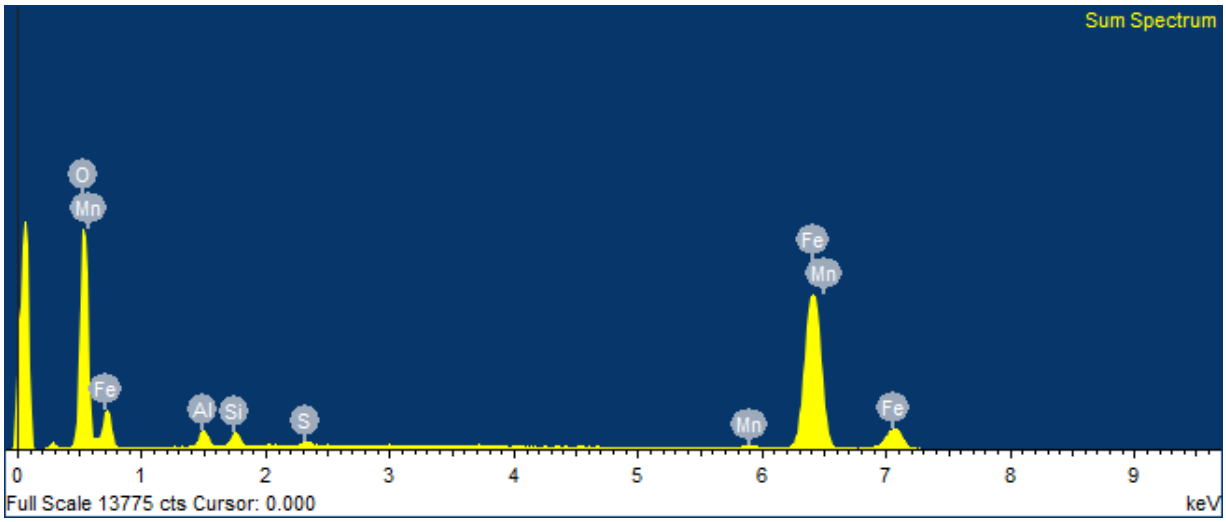


Figure A.844. SEM Image and EDS Spectrum of the Rust Collected from Exterior Web of the Girder.

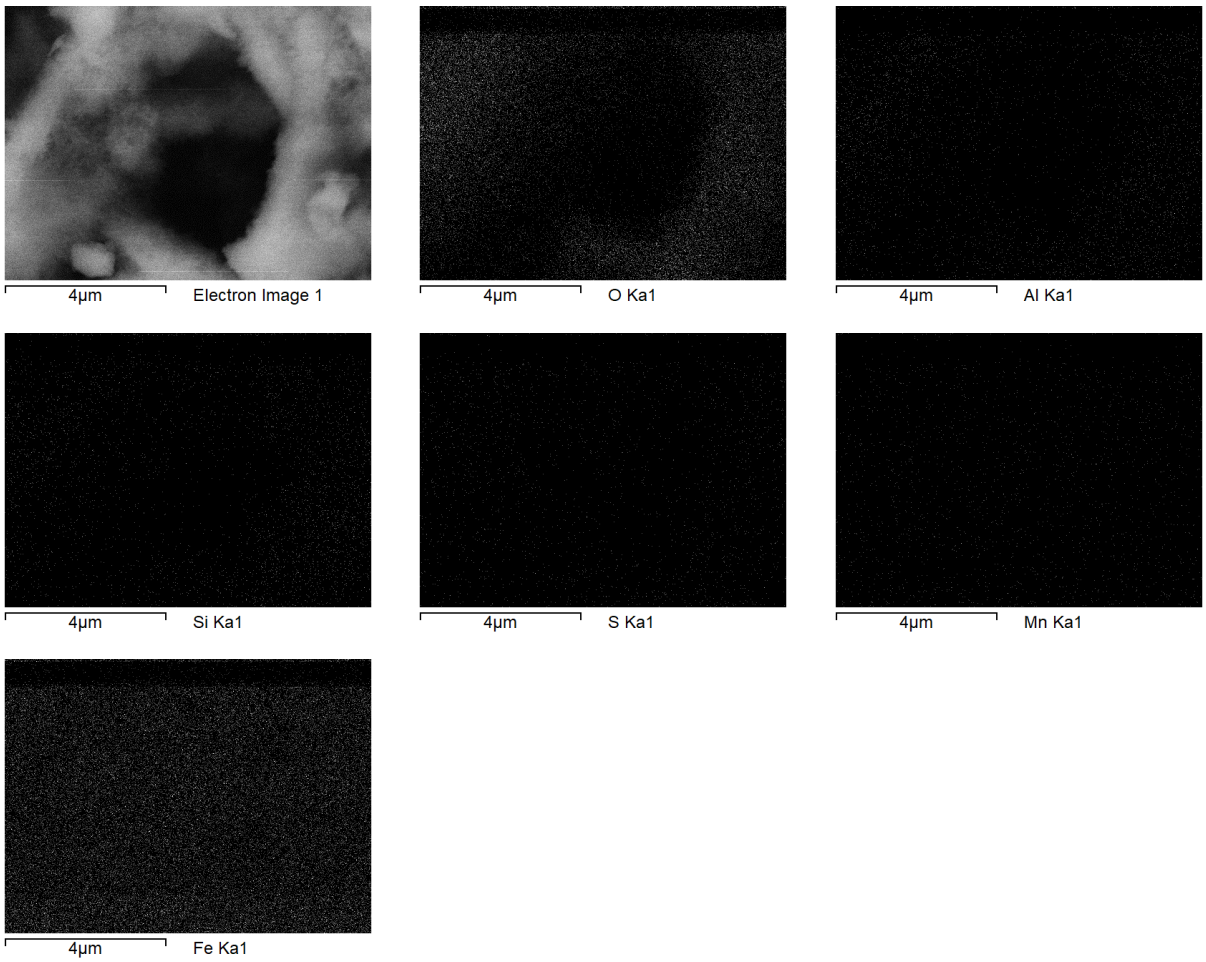
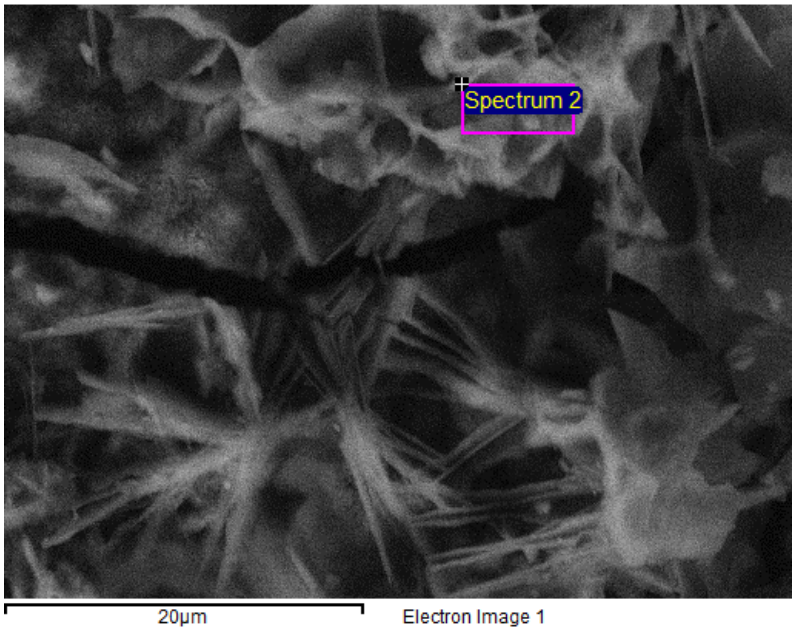


Figure A.845. EDS Elemental Mapping of Rust Collected from Exterior Web.

A.46.4.SEM/EDS Results: Interior Web Girder

Element	Weight %	Atomic %
O K	33.33	62.54
Al K	2.23	2.48
S K	0.95	0.89
Mn K	0.98	0.54
Fe K	61.62	33.13
Ni K	0.27	0.14
Cu K	0.62	0.29
Totals	100.00	



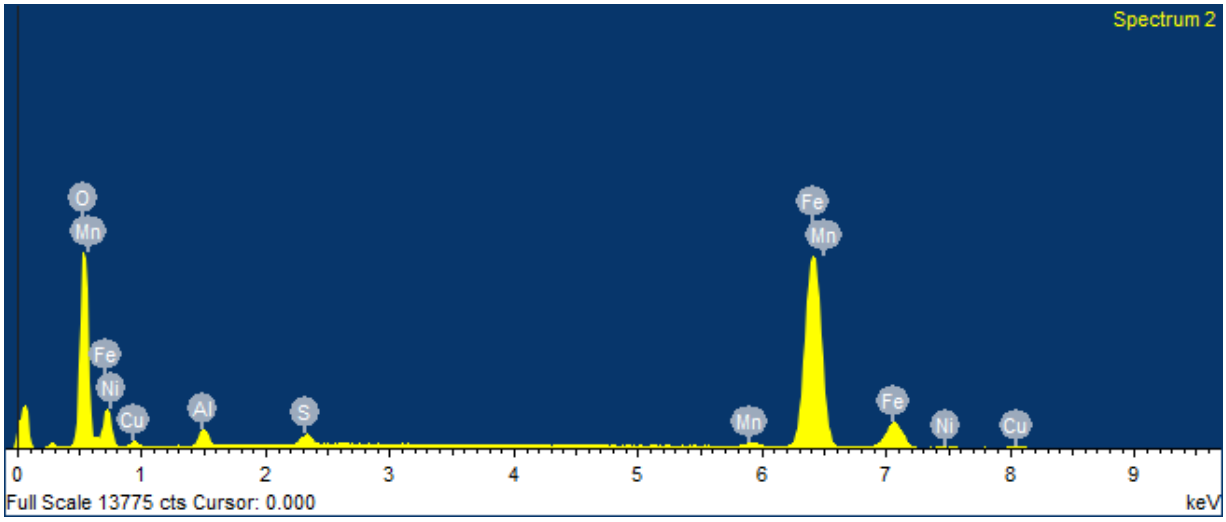
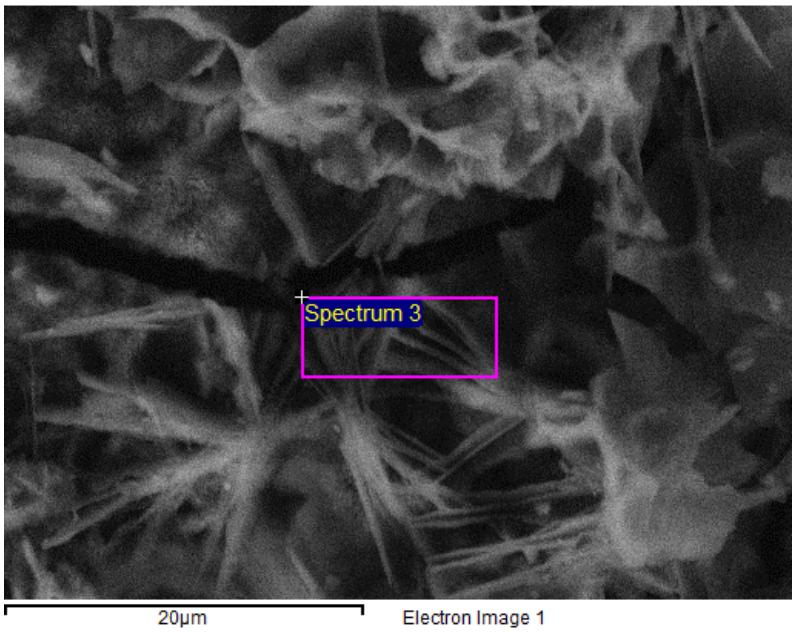


Figure A.846. SEM Image and EDS Spectrum of the Rust Collected from Interior Web of the Girder.

Element	Weight %	Atomic %
O K	44.16	72.78
Al K	1.12	1.10
S K	0.87	0.72
Mn K	0.59	0.29
Fe K	52.95	25.00
Cu K	0.30	0.12
Totals	100.00	



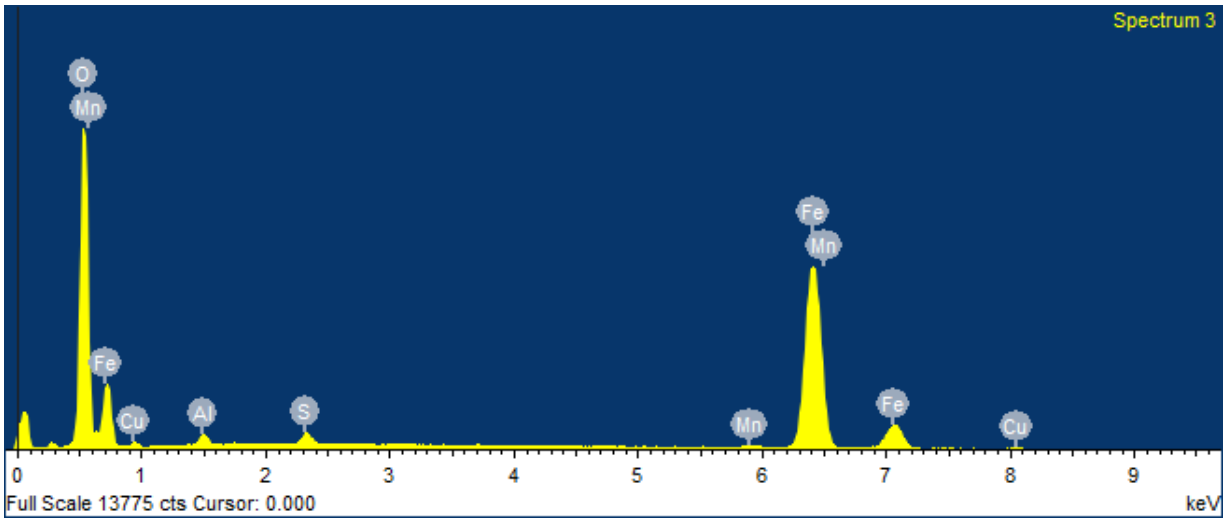
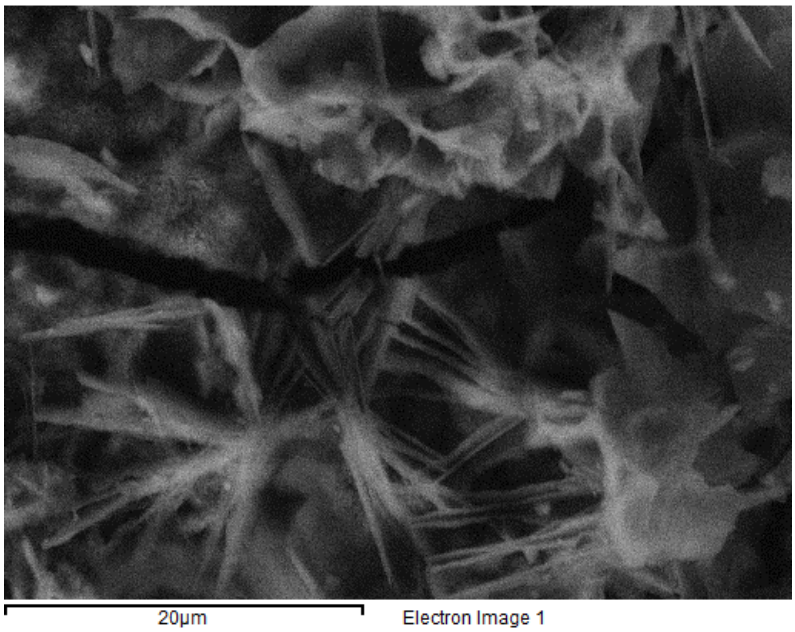


Figure A.847. SEM Image and EDS Spectrum of the Rust Collected from Interior Web of the Girder.

Element	Weight %	Atomic %
O K	36.72	66.16
Al K	1.34	1.43
Si K	0.19	0.20
S K	0.92	0.82
Mn K	0.82	0.43
Fe K	59.68	30.81
Cu K	0.33	0.15
Totals	100.00	



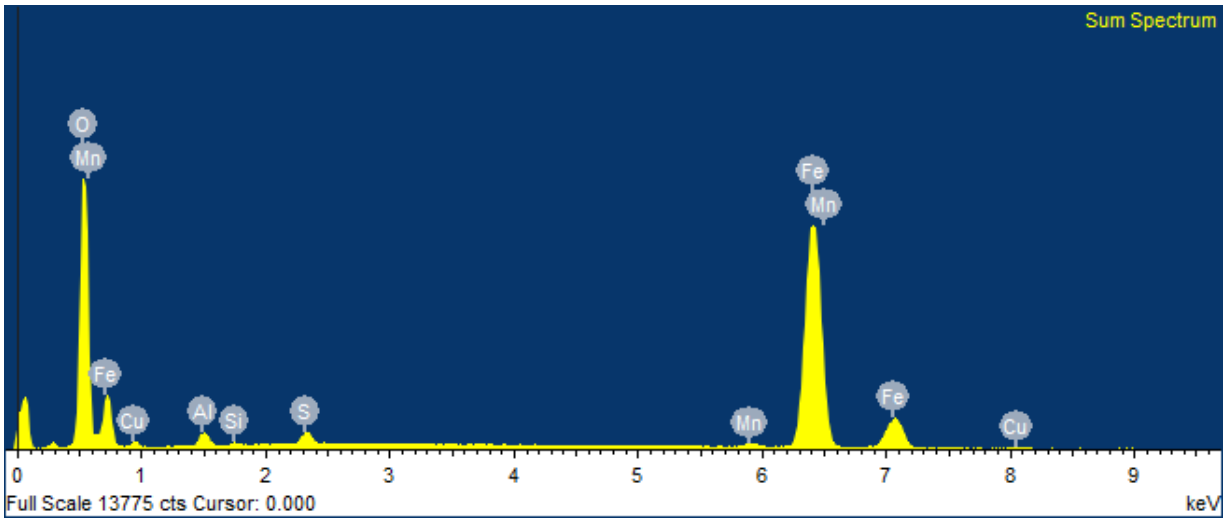


Figure A.848. SEM Image and EDS Spectrum of the Rust Collected from Interior Web of the Girder.

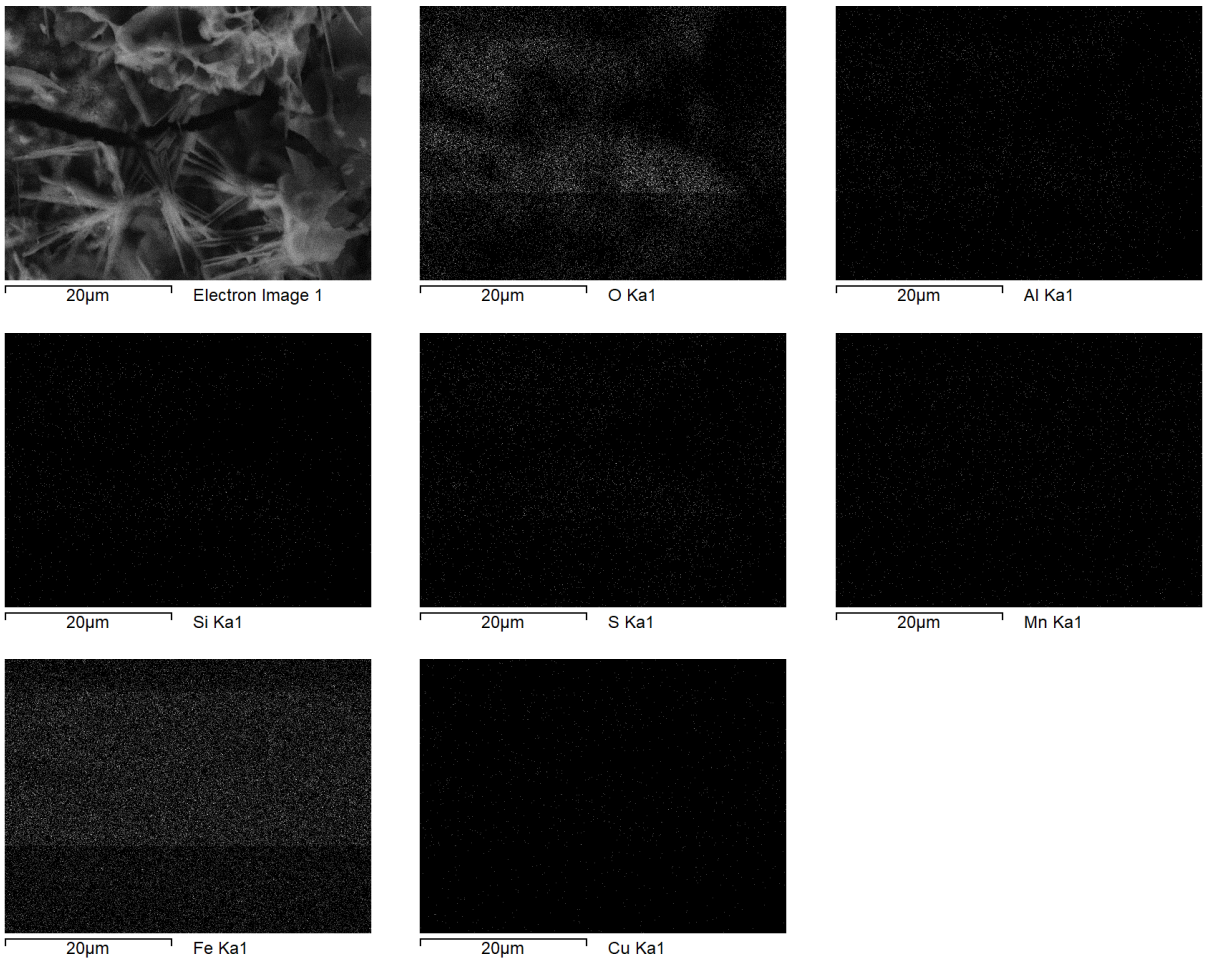
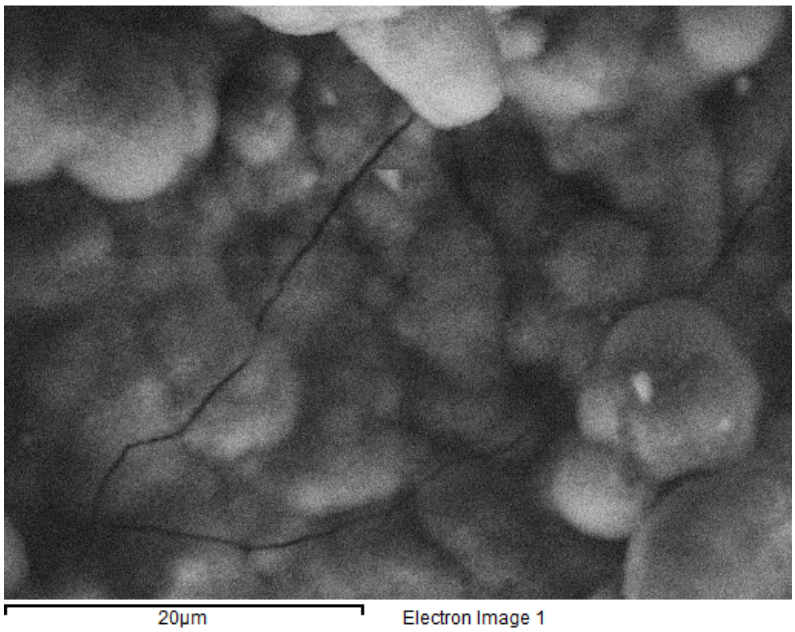


Figure A.849. EDS Elemental Mapping of Rust Collected from Interior Web.

Element	Weight %	Atomic %
O K	19.92	45.66
Al K	1.96	2.66
Si K	0.28	0.36
S K	0.46	0.52
Mn K	0.74	0.50
Fe K	75.95	49.88
Ni K	0.38	0.24
Cu K	0.31	0.18
Totals	100.00	



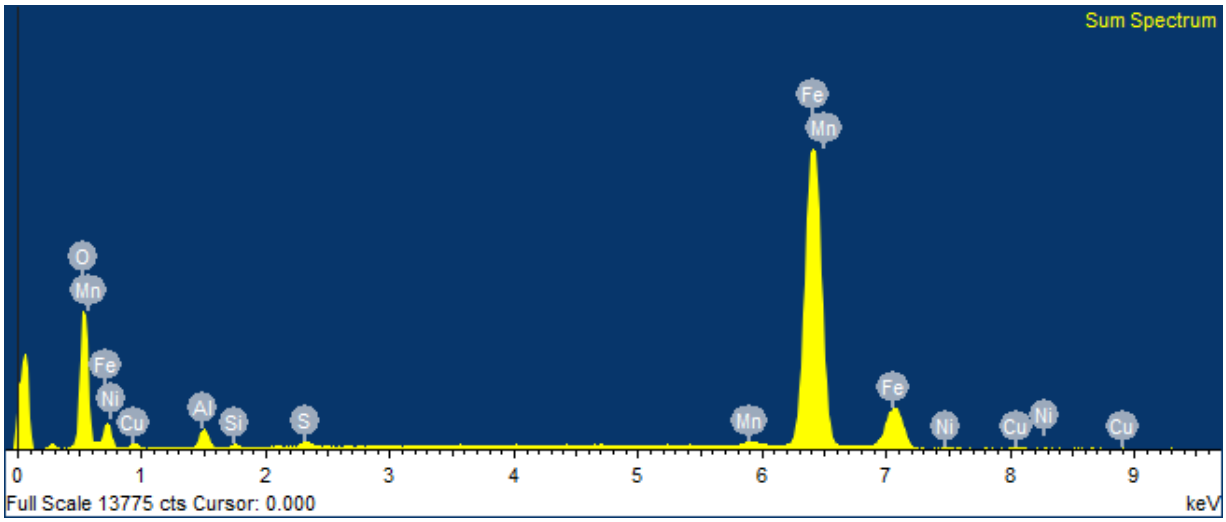


Figure A.850. SEM Image and EDS Spectrum of the Rust Collected from Interior Web of the Girder.

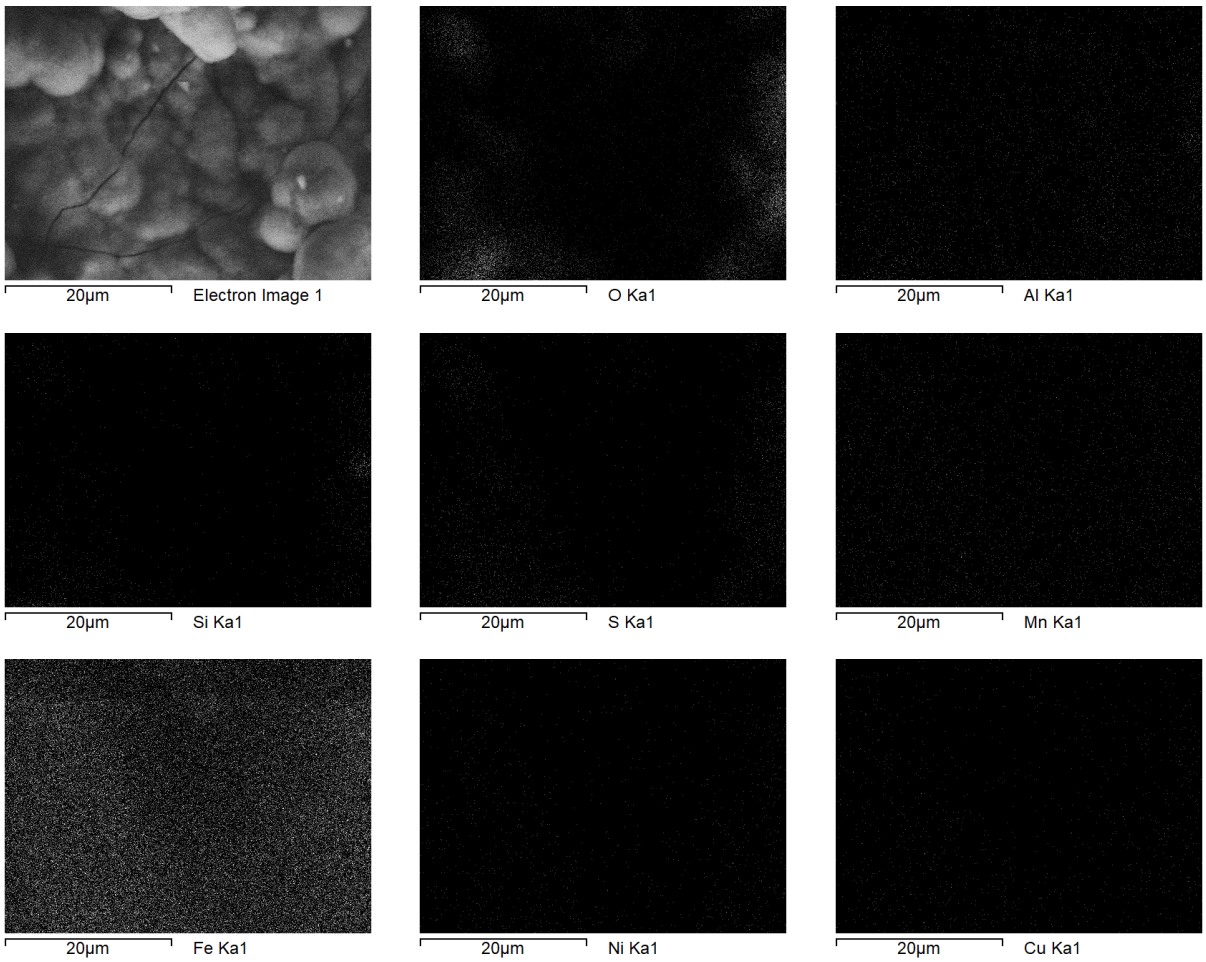
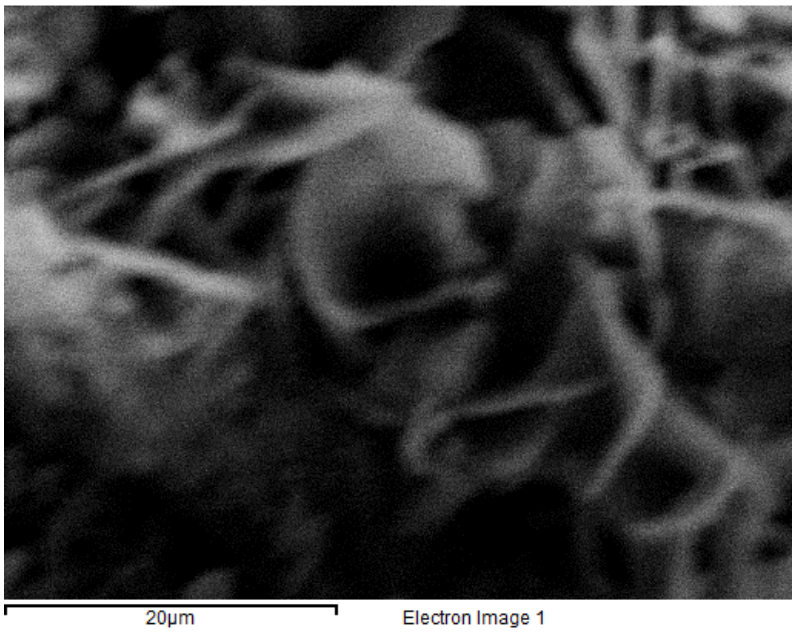


Figure A.851. EDS Elemental Mapping of Rust Collected from Interior Web.

Element	Weight %	Atomic %
O K	23.66	51.22
Al K	1.43	1.84
Si K	0.43	0.53
S K	0.44	0.47
Ca K	0.12	0.10
Mn K	1.13	0.71
Fe K	72.25	44.81
Ni K	0.54	0.32
Totals	100.00	



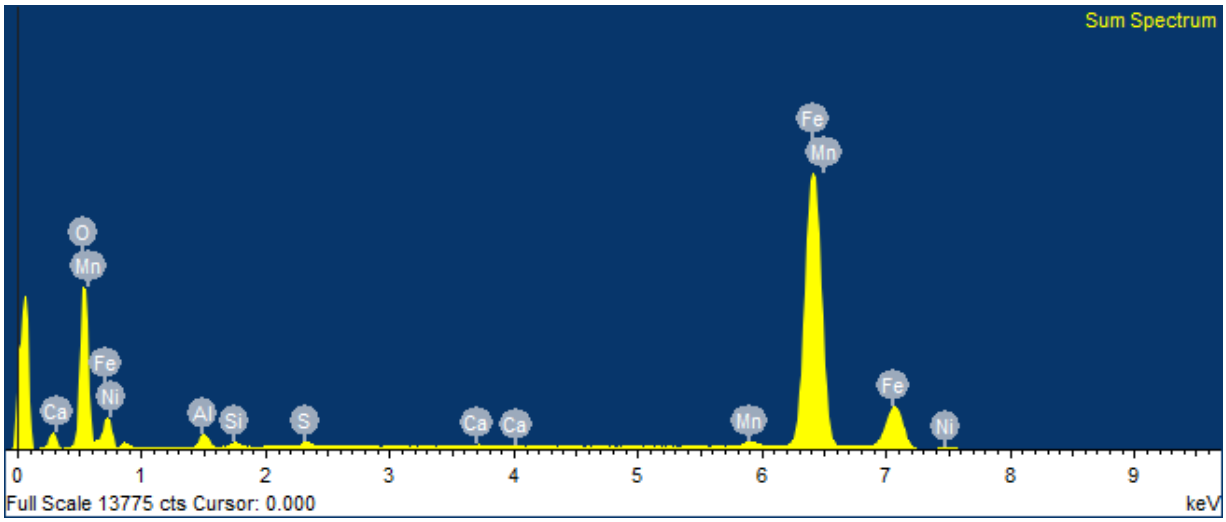


Figure A.852. SEM Image and EDS Spectrum of the Rust Collected from Interior Web of the Girder.

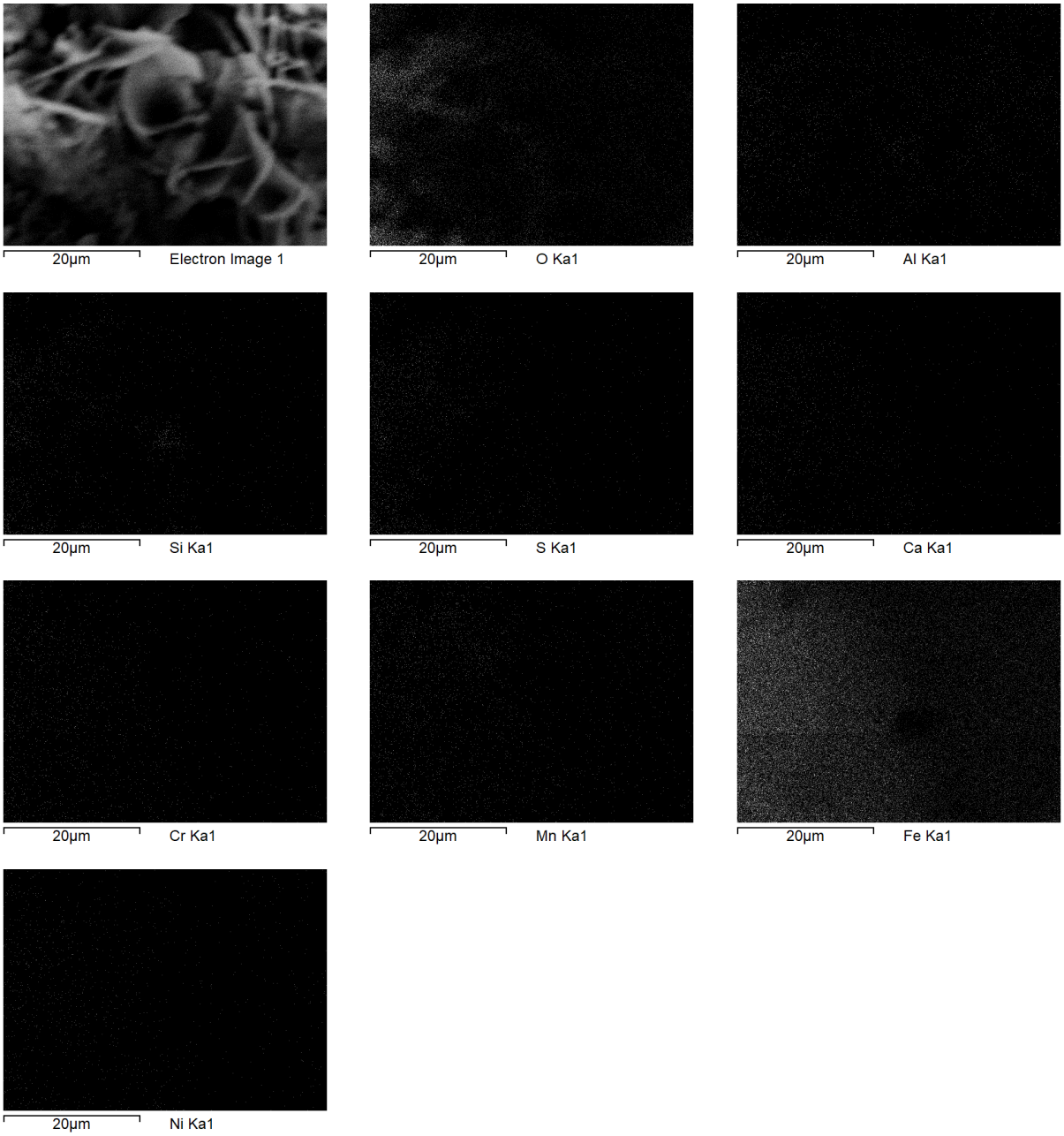


Figure A.853. EDS Elemental Mapping of Rust Collected from Interior Web.

A.46.5.XPS Result: Exterior Girder

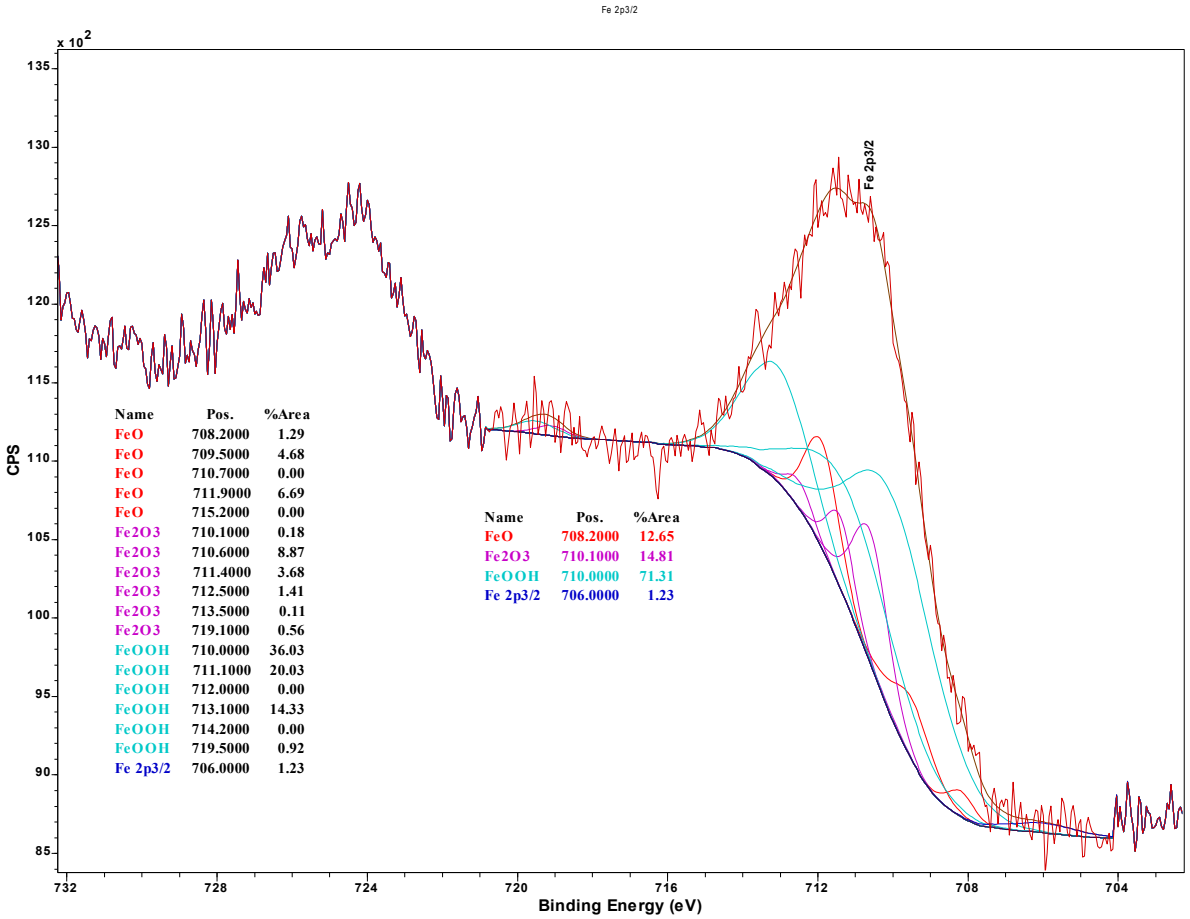


Figure A.854. XPS Spectrum of the Rust Collected from Exterior Web of the Girder.

A.46.6.XPS Result: Interior Girder

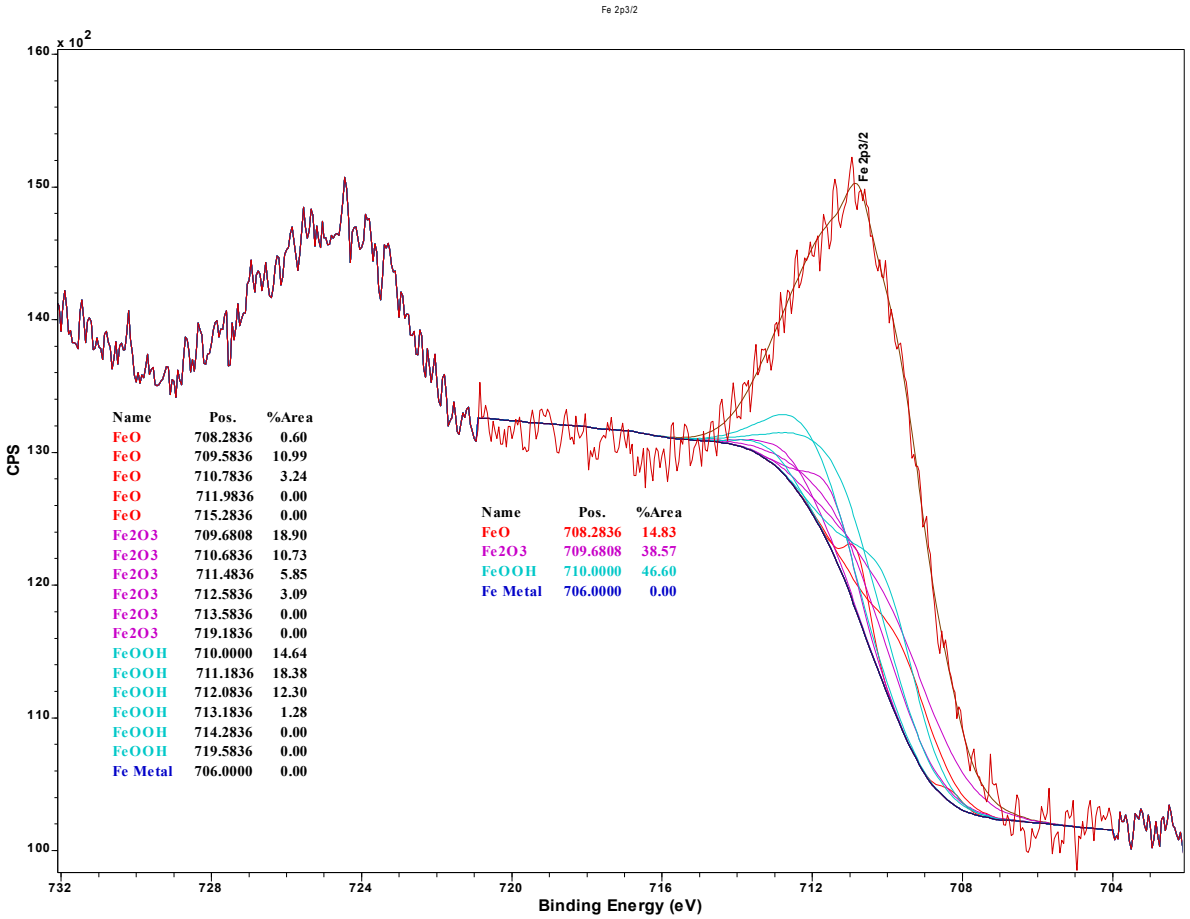


Figure A.855. XPS Spectrum of the Rust Collected from Interior Web of the Girder.

A.46.7.XRD Result: Exterior and Interior Girder

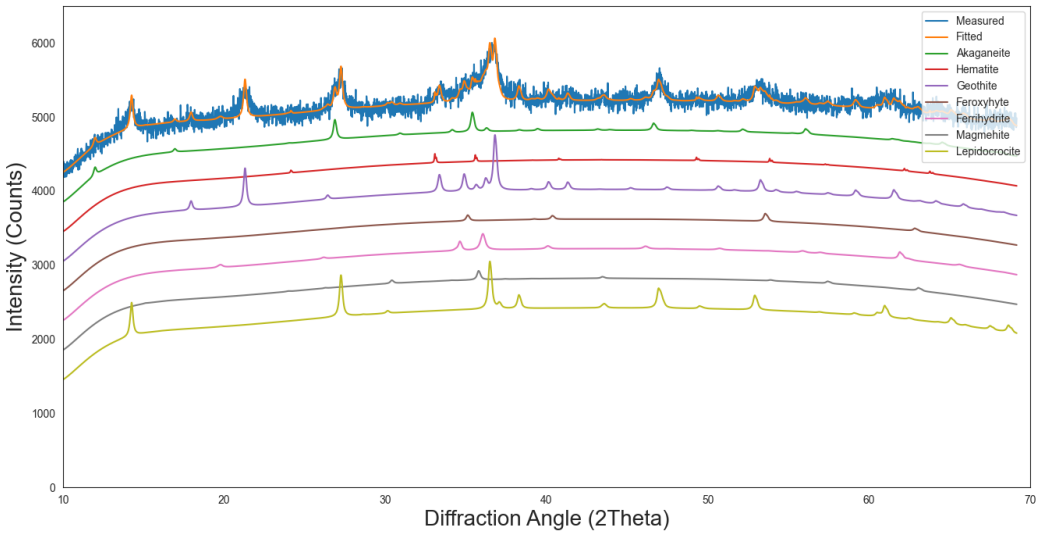


Figure A.856. XRD Pattern of Powdered Rust Collected from Exterior Web of the Girder.

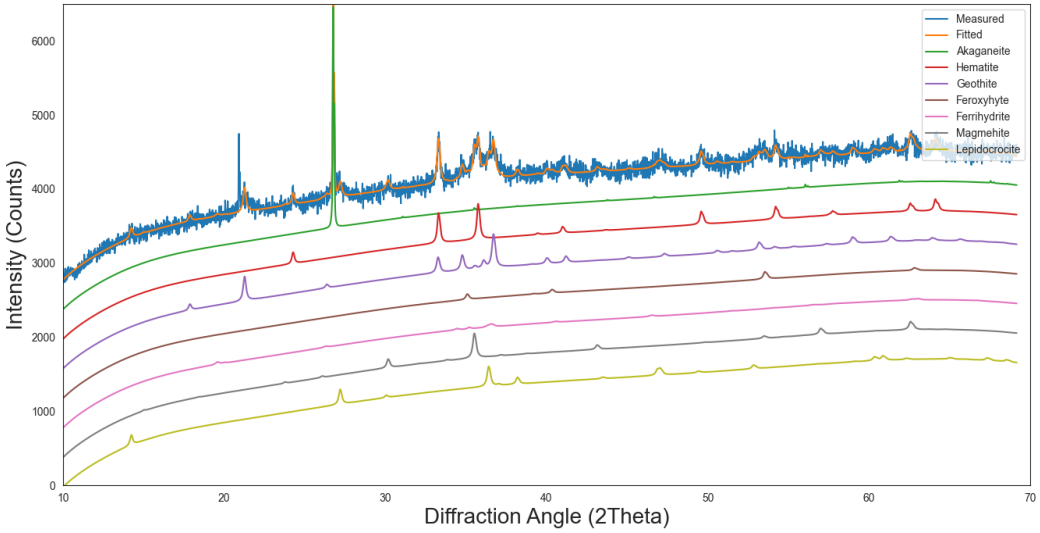


Figure A.857. XRD Pattern of Powdered Rust Collected from Interior Web of the Girder.

A.46.8.Particle Size Analysis: Tape Adhesion Results

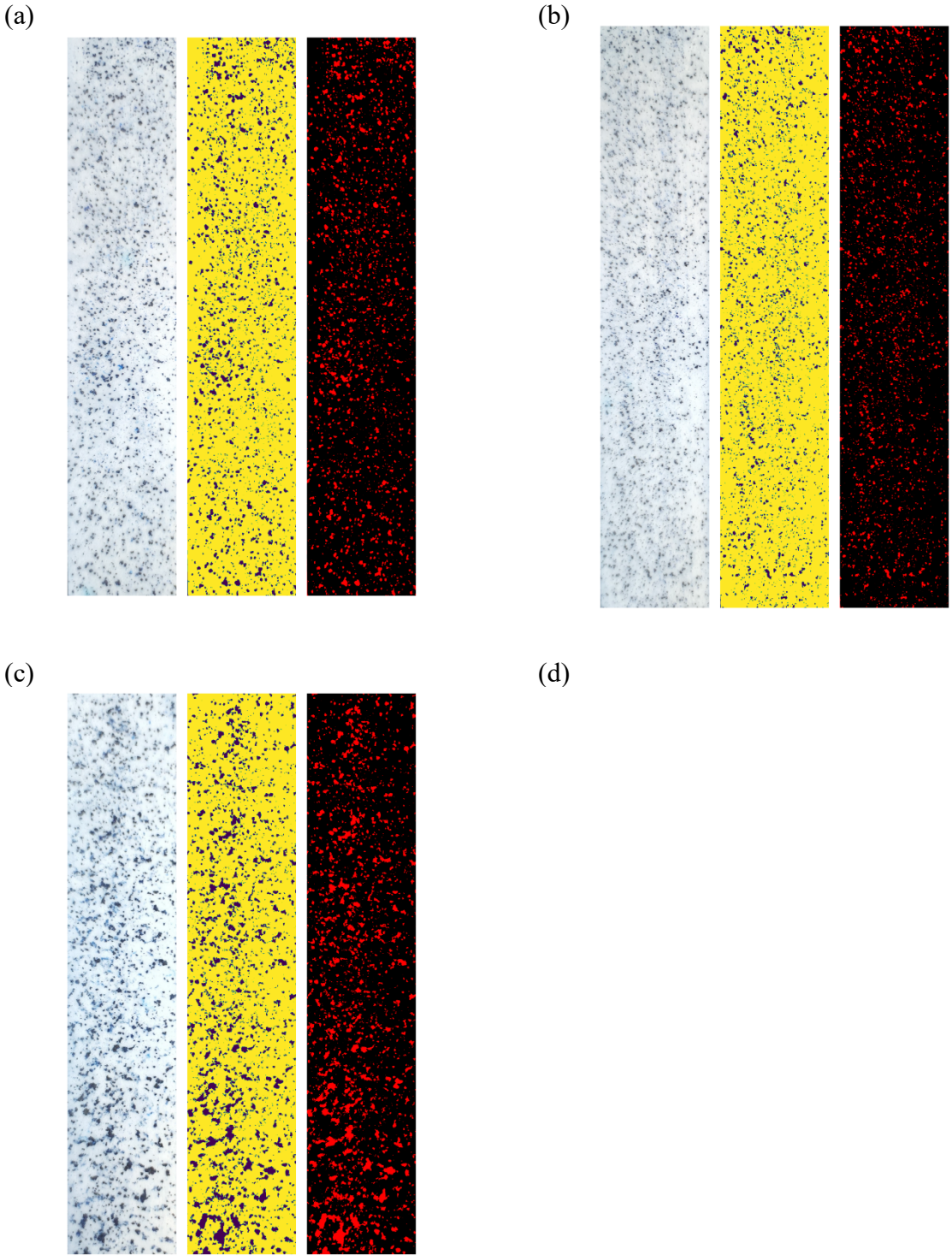
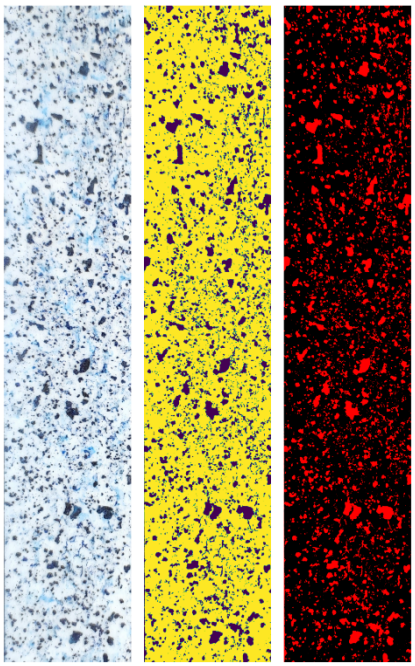
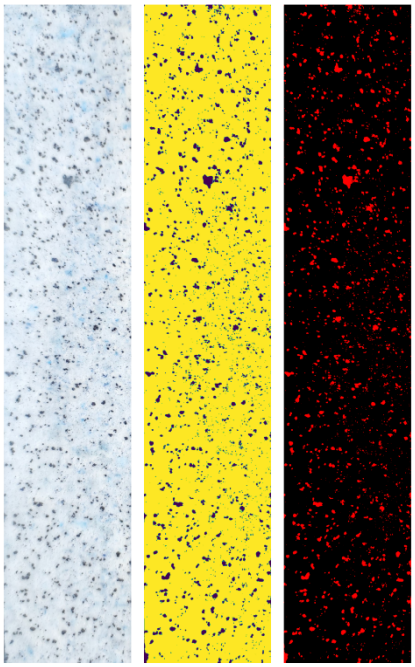


Figure A.858. Particle Size Analysis Results at A6G1F1 (a) Top Flange Bottom, (b) Web, (c) Bottom Flange Bottom (d) Stiffener.

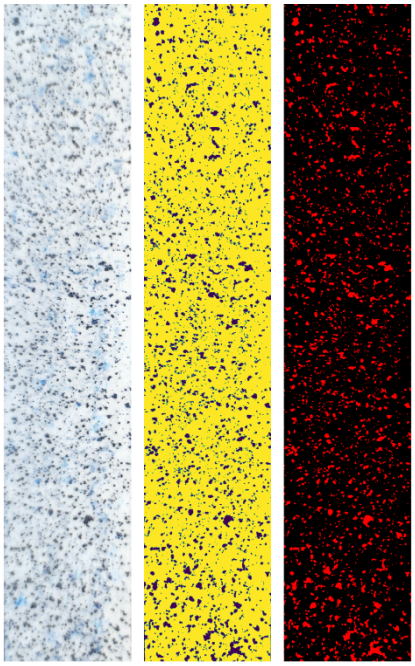
(a)



(b)



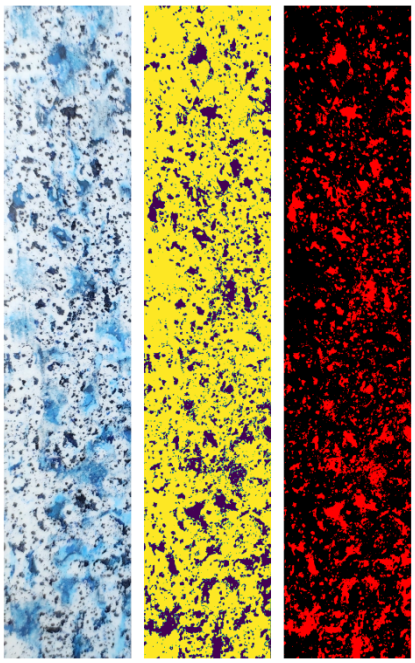
(c)



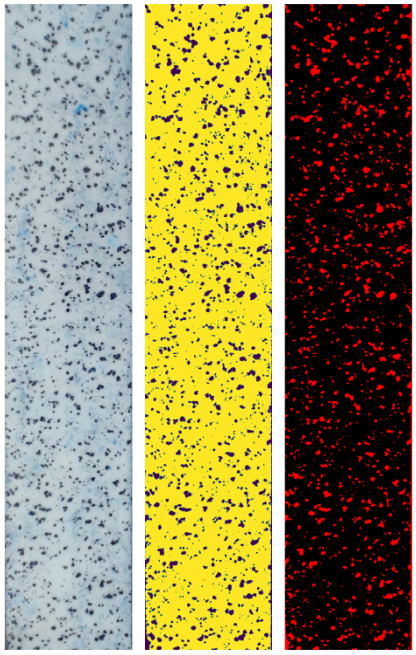
(d)

Figure A.859. Particle Size Analysis Results at A6G3F1 (a) Top Flange Bottom, (b) Web, (c) Bottom Flange Bottom (d) Stiffener.

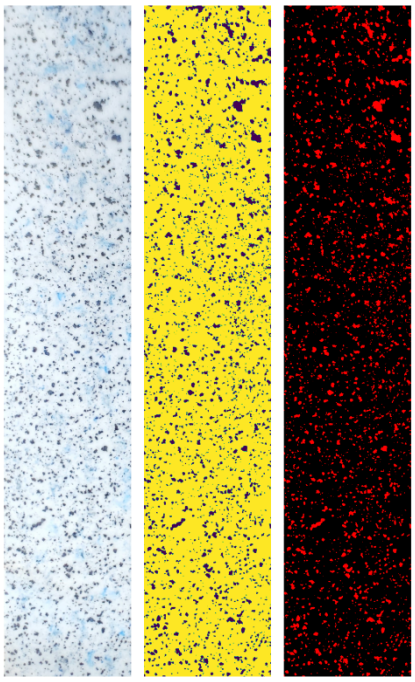
(a)



(b)



(c)



(d)

Figure A.860. Particle Size Analysis Results at A6G5F2 (a) Top Flange Bottom, (b) Web, (c) Bottom Flange Bottom (d) Stiffener.

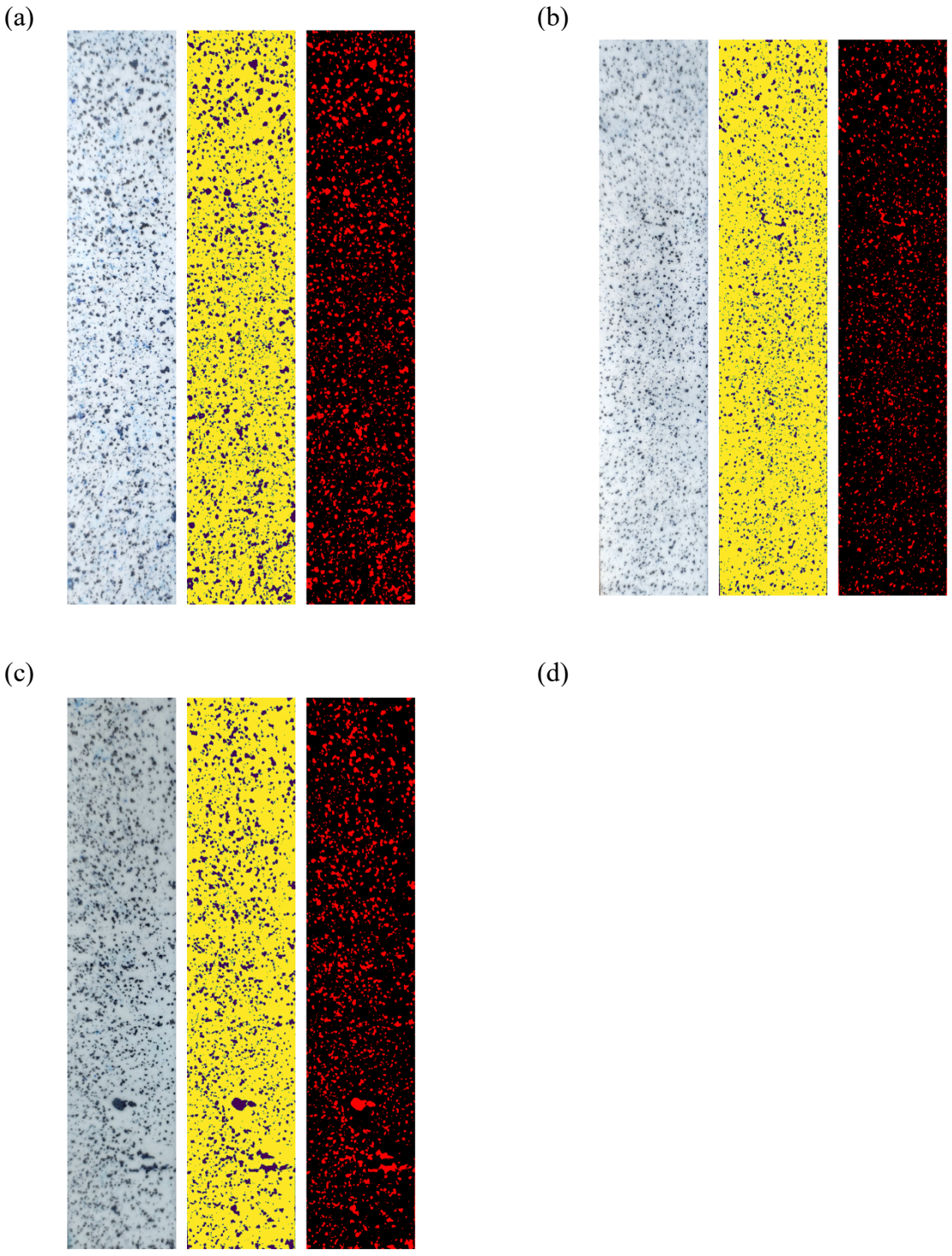


Figure A.861. Particle Size Analysis Results at A6G8F2 (a) Top Flange Bottom, (b) Web, (c) Bottom Flange Bottom (d) Stiffener.

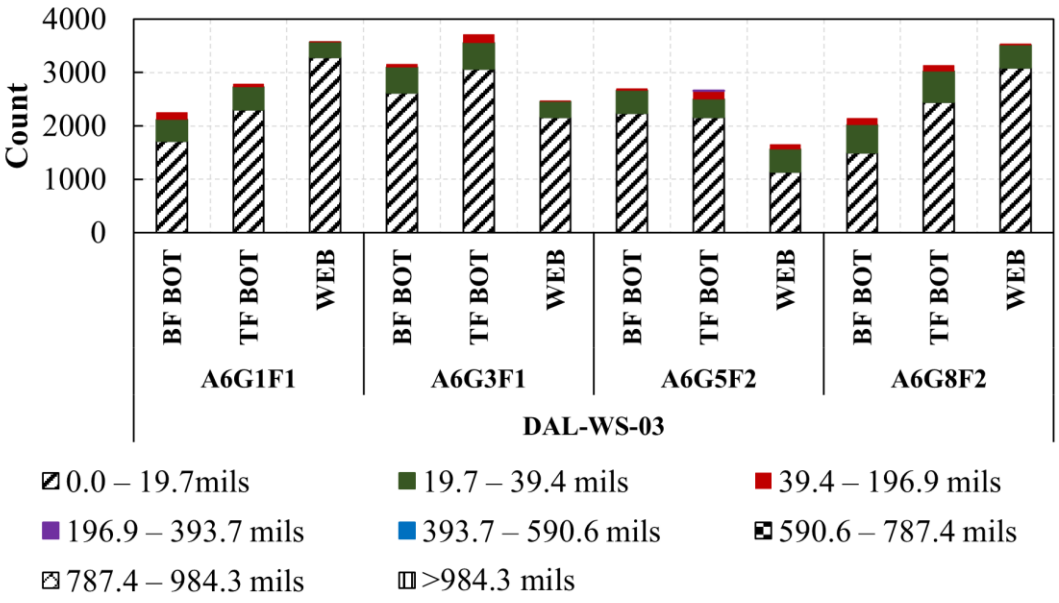


Figure A.862. Particle Size Analysis Showing Different Locations Examined.

A.47. PYTHON CODE FOR TAPE TEST ANALYSIS WITH OPENCV AND SCIKIT LEARN

The following python script developed in this study to analyze the result of tape adhesion test. The python packages required and must be installed before running this code are OpenCV, pandas, numpy, skimage, scipy, and matplotlib. The python script converts the results of the tape adhesion test in grayscale image files that can be used to measure the area diameter, and intensity of dark spots. To improve the final result of this analysis, the script also applies Yen thresholding to each individual sample.

```
import cv2
import os
import pandas as pd
import numpy as np
import skimage
from skimage import measure, color, io
from scipy import ndimage
import matplotlib
import matplotlib.pyplot as plt
from matplotlib import font_manager
matplotlib.rcParams['font.family'] = "Times New Roman"

df = pd.DataFrame()
parent_folder = r'C:\Users\pushk\Desktop\TAPE'
folder_list = []
files_folders = os.listdir(parent_folder)


for item in files_folders:
    item_path = os.path.join(parent_folder, item)
    if os.path.isdir(item_path):
        folder_list.append(item_path)


for path in folder_list:
    foldername = os.path.basename(path)
    folder = path


    for filename in os.listdir(folder):
        img_path = os.path.join(folder, filename)
        img = cv2.imread(img_path)
```

```
height, width,_ = img.shape

if height>=width:
   scale = (5*25.4)/height
else:
   scale = (5*25.4)/width

plt.show()
gray = cv2.cvtColor(img, cv2.COLOR_BGR2GRAY)

ret4,th8 = cv2.threshold(gray,
                         skimage.filters.threshold_yen(gray),
                         255,cv2.THRESH_BINARY)

mask = th8 == 0
s = [[1,1,1],[1,1,1],[1,1,1]]
labeled_mask, num_labels = ndimage.label(mask, structure=s)

colors = [(1, 0, 0)]
rgb_image = color.label2rgb(labeled_mask, colors=colors, bg_label=0)
img2 =color.label2rgb(labeled_mask,colors=colors, bg_label=0)
fig, axes = plt.subplots(nrows=3)

axes[0].imshow(img)
axes[1].imshow(th8)
axes[2].imshow(rgb_image)

font_prop = font_manager.FontProperties(family='Times New Roman', size=14)

for ax in axes.flat:
   ax.set_axis_off()

plt.subplots_adjust(top = 0.8,
                    bottom = 0.2,
                    right = 0.9,
                    left = 0.1,
                    hspace=0.1,
                    wspace=0)


plt.savefig(foldername +'_'+ filename.split('.')[0]+'.png', dpi = 300)
plt.close()

clusters = measure.regionprops(labeled_mask, img)
```

```
propList = ['Area',
          'equivalent_diameter',
          'orientation',
          'MajorAxisLength',
          'MinorAxisLength',
          'Perimeter',
          'MinIntensity',
          'MeanIntensity',
          'MaxIntensity']


output_file = open(foldername +'_'+ filename.split('.')[0]+'.csv', 'w')
output_file.write(',' + ",".join(propList) + '\n')

for cluster_props in clusters:

    output_file.write(str(cluster_props['Label']))
    for i,prop in enumerate(propList):
        if(prop == 'Area'):
            to_print = cluster_props[prop]*scale**2
        elif(prop == 'orientation'):
            to_print = cluster_props[prop]*57.2958
        elif(prop.find('Intensity') < 0):
            to_print = cluster_props[prop]*scale
        else:
            to_print = cluster_props[prop]
        output_file.write(',' + str(to_print))
    output_file.write('\n')
output_file.close()
```